J Membrane Biol (2012) 245:1–13
DOI 10.1007/s00232-011-9408-0

ORIGINAL ARTICLES

Modeling of Cellular Arginine Uptake by More Than One Transporter

Marietha J. Nel · Angela J. Woodiwiss · Geoffrey P. Candy

Received: 29 June 2011 / Accepted: 6 November 2011 / Published online: 24 November 2011

Abstract Determining the kinetic constants of arginine uptake by endothelial cells mediated by more than one transporter from linearization of data as Eadie-Hofstee plots or modeling which does not include the concentration of trace radiolabeled amino acid used to measure uptake may not be correct. The initial rate of uptake of trace [^{3}H]L-arginine by HUVECs and ECV_{304} cells in the presence of a range of unlabeled arginine and modifiers was used in nonlinear models to calculate the constants of arginine uptake using GraphPad Prism. Theoretical plots of uptake derived from constants determined from Eadie-Hofstee graphs overestimated uptake, whereas those from the nonlinear modeling approach agreed with experimental data. The contribution of uptake by individual transporters could be modeled and showed that leucine inhibited the individual transporters differently and not necessarily competitively. *N*-Ethylmaleimide inhibited only y^+ transport, and BCH may be a selective inhibitor of y^+L transport. The absence of sodium reduced arginine uptake by y^+L transport and reduced the K_m', whereas reducing sodium decreased arginine uptake by y^+ transport without affecting the K_m'. The nonlinear modeling approach using raw data avoided the errors inherent in methods deriving constants from the linearization of the uptake processes following Michaelian kinetics. This study provides explanations for discrepancies in the literature and suggests that a nonlinear modeling approach better characterizes the kinetics of amino acid uptake into cells by more than one transporter.

Keywords Amino acid transport · Kinetics · Endothelial cell

M. J. Nel · G. P. Candy (✉)
Department of Surgery, Faculty of Health Sciences, University of the Witwatersrand, 7 York Road, Parktown, Johannesburg 2193, South Africa
e-mail: geoffrey.candy@wits.ac.za

A. J. Woodiwiss
School of Physiology, Faculty of Health Sciences, University of the Witwatersrand, Parktown, Johannesburg 2193, South Africa

Introduction

The semi-essential, cationic amino acid L-arginine plays an important role in cellular function and metabolism and is the known precursor of the vasodilator nitric oxide (NO). Arginine potentiates the release of NO from endothelial cells grown in arginine-depleted medium, thereby regulating NO production (Sessa et al. 1990). Arginine may limit NO production in subjects with normal blood pressure but not in patients with hypertension (Panza et al. 1993). Indeed, fasting plasma arginine concentrations are elevated in patients with hypertension (Penttinen et al. 2000; Moss et al. 2004; Perticone et al. 2005; Naidoo et al. 2009), yet supplemental arginine can decrease blood pressure in such patients (Siani et al. 2000; Ast et al. 2010). One explanation for these data may be that arginine uptake into cells was impaired and therefore would not be available for NO production. In support of such a hypothesis, studies have shown that cellular uptake of arginine is reduced in lymphocytes from patients with hypertension and individuals genetically predisposed to developing hypertension (Schlaich et al. 2004). However, elucidating the kinetics of arginine uptake into endothelial cells is fundamental to determining whether arginine uptake is indeed impaired in these cases.

Studies to date have determined that cationic amino acid uptake into endothelial cells is mediated by the high-

affinity/low-rate y^+L transporter and the low-affinity/high-rate y^+ transporter. Uptake mediated by the y^+ transporter is sodium-independent, pH-insensitive, stereoselective and inhibited by *N*-ethylmaleimide (NEM) and certain neutral amino acids (Devés and Boyd 1998). Transport of arginine and other cationic amino acids by the y^+L transporter is sodium-independent; and in the presence of sodium, neutral amino acids, such as methionine, glutamine and leucine, may also be transported with high affinity (Devés and Boyd 1998; Mann et al. 2003; Bröer 2008). Although recent studies have described the activity and properties of transporter gene products CAT-1, CAT-2A and CAT-2B (y^+) as well as 4F2hc/y^+LAT1 (SLC3A2/SLC7A7) and 4F2hc/y^+LAT2 (SLC3A2/SLC7A6) (y^+L) (Closs et al. 1997; Mann et al. 2003; Bröer 2008), ascribing and reconciling the activities of these gene products to earlier studies which only measured activity can be difficult as the use of different cell types and experimental approaches when determining uptake rates has complicated direct comparison of the data.

Most studies determining the uptake of radiolabeled amino acids have assumed Michaelis–Menten kinetics and have calculated constants from Lineweaver–Burk reciprocal plots, Eadie-Hofstee plots and nonlinear modeling (Christensen and Antonioli 1969; White and Christensen 1982; Closs et al. 1993b; Moss et al. 2004; Brunini et al. 2006). Determining the kinetics, the relative contribution and the physiological importance of individual transporters in cells expressing more than one transporter may be complicated (Rotmann et al. 2007). Indeed, early in vitro kinetic uptake studies that ascribed uptake to only y^+ transport (Christensen et al. 1994) appear to have overlooked the contribution of y^+L transport (Devés et al. 1992). Furthermore, when determining kinetic parameters of individual cationic amino acid transporters operating simultaneously in a cell, studies have made various assumptions.

1. Studies have measured uptake of trace-labeled substrate in the presence of unlabeled substrate, without factoring in the relative concentrations of these when calculating the kinetic parameters (Sobrevia et al. 1995; Durante et al. 1996; Dall'Asta et al. 2000; Casanello and Sobrevia 2002; Hardy and May 2002; Arancibia-Garavilla et al. 2003). In this regard, the rate of uptake of labeled amino acid in the presence of unlabeled amino acid is not linear (Devés et al. 1992).
2. Studies in which radiolabeled tracers have been used with subtraction of nonspecific uptake and then Eadie-Hofstee linearization of data are not suitable to determine the existence of more than one transporter of uptake (Malo and Berteloot 1991).
3. Studies determining relative uptake rates at specific concentrations of the amino acids and their inhibitors (Arancibia-Garavilla et al. 2003; Signorello et al. 2003; Rotoli et al. 2005) may not infer that such rates apply at other substrate and/or inhibitor concentrations.
4. Studies have measured total uptake, then inhibited one of the transporters to determine the residual activity of the other transporter by subtraction. This assumes a linear and additive uptake independent of trace-labeled and unlabeled substrate concentrations (Mendes-Ribeiro et al. 1999; Ayuk et al. 2002; Brunini et al. 2006; Rotmann et al. 2007).
5. Studies have calculated kinetic constants from models of competitive inhibition of cationic amino acid uptake by structurally dissimilar neutral amino acids, such as leucine and glutamine (Devés et al. 1992, 1993), without determining whether noncompetitive or other forms of inhibition significantly improved the fit with the experimental data.
6. Studies determining inhibitor concentrations at which uptake was inhibited by 50% (I_{50}) (Hardy and May 2002; Rotoli et al. 2005) have also only modeled competitive inhibition (Cheng and Prusoff 1973) by these structurally dissimilar neutral amino acids (Angelo et al. 2005; Dall'Asta et al. 2000).

To address these issues, we modeled cationic amino acid uptake into cells using the general nonlinear approach of Malo and Berteloot (1991). This approach allows initial rates of uptake by more than one transporter to be determined and importantly includes the actual concentrations of both the trace-radiolabeled and unlabeled amino acid in the model. Furthermore, no assumptions are made regarding the type of inhibition and the concentrations of inhibitors (or activators) included in the model. As the model was additive, the theoretical contribution of uptake by each transporter could be modeled.

We tested this approach by modeling the initial rate kinetics of arginine uptake by two transporters into ECV_{304} cells, over a range of substrate and inhibitor concentrations, and reproduced the approach in primary human umbilical cord vein endothelial cells (HUVECs). Importantly, the results explain discrepancies in the literature when determining the kinetic parameters of cationic amino acid transport by more than one transporter.

Materials and Methods

Ethical Approval

Although the study did not involve patients, the Human Research Ethics Committee of the University of the Witwatersrand approved it (approval: M03-09-35, October 16, 2003).

Materials

ECV_{304} CRL-1998 and primary HUVECs were obtained from the American Type Culture Collection (Rockville, MD) and Lonza (Walkersville, MD), respectively. Fetal calf serum (FCS) (GIBCO, Carlsbad, CA) and medium 199 (M199) culture medium were obtained in powder form (Highveld Biologicals, Sandringham, Johannesburg, South Africa). The latter was dissolved in double-glass distilled water and filtered through 0.22-μm Millipore filters in a stainless steel filter apparatus (Millipore, Billerica, MA). Costar disposable plastic cell cultureware (Corning, Pittsburgh, PA) was used for all cell culture experiments. Phosphate-buffered saline (PBS), NEM and 2-aminobicyclo[2,2,1] heptane-2-carboxylic acid (BCH) were obtained from Sigma-Aldrich (St. Louis, MO). [^{3}H]L-Arginine was obtained from New England Nuclear and Ultima Gold scintillation fluid from Perkin Elmer (Boston, MA).

Cell Culture and Arginine Uptake Assay

For all experiments, HUVECs or ECV_{304} cells with contact inhibition characteristics were grown to confluence as an adherent monolayer at 37°C in 5% CO_2 according to the suppliers' instructions. Cells were plated out (4×10^5/well) in six-well culture plates with 2 ml complete M199 medium supplemented with 10% FCS (Gazzola et al. 1981) and incubated for 24 h. The medium was removed, cells were washed once in 1 ml PBS (pH 7.4) and 2 ml M199 without FCS, glutamine or arginine was added to deplete the cells of arginine and cells were incubated for a further 24 h as previously described (Sessa et al. 1990). Cell viability was determined by exclusion of trypan blue dye. Cells were then washed twice in 1 ml PBS, and PBS containing freshly diluted labeled 10 nM [^{3}H]L-arginine, with a range of concentrations of unlabeled arginine with or without inhibitors, such as leucine, was added. Uptake was measured for 30 s (Gazzola et al. 1981; White and Christensen 1982; Sala et al. 2002) while agitating the culture plate. The test solution was removed, and the cells were rapidly washed twice with cold PBS before 10% trichloroacetic acid in deionized water was added for 30 min at room temperature, to stop the uptake (Gazzola et al. 1981). Cells were then scraped off the culture plate and resuspended in 800 μl of distilled water. Following this, 200 μl of the cell suspension was added to 4 ml of scintillation fluid and the radioactivity counted (1600CA Tricarb; Canberra Packard, Meriden, IL).

To determine the effect of sodium on arginine uptake, uptake was measured using the following three buffers: (1) Krebs buffer (157 mM sodium), (2) Krebs buffer in which the sodium chloride was replaced with choline chloride (26 mM sodium) and (3) sodium-free buffer in which the other sodium-containing salts in the Krebs buffer were replaced with potassium (Christensen and Antonioli 1969; Mendes-Ribeiro et al. 1999; Arancibia-Garavilla et al. 2003). The effects of the sulfhydryl inhibitor NEM and the neutral amino acid analogue BCH on arginine uptake were determined by preincubating cells with these inhibitors prior to the determination of arginine uptake.

Determination of Uptake Kinetic Constants

In this study, it was assumed that the uptake of ^{3}H-labeled and that of unlabeled arginine were identical. In preliminary experiments we determined the linearity of labeled arginine uptake with time and concentration. Further, uptake of labeled arginine in the presence of unlabeled arginine with time was determined. Uptake of radiolabeled arginine by the cells was expressed as nanomoles per 4×10^5 cells per minute, and these data were used directly in nonlinear models to determine the kinetic constants using methods described previously (Malo and Berteloot 1991).

The rate of uptake (v_T) of undiluted tracer (T) by a single transporter, in the presence of unlabeled substrate (S), may be described by Michaelis–Menten kinetics (Malo and Berteloot 1991):

$$v_T = \frac{V_{\max} * [T]}{(K_m + [T] + [S])} \quad (1)$$

If two independent transporters (denoted by the subscripts "a" and "b") were present, in the presence of unlabeled substrate and diffusion ($K_D * [T]$), the rate of uptake of the labeled substrate was additive:

$$v_T = \frac{V_{maxa} * [T]}{(K_{ma} + [T] + [S])} + \frac{V_{maxb} * [T]}{(K_{mb} + [T] + [S])} + K_D * [T] \quad (2)$$

After correcting for dilution of the isotope, rate versus substrate plots were constructed, assuming an additive model for two transporters following Michaelis–Menten kinetics, and the data were linearized as Eadie-Hofstee plots to determine the kinetic constants, which, if curvilinear, may suggest two independent transporters (Malo and Berteloot 1991).

Statistical Analysis

Equations 1 and 2 were used to model the uptake of the 10 nM labeled arginine in the presence of a range of concentrations of unlabeled arginine and various inhibitors. The maximal rates of uptake (V_{maxa}, V_{maxb}) and the Michaelis constants (K_{ma}, K_{mb}) were adjusted using nonlinear regression analysis (GraphPad Prism®, version 5; GraphPad Software, La Jolla, CA) to best fit the model to

the experimental data. As the rate of uptake was fastest at low substrate concentrations and slowest at high substrate concentrations, the curve was fitted by minimizing the sum of squares of relative distances ($1/Y^2$ weighting to restore equal weighting to all points in the curve) of the data from the curve. Further, after checking for outliers, a D'Agostino and Pearson normality test ($P > 0.20$) was used to ensure that residuals were randomly distributed across the substrate concentrations. A robust fit of data which is less sensitive to outliers was also used. V_{maxa}, V_{maxb}, K_{ma} and K_{mb} were reported as mean ± SEM or mean ± SD, as indicated.

Models of one- versus two-transporter uptake were tested, and it was determined whether the inclusion of a diffusion component improved the fit (Eq. 2). In the presence of inhibitors, the type of inhibition was elucidated by determining whether either V_{max}' and/or K_m' and the ratio K_m'/V_{max}' remained constant. The inhibition constants (K_i) were then calculated for both transporters (Krupyanko 2007). As the results were in agreement with the literature, transport by the higher-affinity/lower-rate transporter (denoted by subscript "a" when K_{ma}, V_{maxa} and K_{ia} were reported) was also referred to as the y^+L transporter. Similarly, the lower-affinity/faster-rate transporter (denoted by subscript "b" when K_{mb}, V_{maxb} and K_{ib} were reported) was referred to as the y^+ transporter.

Results

Preliminary Results

Arginine uptake into ECV_{304} cells was linear up to 50 nM ^{3}H-arginine (Fig. 1a) and for up to 5 min (Fig. 1b). Initial experiments found that 30 s was the shortest time when the rate could be reproducibly measured under the experimental conditions used (data not shown). In the presence of unlabeled arginine, the rate of uptake of 10 nM ^{3}H-labeled arginine decreased in an exponential manner over 5 min and depended on the concentration of unlabeled arginine (Fig. 1c). At 30 s, the nonlinear dependence of the rate of 10 nM ^{3}H-arginine uptake upon the concentration of unlabeled arginine was shown for both ECV_{304} cells (Fig. 2a) and HUVECs (Fig. 3a).

Arginine Uptake by ECV_{304} Cells and HUVECs

Kinetic constants, derived from dilution-corrected, linear-transformed plot intercepts, were used as preliminary estimates in the nonlinear additive models of uptake (Malo and Berteloot 1991). For both ECV_{304} cells (Fig. 2a) and HUVECs (Fig. 3a), after excluding outliers and ensuring residuals between experimental data and the model fit were normally distributed within the range of unlabeled arginine

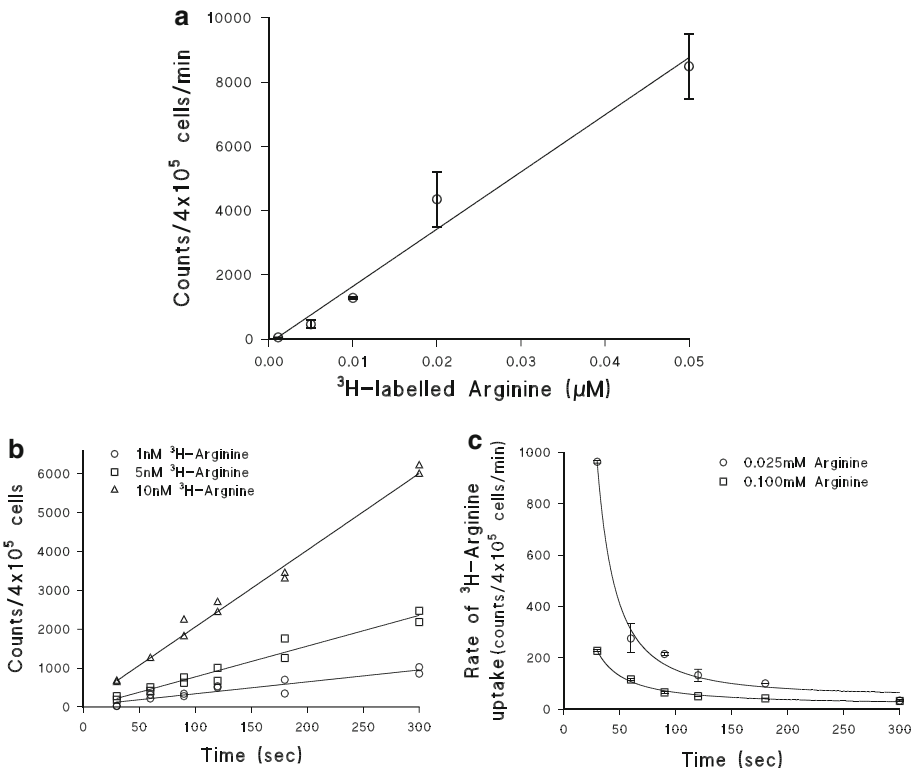

Fig. 1 Uptake of labeled arginine by ECV_{304} cells. **a** Uptake with concentration of ^{3}H-arginine (mean ± SD from triplicate experiments). **b** Uptake over time with concentration of ^{3}H-arginine. **c** Nonlinear decrease in the rate of 10 nM ^{3}H-arginine uptake in the presence of 0.025 and 0.100 mM unlabeled arginine with time. Experimental details are described in Materials and Methods except that uptake was measured for up to 300 s before the reaction was stopped. Data for HUVECs were similar (data not shown)

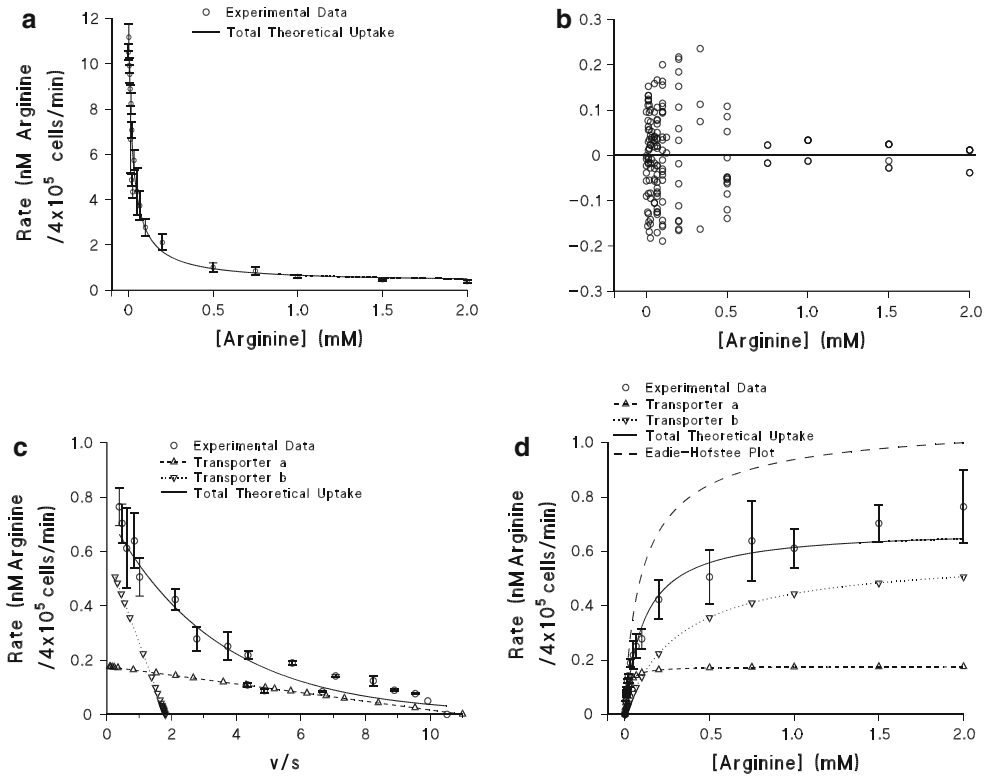

Fig. 2 Data used to determine the kinetic constants of arginine uptake by nonlinear modeling for ECV_{304} cells. **a** Experimental uptake (mean ± SD from 10 experiments) of 10 nM ^{3}H-arginine in the presence of increasing concentrations of unlabeled arginine was used with Eq. 2 to determine the kinetic constants (see Materials and Methods). The curve is the theoretical uptake derived from these constants (see Table 1). **b** Residuals for graph **a**. A D'Agostino and Pearson omnibus K2, $P = 0.383$, indicated a lack of bias for the differences between experimental arginine uptake and the theoretical model contributions. **c** Eadie-Hofstee plots calculated from dilution-corrected data from **a** showing close agreement between total experimental uptake (mean ± SD) and total theoretical uptake calculated from the derived constants of the nonlinear modeling in Table 1. *Straight lines* are the theoretical plots (derived from the constants of nonlinear modeling in Table 1) for each transporter to illustrate the differences between these lines and the theoretical curve of total transport. **d** Michaelis–Menten graphs of dilution-corrected experimental rate of arginine uptake (as mean ± SD) and theoretical contributions of transporters "a" (y^+L, *dotted line*) and "b" (y^+, *short dashed line*) and the combined total theoretical uptake (*solid line*) (derived from the constants obtained by nonlinear modeling, Table 1), which agreed well with the experimental data. Also shown is the curve (*long dashed line*) calculated from the constants derived from the Eadie-Hofstee plots of dilution-corrected data (Table 1), which overestimated the experimental uptake. Experimental details are described in Materials and Methods with uptake measured for 30 s

tested (Figs. 2b, 3b), a model of uptake by two transporters was preferred over that of a single transporter, irrespective of whether the models included a diffusion component ($P < 0.0001$, data not shown). The two-transporter model was also preferred to a single-transporter model with n substrate binding sites and with diffusion (see equation 3 in Chenu and Berteloot 1993; data not shown). Furthermore, the Eadie-Hofstee plots for both ECV_{304} cells (Fig. 2c) and HUVECs (Fig. 3c) were curvilinear, hence supporting a model of uptake by two transporters.

In both ECV_{304} cells and HUVECs, the kinetics program indicated that an uptake model of two transporters without diffusion was preferred, although the difference between the model with and that without diffusion was not significant (Table 1). For both cell types, models including diffusion were found to have large errors (SEM) for the estimates of the kinetic constants (K_{mb}) and the diffusion constant (K_D), with wide confidence intervals for the diffusion constant (Table 1), supporting the indication that the model without diffusion was correct. Furthermore, a robust fit (less sensitive to outliers) of the data found the diffusion parameter was different from that calculated by the least squares fit method, further indicating that the model including diffusion was not stable when fitting this model to the data. Finally, the contribution by diffusion of 10 nM ^{3}H-arginine used in these experiments to the total uptake was small (K_D * 0.00001 mM, Eq. 2). Therefore, for subsequent experiments the diffusion component was excluded.

The V_{maxa} (y^+L transport) calculated for ECV_{304} cells was similar to that of the HUVECs ($P = 0.34$), whereas the V_{maxb} (y^+ transport) was higher for HUVECs compared to ECV_{304} cells ($P = 0.019$). ECV_{304} cell affinity constants for both transporters were similar to those for HUVECs

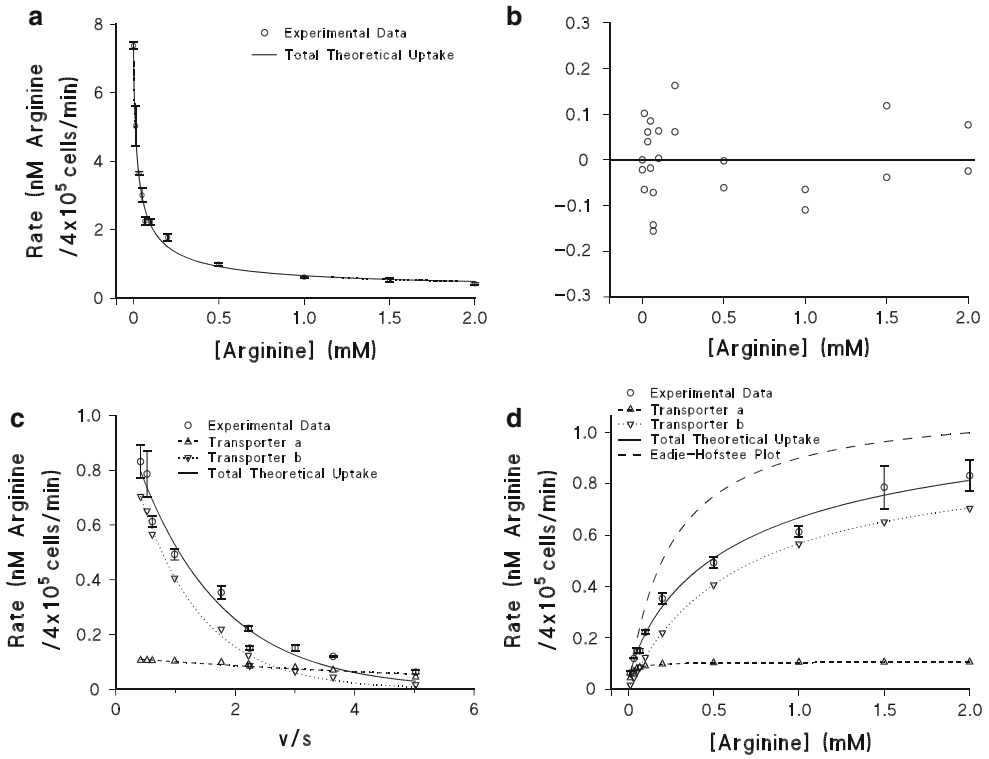

Fig. 3 As for Fig. 2 showing the data used to determine the kinetic constants of arginine uptake by nonlinear modeling for HUVECs. **a** Experimental uptake (mean ± SD from duplicate experiments) of 10 nM ^{3}H-arginine in the presence of increasing concentrations of unlabeled arginine was used with Eq. 2 to determine the kinetic constants (see Materials and Methods). **b** Residuals for graph **a**. A D'Agostino and Pearson omnibus K2, $P = 0.858$, indicated a lack of bias for the differences between experimental arginine uptake and the theoretical model contributions. **c** Eadie-Hofstee plots calculated from dilution-corrected data from **a** showing close agreement between total experimental uptake (mean ± SD) and total theoretical uptake calculated from the derived constants of the nonlinear modeling in Table 1. *Straight lines* are the theoretical plots (derived from the constants of nonlinear modeling in Table 1) for each transporter to illustrate the differences between these lines and the theoretical curve of total transport. **d** Michaelis–Menten graphs of dilution-corrected experimental rate of arginine uptake (mean ± SD) and theoretical contributions of transporters "a" (y^{+}L, *dotted line*) and "b" (y^{+}, *short dashed line*) and the combined total theoretical uptake (*solid line*) (derived from the constants obtained by nonlinear modeling, Table 1), which agreed well with the experimental data. Also shown is the curve (*long dashed line*) calculated from the constants derived from the Eadie-Hofstee plots of dilution-corrected data (Table 1), which overestimated the experimental uptake. Experimental details are described in Materials and Methods with uptake measured for 30 s

(K_{ma} and K_{mb}; Table 1; Figs. 2d, 3d). The relative maximum uptake (V_{maxb}/V_{maxa}) of the faster/lower-affinity transporter (y^{+}) relative to the slower/higher-affinity (y^{+}L) transporter was 3.6 in ECV_{304} cells and 8.8 in HUVECs. The kinetic parameters determined by the nonlinear modeling approach were similar to those determined using a model of Michaelis–Menten uptake with two transporters, after correcting uptake for dilution of the isotope (Figs. 2d, 3d).

The additive model approach allowed for the theoretical contribution of uptake by the individual transporters into ECV_{304} cells (Fig. 2d) and HUVECs (Fig. 3d). Theoretical total uptake calculated from the kinetic constants, derived from dilution-corrected, linear-transformed plot intercepts (Eadie-Hofstee plots, Table 1), significantly overestimated the experimental data, whereas theoretical uptake calculated from nonlinear modeling closely matched the experimental data (Table 1; Fig. 2d for ECV_{304} cells and Fig. 3d for HUVECs). For both cell lines, the y^{+}L transporter (transporter a) was the major contributor of uptake at low arginine concentrations and approached V_{maxa} above 0.300 mM with near zero order kinetics above this concentration. The y^{+} transporter (transporter b) accounted for most of the transport above this concentration.

Finally, we recalculated the kinetic constants using dilution-corrected data, modeling an additive Michaelis–Menten equation to best fit the experimental data, to compare the results obtained with equation 2 of the nonlinear modeling using the raw data as described above. From the Michaelis–Menten graph (Fig. 2d), the constants determined for ECV_{304} cells were $V_{maxa} = 0.176 \pm 0.027$ nM arginine/4×10^5 cells/min, $K_{ma} = 0.016 \pm 0.002$ mM, $V_{maxb} = 0.589 \pm 0.028$ nM arginine/4×10^5 cells/min and $K_{mb} = 0.326 \pm 0.072$ mM, which were similar to those obtained from the nonlinear modeling (i.e., the kinetic constants obtained from the model fit of Fig. 2d matched those of the fit of Fig. 2a; Table 1). Similar

Table 1 Comparison of kinetic constants obtained from Eadie-Hofstee plots (from dilution corrected data) and nonlinear models (using raw data) of arginine uptake by ECV_{304} cells and HUVECs

	ECV_{304} cells			HUVECs		
	Eadie-Hofstee plot	Model without diffusion[a]	Model with diffusion	Eadie-Hofstee plot	Model without diffusion[b]	Model with diffusion
V_{maxa} (nM arginine/ 4×10^5 cells/min)	0.294 ± 0.042*	0.176 ± 0.026 (0.243)	0.136 ± 0.034 (0.235)	0.225 ± 0.019**	0.106 ± 0.026 (0.122)	0.091 ± 0.037 (0.120)
K_{ma} (mM)	0.024 ± 0.006	0.016 ± 0.002 (0.021)	0.013 ± 0.003 (0.021)	0.030 ± 0.005	0.018 ± 0.004 (0.020)	0.016 ± 0.005 (0.020)
V_{maxb} (nM arginine/ 4×10^5 cells/min)	0.768 ± 0.035***	0.589 ± 0.028 (0.558)	0.459 ± 0.054 (0.407)	1.038 ± 0.09	0.933 ± 0.077† (0.902)	0.646 ± 0.259 (0.841)
K_{mb} (mM)	0.177 ± 0.024	0.326 ± 0.072 (0.504)	0.175 ± 0.062 (0.348)	0.562 ± 0.134	0.647 ± 0.170 (0.659)	0.401 ± 0.264 (0.613)
K_D (diffusion constant)		–	8,515 ± 4,089 (7,801)		–	10,353 ± 10,718 (2,270)

Subscript a, lower-rate/higher-affinity transporter (y^+L); subscript b, higher-rate/lower-affinity transporter (y^+)

[a] Preferred model in ECV_{304} cells ($F = 0.641$ [$n = 180$], $P = 0.42$); note the high SEM for K_D

[b] Preferred model in HUVECs ($F = 0.857$ [$n = 23$], $P = 0.37$); note the high SEM for K_D

*, **, *** Differences in the V_{max} values of the Eadie-Hofstee plot and the Model without diffusion; † Differences in the V_{maxb} values of the ECV and HUVEC Models without diffusion

equivalent results were obtained for HUVECs: $V_{maxa} = 0.103 \pm 0.012$ nM arginine/4×10^5 cells/min, $K_{ma} = 0.017 \pm 0.002$ mM, $V_{maxb} = 0.907 \pm 0.034$ nM arginine/4×10^5 cells/min, $K_{mb} = 0.612 \pm 0.073$ mM (i.e., the kinetic constants obtained from the model fit of Fig. 3d matched those of the fit of Fig. 3a; Table 1).

Inhibition of Arginine Uptake by Leucine

Leucine decreased both V_{maxa}' and K_{ma}' of tracer uptake by the high-affinity/low-rate transporter in ECV_{304} cells at all concentrations of leucine tested (Fig. 4). V_{maxa}' decreased significantly until leucine concentrations reached 0.200 mM ($P < 0.0005$) and then was increased at 0.500 mM leucine (0.200 vs. 0.500 mM, $P = 0.0031$; Fig. 4a). Similarly, K_{ma}' was also minimal at a concentration of approximately 0.200 mM leucine ($P < 0.005$ vs. leucine = 0 mM) and was increased at 0.500 mM leucine (0.200 vs. 0.500 mM, $P < 0.0001$; Fig. 4b). To determine the type of inhibition, the ratio K_{ma}'/V_{maxa}' increased linearly with the concentration of leucine ($r^2 = 0.973$) and as both K_{ma}' and V_{maxa}' were decreased (i.e., neither were constant), the results suggested that the inhibition of this transporter by leucine was mixed. These data were consistent with "discoordinated inhibition" (Krupyanko 2007) with a $K_{ia} = 0.024 \pm 0.003$ and 0.159 mM when leucine was < 0.500 mM and equal to 0.500 mM, respectively.

The maximum rate of uptake (V_{maxb}') of the low-affinity/high-rate transporter in ECV_{304} cells was unchanged in the presence of leucine, except at 0.500 mM leucine when V_{maxb}' was significantly lower ($P < 0.0001$ for all leucine concentrations versus 0.500 mM, Fig. 4a). Compared to the uninhibited reaction, K_{mb}' was significantly reduced at leucine concentrations of 0.033–0.200 mM ($P < 0.05$) but was not different from the uninhibited reaction at 0.500 mM leucine ($P = 0.35$, Fig. 4b). The data suggest that such inhibition/activation was competitive for leucine concentrations of 0.033–0.200 mM and were consistent with a model of "competitive activation" (Krupyanko 2007), with $K_{ib} = 0.0.040 \pm 0.005$ and $K_{ib} = 1.554$ mM when leucine was < 0.500 and 0.500 mM, respectively. There were insufficient data to determine whether V_{maxb} simply decreased linearly with increasing leucine, which would suggest uncompetitive inhibition (unassociative; Krupyanko 2007).

Nonlinear modeling suggested that leucine affected both transporters differently without either transporter being completely inhibited at any of the concentrations of leucine tested. These kinetic constants were not determined at higher leucine concentrations.

Effect of NEM on Arginine Uptake in ECV_{304} Cells

NEM (0.200 mM) incubated with ECV_{304} cells for 10 min prior to the uptake of labeled arginine completely inhibited the low-affinity/higher-rate y^+ transporter. The result was tested using a single model of transport, which was preferred to a two-transporter model of uptake, with the results for the latter model being ambiguous and both K_{mb}' and

V_{maxb}' defaulting to a large value (infinity) when using GraphPad Prism (see Materials and Methods, Table 2), suggesting noncompetitive inhibition.

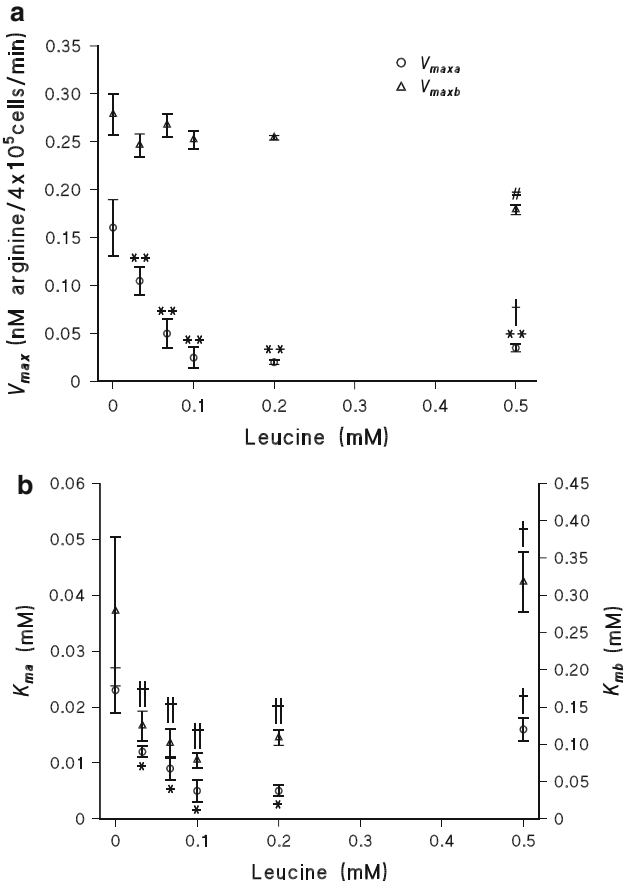

Fig. 4 The effect of leucine on (**a**) the rate (V_{max}') of 10 nM ^{3}H-arginine uptake and (**b**) Michaelis constant (K_m') for the individual transporters, as determined by nonlinear modeling described above. Results are mean ± SD from triplicate experiments. The experimental method is described in Materials and Methods, with the PBS test solution containing 10 nM ^{3}H-arginine; various concentrations of unlabeled arginine with the concentrations of leucine as indicated in the graphs. $^*P < 0.005$ and $^{**}P < 0.0005$ versus no leucine; †$P < 0.005$ versus 0.2 mM leucine; $^{\#}P < 0.0001$ versus all other leucine concentrations; ††$P < 0.05$ versus no leucine

Effect of BCH on Arginine Uptake in ECV_{304} Cells

BCH (30 mM) was preincubated with ECV_{304} cells for 60 min prior to determining tracer uptake. A two-transport model was preferred over a single-transport system ($P < 0.0001$). V_{maxa}' and K_{ma}' were both significantly reduced ($P < 0.0001$), whereas V_{maxb}' and K_{mb}' were unchanged (Table 2), suggesting that only the y^+L transport was affected by BCH.

Sodium Dependence of L-Arginine Uptake

Reducing sodium from 157 to 26 mM affected neither V_{maxa}' nor K_{ma}', whereas the absence of sodium decreased both constants (Table 3) (157 vs. 0 mM, V_{maxa} $P < 0.001$ and K_{ma} $P < 0.01$; 26 vs. 0 mM, V_{maxa} $P < 0.01$ and K_{ma} $P < 0.05$). K_{ma}'/V_{maxa}' was unchanged, suggesting that the absence of sodium affected transport by y^+L uncompetitively. V_{maxb}' of the low-affinity/high-rate transporter was significantly reduced when sodium was reduced or absent ($P < 0.0005$, 26 vs. 0 mM, P = ns), whereas K_{mb}' was unchanged, suggesting noncompetitive inhibition of y^+ transport when sodium was reduced.

Discussion

The present study used raw, rather than transformed, data in nonlinear regression analysis to characterize the kinetics of arginine uptake into cells by more than one transporter, thereby avoiding the potential difficulties and errors of methods deriving constants from the linearization of the uptake process following Michaelian kinetics (Malo and Berteloot 1991). Importantly, the approach allowed for the concentrations of both labeled and unlabeled arginine to be included and by determining changes in V_{max}' or K_m' was able to determine the inhibition type for either transporter in the presence of effector molecules.

Table 2 Effect of preincubation of the inhibitors NEM (0.2 mM) and BCH (30 mM) on arginine uptake by ECV_{304} cells

	NEM		BCH	
	0 mM	0.2 mM	0 mM	30 mM
V_{maxa} (nM/4 × 10^5 cells/min)	0.166 ± 0.0265 (0.224)	0.371 ± 0.011 (—)	0.294 ± 0.029 (0.362)	0.012 ± 0.004*** (0.010)
K_{ma} (mM)	0.024 ± 0.003 (0.032)	0.059 ± 0.003 (—)	0.026 ± 0.002 (0.030)	0.002 ± 0.001*** (0.002)
V_{maxb} (nM/4 × 10^5 cells/min)	0.268 ± 0.026 (0.3)	~5.10 × 10^{14}***,[a] (—)	1.509 ± 0.071 (1.867)	2.109 ± 0.102 (2.084)
K_{mb} (mM)	0.272 ± 0.083 (0.762)	~2.08 × 10^{15}***,[a] (—)	0.598 ± 0.085 (1.024)	0.602 ± 0.049 (0.595)

Results are mean ± SEM from triplicate experiments, with robust values in parentheses

[a] After preincubation with NEM, the best fit of V_{maxb} and K_{mb} defaulted to a large value (∞), with an ambiguous result. Hence, a single-transport model with diffusion was preferred

Difference between uptake with and without inhibitor: *** $P < 0.0001$

Table 3 Kinetic constants for ECV_{304} cells determined at various sodium concentrations

	Sodium 157 mM	Sodium 26 mM	Sodium 0 mM
V_{maxa} (nM arginine/4 × 10^5 cells/min)	0.142 ± 0.027 (0.184)	0.201 ± 0.036 (0.236)	0.100 ± 0.007**† (0.118)
K_{ma} (mM)	0.016 ± 0.002 (0.019)	0.018 ± 0.003 (0.021)	0.011 ± 0.001*†† (0.012)
K_{ma}/V_{maxa}	1.09 ± 0.05 × 10^{-3}	0.92 ± 0.04 × 10^{-3}	1.07 ± 0.02 × 10^{-3}
	[0.99 to 1.20 × 10^{-3}]	[0.82 to 1.00 × 10^{-3}]	[1.03 to 1.11 × 10^{-3}]
V_{maxb} (nM arginine/4 × 10^5 cells/min)	0.660 ± 0.022 (0.695)	0.313 ± 0.028*** (0.356)	0.350 ± 0.009*** (0.403)
K_{mb} (mM)	0.193 ± 0.027 (0.283)	0.210 ± 0.073 (0.400)	0.204 ± 0.020 (0.315)
K_{mb}/V_{maxb}	2.93 ± 0.46 × 10^{-3}	6.70 ± 2.72 × 10^{-3}	5.85 ± 0.54 × 10^{-3}
	[2.01 to 3.84 × 10^{-3}]	[1.31 to 12.08 × 10^{-3}]	[4.78 to 6.91 × 10^{-3}]

Results are mean ± SEM from triplicate experiments, with robust value in parentheses and 95% CI for the slope in brackets

Significant differences: * $P < 0.05$, ** $P < 0.005$, *** $P < 0.0005$ for 0 or 26 mM versus 157 mM sodium; † $P < 0.005$, †† $P < 0.0005$ for 0 versus 26 mM sodium

The results show that (1) the effect of the unlabeled amino acid on the rate of uptake of the "trace" labeled amino acid was not linear and depended on the relative concentrations of unlabeled to labeled amino acid; (2) the theoretical plot of the total rate of uptake, derived from the kinetic constants of arginine uptake estimated from Eadie-Hofstee plots, significantly overestimated the experimental data; and (3) when the constants were estimated from the nonlinear modeling (Malo and Berteloot 1991), there was good agreement. The results suggest that values of kinetic constants calculated from linearized data reported for cationic amino acids in the literature (Devés and Boyd 1998; Mann et al. 2003) may have overestimated the true values. Although Malo and Berteloot (1991) developed this approach for glucose uptake by more than one transporter, as far as we are aware this is the first report to show the discrepancy between theoretical and experimental data for amino acid uptake by more than one transporter.

Nonlinear regression analysis allowed comparison between models of one or two transporters, the presence of diffusion (Malo and Berteloot 1991) and the possibility of uptake by a single transporter with multiple binding sites (Chenu and Bertloot 1993). The results consistently determined that, in the absence of inhibitors, a model of uptake by two independent transporters was preferred over other models. This conclusion was supported by curvilinear Eadie-Hofstee plots using transformed data.

Studies have suggested that the uptake in HUVECs was facilitated by a single high-affinity transporter with a diffusion component, rather than two simultaneously operating transporters (Arancibia-Garavilla et al. 2003; Speake et al. 2003); however, expression data suggest that additional cationic transporters were operational in these cells (Rotmann et al. 2007), and thus the activity ascribed to the y^+L transporter could in fact be ascribed to more than one such transporter (Arancibia-Garavilla et al. 2003).

Differences between the results of various studies may be partly explained by variations in study methodology as studies have determined uptake in the presence of labeled amino acid alone (Sobrevia et al. 1995; Rotoli et al. 2005; Brunini et al. 2006), specified the activity but not the concentration of trace labeled amino acid (Closs et al. 1993a; Casanello and Sobrevia 2002; Hardy and May 2002; Arancibia-Garavilla et al. 2003; Signorello et al. 2003; Martín et al. 2006; Rotmann et al. 2007) and reported results from studies using 0.1–0.2 μM (Ayuk et al. 2002; Schlaich et al. 2004) to 50 μM (Durante et al. 1996) labeled arginine in the presence of fixed or varying concentrations of unlabeled substrate or inhibitors. Our data showing nonlinear uptake of tracer in the presence of unlabeled amino acid underscore the importance of including the concentrations of both the labeled and unlabeled amino acids when determining the rate of uptake.

Uptake by diffusion has been demonstrated as the nonsaturable uptake of labeled arginine (0.05 mM), measured in the presence of excess unlabeled arginine (10 mM) (Speake et al. 2003; Martín et al. 2006). Subtracting this nonsaturable uptake from the total transport (Dall'Asta et al. 2000; Arancibia-Garavilla et al. 2003) may exceed the contribution of the higher-affinity/lower-rate transporter (y^+L) (Dall'Asta et al. 2000), which may be among the reasons that this transporter has been overlooked (Devés et al. 1992). Subtracting the diffusion component from transformed data results in the loss of statistical information, whereas when using the nonlinear approach, such information is retained, allowing error in the calculated kinetic constants to be determined (Malo and Berteloot 1991). In our experiments using 10 nM labeled arginine, the inclusion of the diffusion term did not improve the fit of the models and the contribution of diffusion to the total counts was insignificant. This does not suggest that diffusion or the contribution of a nonsaturable

component is not important but, rather, that under the experimental conditions used, this contribution was small.

Inhibitors and Effector Molecules

The nonlinear approach makes no assumptions regarding the type of inhibition or activation of transport by effector molecules. We investigated the inhibition of arginine uptake by leucine, which has been used to differentiate between y^+L and y^+ transport; NEM, which inhibits y^+ transport; and the neutral amino acid analogue BCH, an inhibitor of sodium-independent transport (White et al. 1982). Furthermore, the effects of sodium on uptake were determined.

Leucine

Studies have used fitted models of competitive inhibition of one or both transporters to experimental data when determining the effects of neutral amino acid on cationic amino acid uptake (Devés et al. 1992; Devés and Boyd 1998; Hardy and May 2002; Rotoli et al. 2005). As the side chain of leucine and other neutral amino acids differs from that of arginine and lysine, it appears that models which included noncompetitive and uncompetitive inhibition were not tested. Indeed, data showing K_i coinciding with I_{50} (Angelo et al. 2005) would be consistent with noncompetitive or uncompetitive inhibition of the transport of leucine (Cheng and Prusoff 1973).

Our data showing that leucine affected y^+L transport by mixed inhibition ("discoordinated inhibition") and y^+ transport by "competitive activation" (Krupyanko 2007) are in contrast to previous studies which determined that leucine competitively inhibited y^+L transport in erythrocytes (Devés et al. 1992), HUVECs (Arancibia-Garavilla et al. 2003) and platelets (Signorello et al. 2003). However, these reports did not determine inhibition by leucine at low and physiological concentrations.

Although leucine did not completely inhibit transport at any of the concentrations tested, other studies, using higher leucine concentrations (1–10 mM leucine in the presence of sodium), determined uptake of leucine-sensitive transport (i.e., the contribution of y^+L transport) by subtracting leucine-insensitive uptake (i.e., the contribution by y^+) from the total uptake (Mendes-Ribeiro et al. 1999; Arancibia-Garavilla et al. 2003; Martín et al. 2006; Rotmann et al. 2007). However, as stressed above, the results of such studies would depend on the relative concentrations of the added labeled tracer versus the unlabeled arginine present and were included in the models used in our study.

Different neutral amino acids affect arginine uptake differently (Closs et al. 1993a; Bröer et al. 2000; Rotmann et al. 2007), and results may not be consistent if, for example, leucine was replaced by glutamine (Ayuk et al. 2002; Speake et al. 2003). In addition, there appear to be no data suggesting that leucine and glutamine inhibit cationic transport in the same manner, and such studies could be tested using this nonlinear modeling approach.

NEM and BCH

The nonlinear modeling approach determined that the y^+L transporter was unaffected by NEM, whereas the y^+ transporter was completely inhibited, which was consistent with the literature (Devés and Boyd 1998; Babu et al. 2003). Almost three decades ago, BCH was developed as a model substrate for the sodium-independent system for neutral amino acids (White and Christensen 1982). Interestingly, the results of the present study show that BCH significantly reduced the activity of the y^+L transporter without affecting the y^+ transporter. In the absence of a y^+L transporter inhibitor, BCH or structurally related analogues may be of interest in the quest to obtain a selective inhibitor for this transporter.

Sodium Dependence of Arginine Transport

Cationic y^+L and y^+ amino acid transport is accepted as being independent of sodium concentration (Devés and Boyd 1998; Mann et al. 2003; Bröer 2008). White et al. (1982) originally noted inhibition of cationic amino acid transport by neutral amino acids, such as leucine, glutamine, methionine and, to a lesser extent, homoserine and serine (see also Devés et al. 1992). Such sodium-dependent inhibition of cationic transporters was used to identify the y^+L transporter (Devés et al. 1992) and has been used to differentiate this transporter from the y^+ transporter (Mendes-Ribeiro et al. 1999; Rojas and Devés 1999; Arancibia-Garavilla et al. 2003; Martín et al. 2006; Rotmann et al. 2007). However, data suggest that neutral amino acids also inhibit uptake of cationic amino acids by y^+ transport (Christensen 1990), with some 30% of lysine uptake into HUVECs (Hardy and May 2002) and bovine aortic endothelial cells (Durante et al. 1996) being sodium-dependent. The latter could be explained if other transporters were operational in these cells, but such discrepancies in the literature highlight the difficulties in comparing cationic transport studies and appear to be similar to those noted for epithelial cells (reviewed by Bröer 2008).

Although it was suggested that sodium occupies the site normally occupied by the ω-amino group of cationic amino acids to facilitate neutral amino acid transport (Christensen and Antonioli 1969), if sodium was already occupying the ω-amino group site, it is not clear how these transporters facilitate cationic amino acid uptake. Our results may

suggest that sodium ions are necessary for the conformational integrity of the transporters or were required for transport of arginine; i.e., sodium interacts with the arginine–transporter complex.

Three concentrations of sodium were used to determine its effects on arginine uptake in ECV_{304} cells. In contrast to earlier findings, the results suggest that y^+L transport was relatively unaffected by sodium concentration unless sodium was absent when transport was uncompetitively inhibited. In contrast, the rate of arginine uptake by the y^+ transporter was significantly reduced as sodium was decreased, without affecting the affinity of this transporter (i.e., noncompetitively inhibited). The results suggest that the absence of sodium would decrease the total rate of uptake by both transporters but would only affect the affinity of the y^+L transporter. These data underscore the advantage of measuring uptake over a wide range, not single concentrations of unlabeled substrate, and to determine the kinetic constants of both transporters, which is possible using this nonlinear approach.

Study Limitations

Although the origin of ECV_{304} cells is controversial (Brown et al. 2000; Drexler et al. 2002; Mann et al. 2003), these cells express hCAT1 (y^+) and y^+LAT2 (y^+L) transporters (Rotmann et al. 2007) and were therefore used as a model to determine uptake by more than one transporter.

We depleted cells of arginine for 24 h (Sessa et al., 1990), with other studies using times between 1 and 24 h (Mann et al. 2003). Intracellular arginine levels appear to be maintained in HUVECs over this time (Mann et al. 2003), and we did not determine whether shorter depletion periods affected the rate of arginine uptake. The initial rate of arginine uptake was then measured for 30 s, assuming that both the conversion of labeled arginine to metabolites, which may be exported, and the export of arginine via trans-stimulation (Flores et al. 2003) were insignificant. Furthermore, our results were in agreement with the literature (Mann et al. 2003).

Although HUVECs also express other transporters, hCAT1, -2B, y + LAT1 and -2 (Rotmann et al. 2007), under the experimental conditions, the study showed statistically that a two-transporter model was preferred over those of a single- or three- (six unknowns) transporter model, with or without multiple binding sites. The possibility of a single transporter modified by the binding of a regulatory subunit or by forming a dimeric transporter (Oulianova and Berteloot 1996) may explain many of the findings and will be the subject of future investigations.

The effects of sodium on uptake of arginine in the presence of leucine, particularly at 1–10 mM leucine concentrations, and other neutral amino acids remain to be determined by this method. In the absence of data measuring labeled arginine uptake in the presence of millimolar leucine concentrations, at this time we have no explanation for the observation of a change in the rate of arginine uptake at 0.5 mM leucine. As V_{maxb} appeared to decrease with increasing leucine concentrations, the inhibition may simply be uncompetitive (unassociative; Krupyanko 2007); but there were insufficient data to substantiate this possibility. Moreover, the possibility that leucine and sodium affect the membrane potential (or pH in the case of sodium), thereby influencing arginine transport, was not investigated in our study and cannot be excluded (Devés and Boyd 1998).

Summary

This nonlinear modeling approach to characterize the uptake of arginine in cells using raw, rather than transformed data, avoids the difficulties and errors of methods deriving constants from the linearization of uptake processes following Michaelian kinetics. Moreover, the model allows for more than one transporter to be modeled, accounts for the concentrations of both labeled and unlabeled arginine and allows the constants to be determined over a range of unlabeled, not single, substrate or inhibitor concentrations, without making assumptions regarding the type of inhibition/activation present. The theoretical models of total uptake closely matched the experimental data, uptake curves could be obtained for the individual transporters and the effects of inhibitors and sodium on the individual transporters determined. In conclusion, we have shown that the use of a nonlinear regression modeling approach may more accurately represent the kinetics of cationic amino acid uptake, activation and inhibition into cells and, hence, provides explanations for discrepancies in the literature.

Acknowledgements We thank Robyn van Zyl from the Department of Clinical and Experimental Pharmacology, Faculty of Health Sciences, University of the Witwatersrand, and Craig Griffiths from the Department of Chemical Engineering, Faculty of Engineering, University of the Witwatersrand, for helpful comments and advice on the initial kinetic analysis. Dr. Deidre Kruger provided valuable comment on the final revisions of the manuscript. We are grateful to the Percy Fox Foundation (grant 011-309-8441101-5121506-190035) and the Iris Hodges Cardiovascular Research Grant (001-8441101-410-5121506 NELM000) for generous financial assistance.

References

Angelo S, Cabrera S, Rojas AM, Rodriguez N, Devés R (2005) Testing the hypothesis that system y^+L accounts for high- and low-transport phenotypes in chicken erythrocytes using L-leucine as substrate. J Membr Biol 204:93–100

Arancibia-Garavilla Y, Toledo F, Casanello P, Sobrevia L (2003) Nitric oxide synthesis requires activity of the cationic amino acid transport system y^+L in human umbilical vein endothelium. Exp Physiol 88:699–710

Ast J, Jablecka A, Bogdanski P, Smolarek I, Krauss H, Chmara E (2010) Evaluation of the antihypertensive effect of L-arginine supplementation in patients with mild hypertension assessed with ambulatory blood pressure monitoring. Med Sci Monit 16:CR266–CR271

Ayuk PT-Y, Theophanous D, D'Souza SW, Sibley CP, Glazier JD (2002) L-Arginine transport by microvillous plasma membrane. J Clin Endocrinol Metab 87:747–751

Babu E, Kanai Y, Chairoungdua A, Kim DK, Iribe Y, Tangtrongsup S, Jutabha P, Li Y, Ahmed N, Sakamoto S, Anzai N, Nagamori S, Endou H (2003) Identification of a novel system L amino acid transporter structurally distinct from heterodimeric amino acid transporters. J Biol Chem 278:43838–43845

Bröer S (2008) Amino acid transport across mammalian intestinal and renal epithelia. Physiol Rev 88:249–286

Bröer A, Wagner CA, Lang F, Bröer S (2000) The heterodimeric amino acid transporter 4F2hc/y^+LAT2 mediates arginine efflux in exchange with glutamine. Biochem J 349:787–795

Brown J, Reading SJ, Jones S, Fitchett CJ, Howl J, Longland CL, Michelangeli F, Dubrova YE, Brown CA (2000) Critical evaluation of ECV304 as a human endothelial cell model defined by genetic analysis and functional responses: a comparison with the human bladder cancer derived epithelial cell line T24/83. Lab Invest 80:37–45

Brunini TMC, Yaqoob MM, Roberts NB, Ellory JC, Moss MB, Siqueira MAS, Mann GE, Mendes Ribeiro AC (2006) Characterization of cationic amino acid transport systems in rat erythrocytes: lack of effect of uraemia on L-arginine influx. Clin Exp Pharmacol Physiol 33:702–707

Casanello B, Sobrevia L (2002) Intrauterine growth retardation is associated with reduced activity and expression of the cationic amino acid transport systems y +/hCAT-1 and y +/CAT-2B and lower activity of nitric oxide synthase in human umbilical vein endothelial cells. Circ Res 91:127–134

Cheng Y-C, Prusoff WH (1973) Relationship between the inhibition constant (K_i) and the concentration of inhibitor which causes 50 per cent inhibition (I_{50}) of an enzymatic reaction. Biochem Pharmacol 22:3099–3108

Chenu C, Bertloot A (1993) Glucose cotransport allosteric kinetics. J Membr Biol 132:95–113

Christensen HN (1990) Role of amino acid transport and counter transport in nutrition and metabolism. Physiol Rev 70:43–77

Christensen HN, Antonioli JA (1969) Cationic amino acid transport in the rabbit reticulocyte. J Biol Chem 244:1497–1504

Christensen HN, Albritton LM, Kakuda DK, MacLeod CL (1994) Gene-product designations for amino acid transporters. J Exp Biol 196:51–57

Closs EI, Albritton LM, Kim JW, Cunningham JM (1993a) Identification of a low affinity, high capacity transporter of cationic amino acids in mouse liver. J Biol Chem 268:7536–7544

Closs EI, Lyons CR, Kelly C, Cunningham JM (1993b) Characterization of the third member of the mCAT family of cationic amino acid transporters. J Biol Chem 268:20796–20800

Closs EI, Basha FZ, Habermeier A, Förstermann U (1997) Interference of L-arginine analogues with L-arginine transport mediated by the y + carrier hCAT-2B. Nitric Oxide Biol Chem 1:65–73

Dall'Asta V, Bussolati O, Sala R, Rotoli BM, Sebastio G, Sperandeo MP, Andria G, Gazzola GC (2000) Arginine transport through system y + L in cultured human fibroblasts: normal phenotype of cells from LPI subjects. Am J Physiol Cell Physiol 279:C1829–C1837

Devés R, Boyd CAR (1998) Transporters for cationic amino acids in animal cells: discovery, structure and function. Physiol Rev 78:487–545

Devés R, Chavez P, Boyd CAR (1992) Identification of a new transport system (y + l) in human erythrocytes that recognizes lysine and leucine with high affinity. J Physiol 454:491–501

Devés R, Angelo S, Chavez P (1993) *N*-Ethylmaleimide discriminates between two lysine transport systems in human erythrocytes. J Physiol 468:753–766

Drexler HG, Dirks WG, Quentmeier H, MacLoed RAF (2002) Bladder carcinoma cell line ECV304 is not a model system for endothelial cells. In Vitro Cell Dev Biol Anim 38:185–186

Durante W, Laio L, Iftikhar I, O'Brien WE, Schafer AI (1996) Differential regulation of L-arginine transport and nitric oxide production by vascular smooth muscle and endothelium. Circ Res 78:1075–1082

Flores C, Rojas S, Aguayo C, Parodi J, Mann G, Pearson JD, Casanello P, Sobrevia L (2003) Cellular biology: rapid stimulation of L-arginine transport by D-glucose involves $p24/44^{mapk}$ and nitric oxide in human umbilical vein endothelium. Circ Res 92:64–72

Gazzola GC, Dall'Asta V, Fracchi-Gazzola R, White MF (1981) The cluster-tray method for rapid measurement of solute fluxes in adherent cultured cells. Anal Chem 115:368–874

Hardy TA, May JM (2002) Coordinate regulation of L-arginine uptake and nitric oxide synthase activity in cultured endothelial cells. Free Radic Biol 32:122–131

Krupyanko VI (2007) Corrected equations for calculation of constants in enzyme inhibition and activation. Biochemistry (Moscow) 72:380–391

Malo C, Berteloot A (1991) Analysis of kinetic data in transport studies: new insights from kinetic studies of Na^+-D-glucose cotransport in human intestinal brush-border membrane vesicles using a fast sampling, rapid filtration apparatus. J Membr Biol 122:127–241

Mann G, Yudilevich DL, Sobrevia L (2003) Regulation of amino acid and glucose transporters in endothelial and smooth muscle cells. Physiol Rev 83:183–252

Martín L, Comalada M, Marti L, Closs EI, MacLeod CL, de Rio RM, Zorzano A, Modolell M, Celada A, Palacin M, Bertan J (2006) Granulocyte-macrophage colony-stimulating factor increases L-arginine transport through induction of CAT2 in bone marrow-derived macrophages. Am J Physiol Cell Physiol 290:C1364–C1372

Mendes-Ribeiro AC, Brunini TMC, Yaqoob M, Aronson JK, Mann GE, Ellory JC (1999) Identification of system y + L as the high affinity transporter of L-arginine in human platelets: upregulation of L-arginine influx in human uremia. Pflugers Arch 438: 573–575

Moss MB, Brunini TMC, Soares de Moura R, Novaes Malagris LE, Roberts NB, Ellory JC, Mann GE, Mendes-Ribeiro AC (2004) Diminished L-arginine bioavailability in hypertension. Clin Sci (Lond) 107:391–397

Naidoo C, Cromarty AD, Snyman T, Sliwa K, Libhaber E, Essop MR, Candy GP (2009) Relationships between plasma amino acids and blood pressure in South Africans of African descent. SA Heart J 6:142–147

Oulianova N, Berteloot A (1996) Sugar transport heterogeneity in the kidney: two independent transporters or different transport modes through an oligomeric protein? 1. Glucose transport studies. J Membr Biol 153:181–194

Panza JA, Casino PR, Badar DM, Quyyumi AA (1993) Effect of increased availability of endothelium-derived nitric oxide precursor on endothelium-dependent vascular relaxation in normal subjects and in patients with essential hypertension. Circulation 87:1475–1481

Penttinen J, Pennanen S, Liesivuori J (2000) Indicators of L-arginine metabolism and cardiovascular risk factors: a cross-sectional study in healthy middle-aged men. Amino Acids 18:199–206

Perticone F, Sciacqua A, Maio R, Perticone M, Maas R, Boger RH, Tripepi G, Sesti G, Zoccali C (2005) Asymmetric dimethylarginine, L-arginine, and endothelial dysfunction in essential hypertension. J Am Coll Cardiol 46:518–523

Rojas AM, Devés R (1999) Mammalian amino acid transport system y^+ revisited: specificity and cation dependence of the interaction with neutral amino acids. J Membr Biol 168:199–208

Rotmann A, Simon A, Martiné U, Habermeier A, Closs EI (2007) Activation of classical protein kinase C decreases transport via systems y + and y + L. Am J Physiol Cell Physiol 292:C2259–C2268

Rotoli BM, Bussolati O, Sala R, Gazzola GC, Dall'Asta V (2005) The transport of cationic amino acids in human airway cells: expression of system y + L activity and transepithelial delivery of NOS inhibitors. FASEB J 19:810–812

Sala R, Rotoli BM, Colla E, Visigalli R, Parolari A, Bussolati O, Gazzola GC, Dall'Asta V (2002) Two way arginine Transport in human endothelial cells: TNF-α stimulation is restricted to system y^+. Am J Physiol Cell Physiol 282:C134–C143

Schlaich MP, Parnell M, Ahlers BA, Finch S, Marshall T, Zhang W-Z, Kaye D (2004) Impaired L-arginine transport and endothelial function in hypertensive and genetically predisposed normotensive subjects. Circulation 110:3680–3686

Sessa WC, Hecker M, Mitchell JA, Vane JR (1990) The metabolism of L-arginine and its significance for the biosynthesis of endothelium-derived relaxing factor: L-glutamine inhibits the generation of L-arginine by cultured endothelial cells. Proc Natl Acad Sci USA 87:8607–8611

Siani A, Pagano E, Lacone R, Iacoviello L, Scopacasa F, Strazzullo P (2000) Blood pressure and metabolic changes during L-arginine supplementation in humans. Am J Hypertens 13:547–551

Signorello MG, Pascale R, Leoncini G (2003) Transport of L-arginine and nitric oxide formation in human platelets. Eur J Biochem 270:2005–2012

Sobrevia L, Cesare P, Yudilevich DL, Mann GE (1995) Diabetes-induced activation, of system y + and nitric oxide synthase in human endothelial cells: association with membrane hyperpolarization. J Physiol 489:183–192

Speake PF, Glazier JD, Ayuk PT-Y, Reade M, Sibley CP, D'Souza SW (2003) L-Arginine transport across the basal plasma membrane of the syncytiotrophoblast of the human placenta from normal and pre-eclamptic pregnancies. J Clin Endocronol Metab 88:4287–4292

White MF, Christensen HN (1982) The two-way influx of cationic amino acids across the plasma membrane of mammalian cells is largely explained by a single transport system. J Biol Chem 257:10069–10080

White MF, Gazzola GC, Christensen HN (1982) Cationic amino acid transport into cultured animal cells. J Biol Chem 257:4443–4449

J Membrane Biol (2012) 245:15–22
DOI 10.1007/s00232-011-9409-z

The Effect of Contrast Medium SonoVue® on the Electric Charge Density of Blood Cells

Aneta D. Petelska · Jacek R. Janica · Joanna Kotynska · Urszula Łebkowska · Zbigniew A. Figaszewski

Received: 31 May 2011 / Accepted: 9 November 2011 / Published online: 24 November 2011

Abstract The effect of contrast medium SonoVue® on the electric charge density of blood cells (erythrocytes and thrombocytes) was measured using a microelectrophoretic method. We examined the effect of adsorbed H^+ and OH^- ions on the surface charge of erythrocytes or thrombocytes. Surface charge density values were determined from electrophoretic mobility measurements of blood cells performed at various pH levels. The interaction between solution ions and the erythrocyte's or thrombocyte's surface was described by a four-component equilibrium model. The agreement between the experimental and theoretical charge variation curves of the erythrocytes and thrombocytes was good at pH 2–9. The deviation observed at a higher pH may be caused by disregarding interactions between the functional groups of blood cells.

Keywords SonoVue · Erythrocyte · Thrombocyte · pH measurement · Surface charge density · Association constant

A. D. Petelska (✉) · J. Kotynska · Z. A. Figaszewski
Institute of Chemistry, University in Bialystok,
Al. J. Pilsudskiego 11/4, 15-443 Bialystok, Poland
e-mail: aneta@uwb.edu.pl

J. R. Janica · U. Łebkowska
Department of Radiology, Medical University of Bialystok,
M. Skłodowskiej-Curie 24A, 15-276 Bialystok, Poland

Z. A. Figaszewski
Faculty of Chemistry, Laboratory of Electrochemical Power Sources, University of Warsaw, Pasteur Street 1,
02-093 Warsaw, Poland

Introduction

Hepatic hemangiomas (congenital vascular malformations) are the most common benign tumors, accounting for 9.4–22.7% of all diagnosed hepatic tumors (Numata et al. 2006; Tranquart et al. 2009; Tani et al. 2010; von Herbay et al. 2010). Most of them are asymptomatic and require no treatment; therefore, differentiation between hepatic hemangiomas and hepatic malignant lesions is a frequent challenge. Radiologists can use numerous methods to diagnose hepatic tumors. Ultrasound is considered to be inferior in comparison to computed tomography (CT), and magnetic resonance imaging (MRI) using contrast agents allows for an evaluation of its nature (Soyer et al. 1998; Herman et al. 2005; Dietrich et al. 2007; Zviniene et al. 2010). The introduction of contrast medium for diagnosis of various medical conditions has been associated with a number of adverse effects such as nephropathy, thrombosis and nephrogenic systemic fibrosis (Carr et al. 1995; Broome 2008; Feldkamp and Kribben 2008; Van Linden et al. 2011). Currently, a growing number of centers perform contrast-enhanced ultrasonography (CEUS) with the contrast agent SonoVue®. Although the use of SonoVue is characterized by a small amount of contraindications, compared to other contrast media it has a good safety profile in abdominal applications, myocardial perfusion assessment and transcranial ultrasound diagnostic (Kaps et al. 1999; Bokor et al. 2001; Piscaglia and Bolondi 2006; Dijkmans et al. 2009; Gaibazzi et al. 2009; Beaton et al. 2010). CEUS achieves comparable sensitivity and specificity to CT and MRI (Bartolotta et al. 2007; Dietrich et al. 2007; Li et al. 2007; Tranquart et al. 2009; Beaton et al. 2010; von Herbay et al. 2010). We have used this method since 2006, especially in people in whom CT or MRI is contraindicated. No complications have been observed.

This study was designed to assess the effects of SonoVue on erythrocytes and thrombocytes.

SonoVue is for diagnostic use only. It is a contrast agent (it helps make internal body structures visible during imaging tests). SonoVue is used in tests that measure how ultrasound travels within the body because it improves the ability of the blood to create an echo. It is only used when the results of the test without a contrast agent are inconclusive.

SonoVue is used in the following:

- Echocardiography (a diagnostic test where an image of the heart is obtained), to obtain a clearer scan of the chambers of the heart, especially of the left ventricle, in patients with suspected or confirmed coronary artery disease.
- Doppler (a diagnostic test that measures the speed of blood flow), in tests for large blood vessels, such as those in the head and those leading to the head or the main vein to the liver, or for smaller blood vessels, such as those in lesions (areas of disease) in the breast or liver.

A microscopic picture SonoVue microbubbles and a schematic representation of the SonoVue microbubble structure are presented in Fig. 1.

The total amount of sulfur hexafluoride (SF_6) administered in a clinical dose is extremely small (in a 2-ml dose the microbubbles contain 16 µl of gas). SF_6 is an inert, innocuous gas, poorly soluble in aqueous solutions. It dissolves in the blood and is subsequently exhaled. More than 80% of the administered SF_6 was recovered in exhaled air within 2 min after injection and almost 100% after 15 min (Schneider et al. 1995; Schneider 1999a, 1999b; Greis 2004). SonoVue is a contrast agent of the second generation that contains phospholipid-stabilized microbubbles filled with SF_6 with a diameter <8 µm (mean 2.5 µm). The physicochemical parameters of SonoVue are presented in Table 1.

Biological membranes are characterized by a markedly ordered structure and can be considered to be a distinct phase from the physical point of view, separated from surrounding cytoplasm or intermolecular biological fluid. Thus, the membrane surface can be approximated to an interface. The membrane–medium interface is the site where some physicochemical processes occur which are characteristic of a typical interface, e.g., asymmetric distribution of electric charge (Nalecz and Wojtczak 1982).

Examining the electrical charge could reveal substantial information about the balance between membrane components but also between membrane components and the surrounding solution. The electrical charge is determined by structural positive charge carriers (free amino groups of proteins and aminophospholipids) and by negative charge carriers (some phospholipids, especially phosphatidylserine, sialic acid, glycophorins and free carboxy groups of polypeptide chains) (Szachowicz-Petelska et al. 2010).

The effect of contrast medium SonoVue on the electric charge density of blood cells (erythrocytes and thrombocytes) was measured using a microelectrophoretic method. We describe the changes of electric charge density of the

Table 1 SonoVue physicochemical parameters

Concentration	1–5 × 10^8 ml^{-1}
Mean microbubble diameter	2.5 (µm)
SF_6 encapsulated volume	8 (µl/ml)
SF_6 volume in a 2.4-ml dose	0.02 (ml)
Osmolarity	290 (mOs/kg)
Viscosity	2 (mPa s)
pH	6.0–6.5
Stability after reconstitution	6 (h)

Data from Schneider et al. 1995; Schneider 1999a, 1999b

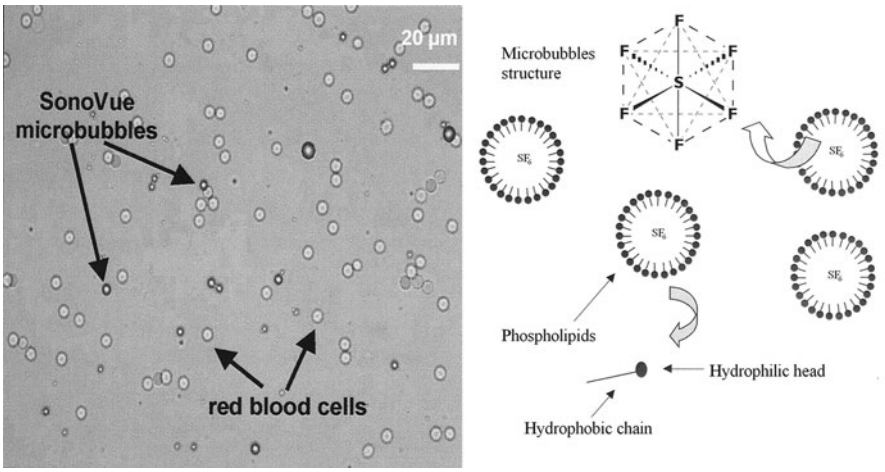

Fig. 1 Microscopic picture and schematic representation of SonoVue microbubble structure (Schneider et al. 1995; Schneider 1999a, 1999b; Greis 2004)

erythrocytes and thrombocytes after the SonoVue effect over the pH range 2–11.

Theory

The dependence of the surface charge density of erythrocytes or thrombocytes as a result of SonoVue on the pH of the electrolyte solution can be described using four equilibrium equations. Two are connected with positive groups (e.g., phospholipids or proteins and sodium and hydrogen ions), and two concern the negative species of phospholipids or proteins and hydroxide and chloride ions. The H^+, OH^-, Na^+ and Cl^- ions are adsorbed at the cell membranes (erythrocytes or thrombocytes), and the adsorption equilibria can be presented in the following form (Dobrzynska et al. 2006, 2007):

$$A^- + H^+ \Leftrightarrow AH \quad (1)$$

$$A^- + Na^+ \Leftrightarrow ANa \quad (2)$$

$$B^+ + OH^- \Leftrightarrow BOH \quad (3)$$

$$B^+ + Cl^- \Leftrightarrow BCl \quad (4)$$

Therefore, the association constants of the H^+, Na^+, OH^- and Cl^- ions with functional groups are expressed in the following manner (Dobrzynska et al. 2006, 2007):

$$K_{AH} = \frac{a_{AH}}{a_{A^-} \cdot a_{H^+}} \quad (5)$$

$$K_{ANa} = \frac{a_{ANa}}{a_{A^-} \cdot a_{Na^+}} \quad (6)$$

$$K_{BOH} = \frac{a_{BOH}}{a_{B^+} \cdot a_{OH^-}} \quad (7)$$

$$K_{BCl} = \frac{a_{BCl}}{a_{B^+} \cdot a_{Cl^-}} \quad (8)$$

where K_{AH}, K_{ANa}, K_{BOH} and K_{BCl} are association constants; a_{AH}, a_{ANa}, a_{A^-}, a_{BOH}, a_{BCl} and a_{B^+} are surface concentrations of corresponding groups on the membrane surface; and a_{H^+}, a_{Na^+}, a_{OH^-} and a_{Cl^-} are volume concentrations of solution ions. The concentration balances are expressed as follows (Dobrzynska et al. 2006):

$$C_A = a_{A^-} + a_{AH} + a_{ANa} \quad (9)$$

$$C_B = a_{B^+} + a_{BOH} + a_{BCl} \quad (10)$$

where C_A is the total surface concentration of the membrane acidic groups and C_B is the total surface concentration of the membrane basic groups.

Surface charge density of the membrane is given by the equation presented by Dobrzynska et al. (2006):

$$\delta = (a_{B^+} - a_{A^-}) \cdot F \quad (11)$$

where $F = 96,487\,\mathrm{C/mol}$ is the Faraday constant.

Elimination of a_{AH}, a_{ANa}, a_{A^-}, a_{BOH}, a_{BCl} and a_{B^+} from the above equations yields the following formula (Dobrzynska et al. 2006):

$$\frac{\delta}{F} = \frac{C_B}{1 + K_{BOH}a_{OH^-} + K_{BCl}a_{Cl^-}} - \frac{C_A}{1 + K_{AH}a_{H^+} + K_{ANa}a_{Na^+}} \quad (12)$$

Determination of the searching parameters requires a simplification of the above equation to a linear form at high H^+ ($a_{H+} \to \infty$) and low H^+ ($a_{H+} \to 0$) concentrations, which were presented by Dobrzynska et al. (2006). In the former case Eq. 12 was rewritten as a decreasing exponential function of H^+ concentration (Eq. 13) and in the latter case, as an increasing exponential function of H^+ concentration (Eq. 14) (Dobrzynska et al. 2006).

$$\frac{\delta}{F} = \frac{C_B a_{H^+}}{a_{H^+}(1 + K_{BCl}a_{Cl^-}) + K_{BOH}K_W} - \frac{C_A}{K_{AH}a_{H^+} + K_{ANa}a_{Na^+} + 1} \quad (13)$$

$$\frac{\delta}{F} = \frac{C_B a_{H^+}}{K_{BOH}K_W + a_{H^+}(1 + K_{BCl}a_{Cl^-})} - \frac{C_A}{K_{ANa}a_{Na^+} + 1 + K_{AH}a_{H^+}} \quad (14)$$

The numerator of each term in Eq. 13 was divided by the denominator to yield two terms. These operations resulted in a linear equation in the a_{H+} and $(\delta a_{H^+})/F$ coordinate system, which was correct for high hydrogen ion concentrations ($a_{H+} \to \infty$) (Dobrzynska et al. 2006).

$$\frac{\delta a_{H^+}}{F} = \frac{C_B}{1 + K_{BCl}a_{Cl^-}} a_{H^+} - \left(\frac{C_B K_{BOH} K_W}{(1 + K_{BCl}a_{Cl^-})^2} + \frac{C_A}{K_{AH}} \right) \quad (15)$$

Applying the same procedure to Eq. 14 resulted in a linear equation in the $1/(a_{H^+})$ and $\delta/(Fa_{H^+})$ coordinate system, which was correct for low hydrogen ion concentrations ($a_{H+} \to 0$) (Dobrzynska et al. 2006):

$$\frac{\delta}{Fa_{H^+}} = -\left(\frac{C_A}{1 + K_{ANa}a_{Na^+}} \right) \frac{1}{a_{H^+}} + \left(\frac{C_B}{K_{BOH}K_W} + \frac{C_A K_{AH}}{(1 + K_{ANa}a_{Na^+})^2} \right) \quad (16)$$

The coefficients describing these linear functions may be easily obtained using linear regression and subsequently applied to calculate the parameters. Calculation of C_A, C_B, K_{AH} and K_{BOH} is possible owing to knowledge of the association constants K_{ANa} and K_{BCl} obtained for phosphatidylcholine liposome membrane (Dobrzynska et al. 2007). Defining the value of these parameters permits calculation of the theoretical cell membrane surface charge from Eq. 12 for comparison to experimental data.

Materials and Methods

Contrast Medium SonoVue

SonoVue (Bracco, Milan, Italy) contains the active substance SF_6 gas. It is available as a kit containing one vial of gas and powder and one prefilled syringe containing the solvent. SonoVue solution was prepared according to the manufacturer's instructions by mixing the solvent with the powder and gas. The solution contains SF_6 gas as microbubbles.

Blood Cell Preparation

Approval for this study was granted by the Ethics Review Board of Medical University of Bialystok, and informed consent was obtained from all patients at the time of scanning after the nature of the procedure had been fully explained.

The examination was based on 20 selected individuals (12 women and 8 men; mean age 33.2 years, range 18–49) with hepatic hemangioma size up to 30 mm (19 ± 7.5 mm), without any other diseases. The size was limited to 30 mm because hemangiomas of at least 4 cm in diameter are defined as giant hemangiomas and in some cases give rise to symptoms because of Kasabach–Merritt syndrome (tumor leads to decreased platelet counts) (Tani et al. 2010).

There were two control groups. Both consisted of 20 healthy volunteers. The first (14 women and 6 men; mean age 33.3 years, range 18–50) was used to assess the impact of only ultrasound on the red blood cells and platelets, and the second (12 women and 8 men; mean age 33.2 years, range 18–49) was used to compare blood cells.

Blood in the amount of 2 ml was taken immediately before and 10 min after administration of SonoVue into biologically clean glass containers containing anticoagulant (sodium citrate) from a separate puncture antecubital vein without stasis.

All sonographic examinations were performed by a senior radiologist using Toshiba Aplio (Toshiba Medical Systems, Otawara, Japan) equipped with pulse subtraction harmonic imaging software, with the use of a wide-band, multifrequency convex array abdominal transducer (3.5 MHz PVT 375BT). A bolus of 2.4 ml of SonoVue was administered with a 21-gauge peripheral intravenous cannula, followed by a 10-ml saline flush. Dynamic real-time CEUS was then performed using a low mechanical index (MI 0.08) to avoid microbubble disruption. After SonoVue injection, the lesion was scanned continuously for up to 8 min until the enhancement effect began to subside. CEUS recognition of hemangiomas was based on enhancement and washing and washout patterns of the lesion relative to normal hepatic parenchyma during the three vascular contrast phases: arterial, portal-venous and late (Lencioni 2006; Correas et al. 2009). Static image captures as well as dynamic video clips were stored on digital video disc.

Preparation of Erythrocytes from Blood

Erythrocytes were isolated from 2 ml of anticoagulated whole blood by centrifugation at $900\times g$ for 8 min at room temperature. The supernatant, thrombocyte-rich plasma was removed and saved for subsequent processing, while the erythrocytes were washed three times with isotonic saline (0.9% NaCl) at $3{,}000\times g$ for 15 min. After the final wash, the erythrocyte pellet was resuspended in isotonic saline for electrophoretic measurement.

Preparation of Thrombocytes from Plasma

The thrombocyte-rich plasma was centrifuged at $4{,}000\times g$ for 8 min. The supernatant plasma was removed and discarded. The thrombocyte pellet was washed three times with isotonic saline by centrifugation at $3{,}000\times g$ for 15 min. After the final wash, thrombocytes were resuspended in isotonic saline for electrophoretic measurement.

All solutions and cleaning procedures were performed with water purified using a Milli-Qll system (18.2; Millipore, Billerica, MA).

Microelectrophoretic Mobility Measurements

The electrophoretic mobility of erythrocyte or thrombocyte cells in suspension was measured using laser Doppler velocimetry and a Zetasizer Nano ZS (Malvern Instruments, Malvern, UK) apparatus. Measurements were carried out as a function of pH. Cell membranes were suspended in NaCl solution and titrated to the desired pH using (HCl + NaCl or NaOH + NaCl). The reported values represent the average of at least six measurements performed at a given pH.

From electrophoretic mobility measurements the surface charge density was determined using the following equation (Alexander and Johnson 1949):

$$\delta = \frac{\eta \cdot u}{d} \tag{17}$$

where η is the viscosity of solution, u is electrophoretic mobility and d is the diffuse layer thickness. The diffuse layer thickness was determined from the following formula (Barrow 1996):

$$d = \sqrt{\frac{\varepsilon \cdot \varepsilon_0 \cdot R \cdot T}{2 \cdot F^2 \cdot I}} \tag{18}$$

where R is the gas constant, T is the temperature, F is the Faraday number, I is the ionic strength of 0.9% NaCl and ε_o is the permeability of the electric medium.

Results and Discussion

The electrophoretic mobility measurements of the blood cells containing SonoVue formed the basis for investigations of ion/membrane association phenomena. Experiments were performed at several pH values using 0.155 M NaCl as a supporting electrolyte. The electrophoretic mobility values were converted to surface charge density using Eq. 17. The theoretical values of the surface charge density were determined by applying Eq. 12 to the experimental data. The association constants of blood cell surface groups with Na^+ and Cl^- [$K_{A_1Na} = 0.230$ (m^3/mol), $K_{B_1Cl} = 0.076$ (m^3/mol)] have been previously reported (Dobrzynska et al. 2007). The calculated association constants were substituted into Eq. 12 to produce a theoretical curve. The surface charge densities of the control and SonoVue erythrocytes are plotted as a function of pH in Fig. 2. The points denote the experimental values, and the continuous lines represent the theoretical values obtained from Eq. 12. The theoretical and experimental surface charge density values agree between pH 2 and 9 but diverge slightly in the high pH range. Deviations from the theoretical curve may be caused by interactions between the functional groups of the blood cell components.

If we considered an acid solution, a small decrease in positive charge was observed in erythrocytes after SonoVue use in comparison to control erythrocytes. In basic solutions we also observed a small change in the negative charge in erythrocytes after SonoVue in comparison to control erythrocytes and a small shift of the isoelectric point of the membrane to high pH values.

The surface charge densities of the control and SonoVue thrombocytes are plotted as a function of pH in Fig. 3. The points denote experimental values, and the continuous lines represent theoretical values obtained from Eq. 12. The theoretical and experimental surface charge density values agree between pH 2 and 9 but diverge slightly in the high pH range.

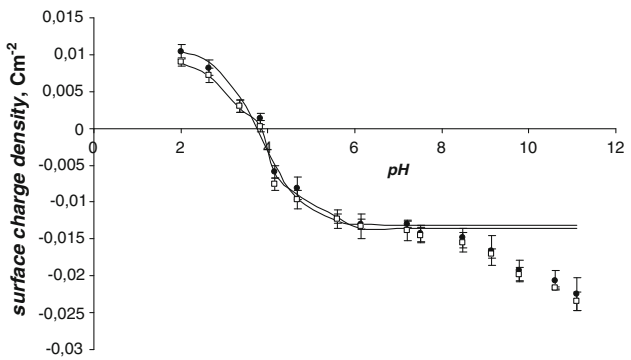

Fig. 2 pH dependence of surface charge density of erythrocytes: *filled circle* control; *open square* SonoVue effect (experimental values are indicated by *points* and theoretical values, by the *curve*)

If we consider an acid solution, any change in positive charge is observed in thrombocytes with SonoVue in comparison to control thrombocytes. In basic solutions we observed an increase of the negative charge in thrombocytes with SonoVue in comparison to control thrombocytes and a small shift of the isoelectric point of the membrane to low pH values.

The isoelectric point and surface charge density values for human erythrocytes and thrombocytes determined using electrophoresis are presented in Tables 2 and 3, respectively. Data are expressed as mean ± standard deviation. These data were analyzed using standard statistical analysis.

The surface charge density values at low pH values in erythrocytes with SonoVue decreased compared with control groups (14%); however, at high pH values they increased compared with the control group (3%, Table 2). The isoelectric point of SonoVue erythrocyte membranes (3.60) compared to controls (3.80) slightly shifted to low pH values.

The surface charge density values at low pH values as well as at high pH values in thrombocytes with SonoVue decreased compared with controls (15%); however, at high pH values they increased compared to controls (33%), which is presented in Table 3. The isoelectric point of SonoVue thrombocyte membranes (4.40) compared with the control group (4.65) showed a considerable shift to low pH values.

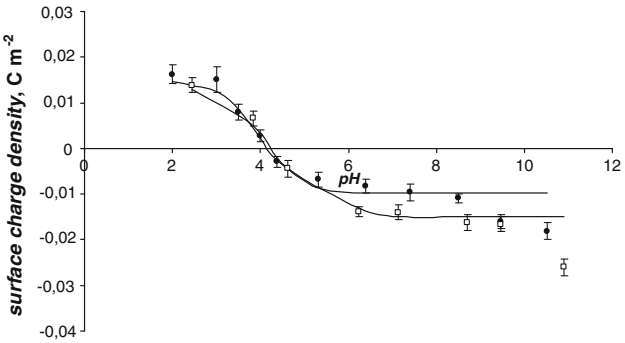

Fig. 3 pH dependence of surface charge density of thrombocytes: *filled circle* control; *open square* SonoVue effect (experimental values are indicated by *points* and theoretical values, by the *curve*)

Table 2 Surface charge density and isoelectric point values for human erythrocytes (control and SonoVue effect)

Groups	Isoelectric point	Surface charge density (10^{-2} C/m^2)	
		Low pH values	High pH values
Control	3.80	1.04 ± 0.11	–1.31 ± 0.08
SonoVue effect	3.60	0.89 ± 0.09	–1.35 ± 0.09

Table 3 Surface charge density and isoelectric point values for human thrombocytes (control and SonoVue effect)

Groups	Isoelectric point	Surface charge density (10^{-2} C/m^2)	
		Low pH values	High pH values
Control	4.65	1.63 ± 0.10	–1.09 ± 0.19
SonoVue effect	4.40	1.39 ± 0.13	–1.62 ± 0.32

Table 4 Acidic and basic functional group concentrations and association constants for erythrocyte functional groups and H^+ and OH^- ions

Groups	Parameters			
	C_A (10^{-6} mol/m^2)	C_B (10^{-6} mol/m^2)	K_{AH} (10^2 m^3/mol)	K_{BOH} (10^7 m^3/mol)
Control	7.06 ± 0.42	1.54 ± 0.47	3.39 ± 1.12	3.65 ± 0.84
SonoVue effect	6.82 ± 0.10	1.46 ± 0.08	3.95 ± 0.73	4.07 ± 0.60

Acidic (C_A) and basic (C_B) functional group concentrations and their average association constants with hydrogen (K_{AH}) and hydroxyl (K_{BOH}) ions of erythrocyte and thrombocyte surface groups were determined as described previously by Dobrzynska et al. (2006). These values are presented in Tables 4 and 5, respectively. Data are expressed as mean ± standard deviation. These data were analyzed using standard statistical analysis.

The concentration of acidic (4%) functional groups in erythrocytes with SonoVue decreased compared to controls, and the basic (5%) groups in erythrocytes also decreased compared to controls (Table 4). The K_{AH}, the association constant of the acidic groups of the erythrocyte membrane, increased (15%) with SonoVue compared to controls; and the K_{BOH} value was only 10% higher compared with the control group.

The experimental results indicate that SonoVue caused a small decrease in negative and positive charge numbers at the erythrocyte surface. This corresponded to a slightly decreased surface concentration of acidic groups (C_A) and basic groups (C_B). Changes in functional group composition on the membrane surface are due to the appearance of new functional groups and/or to the disappearance of existing ones as the result of a reaction of SonoVue with erythrocyte components. Variations in the number and kind of functional groups bring about variations in C_A and C_B and, in turn, in their association constant values. SonoVue increases the association constants of negatively charged (K_{AH}) and positively charged (K_{BOH}) groups.

In thrombocytes with SonoVue we observed an increase of the acidic group's concentration, C_A (3%), and an increase of the basic functional concentration, C_B (11%), compared with the control group (Table 5). SonoVue induces an increase in K_{AH} (6%) and K_{BOH} values (11%) in the thrombocytes compared with the control groups.

Table 5 Acidic and basic functional group concentrations and association constants for thrombocyte functional groups and H^+ and OH^- ions

Groups	Parameters			
	C_A (10^{-6} mol/m^2)	C_B (10^{-6} mol/m^2)	K_{AH} (10^2 m^3/mol)	K_{BOH} (10^7 m^3/mol)
Control	3.67 ± 0.79	1.17 ± 0.21	2.81 ± 1.70	2.04 ± 0.59
SonoVue effect	3.98 ± 0.08	1.31 ± 0.07	2.98 ± 0.43	2.29 ± 0.56

The experimental results indicate that SonoVue causes a small increase in negative and positive charge numbers at the thrombocyte surface. This corresponded to a slightly increased surface concentration of acidic groups (C_A) and basic groups (C_B). Changes in functional group composition on the membrane surface are due to the appearance of new functional groups and/or to the disappearance of existing ones as the result of a reaction of SonoVue with thrombocyte components. Variations in the number and kind of functional groups bring about variations in C_A and C_B and, in turn, in their association constant values. SonoVue increases the association constants of negatively charged (K_{AH}) and positively charged (K_{BOH}) groups.

The current results demonstrate that SonoVue causes a small change in the levels of all membrane components (phospholipids and integral membrane proteins) in erythrocytes and thrombocytes (Tables 4, 5). In addition, our results have shown that the electrical properties of erythrocyte and thrombocyte membranes are not affected by SonoVue. An essential property of the electric double layer is its electrokinetic potential, the potential difference between the membrane and its environment and the surface charge. Changes in cell membrane charge are connected with changes in membrane composition (Szachowicz-Petelska et al. 2008; Dobrzynska et al. 2008). An increase in the amount of specific phospholipids results in the appearance of additional functional groups, both positively and negatively charged, at the membrane surface (Dobrzynska et al. 2010).

In our results we did not observe any changes in surface charge density of erythrocytes after addition of SonoVue, but in thrombocytes we observed changes of surface charge density at high pH values. The changes of negative surface charge density of thrombocytes probably are connected with adsorption of the remaining phospholipids from the SonoVue contrast agent. In our opinion the problem could be studied by means of model experiments (e.g., bilayer lipid membranes) as well as in vitro examination of the SonoVue effect in blood cells.

Our CEUS results are in agreement with the literature that typical small hemangiomas show peripheral nodular enhancement in the arterial phase and from portal to late phase nodules have progressive centripetal enhancement (Dietrich et al. 2007; von Herbay et al. 2010; Zviniene et al. 2010). There have been no adverse events or technical difficulties encountered in this patient population, and many authors have also reported no adverse effects of SonoVue (Bokor et al. 2001; Piscaglia and Bolondi 2006; Gaibazzi et al. 2009; Tranquart et al. 2009; Beaton et al. 2010).

The normal blood pH is tightly regulated between 7.35 and 7.45. Virtually all degenerative diseases, including cancer, heart disease, osteoporosis, arthritis, kidney and gall stones and tooth decay, are associated with excess acidity in the body. We observed no large changes of the surface charge density of blood cells in a wide pH range. We see no reason for limiting the use of SonoVue contrast medium in clinical diagnostics.

Conclusions

The interaction between blood cell membranes and solution ions has been well characterized. The dependence of the surface charge density of the erythrocytes and thrombocytes as a SonoVue effect on pH was described using a mathematical model derived from experimental electrophoretic data. The theoretical estimates of electric charge enabled the determination of association constants for the functional groups of erythrocytes or thrombocytes and electrolyte ions. The agreement of the experimental and theoretical charge variation curves of the erythrocytes as well as thrombocytes is good between pH 2 and 9. The deviation observed at a higher pH may be caused by disregarding interactions between the functional groups of blood cells.

No adverse events or technical difficulties were encountered in the patient population presented in this study. In our opinion, SonoVue is a safe contrast medium.

References

Alexander AE, Johnson P (1949) Colloid science. Clarendon Press, Oxford

Barrow GM (1996) Physical chemistry. McGraw-Hill, New York

Bartolotta TV, Midiri M, Galia M, Rollandi GA, Cademartiri F, Lagalla R, Cardinale AE (2007) Characterization of benign hepatic tumors arising in fatty liver with SonoVue and pulse inversion US. Abdom Imaging 32:84–91

Beaton C, Cochlin D, Kumar N (2010) Contrast enhanced ultrasound should be the initial radiological investigation to characterise focal liver lesions. Eur J Surg Oncol 36:43–46

Bokor D, Chambers JB, Rees PJ, Rees PJ, Mant TGK, Luzzani F, Spinazzi A (2001) Clinical safety of SonoVue, a new contrast agent for ultrasound imaging, in healthy volunteers and in patients with chronic obstructive pulmonary disease. Invest Radiol 36:104–109

Broome DR (2008) Nephrogenic systemic fibrosis associated with gadolinium based contrast agents: a summary of the medical literature reporting. Eur J Radiol 66:230–234

Carr ME Jr, Carr SL, Merten SR (1995) Effects of ionic and nonionic contrast media on clot structure, platelet function and thrombolysis mediated by tissue plasminogen activator in plasma clots. Haemostasis 25:172–181

Correas JM, Tranquart F, Claudon M (2009) Guidelines for contrast enhanced ultrasound (CEUS)—update 2008. J Radiol 90:123–138

Dietrich CF, Mertens JC, Braden B, Schuessler G, Ott M, Ignee A (2007) Contrast-enhanced ultrasound of histologically proven liver hemangiomas. Hepatology 45:1139–1145

Dijkmans PA, Juffermans LJ, van Dijk J, Musters RJP, Spreeuwenberg MD, Kamp O (2009) Safety and feasibility of real time adenosine myocardial contrast echocardiography with emphasis on induction of arrhythmias: a study in healthy volunteers and patients with stable coronary artery disease. Echocardiography 26:807–814

Dobrzynska I, Skrzydlewska E, Figaszewski Z (2006) Parameters characterizing acid–base equilibria between cell membrane and solution and their application to monitoring the effect of various factors on the membrane. Bioelectrochemistry 69:142–147

Dobrzynska I, Kotyńska J, Figaszewski Z (2007) Changes in electrical charge of phosphatidylcholine and phosphatidylserine liposomal membranes caused by adsorption of monovalent ions. Chem Anal 52:931–944

Dobrzynska I, Szachowicz-Petelska B, Skrzydlewska E, Figaszewski ZA (2008) Effects of green tea on physico-chemical properties of liver cell membrane of different age rats intoxicated with ethanol. Pol J Environ Stud 17:327–333

Dobrzynska I, Szachowicz-Petelska B, Skrzydlewska E, Figaszewski ZA (2010) Effect of L-carnitine on liver cell membranes in ethanol-intoxicated rats. Chem Biol Interact 188:44–51

Feldkamp T, Kribben A (2008) Contrast media induced nephropathy: definition, incidence, outcome, pathophysiology, risk factors and prevention. Minerva Med 99:177–196

Gaibazzi N, Squeri A, Ardissino D, Reverberi C (2009) Safety of contrast flash-replenishment stress echocardiography in 500 patients with a chest pain episode of undetermined origin within the last 5 days. Eur J Echocardiogr 10:726–732

Greis C (2004) Technology overview: SonoVue (Bracco, Milan). Eur Radiol Suppl 14:P11–P15

Herman P, Costa ML, Machado MA et al (2005) Management of hepatic hemangiomas: a 14-year experience. J Gastrointest Surg 9:853–859

Kaps M, Seidel G, Bokor D, Modrau B, Algermissern C (1999) Safety and ultrasound-enhancing potentials of a new sulfur hexafluoride-containing agent in the cerebral circulation. J Neuroimaging 9:150–154

Lencioni R (2006) European federation of societies for ultrasound in medicine and biology (EFSUMB). Impact of European federation of societies for ultrasound in medicine and biology (EFSUMB) guidelines on the use of contrast agents in liver ultrasound. Eur Radiol 16:1610–1613

Li R, Guo Y, Hua X, He Y, Ding J, Guo A, Luo M (2007) Characterization of focal liver lesions: comparison of pulse-inversion harmonic contrast-enhanced sonography with contrast-enhanced CT. J Clin Ultrasound 35:109–117

Nalecz MJ, Wojtczak L (1982) Surface charge of biological membranes and its regulatory functions. Post Biochem 28:191–225

Numata K, Isozaki T, Morimoto M, Sugimori K, Kunisaki R, Morizane T, Tanaka K (2006) Prospective study of differential diagnosis of hepatic tumors by pattern-based classification of contrast-enhanced sonography. World J Gastroenterol 12:6290–6298

Piscaglia F, Bolondi L (2006) Italian society for ultrasound in medicine and biology (SIUMB) study group on ultrasound contrast agents. The safety of Sonovue in abdominal applications: retrospective analysis of 23188 investigations. Ultrasound Med Biol 32:1369–1375

Schneider M (1999a) Characteristics of SonoVue™. Echocardiography 16:743–746

Schneider M (1999b) SonoVue, a new ultrasound contrast agent. Eur Radiol 9:S347–S348

Schneider M, Arditi M, Barrau MB, Brochot J, Broillet A, Ventrone R, Feng Y (1995) BR1: a new ultrasonographic contrast agent based on sulfur hexafluoride-filled microbubbles. Invest Radiol 30:451–457

Soyer P, Dufresne AC, Somveille E, Lenormand S, Scherrer A, Rymer R (1998) Differentiation between hepatic cavernous hemangioma and malignant tumor with T2-weighted MRI: comparison of fast spin-echo and breathhold fast spin-echo pulse sequences. Clin Imaging 22:200–210

Szachowicz-Petelska B, Dobrzynska I, Skrzydlewska E, Figaszewski ZA (2008) Changes in phospholipids composition studied by HPLC and electric properties of liver cell membrane of ethanol-poisoned rats. Toxicol Mech Methods 18:525–530

Szachowicz-Petelska B, Dobrzynska I, Sulkowski S, Figaszewski ZA (2010) Characterization of the cell membrane during cancer transformation. J Environ Biol 31:845–850

Tani A, Yoshida H, Mamada Y, Taniai N, Kawano Y, Uchida E (2010) Extrahepatic portal venous obstruction due to a giant hepatic hemangioma associated with Kasabach–Merritt syndrome. J Nippon Med Sch 77:269–272

Tranquart F, Correas JM, Ladam Marcus V, Manzoni P, Vilgrain V, Aube C, Elmaleh A, Chami L, Claudon M, Cuilleron M, Diris B, Garibaldi F, Lucidarme O, Marion D, Beziat C, Rode A, Tasu JP, Trillaud H, Bleuzen A, Le Gouge A, Giraudeau B, Rusch E (2009) Real-time contrast-enhanced ultrasound in the evaluation of focal liver lesions: diagnostic efficacy and economical issues from a French multicentric study. J Radiol 90:109–122

Van Linden A, Kempfert J, Rastan AJ, Holzhey D, Blumenstein J, Schuler G, Mohr FW, Walther T (2011) Risk of acute kidney injury after minimally invasive transapical aortic valve implantation in 270 patients. Eur J Cardiothorac Surg 39:835–843

von Herbay A, Westendorff J, Gregor M (2010) Contrast-enhanced ultrasound with SonoVue: differentiation between benign and malignant focal liver lesions in 317 patients. J Clin Ultrasound 38:1–9

Zviniene K, Zaboriene I, Basevicius A, Jurkiene N, Barauskas G, Pundzius J (2010) Comparative diagnostic value of contrast-enhanced ultrasonography, computed tomography, and magnetic resonance imaging in diagnosis of hepatic hemangiomas. Medicina (Kaunas) 46:329–335

J Membrane Biol (2012) 245:23–28
DOI 10.1007/s00232-011-9411-5

Headgroup Conformations of Phospholipids from Molecular Dynamics Simulation: Sampling Challenges and Comparison to Experiment

Alexander Vogel · Scott E. Feller

Received: 14 October 2011 / Accepted: 19 November 2011 / Published online: 9 December 2011

Abstract The preferred conformations of the glycerol region of a phospholipid have been explored using replica exchange molecular dynamics (MD) simulations and compared with the results of standard MD approaches and with experiment. We found that due to isomerization rates in key torsions that are slow on the timescale of atomistic MD simulations, standard MD is not able to produce accurate equilibrium conformer distributions from reasonable trajectory lengths (e.g., on the 100 ns) timescale. Replica exchange MD, however, results in quite efficient sampling due to the rapid increase in isomerization rate with temperature. The equilibrium distributions obtained from replica exchange MD have been compared with the results of experimental nuclear magnetic resonance observations. This comparison suggests that the sampling approach demonstrated here is a valuable tool that can be used in evaluating force fields for molecular simulation of lipids.

Keywords Molecular dynamics · Model membrane · Replica exchange · NMR study · Artificial bilayer membrane

Introduction

Phospholipids constitute an important class of biomolecules, providing the basis for cellular membranes and creating nanoscopic interfaces with extreme variations in polarity over a length scale of angstroms. The backbone of the phospholipid is a substituted glycerol with the hydrophilic phosphate headgroup connected to carbon atom C1 via a phosphate ester bond and two hydrophobic fatty acid chains connected at C2 and C3 via ester bonds (see Fig. 1). Situated in a unique region of astounding chemical heterogeneity (Wiener and White 1992), the conformational preferences of the glycerol region of the phospholipid determine important details of headgroup and tail orientations, influencing properties such as the dipole orientation and dipole potential (Gawrisch et al. 1992) and the packing of the aliphatic chains that are critical determinants of membrane structure and function (Israelachvili 1977). Hauser et al. (1980, 1988) have described how the values of the θ_3/θ_4 torsion angles (see Fig. 1 for definitions of these angles) determine the relative orientation of the acyl chains and compared the torsional states of a variety of phospholipids as crystalline solids, as fluid phase (L_α) bilayers and as individual monomers dissolved in a range of solvents. While the crystal structure indicates a single conformation (θ_3 = trans, θ_4 = gauche+), under physiological temperature, in both the monomeric and bilayer forms, several conformations are observed by nuclear magnetic resonance (NMR). Hauser et al. labeled the global free energy minimum conformer observed in the crystal structures "A" and identified by NMR analysis the "B" conformer (θ_3 = gauche+, θ_4 = gauche–) and the "C" conformer (θ_3 = gauche-, θ_4 = trans). The relative population of these rotational isomers depends somewhat on acyl chain composition, aggregation state and solvent polarity; but for glycerophosphatidylcholines the A conformer always predominates (50–60%) and the C conformer constitutes only a small fraction (1–10%).

A. Vogel
Institute of Medical Physics and Biophysics,
University of Leipzig, Leipzig, Germany

S. E. Feller (✉)
Department of Chemistry, Wabash College,
301 W. Wabash Avenue, Crawfordsville, IN 47933, USA
e-mail: fellers@wabash.edu

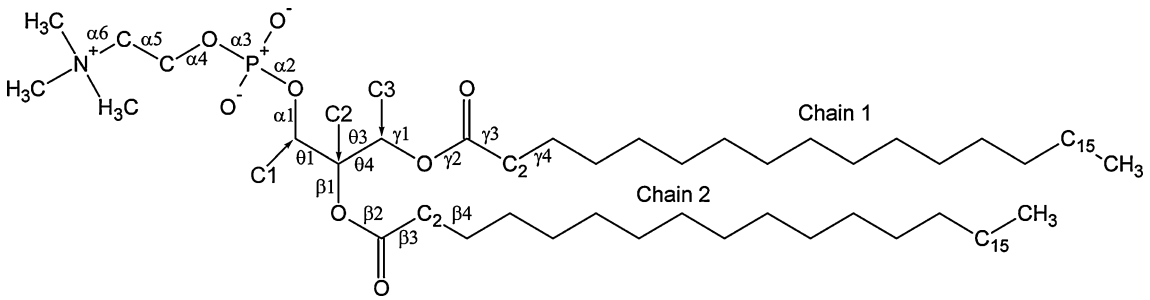

Fig. 1 Structure of DPPC using the torsion angle notation of Sundaralingam (1972)

In the recent past molecular dynamics (MD) computer simulations have emerged as a powerful tool for providing structural, dynamic and thermodynamic descriptions of lipid bilayer membranes at the atomic level (Brandt and Edholm 2009; Lyubartsev and Rabinovich 2011; Marrink et al. 2009). These calculations have been found to complement experimental techniques such as X-ray scattering and NMR and are finding widespread use in membrane biophysics research programs. There are, however, many details that must be considered in carrying out such computer simulations, such as the time and length scales of the processes under study, the statistical mechanical ensemble to be employed, the algorithm used to integrate the equations of motion and the form of the energy function and its parameterization. A key quantity that must be assessed in evaluating such simulations is the degree to which the results can be said to be converged; i.e., the observed conformations correspond to the equilibrium distribution and the number of transitions between states is sufficiently large that reliable statistics on the dynamics of fluctuations are obtained (Grossfield and Zuckerman 2009). For degrees of freedom with long correlation times, it may be difficult to determine accurate equilibrium distributions and it may be unclear whether discrepancies with experiment arise from a systematic error, e.g., deficiencies in the potential energy function, or from statistical error. A powerful algorithm for accelerating the sampling in MD simulations is the replica exchange (REX) technique. In its most frequent implementation, a series of MD simulations (system replicas) are run in parallel at different temperatures. The temperature range typically begins at or near the temperature of primary interest and increases to a significantly higher temperature, where rates for crossing energetic barriers are significantly higher. A Monte Carlo procedure is applied periodically to swap configurations among the various temperatures; thus, each replica spends time at higher temperatures, accelerating processes that have long correlation times at the temperature of interest. For a detailed description of REX MD, the reader is referred to Sugita and Okamoto (1999).

Here, we describe the application of REX MD to a dipalmitoylphosphatidylcholine (DPPC) monomer in aqueous solution. While many simulations of DPPC as a bilayer or monolayer have been reported in the literature, few have examined the monomeric form. We chose this system composition because it more closely matches the conditions of the NMR experiments we seek to connect to and because it allows extremely efficient sampling using the REX MD technique. Our results, however, have important implications for simulations of the phospholipid bilayers that are our ultimate goal.

Procedure

The program CHARMM (Brooks et al. 1983) was employed for all simulations, using the CHARMM c32b2 all-atom force field (Feller and MacKerell 2000; Schlenkrich et al. 1996). A single DPPC molecule was built with all bond lengths, angles and dihedrals generated from internal coordinates. In that process the dihedral angles θ_3 and θ_4 were generated as 180° and 60°, respectively. After hydration with 898 TIP3P water molecules, the system consisted of 2,725 atoms in cubic periodic boundary conditions with a side length that fluctuated about a value of 30.1 Å during the conventional simulation. Constant pressure (1 atm) was maintained using the Langevin piston (Feller et al. 1995) algorithm, while constant temperature (300 K) was maintained via a Hoover (1985) thermostat. All bonds to hydrogen atoms were fixed at their equilibrium lengths using the SHAKE (Ryckaert et al. 1977) procedure.

The conventional MD simulation was equilibrated for 1.2 ns and subsequently run for 110 ns with a 1-fs time step in the NPT ensemble. The coordinates produced after 3.9 ns of this simulation were used as a starting configuration of a REX MD simulation that ran for 35.7 ns with a 1-fs time step. In this simulation, 20 replicas of the system were simulated at constant volume at the following temperatures: 300, 306, 312, 320, 328, 336, 346, 356, 366, 378, 390, 402, 416, 430, 444, 460, 476, 492, 510, and 528 K. Systems at neighboring temperature baths were allowed to swap in 250-fs intervals of MD simulation. With this temperature spacing the swap probability was approximately 10%.

Results

Figure 2 shows the time evolution of the θ_4 torsion angle over more than 100 ns of standard MD simulation. The majority of the simulation time is spent in conformation A. The number of isomerizations is small ($\sim$0.8/ns), with many producing only short periods in conformations B and C. The B conformation in particular is rarely observed in the simulation, making up only $\sim$1% of the states, much less than observed experimentally. The single transition to the B state observed in over 100 ns of simulation powerfully demonstrates the challenge in sampling lipid headgroup conformations. While the lifetimes of rotational isomers along the acyl chain are in the range of tens to hundreds of picoseconds (Venable et al. 1993), the dramatically longer lifetimes observed in the headgroup lead to a situation where lipid simulations begun from arbitrary initial conditions may not achieve an equilibrium distribution on the timescale of current MD simulations. While it might be argued that in a typical lipid bilayer simulation with $\sim$100 lipid molecules taken from preequilibrated libraries the equilibrium distribution may still be obtained when averaging over all molecules, this will not be the case for an inhomogenous membrane such as one containing a transmembrane protein or membrane-bound peptide where the distribution of glycerol backbone dihedrals might be shifted.

The time evolution of θ_4 in the lowest temperature replica of the REX MD simulation is plotted in Fig. 3. The dramatically shorter lifetimes arise primarily from swap moves between the $T = 300$ K bath and higher-temperature baths. While the long standard MD run retained

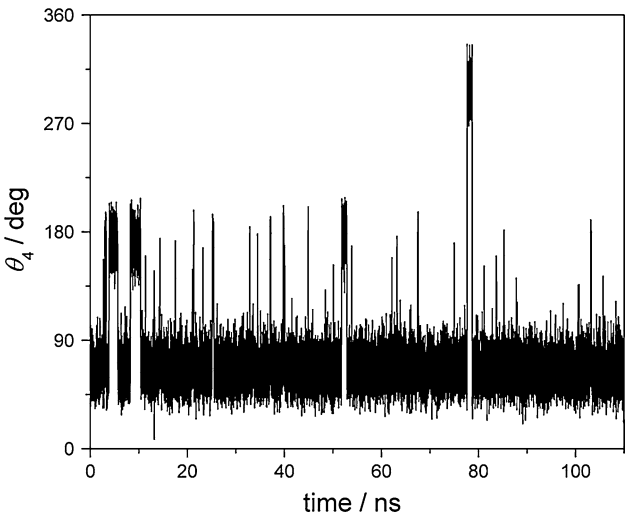

Fig. 2 Time evolution of the θ_4 torsion in the conventional MD simulation showing the small number of transitions observed in over 100 ns of simulation ($\sim$0.8/ns), with many having a lifetime of only a few picoseconds

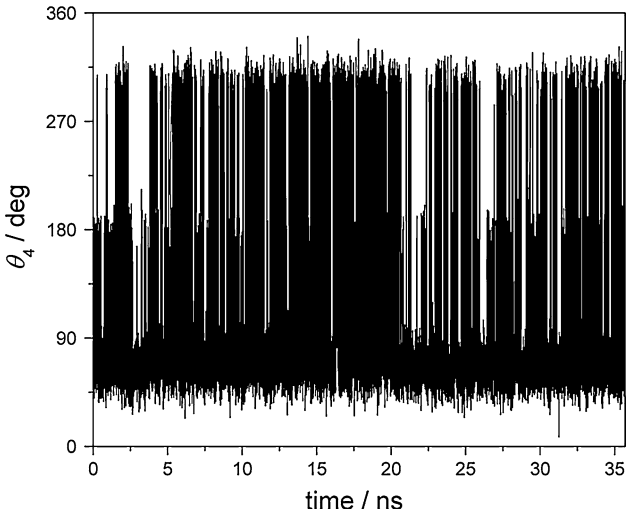

Fig. 3 Time evolution of the θ_4 torsion in the REX MD simulation at the lowest (300 K) temperature. The high rate of conformational transitions observed in the simulation at this temperature arises primarily from swaps with other temperature baths

significant memory of the initial condition, spending $\sim$93% in the A conformation that began the production run, new conformers emerge immediately in the REX MD run. By following the individual replicas, the isomerization rate occurring at each temperature, i.e., true transitions occurring at a given temperature rather than changes in a torsion arising from a swap move, was computed; and the results are plotted in Fig. 4. Over the temperature range investigated the transition rate increased by approximately 15-fold. The solid line in Fig. 5 gives the best fit of the observed rates to the Arrhenius equation, yielding activation energy of 4.5 kcal/mol. The small transition rate ($\sim$1/ns) in the low-temperature bath of the REX MD simulations is consistent with the observations from the standard MD run and reemphasizes the challenge in equilibrating the lipid headgroup structure.

While the slow dynamics of glycerol group isomerization provides a challenge to the successful implementation of atomistic MD simulation, it is not the case that the simulated dynamics are necessarily incorrect. In other words, the potential energy surface may be accurate even if it is not sufficiently well sampled in a finite-length simulation. The situation is analogous to the difficulties of folding a protein from the denatured state using atomic-level MD. Folding may be unsuccessful; i.e., the correct equilibrium structure is not obtained, even when the potential function is highly accurate, simply because insufficient time is available in the simulation. Errors are readily introduced into the interpretation of the simulation, however, when the distribution functions produced by the simulation are blindly assumed to represent the equilibrium distribution. For the glycerol θ_4 torsion, Fig. 6 shows the

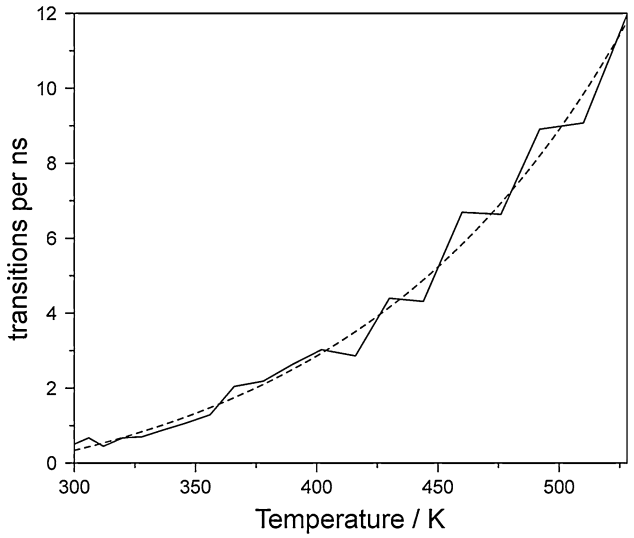

Fig. 4 Transition rates for the θ_4 torsion in the REX MD simulation as a function of temperature showing greater than order of magnitude acceleration in conformational transitions. The transition rates reported here are actual conformational changes, i.e., not changes arising from swaps between baths

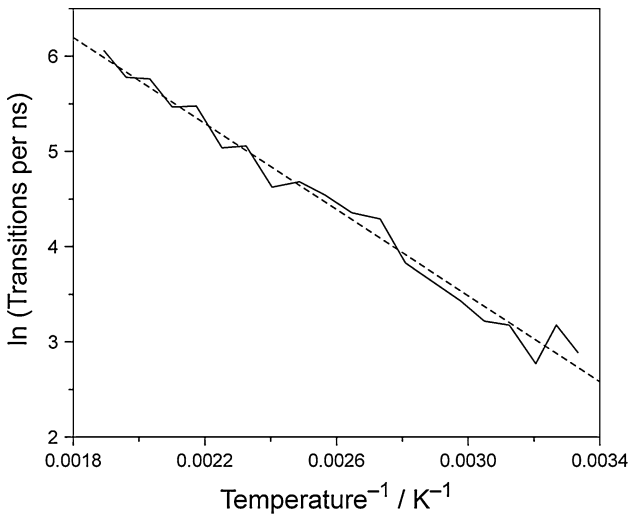

Fig. 5 Arrhenius plot of natural log of transition rates versus inverse Kelvin temperature (using data from Fig. 4), showing activation energy of $\sim$4.5 kcal/mol

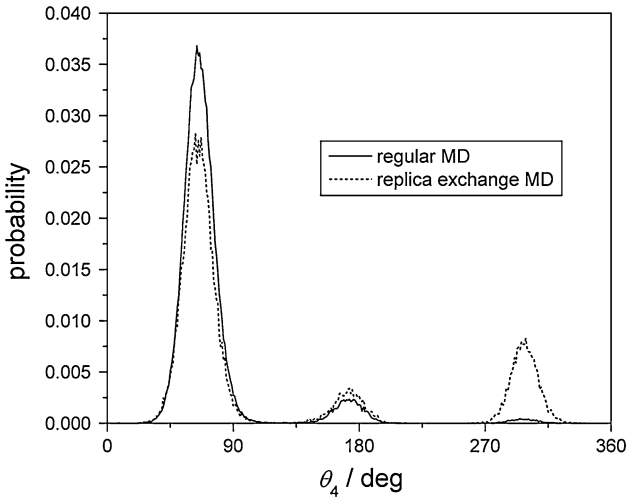

Fig. 6 Probability distribution for the θ_4 torsion observed in the REX MD and conventional MD simulations at 300 K, showing significant differences in the conformer distributions, particularly the frequency of observing the B conformation

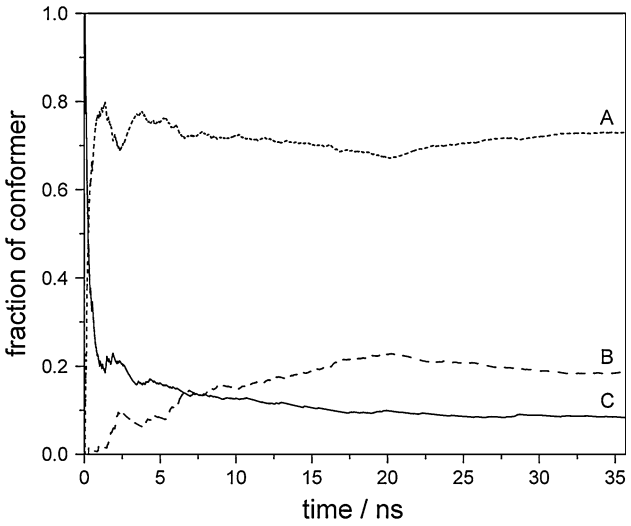

Fig. 7 Cumulative probability distribution of the θ_4 torsion in the REX MD simulation at the lowest (300 K) temperature. Compared to experiment, the A conformation is overrepresented in the simulation, while the B conformation is underrepresented (though much closer to experiment than was observed in the conventional MD calculation)

distribution of conformers observed in the REX MD and standard MD simulations. The plot shows that the calculated histograms differ significantly from one another with the relative populations in different orders, even though both simulations employed the identical potential energy function. Especially poorly sampled is the B conformation in the standard MD run, where it makes up only $\sim$1%, while the REX MD spends $\sim$18.5% in this state.

The results in Fig. 6 clearly show that a conventional simulation of 100 ns is insufficient to generate an equilibrium distribution of conformers, but it must also be noted that the REX MD simulations are more computationally expensive per unit of simulation time because they involve integrating the equations of motion of many systems. Thus, one must compare the computational cost of running an ensemble of, e.g., 20 exchanging replicas for a short period with the cost of running a single system for a long period. Figure 7 demonstrates the timescale required for convergence in the REX MD simulation. While the simulation time needed is relatively short, e.g., at approximately 25 ns reasonable convergence is obtained, this required 500 ns of total simulation time for the present case

of 20 replicas. The time series for the conventional simulation shown in Fig. 2 suggests that even after 500 ns of conventional MD the equilibrium distribution would not have converged. Another telling comparison is between the cumulative probability distribution from the REX MD simulation at 5 ns and the conventional result based on 100 ns. Even though every replica was started in the lowest probability conformation (*C*), in just a few nanoseconds a very reasonable distribution function is obtained. It also should be noted that scaling on a parallel computer is excellent with a REX simulation; thus, this approach can make good use of multiple processor systems. A potential downside for REX when simulating membrane systems is that the number of replicas must increase with system size in order to obtain reasonable swap probabilities; and given that membrane systems typically contain many atoms, this is a considerable challenge.

Conclusions

We have focused here on a single degree of freedom, namely, the θ_4 torsion angle found in the glycerol backbone region of a phospholipid, to illustrate the enormous challenge in determining the equilibrium conformer distribution in a molecule that possesses multiple rotational isomers having lifetimes that are long on the timescale of atomistic MD simulations. When compared to the other major classes of biomolecules, phospholipids are generally considered small and flexible because they consist of just a few monomeric units, e.g., a headgroup and two acyl chains, while proteins and DNA are orders of magnitude larger in terms of the number of monomers they contain. It has been shown that not only large proteins (Grossfield and Zuckerman 2009) but even small peptides (Vogel et al. 2010) pose considerable challenges for conformational sampling. Less appreciated is a property that the much smaller phospholipids nonetheless share with proteins and DNA, namely, that sampling their backbone conformations is a huge challenge for conventional MD simulations. One outcome of the present study is to demonstrate clearly and to quantify the difficulty in sampling lipid backbone conformations. This is important in particular for the setup of membrane simulations that most often rely on libraries of preequilibrated lipid structures (Jo et al. 2007). Our results demonstrate that equilibration simulations of tens of nanoseconds that were typical in the past are not sufficient for complete sampling of lipid backbone conformations. A membrane consisting of lipid structures from such relatively short preequilibrated lipid structures will at the beginning still lack a good distribution of these backbone conformations. Therefore, such libraries should be equilibrated either by very long classical simulations (possibly at high temperatures) or by approaches that improve sampling speed such as REX (Sugita and Okamoto 1999) or accelerated MD (Hamelberg et al. 2004) simulations. A second result is to show that simulations of monomeric phospholipids are potentially valuable in the refinement of potential energy parameters, i.e., force fields, for molecular simulations of lipid bilayer membranes. For example, it appears that the B conformation is less prevalent in our simulations than the NMR experiments (Hauser et al. 1988) indicate. This is indicative of inaccuracies in the torsional potential employed in this force field, and the most recent refinement of the CHARMM lipid force field (Klauda et al. 2010) alters the θ_4 torsional potential to make the B conformation more favorable. While their approach was to analyze NMR deuterium order parameters (and to carry out high-level quantum chemical computations on the relative gas-phase energies of model compounds containing this torsion), it is interesting to note that the analysis of monomeric lipids may have been a more efficient approach for this important element of the force field.

Acknowledgments S. E. F. thanks the National Science Foundation for support under award MCB0950258. The authors thank Richard Venable for providing the scripts for implementing REX MD using CHARMM.

References

Brandt EG, Edholm O (2009) Dynamic structure factors from lipid membrane molecular dynamics simulations. Biophys J 96: 1828–1838

Brooks BR, Bruccoleri RE, Olafson BD, States DJ, Swaminathan S, Karplus M (1983) CHARMM—a program for macromolecular energy, minimization, and dynamics calculations. J Comput Chem 4:187–217

Feller SE, MacKerell AD (2000) An improved empirical potential energy function for molecular simulations of phospholipids. J Phys Chem B 104:7510–7515

Feller SE, Zhang YH, Pastor RW, Brooks BR (1995) Constant-pressure molecular-dynamics simulation—the Langevin piston method. J Chem Phys 103:4613–4621

Gawrisch K, Ruston D, Zimmerberg J, Parsegian VA, Rand RP, Fuller N (1992) Membrane dipole potentials, hydration forces, and the ordering of water at membrane surfaces. Biophys J 61:1213–1223

Grossfield A, Zuckerman DM (2009) Quantifying uncertainty and sampling quality in biomolecular simulations. In: Wheeler R, Spellmeyer D (eds) Annual reports in computational chemistry. Elsevier, Amsterdam, pp 23–48

Hamelberg D, Mongan J, McCammon JA (2004) Accelerated molecular dynamics: a promising and efficient simulation method for biomolecules. J Chem Phys 120:11919–11929

Hauser H, Guyer W, Pascher I, Skrabal P, Sundell S (1980) Polar group conformation of phosphatidylcholine. Effect of solvent and aggregation. Biochemistry 19:366–373

Hauser H, Pascher I, Sundell S (1988) Preferred conformation and dynamics of the glycerol backbone in phospholipids. An NMR and X-ray single-crystal analysis. Biochemistry 27:9166–9174

Hoover WG (1985) Canonical dynamics—equilibrium phase-space distributions. Phys Rev A 31:1695–1697

Israelachvili JN (1977) Refinement of fluid-mosaic model of membrane structure. Biochim Biophys Acta 469:221–225

Jo S, Kim T, Im W (2007) Automated builder and database of protein/membrane complexes for molecular dynamics simulations. PloS One 2:e880

Klauda JB, Venable RM, Freites JA, O'Connor JW, Tobias DJ, Mondragon-Ramirez C, Vorobyov I, MacKerell AD, Pastor RW (2010) Update of the CHARMM all-atom additive force field for lipids: validation on six lipid types. J Phys Chem B 114:7830–7843

Lyubartsev AP, Rabinovich AL (2011) Recent development in computer simulations of lipid bilayers. Soft Matter 7:25–39

Marrink SJ, de Vries AH, Tieleman D (2009) Lipids on the move: simulations of membrane pores, domains, stalks and curves. Biochim Biophys Acta 1788:149–168

Ryckaert JP, Ciccotti G, Berendsen HJC (1977) Numerical integration of Cartesian equations of motion of a system with constraints—molecular-dynamics of *n*-alkanes. J Comput Phys 23:327–341

Schlenkrich M, Brickmann J, MacKerell AD, Karplus M (1996) An empirical potential energy function for phospholipids: criteria for parameter optimization and applications. In: Merz KM, Roux B (eds) Biological membranes: a molecular perspective from computation and experiment. Birkhauser, Boston, pp 31–81

Sugita Y, Okamoto Y (1999) Replica-exchange molecular dynamics method for protein folding. Chem Phys Lett 314:141–151

Sundaralingam M (1972) Molecular structures and conformations of the phospholipids and sphingomyelins. Ann N Y Acad Sci 195: 324–355

Venable RM, Zhang YH, Hardy BJ, Pastor RW (1993) Molecular-dynamics simulations of a lipid bilayer and of hexadecane—an investigation of membrane fluidity. Science 262:223–226

Vogel A, Reuther G, Roark MB, Tan KT, Waldmann H, Feller SE, Huster D (2010) Backbone conformational flexibility of the lipid modified membrane anchor of the human N-Ras protein investigated by solid-state NMR and molecular dynamics simulation. Biochim Biophys Acta 1798:275–285

Wiener MC, White SH (1992) Structure of a fluid dioleoylphosphatidylcholine bilayer determined by joint refinement of X-ray and neutron-diffraction data. 3. Complete structure. Biophys J 61:434–447

J Membrane Biol (2012) 245:29–50
DOI 10.1007/s00232-011-9413-3

Efficiency of Primary Saliva Secretion: An Analysis of Parameter Dependence in Dynamic Single-Cell and Acinus Models, with Application to Aquaporin Knockout Studies

Oliver J. Maclaren · James Sneyd · Edmund J. Crampin

Received: 24 February 2011 / Accepted: 15 December 2011 / Published online: 19 January 2012

Abstract Secretion from the salivary glands is driven by osmosis following the establishment of osmotic gradients between the lumen, the cell and the interstitium by active ion transport. We consider a dynamic model of osmotically driven primary saliva secretion and use singular perturbation approaches and scaling assumptions to reduce the model. Our analysis shows that isosmotic secretion is the most efficient secretion regime and that this holds for single isolated cells and for multiple cells assembled into an acinus. For typical parameter variations, we rule out any significant synergistic effect on total water secretion of an acinar arrangement of cells about a single shared lumen. Conditions for the attainment of isosmotic secretion are considered, and we derive an expression for how the concentration gradient between the interstitium and the lumen scales with water- and chloride-transport parameters. Aquaporin knockout studies are interpreted in the context of our analysis and further investigated using simulations of transport efficiency with different membrane water permeabilities. We conclude that recent claims that aquaporin knockout studies can be interpreted as evidence against a simple osmotic mechanism are not supported by our work. Many of the results that we obtain are independent of specific transporter details, and our analysis can be easily extended to apply to models that use other proposed ionic mechanisms of saliva secretion.

Keywords Fluid and electrolyte secretion in salivary glands · Epithelial transport · Mathematical modeling · Efficiency · Aquaporin

Introduction

Appropriate control of salivary fluid secretion is required for effective speech, mastication and general oral health. Salivary gland dysfunction affects a significant number of people (around 20% in the United States) and is often a consequence of certain medications or irradiation therapy, as well as being associated with diseases such as cystic fibrosis and Sjögren syndrome. Dysfunction can lead to oral pain, dental cavities and infections, as well as difficulties with eating and speaking.

Anatomically, there are three major pairs of salivary glands expressed in mammals: the parotid, submandibular and sublingual glands. These glands are primarily composed of two epithelial cell types—the acinar cells, which are arranged in clusters around a lumenal space forming the acini responsible for the secretion of salivary fluid and most salivary proteins, and the ductal cells, which modify

Electronic supplementary material The online version of this article (doi:10.1007/s00232-011-9413-3) contains supplementary material, which is available to authorized users.

O. J. Maclaren (✉) · E. J. Crampin
Auckland Bioengineering Institute, The University of Auckland, 70 Symonds Street, 1010 Auckland, New Zealand
e-mail: omac010@aucklanduni.ac.nz

J. Sneyd
Department of Mathematics, The University of Auckland, Auckland, New Zealand

E. J. Crampin (✉)
Department of Engineering Science, The University of Auckland, Auckland, New Zealand
e-mail: e.crampin@auckland.ac.nz

the composition of the saliva and secrete additional proteins as the saliva travels to the mouth. Most saliva secretion is due to the parotid and submandibular glands, with the parotid gland supplying the larger share.

Thaysen et al. (1954) proposed that saliva secretion is a two-stage process. The first step consists of the secretion of an isotonic, plasma-like primary fluid by the acini. This is followed by a modification of the ionic composition of this primary secretion by the ductal cells, during which there is little or no additional secretion or absorption of water. The final solution is then hypotonic by the time it enters the mouth.

A variety of ionic mechanisms have been proposed to account for the primary secretion by the acinar cells (see, e.g., Turner et al. 1993; Cook and Young 2010). Each of these mechanisms involves active ion transport, with ions taken up at one end of a cell and secreted at the other, establishing a transepithelial osmotic gradient which water follows. For two of the mechanisms discussed by Turner et al. (1993) and Cook and Young (2010), the secreted anion is chloride, while another involves the secretion of bicarbonate (the authors also discuss the experimental evidence for each of these processes). Rather than being strictly competing, it appears that a variety of processes act concurrently in the same gland, and possibly even in the same cell, to secrete fluid, with the relative importance varying over species, gland type and physiological condition. The chloride-based mechanism adopted in this report is thought to account for the majority of saliva secretion from the major salivary glands (Turner and Sugiya 2002).

Regardless of the particular ionic mechanism, the common feature of these explanations for fluid secretion is that salivary fluid flow is due to an osmotic gradient established between the lumenal region (surrounded by the acinar cells) and the intracellular space as well as between the intracellular space and the interstitium. This gives rise to a directed transcellular flow of water, from the interstitium into the intracellular region, then from the intracellular space into the lumen and out into the duct (see Fig. 1). The possibility of water moving via a paracellular pathway utilizing either the osmotic gradient between the lumen and the interstitium (established by the same mechanisms) or some alternative mechanism has also been much discussed in the literature on epithelial transport (Spring 1999; Hill et al. 2004; Hill 2008).

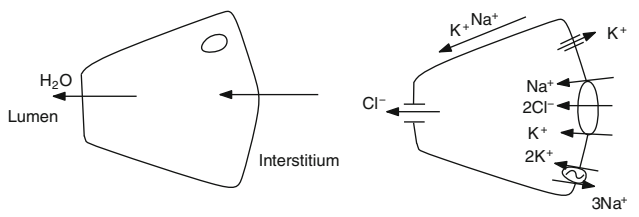

Fig. 1 Transcellular fluid secretion. *Left* direction of fluid flow. *Right* one mechanism, utilizing secretion of chloride, involved in fluid secretion

Notable models of osmotically driven fluid transport include the three-compartment model of Curran (1960) and the "standing-gradient" model of Diamond and Bossert (1967), both of which have been the basis of much of the work in this area. The primary motivation of the Curran (1960) model was to explain transport against an adverse osmotic gradient (between bathing solutions) by utilizing a middle coupling compartment bounded by membranes with differing solute and solvent-transport properties (Friedman 2008). Diamond (1964) criticized the ability of this model to represent isotonic transport, and this led to the development of the Diamond and Bossert (1967) model, which includes spatial gradients of concentration in the coupling compartment. Weinstein and Stephenson (1979, 1981a, b) emphasized that the issues of approximate isotonic transport and transport in the complete absence of, or against (uphill), osmotic gradients need to be distinguished and that each depends on a different combination of parameters. Of particular relevance here, Weinstein and Stephenson (1979, 1981a, b) recognized that the attainment of approximate isotonicity of transport depends essentially only on the cell membrane water permeability, which must be sufficiently high (while the ability to transport in the absence of, or against, an adverse osmotic gradient depends on restrictions of solute movement, e.g., via a basement membrane for absorptive epithelia and/or restricted diffusion in the relevant coupling compartment). Mathias and Wang (2005) considered a simple model of isotonic secretion and similarly demonstrated how small osmotic gradients between the cell and the compartments on either side of the cell which are close to, but not exactly, zero can produce near-isotonic fluid transport. Both sets of authors note that when the gradients are forced to be exactly zero, the secretion drops significantly and becomes much less isotonic.

As pointed out by a number of authors, models based on the standing-gradient model reduce in many cases to approximate mappings of the original compartment Curran (1960) model onto the appropriate physiological system (Weinstein and Stephenson 1981a; Spring 1999; Mathias and Wang 2005; Friedman 2008). Furthermore, although most models have been primarily concerned with fluid-absorbing epithelia, fluid secretion can also be understood using the basic conceptual scheme of the Curran (1960) model, as explained by Spring (1999). The resulting explanation of isotonic transport is thus given in terms of an osmotic coupling mechanism operating in the presence of small, but non-zero, gradients. This osmotic model is considered the "normal science" in epithelial transport (Schultz 2001); but as mentioned, this view has been and continues to

be criticized (Hill 2008; Fischbarg 2010), and many other mechanisms have been proposed for the process of fluid transport (e.g., Hill (2008) discusses various proposed mechanisms). In particular, Fischbarg (2010), Shachar-Hill and Hill (2002), Hill et al. (2004), and Hill (2008) have criticized the interpretation of aquaporin knockout studies, such as those of Ma et al. (1999), which are commonly used as support for the osmotic mechanism, and even suggest that aquaporins have gone from "saviors" of the osmotic theory to "its major problem" (Hill 2008). In the discussion we consider the results of aquaporin knockout studies and their various interpretations in the context of our analysis and simulations of a model of osmotically driven transcellular fluid flow. Furthermore, a common argument of those who accept the osmotic mechanism but reject the paracellular pathway is that the area of the tight junctions is too small to be permeable enough to admit a significant osmotic water flux (e.g., Spring (2010) offers a good discussion of this). In response to this, the main advocates of a paracellular water pathway tend to argue that a paracellular flux must be driven by nonosmotic mechanisms (Shachar-Hill and Hill 2002). Since we adopt the osmotic mechanism for this model, for consistency we initially ignore the paracellular route but come back to this in the discussion.

As discussed above, the modeling literature includes many primarily osmotically driven models of fluid transport, which have been analyzed by a number of authors, e.g., Weinstein and Stephenson (1979, 1981a, b) and Mathias and Wang (2005) (and both include aspects based on the earlier analysis of Segel (1970) of the Diamond and Bossert (1967) model). Both sets of authors utilize linearizations/perturbation expansions about the condition of isotonic/isosmotic transport and consider steady-state conditions. Our work takes a similar approach to analysis of the model behavior and conditions for (approximate) isotonic secretion. The main points of difference of our work are that (1) we focus on the problem of secretion into a small compartment, rather than the more common absorption from a small compartment (and into a larger bath); (2) we consider not only linearized/perturbation approximations to the model equations about the condition of isotonic/isosmotic secretion but also significant deviations from this state; and (3) our analysis applies directly to a (physiologically detailed) dynamic model, and hence, we work mostly in terms of scales and quasi-steady states as opposed to steady-state fluxes. In regard to point (1), while authors such as Weinstein and Stephenson (1979, 1981a, b) make reference to, and perform some calculations for, absorption from a mucosal (apical/lumenal) compartment into a small serosal (basal) compartment, which is an arrangement essentially equivalent to the secretion problem, they give more emphasis to the problem of absorption from a small mucosal bath into a large serosal bath. After linearization, these cases become more symmetric; but for larger deviations the interaction of the secretion into the small bath, convective removal from the bath and the concentration of the bath become important. Mathias and Wang (2005) gave more attention to this arrangement; however, they focused primarily on a perturbation solution to steady-state equations and applications to the renal proximal tubule. In regard to point (2), we only consider the standard linear phenomenological relationship for osmosis (described, e.g., in Schultz 1980); but we consider the effects of retaining nonlinear terms in the resulting model equations, in particular the term, discussed above, resulting from convective removal out of the lumen.

The model we consider is a physiologically based, dynamic, calcium-regulated model of primary saliva secretion, previously published by Gin et al. (2007), which consists of a system of nonlinear ordinary differential equations. Utilizing the approximation methods described above (scaling and singular perturbation methods) in combination with simulations of the full model, we explore fluid secretion as water permeability is decreased and secretion is no longer near the isotonic/isosmotic regime. This enables us to consider the consistency of the osmotic mechanism adopted here with aquaporin knockout studies such as those of Ma et al. (1999), in light of the criticisms by authors such as Hill et al. (2004) of the traditional interpretations of these studies.

Transcellular Fluid Secretion Model

Here, we consider a single-cell model based on Gin et al. (2007) for primary fluid secretion through a transcellular pathway. The ionic mechanism represented is that thought to be responsible for the bulk of the secretion in the major salivary glands (Turner and Sugiya 2002). In this model, the movement of Cl^- through the transcellular pathway, as well as the movement of Na^+ and K^+ via a paracellular pathway, sets up the required osmotic gradients between the three spaces. Based on the schematic model illustrated in the right panel of Fig. 1, we can write down the governing equations for conservation of ions and water volume. In what follows, the subscripts "e," "i" and "l" denote interstitial (extracellular), intracellular and lumenal compartments, respectively, which we assume to be well mixed. We do, however, allow a variable cell volume, w.

Cell Equations

The conservation of Cl^- ions in the intracellular region gives

$$\frac{\mathrm{d}([\mathrm{Cl}]_i w)}{\mathrm{d}t} = -\frac{I_{\mathrm{Cl}}}{z_{\mathrm{Cl}} F} + 2J_{\mathrm{NKCC}} \tag{1}$$

where F is the Faraday constant and $z_{\mathrm{Cl}} = -1$ is the valence of Cl^-. Here, Cl^- is brought into the cell via the Na^+–K^+–$2Cl^-$ cotransporter (J_{NKCC}) in the basolateral membrane, and efflux is via the apical Cl^- channel (I_{Cl}). The cotransporter moves two Cl^- ions for every K^+ and Na^+ ion. Similarly, conservation of Na^+ ions in the intracellular region gives

$$\frac{\mathrm{d}([\mathrm{Na}]_i w)}{\mathrm{d}t} = -3J_{\mathrm{NaK}} + J_{\mathrm{NKCC}} \tag{2}$$

Influx of Na^+ is due to the cotransporter, while efflux is due to the Na^+–K^+–ATPase (J_{NaK}), which pumps three Na^+ ions out for every two K^+ ions pumped in. Conservation of K^+ ions in the intracellular region gives

$$\frac{\mathrm{d}([\mathrm{K}]_i w)}{\mathrm{d}t} = 2J_{\mathrm{NaK}} + J_{\mathrm{NKCC}} - \frac{I_{\mathrm{K}}}{z_{\mathrm{K}} F} \tag{3}$$

These fluxes are due to the ATPase, the cotransporter and the K^+ channel (I_{K}) in the basolateral membrane.

Since we allow a variable cell volume, conservation of water in the intracellular region must be taken into account, giving

$$\frac{\mathrm{d}w}{\mathrm{d}t} = q_{\mathrm{b}} - q_{\mathrm{a}} \tag{4}$$

where

$$q_{\mathrm{a}} = R\Theta L_{\mathrm{pa}}(c_{\mathrm{l}} - c_{\mathrm{i}}) \tag{5}$$

$$q_{\mathrm{b}} = R\Theta L_{\mathrm{pb}}(c_{\mathrm{i}} - c_{\mathrm{e}}) \tag{6}$$

are the apical and basolateral water volume fluxes, respectively, and c_{e}, c_{i} and c_{l} are the total osmolyte concentrations in each region. L_{pa} and L_{pb} are the total water permeabilities of each membrane (area-weighted as in Gin et al. (2007), see Appendix A), R is the universal gas constant and Θ is the temperature. Note that the total intracellular concentration includes cell-impermeant X at concentration X/w and intracellular messengers such as Ca^{2+}.

Lumen Compartment

We assume that all external concentrations (composing c_{e}) surrounding the basolateral membrane remain unchanged; however, we allow variable lumenal concentrations. The lumenal region into which the primary secretion occurs is a small region surrounded by a spherical arrangement of acinar cells located in a secretory end piece (acinus). The primary secretion produced from the acinar cells then flows from the acinus lumen into a system of ducts of increasing size, beginning with the intercalated ducts. Due to the small dimensions of the lumenal region, we model this as well mixed. If we assume no volume change of the lumen and no pressure buildup, the water flux leaving the lumen is equal to q_{a}, the rate of secretion into the lumen. Furthermore, since the primary secretion is isotonic (in accordance with the two-stage hypothesis of Thaysen et al. 1954) and is pushed out as a combined bulk flow into the duct system, we assume that the removal of all ions, in particular Cl^-, from the lumen is dominated by convection by water. The second stage of transport, when the saliva is in the duct system, involves modification of the saliva composition along the duct length. However, here we model only the primary secretion from the secretory end pieces, and ductal transport and associated concentration changes are not considered further. This gives the lumenal Cl^- conservation equation

$$w_{\mathrm{l}} \frac{\mathrm{d}[\mathrm{Cl}]_{\mathrm{l}}}{\mathrm{d}t} = \frac{I_{\mathrm{Cl}}}{z_{\mathrm{Cl}} F} - q_{\mathrm{a}}[\mathrm{Cl}]_{\mathrm{l}} \tag{7}$$

where w_{l} is the lumenal volume surrounded by the acinar cells, which has an opening into the duct system.

Bicarbonate secretion is also thought to be involved in primary saliva secretion, although to a lesser extent than the chloride-based mechanism represented here (Turner and Sugiya 2002). It is not included in this model, and we briefly consider this assumption in the Discussion.

Voltage and Paracellular Ion Fluxes

In our model Na^+ and K^+ travel via the paracellular pathway, which are assumed to be cation-selective in accordance with the basic proposed mechanisms of saliva secretion (Cook and Young 2010). We consider the tight junction to be a simple membrane, with no ion–ion interactions. Furthermore, as discussed in the Introduction, we assume a fully transcellular pathway for water (and via an independent route—the aquaporins—to the chloride ions), so there is no convective transport. We return to these assumptions in the Discussion.

Assuming electrochemically driven fluxes, the K^+ tight junction flux could, e.g., be represented as

$$I^t_{\mathrm{K}} = g_{t,\mathrm{K}}(V_t - V_{\mathrm{K}}) \tag{8}$$

$$I^t_{\mathrm{Na}} = g_{t,\mathrm{Na}}(V_t - V_{\mathrm{Na}}) \tag{9}$$

where $g_{t,K}$, $g_{t,\mathrm{Na}}$, V_{K} and V_{Na} are the tight junction potassium and sodium conductances and Nernst potentials (between the interstitium and lumenal compartments), respectively, and V_t is the voltage difference between the lumen and interstitium.

Palk et al. (2010) discuss how to complete an electrophysiological model of this type, and they include differential equations for distinct apical and basolateral membrane

voltages. However, to good approximation (due to the small membrane capacitances), we replace these differential equations by electroneutrality constraints in each region. This is equivalent to taking a quasi-steady-state approximation of the differential equations, in which the voltage variables are slaved to the remaining variables. Based on these constraints, the total cation ion current ($I^t_{Na} + I^t_K$) must be such that it is equal to the total anion current (here, I_{Cl}).

$$I^t_{Na} + I^t_K = I_{Cl} \tag{10}$$

at all times. Given an initially electroneutral lumen, this implies

$$[Na]_l + [K]_l = [Cl]_l \tag{11}$$

Furthermore, when the lumenal fluid is approximately isotonic to the interstitium, the Nernst potential terms in (8) and (9) are negligible, and the currents are driven primarily by the same voltage difference. In this case, the relative amount of flux of Na^+ to K^+ is simply determined by the ratio of the respective conductances. Since the convective removal of a given ion from the lumen is proportional to its lumenal concentration and since $[K]_l \ll [Na]_l$. (from isotonicity we expect these concentrations to be close to their interstitial values), we would expect that $g_{t,K} \ll g_{t,Na}$.

The relative tight junction conductances are, in fact, not important here—the model behavior is independent of the actual proportion of cation current due sodium or potassium, respectively (other than in determining the proportions themselves, of course). Only (11) is actually required in the analysis that follows. For simplicity of simulation, we assume that the amount of potassium flux is such that the lumenal potassium concentration, $[K]_l$, is maintained at a value exactly equal to the interstitial potassium concentration, $[K]_e$ (noting that K^+ must be removed into the duct system along with the secreted fluid). This leaves the sodium flux as a variable to be determined by the electroneutrality constraint. These assumptions give

$$[K]_l = [K]_e \tag{12}$$

$$[Na]_l = [Cl]_l - [K]_l \tag{13}$$

though again we emphasize that, here, neither (12) nor (13) is required in the analysis that follows and the model results do not depend on either. Gin et al. (2007) used a constraint of electroneutrality between the lumen and the interstitium, i.e., $[Na]_l = [Na]_e - [Cl]_e + [Cl]_l$ instead of (13), which is in fact an equivalent assumption, given (12). Palk et al. (2010) considered the effects of adding a small apical potassium channel density, in which case the proportion of the cation concentration made up by sodium and potassium, respectively, does matter. This is beyond the scope of the present study, though extensions of our analysis are possible, e.g., by using assumptions on the potassium-to-sodium conductance ratio.

An electroneutrality constraint must also be specified for the cell compartment and, as for the lumenal region, this simply states that the fluxes of positive and negative charge must balance to give no net charge imbalance inside the cell. This allows the cell membrane voltage to be determined as an implicit function of the concentrations and volume, in terms of an equation of analogous form to (10). This equation also requires including calcium fluxes through the basolateral membrane (calcium signaling is discussed in the following section), and it is not required for the analysis that follows (though it is required in the full simulation model).

This completes our fluid flow model, without concern for the underlying details of channel/transporter activity and messenger dynamics. We can obtain some conclusions about this model irrespective of these details, while for full simulations and additional analysis we require explicit functional forms for these model aspects. The details used in that case follow Gin et al. (2007) and are briefly outlined in the next section. The full model equations and parameters are provided in the supplementary material.

Channels, Transporters and Signaling

The model we consider here is based on that of Gin et al. (2007). This model can conceptually be broken into two main parts—a three-compartment electrophysiological model of ion and water fluxes, which was described in the previous section, and a model of an oscillating calcium signal. We outline some of the properties of the model components here.

Ion and Water Transport

Here, we use the ion- and water-transport model of Gin et al. (2007, as detailed on pages 65–68, Tables 1–3 and the Appendices A and B).

Calcium-Dependent Channels

The ionic mechanism used in this model involves a Ca^{2+}-activated Cl^- channel in the apical membrane and a Ca^{2+}-activated K^+ channel in the basolateral membrane, in accordance with the literature (Turner et al. 1993; Cook and Young 2010). The steady-state open probability of the Cl^- channel is Ca^{2+}-dependent and includes voltage-dependent equilibrium constants. Gin et al. (2007) based this on a model developed for rat parotid acinar cells by Arreola et al. (1996). The K^+ channel open probability is Ca^{2+}-dependent but voltage-independent, in accordance

with the study of Takahata et al. (2003) on bovine parotid acinar cells.

ATPase

The model includes an Na^+–K^+–ATPase, which maintains low $[Na^+]$ and high $[K^+]$ in the cell, relative to the interstitium. It exchanges three Na^+ for two K^+ at the expenditure of ATP. Gin et al. (2007) used a reduced model by Smith and Crampin (2004), originally based on a model by Läuger and Apell (1986).

Cotransporter

The model includes a Na^+–K^+–$2Cl^-$ electroneutral cotransporter, a secondary active transport system which is the main uptake pathway for Cl^-. Gin et al. (2007) considered a 10-state scheme proposed by Lytle and McManus (1986) and formulated as a system of differential equations by Benjamin and Johnson (1997). They reduced this to a two-state model and then took the steady-state flux. We use this here.

Calcium Signaling Model

Here, we are primarily concerned with the ion and fluid transport, though under the influence of an oscillating Ca^{2+} signal. We are not as concerned with how the Ca^{2+} signal is generated. For this we refer to Palk et al. (2010), who describe modifications to the Gin et al. (2007) model. Our model has one slight difference again from the Palk et al. (2010) model, which is described in our Appendix B. Other than this, the signaling model is identical to that of Palk et al. (2010) and follows the details given in their article (see pp. 626–628 and Tables 1–3).

Analysis of a Single-Cell Model

The primary secretion formed in the lumen is known to be approximately isotonic to the source bath. This is usually viewed as being due to the relatively high water permeability for epithelial fluid transport (Turner and Sugiya 2002; Spring 1998). It is also known that the geometry of the acinus is such that the lumenal space is significantly smaller in volume than the acinar cells themselves. Here, we use the mathematical model to investigate the implications of these physiological observations.

Fluid Secretion and Scales

We first consider the equation governing the lumenal chloride concentration, $[Cl]_l$ (7), and the implications of a large water permeability (relative to other cell transport parameters) and a small lumen volume (relative to cell volume).

Estimate of Scale for Lumenal Concentration Increase

To begin, we will perform a scaling analysis and nondimensionalization of Eq. 7. Perspectives and case studies on scaling methods are offered in, e.g., Segel (1972), Segel and Slemrod (1989), Segel and Goldbeter (1994) and Krantz (2007). The results we obtain from this analysis will be compared in detail with simulations of the full model.

To be consistent with the requirement of (approximate) isotonicity of the secretion, the change in the lumenal concentrations must be small. In this model, the chloride current is the primary driver of the change in lumenal concentrations as the total cation ion concentration is determined by the lumen electroneutrality constraint (11). Thus, the change in total ion concentration in the lumen will be twice that of the chloride concentration, and both should be small for the model to reproduce expected results. In order to account for this in our scale for lumenal chloride concentration, we first define the new variable

$$[Cl]_{ld} = [Cl]_l - [Cl]_e \tag{14}$$

which represents the increase of $[Cl]_l$ above $[Cl]_e$. We now wish to define a scale for the change in $[Cl]_{ld}$ between stimulated and unstimulated conditions. We estimate this by considering the prestimulation steady state and poststimulation steady state of (7), without yet considering the dynamics in between or the effect of oscillations. Using (14), the steady-state relation obtained from (7) can be written as

$$\frac{I_{Cl}}{z_{Cl}F} = q_a\left([Cl]_{ld} + [Cl]_e\right) \tag{15}$$

To estimate the change in $[Cl]_{ld}$, we will assume for now that (15) holds both pre- and poststimulation, which we will denote by using a superscript "s" to indicate the poststimulation values ("stimulated") and a superscript "u" to represent the prestimulation values ("unstimulated"). Later, we will consider conditions for the steady state to hold during cell stimulation and an oscillating calcium signal, i.e., conditions for a quasi-steady state to hold for the actual variables (no superscript). Since $c_l - c_i < c_l - c_e = \Delta c$ and from electroneutrality $\Delta c = 2[Cl]_{ld}$, we can define a scale for the poststimulation fluid secretion rate as

$$q_a^s \sim 2R\Theta L_{pa}\delta \tag{16}$$

where δ is a scale parameter representing the maximum change in lumenal chloride concentrations (and is also a representative scale for total concentration changes since

these only differ by a factor of 2) and for which we will next determine an estimate in terms of the fluid- and chloride-transport parameters. Nondimensional quantities (represented by asterisks) can now be introduced for q_a^s, $[Cl]_{ld}^s$, and I_{Cl}^s, defined via

$$\begin{aligned} &[Cl]_{ld}^s = \delta [Cl]_{ld}^{s*}, \qquad I_{Cl}^s = \frac{z_{Cl} g_{Cl} R\Theta}{F} I_{Cl}^{s*}, \\ &q_a^s = 2R\Theta L_{pa} \delta q_a^{s*}; \end{aligned} \tag{17}$$

where g_{Cl} is a chloride conductivity parameter and δ is the chloride concentration change scale as defined above. The open probability of the chloride channel is typically much lower than 1—e.g., based on Palk et al. (2010) a value of around 0.1 is typical—hence, for simplicity of analysis, we take g_{Cl} to represent the product of the whole-cell chloride conductivity and the maximum open probability. Thus, for cells with identical physical characteristics, a higher g_{Cl} will represent a higher open probability, i.e., a higher stimulation level. We have also included the valency $z_{Cl} = -1$ in the nondimensionalization of I_{Cl} so that I_{Cl}^* is the magnitude of the chloride flux into the lumen. These scalings will ensure that the nondimensional poststimulation chloride current into the lumen and the poststimulation convective chloride removal out of the lumen have a nondimensional magnitude of about one. Using the same scalings for prestimulation values will mean that the resulting nondimensional values are small compared to one as we will assume that prestimulation values are at least an order of magnitude smaller than poststimulation values. Applying the steady-state equation to both cases and combining, we obtain

$$\begin{aligned} &\left(\frac{g_{Cl}}{(2L_{pa}[Cl]_e^2 F^2}\right)\left[I_{Cl}^{s*} + I_{Cl}^{u*}\right] = \left(\frac{\delta}{[Cl]_e}\right) \\ &\times \left[\frac{\delta}{[Cl]_e}\left(q_a^{s*}[Cl]_{ld}^{s*} + q_a^{u*}[Cl]_{ld}^{u*}\right) + \left(q_a^{s*} + q_a^{u*}\right)\right] \end{aligned} \tag{18}$$

By neglecting the nondimensional prestimulation values (setting to zero) and setting the nondimensional poststimulation terms to exactly one, we can obtain an estimate of δ, the scale of lumenal (chloride) concentration change. Solving (18) with these conditions (and taking the positive solution) gives

$$\frac{\delta}{[Cl]_e} = \frac{1}{2}\left(\sqrt{1+4\epsilon_d} - 1\right) = \epsilon_d - \epsilon_d^2 + 2\epsilon_d^3 + O(\epsilon_d^4) \tag{19}$$

where the series is derived from a binomial series (converging for $|\epsilon_d| < 1/4$), and we have defined

$$\epsilon_d \equiv \frac{g_{Cl}}{2L_{pa}[Cl]_e^2 F^2} \tag{20}$$

For $\epsilon_d \ll 1$, we see from the series expansion that

$$\frac{\delta}{[Cl]_e} \approx \epsilon_d \tag{21}$$

This will represent our scale under near-isotonic conditions. Note that this also represents the scale of total lumenal concentration change since $\frac{\delta}{[Cl]_e} = \frac{2\delta}{2[Cl]_e} = \frac{2\delta}{C_e} \sim \frac{\Delta C}{C_e}$. Considering this preliminary result, it is apparent that when the permeability is relatively large the fluid secretion term requires only very small differences in concentrations to balance the ion transport, and we obtain the isosmotic/isotonic case. This implies not only that isosmotic secretion requires large permeabilities (to generate enough fluid transport) but also that large permeabilities tend to produce isosmotic secretion. This is consistent with the conditions for iso-osmoticity given by Mathias and Wang (2005) (their Eq. 2) and Weinstein and Stephenson (1981b) (their Eq. 1-21). Later, we will consider the water permeability to be the main physical parameter controlling the size of these dimensionless groups since it is the large permeability of salivary cells (compared to other non-water-transporting cell types) that is most noteworthy. In addition to the near-isosmotic regime (ϵ_d, $\frac{\delta}{[Cl]_e} \ll 1$), we will consider how fluid secretion is affected when the ratio of chloride to water-transport parameters is no longer small, i.e., ϵ_d not negligible compared to 1, and hence significant osmotic gradients develop, i.e., $\frac{\delta}{[Cl]_e}$ no longer negligible compared to 1. Based on (19), we expect osmotic gradients ($\frac{\delta}{[Cl]_e}$) to grow more slowly than the ratio of transport parameters (ϵ_d).

Nondimensional Equation and Identification of Small Parameters

Returning to the main scaling analysis of (7) and considering (21), we can now introduce the following scalings, based on the isosmotic scales:

$$\begin{aligned} &[Cl]_{ld} = \frac{g_{Cl}}{2L_{pa}[Cl]_e F^2}[Cl]_{ld}^*, \quad I_{Cl} = \frac{z_{Cl} g_{Cl} R\Theta}{F} I_{Cl}^*, \\ &q_a = \frac{g_{Cl} R\Theta}{[Cl]_e F^2} q_a^*, \quad t = Tt^*; \end{aligned} \tag{22}$$

where T represents an as yet unspecified time scale of interest (the observation scale [Krantz 2007]), and the rest is consistent with the preceding analysis. As mentioned, the scale chosen for q_a is now fixed at the isosmotic scale, so q_a^* here will represent the ratio of q_a to its isosmotic value (which we will see is between 0 and 1). This scale is based on that of the poststimulation scale (16) combined with our scale for lumenal concentration changes in the limit of

$\epsilon_d \to 0$ (21). By first writing (7) in terms of $[Cl]_{ld}$ and then substituting the scalings (22) into the result, we obtain

$$\left(\frac{1}{T}\right)\left(\frac{w_l}{2R\Theta L_{pa}[Cl]_e}\right)\frac{d[Cl]^*_{ld}}{dt^*} = I^*_{Cl} - q^*_a\left(\frac{g_{Cl}}{2L_{pa}[Cl]^2_e F^2}[Cl]^*_{ld} + 1\right) \quad (23)$$

The term $\frac{w_l}{2R\Theta L_{pa}[Cl]_e}$ occurring on the left-hand side has dimensions of time, and we will call it T_t, taking it to represent a transient time scale. If this is small compared to our time scale of interest, i.e., $\frac{T_t}{T} \equiv \epsilon_t \ll 1$, then we obtain the singular problem

$$\epsilon_t \frac{d[Cl]^*_{ld}}{dt^*} = I^*_{Cl} - q^*_a\left(\epsilon_d[Cl]^*_{ld} + 1\right) \quad (24)$$

where $\epsilon_d \equiv \frac{g_{Cl}}{2L_{pa}[Cl]^2_e F^2} = \frac{\delta}{[Cl]_e} \sim \frac{\Delta c}{c_e}$, as before.

Time Scales of Interest

In order to determine under what circumstances we obtain the singular form (24), i.e., under what circumstances the condition $\frac{T_t}{T} \equiv \epsilon_t \ll 1$ holds, we need to consider what our time scale(s) of interest is.

We first use the equation for volume dynamics (4) to estimate the time scale over which significant changes in volume occur. Employing the same scaling for q_a and q_b as that used for q_a in (22), using $w = w_0 w^*$ to define the scaling of cell volume and $t = Tt^*$ for the time scale to be estimated, (4) becomes

$$\frac{w_0}{T}\frac{dw^*}{dt^*} = \frac{g_{Cl}R\Theta}{[Cl]_e F^2}(q^*_b - q^*_a) \quad (25)$$

During cell volume decrease, the volume flux out of the cell will dominate over the volume uptake. A balance of the left-hand side with the q_a term gives an estimate of the time scale for significant volume change. This can be achieved by setting $\frac{dw^*}{dt^*} = q^*_a = 1,\ q^*_b = 0$ and equating the scale factors, giving an estimate for the volume change time scale:

$$T_0 = \frac{w_0[Cl]_e F^2}{g_{Cl}R\Theta} \quad (26)$$

We can then use this time scale as our time scale of interest in (24), to obtain

$$(\epsilon_w)(\epsilon_d)\frac{d[Cl]^*_{ld}}{dt^*} = I^*_{Cl} - q^*_a\left(\epsilon_d[Cl]^*_{ld} + 1\right) \quad (27)$$

where $\epsilon_w \equiv \frac{w_l}{w_0}$ and $\epsilon_d \equiv \frac{g_{Cl}}{2L_{pa}[Cl]^2_e F^2}$ are each expected to be small under physiological conditions, due to the small lumenal volume (relative to cell volume) and the large water permeability (relative to chloride-transport parameters). Hence, we expect their product, ϵ_t, to be even smaller. This indicates a wide separation of scales, so we will assume (27) moves quickly (relative to the volume dynamics) to its quasi-steady state, given by

$$I^*_{Cl} - q^*_a\left(\epsilon_d[Cl]^*_{ld} + 1\right) = 0 \quad (28)$$

Since q_a increases/decreases with increases/decreases of $[Cl]_{ld}$, we expect sufficiently small perturbations of $[Cl]_{ld}$ (which leave I_{Cl} relatively unchanged, with any small changes in I_{Cl} expected to occur in the opposite direction) to return to the quasi-steady-state value. However, we do not consider the stability of the quasi-steady state in any more detail here. The equation of the steady state relating q_a and I_{Cl} will be exactly linear when $\epsilon_d \to 0$, while for small values (i.e., small deviations from iso-osmoticity) the relationship falls below this curve. The dependence of fluid secretion on chloride secretion is perhaps clearer if (28) is rewritten as

$$q^*_a = \left(1 - \epsilon_d[Cl]^*_{ld}\right)I^*_{Cl} \quad (29)$$

which is valid to first order for small ϵ_d (taking a Taylor series in ϵ_d). Hence, $q^*_a < I^*_{Cl}$ for nonzero ϵ_d and has the upper limit $q^*_a < I^*_{Cl}$ for $\epsilon_d \to 0$. This relationship will be discussed in detail later, and we also consider how it changes with non-negligible ϵ_d.

In order to consider the effects of an oscillating calcium signal, we need to consider another time scale of interest, a characteristic scale for the calcium spikes/oscillations. Based on the results of the models of Gin et al. (2007) and Palk et al. (2010) (which is the calcium signaling model used here), we estimate this to be about one to two orders of magnitude smaller than T_0 as given in (26), i.e., between $0.1T_0$ and $0.01T_0$. Using this scale in (27) instead of T_0 will still result in a singular equation as long as the product of ϵ_w and ϵ_d is sufficiently small, less than about 10^{-2}–10^{-3}. Based on typical parameter values used in later simulations, $\epsilon_w \approx \times 10^{-2}$, and $\epsilon_d \approx 10^{-3}$, up to a value of 1 for "low permeability" (relative to usual high values) ranges, giving a product of $\epsilon_t \approx 10^{-5}$ to 10^{-2}. This includes values of the desired order of smallness. However, as the permeability decreases, the system would be expected to still follow the general trend of the quasi-steady state on the time scale T_0 but may fail to fully follow the quasi-steady state exactly on the time scale of the calcium oscillations. The accuracy of the quasi-steady-state approximation will be tested by checking the correspondence to full simulations, and we will also consider consequences of any failure to exactly follow the oscillating quasi-steady state for low permeability values.

Cell Volume Quasi-Steady State

Although, as mentioned, the cell volume takes significantly longer to reach a new steady state after stimulation than the

lumenal concentrations, its steady state is still a useful tool for analysis. In particular, we will use it to obtain an approximation relating the fluid secretion to the change in total lumenal concentrations, which is independent of the internal cell concentrations. This will allow us to construct a good analytic approximation to the quasi-steady state of (27) relating q_a to I_{Cl} only, which captures the dependence on key parameters. The error in using the volume steady state for this purpose will be assessed in comparisons to simulations.

Expanding the expressions for q_a and q_b in (4) gives the quasi-steady-state condition for the volume ($q_a = q_b$) as

$$\frac{L_{pb}}{L_{pa}} = \frac{(c_l - c_i)}{(c_i - c_e)} \tag{30}$$

which can be rearranged to give an expression for c_i as a weighted average of c_l and c_e

$$c_i = \frac{L_{pa}c_l + L_{pb}c_e}{L_{pa} + L_{pb}} \tag{31}$$

when L_{pb} is greater than L_{pa}, the steady-state total osmolarity of the cell is closer to its initial value; and in the converse case, the steady-state total osmolarity of the cell is closer to that of the lumen. In either case the change is small. Since the net fluid secretion is equal to q_a, this gives an approximate expression for the fluid secreted:

$$q_a = R\Theta L_T(c_l - c_e), \tag{32}$$

where

$$L_T = \frac{L_{pa}L_{pb}}{L_{pa} + L_{pb}} \tag{33}$$

This expression for q_a is consistent with our previous scaling assumption for q_a. Using $c_l - c_e = 2([Cl]_l - [Cl]_e) = 2[Cl]_{ld}$ in (32) and using the result to eliminate $[Cl]^*_{ld}$ in the lumen quasi-steady-state relation (28) gives the quadratic relationship

$$\alpha q_a^{*2} + q_a^* - I^*_{Cl} = 0 \tag{34}$$

where $\alpha \equiv \left(\frac{g_{Cl}}{2L_T F^2 [Cl]_e^2}\right)$. The importance of the quadratic deviation from the linear approximation (the isosmotic case) is indicated by α, which measures the relative magnitudes of the chloride secretion and the fluid secretion and is proportional to $\epsilon_d = \frac{\delta}{[Cl]_e}$ (α has L_T instead of L_{pa}). We can use this expression to gain insight into the model, and we compare the accuracy of this approximation against simulations of the full model.

Efficiency of Secretion

Here, we consider the degree of deviations from the linear relationship between q_a^* and I^*_{Cl} arising from keeping the quadratic term in the quasi-steady-state relation (34). We can solve (34) for q_a^* in terms of I^*_{Cl}, giving

$$\begin{aligned} q_a^* &= \left(\frac{1}{\alpha}\right)\left(\frac{1}{2}\right)\left[\sqrt{1 + 4\alpha I^*_{Cl}} - 1\right] \\ &= I^*_{Cl}\left[1 - \alpha I^*_{Cl} + 2\alpha^2 I^*_{Cl}\right] + O(\alpha^3) \end{aligned} \tag{35}$$

which for $I^*_{Cl} = 1$ is

$$q_a^* = \left(\frac{1}{\alpha}\right)\left(\frac{1}{2}\right)\left[\sqrt{1 + 4\alpha} - 1\right] = 1 - \alpha + 2\alpha^2 + O(\alpha^3) \tag{36}$$

These series expansions illustrate the behavior for small α and converge for $\left|\alpha I^*_{Cl}\right| \leq 1/4$. Note also that the limits for $\alpha \to 0$ exist and are equal to 1. When α is non-negligible, we obtain the square-root relationship illustrated by the red line in panel 1 of Fig. 2, which is bounded by the linear, isosmotic limit. In the analysis here (and in following sections) we consider the difference between a system exactly following the linear form of the quasi-steady-state relation and the system exactly following the quadratic form of the quasi-steady-state relation. We include some consideration of deviations from quasi-steady state in comparisons to simulations, as well as later, in the discussion of aquaporin knockout studies.

This analysis demonstrates that for a given chloride current I_{Cl}, a larger L_T, i.e., a secretion closer to isosmotic, gives a larger fluid flow. The decrease in q_a^*, for a fixed chloride current (here, $I^*_{Cl} = 1$), as L_T is decreased is illustrated in panel 2 of Fig. 2. Starting from a small a value, e.g., 10^{-3}, L_T can be decreased by several orders of magnitude before changes in q_a^* become significant. As α approaches 1, we see that fluid flow drops to $1/\phi \approx 0.62\%$ of its isosmotic value (where ϕ is the golden ratio), for

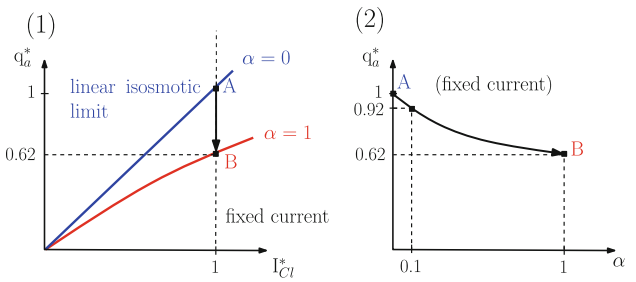

Fig. 2 Efficiency of fluid secretion. Two representations of the behavior of the solution (35) of the quasi-steady-state equation (34) relating fluid flow to chloride current for the large permeability limit (upper bound, *blue*) and finite permeability (*red*). The singular (large permeability, $\alpha = 0$) isosmotic case is an upper bound for fluid secretion and gives a greater flow at a fixed chloride current (1). For fixed chloride current, the dependence of fluid flow on the ratio (α) of the chloride and fluid transport parameters can be seen in *2*, while the change in shape of the whole solution is illustrated in *1*. For small α values, the decrease in fluid flow is roughly proportional, while the rate of decrease is lower for larger α values (Color figure online)

fixed chloride current. The chloride current is the main driver of the change in lumenal concentrations (electroneutrality or a similar constraint gives the concentration of the lumenal sodium), and maintaining this requires active processes operating at the basolateral end of the cell. Hence, we can consider (the isosmotic value of) I_{Cl} as a measure of the energy used in secretion. Since isosmotic secretion maximizes the flow for a given current, it is more efficient by this measure than nonisosmotic secretion at this same current. Although in this limit we are increasing the permeability L_T, we are also decreasing the concentration gradient available since the scale of the concentration difference is $\delta \propto 1/L_T$ (see the definition of α in Eq. 34). By this interpretation, panel 2 of Fig. 2 illustrates the change in fluid flow due to decreases in efficiency. Weinstein and Stephenson (1981b) and Hill and Hill (1978) defined similar measures of efficiency and coupling between solute and water fluxes in their studies of epithelial fluid transport. However, in their definitions of efficiency the authors required that the observed volume flow be that obtained for exactly equal bathing media. We do not make this restriction since we are interested in the volume flow observed for small but non-zero osmotic gradients.

The explanation for this maximal efficiency at isosmotic secretion lies in the natural balance between the transport of ions into the lumen and the removal of ions out of lumen, given in nondimensional form by (28). In this balance, the number of ions removed from the lumen per unit saliva is determined by the osmotic gradient, with a larger gradient giving a larger number of ions removed per unit saliva. When the total ion removal rate is constrained to balance a fixed ion current into the lumen, the largest fluid flow rate satisfying this is achieved when the number of ions removed per unit saliva is smallest; i.e., the osmotic gradient is smallest. As shown in the previous subsection, the size of the gradient, and hence the number of ions removed per unit saliva, is determined by the ratio of the chloride conductance g_{Cl} and the water permeability L_T.

Also of note is that once the permeability L_T is sufficiently large, and hence α is sufficiently small, the secretion is no longer dependent on L_T and is essentially proportional to the chloride current. Thus, the amount of fluid secreted under isosmotic conditions is less affected by variations in permeability than is nonisosmotic secretion. We will consider this feature more in the Discussion, in particular in the context of aquaporin knockout studies.

Numerical Simulations

We specify particular formulations for J_{NKCC}, J_{NaK}, I_{Cl} and I_K to complete the model discussed at a more general level thus far. These fluxes/currents depend on calcium signaling, IP_3 dynamics and voltage. For these dependencies, we follow Gin et al. (2007), with modifications described in our Appendix B. In these simulations none of the model approximations derived previously are used.

Baseline Behavior—Ion Concentrations and Volume

The basic behavior of the model is illustrated in Fig. 3. Following stimulation, chloride is secreted and the ion concentrations adjust to new levels, while the volume changes according to the secretion rate. The oscillations are due to the oscillatory nature of the calcium signaling (not shown).

The main intuitive features of the model response to stimulation are the increased calcium signal, which increases the open probability of the chloride channel and hence chloride flows from the cell, decreasing its concentration inside the cell; this decrease in chloride levels causes a compensating increase in the rate of chloride uptake via the cotransporter; this in turn increases the rate of sodium and potassium uptake via the cotransporter; the increase in cell sodium is offset by an increase in the ATPase pump rate; the increases in potassium uptake and pump rate are offset by the basolateral potassium channel, the open probability of which is also increased by the calcium increase.

Secretion, Efficiency and Variation in Permeabilities

Next we consider the question of efficiency and total secretion for varying permeabilities (Fig. 4). It can be seen that the quasi-steady-state expression relating fluid secretion (q_a) and chloride current (I_{Cl}) derived previously (34) accurately accounts for the changes in fluid flow for the different permeabilities. As expected, if the permeability is large (Fig. 4a), the linear quasi-steady-state approximation (the isosmotic limit) is sufficient to capture the behavior. As the permeability is decreased (Fig. 4b, c), the drop in secretion is accounted for simply and to reasonable accuracy by using the quadratic quasi-steady-state relation derived. Thus, the drop in fluid secretion is mainly due to a drop in efficiency (for bigger concentration gradients), the effect of which can be estimated by comparing, in each case, the linear approximation to the quadratic approximation (where the quadratic approximation closely follows the actual simulations). The difference in total secretion between the panels also includes a part due to a decrease in chloride current, which can be seen by the slight difference in the respective fluid flows as calculated from linear quasi-steady-state relation in each case. This decrease is also due to the inefficiency of an increase in lumenal concentrations since the stimulation levels remain the same, though the fixed-current drop in efficiency represents the dominant effect.

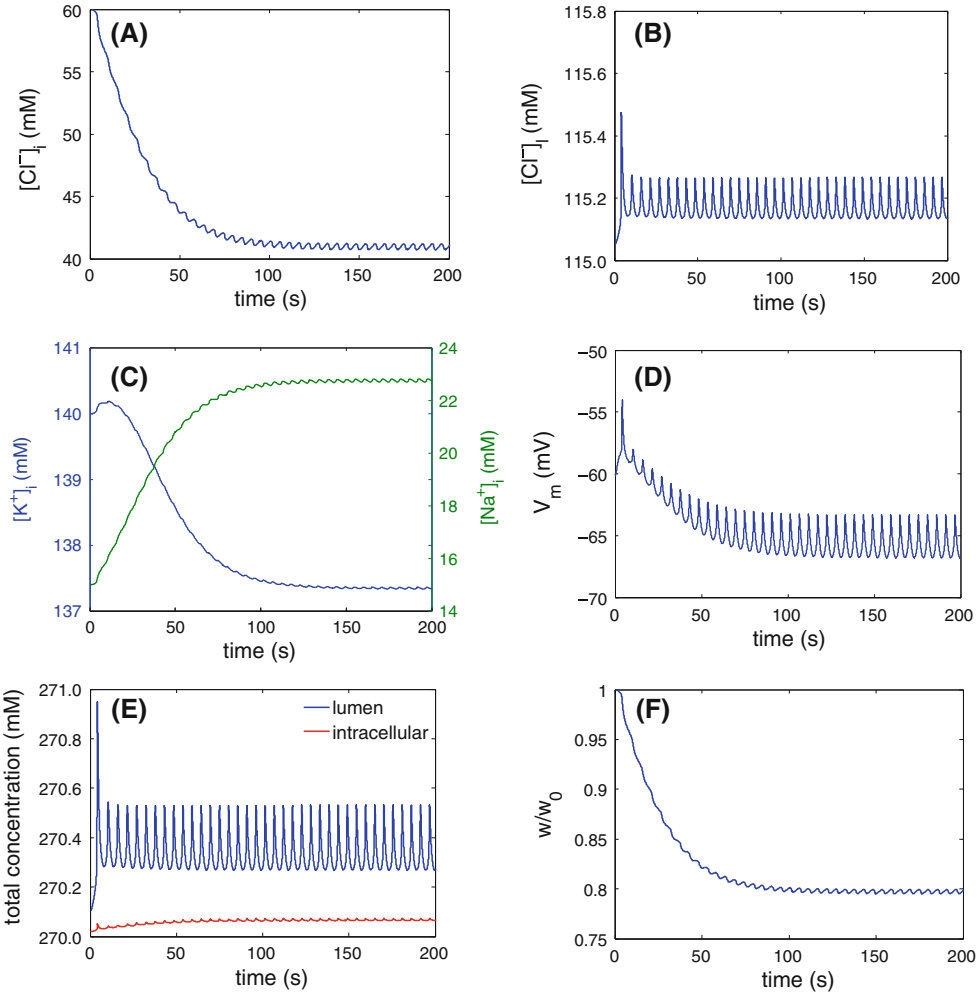

Fig. 3 Baseline behavior. There are oscillatory shifts to new levels for the ions ($[Cl]_i$, $[Na]_i$, $[K]_i$, $[Cl]_l$), membrane voltage, total concentrations and cell volume (**a**–**f**, respectively)

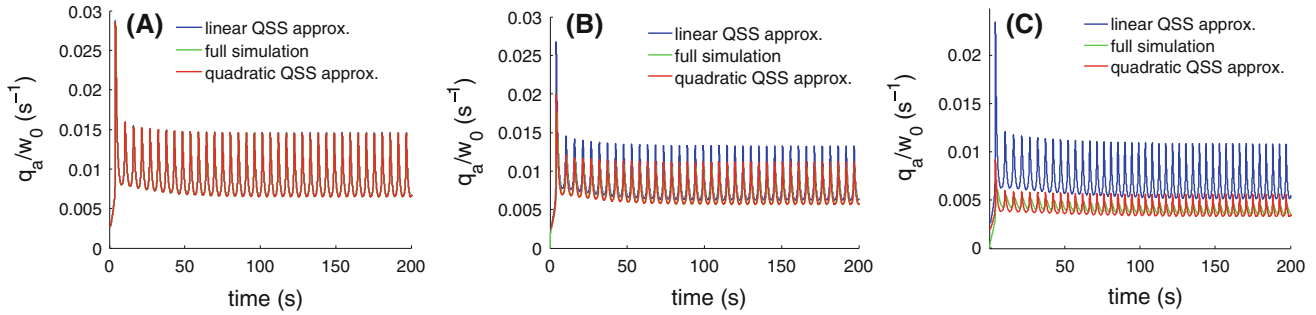

Fig. 4 Simulation plots of fluid secretion for a range of permeabilities. **a** $L_{pa} = 1.23 \times 10^{-14}$ L^2 J^{-1} s^{-1}. **b** $L_{pa} = 1.23 \times 10^{-16}$ L^2 J^{-1} s^{-1}. **c** $L_{pa} = 1.23 \times 10^{-17}$ L^2 J^{-1} s^{-1}. $L_{pb} = 4L_{pa}$ in all cases. In **a** all the traces are indistinguishable. As the permeability is decreased (**b**, **c**), the quadratic quasi-steady-state approximation follows the full simulation results, while the linear quasi-steady-state approximation overestimates the secretion, consistent with our prediction of it as an upper bound. In the lower-permeability range, the quadratic steady state slightly overestimates the true water-transport rate during rapid spikes

The accuracy of the lumenal chloride transport quasi-steady-state Eq. (28) decreases with decreasing permeability since the time for the lumen concentrations to reach their quasi-steady state depends on the size of the lumen changes (see 27). As the permeability decreases and the size of the lumenal concentration changes increase, the lumen does not reach the quasi-steady state as fast. This means that the convective chloride removal does not

increase fast enough to balance the fastest spikes in chloride current, and the quasi-steady state overestimates the actual chloride removal during these spikes. This deviation from the quasi-steady-state case represents another (dynamic) form of inefficiency and needs to be taken into account when considering any experimentally determined drop in salt secretion since it is the convective quantity that corresponds to what would be collected experimentally from inside (or at the end of) ducts. This will be discussed further in the context of aquaporin knockouts.

The derivation of the approximate quasi-steady-state Eq. (34), relating q_a and I_{Cl} directly, involved the use of the quasi-steady-state fluid secretion rate obtained from consideration of the volume Eq. (4), along with the assumption of a fast transition to the quasi-steady state of the lumenal chloride Eq. (7), given by (28). As discussed, the time for the volume to reach a quasi-steady state is much longer than for the lumenal concentrations. Since the size of the error depends on how close q_a is to its steady-state value during dynamic changes, the error depends on the relative size of the large, fast increase in q_a due to fast lumenal increases in concentration and the size of the smaller decrease in q_a due to slower increases in total cell concentrations. This error decreases on the slow time scale. Furthermore, the importance of this error is reduced due to the approximation being used in the term multiplied by the small parameter ϵ_d.

These errors account for the deviations of the approximation from the actual simulated values, although it still appears to give a good characterization of the model behavior. Additionally, we note that since the volume takes some time to reach a quasi-steady state and has slight variations about it, we cannot simply assume that the volume variable becomes slaved to others in the same way as we might for a truly singular equation. Computing the volume variable in this way underestimates the total volume decrease due to the initial larger flux of water from the apical membrane (calculations not shown). Instead, we must include the full volume differential Eq. (4).

Acinus Model—Lumenal Coupling

Above, we have discussed the efficiency of saliva secretion in a single cell; however, the main secretory unit of a salivary gland is an acinus end piece—a spherically arranged clump of cells surrounding a shared lumen. A simple schematic of a section through an acinus illustrating the arrangement of cells is given in Fig. 5. Secretions into the lumen are then pushed out into the duct system. The geometric arrangement of cells in an acinus leads to the possibility of coupling effects being induced via the (shared) NaCl concentration in the lumen.

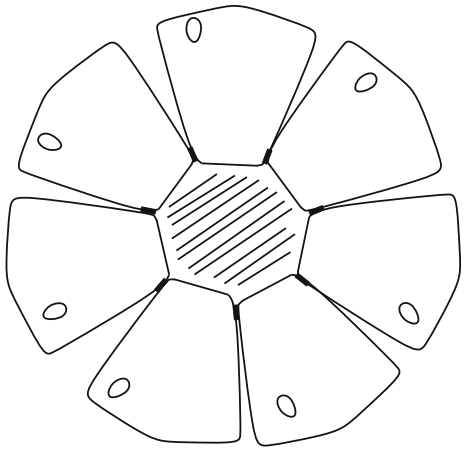

Fig. 5 Salivary acinus (not to scale). Cells are arranged about a shared lumenal region (*hatched*)

We model an acinus as an arrangement of n cells secreting into a single lumen by taking a copy of Eqs. 1–6 for each cell, giving for the jth cell:

$$\frac{d([Cl]_i^j w^j)}{dt} = -\frac{I_{Cl}^j([Cl]_l, \ldots)}{z_{Cl}F} + 2J_{NKCC}^j \tag{37}$$

$$\frac{d([Na]_i^j w^j)}{dt} = -3J_{NaK}^j + J_{NKCC}^j \tag{38}$$

$$\frac{d([K]_i^j w^j)}{dt} = 2J_{NaK}^j + J_{NKCC}^j - \frac{I_K^j}{z_K F} \tag{39}$$

$$\frac{dw^j}{dt} = q_b^j - q_a^j \tag{40}$$

Equation 7 for the lumenal chloride concentration, $[Cl]_l$, is modified to take into account the chloride flux from each cell, giving

$$w_l \frac{d[Cl]_l}{dt} = \frac{\sum_{i=1}^n I_{Cl}^i}{z_{Cl}F} - \left(\sum_{i=1}^n q_a^i\right)[Cl]_l \tag{41}$$

again assuming no pressure buildup in the lumen. Each cell is modeled in the same way, but we allow for different parameters and/or different constitutive equations as desired. Here, we will consider the results from identical cells with heterogeneous levels of cell stimulation (as would be expected from the spatial arrangement and separation of the cells), which manifests as a difference in the chloride currents, I_{cl}^j, for each cell $j = 1 \ldots n$.

Volume Quasi-Steady State

The analysis of the volume equation for a single cell can be immediately carried over to each cell in the acinus arrangement (though, as for a single cell, this quasi-steady-state assumption must be verified by simulation). In

particular, for each cell, the quasi-steady-state result (32), $q_a = R\Theta L_T(c_l - c_e)$, applies, i.e., for the jth cell:

$$q_a^j = R\Theta L_T^j(c_l - c_e) = 2R\Theta L_T^j[\mathrm{Cl}]_{ld} \tag{42}$$

where

$$L_T^j = \frac{L_{pa}^j L_{pb}^j}{L_{pa}^j + L_{pb}^j} \tag{43}$$

Since this expression depends only on the shared lumenal concentration and the homogeneous external environment, it follows that at the quasi-steady state, cells with the same water permeabilities secrete water at the same rate, even when the cells have different chloride (and sodium) secretion rates. This indicates that the coupling arising from the geometric arrangement leads to results that differ from what would be obtained from a collection of independent cells, in this case resulting in similar water secretions from differently stimulated cells.

Efficiency

Here, we extend the analysis of efficiency to the multicell case, yielding an analogous result for coupled cells, and consider the size of coupling effects.

Quasi-Steady State

Firstly, the (quasi-) steady state of (41) can be written as

$$\frac{\sum_{i=1}^n I_{Cl}^i}{z_{Cl}F} = (\sum_{i=1}^n q_a^i)([\mathrm{Cl}]_{ld} + [\mathrm{Cl}]_e) \tag{44}$$

which can be rewritten as

$$\frac{\bar{I}_{Cl}}{z_{Cl}F} = \bar{q}_a^c([\mathrm{Cl}]_{ld}^c + [\mathrm{Cl}]_e) \tag{45}$$

where we have used a superscript c to indicate coupled cell quantities (we do not include a superscript on $\bar{I}_{Cl}$ since we will be interested in fixed currents, regardless of coupling). Now (42) can be used to write

$$\bar{q}_a^c = 2R\Theta\bar{L}_T[\mathrm{Cl}]_{ld}^c \tag{46}$$

Scaling each I_{Cl}^j as usual (as in 22) but using the conductivity g_{Cl}^j appropriate to cell j, we can obtain a scale for the average current $\bar{I}_{Cl}$:

$$\bar{I}_{Cl} = \frac{z_{Cl}R\Theta}{F}\left(\frac{\sum_{i=1}^n g_{Cl}^i I_{Cl}^{i*}}{n}\right) \sim \frac{z_{Cl}R\Theta}{F}\bar{g}_{Cl} \tag{47}$$

where the last scale can be obtained by setting the individual nondimensionalized chloride currents to one. Following the same procedures as in the single-cell case to determine the $[\mathrm{Cl}]_{ld}^c$ scale (using [46] to define the relationship between $\bar{q}_a^c$ and $[\mathrm{Cl}]_{ld}^c$ scales), the appropriate isosmotic scalings are

$$\begin{aligned}[\mathrm{Cl}]_{ld}^c &= \frac{\bar{g}_{Cl}}{2\bar{L}_T[\mathrm{Cl}]_e F^2}[\mathrm{Cl}]_{ld}^{c*}, \quad \bar{I}_{Cl} = \frac{z_{Cl}\bar{g}_{Cl}R\Theta}{F}\bar{I}_{Cl}^*, \\ \bar{q}_a^c &= \frac{\bar{g}_{Cl}R\Theta}{[\mathrm{Cl}]_e F^2}\bar{q}_a^*;\end{aligned} \tag{48}$$

Using (46) to eliminate $[\mathrm{Cl}]_{ld}^c$ in (45) and substituting the scales (48) into the result, we then obtain the nondimensionalized quasi-steady-state equation:

$$\left(\frac{\bar{g}_{Cl}}{2\bar{L}_T F^2[\mathrm{Cl}]_e^2}\right)\bar{q}_a^{c*2} + \bar{q}_a^{c*} - \bar{I}_{Cl}^* = 0 \tag{49}$$

we see from this equation that a group of n lumenally coupled cells behave like (n copies of) a single cell secreting chloride at a rate equal to the average chloride secretion rate of the group. Here, we will denote the small parameter by $\alpha_c \equiv \frac{\bar{g}_{Cl}}{2\bar{L}_T F^2[\mathrm{Cl}]_e^2}$, which is the ratio of the average of the chloride-transport parameters to the average of the fluid-transport parameters (not the average of the ratio for each cell). As noted in the previous subsection, if the cells have the same water permeability, L_T, then each cell itself behaves (approximately) like a single cell secreting chloride at a rate equal to the average secretion rate of the group. The solution to this equation is analogous to the single-cell case

$$\begin{aligned}\bar{q}_a^{c*} &= \left(\frac{1}{\alpha_c}\right)\left(\frac{1}{2}\right)\left[\sqrt{1 + 4\alpha_c\bar{I}_{Cl}^*} - 1\right] \\ &= \bar{I}_{Cl}^*\left[1 - \alpha_c\bar{I}_{Cl}^* + 2\alpha_c^2\bar{I}_{Cl}^*\right] + O(\alpha_c^3)\end{aligned} \tag{50}$$

so the dimensional flow is

$$\bar{q}_a^c = \left(\frac{\bar{g}_{Cl}R\Theta}{[\mathrm{Cl}]_e F^2}\right)q_a^{c*} \equiv \bar{Q}_s^c q_a^{c*} \tag{51}$$

where $\bar{Q}_s^c \equiv \frac{\bar{g}_{Cl}R\Theta}{[\mathrm{Cl}]_e F^2} = \frac{1}{n}\sum_{i=1}^n Q_s^i$ is the scale for coupled secretion.

Coupling Effects on Efficiency

To compare the efficiency of secretion between isolated and lumenally coupled cells, we consider each cell to have a fixed chloride-secretion rate (whether coupled or not) which differs from its neighbors. We then define the efficiency of fluid secretion (in a way consistent with our single-cell analysis) as how much fluid is secreted for these fixed chloride-secretion rates for each cell. It is clear that, as in the single-cell case, the isosmotic limiting case is an upper bound on the efficiency of coupled cells.

We address the question of whether, as far as efficiency is concerned, there is any effect due to the shared lumen which goes beyond the results obtained for a single cell.

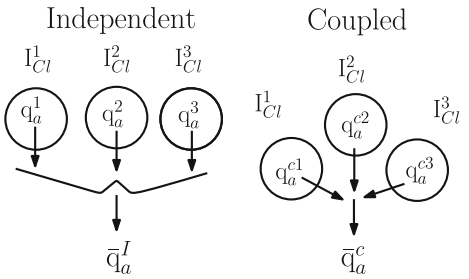

Fig. 6 Illustration of the comparison of the secretion from n independent cells to the secretion from n lumenally coupled cells, for fixed chloride currents. For simplicity, the diagram shows the case of three cells when independent compared to the same three cells (with fixed chloride currents) when lumenally coupled

Therefore, the question becomes, Is the total fluid secretion higher for n lumenally coupled cells or for n independent cells (and does this change between isosmotic and non-isosmotic regimes)? Since the number of cells is the same in each case, we can rephrase this as follows: Is the average fluid secretion higher for n lumenally coupled cells or for n independent cells (and does this change between isosmotic and nonisosmotic regimes)? This comparison is illustrated in Fig. 6. We can calculate the average fluid secretion for coupled cells using (49). The average for the uncoupled case is computed by first calculating the n independent fluid secretions for the n chloride currents and then averaging. To define this latter quantity, we first apply (35) to each independent cell j with current I_{Cl}^{j*} and transport parameters g_{Cl}^{j}, L_{T}^{j}. This gives

$$q_{\mathrm{a}}^{j} = \left(\frac{g_{\mathrm{Cl}}^{j} R\Theta}{[\mathrm{Cl}]_{\mathrm{e}} F^2}\right) q_{\mathrm{a}}^{j*} \equiv Q_{\mathrm{s}}^{j} q_{\mathrm{a}}^{j*} \tag{52}$$

for each of the dimensional fluid flows, where $Q_{\mathrm{s}}^{j} \equiv \frac{g_{\mathrm{Cl}}^{j} R\Theta}{[\mathrm{Cl}]_{\mathrm{e}} F^2}$ is the scale for the jth secretion, and

$$\begin{aligned} q_{\mathrm{a}}^{j*} &= \left(\frac{1}{\alpha_j}\right)\left(\frac{1}{2}\right)\left[\sqrt{1+4\alpha_j I_{\mathrm{Cl}}^{j*}} - 1\right] \\ &= I_{\mathrm{Cl}}^{j*}\left[1 - \alpha_j I_{\mathrm{Cl}}^{j*} + 2\alpha_j^2 I_{\mathrm{Cl}}^{j*}\right] + O(\alpha_j^3) \end{aligned} \tag{53}$$

for the nondimensional parts. We can then define the average fluid secretion for n independent cells, $\bar{q}_{\mathrm{a}}^{\mathrm{I}}$, as

$$\begin{aligned} \bar{q}_{\mathrm{a}}^{\mathrm{I}} &\equiv \frac{\sum_{\mathrm{i}=1}^{n} Q_{\mathrm{s}}^{i} q_{\mathrm{a}}^{i*}}{n} \\ &= \frac{1}{n}\sum_{i=1}^{n}\left[Q_{\mathrm{s}}^{i}\left(\frac{1}{\alpha_i}\right)\left(\frac{1}{2}\right)\left[\sqrt{1+4\alpha_i I_{\mathrm{Cl}}^{i*}} - 1\right]\right] \end{aligned} \tag{54}$$

Now, we wish to use these two expressions $\bar{q}_{\mathrm{a}}^{\mathrm{I}}$ and $\bar{q}_{\mathrm{a}}^{c}$ to compare the different average fluid secretions, i.e., to consider the difference in the average (and hence total) secretion in the coupled and independent cases. Since $q_{\mathrm{a}}^{j*} \to 1$ as $\alpha_i \to 0$ and $q_{\mathrm{a}}^{c*} \to 1$ as $\alpha_c \to 0$

$$\bar{q}_{\mathrm{a}}^{\mathrm{I}} = \frac{\sum_{\mathrm{i}=1}^{\mathrm{n}} Q_{\mathrm{s}}^{\mathrm{i}}}{n} \equiv \bar{Q}_{\mathrm{s}}^{\mathrm{c}} \equiv \frac{1}{n}\sum_{\mathrm{i}=1}^{\mathrm{n}} Q_{\mathrm{s}}^{\mathrm{i}} \qquad \text{for isosmotic secretion} \tag{55}$$

and

$$\bar{q}_{\mathrm{a}}^{c} = \bar{Q}_{\mathrm{s}}^{c} \equiv \frac{1}{n}\sum_{i=1}^{n} Q_{\mathrm{s}}^{i} \qquad \text{for isosmotic secretion} \tag{56}$$

These expressions are identical, and hence, the coupled and independent cell secretions are the same for isosmotic cases. This value is simply the average of the independent isosmotic secretions. We now wish to make the comparison in the nonisosmotic case. Since we are considering fixed chloride currents, while allowing the permeabilities to vary, we can set each of the nondimensional chloride currents to 1 so that the fixed value of each current is determined solely by its associated scaling factor. Next, we normalize each of the expressions for average fluid flow (the coupled and independent cases, respectively) relative to the shared isosmotic upper bound $\frac{\sum_{i=1}^{n} Q_{\mathrm{s}}^{i}}{n}$. These two normalized averages can then be expressed as

$$\left(\bar{q}_{\mathrm{a}}^{\mathrm{I}}\right)^{*} \equiv \frac{\bar{q}_{\mathrm{a}}^{\mathrm{I}}}{\left(\frac{\sum_{i=1}^{n} Q_{\mathrm{s}}^{i}}{n}\right)} = \frac{\sum_{k=1}^{n} Q_{\mathrm{s}}^{k} f(\alpha_k)}{\sum_{i=1}^{n} Q_{\mathrm{s}}^{i}} = \frac{\sum_{k=1}^{n} g_{\mathrm{Cl}}^{k} f\left(\frac{g_{\mathrm{Cl}}^{k}}{L_{\mathrm{T}}^{k}}\right)}{\sum_{i=1}^{n} g_{\mathrm{Cl}}^{i}} \tag{57}$$

(note this quantity is nondimensionalized as a whole since adding individually nondimensionalized quantities of the same type makes no physical sense when the scales are chosen differently—e.g., adding the numerical value of two lengths, one in centimeters and the other in meters, is physically meaningless) and

$$\bar{q}_{\mathrm{a}}^{c*} \equiv \frac{\bar{q}_{\mathrm{a}}^{c}}{\left(\frac{\sum_{i=1}^{n} Q_{\mathrm{s}}^{i}}{n}\right)} = f(\alpha_{\mathrm{c}}) \equiv f\left(\frac{\sum_{k=1}^{n} g_{\mathrm{Cl}}^{k}}{\sum_{i=1}^{n} L_{\mathrm{T}}^{i}}\right) \tag{58}$$

respectively. As mentioned, the nondimensional chloride currents are fixed at a value of 1 in the function f so that its argument is simply an α value. This function is the same as that represented in panel 2 of Fig. 2. A beneficial coupling effect on secretion will be indicated by $\bar{q}_{\mathrm{a}}^{c*} > \left(\bar{q}_{\mathrm{a}}^{\mathrm{I}}\right)^{*}$, and conversely, if $\left(\bar{q}_{\mathrm{a}}^{\mathrm{I}}\right)^{*} > \bar{q}_{\mathrm{a}}^{\mathrm{c}*}$, then coupling has a detrimental effect on total secretion. In Appendix C we show that

$$\bar{q}_{\mathrm{a}}^{c*} \geq \left(\bar{q}_{\mathrm{a}}^{\mathrm{I}}\right)^{*} \qquad \text{for non-isosmotic secretion} \tag{59}$$

follows from the convex, strictly decreasing nature of $f(\alpha)$—or, equivalently, the concave, strictly increasing nature of $F(\beta) = f\left(\frac{1}{\alpha}\right)$. Equality in (59) only holds when the α_j are all identical. Hence, in general, for nonisosmotic

secretion there is a beneficial effect on the average (and hence the total) secretion due to the lumenal coupling.

Despite the possibility of a beneficial coupling effect, the effect on secretion is never enough to make up for the difference in secretion between isosmotic and nonisosmotic regimes. As shown, the isosmotic case is an upper bound for both coupled and uncoupled secretion. Since the coupling effect is mathematically due to the convexity (concavity) of the function $f(\alpha)$ $(F(\beta))$, we expect the effect to be greater for greater ranges of α (β) values (for small ranges any differentiate function is close to linear). Thus, this coupling benefit plays an essentially compensatory role for deviations from normal function—a positive coupling effect requires nonisosmotic secretion and a significant spread in parameter values. We can summarize these results with the ordering isosmotic independent = isosmotic coupled > nonisosmotic coupled > nonisosmotic independent, where the ordering is with respect to efficiency.

This does not quite complete the analysis, however, since we have compared cases at fixed chloride currents. As mentioned, it may be the case that coupling significantly modifies the chloride currents; i.e., a coupled arrangement may have a higher or lower total fluid secretion than that calculated for fixed chloride currents if the average chloride current increases or decreases due to interactions via the shared lumen. We can easily rule this out in the isosmotic case—although the fluid-secretion rates change when coupled (to close to a common rate as shown in the previous section), we would expect no change in the chloride secretion. The difference between the two is that the fluid secretion depends very sensitively on small changes in lumenal concentrations due to the large permeability, while changes in chloride secretion require much larger lumenal changes for non-negligible effects. Since, by assumption, in the isosmotic case all changes in the lumen are negligible, the cells do not "see" each other via the lumen and, thus, each cell continues to secrete chloride as it did before.

The nonisosmotic case is not so straightforward—although it may be reasonable to simply assume the average chloride current will not change significantly when cells are coupled (although some individual currents may go up or down), it depends on the details of the model. To check the reasonableness of this assumption and to verify some of our results obtained so far, we turn next to simulation.

Simulations

As in the single-cell case, we now validate and extend the analysis we have undertaken by considering a particular model with specific flux equations, signaling dynamics and parameters, allowing model simulation. Each cell in the multicell simulation is identical (other than initial conditions and/or "stimulation parameter" v) to that discussed in the single-cell case. For simplicity of presentation, we illustrate the results here with the case of three cells; however, the results hold for any number.

Individual Secretions

Figure 7 illustrates the individual secretions from differently stimulated cells in an acinus arrangement. The choices of stimulation parameter (v, the maximum rate of IP_3 production) correspond to a representative range between the minimum and maximum values used by Palk et al. (2010) in their calcium model. The details here are unimportant; essentially, higher parameter choices correspond to a more stimulated cell. Although each cell is stimulated differently and has different chloride and sodium currents from each cell as well as different ion levels, we see that, consistent with our analysis, the fluid secretions change and are close to identical in this case. The two more highly stimulated cells each have decreases in their time-averaged fluid secretion rate of between 12 and 13% when lumenally coupled compared to their secretion rates when uncoupled, while the cell with the lower stimulation has an increase in secretion of about 25%. In accordance with the discussion of efficiency, the effect on total secretion appears to be small, if any. In the subsection following the next, we consider whether there are any coupling effects on chloride currents, and hence fluid secretion, as the permeability is decreased and lumenal concentrations increase.

Efficiency of Secretion

As in the single-cell case, simulations verify that a change in efficiency for different sizes of concentration gradient

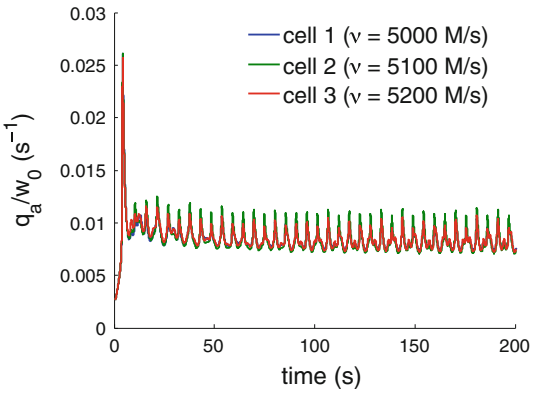

Fig. 7 Individual secretions from differently stimulated cells. Each cell is stimulated differently, but, due to the shared lumen, they secrete saliva at close to the same rate. $L_{pa} = 1.23 \times 10^{-14}$ L^2 J^{-1} s^{-1} and $L_{pb} = 4L_{pa}$ in all cases

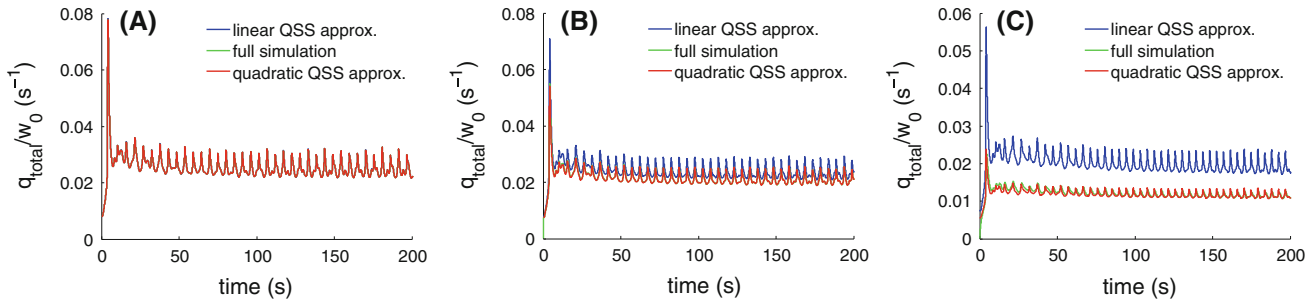

Fig. 8 Efficiency of total secretion under coupled conditions. **a** $L_{pa} = 1.23 \times 10^{-14}$ L^2 J^{-1} s^{-1}. **b** $L_{pa} = 1.23 \times 10^{-16}$ L^2 J^{-1} s^{-1}. **c** $L_{pa} = 1.23 \times 10^{-17}$ L^2 J^{-1} s^{-1}. $L_{pb} = 4L_{pa}$ in all cases

accounts for the majority of changes in total fluid secretion under coupled conditions (Fig. 8). Each cell still secretes at close to a common rate (not shown), but this common rate decreases away from the isosmotic regime, accounting for the reduction in total secretion. During rapid spikes, the difference between the quadratic quasi-steady state and the actual simulations for lower permeability values appears less than in the single-cell case; however, this is due to each cell being stimulated differently—some cells are oscillating less than they would be for the typical v value (the calcium oscillations decrease either side of the typical stimulation value). When each cell is stimulated at the same, typical, value (producing the largest oscillations) the actual secretion again fails to full reach the quasi-steady-state value during rapid spikes, for lower-permeability cases.

Secretion from an Acinus Versus Independent Secretion

Finally, we consider comparisons between coupled and uncoupled cells. As discussed previously, it is relatively easy to compare fluid secretions analytically at fixed chloride currents to analyze efficiency. Whether or not there is any net change due to a change in average or total chloride secretion, e.g., is a harder question and depends on the model details chosen. Figure 9 shows comparisons between independent cells and coupled cells for a range of permeabilities (i.e., for secretion under different conditions, isosmotic/high permeability and nonisosmotic/lower permeability). From these simulations, we see that, as predicted, the total fluid secretion is identical under isosmotic conditions, while there are small but essentially negligible changes in the total fluid secretion under non-isosmotic conditions, even though the individual secretions change to a common rate. For the model chosen the average chloride current did not show any significant differences between the coupled and uncoupled cases, though there was a small (around 1%) decrease in average current between coupled and uncoupled cases, for the lower-permeability values. The range of chloride currents—a range

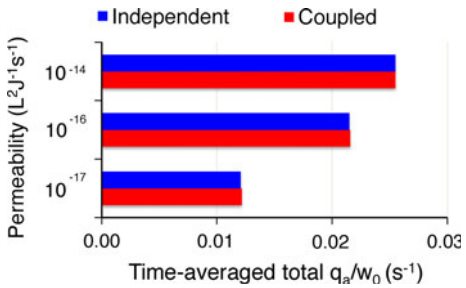

Fig. 9 Comparison of the time-averaged total secretion from independent and coupled cells for a range of permeabilities. *Top group* $L_{pa} = 1.23 \times 10^{-14}$ L^2 J^{-1} s^{-1}. *Middle group* $L_{pa} = 1.23 \times 10^{-16}$ L^2 J^{-1} s^{-1}. *Bottom group* $L_{pa} = 1.23 \times 10^{-17}$ L^2 J^{-1} s^{-1}. $L_{pb} = 4L_{pa}$ in all cases

of about 23% of the current at normal stimulation—means that the convexity/concavity effects are not expected to be large. This, combined with the negligible decrease in total current, means that only a negligible coupling effect of any sort is observed on total secretion. Thus, under typical parameter variations, we do not expect non-negligible lumenal-coupling effects.

Discussion

Recent models of salivary secretion, e.g., those of Gin et al. (2007) and Palk et al. (2010), are relatively easy to simulate using appropriate computational tools; but it can be difficult to understand the results in a simple manner. Weinstein and Stephenson (1979, 1981a, b) combined analysis of a high-level model of a single neutral solute with more comprehensive simulation models in a particularly careful and insightful manner. The work we have presented follows in this spirit by focusing on key general features of water transport, combining both approximate analysis and simulations. We have focused attention on a physiologically detailed, dynamic saliva-secretion model. Most of the prior work has placed more emphasis on fluid absorption, often from a small compartment into a larger compartment;

and the analytic work has focused on steady-state conditions, as opposed to quasi-steady-state conditions. Furthermore, most of the prior analytic work considers linearizations/perturbation expansions about isotonic/isosmotic conditions. In the context of saliva secretion into a small lumenal space, we have considered conditions for, and deviations from, quasi-steady-state conditions, deviations from isotonic/isosmotic secretion as well as effects of lumenal coupling. The main physiological application we discuss here, beyond consideration of conditions for isotonic/isosmotic secretion discussed in the next subsection, is to the interpretation of, and debate surrounding, aquaporin knockout studies, discussed below.

Isotonic/Isosmotic Water Transport: Relationship to Previous Studies

A consistent theme in discussion about fluid transport in epithelia is how isotonic/isosmotic water transport is achieved. The most commonly accepted view is that water follows salt secretion osmotically, and this, combined with relatively large water permeabilities (due to the presence of aquaporins), is sufficient to account for the basic phenomenon of saliva secretion (Spring 1999). As discussed by Turner and Sugiya (2002), one of the main problems with this hypothesis is that it is very difficult to demonstrate the existence of osmotic gradients between the interstitium and lumen. However, due to the high water permeability, it is supposed that only very small gradients are required (Spring 1999), so this becomes a problem of verifiability rather than an inconsistency with the hypothesis itself. Other evidence, in particular that based on aquaporin knockout studies (e.g., Ma et al. 1999), is usually taken to weight the evidence in favor of the osmotic hypothesis. However, the interpretation of these knockout studies has been criticized by researchers such as Hill et al. (2004) and Fischbarg (2010). We discuss this further below.

Our model is a compartment model based on an osmotic coupling mechanism. In terms of the original Curran (1960) model for epithelial transport, mapped onto the physiology of saliva secretion, the lumen plays the role of the "middle" compartment for the secretion out of the cell, though the cell itself also draws water through the basolateral membrane. Friedman (2008) offers a good discussion of how the Curran (1960) model can be used as the basic model for various physiological systems. Weinstein and Stephenson (1979, 1981a, b) emphasized a number of important distinctions relevant to key questions of epithelial transport, in particular the different parameter and boundary condition dependencies of the cases of approximate isotonicity and exact isotonicity/uphill transport. Similarly, Mathias and Wang (2005) presented a series of simple theoretical models, also based on the Curran (1960) compartment model, to investigate conditions for the generation of isotonic water transport using the osmotic mechanism. They analyzed two variations of a simple two-membrane steady-state model, one without an imposed boundary condition on the secretion (i.e., the osmolarity of the secretion is determined from the balance of salt and water transport) and one with an imposed boundary condition, setting the osmolarity to be exactly equal at each end. Due to the large permeabilities, the model behavior has a strong dependence on the selection of boundary conditions. This observation is consistent with the earlier work of Weinstein and Stephenson (1979, 1981a, b).

The first case considered by Mathias and Wang (2005) is most appropriate for models of saliva secretion due to our assumption of no pressure buildup in the lumen of a secretory end piece; i.e., any saliva previously secreted is pushed out of the lumen by newly secreted saliva (and then travels through a system of ducts before exiting into the mouth). This corresponds to the case discussed by Weinstein and Stephenson (1979, 1981a, b) of transport into a small serosal bath from a larger mucosal bath (which they discuss in reference to a hanging gallbladder experimental arrangement). For saliva secretion, this means that concentrations in the lumen are determined by a balance of salt and water transport. This is consistent with recent models published for saliva secretion (Gin et al. 2007; Palk et al. 2010).

These single-cell models of saliva secretion explicitly account for changes over time (i.e., are dynamic models), while the cells are modeled as well mixed. The model of Mathias and Wang (2005) does not include time, and in the case of interest, the spatial gradients are negligible. Weinstein and Stephenson (1979, 1981a, b) include some dynamics in their simulation model, but their corresponding theoretical treatment focuses on steady states (as opposed to quasi-steady states). Our analysis of the Gin et al. (2007) model of saliva secretion from a parotid acinar cell allows us to consider how (linearized/perturbation) analysis such as that of Mathias and Wang (2005) and those of Weinstein and Stephenson (1979, 1981a, b) carries over to a dynamic, physiologically based model of fluid secretion, regulated by an oscillating calcium signal. Our analysis shows that a large membrane permeability (relative to chloride conductivity) both is required for and leads to isosmotic secretion for osmotically driven saliva secretion. The scale of small deviations from iso-osmolarity is shown to be inversely proportional to the membrane permeability and proportional to the ratio of chloride-transport and fluid-transport terms. Furthermore, the case of isosmotic secretion provides an upper bound on saliva secretion efficiency for both single cells and cells arranged in an acinus. These results are in agreement with the work of the

aforementioned authors in their particular models. As discussed in Gin et al. (2007) and Palk et al. (2010), the basic model used here is in good agreement with estimates of total saliva secretion and of other quantities of interest such as membrane potential.

Aquaporin Knockout Studies

Overview

Hill et al. (2004) and Fischbarg (2010) (among others) have criticized the usual interpretation of aquaporin knockout studies in the context of epithelial fluid transport. In particular they focus on the fact that, in aquaporin knockout animals, water permeability is often reduced by a larger proportion than is the water transport. Although some studies, such as that of aquaporin-5-deficient mice by Krane et al. (2001), do not appear to suffer this issue, we will consider the more extreme cases of apparent conflict from a general point of view informed by our modeling work and give a representative quantitative comparison to the results of Ma et al. (1999) for aquaporin-5 knockout mice, as they are summarized in Hill et al. (2004). This requires consideration of cases for which the osmotic gradients become more significant than can be appropriately treated with a perturbation expansion near the isotonic/isosmotic secretion regime.

Hill et al. (2004) emphasize two interconnected points in their critique of the "simple permeability hypothesis" (SPH, the hypothesis being that the main role of aquaporins is to provide a path of increased water permeability to increase water transport). This hypothesis plays a crucial role in providing the large permeabilities required for the osmotic mechanism. The first, and main, point the authors raise is that the differing magnitudes of the reduction of permeability, on the one hand, and the reduction of water transport, on the other, raises problems for this hypothesis—as they say, "SPH would predict that the removal of a major pathway of water flux across membranes would have drastic effects on biological function at the cellular, tissue and whole animal level" (Hill et al. 2004, p. 8), and "where fluid flow has been significantly reduced… it has only been partial where it should have been substantial" (p. 11). The second point they raise is that there often appears to be a reduction in the total salt transport, which would by itself be enough to account for a significant portion of the reduction in fluid transport, without leaving much to be accounted for by the reduced water permeability. Though they acknowledge that their calculation of the reduction in salt transport is complicated by the possibility of changes in ductal absorption, the point remains that any reduction in salt transport leaves less reduction in fluid transport to be directly attributable to the decreased membrane permeabilities. Thus, the overall point raised is that large reductions in water permeability due to aquaporin knockouts do not appear to be having a significant enough effect on water-transport rates. Representative changes cited by Hill et al. (2004) are around 40–60% for both fluid and salt transport and up to 90% for membrane permeability, although these vary across the range of studies they consider.

Here, we consider whether such changes really are inconsistent with a model such as ours, which is based on the SPH and the corresponding osmotic mechanism for saliva secretion. Quantitative comparisons of model and experiment are discussed in the following subsection; however, we first note that according to the relationship (35) (illustrated in Fig. 2), a drop in fluid transport essentially has two components—one due to a decrease in the chloride current and one due to a drop in efficiency (i.e., when permeability is lowered and the osmotic gradient increased). As the isosmotic regime is approached (the large permeability limit), these effects become essentially independent. Furthermore, as this regime is approached, the fluid transport loses all dependence on permeability—the dependence disappears according to an inverse relationship in permeability (since $\alpha \sim 1/L_T$). So when the physiological system is in this parameter range, a drop in chloride current is associated with a direct linear decrease in fluid transport, while a significant drop in permeability may not have much effect at all. As long as the ratio of chloride conductance to water permeability is sufficiently small, the system will remain in this regime. Thus, the role of aquaporins may be not only to increase the fluid transported for a given amount of salt transport but also to push the system into a regime where it is more robust to variations in permeability.

Comparison to Experiments

The water permeability used in the simulation shown in Fig. 4c is an order of magnitude lower than the water permeability used in the simulation shown in Fig. 4b. This corresponds to a drop in water permeability of 90%. At the same time, the drop in fluid flow (here denoted by J_v instead of q_a) is only about 51%. A comparison of these results with those of Ma et al. (1999) as summarized by Hill et al. (2004) is given in Table 1. As can be seen, these results are of a similar scale to those of Ma et al. (1999), which Hill et al. (2004) cite as being in conflict with the SPH. In particular, the large drop in water permeability (of 90%) produces a much less marked drop in fluid secretion (51% in the model, 59% observed experimentally), along with a drop in convective salt collection rate (J_s) (27% compared to 41% observed experimentally). It is apparent that a large reduction in water permeability is not

Table 1 Comparison of aquaporin knockout studies and representative model dependence on water permeability

Knockout				Model				
ΔPosm	ΔJ_v	ΔOsm	ΔJ_s	ΔPosm	ΔJ_v	ΔOsm	ΔJ_s	ΔI_{Cl}
−65 to −90%[a]	−59%	+43%	−41%	−90%	−51%	+41%	−27%	−19%

Data are from Ma et al. (1999) and include an estimate of J_v changes as calculated by Hill et al. (2004)

[a] Ma et al. (1999) did not measure the decrease in cell membrane permeability in their knockout experiment. Krane et al. (2001) found a relative decrease in permeability (as measured by changes in swelling/shrinking rates) in aquaporin-knockout mice of 65% for parotid and 77% for sublingual cells. Aquaporins are estimated to account for up to 90% of cell water permeability in various physiological systems, as summarized by Hill et al. (2004)

inconsistent with a smaller reduction in fluid secretion, according to results produced entirely according to the SPH mechanism. The drop in (measured) salt transport is also largely accounted for, and actually corresponds to a much lower decrease in the chloride current (I_{Cl}) itself (19%), due to deviations from quasi-steady-state behavior (as discussed above, Numerical Simulations). Further decreases in chloride-transport rates not accounted for in the model could be due to changes in duct absorption rates in knockouts (affecting J_s) or other changes in cell chloride secretion (affecting I_{Cl} and J_s) in knockouts.

The effect of a 99% permeability decrease on water transport is even less going from Fig. 4a, b as these are further in the isosmotic parameter range, and hence, the results are even less susceptible to variations in permeability. The water permeability values used here were originally model fits by Gin et al. (2007), and the largest value used is probably one to two orders of magnitude too large, based on the range for typical epithelia (Spring 2010). The exact membrane water permeabilities are difficult to measure in glandular acini (Hill et al. 2004), and we are not aware of any values for parotid glands in the literature. However, in our representative comparison with aquaporin studies given above we used a baseline permeability of two orders of magnitude less than that of Gin et al. (2007) (Fig. 4b) and then considered a further order of magnitude decrease (Fig. 4c), consistent with the expected range of permeability values (we present a conversion from our units for water permeability to an equivalent P_f value in Appendix A). Based on our results (including those given below), we would expect the permeability of parotid acinar cells to be similar to that of other high-permeability cells in other water-transporting epithelia such as the lung (Dobbs et al. 1998) and renal proximal tubule (Meyer and Verkman 1987), i.e., a P_f of the order 10^{-2} cm s^{-1}.

Acinus Geometry

Mathematical models of saliva secretion (e.g., Gin et al. 2007; Palk et al. 2010) have so far focused on single cells. However, in this analysis we have begun to consider the effects of acinus geometry on secretion. In particular, we considered the coupling effect induced by the shared lumen of an acinus on the dynamics of the cells making up that acinus. We demonstrated how to carry over the results for efficiency and isosmotic/nonisosmotic secretion to this case. Furthermore, we illustrated two key points. Firstly, the individual fluid secretions of member cells in an acinus are in fact modified by the arrangement of the cells around a single shared lumen. Differently stimulated cells can secrete fluid at close to identical rates when arranged into an acinus, while this is not the case for isolated cells. However, the total fluid secreted from an acinus is not affected by this lumenal coupling. It is worth noting that in real salivary glands the lumenal structure can be more convoluted and is continuous with intercellular canaliculi (Riva et al. 1993).

Calcium Signaling

In this work we included an oscillating calcium signal which, e.g., leads to deviations from (quasi-) steady-state behavior. We have not considered effects of the acinus geometry on this calcium signaling. Work in progress includes, from the single-cell perspective, incorporating calcium waves (originating at the apical end) to explore the observation of the relatively rapid calcium wave speed (e.g. compared to that in the pancreas [Giovannucci et al. 2002]) in the context of the type of signaling that works best for fluid secretion. In the multicellular case, work has begun to explore the effects of the inclusion of gap junctions on calcium signaling and hence fluid secretion. In each of these cases, the analysis of the salt and water coupling effects carried out here forms a foundation from which to consider these extensions. The effects of variations in calcium signaling, in both a single cell and an acinus, can profit from the reduction in complexity of the fluid secretion model, e.g., utilizing the simple relations derived between fluid secreted and chloride current. Changes in transporters and ionic mechanisms can also be understood using modifications of the analysis carried out here.

Transport Routes and Ionic Mechanisms

The chloride-based mechanism adopted in this report is thought to account for the majority of saliva secretion from the major salivary glands. But it is also thought possible that bicarbonate exits the cell via the same apical anion channel as chloride (Turner and Sugiya 2002), and we have not represented this mechanism in our model. There may be interesting consequences of including this additional mechanism; however, the essential feature of anion secretion via the apical membrane and cation flow via the tight junctions (establishing an osmotic gradient in the lumen) is the same. Since the water secretion into the lumen washes all ions away, in principle there must be a bicarbonate current into the lumen; here, it is essentially assumed that it would in reality make up some fraction of the total apical anion current into the lumen, which for the same osmotic gradient would mean a slightly lower chloride current than is present in this model. The proper inclusion of bicarbonate in the model remains future work, as does the inclusion of details from other suggested ionic mechanisms (Turner and Sugiya 2002; Cook and Young 2010).

The effect on secretion of a possible apical K^+ channel was considered by Cook and Young (1989) and more recently by Palk et al. (2010). While our analysis could be extended to cover this, it is beyond the scope of the present study. In our model Na^+ and K^+ travel only via the paracellular pathway, which is assumed to be cation-selective in accordance with the basic proposed mechanisms of saliva secretion (Cook and Young 2010). In general, these ionic fluxes will be driven by their electrochemical gradients, as well as by convection by any water traveling via this same pathway. We ignore direct ion–ion interactions; however, if solute reflectivities differ between two (or more) parallel pathways (e.g., the paracellular pathway and the cell) through which water also travels, then cross-terms in overall (or "composite") epithelium system equations can still occur. These represent formal ion–ion interactions and can have important consequences for the interpretation of tracer flux experiments and the determination of permeabilities (Weinstein 1987). Since in our model we assume a fully transcellular pathway for water (consistent with the assumption of an osmotic mechanism as discussed in the Introduction), these formal composite-system interactions are not present (Weinstein 1987; Friedman 2008).

Despite this, it still may be of interest to consider a paracellular water flux, via either an osmotic mechanism or some other mechanism, to better clarify and understand the model dependence on this assumption and the consequences for determining parameter values experimentally. Gin et al. (2007) and Palk et al. (2010) both considered a paracellular water flux; however, they did not consider an explicit convective solute flux (or any other similar paracellular flux coupling, as can be formalized using the framework of nonequilibrium thermodynamics [Schultz 1980]). Without this, they found no qualitative differences in model behavior. This can be explained by the expression we derived for the secretion from a cell (32) (which applies for both isolated cells and cells in an acinus), which is dependent only on the lumenal and interstitial concentrations and thus has the same form as a simple paracellular flux. Finally, we note that the specific equations representing the paracellular ion fluxes will change depending on the included mechanisms, but the electroneutrality equation that we use (11) holds (approximately) regardless of the mechanism of ion flux.

Acknowledgement We thank Ted Begenisich, David Yule and Trevor Shuttleworth at the University of Rochester; James Melvin and Marcelo Catalan at the National Institutes of Health (NIH); and Laurence Palk, Kate Patterson, Katie Sharp, Shawn Means, Ivo Siekmann and Vivien Kirk from the University of Auckland for helpful discussions and feedback. We also thank the anonymous referees for detailed and helpful comments that we feel significantly improved this work. O. M. was supported by the Tertiary Education Commission's Top Achiever Doctoral Scholarship. This work was supported by NIH grant R01 DE19245-01.

Appendix A: Water Permeability

We have used the units $L^2\ J^{-1}\ s^{-1}$ for water permeability, in line with Palk et al. (2010) and which we found convenient for simulation and analysis but which are not as common among physiologists. A variety of quantities characterizing water permeability are in use in epithelial water-transport studies; here, we give a conversion from our water permeability to an equivalent P_f ("osmotic water permeability") quantity, which is measured in centimeters per second.

We first note that our permeability is an area-weighted quantity, as employed by Gin et al. (2007) and Palk et al. (2010). We use the data from Cope and Williams (1974) and Poulsen and Bundgaard (1994) to give a typical value for apical membrane area of about $A = 1.25 \times 10^{-6}$ cm^2. The remaining quantities required for conversion are $R = 8.315$ J mol^{-1} K^{-1}, $\Theta = 310$ K, $V_w = 18 \times 10^{-3}$ L mol^{-1} and 10^3 cm^3 = 1 L. The relationship between our L_{pa} and the quantity P_f, expressed using these quantities, is (Persson and Spring 1982)

$$P_f = \frac{10^3 R\Theta L_{pa}}{A V_w} \tag{60}$$

where 10^3 is a conversion factor for $\frac{L_{pa}}{V_w}$ (the ratio of which has units L mol J^{-1} s^{-1}) from liters to centimeters cubed. This gives an equivalent value for P_f of about 1.41 cm s^{-1} for our highest permeability ($L_{pa} = 1.23 \times 10^{-14}$ L^2 J^{-1} s^{-1}) and a value of about 1.41×10^{-2} cm s^{-1} for the

value we take as representative in our comparisons to aquaporin knockout studies ($L_{pa} = 1.23 \times 10^{-16}$ L^2 J^{-1} s^{-1}). This latter value is similar to those of other water-transporting epithelia, as discussed in the main text, while the higher value represents a limiting case.

Appendix B: Calcium Signaling Model Modification

As noted by Palk et al. (2010), the Gin et al. (2007) model appeared to have a dependence of calcium oscillations on volume oscillations, which they deemed undesirable. Because of this, our calcium model follows that of Palk et al. (2010). The only difference is that our model uses a Hill function expression for IP_3 production

$$J_{\text{IP3prod}} = v_{w_0} \frac{[\text{Ca}]_i^2}{[\text{Ca}]_\text{i}^2 + \text{K}^2} \tag{61}$$

where K = 5 nM and v is a control parameter with a typical value of 5,100 M s^{-1}, while their model has a constant production rate:

$$J_{\text{IP3prod}} = v_{w_0} \tag{62}$$

This makes no difference to the results. The rest of the signaling model is identical and follows the details given in their paper (see pp. 626–628 and Tables 1–3).

Appendix C: Beneficial Coupling Effect

Function Properties

We state without proof that, for $\alpha \in [0, \infty)$, the function $f(\alpha) = \left(\frac{1}{\alpha}\right)\left(\frac{1}{2}\right)\left[\sqrt{1+4\alpha} - 1\right]$ is (1a) convex and (2a) strictly decreasing. We define the value at $\alpha = 0$ to be the limit as $\alpha \to 0$, which exists and is equal to 1. Defining the new variable $\beta = 1/\alpha$, we can define the new function:

$$F(\beta) = (\beta)\left(\frac{1}{2}\right)\left[\sqrt{1+4\left(\frac{1}{\beta}\right)} - 1\right] = f(1/\beta)$$

Over $\beta \in [0, \infty)$, this function is (1b) concave and (2b) strictly increasing. We again state this without proof. However, these function properties can be verified simply, by plotting the functions (for positive values) along with the first and second derivatives. A negative (positive) first derivative indicates a decreasing (increasing) function, and a positive (negative) second derivative indicates a convex (concave) function. The freely available computational tool Wolfram Alpha (www.wolframalpha.com), e.g., can be used. This can compute the derivatives and handle the singularity at zero automatically.

Positive Coupling Effect

Now we can write (57) and (58) (derived for fixed chloride currents) as

$$\left(\bar{q}_\text{a}^\text{I}\right)^* = \frac{\sum_{k=1}^n g_\text{Cl}^k F\left(\frac{L_\text{T}^k}{g_\text{Cl}^k}\right)}{\sum_{i=1}^n g_\text{Cl}^i} \tag{63}$$

and

$$\bar{q}_\text{a}^{c*} = F\left(\frac{\sum_{k=1}^n L_\text{T}^k}{\sum_{i=1}^n g_\text{Cl}^i}\right) = F\left(\sum_{k=1}^n \frac{g_\text{Cl}^k}{\sum_{i=1}^n g_\text{Cl}^i}\left(\frac{L_\text{T}^k}{g_\text{Cl}^k}\right)\right) \tag{64}$$

Thus, (63) is a weighted average of F evaluated at each $\left(\frac{L_\text{T}^j}{g_\text{Cl}^j}\right)$ value, while (64) is equal to F evaluated at the weighted average of the $\left(\frac{L_\text{T}^j}{g_\text{Cl}^j}\right)$ values. By Jensen's inequality (Hardy et al. 1997) applied to concave, strictly increasing $F\left(\frac{L_\text{T}^j}{g_\text{Cl}^j}\right)$, it follows that

$$\bar{q}_\text{a}^{c*} \geq \left(\bar{q}_\text{a}^\text{I}\right)^* \tag{65}$$

where the inequality is strict when the $\left(\frac{L_\text{T}^j}{g_\text{Cl}^j}\right)$ values are not all identical. This gives the required result.

References

Arreola J, Melvin JE, Begenisich T (1996) Activation of calcium-dependent chloride channels in rat parotid acinar cells. J Gen Physiol 108:35–47

Benjamin BA, Johnson EA (1997) A quantitative description of the Na–K–2Cl cotransporter and its conformity to experimental data. Am J Physiol 273:F473–F482

Cook DI, Young JA (1989) Effect of K^+ channels in the apical plasma membrane on epithelial secretion based on secondary active Cl^- transport. J Membr Biol 110:139–146

Cook DI, Young JA (2010) Fluid and electrolyte secretion by salivary glands. In comprehensive physiology. John Wiley & Sons, Hoboken

Cope GH, Williams MA (1974) Improved preservation of parotid tissue for electron microscopy: a method permitting the collection of valid stereological data. J Cell Biol 60(1):292–297

Curran PF (1960) Na, Cl, and water transport by rat ileum in vitro. J Gen Physiol 43:1137–1148

Diamond JM (1964) The mechanism of isotonic water transport. J Gen Physiol 48:15–42

Diamond JM, Bossert WH (1967) Standing-gradient osmotic flow. J Gen Physiol 50(8):2061–2083

Dobbs LG, Gonzalez R, Matthay MA, Carter EP, Allen L, Verkman AS (1998) Highly water-permeable type I alveolar epithelial cells confer high water permeability between the airspace and vasculature in rat lung. Proc Natl Acad Sci USA 95:2991–2996

Fischbarg J (2010) Fluid transport across leaky epithelia: central role of the tight junction and supporting role of aquaporins. Physiol Rev 90:1271–1290

Friedman M (2008) Principles and models of biological transport. Springer, New York

Gin E, Crampin EJ, Brown DA, Shuttleworth TJ, Yule DI, Sneyd J (2007) A mathematical model of fluid secretion from a parotid acinar cells. J Theor Biol 248:64–80

Giovannucci DR, Bruce JIE, Straub SV, Arreola J, Sneyd J, Shuttleworth TJ, Yule DI (2002) Cytosolic Ca^{2+} and Ca^{2+}-activated Cl^{-} current dynamics: insights from two functionally distinct mouse exocrine cells. J Physiol 540(2):469–484

Hardy G, Littlewood J, Polya G (1997) Inequalities. Cambridge mathematical library. Cambridge University Press, Cambridge

Hill AE (2008) Fluid transport: a guide for the perplexed. J Membr Biol 223(1):1–11

Hill AE, Hill BS (1978) Sucrose fluxes and junctional water flow across *Necturus* gall bladder epithelium. Proc R Soc Lond B 200(1139):163–174

Hill AE, Shachar-Hill B, Shachar-Hill Y (2004) What are aquaporins for? J Membr Biol 197:1–32

Krane CM, Melvin JE, Nguyen HV, Richardson L, Towne JE, Doetschman T, Menon AG (2001) Salivary acinar cells from aquaporin 5-deficient mice have decreased membrane water permeability and altered cell volume regulation. J Biol Chem 276:23413–23420

Krantz W (2007) Scaling analysis in modeling transport and reaction processes: a systematic approach to model building and the art of approximation. Wiley-Interscience, Hoboken

Läuger P, Apell HJ (1986) A microscopic model for the current–voltage behaviour of the Na, K-pump. Eur Biophys 13:309–321

Lytle C, McManus T (1986) A minimal kinetic model of Na^{+} K^{+} 2Cl co-transport with ordered binding and glide symmetry. J Gen Physiol 88:36a

Ma T, Song Y, Gillespie A, Carlson EJ, Epstein CJ, Verkman AS (1999) Defective secretion of saliva in transgenic mice lacking aquaporin-5 water channels. J Biol Chem 274(29):20071–20074

Mathias RT, Wang H (2005) Local osmosis and isotonic transport. J Membr Biol 208:39–53

Meyer MM, Verkman AS (1987) Evidence for water channels in renal proximal tubule cell membranes. J Membr Biol 96:107–119

Palk L, Sneyd J, Shuttleworth TJ, Yule DI, Crampin EJ (2010) A dynamic model of saliva secretion. J Theor Biol 266(4):625–640

Persson BE, Spring KR (1982) Gallbladder epithelial cell hydraulic water permeability and volume regulation. J Gen Physiol 79:481–505

Poulsen JH, Bundgaard M (1994) Quantitative estimation of the area of luminal and basolateral membranes of rat parotid acinar cells: some physiological applications. Pflugers Arch 429(2):240–244

Riva A, Valentino L, Lantini MS, Floris A, Riva FT (1993) 3D structure of cells of human salivary glands as seen by SEM. Microsc Res Tech 26(1):5–20

Schultz S (1980) Basic principles of membrane transport. IUPAB biophysics series. Cambridge University Press, Cambridge

Schultz SG (2001) Epithelial water absorption: osmosis or cotransport? Proc Natl Acad Sci USA 98:3628–3630

Segel LA (1970) Standing-gradient flows driven by active solute transport. J Theor Biol 29(2):233–250

Segel LA (1972) Simplification and scaling. SIAM Rev 14(4): 547–571

Segel L, Goldbeter A (1994) Scaling in biochemical kinetics: dissection of a relaxation oscillator. J Math Biol 32:147–160

Segel LA, Slemrod M (1989) The quasi-steady-state assumption: a case study in perturbation. SIAM Rev 31(3):446–477

Shachar-Hill B, Hill AE (2002) Paracellular fluid transport by epithelia. In: Thomas Zeuthen WDS (ed) Molecular mechanisms of water transport across biological membranes. International review of cytology, vol 215. Academic Press, San Diego, pp 319–350

Smith NP, Crampin EJ (2004) Development of models of active ion transport for whole-cell modeling: cardiac sodium-potassium pump as a case study. Prog Biophys Mol Biol 85:387–405

Spring KR (1998) Routes and mechanism of fluid transport by epithelia. Annu Rev Physiol 60:105–119

Spring KR (1999) Epithelial fluid transport—a century of investigation. News Physiol Sci 14(3):92–98

Spring KR (2010) Mechanism of fluid transport by epithelia. John Wiley & Sons, Hoboken

Takahata T, Hayashi M, Ishikawa T (2003) SK4/IK1-like channels mediate TEA-insensitive, Ca^{2+}-activated K^{+} currents in bovine parotid acinar cells. Am J Physiol 284:C127–C144

Thaysen JH, Thorn NA, Schwartz IL (1954) Excretion of sodium, potassium, chloride and carbon dioxide in human parotid saliva. Am J Physiol 178(1):155–159

Turner RJ, Sugiya H (2002) Understanding salivary fluid and protein secretion. Oral Dis 8:3–11

Turner RJ, Paulais M, Manganel M, Lee SI, Moran A, Melvin JE (1993) Ion and water transport mechanisms in salivary glands. Crit Rev Oral Biol Med 4:385–391

Weinstein AM (1987) Convective paracellular solute flux. A source of ion–ion interaction in the epithelial transport equations. J Gen Physiol 89:501–518

Weinstein AM, Stephenson JL (1979) Electrolyte transport across a simple epithelium. Steady-state and transient analysis. Biophys J 27(2):165–186

Weinstein AM, Stephenson JL (1981a) Coupled water transport in standing gradient models of the lateral intercellular space. Biophys J 35(1):167–191

Weinstein AM, Stephenson JL (1981b) Models of coupled salt and water transport across leaky epithelia. J Membr Biol 60:1–20

J Membrane Biol (2012) 245:51–68
DOI 10.1007/s00232-011-9412-4

REVIEW

Functions of Cholesterol and the Cholesterol Bilayer Domain Specific to the Fiber-Cell Plasma Membrane of the Eye Lens

Witold K. Subczynski · Marija Raguz · Justyna Widomska · Laxman Mainali · Alexey Konovalov

Received: 30 August 2011 / Accepted: 29 November 2011 / Published online: 30 December 2011

Abstract The most unique feature of the eye lens fiber-cell plasma membrane is its extremely high cholesterol content. Cholesterol saturates the bulk phospholipid bilayer and induces formation of immiscible cholesterol bilayer domains (CBDs) within the membrane. Our results (based on EPR spin-labeling experiments with lens-lipid membranes), along with a literature search, have allowed us to identify the significant functions of cholesterol specific to the fiber-cell plasma membrane, which are manifest through cholesterol–membrane interactions. The crucial role is played by the CBD. The presence of the CBD ensures that the surrounding phospholipid bilayer is saturated with cholesterol. The saturating cholesterol content in fiber-cell membranes keeps the bulk physical properties of lens-lipid membranes consistent and independent of changes in phospholipid composition. Thus, the CBD helps to maintain lens-membrane homeostasis when the membrane phospholipid composition changes significantly. The CBD raises the barrier for oxygen transport across the fiber-cell membrane, which should help to maintain a low oxygen concentration in the lens interior. It is hypothesized that the appearance of the CBD in the fiber-cell membrane is controlled by the phospholipid composition of the membrane. Saturation with cholesterol smoothes the phospholipid-bilayer surface, which should decrease light scattering and help to maintain lens transparency. Other functions of cholesterol include formation of hydrophobic and rigidity barriers across the bulk phospholipid-cholesterol domain and formation of hydrophobic channels in the central region of the membrane for transport of small, nonpolar molecules parallel to the membrane surface. In this review, we provide data supporting these hypotheses.

Keywords Lens lipid · Lens cortex · Lens nucleus · Cholesterol bilayer domain · Spin label · Electron paramagnetic resonance

W. K. Subczynski (✉) · M. Raguz · J. Widomska · L. Mainali · A. Konovalov
Department of Biophysics, Medical College of Wisconsin, 8701 Watertown Plank Road, Milwaukee, WI 53226, USA
e-mail: subczyn@mcw.edu

M. Raguz
Department of Medical Physics and Biophysics, School of Medicine, University of Split, Split, Croatia

J. Widomska
Department of Biophysics, Medical University, Lublin, Poland

Introduction

The eye lens is an avascular structure which, in conjunction with the cornea, focuses light on the retina and, thus, must remain transparent throughout an individual's life. The human lens is 9 mm in diameter and 4 mm thick and contains 1,000–3,000 layers of fiber cells (Fig. 1). To prevent excessive light scattering and compromised lens transparency, fiber cells lose all of their subcellular organelles during maturation (Beebe 2003). Newly formed fiber cells in the periphery displace existing fiber cells near the center of the lens (Beebe 2003). Thus, the line from the lens surface to its center is the age axis. Fiber cells are not homogeneous in terms of composition, metabolism or age. The adult lens contains two kinds of fiber cells: those located in the cortex (the outer layers of the lens), which are not yet mature and still contain organelles (including mitochondria), and those located in the nucleus (the core of the lens), which are mature and do not contain organelles (Fig. 1). The nuclear region contains the embryonic lens,

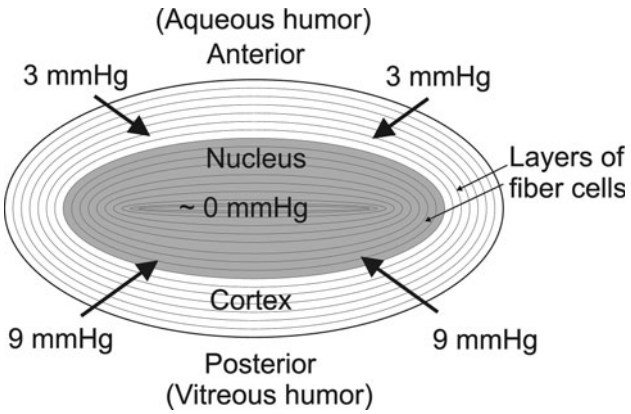

Fig. 1 Diagram of the eye lens section showing the location of the lens cortex and nucleus. Values of the oxygen partial pressure at the surface of the anterior and posterior cortex of the lens in the healthy eye are taken from Siegfried et al. (2010). *Arrows* indicate the oxygen flux into the lens, toward the lens center. The Chol/PL mole ratio in cortical fiber-cell membranes is from 1 to 2 and that in nuclear membranes is from 3 to 4 (Li et al. 1987). The basic phospholipid composition (taken from Yappert et al. 2003 for a 25 year old human) of the cortical and nuclear lens lipid membrane is 3.2% PC, 14% PE, 1.5% PS and 42.8% (DHSM + SM) and 0.7% PC, 6% PE, 3.1% PS and 49.8% (DHSM + SM), respectively. PC, phosphatidylcholine; PE, phosphatidylethanolamine; PS, phosphatidylserine; SM, sphingomyelin (including dihydrosphingomyelin)

the fetal fibers and the juvenile and adult nuclear fibers (Li et al. 1985). Due to minimal cell turnover, cells in the nucleus of the human lens are considered the longest-living cells in the human body (Peterson and Delamere 1992). Consequently, they require functional mechanisms to protect them from damage.

Membranes of fiber cells, which build the human eye lens (Fig. 1), are overloaded with cholesterol, which not only saturates the phospholipid bilayer but also leads to the formation of cholesterol bilayer domains (CBDs) within these membranes (Jacob et al. 1999, 2001). The appearance of these domains is usually a sign of pathology (Tulenko et al. 1998). However, only in the eye lens can CBDs play a positive physiological function, maintaining lens transparency (Borchman et al. 1996; Jacob et al. 1999; Mason et al. 2003) and, therefore, possibly protecting against cataract formation (Jacob et al. 1999; Mason et al. 2003). The significance of cholesterol in the eye lens is further emphasized by observations that inherited defects in enzymes of cholesterol metabolism and the use of cholesterol biosynthesis–inhibiting drugs cause cataract formation in humans and other animals (Borchman et al. 1989; Cenedella 1996; de Vries and Cohen 1993; Kirby 1967; Mosley et al. 1989). These effects indicate that cholesterol plays an important physiological role in the eye lens. A better understanding of the physiological functions of cholesterol requires an increased understanding of cholesterol function at the molecular level, which can be shown through cholesterol-induced changes in the properties of the lipid-bilayer portion of the fiber-cell plasma membrane. Changes in cholesterol content in the fiber-cell plasma membrane, which occur during aging, are indicated by an increase in the total cholesterol/phospholipid (Chol/PL) molar ratio and as a higher Chol/PL molar ratio in the nucleus compared to the cortex (Borchman et al. 1989; Fleschner and Cenedella 1991; Li and So 1987; Raguz et al. 2009; Rujoi et al. 2003). Interestingly, animals with a long life span exhibit a higher Chol/PL molar ratio than animals with a shorter life span (Borchman et al. 1989; Fleschner and Cenedella 1991; Li et al. 1987). Also, the phospholipid composition of the eye-lens membrane changes significantly with age (Huang et al. 2005; Paterson et al. 1997; Truscott 2000; Yappert et al. 2003), between regions of the lens (Raguz et al. 2009, 2004) and between animal species (Borchman et al. 2004; Deeley et al. 2008). In contrast, there is not much difference in the lipid composition of most organs from one species to another (Rouser et al. 1969, 1971) or with age (Rouser and Solomon 1969). Such great variation with age in phospholipid composition and cholesterol content suggests difficulties in maintaining fiber-cell-membrane homeostasis as well as homeostasis within the fiber cell, which is required for lens transparency. This is especially true for fiber cells in which the plasma membrane is basically the only membranous structure. Lens fiber cells lose their intracellular organelles soon after they are formed (Rafferty 1985), and the plasma membrane accounts for essentially all lens lipids.

The need for a high cholesterol content in the lens is unclear. Borchman et al. (2004), based on their measurements and data from the literature, hypothesized that lens membranes are highly ordered because of high sphingolipid and cholesterol contents and suggested that cholesterol provides buffering properties for membrane fluidity by ordering fluid phospholipids and disordering ordered lipids (Li et al. 1987; Truscott 2000). They concluded that the physiological role of cholesterol is to increase the structural order of cortical membrane lipids and decrease the order of nuclear lipids so that the two membranes have a similar order (Borchman et al. 1996). Because cholesterol is relatively stable and resistant to oxidation compared with unsaturated phospholipids, it is suggested that it may also add chemical stability to the membrane (Borchman and Yappert 2010). Additionally, the high cholesterol level may be related to gap junctions. Cholesterol is understood to be associated with gap junctions (Biswas et al. 2009, 2010; Biswas and Lo 2007), and the lens contains more gap junctions than any other tissue. Cholesterol content in protrusions, which are specialized, interlocking membrane domains between lens fiber cells, is very high. It has been suggested (Biswas et al. 2010) that the high cholesterol content in protrusion membranes makes them less

deformable and more suitable to maintain fiber-to-fiber stability during visual accommodation. The relationship between lens cholesterol and lens cataracts has been reviewed (Cenedella 1996) with an ultimate focus on the effect of statin drugs on the lens in humans and other animals.

We present data that support the main hypothesis of this review: a high cholesterol content and the presence of the CBD are necessary to maintain lens-membrane homeostasis throughout the life of an individual. It should be stressed here that, due to minimal cell turnover, cells in the lens nucleus may be the longest-lived cells in the human body (Peterson and Delamere 1992). Please note that hypotheses presented in this review regarding the purported functions of cholesterol and CBDs are based on measurements for lens-lipid membranes and model lipid membranes—i.e., membranes without a protein component. In these measurements, we have mostly used electron paramagnetic resonance (EPR) spin-labeling methods. The unique abilities of these methods will first be described, to provide guidelines for a clear understanding of our experimental results and our interpretation of data.

EPR Spin-Labeling Approaches for Profiles of Lens-Lipid Membrane Properties

EPR spin-labeling methods provide a unique opportunity to determine the lateral organization of lipid bilayer membranes, including coexisting membrane domains or coexisting membrane phases (Ashikawa et al. 1994; Kawasaki et al. 2001; Raguz et al. 2008; Subczynski et al. 2007a, 2007b). These methods also provide a number of approaches to determine several important membrane properties as a function of bilayer depth, including alkyl-chain order (Marsh 1981), fluidity (Subczynski et al. 2010), hydrophobicity (Subczynski et al. 1994) and the oxygen diffusion-concentration product (called the "oxygen transport parameter") (Kusumi et al. 1982). In some cases, these properties can be obtained in coexisting membrane domains without the need for their physical separation (Subczynski et al. 2007a, 2010). We will briefly explain how EPR spin-labeling methods can be used to obtain profiles of the above-mentioned properties across lens-lipid membranes and simple model membranes, which resemble the basic lipid composition of lens membranes (Mainali et al. 2011b; Raguz et al. 2008, 2009; Widomska et al. 2007a).

In these studies, phospholipid- and cholesterol-analogue spin labels are incorporated in the membrane with the nitroxide moiety, which gives rise to the observed EPR signal, at specific depths and in specific membrane domains. The physical/chemical properties of the microenvironment in the immediate vicinity of the nitroxide are then characterized using EPR spectroscopic methods. The spin labels used here have molecular structures similar to phospholipids or cholesterol and, therefore, should approximate cholesterol–phospholipid and cholesterol–cholesterol interactions in the membrane as well as be distributed between different membrane domains similarly to parent molecules (Raguz et al. 2008, 2009; Widomska et al. 2007a). Figure 2 is a schematic drawing that shows possible cases of spin-label distribution that may be relevant to eye-lens-lipid membranes.

When the cholesterol concentration in the membrane is close to its solubility threshold, the entire membrane should be in the liquid-ordered-like phase. In this case, separate domains are not expected (Fig. 2a). Profiles of the order parameter, fluidity, hydrophobicity and the oxygen transport parameter can be obtained in this homogeneous membrane. In the case of membranes oversaturated with

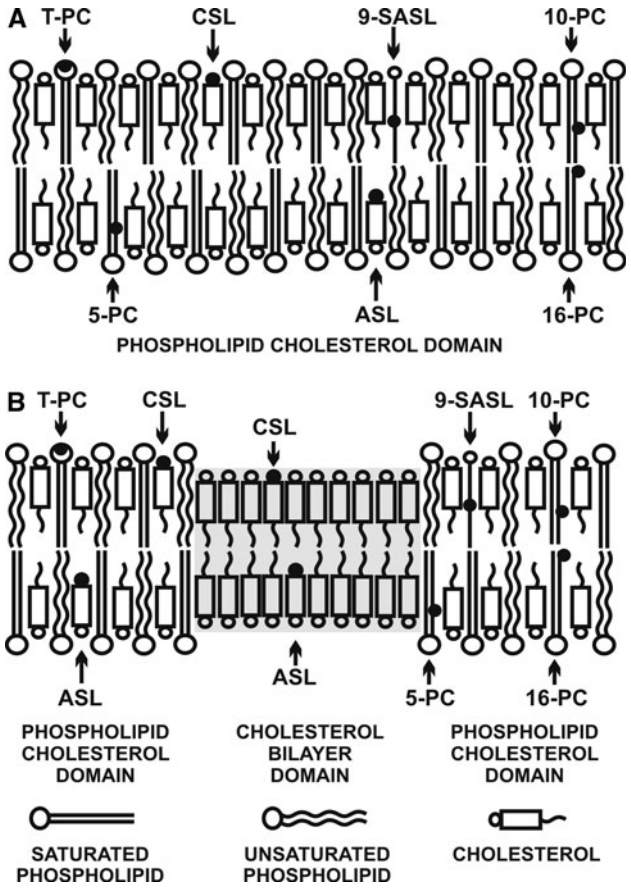

Fig. 2 Schematic drawings showing organization of lipids and spin-label distributions that may be relevant to eye-lens lipid membranes. The distribution and approximate localization of the nitroxide moiety of lipid spin labels (phospholipid analogues 5-, 10-, 16- T-PC and 9-SASL and cholesterol analogues ASL and CSL) in membranes with a cholesterol content close to the CST (**a**, model of the lens lipid membrane from young animals and the cortical membrane) and in membranes oversaturated with cholesterol, when the bulk PCD coexists with the CBD (**b**, model of the nuclear membrane). The nitroxide moieties of spin labels are indicated by *black dots*

cholesterol, in which CBDs are formed, the distribution of lipid spin labels is unique (Fig. 2b). The phospholipid-analogue spin labels should partition only into the bulk phospholipid cholesterol domain (PCD, the phospholipid cholesterol membrane saturated with cholesterol before formation of the CBD or the phospholipid cholesterol membrane coexisting with the CBD), and the cholesterol analogues should distribute between the two domains. Thus, only cholesterol-analogue spin labels can discriminate the two coexisting domains. The unique distribution of phospholipid-analogue spin labels allows profiles of the order parameter, fluidity, hydrophobicity and oxygen transport parameter to be obtained in the bulk PCD without "contamination" from the CBD. These two cases are relevant to lens-lipid membranes that are near the cholesterol solubility threshold (CST) in the lenses of young animals and in the cortex of lenses from older animals and humans (Fig. 2a) and are oversaturated with cholesterol (the coexisting CBD and PCD are present) in the lens nucleus (Fig. 2b).

The CBD Saturates the Surrounding Phospholipid Bilayer with Cholesterol

The lipid composition of the lens fiber-cell membrane changes as both humans and other animals age (Borchman et al. 1994; Broekhuyse 1973; Broekhuyse and Kuhlmann 1974, 1978; Huang et al. 2005; Li and So 1987; Li et al. 1985, 1987; Roy et al. 1982; Rujoi et al. 2003; Truscott 2000; Yappert et al. 2003). Usually, such notable changes would result in alteration of the physical properties of the membrane, which would then affect the function of proteins immersed in the lipid bilayer (Epand 2005). Based on results obtained for lens-lipid membranes from different species (a 6 month old calf and pig [Raguz et al. 2008; Widomska et al. 2007a]), from animals at different ages (6 month old and 2 year old cow and pig [Mainali et al. 2011b; Raguz et al. 2009; Widomska et al. 2007a]) and from different eye regions (the cortex and nucleus of a 2 year old cow and pig [Mainali et al. 2011b; Raguz et al. 2009]), we conclude that the extremely high (saturating) content of cholesterol in the fiber-cell membrane keeps the bulk physical properties of the lipid-bilayer portion of the membrane consistent and independent of changes in the phospholipid composition. The phospholipid composition of fiber-cell membranes significantly changes not only between species (Deeley et al. 2008; Yappert and Borchman 2004; Yappert et al. 2003) and with age (Yappert and Borchman 2004) but also between different regions of the lens (Li and So 1987; Li et al. 1987; Raguz et al. 2009). Surprisingly, independent of these differences, profiles of the bulk membrane properties across PCDs were very similar (practically identical) in all of the investigated membranes. Bulk membrane properties included the order parameter, fluidity, hydrophobicity and the oxygen transport parameter (oxygen diffusion-concentration product). As we stated in the Introduction, a similar conclusion was made by Borchman et al. (1996) using the structural order parameter as a measure of fluidity in bovine cortical and nuclear lens-lipid membranes. They showed that at a saturating amount of cholesterol the structural orders of nuclear and cortical membranes are very similar and concluded that the physiological role of cholesterol is to increase the structural order of cortical membrane lipids and to decrease the order of nuclear lipids so that the two membranes have a similar order. This finding agrees with our main conclusion.

To illustrate this conclusion, profiles of the order parameter (Fig. 3a–d), fluidity (Fig. 3e–h), hydrophobicity (Fig. 4a–d) and the oxygen transport parameter (Fig. 4e–h) across the PCD of the lens-lipid membrane from a 6 month old pig and calf (Figs. 3a, e and 4a, e) and from the cortex and nucleus of a 2 year-old pig (Figs. 3c, g and 4c, g) and cow (Figs. 3d, h and 4d, h) are presented. With this method, we can compare the differences between species as well as age-related and/or topographical differences, if any, in the bulk properties of the lens-lipid membrane. All profiles were obtained with phospholipid-type spin labels, which describe properties of the PCD. We should reiterate that in all investigated membranes the cholesterol content was close to or in excess of the CST. Small differences in the hydrophobicity profiles shown in Fig. 4a, d suggest that 6 month old pig and 2 year old cow cortex membranes are not yet saturated with cholesterol (Raguz et al. 2008, 2009).

All profiles for membranes with a saturating amount of cholesterol differ drastically from profiles across membranes without cholesterol. This is illustrated in Figs. 5a, d

Fig. 3 Independently of the differences in the phospholipid composition of lens-lipid membranes derived from the eyes of different species, different animal ages and different region of the lens, the profiles of the membrane order (the alkyl-chain order parameter) and the membrane dynamics (spin–lattice relaxation time) across these membranes are very similar. Profiles of the alkyl-chain order parameter (**a**–**d**) and the membrane fluidity (spin–lattice relaxation time, T_1, for deoxygenated samples) (**e**–**h**) obtained at 35°C across the PCD of lens-lipid membranes made of lipids extracted from a 6 month old pig and calf (**a**, **e**), a 6 month old pig after addition of excess cholesterol (**b**, **f**) and the cortex and nucleus of a 2 year old pig (**c**, **g**) and cow (**d**, **h**). Approximate localizations of the nitroxide moieties of spin labels are indicated by *arrows*. The order parameter is a measure of the amplitude of the wobbling motion of the alkyl-chain fragment to which the nitroxide moiety is attached (Hubbel and McConnell 1968), while T_1 depends primarily on the rate of motion of the nitroxide moiety within the lipid bilayer and, thus, describes the dynamics of the membrane environment at a depth at which the nitroxide fragment is located (Mainali et al. 2011a). Data compiled from Raguz et al. (2008, 2009) and Widomska et al. (2007a)

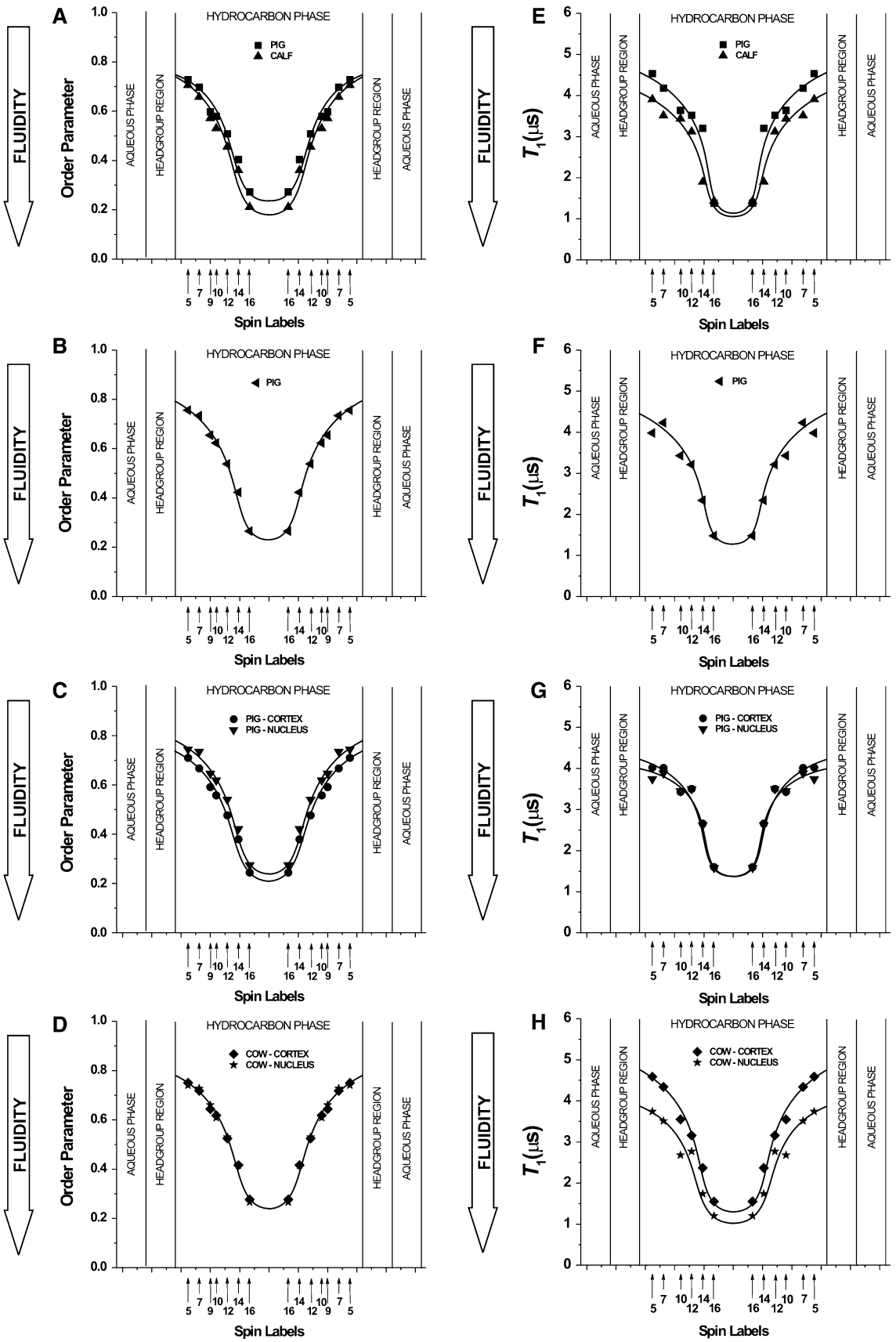
A
B
C
D
E
F
G
H
FLUIDITY
Order Parameter
T_1(μs)
HYDROCARBON PHASE
AQUEOUS PHASE
HEADGROUP REGION
HEADGROUP REGION
AQUEOUS PHASE
PIG
CALF
PIG - CORTEX
PIG - NUCLEUS
COW - CORTEX
COW - NUCLEUS
Spin Labels
5 7 9 10 12 14 16 16 14 12 10 9 7 5

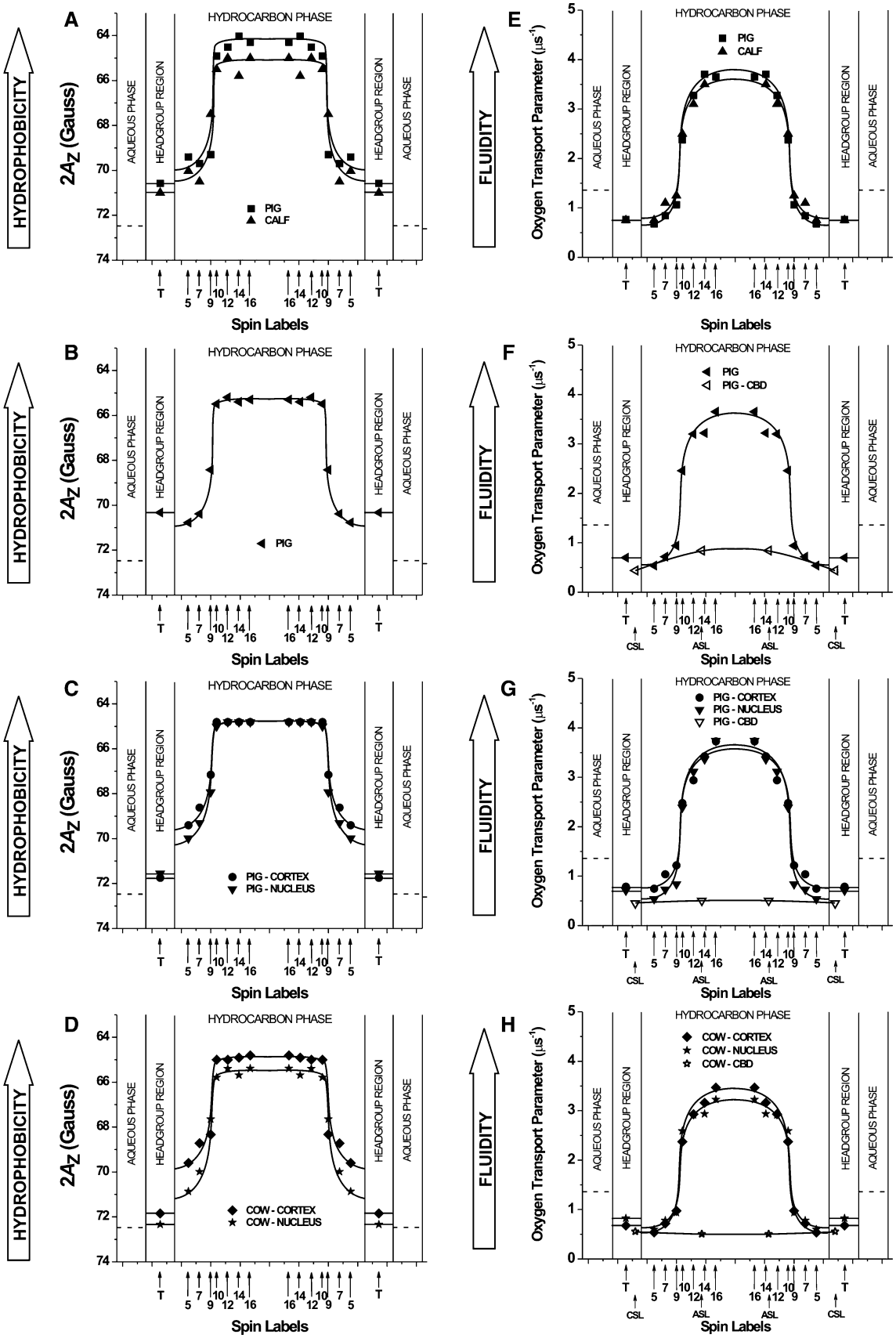
A
B
C
D
E
F
G
H
HYDROCARBON PHASE
AQUEOUS PHASE
HEADGROUP REGION
HYDROPHOBICITY
FLUIDITY
2Az (Gauss)
Oxygen Transport Parameter (μs-1)
Spin Labels
PIG
CALF
PIG - CBD
PIG - CORTEX
PIG - NUCLEUS
COW - CORTEX
COW - NUCLEUS
COW - CBD
CSL
ASL

◀ **Fig. 4** Independently of the differences in the phospholipid composition of lens-lipid membranes, all these membranes have a very similar shape of the hydrophobic barrier, with hydrophobicity in the membrane center close to that of hexane ($\varepsilon = 2$). Also, profiles of the oxygen transport parameters are nearly identical with low oxygen transport close to the membrane surface and high oxygen transport in the membrane center. Hydrophobicity profiles (obtained at −165°C) (**a**–**d**) and profiles of the oxygen transport parameter (obtained at 35°C) (**e**–**h**) across the PCD of lens-lipid membranes made of lipids extracted from a 6 month old pig and calf (**a**, **e**), a 6 month old pig after addition of cholesterol (**b**, **f**), and the cortex and nucleus of a 2 year old pig (**c**, **g**) and cow (**d**, **h**). Profiles of the oxygen transport parameter across the CBD, which is formed in lens-lipid membranes made of lipids extracted from a 6 month old pig after addition of cholesterol (**f**) and from the nucleus of a 2 year old pig (**g**) and a 2 year old cow (**h**), are also included. *Broken lines* indicate the appropriate value in the aqueous phase. Approximate localizations of nitroxide moieties of spin labels are indicated by *arrows*. Hydrophobicity profiles ($2A_Z$) are obtained for frozen samples to eliminate the motional contribution. Smaller $2A_Z$ values (upward changes in the profiles) indicate higher hydrophobicity. Usually, the local hydrophobicity as observed by $2A_Z$ is related to the hydrophobicity (or ε) of the bulk organic solvent by referring to Fig. 2 in Subczynski et al. (1994). An oxygen transport parameter was introduced as a convenient quantitative measure of the collision rate between the spin label and molecular oxygen (Kusumi et al. 1982). It is useful to monitor membrane fluidity, which reports on translational diffusion of small molecules. The oxygen transport parameter is normalized to an oxygen concentration that corresponds to the sample equilibrated with atmospheric air. Data compiled from Raguz et al. 2008, 2009) and Widomska et al. (2007a)

and 6a, d, where profiles for the POPC membrane and the POPC membrane saturated with cholesterol are shown; in Figs. 5b, e and 6b, e, which show profiles for the egg sphingomyelin (ESM) membrane and the ESM membrane saturated with cholesterol; and in Figs. 5c, f and 6c, f, which display profiles across the model membrane, made from a phospholipid mixture that resembles the composition of the pig lens-lipid membrane (Deeley et al. 2008), without cholesterol and saturated with cholesterol.

Profiles of the order parameter (Fig. 5a–c) indicated that in membranes saturated with cholesterol, including lens-lipid membranes (Fig. 3a–d), lipids are strongly ordered at all depths, which is in contrast to the low order of membranes without cholesterol (Fig. 5a–c). All profiles show a gradual decrease in alkyl-chain order with an increasing depth in the membrane. Values of the order parameter measured at the same depth are always significantly greater for membranes saturated with cholesterol than for membranes without cholesterol. Thus, an ordering effect of cholesterol in fluid-phase membranes is observed at all depths from the membrane surface to the membrane center. The order parameter, which is most often used as a measure of membrane fluidity, describes the amplitude of the wobbling motion of alkyl chains relative to the membrane normal and does not explicitly contain time or velocity (Hubbell and McConnell 1968). Thus, this parameter can be considered nondynamic.

The structural order determined by the static value of the *trans*/gauche rotamer ratio in the hydrocarbon chains (with special attention paid to the role of cholesterol) has been evaluated by other groups for lens-lipid membranes (Borchman et al. 1993, 1996, 1999). Thus, the structural order describes membrane properties averaged across membrane depths and domains, which is less informative than the profiles of the order parameter presented here. These profiles reflect the local order of hydrocarbon chains at different depths in the membrane.

The spin–lattice relaxation time (T_1) obtained from saturation-recovery EPR measurements of lipid spin labels in deoxygenated samples depends primarily on the rotational correlation time of the nitroxide moiety within the lipid bilayer. Thus, T_1 can be used as a convenient quantitative measure of membrane fluidity that reflects local membrane dynamics (Mainali et al. 2011a, b, c). T_1 profiles, which we call "profiles of membrane fluidity," obtained for membranes saturated with cholesterol (Fig. 5d–f), including lens-lipid membranes (Fig. 3e–h), are very similar. When compared with fluidity profiles without cholesterol (Fig. 5d–f), they reveal that cholesterol has a rigidifying effect only to the depth occupied by the rigid steroid-ring structure and a fluidizing effect at deeper locations. These effects cannot be differentiated by profiles of the order parameter.

Profiles of hydrophobicity (Fig. 6a–c) and the oxygen transport parameter (Fig. 6d–f) in membranes saturated with cholesterol and in lens-lipid membranes (Fig. 4a–h) have a characteristic rectangular shape with an abrupt change between the C9 and C10 positions, which is approximately where the rigid steroid-ring structure of cholesterol reaches into the membrane. At this position, hydrophobicity increases from the level of methanol to that of hexane and the oxygen transport parameter increases by a factor of ∼2.5 (from the level observed in gel-phase membranes to that observed in fluid-phase membranes). These profiles are bell-shaped in phospholipid membranes without cholesterol (Fig. 6a–f). These results indicate that a high, saturating cholesterol content is responsible for these unique profiles and unique properties of lens-lipid membranes. These profiles are also characteristic of liquid-ordered-phase membranes saturated with cholesterol (Mainali et al. 2011c, d; Subczynski et al. 1994, 2007b; Widomska et al. 2007a), which allows us to conclude that the entire PCD in the lens-lipid membrane is in the liquid-ordered-like phase.

The above conclusions were based on profiles obtained for lens-lipid membranes with Chol/PL molar ratios of ∼1, in which the CBD was not observed and lipids were organized as in Fig. 2a. Figures 3 and 4 contain profiles obtained for lens-lipid membranes with Chol/PL molar ratios of ∼2 (from the nucleus of 2 year old cow and pig

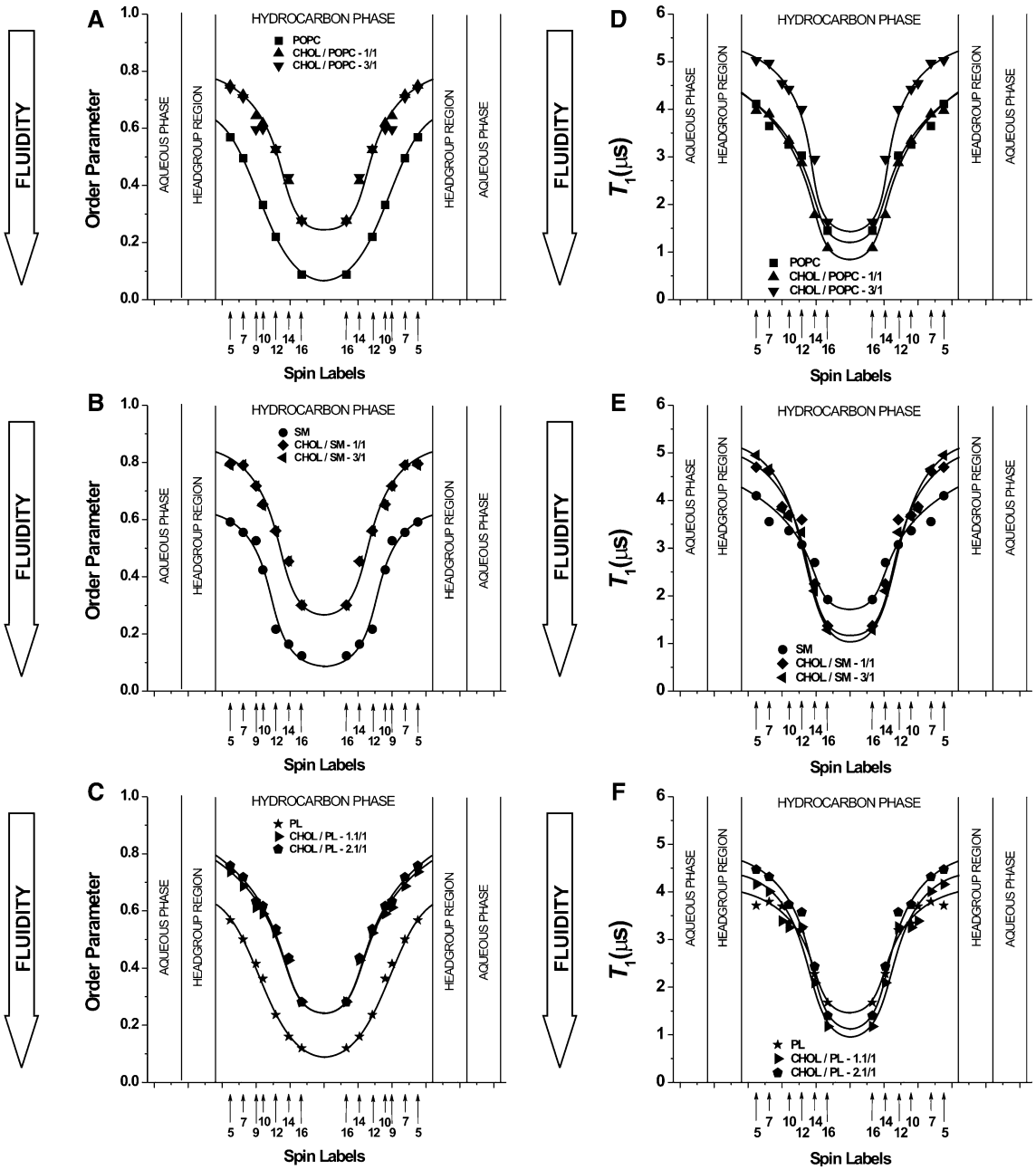

Fig. 5 An ordering effect of the saturating amount of cholesterol is observed at all depths from the membrane surface to the membrane center. However, profiles of membrane dynamics reveal that cholesterol has a rigidifying effect only to the depth occupied by the rigid steroid-ring structure and a fluidizing effect at deeper locations. Profiles of the alkyl-chain order parameter (**a**–**c**) and membrane fluidity (spin–lattice relaxation time, T_1, for deoxygenated samples) (**d**–**f**) obtained at 35°C across POPC membranes (**a**, **d**) without cholesterol (POPC) and with cholesterol at cholesterol/POPC mixing ratios of 1/1 (CHOL/POPC-1/1) and 3/1 (CHOL/POPC-3/1), across ESM membranes (**b**, **e**) without cholesterol (SM) and with cholesterol at cholesterol/SM mixing ratios of 2/1 (CHOL/SM-2/1) and 3/1 (CHOL/SM-3/1) and across model membranes made from a phospholipid mixture resembling the composition of the pig lens-lipid membrane (PL, 30% SM, 36% PC, 12% PE, 22% PS) (**c**, **f**) without cholesterol (PL), saturated with cholesterol at a cholesterol/PL mixing ratio of 1.1/1 (CHOL/PL-1.1/1) and oversaturated with cholesterol at a cholesterol/PL mixing ratio of 2.1/1 (CHOL/PL-2.1/1). Approximate localizations of nitroxide moieties of spin labels are indicated by *arrows*. Data compiled from Widomska et al. (2007a)

lens and from 6 month old pig lenses with the addition of excess cholesterol), in which the CBD was present and lipids were organized as in Fig. 2b. Profiles of the order parameter, fluidity, hydrophobicity and the oxygen transport parameter across the bulk PCD surrounding the CBD are very similar to those observed for membranes with a lower cholesterol content when the CBD is not yet observed. Similarly, profiles presented in Figs. 5 and 6 for

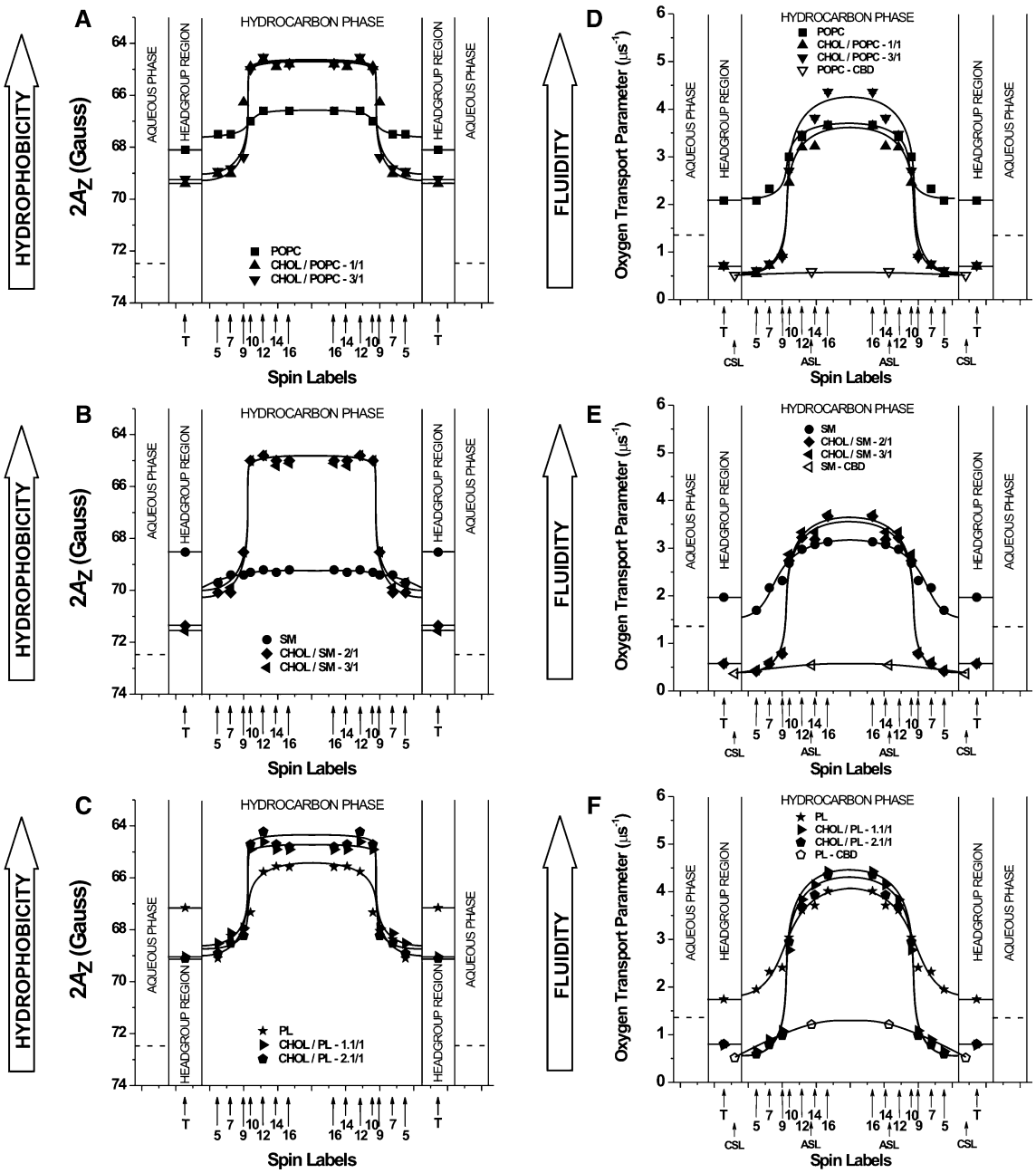

Fig. 6 The saturating amount of cholesterol is responsible for changing the bell-shaped hydrophobicity and oxygen transport parameter profiles to the rectangular shape with an abrupt change between C9 and C10 positions, which is approximately where the rigid steroid-ring structure of cholesterol reaches into the membrane. Hydrophobicity profiles (obtained at −165°C) (**a**–**c**) and profiles of the oxygen transport parameter (obtained at 35°C) (**d**–**f**) across POPC membranes (**a**, **d**), SM membranes (**b**, **e**) and model membranes resembling the pig lens-lipid membrane (**c**, **f**) with different cholesterol contents (see the caption for Fig. 5 for details). Profiles are also included of the oxygen transport parameter across the CBD, which is formed in the POPC membrane, with a cholesterol/POPC mixing ratio of 3/1 (**d**, POPC-CBD), the ESM membrane with a cholesterol/SM mixing ratio of 3 (**e**, SM-CBD) and across model membranes resembling the pig lens-lipid membrane oversaturated with cholesterol at a cholesterol/PL mixing ratio of 2.1/1 (**f**, PL-CBD). *Broken lines* indicate the appropriate value in the aqueous phase. Approximate localizations of nitroxide moieties of spin labels are indicated by *arrows*. Data compiled from Widomska et al. (2007a) and Mainali et al. (2011b)

model membranes with saturating amounts of cholesterol (the CBD was not yet present) and profiles for the same membranes containing coexisting PCDs and CBDs were nearly indistinguishable.

These data suggest that the CBD has some function specific to the fiber-cell plasma membrane. The CBD provides buffering capacity for cholesterol concentration in the surrounding phospholipid bilayer, keeping it at a

constant saturating level and, thus, keeping the physical properties of the membrane consistent and independent of changes in phospholipid composition. Our conclusions are especially significant for human lenses because among mammalian lenses those from humans are of the longest life span and changes in lens phospholipid composition with age are most pronounced (Estrada et al. 2010). Human lens fiber cells undergo minimal cell turnover. They do not regenerate, and cells in the center of the nucleus of an adult human lens are as old as the individual. Membrane proteins that perform several functions in young human lenses perform the same functions in older lenses with altered phospholipid compositions. Thus, the CBD plays a crucial role in maintaining homeostasis of the lens membrane, the only membranous structure of mature fiber cells.

Phospholipid Composition Controls Formation of the CBD

Phospholipids surrounding the CBD cannot affect the properties of its interior because it is a pure cholesterol bilayer (Raguz et al. 2011a, b). However, the phospholipid composition of the fiber-cell plasma membrane can determine the cholesterol concentration at which the CBD is formed. This is a new and uninvestigated mechanism through which cholesterol-dependent processes in the eye lens could be regulated. Our hypothesis is based on the fact that the threshold of cholesterol solubility (expressed here as a Chol/PL molar ratio) differs significantly for simple phospholipid membranes. The values for Chol/PS, Chol/PC, Chol/PE and Chol/SM are 1/2, 1/1, 1/1 and 2/1, respectively (Bach and Wachtel 2003; Epand 2003; Epand et al. 2002; Huang et al. 1999). Here, PS, PC, PE and SM are phosphatidylserine, phosphatidylcholine, phosphatidylethanolamine and ESM, respectively. Above these concentrations, cholesterol forms CBDs in these membranes. PS, PC, PE and SM are major lens phospholipids in humans and other animals (Deeley et al. 2008). Figure 7 presents the hypothetical phase diagram for the mixtures of these lens phospholipids, which shows the cholesterol concentration above which the CBD is formed. It is assumed that the CST value in the phospholipid mixture is a weighted sum of individual thresholds with a weight equal to the mole fraction of the individual phospholipid in the mixture. Thus, the CBD can be formed, depending on the composition of the mixture, already at a cholesterol concentration of 33 mol% (for PS membranes [Raguz et al. 2011a]) up to a cholesterol concentration of 66 mol% (for SM membranes [Mainali et al. 2011d]).

Based on these differences in the CST in different phospholipid bilayers, we can speculate that in animals with a long life span the phospholipid composition of the

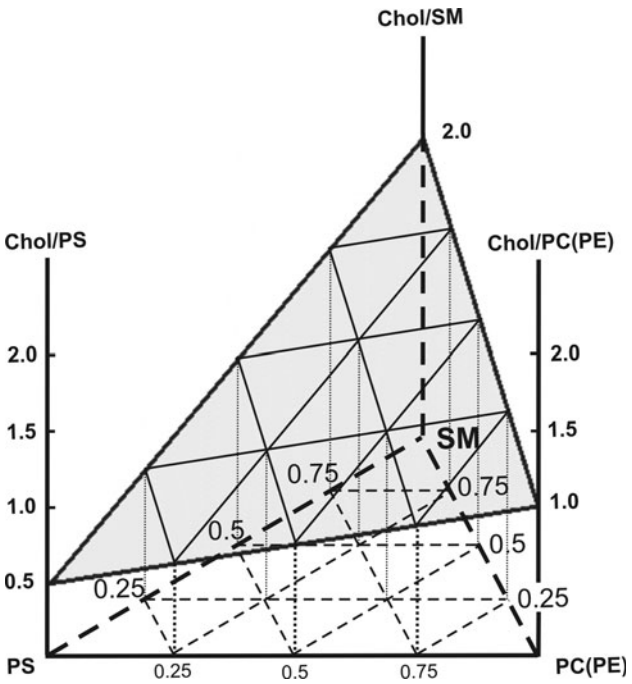

Fig. 7 Hypothetical phase diagram for mixtures of the most abundant lens phospholipids (PS, PC, PE and SM, including dihydrosphingomyelin) and cholesterol. *Shaded surface* indicates the CST for the mixture. For cholesterol contents above this surface, the CBD is formed. It is assumed that the CST value in the phospholipid mixture is a weighted sum of CSTs for individual phospholipids with a weight equal to the mole fraction of the individual phospholipid in the mixture. CSTs in PS, PC, PE and SM membranes are taken from Bach and Wachtel (2003), Epand (2003), Epand et al. (2002) and Huang et al. (1999)

lens membrane (Deeley et al. 2008) ensures formation of CBDs at significantly higher cholesterol concentrations than in animals with a shorter life span. This is illustrated in Fig. 8, where the evaluated value of the CST in the lens-lipid membranes of different animals is plotted as a function of animal life span. It is worth noting that in animals (including humans), the lens phospholipid composition changes with age in a way that delays formation of the CBD. For example, in human lenses the most notable age-related trend is the preferential depletion of glycerophospholipids in older fiber cells and the consequent enrichment of sphingolipids (Yappert and Borchman 2004; Yappert et al. 2003). Thus, the CST in lens-lipid membranes from old donors should be greater than that for young donors. The cholesterol content in lens membranes also increases with age, reaching conditions for CBD formation at a certain age. Thus, the delicate balance between changes in the lens-membrane phospholipid composition and changes in the cholesterol content controls the formation of the CBD. It is also possible that the size of the CBD and the cholesterol exchange rate between the CBD and the PCD are controlled by the lens-membrane phospholipid composition. Most unexpectedly, recent

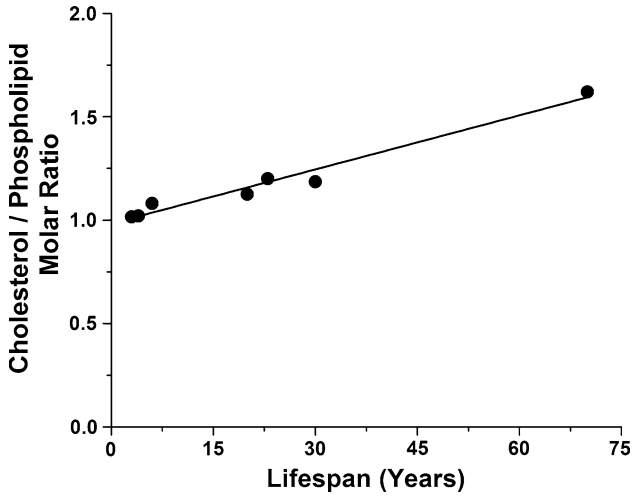

Fig. 8 The relationship between the CST in the lens-lipid membrane and the maximum life spans for different species. CSTs (above these cholesterol contents the CBD should be formed) for lens-lipid membranes were evaluated based on the phospholipid compositions taken from Deeley et al. (2008) and the phase diagram presented in Fig. 7. Points are for mouse (3), rat (4), chick (6), sheep (20), pig (23), cow (30) and human (70) (maximum life-span values are indicated in *parentheses*)

results have shown the high dynamics of cholesterol molecules in the CBD (Raguz et al. 2011a, b), which differ from the rigid organization of cholesterol molecules in cholesterol crystals (Borochov et al. 1995; Cheetham et al. 1989; Epand 2003; Knoll et al. 1985; Mason et al. 2003; Wachtel et al. 1991). This new molecular-level data will help us to better understand the physiological functions of CBDs.

Adult human lenses exhibit extremely high cholesterol contents, with a Chol/PL molar ratio as high as 4, which is much higher than in the lenses of other animals and young humans (Li et al. 1985, 1987; Rujoi et al. 2003; Zelenka 1984). This suggests that in humans, because of an increased amount of sphingolipids, CBDs are formed in aged lenses (first in the lens nucleus, where the cholesterol content is extremely high), while in animals with a shorter life span, the phospholipid composition (high amounts of PS, PC and PE) allows formation of CBDs at much lower cholesterol concentrations (see Deeley et al. 2008 for animal-lens phospholipid compositions).

The CBD Forms a Barrier to Oxygen Transport

Oxygen concentration in the lens is very low, reaching a value close to zero in the lens nucleus (Eaton 1991; Harding 1991; McNulty et al. 2004). Detailed information about oxygen distribution within the lens is scarce: a few measurements have been made that report oxygen partial pressures in the human anterior cortex as low as 0.8–4.0 mmHg (Helbig et al. 1993). At the lens surface, oxygen concentration is low as well (Fig. 1); values of ~ 3 and ~ 9 mmHg have been reported, respectively, at the surface of the anterior and posterior cortex of the lens in the healthy eye (Barbazetto et al. 2004; Bassnett and McNulty 2003; Beebe 2008; Briggs and Rodenhauser 1973; Fitch et al. 2000; Jacobi and Driest 1966; Ormerod et al. 1987; Shui et al. 2006; Siegfried et al. 2010). An increase in oxygen concentration in the lens is thought to be responsible for cataract formation (Borchman et al. 2000; Chung et al. 2001; Freel et al. 2003; Harocopos et al. 2004; Hsuan et al. 2001; Huang et al. 2006, 2008; Palmquist et al. 1984). Thus, understanding the processes that control oxygen transport, concentration and distribution in the lens is very important.

Because oxygen is constantly consumed and oxygen consumption reactions are located inside the eye lens (McNulty et al. 2004), it is concluded that there must be a gradient in the oxygen concentration across fiber-cell layers that builds the eye lens and creates oxygen flux into the lens interior (Fig. 1). Oxygen consumption is necessary to maintain a low oxygen concentration inside the eye lens (otherwise the concentration of oxygen would be equal to that outside the lens). Mitochondrial respiration accounts for approximately 90% of oxygen consumption by the lens (McNulty et al. 2004). This suggests that the outer layers of cortical fiber cells (not yet mature and containing organelles, including mitochondria) could be responsible for a low oxygen concentration in the lens nucleus. Some investigators have proposed that the major function of mitochondria in the lens cortex is not to generate ATP but to maintain lens clarity by keeping the oxygen content very low and preventing proteins and lipids from being oxidized (McNulty et al. 2004). The value of the oxygen concentration difference across certain fiber-cell layers is determined by the rate of oxygen consumption by cells confined inside this concentric fiber-cell layer and the oxygen permeability coefficient of the cell layer. A hypothetical high barrier to oxygen permeation located at the fiber-cell plasma membrane should help to keep oxygen concentration within the eye lens at a very low level. This is especially important for the lens nucleus. A high barrier to oxygen permeation can help to lower oxygen partial pressure in this region to even below that in the cortex if a system to remove oxygen from the nucleus exists. This system should depend on nonmitochondrial oxygen consumption and can be formed by ascorbate- (Eaton 1991; McNulty et al. 2004) or glutathione-dependent oxygen consumption reactions (Beebe et al. 2011). High barriers formed by the membranes of nuclear fiber cells can help to maintain a low oxygen partial pressure in the lens nucleus even at a very low oxygen consumption rate (Fig. 1 helps to illustrate oxygen diffusion into the lens). It should be

stressed that oxygen must pass through thousands of fiber-cell membranes on its way from the lens surface to its center and a very small oxygen concentration difference across each membrane can significantly contribute to the oxygen concentration gradient across the eye lens. Evaluation of how the main lipid domains of fiber-cell membranes contribute to the resistance to oxygen transport into the lens interior is a timely task.

Values of the permeability coefficients for oxygen across the calf (Widomska et al. 2007b), porcine (Raguz et al. 2008), bovine (Raguz et al. 2009) and pig (Mainali personal communication) bulk PCD of the lens-lipid membrane have been reported. At 37°C, they lay in the region from 57.2 to 69.2 cm/s, compared with a value of 69.3 cm/s across a water layer of the same thickness as the membrane. These measurements provide the upper limits for oxygen permeability across the PCD in intact fiber-cell membranes because proteins located in native membranes can decrease oxygen permeability. These problems were discussed by Widomska et al. (2007a).

Oxygen transport across the lens membrane is also affected by CBDs that are formed in the oxygen-permeable lipid bilayer portion of the fiber-cell membrane (Raguz et al. 2008, 2009). However, details of oxygen transport across the CBD are not known and need explanation. As indicated in Fig. 2b, only cholesterol-analogue spin labels, androstane spin label (ASL) and cholestane spin label (CSL), can probe the CBD located within the bulk PCD. Values of the oxygen transport parameter obtained with ASL and CSL for the CBD allowed us to draw an approximate profile of the oxygen transport parameter across this domain (Figs. 4f–h and 6d–f) and calculate its permeability coefficient for oxygen as described in Raguz et al. (2008) and Widomska et al. (2007b). At 37°C, these values lay in the region from 34.4 to 42.5 cm/s, compared with the value of 85.9 cm/s across a water layer of the same thickness as the CBD. The CBD is significantly thinner than the bulk PCD. These data strongly suggest that the major permeability barrier for oxygen transport into the lens interior in the lipid bilayer portion of the fiber-cell plasma membrane is located at the CBD. This should help to maintain a low oxygen concentration in the lens interior and, especially, in the human lens nucleus, where the Chol/PL mole ratio is as high as 4 (Li et al. 1985, 1987) and the CBD should occupy a significant part of the membrane surface. Interestingly, age-related changes in the lipid composition of the human lens (Borchman et al. 1994; Huang et al. 2005; Li et al. 1985, 1987; Rujoi et al. 2003; Truscott 2000) indicate that the resistance of the fiber-cell plasma membrane to oxygen permeation should increase with age and should be greater in the lens nucleus than in the lens cortex (see also discussions in Raguz et al. 2008, 2009; Widomska et al. 2007a, b).

Saturation with Cholesterol Smoothes the Surface of Lens-Lipid Membranes

Another significant structural feature of lens-lipid membranes is the notable steepness of the profiles of the oxygen transport parameter (Fig. 4e–h). These profiles were obtained at 37°C when the lens-lipid membranes (which are saturated with cholesterol) were in the fluid phase. In these membranes, the oxygen transport parameter from the membrane surface to the depth of the ninth carbon is as low as in gel-phase membranes and at locations deeper than the ninth carbon as high as in fluid-phase model membranes without cholesterol. This very sharp (~2.5 times) increase in the oxygen transport parameter occurs within the distance of one carbon–carbon bond (i.e., 1.3–1.5 Å) along the alkyl chain. This transition is smooth and bell-shaped for membranes without cholesterol (Fig. 6d–f) or that contain a small cholesterol concentration (~30 mol%) (Subczynski et al. 1989, 1991, 1998, 2003, 2007b). Abrupt changes that occur in the properties of the fluid-phase membrane are difficult to explain unless it is assumed that at a saturating cholesterol content (1) vertical fluctuations of membrane components are much smaller than in membranes without cholesterol, (2) alignment of all membrane components is high and (3) all cholesterol rings are immersed to the same membrane depth, which is close to the position of C9 in phospholipid alkyl chains. These findings also indicate that by using saturation-recovery EPR and lipid spin labels the main features of the oxygen transport parameter profile can practically be obtained at atomic resolution. Models created through molecular-dynamics simulations (Plesnar et al. 2011) also confirm that saturation with cholesterol narrows the distribution of vertical positions of atoms in phospholipid and cholesterol molecules at any bilayer depth and, as a result, smoothes the membrane surface. Bettelheim and Paunovic (1979) suggested that in a clear human lens most light scattering comes from fiber-cell membranes, whose refractive index is higher than that of the surrounding cytoplasm. Based on this suggestion and data described above, we hypothesize that cholesterol-induced smoothing of the membrane surface should decrease light scattering and help to maintain lens transparency.

Permeability Barriers and Hydrophobic Channels in Membranes Saturated with Cholesterol

The lipid bilayer represents the fundamental permeability barrier to the nonspecific passage of polar molecules into and out of a cell due to its high hydrophobicity. The incorporation of saturating amounts of cholesterol into lens-lipid membranes ensures the rectangular shape of the

hydrophobicity profile across the PCD, with the hydrophobicity in the membrane center comparable to that in hexane and dipropylamine (ε from 2 to 3) (Fig. 4a–d). This greatly increases the activation energy required for polar and small ionic molecules to pass through the membrane. Thus, the rate-limiting step for the permeability of small polar molecules is likely to be the process of crossing the hydrophobic barrier at the membrane center.

The incorporation of saturating amounts of cholesterol also creates resistance to the permeation of small hydrophobic molecules (like oxygen) across the membrane. To better illustrate the transport of oxygen and other small hydrophobic molecules within the lens-lipid membrane saturated and oversaturated with cholesterol, we constructed Fig. 9, in which the inverse of the oxygen transport parameter (which is a measure of resistance to oxygen permeation [Widomska et al. 2007b]) is plotted as a function of the position across the lens-lipid cortical and nuclear membrane of a 2 year old cow. It can be seen that in the PCD of cortical and nuclear membrane, a rather high permeability barrier to oxygen transport is located in the polar headgroup region and, in the hydrophobic region, to the depth of the ninth carbon, which is approximately where the rigid steroid-ring structure of cholesterol reaches into the membrane. Resistance to oxygen permeation in this region is much higher than resistance in the water phase. However, resistance to oxygen permeation in the membrane center is much less than in the water phase and comparable to the resistance in pure phospholipid membranes (see profile for pure POPC bilayer included in Fig. 9). Thus, the rate-limiting step for permeation of small, nonpolar molecules across the membrane (including molecular oxygen) is likely to be the process of crossing the rigidity barrier located near the membrane surface (Raguz et al. 2008, 2009; Widomska et al. 2007b). Similar conclusions can be made for the PCDs of other lens-lipid membranes.

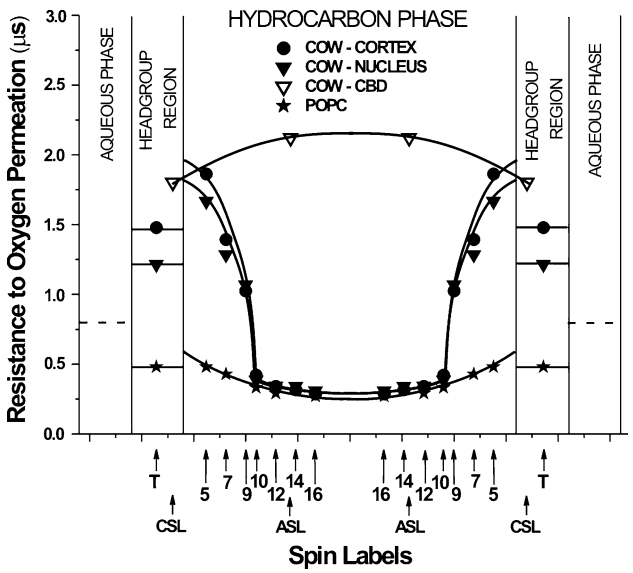

Fig. 9 Profiles of the resistance to oxygen permeation (the inverse of the oxygen transport parameter) across the PCD of lens-lipid membranes made of lipids extracted from the cortex and nucleus of a 2 year old cow at 35°C are plotted to show the oxygen permeability barriers. The profile across the CBD that is formed in lens-lipid membranes made of lipids extracted from a 2 year old cow is also included. To emphasize the effect of cholesterol, the profile of the resistance to oxygen permeation across the pure POPC membrane is shown. The resistance to oxygen permeation in the aqueous phase is indicated as a *broken line*. Oxygen transport parameter values were taken from Fig. 4d, h

These results indicate that the locations of permeation barriers are different for polar and nonpolar molecules. For polar molecules, the major resistance to permeation is the hydrophobic barrier in the central part of the membrane. For nonpolar molecules, the major resistance to permeation is the rigidity barrier near the membrane surface. We can conclude that cholesterol has some functions specific to lens fiber-cell membranes, which are saturated or oversaturated with cholesterol. Since the layers of fiber cells separate the lens interior from the external environment, the membrane barrier must be very high to block nonspecific permeation of small molecules across the membrane into the lens interior. Incorporation of cholesterol into the membrane serves this purpose well because cholesterol simultaneously raises the hydrophobic barrier for polar molecules and increases the rigidity barrier for nonpolar molecules.

Figure 9 also includes the profile of resistance to oxygen permeation across the CBD, coexisting with the PCD, in the nuclear membrane. The resistance to oxygen permeation in this domain is higher than in water and in the surrounding PCD at all depths. In the membrane center, the difference between resistance in the CBD and the PCD is as great as seven times.

Results presented in this review can help us to better understand the molecular nature of the internal barrier to diffusion of small molecules that is formed in the human lens during middle age and is hypothesized to be a key event in the development of age-related nuclear cataract (Moffat et al. 1999; Sweeney and Truscott 1998). The binding of denatured proteins to the fiber-cell membrane as the mechanism responsible for the barrier (Friedrich and Truscott 2009) (possibly by occluding membrane pores and channels) is more probable than a recent hypothesis which states that changes in membrane lipids with age may be responsible (Deeley et al. 2010). The latter mechanism was proposed based on results that revealed that sphingomyelin levels increased with age in the barrier region, until reaching a plateau at approximately 40 years of age. Deeley et al. state that such changes in lipid composition will have a significant impact on the physical properties of

fiber-cell membranes. This contrasts with our conclusion that membrane properties, including barrier properties, are independent of phospholipid composition until the membrane is saturated with cholesterol. However, when the cholesterol concentration is low (~30 mol%), these membranes (especially those composed of saturated sphingomyelin) can be very rigid (Borchman et al. 1996; Kusumi et al. 1986; Wisniewska and Subczynski 2008).

The striking similarity between profiles of the oxygen transport parameter (Figs. 4e–h and 6d–f) and profiles of hydrophobicity (Figs. 4a–d and 6a–c) in lens-lipid membranes and model membranes saturated with cholesterol suggests a possibility for lateral transport of molecular oxygen and other small, nonpolar molecules along the inner core of the membrane (parallel to the membrane surface), which is referred to as "hydrophobic channeling." As shown in Fig. 9, the resistance to the transport of oxygen and other small, hydrophobic molecules in the membrane center is much lower than in the water phase and the solubility of small, hydrophobic molecules is much higher (as indicated by the high hydrophobicity in this region [Figs. 4a–d and 6a–c]). To better illustrate the phenomenon of hydrophobic channeling in lens-lipid membranes, we constructed Fig. 10, in which we display the temperature dependence of the permeability coefficient for oxygen across the membrane region, where the major

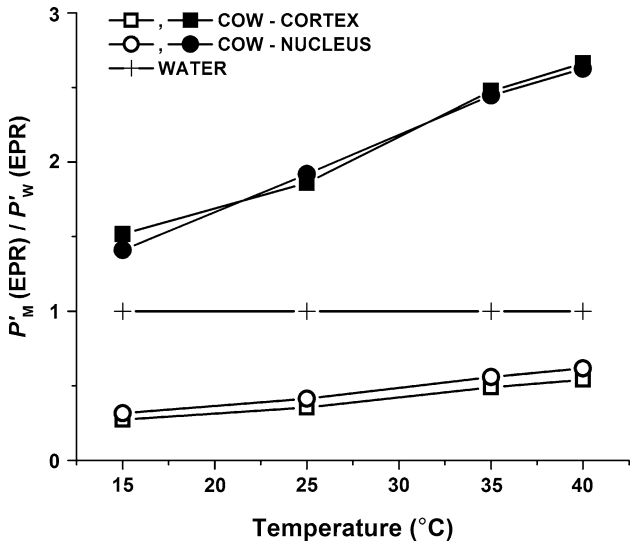

Fig. 10 The permeability coefficient for oxygen across a specific membrane region, P'_M(EPR), relative to that across a water layer of the same thickness as the membrane region, P'_W(EPR)—i.e., P'_M(EPR)/P'_W(EPR)—for cortical and nuclear lens-lipid membranes of a 2 year old cow plotted as a function of temperature. Both P'_M(EPR) and P'_W(EPR) were obtained by the EPR method. *Open symbols* indicate the membrane region from the membrane surface to the depth of the ninth carbon (measurements with T-PC, 5-PC, 7-PC and 9-SASL), and *closed symbols* indicate the membrane region between the tenth carbons in each membrane leaflet (measurements with 10-, 12-, 14- and 16-PC)

resistance to oxygen permeation is located (from the membrane surface to the depth of the ninth carbon), and for the membrane center, where oxygen transport is enhanced (between the tenth carbons in each leaflet). To compare the permeability properties of certain membrane regions with those of water, we display these data as a ratio of oxygen permeability across the appropriate membrane region to oxygen permeability across a water layer of the same thickness. We observed that centers of membranes saturated with cholesterol (both lens lipid and model) can serve as channels for oxygen transport as they have a much higher oxygen permeability than water. To escape from these channels, oxygen has to cross high barriers, with low oxygen permeability existing on both sides of the membrane. Additionally, the activation energy for oxygen translational diffusion in the lens-lipid membrane is significantly greater in the region where the rigidity barrier is located than in the membrane center (Raguz et al. 2009). This supports our hypothesis that in the lens-lipid membrane a high cholesterol content is responsible for creating hydrophobic channels for oxygen transport parallel to the membrane surface and, at the same time, a high cholesterol content is responsible for creating the rigidity barrier to oxygen transport across the membrane.

Finally, the following question is raised: Is high cholesterol content in the fiber-cell plasma membrane beneficial or harmful to the lens? We addressed this "conflict" of membrane properties in the paper entitled "Membranes: Barriers or Pathways for Oxygen Transport" (Subczynski and Hyde 1998). This conflict is evident in the eye lens, where the barrier to oxygen transport created by fiber-cell plasma membranes can be beneficial, helping to maintain low oxygen partial pressure in the lens nucleus. On the other hand, the hydrophobic channel makes it possible for the system of fiber-cell membranes to form conduits for oxygen molecules from the anterior and posterior surfaces into the deeper regions of the lens. This phenomenon could be harmful to the lens, especially when the low oxygen level around the lens is disturbed. Such an event can occur after vitrectomy, when the partial pressure of oxygen at the posterior of the human lens increases to ~13 mmHg (Siegfried et al. 2010). This increase in oxygen partial pressure is associated with rapid (less than 2 years) opacification of the lens nucleus. Also, in older individuals, when the structure of the vitreous body breaks down (Harocopos et al. 2004), decreasing the rate of ascorbate-dependent oxygen consumption within the vitreous fluid (Shui et al. 2009), the posterior of the lens is exposed to the increased oxygen partial pressure (Beebe et al. 2011). In these conditions, pathways for oxygen transport provided by the fiber-cell membranous system supply more oxygen to the lens center, disturbing the delicate balance between oxygen consumption and oxygen delivery and increasing

oxygen partial pressure in the lens nucleus, which, as a consequence, leads to cataract development.

Concluding Remarks

In our opinion, the amount of data collected for lens-lipid membranes and model membranes saturated and oversaturated with cholesterol is sufficient to determine the significant functions of cholesterol and CBDs specific to the fiber-cell plasma membranes of the eye lens. Mechanisms of these functions, which manifest themselves through cholesterol-induced changes in the properties and organization of the lipid bilayer portion of the fiber-cell plasma membrane, are explained on the molecular level. This was possible thanks to the abilities of molecular probe methods (EPR spin labeling) using phospholipid- and cholesterol-analogue spin labels. The local information coming from the small nitroxide moiety (attached to a specific position of the lipid molecules) allowed us to build a fairly complete three-dimensional dynamic structure of the lens lipid membrane and to obtain three-dimensional distribution of membrane properties. In this case, "three-dimensional" means the ability to get information about the lateral organization of the membrane (including coexisting domains) and to obtain membrane properties in each domain as a function of the third dimension (namely, the membrane depth).

We are aware of the limitations of the conclusions and hypotheses presented in this review, which were made based on measurements using lens-lipid membranes formed from lipids extracted from eye lenses. Intact eye-lens membranes are loaded with membrane proteins, which raises questions and concerns as to what extent the conclusions presented above can apply. These concerns outline the future direction of our work, which requires that experiments are performed with intact membranes and, possibly, with simple reconstituted membranes made of lens-lipid extracts and lens-membrane proteins.

Our study of the functions of cholesterol in simple models should also help us to better understand its functions in intact membranes. Such steps in the investigation of the properties and organization of the lipid-bilayer portion of fiber-cell plasma membranes are necessary. Without this research, it is not possible to understand clearly the mechanisms by which intrinsic proteins affect the properties of the lipid bilayer. We will investigate the properties of the lipid-bilayer portion of intact lens membranes further; but it is not an easy task, and it will take some time to clarify existing methodological problems before results can be obtained with the same confidence we have in our lens-lipid membrane measurements. However, based on data from the literature and our own studies, we can predict major changes in the properties of the lipid-bilayer portion of intact fiber-cell plasma membranes (which are dense with integral membrane proteins) compared to the properties of lens-lipid membranes. Lipids around monomers of integral membrane proteins are more immobilized than bulk lipids (Jost et al. 1973; Ryba et al. 1987), and even more immobilized are lipids trapped within aggregates of integral membrane proteins (Ashikawa et al. 1994). Additionally, oxygen permeability across boundary and bulk lipid domains is strongly reduced (Ashikawa et al. 1994; Kawasaki et al. 2001). Because proteins are nearly impermeable to oxygen (Altenbach et al. 1994; Subczynski et al. 1992), the effective oxygen permeability coefficient across the fiber-cell plasma membrane should be equal to the oxygen permeability coefficient evaluated for the lipid-bilayer portion of the membrane multiplied by a factor proportional to the surface area of the lipid-bilayer portion and divided by the surface area of the entire membrane. Thus, we can conclude that the intact fiber-cell membrane forms a significantly greater barrier to oxygen permeation than the lens-lipid membrane.

At this stage, the conclusions presented here are valid for model membranes, and our investigations have filled a gap in membrane research by providing profiles of physical properties across membranes saturated and oversaturated with cholesterol. Profiles are also valid for membranes that contain a small amount of membrane proteins, where the amount of bulk lipids exceeds the amount of lipids in immediate contact with proteins.

Acknowledgements This work was supported by grants EY015526, TW008052, EB002052 and EB001980 of the National Institutes of Health.

References

Altenbach C, Greenhalgh DA, Khorana HG, Hubbell WL (1994) A collision gradient method to determine the immersion depth of nitroxides in lipid bilayers: application to spin-labeled mutants of bacteriorhodopsin. Proc Natl Acad Sci USA 91:1667–1671

Ashikawa I, Yin J-J, Subczynski WK, Kouyama T, Hyde JS, Kusumi A (1994) Molecular organization and dynamics in bacteriorhodopsin-rich reconstituted membranes: discrimination of lipid environments by the oxygen transport parameter using a pulse ESR spin-labeling technique. Biochemistry 33:4947–4952

Bach D, Wachtel E (2003) Phospholipid/cholesterol model membranes: formation of cholesterol crystallites. Biochim Biophys Acta 1610:187–197

Barbazetto IA, Liang J, Chang S, Zheng L, Spector A, Dillon JP (2004) Oxygen tension in the rabbit lens and vitreous before and after vitrectomy. Exp Eye Res 78:917–924

Bassnett S, McNulty R (2003) The effect of elevated intraocular oxygen on organelle degradation in the embryonic chicken lens. J Exp Biol 206:4353–4361

Beebe DC (2003) The lens. In: Kaufman PL (ed) Physiology of the eye. Mosby-Year Book, St. Louis, pp 117–158

Beebe DC (2008) Maintaining transparency: a review of the developmental physiology and pathophysiology of two avascular tissues. Semin Cell Dev Biol 19:125–133

Beebe DC, Holekamp NM, Siegfried C, Shui YB (2011) Vitreoretinal influences on lens function and cataract. Phil Trans R Soc Lond B Biol Sci 366:1293–1300

Bettelheim FA, Paunovic M (1979) Light scattering of normal human lens I. Application of random density and orientation fluctuation theory. Biophys J 26:85–99

Biswas SK, Lo WK (2007) Gap junctions contain different amounts of cholesterol which undergo unique sequestering processes during fiber cell differentiation in the embryonic chicken lens. Mol Vis 13:345–359

Biswas SK, Jiang JX, Lo WK (2009) Gap junction remodeling associated with cholesterol redistribution during fiber cell maturation in the adult chicken lens. Mol Vis 15:1492–1508

Biswas SK, Lee JE, Brako L, Jiang JX, Lo WK (2010) Gap junctions are selectively associated with interlocking ball-and-sockets but not protrusions in the lens. Mol Vis 16:2328–2341

Borchman D, Yappert MC (2010) Lipids and the ocular lens. J Lipid Res 51:2473–2488

Borchman D, Delamere NA, Cauley LA, Paterson CA (1989) Studies on the distribution of cholesterol, phospholipid and protein in the human and bovine lens. Lens Eye Exp Res 6:703–724

Borchman D, Lamba OP, Yappert MC (1993) Structural characterization of lipid membranes from clear and cataractous human lenses. Exp Eye Res 57:199–208

Borchman D, Byrdwell WC, Yappert MC (1994) Regional and age-dependent differences in the phospholipid composition of human lens membranes. Invest Ophthalmol Vis Sci 35:3938–3942

Borchman D, Cenedella RJ, Lamba OP (1996) Role of cholesterol in the structural order of lens membrane lipids. Exp Eye Res 62:191–197

Borchman D, Tang D, Yappert MC (1999) Lipid composition, membrane structure relationships in lens and muscle sarcoplasmic reticulum membranes. Biospectroscopy 5:151–167

Borchman D, Giblin FJ, Leverenz VR, Reddy VN, Lin LR, Yappert MC, Tang D, Li L (2000) Impact of aging and hyperbaric oxygen in vivo on guinea pig lens lipids and nuclear light scatter. Invest Ophthalmol Vis Sci 41:3061–3073

Borchman D, Yappert MC, Afzal M (2004) Lens lipids and maximum lifespan. Exp Eye Res 79:761–768

Borochov N, Wachtel EJ, Bach D (1995) Phase behavior of mixtures of cholesterol and saturated phosphatidylglycerols. Chem Phys Lipids 76:85–92

Briggs D, Rodenhauser JH (1973) Distribution and consumption of oxygen in the vitreous body of cats. In: Kessler M (ed) Oxygen supply: theoretical and practical aspects of oxygen supply and microcirculation of tissue. University Park Press, Baltimore, pp 265–269

Broekhuyse RM (1973) Membrane lipids and proteins in aging lens and cataract. Ciba Found Symp 19:135–149

Broekhuyse RM, Kuhlmann ED (1974) Lens membranes 1. Composition of urea-treated plasma membranes from calf lens. Exp Eye Res 19:297–302

Broekhuyse RM, Kuhlmann ED (1978) Lens membranes. IV. Preparative isolation and characterization of membranes and various membrane proteins from calf lens. Exp Eye Res 26:305–320

Cenedella RJ (1996) Cholesterol and cataracts. Surv Ophthalmol 40:320–337

Cheetham JJ, Wachtel E, Bach D, Epand RM (1989) Role of the stereochemistry of the hydroxyl group of cholesterol and the formation of nonbilayer structures in phosphatidylethanolamines. Biochemistry 28:8928–8934

Chung CP, Hsu SY, Wu WC (2001) Cataract formation after pars plana vitrectomy. Kaohsiung J Med Sci 17:84–89

de Vries AC, Cohen LH (1993) Different effects of the hypolipidemic drugs pravastatin and lovastatin on the cholesterol biosynthesis of the human ocular lens in organ culture and on the cholesterol content of the rat lens in vivo. Biochim Biophys Acta 1167: 63–69

Deeley JM, Mitchell TW, Wei X, Korth J, Nealon JR, Blanksby SJ, Truscott RJ (2008) Human lens lipids differ markedly from those of commonly used experimental animals. Biochim Biophys Acta 1781:288–298

Deeley JM, Hankin JA, Friedrich MG, Murphy RC, Truscott RJ, Mitchell TW, Blanksby SJ (2010) Sphingolipid distribution changes with age in the human lens. J Lipid Res 51:2753–2760

Eaton JW (1991) Is the lens canned? Free Radic Biol Med 11: 207–213

Epand RM (2003) Cholesterol in bilayers of sphingomyelin or dihydrosphingomyelin at concentrations found in ocular lens membranes. Biophys J 84:3102–3110

Epand RM (2005) Role of membrane lipids in modulating the activity of membrane-bound enzymes. In: Yeagle PL (ed) The structure of biological membrane. CRC Press, Boca Raton, pp 499–509

Epand RM, Bain AD, Sayer BG, Bach D, Wachtel E (2002) Properties of mixtures of cholesterol with phosphatidylcholine or with phosphatidylserine studied by ^{13}C magic angle spinning nuclear magnetic resonance. Biophys J 83:2053–2063

Estrada R, Puppato A, Borchman D, Yappert MC (2010) Reevaluation of the phospholipid composition in membranes of adult human lenses by ^{31}P NMR and MALDI MS. Biochim Biophys Acta 1798:303–311

Fitch CL, Swedberg SH, Livesey JC (2000) Measurement and manipulation of the partial pressure of oxygen in the rat anterior chamber. Curr Eye Res 20:121–126

Fleschner CR, Cenedella RJ (1991) Lipid composition of lens plasma membrane fractions enriched in fiber junctions. J Lipid Res 32: 45–53

Freel CD, Gilliland KO, Mekeel HE, Giblin FJ, Costello MJ (2003) Ultrastructural characterization and Fourier analysis of fiber cell cytoplasm in the hyperbaric oxygen treated guinea pig lens opacification model. Exp Eye Res 76:405–415

Friedrich MG, Truscott RJ (2009) Membrane association of proteins in the aging human lens: profound changes take place in the fifth decade of life. Invest Ophthalmol Vis Sci 50:4786–4793

Harding JJ (1991) Cataract, biochemistry, epidemiology and pharmacology. Chapman and Hall, London

Harocopos GJ, Shui YB, McKinnon M, Holekamp NM, Gordon MO, Beebe DC (2004) Importance of vitreous liquefaction in age-related cataract. Invest Ophthalmol Vis Sci 45:77–85

Helbig H, Hinz JP, Kellner U, Foerster MH (1993) Oxygen in the anterior chamber of the human eye. Ger J Ophthalmol 2:161–164

Hsuan JD, Brown NA, Bron AJ, Patel CK, Rosen PH (2001) Posterior subcapsular and nuclear cataract after vitrectomy. J Cataract Refract Surg 27:437–444

Huang J, Buboltz JT, Feigenson GW (1999) Maximum solubility of cholesterol in phosphatidylcholine and phosphatidylethanolamine bilayers. Biochim Biophys Acta 1417:89–100

Huang L, Grami V, Marrero Y, Tang D, Yappert MC, Rasi V, Borchman D (2005) Human lens phospholipid changes with age and cataract. Invest Ophthalmol Vis Sci 46:1682–1689

Huang L, Estrada R, Yappert MC, Borchman D (2006) Oxidation-induced changes in human lens epithelial cells. 1. Phospholipids. Free Radic Biol Med 41:1425–1432

Huang L, Yappert MC, Jumblatt MM, Borchman D (2008) Hyperoxia and thyroxine treatment and the relationships between reactive oxygen species generation, mitochondrial membrane potential, and cardiolipin in human lens epithelial cell cultures. Curr Eye Res 33:575–586

Hubbell WL, McConnell HM (1968) Spin-label studies of the excitable membranes of nerve and muscle. Proc Natl Acad Sci USA 61:12–16

Jacob RF, Cenedella RJ, Mason RP (1999) Direct evidence for immiscible cholesterol domains in human ocular lens fiber cell plasma membranes. J Biol Chem 274:31613–31618

Jacob RF, Cenedella RJ, Mason RP (2001) Evidence for distinct cholesterol domains in fiber cell membranes from cataractous human lenses. J Biol Chem 276:13573–13578

Jacobi KW, Driest J (1966) Oxygen determinations in the vitreous body of the living eye [in German]. Ber Zusammenkunft Dtsch Ophthalmol Ges 67:193–198

Jost PC, Griffith OH, Capaldi RA, Vanderkooi G (1973) Evidence for boundary lipid in membranes. Proc Natl Acad Sci USA 70:480–484

Kawasaki K, Yin J–J, Subczynski WK, Hyde JS, Kusumi A (2001) Pulse EPR detection of lipid exchange between protein rich raft and bulk domains in the membrane: methodology development and its application to studies of influenza viral membrane. Biophys J 80:738–748

Kirby TJ (1967) Cataracts produced by triparanol (MER-29). Trans Am Ophthalmol Soc 65:494–543

Knoll W, Schmidt G, Ibel K, Sackmann E (1985) Small-angle neutron scattering study of lateral phase separation in dimyristoylphosphatidylcholine-cholesterol mixed membranes. Biochemistry 24:5240–5246

Kusumi A, Subczynski WK, Hyde JS (1982) Oxygen transport parameter in membranes as deduced by saturation recovery measurements of spin-lattice relaxation times of spin labels. Proc Natl Acad Sci USA 79:1854–1858

Kusumi A, Subczynski WK, Pasenkiewicz-Gierula M, Hyde JS, Merkle H (1986) Spin-label studies on phosphatidylcholine-cholesterol membranes: effects of alkyl chain length and unsaturation in the fluid phase. Biochim Biophys Acta 854:307–317

Li LK, So L (1987) Age dependent lipid and protein changes in individual bovine lenses. Curr Eye Res 6:599–605

Li LK, So L, Spector A (1985) Membrane cholesterol and phospholipid in consecutive concentric sections of human lenses. J Lipid Res 26:600–609

Li LK, So L, Spector A (1987) Age-dependent changes in the distribution and concentration of human lens cholesterol and phospholipids. Biochim Biophys Acta 917:112–120

Mainali L, Feix JB, Hyde JS, Subczynski WK (2011a) Membrane fluidity profiles as deduced by saturation-recovery EPR measurements of spin-lattice relaxation times of spin labels. J Magn Reson 212:418–425

Mainali L, Raguz M, Camenisch TG, Hyde JS, Subczynski WK (2011b) Spin-label saturation-recovery EPR at W-band: applications to eye lens lipid membranes. J Magn Reson 212:86–94

Mainali L, Raguz M, Subczynski WK (2011c). Phases and domains in sphingomyelin-cholesterol membranes: structure and properties using EPR spin-labeling methods. Eur Biophys J. doi:10.1007/s00249-011-0766-4

Mainali L, Raguz M, Subczynski WK (2011d) Phase-separation and domain-formation in cholesterol-sphingomyelin mixture: pulse-EPR oxygen probing. Biophys J 101:837–846

Marsh D (1981) Electron spin resonance: spin labels. In: Grell E (ed) Membrane spectroscopy. Springer-Verlag, Berlin, pp 51–142

Mason RP, Tulenko TN, Jacob RF (2003) Direct evidence for cholesterol crystalline domains in biological membranes: role in human pathobiology. Biochim Biophys Acta 1610:198–207

McNulty R, Wang H, Mathias RT, Ortwerth BJ, Truscott RJ, Bassnett S (2004) Regulation of tissue oxygen levels in the mammalian lens. J Physiol 559:883–898

Moffat BA, Landman KA, Truscott RJ, Sweeney MH, Pope JM (1999) Age-related changes in the kinetics of water transport in normal human lenses. Exp Eye Res 69:663–669

Mosley ST, Kalinowski SS, Schafer BL, Tanaka RD (1989) Tissue-selective acute effects of inhibitors of 3-hydroxy-3-methylglutaryl coenzyme A reductase on cholesterol biosynthesis in lens. J Lipid Res 30:1411–1420

Ormerod LD, Edelstein MA, Schmidt GJ, Juarez RS, Finegold SM, Smith RE (1987) The intraocular environment and experimental anaerobic bacterial endophthalmitis. Arch Ophthalmol 105: 1571–1575

Palmquist BM, Philipson B, Barr PO (1984) Nuclear cataract and myopia during hyperbaric oxygen therapy. Br J Ophthalmol 68:113–117

Plesnar E, Subczynski WK, Pasenkiewicz-Gierula, M (2011). Saturation with cholesterol increases vertical order and smoothes the surface of the phosphatidylcholine bilayer: a molecular simulation study. Biochim Biophys Acta. doi:10.1016/j.bbamem.2011.10.023

Paterson CA, Zeng J, Husseini Z, Borchman D, Delamere NA, Garland D, Jimenez-Asensio J (1997) Calcium ATPase activity and membrane structure in clear and cataractous human lenses. Curr Eye Res 16:333–338

Peterson CA, Delamere NA (1992) The lens. In: Hart WM Jr (ed) Physiology of the eye. Mosby-Year Book, St. Louis, pp 348–390

Rafferty NS (1985) Lens morphology. In: Maisel H (ed) The ocular lens: structure, function and pathology. Marcel Dekker, New York, pp 1–60

Raguz M, Widomska J, Dillon J, Gaillard ER, Subczynski WK (2008) Characterization of lipid domains in reconstituted porcine lens membranes using EPR spin-labeling approaches. Biochim Biophys Acta 1778:1079–1090

Raguz M, Widomska J, Dillon J, Gaillard ER, Subczynski WK (2009) Physical properties of the lipid bilayer membrane made of cortical and nuclear bovine lens lipids: EPR spin-labeling studies. Biochim Biophys Acta 1788:2380–2388

Raguz M, Mainali L, Widomska J, Subczynski WK (2011a) The immiscible cholesterol bilayer domain exists as an integral part of phospholipid bilayer membranes. Biochim Biophys Acta 1808:1072–1080

Raguz M, Mainali L, Widomska J, Subczynski WK (2011b). Using spin-label electron paramagnetic resonance (EPR) to discriminate and characterize the cholesterol bilayer domain. Chem Phys Lipids 164:819–829

Rouser G, Solomon RD (1969) Changes in phospholipid composition of human aorta with age. Lipids 4:232–234

Rouser G, Simon G, Kritchevsky G (1969) Species variations in phospholipid class distribution of organs. I. Kidney, liver and spleen. Lipids 4:599–606

Rouser G, Yamamoto A, Kritchevsky G (1971) Cellular membranes. Structure and regulation of lipid class composition species differences, changes with age, and variations in some pathological states. Arch Intern Med 127:1105–1121

Roy D, Rosenfeld L, Spector A (1982) Lens plasma membrane: isolation and biochemical characterization. Exp Eye Res 35: 113–129

Rujoi M, Jin J, Borchman D, Tang D, Yappert MC (2003) Isolation and lipid characterization of cholesterol-enriched fractions in cortical and nuclear human lens fibers. Invest Ophthalmol Vis Sci 44:1634–1642

Rujoi M, Estrada R, Yappert MC (2004) In situ MALDI-TOF MS regional analysis of neutral phospholipids in lens tissue. Anal Chem 76:1657–1663

Ryba NJ, Horvath LI, Watts A, Marsh D (1987) Molecular exchange at the lipid–rhodopsin interface: spin-label electron spin resonance studies of rhodopsin-dimyristoylphosphatidylcholine recombinants. Biochemistry 26:3234–3240

Shui YB, Fu JJ, Garcia C, Dattilo LK, Rajagopal R, McMillan S, Mak G, Holekamp NM, Lewis A, Beebe DC (2006) Oxygen distribution in the rabbit eye and oxygen consumption by the lens. Invest Ophthalmol Vis Sci 47:1571–1580

Shui YB, Holekamp NM, Kramer BC, Crowley JR, Wilkins MA, Chu F, Malone PE, Mangers SJ, Hou JH, Siegfried CJ, Beebe DC (2009) The gel state of the vitreous and ascorbate-dependent oxygen consumption: relationship to the etiology of nuclear cataracts. Arch Ophthalmol 127:475–482

Siegfried CJ, Shui YB, Holekamp NM, Bai F, Beebe DC (2010) Oxygen distribution in the human eye: relevance to the etiology of open-angle glaucoma after vitrectomy. Invest Ophthalmol Vis Sci 51:5731–5738

Subczynski WK, Hyde JS (1998) Membranes. Barriers or pathways for oxygen transport. Adv Exp Med Biol 454:399–408

Subczynski WK, Hyde JS, Kusumi A (1989) Oxygen permeability of phosphatidylcholine-cholesterol membranes. Proc Natl Acad Sci USA 86:4474–4478

Subczynski WK, Hyde JS, Kusumi A (1991) Effect of alkyl chain unsaturation and cholesterol intercalation on oxygen transport in membranes: a pulse ESR spin labeling study. Biochemistry 30:8578–8590

Subczynski WK, Renk GE, Crouch RK, Hyde JS, Kusumi A (1992) Oxygen diffusion-concentration product in rhodopsin as observed by a pulse ESR spin labeling method. Biophys J 63: 573–577

Subczynski WK, Wisniewska A, Yin J-J, Hyde JS, Kusumi A (1994) Hydrophobic barriers of lipid bilayer membranes formed by reduction of water penetration by alkyl chain unsaturation and cholesterol. Biochemistry 33:7670–7681

Subczynski WK, Lewis RN, McElhaney RN, Hodges RS, Hyde JS, Kusumi A (1998) Molecular organization and dynamics of 1-palmitoyl-2-oleoylphosphatidylcholine bilayers containing a transmembrane alpha-helical peptide. Biochemistry 37:3156–3164

Subczynski WK, Pasenkiewicz-Gierula M, McElhaney RN, Hyde JS, Kusumi A (2003) Molecular dynamics of 1-palmitoyl-2-oleoylphosphatidylcholine membranes containing transmembrane alpha-helical peptides with alternating leucine and alanine residues. Biochemistry 42:3939–3948

Subczynski WK, Widomska J, Wisniewska A, Kusumi A (2007a) Saturation-recovery electron paramagnetic resonance discrimination by oxygen transport (DOT) method for characterizing membrane domains. Methods Mol Biol 398:143–157

Subczynski WK, Wisniewska A, Hyde JS, Kusumi A (2007b) Three-dimensional dynamic structure of the liquid-ordered domain as examined by a pulse-EPR oxygen probing. Biophys J 92:1573–1584

Subczynski WK, Raguz M, Widomska J (2010) Studying lipid organization in biological membranes using liposomes and EPR spin labeling. Methods Mol Biol 606:247–269

Sweeney MH, Truscott RJ (1998) An impediment to glutathione diffusion in older normal human lenses: a possible precondition for nuclear cataract. Exp Eye Res 67:587–595

Truscott RJ (2000) Age-related nuclear cataract: a lens transport problem. Ophthalmic Res 32:185–194

Tulenko TN, Chen M, Mason PE, Mason RP (1998) Physical effects of cholesterol on arterial smooth muscle membranes: evidence of immiscible cholesterol domains and alterations in bilayer width during atherogenesis. J Lipid Res 39:947–956

Wachtel EJ, Borochov N, Bach D (1991) The effect of protons or calcium ions on the phase behavior of phosphatidylserine-cholesterol mixtures. Biochim Biophys Acta 1066:63–69

Widomska J, Raguz M, Dillon J, Gaillard ER, Subczynski WK (2007a) Physical properties of the lipid bilayer membrane made of calf lens lipids: EPR spin labeling studies. Biochim Biophys Acta 1768:1454–1465

Widomska J, Raguz M, Subczynski WK (2007b) Oxygen permeability of the lipid bilayer membrane made of calf lens lipids. Biochim Biophys Acta 1768:2635–2645

Wisniewska A, Subczynski WK (2008) The liquid-ordered phase in sphingomyelin-cholesterol membranes as detected by the discrimination by oxygen transport (DOT) method. Cell Mol Biol Lett. 13:430–451

Yappert MC, Borchman D (2004) Sphingolipids in human lens membranes: an update on their composition and possible biological implications. Chem Phys Lipids 129:1–20

Yappert MC, Rujoi M, Borchman D, Vorobyov I, Estrada R (2003) Glycero- versus sphingo-phospholipids: correlations with human and non-human mammalian lens growth. Exp Eye Res 76:725–734

Zelenka PS (1984) Lens lipids. Curr Eye Res 3:1337–1359

J Membrane Biol (2012) 245:69–75
DOI 10.1007/s00232-011-9414-2

ORIGINAL ARTICLES

Liposomes as a Model for the Biological Membrane: Studies on Daunorubicin Bilayer Interaction

Carla Matos · Carla Moutinho · Paulo Lobão

Received: 14 July 2011 / Accepted: 15 December 2011 / Published online: 1 January 2012

Abstract In this study the interaction of the antitumoral drug daunorubicin with egg phosphatidylcholine (EPC) liposomes, used as a cell membrane model, was quantified by determination of the partition coefficient (K_p). The liposome/aqueous-phase K_p of daunorubicin was determined by derivative spectrophotometry and measurement of the zeta-potential. Mathematical models were used to fit the experimental data, enabling determination of K_p. In the partition of daunorubicin within the membrane both superficial electrostatic and inner hydrophobic interactions seem to be involved. The results are affected by the two types of interaction since spectrophotometry measures mainly hydrophobic interactions, while zeta-potential is affected by both interpenetration of amphiphilic charged molecules in the bilayer and superficial electrostatic interaction. Moreover, the degree of the partition of daunorubicin with the membrane changes with the drug concentration, due mainly to saturation factors. Derivative spectrophotometry and zeta-potential variation results, together with the broad range of concentrations studied, revealed the different types of interactions involved. The mathematical formalism applied also allowed quantification of the number of lipid molecules associated with one drug molecule.

Keywords Biomimetics · Membrane · Drug interaction · Liposome · Absorption spectroscopy · Zeta-potential

C. Matos (✉) · C. Moutinho
Grupo de Investigação em Bioengenharia e Química Biofarmacêutica, Faculdade de Ciências da Saúde, Universidade Fernando Pessoa, Praça 9 de Abril no 349, 4249-004 Porto, Portugal
e-mail: cmatos@ufp.edu.pt

C. Moutinho
IBB–Instituto para a Biotecnologia e a Bioengenharia, Centro de Engenharia Biológica, Universidade do Minho, Campus de Gualtar, Braga, Portugal

P. Lobão
Laboratório de Tecnologia Farmacêutica, Faculdade de Farmácia da, Universidade do Porto, Rua Aníbal Cunha 164, 4050 Porto, Portugal

Introduction

Biological membranes act as a physiological barrier for a drug in its path to reach the site of action. The diffusion (through the phospholipidic cell membrane) is a key step in the absorption and distribution of a drug as well as, ultimately, its action in the organism. The molecule must enter the membrane within the polar headgroup region, diffuse through the lipophilic hydrocarbon double layer and emerge throughout the headgroup region on the inner side. Even in cases where a specific transporter is involved, the drug's ability to interact with the membrane is often highly correlated with the velocity or extent of the transportation. This ability depends on the drug's hydrophilic/lipophilic equilibrium, which can be quantitatively expressed as a partition coefficient.

The *n*-octanol/water partition coefficient ($K_{O/W}$) has been correlated with the hydrophobicity of drugs since the studies of Hansch and coworkers in the 1970s (Leo et al. 1971; Hansch and Dunn 1972). The *n*-octanol/water system, however, is only an approximation of the actual environment found in the interface between the cellular membranes and extracellular/intracellular fluids since it is an isotropic environment.

Liposomes are self-closed structures composed of amphiphilic lipids that form a bilayer encompassing an

aqueous compartment and have been extensively used as cell membrane models (Peetla et al. 2009). Liposomes present a membrane structure similar to the cellular one, in which the lipophilic hydrocarbon region is sandwiched between two ordered polar headgroup regions, and a system more appropriate for determining partition coefficients than the traditional *n*-octane/water method.

We studied the interaction of the antitumoral drug daunorubicin with the membrane of unilamellar liposomes composed of phosphatidylcholine. Daunorubicin (Fig. 1) is a natural antitumoral drug classified as an anthracycline, widely used to treat acute lymphocytic and granulocytic leukemia; but its use is restricted by its toxicity and multidrug resistance (MDR) (Agrawal et al. 2005). MDR is greatly dependent on the overexpression of P-glycoprotein (P-gp) multidrug transporter, which acts by decreasing intracellular drug concentrations through an ATP-dependent efflux of drug throughout the lipid bilayer (Romsicki and Sharom 1999). Being an integral membrane protein, the partition of the substrate into the bilayer before it interacts with the transporter is probably a requirement. Therefore, the binding affinity of drugs to P-gp is highly correlated with their ability to partition into the lipid membrane (Romsicki and Sharom 1999). Moreover, this ability determines the amount of drug which is able to effectively cross the cellular and nuclear membranes and reach the DNA and topoisomerase II, which are the main sites of action of daunorubicin (Gallois et al. 1996).

As daunorubicin is a positively charged molecule at physiological pH, it can interact electrostatically with the biological membrane and will probably display a much higher affinity for the lipid bilayer than supposed from the $K_{O/W}$. Electrostatic interaction of the positively charged anthracycline antibiotics with the negatively charged cardiolipin, a lipid abundant in heart tissue, is thought to be involved in drug localization in heart tissue and in the high cardiotoxicity observed with these drugs (Ratna and Burke 1995). On the other hand, the incorporation of an ionized drug into a neutral membrane modifies the membrane's surface charge density, restraining the access of more drug molecules to be incorporated and thus decreasing the apparent partition coefficient.

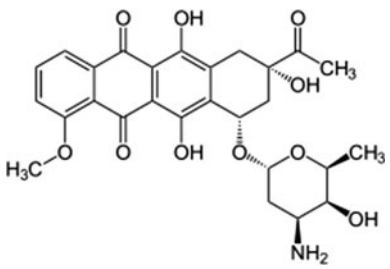

Fig. 1 Chemical structure of daunorubicin

In this context, the study of the mechanisms governing daunorubicin membrane interaction, either partitioning or electrostatic, is crucial.

Liposome/buffer partition coefficients (K_p) can be determined by different methods, including phase separation (for a comparative review on phase separation methods, consult Dipali et al. 1996). Since techniques used to separate the free drug from the liposome-encapsulated drug can potentially cause leakage of contents and, in some cases, uncertainty in the extent of separation, research using methods that do not rely on separation are of interest (Edwards and Baeumner 2006).

We used two different techniques to evaluate the K_p of daunorubicin without separation of phases: derivative spectrophotometry and zeta-potential evaluation.

Materials and Methods

Materials

Egg phosphatidylcholine (EPC) and daunorubicin were from Sigma (St. Louis, MO) and used as received. All other chemicals were from Merck (Darmstadt, Germany). Solutions were prepared with HEPES buffer (10 mM, $I = 0.1$ M, pH 7.4). The ionic strength was adjusted with NaCl.

Vesicle Preparation

Liposomes were prepared by the thin film hydration method. In this method, a solution of lipid in chloroform was evaporated to dryness with a stream of nitrogen. The lipid film, in an amount that would provide a final lipid concentration of around 2 mM, was then left under vacuum overnight to remove all traces of the organic solvent. The resultant dried lipid film was dispersed using HEPES buffer and the mixture vortexed to yield multilamellar vesicles (MLVs).

Lipid suspensions were equilibrated at 25°C for 30 min and further extruded 10 times (10 ml Lipex^{TM} Thermobarrel Extruder; Northern Lipids, Burnaby, Canada) through polycarbonate filters (Nucleopore, Pleasanton, CA) with a diameter pore of 100 nm, to form large unilamellar vesicles (LUVs, stock solution). The EPC concentration in all vesicle suspensions was determined by phosphate analysis using the Fiske and Subbarow phosphomolybdate method (McClare 1971).

Derivative Spectrophotometry

The EPC stock suspension was diluted to prepare a set of suspensions with different EPC concentrations (range

0–1,400 μM), in which the drug concentration was kept constant in each assay but varied between assays (10–85 μM). A set of "blank" suspensions was prepared for each assay. After a period of 2 h in the dark, at 25°C, to allow drug partition equilibrium to be established, the spectra of all suspensions were collected by means of a double-beam spectrophotometer (V-650; Jasco, Easton, MD), at 25°C. The second derivative spectra were calculated after spectra smoothing, with Origin 8.5.1 software (OriginLab, Northampton, MA), using 13 points for the derivative calculus. Partition coefficients were determined by performing a nonlinear fitting of the proposed mathematical model (Eq. 2) to the experimental data using the same computer software.

Zeta-Potential and Size Determinations

For these studies, EPC concentration was kept constant (460 μM) in all the suspensions of the set and drug concentration ranged from 0 to approximately 200 μM across the set.

Size distribution of the extruded vesicles was determined by quasi-elastic light scattering analysis (Malvern ZetaSizer 5000; Malvern Instruments, Malvern, UK), using a helium-neon laser (633 nm) as a source of incident light, operating at a scattering angle of 90° and a temperature of 25.0°C, assuming a medium viscosity of 0.89 cP and a medium refractive index of 1.33.

Theory/Calculations

Determination of Partition Coefficients by Derivative Spectrophotometry

The theoretical background for the determination of partition coefficients by derivative spectrophotometry has been described previously (Castro et al. 2001; Marcelino et al. 2007). Briefly, the technique is based on the evaluation of the discrete spectral variations presented by the drug in the presence of increasing lipid concentrations. The main drawback is the high degree of scattering presented by the lipid solutions in the ultraviolet region, which can be attenuated by spectra derivation, since scattering has a negligible effect on derivatives. Moreover, this technique increases the sensitivity of spectroscopy since spectral details are enhanced and overlapping bands are separated.

The liposome/buffer partition coefficient is defined as the ratio between the number of moles of membrane-bound drug (n_m) per liter of phospholipid and the number of moles of free drug (n_w) per liter of buffer. This relation can be expressed as a function of bound drug ($[A_m]$), free drug ($[A_w]$) and lipid ($[L]$) concentrations and the lipid molar volume (V_Φ).

$$K_p = \frac{n_m/V_L}{n_w/V_w} = \frac{[A_m]}{[A_w]\,[L]V_\Phi} \tag{1}$$

The derivative intensities can be related with the partition coefficient by the following expression (Castro et al. 2001):

$$\mathrm{Abs_T} = \mathrm{Abs_w} + \frac{(\mathrm{Abs_m} - \mathrm{Abs_w})\,K_p[L]\,V_\Phi}{1 + K_p[L]V_\Phi} \tag{2}$$

where $\mathrm{Abs_T}$, $\mathrm{Abs_m}$ and $\mathrm{Abs_w}$ are the total (solution of the drug-containing lipid), lipid and aqueous derivative absorbance of the drug, respectively; K_p is the partition coefficient; $[L]$ is the lipid concentration; and V_Φ is the lipid molar volume. For EPC, the mean molecular weight was considered to be 770 and $V_\Phi = 0.688\ \mathrm{M}^{-1}$ (White et al. 1987).

Determination of Partition Coefficients by Zeta-Potential

The experimentally determined zeta-potential values can also be used to calculate partition coefficients, using a mathematical formalism fully explained in Matos et al. (2004) and used with other charged molecules previously (Ferreira et al. 2005a, b). Basically, the theory is based on the assumption that the membrane charging is a consequence of the stepwise incorporation of the charged drug. The use of Gouy-Chapman theory allows for the calculation of the amount of charged drug that has entered the membrane. Considering that zeta-potential is the potential measured at 2 Å from the particle surface (Winiski et al. 1988; Eisenberg et al. 1979), one can calculate the parameter α, the membrane potential at 0 nm (Ψ_0), and the surface charge density (σ), using the set of mathematical relations described in detail in Matos et al. (2004). The number of charged molecules per area unit (σ^*) can be calculated since $\sigma^* = \sigma.\mathrm{N/F}$. The σ^* value can be used to calculate the molar concentration of a positively charged drug in the membrane ($[A_m^+]$) as

$$[A_m^+] = \frac{\sigma^*\,[L]a_L}{1 - \sigma^*\,a_A} \tag{3}$$

where a_L is the molecular surface area of the lipid, a_A is the molecular surface area of the drug (daunorubicin), N is the Avogadro number and F is the Faraday constant. The value used for a_L was 60 $\mathrm{Å}^2$ (Rooney et al. 1983) and that for a_A was 75 $\mathrm{Å}^2$ (Heywang et al. 1998).

The calculation of the free drug concentration can now be achieved using a mass balance ($[A^T] = [A_m^+] + [A_w^+]$) since the total amount of drug added to the system, $[A^T]$, is known

and the drug is mainly (94%) in its ionized form. The value for the partition coefficient, K_p, can be obtained using Eq. 1.

The values of σ^*_{max} (maximum number of charged molecules per area unit) can be obtained from the plot of σ^* versus $[A^T]$, fitting the binding isotherm (Connors 1987):

$$\theta = \frac{K_b[A^T]}{1 + K_b[A^T]} \quad (4)$$

in which θ, the degree of saturation, is given by $\theta = \sigma^*/\sigma^*_{max}$.

Knowledge of σ^*_{max} allows calculation of $\bar{n}$, the mole ratio of lipid/drug (Matos et al. 2004):

$$\sigma^*_{max} = \frac{1}{(a_A + \bar{n}\, a_L)} \quad (5)$$

Results

Determination of Partition Coefficients by Derivative Spectrophotometry

Second derivative absorption spectra of daunorubicin in the presence of increasing lipid concentrations are shown in Fig. 2, together with the second derivative spectra of the "blank" lipid suspensions. As can be observed, the interference caused by the presence of liposomes was completely eliminated with the second derivative. Usually, LUV suspensions cause strong Rayleigh light scattering, especially in the UV region, hampering spectroscopic data collection and making necessary the use of high derivative orders (third or fourth), with consequent loss of signal to noise ratio. However, as daunorubicin absorbs in the visible region, where scattering is minimal, the second derivative provides an adequate elimination of lipid effect.

An increase in the derivative peaks is observed when the lipid concentration changes from 0 to ca. 1,400 μM (drug concentration kept constant). The derivative spectra show the existence of isosbestic points, which can indicate the existence of equilibrium between drug in polar aqueous and in nonpolar EPC bilayer phases (Castro et al. 2001).

Data points from the drug spectra (Abs_T in Eq. 2) were collected at 539 nm, a wavelength where scattering elimination was effective and the drug presented an intense peak, in order to achieve the best signal to noise ratio.

Equation 2 was fitted to the experimental second derivative spectrophotometric data, using a nonlinear least-squares regression method (Fig. 3), at wavelengths where the scattering is completely eliminated. The value of K_p obtained in HEPES buffer (pH 7.4) for daunorubicin was 1,084 ± 206 (mean and standard deviation of seven independent assays), but there appeared to be a decrease in partition as drug concentration increased, as can be observed in Fig. 4.

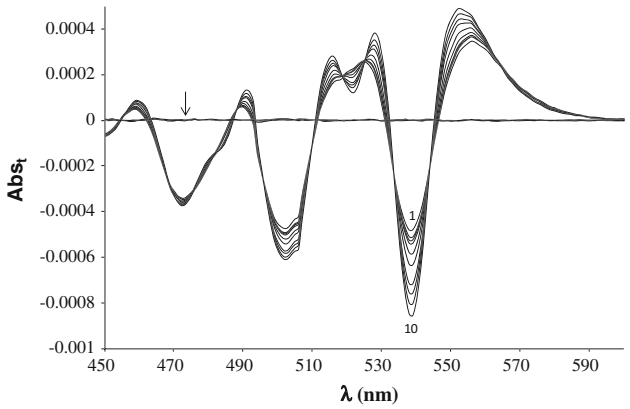

Fig. 2 Second derivative spectra of daunorubicin in different concentrations of EPC liposomes (from 0 [*1*] to 1,400 [*10*] μM), and of "blank" EPC liposomes (*arrow*)

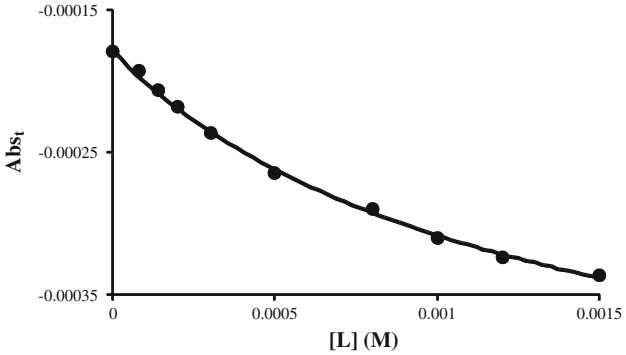

Fig. 3 Second-derivative spectrophotometric data at $\lambda = 539$ nm for daunorubicin in different concentrations of EPC liposomes. *Curve* represents best fit to Eq. 2

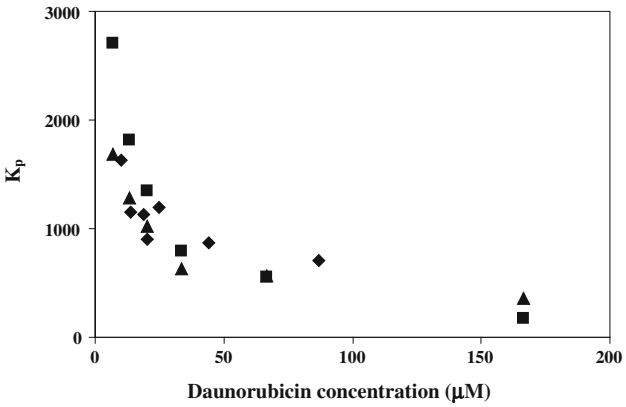

Fig. 4 Variation of partition coefficients on the concentration of daunorubicin obtained by derivative spectrophotometric (*diamonds*) and by zeta-potential measurements with (*triangles*) and without (*squares*) electrostatic effect corrections

Zeta-Potential and Size Determinations

The mean particle size of "blank" liposomes was 125 nm. Suspensions of liposomes with increasing concentrations of daunorubicin show a stepwise increase in vesicle diameter, reaching 305 nm for higher drug amounts. Similarly, results of zeta-potential for daunorubicin-incubated liposomes showed an increase from −7.2 to 1.3 mV (from 0 to 170 μM drug).

The variation of zeta-potential indicates that daunorubicin interacts with the membrane, causing a shift in its surface potential. The observed increase in size is too large to be considered only an expansion of the liposome due to drug incorporation and is probably affected by vesicle aggregation.

Comparison of Partition Coefficients Determined by Derivative Spectrophotometry and Zeta-Potential Variation

The results for partition coefficients determined by derivative spectrophotometry and zeta-potential variation are represented in Fig. 4 and Table 1, and two conclusions can be extracted:

1. For the lower drug concentrations (<20 μM), the K_p values obtained by zeta-potential evaluation (Fig. 4, squares) are around one-third higher than the ones obtained by derivative spectrophotometry (Fig. 5, diamonds). Since the liposome membrane is slightly negative in the absence of daunorubicin, the electrostatic superficial interaction (sensed mainly by zeta-potential) can be responsible for this difference. For higher drug concentrations, the partition of the positively charged daunorubicin, A^+, will lead to a neutralization of the membrane charge, this electrostatic attraction is diminished and the K_p values obtained by the two techniques are similar. Calculations of K_p were made (corrected) using the concentration of the charged form at the interface, $[A_i^+]$, instead of its bulk concentration, $[A_w^+]$. The value for $[A_i^+]$ can be obtained by the Boltzmann equation (McLaughlin and Harary 1976), and it is higher than $[A_w^+]$ due to the ionic attraction. Results for the corrected K_p (Fig. 4, triangles) show that the values obtained with this correction are not very different from the ones obtained with derivative spectrophotometry (diamonds).
2. A decrease in the partition coefficients can be observed as the drug concentration is increased. This decrease, although often described in the literature (Takegami et al. 2008), can be considered a deviation to the Nernst partition law since partition is an equilibrium state and the partition coefficient should be a constant. Such a decrease is probably due to a saturation effect: as the concentration of drug in the membrane increases, the maximum solubility of the drug in lipid is achieved and a minimum lipid/drug ratio is attained.

Table 1 Values for the liposome/buffer partition coefficients (K_p) obtained by two different methods: derivative spectrophotometry and zeta-potential determination

Derivative spectrophotometry		Zeta-potential determination		
Daunorubicin concentration (μM)	K_p	Daunorubicin concentration (μM)	K_p^a	K_p^b
10	1,631	7	2,702	1,690
14	1,150	13	1,820	1,284
19	1,131	20	1,349	1,024
25	1,198	33	796	628
44	872	67	551	568
87	703	167	174	356

In the case of results obtained with zeta-potential, K_p^a were calculated using the bulk drug concentration and K_p^b were calculated using the interfacial drug concentration, calculated by the Boltzmann equation

The values of σ^*_{max} (maximum number of charged molecules per area unit) can be obtained from the plot of σ^* versus $[A^T]$, fitting the binding isotherm (Eq. 4). Fitting is shown in Fig. 5. The value of σ^*_{max} obtained was 4.7×10^{-3} molecules/Å^2, while $\bar{n}$ was 29 molecules of lipid per molecules of drug.

Discussion

Daunorubicin is an amphoteric molecule, containing acidic functions (the ring phenolic groups) and a basic function (the sugar amino group). It is amphiphilic, the anthracycline ring being lipophilic and the sugar amino together with the hydroxyl groups being hydrophilic. The sugar amino group has a pK_a of 8.6 (Gallois et al. 1996), which, applying the

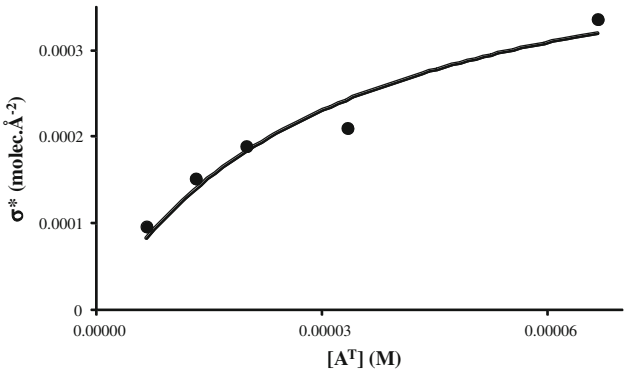

Fig. 5 Dependence of number of charged molecules per unit area (σ^*) on the concentration of daunorubicin at pH 7.4 in the presence of EPC. *Curve* represents best fit to Eq. 4

Henderson-Hasselbalch equation, gives a 94% positive ionization at the working pH value (7.4). Amphiphilic drugs that carry a positive charge can interact electrostatically with the negatively charged phosphate of the headgroup region of the bilayer, while the nonpolar portion inserts into the hydrophobic core. The overall result is an interfacial partitioning of the drug.

The daunorubicin partition in the membrane reflects the different types of interaction that an amphiphilic molecule can perform with a lipidic membrane, as a result of the structured bidimensional membrane, that holds a polarized superficial layer and a nonpolar inner core. This structure allows amphiphilic molecules to penetrate and orientate their polar part to the surface and nonpolar part to an inner position. Such an inner interaction can lead to a spectral modification as electronic distribution in the drug molecule is perturbed by the nonpolar environment, which can in extent lead to bathochromic effects, visible in the derivative spectra here presented.

On the other hand, a drug bearing a charged group can establish electrostatically driven interactions with positive or negative groups of the membrane, such as the negative phosphate or the positive amine groups. Such interactions appear, in the case of anthracyclines, to play a very important role in cardiotoxic effects (Ratna and Burke 1995).

Daunorubicin presents a spectral variation when it interacts with the membrane, which is an indication that the molecule establishes an inner partition. Nevertheless, an electrostatic interaction is also likely to occur, especially for lower drug concentrations, before membrane charging begins to cause electrostatic repulsion. Figure 4 shows that the results (squares) obtained by zeta-potential are higher than the results from derivative spectrophotometry (diamonds) for lower drug concentrations, possibly because of a superficial electrostatic attraction of the positive drug by the negative liposome. As drug concentration increases, this effect diminishes due to neutralization and then inversion of the liposome charge. When corrected for electrostatic effects, both techniques yield similar results. It appears that for lower drug concentrations (<20 μM), electrostatic interaction plays an important role in the interaction; for higher drug concentrations (>20 μM) the process is hydrophobically driven. Another finding was the decrease in K_p as drug concentration increases. That can be observed with the two techniques used and attributed to a saturation effect of the membrane, which is achieved when the lipid/drug ratio is around 30.

Gallois et al. (1996) determined the K_p for daunorubicin using negatively charged liposomes and found a value of 1,900 ± 540, which is higher than the values obtained in our study, probably due to some degree of electrostatic interaction as the positive drug can be attracted to the negative lipid. These authors also concluded that daunorubicin interaction does not depend on the drug's or liposome's charge, and in another study Gallois et al. (1998) detected only hydrophobic interactions by this molecule. These findings are probably due to the techniques used (fluorimetry and circular dichroism) or the drug concentration used (in fact, for higher drug concentrations there is only hydrophobic partition).

Conclusions

This article describes the interaction of daunorubicin with the membrane of EPC liposomes. In the interaction of daunorubicin with the membrane, both electrostatic and hydrophobic forces seem necessary for the stabilization of anthracyclines in the lipid bilayer. The determination of K_p by derivative spectrophotometry is based on the spectral changes occurring when drug and membrane interact and thus must reflect mostly the hydrophobic interaction. On the other hand, zeta-potential variations reflect a charge increase, caused by the partition of a charged molecule in the lipid bilayer.

Our results show that for lower drug concentrations (<20 μM) the electrostatic attraction to the membrane strongly accounts for the global partition coefficient, while for higher drug concentrations the hydrophobic interpenetration is the main single driven force for the interaction.

Another finding was the saturable nature of daunorubicin interaction within the membrane. In fact, a minimum of 30 lipid molecules seems to be necessary to dissolve each drug molecule in the bilayer environment.

References

Agrawal V, Paul MK, Mukhopadhyay AK (2005) 6-Mercaptopurine and daunorubicin double drug liposomes-preparation, drug–drug interaction and characterization. J Liposome Res 15:141–155

Castro B, Gameiro P, Lima JLFC, Matos C, Reis S (2001) A fast and reliable spectroscopic method for the determination of membrane–water partition coefficients of organic compounds. Lipids 36:89–96

Connors KA (ed) (1987) Binding constants. The measurement of molecular complex stability. Wiley, New York

Dipali SR, Kulkarni SB, Betageri GV (1996) Comparative study of separation of non-encapsulated drug from unilamellar liposomes by various methods. J Pharm Pharmacol 48:1112–1115

Edwards KA, Baeumner AJ (2006) Analysis of liposomes. Talanta 68:1432–1441

Eisenberg M, Gresalfi T, Riccio T, McLaughlin S (1979) Adsorption of monovalent cations to bilayer membranes containing negative phospholipids. Biochemistry 18:5213–5223

Ferreira H, Lucio M, Lima JLFC, Matos C, Reis S (2005a) Effects of diclofenac on EPC liposome membrane properties. Anal Bioanal Chem 382:1256–1264

Ferreira H, Lucio M, Lima JLFC, Matos C, Reis S (2005b) Interaction of clonixin with EPC liposomes used as membrane models. J Pharm Sci 94:1277–1287

Gallois L, Fiallo M, Laigle A, Priebe W, Garnier-Suillerot A (1996) The overall partitioning of anthracyclines into phosphatidyl-containing model membranes depends neither on the drug charge nor the presence of anionic phospholipids. Eur J Biochem 241: 879–887

Gallois L, Fiallo M, Garnier-Suillerot A (1998) Comparison of the interaction of doxorubicin, daunorubicin, idarubicin and idarubicinol with large unilamellar vesicles. Circular dichroism study. Biochim Biophys Acta 1370:31–40

Hansch C, Dunn WJ (1972) Linear relationships between lipophilic character and biological activity of drugs. J Pharm Sci 61:1–19

Heywang C, Chazalet MS, Masson M, Bolard J (1998) Orientation of anthracyclines in lipid monolayers and planar asymmetrical bilayers: a surface-enhanced resonance Raman scattering study. Biophys J 75:2368–2381

Leo A, Hansch C, Elkins D (1971) Partition coefficients and their uses. Chem Rev 71:525–552

Marcelino J, Lima JLFC, Reis S, Matos C (2007) Assessing the effects of surfactants on the physical properties of liposome membranes. Chem Phys Lipids 146:94–103

Matos C, Castro B, Gameiro P, Lima JLFC, Reis S (2004) Zeta-potential measurements as a tool to quantify the effect of charged drugs on the surface potential of EPC liposomes. Langmuir 20:369–377

McClare CWF (1971) An accurate and convenient organic phosphorus assay. Anal Biochem 39:527–530

McLaughlin S, Harary H (1976) The hydrophobic adsorption of charged molecules to bilayer membranes: a test of the applicability of the Stern equation. Biochemistry 15:1941–1948

Peetla C, Stine A, Labhasetwar V (2009) Biophysical interactions with model lipid membranes: applications in drug discovery and drug delivery. Mol Pharm 6:1264–1276

Ratna M, Burke TG (1995) Anthracycline antibiotics. New analogues methods of delivery and mechanisms of action. American Chemical Society, Washington, DC

Romsicki Y, Sharom FJ (1999) The membrane lipid environment modulates drug interactions with the P-glycoprotein multidrug transporter. Biochemistry 38:6887–6896

Rooney EK, East JM, Jones OT, McWhirter J, Simmonds AC, Lee AG (1983) Interaction of fatty acids with lipid bilayers. Biochim Biophys Acta 728:159–170

Takegami S, Kitamura K, Funakoshi T, Kitade T (2008) Partitioning of anti-inflammatory steroid drugs into phosphatidylcholine and phosphatidylcholine-cholesterol small unilamellar vesicles as studied by second-derivative spectrophotometry. Chem Pharm Bull 56:663–667

White SH, Jacobs RE, King GI (1987) Partial specific volumes of lipid and water in mixtures of egg lecithin and water. Biophys J 52:663–665

Winiski AP, Eisenberg M, Langner M, McLaughlin S (1988) Fluorescent probes of electrostatic potential 1 nm from the membrane surface. Biochemistry 27:386–392

J Membrane Biol (2012) 245:77–87
DOI 10.1007/s00232-012-9416-8

Downregulation of the Taurine Transporter TauT During Hypo-Osmotic Stress in NIH3T3 Mouse Fibroblasts

Daniel Bloch Hansen · Martin Barfred Friis · Else Kay Hoffmann · Ian Henry Lambert

Received: 8 July 2011 / Accepted: 26 January 2012 / Published online: 2 March 2012

Abstract The present work was initiated to investigate regulation of the taurine transporter TauT by reactive oxygen species (ROS) and the tonicity-responsive enhancer binding protein (TonEBP) in NIH3T3 mouse fibroblasts during acute and long-term (4 h) exposure to low-sodium/hypo-osmotic stress. Taurine influx is reduced following reduction in osmolarity, keeping the extracellular Na^+ concentration constant. TonEBP activity is unaltered, whereas TauT transcription as well as TauT activity are significantly reduced under hypo-osmotic conditions. In contrast, TonEBP activity and TauT transcription are significantly increased following hyperosmotic exposure. Swelling-induced ROS production in NIH3T3 fibroblasts is generated by NOX4 and by increasing total ROS, by either exogenous application of H_2O_2 or overexpressing NOX4, we demonstrate that TonEBP activity and taurine influx are regulated negatively by ROS under hypo-osmotic, low-sodium conditions, whereas the TauT mRNA level is unaffected. Acute exposure to ROS reduces taurine uptake as a result of modulated TauT transport kinetics. Thus, swelling-induced ROS production could account for the reduced taurine uptake under low-sodium/hypo-osmotic conditions by direct modulation of TauT.

Keywords NADPH oxidase · Hyponatremia · Osmolyte transport · Hypo-osmolal

Introduction

The ability to restore cell volume following osmotic perturbation is pivotal for cell function, and we have recently reviewed the intracellular signaling events evoked by cell swelling and cell shrinkage, as well as the biophysical and pharmacological characteristics of volume-sensitive transporters for organic and inorganic osmolytes (Hoffmann et al. 2009; Lambert et al. 2008). Mammalian cells restore their cell volume following osmotic perturbation; i.e., KCl, organic osmolytes (amino acids/sugars), and water are released to or taken up from the extracellular compartment following cell swelling and cell shrinkage, respectively (Hoffmann et al. 2009). The organic acid taurine is quantitatively an important osmolyte in mammalian cells, and even though taurine is mainly recognized through its contribution to the cellular pool of organic osmolytes, it has in recent years turned out that taurine modulates multiple cellular functions through stabilization of membrane integrity, modulation of ion channel activity, shifts in membrane phospholipid content and, hence, activity of enzymes embedded in the membrane (Jong et al. 2010) or elimination of reactive oxygen species (ROS) and thereby limitation in lipid peroxidation (Goodman et al. 2009). Taurine is taken up from the extracellular compartment via the Na^+-dependent taurine transporter TauT and released via a volume-sensitive leak pathway which is permeable to a range of organic osmolytes (Lambert and Hansen 2011; Hall et al. 1996; Lambert 2004). Expression of TauT is regulated by p53, c-Jun, WT1 (Wilms tumor gene 1) and TonEBP (Chesney et al. 2010; Lambert 2004), whereas

Electronic supplementary material The online version of this article (doi:10.1007/s00232-012-9416-8) contains supplementary material, which is available to authorized users.

D. B. Hansen · M. B. Friis · E. K. Hoffmann · I. H. Lambert (✉)
Department of Biology, Section of Cellular and Developmental Biology, University of Copenhagen, The August Krogh Building, Universitetsparken 13, 2100 Copenhagen Ø, Denmark
e-mail: ihlambert@bio.ku.dk

TauT activity is acutely controlled through direct phosphorylation/dephosphorylation of TauT and/or a regulator of TauT (Hansen et al. 2011; Jacobsen et al. 2008; Voss et al. 2004; Lambert 2004). The volume-sensitive leak pathway has not been cloned but is often referred to as the volume-sensitive organic anion channel (VSOAC) (Hansen et al. 2011; Lambert 2004).

ROS in limited quantities are considered essential second messengers, whereas ROS in larger quantities become harmful to cell function and cause cell damage and cell death. ROS production increases following osmotic cell swelling (Supplementary Fig. 2) (Diaz-Elizondo et al. 2006; Friis et al. 2008; Lambert 2003; Varela et al. 2004; Ørtenblad et al. 2003; Hansen et al. 2011) as well as osmotic cell shrinkage (Zhou et al. 2006; Yang et al. 2005; Eisner et al. 2006), and it has previously been shown that ROS potentiate the swelling-induced taurine release, presumably through inactivation of protein tyrosine phosphatases and, hence, an increase in the phosphorylation of tyrosine residues of enzymes involved in the activation of the volume-sensitive taurine transporter or the transporter itself (Hansen et al. 2011; Lambert 2003). It appears that NADPH oxidases constitute the catalytic core for ROS production under hypo-osmotic conditions (Friis et al. 2008), whereas ROS under hyperosmotic conditions are of mitochondrial origin (Zhou et al. 2006). Hyperosmotically induced transcription of TauT is under the control of the tonicity-responsive enhancer binding protein (TonEBP). TonEBP is transactivated by ROS under hyperosmotic conditions (Zhou et al. 2006), whereas TonEBP mRNA is reduced and TonEBP retained in the cytoplasm under hypo-osmotic conditions (Woo et al. 2000).

Hyponatremia involves several clinical conditions that affect as much as 22% of hospitalized patients (see Loh and Verbalis 2008). Hyponatremia results in decreased sodium plasma levels from approximately 150 to <135 mM and is often associated with hypo-osmolarity caused by excessive renal water retention (Wakil et al. 2011; Upadhyay and Gormley 2011). Hyponatremia and generally cell swelling have been associated with increased oxidative stress (Barsony et al. 2011; Haussinger and Schliess 2008; Friis et al. 2008). Previous studies have demonstrated depletion of organic osmolytes, e.g., the brain taurine pool being reduced to 17% following chronic hyponatremia (Clark et al. 1996; Massieu et al. 2004). We initiated the present work to test whether hyponatremic/swelling-induced ROS production, besides initial potentiation of the swelling-induced taurine release, would modulate TauT activity directly or indirectly through TonEBP activity and TauT transcription, altering taurine uptake following hypo-osmotic hyponatremic exposure.

Materials and Methods

Cell Culture

NIH3T3 fibroblasts were grown at 37°C, 5% CO_2 in 75 cm^2 tissue culture flasks (Cellstar; Greiner Bio-One, Frickenhausen, Germany) in DMEM (335 mOsm) supplemented with 10% fetal bovine serum (FBS) and 1% penicillin/streptomycin. Cells were subcultured every 3–4 days using 0.25% trypsin in phosphate-buffered saline (PBS) containing 137 mM NaCl, 2.6 mM KCl, 6.5 mM Na_2HPO_4, and 1.5 mM KH_2PO_4. Penicillin, streptomycin, Dulbecco's modified Eagle medium (DMEM), fetal calf serum and trypsin were from Invitrogen (Naerum, Denmark).

Media

Media for Taurine Influx and Estimation of ROS

iso-osmotic DMEM (335 mOsm) contained (in mM) 1.4 $CaCl_2$, 0.4 $MgSO_4$, 5.4 KCl, 44 $NaHCO_3$, 110 NaCl, 0.79 NaH_2PO_4, and 25 D-glucose supplemented with 2 ml amino acid solution (Sigma R7131; Sigma, St. Louis, MO) per liter. Low Na^+ hypo-osmotic DMEM (200 mOsm) was obtained by reduction of NaCl to 34 mM. Low Na^+ iso-osmotic DMEM (335 mOsm) was obtained from the low Na^+ hypo-osmotic DMEM by supplementation with 0.85 mmol sucrose per millimole reduction in NaCl (21.8 g/l) (Hoffmann and Lambert 1983). Iso-osmotic NaCl Ringer (335 mOsm) contained (in mM) 158 NaCl, 5 KCl, 1 Na_2HPO_4, 1 $CaCl_2$, 0.1 $MgSO_4$, and 10 HEPES (*N*-2-hydroxyethyl piperazine-*N*′-2-ethanesulfonic acid). Low Na^+ hypo-osmotic NaCl Ringer (200 mOsm) was prepared by reduction of the NaCl concentration in the iso-osmotic NaCl medium to 91 mM. Low Na^+ iso-osmotic NaCl Ringer (335 mOsm) was prepared from low Na^+ hypo-osmotic NaCl Ringer by supplementation with sucrose as described above for DMEM. Ringer for Na^+ kinetic experiments was prepared by substituting *N*-methyl-D-glucamine for Na^+.

Media for TonEBP/mRNA Assays

Hypo-osmotic DMEM (200 mOsm) and hyperosmotic DMEM (500 mOsm) were obtained by dilution of DMEM (iso-osmotic, Invitrogen) with buffered water (5 mM HEPES) and addition of 80 mM NaCl, respectively. All media were supplemented with 10% FBS and 1% penicillin/streptomycin.

Taurine Influx

NIH3T3 cells were grown to 80% confluence in six-well polyethylene dishes (9.6 cm^2/well). Influx was estimated in cells preincubated for 4 h with the indicated DMEM medium or exposed acutely to the indicated NaCl Ringer. Prior to influx, cells were washed two times by gentle aspiration/addition of 600 µl of the respective medium/Ringer. ^{3}H-taurine (Amersham, Aylesbury, UK; 629 GBq/mmol) was added to cells in well 1.5 at 0, 3, 6, 9, and 12 min, respectively (final taurine concentration 4.5 nM). At 15 min taurine uptake was terminated by removal of the extracellular medium, rapid addition/aspiration of 1 ml ice-cold $MgCl_2$ (115 mM), followed by cell lysis with 200 µl 96% ethanol. The ethanol was blown off and the cellular ^{3}H-taurine extracted by addition of 600 µl ddH_2O (30 min), which was transferred to a scintillation vial for estimation of ^{3}H activity (β-scintillation counting, Ultima Gold™; Perkin-Elmer, Waltham, MA). Each well was washed twice with ddH_2O. The total ^{3}H-taurine (cpm) taken up by the cells at a given time point was in each case estimated as the sum of ^{3}H activity in the cell extract and water washouts. Uptake (cycles per minute in each well) was converted to nanomoles per gram of protein using the extracellular specific activity and the protein content (milligrams of protein per well). The latter was estimated in the sixth well by the Lowry et al. (1951) method using BSA as standard. TauT affinity for Na^+, maximal transport rate and Na^+:taurine stoichiometry were estimated by fitting taurine uptake at various Na^+ concentrations in *N*-methyl-D-glucamine chloride to a Hill-type equation as previously described (Hansen et al. 2011).

TonEBP Activity—Luciferase Assay

The -1233-1105 TonEBP-luciferase plasmid (-1233-1105) and the -1233-1105 TonEBP-luciferase mutant plasmid (-1233-1105 M) were kind gifts from Dr. J. D. Ferraris (National Institutes of Health, Bethesda, MD). The constructs were made as outlined (Trama et al. 2000; Zhou et al. 2005). Briefly, the -1233-1105 construct contains the binding motif for TonEBP, fused upstream to the luciferase gene, whereas the mutant has a nonfunctional binding motif. The constructs were transformed into DH10α-competent cells and subsequently isolated using E.Z.N.A Fastfilter Midi Kit (Omega Bio-Tek, Norcross, GA; cat. no. D690503). NIH3T3 cells were grown to 50% confluence in a six-well dish prior to transfection. Transient transfection was performed using Lipofectamine 2000 (Invitrogen, cat. no. 11668-027) according to the manufacturer's instructions. Briefly, 1 µg of plasmid was mixed with 5 µl Lipofectamine 2000 and 200 µl serum-free DMEM without penicillin/streptomycin and left at room temperature for 30 min. The cells in one well of the six-well dish were incubated in 1.8 ml serum-free DMEM without penicillin/streptomycin, and 200 µl transfection solution was added. The transfection medium was substituted with 2 ml of DMEM containing serum 2.5 h later. Cells were transfected 48 h before experimental use.

All luciferase measurements were performed following 4 h incubation in iso-osmotic, hyperosmotic, or hypo-osmotic DMEM. Transfected cells (-1233-1105) were lysed in 120 µl cell culture lysis buffer (Sigma, cat. no. C-4707) and left for 15 min at room temperature. Cell debris was removed and protein content estimated according to the principles of the Lowry et al. (1951) method. Luciferin assay reagent (100 µl; luciferase assay buffer plus luciferase assay substrate; Promega, Madison, WI; cat. no. E1501) was added to 20 µl cell lysates and the luciferase activity estimated with a RamCon (Birkerod, Denmark) Fluostar Optima plate reader. Luminescence was normalized by background subtraction (-1233-1105 M-transfected cells) and calculated relative to the amount of protein in the sample.

TauT mRNA—qPCR

NIH3T3 fibroblasts were grown to 70–80% confluence in tissue culture flasks (75 cm^2). Cells were washed once in PBS, trypsinized and spun down (600×*g*) and total mRNA was isolated according to the manufacturer's instructions, using the GenElute Mammalian Total RNA miniprep kit (Sigma). Total mRNA (1,500 ng) was used for cDNA synthesis using random nonamers (Sigma) and Superscript II avian reverse transcriptase (Invitrogen). cDNA was synthesized under the following conditions: 500 nM dNTP (each) and 1,500 ng total mRNA were mixed with 2.5 µM random nonamers, incubated for 10 min at 25°C, heated to 65°C for 10 min and finally transferred to ice. Reaction buffer, 200 units Superscript II (Invitrogen) and 10 µM dithiothreitol (DTT) were added to the sample, which was incubated at 25°C for 10 min, 42°C for 50 min and finally 72°C for 10 min. Following incubations, samples were transferred to ice.

qPCR was performed using the Brilliant SYBR® green qPCR Master Mix (Agilent, Palo Alto, CA). Triplet measurements of TauT and β-actin expression were performed on each sample. Briefly, 25 µl reaction mixtures were made containing 112.5 ng cDNA, 1× master mix, 30 nM reference dye and 100 nM primer mix (TauT: forward 5′-ATCCTGGGCTTCATGGCACAAG-3′, reverse 5′-ATAGACCAAAAGGTGGGCAGCG-3′; β-actin: forward 5′-AGAGCTATGAGCTGCCTGAC-3′, reverse 5′-GGATGCCACAGGATTCCATAC-3′). qPCR was performed under the following conditions: 10 min at 95°C, followed by 40 cycles of 30 s at 95°C, 1 min at 60°C, 1 min at 72°C and a

single final elongation step for 3 min at 72°C. The mean C_T value was calculated. TauT expression in each sample was calculated relative to β-actin expression to normalize differences in cDNA in each sample. Subsequently, values from each sample were calculated relative to the iso-osmotic control.

NOX4 Construct

Total RNA was isolated from mouse kidney renal cortex, using GenElute mammalian total RNA mini prep (Sigma, cat. no. RTN70). NOX4 was cloned using the Superscript III One-step RT-PCR system with Platinum Taq High Fidelity (Invitrogen, cat. no. 12574-030) with specific NOX4 primers (forward 5′-GAGAATTCTGGCGGTGTC CTGGAGG-3′, reverse 5′-GGGGTACCTCAGCTGAAG GATTCTTTATTGTATTC-3′). An *Eco*RI site was incorporated at the 5′ end and a *Kpn*I site at the 3′ end, and whole NOX4 PCR fragment was cloned into a pCMV-HA vector (Clontech, Palo Alto, CA; cat. no. 631604). The constructs were transformed into DH10α-competent cells and subsequently isolated using E.Z.N.A Fastfilter Midi kit. The constructs were sequenced by MWG-Biotech (Milton-Keynes, UK). NIH3T3 fibroblasts were mock-transfected (transfection medium only) or transfected with the NOX4 construct using Lipofectamine 2000 (see above) or L-PEI. In the latter case, 3 μg of plasmid was mixed with 150 mM NaCl to a final volume of 100 μl and 9.6 μl L-PEI was mixed with 150 mM NaCl to a final volume of 100 μl. The L-PEI solution was added to the plasmid solution during vortexing. The final solution was mixed for 15 s and left at room temperature for 20 min Growth medium was changed to 1,300 μl DMEM without serum or antibiotics. Plasmid solution (200 μl) was added per well dropwise. Cells were left with the plasmid solution for 3–4 h before changing medium back to DMEM with serum. Cells were left for transfection 48 h before experimental use.

Estimation of ROS Production

ROS production was estimated as previously described (Hansen et al. 2011). Cells grown on pretreated coverslips were preincubated in serum-free growth medium containing the ROS-sensitive fluorescent probe carboxy-H2DCFDA (25 lM, 2 h). Coverslips were washed with iso-osmotic NaCl medium and placed in iso-osmotic, hyper-osmotic or hypo-osmotic NaCl medium. ROS was estimated at 37°C on a thermostatic PTI (Princeton, NJ) Ratio Master spectrophotometer using excitation and emission wavelengths of 490 and 515 nm, respectively. ROS production was estimated from the initial increase in fluorescence from 0 to 20 s.

Western Blotting

Cell lysates were prepared in lysis buffer (1% SDS, 150 mM NaCl, 20 mM HEPES, 1 mM EDTA, 0.5% Triton X-100, 1 mM $NaVO_3$, and 1% protease inhibitor mix). SDS-PAGE gel electrophoresis was carried out in 10% Bis–Tris gels using NuPAGE MOPS SDS running buffer (Invitrogen). Proteins were transferred to nitrocellulose membranes using NuPAGE transfer buffer (Invitrogen) and the membranes blocked in TBST (0.01 M Tris–HCl, 0.15 M NaCl, 0.1% Tween 20, pH 7.4) containing 5% nonfat dry milk. Proteins were probed with antibodies against NOX4 (Novus Biologicals, Littleton, CO) or histone H3 (Santa Cruz Biotechnology, Santa Cruz, CA). Protein–antibody complexes were visualized using BCIP/NBT (KPL, Gaithersburg, MD).

MTT Assay—Cell Viability

The MTT calorimetric assay was used to estimate the ability of cells to convert the yellow soluble tetrazolium salt 3-(4,5-dimethylthiazol-2-yl)-2,5-diphenyltetrazolium bromide (MTT) into a blue insoluble formazan precipitate. Cells were seeded in 96-well microplates (16×10^3 in 200 μl medium) and incubated overnight (37°C, 5% CO_2). H_20_2 was added, and cells were incubated for 4 h. The MTT solution (5 mg/ml sterilized PBS) was added (25 μl/well) and the plate incubated (37°C, 5% CO_2) for 3 h. One hundred microliters of SDS–HCl solution (5 ml 0.01 M HCl, 0.5 g SDS) was added to each well and mixed to lyse the cells and solubilize the colored formazan crystals. Samples were measured at 570 nm using a FLUOstar OPTIMA 96-well microplate plate reader (BMG Lab Technologies, Offenburg, Germany). Data are reported in terms of relative cell viability compared to control cells with no H_2O_2. Absorbance values were assumed to be directly proportional to the number of viable cells. Each experiment was performed in triplicate.

Statistics

All data are presented either as individual experiments or as mean values ± standard error of the mean (SEM). Statistical evaluation is based on two-way ANOVA or a Student's *t*-test (specified in legends).

Results

Taurine Uptake is Reduced by Osmotic Cell Swelling *per se*

Taurine uptake in NIH3T3 mouse fibroblasts was previously shown to be totally Na^+-dependent and eliminated in

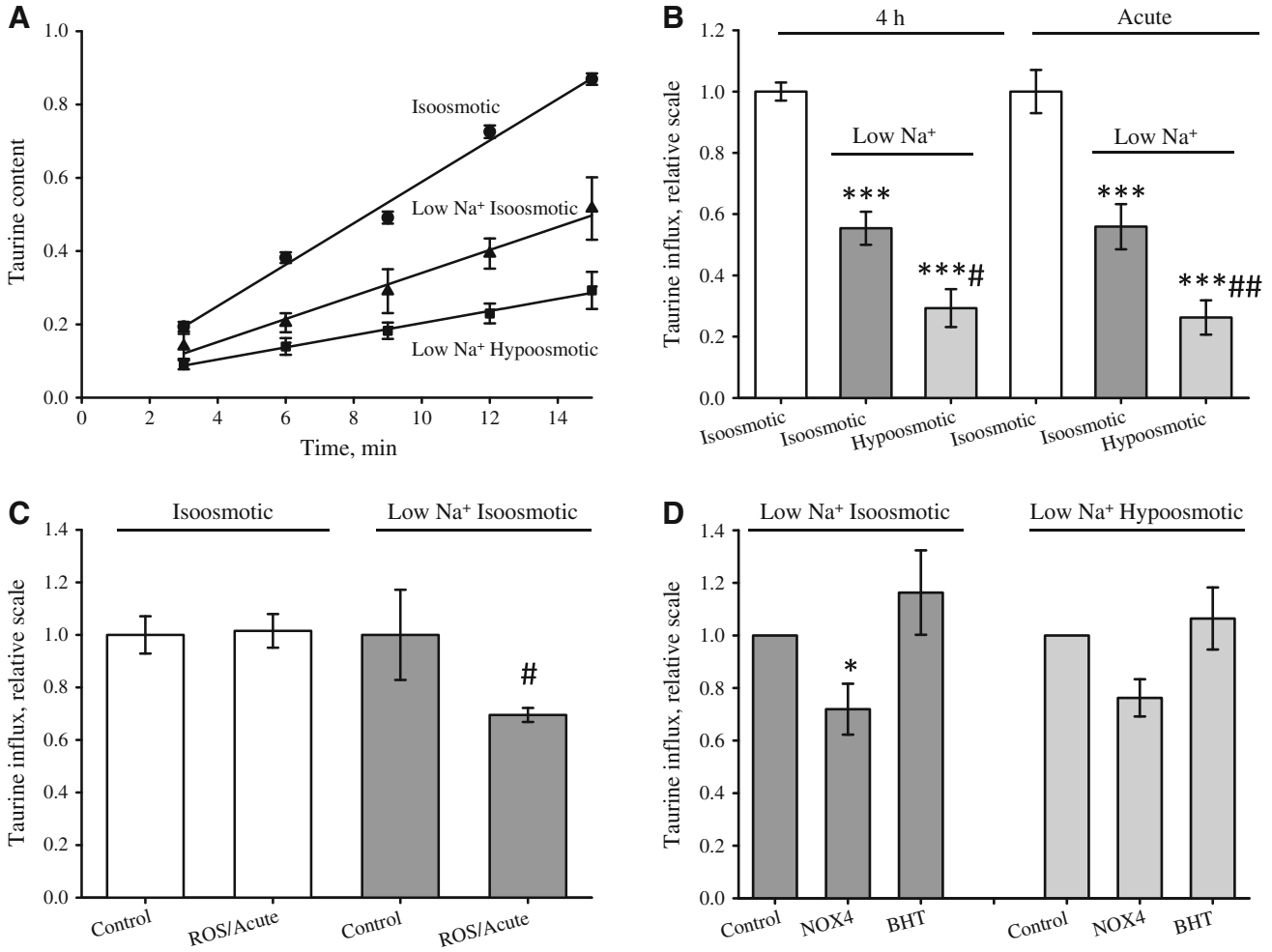

Fig. 1 The reduction in taurine uptake following hypo-osmotic exposure is independent of NOX4 activity. Taurine uptake (nmol g protein^{-1}) was estimated by the tracer technique in NIH3T3 cells exposed to either 4 h iso-osmotic DMEM, low Na^+ hypo-osmotic DMEM (200 mOsm) and low Na^+ iso-osmotic DMEM (335 mOsm, adjusted to osmolarity by addition of sucrose) or acutely (*Acute*) to iso-osmotic NaCl, low Na^+ hypo-osmotic NaCl and low Na^+ iso-osmotic NaCl (335 mOsm, adjusted to osmolarity by addition of sucrose), as described in Materials and Methods. Taurine influx (nmol g protein^{-1} min^{-1}) was estimated by linear regression of taurine uptake within 15 min. **a** Taurine uptake following 4 h incubation in the respective DMEM solutions. Data represent three sets of paired experiments. **b** Taurine influx (4 h and acute) in cells exposed for 4 h to the DMEM solutions (4 h) or acutely to the NaCl medium. Absolute values for controls are 0.056 ± 0.002 nmol g protein^{-1} min^{-1} (4 h, n = 3) and 0.222 ± 0.019 nmol g protein^{-1} min^{-1} (acute, n = 4). Significance was determined using two-way ANOVA with Bonferroni post test, comparing treatments within the acute and 4 h groups, respectively. **c** Taurine influx in cells exposed acutely to iso-osmotic and low Na^+ iso-osmotic NaCl with or without acute exposure to 0.5 mM H_2O_2. Absolute values for controls are 0.230 ± 0.016 nmol g protein^{-1} min^{-1} (iso-osmotic, n = 3) and 0.089 ± 0.015 nmol g protein^{-1} min^{-1} (low Na^+ iso-osmotic, n = 3). Significance was determined with Student's t-test (paired, one-sided) comparing influx with and without ROS/acute with the respective control. **d** Taurine influx estimated in cells acutely exposed to low Na^+ iso-osmotic or low Na^+ hypo-osmotic NaCl. NOX4 overexpression was carried out as described in Materials and Methods. BHT (0.5 mM) was present during the influx experiments. Statistical evaluation by two-way ANOVA with Bonferroni post test comparing influx from each treatment with the respective control; e.g., BHT-treated cells were compared with untreated, whereas NOX4-overexpressing cells were compared with mock-treated cells under iso-osmotic and hypo-osmotic conditions. All values are given relative to the respective control ± SEM. $^{*}P < 0.05$, $^{**}P < 0.01$, $^{***}P < 0.001$ compared to the respective control; $^{\#}P < 0.05$, $^{\#\#}P < 0.01$ compared to low Na^+ iso-osmotic

the presence of the taurine analog β-alanine (Voss et al. 2004), indicating that taurine uptake in the fibroblasts is mediated by TauT. From Fig. 1a, b it is seen that reduction in the total extracellular Na^+ concentration from 150 to 80 mM for 4 h, keeping osmolarity constant with sucrose, results in a significant reduction in the taurine influx in NIH3T3 cells to 56% of the iso-osmotic value (compare "iso-osmotic" to "low Na^+ iso-osmotic"). From Fig. 1a, b it is also seen that reduction in the extracellular osmolarity from 335 to 200 mOsm, keeping the extracellular Na^+ concentration constant at 80 mM, leads to an additional 50% reduction in taurine uptake (compare "low Na^+

iso-osmotic" to "low Na^+ hypo-osmotic"). Hence, TauT activity is reduced by 4 h exposure to hypo-osmotic conditions due to reduction in the extracellular Na^+ concentration as well as reduction in the extracellular osmolarity, i.e., osmotic cell swelling. This is similar to observations in Ehrlich ascites tumor cells (Hoffmann and Lambert 1983). To test whether reduced expression or membrane localization of TauT is responsible for the decreased taurine uptake under long-term hypo-osmotic conditions (4 h), we compared taurine uptake in cells exposed to 4 h reduction in the extracellular osmolarity with cells exposed acutely to hypo-osmotic conditions. From Fig. 1b it is seen that taurine uptake is reduced to the same extent following 4 h and acute reduction in the extracellular Na^+ concentration (compare dark gray bars at 4 h and acute) and in extracellular osmolarity (compare light gray bars at 4 h and acute). As acute and 4 h reduction in Na^+ and osmolarity give the same reduction in influx, it is suggested that the reduction in taurine uptake is most likely caused by direct inhibition of TauT. Similarly, it was previously shown in Ehrlich ascites cells that the regulation of the activity of another osmoregulatory transporter, NKCC1, by changes in osmolarity is not related to the number of transport molecules present in the membrane (Hoffmann et al. 1986).

ROS Reduce Taurine Uptake under Conditions with Low Extracellular Na^+

Protein phosphorylation is modulated by ROS as protein phosphatases contain a redox-sensitive cysteine group in the catalytic site, rendering them inactive when oxidized by otherwise weak oxidants, such as H_2O_2 (Sommer et al. 2002; Meng et al. 2002; Wright et al. 2009; Barchowsky et al. 1995; Lee et al. 1998). ROS production in NIH3T3 cells is increased under hyperosmotic (Supplementary Fig. 1) as well as hypo-osmotic (Supplementary Fig. 2) conditions, and we speculated whether the reduced taurine uptake following hypo-osmotic cell swelling (Fig. 1b) reflects a ROS-induced shift in TauT's Na^+ sensitivity. From Supplementary Fig. 3a and Fig. 1c it is seen that acute exposure to 0.5 mM H_2O_2 has no detectable effect on taurine uptake under either hyperosmotic or iso-osmotic conditions, respectively, whereas 0.5 mM H_2O_2 results in a significant reduction in taurine influx under iso-osmotic conditions with low extracellular Na^+ concentration. It is emphasized that the effect of ROS in the latter case was tested in a medium with low Na^+ concentration, which was supplemented to isotonicity with sucrose in order to avoid taurine influx via the swelling-induced and ROS-sensitive taurine release pathway (Hansen et al. 2011; Lambert 2007). Exposure to 2 mM H_2O_2 was previously reported to reduce taurine uptake in NIH3T3 cells under iso-osmotic conditions (Voss et al. 2004). However, long-term exposure (4 h) to 0.5 mM H_2O_2 is accompanied by a reduction in taurine uptake as well as cell survival; i.e., acute exposure to a high dose or long-term exposure to a low dose of H_2O_2 is likely to kill NIH3T3 cells (Supplementary Fig. 3b).

Kinetic analysis of taurine uptake versus the extracellular Na^+ concentration (medium supplemented to isotonicity with NMDG) revealed that acute exposure to 0.5 mM H_2O_2 increased the Na^+:taurine stoichiometry significantly by $17 \pm 7\%$ (control 1.93 ± 0.14, H_2O_2-treated 2.24 ± 0.06, $n = 4$), whereas it had no significant effect on the TauT affinity for Na^+ (control 81 ± 13 mM, H_2O_2-treated 72 ± 2 mM, $n = 4$) or the maximal transport rate (H_2O_2 relative to control 0.94 ± 0.11, $n = 4$). ROS is generated by NOX4 under hypo-osmotic conditions in NIH3T3 cells (Supplementary Fig. 2), and in order to determine whether ROS produced by NOX4 could mimic the effect of acute exposure to H_2O_2 and cause a reduction in TauT taurine transport under conditions with low extracellular Na^+ concentration, we used ROS scavenging by butylated hydroxytoluene (BHT) (Lambert 2003) and overexpression of NOX4. There is a roughly similar reduction in taurine uptake with ROS acute and NOX4 (compare Fig. 1c, d). ROS scavenging with BHT has no significant effect on taurine uptake at low extracellular Na^+ concentration under iso-osmotic and hypo-osmotic conditions (Fig. 1d), indicating that ROS scavenging has no effect on taurine uptake at low extracellular Na^+ concentrations.

TauT mRNA is Reduced under Hypo-Osmotic Conditions

TauT transcription in mammalian cells is upregulated by TonEBP under hyperosmotic conditions (Miyakawa et al. 1998, 1999b), and we have previously shown that 4 h hyperosmotic exposure increases TauT activity in, e.g., NIH3T3 cells (Voss et al. 2004). As the effects of hypo-osmotic exposure on taurine uptake appeared to be acute and independent of TauT transcription, we tested whether TonEBP activity and TauT transcription were actually unaffected by prolonged exposure to hypo-osmotic conditions. From Fig. 2 it is seen, in accordance with previous data, that exposure of NIH3T3 cells to hyperosmotic conditions results in a significant 16-fold increase in TonEBP activity within 16 h (Fig. 2a) and an almost twofold increase in TauT mRNA within 4 h (Fig. 2b). However, TonEBP activity is unaffected by 16 h hypo-osmotic exposure (Fig. 2a), which is in agreement with previously demonstration of a reduction in TonEBP mRNA and retention of TonEBP in the cytoplasm under hypo-osmotic conditions (Woo et al. 2000). However, despite the unaffected TonEBP activity, TauT mRNA is reduced after 4 h

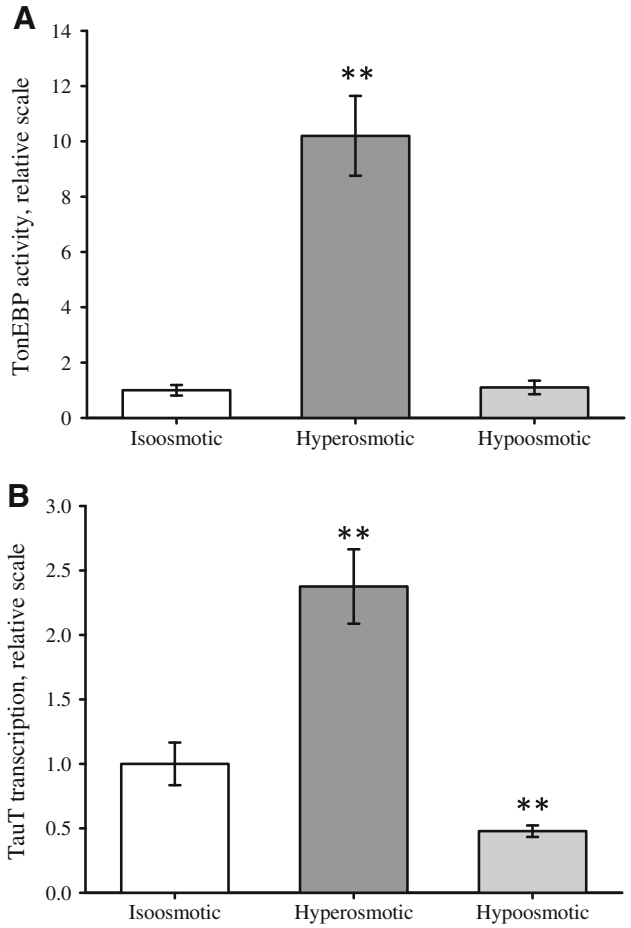

Fig. 2 Effect of long-term hyper- and hypo-osmotic conditions on TonEBP activity and TauT transcription. TonEBP activity and TauT transcription were estimated in NIH3T3 cells exposed to iso-osmotic, hyperosmotic or hypo-osmotic medium (DMEM) for 16 and 4 h, respectively. **a** For estimation of TonEBP activity, cells were transfected with luciferase-plasmid and incubated with the indicated medium and luciferase activity was estimated as indicated in Materials and Methods. **b** TauT mRNA transcription was estimated by qPCR. cDNA was generated from mock-transfected NIH3T3 cells, and qPCR was performed using primers specific for TauT mRNA as indicated in Materials and Methods. Values are given relative to their respective iso-osmotic control ± SEM. Data in (**a**) represent seven sets of paired experiments. Data in (**b**) represent four and five sets of paired experiments for hyperosmotic and hypo-osmotic, respectively. Statistical evaluation for (**a**) and (**b**) by Student's *t*-test (paired, one-sided) comparing hyperosmotic or hypo-osmotic to iso-osmotic control, respectively. $*P < 0.05$, $**P < 0.01$ compared to iso-osmotic control

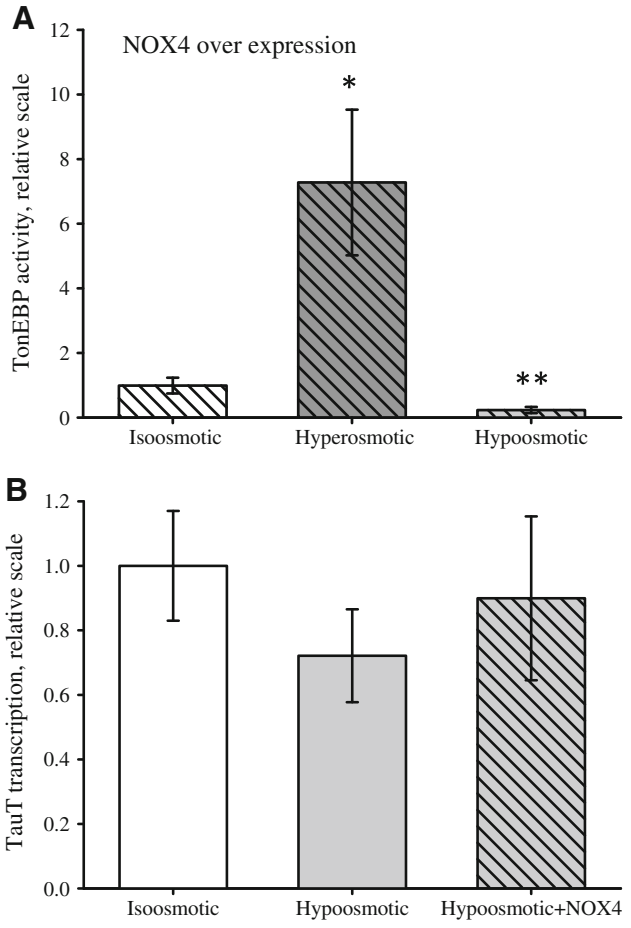

Fig. 3 NOX4 regulates TonEBP activity, but not TauT transcription, under hypo-osmotic conditions. TonEBP activity and TauT transcription were estimated in NIH3T3 cells exposed for 4 h to iso-osmotic or hypo-osmotic medium (DMEM). Cells were transfected with NOX4 (*hatched bars*) or mock-transfected (*open bars*) as described in Materials and Methods. TonEBP activity and TauT mRNA were estimated as described in the legend to Fig. 2 and Materials and Methods. **a** TonEBP activity in NOX4-transfected cells relative to non-transfected iso-osmotic control. **b** TauT mRNA transcription in mock- and NOX4-transfected cells. Values are given relative to their respective iso-osmotic control ± SEM. Data in (**a**) represent seven sets of experiments. Data in (**b**) represent four (hypo-osmotic) and three (NOX4) sets of experiments. Statistical evaluation for (**a**) and (**b**) by Student's *t*-test (paired, one-sided) comparing hyperosmotic, hypo-osmotic or hypo-osmotic+NOX4 to the respective iso-osmotic control. Values are given relative to iso-osmotic control ± SEM. $*P < 0.05$, $**P < 0.01$ compared to iso-osmotic control

hypo-osmotic exposure (Fig. 2b). A selection of cells expressing low TauT as the cause of the observed data is most unlikely as kinetic analysis (Voss et al. 2004) revealed that there is only one population of NIH3T3 cells (one K_m value for taurine) and that the time frame of our experiments is very short. Hence, TauT mRNA levels correlate with TonEBP activity under long-term hyperosmotic conditions but not under long-term hypo-osmotic conditions.

Using NOX4-overexpressing cells, we tested whether ROS generated by NOX4 could affect TonEBP activity and TauT transcription. It is seen that the increase in TonEBP activity following hypertonic exposure in NOX4-overexpressing cells is comparable to that in native cells, whereas there is a significant decrease in TonEBP activity under hypo-osmotic conditions (4 h) (Fig. 3a). The significant reduction in TonEBP activity under hypo-osmotic conditions compared to iso-osmotic conditions is taken to indicate that TonEBP is negatively regulated by excess

ROS produced by NOX4 under hypo-osmotic conditions. From Fig. 3b it is seen that TauT mRNA transcription is unaltered under hypo-osmotic conditions when over-expressing NOX4. Thus, the increased ROS availability generated from NOX4 under hypo-osmotic conditions does not seem to suppress *TauT* transcription via the altered TonEBP activity.

To test these results, we applied ROS (H_2O_2) and the phosphatase inhibitor vanadate and estimated TonEBP activity. Unexpectedly, we found that both ROS and vanadate reduced TonEBP activity significantly when added acutely to NIH3T3 cells preincubated under hyperosmotic conditions (16 h, 500 mOsm), i.e., immediately before lysis and estimation of luciferase activity (Supplementary Fig. 4a). Mg^{2+}-dependent ATPases are inhibited by vanadate (Bond and Hudgins 1980; Hanocq-Quertier et al. 1988), and as the luciferase used in this assay requires Mg^{2+} as cosubstrate (Promega technical bulletin 281), the observed acute effect of vanadate on the TonEBP assay is most likely a result of luciferase inhibition. Thus, H_2O_2 and vanadate most likely interfere directly with luciferase activity. Furthermore, prolonged exposure to H_2O_2 (0.5 mM) under hyperosmotic conditions results in significantly reduced TauT transcription (Supplementary Fig. 4b); this is, however, most likely an effect of the significant cell death following prolonged exposure to H_2O_2 (Supplementary Fig. 3b). The effect of H_2O_2 and vanadate on TonEBP activity and TauT transcription will therefore not be discussed further.

Discussion

Active taurine uptake in mammalian cells is fueled by the prevailing Na^+ gradient, and TauT activity is regulated by various protein kinases, e.g., protein kinase A (PKA) and PKC plus casein kinase 2 (CK2) (Hansen et al. 2011; Jacobsen et al. 2008; Voss et al. 2004). We find here, in agreement with previous results (Hoffmann and Lambert 1983), that osmotic cell swelling per se results in an inhibition of taurine uptake. Acute regulation of TauT often involves a shift in the maximal transport capacity (V_{max}), the substrate concentration required for half-maximal transport activity (K_m values for taurine [$K_{m\ taurine}$] and Na^+ [$K_{m\ Na}$]) and/or the Na^+:taurine transport stoichiometry (Lambert 2004). In the case of NIH3T3 fibroblasts, we recently demonstrated that phosphorylation, mediated by the constitutively active serin/threonine kinase CK2, reduces the affinity of TauT toward Na^+ plus the maximal transport activity and increases the Na^+:taurine stoichiometry and that the effect of CK2 inhibition on TauT activity was more pronounced at an extracellular Na^+ concentration close to $K_{m\ Na}$ (Hansen et al. 2011). Osmotic cell swelling is accompanied by an increase in the production of ROS in NIH3T3 mouse fibroblasts, porcine myotubes, HTC cells (liver-derived cell line), HEK293 cells, collecting duct cells and neonatal rat cardiomyocytes (Zhou et al. 2006; Diaz-Elizondo et al. 2006; Friis et al. 2008; Lambert 2003; Varela et al. 2004; Ørtenblad et al. 2003; Hansen et al. 2011); and we have recently shown that a NOX4/p22phox complex constitutes the catalytic core of the volume-sensitive NADPH oxidase in NIH3T3 fibroblasts (Friis et al. 2008). Furthermore, NADPH-oxidase activity has been assigned a role in the increased ROS production during hyponatremia (Haussinger and Schliess 2008). It thus seemed likely that taurine uptake could be modulated by ROS following hypo-osmotic/hyponatremic conditions.

The present data indicate that acute exposure to 0.5 mM H_2O_2 under iso-osmotic conditions has no detectable effect on taurine uptake at standard extracellular Na^+ concentration, whereas H_2O_2 reduces uptake under conditions with low extracellular Na^+ (Fig. 1c). NOX4 overexpression increases the swelling-induced ROS production in NIH3T3 cells and, similar to H_2O_2 exposure, appears to reduce taurine uptake under conditions with low extracellular Na^+ concentration (Fig. 1c, d). We also find that the Na^+:taurine transport stoichiometry is increased by addition of 0.5 mM H_2O_2; i.e., lower concentrations of Na^+ are required for equivalent taurine uptake following addition of H_2O_2 as long as the concentration of sodium is above $K_{m\ Na}$. Increased availability of ROS under hypo-osmotic conditions can partly explain the observed reduction in taurine uptake when the extracellular Na^+ concentration is reduced. However, the increased Na^+:taurine stoichiometry by ROS will only reduce the uptake of taurine at Na^+ concentrations below $K_{m\ Na}$. As the Na^+ concentration is not reduced below $K_{m\ Na}$ even under severe hyponatremia, this effect is probably not pathophysiologically relevant.

ROS—TonEBP—Tonicity Sensitivity

Long-term regulation in NIH3T3 cells, following continuous exposure to hyperosmotic stress or substrate (taurine), relies on the transcriptional modulation of the gene encoding TauT (Voss et al. 2004). The transcriptional increase in the expression of the Na^+-dependent co-transporters, sodium/*myo*-inositol co-transporter (SMIT), sodium/chloride/betaine co-transporter (BGT1), and TauT is facilitated by the *cis*-element tonicity-response enhancer (TonE) (Miyakawa et al. 1998; Rim et al. 1998), which is regulated by TonEBP (Han et al. 2006; Ito et al. 2004; Jeon et al. 2006; Miyakawa et al. 1999b). TonEBP plays a key role in the protection of cells from prolonged increase in the extracellular osmolarity by increasing the cellular content of osmolytes through transcription of co-transporters for organic and inorganic osmolytes (Han et al.

2006; Ito et al. 2004; Jeon et al. 2006; Miyakawa et al. 1999a, 1999b). Mice lacking functional TonEBP ($TonEBP^{-/-}$) have a severe renal medulla degeneration caused by low levels of SMIT, aldose reductase and TauT expression (Lopez-Rodriguez et al. 2004). TonEBP is evenly distributed between the cytosol and nucleus under iso-osmotic conditions, whereas hyperosmolarity increases and hypo-osmolarity decreases the nuclear fraction (Woo et al. 2000; Miyakawa et al. 1999b; Cha et al. 2001; Tong et al. 2006). In accordance, hyperosmotic stress results in increased expression and activation of TonEBP (Lopez-Rodriguez et al. 2004; Woo et al. 2002; Zhou et al. 2006; Cai et al. 2005), whereas TonEBP transcription is reduced and nuclear export accelerated during hypo-osmotic stress (Woo et al. 2000; Tong et al. 2006). TonEBP activity and nuclear translocation are regulated by serine and tyrosine phosphorylation (reviewed in Burg et al. 2007; Aramburu et al. 2006). The increased TonEBP activity following hyperosmotic exposure involves mitochondrial release of ROS (Zhou et al. 2005, 2006; Ferraris et al. 2002). In the present study we demonstrate that TonEBP activity is similarly stimulated under hyperosmotic conditions but unaffected under hypo-osmotic conditions (Fig. 2). In NOX4-overexpressing NIH3T3 cells TonEBP activity is still increased under hyperosmotic conditions, whereas TonEBP activity is significantly reduced under hypo-osmotic conditions (Fig. 3).

Figure 4 summarizes data and illustrates modulation of taurine uptake by TauT in NIH3T3 cells following osmotic stress. TauT transcription is generally assumed to follow TonEBP activity. This is also the case for TauT transcription under hyperosmotic conditions (Fig. 2). However, we find that under long-term hypo-osmotic exposure the downregulation of TauT transcription is not secondary to reduced TonEBP activity as (1) TonEBP activity is unaltered whereas TauT mRNA is reduced (Fig. 2) and (2) stimulation and hindrance of TonEBP activity by increased NOX4 expression do not correlate with TauT transcription level (Fig. 3). The lack of correlation between TonEBP activity and TauT transcription under hypo-osmotic conditions could indicate that TauT transcription is dependent on other transcription factors inactivated by hypo-osmolarity. Under hyperosmotic conditions, ROS generated from the mitochondria are reported to stimulate TonEBP transactivation via a hyper-osmotically induced transactivation domain (TAD) (Zhou et al. 2006), and we hypothesize that the primary effect of ROS on TonEBP-TAD is an increased sensitivity toward tonicity. In this scenario ROS stimulate TonEBP transactivation under conditions with high extracellular ion concentrations, whereas TonEBP transactivation is further suppressed by NOX4-generated ROS under conditions with low extracellular ion concentrations. Our current hypothesis is that ROS-mediated

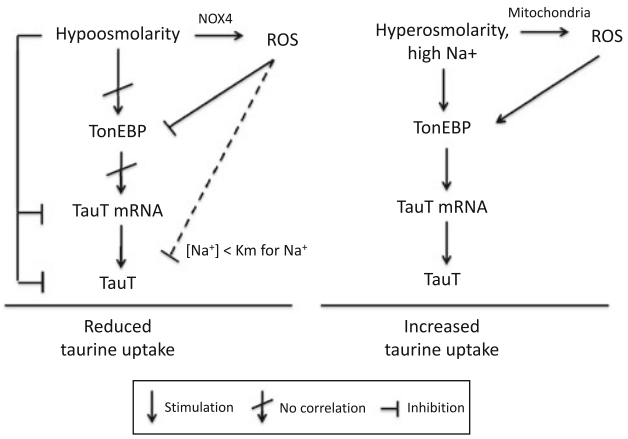

Fig. 4 Modulation of taurine uptake by TauT following osmotic stress. The model is described in the text

interference with TauT kinetics is only visible under conditions with very low Na^+ concentrations, i.e., concentrations significantly lower than those observed under hypo-osmotic hyponatremia, but will have no effect on taurine transport under conditions with high or normal extracellular Na^+ concentrations. The hypo-osmotically induced reduction in TauT mRNA will reduce TauT activity following prolonged osmotic stress. The reduction in cellular taurine content following hyponatremia is probably dominated by increased taurine leak, whereas more chronic conditions can involve the reduction in TauT mRNA.

Acknowledgments The present work was supported by The Danish Natural Sciences Research Council (grants 21-04-0535, 272-07-0530, 272-08-0170, 271-08-0520). Dr. J. D. Ferraris (National Institutes of Health, Bethesda, MD) is acknowledged for donation of the -1233-1105 TonEBP-luciferase plasmid (-1233-1105) and the -1233-1105 TonEBP-luciferase mutant plasmid (-1233-1105 M). Tina Rødgaard is acknowledged for contributing to experiments included in Fig. 2a. The technical assistance of Dorthe Nielsen is gratefully acknowledged.

References

Aramburu J, Drews-Elger K, Estrada-Gelonch A, Minguillon J, Morancho B, Santiago V, Lopez-Rodriguez C (2006) Regulation of the hypertonic stress response and other cellular functions by the Rel-like transcription factor NFAT5. Biochem Pharmacol 72:1597–1604

Barchowsky A, Munro SR, Morana SJ, Vincenti MP, Treadwell M (1995) Oxidant-sensitive and phosphorylation-dependent activation of NF-kappa B and AP-1 in endothelial cells. Am J Physiol Lung Cell Mol Physiol 269:L829–L836

Barsony J, Sugimura Y, Verbalis JG (2011) Osteoclast response to low extracellular sodium and the mechanism of hyponatremia-induced bone loss. J Biol Chem 286:10864–10875

Bond GH, Hudgins PM (1980) Inhibition of red cell Ca^{2+}-ATPase by vanadate. Biochim Biophys Acta 600:781–790

Burg MB, Ferraris JD, Dmitrieva NI (2007) Cellular response to hyperosmotic stresses. Physiol Rev 87:1441–1474

Cai Q, Ferraris JD, Burg MB (2005) High NaCl increases TonEBP/OREBP mRNA and protein by stabilizing its mRNA. Am J Physiol Renal Physiol 289:F803–F807

Cha JH, Woo SK, Han KH, Kim YH, Handler JS, Kim J, Kwon HM (2001) Hydration status affects nuclear distribution of transcription factor tonicity responsive enhancer binding protein in rat kidney. J Am Soc Nephrol 12:2221–2230

Chesney RW, Han X, Patters AB (2010) Taurine and the renal system. J Biomed Sci 17(Suppl 1):S4

Clark EC, Thomas D, Baer J, Sterns RH (1996) Depletion of glutathione from brain cells in hyponatremia. Kidney Int 49: 470–476

Diaz-Elizondo J, Chiong M, Rojas-Rivera D, Olea-Azar C, Kwon HM, Lavandero S (2006) Reactive oxygen species inhibit hyposmotic stress-dependent volume regulation in cultured rat cardiomyocytes. Biochem Biophys Res Commun 350: 1076–1081

Eisner V, Criollo A, Quiroga C, Olea-Azar C, Santibanez JF, Troncoso R, Chiong M, az-Araya G, Foncea R, Lavandero S (2006) Hyperosmotic stress-dependent NFkappaB activation is regulated by reactive oxygen species and IGF-1 in cultured cardiomyocytes. FEBS Lett 580:4495–4500

Ferraris JD, Williams CK, Persaud P, Zhang Z, Chen Y, Burg MB (2002) Activity of the TonEBP/OREBP transactivation domain varies directly with extracellular NaCl concentration. Proc Natl Acad Sci USA 99:739–744

Friis MB, Vorum KG, Lambert IH (2008) Volume-sensitive NADPH oxidase activity and taurine efflux in NIH3T3 mouse fibroblasts. Am J Physiol Cell Physiol 294:C1552–C1565

Goodman CA, Horvath D, Stathis C, Mori T, Croft K, Murphy RM, Hayes A (2009) Taurine supplementation increases skeletal muscle force production and protects muscle function during and after high-frequency in vitro stimulation. J Appl Physiol 107: 144–154

Hall JA, Kirk J, Potts JR, Rae C, Kirk K (1996) Anion channel blockers inhibit swelling-activated anion, cation, and nonelectrolyte transport in HeLa cells. Am J Physiol Cell Physiol 271:C579–C588

Han X, Patters AB, Jones DP, Zelikovic I, Chesney RW (2006) The taurine transporter: mechanisms of regulation. Acta Physiol 187:61–73

Hanocq-Quertier J, Baltus E, Schram E (1988) Bioluminescent assay of ATPase activity in embryonic material using firefly luciferase. J Biolumin Chemilumin 2:17–24

Hansen DB, Guerra B, Jacobsen JH, Lambert IH (2011) Regulation of taurine homeostasis by protein kinase CK2 in mouse fibroblasts. Amino Acids 40:1091–1106

Haussinger D, Schliess F (2008) Pathogenetic mechanisms of hepatic encephalopathy. Gut 57:1156–1165

Hoffmann EK, Lambert IH (1983) Amino acid transport and cell volume regulation in Ehrlich ascites tumour cells. J Physiol 338:613–625

Hoffmann EK, Schiodt M, Dunham P (1986) The number of chloride-cation cotransport sites on Ehrlich ascites cells measured with ^{3}H-bumetanide. Am J Physiol Cell Physiol 250:C688–C693

Hoffmann EK, Lambert IH, Pedersen SF (2009) Physiology of cell volume regulation in vertebrates. Physiol Rev 89:193–277

Ito T, Fujio Y, Hirata M, Takatani T, Matsuda T, Muraoka S, Takahashi K, Azuma J (2004) Expression of taurine transporter is regulated through the TonE (tonicity-responsive element)/TonEBP (TonE-binding protein) pathway and contributes to cytoprotection in HepG2 cells. Biochem J 382:177–182

Jacobsen JH, Clement CA, Friis MB, Lambert IH (2008) Casein kinase 2 regulates the active uptake of the organic osmolyte taurine in NIH3T3 mouse fibroblasts. Pflugers Arch 457:327–337

Jeon US, Kim JA, Sheen MR, Kwon HM (2006) How tonicity regulates genes: story of TonEBP transcriptional activator. Acta Physiol (Oxf) 187:241–247

Jong CJ, Ito T, Mozaffari M, Azuma J, Schaffer S (2010) Effect of beta-alanine treatment on mitochondrial taurine level and 5-taurinomethyluridine content. J Biomed Sci 17(Suppl 1):S25

Lambert IH (2003) Reactive oxygen species regulate swelling-induced taurine efflux in NIH3T3 mouse fibroblasts. J Membr Biol 192:19–32

Lambert IH (2004) Regulation of the cellular content of the organic osmolyte taurine in mammalian cells. Neurochem Res 29:27–63

Lambert IH (2007) Activation and inactivation of the volume-sensitive taurine leak pathway in NIH3T3 fibroblasts and Ehrlich Lettre acites cells. Am J Physiol Cell Physiol 293:C390–C400

Lambert IH, Hansen DB (2011) Regulation of taurine transport systems by protein kinase CK2 in mammalian cells. Cell Physiol Biochem 28:1099–1110

Lambert IH, Hoffmann EK, Pedersen SF (2008) Cell volume regulation: physiology and pathophysiology. Acta Physiol Scand 194:255–282

Lee SR, Kwon KS, Kim SR, Rhee SG (1998) Reversible inactivation of protein-tyrosine phosphatase 1B in A431 cells stimulated with epidermal growth factor. J Biol Chem 273:15366–15372

Loh JA, Verbalis JG (2008) Disorders of water and salt metabolism associated with pituitary disease. Endocrinol Metab Clin North Am 37:213–234

Lopez-Rodriguez C, Antos CL, Shelton JM, Richardson JA, Lin F, Novobrantseva TI, Bronson RT, Igarashi P, Rao A, Olson EN (2004) Loss of NFAT5 results in renal atrophy and lack of tonicity-responsive gene expression. Proc Natl Acad Sci USA 101:2392–2397

Lowry OH, Rosebrough NJ, Farr AL, Randall RJ (1951) Protein measurement with the folin phenol reagent. J Biol Chem 193: 265–275

Massieu L, Montiel T, Robles G, Quesada O (2004) Brain amino acids during hyponatremia in vivo: clinical observations and experimental studies. Neurochem Res 29:73–81

Meng TC, Fukada T, Tonks NK (2002) Reversible oxidation and inactivation of protein tyrosine phosphatases in vivo. Mol Cell 9:387–399

Miyakawa H, Woo SK, Chen CP, Dahl SC, Handler JS, Kwon HM (1998) *Cis*- and *trans*-acting factors regulating transcription of the *BGT1* gene in response to hypertonicity. Am J Physiol Renal Physiol 274:F753–F761

Miyakawa H, Rim JS, Handler JS, Kwon HM (1999a) Identification of the second tonicity-responsive enhancer for the betaine transporter (*BGT1*) gene. Biochim Biophys Acta 1446:359–364

Miyakawa H, Woo SK, Dahl SC, Handler JS, Kwon HM (1999b) Tonicity-responsive enhancer binding protein, a rel-like protein that stimulates transcription in response to hypertonicity. Proc Natl Acad Sci USA 96:2538–2542

Ørtenblad N, Young JF, Oksbjerg N, Nielsen JH, Lambert IH (2003) Reactive oxygen species are important mediators of taurine release from skeletal muscle cells. Am J Physiol Cell Physiol 284:C1362–C1373

Rim JS, Atta MG, Dahl SC, Berry GT, Handler JS, Kwon HM (1998) Transcription of the sodium/myo-inositol cotransporter gene is regulated by multiple tonicity-responsive enhancers spread over 50 kilobase pairs in the 5′-flanking region. J Biol Chem 273:20615–20621

Sommer D, Coleman S, Swanson SA, Stemmer PM (2002) Differential susceptibilities of serine/threonine phosphatases to oxidative and nitrosative stress. Arch Biochem Biophys 404:271–278

Tong EH, Guo JJ, Huang AL, Liu H, Hu CD, Chung SS, Ko BC (2006) Regulation of nucleocytoplasmic trafficking of transcription factor OREBP/TonEBP/NFAT5. J Biol Chem 281:23870–23879

Trama J, Lu Q, Hawley RG, Ho SN (2000) The NFAT-related protein NFATL1 (TonEBP/NFAT5) is induced upon T cell activation in a calcineurin-dependent manner. J Immunol 165:4884–4894

Upadhyay UM, Gormley WB (2011) Etiology and management of hyponatremia in neurosurgical patients. J Intensive Care Med. doi:10.1177/0885066610395489

Varela D, Simon F, Riveros A, Jorgensen F, Stutzin A (2004) NAD(P)H oxidase-derived H_2O_2 signals chloride channel activation in cell volume regulation and cell proliferation. J Biol Chem 279:13301–13304

Voss JW, Pedersen SF, Christensen ST, Lambert IH (2004) Regulation of the expression and subcellular localisation of the taurine transporter TauT in mouse NIH3T3 fibroblasts. Eur J Biochem 271:4646–4658

Wakil A, Ng JM, Atkin SL (2011) Investigating hyponatraemia. BMJ 342:d1118

Woo SK, Dahl SC, Handler JS, Kwon HM (2000) Bidirectional regulation of tonicity-responsive enhancer binding protein in response to changes in tonicity. Am J Physiol Renal Physiol 278:F1006–F1012

Woo SK, Lee SD, Na KY, Park WK, Kwon HM (2002) TonEBP/NFAT5 stimulates transcription of HSP70 in response to hypertonicity. Mol Cell Biol 22:5753–5760

Wright VP, Reiser PJ, Clanton TL (2009) Redox modulation of global phosphatase activity and protein phosphorylation in intact skeletal muscle. J Physiol 587:5767–5781

Yang T, Zhang A, Honeggar M, Kohan DE, Mizel D, Sanders K, Hoidal JR, Briggs JP, Schnermann JB (2005) Hypertonic induction of COX-2 in collecting duct cells by reactive oxygen species of mitochondrial origin. J Biol Chem 280:34966–34973

Zhou X, Ferraris JD, Cai Q, Agarwal A, Burg MB (2005) Increased reactive oxygen species contribute to high NaCl-induced activation of the osmoregulatory transcription factor TonEBP/OREBP. Am J Physiol Renal Physiol 289:F377–F385

Zhou X, Ferraris JD, Burg MB (2006) Mitochondrial reactive oxygen species contribute to high NaCl-induced activation of the transcription factor TonEBP/OREBP. Am J Physiol Renal Physiol 290:F1169–F1176

J Membrane Biol (2012) 245:89–95
DOI 10.1007/s00232-012-9417-7

Exploration of Respiratory Chain of *Nocardia asteroides*: Purification of Succinate Quinone Oxidoreductase

Waqar Ahmad · Khadija Shabbiri · Ahmad Adnan

Received: 5 December 2011 / Accepted: 26 January 2012 / Published online: 23 February 2012

Abstract *Nocardia asteroides* is a pathogenic bacterium that causes severe pulmonary infections and plays a vital role in HIV development. Its electron transport chain containing cytochromes as electron carriers is still undiscovered. Information regarding cytochromes is important during drug synthesis based on cytochrome inhibitions. In this study we explored the electron transport of *N. asteroides*. Spectroscopic analysis of cytoplasm and membranes isolated from *N. asteroides* indicates the presence of soluble cytochrome-*c*, complex-II and the modified a_1c_1 complex as the terminal oxidase. The molecular weight of the respiratory complex-II isolated and purified from the given bacterium was 103 kDa and was composed of three subunits, of 14, 26 and 63 kDa. Complex-II showed symmetrical α-absorption peaks at 561 nm in the reduced state. Spectral analysis revealed the presence of only one heme *b* molecule (14-kDa subunit) in complex-II, which was confirmed by heme staining. Heme *b* content was found to be 9.5 nmol/mg in complex-II. The electron transport chain of *N. asteroides* showed the presence of soluble cytochrome-*c*, cytochrome-a_1c_1 and cytochrome-*b*.

Keywords Cytochrome · Complex-II · SQR activity · Electron transport chain

W. Ahmad · K. Shabbiri · A. Adnan
Department of Chemistry, GC University, Lahore 54000, Pakistan

W. Ahmad (✉)
Centre of Excellence in Molecular Biology, 87-West Canal Road, Lahore 53700, Pakistan
e-mail: waqarchemist@hotmail.com; waqarchemist123@yahoo.com

Introduction

Nocardia asteriodes is a member of the family Nocardiaceae, order Actinomycetales (Bordet et al. 1972). It is the most common pathogen that can cause pulmonary disease, followed by *Nocardia brasiliensis*. It is a gram-positive, partially acid-fast, aerobic organism that causes suppurative and granulomatous lesions in humans. An increasing number of *Nocardia* infections have been noted in the past 20 years as a result of increasing numbers of immunocompromised hosts and improvement in laboratory identification techniques (Welsh et al. 1995). This enhancement has also been associated with advances in organ transplantation and increases in HIV infections in the past two decades (Brown-Elliott et al. 2006).

The respiratory electron transfer chain of bacteria is usually composed of enzyme complexes I–IV, cytochromes, ubiquinone and complex V (ATP synthase). Electrons are transferred from NADH and succinate (cytoplasmic electron carriers) to membrane-bound reductases, which in turn reduce quinone. These electrons are then transferred directly to the cytochrome-*c* oxidase pathway or through the quinol-O_2 oxidoreductase pathway (Dudkina et al. 2005; Megehee et al. 2006; Schultz and Chan 2001; Adams and Turnbull 1996; Shabbiri et al. 2010). Complex-I of the electron transport chain is composed of NADH-quinone oxidoreductase, complex-II is composed of succinate coenzyme O reductase (SQR), complex-III is generally composed of ubiquinone–cytochrome-*c* oxidoreductase, while cytochrome *c*-oxidase acts as complex-IV, also known as the terminal enzyme of the respiratory chain (Loskovich et al. 2005; Ferguson 2001).

The electron transfer mechanism in gram-positive bacteria is still poorly understood, whereas detailed information on gram-negative bacteria is available (Croal et al.

2004; Rabaey et al. 2007). Several types of cytochrome-*c* of low molecular mass have been reported. In gram-positive bacteria there is much less of a chance of finding soluble cytochrome because of the absence of an outer membrane or periplasmic space. The cytochrome-*c* binding surface of the oxidase is topologically outside the cell (Megehee et al. 2006). However, *N. asteroides* is a partially acid-fast bacterium and can have structural similarities to both gram-positive and -negative bacteria (Beaman 1973), so there might be a chance of finding soluble cytochrome-*c*.

In bacteria, complex-II acts as a dehydrogenase and plays a role in the tricarboxylic acid cycle. It serves as the only direct link between activity in the citric acid cycle and electron transport in membranes. This complex is composed of membrane-bound and water-soluble moieties. Heme cytochrome-*b* is present in a membrane-bound moiety, while flavin adenine dinucleotide (FAD) and iron sulfur clusters are present in a water-soluble moiety (Brown 2000; Cecchini et al. 2002; Doi et al. 1983). Although cytochrome-*b* is generally present in association with SQR, the exact role of this component is yet to be determined. Previous studies have shown that complex-II can contain one or two heme *b*s per SQR (Qureshi et al. 1996; Melo et al. 2004).

Complex-IV or terminal oxidase is usually heme-Cu-oxidase, composed of two catalytic subunits, I and II. Subunit-I contains two heme clusters. The first heme, usually heme "*a*," acts as an electron input device to the second heme "a_3" with copper (Michel et al. 1998; Palmer 1987). Subunit-II processes the electron donation and contains a Cu center. These vertically arranged enzymes transfer charge across the membrane, and electrons are passed to O_2. Some variations in complex-IV have been reported, such as replacement of heme *b* or *o* with heme *a* and heme *c* in place of a_3 (Michel 1998; Berg et al. 2002).

In the present study, we analyzed the cytoplasmic and membrane proteins of *N. asteroides* and report the presence of soluble cytochrome-*c*, membrane-bound heme *b* and terminal oxidase a_1c_1. Furthermore, we also purified and characterized membrane-bound complex-II from *N. asteroides*.

Materials and Methods

Materials

Sodium succinate and DEAE-Sephadex were purchased from Sigma (St. Louis, MO, USA). DEAE-Bio-Gel and Bio-Gel-P100 were from Bio-Rad (Richmond, CA, USA). Commassie brilliant blue dye was from Fischer (Fairlawn, NJ, USA). Triton X-100, Tris-salt and DCPIP were from Fluka (Buchs, Switzerland). Pyridine and sodium dithionate were from BDH (Toronto, Canada). Nutrient agar, nutrient broth, SDS, EDTA and potassium dochromate were purchased from Merck (Darmstadt, Germany). All other chemicals used in this study were of extra-pure grade.

Organism and Culture Conditions

N. asteroides strain NRRL-B-3828 was kindly given by Dr. Quratulain Syed (Pakistan Council of Scientific and Industrial Research Laboratories Complex, Lahore, Pakistan). *N. asteroides* was cultivated aerobically in nutrient medium at 37°C in conical flasks on a shaker incubator at 250 rpm. Cells were harvested at early exponential stage after 20 h of growth (data not shown) by centrifugation at 6,000 rpm for 20 min and suspended in 50 mM Tris–HCl buffer (pH 8.4) containing 50 mM EDTA.

Preparation of Membrane

All steps from membrane preparation to enzyme assay were performed with some modifications according to protocols previously described (Shabbiri et al. 2010). Briefly, about 25*g* centrifugally packed frozen cells suspended in a mixture of 400 ml of 50 mM Tris–HCl buffer (pH 8.4) and 20 ml of 50 mM EDTA were disrupted with a sonic oscillator at 15 kHz at 4°C for 20 min with intervals of 2 min. After removal of unbroken cells by centrifugation at 15,000 rpm at 4°C for 15 min, supernatant-containing broken cells were ultracentrifuged at 45,000 rpm for 45 min at 4°C. After centrifugation, cytoplasm was obtained as supernatant, while a reddish brown pellet indicated cell membranes. This pellet was resuspended in a solution mixture containing 25 ml of 50 mM Tris–HCl buffer (pH 8.4), 2.5 ml of 50 mM EDTA and 4.2 ml of 20% (wt/vol) Triton X-100. This suspension was then subjected to ultracentrifugation at 45,000 rpm for 60 min at 4°C. The reddish brown supernatant of membrane proteins was collected and frozen, while the white pellet of membrane lipids was discarded.

Elution of Membrane Proteins and Purification of Complex-II

The reddish brown supernatant of membrane proteins was subjected to ion-exchange chromatography (Biologic LP system, Bio-Rad) on a DEAE-Sephadex column (4 × 16 cm), washed and equilibrated with 500 ml buffer A (50 mM Tris–HCl buffer, 50 mM EDTA and 1% Triton X-100). Membrane proteins were eluted using a linear gradient solution of 1 liter each of buffer A and buffer B (1 M NaCl and 1% Triton X-100). Elutes were dialyzed after verifying their enzymatic activity against 1 liter of buffer A. Dialyzed elutes were subjected to a second ion-exchange chromatography on a DEAE-Bio-Gel column (1.5 × 8.0 cm) and equilibrated with

buffer A. The adsorbed membrane proteins were eluted with a linear gradient of NaCl (0–1.0 M NaCl) produced in 600 ml of buffer A. Two peaks of fractions 20–25 and 32–37 (5 ml each) were collected and concentrated by lyophilization to an appropriate size. The lyophilized fraction was subjected to gel filtration with a Bio-Gel-P-100 column equilibrated with solution containing 50 mM Tris–HCl buffer (8.4), 1% Triton X-100 and 0.5 M NaCl. The yellowish red fraction of complex-II was collected and used as purified preparation.

Spectrophotometric Measurements of Cytoplasmic and Membrane Proteins

Absorption spectra of cytoplasm and eluted membrane proteins were studied using a quartz cuvette at room temperature in the visible range (380–700 nm) using a Cecil Instruments (Cambridge, UK) UV–Visible spectrophotometer. Cytoplasm and eluted proteins were oxidized with 1 M potassium dichromate and reduced by adding 1 M of sodium dithionate. Ferrohemochrome spectra were obtained by adding 0.5 ml of 0.2 N NaOH, 1.8 ml distilled water and 0.5 ml of pyridine in 0.7 ml of purified proteins and cytoplasm, then reduced with 500 mg of sodium dithionate.

Gel Electrophoresis of Complex-II and Molecular Weight Determination of Cytochrome-*b*

Nondenaturing polyacrylamide gel electrophoresis was performed in the presence of 0.4% Triton X-100 at 4°C, while polyacrylamide gel electrophoresis in the presence of sodium dodecyl sulfate (SDS-PAGE) was performed at room temperature as described by Schagger and von Jagow (1987). The presence of native heme (cytochrome-*b*) for complex-II was detected by heme staining reagent (Connelly et al. 1958). The apparent molecular weight of complex-II and cytochrome-*b* was determined with a set of protein markers (PAGE ruler prestained ladder; Fermentas; Burlington, Canada).

Measurement of Enzymatic Activity

Complex-II (SQR) activity was measured at room temperature spectrophotometrically in time-scanned mode by following the change of absorbance due to reduction of succinate-ubiquinone 1 (UQ_1). Succinate-2,6-dichlorophenolindophenol (DCPIP) was used as a terminal electron acceptor, and the oxidation of succinate to fumarate was determined by monitoring the decrease in absorbance at 600 nm for 5 min. The reaction mixture contained 3 ml 50 mM Tris–HCl buffer (pH 8.4), 9 µl 0.1 M EDTA, 159 µl DCPIP/UQ_1 and 60 µl 0.1 M sodium succinate. The reaction was initiated by adding 40 µl isolated purified complex-II.

Results

Spectral Properties of Cytoplasmic and Purified Membrane Proteins

The absorption spectrum of the *N. asteroides* crude cytoplasm (Fig. 1a) showed the presence of auto-oxidizable cytochrome, while in reduced spectrum of cytoplasm, the α-peak at 549 nm appeared (Fig. 1b). In pyridine spectrum of cytoplasm (Fig. 1c), the α-peak shifted to 553.5. The absorption spectrum of crude membrane proteins at resting and oxidized stages (Fig. 2a, b) showed one peak each at 409 and 387.5 nm, respectively. Partial purification of

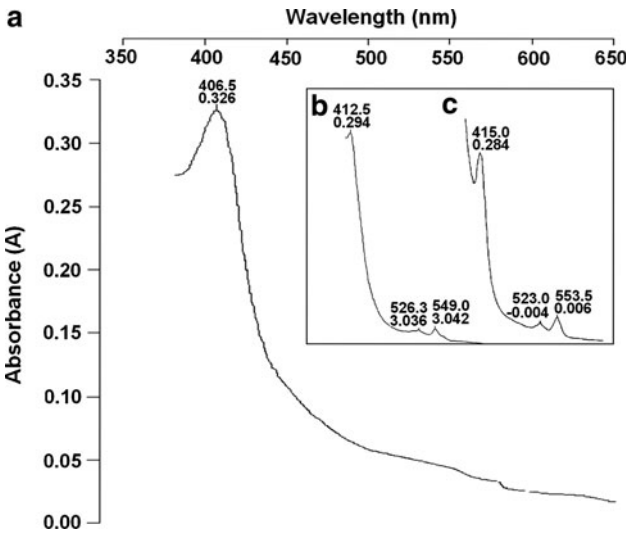

Fig. 1 Absorption spectrum of the *N. asteroides* cytoplasm as (**a**) crude, (**b**) reduced and (**c**) with pyridine

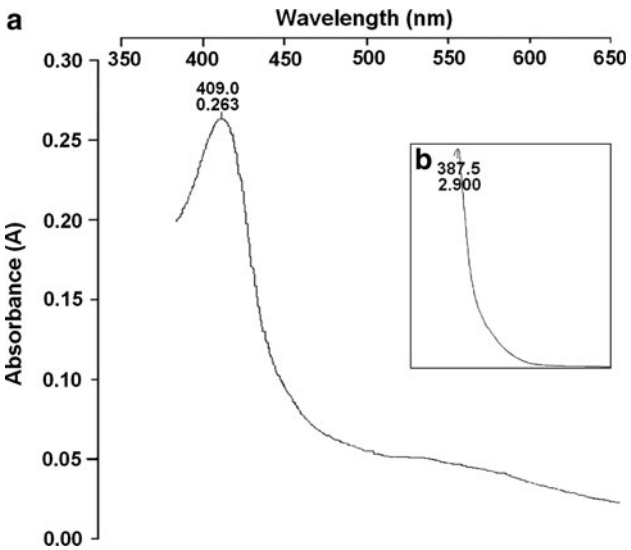

Fig. 2 Absorption spectrum of crude membrane proteins at resting (**a**) and oxidized (**b**) stages

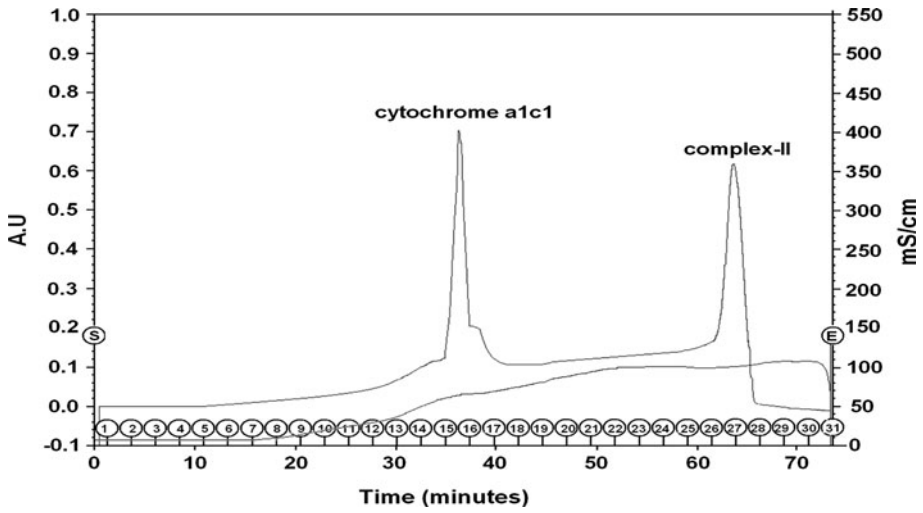

Fig. 3 Partial purification of membrane proteins with ion-exchange chromatography. Complex-II was eluted using a linear gradient solution of 600 ml each of buffer A containing 1% of Triton X-100 and buffer B containing 1% Triton X-100 and 1.0 M NaCl

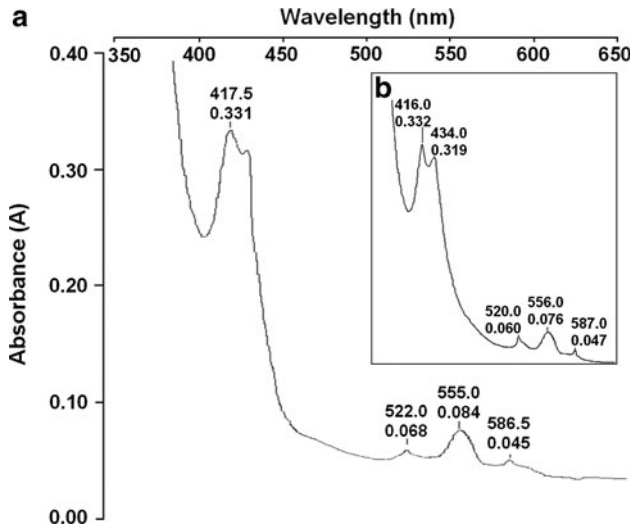

Fig. 4 Reduced (**a**) and pyridine (**b**) spectra of cytochrome-a_1c_1

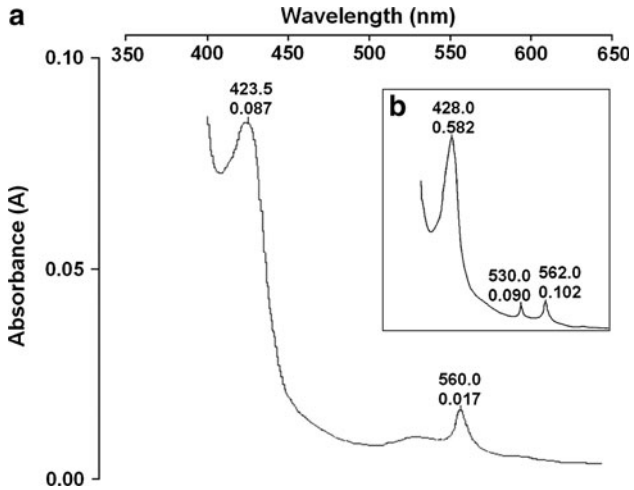

Fig. 5 Reduced (**a**) and pyridine (**b**) spectra of complex-II

membrane proteins with ion-exchange chromatography showed the presence of two membrane-bound cytochromes (Fig. 3). When purified membrane protein fraction 1 was reduced with sodium dithionate, it showed prominent peaks at 586.0, 555.5, 524.5 and 418.5 nm (Fig. 4a). In pyridine spectra shifting of peaks was observed at 587.0, 556.0, 520 and 416.0 nm, while a new peak at 434.0 nm also appeared (Fig. 4b). Reduced spectra of fraction 2 (Fig. 5a) showed peaks at 561.0 and 425.0 nm. It also showed a trough at 525–535 nm. Pyridine spectra showed three peaks, at 562.0, 530.0 and 428.0 nm (Fig. 5b).

Purification of Complex-II from *N. asteroides* Strain NRRL-B-3828

The Triton X-100 solublized *N. asteroides* membrane-bound complex-II in active form was purified by ion-exchange chromatography and gel filtration. The representative purification factors and purification yield are summarized in Table 1. Complex-II was found to be purified to an electrophoretically homogenous state when subjected to PAGE and stained with Coomassie brilliant blue, and one single band was observed after heme staining.

Enzymatic Properties of Complex-II

The enzymatic properties of the complex-II isolated and purified from *N. asteroides* were analyzed spectrophotometrically at 660 nm using artificial electron donor DCPIP. The heme *b* moiety of oxidized complex-II was fully reduced in 5 min when succinate was added to complex-II (Fig. 6). The optimal pH of the reaction was 8.4.

Gel Electrophoresis of Complex-II

Three protein bands appeared on the 12.5% SDS-PAGE; when isolated, complex-II was analyzed for subunit

Table 1 Purification of complex-II

Step	Total vol. (ml)	Total protein (mg)	Total heme *b* (nmol)	Heme *b* protein (nmol/mg)	Yield (%)
Solublized membranes	80.0	235	310	1.3	100
DEAE-Sephadex	25.0	39	119	3.05	38.34
DEAE-Bio-Gel	10.0	8.7	41.3	4.08	13.3
Gel filtration	8.0	4.2	35.6	8.5	11.48
Purified enzyme	1.0	2.9	27.4	9.5	8.7

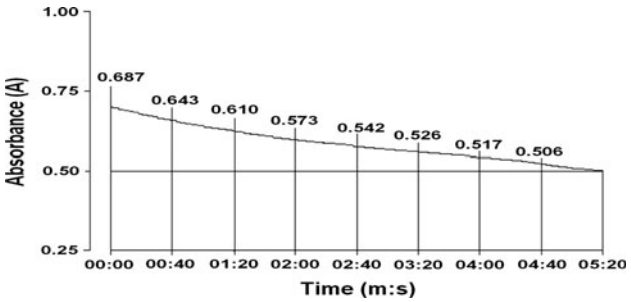

Fig. 6 Enzyme assay of complex-II from *N. asteroides*. The enzymatic reaction was time-scanned for 5 min at 660 nm to observe the decrease in absorption of DCPIP dye, which acts as artificial electron acceptor in vitro

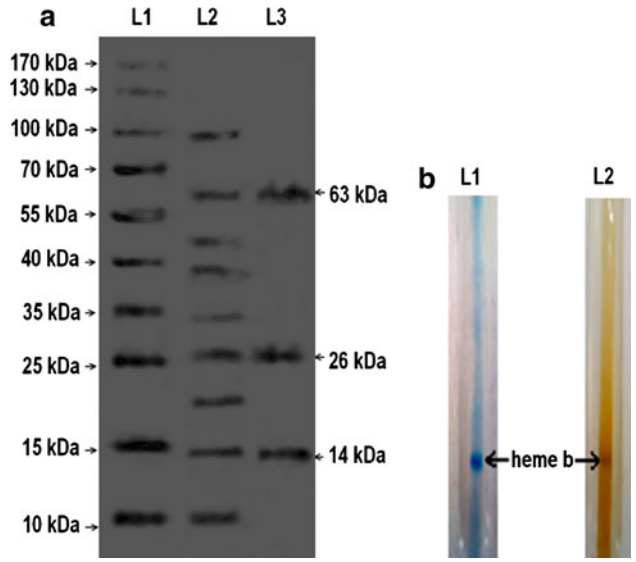

Fig. 7 SDS-PAGE (**a**) and Native PAGE (**b**) of complex-II isolated from *N. asteroides*. Purified cytochrome-*b* was loaded on a 12.5% gel. The gel was stained with Coomassie brilliant blue after electrophoresis. *Lane 1*, molecular mass marker proteins; *lane 2*, sample 1, partially purified complex-II after ion-exchange chromatography; *lane 3*, sample 2, purified complex-II. Total approximate size of the complex-II was 113 kDa. The molecular masses of three subunits of the *N. asteroides* complex-II were estimated to be 63, 26 and 14 kDa. Purified cytochrome-*b* was run on Native PAGE and stained. **a** Coomassie brilliant blue staining of heme *b*, **b** heme staining of heme *b*

composition and denatured at room temperature for 15 min in 5% mercaptoethanol and 2% SDS (Fig. 7a). The molecular masses of the subunits were estimated to be 63, 26 and 14 kDa, respectively. This purified complex-II was also subjected to Native PAGE, followed by Coomassie brilliant blue and heme staining. A single band corresponding to a molecular mass of 14 kDa was stained (Fig. 7b).

Discussion

N. asteroides belongs to a subgroup of aerobic nocardioform actinomycetes and causes severe human urinary tract diseases. The electron transport chain of *N. asteroides* is still undiscovered. In this study, for the first time, we report the presence of certain cytochromes and purification of complex-II containing cytochrome-*b*.

Absorption spectra of cytoplasm showed the presence of cytochromes (Fig. 1a), while reduced spectra of cytoplasm confirmed the presence of soluble cytochrome-*c* having an α-peak at 549 nm (Fig. 1b). Cytochrome-*c* acts as the direct electron donor for cytochrome-*c* oxidase or for the enzyme which performs functions similar to those performed by oxidase. However, in pyridine spectra, shifting of the α-peak to 553.5 nm indicated the presence of heme *c* (Fig. 1c) (Connelly et al. 1958; Trudinger et al. 1985; Basu et al. 2008).

Absorption spectra of membrane at resting stage showed the presence of some autoredox state cytochromes (Fig. 2a), while the absorption spectra of oxidized membrane revealed that all the respiratory redox proteins were in oxidized stage as the characteristic α-peak of cytochromes was absent (Fig. 2b). The characteristic peak at 586 nm in reduced spectra showed the presence of cytochromes *a* and *c* in combined form. Cytochrome-a_1c_1 has been purified from *N. winogradskyi* by Tanaka et al. (1983). Its reduced form shows absorption peaks at 416, 521 and 556 nm (attributed to heme *c*) and at 434 and 587 nm (attributed to heme *a*). This cytochrome was not autoxidizable, so it is not a terminal oxidase as earlier believed. Furthermore, its spectral properties due to heme *a* are really those of a_1 (Mogi 2009; Tanaka et al. 1983).

The presence of SQR and any type of cytochrome-*b* has been reported in many bacteria. Cytochrome-*b* is a component of complex-II and is required for electron transfer

from succinate to ubiquinone. Many workers have reported the presence of complex-II and many types of cytochrome-*b* in several bacteria (Shabbiri et al. 2010; Qureshi et al. 1996; Tamegai et al. 1993). In this study we isolated and purified complex-II from *N. asteroides*. Complex-II was highly active and best solubilized in non-ionic detergent Triton X-100. The α-peak at 561.0 nm that appeared during the reduced spectrum of purified fraction 2 revealed the presence of the respiratory bound complex of oxidoreductase (complex-II), which was confirmed by pyridine spectra. These absorption peaks were very close to the isolated complex-II from other bacteria.

Bacterial SQR can contain one or two heme *b* molecules in the complex (Qureshi et al. 1996). *Proteus mirabilis* and *Escherichia coli* complex-II showed only one heme *b*, while *Bacillus subtilis* contains two heme proteins (Shabbiri et al. 2010; Qureshi et al. 1996). A symmetrical α-peak at 562.0 nm revealed the presence of a single cytochrome-*b*, which was confirmed by gel electrophoresis. The molecular weight of the purified complex-II was 103 kDa, very near the purified complex-II by other bacteria (Qureshi et al. 1996; Xin et al. 2009; Yariv et al. 1981). Heme staining of only the 14-kDa subunit confirmed the presence of one heme *b* molecule in *N. asteroides* complex-II. Recovery in the purification on the basis of total heme *b* content was calculated to be about 9.5 nmol/mg, which yields 8.6% of the total solubilized protein. SQR was also very active when analyzed using the artificial electron acceptor DCPIP. A decrease in absorbance of DCPIP in 5 min confirmed the reduction ability of enzyme.

In conclusion, our study revealed that the electron transport chain of *N. asteroides* contains highly active complex-II, while the presence of terminal oxidase a_1c_1 and soluble cytochrome-*c* was also observed.

References

Adams PL, Turnbull DM (1996) Disorders of the electron transport chain. J lnherit Metab Dis 19:463–469

Basu S, Azarova NA, Font MD, King SB, Hogg N, Gladwin MT, Shiva S, Kim-Shapiro DB (2008) Nitrite reductase activity of cytochrome *c*. J Biol Chem 283(47):32590–32597

Beaman BL (1973) An ultrastructural analysis of *Nocardia* during experimental infections in mice. Infect Immun 8(5):828–840

Berg JM, Tymoczko JL, Stryer L (2002) Biochemistry, 5th edn. W H Freeman, New York

Bordet C, Karahjoli M, Gateau O, Michel G (1972) Cell walls of *Nocardia* and related actinomycetes: identification of the *Nocardia* by cell wall analysis. Int J Syst Bacteriol 22:251–259

Brown S (2000) Does succinate oxidation yield FADH2 or ubiquinol? Biochem Educ 28:52–54

Brown-Elliott BA, Brown JM, Conville PS, Wallace RJ Jr (2006) Clinical and laboratory features of the *Nocardia* spp. based on current molecular taxonomy. Clin Microbiol Rev 19(2):259–282

Cecchini G, Schroder I, Gunsalus RP, Maklashina E (2002) Succinate dehydrogenase and fumarate reductase from *Escherichia coli*. Biochim Biophys Acta 1553:140–157

Connelly JL, Morrison M, Stotz E (1958) Hemins of beef heart muscle. J Biol Chem 233:743–747

Croal LR, Gralnick JA, Malasarn D, Newman DK (2004) The genetics of geochemistry. Annu Rev Genet 38:175–202

Doi M, Takamiya KI, Nishimura M (1983) Isolation and properties of membrane-bound cytochrome *c*-552 from photosynthetic bacterium *Chromatium vinosum*. Photosynth Res 4:49–60

Dudkina NV, Eubel H, Keegstra W, Boekema EJ, Braun HP (2005) Structure of a mitochondrial supercomplex formed by respiratory-chain complexes I and III. Proc Natl Acad Sci USA 102: 3225–3229

Ferguson SJ (2001) Keilin's cytochromes: how bacteria use them, vary them and make them. Biochem Soc Trans 29:629–640

Loskovich MV, Grivennikova VG, Cecchini G, Vinogradov AD (2005) Inhibitory effect of palmitate on the mitochondrial NADH: ubiquinone oxidoreductase (complex I) as related to the active-de-active enzyme transition. Biochem J 387:677–683

Megehee JA, Hosler JP, Lundrigan MD (2006) Evidence for a cytochrome bcc–aa_3 interaction in the respiratory chain of *Mycobacterium smegmatis*. Microbiology 152:823–829

Melo AM, Bandeiras TM, Teixeira M (2004) New insights into type II NAD(P)H: quinone oxidoreductases. Microbiol Mol Biol Rev 68(4):603–616

Michel H (1998) The mechanism of proton pumping by cytochrome *c* oxidase. Proc Natl Acad Sci USA 95:12819–12824

Michel H, Behr J, Harrenga A, Kannt A (1998) Cytochrome *c* oxidase: structure and spectroscopy. Annu Rev Biophys Biomol Struct 27:329–356

Mogi T (2009) Probing structure of heme *a* synthase from *Bacillus subtilis* by site-directed mutagenesis. J Biochem 145(5):625–633

Palmer G (1987) Cytochrome oxidase: a perspective. Pure Appl Chem 59(6):749–758

Qureshi MH, Fujiwara T, Fukumori Y (1996) Succinate: quinone oxidoreductase (complex II) containing a single heme *b* in facultative alkaliphilic *Bacillus* sp. strain YN-2000. J Bacteriol 178(11):3031–3036

Rabaey K, Rodríguez J, Blackall LL, Keller J, Gross P, Batstone D, Verstraete W, Nealson KH (2007) Microbial ecology meets electrochemistry: electricity-driven and driving communities. ISME J 1(1):9–18

Schagger H, von Jagow G (1987) Tricine-sodium dodecylsulfate polyacrylamide gel electrophoresis for the separation of proteins in the range from 1 to 100 kDa. Anal Biochem 166:368–379

Schultz BE, Chan SI (2001) Structures and proton-pumping strategies of mitochondrial respiratory enzymes. Annu Rev Biophys Biomol Struct 30:23–65

Shabbiri K, Ahmad W, Syed Q, Adnan A (2010) Isolation and purification of complex II from *Proteus mirabilis* strain ATCC 29245. Braz J Microbiol 41(3):796–804

Tamegai H, Yamanaka T, Fukumori Y (1993) Purification and properties of a "cytochrome a_1"-like hemoprotein from a magnetotactic bacterium, *Aquaspirillum magnetotacticum*. Biochim Biophys Acta 1158:237–243

Tanaka Y, Fukumori Y, Yamanaka T (1983) Purification of cytochrome a_1c_1 from *Nitrobacter agilis* and characterization of nitrite oxidase system of the bacterium. Arch Microbiol 135:265–271

Trudinger PA, Meyer TE, Bartsch RG, Kamen MD (1985) The major soluble cytochromes of the obligately aerobic sulfur bacterium, *Thiobacillus neapolitanus*. Arch Microbiol 141:273–278

Welsh O, Salinas MC, Rodriguez MA (1995) Treatment of eumycetoma and actinomycetoma. Curr Top Med Mycol 6:47–71

Xin Y, Lu YK, Fromme P, Blankenship RE (2009) Purification, characterization and crystallization of menaquinol: fumarate oxidoreductase from the green filamentous photosynthetic bacterium *Chloroflexus aurantiacus*. Biochim Biophys Acta 1787:86–96

Yariv J, Kalb AJ, Sperling R, Bauminger ER, Cohen SG, Ofer S (1981) The composition and the structure of bacterioferritin of *Escherichia coli*. Biochem J 197:171–175

J Membrane Biol (2012) 245:97–105
DOI 10.1007/s00232-012-9418-6

Hyperpolarization of the Membrane Potential in Cardiomyocyte Tissue Slices by the Synchronization Modulation Electric Field

Robin Dando · Zhihui Fang · Wei Chen

Received: 20 June 2011 / Accepted: 31 January 2012 / Published online: 23 February 2012

Abstract Our previous studies have shown that a specially designed, so-called synchronization modulation electric field can entrain active transporter Na/K pumps in the cell membrane. This approach was previously developed in a study of single cells using a voltage clamp to monitor the pump currents. We are now expanding our study from isolated single cells to aggregated cells in a 3-dimensional cell matrix, through the use of a tissue slice from the rat heart. The slice is about 150 μm in thickness, meaning the slices contain many cell layers, resulting in a simplified 3-dimensional system. A fluorescent probe was used to identify the membrane potential and the ionic concentration gradients across the cell membrane. In spite of intrinsic cell-to-cell interactions and the difficulty in stimulating cell aggregation in the tissue slice, the oscillating electric field increased the intracellular fluorescent intensity, indicating elevation of the cell ionic concentration and hyperpolarization of the cell membrane. Blockage of these changes by ouabain confirmed that the results are directly related to Na/K pumps. These results along with the backward modulation indicate that the synchronization modulation electric field can influence the Na/K pumps in tissue cells of a 3-dimensional matrix and therefore hyperpolarize the cell membrane.

Keywords Cardiac tissue slice · Hyperpolarization · Synchronization · Modulation · Na/K pump

R. Dando · Z. Fang · W. Chen (✉)
Cellular and Molecular Biophysics Lab, Department of Physics, University of South Florida, 4202 E. Fowler Ave., Tampa, FL 33620, USA
e-mail: wchen@cas.usf.edu

Introduction

The electrogenic action of the Na/K-ATPase or Na/K pump has been thoroughly documented since its initial characterization around 50 years ago (Skou 1957; Post and Jolly 1957; Albers 1967). The pump molecule, in each pumping cycle, extrudes 3 Na ions and pumps in 2 K ions against their electrochemical potential barriers by consuming metabolic energy from hydrolysis of one ATP molecule. The major function of the Na/K pump is to maintain the intracellular ionic concentration and the potential difference across the cell membrane. The ionic concentration gradient and the membrane potential play a significant role in many cell functions.

Many diseases and disorders are associated with dysfunction of Na/K pumps due to either lack of metabolic energy to fuel the pump molecules, a defect in the mechanism to control the pumps or deficiency of the pump contents. Heart failure often involves a shortage of blood and oxygen, which may result in a deficiency of ATP molecules (Conway et al. 1974). Membrane electroporation in lightning and electric shock will result in loss of ionic concentration gradients (Lee and Kolodncy 1987; Lee et al. 1988). Without quick reinstatement of the ionic concentration gradient, cell excitability may be lost and cells may swell and undergo necrosis. Diminished Na/K pump activity has been observed in several tissues prone to diabetic complications, including peripheral nerves (Stevens et al. 1993; Sima et al. 2004), blood vessels (Wahren et al. 2000), skeletal and cardiac muscles (Yuk-Chow et al. 1993), retinal cells (Phipps et al. 2006) and kidney renal tubules (Scherzer et al. 2000). In addition, in many diseases, Na/K pump functions are impaired by a significant deficiency in the pump itself, such as Alzheimer disease (Evertsen et al. 1997), Huntington disease (Everts et al. 1990), myotonic

dystrophy (Desnuelle et al. 1982), phosphorylase deficiency (De Paoli et al. 2002) and McArdle disease (Haller et al. 1998). How to activate the pump functions is an important scientific question relevant to disease treatment and emergency management.

Significant efforts have been made in the past to electrically modulate the pump function. Many investigators have focused on the interaction of the oscillating electric field resonance with the pump's intrinsic oscillating frequency, where the intrinsic frequencies are assumed to exist (Teissie and Tsong 1980; Serpersu and Tsong 1983; Tsong and Astumian 1987; Blank and Soo 1989; Xie et al. 1994). Several theoretical models have been developed, including a thermal noise model of weak electric field–induced pump activation (Weaver and Astumian 1990), a brownian motion model (Astumian 1997; Tsong 2002) and an adiabatic pump model (Astumian 2003).

Recently, a practical technique was developed by our group to effectively control the pump function. Theoretical analysis of the synchronization modulation (Chen 2008), computer simulation (Chen and Huang 2008; Huang et al. 2009) and experimental results (Chen et al. 2007, 2008) have been reported previously. Here, we only briefly describe the underlying mechanisms involved in the technique and the technique protocol. The technique was developed by introducing the concept from an electronic synchrotron accelerator to the biological system. The technique consists of two steps: first, a specially designed pulsed oscillating electric field is applied to force or synchronize the individual pump molecules to run at the same pace as the field oscillation so that the Na transport from individual pumps is entrapped into the positive half-cycle, while all the K transporters are similarly entrapped in the negative half-cycle; second, the field frequency is gradually changed, either increased or decreased following a step-change pattern. By carefully maintaining the pump synchronization, the pump molecules can be entrained and either accelerated or decelerated, to a defined pumping rate (Chen et al. 2007, 2008).

Our whole-cell patch-clamp experiments on single skeletal muscle cells have demonstrated effective synchronization of the Na/K pumps and realized significant acceleration of the pumping rate up to 10-fold (Chen et al. 2007, 2008). We also showed that the oscillating electric field can elevate or hyperpolarize the membrane resting potential of single intact skeletal muscle fibers (Chen and Dando 2007, 2008).

When single cells are organized into tissues, these natural cell aggregations have resultant electrical properties through tissue matrix structure, cell-to-cell interactions and regulatory mechanisms associated with specific physiological functions. In addition, the cell aggregations with narrow intercellular spaces may obstruct the pathway of the field application to generate an oscillating membrane potential across each individual cell membrane. Our postulation is that the oscillating electric field should be able to penetrate the tissue through the interstitial fluid between the cells, alternating the membrane potential and hence activating the Na/K pumps in inner-layer cells. Because of active entrainment of the pump molecules, the technique should be able to increase the cell ionic concentration gradients and hyperpolarize the membrane potential in tissues.

Here, we report our experimental results in application of the synchronization modulation electric field to cardiomyocytes in tissue slices. Mammalian cardiomyocytes contain some of the highest expression of Na/K-ATPase outside of the CNS. The sliced tissue is estimated to be around five to eight cells thick. Confocal microscopic imaging with slow fluorescent probes was used to monitor the field-induced potential changes. The study demonstrated that the synchronization modulation electric field can effectively hyperpolarize the cell membrane beyond the normal resting potential by activating the Na/K pumps in tissue cells.

Methods

All animal work was carried out under full Institutional Animal Care and Use Committee approval. Adult male Sprague–Dawley rats weighing 200–300 g were anesthetized using 100 mg/kg thiobutabarbitol (Inactin; Sigma-Aldrich, St. Louis, MO), injected intraperitoneally; and the hearts were quickly dissected from the pericardium and placed in cooled phosphate-buffered saline (PBS) solution, oxygenated with 95% oxygen, 5% CO_2. The fat, arteries and aorta were removed in solution; and the atria were dissected away. Dissected tissue from the left ventricle was briefly dried and brought into contact with the stage of an Electron Microscopy Sciences OTS 4500 oscillating tissue slicer (Warner Instruments, Hamden, CT), which was previously coated with industrial adhesive. Fifteen seconds was deemed sufficient to assure adequate adhesion, with the tissue subsequently resubmerged in oxygenated PBS, this time in the slicer bath. For our application, slices of 150 μm were deemed to be adequate, allowing a thin enough slice for the application but ensuring that the slice was still thick enough to approximate a 3-dimensional region of tissue.

Slices were then placed in a custom-made experimental chamber (a modified Ussing chamber) filled with cell culture solution. A schematic of the chamber is displayed in Fig. 1, with a transparent base to allow fluorescence to pass, with a small working distance from the microscope objective. The slice was sealed airtight (around 1 MΩ

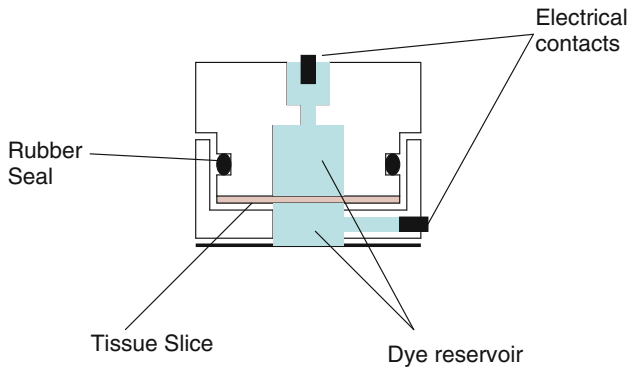

Fig. 1 Modified Ussing chamber, with slice surrounded by two dye reservoirs and electrical contacts made to *top* and *bottom*

sealing resistance) into two compartments, the top and bottom, ensuring the voltage drop of the electric field applied to the two compartments was mainly across the tissue slice. Electrical contacts were made with agar bridges to two compartments in order to minimize junction potential. Adequate dye reservoirs were maintained on either side of the tissue slice, to provide enough dye molecules for the cells, while still being small enough to not interfere with the microscope depth of field.

Membrane potential was measured using fluorescence probe tetramethylrhodamine ethyl ester (TMRE). Fluorescence images were taken using standard rhodamine optics, employing 488 nm argon laser excitation and 505 nm long pass emission filter and a fully computer-controlled Olympus (Center Valley, PA) IX81 confocal microscope system, running the Fluoview Tiempo (Olympus, Tokyo, Japan) analysis package. The confocal microscope is able to focus on a specific cell layer inside the tissue in order to accurately and efficiently monitor the field-induced fluorescence-intensity changes inside the tissue. A 10× dry objective and a confocal aperture of 80 nm was used in each of these readings.

Potentiometric dye, TMRE, was selected due to its superior potential sensitivity. TMRE dye belongs to a class known as Nernstian dyes, initially developed by Waggoner (1976). In contrast to many other fluorescent dyes that exhibit fluorescence only when binding with specific molecules, TMRE always fluoresces. The lipophilicity of TMRE, combined with the delocalization of the positive charge on the dye molecules, renders them membrane-permeant (Tsien and Waggoner 1990; Loew 1993). The high membrane permeability and the positive charge allow the TMRE molecules to easily penetrate the membrane into the cells due to the negative intracellular membrane potential. When reaching equilibrium, the ratio of the intracellular dye molecules, and hence fluorescence intensity, over those on the extracellular side is governed by the membrane potential difference. Whenever the membrane potential changes, the TMRE molecules redistribute themselves, crossing the membrane and exhibiting a different fluorescent intensity ratio.

It takes time for TMRE molecule redistribution. Therefore, TMRE is called a "slow dye," which fit our purpose well because we were not interested in the oscillating membrane potential induced by the applied electric field. Instead, we were interested in the DC shift, especially the hyperpolarization, of the membrane potential, which is a result of ionic concentration changes due to continuous activation of the Na/K pumps.

TMRE fluorescence probe and confocal microscope imaging have long been used to study membrane potential changes in our lab (Chen and Dando 2007, 2008). In this article, no attempt is made to measure the absolute value of the membrane potential. Instead, we demonstrate the capability of the oscillating electric field to hyperpolarize the membrane potential of a 3-dimensional cellular aggregation in a superfused tissue slice.

Solutions used were as follows (in mM), with chemicals obtained from Sigma unless otherwise noted: Krebs HEPES (KH) solution, 118 NaCl, 10 HEPES, 4.7 KCl, 1.5 $CaCl_2$, 1.1 $MgSO_4$, 1.2 KH_2PO_4, 5.6 glucose; experimental solution, same as KH solution with 1 μM TMRE, 1 μM TTX; culture medium, DMEM with 15% FBS and 1% penicillin/streptomycin. All solutions were titrated to pH 7.4 at 25°C.

Stimulation was provided through a purpose-designed LabVIEW program (Texas Instruments, Dallas, TX), providing an oscillating field empirically calibrated to 50 mV across the cell membrane. This potential difference is within physiological range, far below the thresholds of membrane electroporation (O'Neil and Tung 1991; Chen and Lee 1994) or membrane protein denaturation (Chen and Lee 1994). The initial oscillating frequency was 30 Hz, which is comparable to the natural Na/K pumping rates (Rakowski et al. 1989). After a synchronization period of 3 s (90 oscillating pulses), determined in earlier work to be sufficient to synchronize the pump molecules (Chen et al. 2007), the field frequency was gradually increased by 3% for every 10 pulses, to a final value of 400 Hz, which took about 20 s. Then, the frequency was held at 400 Hz for a period of 400–1,000 s. Fluorescence intensity was measured during the whole stimulation period, from an area on the confocal plane within the tissue slice, and plotted with time. In all experiments, the voltage-gated sodium channels were blocked using TTX so that we could focus on the field effects on the Na/K pumps.

Results

Tissue slicing is tedious, and special care and practice are needed, especially for thin slices. The unhealthy slice may

show some changes or deterioration in the preparation over the time course of the experiments. Identifying a healthy slice is important. Figure 2 is an image of a typical healthy slice, with individual myocytes observable. Striations are visible within the individual cells, and some outer cells are observed to beat during imaging. This would indicate that the cells are still alive and healthy and that the slice is viable for experimentation.

The results of measurement of TMRE fluorescence intensity presented here are averaged values. We measured the average fluorescence intensity in several regions, each containing over 100 cells. When comparing the results from a whole region with individual regions, the pattern of changes was very similar for a healthy slice, validating this averaging method. When the pattern of changes was noticeably different, the slice was considered unhealthy and abandoned.

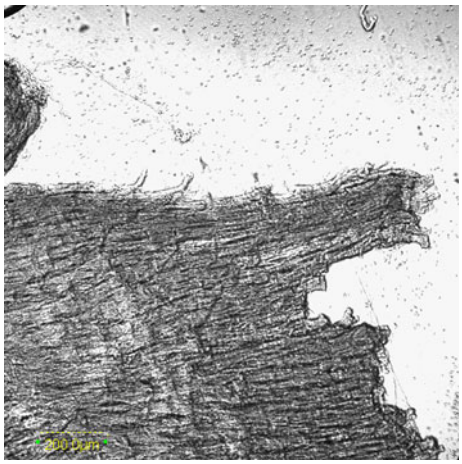

Fig. 2 Transmission image of tissue slice. Many individual cells are evident, woven into a 2-dimensional lattice

Fluorescence intensity was measured before and during the field application. In order to demonstrate the field-induced changes in the membrane potential and especially for the purpose of comparison of the results from different slices, the averaged fluorescence intensity measured before the field application functioned as a control of the slice. All results measured during the field application were normalized to this control value.

We first measured the field-induced fluorescence-intensity changes from the surface of the tissue slice. Seven tissue slices from individual rats were studied. The fluorescence changes due to the field application were averaged and plotted with standard deviation as a trace vs. the field application time, as shown in Fig. 3.

The results show that the fluorescence intensity was gradually and monotonically increased with a few seconds' time delay through the whole procedure of the field application, showing that more dye molecules penetrate the cell membrane into the cells due to the synchronization modulation electric field. Because the number of dye molecules penetrating the cell membrane into the cells depends on the membrane potential changes, this result indicates that the cell membrane potential is progressively hyperpolarized upon the field application.

At the end of the 16-min field application, the average hyperpolarization was about 9%. This value is in agreement with our earlier results taken in single skeletal muscle fibers (Chen and Dando 2007) and slightly less than that measured in single cardiomyocytes (Chen and Dando 2008). We would expect it to be more difficult to hyperpolarize the membrane potential of the aggregated cells in tissue than individual

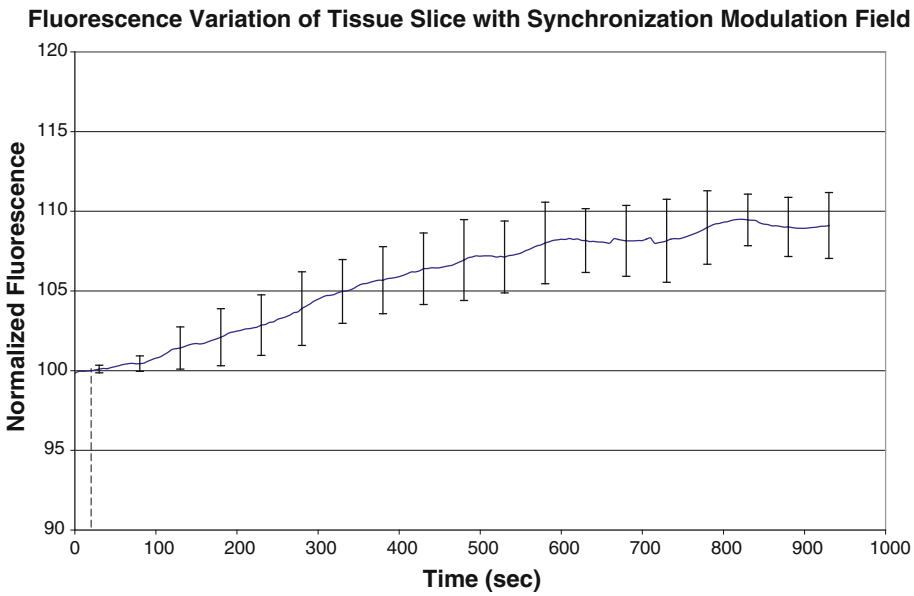

Fig. 3 Fluorescence-intensity changes measured form the surface of the tissue slice upon application of the synchronization modulation electric field, starting from the *dashed line* and lasting for about 15 min. The field frequency was initially 30 Hz and finally modulated to 400 Hz. All intensities were normalized to the value of the control measured before the field application (*dashed line*). Significant increase in fluorescence intensity within the slice is observed. Average of seven cells, with SD indicated

isolated cells. This would be due to gap junction interactions of cardiomyocytes and the difficulty in applying the electric field on individual cells due to their tight adjunction.

In the next step, we investigated the field-induced changes in the membrane potential of the interior cells in the tissue slice. Due to tight adjunction among cardiomyocytes, it may be difficult for the dye molecules to penetrate into the tissue slice. We extended our TMRE dye staining time to 30 min. Then, we measured the fluorescent intensity from the cell layers at the tissue surface and at 20 and 40 μm inside the tissues by adjusting the focus plane of the confocal microscope to the corresponding planes. The fluorescence intensities from all three cell layers were relatively consistent, though slightly lower in the deeper plane. This result implies that the dye molecules can indeed enter the slice from the surrounding reservoir solution and penetrate the cell membrane into the cells. Considering the penetration time of the dye molecules, the field application was also extended to 20 min. The field-induced changes in fluorescence intensity in three cell layers of individual slices were continuously monitored during the field application. Again, the measured fluorescence intensities were normalized to the corresponding control values measured before the field application. The results are plotted in Fig. 4.

The results show that the fluorescence intensities for all three cell layers gradually increased throughout the field application. The fluorescence intensity from the surface cell layer had the highest increment up to about 10% for 15 min field application, while the increments from the 20 and 40 μm interior cell layers were about 5% and 3%, respectively. These results indicate that the oscillating electric field can hyperpolarize the membrane potential beyond the natural resting potential even in the cell layers inside the tissue. Although there is a higher level of hyperpolarization observed at the layers proximal to the edge of the tissue slice, these are undoubtedly evidence that the oscillating electric field can penetrate into the 3-dimensional tissue matrix to hyperpolarize the membrane potential at least several cell layers into the slice.

These results were expected. Because of the voltage drop through the interstitial fluid and the tight adjunction among the cardiomyocytes in the pathway of the field application, the field-induced membrane potential on individual cells may not be the same. The deeper the cell layer is, the less the field-induced membrane potential. In addition, the series resistance in the pathway of the electric field slows down the process in charging the membrane capacitance or increases the charging time constant. Again, the deeper the cell layer is, the larger the time constant and, therefore, the more distortion of the field-induced membrane potential from the applied pulsed oscillating electric field. Our previous studies have shown that the pulsed oscillating membrane potential has the best effect in the pump synchronization, even though for those complications the results show that the synchronization modulation electric field can still noticeably hyperpolarize the membrane potential beyond the physiological value of the cell layers interior the tissue.

The above experiments were repeated seven times with different slices. A sizeable variation from slice to slice would be expected, due to differing geometry of slice arrangements, a slight variation in the direction of slicing within the heart and differing health of individual slices. However, all seven slices showed hyperpolarization of the membrane potential in interior layers upon the field application: the deeper the cell layer, the less the effect.

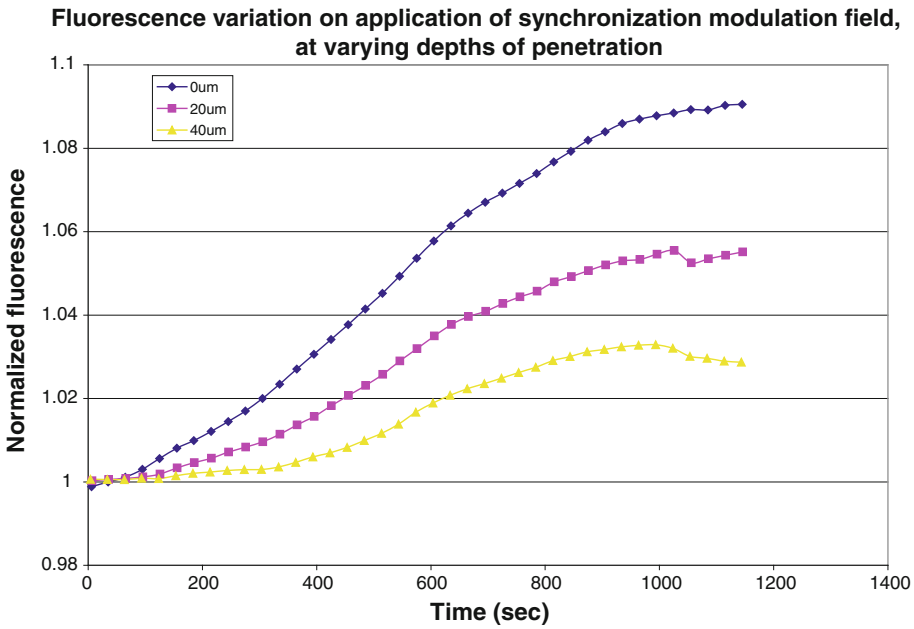

Fig. 4 Normalized fluorescence intensity vs. time of a single tissue slice, showing the relative hyperpolarization variation with different depths into the slice. Maximal effect is observed close to the surface; however, hyperpolarization is nevertheless still observed within the slice

In order to identify that the field-induced increase in the fluorescence intensity and hyperpolarization of the cell membrane were due to activation of the Na/K pump molecules, ouabain, a specific inhibitor of the Na/K pumps, was used in the following experiments. After the tissue slices were stained by the fluorescence dye, the bathing solution was changed to that with 1 mM ouabain (Sigma). Considering the penetration time of ouabain into the tissues, the oscillating electric field was not applied until 30 min later. During the field application, fluorescence intensity was monitored. Seven experiments were conducted from different tissue slices at different depths. No single slice showed an increase in fluorescence intensity upon the field application, while all seven slices exhibited some kind of decrease in intensity. The average of the seven slices is shown in Fig. 5 with standard deviation, where the dashed line represents the starting time of the field application. In 6 min of the field application, the averaged fluorescence intensity decreased over 5%. These results indicate that the field-induced membrane potential hyperpolarization is related to the Na/K pumps. Blockage of the pump functions by ouabain fully eliminated the membrane potential hyperpolarization.

In terms of the consistent decrease in the fluorescence intensity or depolarization of the membrane potential in response to the oscillating electric field, it may be due to opening of the voltage-gated potassium channels. The repeated opening in the K channels without the pump acceleration to compensate the channel currents gradually reduces the intracellular K concentration and therefore depolarizes the membrane potential.

It is also noticeable that the standard deviation of the measurements, especially to the end of the field application, is larger than that without the ouabain, as shown in Fig. 3. This may be due to the ouabain's difficulty in penetrating into the tissues to different depths of different slices. Considering that the sensitivity of the Na/K pump in cardiomyocytes to ouabain is not as high as that in skeletal muscles, we purposely used a 1 mM concentration of oubain and increased the bathing time of ouabain solution to 30 min before the field application.

Figure 6 shows the statistical distribution of tissue slice variance in response to synchronization modulation electric field in the presence and absence of ouabain. The results show that the effect of ouabain is statistically significant in response to the synchronization modulation electric field. In the control without ouabain the field-induced variance was positive and close to 10%, while in the presence of

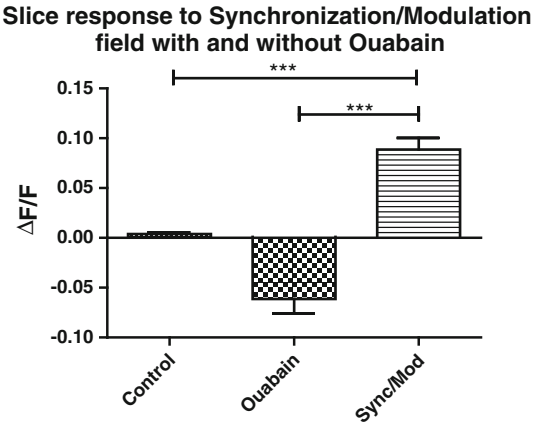

Fig. 6 Statistical distribution of tissue slice variance in response to synchronization/modulation electric field, in the presence and absence of ouabain. The results in both situations show a statistically significant response to the synchronization/modulation electric field, $***P < 0.0001$

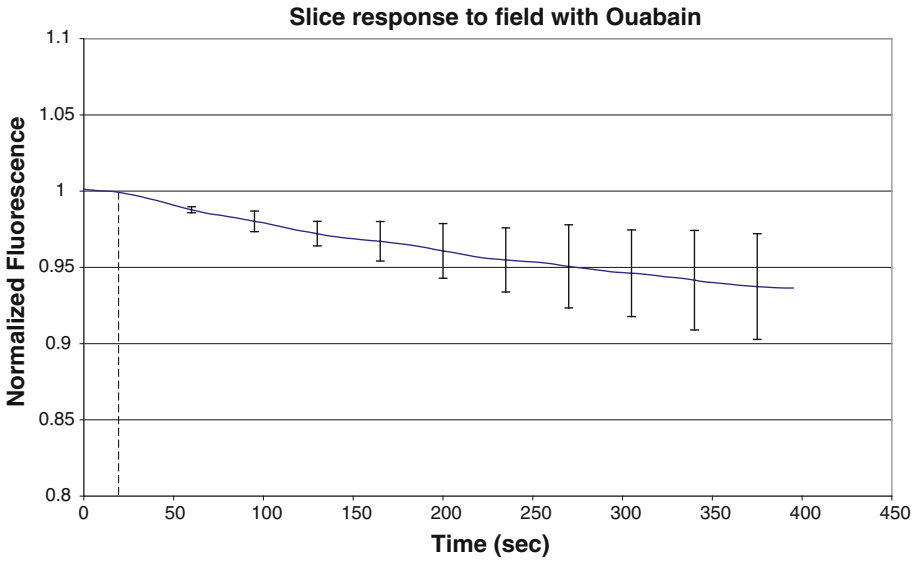

Fig. 5 Tissue slice with ouabain blocking action of Na/K-ATPase molecules, displaying normalized fluorescence intensity vs. time. Decrease in membrane potential is evident upon stimulation of slice

ouabain the variance became negative, –6%, with $P < 0.0001$. In statistical analysis carried out with GraphPad Prism (GraphPad, La Jolla, CA), P values were calculated using both repeated measures t-test for paired analysis and one-way ANOVA for unpaired analysis.

The last concern is that the field-induced hyperpolarization of the cell membrane may not be due to acceleration of the pumping rate but simply to the field application. We further conducted experiments using the backward modulation electric field, where all the field parameters and application protocol were exactly the same as forward modulation except for the modulation direction. That is, after the pump synchronization, the field oscillating frequency, instead of increasing, gradually reduced to slow down the pumping rate. Our previous studies of skeletal muscle fibers by directly monitoring the pump currents with a whole-cell patch clamp have shown that backward modulation can slow down the turnover rate of Na/K pumps.

In contrast to the use of ouabain to inhibit the pump functions, the backward modulation electric field reduces the pumping rate. This group of experiments acts as a second control whereby the tissue experiences the same magnitude of the oscillating electric field as the forward modulation. The side effect, if any, induced by the electric field on the tissue should remain the same. Any different changes in the intracellular fluorescence intensity or any alterations in the membrane potential of the tissue cells will be attributed to the method of modulation.

Similar to the forward modulation, the oscillating electric field with an initial frequency of 40 Hz and 100 oscillating pulses was first to synchronize the pump molecules. Then, the frequency gradually reduced in a stepwise pattern to 10 Hz with a step change of 3% for every 10 pulses. Once determining the minimum frequency (10 Hz), the field remained at this frequency until removal of the field.

We studied seven tissue slices from five rats. Again, no increase in fluorescence intensity was observed in all slices regardless of the depth of the cell layers upon application of the backward modulation electric field. Out of seven slices, six showed a noticeable decrease in the fluorescence intensity. The average of the seven results with standard deviation is shown in Fig. 7. The fluorescence intensity reduced about 4% in response to 6 min of backward modulation. The results indicate that the backward modulation of the oscillating electric field cannot hyperpolarize the membrane potential at all. Instead, the electric field slightly depolarized the membrane potential. This result would be again attributed to the opening of the voltage-gated potassium channels. The pump molecules with the slowed down pumping rate cannot fully compensate the channel currents and, therefore, would be unable to maintain the membrane resting potential.

From Figs. 5 and 7, it is noticed that the backward modulation shows a lesser decrease in the fluorescence intensity and therefore lesser depolarization of the membrane potential than that due to the presence of ouabain. This would make sense as in the case of ouabain the pump molecules are largely, if not entirely, inhibited from functioning and the channel currents can easily reduce the intracellular K concentration and therefore depolarize the membrane potential. Figure 5 shows the fluorescence intensity continuously reduced upon the field application. This would not be the case for the backward modulation. The pumps are still running even though significantly slowed down, which may partially compensate the channel currents. At some stage, a little over 300 s as shown in Fig. 7, the fluorescence intensity remains unchanged.

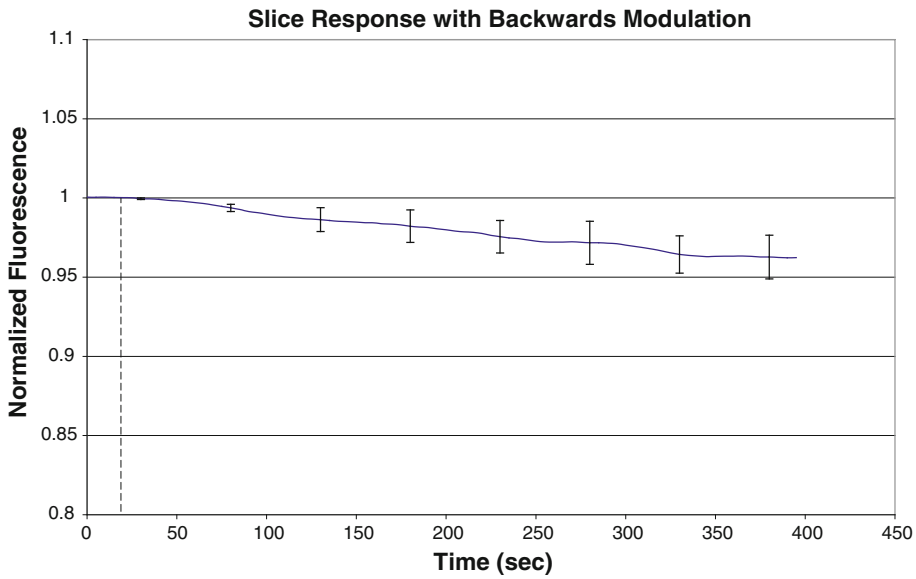

Fig. 7 Tissue slice stimulated with backward modulation, showing normalized fluorescence intensity against time. Again, slice fluorescence intensity is decreased with the stimulation

The opposite effects on the intracellular fluorescence intensity due to the two modulation electric fields, combined with the results using ouabain, provide strong evidence that the electric field alters the function of the Na/K pumps. The change of the pumping rates depends on the direction of the frequency modulation. Because all the parameters of the electric fields, as well as the protocol and configuration of the field applications, are exactly the same except for the direction of the frequency modulation, the reversal effects in the fluorescence intensity and, therefore, in the membrane potential show that the synchronization modulation electric field can effectively entrain, either accelerated or decelerated, the Na/K pumping rate.

Discussion

In this study we investigated whether the synchronization modulation electric field, which has been previously shown to effectively control the pumping rate of the Na/K pumps on single isolated cells, can manipulate the membrane potential in a 3-dimensional tissue slice.

When applying an oscillating electric field to aggregated cells in 3-dimensional tissues to activate the Na/K pump functions, we have to consider two things. One is the possible side effects of the applied electric field on other membrane proteins, especially the voltage-dependent membrane proteins. Another is how the applied electric field generates the necessary oscillating membrane potential for both magnitude and waveform in individual cells of the tissues and effectively activates the pumps in the presence of cell-to-cell interaction and regulatory mechanisms.

In terms of side effects, the major voltage-dependent membrane proteins in cardiac muscle cells are the voltage-gated Na channels, delayed rectifier K channels, inward rectifier K channel and L-type Ca channels. Our previous voltage-clamp studies have shown that an oscillating membrane potential can effectively inactivate the delayed rectifier K channel. The rectifier K channel currents can be significantly reduced even within the synchronization period (not published). In this study, the voltage-gated Na channels were blocked by TTX. In fact, the inactivation of the Na channel is well known and more obvious than that in the K channel. In terms of inward rectifier K channels, indeed, we did not specifically study their inactivation. However, the inward rectifier K channel opens when the membrane potential is hyperpolarized, resulting in K ion influx. If the oscillating electric field cannot inactivate the inward rectifier K channels, the channel opening and the resultant K ion influx will hyperpolarize the membrane potential, which is consistent with the effects of Na/K pump activation. For other membrane proteins, such as the L-type Ca channels, even if they cannot be inactivated, the ion flux is much smaller than in the Na and K channels; and these will not affect the membrane potential significantly.

In fact, our previous studies have shown that the synchronization modulation electric field can hyperpolarize membrane potential of single skeletal muscle fibers in physiological solution without any channel blockers (Chen and Dando 2007). We observed that upon the field application, the membrane potential was initially and quickly depolarized for a short period due to opening of Na channels and then gradually hyperpolarized until removal of the field. Here, we show the field-induced slow hyperpolarization of the membrane potential without transient initial depolarization, which is consistent with our previous studies.

In terms of the difficulty in alternating the membrane potential in individual cells of 3-dimensional tissue and the cell-to-cell interaction, the results clearly show that the electric field can effectively increase the fluorescence intensity and, therefore, the hyperpolarizing membrane potential of the cells persisted to a level of several cell layers into the slice. Indeed, the deeper into the tissues, the less hyperpolarization of the membrane potential was observed.

The fact that the hyperpolarizing effect was eliminated when either the Na/K pumps are chemically blocked with ouabain or the modulation is performed backward would suggest not only that are the effects attributable to the activation on the Na/K pumps but also that the pump molecules can be entrained oppositely. This, in turn, would suggest that we are exhibiting a degree of control over the action of these critical physiological housekeeping molecules at the tissue level, which would provide promise for the future application of the technique.

The transposing of the field application on single cells to cell aggregation in the tissue matrix has a great deal of promise. The contribution of interactions between neighboring cells in the matrix (i.e., connexons) was found to be trivial in front of active entrainment of the pump molecules, with the cell membrane hyperpolarization at a rate and to a level approximated to the behavior observed from single isolated cells.

The success from single cells to tissue slices without much detriment to the level of measured effectiveness suggests that the next logical step would be to apply the technique to a large tissue sample or even a small organ.

Acknowledgement This study was partially supported by research grants from the National Institutes of Health (GM R01 50785) and National Science Foundation (0515787).

References

Albers RW (1967) Biochemical aspects of active transport. Annu Rev Biochem 36:727–756

Astumian RD (1997) Thermodynamics and kinetics of a brownian motor. Science 276:917

Astumian RD (2003) Adiabatic pumping mechanism for ion motive ATPases. Phys Rev Lett 91(11):118102

Blank M, Soo L (1989) The effects of alternating current on Na, K ATPase function. Bioelectrochem Bioenerg 22:313–322

Chen W (2008) Synchronization of ion exchangers by an oscillating electric field: theory. J Phys Chem B 112(32):10064–10070

Chen W, Dando R (2007) Electrical activation of Na/K pumps can increase ionic concentration gradient and membrane resting potential. J Membr Biol 39:117–126

Chen W, Dando R (2008) Membrane potential hyperpolarization in mammalian cardiac cells by synchronization modulation of Na/K Pumps. J Membr Biol 221(3):165–173

Chen W, Huang F (2008) Computer simulation of synchronization of Na/K pump molecules. J Bioenerg Biomembr 40:337–345

Chen W, Lee RC (1994) An improved double vaseline gap voltage clamp to study electroporated skeletal muscle fibers. Biophys J 66:700–709

Chen W, Zhang ZS, Huang F (2007) Entrainment of Na/K pumps by synchronization modulation electric field. J Bioenerg Biomembr 39:331–339

Chen W, Zhang ZS, Huang F (2008) Synchronization of the Na/K pumps by an oscillating electric field. J Bioenerg Biomembr 40:347–357

Conway MJ, Seibel JA, Eaton RP (1974) Thyrotoxicosis and periodic paralysis: improvement with beta blockade. Ann Intern Med 81:332–336

De Paoli F, Overgaard K, Nielsen OB (2002) Protective effects of acidosis and Na/K pump activation on force in K depressed skeletal muscle. J Physiol (Lond) 544:82P

Desnuelle C, Lombet A, Serratrice G, Lazdunski M (1982) Sodium channel and sodium pump in normal and pathological muscles from patients with myotonic muscular dystrophy and lower motor neuron impairment. J Clin Invest 69:358–367

Everts ME, Skajaa K, Hansen K (1990) The concentration of ouabain biding sites in biopsies of uterine muscle. Acta Physiol Scand 139:503–510

Evertsen F, Medlbo JI, Jebens E, Nicolaysen K (1997) Hard training for 5 mo increases Na/K pump concentration in skeletal muscle of cross-country skiers. Am J Physiol Regul Integr Comp Physiol 272:R1417–R1424

Haller RG, Clausen T, Vissing J (1998) Reduced levels of skeletal muscle Na^+, K^+-ATPase in McArdle disease. Neurology 50: 37–40

Huang F, Rabson D, Chen W (2009) Distribution of the Na/K pumps' turnover rates as a function of membrane potential, temperature, and ion concentration gradients and effect of fluctuations. J Phys Chem B 113(23):8096–8102

Lee RC, Kolodncy MS (1987) Electrical injury mechanisms: dynamics of the thermal response. Plast Surg 80:663

Lee RC, Gaylor DG, Bhatt DL, Israel DA (1988) Role of cell membrane rupture in the pathogenesis of electrical trauma. J Surg Res 44(6):709

Loew LM (1993) Confocal microscopy of potentiometric fluorescent dyes. Methods Cell Biol 38:195–209

O'Neil RJ, Tung L (1991) Cell-attached patch clamp study of the electropermeabilization of amphibian cardiac cells. Biophys J 59:1028–1039

Phipps J, Yee P, Fletcher E, Vingrys A (2006) Rod photoreceptor dysfunction in diabetes: activation, deactivation, and dark adaptation. Invest Ophthalmol Vis Sci 47(7):3187–3194

Post RL, Jolly PC (1957) The linkage of sodium, potassium and ammonium active transport across the human erythrocyte membrane. Biochim Biophys Acta 25:118–128

Rakowski RF, Gadsby DC, De Weer P (1989) Stoichiometry and voltage dependence of the sodium pump in voltage-champed, internally dialyzed squid giant axon. J Gen Physiol 93:903–941

Scherzer P, Nachlie I, Bar-On H, Popovtzer M, Ziv E (2000) Renal Na/K ATPase hyperactivity in diabetic psammomys obesus is related to glomerular filtration but is insulin-independent. J Endocrinol 167:347–354

Serpersu EH, Tsong TY (1983) Stimulation of a ouabain-sensitive Rb^+ uptake in human erthrocytes with an external electric field. J Membr Biol 74:191–201

Sima AA, Zhang W, Li ZG, Murakawa Y, Pierson CR (2004) Molecular alterations underlie nodal and paranodal degeneration in type 1 diabetic neuropathy and are prevented by C-peptide. Diabetes 53:1556–1563

Skou J (1957) The influence of some cations on an adenosine triphosphatase from peripheral nerves. Biochim Biophys Acta 23(2):394–401

Stevens MJ, Lattimer SA, Kamijo M, Van Huysen C, Sima AA, Greene DA (1993) Osmotically-induced nerve taurine depletion and the compatible osmolyte hypothesis in experimental diabetic neuropathy in the rat. Diabetologia 36:608–614

Teissie J, Tsong TY (1980) Evidence of voltage-induced channel opening in Na/K ATPase of human erythrocyte membrane. J Membr Biol 55:133–140

Tsien RY, Waggoner AS (1990) Fluorophors for confocal microcopy. In Handbook of confocal microscopy. Plenum Press, New York, pp 169–178

Tsong TY (2002) Na, K-ATPase as a brownian motor: electric field-induced conformational fluctuation leads to uphill pumping of cation in the absence of ATP. J Biol Phys 28(2):309–325

Tsong TY, Astumian RD (1987) Electroconformational coupling and membrane protein function. Prog Biophys Mol Biol 50:1–45

Waggoner AS (1976) Optical probes of membrane potential. J Membr Biol 27(4):317–334

Wahren J, Ekberg K, Johansson J, Henriksson M, Pramanik A, Johansson BL (2000) Role of C-peptide in human physiology. Am J Physiol Endocrinol Metab 278:E759–E768

Weaver JC, Astumian RD (1990) The response of living cells to very weak electric fields: the thermal noise limit. Science 247:459

Xie TD, Marxzalek P, Chen YD, Tsong TY (1994) Recognition and processing of randomly fluctuating electric signals by Na, K-ATPase. Biophys J 67:1247–1251

Yuk-Chow NG, Tolerico PH, Book CBS (1993) Alternations in levels of Na/K ATPase isoforms in heart, skeletal muscle, and kidney of diabetic rats. Am J Physiol Endocrinol Metab 265:E243–E251

J Membrane Biol (2012) 245:107–115
DOI 10.1007/s00232-012-9419-5

Volume-Activated Chloride Currents in Fetal Human Nasopharyngeal Epithelial Cells

Xuerong Sun · Lixin Chen · Haibing Luo · Jianwen Mao · Linyan Zhu · Sihuai Nie · Liwei Wang

Received: 16 September 2011 / Accepted: 31 January 2012 / Published online: 21 February 2012

Abstract Volume-activated chloride channels have been studied by us extensively in human nasopharyngeal carcinoma cells. However, the chloride channels in the counterpart of the carcinoma cells have not been investigated. In this study, volume-activated chloride currents ($I_{cl,vol}$) were characterized in normal fetal human nasopharyngeal epithelial cells using the whole-cell patch-clamp technique. Under isotonic conditions, nasopharyngeal epithelial cells displayed only a weak background current. Exposure to 47% hypotonic solution activated a volume-sensitive current. The reversal potential of the current was close to the calculated equilibrium potential for Cl^-. The peak values of the hypotonicity-activated current at +80 mV ranged from 0.82 to 2.71 nA in 23 cells. Further analysis indicated that the density of the hypotonicity-activated current in most cells (18/23) was smaller than 60 pA/pF. Only five cells presented a current larger than 60 pA/pF. The hypotonicity-activated current was independent of the exogenous ATP. Chloride channel inhibitors ATP, tamoxifen and 5-nitro-2-(3-phenylpropylamino) benzoic acid (NPPB), inhibited the current dramatically. The anion permeability of the hypotonicity-activated chloride channels was $I^- > Br^- > Cl^- >$ gluconate. Unexpectedly, in isotonic conditions, ATP (10 mM) activated an inward-rectified current, which had not been observed in the nasopharyngeal carcinoma cells. These results suggest that, under hypotonic challenges, fetal human nasopharyngeal epithelial cells can produce $I_{cl,vol}$, which might be involved in cell volume regulation.

Keywords Patch-clamp technique · Regulation of ion transport by cell volume · Ion channel/epithelial cell · Epithelial chloride transport

X. Sun
Institute of Aging Research, Key Laboratory for Medical Molecular Diagnostics of Guangdong Province, Guangdong Medical College, Dongguan 523808, China
e-mail: xuerongsun@126.com

X. Sun · H. Luo · S. Nie
Department of Physiology, Guangdong Medical College, Zhanjiang 524023, China

L. Chen (✉) · L. Zhu
Department of Pharmacology, Medical College, Jinan University, Guangzhou 510632, China
e-mail: chenlixinw@sohu.com

J. Mao
Department of Biology, Guangdong Key Laboratory for Bioactive Drugs Research, Guangdong Pharmaceutical University, Guangzhou 510006, China

L. Wang (✉)
Department of Physiology, Medical College, Jinan University, Guangzhou 510632, China
e-mail: wangliweic@sohu.com

Introduction

Regulation of cell volume under osmotic challenges is one of the most fundamental functions of cellular homeostatic mechanisms. In response to osmotic swelling, most cells extrude cytoplasmic solutes, and water resulting in a regulatory volume decrease (RVD). Activation of volume-activated chloride channels and the consequent Cl^- efflux play a key role in the RVD in many cells (Chen et al. 2010; Harvey et al. 2010; Okada et al. 2009).

The characteristics of the volume-activated chloride current $I_{cl,vol}$ have been intensively investigated in many kinds of cells derived from different tissues (Chen et al. 2010; Inoue et al. 2010; Mao et al. 2010; Okada 2006). Besides cell volume regulation, the volume regulatory

chloride channels underpinning $I_{cl,vol}$ play extensive roles in various biological functions, including fluid secretion, maintenance of resting membrane potential, cell proliferation, and cell migration, among others (Mao et al. 2007; Okada et al. 2009).

Epithelial cells derived from the ectodermal blastoderm during embryonic development share many similar functions, such as barrier function and secretion, and activate $I_{cl,vol}$ in response to hypotonic challenges, except in normal cervical epithelial cells (Chou et al. 1995). We previously reported that fetal nasopharyngeal epithelial cells possess background chloride currents under isotonic conditions (Sun et al. 2005b), which implied potential physiological roles of the related channels in the cells. However, whether nasopharyngeal epithelial cells can produce $I_{cl,vol}$ under hypotonic conditions and whether the background chloride current and the $I_{cl,vol}$ share similar characteristics are still unknown.

During the development of the nasopharyngeal epithelium, cell proliferation and differentiation are vigorous; and the frequent flow of ions and water is necessary for these biological processes. Volume-activated chloride channels probably play an important role during the processes, though the characteristics of the $I_{cl,vol}$ in these cells have not been explored. In previous studies, we have explored the characteristics and roles of the $I_{cl,vol}$ in the human nasopharyngeal carcinoma cell line CNE-2Z (Chen et al. 2002, 2007). However, the $I_{cl,vol}$ in the counterpart of the carcinoma cell, the normal human nasopharyngeal epithelial cell, has not been investigated, mostly due to the difficulty in harvesting enough normal nasopharyngeal epithelial cells. In this study, we explored the characteristics of the $I_{cl,vol}$ in primary cultured fetal human nasopharyngeal epithelial cells.

Materials and Methods

Cell Preparation

Fetal human nasopharyngeal epithelial cells were prepared as previously described (Sun et al. 2005b). Briefly, nasopharyngeal epithelia were obtained from 4-month-old fetuses of induced labor. Dissected tissues were explanted onto round coverslips and supplied with Dulbecco's modified Eagle medium/F12 medium containing 5 ng/ml epidermal growth factor (PeproTech, Rocky Hill, NJ), 5×10^{-7} mol/l hydrocortisone (Sigma, St. Louis, MO) and 5 μg/ml insulin (Sigma). Nasopharyngeal epithelial cells in primary culture of 1–2 weeks were used for experiments. The protocol of the study adhered to the tenets of the Declaration of Helsinki and was approved by the local ethics committee.

Electrophysiological Experiments

Whole-cell currents were recorded using the patch-clamp technique with a List EPC-7 patch-clamp amplifier (List Electronic, Darmstadt, Germany). Electrodes with 5–10 MΩ when filled with pipette solution were pulled from standard wall borosilicate glass capillaries. The liquid junction potential was corrected when the electrode entered the bath. After digitization at 3 kHz using a CED 1401 laboratory interface (CED, Cambridge, UK), voltage and current signals from the amplifier together with synchronizing pulses were stored in a computer. For the majority of experiments, cells were held at 0 mV and stepped to ±40, 0 and ±80 mV for 200 ms with a 4 s interval repeatedly. Occasionally, the responses to stepwise (20 mV) pulses from −120 to +120 mV were examined. All current measurements were made 20 ms after the onset of each voltage pulse. All patch-clamp recordings were made at room temperature (20–24°C). Cell capacitance was detected using the methods described previously by us (Chen et al. 2002). Current density was obtained by dividing the current value with cell capacitance. The reversal potential of the current was calculated according to the linear equation $y = ax + b$, and the equilibrium potential for each ion was obtained from the Nernst formula.

Solutions and Chemicals

The pipette solution contained 70 mM *N*-methyl-D-glucamine chloride (NMDG- Cl), 1.2 mM $MgCl_2$, 10 mM HEPES, 1 mM EGTA, 140 mM D-mannitol, and 2 mM Na_2ATP. The isotonic bath solution contained 70 mM NaCl, 0.5 mM $MgCl_2$, 2 mM $CaCl_2$, 10 mM HEPES, and 140 mM D-mannitol. The osmolarity in the pipette and isotonic bath solutions was measured with a freezing-point osmometer (Osmomat 030; Gonotec, Berlin, Germany) and adjusted to 300 mOsm/l with D-mannitol. The hypotonic bath solution was obtained by omitting the D-mannitol from the solution, giving an osmolarity of 160 mOsm/l. In some experiments, the chloride channel blocker tamoxifen, 5-nitro-2-(3- phenylpropylamino) benzoic acid (NPPB) or ATP was added to hypotonic bath solutions to investigate their effects on hypotonicity-activated currents. Tamoxifen, NPPB, and ATP were purchased from Sigma-Aldrich (Poole, UK), and preparation of the stock solution was referred to the method previously described (Chen et al. 2002).

Anion Substitution Experiments

In anion substitution experiments, an agar bridge was used to connect the reference electrode to the bath solution. When the hypotonicity-activated current reached the peak and leveled off, 70 mM NaCl in the 47% hypotonic solution was

replaced by equimolar of NaI, NaBr, or sodium gluconate. The permeability ratio (P_X/P_{Cl}) of various anions relative to that of Cl^- was calculated using the modified Goldman-Hodgkin-Katz equation, $P_X/P_{Cl} = \{[Cl^-]_n \exp(-\Delta V_{rev}F/RT) - [Cl^-]_s\}/[X^-]_s$ (Chen et al. 2002), where $[Cl^-]_n$ and $[Cl^-]_s$ are the Cl^- concentration in the normal and the substituted bath solutions, $[X^-]_s$ is the concentration of the substituted anion, ΔV_{rev} is the difference of the reversal potentials for Cl^- and X^-, F is the Faraday constant, R is the gas constant and T is the absolute temperature.

Statistics

Values are expressed as mean ± standard error (number of observations). Analysis of variance (ANOVA) or Student's *t*-test was used to test for significant differences, and $P < 0.05$ was taken to be significant.

Results

$I_{cl,vol}$ in Nasopharyngeal Epithelial Cells

Coverslips with fetal nasopharyngeal epithelial cells were placed in a perfusion recording chamber. Whole-cell currents were recorded using the patch-clamp technique. Cells were clamped at 0, ± 40, and ± 80 mV (Fig. 1a). When cells were bathed in the isotonic solution, currents were small and stable (Fig. 1b). The current value at ±80 mV was 0.16 ± 0.02 nA ($n = 23$). A large current was activated when cells were exposed to 47% hypotonic bath solution for 1–2 min (Fig. 1c). The current reached a peak and leveled off 3–5 min after exposure to hypotonic solution. Clamped cells remained in a swollen state in hypotonic solution. When hypotonic bath solution was replaced with control isotonic solution, cells shrank toward normal size while the current declined gradually to the basal level. These results indicated that the hypotonicity-activated current was sensitive to cell volume changes.

As shown in Fig. 1c, the hypotonicity-activated current presented mild outward rectification. There was no, or negligible, time-dependent inactivation of the current at +80 mV. When the voltage was stepped to +120 mV from −120 mV, the current still showed no obvious time-dependent inactivation (data not shown). The current–voltage relationships under isotonic and hypotonic conditions are shown in Fig. 1d. The reversal potential of the hypotonicity-activated current was −7.31 ± 0.64 mV ($n = 23$), which was close to the calculated equilibrium potential for Cl^-. In our experiments, the concentration of Cl^- in pipette solution was almost equal to that in bath solution. The calculated equilibrium potential for Cl^- was −0.9 mV. The results suggest that the main component of the current was $I_{cl,vol}$ (details in Discussion).

At +80 mV step, the peak values of the $I_{cl,vol}$ displayed great variation, changing from 0.82 to 2.71 nA in the 23 cells detected. To analyze further the hypotonicity-activated currents recorded in different cells, the current was normalized with cell capacitance, which is directly correlated with the area of cell surface. The results showed that the density of the hypotonicity-activated current in most cells (18/23) was smaller than 60 pA/pF. Only five cells presented a current larger than 60 pA/pF.

Independence of $I_{cl,vol}$ on Exogenous ATP

To investigate the dependence of $I_{cl,vol}$ activation on ATP in fetal nasopharyngeal epithelial cells, ATP was excluded from

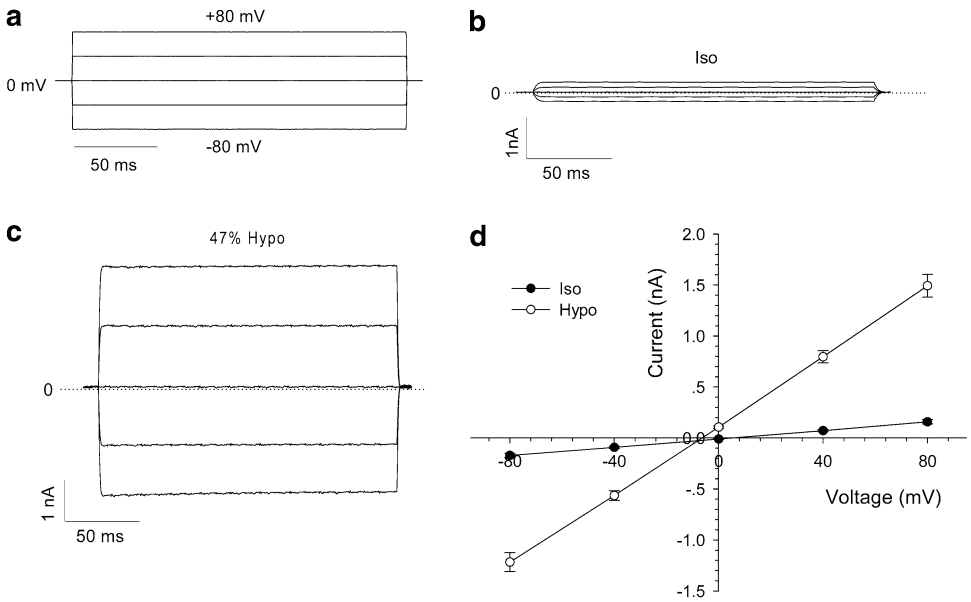

Fig. 1 Whole-cell currents under isotonic and 47% hypotonic conditions. **a** The voltage protocol used to generate the current traces in (**b**) and (**c**). Cells were held at 0 mV and stepped to ±40, 0 and ±80 mV for 200 ms with a 4 s interval repeatedly. The basal current recorded under isotonic conditions (*Iso*) was small (**b**), and exposure to 47% hypotonic bath solution (*Hypo*) activated a large current (**c**). Current values were measured 20 ms after the start of each voltage pulse, and the current–voltage relationships under isotonic and hypotonic conditions are shown in (**d**) (mean ± SE, $n = 23$)

the pipette solution. After the whole-cell configuration was formed, the cell was dialyzed with the ATP-free pipette solution for more than 3 min before exposure to 47% hypotonic bath solution. The results indicated that the volume-activated chloride channels could be activated by the hypotonic challenge in the absence of exogenous ATP (Fig. 2). A hypotonicity-induced chloride current was recorded with the pipette containing the ATP-free solution. The current possessed properties similar to those recorded in the presence of intracellular ATP. The current showed a mild outward rectification and was not inactivated in the observed period. The reversal potential of the current was -7.17 ± 1.05 mV ($n = 9$), which was close to the Cl^- equilibrium potential. There was no significant difference in the current density between the currents recorded in the presence and absence of ATP in the pipette solution ($P > 0.05$, Fig. 2c).

In addition, when ATP was omitted from the pipette solution, the $I_{cl,vol}$ could still be activated repeatedly (Fig. 2b). However, the $I_{cl,vol}$ activated a second time was somewhat smaller than that the first time, whether ATP was included in or excluded from the pipette solution (Fig. 2a, b). We defined the ratio of the currents elicited between the second time and the first time as the "recovery ratio." That is, recovery ratio (%) = (current density induced the second time/current density induced the first time) × 100%. Results showed that when ATP was omitted from the pipette solution the recovery ratios ($65.3 \pm 5.0\%$ at +80 mV, $68.4 \pm 10.3\%$ at −80 mV, $n = 5$) were slightly smaller than those when ATP was included in the pipette solution ($82.5 \pm 6.3\%$ at +80 mV, $80.9 \pm 8.0\%$ at −80 mV, $n = 5$), but the differences were not significant ($P > 0.05$).

Inhibition of $I_{cl,vol}$ by Extracellular ATP

ATP in high concentrations has been proven to be a strong blocker of chloride channels in nasopharyngeal carcinoma cells (Chen et al. 2002). To characterize the $I_{cl,vol}$ further, the effect of extracellular ATP on the current was tested in

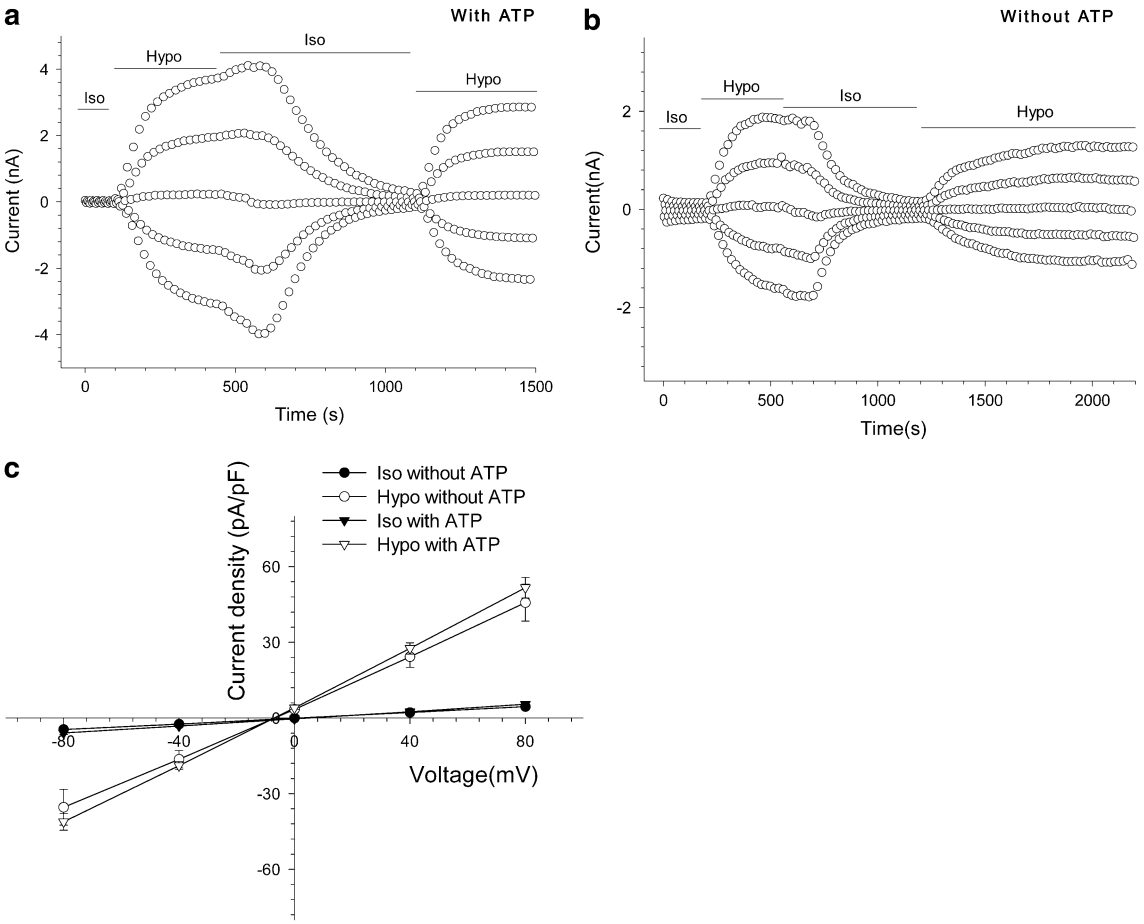

Fig. 2 Volume-activated chloride currents recorded with ATP-rich (2 mM) or ATP-free pipette solutions. Values of the whole-cell currents were obtained 20 ms after the start of each voltage step (0, ±40, and ±80 mV). Large currents were activated repeatedly by the 47% hypotonic solution in both the presence (**a**) and the absence (**b**) of ATP in the pipette solutions. The current–voltage relationships under isotonic (*Iso*) and hypotonic (*Hypo*) conditions with or without ATP in the pipette solution are shown in (**c**) (mean ± SE of 11 cells without ATP or 23 cells with ATP). The difference in current density between the two groups was not significant

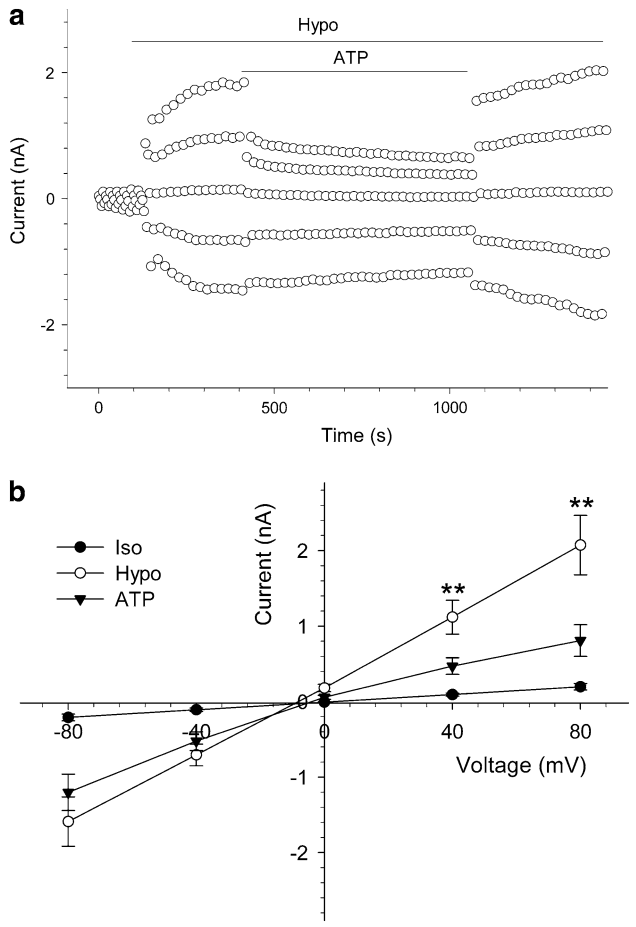

Fig. 3 Inhibition of volume-activated Cl^- currents by extracellular ATP. **a** Typical time course of volume-activated Cl^- currents induced by 47% hypotonic solution, indicated by the *Hypo* bar; and the effect of 10 mM extracellular ATP on the currents, indicated by the *ATP* bar. **b** Current–voltage relationships under isotonic (*Iso*) and hypotonic (*Hypo*) conditions and after treatment with the hypotonic solution containing 10 mM ATP (*ATP*). Data in (**b**) are mean ± SE ($n = 7$). $^{**}P < 0.01$ (vs. current value in ATP group)

fetal human nasopharyngeal epithelial cells. After $I_{cl,vol}$ were induced and leveled off, ATP was added to the hypotonic bath solution to a final concentration of 10 mM. As shown in Fig. 3, 10 mM ATP inhibited the $I_{cl,vol}$. The outward currents were more sensitive to ATP than the inward currents ($P < 0.01$). ATP (10 mM) inhibited 68.4 ± 7.8% ($P < 0.01$) of the outward current at +80 mV and only 22.8 ± 8.2% ($P > 0.05$) of the inward current at −80 mV ($n = 7$). The inhibitory effect of ATP was reversible upon washout.

Compared with the nasopharyngeal carcinoma cell line CNE-2Z (Chen et al. 2002), the inhibition effect of ATP on $I_{cl,vol}$ was much weaker in the current study. To confirm the difference, we investigated the effect of ATP on the background currents under isotonic conditions. Our recent research in nasopharyngeal carcinoma CNE-2Z cells showed that ATP at 10 mM could obviously inhibit the background currents (Yang et al. 2011). Unexpectedly, in fetal nasopharyngeal epithelial cells, ATP at the same concentration activated an inward-rectification current. In six cells, ATP increased the inward current by 232.3 ± 64.3 pA at −80 mV and the outward current by 91.9 ± 35.0 pA at +80 mV (Fig. 4). The calculated reverse potential was +15.7 mV, which was far from the calculated Cl^- equilibrium potential. Furthermore, the chloride channel blockers NPPB (100 μM) and tamoxifen (20 μM) could not inhibit the inward-rectification current activated by ATP (Fig. 4e, f).

Sensitivity of $I_{cl,vol}$ to Tamoxifen

Figure 5a shows an example of the effect of tamoxifen, a Cl^- channel blocker, at 20 μM on the $I_{cl,vol}$. Tamoxifen (20 μM) inhibited 102.6 ± 5.4% of the outward current at +80 mV and 105.4 ± 8.6% of the inward current at −80 mV (Fig. 5b, $P < 0.01$, $n = 5$). The inhibition ratios on the outward and inward currents were similar ($P > 0.05$). The reason the inhibition ratios exceeded 100% was that tamoxifen not only inhibited $I_{cl,vol}$ completely but also inhibited the basic background currents (Sun et al. 2005b).

Inhibition of $I_{cl,vol}$ by Extracellular NPPB

NPPB is a classic chloride channel inhibitor. To explore its effect on $I_{cl,vol}$, NPPB was added into the perfusion solution after the activation of $I_{cl,vol}$. The results showed that $I_{cl,vol}$ was attenuated by extracellular applications of NPPB (Fig. 6). NPPB (100 μM) inhibited the $I_{cl,vol}$ by 45.48 ± 9.02% at +80 mV and 45.97 ± 9.40% at −80 mV ($n = 5$, $P < 0.01$). Increasing the concentration of NPPB to 200 μM further inhibited the $I_{cl,vol}$, with inhibition rates of 95.59 ± 6.55% at +80 mV and 86.95 ± 9.61% at −80 mV ($n = 5$, $P < 0.01$). At either 100 or 200 μM, NPPB inhibited outward and inward currents to similar degrees ($P > 0.05$).

It should be noted that NPPB, at a concentration of 200 μM, could obviously accelerate the time-dependent inactivation of the $I_{cl,vol}$ at +80 mV (Fig. 6c). This phenomenon could hardly be detected in the application of ATP, tamoxifen and low-concentration NPPB (100 μM).

Permeability of Volume-Activated Chloride Channels

When the $I_{cl,vol}$ was activated and had reached a peak, the hypotonic solution containing 70 mM of Cl^- was replaced with hypotonic solution containing equimolar I^-, Br^- or gluconate. The anion substitution shifted the reversal potential. The permeability ratios of P_I/P_{Cl}, P_{Br}/P_{Cl}, and $P_{gluconate}/P_{Cl}$ calculated from the shifts in reversal potential by the modified Goldman-Hodgkin-Katz equation are

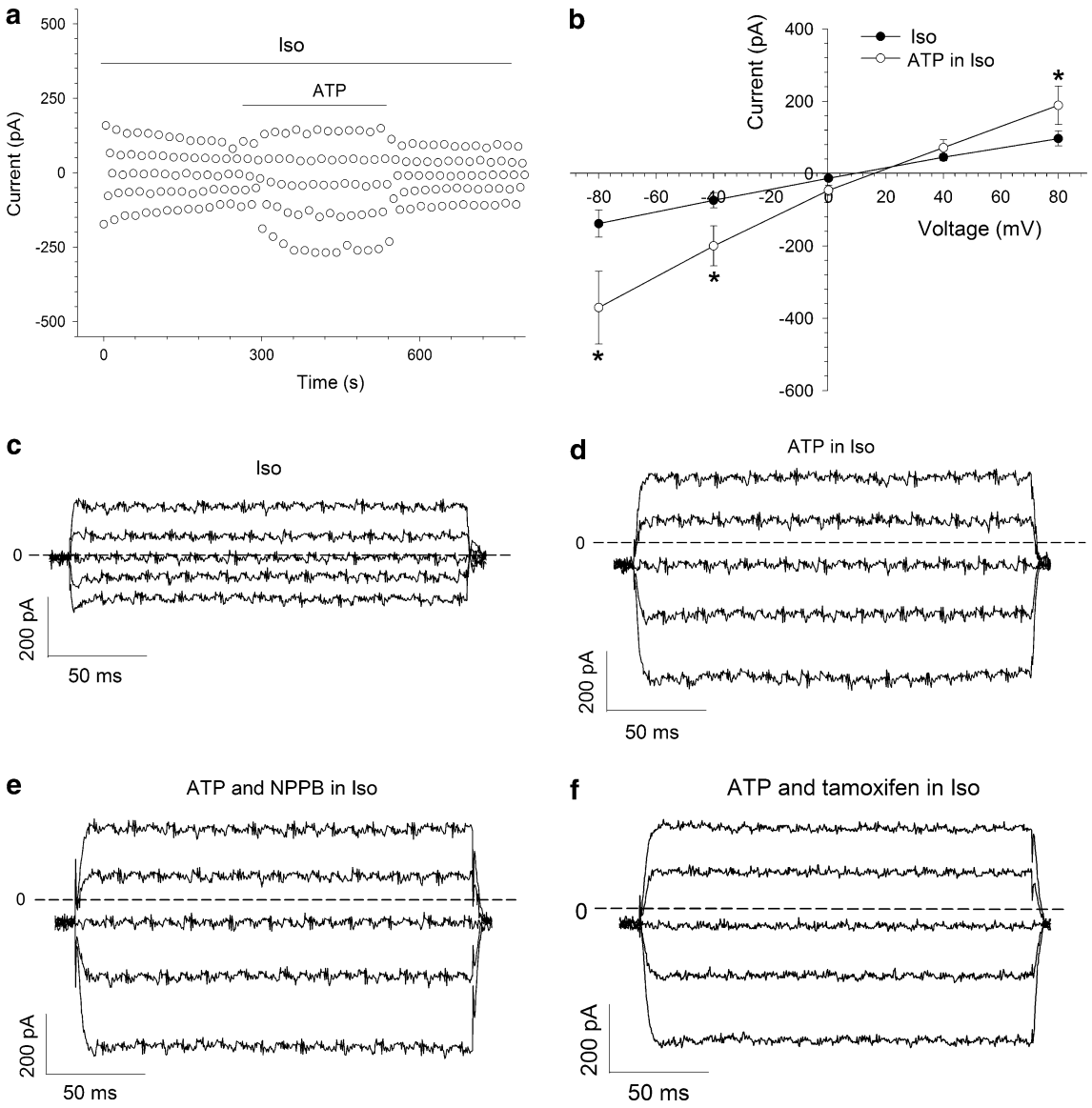

Fig. 4 Currents activated by 10 mM ATP in isotonic conditions. A typical time course of the ATP-activated, inward-rectified current in isotonic solution (*Iso*) is shown in (**a**). The current declined upon ATP washout. Current–voltage relationships of the background current in the isotonic solution and the ATP-activated current are presented in (**b**) (mean ± SE, $n = 6$). **c–f** Typical current traces of the background current in isotonic solution (**c**), inward-rectified current activated by ATP (**d**) and effects of NPPB (100 μM) (**e**), and tamoxifen (20 μM) (**f**) on the ATP–activated current. *$P < 0.05$ (vs. current value in Iso group)

shown in Fig. 7. The sequence of anion permeability was $I^- > Br^- > Cl^- >$ gluconate.

Discussion

The current study demonstrated that hypotonic challenges activated a volume-sensitive current in fetal human nasopharyngeal epithelial cells. The current direction and reversal potential for the current were consistent with those of the current carried by Cl^-. The sensitivity to chloride channel blockers and the anion permeability of the channels were similar to the $I_{cl,vol}$ recorded in other cells (Inoue et al. 2005; Stutzin and Hoffmann 2006). Therefore, fetal human nasopharyngeal epithelial cells can produce $I_{cl,vol}$ under hypotonic conditions.

The $I_{cl,vol}$ in this study shared most of the characteristics with the background chloride current recorded by us previously under isotonic conditions in fetal nasopharyngeal epithelial cells (Sun et al. 2005b). Our recent research suggests that both the background chloride current and the $I_{cl,vol}$ in nasopharyngeal carcinoma CNE-2Z cells are mediated by the same volume-activated chloride channels (Yang et al. 2011); the volume-activated chloride channels

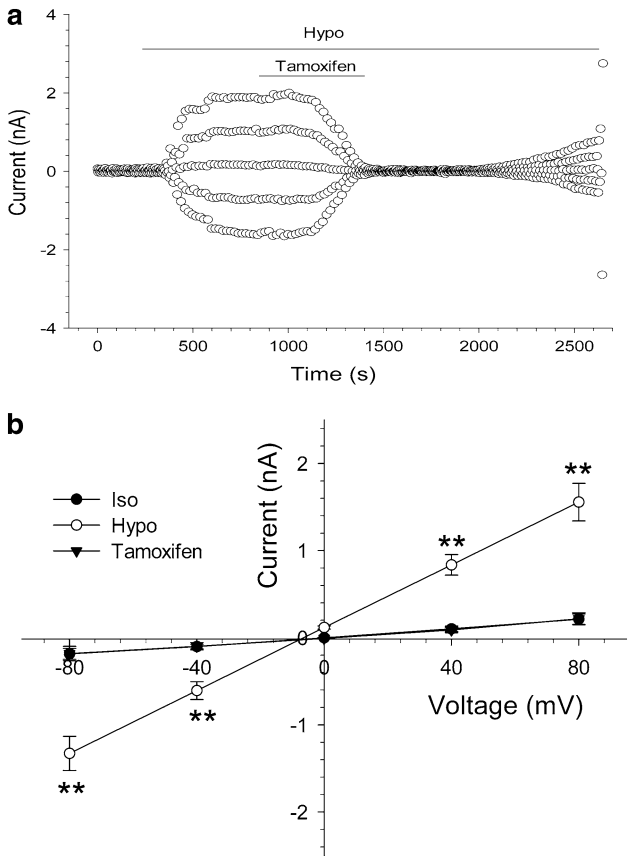

Fig. 5 Inhibition of volume-activated Cl^- currents by the chloride channel blocker tamoxifen. **a** Typical time course of the volume-activated Cl^- current induced by 47% hypotonic solution, indicated by the *Hypo* bar; and the effect of 20 μM extracellular tamoxifen on the current, indicated by the *Tamoxifen* bar. **b** Current–voltage relationships under isotonic (*Iso*) and hypotonic (*Hypo*) conditions and after treatment with the hypotonic solution containing 20 μM tamoxifen (*Tamoxifen*). Data in (**b**) are mean ± SE ($n = 5$). $^{**}P < 0.01$ (vs. current value in tamoxifen group)

in fetal nasopharyngeal epithelial cells probably underpins both the $I_{cl,vol}$ in hypotonic conditions and the background chloride currents in isotonic conditions (Sun et al. 2005b). A functional role of the channels should exist in both hypotonic and isotonic conditions.

Our previous work indicated that the fetal human nasopharyngeal epithelial cells swelled and underwent a process of RVD when exposed to a hypotonic challenge (Sun et al. 2005a). Inhibition of the RVD by the chloride channel blockers ATP, NPPB and tamoxifen suggests a fundamental role of the volume-sensitive chloride channels in RVD (Sun et al. 2005a). The current study validates that $I_{cl,vol}$ can be activated by the same hypotonic challenge and can also be inhibited by ATP, NPPB, and tamoxifen. Besides, the degree of inhibition of the chloride channel blockers on the RVD is similar to that on $I_{cl,vol}$ presented in the current study. These results confirm that the $I_{cl,vol}$ plays a key role in the RVD in fetal human nasopharyngeal epithelial cells.

Based on the morphology described by us previously (Sun et al. 2005a), cultured fetal nasopharyngeal epithelial cells were heterogeneous, mainly due to their dynamic and asynchronous development. It is well known that all somatic cells are derived from stem cells. During the process of histogenesis, a few self-renewing stem cells give rise to a limited number of committed progenitors. Progenitor cells have limited proliferation ability, subsequently differentiate into precursor cells, and eventually become terminally mature cells (Alison et al. 2006). Therefore, the primary cultured nasopharyngeal epithelial cells in the current study might be a mixture of stem cells, progenitor cells, precursor cells, and fully differentiated mature cells.

On the basis of current density of $I_{cl,vol}$ and cell size distribution, our results in this study reveal that the current density and cell size vary greatly among the cells observed; but the exact significance of the variation remains to be clarified in future studies. It has been reported that stem or progenitor cells usually display smaller size relative to the corresponding mature cells (De Paiva et al. 2006; Greene et al. 2010; Izumi et al. 2009) and that the primitive immature cells, such as progenitor cells or tumor cells, generally possessed stronger $I_{cl,vol}$ compared with the differentiated ones (Chou et al. 1995; Qian et al. 2009; Voets et al. 1997). Thus, it is possible that the variation of current density may be caused by the difference of the stages of cells situated. It should be noted that cell cycle distribution and cell apoptosis also have great influence on both cell size and current density (Chen et al. 2002; Stutzin and Hoffmann 2006; Zuo et al. 2009). Therefore, these factors should be taken into account in future research.

Most reports indicate that the activation of $I_{cl,vol}$ depends on intracellular ATP (Okada et al. 2009; Poletto Chaves and Varanda 2008; Stutzin and Hoffmann 2006). However, the degree of dependence is variable under different conditions. A study on rat IMCD cells showed that intracellular ATP was necessary to evoke $I_{cl,vol}$ when the hypotonic stimulus was modest but was not when the stimulus was stronger (Volk et al. 1996). In N1E115 neuroblastoma cells and human prostate cancer epithelial cells, the results suggest that volume-sensitive Cl^- channels can be activated via two different mechanisms, i.e., ATP-dependent and ATP-independent mechanisms, and that increasing the rate of cell swelling appears to increase the proportion of channels activated via the ATP-independent pathway (Bond et al. 1999; Lazarenko et al. 2005). In our study, deletion of ATP from the pipette solution did not significantly change the original activation, the current density, and the repeated activation (embodied by the recovery ratio) of $I_{cl,vol}$, suggesting that exogenous ATP seems to be not necessary for activation of $I_{cl,vol}$. However, our results do not exclude the dependence of $I_{cl,vol}$ on endogenous ATP. The first reason is that the production of ATP by the clamped cells was not inhibited by the

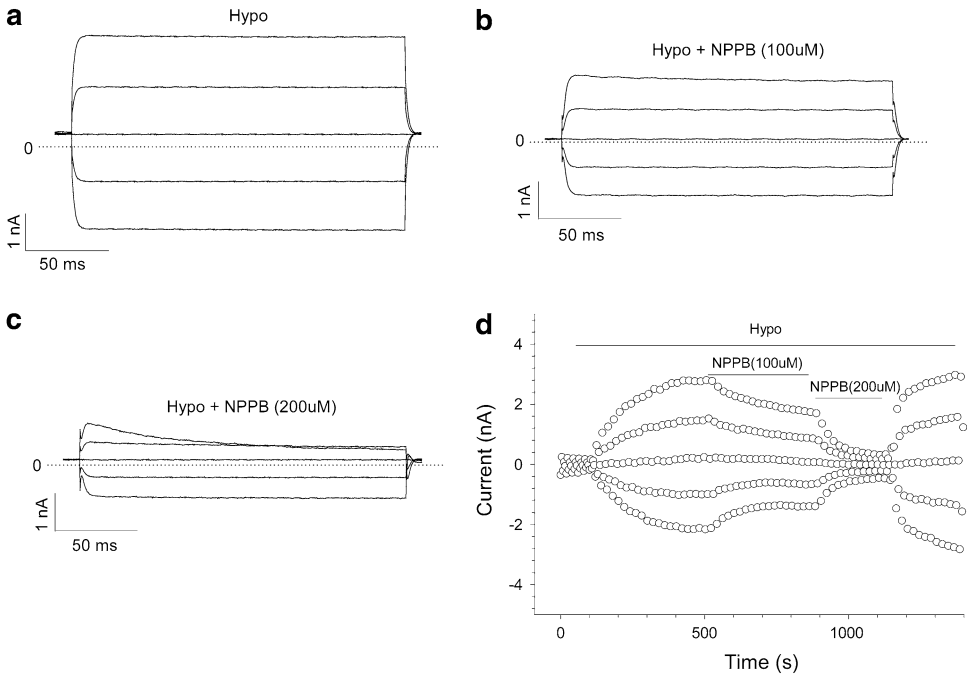

Fig. 6 Inhibition of volume-activated chloride currents by the chloride channel blocker NPPB. Cells were clamped at 0, ±40 and ±80 mv for 200 ms with an interval of 4 s. **a–c** Typical current traces recorded in 47% hypotonic control solution (**a**) and in 47% hypotonic solution containing 100 μM (**b**), or 200 μM NPPB (**c**), respectively. **d** Time course of activation of $I_{cl,vol}$ induced by 47% hypotonic challenge (*Hypo*) and inhibition of the current by 100 and 200 μM NPPB. NPPB inhibited $I_{cl,vol}$ in a dose–dependent manner and obviously accelerated the time-dependent inactivation at +80 mV in higher concentrations (**c**)

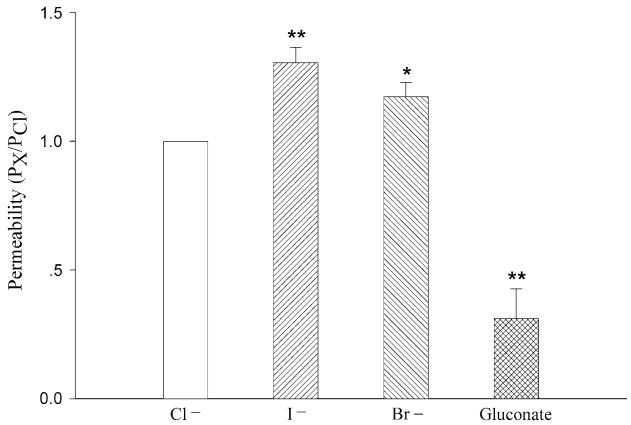

Fig. 7 Anion permeability of volume-activated chloride channels. The permeability ratios (P_X/P_{Cl}) of various anions (X^-), including I^-, Br^-, and gluconate, relative to Cl^- were calculated as described in Materials and Methods. Data represent mean ± SE ($n = 5$). $^{**}P < 0.01$ and $^{*}P < 0.05$, respectively (vs. Cl^-)

metabolic inhibitors, as in other reports (Bond et al. 1999; Lazarenko et al. 2005). The second is that the 47% hypotonic bath solution used in our study represents a strong hypotonic stimulus, which would induce cell swelling at a high rate and, thus, might activate the $I_{cl,vol}$ mainly through the ATP-independent pathway (Bond et al. 1999).

The $I_{cl,vol}$ in fetal nasopharyngeal epithelial cells shared many similar characteristics with those in nasopharyngeal carcinoma cells (Chen et al. 2002). However, under isotonic conditions, 10 mM ATP activated an inward-rectified current in fetal nasopharyngeal epithelial cells, which has not been observed in nasopharyngeal carcinoma cells (Yang et al. 2011). The reversal potential of the ATP-activated current (+15.7 mV) was far from the Cl^- equilibrium potential. The current showed inward rectification and was insensitive to NPPB and tamoxifen. All of these characteristics are different from those of the $I_{cl,vol}$, the cAMP-activated chloride current or the Ca^{2+}-activated chloride current (Morris 1999). Therefore, the ATP-activated current should not be mediated by Cl^-. Based on the ion concentration in the pipette and the bath solution, the equilibrium potential of Na^+ is +73.5 mV and the equilibrium potential of Mg^{2+} is −11.2 mV. Both are far from the reversal potential. Therefore, the ATP-activated current is probably mediated mainly by Ca^{2+}, though the coexistence of a magnesium current cannot be excluded. Activation of the ATP-activated current might be mediated by the ionotropic purinoceptor P2X (Browne et al. 2010), which needs to be explored further. In this study, the mild inhibition of ATP on the $I_{cl,vol}$ might be the conjunct result of the inhibition of $I_{cl,vol}$ and the activation of cation currents. Since the ATP (10 mM)–activated current could not be observed in nasopharyngeal carcinoma CNE-2Z cells (Yang et al. 2011), the current study implies that normal fetal nasopharyngeal epithelial cells and nasopharyngeal carcinoma cells might have a great difference in the expression of purinergic receptors.

The molecular identity of $I_{cl,vol}$ is still unknown. Several proteins, including pIcln, ClC-3, and P-glycoprotein (the MDR1 gene product), have been described as possible molecular candidates. However, many results suggest that these proteins might only be channel regulators, not the real channels (Okada 2006; Verkman and Galietta 2009). ClC-3

belongs to the highly evolutionarily conserved ClC family. Our previous studies in nasopharyngeal carcinoma cells have shown that ClC-3 is a key protein in the activation of $I_{cl,vol}$ and that ClC-3 is also a main component of the background chloride channels activated under isotonic conditions (Mao et al. 2008; Wang et al. 2004; Yang et al. 2011). The role of ClC-3 in fetal nasopharyngeal epithelial cells is not clear and will be one of the targets of our next study.

As a summary, our study demonstrated that, in response to hypotonic challenges, fetal human nasopharyngeal epithelial cells could produce $I_{cl,vol}$, which was sensitive to the chloride channel inhibitors and independent of exogenous ATP. Compared with nasopharyngeal carcinoma CNE-2Z cells, ATP displayed a weaker inhibition of $I_{cl,vol}$ in fetal nasopharyngeal epithelial cells, due to the activation of another inward-rectified current.

Acknowledgments This work was supported by the National Natural Science Foundation of China (30771106, 30870567, 30871267, 90913020 and U0932004) and the Science & Technology Innovation Fund of Guangdong Medical College (STIF201102).

References

Alison MR, Brittan M, Lovell MJ, Wright NA (2006) Markers of adult tissue-based stem cells. Handb Exp Pharmacol 174:185–227

Bond T, Basavappa S, Christensen M, Strange K (1999) ATP dependence of the ICl, swell channel varies with rate of cell swelling. Evidence for two modes of channel activation. J Gen Physiol 113:441–456

Browne LE, Jiang LH, North RA (2010) New structure enlivens interest in P2X receptors. Trends Pharmacol Sci 31:229–237

Chen L, Wang L, Zhu L, Nie S, Zhang J, Zhong P, Cai B, Luo H, Jacob TJ (2002) Cell cycle–dependent expression of volume-activated chloride currents in nasopharyngeal carcinoma cells. Am J Physiol Cell Physiol 283:C1313–C1323

Chen LX, Zhu LY, Jacob TJ, Wang LW (2007) Roles of volume-activated Cl^- currents and regulatory volume decrease in the cell cycle and proliferation in nasopharyngeal carcinoma cells. Cell Prolif 40:253–267

Chen B, Jefferson DM, Cho WK (2010) Characterization of volume-activated chloride currents in regulatory volume decrease of human cholangiocyte. J Membr Biol 235:17–26

Chou CY, Shen MR, Wu SN (1995) Volume-sensitive chloride channels associated with human cervical carcinogenesis. Cancer Res 55:6077–6083

De Paiva CS, Pflugfelder SC, Li DQ (2006) Cell size correlates with phenotype and proliferative capacity in human corneal epithelial cells. Stem Cells 24:368–375

Greene SB, Gunaratne PH, Hammond SM, Rosen JM (2010) A putative role for microRNA-205 in mammary epithelial cell progenitors. J Cell Sci 123:606–618

Harvey VL, Saul MW, Garner C, McDonald RL (2010) A role for the volume regulated anion channel in volume regulation in the murine CNS cell line, CAD. Acta Physiol (Oxf) 198:159–168

Inoue H, Mori S, Morishima S, Okada Y (2005) Volume-sensitive chloride channels in mouse cortical neurons: characterization and role in volume regulation. Eur J Neurosci 21:1648–1658

Inoue H, Takahashi N, Okada Y, Konishi M (2010) Volume-sensitive outwardly rectifying chloride channel in white adipocytes from normal and diabetic mice. Am J Physiol Cell Physiol 298:C900–C909

Izumi K, Inoki K, Fujimori Y, Marcelo CL, Feinberg SE (2009) Pharmacological retention of oral mucosa progenitor/stem cells. J Dent Res 88:1113–1118

Lazarenko RM, Kondrats'kyi AP, Pohoriela N, Shuba IM (2005) Alterations in ATP dependence of swelling-activated Cl^- current associated with neuroendocrine differentiation of LNCaP human prostate cancer epithelial cells [in Russian]. Fiziol Zh 51:57–66

Mao J, Wang L, Fan A, Wang J, Xu B, Jacob TJ, Chen L (2007) Blockage of volume-activated chloride channels inhibits migration of nasopharyngeal carcinoma cells. Cell Physiol Biochem 19:249–258

Mao J, Chen L, Xu B, Wang L, Li H, Guo J, Li W, Nie S, Jacob TJ, Wang L (2008) Suppression of ClC-3 channel expression reduces migration of nasopharyngeal carcinoma cells. Biochem Pharmacol 75:1706–1716

Mao J, Xu B, Li H, Chen L, Jin X, Zhu J, Wang W, Zhu L, Zuo W, Chen W, Wang L (2010) Lack of association between stretch-activated and volume-activated Cl^- currents in hepatocellular carcinoma cells. J Cell Physiol 226:1176–1185

Morris AP (1999) The regulation of epithelial cell cAMP- and calcium-dependent chloride channels. Adv Pharmacol 46:209–251

Okada Y (2006) Cell volume–sensitive chloride channels: phenotypic properties and molecular identity. Contrib Nephrol 152:9–24

Okada Y, Sato K, Numata T (2009) Pathophysiology and puzzles of the volume-sensitive outwardly rectifying anion channel. J Physiol 587:2141–2149

Poletto Chaves LA, Varanda WA (2008) Volume-activated chloride channels in mice Leydig cells. Pflugers Arch 457:493–504

Qian JS, Pang RP, Zhu KS, Liu DY, Li ZR, Deng CY, Wang SM (2009) Static pressure promotes rat aortic smooth muscle cell proliferation via upregulation of volume-regulated chloride channel. Cell Physiol Biochem 24:461–470

Stutzin A, Hoffmann EK (2006) Swelling-activated ion channels: functional regulation in cell-swelling, proliferation and apoptosis. Acta Physiol (Oxf) 187:27–42

Sun XR, Chen LX, Mao JW, Zhu LY, Nie SH, Zhong P, Li P, Wang LW (2005a) Regulatory volume decrease and its mechanism in nasopharyngeal epithelial cells [in Chinese]. Shi Yan Sheng Wu Xue Bao 38:353–358

Sun XR, Wang LW, Mao JW, Zhu LY, Nie SH, Zhong P, Chen LX (2005b) Background chloride currents in fetal human nasopharyngeal epithelial cells [in Chinese]. Sheng Li Xue Bao 57:349–354

Verkman AS, Galietta LJ (2009) Chloride channels as drug targets. Nat Rev Drug Discov 8:153–171

Voets T, Wei L, De Smet P, Van Driessche W, Eggermont J, Droogmans G, Nilius B (1997) Downregulation of volume-activated Cl^- currents during muscle differentiation. Am J Physiol Cell Physiol 272:C667–C674

Volk KA, Zhang C, Husted RF, Stokes JB (1996) Cl^- current in IMCD cells activated by hypotonicity: time course, ATP dependence, and inhibitors. Am J Physiol Renal Physiol 271:F552–F559

Wang LW, Chen LX, Jacob T (2004) ClC-3 expression in the cell cycle of nasopharyngeal carcinoma cells. Sheng Li Xue Bao 56:230–236

Yang L, Ye D, Ye W, Jiao C, Zhu L, Mao J, Jacob TJ, Wang L, Chen L (2011) ClC-3 is a main component of background chloride channels activated under isotonic conditions by autocrine ATP in nasopharyngeal carcinoma cells. J Cell Physiol 226:2516–2526

Zuo W, Zhu L, Bai Z, Zhang H, Mao J, Chen L, Wang L (2009) Chloride channels involve in hydrogen peroxide-induced apoptosis of PC12 cells. Biochem Biophys Res Commun 387:666–670

J Membrane Biol (2012) 245:117–123
DOI 10.1007/s00232-012-9415-9

BRIEF COMMUNICATION

Ancient Origin of Four-Domain Voltage-gated Na^+ Channels Predates the Divergence of Animals and Fungi

Xinjiang Cai

Received: 9 August 2011 / Accepted: 3 January 2012 / Published online: 19 January 2012

Abstract The four-domain voltage-gated Na^+ channels are believed to have arisen in multicellular animals, possibly during the evolution of the nervous system. Recent genomic studies reveal that many ion channels, including Na^+ channels and Ca^{2+} channels previously thought to be restricted to animals, can be traced back to one of the unicellular ancestors of animals, *Monosiga brevicollis*. The eukaryotic supergroup Opisthokonta contains animals, fungi, and a diverse group of their unicellular relatives including *M. brevicollis*. Here, we demonstrate the presence of a putative voltage-gated Na^+ channel homolog ($TtrNa_V$) in the apusozoan protist *Thecamonas trahens*, which belongs to the unicellular sister group to Opisthokonta. $TtrNa_V$ displays a unique selectivity motif distinct from most animal voltage-gated Na^+ channels. The identification of $TtrNa_V$ suggests that voltage-gated Na^+ channels might have evolved before the divergence of animals and fungi. Furthermore, our analyses reveal that Na_V channels have been lost independently in the amoeboid holozoan *Capsaspora owczarzaki* of the animal lineage and in several basal fungi. These findings provide novel insights into the evolution of four-domain voltage-gated ion channels, ion selectivity, and membrane excitability in the Opisthokonta lineage.

Keywords Channel evolution · Channel pore · Genomics · Na^+ channel · Protists · Selectivity motif

Voltage-gated Na^+ (Na_V) channels in animals initiate and propagate action potentials in many excitable cells such as neurons, myocytes, and neuroendocrine cells (Catterall et al. 2005a). Similar to animal voltage-gated Ca^{2+} (Ca_V) channels, Na_V channels possess four homologous domains, each of which contains six transmembrane segments (TMS) and a pore loop resembling the single-domain 6-TMS voltage-gated K^+ channels (Armstrong and Hille 1998; Cai 2008a; Hille 2001; Strong et al. 1993). It was hypothesized that primordial Ca_V channels were likely derived from an ancestral single-domain channel by two rounds of intragenic duplication (Armstrong and Hille 1998; Hille 2001; Strong et al. 1993). Na_V channels then diverged from some primitive Ca_V channels during the development of the nervous system and fast-conducting axons in ancestral multicellular animals (Fig. 1a) (Armstrong and Hille 1998; Hille 2001; Strong et al. 1993). Indeed, putative evolutionary intermediate two-pore channels (TPCs) with two homologous 6-TMS domains have recently been identified (Ishibashi et al. 2000) and characterized to be involved in Ca^{2+} signaling in animals (Brailoiu et al. 2009; Cai and Patel 2010; Calcraft et al. 2009).

The evolution of animal Na_V channels has been intensively studied because of its relevance not only for understanding the structure and function relationship of Na_V channels, but also for exploring the origin of membrane excitability and the nervous system (Arnegard et al. 2010; Goldin 2002; Lopreato et al. 2001; Plummer and Meisler 1999; Strong et al. 1993; Widmark et al. 2011; Zakon et al. 2006, 2011). However, little is known about

Electronic supplementary material The online version of this article (doi:10.1007/s00232-012-9415-9) contains supplementary material, which is available to authorized users.

X. Cai (✉)
Department of Molecular Pathogenesis, New York University Langone Medical Center, 540 First Avenue, SK Lab 3-9, New York, NY 10016, USA
e-mail: xinjiang.cai@med.nyu.edu

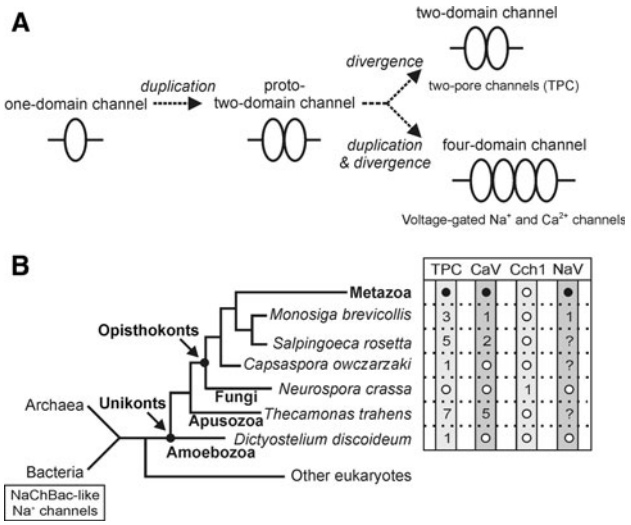

Fig. 1 Schematic representation of ion channel evolution. **a** Schematic diagram illustrating the hypothesis of intragenic duplications resulting in two-domain two-pore channels (Ishibashi et al. 2000; Patel et al. 2010) and four-domain Na^+ and Ca^{2+} channels (Armstrong and Hille 1998; Strong et al. 1993). **b** Phylogeny of select species in Opisthokonta and its relationship within eukaryotes and with prokaryotes, inferred from the Tree of Life project (http://www.tolweb.org/) and recent references (Ruiz-Trillo et al. 2007; Sebe-Pedros et al. 2010). The number of protein homologs derived from currently available genomic databases is shown, while a *black dot* indicates the presence of protein homolog(s) and a *white circle* indicates the absence of related protein homolog. An interrogation mark "?" indicates the unknown status of protein homolog(s) in the genomes. Ca_V, voltage-gated Ca^{2+} channel; Cch1, fungal Ca^{2+} channel protein 1; NaV, voltage-gated Na^+ channel; TPC, two-pore channel

the evolution of Na_V channels outside of the metazoan lineage. A family of prokaryotic 6-TMS Na_V channels have been functionally characterized (Koishi et al. 2004), the first of which is the NaChBac channel isolated from the salt-loving bacterium *Bacillus halodurans* (Durell and Guy 2001; Ren et al. 2001). These prokaryotic Na_V channels appear to be missing in the currently available eukaryotic genomes. The apparent absence of Na_V channel homologues in the genomes of fungi, plants and many protists suggested that 24-TMS Na_V channels might be animal specific (Armstrong and Hille 1998).

Animals, fungi, and a diverse group of their unicellular relatives belong to the same eukaryotic supergroup Opisthokonta (Cavalier-Smith and Chao 2003; Rokas 2008; Ruiz-Trillo et al. 2007; Steenkamp et al. 2006). *Monosiga brevicollis*, one of the closest unicellular relatives of animals (Carr et al. 2008; Ruiz-Trillo et al. 2008; Steenkamp et al. 2006), has been shown to possess cell surface adhesion molecules, receptor tyrosine kinases, and several other signaling molecules previously thought to be restricted to animals (King and Carroll 2001; King et al. 2003, 2008; Li et al. 2008). We also demonstrated in *M. brevicollis* the presence of various ion channels and transporters involved in animal Ca^{2+} signaling (Cai 2008b). Interestingly, a putative 24-TMS Na_V channel homolog with an ion selectivity filter conserved in many invertebrates has recently been cloned in *M. brevicollis* (Liebeskind et al. 2011), which suggests that the evolution of 24-TMS Na_V channels occurred before the emergence of the nervous system in animals (Liebeskind et al. 2011).

Animals and fungi display lineage-specific diversifications in the components of many signaling pathways after having diverged from a common unicellular ancestor approximately 1 billion years ago (Rokas 2008; Ruiz-Trillo et al. 2007). The evolutionary origin of the integrin adhesion complex critical for intercellular communications in animals was recently shown to predate the divergence of Opisthokonta, with the key component being lost in fungi (Sebe-Pedros et al. 2010). We also showed that many components of the animal Ca^{2+} signaling machinery originated in the apusozoan protist *Thecamonas trahens* (Cai and Clapham 2012), which belongs to the putative unicellular sister group to Opisthokonta (Fig. 1b) (Cavalier-Smith and Chao 2010).

In this study, we aimed to identify ancestral Na^+ channel homologs in the Opisthokonta lineage by examining genomic data from *T. trahens* and several close relatives of animals and fungi. We show that a putative 24-TMS Na_V channel homolog is present in *T. trahens*, suggesting 24-TMS Na_V channels might have evolved before the divergence of animals and fungi, much earlier than previously thought.

Materials and Methods

Database Searches

Protein sequences of Na_V and Ca_V channels from *Homo sapiens* were used as queries to perform initial BlastP and TBlastN searches (Altschul et al. 1997) against the Origins of Multicellularity Database (http://www.broadinstitute.org/annotation/genome/multicellularity_project/MultiHome.html), the Broad Institute Genomic Database (http://www.broadinstitute.org/scientific-community/data), and the National Center for Biotechnology Information Genome Database (http://www.ncbi.nlm.nih.gov/blast/). In order to identify potential distantly related homologs in nonmetazoan organisms that might not be detected by using *H. sapiens* query proteins, repeated BLAST searches using hit sequences from the first round of searches were also performed against the above databases. In addition, PHMMER searches (HMMER 3.0, http://hmmer.janelia.org/) were also performed against protein data sets downloaded from the Origins of Multicellularity Database.

Multiple Sequence Alignments and Phylogeny Reconstruction

Nonredundant protein sequences were aligned by MAFFT (Katoh and Toh 2008) or PRANK (Loytynoja and Goldman 2010) programs and were subsequently manually edited to improve alignments displayed with the Blosum62 Similarity Scoring Table in Genedoc (Nicholas et al. 1997). Poorly aligned sites from the multiple sequence alignments were eliminated by using Gblocks (Talavera and Castresana 2007), and unambiguous sequence alignments were then exported to files in PHYLIP format. Next, ProtTest (Darriba et al. 2011) was used to select the best-fit evolution model and parameter estimates for the phylogeny reconstruction.

Maximum likelihood phylogenies were estimated by PHYML 3.0 (Guindon et al. 2010), with 100 resampled data sets obtained by SEQBOOT (PHYLIP package, v. 3.69) (Felsenstein 1996), the LG amino acid substitution matrix (Le and Gascuel 2008), the four-category discrete-gamma model and empirical amino acid frequencies (LG + G + F) selected by ProtTest. Bootstrap is a commonly used method to assess confidence in phylogenetic analyses by resampling sites from the multiple sequence alignment with replacements and assigning a bootstrap value for each clade of the reconstructed tree (Felsenstein 1985). A bootstrap value of $\geq$70 is considered to define a true clade in the phylogenetic tree with a probability of $\geq$95% (Hillis and Bull 1993). An outgroup is a protein sequence that is outside the sequences of interest (ingroup protein sequences) but is also closely related to ingroup proteins. The outgroup sequence provides a reference point for the determination of the evolutionary relationships among ingroup proteins. The TREEVIEW program (v. 1.6.6) (Page 1996) were used to display the phylogenetic trees.

Results and Discussion

Identification of a Putative 24-TMS Na_V Channel Homolog in the Apusozoan *Thecamonas trahens*

The apparent absence of 24-TMS Na_V channels in fungi suggests that 24-TMS Na_V channels might have evolved to modulate membrane excitability specifically in the lineage leading to animals, possibly as early as in the choanoflagellate *M. brevicollis* (Liebeskind et al. 2011). Alternatively, Na_V channels could have been developed in the common ancestors of animals and fungi but were subsequently lost in fungi following the animal–fungal divergence. To better understand the evolutionary origin of Na_V channels, we searched for Na_V channel homologs in several genomes at the Origins of Multicellularity Database (Ruiz-Trillo et al. 2007; Sebe-Pedros et al. 2010), including the apusozoan *T. trahens,* the amoeboid holozoan *Capsaspora owczarzaki,* the choanoflagellate *Salpingoeca rosetta*, the basal chytridiomycete fungi *Allomyces macrogynus*, and *Spizellomyces punctatus*, as well as other select genomes in the NCBI genomic databases.

12-TMS TPC channels are widely distributed among eukaryotes except in fungi (Fig. 1b) (Brailoiu et al. 2009; Galione et al. 2009). In contrast, 24-TMS Ca_V channel homologs are present in animals, fungi (Cch1 channels), and some protists (Fig. 1b). We found the presence of a 24-TMS Na_V channel homolog in the colonial choanoflagellate *S. rosetta* (Fig. 2), further confirming that Na_V channels had evolved in Choanoflagellata. However, the amoeboid holozoan *C. owczarzaki*, one of the unicellular lineages branching close to choanoflagellates and animals (Ruiz-Trillo et al. 2007, 2008), does not possess Na_V channel homologs. Ca_V channels also appear to be lost in *C. owczarzaki* (Cai and Clapham 2012), and therefore, the absence of Na_V channel homologs in *C. owczarzaki* could be related to lineage-specific gene loss.

We next examined the genome of the apusozoan *T. trahens* for potential Na_V channel homologs that might exist before the divergence of the animal and fungal lineages. Indeed, a putative 24-TMS Na_V homolog with a unique selectivity filter was detected in *T. trahens* ($TtrNa_V$) (Figs. 2, 3; Supplemental Figs. S1, S2). Na_V and Ca_V channels display a certain degree of structural and sequence similarity and are speculated to share common evolutionary origins (Hille 2001; Strong et al. 1993). Nevertheless, robust phylogenetic analyses coupled with strong bootstrap support can be utilized to identify critical clades for the Na_V/Ca_V channel phylogeny and thus provide evolutionary evidence to distinguish between Na_V and Ca_V homologs, as shown previously in analyzing channel homologs from the cnidarian jellyfish *Cyanea capillata* (Anderson et al. 1993) and the choanoflagellate *M. brevicollis* (Liebeskind et al. 2011). To delineate the evolutionary relationships of $TtrNa_V$ with other Na_V and Ca_V channels from select animal species and two choanoflagellates, maximum likelihood analyses were performed by using three different outgroups that are closely related to animal 24-TMS voltage-gated Na^+ and Ca^{2+} channels but possess distinct evolutionary histories and functional properties: (1) 24-TMS channels—two fungal Ca^{2+}-selective Cch1 channels (Fig. 2a), presumably voltage independent (Hong et al. 2010), and a 24-TMS voltage-independent and nonselective cation channel NALCN (Lu et al. 2007) (Supplemental Fig. S1); (2) a 12-TMS TPC channel (Fig. 2b); and (3) 6-TMS channels, two prokaryotic voltage-dependent Na^+ channels (Supplemental Fig. S2). In all four phylogenetic trees with different outgroups

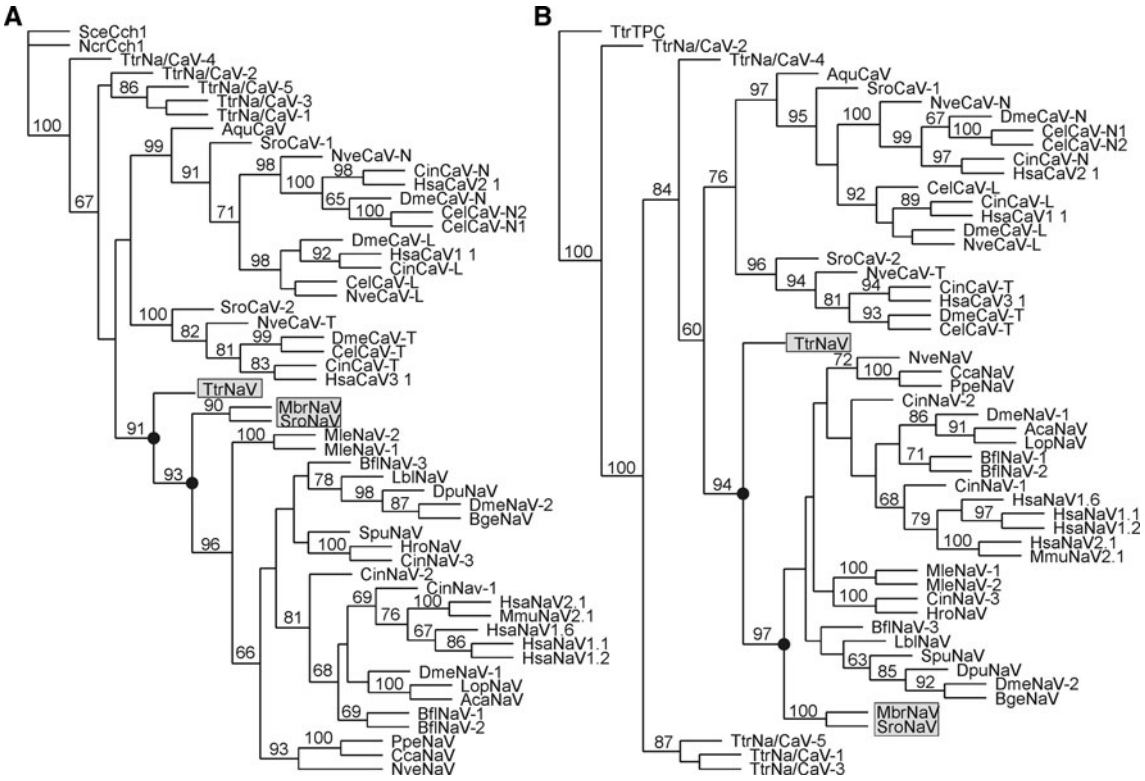

Fig. 2 Phylogenetic analysis of Na_V and Ca_V channel homologs by using two four-domain fungal Ca^{2+} channels (**a**) or a two-domain TPC Ca^{2+} channel (**b**) as the outgroup. The phylogenetic tree was built by using the maximum likelihood approach, as described in Section "Materials and Methods". *Bootstrap values* greater than 60 are shown at the nodes. The Na_V branches containing protist Na_V channel homologs ($TtrNa_V$, $MbrNa_V$, and $SroNa_V$) are highlighted by *black circles*. Abbreviations used for species: *Aplysia californica* (Aca); *A. queenslandica* (Aqu); *Branchiostoma floridae* (Bfl); *Blattella germanica* (Bge); *Caenorhabditis elegans* (Cel); *Cyanea capillata* (Cca); *Ciona intestinalis* (Cin); *Drosophila melanogaster* (Dme); *Daphnia pulex* (Dpu); *Halocynthia roretzi* (Hro); *H. sapiens* (Hsa); *Loligo bleekeri* (Lbl); *Loligo opalescens* (Lop); *M. brevicollis* (Mbr); *Mnemiopsis leidyi* (Mle); *Mus musculus* (Mmu); *Neurospora crassa* (Ncr); *N. vectensis* (Nve); *Polyorchis penicillatus* (Ppe); *Saccharomyces cerevisiae* (Sce); *Strongylocentrotus purpuratus* (Spu); *S. rosetta* (Sro); *T. trahens* (Ttr)

(Fig. 2; Supplemental Figs. S1, S2), $TtrNa_V$ is consistently grouped with the Na_V channel protein family including the two choanoflagellate Na_V channel homologs ($MbrNa_V$ and $SroNa_V$), not with the Ca_V channel protein family in the animal lineage. TtrNaV is placed at the base of the Na_V protein family in the animal lineage (strong bootstrap values ranging from 88 to 97 depending on the outgroup used). In addition, the phylogeny of Na_V and Ca_V channels is well correlated with the known evolutionary history of the species analyzed here. Thus, the identification of a putative 24-TMS Na_V channel homolog in *T. trahens* suggests that Na_V channels might have originated not only before the evolution of animal multicellularity and the nervous system (Liebeskind et al. 2011), but also before the divergence of the animal and fungal lineages.

Interestingly, five 24-TMS channel homologs from *T. trahens* are not grouped with either animal Na_V or Ca_V protein families in the trees using 24-TMS and 12-TMS channel outgroups (Fig. 2a, b; Supplemental Fig. S1) and are therefore named as Na_V and Ca_V-like homologs ($TtrNa/Ca_V$-1–5). Indeed, if only based on sequence homology and BLASTP (Altschul et al. 1997) searches, $TtrNa/Ca_V$ homologs show high similarity not only to animal Ca_V channels and fungal Cch1 Ca^{2+} channels, but also to a lesser extent to animal Na_V channels. $TtrNa/Ca_V$ channel homologs could represent ancestral Ca^{2+}-permeable ion channel homologs from which Na_V channels had evolved, as proposed previously (Armstrong and Hille 1998; Hille 2001; Strong et al. 1993).

Na_V channel homologs are absent in the basal fungi *A. macrogynus,* S. *punctatus*, *Rhizopus oryzae*, and *Batrachochytrium dendrobatidis*. Similar to the evolution of the integrin adhesion complex (Sebe-Pedros et al. 2010), Na_V channels appear to have been subsequently lost in the fungal lineage after its divergence from animals (Liebeskind et al. 2011).

Selectivity Filter Motif of Na_V Channels

The ion selectivity of Na_V and Ca_V channels is primarily determined by the pore loops, particularly a ring of four key residues that form the selectivity filter motif—

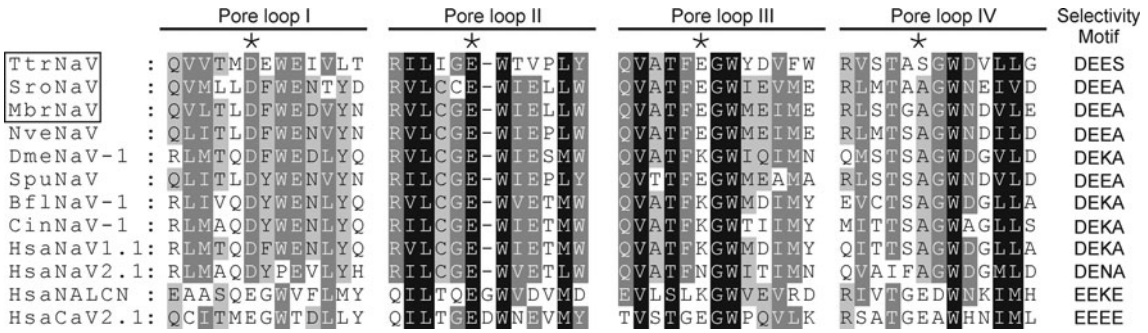

Fig. 3 Evolution of the pore loop region and the selectivity filter motif in Na_V channels. The amino acid sequences of the pore loop regions from each homologous domain of select Na_V channels and the human Ca_V 2.1 and NALCN channels are aligned, with the four key residues of the selectivity motif indicated by an *asterisk* and listed on the *right side* of the alignment

D/E/K/A for Na_V channels and E/E/E/E for Ca_V channels (Heinemann et al. 1992). Although these selectivity motifs are generally conserved in animals, variations have been observed in some species, for example, D/E/E/A in the α isoform of the cnidarian *Nematostella vectensis* and the choanoflagellates *M. brevicollis* (Liebeskind et al. 2011) and *S. rosetta* (Fig. 3), and D/K/E/A in the cnidarian jellyfish *C. capillata* (Anderson et al. 1993). Surprisingly, the selectivity motif in $TtrNa_V$ is D/E/E/S, which contains an unusual Ser residue in the fourth loop, instead of an Ala residue conserved in most Na_V channels. So far, there are only two Na_V channel homologs shown to possess a hydrophilic residue in the fourth loop—D/E/E/T in *N. vectensis* (β isoform) (Liebeskind et al. 2011) and D/E/E/S in *T. trahens* (Fig. 3).

The structure of a prokaryotic 6-TMS Na_V channel from *Arcobacter butzleri* has recently been determined (Payandeh et al. 2011), which showed that the four acidic side chains of E/E/E/E (one from each 6-TMS subunit) coordinate to form the strongly negatively charged and the narrowest part of the ion conduction pathway. Previous studies have demonstrated that a single mutation of Glu to Asp converts NaChBac from a highly Na^+-selective channel to a Ca^{2+}- and Na^+-permeable channel (D/D/D/D) and incorporating two additional Asp residues in the pore loop region of NaChBac results in a highly Ca^{2+}-selective channel (Yue et al. 2002). Conversely, mutations in the selectivity filter of the 24-TMS Na_V and Ca_V channels in animals also modulate the Na^+ and Ca^{2+} ion selectivity (Heinemann et al. 1992; Yang et al. 1993). Therefore, it is conceivable that in the four homologous channel domains of ancestral 24-TMS Ca_V and Na_V channels, the selectivity filters and the pore loop regions underwent evolutionary selection pressures to modulate ion selectivity. Furthermore, Ca_V and Na_V channels are likely also subject to changes in other conserved regions in the channel domains, which are often related to their different functional properties and pharmacological characteristics (Catterall et al. 2005a, 2005b). By taking into account not only the pore loop/selectivity filter regions but also other conserved regions in the channel domains, our phylogenetic analyses with three evolutionarily distinct outgroups (Fig. 2; Supplemental Figs. S1, S2) distinguish the ancestral Na_V channel homolog from Ca_V channels by consistently grouping the $TtrNa_V$ homolog with the animal Na_V family.

It should be noted that phylogenetic analyses used to reconstruct the evolutionary relationships of ion channel families can provide strong support for, but may not necessarily define, the nature of their functional properties, especially for these ancestral channel homologs. None of these putative protist Na_V channel homologs from *T. trahens* and the choanoflagellates *M. brevicollis* (Liebeskind et al. 2011) and *S. rosetta* have been functionally characterized so far. It remains possible that these ancestral Na_V channel homologs could represent the putative channel intermediates between Ca_V and Na_V channels as proposed previously (Hille 2001; Liebeskind et al. 2011), or display previously undescribed properties, as shown in recent characterization of two protist P2X receptors (Fountain et al. 2007, 2008). Sequence alignment, domain assignment and phylogenetic analyses support the grouping of these protist P2X receptors with their animal counterparts (Cai 2011; Fountain and Burnstock 2009). In animals, P2X receptors sense extracellular ATP and induce the flux of cations across the plasma membrane (Khakh and North 2006). In contrast, P2X receptors in the dictyostelid social amoeba *Dictyostelium discoideum* (Fountain et al. 2007) and the green alga *Ostreococcus tauri* (Fountain et al. 2008) appear to serve functional roles on intracellular organelle membranes with distinct properties, presumably sensing the changes in intracellular ATP.

Conclusion

Together with the seminal report on the first cloning and phylogenetic characterization of a protist 24-TMS Na_V channel homolog from the choanoflagellates *M. brevicollis*

(Liebeskind et al. 2011), the identification of $TtrNa_V$ from the apusozoan protist *T. trahens* with a unique pore sequence provides an exciting opportunity to study the evolution of ion selectivity in voltage-gated ion channels and the role of ion channels in the eukaryotic evolution leading to multicellular organisms. Little is known about the biology of the phylum Apusozoa, including *T. trahens* (Cavalier-Smith and Chao 2003, 2010). *T. trahens* are unicellular and biflagellate eukaryotes living in soils and aquatic environments, where they glide on the surface and feed on bacteria. Flagellar movement promotes motility in search for food, which is ingested by pseudopodia-like locomotion. Presumably, the emergence of a 24-TMS Na_V channel could provide a new means of controlling membrane excitability and enabling Ca^{2+} to function more specifically as a signaling molecule to regulate diverse cellular processes (Clapham 2007). Indeed, *T. trahens* had acquired a set of Ca^{2+} signaling molecules conserved in the animal lineage such as voltage-gated CatSper Ca^{2+} channels and Na^+/Ca^{2+} exchangers (Cai and Clapham 2012).

Determining the biophysical properties and ion selectivity of these protist Na_V homologs will no doubt broaden our current knowledge on the evolution of the electrophysiological properties in protists and in excitable cells such as neurons and cardiomyocytes (Armstrong and Hille 1998; Rosati and McKinnon 2009). Further evolutionary systems biology studies (Medina 2005) of ion channel protein families will also shed novel evolutionary and mechanistic insights into signaling pathways mediated by different ion channels.

Acknowledgments This project was initiated as part of the Ion Channel Genomics Study when I was at Duke University Medical Center. I thank the Broad Institute and the investigators of the Origins of Multicellularity Sequencing Project, Broad Institute of Harvard, and MIT (http://www.broadinstitute.org/) for making data publicly available, and several anonymous reviewers for their valuable suggestions and insightful comments. I also thank Yanhong Zhang for technical assistance and critical reading.

References

Altschul SF, Madden TL, Schaffer AA, Zhang J, Zhang Z, Miller W, Lipman DJ (1997) Gapped BLAST and PSI-BLAST: a new generation of protein database search programs. Nucleic Acids Res 25:3389–3402

Anderson PA, Holman MA, Greenberg RM (1993) Deduced amino acid sequence of a putative sodium channel from the scyphozoan jellyfish *Cyanea capillata*. Proc Natl Acad Sci USA 90:7419–7423

Armstrong CM, Hille B (1998) Voltage-gated ion channels and electrical excitability. Neuron 20:371–380

Arnegard ME, Zwickl DJ, Lu Y, Zakon HH (2010) Old gene duplication facilitates origin and diversification of an innovative communication system—twice. Proc Natl Acad Sci USA 107:22172–22177

Brailoiu E, Churamani D, Cai X, Schrlau MG, Brailoiu GC, Gao X, Hooper R, Boulware MJ, Dun NJ, Marchant JS, Patel S (2009) Essential requirement for two-pore channel 1 in NAADP-mediated calcium signaling. J Cell Biol 186:201–209

Cai X (2008a) Subunit stoichiometry and channel pore structure of ion channels: all for one, or one for one? J Physiol 586:925–926

Cai X (2008b) Unicellular Ca^{2+} signaling "toolkit" at the origin of Metazoa. Mol Biol Evol 25:1357–1361

Cai X (2011) P2X receptor homologs in basal fungi. Purinergic Signal. doi:10.1007/s11302-011-9261-8

Cai X, Clapham DE (2012) Ancestral Ca^{2+} signaling machinery in early animal and fungal evolution. Mol Biol Evol 29:91–100

Cai X, Patel S (2010) Degeneration of an intracellular ion channel in the primate lineage by relaxation of selective constraints. Mol Biol Evol 27:2352–2359

Calcraft PJ, Ruas M, Pan Z, Cheng X, Arredouani A, Hao X, Tang J, Rietdorf K, Teboul L, Chuang KT, Lin P, Xiao R, Wang C, Zhu Y, Lin Y, Wyatt CN, Parrington J, Ma J, Evans AM, Galione A, Zhu MX (2009) NAADP mobilizes calcium from acidic organelles through two-pore channels. Nature 459:596–600

Carr M, Leadbeater BS, Hassan R, Nelson M, Baldauf SL (2008) Molecular phylogeny of choanoflagellates, the sister group to Metazoa. Proc Natl Acad Sci USA 105:16641–16646

Catterall WA, Goldin AL, Waxman SG (2005a) International union of pharmacology. XLVII. Nomenclature and structure-function relationships of voltage-gated sodium channels. Pharmacol Rev 57:397–409

Catterall WA, Perez-Reyes E, Snutch TP, Striessnig J (2005b) International union of pharmacology. XLVIII. Nomenclature and structure-function relationships of voltage-gated calcium channels. Pharmacol Rev 57:411–425

Cavalier-Smith T, Chao EE (2003) Phylogeny of choanozoa, apusozoa, and other protozoa and early eukaryote megaevolution. J Mol Evol 56:540–563

Cavalier-Smith T, Chao EE (2010) Phylogeny and evolution of apusomonadida (protozoa: apusozoa): new genera and species. Protist 161:549–576

Clapham DE (2007) Calcium signaling. Cell 131:1047–1058

Darriba D, Taboada GL, Doallo R, Posada D (2011) ProtTest 3: fast selection of best-fit models of protein evolution. Bioinformatics 27:1164–1165

Durell SR, Guy HR (2001) A putative prokaryote voltage-gated Ca(2+) channel with only one 6TM motif per subunit. Biochem Biophys Res Commun 281:741–746

Felsenstein J (1985) Confidence limits on phylogenies: an approach using the bootstrap. Evolution 39:783–791

Felsenstein J (1996) Inferring phylogenies from protein sequences by parsimony, distance, and likelihood methods. Meth Enzymol 266:418–427

Fountain SJ, Burnstock G (2009) An evolutionary history of P2X receptors. Purinergic Signal 5:269–272

Fountain SJ, Parkinson K, Young MT, Cao L, Thompson CR, North RA (2007) An intracellular P2X receptor required for osmoregulation in *Dictyostelium discoideum*. Nature 448:200–203

Fountain SJ, Cao L, Young MT, North RA (2008) Permeation properties of a P2X receptor in the green algae *Ostreococcus tauri*. J Biol Chem 283:15122–15126

Galione A, Evans AM, Ma J, Parrington J, Arredouani A, Cheng X, Zhu MX (2009) The acid test: the discovery of two-pore channels (TPCs) as NAADP-gated endolysosomal Ca(2+) release channels. Pflugers Arch 458:869–876

Goldin AL (2002) Evolution of voltage-gated Na(+) channels. J Exp Biol 205:575–584

Guindon S, Dufayard JF, Lefort V, Anisimova M, Hordijk W, Gascuel O (2010) New algorithms and methods to estimate

maximum-likelihood phylogenies: assessing the performance of PhyML 3.0. Syst Biol 59:307–321

Heinemann SH, Terlau H, Stuhmer W, Imoto K, Numa S (1992) Calcium channel characteristics conferred on the sodium channel by single mutations. Nature 356:441–443

Hille B (2001) Ionic channels of excitable membranes. Sinauer Associates, Sunderland

Hillis DM, Bull JJ (1993) An empirical test of bootstrapping as a method for assessing confidence in phylogenetic analysis. Syst Biol 42:182–192

Hong MP, Vu K, Bautos J, Gelli A (2010) Cch1 restores intracellular Ca^{2+} in fungal cells during endoplasmic reticulum stress. J Biol Chem 285:10951–10958

Ishibashi K, Suzuki M, Imai M (2000) Molecular cloning of a novel form (two-repeat) protein related to voltage-gated sodium and calcium channels. Biochem Biophys Res Commun 270:370–376

Katoh K, Toh H (2008) Recent developments in the MAFFT multiple sequence alignment program. Brief Bioinform 9:286–298

Khakh BS, North RA (2006) P2X receptors as cell-surface ATP sensors in health and disease. Nature 442:527–532

King N, Carroll SB (2001) A receptor tyrosine kinase from choanoflagellates: molecular insights into early animal evolution. Proc Natl Acad Sci USA 98:15032–15037

King N, Hittinger CT, Carroll SB (2003) Evolution of key cell signaling and adhesion protein families predates animal origins. Science 301:361–363

King N, Westbrook MJ, Young SL, Kuo A, Abedin M, Chapman J, Fairclough S, Hellsten U, Isogai Y, Letunic I, Marr M, Pincus D, Putnam N, Rokas A, Wright KJ, Zuzow R, Dirks W, Good M, Goodstein D, Lemons D, Li W, Lyons JB, Morris A, Nichols S, Richter DJ, Salamov A, Sequencing JG, Bork P, Lim WA, Manning G, Miller WT, McGinnis W, Shapiro H, Tjian R, Grigoriev IV, Rokhsar D (2008) The genome of the choanoflagellate *Monosiga brevicollis* and the origins of metazoan multicellularity. Nature 451:783–788

Koishi R, Xu H, Ren D, Navarro B, Spiller BW, Shi Q, Clapham DE (2004) A superfamily of voltage-gated sodium channels in bacteria. J Biol Chem 279:9532–9538

Le SQ, Gascuel O (2008) An improved general amino acid replacement matrix. Mol Biol Evol 25:1307–1320

Li W, Young SL, King N, Miller WT (2008) Signaling properties of a non-metazoan Src kinase and the evolutionary history of Src negative regulation. J Biol Chem 283:15491–15501

Liebeskind BJ, Hillis DM, Zakon HH (2011) Evolution of sodium channels predates the origin of nervous systems in animals. Proc Natl Acad Sci USA 108:9154–9159

Lopreato GF, Lu Y, Southwell A, Atkinson NS, Hillis DM, Wilcox TP, Zakon HH (2001) Evolution and divergence of sodium channel genes in vertebrates. Proc Natl Acad Sci USA 98:7588–7592

Loytynoja A, Goldman N (2010) webPRANK: a phylogeny-aware multiple sequence aligner with interactive alignment browser. BMC Bioinformatics 11:579

Lu B, Su Y, Das S, Liu J, Xia J, Ren D (2007) The neuronal channel NALCN contributes resting sodium permeability and is required for normal respiratory rhythm. Cell 129:371–383

Medina M (2005) Genomes, phylogeny, and evolutionary systems biology. Proc Natl Acad Sci USA 102(1):6630–6635

Nicholas K, Nicholas H, Deerfield D (1997) Genedoc: analysis and visualization of genetic variation. EMBNET News 4:1–4

Page RD (1996) TREEVIEW: an application to display phylogenetic trees on personal computers. Comput Appl Biosci 12:357–358

Patel S, Marchant JS, Brailoiu E (2010) Two-pore channels: regulation by NAADP and customized roles in triggering calcium signals. Cell Calcium 47:480–490

Payandeh J, Scheuer T, Zheng N, Catterall WA (2011) The crystal structure of a voltage-gated sodium channel. Nature 475:353–358

Plummer NW, Meisler MH (1999) Evolution and diversity of mammalian sodium channel genes. Genomics 57:323–331

Ren D, Navarro B, Xu H, Yue L, Shi Q, Clapham DE (2001) A prokaryotic voltage-gated sodium channel. Science 294: 2372–2375

Rokas A (2008) The origins of multicellularity and the early history of the genetic toolkit for animal development. Annu Rev Genet 42:235–251

Rosati B, McKinnon D (2009) Structural and regulatory evolution of cellular electrophysiological systems. Evol Dev 11:610–618

Ruiz-Trillo I, Burger G, Holland PW, King N, Lang BF, Roger AJ, Gray MW (2007) The origins of multicellularity: a multi-taxon genome initiative. Trends Genet 23:113–118

Ruiz-Trillo I, Roger AJ, Burger G, Gray MW, Lang BF (2008) A phylogenomic investigation into the origin of metazoa. Mol Biol Evol 25:664–672

Sebe-Pedros A, Roger AJ, Lang FB, King N, Ruiz-Trillo I (2010) Ancient origin of the integrin-mediated adhesion and signaling machinery. Proc Natl Acad Sci USA 107:10142–10147

Steenkamp ET, Wright J, Baldauf SL (2006) The protistan origins of animals and fungi. Mol Biol Evol 23:93–106

Strong M, Chandy KG, Gutman GA (1993) Molecular evolution of voltage-sensitive ion channel genes: on the origins of electrical excitability. Mol Biol Evol 10:221–242

Talavera G, Castresana J (2007) Improvement of phylogenies after removing divergent and ambiguously aligned blocks from protein sequence alignments. Syst Biol 56:564–577

Widmark J, Sundstrom G, Ocampo Daza D, Larhammar D (2011) Differential evolution of voltage-gated sodium channels in tetrapods and teleost fishes. Mol Biol Evol 28:859–871

Yang J, Ellinor PT, Sather WA, Zhang JF, Tsien RW (1993) Molecular determinants of Ca^{2+} selectivity and ion permeation in L-type Ca^{2+} channels. Nature 366:158–161

Yue L, Navarro B, Ren D, Ramos A, Clapham DE (2002) The cation selectivity filter of the bacterial sodium channel, NaChBac. J Gen Physiol 120:845–853

Zakon HH, Lu Y, Zwickl DJ, Hillis DM (2006) Sodium channel genes and the evolution of diversity in communication signals of electric fishes: convergent molecular evolution. Proc Natl Acad Sci USA 103:3675–3680

Zakon HH, Jost MC, Lu Y (2011) Expansion of voltage-dependent Na^+ channel gene family in early tetrapods coincided with the emergence of terrestriality and increased brain complexity. Mol Biol Evol 28:1415–1424

J Membrane Biol (2012) 245:125–129
DOI 10.1007/s00232-012-9420-z

BRIEF COMMUNICATION

Assignment of Putative Functions to Membrane "Hypothetical Proteins" from the *Trypanosoma cruzi* Genome

Ariel Mariano Silber · Claudio Alejandro Pereira

Received: 20 December 2011 / Accepted: 31 January 2012 / Published online: 22 February 2012

Abstract Protozoan parasites cause thousands of deaths each year in developing countries. The genome projects of these parasites opened a new era in the identification of therapeutic targets. However, the putative function could be predicted for fewer than half of the protein-coding genes. In this work, all *Trypanosoma cruzi* proteins containing predicted transmembrane spans were processed through an automated computational routine and further analyzed in order to assign the most probable function. The analysis consisted of dissecting the whole predicted protein in different regions. More than 5,000 sequences were processed, and the predicted biological functions were grouped into 19 categories according to the hits obtained after analysis. One focus of interest, due to the scarce information available on trypanosomatids, is the proteins involved in signal-transduction processes. In the present work, we identified 54 proteins belonging to this group, which were individually analyzed. The results show that by means of a simple pipeline it was possible to attribute probable functions to sequences annotated as coding for "hypothetical proteins." Also, we successfully identified the majority of candidates participating in the signal-transduction pathways in *T. cruzi*.

Keywords *Trypanosoma cruzi* · Hypothetical protein · Membrane protein · Signal transduction · Receptor · Chagas disease

Introduction

Trypanosomes are etiological agents of several veterinary infections, but only two of them cause important human diseases. In sub-Saharan Africa, *Trypanosoma brucei* causes sleeping sickness, and in America *Trypanosoma cruzi* causes Chagas disease. Both trypanosomiases affect mainly poor and marginalized populations. Chagas disease is limited to Central and South America, where about 7.7 million people are infected (Rassi et al. 2010). It is also the first cause of cardiac lesions in young, economically productive adults in endemic countries (Aufderheide et al. 2004).

In 2005, the genomes of the trypanosomatids *T. brucei*, *T. cruzi* and *Leishmania major* were partially completed by the TriTryp sequencing consortium (El-Sayed et al. 2005b). A major problem that occurs in the genome projects in general, and particularly in the TriTryp genomes, is failure to predict gene function; consequently, more than half of the gene products have been annotated as "hypothetical proteins." Genes coding for hypothetical proteins are predominant in trypanosomatid genomes. For example, in the TriTryp database, there are over 105,060 protein-coding genes, with 62,068 codes for hypothetical proteins (59%). In the specific case of *T. cruzi*, there are 11,062 hypothetical proteins (56%) in the genome database, corresponding to 6,526 different genes (Aslett et al. 2010). Considering the present situation, development of novel

Electronic supplementary material The online version of this article (doi:10.1007/s00232-012-9420-z) contains supplementary material, which is available to authorized users.

A. M. Silber
Departamento de Parasitologia, Instituto de Ciências Biomédicas, Universidade de São Paulo, São Paulo, Brazil

C. A. Pereira (✉)
Laboratorio de Biología Molecular de Trypanosoma Cruzi (LBMTC), Instituto de Investigaciones Médicas "Alfredo Lanari", Universidad de Buenos Aires and CONICET, Combatientes de Malvinas 3150, 1427 Buenos Aires, Argentina
e-mail: cpereira@retina.ar

strategies for automated gene-function prediction is especially relevant in protozoan parasites. Putative functions could be assigned to fewer than half of the genes, and these predictions were based on the similarity to previously characterized proteins or known functional domains. For example, many of the predicted metabolic pathways are truncated or incomplete, where the end products would not be used by the parasite (Kanehisa and Goto 2000). Probably, some of these "missing enzymes" exist, but they have been annotated as hypothetical proteins.

Membrane proteins constitute the connecting interface between the intra- and extracellular environments, which mediates the interchange of molecules, medium sensing and cell communication. To date, studies on the membrane components of signal-transduction pathways in protozoan parasites are very scarce. In addition, little is known about the nature of macromolecules with regard to the extracellular environment and their ability to recognize specific environmental signals. The identification of surface proteins able to recognize molecules secreted by the host, which would alter parasite behavior, and the type of response that is expected are critical issues to understand host–parasite interactions (Parsons and Ruben 2000).

In this work, using an automated bioinformatic routine, we determined the distribution of *T. cruzi* membrane proteins according to the transmembrane span number. Based on this initial information, the whole proteins as well as the N- and C-terminal regions were analyzed by BLAST, which allowed prediction of functions for a relevant subpopulation. Novel groups of membrane proteins, including putative receptors, were identified.

Materials and Methods

Databanks Employed

T. cruzi sequence data were obtained from TriTrypDB version 3.3. The Swiss Prot Database, used as a reference for protein alignment, was obtained at the NCBI FTP Databases Repository (ftp://ftp.ncbi.nih.gov/blast/db/). This database, containing 303,518 amino acid sequences, was chosen because it includes only high-quality annotated and nonredundant protein sequences. Other sequences used in this work are from the DNA Database from Japan (DDBJ, http://www.ddbj.nig.ac.jp/) and Interpro Database (http://www.ebi.ac.uk/InterProScan/).

Automated Routines for Sequence Processing

Automated routines were programmed in Perl language (http://www.perl.org/) using Bioperl (http://www.bioperl.org/) code and proceed as indicated in the scheme in Fig. 1a. The routine input was a text report from TriTrypDB for all 5,174 predicted membrane proteins, containing the following data: gene ID, protein length, transmembrane spans (TMS) count, sequence type (gene or pseudogene), amino acid sequence and a table containing the TMS positions. Protein sequences were divided into 37 groups according to TMS number, and then each group was subdivided into three individual fasta files containing the full-length sequence, the N- and C-terminal domains defined as the sequences before the first TMS and after the last TMS. Sequences were compared using the standalone BLAST and the Swissprot protein database. BLASTP version 2.2.24 (Altschul et al. 1997) was run under default parameters using a cut-off score for sequence hits with E values $<10^{-10}$. The final report of the functional groups of hits associated to each query was manually created. Sequences were grouped into 19 categories according to the predicted biological process. Hits related to proteins of particular interest were individually analyzed.

Other Bioinformatic Tools

Further sequence analysis were performed using different resources: TMpred (http://www.ch.embnet.org/), TMHMM version 2.0 (http://www.cbs.dtu.dk/) for topology prediction (Krogh et al. 2001), PredGPI (http://gpcr.biocomp.unibo.it/predgpi/pred.htm) for glycosylphosphatidylinositol PredGPI (http://gpcr.biocomp.unibo.it/predgpi/pred.htm)-anchor sites and Vector NTI 10 package (Invitrogen Corporation, Carlsbad, California) for general sequence analysis.

Results and Discussion

Ordering Membrane Hypothetical Proteins

About 26% of the *T. cruzi* genes code for putative membrane proteins (5,174 out of 19,673 protein-coding genes), of which 48% (2,499) are annotated as hypothetical proteins. Taking as a starting point all the 5,174 genes coding for putative membrane proteins available on TriTrypDB, an automated TMS prediction was performed and the proteins were classified according to the number of TMS, ranging from 1 to 37.

About 74% of the predicted proteins have one or two TMS, belonging to few multigene families of surface proteins including *trans*-sialidases, gp63, Tc85, mucin-associated surface proteins (MASP) and related proteins (El-Sayed et al. 2005a). In a preliminary analysis we found that many sequences within this group, annotated as "hypothetical proteins," had high-identity values with known soluble proteins. Therefore, proteins with one or two TMS were excluded from further analyses because the

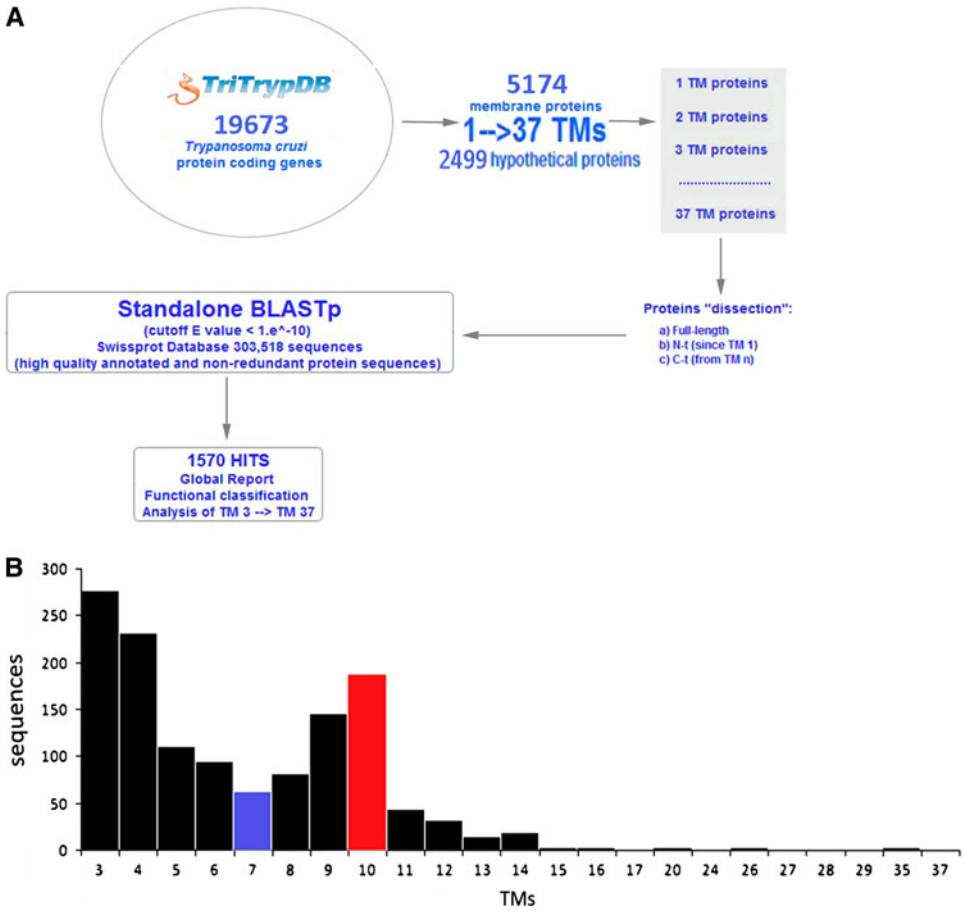

Fig. 1 **a** Schematic representation of the automated routine for functional classification of proteins. Input files are text reports obtained from TriTrypDB (http://tritrypdb.org/) containing the following data: gene ID, protein length, transmembrane span (TMS) count, sequence type (gene or pseudogene), predicted amino acid sequence and a table containing the TMS positions. Protein sequences have been divided into 37 groups according the TMS number, and then each group was subdivided in individual fasta files containing the full-length sequence and the N- and C-terminal domains, defined as the sequences before the first TMS and after the last TMS. Sequences were compared using the standalone BLAST and the Swissprot protein database. BLASTP version 2.2.24 was run under default parameters using a cut-off score for sequence hits of $E < 10^{-10}$. **b** Protein classification according to TMS count. Proteins containing 3–37 TMS were graphically represented as a function of sequence number

data obtained from these sequences were not reliable, an error in the prediction of one TMS leading to the inclusion of soluble proteins in this group (see Supplementary Table S1).

The distribution of membrane proteins is shown in Fig. 1b. Interestingly, the number of proteins in each group as a function of the number of TMS presents a regular pattern, which continuously decreases up to seven TMS, presenting a second "peak" at 10 TMS (Fig. 1b, blue and red bars, respectively). This pattern is probably related to protein function because loops are variable regions submitted to the selective pressure of the immune system of the hosts, but the TMS present a more restrictive degree of freedom in terms of variation during evolution due to the fact that they constitute the structural basis for protein function.

Predicting Functions of Membrane Proteins

The second part of the algorithm designed in this work is oriented to function prediction based on the subdivision of proteins in their N- and C-terminal domains for local sequence alignment using BLAST. All 1,570 proteins with BLAST hits under the cut-off score ($E < 10^{-10}$) were classified in 18 different groups according to their functions (Fig. 2a, b). Of the total analyzed, 918 proteins were above the cut-off E value and excluded, to maintain the stringency of the analysis. The largest protein group identified comprises different transporter proteins, including ion channels, amino acid permeases, ABC and MDR pumps (constituting about 50% of the membrane proteins analyzed) and enzymes related to lipid metabolism (18.8%). Amino acids and related transporters are those

A

Classification/TMs number	3	4	5	6	7	8	9	10	11	12	13	14	15	16	17	20	26	27	29	35	37	TOTAL	%
Lipid metabolism	8	22	10	5	8	6	3	4	2								2	1				71	18.8
Unclassified transporters	11	12	10	3	3	1	6	8	4	3												61	16.1
Ion transporters	2	8	1	2	2	5	2	2	8	1				1		1						35	9.3
ABC/MDR transporters	2	4	4	6	1		1	3	4	4	1	1	1	1								33	8.7
Surface proteins	24	3	1		1																	29	7.7
Unexpected hits	8	4	2	1	3	1		1	1	1					1							23	6.1
Amino Acid transporters		1			1	1		8	7	3												21	5.6
Unclassified non-transporter proteins	5	4	9	2																		20	5.3
Zinc transporters		1	1	2	2	3		1				1	1									12	3.2
Putative receptors	1	1	2		3		1		1	2	1											12	3.2
Carbohydrate transporters		2	1			2	3	1	1	2												12	3.2
F/P-type ATPases	2		4	3	1																	10	2.6
Lipid transporters			1		3	2				3												9	2.4
Carbohydrate metabolism	1	3		1			2	1														8	2.1
Protein kinases	2	1	2			1	1															7	1.9
Respiratory chain	2	1	1			1				1												6	1.6
Aquaporines				5																		5	1.3
Structural proteins																			1	2	1	4	1.1
TOTAL	68	67	49	30	28	23	19	29	28	20	2	2	2	2	1	1	2	1	1	2	1	378	100.0

B

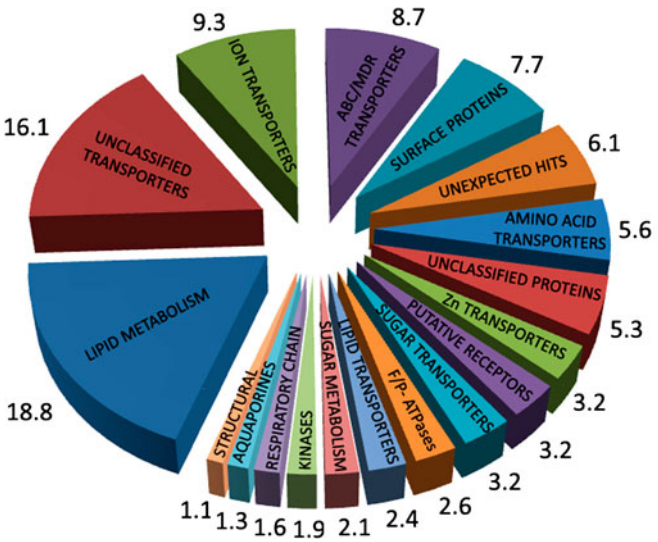

Fig. 2 Functional classification of membrane proteins. **a** Predicted protein sequences ordered according to TMS number and classified in 19 functional groups based on the corresponding BLAST hits report. *Gray rows* indicate groups analyzed in proof in 3.3. **b** Graphical representation of each functional group. A pie chart was constructed using the data shown in **a**. Numbers next to each triangle are the percentage of sequences corresponding to each functional group

sequences that constitute the "peak" at 9 or 10 TMS in Fig. 1. A special case are zinc transporters, which are interesting not for their function but for the large number of them found in the sequence analysis—about 25% of the protein involved in ion uptake in *T. cruzi* are putative zinc transporters. However, the physiological role of zinc in the parasites remains unknown. A group named "unexpected hits" contained proteins not previously found in this organism or unusual membrane proteins. For example, proteins related to nucleic acid remodeling, including those involved in DNA excision/repair process, DEAD-box ATP-dependent RNA helicases and endo- and exonucleases. These putative proteins are probably associated with the nuclear membrane.

Proteins Related to Signal-Transduction Processes

We specifically analyzed all the protein hits related to sensing or transducing extracellular signals. A total of 55 proteins were selected. The most interesting subgroups found are proteins involved in processes such as autophagy, programmed cell death, inositol 1,4,5-trisphosphate (IP3) receptors and components of the mitogen-activated protein kinase (MAPK) cascade (Supplementary Table S2). Finally, one group, belonging to the seven transmembrane receptors family (7TMR), is composed of adiponectin receptors. Adiponectin is an essential hormone secreted by adipocytes, which acts as an antidiabetic factor and is involved in metabolic pathways that regulate lipid metabolism such as fatty acid oxidation and glucose uptake throughout the AMP-activated protein kinase (AMPK) (Goldstein and Scalia 2004). Three different sequences belonging to the PAQR (progestin and adipoQ receptors) family were identified as putative adiponectin receptors. Considering that adipose tissue is one of the major sites of inflammation in Chagas disease and that a *T. cruzi* infection–associated decrease in adiponectin has been demonstrated (Nagajyothi et al. 2008), future studies on these

putative receptors can reveal new host–parasite interaction mechanisms.

Acknowledgements This work was supported by grants from the Consejo Nacional de Investigaciones Científicas y Técnicas (CONICET, PIP grant 0685 to C. A. P.), Agencia Nacional de Promoción Científica y Tecnológica (FONCYT PICT grant 2008-1209 to C. A. P.), Fundação de Amparo à Pesquisa do Estado de São Paulo (FAPESP grant 11/50631-1 to A. M. S.) and Instituto Nacional de Biologia Estrutural e Química Medicinal em Doenças Infecciosas (INBEQMeDI). C. A. P. is a career scientific investigator of CONICET (Argentina). The funders had no role in study design, data collection and analysis, the decision to publish or preparation of the manuscript.

References

Altschul SF, Madden TL, Schaffer AA, Zhang J, Zhang Z, Miller W, Lipman DJ (1997) Gapped BLAST and PSI-BLAST: a new generation of protein database search programs. Nucleic Acids Res 25:3389–3402

Aslett M, Aurrecoechea C, Berriman M, Brestelli J, Brunk BP, Carrington M, Depledge DP, Fischer S, Gajria B, Gao X, Gardner MJ, Gingle A, Grant G, Harb OS, Heiges M, Hertz-Fowler C, Houston R, Innamorato F, Iodice J, Kissinger JC, Kraemer E, Li W, Logan FJ, Miller JA, Mitra S, Myler PJ, Nayak V, Pennington C, Phan I, Pinney DF, Ramasamy G, Rogers MB, Roos DS, Ross C, Sivam D, Smith DF, Srinivasamoorthy G, Stoeckert CJ Jr, Subramanian S, Thibodeau R, Tivey A, Treatman C, Velarde G, Wang H (2010) TriTrypDB: a functional genomic resource for the Trypanosomatidae. Nucleic Acids Res 38:D457–D462

Aufderheide AC, Salo W, Madden M, Streitz J, Buikstra J, Guhl F, Arriaza B, Renier C, Wittmers LE Jr, Fornaciari G, Allison M (2004) A 9,000-year record of Chagas' disease. Proc Natl Acad Sci USA 101:2034–2039

El-Sayed NM, Myler PJ, Bartholomeu DC, Nilsson D, Aggarwal G, Tran AN, Ghedin E, Worthey EA, Delcher AL, Blandin G, Westenberger SJ, Caler E, Cerqueira GC, Branche C, Haas B, Anupama A, Arner E, Aslund L, Attipoe P, Bontempi E, Bringaud F, Burton P, Cadag E, Campbell DA, Carrington M, Crabtree J, Darban H, da Silveira JF, de Jong P, Edwards K, Englund PT, Fazelina G, Feldblyum T, Ferella M, Frasch AC, Gull K, Horn D, Hou L, Huang Y, Kindlund E, Klingbeil M, Kluge S, Koo H, Lacerda D, Levin MJ, Lorenzi H, Louie T, Machado CR, McCulloch R, McKenna A, Mizuno Y, Mottram JC, Nelson S, Ochaya S, Osoegawa K, Pai G, Parsons M, Pentony M, Pettersson U, Pop M, Ramirez JL, Rinta J, Robertson L, Salzberg SL, Sanchez DO, Seyler A, Sharma R, Shetty J, Simpson AJ, Sisk E, Tammi MT, Tarleton R, Teixeira S, Van Aken S, Vogt C, Ward PN, Wickstead B, Wortman J, White O, Fraser CM, Stuart KD, Andersson B (2005a) The genome sequence of *Trypanosoma cruzi*, etiologic agent of Chagas disease. Science 309:409–415

El-Sayed NM, Myler PJ, Blandin G, Berriman M, Crabtree J, Aggarwal G, Caler E, Renauld H, Worthey EA, Hertz-Fowler C, Ghedin E, Peacock C, Bartholomeu DC, Haas BJ, Tran AN, Wortman JR, Alsmark UC, Angiuoli S, Anupama A, Badger J, Bringaud F, Cadag E, Carlton JM, Cerqueira GC, Creasy T, Delcher AL, Djikeng A, Embley TM, Hauser C, Ivens AC, Kummerfeld SK, Pereira-Leal JB, Nilsson D, Peterson J, Salzberg SL, Shallom J, Silva JC, Sundaram J, Westenberger S, White O, Melville SE, Donelson JE, Andersson B, Stuart KD, Hall N (2005b) Comparative genomics of trypanosomatid parasitic protozoa. Science 309:404–409

Goldstein BJ, Scalia R (2004) Adiponectin: a novel adipokine linking adipocytes and vascular function. J Clin Endocrinol Metab 89:2563–2568

Kanehisa M, Goto S (2000) KEGG: Kyoto encyclopedia of genes and genomes. Nucleic Acids Res 28:27–30

Krogh A, Larsson B, von Heijne G, Sonnhammer EL (2001) Predicting transmembrane protein topology with a hidden Markov model: application to complete genomes. J Mol Biol 305:567–580

Nagajyothi F, Desruisseaux MS, Thiruvur N, Weiss LM, Braunstein VL, Albanese C, Teixeira MM, de Almeida CJ, Lisanti MP, Scherer PE, Tanowitz HB (2008) *Trypanosoma cruzi* infection of cultured adipocytes results in an inflammatory phenotype. Obesity (Silver Spring) 16:1992–1997

Parsons M, Ruben L (2000) Pathways involved in environmental sensing in trypanosomatids. Parasitol Today 16:56–62

Rassi A Jr, Rassi A, Marin-Neto JA (2010) Chagas disease. Lancet 375:1388–1402

J Membrane Biol (2012) 245:131–140
DOI 10.1007/s00232-012-9421-y

ORIGINAL ARTICLES

Effect of Simultaneously Replacing Putative TM6 and TM12 of Human NBCe1-A with Those from NBCn1 on Surface Abundance in *Xenopus* Oocytes

Li-Ming Chen · Xue Qin · Fraser J. Moss · Ying Liu · Walter F. Boron

Received: 28 October 2011 / Accepted: 4 February 2012 / Published online: 2 March 2012

Abstract HCO_3^- translocation across the plasma membrane via the electrogenic Na/HCO_3^- cotransporter NBCe1 plays an important role in intracellular pH regulation and transepithelial HCO_3^- transport. However, the structural determinants of transporter function remain largely unknown. A previous study showed that the putative fourth extracellular loop (EL4) plays an essential role in determining the electrogenicity of NBCe1. In the present study, we generated eight new chimeras of human NBCe1-A and NBCn1-A. All possess the putative NBCe1 EL4 and are electrogenic. Chimera O, in which the putative sixth transmembrane segment (TM6) and EL5 through the C terminus (Ct) of NBCe1 was replaced by corresponding NBCn1 sequence, produces the smallest hyperpolarization (1–2 mV) when CO_2/HCO_3^- is added to the extracellular solution. Biotinylation experiments show that O has a very low abundance at the plasma membrane. However, chimeras in which we simultaneously replaced the putative TM6 and smaller subdomains of the EL5-Ct region for the NBCn1 sequence were strongly electrogenic except for chimera T, in which we replaced TM6 and TM12 of NBCe1 with the corresponding regions of NBCn1. T exhibited greatly reduced transporter surface expression compared to wild-type NBCe1-A, while retaining at least some electrogenic character. We hypothesize that putative TM6 and TM12 are part of a functional unit and that if the two TMs are replaced by those of the same transporter type, high surface expression would require that the surrounding TMs are also from the same transporter type.

Keywords *Xenopus* oocyte · SLC4A4 · SLC4A7 · Intracellular pH · Biotinylation · Bicarbonate transporter

Xue Qin and Fraser J. Moss contributed equally to this work.

L.-M. Chen (✉) · Y. Liu
Department of Biological Sciences, Key Laboratory of Molecular Biophysics of the Ministry of Education, College of Life Science and Technology, Huazhong University of Science & Technology, Wuhan 430074, Hubei Province, China
e-mail: liming.chen@mail.hust.edu.cn

X. Qin · F. J. Moss · W. F. Boron (✉)
Department of Physiology and Biophysics, Case Western Reserve University School of Medicine, 10900 Euclid Avenue, Cleveland, OH 44106, USA
e-mail: walter.boron@case.edu

Introduction

For secondary active transport, substrate stoichiometry is a fundamentally important property. Among the five Na-coupled HCO_3^- transporters (NCBTs) of the SLC4 family, differences in stoichiometry cause them to fall into two groups based on net charge movement: (1) the electrogenic Na/HCO_3 cotransporters NBCe1 (Romero et al. 1997) and NBCe2 (Virkki et al. 2002; Sassani et al. 2002) and (2) the electroneutral NCBTs, which include NBCn1 (Choi et al. 2000; Pushkin et al. 1999) and NBCn2 (aka NCBE, see Parker et al. 2008; Wang et al. 2000) as well as the Na^+-driven Cl-HCO_3^- exchanger NDCBE (Grichtchenko et al. 2001). On the one hand, electrogenic transport can have profound effects on the membrane potential (V_m) and, thus, could affect a wide range of voltage-sensitive biological processes, such as gating of and flux through ion channels. On the other hand, the electrogenicity (or lack thereof) impacts the thermodynamics of the transporter even to the extent that it can determine the direction of net transport.

The electrogenic NBCe1 and electroneutral NBCn1 have broad physiological relevance. Mutations in NBCe1 have been associated with proximal renal tubular acidosis, mental retardation as well as ocular and dental defects (for review, see

Boron et al. 2009). A carboxyl-terminally truncated NBCe1 mutant with impaired trafficking to the plasma membrane is associated with hemiplegic migraine (Suzuki et al. 2010). Targeted disruption of *Slc4a4* in mice severely impairs the formation of dental enamel, indicating that NBCe1 is essential for normal development of dentition (Lacruz et al. 2010). The complex expression and distribution of at least five NBCe1 variants in the reproductive tract tissues suggest that the transporter plays important roles in mammalian reproduction (Liu et al. 2011).

NBCn1 appears to be important in both normal physiology and pathophysiology. In osteoclasts, NBCn1 is responsible for the increase in intracellular pH (pH_i) triggered by colony-stimulating factor 1, resulting in enhanced cell survival (Bouyer et al. 2007). NBCn1 is also necessary for the degradation of hydroxyapatite by osteoclasts (Riihonen et al. 2010). Polymorphisms in NBCn1 are associated with an increase in susceptibility to breast cancer (Antoniou et al. 2010; Ahmed et al. 2009). Moreover, in a human breast-cancer cell line, NBCn1 abundance is substantially enhanced by the expression of a constitutively active, truncated receptor tyrosine kinase, ErbB2, that is commonly expressed in breast cancer (Lauritzen et al. 2010). In addition, knockout of NBCn1 in mice is associated with blindness and deafness (Bok et al. 2003). Boedtkjer et al. (2011) have shown that NO-mediated vasorelaxation as well as hypertension development are inhibited in NBCn1-null mice. Moreover, a genomewide association study has shown that variations in *SLC4A7* are associated with hypertension and increased cardiovascular disease risk in humans (Ehret et al. 2011). Finally, allelic variants of *SLC4A7* could contribute to the vulnerability to drug addiction (Ishiguro et al. 2007).

Interestingly, the electrogenic NBCe1 and electroneutral NBCn1 appear to have opposite roles in the heart. Inhibition of NBCe1 reduces ischemic injury in rat cardiac myocytes (Khandoudi et al. 2001). In contrast, knock-down of NBCn1 increases ischemia-induced apoptosis of coronary endothelial cells (Kumar et al. 2010). This last observation, which is consistent with an antiapoptotic effect of NBCn1, is in harmony with the aforementioned osteoclast data. De Giusti et al. (2009) demonstrated that angiotensin II stimulates Na-coupled HCO_3^- transport and presumably electroneutral NBC activity in cardiac myocytes. On the other hand, the same group showed that angiotensin II inhibits electrogenic Na-coupled HCO_3^- transport in cardiac myocytes (De Giusti et al. 2010).

Given the physiological significance of NBCe1 and NBCn1, it is important to understand the molecular mechanism of ion transport by these two transporters. Based upon a study with AE1 (Zhu et al. 2003), Romero et al. (2004) proposed that all SLC4 family members consist of a large soluble cytosolic N-terminal domain (Nt), followed by a transmembrane domain (TMD) containing 14 transmembrane segments (TMs), including 13 helices and one reentrant loop connecting the extracellular end of TM11 and the intracellular end of TM13, and a short cytosolic C-terminal domain (Ct). The putative large third extracellular loop (EL3) between TM5 and TM6 divides the TMD into two parts, the front half (TMD_F) consisting of TM1–TM5 and the back half (TMD_B) consisting of TM6–TM14. Choi et al. (2007) demonstrated that the electrogenicity of rat NBCe1 requires the simultaneous presence of TMD_F and TMD_B. Chen et al. (2011) later demonstrated that the putative fourth extracellular loop (EL4) plays a critical role in determining the electrogenicity vs. electroneutrality of human NBCe1-n1 chimeras. Simply replacing EL4 of NBCe1 with that of NBCn1 (construct M in that study) virtually eliminated electrogenicity, while retaining substantial HCO_3^- transport activity. Moreover, the reverse replacement engendered electrogenicity in an electroneutral chimera.

In the present study, we generated eight new NBCe1-n1 chimeras in the TMD_B, all of which contained the EL4 of NBCe1. We demonstrate that all chimeras are electrogenic. However, the simultaneous replacement of TM6 and TM12 of NBCe1-A with those from NBCn1—but not the simultaneous replacements of TM6 with EL5, TM10, TM11, TM13 or TM14—greatly reduced the surface expression of the chimera when expressed in *Xenopus* oocytes. We hypothesize that TM6 and TM12 are part of a functional unit and that, when they are replaced together, normal surface expression requires that the surrounding TMs be from the same transporter type.

Methods

Construct, Oocyte Injection and Electrophysiologic Measurements

As previously described (Chen et al. 2011), chimeras were generated by polymerase chain reaction using human NBCe1-A (accession NM_003759) and human NBCn1-A (accession AF047033) as templates. All constructs were tagged at amino termini with enhanced green fluorescent protein (EGFP). Although it is possible that this tag could have influenced our results, a comparison with historical transport rates suggests that the Nt-EGFP tag did not reduce activity. In the data set for our previous study (Chen et al. 2011), construct A had a mean slope conductance of $\sim$ 35 μS in 5% CO_2/33 mM HCO_3^- (not previously published), which is modestly higher than the value of $\sim$24 μS observed under similar conditions with untagged rat NBCe1-A (Choi et al. 2007).

Figure 1 shows the putative topology—proposed by Romero et al. (2004) based on the AE1 model of Zhu et al.

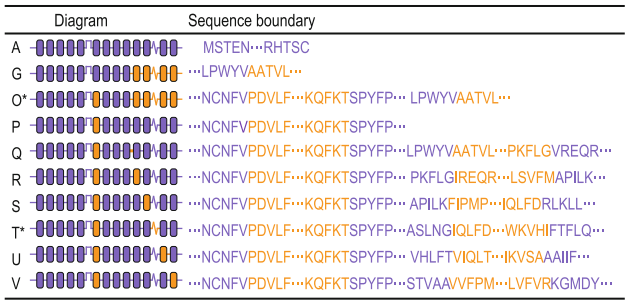

Fig. 1 Diagrams and sequence boundaries of constructs. Regions that contributed human NBCe1-A are in *violet*, whereas regions that contributed by human NBCn1 are in *orange*

(2003)—and sequence boundaries for all constructs that we used in the present study. For the convenience of readers, each construct is designated an alphabetical code consistent with that of our previous article (Chen et al. 2011). The construct cDNAs were linearized by restriction digestion with *Not*I for cRNA synthesis. cRNA was transcribed with T7 RNA polymerase using the mMessage mMachine kit (Ambion, Austin, TX) and stored at –80°C until injected.

In most cases, we obtained *Xenopus laevis* oocytes from an ovarian lobe following a protocol approved by the Institutional Animal Care and Use Committee at Case Western Reserve University. In some cases, we purchased ovaries from NASCO (Fort Atkinson, WI). Each oocyte was injected with 50 nl of cRNA (0.5 µg/µl), encoding a transporter or 50 nl H_2O as a control, and incubated at 18°C for 4–5 days until used for assay.

For 4,4-diisothiocyanatostilbene-2,2-disulfonic acid (DIDS) experiments, we used a nominally CO_2/HCO_3^--free ND96 solution that contained in (mM) 93.5 NaCl, 2 KCl, 1 $MgCl_2$, 1.8 $CaCl_2$ and 5 HEPES. DIDS-containing solutions (400 µM) were made freshly by adding DIDS powder to ND96 or 1.5% CO_2. A 0.2% BSA solution was made freshly by adding albumin powder (0.2 g/100 ml) to ND96 or 1.5% CO_2. Preparation of all other solutions as well as the measurements of V_m and pH_i were performed as previously described (Chen et al. 2011).

Examination of Total and Membrane Proteins Expressed in *Xenopus* Oocytes

For the detection of transporter proteins expressed at the plasma membrane, we biotinylated and then isolated proteins on the extracellular surface of *Xenopus* oocytes using the Pinpoint™ Cell Surface Protein Isolation Kit (catalog 89881; Pierce, Rockford, IL), modifying the manufacturer's protocol for use with oocytes. For each group, 15 oocytes were washed with ice-cold phosphate-buffered saline (PBS, diluted to ~200 mOsm) and incubated in 5 ml PBS containing 1.2 mg Sulfo-NHS-SS-Biotin on a rocker for 1 h at 4°C. The reaction was stopped by adding 250 µl quenching solution. Oocytes were next washed in TRIS-buffered saline (TBS, diluted to ~200 mOsm) for 5 min, then homogenized with a pellet pestle (Kimble Chase Kontes, Vineland, NJ) in 450 µl lysis buffer, which consisted of 1% Triton X-100 (Sigma-Aldrich, St. Louis, MO) and one tablet EDTA-free proteinase inhibitors (Roche Diagnostics, Indianapolis, IN) per 10 ml of TBS. Lysates were centrifuged for 10 min at 1,000×*g* and 4°C. The lipid layer on the top of the supernatant was carefully removed. Some of the supernatant was withheld at this stage and used to assay the amount of total protein fraction. The remaining material was incubated with 500 µl Immobilized Neutravidin™ Gel (Pierce) and incubated for 1 h at room temperature. After five washes with 500 µl lysis buffer, biotinylated proteins were eluted by incubation for 1 h at room temperature in 1 × SDS polyacrylamide gel electrophoresis (SDS-PAGE) sample buffer containing 50 mM DTT. The resulting preparation represents the surface-protein fraction of *Xenopus* oocytes.

The total and surface-protein fractions were separated on SDS-PAGE and then transferred onto an Immobilon™ PVDF membrane (Millipore, Bedford, MA). The blot was probed with monoclonal mouse anti-EGFP primary antibody (Clontech, Palo Alto, CA) at 1:2,000 dilution and then with HRP-conjugated goat anti-mouse secondary antibody (MP Biomedicals, Solon, OH) at 1:5,000. Chemiluminescence was performed with the Amersham ECL Plus Western Blotting Detection Reagents (GE Healthcare, Aylesbury, UK) prior to X-ray film exposure.

Results

V_m and pH_i Measurements of Oocytes Expressing Transporters

Figure 2a shows typical V_m and pH_i records from an oocyte expressing wild-type (wt) human NBCe1-A (construct A). The oocyte was superfused with nominally HCO_3^--free ND96 solution and then with 1.5% CO_2/10 mM HCO_3^-. The addition of CO_2/HCO_3^- caused an abrupt hyperpolarization (V_m, red trace), a change characteristic of an electrogenic NBC. Moreover, after rapid CO_2-induced intracellular acidification, pH_i recovered robustly (green trace). The rate of pH_i recovery (dpHi/dt) reflects the rate of transporter-mediated uptake of HCO_3^- or a related ion (e.g., $CO_3^=$) and is thus an index of NBC activity. Note also that removing Na^+ from the extracellular solution produced the opposite set of changes: an instantaneous depolarization and a rapid fall in pH_i; the depolarization is indicative of electrogenic NBC activity. In the control oocyte injected with H_2O (Fig. 2b), the switch to CO_2/

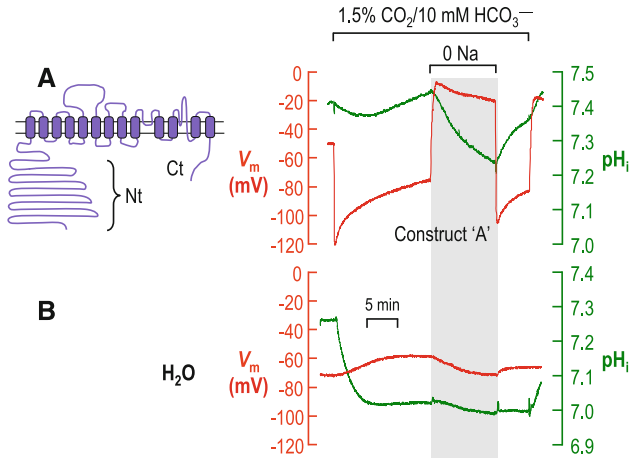

Fig. 2 Typical recordings of pH_i (*green*) and V_m (*red*, in mV). **a** Oocyte expressing human NBCe1-A (construct A). **b** Control oocyte injected with H_2O. The oocyte was first exposed to ND96 (CO_2/HCO_3^--free) solution, and then to 1.5% CO_2/10 mM HCO_3^- for 15 min, all at an extracellular pH of 7.50. Extracellular Na^+ was temporarily replaced with *N*-methyl-D-glucamine for 10 min, and returned for 5 min in the continued presence of CO_2/HCO_3^-

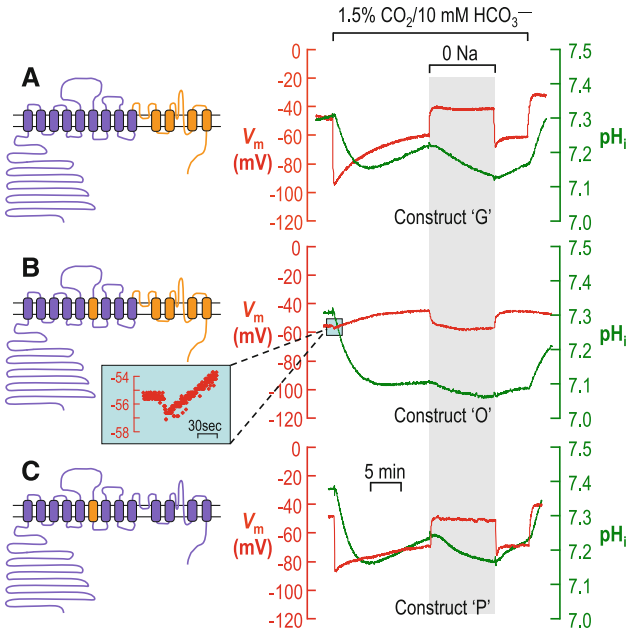

Fig. 3 Typical recordings of pH_i (*green*) and V_m (*red*, in mV) of oocytes expressing chimeric transporters. **a** Construct G. **b** Construct O. **c** Construct P. The experimental protocols are the same as for Fig. 2. The sequence boundaries of the constructs are provided in Fig. 1. *Inset* in *b* shows, in a magnified scale, the small hyperpolarization upon the switch from the ND96 to the CO_2/HCO_3^- solution

HCO_3^- failed to elicit either an instantaneous hyperpolarization or a pH_i recovery from the acid load.

As shown in our previous article (Chen et al. 2011), on the background of wt human NBCe1-A, replacing the fragment from the putative EL5 through the Ct, inclusive, with the corresponding region of human NBCn1-A resulted in an electrogenic chimera (construct G). Representative recordings of V_m and pH_i from an oocyte expressing construct G are shown in Fig. 3a.

On the background of construct G, we created the novel construct O by replacing TM6 of NBCe1 with TM6 of NBCn1. This manipulation had a severe effect on the functional expression. As shown in Fig. 3b, the oocyte expressing construct O exhibited virtually no pH_i recovery. The dominant effect on V_m was a sustained depolarization that was reminiscent of the H_2O-injected oocyte in Fig. 2b. However, closer examination of Fig. 3b reveals that the switch to CO_2/HCO_3^- caused a small transient hyperpolarization. Moreover, we observed similar transient hyperpolarizations of 1–2 mV in each of the nine oocytes that we injected with cRNA encoding construct O and then later examined electrophysiologically. Thus, construct O has at least some electrogenic character.

On the background of wt human NBCe1-A, we created construct P by simply replacing TM6 of NBCe1 with TM6 of NBCn1. This construct retained obvious electrogenicity as well as robust HCO_3^--transport activity (Fig. 3c). Taken together, the data from Fig. 3 show that, although the replacement of only one of the two NBCe1 structural elements at a time (Fig. 3a, c) produces an electrogenic chimera that expresses robustly, the simultaneous replacement of the two structural elements together results in a chimera with at least some electrogenic character but extremely low functional expression in *Xenopus* oocytes.

The above observations are consistent with the hypothesis that putative TM6 interacts with a structural component between putative EL5 and Ct, inclusive. In order to define this latter structural element, we created a series of chimeras on the background of construct P by replacing single putative loops or TMs from EL5 through TM14 of NBCe1-A with the corresponding element of human NBCn1. As shown in Fig. 4a, construct Q, in which we simultaneously replaced putative TM6 and EL5 of NBCe1-A, retained electrogenicity and robust HCO_3^--transport activity. We made similar observations for construct R (Fig. 4b, putative TM6 and TM10) and construct S (Fig. 4c, putative TM6 and TM11). We did not swap the intervening putative intracellular loop 5, which is only three amino acids long.

Simultaneously replacing putative TM6 and TM12 of NBCe1-A to produce construct T virtually eliminated functional expression, as judged by the pH_i-recovery rate (Fig. 5a). However, construct T was not totally inactive because the switch to CO_2/HCO_3^- elicited a modest instantaneous hyperpolarization. On the other hand, construct U (Fig. 5b, TM6 and TM13-EL6) and construct V (Fig. 5c, TM6 and TM14) retained electrogenicity as well as substantial HCO_3^--transport activity.

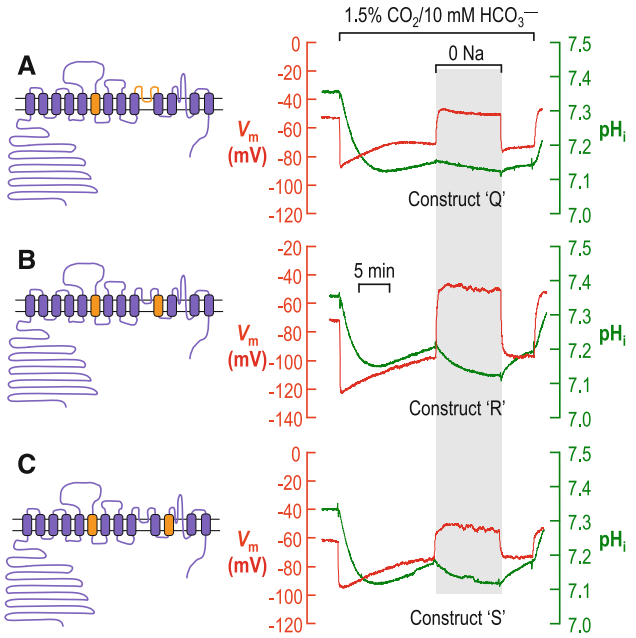

Fig. 4 Typical recordings of pH_i (*green*) and V_m (*red*, in mV) of oocytes expressing chimeric transporters. **a** Construct Q. **b** Construct R. **c** Construct S. The experimental protocols are the same as for Figs. 2 and 3. The sequence boundaries of the constructs are provided in Fig. 1

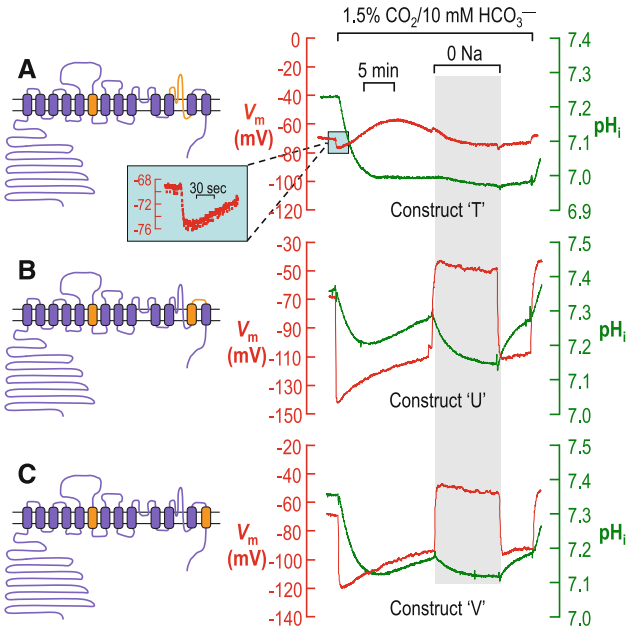

Fig. 5 Typical recordings of pH_i (*green*) and V_m (*red*, in mV) of oocytes expressing chimeric transporters. **a** Construct T. **b** Construct U. **c** Construct V. The experimental protocols are the same as for Figs. 2, 3, and 4. The sequence boundaries of the constructs are provided in Fig. 1. *Inset* in *a* shows, in magnified scale, the small hyperpolarization upon the switch from the ND96 to the CO_2/HCO_3^- solution

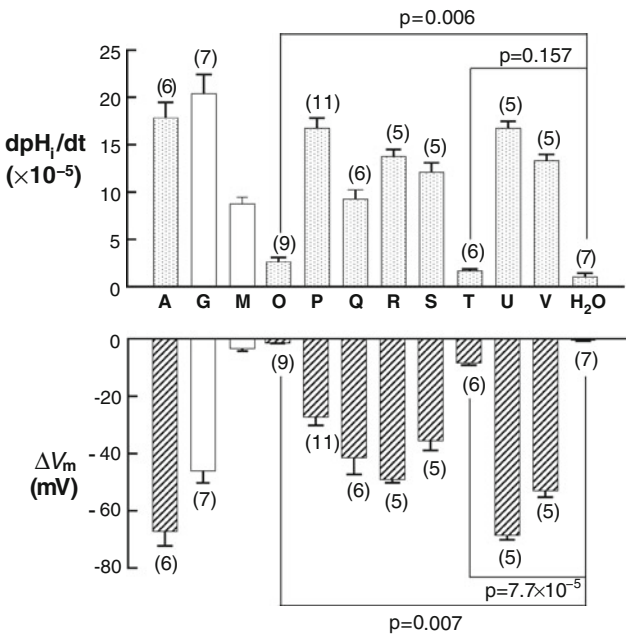

Fig. 6 Summary of pH_i recovery rates and maximum V_m changes of oocytes. Bars for constructs G and M are reproduced from Chen et al. (2011). All data for other bars are new and were collected from experiments like those shown in Figs. 2, 3, 4, and 5. *dpH_i/dt* represents the maximal pH_i recovery rates of oocytes after the initial CO_2-induced acidification. ΔV_m represents the maximum instantaneous V_m changes upon the switch to 1.5% CO_2/10 mM HCO_3^- during the first CO_2/HCO_3^- pulse. Data are presented as mean ± SEM. Welch's unpaired *t*-test was performed to examine if the dpH_i/dt or ΔV_m of oocytes expressing transporters was significantly different from that of control oocytes injected with H_2O. The difference was considered significant if $P \leq 0.01$

Figure 6 summarizes the data on pH_i recovery rate and ΔV_m for CO_2/HCO_3^- exposure experiments like those shown in Figs. 2, 3, 4, and 5. Although very small, both the mean ΔV_m (-1.4 ± 0.2 mV) and the mean dpH_i/dt ($[3.0 \pm 0.3] \times 10^{-5}$ pH units/s) of oocytes expressing construct O were significantly different from those of H_2O-injected oocytes (-0.6 ± 0.2 mV, $P = 0.007$; $[1.0 \pm 0.4] \times 10^{-5}$ pH units/s, $P = 0.006$). For oocytes expressing construct T, the mean ΔV_m was -8.0 ± 0.7 mV, which was significantly greater than that of H_2O-injected oocytes ($P = 7.7 \times 10^{-5}$), although dpH_i/dt was not significantly different ($P = 0.16$). This discordance is not surprising inasmuch as, in oocytes, ΔV_m is the most sensitive indicator of electrogenic NBC activity. Thus, we conclude that construct T retains at least some electrogenic character but has low functional activity. Note that construct M from the previous study (Chen et al. 2011), which has a predominantly electroneutral character, had a far smaller ΔV_m (-3.6 mV) than T but a substantially greater dpH_i/dt (6.8×10^{-5} pH units/s).

Returning to Fig. 6, we see that both ΔV_m and dpH_i/dt of other groups are, of course, significantly different from

those of H_2O-injected oocytes ($P < 0.001$ for all other cases).

Effects of DIDS on Construct O and T

A major feature of NBCe1 is the sensitivity to DIDS. The DIDS-binding motif KKMIK of NBCe1, thought to be near the extracellular end of putative TM5 (Lu and Boron 2007), is present in all chimeras. Because the ΔV_m values for constructs O and T were small, we assayed the inhibitory effect of DIDS (Fig. 7) to test the hypothesis that the small V_m changes were indeed mediated by NBCe1/n1 chimeras O and T and not by some conductance native to the oocyte.

Consistent with the result shown in Fig. 3b, exposing an oocyte expressing construct O to 1.5% CO_2/10 mM HCO_3^- caused a hyperpolarization of ~1 mV (Fig. 7a). Administration of DIDS elicited a negative shift in the V_m of ~5 mV, presumably due to the blockade of endogenous conductance. In the continued presence of DIDS, a second exposure to CO_2/HCO_3^- caused no further hyperpolarization. After the removal of DIDS, which was present for <50 s, a third exposure to CO_2/HCO_3^- again elicited a hyperpolarization larger than the first. We made similar observations for two other oocytes expressing construct O.

For the oocyte expressing construct T (Fig. 7c), the first and third CO_2/HCO_3^--induced V_m changes were larger than for construct O and more sustained. These changes were typical of three oocytes.

In the control oocyte injected with H_2O (Fig. 7c), we observed no hyperpolarizations during the first two applications of CO_2/HCO_3^-. After the removal of DIDS, the third application of CO_2/HCO_3^- elicited a slight, transient CO_2/HCO_3^--induced hyperpolarization that was typical of three oocytes. This slight hyperpolarization during the post-DIDS CO_2/HCO_3^- pulse appears to be common to all three oocyte groups (O, T, H_2O) and presumably represents an endogenous conductance that arises after pretreatment with DIDS.

In summary, the data in Fig. 7 demonstrate that, for both constructs O and T, the small CO_2/HCO_3^--induced hyperpolarizations are blocked by DIDS, indicating that they are mediated by the chimeric transporters.

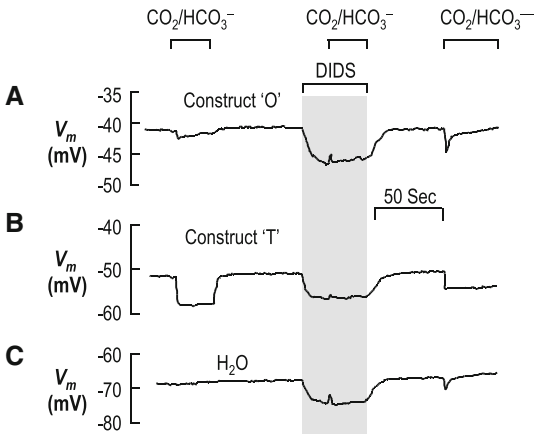

Fig. 7 Effect of DIDS on CO_2/HCO_3^--induced changes in V_m of *Xenopus* oocytes. **a** Construct O. **b** Construct T. **c** Control oocyte injected with H_2O. The extracellular solution was alternated between ND96 (CO_2/HCO_3^--free) solution and 1.5% CO_2/10 mM HCO_3^-, all at an extracellular pH of 7.50. All solutions were supplemented with 0.2% BSA if 400 μM DIDS was not present. Shown here are V_m traces representative of three independent experiments for each case

Membrane Expression of Transporters

We have demonstrated that simultaneously replacing TM6 and TM12 severely reduces the functional expression of the transporter. The reduced functional expression reflects some combination of reduced transporter activity and a reduced number of transporters at the cell surface. We performed biotinylation assays to compare the surface-membrane expression of wt NBCe1-A with that of constructs O and T, the two chimeras that yielded the small transient hyperpolarizations upon switching the perfusing solution from ND96 to CO_2/HCO_3^-. As shown in Fig. 8a, b, compared to oocytes expressing wt NBCe1-A, those expressing constructs O and T had extremely low NBC protein abundance in the plasma membrane. The background signal of membrane preparations from nonbiotinylated oocytes expressing construct O or T was substantially less than that from biotinylated oocytes at these long exposures (data not shown).

We further examined the total transporter protein level by Western blotting with the whole lysate of *Xenopus* oocytes. Figure 8c shows that the total protein levels of construct O and construct T are less than that of wt NBCe1-A. Moreover, the densitometric analysis in Fig. 8d shows that the total protein levels of constructs O and T are ~50% and ~65%, respectively, that of wt NBCe1-A, indicating that the reduction in total construct O and T protein relative to wt NBCe1-A is far less than the reduction in surface abundance.

Note that the molecular weight of the band in the wt NBCe1-A total protein lane (indicated by the arrow in Fig. 8c) is similar to that of the biotinylated band in Fig. 8a (also indicated by an arrow), which represents the fraction localized on the plasma membrane. This band represents the mature glycosylated form of NBCe1 (Chen et al. 2011) and is the major species present in the plasma membrane, consistent with previously published deglycosylation assays (Chen et al. 2011). The lower–molecular weight bands in Fig. 8c (indicated by an arrowhead) represent the immature or nonglycosylated forms of the transporter that predominantly resides in cytosolic compartments and is the major species present in the total lysate. Importantly, the

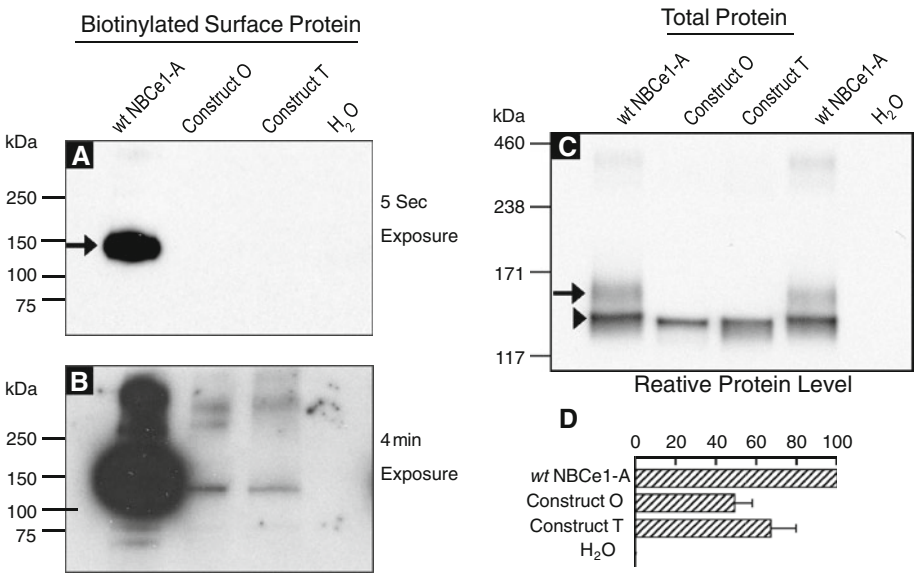

Fig. 8 Protein expression of transporters in expressed *Xenopus* oocytes. **a** Surface expression of transporter protein, detected with short exposure. **b** Longer exposure from the same blot as in **a**. **c** Total protein level of transporters expressed in *Xenopus* oocytes. **d** Summary of densitometric analysis for total protein levels. The surface protein was obtained using a biotinylation approach. In each lane, the same amount of surface protein or total protein was loaded and resolved by SDS-PAGE, then analyzed by Western blot. *Arrows* in **a** and **c** indicate the glycosylated form of NBCe1-A, whereas *arrowhead* in c indicates the immature or nonglycosylated form of the transporter. Densitometric analysis was performed for three independent blots like that shown in **c**. The density of each lane was normalized to that of wt NBCe1-A, which was arbitrarily set to 100

very small fraction of constructs O and T that is expressed at the cell surface also has a molecular weight consistent with that of mature glycosylated NBCe1-A.

Collectively, the data in Fig. 8 suggest that the predominant effect of the dual replacement of TM6 and TM12 of NBCe1 with the comparable portions of NBCn1 severely reduces the presence of the chimeric transporters at the plasma membrane.

Discussion

Topology Model of NCBT

The consensus is that the TMD of NCBTs contains 14 TM segments. No fine structures are available for members of the SLC4 family; and the topology, particularly the back half of TMD, of these transporters is a subject of debate. In the topology model proposed by Romero et al. (2004)—in turn based on the AE1 model by Zhu et al. (2003)—13 of these 14 TMs are helices, whereas TM12 is an extended structure, extending from the extracellular to the intracellular side. This Romero model is the basis of all folding diagrams presented in this investigation as well as the previous one (Chen et al. 2011). In a more recent study, Zhu et al. (2010) proposed that the TMD of NBCe1 contains 14 TM helices. The sequence assignments of Zhu et al. (2010) from Nt through TM9 are basically consistent with the Romero model. A major difference in the model of Zhu et al. (2010) is that the segment from Val^{798} to Lys^{812}, which in the Romero model (2004) is a portion of a loop between TM9 and TM10, forms a Tm helix from the extracellular to the intracellular side. Therefore, the orientations of TM11 and TM12 in the Zhu model are inverted compared to the corresponding TM10 and TM11 in the Romero model. As a result, the extended structure (TM12) in the Romero model—identified as a key element in the present study—would, in the Zhu model, become the intracellular half of TM12, the sixth intracellular loop (IL6) and the intracellular half of TM13.

Electrogenicity of Chimeras

In the previous study, we demonstrated that the fourth extracellular loop—the sequence assignment for which is virtually identical in the Romero and Zhu models—plays a critical role in determining the electrogenicity of NBCe1. In the present study, we made eight additional chimeras of human NBCe1-A and human NBCn1-A, all of which include EL4 of NBCe1. Consistent with our previous study, we find that all eight new chimeras have a CO_2/HCO_3^--induced ΔV_m, which is significantly different from that of H_2O-injected oocytes. In other words, they all appear to have a significant electrogenic component to their cotransport activity. Note that we cannot rule out the possibility that an electrically silent component exists in parallel with the electrogenic component.

Our previous article (Chen et al. 2011) showed that pairing EL5-Ct of NBCn1 with TM9 (construct F), TM8 (construct L) or TM7 (construct J) yields good functional expression. In the present series of chimeras, it is only the combination of EL5-Ct of NBCn1 with TM6 (construct O) that is problematic. Viewed from the opposite perspective, the present report shows that pairing the TM6 of NBCn1 with any of five other downstream elements from NBCn1—EL5 (construct Q), TM10 (construct R), TM11 (construct S), TM13-EL6 (construct U) and TM14 (construct V)—yields constructs with reasonably robust functional expression. It is specifically the combination of TM6 with TM12 from NBCn1 (construct T) that is problematic.

Our biotinylation data (Fig. 8a, b) show that, compared to wt NBCe1-A, the protein abundance of constructs O and T at the cell surface is substantially reduced. Nevertheless, when we switched from ND96 to CO_2/HCO_3^- in our electrophysiologic experiments, the oocytes expressing construct O or T consistently showed a small, abrupt hyperpolarization, which was not observed in oocytes injected with H_2O or expressing the electroneutral NBCn1 (for NBCn1, see Chen et al. 2011). Moreover, treatment with DIDS abolished these small hyperpolarizations (Fig. 7). Together, these observations are consistent with the notion that, although very low abundance of constructs O and T is present in the plasma membrane, they have at least a partial electrogenic character. Our data are not sufficiently quantitative to judge whether the per molecule (or intrinsic) acid-extrusion rates of these constructs are approximately normal.

Surface Expression of Chimeras

Analysis of the total transporter expression in *Xenopus* oocyte whole-cell lysate (Fig. 8c) indicates that the total protein levels of constructs O and T are modestly reduced compared to wt NBCe1-A and their mature glycosylated forms are barely detectable in this fraction. However, the reduction in total transporter expression compared to wt is far less than the reduction in biotinylated O and T detected at the surface relative to wt (Fig. 8b). The molecular weights of the construct O and T bands in the biotinylated fractions (Fig. 8a, b) are consistent with the size of mature glycosylated NBCe1-A. Therefore, the main cause of the functional impairment of NCBT chimeras with the TM6 and TM12 of NBCe1-A replaced by those from NBCn1 is to reduce the plasma membrane abundance of mature glycosylated, functional transporters. The molecular masses of O and T indicate that these proteins are mainly intact, providing no evidence of reduced protein stability. The presence of large amounts of immature or nonglycosylated protein is consistent with retention of the chimeras in intracellular compartments (e.g., ER, Golgi) rather than enhanced retrieval of the proteins from the plasma membrane.

It is interesting that simultaneous replacement of the putative TM6 and TM12 has such a great impact on the plasma membrane abundance of the transporter. If the topology of the NBCe1-A more closely follows that proposed by Zhu et al. (2010) than that by Romero et al. (2004), it is possible that the creation of constructs O and T has disrupted trafficking information predicted to reside in the cytoplasmic domains (in particular IL5, IL6 and the Ct). The region that we refer to as "TM12" contains motifs that, if exposed to the cytosol, could influence the trafficking of the transporter through intracellular organelles on its way to the surface. We expect SLC4 transporters—like other transporters and ion channels expressed at the plasma membrane, after folding and assembly—to enter the transitional ER. There, the SLC4 proteins would associate with Sec24 isoforms (A, B, C and D) that recognize distinct ER exit codes in cargo proteins and participate in the formation of coat protein complex II (COPII) export vesicles (Russell and Stagg 2010; Farhan et al. 2007; Srinivasan et al. 2011; Fernández-Sanchez et al. 2008). Impairing the association of the Sec proteins with plasma membrane proteins severely disrupts subsequent surface expression. The replacement of NBCe1-A TM12 with NBCn1 TM12 removes two putative ER exit codes (Mancias and Goldberg 2008; Wendeler et al. 2007) and introduces a YXXØ internalization motif that is not present in NBCe1-A (Bonifacino and Traub 2003). However, the differences in the TM12 region alone cannot explain the surface-expression deficits of constructs O and T because construct G (the only other construct possessing the NBCn1 TM12) functions almost as well as wt NBCe1-A.

The difference between construct G (with almost normal function) and construct O (barely expressed at the surface) is the presence of TM6 from NBCn1 in construct O. Although no refined crystal structure exists for an SLC4 protein, recently the structure of an SLC23 family member, the 14-transmembrane-segment *Escherichia coli* uracil/H^+ symporter UraA, was reported at a resolution of 2.8 Å (Lu et al. 2011). UraA possesses its own novel fold, but like other transporter families with solved structures, the UraA protomer is similarly formed by two inverted structural repeats, in this case TM1–7 and TM8–14 (Abramson and Wright 2009). Most interestingly, the hydropathic plot of UraA aligns well with that of NBCe1. TM5 and TM12 of UraA are at the center of a gating unit, which also contains TM6, TM7, TM13 and TM14. Let us hypothesize that NCBT structures adopt a 14-TM, UraA-like fold in which what we call "TM6" of NBCe1 (analogous to TM6 of UraA) is juxtaposed to what we call "TM12" of NBCe1 (analogous to TM12 of UraA). If true, it is reasonable to suggest that proper surface expression requires that the

TM6/TM12 dihelical unit—if contributed by TMs of the same transporter type—be surrounded by gating-unit TMs (i.e., TM5 and TM7) that are also contributed by the same transporter type. According to the UraA model, what chimeras O and T have in common is a TM6/TM12 dihelical unit contributed by NBCn1 and adjacent gating-unit TMs contributed by NBCe1.

It is also constructive to consider NBCe1-A residue R881, which is highly conserved among members of the SLC4 family, with the exception of NBCe2. In humans, the mutation R881C causes severe proximal-type renal tubule acidosis (Horita et al. 2005). The mutation does not reduce the activity of NBCe1-A but does decrease the surface expression of NBCe1 transporters when expressed in *Xenopus* oocytes and causes retention in the ER when transiently expressed in Madin-Darby canine kidney cells (Toye et al. 2006). The proposed location of the R881 is at the interface between the plasma membrane and cytosol, within TM12. If NCBT structures approximate a UraA-like fold, then R881 on TM12 would be near the cytosolic end of TM6.

In conclusion, the present study is consistent with the hypothesis that EL4 is necessary for the electrogenicity of NBCe1. In addition, simultaneous switching of the putative TM6 and TM12 of NBCe1 for those from NBCn1 severely impairs the expression of the transporter at the plasma membrane. We hypothesize that TM6 and TM12 are closely associated and part of a functional unit.

Acknowledgements We are thankful to Dr. Mark D. Parker for his helpful discussions. This work was supported by NIH grants DK30344 and NS18400 to W. F. B. L.-M. C. was supported by grant 31000517 from the National Natural Science Foundation of China (NSFC). X. Q. was supported by grants 09POST2060873 and 11POST7670014 from the American Heart Association. Y. L. was supported by grant 30900513 from the NSFC. W. F. B. gratefully acknowledges the support of the Myers/Scarpa endowed chair.

References

Abramson J, Wright EM (2009) Structure and function of Na^+-symporters with inverted repeats. Curr Opin Struct Biol 19:425–432

Ahmed S, Thomas G, Ghoussaini M et al (2009) Newly discovered breast cancer susceptibility loci on 3p24 and 17q23.2. Nat Genet 41:585–590

Antoniou AC, Beesley J, McGuffog L et al (2010) Common breast cancer susceptibility alleles and the risk of breast cancer for BRCA1 and BRCA2 mutation carriers: implications for risk prediction. Cancer Res 70:9742–9754

Boedtkjer E, Praetorius J, Matchkov VV, Stankevicius E, Mogensen S, Füchtbauer AC, Simonsen U, Fuchtbauer EM, Aalkjaer C (2011) Disruption of Na^+, HCO_3^- cotransporter NBCn1 (slc4a7) inhibits NO-mediated vasorelaxation, smooth muscle Ca^{2+} sensitivity, and hypertension development in mice. Circulation 124:1819–1829

Bok D, Galbraith G, Lopez I et al (2003) Blindness and auditory impairment caused by loss of the sodium bicarbonate cotransporter NBC3. Nat Genet 34:313–319

Bonifacino JS, Traub LM (2003) Signals for sorting of transmembrane proteins to endosomes and lysosomes. Annu Rev Biochem 72:395–447

Boron WF, Chen L, Parker MD (2009) Modular structure of sodium-coupled bicarbonate transporters. J Exp Biol 212:1697–1706

Bouyer P, Sakai H, Itokawa T, Kawano T, Fulton CM, Boron WF, Insogna KL (2007) Colony-stimulating factor-1 increases osteoclast intracellular pH and promotes survival via the electroneutral Na/HCO_3 cotransporter NBCn1. Endocrinology 148:831–840

Chen LM, Liu Y, Boron WF (2011) Role of an extracellular loop in determining the stoichiometry of Na/HCO_3 cotransporters. J Physiol 589:877–890

Choi I, Aalkjaer C, Boulpaep EL, Boron WF (2000) An electroneutral sodium/bicarbonate cotransporter NBCn1 and associated sodium channel. Nature 405:571–575

Choi I, Yang HS, Boron WF (2007) The electrogenicity of the rat sodium-bicarbonate cotransporter NBCe1 requires interactions among transmembrane segments of the transporter. J Physiol 578:131–142

De Giusti VC, Garciarena CD, Aiello EA (2009) Role of reactive oxygen species (ROS) in angiotensin II-induced stimulation of the cardiac Na^+/HCO_3^- cotransport. J Mol Cell Cardiol 47:716–722

De Giusti VC, Orlowski A, Aiello EA (2010) Angiotensin II inhibits the electrogenic Na^+/HCO_3^- cotransport of cat cardiac myocytes. J Mol Cell Cardiol 49:812–818

Ehret GB, Munroe PB, Rice KM et al (2011) Genetic variants in novel pathways influence blood pressure and cardiovascular disease risk. Nature 478:103–109

Farhan H, Reiterer V, Korkhov VM, Schmid JA, Freissmuth M, Sitte HH (2007) Concentrative export from the endoplasmic reticulum of the γ-aminobutyric acid transporter 1 requires binding to SEC24D. J Biol Chem 282:7679–7689

Fernández-Sánchez E, Díez-Guerra FJ, Cubelos B, Giménez C, Zafra F (2008) Mechanisms of endoplasmic-reticulum export of glycine transporter-1 (GLYT1). Biochem J 409:669–681

Grichtchenko II, Choi I, Zhong X, Bray-Ward P, Russell JM, Boron WF (2001) Cloning, characterization, and chromosomal mapping of a human electroneutral Na^+-driven $Cl\text{-}HCO_3$ exchanger. J Biol Chem 276:8358–8363

Horita S, Yamada H, Inatomi J, Moriyama N, Sekine T, Igarashi T, Endo Y, Dasouki M, Ekim M, Al Gazali L, Shimadzu M, Seki G, Fujita T (2005) Functional analysis of NBC1 mutants associated with proximal renal tubular acidosis and ocular abnormalities. J Am Soc Nephrol 16:2270–2278

Ishiguro H, Walther D, Arinami T, Uhl GR (2007) Variation in a bicarbonate co-transporter gene family member SLC4A7 is associated with propensity to addictions: a study using fine-mapping and three samples. Addiction 102:1320–1325

Khandoudi N, Albadine J, Robert P, Krief S, Berrebi-Bertrand I, Martin X, Bevensee MO, Boron WF, Bril A (2001) Inhibition of the cardiac electrogenic sodium bicarbonate cotransporter reduces ischemic injury. Cardiovasc Res 52:387–396

Kumar S, Flacke JP, Kostin S, Appukuttan A, Reusch HP, Ladilov Y (2010) SLC4A7 sodium bicarbonate co-transporter controls mitochondrial apoptosis in ischaemic coronary endothelial cells. Cardiovasc Res 89:392–400

Lacruz RS, Nanci A, White SN, Wen X, Wang H, Zalzal SF, Luong VQ, Schuetter VL, Conti PS, Kurtz I, Paine ML (2010) The sodium bicarbonate cotransporter (NBCe1) is essential for normal development of mouse dentition. J Biol Chem 285:24432–24438

Lauritzen G, Jensen MB, Boedtkjer E, Dybboe R, Aalkjaer C, Nylandsted J, Pedersen SF (2010) NBCn1 and NHE1 expression and activity in ΔNErbB2 receptor-expressing MCF-7 breast cancer cells: contributions to pHi regulation and chemotherapy resistance. Exp Cell Res 316:2538–2553

Liu Y, Xu JY, Wang DK, Wang L, Chen LM (2011) Cloning and identification of two novel NBCe1 splice variants from mouse reproductive tract tissues: a comparative study of NCBT genes. Genomics 98:112–119

Lu J, Boron WF (2007) The reversible and irreversible interactions of DIDS with the human electrogenic Na/HCO_3 cotransporter (hNBCe1-A): importance of K558, K559 and K562 within the KKMIK motif of transmembrane segment 5. Am J Physiol Cell Physiol 292:C1787–C1798

Lu F, Li S, Jiang Y, Jiang J, Fan H, Lu G, Deng D, Dang S, Zhang X, Wang J, Yan N (2011) Structure and mechanism of the uracil transporter UraA. Nature 472:243–246

Mancias JD, Goldberg J (2008) Structural basis of cargo membrane protein discrimination by the human COPII coat machinery. EMBO J 27:2918–2928

Parker MD, Musa-Aziz R, Rojas JD, Choi I, Daly CM, Boron WF (2008) Characterization of human SLC4A10 as an electroneutral Na/HCO_3 cotransporter (NBCn2) with Cl^- self-exchange activity. J Biol Chem 283:12777–12788

Pushkin A, Abuladze N, Lee I, Newman D, Hwang J, Kurtz I (1999) Cloning, tissue distribution, genomic organization, and functional characterization of NBC3, a new member of the sodium bicarbonate cotransporter family. J Biol Chem 274:16569–16575

Riihonen R, Nielsen S, Vaananen HK, Laitala-Leinonen T, Kwon TH (2010) Degradation of hydroxyapatite in vivo and in vitro requires osteoclastic sodium-bicarbonate co-transporter NBCn1. Matrix Biol 29:287–294

Romero MF, Hediger MA, Boulpaep EL, Boron WF (1997) Expression cloning and characterization of a renal electrogenic Na^+/HCO_3^- cotransporter. Nature 387:409–413

Romero MF, Fulton CM, Boron WF (2004) The SLC4 family of HCO_3^- transporters. Pflugers Arch 447:495–509

Russell C, Stagg SM (2010) New insights into the structural mechanisms of the COPII coat. Traffic 11:303–310

Sassani P, Pushkin A, Gross E, Gomer A, Abuladze N, Dukkipati R, Carpenito G, Kurtz I (2002) Functional characterization of NBC4: a new electrogenic sodium-bicarbonate cotransporter. Am J Physiol Cell Physiol 282:C408–C416

Srinivasan R, Pantoja R, Moss FJ, Mackey ED, Son CD, Miwa J, Lester HA (2011) Nicotine up-regulates $\alpha4\beta2$ nicotinic receptors and ER exit sites via stoichiometry-dependent chaperoning. J Gen Physiol 137:59–79

Suzuki M, Van Paesschen W, Stalmans I et al (2010) Defective membrane expression of the Na^+-HCO_3^- cotransporter NBCe1 is associated with familial migraine. Proc Natl Acad Sci USA 107:15963–15968

Toye AM, Parker MD, Daly CM, Lu J, Virkki LV, Pelletier MF, Boron WF (2006) The human NBCe1-A mutant R881C, associated with proximal renal tubular acidosis, retains function but is mistargeted in polarized renal epithelia. Am J Physiol Cell Physiol 291:C788–C801

Virkki LV, Wilson DA, Vaughan-Jones RD, Boron WF (2002) Functional characterization of human NBC4 as an electrogenic Na^+-HCO_3^- cotransporter (NBCe2). Am J Physiol Cell Physiol 282:C1278–C1289

Wang CZ, Yano H, Nagashima K, Seino S (2000) The Na^+-driven Cl^-/HCO_3^- exchanger: cloning, tissue distribution, and functional characterization. J Biol Chem 275:35486–35490

Wendeler MW, Paccaud JP, Hauri HP (2007) Role of Sec24 isoforms in selective export of membrane proteins from the endoplasmic reticulum. EMBO Rep 8:258–264

Zhu Q, Lee DW, Casey JR (2003) Novel topology in C-terminal region of the human plasma membrane anion exchanger, AE1. J Biol Chem 278:3112–3120

Zhu Q, Kao L, Azimov R, Abuladze N, Newman D, Pushkin A, Liu W, Chang C, Kurtz I (2010) Structural and functional characterization of the C-terminal transmembrane region of NBCe1-A. J Biol Chem 285:37178–37187

J Membrane Biol (2012) 245:141–150
DOI 10.1007/s00232-012-9422-x

Differential Expression of Potassium Channels in Placentas from Normal and Pathological Pregnancies: Targeting of the K_{ir} 2.1 Channel to Lipid Rafts

Gloria Riquelme · Nicole de Gregorio · Catalina Vallejos · Macarena Berrios · Bárbara Morales

Received: 13 June 2011 / Accepted: 16 February 2012 / Published online: 4 March 2012

Abstract Potassium channels play important physiological roles in human syncytiotrophoblasts (hSTBs) from placenta, an epithelium responsible for maternal–fetal exchange. Basal and apical plasma membranes differ in their lipid and protein composition, and the latter contains cholesterol-enriched microdomains. In placental tissue, the specific localization of potassium channels is unknown. Previously, we described two isolated subdomains from the apical membrane (MVM and LMVM) and their respective microdomains (lipid rafts). Here, we report on the distribution of K_{ir}2.1, K_v2.1, TASK-1, and TREK-1 in hSTB membranes and the lipid rafts that segregate them. Immunoblotting experiments showed that these channels are present mainly in the apical membrane from healthy hSTBs. Apical expression versus basal membrane was 84 and 16% for K_{ir}2.1 and K_v2.1, 60 and 30% for TREK-1, and 74 and 26% for TASK-1. Interestingly, K_v2.1 showed differences between apical membrane subdomains: $26 \pm 8\%$ was located in the LMVM and $59 \pm 9\%$ in MVM. In pathological placentas, the expression distribution changed in the basal membrane: preeclampsia shifted to 50% and intrauterine growth restriction to 42% for TASK-1 and both pathologies increased to 25% for K_{ir}2.1 and K_v2.1, K_{ir}2.1 appeared to be associated with rafts that were sensitive to cholesterol depletion in healthy, but not in pathological, placentas. K_v2.1 and TREK-1 emerged in the nonraft fractions. The precise membrane localization of ion channels in hSTB membranes is necessary to understand the physiological events.

Keywords Potassium channel · Placenta · Apical membrane · Basal membrane · Lipid raft

G. Riquelme (✉) · N. de Gregorio · C. Vallejos · M. Berrios · B. Morales
Departamento de Fisiología y Biofísica, Instituto de Ciencias Biomédicas (ICBM), Facultad de Medicina, Universidad de Chile, Casilla, 70005 Santiago 7, Chile
e-mail: griquelm@med.uchile.cl

Introduction

Potassium channels exist in almost all epithelial and non-epithelial cells, and they are involved in several physiological functions, including membrane potential through the control of membrane permeability to K^+ ions, volume regulation, electrogenic solute transport, and hormone secretion, among many other functions (Warth 2003). Together with knowledge about the structure and function of K^+ channels, the possible role of lipid membrane composition in the regulation of channel localization and function has garnered increasing interest (Levitan et al. 2010). Human placental syncytiotrophoblasts (hSTBs) comprise the continuous epithelial layer that forms the main barrier for maternal–fetal exchange (Stulc 1997). The activity of K^+ channels in the hSTB includes similar functions to those mentioned above for epithelial cells. K^+ transport via the conductance pathway has been studied through flux experiments in vesicles prepared from membranes of placental hSTB (Illsley and Sellers 1992) and in isolated placental villi (explants) of hSTB (Birdsey et al. 1999). In addition, electrophysiological experiments performed in cytotrophoblast cells (Clarson et al. 2001) and on term placental membranes reconstituted in giant liposomes or transplanted in *Xenopus laevis* oocytes (Diaz et al. 2008) showed the presence of potassium conductance. Diaz et al. (2008) used single-channel recordings (patch-clamp method) and total current recordings (voltage-clamp method) to demonstrate the

existence of a Ba^{+2}-sensitive K^+ channel, a subpopulation of TEA-sensitive channels and some Na^+-sensitive K^+ channels in apical membranes purified from term placental hSTBs. Clarson et al. (2001) demonstrated that cytotrophoblast cells express an inwardly rectifying K^+ current that is typical of $K_{ir}2.1$, whose incidence increases with cytotrophoblast cell differentiation. Bai et al. (2005, 2006) described the expression and activity of TASK (1 and 2) and TREK, which are two pore domain K^+ channels (K2p), in the villous tissue from human placenta and in cultured human cytotrophoblast cells. Williams et al. (2008) suggest the presence of potassium channels sensitive to K_v channel blockers 4-AP and TEA in cytotrophoblast cells and human placental villous explants.

hSTBs, similar to all epithelial cells, polarize during differentiation, forming the apical and basal domains, which are two distinct plasma membrane domains with different protein and lipid compositions (Stulc 1997). In addition, there are two subdomains within the apical hSTB domain: the classical microvillous membrane (MVM), which has been used in our studies and by other authors to study transport mechanisms, and the light microvillous membrane (LMVM) (Jimenez et al. 2004; Riquelme 2011). In both purified fractions, we observed lipid rafts. These membrane microdomains are characterized by their resistance to detergent extraction and their ability to float in density gradient centrifugation (Godoy and Riquelme 2008; Riquelme 2011). The domains, subdomains, and microdomains were also characterized in placentas from pregnancy pathology, including preeclampsia (PE) and intrauterine growth restriction (IUGR) (Jimenez et al. 2004; Riquelme et al. 2011). PE is a hypertensive disease associated with proteinuria, sometimes with edemas (Lindheimer and Katz 1989), and affects up to 6% of all gestations beyond 20 weeks, especially in primiparous women. IUGR constitutes another group of complex diseases that affect 8–14% of pregnancies in which the fetus fails to achieve its genetically determined growth (Cetin and Alvino 2009).

The interaction between the transporter proteins, including ion channels, and membrane lipids can be highly specific and is often essential for the functional and structural integrity of the membranes (Tillman and Cascio 2003). Many of these studies have demonstrated that membrane cholesterol is a major regulator of ion channels (Levitan et al. 2010).

In general, the organization and maintenance of ion channels within a specific plasma membrane domain, subdomain, and microdomain play an important role in determining the ion channels' physiological functions. For that reason, it is important to study the relationship between K^+ channels and these specific regions in the normal placenta and in pathological placentas and to determine whether alterations in their segregation can be related to pathology, which occurs in other cells and tissues (Michel and Bakovic 2007). The present work aimed to examine the expression of the K^+ channels $K_{ir}2.1$, $K_v2.1$, TASK-1, and TREK-1; their relationship to the domains, subdomains, and microdomains of hSTB membranes from normal, PE and IUGR placentas was also investigated.

Materials and Methods

Placenta Collection

At the San José Hospital Maternity Unit, placentas obtained from normal pregnancies and from pregnancies with moderate PE and IUGR were collected immediately after delivery and transported to the laboratory on ice. Diagnosis of moderate PE was based on the classic criteria of systolic and diastolic blood pressure $\geq$140/90 mmHg on at least two occasions and proteinuria $\geq$300 mg/24 h. Patients with severe PE, defined as diastolic blood pressure >110 mmHg and/or proteinuria >5 g/day, were excluded from our study sample (Centro de Diagnóstico e Investigaciones Perinatales, Chile; www.cedip.cl/Guias/Guia 2003). Placentas from patients with HELLP syndrome were also excluded, as well as placentas from patients with moderate PE accompanied by any other pathology. An idiopathic diagnosis of IUGR was established by the attending physician via the clinical estimation of the fetal weight corresponding to the growth rate under the 10th percentile for each sex and the gestational age according to the curve selected by the Ministry of Health of Chile (curve of intrauterine growth (Juez 1989)). Fetuses that were at the 10th percentile but had halted growth during a reasonable observation period of at least 14 days were also considered IUGR (Juez 1989). The IUGR exclusion criteria included fetal or maternal infections, maternal drug use or alcohol abuse, multiple pregnancies, fetal malformations, chromosomal abnormalities, maternal chronic hypertension, maternal cardiovascular or autoimmune diseases, diabetes, and moderate PE. Placentas with IUGR from PE pregnancies were excluded. All of the placentas we used were obtained from term pregnancies.

Preparation of Placental Membranes

Human placental apical or MVM, LMVM, and basal membrane (BM) vesicles were prepared from fresh human placenta by a method that we previously described and that enables the simultaneous isolation of apical and basal membranes from the same placenta (Jimenez et al. 2004). The purification method included the precipitation of non-microvillous membrane with magnesium ions, differential

centrifugation, and a sucrose step gradient; this assured that the isolated fractions were enriched and free of contamination (Jimenez et al. 2004). The solutions used were as follows: buffer A (in mmol/l), 250 sucrose, 0.7×10^{-3} pepstatin, 1.1×10^{-3} leupeptin, 80×10^{-6} aprotinin, and buffer B (in mmol/l), 300 sucrose; all solutions were buffered with 20 mM Tris-maleate, pH 7.4. The microvillous and basal enriched preparations containing about 10–15 mg and 6–8 mg of apical and basal protein, respectively, were overlaid on the sucrose gradient. Bands were obtained at the 10/37 and 37/45% sucrose interfaces, which correspond to the LMVM apical fraction and to the classical MVM apical fraction, respectively (Jimenez et al. 2004). The band at the 47/52% (w/v) sucrose interface was collected, corresponding to the BM fraction. These fractions were collected and diluted tenfold with 20 mM Tris-maleate (apical fractions) and 20 mM Tris-HEPES (basal fractions), both at pH 7.4, before centrifugation at 110,000×*g* for 30 min. The final pellet was resuspended in 300 mM sucrose and 20 mM Tris-maleate, pH 7.4 buffer, and stored in liquid nitrogen.

The protein concentration was determined using a bicinchoninic acid (BCA) protein assay kit (Pierce Biotechnology, Rockford, IL) for the colorimetric detection and quantification of total protein (Smith et al. 1985; Wiechelman et al. 1988). The purity and enrichment of the apical fractions were determined routinely by assaying for alkaline phosphatase activity, an apical membrane marker. Enrichment of alkaline phosphatase activity was over 20-fold for MVM and LMVM; both preparations were essentially free of basal membranes and mitochondrial membranes. The purity and cross-contamination of the membranes were similar to those previously observed (Jimenez et al. 2004). The purity and enrichment of the basal membrane fraction were routinely determined by assaying for classic marker protein activities as described by Jimenez et al. (2004). Placental alkaline phosphatase (PLAP) was used as an apical membrane contamination marker. The degree of cross-contamination of the purified basal membranes with apical membranes, quantified using a ratio of PLAP activity enrichment of the BM compared with the MVM (BM/MVM), was approximately 0.1 for the placentas used in this study; this ratio was lower than or equivalent to that from several other reports for single or paired apical and basal membrane preparations, as demonstrated by Jimenez et al. (2004).

Preparation of Apical Lipid Microdomains

Apical plasma membrane microdomains were isolated separately from MVM and LMVM enriched membrane fractions as detergent-resistant membranes (DRMs) through extraction with Triton X-100 using a modified protocol based on that described by Brown and Rose (1992). As we described in Godoy and Riquelme (2008) and Riquelme et al. (2011), normal placenta (NP)/PE/IUGR DRMs from isolated apical fractions (MVM and LMVM) were extracted with 1% Triton X-100 on ice and subjected to ultracentrifugation and sucrose flotation. After centrifugation, the gradients were divided into 10 fractions (0.5 ml each) from the top of the gradient and the pellet was resuspended in 0.5 ml MBS-buffered saline (25 mM morpholinoethanesulfonic acid, 150 mM NaCl, pH 6.5; fraction 11) for subsequent analysis. Throughout this article, we use the terms "lipid microdomains" and "lipid rafts" to refer to the membrane material that floats on the sucrose gradient around the 5/35% interface (fractions 1–5). All flotation fractions from MVM and LMVM were characterized by specific markers for protein, alkaline phosphatase as a positive marker for apical lipid microdomain fractions and human transferrin receptor (hTf-R) as a nonraft marker.

Depletion of Membrane Cholesterol by Methyl-β-Cyclodextrin Treatment

Cyclodextrin treatment was carried out as described previously by Danielsen and Hansen (2003). Placental apical vesicles (0.6 mg of total protein) were incubated with 2% w/v methyl β-cyclodextrin (mβ-CD) in MBS buffer at 37°C for 30 min and centrifuged at 21,000×*g* for 2 h at 4°C. The pellet was resuspended in 1 ml of 1% Triton X-100 in MBS-buffered saline, and microdomain preparation was carried out as described above.

Electrophoresis, Western Blotting, and Densitometric Analysis

Placental Membrane Fractions

For each potassium channels ($K_{ir}2.1$, $K_v2.1$, TREK-1, and TASK-1), 20 µg of total protein of LMVM, MVM, and BM were loaded on a 10% SDS–polyacrylamide gel. Routinely, all four proteins were probed in membrane fractions isolated from the same placenta.

Apical Lipid Microdomains

Aliquots of 50 µl each were incubated with 10% trichloroacetic acid (TCA, v/v) for 30 min on ice and centrifuged at 21,000×*g* for 30 min at 4°C. The pellet was resuspended in sample buffer, boiled for 5 min and sonicated for 30 min. For each potassium channel ($K_{ir}2.1$, $K_v2.1$, TREK-1, and TASK-1) and raft (PLAP) and nonraft markers (hTf-R), 20 µl of each flotation gradient fraction from LMVM and MVM were used.

These samples and the molecular weight marker (PageRuler™ Prestained Protein Ladder; Fermentas, Glen Burnie, MD) were loaded on a 10% SDS–polyacrylamide gel. Electrophoresis was performed at 100 V, and the gel was transferred to a nitrocellulose membrane (BioRad, Richmond, CA; 162-0115) for 2 h at 100 V. The nitrocellulose membrane was blocked for 2 h at room temperature with 3% non-fat milk in Tween/saline buffer (138 mM NaCl, 270 mM KCl, and 0.05% Tween-20) and washed in Tween/saline buffer. Membranes were incubated with primary antibody for 2 h at room temperature. Potassium channel antibodies were diluted as follows in bovine serum albumin (BSA) 1%: anti-$K_{ir}2.1$ 1:500, anti-$K_v2.1$ 1:100, anti-TREK-1 1:1,000, anti-TASK-1 1:500. Each antibody was probed with its control antigen. The specificity of the primary antibodies was evaluated in competition experiments (1:1 antibody/antigen) in which incubation with the corresponding antigens partially neutralized the antibody. The mark of the band identified by the weights provided in the data sheet for each antibody decreased in all the experiments. Such a control was done in the initial stage of this study with all potassium channel antibodies used (data not shown).

Raft and nonraft marker antibodies were diluted as follows in distilled water: anti-PLAP 1:1,000 and anti-hTf-R 1:500. After washing with Tween/saline buffer, membranes were incubated with specific horseradish peroxidase (HRP)-linked secondary antibody: anti-rabbit 1:5,000 or anti-mouse 1:10,000, both diluted in Tween/saline buffer and incubated for 1 h at room temperature. Bands were detected with the enhanced chemiluminescence Western Blotting Analysis System (EZ-ECL; Biological Industries, Kibbutz Beit Haemek, Israel), and measurements were performed according to molecular weight given by a data sheet for each antibody and the band affected by the antigenic peptide. Protein content was quantified with Image J 1.43i (Wayne Rasband, National Institutes of Health, Bethesda, MD).

Reagents and Antibodies

All chemicals were analytical grade. Buffers were made with distilled water, and pH values were determined at room temperature. The following polyclonal antibodies were used: anti-$K_{ir}2.1$, anti-$K_v2.1$, anti-TREK-1, anti-TASK-1 (Alomone Labs, Jerusalem, Israel); mouse monoclonal antibody against human alkaline phosphatase, PLAP (clone 8B6; Sigma, St. Louis, MO); hTf-R (clone H68.4; Zymed, San Francisco, CA); and HRP-conjugated secondary goat anti-mouse (Amersham, Aylesbury, UK) for monoclonal antibodies and rabbit (Santa Cruz Biotechnology, Santa Cruz, CA) for all potassium channels.

Statistical Analysis

Results are expressed as means ± standard deviation (SD). Statistical significance was measured using the one-way ANOVA plus Bonferroni's multiple comparison test and Student's *t*-test. $P < 0.05$ was considered significant.

Results

Expression of K^+ Channels in Domains and Subdomains from Placental hSTB

Apical (MVM, LMVM) and basal membranes (BM) from NP and from PE and IUGR placentas were isolated and purified using the protocol described in ''Materials and Methods'' section. We found similar enrichment markers and cross-membrane contamination markers as described fully in previous work (Jimenez et al. 2004; Riquelme et al. 2011). We purified the membranes from 11 NPs, 4 PE placentas, and 5 IUGR placentas. In these purified membranes, we performed expression experiments using western blotting with specific antibodies for $K_{ir}2.1$, $K_v2.1$, TASK-1, and TREK-1. Figure 1 shows the expression distributions of these four K^+ channels in LMVM and MVM apical subdomains and BM domains. The results are expressed as the percent relative to the expression associated with MVM + LMVM + BM (set at 100%). As shown in Fig. 1a, no significant difference was found in the distribution of $K_{ir}2.1$ in LMVM and MVM between normal and pathological placentas; however, the total expression of this type of channel was higher in apical membrane domains compared with BM. The LMVM + MVM results were 84, 76 and 75% for NP, PE, and IUGR, respectively, in contrast to the BM results, which were 16, 24 and 25%, respectively. For $K_v2.1$ (Fig. 1b), the difference between the total apical (MVM + LMVM) and BM was maintained: 85 vs. 15% in NP, 78 vs. 22% in PE, and 77 vs. 23% in IUGR. However, there was a large difference between the LMVM and MVM. Interestingly, approximately 60% of the total expression in placental hSTB was found in the LMVM apical subdomains from normal and pathological placentas. In contrast, the distribution of TREK-1 was approximately 33%, on average, for all of the membrane fractions from either normal or pathological placentas. As observed for $K_{ir}2.1$, $K_v2.1$, and TREK-1, there was greater expression in the apical domain compared with the basal domain, although there were differences in the distribution between the apical subdomains, as in the case of $K_v2.1$. In contrast, the expression of TASK-1 in PE was similar in both domains, with values of 50 and 49% for MVM + LMVM and BM, respectively. Interestingly, there was an increasing

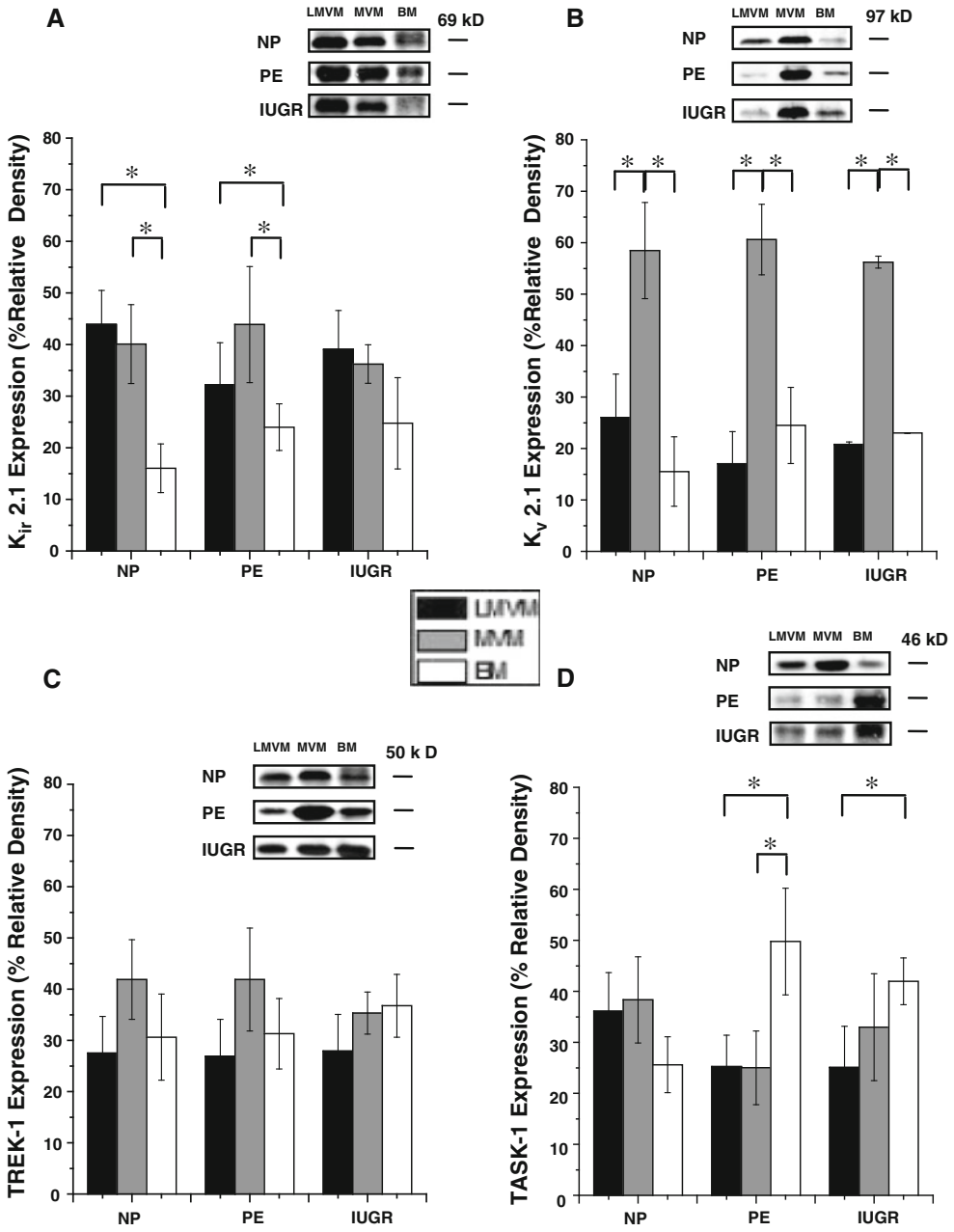

Fig. 1 Expression and distribution of potassium channels ($K_{ir}2.1$, $K_v2.1$, TREK-1, and TASK-1) in hSTB membranes from NP, PE, and IUGR placentas. **a** $K_{ir}2.1$, **b** $K_v2.1$, **c** TREK-1, and **d** TASK-1, tested in LMVM, MVM, and BM purified membranes from NP ($n = 8$), PE ($n = 4$), and IUGR ($n = 4$) placentas (means ± SD, $^*P < 0.05$). The density of the signal in each membrane fraction is expressed as a percentage of the sum of densities (MVM + LMVM = 100%). Representative western blots are shown in *insets*

trend in the expression of these channels in the BM domain from pathological placentas.

Partition of $K_{ir}2.1$ into Lipid Rafts in the Apical Domains of Normal and Pathological Placentas

Apical membranes from normal and pathological placentas were incubated with 1% Triton X-100 and separated by flotation in a discontinuous sucrose gradient. They were tested for the presence of specific raft and nonraft markers as described in Godoy and Riquelme (2008) and Riquelme et al. (2011). We confirmed the quality of our preparations using immunoblotting. All of the fractions in each raft preparation were probed for PLAP, which is a specific apical and raft marker. In Fig. 2a, b the representative western blot and graphic show the distribution of this marker in the flotation gradient fractions. PLAP was present in the first five fractions corresponding to the lipid

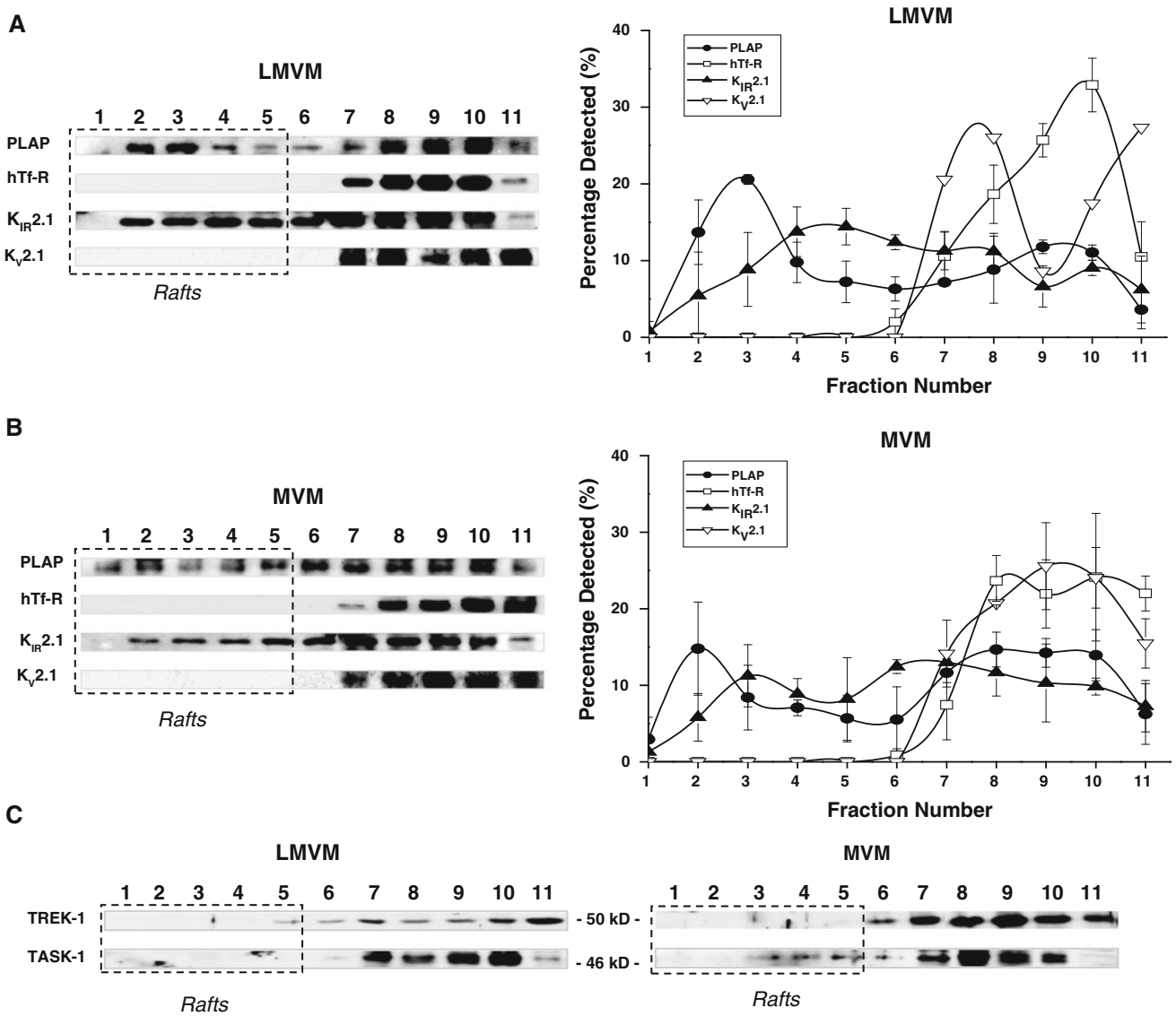

Fig. 2 Differential distribution of potassium channels in the flotation gradient fractions of LMVM and MVM subdomains from normal placentas. Quantification of western blot analysis, and representative images are shown for PLAP (raft marker, $n = 4$), hTf-R (nonraft marker, $n = 4$), $K_{ir}2.1$ ($n = 4$), and $K_v2.1$ ($n = 9$) of LMVM (**a**) and MVM (**b**). **c** Representative western blots for TREK-1 and TASK-1 corresponding to LMVM and MVM

rafts from normal LMVM and MVM (Godoy and Riquelme 2008). To ensure that these lipid rafts were free of nonraft fractions, we routinely probed these fractions for hTf-R, which is a protein known to reside in nonraft areas. As Fig. 2a, b show, this protein was not found in fractions 1–6 in both LMVM and MVM, indicating that those fractions were free of nonraft components.

$K_{ir}2.1$, $K_v2.1$, TASK-1, and TREK-1 antibodies were used to study the possible segregation of these channels in raft and nonraft fractions. Immunoblots of the sucrose density gradient–derived fractions prepared from LMVM and MVM showed that some $K_{ir}2.1$ protein from NPs was localized in the low-density fractions, which corresponded to the first five fractions (Fig. 2a for LMVM and Fig. 2b for MVM). In contrast, $K_v2.1$ was present only in the nonraft microdomains. The behaviors of TASK-1 and TREK-1 are illustrated in Fig. 2c. TREK-1 in LMVM and MVM was found mainly in nonraft areas, 75 and 100%, respectively ($n = 8$ experiments from six independent placentas). For TASK, either in LMVM or in MVM, the results were not conclusive ($n = 6$ from three independent placentas). In general, the western blot suggested mainly nonraft markers for this type of channel; however, a weak band appeared in some of the raft areas.

In summary, the results described here suggested that some $K_{ir}2.1$ was localized in the first five fractions (the raft fractions).

Cholesterol-Depletion Effects

As a control, LMVM and MVM were treated with mβ-CD, a specific cholesterol-removal agent, to deplete cholesterol levels prior to detergent extraction and density ultracentrifugation, as described in "Materials and Methods". As shown in Fig. 3a, this treatment eliminated $K_{ir}2.1$ immunoreactivity from the low-density fractions, as expected for a protein localized to cholesterol-rich areas, such as lipid rafts.

Additionally, immunoblots of fractions separated by sucrose density gradients from LMVM and MVM of PE and IUGR placenta were assayed for $K_{ir}2.1$, and partitioning into raft fractions occurred in both pathologies. However, the association between $K_{ir}2.1$ and the low-density fractions from MVM and LMVM was not as clear and reproducible as in NPs and was not affected by the removal of cholesterol (Fig. 3b, c).

Discussion

This study is the first to demonstrate the expression distribution of potassium channels in the domain and subdomain regions of placental hSTB from normal and pathological pregnancies. The four potassium channels examined ($K_{ir}2.1$, $K_v2.1$, TREK-1, and TASK-1) were previously characterized in multiple placenta studies (Clarson et al. 2001; Bai et al. 2005, 2006; Williams et al. 2008). In addition, this study is the first to demonstrate that $K_{ir}2.1$ is

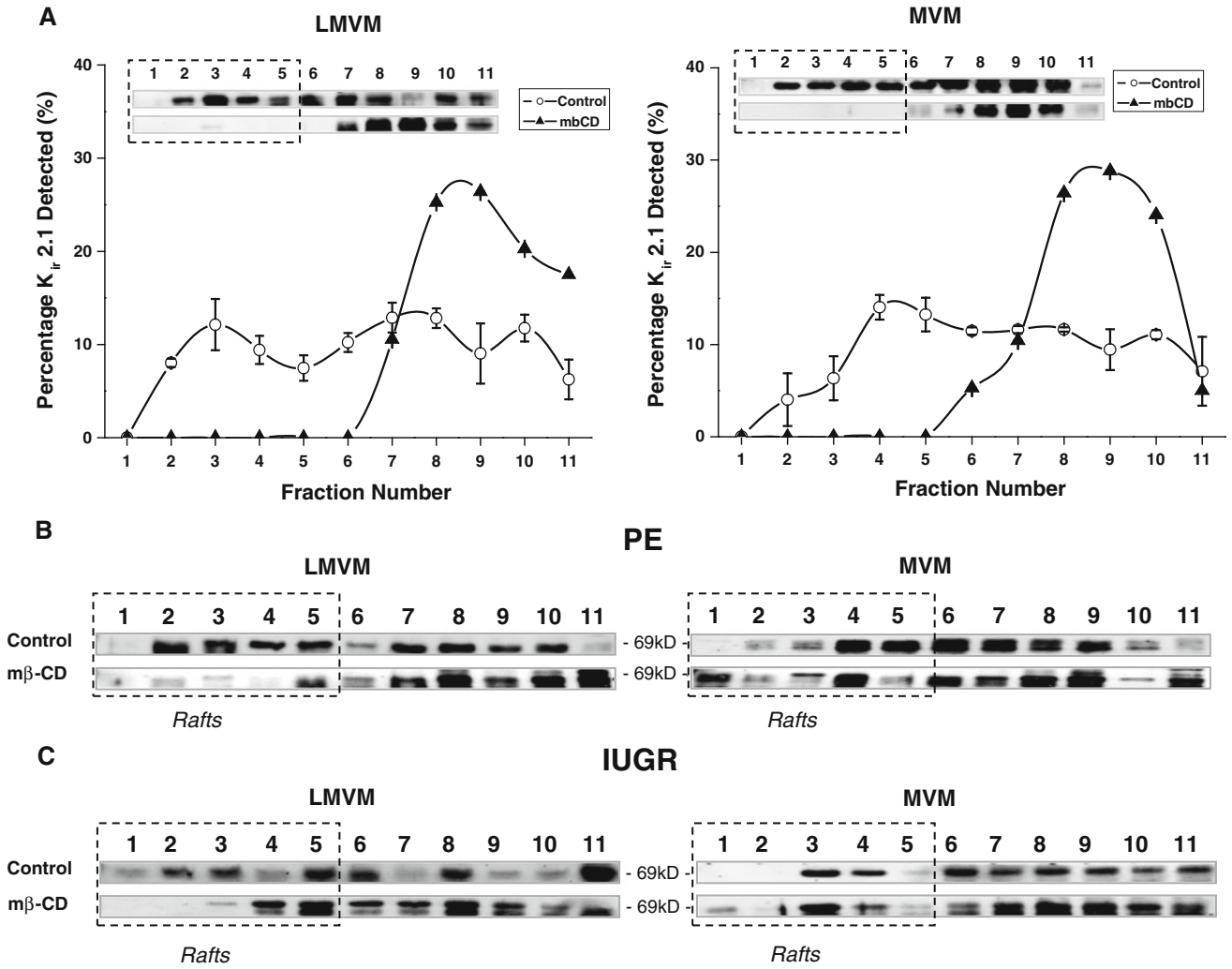

Fig. 3 Effect of cholesterol depletion on $K_{ir}2.1$ segregation into the lipid rafts in LMVM and MVM from NP, PE, and IUGR placentas. **a** Graphical quantification and representative image of western blot for $K_{ir}2.1$ in the flotation gradient fractions of LMVM and MVM subdomains from normal placenta before (control) and after the apical fractions were preincubated with 2% mβ-CD ($n = 2$). **b**, **c** Representative western blots reflecting the effect of cholesterol depletion on the association between $K_{ir}2.1$ (**b**) and the rafts from PE and IUGR apical membrane fractions ($n = 3$ for each condition)

partitioned into lipid rafts in the apical membranes (LMVM and MVM) in both normal and pathological term placentas.

Comparisons of the channel expression distribution between the apical and basal membranes from healthy hSTB revealed that $K_{ir}2.1$, $K_v2.1$, TASK-1, and TREK-1 channels were significantly more abundant in apical than in basal membranes. Expression of $K_{ir}2.1$ and $K_v2.1$ showed that approximately 84 vs. 16% were present in the apical membranes versus basal membranes, respectively; for TREK-1, the expression was 60 vs. 30% and for TASK-1, 74 vs. 26%. However, there was a difference between MVM and LMVM, which are the two subdomains from apical membranes, in that $K_v2.1$ expression was $26 \pm 8\%$ in the LMVM and $59 \pm 9\%$ in the MVM. In previous reports (see brief review in Riquelme 2011), we suggested that the two subdomains from the apical hSTB membranes were correlated: MVM corresponded to the microvillous finger-like region of the apical subdomain, and LMVM corresponded to the apical subdomain that constituted the base of the finger-like projections (Godoy and Riquelme 2008; Riquelme et al. 2011; Riquelme 2011). Then, we determined that most of the K_v was located in the microvillous finger-like region. The differential cell-surface distribution of these K^+ channels is due to the isoform-specific mechanisms that exist for the localization of these proteins (Tikku et al. 2007; Martens et al. 2001; Melnyk et al. 2002; O'Connell and Tamkun 2005).

The results of our equivalent studies in membranes from pathological placentas showed a tendency to maintain the distribution among the apical membrane subdomains for all types of channels studied. However, expression of these channels in the BM increased compared to that in the entire apical membrane. Expression of $K_{ir}2.1$ and $K_v2.1$ increased from 16 to 25% in the BM of PE and IUGR placentas. The most dramatic change was observed for TASK-1, the expression of which was shifted in the BM from 25% in NP to 50% in PE and to 42% in IUGR.

The preferential distribution of these potassium channels in one or more domains of this epithelium as well as their distribution in the apical membrane subdomains are indicative of their role in the transplacental transport model. These compartments are also composed of lipids and proteins, which optimize the environment surrounding these channels for their function, as observed in other epithelia (Levitan et al. 2010). Of note, the distribution of some of these channels is altered in pathologies such as PE and IUGR. These results are consistent with other studies that detected expression changes in proteins, such as syncytin, between the apical and basal membranes in PE (Lee et al. 2001). Those changes are associated with dysfunction of the PE placenta; potassium channels described herein could have an impact on transport through the placenta.

However, the current knowledge about the membrane lipid heterogeneity with the existence of lipid rafts as the specialized membrane microdomains rich in sphingolipids and cholesterol permits a closer examination of the relationship between the channels and the lipids. There was no information about the localization of these placental potassium channels or their membrane partitioning. The immunodetection of $K_{ir}2.1$, $K_v2.1$, TREK-1, and TASK-1 proteins using specific antibodies showed that only $K_{ir}2.1$ appeared to be associated with lipid rafts, whereas $K_v2.1$ and TREK-1 emerged in the nonraft fractions. The data on the TASK-1 channels were not conclusive.

The results, which demonstrate the segregation of placental $K_{ir}2.1$ to raft microdomains, represent a novel finding in the placenta. These results are consistent with several studies that showed that a variety of ion channels, including potassium channels, from other cells and tissues are regulated by the level of cholesterol in the membrane (Levitan et al. 2010). In addition, these studies showed that the depletion of membrane cholesterol by mβ-CD removed several channels from the raft fractions to the nonraft fractions (Tikku et al. 2007; Romanenko et al. 2004). The inwardly rectifying potassium channel (K_{ir}) is a ubiquitous channel that is expressed in many tissues (Kubo et al. 2005; Nichols and Lopatin 1997; Reimann and Ashcroft 1999); in particular Mylona et al. (1998) reported expression of the $K_{ir}2.1$ gene in the human placenta and in cultured cytotrophoblast cells at all different stages of differentiation. This family of potassium channels constituted a major type of ion channel involved in the maintenance of the resting potential in several cells; in particular, there are many reports about the link between the alteration of this type of channel and pathologies. For example, human mutations on $K_{ir}2.1$ may induce Andersen disease, and the targeted disruption of $K_{ir}2.1$ in mice induces death within a few hours after birth (Zaritsky et al. 2000), among other pathological syndromes associated with K_{ir} (Tristani-Firouzi and Etheridge 2010; Decher et al. 2007; Plaster et al. 2001).

Tikku et al. (2007) reported in 2007 that $K_{ir}2.1$ from the Chinese hamster ovary (CHO) K1 cell line had a double distribution between cholesterol-rich (raft) fractions, which are sensitive to cholesterol removal by mβ-CD, and nonraft fractions, indicating that the channels exist in two different types of lipid environment. Our results from normal placental membranes are comparable with those described by Tikku et al. (2007). When we studied this type of channel from PE and IUGR membranes, the segregation into rafts was similar to that obtained from healthy membranes; however, $K_{ir}2.1$ lost its cholesterol sensitivity, and mβ-CD did not remove the channels from the raft fractions. This result was very important because, for these channels and others, it is known that cholesterol enrichment modulates

channel activities (Tikku et al. 2007; Levitan et al. 2010). In general, the organization and maintenance of ion channels within a specific plasma membrane domain, subdomain, and microdomain play an important role in determining their physiological functions (Riquelme 2011). In placentas, the physiological relevance of the localization of potassium channels has not been established, so the relationship between the K^+ channels with these specific regions in normal and pathological placentas may explain whether alterations in their segregation may be related to pathology, as is explained in other cells and tissues (Michel and Bakovic 2007).

Acknowledgments We are grateful to Dr. M. Pérez and the staff at the San José Hospital Maternity Unit for assistance in obtaining the biological material. We also thank American Journal Express for language correction of this manuscript and Mr. Aldo Valdebenito for technical assistance. This research was supported by grant Fondecyt-Chile 1070695.

References

Bai X, Greenwood SL, Glazier JD, Baker PN, Sibley CP, Taggart MJ, Fyfe GK (2005) Localization of TASK and TREK, two-pore domain K^+ channels, in human cytotrophoblast cells. J Soc Gynecol Investig 12:77–83

Bai X, Lacey HA, Greenwood SL, Baker PN, Turner MA, Sibley CP, Fyfe GK (2006) TASK channel expression in human placenta and cytotrophoblast cells. J Soc Gynecol Investig 13:30–39

Birdsey TJ, Boyd RD, Sibley CP, Greenwood SL (1999) Effect of hyposmotic challenge on microvillous membrane potential in isolated human placental villi. Am J Physiol Regul Integr Comp Physiol 276:R1479–R1488

Brown DA, Rose JK (1992) Sorting of GPI-anchored proteins to glycolipid-enriched membrane subdomains during transport to the apical cell surface. Cell 68:533–544

Cetin I, Alvino G (2009) Intrauterine growth restriction: implications for placental metabolism and transport. A review. Placenta 30(suppl A):S77–S82

Clarson LH, Greenwood SL, Mylona P, Sibley CP (2001) Inwardly rectifying K^+ current and differentiation of human placental cytotrophoblast cells in culture. Placenta 22:328–336

Danielsen EM, Hansen GH (2003) Lipid rafts in epithelial brush borders: atypical membrane microdomains with specialized functions. Biochim Biophys Acta 1617:1–9

Decher N, Renigunta V, Zuzarte M, Soom M, Heinemann SH, Timothy KW, Keating MT, Daut J, Sanguinetti MC, Splawski I (2007) Impaired interaction between the slide helix and the C-terminus of Kir2.1: a novel mechanism of Andersen syndrome. Cardiovasc Res 75:748–757

Diaz P, Vallejos C, Guerrero I, Riquelme G (2008) Barium, TEA and sodium sensitive potassium channels are present in the human placental syncytiotrophoblast apical membrane. Placenta 29: 883–891

Godoy V, Riquelme G (2008) Distinct lipid rafts in subdomains from human placental apical syncytiotrophoblast membranes. J Membr Biol 224:21–31

Illsley NP, Sellers MC (1992) Ion conductances in the microvillous and basal membrane vesicles isolated from human placental syncytiotrophoblast. Placenta 13:25–34

Jimenez V, Henriquez M, Llanos P, Riquelme G (2004) Isolation and purification of human placental plasma membranes from normal and pre-eclamptic pregnancies. A comparative study. Placenta 25:422–437

Juez G (1989) Intrauterine growth curve for the appropriate diagnosis of intrauterine growth retardation [in Spanish]. Rev Med Chil 117:1311

Kubo Y, Adelman JP, Clapham DE, Jan LY, Karschin A, Kurachi Y, Lazdunski M, Nichols CG, Seino S, Vandenberg CA (2005) International Union of Pharmacology. LIV. Nomenclature and molecular relationships of inwardly rectifying potassium channels. Pharmacol Rev 57:509–526

Lee X, Keith JC Jr, Stumm N, Moutsatsos I, McCoy JM, Crum CP, Genest D, Chin D, Ehrenfels C, Pijnenborg R, van Assche FA, Mi S (2001) Downregulation of placental syncytin expression and abnormal protein localization in pre-eclampsia. Placenta 22:808–812

Levitan I, Fang Y, Rosenhouse-Dantsker A, Romanenko V (2010) Cholesterol and ion channels. Subcell Biochem 51:509–549

Lindheimer MD, Katz AI (1989) Preeclampsia: pathophysiology, diagnosis, and management. Annu Rev Med 40:233–250

Martens JR, Sakamoto N, Sullivan SA, Grobaski TD, Tamkun MM (2001) Isoform-specific localization of voltage-gated K^+ channels to distinct lipid raft populations. Targeting of Kv1.5 to caveolae. J Biol Chem 276:8409–8414

Melnyk P, Zhang L, Shrier A, Nattel S (2002) Differential distribution of Kir2.1 and Kir2.3 subunits in canine atrium and ventricle. Am J Physiol Heart Circ Physiol 283:H1123–H1133

Michel V, Bakovic M (2007) Lipid rafts in health and disease. Biol Cell 99:129–140

Mylona P, Clarson H, Greenwood SL, Sibley CP (1998) Expression of the Kir2.1 (inwardly rectifying potassium channel) gene in the human placenta and in cultured cytotrophoblast cells at different stages of differentiation. Mol Hum Reprod 4:195–200

Nichols CG, Lopatin AN (1997) Inward rectifier potassium channels. Annu Rev Physiol 59:171–191

O'Connell KM, Tamkun MM (2005) Targeting of voltage-gated potassium channel isoforms to distinct cell surface microdomains. J Cell Sci 118:2155–2166

Plaster NM, Tawil R, Tristani-Firouzi M, Canun S, Bendahhou S, Tsunoda A, Donaldson MR, Iannaccone ST, Brunt E, Barohn R, Clark J, Deymeer F, George AL Jr, Fish FA, Hahn A, Nitu A, Ozdemir C, Serdaroglu P, Subramony SH, Wolfe G, Fu YH, Ptacek LJ (2001) Mutations in Kir2.1 cause the developmental and episodic electrical phenotypes of Andersen's syndrome. Cell 105:511–519

Reimann F, Ashcroft FM (1999) Inwardly rectifying potassium channels. Curr Opin Cell Biol 11:503–508

Riquelme G (2011) Placental syncytiotrophoblast membranes: domains, subdomains and microdomains. Placenta 32(suppl 2):S196–S202

Riquelme G, Vallejos C, de Gregorio N, Morales B, Godoy V, Berrios M, Bastias N, Rodriguez C (2011) Lipid rafts and cytoskeletal proteins in placental microvilli membranes from preeclamptic and IUGR pregnancies. J Membr Biol 241:127–140

Romanenko VG, Fang Y, Byfield F, Travis AJ, Vandenberg CA, Rothblat GH, Levitan I (2004) Cholesterol sensitivity and lipid raft targeting of Kir2.1 channels. Biophys J 87:3850–3861

Smith PK, Krohn RI, Hermanson GT, Mallia AK, Gartner FH, Provenzano MD, Fujimoto EK, Goeke NM, Olson BJ, Klenk DC (1985) Measurement of protein using bicinchoninic acid. Anal Biochem 150:76–85

Stulc J (1997) Placental transfer of inorganic ions and water. Physiol Rev 77:805–836

Tikku S, Epshtein Y, Collins H, Travis AJ, Rothblat GH, Levitan I (2007) Relationship between Kir2.1/Kir2.3 activity and their

distributions between cholesterol-rich and cholesterol-poor membrane domains. Am J Physiol Cell Physiol 293:C440–C450

Tillman TS, Cascio M (2003) Effects of membrane lipids on ion channel structure and function. Cell Biochem Biophys 38: 161–190

Tristani-Firouzi M, Etheridge SP (2010) Kir2.1 channelopathies: the Andersen-Tawil syndrome. Pflugers Arch 460:289–294

Warth R (2003) Potassium channels in epithelial transport. Pflugers Arch 446:505–513

Wiechelman KJ, Braun RD, Fitzpatrick JD (1988) Investigation of the bicinchoninic acid protein assay: identification of the groups responsible for color formation. Anal Biochem 175:231–237

Williams JL, Fyfe GK, Sibley CP, Baker PN, Greenwood SL (2008) K^+ channel inhibition modulates the biochemical and morphological differentiation of human placental cytotrophoblast cells in vitro. Am J Physiol Regul Integr Comp Physiol 295:R1204–R1213

Zaritsky JJ, Eckman DM, Wellman GC, Nelson MT, Schwarz TL (2000) Targeted disruption of Kir2.1 and Kir2.2 genes reveals the essential role of the inwardly rectifying K^+ current in K^+-mediated vasodilation. Circ Res 87:160–166

J Membrane Biol (2012) 245:151–156
DOI 10.1007/s00232-012-9423-9

Cl Anion-Dependent Mg-ATPase

Sopio Dzneladze · Leila Tsakadze · Marina Leladze · Zurab Kometiani

Received: 27 September 2011 / Accepted: 16 February 2012 / Published online: 8 March 2012

Abstract We studied, in the rat brain, the synaptosomal and microsomal membrane fractions of Cl^- ion-activated, Mg^{2+}-dependent ATPase, satisfying the necessary kinetic peculiarities of transport ATPases, by a novel method of kinetic analysis of the multisite enzyme systems: (1) the [Mg-ATP] complex constitutes the substrate of the enzymic reaction; (2) the $V = f(Cl^-)$ dependence-reflecting curve is bell-shaped; (3) substrate dependence, $V = f(S)$, curves at a constant concentration of free ligands (Mg_f, ATP_f, Cl^-); (4) as known from the literature, in the process of reaction a phosphorylated intermediate is formed (Gerencser, Crit Rev Biochem Mol Biol 31:303–337, 1996). We report on the Cl-ATPase molecular mechanism and its place in the "P-type ATPase" classification.

Keywords Plasma membrane · P-type ATPase · Transport-ATPase · Anion dependence ATPase (Cl-ATPase) free ligand · Molecular mechanism

Introduction

Anion-dependent, Mg^{2+}-activated ATP hydrolysis, namely, HCO_3^- and activation by Cl^- ions, is known from the literature. The activity has been mainly identified in bacteria and eukaryotes, some organs of *Aplysia californica* and toad (*Bufo bufo*) such as the epithelial tissue basolateral membrane of the small intestine (Gerencser and Dept 2003), membrane fraction of freshwater eel fins (Bornancin et al. 1977), the plasma membrane of *Aplysia* vesicles and rat pancreatic canals (Zhao et al. 1994), membrane vesicles of rat brain (Gerencser 1996), liver plasma membrane cells (Izutsu and Siegel 1980) and brain plasma membrane cells (Gerencser and Dept 2003).

The asymmetric distribution of anions (mainly HCO_3^- and Cl^-) in the membrane (out $\gg$ in) accounts for their passive transport down the concentration gradient, whose reverse system appears to be an active transport mechanism. Transport ATPases are known to have a particularly important role in cell functioning. Providing the asymmetric arrangement of cations in the membrane at the expense of ATP hydrolysis, they represent a complex biological mechanism.

Among the transport ATPases worth mentioning are the "P-type" ATPases, which possess a phosphorylated intermediate and accomplish a two-step catalysis of phosphorylation and dephosphorylation with the participation of the Mg-ATP complex.

P-type ATPases belong to the plasma membrane ATPases, such as Na, K-ATPase, H-ATPase, K, H-ATPase and bivalent cation-activated ATPases. The ATP hydrolysis activation by anions can also be attributed to P-type ATPases.

The goal of the present work was to identify Cl-ATPase activity in rat brain plasma membrane fractions, to study the enzyme molecular mechanism using the method of composite geometric curve shape analysis and to determine its place in the general classification of ATPases.

Materials and Methods

Sections of albino rat brain from different membranes of both sexes, weighing 200–300 g, served as the experimental material. Sections were obtained via osmotic shock

S. Dzneladze (✉) · L. Tsakadze · M. Leladze · Z. Kometiani
Beritashvili Institute of Physiology, 14 Gotua str,
0160 Tbilisi, Georgia
e-mail: dsopio@yahoo.com

to the synaptosomes at 0.9–1.2 M sucrose (Kometiani 1982), as well as fractions of microsomes (0.32 M sucrose). The preparations were washed in 2.5 mM EGTA and 2.5 mM EDTA solutions.

ATPase activity was determined by a volume of liberated inorganic phosphorus (P_i) (Kazanov and Maslova 1980), and protein was determined according to the method of Lowry et al. (1951). ATPase activity was represented as micromoles of P_i per hour, with milligram protein units. Reagent medium always contained 30 mM Tris–Malate (pH 7.65), 0.4 mM EGTA, 0.2 mM ouabain and 0.3 mM ethacrynic acid (the specific inhibitor of Cl-ATPase (Gassnez and Komnick 1981; Tanaka et al. 1986). Concentrations of other ligands in incubation solution are given in the text.

Cl-ATPase was measured as the difference between Cl^--containing incubation and ethacrynic acid-containing media. Experimental data were processed statistically.

In the Cl-ATPase study we applied kinetic analysis of multisited enzyme systems (Kometiani et al. 1984), which is a single method used from kinetic investigation of multisited enzyme systems.

Concentration estimates of free ATP_f, Mg_f^{2+} and Mg-ATP complex were made by application of the following equations:

$$[ATP_f] \cdot \left[Mg_f^{2+}\right] = [\text{Mg-ATP}] \cdot K_{Mg}$$

$$\sum Mg^{2+} = \left[Mg_f^{2+}\right] + [\text{Mg-ATP}]$$

$$\sum ATP = [ATP_f] + [\text{Mg-ATP}]$$

where K_{Mg} is the dissociation constant of the Mg-ATP complex (0.0603 mM).

To analyze the experimental curves, the method of kinetic analysis of multisited enzyme systems was applied. This kinetic method of complex geometric shape curves was used to establish a "minimal model" for the enzyme system. The reaction velocity of the Cl-ATPase enzyme system is a function of at least three physiological ligands, Mg-ATP, Mg_f^{2+} and ATP_f, each of which may exert on the enzyme an activating or inhibiting action. To analyze the initial velocity of an enzymatic reaction, it is required to obtain $V = f([\text{Mg-ATP}], [ATP]\ [Mg_f^{2+}])$ as a function of one variable, when the values of other ligands are constant. Therefore, in the experiment the concentrations of the mentioned ligands were chosen so that the enzyme reaction velocity was actually represented by a one-variable ligand function. In particular, in each experiment the concentrations of three ligands represented constant quantities. Then, in each particular case, the conditions of the reaction being invariable and the enzyme functional unit structure being in a steady state, the initial velocity would be a one-variable function and would be described by the following analytical formula:

$$V = e_0 \frac{x^n \sum_{i=0}^{p} \alpha_i x^i}{\sum_{i=0}^{S} \beta_i x^i};\ S = n + m + p$$

where α_i and β_i are the sum of products of individual velocity coefficients and steady-state ligand concentrations; X is a variable ligand concentration; e_0 is the enzyme overall concentration; and n, m and p represent power parameters and are positive integers: n is the number of sites for essential activators, m is the number of sites assigned for full-effect inhibitors and p is the number of sites for partial-effect modifiers. To determine numerical values for the parameters n, m and p, a special computer program was used (Kometiani 2007).

Results

From primary evidence it follows that ATP hydrolysis with Cl^- participation proceeds only in Mg^{2+} medium. When $Mg^{2+} = 0$, activation by Cl^- does not manifest itself. Consequently, Cl-ATPase activity implies Cl^- anion Mg^{2+}-activated ATP hydrolysis.

Figure 1 shows the relation of Mg^{2+}-dependent ATP hydrolysis with Cl^- ion concentration in synaptic membrane and microsomal fractions. The shape of the $V = f(Cl^-)$ curve is similar in both cases. Only the specific activity of the enzyme is altered. Synaptic membranes are characterized by a high Cl-ATPase activity compared to microsomes. Analysis of the curve's geometric shape clearly reveals its bell shape, with ascending and descending phases of Cl^- concentration dependence.

Study of Cl^- ion activity mechanisms on Cl-ATPase has revealed that when $[Cl^-] < 10$ mM the enzyme activity

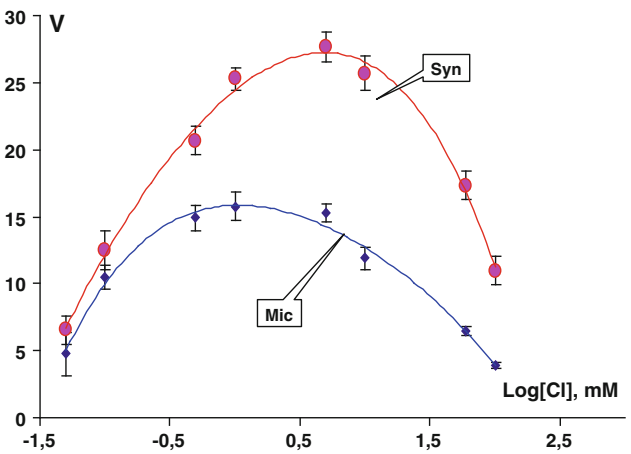

Fig. 1 Dependence of Cl-ATPase activity (V) on Cl ion concentration (decimal logarithms) in synaptic and microsomal fraction. Protein: 0.022 mg/ml, ATP = 2 mM, Tris–Malate = 30 mM (pH 7.7), ouabain = 0.2 mM

dependence on a variable ligand is increasing. With a further increase of Cl^- concentration the enzyme activity is reduced and approximates zero. For the transport to be effected, at the very beginning the enzyme with high affinity should bind an ion, whereas after the transport has been effected, due to the decay of ion affinity, the enzyme should get released from that ion. Such a geometric shape of the kinetic $V = f(Cl^-)$ curve is certainly specific to all Tr-ATPases and is a necessary but insufficient condition for the identification of Tr-ATPase system.

Qualitative conversion results in linearization of the function when $r = 1$ (r is a power index whose numerical value is determined by the curve's shape; when the function has a horizontal asymptote, $r = n$). This means that each molecule of Cl-ATPase has one ligand-binding site for Cl^- as for an essential activator (i.e., $n = 1$). To determine the number of sites for Cl^- as a full inhibitor, a high variable concentration of Cl^- was taken ([Cl] $\geq$ 40 mM). Linearization of function was achieved when $r = 1$, i.e., number of sites for Cl^- as a full inhibitor, $m = 1$.

Figure 2 represents in double reciprocal values the Cl-ATPase activity dependence on Mg-ATP concentration. In both cases $1/V = f(1/\text{Mg-ATP})$ function has an asymptote at high values. At medium Mg-ATP concentrations the function has turning and inflexion points, while at small values the enzyme system undergoes inhibition. At high values (with extremely small Mg-ATP concentration) the linearity of $1/V = f(1/\text{Mg-ATP})$ function is a necessary and sufficient condition for maintaining that the [Mg-ATP] complex represents a true substrate for the enzyme system (Kometiani 1982).

Free ligands (Mg_f and ATP_f) are known to be modifiers of transport ATPases (for Na, K-ATPase, in particular). The effect of the given ligands on Cl-ATPase was studied at various fixed substrate concentrations. Figure 3 shows the pattern of ATPase activity change from Mg_f concentration under conditions of various fixed substrate concentration (0.5, 1.5 mM).

As is evident from the figure, at low Mg-ATP fixed concentration the curve has a simple concave shape. At a high fixed concentration the curve has a composite geometric shape: at modest values one can see activation of the enzyme system, while at high concentrations the enzyme system is inhibited. Therefore, in the 0.2–1.2 mM range of Mg, enzyme activity is homogeneous and a "plateau" is seen on the curve (Fig. 2).

A similar dependence was observed upon studying $V = f(ATP_f)$ when S = const. The inhibition pattern by free ligands (Mg_f and ATP_f) appeared to be qualitatively identical.

Figure 4 shows the Cl-ATPase activity dependence on substrate concentration, in double reciprocal coordinates, at various Mg_f fixed concentrations. The substrate experimental concentrations were chosen so that $V = f(S)$ had a rectilinear dependence at small concentrations. Under these conditions, with a rise in [Mg_f], the slope and intercept increase; the lines intersect on the abscissa, which indicates that the enzyme affinity for the substrate does not alter at various fixed Mg_f concentrations; the reaction maximum velocity increases in parallel with Mg_f concentration rise, within the concentration range; and a further rise in Mg_f concentration (>0.8 mM) causes a decline in activity.

Figure 5 represents Cl-ATPase activity dependence on Cl^- ions (x) at different fixed substrate concentrations in double-reciprocal values. The $1/V = f(1/x)$ function is a straight line and has an asymptote; i.e., Cl^- ions are activators of Cl-ATPase. Calculation of regression coefficients and determination of line intersection points allows us to ascertain the character of modifier (Cl^- ions in particular)

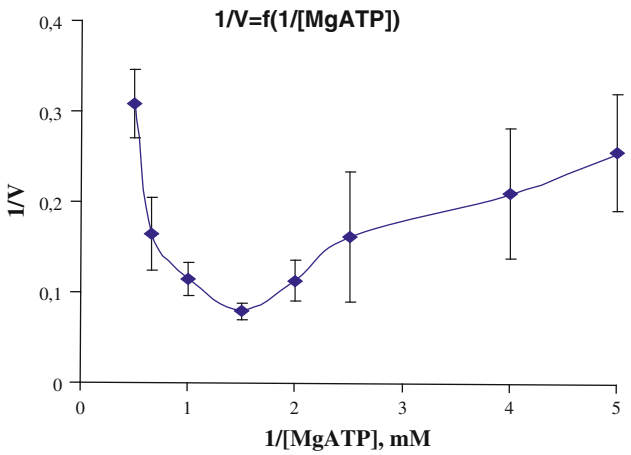

Fig. 2 Dependence of Cl-ATPase upon substrate (S = Mg-ATP) contentration, in double inverse values, when $Mg_f = ATP_f$

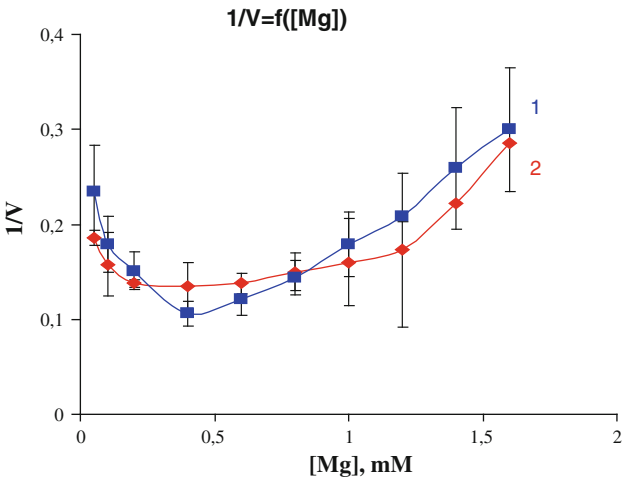

Fig. 3 Dependence of Cl-ATPase activity upon Mg_f concentration at fixed substrate concentrations ($S_1 = 0.5$ mM, $S_2 = 1.5$ mM). Microsomal fraction protein = 0.025 mg/ml

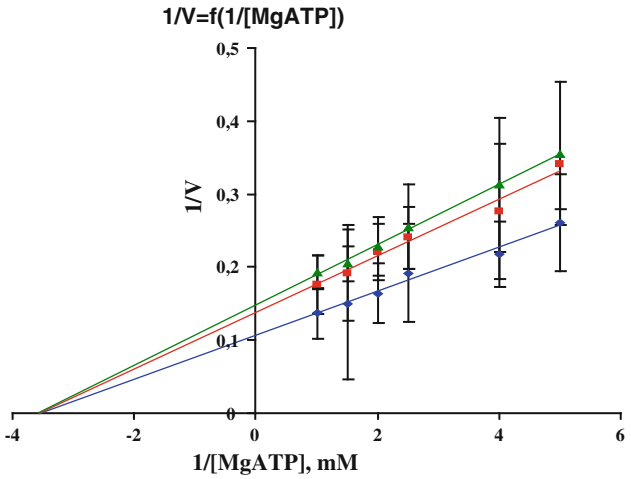

Fig. 4 Dependence of Cl-ATPase activity upon substrate concentration on double inverse values at different fixed Mg_f concentrations: 0.2, 0.5, 1.2 mM

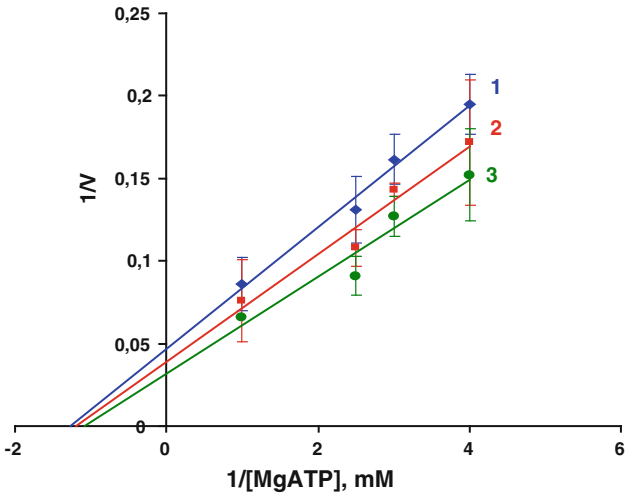

Fig. 5 Dependence of Cl-ATPase activity on substrate concentration on double inverse values at different fixed Cl^- concentrations: 5, 10, 15 mM

activity for the enzyme system. Computation of regression coefficients for asymptotes revealed that this parameter is identical at various substrate fixed concentrations; i.e., linear functions intersect at one point on the abscissa. And this indicates that the enzyme affinity for the substrate remains unchanged with a Cl^- concentration change. Binding of the substrate and Cl^- ion is mediated by a randomized mechanism.

Discussion

The "P-type" cations appear to be multisited, complex enzyme systems. Less known is the role and place in the general classification of anionic ATPases (Cl-ATPase, in particular). To determine this, study of the molecular mechanism of its activity is necessary. First of all, a question is raised as to whether Cl-ATPase belongs to the transport ATPase system or not. The principal demands posed to the transport ATPases are known from the literature (Kometiani and Nozadze 2007). Among them, the most important is to define the shape of the curve reflecting the transportable ion-dependent velocity of $V = f(Cl^-)$ and the Mg-ATP complex as a true substrate.

For all transport ATPases, the curve reflecting the enzyme reaction velocity dependence on the transportable ion concentration has a bell shape, where the ascending phase corresponds to the ion binding process and the descending one corresponds to its release. According to our data, this condition is satisfied for Cl-ATPase only in the case when the reaction proceeds against the background of Mg^{2+} ions.

From our findings it emerges that Cl^- ion-activated, Mg^{2+}-dependent ATPase satisfies the essential kinetic peculiarities of transport ATPases:

1. The curve for $V = f(Cl^-)$ dependence has a bell shape (Fig. 1).
2. The optimal regimen for the system to work provides for the inevitable existence of the [Mg-ATP] complex (Figs. 2, 3).
3. In the course of the catalytic reaction a phosphorylated intermediate is formed (Gerencser 1996).

The rectilinearity of the $1/V = f(1/Mg\text{-}ATP)$ function at small Mg-ATP concentrations (Fig. 2) indicates that the number of sites for Mg-ATP as an essential activator is $n = 1$. If we take into account that Cl-ATPase activity manifests only in the presence of Mg^{2+} and Mg-ATP is an essential activator for the enzyme system, it may be said that Mg-ATP constitutes a substrate for the Cl-ATPase system. It is remarkable that at high concentrations of Mg-ATP its number of sites assigned for full inhibitors is $m = 1$. Under these conditions, on the $1/V = f(1/Mg\text{-}ATP)$ curve at medium values the existence of turning and inflexion points indicates that the minimal number of sites for Mg-ATP as for the partial effect modifiers is $P \geq 1$. Since in the case of other P-type ATPases, for Na, K-ATPase in particular, it is known that for each subunit of the enzyme there is one substrate binding site, it can be assumed that for Cl-ATPase as well the functional unit is minimum a dimmer with two identical subunits.

At various Mg^{2+} fixed concentrations, analysis of $V = f(1/S)$ revealed its modifier nature as having an enzyme system-inhibiting effect. The result given in Fig. 4 together with the above-mentioned may be considered as verification that Mg^{2+} is a component of Cl-ATPase substrate, though it is more complex in nature. On one

functional unit of the Cl-ATPase molecule there may be a special binding site where Mg^{2+} may display its potent modifying nature. The straight line intersection at the abscissa (Fig. 4) indicates that for Mg-ATP Mg is an inhibitor with invariable affinity and Mg^{2+}-bound forms of the enzyme have no catalytic ability.

By analysis of the straight line arrangement (Fig. 5) reflecting substrate concentration dependence of Cl-ATPase in double-reciprocal coordinates at varying fixed Cl^- concentrations, a conclusion is drawn that Cl^- ions are activators of the enzyme system that stimulate preferential activity of the partial effect sites. Cl^- is at the same time a modifier of the system. By increasing its concentration, activation passes into inhibition. Similar alignment is possible only in the case of a multisited enzyme system and depends on the parameters resulting from multisitedness.

Thus, Cl^- ions must belong to the group of modifiers whose activity results in reduction of the slope of rectilinear function, though the ordinate axis intersection point is unchanged, which is the necessary condition for specific modifiers. This means that Cl^- ions are specific effect activators.

Free ligands (Mg_f and ATP_f) are the system's modifiers, with activating and inhibiting effects, with invariable affinity for the substrate. As to Cl^- ions, they are a specific type of modifier with invariable affinity for the substrate. Thus, it may be concluded that all P-type transport ATPases, cations as well as anions, are characterized by a similar molecular mechanism.

The mechanism of dead-end branch formation has been studied in the Na, K-ATPase reaction. During the ATPase reaction, not only the Mg-ATP complex formed in the solution but also the one set up on the enzyme molecule is hydrolyzed. For this to be realized the necessary condition is binding in the enzyme active center, first of ATP and then of Mg^{2+}. In case this process takes place in reverse (first Mg^{2+}, then ATP), a "dead-end" complex is formed.

In accordance with the data reported (Robinson and Flasher 1979; Kometiani et al. 1984), the presence of only one catalytic site per α-subunit has been identified for the Na, K-ATPase system. Therefore, the molecule has a dimeric nature with two identical subunits, $2(\alpha\beta)$, that must be a universal system for all P-type transport ATPases.

Study of the interrelation of membrane Cl-ATPase with other ATPases will assist to some extent in deciphering the mechanism and function of its activity. To this end, we have reveled anion interaction in the membrane in ATP hydrolysis. In the living cell an excessive amount of anions was found on the external surface of the membrane compared to the internal one. This fact determines their movement within a concentration gradient from outward to inward. There is an indication in the literature that there may also be cotransport of Cl^- and other anions at the expense of ATP hydrolyzing energy (cotransport of Cl^-/HCO_3^- in particular). Cl^- is directed from inside the cell, in contrast to HCO_3^-. The process may be due to the existence of an Mg-nondependent HCO_3-ATPase in the plasma membrane (Tsakadze et al. 2007), whose substrate (as distinct from Mg-dependent HCO_3-ATPase) is only free ATP. This ATPase is likely to be attributed to the so-called Ecto-ATPase group, which function on the external side of the membrane and do not require Mg ions.

Conclusion

In conclusion, it can be said that the study of Cl-ATPase revealed an interesting analogy of transport ATPases with general kinetic peculiarities. Cl-ATPase, like the P-type ATPases, is a transport system which carries out active movement of Cl^- anions from inward to outward of the synaptosomal and microsomal membranes. The kinetic parameters of both membranes are identical. On the basis of the evidence and theoretical calculation, we suggest a scheme for the operation of the Cl-ATPase system.

References

Bornancin M, De Renzis G, Maetz I (1977) Branchial Cl transport, anion stimulated ATPase and acid–base balance in *Anguilla anguilla* adapted to freshwater: effects of hyperoxia. J Comp Physiol B Biochem Syst Environ Physiol 117(3):313–322

Gassnez D, Komnick H (1981) Inhibition of a Cl^-/HCO_3-ATPase in the avian salt gland by furosemide and ethacrynic acid. Cell Biol Int Rep 5:239–246

Gerencser GA (1996) The chloride pump: a Cl^- translocating P-type ATPase. Crit Rev Biochem Mol Biol 31:303–337

Gerencser GA, Dept ZI (2003) Existence and nature of the chloride pump. Comp Biochem Physiol A 137:S1–S237

Izutsu KT, Siegel IA (1980) A microsomal HCO_3^--stimulated ATPase in the rat liver plasma membrane cells. Biocemistry 45:424–429

Kazanov A, Maslova M (1980) Peculiarities of detergent-induced activation of the brain Na, K-ATPase in vertebrates. Zh Evol Biokhim Fiziol 16(5):81–87

Kometiani Z (1982) Method for the analysis of kinetic curves for multisite enzyme systems. Bull Ga Acad Sci 105:401–404

Kometiani Z (2007) Methods for kinetic analysis of multi-sited enzyme systems. Sakartvelos Matsne, Tbilisi, Georgia

Kometiani Z, Nozadze E (2007) Kinetic singularities of transport ATPases. Bull Ga Acad Sci 175(4):106–109

Kometiani Z, Tsakadze L, Jariashvili T (1984) Functional significance of the effects of neurotransmitters on the Na, K-ATPase system. J Neurochem 42(5):1246–1250

Lowry OH, Rosebroygh NL, Fazz AU, Randall RY (1951) Protein measurement with the folin phenol reagent. J Biol Chem 193:265–276

Robinson ID, Flasher MS (1979) The (Na^+, K^+) activated ATPase. Biochem Biophys Acta 549:145–176

Tanaka T, Inagaki C, Matsuda K, Takaori S (1986) Characteristics of ethacrynic acid highly sensitive Mg^{2+}-ATPase in microsomal fractions of the rat brain: functional molecular size, inhibition by SITS and stimulation by Cl^-. Jpn J Pharmacol 42:351–359

Tsakadze L, Dzneladze S, Kometiani Z (2007) Mg-independent HCO_3-ATPase. Ga Acad Sci Biol Ser B 5(2):9–13

Zhao H, Star RA, Muallem S (1994) Membrane localization of H^+ and HCO_3^- transporters in the rat pancreatic duct. J Gen Physiol 104:57–85

J Membrane Biol (2012) 245:157–163
DOI 10.1007/s00232-012-9424-8

Downregulation of the Creatine Transporter SLC6A8 by JAK2

Manzar Shojaiefard · Zohreh Hosseinzadeh · Shefalee K. Bhavsar · Florian Lang

Received: 4 November 2011 / Accepted: 16 February 2012 / Published online: 11 March 2012

Abstract Janus-activated kinase-2 (JAK2) participates in the regulation of the Na^+-coupled glucose transporter SGLT1 and the Na^+-coupled amino acid transporter SLC6A19. Concentrative cellular creatine uptake is similarly accomplished by Na^+-coupled transport. The carrier involved is SLC6A8 (CreaT). The present study thus explored whether JAK2 regulates the activity of SLC6A8. To this end, cRNA encoding SLC6A8 was injected into *Xenopus* oocytes with or without cRNA encoding wild-type JAK2, constitutively active ^{V617F}JAK2 or inactive ^{K882E}JAK2. Electrogenic creatine transport was determined in those oocytes by dual-electrode voltage-clamp experiments. In oocytes injected with cRNA encoding SLC6A8 but not in oocytes injected with water or with cRNA encoding JAK2 alone, addition of 1 mM creatine to the extracellular bath generated an inward current (I_{crea}). In SLC6A8 expressing oocytes I_{crea} was significantly decreased by coexpression of JAK2 or ^{V617F}JAK2 but not by coexpression of ^{K882E}JAK2. According to kinetic analysis, coexpression of JAK2 decreased the maximal transport rate without significantly modifying the affinity of the carrier. In oocytes expressing SLC6A8 and ^{V617F}JAK2 I_{crea} was gradually increased by the JAK2 inhibitor AG490 (40 μM). In SLC6A8 and JAK2 coexpressing oocytes the decline of I_{crea} following disruption of carrier insertion with brefeldin A (5 μM) was similar in the absence and presence of JAK2. In conclusion, JAK2 is a novel regulator of the creatine transporter SLC6A8, which downregulates the carrier, presumably by interference with carrier protein insertion into the cell membrane.

Keywords Creatine uptake · Energy depletion · Brefeldin · AG490 · Erythropoietin · Leptin

Introduction

Janus-activated kinase-2 (JAK2) participates in the signaling of several hormones, such as leptin (Morris and Rui 2009), growth hormone (Brooks and Waters 2010), erythropoietin (Spivak 2010), thrombopoietin (Spivak 2010), granulocyte colony-stimulating factor (Spivak 2010) and further cytokines (Lopez et al. 2010; Spivak 2010). JAK2 is activated by oxidative stress, ischemia, and hypertonicity (Kurdi and Booz 2009; Garnovskaya et al. 2003; Gatsios et al. 1998). Enhanced JAK2 activity may foster the development of malignancy, and JAK2 inhibitors are considered potential drugs in the treatment of myeloproliferative disorders (Baskin et al. 2010; Ho et al. 2010; Oh and Gotlib 2010; Pardanani et al. 2011; Santos and Verstovsek 2011; Tefferi et al. 2009; Tefferi 2010). The gain-of-function mutation ^{V617F}JAK2 is found in, and presumably contributes to, the development of myeloproliferative disease (Mahfouz et al. 2011). The pleiotropic effects of JAK2 include transport regulation (Gong et al. 1998; Yokota et al. 1998). Recently, JAK2 has been shown

M. Shojaiefard and Z. Hosseinzadeh contributed equally to this work and share the position of first author.

M. Shojaiefard · Z. Hosseinzadeh · S. K. Bhavsar · F. Lang (✉)
Department of Physiology I, University of Tübingen, Gmelinstr. 5, 72076 Tübingen, Germany
e-mail: florian.lang@uni-tuebingen.de

M. Shojaiefard
Department of Physiology, Fasa University of Medical Science, Fasa, Iran

Z. Hosseinzadeh
Department of Science, Shahid Chamran University, Ahwaz, Iran

to upregulate Na^+-coupled glucose transport (Hosseinzadeh et al. 2011) and the Na^+-coupled amino acid transporter SLC6A19 (Bhavsar et al. 2011).

The creatine transporter SLC6A8 (CreaT) belongs to a superfamily of Na^+, Cl^--coupled transporters for neurotransmitters (e.g., dopamine, GABA, serotonin and norepinephrine), amino acids (e.g., glycine) (Christie 2007; Dodd and Christie 2001; Sora et al. 1994) and the organic osmolytes betaine (Takenaka et al. 1995) and taurine (Uchida et al. 1992).

SLC6A8 is expressed in a wide variety of tissues, such as skeletal muscle, kidney, small intestine, heart, brain, and retina (Braissant and Henry 2008; Guimbal and Kilimann 1993; Mak et al. 2009; Mellott et al. 2007). Genetic defects affecting SLC6A8 result in mental retardation with seizures (Alcaide et al. 2010, 2011; Ardon et al. 2010; Battini et al. 2007, 2011; Braissant et al. 2010, 2011; Hahn et al. 2002; Jensen et al. 2011; Longo et al. 2011; Mancardi et al. 2007; Mercimek-Mahmutoglu et al. 2010; Puusepp et al. 2009; Rosenberg et al. 2007; Salomons et al. 2003; Skelton et al. 2011; Stockler et al. 2007; van de Kamp et al. 2011). Decreasing SLC6A8 protein abundance has been observed in the failing heart (Neubauer et al. 1999), and SLC6A8 deficiency may compromise cardiac function (Anselm et al. 2008). SLC6A8 activity is regulated by AMP-activated kinase AMPK (Li et al. 2010), cyclosporin A (Tran et al. 2000), mammalian target of rapamycin (mTOR) (Shojaiefard et al. 2006), serum and glucocorticoid inducible kinase isoforms (Shojaiefard et al. 2005) and PIKfyve (Strutz-Seebohm et al. 2007). SLC6A8 has been suggested to be phosphorylated by Src (Wang et al. 2002). SLC6A8 is further regulated by extracellular and cytosolic creatine levels (Brault et al. 2003; Loike et al. 1988). Expression of the creatine transporter is increased by growth hormone (Omerovic et al. 2003).

The present study explored whether SLC6A8 is regulated by JAK2. SLC6A8 was expressed in *Xenopus* oocytes with or without wild-type JAK2, constitutively active ^{V617F}JAK2 or inactive ^{K882E}JAK2; and the electrogenic creatine transport was determined utilizing dual-electrode voltage-clamp.

Materials and Methods

Constructs

Constructs were used encoding wild-type bovine SLC6A8 (CreaT) (Dodd and Christie 2001) and wild-type human JAK2 (Imagenes, Berlin, Germany). Further, an inactive ^{K882E}JAK2 mutant (Feng et al. 1997) and the ^{V617F}JAK2 mutant (Mahfouz et al. 2011) were generated by site-directed mutagenesis (QuikChange II XL Site-Directed Mutagenesis Kit; Stratagene, Heidelberg, Germany) according to the manufacturer's instructions (Mohamed et al. 2010). The following primers were used: ^{V617F}JAK2, 5′-AGCATTTGGTTTTAAATTATGGAGTATGTTTCTG TGGAGACGAGA-3′; ^{V617F}JAK2, 5′-TCTCGTCTCCAC AGAAACATACTCCATAATTTAAAACCAAATGCT-3′; ^{K882E}JAK2, 5′-GGGAGGTGGTCGCTGTAGAAAAGCT TCAGCATAGT-3′; and ^{K882E}JAK2, 5′-ACTATGCTGAA GCTTTTCTACAGCGACCACCTCCC-3′. Underlined bases indicate mutation sites. The mutants were sequenced to verify the presence of the desired mutation. The mutants were used for generation of cRNA as described previously (Gehring et al. 2009).

Voltage Clamp in *Xenopus* Oocytes

Xenopus oocytes were prepared as previously described (Bohmer et al. 2010). We injected SLC6A8 cRNA (15 ng) on the 1st day and wild-type JAK2 cRNA (10 ng) on the 2nd day or the same day after preparation of oocytes. Oocytes were maintained at 17°C in ND96 solution containing (in mM) 96 NaCl, 4 KCl, 1.8 $MgCl_2$, 0.1 $CaCl_2$, 5 HEPES (pH 7.4) (Rexhepaj et al. 2010). Gentamycin (100 mg/l), theophylline (90 mg/l), tetracyclin (50 mg/l), ciprofloxacin (1.6 mg/l) and, where indicated, the JAK2 inhibitor AG490 (40 μM), actinomycin D (10 μM) or brefeldin A (5 μM) were added to the respective solutions. Voltage-clamp experiments were performed at room temperature 4 days after injection. Two-electrode voltage-clamp recordings were performed at a holding potential of −60 mV. The data were filtered at 10 Hz and recorded with a Digidata A/D–D/A converter and Clampex V.9 software for data acquisition and analysis (Axon Instruments, Foster City, CA). The control superfusate (ND96) contained (in mM) 96 NaCl, 2 KCl, 1.8 $CaCl_2$, 1 $MgCl_2$ and 5 HEPES (pH 7.4). Creatine was added to the solutions at a concentration of 1 mM, unless otherwise stated. The flow rate of the superfusion was approximately 20 ml/min, and a complete exchange of the bath solution was reached within about 10 s.

Statistical Analysis

Data are provided as means ± SEM, and n represents the number of oocytes investigated. All experiments were repeated with at least two to three batches of oocytes; in all repetitions qualitatively similar data were obtained. Data were tested for significance using ANOVA or t-test, as appropriate. Results with $P < 0.05$ were considered statistically significant.

Results

To explore whether JAK2 influences SLC6A8, the carrier was expressed with or without additional expression of the

kinase and SLC6A8-mediated transport was estimated from the creatine (1 mM)—induced inward current (I_{crea}). Addition of 1 mM creatine to the extracellular fluid did not induce an appreciable I_{crea} in non-injected or water-injected *Xenopus* oocytes. Thus, *Xenopus* oocytes do not express appreciable endogenous electrogenic creatine transport (Fig. 1a). Moreover, I_{crea} was negligible in *Xenopus* oocytes expressing wild-type JAK2 alone (Fig. 2b). A sizable I_{crea} was, however, observed in *Xenopus* oocytes injected with cRNA encoding SLC6A8 (CreaT). The coexpression of wild-type JAK2 was followed by a significant decrease of I_{crea} in *Xenopus* oocytes expressing SLC6A8 (Fig. 1b).

Additional experiments were performed to elucidate whether JAK2 was effective by modifying the maximal transport rate or the affinity of the carrier. As revealed by kinetic analysis of the creatine-induced currents in SLC6A8-expressing *Xenopus* oocytes (Fig. 1c), the maximal current approached 21.7 ± 1.1 nA ($n = 3$) in *Xenopus* oocytes expressing SLC6A8 alone and 10.3 ± 0.6 nA ($n = 3$) in *Xenopus* oocytes expressing SLC6A8 together with ^{V617F}JAK2. Thus, the maximal transport rate was significantly lower in *Xenopus* oocytes expressing SLC6A8 together with ^{V617F}JAK2 than in *Xenopus* oocytes expressing SLC6A8 alone. The creatine concentration required for half-maximal current (K_m) approached 167.4 ± 33.6 µM ($n = 3$) in *Xenopus* oocytes expressing SLC6A8 alone and 101.6 ± 25.2 µM ($n = 3$) in *Xenopus* oocytes expressing SLC6A8 together with ^{V617F}JAK2. The K_m was not significantly different between *Xenopus* oocytes expressing SLC6A8 together with ^{V617F}JAK2 and those expressing SLC6A8 alone. Accordingly, coexpression of JAK2 decreased SLC6A8 activity at least in part by reducing the maximal current.

As illustrated in Fig. 2, the effect of JAK2 was mimicked by the gain-of-function mutant ^{V617F}JAK2 but not by the inactive mutant ^{K882E}JAK2. The effect of ^{V617F}JAK2 tended to be higher than the effect of wild-type JAK2, though it did not reach statistical significance. Possibly, wild-type JAK2 is not fully activated in *Xenopus* oocytes.

Treatment of *Xenopus* oocytes expressing both SLC6A8 and ^{V617F}JAK2 with the JAK2 inhibitor AG490 (40 µM) was followed by a gradual increase of I_{crea} (Fig. 3). The effect of the inhibitor on I_{crea} reached statistical significance within 24 h of preincubation with AG490. At 6 h incubation, however, the inhibitor did not appreciably affect I_{crea}.

The decrease of I_{crea} in SLC6A8-expressing *Xenopus* oocytes by coexpression of ^{V617F}JAK2 could have resulted from accelerated clearance of carrier protein from the cell membrane. To test this possibility, SLC6A8-expressing *Xenopus* oocytes were treated with 5 µM brefeldin A, a substance that blocks the insertion of new carrier protein into the cell membrane. As shown in Fig. 4a, the creatine-induced current of SLC6A8 and ^{V617F}JAK2-expressing *Xenopus*

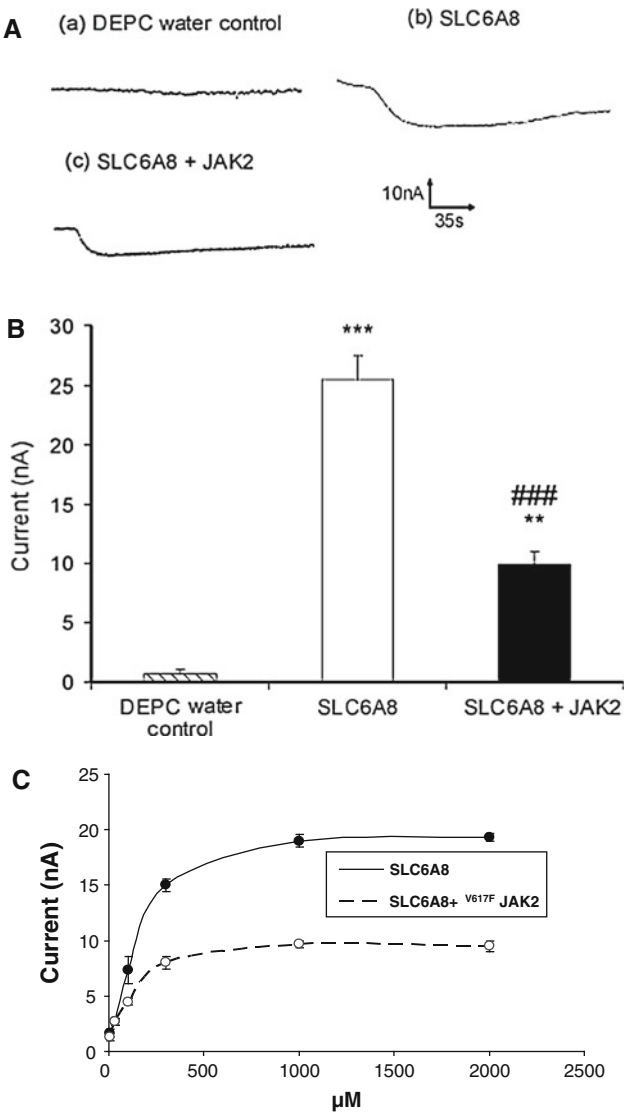

Fig. 1 Coexpression of JAK2 inhibits electrogenic creatine transport in SLC6A8-expressing *Xenopus* oocytes. **a** Representative original tracings showing creatine (1 mM)—induced current (I_{crea}) in *Xenopus* oocytes injected with water (*a*), expressing SLC6A8 without (*b*) or with (*c*) additional coexpression of wild-type JAK2. **b** Arithmetic means ± SEM (n = 16–33) of I_{crea} in *Xenopus* oocytes injected with water and expressing JAK2 alone (DEPC water control) or SLC6A8 without (SLC6A8) or with (SLC6A8 + JAK2) additional coexpression of wild-type JAK2. $^{**}P < 0.01$, $^{***}P < 0.001$ vs. absence of SLC6A8; $^{\#\#\#}P < 0.001$ vs. absence of JAK2. **c** Arithmetic means ± SEM ($n = 3$) of I_{crea} as a function of creatine concentration in *Xenopus* oocytes expressing SLC6A8 without (*closed circles, solid line*) or with (*open circles, dashed line*) additional coexpression of wild-type JAK2

oocytes declined at similarly rapid rates in the presence of brefeldin A. The observation suggests that ^{V617F}JAK2 decreases SLC6A8 activity by a mechanism other than accelerating carrier clearance from the cell membrane.

Inhibition of transcription by incubation (1–3 days) with actinomycin D (10 µM) did not significantly modify the

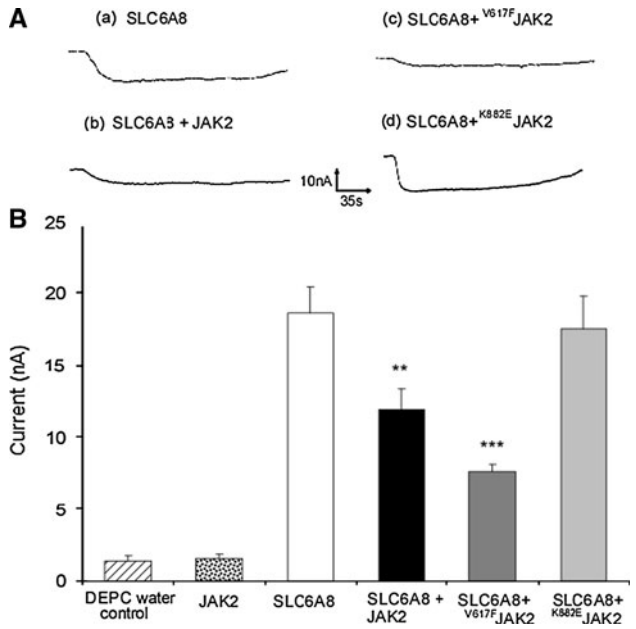

Fig. 2 Effect of JAK2 is mimicked by ^{V617F}JAK2 but not by the inactive mutant ^{K882E}JAK2. **a** Representative original tracings showing creatine (1 mM)—induced current (I_{crea}) in *Xenopus* oocytes injected with SLC6A8 alone (*a*) or coexpressing SLC6A8 with JAK2 (*b*), ^{V617F}JAK2 (*d*) or SLC6A8 with the inactive mutant ^{K882E}JAK2 (*c*). **b** Arithmetic means ± SEM (n = 13–23) of I_{crea} in *Xenopus* oocytes expressing SLC6A8 without (SLC6A8) or with wild-type JAK2 or SLC6A8 with constitutively active ^{V617F}JAK2 (SLC6A8 + ^{V617F}JAK2) or SLC6A8 with the inactive mutant ^{K882E}JAK2 (SLC6A8 + ^{K882E}JAK2). $^{**}P < 0.01$, $^{***}P < 0.001$ vs. expression of SLC6A8 alone

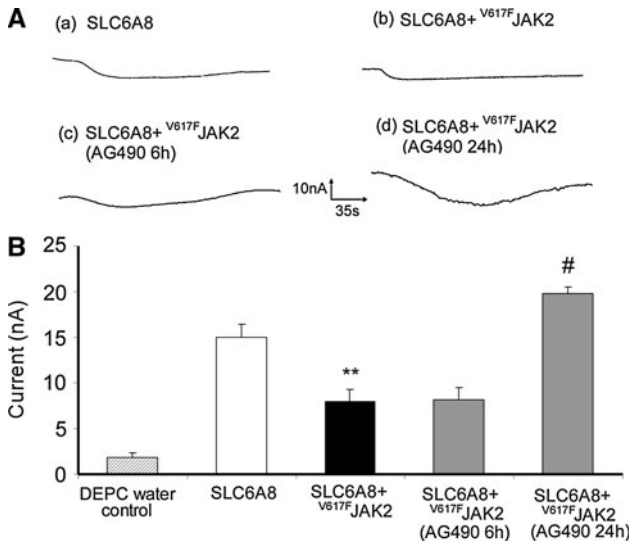

Fig. 3 Effect of ^{V617F}JAK2 is reversed by the JAK2 inhibitor AG490. **a** Representative original tracings showing creatine (1 mM)—induced current (I_{crea}) in *Xenopus* oocytes injected with SLC6A8 (*a*) or SLC6A8 + ^{V617F}JAK2 without (*b*) or with 6 h (*c*) or 24 h (*d*) pretreatment with AG490 (40 μM). **b** Arithmetic means ± SEM (n = 4–5) of I_{crea} in *Xenopus* oocytes expressing SLC6A8 with constitutively active ^{V617F}JAK2 in the absence of inhibitor (0 h) or following pretreatment with AG490 (40 μM) for the indicated time periods. $^{**}P < 0.001$ vs. expression of SLC6A8 alone, $^{\#}P < 0.001$ vs. absence of AG490 (SLC6A8 + ^{V617F}JAK2)

current induced by SLC6A8 either in the presence or in the absence of JAK2 (Fig. 4b).

Discussion

The present study uncovers a novel mechanism in the regulation of the creatine transporter SLC6A8 (CreaT). JAK2 decreased the electrogenic transport of creatine in SLC6A8-expressing *Xenopus* oocytes. The effect was mimicked by the gain-of-function mutant ^{V617F}JAK2 but not by the inactive ^{K882E}JAK2, indicating that kinase activity was required for this effect. Coexpression of ^{V617F}JAK2 did not significantly affect the affinity for creatine but rather decreased the maximal transport rate. According to the experiments in the presence of brefeldin A, JAK2 did not accelerate carrier retrieval from the cell membrane. Thus, JAK2 was presumably effective through inhibition of the carrier or interference with transporter protein insertion into the cell membrane. However, as brefeldin A is expected to affect the trafficking of a wide variety of molecules, which could at least in theory participate in the regulation of SLC6A8, the interpretation of experiments in the presence of brefeldin A may involve some uncertainty. The inefficacy of the inhibitor following short incubation may result from delayed access of the inhibitor to the kinase or may be an indirect effect of the kinase on carrier activity. For instance, the slow effect of the inhibitor could result from regulation of protein abundance rather than direct inactivation of the transporter. The insensitivity of the JAK2 effect to the presence of actinomycin suggests that the observed effect of JAK2 does not depend on transcription.

Given the close relation of SLC6A8 to the osmolyte transporters BGT and TAUT (Nash et al. 1994), the downregulation of SLC6A8 by JAK2 appears somewhat surprising. JAK2 activity is stimulated by hypertonicity (Garnovskaya et al. 2003; Gatsios et al. 1998) and the kinase enhances the activity of the cell volume regulatory Na^+/H^+ exchanger (NHE) (Coaxum et al. 2009). Osmotic cell shrinkage upregulates the activity of osmolyte transporters (Handler and Kwon 1996; Hoffmann and Pedersen 2006; Pasantes-Morales and Cruz-Rangel 2010), a regulation opposite to the presently observed JAK2-dependent downregulation of SLC6A8. It must be kept in mind that the osmolyte carriers are regulated by gene expression (Handler and Kwon 1996) and by cell volume–sensitive signaling involving the mTOR (Shojaiefard et al. 2006), serum and glucocorticoid inducible kinase (SGK1) (Shojaiefard et al. 2005) and phosphatidylinositol-3-phosphate-5-kinase (PIKfyve) (Strutz-Seebohm et al. 2007). Those mechanisms could upregulate SLC6A8 during cell

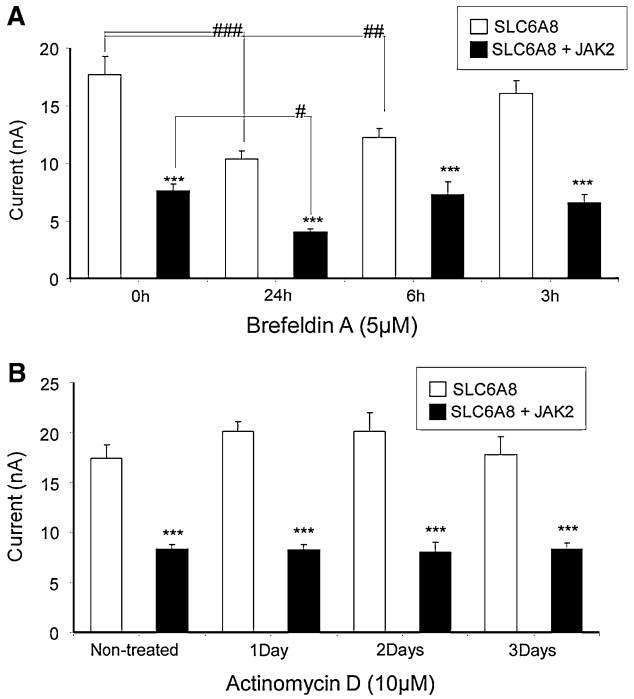

Fig. 4 Effects of brefeldin A and actinomycin D on SLC6A8 and SLC6A8 + JAK2 expressing *Xenopus* oocytes. **a** Arithmetic means ± SEM ($n = 7$–16) of creatine (1 mM)—induced current (I_{crea}) in *Xenopus* oocytes injected with cRNA encoding SLC6A8 without (*white bars*) and with (*black bars*) JAK2 in the presence and absence of 5 μM brefeldin A for 0–24 h prior to measurement. $^{***}P < 0.001$ vs. absence of JAK2, $^{\#}P < 0.05$, $^{\#\#}P < 0.01$, $^{\#\#\#}P < 0.001$ vs. absence of brefeldin A. **b** Arithmetic means ± SEM ($n = 8$–9) of I_{crea} in *Xenopus* oocytes injected with cRNA encoding SLC6A8 without (*white bars*) and with (*black bars*) JAK2 in the presence and absence of 10 μM actinomycin D 1–3 days prior to measurement. $^{***}P < 0.001$ vs. absence of JAK2

shrinkage. The creatine transporter is further regulated by Src (Wang et al. 2002) and AMP-activated kinase AMPK (Li et al. 2010). Nevertheless, the present observations raise a question about the functional significance of JAK2-sensitive SLC6A8 downregulation. The decrease of carrier activity would decrease Na^+ entry, which may be protective during energy depletion or otherwise compromised Na^+ extrusion by the Na^+/K^+-ATPase. On the other hand, creatine may reversibly bind phosphate (Speer et al. 2004), and decreased abundance of cytosolic creatine may decrease the ability of the cell to replenish ATP upon energy depletion.

Summary

This study presents evidence, for the first time, that JAK2 regulates the creatine transporter SLC6A8 (CreaT). It appears that JAK2 associates with the carrier and regulates its trafficking to the surface and, thus, cell membrane abundance.

Acknowledgments The authors acknowledge the meticulous preparation of the manuscript by Lejla Subasic and Sari Rübe and technical support by Elfriede Faber. This study was supported by the Deutsche Forschungsgemeinschaft (GRK 1302, SFB 773 B4/A1, La 315/13-3).

References

Alcaide P, Rodriguez-Pombo P, Ruiz-Sala P, Ferrer I, Castro P, Ruiz MY, Merinero B, Ugarte M (2010) A new case of creatine transporter deficiency associated with mild clinical phenotype and a novel mutation in the SLC6A8 gene. Dev Med Child Neurol 52:215–217

Alcaide P, Merinero B, Ruiz-Sala P, Richard E, Navarrete R, Arias A, Ribes A, Artuch R, Campistol J, Ugarte M, Rodriguez-Pombo P (2011) Defining the pathogenicity of creatine deficiency syndrome. Hum Mutat 32:282–291

Anselm IA, Coulter DL, Darras BT (2008) Cardiac manifestations in a child with a novel mutation in creatine transporter gene SLC6A8. Neurology 70:1642–1644

Ardon O, Amat di San FC, Salomons GS, Longo N (2010) Creatine transporter deficiency in two half-brothers. Am J Med Genet A 152A:1979–1983

Baskin R, Majumder A, Sayeski PP (2010) The recent medicinal chemistry development of Jak2 tyrosine kinase small molecule inhibitors. Curr Med Chem 17:4551–4558

Battini R, Chilosi A, Mei D, Casarano M, Alessandri MG, Leuzzi V, Ferretti G, Tosetti M, Bianchi MC, Cioni G (2007) Mental retardation and verbal dyspraxia in a new patient with de novo creatine transporter (SLC6A8) mutation. Am J Med Genet A 143A:1771–1774

Battini R, Chilosi AM, Casarano M, Moro F, Comparini A, Alessandri MG, Leuzzi V, Tosetti M, Cioni G (2011) Language disorder with mild intellectual disability in a child affected by a novel mutation of SLC6A8 gene. Mol Genet Metab 102: 153–156

Bhavsar SK, Hosseinzadeh Z, Merches K, Gu S, Broer S, Lang F (2011) Stimulation of the amino acid transporter SLC6A19 by JAK2. Biochem Biophys Res Commun 414:456–461

Bohmer C, Sopjani M, Klaus F, Lindner R, Laufer J, Jeyaraj S, Lang F, Palmada M (2010) The serum and glucocorticoid inducible kinases SGK1-3 stimulate the neutral amino acid transporter SLC6A19. Cell Physiol Biochem 25:723–732

Braissant O, Henry H (2008) AGAT, GAMT and SLC6A8 distribution in the central nervous system, in relation to creatine deficiency syndromes: a review. J Inherit Metab Dis 31:230–239

Braissant O, Beard E, Torrent C, Henry H (2010) Dissociation of AGAT, GAMT and SLC6A8 in CNS: relevance to creatine deficiency syndromes. Neurobiol Dis 37:423–433

Braissant O, Henry H, Beard E, Uldry J (2011) Creatine deficiency syndromes and the importance of creatine synthesis in the brain. Amino Acids 40:1315–1324

Brault JJ, Abraham KA, Terjung RL (2003) Muscle creatine uptake and creatine transporter expression in response to creatine supplementation and depletion. J Appl Physiol 94:2173–2180

Brooks AJ, Waters MJ (2010) The growth hormone receptor: mechanism of activation and clinical implications. Nat Rev Endocrinol 6:515–525

Christie DL (2007) Functional insights into the creatine transporter. Subcell Biochem 46:99–118

Coaxum SD, Garnovskaya MN, Gooz M, Baldys A, Raymond JR (2009) Epidermal growth factor activates Na^+/H^+ exchanger in podocytes through a mechanism that involves Janus kinase and calmodulin. Biochim Biophys Acta 1793:1174–1181

Dodd JR, Christie DL (2001) Cysteine 144 in the third transmembrane domain of the creatine transporter is located close to a substrate-binding site. J Biol Chem 276:46983–46988

Feng J, Witthuhn BA, Matsuda T, Kohlhuber F, Kerr IM, Ihle JN (1997) Activation of Jak2 catalytic activity requires phosphorylation of Y1007 in the kinase activation loop. Mol Cell Biol 17:2497–2501

Garnovskaya MN, Mukhin YV, Vlasova TM, Raymond JR (2003) Hypertonicity activates Na^+/H^+ exchange through Janus kinase 2 and calmodulin. J Biol Chem 278:16908–16915

Gatsios P, Terstegen L, Schliess F, Haussinger D, Kerr IM, Heinrich PC, Graeve L (1998) Activation of the Janus kinase/signal transducer and activator of transcription pathway by osmotic shock. J Biol Chem 273:22962–22968

Gehring EM, Zurn A, Klaus F, Laufer J, Sopjani M, Lindner R, Strutz-Seebohm N, Tavare JM, Boehmer C, Palmada M, Lang UE, Seebohm G, Lang F (2009) Regulation of the glutamate transporter EAAT2 by PIKfyve. Cell Physiol Biochem 24:361–368

Gong TW, Meyer DJ, Liao J, Hodge CL, Campbell GS, Wang X, Billestrup N, Carter-Su C, Schwartz J (1998) Regulation of glucose transport and c-fos and egr-1 expression in cells with mutated or endogenous growth hormone receptors. Endocrinology 139:1863–1871

Guimbal C, Kilimann MW (1993) A Na^+-dependent creatine transporter in rabbit brain, muscle, heart, and kidney: cDNA cloning and functional expression. J Biol Chem 268:8418–8421

Hahn KA, Salomons GS, Tackels-Horne D, Wood TC, Taylor HA, Schroer RJ, Lubs HA, Jakobs C, Olson RL, Holden KR, Stevenson RE, Schwartz CE (2002) X-linked mental retardation with seizures and carrier manifestations is caused by a mutation in the creatine-transporter gene (SLC6A8) located in Xq28. Am J Hum Genet 70:1349–1356

Handler JS, Kwon HM (1996) Regulation of the myo-inositol and betaine cotransporters by tonicity. Kidney Int 49:1682–1683

Ho K, Valdez F, Garcia R, Tirado CA (2010) JAK2 translocations in hematological malignancies: review of the literature. J Assoc Genet Technol 36:107–109

Hoffmann EK, Pedersen SF (2006) Sensors and signal transduction pathways in vertebrate cell volume regulation. Contrib Nephrol 152:54–104

Hosseinzadeh Z, Bhavsar SK, Shojaiefard M, Saxena A, Merches K, Sopjani M, Alesustan I, Lang F (2011) Stimulation of the glucose carrier SGLT1 by JAK2. Biochem Biophys Res Commun 408:208–213

Jensen LR, Chen W, Moser B, Lipkowitz B, Schroeder C, Musante L, Tzschach A, Kalscheuer VM, Meloni I, Raynaud M, van Esch H, Chelly J, de Brouwer AP, Hackett A, van der Haar S, Henn W, Gecz J, Riess O, Bonin M, Reinhardt R, Ropers HH, Kuss AW (2011) Hybridisation-based resequencing of 17 X-linked intellectual disability genes in 135 patients reveals novel mutations in ATRX, SLC6A8 and PQBP1. Eur J Hum Genet 19:717–720

Kurdi M, Booz GW (2009) JAK redux: a second look at the regulation and role of JAKs in the heart. Am J Physiol Heart Circ Physiol 297:H1545–H1556

Li H, Thali RF, Smolak C, Gong F, Alzamora R, Wallimann T, Scholz R, Pastor-Soler NM, Neumann D, Hallows KR (2010) Regulation of the creatine transporter by AMP-activated protein kinase in kidney epithelial cells. Am J Physiol Renal Physiol 299:F167–F177

Loike JD, Zalutsky DL, Kaback E, Miranda AF, Silverstein SC (1988) Extracellular creatine regulates creatine transport in rat and human muscle cells. Proc Natl Acad Sci USA 85:807–811

Longo N, Ardon O, Vanzo R, Schwartz E, Pasquali M (2011) Disorders of creatine transport and metabolism. Am J Med Genet C Semin Med Genet 157:72–78

Lopez AF, Hercus TR, Ekert P, Littler DR, Guthridge M, Thomas D, Ramshaw HS, Stomski F, Perugini M, D'Andrea R, Grimbaldeston M, Parker MW (2010) Molecular basis of cytokine receptor activation. IUBMB Life 62:509–518

Mahfouz RA, Hoteit R, Salem Z, Bazarbachi A, Mugharbel A, Farhat F, Ziyadeh A, Ibrahim A, Taher A (2011) JAK2 V617F gene mutation in the laboratory work-up of myeloproliferative disorders: experience of a major referral center in Lebanon. Genet Test Mol Biomarkers 15:263–265

Mak CS, Waldvogel HJ, Dodd JR, Gilbert RT, Lowe MT, Birch NP, Faull RL, Christie DL (2009) Immunohistochemical localisation of the creatine transporter in the rat brain. Neuroscience 163: 571–585

Mancardi MM, Caruso U, Schiaffino MC, Baglietto MG, Rossi A, Battaglia FM, Salomons GS, Jakobs C, Zara F, Veneselli E, Gaggero R (2007) Severe epilepsy in X-linked creatine transporter defect (CRTR-D). Epilepsia 48:1211–1213

Mellott TJ, Kowall NW, Lopez-Coviella I, Blusztajn JK (2007) Prenatal choline deficiency increases choline transporter expression in the septum and hippocampus during postnatal development and in adulthood in rats. Brain Res 1151:1–11

Mercimek-Mahmutoglu S, Connolly MB, Poskitt KJ, Horvath GA, Lowry N, Salomons GS, Casey B, Sinclair G, Davis C, Jakobs C, Stockler-Ipsiroglu S (2010) Treatment of intractable epilepsy in a female with SLC6A8 deficiency. Mol Genet Metab 101: 409–412

Mohamed MR, Alesutan I, Foller M, Sopjani M, Bress A, Baur M, Salama RH, Bakr MS, Mohamed MA, Blin N, Lang F, Pfister M (2010) Functional analysis of a novel I71 N mutation in the GJB2 gene among southern Egyptians causing autosomal recessive hearing loss. Cell Physiol Biochem 26:959–966

Morris DL, Rui L (2009) Recent advances in understanding leptin signaling and leptin resistance. Am J Physiol Endocrinol Metab 297:E1247–E1259

Nash SR, Giros B, Kingsmore SF, Rochelle JM, Suter ST, Gregor P, Seldin MF, Caron MG (1994) Cloning, pharmacological characterization, and genomic localization of the human creatine transporter. Recept Channels 2:165–174

Neubauer S, Remkes H, Spindler M, Horn M, Wiesmann F, Prestle J, Walzel B, Ertl G, Hasenfuss G, Wallimann T (1999) Downregulation of the Na^+-creatine cotransporter in failing human myocardium and in experimental heart failure. Circulation 100: 1847–1850

Oh ST, Gotlib J (2010) JAK2 V617F and beyond: role of genetics and aberrant signaling in the pathogenesis of myeloproliferative neoplasms. Expert Rev Hematol 3:323–337

Omerovic E, Bollano E, Lorentzon M, Walser M, Mattsson-Hulten L, Isgaard J (2003) Growth hormone induces myocardial expression of creatine transporter and decreases plasma levels of IL-1beta in rats during early post-infarct cardiac remodeling. Growth Horm IGF Res 13:239–245

Pardanani A, Vannucchi AM, Passamonti F, Cervantes F, Barbui T, Tefferi A (2011) JAK inhibitor therapy for myelofibrosis: critical assessment of value and limitations. Leukemia 25:218–225

Pasantes-Morales H, Cruz-Rangel S (2010) Brain volume regulation: osmolytes and aquaporin perspectives. Neuroscience 168: 871–884

Puusepp H, Kall K, Salomons GS, Talvik I, Mannamaa M, Rein R, Jakobs C, Ounap K (2009) The screening of SLC6A8 deficiency among Estonian families with X-linked mental retardation. J Inherit Metab Dis. doi:10.1007/s10545-008-1063-y

Rexhepaj R, Dermaku-Sopjani M, Gehring EM, Sopjani M, Kempe DS, Foller M, Lang F (2010) Stimulation of electrogenic glucose

transport by glycogen synthase kinase 3. Cell Physiol Biochem 26:641–646

Rosenberg EH, Martinez MC, Betsalel OT, van Dooren SJ, Fernandez M, Jakobs C, Degrauw TJ, Kleefstra T, Schwartz CE, Salomons GS (2007) Functional characterization of missense variants in the creatine transporter gene (SLC6A8): improved diagnostic application. Hum Mutat 28:890–896

Salomons GS, van Dooren SJ, Verhoeven NM, Marsden D, Schwartz C, Cecil KM, Degrauw TJ, Jakobs C (2003) X-linked creatine transporter defect: an overview. J Inherit Metab Dis 26:309–318

Santos FP, Verstovsek S (2011) JAK2 inhibitors: what's the true therapeutic potential? Blood Rev 25:53–63

Shojaiefard M, Christie DL, Lang F (2005) Stimulation of the creatine transporter SLC6A8 by the protein kinases SGK1 and SGK3. Biochem Biophys Res Commun 334:742–746

Shojaiefard M, Christie DL, Lang F (2006) Stimulation of the creatine transporter SLC6A8 by the protein kinase mTOR. Biochem Biophys Res Commun 341:945–949

Skelton MR, Schaefer TL, Graham DL, Degrauw TJ, Clark JF, Williams MT, Vorhees CV (2011) Creatine transporter (CrT; Slc6a8) knockout mice as a model of human CrT deficiency. PLoS ONE 6:e16187

Sora I, Richman J, Santoro G, Wei H, Wang Y, Vanderah T, Horvath R, Nguyen M, Waite S, Roeske WR (1994) The cloning and expression of a human creatine transporter. Biochem Biophys Res Commun 204:419–427

Speer O, Neukomm LJ, Murphy RM, Zanolla E, Schlattner U, Henry H, Snow RJ, Wallimann T (2004) Creatine transporters: a reappraisal. Mol Cell Biochem 256–257:407–424

Spivak JL (2010) Thrombocytosis, polycythemia vera, and JAK2 mutations: the phenotypic mimicry of chronic myeloproliferation. Ann Intern Med 152:300–306

Stockler S, Schutz PW, Salomons GS (2007) Cerebral creatine deficiency syndromes: clinical aspects, treatment and pathophysiology. Subcell Biochem 46:149–166

Strutz-Seebohm N, Shojaiefard M, Christie D, Tavare J, Seebohm G, Lang F (2007) PIKfyve in the SGK1 mediated regulation of the creatine transporter SLC6A8. Cell Physiol Biochem 20:729–734

Takenaka M, Bagnasco SM, Preston AS, Uchida S, Yamauchi A, Kwon HM, Handler JS (1995) The canine betaine gamma-amino-*n*-butyric acid transporter gene: diverse mRNA isoforms are regulated by hypertonicity and are expressed in a tissue-specific manner. Proc Natl Acad Sci USA 92:1072–1076

Tefferi A (2010) Novel mutations and their functional and clinical relevance in myeloproliferative neoplasms: JAK2, MPL, TET2, ASXL1, CBL, IDH, and IKZF1. Leukemia 24:1128–1138

Tefferi A, Skoda R, Vardiman JW (2009) Myeloproliferative neoplasms: contemporary diagnosis using histology and genetics. Nat Rev Clin Oncol 6:627–637

Tran TT, Dai W, Sarkar HK (2000) Cyclosporin A inhibits creatine uptake by altering surface expression of the creatine transporter. J Biol Chem 275:35708–35714

Uchida S, Kwon HM, Yamauchi A, Preston AS, Marumo F, Handler JS (1992) Molecular cloning of the cDNA for an MDCK cell Na^+- and Cl^--dependent taurine transporter that is regulated by hypertonicity. Proc Natl Acad Sci USA 89:8230–8234

van de Kamp JM, Mancini GM, Pouwels PJ, Betsalel OT, van Dooren SJ, de Koning I, Steenweg ME, Jakobs C, van der Knaap MS, Salomons GS (2011) Clinical features and X-inactivation in females heterozygous for creatine transporter defect. Clin Genet 79:264–272

Wang W, Jobst MA, Bell B, Zhao CR, Shang LH, Jacobs DO (2002) Cr supplementation decreases tyrosine phosphorylation of the CreaT in skeletal muscle during sepsis. Am J Physiol Endocrinol Metab 282:E1046–E1054

Yokota I, Hayashi H, Matsuda J, Saijo T, Naito E, Ito M, Ebina Y, Kuroda Y (1998) Effect of growth hormone on the translocation of GLUT4 and its relation to insulin-like and anti-insulin action. Biochim Biophys Acta 1404:451–456

J Membrane Biol (2012) 245:165–176
DOI 10.1007/s00232-012-9426-6

ORIGINAL ARTICLES

Unsaturation of Mitochondrial Membrane Lipids is Related to Palmitate Oxidation in Subsarcolemmal and Intermyofibrillar Mitochondria

Graham P. Holloway · Val Andrew Fajardo · Lauren McMeekin · Paul J. LeBlanc

Received: 22 August 2011 / Accepted: 1 April 2012 / Published online: 18 April 2012

Abstract Membrane lipid composition is thought to influence the function of integral membrane proteins; however, the potential for lipid composition to influence overall mitochondrial long-chain fatty acids (LCFA) oxidation is currently unknown. Therefore, the naturally occurring variability of LCFA oxidation rates within subsarcolemmal (SS) and intermyofibrillar (IMF) mitochondria in muscles with varying oxidative potentials (heart → red → white) was utilized to examine this relationship. To this end, SS and IMF mitochondria were isolated and palmitate oxidation rates were compared to membrane phospholipid composition. Among tissues, rates of palmitate oxidation in mitochondria displayed a 2.5-fold range, creating the required range to determine potential relationships with membrane lipid composition. In general, the percent mole fraction of phospholipid head groups and major fatty acid subclasses were similar in all mitochondria studied. However, rates of palmitate oxidation were positively correlated with both the unsaturation index and relative abundance of cardiolipin within mitochondria ($r = 0.57$ and 0.49, respectively; $p < 0.05$). Thus, these results suggest that mitochondrial LCFA oxidation may be significantly influenced by the total unsaturation and percent mole fraction of cardiolipin of the mitochondrial membrane, whereas other indices of membrane structure (e.g., percent mole fraction of other predominant membrane phospholipids, chain length, and ratio of phosphatidylcholine to phosphatidylethanolamine) were not significantly correlated.

Keywords Cardiac muscle · Cardiolipin · LCFA oxidation · Lipid composition · Mitochondrial membranes · Red muscle · Unsaturation index · White muscle

G. P. Holloway
Department of Human Health and Nutritional Sciences, University of Guelph, Guelph, ON, Canada

V. A. Fajardo · L. McMeekin · P. J. LeBlanc (✉)
Centre for Bone and Muscle Health, Faculty of Applied Health Sciences, Brock University, 500 Glenridge Avenue, St. Catharines, ON L2S 3A1, Canada
e-mail: pleblanc@brocku.ca

In both skeletal and cardiac muscle, the oxidation of long-chain fatty acids (LCFA) represents a substantial contribution of the reducing equivalents required for the maintenance of adenosine triphosphate homeostasis, a process that exclusively occurs within the mitochondrial matrix. Regardless of the restricted location of LCFA oxidation, over the past two decades evidence has accumulated to show that rates of fatty acid oxidation within muscle is regulated at several sites, including the transport of LCFA across both the sarcolemmal (reviewed in Glatz et al. 2010) and mitochondrial membranes (Fritz and Yue 1963; Smith et al. 2011; Winder et al. 1989). However, the understanding of potential mechanisms regulating fatty acid oxidation at the level of the mitochondria is in its infancy.

The regulation of mitochondrial LCFA oxidation has historically been ascribed to malonyl-CoA inhibition of carnitine palmitoyltransferase I (CPTI) (Saggerson and Carpenter 1981; Winder et al. 1989). However, it is now recognized that the malonyl-CoA/CPTI axis cannot entirely account for the regulation of LCFA oxidation (Alkhateeb et al. 2011; Dzamko et al. 2008; Odland et al. 1996, 1998; Roepstorff et al. 2004). As a result, in recent years a renewed interest has emerged to unravel novel sites of regulation in mitochondrial fatty acid oxidation. Since then, several additional sites of regulation have been found, including, but not limited to, fatty acid translocase (FAT/CD36) suggested interaction with acyl-CoA synthetase

(Smith et al. 2011); NAD-dependent deacetylase sirtuin-3 deacetylation of long-chain acyl CoA dehydrogenase (Hirschey et al. 2010); and complex I of the electron transport chain (Ahn et al. 2008).

Creating another level of complexity within muscle is the fact there are two spatially distinct mitochondrial subpopulations, known as subsarcolemmal (SS) and intermyofibrillar (IMF) because they are located directly beneath the sarcolemmal membrane and between the myofibrillar apparatus, respectively. These mitochondrial subpopulations are known to have different characteristics, including size and various enzymatic activities, both of which may account for the higher rates of LCFA oxidation within IMF mitochondria (Cogswell et al. 1993; Holloway et al. 2009a, 2010; Hoppel et al. 2002; Kelley et al. 2002; Palmer et al. 1985). In addition to these reported differences between mitochondrial subpopulations, additional mechanisms that regulate LCFA oxidation within muscle mitochondria, including the unsaturation index (UI) of the mitochondrial membranes, may exist. However, to date the influence of membrane saturation in SS and IMF mitochondrial LCFA oxidation has not been examined in skeletal or cardiac muscles.

Although most of the regulation of mitochondrial LCFA oxidation studied to date involves integral mitochondrial membrane proteins, structural properties of membranes can also influence fundamental physiological processes, and changes in membrane phospholipid or fatty acid composition can influence integral membrane protein function (Lee 2004; McIntosh and Simon 2006). Specifically, lower phosphatidylcholine (PC) and cardiolipin (CL), higher phosphatidylethanolamine (PE), and fatty acid chain length and degree of saturation (Spector and Yorek 1985), and lower PC/PE ratio (Hazel and Williams 1990) are all positively correlated with membrane rigidity. In the context of LCFA oxidation, it has previously been shown that membrane UI is positively related to CPTI activity in hepatic mitochondria (Power et al. 1994). However, it remains to be determined whether these potential relationships exist in muscle mitochondria.

Past studies have successfully utilized diet manipulation (altering fat composition but not content) to alter SS and IMF cardiac mitochondrial membrane lipid composition (Khairallah et al. 2010a, b; O'Shea et al. 2009). However, this is no evidence in the literature to suggest that this approach is effective in skeletal muscle. Therefore, in the current study we took a different approach and utilized the naturally occurring variation of intrinsic rates of LCFA oxidation within SS and IMF mitochondria in muscles with varying oxidative potentials (white, red, and cardiac muscles) to examine the potential that mitochondrial membrane lipid composition is associated with rates of LCFA oxidation. Specifically, we hypothesized that greater rates of LCFA oxidation would correlate with mitochondria with higher membrane contents of PC, CL, and PC/PE, and lower PE, and shorter and more unsaturated fatty acids.

Methods

Animals

Male Sprague Dawley rats (250–300 g, $n = 5$) were used. The rats were housed in a controlled environment on a reverse 12:12 h light–dark cycle. Animals were provided with standard rat chow (Teklad Global 18 % Protein Rodent Diet; Harland Laboratories, Madison, WI; ingredients include ground wheat, ground corn, wheat middlings, dehulled soybean meal, corn gluten meal, and soybean oil fortified with essential vitamins and minerals, resulting in a percent weight contribution of 18.6 % protein, 75.2 % carbohydrates, and 6.2 % fat, which was made up predominately of 3.1 % linoleic, 1.2 % oleic, 0.7 % palmitic, 0.3 % linolenic, and 0.2 % steric) and water ad libitum. Ethical approval for this work was obtained from the Animal Care Committee at the University of Guelph and conformed to all Canadian Council on Animal Care guidelines.

Tissue Collection and Mitochondrial Isolation

Animals were euthanized [pentobarbital sodium (Somnotol), 6 mg/100 g body wt]. Heart (left ventricle) and red (red gastrocnemius and red vastus lateralis) and white (white gastrocnemius and white vastus lateralis) muscles from both hind limbs were excised and used for whole muscle determinants of citrate synthase (CS) and isolation of SS and IMF mitochondria as described below.

Citrate Synthase

Muscle samples ($\sim$10 mg wet tissue) were homogenized in 100 vol/wt of a 100 mM potassium phosphate buffer, while isolated mitochondria were diluted 20$\times$ in a sucrose mannitol buffer, for the measurements of CS. Total CS activity was assayed spectrophotometrically at 412 nm (37 °C) after ensuring intact mitochondria were lysed with 0.04 % Triton X-100 and repeated freeze-thawing (Srere 1969).

Mitochondrial Isolation

Differential centrifugation was used to obtain both SS and IMF mitochondrial fractions (Benton et al. 2008; Bezaire et al. 2004; Campbell et al. 2004). All procedures were identical to those previously published by our group

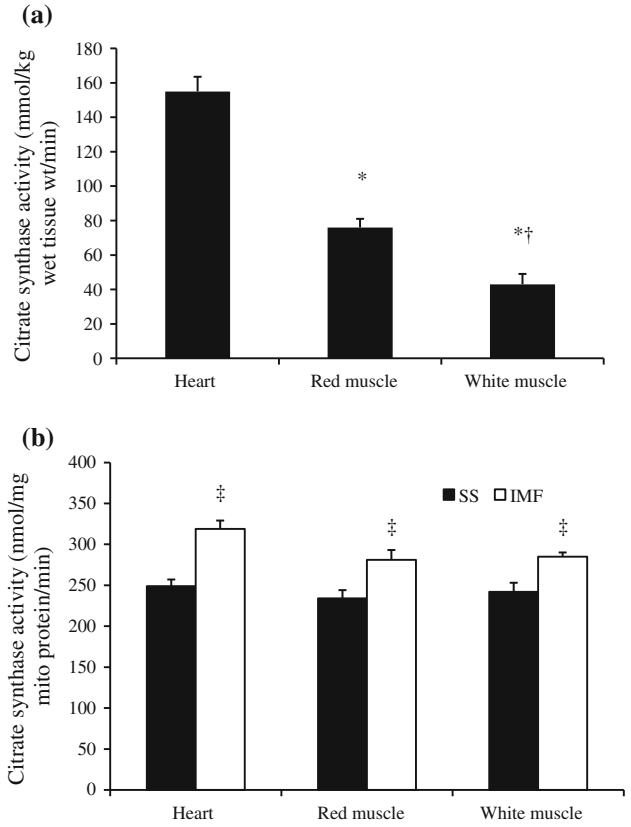

Fig. 1 Maximal citrate synthase (CS) activity in **a** whole muscle homogenates and **b** isolated subsarcolemmal (SS) and intermyofibrillar (IMF) mitochondria from rat heart, red (gastrocnemius), and white (gastrocnemius) muscle. Values are means ± SE ($n = 5$); *and †denote significance from heart and red muscle, respectively; ‡ denotes significance from SS mitochondria within the same tissue

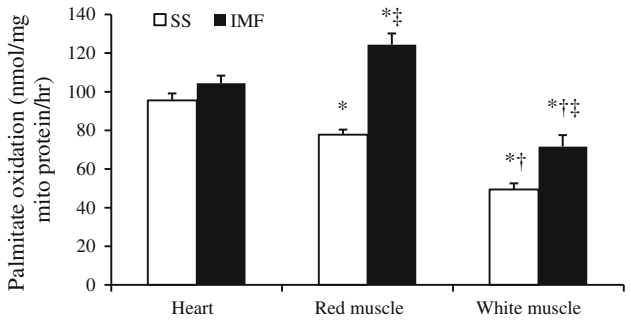

Fig. 2 In vitro palmitate oxidation rates in subsarcolemmal (SS) and intermyofibrillar (IMF) mitochondria in rat heart, red (gastrocnemius and vastus lateralis), and white (gastrocnemius and vastus lateralis) muscle. Values are means ± SE ($n = 5$); *and †denote significance from heart and red muscle, respectively, within the same mitochondrial subpopulation; ‡denotes significance from SS mitochondria within the same tissue

(Bezaire et al. 2006; Campbell et al. 2004; Holloway et al. 2006). Briefly, muscle was homogenized with a Polytron (PT3100, Kinematica) for exactly 5 s at a setting of 7. The

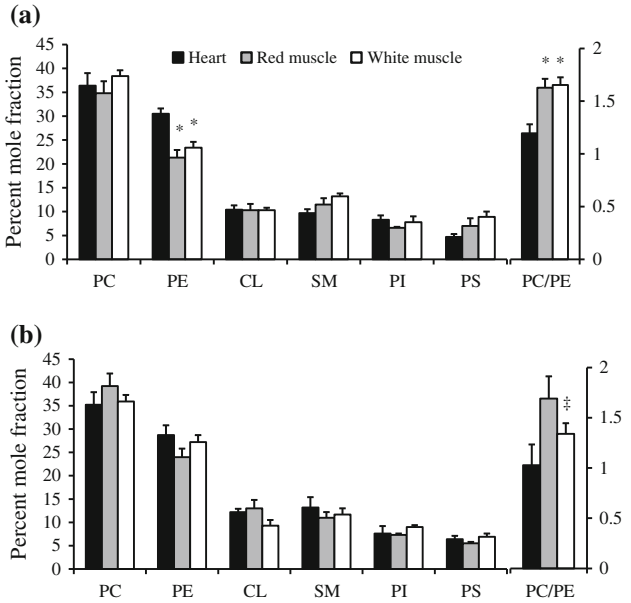

Fig. 3 Percent mole fraction of major phospholipid species of **a** subsarcolemmal and **b** intermyofibrillar mitochondrial membranes in rat heart, red (gastrocnemius and vastus lateralis), and white (gastrocnemius and vastus lateralis) muscle. Values are expressed as means ± SE ($n = 5$); *denotes significance from heart within the same mitochondrial subpopulation, ‡denotes significance from subsarcolemmal (SS) mitochondria within the same tissue. *PC* phosphatidylcholine, *PE phosphatidylethanolamine*, *CL* cardiolipin, *PI* phosphatidylinositol, *SM* sphingomyelin, *PS* phosphatidylserine

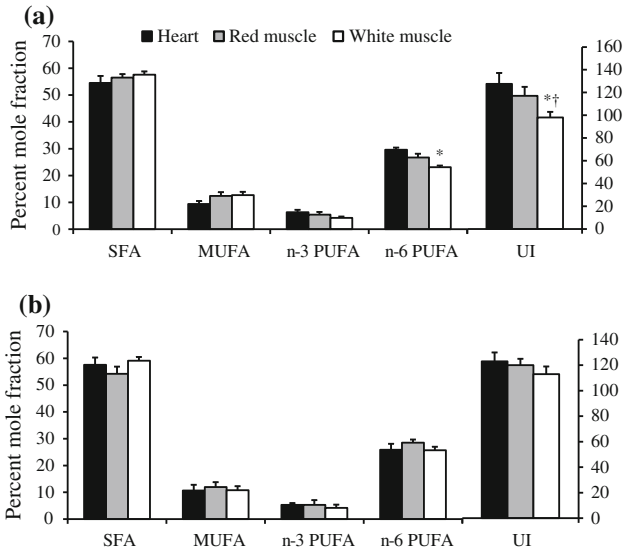

Fig. 4 Percent mole fraction of total fatty acid subclasses of total phospholipids of **a** subsarcolemmal and **b** intermyofibrillar mitochondrial membranes in rat heart, red (gastrocnemius and vastus lateralis), and white (gastrocnemius and vastus lateralis) muscle. Values are expressed as means ± SE ($n = 5$) with SFA, MUFA, n3, and n6 represented on the left y-axis and UI represented on the right. *SFA* saturated fatty acids, *MUFA* monounsaturated fatty acids, *PUFA* polyunsaturated fatty acids, *UI* unsaturation index $= \sum m_i \times n_i$, where m_i is the mole percent and n_i is the number of carbon–carbon double bonds of the fatty acid

Table 1 Percent mole fraction of total phospholipid fatty acids of subsarcolemmal (SS) and intermyofibrillar (IMF) mitochondrial membranes in rat heart, red (gastrocnemius and vastus lateralis), and white (gastrocnemius and vastus lateralis) muscle

Fatty acid	Heart		Red muscle		White muscle	
	SS	IMF	SS	IMF	SS	IMF
14:0	2.2 ± 0.3	2.6 ± 0.2	3.2 ± 0.4	2.7 ± 0.2	3.9 ± 0.8	2.6 ± 0.4
15:0	1.3 ± 0.2	1.5 ± 0.2	1.9 ± 0.3	1.5 ± 0.1	2.2 ± 0.4	1.7 ± 0.2
16:0	18.3 ± 1.2	21.0 ± 1.1	26.5 ± 1.0*	25.4 ± 1.0	24.7 ± 3.3*	24.5 ± 3.2
17:0	1.9 ± 0.2	2.4 ± 0.4	2.6 ± 0.3	2.3 ± 0.3	2.7 ± 0.3	2.7 ± 0.2
18:0	24.8 ± 0.6	27.0 ± 0.7	19.5 ± 0.3*	19.7 ± 0.7*	16.2 ± 2.0*	19.2 ± 1.8*
14:1	1.4 ± 0.4	1.3 ± 0.2	2.1 ± 0.5	1.3 ± 0.2	3.6 ± 2.0	1.3 ± 0.2
16:1	1.7 ± 0.4	2.3 ± 0.6	2.6 ± 0.3*	2.4 ± 0.3	3.4 ± 0.4*	2.4 ± 0.7
18:1	3.6 ± 0.3	4.0 ± 0.3	4.5 ± 0.7	6.3 ± 2.4	6.6 ± 1.6	4.1 ± 0.8
22:6n3	5.3 ± 0.4	4.8 ± 0.5	4.5 ± 0.6	4.5 ± 0.3	2.7 ± 0.4	3.1 ± 0.6
18:2n6	14.2 ± 1.8	11.6 ± 1.0	14.0 ± 0.7	15.4 ± 0.9	9.6 ± 1.5* †	10.6 ± 1.6
18:3n6	1.4 ± 0.3	1.7 ± 0.3	1.3 ± 0.3	1.3 ± 0.3	1.5 ± 0.2	3.3 ± 1.4
20:4n6	11.9 ± 1.7	12.0 ± 1.1	9.1 ± 0.8	9.3 ± 0.5	7.0 ± 1.3*	8.7 ± 1.1
Chain length	16.7 ± 0.1	16.8 ± 0.1	16.5 ± 0.1	16.7 ± 0.1	16.7 ± 0.1	16.7 ± 0.1

Values are expressed as means ± SE

Fatty acids with a percent mole fractions below 1 % are not shown

SS subsarcolemmal mitochondria, *IMF* intermyofibrillar mitochondria, *UI* unsaturation index = $\sum m_i \times n_i$, where m_i is the mole percent and n_i is the number of carbon–carbon double bonds of the fatty acid

* and † denote significance from heart and red muscle, respectively, within the same mitochondrial subpopulation

Table 2 Percent mole fraction of phosphatidylcholine fatty acids of subsarcolemmal (SS) and intermyofibrillar (IMF) mitochondrial membranes in rat heart, red (gastrocnemius and vastus lateralis), and white (gastrocnemius and vastus lateralis) muscle

Fatty acid	Heart		Red muscle		White muscle	
	SS	IMF	SS	IMF	SS	IMF
14:0	1.3 ± 0.3	1.3 ± 0.1	1.4 ± 0.2	1.3 ± 0.1	1.7 ± 0.2	1.4 ± 0.1
15:0	1.0 ± 0.1	1.0 ± 0.1	1.0 ± 0.1	1.0 ± 0.1	1.0 ± 0.1	1.1 ± 0.2
16:0	24.1 ± 1.0	24.2 ± 0.9	38.8 ± 0.8*	37.3 ± 1.1*	42.5 ± 1.0* †	39.7 ± 3.2*
17:0	1.1 ± 0.1	1.3 ± 0.1	1.4 ± 0.2	1.3 ± 0.1	1.5 ± 0.1	1.4 ± 0.1
18:0	26.5 ± 0.7	28.0 ± 0.4	11.2 ± 0.5*	10.5 ± 0.8*	8.4 ± 0.2* †	7.1 ± 0.6* †
16:1	1.2 ± 0.3	1.6 ± 0.3	1.8 ± 0.3	1.5 ± 0.4	2.0 ± 0.6	2.3 ± 0.5
18:1	3.2 ± 0.1	3.4 ± 0.3	4.0 ± 0.2	4.8 ± 1.1	3.3 ± 0.8	3.6 ± 0.4
22:6n3	2.9 ± 0.1	2.8 ± 0.2	2.6 ± 0.3	2.8 ± 0.2	2.0 ± 0.5	1.4 ± 0.2
18:2n6	12.9 ± 0.5	13.1 ± 1.0	18.2 ± 1.0*	19.6 ± 1.0*	16.4 ± 0.2*	16.0 ± 1.4
20:4n6	20.0 ± 1.5	18.8 ± 0.8	13.7 ± 0.6*	14.4 ± 0.7*	13.5 ± 0.8*	13.3 ± 1.2*
Total saturates	55.4 ± 1.7	58.0 ± 1.7	56.2 ± 1.6	52.6 ± 1.4*	56.8 ± 1.0	56.1 ± 0.9
Total monoenes	6.5 ± 1.0	6.7 ± 0.8	7.6 ± 0.3	7.6 ± 1.2	7.0 ± 0.5	7.8 ± 0.6
n3 polyenes	3.2 ± 0.2	3.1 ± 0.3	3.1 ± 0.3	3.4 ± 0.3	3.5 ± 1.1	2.0 ± 0.2* †
n6 polyenes	34.8 ± 1.7	32.2 ± 1.6	34.3 ± 1.5	36.3 ± 1.5	32.7 ± 0.7	34.0 ± 0.7
UI	136 ± 7	130 ± 6	122 ± 6	129 ± 5	119 ± 4	128 ± 12
Chain length	17.3 ± 0.1	17.3 ± 0.1	16.9 ± 0.1*	16.9 ± 0.1*	16.9 ± 0.1*	17.0 ± 0.1*

Values are expressed as means ± SE

Fatty acids with a percent mole fraction below 1 % are not shown

SS subsarcolemmal mitochondria, *IMF* intermyofibrillar mitochondria, *UI* unsaturation index = $\sum m_i \times n_i$, where m_i is the mole percent and n_i is the number of carbon–carbon double bonds of the fatty acid

* and † denote significance from heart and red muscle, respectively, within the same mitochondrial subpopulation

Table 3 Percent mole fraction of phosphatidylethanolamine fatty acids of subsarcolemmal (SS) and intermyofibrillar (IMF) mitochondrial membranes in rat heart, red (gastrocnemius and vastus lateralis), and white (gastrocnemius and vastus lateralis) muscle

Fatty acid	Heart		Red muscle		White muscle	
	SS	IMF	SS	IMF	SS	IMF
14:0	1.5 ± 0.1	2.0 ± 0.1‡	2.0 ± 0.2	2.0 ± 0.2	2.3 ± 0.4	2.2 ± 0.3
15:0	1.0 ± 0.2	1.0 ± 0.3	1.5 ± 0.3	1.1 ± 0.2	1.9 ± 0.2*	1.4 ± 0.2
16:0	15.2 ± 1.1	16.7 ± 0.9	14.0 ± 1.2	13.2 ± 0.6*	15.6 ± 0.5	14.2 ± 0.7
17:0	1.7 ± 0.2	1.9 ± 0.2	1.9 ± 0.2	1.7 ± 0.2	2.3 ± 0.3	1.9 ± 0.2
18:0	34.3 ± 1.2	34.5 ± 0.3	36.6 ± 1.0	38.2 ± 1.1*	34.0 ± 1.4	36.9 ± 0.6
16:1	1.1 ± 0.3	1.2 ± 0.4	1.1 ± 0.2	1.3 ± 0.3	1.8 ± 0.6	1.1 ± 0.5
17:1	1.0 ± 0.1	1.2 ± 0.1	1.1 ± 0.1	1.0 ± 0.1	1.1 ± 0.2	1.0 ± 0.1
18:1	3.8 ± 0.1	3.8 ± 0.1	3.7 ± 0.1	5.4 ± 1.5	6.1 ± 2.3	4.1 ± 0.2
22:6n3	12.4 ± 1.0	10.7 ± 0.9	11.7 ± 1.2	11.5 ± 0.4	6.2 ± 0.4* †	8.9 ± 0.9‡
18:2n6	7.7 ± 0.3	7.4 ± 0.6	9.0 ± 0.6	8.0 ± 0.8	6.8 ± 0.2 †	7.7 ± 0.2‡
18:3n6	1.2 ± 0.7	1.0 ± 0.3	1.0 ± 0.3	1.1 ± 0.2	1.0 ± 0.3	1.2 ± 0.2
20:4n6	13.1 ± 3.3	13.8 ± 0.9	11.3 ± 0.5	10.7 ± 0.8	11.4 ± 0.8	13.6 ± 0.7 †
Total saturates	57.2 ± 3.5	59.1 ± 1.3	59.0 ± 1.7	57.7 ± 1.6	59.4 ± 1.7	59.3 ± 1.0
Total monoenes	7.3 ± 0.5	8.3 ± 0.7	7.6 ± 0.1	9.0 ± 1.8	11.2 ± 2.9	7.9 ± 0.6
n3 polyenes	12.7 ± 0.9	10.5 ± 0.7	12.3 ± 1.2	12.0 ± 0.4	7.4 ± 0.2* †	9.2 ± 0.8 †
n6 polyenes	22.8 ± 2.8	22.1 ± 0.7	22.5 ± 1.2	21.4 ± 1.3	21.8 ± 1.3	23.5 ± 0.8
UI	156 ± 15	149 ± 9‡	149 ± 9	146 ± 4	121 ± 2	138 ± 6
Chain length	15.7 ± 0.1	16.0 ± 0.1	15.7 ± 0.2	15.7 ± 0.1	16.7 ± 0.1* †	16.2 ± 0.1 †

Values are expressed as means ± SE

Fatty acids with a percent mole fractions below 1 % are not shown

SS subsarcolemmal mitochondria, *IMF* intermyofibrillar mitochondria, *UI* unsaturation index = $\sum m_i \times n_i$, where m_i is the mole percent and n_i is the number of carbon–carbon double bonds of the fatty acid

‡ Denotes significance from SS within the same tissue

* and † denote significance from heart and red muscle, respectively, within the same mitochondrial subpopulation

homogenate was centrifuged at 800×*g* for 10 min to separate the SS and IMF mitochondria. The IMF mitochondria were released by treating the pellet with a protease (0.025 ml/g Subtilisin A (P-5380); Sigma, St. Louis, MO, USA) for exactly 5 min to digest the myofibrils. Further centrifugation was used to remove the myofibrils, and mitochondria were finally recovered by centrifuging twice at 10,000×*g* for 10 min and resuspending the final pellet in 500 µl of buffer (220 mM sucrose, 70 mM mannitol, 10 mM Tris HCl, and 1 mM EDTA). A portion of the mitochondria (200 µl) was used immediately for determinations of palmitate oxidation, while the remaining mitochondrial protein was purified through the use of a Percoll gradient (Benton et al. 2004) and frozen for future phospholipid analyses. Mitochondrial protein concentration was determined by bicinchoninic acid assay.

Mitochondrial Palmitate Oxidation

Palmitate oxidation was measured in a sealed system, as described previously (Benton et al. 2008; Holloway et al. 2009b). Briefly, mitochondria were added to a pregassed modified Krebs-Ringer buffer at 37 °C. The reaction (30 min) was initiated by addition of palmitate–bovine serum albumin complex (75 µM, 1-[^{14}C]palmitate [0.5 µCi/vial, 30 min, 37 °C, pH 7.4]). Oxidation was determined from trapping of the $^{14}CO_2$ produced and the ^{14}C label released from acidified buffer, as we have reported previously (Benton et al. 2008; Campbell et al. 2004; Holloway et al. 2009b; Yoshida et al. 2007).

Phospholipid Analysis

Total lipids were extracted (Folch et al. 1957), and thin-layer chromatography (Mahadevappa and Holub 1987) was used to separate individual phospholipids (PC, PE, CL, phosphatidylinositol, phosphatidylserine, phosphatidic acid, sphingomyelin) from isolated SS and IMF mitochondria. Briefly, isolated phospholipids were methylated (Mahadevappa and Holub 1987), and the fatty acid composition of each phospholipid was analyzed by gas chromatography (Bradley et al. 2008; Stefanyk et al. 2010). A 0.1–1.0 µl sample of methyl esters from each sample was injected into a gas chromatograph (Trace GC Ultra, Thermo Electron, Milan,

Table 4 Percent mole fraction of cardiolipin fatty acids of subsarcolemmal (SS) and intermyofibrillar (IMF) mitochondrial membranes in rat heart, red (gastrocnemius and vastus lateralis), and white (gastrocnemius and vastus lateralis) muscle

Fatty acid	Heart		Red muscle		White muscle	
	SS	IMF	SS	IMF	SS	IMF
14:0	2.5 ± 0.3	4.3 ± 0.8	4.4 ± 0.8	3.1 ± 0.2	6.5 ± 1.7	3.9 ± 0.2
15:0	1.7 ± 0.4	1.9 ± 0.3	3.0 ± 0.9	1.4 ± 0.1	3.2 ± 1.1	3.2 ± 0.8
16:0	11.7 ± 1.6	20.5 ± 3.6	14.5 ± 2.5	14.5 ± 1.5	17.4 ± 3.3	17.4 ± 1.7
17:0	2.4 ± 0.5	3.1 ± 0.4	3.2 ± 0.8	3.3 ± 0.7	2.8 ± 0.5	3.9 ± 0.3
18:0	5.8 ± 0.8	11.5 ± 1.4‡	6.8 ± 1.6	6.8 ± 0.5	7.6 ± 1.9	10.7 ± 1.4
16:1	2.5 ± 0.6	3.0 ± 0.5	2.9 ± 1.0	3.1 ± 0.6	5.7 ± 1.1	3.1 ± 0.8
18:1	3.9 ± 0.7	5.0 ± 1.5	7.5 ± 4.3	7.4 ± 3.6	10.0 ± 4.2	5.6 ± 1.6
18:2n6	57.8 ± 5.4	32.1 ± 9.1	34.9 ± 7.1*	38.3 ± 3.5	25.8 ± 5.7*	29.0 ± 7.8
18:3n6	2.2 ± 0.5	3.2 ± 1.8	1.4 ± 0.6	2.2 ± 1.2	1.3 ± 0.6	4.4 ± 1.9
20:3n6	1.3 ± 0.4	1.6 ± 0.6	1.8 ± 0.5	2.2 ± 1.0	1.3 ± 0.3	1.1 ± 0.5
Total saturates	26.5 ± 3.7	39.5 ± 6.4	35.7 ± 4.8	35.8 ± 4.0	42.5 ± 3.5	45.3 ± 5.2
Total monoenes	9.5 ± 1.6	11.0 ± 1.0	21.2 ± 5.4	15.5 ± 4.3	20.1 ± 5.7	15.4 ± 1.7
n3 polyenes	1.1 ± 0.1	1.2 ± 0.3	2.1 ± 0.5	2.0 ± 0.5	1.6 ± 0.5	2.1 ± 0.2
n6 polyenes	62.7 ± 5.0	48.3 ± 6.5	40.8 ± 6.4	46.6 ± 3.0	30.3 ± 6.2*	37.1 ± 6.3
UI	144 ± 9	118 ± 13	115 ± 9*	124 ± 7	98 ± 4*	105 ± 9
Chain length	17.4 ± 0.1	17.4 ± 0.1	17.1 ± 0.2	17.6 ± 0.1‡	17.1 ± 0.1	17.1 ± 0.1* †

Values are expressed as means ± SE. Fatty acids with a percent mole fractions below 1 % are not shown

SS subsarcolemmal mitochondria, *IMF* intermyofibrillar mitochondria, *UI* unsaturation index = $\sum m_i \times n_i$, where m_i is the mole percent and n_i is the number of carbon–carbon double bonds of the fatty acid

* and † denote significance from heart and red muscle, respectively, within the same mitochondrial subpopulation; ‡ denotes significance from SS within the same tissue

Italy) fitted with a split/splitless injector, a fast flame ionization detector, and Triplus AS autosampler (Trace GC Ultra, Thermo Electron). Fatty acid methyl esters were separated on a UFM RTX-WAX analytical column (Thermo Electron) using helium as a carrier gas. Fatty acids were identified by comparison of retention times with those of a known standard (Supelco 37 component FAME mix, Supelco, Bellefonte, PA), and absolute amounts of individual fatty acids were calculated with the aid of the internal standard, tridecanoic acid (13:0), added to the samples before the methylation process (Lepage and Roy 1986). Preliminary analyses indicated no detectable endogenous 13:0 in the samples analyzed (data not shown). The molar amount of each fatty acid was then used to calculate its relative percentage. Total amounts of each phospholipid were determined from the summed amount of fatty acids in each phospholipid. The UI was calculated as $\sum m_i \times n_i$, where m_i is the mole percentage and n_i is the number of carbon–carbon double bonds of the fatty acid.

Statistical Analysis

All values are expressed as the mean ± standard error (SE). Differences in CS activity were examined by an analysis of variance (ANOVA). A two-way ANOVA was used to establish differences between tissue and mitochondrial subpopulations for palmitate oxidation rates and membrane lipid composition data. Tukey's post hoc test was used to determine significance ($p < 0.05$). Assumption for normality were verified and data transformed (log, square root, and inverse square) to meet this assumption. Pearson correlations were used to test the relationship between palmitate oxidation rates and membrane lipid components. SPSS software (Chicago, IL) was used for all statistical analyses.

Results

Total CS and Mitochondrial Palmitate Oxidation Hierarchy

Total homogenate CS enzymatic activity displayed the expected hierarchy between heart → red → white muscles (Fig. 1a), confirming the oxidative potential of muscles subsequently used to isolate SS and IMF mitochondria. Isolated mitochondrial CS values were not significantly different between muscles, but were significantly higher in IMF mitochondria within tissues (Fig. 1b). In general, mitochondrial rates of palmitate oxidation displayed the

Table 5 Percent mole fraction of sphingomyelin fatty acids of subsarcolemmal (SS) and intermyofibrillar (IMF) mitochondrial membranes in rat heart, red (gastrocnemius and vastus lateralis), and white (gastrocnemius and vastus lateralis) muscle

Fatty acid	Heart		Red muscle		White muscle	
	SS	IMF	SS	IMF	SS	IMF
12:0	1.3 ± 0.3	1.8 ± 0.7	1.3 ± 0.3	1.6 ± 0.2	1.5 ± 0.1	1.3 ± 0.2
14:0	7.4 ± 0.6	8.3 ± 0.9	8.0 ± 0.4	7.5 ± 0.7	8.3 ± 0.4	7.7 ± 1.0
15:0	3.3 ± 0.3	4.0 ± 0.8	3.5 ± 0.3	3.7 ± 0.6	3.5 ± 0.3	4.0 ± 0.5
16:0	29.1 ± 2.6	23.0 ± 2.2	31.0 ± 1.0	26.3 ± 2.0	31.0 ± 1.0	23.9 ± 4.1
17:0	5.2 ± 0.4	5.1 ± 1.2	5.6 ± 0.5	5.0 ± 0.7	5.6 ± 0.5	4.5 ± 1.2
18:0	15.4 ± 0.6	10.5 ± 3.6	18.4 ± 0.5	17.2 ± 1.7	18.4 ± 0.5	23.5 ± 4.1
14:1	4.2 ± 0.4	4.0 ± 0.4	4.7 ± 0.4	3.8 ± 0.6	4.7 ± 0.4	6.7 ± 3.4
15:1	2.3 ± 0.2	2.2 ± 0.3	2.6 ± 0.1	2.1 ± 0.3	2.4 ± 0.2	2.1 ± 0.4
16:1	5.7 ± 1.6	6.3 ± 1.0	7.8 ± 1.3	7.1 ± 1.0	7.8 ± 1.3	5.3 ± 1.5
17:1	1.0 ± 0.2	1.8 ± 0.5	1.8 ± 0.3	1.0 ± 0.3	1.5 ± 0.2	2.0 ± 0.8
18:1	3.6 ± 1.0	10.1 ± 5.7	3.1 ± 1.1	9.9 ± 5.9	3.1 ± 1.1	4.6 ± 2.0
18:2n6	1.9 ± 0.4	1.3 ± 0.5	1.3 ± 0.4	3.2 ± 0.5‡	1.8 ± 0.5	1.9 ± 0.8
18:3n6	4.4 ± 1.9	5.7 ± 0.5	2.8 ± 1.1	2.7 ± 1.1	2.6 ± 0.7	3.5 ± 1.0
20:3n6	1.7 ± 0.6	2.1 ± 0.7	2.9 ± 0.5	2.1 ± 0.4	1.4 ± 0.4	1.5 ± 0.5
Total saturates	66.9 ± 2.9	62.0 ± 2.9	69.0 ± 2.9	63.2 ± 4.7	70.5 ± 1.9	68.5 ± 5.8
Total monoenes	17.8 ± 2.5	20.3 ± 2.7	19.4 ± 1.7	24.7 ± 5.5	20.8 ± 1.3	21.1 ± 5.3
n3 polyenes	4.6 ± 1.2	3.7 ± 1.1	2.2 ± 0.7	1.9 ± 0.5	1.1 ± 0.3	1.4 ± 0.5
n6 polyenes	10.4 ± 1.1	13.4 ± 1.1	8.7 ± 1.1	10.1 ± 1.2	7.5 ± 0.8	8.9 ± 0.8
UI	67 ± 8	69 ± 5	54 ± 7	60 ± 5	46 ± 3	51 ± 7
Chain length	16.6 ± 0.1	16.6 ± 0.1	16.6 ± 0.1	16.6 ± 0.1	16.4 ± 0.1	16.7 ± 0.2

[a] Values are expressed as means ± SE

Fatty acids with a percent mole fractions below 1 % are not shown

SS subsarcolemmal mitochondria, *IMF* intermyofibrillar mitochondria, *UI* unsaturation index = $\sum m_i \times n_i$, where m_i is the mole percent and n_i is the number of carbon–carbon double bonds of the fatty acid

* and † denote significance from heart and red muscle, respectively, within the same mitochondrial subpopulation; ‡ denotes significance from SS within the same tissue

expected hierarchy (heart → red → white), and as a result, rates of palmitate oxidation in mitochondria across all muscles displayed a 2.5-fold range (Fig. 2), creating the required continuum to determine potential relationships between membrane lipid composition and rates of mitochondrial fatty acid oxidation.

Membrane Lipid Composition

The hierarchy of the membrane lipid results presented is the phospholipid species independent of fatty acid subclasses (Fig. 3), the major fatty acids independent of phospholipid species in SS (Fig. 4a), and IMF (Fig. 4b) mitochondria, and finally a more in-depth examination of the individual fatty acids represented in individual phospholipid species.

In general, mitochondrial membrane phospholipid head group composition did not differ between tissues types or mitochondrial subpopulations, with the exception of heart SS mitochondria, which displayed higher relative abundance of PE and a lower PC/PE ratio compared to red and white muscle (Fig. 3), whereas SS mitochondria had a higher PC/PE compared to IMF mitochondria within white muscle. White muscle SS mitochondrial membranes had a lower relative abundance of n6 polyunsaturated fatty acid (Fig. 4a) compared to heart, which was mainly due to lower 18:2n6 and 20:4n6 (Table 1), and to lower UI compared to the other muscle tissues.

The fatty acid composition of the predominant (PC and PE) and mitochondrial-specific (CL) phospholipid species demonstrated unique trends between muscle types. PC of heart mitochondria demonstrated longer chain length, whereas red muscle IMF mitochondria had slightly less total saturates (mainly 18:0; Table 2). PE of white muscle mitochondria had longer chain lengths and less n3 polyunsaturates (mainly 22:6n3; Table 3), whereas CL of heart SS mitochondria had higher n6 polyunsaturates (mainly 18:2n6), resulting in a higher UI (Table 4) compared to other muscle types. Few differences were seen in the other phospholipid species (Tables 5, 6, 7).

Table 6 Percent mole fraction of phosphatidylinositol fatty acids of subsarcolemmal (SS) and intermyofibrillar (IMF) mitochondrial membranes in rat heart, red (gastrocnemius and vastus lateralis), and white (gastrocnemius and vastus lateralis) muscle

Fatty acid	Heart		Red muscle		White muscle	
	SS	IMF	SS	IMF	SS	IMF
14:0	5.7 ± 1.0	4.5 ± 1.1	6.3 ± 0.5	5.9 ± 0.3	4.2 ± 1.3	4.5 ± 0.8
15:0	2.7 ± 0.4	3.2 ± 0.3	3.1 ± 0.3	2.5 ± 0.3	2.2 ± 0.8	2.9 ± 0.5
16:0	15.8 ± 2.4	21.4 ± 2.7	24.1 ± 2.1	22.3 ± 2.3	17.8 ± 3.8	18.7 ± 1.9
17:0	3.5 ± 0.6	4.2 ± 0.8	4.6 ± 0.3	4.1 ± 0.5	4.4 ± 0.5	5.3 ± 0.3
18:0	26.8 ± 4.6	27.7 ± 4.3	26.4 ± 2.4	27.3 ± 2.1	21.6 ± 3.0	29.2 ± 3.9
14:1	5.7 ± 2.4	2.2 ± 0.5	3.3 ± 0.3	2.8 ± 0.3	1.9 ± 0.6	2.3 ± 0.5
15:1	1.8 ± 0.2	1.7 ± 0.3	2.0 ± 0.2	1.7 ± 0.2	1.2 ± 0.4	1.8 ± 0.3
16:1	2.4 ± 1.0	4.7 ± 1.0	5.5 ± 1.3	5.7 ± 1.1	2.5 ± 1.1	3.9 ± 0.8
18:1	5.5 ± 1.5	4.1 ± 1.1	4.2 ± 0.7	9.3 ± 4.8	10.5 ± 5.3	3.4 ± 1.0
20:3n3	5.3 ± 2.3	1.9 ± 0.8	4.5 ± 1.4	4.4 ± 0.8	2.2 ± 0.9	2.7 ± 1.1
18:2n6	1.7 ± 0.6	1.4 ± 0.4	2.0 ± 0.3	1.7 ± 0.2	1.6 ± 0.5	1.2 ± 0.3
18:3n6	2.5 ± 0.9	4.6 ± 0.6	2.1 ± 0.7	1.1 ± 0.7*	1.9 ± 0.5	3.7 ± 1.0 †
20:3n6	1.3 ± 0.5	1.9 ± 0.5	2.4 ± 0.1	2.2 ± 0.3	1.4 ± 0.2	1.9 ± 0.8
Total saturates	61.2 ± 3.7	65.0 ± 3.6	68.7 ± 2.0	66.5 ± 5.2	57.3 ± 9.5	69.9 ± 3.0
Total monoenes	18.3 ± 4.4	19.3 ± 1.8	17.0 ± 2.0	21.9 ± 4.9	22.9 ± 6.2	13.3 ± 2.5
n3 polyenes	5.3 ± 3.4	3.8 ± 1.4	2.1 ± 0.3	1.4 ± 0.3	3.7 ± 1.5	2.9 ± 1.2
n6 polyenes	15.1 ± 3.1	11.7 ± 0.7	11.9 ± 2.4	10.3 ± 1.4	15.1 ± 5.1	11.6 ± 2.5
UI	83 ± 9	66 ± 11	64 ± 8	61 ± 8	63 ± 13	61 ± 12
Chain length	17.2 ± 0.2	17.1 ± 0.2	16.9 ± 0.1	17.0 ± 0.1	16.7 ± 0.1	17.4 ± 0.2‡

Values are expressed as means ± SE

Fatty acids with a percent mole fractions below 1 % are not shown

SS subsarcolemmal mitochondria, *IMF* intermyofibrillar mitochondria, *UI* unsaturation index $= \sum m_i \times n_i$, where m_i is the mole percent and n_i is the number of carbon–carbon double bonds of the fatty acid

* and † denote significance from heart and red muscle, respectively, within the same mitochondrial subpopulation, ‡ denotes significance from SS within the same tissue

Relationship between Palmitate Oxidation Rate and Membrane Lipids

In SS and IMF mitochondria from heart, red, and white muscle, there was a significant positive correlation between palmitate oxidation rates and the UI ($r = 0.57$, $p < 0.05$, Fig. 5a). Rates of palmitate oxidation were also positively correlated with the percent mole fraction of CL ($r = 0.49$, $p < 0.05$, Fig. 5b). There were no significant correlations between palmitate oxidation and the percent mole fraction of other phospholipid head groups (PC, PE, sphingomyelin, phosphatidylinositol, and phosphatidylserine), average fatty acid chain length, or PC/PE ratio of mitochondrial membranes (data not shown).

Discussion

Our primary focus was to determine the potential association between rates of LCFA oxidation and membrane lipid composition in isolated mitochondria. We examined rates of fatty acid oxidation in SS and IMF mitochondria from muscles with variable oxidative capacities (heart, and red and white skeletal muscles) and related these values to membrane lipid composition. Our data demonstrate that regardless of subpopulation or muscle origin, mitochondria are similar in lipid composition, and that rates of mitochondrial palmitate oxidation are positively related to the lipid unsaturation and CL abundance. These data suggest that mitochondrial membrane lipid composition may influence mitochondrial substrate utilization in a structure–function relationship.

Mitochondrial Membrane Lipid Composition

In the current study, PC, PE, and CL comprised the majority of the phospholipid profiles in all mitochondria, accounting for ~80 % of the phospholipid content. This is comparable to what we (Stefanyk et al. 2010) and others (Daum 1985) have previously reported. However, previous literature has exclusively examined SS mitochondrial lipid composition, and to our knowledge this is the first report

Table 7 Percent mole fraction of phosphatidylserine fatty acids of subsarcolemmal (SS) and intermyofibrillar (IMF) mitochondrial membranes in rat heart, red (gastrocnemius and vastus lateralis), and white (gastrocnemius and vastus lateralis) muscle

Fatty acid	Heart		Red muscle		White muscle	
	SS	IMF	SS	IMF	SS	IMF
12:0	2.4 ± 0.5	1.8 ± 0.5	1.7 ± 0.3	1.7 ± 0.3	1.1 ± 0.2	1.2 ± 0.3
14:0	7.0 ± 0.6	7.3 ± 1.1	8.4 ± 0.7	6.7 ± 0.7	5.1 ± 1.2	4.9 ± 1.3
15:0	3.3 ± 0.3	3.6 ± 0.3	4.5 ± 0.5	3.0 ± 0.5‡	2.9 ± 0.9	2.4 ± 0.5
16:0	25.2 ± 2.1	25.6 ± 3.0	24.9 ± 1.6	26.5 ± 3.2	18.5 ± 3.7	23.4 ± 5.4
17:0	5.4 ± 0.7	5.6 ± 1.0	5.7 ± 0.3	4.6 ± 0.6*	3.7 ± 0.8	4.3 ± 0.4*
18:0	22.5 ± 3.3	22.7 ± 4.5	18.9 ± 2.1	20.4 ± 1.5	14.4 ± 3.1	21.4 ± 4.0
14:1	3.5 ± 0.7	3.5 ± 0.6	5.4 ± 0.7	3.6 ± 0.5	2.8 ± 0.6 †	2.3 ± 0.8
15:1	2.3 ± 0.2	2.0 ± 0.4	2.7 ± 0.2	2.0 ± 0.4	1.6 ± 0.3 †	1.5 ± 0.4
16:1	5.0 ± 1.0	5.4 ± 1.1	6.2 ± 1.3	4.7 ± 1.1	5.7 ± 1.5	4.0 ± 1.6
18:1	3.9 ± 1.2	3.6 ± 1.1	4.8 ± 0.7	11.0 ± 6.2	8.7 ± 5.4	7.5 ± 4.1
18:2n6	1.3 ± 0.8	0.9 ± 0.3	1.5 ± 0.1	2.0 ± 0.4	1.4 ± 0.3	1.0 ± 0.3
18:3n6	3.9 ± 0.4	3.6 ± 0.9	2.5 ± 0.9	3.1 ± 1.0	3.3 ± 0.6	5.5 ± 2.7
20:3n6	1.5 ± 0.6	2.1 ± 0.6	2.9 ± 0.5	2.2 ± 0.3	2.7 ± 0.5	5.5 ± 4.5
Total saturates	70.2 ± 3.4	67.2 ± 2.6	67.3 ± 2.7	65.5 ± 6.1	57.5 ± 5.5	73.8 ± 3.9‡
Total monoenes	16.9 ± 3.1	19.5 ± 2.5	21.1 ± 2.4	22.9 ± 6.4	22.5 ± 6.0	18.7 ± 3.5
n3 polyenes	2.3 ± 0.8	3.2 ± 0.7	3.2 ± 0.5	2.1 ± 0.6	5.1 ± 3.6	1.1 ± 0.1
n6 polyenes	10.4 ± 0.9	10.1 ± 0.8	8.1 ± 1.3	9.3 ± 1.0	15.8 ± 4.6	6.4 ± 1.3
UI	56 ± 3	54 ± 9	60 ± 5	59 ± 7	79 ± 20	60 ± 17
Chain length	16.7 ± 0.1	16.7 ± 0.1	16.5 ± 0.1	16.6 ± 0.1	17.1 ± 0.3	16.5 ± 0.3

Values are expressed as means ± SE

Fatty acids with a percent mole fractions below 1 % are not shown

SS subsarcolemmal mitochondria, *IMF* intermyofibrillar mitochondria, *UI* unsaturation index = $\sum m_i \times n_i$, where m_i is the mole percent and n_i is the number of carbon–carbon double bonds of the fatty acid

* and † denote significance from heart and red muscle, respectively, within the same mitochondrial subpopulation, ‡ denotes significance from SS within the same tissue

comparing membrane lipid analysis in SS and IMF mitochondria. In general, the lipid composition between SS and IMF mitochondria was similar across all muscles, and therefore the well-established observation that IMF mitochondria display higher rates of respiration cannot be explained by variances in lipid membrane composition. We have previously shown that the lipid composition of SS mitochondria from the soleus muscle differs from that isolated from either the red gastrocnemius or plantaris muscles (Stefanyk et al. 2010). Taken together with the current data, it appears that the soleus muscle may represent a unique muscle, as all other muscles studied from our group have similar lipid composition (current study and Stefanyk et al. 2010).

Relationships between Mitochondrial Membrane Lipid Composition and Fatty Acid Oxidation

There is controversy in the literature regarding the association between metabolic function and membrane lipids in muscle (Blackard et al. 1997; Kriketos et al. 1995). Past literature has limited membrane lipid analysis to whole muscle and does not provide a direct measure of substrate utilization. Therefore, we compared LCFA oxidation rates with various lipid composition determinants of isolated and purified mitochondria.

We have observed that the rates of fatty acid oxidation may in part be influenced by the degree of membrane lipid unsaturation, as across all muscles, the total phospholipid UI (influenced mainly by 18:2n6 and 20:4n6) was positively correlated with rates of LCFA oxidation. This observation may largely reflect the relationship between CL content and fatty acid oxidation, which mirrored that of the UI. CL is highly unsaturated, with polyunsaturated fatty acids (mainly 18:2n6) being the predominant fatty acid class. In contrast, while membranes with a higher composition of PC are more fluid than those composed primarily of PE (reviewed in Spector and Yorek 1985), PC and PE abundance, or the PC/PE ratio did not significantly correlate with LCFA oxidation rates. Therefore, tissue differences in PE and PC/PE cannot

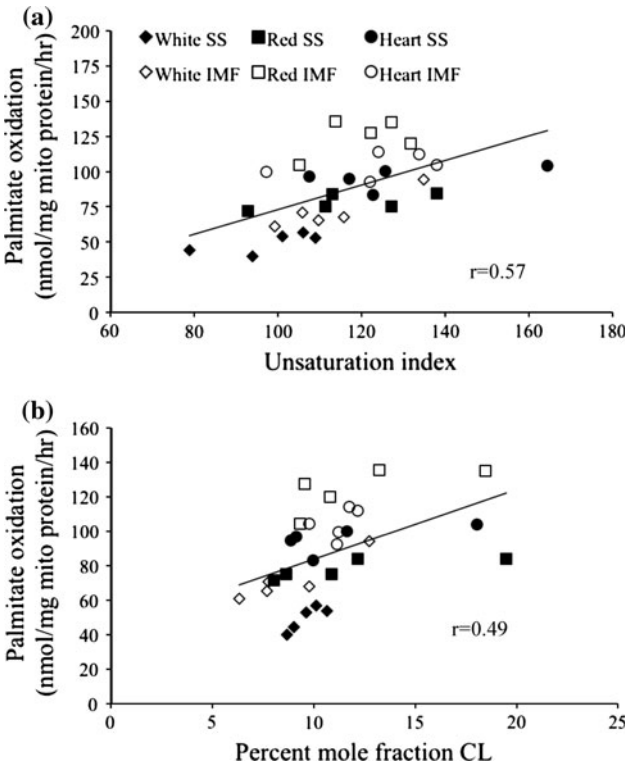

Fig. 5 Correlation between **a** palmitate oxidation rate and unsaturation index (UI) ($r = 0.57$; $p < 0.05$) and **b** palmitate oxidation rate and percent mole fraction of cardiolipin (CL) ($r = 0.49$; $p < 0.05$) in subsarcolemmal (SS) and intermyofibrillar (IMF) mitochondria isolated from heart (H), red (R; gastrocnemius and vastus lateralis), and white (W; gastrocnemius and vastus lateralis) muscle. Values are means ± SE ($n = 5$)

account for the observed variance in basal rates of LCFA oxidation in the current study. Altogether, we demonstrate and association between rates of fatty acid oxidation and the degree of membrane total phospholipid unsaturation and percent mole fraction of CL, but not percent mole fraction of PC or PE, in muscle tissue.

In the current study, the relationship between LCFA oxidation and some lipid composition surrogates of membrane fluidity (specifically percent mole fraction of CL and total phospholipid unsaturation) indicates that membrane structure may influences function of integral membrane proteins. In support of this, previous studies utilizing diet, exercise, or both to increase unsaturated lipids within mitochondrial membranes have demonstrated increased CPTI activity in liver (Karanth and Jeevaratnam 2010; Power et al. 1994). In addition, hepatic mitochondrial CL content has been shown to be positively correlated with CPTI activity (Mynatt et al. 1994) as well as the rate of accumulation palmitoylcarnitine, the CPTI reaction product (Pande et al. 1986). Therefore, previous data exist to suggest that mitochondrial membrane lipid composition can influence CPTI activity. This study is the first to examine this specific relationship in muscle tissue. In addition, CPTI is not the only site of regulation in mitochondrial LCFA oxidation, and therefore the current approach provides further support that percent mole fraction of CL and total phospholipid unsaturation can influence overall mitochondrial function. However, a limitation to this approach is that the exact location of influence cannot be determined, and it remains to be determined whether membrane lipid unsaturation and percent mole fraction of CL influences several integral proteins. In addition, only 33 % and 24 % of the variation can be attributed to CL percent mole fraction and total phospholipid unsaturation, respectively, leaving 67–76 % of the variation unexplained. Future research specifically examining the relative abundance of CL, fatty acid unsaturation, and function of integral membrane proteins located within the inner mitochondrial membrane will, we hope, rectify these issues.

In conclusion, the current data demonstrate a significant positive relationship between rates of mitochondrial palmitate oxidation, CL abundance, and unsaturation in SS and IMF mitochondria isolated from muscles with varying oxidative potential. These data suggest that mitochondrial membrane lipid composition may influence mitochondrial substrate utilization in a structure–function relationship.

Acknowledgments This study was supported by the Natural Sciences and Engineering Research Council of Canada (G. P. H., P. J. L.). V. A. F. was supported by a Natural Sciences and Engineering Research Council of Canada Undergraduate Student Research Award.

Bibliography

Ahn BH, Kim HS, Song S, Lee IH, Liu J, Vassilopoulos A, Deng CX, Finkel T (2008) A role for the mitochondrial deacetylase Sirt3 in regulating energy homeostasis. Proc Natl Acad Sci USA 105:14447–14452

Alkhateeb H, Holloway GP, Bonen A (2011) Skeletal muscle fatty acid oxidation is not directly associated with AMPK or ACC2 phosphorylation. Appl Physiol Nutr Metab 36:361–367

Benton CR, Campbell SE, Tonouchi M, Hatta H, Bonen A (2004) Monocarboxylate transporters in subsarcolemmal and intermyofibrillar mitochondria. Biochem Biophys Res Comm 323:249–253

Benton CR, Nickerson JG, Lally J, Han XX, Holloway GP, Glatz JFC, Luiken JJFP, Graham TE, Heikkila JJ, Bonen A (2008) Modest PGC-1alpha overexpression in muscle in vivo is sufficient to increase insulin sensitivity and palmitate oxidation in subsarcolemmal, not intermyofibrillar, mitochondria. J Biol Chem 283:4228–4240

Bezaire V, Heigenhauser GJF, Spriet LL (2004) Regulation of CPT1 activity in intermyofibrillar and subsarcolemmal mitochondria isolated from human and rat skeletal muscle. Am J Physiol 286:E85–E91

Bezaire V, Bruce CR, Heigenhauser GJF, Tandon NN, Glatz JFC, Luiken JJJF, Bonen A, Spriet LL (2006) Identification of fatty

acid translocase on human skeletal muscle mitochondrial membranes: essential role in fatty acid oxidation. Am J Physiol 290:E509–E515

Blackard WG, Li J, Clore JN, Rizzo WB (1997) Phospholipid fatty acid composition in type I and type II rat muscle. Lipids 32:193–198

Bradley NS, Heigenhauser GJF, Roy BD, Staples EM, Inglis JG, LeBlanc PJ, Peters SJ (2008) The acute effects of differential dietary fatty acids on human skeletal muscle pyruvate dehydrogenase activity. J Appl Physiol 104:1–9

Campbell SE, Tandon NN, Woldegiorgis G, Luiken JJFP, Glatz JFC, Bonen A (2004) A novel function for fatty acid translocase (FAT)/CD36. Involvement in long chain fatty acid transfer into the mitochondria. J Biol Chem 279:36235–36241

Cogswell AM, Stevens RJ, Hood DA (1993) Properties of skeletal muscle mitochondria isolated from subsarcolemmal and intermyofibrillar regions. Am J Physiol 264:C383–C389

Daum G (1985) Lipids of mitochondria. Biochim Biophys Acta 822:1–42

Dzamko N, Schertzer JD, Ryall JG, Steel R, Macaulay SL, Wee S, Chen ZP, Michell BJ, Oakhill JS, Watt MJ, Jorgensen SB, Lynch GS, Kemp BE, Steinberg GR (2008) AMPK-independent pathways regulate skeletal muscle fatty acid oxidation. J Physiol 586:5819–5831

Folch J, Lees M, Stanley GHS (1957) A simple method for the isolation and purification of total lipides from animal tissues. J Biol Chem 226:497–509

Fritz IB, Yue KT (1963) Long-chain carnitine acyl transferase and the role of acylcarnitine derivatives in the catalytic increase of fatty acid oxidation induced by carnitine. J Lipid Res 4:279–288

Glatz JF, Luiken JJ, Bonen A (2010) Membrane fatty acid transporters as regulators of lipid metabolism: implications for metabolic disease. Physiol Rev 90:367–417

Hazel JR, Williams EE (1990) The role of alterations in membrane lipid composition in enabling physiological adaptation of organisms to their physical environment. Prog Lipid Res 29:167–227

Hirschey MD, Shimazu T, Goetzman E, Jing E, Schwer B, Lombard DB, Grueter CA, Harris C, Biddinger S, Ilkayeva OR, Stevens RD, Li Y, Saha AK, Ruderman NB, Bain JR, Newgard CB, Farese RV Jr, Alt FW, Kahn CR, Verdin E (2010) SIRT3 regulates mitochondrial fatty-acid oxidation by reversible enzyme deacetylation. Nature 464:121–125

Holloway GP, Bezaire VL, Heigenhauser GJ, Tandon NN, Glatz JFC, Luiken JJFP, Bonen A, Spriet LL (2006) Mitochondrial long chain fatty acid oxidation, fatty acid translocase/CD36 content and carnitine palmitoyltransferase I activity in human skeletal muscle during aerobic exercise. J Physiol 571:201–210

Holloway GP, Benton CR, Mullen KL, Yoshida Y, Snook LA, Han XX, Glatz JF, Luiken JJ, Lally J, Dyck DJ, Bonen A (2009a) In obese rat muscle transport of palmitate is increased and is channeled to triacylglycerol storage despite an increase in mitochondrial palmitate oxidation. Am J Physiol 296:E738–E747

Holloway GP, Jain SS, Bezaire V, Han XX, Glatz JFC, Luiken JJFP, Harper ME, Bonen A (2009b) FAT/CD36-null mice reveal that mitochondrial FAT/CD36 is required to upregulate mitochondrial fatty acid oxidation in contracting muscle. Am J Physiol 297:R960–R967

Holloway GP, Gurd BJ, Snook LA, Lally J, Bonen A (2010) Compensatory increases in nuclear PGC1alpha protein are primarily associated with subsarcolemmal mitochondrial adaptations in ZDF rats. Diabetes 59:819–828

Hoppel CL, Moghaddas S, Lesnefsky EJ (2002) Interfibrillar cardiac mitochondrial comples III defects in the aging rat heart. Biogerontology 3:41–44

Karanth J, Jeevaratnam K (2010) Effect of carnitine supplementation on mitochondrial enzymes in liver and skeletal muscle of rat after dietary lipid manipulation and physical activity. Indian J Exp Biol 48:503–510

Kelley DE, He J, Menshikova EV, Ritov VB (2002) Dysfunction of mitochondria in human skeletal muscle in type 2 diabetes. Diabetes 51:2944–2950

Khairallah RJ, O'Shea KM, Brown BH, Khanna N, Des Rosiers C, Stanley WC (2010a) Treatment with docosohexaenoic acid, but not eicosapentaenoic acid, delays Ca^{2+}-induced mitochondria permeability transition in normal and hypertrophied myocardium. J Pharmacol Exp Ther 335:155–162

Khairallah RJ, Sparagna GC, Khanna N, O'Shea KM, Hecker PA, Kristian T, Fiskum G, Des Rosiers C, Polster BM, Stanley WC (2010b) Dietary supplementation with docosahexaenoic acid, but not eicosapentaenoic acid, dramatically alters cardiac mitochondrial phospholipid fatty acid composition and prevents permeability transition. Biochim Biophys Acta 1797:1555–1562

Kriketos AD, Pan DA, Sutton JR, Hoh JF, Baur LA, Cooney GJ, Jenkins AB, Storlien LH (1995) Relationships between muscle membrane lipids, fiber type, and enzyme activities in sedentary and exercised rats. Am J Physiol 269:R1154–R1162

Lee AG (2004) How lipids affect the activities of integral membrane proteins. Biochim Biophys Acta 1666:62–87

Lepage G, Roy CC (1986) Direct transesterification of all classes of lipids in a one-step reaction. J Lipid Res 27:114–120

Mahadevappa VG, Holub BJ (1987) Quantitative loss of individual eicosapentaenoyl-relative to arachidonoyl-containing phospholipids in thrombin-stimulated human platelets. J Lipid Res 28:1275–1280

McIntosh TJ, Simon SA (2006) Roles of bilayer material properties in function and distribution of membrane proteins. Ann Rev Biophys Biomol Struc 35:177–198

Mynatt RL, Greenhaw JJ, Cook GA (1994) Cholate extracts of mitochondrial outer membranes increase inhibition by malonyl-CoA of carnitine palmitoyltransferase-I by a mechanism involving phospholipids. Biochem J 299:761–767

O'Shea KM, Khairallah RJ, Sparagna GC, Xu W, Hecker PA, Robillard-Frayne I, Des Rosiers C, Kristian T, Murphy RC, Fiskum G, Stanley WC (2009) Dietary ω-3 fatty acids alter cardiac mitochondrial phospholipid composition and delay Ca^{2+}-induced permeability transition. J Mol Cell Cardiol 47:819–827

Odland LM, Heigenhauser GJF, Lopaschuk GD, Spriet LL (1996) Human skeletal muscle malonyl-CoA at rest and during prolonged submaximal exercise. Am J Physiol 270:E541–E544

Odland LM, Howlett RA, Heigenhauser GJF, Hultman E, Spriet LL (1998) Skeletal muscle malonyl-CoA content at the onset of exercise at varying power outputs in humans. Am J Physiol 274:E1080–E1085

Palmer JW, Tandler B, Hoppel CL (1985) Biochemical differences between subsarcolemmal and interfibrillar mitochondria from rat cardiac muscle: effects of procedural manipulations. Arch Biochem Biophys 236:691–702

Pande SV, Murthy MSR, Noel H (1986) Differential effects of phosphatidylcholine and cardiolipin on carnitine palmitoyltransferase activity. Biochim Biophys Acta 877:223–230

Power GW, Yaqoob P, Harvey DJ, Newsholme EA, Calder PC (1994) The effect of dietary lipid manipulation on hepatic mitochondrial phospholipid fatty acid composition and carnitine palmitoyltransferase I activity. Biochem Mol Biol Int 34:671–684

Roepstorff C, Halberg N, Hillig T, Saha AK, Ruderman NB, Wojtaszewski JFP, Richter EA, Kiens B (2004) Malonyl-CoA and carnitine in regulation of fat oxidation in human skeletal muscle during exercise. Am J Physiol 288:E133–E142

Saggerson ED, Carpenter CA (1981) Carnitine palmitoyltransferase and carnitine octanoyltransferase activities in liver, kidney

cortex, adipocyte, lactating mammary gland, skeletal muscle and heart. FEBS Lett 129:229–232

Smith BK, Jain SS, Rimbaud S, Dam A, Quadrilatero J, Ventura-Clapier R, Bonen A, Holloway GP (2011) FAT/CD36 is located on the outer mitochondrial membrane, upstream of long-chain acyl-CoA synthetase, and regulates palmitate oxidation. Biochem J 437:125–134

Spector AA, Yorek MA (1985) Membrane lipid composition and cellular function. J Lipid Res 26:1015–1035

Srere PA (1969) Citrate synthase. In: Lowenstein JM (ed) Methods in Enzymology, vol 13. Academic Press, New York, pp 3–11

Stefanyk LE, Coverdale N, Roy BD, Peters SJ, LeBlanc PJ (2010) Skeletal muscle type comparison of subsarcolemmal mitochondrial membrane phospholipid fatty acid composition in rat. J Mem Biol 234:207–215

Winder WW, Arogyasami J, Barton RJ, Elayan IM, Vehrs PR (1989) Muscle malonyl-CoA decreases during exercise. J Appl Physiol 67:2230–2233

Yoshida Y, Holloway GP, Ljubicic V, Hatta H, Spriet LL, Hood DA, Bonen A (2007) Negligible direct lactate oxidation in subsarcolemmal and intermyofibrillar mitochondria obtained from red and white rat skeletal muscle. J Physiol 582:1317–1335

J Membrane Biol (2012) 245:177–183
DOI 10.1007/s00232-012-9427-5

Expression of Transcriptional Factor Genes (*Oct-4*, *Nanog*, and *Sox-2*) and Embryonic Stem Cell-Like Characters in Placental Membrane of Buffalo (*Bubalus bubalis*)

Kapil Dev · Shiv Kumar Giri · Anil Kumar · Anita Yadav · Birbal Singh · Sanjeev Kumar Gautam

Received: 11 November 2011 / Accepted: 1 April 2012 / Published online: 22 April 2012

Abstract The aim of the study was to assess the expression of transcriptional factor genes and embryonic stem cell-like characters in the placental membrane of buffalo (*Bubalus bubalis*). Along with the placenta, amniotic fluid, maternal peripheral blood, and umbilical cord blood samples were taken for the future study. The isolation and culture of cells from the placental membrane was followed by the determination of RT-PCR-based markers (Oct-4, Nanog, Sox-2, alkaline phosphatase, stem cell factor, and Nestin) of these cells. Placental membrane cells also positively expressed alkaline phosphatase staining. We isolated adherent cells from trypsin–EDTA-digested placentas and examined these cells for morphology, surface markers, and differentiation potential and found that they expressed several stem cell markers. They also showed neurogenic and adipogenic differentiation potentials under appropriate guided conditions. We suggest that placenta-derived cells have multilineage differentiation potential similar to mesenchymal stem cells in terms of morphology and cell-surface antigen expression. The placenta may prove to be a useful source of mesenchymal stem cells.

Keywords Amniotic membrane · Differentiation · Placenta · Stem cells

K. Dev · S. K. Giri · A. Kumar · A. Yadav · S. K. Gautam (✉)
Department of Biotechnology, Kurukshetra University, Kurukshetra 136119, Haryana, India
e-mail: sgautam@kuk.ac.in

K. Dev
e-mail: kapildchauhan@rediffmail.com

B. Singh
Regional Station, Indian Veterinary Research Institute, Palampur 176061, Himachal Pradesh, India

Introduction

Regenerative medicine based on cell therapy and tissue engineering methodologies is a newly emerging, multidisciplinary field involving biology, medicine, and genetic manipulation (Parolini and Soncini 2006). Modern improvement in the study of stem cells has unlocked new perspective for their application in cell treatment. The present resources of stem cells are embryonic stem cells and adult-type stem cells; however, their use poses both ethical and technical problems. The finding of other stem cell sources that do not raise ethical problems, that are easily accessible, and that are sufficiently numerous to be used for therapeutic purposes has been attempted (Mihu et al. 2009). A new source that meets all these requirements is placenta.

In this study, we focused on the presence of stem cell characters in the placental membrane because these are less studied in the bubaline species and are speculated to have good differentiation related to a high number of cell varieties—significantly greater than that of adult-type stem cells. Because they are located at the maternal–fetal border, they appear to have high immunological acceptance, which makes them simple to apply in the transplantation process. The aim of this study was to isolate placental membrane cells and to assess the evidence of their stem cell like properties.

The water buffalo is an important livestock species contributing significantly to dairy, agriculture, leather and meat production in several countries (Singh et al. 2009), and research is going on to enhance its production efficiency and conservation of elite and native genotypes (Gautam et al. 2008; Singh et al. 2009). Establishing stem cells for assisted reproduction and health application has been emphasized in this species (Dev et al. 2011a, b; Singh et al. 2011;

Yadav et al. 2012). In this study, we report characterization of pluripotency molecular markers and embryonic stem cells like characters in placental membrane from bubaline. Ability of prolonged cultured cells to differentiate in vitro into various cell lineages is investigated.

Materials and Methods

Chemicals and Media

All chemicals, reagents, culture media, and antibiotics used in this study were of cell culture grade and were obtained from Sigma Chemical Company (USA) unless otherwise indicated. Fetal bovine serum (FBS) was from Hyclone (Thermo Scientific, USA), and Trizol was from Invitrogen (USA). Disposable 35 × 10 mm cell culture petri dishes, six-well tissue culture plates, and centrifuge tubes were procured from Tarsons Products (India). Membrane filters were from Advanced Micro-Devices (India). The primers were synthesized by GenxBio (India). The culture media was filter sterilized (0.22 μm) before use.

Sampling and Transportation

Of all the placentas gathered, six were from natural deliveries and one was from a dead fetus. They were transported in cold Dulbecco phosphate-buffered saline (DPBS) solution in a thermally insulated container on ice. Along with the placentas, different samples from amniotic fluid and umbilical cord blood were taken. All the samples were directly processed following laboratory-standardized protocols. Some of samples were separated by centrifugation with a Ficoll density gradient and amassed in liquid nitrogen awaiting its later use. The placentas were assessed macroscopically and microscopically. Stained histologic preparations for placenta were completed.

Isolation and Culturing of Placental Membrane Cells

The placental cells were separated by chopping followed by centrifugation (5000*g*, 10 min), then washed three times with DPBS. The cells were seeded at a density of 10^3 cells/cm^2 in six-well culture plates containing cell culture medium (Dulbecco modified Eagle medium supplemented with 16 % FBS, 1 % penicillin/streptomycin, and 1 % vitamin solution) and incubated in a humidified CO_2 incubator (Lark, China) at 38.5 °C in the presence of 5 % CO_2 (Dev et al. 2010).

The placental cells were allowed to grow and were subcultured by passaging after achieving >80 % confluence. Viability of the cells was monitored by standard protocols of exclusion of trypan blue dye, and the cells were counted with a hemocytometer (Rohem, India). Morphologic features of the cells and their anchorage to culture plates were monitored and recorded regularly.

Characterization of Stem Cells

Alkaline Phosphatase (AP) Expression

The cultured placental cells were screened for embryonic stem cell-like cells and AP expression with an AP staining kit (Sigma Chemical Company, catalog no. 86C). For this, cell culture medium was removed and the cells were fixed using the fixative 157 μl citrate solution, 50 μl formaldehyde, and 406 μl acetone for 30 s. After fixation, the cells were washed three times with DPBS for 60 s, and 60 μl alkaline dye (10 μl sodium nitrate, 10 μl fast blue base alkaline, 10 μl naphthalene, and 470 μl water) was added. The cells were left at room temperature for 15 min. The treated cells were washed 8–10 times with DPBS. Natural red dye was added and removed after 30 s. The cells were observed under an inverted microscope (Radical Instruments, India).

Oct-4, Sox-2, Nanog, AP, and Nestin Expression with RT-PCR

The method proposed by Hummon et al. (2007), with minor modifications, was used for extracting total cellular RNA. RNA was extracted from approximately 0.6 × 107 cells with Trizol (Invitrogen, USA) reagent. The Trizol extract (with the cell pellet) was transferred to 2 ml centrifuge tubes and mixed with 200 μl chloroform and isoamyl alcohol (24:1). Aqueous and organic phases were mixed by gentle shaking followed by centrifugation at 12,000×*g* for 15 min at room temperature. The supernatant was collected, and 500 μl of isopropyl alcohol was added to 1 ml of Trizol extract. The contents were remixed gently and centrifuged at 9500×*g* for 15 min. The RNA pellet was washed with 500 μl of 70 % chilled ethanol, then dried at room temperature. The dried RNA pellet was dissolved in 190 μl of diethylpyrocarbonate-treated water and treated with RNase-free DNase for removing DNA, if any. The RNA concentration was measured with a spectrophotometer (ND-1000; NanoDrop Technologies, USA).

The cDNA was synthesized by reverse transcription of mRNA purified from the cultured placental cells. The reaction mixture was composed of total cellular 5 ng RNA, 0.2 μg/μl random hexamer, 7 μg/μl cDNA direct RT, 10 μM/ μl AMV reverse transcriptase, and 40 U/μl RNase inhibitor in a total volume of 20 μl. RT-PCR was carried out at 42 °C for 60 min followed by denaturation at 95 °C for 8 min. The cDNA taken was generally 5–10 ng/μL, and

Table 1 Primer sequences, size of amplification products, and annealing temperatures

Gene	Primer sequence	Product size (bp)	Accession no.	Annealing temperature (°C)
Octamer binding-4 (*Oct-4*)	CTTCAATCGCATATTCTTTAACCA GGAGGAAGCTGACAACAACG	314	FI907061	58.0
Nanog	GCCCCTTAGTAAGCTGCTTTT GGGGTGGTGGAAATCAGTAA	317	DQ487022	58.0
Sox-2	AACCAAGACGCTCATGAAGAA GTACTGCAGGGCGCTCAC	277	EU627692	61.0
Alkaline phosphatase (*AP*)	ACCAATGGCAACCTGCTGTA CTCCTCCAGGATCTTGGCTA	180	X93604	60.0
Stem cell factor (*SCF*)	TCCCTGCTACCATCCCTATG GCTTCCCAAATCTGGATCAT	216	AY667192	59.5
Nestin	ACC TGC TGT ACA TCG GCT TT GAGGATGGTGAAGACGGAGA	307	X93604	60.0

ultrapure water instead of standard DNA was taken as negative control. The final volume of the PCR reaction consisted of 60 ng cDNA, 20 pmol of each primer (GenxBio, India), 10 mM dNTPs mixture, 25 mM of $MgCl_2$, and 3 U of Taq polymerase (all from Bangalore GeNei, India). The primer sequences used were for Oct-4, Sox-2, Nanog, AP, stem cell factor, and Nestin (Table 1). The PCR conditions were the same except for the annealing temperature (Table 1): 94 °C for 5 min for initial denaturation, denaturation at 94 °C for 30 s, elongation at 72 °C for 1 min (35 cycles), and final extension at 72 °C for 10 min. The amplified DNA fragments were resolved on a 2 % agarose gel containing 10 mg/ml ethidium bromide.

Karyotyping

Standard protocols were used to investigate the chromosomal profiles of the fibroblastic cells at different passages. The actively growing cells were incubated with colchicine (0.1 μg/ml) for 4 h at 37 °C. The treated cultures were washed twice with DPBS and trypsinized (as above). The cells were suspended and incubated in a hypotonic solution (68 mM KCl) for 20 min at 37 °C. The cells were collected by centrifugation and fixed in a chilled fixative (methanol and glacial acetic acid, 3:1) for 10 min. The cell pellet was obtained and suspended in 5 ml of chilled fixative for another 10 min. The metaphase spreads were prepared by dropping the cell suspension onto prechilled glass slides. The air-dried cell spreads were stained with Giemsa stain and observed under oil immersion. Additionally, the cells were also examined for appearance of micronuclei as indicators of genetic abnormalities during culturing (Thomas et al. 2009).

Results

Isolation and Culturing of Placental Membrane Cells

After collection, all the cells were in network form and were similar in size and shape (Fig. 1). Some of the cells were rounded and some were edge-pointed after 5 days of culturing. All the cells displayed anchorage after 9 days of culturing. After day 14, there was <80 % confluence with morphologically similar cells (fibroblastic cells).

Instead of forming uniform cell monolayers, cell clumps were also observed. Initially the cells reached 70–80 % confluence after 2 weeks. However, the passaged cells exhibited a higher growth rate, reaching 90–100 % confluence after day 16 of culturing.

Characterization of Placental Membrane Cells by AP Staining

The placental cells were found to expand extensively in fibroblast appearance. The cells were found to stain positive for AP. Cells showed embryonic stem cell-like cells properties by AP staining. Whereas the other cell (Pinna)-cultured fibroblasts did not acquire stain, the cultured cells stained red and were considered positive for AP expression (Fig. 2).

Karyotyping

The cells had a standard karyotype at different passages. No noticeable genomic aberrations (e.g., appearance of micronuclei, chromosomal fragmentation) were observed (Fig. 3).

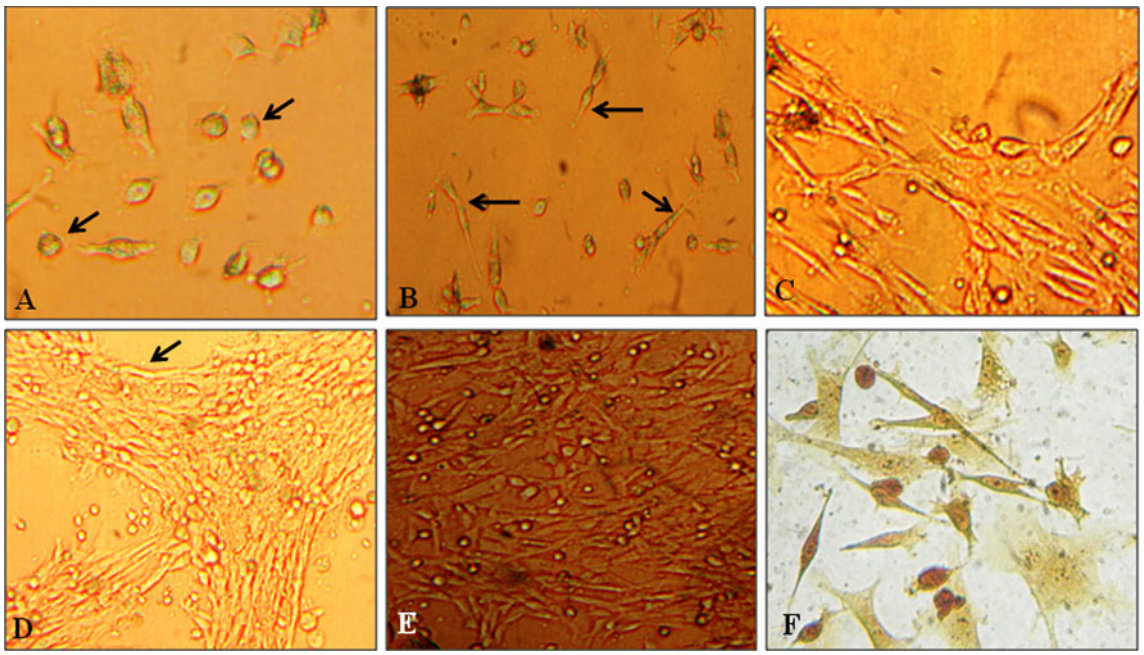

Fig. 1 Culturing of placental membrane-derived cells. **a** All the cells appear rounded on day 2. **b** Edge and connective bridge formation start on day 3. **c** Cells start to regularly proliferate in the whirlpool on day 5. **d** About 50 % confluence take place on day 8 of culturing. **e** Less than 90 % confluence is reached on day 14. **f** Cells after the second day of the trypsin–EDTA step. After each 5-day interval, cells were in need of feeding with the same concentration and composition of supplements as the last cultured cells

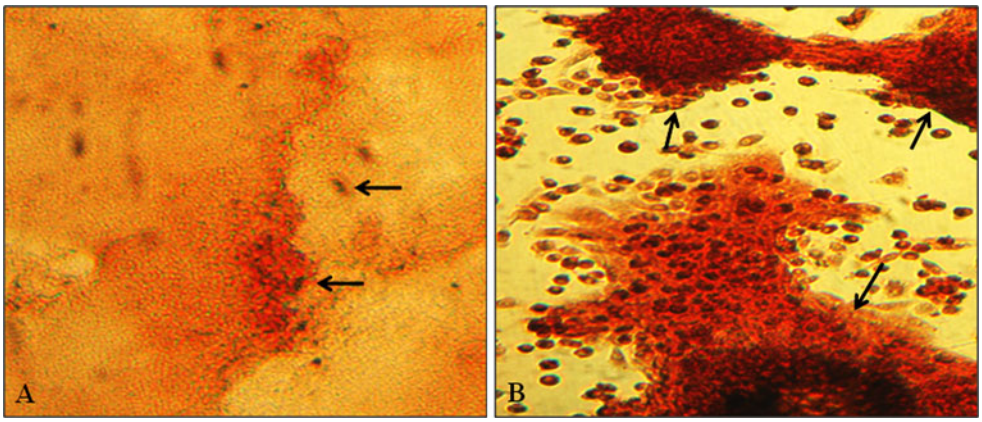

Fig. 2 Expression of strong positive alkaline phosphatase staining at passages 3 and 5. Placental membrane cells revealed a strong positive staining (*red*), showing that cells have an embryonic cell-like character. **a** Placental membrane cells at low magnification appear as clumps (×100). **b** A clear embryonic stem cell-like colony formation appears at high magnification (×250)

Characterization of Placental Membrane Cells for Oct-4-, Sox-2-, Nanog-, AP-, and Nestin-positive RT-PCR Expression

At passages 2–4, cells were collected to analyze different gene expressions. RT-PCR-based studies showed strong positive expression for *Oct-4*, *Sox-2*, *Nanog*, *AP*, and *Nestin* genes. Agarose gel electrophoresis of RT-PCR product revealed PCR amplicons of 314, 277, 317, 180, and 307, respectively (Fig. 4).

Discussion

The mesenchymal cells of the placental membrane can represent an important source of cells with pluripotential characteristics (Benirschke and Kaufmann 2000; Bieback et al. 2004; In 'T Anker et al. 2004; Matikainen and Laine 2005; Strom and Miki 2003; Yen et al. 2005). During this study, we succeeded in isolating, culturing, and characterizing these cells by RT-PCR and by AP staining. To our knowledge, this provides the first evidence of RT-PCR- and

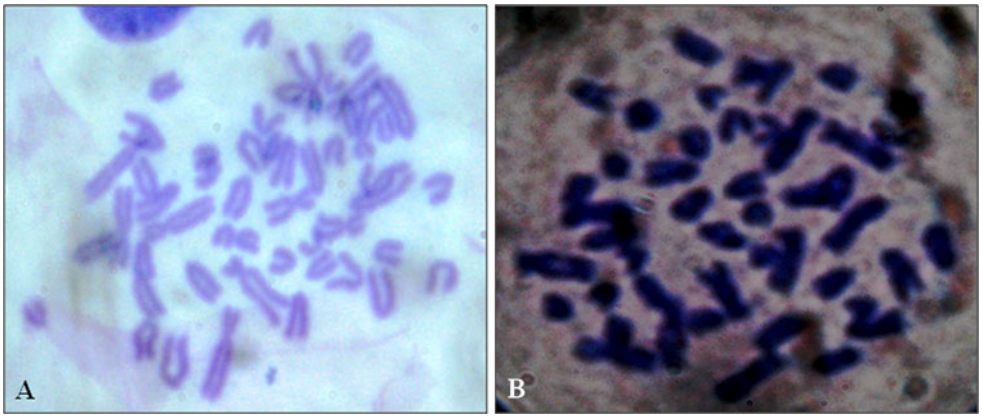

Fig. 3 Cells were found to have a normal karyotype during the different passages. **a** Passage 2 (×1000). **b** Passage 5 (×1000)

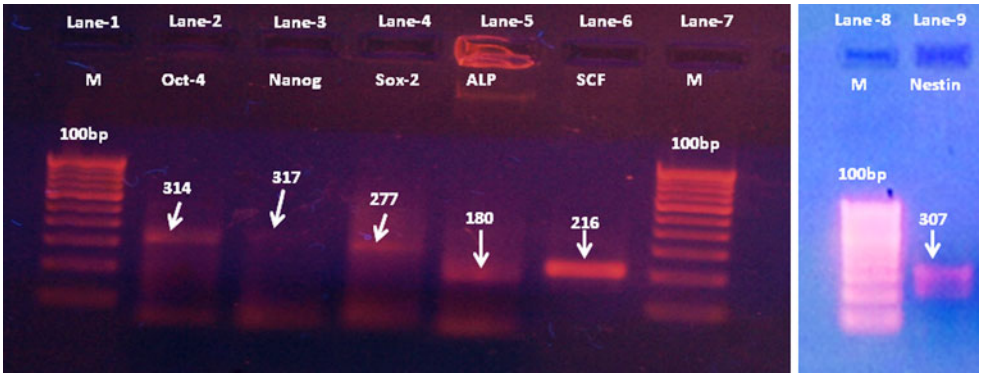

Fig. 4 RT-PCR-based studies showed the strong positive expression for *Oct-4, Nanog, Sox-2,* alkaline phosphatase (*ALP*), stem cell factor (*SCF*), and *Nestin* genes. Agarose gel electrophoresis of analysis of RT-PCR product revealed PCR amplicons of 314, 317, 277, 180, 216, and 307, respectively

AP staining-based characterization of placental membrane cells in in vitro bubaline species. Even though stem cells and their potential applications have emerged as a potential oasis in the field of disease treatment, there is a difference of opinion among scientists even in the definition of the term *stem cell*, which is still clearly an evolving concept (Parker and Cotanche 2004). The main characteristic of stem cells is their pluripotency and their self-regeneration capacity, properties conferred by the presence of some cell transcription factors, of which the most studied are Oct-3/4 and Nanog. Oct-3/4 and Nanog are expressed in embryonic stem cells, tumor germ cells, and adult stem cells. They are essential in the formation of the internal cell mass and are necessary for the self-regeneration function (Barry et al. 2005; Matikainen and Laine 2005). AP, or TRA-2-39, is also a glycoprotein expressed by nondifferentiated cells and teratocarcinoma cells (Erices et al. 2000; Niyibizi et al. 2004; Thellin et al. 2000; Zhang et al. 2004a, b).

Various approaches have been reported to isolate cells with stem and progenitor cell characteristics from placental tissues, as summarized in a recent review by Matikainen and Laine (2005). Such cells have been isolated from the intact human term placenta (Yen et al. 2005), fetal and the maternal portions of the placenta (In 'T Anker et al. 2004), internal regions of the placental lobules (Fukuchi et al. 2004), amniochorionic fetal membrane (Bailo et al. 2004), amniotic epithelium (Sakuragawa et al. 1996), and amniotic mesenchymal cells (Sakuragawa et al. 1997). Mesenchymal cells have also been isolated from human (Elwan and Sakuragawa 1997) and porcine amniotic fluid (Ishii et al. 1999).

Efforts are being made to study various types of pluripotent stem cells (Huang et al. 2010; Sritanaudomchai et al. 2007; Verma et al. 2007) in buffalo (*Bubalus bubalis*), the mainstay of the dairy and meat industries in many countries. The present study is a preliminary effort to investigate whether the cells in bubaline placental membrane cells can be cultured and whether they exhibit stem cell-like attributes. Our results show that placental membrane cells strongly expressed Oct-4 during the earlier passages, then displayed poor expression as the cell differentiation passed away. Mihu et al. (2009) found Oct-4 expression in placental membrane cells; our finding similarly supports Oct-4 expression. Pluripotency markers, AP,

Oct-3/4, and SSEA-4 had an intensely positive expression and SOX-2 and Nanog a weakly positive expression (In 'T Anker et al. 2004; Mihu et al. 2009; Pittenger et al. 1999). Our result also support the same finding that the placental membrane strongly expresses Oct-4 and AP, and weakly positively expresses Sox-2 and Nanog.

In conclusion, placental membrane cells may be isolated and maintained in vitro for prolonged periods of time. Many important features of pluripotent stem cells, including Oct-4, Sox-2, Nanog, AP, stem cell factor, cyclin A, Nestin, and FGF-5, indicating their pluripotency and the capacity for in vitro differentiation, were demonstrated. This analysis showed that the placenta-derived mesenchymal stem cell-like cells could be simply isolated and prolonged without morphologic and quality changes in medium supplemented only with FBS. Therefore, the placenta may prove to be an attractive and rich source of mesenchymal stem cells. The presence of stem cells in the placenta may be quite useful. Amniotic membrane transplantation has been successfully used in a variety of ocular surface conditions. Further studies are required to better understand the precise nature of placenta-derived cells and to explore their potential clinical applications.

This membrane has unique properties such as promotion of normal epithelialization and suppression of inflammation and scar formation. These properties are beneficial for treatment of various conjunctival and corneal disorders such as retinal pigment epithelial (RPE) detachment, neurotrophic ulcers, shield ulcers, chemical injuries, pterygium surgery, and conjunctival surface reconstruction.

Acknowledgments Financial assistance for the research project under SERC FAST Track scheme (SR/FT/035/2008) by the Department of Science and Technology, Government of India, is duly acknowledged.

References

Bailo M, Soncini M, Vertua E, Signoroni PB, Sanzone S, Lombardi G, Arienti D, Calamani F, Zatti D, Paul P, Albertini A, Zorzi F, Cavagnini A, Candotti F, Wengler GS, Parolini O (2004) Engraftment potential of human amnion and chorion cells derived from term placenta. Transplantation 78:1439–1448

Barry FP, Murphy JM, English K, Mahon BP (2005) Immunogenicity of adult mesenchymal stem cells: lessons from the fetal allograft. Stem Cells Dev 14:252–265

Benirschke K, Kaufmann P (eds) (2000) Pathology of the human placenta, 4th edn. Springer, New York

Bieback K, Kern S, Kluter H, Eichler H (2004) Critical parameters for the isolation of mesenchymal stem cells from umbilical cord blood. Stem Cells 22:625–634

Dev K, Khuttan A, Giri SK, Kumar A, Yadav A, Singh B, Verma V, Aggarwal NK, Gautam SK (2010) Isolation and culturing of putative amniotic fluid stem cells in water buffalo (*Bubalus bubalis*). Presented at the 25th International Conference on Buffalo, New Delhi, India, February 1–4). p 50

Dev K, Gautam SK, Giri SK, Kumar A, Yadav A, Verma V, Kumar P, Singh B (2011a) Isolation, culturing and characterization of feeder-independent amniotic fluid stem cells in buffalo (*Bubalus bubalis*). Res Vet Sci. doi:10:1016/j.rvsc.2011.09.007

Dev K, Gautam SK, Giri SK, Kumar A, Yadav A, Singh B (2011b) Derivation, characterization and differentiation of buffalo (*Bubalus bubalis*) amniotic fluid derived stem cells. Reprod Domest Anim. doi:10.1111/j.1439-0531.2011.01947.x

Elwan MA, Sakuragawa N (1997) Evidence for synthesis and release of catecholamines by human amniotic epithelial cells. Neuroreport 8:3435–3438

Erices A, Conget P, Minguell JJ (2000) Mesenchymal progenitor cells in human umbilical cord blood. Br J Haematol 109:235–242

Fukuchi Y, Nakajima H, Sugiyama D, Hirose I, Kitamura T, Tsuji K (2004) Human placenta-derived cells have mesenchymal stem/progenitor ell potential. Stem Cells 22:649–658

Gautam SK, Verma V, Palta P, Chauhan MS, Manik RS (2008) Effect of type of cryoprotectant on morphology and developmental competence of in vitro-matured buffalo (*Bubalus bubalis*) oocytes subjected to slow freezing or vitrification. Reprod Fert Develop 20(4):490–496

Huang B, Li T, Wang XL, XIE TS, Lu YQ, Da Silva FM, Shi DS (2010) Generation and characterization of embryonic stem-like cell lines derived from in vitro fertilization in buffalo (*Bubalus bubalis*) embryos. Reprod Domest Anim 45:122–128

Hummon AB, Lim SR, Difilippantonio MJ, Ried T (2007) Isolation and solubilization of proteins after TRIzol extraction of RNA and DNA from patient material following prolonged storage. Biotechniques 42:467–470

In 'T Anker PS, Scherjon SA, Kleijburg-Van Der Keur C, De Groot-Swings GM, Claas FH, Fibbe WE, Kanhai HH (2004) Isolation of mesenchymal stem cells of fetal or maternal origin from human placenta. Stem Cells 22:1338–1345

Ishii T, Ohsugi K, Nakamura S, Sato K, Hashimoto M, Mikoshiba K, Sakuragawa N (1999) Gene expression of oligodendrocyte markers in human amniotic epithelial cells using neural cell-type-specific expression system. Neurosci Lett 268:131–134

Matikainen T, Laine J (2005) Placenta—an alternative source of stem cells. Toxicol Appl Pharmacol 207:544–549

Mihu CM, Ciuca DR, Soritau O, Susman S, Mihu D (2009) Isolation and characterization of senchymal stem cells from the amniotic membrane. Rom J Morphol Embryol 50:73–77

Niyibizi C, Wang S, Mi Z, Robbins PD (2004) The fate of mesenchymal stem cells transplanted into immunocompetent neonatal mice: implications for skeletal gene therapy via stem cells. Mol Ther 9:955–963

Parker MA, Cotanche DA (2004) The potential use of stem cells for cochlear repair. Audiol Neurootol 9:72–80

Parolini O, Soncini M (2006) Human placenta: a source of progenitor/stem cells. J Reprod Med Endocrinol 3:117–126

Pittenger MF, Mackay AM, Beck SC, Jaiswal RK, Douglas R, Mosca JD, Moorman MA, Simonetti DW, Craig S, Marshak DR (1999) Multilineage potential of adult human mesenchymal stem cells. Science 284(5411):143–147

Sakuragawa N, Thangavel R, Mizuguchi M, Hirasawa M, Kamo I (1996) Expression of markers for both neuronal and glial cells in human amniotic epithelial cells. Neurosci Lett 209:9–12

Sakuragawa N, Misawa H, Ohsugi K, Kakishita K, Ishii T, Thangavel R, Tohyama J, Elwan M, Yokoyama Y, Okuda O, Arai H, Ogino I, Sato K (1997) Evidence for active acetylcholine metabolism in human amniotic epithelial cells: applicable to intracerebral allografting for neurologic disease. Neurosci Lett 232:53–56

Singh B, Chauhan MS, Singla SK, Gautam SK, Verma V, Singh AK, Manik RS, Sodhi M, Mukesh M (2009) Reproductive biotechniques in buffalo: status, prospects and challenges. Reprod Fert Develop 14:499–507

Singh B, Gautam SK, Verma V, Chauhan MS, Singla SK, Yadav PS, Singh RK (2011) Stem cell technology: a perspective on promises and challenges for applications in livestock health and production. Int J Anim Biotechnol 1:116–125

Sritanaudomchai H, Pavasuthipaisit K, Kitiyanant Y, Kupradinum P, Mitalipov S, Kusamran T (2007) Characterization and multilineage differentiation of embryonic stem cells derived from a buffalo parthenogenetic embryo. Mol Reprod Dev 74:1295–1302

Strom S, Miki T (2003) Placental derived stem cells and uses thereof. United States Patent Application Publication US2003/02355 63A1

Thellin O, Coumans B, Zorzi W, Igout A, Heinen E (2000) Tolerance to the foeto-placental "graft": ten ways to support a child for nine months. Curr Opin Immunol 12:731–737

Thomas P, Holland N, Bolognesi C, Kirsch-Volders M, Bonassi S, Zeiger E, Knasmueller S, Fenech M (2009) Buccal micronucleus cytome assay. Nat Prot 4:825–837

Verma V, Gautam SK, Singh B, Manik RS, Palta P, Singla SK, Goswami SL, Chauhan MS (2007) Isolation and characterization of embryonic stem cell-like cells from in vitro produced buffalo (*Bubalus bubalis*) embryo. Mol Reprod Dev 74:520–529

Yadav PS, Singh RK, Singh B (2012) Animal fetal stem cells-potential health applications. Review. Agr Res. doi:10.1007/s40003-011-0001-7

Yen BL, Huang HI, Chien CC, Jui HY, Ko BS, Yao M, Shun CT, Yen ML, Lee MC, Chen YC (2005) Isolation of multipotent cells from human term placenta. Stem Cells 23:3–9

Zhang W, Ge W, Li C, You S, Liao L, Han Q, Deng W, Zhao RC (2004a) Effects of mesenchymal stem cells on differentiation, maturation, and function of human monocyte-derived dendritic cells. Stem Cells Dev 13:263–271

Zhang Y, Li C, Jiang X, Zhang S, Wu Y, Liu B, Tang P, Mao N (2004b) Human placenta-derived mesenchymal progenitor cells support culture expansion of long-term culture initiating cells from cord blood $CD34^+$ cells. Exp Hematol 32:657–664

J Membrane Biol (2012) 245:185–190
DOI 10.1007/s00232-012-9428-4

Changes in Surface-Charge Density of Blood Cells After Sudden Unexpected Death

Joanna Kotyńska · Aneta D. Petelska · Michał Szeremeta · Anna Niemcunowicz-Janica · Zbigniew A. Figaszewski

Received: 6 December 2011 / Accepted: 1 April 2012 / Published online: 20 April 2012

Abstract The objective of the investigation was evaluation of postmortem changes of electric charge of human erythrocyte and thrombocyte membranes after sudden unexpected death. The surface charge density values were determined on the basis of the electrophoretic mobility measurements of the cells carried out at various pHs of electrolyte solution. The interactions between both erythrocyte and thrombocyte membranes and electrolyte ions were studied. Values of parameters characterizing the membrane—that is, the total surface concentrations of both acidic and basic groups and their association constants with solution ions—were calculated on the basis of a four-equilibria mathematical model. The model was validated by comparison of these values to experimental data. We established that examined electric properties of the cell membranes are affected by sudden unexpected death. Postmortem processes occurring in the cell membranes can lead to disorders of existing equilibria, which in turn result in changes in values of all the above-mentioned parameters.

J. Kotyńska · A. D. Petelska (✉) · Z. A. Figaszewski
Institute of Chemistry, University of Bialystok, Al. J. Pilsudskiego 11/4, 15-443 Bialystok, Poland
e-mail: aneta@uwb.edu.pl

M. Szeremeta · A. Niemcunowicz-Janica
Department of Forensic Medicine, Medical University of Bialystok, Waszyngtona St. 13, 15-230 Bialystok, Poland

Z. A. Figaszewski
Laboratory of Electrochemical Power Sources, Faculty of Chemistry, University of Warsaw, Pasteur St. 1, 02-093 Warsaw, Poland

Keywords Erythrocytes · Microelectrophoresis · pH measurement · Sudden unexpected death · Surface charge density · Thrombocytes

Introduction

The surface electric charge density of biological membranes is an important parameter for the maintenance of normal physiological functions of cells. It controls several processes in biological membranes, such as membrane-bound enzymes, insertion of newly synthesized proteins into membranes, and host–pathogen interactions (Yermiyahu et al. 1999). Apart from this, knowledge of surface electric charge values can provide valuable information about the equilibria existing within the membrane and between the membrane and its surroundings.

Biological membranes are negatively charged in physiological pH, mainly as a result of the presence of acidic phospholipids; about 10–20 % of total membrane lipids are anionic ones. Other membranes constituents such as proteins or gangliosides also contribute to the negative charge (Nałęcz and Wojtczak 1982; Gennis 1989). Because the membrane is exposed to surrounding aqueous buffer, specific interactions with outer medium components occur. The resulting equilibria, in which charged groups of membrane components and solutions ions are involved, can be affected by different factors and processes leading to a membrane surface charge density variation. The parameter is also influenced by membrane composition, ionic strength of electrolytes, and solution pH (Deshiikan and Papadopoulos 1998). Changes in pH alter the surface charge of a membrane, with the membrane becoming more positive at a lower pH and more negative at a higher pH (Mullet et al. 1997; Dobrzyńska et al. 2006; Petelska et al. 2012).

In vitro, the surface charge density of biological membranes can be changed either by adding, for example, ionizable surfactants (McLaughlin and Harary 1976) or divalent ions (Mg^{2+}, Ca^{2+}) (Barber 1980) to the membrane suspension, or by altering the membrane lipid composition (Nałęcz et al. 1980). In certain conditions, the surface charge density may be subject to in vivo modification. It was observed that changes in cell surface components (e.g., proteoglycans or sialic acids, which are typical for cancer transformations or other pathologies) are accompanied by changes in surface charge of a cell membrane (Dobrzyńska et al. 2010; Monteggia et al. 2000). Therefore, it seems that variation in membrane surface charge density can commonly occur in living cells, and the resultant membrane charge is the result of a number of various overlapping processes (Nałęcz and Wojtczak 1982).

The most common cause of sudden unexpected death is cardiovascular disease due to sudden cardiac death, acute myocardial ischemia resulting from coronary atherosclerosis, or lethal arrhythmia (Langlois 2009). Biochemical processes, which are controlled in the living organism, can be significantly altered during the course of disease (Kała and Chudzikiewicz 2003). Concentrations of many substances that occur in living organism at normal levels can be influenced after sudden unexpected death. After cessation of circulation, the physiology of the blood and the vascular system completely changes. In cadaveric blood, a rapid increase of catecholamine levels is also observed, with a higher level of adrenaline than noradrenalin (Takeichi et al. 1984), a high level of K^+ ions (Takeichi et al. 1985), and a lower level of pH, and base excess (BE) and HCO_3^- ions (Takeichi et al. 1986). In the early postmortem phase, the dead body is exposed to autolysis—that is, dissolution of organs under the impact of endogenous enzymes. The autolysis of blood (hemolysis) can generate many new chemical compounds, leading to disorders of equilibria describing the specific membranes. Quantitative estimates of the equilibria and numerical determination of the membrane characterizing parameters are extremely important for the interpretation of changes in physicochemical processes. Appearance of new groups on the surface of membranes or loss of existing ones causes changes not only the membrane's electric charge, but also the total surface concentrations of both acidic and basic groups and their association constants with solution ions.

This work continues the systematic study of electrical properties of membranes both model and biological realized by Figaszewski and coworkers (Dobrzyńska et al. 2007, 2008; Kotyńska et al. 2008; Naumowicz et al. 2006; Petelska and Figaszewski 2011; Szachowicz-Petelska et al. 2010). We examined postmortem changes of the surface charge of erythrocyte and thrombocyte membranes after sudden unexpected death. Our experiment was performed using the microelectrophoresis method, which is one of the basic analytical tools for biological studies. The electrophoretic mobility measurements were done over the pH range 2–11. On the basis of a mathematical model describing the equilibria between a cell membrane and surrounding ions, the parameters characterizing the equilibria were determined. In our opinion, the quantitative description of cell membrane surface properties can help in interpreting and understanding the processes that take place on biological membrane surfaces after sudden unexpected death.

Theory

The model, which has been presented in full detailed by Dobrzyńska et al. (2006), assumes that dependence of surface charge density of the cell membrane on the pH of electrolyte solution can be described with the help of four equilibria. Two are connected with positive groups (e.g., phospholipids or proteins and sodium and hydrogen ions), and two concern the negative species of phospholipids or proteins and hydroxide and chloride ions. The H^+, OH^-, Na^+, and Cl^- ions are adsorbed at the cell membrane (erythrocyte or thrombocyte), and the adsorption equilibria (Eqs. 1–4) can be presented in the following form:

$$A^- + H^+ \Leftrightarrow AH \quad (1)$$

$$A^- + Na^+ \Leftrightarrow ANa \quad (2)$$

$$B^+ + OH^- \Leftrightarrow BOH \quad (3)$$

$$B^+ + Cl^- \Leftrightarrow BCl \quad (4)$$

Therefore, the association constants of the H^+, Na^+, OH^-, and Cl^- ions with functional groups are expressed in the following manner (Dobrzyńska et al. 2006, 2007):

$$K_{AH} = \frac{a_{AH}}{a_{A^-} \cdot a_{H^+}} \quad (5)$$

$$K_{ANa} = \frac{a_{ANa}}{a_{A^-} \cdot a_{Na^+}} \quad (6)$$

$$K_{BOH} = \frac{a_{BOH}}{a_{B^+} \cdot a_{OH^-}} \quad (7)$$

$$K_{BCl} = \frac{a_{BCl}}{a_{B^+} \cdot a_{Cl^-}} \quad (8)$$

where, K_{AH}, K_{ANa}, K_{BOH} and K_{BCl} are association constants; a_{AH}, a_{ANa}, a_{A^-}, a_{BOH}, a_{BCl}, and a_{B^+} are surface concentrations of corresponding groups on the membrane surface; a_{H^+}, a_{Na^+}, a_{OH^-} and a_{Cl^-} are a_{Cl^+} are volume concentrations of solution ions.

The concentrations balances are expressed as follows (Dobrzyńska et al. 2006):

$$C_A = a_{A^-} + a_{AH} + a_{ANa} \quad (9)$$

$$C_B = a_{B^+} + a_{BOH} + a_{BCl} \tag{10}$$

where C_A is the total surface concentration of the membrane acidic groups and C_B is the total surface concentration of the membrane basic groups.

Surface charge density of the membrane is given by the following equation (Dobrzyńska et al. 2006):

$$\delta = (a_{B^+} - a_{A^-}) \cdot F \tag{11}$$

where

$$F = 96487 \left[\frac{C}{\text{mol}}\right] - \text{Faraday constant}$$

Elimination of, a_{AH}, a_{ANa}, a_{A^-}, a_{BOH}, a_{BCl}, and a_{B^+} from the above equations yields the following formula (Dobrzyńska et al. 2006):

$$\frac{\delta}{F} = \frac{C_B}{1 + K_{BOH}a_{OH^-} + K_{BCl}a_{Cl^-}} - \frac{C_A}{1 + K_{AH}a_{H^+} + K_{ANa}a_{Na^+}} \tag{12}$$

Determination of the searching parameters requires a simplification of the above equation to a linear form at high H^+ ($a_{H+} \to \infty$) and low H^+ ($a_{H+} \to 0$) concentrations, which appeared previously (Dobrzyńska et al. 2006). In the former case, Eq. 12 was rewritten as a decreasing exponential function of H^+ concentration (Eq. 13), and in the latter case, it was rewritten as an increasing exponential function of H^+ concentration (Eq. 14) (Dobrzyńska et al. 2006).

$$\frac{\delta}{F} = \frac{C_B a_{H^+}}{a_{H^+}(1 + K_{BCl}a_{Cl^-}) + K_{BOH}K_W} - \frac{C_A}{K_{AH}a_{H^+} + K_{ANa}a_{Na^+} + 1} \tag{13}$$

$$\frac{\delta}{F} = \frac{C_B a_{H^+}}{K_{BOH}K_W + a_{H^+}(1 + K_{BCl}a_{Cl^-})} - \frac{C_A}{K_{ANa}a_{Na^+} + 1 + K_{AH}a_{H^+}} \tag{14}$$

The numerator of each term in Eq. 13 was divided by the denominator to yield two terms. These operations resulted in a linear equation in the a_{H+} and $\frac{\delta a_{H^+}}{F}$ coordinate system, which was correct for high hydrogen ion concentrations ($a_{H+} \to \infty$) (Dobrzyńska et al. 2006):

$$\frac{\delta a_{H^+}}{F} = \frac{C_B}{1 + K_{BCl}a_{Cl^-}} a_{H^+} - \left(\frac{C_B K_{BOH} K_W}{(1 + K_{BCl}a_{Cl^-})^2} + \frac{C_A}{K_{AH}}\right) \tag{15}$$

Applying the same procedure to Eq. 14 resulted in a linear equation in the $\frac{1}{a_{H^+}}$ and $\frac{\delta}{F a_{H^+}}$ coordinate system, which was correct for low hydrogen ion concentrations ($a_{H+} \to 0$) (Dobrzyńska et al. 2006):

$$\frac{\delta}{F a_{H^+}} = -\left(\frac{C_A}{1 + K_{ANa}a_{Na^+}}\right)\frac{1}{a_{H^+}} + \left(\frac{C_B}{K_{BOH}K_W} + \frac{C_A K_{AH}}{(1 + K_{ANa}a_{Na^+})^2}\right) \tag{16}$$

The coefficients describing these linear functions may be easily obtained by linear regression and subsequently applied to calculate the parameters. The calculation of the parameters; C_A, C_B, K_{AH}, and K_{BOH} is possible as a result of knowledge of the association constants-K_{ANa}, and K_{BCl} obtained for phosphatidylcholine liposome membrane (Dobrzyńska et al. 2007). Defining the value of these parameters permits the calculation of the theoretical cell membrane surface charge from Eq. 12 for comparison to experimental data.

Materials and Methods

Materials

Approval for this study was granted by the Ethics Review Board of the Medical University of Bialystok (No. R-I-002/533/2010). Blood was obtained from all individuals during autopsies performed at the Forensic Medicine Department at the Medical University of Bialystok in the year 2010. The subject of the examination was based on 28 cases of selective sudden unexpected death (20 men, eight women; mean age 34.3 years; range 22–41 years; all causes of death due to sudden cardiac death, without coagulation disorders). Blood was routinely obtained from the femoral vein and placed into chemically and biologically clean glass containers, then donated to the Department of Electrochemistry at the University of Bialystok. The donated samples were comparatively analyzed to the control samples taken from live individuals from the blood service center in Bialystok.

Preparation of Erythrocytes from Blood

Erythrocytes were isolated from blood by centrifugation at 900×*g* for 8 min at room temperature. The supernatant thrombocyte-rich plasma was removed and saved for subsequent processing, while the erythrocytes were washed three times with isotonic saline (0.9 % NaCl) at 3,000×*g* for 15 min. After the final wash, the erythrocyte pellet was resuspended in isotonic saline for electrophoretic measurement.

Preparation of Thrombocytes from Plasma

The thrombocyte-rich plasma was centrifuged at 900×*g* for 8 min. The supernatant plasma was removed and discarded.

The thrombocyte pellet was washed three times with isotonic saline by centrifugation at 3,000×g for 15 min. After the final wash, the thrombocytes were resuspended in isotonic saline for electrophoretic measurement.

All solutions and cleaning procedures were performed with purified water with a Milli-Q system (18.2; Millipore, USA).

Microelectrophoretic Mobility Measurements

The electrophoretic mobility of erythrocytes or thrombocytes was measured with Zetasizer Nano ZS (Malvern Instruments, UK) apparatus. The measurements were carried out as a function of pH. The cell membranes were suspended in NaCl solution and titrated to the desired pH with HCl or NaOH. The reported values represent the average of at least six measurements performed at a given pH.

From electrophoretic mobility measurements, the surface charge density was determined by the following equation (Alexander and Johnson 1949):

$$\delta = \frac{\eta \cdot u}{d} \tag{17}$$

where η is viscosity of solution, u is electrophoretic mobility, and d is diffuse layer thickness.

The diffuse layer thickness was determined from the following formula (Barrow 1996):

$$d = \sqrt{\frac{\varepsilon \cdot \varepsilon_0 \cdot R \cdot T}{2 \cdot F^2 \cdot I}} \tag{18}$$

where R is the gas constant, T is the temperature, F is the Faraday number, I is the ionic strength of 0.9 % NaCl, and ε and ε_0 refer to the permeability of the electric medium.

Results and Discussion

The influence of postmortem changes in surface charge of erythrocyte and thrombocyte as a result of sudden unexpected death was examined. The experimental data of surface charge density were calculated from measured electrophoretic mobility values using Eq. 17, presented in Materials and Methods. The measurements were performed at several pH values, using 0.155 M NaCl as a supporting electrolyte. The theoretical values of surface charge density were determined by applying Eq. 12 to the experimental data.

Both experimental and theoretical surface charge density values of the cell membranes as a function of pH are presented in Figs. 1 and 2. The former are indicated by points, and the latter are indicated by curves.

The surface charge densities of the control and the sudden unexpected death erythrocytes are plotted in Fig. 1.

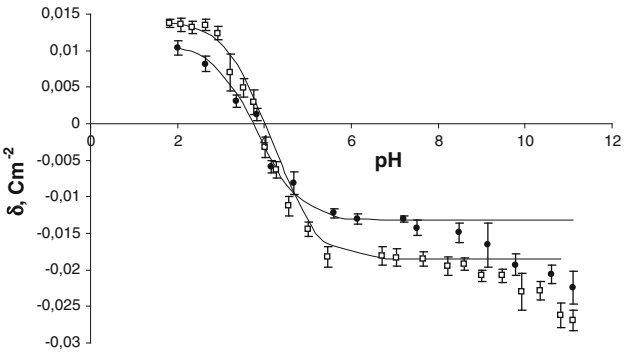

Fig. 1 pH dependence of surface charge density of erythrocytes. *Circles* control, *squares* sudden unexpected death. Experimental values are indicated by *points* and the theoretical values by the *curve*

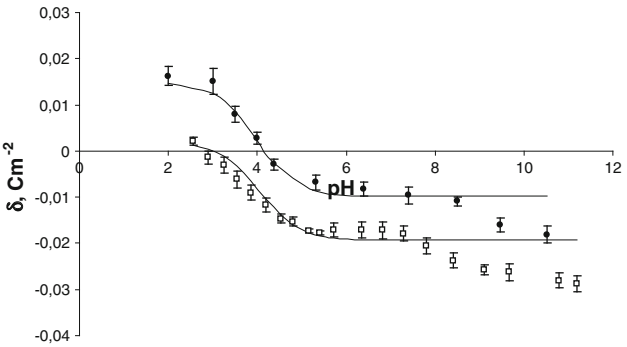

Fig. 2 pH dependence of surface charge density of thrombocytes. *Circles* control, *squares* sudden unexpected death. Experimental values are indicated by *points* and the theoretical values by the *curve*

If we consider an acid solution, an increased positive charge is observed in erythrocytes after sudden unexpected death in comparison to control erythrocytes. In a basic solution, we also observed an increase in negative charge in erythrocytes after sudden unexpected death in comparison to control erythrocytes and a small shift of the isoelectric point of the membrane to high pH values.

The surface charge densities of the control and the sudden unexpected death thrombocytes are plotted in Fig. 2. In the thrombocytes case, if we consider an acid solution, a decreased positive charge is observed in thrombocytes after sudden unexpected death in comparison to control thrombocytes. In basic solutions, we also observed an increase in the negative charge in thrombocytes after sudden unexpected death in comparison to control thrombocytes and a shift of the isoelectric point of the membrane to a low pH values.

Mathematical calculations based on the four equilibria model (presented in Theory), describing adsorption of electrolyte ions on a cell membrane surface, enabled to quantitative evaluation of the membranes characterizing parameters. The total concentrations of functional acidic (c_A) and basic (c_B) groups on the erythrocyte as well as

thrombocyte surface and their average association constants with hydrogen (K_{AH}) and hydroxyl (K_{BOH}) ions were calculated based on Eqs. 15 and 16, as described previously by Dobrzyńska et al. (2006). The determination of all above parameters was feasible by making an assumption that the K_{ANa} and K_{BCl} association constants values are the same as those obtained for phosphatidylcholine liposomes. The K_{ANa} and K_{BCl} values of phosphatidylcholine surface groups with sodium and chloride ions were previously reported and are equal to 0.230 and 0.076 m^3/mol, respectively (Dobrzyńska et al. 2007). The obtained c_A, c_B, K_{AH} and K_{BOH} values were substituted into Eq. 12 to produce a surface charge density versus pH theoretical curves for the studied cell membranes. The parameters characterizing both erythrocyte and thrombocyte surfaces are presented in Tables 1 and 2, respectively. These data were analyzed by standard statistical analyses and are expressed as mean and standard deviation.

As can be seen from Figs. 1 and 2, the theoretical and the experimental surface charge density values agree between pH 2 and 9 but diverge in the high pH range. The association equilibria depend on pH that is related to changes of ionic forms of the functional groups involved in the equilibria. Therefore, the observed deviation may be caused by the interactions occurring between the functional groups of the blood cell membrane components, which were not taken into account in the proposed theoretical model. The model describes the equilibria with electrolyte ions only. Biological membranes are complex systems, so it is currently difficult to indicate exactly what interactions may cause the effect of incompatibility of both curves only in the reliable pH range.

The concentration of acidic functional groups in erythrocytes after sudden unexpected death decreased compared with control groups; however, the concentration of basic groups did not change in a statistically significant manner (Table 1). The K_{AH} increased two times after sudden unexpected death compared with the control group, whereas the K_{BOH} value is eight times higher compared with the control group.

In thrombocytes after sudden unexpected death, we observed an increase in the acidic group's concentration c_A and an increase of the basic functional concentration c_B compared with the control group (Table 2). Sudden unexpected death induces an increase in K_{AH} and K_{BOH} values in thrombocytes compared with control groups.

Biochemical profiles at autopsy may show considerable case variations due to various factors involving preexisting disorders, cause of death, complications, and environment (Maeda et al. 2009). Luna (2009) postulated that forensic examiners need a real model of cadaveric physiology to understand the differences between living and cadaveric tissue. One of the most important elements of this model is evaluation of membrane changes in blood cells. Our results here demonstrate that the electrical properties of both erythrocyte and thrombocyte membranes are affected by sudden unexpected death. Our experiment demonstrates that alterations in surface charge of the human cell membranes results in variations of all analyzed parameters (c_A, c_B, K_{AH}, and K_{BOH}). It is well known that a surface charge is dependent on molecular composition of the cell membrane, particularly of the type and number of surface functional groups. Numerous experiments studying such relationships have been previously performed with on model (Kotyńska et al. 2008; Dobrzyńska et al. 2007) as well as on biological membranes (Dobrzyńska et al. 2008; Szachowicz-Petelska et al. 2008). The analyzed post-mortem changes in the surface charge of the membranes compared to control are probably the result of a number of processes occurring in the cells membranes after sudden unexpected death. We suppose that existing interactions between the cell membrane components and between them and their surroundings lead to the appearance of new functional groups on the membrane surfaces and/or to the

Table 1 Total concentrations of acidic and basic functional groups of erythrocytes and their association constants with H^+ and OH^- ions

Group	Parameter			
	c_A (10^{-6} mol/m^2)	c_B (10^{-6} mol/m^2)	K_{AH} (10^2 m^3/mol)	K_{BOH} (10^7 m^3/mol)
Control	7.06 ± 0.42	1.54 ± 0.47	3.39 ± 1.12	3.65 ± 0.84
Sudden unexpected death	5.34 ± 0.10	1.68 ± 0.08	6.95 ± 0.73	30.7 ± 0.60

Table 2 Total concentrations of acidic and basic functional groups of thrombocytes and their association constants with H^+ and OH^- ions

Group	Parameter			
	c_A (10^{-6} mol/m^2)	c_B (10^{-6} mol/m^2)	K_{AH} (10^2 m^3/mol)	K_{BOH} (10^7 m^3/mol)
Control	3.67 ± 0.79	1.17 ± 0.21	2.81 ± 1.70	2.04 ± 0.59
Sudden unexpected death	6.44 ± 0.08	2.71 ± 0.07	4.67 ± 0.43	25.4 ± 0.56

disappearance of the existing ones, which in turn causes alterations in all analyzed parameters characterizing the cell membrane.

To our knowledge, this is the first report to describe the quantitative changes in cell membrane surface properties after sudden unexpected death. However, our study is preliminary. More in-depth research will provide essential information for understanding biological phenomena.

In conclusion, the interactions between erythrocyte and thrombocyte membranes after sudden unexpected death and solution ions have been characterized. The dependence of the surface charge density of the blood cells on pH was described by using a mathematical model derived from experimental electrophoretic data. The theoretical estimates of electric charge enabled the determination of both total concentrations of acidic and basic functional groups of the analyzed cell membranes and their association constants with electrolyte ions.

We emphasize that there are many problems in diagnosis in forensic medicine—for example, estimation of the time of death. Therefore, we are convinced that knowledge of the equilibria existing within postmortem cell membranes and the processes accompanying them can be helpful in understanding the results obtained by forensic analyses.

Acknowledgments The research was supported by the Medical University of Bialystok (grant ANZ-0604-113-21677L).

References

Alexander AE, Johnson P (1949) Colloid science. Clarendon Press, Oxford

Barber J (1980) Membrane-surface charges and potentials in relation to photosynthesis. Biochim Biophys Acta 594:253–308

Barrow GM (1996) Physical chemistry. McGraw-Hill, New York

Deshiikan SR, Papadopoulos KD (1998) Modified booth equation for the calculation of zeta potential. Colloid Polym Sci 276:117–124

Dobrzyńska I, Skrzydlewska E, Figaszewski Z (2006) Parameters characterizing acid–base equilibria between cell membrane and solution and their application to monitoring the effect of various factors on the membrane. Bioelectrochemistry 69:142–147

Dobrzyńska I, Kotyńska J, Figaszewski Z (2007) Changes in electrical charge of phosphatidylcholine and phosphatidylserine liposomal membranes caused by adsorption of monovalent ions. Chem Anal 52:931–944

Dobrzyńska I, Szachowicz-Petelska B, Skrzydlewska E, Figaszewski ZA (2008) Effects of green tea on physico-chemical properties of liver cell membrane of different age rats intoxicated with ethanol. Pol J Environ Stud 17:327–333

Dobrzyńska I, Szachowicz-Petelska B, Sulkowski S, Figaszewski ZA (2010) Characterization of the cell membrane during cancer transformation. J Environ Biol 31:845–850

Gennis RB (1989) Biomembranes: molecular structure and function. Springer-Verlag, New York

Kała M, Chudzikiewicz E (2003) The influence of post-mortem changes in biological material on interpretation of toxicological analysis results. Probl Forensic Sci 54:32–59

Kotyńska J, Dobrzyńska I, Figaszewski Z (2008) Effect of monovalent ion adsorption on the electric charge of phosphatidylcholine–decylamine liposomal membranes. J Bioenerg Biomembr 40:637–641

Langlois NE (2009) Sudden adult death. Forensic Sci Med Pathol 5:210–232

Luna A (2009) Is postmortem biochemistry really useful? Why is it not widely used in forensic pathology? Legal Med 11:27–30

Maeda H, Zhu BL, Ishikawa T, Quan L, Michiue T (2009) Significance of postmortem biochemistry in determining the cause of death. Legal Med 11:46–49

McLaughlin S, Harary H (1976) The hydrophobic adsorption of charged molecules to bilayer membranes. A test of the applicability of the Stern equation. Biochemistry 15:1941–1948

Monteggia E, Colombo I, Guerra A, Berra B (2000) Phospholipid distribution in murine mammary adenocarcinomas inducted by activated neu oncogene. Cancer Detect Prev 24:207–211

Mullet M, Fievet P, Reggiani JC, Pagetti J (1997) Surface electrochemical properties of mixed oxide ceramic membranes: zeta-potential and surface charge density. J Membr Sci 123:255–265

Nałęcz MJ, Wojtczak L (1982) Surface charge of biological membranes and its regulatory functions. Postepy Biochem 28:191–225

Nałęcz MJ, Zborowski J, Famulski KS, Wojtczak L (1980) Effect of phospholipid composition on the surface potential of liposomes and the activity of enzymes incorporated. Eur J Biochem 112:75–80

Naumowicz M, Kotyńska J, Petelska AD, Figaszewski ZA (2006) Impedance analysis of phosphatidylcholine membranes modified with valinomycin. Eur Biophys J 35:239–246

Petelska AD, Figaszewski ZA (2011) The equilibria of phosphatidylcholine–fatty acid and phosphatidylcholine–amine in monolayers at the air/water interface. Colloids Surf B 82:340–344

Petelska AD, Janica JR, Kotynska J, Łebkowska U, Figaszewski ZA (2012) The effect of contrast medium SonoVue® on the electric charge density of blood cells. J Membr Biol 245:15–22

Szachowicz-Petelska B, Dobrzyńska I, Skrzydlewska E, Figaszewski ZA (2008) Changes in phospholipids composition studied by HPLC and electric properties of liver cell membrane of ethanol-poisoned rats. Toxicol Mech Methods 18:525–530

Szachowicz-Petelska B, Skrzydlewska E, Figaszewski ZA (2010) Changes in protein composition in erythrocyte membrane of ethanol poisoned rats after administration of teas. Anal Lett 43:721–734

Takeichi S, Wakasugi C, Shikata I (1984) Fluidity of cadaveric blood after sudden death: part I. Posmorten fibrinolysis and plasma catecholamine level. Am J Forensic Med Pathol 5:223–227

Takeichi S, Wakasugi C, Shikata I (1985) Fluidity of cadaveric blood after sudden death: part II. Mechanism of release of plasminogen activator from blood vessels. Am J Forensic Med Pathol 6:25–29

Takeichi S, Wakasugi C, Shikata I (1986) Fluidity of cadaveric blood after sudden death: part III. Acid–base balance and fibrinolysis. Am J Forensic Med Pathol 7:35–38

Yermiyahu U, Ben-Hayyim S, Nir G, Kafkafi U, Scherer GFE, Kinraide TB (1999) Surface properties of plasma membrane vesicles isolated from melon (*Cucumus melo* L.) root cells differing in salinity tolerance. Colloids Surf B 14:237–249

J Membrane Biol (2012) 245:191–200
DOI 10.1007/s00232-012-9429-3

Protective Effect of Blackcurrant on Liver Cell Membrane of Rats Intoxicated with Ethanol

Barbara Szachowicz-Petelska · Izabela Dobrzyńska · Elżbieta Skrzydlewska · Zbigniew Figaszewski

Received: 12 December 2011 / Accepted: 1 April 2012 / Published online: 20 April 2012

Abstract Chronic ethanol intoxication oxidative stress participates in the development of many diseases. Nutrition and the interaction of food nutrients with ethanol metabolism may modulate alcohol toxicity. One such compound is blackcurrant, which also has antioxidant abilities. We investigated the effect of blackcurrant as an antioxidant on the composition and electrical charge of liver cell membranes in ethanol-intoxicated rats. Qualitative and quantitative phospholipid composition and the presence of integral membrane proteins were determined by high-performance liquid chromatography. Electrophoresis was used to determine the surface charge density of the rat liver cell membranes. Ethanol intoxication is characterized by changes in cell metabolism that alter the structure and function of cell membrane components. Ethanol increased phospholipid levels and altered the level of integral proteins as determined by decreased phenylalanine, cysteine, and lysine. Ethanol significantly enhanced changes in the surface charge density of the liver cell membranes. Administration of blackcurrant to rats intoxicated with ethanol significantly protected lipids and proteins against oxidative modifications. It is possible that the beneficial effect of blackcurrant is connected with its abilities to scavenge free radicals and to chelate metal ions.

Keywords Amino acids · Blackcurrant · Ethanol · Liver cell membrane proteins · Peptides · Phospholipids · Surface charge density

B. Szachowicz-Petelska · I. Dobrzyńska · Z. Figaszewski (✉)
Institute of Chemistry, University in Białystok,
Al. Piłsudskiego 11/4, 15-443 Białystok, Poland
e-mail: elchem@uwb.edu.pl

E. Skrzydlewska
Department of Analytical Chemistry, Medical University of Białystok, Mickiewicza 2, 15-230 Białystok, Poland

Z. Figaszewski
Laboratory of Electrochemical Power Sources, Faculty of Chemistry, University of Warsaw, Pasteur St. 1, 02-093 Warsaw, Poland

Several exterior factors could be implicated in the oxidative stress formation and cell injury, for example, chronic consumption of ethanol that induces reactive oxygen species (ROS) production (Ponappa and Rubin 2000; Vallet et al. 1997).

The oxidative stress induced by chronic ethanol consumption has been implicated in changes in the structure and function of liver cell components, including membrane phospholipids and proteins. Any perturbation in the action of the cell is manifested by variations in the action of the cell membrane, i.e., in its electric double layer (Szachowicz-Petelska et al. 2010; Dobrzyńska et al. 2010). An essential property of the electric double layer is its electric charge, which can be altered by various xenobiotics or by metabolic transformations.

Ethanol is rapidly absorbed from the gastrointestinal tract, and about 90 % of it is metabolized in the liver. There, ethanol is oxidized into acetaldehyde and then into acetate. These processes are accompanied by free radical generation (Ponappa and Rubin 2000; Vallet et al. 1997). Acetaldehyde and ROS can react with amino acids, peptides, and proteins, modifying their composition and function (Grimsrud et al. 2008; Dorn and Petersen 2002). ROS can also react with lipids causing peroxidation (Kato et al. 1990). Free radical peroxidation, especially of unsaturated lipids, disrupts the important structural and protective functions associated with

biomembranes. Certain in vivo pathological events result from this oxidation (Wagner et al. 1994). Therefore, alcohol abuse has been related to a number of biochemical changes and disorders in humans and animals (Ward et al. 2009).

Nutrition and the interaction of food nutrients with ethanol metabolism may modulate alcohol toxicity. Diets rich in fruits are associated with a reduced risk for this pathology, and protection has often been attributed to antioxidant vitamins such as vitamin C, vitamin E, and β-carotene. Although fruits are primary sources for these nutrient antioxidant, other dietary components may also be important protective agents. Flavonoids are plant polyphenolic compounds ubiquitous in fruits. Flavonoids are primarily categorized into flavonols, flavones, flavanols, flavanones, and anthocyanins (Prior 2003). Anthocyanins are the largest group of phenolics in blackcurrants, and they have shown a high antioxidant activity, which influences the oxidation of low-density lipoprotein and food lipids (Satué-Gracia et al. 1997; Fukumoto and Mazza 2000; Smith et al. 2000). Blackcurrants, which are rich in anthocyanins and other phenolics, have been found to posses a varying antioxidant ability (Fukumoto and Mazza 2000; Kähkönen et al. 2001; Moyer et al. 2002).

Therefore, we investigated whether blackcurrant consumption affects the phospholipid and integral membrane protein content as well as the electrical properties of liver cell membranes of ethanol-intoxicated rats.

Materials and Methods

Blackcurrant (*Ribes nigrum* L.) was used as a juice (containing 28 % pure blackcurrant juice). Blackcurrant juice was purchased in the local supermarket. Rats drank this commercial blackcurrant juice ad libitum instead of water. The content of drinking vessels was renewed every day with 250 ml of fresh juice. The total amount of phenols in the juice was spectrophotometrically determined by using Folin–Ciocatleu's phenol reagent (Kapasakalidis et al. 2006). The total amount of polyphenols in blackcurrant juice was 1,269 mg of gallic acid equivalents per liter. Anthocyanin concentration was determined by high-performance liquid chromatography (HPLC) with a diode-array detector; detection was at 520 nm (Kapasakalidis et al. 2006). The concentration of four main anthocyanins in blackcurrant juice was 18.28, 14.06, 2.33, and 1.61 µmol/l for delphinidin-3-rutinoside, cyaniding-3-rutinoside, delphinidin-3-glucoside, and cyanidnin-3-glucoside, respectively. The level of vitamin C in the juice was determined by HPLC with a UV detector (Ivanović et al. 1999). The concentration of vitamin C was 50.03 mg/l.

Animals

Twelve-month-old male Wistar rats were used for the experiment. They were housed in groups with free access to a granular standard diet and water and maintained under a normal light–dark cycle. All experiments were approved by the local ethics committee in Białystok, Poland, according to the Polish Act Protecting Animals of 1997.

The animals were divided into the following groups. The control group was treated intragastrically with 1.8 ml of physiological saline every day for 4 weeks ($n = 6$). The blackcurrant group received blackcurrant juice ad libitum instead of water for 1 week. Next, animals in this group were treated intragastrically with 1.8 ml of physiological saline and received black tea solution ad libitum instead of water every day for 4 weeks ($n = 6$). The ethanol group was treated intragastrically with 1.8 ml of ethanol in doses from 2.0 to 6.0 g/kg body weight every day for 4 weeks. The dose of ethanol was gradually increased by 0.5 g/kg body weight every 3 days ($n = 6$).

The ethanol and blackcurrant groups were given blackcurrant juice ad libitum instead of water for 1 week. Next the animals were treated intragastrically with 1.8 ml of ethanol in doses from 2.0 to 6.0 g/kg body weight and received blackcurrant juice ad libitum instead of water every day for 4 weeks.

Isolation of Liver Cell Membranes

Livers (approximately 1.5 g) were homogenized in a solution containing 1 mM $NaHCO_3$ (pH 7.6) and 0.5 mM $CaCl_2$ in a loose-fitting Dounce homogenizer. The addition of 0.5 mM $CaCl_2$ increased the cell membrane sedimentation, as determined by measurement of 5′-nucleotidase activity (Ipata 1967). Membrane fragments were separated from nuclei and mitochondria by rate-zonal centrifugation of the low-speed pellet, as described previously (Evans 1970). The sediment was homogenized in sucrose (1.22 g/cm^3 density) and in the next step was covered with sucrose (1.16 g/cm^3 density). The cell membranes were separated by centrifugation at 2,000×g for 25–35 min. Membrane purity was determined by spectrophotometric determination of 5′-nucleotidase (EC 3.1.3.5) activity as described previously (Ipata 1967).

Isolation and Analysis of Phospholipids by HPLC

The Folch method was used to extract phospholipids (Folch et al. 1957). The cell membrane was homogenized in a chloroform–methanol mixture (2:1 volume ratio). The solution was then filtered with degreased paper filters, and the precipitate was washed with an extracting solution (8:4:3 chloroform:methanol:aqueous calcium chloride

solution 0.05 M calcium chloride). The suspension was centrifuged at 500×*g* for 2 min, the organic and the aqueous phases were separated, and the aqueous phase was shaken again with a chloroform, methanol, and water mixture (3:48:47 volume ratio), and the phases were separated. The organic phases were combined and evaporated to dryness. The extract was dissolved in 200 µl of hexane:isopropanol mixture (3:2) (Ostrowska et al. 2000). Addition of 0.03 % tert-butylhydroxytoluene and flushing with nitrogen at each step in the procedure were used to prevent oxidation during lipid extraction.

HPLC analysis was performed on the extracted phospholipids to assess the quantities phosphatidylinositol (PI), phosphatidylserine (PS), phosphatidylethanolamine (PE), and phosphatidylcholine (PC). The isolated phospholipids were separated by group analysis in a silica gel column using normal phase (NP) HPLC; acetonitrile–methanol–phosphoric acid (85 %) mixture (130:5:1.5 volume ratio) by isocratic elution at 1 ml/s flow rate and 214 nm wavelength (Dobrzyńska et al. 2005b).

Extraction of Membrane Proteins

The liver cell membranes were homogenized in 5 mM NaOH. PMSF (phenyl–methyl–sulfonyl fluoride) was added to a final concentration of 1 µM to inhibit proteolysis. The suspension was centrifuged for 45 min at 1,000×*g* (Josić et al. 1985).

The residual cell membranes were solubilized in 30 ml buffer containing 20 mM Tris/HCl (pH 7.4) and 1 % Triton X-100 at 4 °C. The suspension was centrifuged at 1,000×*g* for 10 min. The supernatant was incubated at 32 °C for 2 h (Tani et al. 1997) and was then dialyzed against distilled water and evaporated until dry.

Trypsin Hydrolysis of Proteins

The protein extract was weighed and dissolved in phosphate buffer (pH 7.4) to yield a final protein concentration of approximately 0.10 mg/ml. A stock solution of trypsin (0.05 mg/ml in H_2O) was added at an enzyme:substrate ratio of 1:25. The reaction mixtures were incubated at 37 °C for 1 h. Hydrolysis was stopped by the addition of PMSF to a final concentration of 1 µM) (Persaud et al. 2000), and the hydrolysate was then evaporated until dry and dissolved in 200 µl H_2O.

Separation of the Peptide Mixture of Integral Membrane Proteins by HPLC

After hydrolysis, the peptides were separated by HPLC on a LichroCART RP-18 column 100A (5 µm, 250 × 4.0 mm) equilibrated with solvent A (0.1 % trifluoroacetic acid (TFA) in H_2O) and eluted with a linear gradient to 20 % solvent B (0.1 % TFA in acetonitrile) during the first 8 min, to 70 % solvent B during the next 20 min, and to 100 % solvent B during the final 4 min at 220 nm. The flow rate was 1 ml/min (Skrzydlewska et al. 1998). The Merck HPLC system was equipped with a pump, a UV detector, an analog interface module D-6000 A, and System Manager software. A typical separation of the peptide mixture containing liver integral membrane proteins is provided in Fig. 1.

Peptide Assignment

The amino acid compositions of isolated peptides (6.2, 8.2, 9.1, 11.7, 12.6, 14, 17.1, 27.4, 28.9, and 30.7 min) were determined by HPLC after acid hydrolysis under vacuum in

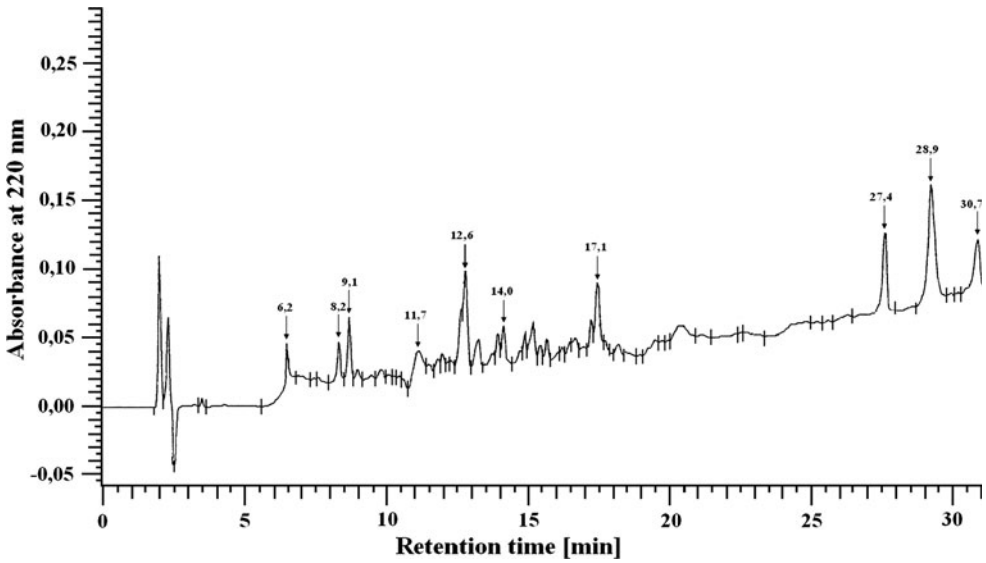

Fig. 1 Typical separation of peptides from liver integral membrane proteins (UV detected at 220 nm)

the presence of 6 M HCl for 24 h at 110 °C. The amino acid separation was performed on a Lichrosorb NH_2 column 100A (5 μm, 250 × 4.6 mm). The mobile phase consisted of solvents A (0.01 M KH_2PO_4, pH 4.3) and B (a 500:70 mixture of acetonitrile/water). All separations were performed with a 5–50 % gradient of solvent A using a flow rate of 1 ml/min. The amino acids were detected at a wavelength of 200 nm (Schuster 1980). All the peptides originated from different groups that consistently contained the following three amino acids: phenylalanine (Phe), cysteine (Cys), and lysine (Lys). Figure 2 shows the separation of these amino acids from a typical peptide mixture after the hydrolysis of proteins isolated from liver cell membranes.

Under the chromatographic conditions tested, a linear relationship was verified in the ranges 20–80 μg/ml for Phe, 0.15–1.0 μg/ml for Cys, and 250–400 mg/ml for Lys using standardized solutions and analysis of variance of the regression (r^2). The r^2 values for all of these compounds were 0.990.

Electrochemical Methods

To determine the surface charge density of the cell membrane, liver tissue was exposed to trypsin action. Received cells were put into the measuring vessel, and then electrophoretic mobility on dependent pH was measured with a Zetasizer Nano ZS (Malvern Instruments, UK).

The surface charge density has been determined by the equation $\sigma = \eta u/d$, where u is the electrophoretic mobility, η is the viscosity of the solution, and d is the diffuse layer thickness (Krysiński and Tien 1986). The diffuse layer thickness was determined by a formula from Barrow (1996):

$$d = \sqrt{\frac{\varepsilon\varepsilon_0 RT}{2F^2 I}}$$

where R is the gas constant, T is the temperature, F is the Faraday number, I is the ionic strength of 0.9 % NaCl, and ε and ε_o are the relative and absolute permittivities of the medium.

Acidic (C_{TA}) and basic (C_{TB}) functional group concentrations and their average association constants with hydrogen (K_{AH}) or hydroxyl (K_{BOH}) ions were determined as described previously (Dobrzyńska et al. 2005a).

Statistical Analysis

Data are expressed as mean ± standard deviation. These data were analyzed by standard statistical techniques, specifically one-way analysis of variance with Tukey's test for multiple comparisons, to determine significant differences between different groups. The data were analyzed separately for treatment groups. A P value of less than 0.05 was considered statistically significant.

Results

Blackcurrant Administration Affects the Phospholipid Composition of Liver Cell Membranes from Ethanol-Intoxicated Rats

Ethanol intoxication caused an increase in the phospholipid content in the liver cell membrane compared with the control group (Fig. 3). The content of the individual phospholipids—phosphatidylinositol (PI), phosphatidylserine (PS), phosphatidylethanolamine (PE), and phosphatidylcholine (PC)—increased by about 60, 90, 100, and 80 %, respectively. Administration of alcohol to blackcurrant-exposed rats caused a smaller increase in PI, PS, PE, and PC than administration of ethanol alone. In the rats treated with blackcurrant alone and the control rats, no essential differences were observed in the phospholipid content.

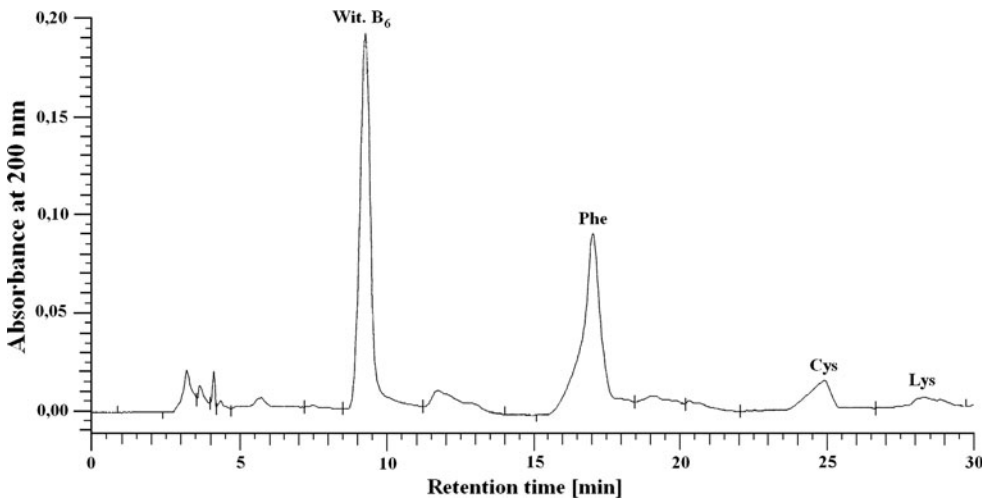

Fig. 2 Chromatogram for the amino acids Phe, Cys, and Lys, which occurred in the all of the peptides for each treatment group after hydrolysis of liver cell membrane protein isolates (UV detected at 200 nm)

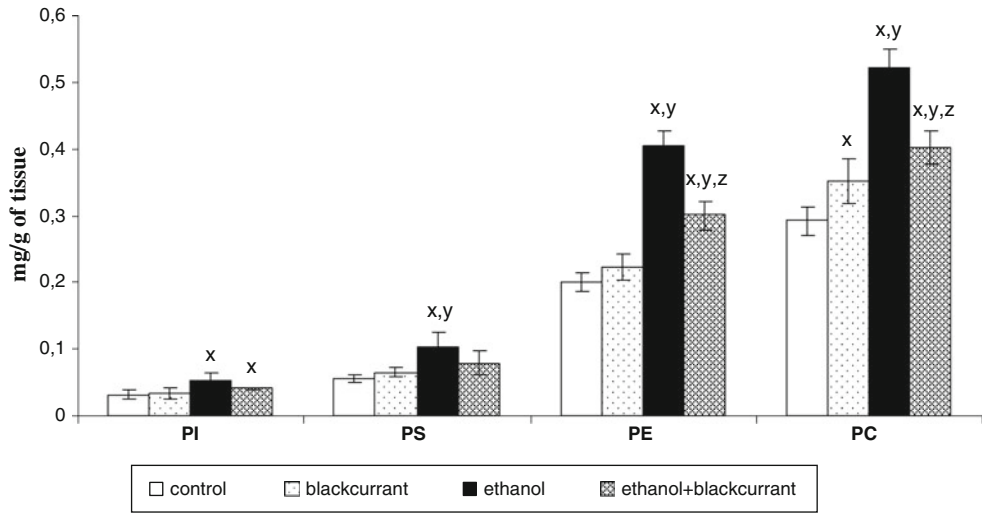

Fig. 3 Blackcurrant affects the liver cell membrane content of four phospholipid classes. After exposure to ethanol, blackcurrant, both, or neither, rat liver cell membranes were isolated and the phospholipid content assessed as described in "Materials and Methods" section. Data points represent mean ± SD, $n = 6$ ($^{x}P < 0.05$ in comparison with values for control group; $^{y}P < 0.05$ in comparison with values for blackcurrant group; $^{z}P < 0.05$ in comparison with values for ethanol group)

Blackcurrant Administration Affects Integral Membrane Proteins of Liver Cell Membranes from Ethanol-Intoxicated Rats

Selective hydrolysis of integral membrane proteins to peptides, resolution by HPLC, and subsequent determination of the amount of specific amino acids within individual peptides is one method used to study pathological changes in integral membrane proteins. Up to a 40 % decrease in integral membrane protein levels was observed in the ethanol group relative to the control and blackcurrant groups (Table 1). In contrast, the group that consumed both blackcurrant and ethanol had integral membrane protein levels that were higher than the ethanol group but lower than the control and blackcurrant-alone groups.

Figure 4 shows changes in peptide content after hydrolysis of proteins isolated from liver cell membranes of the control, ethanol, blackcurrant, and ethanol with blackcurrant groups. Ethanol intoxication caused an decrease in peptide levels in the ethanol group relative to the control, blackcurrant, and ethanol with blackcurrant groups. The peptide contents at the retention times of 6.2, 8.2, 9.1, 11.7, 12.6, 14, 17.1, 27.4, 28.9, and 30.7 min decreased approximately 20, 10, 30, 30, 20, 20, 25, 25, 20, and 15 %, respectively, in the ethanol group relative to the control group. Rats that consumed blackcurrant with ethanol had higher integral membrane protein content than those that consumed ethanol alone. No significant differences were observed between the control group and the blackcurrant-alone group.

No significant differences in the content of Phe, Cys, and Lys individually were observed in rats treated with blackcurrant relative to the control group. The ethanol group showed a decrease in the amount of individual amino acids relative to the control group (Figs. 5, 6, 7). The amino acid contents at the retention times 6.2, 8.2, 9.1, 11.7, 12.6, 14, 17.1, 27.4, 28.9, and 30.7 min decreased by approximately 45, 30, 20, 20, 10, 35, 20, 30, 30, and 15 %, respectively for Phe; decreased by approximately 20, 30, 20, 20, 30, 40, 30, 40, 30, and 20 %, respectively, for Cys; and decreased by approximately 35, 60, 20, 40, 50, 10, 10, 40, 50, and 30 %, respectively, for Lys. The largest decrease was seen with Lys, which was reduced by 60 % (8.2 min), 40 % (11.7 min), 50 % (12.6 min), 40 % (27.4 min), and 50 % (28.9 min). Administration of alcohol to rats consuming blackcurrant led to an increase in the amount of Phe, Cys, and Lys relative to the ethanol-alone group.

Table 1 Effect of blackcurrant on integral membrane protein content in liver cell membranes of rats receiving ethanol, blackcurrant, or both

Group	Integral protein (mg/g tissue)
Control	4.4 ± 0.35
Blackcurrant	4.0 ± 0.34
Ethanol	$2.81 \pm 0.22^{x,y}$
Ethanol + blackcurrant	$3.52 \pm 0.28^{x,y,z}$

Data points represent mean ± SD, $n = 6$

^{x} $P < 0.05$ in comparison with values for control group

^{y} $P < 0.05$ in comparison with values for blackcurrant group

^{z} $P < 0.05$ in comparison with values for ethanol group

Effect of Blackcurrant on Electric Properties of Liver Cell Membrane of Ethanol-Intoxicated Rats

Administering ethanol to the rats provokes an increase in liver cell membrane C_{TA} (26 %) and C_{TB} (31 %) compared

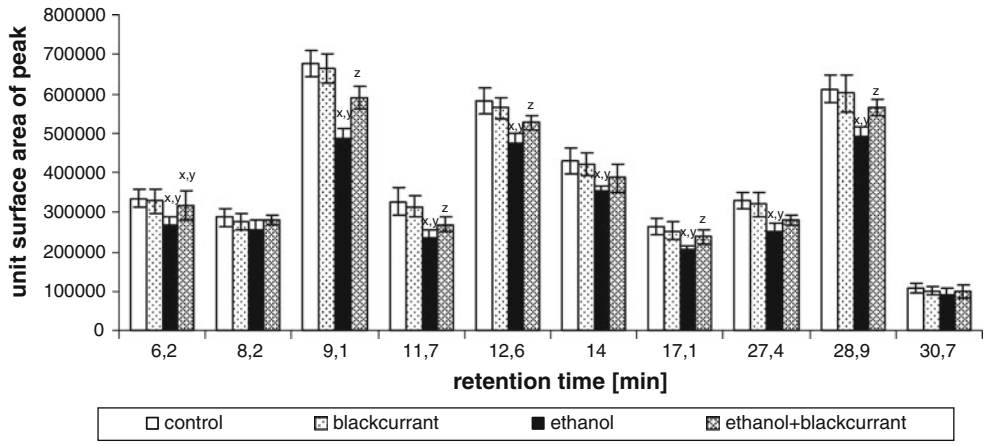

Fig. 4 Blackcurrant affects the peptide content of hydrolyzed liver cell membranes from rats fed ethanol. Data points represent mean ± SD, $n = 6$ ($^{x}P < 0.05$ in comparison with values for control group; $^{y}P < 0.05$ in comparison with values for blackcurrant group; $^{z}P < 0.05$ in comparison with values for ethanol group)

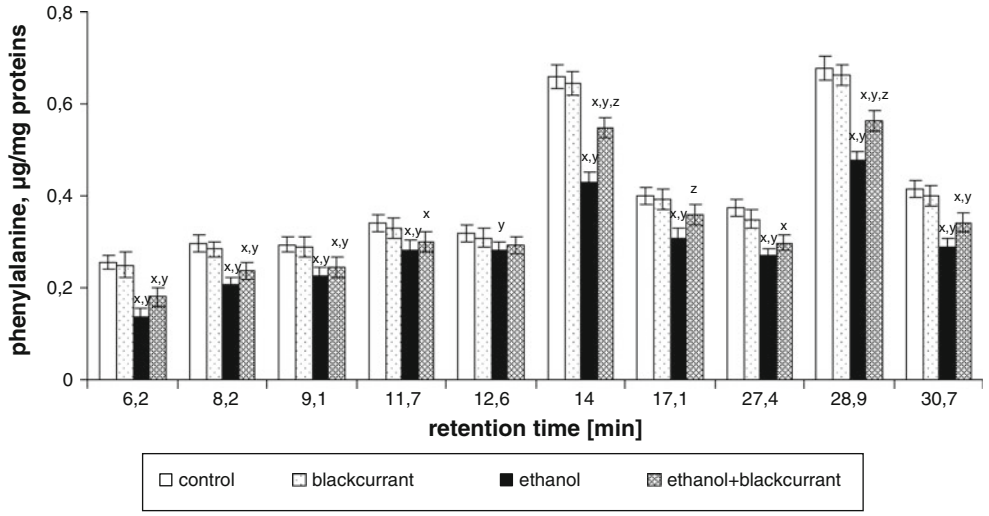

Fig. 5 Blackcurrant affects Phe levels in integral membrane proteins from liver cell membranes. Data points represent mean ± SD, $n = 6$ ($^{x}P < 0.05$ in comparison with values for control group; $^{y}P < 0.05$ in comparison with values for blackcurrant group; $^{z}P < 0.05$ in comparison with values for ethanol group)

with the control group (Table 2). The concentration of acidic (11 %) and basic (10 %) groups in the liver cell membrane decreased in animals fed ethanol and blackcurrant compared with animals fed ethanol only. Administering blackcurrant to the rats increased the association constant of the acidic groups (K_{AH}) of the liver cell membrane compared to the control groups. In both groups, K_{BOH}, the association constant of the basic groups of the liver cell membrane, decreased after administering blackcurrant compared with the control group. Administering ethanol induces a decrease in K_{AH} (49 %) and an increase in K_{BOH} (48 %) in the rat liver cell membranes compared with the control groups. Administering blackcurrant with ethanol also induced an increase in the K_{AH} value (15 %) and a decrease in the K_{BOH} value (45 %) compared with the ethanol groups.

Discussion

The liver is the main organ responsible for metabolism of both endogenous and exogenous compounds, and therefore it is also one of the first target organs for the toxic action of xenobiotics or their reactive metabolites.

Ethanol intoxication causes a wide variety of metabolic disorders in human and animals, mainly caused by free radicals, and hydroxyl radicals in particular. Hydroxyl radicals readily react with cell components, especially with lipids and proteins (Gieseg et al. 2000). This is manifested by an increase in lipid peroxidation and protein oxidative modification products observed in this study. Oxidative modifications of proteins are usually initiated by hydroxyl radicals, as a result of which oxidation of amino acid

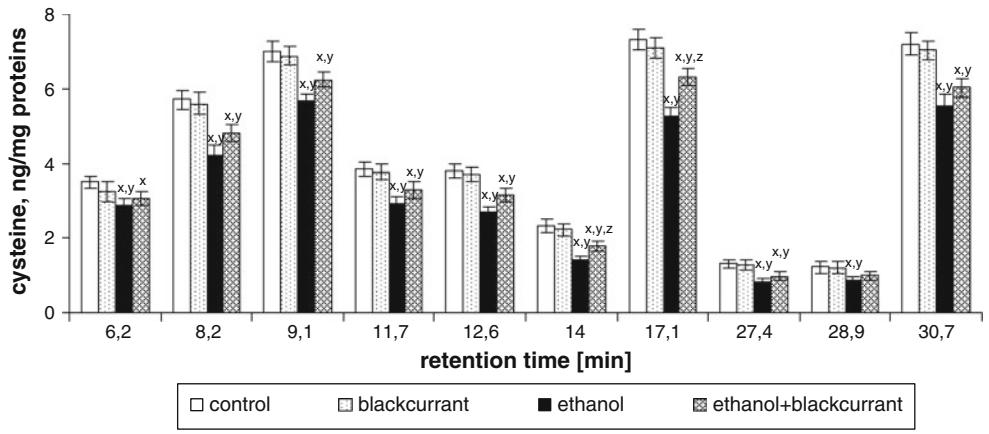

Fig. 6 Blackcurrant affects Cys levels in integral membrane proteins from liver cell membranes. Data points represent mean ± SD, $n = 6$ ($^{x}P < 0.05$ in comparison with values for control group; $^{y}P < 0.05$ in comparison with values for blackcurrant group; $^{z}P < 0.05$ in comparison with values for ethanol group)

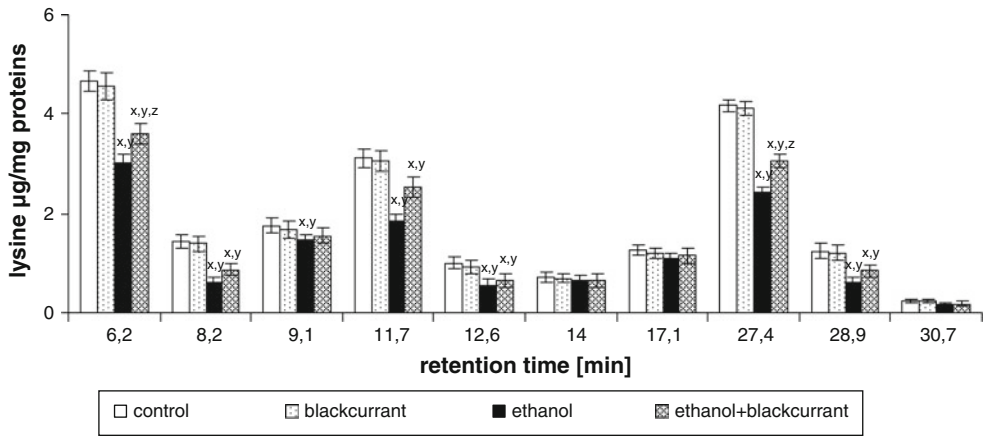

Fig. 7 Blackcurrant affects Lys levels in integral membrane proteins from liver cell membranes. Data points represent mean ± SD, $n = 6$ ($^{x}P < 0.05$ in comparison with values for control group; $^{y}P < 0.05$ in comparison with values for blackcurrant group; $^{z}P < 0.05$ in comparison with values for ethanol group)

residues and oxidation in polypeptide chain of protein take place that lead to fragmentation and/or formation of cross-link bindings (Davies 1987; Stefek et al. 2005; Wu et al. 2009). All amino acids are susceptible to attack by free radicals, although some of them are more vulnerable than others—those that are most sensitive to oxidation include aromatic amino acids such as phenylalanine and tyrosine. Moreover, the levels of bistyrosine—the product of a reaction between free radicals and tyrosine—are known to increase during ethanol ingestion (Łuczaj et al. 2006). As such, bistyrosine production is a useful marker for protein modification by hydroxyl radicals (Giulivi et al. 2003). As a sulfydryl amino acid, Cys is also extremely sensitive to free radicals. Reports have shown that the cysteine:cystine ratio of proteins is altered under oxidizing conditions (Kalyanaraman 1995). The occurrence of these types of reactions would explain the decrease in the number of Phe and Cys amino acids detected in our study (Figs. 5, 6).

Ethanol-induced oxidative modifications of membrane cell phospholipids were also observed in this and earlier studies. This was manifested by an increase in the level of all phospholipids in liver cell membranes (Fig. 3).

Therefore, the increase in phospholipids caused by ethanol intoxication is accompanied by decreased integral membrane proteins in liver cell membranes. Changes in membrane composition are connected with changes in cell membrane charge. Our results demonstrate that the electrical properties of liver cell membranes are affected by ethanol intoxication (Fig. 8; Table 2). An increase in the amount of specific phospholipids results in the appearance of additional functional groups, both positively and negatively charged, at the membrane surface. Changes in

Table 2 Effect of blackcurrant on the C_{TA}, C_{TB}, K_{AH}, and K_{BOH} of liver cell membranes from ethanol-intoxicated rats

Group	C_{TA} (10^{-7}−mol/m^2)	C_{TB} (10^{-7} mol/m^2)	K_{AH} (m^3/mol)	K_{BOH} (10^6 m^3/mol)
Control	2.31 ± 0.08	0.96 ± 0.08	34.04 ± 1.10	7.10 ± 0.21
Blackcurrant	2.28 ± 0.07	0.95 ± 0.07	33.54 ± 1.01	7.55 ± 0.20^{x}
Ethanol	2.92 ± 0.10^{x,y}	1.28 ± 0.06^{x,y}	22.81 ± 1.27^{x,y}	10.51 ± 0.24^{x,y}
Ethanol + blackcurrant	2.62 ± 0.09^{x,y,z}	1.17 ± 0.05^{x,y,z}	27.12 ± 1.11^{x,y,z}	8.90 ± 0.25^{x,y,z}

Data points represent mean ± SD, $n = 6$

^{x} $P < 0.05$ in comparison with values for control group

^{y} $P < 0.05$ in comparison with values for blackcurrant group

^{z} $P < 0.05$ in comparison with values for ethanol group

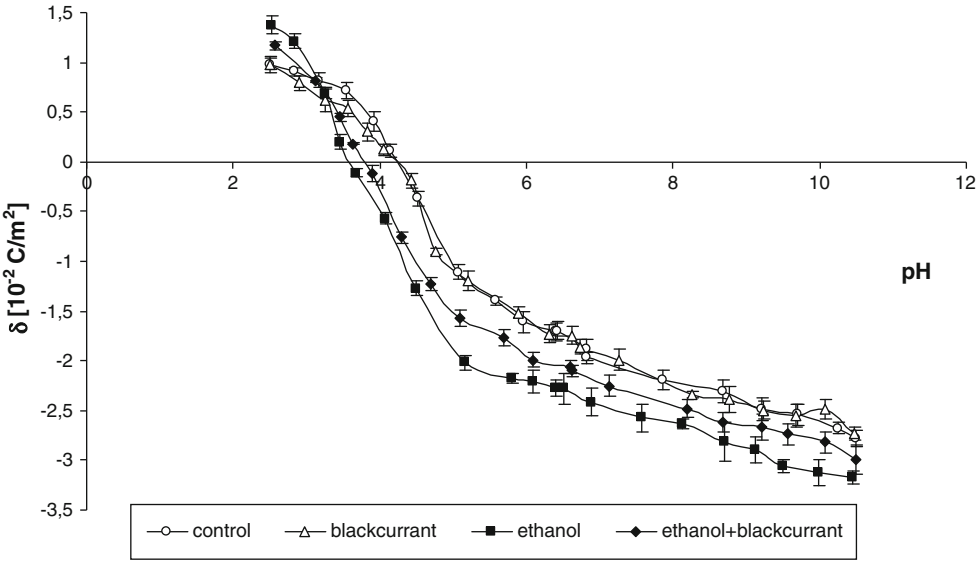

Fig. 8 Blackcurrant prevents changes in electrical properties of liver cell membranes from rats fed ethanol

membrane structure caused by the modification of protein structure lead to yield higher negative electric charge at high pH values and lower positive electric charges at low pH values (Szachowicz-Petelska et al. 2005, 2008; Dobrzyńska et al. 2008). Variations in the number and kind of functional groups result in changes in C_{TA} and C_{TB} and, in turn, in their association constant values (Table 2).

Oxidative stress and oxidative damage of cell components caused by ethanol are also counteracted by compounds that have antioxidant properties, which are able to modulate ethanol metabolism in the organism. One of such potent antioxidant is blackcurrant, which is known as a fruit with a strong in vitro antioxidative capacity, but its in vivo antioxidant efficacy has not yet been characterized (Salobir et al. 2010; Viljanen et al. 2004; Valentova et al. 2007). In this study, it has been shown that blackcurrant significantly protects phospholipids as well as protein against oxidative modification of Phe, Cys, and Lys.

Blackcurrant is rich in monomeric and polymeric phenolic compounds providing protection toward both lipid and protein oxidation (Viljanen et al. 2004). Phenolic compounds have been shown to be effective antioxidants in inhibiting lipid oxidation (Kähkönen et al. 2001; Mullen et al. 2002; Kähkönen and Heinonen 2003) as well as potent radical scavengers (Riedl and Hagerman 2001). In addition, anthocyanins have been shown to chelate metal ions at moderate pH with their ionized hydroxyl groups of the B ring (Prior 2003). It was postulated that phenolic compounds inhibit oxidation of proteins both by retarding the oxidation reactions by binding to the proteins and by forming complexes between protein molecules (Viljanen et al. 2005).

Our results provide evidence for the effectiveness of blackcurrant in the prevention of ethanol-induced oxidative stress. This indicates the possibility of the use of this natural antioxidant in preventing disorders initiated by oxidative stress.

References

Barrow GM (1996) Physical chemistry. McGraw-Hill, New York

Davies KJA (1987) Protein damage and degradation by oxygen radicals: I. General aspects. J Biol Chem 262:9895–9901

Dobrzyńska I, Skrzydlewska E, Figaszewski ZA (2005a) Parameters characterizing acid–base equilibria between cell membrane and solution and their application to monitoring the effect of various factors on the membrane. Bioelectrochemistry 276:113–119

Dobrzyńska I, Szachowicz-Petelska B, Sulkowski S, Figaszewski ZA (2005b) Changes in electric charge and phospholipid composition in human colorectal cancer cells. Mol Cell Biochem 276:113–119

Dobrzyńska I, Szachowicz-Petelska B, Skrzydlewska E, Figaszewski ZA (2008) Effects of green tea on physico-chemical properties of liver cell membrane of different age rats intoxicated with ethanol. Pol J Environ Stud 17:327–333

Dobrzyńska I, Szachowicz-Petelska B, Skrzydlewska E, Figaszewski ZA (2010) Effect of L-carnitine on liver cell membranes in ethanol-intoxicated rats. Chem Biol Interact 188:44–51

Dorn JA, Petersen DR (2002) Covalent modification of amino acid nucleophiles by the lipid peroxidation products 4-hydroxy-2-nonenal and 4-oxo-2-nonenal. Chem Res Toxicol 15:1445–1450

Evans WH (1970) Fractionation of liver plasma membranes prepared by zonal centrifugation. Biochem J 166:833–842

Folch J, Lees M, Stanley GHS (1957) A simple method for the isolation and purification of total lipids from animal tissues. J Biol Chem 226:497–509

Fukumoto L, Mazza G (2000) Assessing antioxidant and prooxidant activity of phenolic compounds. J Agric Food Chem 48: 3597–3604

Gieseg S, Duggan S, Gebicki JM (2000) Peroxidation of proteins before lipids in U937 cells exposed to peroxyl radicals. Biochem J 350:215–218

Giulivi C, Traaseth NJ, Davies KJ (2003) Tyrosine oxidation products: analysis and biological relevance. Amino Acids 25: 227–232

Grimsrud PA, Xie H, Griffin TJ, Bernlohr DA (2008) Oxidative stress and covalent modification of protein with bioactive aldehydes. J Biol Chem 283:21837–21841

Ipata PL (1967) A coupled optical enzyme assay for 5′-nucleotidase. Anal Biochem 20:30–36

Ivanović D, Popović A, Radulović D, Medenica M (1999) Reversed-phase ion-pair HPLC determination of some water-soluble vitamins in pharmaceuticals. J Pharm Biomed Anal 18:999–1004

Josić D, Schuett W, Neumeier R, Reutter W (1985) Purification of liver and hepatoma membrane proteins by high-performance liquid chromatography. FEBS Lett 185:182–186

Kähkönen MP, Heinonen M (2003) Antioxidant activity of anthocyanins and their aglycones. J Agric Food Chem 51:628–633

Kähkönen MP, Hopia AI, Heinonen M (2001) Berry phenolics and their antioxidant activity. J Agric Food Chem 49:4076–4082

Kalyanaraman B (1995) Radical intermediates during degradation of lignin-model compounds and environmental pollutants: an electron spin resonance study. Xenobiotica 25:667–675

Kapasakalidis PG, Rastall RA, Gordon MH (2006) Extraction of polyphenols from processed blackcurrant (*Ribes nigrum* L.) residues. J Agric Food Chem 54:4016–4021

Kato S, Kawase T, Alderman J, Inatori N, Lieber CS (1990) Role of xanthine oxidase in ethanol-induced lipid peroxidation. Gastroenterology 98:203–210

Krysiński P, Tien HY (1986) Membrane electrochemistry. Prog Surf Sci 23:17–412

Łuczaj W, Siemieniuk E, Roszkowska-Jakimiec W, Skrzydlewska E (2006) Protective effect of black tea against ethanol-induced oxidative modifications of liver proteins and lipids. J Stud Alcohol 67:510–518

Moyer RA, Hummer KE, Finn CE, Frei B, Wrolstad RE (2002) Anthocyanins, phenolics, and antioxidant capacity in diverse small fruits: vaccinum, rubus, and ribes. J Agric Food Chem 50:519–525

Mullen W, McGinn J, Lean MEJ, MacLean MR, Gardner P, Duthie GG, Yokota T, Crozier A (2002) Ellagitannins, flavonoids, and other phenolics in red raspberries and their contribution to antioxidant capacity and vasorelaxation properties. J Agric Food Chem 50:5191–5196

Ostrowska J, Skrzydlewska E, Figaszewski Z (2000) Isolation and analysis of phospholipids. Chem Anal 45:613–618

Persaud DR, Dalgleish DG, Nadeau L, Gauthier S (2000) Isolation and purification of serum and interfacial peptides of a trypsin-olyzed beta-lactoglobulin oil-in-water emulsion. J Chrom B Biomed Sci Appl 744:389–397

Ponappa BC, Rubin E (2000) Modeling alcohol's effects on organs in animal models. Alcohol Res Health 24:93–104

Prior RL (2003) Fruits and vegetables in the prevention of cellular oxidative damage. Am J Clin Nutr 78:570S–578S

Riedl KM, Hagerman AE (2001) Tannin–protein complexes as radical scavengers and radical sinks. J Agric Food Chem 49:4917–4923

Salobir J, Zontar TP, Lewart A, Rezar V (2010) The comparison of black currant juice and vitamin E for the prevention of oxidative stress. Int J Vitam Nutr Res 80:5–11

Satué-Gracia MT, Heinonen M, Frankel EN (1997) Anthocyanins as antioxidants on human low-density lipoprotein and lecithin–liposome systems. J Agric Food Chem 45:3362–3367

Schuster R (1980) Determination of free amino acids by high performance liquid chromatography. Anal Chem 52:617–620

Skrzydlewska E, Ostrowska J, Figaszewski Z (1998) Peptide mapping by high-performance liquid chromatography. Acta Chrom 8:70–85

Smith MAL, Marley KA, Seigler D, Singletary KW, Meline B (2000) Bioactive properties of wild blueberry fruits. J Food Sci 65: 352–356

Stefek M, Kyselova Z, Rackowa L, Krizanowa L (2005) Oxidative modification of rat eye lens proteins by peroxyl radicals in vitro: protection by the chain-breaking antioxidants stobadine and trolox. Biochim Biophys Acta 1741:183–190

Szachowicz-Petelska B, Dobrzyńska I, Skrzydlewska E, Figaszewski ZA (2005) Influence of green tea on surface charge density and phospholipid composition of erythrocytes membrane in ethanol intoxicated rats. Cell Biol Toxicol 21:61–70

Szachowicz-Petelska B, Dobrzyńska I, Skrzydlewska E, Figaszewski ZA (2008) Changes in phospholipids composition studied by HPLC and electric properties of liver cell membrane of ethanol-poisoned rats. Toxicol Mech Methods 18:525–530

Szachowicz-Petelska B, Skrzydlewska E, Figaszewski ZA (2010) Changes in protein composition in erythrocyte membrane of ethanol-poisoned rats after administration of teas. Anal Lett 43:721–734

Tani H, Kamidate T, Watanabe H (1997) Micelle-mediated extraction. J Chromatogr A 780:229–241

Valentova K, Ulrichova J, Cvak L, Simanek V (2007) Cytoprotective effect of a bilberry extract against oxidative damage of rat hepatocytes. Food Chem 101:912–917

Vallet M, Tabatabale T, Briscoe RJ, Baird TJ, Beatty WW, Floyd RA (1997) Free radical production during ethanol intoxication, dependence, and withdrawal. Alcohol Clin Exp Res 21: 275–285

Viljanen K, Kylli P, Kivikari R, Heinonen M (2004) Inhibition of protein and lipid oxidation in liposomes by berry phenolics. J Agric Food Chem 52:7419–7424

Viljanen K, Halmos AL, Sinclair A, Heinonen M (2005) Effect of blackberry and raspberry juice on whey protein emulsion stability. Eur Food Res Technol 221:602–609

Wagner BA, Buettner GB, Burns CP (1994) Free radical–mediated lipid peroxidation in cells: oxidizability is a function of cell lipid bis-allylic hydrogen content. Biochemistry 33:4449–4453

Ward RJ, Lallemand F, de Witte P (2009) Biochemical and neurotransmitter changes implicated in alcohol-induced brain damage in chronic or binge drinking alcohol abuse. Alcohol Alcohol 44:128–135

Wu W, Zhang C, Kong X, Hua Y (2009) Oxidative modification of soy protein by peroxyl radicals. Food Chem 116:295–301

J Membrane Biol (2012) 245:201–215
DOI 10.1007/s00232-012-9431-9

Kinetic Analysis of Gill (Na^+,K^+)-ATPase Activity in Selected Ontogenetic Stages of the Amazon River Shrimp, *Macrobrachium amazonicum* (Decapoda, Palaemonidae): Interactions at ATP- and Cation-Binding Sites

Francisco Assis Leone · Douglas Chodi Masui · Thais Milena de Souza Bezerra · Daniela Pereira Garçon · Wagner Cotroni Valenti · Alessandra Silva Augusto · John Campbell McNamara

Received: 24 November 2011 / Accepted: 9 April 2012 / Published online: 28 April 2012

Abstract We investigated modulation by ATP, Mg^{2+}, Na^+, K^+ and NH_4^+ and inhibition by ouabain of (Na^+,K^+)-ATPase activity in microsomal homogenates of whole zoeae I and decapodid III (formerly zoea IX) and whole-body and gill homogenates of juvenile and adult Amazon River shrimps, *Macrobrachium amazonicum*. (Na^+,K^+)-ATPase-specific activity was increased twofold in decapodid III compared to zoea I, juveniles and adults, suggesting an important role in this ontogenetic stage. The apparent affinity for ATP ($K_M = 0.09 \pm 0.01$ mmol L^{-1}) of the decapodid III (Na^+,K^+)-ATPase, about twofold greater than the other stages, further highlights this relevance. Modulation of (Na^+,K^+)-ATPase activity by K^+ also revealed a threefold greater affinity for K^+ ($K_{0.5} = 0.91 \pm 0.04$ mmol L^{-1}) in decapodid III than in other stages; NH_4^+ had no modulatory effect. The affinity for Na^+ ($K_{0.5} = 13.2 \pm 0.6$ mmol L^{-1}) of zoea I (Na^+,K^+)-ATPase was fourfold less than other stages. Modulation by Na^+, Mg^{2+} and NH_4^+ obeyed cooperative kinetics, while K^+ modulation exhibited Michaelis-Menten behavior. Rates of maximal Mg^{2+} stimulation of ouabain-insensitive ATPase activity differed in each ontogenetic stage, suggesting that Mg^{2+}-stimulated ATPases other than (Na^+,K^+)-ATPase are present. Ouabain inhibition suggests that, among the various ATPase activities present in the different stages, Na^+-ATPase may be involved in the ontogeny of osmoregulation in larval *M. amazonicum*. The NH_4^+-stimulated, ouabain-insensitive ATPase activity seen in zoea I and decapodid III may reflect a stage-specific means of ammonia excretion since functional gills are absent in the early larval stages.

Keywords (Na^+,K^+)-ATPase activity · Gill microsome · Cation-binding site · *Macrobrachium amazonicum* · Ontogenetic stage · Environmental salinity

F. A. Leone (✉) · D. C. Masui · T. M. de Souza Bezerra · D. P. Garçon
Departamento de Química, Faculdade de Filosofia, Ciências e Letras de Ribeirão Preto, Universidade de São Paulo, Avenida Bandeirantes, 3900, Ribeirão Prêto, SP 14040-901, Brazil
e-mail: fdaleone@ffclrp.usp.br

Present Address:
D. P. Garçon
Departamento de Biologia Molecular, Centro de Ciências Exatas e da Natureza, Universidade Federal da Paraíba, João Pessoa, PB 58059-900, Brazil

W. C. Valenti · A. S. Augusto
Campus Experimental do Litoral Paulista, Universidade Estadual Paulista Júlio de Mesquita Filho, São Vicente, SP 11330-900, Brazil

J. C. McNamara
Departamento de Biologia, Faculdade de Filosofia, Ciências e Letras de Ribeirão Preto, Universidade de São Paulo, Ribeirão Prêto, SP 14040-901, Brazil

Introduction

The success of a particular crustacean species in a given biotope depends on the adjustment of each ontogenetic stage to its specific surroundings. In aquatic environments, salt content constitutes the main factor with which organisms must contend (Charmantier 1998; Anger 2003). While some crustaceans spend their life cycles in waters where salinity varies little, others migrate between fresh- and brackish-water biotopes during development, exposing their successive ontogenetic stages to widely different salinity regimes (Charmantier 1998; Freire et al. 2003; Short 2004).

Crustaceans are predominantly marine organisms. Although many have become independent of seawater, completing their entire life cycles in freshwater, others still appear to be invading this medium, as suggested by their larval developmental sequence being dependent on brackish water and by their characteristic metabolic, osmotic and ion regulatory mechanisms (Sandifer et al. 1975; Read 1984; Moreira et al. 1986; McNamara et al. 1986; Freire et al. 2003; Faria et al. 2011). Marine crustaceans essentially osmoconform with their environment and only weakly regulate their hemolymph ionic concentrations. Brackish and freshwater habitats, however, represent challenging environments since hemolymph osmotic and ionic concentrations are held fairly constant at levels much higher than the surrounding medium, leading to passive ion loss and water gain. Crustaceans inhabiting these media have evolved mechanisms that regulate their hemolymph Na^+ and Cl^- concentrations, both by compensatory ion uptake and by diminishing passive ion loss across the gills and other body-surface epithelia (Onken et al. 1995; Péqueux 1995; Riestenpatt et al. 1996; Lucu and Towle 2003; Kirschner 2004; Freire et al. 2008; Faria et al. 2011; McNamara and Faria 2012).

All crustacean Na^+-absorbing epithelia appear to express (Na^+,K^+)-ATPase, an ion-transporting enzyme located in the basal membrane, together with basal K^+ and Cl^- channels. However, in strongly hyperosmoregulating crabs like *Eriocheir sinensis* and *Dilocarcinus pagei*, Na^+ channels, the V-type H^+ pump and Cl^-/HCO_3^- exchangers, located in the apical membrane, are also key components of salt uptake (Onken and Riestenpatt 1998; Onken and McNamara 2002; Weihrauch et al. 2004a). Salt-uptake models for freshwater palaemonid shrimps like *Macrobrachium amazonicum* propose that active Na^+ absorption ensues through Na^+ channels in the apical flange membranes of gill pillar cells in concert with the (Na^+,K^+)-ATPase located in the basal membrane of ion-transporting, septal cell ionocytes to which the pillar cells are structurally coupled (McNamara and Lima 1997; McNamara and Torres 1999; Belli et al. 2009; Faleiros et al. 2010). H^+ extrusion via the apical pillar cell V(H^+)-ATPase appears to drive Na^+ influx, leading to cellular hyperpolarization that facilitates basal Cl^- extrusion (Torres et al. 2003; Faleiros et al. 2010). Apical Cl^-/HCO_3^- exchangers, using HCO_3^- derived from CO_2 hydration by carbonic anhydrase, transport Cl^- into the pillar cell flanges, while Cl^- efflux to the septal cells proceeds through basal Cl^- channels. Together with active Na^+ transport to the hemolymph by the electrogenic (Na^+,K^+)-ATPase, K^+ recycling through basal membrane K^+ channels in the septal cells generates a negative electrical potential that drives Cl^- efflux to the hemolymph (for review, see Freire et al. 2008).

The (Na^+,K^+)-ATPase, found in the plasma membranes of all animal cells, underpins many homeostatic processes and is directly responsible for the asymmetrical, electrogenic countertransport of Na^+ and K^+ that results in strong ionic gradients across their membranes; i.e., the energy provided by ATP hydrolysis powers the countertransport of $3Na^+$ out of and $2K^+$ into the cytosol (Kaplan 2002; Jorgensen et al. 2003; Martin 2005; Sáez et al. 2009). Such gradients generate transmembrane electrical potential and drive transport processes like active transepithelial salt and passive water movement, Na^+/glucose/amino acid/nucleotide cotransport and cell volume regulation (Jorgensen and Pedersen 2001; Jorgensen et al. 2003; Martin 2005; Sáez et al. 2009). (Na^+,K^+)-ATPase is an oligomeric protein belonging to the P_{2C} subfamily of membrane-embedded P-type ATPases, whose hallmark is the formation of an acyl-phosphate intermediate during the catalytic cycle (Axelsen and Palmgren 1998; Jorgensen and Pedersen 2001; Kaplan 2002; Poulsen et al. 2010). The protein's X-ray crystal structure reveals a catalytic 110 kDa α-subunit and a 50 kDa β-subunit that constitute the active moiety of the enzyme, together with a regulatory FXYD protein (Morth et al. 2007; Geering 2008). Phosphorylation and dephosphorylation at the D376 residue in the α-subunit results in the transition between two main conformational changes: E_1, with a high affinity for intracellular Na^+, and E_2, characterized by high affinity for extracellular K^+ (reviewed by Jorgensen et al. 2003; Martin 2005; Morth et al. 2007; Sáez et al. 2009). Different tissue-specific α- and β-isoforms exhibit distinct transport and pharmacological properties (Blanco and Mercer 1998; Crambert et al. 2000; Blanco 2005).

Studies of crustacean ontogeny have dealt mainly with marine and estuarine decapods (Charmantier 1998), while osmoregulatory studies in freshwater Crustacea have focused mostly on adult crab, shrimp and crayfish species, mainly owing to their large size, which is convenient for in vivo and in vitro experiments (Péqueux 1995; Onken and McNamara 2002; Lucu and Towle 2003; Kirschner 2004; Freire et al. 2008). The larval stages have been neglected (Read 1984; Charmantier 1998; Haond et al. 1999; Khodabandeh et al. 2006) due to their small dimensions and reduced hemolymph volume (Charmantier 1998; Anger 2003; Augusto et al. 2007). The few studies that do correlate the salinity tolerance of early ontogenetic stages with their osmoregulatory capabilities have been hampered by a lack of information on the kinetic characteristics of the transporters involved in osmoregulation during larval development (Conte et al. 1977; Read 1984; Sun et al. 1991; Lee and Watts 1994; Escalante et al. 1995; Augusto et al. 2007; Ituarte et al. 2008).

The ontogeny of osmoregulation has been examined in *M. petersi* (Read 1984), and recently Charmantier and Anger (2010) explored ontogenetic osmoregulatory ability in two geographically isolated populations of

M. amazonicum from different Brazilian biomes. This species embraces both hololimnetic populations, in which the life cycle is entirely restricted to freshwater (Magalhães 1985; Collart and Rabelo 1996; Zanders and Rodriguez 1992), and diadromous populations, which are dependent on brackish water for larval development (McNamara et al. 1983, 1986; Charmantier 1998). *M. amazonicum* is widely distributed throughout neotropical South America, inhabiting inland and estuarine waters of the major hydrographic basins, such as the Amazon, Orinoco, São Francisco, Araguaia-Tocantins, Paraná and Paraguay watersheds, as well as coastal rivers in north and northeastern Brazil (Pettovello 1996; Ramos-Porto and Coelho 1998). Despite this ample geographical distribution and economic importance for fisheries (Maciel and Valenti 2009) and aquaculture (Moraes-Valenti and Valenti 2010), the larval biology of *M. amazonicum* is not well known (see Anger et al. 2009). The adult shrimp is a good hyperosmotic regulator, including excellent chloride regulatory capability, and has been used as a model organism for physiological studies of salinity tolerance and osmoregulatory mechanisms (McNamara et al. 1983; Zanders and Rodriguez 1992; Augusto et al. 2007; Santos et al. 2007; Faleiros et al. 2010). Larval growth patterns (Moreira et al. 1986), chemical composition (Anger et al. 2009) and osmoregulatory ability (Charmantier and Anger 2010) also have been investigated.

The life cycle of *M. amazonicum* consists of egg, larval, juvenile and adult stages; and the species has been well studied in its natural environment and under aquaculture and laboratory conditions (for review, see Maciel and Valenti 2009). In *M. amazonicum* from the Amazon delta, only newly hatched zoea I tolerate exposure to freshwater, maintaining a hemolymph osmolality of ≈300 mOsm/kg H_2O; larval instars II–IX and first-stage juveniles do not survive freshwater (Charmantier and Anger 2010). However, later juveniles and adults exhibit strong osmoregulatory capability in this medium compared to zoea I, a stage that also survives well at low salinities compared to instars II–IX, showing stronger osmoregulatory ability, which becomes maximal in juveniles and adults. In seawater (32 ‰ salinity), zoeae I–V and adults survive very well, in contrast to larval instars VI–IX, while late juveniles and adults hypo-osmoregulate slightly. Under strong hyperosmotic challenge (44 ‰ salinity), a few stage II–VII instars survive, showing hypo-osmoregulatory capability; however, zoea I, instars VIII and IX, juveniles and adults cannot tolerate this salinity (Charmantier and Anger 2010).

A kinetic characterization of (Na^+,K^+)-ATPase in such a diadromous species should allow insight into the development of osmoregulatory capability. Thus, in this study we investigated the modulation by ATP, Mg^{2+}, K^+, Na^+ and NH_4^+ and inhibition by ouabain of (Na^+,K^+)-ATPase from several ontogenetic stages of the freshwater shrimp *M. amazonicum*.

Materials and Methods

Material

All solutions were prepared using Millipore (Billerica, MA) MilliQ ultrapure apyrogenic water, and all reagents were of the highest purity commercially available. Imidazole, *N*-(2-hydroxyethyl) piperazine-N19-ethanesulfonic acid (HEPES), triethanolamine, ATP ditris salt, pyruvate kinase (PK), phosphoenolpyruvate (PEP), NAD^+, NADH, phosphoglycerate kinase (PGK), alamethicin, lactate dehydrogenase (LDH), glyceraldehyde-3-phosphate dehydrogenase (GAPDH), glyceraldehyde-3-phosphate (G3P), ouabain and 3-phosphoglyceraldehyde diethyl acetal were purchased from Sigma (St. Louis, MO). The protease inhibitor cocktail (5 mmol L^{-1} leupeptin, 5 mmol L^{-1} antipain, 1 mmol L^{-1} benzamidine, 1 mmol L^{-1} pepstatin A and 5 µmol L^{-1} phenyl-methane-sulfonyl-fluoride) was from Calbiochem (Darmstadt, Germany).

Reagents

G3P was prepared by hydrolysis of 3-phosphoglyceraldehyde diethyl acetal, barium salt with 150 µl HCl (d = 1.18 g/mL) in a boiling water bath for 2 min, after removal of the barium salt with Dowex $50H^+$ resin, as recommended by the manufacturer (see Sigma product information for G5376). Final pH was adjusted to 7.0 with 50 µl triethanolamine just before use. Ammonium-free suspensions were prepared by centrifuging 200 µl of 2.9 mol L^{-1} ammonium sulfate containing crystalline suspensions of LDH and PK at 20,000×*g* for 15 min, at 4 °C, in Eppendorf tubes. The pellet was resuspended in 300 µl of 50 mmol L^{-1} HEPES buffer (pH 7.5), transferred to a YM-30 Amicon (Billerica, MA) Microcon filter and centrifuged five times at 10,000×*g* in 300 µl of the same buffer until depletion of ammonium ions (tested with Nessler reagent). Finally, the pellet was resuspended to the original volume. For PGK and GAPDH, the suspension was treated as above with 50 mmol L^{-1} triethanolamine buffer, pH 7.5, containing 1 mmol L^{-1} dithiothreitol. When necessary, enzyme solutions were concentrated using YM-30 Amicon Microcon filters. Ammonium-depleted enzyme solutions were used within 2 days of preparation.

Shrimps

Amazon River shrimps, *M. amazonicum*, were produced at the Aquaculture Center, UNESP, Jaboticabal, São Paulo,

Brazil, from broodstock collected in freshwater at Furo das Marinhas near Santa Bárbara do Pará (1° 13.450′ S, 48° 17.632′ W), northeastern Pará State, Brazil, in 2001 (Araujo and Valenti 2007). The larval stages were identified according to Guest (1979); however, zoeae VII, VIII and IX are now termed decapodid I, II and III, respectively, according to the nomenclature proposed by Anger (2001).

Zoeae I (approximately 6,000 individuals/preparation, ≈60 μg wet mass) were obtained from hatching tanks (6 ‰ salinity) just after eclosion, guaranteeing that all individuals were in the same stage. The decapodid III stage was obtained from larviculture tanks (12 ‰ salinity), and individuals were separated under a stereomicroscope using morphological and behavioral characteristics. Groups of decapodid III (approximately 300 individuals/preparation, ≈650 μg wet mass) were held in aerated carboys containing 32 L water from the larviculture tanks. Juveniles (20 individuals/preparation, ≈700 μg wet gill mass) were collected from freshwater rearing tanks and held in carboys containing 32 L aerated freshwater. Adult male and non-ovigerous female shrimps (20 individuals/preparation, ≈6 g wet gill mass) were collected from freshwater ponds and maintained in carboys containing 32 L aerated pond water. These particular stages were chosen as they typify the different ontogenetic phases. Zoea I is a newly hatched, small, free-swimming larva that uses only internal yolk reserves as an energetic substrate. Decapodid III is the last larval stage; it requires brackish water for survival, its yolk supply has been long exhausted and exogenous feeding is necessary (Araujo and Valenti 2007). The juvenile represents the first benthonic freshwater stage, while adult shrimps are sexually mature.

The various salinities in which the different stages were reared represent those encountered by each ontogenetic stage in the natural environment. To avoid possible effects of the molting cycle, zoeae I were collected in the evening shortly after hatching. The decapodid III, juvenile and adult stages were used in intermolt, confirmed by stereoscopic microscopy. Individuals in the different stages were transported in their respective carboys to the laboratory and used immediately for microsomal preparation.

Preparation of Microsomal Fractions

For each homogenate prepared, shrimps were anesthetized by chilling on crushed ice immediately before dissection and homogenization. The gills of juvenile and adult shrimps were rapidly dissected, diced and homogenized in a Potter homogenizer in 20 mmol L^{-1} imidazole homogenization buffer, pH 6.8, containing 6 mmol L^{-1} EDTA, 250 mmol L^{-1} sucrose and a protease inhibitor cocktail (20 mL buffer/g wet tissue). For zoeae I and decapodid III, whole larvae were homogenized similarly; homogenates of whole juveniles and adults were prepared after removing the appendages and exoskeleton.

After centrifuging the crude homogenate at 10,000×*g* for 35 min at 4 °C, the supernatant was placed on crushed ice and the pellet was resuspended in an equal volume of homogenization buffer. After further centrifugation as above, the two supernatants were pooled and centrifuged at 100,000×*g* for 2 h at 4 °C. The resulting pellet containing the microsomal fraction was homogenized in 20 mmol L^{-1} imidazole buffer, pH 6.8, containing 250 mmol L^{-1} sucrose (15 mL buffer/g wet tissue). Finally, 0.5 mL aliquots were rapidly frozen in liquid nitrogen and stored at −20 °C. No appreciable loss of (Na^+,K^+)-ATPase activity was seen after 2 month storage of the microsomal enzyme prepared from either whole larvae or gill tissue. When required, the aliquots were thawed, placed on crushed ice and used immediately.

Measurement of ATP Hydrolysis

Total ATPase activity was routinely assayed at 25 °C using the PK/LDH linked system (Rudolph et al. 1979) in which the hydrolysis of ATP was coupled to the oxidation of NADH (Masui et al. 2008). The oxidation of NADH was monitored at 340 nm ($\varepsilon_{340\ nm,\ pH\ 7.5} = 6{,}200\ mol^{-1}\ L\ cm^{-1}$) in a Hitachi (Tokyo, Japan) U-3000 spectrophotometer equipped with thermostatted cell holders. Standard conditions were as follows: 50 mmol L^{-1} HEPES buffer (pH 7.5), 2 mmol L^{-1} ATP, containing 5 mmol L^{-1} $MgCl_2$, 20 mmol L^{-1} KCl, 0.14 mmol L^{-1} NADH, 2 mmol L^{-1} PEP, 82 μg PK (49 U) and 110 μg LDH (94 U), 50 mmol L^{-1} NaCl (for zoea I and juveniles) and 20 mmol L^{-1} NaCl (for decapodid III and adults), in a final volume of 1 mL. ATP hydrolysis was also estimated with 3 mmol L^{-1} ouabain to assess ouabain-insensitive activity. The difference in activity measured in the absence (total ATPase activity) or presence (ouabain-insensitive activity) of ouabain represents the (Na^+,K^+)-ATPase activity. Alternatively, ATPase activity was estimated using a GAPDH/PGK-linked system coupled to the reduction of NAD^+ at 340 nm (Masui et al. 2008). Standard conditions were 50 mmol L^{-1} triethanolamine buffer (pH 7.5), 2 mmol L^{-1} ATP, containing 5 mmol L^{-1} $MgCl_2$, 20 mmol L^{-1} KCl, 1 mmol L^{-1} NAD^+, 0.5 mmol L^{-1} sodium phosphate, 1 mmol L^{-1} G3P, 150 μg GAPDH (12 U), 20 μg PGK (9 U), 50 mmol L^{-1} NaCl (for zoea I and juveniles) and 20 mmol L^{-1} NaCl (for decapodid III and adults), in a final volume of 1 mL. The two coupling systems gave equivalent results, with a difference of $< 10\%$. ATP hydrolysis was also estimated at 25 °C after 10 min preincubation with alamethicin (1 mg/mg protein) to provide leaky and/or disrupted vesicles (Masui et al. 2008). Controls without added enzyme were included in each experiment to quantify the nonenzymatic hydrolysis of

substrate. Initial velocities were constant for at least 15 min provided that <5 % of the total NADH (or NAD^+) was oxidized (or reduced). The reaction rate for each modulator was estimated in duplicate using identical aliquots from the same preparation. Mean values were used to fit each corresponding saturation curve, which was repeated three times utilizing different microsomal homogenates ($n = 3$). One enzyme unit (U) is defined as the amount of enzyme that hydrolyzes 1.0 nmol of ATP per minute, at 25 °C; and (Na^+,K^+)-ATPase specific activity is given as U mg^{-1} total protein.

Protein Measurement

Protein concentration was estimated according to the Coomassie Blue G dye–binding assay of Read and Northcote (1981), using bovine serum albumin as the standard.

Estimation of Kinetic Parameters

The kinetic parameters V_M (maximum velocity), $K_{0.5}$ (apparent dissociation constant), K_M (Michaelis-Menten constant) and n_H (Hill coefficient) for ATP hydrolysis under the different assay conditions were calculated using SigrafW software (Leone et al. 2005a). The figures provide representative curves, each obtained from a single microsomal preparation. The kinetic parameters provided are calculated values, expressed as the mean ± SD, and represent the number of experiments performed with different preparations ($n = 3$). The apparent dissociation constant, K_I, of the enzyme-inhibitor complex was estimated as described by Marks and Seeds (1978). SigrafW software can be obtained from http://portal.ffclrp.usp.br/sites/fdaleone/downloads.

Results

(Na^+,K^+)-ATPase Activity in Whole Adult and Juvenile Shrimps

(Na^+,K^+)-ATPase activity assayed in the microsomal fraction of whole juveniles was 87.7 U mg^{-1}, ≈50 % less than in the corresponding gill microsomal preparation (176.2 U mg^{-1}). In whole adult shrimps, activity was 62.8 U mg^{-1}, representing ≈40 % of microsomal gill (Na^+,K^+)-ATPase activity (156.7 U mg^{-1}).

Modulation of (Na^+,K^+)-ATPase Activity by ATP

Figure 1 shows the effect of ATP concentration on (Na^+,K^+)-ATPase activity in microsomal fractions of *M. amazonicum* tissues from the four ontogenetic stages. Independent of stage, 70–85 % of total ATPase activity corresponds to (Na^+,K^+)-ATPase (insets to figures). Further, under saturating Mg^{2+}, Na^+ and K^+ concentrations, only a single ATP saturation curve, obeying Michaelis-Menten kinetics, was seen for the enzyme in the four stages (Table 1). Although the maximum (Na^+,K^+)-ATPase activities for zoea I and adult enzymes are similar, that for decapodid III is almost twofold greater (Table 1). The considerable ouabain-insensitive ATPase activity (54.0 ± 1.4, 104.5 ± 5.2, 49.3 ± 2.5 and 31.2 ± 1.8 U mg^{-1} for zoea I, decapodid III, juvenile and adult shrimps, respectively) also was stimulated over the same ATP concentration range, strongly suggesting Mg^{2+}-stimulated ATPase activities other than (Na^+,K^+)-ATPase. K_M values for the enzymes from the zoea I, decapodid III, juvenile and adult stages were fairly similar (Table 1). For ATP concentrations as low as 10^{-6} mol L^{-1}, a residual ATPase activity ranging 5–10 % of total ATPase activity was found for all stages (insets to figures).

Effect of Magnesium Ions

Figure 2 shows the modulation by Mg^{2+} of (Na^+,K^+)-ATPase activity in the four ontogenetic stages. A single saturation curve exhibiting positive cooperative effects ($n_H > 1.0$) was found over the range from 10^{-5} to 5×10^{-2} mol L^{-1}, independently of ontogenetic stage. The maximum stimulation rates for zoea I, juvenile and adult shrimps were similar; however, that for decapodid III was considerably greater (Table 1). $K_{0.5}$ values for Mg^{2+} stimulation of (Na^+,K^+)-ATPase activity varied very little (Table 1). Stimulation of ouabain-insensitive ATPase activity by Mg^{2+} varied considerably (see insets to figures), resulting in maximum stimulation rates of 51.6 ± 2.8 U mg^{-1} for zoea I, 104.6 ± 6.3 U mg^{-1} for decapodid III, 57.2 ± 2.9 U mg^{-1} for juvenile and 22.7 ± 0.8 U mg^{-1} for adult enzymes (insets to figures). A residual Mg^{2+}-stimulated ATPase activity of around 10 % of total ATPase activity for Mg^{2+} concentrations as low as 10^{-5} mol L^{-1} was detected in both zoea I and decapodid III but not in juveniles and adults. Interestingly, these Mg^{2+}-stimulated, ouabain-insensitive ATPase activities are similar to the ATP-stimulated, ouabain-insensitive ATPase activities (insets to figures), corroborating the likelihood of Mg^{2+}-stimulated ATPases other than (Na^+,K^+)-ATPase in the preparation. Independent of ontogenetic stage, stimulation by Mg^{2+} obeyed cooperative kinetics (Table 1), and Mg^{2+} concentrations >5 mmol L^{-1} markedly inhibited (Na^+,K^+)-ATPase activity (data not shown).

Effect of Sodium Ions

Under saturating ATP, Mg^{2+} and K^+ concentrations, stimulation of (Na^+,K^+)-ATPase activity by Na^+ resulted

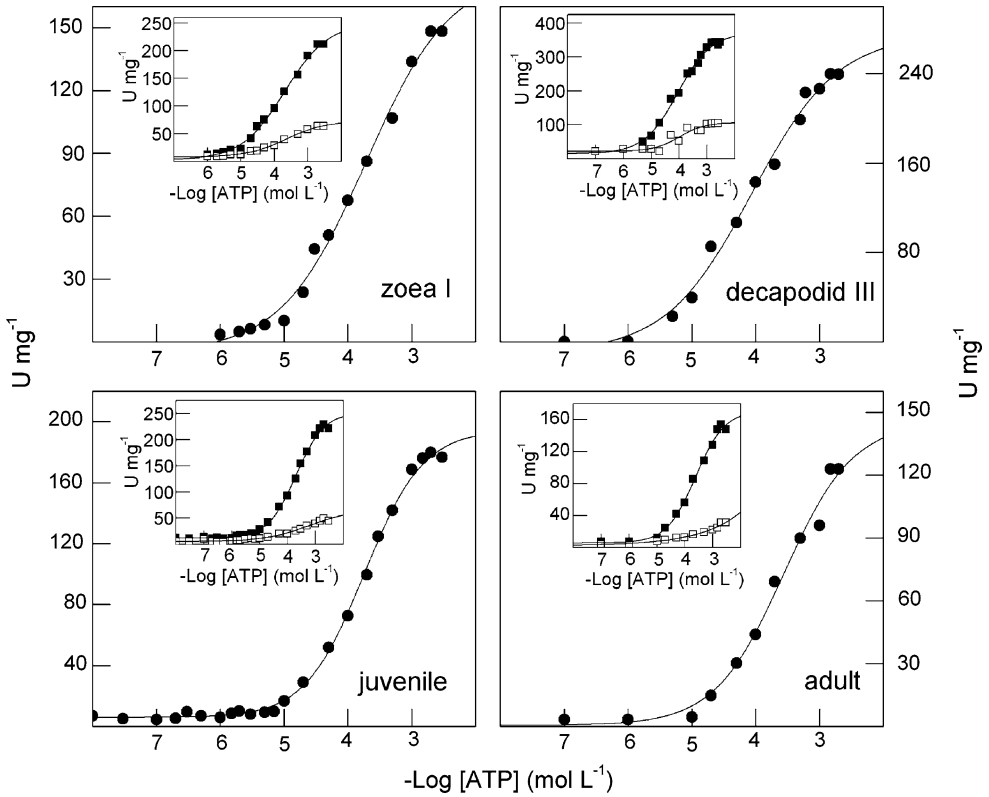

Fig. 1 Effect of ATP concentration on (Na^+,K^+)-ATPase activity in microsomal fractions from *M. amazonicum* at different ontogenetic stages. Activity was assayed continuously at 25 °C in 50 mmol L^{-1} HEPES buffer, pH 7.5, containing 5.0 mmol L^{-1} $MgCl_2$, 20.0 mmol L^{-1} KCl, 0.14 mmol L^{-1} NADH, 2.0 mmol L^{-1} PEP, 82 μg PK (49 U), 110 μg LDH (94 U) and NaCl 50 mmol L^{-1} for zoea I and juvenile enzymes or 20 mmol L^{-1} for decapodid III and adult enzymes. Enzyme activity was assayed using 13.4, 7.2, 9.8 and 31.4 μg protein from homogenates of whole zoeae I and decapodid III, and gill homogenates of juvenile and adult shrimps, respectively. Experiments were performed using duplicate aliquots from three different homogenates; representative curves obtained from one homogenate are given. *Insets* effect of ATP concentration on ouabain-insensitive (*open square*) and total ATPase activities (*filled square*)

in single saturation curves, showing positive cooperativity (Fig. 3). Maximum rates for zoea I, decapodid III, juvenile and adult shrimps were similar to those for K^+ (Table 1). Except for zoea I, showing the highest $K_{0.5}$, the affinity constants of the enzymes in the other stages were about 4 mmol L^{-1} (Table 1). The ouabain-insensitive activity of zoea I was stimulated up to 15 % of total ATPase activity over the range 10^{-4} to 7×10^{-2} mol L^{-1} Na^+; however, stimulation by Na^+ was negligible in the other stages (insets to figures).

Effect of Potassium Ions

Figure 4 shows the effect of K^+ on (Na^+,K^+)-ATPase activity in the four different ontogenetic stages. Under saturating ATP, Mg^{2+} and Na^+ concentrations, enzyme activity is notably stimulated by K^+. Maximal stimulation rates were fairly similar for zoea I, juvenile and adult enzymes but about twofold less than for decapodid III (Table 1). Michaelis-Menten kinetics prevailed for K^+ stimulation of (Na^+,K^+)-ATPase in all stages (Table 1). The decapodid III enzyme exhibited the highest affinity for K^+ ($K_M = 0.91 \pm 0.04$ mmol L^{-1}). Except for zoea I, which showed maximal stimulation of ouabain-insensitive activity of 54.0 ± 1.3 U mg^{-1} (inset to figure), the decapodid III, juvenile and adult (insets to figure) enzymes were not stimulated by K^+, suggesting the absence of K^+-dependent ATPase activity. Considerable residual Mg^{2+}-ATPase activity, ranging 10–20 % of total ATPase activity, was found for K^+ concentrations as low as 10^{-5} mol L^{-1} (insets to figures).

Stimulation by Ammonium Ions

(Na^+,K^+)-ATPase activity in all four ontogenetic stages was stimulated by NH_4^+ under saturating ATP (2 mmol L^{-1}), Na^+ (50 mmol L^{-1} for zoea I and juvenile enzymes, 20 mmol L^{-1} for decapodid III and adult enzymes) and Mg^{2+} (5 mmol L^{-1}) concentrations, in the absence of K^+ (Fig. 5). Increasing NH_4^+ concentrations from 10^{-3} to 7×10^{-2} mol L^{-1} stimulated (Na^+,K^+)-ATPase activity to a maximum of ≈270 U mg^{-1} in zoea I

Table 1 Kinetic parameters for stimulation by ATP, Mg^{2+}, K^+, Na^+ or NH_4^+ and K_I values for ouabain inhibition of microsomal (Na^+,K^+)-ATPase activity in four ontogenetic stages (zoea I, decapodid III, juvenile and adult) of the Amazon River shrimp, *M. amazonicum*

Effector	V (U mg^{-1})				$K_{0.5}$ or K_M (mmol L^{-1})				n_H			
	Z I	D III	Juvenile	Adult	Z I	D III	Juvenile	Adult	Z I	DIII	Juvenile	Adult
ATP	140.4 ± 6.7	266.8 ± 12.6	194.4 ± 9.6	133.3 ± 6.4	0.19 ± 0.01	0.09 ± 0.01	0.18 ± 0.01	0.21 ± 0.01	0.8	0.7	1.0	1.0
Mg^{2+}	133.2 ± 6.2	245.0 ± 12.0	181.3 ± 7.7	139.4 ± 6.7	0.68 ± 0.03	0.56 ± 0.03	0.51 ± 0.02	1.03 ± 0.05	2.2	1.8	1.3	1.7
K^+	150.5 ± 7.3	247.0 ± 12.3	196.5 ± 10.1	137.1 ± 7.0	3.2 ± 0.16	0.91 ± 0.04	2.35 ± 0.12	2.02 ± 0.10	1.0	1.0	1.0	1.0
Na^+	144.4 ± 6.9	249.1 ± 11.9	186.8 ± 9.3	126.4 ± 6.3	13.2 ± 0.60	4.20 ± 0.20	4.06 ± 0.20	3.00 ± 0.15	1.5	2.2	1.3	2.2
NH_4^+	271.9 ± 11.8	273.8 ± 12.5	205.9 ± 9.4	194.2 ± 8.5	6.3 ± 2.1	3.12 ± 0.18	1.88 ± 0.08	4.76 ± 0.23	3.4	3.3	1.0	1.9
Ouabain inhibition												
	Z I				D III		Juvenile				Adult	
K_I (μmol L^{-1})	104.3 ± 5.3				92.0 ± 4.5		85.0 ± 4.1				126.4 ± 6.6	

Assays were performed in 50 mmol L^{-1} HEPES or triethanolamine buffer, pH 7.5, in a final volume of 1 mL. Microsomes were obtained by homogenizing whole zoeae I (Z I) and decapodid III (D III) or gill tissue (juveniles and adults). The effect of each modulator was evaluated under optimal concentrations of the others. Data are the mean ± SD from three different microsomal preparations

and decapodid III and to ≈200 U mg^{-1} in juveniles and adults (Table 1). Cooperative kinetics prevailed independently of developmental stage for stimulation by NH_4^+, although calculated $K_{0.5}$ values differed considerably (Table 1). Ouabain-insensitive ATPase activity was not stimulated by NH_4^+ in juveniles and adults, in contrast to zoea I and decapodid III, representing 15 and 45 %, respectively, of total ATPase activity (insets to Fig. 5).

Inhibition by Ouabain

Inhibition by 3 mmol L^{-1} ouabain of total ATPase activity in the four ontogenetic stages is shown in Fig. 6 with the corresponding K_I values in Table 1. In adult shrimps, ouabain inhibited 87 % of total ATPase activity (154.1 U mg^{-1}), resulting in ouabain-insensitive activity of 19.8 U mg^{-1}. For zoea I, the maximum ATPase activity of 180.1 U mg^{-1} decreased to 52.8 U mg^{-1} with ouabain. Total ATPase activities of both decapodid III and juveniles (344.0 and 231.1 U mg^{-1}, respectively) were inhibited by ouabain to about 50 U mg^{-1}.

Discussion

This is the first kinetic characterization of modulation by ATP, Mg^{2+}, Na^+, K^+ and NH_4^+ and inhibition by ouabain of a gill microsomal (Na^+,K^+)-ATPase in selected ontogenetic stages of the palemonid shrimp *M. amazonicum*. Our findings reveal considerable differences in modulation by Na^+ (zoea I), K^+ and ATP (decapodid III) of (Na^+,K^+)-ATPase activity, suggesting an important role in the osmoregulatory capability of the larval stages. While the similar K_M values estimated for ATP exclude the likelihood of different (Na^+,K^+)-ATPase isoforms, ouabain inhibition suggests that among the various ATPases expressed in the different ontogenetic stages, Na^+-ATPase may be involved in the ontogeny of osmoregulatory capability in larval *M. amazonicum*. Further, the NH_4^+-stimulated, ouabain-insensitive ATPase activity seen in zoea I and decapodid III may reflect a stage-specific means of ammonia excretion since functional gills are absent in the early larval stages.

Maximum specific activities estimated for tank-reared *M. amazonicum* zoea I, decapodid III and juvenile enzymes are considerably greater than in homogenates of whole *M. rosenbergii* larvae (Huong et al. 2004). Maximum activities lie between 3 and 100 U mg^{-1} in other shrimp species (Felder et al. 1986; Ituarte et al. 2008) and are approximately 50 U mg^{-1} in cephalothorax homogenates of larval *Homarus gammarus* (Thuet et al. 1988). Maximum rates of ATP hydrolysis for the gill enzyme in adult, pond-reared *M. amazonicum* are twofold less than in wild

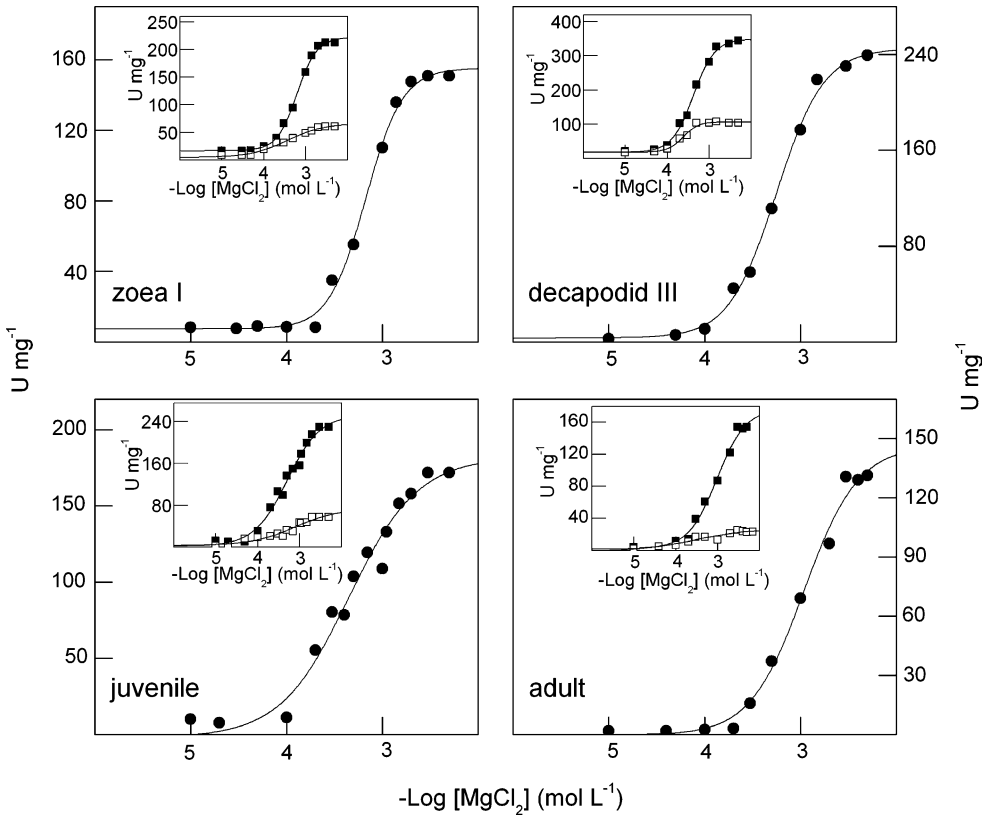

Fig. 2 Effect of Mg^{2+} concentration on (Na^+,K^+)-ATPase activity in microsomal fraction from *M. amazonicum* at different ontogenetic stages. Activity was assayed continuously at 25 °C in 50 mmol L^{-1} HEPES buffer, pH 7.5, containing 2.0 mmol L^{-1} ATP, 20.0 mmol L^{-1} KCl, 0.14 mmol L^{-1} NADH, 2.0 mmol L^{-1} PEP, 82 µg PK (49 U), 110 µg LDH (94 U) and 50 mmol L^{-1} NaCl for zoea I and juvenile enzymes or 20 mmol L^{-1} NaCl for decapodid III and adult enzymes. Enzyme activity was assayed using 13.4, 7.2, 9.8 and 31.4 µg protein from homogenates of whole zoeae I and decapodid III, and gill homogenates of juvenile and adult shrimps, respectively. Experiments were performed using duplicate aliquots from three different homogenates; representative curves obtained from one homogenate are given. *Insets* effect of Mg^{2+}concentration on ouabain-insensitive (*open square*) and total ATPase activities (*filled square*)

M. amazonicum (Santos et al. 2007). Further, the single ATP stimulation curve seen in pond-reared adults also contrasts markedly with the biphasic stimulation by ATP of (Na^+,K^+)-ATPase activity seen in wild adult *M. amazonicum* (Santos et al. 2007). Whether this difference is a response to rearing conditions remains to be elucidated. Several *Macrobrachium* species show (Na^+,K^+)-ATPase activities ranging from 70 to 100 U mg^{-1} in gill homogenates (Moretti et al. 1991; Proverbio et al. 1991) and from 120 to 200 U mg^{-1} in microsomal fractions (Stern et al. 1984; Lima et al. 1997), including adult freshwater shrimp, *M. olfersi* (690 U mg^{-1}) (Furriel et al. 2000). While establishing the number of ATP binding sites on the gill enzyme in crustaceans is still controversial, K_M values for ATP hydrolysis are known for some species (Leone et al. 2005b; Lucu and Towle 2003) and may constitute a valuable tool to better compare enzyme modulation by its physiological substrate during ontogeny. The K_M for ATP binding sites on the gill (Na^+,K^+)-ATPase from adult, pond-reared *M. amazonicum* is comparable to wild adult *M. amazonicum* (Santos et al. 2007), *M. olfersi* (Furriel et al. 2000) and *M. rosenbergii* (Stern et al. 1984). However, the K_M for *M. amazonicum* decapodid III is about twofold less than the other stages, suggesting a greater affinity of the enzyme for its physiological substrate.

The crustacean (Na^+,K^+)-ATPase is a Mg^{2+}-dependent, Na^+ and K^+/NH_4^+-stimulated enzyme, Mg^{2+} being a cofactor required for enzyme phosphorylation and ATP hydrolysis either as free Mg^{2+} or as a Mg^{2+}-nucleotide complex (Robinson and Pratap 1991; Tentes and Stratakis 1991; Jorgensen et al. 2003; Leone et al. 2005b). Stimulation by Mg^{2+} was independent of ontogenetic stage in *M. amazonicum*, and $K_{0.5}$ values were similar to adult *M. olfersi* (Furriel et al. 2000) and wild adult *M. amazonicum* (Santos et al. 2007). A characteristic feature of crustacean (Na^+,K^+)-ATPase is inhibition by excess Mg^{2+} (Leone et al. 2005b) due to free Mg^{2+} binding to the E_2K enzyme form and to the decreased ATP affinity that occurs during the K^+-releasing step (Fontes et al. 1992). However, this is not the case for the ouabain-insensitive ATPase activity estimated here for the

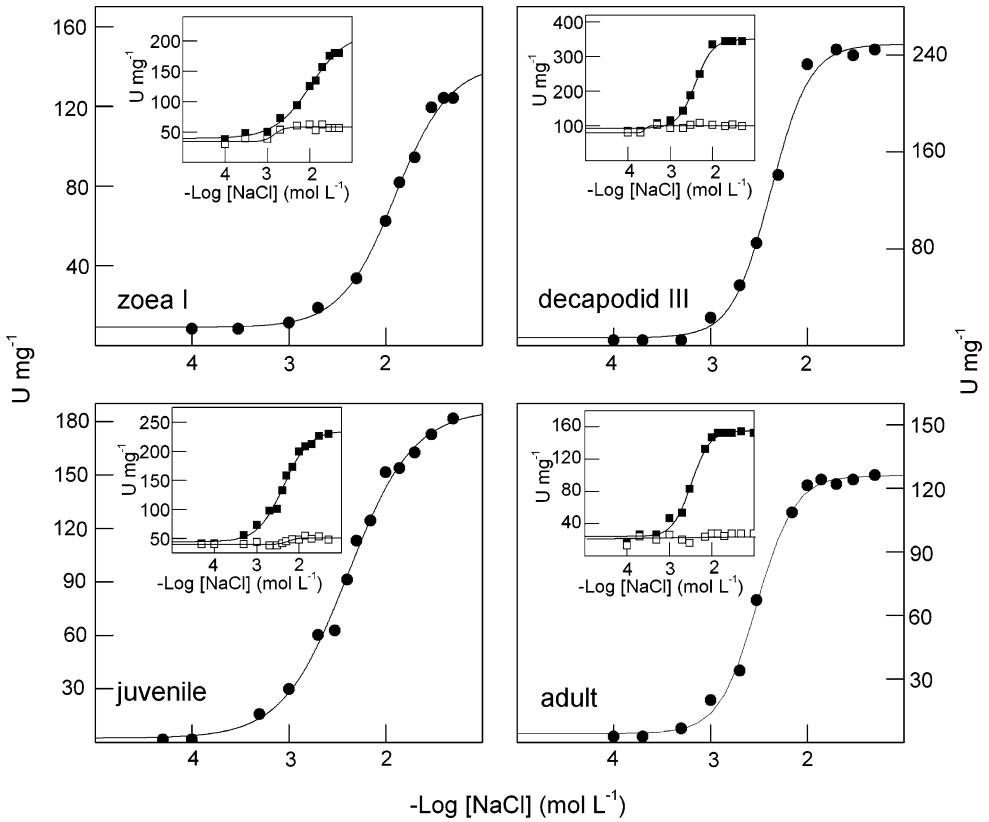

Fig. 3 Effect of Na^+ concentration on (Na^+,K^+)-ATPase activity in microsomal fractions from *M. amazonicum* at different ontogenetic stages. Activity was assayed continuously at 25 °C in 50 mmol L^{-1} HEPES buffer, pH 7.5, containing 2.0 mmol L^{-1} ATP, 5.0 mmol L^{-1} $MgCl_2$, 20.0 mmol L^{-1} KCl, 0.14 mmol L^{-1} NADH, 2.0 mmol L^{-1} PEP, 82 μg PK (49 U), 110 μg LDH (94 U) and 50 mmol L^{-1} NaCl for zoea I and juvenile enzymes or 20 mmol L^{-1} NaCl for decapodid III and adult enzymes. Enzyme activity was assayed using 13.4, 7.2, 9.8 and 31.4 μg protein from homogenates of whole zoeae I and decapodid III, and gill homogenates of juvenile and adult shrimps, respectively. Experiments were performed using duplicate aliquots from three different homogenates; representative curves obtained from one homogenate are given. *Insets* effect of Na^+ concentration on ouabain-insensitive (*open square*) and total ATPase activities (*filled square*)

different ontogenetic stages, which remains virtually unchanged over a wide range of Mg^{2+} concentrations. The (Na^+,K^+)-ATPase and ouabain-insensitive ATPase activities estimated in the different stages of pond-reared *M. amazonicum* also reflect this typical behavior. The different rates of maximal stimulation of ouabain-insensitive ATPase activity by millimolar Mg^{2+} also suggest the presence of Mg^{2+}-stimulated ATPases other than (Na^+,K^+)-ATPase in the different ontogenetic stages of *M. amazonicum*. Whether these activities correspond to the same or to different Mg^{2+}-stimulated ATPases is unclear.

The kinetic characteristics of specific α-subunit (Na^+,K^+)-ATPase isoforms such as apparent affinity for Na^+ and K^+ when ATP is used as a substrate depend on the organism and tissue, membrane factors and posttranslational modifications (Therien et al. 1996; Sáez et al. 2009). The apparent affinity for Na^+ of the (Na^+,K^+)-ATPase from various species varies widely (4–25 mmol L^{-1}) among the Crustacea, although that for K^+ (0.5–2.5 mmol L^{-1}) is less so (for review, see Leone et al. 2005b). In *M. amazonicum*, (Na^+,K^+)-ATPase shows far lower Na^+ affinity in the earlier ontogenetic stages. Further, modulation by Na^+ obeys cooperative kinetics, in contrast to the Michaelis-Menten behavior seen for K^+ modulation, independently of ontogenetic stage. Except for decapodid III all stages show $K_{0.5}$ values of around 2.0 mmol L^{-1} for K^+ (see Table 1). The apparent affinity for K^+ of the enzyme from adult, pond-reared shrimps was about 2.5-fold less than in wild *M. amazonicum* (Santos et al. 2007) but similar to *M. olfersi* (Furriel et al. 2000). However, zoea I exhibited a considerably higher $K_{0.5}$ value, revealing low affinity for Na^+, possibly a consequence of protection against osmotic stress in the embryonic stage (Susanto and Charmantier 2001). Compared to juvenile and adult shrimps, the larval stages exhibit ATPase activities other than (Na^+,K^+)-ATPase. From the physiological standpoint, the 15 % stimulation of ouabain-insensitive ATPase activity, suggesting the presence of a Na^+-ATPase, warrants future investigation. Like the rat kidney cortex, this Na^+-ATPase activity may compensate for diminished Na^+

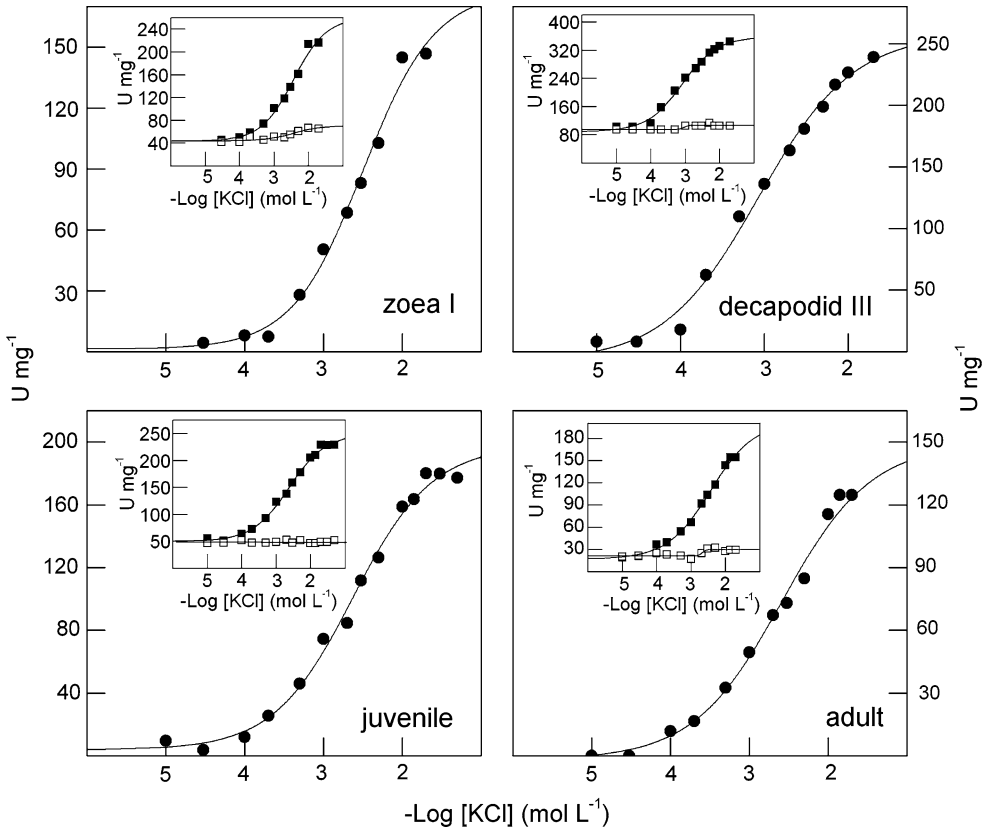

Fig. 4 Effect of K^+ concentration on (Na^+,K^+)-ATPase activity in microsomal fractions from *M. amazonicum* at different ontogenetic stages. Activity was assayed continuously at 25 °C in 50 mmol L^{-1} HEPES buffer, pH 7.5, containing 2.0 mmol L^{-1} ATP, 5.0 mmol L^{-1} $MgCl_2$, 1.0 mmol L^{-1} NAD^+, 0.5 mmol L^{-1} sodium phosphate, 1.0 mmol L^{-1} G3P, 150 µg GAPDH (12 U), 20 µg PGK (9 U) and 50 mmol L^{-1} NaCl for zoea I and juvenile enzymes or 20 mmol L^{-1} NaCl for decapodid III and adult enzymes. Enzyme activity was assayed using 13.4, 7.2, 9.8 and 31.4 µg protein from homogenates of whole zoeae I and decapodid III, and gill homogenates of juvenile and adult shrimps, respectively. Experiments were performed using duplicate aliquots from three different homogenates; representative curves obtained from one homogenate are given. *Insets* Effect of K^+ concentration on ouabain-insensitive (*open square*) and total ATPase activities (*filled square*)

transport consequent to oscillation in (Na^+,K^+)-ATPase activity (Reyes et al. 2009).

The monophasic ouabain inhibition curves obtained suggest the absence of different (Na^+,K^+)-ATPase isoforms in the ontogenetic stages of pond-reared *M. amazonicum* as also seen in wild adult *M. amazonicum* (Santos et al. 2007) and *M. olfersi*, in which K_I is 2.5-fold less (Furriel et al. 2000). The comparable K_I values for ouabain inhibition of (Na^+,K^+)-ATPase in the early ontogenetic stages of *M. amazonicum*, considerably different from adult shrimps, may reflect the expression of different isoforms before larval metamorphosis. While different isoenzymes are expressed in crustacean gill tissues in response to salinity acclimation (Harris and Bayliss 1988; Genovese et al. 2004; Masui et al. 2005; Mendonça et al. 2007), no information is available on (Na^+,K^+)-ATPase isoform expression in the different ontogenetic stages. That newly hatched zoeae I of *Palaemonetes argentinus*, *M. petersi* and *M. amazonicum* hyperosmoregulate (Read 1984; Ituarte et al. 2008; Charmantier and Anger 2010), although functional gills are absent, suggests that the ion-transporting cells must be located elsewhere during the early stages, probably in the branchiostegite epithelium.

Owing to the absence of gills (zoea I) or their diminutive size (decapodid III), microsomal fractions of these stages were prepared using whole animals. While this procedure may occasion differences in enzyme-specific activity, the (Na^+,K^+)-ATPase activity of the decapodid III can be compared with that of zoea I and with the gill and whole-body preparations from juvenile and adult shrimps. Since we employed microsomal preparations rather than crude tissue homogenates, the activity increase in decapodid III cannot be attributed to a decrease in soluble proteins in the body fluids or associated with structural protein synthesis during metamorphosis. Further, any newly expressed structural proteins in the microsomal fraction from decapodid III would tend to decrease rather than increase (Na^+,K^+)-ATPase-specific activity. Thus, (Na^+,K^+)-ATPase activity in homogenates of whole adult and juvenile *M. amazonicum* is about one-third that of *P. argentinus*

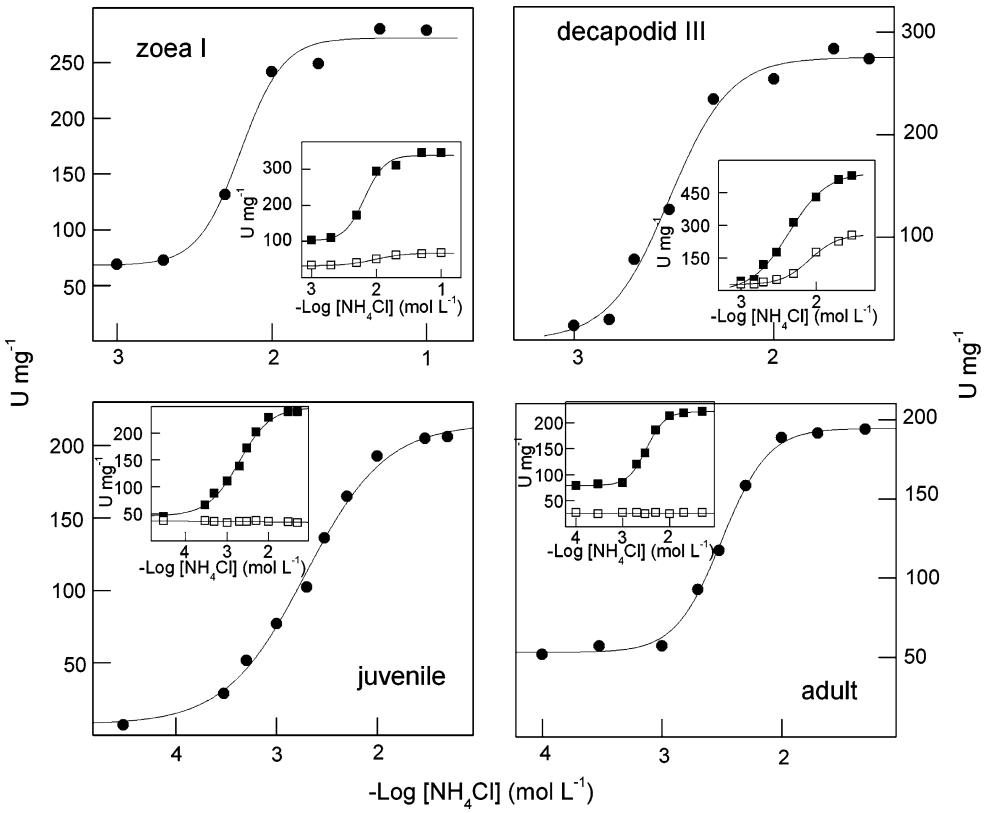

Fig. 5 Effect of NH_4^+ concentration on (Na^+,K^+)-ATPase activity in microsomal fractions from *M. amazonicum* at different ontogenetic stages. Activity was assayed continuously at 25 °C in 50 mmol L^{-1} HEPES buffer, pH 7.5, containing 2.0 mmol L^{-1} ATP, 5.0 mmol L^{-1} $MgCl_2$, 1.0 mmol L^{-1} NAD^+, 0.5 mmol L^{-1} sodium phosphate, 1.0 mmol L^{-1} G3P, 150 μg GAPDH (12 U), 20 μg PGK (9 U) and 50 mmol L^{-1} NaCl for zoea I and juvenile enzymes or 20 mmol L^{-1} NaCl for decapodid III and adult enzymes. Enzyme activity was assayed using 13.4, 7.2, 9.8 and 31.4 μg protein from homogenates of whole zoeae I and decapodid III, and gill homogenates of juvenile and adult shrimps, respectively. Experiments were performed using duplicate aliquots from three different homogenates; representative curves obtained from one homogenate are given. *Insets* effect of NH_4^+ concentration on ouabain-insensitive (*open square*) and total ATPase activities (*filled square*)

gill tissue (Ituarte et al. 2008) and considerably lower than for zoea I and decapodid III. The few studies correlating the salinity tolerance of early ontogenetic stages with (Na^+,K^+)-ATPase activity have been undertaken mainly using crude tissue homogenates (Conte et al. 1977; Sun et al. 1991; Lee and Watts 1994; Escalante et al. 1995; Wilder et al. 2001; Huong et al. 2004; Ituarte et al. 2008) and not isolated microsomal fractions as employed here, and direct comparison is not possible.

The $K_{0.5}$ values for modulation by NH_4^+ of (Na^+,K^+)-ATPase activity in zoea I, decapodid III, juvenile and adult *M. amazonicum* are similar to those for *Callinectes danae* ($K_{0.5}$ = 4.61 ± 0.27 mmol L^{-1}, Masui et al. 2002), *Xiphopenaeus kroyeri* ($K_{0.5}$ = 3.7 ± 0.6 mmol L^{-1}, Leone et al. 2005b), *Clibanarius vittatus* ($K_{0.5}$ = 4.5 ± 0.2 mmol L^{-1}, Gonçalves et al. 2006), *Callinectes ornatus* ($K_{0.5}$ = 5.4 ± 0.2 mmol L^{-1}, Garçon et al. 2007), *M. amazonicum* ($K_{0.5}$ = 5.0 ± 0.2 mmol L^{-1}, Santos et al. 2007), *D. pagei* ($K_{0.5}$ = 1.92 ± 0.11 mmol L^{-1}, Furriel et al. 2010) and *M. olfersi* ($K_{0.5}$ = 8.4 ± 0.2 mmol L^{-1}, Furriel et al. 2004). NH_4^+ can replace K^+ in sustaining ATP hydrolysis in crustacean (Holliday 1985; Furriel et al. 2000; Masui et al. 2002; Gonçalves et al. 2006; Santos et al. 2007; Garçon et al. 2007; Furriel et al. 2010) and mollusk (Pagliarani et al. 2008) gill (Na^+,K^+)-ATPases, and NH_4^+ can substitute for K^+ as a counter ion in Na^+ transport in *Callinectes sapidus* (Towle and Holleland 1987). Like K^+, NH_4^+ can be actively transported by vertebrate (Na^+,K^+)-ATPase (Wall 1996). Synergistic stimulation by K^+ and NH_4^+ of crustacean (Na^+,K^+)-ATPase was first shown in *C. danae* (Masui et al. 2002, 2005) and now has been demonstrated in various crustaceans (Furriel et al. 2000; Gonçalves et al. 2006; Garçon et al. 2007, 2009; Santos et al. 2007; Furriel et al. 2010). While NH_4^+ excretion and active transport are not necessarily directly coupled in crabs (Weihrauch et al. 1999), exposure to elevated NH_3 may lead to substitution of K^+ by NH_4^+, decreasing intracellular K^+ (Towle and Holleland 1987). Further, acute exposure to NH_3 of *Neohelice* (=*Chasmagnathus*) *granulata* reveals hemolymph NH_3 to

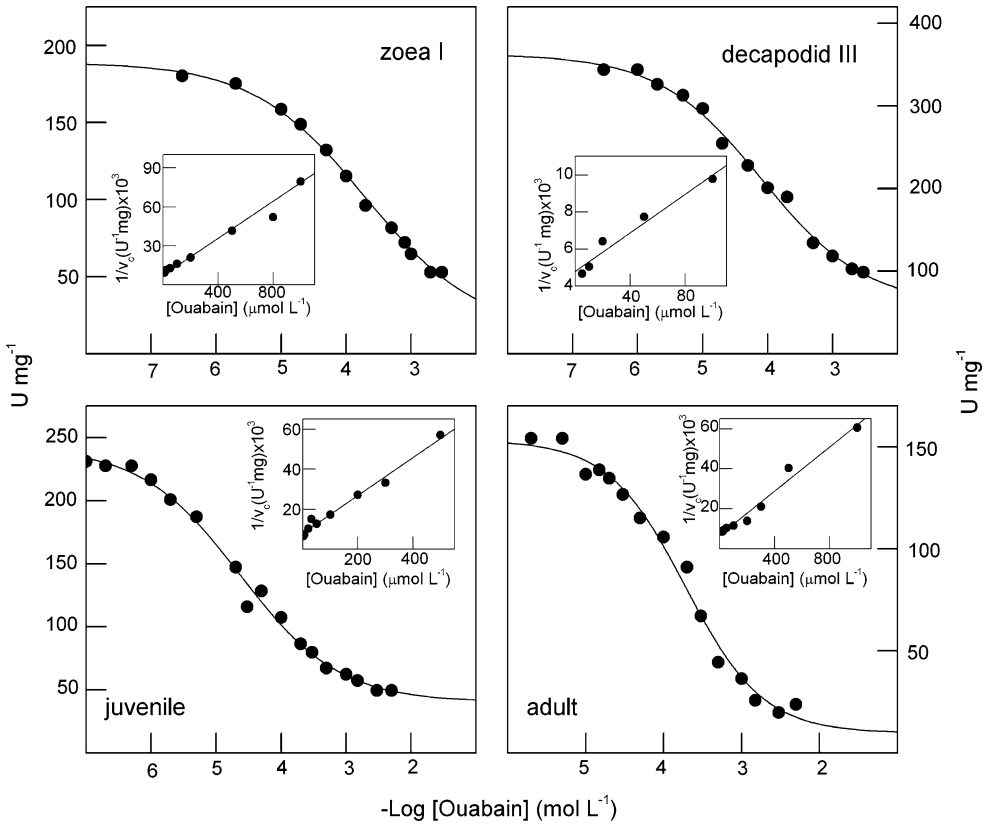

Fig. 6 Effect of ouabain on total ATPase activity in microsomal fractions from *M. amazonicum* at different ontogenetic stages. Activity was assayed continuously at 25 °C in 50 mmol L^{-1} HEPES buffer, pH 7.5, containing 2.0 mmol L^{-1} ATP, 5.0 mmol L^{-1} $MgCl_2$, 20.0 mmol L^{-1} KCl, 0.14 mmol L^{-1} NADH, 2.0 mmol L^{-1} PEP, 82 μg PK (49 U), 110 μg LDH (94 U) and 50 mmol L^{-1} NaCl for zoea I and juvenile enzymes or 20 mmol L^{-1} NaCl for decapodid III and adult enzymes. Enzyme activity was assayed using 13.4, 7.2, 9.8 and 31.4 μg protein from homogenates of whole zoeae I, and decapodid III, and gill homogenates of juvenile and adult shrimps, respectively. Experiments were performed using duplicate aliquots from three different homogenates; representative curves obtained from one homogenate are given. *Insets* dixon plots for estimation of K_I, the enzyme-inhibitor complex dissociation constant, in which v_c is the reaction rate corresponding to (Na^+,K^+)-ATPase activity alone

be less than ambient (Rebelo et al. 1999). Consequently, and given that the NH_4^+ binding sites on the Na^+,K^+-ATPase molecule face the hemolymph, when hemolymph NH_3 exceeds physiological concentrations (100 μM), (Na^+,K^+)-ATPase may be stimulated, maintaining steady-state ammonia titers within physiological limits (Masui et al. 2002, 2005). In aquatic animals facing an inwardly directed ammonia gradient in their natural environment, the active component of an exocytotic ammonia excretion mechanism (Weihrauch et al. 2002) may provide protection for both the gill epithelial cells and the organism as a whole against passive NH_4^+ influx. The existence of such an excretion mechanism seems highly likely since, rather than diffusing freely across the cytoplasm, toxic ammonia would be trapped in intracellular vesicles, avoiding cytoplasmic damage (Weihrauch et al. 2002, 2004b).

Although these findings show that (Na^+,K^+)-ATPase activity in *M. amazonicum* is strongly modulated by Na^+, K^+, Mg^{2+} and NH_4^+ concentrations, further investigation is necessary to better comprehend modulation by ATP and ions of (Na^+,K^+)-ATPase activity during the ontogenesis of palemonid shrimps. We are undertaking a systematic investigation of Mg^{2+}-stimulated, ouabain-insensitive ATPase activities in addition to salinity acclimation studies to gather information on the different ATPases expressed during ontogeny. Such investigations should allow a better understanding of the marked, transitory increase in (Na^+,K^+)-ATPase activity in the decapodid III stage.

Acknowledgements This investigation was supported by research grants from the Fundação de Amparo à Pesquisa do Estado de São Paulo (FAPESP), Conselho de Desenvolvimento Científico e Tecnológico (CNPq), Coordenação de Aperfeiçoamento de Pessoal de Nível Superior (CAPES) and Instituto Nacional de Ciência e Tecnologia (INCT) ADAPTA/Fundação de Amparo à Pesquisa do Estado do Amazonas (FAPEAM, 573976/2008-2). T. M. S. B. received undergraduate scholarships from CNPq; A. S. A., D. C. M. and D. P. G. received postdoctoral scholarships from FAPESP. F. A. L., W. C. V. and J. C. M. received research scholarships from CNPq. We thank Nilton Rosa Alves and Roberto Polachini for technical assistance. This laboratory (F. A. L.) is integrated with the Amazon Shrimp Network (Rede de Camarão da Amazônia) and with ADAPTA (Centro de Estudos de Adaptações da Biota Aquática da Amazônia).

References

Anger K (2001) The biology of decapod crustacean larvae. Crustacean issues 14. Balkema, Lisse

Anger K (2003) Salinity as a key parameter in the larval biology of decapod crustaceans. Invertebr Reprod Dev 43:29–45

Anger K, Hayd L, Knott J, Nettelmann U (2009) Patterns of larval growth and chemical composition in the Amazon River prawn, *Macrobrachium amazonicum*. Aquaculture 287:341–348

Araujo MC, Valenti WC (2007) Feeding habit of the Amazon River prawn *Macrobrachium amazonicum* larvae. Aquaculture 265:187–193

Augusto A, Greene LJ, Laure HJ, McNamara JC (2007) The ontogeny of isosmotic intracellular regulation in the diadromous, freshwater palaemonid shrimps, *Macrobrachium amazonicum* and *M. olfersi* (Crustacea, Decapoda). J Crust Biol 27:626–634

Axelsen MG, Palmgren KB (1998) Evolution of P-type ATPases. Biochim Biophys Acta 1365:37–45

Belli NM, Faleiros RO, Firmino KCS, Masui DC, Leone FA, McNamara JC, Furriel RPM (2009) Na,K-ATPase activity and epithelial interfaces in gills of the freshwater shrimp *Macrobrachium amazonicum* (Decapoda, Palaemonidae). Comp Biochem Physiol A 152:431–439

Blanco G (2005) Na,K-ATPase subunit heterogeneity as a mechanism for tissue-specific ion regulation. Semin Nephrol 25:292–303

Blanco G, Mercer RW (1998) Isozymes of the Na-K-ATPase: heterogeneity in structure, diversity in function. Am J Physiol Renal Physiol 275:F633–F650

Charmantier G (1998) Ontogeny of osmoregulation in crustaceans: a review. Invertebr Reprod Dev 33:177–190

Charmantier G, Anger K (2010) Ontogeny of osmoregulatory patterns in the South American shrimp *Macrobrachium amazonicum*: loss of hypo-regulation in a land-locked population indicates phylogenetic separation from estuarine ancestors. J Exp Mar Biol Ecol 396:89–98

Collart OO, Rabelo H (1996) Variation in egg size of the fresh-water prawn *Macrobrachium amazonicum* (Decapoda: Palaemonidae). J Crust Biol 16:684–688

Conte FP, Droukas PC, Ewing RD (1977) Development of sodium regulation and de novo synthesis of Na^+,K^+-activated ATPase in larval brine shrimp, *Artemia salina*. J Exp Zool 202:339–362

Crambert G, Hasler U, Beggah AT, Yu C, Modyanov NN, Horisberger JD, Lelievre L, Geering K (2000) Transport and pharmacological properties of nine different human Na,K-ATPase isozymes. J Biol Chem 275:1976–1986

Escalante R, Garcia-Sáez A, Sastre L (1995) In situ hybridization analyses of Na,K-ATPase α-subunit expression during early larval development of *Artemia franciscana*. J Histochem Cytochem 43:391–399

Faleiros RO, Goldman MH, Furriel RP, McNamara JC (2010) Differential adjustment in gill Na^+/K^+- and V-ATPase activities and transporter mRNA expression during osmoregulatory acclimation in the cinnamon shrimp *Macrobrachium amazonicum* (Decapoda, Palaemonidae). J Exp Biol 213:3894–3905

Faria SC, Augusto AS, McNamara JC (2011) Intra- and extracellular osmotic regulation in the hololimnetic Caridea and Anomura: a phylogenetic perspective on the conquest of fresh water by the decapod Crustacea. J Comp Physiol B 181:175–186

Felder JM, Felder DL, Hand SC (1986) Ontogeny of osmoregulation in the estuarine ghost shrimp *Callianassa jamaicense* var. louisianensis Schmitt (Decapoda, Thalassinidea). J Exp Mar Biol Ecol 99:91–105

Fontes CFL, Barrabin H, Scofano HM, Norby JG (1992) The role of Mg^{2+} and K^+ in the phosphorylation of Na^+,K^+-ATPase by ATP in the presence of dimethylsulfoxide but in the absence of Na^+. Biochim Biophys Acta 1104:215–225

Freire CA, Cavassin F, Rodrigues EN, Torres AH, McNamara JC (2003) Adaptive patterns of osmotic and ionic regulation, and the invasion of fresh water by the palaemonid shrimps. Comp Biochem Physiol A 136:771–778

Freire CA, Onken H, McNamara JC (2008) A structure-function analysis of ion transport in crustacean gills and excretory organs. Comp Biochem Physiol A 151:272–304

Furriel RPM, McNamara JC, Leone FA (2000) Characterization of (Na^+,K^+)-ATPase in gill microsomes of the freshwater shrimp *Macrobrachium olfersi*. Comp Biochem Physiol B 126: 303–315

Furriel RPM, Masui DC, McNamara JC, Leone FA (2004) Modulation of gill Na^+,K^+-ATPase activity by ammonium ions: putative coupling of nitrogen excretion and ion uptake in the freshwater shrimp *Macrobrachium olfersii*. J Exp Zool A 301:63–74

Furriel RPM, Firmino KCS, Masui DC, Faleiros RO, Torres AH, McNamara JC (2010) Structural and biochemical correlates of Na^+,K^+-ATPase driven ion uptake across the posterior epithelium of the true freshwater crab, *Dilocarcinus pagei* (Brachyura, Trichodactylidae). J Exp Zool A 313:508–523

Garçon DP, Masui DC, Mantelatto FLM, McNamara JC, Furriel RPM, Leone FA (2007) K^+ and NH_4^+ modulate gill (Na^+,K^+)-ATPase activity in the blue crab, *Callinectes ornatus*: fine tuning of ammonia excretion. Comp Biochem Physiol A 147:145–155

Garçon DP, Masui DC, Mantelatto FLM, McNamara JC, Furriel RPM, Leone FA (2009) Hemolymph ionic regulation and adjustments in gill (Na^+,K^+)-ATPase activity during salinity acclimation in the swimming crab *Callinectes ornatus* (Decapoda, Brachyura). Comp Biochem Physiol A 154:44–55

Geering K (2008) Functional roles of Na-K-ATPase subunits. Curr Opin Nephrol Hypertens 17:526–532

Genovese G, Luchetti CG, Luquet CM (2004) Na^+/K^+-ATPase activity and gill ultrastructure in the hyper-hypo-regulating crab *Chasmagnathus granulatus* acclimated to dilute, normal, and concentrated seawater. Mar Biol 144:111–118

Gonçalves RR, Masui DC, McNamara JC, Mantelatto FLM, Garçon DP, Furriel RPM, Leone FA (2006) A kinetic study of the gill (Na^+,K^+)-ATPase, and its role in ammonia excretion in the intertidal hermit crab, *Clibanarius vittatus*. Comp Biochem Physiol A 145:346–356

Guest WC (1979) Laboratory life history of the palaemonid shrimp *Macrobrachium amazonicum* (Heller) (Decapoda, Palaemonidae). Crustaceana 37:141–152

Haond C, Bonnal L, Charmantier G, Trilles JP (1999) Ontogeny of intracellular isosmotic regulation in the European lobster *Homarus gammarus*. Physiol Biochem Zool 72:534–544

Harris RR, Bayliss D (1988) Gill (Na^+/K^+)-ATPases in decapod crustaceans: distribution and characteristics in relation to Na^+ regulation. Comp Biochem Physiol A 90:303–308

Holliday CW (1985) Salinity-induced changes in gill Na,K-ATPase activity in the mud fiddler crab *Uca pugnax*. J Exp Zool 233: 199–208

Huong DTT, Jayasankar V, Jasmani S, Saido-Sakanaka H, Wigginton AJ, Wilder MN (2004) Na/K-ATPase activity during larval development in the giant freshwater prawn *Macrobrachium rosenbergii* and the effects of salinity on survival rates. Fish Sci 70:518–520

Ituarte RB, Mañanes AAL, Spivak ED, Anger K (2008) Activity of Na^+,K^+-ATPase in a freshwater shrimp, *Palaemonetes argentinus* (Caridea, Palaemonidae): ontogenetic and salinity-induced changes. Aquat Biol 3:283–290

Jorgensen PL, Pedersen PA (2001) Structure–function relationships of Na^+,K^+, ATP, or Mg^{2+} binding and energy transduction in Na^+,K^+-ATPase. Biochim Biophys Acta 1505:57–74

Jorgensen PL, Hakansson KO, Karlish SJD (2003) Structure and mechanism of Na,K-ATPase: functional sites and their interactions. Annu Rev Physiol 65:817–849

Kaplan JH (2002) Biochemistry of Na,K-ATPase. Annu Rev Biochem 30:511–533

Khodabandeh S, Charmantier G, Charmantier-Daures M (2006) Immunolocalization of Na,K-ATPase in osmoregulatory organs during the embryonic and post-embryonic development of the lobster *Homarus gammarus*. J Crust Biol 26:515–523

Kirschner LB (2004) The mechanism of sodium chloride uptake in hyperregulating aquatic animals. J Exp Biol 207:1439–1452

Lee KJ, Watts SA (1994) Specific activity of Na^+,K^+ ATPase is not altered in response to changing salinities during early development of the brine shrimp, *Artemia franciscana*. Physiol Zool 67:910–924

Leone FA, Baranauskas JA, Furriel RPM, Borin IA (2005a) SigrafW: an easy-to-use program for fitting enzyme kinetic data. Biochem Mol Biol Educ 33:399–403

Leone FA, Furriel RPM, McNamara JC, Mantelatto FLM, Masui DC, Rezende LA, Gonçalves RR, Garçon D (2005b) (Na^+,K^+)-ATPase from crustacean gill microsomes: a molecular marker to evaluate adaptation to biotopes of different salinity. Trends Comp Biochem Physiol 11:1–15

Lima AG, McNamara JC, Terra WR (1997) Regulation of hemolymph osmolytes and gill (Na^+,K^+)-ATPase activities during acclimation to saline media in the freshwater shrimp *Macrobrachium olfersi* (Wiegmann 1836) (Decapoda Palaemonidae). J Exp Mar Biol Ecol 215:81–91

Lucu C, Towle DW (2003) Na^+,K^+-ATPase in gills of aquatic crustacea. Comp Biochem Physiol A 135:195–214

Maciel CR, Valenti WC (2009) Biology, fisheries and aquaculture of the Amazon River prawn *Macrobrachium amazonicum*: a review. Nauplius 17:61–79

Magalhães C (1985) Desenvolvimento larval obtido em laboratório de palemonídeos da Região Amazônica. I. *Macrobrachium amazonicum* (Heller, 1862) (Crustacea, Decapoda). Amazoniana 9:247–274

Marks MJ, Seeds NW (1978) A heterogeneous ouabain-ATPase interaction in mouse brain. Life Sci 23:2735–2744

Martin DW (2005) Structure–function relationships in the Na^+,K^+-pump. Semin Nephrol 25:282–291

Masui DC, Furriel RPM, McNamara JC, Mantelatto FLM, Leone FA (2002) Modulation by ammonium ions of gill microsomal (Na^+,K^+)-ATPase in the swimming crab *Callinectes danae*: a possible mechanism for regulation of ammonia excretion. Comp Biochem Physiol C 132:471–482

Masui DC, Furriel RPM, Silva ECC, Mantelatto FLM, McNamara JC, Barrabin H, Scofano HM, Fontes CFL, Leone FA (2005) Gill microsomal (Na^+,K^+)-ATPase from the blue crab *Callinectes danae*: interactions at cationic sites. Int J Biochem Cell Biol 37:2521–2535

Masui DC, Silva ECC, Mantelatto FLM, McNamara JC, Barrabin H, Scofano HM, Fontes CFL, Furriel RPM, Leone FA (2008) The crustacean gill (Na^+,K^+)-ATPase: allosteric modulation of high- and low-affinity ATP-binding sites by sodium and potassium. Arch Biochem Biophys 479:139–144

McNamara JC, Faria SC (2012) Evolution of osmoregulatory patterns and gill ion transport mechanisms in the decapod Crustacea: a review. J Comp Physiol B. doi:10.1007/s00360-012-0665-8

McNamara JC, Lima AG (1997) The route of ion water movements across the gill epithelium of the freshwater shrimp *Macrobrachium olfersii* (Decapoda, Palaemonidae): evidence from ultrastructural changes induced by acclimation to saline media. Biol Bull 192:321–331

McNamara JC, Torres AH (1999) Ultracytochemical location of Na^+/K^+-ATPase activity and effects of high salinity acclimation in gill and renal epithelia of the freshwater shrimp *Macrobrachium olfersii* (Crustacea, Decapoda). J Exp Zool 284:617–628

McNamara JC, Moreira GS, Moreira OS (1983) The effect of salinity on respiratory metabolism, survival and moulting in the first zoea of *Macrobrachium amazonicum* (Heller) (Crustacea, Palaemonidae). Hydrobiologia 101:239–242

McNamara JC, Moreira GS, Souza SCR (1986) The effect of salinity on respiratory metabolism in selected ontogenetic stages of the freshwater shrimp *Macrobrachium olfersii* (Decapoda, Palaemonidae). Comp Biochem Physiol A 83:359–363

Mendonça NN, Masui DC, McNamara JC, Leone FA, Furriel RPM (2007) Long-term exposure of the freshwater shrimp *Macrobrachium olfersi* to elevated salinity: effects on gill (Na^+,K^+)-ATPase α-subunit expression and K^+-phosphatase activity. Comp Biochem Physiol A 146:534–543

Moraes-Valenti P, Valenti WC (2010) Culture of the Amazon River prawn *Macrobrachium amazonicum*. In: New MB, Valenti WC, Tidwel JH, Abramo LR, Kutty MN (eds) Freshwater prawns: biology and farming. Wiley, Oxford, pp 485–501

Moreira GS, McNamara JC, Moreira PS (1986) The effect of salinity on the upper thermal limits of survival and metamorphosis during larval development in *Macrobrachium amazonicum* (Heller) (Decapoda, Palaemonidae). Crustaceana 50:231–238

Moretti R, Martin M, Proverbio T, Proverbio F, Marin R (1991) Ouabain-insensitive Na-ATPase activity in homogenates from different animal tissues. Comp Biochem Physiol B 98:623–626

Morth JP, Pedersen BP, Toustrup-Jensen MS, Sorensen TLM, Petersen J, Andersen JP, Vilsen B, Nissen P (2007) Crystal structure of the sodium–potassium pump. Nature 450:1043–1050

Onken H, McNamara JC (2002) Hyperosmoregulation in the red freshwater crab *Dilocarcinus pagei* (Brachyura, Trichodactylidae): structural and functional asymmetries of the posterior gills. J Exp Biol 205:167–175

Onken H, Riestenpatt S (1998) NaCl absorption across split gill lamellae of hyperregulating crabs, transport mechanisms and their regulation. Comp Biochem Physiol A 119:883–893

Onken H, Graszynski K, Johansen A, Putzenlechner M, Riestenpatt S, Schirmer C, Siebers D, Zeiske W (1995) How to overcome osmotic stress: marine crabs conquer fresh-water. New insights from modern electrophysiology. Helgol Meeresunters 49: 715–725

Pagliarani A, Bandiera P, Ventrella V, Trombetti F, Manuzzi MP, Pirini M, Borgatti AR (2008) Response of Na^+-dependent ATPase activities to the contaminant ammonia nitrogen in *Tapes philippinarum*: possible ATPase involvement in ammonium transport. Arch Environ Contam Toxicol 55:49–56

Péqueux A (1995) Osmotic regulation in crustaceans. J Crust Biol 15:1–60

Pettovello AD (1996) First record of *Macrobrachium amazonicum* (Decapoda, Palaemonidae) in Argentina. Crustaceana 69:113–116

Poulsen H, Morth PO, Egebjerg J, Nissen P (2010) Phosphorylation of the Na^+,K^+-ATPase and the H^+,K^+-ATPase. FEBS Lett 584: 2589–2595

Proverbio F, Marin R, Proverbio T (1991) The ouabain-insensitive sodium pump. Comp Biochem Physiol A 99:279–283

Ramos-Porto M, Coelho PA (1998) Malacostraca Eucarida Caridea (Alpheoidea). In: Young PS (ed) Catalogue of Crustacea of Brazil. Museu Nacional, Rio de Janeiro, pp 325–350

Read GHL (1984) Intraspecific variation in the osmoregulatory capacity of larval, post larval, juvenile and adult *Macrobrachium petersi* (Hilgendorf). Comp Biochem Physiol A 78:501–506

Read SM, Northcote DH (1981) Minimization of variation in the response to different proteins of the Coomassie blue G dye-binding assay for protein. Anal Biochem 116:53–64

Rebelo MF, Santos EA, Monserrat JM (1999) Ammonia exposure of *Chasmagnathus granulata* (Crustacea, Decapoda) Dana, 1851:

accumulation in haemolymph and effects on osmoregulation. Comp Biochem Phys A 122:429–435

Reyes A, Galindo MM, Garcia L, Segura-Pena D, Caruso-Neves C, Eblen-Zajjur A, Proverbio T, Marini R, Proverbio F (2009) Ouabain-insensitive, Na^+-stimulated ATPase of several rat tissues: activity during a 24 h period. Physiol Res 58:693–699

Riestenpatt S, Onken H, Siebers D (1996) Active absorption of Na^+ and Cl^- across the gill epithelium of the shore crab *Carcinus maenas*: voltage-clamp and ion-flux studies. J Exp Biol 199: 1545–1554

Robinson JD, Pratap PR (1991) Na^+/K^+-ATPase—modes of inhibition by Mg^{2+}. Biochim Biophys Acta 1061:267–278

Rudolph FB, Baugher BW, Beissner RS (1979) Techniques in coupled enzyme assays. Methods Enzymol 63:22–42

Sáez AG, Lozano E, Zaldívar-Riverón A (2009) Evolutionary history of Na,K-ATPases and their osmoregulatory role. Genetica 136:479–490

Sandifer PA, Hopkins JS, Smith TIJ (1975) Observations on salinity tolerance and osmoregulation in laboratory reared *Macrobrachium rosenbergii* post-larvae (Crustacea, Caridea). Aquaculture 6:103–114

Santos LCF, Belli NM, Augusto A, Masui DC, Leone FA, McNamara JC, Furriel RPM (2007) Gill (Na^+,K^+)-ATPase in diadromous, freshwater palaemonid shrimps: species specific kinetic characteristics and α-subunit expression. Comp Biochem Physiol A 148:178–188

Short JW (2004) A revision of Australian river prawns, *Macrobrachium* (Crustacea: Decapoda: Palaemonidae). Hydrobiologia 525:1–100

Stern S, Borut A, Cohen D (1984) Characterization of (Na,K)-ATPase from the gills of the freshwater prawn *Macrobrachium rosenbergii* (De Man). Comp Biochem Physiol B 79:47–50

Sun DY, Guo JZ, Hartman HA, Uno H, Hokin LE (1991) Na,K-ATPase expression in the developing brine shrimp *Artemia*. Immunochemical localization of the alpha- and beta-subunits. J Histochem Cytochem 39:1455–1460

Susanto GN, Charmantier G (2001) Crayfish freshwater adaptation starts in eggs: ontogeny of osmoregulation in embryos of *Astacus leptodactylus*. J Exp Zool 289:433–440

Tentes I, Stratakis E (1991) Partial purification and properties of Na,K-ATPase from *Potamon potamios*. Comp Biochem Physiol C 100:619–624

Therien AG, Nestor NB, Ball NJ, Blostein R (1996) Tissue-specific versus isoform-specific differences in cation activation kinetics of the Na,K-ATPase. J Biol Chem 271:7104–7112

Thuet P, Charmantier-Daures M, Charmantier G (1988) Relation entre osmorégulation et activité d'ATPase Na^+–K^+ et d'anhydrase carbonique chez les larves et post-larves de *Homarus gammarus* (L.) (Crustacea, Decapoda). J Exp Mar Biol Ecol 115:249–261

Torres AH, Onken H, McNamara JC (2003) Como as brânquias de um camarão de água doce capturam Na^+, Ca^{2+} e Cl^- do meio ambiente: uma abordagem eletrofisiológica qualitativa. In: XVIII Reunião Anual da Federação das Sociedades de Biologia Experimental, Curitiba, Brazil, 23–27 August 2003. Abstract 11.022

Towle DW, Holleland T (1987) Ammonium ion substitutes for K^+ in ATP-dependent Na^+ transport by basolateral membrane vesicles. Am J Physiol Regul Integr Comp Physiol 252:R427–R489

Wall SM (1996) Ammonium transport and the role of the Na,K-ATPase. Miner Electrolyte Metab 22:311–317

Weihrauch D, Becker W, Postel U, Luck-Kopp S, Siebers D (1999) Potential of active excretion of ammonia in three different haline species of crabs. J Comp Physiol B 169:364–376

Weihrauch D, Ziegler A, Siebers D, Towle DW (2002) Active ammonia excretion across the gills of the green shore crab *Carcinus maenas*: participation of Na^+/K^+-ATPase, V-type H^+-ATPase and functional microtubules. J Exp Biol 205:2765–2775

Weihrauch D, McNamara JC, Towle D, Onken H (2004a) Ion-motive ATPases and active transbranchial NaCl uptake in the red freshwater crab *Dilocarcinus pagei* (Decapoda, Trichodactylidae). J Exp Biol 207:4623–4631

Weihrauch D, Morris S, Towle DW (2004b) Ammonia excretion in aquatic and terrestrial crabs. J Exp Biol 207:4491–4504

Wilder MN, Huong DTT, Okuno A, Atmomarsono M, Yang WJ (2001) Ouabain-sensitive Na/K-ATPase activity increases during embryogenesis in the giant freshwater prawn *Macrobrachium rosenbergii*. Fish Sci 67:182–184

Zanders IP, Rodriguez JM (1992) Effects of temperature and salinity stress on osmoionic regulation in adults and on oxygen-consumption in larvae and adults of *Macrobrachium amazonicum* (Decapoda, Palaemonidae). Comp Biochem Physiol A 101: 505–509

J Membrane Biol (2012) 245:217–219
DOI 10.1007/s00232-012-9486-7

INTRODUCTION

Introduction Paper of the Special Issue on Gap Junctions in Honor of Ross Johnson

Paul D. Lampe · Dale W. Laird

Published online: 8 July 2012

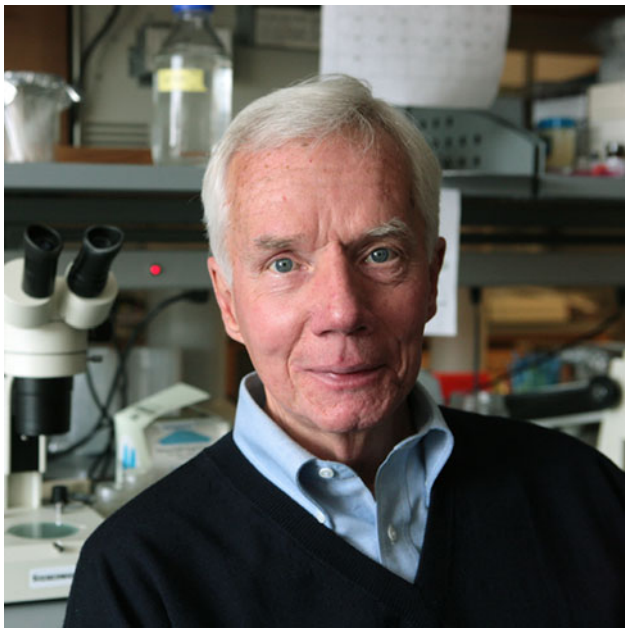

On a hot Saturday evening in August of 2009, the gap junction community gathered at the Hilton in Sedona, AZ in anticipation of the biennial International Gap Junction Conference. This meeting was particularly special as it was an opportunity to honor and pay tribute to one of the long time leaders and life-time contributors to the field, Dr. Ross Johnson. After Dr. Paul Lampe recapped Ross' notable and seminal contributions to the field, Ross spoke elegantly and humbly about his joy of science and the love of this community. Ross was accompanied by his lovely wife Esther, who often joined him in his travels and who has become endeared to the community in her own right. Phrases like "he is one of the really good guys", "I know he respects my work" and "he gives generously of his time" echoed in the halls of the Sedona meeting as colleagues recounted their interactions with Ross over four decades. It is a privilege and honor for us to know Ross and to spearhead and act as guest editors for this special *Journal of Membrane Biology* issue dedicated equally to Ross' achievements in science and to the mentorship and friendship he has extended to many of us in the field. A testament to Ross' impact on the community was evidenced by the fact that over 95 % of the colleagues asked to contribute to this issue agreed without hesitation and with comments like "I would only do it for Ross", "Definitely, for Ross" and "Count me in". To all of you, we say thank you for your timely contributions. We also wish to express our gratitude and thanks to Dr. Tom Woolf, Editor-in-Chief, for supporting this initiative and for taking a leading role in seeing that this endeavor is executed with the highest level of professionalism. Finally, to Dr. Jan Hoh, Ross' long-time friend and ours as well, we also say thanks for seeding this idea with Tom.

Ross began his academic career at Augustana College from which he graduated with a BA before moving to Iowa State University, where he obtained a NIH predoctoral Fellowship to complete his PhD. It was here that he fell in love with cell biology. Success came quickly for Ross as he was immediately recruited as an Assistant Professor in the Department of Zoology at the University of Minnesota

P. D. Lampe (✉)
Fred Hutchinson Cancer Research Center, 1100 Fairview Avenue North, M5C800, Box 19024, Seattle, WA 98109, USA
e-mail: plampe@fhcrc.org

D. W. Laird
Department of Anatomy and Cell Biology, Western University, London, ON, Canada
e-mail: dale.laird@schulich.uwo.ca

(later joining Genetics and Cell Biology after a reorganization), where he would spend his entire scientific career and rise through the ranks to Professor and Head of the Department. It was during his early years as an independent investigator that Ross engaged in a newly emerging field called gap junction biology. At the outset, Ross chose to establish formidable collaborations with two pioneers of the field, Minnesota colleague Dr. Judd Sheridan, who introduced Ross to gap junctions, and Dr. Jean-Paul Revel. Jean-Paul, who was instrumental in naming gap junctions, has frequently been recognized as the first to use electron microscopy to describe their distinctive structure, although the widespread distribution of gap junctions was under appreciated in these early days. Together with Judd, Ross entered the gap junction literature in 1971 with a splash as his first paper was published in *Science* and depicted gap junctions in hepatoma cells, indicating that junctions were not absent in all cancer cells as some believed at that time. Later Ross' team used freeze-fracture electron microscopy to clearly show that gap junctions could form between cells of different types, further expanding the versatility and importance of gap junctions in tissue biology. However, with Jean-Paul, Ross reported in *Science* that there were limitations as to where gap junctions would form, noting that they were not observed in *Dictostelium discoideum* (slime molds).

Throughout his career, one of the most prominent research themes developed by Ross and his team was related to the mechanisms of gap junction assembly. Ross and Judd coined the term "formation plaque" to describe the specialized membrane areas present in both opposed cells at the early stages of gap junction assembly. This theme persisted from an early paper in 1974 published in *Proceedings of the National Academy of Science* to his most recent paper published in the *Molecular Biology of the Cell* in 2012, the latter with microscopy by Dr. Jim Reynhout that was pivotal. These papers book-ended nearly 40 years of studies that highlight the power of high resolution freeze-fracture electron microscopy and, more recently, freeze-fracture replica immunolabeling. In this special issue, Dr. Rash, another collaborator of Ross' highlights novel insights that can be deduced from these morphological studies. In 1976 Ross used his sabbatical year to study with his long-time friend Jean-Paul Revel at Caltech and it was there that he started to complement his cell biological and morphological approaches with cell fractionation and biochemical studies. In those days, the connexin proteins had not yet been identified and candidate proteins that constituted gap junction channels were constantly being evaluated.

As Ross entered the 80's he continued to expand the scope of his laboratory by establishing new collaborations. He turned his eye to the lens (no pun intended) as a rich source of gap junction proteins, and had productive collaborations with Dr. Charles Louis. Together with Dr. Sue Menko, he developed methods to culture lens fiber cells that are still used today and are featured in Dr. Linda Musil's article in this issue. Together with Dr. Elliot Hertzberg, in 1987 Ross co-organized the first ever International Gap Junction Conference (IGJC) at Asilomar, CA. With Ross' guidance this meeting evolved into the primary conference series serving the field that would be held every two years to this day. During this decade Ross also began to mentor Dr. Paul Lampe who brought his considerable biochemical skills to the ever expanding arsenal of approaches used in Ross' laboratory. Together as friends and colleagues, they built on the work of Dr. Keith Johnson, a former student in the lab, and pioneered studies on the phosphorylation of lens MIP. They then applied these approaches to phosphorylation events associated with the newly emerging connexin family of gap junction proteins. Importantly, Ross' group discovered that different kinase activators and inhibitors could regulate gap junction assembly at multiple stages in a series of elegant reports; many lab members, especially Dr. Erica TenBroek, were involved in this work. Dr. Lampe would eventually move on to the Fred Hutchison Cancer Research Center where he continues to identify, characterize and assign function to many of the connexin43 phosphorylation events. Further testament to Ross as a gentleman, scholar and mentor was evidenced in 1989 when he reached-out to befriend an unknown new Postdoctoral Fellow, Dr. Dale Laird, at a cell biology meeting in Houston. As collaborators and friends in the years to follow, Dale frequently sought mentorship from Ross in both his professional and personal life.

The 90's brought a new era of discovery for Ross. His 1996 paper in the *Journal of Cell Biology* solidified the existence and importance of gap junction hemichannels. This highly-cited paper was a rigorous, compelling and extensive study that placed hemichannels clearly on the map. Currently hemichannel studies constitute a large proportion of activity in the field and every Gap Junction Conference since the mid 90's features one or more hemichannel sessions. In addition, with the support of his University of Minnesota zebrafish colleagues, Drs. Perry Hackett and Steve Ekker, Ross continued to expand his research boundaries by turning his attention to the role of connexins in early zebrafish development. This all started when Ross' friend and collaborator, Dr. Jeff Essner, while still a student with Perry, stumbled onto a cDNA clone for Cx43.4. Later Dr. Julia Hatler, while a graduate student in Ross' group, used morpholino approaches to make seminal discoveries evoking Cx43.4 as an essential and evolutionarily-conserved component in left–right patterning of the early vertebrate embryo. Ross' interests in zebrafish connexins brought him together with Dr. Gunnar

Valdimarsson who some years later died tragically of a brain tumor. Through the zebrafish work of Ross, Gunnar and others, there is little doubt that connexins are at the cornerstone of early development.

In the last few years Ross has returned to freeze-fracture electron microscopy technology. Through his collaboration with Dr. John Rash, they brought the power of freeze-fracture replica immunolabeling analysis to bear on the assembly problem. Having established a detailed and linear analysis of morphological and mechanistic events that lead to gap junction assembly, Ross and John, along with Drs. Jim Nagy and Alberto Pereda, plan to extend this analysis even further. In 2008, after 40 years at the University of Minnesota, Ross entered phased retirement and together with Esther migrated out west to be close to their two daughters and grandchildren in the San Francisco Bay area close to the beautiful wine country. However, Ross continues to be an active member of the gap junction community. As examples: he spearheaded the successful NIH grant in support of the 2009 IGJC meeting, described recent research findings at the 2011 IGJC meeting in Belgium, and continues to work on manuscripts and sustain collaborations—all testament to the fact that Ross remains an important and vibrant contributor to the field.

Threaded through Ross's career has been a constant love for and excitement over the science and, more importantly, a love of people and teaching. Whether it is through his mentorship of over 20 PhD students and postdoctoral fellows or his decade as department head or service on graduate student advisory committees at the University of Minnesota ($\sim$200 we have learned), Ross has often said how he thoroughly enjoys the people in his life and the life of a scientist. The University of Minnesota feted Ross spectacularly for his retirement, focusing in his honor its annual Developmental Biology Symposium on "The Ties That Bind: Cell Junctions and Adhesion in Development". Now on behalf of the authors of this special issue and the gap junction community in general, we thank you, Ross, for touching all of our lives and we thank you most of all for your friendship. You are unquestionably "one of the really good guys".

J Membrane Biol (2012) 245:221–230
DOI 10.1007/s00232-012-9443-5

ORIGINAL ARTICLES

Cytoplasmic Amino Acids within the Membrane Interface Region Influence Connexin Oligomerization

Tekla D. Smith · Aditi Mohankumar · Peter J. Minogue · Eric C. Beyer · Viviana M. Berthoud · Michael Koval

Received: 27 February 2012 / Accepted: 1 June 2012 / Published online: 22 June 2012

Abstract Gap junction channels composed of connexins connect cells, allowing intercellular communication. Their cellular assembly involves a unique quality-control pathway. Some connexins [including connexin43 (Cx43) and Cx46] oligomerize in the *trans*-Golgi network following export of stabilized monomers from the endoplasmic reticulum (ER). In contrast, other connexins (e.g., Cx32) oligomerize early in the secretory pathway. Amino acids near the cytoplasmic aspect of the third transmembrane domain have previously been shown to determine this difference in assembly sites. Here, we characterized the oligomerization of two connexins expressed prominently in the vasculature, Cx37 and Cx40, using constructs containing a C-terminal dilysine-based ER retention/retrieval signal (HKKSL) or treatment with brefeldin A to block ER vesicle trafficking. Both methods led to intracellular retention of connexins, since the cells lacked gap junction plaques. Retention of Cx40 in the ER prevented it from oligomerizing, comparable to Cx43. By contrast, ER-retained Cx37 was partially oligomerized. Replacement of two amino acids near the third transmembrane domain of Cx43 (L152 and R153) with the corresponding amino acids from Cx37 (M152 and G153) resulted in early oligomerization in the ER. Thus, residues that allow Cx37 to oligomerize early in the secretory pathway could restrict its interactions with coexpressed Cx40 or Cx43 by favoring homomeric oligomerization, providing a structural basis for cells to produce gap junction channels with different connexin composition.

Keywords Endothelium · Membrane traffic · Quality control · Chaperone · ERp29

Electronic supplementary material The online version of this article (doi:10.1007/s00232-012-9443-5) contains supplementary material, which is available to authorized users.

T. D. Smith · M. Koval (✉)
Division of Pulmonary, Allergy, and Critical Care Medicine, Department of Medicine, Emory University School of Medicine, Whitehead Biomedical Research Building, 615 Michael St., Suite 205, Atlanta, GA 30022, USA
e-mail: mhkoval@emory.edu

A. Mohankumar · P. J. Minogue · E. C. Beyer · V. M. Berthoud
Department of Pediatrics, Section of Hematology/Oncology, University of Chicago, Chicago, IL 60637, USA

M. Koval
Department of Cell Biology, Emory University School of Medicine, Atlanta, GA 30322, USA

Introduction

Cell–cell contact sites known as "gap junctions" facilitate intercellular communication by enabling the direct transfer of small metabolites and ions between adjacent cells. Gap junctions consist of arrays of channels formed by proteins in the connexin (Cx) family (Beyer and Berthoud 2009). A complete gap junction channel is formed by two hexameric hemichannels, one in each cell, that are transported to the plasma membrane, where they dock to form a complete intercellular channel (Laird 2006) and then assemble into semicrystaline arrays known as "gap junction plaques" (Johnson et al. 1974, 2012).

Oligomerization of connexin hemichannels is regulated by a unique quality-control pathway, which is still being elucidated (Koval 2006; Laird 2010). Different connexins show substantial differences in oligomerization. One connexin, Cx43, is stabilized in the endoplasmic reticulum (ER) by a chaperone protein, ERp29, that enables it to be transported as a monomer through the secretory pathway to the *trans*-Golgi

apparatus, where it oligomerizes into hexameric hemichannels (Das et al. 2009; Musil and Goodenough 1993). In contrast, Cx32 does not interact with ERp29 and oligomerizes in the ER (Das et al. 2009). The quality control of Cx43 depends upon the amino acids flanking the third transmembrane (TM3) domain. Specifically, substituting tryptophan for arginine at amino acid position 153 in the cytosolic aspect of TM3 destabilizes monomeric Cx43 and causes its early oligomerization in the ER (Maza et al. 2003, 2005). Moreover, two dominant Cx43 mutations adjacent to R153 (T154A and T154N) are associated with oculodentodigital dysplasia (ODDD), underscoring the importance of this motif in the proper function of Cx43 (Paznekas et al. 2009).

Analysis of the cytoplasmic aspect of TM3 in the members of the connexin family reveals conserved motifs among subgroups of connexins that may determine cellular sites of oligomerization (Fig. 1). These connexin motifs fall into three subcategories: R-type, such as Cx43; W-type, including Cx32; and a third group that does not have clear homology with either the R- or W-type connexins (Table 1). Based on previous analysis of Cx43 and Cx32 (Maza et al. 2005), connexins in the R group are predicted to be highly stabilized as monomers in the ER, whereas connexins in the W group would oligomerize early within the secretory pathway. However, it is difficult to predict a priori whether connexins containing a cytoplasmic membrane interface region of TM3 that does not conform to either the R or the W motif would behave more like Cx43 or Cx32 in the ER.

We sought to determine the oligomerization properties of two connexins, Cx37 and Cx40, that do not contain either an R or a W motif. Cx37 and Cx40 are among the four major connexins expressed throughout the vasculature (Cx37, Cx40, Cx43 and Cx45) (Johnstone et al. 2009; Brisset et al. 2009). Connexin expression in the major cell types of blood vessels, endothelial cells and smooth muscle cells, is heterogeneous. Moreover, connexin composition of different classes of vascular gap junctions varies depending upon the vascular bed examined (Severs et al. 2001). For example, myoendothelial junctions of mesentery and cremaster microvessels both contain abundant Cx40 and low levels of Cx45 but differ dramatically in Cx37 and Cx43 content (Isakson et al. 2008; Heberlein et al. 2009). Thus, endothelial cells differentially process and sort connexins between myoendothelial junctions and endothelial–endothelial cell junctions. Since Cx37, Cx40 and Cx45 are all compatible to form mixed (heteromeric) connexons with Cx43 (Beyer et al. 2001), the ability to alter myoendothelial connexin content requires that endothelial cells regulate oligomerization.

Since Cx37 and Cx40 have TM3 interface regions that do not fit well into either the R or W subcategories (Table 1) (Figueroa et al. 2004), we could not predict how their oligomerization would be regulated. In the current study, we assessed the oligomerization state of Cx37 and Cx40 in the ER and found that they differed in monomer stability and in the subcellular compartments where oligomerization occurs. These connexin-specific differences likely affect connexin targeting and hetero-oligomerization.

Methods

Antibodies and Reagents

Polyclonal rabbit anti-Cx37 antibodies were generated against a maltose binding protein-Cx37 fusion protein

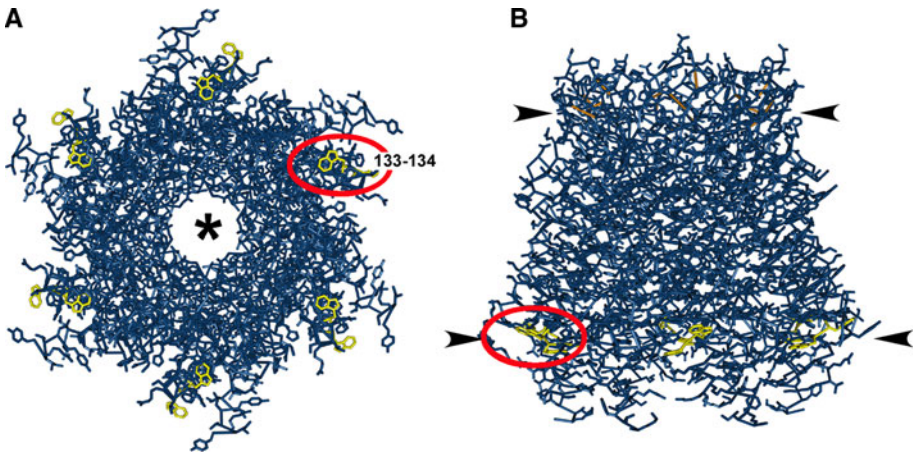

Fig. 1 Localization of the Cx26 ditryptophan (WW) motif to the cytoplasmic membrane–aqueous interface based on the structural model. A tube-style structural model of Cx26 including side chains (Maeda et al. 2009) was produced using the Molecular Modeling Database (Wang et al. 2007; Chen et al. 2003). The WW motif at amino acids 133–134 (*red oval*) is highlighted in *yellow*. Disulfide bonds in the EL domains are highlighted in *orange*. **a** View from the cytosolic aspect of a Cx26 hemichannel looking up through the aqueous pore (*). **b** Side view of a Cx26 hemichannel in a membrane bilayer. Positions of the membrane–aqueous interfaces are denoted by *arrowheads*. Note that the WW motif is located at the membrane interface of the cytoplasmic leaflet

Table 1 Connexin motifs in the cytoplasmic membrane interface region of TM3

Connexin		Amino acids	Motif
R type			
Cx43	GJA1	151–155	LLRTY
Cx46	GJA3	145–149	LLRTY
Cx50	GJA8	147–151	LLRTY
Cx62	GJA10	153–157	LLRTY
Cx45	GJC1	173–177	LMKIY
Cx47	GJC2	209–213	LMRVY
Cx36	GJD2	195–199	ISRFY
Cx31.9	GJD3	132–136	ARRCY
W type			
Cx32	GJB1	131–135	LWWTY
Cx26	GJB2	132–136	LWWTY
Cx31	GJB3	127–131	LWWTY
Cx30.3	GJB4	127–131	LWWTY
Cx31.1	GJB5	127–131	LWWTY
Cx30	GJB6	132–136	LWWTY
Cx25	GJB7	120–124	LWYAY
Cx30.2	GJC3	133–137	LLWAY
Other			
Cx37	GJA4	151–155	LMGTY
Cx40	GJA5	149–153	LLNTY
Cx59	GJA9	153–157	LLCTY
Cx40.1	GJD4	139–143	FSAGY
Cx23	GJE1	112–116	YTIIY

containing amino acids 80–333 of human Cx37. Anti-PDIA1 (PDI), -GM130 and -Cx43 antibodies were from Sigma (St. Louis, MO). Anti-Cx40 antibodies and monoclonal anti-Cx43 antibody were obtained from Chemicon (Temecula, CA). Fluorescent and horseradish peroxidase (HRP)-conjugated secondary antibodies were from Jackson ImmunoResearch (West Grove, PA). Triton X-100 was from Roche Molecular Biochemicals (Indianapolis, IN). Unless otherwise specified, all other reagents were from Sigma.

Generation of Connexin Constructs

Wild-type and HKKSL-containing Cx37 and Cx40 constructs were generated by PCR using human Cx37 in pSFFV-neo (Reed et al. 1993) or human Cx40 in pBScript (Kanter et al. 1994) as templates, the corresponding primers (Supplementary Table 1) and LA Taq DNA polymerase (Takara Mirus Bio, Madison, WI) or Phusion DNA polymerase (New England BioLabs, Ipswitch, MA). Primers were designed to incorporate *Hin*dIII and *Bam*HI restriction sites flanking the coding region. In the case of the HKKSL-containing constructs, primers were designed to incorporate the ER-retention signal HKKSL appended to the carboxyl terminus of the connexin. PCR products were subcloned in pGEM-T Easy (Promega, Madison, WI) or pCR4Blunt-TOPO vector (Life Technologies, Grand Island, NY); then, the *Bam*HI–*Hin*dIII inserts from these plasmids were subcloned into the corresponding sites of pcDNA3.1/Hygro (+) (Invitrogen).

To obtain the HKKSL-containing Cx43 mutants, primers facing opposite directions and spanning the DNA region encoding the mutated amino acids were designed to amplify the sequence of the full construct (Cx43-HKKSL including the vector sequence) according to the strategy used previously (Minogue et al. 2005); the plasmid was regenerated by religation of the PCR product. Cx43R153G and Cx43L152MR153G without the ER-retention signal were obtained by PCR using the HKKSL-containing constructs as templates and the primers listed in Supplementary Table 1; PCR products were subcloned in pCR-Blunt II-TOPO vector. The *Bam*HI–*Xho*I inserts of all Cx43 mutants were subcloned into the *Bam*HI-*Xho*I sites of pcDNA3.1/Hygro (+) vector.

The coding region of all constructs was fully sequenced at the Cancer Research Center DNA Sequencing Facility of the University of Chicago to ensure that PCR amplification did not introduce additional unwanted mutations.

Cell Culture

HeLa cells transfected with connexin constructs were prepared as previously described (Daugherty et al. 2007; Maza et al. 2003) and cultured in minimum essential medium containing Earle's salts, L-glutamine, 10 % heat-inactivated bovine calf serum, 100 IU/ml penicillin, 100 μg/ml streptomycin and 0.5 mg/ml Geneticin (Invitrogen) or 132 μg/ml hygromycin (EMD Millipore, Billerica, MA).

Immunofluorescence

For immunofluorescence, cells cultured on glass coverslips were fixed and permeabilized with methanol/acetone (1:1), then washed three times with PBS, followed by PBS + 0.5 % Triton X-100 and PBS + 0.5 % Triton X-100 + 2 % goat serum (PBS/GS). Cells were incubated with primary antibodies diluted into PBS/GS for 1 h, rinsed and then labeled with secondary antibodies diluted into PBS/GS. Cells were then rinsed with PBS, and coverslips were mounted on microscope slides with MOWIOL (Polysciences, Warren, PA). Images of the fluorescence signal were obtained using an Olympus (Tokyo, Japan) IX-70 microscope system with a Hamamatsu (Shizuoka, Japan) Orca-1 CCD camera and Image-Pro image analysis software (Media Cybernetics, Silver Spring, MD).

Sucrose Gradient Fractionation

Postnuclear homogenates were prepared with a ball-bearing homogenizer and centrifugation as previously described (Koval et al. 1995, 1997; Das Sarma et al. 2002). Postnuclear homogenates were solubilized in 1 % Triton X-100 for 30 min at 4 °C as described (Maza et al. 2005). Samples were then centrifuged at 100,000×*g* for 30 min, and the resulting Triton X-100-soluble fraction was overlaid onto a 5–18 % sucrose gradient on a 25 % sucrose cushion. Gradients were centrifuged at 148,000×*g* for 16 h at 4 °C in a Sorvall Ultra Pro 80 centrifuge (Thermo Scientific, Asheville, NC) using an AH-650 swinging bucket rotor. Following centrifugation, 0.2-ml fractions were collected from the bottom of the gradient at 4 °C. Samples were added to 2× sample buffer containing 50 mM DTT, resolved by SDS-PAGE, transferred to Immobilon P membranes and blotted. Specific signals corresponding to a given protein were detected by immunoblot using enhanced chemiluminescence (ECL) reagent (GE Healthcare, Piscataway, NJ) and quantified with a BioRad Image Lab system (Hercules, CA). The extent of oligomerization was calculated as the percentage of the total area under the curve from the sucrose gradient curves corresponding to the hexamer peak. Statistical significance was assessed by Student's *t* test.

Blue Native Gel Electrophoresis

Nondenaturing, blue native gel electrophoresis was done using a method based on that of Wittig et al. (2006). Cells were either untreated or treated for 5 h with 6 μg/ml brefeldin A. Cells were homogenized and postnuclear supernatants were diluted into BN Sample Buffer [50 mg/ml Serva G (coomassie blue, G250), 30 % glycerol in ddH_2O]. Blue native gels consisted of a 4.2 % polyacrylamide stacking gel on a 7.5 % resolving gel in Bis Tris–HCl, pH 7.0. Five microliters of each sample were loaded per lane, and the gels were run using 50 mM Tricine/15 mM Bis Tris (pH 7.0) cathode buffer containing 0.01 % Serva G and 50 mM Bis Tris–HCl on ice. Gels were run at constant voltage (100 V) on ice for 3–6 h until the blue dye migrated approximately two-thirds of the way along the resolving gel. The cathode buffer was replaced with a dye-free cathode buffer and the gel run to completion at 150 V constant voltage for 2 h. Gels were removed and incubated in transfer buffer (50 mM Tris, 380 mM glycine, 0.025 % SDS, 20 % MeOH) for 30 min at room temperature, and proteins were transferred to Immobilon P using a BioRad semidry apparatus. Blots were processed using a standard immunoblot protocol, using appropriate primary antibodies, HRP-conjugated goat anti-rabbit IgG secondary antibodies and ECL for detection. Lanes were scanned and analyzed using Image-Pro software.

Results

To examine the cellular sites of oligomerization of Cx40 and Cx37, we applied an approach previously used to study early events in Cx43 and Cx32 oligomerization by producing connexin constructs tagged with a C-terminal HKKSL ER-retention/retrieval motif, Cx40-HKKSL and Cx37-HKKSL (Das Sarma et al. 2002, 2005, 2008; Maza et al. 2003, 2005). Using transfected HeLa cells, we found that wild-type (untagged) Cx40 was transported to the plasma membrane, where it formed gap junction plaques. However, Cx40-HKKSL was retained in the ER (Fig. 2). Sucrose gradient fractionation revealed that the sedimentation profile of Cx40-HKKSL was indistinguishable from that of Cx43-HKKSL (Fig. 2). Thus, Cx40-HKKSL is retained in the ER as stabilized monomers, suggesting that the itinerary of Cx40 oligomerization is comparable to that of Cx43.

We performed a similar analysis of Cx37 and Cx37-HKKSL. As expected, untagged Cx37 was transported to the plasma membrane, while Cx37-HKKSL was retained in the ER (Fig. 3). To further confirm that Cx37-HKKSL was

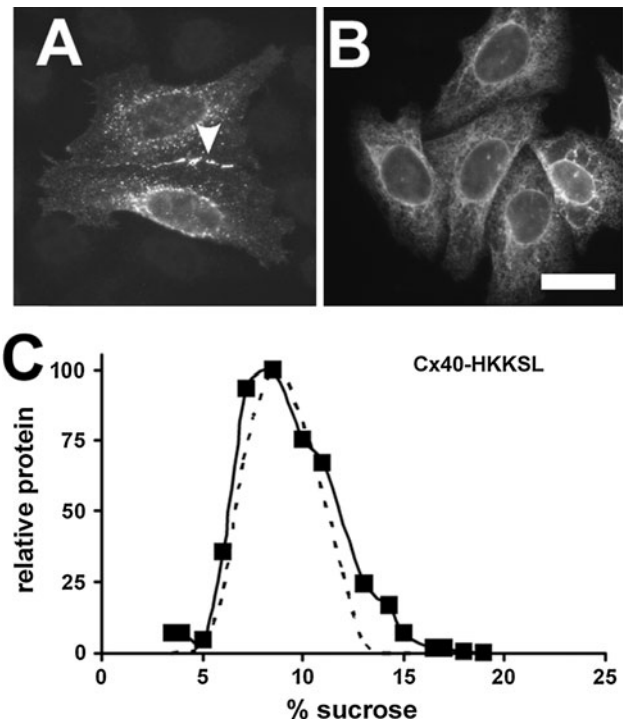

Fig. 2 ER-retained Cx40 is monomeric. **a**, **b** HeLa cells transfected with either Cx40 (**a**) or Cx40-HKKSL (**b**) were fixed and immunostained. Untagged Cx40 was transported to the plasma membrane, where it formed gap junction plaques (*arrowhead*). By contrast, Cx40-HKKSL was retained in the ER. **c** HeLa/Cx40-HKKSL cells (*squares*) or HeLa/Cx43-HKKSL cells (*dashed line*) were processed and analyzed by sucrose gradient fractionation. Cx40-HKKSL had a similar profile on the gradient as Cx43-HKKSL, indicating that the ER-resident pool was monomeric. *Bar* 10 μm

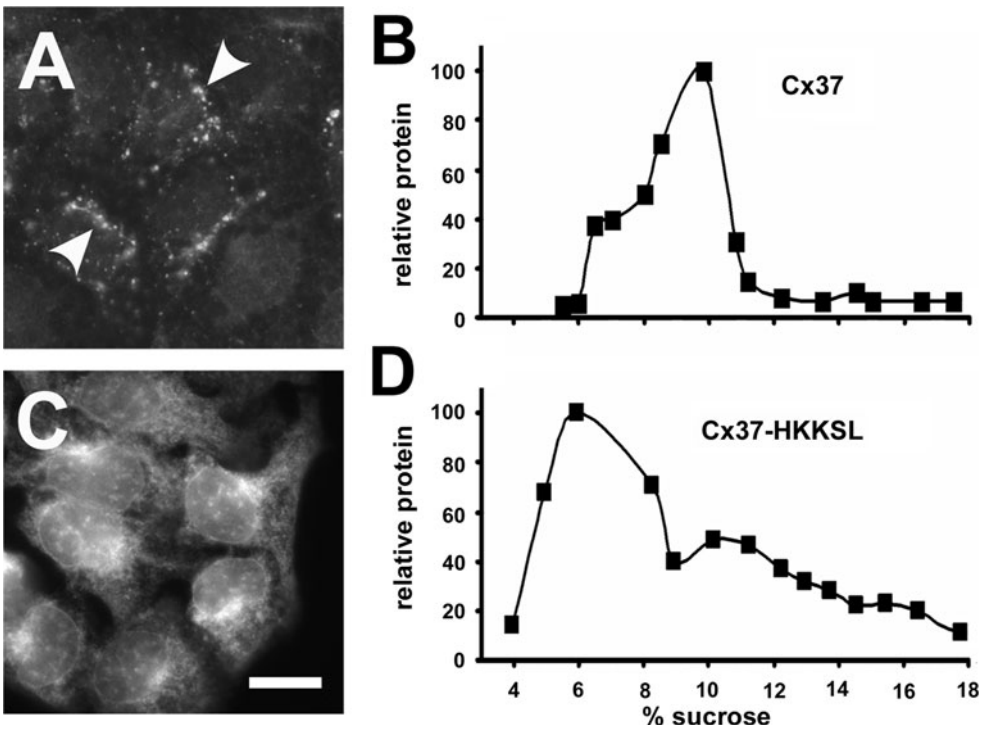

Fig. 3 ER-retained Cx37 is partially oligomerized. **a**, **c** HeLa cells transfected with either Cx37 (**a**) or Cx37-HKKSL (**c**) were fixed and immunostained. Untagged Cx37 was transported to the plasma membrane, where it formed gap junction plaques (*arrowheads*). By contrast, Cx37-HKKSL was retained in the ER. *Bar* 10 μm. **b**, **d** HeLa/Cx37 (**b**) and HeLa/Cx37-HKKSL (**d**) cells were processed and analyzed by sucrose gradient fractionation. About one-third of Cx37-HKKSL migrated as oligomers at a peak centered at 10 % sucrose that comigrated with the predominant peak of untagged Cx37

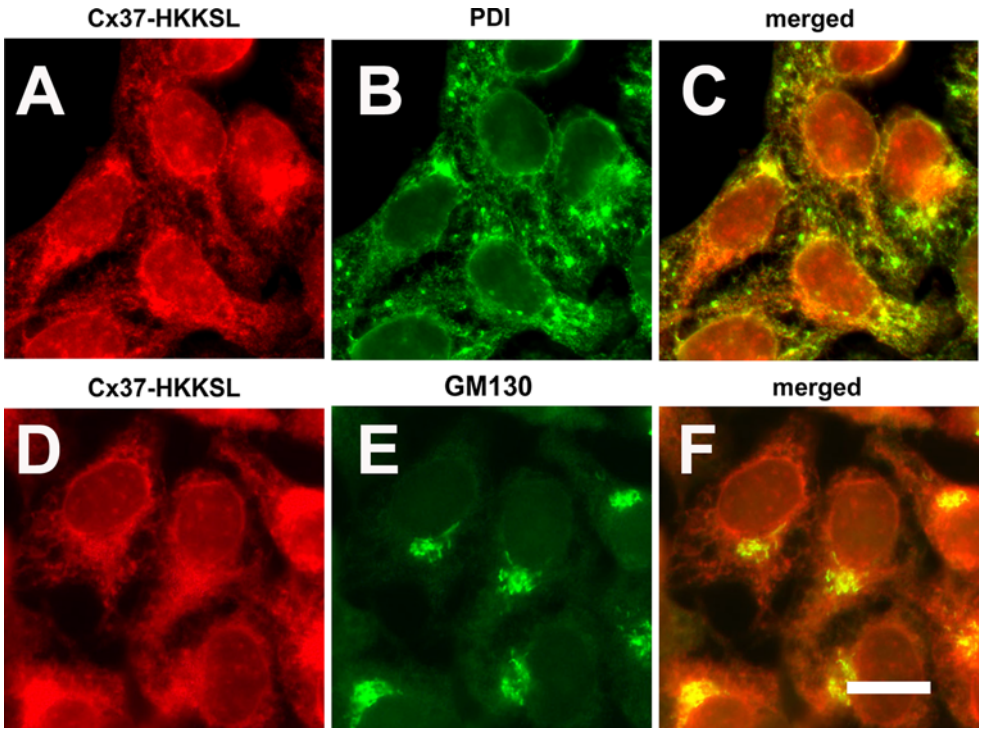

Fig. 4 Cx37-HKKSL localized to the ER and Golgi apparatus. HeLa cells transfected with Cx37-HKKSL were fixed, permeabilized and then immunolabeled for Cx37 (**a**, **d**; *red*) and an ER marker, protein sulfide isomerase (PDI) (**b**, *green*) or a marker for the *cis* Golgi apparatus (GM130) (**e**, *green*). Merged images are shown in (**c**, **f**). Most Cx37-HKKSL colocalized with PDI, consistent with ER localization. A small fraction of Cx37-HKKSL colocalized with GM130, suggesting low levels of transport to the *cis* aspect of the Golgi apparatus. *Bar* 10 μm

predominantly localized to the ER, immunofluorescence colocalization was performed using markers for the ER (PDI) and *cis*-Golgi apparatus (GM130). Cx37-HKKSL predominantly colocalized with PDI, consistent with ER retention (Fig. 4). There was also some colocalization with GM130; however, this appeared to be a relatively minor intracellular component of Cx37-HKKSL.

In contrast to Cx40-HKKSL and Cx43-HKKSL, the sucrose gradient fractionation profile of Cx37-HKKSL had a more complex pattern. One peak sedimented at the same

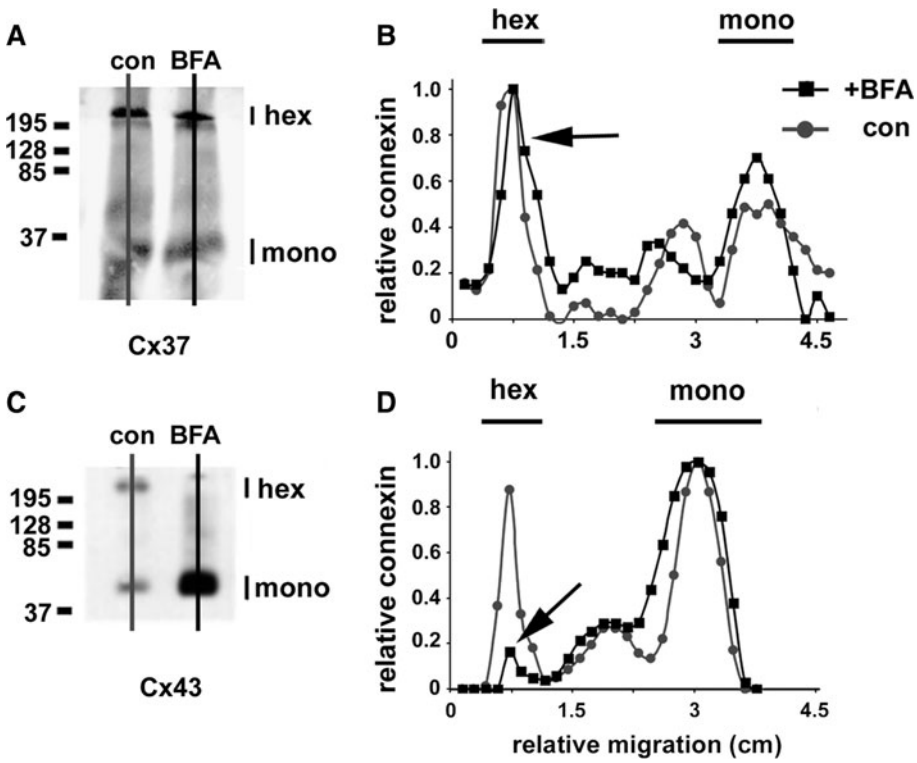

Fig. 5 Cx37 oligomerization is insensitive to brefeldin A. HeLa cells transfected with either Cx37 (**a**, **b**) or Cx43 (**c**, **d**) were incubated in either the presence (*squares*) or the absence (*circles*) of 6 μg/ml brefeldin A (*BFA*) for 5 h, then harvested and solubilized in 0.1 % Triton X-100. Proteins were resolved by blue native gel electrophoresis and then transferred to Immobilon membranes. Cx37 and Cx43 were visualized by immunoblot. The Cx43 hexamer peak was considerably reduced by BFA treatment (**d**, *arrow*). In contrast to Cx43, the electrophoretic migration pattern for native Cx37 was not affected by BFA. Comparable levels of hexamers were detected in the presence and absence of the drug (**b**, *arrow*)

percentage of sucrose (10 %) as the predominant peak of untagged Cx37 representing oligomerized Cx37 (Fig. 3). These results suggest that Cx37-HKKSL retained in the ER was partially oligomerized.

As an independent method to examine the oligomerization state of Cx37 retained in the ER, we examined HeLa cells transfected with untagged Cx37 by blue native gel electrophoresis (Fig. 5). In control HeLa/Cx37 cells, Cx37 exhibited comparable hexamer and monomer peaks. Importantly, when these cells were treated with brefeldin A for 5 h to inhibit membrane efflux from the ER, Cx37 oligomerization was not affected. In contrast, this treatment significantly inhibited Cx43 oligomerization (Fig. 5).

The cytoplasmic interface region of TM3 is necessary to stabilize monomeric Cx43 in the ER (Maza et al. 2005). Since Cx37 has a distinct motif in this region, we examined whether changing the Cx43 LR motif to the MG motif found in Cx37 would affect the extent of Cx43 oligomerization in the ER. As shown in Fig. 6, this was indeed the case for the two mutant Cx43 constructs, Cx43R153G-HKKSL and Cx43L152MR153G-HKKSL. In fact, the sedimentation profile and amount of ER oligomerized protein were equivalent for Cx43L152MR153G-HKKSL and Cx37-HKKSL. As a control for misfolding induced by these point mutations, we examined the ability of untagged Cx43R153G and Cx43L152MR153G to form gap junction plaques (Fig. 7). Both of these proteins were transported to the plasma membrane, where they assembled into gap junction plaques, suggesting that the proteins were properly processed. Taken together, these data suggest that the MG motif plays an important role in promoting early oligomerization of Cx37.

Discussion

We found that Cx37, unlike Cx43, has the capacity to oligomerize in the ER. We could mimic this behavior by mutating two key amino acid residues of Cx43 in the cytoplasmic interface region of TM3 to the corresponding amino acids of Cx37. This observation extends previous studies demonstrating that R153 was required to stabilize monomeric Cx43 in the ER (Maza et al. 2005). In the present study, we consistently observed an increase in ER oligomerization of Cx43 when both L152 and R153 were mutated to MG. Moreover, mutation of only R153 to glycine in Cx43-HKKSL resulted in variable ER oligomerization compared with Cx40 or Cx43. However, the cytoplasmic arginine residue is not an absolute requirement to stabilize connexin monomers in the ER since Cx40-HKKSL was retained as monomers in the ER, despite the presence of an asparagine at the corresponding position in this connexin. Thus, the amino group of the carboxamide in the N151 side chain of Cx40 can substitute for the function of a guanidinium amino group in R153 of Cx43.

By sequence analysis, we defined three classes of motifs in the plasma membrane–cytoplasm interface of TM3. Several connexins have a conserved, positively charged arginine or lysine residue in this region of TM3 (Table 1),

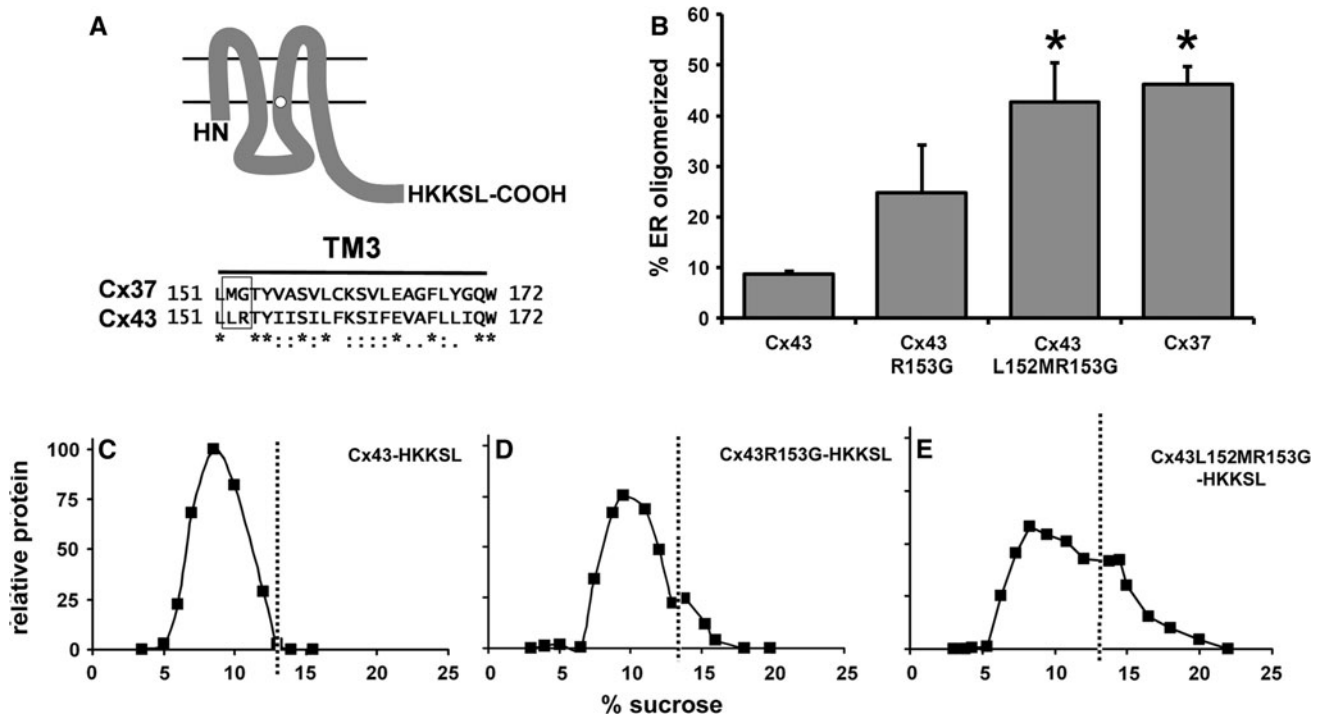

Fig. 6 Mutating the cytoplasmic membrane interface region of the Cx43 TM3 from LR to MG destabilizes ER-retained monomers. **a** *Top* Diagram showing the plasma membrane topology of a connexin monomer (with an HKKSL tag appended to its C terminus). *Bottom* Sequence alignment of the TM3 domains of Cx37 and Cx43 shows the cytoplasmic interface motif surrounded by a *box*. **b** *Graph* shows the percentage of ER oligomerization calculated from profiles of sucrose gradient fractionation of HeLa cells transfected with Cx43-HKKSL, Cx43R153G-HKKSL, Cx43L152MR153G-HKKSL or Cx37-HKKSL (average ± SE, $n = 3$). The sucrose gradient profiles of Cx43L152-MR153G-HKKSL and Cx37-HKKSL were comparable and contained significantly more oligomerized connexins than Cx43-HKKSL ($*p < 0.01$). **c–e** Representative sucrose gradient profiles are shown for HeLa cells transfected with Cx43-HKKSL (**c**), Cx43R153G-HKKSL (**d**) or Cx43L152MR153G-HKKSL (**e**) dashed lines indicate the upper limit of the monomer peak in the gradient profiles (A representative sucrose gradient fractionation profile for Cx37-HKKSL is shown in Fig. 3)

which we have designated as the R motif. Based on the behavior of Cx43, we anticipate that other R-motif connexins are highly stabilized as monomers in the ER and subsequently oligomerized in the *trans*-Golgi network (Maza et al. 2005). Consistent with this hypothesis, Cx46, which contains an R-motif sequence identical to that of Cx43 (LLRTY), oligomerizes in the Golgi apparatus (Koval et al. 1997). We anticipate that the other R-type connexins will also remain monomeric in the ER, due to the presence of the conserved arginine/lysine residue; however, the stability of connexins containing R-type motifs that are not identical to Cx43 could be influenced by surrounding amino acids as well.

Our results imply that Cx43 domains on both sides of the ER membrane are critical for regulating monomer stability and oligomerization. Stabilization of monomeric Cx43 in the ER requires an interaction of ERp29 (a luminal chaperone) with the second extracellular loop domain of Cx43 (Das et al. 2009). Our current and previous results also emphasize the importance of L152 and R153 at the cytoplasmic side of TM3 in regulating oligomerization. These results suggest a sequence of events in which the dissociation of ERp29 from monomeric Cx43 leads to conformational changes involving TM3 that alter the exposure of L152 and R153, which in turn allows oligomerization with other Cx43 monomers.

We anticipate that ERp29 will interact with other connexins as well. Interestingly, development of cataracts in Cx46-deficient mice is sensitive to strain background; cataracts are more severe in lenses of mice that are deficient in ERp29 (129/SvJ) than in lenses of mice with high levels of ERp29 (C57Bl6) (Gong et al. 1999; Hoehenwarter et al. 2008). This difference may be explained by a role for ERp29 in regulating oligomerization and trafficking of the second connexin (Cx50, which has an LLRTY motif) that is also expressed in lens fiber cells and may partially compensate for the loss of Cx46. Whether other R-type connexins can bind to ERp29 remains to be determined. It is likely that interactions between connexins and ERp29 will be influenced by the identity of amino acids in the extracellular loop domains in addition to those in the membrane interface regions of the TM3 domain.

In contrast with Cx43, Cx32, which has a WW motif instead of the LR motif, oligomerizes in the ER. By

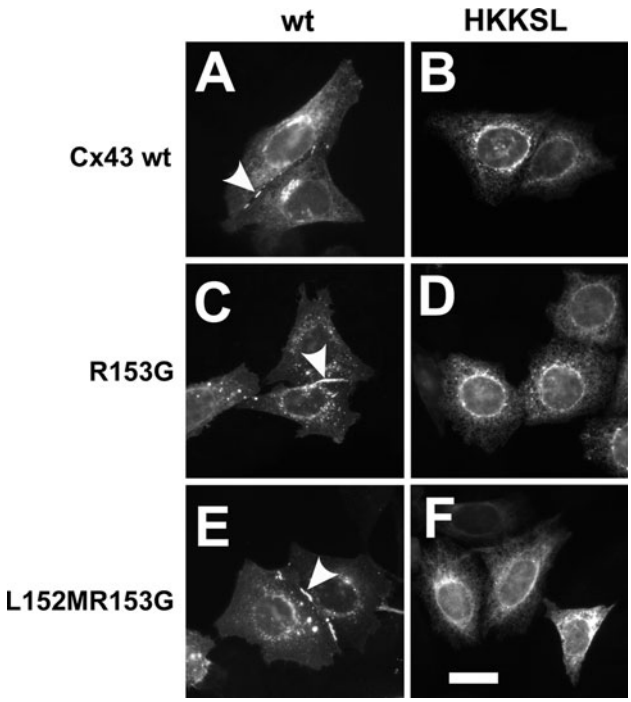

Fig. 7 Cx43 mutants at the cytoplasmic membrane interface region of TM3 lacking the ER retention signal form gap junction plaques. HeLa cells transfected with Cx43 (**a**), Cx43-HKKSL (**b**), Cx43R153G (**c**), Cx43R153G-HKKSL (**d**), Cx43L152MR153G (**e**) or Cx43L152-MR153G-HKKSL (**f**) were fixed, permeabilized and then immunolabeled for Cx43. All untagged constructs formed gap junction plaques (*arrowheads*), indicating that they were properly folded and transported to the plasma membrane (**a**, **c**, **e**). By contrast, the HKKSL-tagged constructs showed ER localization (**b**, **d**, **f**). *Bar* 10 μm

analogy, this suggests that other W-type connexins may also oligomerize in the ER. We propose that the presence of a highly charged arginine (rather than a bulky hydrophobic residue) at the TM3–membrane interface in R-type connexins determines their subcellular site of oligomerization by allowing TM3 the conformational flexibility needed to stabilize monomers in the ER membrane and, thus, restrict oligomerization until they reach the *trans*-Golgi. Moreover, the lack of a highly charged residue in the "MG" motif of Cx37 is likely to have a destabilizing effect since introduction of this motif into Cx43 destabilized it in the ER as well. In addition, the finding that Cx40 and Cx43 remain monomeric in the ER suggests that in order to completely block ER oligomerization, the side chain of the amino acid corresponding to R153 in Cx43 at the TM3–membrane interface may require an amino group (R, K or N). Distinguishing between these possibilities will require structural models for monomeric Cx43 and further experimentation.

Cells expressing multiple connexin genes have the potential to form heteromeric hexamers in addition to homomeric hexamers. Hetero-oligomerization is a regulated process, and connexins must be compatible to interact in order to form a heteromeric hemichannel (Cottrell and Burt 2005; Koval 2006). For instance, Cx26 and Cx43 are incompatible to hetero-oligomerize; however, replacing the TM3 domain of Cx26 with amino acids 154–174 from the TM3 domain of Cx43 creates a chimera that can hetero-oligomerize with both Cx26 and Cx43 (Martinez et al. 2011). While the dual compatibility for this chimera indicates an important role for TM3 in defining connexin compatibility, it also suggests that other residues contribute to the control of connexin oligomerization. Consistent with this, N-terminal variants of Cx43 (e.g., D12S, K13G) interact with Cx32 (Lagree et al. 2003). However, these mutations did not support hetero-oligomerization with Cx26, indicating that other, as yet to be determined structural motifs promote an interaction with Cx26 (Gemel et al. 2004). However, mechanisms that favor homo-oligomerization are also important. For instance, the C-terminal domain of Cx43 dimerizes as well as interacts with the cytoplasmic loop domain in a pH-dependent manner (Hirst-Jensen et al. 2007).

Although Cx37, Cx40 and Cx43 can hetero-oligomerize, incorporation of these three connexins into gap junctions in the vascular bed is regulated. Using a coculture model where cells maintained polarity and phenotype, Isakson and Duling (2005) found that Cx37 was specifically excluded from myoendothelial junctions between aortic endothelial cells and vascular smooth muscle cells. Instead, Cx37 was incorporated into junctions interconnecting either two adjacent endothelial cells or two adjacent smooth muscle cells. Immunohistochemical analysis is consistent with this result since there is partial colocalization between Cx37 and Cx40 or Cx43 in situ (Gabriels and Paul 1998; Severs et al. 2001). Triple heteromers consisting of Cx37, Cx40 and Cx43 have not been biochemically isolated, although there is immunohistochemical evidence showing all three connexins in the same endothelial gap junction plaque (Yeh et al. 1998). We speculate that differences in subcellular sites of oligomerization between Cx37, Cx40 and Cx43 and in their ability to interact with the connexin quality-control pathway play key roles in determining connexin sorting to different plasma membrane domains. Given that Cx40 and Cx43 oligomerization are comparably regulated, there is likely to be a prevalence of Cx40/Cx43 hetero-oligomers over those containing Cx37. In particular, since different types of microvessels exhibit differences in myoendothelial junction composition (Isakson et al. 2008), cells require the ability to regulate connexin homo- and hetero-oligomerization. Identifying elements of the connexin quality-control pathway that differentially control connexin oligomerization and trafficking will help to define the cellular mechanisms used to regulate gap junction composition.

Acknowledgments This work was supported by the Emory Alcohol and Lung Biology Center/National Institutes of Health grants P50-AA013757 (M. K.), R01-HL083120 (M. K.), RO1-HL59199 (E. C. B.) and RO1-EY08368 (E. C. B.) and by the Emory University Research Committee (M. K.).

References

Beyer EC, Berthoud VM (2009) The family of connexin genes. In: Harris AL, Locke D (eds) Connexins: a guide. Humana Press, New York, pp 3–26

Beyer EC, Gemel J, Martinez A, Berthoud VM, Valiunas V, Moreno AP, Brink PR (2001) Heteromeric mixing of connexins: compatibility of partners and functional consequences. Cell Commun Adhes 8:199–204

Brisset AC, Isakson BE, Kwak BR (2009) Connexins in vascular physiology and pathology. Antioxid Redox Signal 11:267–282

Chen J, Anderson JB, DeWeese-Scott C, Fedorova ND, Geer LY, He S, Hurwitz DI, Jackson JD, Jacobs AR, Lanczycki CJ, Liebert CA, Liu C, Madej T, Marchler-Bauer A, Marchler GH, Mazumder R, Nikolskaya AN, Rao BS, Panchenko AR, Shoemaker BA, Simonyan V, Song JS, Thiessen PA, Vasudevan S, Wang Y, Yamashita RA, Yin JJ, Bryant SH (2003) MMDB: Entrez's 3D-structure database. Nucleic Acids Res 31:474–477

Cottrell GT, Burt JM (2005) Functional consequences of heterogeneous gap junction channel formation and its influence in health and disease. Biochim Biophys Acta 1711:126–141

Das Sarma J, Wang F, Koval M (2002) Targeted gap junction protein constructs reveal connexin-specific differences in oligomerization. J Biol Chem 277:20911–20918

Das S, Smith TD, Das Sarma J, Ritzenthaler JD, Maza J, Kaplan BE, Cunningham LA, Suaud L, Hubbard MJ, Rubenstein RC, Koval M (2009) ERp29 restricts connexin43 oligomerization in the endoplasmic reticulum. Mol Biol Cell 20:2593–2604

Das Sarma J, Das S, Koval M (2005) Regulation of connexin43 oligomerization is saturable. Cell Commun Adhes 12:237–247

Das Sarma J, Kaplan BE, Willemsen D, Koval M (2008) Identification of rab20 as a potential regulator of connexin43 trafficking. Cell Commun Adhes 15:65–74

Daugherty BL, Ward C, Smith T, Ritzenthaler JD, Koval M (2007) Regulation of heterotypic claudin compatibility. J Biol Chem 282:30005–30013

Figueroa XF, Isakson BE, Duling BR (2004) Connexins: gaps in our knowledge of vascular function. Physiology (Bethesda) 19: 277–284

Gabriels JE, Paul DL (1998) Connexin43 is highly localized to sites of disturbed flow in rat aortic endothelium but connexin37 and connexin40 are more uniformly distributed. Circ Res 83: 636–643

Gemel J, Valiunas V, Brink PR, Beyer EC (2004) Connexin43 and connexin26 form gap junctions, but not heteromeric channels in co-expressing cells. J Cell Sci 117:2469–2480

Gong X, Agopian K, Kumar NM, Gilula NB (1999) Genetic factors influence cataract formation in α3 connexin knockout mice. Dev Genet 24:27–32

Heberlein KR, Straub AC, Isakson BE (2009) The myoendothelial junction: breaking through the matrix? Microcirculation 16:307–322

Hirst-Jensen BJ, Sahoo P, Kieken F, Delmar M, Sorgen PL (2007) Characterization of the pH-dependent interaction between the gap junction protein connexin43 carboxyl terminus and cytoplasmic loop domains. J Biol Chem 282:5801–5813

Hoehenwarter W, Tang Y, Ackermann R, Pleissner KP, Schmid M, Stein R, Zimny-Arndt U, Kumar NM, Jungblut PR (2008) Identification of proteins that modify cataract of mouse eye lens. Proteomics 8:5011–5024

Isakson BE, Duling BR (2005) Heterocellular contact at the myoendothelial junction influences gap junction organization. Circ Res 97:44–51

Isakson BE, Best AK, Duling BR (2008) Incidence of protein on actin bridges between endothelium and smooth muscle in arterioles demonstrates heterogeneous connexin expression and phosphorylation. Am J Physiol Heart Circ Physiol 294:H2898–H2904

Johnson R, Hammer M, Sheridan J, Revel JP (1974) Gap junction formation between reaggregated Novikoff hepatoma cells. Proc Natl Acad Sci USA 71:4536–4540

Johnson RG, Reynhout JK, Tenbroek EM, Quade BJ, Yasumura T, Davidson KG, Sheridan JD, Rash JE (2012) Gap junction assembly: roles for the formation plaque and regulation by the C-terminus of connexin43. Mol Biol Cell 23:71–86

Johnstone S, Isakson B, Locke D (2009) Biological and biophysical properties of vascular connexin channels. Int Rev Cell Mol Biol 278:69–118

Kanter HL, Saffitz JE, Beyer EC (1994) Molecular cloning of two human cardiac gap junction proteins, connexin40 and connexin45. J Mol Cell Cardiol 26:861–868

Koval M (2006) Pathways and control of connexin oligomerization. Trends Cell Biol 16:159–166

Koval M, Geist ST, Westphale EM, Kemendy AE, Civitelli R, Beyer EC, Steinberg TH (1995) Transfected connexin45 alters gap junction permeability in cells expressing endogenous connexin43. J Cell Biol 130:987–995

Koval M, Harley JE, Hick E, Steinberg TH (1997) Connexin46 is retained as monomers in a *trans*-Golgi compartment of osteoblastic cells. J Cell Biol 137:847–857

Lagree V, Brunschwig K, Lopez P, Gilula NB, Richard G, Falk MM (2003) Specific amino-acid residues in the N-terminus and TM3 implicated in channel function and oligomerization compatibility of connexin43. J Cell Sci 116:3189–3201

Laird DW (2006) Life cycle of connexins in health and disease. Biochem J 394:527–543

Laird DW (2010) The gap junction proteome and its relationship to disease. Trends Cell Biol 20:92–101

Maeda S, Nakagawa S, Suga M, Yamashita E, Oshima A, Fujiyoshi Y, Tsukihara T (2009) Structure of the connexin 26 gap junction channel at 3.5 Å resolution. Nature 458:597–602

Martínez AD, Maripillán J, Acuña R, Minogue PJ, Berthoud VM, Beyer EC (2011) Different domains are critical for oligomerization compatibility of different connexins. Biochem J 436: 35–43

Maza J, Mateescu M, Sarma JD, Koval M (2003) Differential oligomerization of endoplasmic reticulum-retained connexin43/connexin32 chimeras. Cell Commun Adhes 10:319–322

Maza J, Das Sarma J, Koval M (2005) Defining a minimal motif required to prevent connexin oligomerization in the endoplasmic reticulum. J Biol Chem 280:21115–21121

Minogue PJ, Liu X, Ebihara L, Beyer EC, Berthoud VM (2005) An aberrant sequence in a connexin46 mutant underlies congenital cataracts. J Biol Chem 280:40788–40795

Musil LS, Goodenough DA (1993) Multisubunit assembly of an integral plasma membrane channel protein, gap junction connexin43, occurs after exit from the ER. Cell 74:1065–1077

Paznekas WA, Karczeski B, Vermeer S, Lowry RB, Delatycki M, Laurence F, Koivisto PA, Van Maldergem L, Boyadjiev SA, Bodurtha JN, Jabs EW (2009) *GJA1* mutations, variants, and connexin 43 dysfunction as it relates to the oculodentodigital dysplasia phenotype. Hum Mutat 30:724–733

Reed KE, Westphale EM, Larson DM, Wang HZ, Veenstra RD, Beyer EC (1993) Molecular cloning and functional expression of human connexin37, an endothelial cell gap junction protein. J Clin Invest 91:997–1004

Severs NJ, Rothery S, Dupont E, Coppen SR, Yeh HI, Ko YS, Matsushita T, Kaba R, Halliday D (2001) Immunocytochemical analysis of connexin expression in the healthy and diseased cardiovascular system. Microsc Res Tech 52:301–322

Wang Y, Addess KJ, Chen J, Geer LY, He J, He S, Lu S, Madej T, Marchler-Bauer A, Thiessen PA, Zhang N, Bryant SH (2007) MMDB: annotating protein sequences with Entrez's 3D-structure database. Nucleic Acids Res 35:D298–D300

Wittig I, Braun HP, Schagger H (2006) Blue native PAGE. Nat Protoc 1:418–428

Yeh HI, Rothery S, Dupont E, Coppen SR, Severs NJ (1998) Individual gap junction plaques contain multiple connexins in arterial endothelium. Circ Res 83:1248–1263

J Membrane Biol (2012) 245:231–241
DOI 10.1007/s00232-012-9444-4

Inducible Coexpression of Connexin37 or Connexin40 with Connexin43 Selectively Affects Intercellular Molecular Transfer

Joanna Gemel · Tasha K. Nelson · Janis M. Burt · Eric C. Beyer

Received: 21 March 2012 / Accepted: 1 June 2012 / Published online: 23 June 2012

Abstract Many tissues express multiple gap junction proteins, or connexins (Cx); for example, Cx43, Cx40, and Cx37 are coexpressed in vascular cells. This study was undertaken to elucidate the consequences of coexpression of Cx40 or Cx37 with Cx43 at different ratios. EcR-293 cells (which endogenously produce Cx43) were transfected with ecdysone-inducible plasmids encoding Cx37 or Cx40. Immmunoblotting showed a ponasterone dose-dependent induction of Cx37 or Cx40 while constant levels of Cx43 were maintained. The coexpressed connexins colocalized at appositional membranes. Double whole-cell patch clamp recordings showed no significant change in total junctional conductances in cells treated with 0, 0.5, or 4 μM ponasterone; however, they did show a diversity of unitary channel sizes consistent with the induced connexin expression. In cells with induced expression of either Cx40 or Cx37, intercellular transfer of microinjected Lucifer yellow was reduced, but transfer of NBD-TMA (2-(4-nitro-2,1,3-benzoxadiol-7-yl)[aminoethyl]trimethylammonium) was not affected. In cocultures containing uninduced EcR cells together with cells induced to coexpress Cx37 or Cx40, Lucifer yellow transfer was observed only between the cells expressing Cx43 alone. These data show that induced expression of either Cx37 or Cx40 in Cx43-expressing cells can selectively alter the intercellular exchange of some molecules without affecting the transfer of others.

Keywords Connexins · Electrophysiology · Gap junction · Gap junctions · Gap junctions/cell–cell channels

J. Gemel · E. C. Beyer
Department of Pediatrics, University of Chicago, Chicago, IL, USA

T. K. Nelson · J. M. Burt
Department of Physiology, University of Arizona, Tucson, AZ, USA

E. C. Beyer (✉)
Section of Pediatric Hematology/Oncology,
University of Chicago, 900 E 57th St., KCBD 5152,
Chicago, IL 60637, USA
e-mail: ebeyer@peds.bsd.uchicago.edu

The intercellular channels in gap junctions are formed by docking of two hemichannels (connexons), each composed of six subunit proteins called connexins (Cx) (for reviews, see Harris 2001; Saez et al. 2003). Each connexin can form channels by itself (homomeric/homotypic channels), and different connexins form channels with different conductance, permeability, and gating properties. In cells coexpressing more than one connexin, heteromeric channels (containing different connexins in the same connexon) can potentially be formed.

Most cells contain multiple connexins. Cx37, Cx40, and Cx43 are abundant components of the gap junctions in various cells of the cardiovascular system, and they are coexpressed in some of these cells. In ventricular myocytes, Cx43 is the predominant connexin; however, in atrial myocytes, the abundances of Cx40 and Cx43 are approximately equal (Lin et al. 2010). In diseased myocardium, gap junctions may undergo remodeling, and the levels of Cx40 and Cx43 may be altered (reviewed by Severs et al. 2008). Endothelial cells from different sources or vascular beds contain Cx37, Cx40, and/or Cx43 (Johnstone et al. 2009). The relative abundances of these proteins and their coexpression are dynamic and may vary depending on a number of factors, including developmental stage (Delorme et al. 1997; Gabriels and Paul 1998), aging (Yeh et al. 2000), hemodynamics or shear stress (Gabriels and Paul

1998; Chang et al. 2010), and pathologies including inflammation, atherosclerosis, and hypertension (Haefliger et al. 2004; Chanson et al. 2005; Brisset et al. 2009).

Coexpression of connexins and heteromeric channel formation may have profound effects on conductance, permeability/selectivity, and regulation of gap junction channels (reviewed by Cottrell and Burt 2005). Cx43 is one of the most widely expressed gap junction proteins, and channels formed of this protein show little selectivity in the intercellular passage of positively or negatively charged ions or dye tracers (Veenstra et al. 1995; Weber et al. 2004). In contrast, despite forming channels with larger unitary conductances, both Cx37 and Cx40 form channels with substantially less permeability to some negatively charged molecules than to positive ones (Veenstra et al. 1994, 1995; Weber et al. 2004; Beblo et al. 1995). As examples, homomeric Cx43 channels exhibit substantial permeability to both Lucifer yellow (net charge = −2, molecular weight 457) and NBD-TMA (2-(4-nitro-2,1,3-benzoxadiol-7-yl)[aminoethyl]trimethylammonium; net charge = +1; molecular weight 280) (Ek-Vitorin and Burt 2005; Heyman and Burt 2008); in contrast, while homomeric Cx37 and Cx40 channels also allow permeation by NBD-TMA, the permeation of Lucifer yellow is much less (Cottrell et al. 2002; Valiunas et al. 2002; Heyman et al. 2009).

Because Cx37 and Cx40 are often coexpressed with Cx43 in different cells (especially those of the cardiovascular system), the properties of intercellular communication will be determined by the channel properties of each connexin and by their formation of heteromeric and heterotypic channels. Strong evidence suggests that coexpressed Cx37 and Cx43 mix to form many different heteromeric channels (Brink et al. 1997). Previous studies have emphasized the effects of Cx40 and Cx43 coexpression on intercellular communication (Valiunas et al. 2000, 2001; Burt et al. 2001; Cottrell et al. 2002), although there are lingering controversies about the extent or ability of these two connexins to form heterotypic channels (Valiunas et al. 2000; Cottrell and Burt 2001; Rackauskas et al. 2007). Some previous studies have examined different clones of the same cells that had been manipulated to express different relative amounts of two connexins. Burt et al. (2001) studied A7r5 cells (that naturally coexpress Cx40 and Cx43) after stable transfection with a vector coding for Cx43 in an antisense orientation; they identified different clones with different Cx43/Cx40 ratios depending on the number of copies of antisense Cx43 incorporated into genome.

The current study was designed to characterize (and contrast) the effects of induced expression of Cx37 or Cx40 with Cx43 to allow regulated expression of different ratios of the two coexpressed connexins.

Materials and Methods

Connexin Expression Plasmids, Cell Culture, and Transfections

Unless otherwise specified, plasmids, EcR293 cells (HEK-293 cells stably transfected with the ecdysone receptor), and culture medium ingredients were obtained from Invitrogen (Carlsbad, CA). Connexin DNAs were generated by PCR methods. Human Cx37 (T1019/Ser-319 polymorphic variant) with a C-terminal FLAG epitope tag was subcloned into pIND/V5-His-A; Cx37 with a C-terminal HA tag was subcloned into pcDNA3.1/hygro; and rat Cx40 was subcloned into pIND(Sp1)/hygro. Plasmids were purified using a high-purity plasmid purification kit (Marligen Biosciences, Ijamsville, MD) and fully sequenced. EcR293 cells were grown in Dulbecco modified Eagle medium supplemented with 10 % fetal calf serum, 2 mM L-glutamine, 100 U/ml penicillin, and 100 μg/ml streptomycin. Cells were stably transfected with linearized DNA with lipofectamine 2000. Stable clones were selected by culturing in medium containing 400 μg/ml G418 or 50 μg/ml hygromycin (EMD/Calbiochem, San Diego, CA).

Immunochemical Detection of Connexins

Cx43 was detected using a mouse monoclonal antibody (MAB 3068; Millipore/Chemicon, Billerica, MA) or rabbit antibodies (C6219, Sigma Chemical Company, St. Louis, MO). Cx40 was detected using rabbit antibodies directed against a bacterially expressed Cx40 carboxyl tail fusion protein (Kwong et al. 1998) or directed against a 19 amino acid peptide sequence within its C-terminal domain (AB 1726; Millipore/Chemicon). Epitope-tagged Cx37 was detected using anti-FLAG M2 monoclonal antibody (F3165; Sigma) or rabbit anti-HA antibodies (71-5500; Invitrogen/Zymed).

Immunoblotting was performed similarly to our previous studies (Valiunas et al. 2001) using protein extracts from cells prepared as described by Laing and Beyer (1995) resolved on 10 % polyacrylamide gels containing SDS, and blotted onto Immobilon-P (Millipore, Bedford, MA). Immunoblots were developed with ECL chemiluminescence reagents. Rainbow molecular weight marker standards (GE Healthcare, Piscataway, NJ) were used to calibrate the gels.

Immunofluorescence was performed by staining cells cultured on multiwell slides essentially as described previously (Valiunas et al. 2001; Gemel et al. 2004, 2006). Briefly, EcR293 cells were plated on slides coated for 30 min with 0.01 % poly-L-lysine (Sigma) to increase their adherence, and cells were fixed using 4 % paraformaldehyde for 30 min. For double-labeling experiments, cells

were incubated simultaneously with both mouse anti-Cx43 monoclonal antibody and rabbit anti-Cx40 antibodies or with both mouse anti-FLAG monoclonal antibody and rabbit anti-Cx43 antibodies followed by Cy2- and Cy3-conjugated secondary antibodies (Jackson ImmunoResearch Laboratories, West Grove, PA).

Detergent Solubilization and Affinity Purification of Connexons

Solubilization of connexons with Triton X-100 was performed essentially as described previously (Berthoud et al. 2001; Gemel et al. 2004, 2006). Briefly, cultured cells were harvested in PBS containing protease inhibitors, pelleted, and resuspended in buffer containing 1 % Triton X-100. After incubation on ice for 30 min, samples were centrifuged at 100,000g_{ave} for 30 min. In some experiments, we examined the relative solubilization of total connexins and forms that differ in electrophoretic mobilities by immunoblotting comparable fractions of the initial homogenates, supernatants, and pellets.

The supernatant containing solubilized connexons was also used for purification of HA-tagged connexins and associated proteins. For these experiments, EcR293 cells were transiently transfected with Cx37HA (in pcDNA3.1/hygro) using lipofectamine, and HA-tagged (and associated) proteins were purified 72 h later using the μMACS HA isolation kit (Miltenyi Biotec, Bergisch Gladbach, Germany) (Gemel et al. 2006, 2008). We have previously established this as a system in which a coexpressed connexin that forms heteromeric connexons copurifies with the tagged connexin (e.g., Cx40 and Cx43), (Valiunas et al. 2001) while a connexin that does not participate in heteromers with the tagged connexin does not copurify with it (e.g., Cx43 and Cx26) (Gemel et al. 2004).

Microinjection of Gap Junction Tracers

Cells cultured on coverslips (80–100 % confluent cultures) were impaled with a micropipette filled with 150 mM LiCl and 4 % Lucifer yellow (Sigma Chemical Company) or NBD-TMA (Bednarczyk et al. 2000). Solutions were microinjected with a picospritzer (model PLI-188, Nikon Inc) using 0.2- to 0.3-s pulses of 1–2 psi; cells were impaled for 1 min. The extent of intercellular transfer of both tracers was determined by recording the number of adjacent cells containing the tracer after visualization by epifluorescence and digital microscopy. The statistical significance of differences between treated vs. untreated cells was calculated by Student's *t* test for paired data.

Some dye transfer experiments were also performed in mixed cocultures of EcR293 and EcR293-Cx37 or EcR293-Cx40 cells in which the connexin coexpressing cells were labeled with the red fluorescent dye PKH26 (Sigma) while the EcR293 cells were unlabeled. EcR293-Cx37 (or EcR293-Cx40) cells were trypsinized, counted and labeled with PKH26 for 5 min. They were plated at a 1:1 ratio with unlabeled EcR293 cells. The next day, expression of Cx37 or Cx40 was induced using 4 μM ponasterone. After 20 h, Lucifer yellow was injected into an unlabeled (EcR293) cell that neighbored both unlabeled (EcR293) and labeled (EcR293-Cx37 or EcR293-Cx40) cells; the extent of dye transfer was determined by recording the number of adjacent cells (PKH26 labeled and unlabeled) containing the tracer after visualization by epifluorescence and digital microscopy.

Electrophysiological Measurements

The dual whole cell voltage-clamp technique was used to assess both macroscopic and single-channel conductance between pairs of cells in culture as described previously (Cottrell et al. 2002). Cells were grown to confluence in a 100-mm dish, released with 0.25 % trypsin in Ca^{2+}- and Mg^{2+}-free buffer, and replated at low density on glass coverslips (in the presence or absence of ponasterone). At 20–28 h after plating, coverslips were mounted in a custom-made chamber, and an Olympus inverted (IMT2) microscope with phase contrast optics was used to identify pairs of cells in the dish (typically only two or three pairs of cells were found on any given 25-mm coverslip). Cells were bathed in external solution containing 142.5 mM NaCl, 4 mM KCl, 1 mM $MgCl_2$, 5 mM glucose, 2 mM sodium pyruvate, 10 mM HEPES, 15 mM CsCl, 10 mM TEACl, 1 mM $BaCl_2$, and 1 mM $CaCl_2$, pH 7.2, with an osmolarity of 330 mOsm. Junctional conductance was determined on all pairs within 30 min using dual whole cell voltage-clamp techniques as previously described. The pipette solution contained 124 mM KCl, 14 mM CsCl, 9 mM HEPES, 9 mM EGTA, 0.5 mM $CaCl_2$, 5 mM glucose, 9 mM TEACl, 3 mM $MgCl_2$, and 5 mM disodium ATP, pH 7.2 with an osmolarity of 326 mOsm. Macroscopic junctional conductance (g_j) was evaluated with 10-mV transjunctional pulses. Single-channel events were studied in cell pairs that had been partially uncoupled with halothane such that only one or a few channels were active ($g_j < 0.5$ nS). In all cell pairs, the transjunctional voltage (V_j) applied was 40 mV with pulse durations of >20 s. Records were filtered at 50–100 Hz, and transitions in current amplitude that were of equal amplitude but had opposite polarity in the two current traces and lasted longer than 0.1 s were noted. Amplitude data were binned in 10 pS bins, and the relative frequency of each bin was calculated for each cell pair. Histograms display the mean (±SEM, or range for sample sizes less than 3); the relative frequency of each bin was derived by averaging each bin's frequency across multiple cell pairs.

Results

Generation and Immunological Characterization of EcR293-Cx37 and EcR293-Cx40 Cells that Inducibly Coexpress Cx37 or Cx40 with Cx43

Cx37 (T1019/Ser-319 polymorphic variant) or Cx40 were introduced into EcR293 cells by stable transfection (generating inducible EcR293-Cx37 and EcR293-Cx40 cells). Production of connexin proteins was examined by immunoblotting after 20 h of induction with ponasterone (Fig. 1). The EcR293 cells abundantly produced Cx43 (Fig. 1a, c), as expected, because they are derived from HEK293 cells, which endogenously express Cx43 (Gemel et al. 2006, 2008). The levels of Cx43 were not significantly affected by treatment with different doses of ponasterone (Fig. 1a, c). No immunoreactive Cx37 or Cx40 bands were detected in untreated EcR293-Cx37 or EcR293-Cx40 cells (Fig. 1a, c, lanes marked 0 μM ponasterone). Connexin protein induction was detected after treatment with as little as 0.25 μM ponasterone (Fig. 1). Immunoblots showed that levels of Cx37 (Fig. 1a, b) and Cx40 (Fig. 1c, d) increased linearly when cells were treated with increasing concentrations of ponasterone in the range between 0.5 and 4.0 μM ponasterone.

Acquisition of insolubility in 1 % Triton-X-100 has previously been associated with incorporation of Cx43 into gap junction plaques (Musil and Goodenough 1991). We tested whether induction of a second connexin affected the detergent solubility and electrophoretic mobilities of Cx43 in the EcR293-Cx37 and EcR293-Cx40 cells. Cx43 immunoblots had similar appearances in samples derived from both EcR293-Cx37 and EcR293-Cx40 cells regardless of treatment with any concentrations of ponasterone (Fig. 2). In samples prepared from total cellular homogenates or in TritonX-100-insoluble material, three immunoreactive Cx43 bands were observed (likely representing different phosphorylated forms of Cx43 (Musil et al. 1990; Musil and Goodenough 1991)) (Fig. 2, lanes labeled H and P). In contrast samples prepared from the Triton X-100 soluble material predominantly contained a single Cx43 band (likely representing the "NP" form based on its migration faster than the other Cx43 bands). The bands in these immunoblots were quantified by densitometry. This analysis showed that there was little major variation in the distribution of Cx43 between supernatant (Triton soluble) and pellet (Triton insoluble) material regardless of ponasterone treatments; each varied between 40 and 60 % (data not shown).

We used double label immunofluorescence microscopy to examine the localization of Cx43 and Cx37 or Cx40 in the coexpressing EcR293 cells. No immunoreactive Cx37 or Cx40 was detected in noninduced EcR293-Cx37 or

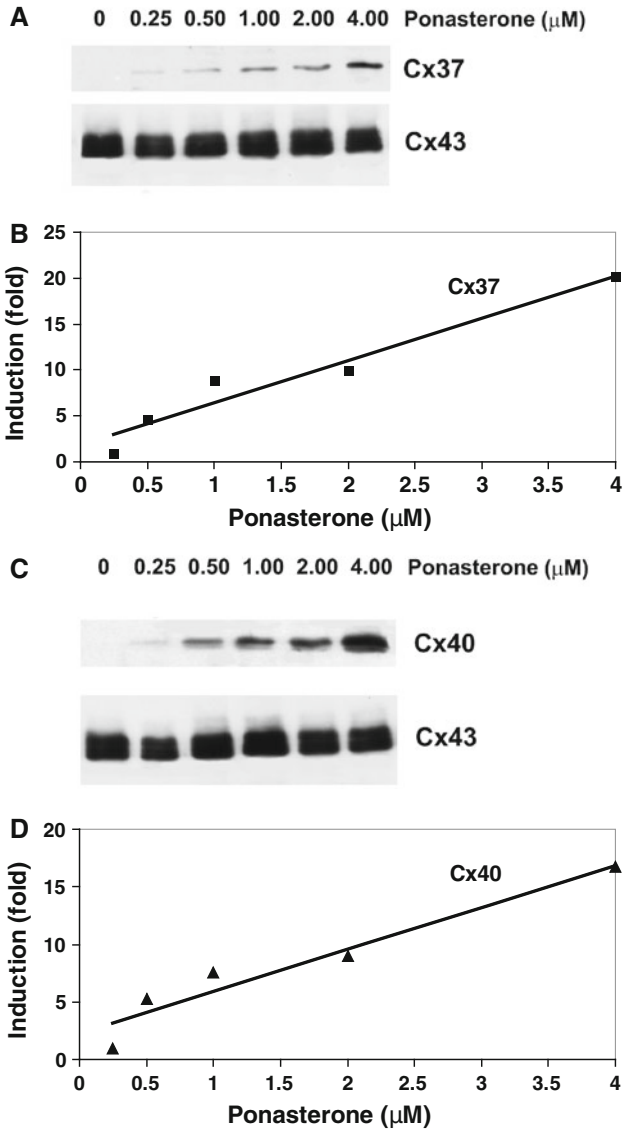

Fig. 1 Treatment of transfected EcR293 cells with ponasterone for 20 h induces a dose-dependent production of Cx37 or Cx40 while relatively stable levels of Cx43 are maintained. Homogenates of EcR293 cells transfected with Cx37 or Cx40 and treated with different doses of ponasterone were analyzed by immunoblotting for Cx37 and Cx43 (**a**) or Cx40 and Cx43 (**b**). Graphs show the densitometric values derived from these blots after induction of Cx37 (**b**) or Cx40 (**d**). These data were fit with lines according to the equations: $y = 4.67x + 1.8$ and $y = 3.7x + 2.3$ with $R^2 = 0.9443$ and $R^2 = 0.9294$ for **b** and **d**, respectively

EcR293-Cx40 cells (not shown). Untreated and ponasterone treated EcR293-Cx37 and EcR293-Cx40 cells abundantly produced Cx43 which localized within the cytoplasm and at appositional membranes in a distribution consistent with that expected for gap junctions (Fig. 3b, d). After treatment with ponasterone, Cx37 was detected in EcR293-Cx37 cells (Fig. 3a) and Cx40 was detected in EcR293-Cx40 cells (Fig. 3e). Cx37 and Cx40 were both

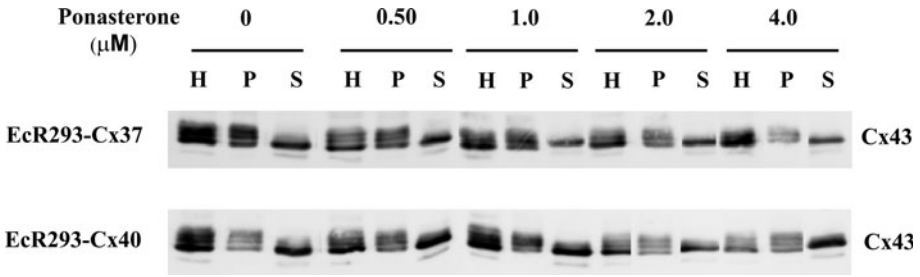

Fig. 2 Induced expression of Cx37 or Cx40 in EcR293 cells does not affect the detergent solubility or electrophoretic mobilities of coexpressed Cx43. EcR293-Cx37 and EcR293-Cx40 cells untreated or treated with different concentrations of ponasterone for 20 h. Then cells were harvested; total homogenates (H) were prepared in Triton X-100 and centrifuged to separate them into material that was detergent insoluble (pellet, P) or detergent soluble (supernatant, S). Cx43 was detected by immunoblotting aliquots of the homogenates containing 30 μg protein and corresponding fractions of the supernatants and pellets

found at appositional membranes where there was substantial overlap with Cx43 (Fig. 3c, f).

Although we have previously published biochemical data suggesting that Cx43 can form heteromeric connexons with other connexins including Cx40 (He et al. 1999; Valiunas et al. 2001), no such analysis has been conducted for the combination of Cx37 with Cx43. Therefore, we examined the potential heteromeric association of Cx37 with Cx43 using an affinity purification strategy similar to that previously used to study formation of heteromeric connexons between Cx43 and other connexins (Gemel et al. 2006, 2008). The 100,000 *g* supernatant was prepared from a 1 % Triton X-100 extract of EcR293 cells stably transfected with HA-tagged Cx37, and it was affinity purified using an anti-HA column, which allowed binding and elution of the tagged connexin and any tightly associated proteins. Both Cx37 and Cx43 were recovered in the eluate from this column (Fig. 4). A reasonable explanation for the copurification of Cx43 with Cx37 is that this pair of connexins can also form heteromeric associations.

Electrophysiological Characterization of Gap Junction Currents and Channels in EcR293-Cx37 and EcR293-Cx40 Cells

We analyzed the gap junctional currents in pairs of parental EcR293, EcR293-Cx37 and EcR293-Cx40 cells using the double whole-cell patch clamp technique. As Cx37 or Cx40 expression was controlled by an inducible promoter, analysis was performed under control conditions (no ponasterone,

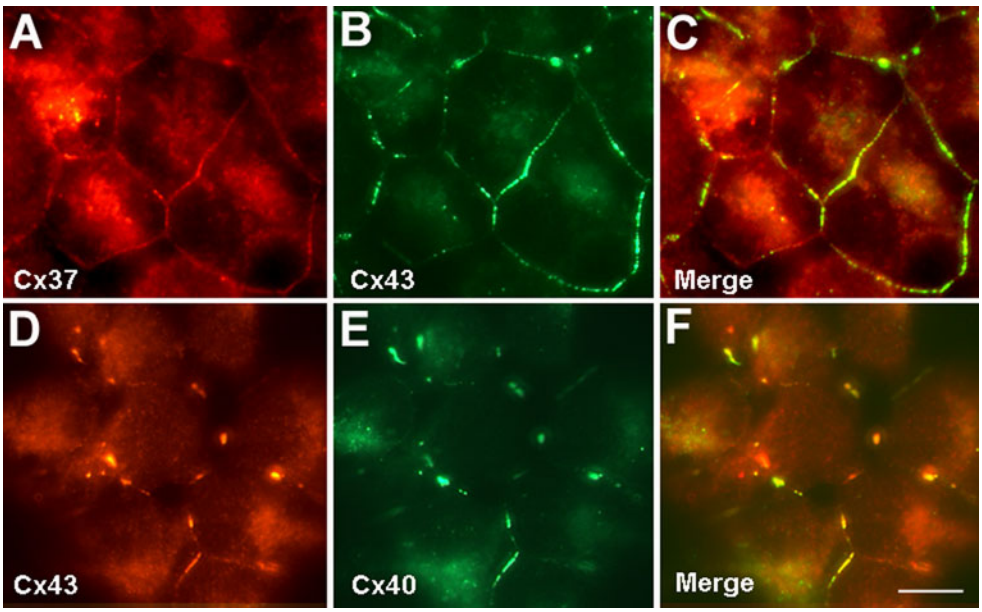

Fig. 3 Induced Cx37 or Cx40 extensively colocalizes with Cx43 at appositional membranes. EcR293-Cx37 (**a**–**c**) and EcR293-Cx40 (**d**–**f**) cells were treated for 20 h with 0.5 μM ponasterone, and Cx37 (*red* in **a** and **c**), Cx40 (*green* in **e** and **f**), and Cx43 (*green* in **b** and **c**; *red* in **d** and **f**) were detected by double label immunofluorescence. The overlap of immunoreactive Cx37 and Cx43 in EcR293-Cx37 cells or Cx40 and Cx43 in EcR293-Cx40 cells appears *yellow* in **c** and **f**, respectively. Bar = 10 μm

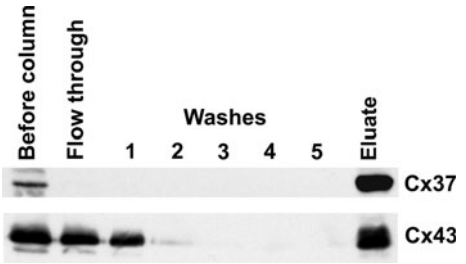

Fig. 4 Copurification of Cx43 and Cx37 suggests that they form heteromeric connexons. Triton X-100 soluble material (containing connexons) from EcR293 cells transfected with HA-tagged Cx37 was affinity purified using an anti-HA resin. Fractions of the initial extract, various column fractions, and the eluate were analyzed by immunoblotting. Even though only Cx37 contained the HA-tag, both Cx37 and Cx43 were detected in the eluate

with or without ethanol treatment) and in cells treated with two different concentrations of ponasterone (0.5 or 4 μM with comparable ethanol concentration). All analyzed cell pairs showed substantial intercellular coupling (Table 1). Although induction of Cx37 by treatment with either 0.5 or 4 μM ponasterone produced an apparent increase (33–60 %) of total conductance, the data did not differ significantly from the mean junctional conductance measured in uninduced EcR293-Cx37 cells. Similarly, mean junctional conductance in EcR293-Cx40 cells was not significantly affected by ponasterone treatment.

Individual channel events were observed in poorly coupled pairs of EcR293, EcR293-Cx37 or EcR293-Cx40 cells. In EcR293 cells and noninduced EcR293-Cx37 or EcR293-Cx40 cells (with or without ethanol exposure), most channel events were between 50 and 100 pS, and very few events larger than 120 pS were observed (Fig. 5a). This range is consistent with the expected conductances of Cx43 channels (approximately 50, 80 and 100 pS) recorded under these conditions (Cottrell and Burt 2001; Cottrell et al. 2002). In cells coexpressing Cx37 and Cx43 (Fig. 5b) or EcR293-Cx40 and Cx43 (Fig. 5c) a diversity of unitary channel conductances were observed many of which were much larger than observed in the absence of induced coexpression.

Properties of Gap Junction Channels in EcR-Cx37 or EcR-Cx40 Cells Assessed by Dye Transfer

To determine how induced coexpression of Cx37 or Cx40 with Cx43 affected intercellular passage of larger molecules, we microinjected two different tracers (Lucifer yellow or NBD-TMA) into noninduced EcR293-Cx37 or EcR293-Cx40 cells or into cells that had been treated with 0.5 or 4 μM ponasterone. Dye transfer was quantified by performing multiple injections and counting dye-filled neighbors (Fig. 6). Microinjected Lucifer yellow transferred to 6.4 ± 0.3 or 6.0 ± 0.4 neighbors (mean ± SEM) for uninduced EcR-Cx37 or EcR-Cx40 cells, respectively. Induction of Cx37 or Cx40 by treatment with 0.5 μM ponasterone significantly reduced Lucifer yellow transfer by nearly 50 %. Induction of greater levels of the second connexin by treatment with 4 μM ponasterone reduced Lucifer yellow transfer to even lower levels; however, differences between dye transfer in cells induced with 0.5 and 4 μM ponasterone did not achieve statistical significance. Uninduced EcR-Cx37 and EcR-Cx40 cells exhibited robust transfer of NBD-TMA, but there was no significant change in NBD-TMA transfer among these cells in response to treatment with either 0.5 or 4 μM ponasterone (Fig. 6).

In vivo, cells expressing one connexin may border cells coexpressing multiple connexins, and these differences in connexin expression might affect intercellular communication within that tissue. We mimicked this situation by coculturing EcR293 cells with ponasterone-induced EcR293-Cx37 or EcR293-Cx40 cells. Lucifer yellow was microinjected into EcR293 cells, and we examined the intercellular transfer of to neighboring EcR293 cells (unlabeled) and to ponasterone-induced EcR293-Cx37 or EcR293-Cx40 cells (labeled with PKH26). Representative photomicrographs obtained after such injections are shown in Fig. 7. In all injections, we observed substantial dye transfer to EcR cell recipients: 7.9 ± 1.0 ($n = 7$) in EcR/EcR-Cx37 coculture and 8.0 ± 0.3 ($n = 16$) in EcR/EcR-Cx40 coculture; however, no Lucifer yellow labeled EcR-Cx37 or EcR-Cx40 cell neighbors were observed.

Table 1 Gap junction conductance in pairs of transfected EcR293 cells

Transfected connexin	Ponasterone concentration (μM)	Junctional conductance		Single channel data	
		Mean ± SEM (nS)	*n*	Events	*n*
None	0 (untreated)	6 ± 3	8	265	6
Cx37	0 (ethanol)	6 ± 2	6	124	2
	0.5	9 ± 2	17	356	8
	4.0	8 ± 2	18	459	12
Cx40	0 (untreated)	5 ± 2	4	127	3
	0 (ethanol)	5 ± 3	7	541	6
	0.5	4 ± 1	16	663	10
	4.0	6 ± 1	17	850	12

nS nanoSiemens

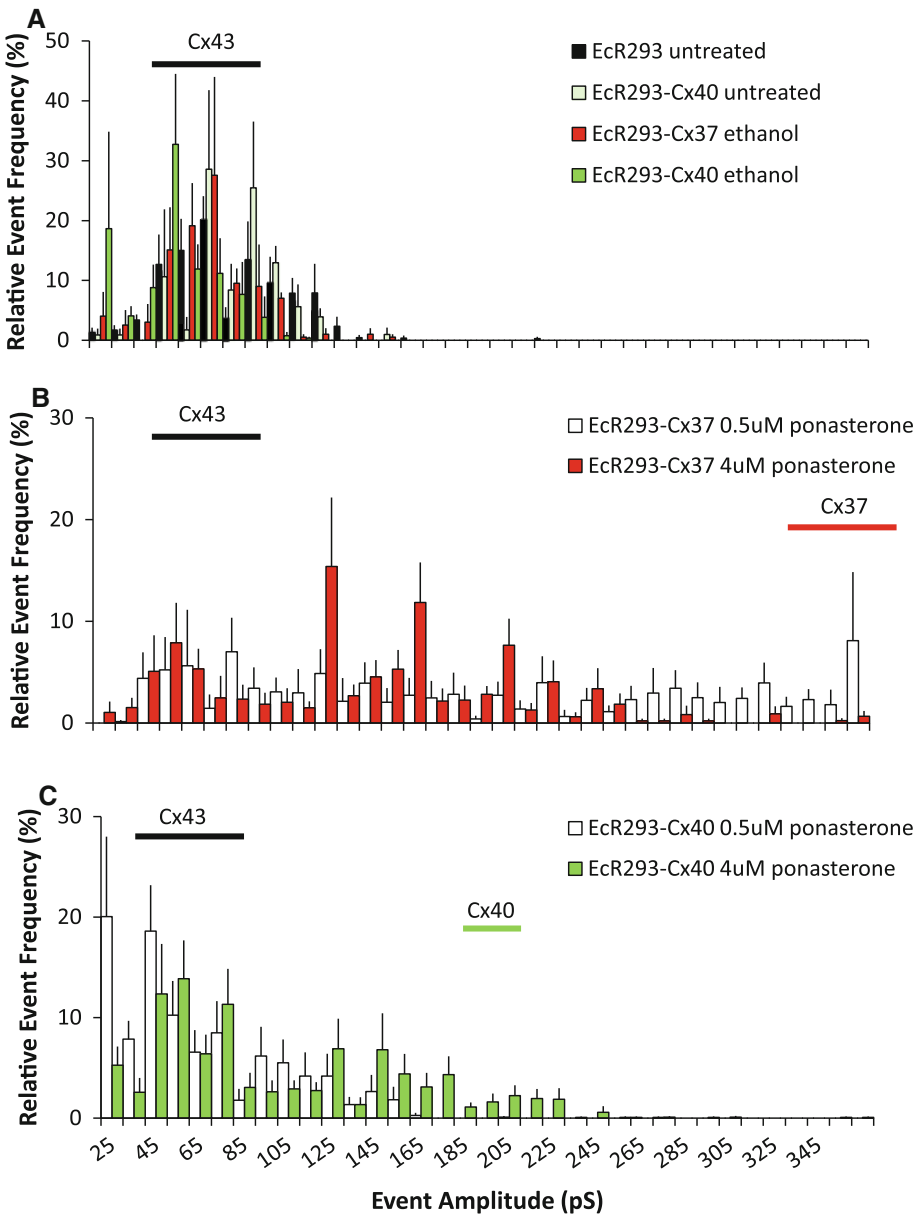

Fig. 5 Induced coexpression of Cx37 or Cx40 with Cx43 alters the distribution of single channel events with a shift toward larger unitary conductances. Single gap junction channel events were recorded in pairs of EcR293 cells, EcR293-Cx37 cells, and EcR293-Cx40 cells. **a** Control experiments including untreated EcR293 (*black bars*) and EcR-Cx40 cells (*light green bars*) and ethanol (vehicle) treated EcR-Cx37 (*red bars*) and EcR-Cx40 cells (*dark green bars*). **b** EcR293-Cx37 cells exposed to 0.5 or 4 μM ponasterone (*white and red bars, respectively*). **c** EcR293-Cx40 cells exposed to 0.5 or 4 μM ponasterone (*white and green bars, respectively*). *Horizontal bars* indicate the distributions of the most common Cx43 single channel events (*black bars* in all panels; 50–110 pS) and the fully open homomeric/homotypic Cx37 channels (*red bar* in **b**; 330–370 pS) or Cx40 channels (*green bar* in **c**; 190–220 pS). Coexpression of either Cx37 (**b**) or Cx40 (**c**) with Cx43 resulted in many events with amplitudes greater than those common in the Cx43 expressing EcR293 cells (**a**), but smaller than fully open homomeric/homotypic Cx37 channels or Cx40 channels. The numbers of cell pairs (n) and events recorded in each data set are shown in Table 1

Discussion

In the current paper, we have developed a system for inducible expression of connexins and used it to examine the functional consequences of their coexpression. Inducible systems have previously been exploited to examine some other aspects of the biology of connexins. Zhong et al. (2003) used a lactose-inducible/regulatable system to study effects of differing amounts of Cx43 on its gating and single channel properties in N2A cells. Burt et al. (2008) used an inducible system to express Cx37 in RIN cells and study the growth properties of Cx37-expressing cells because they were unable to isolate constitutively Cx37-expressing clones (because they would not proliferate). Ours is the first study to use inducible coexpression specifically to study effects of different relative amounts of two coexpressed connexins on the properties of channels in the coexpressing cells. Our transfections of cells derived from human embryonic kidney (HEK293) that endogenously express Cx43 with Cx37 or Cx40 allowed us to mimic the complexity of the intercellular communication present in endothelial cells or atrial myocytes that coexpress differing ratios of these connexins in vivo. Our current studies have expanded upon the data available from previous studies of coexpression of connexins by allowing regulated coexpression.

When we induced Cx37 or Cx40, these connexins extensively colocalized with Cx43, implying that the two connexins were both present in the same gap junction plaques. We have previously studied connexons that were

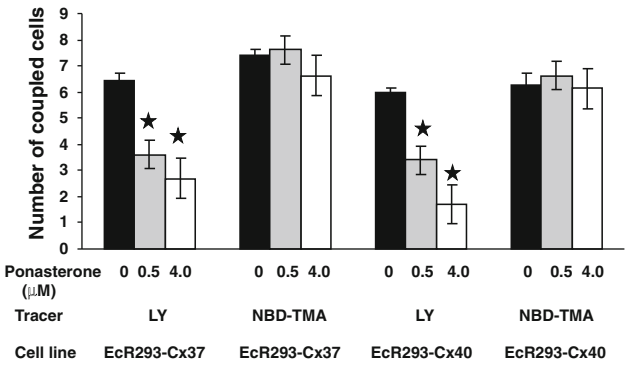

Fig. 6 Induced coexpression of Cx37 or Cx40 with Cx43 selectively affects the intercellular transfer of two different tracers. Intercellular transfer of microinjected dyes was studied in uninduced or induced EcR293-Cx37 or EcR293-Cx40 cells. *Lucifer yellow* or NBD-TMA were microinjected into individual cells within a monolayer. After 1 min, dye-filled neighbors were counted. *Black bars* indicate untreated cells, *gray bars* cells induced with 0.5 μM ponasterone, and *white bars* cells induced with 4 μM ponasterone. Values represent the mean ± SEM ($n \geq 13$ for *Lucifer yellow*; $n = 8$ for NBD-TMA). *$p < 0.05$ as compared to 0 μM ponasterone)

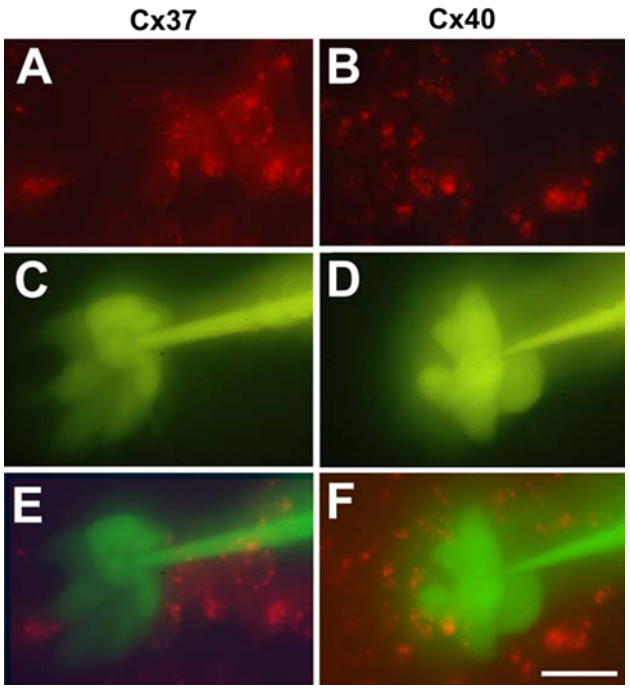

Fig. 7 Coexpression of Cx37 or Cx40 with Cx43 restricts communication with cells expressing Cx43 alone. Intercellular transfer of microinjected Lucifer yellow was studied in EcR293-Cx37 (**a**, **c**, **e**) or EcR293-Cx40 (**b**, **d**, **f**) cells induced with 4 μM ponasterone and cocultured with EcR293 cells. EcR293-Cx37 and EcR293-Cx40 cells were labeled with PKH26 *red* fluorescent cell linker while cocultured EcR293 cells were not labeled (**a**, **b**). Lucifer yellow was injected into an EcR293 cell (unlabeled) that neighbored both other EcR293 cells and labeled EcR293-Cx37 (**c**) or EcR293-Cx40 (**d**) cells. Superimposed images **e**, **f** show dye transfer only among the EcR293 cells, but not to the (*red labeled*) cocultured EcR293-Cx37 or EcR293-Cx40 cells. Bar = 30 μm

enriched by centrifugation, and shown that Cx40 and Cx43 copurify (Valiunas et al. 2001) and can be coimmunoprecipitated (He et al. 1999) suggesting that at least some hemichannels contain both connexins. Similarly, in the current study, we found that Cx37 and Cx43 copurified; this result provides biochemical support for the extensive previous physiological data suggesting that Cx37 and Cx43 can make heteromeric channels with intermediate properties (Brink et al. 1997).

Our biochemical studies suggest that induced coexpression of Cx37 or Cx40 had relatively little effect on the endogenous Cx43. The relative amounts of Cx43 that were insoluble in Triton X-100 were little changed by induced expression of a second connexin (Fig. 2), suggesting little change in the fraction of Cx43 contained in gap junction plaques (Musil and Goodenough 1991). Similarly, the electrophoretic mobility pattern of Cx43 observed in immunoblots (a crude surrogate for phosphorylation; Musil and Goodenough 1991) also showed little change. The absolute amount of Cx43 did not show significant changes with Cx37 or Cx40 induction (Figs. 1, 2).

We observed selective effects on dye transfer after induction of Cx37 or Cx40. Some of these results may be explained by differences in the charge selectivity of channels containing the different connexins: Cx40 and Cx37 channels are cation selective, while Cx43 channels are nonselective. We observed that induced expression of Cx40 or Cx37 reduced the extent of transfer of Lucifer yellow (charge −2) but did not affect transfer of NBD-TMA (charge +1). These data suggest that after induction the intercellular transfer was dominated by the most restrictive connexin. It was previously observed that the properties of a heteromeric channel may be determined by the more selective connexin (Martinez et al. 2002). Interestingly, induction of high levels of Cx37 or Cx40 by treatment with 4 μM ponasterone did not completely abolish Lucifer yellow transfer. This argues that these cells still contained a substantial number of channels that were permeable to this tracer, possibly homomeric or predominantly Cx43-containing channels, although previously published data do suggest that negatively charged molecules as large as ATP can permeate Cx37 hemichannels (and likely intercellular gap junction channels) (Wong et al. 2006; Derouette et al. 2009). Our dye transfer studies also illustrate an obvious consequence of the different molecular permeabilities of these connexins and their heteromeric combinations, boundary formation; when cells expressing only (or predominantly) Cx43 encounter a boundary with cells coexpressing Cx37 or Cx40, the intercellular passage of larger and negatively charged molecules is restricted (Fig. 7).

In both Cx37/Cx43 and Cx40/Cx43 coexpressing cells, we observed a large variety of single channel conductances.

As with previous studies of cells stably coexpressing these connexins, the unitary conductances that differ from the expected sizes of homomeric/homotypic Cx43, Cx37 or Cx40, likely represent "mixed" channels containing both of the coexpressed connexins; we favor the interpretation that many of them are heteromeric Cx37/Cx43 and Cx40/Cx43 channels. The conductance of the fully open Cx37 channel is 330–370 pS (Veenstra et al. 1994; Kumari et al. 2000), and that of Cx40 is 190–220 pS (Cottrell and Burt 2001; Cottrell et al. 2002). Because these are larger than fully open Cx43 channels (~100 pS), the shift toward larger conductances with induced expression of Cx37 or Cx40 matches expectations for production of heteromeric channels (containing Cx43 and the induced connexin). Heterotypic channels represent a special case of "mixed" channels formed by the docking of homomeric connexons containing the two different connexins. Certainly, heterotypic Cx37/Cx43 and Cx40/Cx43 channels might account for some of the diversity of unitary conductances observed after induced coexpression. Indeed, the histograms shown in Fig. 5c do not appear dramatically different from our previous studies of heterotypic Cx40-Cx43 performed using transfected HeLa or RIN cells (Valiunas et al. 2001; Cottrell et al. 2002). As previously stated, determination of the abundance and distributions of channel sizes do not permit us to distinguish unambiguously between homotypic, heterotypic, and heteromeric forms (Valiunas et al. 2001). However, we suspect limited contribution of Cx40-Cx43 heterotypic channels because our studies and those of others have shown very reduced junctional conductances produced by pairing of Cx40- and Cx43-expressing cells (Cottrell et al. 2002; Rackauskas et al. 2007).

When we induced Cx37 expression, the mean values for total junctional conductance in cell pairs appeared to be increased (Table 1) (although not statistically different from the uninduced controls). An increase in total conductance would have been expected if induction led to a greater total amount of connexins in these cells. These cells may have contained a greater number of gap junction channels; or, alternatively, the increased total conductance could be explained by a nearly constant number of total channels that were larger in individual conductance (Fig. 4). That Cx37 expression did not significantly increase electrical coupling could reflect a relatively small sample size in the face of considerable pair to pair variability. However, it could also reflect a decrease in channel permselectivity (as suggested by the parallel dye coupling data) or open probability differences (long duration events were much rarer in Cx37 coexpressing cells than in either the parental cells or Cx40 coexpressing cells). The total junctional conductance of Cx40-expressing cell pairs was certainly not different from uninduced cells. Total conductance might be unchanged if Cx43 was reduced after Cx40 induction; however, we did not observe a statistically significant change in Cx43 levels by immunoblotting. Alternatively, it might reflect the formation of some heteromeric channels with differential permselective properties (or even some that are nonfunctional). It is also possible that the 293 cells have an absolute upper limit (a fixed capacity) to the number of gap junctional channels that they can form thereby preventing an increase in channel number with expression of Cx37 or Cx40.

We have previously observed that expression of Cx37 leads to the death of endothelial cells (Seul et al. 2004) and greatly slows the proliferation of rat insulinoma cells (Burt et al. 2008). The effects of Cx37 on vascular growth require a functional channel (Good et al. 2011). However, in the current study, treatment of our cells with ecdysone (and its ethanol vehicle) and induction of either Cx37 or Cx40 had little or no observed effects on growth or cell viability (data not shown). This lack of effect may represent the brief induction period required to perform the present experiments. It may also reflect our choice of human Cx37 polymorphic variant; we studied the serine-319 polymorphic variant. Morel et al. (2010) have observed that the proline-319 variant slows the proliferation of tumor cells, while the serine-319 variant has no effect. Finally, it may be that our incorporation of an epitope tag (FLAG) at the end of Cx37 reduced its toxicity.

There is certainly substantial biological importance of our observation that altered coexpression of two connexins in the same cell has substantial functional consequences (like alteration of the intercellular exchange of different small molecules). For example, changes in the connexin expression ratio can affect the response of cells to growth factors. Burt and Steele (2003) observed that Cx43 channels were sensitive to PDGF, while Cx40 channels were not; intermediate sensitivity could be achieved by modifying the Cx40/Cx43 expression ratio. In the current study we have generated cell lines in which the stoichiometry of connexin coexpression can be regulated; these cell lines may be useful for elucidating how intercellular exchange of small molecules that differ in charge (and consequent permeation through the endogenous vs. induced intercellular channels) affect various processes such as stimulated proliferation.

Acknowledgments This work was supported by National Institutes of Health grants HL59199 (ECB), 5R01HL058732 (JMB), and 5R01HL077675 (JMB).

References

Beblo DA, Wang HZ, Beyer EC, Westphale EM, Veenstra RD (1995) Unique conductance, gating, and selective permeability properties of gap junction channels formed by connexin40. Circ Res 77:813–822

Bednarczyk D, Mash EA, Aavula BR, Wright SH (2000) NBD-TMA: a novel fluorescent substrate of the peritubular organic cation transporter of renal proximal tubules. Pflugers Arch 440: 184–192

Berthoud VM, Montegna EA, Atal N, Aithal NH, Brink PR, Beyer EC (2001) Heteromeric connexons formed by the lens connexins, connexin43 and connexin56. Eur J Cell Biol 80:11–19

Brink PR, Cronin K, Banach K, Peterson E, Westphale EM, Seul KH, Ramanan SV, Beyer EC (1997) Evidence for heteromeric gap junction channels formed from rat connexin43 and human connexin37. Am J Physiol (Cell Physiol) 273:C1386–C1396

Brisset AC, Isakson BE, Kwak BR (2009) Connexins in vascular physiology and pathology. Antioxid Redox Signal 11:267–282

Burt JM, Steele TD (2003) Selective effect of PDGF on connexin43 versus connexin40 comprised gap junction channels. Cell Commun Adhes 10:287–291

Burt JM, Fletcher AM, Steele TD, Wu Y, Cottrell GT, Kurjiaka DT (2001) Alteration of Cx43:Cx40 expression ratio in A7r5 cells. Am J Physiol Cell Physiol 280:C500–C508

Burt JM, Nelson TK, Simon A, Fang JS (2008) Connexin 37 profoundly slows cell cycle progression in rat insulinoma cells. Am J Physiol Cell Physiol 296:C1103–C1112

Chang CJ, Wu LS, Hsu LA, Chang GJ, Chen CF, Yeh HI, Ko YS (2010) Differential endothelial gap junction expression in venous vessels exposed to different hemodynamics. J Histochem Cytochem 58:1083–1092

Chanson M, Derouette JP, Roth I, Foglia B, Scerri I, Dudez T, Kwak BR (2005) Gap junctional communication in tissue inflammation and repair. Biochim Biophys Acta 1711:197–207

Cottrell GT, Burt JM (2001) Heterotypic gap junction channel formation between heteromeric and homomeric Cx40 and Cx43 connexons. Am J Physiol Cell Physiol 281:C1559–C1567

Cottrell GT, Burt JM (2005) Functional consequences of heterogeneous gap junction channel formation and its influence in health and disease. Biochim Biophys Acta 1711:126–141

Cottrell GT, Wu Y, Burt JM (2002) Cx40 and Cx43 expression ratio influences heteromeric/heterotypic gap junction channel properties. Am J Physiol Cell Physiol 282:C1469–C1482

Delorme B, Dahl E, Jarry-Guichard T, Briand JP, Willecke K, Gros D, Theveniau-Ruissy M (1997) Expression pattern of connexin gene products at the early developmental stages of the mouse cardiovascular system. Circ Res 81:423–437

Derouette JP, Desplantez T, Wong CW, Roth I, Kwak BR, Weingart R (2009) Functional differences between human Cx37 polymorphic hemichannels. J Mol Cell Cardiol 46:499–507

Ek-Vitorin JF, Burt JM (2005) Quantification of gap junction selectivity. Am J Physiol Cell Physiol 289:C1535–C1546

Gabriels JE, Paul DL (1998) Connexin43 is highly localized to sites of disturbed flow in rat aortic endothelium but connexin37 and connexin40 are more uniformly distributed. Circ Res 83: 636–643

Gemel J, Valiunas V, Brink PR, Beyer EC (2004) Connexin43 and connexin26 form gap junctions, but not heteromeric channels in co-expressing cells. J Cell Sci 117:2469–2480

Gemel J, Lin X, Veenstra RD, Beyer EC (2006) N-terminal residues in Cx43 and Cx40 determine physiological properties of gap junction channels, but do not influence heteromeric assembly with each other or with Cx26. J Cell Sci 119:2258–2268

Gemel J, Lin X, Collins R, Veenstra RD, Beyer EC (2008) Cx30.2 can form heteromeric gap junction channels with other cardiac connexins. Biochem Biophys Res Commun 369:388–394

Good ME, Nelson TK, Simon AM, Burt JM (2011) A functional channel is necessary for growth suppression by Cx37. J Cell Sci 124:2448–2456

Haefliger JA, Nicod P, Meda P (2004) Contribution of connexins to the function of the vascular wall. Cardiovasc Res 62:345–356

Harris AL (2001) Emerging issues of connexin channels: biophysics fills the gap. Q Rev Biophys 34:325–472

He DS, Jiang JX, Taffet SM, Burt JM (1999) Formation of heteromeric gap junction channels by connexins 40 and 43 in vascular smooth muscle cells. Proc Natl Acad Sci USA 96: 6495–6500

Heyman NS, Burt JM (2008) Hindered diffusion through an aqueous pore describes invariant dye selectivity of Cx43 junctions. Biophys J 94:840–854

Heyman NS, Kurjiaka DT, Ek Vitorin JF, Burt JM (2009) Regulation of gap junctional charge selectivity in cells coexpressing connexin 40 and connexin 43. Am J Physiol Heart Circ Physiol 297:H450–H459

Johnstone S, Isakson B, Locke D (2009) Biological and biophysical properties of vascular connexin channels. Int Rev Cell Mol Biol 278:69–118

Kumari SS, Varadaraj K, Valiunas V, Ramanan SV, Christensen EA, Beyer EC, Brink PR (2000) Functional expression and biophysical properties of polymorphic variants of the human gap junction protein connexin37. Biochem Biophys Res Commun 274:216–224

Kwong KF, Schuessler RB, Green KG, Laing JG, Beyer EC, Boineau JP, Saffitz JE (1998) Differential expression of gap junction proteins in the canine sinus node. Circ Res 82:604–612

Laing JG, Beyer EC (1995) The gap junction protein connexin43 is degraded via the ubiquitin proteasome pathway. J Biol Chem 270:26399–26403

Lin X, Gemel J, Glass A, Zemlin CW, Beyer EC, Veenstra RD (2010) Connexin40 and connexin43 determine gating properties of atrial gap junction channels. J Mol Cell Cardiol 48:238–245

Martinez AD, Hayrapetyan V, Moreno AP, Beyer EC (2002) Connexin43 and connexin45 form heteromeric gap junction channels in which individual components determine permeability and regulation. Circ Res 90:1100–1107

Morel S, Burnier L, Roatti A, Chassot A, Roth I, Sutter E, Galan K, Pfenniger A, Chanson M, Kwak BR (2010) Unexpected role for the human Cx37 C1019T polymorphism in tumour cell proliferation. Carcinogenesis 31:1922–1931

Musil LS, Goodenough DA (1991) Biochemical analysis of connexin43 intracellular transport, phosphorylation, and assembly into gap junctional plaques. J Cell Biol 115:1357–1374

Musil LS, Cunningham BA, Edelman GM, Goodenough DA (1990) Differential phosphorylation of the gap junction protein connexin43 in junctional communication-competent and -deficient cell lines. J Cell Biol 111:2077–2088

Rackauskas M, Kreuzberg MM, Pranevicius M, Willecke K, Verselis VK, Bukauskas FF (2007) Gating properties of heterotypic gap junction channels formed of connexins 40, 43, and 45. Biophys J 92:1952–1965

Saez JC, Berthoud VM, Branes MC, Martinez AD, Beyer EC (2003) Plasma membrane channels formed by connexins: their regulation and functions. Physiol Rev 83:1359–1400

Seul KH, Kang KY, Lee KS, Kim SH, Beyer EC (2004) Adenoviral delivery of human connexin37 induces endothelial cell death through apoptosis. Biochem Biophys Res Commun 319:1144–1151

Severs NJ, Bruce AF, Dupont E, Rothery S (2008) Remodelling of gap junctions and connexin expression in diseased myocardium. Cardiovasc Res 80:9–19

Valiunas V, Weingart R, Brink PR (2000) Formation of heterotypic gap junction channels by connexins 40 and 43. Circ Res 86:E42–E49

Valiunas V, Gemel J, Brink PR, Beyer EC (2001) Gap junction channels formed by coexpressed connexin40 and connexin43. Am J Physiol Heart Circ Physiol 281:H1675–H1689

Valiunas V, Beyer EC, Brink PR (2002) Cardiac gap junction channels show quantitative differences in selectivity. Circ Res 91:104–111

Veenstra RD, Wang HZ, Beyer EC, Ramanan SV, Brink PR (1994) Connexin37 forms high conductance gap junction channels with subconductance state activity and selective dye and ionic permeabilities. Biophys J 66:1915–1928

Veenstra RD, Wang HZ, Beblo DA, Chilton MG, Harris AL, Beyer EC, Brink P (1995) Selectivity of connexin-specific gap junctions does not correlate with channel conductance. Circ Res 77:1156–1165

Weber PA, Chang HC, Spaeth KE, Nitsche JM, Nicholson BJ (2004) The permeability of gap junction channels to probes of different size is dependent on connexin composition and permeant-pore affinities. Biophys J 87:958–973

Wong CW, Christen T, Roth I, Chadjichristos CE, Derouette JP, Foglia BF, Chanson M, Goodenough DA, Kwak BR (2006) Connexin37 protects against atherosclerosis by regulating monocyte adhesion. Nat Med 12:950–954

Yeh HI, Chang HM, Lu WW, Lee YN, Ko YS, Severs NJ, Tsai CH (2000) Age-related alteration of gap junction distribution and connexin expression in rat aortic endothelium. J Histochem Cytochem 48:1377–1389

Zhong G, Mantel PL, Jiang X, Jarry-Guichard T, Gros D, Labarrere C, Moreno AP (2003) LacSwitch II regulation of connexin43 cDNA expression enables gap-junction single-channel analysis. Biotechniques 34:1034–1046

J Membrane Biol (2012) 245:243–253
DOI 10.1007/s00232-012-9445-3

Neurons and β-Cells of the Pancreas Express Connexin36, Forming Gap Junction Channels that Exhibit Strong Cationic Selectivity

Feliksas F. Bukauskas

Received: 23 March 2012 / Accepted: 1 June 2012 / Published online: 30 June 2012

Abstract We examined the permeability of connexin36 (Cx36) homotypic gap junction (GJ) channels, expressed in neurons and β-cells of the pancreas, to dyes differing in molecular mass and net charge. Experiments were performed in HeLa cells stably expressing Cx36 tagged with EGFP by combining a dual whole-cell voltage clamp and fluorescence imaging. To assess the permeability of the single GJ channel (P_γ), we used a dual-mode excitation of fluorescent dyes that allowed us to measure cell-to-cell dye transfer at levels not resolvable using whole-field excitation solely. We demonstrate that P_γ of Cx36 for cationic dyes (EAM-1^+ and EAM-2^+) is ~10-fold higher than that for an anionic dye of the same net charge and similar molecular mass, Alexa fluor-350 (AFl-350^-). In addition, P_γ for Lucifer yellow (LY^{2-}) is approximately fourfold smaller than that for AFl-350^-, which suggests that the higher negativity of LY^{2-} significantly reduces permeability. The P_γ of Cx36 for AFl-350 is approximately 358, 138, 23 and four times smaller than the P_γs of Cx43, Cx40, Cx45, and Cx57, respectively. In contrast, it is 6.5-fold higher than the P_γ of mCx30.2, which exhibits a smaller single-channel conductance. Thus, Cx36 GJs are highly cation-selective and should exhibit relatively low permeability to numerous vital negatively charged metabolites and high permeability to K^+, a major charge carrier in cell–cell communication.

Keywords Intercellular communication · Connexin · Gap junction · Permeability · Voltage gating · Cationic selectivity

Introduction

The connexins (Cxs) are members of a large family of integral membrane proteins that form gap junction (GJ) channels, which provide a pathway for electrical signaling and metabolic communication (Bukauskas and Verselis 2004; Harris 2007). Each GJ channel is formed of two apposed hemichannels (aHCs) representing hexamers/connexons oligomerized in the endoplasmic reticulum (ER)/Golgi complex and inserted in the plasma membrane. Expression of Cxs is tissue- and organ-specific, and many cells express several Cx isoforms, allowing them to form homotypic, heterotypic and/or heteromeric GJ channels (Bukauskas and Verselis 2004). Cx36 is one of three major neuronal Cxs (m30.2/hCx31.9, Cx36, Cx45) and the sole Cx in β-cells of the pancreas in adults (Condorelli et al. 1998; Serre-Beinier et al. 2000).

Cx-based GJs differ in single-channel conductance, perm selectivity and voltage gating (Goldberg et al. 2004; Harris 2007; Rackauskas et al. 2007a; Palacios-Prado and Bukauskas 2009; Heyman et al. 2009; Veenstra et al. 1995). Each aHC has two gating mechanisms, both sensitive to transjunctional voltage (V_j), the *fast* gate and the *slow* (or *loop*) gate (Bukauskas and Verselis 2004). In addition, GJ channels can be gated by intracellular H^+, Ca^{2+}, posttranslational modifications and a variety of chemical agents (Harris 2001). The mechanisms by which

Electronic supplementary material The online version of this article (doi:10.1007/s00232-012-9445-3) contains supplementary material, which is available to authorized users.

F. F. Bukauskas (✉)
Dominick P. Purpura Department of Neuroscience,
Albert Einstein College of Medicine, 1300 Morris Park Avenue,
Bronx 10461, NY, USA
e-mail: feliksas.bukauskas@einstein.yu.edu

these factors exert their effect on GJs remain unclear, although H^+ and Ca^{2+} ions may both act through the *slow* gate (Peracchia 2004). GJs respond to V_j with decay of junctional conductance (g_j) to a steady state ($g_{j,ss}$) or a minimal conductance (Bennett and Verselis 1992). This property has been explained by single-channel studies showing that GJ channels close with fast transitions from the main open state with conductance, γ_{open}, to a subconducting or residual conductance state, γ_{res}, which is a property of the *fast* gate (Bukauskas and Weingart 1994; Bukauskas and Peracchia 1997). Sensitivity to V_j is Cx type–specific, and Cx36 is one of the least V_j-sensitive Cxs among the 21 members of this family. Typically, homotypic GJs show a maximum g_j at $V_j = 0$ mV and a symmetric $g_{j,ss} - V_j$ dependence, which is due to the presence of two gates in each hemichannel (Harris 2001). Fast and slow V_j-sensitive gating mechanisms have been reported in GJ channels formed of different Cx isoforms (reviewed in Bukauskas and Verselis 2004) as well as in unapposed/nonjunctional Cx46 hemichannels (Trexler et al. 1996).

It is well established that GJs are permeable to second messengers, such as Ca^{2+}, cAMP and IP_3, in a Cx type–dependent manner (Hernandez et al. 2007; Bedner et al. 2006; Ponsioen et al. 2007). For example, Cx43 GJs demonstrate ~15-fold higher permeability than Cx32 GJs for glutamate, glutathione, ADP and AMP and ~10-fold lesser permeability to adenosine (Goldberg et al. 2004). All of the aforementioned molecules are comparable in molecular mass and net charge to the fluorescent dyes used in this study. Cx isoforms exhibit different permeability (P_j) to the same compound, which for some Cxs can differ 1,000-fold (Rackauskas et al. 2007b). Single-channel permeability (P_γ) is not necessarily proportional to single-channel conductance or pore diameter (Goldberg et al. 2004; Rackauskas et al. 2007b). In addition, the fast V_j-sensitive gating mechanism operates as a selectivity filter, restricting metabolic cell–cell communication while preserving electrical coupling (Qu and Dahl 2002; Bukauskas et al. 2002a). In primary β-cells only Cx36 forms GJs that exhibit higher permeability to positively charged tracers (Charpantier et al. 2007). Also, it has been shown that β-cells are able to exchange by negatively charged molecules, such as phosphorylated glucose metabolites and nucleotides (reviewed in Jain and Lammert 2009), suggesting that cationic selectivity of Cx36 GJs is not absolute. It is well documented that Cx36-expressing cells exhibit relatively low cell–cell coupling, low single-channel conductance and low sensitivity of V_j gating (Srinivas et al. 1999; Teubner et al. 2000). However, there are no reported data demonstrating Cx36 permeability at the single-channel level for different dyes, which is necessary to quantify charge selectivity and to compare with permselectivity of other Cxs. Original reports on the permeability of Cx36 GJs demonstrated some disagreement in regard to Lucifer yellow (LY) (Srinivas et al. 1999; Teubner et al. 2000). Due to difficulties with detection of LY transfer between cells expressing Cx36 in brain slices (Campbell et al. 2011) and retina (Pan et al. 2010), these and many similar studies preferentially used neurobiotin. In contrast, it was shown that electrical synapses between Mauthner cells and the club endings of nerve afferents are permeable to LY (Pereda et al. 1995); Mauthner cells express Cx35, the fish ortholog of Cx36 (Pereda et al. 2003). Thus, it is quite possible that Cx36 is permeable to cations and anions but at significantly different rates.

Here, we examined the permselectivity of homotypic GJs formed of Cx36. We demonstrate that Cx36 exhibits ~10-fold higher permeability to cationic than to anionic dyes of approximately the same molecular mass and net charge. Combined electrophysiological and fluorescence imaging studies allowed us to evaluate the permeability of the single Cx36 GJ channel for different dyes and to compare the permeability of Cx36 with that of other connexins.

Materials and Methods

Cells and Culture Conditions

Experiments were performed on HeLa cells (ATCC CCL2) stably transfected with Cx36 tagged with green fluorescence to the C terminus (Cx36-EGFP). Cells were grown in Dulbecco's modified Eagle medium supplemented with 8 % FBS. All media and culture reagents were obtained from Life Technologies (Bethesda, MD). For simultaneous electrophysiological and fluorescence recording, cells were grown on coverslips and then transferred to an experimental chamber (Bukauskas 2001) mounted on the stage of an inverted Olympus (Tokyo, Japan) IX-70 microscope equipped with a Hamamatsu (Bridgewater, NJ) digital camera and filter wheels housing appropriate excitation and emission filters adapted to image EGFP and the fluorescent dyes used in this study.

Electrophysiological Recordings of Cell–Cell Coupling

Junctional conductance, g_j, was measured in selected cell pairs by a dual whole-cell voltage-clamp method. Cells 1 and 2 of a cell pair were voltage-clamped independently with separate patch-clamp amplifiers (EPC8; HEKA Elektronik, Lambrecht, Germany) at the same holding potential, $V_1 = V_2$. By stepping the voltage in cell 1 and keeping the other constant, junctional current was measured as the change in current in the unstepped cell 2, $I_j = I_2$. Thus, g_j was obtained from the ratio $-I_j/V_j$, where

V_j is transjunctional voltage and the negative sign indicates that I_j measured in cell 2 is oppositely oriented to the one measured in cell 1. To minimize the effect of series resistance on measurements of g_j (Wilders and Jongsma 1992), we maintained pipette resistances below 3 MOhm. Patch pipettes were pulled from glass capillary tubes with filaments. Voltages and currents were acquired and analyzed using the MIO-163 A/D converter (National Instruments, Austin, TX) and custom-made software (Trexler et al. 1999). Cells were perfused at room temperature in a modified Krebs-Ringer (MKR) solution containing (in mM) NaCl, 140; KCl, 4; $CaCl_2$, 2; $MgCl_2$, 1; glucose, 5; pyruvate, 2; HEPES, 5 (pH 7.4). Patch pipettes were filled with a solution containing (in mM) KCl, 130; NaAsp, 10; $MgCl_2$, 1; $CaCl_2$, 0.2; EGTA, 2; HEPES, 5 (pH 7.2, $[Ca^{2+}]_i = 5 \times 10^{-8}$ M).

Fluorescence Imaging and Dye Transfer Studies

Fluorescence signals were acquired using an ORCA digital camera (Hamamatsu) with UltraVIEW software for image acquisition and analysis (Perkin Elmer Life Sciences, Boston, MA). For dye transfer studies, a given dye was introduced into cell 1 of a pair through a patch pipette in whole-cell voltage-clamp mode. Typically, this resulted in rapid loading of cell 1, followed by dye transfer to the neighboring cell 2. A whole-cell recording in the dye recipient cell (cell 2) was established ~6–10 min after opening the patch in cell 1. This allowed measurement of g_j and avoided dye leakage into pipette 2 during dye permeability measurements.

Evaluation of GJ permeability of dyes from changes in fluorescence intensity in both cells was previously detailed (Rackauskas et al. 2007b; Palacios-Prado et al. 2009, 2010). In brief, cell-to-cell flux (J_j) of dye in the absence of transjunctional voltage ($V_j = 0$ mV) can be determined from changes of dye concentration in cell 2 (ΔC_2) over time interval (Δt) as follows:

$$J_j = vol_2\ (\Delta C_2/\Delta t) \tag{1}$$

where vol_2 is the volume of cell 2. Then, according to the modified (Verselis et al. 1986) Goldman-Hodgkin-Katz (GHK) equation (Hille 2001), the total junctional permeability (P_j) can be described in consequence:

$$P_j = \frac{J_j}{C_1 - C_2} = \frac{vol_2 \cdot (\Delta C_2/\Delta t)}{C_1 - C_2} \tag{2}$$

where C_1 and C_2 are dye concentrations in cell 1 (dye donor) and cell 2 (dye recipient), respectively. Cell volume was approximated as a hemisphere. The diameter of a hemisphere was determined by averaging the longest and shortest diameters of the cell; on average, the volume of examined HeLa cells was ~1,800 μm^3. Assuming that dye concentration is directly proportional to fluorescence intensity ($C = k{\cdot}FI$), then equation 2 can be modified as follows:

$$P_j = \frac{(vol_2 \cdot \Delta FI_2/\Delta t)}{FI_1 - FI_2} \tag{3}$$

where $\Delta FI_2 = FI_{2,n+1} - FI_{2,n}$ is the change in FI in cell 2 over time, $\Delta t = (t_{n+1} - t_n)$; n is the nth time point in the recording.

Most of the fluorescent dyes and reagents were purchased from Invitrogen (Eugene, OR). EAM-1 and EAM-2 cationic dyes (see below) were obtained from Macrocyclics (Dallas, TX). To minimize dye bleaching, studies were performed using time-lapse imaging, which exposed cells to a low-intensity light for ~0.5 s every 6 s or more. We also used low dye concentrations in the pipette solution, typically 0.1 mM and below, which minimized phototoxicity but still provided satisfactory fluorescence intensities.

Data Analysis and Statistics

The analysis was performed using SigmaPlot software (Systat, Richmond, CA), and averaged data are reported as means ± SEM.

Results

Cell-to-Cell Dye Transfer Studies

The major goal of this study was to determine the permeability of the Cx36 GJ channel to dyes that differ in molecular mass and net charge. To assess the single-channel permeability of Cx36 GJs to fluorescent dyes, we combined dye transfer studies with g_j measurements in HeLaCx36-EGFP cell pairs. Typically, we selected cell pairs exhibiting at least one junctional plaque (see Fig. 2a), which usually yields electrical cell–cell coupling; and g_j was higher at larger junctional plaques. Dyes used include (molecular mass of the fluorescent ion, valence): LY (443, −2), Alexa fluor-350 (AFl-350; 326, −1), EAM-1 (MW 266, +1) and EAM-2 (MW 310, +1), ethidium bromide (EtBr; 314, +1) and DAPI (279, +2). Usually, positively charged dyes bind to nucleotides, and due to this binding, the quantum efficiency of their fluorescence increases substantially. Only one class of compounds that generally remains unbound in the cytoplasm, [2-(4-nitro-2,1,3-benzoxadiazol-7-yl)aminoethyl]trimethylammonium (NBD-TMA$^+$), designed originally as a probe for monitoring renal transport of organic cations, has been reported (Bednarczyk et al. 2000). Furthermore, NBD-TMA$^+$ has been used by Burt and colleagues to measure the cationic permeability of GJs formed of different Cx isoforms

(Ek-Vitorin and Burt 2005; Ek-Vitorin et al. 2006; Heyman and Burt 2008). They showed that NBD-TMA$^+$ fluorescence intensity is linearly proportional to its concentration. Iodide and bromide salts of NBD-TMA are known as EAM-1 and EAM-2, respectively; their molecular formulas are shown in Fig. 1b. To test whether EAM-1 and EAM-2 bind to cytoplasmic constituents, we pemeabilized cells loaded with EAM dyes by applying >200-mV pulses to the patch pipette or exposing cells to alcohol. We observed a decay of fluorescence approaching zero over a several minutes, which indicates that EAM dyes do not bind to cytoplasmic constituents or do so at low levels.

To measure permeability, pipette 1 filled with dye was attached to cell 1 and pipette 2 without dye was attached to cell 2 (Figs. 1, 2). After opening patch-1, dye diffused to cell 1, followed by dye transfer to cell 2. Typically, fluorescence intensity in cell 1 approached steady state during several minutes, but this time was longer at higher dye transfer rates to cell 2. Approximately 5 min later, the patch in cell 2 was open to measure g_j in a dual whole-cell voltage-clamp mode. The total junctional permeability, P_j, was evaluated using equation 3, which accounted for fluorescence intensity changes in cell 1 (FI_1) and cell 2 (FI_2). The single-channel permeability (P_γ) can be found by dividing P_j by the number of open channels ($n = g_j/\gamma_o$, where γ_o is the open single-channel conductance) at a given time as follows:

$$P_\gamma = \frac{P_j}{g_j/\gamma_o} = \frac{(vol_2 \cdot \Delta FI_2/\Delta t)\gamma_o}{(FI_1 - FI_2)\, g_j} \quad (4)$$

Our initial studies revealed that Cx36-expressing cells are permeable to neurobiotin but not to LY and DAPI (Teubner et al. 2000). All these studies were performed using whole-field excitation, which has strong limitations in cells expressing low coupling. The emission light of cell 1 as well as of pipette 1 loaded with dye is relatively intense, and its scattering from cell 2 and surroundings can even exceed the emission light of dye transferred to cell 2 severalfold if the number of operating GJ channels is small and/or channel permeability is low (see Fig. 1a, left). It is assumed that this applies to Cx36 because it exhibits very low single-channel conductance and <1 % of Cx36 GJ channels are functional (F. F. B. unpublished data). To overcome this problem, we used dual excitation, as described earlier (Rackauskas et al. 2007b; Palacios-Prado et al. 2009). In brief, cells were exposed periodically (every

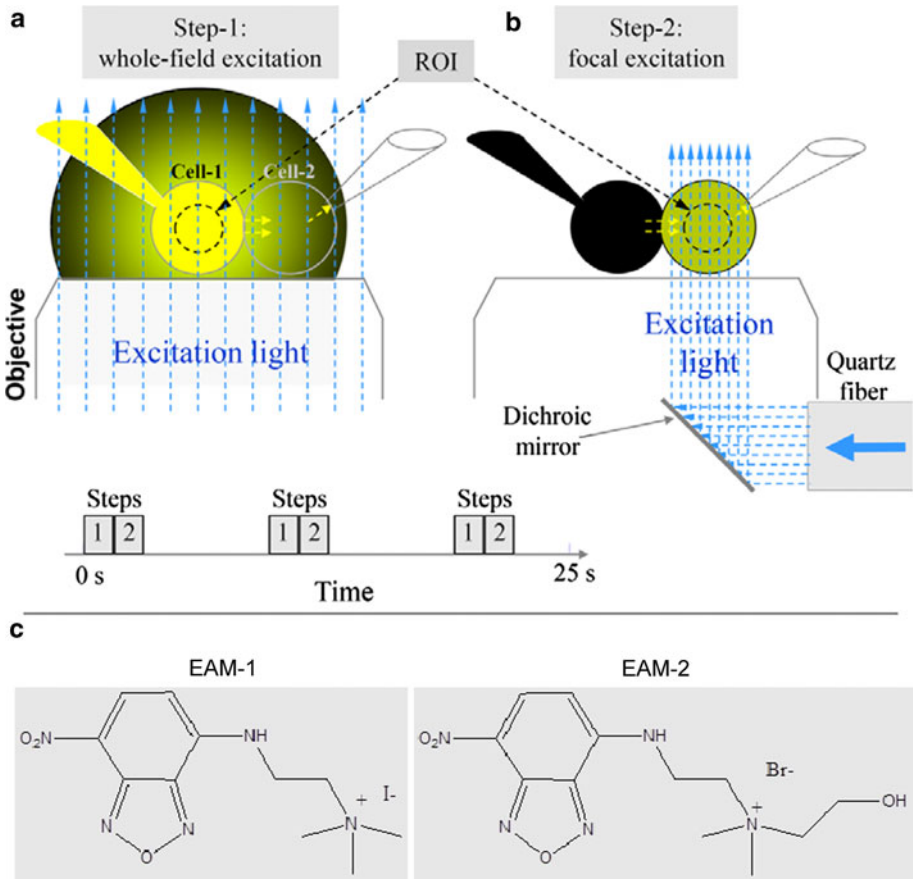

Fig. 1 Schematics of time-lapse imaging using a dual-fluorescence excitation mode. **a** Whole-field excitation (*vertical, blue, dashed arrows*) of the cell pair with two patch pipettes. Emitted light of dye (*yellow*) in the pipette, and cell 1 creates a large background of scattered light around the cell pair. **b** The same as in **a** but excitation light is focused only to cell 2. This eliminates excitation of dye in cell 1 and the pipette attached to it. **c** Molecular formulas of positively charged fluorescent dyes, EAM-1 and EAM-2

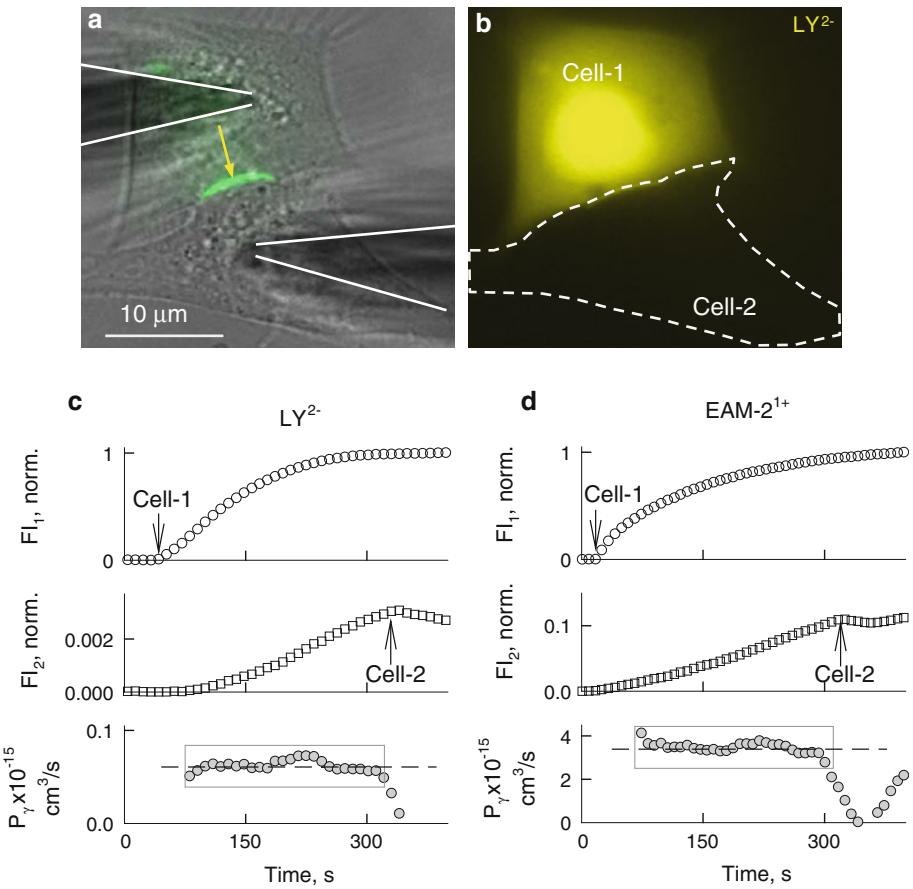

Fig. 2 Permeability of Cx36-EGFP GJ channels. **a**, **b** Images of HeLaCx36-EGFP cell pair. **a** Overlapped phase contrast (*gray*) and EGFP (*green*) images; shadows of two patch pipettes are accentuated by continuous lines, and the *yellow arrow* shows the position of the junctional plaque. **b** Fluorescent image of LY obtained using whole-field excitation 5 min after the patch was open to cell 1. There was no detectable LY signal in cell 2; cells were electrically coupled, $g_j = 5$ nS. **c**, **d** Examples of time course of changes in LY (**c**) and EAM-2 (**d**) fluorescence in cell 1 (FI_1) and cell 2 (FI_2) and in single-channel permeability (P_γ). *Arrows* point to the moments of patch opening in cell 1 and cell 2

6–9 s in time-lapse mode) to whole-field excitation (see Fig. 1a, left), followed by exposure only of cell 2 to a focused light with diameter of ~15 µm (see Fig. 1a, right). The diameter and intensity of focused light were variable, when necessary. The 3-D micromanipulator was used to change the focus and position of the focused light. To assess P_j, we measured changes in FI_1 during whole-field excitation and in FI_2 during focused excitation. To calibrate emission signals obtained during whole-field and focused excitations, cell 1 was exposed to focused light several times during the experiment. A dual-mode excitation increased the resolution of dye transfer measurements at least 100-fold and allowed us to measure dye transfer even in the presence of few GJ channels.

Permeability of Cx36 GJs to Negatively Charged Dyes

Experiments were performed in a HeLaCx36-EGFP cell pair exhibiting one or several junctional plaque (Fig. 2a). Figure 2c shows that after opening the patch in pipette 1 filled with LY (first arrow), FI_1 started to rise, reaching steady state after ~3.5 min. Fluorescence images measured during whole-field excitation (Fig. 2b) did not show detectable LY transfer into cell 2, while the FI_2 trace measured during the focal excitation demonstrates the FI_2 rise, reaching approximately 0.3 % of the FI_1 value at ~320 s (FI_2 trace in Fig. 2c). After opening the patch into cell 2 (second arrow), we applied repeated (1.5 s) voltage ramps, changing during 1 s from −10 to +10 mV to cell 1, to measure I_j, which allowed us to find that $g_j = 6.4$ nS. FI_2 started to decay after opening the patch into cell 2, indicating LY flux from cell 2 to pipette 2. The bottom trace shows P_γ calculated using equation 4. Data points positioned inside the gray rectangle resulted in $P_\gamma = 0.0618 \pm 0.0024 \times 10^{-15}$ cm^3/s ($n = 26$). On average $P_{\gamma,LY} = 0.068 \pm 0.012 \times 10^{-15}$ cm^3/s ($n = 14$). Using AFl-350 instead of LY, we found similar dynamics of FI_1 and FI_2, but on average $P_{\gamma,AFl\text{-}350}$ was fourfold higher: $P_{\gamma,AFl\text{-}350} = 0.27 \pm 0.06 \times 10^{-15}$ cm^3/s ($n = 11$). Fluorescence images obtained using a whole field were similar to the one shown in Fig. 2b; i.e., AFl-350 transfer signals were comparable with background fluorescence. In summary, the data show that on average $P_{\gamma,LY}$ is approximately fourfold smaller than $P_{\gamma,AFl\text{-}350}$, which could be mainly due to two negative charges instead of one. Figure 2c, d shows that P_γ values remained constant during their evaluation

period, which indicates that during the experiment lasting ~5 min, there was no substantial dye bleaching or dye binding to cytoplasmic constituents.

In evaluations of P_γ, the number of GJ channels was calculated assuming that $\gamma_o = 15$ pS (Teubner et al. 2000), which can be even smaller, between 10 and 15 pS (Srinivas et al. 1999). Furthermore, measured g_j is defined by channels that can be only at the main open state but not at the residual state, which is not permeable to dyes and metabolites even in Cxs with significantly higher γ_os, such as Cx43 and Cx46 (Qu and Dahl 2002; Bukauskas et al. 2002a). There are no reports that reliably demonstrate gating of Cx36 GJ channels to the residual state, which is an indication of the *fast* gate. In addition, g_j measurements were performed at small V_js (~10 mV) that cannot induce gating in Cx36 exhibiting exceptionally low sensitivity to V_j (Srinivas et al. 1999; Teubner et al. 2000). To further exploit this aspect, we examined $g_j - V_j$ dependence in HeLaCx36-EGFP cell pairs in response to a slow V_j change from 0 to +100 and −100 mV (Fig. 3a). An averaged ($n = 9$) and normalized $g_j - V_j$ plot is shown as a black solid line in Fig. 3b. The white line is a fitting curve obtained using a stochastic four-state model (S4SM) (Paulauskas et al. 2009; see function of the model online: http://connexons.aecom.yu.edu/Applet.htm). During simulation, we assumed that Cx36 GJs contain two *slow* gates, operating between open and closed states with conductances of 15 and 0 pS, respectively. We used an Exkor algorithm of global optimization to fit an experimental $g_j - V_j$ plot (see movies at http://connexons.aecom.yu.edu/Research.htm, illustrating performance of global optimization) that allowed us to evaluate parameters of the gates and consequently changes of open probability of the A and B hemichannels, $P_{H,A}$ and $P_{H,B}$, depending on V_j (Fig. 3c). The summarized $g_j - V_j$ plot is slightly asymmetric, which is reflected in a small asymmetry of $P_{H,A} - V_j$ and $P_{H,B} - V_j$ plots. At $V_j = 0$, $P_{H,A} = 0.85$ and $P_{H,B} = 0.88$, and consequently the open probability of GJs is 0.75 (0.85 × 0.88). Therefore, under control/normal conditions, ~75 % of functional Cx36 GJs are open at any given time. It is typical for many Cxs to be gated under resting ($V_j = 0$ mV) conditions (Bukauskas et al. 2002b; Palacios-Prado et al. 2009, 2010). If GJs are indeed gated by the *slow* gate, then evaluations of P_γ would be in accordance with equation 4. If a fraction of channels could be gated to the residual state by the *fast* gate, then P_γ could be slightly underevaluated because at the same g_j a smaller number of channels would be in the fully open state.

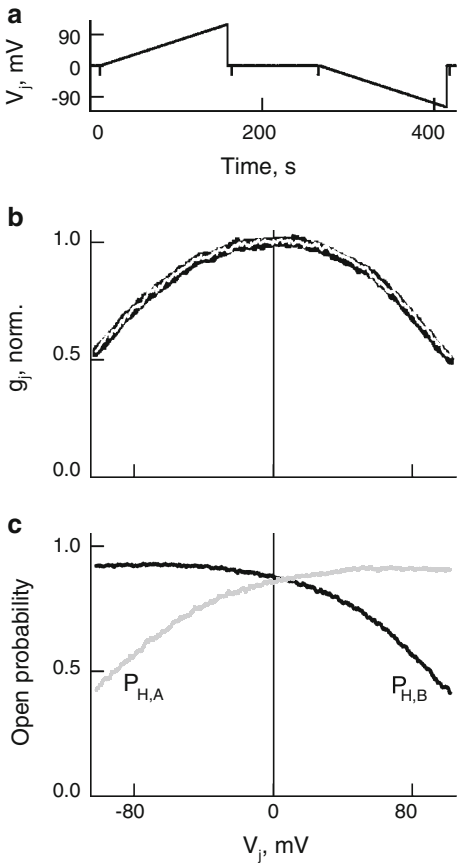

Fig. 3 Voltage gating of HeLaCx36-EGFP GJs. **a**, **b** Averaged and normalized $g_j - V_j$ plot (*black solid line* in **b**) obtained in response to V_j ramps (shown in **a**). *White line* is a fitting curve obtained using a S4SM and global optimization. **c** Dependencies of open probabilities of A ($P_{H,A}$) and B ($P_{H,B}$) hemichannels on V_j derived from the S4SM

Permeability of Cx36 GJs to Positively Charged Dyes

To study permeability to cationic dyes, we used EAM-1 and EAM-2 as well as EtBr and DAPI. Figure 2d shows the dynamics of FI_1 and FI_2 of EAM-2 fluorescence in a HeLaCx36-EGFP cell pair with $g_j = 5$ nS, which corresponds to ~333 channels (5 nS/15 pS). Arrows indicate patch openings in cell 1 and cell 2. The bottom trace shows the calculated values of P_γ. Averaged P_γ values of EAM-1 and EAM-2 are alike ($2.31 \pm 0.562 \times 10^{-15}$ cm^3/s [$n = 9$] and $2.10 \pm 0.67 \times 10^{-15}$ cm^3/s [$n = 9$], respectively), presumably due to a similarity in their structure and the net charge (+1), while a small difference in their MW (266 vs. 310) may explain why $P_{\gamma,EAM\text{-}1}$ is slightly higher than $P_{\gamma,EAM\text{-}2}$. Thus, the P_γs of EAM-1 and EAM-2 are ~10-fold higher than the P_γ of AFl-350, which is of approximately the same molecular mass. The polarity of the net charge should be a major reason for this difference. Movies 1 and 2 in the supplements show a barely detectable transfer of EAM-1 when only whole-field excitation was used (Movie 1), and it was significantly more expressed using a dual-excitation mode (Movie 2) in the cell pair exhibiting g_j of 4.3 nS. To compare the cationic

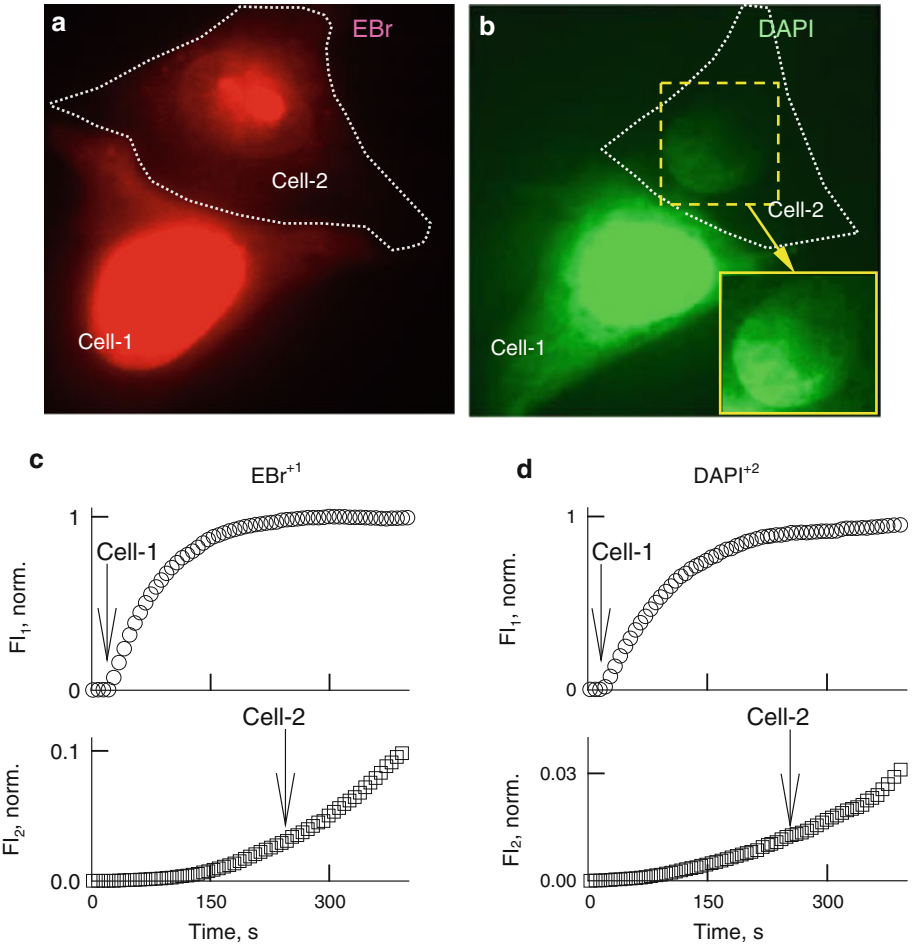

Fig. 4 Permeability of Cx36–EGFP GJ channels to EtBr and DAPI. Representative images of HeLaCx36-EGFP cell pairs showing transfer of EtBr (**a**) and DAPI (**b**) recorded using whole-field excitation. Enhanced view of nucleus in cell 2 (*inset* in **b**) shows a gradient of fluorescence with higher intensity on the junctional side. Examples of time course of changes in EtBr (**c**) and DAPI (**d**) fluorescence in cell 1 (FI_1) and cell 2 (FI_2). *Arrows* point to the moments of patch opening in cell 1 and cell 2

permeability of Cx36 with other Cxs using the same technique, we examined P_γ for EAM-1 in HeLa cells expressing Cx43-EGFP and found that $P_{\gamma,\text{EAM-1}} = 42 \pm 8 \times 10^{-15}$ cm^3/s ($n = 6$), which is between $P_{\gamma,\text{LY}}$ and $P_{\gamma,\text{AFl-350}}$ reported by us earlier (Rackauskas et al. 2007b). Thus, Cx43 GJs in general are not charge-selective, in harmony with earlier reports (Verselis et al. 2000; Heyman and Burt 2008; Kanaporis et al. 2011).

When cell 1 of a Cx36–EGFP cell pair was loaded with $EtBr^+$ or $DAPI^{2+}$, we initially observed increasingly strong fluorescence labeling of the nucleus of cell 1 and, with some delay, labeling of the nucleus of cell 2. When only whole-field excitation was used for EtBr or DAPI transfer, it was barely detectable. Labeling of cell 2 was significantly more expressed using a dual-excitation mode (see Movies 3 and 4 for EtBr transfer in supplemental materials). Typically, we observed

Table 1 Summary of single-channel permeability (P_γ) (mean ± SEM × 10^{-15} cm^3/s) of homotypic GJs for different dyes

Dye	mCx30.2	Cx36	Cx40	Cx43	Cx45	Cx57
$AFl\text{-}350^-$	0.04 ± 0.02	0.27 ± 0.06	33.1 ± 6.4	86 ± 7.4	5.5 ± 1	0.95 ± 0.09
	$n = 5$	$n = 11$	$n = 8$	$n = 5$	$n = 3$	$n = 5$
LY^{2-}	n.p.	0.068 ± 0.012	6.9 ± 1.4	24.6 ± 2.4	1.1 ± 0.6	n.e.
	$n = 8$	$n = 13$	$n = 7$	$n = 6$	$n = 3$	
$EAM\text{-}1^+$		2.31 ± 0.56		42 ± 8		
		($n = 9$)		($n = 6$)		
$EAM\text{-}2^+$		2.10 ± 0.67				
		($n = 9$)				

Data for P_γs of mCx30.2, Cx40, Cx43, Cx45 and Cx57 are from Rackauskas et al. (2007b) and Palacios-Prado et al. (2009)

n.p. nonpermeable, *n.e.* not examined

the spread of the wave across the nucleus starting from the position where pipette 1 is located and in cell 2 starting from the side of the nucleus that was closer to the junction (Fig. 4b and Movies 5 and 6 in supplemental materials).

Figure 4c, d shows FI_1 and FI_2 changes of EtBr and DAPI after opening the patch in cell 1. FI_2 started to rise only after fluorescence intensities of EtBr or DAPI in cell 1 almost reached the steady-state level. During the initial period after patch opening in cell 1, EtBr or DAPI quickly bound to DNA, resulting in a very low free concentration. After saturation of binding to nucleotides, the free concentration of EtBr and DAPI increased, allowing to observe a fluorescence rise in cell 2 (Fig. 3c, d). After transferring cell 2 into a whole-cell voltage-clamp configuration, there were no signs of decay in FI_2, which was well defined in Fig. 2c, d. This may be due to the fact that most of the fluorescence comes from bound dyes, while unbound EtBr or DAPI exhibit very low fluorescence. All examined cell pairs exhibited weak but detectable cell-to-cell transfer of EtBr ($n = 11$) and DAPI ($n = 13$) using whole-field excitation, as seen in Fig. 4a, b, which typically was not achievable for LY and AFl-350. Due to strong binding of EtBr and DAPI to DNA, quantification of P_γs using equation 4 is not possible. These data support the conclusion that permeability of Cx36 channels is significantly higher for positively than negatively charged dyes. This is also supported by an earlier report (Teubner et al. 2000) showing a transfer of positively charged neurobiotin but no transfer of LY from HeLaCx36 cells injected with dye to the first-order neighboring cells. At this time, we did not use a dual-mode excitation to study dye transfer.

Permeability of the single Cx36-EGFP GJ channel for anionic and cationic dyes is summarized in Table 1 and Fig. 5a. Thus, Cx36 GJ channels exhibit strong cationic selectivity, similar to Cx40 (Heyman et al. 2009), but with ~100-fold smaller in absolute values of P_γs.

Discussion

Cx36 is expressed preferentially in neurons and β-cells of the pancreas in adults (Condorelli et al. 1998; Serre-Beinier

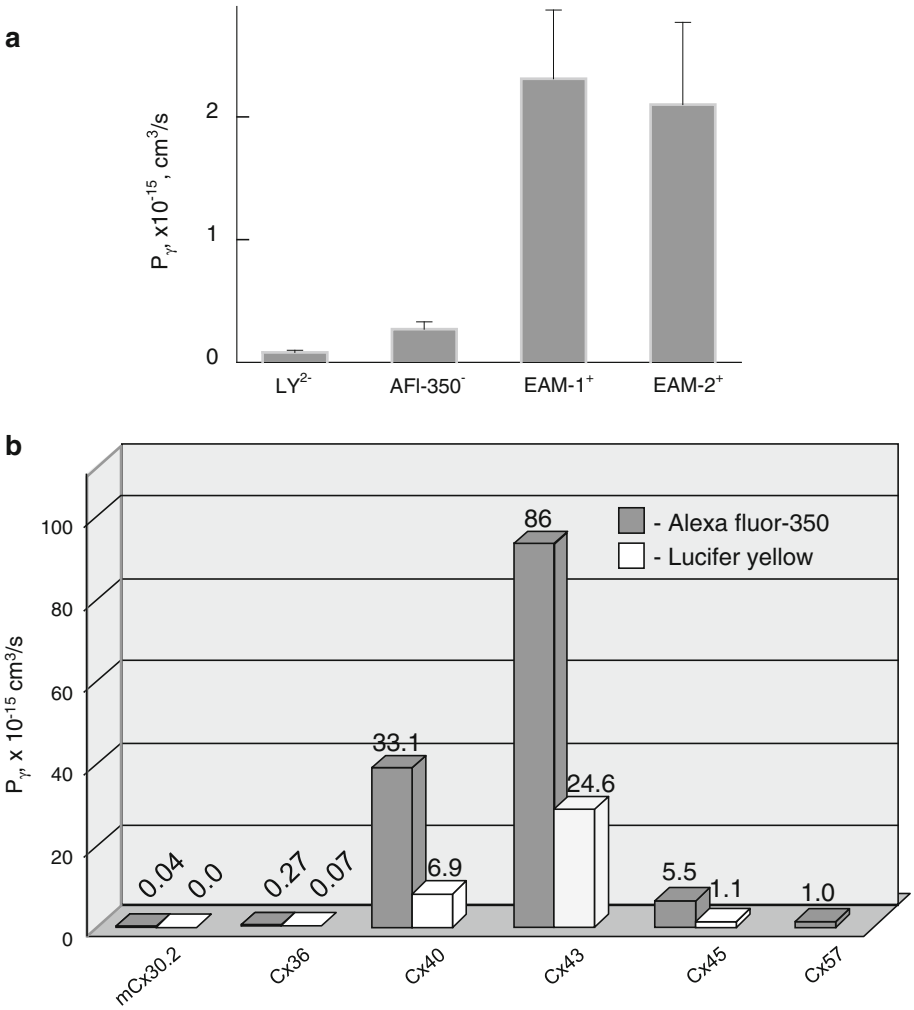

Fig. 5 **a** Averaged single-channel permeability of homotypic Cx36–EGFP GJs for different dyes. **b** Single GJ channel permeabilities of different Cxs. Bars show averaged P_γs of GJ channels for AFl-350 (*gray*) and LY (*white*)

et al. 2000), while its expression could be even broader during embryonic stages and in neonatals (Dobrenis et al. 2005). It was shown, by following the diffusion of microinjected dyes in primary β-cells, that Cx36 GJs are more permeable to positively than negatively charged tracers (Charpantier et al. 2007). Cell-to-cell transfer of dyes depends also on the number of open GJ channels which can be estimated from g_j measurements. One of the key parameters allowing comparison of the permeability of GJ channels formed of different Cx isoforms is single-channel permeability, P_γ. Here, we combined imaging and electrophysiological methods to estimate P_γs for dyes differing in molecular mass and net charge. Many of the fluorescent dyes used resemble, based on size and charge, numerous vital metabolites, which are not fluorescent and whose permeability cannot be measured directly.

Cell-to-cell transfer of atomic ions and metabolites depends also on ionophoresis by V_j, which can accelerate or decelerate the motion of charged molecules in the GJ channel pore (Palacios-Prado and Bukauskas 2012). Thus, metabolic cell–cell communication depends on the permeability of GJs, their number and V_j. We evaluated P_γ before the patch in cell 2 was open, i.e., at $V_j = 0$ mV, thereby preventing dye leak into pipette 2. If the patch of pipette 2 is open during dye transfer measurements, then the following equation for permeability evaluation (Palacios-Prado and Bukauskas 2009) should be used:

$$P_{j,Vj=0} = \frac{\left[vol_2 \cdot (\Delta FI_2/\Delta t) + P_p FI_2\right]}{\left[FI_1 - FI_2\right]} \quad (5)$$

where P_p is a constant characterizing dye diffusion from cell 2 to pipette 2, which can be considered as infinite volume. FI_2 decay after patch opening in cell 2 can be seen in Fig. 2c, d. From that moment, equation 5 should be used to evaluate P_j. Typically, we measured the kinetics of FI_2 decay under rapid chemical uncoupling (heptanol, CO_2, etc.) for P_p estimation. Then, $P_{j,Vj=0} = 0$ and equation 5 can be transformed as follows: $P_p = -\ vol_2 \cdot (\Delta FI_2/\Delta t)/FI_2$ and used to estimate P_p. If dye transfer is performed under the influence of transjunctional voltage, then equation 6 (Palacios-Prado and Bukauskas 2009), derived from the GHK formalism (Hille 2001), should be used:

$$Pj = \frac{\left[(vol_2\, \Delta FI_2/\Delta t) + P_p\, FI_2\right]\ \left[1 - \exp\left(-zFV_j/RT\right)\right]}{\left(zFV_j/RT\right)\ \left[FI_1 - FI_2 \exp\left(-zFV_j/RT\right)\right]} \quad (6)$$

where z is the net charge of the dye molecule, F is Faraday's constant, R is the gas constant and T is the absolute temperature. We used this equation in correlative studies of g_j and permeability modulation by V_j in heterotypic Cx43/Cx45 GJs and in separating ionophoretic and diffusional components in dye transfer (Palacios-Prado and Bukauskas 2009). In neurons, cardiomyocytes and other excitable cells, V_j can reach $\sim$100 mV during asynchronous action potentials and substantially modulate metabolic cell–cell commination. Smaller but long-lasting values of V_js could be due to differences in the resting potential, which typically is small under normal/control conditions and can be substantial in transitional zones between normal and pathological regions.

We found that $P_{\gamma,\text{AFl-350}}$ of Cx36 is smaller than those of Cx43, Cx40, Cx45, and Cx57 by approximately 358, 138, 23 and 4 times, respectively, while $P_{\gamma,\text{LY}}$ is smaller than those for LY of Cx43, Cx40 and Cx45 for $\sim$361, 101 and 16 times, respectively (Rackauskas et al. 2007b; Palacios-Prado et al. 2009). In contrast, $P_{\gamma,\text{AFl-350}}$ of Cx36 is $\sim$6.5-fold higher than that of mCx30.2 (Rackauskas et al. 2007b), which exhibits smaller single-channel conductance ($\sim$10 vs. 15 pS [Srinivas et al. 1999; Teubner et al. 2000; Kreuzberg et al. 2005]). P_γ values of EAM-1 and EAM-2 are $\sim 2.2 \times 10^{-15}$ cm^3/s, which is $\sim$10-fold higher than permeability for anionic dyes AFl-350 and LY. This correlates with transfer of EtBr and DAPI detectable even using whole-field excitation. All these data are summarized in Table 1 and illustrated in Fig. 5b.

Data collected by different groups generally are in a broad agreement that P_γ decreases with an increase in molecular mass (Heyman and Burt 2008; Weber et al. 2004). The relationship between $P_{\gamma,\text{AFl-350}}$ and $P_{\gamma,\text{LY}}$ of different Cxs and the single-channel conductance (Fig. S1 in supplemental materials) shows that the permeability of GJs is not directly proportional to their unitary conductance. There is a tendency for higher P_γs at higher γ_os. Thus, the channel pore cannot be viewed as a simple cylinder due to the interaction of charged permeant molecules with charged domains of the pore. This interaction is reflected in a broad variation of charge selectivity from nonselective to highly cationic or even some anionic selectivity (Veenstra et al. 1994a, 1994b; Verselis and Veenstra 2000; Verselis et al. 2000). It was predicted that an important determinant of charge selectivity is located, at least for Cx32 and Cx46, in the E1 domain (Trexler et al. 2000). Most of the recently collected data support a view that GJs preferentially exhibit no or weak anionic selectivity, while only cationic selectivity can be strong (Heyman et al. 2009; Kanaporis et al. 2011).

Previously, using a dual-mode excitation, we reported that $P_{\gamma,\text{AFl-350}}$ and $P_{\gamma,\text{LY}}$ of Cx43 is $\sim$2.6- and 3.6-fold larger than those of Cx40 and $\sim$16- and 22-fold larger than those of Cx45. These ratios differ from those reported by Kanaporis et al. (2011), demonstrating that $P_{\gamma,\text{AFl-350}}$ and $P_{\gamma,\text{LY}}$ of Cx43 are 11- and 6-fold smaller than those reported by Rackauskas et al. (2007b), respectively. Furthermore, Cx40 and Cx45 exhibit similar $P_{\gamma,\text{LY}}$, while in Rackauskas et al. (2007b) $P_{\gamma,\text{LY}}$ of Cx40 is approximately sixfold higher

than that in Cx45, which exhibits approximately fivefold smaller single-channel conductance. Furthermore, the reported value for $P_{\gamma,\mathrm{AFl\text{-}350}}$ of Cx43 measured using a compartmental model is 180×10^{-15} cm^3/s (Nitsche et al. 2004) and that for $P_{\gamma,\mathrm{LY}}$ measured in HeLa Cx43 transfectants is $\sim 39 \times 10^{-15}$ cm^3/s (Eckert 2006), which are even higher than those in Rackauskas et al. (2007b). Measurements of P_γ are highly complex, and there are several potential sources of error, indicated in Weber et al. (2004) and Eckert (2006). Among them, the most critical are those related to proper measurement of g_j and emitted light of cell 2. A major error in determining g_j is due to a series resistance (Wilders and Jongsma 1992), which can be minimized using low-resistance patch pipettes, and excluding measurements in cell pairs with g_js exceeding $\sim$20 nS. In HeLaCx36-EGFP cell pairs, measured g_j was relatively low, on average $\sim$5 nS. Thus, evaluations of P_γ performed for Cx36 should not be affected substantially by series resistance.

Thus, we demonstrate that Cx36 GJs exhibit strong cationic selectivity, which may explain some unsuccessful attempts to demonstrate LY transfer in between neurons and to some degree reduces existing controversy on this issue. Many signaling molecules and metabolites, such as cAMP, IP_3, ATP, ADP, AMP and PCr (phosphocreatine), are charged negatively, which predicts their relatively low permeability rate through Cx36 GJs. At the same time, permeability to cations, including K^+, which is a major cell-to-cell charge carrier, should be high, which assumes that Cx36 GJs are specialized more for electrical than for metabolic cell–cell communication. Preferential cationic vs. anionic selectivity among Cx isoforms in which permselectivity was examined rigorously suggest that this conclusion has the potential to be applied to more Cx isoforms.

Acknowledgements We thank Dr. Garry E. Kiefer, chief executive officer of Macrocyclics (Dallas, TX), for the kind supply of EAM-1 and EAM-2 dyes; Dr. Klaus Willecke for kindly providing the constructs of Cx36; and PhD student Nerijus Paulauskas and Dr. Angele Bukauskiene for excellent technical assistance. This work was supported by National Institutes of Health grants HL084464 and NS072238 (to F. F. B.).

References

Bednarczyk D, Mash EA, Aavula BR, Wright SH (2000) NBD-TMA: a novel fluorescent substrate of the peritubular organic cation transporter of renal proximal tubules. Pflugers Arch 440:184–192

Bedner P, Niessen H, Odermatt B, Kretz M, Willecke K, Harz H (2006) Selective permeability of different connexin channels to the second messenger cyclic AMP. J Biol Chem 28:6673–6681

Bennett MV, Verselis VK (1992) Biophysics of gap junctions. Semin Cell Biol 3:29–47

Bukauskas FF (2001) Inducing de novo formation of gap junction channels. Method Mol Biol 154:379–393

Bukauskas FF, Peracchia C (1997) Two distinct gating mechanisms in gap junction channels: CO_2-sensitive and voltage-sensitive. Biophys J 72:2137–2142

Bukauskas FF, Verselis VK (2004) Gap junction channel gating. Biochim Biophys Acta 1662:42–60

Bukauskas FF, Weingart R (1994) Voltage-dependent gating of single gap junction channels in an insect cell line. Biophys J 67:613–625

Bukauskas FF, Bukauskiene A, Verselis VK (2002a) Conductance and permeability of the residual state of connexin43 gap junction channels. J Gen Physiol 119:171–186

Bukauskas FF, Bukauskiene A, Verselis VK, Bennett MVL (2002b) Coupling asymmetry of heterotypic connexin 45/connexin 43-EGFP gap junctions: properties of fast and slow gating mechanisms. Proc Natl Acad Sci USA 99:7113–7118

Campbell RE, Ducret E, Porteous R, Liu X, Herde MK, Wellerhaus K, Sonntag S, Willecke K, Herbison AE (2011) Gap junctions between neuronal inputs but not gonadotropin-releasing hormone neurons control estrous cycles in the mouse. Endocrinology 152:2290–2301

Charpantier E, Cancela J, Meda P (2007) Beta cells preferentially exchange cationic molecules via connexin 36 gap junction channels. Diabetologia 50:2332–2341

Condorelli DF, Parenti R, Spinella F, Salinaro AT, Belluardo N, Cardile V, Cicirata F (1998) Cloning of a new gap junction gene (Cx36) highly expressed in mammalian brain neurons. Eur J Neurosci 10(3):1202–1208

Dobrenis K, Chang H, Pina-Benabou MH, Woodroffe A, Lee SC, Rozental R, Spray DC, Scemes E (2005) Human and mouse microglia express connexin36, and functional gap junctions are formed between rodent microglia and neurons. J Neurosci Res 82:306–315

Eckert R (2006) Gap-junctional single-channel permeability for fluorescent tracers in mammalian cell cultures. Biophys J 91:565–579

Ek-Vitorin JF, Burt JM (2005) Quantification of gap junction selectivity. Am J Physiol Cell Physiol 289:C1535–C1546

Ek-Vitorin JF, King TJ, Heyman NS, Lampe PD, Burt JM (2006) Selectivity of connexin 43 channels is regulated through protein kinase C–dependent phosphorylation. Circ Res 98:1498–1505

Goldberg GS, Valiunas V, Brink PR (2004) Selective permeability of gap junction channels. Biochim Biophys Acta 1662:96–101

Harris AL (2001) Emerging issues of connexin channels: biophysics fills the gap. Q Rev Biophys 34:325–427

Harris AL (2007) Connexin channel permeability to cytoplasmic molecules. Prog Biophys Mol Biol 94:120–143

Hernandez VH, Bortolozzi M, Pertegato V, Beltramello M, Giarin M, Zaccolo M, Pantano S, Mammano F (2007) Unitary permeability of gap junction channels to second messengers measured by FRET microscopy. Nat Methods 4:353–358

Heyman NS, Burt JM (2008) Hindered diffusion through an aqueous pore describes invariant dye selectivity of Cx43 junctions. Biophys J 94:840–854

Heyman NS, Kurjiaka DT, Ek-Vitorin JF, Burt JM (2009) Regulation of gap junctional charge selectivity in cells coexpressing connexin 40 and connexin 43. Am J Physiol Heart Circ Physiol 297:H450–H459

Hille B (2001) Ionic channels of excitable membranes. Sinauer Associates, Sunderland

Jain R, Lammert E (2009) Cell–cell interactions in the endocrine pancreas. Diabetes Obes Metab 11:159–167

Kanaporis G, Brink PR, Valiunas V (2011) Gap junction permeability: selectivity for anionic and cationic probes. Am J Physiol Cell Physiol 300:C600–C609

Kreuzberg MM, Sohl G, Kim J, Verselis VK, Willecke K, Bukauskas FF (2005) Functional properties of mouse connexin30.2

expressed in the conduction system of the heart. Circ Res 96:1169–1177

Nitsche JM, Chang H, Weber PA, Nicholson BJ (2004) A transient diffusion model yields unitary gap junctional permeabilities from images of cell-to-cell fluorescent dye transfer between *Xenopus* oocytes. Biophys J 86:2058–2077

Palacios-Prado N, Bukauskas FF (2009) Heterotypic gap junction channels as voltage-sensitive valves for intercellular signaling. Proc Natl Acad Sci USA 106:14855–14860

Palacios-Prado N, Bukauskas FF (2012) Modulation of metabolic communication through gap junction channels by transjunctional voltage; synergistic and antagonistic effects of gating and ionophoresis. Biochim Biophys Acta 1818:1884–1894

Palacios-Prado N, Sonntag S, Skeberdis VA, Willecke K, Bukauskas FF (2009) Gating, permselectivity and pH-dependent modulation of channels formed by connexin57, a major connexin of horizontal cells in the mouse retina. J Physiol 587:3251–3269

Palacios-Prado N, Briggs SW, Skeberdis VA, Pranevicius M, Bennett MV, Bukauskas FF (2010) pH-dependent modulation of voltage gating in connexin45 homotypic and connexin45/connexin43 heterotypic gap junctions. Proc Natl Acad Sci USA 107: 9897–9902

Pan F, Paul DL, Bloomfield SA, Völgyi B (2010) Connexin36 is required for gap junctional coupling of most ganglion cell subtypes in the mouse retina. J Comp Neurol 518:911–927

Peracchia C (2004) Chemical gating of gap junction channels; roles of calcium, pH and calmodulin. Biochim Biophys Acta 1662:61–80

Pereda AE, Bell TD, Faber DS (1995) Retrograde synaptic communication via gap junctions coupling auditory afferents to the Mauthner cell. J Neurosci 15:5943–5955

Pereda A, O'Brien J, Nagy JI, Bukauskas F, Davidson KG, Kamasawa N, Yasumura T, Rash JE (2003) Connexin35 mediates electrical transmission at mixed synapses on Mauthner cells. J Neurosci 23:7489–7503

Ponsioen B, van Zeijl L, Moolenaar WH, Jalink K (2007) Direct measurement of cyclic AMP diffusion and signaling through connexin43 gap junctional channels. Exp Cell Res 313:415–423

Qu Y, Dahl G (2002) Function of the voltage gate of gap junction channels: selective exclusion of molecules. Proc Natl Acad Sci USA 99:697–702

Rackauskas M, Kreuzberg MM, Pranevicius M, Willecke K, Verselis VK, Bukauskas FF (2007a) Gating properties of heterotypic gap junction channels formed of connexins 40, 43 and 45. Biophys J 92:1952–1965

Rackauskas M, Verselis VK, Bukauskas FF (2007b) Permeability of homotypic and heterotypic gap junction channels formed of cardiac connexins mCx30.2, Cx40, Cx43, and Cx45. Am J Physiol Heart Circ Physiol 293(3):H1729–H1736

Serre-Beinier V, Le Gurun S, Belluardo N, Trovato-Salinaro A, Charollais A, Haefliger JA, Condorelli DF, Meda P (2000) Cx36 preferentially connects beta-cells within pancreatic islets. Diabetes 49(5):727–734

Srinivas M, Rozental R, Kojima T, Dermietzel R, Mehler M, Condorelli DF, Kessler JA, Spray DC (1999) Functional properties of channels formed by the neuronal gap junction protein connexin36. J Neurosci 19:9848–9855

Teubner B, Degen J, Sohl G, Guldenagel M, Bukauskas FF, Trexler EB, Verselis VK, De Zeeuw CI, Lee CG, Kozak CA, Petrasch-Parwez E, Dermietzel R, Willecke K (2000) Functional expression of the murine connexin36 gene coding for a neuron-specific gap junctional protein. J Membr Biol 176:249–262

Trexler EB, Bennett MV, Bargiello TA, Verselis VK (1996) Voltage gating and permeation in a gap junction hemichannel. Proc Natl Acad Sci USA 93:5836–5841

Trexler EB, Bukauskas FF, Bennett MVL, Bargiello TA, Verselis VK (1999) Rapid and direct effects of pH on connexins revealed by the connexin46 hemichannel preparation. J Gen Physiol 113: 721–742

Trexler EB, Bukauskas FF, Kronengold J, Bargiello TA, Verselis VK (2000) The first extracellular loop domain is a major determinant of charge selectivity in connexin46 channels. Biophys J 79: 3036–3051

Veenstra RD, Wang HZ, Beyer EC, Brink PR (1994a) Selective dye and ionic permeability of gap junction channels formed by connexin45. Circ Res 75:483–490

Veenstra RD, Wang HZ, Beyer EC, Ramanan SV, Brink PR (1994b) Connexin37 forms high conductance gap junction channels with subconductance state activity and selective dye and ionic permeabilities. Biophys J 66:1915–1928

Veenstra RD, Wang HZ, Beblo DA, Chilton MG, Harris AL, Beyer EC, Brink PR (1995) Selectivity of connexin-specific gap junctions does not correlate with channel conductance. Circ Res 77:1156–1165

Verselis VK, Veenstra RD (2000) Gap junction channels. Permeability and voltage gating. In: Hertzberg E (ed) Advances in molecular and cell biology, vol 30. JAI Press, Greenwich, pp 129–192

Verselis V, White RL, Spray DC, Bennett MV (1986) Gap junctional conductance and permeability are linearly related. Science 234:461–464

Verselis VK, Trexler EB, Bukauskas FF (2000) Connexin hemichannels and cell–cell channels: comparison of properties. Braz J Med Biol Res 33:379–389

Weber PA, Chang H, Spaeth KE, Nitsche JM, Nicholson BJ (2004) The permeability of gap junction channels to probes of different size is dependent on connexin composition and permeant-pore affinities. Biophys J 87:958–973

Wilders R, Jongsma HJ (1992) Limitations of the dual voltage clamp method in assaying conductance and kinetics of gap junction channels. Biophys J 63:942–953

J Membrane Biol (2012) 245:255–262
DOI 10.1007/s00232-012-9446-2

Changes in Connexin43 Expression and Localization During Pancreatic Cancer Progression

Joell L. Solan · Sunil R. Hingorani · Paul D. Lampe

Received: 27 March 2012 / Accepted: 1 June 2012 / Published online: 23 June 2012

Abstract Gap junctions and gap junction communication have long been recognized to play roles in tissue organization and remodeling through both cell autonomous and intercellular means. We hypothesized that these processes become dysregulated during pancreas cancer progression. Molecular and histological characterization of the gap junction protein, connexin43, during progression of pancreatic ductal adenocarcinoma could yield insight into how these events may contribute to or be modulated during carcinogenesis. In a mouse model of pancreatic ductal adenocarcinoma generated through targeted endogenous expression of $Kras^{G12D}$ in the murine pancreas, we examined the evolving expression and localization of connexin43. Overall, connexin43 expression increased over time, and its localization became more widespread. At early stages, connexin43 is found almost exclusively in association with the basolateral membrane of duct cells found in invasive lesions. Connexin43 became increasingly associated with the surrounding stroma over time. Connexin43 phosphorylation was also altered during tumorigenesis, as assessed by migrational changes of the protein in immunoblots. These data suggest a potential role for gap junctions and connexin43 in mediating interactions between and amongst the stromal and epithelial cells in pancreatic ductal adenocarcinoma.

Keywords Connexin · Gap junction · Pancreas cancer · Phosphorylation

J. L. Solan · S. R. Hingorani · P. D. Lampe (✉)
Fred Hutchinson Cancer Research Center, 1100 Fairview Avenue North, M5C800, Box 19024, Seattle, WA 98109, USA
e-mail: plampe@fhcrc.org

Alterations in gap junction biology have long been recognized to contribute to tumor promotion and progression (Cronier et al. 2009; Naus and Laird 2010). Gap junctions are specialized membrane domains containing channels, made up of connexins, that allow exchange of small molecules (<1,000 Da) including ions, metabolites, and second messengers (e.g., Ca^{2+} and IP_3) between neighboring cells (Loewenstein 1981; Saez et al. 2003; Willecke et al. 2002). A wealth of correlative evidence in vivo and in cell lines indicates that gap junctional intercellular communication (GJC) and connexin expression can regulate proliferation and play key tumor prevention roles (Cronier et al. 2009). Loss of GJC is a common feature of transformed cells and tissues (Cronier et al. 2009; Hossain et al. 1989; Naus and Laird 2010). In fact, modulation or loss of connexin expression and localization have been correlated with degree of carcinogenesis in several human tissues including breast, ovary and cervix (Hanna et al. 1999; King et al. 2000; Laird et al. 1999). Mice lacking Cx32 are 25 times more susceptible to carcinogen-induced liver tumors (Moennikes et al. 1999; Temme et al. 1997) and 3 times more susceptible to radiation-induced liver tumors (King and Lampe 2004). Tumor promoters, activated oncogenes (e.g., *src*, *ras*, *mos*, *v-raf*), growth factors (e.g., EGF, PDGF, FGF) and carcinogens all decrease GJC (Fitzgerald and Yamasaki 1990; Jou et al. 1995; Kihara et al. 1990; Trosko et al. 1990). For example, down-regulation of metabolic coupling through gap junctions after treatment with various tumor promoters, such as 12-*O*-tetradecanoylphorbol-13-acetate (TPA), has been observed in a variety of cell systems. Viral infection or transfection of viral encoded oncogenes, such as v-*src* and polyomavirus middle T-antigen into GJC-competent cells results in decreased GJC (Lau et al. 1996). Importantly, connexin mutations do not appear to be common in human tumors

(Yamasaki et al. 1999). Rather, two epigenetic events, silencing of expression via gene methylation (King et al. 2002; Piechocki et al. 1999) and loss of connexin localization from cell-cell interfaces (Krutovskikh et al. 1994), have been observed to correlate with carcinogenesis. Thus, there is the potential to reverse these effects during tumorigenesis. In fact, a chemopreventive role for GJC has been established both in vitro and in vivo by observations that connexin expression and GJC function are up-regulated by several cancer preventive agents including various retinoids and carotenoids (Hossain et al. 1989). Ectopic expression of connexin43 (Cx43) in some tumor cells and cell lines can restore growth control (Chen et al. 1995; Cronier et al. 2009). Paradoxically some tumors, particularly at later stages, can actually begin to overexpress Cx43. For example, malignant gliomas, a tumor which, like pancreatic ductal adenocarcinoma (PDA), is highly aggressive, metastatic and resistant to treatment, shows Cx43 upregulation (Cronier et al. 2009; Zhang et al. 1999). Recently, several studies have raised questions as to whether connexins can play key roles in tumorigenesis independent of gap junction formation (Naus and Laird 2010).

PDA, the most common cancer of the pancreas, is the fourth leading cause of cancer-related death in the United States (Siegel et al. 2012) with an annual incidence and mortality of >40,000 people and a 5 year overall survival rate of <3 % (Hruban 2007). The extremely high mortality occurs primarily because symptoms do not present until tumors are either locally unresectable or widely metastatic. The highly metastatic nature of this cancer is apparent as surgical resection with clean margins in patients diagnosed at "early stages" still inevitably leads to recurrent or metastatic disease (Allison et al. 1998; Yeo et al. 2002). These tumors are also highly resistant to virtually all chemical and radiotherapies (Hruban 2007).

Interestingly and frustratingly, effective treatments have been difficult to achieve despite a fairly good understanding of many of the mutational events present in PDA. Pancreas cancer exhibits activating mutations in *KRAS* in over 90 % of cases (Almoguera et al. 1988) leading to the belief that this is an initiating event in PDA (Hingorani et al. 2003). In addition, overexpression of *ERBB2/HER2,* a member of the family of epidermal growth factor receptors, is a common early event in PDA progression (Hansel et al. 2003; Hingorani et al. 2005). Animal models of preinvasive and invasive PDA (Aguirre et al. 2003; Hingorani et al. 2003, 2005) have been generated through the targeted physiologic expression of oncogenic $Kras^{G12D}$ to the mouse pancreas (hereafter termed K* mouse). These models faithfully mimic the clinical syndrome, histopathology and genetic progression of PDA found in humans. Resected pancreata from these animals demonstrate the full spectrum of preinvasive lesions seen in patients, and the lesions progress histologically over time culminating in fully invasive and metastatic disease. During PDA progression, the cellular makeup of the pancreas changes dramatically; there is a loss of acinar cells with a concomitant increase in glandular epithelial cells. In addition there is a robust fibroinflammatory or desmoplastic reaction in which the stromal components can outnumber the tumor epithelial cells in both the K* model and human cancer. The relevance of the K* mouse models to human pancreas cancer has been validated by an independent panel of human pancreas cancer pathologists assembled by the NCI/MMHCC (Hruban et al. 2006).

Recently, there has been an increased appreciation for the role of the tumor microenvironment in disease progression (Erkan et al. 2010). In particular, increasing attention is being paid to the interaction of pancreatic tumor epithelial cells with the surrounding stroma. Indeed, paracrine interaction between these cell compartments has been observed (Bailey et al. 2008; Brentnall et al. 2012; Tian et al. 2009; Yauch et al. 2008). Cx43 expression in the normal pancreas is quite low and other connexins are responsible for GJC in this tissue. The endocrine cells of the islet express Cx36 (Serre-Beinier et al. 2000), while the exocrine acinar cells are coupled by Cx26 and Cx32 (Meda et al. 1993). The acinar and islet cells make up the mass majority of a normal pancreas. Cx43 is found at low levels in association with endothelial cells or the epithelial duct cells and associated fibroblasts, which only sparsely populate the normal pancreas (Theis et al. 2004). However, as discussed above, these are the cells that expand during PDA. Interestingly, a paracrine-like role for Cx43 in fibroblast activation has recently been suggested, where mast cells could activate fibroblasts via GJC (Pistorio and Ehrlich 2011). It is intriguing to consider that gap junctions and Cx43 could be involved in epithelial: stromal interactions during PDA progression. Here, we present preliminary data indicating that overall Cx43 expression increases and that its localization increasingly shifts to the stromal compartment during cancer progression. This model could help us determine whether increased Cx43 expression during progression is playing a tumor suppressive role and/or a stromal-tumor communication role.

Materials and Methods

Antibodies and Reagents

All general chemicals, unless otherwise noted, were purchased from Fisher Scientific. The rabbit anti-Cx43 antibody (C6219) and anti-α-smooth muscle actin were

purchased from Sigma (St. Louis, MO). The mouse antibody NT1 was raised against amino acids 1–20 of Cx43 at the Fred Hutchinson Cancer Research Center Hybridoma Development Facility (Seattle, WA).

Mouse Strains and Tissue Processing

Mice expressing a single allele of $Kras^{G12D}$ in the pancreas were generated as described previously (Hingorani et al. 2003). Animals were euthanized at the appropriate time points using an overdose of isofluorane followed by cervical dislocation and necropsies were performed. Pancreata were bisected laterally, one half was flash frozen and the other was fixed in 10 % neutral buffered formalin, paraffin embedded and processed for tissue sectioning.

Histology and Immunofluorescence

8 μm sections were analyzed by hematoxylin and eosin staining or immunofluorescence. For immunofluorescence experiments, deparaffinized sections underwent antigen retrieval in a solution of Tris/EDTA pH9.0, were blocked with 10 % normal goat serum (Sigma) and 1 % IgG-free BSA (Jackson Labs, Westgrove, PA). Slides were incubated with primary antibody overnight. Samples were then incubated with anti-rabbit secondary antibodies conjugated to AlexaFluor 635 or anti-mouse IgG2a conjugated to AlexaFluor 546 (Invitrogen, Carlsbad, CA), counterstained with DAPI (4′,6-diamidino-2-phenylindole) and mounted in ProLong Antifade (Invitrogen). Slides were analyzed using a Nikon Eclipse 80i bright field/fluorescence microscope and images collected with a Nikon DS-U1 color camera controlled with NIS Elements (Nikon, v3.1) software.

Immunoblotting

Frozen tissue was weighed and lysed with 5 volumes of lysis buffer [0.5 % deoxycholate, 0.5 % Triton X-100, 10 mM NaF, 1 mM Na_3VO_4, 5 % β-mercaptoethanol, 1 mM PMSF and 1× complete protease inhibitors (Roche Molecular Biochemicals, Alameda, CA) in TBS] and sonicated. We have found that tissue lysates, especially from tumor tissue, often contain large amounts of IgG that can make it difficult to resolve and detect Cx43 phosphoforms by SDS-PAGE. To minimize this effect tissue lysates were incubated with protein G agarose to remove IgG. Protein assays were performed on these clarified lysates and 100 μg loaded per sample. However, because the IgG content likely varied from animal to animal, it may be difficult to make direct comparisons of Cx43 levels across these samples. This depletion of IgG also allowed the use of anti-mouse secondary antibodies on mouse tissue. For the MDCK cell lysate control, cells were lysed directly in sample buffer. After sonication, samples were separated by sodium dodecylsulfate-10 % polyacrylamide gel electrophoresis (SDS-PAGE). After immunoblotting, protein was detected with rabbit and mouse primary antibodies. Primary antibodies were sequentially visualized with fluorescent dye-labeled secondary antibodies AlexaFluor 680 goat anti-rabbit (Invitrogen) followed by IRDye800-conjugated rabbit anti-mouse IgG_1 (Rockland Immunochemicals, Gilbertsville, PA) using the LI-COR Biosciences Odyssey infrared imaging system (Omaha, NE) and associated software.

Results

Cx43 Expression and Localization Change During Pancreatic Cancer Progression

Pancreata from wild-type (WT) mice are made up predominantly of acinar cells but ducts and vessels can be also be visualized by the distinct organization of nuclei when stained with DAPI. In Fig. 1, sections of pancreas from WT and K* mice are shown labeled with DAPI and an antibody to Cx43. In Fig. 1, a typical small duct in WT pancreas can be seen with the characteristic punctate gap junction signal for Cx43 on the basolateral side of the duct. The remaining panels show staining from pancreata of K* mice taken at 6, 12 and 16 months of age. Previous studies have shown there is a progressive loss of acinar cells and an increase in both number and grade of preinvasive lesions as these mice age (Hingorani et al. 2003). This is reflected in Fig. 1 by the organization of the DAPI labeled nuclei, where the glandular structures become more numerous and show increasing cellular and architectural atypia over time. These data also show Cx43 expression increasing during PDA progression. At 6 months, increased Cx43 expression can be found tightly associated with some, but not all, ducts on the basolateral membrane. For example, in the 6 months panel the duct on the right shows Cx43 puncta circumscribing the duct structure, while the one on the left shows very little Cx43 labeling. By 12 months Cx43 can be detected circumscribing many ducts but the association between Cx43 and ductal structures appear looser and less organized (Fig. 1, 12 months). This could reflect changes in the ducts as they become less organized during cancer progression or a change in the cell population expressing Cx43 as the stromal content evolves. By 16 months, Cx43 expression is higher, is much less organized and is found both in association with ducts (Fig. 1, 16 months, lower right) and in the surrounding stroma (Fig. 1, 16 months).

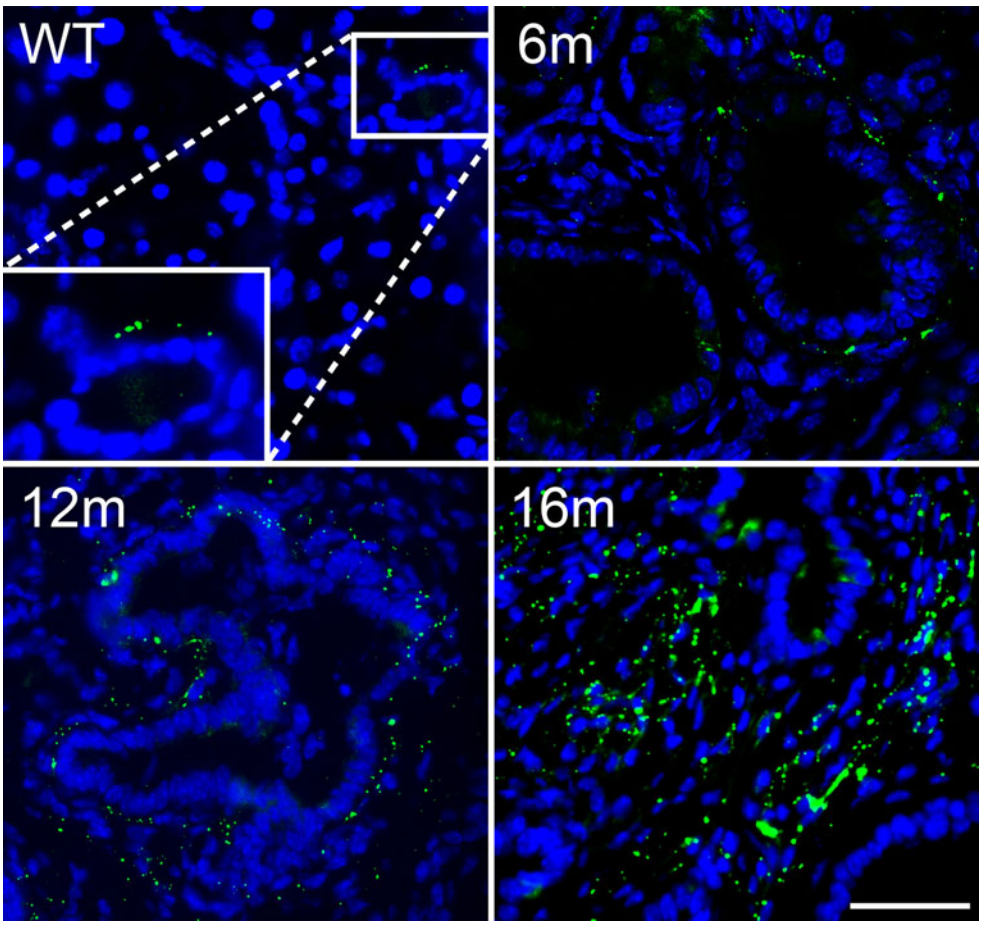

Fig. 1 Cx43 localization changes during PDA progression. Paraffin embedded sections of pancreas from normal (WT) and K* mice taken at 6, 12 and 16 months were colabeled with a rabbit antibody to total Cx43 (punctate signal) and DAPI (signal adjusted to appear *dull grey*). *Bar* is 50 μm

Cx43 Phosphorylation Changes During Pancreatic Cancer Progression

Cx43 normally migrates as several distinct bands that reflect the phosphorylation state of the protein; these are often named P0, P1, P2, etc., with P0 co-migrating with Cx43 that has been dephosphorylated with phosphatases (Musil et al. 1990). Immunoblots were probed with Cx43 antibodies to both the C and N-termini: Rb Cx43, a rabbit polyclonal antibody made to the C terminus and NT1, a mouse monoclonal antibody made to the N terminus. Use of two reliable Cx43 antibodies that yielded overlaying signal gave us confidence that the low signals we observed were, in fact, Cx43.

Expression was very low in WT pancreas though both Rb Cx43 and NT1 detected a faint doublet that may include the P0 form of Cx43 (Fig. 2, WT compared to cell lysate). At 6 months, pancreata from duplicate K* animals show Cx43 migrating as apparent P2, a phosphoisoform associated with functional junctions. At 12 and 16 months an even slower migrating form of Cx43 appears and is maintained. This slow migrating form is also found in the lysate from cells containing activated src, a condition associated with gap junction closure. The samples from the K* mice at 6–16 months shown in this immunoblot demonstrate considerable variation in the levels of Cx43. Because the K* mice need to develop subsequent mutations for tumor progression to proceed and these events are stochastic as demonstrated by their wide ranging lifespan, we believe that this variation in Cx43 expression could be related to the extent of cancer progression. We speculate that these changes in Cx43 phosphorylation and migration are associated with a functional change in gap junction communication between or amongst cancer and stromal cells.

Cx43 Expression Is Increasingly Heterogeneous and Associated with Stromal Cells During PDA Progression

As discussed above, PDA exhibits a distinct and robust stromal response containing a heterogeneous mixture of

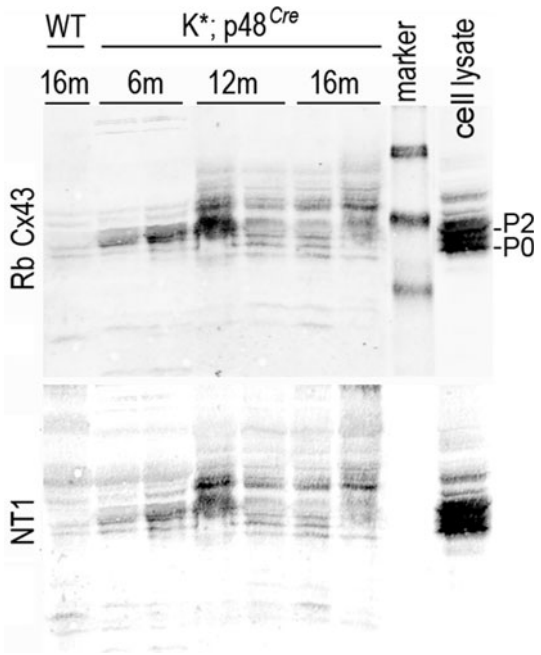

Fig. 2 Cx43 phosphorylation changes during PDA progression. Pancreatic tissue lysates from 1 normal (WT) mouse and 2 each K* mice taken at 6, 12, and 16 months were analyzed by SDS-PAGE and immunoblot. A lysate from MDCK cells expressing Cx43 and activated src is included as a control (cell lysate). Blots were probed with antibodies to the C terminus (Rb Cx43) and N terminus (NT1) of Cx43. Protein marker molecular weights (*from top*): 64, 50, and 38 kDa

immune and connective cells and extracellular material (Cubilla and Fitzgerald 1976; Hruban et al. 2001; Klimstra and Longnecker 1994; Tian et al. 2009). To examine which cells are making apparent gap junctions, we performed Cx43 immunofluorescence and hematoxylin and eosin staining on serial sections from pancreatic tissue harvested at 6 and 16 months. At 6 months Cx43 is closely associated with ducts (Fig. 3a), as described above, but hematoxylin and eosin staining indicates gap junctions are also closely associated with cells surrounding the precursor lesions (Fig. 3c, arrowheads). In 16 month-old animals, Cx43 expression is still found closely associated with some ducts (Fig. 3b, arrowheads) but is also highly expressed in the stroma, seemingly independent of the ducts. Figure 3e, f shows colabeling of tissue with antibodies to Cx43 in green and α-smooth muscle actin (SMA) in red. SMA is used as a marker for blood vessels and activated fibroblasts (Erkan et al. 2012), both of which could be expressing Cx43. In Fig. 3e, SMA clearly defines a blood vessel (arrow); we see little to no association with Cx43 with vessels while we do clearly see Cx43 circumscribing the adjacent duct. In Fig. 3f, SMA is likely marking activated fibroblasts surrounding the duct (arrowhead). Here Cx43 is found in stroma, seemingly independent of SMA staining. Further labeling and histology is required to more fully characterize these cells. One interesting question is whether these apparent gap junctions are being utilized for homocellular communication in the stroma or whether they are used for heterocellular communication, thus allowing interaction between the potential tumor cells and their surrounding environment.

Another question that arises is whether these Cx43 expressing stromal cells are the same cell type found adjacent to ductal cells in younger animals but that have proliferated and migrated or whether this represents a separate communication compartment active during this later stage of tumorigenesis. It is also possible that these cells are not engaged in gap junction communication; the immunoblot data indicates that much of Cx43 at this time point is a slow migrating isoform, which can be associated with closed channels. Further experiments are underway to examine these events.

Discussion

Progression of PDA results in a dramatic change in the cellular makeup of the pancreas. There is a loss of acinar cells with a concomitant increase in glandular epithelial cells and infiltration of connective and immune components, or stroma, which is a distinct feature of PDA. We show here that this shift is accompanied by an increase in expression of Cx43. Initially this increase in Cx43 expression is associated with ductal structures. Changes in the ducts have been well characterized through elaboration of histological (Cubilla and Fitzgerald 1976; Hruban et al. 2001; Klimstra and Longnecker 1994) and genetic mouse models (Hingorani et al. 2003). These models provide evidence that pancreas cancer evolves from definable precursor lesions (Hruban et al. 2000). These preinvasive lesions, collectively termed pancreatic intraepithelial neoplasias, or PanINs, were codified by an assembled working group of pathologists (Kern et al. 2001) into a system of classification originally proposed by Klimstra and Longnecker (1994). In this scheme, the lesions are divided into three discrete stages (PanIN-1, -2, and -3) characterized by increasing degrees of cellular and architectural atypia. It may be that the changes we see in Cx43 expression over time are associated with specific lesions or stages of PDA; to examine this idea a rigorous histological analysis of Cx43 localization is presently underway. Previous studies have indicated that Cx26 is overexpressed in human pancreatic cancer (Garcia-Rodriguez et al. 2011; Kyo et al. 2008). It will be interesting to confirm that this occurs in the mouse model and to compare the Cx26 expression profile to what we see with Cx43.

It is notable that PanIN lesions overexpress *ERBB2/HER2*, a member of the family of epidermal growth factor

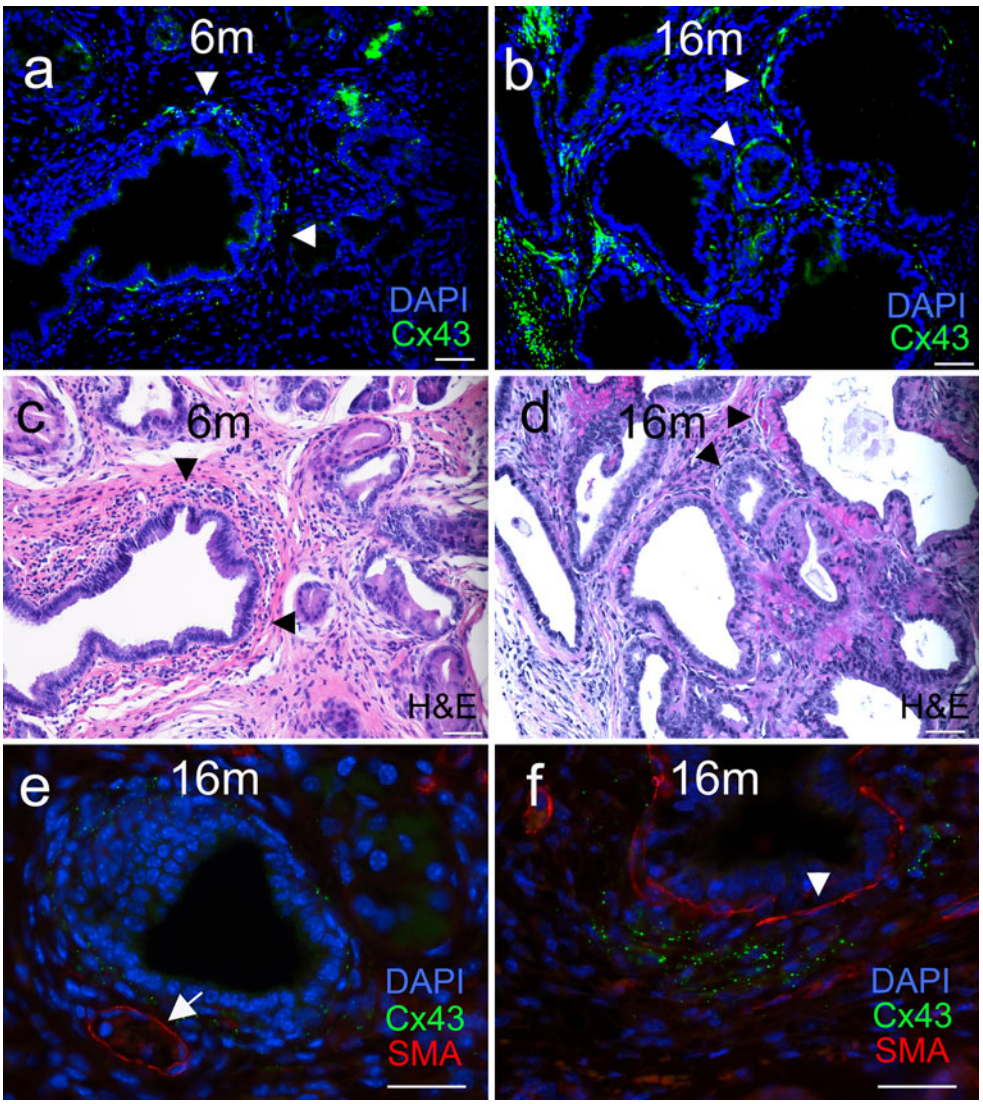

Fig. 3 Gap junctions become increasingly associated with the stroma during PDA progression. Serial paraffin-embedded sections from pancreas taken from K* mice at 6 months (**a**, **c**) and 16 months (**b**, **d**) were labeled with antibody to Cx43 (*green*) and DAPI (*blue*) (**a**, **b**) or hematoxylin and eosin (**c**, **d**). *Arrowheads* point to specific areas of Cx43 expression discussed in Results. **e**, **f** Pancreas tissue from a 16 month mouse was stained with antibodies to Cx43 (*green*) or SMA (*red*) (DAPI is in *blue*). The *arrow* in **e** points to a blood vessel and the *arrowhead* in **f** to a duct. *Bars* = 50 μm

receptors and exhibit increased levels of phosphorylated extracellular signal-related kinase (ERK) (Hingorani et al. 2005). We know that gap junction communication and connexin localization can be modulated via activation of ERK through growth factor stimulation (Kanemitsu and Lau 1993). We also know that a slow migrating isoform of Cx43, similar to that seen in the K* animals at 16 months, is associated with ERK activation. Given the localization of Cx43 at the apparent interface between PanINs and the stroma (Figs. 1 and 3) it is plausible that gap junctions may be regulated or even play a regulatory role in ERK activation.

At the later time points Cx43 expression increases both around the PanINs, where it seems to be expressed through multiple cell layers circumscribing these lesions and is also found increasingly in the stroma, seemingly independent of PanINs. This shift in expression also parallels the progression of PanINs to carcinoma and invasive stages suggesting that gap junctions may play a role in invasion and metastasis. It is possible that these patterns correspond to an epithelial cell-associated communication compartment that is permissive to invasion possibly through Cx43 mediated interaction with stromal cells. The lack of localization with SMA could support this. However, it is also possible that the stromal and PanIN-associated Cx43 expression represent two distinct and independent communication compartments. Several markers used to distinguish different cell types in PDA including those for

epithelial cells (cytokeratin 19), immune cells (CD45), and pancreatic stellate cells (smooth muscle actin and glial fibrillary acidic protein) (Erkan et al. 2012) will be useful to distinguish between these possibilities.

PDA, like other cancers, requires cells to alter not only cell autonomous features but also interactions with neighboring cells and tissue components—functions that connexins fulfill (Laird 2006). If Cx43 is indeed acting to regulate invasion and metastasis through interactions between epithelial tumor cells and the stroma, modulating these interactions could represent a viable therapeutic strategy.

Acknowledgments Supported in part by grants CA149554 and GM55632 from the National Institutes of Health.

Reference

Aguirre AJ, Bardeesy N, Sinha M, Lopez L, Tuveson DA, Horner J, Redston MS, DePinho RA (2003) Activated Kras and Ink4a/Arf deficiency cooperate to produce metastatic pancreatic ductal adenocarcinoma. Genes Dev 17:3112–3126

Allison DC, Piantadosi S, Hruban RH, Dooley WC, Fishman EK, Yeo CJ, Lillemoe KD, Pitt HA, Lin P, Cameron JL (1998) DNA content and other factors associated with ten-year survival after resection of pancreatic carcinoma. J Surg Oncol 67:151–159

Almoguera C, Shibata D, Forrester K, Martin J, Arnheim N, Perucho M (1988) Most human carcinomas of the exocrine pancreas contain mutant c-K-ras genes. Cell 53:549–554

Bailey JM, Swanson BJ, Hamada T, Eggers JP, Singh PK, Caffery T, Ouellette MM, Hollingsworth MA (2008) Sonic hedgehog promotes desmoplasia in pancreatic cancer. Clin Cancer Res 14:5995–6004

Brentnall TA, Lai LA, Coleman J, Bronner MP, Pan S, Chen R (2012) Arousal of cancer-associated stroma: overexpression of palladin activates fibroblasts to promote tumor invasion. PLoS One 7:e30219

Chen S-C, Pelletier DB, Ao P, Boynton AL (1995) Connexin43 reverses the phenotype of transformed cells and alters their expression of cyclin/cyclin dependent kinases. Cell Growth Differ 6:681–690

Cronier L, Crespin S, Strale PO, Defamie N, Mesnil M (2009) Gap junctions and cancer: new functions for an old story. Antioxid Redox Signal 11:323–338

Cubilla AL, Fitzgerald PJ (1976) Morphological lesions associated with human primary invasive nonendocrine pancreas cancer. Cancer Res 36:2690–2698

Erkan M, Reiser-Erkan C, Michalski CW, Kleeff J (2010) Tumor microenvironment and progression of pancreatic cancer. Exp Oncol 32:128–131

Erkan M, Adler G, Apte MV, Bachem MG, Buchholz M, Detlefsen S, Esposito I, Friess H, Gress TM, Habisch HJ, Hwang RF, Jaster R, Kleeff J, Kloppel G, Kordes C, Logsdon CD, Masamune A, Michalski CW, Oh J, Phillips PA, Pinzani M, Reiser-Erkan C, Tsukamoto H, Wilson J (2012) StellaTUM: current consensus and discussion on pancreatic stellate cell research. Gut 61:172–178

Fitzgerald DJ, Yamasaki H (1990) Tumor promotion: models and assay systems. Teratog Carcinog Mutagen 10:89–102

Garcia-Rodriguez L, Perez-Torras S, Carrio M, Cascante A, Garcia-Ribas I, Mazo A, Fillat C (2011) Connexin-26 is a key factor mediating gemcitabine bystander effect. Mol Cancer Ther 10:505–517

Hanna EA, Umhauer S, Roshong SL, Piechocki MP, Fernstrom MJ, Fanning JD, Ruch RJ (1999) Gap junctional intercellular communication and connexin43 expression in human ovarian surface epithelial cells and ovarian carcinomas in vivo and in vitro. Carcinogenesis 20:1369–1373

Hansel DE, Kern SE, Hruban RH (2003) Molecular pathogenesis of pancreatic cancer. Annu Rev Genomics Hum Genet 4:237–256

Hingorani SR, Petricoin EF, Maitra A, Rajapakse V, King C, Jacobetz MA, Ross S, Conrads TP, Veenstra TD, Hitt BA, Kawaguchi Y, Johann D, Liotta LA, Crawford HC, Putt ME, Jacks T, Wright CV, Hruban RH, Lowy AM, Tuveson DA (2003) Preinvasive and invasive ductal pancreatic cancer and its early detection in the mouse. Cancer Cell 4:437–450

Hingorani SR, Wang L, Multani AS, Combs C, Deramaudt TB, Hruban RH, Rustgi AK, Chang S, Tuveson DA (2005) Trp53R172H and KrasG12D cooperate to promote chromosomal instability and widely metastatic pancreatic ductal adenocarcinoma in mice. Cancer Cell 7:469–483

Hossain MZ, Wilkens LR, Mehta PP, Loewenstein WR, Bertram JS (1989) Enhancement of gap junctional communication by retinoids correlates with their ability to inhibit neoplastic transformation. Carcinogenesis 10:1743–1748

Hruban RH (2007) Tumors of the pancreas. In: Hruban RH, Pitman MB, Klimstra DS (eds) Atlas of tumor pathology. Armed Forces Institute of Pathology, Washington DC

Hruban RH, Wilentz RE, Kern SE (2000) Genetic progression in the pancreatic ducts. Am J Pathol 156:1821–1825

Hruban RH, Adsay NV, Albores-Saavedra J, Compton C, Garrett ES, Goodman SN, Kern SE, Klimstra DS, Kloppel G, Longnecker DS, Luttges J, Offerhaus GJ (2001) Pancreatic intraepithelial neoplasia: a new nomenclature and classification system for pancreatic duct lesions. Am J Surg Pathol 25:579–586

Hruban RH, Adsay NV, Albores-Saavedra J, Anver MR, Biankin AV, Boivin GP, Furth EE, Furukawa T, Klein A, Klimstra DS, Kloppel G, Lauwers GY, Longnecker DS, Luttges J, Maitra A, Offerhaus GJ, Perez-Gallego L, Redston M, Tuveson DA (2006) Pathology of genetically engineered mouse models of pancreatic exocrine cancer: consensus report and recommendations. Cancer Res 66:95–106

Jou Y-S, Layhe B, Matesic DF, Chang C-C, de Feijter AW, Lockwood L, Welsch CW, Klaunig JE, Trosko JE (1995) Inhibition of gap junctional intercellular communication and malignant transformation of rat liver epithelial cells by neu oncogene. Carcinogenesis 16:311–317

Kanemitsu MY, Lau AF (1993) Epidermal growth factor stimulates the disruption of gap junctional communication and connexin43 phosphorylation independent of 12-*O*-tetradecanoyl 13-acetate-sensitive protein kinase C: the possible involvement of mitogen-activated protein kinase. Mol Biol Cell 4:837–848

Kern S, Hruban R, Hollingsworth MA, Brand R, Adrian TE, Jaffee E, Tempero MA (2001) A white paper: the product of a pancreas cancer think tank. Cancer Res 61:4923–4932

Kihara K, Fukui I, Higashi Y, Oshima H (1990) Inhibitory effect of testosterone on gap junctional intercellular communication of human transitional cell carcinoma cell lines. Cancer Res 50:2848–2852

King TJ, Lampe PD (2004) Mice deficient for the gap junction protein Connexin32 exhibit increased radiation-induced tumorigenesis associated with elevated mitogen-activated protein kinase (p44/Erk1, p42/Erk2) activation. Carcinogenesis 25:669–680

King TJ, Fukushima LH, Hieber AD, Shimabukuro KA, Sakr WA, Bertram JS (2000) Reduced levels of connexin43 in cervical dysplasia: inducible expression in a cervical carcinoma cell line

decreases neoplastic potential with implications for tumor progression. Carcinogenesis 21:1097–1109

King TJ, Fukushima LH, Yasui Y, Lampe PD, Bertram JS (2002) Inducible expression of the gap junction protein connexin43 decreases the neoplastic potential of HT-1080 human fibrosarcoma cells in vitro and in vivo. Mol Carcinog 35:29–41

Klimstra DS, Longnecker DS (1994) K-ras mutations in pancreatic ductal proliferative lesions. Am J Pathol 145:1547–1550

Krutovskikh V, Mazzoleni G, Mironov N, Omori Y, Aguelon AM, Mesnil M, Berger F, Partensky C, Yamasaki H (1994) Altered homologous and heterologous gap-junctional intercellular communication in primary liver tumors associated with aberrant protein localization but not gene mutation of connexin 32. Int J Cancer 56:87–94

Kyo N, Yamamoto H, Takeda Y, Ezumi K, Ngan CY, Terayama M, Miyake M, Takemasa I, Ikeda M, Doki Y, Dono K, Sekimoto M, Nojima H, Monden M (2008) Overexpression of connexin 26 in carcinoma of the pancreas. Oncol Rep 19:627–631

Laird DW (2006) Life cycle of connexins in health and disease. Biochem J 394:527–543

Laird DW, Fistouris P, Batist G, Alpert L, Huynh HT, Carystinos GD, Alaoui-Jamali MA (1999) Deficiency of connexin43 gap junctions is an independent marker for breast tumors. Cancer Res 59:4104–4110

Lau AF, Kurata WE, Kanemitsu MY, Loo LWM, Warn-Cramer BJ, Eckhart W, Lampe PD (1996) Regulation of connexin43 by activated tyrosine protein kinases. J Bioenerg Biomembr 28:357–365

Loewenstein WR (1981) Junctional intercellular communication: the cell-to-cell membrane channel. Physiol Rev 61:829–913

Meda P, Pepper MS, Traub O, Willecke K, Gros D, Beyer E, Nicholson B, Paul D, Orci L (1993) Differential expression of gap junction connexins in endocrine and exocrine glands. Endocrinology 133:2371–2378

Moennikes O, Buchmann A, Ott T, Willecke K, Schwarz M (1999) The effect of connexin32 null mutation on hepatocarcinogenesis in different mouse strains. Carcinogenesis 20:1379–1382

Musil LS, Beyer EC, Goodenough DA (1990) Expression of the gap junction protein connexin43 in embryonic chick lens: molecular cloning, ultrastructural localization, and post-translational phosphorylation. J Membr Biol 116:163–175

Naus CC, Laird DW (2010) Implications and challenges of connexin connections to cancer. Nat Rev Cancer 10:435–441

Piechocki MP, Burk RD, Ruch RJ (1999) Regulation of connexin32 and connexin43 gene expression by DNA methylation in rat liver cells. Carcinogenesis 20:401–406

Pistorio AL, Ehrlich HP (2011) Modulatory effects of connexin-43 expression on gap junction intercellular communications with mast cells and fibroblasts. J Cell Biochem 112:1441–1449

Saez JC, Berthoud VM, Branes MC, Martinez AD, Beyer EC (2003) Plasma membrane channels formed by connexins: their regulation and functions. Physiol Rev 83:1359–1400

Serre-Beinier V, Le Gurun S, Belluardo N, Trovato-Salinaro A, Charollais A, Haefliger JA, Condorelli DF, Meda P (2000) Cx36 preferentially connects beta-cells within pancreatic islets. Diabetes 49:727–734

Siegel R, Naishadham D, Jemal A (2012) Cancer statistics, 2012. CA Cancer J Clin 62:10–29

Temme A, Buchman A, Babriel HC, Nelles E, Scharz M, Willecke K (1997) High incidence of spontaneous and chemically-induced liver tumors in mice deficient for connexin 32. Curr Biol 7:713–718

Theis M, Mas C, Doring B, Degen J, Brink C, Caille D, Charollais A, Kruger O, Plum A, Nepote V, Herrera P, Meda P, Willecke K (2004) Replacement by a lacZ reporter gene assigns mouse connexin36, 45 and 43 to distinct cell types in pancreatic islets. Exp Cell Res 294:18–29

Tian H, Callahan CA, DuPree KJ, Darbonne WC, Ahn CP, Scales SJ, de Sauvage FJ (2009) Hedgehog signaling is restricted to the stromal compartment during pancreatic carcinogenesis. Proc Natl Acad Sci USA 106:4254–4259

Trosko JE, Chang CC, Madhukar BV, Klaunig JE (1990) Chemical, oncogene, and growth factor inhibition of gap junctional intercellular communication: an integrative hypothesis of carcinogenesis. Pathobiology 58:265–278

Willecke K, Eiberger J, Degen J, Eckardt D, Romualdi A, Guldenagel M, Deutsch U, Sohl G (2002) Structural and functional diversity of connexin genes in the mouse and human genome. Biol Chem 383:725–737

Yamasaki H, Omori Y, Krutovskikh V, Zhu W, Mironov N, Yamakage K, Mesnil M (1999) Connexins in tumour suppression and cancer therapy. Novartis Found Symp 219:241–260

Yauch RL, Gould SE, Scales SJ, Tang T, Tian H, Ahn CP, Marshall D, Fu L, Januario T, Kallop D, Nannini-Pepe M, Kotkow K, Marsters JC, Rubin LL, de Sauvage FJ (2008) A paracrine requirement for hedgehog signalling in cancer. Nature 455:406–410

Yeo CJ, Cameron JL, Lillemoe KD, Sohn TA, Campbell KA, Sauter PK, Coleman J, Abrams RA, Hruban RH (2002) Pancreaticoduodenectomy with or without distal gastrectomy and extended retroperitoneal lymphadenectomy for periampullary adenocarcinoma, part 2: randomized controlled trial evaluating survival, morbidity, and mortality. Ann Surg 236:355–366

Zhang W, Couldwell WT, Simard MF, Song H, Lin JH, Nedergaard M (1999) Direct gap junction communication between malignant glioma cells and astrocytes. Cancer Res 59:1994–2003

J Membrane Biol (2012) 245:263–273
DOI 10.1007/s00232-012-9447-1

Cx36 Is a Target of Beta2/NeuroD1, Which Associates with Prenatal Differentiation of Insulin-producing β Cells

Rachel Nlend Nlend · Aouatef Aït-Lounis · Florent Allagnat · Valentina Cigliola · Anne Charollais · Walter Reith · Jacques-Antoine Haefliger · Paolo Meda

Received: 28 March 2012 / Accepted: 1 June 2012 / Published online: 23 June 2012

Abstract The insulin-producing β cells of pancreatic islets are coupled by connexin36 (Cx36) channels. To investigate what controls the expression of this connexin, we have investigated its pattern during mouse pancreas development, and the influence of three transcription factors that are critical for β-cell development and differentiation. We show that (1) the Cx36 gene (*Gjd2*) is activated early in pancreas development and is markedly induced at the time of the surge of the transcription factors that determine β-cell differentiation; (2) the cognate protein is detected about a week later and is selectively expressed by β cells throughout the prenatal development of mouse pancreas; (3) a 2-kbp fragment of the *Gjd2* promoter, which contains three E boxes for the binding of the bHLH factor Beta2/NeuroD1, ensures the expression of Cx36 by β cells; and (4) Beta2/NeuroD1 binds to these E boxes and, in the presence of the E47 ubiquitous cofactor, transactivates the *Gjd2* promoter. The data identify Cx36 as a novel early marker of β cells and as a target of Beta2/NeuroD1, which is essential for β-cell development and differentiation.

Keywords Beta2/neurod1 · Connexin · Gap junctions · Gene regulation · Pancreas · Promoter · Transcription factor

R. N. Nlend · V. Cigliola · A. Charollais · P. Meda (✉)
Department of Cell Physiology and Metabolism, University of Geneva, CMU, 1 rue Michel Servet CH- 1211, Geneva 4, Switzerland
e-mail: paolo.meda@unige.ch

A. Aït-Lounis
Laboratory of Cellular and Molecular Biology, University of Algiers, USTHB, BP32 El-Alia, Bab Ezzouar, Algiers, Algeria

F. Allagnat · J.-A. Haefliger
Department of Internal Medicine, University of Lausanne, Bugnon 7A, 1005 Lausanne, Switzerland

W. Reith
Department of Pathology and Immunology, University of Geneva, CMU, 1 rue Michel Servet CH- 1211, Geneva 4, Switzerland

The insulin-producing β cells of pancreatic islets are coupled by Cx36 channels (Serre-Beinier et al. 2000; Theis et al. 2004). Although a previous report has documented how this connexin is repressed in most cell types (Martin et al. 2003), the mechanism that accounts for the consistent expression of Cx36 in β cells, neurons and neuron-derived cells (Bosco et al. 2011; Potolicchio et al. 2012) has not yet been investigated. In view of the changes in Cx36 distribution and levels which take place in different areas of the developing brain, and which correlate with critical differentiation steps of neuronal networks (Cina et al. 2007; Gulisano et al. 2000), we hypothesized that important insights about the obligatory expression of Cx36 in β cells could be gained by establishing the expression profile of the protein, as a function of the initiation, differentiation and growth of β cells (Herrera 2000), as well as the subsequent morphogenesis of pancreatic islets (Kim and MacDonald 2002). Therefore, we have studied the temporal and spatial expression of Cx36 during the pre- and postnatal development of the mouse pancreas. To this end, we used real-time PCR to evaluate the transcription of the Cx36 gene (*Gjd2*), and immunofluorescence to investigate the expression of the cognate protein during the development of mouse pancreas.

In view of the tight correlation between the expression of *Gjd2* and the two insulin genes (Carvalho et al. 2010; Serre-Beinier et al. 2009), we also hypothesized that the

expression of Cx36 may be controlled by the same set of transcription factors that regulate β-cell differentiation and function (Kim and MacDonald 2002; Habener et al. 2005; Murtaugh 2007; Jonsson et al. 1994; Naya et al. 1997; Zhang et al. 2005). Given the restricted distribution of Cx36 (Bosco et al. 2011; Potolicchio et al. 2012), we further posited that the expression of Cx36 was likely to be controlled by transcription factor or factors involved in the differentiation and function of both pancreatic β cells (Zhang et al. 2005) and neurons (Cho and Tsai 2004). Therefore, we investigated the effects on Cx36 expression of several transcription factors involved in pancreatic development (Herrera 2000; Kim and MacDonald 2002; Habener et al. 2005). To this end, we used a luciferase reporter system to test different regions of the *Gjd2* promoter, chromatin immunoprecipitation assays to evaluate the binding of Beta2/NeuroD1 to this promoter, and cell transfections, as well as site-directed mutagenesis, to assess the effects of Beta2/NeuroD1 on Cx36 expression. The data show that *Gjd2* is (1) expressed early in the development of the mouse pancreas, as reported in the chicken (Berthoud et al. 2004), and in a recent report (Pérez-Armendariz et al. 2012) published since the submission of this study; (2) encodes the cognate Cx36 protein at the time of the second wave of β-cell differentiation; (3) is a hitherto nonidentified target of Beta2/NeuroD1, which controls its expression by direct binding to the *Gjd2* promoter.

Materials and Methods

Animals

Adult C57Bl/6 mice (Charles Rivers, Lyon, France) were mated, and coupling confirmed by the presence of a vaginal plug on the next morning (E0.5). Embryos were then obtained from pregnant females at E11.5, E13.5, E15.5, and E17.5. Control mice were also sacrificed at stages P0 and P2, and after 1–2 months of life.

Histology

Cryostat sections (5-µm thickness) of pancreas were fixed for 10 min in 4 % paraformaldehyde (PFA) supplemented with 0.1 % Triton X-100. Sections were then incubated 30 min in 0.1 M phosphate-buffered saline (PBS) supplemented with 2 % BSA, and exposed for 2 h at room temperature to one of the following primary antibodies: rabbit polyclonal antibody anti-Cx36 (Zymed 36-4600), diluted 1/50; guinea pig polyclonal antibody anti-insulin (Ventrex Bioreagent 4043580), diluted 1/200; mouse monoclonal antibody anti-glucagon (Sigma G2654), diluted 1/2000. After rinsing, the sections were reacted with one of the following secondary antibodies, whichever appropriate: mouse anti-rabbit IgGs (Boehringer) conjugated to fluorescein isothiocyanate, diluted 1/400; goat anti guinea pig IgGs conjugated to rhodamine, diluted 1/200; goat anti-mouse IgGs conjugated to rhodamine (Boehringer), diluted 1/200. Immunolabeling was visualized under UV illumination.

RT-PCR

Total RNA was extracted from control mouse liver using Trizol (Invitrogen), and from pancreas (E11.5-P0) using the RNeasy micro kit (Qiagen), as recommended by the manufacturers. RNA of adult pancreas was extracted as previously reported (Serre-Beinier et al. 2000; Carvalho et al. 2010). Briefly, samples were exposed to 4 M guanidine isothiocyanate in the presence of 2 M β-mercaptoethanol and 2.5 mM Tris-HCl, layered on a 228 mM CsCl/0.1 M EDTA cushion (pH 7.4), and centrifuged at 35,000 rpm for 20 h at 20 °C. Pelleted RNA was resuspended in 10 mM Tris-HCl containing 5 mM EDTA and 0.1 % SDS. Samples were extracted three times with phenol–chloroform–isoamyl alcohol, and precipitated in ethanol. The dried pellets were resuspended in DEPC-H_2O and stored at −80 °C. Total RNA from Min6, INS1-E, and HeLa cells was extracted using Trizol (Invitrogen), as recommended by the manufacturer. The RNA quality was controlled using a laser Agilent 2100 bioanalyser. A total of 1 µg (standard PCR) or 750 ng (quantitative PCR) total RNA were reverse-transcribed using 200 U Reverse transcriptase Superscript II (Invitrogen), 10 ng/µl random hexamer primers (Promega) and 500 µM each dNTP mix (Invitrogen). The mixture was heated to 65 °C for 5 min and quickly chilled on ice. First strand buffer (5×), 10 mM dithiothreitol and 200 U Superscript II Reverse transcriptase were then added (all reagents purchased from Invitrogen). The samples were heated at 25 °C for 10 min, at 42 °C for 50 min and at 70 °C for a 15 min inactivation. 0.5 U RNase H (Roche) was then added for 20 min at 37 °C.

For real-time PCR, we used a 1:10 (cell lines)–1:16 (tissues) dilution of the cDNA in a mix containing 2× QuantiTect SYBR Green PCR Master Mix (1×; Qiagen) and 300 nM each primer. The amplification protocol consisted of a 10-min initial activation of the Taq polymerase at 95 °C, 40 cycles of denaturation at 95 °C for 15 s, and annealing at 65 °C for 1 min. The following primers were used: for Cx36, 5′-GAC CAT CTT GGA GAG GCT GC-3′ (F) and 5′-ACC ACC ACA GTC AAC AGG ATC C-3′ (R); for insulin2, 5′-GCA GGA AGC CTA TCT TCC AGG-3′ (F) and 5′-GGA CTC CCA GAG GAA GAG CAG-3′ (R); for Beta2/NeuroD1, 5′-ACG CAG AAG GCA AGG TGT C-3′ (F) and 5′-CCG CTC TCG CTG TAT

GAT TT-3′ (R); for Neurogenin3, 5′-AGA ACT AGG ATG GCG CCT CA-3′ (F) and 5′-GTG GCT AGG TGG GGT GGA A-3′ (R); for PDX1, 5′-AAG AGC CCA ACC GCG TC-3′ (F) and 5′-GTG TAA GCA CCT CCT GCC CA-3′ (R); for Cx32, 5′-AGT GCC AGG GAG GTG TGA AT-3′ (F) and 5′-ACA GCC ATA CTC GGC CAA T-3′ (R); for connexin43 (Cx43), 5′-ACT TTC ATT AAG TGA AAG AGA GGT GCC-3′ (F) and 5′-GCC GTC GAG TAG GCT TGG AG-3′ (R); for RSP9, 5′-GAC CAG GAG CTA AAG TTG ATT GGA-3′ (F) and 5′-TCT TGG CCA GGG TAA ACT TGA-3′ (R); for HPRT, 5′-GCT CGA GAT GTC ATG AAG GAG AT-3′ (F) and 5′-AAG AAC TTA TAG CCC CCC TTG A-3′ (R). A melting curve was run at the end of the 40 cycles to test for the presence of a unique PCR reaction product, using the following protocol: 95 °C for 15 s, 60 °C for 1 min and 95 °C for 15 s. The PCR was performed using the 7900HT PCR system (Applied Biosystem). mRNA levels were normalized to those of the two ubiquitous genes *HPRT* and *RPS9*. The stable expression of these control genes in our samples was assessed using the Genorm software.

Bioinformatics

The sequences of mouse, rat and human Cx36 genes were compared using the multi-LAGAN function of the LAGAN Alignment Toolkit Web site (http://lagan.stanford.edu/lagan_web/ index.shtml). Conservation of response elements for Beta2/NeuroD1 was assessed using the Genomatix software (http://www.genomatix.de).

Cloning and Constructs

A −4,946/+485 fragment of *Gjd2* (the transcription start site being referred to as +1) was isolated from the mouse genomic library RP23-230H3 (Invitrogen), and cloned into a pGL3b luciferase reporter vector (Promega). A −2,010/−12 fragment was cloned in plasmid pCR4 (Invitrogen), and used as source of the promoter region. To this end, a *Sna*bI/*Xho*I fragment (−1,524/+474) of pCR4 was amplified by PCR using the Platinum Pfx DNA Polymerase (Invitrogen) and primers 5′-CTA TAC GTA GAA TCA CCG TCC CAT CTG TC-3′ (F) and 5′- CCG CTC GAG GGA GGC AGC AGA CAA AGA CT-3′ (R). The PCR product was first subcloned in TOPO vector pCR2.1 (Invitrogen), before being excised with SacI and XbaI, and inserted by ligation (T4 DNA ligase, Promega) into the reporter vector pGL3b (Promega), upstream of a cDNA coding for luciferase. Using the −1,524/+474 fragment as substrate, and primers 5′-AGA GTG CGG GAG TCC ATC-3′ (F) and 5′-CCG CTC GAG GGA GGC AGC AGA CAA AGA CT-3′ (R), we then generated a +192/+474 fragment, which was also subcloned in TOPO vector pCR2.1 (Invitrogen), excised with KpnI and XhoI, and inserted by ligation (T4 DNA ligase, Promega) into the reporter vector pGL3b (Promega), upstream of a cDNA coding for luciferase. Expression vectors for Beta2/NeuroD1 (pCMV-BETA2), its E47 coactivator (pCR3.1-E47) and the RIPE3 sequence (pINSCAT448) were generously provided by Dr. H. Suh-Kim (Kyonggi University, South Korea).

The mutated constructs 2Kb-E1m, 2Kb-E2m, and 2Kb-E3m were generated using as substrate the −2,010/−12 promoter construct, and the QuikChange Multi Site Directed Mutagenesis Kit (Stratagene), following the instructions of the manufacturer. The primers used for each construct were: for 2 Kb-E1 m, 5′-CGC GGG AGC GCT GGG TGC CCG CTC CAG TGA-3′ (F) and 5′ TCA CTG GAG CGG GCA CCC AGC GCT CCC GCG-3′ (R); for 2 Kb-E2 m, 5′-GCA GGA GCT CGG CTG CCT GCA CGC TGC C-3′ (F) and 5′-GGC AGC GTG CAG GCA GCC GAG CTC CTG C-3′ (R); for 2 Kb-E3 m, 5′-AGA CTG CGG GAG TCT GTC TGA CCC CCG G- 3′ (F) and 5′-CCG GGG GTC AGA CAG ACT CCC GCA GTC T-3′ (R).

Cell Culture

MIN6 and HeLa cells were grown at 37 °C, under 5 % CO_2, in Dulbecco's modified Eagle's medium (DMEM), containing 110 U/ml penicillin, 110 µg/ml streptomycin, and either 5 mM glucose plus 10 % heat-inactivated fetal calf serum (HeLa cells) or 25 mM glucose plus 15 % heat-inactivated FCS and 70 µM β-mercaptoethanol (MIN6 cells). INS-1E cells were grown at 37 °C, under 5 % CO_2, in RPMI-1640 medium containing L-glutamine, 10 mM Hepes, 5 % heat-inactivated fetal calf serum, 100 mM Na-Pyruvate, 5 mM β-mercapto-ethanol, 110 U/ml penicillin, and 110 µg/ml streptomycin

Transfection

Aliquots of 10^5 Min6, 10^5 INS1-E cells or 8×10^4 HeLa cells were plated per well in 12-well plates. The next day, cells were transfected using the Polyfect reagent (Qiagen), as per the manufacturer instructions. Each of the reporter pGL3b plasmids (1 µg) coding for a different Cx36 promoter fragment, was individually transfected with or without the plasmid pCMV-BETA2 (1 µg) coding for Beta2/NeuroD1, and plasmid pCR3.1-E47 (140 ng) coding for the E47 cofactor. In all experiments, 0.1 µg vector pRL-TK (Promega) coding for *Renilla* luciferase was cotransfected with these plasmids, to allow for a normalization of the firefly luciferase activity induced by the promoter reporter constructs. In each experiment, the total DNA amount was adjusted to the same level using an empty pCDNA.3 plasmid (Invitrogen).

Luciferase Assay

Two days after transfection, cells were lysed in PLB, and the activities of firefly (induced by the various pGL3b vectors) and Renilla luciferase (induced by the pRL-TK vector), were monitored using the Dual-luciferase reporter assay kit (Promega), as per the manufacturer instructions. To compare the basal activity of the various *Gjd2* fragments in the different cell lines, results are presented as mean + SEM luciferase activity, normalized to that of the Renilla reporter. To compare the Beta2/NeuroD1 regulation of the *Gjd2* fragments in each cell line, we assessed luciferase activity of cells cotransfected with plasmid pCMV-BETA2 (coding for Beta2/NeuroD1), and plasmid pCR3.1-E47 (coding for the E47 cofactor) or only with a control empty vector. Data are shown as means + SEM, normalized to the luciferase activity of the respective promoter fragment, which was transfected with the empty vector.

Chromatin Immunoprecipitation (ChIP) Assay

ChIP was performed as previously described (Masternak et al. 2003). Briefly, crosslinked chromatin was prepared by exposing 4×10^7 Min 6 cells to 1 % formaldehyde for 8 min at room temperature. Crosslinking was stopped by the addition of 0.2 M glycine. The cells were then lysed in TE buffer (10 mM Tris-HCl, 1 mM EDTA, pH 8) containing protease inhibitors and 0.5 % NP-40. Nuclei were pelleted and lysed in TE containing 0.5 M NaCl, 1 % Triton X-100 and 0.5 % sodium deoxycholate. Crosslinked chromatin was resuspended in TE buffer supplemented with 100 mM NaCl, sheared by sonication, and cleared by two successive centrifugations, first at 4,000 rpm for 10 min and then at 13,000 rpm for 15 min. One aliquot of 10 µg sheared chromatin was saved for the input, while another 10-µg aliquot was used for immunoprecipitation at 4 °C overnight, using 2 µg rabbit polyclonal antibody against NeuroD1 (Abgent AP2021b). The immune complexes were captured at room temperature using protein A-Sepharose beads (GE Healthcare Biosciences).The immunoprecipitated chromatin fragments were eluted for 10 min at 65 °C with 100 mM Tris-HCl containing 1 % SDS (pH 8), digested for 2 h at 42 °C with 150 µg/ml Proteinase K, and incubated overnight at 65 °C to reverse the crosslinks. After extraction with phenol-chloroform and chloroform, DNA was precipitated with isopropanol in the presence of glycogen, washed in 75 % ethanol and resuspended in 50 µl TE buffer. The immunoprecipitated DNA and the input chromatin DNA were analyzed by qPCR using a SYBR-Green kit (Eurogentec) and the following primers: for the Cx36 promoter, 5′-CCTCAGACCGCAA GATCG-3′ (F) and 5′-TGG GGG AAG CAA TCT ATG TG-3′ (R); for the insulin promoter, 5′-TGT TGA CGT CCA ATG AGC GCT TTC-3′ (F) and 5′-TA G GTC AGC AGA TGG CCA GAG G-3′ (R); for TG737, 5′- GCC AAG GCT ACA CAA GAC-3′ (F) and 5′-CAC CAG TGC TTC CGA TTC-3′ (R). A standard curve was generated with the input chromatin, and binding of Beta2/NeuroD1 to the Cx36 promoter was evaluated relative to that of the same transcription factor to the insulin promoter, which was used as positive control.

Statistical Analysis

Student's *t* tests were used for statistical analysis throughout the study. p values <0.05 were considered as statistically significant.

Results

Gjd2 Transcription Starts during Early Pancreas Development and Changes at Selected Time Points

To determine the temporal pattern of Cx36 expression, we amplified RNA extracted from the pancreas of wild type mice, age E11.5 onward. Real-time quantitative PCR showed that the levels of Cx36 mRNA increased ($p < 0.005$) 12-fold between E11.5 and E15.5, and by a further 1.6-fold ($p < 0.01$) from E15.5 to P0 (Fig. 1a). Thereafter, these levels apparently decreased (Fig. 1a) as a result of the dilution of the endocrine transcripts in the total pancreas extracts, as a result of the explosive, postnatal expansion of the exocrine pancreas. This was confirmed by the postnatal 3.5 increase in Cx32, a connexin isoform expressed by the acinar cells of pancreas (Fig. 1a). The mRNA levels of this connexin, as well as those of the Cx43 isoform, which is expressed in the nonendocrine and non-acinar compartments of the pancreas, featured an expression pattern quite different from that of Cx36, during both pre- and postnatal development of pancreas (Fig. 1a).

The first peak of Cx36 expression occurred at the prenatal time (E15.5) of the so called "secondary transition" (Pictet et al. 1972), during which β cells massively differentiate, as revealed by increased transcription of the insulin gene (*Ins;* Fig. 1b). The second peak of Cx36 expression (P0) also occurred at the time of increased transcription of *Ins,* which reached adult levels within the first 2 days of neonatal life (Fig. 1b). Quantitative PCR further showed that the increase in Cx36 expression between E13.5 and E15.5 coincided with that of Beta2/NeuroD1, PDX1 (Fig. 1b) and Ngn3 (data not shown), three transcription factors which are obligatory for proper pancreas development and β-cell function (Itkin-Ansari et al. 2005; Naya et al. 1995; Offield et al. 1996).

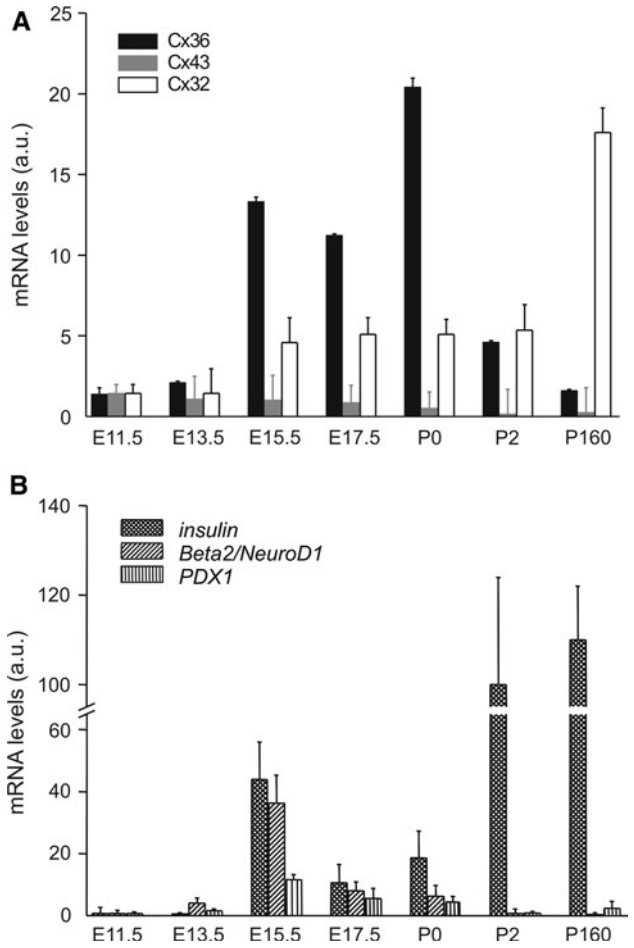

Fig. 1 *Gjd2* transcription is detected in early pancreas development, and changes at selected time points. **a** Real-time PCR showed that the levels of the Cx36 mRNA (*solid columns*) increased sharply between E13.5 and E15.5, and at birth (P0), in contrast to those of both Cx43 (*grey bars*) and Cx32 transcript (*open bars*). **b** Prenatal and neonatal increase in the levels of the insulin mRNA (*cross-hatched bars*) was coincident with that of Cx36 mRNA (*solid bars* in **a**). The increased transcription of Cx36 between E13.5 and E15.5 (*solid bars* in **a**) was also coincident with that of Beta2/NeuroD1 (*diagonally hatched bars*) and PDX1 (*vertically hatched bars*). Bars represent the mean + SEM fold change in mRNA level, relative to the level evaluated at E11.5; $n = 4$ for E13.5–E17.5; $n = 5$ for E11.5 and P times

Thereafter, the levels of these factors decreased up to the adult age (Fig. 1b) as a result of the increasing growth of the exocrine tissue. These experiments show that the expression of Cx36 is initiated during early pancreas development, and follows a temporal pattern which is different from that of other connexins and which is initiated at the time the expression of the insulin gene and of major β-cell transcription factors surges.

To identify the cell types expressing Cx36, we immunostained the pancreas of control C57Bl6 mice. No Cx36 was detected in the pancreas of E11.5, E13.5, and E15.5 mice, when few cells contained detectable levels of either insulin (Fig. 2) or glucagon (data not shown). Later on, Cx36 spots were found on insulin-containing (Fig. 2), but were never observed in glucagon-containing cells (data not shown). These experiments show that Cx36 is expressed during the early development of the mouse pancreas, and later becomes a specific attribute of β cells.

A Fragment of the *Gjd2* Promoter Ensures the Specific Expression of Cx36 in Insulin-producing Cells

To unravel the mechanism controlling the expression of Cx36, we generated luciferase reporter plasmids coding for fragments of the *Gjd2* promoter, and transiently transfected lines of the insulin-producing Min6 and INS1-E cells, as well as the nonendocrine line of HeLa cells. When compared to the void vector, the 282-bp promoter fragment induced a similar increase ($p < 0.001$) in luciferase activity in the three cell types (Fig. 3a). The 2- and 5-kbp fragments also significantly increased ($p < 0.001$) luciferase activity over that seen in cells transfected with the void vector (Fig. 3a). However, this effect was significantly larger ($p < 0.01$) in the two insulin-producing lines than in HeLa cells (Fig. 3a). The results indicate that the 2-kbp fragment of the *Gjd2* promoter is sufficient to ensure a specific expression of Cx36 in insulin-producing cells, and that the region comprised between −2,010 and −294 bp contains elements that regulate its expression level.

In silico analysis identified in this region three E boxes with a CANNTG sequence characteristic of cis-elements binding bHLH factors (Sommer et al. 1996; Robinson et al. 2000), which were referred to as E1, E2 and E3, at position −280, −332, and −445, respectively (Fig. 3b). Comparison of the sequences of these E boxes of mouse, rat and human *Gjd2,* showed a highly conservation of the canonic CANNTG sequence, especially in E1 and E3 (Fig. 3c).

A Fragment of the *Gjd2* Promoter Binds Beta2/NeuroD1, Which Transactivates Cx36 Expression

Beta2/NeuroD1 is a bHLH transcription factor central to the development and differentiation of both β cells (Herrera 2000; Itkin-Ansari et al. 2005; Naya et al. 1995a; Offield et al. 1996; Sommer et al. 1996; Robinson et al. 2000; Naya et al. 1994, 1995) and neurons (Masternak et al. 2003; Lee 1995, 1997; Liu et al. 2000; Poulin et al. 1997), which binds to E boxes to regulate the expression of the insulin gene (*Ins;* Itkin-Ansari et al. 2005; Naya et al. 1995). To test whether Beta2/NeuroD1 also binds to *Gjd2* promoter, we run chromatin immunoprecipitation assays on Min6 cells. We first validated the protocol by assessing the immunoprecipitated chromatin using primers for the promoter of *Ins* (Fig. 4a) which, thereafter, was used as normalization standard. Relative to this standard, the binding of Beta2/NeuroD1 to the region of the *Gjd2*

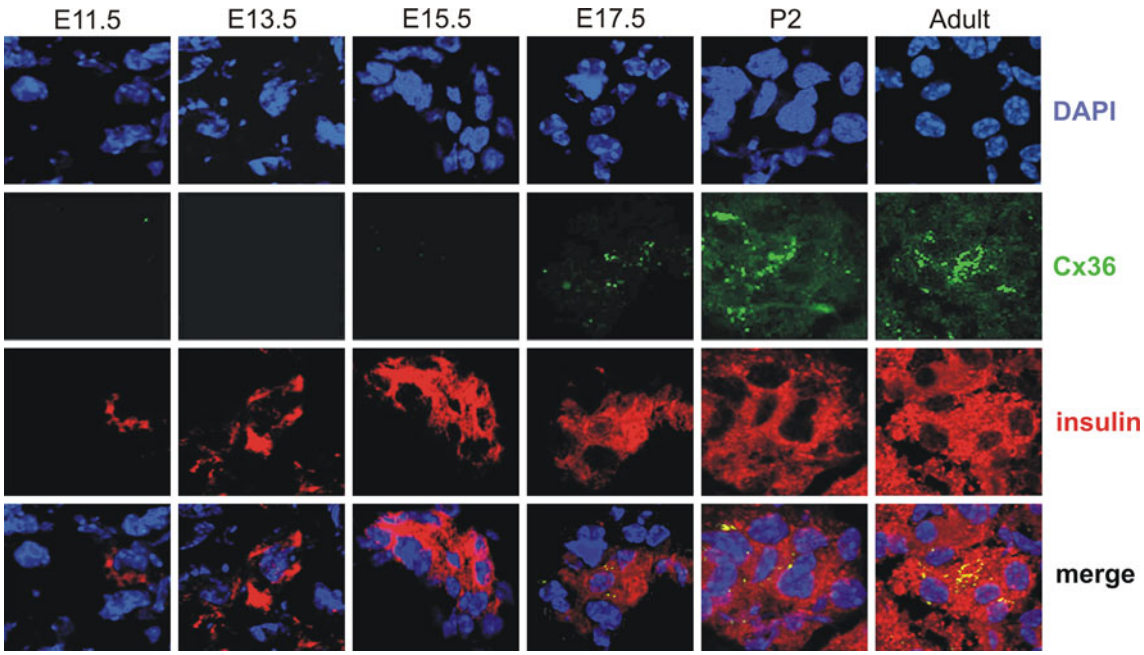

Fig. 2 The Cx36 protein is detected in β cells during late pancreas development. The same area of a control mouse pancreas is shown after staining of cell nuclei (DAPI, *blue*), Cx36 (*green*), and insulin (*red*). Cx36 was immunodetected from E17.5 onward and showed a punctate distribution only in insulin-containing β cells (*red*). *Bars* 15 μm

promoter that contained E boxes represented 43 ± 15 % (Fig. 4a). This binding was significantly higher ($p < 0.05$) than the nonspecific binding of the transcription factor to either a downstream region of the *Gjd2* promoter or to a region of the promoter of the unrelated *TG737,* which served as negative controls (Fig. 4a). The results show that Beta2/NeuroD1 specifically binds to the region of the *Gjd2* promoter containing the three E boxes.

To investigate whether this binding modulated the expression of Cx36, we cotransfected Beta2/NeuroD1, together with the ubiquitous cofactor E47 which is required for its activity (Qiu et al. 2002; Mirasierra and Vallejo 2006; Kim et al. 2002; Docherty et al. 2005), and one of the 5.4-kbp, 2-kbp, or 282-bp *Gjd2* promoter constructs (Fig. 4a) in Min6, INS1-E and HeLa cell lines. Although the former two insulin-producing cell types natively express Beta2/NeuroD1, the latter does not (Fig. 4b) and thus provided for a negative control. The parallel transfection of the RIPE3-luc construct, which contained three multimerized copies of the E box of the rat *Ins* promoter upstream of a luciferase reporter sequence (Kim et al. 2002; Henderson and Stein 1994), provided for a positive control. Relative to the basal luciferase activity observed in cells that had not been transfected with Beta2/NeuroD1 and E47, cells transfected for these factors plus the void pGL3b vector did not show a change in luciferase activity (Fig. 4c). In contrast, transfection of the RIPE3 construct resulted in a significant increase ($p < 0.01$) in luciferase activity in the three cell types (Fig. 4c). Under these conditions, which validated the experimental protocol, the 282-bp fragment of *Gjd2,* which contained the E3 box, did not significantly modify the luciferase activity (Fig. 4c). In contrast, this activity was significantly increased ($p < 0.005$) over basal values after transfection of either the 2-kbp or the 5.4-kbp fragments of *Gjd2,* which contained the E1, E2 and E3 boxes (Fig. 4c). These results show that Beta2/NeuroD1 transactivates the promoter of *Gjd2* via cis-elements of the 5.4-kbp and the 2-kbp fragments, possibly E1 and E2.

To test the role of these sequences, each of the three E boxes was mutated by scrambling the consensus core sequence CANNTG in the 2-kbp fragment of the *Gjd2* promoter, which was chosen because it provided for the largest effect of Beta2/NeuroD1 (Fig. 4c). Thus, four mutated versions of the 2-kbp promoter were constructed, three carrying a single mutated E box and one carrying a combined mutation of the three E boxes (Fig. 4d). The mutated constructs were then tested in INS1-E and HeLa cells after cotransfection with Beta2/NeuroD1 and E47. Compared to the luciferase activity of the wild-type 2-kbp construct, the activity observed after mutation of E1 was significantly reduced ($p < 0.05$), whereas that observed after a mutation of either E2 or E3 had a minimal effect (Fig. 4d). The effect of the E1 mutation was larger ($p < 0.005$) in the presence of a concurrent mutation of E2 and E3 (Fig. 4d). The results indicate that Beta2/NeuroD1 transactivates *Gjd2* via the native E boxes of its promoter.

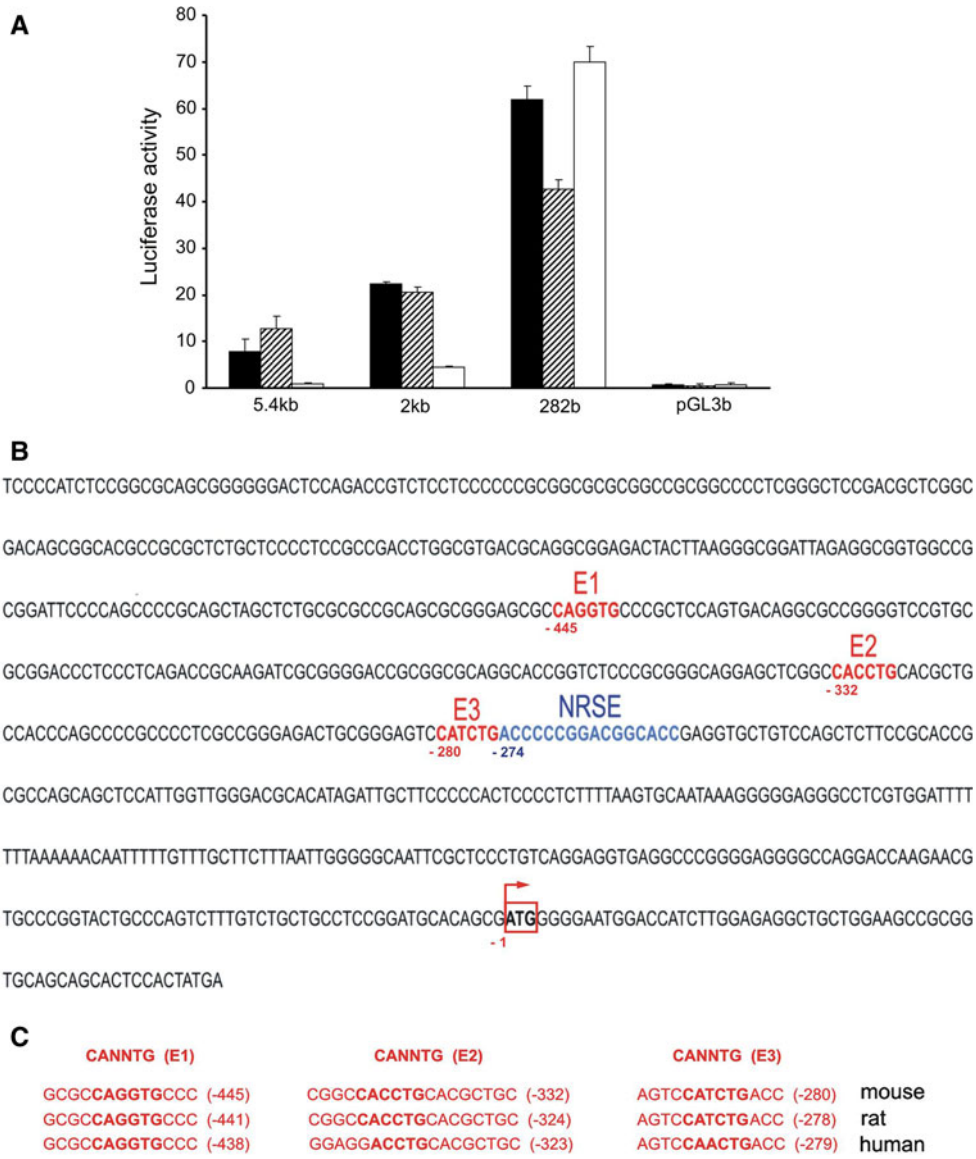

Fig. 3 A promoter fragment ensures the specific expression of *Gjd2* in insulin-producing cells. **a** Three fragments of the *Gjd2* promoter were transiently transfected, using a luciferase reporter plasmid. The 282-bp fragment increased luciferase activity over that provided by an empty pGL3b vector in MIN6 (*solid bars*), INS1E (*hatched bars*), and HeLa cells (*open bars*). The 2-kbp and 5-kbp constructs induced a smaller increase, which was restricted to the insulin-producing MIN6 and INS1E cells. Values are mean + SEM of 3 experiments and are shown after normalization to the luciferase activity observed in cells transfected with pRL-TK. **b** The partial sequence of the *Gjd2* promoter shows the position (relative to that of the translation start site, which is referred to as +1) of the 3 E boxes (*red*). The previously identified NRSE (Martin et al. 2003) is shown in *blue*. **c** Alignment of the mouse, rat, and human Cx36 promoters shows the conservation of the consensus CANNTG sequence of the 3 E boxes

Discussion

We have investigated the pattern of Cx36 expression during pancreas development and the differentiation of pancreatic β cells. Our data confirm that *Gjd2* is transcribed during the early prenatal development of pancreas (Berthoud et al. 2004; Pérez-Armendariz et al. 2012), before the first wave of β cells can be detected (Theis et al. 2004; Herrera 2000; Berthoud et al. 2004; Pérez-Armendariz et al. 2012). Using antibodies, we have further shown that Cx36 becomes detectable at later stages of the prenatal pancreas development, but only in cells containing immunodetectable insulin. Cx36 largely increases in these cells during the neonatal period, when β cells acquire their major differentiation characteristic, i.e. the ability to recognize circulating glucose as a stimulus for insulin secretion (Gulisano et al. 2000; Herrera 2000; Carvalho et al. 2010, 2012). This evolution is consistent with the previous findings that Cx36 is required for the proper functioning of differentiated islets (Ravier et al. 2005; Speier et al. 2007; Klee et al. 2011), and provides the first clue that this requirement actually precedes the functional maturation of these microorgans. Strikingly, immunolabeling showed no association between Cx36 and the glucagon-containing α-cells, extending previous biochemical, immunological and functional observations (Serre-Beinier et al. 2000; Theis et al. 2004; Bosco et al. 2011; Kim and MacDonald 2002), which indicated that, throughout rodent life, Cx36 expression and signalling are solely restricted to the β-cell lineage.

The initial surge of *Gjd2* occurred at the time (E13.5–E15.5), the first wave of β cells is induced (Herrera 2000; Kim and MacDonald 2002; Habener et al. 2005), as evidenced by the concomitant induction of the insulin gene.

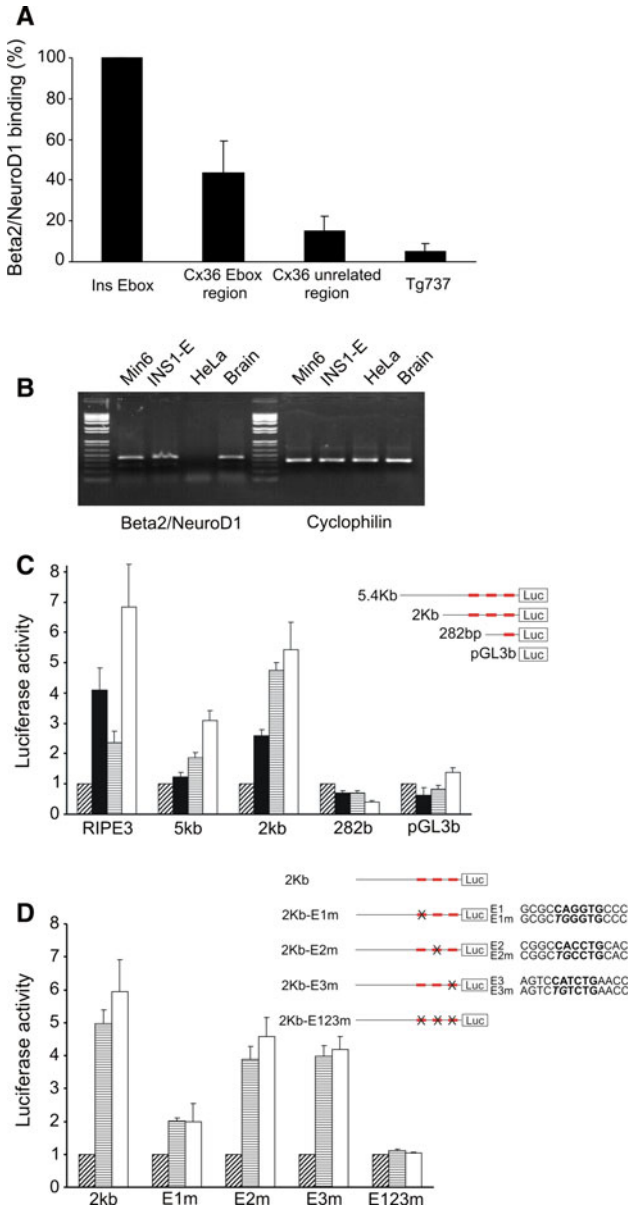

◀ **Fig. 4** Beta2/NeuroD1 binds to E boxes and transactivates the *Gjd2* promoter. **a** DNA of Min6 cells was immunoprecipitated using antibodies to Beta2/NeuroD1, then amplified by qPCR. Beta2/NeuroD1 bound to the region of the *Gjd2* promoter containing the E boxes more than to a Gjd2 region devoid of E boxes and to the unrelated *Tg737* promoter. Data are mean + SEM from 3 independent experiments and are expressed relative to the binding of Beta2/NeuroD1 to the *Ins* promoter, which served as positive control. **b** RT-PCR showed the native expression of Beta2/NeuroD1 in MIN6 and INS1E cells, but not in HeLa cells. Brain served as positive control. **c** After transient cotransfection with Beta2/NeuroD1 and E47, the 282-bp fragment of the *Gjd2* promoter did not increase luciferase activity of Min6 (*solid bars*), INS1-E (*horizontally hatched bars*), and HeLa cells (*open bars*), over the basal level observed in nontransfected cells (*obliquely hatched bars*), whereas the 2-kbp and the 5.4-kbp fragments did. The RIPE3 and the void pGL3B plasmids served as positive and negative controls, respectively. Values are mean + SEM of 3 experiments and are expressed relative to the luciferase activity observed in cells transfected with pRL-TK. **d** After transient cotransfection with Beta2/NeuroD1 and E47, the 2-kbp fragment of *Gjd2* increased the luciferase activity of INS1-E cells (*horizontally hatched bars*) and HeLa cells (*open bars*) over the basal level observed in nontransfected cells (*obliquely hatched bars*). This effect was decreased after mutation of E1, blocked after the combined mutation of the 3 E boxes, but unaffected after mutation of either E2 or E3. Values are mean + SEM luciferase activity of 3 experiments, relative to the basal luciferase activity evaluated in the absence of exogenous Beta2/NeuroD1 (*obliquely hatched bars*)

This coincidence was not observed for either Cx32 or Cx43, showing that the pattern of Cx36 expression is specifically controlled at key moments of β-cell development. In turn, this timing suggests that Cx36 may be implicated in this development and/or be regulated by the very same transcription factors that determine pancreas differentiation. Quantitative PCR indeed documented that the prenatal *Gjd2* expression increases at the same time of the expression surge of the major transcription factors which contribute to the specification and differentiation of pancreatic β cells (Herrera 2000; Kim and MacDonald 2002; Habener et al. 2005). Previous studies have shown that the RE-1 silencing transcription factor (REST) prevents the expression of *Gjd2* in non-insulin-producing and nonneuronal cells (Martin et al. 2003; Hohl and Thiel 2005). However, no transcription factor was so far identified as a transactivator of the expression of this gene. Our data show that a 2-kbp region of mouse *Gjd2* contains cis-regulatory elements that are sufficient to determine the expression of Cx36 in insulin-producing cells. We further document that this region allows for the binding of the transcription factor Beta2/NeuroD1 to a specific E box (E1) of the *Gjd2* promoter. In the presence of its coactivator E47, Beta2/NeuroD1 transfection resulted in the transactivation of this promoter, which was potentiated by the two close-by E2 and E3 boxes. The extent of the transactivation of the 2-kbp and 5.4-kbp fragments induced by Beta2/NeuroD1 was lower in the insulin-producing cells than in the unrelated HeLa cells, suggesting that endogenous Beta2/NeuroD1 resulted in a higher basal transcriptional activity of *Gjd2* in the former cell type. Consistent with this hypothesis, mutation of E1 resulted in loss of the *Gjd2* transactivation dependent on the expression of transfected Beta2/NeuroD1, but not of the basal activity of the Cx36 promoter in INS-1E cells (data not shown). This finding implies that multiple factors converge to regulate the expression of the Cx36 gene in insulin-producing cells, as is the case for the insulin gene *Ins,* which is selectively regulated by the combinatorial effect of Beta2/NeuroD1, PDX1, and MafA transcription factors (Aramata et al. 2005). The *Gjd2* promoter contains putative binding sites for PDX1 (data not shown). However, these sites are not highly conserved, in spite of the consistent β cells expression of Cx36 in all species so far investigated

(Serre-Beinier et al. 2000; Theis et al. 2004; Pérez-Armendariz et al. 2012; Le Gurun et al. 2003), raising concerns that they may be dispensable for Cx36 expression.

An implication of these results is that some of the effects attributable to Beta2/NeuroD1 signaling, which has been shown to be essential for the terminal differentiation and survival of the β cells (Habener et al. 2005; Naya et al. 1995a), may be mediated by Cx36. The validation of this tentative conclusion awaits further studies on the molecular mechanism linking the timely related changes in the expression of these two proteins. Strikingly, mice lacking Beta2/NeuroD1 die around birth, with severe diabetes, ketoacidosis (Naya et al. 1997), and neuronal alterations (Miyata et al. 1999). Future studies should therefore evaluate whether altered Cx36 expression may be implicated in these defects. The previous reports that mice lacking this connexin show altered β-cell function (Carvalho et al. 2010; Ravier et al. 2005; Speier et al. 2007; Klee et al. 2011; Wellershaus et al. 2008) is consistent with this view. The observation that these animals do not feature major alterations in the development of islets and β-cell differentiation (Ravier et al. 2005; Klee et al. 2011; Wellershaus et al. 2008; Degen et al. 2004) only indicates that Cx36 is but one of the many actors that participate in the complex regulation of islet development and β-cell function (MacDonald 2007; MacDonald and Rorsman 2007). Thus, loss of Cx36 signaling may be compensated by other mechanisms, as documented in neurons (Cummings et al. 2008). The key importance of Beta2/NeuroD1 in pancreas development and function is further stressed by the observations that mutations inactivating the Beta2/NeuroD1 gene cause one of the rare monogenic forms of diabetes, referred to as MODY6 (Malecki et al. 1999), and that several variants of this gene confer susceptibility to the much more frequent type I and type II forms of diabetes (Iwata et al. 1999; Malecki et al. 2003; Yamada et al. 2001). The mechanism linking the genetic mutations to the various forms of the disease remains unknown. However, together with the reports that mice lacking Cx36 develop structurally normal islets which cannot sustain normal insulin secretion (Ravier et al. 2005; Speier et al. 2007; Klee et al. 2011; Wellershaus et al. 2008; Head et al. 2012; Meda 2012), the clinical data implicate that the predominant effect of the regulation of Cx36 expression by Beta2/NeuroD1 is likely on the function, rather than on the mass of the insulin-producing β cells (Martin et al. 2003; Bosco et al. 2011; Head et al. 2012; Meda 2012).

Acknowledgments Our team is supported by Grants from the Swiss National Science Foundation (310000-141162, IZ73Z0_127935, CR32I3_129987), the Juvenile Diabetes Research Foundation (40-2011-11, 5-2012-281), and the European Union (BETAIMAGE 222980; IMIDIA C2008-T7, BETATRAIN 289932). We are pleased to dedicate this study to Ross G. Johnson on occasion of the starting of his new life. Ross has been a pioneer in our field, a passionate and influential scholar, and a much appreciated host while Paolo was striving in snowy Minneapolis. We wish him all the best for a new exciting adventure.

Reference

Aramata S, Han SI, Yasuda K, Kataoka K (2005) Synergistic activation of the insulin gene promoter by the beta-cell enriched transcription factors MafA, Beta2, and Pdx1. Biochim Biophys Acta 1730:41–46

Berthoud VM, Singh R, Minogue PJ, Ragsdale CW, Beyer EC (2004) Highly restricted pattern of connexin36 expression in chick somite development. Anat Embryol 209:11–18

Bosco D, Haefliger JA, Meda P (2011) Connexins: key mediators of endocrine function. Physiol Rev 91:1393–1445

Carvalho CP, Barbosa HC, Britan A, Santos-Silva JC, Boschero AC, Meda P, Collares-Buzato CB (2010) Beta cell coupling and connexin expression change during the functional maturation of rat pancreatic islets. Diabetologia 53:1428–1437

Carvalho CP, Oliveira RB, Britan A, Silva-Santos JC, Boschero AC, Meda P, Collares-Buzato CB (2012) Impaired beta-to-beta cell coupling mediated by Cx36 gap junctions in pre-diabetic mice. Am J Physiol Endocrinol Metab 302 (in press)

Cho JH, Tsai MJ (2004) The role of BETA2/NeuroD1 in the development of the nervous system. Mol Neurobiol 30:35–47

Cina C, Bechberger JF, Ozog MA, Naus CC (2007) Expression of connexins in embryonic mouse neocortical development. J Comp Neurol 504:298–313

Cummings DM, Yamazaki I, Cepeda C, Paul DL, Levine MS (2008) Neuronal coupling via connexin36 contributes to spontaneous synaptic currents of striatal medium-sized spiny neurons. J Neurosci Res 86:2147–2158

Degen J, Meier C, Van Der Giessen RS, Sohl G, Petrasch-Parwez E, Urschel S, Dermietzel R, Schilling K, De Zeeuw CI, Willecke K (2004) Expression pattern of lacZ reporter gene representing connexin36 in transgenic mice. J Comp Neurol 473:511–525

Docherty HM, Hay CW, Ferguson LA, Barrow J, Durward E, Docherty K (2005) Relative contribution of PDX-1, MafA and E47/beta2 to the regulation of the human insulin promoter. Biochem J 389:813–820

Gulisano M, Parenti R, Spinella F, Cicirata F (2000) Cx36 is dynamically expressed during early development of mouse brain and nervous system. Neuroreport 11:3823–3828

Habener JF, Kemp DM, Thomas MK (2005) Minireview: transcriptional regulation in pancreatic development. Endocrinology 146:1025–1034

Head WS, Orseth ML, Nunemaker CS, Satin LS, Piston DW, Benninger RK (2012) Connexin-36 gap junctions regulate in vivo first- and second-phase insulin secretion dynamics and glucose tolerance in the conscious mouse. Diabetes 61 (in press)

Henderson E, Stein R (1994) c-jun inhibits transcriptional activation by the insulin enhancer, and the insulin control element is the target of control. Mol Cell Biol 14:655–662

Herrera PL (2000) Adult insulin- and glucagon-producing cells differentiate from two independent cell lineages. Development 127:2317–2322

Hohl M, Thiel G (2005) Cell type-specific regulation of RE-1 silencing transcription factor (REST) target genes. Eur J Neurosci 22:2216–2230

Itkin-Ansari P, Marcora E, Geron I, Tyrberg B, Demeterco C, Hao E, Padilla C, Ratineau C, Leiter A, Lee JE, Levine F (2005) NeuroD1 in the endocrine pancreas: localization and dual function as an activator and repressor. Dev Dyn 233:946–953

Iwata I, Nagafuchi S, Nakashima H, Kondo S, Koga T, Yokogawa Y, Akashi T, Shibuya T, Umeno Y, Okeda T, Shibata S, Kono S, Yasunami M, Ohkubo H, Niho Y (1999) Association of polymorphism in the NeuroD/BETA2 gene with type 1 diabetes in the Japanese. Diabetes 48:416–419

Jonsson J, Carlsson L, Edlund T, Edlund H (1994) Insulin-promoter-factor 1 is required for pancreas development in mice. Nature 371:606–609

Kim SK, MacDonald RJ (2002) Signaling and transcriptional control of pancreatic organogenesis. Curr Opin Genet Dev 12:540–547

Kim JW, Seghers V, Cho JH, Kang Y, Kim S, Ryu Y, Baek K, Aguilar-Bryan L, Lee YD, Bryan J, Suh-Kim H (2002) Transactivation of the mouse sulfonylurea receptor I gene by BETA2/NeuroD. Mol Endocrinol 16:1097–1107

Klee P, Allagnat F, Pontes H, Cederroth M, Charollais A, Caille D, Britan A, Haefliger JA, Meda P (2011) Connexins protect mouse pancreatic β cells against apoptosis. J Clin Invest 121: 4870–4879

Le Gurun S, Martin D, Formenton A, Maechler P, Caille D, Waeber G, Meda P, Haefliger JA (2003) Connexin-36 contributes to control function of insulin-producing cells. J Biol Chem 278: 37690–37697

Lee JE (1997) NeuroD and neurogenesis. Dev Neurosci 19:27–32

Lee JE, Hollenberg SM, Snider L, Turner DL, Lipnick N, Weintraub H (1995) Conversion of Xenopus ectoderm into neurons by NeuroD, a basic helix-loop-helix protein. Science 268:836–884

Liu M, Pereira FA, Price SD, Chu MJ, Shope C, Himes D, Eatock RA, Brownell WE, Lysakowski A, Tsai MJ (2000) Essential role of Beta2/NeuroD1 in development of the vestibular and auditory systems. Genes Dev 14:2839–2854

MacDonald MJ (2007) Synergistic potent insulin release by combinations of weak secretagogues in pancreatic islets and INS-1 cells. J Biol Chem 282:6043–6052

MacDonald PE, Rorsman P (2007) The ins and outs of secretion from pancreatic beta-cells: control of single-vesicle exo- and endocytosis. Physiology (Bethesda) 22:113–121

Malecki MT, Jhala US, Antonellis A, Fields L, Doria A, Orban T, Saad M, Warram JH, Montminy M, Krolewski AS (1999) Mutations in NEUROD1 are associated with the development of type 2 diabetes mellitus. Nat Genet 23:323–328

Malecki MT, Cyganek K, Klupa T, Sieradzki J (2003) The Ala45Thr polymorphism of Beta2/NeuroD1 gene and susceptibility to type 2 diabetes mellitus in a Polish population. Acta Diabetol 40: 109–111

Martin D, Tawadros T, Meylan L, Abderrahmani A, Condorelli DF, Waeber G, Haefliger JA (2003) Critical role of the transcriptional repressor neuron-restrictive silencer factor in the specific control of connexin36 in insulin-producing cell lines. J Biol Chem 278:53082–53089

Masternak K, Peyraud N, Krawczyk M, Barras E, Reith W (2003) Chromatin remodeling and extragenic transcription at the MHC class II locus control region. Nat Immunol 4:132–137

Meda P (2012) The in vivo β-to-β-cell chat room: connexin connections matter. Diabetes 61 (in press)

Mirasierra M, Vallejo M (2006) The homeoprotein Alx3 expressed in pancreatic beta-cells regulates insulin gene transcription by interacting with the basic helix-loop-helix protein E47. Mol Endocrinol 20:2876–2889

Miyata T, Maeda T, Lee JE (1999) NeuroD is required for differentiation of the granule cells in the cerebellum and hippocampus. Genes Dev 13:1647–1652

Murtaugh LC (2007) Pancreas and beta-cell development: from the actual to the possible. Development 134:427–438

Naya FJ, Stellrecht CM, Tsai MJ (1994) Tissue-specific regulation of the insulin gene by a novel basic helix-loop-helix transcription factor. Genes Dev 9:1009–1919

Naya FJ, Stellrecht CM, Tsai MJ (1995) Tissue-specific regulation of the insulin gene by a novel basic helix-loop-helix transcription factor. Genes Dev 9:1009–1019

Naya FJ, Huang HP, Qiu Y, Mutoh H, DeMayo FJ, Leiter AB, Tsai MJ (1997) Diabetes, defective pancreatic morphogenesis, and abnormal enteroendocrine differentiation in BETA2/neuroD-deficient mice. Genes Dev 11:2323–2334

Offield MF, Jetton TL, Labosky PA, Ray M, Stein RW, Magnuson MA, Hogan BL, Wright CV (1996) PDX-1 is required for pancreatic outgrowth and differentiation of the rostral duodenum. Development 122:983–995

Pérez-Armendariz EM, Cruz-Miguel L, Coronel-Cruz C, Esparza-Aguilar M, Pinzon-Estrada E, Rancaño-Camacho E, Zacarias-Climaco G, Olivares PF, Espinosa AM, Becker I, Sáez JC, Berumen J, Pérez-Palacios G (2012) Connexin 36 is expressed in beta and connexins 26 and 32 in acinar cells at the end of the secondary transition of mouse pancreatic development and increase during fetal and perinatal life. Anat Rec 295:980–990

Pictet RL, Clark WR, Williams RH, Rutter WJ (1972) An ultrastructural analysis of the developing embryonic pancreas. Dev Biol 29:436–467

Potolicchio I, Cigliola V, Velazquez-Garcia S, Klee P, Valjevac A, Kapic D, Cosovic E, Lepara O, Hadzovic-Dzuvo A, Mornjacovic Z, Meda P (2012) Connexin-dependent signaling in neurohormonal systems. Biochim Biophys Acta 1818:1919–1936

Poulin G, Turgeon B, Drouin J (1997) NeuroD1/beta2 contributes to cell-specific transcription of the proopiomelanocortin gene. Mol Cell Biol 17:6673–6682

Qiu Y, Guo M, Huang S, Stein R (2002) Insulin gene transcription is mediated by interactions between the p300 coactivator and PDX-1, BETA2, and E47. Mol Cell Biol 22:412–420

Ravier MA, Guldenagel M, Charollais A, Gjinovci A, Caille D, Sohl G, Wollheim CB, Willecke K, Henquin JC, Meda P (2005) Loss of connexin36 channels alters beta-cell coupling, islet synchronization of glucose-induced Ca^{2+} and insulin oscillations, and basal insulin release. Diabetes 54:1798–1807

Robinson KA, Koepke JI, Kharodawala M, Lopes JM (2000) A network of yeast basic helix-loop-helix interactions. Nucleic Acids Res 28:4460–4466

Serre-Beinier V, Le Gurun S, Belluardo N, Trovato-Salinaro A, Charollais A, Haefliger JA, Condorelli DF, Meda P (2000) Cx36 preferentially connects beta-cells within pancreatic islets. Diabetes 49:727–734

Serre-Beinier V, Bosco D, Zulianello L, Charollais A, Caille D, Charpantier E, Gauthier BR, Diaferia GR, Giepmans BN, Lupi R, Marchetti P, Deng S, Buhler L, Berney T, Cirulli V, Meda P (2009) Cx36 makes channels coupling human pancreatic beta-cells, and correlates with insulin expression. Hum Mol Genet 18:428–439

Sommer L, Ma Q, Anderson DJ (1996) Neurogenins, a novel family of atonal-related bHLH transcription factors, are putative mammalian neuronal determination genes that reveal progenitor cell heterogeneity in the developing CNS and PNS. Mol Cell Neurosci 8:221–241

Speier S, Gjinovci A, Charollais A, Meda P, Rupnik M (2007) Cx36-mediated coupling reduces beta-cell heterogeneity, confines the stimulating glucose concentration range, and affects insulin release kinetics. Diabetes 56:1078–1086

Theis M, Mas C, Doring B, Degen J, Brink C, Caille D, Charollais A, Kruger O, Plum A, Nepote V, Herrera P, Meda P, Willecke K (2004) Replacement by a lacZ reporter gene assigns mouse connexin36, 45 and 43 to distinct cell types in pancreatic islets. Exp Cell Res 294:18–29

Wellershaus K, Degen J, Deuchars J, Theis M, Charollais A, Caille D, Gauthier B, Janssen-Bienhold U, Sonntag S, Herrera P, Meda P, Willecke K (2008) A new conditional mouse mutant reveals

specific expression and functions of connexin36 in neurons and pancreatic beta-cells. Exp Cell Res 314:997–1012

Yamada S, Motohashi Y, Yanagawa T, Maruyama T, Kasuga A, Hirose H, Matsubara K, Shimada A, Saruta T (2001) NeuroD/beta2 gene G→A polymorphism may affect onset pattern of type 1 diabetes in Japanese. Diabetes Care 24:1438–1441

Zhang C, Moriguchi T, Kajihara M, Esaki R, Harada A, Shimohata H, Oishi H, Hamada M, Morito N, Hasegawa K, Kudo T, Engel JD, Yamamoto M, Takahashi S (2005) MafA is a key regulator of glucose-stimulated insulin secretion. Mol Cell Biol 25: 4969–4976

J Membrane Biol (2012) 245:275–281
DOI 10.1007/s00232-012-9448-0

Connexin43 Cardiac Gap Junction Remodeling: Lessons from Genetically Engineered Murine Models

Benjamin F. Remo · Steven Giovannone · Glenn I. Fishman

Received: 28 March 2012 / Accepted: 1 June 2012 / Published online: 22 June 2012

Abstract Sudden cardiac death is responsible for several hundred thousand deaths each year in the United States. Multiple lines of evidence suggest that perturbation of gap junction expression and function in the heart, or what has come to be known as cardiac gap junction remodeling, plays a key mechanistic role in the pathophysiology of clinically significant cardiac arrhythmias. Here we review recent studies from our laboratory using genetically engineered murine models to explore mechanisms implicated in pathologic gap junction remodeling and their proarrhythmic consequences, with a particular focus on aberrant posttranslational phosphorylation of connexin43.

Keywords Arrhythmia · Connexins · Gap junctions · Mouse model · Phosphorylation

Connexins and Gap Junctions

Connexins comprise a family of proteins encoded by as many as 20 genes in most mammalian species (Willecke et al. 2002). Substantial experimental evidence has demonstrated that connexins oligomerize into channels, which are organized into arrays at the gap junction. Channels formed from single connexin isoforms (homomeric/homotypic channels) have distinct biophysical properties, which can most easily be studied in heterologous expression systems (Harris 2001). Characteristic biophysical parameters include such properties as unitary conductance, voltage dependence, as well as size and charge selectivity (Spray and Burt 1990; Spray et al. 1992). There is also evidence that individual connexin isoforms may mix and match to form complex heteromeric and/or heterotypic channels; these more complex assemblies may have biophysical properties that differ from those formed from only a single connexin isoform (Harris 2001). Indeed, this molecular diversity is postulated to provide a mechanism for physiological diversity and regulation (Giovannone et al. 2011; Kanno and Saffitz 2001). Importantly, this combinatorial complexity may be directly relevant to understanding the pathophysiology of gap junctions, as aberrant regulation and/or mutations of a single connexin isoform may exert dominant effects on alternative connexin isoforms.

B. F. Remo · S. Giovannone · G. I. Fishman (✉)
Leon H. Charney Division of Cardiology, New York University School of Medicine, 522 First Avenue, Smilow 801, New York, NY 10016, USA
e-mail: glenn.fishman@nyumc.org

Gap Junction Remodeling and Arrhythmogenesis

There is compelling experimental evidence linking abnormalities in gap junctions with a highly proarrhythmic substrate (reviewed in Severs et al. 2008). These data include pathologic studies of hearts from patients with a broad assortment of acquired arrhythmic syndromes including ischemic and hypertrophic cardiomyopathies, inherited diseases such as arrhythmogenic right ventricular cardiomyopathy (ARVC) (Saffitz 2009; Severs 2002; Severs et al. 2004, 2006, 2008), human genetic studies of patients with somatic (Gollob et al. 2006; Thibodeau et al. 2010) or germ line (Paznekas et al. 2003) mutations in connexin genes, as well as genetically engineered murine models created by our own group (Gutstein et al. 2001) and others (van Rijen et al. 2004). Indeed, in recent years a growing body of literature suggests that gap junction remodeling represents a "final common pathway"

predisposing to arrhythmias in response to diverse pathologic insults to the heart. The mechanistic relationship between gap junction remodeling and the increased propensity for arrhythmic activity is multifactorial (Kanno and Saffitz 2001). Abnormal localization and/or gating of intercellular channels disturbs the highly orchestrated temporal and spatial pattern of cardiac excitation, with slow and oftentimes heterogeneous conduction conducive to reentrant activity. Heterogeneous gap junction remodeling may also enhance the dispersion of repolarization (Poelzing et al. 2004), another highly proarrhythmic factor.

Genetically Engineered Murine Models

The carboxyl-terminus of Cx43 contains numerous sites that are subject to posttranslational phosphorylation and these modifications are thought to regulate virtually all aspects of the Cx43 life cycle, including translation, trafficking, degradation, and gating, as reviewed in (Lampe and Lau 2000, 2004; Solan and Lampe 2009). Altered phosphorylation of Cx43 has been observed in response to a variety of pathologic stimuli, including acute ischemia (Beardslee et al. 2000), hypoxic stress (Matsushita et al. 2006), rapid pacing (Akar et al. 2007)

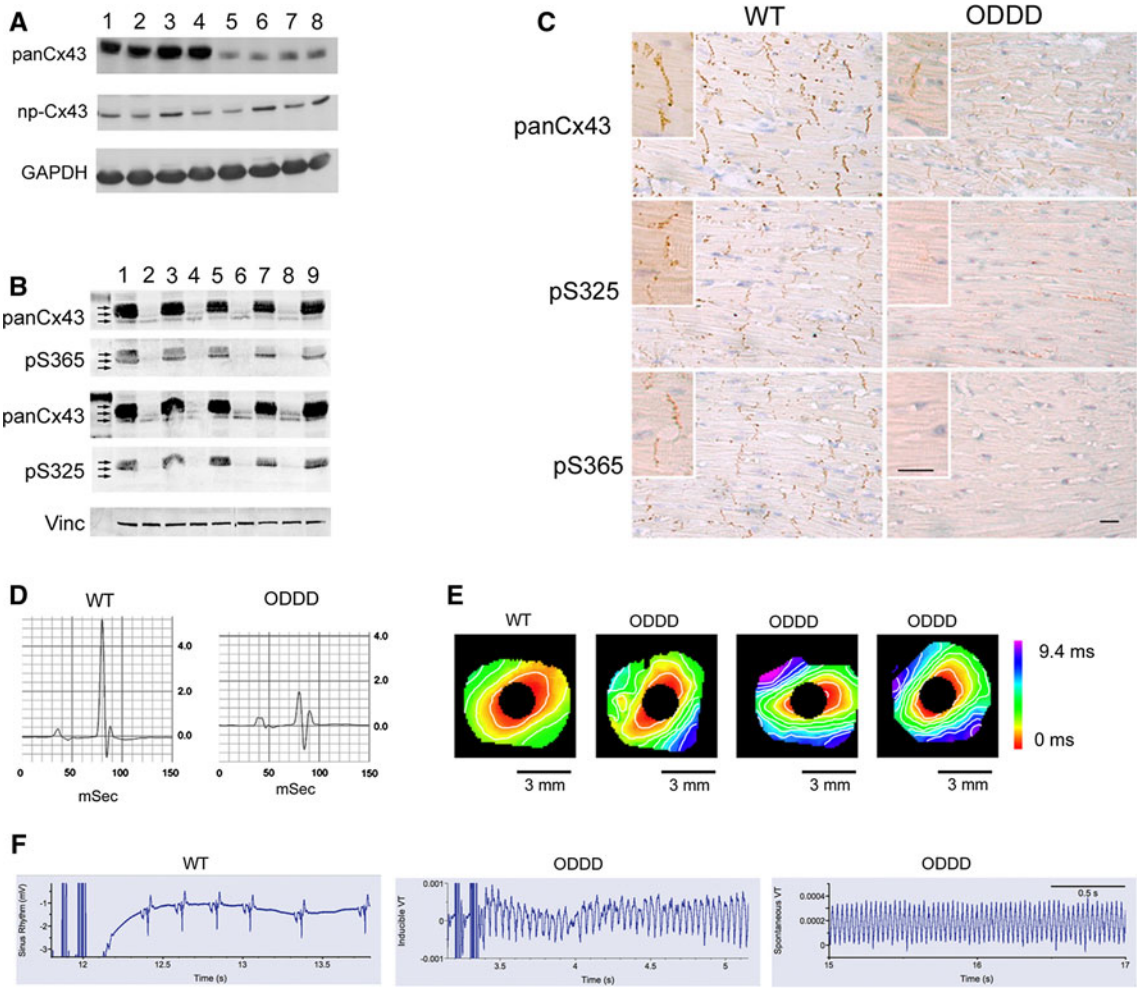

Fig. 1 Aberrant posttranslational phosphorylation of Cx43 in ODDD mutant hearts. **a** Western blot analysis using antibodies recognizing all forms of Cx43 (panCx43) and nonphosphorylated Cx43 (np-Cx43) showing specific loss of phosphorylated Cx43. *Lanes 1–4* are from wild-type hearts and *lanes 5–8* are from ODDD hearts. **b** Western blot analysis using antibodies recognizing all forms of Cx43 (panCx43), phosphoS365-Cx43 (pS365) and phosphoS325/328/330-Cx43 (pS325), showing specific loss of PS365 and pS325. *Lanes 1*, *3*, *5*, *7* and *9* are from wild-type hearts and *lanes 2*, *4*, *6* and *8* are from ODDD hearts. **c** Immunohistochemical staining of wild-type and ODDD mutant hearts with panCx43, pS325 and pS365 antibodies. Phosphorylated forms of Cx43 are virtually absent in ODDD mutant hearts. *Bar* 20 μm. **d** Representative signal-averaged surface electrocardiograms (lead II) from a wild type (WT) and an ODDD mutant mouse. Note the diminished QRS amplitude in the mutant. **e** Optical mapping of the *left* ventricular surface of a representative WT heart and 3 individual ODDD mutant hearts showing significant slowing of conduction in the mutant hearts. **f** Programmed electrical stimulation showing return of sinus rhythm after premature beats in a wild type heart, but induction of sustained VT in an ODDD heart (*middle*), and spontaneous VT in an ODDD heart (*right*). Adapted from Kalcheva et al. (2007)

and other stressors. Several years ago we developed a murine model of the human syndrome oculodentodigital dysplasia (ODDD), an autosomal-dominant systemic disorder caused by mutations in the Cx43 gene (Kalcheva et al. 2007; Paznekas et al. 2003). Unexpectedly, because the missense mutation (I130T) was at a distance from the serine-rich carboxy-terminus, we observed a profound defect in the posttranslational phosphorylation of Cx43 at both serine 365 (a PKA-dependent site) and the triplet of serines at 325, 328, and 330 (CK1δ-dependent sites), as defined by using phospho-specific antibodies generated by the Lampe laboratory. These mice also demonstrated significant abnormalities in cardiac impulse propagation and increased susceptibility to induced cardiac arrhythmias (Fig. 1).

We next sought to extend these results to a more common and arguably more relevant model of cardiac disease, pressure-overload hypertrophy induced by transverse aortic constriction (TAC). Imposition of hemodynamic overload causes a similar time-dependent reduction in posttranslational phosphorylation of Cx43 at these same sites, especially the CK1δ-dependent sites (Qu et al. 2009), and as with the ODDD mutant mice, we observed significant slowing of cardiac impulse propagation and increased arrhythmogenicity (Fig. 2). Importantly, treatment with the aldosterone receptor antagonist spironolactone, a drug which has been shown to diminish sudden arrhythmic death in human clinical trials (Pitt et al. 1999), blunted the development of gap junction remodeling and reversed the functional abnormalities as well. Taken together with our findings in the ODDD mutant mice, these data suggested that aberrant posttranslational phosphorylation of Cx43 might be a common mechanism through which both intrinsic (i.e., genetic) and extrinsic (acquired) stressors result in pathologic gap junction remodeling.

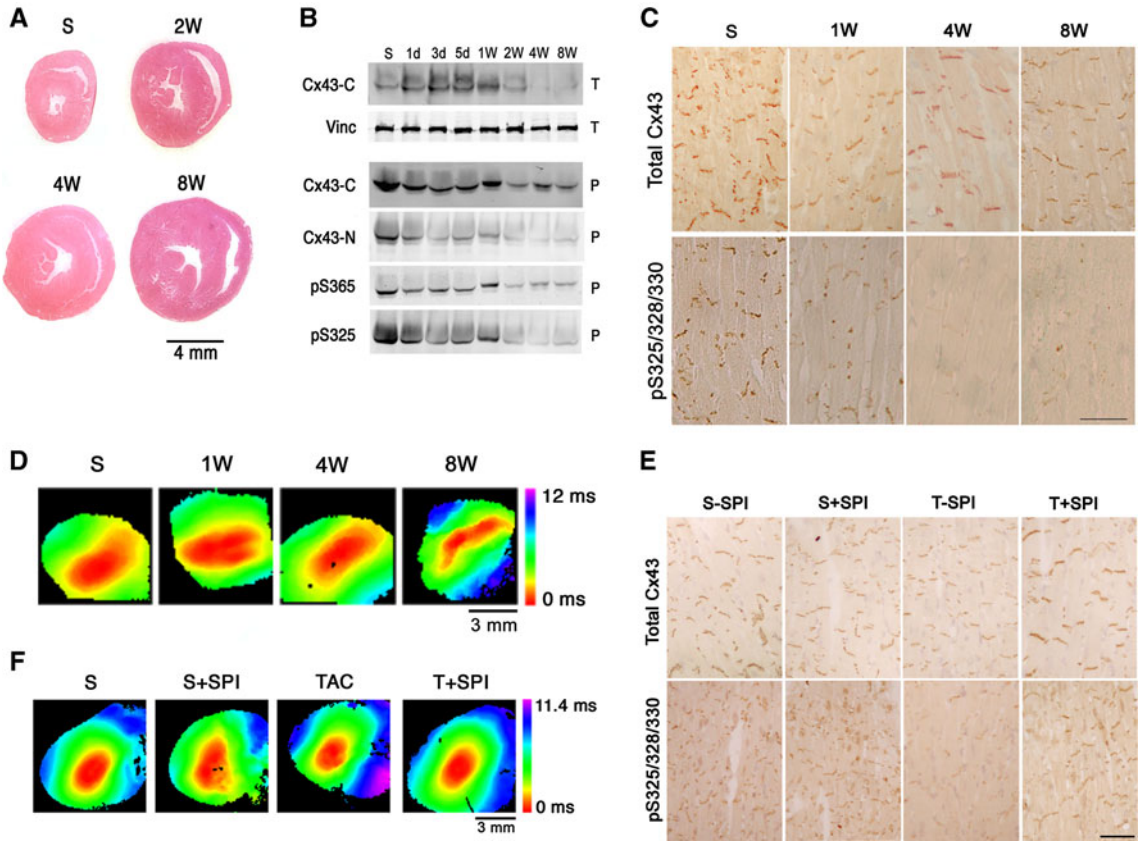

Fig. 2 Structural, molecular and functional gap junction remodeling with pressure overload hypertrophy. **a** Cross-sections of hearts showing progressive hypertrophy after transverse aortic constriction (TAC). **b** Western blot analysis demonstrating progressive reduction in total and phosphoCx43 expression in total cellular lysates (T) or Triton X-100 insoluble pellet fractions (P). Antibodies recognized the Cx43 C-terminus (Cx43-C); Cx43 amino-terminus (Cx43-N); vinculin (Vinc); S365-phosphoCx43 (pS365) or S325/328/330-phospho-Cx43 (pS325). **c** Immunostaining showing progressive loss of junctional Cx43 with TAC, especially S325/328/330-pCx43. **d** Representative optical maps demonstrating progressive slowing of conduction velocity after TAC. **e** Immunostaining showing loss of Cx43 gap junction plaques in TAC mice treated with vehicle alone (T-SPI), but substantial improvement in mice treated with spironolactone (T + SPI), comparable to sham-operated mice receiving vehicle alone (S-SPI) or spironolactone (S + SPI). *Scale bar* 50 μm. **f** Representative optical maps from each of the 4 groups. Adapted from Qu et al. (2009)

Nonetheless, given the multiplicity of kinase target sites that might be affected during acute and chronic stress, these studies alone did not establish a *direct* link between aberrant phosphorylation of Cx43, gap junction remodeling and arrhythmic susceptibility. Therefore, to unequivocally determine the importance of CK1δ-dependent phosphorylation, we created two new strains of mutant mice, in which the serine 325, 328 and 330 (the CK1δ target sites) were mutated to either nonphosphorylatable alanines (S3A mice) or phosphatase-resistant, phosphomimetic glutamic acid residues (S3E mice) (Remo et al. 2011). Both strains of mutant mice were grossly indistinguishable from wild-type (WT) controls at birth and throughout development, and there were no significant differences with regards to baseline physiological and echocardiographic measurements. For many years it has been known that posttranslational phosphorylation of Cx43 influences its electrophoretic mobility by SDS-PAGE (Crow et al. 1990). Interestingly, immunoblotting of total heart homogenates and junctional membrane enriched samples from the mutant mice demonstrated that mutations in the triplet of serines significantly influenced Cx43 mobility. Cx43 immunoreactive bands from Cx43-S3E mutant mice migrated more slowly and conversely those from Cx43-S3A mutant mice migrated more rapidly than those observed in WT hearts. Moreover, immunofluorescent staining demonstrated that Cx43-S3A mice had significantly less junctional Cx43 compared to WT or S3E mice (Fig. 3). These results suggest that the inhibition of CK1δ-dependent phosphorylation of Cx43, as demonstrated in vivo by the Cx43-S3A mutant mice, interferes with either trafficking of Cx43 to the junctional membrane or its stability after assembly into gap junction plaques. These molecular changes were associated with significant functional sequelae. The Cx43-S3A mutant mice displayed significantly increased susceptibility to inducible ventricular tachycardia whereas the Cx43-S3E mice were relatively resistant. Moreover, the Cx43-S3E mutant mice produced gap junctions that were resistant to pathologic gap junction remodeling associated with TAC (Fig. 3). Taken together, these data clearly confirmed a mechanistic link between posttranslational phosphorylation of Cx43 and gap junction formation, pathologic gap junction remodeling and arrhythmic susceptibility within the context of the intact organism.

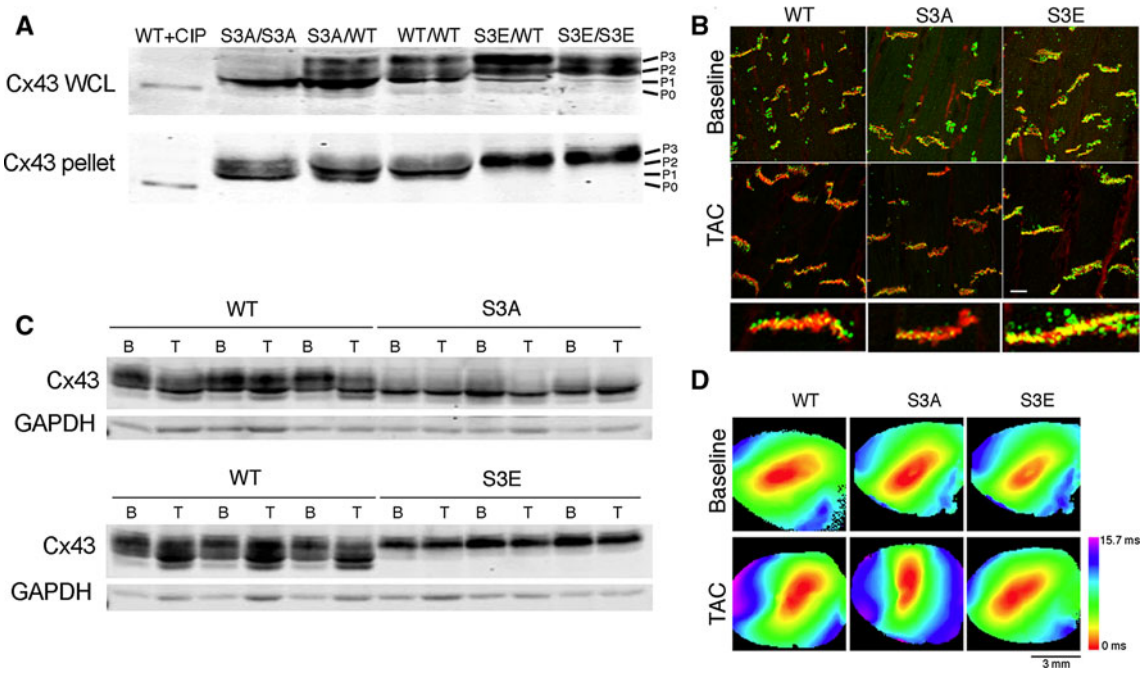

Fig. 3 Molecular and functional analysis of CK1δ mutant mice. **a** High-resolution Western blot analysis of whole cell lysates (WCL) or Triton X-100 insoluble pellets (pellet) prepared from ventricles of mice with the indicated genotypes, probed with polyclonal panCx43 antisera. Wild type Cx43 lysate treated with calf intestine phosphatase (CIP) migrates at P0 and is shown for comparison to various major phosphorylated forms of Cx43 (P1, P2, P3). **b** Representative immunofluorescent staining with panCx43 (Cx43, *green*) and N-cadherin (N-cad, *red*) antibodies at baseline and 4 weeks after TAC. *Scale bar* 10 μm. Magnified views of individual gap junction plaques for each genotype after TAC are shown below. **c** Representative immunoblots of whole cell lysates at baseline (B) and after TAC (T) from each of the indicated genotypes, probed with polyclonal panCx43 and GAPDH antibodies. **d** Representative activation maps from each of the indicated genotypes at baseline and after TAC, showing blunting of conduction slowing in S3E mutant mice. Adapted from Remo et al. (2011)

Regulation by the Nonreceptor Tyrosine Kinase Src

More recently, we have turned our attention to the role of Src kinase-dependent phosphorylation of Cx43 in the heart. Atkinson et al. (1981) originally reported that infection of cells with an avian sarcoma virus resulted in junctional uncoupling; this effect was subsequently shown to be due to the activity of the viral tyrosine kinase *v-src* (Chang et al. 1985) and more specifically, to phosphorylation of Cx43 on tyrosine residues in the carboxy terminus (Swenson et al. 1990; Filson et al. 1990). Subsequently, Toyofuku et al. (1999) reported that endogenous, or cellular c-Src was increased in myopathic BIO 14.6 hamsters and that activated phospho-Src reduced gap junctional coupling between cardiac myocytes, suggesting a role for dysregulated Src signaling and pathologic gap junction remodeling within the context of the intact organism. Moreover, they also showed that Src could directly phosphorylate Cx43 and this posttranslational modification diminished the interactions of Cx43 with ZO-1 (Toyofuku et al. 2001). Conversely, Giepmans et al. (2003) showed that the receptor protein tyrosine phosphatase mu (RPTPmu) also interacted with the carboxy-terminus of Cx43 and could prevent Src-mediated closure of gap junction channels, suggesting dynamic regulation of Cx43 by the opposing actions of tyrosine kinases and phosphatases. Subsequent studies by Pointis and colleagues, although performed in nonexcitable Sertoli cells, have not only confirmed that activated pSrc can bind to Cx43 and displace ZO-1, but also that this molecular reorganization promotes rapid, dynamin2-dependent endocytic internalization of Cx43 GJs (Gilleron et al. 2008, 2011). Sorgen and colleagues have begun to examine the relevance of these molecular events within the context of the intact heart, using the canine infarct model. They found that the pathologic gap junction remodeling in the epicardial border zone was characterized by activation of Src and a molecular reorganization of Src and ZO-1 (Kieken et al. 2009), although the posttranslational status of Cx43 was not examined in detail. Moreover, in apparent contrast to the model of Pointis et al (Gilleron et al. 2008), their studies suggested that activated Src preferentially bound to ZO-1, resulting in an "untethering" of Cx43 from its ZO-1 scaffold, allowing it to migrate from the intercalated disc to the lateral myocyte membrane.

Interestingly, recent evidence suggests that aldosterone signaling, acting through either a genomic or nongenomic mechanism, may increase Src activity (Kobayashi et al. 2006; Shi et al. 2011). These data are intriguing given our recent observation that treatment of aortic banded mice with the aldosterone receptor antagonist spironolactone resulted in significant amelioration of pathologic gap junction remodeling (Qu et al. 2009). Further supporting a fundamental role for Src in pathologic gap junction remodeling is the recent report by Dudley's group examining angiotensin converting enzyme overexpressing transgenic mice, in which Cx43 remodeling and arrhythmias are prevalent. Treatment of ACE-overexpressors with the Src inhibitor PP1 resulted in partial normalization of Cx43 levels and diminished arrhythmic burden (Sovari et al. 2011). Not only is the renin–angiotensin–aldosterone system pathway implicated in pathologic gap junction remodeling, but additional circulating factors including endothelin-1, lipopolysaccharide and TNFα have all been reported to induce Cx43 tyrosine phosphorylation and uncoupling (Huang et al. 2003; Lidington et al. 2002; Postma et al. 1998). To date, gene-targeted murine models that might elucidate the role of Src in cardiac physiology and pathology have not been revealing. Unfortunately, germ line knockout of Src produces osteopetrotic, runted mice that die in the perinatal period, complicating an analysis of potential arrhythmic behavior (Soriano et al. 1991). Recently, however, mice harboring a floxed Src allele have been created by the Muller laboratory (Marcotte et al. 2012), and analysis of their cardiac phenotype should be instructive.

New Directions

Paralleling our strategy to elucidate the role of CK1δ-dependent phosphorylation, we have recently begun replacing tyrosines 247 and 265 in the carboxy-terminus of Cx43 with either nonphosphorylatable phenylalanine residues or phosphomimetic glutamic acids. Mice harboring these mutations should provide a definitive approach to determine the importance of tyrosine-dependent phosphorylation of Cx43 and the role of this modification in the cardiac gap junction lifecycle, both in health and in response to pathologic stressors. Moreover, we have generated mice expressing a Cx43-eGFP fusion protein in the heart. Our preliminary analysis reveals appropriate colocalization of the fusion protein with endogenous Cx43 at the cardiac intercalated disc. Real time fluorescent imaging of cardiomyocytes and myocardial tissue slices from these mice can be used to characterize the numerous signaling pathways (i.e., kinases, phosphatases, acetylases, ubiquitin ligases, etc.) that are thought to regulate gap junction formation and internalization. In the future, we anticipate that these and other genetically engineered murine models will provide important insights into the mechanisms and consequences of pathologic cardiac gap junction remodeling.

Acknowledgments Gap junction research in the Fishman laboratory is supported by grants from the NIH (R01 HL82727, R01 HL105983 and T32 HL098129).

Reference

Akar FG, Nass RD, Hahn S, Cingolani E, Shah M, Hesketh GG, DiSilvestre D, Tunin RS, Kass DA, Tomaselli GF (2007) Dynamic changes in conduction velocity and gap junction properties during development of pacing-induced heart failure. Heart Circul Physiol 293:H1223–H1230

Atkinson MM, Menko AS, Johnson RG, Sheppard JR, Sheridan JD (1981) Rapid and reversible reduction of junctional permeability in cells infected with a temperature-sensitive mutant of avian sarcoma virus. J Cell Biol 91:573–578

Beardslee MA, Lerner DL, Tadros PN, Laing JG, Beyer EC, Yamada KA, Kleber AG, Schuessler RB, Saffitz JE (2000) Dephosphorylation and intracellular redistribution of ventricular connexin43 during electrical uncoupling induced by ischemia. Circ Res 87:656–662

Chang CC, Trosko JE, Kung HJ, Bombick D, Matsumura F (1985) Potential role of the src gene product in inhibition of gap-junctional communication in NIH/3T3 cells. Proc Natl Acad Sci USA 82:5360–5364

Crow DS, Beyer EC, Paul DL, Kobe SS, Lau AF (1990) Phosphorylation of connexin43 gap junction protein in uninfected and Rous sarcoma virus-transformed mammalian fibroblasts. Mol Cell Biol 10:1754–1763

Filson AJ, Azarnia R, Beyer EC, Loewenstein WR, Brugge JS (1990) Tyrosine phosphorylation of a gap junction protein correlates with inhibition of cell-to-cell communication. Cell Growth Differ 1:661–668

Giepmans BN, Feiken E, Gebbink MF, Moolenaar WH (2003) Association of connexin43 with a receptor protein tyrosine phosphatase. Cell Commun Adhes 10:201–205

Gilleron J, Fiorini C, Carette D, Avondet C, Falk MM, Segretain D, Pointis G (2008) Molecular reorganization of Cx43, Zo-1 and Src complexes during the endocytosis of gap junction plaques in response to a non-genomic carcinogen. J Cell Sci 121:4069–4078

Gilleron J, Carette D, Fiorini C, Dompierre J, Macia E, Denizot JP, Segretain D, Pointis G (2011) The large GTPase dynamin2: a new player in connexin 43 gap junction endocytosis, recycling and degradation. Int J Biochem Cell Biol 43:1208–1217

Giovannone S, Remo BF, Fishman GI (2011) Channeling diversity: gap junction expression in the heart. Heart Rhythm. doi:10.1016/j.hrthm.2011.11.040

Gollob MH, Jones DL, Krahn AD, Danis L, Gong XQ, Shao Q, Liu X, Veinot JP, Tang AS, Stewart AF, Tesson F, Klein GJ, Yee R, Skanes AC, Guiraudon GM, Ebihara L, Bai D (2006) Somatic mutations in the connexin 40 gene (GJA5) in atrial fibrillation. N Engl J Med 354:2677–2688

Gutstein DE, Morley GE, Tamaddon H, Vaidya D, Schneider MD, Chen J, Chien KR, Stuhlmann H, Fishman GI (2001) Conduction slowing and sudden arrhythmic death in mice with cardiac-restricted inactivation of connexin43. Circ Res 88:333–339

Harris AL (2001) Emerging issues of connexin channels: biophysics fills the gap. Q Rev Biophys 34:325–472

Huang S, Dudez T, Scerri I, Thomas MA, Giepmans BN, Suter S, Chanson M (2003) Defective activation of c-Src in cystic fibrosis airway epithelial cells results in loss of tumor necrosis factor-alpha-induced gap junction regulation. J Biol Chem 278:8326–8332

Kalcheva N, Qu J, Sandeep N, Garcia L, Zhang J, Wang Z, Lampe PD, Suadicani SO, Spray DC, Fishman GI (2007) Gap junction remodeling and cardiac arrhythmogenesis in a murine model of oculodentodigital dysplasia. Proc Natl Acad Sci USA 104: 20512–20516

Kanno S, Saffitz JE (2001) The role of myocardial gap junctions in electrical conduction and arrhythmogenesis. Cardiovasc Pathol 10:169–177

Kieken F, Mutsaers N, Dolmatova E, Virgil K, Wit AL, Kellezi A, Hirst-Jensen BJ, Duffy HS, Sorgen PL (2009) Structural and molecular mechanisms of gap junction remodeling in epicardial border zone myocytes following myocardial infarction. Circ Res 104:1103–1112

Kobayashi N, Yoshida K, Nakano S, Ohno T, Honda T, Tsubokou Y, Matsuoka H (2006) Cardioprotective mechanisms of eplerenone on cardiac performance and remodeling in failing rat hearts. Hypertension 47:671–679

Lampe PD, Lau AF (2000) Regulation of gap junctions by phosphorylation of connexins. Arch Biochem Biophys 384:205–215

Lampe PD, Lau AF (2004) The effects of connexin phosphorylation on gap junctional communication. Int J Biochem Cell Biol 36:1171–1186

Lidington D, Tyml K, Ouellette Y (2002) Lipopolysaccharide-induced reductions in cellular coupling correlate with tyrosine phosphorylation of connexin 43. J Cell Physiol 193:373–379

Marcotte R, Smith HW, Sanguin-Gendreau V, McDonough RV, Muller WJ (2012) Mammary epithelial-specific disruption of c-Src impairs cell cycle progression and tumorigenesis. Proc Natl Acad Sci USA 109:2808–2813

Matsushita S, Kurihara H, Watanabe M, Okada T, Sakai T, Amano A (2006) Alterations of phosphorylation state of connexin 43 during hypoxia and reoxygenation are associated with cardiac function. J Histochem Cytochem 54:343–353

Paznekas WA, Boyadjiev SA, Shapiro RE, Daniels O, Wollnik B, Keegan CE, Innis JW, Dinulos MB, Christian C, Hannibal MC, Jabs EW (2003) Connexin 43 (GJA1) mutations cause the pleiotropic phenotype of oculodentodigital dysplasia. Am J Hum Genet 72:408–418

Pitt B, Zannad F, Remme WJ, Cody R, Castaigne A, Perez A, Palensky J, Wittes J (1999) The effect of spironolactone on morbidity and mortality in patients with severe heart failure. randomized aldactone evaluation study investigators. N Engl J Med 341:709–717

Poelzing S, Akar FG, Baron E, Rosenbaum DS (2004) Heterogeneous connexin43 expression produces electrophysiological heterogeneities across ventricular wall. Am J Physiol Heart Circ Physiol 286:H2001–H2009

Postma FR, Hengeveld T, Alblas J, Giepmans BN, Zondag GC, Jalink K, Moolenaar WH (1998) Acute loss of cell–cell communication caused by G protein-coupled receptors: a critical role for c-Src. J Cell Biol 140:1199–1209

Qu J, Volpicelli FM, Garcia LI, Sandeep N, Zhang J, Marquez-Rosado L, Lampe PD, Fishman GI (2009) Gap junction remodeling and spironolactone-dependent reverse remodeling in the hypertrophied heart. Circ Res 104:365–371

Remo BF, Qu J, Volpicelli FM, Giovannone S, Shin D, Lader J, Liu FY, Zhang J, Lent DS, Morley GE, Fishman GI (2011) Phosphatase-resistant gap junctions inhibit pathological remodeling and prevent arrhythmias. Circ Res 108:1459–1466

Saffitz JE (2009) Arrhythmogenic cardiomyopathy and abnormalities of cell-to-cell coupling. Heart Rhythm 6:S62–S65

Severs NJ (2002) Gap junction remodeling in heart failure. J Card Fail 8:S293–S299

Severs NJ, Coppen SR, Dupont E, Yeh HI, Ko YS, Matsushita T (2004) Gap junction alterations in human cardiac disease. Cardiovasc Res 62:368–377

Severs NJ, Dupont E, Thomas N, Kaba R, Rothery S, Jain R, Sharpey K, Fry CH (2006) Alterations in cardiac connexin expression in cardiomyopathies. Adv Cardiol 42:228–242

Severs NJ, Bruce AF, Dupont E, Rothery S (2008) Remodelling of gap junctions and connexin expression in diseased myocardium. Cardiovasc Res 80:9–19

Shi G, Fu Y, Jiang W, Yin A, Feng M, Wu Y, Kawai Y, Miyamori I, Fan C (2011) Activation of Src-ATF1 pathway is involved in upregulation of Nox1, a catalytic subunit of NADPH oxidase, by aldosterone. Endocr J 58:491–499

Solan JL, Lampe PD (2009) Connexin43 phosphorylation: structural changes and biological effects. Biochem J 419:261–272

Soriano P, Montgomery C, Geske R, Bradley A (1991) Targeted disruption of the c-src proto-oncogene leads to osteopetrosis in mice. Cell 64:693–702

Sovari AA, Iravanian S, Dolmatova E, Jiao Z, Liu H, Zandieh S, Kumar V, Wang K, Bernstein KE, Bonini MG, Duffy HS, Dudley SC (2011) Inhibition of c-Src tyrosine kinase prevents angiotensin II-mediated connexin-43 remodeling and sudden cardiac death. J Am Coll Cardiol 58:2332–2339

Spray DC, Burt JM (1990) Structure–activity relations of the cardiac gap junction channel. Am J Physiol 258:C195–C205

Spray DC, Moreno AP, Eghbali B, Chanson M, Fishman GI (1992) Gating of gap junction channels as revealed in cells stably transfected with wild type and mutant connexin cDNAs. Biophys J 62:48–50

Swenson KI, Piwnica-Worms H, McNamee H, Paul DL (1990) Tyrosine phosphorylation of the gap junction protein connexin43 is required for the pp 60v-src-induced inhibition of communication. Cell Regul 1:989–1002

Thibodeau IL, Xu J, Li Q, Liu G, Lam K, Veinot JP, Birnie DH, Jones DL, Krahn AD, Lemery R, Nicholson BJ, Gollob MH (2010) Paradigm of genetic mosaicism and lone atrial fibrillation: physiological characterization of a connexin 43-deletion mutant identified from atrial tissue. Circulation 122:236–244

Toyofuku T, Yabuki M, Otsu K, Kuzuya T, Tada M, Hori M (1999) Functional role of c-Src in gap junctions of the cardiomyopathic heart. Circ Res 85:672–681

Toyofuku T, Akamatsu Y, Zhang H, Kuzuya T, Tada M, Hori M (2001) c-Src regulates the interaction between connexin-43 and ZO-1 in cardiac myocytes. J Biol Chem 276:1780–1788

van Rijen HV, Eckardt D, Degen J, Theis M, Ott T, Willecke K, Jongsma HJ, Opthof T, de Bakker JM (2004) Slow conduction and enhanced anisotropy increase the propensity for ventricular tachyarrhythmias in adult mice with induced deletion of connexin43. Circulation 109:1048–1055

Willecke K, Eiberger J, Degen J, Eckardt D, Romualdi A, Guldenagel M, Deutsch U, Sohl G (2002) Structural and functional diversity of connexin genes in the mouse and human genome. Biol Chem 383:725–737

J Membrane Biol (2012) 245:283–290
DOI 10.1007/s00232-012-9449-z

Electrical Transmission between Mammalian Neurons is Supported by a Small Fraction of Gap Junction Channels

Sebastian Curti · Gregory Hoge · James I. Nagy · Alberto E. Pereda

Received: 29 March 2012 / Accepted: 1 June 2012 / Published online: 24 June 2012

Abstract Electrical synapses formed by gap junctions between neurons create networks of electrically coupled neurons in the mammalian brain, where these networks have been found to play important functional roles. In most cases, interneuronal gap junctions occur at remote dendro–dendritic contacts, making difficult accurate characterization of their physiological properties and correlation of these properties with their anatomical and morphological features of the gap junctions. In the mesencephalic trigeminal (MesV) nucleus where neurons are readily accessible for paired electrophysiological recordings in brain stem slices, our recent data indicate that electrical transmission between MesV neurons is mediated by connexin36 (Cx36)-containing gap junctions located at somato–somatic contacts. We here review evidence indicating that electrical transmission between these neurons is supported by a very small fraction of the gap junction channels present at cell–cell contacts. Acquisition of this evidence was enabled by the unprecedented experimental access of electrical synapses between MesV neurons, which allowed estimation of the average number of open channels mediating electrical coupling in relation to the average number of gap junction channels present at these contacts. Our results indicate that only a small proportion of channels ($\sim$0.1 %) appear to be conductive. On the basis of similarities with other preparations, we postulate that this phenomenon might constitute a general property of vertebrate electrical synapses, reflecting essential aspects of gap junction function and maintenance.

Keywords Connexin36 · Electrical coupling · Electrical transmission · Gap junction

S. Curti (✉)
Facultad de Medicina, Departamento de Fisiología, Laboratorio de Neurofisiología Celular, Universidad de la República, Gral. Flores 2125, Montevideo 11800, Uruguay
e-mail: scurti@fmed.edu.uy

G. Hoge · A. E. Pereda (✉)
Dominick P. Purpura Department of Neuroscience, Albert Einstein College of Medicine, Bronx, NY 10461, USA
e-mail: alberto.pereda@einstein.yu.edu

J. I. Nagy
Department of Physiology, University of Manitoba, Winnipeg, Manitoba R3EOJ9, Canada

Gap junctions mediate electrical transmission between neurons by providing a pathway of low resistance for the spread of electrical currents and small metabolites (Bennett 1997). Contrasting initial perceptions and overcoming technical challenges and long-standing prejudices (Bennett and Pereda 2006), electrical synapses are now known to be present in virtually every structure of the mammalian brain, where they usually form networks of electrically coupled neurons (Bennett and Zukin 2004; Connors and Long 2004; Hormuzdi et al. 2004). However, and in marked contrast with some advantageous teleost model synapses (Pereda et al. 2004), the dendro–dendritic location of neuronal gap junctions in most brain structures (Connors and Long 2004) makes it difficult to correlate their physiological properties with anatomical features.

The mesencephalic trigeminal (MesV) nucleus, formed by the somata of primary afferents originating in jaw-closing muscles, constitutes one of the first examples supporting the presence of electrical synapses in the mammalian central nervous system (Hinrichsen and Larramendi 1970; Hinrichsen 1970; Baker and Llinás 1971; Llinas 1975). The demonstration of electrical coupling relied on indirect electrophysiological evidence obtained

by stimulating the peripheral projections of these afferents at a strength that was subthreshold for the recorded neuron, but was suprathreshold to others, thus allowing the detection of a depolarizing coupling potential, which represented the electrotonic spread of action potentials from electrically coupled cells (Hinrichsen 1970; Baker and Llinás 1971). Because of its limitations, this approach precluded a detailed analysis of the properties of these electrical synapses and the organization of electrical coupling within this nucleus. By combining tracer coupling analysis and immunochemistry with current electrophysiological approaches in rodent slices, we recently examined the properties, organization and developmental profile of electrical coupling between MesV neurons (Curti et al. 2012). Interestingly, we demonstrated that coupling between MesV neurons was mostly restricted to pairs (or very small clusters) of neurons and, in contrast with most examples where coupling decreases or disappears with age (Peinado et al. 1993; Meier and Dermietzel 2006), coupling was absent during early development and appeared at about postnatal day 8 to remain as a feature of the mature cellular phenotype of these neurons (Curti et al. 2012). In addition, we demonstrated that electrical transmission between MesV neurons is mediated by anatomically distinct somato–somatic contacts that contained, as with most mammalian electrical synapses (Bennett and Zukin 2004; Connors and Long 2004), the gap junction protein Cx36 (Curti et al. 2012).

Estimates obtained at mixed synapses formed by afferent terminals on the goldfish Mauthner cell (for review, see Pereda et al. 2004), where the number of channels was obtained from direct ultrastructural reconstruction of these terminals (Tuttle et al. 1986), suggested that only a small percentage of channels ($\sim$1 %) support the electrical component of a unitary mixed synaptic potential (Lin and Faber 1988). We review here evidence suggesting that, consistent with this finding, electrical transmission between mammalian neurons is also supported by a very small fraction of gap junction channels. Taking advantage of the uncommon experimental accessibility of MesV, we combined imaging-based estimates of numbers of channels present with physiological measurements and found that electrical coupling is supported by a surprisingly small fraction of conductive channels.

Methods

For these experiments, Sprague Dawley or Wistar rats were used. Slicing and recording techniques were similar to those described previously (Curti et al. 2012). Detailed illustration and interpretation of electrophysiological recordings described here can be found in our previous report (Curti et al. 2012). Methods for tissue preparation and immunolabeling, sources of antibodies, and their specificity and analysis by confocal microscopy were as we previously described in studies of connexins in the central nervous system (Li et al. 2004a, b; Penes et al. 2005). Interpretations of images presented are also extensively described in our previous report (Curti et al. 2012). Statistical analysis is expressed as standard deviation (SD) or standard error of the mean (SEM).

Results

Using in vivo single intracellular recordings, Baker and Llinás (1971) revealed the existence of electrical coupling between neurons of the MesV. We have more recently investigated the presence of electrical coupling between adjacent pairs of these neurons using paired-recordings in slices of rat brain stem visualized by IR-DIC (Fig. 1a). MesV neurons were identified by their large spherical somata and characteristic electrophysiological properties in response to current steps of both polarities (Pedroarena et al. 1999). The presence of electrical coupling was tested by recording membrane responses in two adjacent MesV neurons after the injection of hyperpolarizing current pulses in one of the cells. An example of a coupled pair is illustrated in Fig. 1b, in which a current pulse in the presynaptic cell evokes a membrane response in the postsynaptic cell of the same sign but of lower amplitude and slower temporal course. About 23 % of the explored pairs ($n = 243$) were electrically coupled. For each coupled pair, the coupling coefficient and junctional resistance were estimated and expressed as the average of the values in both directions (see Curti et al. 2012 for details) averaging 0.19 ± 0.14 SD and 6.2 ± 6.33 nS SD, respectively ($n = 47$). Estimates of junctional conductance in both directions for each pair showed a positive correlation with a slope of 1.04 ($R^2 = 0.75$) not significantly different than one ($p = 0.7$), indicating that gap junctional conductance between MesV neurons is largely nonrectifying (Curti et al. 2012).

Somato–Somatic Contact Areas Contain Cx36

We next investigated by immunohistochemical approaches whether Cx36, a widespread neuronal connexin responsible for most electrical coupling in mammalian brain (Nagy et al. 2004; Meier and Dermietzel 2006; Condorelli 1998; Söhl et al. 1998), was expressed by MesV neurons of rats at postnatal day 15, corresponding roughly to the age at which electrophysiological studies of coupling between MesV neurons were conducted. At anterior levels through the MesV nucleus, neuronal somata are somewhat dispersed

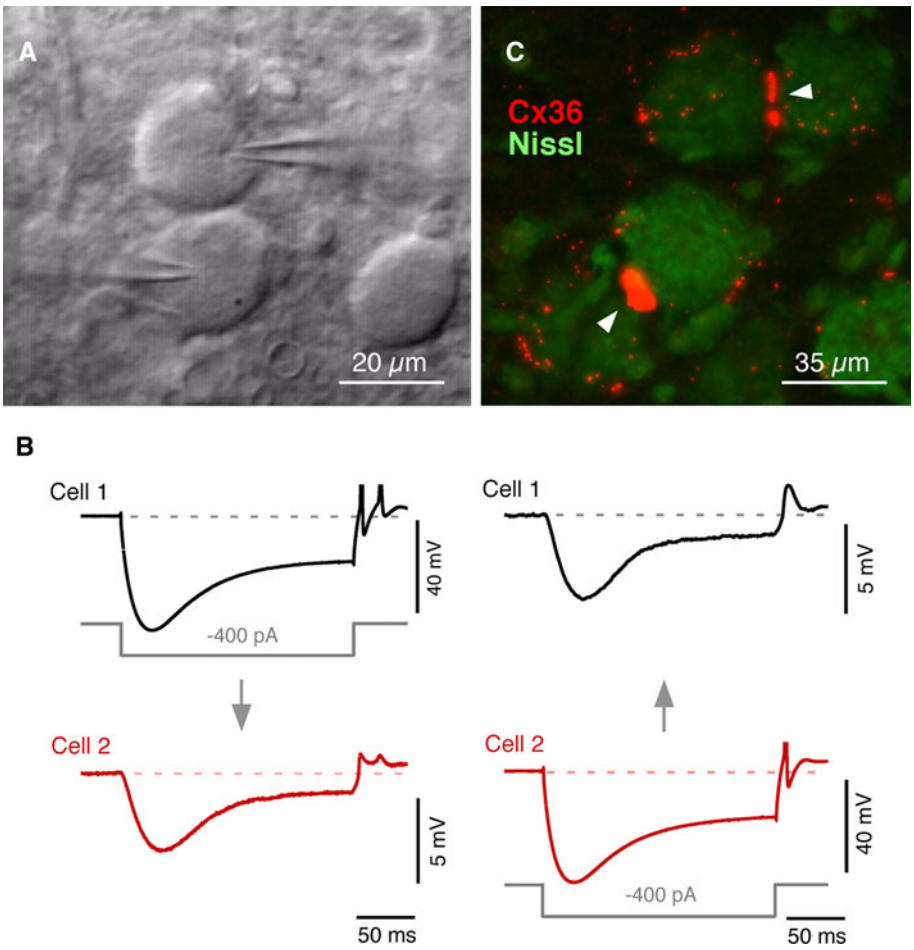

Fig. 1 Electrical transmission between MesV neurons. **a** IR-DIC image of a pair of contiguous MesV neurons during a simultaneous whole-cell recording. **b** Simultaneous recording from a pair of electrically coupled MesV neurons. Voltage responses to 200 ms hyperpolarizing (400 pA) current pulses injected either in cell 1 (*left*) or cell 2 (*right*). **c** Immunofluorescence labeling of Cx36 associated with MesV neurons at postnatal day 15. Labeling for Cx36 is shown with *red fluorochrome* in sections counterstained for Nissl with *green fluorochrome*. Image shows labeling for Cx36 (*arrowheads*) at appositions between pairs of MesV neurons. Modified from Curti et al. (2012)

along a dorsoventral axis, thus reducing the frequency of contacts between them. Nevertheless, most of these neurons were moderately laden with fine Cx36-positive puncta around their periphery. At more posterior levels, the MesV nucleus is much more compact, with constituent somata often appearing in clusters and in close apposition to each other. Labeling associated with MesV somata consisted of both fine Cx36-positive puncta around the somata surfaces and large aggregates of puncta at points of contact (Fig. 1c, arrowheads). Through focus of entire cells by confocal microscopy revealed that virtually all of the fine dispersed puncta were localized to the cell surface rather than intracellularly (Curti et al. 2012).

As shown by confocal analysis (Fig. 2a), immunolabeling at somatic appositions did not consist of a single large immunopositive plaque, but rather of numerous small puncta. Aggregates of puncta at somatic appositions were often visualized on edge but were occasionally captured *en face* (Fig. 2a, top), revealing various features of their organization. Taking advantage of the uncommon opportunity of identifying the junctional area between two neurons (most electrical coupling in mammalian neurons generally occurs at remote dendro–dendritic contacts; Connors and Long 2004), we calculated the average area of labeling for Cx36 at somato–somatic contacts. As determined from *en face* views of Cx36 immunofluorescence at contact sites between MesV somata (Fig. 2a), the average number of Cx36-puncta per apposition was 70.1 ± 9.9 SEM, the puncta diameter was 0.34 ± 0.09 μm SEM, and the average puncta area was 0.36 ± 0.028 μm^2 SEM ($n = 10$) (Fig. 2b–d). Complete confocal reconstruction of these contacts areas allowed us to determine that labeling most frequently appeared at appositions linking pairs or triplets of somata (Curti et al. 2012).

Somatic appositions between MesV neurons at postnatal day 9 and in adult did not display any immunolabeling for all other connexins examined, including connexins found in various peripheral cell types such as Cx30.3, 31.1, Cx31, Cx37, Cx39, Cx40, Cx46 or Cx50 (not shown). Nor did these appositions display labeling for connexins (Cx26, Cx29, Cx30, Cx32, Cx43 and Cx47) expressed in glial cells (Nagy et al. 2004), as shown by examples of double immunofluorescence labeling for some of these connexins in combination with labeling for Cx36 (Fig. 3). Immunolabeling for Cx32 was localized to myelinated fibers traversing a region immediately adjacent laterally to the

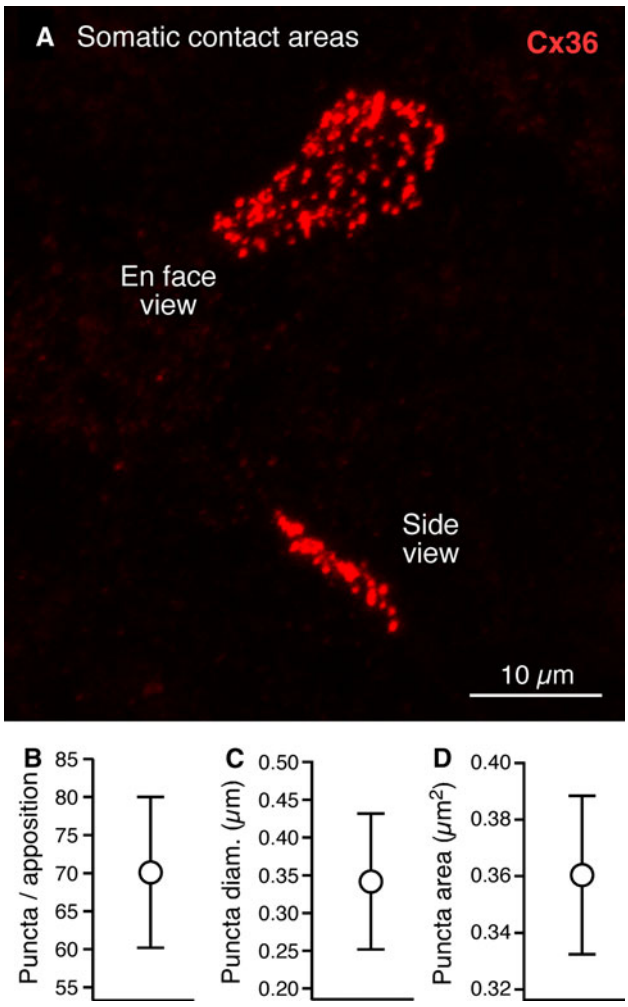

Fig. 2 Quantification of Cx36 labeling at somatic contact areas. **a** Confocal immunofluorescence (z-stack) *en face* view and side view appositions between two different pairs of MesV neurons. Only *en face* views of Cx36-immunopositive clusters were used for quantitation of Cx36-puncta area at appositions between pairs of MesV neurons. **b** Average of puncta per apposition. **c** Average of puncta diameter. **d** Average of puncta area

MesV nucleus, and was absent in the MesV nucleus (Fig. 3a). Punctate labeling for Cx47 was localized to oligodendrocyte cell bodies intermingled with fibers lateral to the MesV nucleus (Fig. 3b). Labeling for Cx30 and Cx43, which occur at astrocyte gap junctions throughout the brain (Nagy et al. 2004), was found around the MesV nucleus and sparsely dispersed within the nucleus (Fig. 3c, d). None of these connexins were found to be colocalized with Cx36 at appositions between MesV neurons, as shown by image overlay of labeling for Cx36 in combination with each of these connexins (Fig. 3a–d). Examination of other connexins reported to be expressed in neurons of adult brain (i.e., Cx30.2, Cx45 and Cx57) also revealed an absence of these at MesV neuronal appositions, as shown in the case of labeling for Cx45, which was instead

Fig. 3 Double immunofluorescence labeling of various connexins in combination with Cx36 in MesV nucleus at postnatal day 15 in rat brain. **a**, **b** Immunolabeling of the oligodendrocyte connexins Cx32 and Cx47 is restricted to myelinated fibers running lateral to the MesV nucleus (**A1**, *arrows*) and to oligodendrocyte cell bodies (**B1**, *arrowheads*), respectively; neither connexin is associated with MesV neurons or with Cx36 (**A2**, **B2**, *arrows*; and **A3**, **B3**, *overlay*). **c**, **d** Sparse immunolabeling of the astrocyte connexins Cx30 (**c**, *arrows*) and Cx43 (**d**, *arrows*) occurs within the MesV nucleus, where Cx36 is concentrated (**c**, **d**, *arrows*), and neither connexin is seen at MesV neuronal appositions or in association with Cx36 (**c**, **d**, *overlay*). **e** Punctate immunolabeling of Cx45 is restricted to blood vessels, in this case to a vessel traversing through the MesV nucleus (**E1**, *arrows*), and no labeling is seen associated with MesV neurons or with Cx36 (**E2**, *arrows*, and **E3** *overlay*). Scale bars = **a**, **b**, 100 μm; **c**, 10 μm; **d** 20 μm; **e**, 50 μm

localized along blood vessels traveling through the MesV nucleus (Fig. 3e), consistent with the expression of Cx45 by smooth muscle cells along vasculature elsewhere in brain (Kruger et al. 2000; Li and Simard 2001).

Estimates of Junctional Conductance under Voltage Clamp

The large spherical cell bodies and the somatic location of the gap junctional area between these cells facilitates recording from these cells and provides unusual advantages for biophysical examination of the properties of native neuronal gap junctions. More specifically, and in contrast with other neuronal types, the somatic location of gap junctions and spherical geometry of MesV neurons as well as the fact they tend to be coupled in pairs, contribute to alleviate space clamp limitations. We therefore obtained direct measurements of junctional conductance from pairs of coupled cells by using the dual whole cell patch clamp technique. Current responses to voltage steps in a presynaptic neuron where recorded in a coupled postsynaptic MesV neuron (Fig. 4a), and the junctional conductance was obtained from the slope of V–I relationships (Fig. 4b) (Curti et al. 2012). Junctional conductance averaged 2.8 ± 2.0 nS SD, $n = 8$ (Fig. 5a). In pairs where it was possible to estimate conductance in both directions the values were largely symmetrical, corroborating the lack of significant rectification at these contacts obtained under current clamp conditions.

Electrical Coupling is Supported by a Small Fraction of Open Gap Junction Channels

From the various measurements of labeled puncta (Fig. 2), we calculated the total Cx36 labeled area (area of all puncta) per apposition, which averaged 25.5 ± 3.9 μm^2 SEM (Fig. 5b). Because Cx36 was the only connexin detected at these contacts (Curti et al. 2012) and assuming

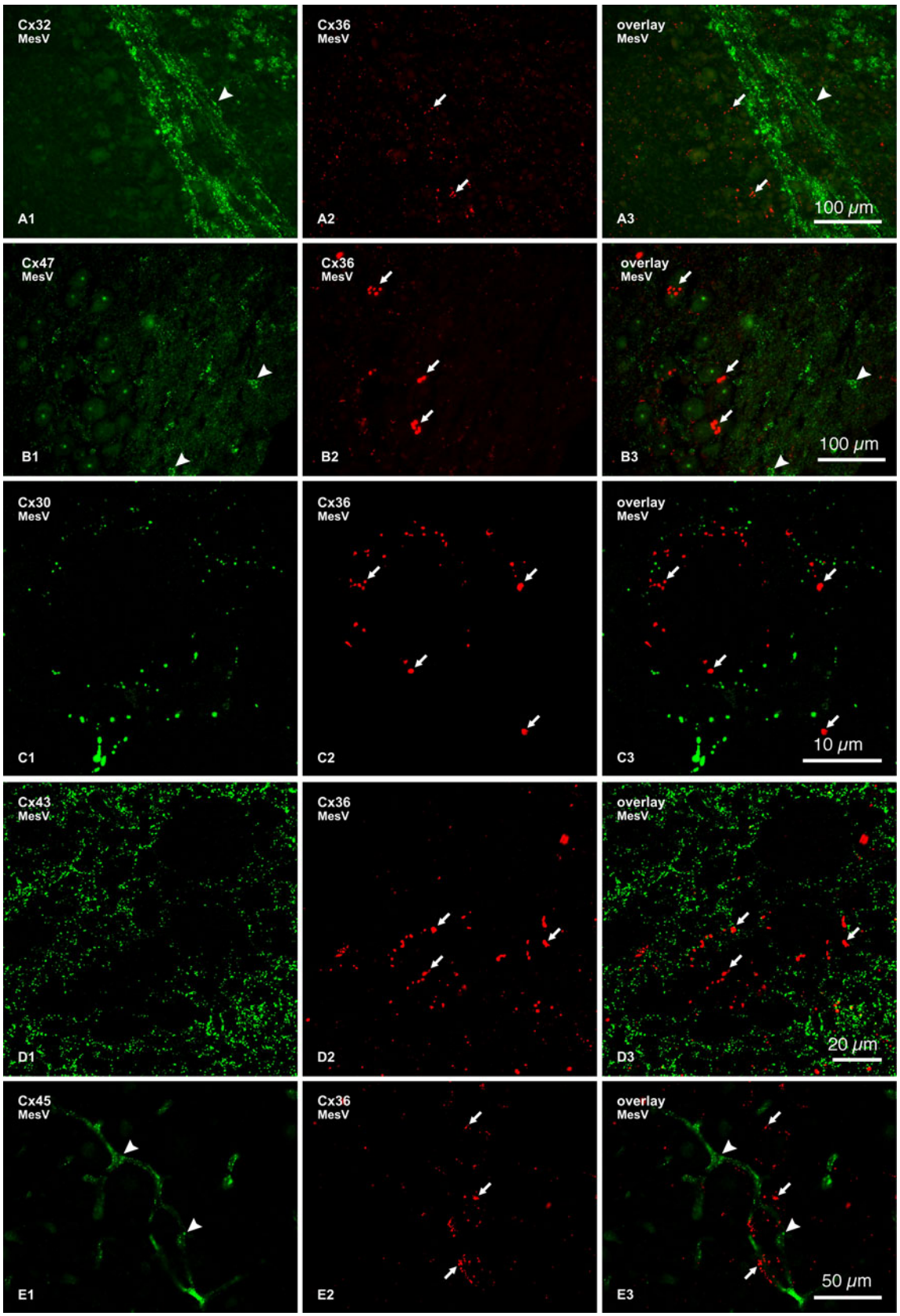
Cx32
MesV
A1
Cx36
MesV
A2
overlay
MesV
A3
100 μm
Cx47
MesV
B1
Cx36
MesV
B2
overlay
MesV
B3
100 μm
Cx30
MesV
C1
Cx36
MesV
C2
overlay
MesV
C3
10 μm
Cx43
MesV
D1
Cx36
MesV
D2
overlay
MesV
D3
20 μm
Cx45
MesV
E1
Cx36
MesV
E2
overlay
MesV
E3
50 μm

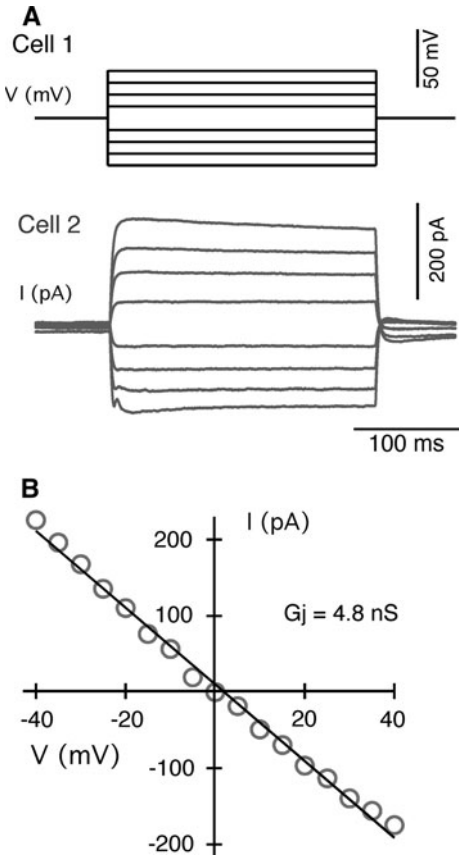

Fig. 4 Determination of junctional conductance between coupled pairs of MesV neurons. **a** Current traces obtained under dual whole cell voltage clamp configuration. Both cells were held at −50 mV and voltage commands of increasing magnitude in steps of 5 mV of both polarities were applied to one of the cells (cell 1, *top*), while monitoring junctional current in the second cell (cell 2, *bottom*). The transient component observed in response to strong positive voltage commands corresponds to an undetermined voltage-dependent conductance of the presynaptic cell that is not blocked by TTX or K^+ channel blockers). **b** Graph of junctional current (ordinates) versus transjunctional voltage (abscissa) for the recordings depicted in (**a**). The data were fitted to a straight-line function and the junctional conductance (Gj) was determined from the slope of this linear regression (4.8 nS in this pair). Modified from Curti et al. (2012)

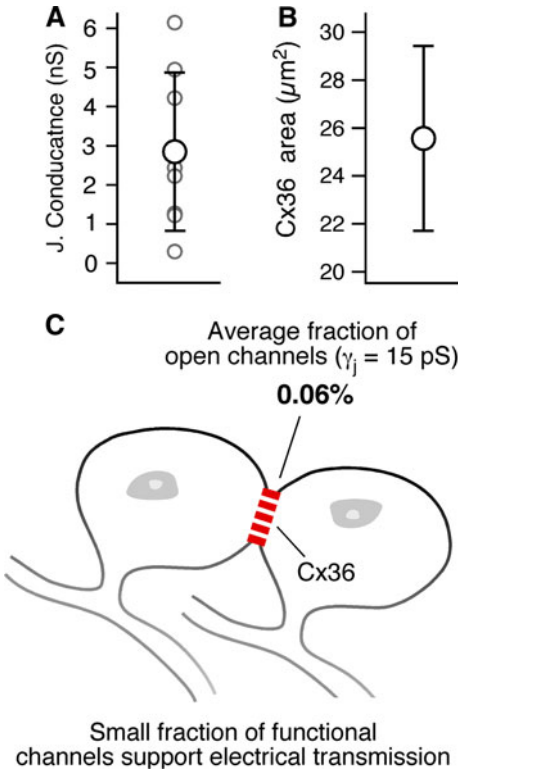

Fig. 5 A small fraction of gap junction channels supports electrical transmission between pairs of MesV neurons. **a** Estimates of junctional conductance obtained under voltage clamp configuration. Individual (*open circles*) and average (*solid circles*) values are illustrated superimposed (*error bars* indicate SD). According to these estimates of macroscopic junctional conductance and assuming a unitary conductance (γ_j) of 10–15 pS, the average number of open channels is 190–280, representing the 0.06–0.09 % of the average total population. **b** Average of Cx36 labeling area per apposition at somatic contacts. Assuming a density of 12,000 connexons per square micrometer, the averaged labeled area represents 306,000 intercellular channels per contact between MesV neurons. **c** The cartoon illustrates that electrical transmission is supported by a small proportion of open gap junction channels at appositions between MesV neurons. Modified from Curti et al. (2012)

that connexons in gap junction plaques between MesV neurons are organized in a crystalline fashion, where the density is reported to be 12,000 connexons per μm^2 (Kamasawa et al. 2006), the labeled area corresponds to about 306,000 channels. Because the single channel conductance of gap junction channels formed by Cx36 was reported to be 10–15 pS (Srinivas et al. 1999b; Teubner et al. 2000), the values of junctional conductance indicate that the average number of open gap junction channels was of 190–280. Given that the opening probability of functional gap junction intercellular channels was reported to be close to 1 (Srinivas et al. 1999a), this estimate indicates that, on average, only 0.06–0.09 % of gap junction channels between MesV neurons are conductive. Independent estimates of junctional conductance between the same pairs of MesV neurons using indirect approaches which involve measurements of coupling coefficient and input resistance provided independent support for the notion that a very low fraction of open channels contribute to electrical coupling. Indirectly estimated junctional conductance averaged 7.3 ± 5.0 nS SD ($n = 9$), representing 0.16–0.24 % of the total population of channels, a value which was also consistent with estimates obtained with current clamp for all the coupled pairs. Finally, the differences in junctional conductance observed between pairs of MesV neurons would indicate that the number of open channels between cells could be varied.

Discussion

Taking advantage of current electrophysiological approaches, our recordings from pairs of MesV neurons provided direct evidence for the existence of electrical coupling between neurons of the MesV nucleus (Curti et al. 2012). Electrical coupling was symmetrical and junctions non-rectifying. Strikingly, although unusually strong (Curti et al. 2012), coupling was supported by a small number of channels ($\sim$200), which represented a very small proportion ($\sim$0.1 %) of the gap junction channels estimated to be present at the contacts (Fig. 5c). These calculations were possible because of the advantageous experimental access of these electrical synapses: (1) unlike most electrical synapses in mammalian brain, which are located at remote dendritic processes, the ability to identify the areas of contact between MesV neurons made it possible to estimate the average number of channels between these neurons, (2) the organization of coupling in the nucleus mostly in pairs of coupled cells facilitated electrophysiological analysis, and (3) the spherical somata and proximity of electrodes to somatic gap junctions permitted more rigorous biophysical analysis, allowing us to estimate the average number of conductive channels responsible for electrical coupling (assuming a unitary conductance of 15 pS; Srinivas et al. 1999a). Because functional gap junction channels characteristically have an open probability of $\sim$1 at a transjunctional voltage of zero (Srinivas et al. 1999b), these results indicate that electrical transmission at these somatic contacts likely results from a small number of channels with a high open probability rather than from larger number of them with low open probability.

The estimated fraction of open channels was similar for independent estimates of junctional conductance, using either indirect (from measurements of coupling coefficient and input resistance) or direct (voltage clamp) approaches, supporting the notion that a small fraction of channels are conductive. On the other hand, it is important to emphasize that these estimates assume a unitary conductance of Cx36 channels, which has been similarly reported by various groups (Srinivas et al. 1999b; Teubner et al. 2000), but which has not been so far validated in a native neuronal gap junction. The small proportion of open channels found is consistent with similar estimates obtained at mixed synapses formed by afferent terminals on the goldfish Mauthner cell, where only a small percentage of channels ($\sim$1 %) support the electrical component of a unitary mixed synaptic potential (Lin and Faber 1988) and where the number of channels was obtained from direct ultrastructural reconstruction of these terminals (Tuttle et al. 1986). Further, a similar fraction of open Cx36 gap junction channels ($\sim$0.1 %) was obtained in expression systems combining electrophysiological and imaging approaches (F. Bukauskas, personal communication). Despite our use of indirect methods, this agreement between the present results and those derived from other approaches in Mauthner cells and transfected cells suggests that our estimates of channel number were not significantly affected by our assumptions.

Docking of connexons requires a specific distance between the membranes of adjoining cells, and cell–cell channels that did not open might therefore contribute to the mechanical stability necessary to maintain functional intercellular channels. In this view both, conductive and nonconductive channels would play important functional roles in electrical transmission. It has been recently shown that the strength of electrical transmission is maintained by a balance between hemichannel insertion, cell–cell channel formation, and channel removal with an overall half-life of $\sim$1–3 h (Flores et al. 2012), a value that is consistent with previous estimates for turnover of gap junctions in expression systems and intact tissue (Beardslee et al. 1998; Herve et al. 2007). The generation of such striking disparity between conductive and nonconductive channels may reflect essential aspects of gap junction formation and maintenance, which include the lifetime of intercellular gap junction channels and the existence of heterogeneous populations of these channels within the plaque.

On the other hand, it is clear that stable interneuronal gap junctions can form with a very small number of connexins present in the junction. At neuronal gap junctions in the retina, for example, linear arrays of scores of connexons in what have been termed string gap junctions consist of only one or two particles in width. These strings constitute true gap junctions because their constituent connexons are seen to be docked across apposing membranes (Kamasawa et al. 2006), although it is not known what proportion, if any, of the channels in string junctions reside in a open conducting state.

Acknowledgments Supported in part by Comisión Sectorial de Investigación Científica (to S.C.), National Institutes of Health (NIH) Grants DC03186 and NS0552827 (to A.E.P.), and NIH Grant NS44395 and Canadian Institutes of Health Research (to J.I.N). Also supported by the program "Vinculación con científicos y tecnólogos uruguayos residentes en el exterior" of Agencia Nacional de Investigación e Innovación, Uruguay.

Reference

Baker R, Llinás R (1971) Electrotonic coupling between neurones in the rat mesencephalic nucleus. J Physiol 212:45–63

Beardslee MA, Laing JG, Beyer EC, Saffitz JE (1998) Rapid turnover of connexin43 in the adult rat heart. Circ Res 83:629–635

Bennett MVL (1997) Gap junctions as electrical synapses. J Neurocytol 26:349–366

Bennett MV, Pereda A (2006) Pyramid power: principal cells of the hippocampus unite! Brain Cell Biol 35:5–11

Bennett MV, Zukin RS (2004) Electrical coupling and neuronal synchronization in the mammalian brain. Neuron 41:495–511

Condorelli DF, Parenti R, Spinella F, Trovato Salinaro A, Belluardo N, Cardile V, Cicirata F (1998) Cloning of a new gap junction gene (Cx36) highly expressed in mammalian brain neurons. Eur J Neurosci 10:1202–1208

Connors BW, Long MA (2004) Electrical synapses in the mammalian brain. Annu Rev Neurosci 27:393–418

Curti S, Hoge G, Nagy JI, Pereda A (2012) Synergy between electrical coupling and membrane properties promotes strong synchronization of neurons of the mesencephalic trigeminal nucleus. J Neurosci 32:4341–4359

Flores C, Nannapaneni S, Davidson K, Yasumura T, Bennett MV, Rash JR, Pereda A (2012) Trafficking of gap junction channels at a vertebrate electrical synapse in vivo. Proc Nat Acad Sci USA 109:E573–E582

Herve JC, Derangeon M, Bahbouhi B, Mesnil M, Sarrouilhe D (2007) The connexin turnover, an important modulating factor of the level of cell-to-cell junctional communication: comparison with other integral membrane proteins. J Membr Biol 217:21–33

Hinrichsen CF (1970) Coupling between cells of the trigeminal mesencephalic nucleus. J Dent Res 49(6 suppl):1369–1373

Hinrichsen CF, Larramendi LM (1970) The trigeminal mesencephalic nucleus II. Electron microscopy. Am J Anat 127:303–319

Hormuzdi SG, Filippov MA, Mitropoulou G, Monyer H, Bruzzone R (2004) Electrical synapses: a dynamic signaling system that shapes the activity of neuronal networks. Biochim Biophys Acta 1662:113–137

Kamasawa N, Furman CS, Davidson KG, Sampson JA, Magnie AR, Gebhardt BR, Kamasawa M, Yasumura T, Zumbrunnen JR, Pickard GE, Nagy JI, Rash JE (2006) Abundance and ultrastructural diversity of neuronal gap junctions in the OFF and ON sublaminae of the inner plexiform layer of rat and mouse retina. Neuroscience 142:1093–1117

Kruger O, Plum A, Kim J-S, Winterhager E, Maxeiner S, Hallas G, Kirchhoff S, Traub O, Lamers WH, Willecke K (2000) Defective vascular development in connexin45-deficient mice. Development 127:4179–4193

Li X, Simard JM (2001) Connexin45 gap junction channels in rat cerebral vascular smooth muscle cells. Am J Physiol 281: H1890–H1898

Li X, Olson C, Lu S, Kamasawa N, Yasumura T, Rash JE, Nagy JI (2004a) Neuronal connexin36 association with zonula occludens-1 protein (ZO-1) in mouse brain and interaction with the first PDZ domain of ZO-1. Eur J Neurosci 19:2132–2146

Li X, Ionescu AV, Lynn BD, Lu S, Kamasawa N, Morita M, Davidson KG, Yasumura T, Rash JE, Nagy JI (2004b) Connexin47, connexin29 and connexin32 co-expression in oligodendrocytes and Cx47 association with zonula occludens-1 (ZO-1) in mouse brain. Neuroscience 126:611–630

Lin JW, Faber DS (1988) Synaptic transmission mediated by single club endings on the goldfish Mauthner cell. I. Characteristics of electrotonic and chemical postsynaptic potentials. J Neurosci 8:1302–1312

Llinas R (1975) Electrical synaptic transmission in the mammalian central nervous system. In: Santini M (ed) Proceedings of the golgi centennial symposium. Raven Press, New York, pp 379–386

Meier C, Dermietzel R (2006) Electrical synapses–gap junctions in the brain. Results Probl Cell Differ 43:99–128

Nagy JI, Dudek FE, Rash JE (2004) Update on connexins and gap junctions in neurons and glia in the mammalian nervous system. Brain Res Rev 47:191–215

Pedroarena CM, Pose IE, Yamuy J, Chase MH, Morales FR (1999) Oscillatory membrane potential activity in the soma of a primary afferent neuron. J Neurophysiol 82:1465–1476

Peinado A, Yuste R, Katz LC (1993) Gap junctional communication and the development of local circuits in neocortex. Cereb Cortex 3:488–498

Penes M, Li X, Nagy JI (2005) Expression of zonula occludens-1 (ZO-1) and the transcription factor ZO-1-associated nucleic acid-binding protein (ZONAB/MsY3) in glial cells and co-localization at oligodendrocyte and astrocyte gap junctions in mouse brain. Eur J Neurosci 22:404–418

Pereda AE, Rash JE, Nagy JI, Bennett MV (2004) Dynamics of electrical transmission at club endings on the Mauthner cells. Brain Res Rev 47:227–244

Söhl G, Degen J, Teubner B, Willecke K (1998) The murine gap junction gene connexin36 is highly expressed in mouse retina and regulated during brain development. FEBS Lett 428:27–31

Srinivas M, Costa M, Gao Y, Fort A, Fishman GI, Spray DC (1999a) Voltage dependence of macroscopic and unitary currents of gap junction channels formed by mouse connexin50 expressed in rat neuroblastoma cells. J Physiol 517:673–689

Srinivas M, Rozental R, Kojima T, Dermietzel R, Mehler M, Condorelli DF, Kessler JA, Spray DC (1999b) Functional properties of channels formed by the neuronal gap junction protein connexin36. J Neurosci 19:9848–9855

Teubner B, Degen J, Söhl G, Güldenagel M, Bukauskas FF, Trexler EB, Verselis VK, De Zeeuw CI, Lee CG, Kozak CA, Petrasch-Parwez E, Dermietzel R, Willecke K (2000) Functional expression of the murine connexin 36 gene coding for a neuron-specific gap junctional protein. J Membr Biol 176:246–249

Tuttle R, Masuko S, Nakajima Y (1986) Freeze-fracture study of the large myelinated club ending synapse on the goldfish Mauthner cell: special reference to the quantitative analysis of gap junctions. J Comp Neurol 246:202–211

J Membrane Biol (2012) 245:291–301
DOI 10.1007/s00232-012-9450-6

Phosphorylation of Serine Residues in the C-terminal Cytoplasmic Tail of Connexin43 Regulates Proliferation of Ovarian Granulosa Cells

Paul W. Dyce · Rachael P. Norris · Paul D. Lampe · Gerald M. Kidder

Received: 30 March 2012 / Accepted: 1 June 2012 / Published online: 24 June 2012

Abstract Connexin43 (Cx43) forms gap junctions that couple the granulosa cells of ovarian follicles. In Cx43 knockout mice, follicle growth is restricted as a result of impaired granulosa cell proliferation. We have used these mice to examine the importance of specific Cx43 phosphorylation sites in follicle growth. Serines at residues 255, 262, 279, and 282 are MAP kinase substrates that, when phosphorylated, reduce junctional conductance. Mutant forms of Cx43 were constructed with these serines replaced with amino acids that cannot be phosphorylated. These mutants were transduced into Cx43 knockout ovarian somatic cells that were combined with wild-type oocytes and grafted into immunocompromised female mice permitting follicle growth in vivo. Despite residues 255 or 262 being mutated to prevent their being phosphorylated, recombinant ovaries constructed with these mutants were able to rescue the null phenotype, restoring complete folliculogenesis. In contrast, Cx43 with serine to alanine mutations at both residues 279 and 282 or at all four residues failed to rescue folliculogenesis; the mutant molecules were largely confined to intracellular sites, with few gap junctions. Using an in vitro proliferation assay, we confirmed a decrease in proliferation of granulosa cells expressing the double mutant construct. These results indicate that Cx43 phosphorylation by MAP kinase at serines 279 and 282 occurs in granulosa cells of early follicles and that this is involved in regulating follicle development.

Keywords Cx43 · Folliculogenesis · Granulosa cell · Oocyte growth · Phosphorylation · Proliferation

P. W. Dyce · G. M. Kidder (✉)
Department of Physiology and Pharmacology, The University of Western Ontario and Children's Health Research Institute, 800 Commissioners Road East, London, ON N6C 2V5, Canada
e-mail: gerald.kidder@schulich.uwo.ca

R. P. Norris · P. D. Lampe
Fred Hutchinson Cancer Research Center, 1100 Fairview Ave. N, PO Box 19024, Seattle, WA 98109, USA

Connexin43 (Cx43), the most widely expressed connexin, is differentially phosphorylated at a dozen or more serine residues throughout its life cycle (Lampe and Lau 2004; Solan and Lampe 2009). Protein kinase C (PKC) (Lampe et al. 2000; Saez et al. 1997), mitogen-activated protein kinase (MAPK) (Warn-Cramer et al. 1996), AKT (Park et al. 2007), casein kinase 1 (CK1) (Cooper and Lampe 2002), $p34^{cdc2}$ (Kanemitsu et al. 1998; Lampe et al. 1998), SRC (Crow et al. 1990; Swenson et al. 1990) and likely other kinases can directly phosphorylate Cx43. Kinase activation can either effect an acute (within minutes) reduction of channel conductance and/or open probability, or over a somewhat longer time frame (tens of minutes to hours) can lead to compromised Cx43 targeting/retention at gap junctions and in some cases, altered Cx43 gene expression. Cx43 has an unusually short half-life in cultured cells and tissues (Beardslee et al. 1998; Crow et al. 1990; Laird et al. 1991; Lampe 1994; Musil et al. 1990). Cx43 turnover appears to be highly regulated with both MAPK- and PKC-mediated phosphorylation implicated in keeping Cx43 hemichannels closed (Goodenough and Paul 2003) and enhancing gap junction turnover (Leithe and Rivedal 2004).

Much of the work exploring the involvement of protein kinases in regulating gap junction assembly and function has come from the use of cultured cells, with little attention to in vivo models. To explore the involvement of Cx43

C-terminal tail phosphorylation in vivo, we have chosen the mouse ovarian follicle. In the mouse, Cx43 is expressed in all stages of follicle development from the primary through the preovulatory stage where it forms gap junctions connecting granulosa cells (both cumulus and mural) with each other; another connexin, Cx37, forms gap junctions coupling the cumulus granulosa cells with the developing oocyte, thus linking the germline and somatic components of the follicle into a functional syncytium allowing diffusional transfer of small molecules throughout (reviewed by Kidder and Vanderhyden 2010). Gene knockout studies have demonstrated that Cx43 is essential for follicle growth because in its absence, granulosa cell proliferation is arrested or impaired, depending on strain background (Ackert et al. 2001; Tong et al. 2006). Furthermore, oocytes developing within Cx43-deficient follicles fail to grow properly and do not achieve meiotic competence (Ackert et al. 2001). This dependency of follicle and oocyte growth on Cx43 provides a testing ground for exploring the importance of C-terminal tail phosphorylation in connexin function.

In the present study, we have exploited the recombinant-reaggregated ovary technique (Eppig and Wigglesworth 2000) to evaluate the importance of specific Cx43 phosphorylation sites in oocyte and follicle growth. Cx43 knockout granulosa cells were transduced with wild-type Cx43 or Cx43 in which specific serines, known to be phosphorylated by MAP kinases, had been replaced with alanine, to prevent phosphorylation, or aspartic acid, to mimic phosphorylation. The transduced granulosa cells were then aggregated with wild-type oocytes to form recombinant ovaries that were grafted under the kidney capsules of immunocompromised adult females to allow for in vivo follicle growth; previous work using this technique had confirmed the ability of transduced wild-type Cx43 to rescue folliculogenesis when Cx43-deficient granulosa cells were combined in grafts with wild-type oocytes (Gittens and Kidder 2005). Using this approach, we were able to identify serines whose phosphorylation is involved in regulating Cx43 function in support of oocyte and follicle growth.

Materials and Methods

Ovary Collection

Ovaries lacking Cx43 were obtained from matings of heterozygous (*Gja1*$^{+}$/*Gja1*$^{-}$) C57BL/6 male and female mice. Immunocompromised adult SCID females (CB17/Icr*Prkdc*^{scid}/IcrIcoCrl, originally obtained from Charles River, St-Constant, QC and maintained in the barrier facility of the Robarts Research Institute at the University of Western Ontario) were used as graft recipients. Fetuses were obtained from pregnant dams at day 17.5–18.5 of gestation after CO_2 anesthesia and cervical dislocation. Fetuses were removed from the uteri and decapitated. A tail snip was collected from each female fetus for genotyping. Ovaries were removed and cleaned of surrounding tissue, then cultured on a 3-μm membrane cell culture insert (VWR USA, Radnor, PA) for 8–10 h in Waymouth MB 752/1 medium (Invitrogen Canada, Burlington, ON) supplemented with 10 % fetal bovine serum and 1 × antibiotic/antimycotic (both from Invitrogen) while the fetuses were genotyped.

Genotyping

The polymerase chain reaction (PCR) was applied to proteinase K-digested tail snips to determine the genotypes of the fetal ovary donors. PCR was carried out utilizing two separate reactions that shared a downstream primer (5′-ACTTTTGCCGCCTAGCTATCCC-3′) specific for a part of the Cx43 C-terminal coding region which is retained in the null allele; see Reaume et al. (1995). To detect the presence of the wild-type *Gja1* allele, an upstream primer (5′-CCCCACTCTCACCTATGTCTCC-3′) was used in conjunction with the downstream primer whereas to detect the null allele, an upstream primer located in the neo cassette (5′-GCTTGCCGAATATCATGGTGGA-3′) was used with the downstream primer. One microliter of the diluted digestions were used per PCR. PCR was carried out using a "touch down" (65–58 °C) protocol for a total of 40 cycles. PCR products were visualized on a 1 % agarose gel containing ethidium bromide and documented using a Bio-Rad imaging system and Quantity One software (Bio-Rad USA, Hercules, CA).

Retroviral Vector Construction

Cloned cDNAs encoding Cx43 with C-terminal mutations at various serine residues were constructed as described (Solan et al. 2007). Serine-to-alanine and serine-to-aspartate mutations were made using the GeneTailor (Invitrogen) or In-Fusion (Clontech Laboratories, Inc. Mountain View, CA) site-directed mutagenesis system applied to full-length Cx43 cDNA that had been cloned into the mammalian expression vector pIREShyg (Clonetech). The mutant cDNAs were inserted into the AP2 retroviral vector that contains an internal ribosomal entry site (IRES) that permits independent translation of the connexin and enhanced green fluorescent protein (EGFP; see Tong et al. 2007 for vector design). Vector lacking connexin cDNA served as negative control and vector encoding wild-type Cx43 served as positive control. The vector was packaged using 293 GPG packaging cells to produce active virus which was concentrated using Amicon Ultra Centrifugal Filter

Devices (Millipore USA, Billerica, MA) according to the manufacturer's protocol.

Construction of Chimeric Ovaries

Chimeric ovaries combining wild-type oocytes with Cx43-deficient (*Gja1*$^{-/-}$), retrovirally transduced ovarian somatic cells were constructed essentially as described by Gittens and Kidder (2005) with minor modifications. Ovaries were grouped on the basis of genotype (four to six per group), washed briefly in HBSS (Invitrogen) supplemented with 1 mg/ml bovine serum albumin (BSA; Sigma, Oakville, ON), and dissociated in trypsin-EDTA (0.05 % trypsin, 0.53 mM EDTA, Invitrogen) for 45 min (Eppig and Wigglesworth 2000). The dissociated cells were plated in TCM199 (Invitrogen) supplemented with 10 % fetal bovine serum (M199-FBS) and antibiotic-antimycotic (Invitrogen) on cell culture-treated 3.5 cm dishes (Falcon) or glass coverslips and cultured overnight at 37 °C in 5 % CO_2/5 % O_2/90 % N_2. After removal of the oocytes, the remaining somatic cells were infected for 48 h with one of the retroviral expression vectors. To prepare reaggregated ovaries, oocytes obtained from wild-type ovaries were washed with M199-FBS and placed in a 15-ml conical tube. The retrovirally transduced somatic cells were trypsinized, washed with M199-FBS, and pelleted by centrifuging at 500×*g* for 5 min. The pelleted cells were then resuspended in 500 µl M199-FBS and added to the washed oocytes at an equal ratio (e.g., wild-type oocytes from four ovaries were combined with the somatic cell pellet from four Cx43-deficient ovaries) along with 7 µl/ml phytohemagglutinin (0.05 %, Sigma) in a 1.5-ml tube, followed by pelleting at 500 x g for 5 min. The pellets were carefully dislodged from the tubes and cultured overnight on 3 µm cell culture inserts at 37 °C in 5 % CO_2 in air. The reaggregated ovaries were transplanted under the kidney capsules of ovariectomized SCID mice (one graft per mouse) and incubated 21–28 days as described previously (Gittens and Kidder 2005; Tong et al. 2007).

Histology

Reaggregated ovaries were recovered from the host kidneys and fixed in Bouin solution, then embedded in paraffin and sectioned at 6 µm onto Superfrost Plus slides (Fisher Canada, Ottawa, ON). The slides were dried, deparaffinized and stained with hematoxylin and eosin using a standard protocol. Measurements of oocyte diameters were taken using an Olympus inverted microscope and Open Lab software (Leica Microsystems Canada, Concord, ON). Three sections were analyzed from each of at least three recombinant ovary grafts.

Immunolocalization of Total and pS279/282 Cx43 in Natural Ovaries

Ovaries from 3 to 4 week old female C57BL/6 mice were placed into cryomolds containing O.C.T. (Tissue Tek), and were frozen on an aluminum block cooled in liquid nitrogen. Eight- to 10-µm-thick sections were cut and left at room temperature to dry 24–48 h before fixing. Sections were fixed in chilled 50:50 methanol/acetone at 4 °C for 10–15 min then dried for 5 min or less. Sections were rinsed twice with 1 × PBS to remove excess OCT and blocked in 1 % BSA in PBS with 5 % normal goat serum (Sigma) for 30 min. Sections were outlined with a PAP pen to minimize the volume of blocking buffer and antibody needed. They were treated for 1 h at room temperature with two primary antibodies: 1 µg/ml CT1 anti-Cx43 (Sosinsky et al. 2007) and 1:5,000 anti-phospho-S279/282 Cx43 prepared at the Fred Hutchinson Cancer Research Center against peptide S279/282 (CAPL(pS)PM(pS)PPGY-amide (Solan and Lampe 2008). Secondary antibody treatment was also carried out for 1 h at room temperature using Alexafluor 488-conjugated goat anti-mouse and Alexafluor 546-conjugated goat anti-rabbit, both from Invitrogen. Nuclei were labeled with DAPI (300 nM, Invitrogen). Sections were imaged using a Nikon E400 epifluorescence microscope with a Nikon DS-Qi1Mc camera.

Immunolocalization of Total Cx43 in Recombinant Ovaries

Grafts were recovered into TCM-FBS and follicles were liberated using 25 gauge needles. The follicles were plated on glass coverslips and cultured 24 to 48 h at 37 °C in M199-FBS in 5 % CO_2/5 % O_2/90 % N_2. The cells were washed with PBS, fixed with 4 % paraformaldehyde (PFA) for 20 min then blocked in PBS containing 5 % BSA (PBS-BSA) for 1 h at room temperature before immunolabeling with Cx43 primary antibody (Sigma cat. no. C6219; 1/5,000 in PBS-BSA) overnight at 4 °C. Excess primary antibody was removed by washing three times with PBS-BSA before the secondary (goat anti-rabbit Alexafluor 488, 1/1,000, Invitrogen) was added for 1 h at room temperature. Secondary antibody was removed by washing three times in PBS-BSA, then the nuclei were labelled with Hoechst 33342 (1 µg/ml in PBS) for 8 min at room temperature. A final PBS wash was performed before the coverslips were mounted on slides with Airvol. The cells were imaged using a Zeiss LSM 510 META confocal microscope and ZEN imaging software (Carl Zeiss Canada, Toronto, ON).

Cell Proliferation Assay

Cx43-deficient ovarian somatic cells, devoid of oocytes, were plated directly onto 13 mm Thermanox plastic coverslips (VWR Canada, Mississauga, ON). The Click-iT EdU Imaging Kit (Invitrogen) was used to measure cell proliferation. After 48-h viral vector infection, cells were cultured with 10 μM EdU (5-ethynyl-2′-deoxyuridine) for 12 h then fixed in 4 % PFA for 20 min. The fixative was washed off using PBS containing 3 % BSA (PBS-BSA) and then the cells were incubated for 20 min with 0.5 % Triton X-100, washed once with PBS-BSA and incubated 30 min with the Click-iT reaction cocktail followed by washing with PBS-BSA. Nuclei were labelled using the Hoechst dye provided in the kit and according to the manufacturer's protocol. The coverslips were mounted onto slides using Airvol and documented using a fluorescence photomicroscope (Leica Microsystems Canada, Concord, ON). The ratio of EdU positive cells to total cells was determined by counting five fields per coverslip and each experiment was conducted three times.

Statistical Analyses

Statistical analysis of follicle stage distributions was performed using a chi-square test and analysis of oocyte size and granulosa cell proliferation rate data was conducted by one way ANOVA followed by Tukey's post test using GraphPad Prism software (La Jolla, CA). Results were considered significant if $P < 0.05$.

Results

Specific Serines in the C-terminal Tail of Cx43 Are Phosphorylated during Follicle Growth

Cx43 phosphorylated at serines 279/282 is located primarily at perinuclear sites in small primary and secondary follicles (top left and bottom right, respectively, of Fig. 1a), overlapping to some extent with total Cx43 (arrowheads). In larger follicles (Fig. 1c), there is increased expression of total Cx43 in plaque-like structures at cell borders (arrows) but reduced expression of Cx43 phosphorylated at serines 279/282, some of which continues to exhibit perinuclear colocalization with Cx43 (arrowhead). This difference in level and localization of Cx43 phosphorylated at serines 279/282 in different follicle stages is clearer when its immunostaining is shown alone (Fig. 1b, d). We conclude that the relative level of Cx43 phosphorylated at serines 279 and 282 is higher in earlier follicle stages where there are fewer gap junctions.

Mutation of Phosphorylation Sites S279 and S282 Abrogates the Ability of Cx43 to Rescue Folliculogenesis in Cx43-deficient Ovaries

To confirm that the recombinant reaggregated ovary system can be used to identify follicle growth differences in the presence or absence of Cx43, reaggregated ovaries were constructed with wild-type oocytes combined with Cx43-deficient somatic cells that had been transduced with either wild-type Cx43 or the empty vector control construct. These were transplanted under the kidney capsules of ovariectomized immunodeficient adult females and allowed to develop for 21–25 days. Ovaries containing Cx43-deficient somatic cells transduced with wild-type Cx43 produced follicles representing all stages of development, from primary to late antral (Fig. 2a, Table 1) demonstrating the ability of the transduced connexin to rescue the Cx43-deficient follicles from growth arrest. Conversely, in ovaries made with Cx43-deficient somatic cells transduced with the empty vector control, only primary stage follicles were observed (Fig. 2b). To confirm that the rescue of folliculogenesis after transduction with wild-type Cx43 did not result from contamination with wild-type granulosa cells, follicles were recovered from the grafts and immunostained for Cx43. Follicles derived from Cx43-transduced somatic cells (Fig. 2c) showed typical punctate immunostaining between granulosa cells whereas follicles derived from empty vector-transduced somatic cells did not show any Cx43 immunofluorescence (Fig. 2d). These results confirmed the validity of the recombinant-reaggregated ovary system for testing the ability of phosphorylation site mutants to support oocyte and follicle growth.

The first mutant phosphorylation site construct tested contained all four MAPK sites in the C-terminal tail (S255, S262, S279, and S282) mutated from serine to alanine. When this construct was used to transduce Cx43-deficient somatic cells for recombinant ovary construction, the resulting follicles were restricted to a single layer of granulosa cells, similar to the results seen in the empty vector controls (Fig. 3a, Table 1). Likewise, mutating both serine 279 and serine 282 to alanine resulted in the majority of follicles remaining restricted to the primary stage with only a few reaching the two layer early secondary stage (Fig. 3b, Table 1). We then tested individual sites for their ability to rescue folliculogenesis. When the transduced connexin contained a single serine to alanine mutation at residue 255, folliculogenesis proceeded to the antral stage suggesting phosphorylation of that residue is not critical in this context (Fig. 3c). When the same serine was mutated to aspartic acid (S255D), the same result was seen (Fig. 3d). Likewise, the S262D mutation supported folliculogenesis to the antral stage, rescuing the null mutant

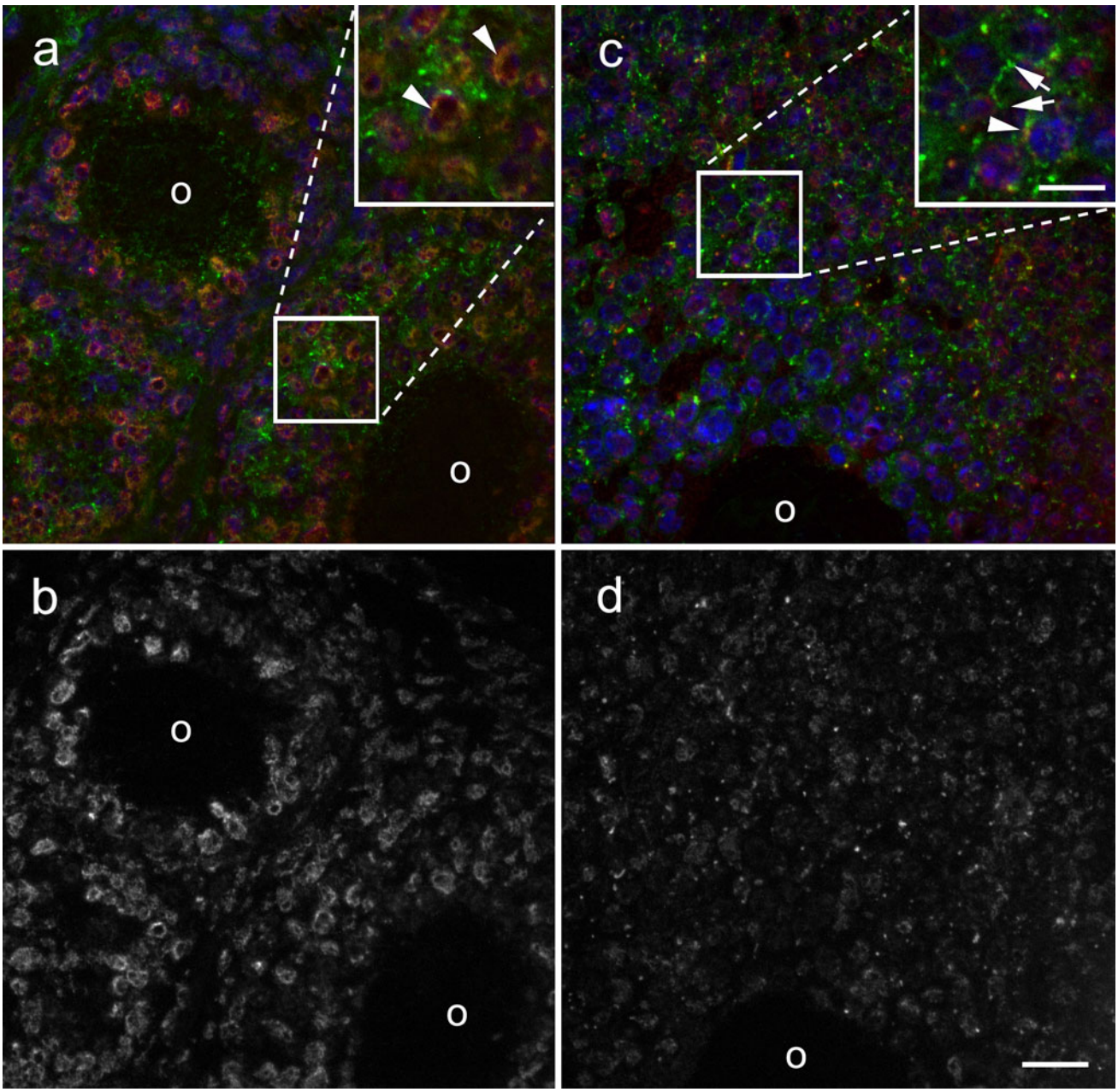

Fig. 1 Cx43 in primary ovarian follicles is mainly perinuclear and phosphorylated at S279/282, whereas secondary follicles show more junctional staining. **a** A primary follicle (*upper left*) and a small secondary follicle (*lower right*) show perinuclear and junctional localization of total Cx43 (*green*) and predominantly perinuclear localization of Cx43 phosphorylated at S279/282 (*red*). *Inset,* magnified view of the colocalization of total Cx43 and Cx43 phosphorylated at S279/282, indicated by *arrowheads.* **b** A single channel image of the field in (a) shows more clearly the perinuclear localization of Cx43 phosphorylated at S279/282. **c** In a larger secondary follicle, a greater proportion of total Cx43 is in junctional plaques and less is perinuclear. The magnified *inset* shows an example of total Cx43 in plaques at a cell–cell interface arrows and colocalization of total Cx43 with Cx43 phosphorylated at S279/282 (*arrowhead*). **d** A single channel image of the field in (c) reveals that there is less perinuclear localization of Cx43 phosphorylated at S279/282 and an overall lower level of immunostaining, presumably reflecting a reduced level of phosphorylation. O, oocyte. Scale bars = **c** 10 μm; **d** 20 μm

phenotype (Fig. 3e, Table 1). Thus, phosphorylation at neither the S255 nor the S262 site is critical for folliculogenesis. Furthermore, the follicle stage distributions in the mutant-expressing recombinant grafts that exhibited limited follicle growth were significantly different from the distribution in grafts expressing wild-type Cx43.

The localization of Cx43 within the recovered follicles was examined to determine if the phosphorylation mutants had an

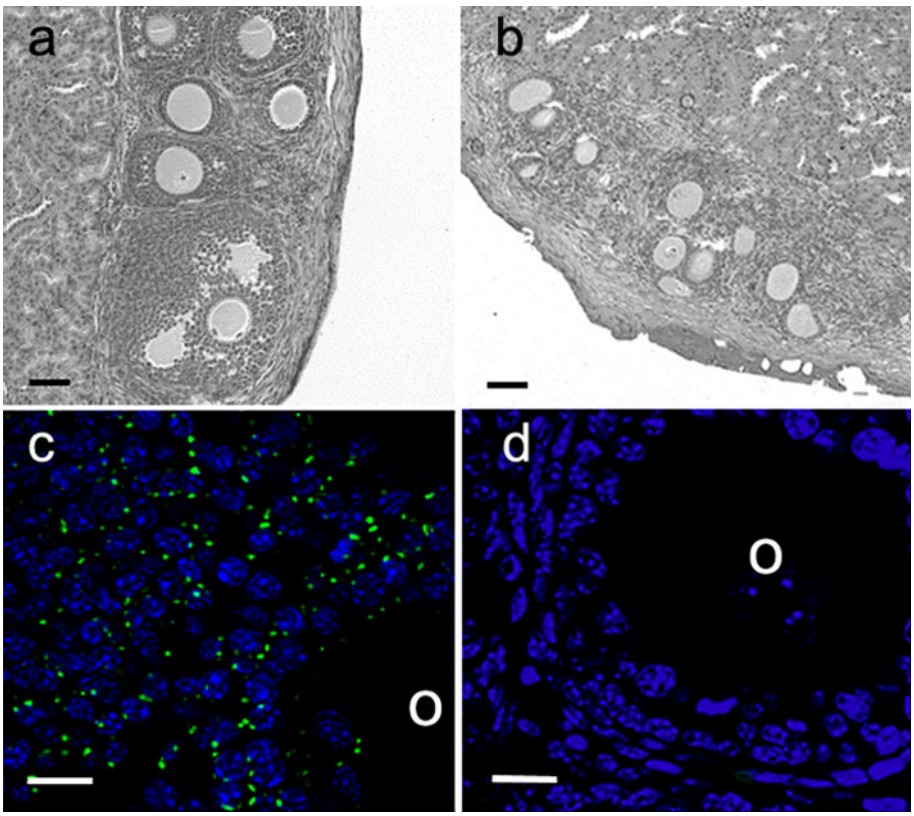

Fig. 2 Folliculogenesis can be rescued by the transduction of wild-type Cx43 into Cx43-deficient ovarian somatic cells and aggregation with wild-type oocytes. **a** Section of a grafted recombinant ovary made with wild-type Cx43-transduced somatic cells. A full range of follicle stages is present in the ovary. **b** Section of a grafted recombinant ovary made with somatic cells transduced with the empty vector. Follicle development was limited to the primary and early secondary stages in these ovaries. **c** Immunofluorescence revealed robust Cx43 expression in gap junction plaques in the cumulus cells of recombinant ovaries made with wild-type Cx43-transduced somatic cells. **d** Cx43 was undetectable in recombinant ovaries made with somatic cells transduced with the empty vector. O, oocyte. Scale bars = **a**, **b** 50 μm; **c**, **d** 10 μm

effect on gap junction plaque formation within the grafted recombinants. Plaques containing Cx43 were found at the junctional membranes of some granulosa cells in all groups tested, although follicles from reaggregated ovaries expressing the quadruple mutant (S255A + S262A + S279A + S282A) exhibited few gap junction plaques and more intracellular Cx43 (Fig. 4a). Similarly, follicles expressing the double mutant (S279A + S282A), while having more membrane plaques than ovaries constructed with the quadruple mutant, also exhibited cytoplasmic immunostaining (Fig. 4b). In contrast, typical punctate membrane immunostaining and little cytoplasmic immunostaining was observed in reaggregated ovaries expressing the single mutants S255A, S255D, and S262D that supported folliculogenesis (Fig. 4c–e).

Oocyte Growth Is Retarded in Reaggregated Ovaries Where Follicle Growth Is Impaired

In order to determine if the inability to phosphorylate the selected MAPK sites in Cx43 had an effect on oocyte growth, oocyte diameters were measured (Table 2). Ovaries constructed of wild-type oocytes and Cx43-deficient somatic cells transduced with wild-type Cx43 had a mean oocyte diameter of 61.34 ± 1.47 μm (Fig. 5). This was significantly ($P < 0.01$) greater than the mean diameter (35.47 ± 1.12 μm) of oocytes obtained from reaggregated ovaries constructed with wild-type oocytes and empty vector-transduced somatic cells. Likewise, the follicles of reaggregated ovaries expressing the quadruple mutant contained oocytes that were significantly smaller (at 47.05 ± 1.63 μm mean diameter) than those expressing wild-type Cx43 ($P < 0.001$); however, they were significantly larger than the oocytes in the empty vector control ovaries ($P < 0.01$) The single mutation S255A resulted in oocytes whose mean diameter (60.43 ± 1.69 μm) was not significantly different from that of follicles transduced with wild-type Cx43. Similarly, oocytes averaged 60.96 ± 1.22 μm and 62.11 ± 1.18 μm in diameter when combined with somatic cells expressing the S255D and S262D mutants, respectively, neither of which was significantly different from oocytes combined with wild-type Cx43-transduced somatic cells. Oocytes within follicles transduced with the double mutant S279A and S282A were significantly ($P < 0.01$) smaller (at 43.99 ± 1.64 μm) than those in follicles expressing wild-type Cx43 indicating that the ability to phosphorylate one or both of those sites is essential for oocyte growth (Fig. 5).

Inability to Phosphorylate S279 and S282 Restricts Proliferation of Granulosa Cells In Vitro

The inability of the transduced S279A/S282A double mutant construct to rescue folliculogenesis in Cx43-deficient reaggregated ovaries suggested failure of the mutant

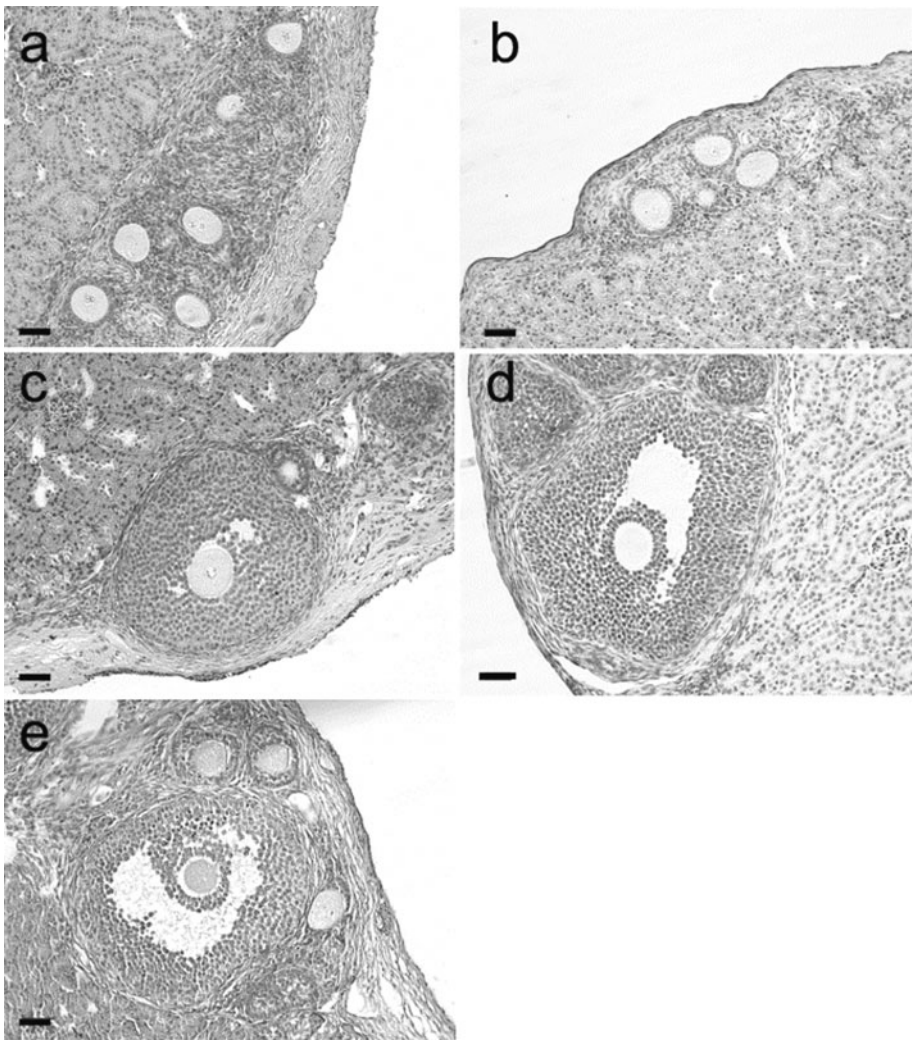

Fig. 3 Folliculogenesis is impaired in recombinant ovaries constructed with somatic cells expressing Cx43 with 2 or more MAPK site mutations. **a** In ovaries constructed with somatic cells expressing the quadruple mutant S255A + S262A + S279A + S282A, folliculogenesis was restricted to the primary stage. **b** When constructed with somatic cells expressing the double mutant S279A + S282A, ovaries were devoid of follicles beyond the primary/early secondary stage. **c–e** In ovaries constructed with somatic cells expressing the single MAPK site mutations S255A (**c**), S255D (**d**), or S262D (**e**), folliculogenesis reached the antral stage. Scale bars = 50 μm

Table 1 Distribution of follicle classes in recombinant ovaries

Transduced connexin	No. of ovary grafts	No. of follicles analyzed	Follicles at stage, *n* (%)			
			Primary (1 layer)	Early secondary (≤2 layers)	Secondary (>2 layers)	Tertiary (antral)
None	3	54	54 (100)	0	0	0
Wild type	4	53	12 (22.6)	10 (18.9)	13 (24.5)	18 (34.0)
S255A + S262A + S279A + S282A	3	69	69 (100)	0	0	0
S279A + S282A	3	52	47 (90.4)	5 (9.6)	0	0
S255A	3	41	16 (39.0)	7 (17.1)	5 (12.2)	13 (31.7)
S255D	4	69	39 (56.5)	9 (13.0)	12 (17.4)	9 (13.0)
S262D	3	46	17 (36.9)	14 (30.4)	5 (10.9)	10 (21.7)

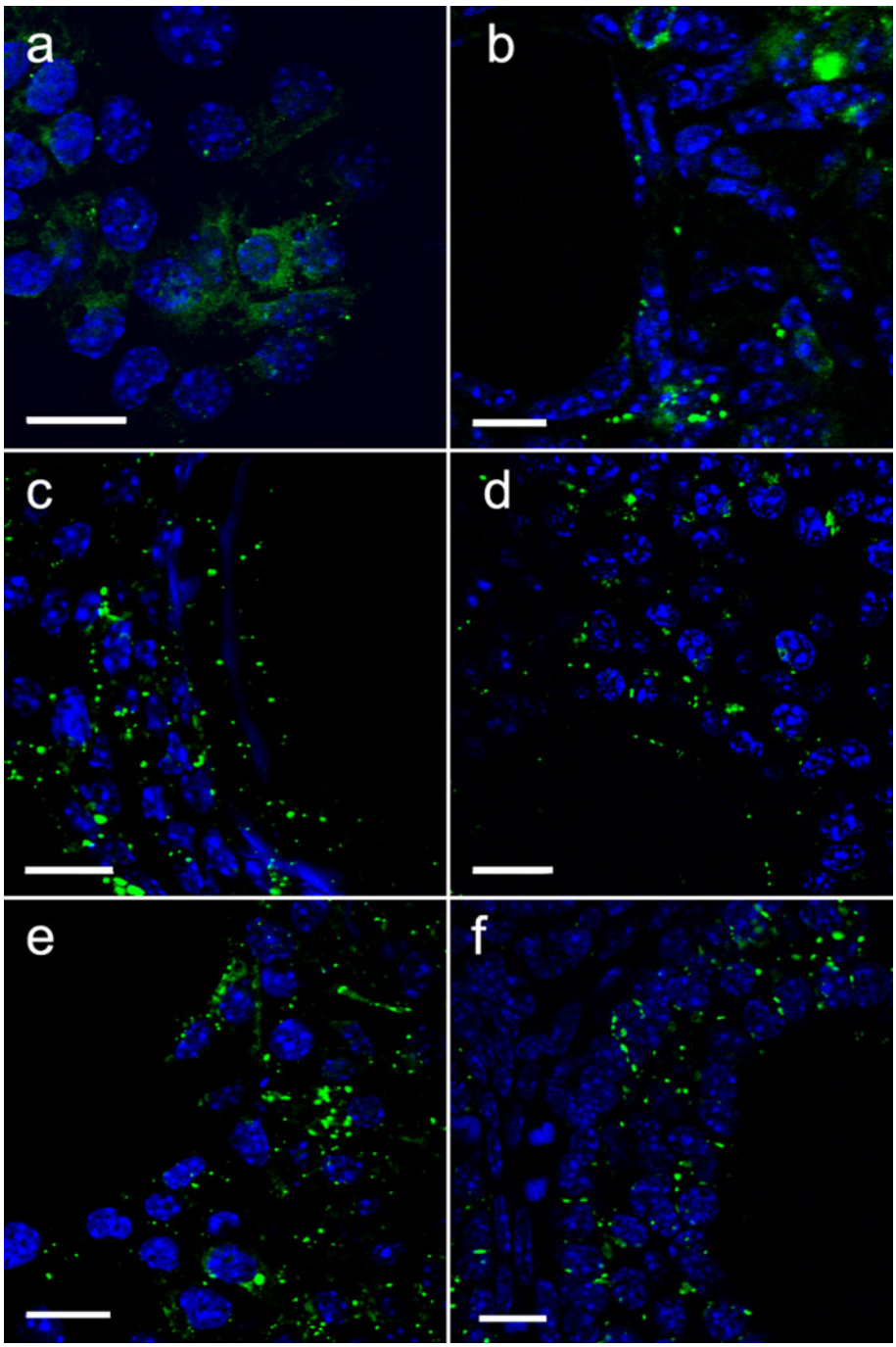

Fig. 4 Immunofluorescence analysis reveals altered Cx43 subcellular distribution in granulosa cells expressing mutants with two or more MAPK site mutations. **a** Ovaries made with somatic cells expressing the quadruple mutation S255A + S262A + S279A + S282A exhibited few membrane plaques in the granulosa cells but ample intracellular staining. **b** Intracellular Cx43 immunostaining was also present in follicles expressing the double mutant S279A + S282A, but membrane plaques were more numerous than with the quadruple mutant. **c–f** Granulosa cells in recombinant ovaries expressing the single mutations S255A (**c**), S255D (**d**), and S262D (**e**) all displayed numerous membrane plaques with little intracellular immunoreactivity as in ovaries made with somatic cells expressing wild-type Cx43 (**f**). Scale bars = 10 μm

to support granulosa cell proliferation. To test this hypothesis directly, we infected Cx43-deficient ovarian somatic cells with the various wild-type and mutant vector constructs and after 48 h, added EdU and allowed the cells to incorporate this fluorescent nucleoside analog for a further 12 h in vitro. Cx43-deficient cells transduced with the quadruple mutant proliferated at a significantly lower rate (8.02 ± 0.35 %; $P < 0.05$) when compared with cells

Table 2 Oocyte diameters (microns) in recombinant ovaries

Transduced connexin	Total oocytes analyzed	Mean ± SEM
None	44	35.47 ± 1.12
Wild type	28	61.34 ± 1.47
S255A + S262A + S279A + S282A	42	47.05 ± 1.63
S279A + S282A	52	43.99 ± 1.64
S255A	28	60.43 ± 1.69
S255D	44	60.96 ± 1.22
S262D	26	62.11 ± 1.18

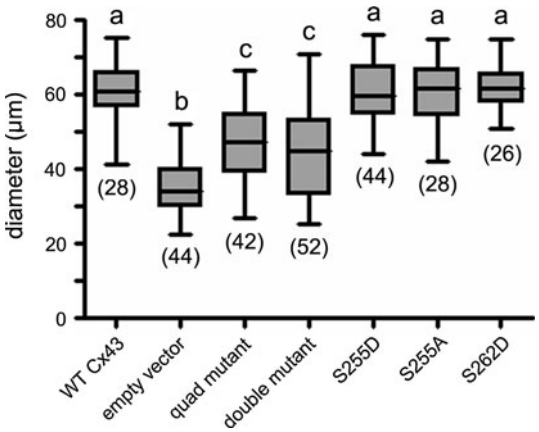

Fig. 5 Oocyte growth was diminished in recombinant follicles that failed to develop beyond the early secondary stage. Oocyte diameters were measured in follicles constructed from ovarian somatic cells transduced with (*left to right*) wild-type Cx43, empty vector, the quadruple mutant S255A + S262A + S279A + S282A, the double mutant S279A + S282A, S255D, S255A, and S262D. The number of oocytes measured for each experimental group is shown in parentheses. Mean diameters with different letters above them differ significantly ($P < 0.05$)

expressing wild-type Cx43 (20.29 ± 2.38 %); indeed, the quadruple mutant construct was not significantly better than the empty vector, which supported a proliferation rate of only 5.74 ± 0.84 % (Fig. 6). Similar results were seen with the S279A/S282A double mutant-transduced ovarian somatic cells: the proliferation rate was significantly lower (4.49 ± 0.30 %) when compared to the wild-type Cx43-transduced cells (Fig. 6, $P < 0.01$) and not significantly different from the empty vector control. The single mutants supporting rescue of folliculogenesis were not significantly different from wild-type Cx43 with S255D proliferating at 24.34 ± 2.82 %, S255A at 28.46 ± 3.70 %, and S262D at 22.07 ± 2.16 %, indicating that the inability of the double and quadruple mutants to rescue folliculogenesis in Cx43-deficient reaggregated ovaries results from diminished granulosa cell proliferation.

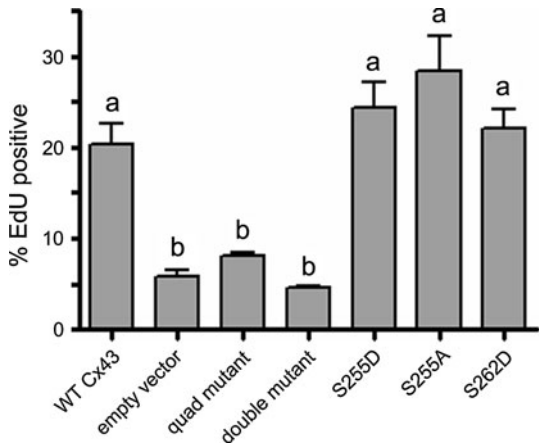

Fig. 6 Failure of recombinant follicles to develop beyond the early secondary stage is due at least in part to reduced granulosa cell proliferation. A 12-h in vitro EdU incorporation assay was used to measure proliferation of Cx43-deficient granulosa cells transduced with (*left to right*) wild-type Cx43, empty vector, the quadruple mutant S255A + S262A + S279A + S282A, the double mutant S279A + S282A, S255D, S255A, and S262D. Mean EdU incorporation frequencies with different letters above them differ significantly ($P < 0.05$)

Discussion

During the development of ovarian follicles, Cx43 expression in granulosa cells is required for both follicle and oocyte growth (Kidder and Vanderhyden 2010). The results of this study allowed us to conclude that phosphorylation of serine residues in the C-terminal cytoplasmic tail of Cx43, known to be targets for MAP kinases, occurs in the early stages of folliculogenesis and is involved in regulating granulosa cell proliferation. To our knowledge, this is the first demonstration that phosphorylation of specific Cx43 serines plays a role in cell proliferation in vivo. Previous work had demonstrated that phosphorylation of Cx43 in mature, preovulatory follicles by MAP kinases occurs in response to luteinizing hormone (LH) (Sela-Abramovich et al. 2005, 2008). LH treatment results in phosphorylation of Cx43 at S255, S262, S279, and S282 (Norris et al. 2008), causing the attenuation of gap junctional communication among the cumulus cells that triggers oocyte maturation. The present work extends to earlier stages of folliculogenesis the importance of MAP kinases in the life cycle of ovarian follicles.

The majority of connexin proteins have been shown to be phosphorylated, with most of the phosphorylated residues residing in the cytoplasmic C-terminal tail (reviewed by Lampe and Lau 2000). However, given that not all connexins have a C-terminal tail long enough to include those sites and that truncated forms of Cx43 lacking the C-terminal tail are still capable of forming functional gap junctions (Maass et al. 2007), it is clear that phosphorylation of

the C-terminal tail is not required for the establishment of intercellular coupling. It has been clear for some time, however, that C-terminal phosphorylation of Cx43 is involved in the regulation of gap junctional communication. For example, S255, S279 and S282 are phosphorylated directly by activated MAPK in EGF-treated cells with phosphorylation of one or both of the S279/S282 sites being adequate to disrupt gap junctional communication (Warn-Cramer et al. 1998). It was further reported in that study that mutating S255, S279, and S282 to alanine abolished the ability of EGF to disrupt communication. In addition to channel activity, EGF treatment leads to internalization of Cx43 (Leithe and Rivedal 2004), potentially in a direct manner through phosphorylation of Cx43 at serines 279 and 282 (Leykauf et al. 2003).

In the present work, Cx43 in primary and early secondary follicles, in contrast to that of more advanced follicles, was found to be predominately intracellular and relatively highly phosphorylated at serines 279 and 282. This is similar to the situation in cells undergoing mitosis, where Cx43 is redistributed to an intracellular location in association with an increase in its phosphorylation (Boassa et al. 2010). Possibly, phosphorylation at serines 279 and 282 in granulosa cells limits the amount of Cx43 within gap junctions and/or decreases the level of gap junctional communication, thereby allowing their entry into M phase.

Our results are consistent with the work of Maass et al. (2004) who found that surviving knock-in female mice homozygous for a truncation mutant of Cx43 ($Cx43^{K258stop}$), one that lacks most of the C-terminal cytoplasmic tail, are infertile as a result of impaired folliculogenesis. The mice analyzed in that study lacked three of the four serines (S262, S279 and S282) that, when collectively mutated to alanine in our study, failed to support folliculogenesis. However, our results must also be considered in the context of the preliminary (unpublished) finding that female knock-in mice homozygous for the same quadruple mutant used in the present study can produce apparently healthy litters. An analysis of follicle growth, ovulation rate, and litter size in those mice has not yet been carried out to determine if they may in fact be subfertile as recently determined in the case of apparently fertile females carrying the dominant loss-of-function G60S substitution in Cx43 (Tong et al. 2009). One possible reason for the apparent discrepancy with the present results is a difference in strain background. It is known that the importance of Cx43-mediated intercellular communication for folliculogenesis in mice is influenced by genetic background: the *Gja1* null mutation in the homozygous state causes follicle development to arrest in the primary stage on the C57BL/6 background (Ackert et al. 2001) whereas some follicles can develop into antral stages when the same mutation is crossed into the CD1 background (Tong et al. 2006). The quadruple mutant mice have to this point been maintained on a mixed C57BL/6 × 129S6SvEV genetic background, and thus, their continued fertility could be explained by strain-specific genetic modifiers that do not come into play in recombinant ovaries when both oocytes and ovarian somatic cells are of the inbred C57BL/6 strain.

In conclusion, the results presented here add yet another level of regulation- that by MAP kinases acting on Cx43- to the list of factors regulating the early stages of folliculogenesis and oocyte growth, raising the possibility that interference with that regulation may contribute to female infertility.

Acknowledgments Supported in part by an operating grant to G.M.K. and a Postdoctoral Fellowship to P.W.D. from the Canadian Institutes of Health Research and grant GM55632 to P.D.L. from the U.S. National Institutes of Health. We thank Kevin Barr, Dan Li, and Tony Y. Li for their expert technical assistance and the University of Western Ontario Health Sciences Animal Facility staff for providing mouse care.

References

Ackert CL, Gittens JEI, O'Brien MJ, Eppig JJ, Kidder GM (2001) Intercellular communication via connexin43 gap junctions is required for ovarian folliculogenesis in the mouse. Dev Biol 233:258–270

Beardslee M, Laing J, Beyer E, Saffitz J (1998) Rapid turnover of connexin43 in the adult rat heart. Circ Res 83:629–635

Boassa D, Solan JL, Papas A, Thornton P, Lampe PD, Sosinsky GE (2010) Trafficking and recycling of the connexin43 gap junction protein during mitosis. Traffic 11:1471–1486

Cooper CD, Lampe PD (2002) Casein kinase 1 regulates connexin43 gap junction assembly. J Biol Chem 277:44962–44968

Crow DS, Beyer EC, Paul DL, Kobe SS, Lau AF (1990) Phosphorylation of connexin43 gap junction protein in uninfected and Rous sarcoma virus-transformed mammalian fibroblasts. Mol Cell Biol 10:1754–1763

Eppig JJ, Wigglesworth K (2000) Development of mouse and rat oocytes in chimeric reaggregated ovaries after interspecific exchange of somatic and germ cell components. Biol Reprod 63:1014–1023

Gittens JEI, Kidder GM (2005) Differential contributions of connexin37 and connexin43 to oogenesis revealed in chimeric reaggregated mouse ovaries. J Cell Sci 118:5071–5078

Goodenough DA, Paul DL (2003) Beyond the gap: functions of unpaired connexon channels. Nat Rev Mol Cell Biol 4:285–294

Kanemitsu MY, Jiang W, Eckhart W (1998) Cdc2-mediated phosphorylation of the gap junction protein, connexin43, during mitosis. Cell Growth Differ 9:13–21

Kidder GM, Vanderhyden BC (2010) Bidirectional communication between oocytes and follicle cells: ensuring oocyte developmental competence. Can J Physiol Pharmacol 88:99–413

Laird DW, Puranam KL, Revel JP (1991) Turnover and phosphorylation dynamics of connexin43 gap junction protein in cultured cardiac myocytes. Biochem J 273:67–72

Lampe PD (1994) Analyzing phorbol ester effects on gap junction communication: a dramatic inhibition of assembly. J Cell Biol 127:1895–1905

Lampe PD, Lau AF (2000) Regulation of gap junctions by phosphorylation. Arch Biochem Biophys 384:205–215

Lampe PD, Lau AF (2004) The effects of connexin phosphorylation on gap junctional communication. Int J Biochem Cell Biol 36:1171–1186

Lampe PD, Kurata WE, Warn-Cramer B, Lau AF (1998) Formation of a distinct connexin43 phosphoisoform in mitotic cells is dependent upon $p34^{cdc2}$ kinase. J Cell Sci 111:833–841

Lampe PD, TenBroek EM, Burt JM, Kurata WE, Johnson RG, Lau AF (2000) Phosphorylation of connexin43 on serine368 by protein kinase C regulates gap junctional communication. J Cell Biol 126:1503–1512

Leithe E, Rivedal E (2004) Epidermal growth factor regulates ubiquitination, internalization and proteasome-dependent degradation of connexin43. J Cell Sci 117:1211–1220

Leykauf K, Dürst M, Alonso A (2003) Phosphorylation and subcellular distribution of connexin43 in normal and stressed cells. Cell Tiss Res 311:23–30

Maass K, Ghanem A, Kim J-S, Saathoff M, Urschel S, Kirfel G, Grümmer R, Kretz M, Lewalter T, Tiemann K, Winterhager E, Herzog V, Willecke K (2004) Defective epidermal barrier in neonatal mice lacking the C-terminal region of connexin43. Mol Biol Cell 15:4597–4608

Maass K, Shibayama J, Chase SE, Willecke K, Delmar M (2007) C-terminal truncation of connexin43 changes number, size, and localization of cardiac gap junction plaques. Circ Res 101:1283–1291

Musil LS, Beyer EC, Goodenough DA (1990) Expression of the gap junction protein connexin43 in embryonic chick lens: molecular cloning, ultrastructural localization, and post-translational phosphorylation. J Membr Biol 116:163–175

Norris RP, Freudzon M, Mehlmann LM, Cowan AE, Simon AM, Paul DL, Lampe PD, Jaffe LA (2008) Luteinizing hormone causes MAP kinase-dependent phosphorylation and closure of connexin43 gap junctions in mouse ovarian follicles: one of two paths to meiotic resumption. Development 135:3229–3238

Park DJ, Wallick CJ, Martyn KD, Lau AF, Jin C, Warn-Cramer BJ (2007) Akt phosphorylates Connexin43 on Ser373, a "mode-1" binding site for 14-3-3. Cell Commun Adhes 14:211–226

Reaume AG, De Sousa PA, Kulkarni S, Langille BL, Zhu D, Davies TC, Juneja SC, Kidder GM, Rossant J (1995) Cardiac malformation in neonatal mice lacking connexin43. Science 267:831–1834

Saez JC, Nairn AC, Czernik AJ, Fishman GI, Spray DC, Hertzberg EL (1997) Phosphorylation of connexin43 and the regulation of neonatal rat cardiac myocyte gap junctions. J Mol Cell Cardiol 29:2131–2145

Sela-Abramovich S, Chorev E, Galiani D, Dekel N (2005) Mitogen-activated protein kinase mediates luteinizing hormone-induced breakdown of communication and oocyte maturation in rat ovarian follicles. Endocrinology 146:1236–1244

Sela-Abramovich S, Galiani D, Nevo N, Dekel N (2008) Inhibition of rat oocyte maturation and ovulation by nitric oxide: mechanism of action. Biol Reprod 78:1111–1118

Solan JL, Lampe PD (2008) Connexin43 in LA-25 cells with active v-src is phosphorylated on Y247, Y265, S262, S279/282 and S368 via multiple signaling pathways. Cell Comm Adhes 15:75–84

Solan JL, Lampe PD (2009) Connexin43 phosphorylation: structural changes and biological effects. Biochem J 419:261–272

Solan JL, Marquez-Rosado L, Sorgen PL, Thornton PJ, Gafken PR, Lampe PD (2007) Phosphorylation of Cx43 at S365 is a gatekeeper event that changes the structure of Cx43 and prevents downregulation by PKC. J Cell Biol 179:1301–1309

Sosinsky GE, Solan JL, Gaietta GM, Ngan L, Mackey M, Lampe PD (2007) The C-terminus of connexin43 adopts different conformations in the Golgi and gap junction as detected with structure specific antibodies. Biochem J 408:375–385

Swenson KI, Piwnica-Worms H, McNamee H, Paul DL (1990) Tyrosine phosphorylation of the gap junction protein connexin43 is required for pp 60src-induced inhibition of communication. Cell Regul 1:989–1002

Tong D, Gittens JEI, Kidder GM, Bai D (2006) Patch clamp study reveals that the importance of connexin43-mediated gap junctional communication for ovarian folliculogenesis is strain-specific in the mouse. Am J Physiol Cell Physiol 290:290–C297

Tong D, Li TY, Naus KE, Bai D, Kidder GM (2007) In vivo analysis of undocked connexin43 gap junction hemichannels in ovarian granulosa cells. J Cell Sci 120:4016–4024

Tong D, Colley D, Thoo R, Li TY, Plante I, Laird DW, Bai D, Kidder GM (2009) Oogenesis defects in a mutant mouse model of oculodentodigital dysplasia. Dis Models Mech 2:157–167

Warn-Cramer BJ, Lampe PD, Kurata WE, Kanemitsu MY, Loo LWM, Eckhart W, Lau AF (1996) Characterization of the MAP kinase phosphorylation sites on the connexin43 gap junction protein. J Biol Chem 271:3779–3786

Warn-Cramer BJ, Cottrell GT, Burt JM, Lau AF (1998) Regulation of connexin43 gap junctional intercellular communication by mitogen-activated protein kinase. J Biol Chem 273:9188–9196

J Membrane Biol (2012) 245:303–317
DOI 10.1007/s00232-012-9451-5

Under Construction: Building the Macromolecular Superstructure and Signaling Components of an Electrical Synapse

B. D. Lynn · Xinbo Li · J. I. Nagy

Received: 2 April 2012 / Accepted: 1 June 2012 / Published online: 22 June 2012

Abstract A great deal is now known about the protein components of tight junctions and adherens junctions, as well as how these are assembled. Less is known about the molecular framework of gap junctions, but these also have membrane specializations and are subject to regulation of their assembly and turnover. Thus, it is reasonable to consider that these three types of junctions may share macromolecular commonalities. Indeed, the tight junction scaffolding protein zonula occluden-1 (ZO-1) is also present at adherens and gap junctions, including neuronal gap junctions. On the basis of these earlier observations, we more recently found that two additional proteins, AF6 and MUPP1, known to be associated with ZO-1 at tight and adherens junctions, are also components of neuronal gap junctions in rodent brain and directly interact with connexin36 (Cx36) that forms these junctions. Here, we show by immunofluorescence labeling that the cytoskeletal-associated protein cingulin, commonly found at tight junctions, is also localized at neuronal gap junctions throughout the central nervous system. In consideration of known functions related to ZO-1, AF6, MUPP1, and cingulin, our results provide a context in which to examine functional relationships between these proteins at Cx36-containing electrical synapses in brain—specifically, how they may contribute to regulation of transmission at these synapses, and how they may govern gap junction channel assembly and/or disassembly.

Keywords AF6 · Cingulin · Connexin36 · Electrical synapse · Gap junctions · MUPP1 · Neurons · PDZ domain

As evident in this special tribute issue of *Journal of Membrane Biology* to the long and distinguished career of Dr. Ross Johnson as a gap junctionologist, gap junctions remain at center stage regarding their relevance in health and disease. As well, these entities continue to entertain the imagination of researchers in the field and still seem to yield endless surprises concerning their myriad functions, their complex regulation, and, as is becoming evident more recently, their rich structural organization. One organ system in which studies of connexins and gap junctions have generated its share of such surprises over the past decade is the central nervous system (CNS). In brain, for example, the large repertoire of connexins expressed by glial cells is unparalleled by any other cell type in the body. In addition, huge advances in understanding the functional importance of widespread electrical synapses formed by gap junctions between neurons in the mammalian CNS (Bennett 1997; Bennett and Zukin 2004; Connors and Long 2004; Nagy et al. 2004) have left many wondering how, in the past, these functionally essential structures could have been overlooked, neglected, or even dismissed as a fundamental means of neurotransmission in higher vertebrates, along with chemical transmission. Three areas of our focus have been documentation of brain regions in which electrical synapses occur, identification of the structural components of neuronal gap junctions that form these synapses, and elucidation of how transmission at these synapses may be regulated.

B. D. Lynn and Xinbo Li contributed equally to this study.

B. D. Lynn · X. Li · J. I. Nagy (✉)
Department of Physiology, Faculty of Medicine, University of Manitoba, Winnipeg, MB R3E 0J9, Canada
e-mail: nagyji@ms.umanitoba.ca

Present Address:
X. Li
Casey Eye Institute, Oregon Health and Science University, Portland, OR, USA

Analogous to protein markers that are used for the identification of nerve terminals that contain specific chemical synaptic transmitters or their cognate postsynaptic receptors, there is a large body of evidence that has led to the acceptance of connexin36 (Cx36) as a reliable immunohistochemical marker for electrical synapses. Cx36 has a broad distribution pattern and is found in many electrically coupled networks in adult rodent brain (Connors and Long 2004; Hormuzdi et al. 2004; Sohl et al. 2004, 2005). Indeed, the typically plasma membrane-associated punctate immunoreactivity for Cx36 widely seen in brain corresponds at the ultrastructural level to sites of interneuronal gap junctions (Kamasawa et al. 2006; Rash et al. 2000, 2007a, b; Li et al. 2008a), and Cx36 is found at locations in brain where functional electrical synapses occur (Fuduka et al. 2006; Baude et al. 2007; Liu and Jones 2003; Muller et al. 2005). Specific examples of electrically coupled neuronal networks wherein Cx36 has been identified, among many others, include interneurons in the cerebral cortex (Bennett and Zukin 2004), principal neurons in the inferior olive (Llinas et al. 1974), the soma of proprioceptive neurons in the trigeminal mesencephalic nucleus (Curti et al. 2012a) and the long-projection noradrenergic neurons in the locus coeruleus (Rash et al. 2007b).

Like other cell–cell junctions, such as tight junctions and adherens junctions, gap junctions including those forming electrical synapses are emerging as multimolecular composites whose structure and regulation is governed in part by their associated proteins. In particular, protein sequence analysis has revealed that most members of the connexin family of gap junction proteins contain a PDZ (postsynaptic density-95/disks large/zonula occludens-1) ligand motif at their C-terminus. By virtue of this motif, many of these connexins have been demonstrated to interact with the PDZ domain-containing protein zonula occludens-1 (ZO-1). ZO-1 is a member of the membrane associated guanylate kinase (MAGUK) family of PDZ proteins, which are hallmarked by multiple PDZ domains, one SH3 domain and one GUK domain. ZO-1 was initially described in peripheral endothelial cells as a tight junction-associated protein. In the context of tight junctions, the PDZ domains of ZO-1 and zonula occludens-2 (ZO-2) have a pivotal role in the formation of claudin-based tight junction strands (Umeda et al. 2006). It is via their C-terminal motif that the claudins interact with the first PDZ domain of the zonula occludens (ZO) family of proteins and with the 10th PDZ domain of multi-PDZ domain protein-1 (MUPP1) (Jeansonne et al. 2003).

In brain, ZO-1 was originally reported to be localized almost exclusively at vascular endothelial cell tight junctions, ostensibly precluding its interaction with connexins found to be expressed in brain parenchyma. With reports of ZO-1 interactions with more and more connexins in peripheral tissues, it began to be inconceivable that none of the numerous connexins in brain had functional requirement for interaction with ZO-1. However, we noted that the extreme C-terminus YV residues in Cx36 are identical to those found in members of tight junction-associated proteins, including the claudins (Itoh et al. 1999). The presence of a potential C-terminus PDZ ligand motif in Cx36, together with reports of the mechanism whereby specific interactions occur between other connexins and ZO-1, prompted us to reevaluate the cellular expression and distribution of ZO-1 in brain. We found punctate immunohistochemical labeling of ZO-1 to be broadly distributed in neurons and glial cells in rodent CNS (Li et al. 2004a; Penes et al. 2005), providing the possibility of its interaction with glial connexins and with neuronal Cx36. We found ZO-1 in association with Cx36-containing gap junctions at virtually all electrical synapses examined and described a specific interaction of Cx36 with ZO-1, which required the C-terminal four amino acid PDZ domain ligand (SAYV) of Cx36 for interaction with the first of the three PDZ domains of ZO-1. This finding was later extended to include all members of the zonula occludens (ZO) family of proteins (ZO-1, ZO-2, ZO-3) (Li et al. 2004a, b, 2009; Ciolofan et al. 2006; Flores et al. 2008). The interaction of Cx36 and its fish ortholog Cx35 with ZO-1 is distinguished from that of other connexins previously examined in that while Cx36 and Cx35 interact with the first PDZ domain in ZO-1, other connexins interact with the second PDZ domain of ZO-1 (Derangeon et al. 2009).

Using the YV motif of Cx36 as a guide for potential Cx36 interactors, together with considerations of structural similarities between gap junctions and other specialized tight and adhesion cell-cell junctions, we searched for additional interacting partners of Cx36. Recently, we demonstrated AF6 and MUPP1 colocalization with Cx36 in many brain areas. Coimmunoprecipitation and pull-down approaches revealed association of Cx36 with AF6 and MUPP1, which required the C-terminus PDZ ligand of Cx36 for interaction with the single PDZ domain of AF6 and with the 10th PDZ domain of MUPP1. As proof of principle for identifying shared proteins at tight, adherens and gap junctions, we examined Cx36-containing electrical synapses for the presence of cingulin. Cingulin is a cytoplasmic protein that is localized to tight junctions via its specific binding to ZO-1 and the actin cytoskeleton, and is emerging as an important participant in the regulation of RhoA signaling at tight junctions.

Materials and Methods

The primary antibodies used here were obtained from Life Technologies (Grand Island, NY, USA) and included

mouse monoclonal anti-Cx36 (Cat. No. 36-4600), rabbit polyclonal anti-cingulin (Cat. No. 36-4401), and rabbit polyclonal anti-MUPP1 (Cat. No. 42-2700). A total of six adult C57BL/6 mice were used in this study and these were handled according to approved protocols by the Central Animal Care Committee of University of Manitoba, with minimization of the numbers of animals used.

Immunohistochemistry was conducted using protocols we have previously described (Li et al. 2012). Animals were deeply anesthetized by intraperitoneal injection of equithesin (3 mL/kg) and then transcardially perfused with 3 mL cold sodium phosphate buffer, pH 7.4 containing 0.9 % NaCl, 100 mM sodium nitrite and 1 U/mL heparin, followed by 40 mL of ice-cold sodium phosphate buffer, pH 7.6, containing 1 % freshly depolymerized paraformaldehyde and 0.2 % picric acid. The brains were removed and transferred to an ice-cold cryoprotectant solution consisting of 10 % sucrose in 25 mM sodium phosphate buffer, pH 7.4 and stored at 4 °C in this solution for 24–72 h.

Brain sections were cut on a cryostat at 10 μm thickness, slide mounted and then incubated for 20 min in 50 mM Tris-HCl, pH 7.4, containing 1.5 % sodium chloride (TBS) and 0.3 % Triton X-100 (TBSTr). For immunofluorescence labeling, brain sections were incubated with primary antibodies in TBSTr supplemented with 5 % normal goat serum for 18 h at 4 °C. Double immunofluorescence was conducted by incubation with anti-Cx36 antibody and simultaneously with a rabbit polyclonal antibody against either MUPP1 or cingulin. All primary antibodies were used at a concentration of 2–3 μg/mL. After incubation with primary antibodies, sections were washed for 1 h in TBSTr, and incubated for 1.5 h at room temperature simultaneously with Cy3-conjugated goat anti-mouse IgG diluted 1:300 (Jackson ImmunoResearch Laboratories, West Grove, PA, USA) and Alexa Flour 488-conjugated goat anti-rabbit IgG diluted 1:1,000 (Molecular Probes, Eugene, Oregon). After secondary antibody incubation, sections were washed in TBSTr for 20 min, then in 50 mM Tris-HCl buffer, pH 7.4 for 30 min, covered with antifade medium and coverslipped. Standard control procedures included omission of one of the primary antibodies with inclusion of each of the secondary antibodies to ensure the absence of inappropriate cross-reactions between primary and secondary antibodies or between different combinations of secondary antibodies. Conventional and confocal immunofluorescence images were acquired on a Zeiss Axioskop2 fluorescence microscope using Axiovision 3.0 software (Carl Zeiss Canada, Toronto, Ontario, Canada) and on an Olympus Fluoview IX70 confocal microscope using Olympus Fluoview software (Olympus Canada, Inc., Markham, ON, Canada). Images were assembled using Adobe Photoshop CS (Adobe Systems, San Jose, CA, USA) and CorelDraw Graphics Suite X5 (Corel Corporation, Ottawa, ON, Canada).

Results

Immunofluorescence Localization of MUPP1 and Cx36

We have previously reported that MUPP1 is broadly distributed in various cell types of the CNS (Li et al. 2008b, 2012). On the basis of our observations, it is almost certain that this thirteen PDZ domain-containing protein will be found at a variety of neural cellular structures at which it serves a scaffolding function. In particular, we have documented its association with gap junctions formed by oligodendrocytes (Li et al. 2008b) and those formed by Cx36 between neurons in some regions of rodent brain (Li et al. 2012). Here, we examined relationships between MUPP1 and Cx36 in another region of brain, namely the mesencephalic trigeminal (MesV) nucleus in the brainstem of mouse. This nucleus was among the first in which electrical synapses in mammalian brain were identified (Hinrichsen and Larramendi 1970; Hinrichsen 1970; Baker and Llinas 1971). Recently, we reported on the localization of Cx36 between MesV neurons and the characteristics of the electrical coupling that Cx36-containing gap junctions mediate between these neurons (Curti et al. 2012a, b). In addition to being gap junctionally coupled, MesV neurons are further unusual because they are primary sensory neurons that convey proprioceptive signals from jaw-closing muscles and periodontal ligaments, but have cell bodies located in the CNS rather than in sensory ganglia. We have noted that the absence of dendrites and the large size of MesV somata, together with the heavy concentration of Cx36 associated with their plasma membranes, make these cells ideal for the analyses of neuronal gap junction structure and function. Further, neuronal gap junctions in the MesV are also unique among electrically coupled neurons because the gap junctions between these cells occur exclusively at somato–somatic locations, allowing easy examination and analysis of the cell types between which gap junctions are found, which is not typically the case for other neuronal gap junctions in the CNS (Curti et al. 2012a, b).

The distribution of immunofluorescence labeling for MUPP1 in the MesV nucleus is shown at low magnification in Fig. 1a, where large MesV somata display a moderate density of intracellular labeling for MUPP1 compared with lower densities in surrounding regions. Pairs and triplets of MesV somata are often seen in apposition to each other, and MUPP1 is invariably seen to be concentrated along the entire length of these appositions (Fig. 1a), shown at higher

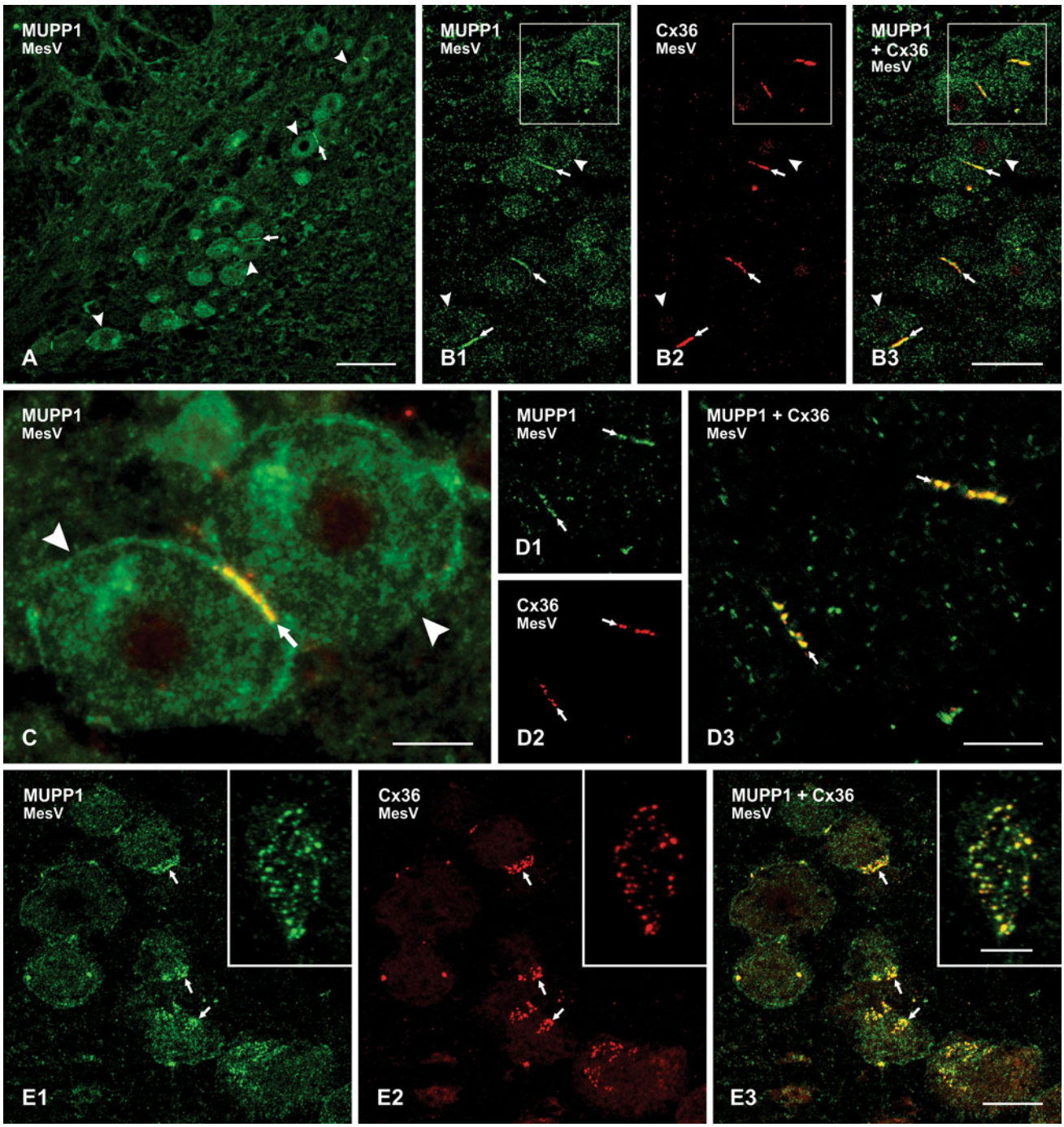

Fig. 1 Immunofluorescence labeling of MUPP1 and Cx36 in the MesV of adult mouse brain. **a** Low magnification of the MesV immunolabeled for MUPP1 showing the distribution of large neuronal somata in the nucleus (*arrowheads*), some of which are closely apposed to each other (*arrows*). **b** Double immunofluorescence showing MesV neurons (*arrowheads*) and dense concentration of labeling for MUPP1 (b1) and Cx36 (b2) at MesV somata appositions (*arrows*). **c** Magnification of two MesV somata (*arrowheads*), with overlay showing colocalization of immunolabeling for MUPP1 (*green*) and Cx36 (*red*) at the somatic apposition (*arrow*). **d** Laser scanning confocal double immunofluorescence of the same field (d1–d3), with labeling of MUPP1 and Cx36 at MesV somatic appositions viewed on edge, showing punctate appearance of immunolabeling (*arrows*). **e** The same field (e1–e3) showing confocal double immunofluorescence labeling of MUPP1 and Cx36 at MesV appositions viewed en face, shown at higher magnification in inset. Clusters of MUPP1-positive (e1, *arrows*) and Cx36-positive (e2, *arrows*) puncta are seen at soma surfaces, with many of these puncta displaying MUPP1/Cx36 colocalization, seen as *yellow* in overlay (E3, *arrows*). Scale bars = a, 100 μm; b, 50 μm; c, d, 10 μm; e, 20 μm; inset in e, 5 μm

magnification in Fig. 1b1. Unlike labeling for MUPP1, immunoreactivity for Cx36 is restricted to areas of MesV somatic appositions, with little detectable intracellular labeling (Fig. 1b2). Specificity of Cx36 labeling has been validated using Cx36 knockout mice, as we have previously described (Curti et al. 2012a). Overlay of double-labeled sections in Fig. 1b reveals a high degree of MUPP1 colocalization with Cx36 at MesV somatic appositions (Fig. 1b3), as shown at higher magnification in image overlay where red/green overlap appears as yellow (Fig. 1c).

Double immunofluorescence labeling for MUPP1 and Cx36 at MesV somatic contacts were subject to more detailed analysis by laser scanning confocal microscopy. Sections through MesV somata often yield on edge views of their somal appositions (i.e., views perpendicular to their plane of contact). In rare cases, these contacts are viewed en face when cells are sectioned tangential to their surface (i.e., parallel to their plane of contact). In edge views, confocal imaging revealed appositions to contain a series of linearly arranged MUPP1-positive (Fig. 1d1) and Cx36-positive puncta (Fig. 1d2), with substantial colocalization (Fig. 1d3). In en face views, the appositions were seen to consist of clusters of individual puncta, with various distances of separation between them (Fig. 1e, with inset showing higher magnification of a cluster). Confocal through focus indicated that the clusters of puncta were located at the cell surface, and image rotation in the y–z axis (not shown) indicated that most MUPP1-immunopositive puncta were also positive for Cx36.

Immunofluorescence Localization of Cingulin and Cx36

On the basis of structural similarities between tight junctions, adherens junctions and gap junctions, each located at plasma membrane appositions with proteinacious substructure, close relationships of the former two junctions with cytoskeletal elements, and the co-occurrence of at least three proteins at these junctions (ZO-1, MUPP1 and AF6), it might be predicted that gap junctions may also harbor cytoskeletal-related proteins. The first of these we have examined in numerous brain structures is cingulin. In the MesV nucleus, labeling for cingulin at cell-cell contacts had an appearance very similar to that of labeling for MUPP1 and Cx36, at both appositions viewed on edge (Fig. 2a) or en face (Fig. 2b). Punctate labeling for cingulin at appositions was robust (Fig. 2a1, b1), and Cx36-puncta (Fig. 2a2, b2) were nearly always colocalized with cingulin-immunopositive puncta (Fig. 2a3, b3). MesV somata contained additional cingulin immunoreactivity that was localized intracellularly and not associated with Cx36 (Fig. 2a1, b1). Further examples of cingulin colocalization with Cx36 are shown in the inner plexiform layer in sections of retina (Fig. 2c), and by image overlay only (cingulin, green; Cx36, red; green/red overlap, yellow) in the mitral cell layer of the olfactory bulb (Fig. 2d), the reticular thalamic nucleus (Fig. 2e) and the inferior olive (Fig. 2f). In these four brain regions, cingulin/Cx36 colocalization was not complete as there appeared to be small subpopulations of Cx36-positive puncta in each region that were devoid of labeling for cingulin, suggesting that cingulin/Cx36 association may be a dynamic process. Similar results concerning colocalization of these two proteins were obtained in numerous other brain regions, including cerebral cortex, hippocampus, striatum, midbrain and various areas of brainstem (not shown).

Discussion

Although ultrastructural confirmation of the localization of AF6, MUPP1, and cingulin to neuronal gap junctions has yet to be conducted, their immunohistochemical colocalization with Cx36 is strongly indicative of their association with electrical synapses. Electrical synapses are found to occur in various neuronal subtypes and appear to have diverse functions and are likely subject to regulation by diverse mechanisms. We previously reported heterogeneous immunolabeling for AF6 and MUPP1 at electrical synapses, which appeared not only across different brain regions, but was also evident within individual brain nuclei. This heterogeneity may reflect differential expression or requirement for these proteins in various electrically coupled neuronal subtypes, or may reflect the dynamic functional and/or structural states of neuronal gap junctions. Cingulin appeared to be more consistently associated with neuronal gap junctions, although the proportion of these junctions containing cingulin remains to be determined by quantitative immunofluorescence approaches.

Like gap junctions between other cell types, it is known that those forming electrical synapses in brain are highly regulated. For example, modulation of gap junctional coupling between neurons is proposed to underlie rapid shifts in neuronal network connectivity (Schmitz et al. 2001). Further, neuronal gap junctions exhibit rapid alteration in coupling state in response to neuromediators (Landisman and Connors 2005; Hatton 1997), and have the same high turnover rate (half-life, 1–5 h) as gap junctions in other cell types (Flores et al. 2012). Various neurotransmitters contained in widespread CNS systems that have a broad influence on cognition are known to alter transmission at electrical synapses. These include dopamine (Cepeda et al. 1989; Hampson et al. 1992; He et al. 2000; Onn and Grace 1994, 1995, 1999; Onn et al. 2000; Rorig et al. 1995), serotonin (Rorig and Sutor 1996),

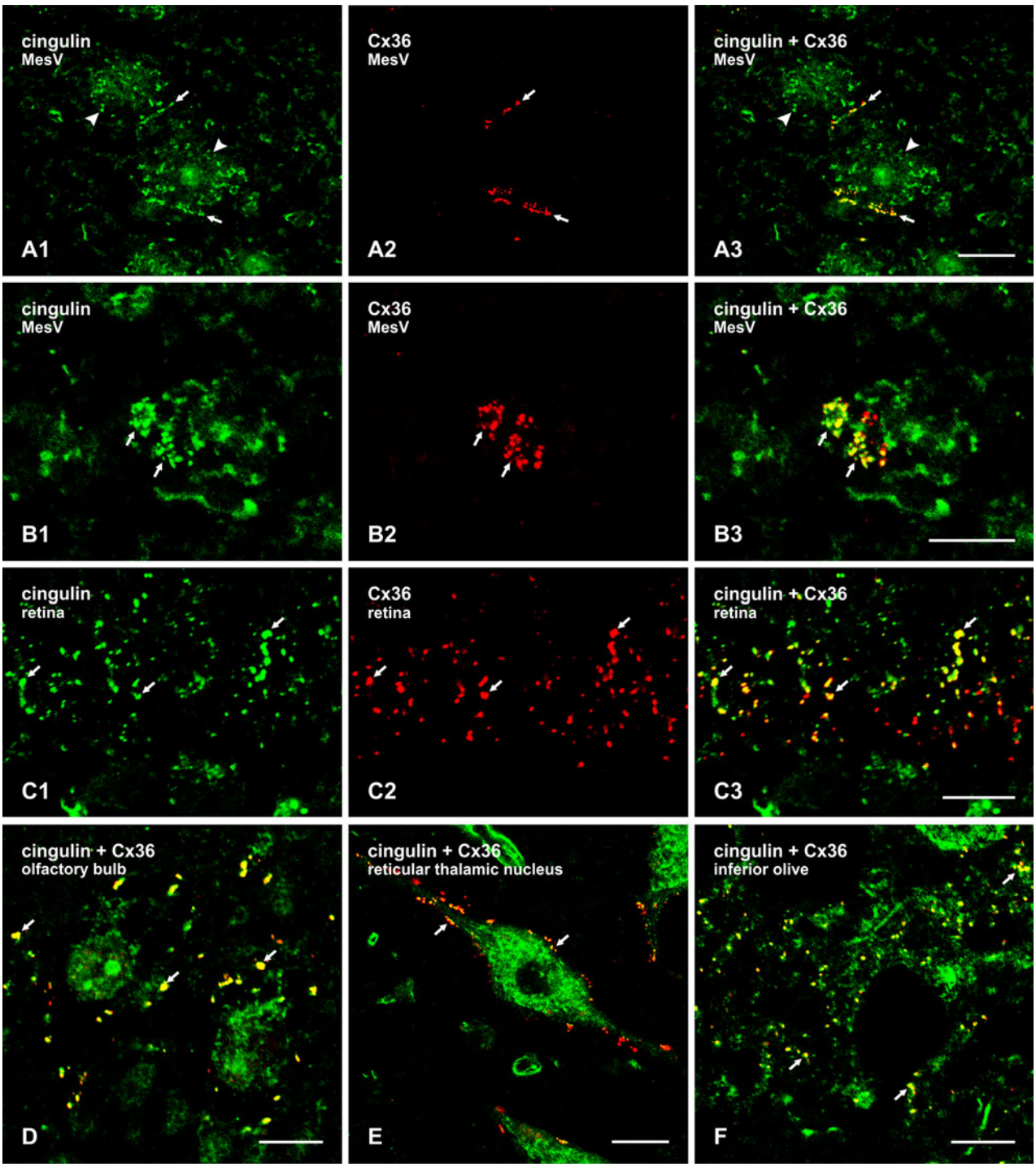

Fig. 2 Laser scanning confocal double immunofluorescence labeling of cingulin and Cx36 in various regions of adult mouse brain. **a** The same field (a1–a3) showing neuronal somata (*arrowheads*) in the MesV, with punctate labeling of cingulin (a1, *arrows*) and Cx36 (a2, *arrows*) at appositions between somata, and colocalization of these puncta, as seen by *red*/*green* overlap in overlay (a3, *arrows*). **b** En face view of MesV neuronal somatic apposition, showing clusters of cingulin-immunopositive (b1, *arrows*) and Cx36-positive puncta (b2, *arrows*), with colocalization of the majority of these puncta. **c** The same field (c1–c3) of a vertical section of retina, showing the inner plexiform layer. Labeling for both cingulin (c1, *arrows*) and Cx36 (c2, *arrows*) is punctate, and the majority of Cx36-immunopositive puncta is also immunopositive for cingulin, as seen by *yellow* in overlay (a3, *arrows*). **d–f** Double immunofluorescence punctate labeling of cingulin (*green*) and Cx36 (*red*), shown only by image overlay in the olfactory bulb at the level of the mitral cell layer (**d**), the reticular thalamic nucleus (**e**), and the inferior olivary nucleus (**f**). Cingulin/Cx36 colocalization seen as *yellow* puncta (*arrows*) are evident in each of the brain areas. Scale bars = a, e, 20 μm; b, c, d, f, 10 μm

histamine (Hatton and Yang 2001; He et al. 2000; Yang and Hatton 2002), acetylcholine (Perez Velazquez et al. 1997) and noradrenaline (Hopkins and Johnston 1988). Some of these transmitters are acted upon by drugs used to treat neurological disorders (e.g., Parkinson's disease, schizophrenia, depression) and by drugs of addiction (e.g., cocaine, amphetamine). In view of these points, therapeutic and addictive drugs may exert their actions in part by modifying the activities of transmitters that regulate signal transmission at electrical synapses. For example, the antipsychotic drug haloperidol and withdrawal from chronic amphetamine increased neuronal gap junctional coupling in the basal ganglia (Onn and Grace 1994, 1995; Onn et al. 2000), and amphetamine and cocaine in animal models of addiction cause altered expression of Cx36 (McCracken et al. 2005a, b).

Just as understanding the biochemical machinery involved in chemical synaptic transmission has served as a basis for deciphering sites and mechanisms of drug action at chemical synapses, so too, knowledge of structural and regulatory components of electrical synapses is expected to provide insight into mechanisms for potential actions of drugs on cellular processes that regulate electrical synapses. Such knowledge is also essential for understanding how malfunction of these synapses may contribute to CNS disease. Despite the wealth of data indicating the dynamic nature of neuronal gap junctions, very little is known about the signaling pathways or the molecular mechanisms that underlie the regulation of electrical synaptic transmission. Indeed, it has been emphasized that a major barrier to progress in understanding electrical synapses in mammalian brain is the paucity of information on mechanisms of their regulation (Bennett and Zukin 2004; Connors and Long 2004; Hormuzdi et al. 2004). Identification of protein components of neuronal gap junctions represents a step toward eliminating that barrier, as discussed below.

Occurrence of ZO-1 at Gap Junctions

In its capacity as a multi-domain scaffolding protein (Fig. 3), ZO-1 interacts with transmembrane structural proteins of intercellular junctions, where it directs the assembly of other adaptor, structural and signaling proteins into functional membrane-associated complexes. ZO-1 is found at various classes of intercellular junctions and, at least in the case of gap junctions formed by connexin43, was found to be essential for gap junctional intercellular communication, gap junction accretion and disassembly (Akoyev and Takemoto 2007; Hunter et al. 2005; Laing et al. 2005). In HeLa cells expressing C-terminal-tagged connexin43 (Cx43) that lacked its capacity for binding of ZO-1, the usual internalization of Cx43 in response to inflammatory mediators did not occur, demonstrating that ZO-1 interactions with Cx43 is required for gap junction internalization (Baker et al. 2008). In lens epithelial cells, silencing of ZO-1 expression caused a stable interaction of protein kinase C-γ (PKC-γ) with Cx43-containing gap junctions, a complete loss of junctional dye transfer, and loss of the usual gap junction disassembly seen in response to TPA activation of PKC-γ, indicating a requirement for ZO-1 in disassembly of these junctions (Akoyev and Takemoto 2007). In lens and *in vitro,* unlike other connexins such as Cx43 that appear able to form gap junctions in the absence of direct interactions with ZO-1 (Hunter et al. 2005; Hunter and Gourdie 2008), the formation of functional gap junctions by Cx50 was recently shown to require the interaction of the C-terminus PDZ ligand of this connexin with ZO-1 (Chai et al. 2011). Although these studies directly address molecular processes that play a role in the essential function of ZO-1 at gap junctions, for the most part little is known at the molecular level regarding the exact mechanisms by which ZO-1 exerts its actions at these structures. Clues to mechanisms involved in ZO-1 actions on junction structure and signaling may be gleaned from studies of the proteins that ZO-1 is known to recruit in other systems.

Molecular Organization of Tight and Adherens Junctions

It is becoming clear that some of the proteins long known to be present at tight and adherens junctions also occur at gap junctions forming electrical synapses, suggesting that there may be other molecular commonalities between these three types of junctions. In considering future directions for deciphering the macromolecular organization of electrical synapses, it may be instructive to take brief account of the somewhat larger body of knowledge concerning the molecular components of tight junctions and adherens junctions. Tight junctions serve to control paracellular permeability across the intercellular space and to maintain cell polarity. They are composed of integral transmembrane proteins (Fig. 4) (for more detailed reviews, see Guillemot et al. 2008; Herve et al. 2011), including claudins, junctional adhesion molecules (JAMS) and the MARVEL family of proteins, of which the occludens are members. In addition, the cytoplasmic "submembrane plaque" of tight junctions contains multimolecular protein complexes that are responsible for anchoring the core proteins within the junction, regulating associations with the actin cytoskeleton (Fanning et al. 1998, 2002) and mediating signals from the plasma membrane to other cellular structures, including the nucleus and to adherens junctions. Many of the protein-protein interactions at tight junctions are mediated by binding of C-terminal PDZ ligands in some proteins to PDZ domains contained in

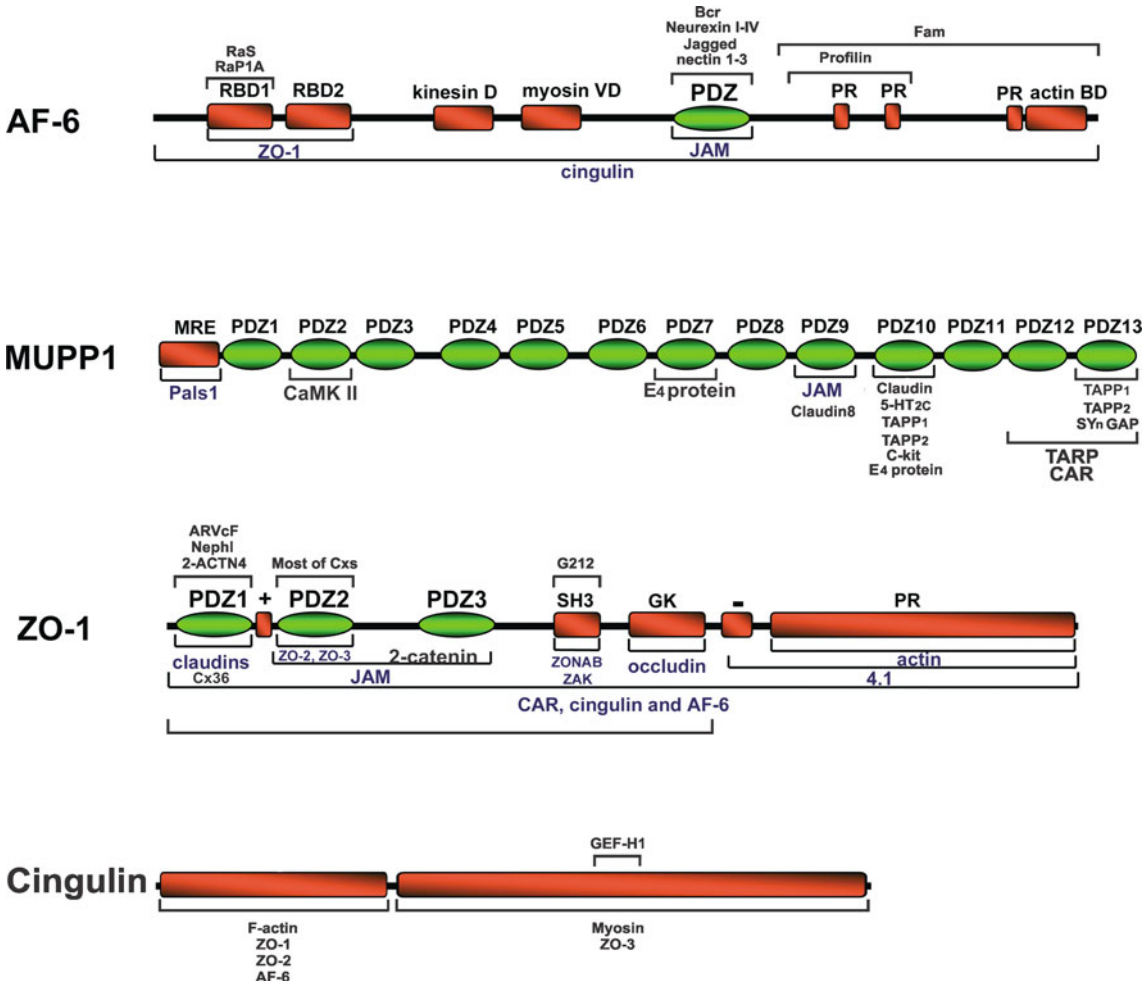

Fig. 3 Diagram of the domain structure of AF6, MUPP1, ZO-1, and cingulin. Bars *above* and *below* protein domain structures indicate known sites of interaction with other proteins. Where interaction has been documented but sites of interaction are not known, the bars span the entire length of the protein. (Modified from Gonzalez-Mariscal et al. 2003)

other proteins. The three members of the ZO family each contain three PDZ domains that mediate a host of interactions. The ZO family members are considered the central scaffolding molecules of tight junctions, as indicated by failure of tight junction strand formation after targeted deletion of ZO-1 and depletion of ZO-2 in cultured epithelial cells (Umeda et al. 2006). In addition to its interaction with other proteins, ZO-1 can undergo self interaction forming a homodimer, which is thought to be mediated via its second PDZ domain (Utepbergenov et al. 2006). Other PDZ domain-containing proteins within the tight junction plaque include AF6 and MUPP1. In addition, there are several non-PDZ proteins in the tight junction cytoplasmic plaque, including cingulin and paracingulin, as well as a growing list of functionally diverse signaling proteins that include: regulators of membrane trafficking, protein kinases and regulators of small GTPases, such as guanine exchange factors (GEFs) and GTPase activating proteins (GAPs) (reviewed in Guillemot et al. 2008). Besides their roles in junction formation and stabilization, some of the tight junction-associated proteins are thought to serve as signaling molecules for regulation of such processes as cell differentiation, proliferation, and gene expression.

Adherens junctions (Fig. 5) (Ogita and Takai 2006) are also molecularly complex structures whose functions include the initiation and stabilization of intercellular adhesion, as well as regulation of intracellular signaling, the cytoskeleton, and gene expression (Niessen and Gottardi 2008). There are several subtypes of adherens junctions, including zonula adherens, which are found in highly polarized epithelial cells, where they encircle the cell in a belt-like fashion. Punctate versions of adherens junctions include puncta adherentia or nascent/primordial junctions, which are formed by interactions of cadherins, the nectin family of adhesion molecules and with the cytoplasmic catenin proteins. ZO-1 is among the PDZ domain proteins found at adherens junctions, where it interacts with various

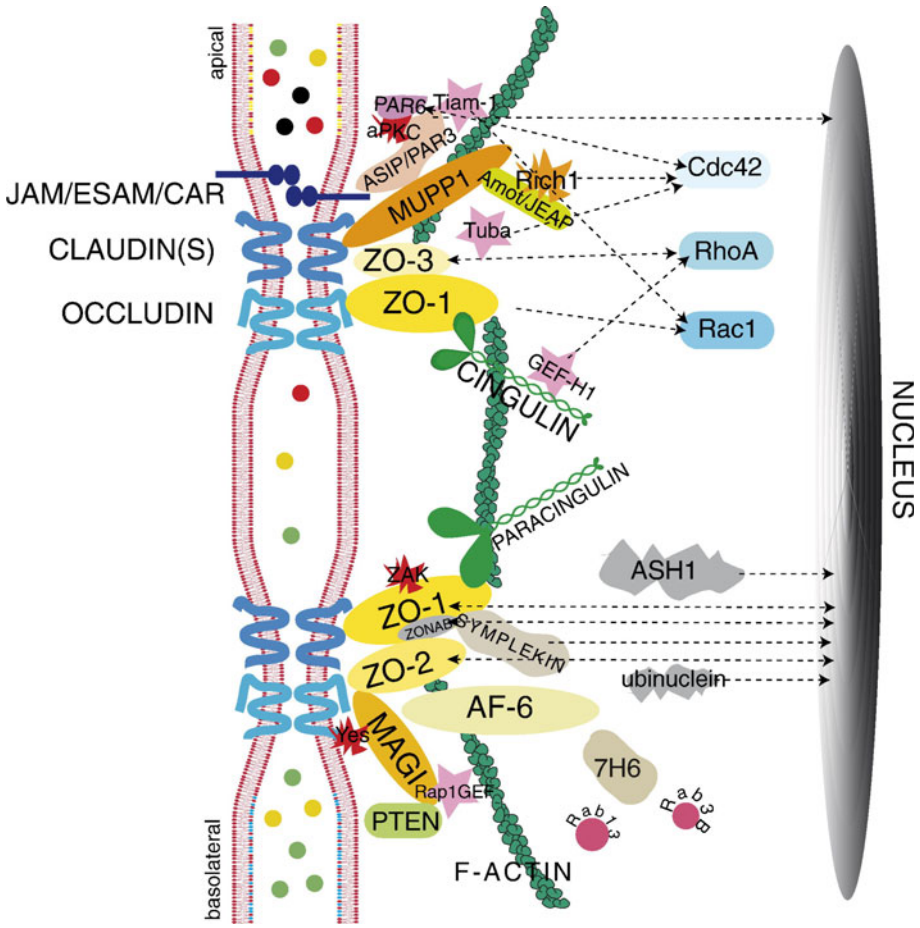

Fig. 4 Diagram of protein organization at tight junctions. The tight junction proteins JAM/ESAM/CAR, claudins, and occludin are shown crossing the membrane bilayers of 2 adjacent cells. These core proteins are shown interacting with various cytoplasmic proteins. Signaling proteins found at tight junctions include kinases (aPKC, ZAK, c-Yes), GEFs (Tiam1, GEF-H1, Tuba, Rap1GEF), and membrane traffic regulators (Rab3B and Rab13). Interactions of cytoplasmic tight junction proteins with signaling proteins (Cdc42, RhoA, and Rac1) are indicated by dotted *arrows*. *Arrows* to the nucleus indicate proteins having a dual nuclear/junctional localization (PAR-3, PAR-6, ASH1, ZO-1, ZO-2, ZONAB, symplekin, ubinuclein). (Reprinted from Guillemot et al. 2008, with permission from Elsevier)

proteins, including alpha catenin and AF6 (aka afadin). These observations on tight and adherens junctions provide the molecular basis for considerations of regulatory and structural proteins as well as intracellular signaling pathways that contribute to modulation of transmission at electrical synapses composed of Cx36.

Scaffolding by MUPP1 at Electrical Synapses

Our previous finding of MUPP1 at neuronal gap junctions and demonstration of its direct interaction with the PDZ ligand of Cx36 added to the list of proteins that associate with PDZ domains of MUPP1 in several cell types and at various cell structures (Ullmer et al. 1998; Becamel et al. 2001; Ebnet et al. 2004; Krapivinsky et al. 2004; Balasubramanian et al. 2007; Guillaume et al. 2008). Presently, we extend that finding to its localization at electrical synapses between sensory neurons of the MesV nucleus in rodent brain, where it has been emphasized that experimental accessibility to the large MesV neuronal cell bodies is ideal for electrophysiological analysis of mechanisms controlling neurotransmission at gap junctions using in vitro preparations (Curti et al. 2012a, b).

Analogous to other systems where MUPP1 serves in an accessory scaffolding capacity for structural and signaling proteins, as indicated by its domain structure (Fig. 3), MUPP1 likely serves to anchor regulatory proteins at gap junctions composed of Cx36. In this context, reports of calcium-calmodulin kinase II (CaMKII) interaction with MUPP1 is of particular interest as various kinases, including protein kinase A (PKA), protein kinase G (PKG) and CaMKII, have an impact on phosphorylation status and coupling state of gap junctions composed of Cx36 or its fish ortholog Cx35 (Pereda et al. 1998; Ouyang et al. 2005; Kothmann et al. 2007; Moreno and Lau 2007). More recently, CaMKII was found to localize at neuronal gap junctions and to interact with specific peptide fragments of Cx36, culminating in phosphorylation of these fragments (Alev et al. 2008). Although phosphorylation of Cx36 mediated by CaMKII would require an effector/ligand interaction, CaMKII is tethered to some of its sites of action in neurons by interacting with the PDZ2 domain of MUPP1 (Krapivinsky et al. 2004). Thus, it is possible that this same CaMKII/MUPP1 interaction occurs at gap junctions, where further interaction of Cx36 with the PDZ10 domain of MUPP1 poises CaMKII in a response-ready position for rapid signaling at electrical synapses.

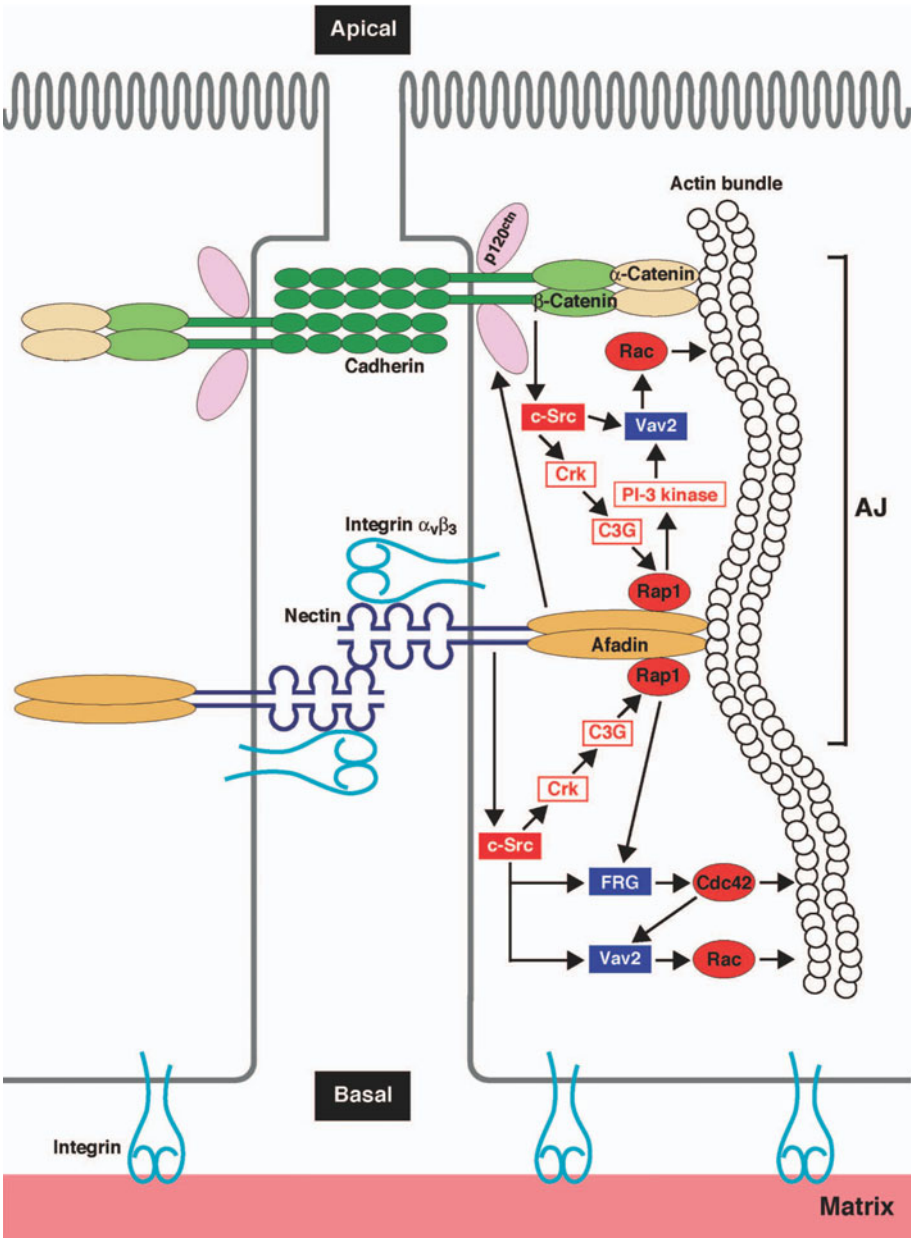

Fig. 5 Diagram of the molecular organization of nectin- and cadherin-based adherens junctions. Core transmembrane proteins cadherin and nectin are shown associated with cytoplasmic proteins, in particular cadherin with catenin anchored to the cytoskeleton, and nectin with cytoskeletal-associated afadin (aka AF6). Afadin is also shown associated with Rap1, which receives signals originating from catenin and c-Src and transmits signals ultimately to Rac and the cytoskeleton. (Reprinted from Ogita and Takai 2006, with permission from John Wiley and Sons)

Signaling and Scaffolding by Cingulin at Electrical Synapses

The current finding of cingulin colocalized with Cx36 adds yet another ZO-1 binding protein found at other types of cell-cell junctions to the roster of proteins at neuronal gap junctions in mouse brain. This provides further clues to the regulation of electrical synapses, although the molecular association of cingulin with Cx36 at neuronal gap junctions is not known and is currently under investigation by biochemical approaches. Cingulin was characterized as a component of the submembranous plaque of tight junctions, where it may be anchored as a parallel homodimer, as predicted by its secondary structure (Citi et al. 1989). It has three distinct structural domains; an *N*-terminal head domain, a central coiled-rod domain and a smaller globular tail (Cordenonsi et al. 1999). Interaction of cingulin with ZO-1 is not through a classical C-terminal PDZ ligand, which cingulin lacks, but rather through a conserved ZO-1 interaction motif (ZIM) located in the cingulin *N*-terminus "head" region (Cordenonsi et al. 1999; D'Atri et al. 2002). In addition to its association with ZO-1, cingulin interacts with other proteins (Fig. 3) at tight junctions, including alpha actin (D'Atri and Citi 2001). Association of actin with gap junctions appears to be important for connexin trafficking, and gap junction stability and channel permeability (Theiss and Meller 2002; Derangeon et al. 2008; Qu et al. 2009; Smyth et al. 2012). Besides its potential

structural roles, cingulin participates in modification of gene expression via its direct binding to the guanine exchange factor GEF-H1, which is an activator of RhoA signaling. It appears that sequestration of GEF-H1 by cingulin at tight junctions contributes to inhibition of RhoA (Citi et al. 2009; Aijaz et al. 2005). In the context of gap junctions, altered RhoA activity in cardiac myocytes leads to rapid changes in gap junctional channel conductance via RhoA actions on the actin cytoskeleton (Derangeon et al. 2008). Although we have not yet determined if cingulin is present at gap junctions composed of other connexins, our finding of cingulin association with neuronal gap junctions raises the possibility that it may influence the stability and channel conductance of electrical synapses by a RhoA dependent mechanism similar to that seen in cardiac myocytes. It remains to be determined whether neuronal gap junctions also serve as platforms for cingulin-mediated signaling to other subcellular sites in neurons.

Electrical Synapses and cAMP/Epac/Rap1 Signaling

AF6 is targeted by the Epac/Rap1-dependant cAMP pathway that is independent of PKA. Although regulation of electrical synapses by cAMP/Epac signaling has not been directly explored, regulatory actions of cAMP on neuronal gap junction coupling have been described (Hampson et al. 1992; Hatton and Yang 2001; Rorig et al. 1995; Urschel et al. 2006; Xia and Mills 2004). Our finding of AF6 at gap junctions composed of Cx36 suggests that the Epac/Rap1 pathway may be operational at electrical synapses. AF6 is targeted by Rap1 after its activation by the cAMP effector Epac (de Rooij et al. 1998; Boettner et al. 2000, 2001, 2003; Caron 2003), a GEF that is distinct from the other major cAMP effector PKA. Epac-Rap1-AF6 signaling has been demonstrated in various cell types and contributes to the regulation of cell-cell contacts (e.g., tight junctions) through its influence on AF6/ZO-1 interaction (Yamamoto et al. 1997, 1999; Kooistra et al. 2006). To date there is one study concerning the impact of Epac on gap junctions, where PKA versus Epac activation had differential, but cooperative actions on cardiomyocyte gap junctions; Epac activation increased the recruitment of Cx43 to junctions, while PKA activation increased dye-coupling (Somekawa et al. 2005). To dissect the specific functions of these two separate pathways, cAMP analogs have been developed that activate either one or the other; 8-CPT-2Me-cAMP (8CPT) specifically activates Epac but not PKA (Enserink et al. 2002; Somekawa et al. 2005), whereas N6-benzoyl-cAMP specifically activates PKA but not Epac (Christensen et al. 2003; Holz et al. 2008; Lorenowicz et al. 2008).

In consideration of the foregoing, the presence of AF6 at electrical synapses suggests that its associated signaling moieties may contribute to the regulation of these synapses. Specifically, as outlined in Fig. 6, we propose that cAMP activation of Epac/Rap1 results in Rap1 targeting to AF6 and ZO-1 at neuronal gap junctions, where it may influence AF6/ZO-1 interaction and dynamically impact junction assembly/disassembly, channel conductance, remodeling and/or turnover. ZO-1 is found at virtually all Cx36-containing electrical synapses that we have examined, suggesting that some of these synapses simultaneously harbor ZO-1, AF6, MUPP1 and cingulin. As yet, we are aware of

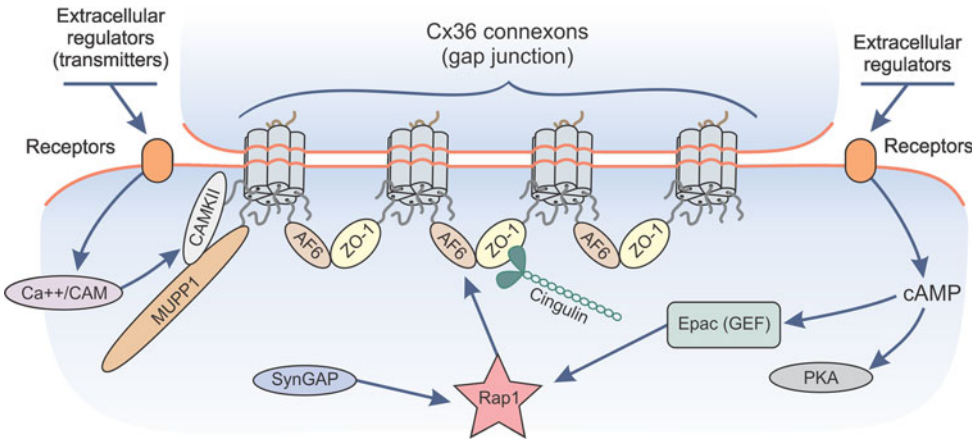

Fig. 6 Hypothesized model for actions of the cAMP-Epac-Rap1 signaling pathway at neuronal gap junctions. The c-terminus PDZ domain ligand of Cx36 within different connexon hexamers are shown associating with ZO-1 and AF6. Association of ZO-1 and AF6 with each other is envisioned to result in clustering of connexons and maintenance of gap junction plaque integrity. Upon cAMP activation of the guanine nucleotide exchange factor (GEF) Epac, which acts on Rap1, Rap1 may be targeted to AF6, where it may either further stabilize junctions or disrupt ZO-1/AF6 association, resulting in untethering of a portion of connexons within a gap junction plaque and internalization of these connexons. SynGAP is shown because it is a GTPase activating protein (GAP) for Rap1 and is known to associate with MUPP1 at other subcellular locations, but as yet, neither Rap1 nor SynGAP has been examined for its presence at neuronal gap junctions

no reports of direct interactions between AF6 and MUPP1 at any cellular structures. But, as indicated in the summary of the domain structures and interactions of these three proteins in Fig. 3, ZO-1 has the capacity to simultaneously interact with AF6 and Cx36, but whether it does so at neuronal gap junctions remains to be determined. It is conceivable that ZO-1, AF6 and MUPP1 simultaneously interact with Cx36 at individual gap junctions, or each of these proteins associate with the constituent connexin molecules within an individual connexon. Additionally, connexins within distinct subregions of a neuronal gap junction plaque may selectively associate with one or more of these proteins. The latter may be of particular relevance to the potentially unique functional roles of ZO-1, AF6, MUPP1 and cingulin at electrical synapses, impacting on the reported segregation of assembly and disassembly of gap junctions that occurs at the periphery and centers, respectively, of the plaque (Segretain and Falk 2004).

The alternatively spliced AF6 isoform lacking the F-actin binding domain influences the interaction of this isoform with the cytoskeleton and may influence the effector functions of AF6 (Lorger and Moelling 2006). We have shown that both of these isoforms coimmunoprecipitate with Cx36 (Li et al. 2012). It remains to be determined if the relative proportion of the full-length and truncated isoforms targeted to gap junctions is dependent on dynamic changes in the requirements of electrical synapses for interactions with cytoskeletal elements to maintain stability or promote turnover.

Acknowledgments Supported in part by grants from the Canadian Institutes of Health Research (MOP 106598) to J.I.N., and from the National Institutes of Health (NS31027, NS44010, NS44395) to J. E. Rash with a subaward to J.I.N. We thank B. McLean for excellent technical assistance.

References

Aijaz S, D'Atri F, Citi S, Balda MS, Matter K (2005) Binding of GEF-H1 to the tight junction-associated adaptor cingulin results in inhibition of Rho signaling and G1/S phase transition. Dev Cell 8:777–786

Akoyev V, Takemoto DJ (2007) ZO-1 is required for protein kinase C gamma-driven disassembly of connexin43. Cell Signal 19: 958–967

Alev C, Urschel S, Sonntag S, Zoidl G, Fort AG, Höher T, Matsubara M, Willecke K, Spray DC, Dermietzel R (2008) The neuronal connexin36 interacts with and is phosphorylated by CaMKII in a way similar to CaMKII interaction with gluamate receptors. Proc Natl Acad Sci (USA) 105:20964–20969

Baker R, Llinas R (1971) Electrotonic coupling between neurons in the rat mesencephalic nucleus. J Physio 212:45–63

Baker SM, Kim N, Gumpert AM, Segretain D, Falk MM (2008) Acute internalization of gap junctions in vascular endothelial cells in response to inflammatory mediator-induced G-protein coupled receptor activation. FEBS Lett 582:4039–4046

Balasubramanian S, Fam SR, Hall RA (2007) GABAb receptor association with the PDZ scaffold MUPP1 alters receptor stability and function. J Biol Chem 282:4162–4171

Baude A, Bleasdale C, Dalezios Y, Somogyi P, Klausberger T (2007) Immunoreactivity for GABAa receptor alpha1 subunit, somatostatin and connexin36 distinguishes axoaxonic, basket and bistratified interneurons of the rat hippocampus. Cereb Cortex 17:2094–2107

Becamel C, Figgs A, Poliak S, Dumuis A, Peles E, Bockaert J, Lubbert H, Ullmer C (2001) Interaction of serotonin 5-hydroxytryptamine type 2C receptors with PDZ10 of the multi-PDZ domain protein MUPP1. J Biol Chem 276:12974–12982

Bennett MVL (1997) Gap junctions as electrical synapses. J Neurocytol 26:349–366

Bennett MVL, Zukin SR (2004) Electrical coupling and neuronal synchronization in the mammalian brain. Neuron 41:495–511

Boettner B, Govek EE, Cross J, Van Aelst L (2000) The junctional multidomain protein AF-6 is a binding partner of the Rap1A GTPase and associates with the actin cytoskeletal regulator profilin. Proc Natl Acad Sci USA 97:9064–9069

Boettner B, Herrmann C, Van Aelst L (2001) Ras and Rap1 interaction with AF-6 effector target. Methods Enzymol 332: 151–168

Boettner B, Harjes P, Ishimaru S, Heke M, Fan HQ, Qin Y, Van Aelst L, Gaul U (2003) The AF-6 homolog canoe acts as a Rap1 effector during dorsal closure of the Drosophila embryo. Genetics 165:159–169

Caron E (2003) Cellular functions of the Rap1 GTP-binding protein: a pattern emerges. J Cell Sci 116:435–440

Cepeda C, Walsh JP, Hull CD, Howard SG, Buchwald NA, Levine MS (1989) Dye-coupling in the neostriatum of the rat: I. Modulation by dopamine-depleting lesions. Synapse 4:229–237

Chai Z, Goodenough DA, Paul DL (2011) Cx50 requires an intact PDZ-binding motif and ZO-1 for the formation of functional intercellular channels. Mol Biol Cell 22:4503–4512

Christensen AE, Selheim F, De Rooij J, Dremier S, Schwede F, Dao KK, Martinez A, Maenhaut C, Bos JL, Genieser H-G, Doskenland SO (2003) cAMP analog mapping of Epac1 and cAMP kinase. J Biol Chem 278:35394–35402

Ciolofan C, Li X, Olson O, Kamasawa N, Yasumura T, Morita M, Rash JE, Nagy JI (2006) Association of Connexin36 and ZO-1 with ZO-2 and the MsY3 transcription factor ZO-1-associated nucleic acid-binding protein (ZONAB) in mouse retina. Neuroscience 140:433–451

Citi S, Sabanay H, Kendrick-Jones J, Geiger B (1989) Cingulin: characterization and localization. J Cell Sci 93:107–122

Citi S, Paschoud S, Pulimeno P, Timolati F, De Robertis F, Jond L, Guillemot L (2009) The tight junction protein cingulin regulates gene expression and RhoA signaling. Ann NY Acad Sci 1165: 88–98

Connors BW, Long MA (2004) Electrical synapses in the mammalian brain. Annu Rev Neurosci 27:393–418

Cordenonsi M, D'Atri F, Hammar E, Parry DA, Kendrick-Jones J, Shore D, Citi S (1999) Cingulin contains globular and coiled-coil domains and interacts with ZO-1, ZO-2, ZO-3, and myosin. J Cell Biol 147:1569–1582

Curti S, Hoge G, Nagy JI, Pereda A (2012a) Synergy between electrical coupling and membrane properties promotes strong synchronization of neurons of the mesencephalic trigeminal nucleus. J Neurosci 32:4341–4359

Curti S, Hoge G, Nagy JI, Pereda A (2012b) Electrical transmission between mammalian neurons is supported by a small fraction of gap junction channels. J Membrane Biol. doi:10.1007/s00232-012-9449-z

D'Atri F, Citi S (2001) Cingulin interacts with F-actin in vitro. FEBS Lett 507:21–24

D'Atri F, Nadalutti F, Citi S (2002) Evidence for a functional interaction between cingulin and ZO-1 in cultured cells. J Biol Chem 277:27757–27764

de Rooij J, Zwartkruis FJ, Verheijen MH, Cool RH, Nijman SM, Wittinghofer A, Bos JL (1998) Epac is a Rap1 guanine-nucleotide-exchange factor directly activated by cyclic AMP. Nature 396:474–477

Derangeon M, Bourmeyster N, Plaisance I, Pinet-Charvet C, Chen Q, Duthe F, Popoff MR, Sarrouilhe D, Hervé JC (2008) RhoA GTPase and F-actin dynamically regulate the permeability of Cx43-made channels in rat cardiac myocytes. J Biol Chem 283:30754–30765

Derangeon M, Spray DC, Bourmeyster N, Sarrouilhe D, Herve JC (2009) Reciprocal influence of connexins and apical junction proteins on their expressions and functions. Biochim Biophys Acta 1788:768–778

Ebnet K, Suzuki A, Ohno S, Vestweber D (2004) Junctional adhesion molecules (JAMs): more molecules with dual functions? J Cell Sci 117:19–29

Enserink JM, Christensen AE, de Rooij J, van Triest M, Schwede F, Genieser HG, Døskeland SO, Blank JL, Bos JL (2002) A novel Epac-specific cAMP analogue demonstrates independent regulation of Rap1 and ERK. Nat Cell Biol 4:901–906

Fanning AS, Jameson BJ, Jesaitis LA, Anderson JM (1998) The tight junction protein ZO-1 establishes a link between the transmembrane protein occludin and the actin cytoskeleton. J Biol Chem 273:29745–29753

Fanning AS, Ma TY, Anderson JM (2002) Isolation and functional characterization of the actin binding region in the tight junction protein ZO-1. FASEB J 16:1835–1837

Flores CE, Li X, Bennett MVL, Nagy JI, Pereda AE (2008) Connexin35 and Zonula Occludens-1 directly interact: implications for the regulation of electrical transmission. Proc Natl Acad Sci USA 105:12545–12550

Flores CE, Nannapaneni S, Davidson KG, Yasumura T, Bennett MV, Rash JE, Pereda AE (2012) Trafficking of gap junction channels at a vertebrate electrical synapse in vivo. Proc Natl Acad Sci USA 109:E573–E582

Fuduka T, Kosaka T, Singer W, Galuske RAW (2006) Gap junctions among dendrites of cortical GABAergic neurons establish a dense and widespread intercolumnar network. J Neurosci 26: 3434–3443

Gonzalez-Mariscal L, Betanzos A, Nava P, Jaramillo BE (2003) Tight junction proteins. Prog Biophys Mol Biol 81:1–44

Guillaume JL, Daulat AM, Maurice P, Levoye A, Migaud M, Brydon L, Malpaux B, Borg-Capra C, Jockers R (2008) The PDZ protein MUPP1 promotes Gi coupling and signaling of the Mt1 melatonin receptor. J Biol Chem 283:16762–16771

Guillemot L, Foglia A, Paschoud S, Pulimeno P, Citi S (2008) The cytoplasmic plaque of tight junctions: a scaffolding and signalling center. Biochim Biophys Acta 1778:601–613

Hampson ECGM, Vaney DI, Weiler R (1992) Dopaminergic modulation of gap junction permeability between amacrine cells in mammalian retina. J Neurosci 12:4911–4922

Hatton GI (1997) Function-related plasticity in hypothalamus. Ann Rev Neurosci 20:375–397

Hatton GI, Yang QZ (2001) Ionotropic histamine receptors and H2 receptors modulate supraoptic oxytocin neuronal excitability and dye coupling. J Neurosci 21:2974–2982

He S, Weiler R, Vaney DL (2000) Endogenous dopaminergic regulation of horizontal cell coupling in the mammalian retina. J Comp Neurol 418:33–40

Herve J-C, Derangeon M, Sarrouilhe D, Geipmans BNG, Bourmeyster N (2011) Gap junctional channels are parts of multiprotein complexes. Biochem Biophys Acta 1818:1844–1865

Hinrichsen CF (1970) Coupling between cells of the trigeminal mesencephalic nucleus. J Dent Res 49(suppl):1369–1373

Hinrichsen CF, Larramendi LM (1970) The trigeminal mesencephalic nucleus. II. Electron microscopy. Am J Anat 127:303–319

Holz GG, Chepurny OG, Schwede F (2008) Epac-selective cAMP analogs; new tools with which to evaluate the signal transduction properties of cAMP-regulated guanine nucleotide exchange factors. Cell Signal 20:10–20

Hopkins WF, Johnston D (1988) Noradrenergic enhancement of long-term potentiation at mossy fiber synapses in the hippocampus. J Neurophysiol 59:667–687

Hormuzdi SG, Filippov MA, Mitropoulon G, Monyer H, Bruzzone R (2004) Electrical synapses: a dynamic signaling system that shapes the activity of neuronal networks. Biochem Biophys Acta 1662:113–137

Hunter AW, Gourdie RG (2008) The second PDZ domain of zonula occludens-1 is dispensable for targeting to connexin 43 gap junctions. Cell Commun Adhes 15:55–63

Hunter AW, Barker RJ, Zhu C, Gourdie RG (2005) Zonula occludens-1 alters connexin43 gap junction size and organization by influencing channel accretion. Mol Biol Cell 16:5686–5698

Itoh M, Furuse M, Morita K, Kubota K, Saitou M, Tsukita S (1999) Direct binding of three tight junction–associated MAGUKs, ZO-1, ZO-2, and ZO-3, with the COOH termini of claudins. J Cell Biol 147:1351–1363

Jeansonne B, Lu Q, Goodenough DA, Chen YH (2003) Claudin-8 interacts with multi-PDZ domain protein 1 (MUPP1) and reduces paracellular conductions in epithelial cells. Cell Mol Biol 49:13–21

Kamasawa N, Furman CS, Davidson KGV, Sampson JA, Magnie AR, Gebhardt BR, Kamasawa M, Yasumura T, Zumbrunnen JR, Pickard GE, Nagy JI, Rash JE (2006) Abundance and ultrastructural diversity of neuronal gap junctions in the OFF and ON sublaminae of the inner plexiform layer of rat and mouse retina. Neuroscience 142:1093–1117

Kooistra MRH, Bube N, Bos JL (2006) Rap1: a key regulator in cell-cell junction formation. J Cell Sci 120:17–22

Kothmann WW, Li X, Burr GS, O'Brien J (2007) Connexin 35/36 is phosphorylated at regulatory sites in the retina. Vis Neurosci 24:363–375

Krapivinsky G, Medina I, Krapininsky L, Gapon S, Clapham DE (2004) SynGAP-MUPP1-CaMKII synaptic complexes regulate p38 MAP kinase activity and NMDA receptor-dependent synaptic AMPA receptor potentiation. Neuron 43:563–574

Laing JG, Chou B, Steinberg TH (2005) ZO-1 alters the plasma membrane localization and function of Cx43 in osteoblastic cells. J Cell Sci 118:2167–2176

Landisman CE, Connors BW (2005) Long-term modulation of electrical synapses in the mammalian thalamus. Science 310: 1809–1813

Li X, Olson C, Lu S, Kamasawa N, Yasumura T, Rash JE, Nagy JI (2004a) Neuronal connexin36 association with zonula occludens-1 protein (ZO-1) in mouse brain and interaction with the first PDZ domain of ZO-1. Eur J Neurosci 19:2132–2146

Li X, Olson C, Lu S, Nagy JI (2004b) Association of connexin36 with zonula occludens-1 in HeLa cells, βTC-3 cells, pancreas and adrenal gland. Histochem Cell Biol 122:485–498

Li X, Kamasawa N, Ciolofan C, Olson CO, Lu S, Davidson KGV, Yasumura T, Shigemoto R, Rash JE, Nagy JI (2008a) Connexin45-containing neuronal gap junctions in rodent retina also contain connexin36 in both apposing hemiplaques, forming bihomotypic gap junctions, with scaffolding contributed by zonula occludens-1. J Neurosci 28:9769–9789

Li X, Penes M, Odermatt B, Willecke K, Nagy JI (2008b) Ablation of Cx47 in transgenic mice leads to the loss of MUPP1, ZONAB

and multiple connexins at oligodendrocyte-astrocyte gap junctions. Eur J Neurosci 28:1503–1517
Li X, Lu S, Nagy JI (2009) Direct association of connexin36 with zonula occludens-2 and zonula occludens-3. Neurochem Int 54:393–402
Li X, Lynn BD, Nagy JI (2012) The effector and scaffolding proteins AF6 and MUPP1 interact with connexin36 and localize at gap junctions that form electrical synapses in rodent brain. Eur J Neurosci 35:166–181
Liu X-B, Jones EG (2003) Fine structural localization of connexin36 immunoreactivity in mouse cerebral cortex and thalamus. J Comp Neurol 466:457–467
Llinas R, Baker R, Sotelo C (1974) Electrotonic coupling between neurons in cat inferior olive. J Neurophysiol 37:560–571
Lorenowicz MJ, Fernandez-Borja M, Kooistra MRH, Bos JL, Hordijk PL (2008) PKA and Epac1 regulate endothelial integrity and migration through parallel and independent pathways. Eur J Cell Biol 87:779–792
Lorger M, Moelling K (2006) Regulation of epithelial wound closure and intercellular adhesion by interaction of AF6 with actin cytoskeleton. J Cell Sci 119:3385–3398
McCracken CB, Hamby SM, Patel KM, Morgan D, Vrana KE, Roberts DC (2005a) Extended cocaine self-administration and deprivation produces region-specific and time-dependent changes in connexin36 expression in rat brain. Synapse 58:141–150
McCracken CB, Patel KM, Vrana KE, Paul DL, Roberts DCS (2005b) Amphetamine withdrawal produces region-specific and time-dependent changes in connexin36 expression in rat brain. Synapse 56:39–44
Moreno AP, Lau AF (2007) Gap junction channel gating modulated through protein phosphorylation. Prog Biophys Mol Biol 94:107–119
Muller JF, Mascagni F, McDonald AJ (2005) Coupled networks of parvalbumin-immunoreactive interneurons in the rat basolateral amygdala. J Neurosci 25:7366–7376
Nagy JI, Dudek FE, Rash JE (2004) Update on connexins and gap junctions in neurons and glia in the mammalian nervous system. Brain Res Rev 47:191–215
Niessen CM, Gottardi CJ (2008) Molecular components of the adherens junction. Biochim Biophys Acta 1778:562–571
Ogita H, Takai Y (2006) Nectins and nectin-like molecules: roles in cell adhesion, polarization, movement, and proliferation. IUBMB Life 58:334–343
Onn SP, Grace AA (1994) Dye coupling between rat striatal neurons recorded in vivo: compartmental organization and modulation by dopamine. J Neurophysiol 71:1917–1934
Onn S-P, Grace AA (1995) Repeated treatment with haloperidol and clozapine exerts differential effects on dye coupling between neurons in subregions of striatum and nucleus accumbens. J Neurosci 15:7024–7036
Onn S-P, Grace AA (1999) Alterations in electrophysiological activity and dye coupling of striatal spiny and aspiny neurons in dopamine-denervated rat striatum recorded in vivo. Synapse 33:1–15
Onn S-P, West AR, Grace AA (2000) Dopamine-mediated regulation of striatal neuronal and network interactions. Trends Neurosci 23:S48–S56
Ouyang X, Winbow VM, Patel LS, Burr GS, Mitchell CK, O'Brien J (2005) Protein kinase A mediates regulation of gap junctions containing connexin35 through a complex pathway. Brain Res Mol Brain Res 135:1–11
Penes MC, Li X, Nagy JI (2005) Expression of zonula occludens-1 (ZO-1) and the transcription factor ZO-1-associated nucleic acid-binding protein (ZONAB)-MsY3 in glial cells and colocalization at oligodendrocyte and astrocyte gap junctions in mouse brain. Eur J Neurosci 22:404–418
Pereda AE, Bell TD, Chang BH, Czernik AJ, Nairn AC, Soderling TR, Faber DS (1998) Ca^{2+}/calmodulin-dependent kinase II mediates simultaneous enhancement of gap-junctional conductance and glutamatergic transmission. Proc Natl Acad Sci USA 95:13272–13277
Perez Velazquez JL, Han D, Carlen PL (1997) Neurotransmitter modulation of gap junctional communication in the rat hippocampus. Eur J Neurosci 9:2522–2531
Qu C, Gardner P, Schrijver I (2009) The role of the cytoskeleton in the formation of gap junctions by Connexin 30. Exp Cell Res 315:1683–1692
Rash JE, Staines WA, Yasumura T, Pate D, Hudson CS, Stelmack GL, Nagy JI (2000) Immunogold evidence that neuronal gap junctions in adult rat brain and spinal cord contain connexin36 (Cx36) but not Cx32 or Cx43. Proc Natl Acad Sci USA 97: 7573–7578
Rash JE, Olson CO, Pouliot WA, Davidson KGV, Yasumura T, Furman CS, Royer S, Kamasawa N, Nagy JI, Dudek FE (2007a) Connexin36, miniature neuronal gap junctions, and limited electrotonic coupling in rodent suprachiasmatic nucleus (SCN). Neuroscience 149:350–371
Rash JE, Olson CO, Davidson KGV, Yasumura T, Kamasawa N, Nagy JI (2007b) Identification of connexin36 in gap junctions between neurons in rodent locus coeruleus. Neuroscience 147: 938–956
Rorig B, Sutor B (1996) Serotonin regulates gap junction coupling in the developing rat somatosensory cortex. Eur J Neurosci 8:1685–1695
Rorig B, Klausa G, Sutor B (1995) Dye coupling between pyramidal neurons in developing rat prefrontal and frontal cortex is reduced by protein kinase A activation and dopamine. J Neurosci 15:7386–7400
Schmitz D, Schuchmann S, Fisahn A, Draguhn A, Buhl EH, Petrasch-Parwez E, Dermietzel R, Heinemann U, Traub RD (2001) Axo-Axonal coupling: a novel mechanism of ultrafast neuronal communication. Neuron 31:831–840
Segretain D, Falk MM (2004) Regulation of connexin biosynthesis, assembly, gap junction formation, and removal. Biochem Biophys Acta 1662:3–21
Smyth JW, Vogan JM, Buch PJ, Zhang SS, Fong TS, Hong TT, Shaw RM (2012) Actin cytoskeleton rest stops regulate anterograde traffic of connexin 43 vesicles to the plasma membrane. Circ Res 2012 Epub ahead of print
Sohl G, Odermatt B, Maxeiner S, Degen J, Willecke K (2004) New insights into the expression and function of neural connexins with transgenic mouse mutants. Brain Res Rev 47:245–259
Sohl G, Maxeiner S, Willecke K (2005) Expresssion and functions of neuronal gap junctions. Nat Rev Neurosci 6:191–200
Somekawa S, Fukuhura S, Nakaoka Y, Fujita H, Saito Y, Mochizuki N (2005) Enhanced functional gap junction neoformation by protein kinase A-dependent and Epac-dependent signals downstream of cAMP in cardiac myocytes. Circ Res 97:655–662
Theiss C, Meller K (2002) Microinjected anti-actin antibodies decrease gap junctional intercellular commmunication in cultured astrocytes. Exp Cell Res 281:197–204
Ullmer C, Schmuck K, Figge A, Lubbert H (1998) Cloning and characterization of MUPP1, a novel PDZ domain protein. FEBS Lett 424:63–68
Umeda K, Kenouchi J, Katahira-Tayama S, Furuse K, Sasaki H, Nakayama M, Matsui T, Tsukita S, Furuse M, Tsukita S (2006) ZO-1 and ZO-2 independently determine where claudins are polymerized in tight-junction strand formation. Cell 126:741–754
Urschel S, Hoher T, Schubert T, Alev C, Sohl G, Worsdorfer P, Asahara T, Dermietzel R, Weiler R, Willecke K (2006) Protein kinase A-mediated phosphorylation of connexin36 in mouse retina results in decreased gap junctional communication between AII amacrine cells. J Biol Chem 281:33163–33171

Utepbergenov DI, Fanning AS, Anderson JM (2006) Dimerization of the scaffolding protein ZO-1 through the second PDZ domain. J Biol Chem 281:24671–24677

Xia XB, Mills SL (2004) Gap junctional regulatory mechanisms in the AII amacrine cell of the rabbit retina. Vis Neurosci 21: 791–805

Yamamoto T, Harada N, Kano K, Taya S-I, Canaani E, Matsuura Y, Mizoguchi A, Ide C, Kaibuchi K (1997) The ras target AF-6 interacts with ZO-1 and serves as a peripheral compoment of tight junctions in epithelial cells. J Cell Biol 139:785–795

Yamamoto T, Harada N, Kawano Y, Taya S, Kaibuchi K (1999) In vivo interaction of AF-6 with activated ras and ZO-1. Biochem Biophys Res Commun 259:103–107

Yang QZ, Hatton GI (2002) Histamine H1-receptor modulation of inter-neuronal coupling among vasopressinergic neurons depends on nitric oxide synthase activation. Brain Res 955:115–122

J Membrane Biol (2012) 245:319–332
DOI 10.1007/s00232-012-9453-3

Posttranslational Modifications in Connexins and Pannexins

Scott R. Johnstone · Marie Billaud · Alexander W. Lohman · Evan P. Taddeo · Brant E. Isakson

Received: 31 March 2012 / Accepted: 8 June 2012 / Published online: 28 June 2012

Abstract Posttranslational modification is a common cellular process that is used by cells to ensure a particular protein function. This can happen in a variety of ways, e.g., from the addition of phosphates or sugar residues to a particular amino acid, ensuring proper protein life cycle and function. In this review, we assess the evidence for ubiquitination, glycosylation, phosphorylation, *S*-nitrosylation as well as other modifications in connexins and pannexin proteins. Based on the literature, we find that posttranslational modifications are an important component of connexin and pannexin regulation.

Keywords Posttranslational modification · Connexin · Pannexin

Introduction

Posttranslational modification is a common method by which proteins can be modulated by intrinsic or extrinsic factors to potentiate or initiate a specific function. It is now well accepted that these modifications are a key way in which a protein can become useful in the context of cellular physiology. This is not different when it comes to the connexin and pannexin family of proteins, where a fairly broad range of modifications has now been described that can alter the function of these proteins, from the dramatic (e.g., opening or closing of the channel/gap junction/hemichannel) to the subtle (e.g., insertion into specialized lipid rafts).

Connexin and pannexin proteins are transmembrane proteins that allow for the passive diffusion of signaling molecules through their pores. Connexins are the key components to gap junctions, linking the cytoplasms of two opposing cells and allowing for rapid electrical or chemical integration among cells in a tissue. These proteins, when composed as a gap junction, allow for several functions, including electrical coordination of cardiac myocytes or ciliary beat frequency between tracheal epithelium, with several mutations in connexins associated with disease states (Boitano and Evans 2000; Johnson and Koval 2009; Kelsell et al. 2001; Lai et al. 2006; Palatinus and Gourdie 2007). Undocked connexin hemichannels have also been hypothesized to play a more paracrine role in cellular communication in more pathological states (De Vuyst et al. 2007; Pearson et al. 2005). While membrane topology is similar to that of connexins, pannexins share no sequence homologies with connexins and are a more recently identified class of transmembrane proteins (Panchin et al. 2000). Pannexins can be found in three different isoforms (Panx1, Panx2 and Panx3) encoded by three different genes, with Panx1 and Panx3 sharing more similarities to each other than to Panx2 (Penuela et al. 2007). In the past decade, a growing body of literature has revealed that pannexins play multiple roles as they have been shown to release ATP and participate in calcium wave propagation and are likely a component of the inflammasome (Dando

S. R. Johnstone · M. Billaud · A. W. Lohman · B. E. Isakson (✉)
Robert M. Berne Cardiovascular Research Center, University of Virginia School of Medicine, Charlottesville, VA 22908, USA
e-mail: brant@virginia.edu

A. W. Lohman · B. E. Isakson
Department of Molecular Physiology and Biological Physics, University of Virginia School of Medicine, PO Box 801394, Charlottesville, VA 22908, USA

E. P. Taddeo
Department of Pharmacology, University of Virginia School of Medicine, Charlottesville, VA 22908, USA

and Roper 2009; Locovei et al. 2006; Silverman et al. 2009; Sridharan et al. 2010). Thus, both connexins and pannexins are critical for cells to coordinate direct and paracrine communication (Fig. 1). In this review, we aim to bring together data focusing on the roles for glycosylation, phosphorylation, *S*-nitrosylation, ubiquitination and other posttranslational modifications in regulating the functions of both connexin and pannexin proteins.

Glycosylation

Glycosylation is a form of posttranslational modification which consists of the enzymatic addition of glycans to form glycosylated proteins. The enzyme glycosyltransferase catalyzes the attachment of glycans to a nitrogen of asparagine (*N*-linked glycosylation) or to a hydroxyl oxygen of threonine or serine (*O*-linked glycosylation) residues (Freeze and Sharma 2010; Reis et al. 2010). Glycosylation mostly occurs in the endoplasmic reticulum (ER) or Golgi apparatus and can affect protein folding and stability, influence protein trafficking and interfere with protein function (Pinho et al. 2011; Reis et al. 2010; Roth et al. 2010).

Connexin proteins are not glycosylated despite identification of the *N*-glycosylation consensus sequence in Cx32 (Martin and Evans 2004; Rahman et al. 1993; Saez et al. 2003). However, it should be noted that a few reports have shown that inhibition of protein glycosylation in cells transfected with Cx43 can increase trafficking of Cx43 to the plasma membrane, its phosphorylation and its opening indirectly via a cAMP pathway (Wang and Mehta 1995; Wang et al. 1995; Wang and Rose 1995).

Currently, the primary identified posttranslational modification in pannexins is glycosylation. Glycosylation of the Panx1 isoforms leads to a migration shift on SDS gel with bands representing three different glycosylation states, whereas the multiple band pattern of Cx43 has been demonstrated to represent different phosphorylated states (Boassa et al. 2007, 2008; Penuela et al. 2007, 2009; Solan and Lampe 2009). The different glycosylation states of Panx1 result in a multiple banding pattern on a Western blot, with the Gly2 species migrating slower than Gly1 as an intermediate band and the Gly0 species being the fastest-migrating form (Boassa et al. 2007, 2008; Penuela et al. 2007, 2009). Of the three pannexin isoforms, Panx1 and Panx3 have been shown to be glycosylated and their glycosylation sites have been defined, whereas the glycosylation site of Panx2 has only been predicted (Boassa et al. 2007, 2008; Penuela et al. 2007, 2009, 2012).

Panx1 and Panx3 are *N*-glycosylated on the amino acids asparagine (N) 254 and N71, respectively, and can be found in three different states: a core unglycosylated protein (Gly0), a high mannose-glycosylated protein (Gly1) and an extensively glycosylated species (Gly2) (Boassa et al. 2007; Penuela et al. 2007, 2009). The role of *N*-glycosylation of Panx1 was explored using site-directed mutagenesis of N254 targeted by *N*-glycosylation ($Panx1^{N254Q}$) (Boassa et al. 2007, 2008; Penuela et al. 2007, 2008). Similarly, the role of Panx3 *N*-glycosylation was investigated using the mutant $Panx3^{N71Q}$ (Penuela et al. 2007, 2008). These glycosylation mutants exhibit reduced trafficking to the plasma membrane when transfected in different cell lines, suggesting an important role for *N*-glycosylation in Panx1 and Panx3 trafficking (Boassa et al. 2007, 2008; Penuela et al. 2007, 2008). However, despite the low amount of $Panx1^{N254Q}$ and $Panx3^{N71Q}$ at the plasma membrane, the mutated proteins still form channels, as evidenced by dye uptake measurements (Penuela et al. 2007, 2009). Additionally, when wild-type Panx1 and $Panx1^{N254Q}$ are cotransfected, the trafficking of the glycosylation mutant to the plasma membrane is rescued, showing that they co-oligomerize and suggesting that *N*-glycosylation does not play a role in oligomerization of Panx1 (Boassa et al. 2008). Altogether, these studies demonstrate that the Gly0 species appears primarily after protein synthesis, whereas Gly1 is associated within the ER and Gly2 is modified in the Golgi apparatus prior to plasma membrane insertion. However, it should be noted that all Panx1 glycosylated species are capable of trafficking to the plasma membrane but the Gly2 form is preferentially trafficked (Gehi et al. 2011).

Fig. 1 Schematic list of posttranslational modifications throughout the life span of connexins and pannexins. *Numbers* are the amino acids in the proteins as indicated in the references. Note that only when amino acids or specific regions on the protein could be identified were they included in the figure; e.g., although palmitoylation has been indicated for Panx2 (Swayne et al. 2010), the exact region on the protein remains unknown. *Shown indirectly through PKA; #this cysteine is assumed to be *S*-nitrosylated in a hemichannel (based on Retamal et al. 2006) but has not been directly shown; +data are now in dispute according to Dunn et al. (2012). *1* Paulson et al. (2000), TenBroek et al. (2001); *2* Locke et al. (2006); *3* Cooper and Lampe (2002); *4* Cottrell et al. (2003), Kanemitsu et al. (1998), Lampe et al. (1998), Norris et al. (2008), Warn-Cramer et al. (1998); *5* Doble et al. (2004), Ek-Vitorin et al. (2006), Lampe et al. (2000); *6* Solan and Lampe (2008); *7* Straub et al. (2011); *8* Kjenseth et al. (2012); *9* Bao et al. (2004b, 2007); *10* Toyofuku et al. (2001); *11* Lampe et al. (2000), Solan et al. (2003); *12* Kanemitsu et al. (1998), Lampe et al. (1998), Xie et al. (1997); *13* Beardslee et al. (2000), Solan et al. (2007); *14* Hertlein et al. (1998); *15* Yin et al. (2001), Yin et al. (2008); *16* Wagner et al. (2011); *17* Boassa et al. (2007), Penuela et al. (2007); *18* Penuela et al. (2007); *19* Chekeni et al. (2010); *20* Kim et al. (2011)

Phosphorylation

Posttranslational modification through phosphorylation acts as a major regulatory pathway in normal protein life

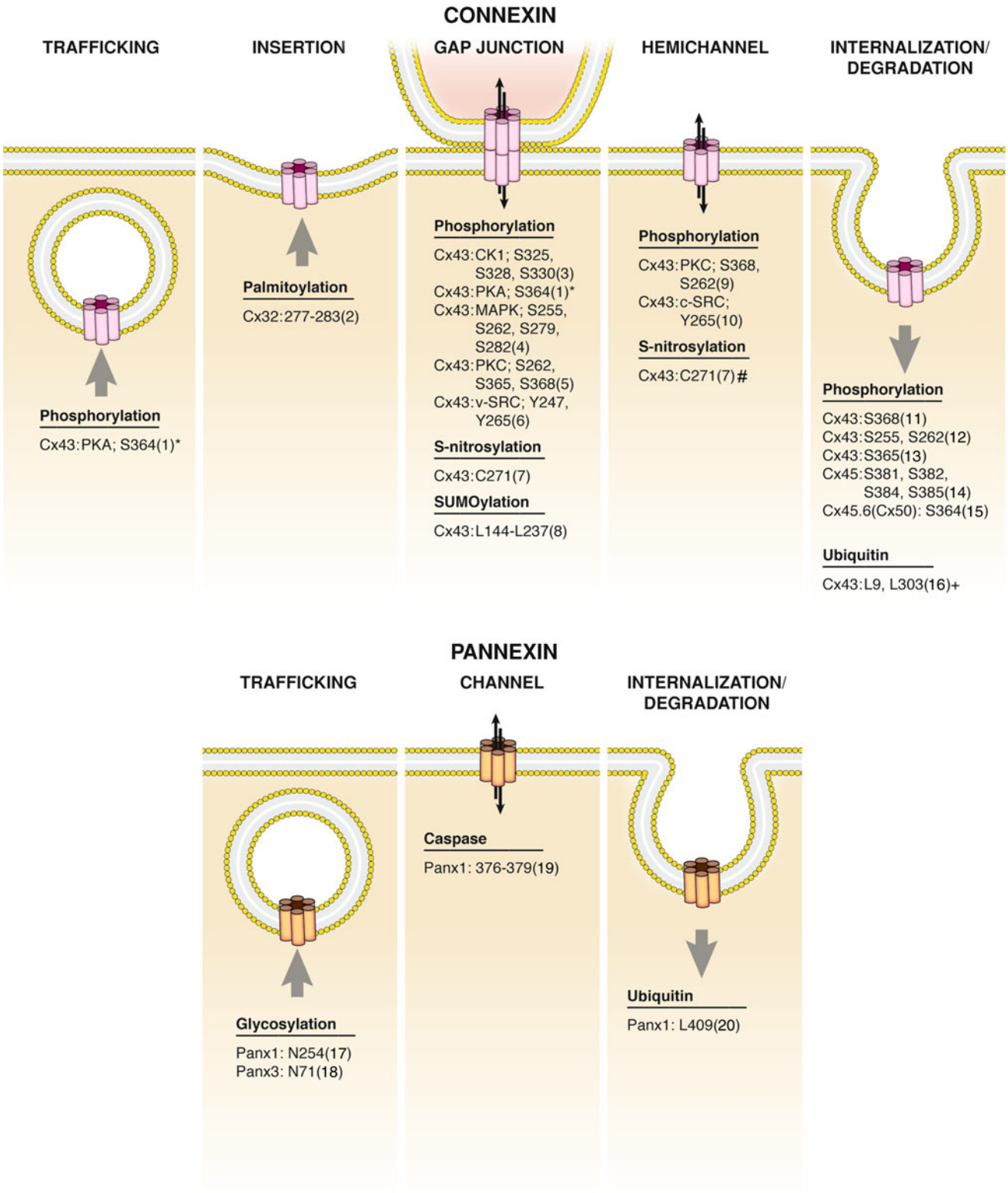

cycles and can be further affected in pathological states by upregulation of kinase pathways. These pathways regulate protein functions through addition of a phosphate group by kinases to serine (S), threonine (T) and tyrosine (Y) sites, which may lead to alterations in the hydrophobicity, charge and potentially structural reorganization of proteins, either promoting or inhibiting normal functions (Davis 2011; Huttlin et al. 2010; Nishi et al. 2011).

Phosphorylation of connexins has been extensively demonstrated and reviewed (particularly for Cx43) and is integral in their life cycle–altering protein oligomerization, trafficking, membrane insertion and aggregation, gap junction communication and internalization from the membrane (Laird 2005; Laird et al. 1995; Marquez-Rosado et al. 2011; Saez et al. 1990, 1998; Solan and Lampe 2005, 2009). Phosphorylation has been demonstrated for multiple S/T/Y sites through c- and v-SRC; mitogen-activated protein kinase (MAPK), protein kinase C (PKC), protein kinase A (PKA), $P34^{cdc}$ (CDC2), casein kinase 1 (CK1) and calmodulin-dependant protein kinase pathways (Lampe and Lau 2004; Saez et al. 1998; Solan and Lampe 2005, 2009).

Posttranslational modification through phosphorylation of cytoplasmic residues primarily occurs within the connexin carboxyl terminus. Additionally, phosphorylation sites in the Cx43 amino terminus (S5) and the Cx56 intracellular loop have been identified as phosphorylated (Berthoud et al. 1997; Chen et al. 2012; Wisniewski et al. 2010). Cx43 does not contain serines within its intracellular loop and is therefore not modified directly by phosphorylation within this region (Solan and Lampe 2005). As a result of a short 19-amino acid carboxyl terminus containing only two serines, Cx26 is the only isoform that is currently considered not to be posttranslationally modified through phosphorylation (Traub et al. 1989). Conversely, Cx43 contains a total of 66 S/T/Y sites (32 in the carboxyl terminus) and has been demonstrated to be highly regulated through phosphorylation primarily at serine residues (Chen et al. 2012; Crow et al. 1990; Marquez-Rosado et al. 2011).

Phosphoproteomic analyses used to determine the incidence of protein phosphorylation in vitro and across multiple tissues, ranging from brain, kidney, lung, spleen and more, derived from mice, rats and humans have demonstrated that Cx43 as well as Cx47, Cx32 and Cx29 are phosphorylated at multiple sites at their carboxyl terminus as well as the amino terminus (Brill et al. 2009; Cooper et al. 2000; Huttlin et al. 2010; Rikova et al. 2007; Wisniewski et al. 2010). These studies and others further suggest that connexins are regulated by complex multisite phosphorylation, which plays an important role in the rapid generation and turnover of connexin proteins in a multitude of tissues and organ systems (Chen et al. 2012; Johnson and Vaillancourt 1994). This area of study will become increasingly important in terms of understanding how multiple phosphorylation events can "tip the balance" one way or another toward a particular protein function.

Connexins are posttranslationally oligomerized to hexameric hemichannels prior to membrane insertion either within the ER (e.g., Cx26, Cx32) (Falk et al. 1997; Falk and Gilula 1998) or in the *trans*-Golgi network (e.g., Cx43, Cx46) (Das Sarma et al. 2001; del Castillo et al. 2009; Koval 2006; Koval et al. 1997; Musil and Goodenough 1993; Puranam et al. 1993). A role for connexin phosphorylation in channel oligomerization has not currently been demonstrated (Solan and Lampe 2005). Pulse-chase studies have shown that newly synthesized Cx43 can be rapidly phosphorylated and dephosphorylated (within 15–30 min) (Crow et al. 1990) in the ER and Golgi compartments (Laird et al. 1995). In addition, monomeric Cx43 phosphoisoforms have been identified, which suggests that Cx43 is phosphorylated prior to insertion into the plasma membrane (Musil and Goodenough 1993). Further, increases in PKA activity can promote Cx43 integration to the membrane and are associated with Cx43-S364 phosphorylation, but Cx43 is a poor substrate for PKA and does not appear to directly increase Cx43 phosphorylation, suggesting that other intermediary pathways mediate the response (Paulson et al. 2000; TenBroek et al. 2001). Data demonstrating nonphosphorylated isoforms of connexins at the membrane suggest that they can be inserted to the membrane without phosphorylation (although transient phosphorylations could occur prior to entry to the membrane (Musil et al. 1990; Musil and Goodenough 1991; Solan and Lampe 2005). This is also evident with truncated mutations of Cx43 (Δ252) oligomerizing and trafficking to the plasma membrane. These truncated channels still form functional channels, suggesting that phosphorylation on the carboxyl tail is not a critical requirement (Johnstone et al. 2009; Martinez et al. 2003). Regardless, deletion mutagenesis studies have demonstrated that a portion of the Cx43 carboxyl terminus is required for trafficking. By creating a carboxyl terminus deletion at amino acid 236, Cx43 cannot traffic to the membrane, while deletions after amino acid 239 (Δ243/Δ239) traffic to the membrane and form gap junctions (De Vuyst et al. 2007; Wayakanon et al. 2012). As with Cx43, Cx45 requires its carboxyl terminus to target the membrane. Phosphorylation does not significantly alter Cx45 trafficking to the membrane but may affect protein half-life (Hertlein et al. 1998). Current data therefore suggest that phosphorylation of connexins is not a critical determinant of oligomerization and membrane insertion but could be involved in efficient gap junction assembly and trafficking.

The open and closed states of connexin hemichannels exist as a balance between inhibition and stimulation of carboxyl terminal residues. Mutagenesis studies of Cx43 have shown that mutations after amino acid 239 in Cx43 can still form functional gap junctions but inhibit hemichannel opening, suggesting that regulatory sites within the carboxyl terminus are required for hemichannel opening (De Vuyst et al. 2007). In general, connexin phosphorylation through PKC (e.g., S368) and MAPK activity maintains a closed hemichannel state (Bao et al. 2004a, 2007; Chandrasekhar and Bera 2012; Contreras et al. 2002;

Ek-Vitorin et al. 2006; Kwak and Jongsma 1996; Schulz and Heusch 2004; Srisakuldee et al. 2009). Indeed, it has been shown that direct phosphorylation of Cx43-S368 by PKC reduces hemichannel opening (Bao et al. 2004b). Similarly, treatments with lipopolysaccharide and basic fibroblast growth factor decrease hemichannel activity in Cx32-, Cx43- and Cx26-expressing HeLa cells (De Vuyst et al. 2007). However, the same treatments enhance hemichannel opening in C6-Cx43 cells (De Vuyst et al. 2007). This diversity in hemichannel signaling has been attributed to a balance between channel inhibition (phosphorylation) and stimulation (dephosphorylation) modifications on the connexin carboxyl terminus (Contreras et al. 2002; De Vuyst et al. 2007).

As described above, the carboxyl terminus of connexins (particularly Cx43) may act to promote efficient gap junction assembly from hemichannels. Once inserted to the membrane, hemichannels aggregate in "formation plaques" prior to incorporation into the gap junctional plaque (Johnson et al. 2012; Segretain and Falk 2004). Truncation mutants of Cx43 result in reduced hemichannel aggregation and gap junction plaque formation, suggesting that phosphorylation of carboxyl-terminal residues may be involved in efficient delivery of hemichannels to the gap junction plaque (Johnson et al. 2012; Palatinus et al. 2011a). Increased formation and stability of gap junctions have been associated with PKA and CK1 activity. Increases in intracellular cAMP levels promote PKA activity, which promotes (indirectly) Cx43-S364 phosphorylation and increases in gap junction assembly and coupling (TenBroek et al. 2001). CK1 phosphorylation of Cx43-S325/S328/S330 also appears to promote gap junction assembly and stability (Cooper and Lampe 2002). Gap junction aggregation occurs through directed trafficking by chaperone proteins, e.g., zonula occludens-1/2 (ZO-1/ZO-2) (Rhett et al. 2011; Singh et al. 2005). Associations between the Cx43 carboxyl terminus and ZO-1 promote targeting to gap junction plaques (Hunter et al. 2005; Jin et al. 2004; Segretain et al. 2004; Toyofuku et al. 1998). This can be disrupted through c-SRC phosphorylation of Cx43-Y265, which appears to be a critical site in the binding of ZO-1 (Toyofuku et al. 2001). Therefore, phosphorylation may allow for efficient and directed movement of connexins within the membrane to sites of gap junction plaques.

In general, for Cx43, CK1 (and PKA) pathways increase and PKC, MAPK, v-SRC, and CDC2 reduce gap junctional communication (Pahujaa et al. 2007; Solan and Lampe 2005, 2008, 2009). Phosphorylation-induced increases in gap junctional communication occur through CK1 phosphorylation of Cx43-S325/S328/S330 (Cooper and Lampe 2002) and by PKA (Cx43-S364, indirectly) (TenBroek et al. 2001). However, as mentioned, these sites are also associated with increased gap junction assembly; and it has been suggested that they may enhance plaque stability, leading to a prolonged life cycle (Remo et al. 2011). In addition, phosphorylation of Cx40 by PKA pathways leads to altered (higher) conductance states (van Rijen et al. 2000).

PKC activity reduces Cx43 gap junctional communication. Reduced unitary conductance occurs following Cx43-S368 phosphorylation (Ek-Vitorin et al. 2006; Lampe et al. 2000), and site-directed mutagenesis demonstrates that Cx43-S262 phosphorylation can reduce gap junctional communication, which in turn may act to promote DNA synthesis and cell cycle progression (Doble et al. 2004). The impact of reduced communication through PKC phosphorylation of Cx43-S368 ranges from promoting wound closure (potentially by isolating cells from surrounding signals and promoting differentiation) (Richards et al. 2004), causing decreased cell-to-cell communication in the vascular wall (Straub et al. 2009) and reducing ischemia–reperfusion injury in hearts (Palatinus et al. 2011b). MAPK phosphorylation of Cx43-S255/S279/S282 leads to reductions in gap junctional communication by inhibiting the ability of the channels to open (Cottrell et al. 2003; Warn-Cramer et al. 1998). It should also be noted that several sites in the Cx43 tail may be phosphorylated through multiple pathways as is demonstrated for PKC induction by phorbol 12-myristate 13-acetate, which promotes Cx43 S279/S282 phosphorylation (Solan and Lampe 2007, 2009). In addition to the classically accepted MAPK sites, Norris et al. (2008) demonstrated that Cx43-S262 sites were phosphorylated (but not S368) through MAPK pathways, leading to reduced gap junctional communication and meiotic resumption in mouse oocytes. Increases in CDC2 promote phosphorylation of Cx43-S255 and reductions in gap junctional communication, which are associated with progression through the cell cycle (Kanemitsu et al. 1998; Lampe et al. 1998). Activation of v-SRC pathways leads to phosphorylation of Cx43-Y247 and Cx43-Y265, which appears to occur in formed gap junctions, leading to a reduction in gap junctional communication (Solan and Lampe 2008). In addition to these sites, active v-SRC can cause phosphorylation at sites associated with PKC and MAPK in Cx43 (Solan and Lampe 2008).

Less is known for the other connexins. Sequence predictions and homology suggest that Cx37 may be similarly phosphorylated through MAPK pathways, potentially at Cx37-S275 and Cx37-S282, which may affect gap junctional assembly and communication; but this has not been directly demonstrated (Burt et al. 2008). Phosphorylation of Cx45 through PKC pathways alters the occupancy time and conductive state of the channel (Kwak et al. 1995; van Veen et al. 2000). Although Cx45 is primarily phosphorylated at serines, substitution of all carboxyl-terminus

serines does not alter gap junctional communication in HeLa cells (Hertlein et al. 1998).

Phosphorylation also plays a role in the internalization of connexins from the gap junctional plaque and has been shown to alter the protein turnover rates for several connexins (Laird 2005). During the cell cycle Cx43 appears to be dynamically regulated at the S, G_1, G_2 and M phases, all represented by alterations in Cx43 phosphorylation and internalization. As the cell cycle progresses, Cx43 appears at more intracellular locations and is highly phosphorylated at CDC2, PKC and MAPK sites, suggesting that phosphorylation may be involved in the removal of the connexins from the membrane gap junction plaques. However, it has not been conclusively demonstrated whether this results from removal of connexins from gap junction plaques or from reduced assembly to plaques (Solan and Lampe 2009). In mitosis, phosphorylation of Cx43 by CDC2 at the S255 and S262 regions is associated with an internalization of the protein (Kanemitsu et al. 1998; Lampe et al. 1998; Xie et al. 1997). During the cell cycle Cx43-S368 phosphorylation is also associated with a reduction in gap junction plaque size and protein internalization (Lampe et al. 2000; Solan et al. 2003). Conversely, it has been noted that dephosphorylation of Cx43 (S365) promotes an intracellular redistribution of Cx43 (Beardslee et al. 2000; Solan et al. 2007) or removal of Cx43 plaques (Laird et al. 1995). Substitution of Cx45-S381/S382/S384/S385 residues, but not the remaining serines from the carboxyl terminus of Cx45, significantly reduces the protein half-life by approximately 50 %, suggesting that these sites are involved in protein degradation (Hertlein et al. 1998). More recently, the MAPK phosphorylation of Cx43 at S255/262/279/282 was identified as critical to binding with cyclin E and promotion through the cell cycle (Johnstone et al. 2012).

While phosphorylation of connexins is integral to their functionality, much less has been demonstrated for modulation of pannexin channels. Despite this, all mammalian forms of pannexins contain multiple S/T/Y sites (Penuela et al. 2007). Currently, there are limited structural data for the pannexins and their carboxyl-terminus regions (Ambrosi et al. 2010). The membrane topology of pannexins appears to resemble that of the connexins with a cytoplasmic amino terminus, intracellular loop and carboxyl terminus, which shows the greatest sequence variability in the Panx2 isoform (Penuela et al. 2012). As with the connexins, the carboxyl-terminus regions are rich in S/T/Y sites. Consensus sequences for S/Y/T phosphorylation have been predicted based on sequence and membrane topology for pannexins 1–3 to occur primarily in the carboxyl terminus with fewer intracellular loop motifs (Barbe et al. 2006; Penuela et al. 2007). It has been shown that Panx1 ATP release can be induced by $P2X_7R$ activation through tyrosine kinase pathways, but it is not clear whether Panx1 is directly phosphorylated or regulated through intermediary pathways (Iglesias et al. 2009). While data on phosphorylation of pannexins are currently in their infancy, there is clearly the potential for this posttranslational modification in the regulation of the protein life cycle or function.

Nitrosylation

Posttranslational modification can also occur through *S*-nitrosylation, in which nitric oxide (NO) can bind to a reactive cysteine (C) thiol, producing an *S*-nitrosothiol (SNO) (Stamler et al. 1992). While proteins often contain multiple cysteine residues, the majority of the observed biological effects imparted by NO occur on single or only a few cysteine residues within a protein. In addition to direct modification of proteins by *S*-nitrosylation, this posttranslational modification can indirectly regulate other protein modifications including acetylation, phosphorylation and ubiquitination (Hess and Stamler 2012; Park et al. 2004; Whalen et al. 2007; Yasukawa et al. 2005).

The effects of NO on hemichannels and gap junctions have primarily been investigated in vascular cell types including vascular endothelial and smooth muscle cells. Of particular note, it was initially shown that exogenous application of the NO donor *S*-nitroso-*N*-acetylpenicillamine to cultured human umbilical vein endothelial cells significantly decreased dye transfer between coupled cells in a Cx37-dependent manner (Kameritsch et al. 2005). The observed decrease in gap junction permeability was independent of the effects of NO on guanylate cyclase and cGMP levels, indicating a separate effect of NO on the channels. In a separate study, NO application significantly reduced electrical coupling between cultured human microvascular endothelial cells mediated by effects on gap junctions composed of Cx37, which was similarly independent of cGMP (McKinnon et al. 2009). Conducted vasoconstriction in cremasteric arterioles has been shown to be dependent on Cx37 gap junctions and, importantly, is impaired during sepsis, a pathology resulting in upregulation of *n*NOS and increased NO production (McKinnon et al. 2006).

While *S*-nitrosylation of gap junctions composed of Cx37 has not been directly observed, evidence has indicated the ability of Cx43 to be *S*-nitrosylated; and this modification has been suggested to regulate gap junction permeability at the myoendothelial junction (MEJ) in the blood vessel wall (Straub et al. 2011). In this study, Cx43 was found to be locally enriched along with eNOS at the MEJ. Importantly, Cx43 was constitutively *S*-nitrosylated at C271. The *S*-nitrosylation of C271 on Cx43 was directly

correlated with an open channel probability as denitrosylation significantly reduced heterocellular communication at the MEJ, namely, the movement of inositol triphosphate from smooth muscle cells to endothelial cells through Cx43 gap junctions. In agreement, pharmacological inhibition or genetic depletion of the denitrosylase GSNOR, which indirectly affects the extent of *S*-nitrosylation in these cells by reducing denitrosylation of the NO donor *S*-nitrosogluathione (GSNO), significantly increased gap junctional communication at the MEJ. Altogether this study suggests the potential for connexin proteins to become *S*-nitrosylated at specific cysteine residues, with the modification affecting channel permeability.

S-nitrosylation has also been proposed to regulate the permeability of undocked Cx43 hemichannels at the plasma membrane. During prolonged periods of ischemia or hypoxia, oxygen deprivation induces the opening of Cx43 hemichannels in cortical astrocytes and cardiomyocytes, leading to cell death (Contreras et al. 2002; John et al. 1999; Kondo et al. 2000). The mechanisms regulating Cx43 hemichannel permeability under these conditions have been suggested to involve dephosphorylation of Cx43 hemichannels (a known stimulus for hemichannel activation (Bao et al. 2004b; Kim et al. 1999) or oxidative modification due to increased production of reactive oxygen species, including NO. A novel study by Retamal et al. (2006) found that metabolic inhibition of cortical astrocytes resulted in both dephosphorylation of Cx43 hemichannels as well as an increase in *S*-nitrosylation, ultimately leading to an increase in cellular permeability as determined by dye uptake. Interestingly, application of reducing agents to these cells did not affect Cx43 phosphorylation but significantly reduced both cell permeability and Cx43 *S*-nitrosylation. In agreement with this, application of exogenous NO donors results in increased cell permeability. Together, these observations indicate a functional role for Cx43 *S*-nitrosylation in regulating hemichannel permeability at the plasma membrane of astrocytes.

The potential regulation of hemichannels composed of Cx46 by NO has also been suggested. When expressed in *Xenopus* oocytes, Cx46 hemichannels exhibited increased voltage sensitivity and current amplitude upon application of GSNO, as assessed by patch-clamp electrophysiology (Retamal et al. 2009). Treatment of these cells with the reducing agent dithiothreitol (DTT) reversed the effects of GSNO on hemichannel currents, and mutation of the two endogenous carboxyl-terminus cysteine residues inhibited the effect of GSNO application. These observations suggest that critical cysteine residues in the carboxyl terminus of Cx46, like C271 in Cx43, may be modified by *S*-nitrosylation to regulate channel permeability.

Of the three pannexin isoforms characterized to date, Panx1 is the most widely expressed and is highly expressed in vascular smooth muscle and endothelial cells in the arterial vasculature (Billaud et al. 2011; Godecke et al. 2012; Lohman et al. 2012) and in multiple cell types in the central and peripheral nervous systems (Ray et al. 2005; Vogt et al. 2005; Xia et al. 2012). Importantly, all these tissues have enriched NOS expression and actively utilize NO for signaling. As Panx1 contains multiple cysteine residues and has been shown to be expressed in tissues with enhanced NO production, it is possible that Panx1 channels in these cells may be regulated posttranslationally by *S*-nitrosylation. Further, it has been shown that mutation of C346 in the carboxyl terminus of Panx1 results in a constitutively leaky channel (Bunse et al. 2010). Also, mutation of C40 in the pore-lining region of the first transmembrane domain of Panx1 produces a constitutively open channel (Bunse et al. 2011). These results indicate the importance of Panx1 cysteine residues in regulating channel gating and permeability. While there are currently no published reports indicating direct modulation of Panx1 channels by *S*-nitrosylation, studies have indicated a role for Panx1 (as well as Panx2) channels in ischemia-induced neuronal cell death, a condition in which NO production is markedly enhanced (Bargiotas et al. 2011). Similarly, oxygen glucose deprivation and metabolic inhibition, conditions similar to ischemia, both induced excessive NO production and neuronal cell death mediated by opening of Panx channels, which was attenuated by pharmacological blockade of *n*NOS or reduction of oxidized cysteine thiols with the reducing agent DTT (Zhang et al. 2008). Importantly, inhibition of guanylate cyclase in these experiments had little effect on Panx channel permeability, suggesting potential effects of NO by *S*-nitrosylation of Panx channels in these cells. Future studies will be essential to directly evaluate the potential for pannexin proteins to be posttranslationally modified by *S*-nitrosylation and how modification of Panx channels in this manner affects channel gating and permeability.

Ubiquitination

The ubiquitin proteasome system regulates the degradation of many proteins. This can occur at the absolute N-terminal primary amine of proteins to induce autophagy (e.g., Lichtenstein et al. 2011). Although this is a relatively new area of connexin research, it could be quite important in multiple disease states. More traditional ubiquitination is comprised of several components, including E1 ubiquitin-activating enzymes, E2 ubiquitin-conjugating enzymes and E3 ubiquitin ligases, that together mediate the transfer of the 76-amino acid protein ubiquitin to specific lysine (K) residues on target proteins (Leithe and Rivedal 2007; Willis et al. 2010). Multiple ubiquitins can be covalently linked via

K48 to form polyubiquitin chains, which target the ubiquitinated protein for degradation by the multisubunit 26S proteasome (Leithe and Rivedal 2007; Voges et al. 1999; Willis et al. 2010). Both connexins and pannexins have multiple lysine residues to which ubiquitin may be conjugated. Connexins can be ubiquitinated on K9 and K303 (Wagner et al. 2011), while pannexins can have ubiquitin conjugated to K409 (Kim et al. 2011). Thus, the possible ubiquitination of connexins and pannexins implies that these proteins may be regulated by proteasomal degradation.

Several studies have suggested that connexins and pannexins are ubiquitinated and degraded by the proteasome. The proteasomal inhibitor *N*-acetyl-L-leucyl-L-leucinyl-norleucinal increased levels of Cx43 (Laing and Beyer 1995) and Cx31 (He et al. 2005) and prolonged Cx43 half-life. Furthermore, immunoprecipitation with antibodies against Cx43 and ubiquitin suggested that Cx43 might be polyubiquitinated (Laing and Beyer 1995), indicating that disrupting the ubiquitin proteasome system could alter connexin turnover. The tumorigenic compound phorbol ester 12-*O*-tetradecanoylphorbol 13-acetate initiated hyperphosphorylation and ubiquitin-mediated degradation of Cx43, which was prevented by proteasomal inhibitors (Leithe and Rivedal 2004), demonstrating the importance of phosphorylation in ubiquitin-mediated connexin degradation. Phosphorylation of connexins facilitates interaction with proteins of the ubiquitin proteasome system, such as the ubiquitin ligase Nedd4 (Leykauf et al. 2006). Disrupting the interaction between connexins and ubiquitin proteasome proteins via proteasomal inhibitors alters the interaction between Cx43 and ZO-1, leading to Cx43 accumulation into enlarged gap junctions at plasma membranes (Girao and Pereira 2007). Therefore, it has been suggested that the ubiquitin proteasome system most likely contributes to the internalization and degradation of connexins.

Despite these findings, there is mounting evidence against ubiquitination and proteasomal degradation of connexins. Degradation of ER-localized Cx43 by the proteasome is partly controlled by Cx43 interactions with the ubiquitin-like protein CIP75, which binds to ubiquitinated substrates. However, immunoprecipitation studies demonstrated that the CIP75-bound Cx43 was not directly ubiquitinated (Su et al. 2010). In addition, a mutant Cx43 construct in which all lysine residues were converted to arginines mimicked the response of wild-type Cx43 to proteasomal inhibitors (Dunn et al. 2012). Taken together, these results indicate that direct ubiquitination may not be required for proteasomal degradation of Cx43. Instead, ubiquitination of connexins may contribute to other pathways regulating turnover. Indeed, recent studies have linked Cx43 monoubiquitination to lysosomal degradation. Following internalization from the plasma membrane, Cx43 can associate with the ubiquitin-binding proteins Hrs (hepatocyte growth factor–regulated tyrosine kinase substrate) and Tsg101 (tumor susceptibility gene 101) and the ubiquitin-binding endocytic adaptor protein Eps15, which shuttle Cx43 along the endocytic pathway for subsequent degradation in lysosomal compartments (Girao et al. 2009; Leithe et al. 2009). Thus, although ubiquitination mediates connexin trafficking and other degradative pathways, it is not clear whether direct ubiquitination is an important step during proteasomal degradation. Connexin turnover by this pathway most likely involves interaction between ubiquitinated substrates, even if connexins themselves are not tagged with ubiquitin.

Perturbation of connexin degradation by the ubiquitin proteasome has physiological and pathological consequences. Connexins are dynamically regulated with a short half-life of 1–6 h (He et al. 2005; Leithe and Rivedal 2004; Musil et al. 2000; Su et al. 2010). Proper connexin turnover rate is vital to maintain normal physiological functions (Li and Wang 2010). Dysregulation of dynamic gap junction protein turnover via inhibition of the ubiquitin proteasome degradation pathway (e.g., from oxidative stress) increases gap junction plaque size and enhances gap junction communication (Girao and Pereira 2007). Inhibition of proteasome-mediated degradation of gap junction proteins and enhanced gap junction communication is associated with several cardiovascular pathologies, such as ischemia–reperfusion injury, cardiac proteinopathy (i.e., irregular protein aggregation), post-myocardial infarct arrhythmias and heart failure (Beardslee et al. 1998; Li and Wang 2010). Thus, the ubiquitin proteasome pathway may provide novel therapeutic targets to treat cardiovascular diseases by restoring proper turnover of cardiac proteins, including connexins.

Much less is known about the involvement of the ubiquitin proteasome system in pannexin degradation. Mass spectrometric screens have identified K409 as a probable site of ubiquitination (Kim et al. 2011). However, biochemical evidence for pannexin ubiquitination and proteasomal degradation is lacking. A recent study has shown that Panx1 internalization and lysosomal degradation are controlled by its carboxyl-terminus region, but Panx1 does not appear to be degraded by traditional endocytic pathways (Gehi et al. 2011). Thus, further studies are needed to investigate the role ubiquitination plays in pannexin turnover (Schalper et al. 2012).

Other Modifications

SUMOylation

It has now been demonstrated that connexins (i.e., Cx43) can be targeted for posttranslation modification by less

characterized pathways, e.g., SUMOylation. The small ubiquitin-like modifier (SUMO) family of proteins acts in most cellular compartments to adapt proteins in multiple processes including transcription, translation, cellular transport, protein interactions, cell growth and programmed cell death (Geiss-Friedlander and Melchior 2007). In Cx43, L144 (intracellular loop) and L237 (carboxyl terminus) can be SUMOylated, leading to a reduction in protein expression and gap junction formation (Kjenseth et al. 2012). Consensus motifs for SUMOylation have been identified in the Panx2 sequence; however, studies of immunoprecipitated Panx2 from mouse neuronal stem cells differentiated to neurospheres showed a lack of detection of SUMO1/2/3, suggesting that Panx2 is not SUMOylated (Swayne et al. 2010). Given the diversity of activity of SUMO proteins, this posttranslational modification could potentially play a significant role in connexins and pannexin protein regulation and channel formation.

Lipid Modification, e.g., Palmitoylation

The correct insertion of transmembrane proteins into the plasma membrane is a delicate process that involves the coordination of protein modifications for the binding of specific phospholipids (termed "palmitoylation"). It has been well described that connexins are associated with lipid rafts, especially those enriched with caveoli (e.g., Langlois et al. 2008; Locke et al. 2005). However, only the carboxyl terminus of Cx32 (amino acids 277–283) has been identified to have a palmitoylation site (Locke et al. 2006). Regardless, this concept was further elucidated by a series of experiments designed to identify all the phospholipids that could be associated with either Cx26 or Cx32 gap junctions. The authors found that the lipids associated with the two homotypic gap junctions were dramatically different, indicating these connexins may reside in very distinct parts of the plasma membrane (Locke and Harris 2009), possibly placed there by palmitoylation modifications.

Thus far, there is no indication that pannexin isoforms associate with caveolin (Gehi et al. 2011). However, it has been demonstrated that Panx2 has distinct depalmitoylated and palmitoylated species that migrate at different molecular weights ($\sim$60 and $\sim$85 kDa, respectively) as determined by treatment of Western blots with hydroxylamine or metabolically labeling cells with BODIPY FL hexadecanoic acid. Swayne et al. (2010) further suggested that the palmitoylated form of Panx2 resides in the Golgi and/or ER, whereas the depalmitoylated form resides primarily at the plasma membrane and indicates these changes are associated with differentiation of neuronal cells. Elucidation of the exact site where Panx2 may be palmitoylated could prove quite interesting.

Caspase Cleavage

The posttranslational modification of proteins is generally considered to be a reversible process. However, a new type of terminal posttranslational modification was recently described where the Panx1 protein was cleaved by caspase 3 during apoptosis, inducing a constitutive open state of the channel for the release of ATP (Chekeni et al. 2010; Dunn et al. 2012). The caspase 3 cleavage site was identified in human Panx1 at amino acids 376–379 (DVVD) (Chekeni et al. 2010). The implications from the work were that the carboxyl terminus of Panx1 could regulate the pore open or closed state. This concept was recently demonstrated in a novel experimental model (Sandilos et al. 2012). In this work the authors inserted a TEV sequence into the Panx1 caspase cleavage site, allowing for controlled enzymatic cleavage of the carboxyl terminus. Next, a disulfide bond between the carboxyl terminus (C426) and an engineered cysteine within the pore of the Panx1 channel prevented removal of the carboxyl terminus from the pore (Sandilos et al. 2012). Finally, cleavage of the carboxyl terminus by TEV protease failed to produce current, and only after disulfide bond removal was current through the Panx1 channel restored (Sandilos et al. 2012). When summed with the caspase cleavage, the data indicate a role for the carboxyl terminus in regulating an open or closed pore and that cleavage of the carboxyl terminus as the specific caspase cleavage site induces a constitutive open channel during apoptosis. Although multiple connexins have been implicated throughout the apoptotic pathway (e.g., Andrade-Rozental et al. 2000; Minogue et al. 2009; Seul et al. 2004), there are no direct links or functional results like that described for the action of caspase 3 on Panx1.

Conclusion

Although much has been learned about how posttranslational modifications can have dramatic or subtle effects on connexin and pannexin function, most of these discoveries have happened only in the last decade. The creation of more specific antibodies toward modified amino acids (e.g., Solan and Lampe 2008) and accessibility of proteomic arrays to more researchers will enable an even greater study of posttranslational modifications associated with connexins and pannexins and their functional effect.

Acknowledgement This study was supported by National Institutes of Health grants HL088554 and HL107963 (to B. E. I.), an American Heart Association Scientist Development Grant (to B. E. I.), American Heart Association postdoctoral fellowships (to M. B. and S. R. J.) and a National Institutes of Health Cardiovascular Training Grant (to A. W. L.).

References

Ambrosi C, Gassmann O, Pranskevich JN, Boassa D, Smock A, Wang J, Dahl G, Steinem C, Sosinsky GE (2010) Pannexin1 and pannexin2 channels show quaternary similarities to connexons and different oligomerization numbers from each other. J Biol Chem 285:24420–24431

Andrade-Rozental AF, Rozental R, Hopperstad MG, Wu JK, Vrionis FD, Spray DC (2000) Gap junctions: the "kiss of death" and the "kiss of life". Brain Res Brain Res Rev 32:308–315

Bao L, Locovei S, Dahl G (2004a) Pannexin membrane channels are mechanosensitive conduits for ATP. FEBS Lett 572:65–68

Bao X, Reuss L, Altenberg GA (2004b) Regulation of purified and reconstituted connexin 43 hemichannels by protein kinase C-mediated phosphorylation of serine 368. J Biol Chem 279:20058–20066

Bao X, Lee SC, Reuss L, Altenberg GA (2007) Change in permeant size selectivity by phosphorylation of connexin 43 gap-junctional hemichannels by PKC. Proc Natl Acad Sci USA 104: 4919–4924

Barbe MT, Monyer H, Bruzzone R (2006) Cell–cell communication beyond connexins: the pannexin channels. Physiology (Bethesda) 21:103–114

Bargiotas P, Krenz A, Hormuzdi SG, Ridder DA, Herb A, Barakat W, Penuela S, von Engelhardt J, Monyer H, Schwaninger M (2011) Pannexins in ischemia-induced neurodegeneration. Proc Natl Acad Sci USA 108:20772–20777

Beardslee MA, Laing JG, Beyer EC, Saffitz JE (1998) Rapid turnover of connexin43 in the adult rat heart. Circ Res 83:629–635

Beardslee MA, Lerner DL, Tadros PN, Laing JG, Beyer EC, Yamada KA, Kleber AG, Schuessler RB, Saffitz JE (2000) Dephosphorylation and intracellular redistribution of ventricular connexin43 during electrical uncoupling induced by ischemia. Circ Res 87:656–662

Berthoud VM, Beyer EC, Kurata WE, Lau AF, Lampe PD (1997) The gap-junction protein connexin 56 is phosphorylated in the intracellular loop and the carboxy-terminal region. Eur J Biochem 244:89–97

Billaud M, Lohman AW, Straub AC, Looft-Wilson R, Johnstone SR, Araj CA, Best AK, Chekeni FB, Ravichandran KS, Penuela S, Laird DW, Isakson BE (2011) Pannexin1 regulates alpha1-adrenergic receptor- mediated vasoconstriction. Circ Res 109:80–85

Boassa D, Ambrosi C, Qiu F, Dahl G, Gaietta G, Sosinsky G (2007) Pannexin1 channels contain a glycosylation site that targets the hexamer to the plasma membrane. J Biol Chem 282:31733–31743

Boassa D, Qiu F, Dahl G, Sosinsky G (2008) Trafficking dynamics of glycosylated pannexin 1 proteins. Cell Commun Adhes 15:119–132

Boitano S, Evans WH (2000) Connexin mimetic peptides reversibly inhibit Ca^{2+} signaling through gap junctions in airway cells. Am J Physiol Lung Cell Mol Physiol 279:L623–L630

Brill LM, Xiong W, Lee KB, Ficarro SB, Crain A, Xu Y, Terskikh A, Snyder EY, Ding S (2009) Phosphoproteomic analysis of human embryonic stem cells. Cell Stem Cell 5:204–213

Bunse S, Schmidt M, Prochnow N, Zoidl G, Dermietzel R (2010) Intracellular cysteine 346 is essentially involved in regulating Panx1 channel activity. J Biol Chem 285:38444–38452

Bunse S, Schmidt M, Hoffmann S, Engelhardt K, Zoidl G, Dermietzel R (2011) Single cysteines in the extracellular and transmembrane regions modulate pannexin 1 channel function. J Membr Biol 244:21–33

Burt JM, Nelson TK, Simon AM, Fang JS (2008) Connexin 37 profoundly slows cell cycle progression in rat insulinoma cells. Am J Physiol Cell Physiol 295:C1103–C1112

Chandrasekhar A, Bera AK (2012) Hemichannels: permeants and their effect on development, physiology and death. Cell Biochem Funct 30:89–100

Chekeni FB, Elliott MR, Sandilos JK, Walk SF, Kinchen JM, Lazarowski ER, Armstrong AJ, Penuela S, Laird DW, Salvesen GS, Isakson BE, Bayliss DA, Ravichandran KS (2010) Pannexin 1 channels mediate "find-me" signal release and membrane permeability during apoptosis. Nature 467:863–867

Chen VC, Gouw JW, Naus CC, Foster LJ (2012) Connexin multi-site phosphorylation: mass spectrometry-based proteomics fills the gap. Biochim Biophys Acta. doi:10.1016/j.bbamem.2012.02.028

Contreras JE, Sanchez HA, Eugenin EA, Speidel D, Theis M, Willecke K, Bukauskas FF, Bennett MV, Saez JC (2002) Metabolic inhibition induces opening of unapposed connexin 43 gap junction hemichannels and reduces gap junctional communication in cortical astrocytes in culture. Proc Natl Acad Sci USA 99:495–500

Cooper CD, Lampe PD (2002) Casein kinase 1 regulates connexin-43 gap junction assembly. J Biol Chem 277:44962–44968

Cooper CD, Solan JL, Dolejsi MK, Lampe PD (2000) Analysis of connexin phosphorylation sites. Methods 20:196–204

Cottrell GT, Lin R, Warn-Cramer BJ, Lau AF, Burt JM (2003) Mechanism of v-Src- and mitogen-activated protein kinase-induced reduction of gap junction communication. Am J Physiol Cell Physiol 284:C511–C520

Crow DS, Beyer EC, Paul DL, Kobe SS, Lau AF (1990) Phosphorylation of connexin43 gap junction protein in uninfected and Rous sarcoma virus-transformed mammalian fibroblasts. Mol Cell Biol 10:1754–1763

Dando R, Roper SD (2009) Cell-to-cell communication in intact taste buds through ATP signalling from pannexin 1 gap junction hemichannels. J Physiol 587:5899–5906

Das Sarma J, Meyer RA, Wang F, Abraham V, Lo CW, Koval M (2001) Multimeric connexin interactions prior to the *trans*-Golgi network. J Cell Sci 114:4013–4024

Davis FP (2011) Phosphorylation at the interface. Structure 19:1726–1727

De Vuyst E, Decrock E, De Bock M, Yamasaki H, Naus CC, Evans WH, Leybaert L (2007) Connexin hemichannels and gap junction channels are differentially influenced by lipopolysaccharide and basic fibroblast growth factor. Mol Biol Cell 18:34–46

del Castillo FJ, Cohen-Salmon M, Charollais A, Caille D, Lampe PD, Chavrier P, Meda P, Petit C (2009) Consortin, a *trans*-Golgi network cargo receptor for the plasma membrane targeting and recycling of connexins. Hum Mol Genet 19:262–275

Doble BW, Dang X, Ping P, Fandrich RR, Nickel BE, Jin Y, Cattini PA, Kardami E (2004) Phosphorylation of serine 262 in the gap junction protein connexin-43 regulates DNA synthesis in cell–cell contact forming cardiomyocytes. J Cell Sci 117:507–514

Dunn CA, Su V, Lau AF, Lampe PD (2012) Activation of Akt, not connexin 43 protein ubiquitination, regulates gap junction stability. J Biol Chem 287:2600–2607

Ek-Vitorin JF, King TJ, Heyman NS, Lampe PD, Burt JM (2006) Selectivity of connexin 43 channels is regulated through protein kinase C-dependent phosphorylation. Circ Res 98:1498–1505

Falk MM, Gilula NB (1998) Connexin membrane protein biosynthesis is influenced by polypeptide positioning within the translocon and signal peptidase access. J Biol Chem 273:7856–7864

Falk MM, Buehler LK, Kumar NM, Gilula NB (1997) Cell-free synthesis and assembly of connexins into functional gap junction membrane channels. EMBO J 16:2703–2716

Freeze HH, Sharma V (2010) Metabolic manipulation of glycosylation disorders in humans and animal models. Semin Cell Dev Biol 21:655–662

Gehi R, Shao Q, Laird DW (2011) Pathways regulating the trafficking and turnover of pannexin1 protein and the role of the C-terminal domain. J Biol Chem 286:27639–27653

Geiss-Friedlander R, Melchior F (2007) Concepts in sumoylation: a decade on. Nat Rev Mol Cell Biol 8:947–956

Girao H, Pereira P (2007) The proteasome regulates the interaction between Cx43 and ZO-1. J Cell Biochem 102:719–728

Girao H, Catarino S, Pereira P (2009) Eps15 interacts with ubiquitinated Cx43 and mediates its internalization. Exp Cell Res 315:3587–3597

Godecke S, Roderigo C, Rose CR, Rauch BH, Godecke A, Schrader J (2012) Thrombin-induced ATP release from human umbilical vein endothelial cells. Am J Physiol Cell Physiol 302:C915–C923

He LQ, Cai F, Liu Y, Liu MJ, Tan ZP, Pan Q, Fang FY, de Liang S, Wu LQ, Long ZG, Dai HP, Xia K, Xia JH, Zhang ZH (2005) Cx31 is assembled and trafficked to cell surface by ER–Golgi pathway and degraded by proteasomal or lysosomal pathways. Cell Res 15:455–464

Hertlein B, Butterweck A, Haubrich S, Willecke K, Traub O (1998) Phosphorylated carboxy terminal serine residues stabilize the mouse gap junction protein connexin45 against degradation. J Membr Biol 162:247–257

Hess DT, Stamler JS (2012) Regulation by *S*-nitrosylation of protein posttranslational modification. J Biol Chem 287:4411–4418

Hunter AW, Barker RJ, Zhu C, Gourdie RG (2005) Zonula occludens-1 alters connexin43 gap junction size and organization by influencing channel accretion. Mol Biol Cell 16:5686–5698

Huttlin EL, Jedrychowski MP, Elias JE, Goswami T, Rad R, Beausoleil SA, Villen J, Haas W, Sowa ME, Gygi SP (2010) A tissue-specific atlas of mouse protein phosphorylation and expression. Cell 143:1174–1189

Iglesias R, Dahl G, Qiu F, Spray DC, Scemes E (2009) Pannexin 1: the molecular substrate of astrocyte "hemichannels". J Neurosci 29:7092–7097

Jin C, Martyn KD, Kurata WE, Warn-Cramer BJ, Lau AF (2004) Connexin43 PDZ2 binding domain mutants create functional gap junctions and exhibit altered phosphorylation. Cell Commun Adhes 11:67–87

John SA, Kondo R, Wang SY, Goldhaber JI, Weiss JN (1999) Connexin-43 hemichannels opened by metabolic inhibition. J Biol Chem 274:236–240

Johnson LN, Koval M (2009) Cross-talk between pulmonary injury, oxidant stress, and gap junctional communication. Antioxid Redox Signal 11:355–367

Johnson GL, Vaillancourt RR (1994) Sequential protein kinase reactions controlling cell growth and differentiation. Curr Opin Cell Biol 6:230–238

Johnson RG, Reynhout JK, TenBroek EM, Quade BJ, Yasumura T, Davidson KG, Sheridan JD, Rash JE (2012) Gap junction assembly: roles for the formation plaque and regulation by the C-terminus of connexin43. Mol Biol Cell 23:71–86

Johnstone SR, Ross J, Rizzo MJ, Straub AC, Lampe PD, Leitinger N, Isakson BE (2009) Oxidized phospholipid species promote in vivo differential cx43 phosphorylation and vascular smooth muscle cell proliferation. Am J Pathol 175:916–924

Johnstone SR, Kroncke BM, Straub AC, Best AK, Dunn CA, Mitchell LA, Peskova Y, Nakamoto RK, Koval M, Lo CW, Lampe PD, Columbus L, Isakson BE (2012) MAPK phosphorylation of connexin 43 promotes binding of cyclin E and smooth muscle cell proliferation. Circ Res

Kameritsch P, Khandoga N, Nagel W, Hundhausen C, Lidington D, Pohl U (2005) Nitric oxide specifically reduces the permeability of Cx37-containing gap junctions to small molecules. J Cell Physiol 203:233–242

Kanemitsu MY, Jiang W, Eckhart W (1998) Cdc2-mediated phosphorylation of the gap junction protein, connexin43, during mitosis. Cell Growth Differ 9:13–21

Kelsell DP, Di WL, Houseman MJ (2001) Connexin mutations in skin disease and hearing loss. Am J Hum Genet 68:559–568

Kim DY, Kam Y, Koo SK, Joe CO (1999) Gating connexin 43 channels reconstituted in lipid vesicles by mitogen-activated protein kinase phosphorylation. J Biol Chem 274:5581–5587

Kim W, Bennett EJ, Huttlin EL, Guo A, Li J, Possemato A, Sowa ME, Rad R, Rush J, Comb MJ, Harper JW, Gygi SP (2011) Systematic and quantitative assessment of the ubiquitin-modified proteome. Mol Cell 44:325–340

Kjenseth A, Fykerud TA, Sirnes S, Bruun J, Kolberg M, Yohannes Z, Omori Y, Rivedal E, Leithe E (2012) The gap junction channel protein connexin43 is covalently modified and regulated by SUMOylation. J Biol Chem 287:15851–15861

Kondo RP, Wang SY, John SA, Weiss JN, Goldhaber JI (2000) Metabolic inhibition activates a non-selective current through connexin hemichannels in isolated ventricular myocytes. J Mol Cell Cardiol 32:1859–1872

Koval M (2006) Pathways and control of connexin oligomerization. Trends Cell Biol 16:159–166

Koval M, Harley JE, Hick E, Steinberg TH (1997) Connexin46 is retained as monomers in a *trans*-Golgi compartment of osteoblastic cells. J Cell Biol 137:847–857

Kwak BR, Jongsma HJ (1996) Regulation of cardiac gap junction channel permeability and conductance by several phosphorylating conditions. Mol Cell Biochem 157:93–99

Kwak BR, Hermans MM, De Jonge HR, Lohmann SM, Jongsma HJ, Chanson M (1995) Differential regulation of distinct types of gap junction channels by similar phosphorylating conditions. Mol Biol Cell 6:1707–1719

Lai A, Le DN, Paznekas WA, Gifford WD, Jabs EW, Charles AC (2006) Oculodentodigital dysplasia connexin43 mutations result in non-functional connexin hemichannels and gap junctions in C6 glioma cells. J Cell Sci 119:532–541

Laing JG, Beyer EC (1995) The gap junction protein connexin43 is degraded via the ubiquitin proteasome pathway. J Biol Chem 270:26399–26403

Laird DW (2005) Connexin phosphorylation as a regulatory event linked to gap junction internalization and degradation. Biochim Biophys Acta 1711:172–182

Laird DW, Castillo M, Kasprzak L (1995) Gap junction turnover, intracellular trafficking, and phosphorylation of connexin43 in brefeldin A-treated rat mammary tumor cells. J Cell Biol 131:1193–1203

Lampe PD, Lau AF (2004) The effects of connexin phosphorylation on gap junctional communication. Int J Biochem Cell Biol 36:1171–1186

Lampe PD, Kurata WE, Warn-Cramer BJ, Lau AF (1998) Formation of a distinct connexin43 phosphoisoform in mitotic cells is dependent upon p34cdc2 kinase. J Cell Sci 111(pt 6):833–841

Lampe PD, TenBroek EM, Burt JM, Kurata WE, Johnson RG, Lau AF (2000) Phosphorylation of connexin43 on serine368 by protein kinase C regulates gap junctional communication. J Cell Biol 149:1503–1512

Langlois S, Cowan KN, Shao Q, Cowan BJ, Laird DW (2008) Caveolin-1 and -2 interact with connexin43 and regulate gap junctional intercellular communication in keratinocytes. Mol Biol Cell 19:912–928

Leithe E, Rivedal E (2004) Ubiquitination and down-regulation of gap junction protein connexin-43 in response to 12-*O*-tetradecanoylphorbol 13-acetate treatment. J Biol Chem 279:50089–50096

Leithe E, Rivedal E (2007) Ubiquitination of gap junction proteins. J Membr Biol 217:43–51

Leithe E, Kjenseth A, Sirnes S, Stenmark H, Brech A, Rivedal E (2009) Ubiquitylation of the gap junction protein connexin-43 signals its trafficking from early endosomes to lysosomes in a process mediated by Hrs and Tsg101. J Cell Sci 122:3883–3893

Leykauf K, Salek M, Bomke J, Frech M, Lehmann WD, Durst M, Alonso A (2006) Ubiquitin protein ligase Nedd4 binds to connexin43 by a phosphorylation-modulated process. J Cell Sci 119:3634–3642

Li YF, Wang X (2010) The role of the proteasome in heart disease. Biochim Biophys Acta 1809:141–149

Lichtenstein A, Minogue PJ, Beyer EC, Berthoud VM (2011) Autophagy: a pathway that contributes to connexin degradation. J Cell Sci 124:910–920

Locke D, Harris AL (2009) Connexin channels and phospholipids: association and modulation. BMC Biol 7:52

Locke D, Liu J, Harris AL (2005) Lipid rafts prepared by different methods contain different connexin channels, but gap junctions are not lipid rafts. Biochemistry 44:13027–13042

Locke D, Koreen IV, Harris AL (2006) Isoelectric points and posttranslational modifications of connexin26 and connexin32. FASEB J 20:1221–1223

Locovei S, Bao L, Dahl G (2006) Pannexin 1 in erythrocytes: function without a gap. Proc Natl Acad Sci USA 103:7655–7659

Lohman AW, Billaud M, Straub AC, Johnstone SR, Best AK, Lee MY, Barr K, Penuela S, Laird DW, Isakson BE (2012) Expression of pannexin isoforms in the systemic murine arterial network. J Vasc Res (in press)

Marquez-Rosado L, Solan JL, Dunn CA, Norris RP, Lampe PD (2011) Connexin43 phosphorylation in brain, cardiac, endothelial and epithelial tissues. Biochim Biophys Acta

Martin PE, Evans WH (2004) Incorporation of connexins into plasma membranes and gap junctions. Cardiovasc Res 62:378–387

Martinez AD, Hayrapetyan V, Moreno AP, Beyer EC (2003) A carboxyl terminal domain of connexin43 is critical for gap junction plaque formation but not for homo- or hetero-oligomerization. Cell Commun Adhes 10:323–328

McKinnon RL, Lidington D, Bolon M, Ouellette Y, Kidder GM, Tyml K (2006) Reduced arteriolar conducted vasoconstriction in septic mouse cremaster muscle is mediated by *n*NOS-derived NO. Cardiovasc Res 69:236–244

McKinnon RL, Bolon ML, Wang HX, Swarbreck S, Kidder GM, Simon AM, Tyml K (2009) Reduction of electrical coupling between microvascular endothelial cells by NO depends on connexin37. Am J Physiol Heart Circ Physiol 297:H93–H101

Minogue PJ, Tong JJ, Arora A, Russell-Eggitt I, Hunt DM, Moore AT, Ebihara L, Beyer EC, Berthoud VM (2009) A mutant connexin50 with enhanced hemichannel function leads to cell death. Invest Ophthalmol Vis Sci 50:5837–5845

Musil LS, Goodenough DA (1991) Biochemical analysis of connexin43 intracellular transport, phosphorylation, and assembly into gap junctional plaques. J Cell Biol 115:1357–1374

Musil LS, Goodenough DA (1993) Multisubunit assembly of an integral plasma membrane channel protein, gap junction connexin43, occurs after exit from the ER. Cell 74:1065–1077

Musil LS, Cunningham BA, Edelman GM, Goodenough DA (1990) Differential phosphorylation of the gap junction protein connexin43 in junctional communication-competent and -deficient cell lines. J Cell Biol 111:2077–2088

Musil LS, Le AC, VanSlyke JK, Roberts LM (2000) Regulation of connexin degradation as a mechanism to increase gap junction assembly and function. J Biol Chem 275:25207–25215

Nishi H, Hashimoto K, Panchenko AR (2011) Phosphorylation in protein–protein binding: effect on stability and function. Structure 19:1807–1815

Norris RP, Freudzon M, Mehlmann LM, Cowan AE, Simon AM, Paul DL, Lampe PD, Jaffe LA (2008) Luteinizing hormone causes MAP kinase-dependent phosphorylation and closure of connexin 43 gap junctions in mouse ovarian follicles: one of two paths to meiotic resumption. Development 135:3229–3238

Pahujaa M, Anikin M, Goldberg GS (2007) Phosphorylation of connexin43 induced by Src: regulation of gap junctional communication between transformed cells. Exp Cell Res 313:4083–4090

Palatinus JA, Gourdie RG (2007) Xin and the art of intercalated disk maintenance. Am J Physiol Heart Circ Physiol 293:H2626–H2628

Palatinus JA, Rhett JM, Gourdie RG (2011a) The connexin43 carboxyl terminus and cardiac gap junction organization. Biochim Biophys Acta 1818:1831–1843

Palatinus JA, Rhett JM, Gourdie RG (2011b) Enhanced PKCepsilon mediated phosphorylation of connexin43 at serine 368 by a carboxyl-terminal mimetic peptide is dependent on injury. Channels (Austin) 5:236–240

Panchin Y, Kelmanson I, Matz M, Lukyanov K, Usman N, Lukyanov S (2000) A ubiquitous family of putative gap junction molecules. Curr Biol 10:R473–R474

Park HS, Yu JW, Cho JH, Kim MS, Huh SH, Ryoo K, Choi EJ (2004) Inhibition of apoptosis signal-regulating kinase 1 by nitric oxide through a thiol redox mechanism. J Biol Chem 279:7584–7590

Paulson AF, Lampe PD, Meyer RA, TenBroek E, Atkinson MM, Walseth TF, Johnson RG (2000) Cyclic AMP and LDL trigger a rapid enhancement in gap junction assembly through a stimulation of connexin trafficking. J Cell Sci 113(pt 17):3037–3049

Pearson RA, Dale N, Llaudet E, Mobbs P (2005) ATP released via gap junction hemichannels from the pigment epithelium regulates neural retinal progenitor proliferation. Neuron 46:731–744

Penuela S, Bhalla R, Gong XQ, Cowan KN, Celetti SJ, Cowan BJ, Bai D, Shao Q, Laird DW (2007) Pannexin 1 and pannexin 3 are glycoproteins that exhibit many distinct characteristics from the connexin family of gap junction proteins. J Cell Sci 120:3772–3783

Penuela S, Celetti SJ, Bhalla R, Shao Q, Laird DW (2008) Diverse subcellular distribution profiles of pannexin 1 and pannexin 3. Cell Commun Adhes 15:133–142

Penuela S, Bhalla R, Nag K, Laird DW (2009) Glycosylation regulates pannexin intermixing and cellular localization. Mol Biol Cell 20:4313–4323

Penuela S, Gehi R, Laird DW (2012) The biochemistry and function of pannexin channels. Biochim Biophys Acta (in press)

Pinho SS, Seruca R, Gartner F, Yamaguchi Y, Gu J, Taniguchi N, Reis CA (2011) Modulation of E-cadherin function and dysfunction by *N*-glycosylation. Cell Mol Life Sci 68:1011–1020

Puranam KL, Laird DW, Revel JP (1993) Trapping an intermediate form of connexin43 in the Golgi. Exp Cell Res 206:85–92

Rahman S, Carlile G, Evans WH (1993) Assembly of hepatic gap junctions. Topography and distribution of connexin 32 in intracellular and plasma membranes determined using sequence-specific antibodies. J Biol Chem 268:1260–1265

Ray A, Zoidl G, Weickert S, Wahle P, Dermietzel R (2005) Site-specific and developmental expression of pannexin1 in the mouse nervous system. Eur J Neurosci 21:3277–3290

Reis CA, Osorio H, Silva L, Gomes C, David L (2010) Alterations in glycosylation as biomarkers for cancer detection. J Clin Pathol 63:322–329

Remo BF, Qu J, Volpicelli FM, Giovannone S, Shin D, Lader J, Liu FY, Zhang J, Lent DS, Morley GE, Fishman GI (2011) Phosphatase-resistant gap junctions inhibit pathological remodeling and prevent arrhythmias. Circ Res 108:1459–1466

Retamal MA, Cortes CJ, Reuss L, Bennett MV, Saez JC (2006) *S*-nitrosylation and permeation through connexin 43 hemichannels in astrocytes: induction by oxidant stress and reversal by reducing agents. Proc Natl Acad Sci USA 103:4475–4480

Retamal MA, Yin S, Altenberg GA, Reuss L (2009) Modulation of Cx46 hemichannels by nitric oxide. Am J Physiol Cell Physiol 296:C1356–C1363

Rhett JM, Jourdan J, Gourdie RG (2011) Connexin 43 connexon to gap junction transition is regulated by zonula occludens-1. Mol Biol Cell 22:1516–1528

Richards TS, Dunn CA, Carter WG, Usui ML, Olerud JE, Lampe PD (2004) Protein kinase C spatially and temporally regulates gap junctional communication during human wound repair via phosphorylation of connexin43 on serine368. J Cell Biol 167:555–562

Rikova K, Guo A, Zeng Q, Possemato A, Yu J, Haack H, Nardone J, Lee K, Reeves C, Li Y, Hu Y, Tan Z, Stokes M, Sullivan L, Mitchell J, Wetzel R, Macneill J, Ren JM, Yuan J, Bakalarski CE, Villen J, Kornhauser JM, Smith B, Li D, Zhou X, Gygi SP, Gu TL, Polakiewicz RD, Rush J, Comb MJ (2007) Global survey of phosphotyrosine signaling identifies oncogenic kinases in lung cancer. Cell 131:1190–1203

Roth J, Zuber C, Park S, Jang I, Lee Y, Kysela KG, Le Fourn V, Santimaria R, Guhl B, Cho JW (2010) Protein *N*-glycosylation, protein folding, and protein quality control. Mol Cells 30:497–506

Saez JC, Nairn AC, Czernik AJ, Spray DC, Hertzberg EL, Greengard P, Bennett MV (1990) Phosphorylation of connexin 32, a hepatocyte gap-junction protein, by cAMP-dependent protein kinase, protein kinase C and Ca^{2+}/calmodulin-dependent protein kinase II. Eur J Biochem 192:263–273

Saez JC, Martinez AD, Branes MC, Gonzalez HE (1998) Regulation of gap junctions by protein phosphorylation. Braz J Med Biol Res 31:593–600

Saez JC, Berthoud VM, Branes MC, Martinez AD, Beyer EC (2003) Plasma membrane channels formed by connexins: their regulation and functions. Physiol Rev 83:1359–1400

Sandilos JK, Chiu YH, Chekeni FB, Armstrong AJ, Walk SF, Ravichandran KS, Bayliss DA (2012) Pannexin 1, an ATP release channel, is activated by caspase cleavage of its pore-associated C terminal autoinhibitory region. J Biol Chem (in press)

Schalper KA, Riquelme MA, Branes MC, Martinez AD, Vega JL, Berthoud VM, Bennett MV, Saez JC (2012) Modulation of gap junction channels and hemichannels by growth factors. Mol BioSyst 8:685–698

Schulz R, Heusch G (2004) Connexin 43 and ischemic preconditioning. Cardiovasc Res 62:335–344

Segretain D, Falk MM (2004) Regulation of connexin biosynthesis, assembly, gap junction formation, and removal. Biochim Biophys Acta 1662:3–21

Segretain D, Fiorini C, Decrouy X, Defamie N, Prat JR, Pointis G (2004) A proposed role for ZO-1 in targeting connexin 43 gap junctions to the endocytic pathway. Biochimie 86:241–244

Seul KH, Kang KY, Lee KS, Kim SH, Beyer EC (2004) Adenoviral delivery of human connexin37 induces endothelial cell death through apoptosis. Biochem Biophys Res Commun 319:1144–1151

Silverman WR, de Rivero Vaccari JP, Locovei S, Qiu F, Carlsson SK, Scemes E, Keane RW, Dahl G (2009) The pannexin 1 channel activates the inflammasome in neurons and astrocytes. J Biol Chem 284:18143–18151

Singh D, Solan JL, Taffet SM, Javier R, Lampe PD (2005) Connexin 43 interacts with zona occludens-1 and -2 proteins in a cell cycle stage-specific manner. J Biol Chem 280:30416–30421

Solan JL, Lampe PD (2005) Connexin phosphorylation as a regulatory event linked to gap junction channel assembly. Biochim Biophys Acta 1711:154–163

Solan JL, Lampe PD (2007) Key connexin 43 phosphorylation events regulate the gap junction life cycle. J Membr Biol 217:35–41

Solan JL, Lampe PD (2008) Connexin 43 in LA-25 cells with active v-src is phosphorylated on Y247, Y265, S262, S279/282, and S368 via multiple signaling pathways. Cell Commun Adhes 15:75–84

Solan JL, Lampe PD (2009) Connexin43 phosphorylation: structural changes and biological effects. Biochem J 419:261–272

Solan JL, Fry MD, TenBroek EM, Lampe PD (2003) Connexin43 phosphorylation at S368 is acute during S and G_2/M and in response to protein kinase C activation. J Cell Sci 116:2203–2211

Solan JL, Marquez-Rosado L, Sorgen PL, Thornton PJ, Gafken PR, Lampe PD (2007) Phosphorylation at S365 is a gatekeeper event that changes the structure of Cx43 and prevents down-regulation by PKC. J Cell Biol 179:1301–1309

Sridharan M, Adderley SP, Bowles EA, Egan TM, Stephenson AH, Ellsworth ML, Sprague RS (2010) Pannexin 1 is the conduit for low oxygen tension-induced ATP release from human erythrocytes. Am J Physiol Heart Circ Physiol 299:H1146–H1152

Srisakuldee W, Jeyaraman MM, Nickel BE, Tanguy S, Jiang ZS, Kardami E (2009) Phosphorylation of connexin-43 at serine 262 promotes a cardiac injury-resistant state. Cardiovasc Res 83:672–681

Stamler JS, Simon DI, Osborne JA, Mullins ME, Jaraki O, Michel T, Singel DJ, Loscalzo J (1992) *S*-nitrosylation of proteins with nitric oxide: synthesis and characterization of biologically active compounds. Proc Natl Acad Sci USA 89:444–448

Straub AC, Johnstone SR, Heberlein KR, Rizzo MJ, Best AK, Boitano S, Isakson BE (2009) Site-specific connexin phosphorylation is associated with reduced heterocellular communication between smooth muscle and endothelium. J Vasc Res 47:277–286

Straub AC, Billaud M, Johnstone SR, Best AK, Yemen S, Dwyer ST, Looft-Wilson R, Lysiak JJ, Gaston B, Palmer L, Isakson BE (2011) Compartmentalized connexin 43 *S*-nitrosylation/denitrosylation regulates heterocellular communication in the vessel wall. Arterioscler Thromb Vasc Biol 31:399–407

Su V, Nakagawa R, Koval M, Lau AF (2010) Ubiquitin-independent proteasomal degradation of endoplasmic reticulum-localized connexin43 mediated by CIP75. J Biol Chem 285:40979–40990

Swayne LA, Sorbara CD, Bennett SA (2010) Pannexin 2 is expressed by postnatal hippocampal neural progenitors and modulates neuronal commitment. J Biol Chem 285:24977–24986

TenBroek EM, Lampe PD, Solan JL, Reynhout JK, Johnson RG (2001) Ser364 of connexin43 and the upregulation of gap junction assembly by cAMP. J Cell Biol 155:1307–1318

Toyofuku T, Yabuki M, Otsu K, Kuzuya T, Hori M, Tada M (1998) Direct association of the gap junction protein connexin-43 with ZO-1 in cardiac myocytes. J Biol Chem 273:12725–12731

Toyofuku T, Akamatsu Y, Zhang H, Kuzuya T, Tada M, Hori M (2001) c-Src regulates the interaction between connexin-43 and ZO-1 in cardiac myocytes. J Biol Chem 276:1780–1788

Traub O, Look J, Dermietzel R, Brummer F, Hulser D, Willecke K (1989) Comparative characterization of the 21-kD and 26-kD gap junction proteins in murine liver and cultured hepatocytes. J Cell Biol 108:1039–1051

van Rijen HV, van Veen TA, Hermans MM, Jongsma HJ (2000) Human connexin40 gap junction channels are modulated by cAMP. Cardiovasc Res 45:941–951

van Veen TA, van Rijen HV, Jongsma HJ (2000) Electrical conductance of mouse connexin45 gap junction channels is modulated by phosphorylation. Cardiovasc Res 46:496–510

Voges D, Zwickl P, Baumeister W (1999) The 26S proteasome: a molecular machine designed for controlled proteolysis. Annu Rev Biochem 68:1015–1068

Vogt A, Hormuzdi SG, Monyer H (2005) Pannexin1 and pannexin2 expression in the developing and mature rat brain. Brain Res Mol Brain Res 141:113–120

Wagner SA, Beli P, Weinert BT, Nielsen ML, Cox J, Mann M, Choudhary C (2011) A proteome-wide, quantitative survey of in vivo ubiquitylation sites reveals widespread regulatory roles. Mol Cell Proteomics 10:M111.013284

Wang Y, Mehta PP (1995) Facilitation of gap-junctional communication and gap-junction formation in mammalian cells by inhibition of glycosylation. Eur J Cell Biol 67:285–296

Wang Y, Rose B (1995) Clustering of Cx43 cell-to-cell channels into gap junction plaques: regulation by cAMP and microfilaments. J Cell Sci 108(pt 11):3501–3508

Wang Y, Mehta PP, Rose B (1995) Inhibition of glycosylation induces formation of open connexin-43 cell-to-cell channels and phosphorylation and triton X-100 insolubility of connexin-43. J Biol Chem 270:26581–26585

Warn-Cramer BJ, Cottrell GT, Burt JM, Lau AF (1998) Regulation of connexin-43 gap junctional intercellular communication by mitogen-activated protein kinase. J Biol Chem 273:9188–9196

Wayakanon P, Bhattacharjee R, Nakahama KI, Morita I (2012) The role of the Cx43 C-terminus in GJ plaque formation and internalization. Biochem Biophys Res Commun 420:456–461

Whalen EJ, Foster MW, Matsumoto A, Ozawa K, Violin JD, Que LG, Nelson CD, Benhar M, Keys JR, Rockman HA, Koch WJ, Daaka Y, Lefkowitz RJ, Stamler JS (2007) Regulation of beta-adrenergic receptor signaling by *S*-nitrosylation of G-protein-coupled receptor kinase 2. Cell 129:511–522

Willis MS, Townley-Tilson WH, Kang EY, Homeister JW, Patterson C (2010) Sent to destroy: the ubiquitin proteasome system regulates cell signaling and protein quality control in cardiovascular development and disease. Circ Res 106:463–478

Wisniewski JR, Nagaraj N, Zougman A, Gnad F, Mann M (2010) Brain phosphoproteome obtained by a FASP-based method reveals plasma membrane protein topology. J Proteome Res 9:3280–3289

Xia J, Lim JC, Lu W, Beckel JM, Macarak EJ, Laties AM, Mitchell CH (2012) Neurons respond directly to mechanical deformation with pannexin-mediated ATP release and autostimulation of P2X7 receptors. J Physiol 590(pt 10):2285–2304

Xie H, Laird DW, Chang TH, Hu VW (1997) A mitosis-specific phosphorylation of the gap junction protein connexin43 in human vascular cells: biochemical characterization and localization. J Cell Biol 137:203–210

Yasukawa T, Tokunaga E, Ota H, Sugita H, Martyn JA, Kaneki M (2005) *S*-nitrosylation-dependent inactivation of Akt/protein kinase B in insulin resistance. J Biol Chem 280:7511–7518

Yin X, Gu S, Jiang JX (2001) The development-associated cleavage of lens connexin 45.6 by caspase-3-like protease is regulated by casein kinase II-mediated phosphorylation. J Biol Chem 276:34567–34572

Yin X, Liu J, Jiang JX (2008) Lens fiber connexin turnover and caspase-3-mediated cleavage are regulated alternately by phosphorylation. Cell Commun Adhes 15:1–11

Zhang L, Deng T, Sun Y, Liu K, Yang Y, Zheng X (2008) Role for nitric oxide in permeability of hippocampal neuronal hemichannels during oxygen glucose deprivation. J Neurosci Res 86:2281–2291

J Membrane Biol (2012) 245:333–344
DOI 10.1007/s00232-012-9454-2

Connexin Composition in Apposed Gap Junction Hemiplaques Revealed by Matched Double-Replica Freeze-Fracture Replica Immunogold Labeling

John E. Rash · Naomi Kamasawa · Kimberly G. V. Davidson · Thomas Yasumura · Alberto E. Pereda · James I. Nagy

Received: 9 April 2012 / Accepted: 8 June 2012 / Published online: 4 July 2012

Abstract Despite the combination of light-microscopic immunocytochemistry, histochemical mRNA detection techniques and protein reporter systems, progress in identifying the protein composition of neuronal versus glial gap junctions, determination of the differential localization of their constituent connexin proteins in two apposing membranes and understanding human neurological diseases caused by connexin mutations has been problematic due to ambiguities introduced in the cellular and subcellular assignment of connexins. Misassignments occurred primarily because membranes and their constituent proteins are below the limit of resolution of light microscopic imaging techniques. Currently, only serial thin-section transmission electron microscopy and freeze-fracture replica immunogold labeling have sufficient resolution to assign connexin proteins to either or both sides of gap junction plaques. However, freeze-fracture replica immunogold labeling has been limited because conventional freeze fracturing allows retrieval of only one of the two membrane fracture faces within a gap junction, making it difficult to identify connexin coupling partners in hemiplaques removed by fracturing. We now summarize progress in ascertaining the connexin composition of two coupled hemiplaques using matched double-replicas that are labeled simultaneously for multiple connexins. This approach allows unambiguous identification of connexins and determination of the membrane "sidedness" and the identities of connexin coupling partners in homotypic and heterotypic gap junctions of vertebrate neurons.

Keywords Astrocyte · Ependymocyte · Glia · Neuron · Oligodendrocyte

Abbreviations

DR	Double replica
E-face	Extraplasmic leaflet
FRIL	Freeze-fracture replica immunogold labeling
P-face	Protoplasmic leafle
RT-PCR	Reverse transcriptase polymerase chain reaction

J. E. Rash (✉) · K. G. V. Davidson · T. Yasumura
Department of Biomedical Sciences, Colorado State University, Fort Collins, CO 80523, USA
e-mail: john.rash@colostate.edu

J. E. Rash
Program in Molecular, Cellular, and Integrative Neurosciences, Colorado State University, Fort Collins, CO 80523, USA

N. Kamasawa
Electron Microscopy Core Facility, Max Planck Florida Institute, Jupiter, FL 33458, USA

A. E. Pereda
Dominick P. Purpura Department of Neuroscience, Albert Einstein College of Medicine, Bronx, NY 10461, USA

J. I. Nagy
Department of Physiology, Faculty of Medicine, University of Manitoba, Winnipeg, MB R3E 0J9, Canada

Introduction and Historical Perspective

Vertebrate gap junctions consist of connexin proteins that assemble as hexamers to form connexon "hemichannels" that link across the extracellular space, forming leakless channels that permit the direct intercellular transport of water, ions and small molecules [≤450 Da (Hu and Dahl 1999)]. Of the 20 or 21 connexins expressed in mammals—named according to their molecular weight, measured in kilodaltons (Willecke et al. 2002)—more than half are

expressed by cells in the central nervous system (CNS). Due to the cellular heterogeneity and morphological complexity of CNS tissue, assignment of connexin expression in, and understanding the formation of gap junctions between, particular cell types has been problematic. Yet, this has become an important issue, especially in recent years by virtue of the identification of several diseases with major neurological damage caused by mutations in connexins expressed in neural tissues. These include X-linked Charcot–Marie–Tooth disease (CMTX) (Bergoffen et al. 1993), resulting from mutations of Cx32; Pelizaeus–Merzbacher-like disease (PMLD), resulting from mutations of Cx47 (Tress et al. 2011; Uhlenberg et al. 2004), oculodentodigital dysplasia (ODDD), resulting from mutations of Cx43 (Paznekas et al. 2003); keratitis–ichthyosis–deafness syndrome, resulting from mutations of Cx26 (Kelsell et al. 1997; Melchionda et al. 2005); and childhood-onset myoclonic epilepsy, resulting from mutations of Cx36 in the noncoding region (Hempelmann et al. 2006; Mas et al. 2004). Understanding how these connexin mutations impact on physiological processes in the CNS and cause severe debilitating disease requires firm knowledge of the cell types expressing the mutated connexins, the subcellular and histological locations at which gap junctions may be disrupted by these abnormal connexins and the nature of the connexin coupling partners normally occurring at those locations. This knowledge acquired in studies of the glial connexins, as well as in studies of defective ion channels and water-transport pathways used for long-distance potassium siphoning and CNS water homeostasis, led to our formulation of the "gateway hypothesis" (Davidson and Rash 2011; Rash 2010) as a working paradigm for a generalized mechanism underlying the physiological and morphological aberrations found in CMTX, ODDD, PMLD, neuromyelitis optica, Alexander disease (van der Knaap et al. 2001) and other "leukodystrophies" (white matter diseases). However, details of the molecular organization of glial gap junctions with their five gap junction-forming connexins, as well as of gap junctions forming electrical synapses in the CNS, is a work in progress. Here, we outline some outstanding difficulties and present a new approach that may help to resolve some of the existing limitations.

Connexon Coupling Patterns

Individual cell types express from one to four different connexins, allowing for the potential formation of "heteromeric" connexons composed of two or more connexins, for which evidence has been obtained in only a few tissues in vivo (Jiang and Goodenough 1996; Sosinsky 1995). Some neurons express only a single connexin isoform (e.g., most express only Cx36), and these often form gap junctions with other neurons singly expressing the same connexin, thereby forming "homomeric" connexins in both cells that link to form "homotypic" intercellular channels (Fig. 1a, showing the simplest type of neuron-to-neuron gap junction, composed of Cx36, only). However, multiple connexin isoforms are expressed in many types of cells, providing for the possible formation of "bihomotypic" and "trihomotypic" gap junctions. For example, astrocyte-to-astrocyte (A:A) gap junctions usually consist of two or three types of homotypic channels, forming, as one example, a Cx43:Cx43 plus Cx30:Cx30 plus Cx26:Cx26 trihomotypic gap junction (Fig. 1b). In addition, when astrocytes (A) couple to oligodendrocytes (O), which express two other gap junction-forming connexins, Cx47 and Cx32, these "heterologous" A:O gap junctions, are necessarily "bi-" or "triheterotypic" (or even multiheterotypic), composed of several combinations of "permissive" coupling partners, three of which are illustrated in Fig. 1c. [Cx29 is also expressed in oligodendrocytes but does not form gap junctions (Altevogt and Paul 2004).] In A:O junctions, a distinct set of connexins on the astrocyte side (i.e., Cx26, Cx30, Cx43) link with a different set of

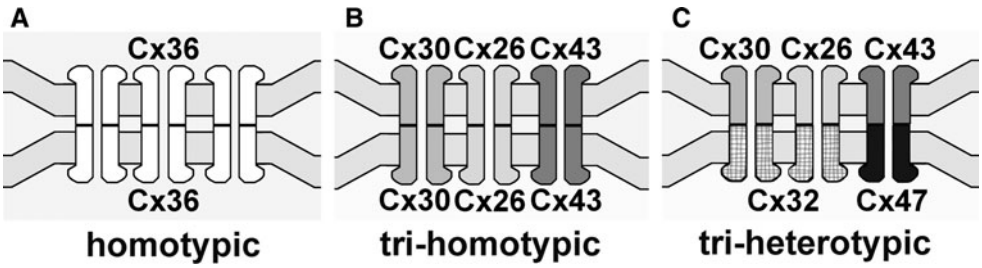

Fig. 1 Generalized models of different connexin coupling patterns in the most common type of gap junctions in the CNS. **a** "Homotypic" neuronal gap junction, with intercellular channels composed of Cx36 coupling with Cx36. **b** "Trihomotypic" astrocyte-to-astrocyte gap junction, with intercellular channels composed of Cx43 coupling with Cx43, Cx30 coupling with Cx30 and Cx26 coupling with Cx26. **c** "Triheterotypic" astrocyte-to-oligodendrocyte gap junction, with astrocyte Cx43 coupling with oligodendrocyte Cx47, astrocyte Cx30 coupling with oligodendrocyte Cx32 and astrocyte Cx26 coupling with oligodendrocyte Cx32. Additional permissive coupling pairs are discussed in the text

connexins on the oligodendrocyte side (i.e., Cx32, Cx47) (Altevogt et al. 2002; Altevogt and Paul 2004; Kleopa et al. 2004; Li et al. 1997; Nagy et al. 2004; Nagy and Rash 2000; Scherer et al. 1995). Recent studies of coupling permissiveness in N2A cells expressing glial connexins indicate that, in addition to permissive homotypic combinations (e.g., Cx30/Cx30, Cx43/Cx43, Cx32/Cx32 and Cx47/Cx47), functional coupling can occur between Cx30 and Cx32 and between Cx43 and Cx47 (Orthmann-Murphy et al. 2007), as well as between Cx30 and Cx47 (Magnotti et al. 2011). Finally, homologous cell types (two neurons, for example) expressing two different connexins at the same gap junction plaque may also form either bihomotypic or heterotypic gap junctions. These several coupling configurations may provide vertebrate gap junctions with the molecular basis for attaining functional diversity, including electrical rectification (directionality of current flow), which has been proposed to require molecular asymmetry of apposed connexon hemichannels (Barrio et al. 1991; Palacios-Prado and Bukauskas 2009; Rubin et al. 1992; Verselis et al. 1994). Currently, these functionally distinct configurations of connexins within apposing hemiplaques can be distinguished in vivo only by the double-replica immunogold labeling technique, as described below.

Sources of Ambiguity in Previous Approaches

False-Positive Identification of Protein Expression in Neural Cells

False-positive identifications of connexin protein expression in cells and misassignment of those connexins to an inappropriate cell type can occur for three main reasons. The first is inadequate confirmation of anticonnexin antibody specificity, which can result in failure to recognize off-target labeling of proteins. The use of connexin knockout (KO) mice can be considered the "gold standard" for confirmation of specificity. Many of the antibodies that we use have been characterized for specificity by comparison of immunofluorescence and/or immunoblotting results in wild-type mice vs. mice with KO of the various connexins. For connexins relevant here, such characterization has included antibodies against Cx26 (Nagy et al. 2011), Cx30 (Lynn et al. 2011), Cx32 (Nagy et al. 2003), Cx36 (Li et al. 2004), Cx47 (Li et al. 2008b) and Cx57 (Ciolofan et al. 2007). In addition, where possible, we have included the use of two different antibodies generated against different sequences within individual connexins, as well as the use of both rabbit polyclonal and mouse monoclonal antibodies generated against the same sequence in some of the connexins. The specificity of antibodies against Cx43 and Cx45 has been established ultrastructurally by showing their detection in gap junction plaques in identified cell types (Rash et al. 2001).

A second source of error derives from the failure to detect a protein target even when using antibodies with proven specificity and proven immunohistochemical applications. This can arise mainly from nonoptimal tissue preparation for immunostaining, particularly if prescribed fixation protocols are not followed. We have previously emphasized that immunofluorescence detection of some connexins requires very weak fixation conditions, where overfixation results in reduced detection or abolition of immunolabeling entirely (Li et al. 2008b).

The third source of connexin misassignment arises from the limited resolution of light microscopy (LM). Because of inherent limits of LM resolution, current immunocytochemical methods applied to complex CNS tissues are unable to discern whether specific connexins, reportedly identified either by diffuse cytoplasmic staining (Colwell 2000) or by the presence of both punctate immunolabeling for connexins and widespread cell-surface immunofluorescence (Nadarajah et al. 1996, 1997), link either neurons or glia or both. When only a single cell type (neuron) is visualized by immunofluorescence in CNS tissue, without companion bright-field or differential interference optics to reveal glial cells (Fig. 2a), it is not possible to assign connexins unambiguously to the visualized neuron, regardless of apparent close proximity of connexin labels. This failure to account for CNS tissue complexity is implicit in representative thin-section transmission electron microscopic (TEM) images (Fig. 2b), wherein all spaces between neurons are seen to be completely filled with the two primary types of macroglial cells (astrocytes and oligodendrocytes) found throughout the neuropil and by their even more pervasive thin processes that are also below the limit of LM resolution. For further clarification, the limits of resolution in the blue and red wavelengths are superimposed on the TEM image (Fig. 2b, blue and red discs), revealing that a single pixel at the limit of LM resolution in those wavelengths would overlap multiple plasma membranes of multiple cell types, with the blue dot overlapping with a neuronal plasma membrane, two astrocyte fingers and an oligodendrocyte soma and nucleus. This image suggests that, in the absence of companion ultrastructural examination, complex interdigitations of neuronal and glial processes preclude or make questionable the LM assignment of specific connexins to specific cell types in convoluted CNS tissue. Of course, this problem of assigning proteins to specific cell margins applies equally well to subcellular localization of all other membrane proteins.

To investigate the basis for putative neuronal gap junctions reportedly containing Cx26, Cx32 and Cx43 by freeze-fracture replica immunogold labeling (FRIL) using knife-

fractured single replicas (procedure described below) revealed that neuronal processes often had thin astrocyte "fingers" interposed, in this case with a small A:A gap junction labeled for both Cx26 and Cx30 (Fig. 2c; 12 nm gold = Cx26, 20 nm gold = Cx30). The nominal LM limits of resolution in the *x*, *y* and *z* axes are indicated in stereoscopic images by the inscribed three-dimensional box, which corresponds to a single "voxel" (volume pixel) at the resolution limit of confocal LM (0.2 × 0.2 × 0.4 μm in the *x*, *y* and *z* axes, respectively). Moreover, in the red wavelength (which had been used to visualize the margins of the neurons in Fig. 2a), the limit of resolution is ∼0.4 μm, or several times the width of the space occupied by the astrocyte fingers (Fig. 2c, crossing red arrows). If this configuration had been

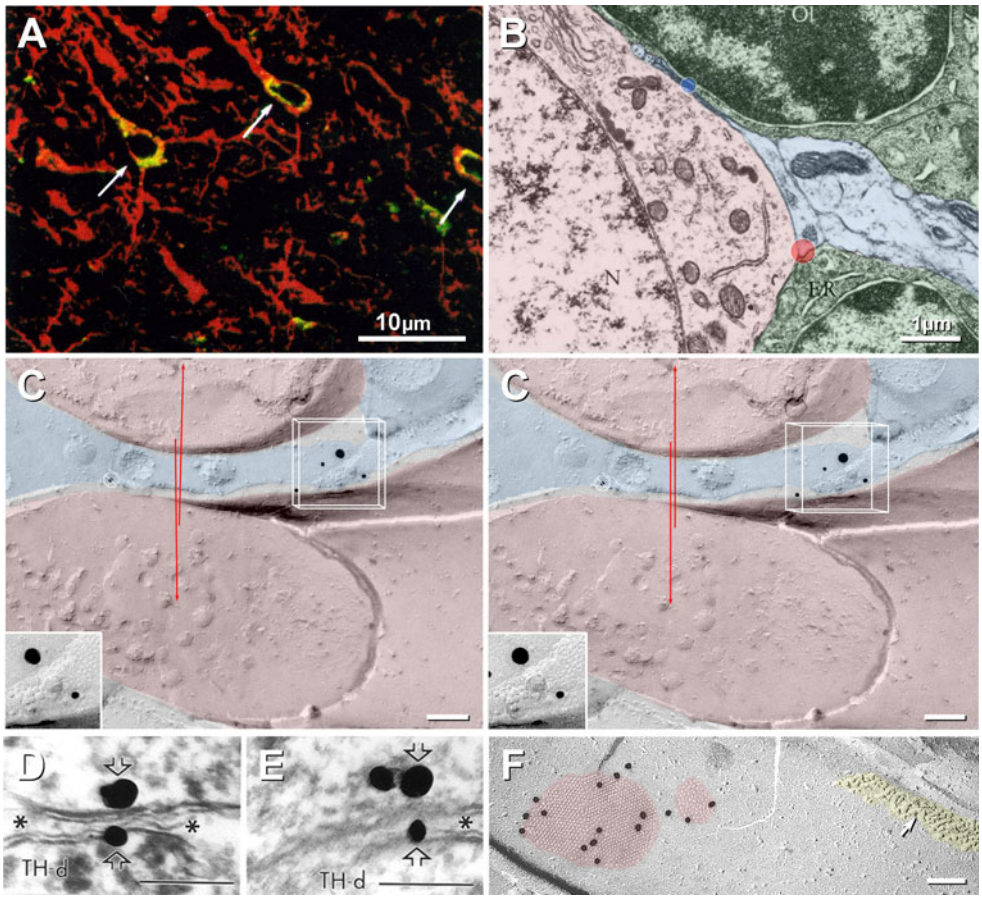

Fig. 2 Comparison of limits of resolution of light microscopy (**a**) with ultrastructural resolution (**b**, **c**). **a** Neurons double-stained for Cx43 (*green fluorescence*) and the neuronal marker MAP-2 (*red fluorescence*) but without visualization of intervening glial cells. Without companion bright-field or differential interference optics to reveal other cell types, it is not possible to assign Cx43 unambiguously to the visualized cells, regardless of apparent close proximity. This deficiency is implicit in representative thin-section TEM images. **b** Modified from Peters et al. (1991). The limits of resolution in the blue and red wavelengths are indicated by superimposed *red* and *blue discs*, each of which overlaps cell margins of all three cell types, as well as multiple cytoplasmic membranes. **c** Two neuronal dendritic processes (*red overlays*), with a gap junction linking two thin intervening astrocyte processes (*blue overlays*). The astrocyte gap junction (shown at higher magnification in the *inset*) is double-labeled for Cx26 (12 nm gold) and Cx30 (20 nm gold). The limits of resolution in the *x*, *y* and *z* axes are indicated by the inscribed *three-dimensional box*, which corresponds to a single voxel (volume pixel) at the limit of resolution of confocal LM. If this region had been visualized by LM, with neurons stained red, astrocytes and oligodendrocytes not stained and connexins visualized using green fluorescence (as in **a**), Cx26 and Cx30 would have appeared to be localized to the decussating, small-diameter neuronal processes. *Crossing red arrows* indicate the limit of LM resolution in the red wavelength, suggesting that these two neuronal processes would have been in direct contact, with no room for intervening astrocyte processes. Barred Circle = gold bead on top of replica, as "noise" (Rash and Yasumura 1999). **d**, **e** "Serial sections in which gold–silver labeling for Cx32 (*straight open arrows*) was identified on the cytoplasmic surface of a peroxidase-labeled TH dendrite and in an apposed glial process (*asterisks*) that separates two TH-positive dendrites from one another" (Alvarez-Maubecin et al. 2000). However, we note that Cx32 is an oligodendrocyte connexin and is not found in astrocytes, nor has it been detected in ultrastructurally defined neuronal gap junctions, so we consider these images to represent background "noise" on two nonserial sections, each showing an astrocyte process between two different sets of TH neurons. *Calibration bars* 0.2 μm. **f** Comparison FRIL image of two neuronal gap junctions (*red overlays*) in adult rat retina that were immunogold-labeled for Cx36 (13- and three 20-nm gold beads). Unlabeled glutamate receptor postsynaptic density (*yellow overlay*). Modified from Rash et al. (2001). *Calibration bars* 0.1 μm, unless otherwise indicated

imaged by LM in red fluorescence (for neuronal markers) and green (for Cx43, Cx32 or Cx26), the overlay would have appeared to support Cx26 (or any other astrocyte connexin) between the two crossing neuronal processes. Thus, this image graphically demonstrates why ultrastructural approaches are essential for eliminating ambiguities of connexin assignment to specific cell types in CNS tissue.

In addition to those early immunofluorescence reports suggesting that neurons express multiple connexins that are now widely recognized to be "glial" [e.g., Cx26, Cx30, Cx32, Cx43 and Cx47 (Chang et al. 1999; Nadarajah et al. 1996, 1997; Nadarajah and Parnavelas 1999; Teubner et al. 2001; Venance et al. 2000; Zhang et al. 2000)], both Cx32 and Cx26 proteins were reported to occur between neurons at putative gap junctions, as identified by the presence of one to three silver-intensified gold beads at areas where membranes "tended to approach" (Fig. 2d, e); but these areas were not otherwise recognizable as gap junctions, even in these purported "consecutive serial sections." Unaccountably, the contacting membranes had reversed contour in the successive sections, and the cytoplasm of one section was heavily stained for tyrosine hydroxylase/peroxidase (Fig. 2d), whereas the successive section had little or no staining (Fig. 2e), suggesting that the samples may have been misidentified as representing consecutive serial sections. In contrast, FRIL (Fig. 2f) unambiguously revealed gap junctions as clusters of 10-nm P-face intramembrane particles (IMPs) and/or 9-nm E-face pits (Goodenough and Revel 1970). [P-face = protoplasmic leaflet, E-face = extraplasmic leaflet; established nomenclature defined in Branton et al. (1975).] By FRIL, both neuronal and glial gap junctions were further confirmed by labeling with multiple immunogold beads for appropriate cell type–specific connexins and only in the appropriate ultrastructurally identified cell types (Rash et al. 2001).

To date, no neuronal gap junctions have been detected by FRIL that were immunogold-labeled for any of the consensus "glial" connexins. However, more than 3,000 neuronal gap junctions have been detected that were labeled for Cx36 (Kamasawa et al. 2006; Rash et al. 2005, 2007a, b), and ~100 have been detected in rodent retina that were labeled for Cx45 (Li et al. 2008a) (see the following); but none were labeled for glial connexins, either within neuronal hemiplaques or within the hemiplaques of neuronal coupling partners. This latter observation means that in normal CNS tissues neurons do not couple with glial cells, regardless of the connexins present in each. Presumably, the neuronal connexins are nonpermissive with glial connexins. In contrast, in many of the same double- and triple-labeled samples, many thousands of glial gap junctions were cumulatively labeled by tens of thousands of gold beads for glial connexins, each gold bead representing a separate confirmation of the target connexin in those gap junctions (Nagy et al. 2004; Rash et al. 2001). With no consensus glial connexins ever detected in ultrastructurally identified gap junctions of neurons and with thousands of glial gap junctions labeled for consensus glial connexins and never for neuronal connexins (Nagy et al. 2003, 2004; Nagy and Rash 2000; Rash et al. 2001), it is no longer appropriate to invoke those early reports as evidence for Cx26, Cx30, Cx32, Cx43 or Cx47 in neurons. On the other hand, Cx36 has been identified in sufficient numbers of neuronal gap junctions and in sufficient areas of the CNS to qualify as a reliable immunofluorescence marker for electrical synapses in widespread brain regions [see companion paper (Lynn et al. 2012), this issue].

False Positives Arising from mRNA Detection Methods

Even when combined with mRNA detection methods (e.g., in situ hybridization, RT-PCR or LacZ reporter methods), detection is common for multiple connexin mRNAs, including multiple glial connexin mRNAs in neurons (Chang et al. 1999; Venance et al. 2000; Zhang et al. 2000; Zhang 2010). In the decade since Fire et al. (1998) first described mRNA suppression by microinterfering RNA (miRNA), it has become clear that most classes of connexin mRNAs appear to be actively prevented from translation into protein by multiple miRNAs, which are particularly abundant in the mammalian brain (Bartel 2004; Berezikov et al. 2006; Farh et al. 2005; Krichevsky et al. 2003; Lim et al. 2005; Miska et al. 2004; Sempere et al. 2004), with some of the "seed matching sequences" for glial vs. neuronal connexins having been identified, consistent with active suppression of glial connexin mRNAs in neurons (Rash et al. 2005). We conclude that in CNS tissues there is such a high incidence of detection of diverse connexin mRNAs without detection of the corresponding connexin protein that such methods have been especially misleading in the identification of the neuronal connexins that are actually expressed (i.e., false correlation of mRNA detection with protein detection). Specifically, one or two neuronal connexin mRNAs but at least five glial connexin mRNAs are routinely detected in neurons by single-cell RT-PCR and by in situ hybridization (Chang et al. 1999; Rash et al. 2005; Venance et al. 2000; Zhang et al. 2000; Zhang 2010). However, none of the five glial connexins that are routinely detected by these mRNA methods appear to be translated into proteins as none were detected by FRIL at ultrastructurally identified gap junctions, even in the same tissues and animal ages as examined by others (Li et al. 2008a; Rash et al. 2005, 2007a, b).

To address these important issues of gap junction connexin composition and the "sidedness" of connexin expression, ultrastructural approaches have been employed,

including thin-section TEM (Nagy et al. 1999, 2001; Ochalski et al. 1997; Yamamoto et al. 1990a, b), FRIL and, more recently, double-replica FRIL (DR-FRIL). [FRIL is the abbreviation originally introduced by Gruijters et al. (1987) for "fracture-replica-immunogold labeling" by a method not using the breakthrough SDS detergent washing procedure (Fujimoto 1995, 1997).] Alternative replica labeling procedures and nomenclature include SDS-FRL (Fujimoto 1995, 1997) and double-replica SDS-FRL (Li et al. 2008a). Our version of FRIL originally was distinguished from SDS-FRL by the additional steps of Lexan plastic stabilization of replicas and by confocal grid mapping to the limit of resolution of LM, prior to tissue removal by SDS washing and subsequent immunogold labeling (Rash et al. 1995, 1996). We found the added steps of FRIL to be essential for the analysis of gap junctions in complex CNS tissues. Regardless, we used both DR-SDS-FRL and DR-FRIL methods in this report.

False Negatives Arising from LacZ mRNA Detection Methods

Data from LacZ reporter systems have been interpreted as showing that a small percentage of neurons in the inner plexiform layer of the retina (i.e., cone bipolar cells) express only Cx45 and not Cx36 (Schubert et al. 2005), whereas the AII amacrine cells to which bipolar cells are known to couple reportedly express only Cx36. This appeared to pose a problem because Cx45 and Cx36 are reported to be "nonpermissive" for forming gap junctions (Teubner et al. 2000). Moreover, three groups using RT-PCR and immunocytochemistry (Han and Massey 2005; Lin et al. 2005) and immunofluorescence of cryosections (Dedek et al. 2006) concluded that Cx45 and Cx36 were never coexpressed in the same neuron, with the further assertion (Han and Massey 2005) that Cx45 and Cx36 proteins are never detected in the same fluorescent punctum. However, Dedek and coworkers reported that where Cx45 was present, it was present along with Cx36 in 30 % of puncta. Thus, those three groups separately concluded that because those cells are known to be coupled via gap junctions, their coupling required either (1) heterotypic coupling of Cx45 and Cx36 (i.e., that some additional factor allowed permissive coupling in vivo) or (2) that there must exist two additional connexin coupling partners to which Cx45 and Cx36 can separately couple.

In our initial FRIL studies of Cx36 vs. Cx45 in 671 double-labeled gap junctions in the inner plexiform layer of rat and mouse retina (Li et al. 2008a), single-replica FRIL showed that ca. 90 % (607) contained only Cx36, whereas ca. 9 % (58) contained both Cx45 and Cx36 in the same hemiplaques (and a statistically insignificant <1 %, mostly very small, contained minimal labeling for Cx45 without labeling for Cx36). Those data demonstrated conclusively that the 58 neurons with hemiplaques containing labeling for Cx45 and Cx36 must have synthesized both Cx45 and Cx36 proteins, conceivable at different times (thereby possibly accounting for failure to detect one or the other connexin), or alternatively, suggesting that the failure to simultaneously detect both connexins in any neurons represented a limitation of the detection method. Nevertheless, by single-replica FRIL, we were unable to ascertain whether the coupling partners of the double-labeled gap junction hemiplaques expressed either or both of those same connexins in the apposed hemiplaque. This question could be answered only by DR-FRIL, as developed and applied below.

In this article we discuss the advantages of matched DR-FRIL in identifying the cellular types contributing specific connexins to neuronal gap junctions in retina and goldfish hindbrain.

Materials and Methods

Animals used in this study were prepared under protocols approved by the Institutional Animal Care and Use Committee of Colorado State University and conducted according to *Principles of Laboratory Animal Care* (U.S. National Institutes of Health publication 86-23, rev. 1985). These protocols included minimization of stress to animals and minimization of the number of animals used. One formaldehyde-fixed rat retina and several formaldehyde-fixed goldfish hindbrains were prepared for DR-SDS-FRL and DR-FRIL, as previously described (Li et al. 2008a; Pereda et al. 2003). Fixed tissues were sliced to 150 μm thickness at 4 °C in a refrigerated vibrating microslicer (DTK-1000; Dosaka, Kyoto, Japan) or a Lancer Vibratome 3000 (Leica Microsystems, Buffalo Grove, IL), infiltrated with 30 % glycerol as a cryoprotectant to reduce freezing damage by ice crystals, placed between two 4.6-mm gold planchettes and either frozen in a BalTec (BalTec, Balzers, Liechtenstein) 010 High-pressure Freezing Device (retina) or plunge-frozen in a mixture of 2:1 propane/ethane at −195 °C (hindbrain). Sandwich samples were placed in a prototype double-replica device (Fig. 3a), the two planchettes were mechanically separated (fractured) and the two newly created mirror complements were coated with 2–5 nm of carbon and shadowed with ~1.5 nm of platinum, thereby creating matched double-replicas (Li et al. 2008a). These samples were either thawed, with the tissues picked up on copper "thin-bar grids" and mapped by reflectance microscopy (Fig. 3b, b′, showing matching complements of adult rat retina), or bonded to a gold "index grid" [not shown but see Pereda et al. (2003)] before SDS washing and immunogold labeling. Both

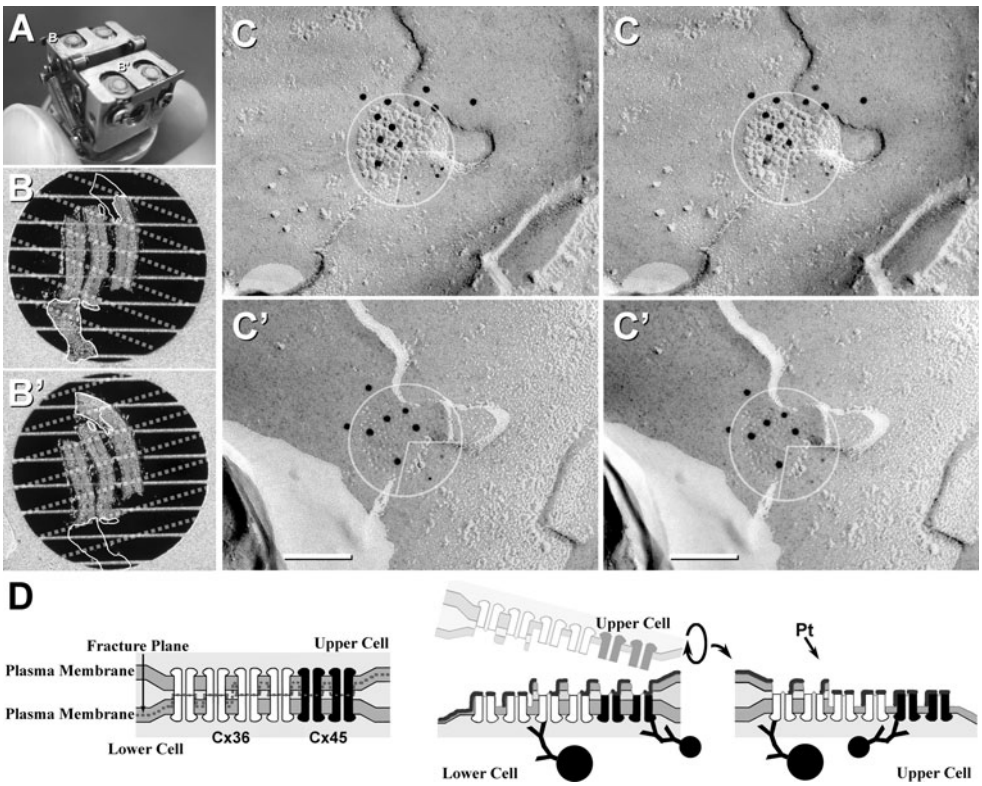

Fig. 3 Explanation of the DR-FRIL technique. **a** Photograph of the DR stage after fracturing of two specimens. Matched DR samples (indicated by *B* and *B′* in **a**) are shown at higher magnification in **b**, **b′**), after floating off into buffer. **b**, **b′** Replicated but undigested samples were mounted on thin-bar grids, with matching outlines indicated. Small tissue fragments were lost during washing (*open outlines* opposite corresponding *outlined tissues*). Bars occluding matching areas are indicated by *dotted lines*. **c**, **c′** One of 11 pairs of matched gap junction hemiplaques (*circles with inscribed quadrants*) from the samples indicated in **b**, **b′**. Cx45 is labeled with 5-nm gold beads (*lower right quadrants*), whereas Cx36 is labeled with 10-nm gold beads (*upper left three quadrants* **c**, **c′**). Labeling for Cx45 is aligned with (i.e., opposite) labeling for Cx45 in the matching areas of the two hemiplaques. Likewise, labeling for Cx36 is aligned with labeling for Cx36. These matching hemiplaques demonstrate bihomotypic gap junctions. **b**, **c** Modified from Li et al. (2008a). **d** Diagram showing production of matched DRs and the subsequent immunogold labeling of bihomotypic plaques containing mostly Cx36 (*white connexons* labeled with *large gold beads*) and fewer Cx45 (*black connexons*, labeled with *small gold beads*)

matched replica complements of retina were immungold-labeled simultaneously according to our previous descriptions (Li et al. 2008a), with 5-nm gold beads used to label Cx45 and 10-nm gold beads used to label Cx36. Matched replicas of goldfish hindbrain were labeled with monoclonal MAB3045 (Biosciences Research Reagents; Millipore, Temecula, CA) against Cx35 and polyclonal rabbit antibody against Cx34.7 [lot 2930-1 IL, from O'Brien et al. (2004)], with a single size of gold bead (5 nm) on goat anti-rabbit IgG for Cx45 and a different size of gold bead (10 nm) on goat anti-mouse IgG against Cx36.

Results

Procedures and Applications of DR-FRIL

We have previously described the method of FRIL and details of its applications (Rash et al. 2001; Rash and Yasumura 1999). DR-FRIL differs from FRIL in several respects. First, both sides of the fracture plane are retrieved and, not incidentally, may be matched by laborious repeated examination and matching of corresponding "fiduciary marks" that nevertheless may be difficult to recognize because they have opposite structural contour, or they may be covered by grid bars or damaged during SDS washing and labeling. Nevertheless, the rewards in obtaining definitive information regarding the connexin content, for example, of matched mirror complements are unequaled by any other technique. Equally important, a wide variety of scaffolding and accessory proteins can now be mapped and correlated with the biochemical composition and functional state of individual gap junctions in two apposed cells, as shown next.

DR-FRIL Reveals Connexin Coupling Partners in Retinal Gap Junctions

To determine whether Cx45-containing gap junctions are heterotypic vs. homotypic (and, hence, to identify connexin coupling partners in individual gap junctions), three cross

sections of adult rat replica were prepared by DR-SDS-FRL and simultaneously double-labeled for Cx36 and Cx45. We found more than 160 gap junctions labeled for Cx36, 12 of which also contained Cx45. Eleven of those were found in the matched complementary replica (Fig. 3c, c′), and all 11 of the complements also had Cx45, along with Cx36. None were found with Cx45 alone, and no additional Cx45-labeled gap junctions were found in the other complement. This means that of 11 examples of Cx45-containing gap junctions encountered, all contained both Cx36 and Cx45 on both sides, thereby demonstrating that 100 % of those 22 coupled cells synthesized both Cx45 and Cx36. Moreover, the two connexins appeared to reside in separate domains, with labeling for Cx45 aligned with (i.e., was opposite) labeling for Cx45 in the matched hemiplaque and labeling for Cx36 aligned with labeling for Cx36 (Fig. 3, matching inscribed quadrants). Thus, these gap junctions were not heterotypic, as proposed by others, nor did either side need to contain additional unidentified connexins for establishing permissive connexon channels. Rather, those 11 gap junctions were bihomotypic, with Cx45 apparently coupling to Cx45 and Cx36 apparently coupling to Cx36. This overcame the problem of what had previously appeared to be heterotypic coupling between nonpermissive Cx45 and Cx36. Finally, the fortuitous segregation of connexin labels within gap junctions (rather than labels being completely intermixed) was consistent with suggestions that the connexons were in homomeric domains (i.e., each domain within an individual gap junction plaque contained only a single connexin type).

DR-FRIL Revealed Heterotypic Gap Junctions at Synapses on Neurons of Goldfish Hindbrain

Neurons in the tetrapod lineage have Cx36 as their primary connexin. In contrast, teleost fish duplicated their entire genomes from the parent vertebrate lineage, resulting in two homologs of mammalian Cx36, which diverged slightly as Cx34.7 and Cx35 (>85 % homology). These connexins vary primarily in their phosphorylation sequences [Cx34.7 lacks a phosphorylation site for CaMKII (Flores et al. 2010)] and in their membrane targeting sequences (O'Brien et al. 1998). In a first step toward investigating the presence of these two homologs in goldfish, we applied DR-FRIL to the analysis of gap junctions in a wide variety of neurons in the hindbrain.

For comparison to our previous thin-section TEM images of heterotypic coupling at O:A gap junctions (Fig. 4a, inset), we show a rare cross-fractured gap junction with heterotypic labeling (Cx35 presynaptic and Cx34.7 postsynaptic, Fig. 4b) and matched DR complements of the an en face view of a gap junction on a reticulospinal neuron (Fig. 4c, d), with only small (5 nm) gold beads labeling postsynaptic connexins and only larger (10 nm) gold beads labeling presynaptic connexins. A diagram depicting the formation of a corresponding DR-FRIL replica is shown (Fig. 4e, f).

These preliminary data document expression of Cx34.7 without Cx35 in hemiplaques of a goldfish reticulospinal neuron, as well as Cx35 without Cx34.7 in the matching hemiplaques of its apposed axon terminal (Fig. 4c, d). In these matching complementary replicas, only Cx34.7 is detected in the reticulospinal neuron hemiplaque (Fig. 4c, arrowheads), whereas Cx35 is detected without Cx34.7 in the presynaptic hemiplaque that underlies the gap junction E-face pits (Fig. 4d). E-face pits are only faintly resolvable because of the 4- to 5-nm-thick carbon "precoat." Although it is not yet determined whether the two types of coupled neurons (sensory and motor neurons) synthesize both connexins (with Cx35 targeted to axon terminals and Cx34.7 targeted to neuron soma and dendrites) or whether each neuronal subtype synthesizes only a single connexin isoform (Cx35 in sensory neurons and Cx34.7 in motor neurons), these data from DR-FRIL provide the molecular basis for a potential rectification of electrical transmission between these neurons.

Heterotypic gap junctions between neurons may contribute to the functional diversity of electrical transmission and provide a mechanism for preferred directionality of signaling (including electrical rectification), while bi- and trihomotypic gap junctions may provide for bidirectional signaling but with the added property of differential modulation of multiple conductance states for ions and small signaling molecules.

Summary

DR-FRIL and DR-SDS-FRL have unambiguously revealed individual gap junctions expressing two connexins—on the one hand, forming bihomotypic and, on the other hand, forming heterotypic junctions. As a now widely recognized type of synapse between neurons in the mammalian CNS, the conductance properties of electrical synapses and their regulation take on new importance. The two different connexin distributions demonstrated by DR-FRIL (i.e., bihomotypic vs. heterotypic) suggest the existence of previously unrecognized mechanisms for regulating gap junction conductance states. Bi- and trihomotypic gap junctions are likely to increase the complexity and enhance the quality of synaptic communication provided by gap junctions. Likewise, heterotypic gap junctions provide not only for differential modulation on opposite sides of the same gap junction but also for the possibility of electrical rectification in teleost CNS neurons. Because there appears so far to be only one connexin (Cx36) widely expressed in

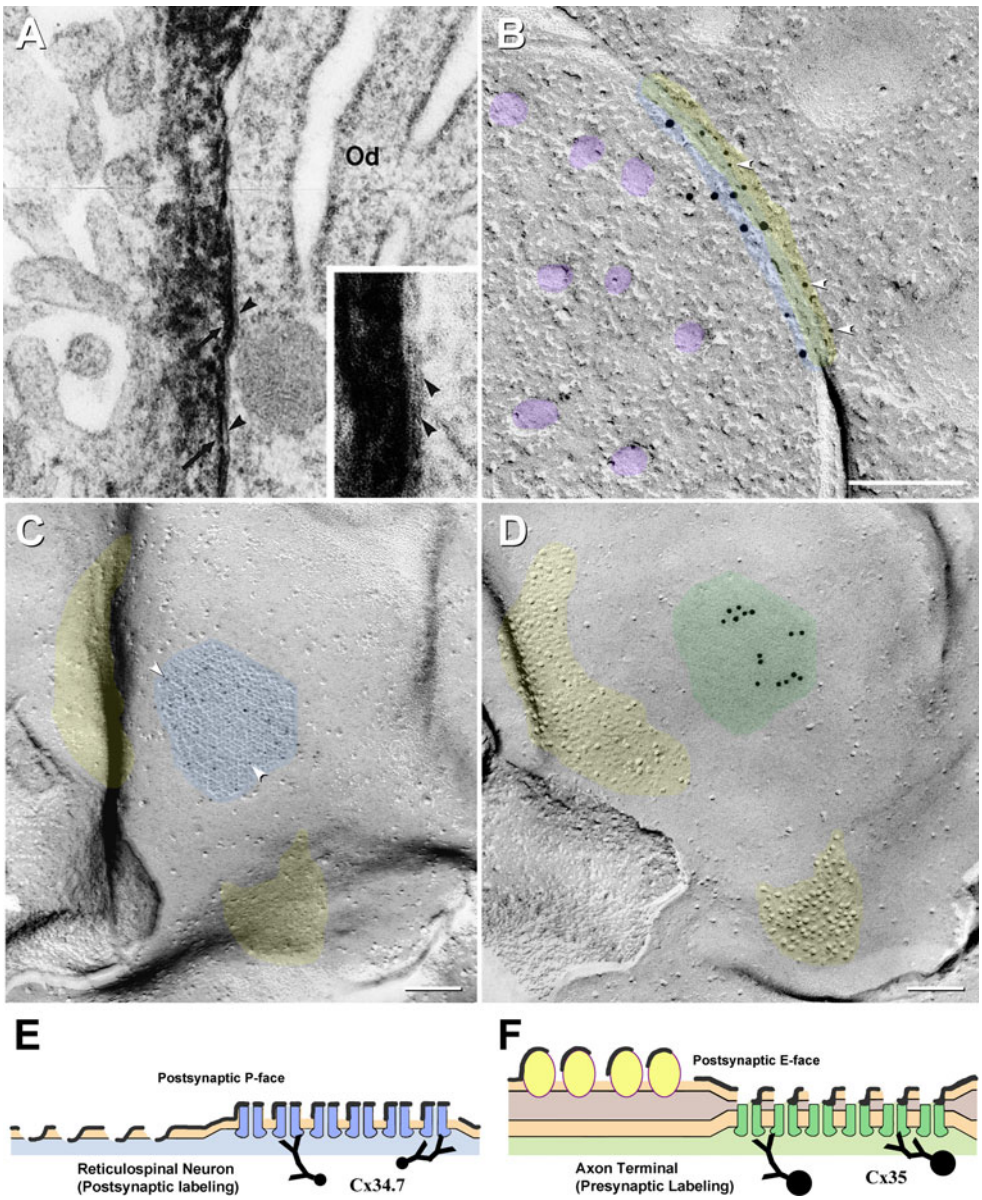

Fig. 4 Comparison of heterotypic labeling in TEM thin sections (**a**), cross-fractured FRIL images (**b**) and by the DR-FRIL technique (**c**, **d**), with explanatory drawing (**e**, **f**). **a** Thin-section immunocytochemical demonstration of Cx43 in the astrocyte side of an O:A gap junction, labeled by the peroxidase–antiperoxidase method, leaving DAB deposition on the astrocyte side (*arrows*) and the oligodendrocyte side (*Od*) unlabeled (*arrowheads*). [This image was obtained 10 years before Cx47 was identified as the coupling partner for Cx43; modified from Ochalski et al. (1997)]. **b** Cross-fractured "mixed" (electrical plus chemical synapse), presumably from an auditory afferent onto an unidentified reticulospinal neuron in goldfish hindbrain. In this companion image to (**c**), 5-nm gold beads labeled postsynaptic connexin Cx34.7 (*arrowheads*), whereas 10-nm gold beads for Cx35 labeled presynaptic connexins. (Synaptic vesicles are indicated by *purple overlays*.) The *yellow overlay* indicates the radius of uncertainty of immunogold labeling for small gold beads, the *blue overlay* indicates the radius of uncertainty for large gold beads and the *green overlay* indicates the region of potential overlap. This asymmetric distribution of gold labels reveals that this gap junction between a sensory afferent and the reticulospinal neuron is heterotypic. **c, d** Matching complementary replicas at club ending synapse on reticulospinal neuron. The postsynaptic hemiplaque (**c**, designated by *blue overlay*) is labeled for Cx34.7 by approximately three 5-nm gold beads (*arrowheads*), whereas the complementary E-face (*green overlay*) is labeled for Cx35 by 15 10-nm gold beads. Areas corresponding to glutamate receptor–containing postsynaptic densities are indicated by *yellow overlays*, with the P-face pits in **c** matching the E-face particles in (**b**), as previously shown by labeling for glutamate receptors (Pereda et al. 2003). **e**, **f** Diagram of matching replica complements, showing Cx34.7 without Cx35 in the reticulospinal neuron (**e**) and Cx35 labeling without labeling for Cx34.7 in the E-face of the matching hemiplaque of the apposed club ending. Labeling in (**d**) and (**f**) is for connexins in the cytoplasm of the underlying axon terminal ending, even though only the E-face pits of the reticulospinal neuron are visualized in the replica

neurons in tetrapods, heterotypic coupling may seem at first glance to preclude rectification. However, functional asymmetry between apposed hemichannels could perhaps be achieved by differences in posttranslational modifications between these two channels. Supporting this possibility, Cx36-containing junctions have been shown to coexist at different degrees of phosphorylation in the retina (Kothmann et al. 2009). If found in the mammalian CNS, electrical rectification and modulation of rectification would open up new pathways for synaptic communication that may be of particular relevance in the human CNS and in human neurological disease.

Future Directions

As powerful as FRIL has proven to be, there are two limitations that make it and DR-FRIL less inviting for the novice. First, freeze-fracture and FRIL require complex, costly equipment that is at the cutting edge of high-vacuum, cryopreservation and metal evaporation technologies. Second, with more than a dozen discrete steps, all of which must be performed flawlessly to obtain the matching complementary replicas, DR-FRIL is particularly demanding of its technological practitioners. Third, freeze-fracture electron microscopy requires considerable time to gain expertise in obtaining and interpreting FRIL images. The training period for FRIL is several years because the researcher must learn conventional electron microscopy as well as interpretation of tissue ultrastructure in freeze-fracture replicas before learning FRIL methods. In these days of automated molecular biology, few students are willing to make this long-term commitment. With few laboratories remaining that are capable of conducting FRIL and DR-FRIL, there is a narrowing window of opportunity for the application of simultaneous ultrastructural and immunocytochemical approaches, not just to gap junctions and mixed synapses at EM resolution but also to other key questions in neuroscience requiring this level of resolution.

Acknowledgments This work was funded by grants from the National Institutes of Health (NS044395, S10 RR08329 and S10 RR015706 to J.E.R. and DC03186 and NS0552827 to A.E.P.) and the Canadian Institute for Health Research (J.I.N.).

References

Altevogt BM, Paul DL (2004) Four classes of intercellular channels between glial cells in the CNS. J Neurosci 24:4313–4323

Altevogt BM, Kleopas KA, Postma FR, Scherer SS, Paul D (2002) Connexin29 is uniquely distributed within myelinating glial cells of the central and peripheral nervous systems. J Neurosci 22:6458–6470

Alvarez-Maubecin V, Garcia-Hernandez F, Williams JT, Van Bockstaele EJ (2000) Functional coupling between neurons and glia. J Neurosci 20:4091–4098

Barrio LC, Suchyna T, Bargiello T, Xu LX, Roginski RS, Bennett MVL, Nicholson BJ (1991) Gap junctions formed by connexins26 and 32 alone and in combination are differently affected by applied voltage. Proc Natl Acad Sci USA 88:8410–8414

Bartel DP (2004) MicroRNAs: genomics, biogenesis, mechanism, and function. Cell 116:281–297

Berezikov E, Thuemmler F, van Laake LW, Kondova I, Bontrop R, Cuppen E, Plasterk RHA (2006) Diversity of microRNAs in human and chimpanzee brain. Nat Genet 38:1375–1377

Bergoffen J, Scherer SS, Wang S, Oronzi-Scott M, Paul D, Chen K, Lensch MW, Chance P, Fischbeck K (1993) Connexin mutations in X-linked Charcot–Marie–Tooth disease. Science 262: 2039–2042

Branton D, Bullivant S, Gilula NB, Karnovsky MJ, Moor H, Northcote DH, Packer L, Satir B, Satir P, Speth V, Staehelin LA, Steere RL, Weinstein RS (1975) Freeze-etching nomenclature. Science 190:54–56

Chang Q, Gonzalez M, Pinter MJ, Balice-Gordon RJ (1999) Gap junctional coupling and patterns of connexin expression among neonatal rat lumbar spinal neurons. J Neurosci 19:10813–10828

Ciolofan C, Lynn BD, Wellershaus K, Willecke K, Nagy JI (2007) Spatial relationships of connexin36, connexin57 and zonula occludens-1 (ZO-1) in the outer plexiform layer of mouse retina. Neuroscience 148:473–488

Colwell CS (2000) Rhythmic coupling among cells in the suprachiasmatic nucleus. J Neurobiol 43:379–388

Davidson KGV, Rash JE (2011) Oligodendrocytes: gateway to the panglial syncytium. In: Scemes E, Spray DC (eds) Astrocytes: wiring the brain. Taylor & Francis, Boca Raton

Dedek K, Schultz K, Pieper M, Dirks P, Maxeiner S, Willecke K, Weiler R, Janssen-Bienhold U (2006) Localization of heterotypic gap junctions composed of connexin45 and connexin36 in the rod pathway of the mouse retina. Eur J Neurosci 24:1675–1686

Farh KK, Grimson A, Jan C, Lewis BP, Johnston WK, Lim LP, Burge CB, Bartel DP (2005) The widespread impact of mammalian microRNAs on mRNA repression and evolution. Science 310: 1817–1821

Fire A, Xu SQ, Montgomery MK, Kostas SA, Driver SE, Mello CC (1998) Potent and specific genetic interference by double-stranded RNA in *Caenorhabditis elegans*. Nature 391:806–811

Flores CE, Cachope R, Nannapaneni S, Ene S, Nairn AC, Pereda AE (2010) Variability of distribution of Ca^{2+}/calmodulin-dependent kinase ii at mixed synapses on the Mauthner cell: colocalization and association with connexin35. J Neurosci 30:9488–9499

Fujimoto K (1995) Freeze-fracture replica electron microscopy combined with SDS digestion for cytochemical labeling of integral membrane proteins. Application to the immunogold labeling of intercellular junctional complexes. J Cell Sci 108:3443–3449

Fujimoto K (1997) SDS-digested freeze-fracture replica labeling electron microscopy to study the two-dimensional distribution of integral membrane proteins and phospholipids in biomembranes: practical procedure, interpretation and application. Histochem Cell Biol 107:87–96

Goodenough DA, Revel JP (1970) A fine structural analysis of intercellular junctions in the mouse liver. J Cell Biol 45:272–290

Gruijters WTM, Kistler J, Bullivant S, Goodenough DA (1987) Immunolocalization of MP70 in lens fiber 16–17-nm intercellular junctions. J Cell Biol 104:565–572

Han Y, Massey SC (2005) Electrical synapses in retinal ON cone bipolar cells: subtype-specific expression of connexins. Proc Natl Acad Sci USA 102:13313–13318

Hempelmann A, Heils A, Sander T (2006) Confirmatory evidence for an association of the connexin-36 gene with juvenile myoclonic epilepsy. Epilepsy Res 71:223–228

Hu X, Dahl G (1999) Exchange of conductance and gating properties between gap junction hemichannels. FEBS Lett 451:113–117

Jiang JX, Goodenough DA (1996) Heteromeric connexons in lens gap junction channels. Proc Natl Acad Sci USA 93:1287–1291

Kamasawa N, Furman CS, Davidson KGV, Sampson JA, Magnie AR, Gebhardt B, Kamasawa M, Morita M, Yasumura T, Pieper M, Zumbrunnen JR, Pickard GE, Nagy JI, Rash JE (2006) Abundance and ultrastructural diversity of neuronal gap junctions in the OFF and ON sublaminae of the inner plexiform layer of rat and mouse retina. Neuroscience 142:1093–1117

Kelsell DP, Dunlop J, Stevens HP, Lench NJ, Liang JN, Parry G, Mueller MF, Leigh IM (1997) Connexin26 mutations in hereditary non-sydromic sensorineural deafness. Nature 387:80–83

Kleopa KA, Orthmann JL, Enriquez A, Paul DL, Scherer SS (2004) Unique distributions of the gap junction proteins connexin29, connexin32, and connexin47 in oligodendrocytes. Glia 47: 346–357

Kothmann WW, Massey SC, O'Brien J (2009) Dopamine-stimulated dephosphorylation of connexin36 mediates AII amacrine cell uncoupling. J Neurosci 29:14903–14911

Krichevsky AM, King KS, Donahue CP, Khrapko K, Kosik KS (2003) A microRNA array reveals extensive regulation of microRNAs during brain development. RNA 9:1274–1281

Li J, Hertzberg EL, Nagy JI (1997) Connexin32 in oligodendrocytes and association with myelinated fibers in mouse and rat brain. J Comp Neurol 379:571–591

Li X, Olson C, Lu S, Kamasawa N, Yasumura T, Rash JE, Nagy JI (2004) Neuronal connexin36 association with zonula occludens-1 protein (ZO-1) in mouse brain and interaction with the first PDZ domain of ZO-1. Eur J Neurosci 19:2132–2146

Li X, Kamasawa N, Ciolofan C, Olson CO, Lu S, Davidson KGV, Yasumura T, Shigemoto R, Rash JE, Nagy JI (2008a) Connexin45-containing neuronal gap junctions in rodent retina also contain connexin36 in both apposing hemiplaques, forming bihomotypic gap junctions, with scaffolding contributed by zonula occludens-1. J Neurosci 28:9769–9789

Li X, Penes M, Odermatt B, Willecke K, Nagy JI (2008b) Ablation of Cx47 in transgenic mice leads to the loss of MUPP1, ZONAB and multiple connexins at oligodendrocyte–astrocyte gap junctions. Eur J Neurosci 28:1503–1517

Lim LP, Lau NC, Garrett-Engele P, Grimson A, Schelter JM, Castle J, Bartel DP, Linsley PS, Johnson JM (2005) Microarray analysis shows that some microRNAs downregulate large numbers of target mRNAs. Nature 433:769–773

Lin B, Jakobs TC, Masland RH (2005) Different functional types of bipolar cells use different gap-junctional proteins. J Neurosci 25:6696–6701

Lynn BD, Tress O, May D, Willecke K, Nagy JI (2011) Ablation of connexin30 in transgenic mice alters expression patterns of connexin26 and connexin32 in glial cells and leptomeninges. Eur J Neurosci 34:1783–1793

Lynn BD, Li X, Nagy JI (2012) Under construction: building the macromolecular superstructure and signaling components of an electrical synapse. J Membr Biol. doi:10.1007/s00232-012-9451-5

Magnotti LM, Goodenough DA, Paul DL (2011) Functional heterotypic interactions between astrocyte and oligodendrocyte connexins. Glia 59:26–34

Mas C, Taske N, Deutsch S, Guipponi M, Thomas P, Covanis A, Friis M, Kjeldsen MJ, Pizzolato GP, Villemure JG, Buresi C, Rees M, Malafosse A, Gardiner M, Antonarakis SE, Meda P (2004) Association of the connexin36 gene with juvenile myoclonic epilepsy. J Med Genet 41:e93

Melchionda S, Bicego M, Marciano E, Franze A, Morgutti M, Bortone G, Zelante L, Carella M, D'Andrea P (2005) Functional characterization of a novel Cx26 (T55N) mutation associated to non-syndromic hearing loss. Biochem Biophys Res Comm 337:799–805

Miska EA, Alvarez-Saavedra E, Townsend M, Yoshii A, Sestan N, Rakic P, Constantine-Paton M, Horvitz HR (2004) Microarray analysis of microRNA expression in the developing mammalian brain. Genome Biol 5:R68

Nadarajah B, Parnavelas JG (1999) Gap junction-mediated communication in the developing and adult cerebral cortex. Novartis Found Symp 219:157–170

Nadarajah B, Thomaidou D, Evans WH, Parnavelas JG (1996) Gap junctions in the adult cerebral cortex: regional differences in their distribution and cellular expression of connexins. J Comp Neurol 376:326–342

Nadarajah B, Jones AM, Evans WH, Parnavelas JG (1997) Differential expression of connexins during neocortical development and neuronal circuit formation. J Neurosci 17:3096–3111

Nagy JI, Rash JE (2000) Connexins and gap junctions of astrocytes and oligodendrocytes in the CNS. Brain Res Brain Res Rev 32:29–44

Nagy JI, Patel D, Ochalski PAY, Stelmack GL (1999) Connexin30 in rodent, cat and human brain: selective expression in gray matter astrocytes, co-localization with connexin43 at gap junctions and late developmental appearance. Neuroscience 88:447–468

Nagy JI, Li X, Rempel J, Stelmack GL, Patel D, Staines WA, Yasumura T, Rash JE (2001) Connexin26 in adult rodent CNS: demonstration at astrocytic gap junctions and co-localization with connexin30 and connexin43. J Comp Neurol 441:302–323

Nagy JI, Ionescu AV, Lynn BD, Rash JE (2003) Coupling of astrocyte connexins Cx26, Cx30, Cx43 to oligodendrocyte Cx29, Cx32, Cx47: implications from normal and connexin32 knockout mice. Glia 44:205–218

Nagy JI, Dudek FE, Rash JE (2004) Update on connexins and gap junctions in neurons and glia in the mammalian central nervous system. Brain Res Brain Res Rev 47:191–215

Nagy JI, Lynn BD, Tress O, Willecke K, Rash JE (2011) Connexin26 expression in brain parenchymal cells demonstrated by targeted connexin ablation in transgenic mice. Eur J Neurosci 34:263–271

O'Brien J, Bruzzone R, White TW, Al-Ubaidi MR, Ripps H (1998) Cloning and expression of two related connexins from the perch retina define distinct subgroups of the connexin family. J Neurosci 18:7625–7637

O'Brien J, Nguyen HB, Mills SL (2004) Cone photoreceptors in bass retina use two connexins to mediate electrical coupling. J Neurosci 24:5632–5642

Ochalski PAY, Frankenstein UN, Hertzberg EL, Nagy JI (1997) Connexin-43 in rat spinal cord: localization in astrocytes and identification of heterotypic astro-oligodendrocytic gap junctions. Neuroscience 76:931–945

Orthmann-Murphy JL, Freidin M, Fischer E, Scherer SS, Abrams CK (2007) Two distinct heterotypic channels mediate gap junction coupling between astrocyte and oligodendrocyte connexins. J Neurosci 27:13949–13957

Palacios-Prado N, Bukauskas FF (2009) Heterotypic gap junction channels as voltage-sensitive valves for intercellular signaling. Proc Natl Acad Sci USA 106:14855–14860

Paznekas WA, Boyadjiev SA, Shapiro RE, Daniels O, Wollnik B, Keegan CE, Innis JW, Dinulos MB, Christian C, Hannibal MC, Jabs EW (2003) Connexin43 (GJA1) mutations cause the pleiotropic phenotype of oculodentodigital dysplasia. Am J Hum Genet 72:408–418

Pereda A, O'Brien J, Nagy JI, Bukauskas F, Davidson KGV, Kamasawa N, Yasumura T, Rash JE (2003) Connexin35 mediates electrical transmission at mixed synapses on Mauthner cells. J Neurosci 23:7489–7503

Peters A, Palay SL, Webster HD (1991) The fine structure of the nervous system: neurons and their supporting cells. Oxford University Press, New York

Rash JE (2010) Molecular disruptions of the panglial syncytium block potassium siphoning and axonal saltatory conduction: pertinence to neuromyelitis optica and other demyelinating diseases of the central nervous system. Neuroscience 168:982–1008

Rash JE, Yasumura T (1999) Direct immunogold labeling of connexins and aquaporin 4 in freeze-fracture replicas of liver, brain and spinal cord: factors limiting quantitative analysis. Cell Tissue Res 296:307–321

Rash JE, Dillman RK, Morita M, Whalen LR, Guthrie PB, Fay-Guthrie D, Wheeler DW (1995) Grid-mapped freeze fracture: correlative confocal laser scanning microscopy and freeze-fracture electron microscopy of preselected cells in tissue slices. In: Severs NJ, Shotton DM (eds) Rapid freezing, freeze fracture and deep etching. Wiley-Liss, New York, pp 127–150

Rash JE, Dillman RK, Bilhartz BL, Duffy HS, Whalen LR, Yasumura T (1996) Mixed synapses discovered and mapped throughout mammalian spinal cord. Proc Natl Acad Sci USA 93:4235–4239

Rash JE, Yasumura T, Dudek FE, Nagy JI (2001) Cell-specific expression of connexins, and evidence for restricted gap junctional coupling between glial cells and between neurons. J Neurosci 21:1983–2001

Rash JE, Davidson KGV, Kamasawa N, Yasumura T, Kamasawa M, Zhang C, Michaels R, Restrepo D, Ottersen OP, Olson C, Nagy JI (2005) Ultrastructural localization of connexins (Cx36, Cx43, Cx45), glutamate receptors and aquaporin-4 in rodent olfactory mucosa, olfactory nerve and olfactory bulb. J Neurocytol 34:307–341

Rash JE, Olson C, Davidson KGV, Yasumura T, Kamasawa N, Nagy JI (2007a) Identification of connexin36 in gap junctions between neurons in rodent locus coeruleus. Neuroscience 147:938–956

Rash JE, Olson CO, Pouliot WA, Davidson KGV, Yasumura T, Furman CS, Royer S, Kamasawa N, Nagy JI, Dudek FE (2007b) Connexin36, miniature neuronal gap junctions, and limited electrotonic coupling in rodent suprachiasmatic nucleus. Neuroscience 149:350–371

Rubin JB, Verselis VK, Bennett MV, Bargiello TA (1992) Molecular analysis of voltage dependence of heterotypic gap junctions formed by connexins26 and 32. Biophys J 62:183–195

Scherer SS, Deschenes SM, Xu YT, Grinspan JP, Fischbeck KH, Paul DL (1995) Connexin32 is a myelin-related protein in the PNS and CNS. J Neurosci 15:8281–8294

Schubert T, Maxeiner S, Kruger O, Willecke K, Weiler R (2005) Connexin45 mediates gap junctional coupling of bistratified ganglion cells in the mouse retina. J Comp Neurol 490:29–39

Sempere L, Freemantle S, Pitha-Rowe I, Moss E, Dmitrovsky E, Ambros V (2004) Expression profiling of mammalian microRNAs uncovers a subset of brain-expressed microRNAs with possible roles in murine and human neuronal differentiation. Genome Biol 5:R13

Sosinsky G (1995) Mixing of connexins in gap junction membrane channels. Proc Natl Acad Sci USA 92:9210–9214

Teubner B, Degen J, Sohl G, Guldenagel M, Bukauskas FF, Trexler EB, Verselis VK, DeZeeuw CI, Lee CG, Kozak CA, Petrasch-Parwez E, Dermietzel R, Willecke K (2000) Functional expression of the murine connexin36 gene coding for a neuron-specific gap junctional protein. J Membr Biol 176:249–262

Teubner B, Odermatt B, Guldenagel M, Sohl G, Degen J, Bukauskas FF, Kronengold J, Veselis VK, Jung YT, Kosak CA, Schilling K, Willecke K (2001) Functional expression of the new gap junction gene connexin47 transcribed in mouse brain and spinal cord neurons. J Neurosci 21:1117–1126

Tress O, Maglione M, Zlomuzica A, May D, Dicke N, Degen J, Dere E, Kettenmann H, Hartmann D, Willecke K (2011) Pathologic and phenotypic alterations in a mouse expressing a connexin47 missense mutation that causes Pelizaeus–Merzbacher-like disease in humans. PLoS Genet 7:e1002146

Uhlenberg B, Schuelke M, Ruschendorf F, Rug N, Kaindl AM, Henneke M, Thiele H, Stoltenburg-Didinger G, Aksu F, Topaloglu H, Hubner C, Weschke B, Gartner J (2004) Mutations in the gene encoding gap junction protein alpha 12 (connexin46.6) cause Pelizaeus–Merzbacher-like disease. Am J Hum Genet 75:251–260

van der Knaap MS, Naidu S, Breiter SN, Blaser S, Stroink H, Springer S, Begeer JC, van Coster R, Barth PG, Thomas NH, Valk J, Powers JM (2001) Alexander disease: diagnosis with MR imaging. Am J Neuroradiol 22:541–552

Venance L, Rosov A, Blatow M, Burnashev N, Feldmeyer D, Monyer H (2000) Connexin expression in electrically coupled postnatal rat brain neurons. Proc Natl Acad Sci USA 97:10260–10265

Verselis VK, Ginter CS, Bargiello TA (1994) Opposite voltage gating polarities of two closely related connexins. Nature 368:348–351

Willecke K, Eiberger J, Degen J, Eckardt D, Romualdi A, Guldenagel M, Deutsch U, Soehl G (2002) Structural and functional diversity of connexin genes in the mouse and human genome. Biol Chem 383:725–737

Yamamoto T, Ochalski A, Hertzberg EL, Nagy JI (1990a) LM and EM immunolocalization of the gap junctional protein connexin43 in rat brain. Brain Res 508:313–319

Yamamoto T, Ochalski A, Hertzberg EL, Nagy JI (1990b) On the organization of astrocytic gap junctions in the brain as suggested by LM and EM immunocytochemistry of connexin43 expression. J Comp Neurol 302:853–883

Zhang C (2010) Gap junctions in olfactory neurons modulate olfactory sensitivity. BMC Neurosci 11:108–123

Zhang C, Finger TE, Restrepo D (2000) Mature olfactory receptor neurons express connexin43. J Comp Neurol 426:1–12

J Membrane Biol (2012) 245:345–355
DOI 10.1007/s00232-012-9455-1

Characterization of Gap Junction Proteins in the Bladder of Cx43 Mutant Mouse Models of Oculodentodigital Dysplasia

R. Lorentz · Q. Shao · T. Huang · G. I. Fishman · D. W. Laird

Received: 9 April 2012 / Accepted: 8 June 2012 / Published online: 3 July 2012

Abstract Oculodentodigital dysplasia (ODDD) is a rare developmental disease resulting from germline mutations in the *GJA1* gene that encodes the gap junction protein connexin43 (Cx43). In addition to the classical ODDD symptoms that affect the eyes, teeth, bone and digits, in some cases ODDD patients have reported bladder impairments. Thus, we chose to characterize the bladder in mutant mouse models of ODDD that harbor two distinct Cx43 mutations, G60S and I130T. Histological assessment revealed no difference in bladder detrusor wall thickness in mutant compared to littermate control mice. The overall localization of Cx43 in the lamina propria and detrusor also appeared to be similar in the bladders of mutant mice with the exception that the G60S mice had more instances of intracellular Cx43. However, both mutant mouse lines exhibited a significant reduction in the phosphorylated P1 and P2 isoforms of Cx43, while only the I130T mice exhibited a reduction in total Cx43 levels. Interestingly, Cx26 levels and distribution were not altered in mutant mice as it was localized to intracellular compartments and restricted to the basal cell layers of the urothelium. Our studies suggest that these two distinct genetically modified mouse models of ODDD probably mimic patients who lack bladder defects or other factors, such as aging or co-morbidities, are necessary to reveal a bladder phenotype.

Keywords Connexin · Cx43 · Mutant · Bladder · Mutant mouse · Gap junction

R. Lorentz · Q. Shao · T. Huang · D. W. Laird (✉)
Department of Anatomy and Cell Biology,
Western University, London, ON, Canada
e-mail: dale.laird@schulich.uwo.ca

G. I. Fishman
Leon H. Charney Division of Cardiology, New York University School of Medicine, New York, NY, USA

Introduction

Overactive bladder (OAB) is a syndrome that affects millions of men and women worldwide, generally manifesting itself in some degree of incontinence. Stress-related incontinence is caused by increased intra-abdominal pressure, resulting from physical activity or coughing/sneezing. Urge-related incontinence can be subdivided into neurogenic and idiopathic types. The neurogenic type is related to altered afferent and efferent neuronal bladder stimuli, which is common in conditions such as spinal cord injury, Parkinson disease and multiple sclerosis (Christ et al. 2003). Idiopathic incontinence has no known pathological cause (Christ et al. 2003; Miller and Hoffman 2006); however, there is a growing body of evidence to suggest a myogenic origin for at least some forms (Brading 1997; Haferkamp et al. 2004). It has been proposed that altered gap junctional intercellular communication (GJIC) or cell signaling may be the cause of idiopathic incontinence, resulting in an increased sensitivity to acetylcholine or changes in how cells communicate (Imamura et al. 2009; Kuhn et al. 2008).

Gap junctions are formed from specialized proteins known as connexins (Cxs). Six connexins that have oligomerized to form a connexon are delivered to the plasma membrane, where they can function as a hemichannel or dock to a connexon from an adjacent cell to form a gap junction channel (Laird 2006). Hemichannels and gap

junction channels can selectively pass small molecules of <1 kDa in size to the extracellular matrix or between connected cytoplasms, respectively (Alexander and Goldberg 2003; Evans et al. 2006). The selectivity of a gap junction channel or hemichannel is highly dependent on its connexin constituents. The 21 human and 20 mouse connexins all share similar membrane topologies and can selectively intermix to create a plethora of channel variations that exhibit unique characteristics (Laird 2005, 2006; Sohl and Willecke 2003).

In the bladder, the urothelial layer is composed of transitional epithelium, which acts as a passive barrier and actively responds to urine composition and bladder distension (Apodaca 2004). ATP, which is known to be released from the urothelium, is thought to signal adjacent urothelial cells and/or bladder nerves through P2X receptor stimulation within the underlying lamina propria, therefore acting in both an autocrine and a paracrine fashion (Apodaca 2004; Cockayne et al. 2000). Both Cx26 and Cx43 have been localized to the urothelium, although their roles in bladder function have yet to be elucidated (Grossman et al. 1994; Haefliger et al. 2002). The lamina propria, composed of loose fibroelastic connective tissue, expresses Cx43, which is localized to fibroblasts and myofibroblasts (Fry et al. 2007; Neuhaus et al. 2007; Sui et al. 2002; Wiseman et al. 2003). Myofibroblasts have been shown to be in close proximity with both afferent and efferent neurons and are therefore thought to aid in bladder signaling (Sui et al. 2002; Wiseman et al. 2003). The detrusor layer of the bladder is composed of smooth muscle cells that express both Cx43 and Cx45, which collectively act to facilitate bladder contractions (Heinrich et al. 2011; Ikeda et al. 2007). Specifically, Cx43 has been localized to the border of smooth muscle cell bundles, suggesting its importance in the transmission of electrical stimulus from one muscle bundle to the next, while Cx45 has been localized to the plasma membrane of cells within the muscle bundles (Hashitani et al. 2004; John et al. 2003; Sui et al. 2003).

To date, over 65 mutations in the gene encoding Cx43 have been linked to the rare autosomal dominant disease oculodentodigital dysplasia (ODDD) (Paznekas et al. 2003, 2009). All mutants examined to date have been shown to have reduced channel function and to act as dominant-negatives to the function of coexpressed wild-type Cx43 (Gong et al. 2007; McLachlan et al. 2005; Roscoe et al. 2005). Patients harboring Cx43 mutants share common clinical characteristics, such as syndactyly and camptodactyly of the digits, microdontia, enamel loss, ophthalmic defects and craniofacial abnormalities (Paznekas et al. 2003, 2009). Bladder defects have been reported in ~12 % of ODDD patients, although the mechanism behind these defects remains poorly understood (Loddenkemper et al. 2002; Paznekas et al. 2003, 2009). Although the percentage of ODDD patients suffering from bladder defects appears lower than that in the general population at ~17 % (Abrams et al. 2003), many of these patients develop bladder defects early in life (Paznekas et al. 2003, 2009), a trait rarely seen in the general population. Since Cx43 is broadly distributed throughout the bladder and is thought to play a critical role in bladder contraction, we hypothesized that the reason ODDD patients suffer from bladder problems may be rooted in how specific ODDD-linked mutants affect the distribution and function of Cx43-based gap junctions within the bladder. To test this hypothesis, we employed two heterozygous Cx43 mutant mouse lines harboring the G60S or I130T mutant (Flenniken et al. 2005; Kalcheva et al. 2007). Upon examination of several cell types obtained from these mice, all were found to exhibit reduced Cx43-based GJIC and the mutant proteins were found to act as dominant-negatives to coexpressed wild-type Cx43 (Flenniken et al. 2005; Kalcheva et al. 2007; Lai et al. 2006; Manias et al. 2008; Shibayama et al. 2005). In the present study, we examined the distribution and spatial localization of Cx43 in the bladders of these two Cx43 mutant mouse lines to assess if Cx43 was perturbed in a manner that might suggest the bladder is functionally compromised.

Materials and Methods

Animals

Animal studies were conducted on two mutant mouse lines harboring heterozygous mutations, G60S or I130T, in the gene *Gja1*, which encodes Cx43. Therefore, the mice are expected to translate a 1:1 ratio of mutant to wild-type Cx43 protein and, thus, genetically match human ODDD patients. G60S, also known as $Gja1^{Jrt/+}$, mice were supplied by the Centre for Modeling Human Disease, University of Toronto (Toronto, Canada), on a mixed C57BL/6J and C3H/HeJ background (Flenniken et al. 2005). After confirming 100 % penetrance of the syndactyly feature in all mutant mice as determined by PCR genotyping (Flenniken et al. 2005), genotype determination was completed by visual inspection of the pups. I130T, also known as $Gja1^{I130T/+}$, mice were obtained from Dr. Glenn Fishman (New York University School of Medicine, New York, NY). These mice, which were on a mixed CD1/C57BL6 background, were further backcrossed onto a C57BL6 background for an additional one to three generations. A 100 % incidence rate of syndactyly ($n = 203$) in I130T mice was confirmed by PCR genotyping. However, while syndactyly was found on the front limbs of all mice, the back limbs did not always exhibit this phenotype.

Tissue Harvesting and Preparation

Whole bladder, heart and liver samples were collected from G60S, I130T and wild-type littermate mice at 3 months of age. All mice used in this study were killed using a carbon dioxide chamber followed by cervical dislocation, in accordance with the University of Western Ontario Guide for Care and Use of Laboratory Animals. Tissue samples assigned to hematoxylin and eosin (H and E) staining were fixed overnight at 4 °C in 10 % neutral buffered formalin (NFB) (EMD, Mississauga, Canada), dehydrated, embedded in paraffin blocks and sectioned longitudinally at 5-μm intervals. Tissue samples assigned to immunohistochemistry were snap-frozen in liquid nitrogen; embedded in 10.2 % polyvinyl alcohol, 4.3 % polyethylene glycol Optimal Cutting Temperature Compound (Sakura, Torrance, CA); sectioned longitudinally at 5 μm thickness; and stored at −80 °C. Tissue samples assigned to immunoblotting were snap-frozen in liquid nitrogen and stored at −80 °C for future use.

Histology

To assess the histology of the mouse bladders, 5-μm paraffin-embedded sections from G60S and I130T mice and their wild-type littermates were stained with H (0.4 %) and E (0.5 %). Briefly, paraffin-embedded bladder sections were deparaffinized in xylene, rehydrated in a descending gradient of ethanol baths and stained with hematoxylin (5 min), then washed and stained with eosin (5 min). Sections were then dehydrated in an ascending gradient of ethanol baths followed by xylene and mounted with Cytoseal (Thermo Scientific, Rockford, IL). Bladder sections were imaged on a Leica (Deerfield, IL) DM IRE2 inverted microscope equipped with a Micropublisher 5.0 RTV CCD color, cooled camera. Linear measurements were made perpendicularly through the detrusor layer using ImageJ software (http://rsbweb.nih.gov/ij/). In total, 405 measurements were made on each of four bladders from G60S and I130T mice and their wild-type littermates, corresponding to three slides per mouse, nine sections per slide and 15 measurements per section. Statistical analysis included standard error and comparison between G60S and I130T mice and their wild-type littermates.

Immunofluorescence

To assess the localization of Cx43 and Cx26 in mouse bladders, hearts and livers, 5-μm cryosections from G60S and I130T mice and their wild-type littermates were first fixed in 10 % NBF for 30 min at room temperature. Tissues sections were blocked with 3% BSA (Sigma-Aldrich, St. Louis, MO) and 0.02 % Triton X-100 in PBS for 45 min at room temperature. Cx43, Cx26 and actin were all detected using rabbit anti-Cx43 (2 μg/ml, Sigma C6219), rabbit anti-Cx26 (0.5 μg/ml; Invitrogen 51-2800; Invitrogen, Carlsbad, CA) and mouse anti-phalloidin (2 U/ml, Invitrogen A12379), respectively. All antibodies were diluted in PBS containing 3 % BSA and 0.02 % Tween-20 and allowed to incubate on tissue sections for 1 h. After repeated washings with PBS, tissues were incubated with secondary anti-rabbit AlexaFluor 555 antibody (4 μg/ml, Invitrogen A-21428), followed by repeated washings. Nuclear staining was performed using Hoechst 33342 (10 μg/ml; Molecular Probes, Eugene, OR) for 5 min at room temperature, followed by a 5-min wash with ddH_2O. Tissues sections were mounted using glass coverslips and allowed to sit overnight at 4 °C. Tissue sections were imaged on a Zeiss (Thornwood, NY) LSM 510 Meta confocal microscope as previously described (Roscoe et al. 2005). Digital images were prepared using Zeiss LSM and CorelDraw 12 software.

To quantify the percentage of cells in the detrusor layer of wild-type and G60S mice that exhibited intracellular Cx43, we randomly selected 10 fields (215 × 215 μm) from immunofluorescently labeled Cx43 bladder sections. The total number of Cx43-positive cells in the detrusor layer per field was counted, as was the number of cells that displayed primarily paranuclear Cx43 staining indicative of intracellular Cx43. The total number of Cx43-positive cells was divided by the number of intracellular Cx43-positive cells from wild-type and G60S mouse bladder sections. Data are presented as the mean percent of cells displaying intracellular Cx43 ± SEM ($^{**}P < 0.01$).

Western Blot Analysis

Tissue samples stored at −80 °C were homogenized in RIPA lysis buffer (50 mM Tris-HCl [pH 8.0], 150 mM NaCl, 1.0 % Triton X-100, 0.5 % sodium deoxycholate, 0.1 % SDS, 1 mM sodium orthovanadate, 1 mM sodium fluoride), and homogenates were removed from cell debris via a 10-min, 6,000-rpm centrifugation at 4 °C.

Immunoblotting was performed as previously described (Gehi et al. 2011) using 10 or 12 % SDS-PAGE. Cx43, Cx26 and GAPDH were detected using polyclonal rabbit anti-Cx43 (0.02 μg/ml, Sigma C6219), polyclonal rabbit anti-Cx26 (0.05 μg/ml, Invitrogen 710500) and polyclonal mouse anti-GAPDH (1 μg/ml; Millipore, Temecula, CA), respectively. Primary antibodies were detected using either anti-rabbit AlexaFluor 680 (0.2 μg/ml, Invitrogen) or anti-mouse IRDye 800 (1:10,000; Rockland, Gilbertsville, PA) antibodies. Membranes were developed using an Odyssey infrared imaging system (LiCor, Lincoln, NE) and analyzed under unsaturated conditions using Odyssey 2.0.4 software (Licor).

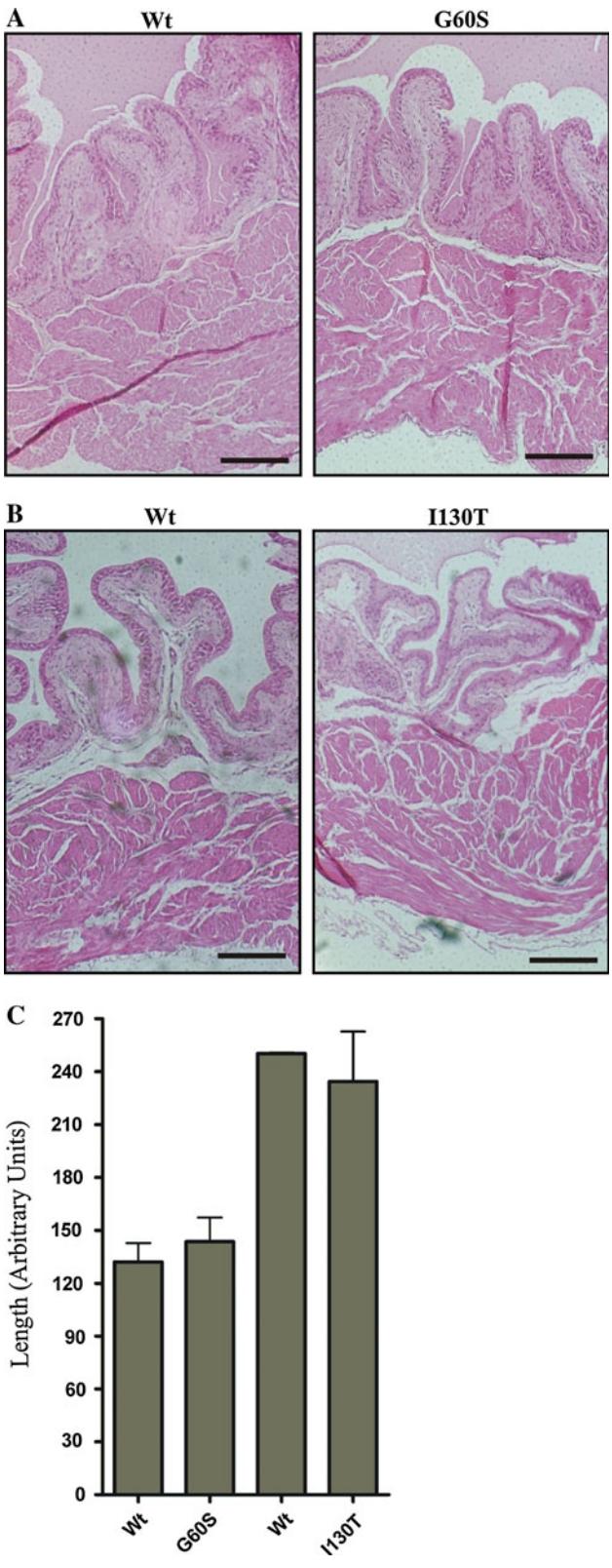

Fig. 1 G60S and I130T mouse bladders have similar histology and detrusor thickness as their wild-type littermate controls. Paraffin-embedded bladders were sectioned, stained with H and E and measured for detrusor thickness. In all mice, bladder histology was similar between mutant and matched wild-type (*Wt*) littermate controls (**a**, **b**). Subsequent detrusor measurements revealed that G60S and I130T mouse bladders have similar detrusor thicknesses as their respective wild-type littermates (**c**). *Bars* 200 μm (**a**, **b**), *error bars* ± SEM (**c**). $n = 4$ mice

Statistics

All results were analyzed using Student's two-tailed independent sample *t*-test, using a $P < 0.05$ value to denote significance. All results were analyzed using GraphPad (San Diego, CA) Prism 4.03 software and are presented as mean ± standard error.

Results

G60S and I130T Bladders Have Similar Histology and Detrusor Thickness as Wild-Type Littermates

Increased detrusor thickness is a known indicator of OAB syndrome, a condition commonly seen in patients suffering from bladder abnormalities (Miyazato et al. 2009; Uvelius et al. 1984). H and E staining revealed that G60S and I130T mice display similar bladder histology as seen in wild-type littermate controls, with no disruption in any of the three bladders layers (Fig. 1a, b). Subsequent detrusor measurements revealed that detrusor thickness was similar between G60S and I130T mutant mice and their respective wild-type littermate controls (Fig. 1c). It is likely that the difference in detrusor thickness between wild-type mice used as controls is due, at least in part, to differences in the mouse strains.

G60S and I130T Bladders Have Reduced Levels of the Highly Phosphorylated Cx43 Species

Previous studies have indicated that total Cx43 levels and levels of the highly phosphorylated Cx43 species are reduced in various tissues of the G60S mouse (Flenniken et al. 2005; Manias et al. 2008; Tong et al. 2009; Toth et al. 2010), while aside from heart, much less is known about the Cx43 species status in I130T mice. Western blots were used to assess the levels and phosphorylation status of Cx43 in the mutant mouse bladders. As positive and negative controls, Cx43 was examined in heart and liver lysates, respectively, from wild-type mice. Cx43 generally resolves in SDS-PAGE as multiple bands representing different phosphorylated species (P0, P1 and P2). Immunoblotting for Cx43 in lysates from G60S and I130T mice and their wild-type littermates revealed low levels in the bladder samples of all mice (Fig. 2a–c). Quantification revealed that total Cx43 levels were reduced in I130T mice, while levels remained similar in G60S mice

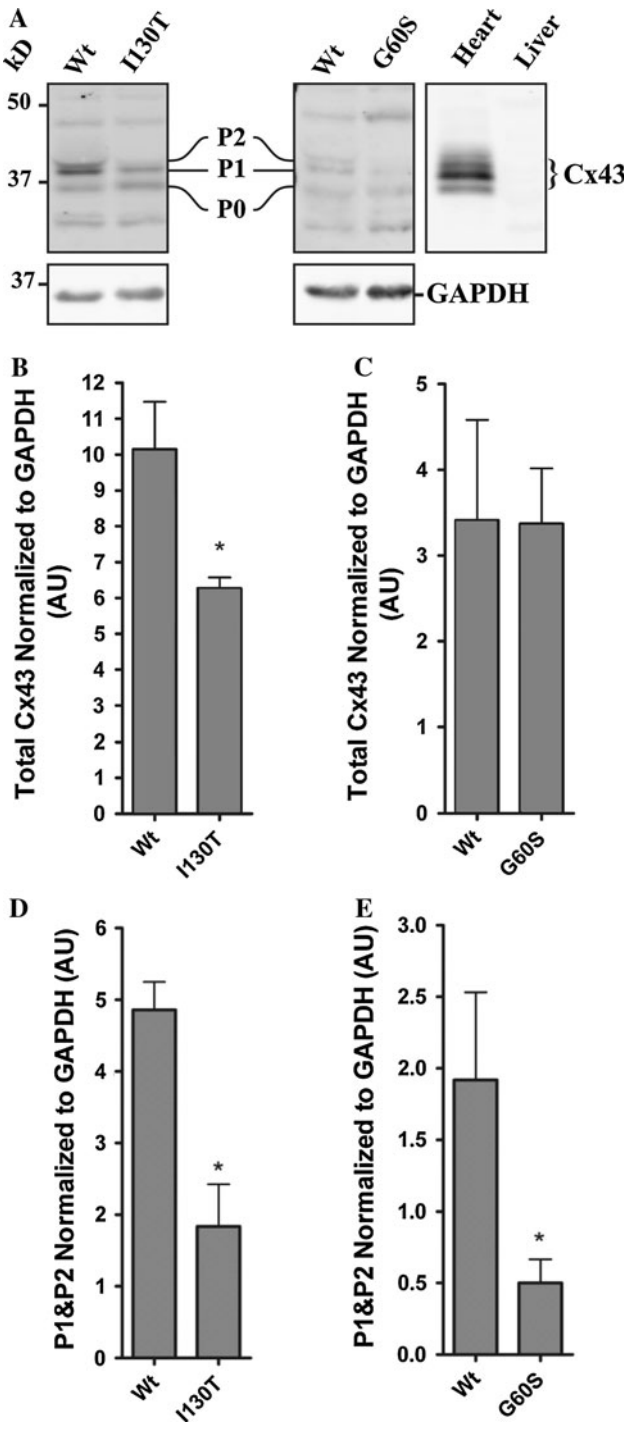

Fig. 2 G60S and I130T mouse bladders exhibit a reduction in the phosphorylated species of Cx43. Cx43 normally resolves as a triplet band representing different phosphorylated species of Cx43 (P0, P1 and P2), as seen in heart tissue (**a**). Cx43 was detected in the bladders of G60S and I130T mutant mice, as well as in wild-type (*Wt*) littermate mouse bladders but not in the mouse liver (**a**). Total Cx43 (P0, P1 and P2) expression was lower in I130T mouse bladders compared to littermate controls (**b**), a condition not observed in G60S mouse bladders (**c**). Lower levels of the phosphorylated Cx43 species (P1 and P2) were found in I130T (**d**) and G60S (**e**) mouse bladders compared to wild-type littermates. Nonspecific bands were noted at ~47–50 and ~30 kDa. *Bars* represent ±SEM (**b**–**e**). $*P < 0.05$. $n = 5$ (I130T mice) and 6 (G60S mice). *AU* arbitrary units

compared to their wild-type littermates (Fig. 2b, c). Further analysis revealed that the slower-migrating Cx43 P1 and P2 species were reduced in both G60S and I130T mice compared to their wild-type littermates (Fig. 2d, e). These phosphorylated Cx43 species have previously been correlated with fully assembled gap junction plaques and channel function. Immunoblotting also revealed nonspecific bands at ~47–50 and ~30 kDa in lysates from all bladder samples. Although these bands were present in only the bladder samples, it is unclear as to what they represent; therefore, they were not quantified.

Cx43 Distribution in the Lamina Propria and Detrusor Layers of Wild-Type and Mutant Mice

As a result of reduced Cx43 phosphorylated species detected in bladder lysates of G60S and I130T mice, we postulated that Cx43 localization and/or distribution may be disrupted in the bladder. Immunofluorescence revealed that Cx43 was highly expressed in the lamina propria of G60S and I130T mice, similar to their wild-type littermates (Fig. 3a, b). The Cx43 distribution at sites of cell to cell apposition in I130T and G60S mice appeared similar to that found in wild-type littermates (Fig. 3a, b, arrowheads). However, G60S mice exhibited significantly more intracellular Cx43 distribution, which was not readily detected in wild-type littermates (Fig. 3a, histogram). Immunofluorescence also revealed that Cx43 was localized to smooth muscle cells and fibroblasts surrounding smooth muscle bundles as revealed by F-actin localization in the detrusor layer of both mutant mice and their wild-type littermates (Fig. 4a, b). Thus, in both wild-type and mutant mice Cx43 was appropriately positioned in the muscle of the detrusor layer to allow for regulated bladder contraction.

G60S and I130T Mouse Bladders Have Similar Cx26 Levels as Wild-Type Littermate Control Mice

The bladder urothelium has previously been shown to express Cx26, and it is thought to play a role in bladder signaling during filling (Ikeda et al. 2007). As controls, Cx26 was detected in liver lysates, while it was absent in heart lysates from wild-type mice (Fig. 5a). Cx26 generally resolves in SDS-PAGE at ~21 kDa, with a dimer species appearing in the liver at ~35–37 kDa. Immunoblotting of Cx26 in bladder lysates from G60S and I130T mice and their wild-type littermates revealed low

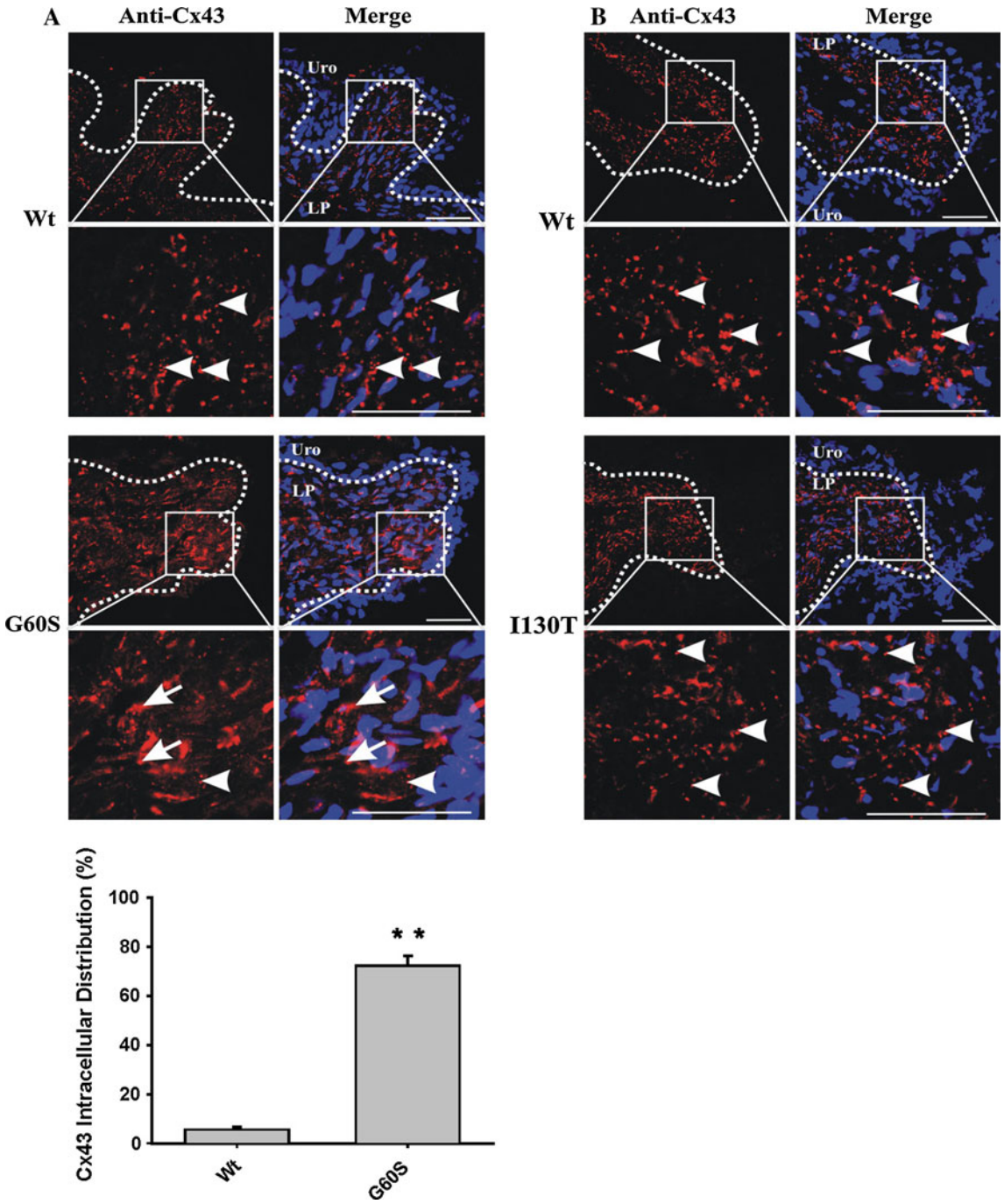

Fig. 3 The distribution of Cx43 in the lamina propria of wild-type and mutant mice. Cx43 was localized in the lamina propria of G60S (**a**) and I130T (**b**) mutant mice and compared to wild-type (*Wt*) littermate mouse bladder controls. G60S mouse bladders displayed significantly more intracellular Cx43 (*arrows*), as opposed to the punctate distribution (*arrowheads*) seen in wild-type littermates (**a**, histogram). I130T mouse bladders displayed a similar punctate Cx43 distribution pattern (*arrowheads*) as seen in wild-type littermates (**b**). *Uro* urothelium, *LP* lamina propria. *Red* indicates Cx43, *blue* indicates Hoechst nuclear stain. *Bars* 50 μm. *Histogram error bars* represent ±SEM. $^{**}P < 0.01$

levels in all mice (Fig. 5a). Quantification revealed similar Cx26 levels in the bladders of G60S and I130T mice compared to their wild-type littermates (Fig. 5b, c). Immunoblotting also revealed nonspecific bands located at ~32–34 kDa in lysates from all bladder samples. Although the band was present in only the bladder samples, it is unclear as to what this band represents; therefore, it was not quantified.

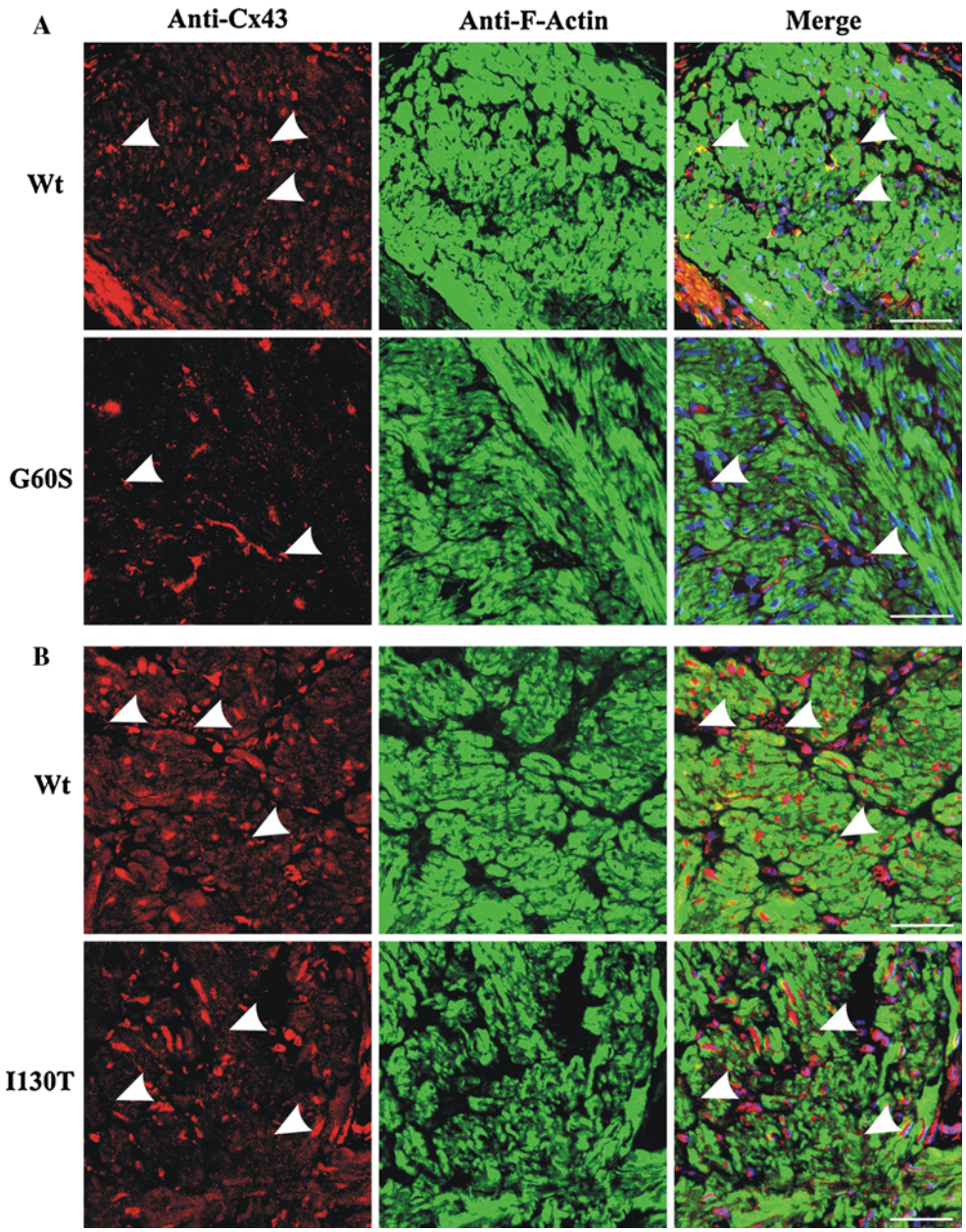

Fig. 4 Cx43 was localized to resident cell types of the detrusor in G60S and I130T mutant mice and their wild-type littermates. In the detrusor layer, immunolabeling revealed that Cx43 was predominantly localized to cells of connective tissue surrounding smooth muscle bundles and smooth muscle cells in G60S (**a**) and I130T (**b**) mice and their respective wild-type (*Wt*) littermates. Cx43 displays punctate structures (*arrowheads*) in G60S (**a**), I130T (**b**) and wild-type littermates. *Red* indicates Cx43, *green* indicates F-actin, and *blue* indicates Hoechst nuclear stain. *Bar* 50 μm

Cx26 Is Localized to Intracellular Compartments in the Basal Urothelium of Mutant Mice and Wild-Type Littermates

Immunoblotting revealed that Cx26 levels remain similar between wild-type and mutant mice; however, it was unclear if Cx26 localization and/or distribution were altered. As a positive control Cx26 was clearly detected at the cell–cell apposition of liver hepatocytes (data not shown). Immunofluorescence revealed that Cx26 was predominantly localized to the basal urothelium in G60S and I130T mutant mice and their wild-type littermate controls (Fig. 6a, b). Surprisingly, Cx26 was localized to intracellular locations and not, as expected, to intercellular boundaries.

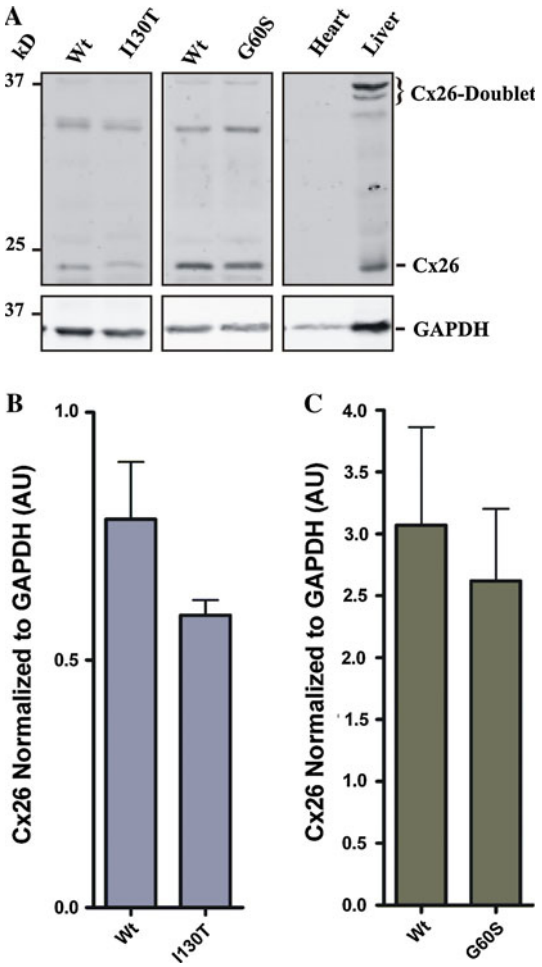

Fig. 5 G60S and I130T mutant mouse bladders have similar Cx26 levels as wild-type littermates. Cx26 generally resolves at ~21 kDa, with the dimer resolving at ~37 kDa as seen in liver lysates (**a**). G60S, I130T and wild-type (*Wt*) littermate mouse bladders were all positive for Cx26 expression (**a**). Total Cx26 expression was similar in I130T and G60S mice and their wild-type littermates (**b**, **c**). A nonspecific band located at ~32–34 kDa was noted. *Bars* represent ±SEM (**b**, **c**). $n = 5$ (I130T mice) and 6 (G60S mice)

Discussion

GJIC is thought to contribute to normal bladder function by allowing for coordinated contraction and ejection of urine from the bladder lumen (Fry et al. 2007; Hashitani et al. 2004; Neuhaus et al. 2007; Sui et al. 2002). Cx43 is the most prevalent connexin expressed in the bladder as it is found in both the lamina propria and the detrusor layer (Fry et al. 2007; Neuhaus et al. 2007; Sui et al. 2002, 2003; Wang et al. 2006). Therefore, any alteration in Cx43 function may ultimately lead to bladder defects. ODDD patients are prime candidates for dysfunctional bladders as Cx43 function in the bladder is expected to be well below 50 % given that these patients harbor loss-of-function Cx43 mutants that dominantly inhibit coexpressed wild-type Cx43 (Churko et al. 2011; Flenniken et al. 2005; Manias et al. 2008; Tong et al. 2009; Toth et al. 2010). Bladder impairments in ODDD patients often do not manifest until the second half of life (Goepel et al. 2010), long after the original diagnosis of ODDD. However, other ODDD patients suffer from bladder defects at a young age, a condition rarely found in the general population (Paznekas et al. 2003, 2009). It remains possible that the number of ODDD patients with bladder impairment is under-reported as symptoms may not be archived as an ODDD-associated disease. It is also not clear if only some ODDD-associated Cx43 mutations result in bladder impairments and whether the location of the mutation, the resulting amino acid change and/or the patient's genetic background all contribute to the development of bladder impairment. Adding to the complexity, it is further unclear if bladder abnormalities reported by ODDD patients are due to neurogenic or myogenic defects (Christ et al. 2003; Haefliger et al. 2002). In the present study we assessed connexin status in the bladders of two genetically distinct Cx43 mutant mouse models of ODDD (G60S and I130T) and found that mice harboring systemic Cx43 mutants have an anatomically and histologically normal bladder even though Cx43 exists primarily as a species that is incompletely phosphorylated.

Characterization of Cx43 in the Bladder of G60S and I130T Mutant Mice

Bladder abnormalities have been reported in ~12 % of ODDD patients and, in a couple of cases, have been putatively linked to neurological defects (Paznekas et al. 2003, 2009). However, there is increasing evidence that suggests some bladder abnormalities are the result of myogenic defects (Christ et al. 2003; Haefliger et al. 2002). Past reports have localized Cx43 within the lamina propria and detrusor layers of the bladder, and other studies have linked Cx43-based gap junctions to various bladder syndromes (Christ et al. 2003; Mori et al. 2005; Neuhaus et al. 2007). It therefore remains possible that ODDD mutants which disrupt Cx43 function (Churko et al. 2011; Dobrowolski et al. 2007; Flenniken et al. 2005; Manias et al. 2008; Shibayama et al. 2005; Tong et al. 2009; Toth et al. 2010) may ultimately affect bladder function. In order to assess this possibility, we examined two Cx43 mutant mouse lines, G60S and I130T, both of which have been shown to phenotypically resemble ODDD patients (Flenniken et al. 2005; Kalcheva et al. 2007; Langlois et al. 2007; Toth et al. 2010); but it is unknown if they suffer from incontinence or any bladder abnormalities. Importantly, both mutant mice are predicted to possess a 1:1 ratio of mutant to wild-type Cx43, matching the genotype of human ODDD patients. As well, the two mutant mouse lines were generated on different genetic backgrounds, more readily mimicking the diverse genetic background of ODDD patients. Previous studies revealed that both mutant mouse

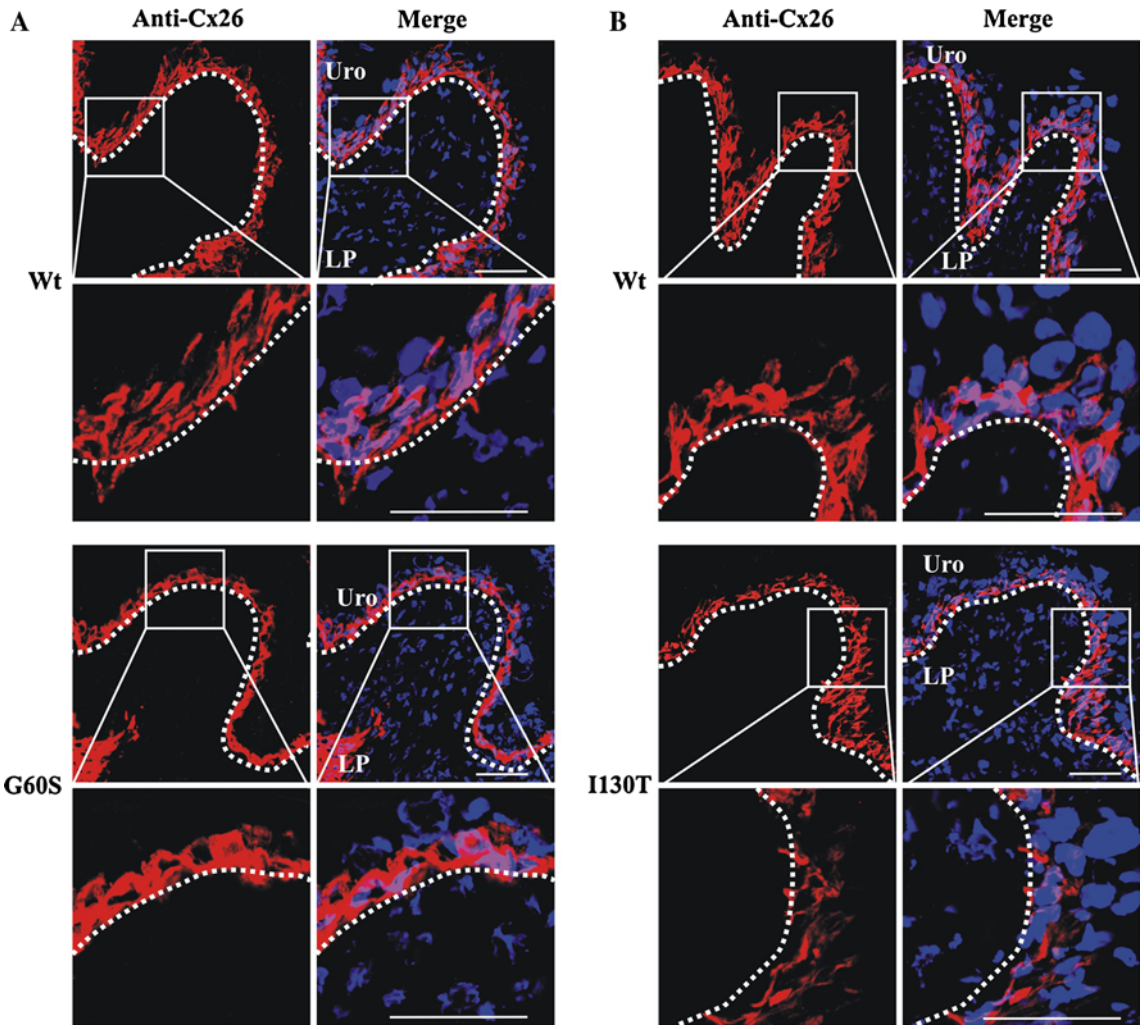

Fig. 6 Cx26 was localized to intracellular compartments of basal urothelial cells of mutant and wild-type (*Wt*) mice. Immunolabeling revealed that Cx26 was localized to intracellular compartments of the basal urothelium cells in all mice (**a**, **b**). *Uro* urothelium, *LP* lamina propria. *Red* indicates Cx26, and *blue* indicates Hoechst nuclear stain. *Bar* 50 μm

lines have altered tissue function and/or development (Flenniken et al. 2005; Kalcheva et al. 2007; Langlois et al. 2007; Toth et al. 2010); however, no studies have assessed the connexin status within the bladder. Here, we aimed to determine the connexin localization and expression profile as possible indicators of altered bladder function.

One of the simplest indicators of OAB syndrome is detrusor hypertrophy (Miyazato et al. 2009; Uvelius et al. 1984). Assessment of mutant mice and their wild-type counterparts revealed anatomically similar bladders as no differences were observed in the appearance or thickness of the detrusor layer. Within the lamina propria, we found Cx43-positive staining in all mice localized to a combination of fibroblasts and myofibroblasts. Myofibroblasts, in particular, are important in forming a functional syncytium for the rapid transmission of chemical and electrical stimuli, required for normal bladder function (Fry et al. 2007; Sui et al. 2002; Wiseman et al. 2003). Cx43 in the detrusor is thought to mediate the propagation of action potentials from one smooth muscle bundle to the next, allowing for a uniform bladder contraction (Hashitani et al. 2004). Our results revealed that while wild-type and all mutant mice displayed punctate, gap junction–like structures, G60S mutant mice frequently displayed a more diffuse intracellular Cx43 expression profile. This localization profile correlated with a reduction in the highly phosphorylated Cx43 species (P1 and P2), known to be important in gap junction plaque formation and GJIC (Solan and Lampe 2009). Interestingly, the I130T mouse bladders also exhibited a reduction in the highly phosphorylated Cx43 species, as well as reduced total Cx43 protein levels. Thus, we conclude that in both mutant mouse lines Cx43 does not likely form a complete complement of fully assembled functional gap junctions in the resident cells of the bladder, not unlike what is seen in other cell types that express ODDD-linked Cx43 mutants

(Churko et al. 2011; Dobrowolski et al. 2007; Flenniken et al. 2005; Manias et al. 2008; Shibayama et al. 2005; Tong et al. 2009; Toth et al. 2010).

Even though bladder abnormalities are most commonly linked to increases in Cx43 (Christ et al. 2003; Imamura et al. 2009; Mori et al. 2005), it remains possible that a reduction in Cx43 levels and/or a resulting decrease in GJIC may also alter bladder function. For instance, reduced GJIC may alter electrical and chemical stimulus propagation within the bladder, resulting in incomplete bladder contractions and increased residual urine levels, ultimately leading to increased urinary frequency. Additional behavioral studies are necessary to see if Cx43 mutant mice suffer from frequent urination and/or bladder leakage.

While our study revealed no Cx43 staining in the bladder urothelium, other groups have localized both Cx43 and Cx26 within this tissue layer (Grossman et al. 1994; Haefliger et al. 2002). Therefore, as a result of Cx26 being localized to the urothelial layer (Grossman et al. 1994; Haefliger et al. 2002; Ikeda et al. 2007), we speculated that Cx26 may be upregulated in the urothelium through potential signaling cross-talk mechanisms to compensate for the overall reduction in Cx43 function. The function of Cx26 within the urothelium is still unknown, although it has been proposed to play a role in signal transduction during bladder filling (Ikeda et al. 2007). Cx26 localization in the urothelium has been reported to be typically at sites of cell to cell apposition (Haefliger et al. 2002; Ikeda et al. 2007); however, similar to our findings, one group has reported the intracellular localization of Cx26 (Gee et al. 2003). Other reports have also indicated that Cx26 hemichannels can release ATP into the extracellular environment (Huckstepp et al. 2010; Majumder et al. 2010), which may alter bladder function. In our study, the levels of Cx26 were similar between the mutant and control groups. Interestingly, Cx26 displayed a unique intracellular urothelium expression profile localized to only the basal one or two cell layers of the urothelium, suggesting that few, if any, Cx26 gap junction channels or hemichannels are formed in these cell layers. The lack of Cx26 in the more luminally localized epithelial cells would suggest that Cx26 serves no role in the more differentiated cells of the urothelium. Nevertheless, we found no evidence that Cx26 was upregulated to compensate for the proposed reduction of Cx43 function in the bladder. Future studies will require the inclusion of additional mutant mice that harbor specific mutations that have strong linkages to patients with bladder abnormalities.

Acknowledgments The authors thank Kevin Barr for breeding and maintaining the genetically modified mice used in the current study. D.W.L. was funded by the Canadian Institutes of Health Research and the Canada Research Chair Program.

References

Abrams P, Cardozo L, Fall M, Griffiths D, Rosier P, Ulmsten U, Van Kerrebroeck P, Victor A, Wein A (2003) The standardisation of terminology in lower urinary tract function: report from the standardisation sub-committee of the International Continence Society. Urology 61:37–49

Alexander DB, Goldberg GS (2003) Transfer of biologically important molecules between cells through gap junction channels. Curr Med Chem 10:2045–2058

Apodaca G (2004) The uroepithelium: not just a passive barrier. Traffic 5:117–128

Brading AF (1997) A myogenic basis for the overactive bladder. Urology 50:57–73

Christ GJ, Day NS, Day M, Zhao W, Persson K, Pandita RK, Andersson KE (2003) Increased connexin43-mediated intercellular communication in a rat model of bladder overactivity in vivo. Am J Physiol Regul Integr Comp Physiol 284:R1241–R1248

Churko JM, Shao Q, Gong XQ, Swoboda KJ, Bai D, Sampson J, Laird DW (2011) Human dermal fibroblasts derived from oculodentodigital dysplasia patients suggest that patients may have wound-healing defects. Hum Mutat 32:456–466

Cockayne DA, Hamilton SG, Zhu QM, Dunn PM, Zhong Y, Novakovic S, Malmberg AB, Cain G, Berson A, Kassotakis L, Hedley L, Lachnit WG, Burnstock G, McMahon SB, Ford AP (2000) Urinary bladder hyporeflexia and reduced pain-related behaviour in P2X3-deficient mice. Nature 407:1011–1015

Dobrowolski R, Sommershof A, Willecke K (2007) Some oculodentodigital dysplasia–associated Cx43 mutations cause increased hemichannel activity in addition to deficient gap junction channels. J Membr Biol 219:9–17

Evans WH, De Vuyst E, Leybaert L (2006) The gap junction cellular internet: connexin hemichannels enter the signalling limelight. Biochem J 397:1–14

Flenniken AM, Osborne LR, Anderson N, Ciliberti N, Fleming C, Gittens JE, Gong XQ, Kelsey LB, Lounsbury C, Moreno L, Nieman BJ, Peterson K, Qu D, Roscoe W, Shao Q, Tong D, Veitch GI, Voronina I, Vukobradovic I, Wood GA, Zhu Y, Zirngibl RA, Aubin JE, Bai D, Bruneau BG, Grynpas M, Henderson JE, Henkelman RM, McKerlie C, Sled JG, Stanford WL, Laird DW, Kidder GM, Adamson SL, Rossant J (2005) A Gja1 missense mutation in a mouse model of oculodentodigital dysplasia. Development 132:4375–4386

Fry CH, Sui GP, Kanai AJ, Wu C (2007) The function of suburothelial myofibroblasts in the bladder. Neurourol Urodyn 26:914–919

Gee J, Tanaka M, Grossman HB (2003) Connexin 26 is abnormally expressed in bladder cancer. J Urol 169:1135–1137

Gehi R, Shao Q, Laird DW (2011) Pathways regulating the trafficking and turnover of pannexin1 protein and the role of the C-terminal domain. J Biol Chem 286:27639–27653

Goepel M, Kirschner-Hermanns R, Welz-Barth A, Steinwachs KC, Rubben H (2010) Urinary incontinence in the elderly: part 3 of a series of articles on incontinence. Dtsch Arztebl Int 107:531–536

Gong XQ, Shao Q, Langlois S, Bai D, Laird DW (2007) Differential potency of dominant negative connexin43 mutants in oculodentodigital dysplasia. J Biol Chem 282:19190–19202

Grossman HB, Liebert M, Lee IW, Lee SW (1994) Decreased connexin expression and intercellular communication in human bladder cancer cells. Cancer Res 54:3062–3065

Haefliger JA, Tissieres P, Tawadros T, Formenton A, Beny JL, Nicod P, Frey P, Meda P (2002) Connexins 43 and 26 are differentially increased after rat bladder outlet obstruction. Exp Cell Res 274:216–225

Haferkamp A, Mundhenk J, Bastian PJ, Reitz A, Dorsam J, Pannek J, Schumacher S, Schurch B, Buttner R, Muller SC (2004) Increased expression of connexin 43 in the overactive neurogenic detrusor. Eur Urol 46:799–805

Hashitani H, Yanai Y, Suzuki H (2004) Role of interstitial cells and gap junctions in the transmission of spontaneous Ca^{2+} signals in detrusor smooth muscles of the guinea-pig urinary bladder. J Physiol 559:567–581

Heinrich M, Oberbach A, Schlichting N, Stolzenburg JU, Neuhaus J (2011) Cytokine effects on gap junction communication and connexin expression in human bladder smooth muscle cells and suburothelial myofibroblasts. PLoS ONE 6:e20792

Huckstepp RT, Bihi R, Eason R, Spyer KM, Dicke N, Willecke K, Marina N, Gourine AV, Dale N (2010) Connexin hemichannel-mediated CO_2-dependent release of ATP in the medulla oblongata contributes to central respiratory chemosensitivity. J Physiol 588:3901–3920

Ikeda Y, Fry C, Hayashi F, Stolz D, Griffiths D, Kanai A (2007) Role of gap junctions in spontaneous activity of the rat bladder. Am J Physiol Renal Physiol 293:F1018–F1025

Imamura M, Negoro H, Kanematsu A, Yamamoto S, Kimura Y, Nagane K, Yamasaki T, Kanatani I, Ito N, Tabata Y, Ogawa O (2009) Basic fibroblast growth factor causes urinary bladder overactivity through gap junction generation in the smooth muscle. Am J Physiol Renal Physiol 297:F46–F54

John H, Wang X, Hauri D, Maake C (2003) Gap junctions in the human urinary bladder [in German]. Aktuel Urol 34:328–332

Kalcheva N, Qu J, Sandeep N, Garcia L, Zhang J, Wang Z, Lampe PD, Suadicani SO, Spray DC, Fishman GI (2007) Gap junction remodeling and cardiac arrhythmogenesis in a murine model of oculodentodigital dysplasia. Proc Natl Acad Sci USA 104: 20512–20516

Kuhn A, Stadlmayr W, Monga A, Cameron I, Anthony F (2008) A pilot study of connexin 43 (Cx43) in human bladder tissue in patients with idiopathic detrusor overactivity. Eur J Obstet Gynecol Reprod Biol 141:83–86

Lai A, Le DN, Paznekas WA, Gifford WD, Jabs EW, Charles AC (2006) Oculodentodigital dysplasia connexin43 mutations result in non-functional connexin hemichannels and gap junctions in C6 glioma cells. J Cell Sci 119:532–541

Laird DW (2005) Connexin phosphorylation as a regulatory event linked to gap junction internalization and degradation. Biochim Biophys Acta 1711:172–182

Laird DW (2006) Life cycle of connexins in health and disease. Biochem J 394:527–543

Langlois S, Maher AC, Manias JL, Shao Q, Kidder GM, Laird DW (2007) Connexin levels regulate keratinocyte differentiation in the epidermis. J Biol Chem 282:30171–30180

Loddenkemper T, Grote K, Evers S, Oelerich M, Stogbauer F (2002) Neurological manifestations of the oculodentodigital dysplasia syndrome. J Neurol 249:584–595

Majumder P, Crispino G, Rodriguez L, Ciubotaru CD, Anselmi F, Piazza V, Bortolozzi M, Mammano F (2010) ATP-mediated cell–cell signaling in the organ of Corti: the role of connexin channels. Purinergic Signal 6:167–187

Manias JL, Plante I, Gong XQ, Shao Q, Churko J, Bai D, Laird DW (2008) Fate of connexin43 in cardiac tissue harbouring a disease-linked connexin43 mutant. Cardiovasc Res 80:385–395

McLachlan E, Manias JL, Gong XQ, Lounsbury CS, Shao Q, Bernier SM, Bai D, Laird DW (2005) Functional characterization of oculodentodigital dysplasia-associated Cx43 mutants. Cell Commun Adhes 12:279–292

Miller J, Hoffman E (2006) The causes and consequences of overactive bladder. J Womens Health 15:251–260

Miyazato M, Sugaya K, Nishijima S, Kadekawa K, Machida N, Oshiro Y, Saito S (2009) Changes of bladder activity and connexin 43-derived gap junctions after partial bladder-outlet obstruction in rats. Int Urol Nephrol 41:815–821

Mori K, Noguchi M, Matsuo M, Nomata K, Suematsu T, Kanetake H (2005) Decreased cellular membrane expression of gap junctional protein, connexin 43, in rat detrusor muscle with chronic partial bladder outlet obstruction. Urology 65:1254–1258

Neuhaus J, Heinrich M, Schlichting N, Oberbach A, Fitzl G, Schwalenberg T, Horn LC, Stolzenburg JU (2007) Structure and function of suburothelial myofibroblasts in the human urinary bladder under normal and pathological conditions [in German]. Urologe A 46:1197–1202

Paznekas WA, Boyadjiev SA, Shapiro RE, Daniels O, Wollnik B, Keegan CE, Innis JW, Dinulos MB, Christian C, Hannibal MC, Jabs EW (2003) Connexin 43 (GJA1) mutations cause the pleiotropic phenotype of oculodentodigital dysplasia. Am J Hum Genet 72:408–418

Paznekas WA, Karczeski B, Vermeer S, Lowry RB, Delatycki M, Laurence F, Koivisto PA, Van Maldergem L, Boyadjiev SA, Bodurtha JN, Jabs EW (2009) GJA1 mutations, variants, and connexin 43 dysfunction as it relates to the oculodentodigital dysplasia phenotype. Hum Mutat 30:724–733

Roscoe W, Veitch GI, Gong XQ, Pellegrino E, Bai D, McLachlan E, Shao Q, Kidder GM, Laird DW (2005) Oculodentodigital dysplasia-causing connexin43 mutants are non-functional and exhibit dominant effects on wild-type connexin43. J Biol Chem 280:11458–11466

Shibayama J, Paznekas W, Seki A, Taffet S, Jabs EW, Delmar M, Musa H (2005) Functional characterization of connexin43 mutations found in patients with oculodentodigital dysplasia. Cir Res 96:e83–e91

Sohl G, Willecke K (2003) An update on connexin genes and their nomenclature in mouse and man. Cell Commun Adhes 10: 173–180

Solan JL, Lampe PD (2009) Connexin43 phosphorylation: structural changes and biological effects. Biochem J 419:261–272

Sui GP, Rothery S, Dupont E, Fry CH, Severs NJ (2002) Gap junctions and connexin expression in human suburothelial interstitial cells. BJU Int 90:118–129

Sui GP, Coppen SR, Dupont E, Rothery S, Gillespie J, Newgreen D, Severs NJ, Fry CH (2003) Impedance measurements and connexin expression in human detrusor muscle from stable and unstable bladders. BJU Int 92:297–305

Tong D, Lu X, Wang HX, Plante I, Lui E, Laird DW, Bai D, Kidder GM (2009) A dominant loss-of-function GJA1 (Cx43) mutant impairs parturition in the mouse. Biol Reprod 80:1099–1106

Toth K, Shao Q, Lorentz R, Laird DW (2010) Decreased levels of Cx43 gap junctions result in ameloblast dysregulation and enamel hypoplasia in $Gja1^{Jrt/+}$ mice. J Cell Physiol 223:601–609

Uvelius B, Persson L, Mattiasson A (1984) Smooth muscle cell hypertrophy and hyperplasia in the rat detrusor after short-time infravesical outflow obstruction. J Urol 131:173–176

Wang HZ, Brink PR, Christ GJ (2006) Gap junction channel activity in short-term cultured human detrusor myocyte cell pairs: gating and unitary conductances. Am J Physiol Cell Physiol 291: C1366–C1376

Wiseman OJ, Fowler CJ, Landon DN (2003) The role of the human bladder lamina propria myofibroblast. BJU Int 91:89–93

J Membrane Biol (2012) 245:357–368
DOI 10.1007/s00232-012-9458-y

ORIGINAL ARTICLES

Primary Cultures of Embryonic Chick Lens Cells as a Model System to Study Lens Gap Junctions and Fiber Cell Differentiation

Linda S. Musil

Received: 14 March 2012 / Accepted: 20 June 2012 / Published online: 15 July 2012

Abstract A major limitation in lens gap junction research has been the lack of experimentally tractable ex vivo systems to study the formation and regulation of fiber-type gap junctions. Although immortalized lens-derived cell lines are amenable to both gene transfection and siRNA-mediated knockdown, to our knowledge none are capable of undergoing appreciable epithelial-to-fiber differentiation. Lens central epithelial explants have the converse limitation. A key advance in the field was the development of a primary embryonic chick lens cell culture system by Drs. Sue Menko and Ross Johnson. Unlike central epithelial explants, these cultures also include cells from the peripheral (preequatorial and equatorial) epithelium, which is the most physiologically relevant population for the study of fiber-type gap junction formation. We have modified the Menko/Johnson system and refer to our cultures as dissociated cell-derived monolayer cultures (DCDMLs). We culture DCDMLs without serum to mimic the avascular lens environment and on laminin, the major matrix component of the lens capsule. Here, I review the features of the DCDML system and how we have used it to study lens gap junctions and fiber cell differentiation. Our results demonstrate the power of DCDMLs to generate new findings germane to the mammalian lens and how these cultures can be exploited to conduct experiments that would be impossible, prohibitively expensive and/or difficult to interpret using transgenic animals in vivo.

Keywords Gap junction · Lens · FGF · Connexin

L. S. Musil (✉)
Department of Biochemistry and Molecular Biology, Oregon Health & Science University, 3181 Southwest Sam Jackson Park Road, Portland, OR 97239, USA
e-mail: musill@ohsu.edu

Preface

It is a pleasure and privilege to be invited to contribute to this special issue in honor of Ross Johnson. I have used this opportunity to write about the contribution that Ross has made to the gap junction field that has had the most direct impact on my career as a principal investigator.

In 1979, Willingham et al. 1979 reported that pp60^{src} from avian sarcoma virus is concentrated at gap junctions in NRK cells. Sue Menko had studied v-src as a postdoctoral fellow with David Boettiger and approached Johnson about working in his laboratory to investigate the potential functional significance of its association with gap junctions. The logical system to conduct such studies was the lens because of the abundance of gap junctions between lens fiber cells. Unfortunately, at the time there was no good culture system that met the criteria required for Menko's intended studies. During her stay in the Johnson lab, Menko developed a methodology to make primary epithelial cell cultures from E8-11 chick lenses. Although the choice of species was made in part because of practical considerations (fertilized eggs could be obtained at the University of Minnesota for free), in retrospect it was an excellent choice given that the chicken embryo has been one of the most useful and powerful systems in developmental biology (Stern 2005). In 1984, Menko and Johnson (Menko et al. 1984) published the initial characterization of this culture system, describing the remarkable extent to which these cells undergo the morphological and biochemical changes associated with lens epithelial-to-fiber cell differentiation in vivo. A subsequent paper (Menko et al. 1987) focused on gap junctions and showed, using both thin section and freeze-fracture electron microscopy, how closely these cultures recapitulate the in vivo process of fiber-type gap junction formation. I learned a variation

of the Menko/Johnson prep from Dan Goodenough when I was a postdoctoral fellow in his laboratory and used these cultures to carry out the first study of the biosynthesis and posttranslational processing of a connexin (Cx43) in lens cells (Musil et al. 1990). In my own laboratory, we have modified this preparation, which we refer to as dissociated cell-derived monolayers (DCDMLs) to distinguish them from related, but functionally distinct, systems such as central epithelial explants and immortalized lens-derived cell lines. This article reviews key features of DCDMLs, summarizes what we have learned about the regulation and role of lens cell gap junctions and fiber differentiation using this system and discusses how these findings apply to the mammalian lens in vivo. Importantly, other lens researchers continue to use primary cultures of embryonic avian lens cells in their own work, with very recent examples from the labs of Drs. Jean Jiang (Liu et al. 2011) and Menko herself (Basu et al. 2012).

Introduction

Lens Structure and Development

Let us begin with a brief primer on the lens. Although the time course and anatomical details differ between species, the general process by which the vertebrate lens develops is remarkably conserved between amphibians, birds and mammals including humans (reviewed by Piatigorsky 1981; Wride 1996; Robinson 2006). Following induction, the embryonic ectoderm overlying the optic vesicle thickens to form the lens placode. The lens placode invaginates and eventually pinches off as the lens vesicle, a hollow sphere of epithelial cells. The cells at the posterior of the lens vesicle then differentiate into the primary fiber cells, which elongate to fill the lumen of the lens vesicle. The cells at the anterior pole remain as a monolayer of undifferentiated epithelial cells. All subsequent growth of the lens is due to differentiation of epithelial cells into so-called secondary fiber cells and takes place at the border of the anterior and posterior faces of the organ in a region referred to as the lens equator (see Fig. 1 for a diagram of the lens). Secondary fiber differentiation is characterized by a dramatic increase in cell volume, extensive restructuring of the cell surface and cytosol and upregulation of fiber-specific proteins including crystallins and fiber connexins. Eventually, intracellular organelles are lost and synthesis of both DNA and protein ceases. Epithelial-to-(secondary) fiber differentiation continues throughout life, and lens cells do not turn over, resulting in the oldest and most differentiated fiber cells being located in the center (nuclear region) of the organ. The younger fiber cells that surround these mature fibers form the lens cortex and are referred to as cortical fiber cells. The lens is surrounded by a capsule of extracellular matrix that forms the thickest basement membrane in the body and is connected to the ciliary body via suspensory ligaments anchored to the lens capsule.

Lens Gap Junctions

The unique optical properties of the lens are due in part to the absence of blood vessels and to the extraordinarily tight cell-to-cell packing of the lens fibers. How, then, does this solid, ever-expanding mass of cells stay in ionic and metabolic homeostasis (and thus transparent) throughout a life span that can exceed 100 years? A major mechanism by which this is accomplished is an extensive network of gap junctional intercellular channels that physically and functionally link the cells of the lens (for review, see Goodenough 1992). Gap junctional intercellular coupling (GJIC) is much higher at the lens equator than at either pole (Baldo and Mathias 1992; Mathias et al. 1997). This pole-to-equator gradient in GJIC is believed to direct the overall pattern of current and solute flow in the lens, allowing metabolites and ions to be circulated between the peripheral (anterior epithelium and cortical fibers) and interior (nuclear region fibers) cell populations (Mathias et al. 1997; Donaldson et al. 2001). Others have suggested that the high level of GJIC at the lens equator is required to facilitate the uptake of essential substances (e.g., cysteine) into the organ (Sweeney et al. 2003).

In all species examined, lens epithelial cells express Cx43. During differentiation of epithelial cells to fibers at the lens equator, Cx43 disappears and two other connexins are upregulated, Cx46 and Cx50 in rodents and their avian orthologs Cx56 and Cx45.6 in the chick (Musil et al. 1990; Paul et al. 1991; White et al. 1992; Rup et al. 1993; Jiang et al. 1994). Mice with homozygous targeted deletions of either of the two fiber-type connexins (Gong et al. 1997; White et al. 1998) and humans with point mutations in these proteins (Shiels et al. 1998; Mackay et al. 1999) develop vision-destroying cataracts early in life (reviewed in Mathias et al. 2010).

The DCDML Prep

It is relatively easy to manually dissect out intact lenses from the eyes of E10 chick embryos. Any extralenticular tissue (e.g., suspensory ligaments, ciliary epithelium) is removed without destroying the capsular barrier by incubating the lenses in 0.08 % trypsin. The cleaned lenses are then broken by vigorous trituration into a single-cell suspension and filtered through three layers of lens paper to remove capsule material and any cell clumps. Mature nuclear and cortical fiber cells do not survive the

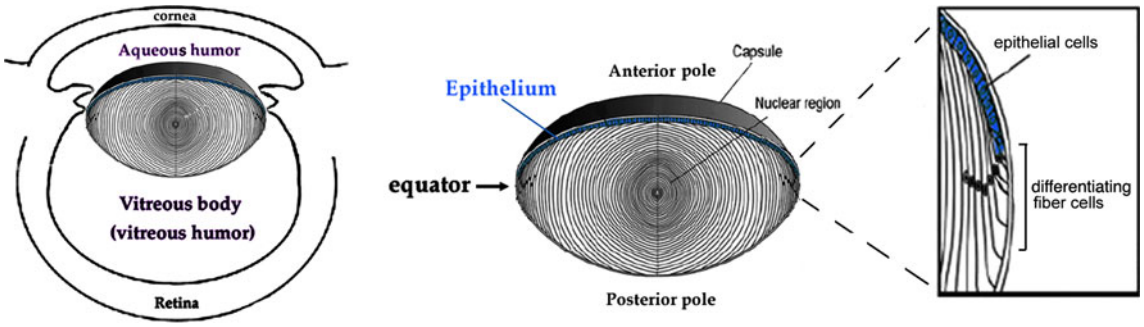

Fig. 1 Schematic of the vertebrate lens, showing its orientation in the eye and identifying key features of lens anatomy. Lens epithelial cells differentiate into secondary fiber cells at the lens equator. Adapted from Garcia et al. (2005)

dissociation process, leaving behind only less differentiated lens epithelial cells. These cells are then plated at 1.2×10^5 cells/well in 96-well tissue culture plates in M199 tissue culture medium plus BOTS (2.5 mg/ml BSA, 25 μg/ml ovotransferrin, 30 nM selenium) with penicillin G and streptomycin (Le and Musil 1998). The wells are precoated with laminin, the major component of the avian and mammalian lens capsule. As described by Menko et al. (1984), embryonic chick lens epithelial cells initially proliferate to form a flattened epithelial monolayer. Beginning at approximately 3–4 days of culture, discrete areas within these sheets differentiate into multilayered clusters of enlarged cells referred to as lentoids, which increase in number and size during the remaining culture period. Ultrastructural analysis by Menko et al. (1984, 1987) demonstrated that the cells contained in such lentoids have acquired many of the defining characteristics of fiber cells in the intact lens, including increased cell volume, loss of intracellular organelles and extensive formation of gap junctions. Thin-section electron micrographs of the lentoid cells closest to the substrate are indistinguishable from those obtained from the differentiated region of the embryonic lens, whereas the lentoid cells farthest from the plate closely resemble the elongating cells of the equatorial region. Lentoids also accumulate high levels of fiber-specific proteins including δ-crystallin, the beaded filament proteins CP49 and CP115 and aquaporin-0/MP28, the latter of which is expressed in vivo only by differentiating and differentiated primary and secondary lens fiber cells (Sas et al. 1985; Yancey et al. 1988).

Advantages of the DCDML System

(1) DCDMLs consist of primary, unpassaged lens cells. Several investigators have succeeded in establishing permanent cell lines from mammalian lens epithelial cells (e.g., N/N1003A, αTN4, HLE B-3). Although some of these lines maintain features characteristic of lens epithelial cells in vivo and are valuable for certain types of studies (e.g., gene promoter analysis), to my knowledge none of them undergo appreciable epithelial-to-fiber differentiation as evidenced by their inability to synthesize more than nominal levels of β- and γ-crystallins and other fiber-specific proteins even when cultured under differentiation-promoting conditions (Krausz et al. 1996; Fleming et al. 1998; Wang-Su et al. 2003). As might therefore be expected, we have been unable to detect significant expression of fiber-type connexins in the lens cell lines we have tested.

(2) DCDMLs consist of equatorial as well as central epithelial cells. It has been well documented that epithelial cells from the center of the anterior epithelial monolayer (i.e., those at the anterior pole of the organ) are biochemically, structurally and functionally distinct from more peripherally located populations (i.e., at or near the lens equator) (Ong et al. 2003). Notably, central epithelial cells require higher levels of growth factor to stimulate epithelial-to-fiber differentiation (Richardson et al. 1992, 1993) and do not express Cx46 (Rong et al. 2002). Because it is the cells at the lens equator that are the direct precursors of cortical fiber cells, it would follow that equatorial epithelial cells are the most physiologically relevant population in which to study fiber-type gap junction formation and fiber differentiation. DCDMLs contain cells from both the central and peripheral regions of the epithelial monolayer, with the latter predominating based on their greater abundance in vivo (Bassnett and Shi 2010) and on the number of cells in DCDMLs with early fiber-type features on day 1 of culture (e.g., low level expression of aquaporin-0/MP28) (Menko et al. 1984; Le and Musil 1998; Ong et al. 2003). In this regard, DCDMLs are very different from the other main primary lens cell culture system, central epithelial explants. Central epithelial explants are prepared by manually excising the intact central epithelial monolayer from the whole

lens and consequently consist exclusively of cells from the region of the lens where fibers normally never form (Philpott and Coulombre 1968; Piatigorsky 1973). Central epithelial explants may therefore be best suited for investigations of the initiation of epithelial-to-fiber differentiation, whereas DCDMLs are a more appropriate system for the study of the subsequent steps in this process.

(3) DCDMLs are cultured under serum-free, defined conditions. A key feature of the lens is the absence of blood vessels within the organ, a specialization essential for lens transparency. Lens cells produce their own survival factors (Ishizaki et al. 1993) and are stimulated to divide or to differentiate by factors in their local environment (e.g., either aqueous or vitreous humor). We therefore believe that culturing lens cells in more than trace amounts of serum (regardless of the source) can be considered non-physiological/pathological. Moreover, exposing lens epithelial cells even temporarily to the myriad defined and undefined substances in serum inevitably confounds interpretation of experiments intended to study the response of these cells to individual growth factors. For these reasons, we culture DCDMLs in serum-free defined medium. In otherwise unsupplemented M199/BOTS, DCDMLs gradually increase the expression of fiber differentiation markers, although not to the extent obtained with vitreous humor or other differentiation-promoting factors (Le and Musil 1998). It is not yet clear whether this limited upregulation reflects initiation of fiber differentiation in response to autocrine/paracrine signaling by endogenously produced growth factors or is instead attributable to the time-dependent expression of fiber markers by a population of cells that became committed to fiber differentiation in vivo.

(4) DCDMLs synthesize functional, fiber-type gap junctions. As demonstrated by Menko et al. (1984, 1987), using thin-section and freeze-fracture electron microscopy, lentoids in primary cultures of E9-11 chick lens cells form extensive (covering ~26 % of the lens cell membrane) gap junctions with fiber-type characteristics (e.g., loosely packed 9 nm particles on membrane P-faces). They also documented gap junction-mediated intercellular transfer of Lucifer yellow in both lentoid and monolayer epithelial cells. Later studies showed that these cultures synthesize, in addition to Cx43, the fiber cell connexins Cx45.6 (considered to be the ortholog of mammalian Cx50) and Cx56 (the ortholog of mammalian Cx46) (Le and Musil 1998; Berthoud et al. 1999; Jiang and Goodenough 1998). As in the lenses of all avian and mammalian species examined to date, Cx43 in DCDMLs is present at cell–cell interfaces throughout the epithelial monolayer. In contrast, Cx45.6 and Cx56 are most concentrated in lentoids, consistent with their accumulation in fiber cells in vivo. Based on the success of the chick system, several groups (including our own) have tried to develop a rodent lens culture system to study fiber-type gap junctions. Unfortunately, and for unknown reasons, these attempts have largely failed. Although dissociated cell-derived primary cultures of P21 rat lens cells form lentoid-like structures that express fiber cell markers such as crystallins and aquaporin-0, these otherwise differentiated lentoid cells rarely formed gap junctions and consequently did not mediate intercellular transfer of Lucifer yellow (FitzGerald and Goodenough 1986).

(5) DCDMLs are amenable to many of the same tools and techniques routinely used to study gap junctions, signal transduction and cellular differentiation in mammalian systems. We have reported that transient transfection of DCDMLs is efficient (>70 %) and long-lasting (>6 days) (Boswell et al. 2009). Most signaling molecules relevant to the lens are highly evolutionarily conserved, thereby allowing mammalian forms to be functionally expressed in chick cells and antibodies raised against mammalian proteins to recognize their avian counterparts. Among the antibodies that were raised against mammalian signaling proteins that we routinely use to detect their chick orthologs are polyclonal and monoclonal reagents against total or phosphorylated forms of ERK, p38, AKT, GSK3β, MEK, Raf-1, JNK, FRS2, S6 kinase 1, Smad1/5/8, Smad2, Smad3 and CREB. Recently, we have developed techniques to carry out RNA interference in DCDMLs. Proof-of-principle experiments are shown in Fig. 2. DCDMLs were transfected on day 1 of culture with an EGFP-encoding plasmid in the presence of either a chemically synthesized 21-mer siRNA duplex (GFP-22 siRNA) (Castel et al. 2007) designed to silence EGFP (siGFP) or a mixture of four similarly sized scrambled (scr) siRNA duplexes. The anti-GFP siRNA very strongly knocked down expression of cotransfected EGFP, but not that of cotransfected LacZ, on day 3–6 of culture (Fig. 2a). We also conducted experiments in which DCDMLs were cotransfected on day 1 with a LacZ expression plasmid (pcDNA1.2/V5-GW/lacZ) and a plasmid (pENTR-GW/H1/TO-lacz2.1^{shRNA}) encoding a shRNA (short hairpin RNA) designed to silence expression of LacZ, constructed using the Invitrogen (Carlsbad, CA) BLOCK-iT H1 RNAi entry vector kit (the RNA polymerase III promoter H1 effectively drives expression of shRNAs in primary chicken cells) (Yuan et al.

2006). Two to 5 days later, anti-LacZ immunostaining and immunoblotting (inset) demonstrated that expression of LacZ was much lower (by >85 %) in pENTR-GW/H1/TO-lacz2.1^{shRNA} (shLacZ)-cotransfected cells than in cells cotransfected with an irrelevant pENTR-GW/H1/TO-based construct designed to silence human (but not chick) survivin (shSur) (Fig. 2b). All samples had the same protein content. Importantly, transfection of siRNA duplexes or shRNA-encoding plasmids into DCDMLs had no detectable effect on: (1) cell survival, morphology or proliferation; (2) basal or growth factor-induced expression of the fiber cell marker δ-crystallin or CP49; or (3) FGF-induced activation of ERK (not shown). We conclude that si- and shRNA-efficiently and specifically block expression of their target in DCDMLs under serum-free conditions, without any evidence of the toxic effects reported after electroporation of siRNAs into very early (<48 h) intact chick embryos (Mende et al. 2008). Using this methodology, we have also successfully and specifically knocked down the function of an endogenous protein in DCDMLs, the TGFβ-dependent transcription factor Smad3 (unpublished results).

Potential Limitations of the DCDML System

(1) DCDMLs contain cells from the central as well as the peripheral regions of the lens epithelium. Because peripheral epithelial cells predominate in DCDML cultures, it is likely that central epithelial cells make only a small contribution to results obtained in most experimental paradigms. Nonetheless, it is conceivable that central epithelial cells could have a disproportionate influence on some aspects of DCDML culture behavior. In some cases, this possibility could be addressed by comparing results obtained in DCDMLs with those from experiments conducted in lens central epithelial explants. Methodology for the use of such explants for studies of GJIC has been developed by Tom White and colleagues (DeRosa et al. 2009).

(2) DCDMLs are plated as a monolayer with a free apical surface. In vivo, the lens consists of concentric layers of cells, with the oldest, most differentiated fiber cells in the center. Thus, any aspects of lens cell biology that require the architecture of the intact lens cannot be recapitulated in DCDMLs. These cultures are therefore unlikely to be a good model system to study the final stages of fiber differentiation in which cortical fibers are transformed into mature (nuclear) fiber cells. Unfortunately, attempts to induce epithelial-to-fiber differentiation in cultured intact isolated lenses have failed (personal communication, Steve Bassnett, Washington University School of Medicine), eliminating them as an alternative system.

(3) DCDMLs are derived from embryos. Although the processes of epithelial-to-fiber differentiation and fiber-type gap junction formation continue throughout life, it could in principle be argued that DCDMLs might behave differently from cells of postnatal origin.

(4) DCDMLs are derived from chicken. Despite the similarities in their formation and function, the avian lens has at least one histological feature not present in mammals, the annular pad. This population of lens epithelial cells is located immediately anterior to the anatomic equator of the lens and is defined as "postmitotic cells committed to and undergoing initial stages of lens fiber formation" (Ireland and Mrock 2000). By these criteria, they are developmentally equivalent to other more differentiated epithelial cells in the equatorial region and would therefore be expected to have similar properties.

Most mammalian cells, including lens epithelial cells, synthesize both ERK1 and ERK2, whereas chick cells have only ERK2. FGF receptor 2 (FGFR2) is reportedly not expressed in chick lens, unlike in rodents (Walshe and Mason 2000). There could be concern that these species-specific differences in gene expression could have some bearing on lens cell differentiation and/or function. However, genetic ablation studies have shown that neither ERK1 nor FGFR2 appears to have a unique, essential role in mammalian lens formation that cannot be compensated for by coexpressed isoforms that are present in chick (i.e., ERK2, FGFR3 and/or FGFR1) (Reneker et al. 2007; Zhao et al. 2008).

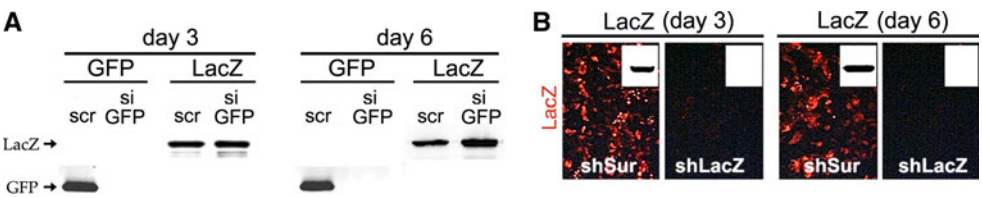

Fig. 2 RNA interference in DCDMLs. Knockdown of GFP using siRNA duplexes (**a**, si GFP) or of LacZ after transfection with shRNA-encoding plasmid (**b**, shLacZ). See text for details

Results

Role of Gap Junctions in Epithelial-to-Fiber Differentiation

In mammalian and avian lenses, both fiber-type gap junction formation and epithelial-to-secondary fiber differentiation take place at the lens equator. In other organs, gap junctions have been shown to play an important role in tissue development and differentiation, raising the possibility that this may also be the case in the lens. We examined the role of gap junctions in lens fiber formation in DCDMLs using βGA, one of several glycyrrhetinic acid derivatives that have been used to block gap junction permeability in cultured cells (Davidson et al. 1986; Goldberg et al. 1996; Guan et al. 1996). βGA has been shown (as were two other unrelated inhibitors of gap junction function) to inhibit cell–cell coupling and myogenesis of cultured rat L6 myoblasts and of primary embryonic chick myoblasts, illustrating the utility of this compound for addressing the role of gap junctions in differentiation processes in vitro (Mege et al. 1994; Proulx et al. 1997). As documented for other cell types, βGA rapidly (within 30 min) and continuously (if replaced every 2 days) suppressed gap junction-mediated intercellular transfer of Lucifer yellow and biocytin in DCDMLs without noticeable toxic effects (Le and Musil 1998). Inhibition of GJIC with βGA did not affect the expression of lens connexins or of molecules associated with other types of cell–cell junctions (*N*-cadherin, β-catenin, NCAM, aquaporin-0/MP28, ZO-1, occludin). Most importantly, there was also no effect on upregulation of markers of fiber differentiation (formation of aquaporin-0/MP28-positive lentoids and increased δ-crystallin synthesis). Gap junction blockade also failed to inhibit epithelial-to-fiber differentiation in E6 chick central epithelial explants as assessed by cell elongation, aquaporin-0/MP28 expression and δ-crystallin synthesis (Le and Musil 1998). This study provided the first evidence that secondary fiber formation is not dependent on the high level of GJIC characteristic of the lens equator. This concept has subsequently been supported by the phenotype of knockout mice in which expression of one, two or all three lens connexins has been eliminated (White et al. 1998, 2001; Xia et al. 2006). Upregulation of gap junctions at the lens equator may therefore primarily play a role in lens physiology.

Although proving that the massive upregulation of GJIC at the lens equator is not an absolute requirement for epithelial-to-fiber differentiation, our findings did not rule out the possibility that gap junctions could play a more subtle, secondary role in this process. Indeed, Rong et al. (2002) reported that fiber maturation is delayed in Cx50 knockout mice. A role for low levels of gap junctional coupling in facilitating optimal fiber differentiation would have been missed in our studies because βGA does not totally abolish all gap junction-mediated intercellular communication in DCDMLs, in keeping with results in nonlenticular cells (Martin et al. 1991; Goldberg et al. 1996).

Role of FGF in Epithelial-to-Fiber Differentiation

In addition to being the region in which fiber differentiation and GJIC are upregulated, the equator of the lens is where lens epithelial cells are first exposed to the high levels of FGF in the vitreous body (the vitreous body contains vitreous humor, a heparin sulfate–rich gel in which growth factors produced by other ocular tissues, especially the retina, accumulate). Over 20 years of research has led to the widely accepted concept that one or more FGFs play a central role in the early stages of epithelial-to-fiber differentiation in the mammalian lens and that the presumptive in vivo source of this FGF is the vitreous humor (reviewed by McAvoy et al. 1999; Lovicu and McAvoy 2005; Robinson 2006). FGFs have been purified from chick vitreous humor (Mascarelli et al. 1987), and avian lenses express FGFR1 and FGFR3 (Potts et al. 1993; Ohuchi et al. 1994). It is therefore remarkable that the prevailing view in the literature for over a decade had been that chick lens epithelial cells are unresponsive to FGF and are instead induced to differentiate by IGF-I or an IGF-like growth factor (Beebe et al. 1987; Caldes et al. 1991; Lang 1999). Using DCDMLs and central epithelial explants, we showed that chick lens cells in fact undergo differentiation when cultured in the presence of purified FGF1 or FGF2 for periods longer than the 5 h used in prior investigations (Le and Musil 2001a). Such longer-term treatments have been routinely used in studies with mammal-derived lens cultures and are physiologically relevant given that the lens is continuously exposed to growth factors in the ocular environment. We showed that a factor with the defining properties of an FGF is capable of diffusing out of the intact vitreous body and inducing fiber marker expression (Le and Musil 2001a). The importance of FGF in secondary fiber differentiation has largely been supported by the phenotype of mice in which FGF signaling has been altered at the lens equator by either dominant negative inhibition of FGF receptor function (Chow et al. 1995; Robinson et al. 1995; Stolen and Griep 2000; Govindarajan and Overbeek 2001), exogenous overexpression of various FGF isoforms (reviewed in Lovicu and Overbeek 1998) or conditional deletion of FGFR 1, 2 and 3 (Zhao et al. 2008). In contrast, overexpression of IGF-I in transgenic mice does not promote fiber differentiation (indeed, differentiation is delayed; Shirke et al. 2001) and lens defects have not been reported in IGF-I receptor knock-out animals. The in vivo significance of IGF-I in the lens remains unclear.

Role of FGF in Lens GJIC

As assessed by immunofluorescence microscopy, none of the known fiber connexins are markedly more concentrated throughout the equatorial axis of the lens than at the poles (Gruijters et al. 1987; Berthoud et al. 1994; Dahm et al. 1999). A study in human lens using freeze-fracture electron microscopy failed to reveal quantitative differences in gap junction channel content between equatorial region and polar fiber cells (Vrensen et al. 1992). There is therefore no compelling evidence that the estimated 14- to 335-fold increase in intercellular electrical conductance in the lens equatorial region (Baldo and Mathias 1992; Rae et al. 1996) is accompanied by a proportional increase in the number of channels assembled from either previously characterized or novel connexin species. Instead, the enhanced coupling at the equator appears to be due at least in part to greater flux through gap junctional channels in this region. The evolutionarily conserved response of lens cells to FGF and the high concentrations of this growth factor in vitreous humor led us to consider whether FGF might be involved in the upregulation of gap junctional function in the lens equatorial region thought to be essential for lens homeostasis and clarity (Le and Musil 2001b). We showed that FGF (either recombinant FGF 1 or 2 or purified from vitreous body-conditioned medium) upregulated gap junction-mediated intercellular communication in DCDMLs in a reversible manner that does not involve an increase in either connexin expression or gap junctional assembly. Upregulation of GJIC by FGF in DCDMLs occurs prior to, and is not a prerequisite for, fiber differentiation. Moveover, insulin and IGF-I, as potent as FGF at inducing lens cell differentiation, have no effect on gap junctional coupling in DCDMLs. These observations demonstrated that enhanced intercellular coupling in FGF-treated DCDML cultures is not a passive downstream consequence of increased fiber differentiation.

Which of the three connexin species expressed in DCDMLs (Cx43 and the fiber-type connexins Cx45.6 and Cx56) are functionally upregulated by FGF? Dong et al. (2006) reported that gap junction channels composed of Cx43, but not of Cx45.6, are permeable to the dye Alexa594 (Cx56 was not assessed). Unlike in fibroblastic cells expressing only Cx43, we found that cell-to-cell transfer of Alexa594 was very low in DCDMLs cultured either with or without purified FGF or vitreous body conditioned medium despite robust growth factor-stimulated intercellular transfer in the same cells of the less connexin type-specific, gap junction–permeant Lucifer yellow (Boswell et al. 2009). We concluded that Cx43 plays a minor role in GJIC in chick lens epithelial cells, in keeping with a report that most gap junction coupling in newborn mouse lens epithelium is due to Cx50 (the mammalian ortholog of Cx45.6) instead of Cx43 (White et al. 2007). FGF must therefore enhance GJIC in DCDMLs by acting on one or both fiber connexins. This is also likely to be true in the mammalian lens, given that FGF increases intercellular coupling mediated by Cx50 (Shakespeare et al. 2009; Cx46 was not assessed).

If FGF is responsible for upregulation of GJIC at the lens equator in vivo, then it would be expected that inhibiting FGF–FGFR interactions in the lens would disrupt the pole-to-equator gradient of cell coupling. Unfortunately, experimental manipulations that block FGF signaling in transgenic mice cause severe defects in lens development (including epithelial-to-fiber differentiation), thereby precluding a meaningful evaluation of gap junction function (Pan et al. 2006; Zhao et al. 2008).

Role of ERK in FGF Signaling in Lens GJIC and Fiber Differentiation

FGF is the main activator of the ERK MAP kinase in the lens in vivo (Govindarajan and Overbeek 2001; Zhao et al. 2008). At concentrations at which it upregulates GJIC and epithelial-to-fiber differentiation in DCDMLs and is able to diffuse out of the vitreous body, FGF induces sustained ($\geq$24 h) activation of ERK as assessed by elevated levels of phospho-ERK. In contrast, FGF at the lower levels thought to be present in the aqueous humor activates ERK only transiently (<1 h) (Le and Musil 2001b). It has been well established in other cell types that one of the most important determinants of the biological outcome of MAP kinase signaling is the length of time that a stimulus activates ERKs (Marshall 1995). We therefore examined whether the duration of ERK phosphorylation played a role in the upregulation of GJIC in DCDMLs. In the first set of experiments, DCDMLs were exposed to GJIC-inducing levels of FGF for various periods of time before the addition of UO126, a highly specific inhibitor of the kinase immediately upstream of ERK in the MAPK cascade (MEK 1/2). In other experiments, DCDMLs were transiently transfected with a constitutively active form of MEK. Together, these studies revealed that sustained ($\geq$12 h) activation of ERK is necessary for FGF to enhance gap junctional coupling in DCDMLs as well as sufficient to increase GJIC in the absence of FGF (Le and Musil 2001b).

The stimulatory effect of ERK on GJIC in DCDMLs was initially surprising given that lens epithelial cells express high levels of Cx43, a connexin that is phosphorylated and inactivated by ERK in other cell types (Hossain et al. 1998; Warn-Cramer et al. 1998; Zhou et al. 1999). This paradox was resolved when it was shown that lens cell coupling does not rely on Cx43 activity (see above) and is instead predominantly mediated by a fiber connexin whose channel function is apparently enhanced by

FGF-stimulated ERK. Subsequently published studies by the White group (Shakespeare et al. 2009) reported that electrical coupling mediated by Cx50 (the mammalian ortholog of Cx45.6) between paired *Xenopus* oocytes is increased by coexpression of constitutively active MEK, whereas coupling by Cx46 (the ortholog of Cx56) is insensitive to ERK. In the same system, FGF enhanced GJIC mediated by Cx50 in an ERK-dependent manner. Although the mechanism by which ERK increases the function of Cx50/Cx45.6 is not known, it is not associated with an increase in connexin expression (Le and Musil 2001b; Shakespeare et al. 2009). It is also unlikely to involve direct modification by ERK, given that the avian, murine and human forms of Cx50 do not contain high-probability sites for ERK binding or phosphorylation (Obenauer et al. 2003; Shakespeare et al. 2009).

Studies with whole chick lenses demonstrated that FGF-induced activation of ERK is much higher in the equatorial region than in polar cortical fibers or in the lens core (Le and Musil 2001b), similar to the distribution of phospho-ERK reported in the mammalian lens (Lovicu and McAvoy 2001; Pan et al. 2010). These and additional results led to a novel model of the role of FGF in establishing the asymmetry in gap junctional coupling in the vertebrate lens believed to be required for lens clarity (Le and Musil 2001b): (1) cells in the central epithelium only have access to the low levels of FGF in the aqueous humor and consequently have relatively low levels of GJIC; (2) cells in the equatorial region of the lens respond to the FGF that diffuses out of the vitreous body by sustained activation of ERK and upregulation of GJIC, most likely at the level of gap junction channel gating; and (3) fiber cells at the lens posterior pole activate ERK in response to FGF only poorly, most likely because of downregulation of FGF receptors or of downstream signaling components.

Long-term activation of ERK by FGF was also shown to play a role in GJIC-independent processes in DCDMLs, including upregulation of expression of the beaded intermediate filament proteins CP49 and CP115. In contrast, synthesis of certain other markers of fiber cell differentiation such as crystallins is UO126-insensitive (Le and Musil 2001a). Similar studies conducted by others using rat central epithelial explants (Lovicu and McAvoy 2001) came to the same conclusion, demonstrating that the role of ERK in FGF-regulated gene expression in the lens is evolutionarily conserved. Genetic ablation of ERK1/2 signaling in the mouse lens blocks fiber differentiation and severely inhibits cell proliferation after E15, leading to lens degeneration and microphthalmia (Reneker 2008). Transgenic overexpression of constitutively active MEK in the lens also causes pleiotropic structural and developmental abnormalities that precluded an interpretable analysis of GJIC or epithelial-to-fiber differentiation in the postnatal lens (Gong et al. 2001).

Role of BMPs in Lens GJIC and Fiber Differentiation

First identified as inducers of ectopic bone formation, bone morphogenetic proteins (BMPs) have since been shown to be key regulators of the development and function of a wide variety of tissues and organs (reviewed by Whitman 1998). Both the ligands and their receptors are highly conserved across animal species. Although the components of the canonical FGF and BMP signaling pathways are distinct, cross-talk between the two classes of growth factors has been described in many systems. In the large majority of cases, FGF inhibits BMP signaling, regulating a myriad of processes including limb growth, neural induction and digit formation (Massague 2003). In contrast, we found that FGF and BMP positively cooperate in lens cells via a unique nonreciprocal interaction (Boswell et al. 2008a, 2008b; reviewed in Lovicu et al. 2011; Mathias et al. 2010). We found that the ability of FGF to upregulate gap junction-mediated dye coupling (Boswell et al. 2008a) or expression of markers of epithelial-to-fiber differentiation (Boswell et al. 2008b) is blocked by coincubation with the function-blocking anti-BMP2, -4 and -7 antibodies or with noggin, a highly specific protein antagonist of BMP2, -4 and -7 binding to BMP receptors (Fig. 3). This effect is attributable to inhibition of BMP4 and -7 produced by the lens cells themselves. Importantly, neither noggin nor anti-BMP antibodies induce cell death, block cell proliferation or prevent upregulation of GJIC or fiber marker expression by the nonphysiological activator fetal calf serum, demonstrating the specificity of their effect. In other studies, we showed that treating DCDMLs with relatively high levels of purified BMP2, -4 and -7 ($\geq$4 ng/ml) upregulates GJIC (Boswell et al. 2008a) and fiber differentiation (Boswell et al. 2008b) in a process that does not require signaling from endogenously produced FGF. We are not aware of a precedent for this type of nonmutual interaction between FGF and BMP in any system. More recent work demonstrated that two types of mechanisms are operative. In the first, signaling from lens-derived BMPs is required to maintain lens cells in an optimally FGF-responsive state. In the second, FGF potentiates endogenous BMP signaling to a level approaching that obtained when BMP is added exogenously (Musil and Boswell 2010).

It has been well established that differentiation of the lens placode, as well as formation of primary lens fibers, requires BMPs (Furuta and Hogan 1998; Wawersik et al. 1999; Faber et al. 2002). Consequently, mice in which BMP signaling has been blocked at early stages of lens development are unsuitable to address the role of BMP in lens GJIC or in secondary fiber differentiation. We therefore used a previously generated strain of transgenic mice (OVE1196; Zhao et al. 2002) in which noggin is exogenously overexpressed under the control of a lens-specific

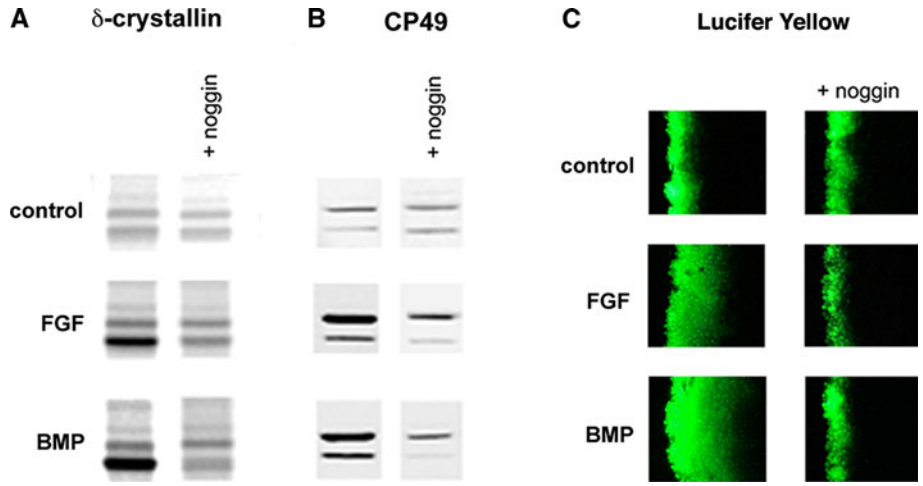

Fig. 3 Inhibition of BMP signaling with noggin blocks FGF from enhancing expression of fiber differentiation markers and upregulating gap junction-mediated dye transfer. DCDMLs were cultured for 6 days (**a**, **b**) or 48 h (**c**) without additions (control), with 10 ng/ml BMP4 or with 15 ng/ml FGF2 in either the absence or the continuous presence of 0.5 μg/ml noggin. **a** Cells were labeled with [^{35}S] methionine for 4 h, and SDS-solubilized lysates were analyzed by SDS-PAGE followed by phosphorimaging. **b** SDS-solubilized whole-cell lysates (2 μg protein/lane) were probed for CP49 by immunoblotting. **c** DCDMLs were assessed for their ability to mediate the intercellular transfer of the gap junction tracer Lucifer yellow using the scrape-loading/dye transfer assay. *Each panel* depicts a portion of the right half of the scrape/load wound. Although not shown, $M_r = 10$ kDa rhodamine dextran remained confined to the cells at the wound edge into which dye had been directly introduced during the scrape-loading process

promoter that becomes active after the formation of the lens placode and primary fibers. We found that these animals displayed a postnatal block of epithelial-to-fiber differentiation, with loss of the equatorial bow region and extension of the epithelial monolayer to the posterior pole of the organ (Boswell et al. 2008b). Morphological abnormalities were also obvious in other ocular tissues (e.g., ciliary body, absence of the vitreous body), likely due to the fact that noggin is a secreted protein and therefore has access to other organs. Because of these extralenticular effects, a direct cause-and-effect relationship between disruption of BMP signaling in the lens and inhibition of secondary fiber formation could not be drawn. Moreover, the rapid onset and severity of noggin-induced defects within and outside of the lens prevented a meaningful assessment of the role of lens-derived BMP in gap junctional coupling. These studies provide another example of the current limitations to the use of transgenic mice to study growth factor signaling in the lens. Although lacking the context of the whole animal, DCDMLs provide a system in which lens epithelial cells that developed within a wild-type eye can be manipulated in the absence of any confounding nonlenticular effects.

Conclusion

As illustrated by the aforementioned studies, results obtained using the DCDML system are consistent with (and, in several cases, predictive of) experimental findings acquired in the mammalian lens in vivo or with mammalian connexins expressed ex vivo. We conclude that DCDMLs are an appropriate and powerful system to study processes localized to the equatorial region of the lens in vivo, including epithelial-to-fiber differentiation and fiber-type gap junction formation, regulation and function. Importantly, there is no convincing justification for the concern that the embryonic or avian origins of DCDMLs preclude their use as a model system for the mammalian lens in vivo. In principle, the most direct test would be to compare results obtained in transgenic/conditional knockout mice with those from comparably modified chickens. Unfortunately, current limitations in genetic engineering in poultry make such experiments untenable. The closest alternative would be to prepare dissociated cell-derived monolayer cultures from mice on day E16 (roughly equivalent to E10 in the chick). Given that an adult mouse lens contains ~40,000–50,000 epithelial cells (Bassnett and Shi 2010) and assuming that the number of epithelial cells in a mouse lens is proportional to lens diameter, one would have to harvest the lenses of ~400 mouse embryos to obtain as many cells as we do from eight dozen E10 eggs, even if the yield approached 100 %. The outlay of time and money required to generate such murine cultures on a weekly basis would exceed most NIH budgets (certainly mine). A potentially promising system is currently being developed by Ales Cvekl and colleagues (Yang et al. 2010). They reported that human embryonic stem cells can

be differentiated in vitro to lens progenitor-like cells using a mixture of BMP4/7 and FGF2 and that these cells can then be induced to form lentoid bodies that express many of the key markers of fiber differentiation (e.g., CP49, CP115, aquaporin-0, β- and γ-crystallins). However, more than 28 days of culture was required for most of these proteins to become detectable by Western blot, and nonlens cell fates were also induced (mostly of neuroectodermal and mesodermal origin). We anticipate that DCDMLs will continue to be a useful system for the study of gap junctions and other fundamental aspects of lens cell biology for the foreseeable future.

Acknowledgements This work was supported by grant R01 2EY014622 from the National Eye Institute (to L.S.M.). I thank Ross Johnson for generously providing antibodies to lens proteins and for many interesting and helpful discussions over the years.

References

Baldo GJ, Mathias RT (1992) Spatial variations in membrane properties in the intact rat lens. Biophys J 63:518–529

Bassnett S, Shi Y (2010) A method for determining cell number in the undisturbed epithelium of the mouse lens. Mol Vis 16:2294–2300

Basu S, Rajakaruna S, Menko AS (2012) Insulin-like growth factor receptor-1 and nuclear factor kappa B are crucial survival signals that regulate caspase-3 mediated lens epithelial cell differentiation initiation. J Biol Chem 287:8384–8397

Beebe DC, Silver MH, Belcher KS, Van Wyk JJ, Svoboda ME, Zelenka PS (1987) Lentropin, a protein that controls lens fiber formation, is related functionally and immunologically to the insulin-like growth factors. Proc Natl Acad Sci USA 84:2327–2330

Berthoud VM, Cook AJ, Beyer EC (1994) Characterization of the gap junction protein connexin56 in the chicken lens by immunofluorescence and immunoblotting. Invest Ophthalmol Vis Sci 35:4109–4117

Berthoud VM, Bassnett S, Beyer EC (1999) Cultured chicken embryo lens cells resemble differentiating fiber cells in vivo and contain two kinetic pools of connexin56. Exp Eye Res 68:475–484

Boswell BA, Lein PJ, Musil LS (2008a) Cross-talk between fibroblast growth factor and bone morphogenetic proteins regulates gap junction-mediated intercellular communication in lens cells. Mol Biol Cell 19:2631–2641

Boswell BA, Overbeek PA, Musil LS (2008b) Essential role of BMPs in FGF-induced secondary lens fiber differentiation. Dev Biol 324:202–212

Boswell BA, Le AC, Musil LS (2009) Upregulation and maintenance of gap junctional communication in lens cells. Exp Eye Res 88:919–927

Caldes T, Alemany J, Robcis HL, de Pablo F (1991) Expression of insulin-like growth factor I in developing lens is compartmentalized. J Biol Chem 266:20786–20790

Castel D, Debily MA, Pitaval A, Gidrol X (2007) Cell microarray for functional exploration of genomes. Methods Mol Biol 381:375–384

Chow RL, Roux GD, Roghani M, Palmer MA, Rifkin DB, Moscatelli DA, Lang RA (1995) FGF suppresses apoptosis and induces differentiation of fibre cells in the mouse lens. Development 121:4383–4393

Dahm R, van Marle J, Prescott AR, Quinlan RA (1999) Gap junctions containing alpha8-connexin (MP70) in the adult mammalian lens epithelium suggests a re-evaluation of its role in the lens. Exp Eye Res 69:45–56

Davidson JS, Baumgarten IM, Harley EH (1986) Reversible inhibition of intercellular junctional communication by glycyrrhetinic acid. Biochem Biophys Res Commun 134:29–36

DeRosa AM, Mese G, Li L, Sellitto C, Brink PR, Gong X, White TW (2009) The cataract causing Cx50-S50P mutant inhibits Cx43 and intercellular communication in the lens epithelium. Exp Cell Res 315:1063–1075

Donaldson P, Kistler J, Mathias RT (2001) Molecular solutions to mammalian lens transparency. News Physiol Sci 16:118–123

Dong L, Liu X, Li H, Vertel BM, Ebihara L (2006) Role of the N-terminus in permeability of chicken connexin45.6 gap junctional channels. J Physiol 576:787–799

Faber SC, Robinson ML, Makarenkova HP, Lang RA (2002) Bmp signaling is required for development of primary lens fiber cells. Development 129:3727–3737

FitzGerald PG, Goodenough DA (1986) Rat lens cultures: MIP expression and domains of intercellular coupling. Invest Ophthalmol Vis Sci 27:755–771

Fleming TP, Song Z, Andley UP (1998) Expression of growth control and differentiation genes in human lens epithelial cells with extended life span. Invest Ophthalmol Vis Sci 39:1387–1398

Furuta Y, Hogan BL (1998) BMP4 is essential for lens induction in the mouse embryo. Genes Dev 12:3764–3775

Garcia CM, Yu K, Zhao H, Ashery-Padan R, Ornitz DM, Robinson ML, Beebe DC (2005) Signaling through FGF receptor-2 is required for lens cell survival and for withdrawal from the cell cycle during lens fiber cell differentiation. Dev Dyn 233:516–527

Goldberg GS, Moreno AP, Bechberger JF, Hearn SS, Shivers RR, MacPhee DJ, Zhang YC, Naus CC (1996) Evidence that disruption of connexon particle arrangements in gap junction plaques is associated with inhibition of gap junctional communication by a glycyrrhetinic acid derivative. Exp Cell Res 222:48–53

Gong X, Li E, Klier G, Huang Q, Wu Y, Lei H, Kumar NM, Horwitz J, Gilula NB (1997) Disruption of alpha3 connexin gene leads to proteolysis and cataractogenesis in mice. Cell 91:833–843

Gong X, Wang X, Han J, Niesman I, Huang Q, Horwitz J (2001) Development of cataractous macrophthalmia in mice expressing an active MEK1 in the lens. Invest Ophthalmol Vis Sci 42:539–548

Goodenough DA (1992) The crystalline lens. A system networked by gap junctional intercellular communication. Semin Cell Biol 3:49–58

Govindarajan V, Overbeek PA (2001) Secreted FGFR3, but not FGFR1, inhibits lens fiber differentiation. Development 128:1617–1627

Gruijters WT, Kistler J, Bullivant S (1987) Formation, distribution and dissociation of intercellular junctions in the lens. J Cell Sci 88:351–359

Guan X, Wilson S, Schlender KK, Ruch RJ (1996) Gap-junction disassembly and connexin 43 dephosphorylation induced by 18 beta-glycyrrhetinic acid. Mol Carcinog 16:157–164

Hossain MZ, Ao P, Boynton AL (1998) Platelet-derived growth factor-induced disruption of gap junctional communication and phosphorylation of connexin43 involves protein kinase C and mitogen-activated protein kinase. J Cell Physiol 176:332–341

Ireland ME, Mrock LK (2000) Differentiation of chick lens epithelial cells: involvement of the epidermal growth factor receptor and endogenous ligand. Invest Ophthalmol Vis Sci 41:183–190

Ishizaki Y, Voyvodic JT, Burne JF, Raff MC (1993) Control of lens epithelial cell survival. J Cell Biol 121:899–908

Jiang JX, Goodenough DA (1998) Phosphorylation of lens-fiber connexins in lens organ cultures. Eur J Biochem 255:37–44

Jiang JX, White TW, Goodenough DA, Paul DL (1994) Molecular cloning and functional characterization of chick lens fiber connexin 45.6. Mol Biol Cell 5:363–373

Krausz E, Augusteyn RC, Quinlan RA, Reddan JR, Russell P, Sax CM, Graw J (1996) Expression of crystallins, Pax6, filensin, CP49, MIP, and MP20 in lens-derived cell lines. Invest Ophthalmol Vis Sci 37:2120–2128

Lang RA (1999) Which factors stimulate lens fiber cell differentiation in vivo? Invest Ophthalmol Vis Sci 40:3075–3078

Le AC, Musil LS (1998) Normal differentiation of cultured lens cells after inhibition of gap junction-mediated intercellular communication. Dev Biol 204:80–96

Le AC, Musil LS (2001a) FGF signaling in chick lens development. Dev Biol 233:394–411

Le AC, Musil LS (2001b) A novel role for FGF and extracellular signal-regulated kinase in gap junction-mediated intercellular communication in the lens. J Cell Biol 154:197–216

Liu J, Ek Vitorin JF, Weintraub ST, Gu S, Shi Q, Burt JM, Jiang JX (2011) Phosphorylation of connexin 50 by protein kinase A enhances gap junction and hemichannel function. J Biol Chem 286:16914–16928

Lovicu FJ, McAvoy JW (2001) FGF-induced lens cell proliferation and differentiation is dependent on MAPK (ERK1/2) signalling. Development 128:5075–5084

Lovicu FJ, McAvoy JW (2005) Growth factor regulation of lens development. Dev Biol 280:1–14

Lovicu FJ, Overbeek PA (1998) Overlapping effects of different members of the FGF family on lens fiber differentiation in transgenic mice. Development 125:3365–3377

Lovicu FJ, McAvoy JW, de Iongh RU (2011) Understanding the role of growth factors in embryonic development: insights from the lens. Philos Trans R Soc Lond B Biol Sci 366:1204–1218

Mackay D, Ionides A, Kibar Z, Rouleau G, Berry V, Moore A, Shiels A, Bhattacharya S (1999) Connexin46 mutations in autosomal dominant congenital cataract. Am J Hum Genet 64:1357–1364

Marshall CJ (1995) Specificity of receptor tyrosine kinase signaling: transient versus sustained extracellular signal-regulated kinase activation. Cell 80:179–185

Martin W, Zempel G, Hulser D, Willecke K (1991) Growth inhibition of oncogene-transformed rat fibroblasts by cocultured normal cells: relevance of metabolic cooperation mediated by gap junctions. Cancer Res 51:5348–5351

Mascarelli F, Raulais D, Counis MF, Courtois Y (1987) Characterization of acidic and basic fibroblast growth factors in brain, retina and vitreous chick embryo. Biochem Biophys Res Commun 146:478–486

Massague J (2003) Integration of Smad and MAPK pathways: a link and a linker revisited. Genes Dev 17:2993–2997

Mathias RT, Rae JL, Baldo GJ (1997) Physiological properties of the normal lens. Physiol Rev 77:21–50

Mathias RT, White TW, Gong X (2010) Lens gap junctions in growth, differentiation, and homeostasis. Physiol Rev 90:179–206

McAvoy JW, Chamberlain CG, de Iongh RU, Hales AM, Lovicu FJ (1999) Lens development. Eye 13:425–437

Mege RM, Goudou D, Giaume C, Nicolet M, Rieger F (1994) Is intercellular communication via gap junctions required for myoblast fusion? Cell Adhes Commun 2:329–343

Mende M, Christophorou NA, Streit A (2008) Specific and effective gene knock-down in early chick embryos using morpholinos but not pRFPRNAi vectors. Mech Dev 125:947–962

Menko AS, Klukas KA, Johnson RG (1984) Chicken embryo lens cultures mimic differentiation in the lens. Dev Biol 103:129–141

Menko AS, Klukas KA, Liu TF, Quade B, Sas DF, Preus DM, Johnson RG (1987) Junctions between lens cells in differentiating cultures: structure, formation, intercellular permeability, and junctional protein expression. Dev Biol 123:307–320

Musil LS, Boswell BA (2010) Molecular mechanism of cross-talk between FGFs and BMPs in lens cell differentiation. Invest Ophthalmol Vis Sci 51; abstract 1213

Musil LS, Beyer EC, Goodenough DA (1990) Expression of the gap junction protein connexin43 in embryonic chick lens: molecular cloning, ultrastructural localization, and post-translational phosphorylation. J Membr Biol 116:163–175

Obenauer JC, Cantley LC, Yaffe MB (2003) Scansite 2.0: proteome-wide prediction of cell signaling interactions using short sequence motifs. Nucleic Acids Res 31:3635–3641

Ohuchi H, Koyama E, Myokai F, Nohno T, Shiraga F, Matsuo T, Matsuo N, Taniguchi S, Noji S (1994) Expression patterns of two fibroblast growth factor receptor genes during early chick eye development. Exp Eye Res 58:649–658

Ong MD, Payne DM, Garner MH (2003) Differential protein expression in lens epithelial whole-mounts and lens epithelial cell cultures. Exp Eye Res 77:35–49

Pan Y, Woodbury A, Esko JD, Grobe K, Zhang X (2006) Heparan sulfate biosynthetic gene Ndst1 is required for FGF signaling in early lens development. Development 133:4933–4944

Pan Y, Carbe C, Powers A, Feng GS, Zhang X (2010) Sprouty2-modulated Kras signaling rescues Shp2 deficiency during lens and lacrimal gland development. Development 137:1085–1093

Paul DL, Ebihara L, Takemoto LJ, Swenson KI, Goodenough DA (1991) Connexin46, a novel lens gap junction protein, induces voltage-gated currents in nonjunctional plasma membrane of *Xenopus* oocytes. J Cell Biol 115:1077–1089

Philpott GW, Coulombre AJ (1968) Cytodifferentiation of precultured embryonic chick lens epithelial cells in vitro and in vivo. Exp Cell Res 52:140–146

Piatigorsky J (1973) Insulin initiation of lens fiber differentiation in culture: elongation of embryonic lens epithelial cells. Dev Biol 30:214–216

Piatigorsky J (1981) Lens differentiation in vertebrates. A review of cellular and molecular features. Differentiation 19:134–153

Potts JD, Harocopos GJ, Beebe DC (1993) Identification of receptor tyrosine kinases in the embryonic chicken lens. Curr Eye Res 12:759–763

Proulx A, Merrifield PA, Naus CC (1997) Blocking gap junctional intercellular communication in myoblasts inhibits myogenin and MRF4 expression. Dev Genet 20:133–144

Rae JL, Bartling C, Rae J, Mathias RT (1996) Dye transfer between cells of the lens. J Membr Biol 150:89–103

Reneker LW (2008) ERK1/2 signaling is required for epithelial-to-fiber differentiation in lens development. Invest Ophthalmol Vis Sci 49; abstract 1135

Reneker LW, Robinson ML, Ogata M, Sanjo H, Pages G (2007) The role of ERK mitogen-activated protein kinase (MAPK) in lens development. Invest Ophthalmol Vis Sci 48; abstract 1119

Richardson NA, McAvoy JW, Chamberlain CG (1992) Age of rats affects response of lens epithelial explants to fibroblast growth factor. Exp Eye Res 55:649–656

Richardson NA, Chamberlain CG, McAvoy JW (1993) IGF-1 enhancement of FGF-induced lens fiber differentiation in rats of different ages. Invest Ophthalmol Vis Sci 34:3303–3312

Robinson ML (2006) An essential role for FGF receptor signaling in lens development. Semin Cell Dev Biol 17:726–740

Robinson ML, MacMillan-Crow LA, Thompson JA, Overbeek PA (1995) Expression of a truncated FGF receptor results in defective lens development in transgenic mice. Development 121:3959–3967

Rong P, Wang X, Niesman I, Wu Y, Benedetti LE, Dunia I, Levy E, Gong X (2002) Disruption of Gja8 (alpha8 connexin) in mice leads to microphthalmia associated with retardation of lens growth and lens fiber maturation. Development 129:167–174

Rup DM, Veenstra RD, Wang HZ, Brink PR, Beyer EC (1993) Chick connexin-56, a novel lens gap junction protein. Molecular cloning and functional expression. J Biol Chem 268:706–712

Sas DF, Sas MJ, Johnson KR, Menko AS, Johnson RG (1985) Junctions between lens fiber cells are labeled with a monoclonal antibody shown to be specific for MP26. J Cell Biol 100:216–225

Shakespeare TI, Sellitto C, Li L, Rubinos C, Gong X, Srinivas M, White TW (2009) Interaction between connexin50 and mitogen-activated protein kinase signaling in lens homeostasis. Mol Biol Cell 20:2582–2592

Shiels A, Mackay D, Ionides A, Berry V, Moore A, Bhattacharya S (1998) A missense mutation in the human connexin50 gene (GJA8) underlies autosomal dominant "zonular pulverulent" cataract, on chromosome 1q. Am J Hum Genet 62:526–532

Shirke S, Faber SC, Hallem E, Makarenkova HP, Robinson ML, Overbeek PA, Lang RA (2001) Misexpression of IGF-I in the mouse lens expands the transitional zone and perturbs lens polarization. Mech Dev 101:167–174

Stern CD (2005) The chick: a great model system becomes even greater. Dev Cell 8:9–17

Stolen CM, Griep AE (2000) Disruption of lens fiber cell differentiation and survival at multiple stages by region-specific expression of truncated FGF receptors. Dev Biol 217:205–220

Sweeney MH, Garland DL, Truscott RJ (2003) Movement of cysteine in intact monkey lenses: the major site of entry is the germinative region. Exp Eye Res 77:245–251

Vrensen G, Van Marle J, Van Veen H, Willekens B (1992) Membrane architecture as a function of lens fibre maturation: a freeze fracture and scanning electron microscopic study in the human lens. Exp Eye Res 54:433–446

Walshe J, Mason I (2000) Expression of FGFR1, FGFR2 and FGFR3 during early neural development in the chick embryo. Mech Dev 90:103–110

Wang-Su ST, McCormack AL, Yang S, Hosler MR, Mixon A, Riviere MA, Wilmarth PA, Andley UP, Garland D, Li H, David LL, Wagner BJ (2003) Proteome analysis of lens epithelia, fibers, and the HLE B-3 cell line. Invest Ophthalmol Vis Sci 44:4829–4836

Warn-Cramer BJ, Cottrell GT, Burt JM, Lau AF (1998) Regulation of connexin-43 gap junctional intercellular communication by mitogen-activated protein kinase. J Biol Chem 273:9188–9196

Wawersik S, Purcell P, Rauchman M, Dudley AT, Robertson EJ, Maas R (1999) BMP7 acts in murine lens placode development. Dev Biol 207:176–188

White TW, Bruzzone R, Goodenough DA, Paul DL (1992) Mouse Cx50, a functional member of the connexin family of gap junction proteins, is the lens fiber protein MP70. Mol Biol Cell 3:711–720

White TW, Goodenough DA, Paul DL (1998) Targeted ablation of connexin50 in mice results in microphthalmia and zonular pulverulent cataracts. J Cell Biol 143:815–825

White TW, Sellitto C, Paul DL, Goodenough DA (2001) Prenatal lens development in connexin43 and connexin50 double knockout mice. Invest Ophthalmol Vis Sci 42:2916–2923

White TW, Gao Y, Li L, Sellitto C, Srinivas M (2007) Optimal lens epithelial cell proliferation is dependent on the connexin isoform providing gap junctional coupling. Invest Ophthalmol Vis Sci 48:5630–5637

Whitman M (1998) Smads and early developmental signaling by the TGFbeta superfamily. Genes Dev 12:2445–2462

Willingham MC, Jay G, Pastan I (1979) Localization of the ASV src gene product to the plasma membrane of transformed cells by electron microscopic immunocytochemistry. Cell 18:125–134

Wride MA (1996) Cellular and molecular features of lens differentiation: a review of recent advances. Differentiation 61:77–93

Xia CH, Cheng C, Huang Q, Cheung D, Li L, Dunia I, Benedetti LE, Horwitz J, Gong X (2006) Absence of alpha3 (Cx46) and alpha8 (Cx50) connexins leads to cataracts by affecting lens inner fiber cells. Exp Eye Res 83:688–696

Yancey SB, Koh K, Chung J, Revel JP (1988) Expression of the gene for main intrinsic polypeptide (MIP): separate spatial distributions of MIP and beta-crystallin gene transcripts in rat lens development. J Cell Biol 106:705–714

Yang C, Yang Y, Brennan L, Bouhassira EE, Kantorow M, Cvekl A (2010) Efficient generation of lens progenitor cells and lentoid bodies from human embryonic stem cells in chemically defined conditions. FASEB J 24:3274–3283

Yuan J, Wang X, Zhang Y, Hu X, Fei J, Li N (2006) Mammalian *Pol*III promoter H1 can transcribe shRNA inducing RNAi in chicken cells. Mol Biol Rep 33:33–41

Zhao S, Chen Q, Hung FC, Overbeek PA (2002) BMP signaling is required for development of the ciliary body. Development 129:4435–4442

Zhao H, Yang T, Madakashira BP, Thiels CA, Bechtle CA, Garcia CM, Zhang H, Yu K, Ornitz DM, Beebe DC, Robinson ML (2008) Fibroblast growth factor receptor signaling is essential for lens fiber cell differentiation. Dev Biol 318:276–288

Zhou L, Kasperek EM, Nicholson BJ (1999) Dissection of the molecular basis of pp 60(v-src) induced gating of connexin 43 gap junction channels. J Cell Biol 144:1033–1045

J Membrane Biol (2012) 245:369–380
DOI 10.1007/s00232-012-9459-x

Extracellular Loop Cysteine Mutant of Cx37 Fails to Suppress Proliferation of Rat Insulinoma Cells

Miranda E. Good · José F. Ek-Vitorín · Janis M. Burt

Received: 29 March 2012 / Accepted: 20 June 2012 / Published online: 15 July 2012

Abstract Although a functional pore domain is required for connexin 37 (Cx37)–mediated suppression of rat insulinoma (Rin) cell proliferation, it is unknown whether functional hemichannels would be sufficient or if Cx37 gap junction channels are required for growth suppression. To test this possibility, we targeted extracellular loop cysteines for mutation, expecting that the mutated protein would retain hemichannel, but not gap junction channel, functionality. Cysteines at positions 61 and 65 in the first extracellular loop of Cx37 were mutated to alanine and the mutant protein (Cx37-C61,65A) expressed in Rin cells. Although the resulting iRin37-C61,65A cells expressed the mutant protein comparably to Cx37 wild-type (Cx37-WT)–expressing Rin cells (iRin37), Cx37-C61,65A expression did not suppress the proliferation of Rin cells. As expected, iRin37-C61,65A cells did not form functional gap junction channels. However, functional hemichannels also could not be detected in iRin37-C61,65A cells by either dye uptake or electrophysiological approaches. Thus, failure of Cx37-C61,65A to suppress the proliferation of Rin cells is consistent with previous data demonstrating the importance of channel functionality to Cx37's growth-suppressive function. Moreover, failure of the Cx37-C61,65A hemichannel to function, even in low external calcium, emphasizes the importance of extracellular loop cysteines not only in hemichannel docking but also in determining the ability of the hemichannel to adopt a closed configuration that can open in response to triggers, such as low external calcium, effective at opening Cx37-WT hemichannels.

M. E. Good · J. F. Ek-Vitorín · J. M. Burt (✉)
Department of Physiology, University of Arizona,
PO Box 245051, Tucson, AZ 85724, USA
e-mail: jburt@u.arizona.edu

Keywords Gap junction · Connexin · Hemichannel · Growth suppression · Insulinoma · Cx37

Introduction

Connexins, the protein products of the gap junction gene family, facilitate coordinated cell and tissue function by influencing and mediating intracellular, transmembrane and intercellular signaling. Intracellular signaling via connexins involves their interaction with a diverse array of proteins, the consequence of which can be regulated connexin function as well as regulation of intracellular signaling cascades (Kardami et al. 2007). The transmembrane signaling function of connexins is mediated by hemichannels (connexons). Hemichannels comprise a hexamer of connexin monomers that, when these channels are open, mediate transmembrane diffusion of ions and small molecules (Goodenough and Paul 2003). The intercellular signaling function of connexins is mediated by gap junction channels, which are formed when two hemichannels from neighboring cells dock to form an intercellular channel that connects the cytosols of those cells. These gap junction channels support the diffusive exchange of ions and small molecules (Harris 2001). Although each connexin isoform is likely able to participate in intracellular, transmembrane and intercellular signaling, isoform-specific differences in their regulation as well as the signaling they mediate suggest the possible cell- and tissue-specific benefits of coexpressing multiple connexin isoforms (Sohl and Willecke 2004). Indeed, based on phenotypic differences in animals with connexin isoform deletion or substitution (Plum et al. 2000; Scherer et al. 1998; Simon et al. 1997), it is clear that connexins serve to facilitate the coordinated function of cells and the

tissues they comprise in both a cell type and connexin isoform specific manner (Kardami et al. 2007).

Isoform and cell type specific growth suppression by connexins is well documented (e.g., Kardami et al. 2007; King and Bertram 2005), although the precise mechanisms underlying growth suppression by any given connexin are less clear. For example, connexin 37 (Cx37), but not Cx40 or Cx43, suppresses the proliferation of rat insulinoma (Rin) cells (Burt et al. 2008). A mutant form of Cx37 (Cx37-T154A) that does not form functional channels but retains the capacity to localize properly and form gap junction plaques, fails to suppress Rin cell proliferation, indicating that the capacity of Cx37 to form functional channels is necessary and the normal localization of the carboxyl terminus is insufficient for Cx37-mediated growth suppression of this cell type (Good et al. 2011). Since the T154A site likely renders both hemichannel and gap junction channel nonfunctional (Beahm et al. 2006), these studies leave unresolved which channel type is necessary for Cx37-mediated growth suppression.

Although the formation of gap junction channels depends upon the structural integrity of the extracellular loops, the formation of hemichannels does not (Foote et al. 1998). These loops share a high degree of sequence homology across connexin isoforms (Dahl et al. 1992; Nakagawa et al. 2010), with the six cysteines conserved in all gap junction–competent connexin isoforms (Sonntag et al. 2009). These cysteines are essential to the formation of functional gap junction channels, likely through interloop disulfide bond formation (Foote et al. 1998; Dahl et al. 1991, 1992). Specifically, disulfide bond formation between cysteines in the first and second extracellular loops, which occurs in a site- and position-specific manner, probably stabilizes the conformation of the extracellular domain such that proper docking of two hemichannels can occur (Foote et al. 1998). In Cx32, mutation of a single cysteine to serine was sufficient to prevent gap junction channel formation and function (Dahl et al. 1992). Bao and colleagues (2004) and more recently Tong and colleagues (2007) demonstrated that Cx43 with all six extracellular loop cysteines mutated to alanines fails to form functional gap junction channels but retains hemichannel function as determined by dye uptake. Together, these studies suggest that cells expressing a connexin with one or more of the cysteines in the extracellular loops mutated to alanine would be unable to form functional gap junction channels but would be able to form functional hemichannels.

In the current study we examined the functional consequences of mutating cysteine residues 61 and 65 in Cx37 to alanine (Cx37-C61,65A) on both the growth-suppressive and channel functions of Cx37. We demonstrate that Cx37-C61,65A does not suppress the proliferation of Rin cells, despite localizing to appositional and nonappositional membranes in a manner comparable to wild-type Cx37 (Cx37-WT) and Cx37-T154A. However, contrary to expectation, Cx37-C61,65A does not form functional hemichannels (or gap junction channels). Thus, consistent with previous data, the current results demonstrate that the growth-suppressive properties of Cx37 depend on the capacity of the protein to adopt a conformation able to support channel function.

Materials and Methods

Antibodies and Reagents

Reagents were purchased from Sigma-Aldrich (St. Louis, MO), except where noted. Anti-Cx37 antibody [αCx37-18264 (Simon et al. 2006)] was used for immunoblots and immunofluorescence. Secondary antibodies to anti-Cx37 antibody were horseradish peroxidase (HRP) conjugated to goat anti-rabbit antibodies (Amersham, Arlington Heights, IL) for immunoblotting and Cy3-conjugated anti-rabbit-IgG (Jackson ImmunoResearch, West Grove, PA) for immunofluorescence.

Mutant Connexin and Expression Vectors

Using the QuikChange Site-Directed Mutagenesis kit (Stratagene, San Diego, CA), the C61,65A mutation was introduced into the pTRE2h-mCx37 plasmid (Burt et al. 2008) using the following oligonucleotide primers (Operon Biotechnologies, Huntsville, AL): 5′-GCCCAGCCGGGC GCCACCAACGTCGCCTATGACCAGGC-3′ and 5′-CG GGTCGGCCCGCGGTGGTTGCAGCGGATACTGGTCC G-3′. Sequence was confirmed by the Genomic Analysis and Technology Core at the University of Arizona. The Cx37-WT and Cx37-C61,65A sequences were subcloned into the pcDNA3.1h vector

Cell Culture and Expression Vectors

iRin cells (Burt et al. 2008), cultured in RPMI 1640 medium supplemented with 10 % Fetal Plex (Gemini Bioproducts, Sacramento, CA), 300 μg/ml penicillin, 500 μg/ml streptomycin and 300 μg/ml G418 (GIBCO Invitrogen, Grand Island, NY), were transfected with the pTRE2h-mCx37-C61,65A plasmid using Lipofectamine (Invitrogen, Carlsbad, CA) and stably expressing cells selected by culturing in the same RPMI medium but also containing 100 μg/ml hygromycin. Clonal cell lines (iRin37-C61,65A) were isolated by dilution cloning. Connexin-deficient MDCK cells [obtained from Paul Lampe (Solan and Lampe 2007)] were transiently transfected with either the Cx37WT or the Cx37-C61,65A

sequence using the pcDNA3.1h vector. Cells were cultured in DMEM supplemented with 10 % Gem Cell Fetal Bovine Serum (Gemini Bioproducts). All cells were maintained at 37 °C in a humidified, 5 % CO_2 incubator.

Immunoblotting

Whole-cell protein was isolated as previously described (Burt et al. 2008), and protein concentration was determined using the BCA Assay (Pierce, Rockford, IL). Samples (50 µg of total protein) were loaded onto 12 % SDS-PAGE gels (Bio-Rad, Richmond, CA), electrophoresed and then transferred to nitrocellulose using the Trans-Blot Turbo Transfer System (Bio-Rad). Blots were blocked using 5 % nonfat dried milk. Enhanced chemiluminescence strategies, with SuperSignal West Dura and Femto Systems (mixed at a 2:1 ratio; Thermo Scientific, Waltham, MA), were used to visualize (Kodak Imagestation 2000; Kodak, Rochester, NY) connexin expression. Cx37 expression levels were quantified as previously described (Burt et al. 2001) by comparing sample band intensity to a standard curve generated with GST-Cx37 fusion protein (residues 233–329). This fusion protein runs as three distinct bands; their collective intensities were used to generate the standard curve.

Immunofluorescence

Cx37 localization was determined as previously described (Good et al. 2011). Briefly, iRin37 and iRin37-C61,65A cells, plated on glass coverslips and induced (2 µg/ml doxycycline) to express Cx37, were rinsed with divalent cation containing phosphate-buffered saline (PBS) and treated with 1 mM Sulfo-NHS-SS-Biotin (Thermo Scientific) to label lysine residues in the extracellular portions of membrane proteins. Excess biotin was quenched with 100 mM glycine in PBS, and the cells were fixed in cold methanol and treated with 0.2 % Triton X-100 followed by 0.5 M NH_4Cl, each for 15 min. Cells were then rinsed with divalent cation-free PBS (DCF-PBS), blocked (in 4 % fish skin gelatin, 1 % normal goat serum and 0.1 % Triton X-100 in DCF-PBS) and exposed to primary antibody for 2 h. After rinsing, secondary antibodies were applied (Cy3-conjugated, diluted 1:200 in blocking reagent for Cx37; Cy5-conjugated streptavidin, diluted 1:250 in blocking reagent, for detection of biotinylated surface proteins). Labeled proteins were visualized with a Zeiss (Thornwood, NY) LSM510meta-NLO confocal/multiphoton fluorescence microscope (lasers set at 514 nm for Cy3 and 633 nm for Cy5 detection).

MDCK cells, plated at low density, were transfected with pcDNA3.1h-mCx37 or pcDNA3.1h-mCx37-C61,65A using Lipofectamine and 24 h later processed as described for labeling and visualization of Cx37.

Immunoprecipitation of Surface Biotinylated Proteins

Subconfluent cells induced to express Cx37 were rinsed with either PBS or DCF-PBS and treated with 10 mM dithiothreitol (DTT) in PBS or DCF-PBS for 20 min at room temperature. Cells in DCF-PBS were rinsed with EGTA-supplemented (5 mM) external solution [in mM: 142.5 NaCl, 4 KCl, 1 $MgCl_2$, 5 glucose, 2 sodium pyruvate, 10 HEPES, 15 CsCl, 10 TEACl, 1 $CaCl_2$ (pH 7.2), 320 mOsM] and rinsed again with DCF-PBS. These cells and those not exposed to low-Ca^{2+} washes (in PBS) were then incubated in 0.5 mg/ml maleimide-PEG_2-biotin (Thermo Scientific) in PBS or DCF-PBS, as appropriate, for 1 h at 4 °C on a rotator. After quenching excess biotin with 100 mM glycine (in PBS or DCF-PBS), cell protein was harvested with immunoprecipitation (IP) buffer [containing 150 mM NaCl, 10 mM Tris HCl, 1 % Triton X-100, 1 % Na deoxycholate, 0.1 % SDS and a protease inhibitor cocktail tablet (catalog no. 11836153001, Roche, Indianapolis, IN; pH 6.8), pH 7.4]. Streptavidin-coupled resin (Thermo Scientific) preequilibrated in IP buffer was added to harvested cell protein and incubated overnight at 4 °C. The mixture was centrifuged (2,500×*g* for 15 s at 4 °C) and the resin washed three times with cold IP buffer and once with PBS. Resin-coupled proteins were then resuspended in sample buffer (100 mM Tris, 4 % SDS, 10 % glycerol, 5 mM NaF, 0.25 mM Na_3VO_4, 2 mM PMSF and 0.02 % bromophenol blue with added protease inhibitor cocktail, pH 6.8), boiled, vortexed and centrifuged (15,000×*g* for 1 min); and the immunoprecipitated proteins were electrophoretically separated [25 µl per sample, 12 % SDS-PAGE gels (Bio-Rad)] and immunoblotted for Cx37 expression, as described above.

Proliferation

As previously described (Burt et al. 2008; Good et al. 2011), iRin37 or iRin37-C61,65A cells were plated at an initial density of 3×10^4/well in six-well plates. 24 h after plating (day zero of proliferation curve), cells were induced (dox+) or not (dox–) with 2 µg/ml doxycycline. Medium was refreshed every 48 h (with or without added doxycycline, as appropriate). Triplicate wells were harvested and counted (Cellometer Auto T4; Nexcelom Bioscience, Lawrence, MA) every 3 days over a 21-day period.

Dye-Uptake Studies

iRin37 or iRin37-C61,65A clone 1C3 cells were plated at low density and induced or not for 24–48 h. Cells were rinsed with medium, external solution and external solution containing 5 mM EGTA. Two rings [made from the tops of

14-ml BD Falcon (Franklin Lakes, NJ) tubes] were adhered to the dish with Vaseline, creating two wells; dye was added to each well, and the dish was placed on ice and protected from ambient light. The dye solution contained 1.25 mg/ml *N*,*N*,*N*-trimethyl-2-[methyl-(7-nitro-2,1,3-benzoxadiol-4-yl)amino]ethanaminium (NBD-M-TMA) (Bednarczyk et al. 2000) and 0.125 mg/ml tetramethylrhodamine dextran (rhodamine, molecular weight 3,000; Molecular Probes, Eugene, OR) added to Ca-free external solution supplemented or not with 5 mM EGTA. Dye and the rings were removed after a 15-min dye-uptake period, and cells were rinsed with culture medium followed by external solution. Cells were imaged with an Olympus (Tokyo, Japan) IX71 or BX50WI fluorescence microscope; differential interference contrast (DIC) and fluorescence images of multiple fields within each ringed area of cells were acquired [CoolSnap ES camera (Photometrics, Tucson, AZ) and V++ software (Digital Optics, Auckland, New Zealand); 41001HQ filter for imaging NBD-M-TMA and U-MWIGA3 filter for imaging rhodamine (both from Olympus)]. Each set of images was scored for NBD-M-TMA-positive and rhodamine-dextran-negative cells and the total number of cells. Multiple fields were imaged for each well. Totals from each field within a well were combined to calculate a percent NBD-M-TMA-positive value. We performed *t*-tests on the dox+ versus dox- groups.

Electrophysiology

iRin parental, iRin37 or iRin37-C61,65A cells were plated onto glass coverslips at low densities such that single cells and cell pairs predominated. One hour after plating doxycycline (2 μg/ml) was added or not to the cells, and 24–48 h later junctional (cell pairs) or membrane (single cells) conductance was evaluated. Coverslips were placed in a custom-made chamber and bathed in external solution. Patch pipettes were fabricated as previously described (Burt et al. 2008; Ek-Vitorín and Burt 2005) and back-filled with internal solution (in mM: 124 KCl, 14 CsCl, 9 HEPES, 9 EGTA, 0.5 $CaCl_2$, 5 glucose, 9 TEACl, 3 $MgCl_2$, 5 Na_2ATP).

Junctional and single gap junction channel conductances were measured as previously described (Burt et al. 2008; Ek-Vitorín and Burt 2005), using either discontinuous single electrode voltage clamp (NPI SEC-05LX) or traditional patch-clamp (Axopatch 1D) amplifiers. In either case, transjunctional voltages (V_j) of 25–50 mV (non-pulsed cell held at 0 mV, while the pulsed cell was clamped to the indicated membrane potential) were applied to reveal the activity of Cx37 gap junction channels.

Hemichannel data were collected in single whole-cell voltage-clamp configuration; depolarizing or hyperpolarizing voltage ramps (between +50 or +100 and −100 mV, 7 s) or square pulses of variable magnitude and duration were applied. Ramps were run every 15–20 s over a period of 5–40 min. Typically, steady transmembrane potentials were continuously applied (10–40 min), with only short interruptions to evince the baseline. The longer recordings were performed while exchanging the external solution (at least twice the chamber volume over 1–2 min); thus, any event appearing while lowering external calcium was likely captured.

Results

To determine whether functional hemichannels would be sufficient to support Cx37-mediated growth suppression, we mutated two of the three cysteines in the first extracellular loop of Cx37 to alanines, with the expectation that the mutant protein would be unable to form functional gap junction channels but retain its ability to form functional hemichannels. Three hygromycin-resistant iRin37-C61,65A subclones (1B3, 1C3 and 1D2) were selected for further study. Cx37 expression levels in these subclones were comparable to that observed in iRin37 cells (Fig. 1A).

Since we previously demonstrated that channel function was necessary for Cx37-mediated growth suppression, we next determined, using two approaches, whether the Cx37-C61,65A protein localized to the plasma membrane in a manner comparable to Cx37-WT. First, immunofluorescence and confocal microscopy were used to examine the localization of WT and mutant Cx37 in both iRin cells and transiently transfected MDCK cells. iRin37 and iRin37-C61,65A clone 1C3 and 1D2 cells (Fig. 1B, panels a, b and c, respectively) induced for 24 h with 2 μg/ml doxycycline revealed Cx37 expression in the cytoplasm and as punctate and diffuse labeling at appositional and nonappositional plasma membranes (arrows). Similarly, Cx-deficient MDCK cells transiently transfected to express Cx37-WT or Cx37-C61,65A (Fig. 1B, panels d and e, respectively) expressed Cx37 in the cytoplasm and both appositional and nonappositional plasma membrane. Second, biotin-coupled maleimide was used to label reactive cysteines exposed (by DTT treatment in the presence or absence of extracellular calcium) on the extracellular surface of Cx37-WT- and Cx37-C61,65A-expressing cells. Biotinylated protein was immunoprecipitated from total protein with streptavidin-conjugated resin and Cx37 protein detected by immunoblotting. Cx37 was detected with this strategy in both the WT and mutant-expressing cell lines (Fig. 1C), indicating that both the WT and Cx37-C61,65A proteins were present in the plasma membrane. Together, the immunofluorescence and biotinylation results indicated that both proteins (mutant and WT) localize to and insert into the plasma membrane.

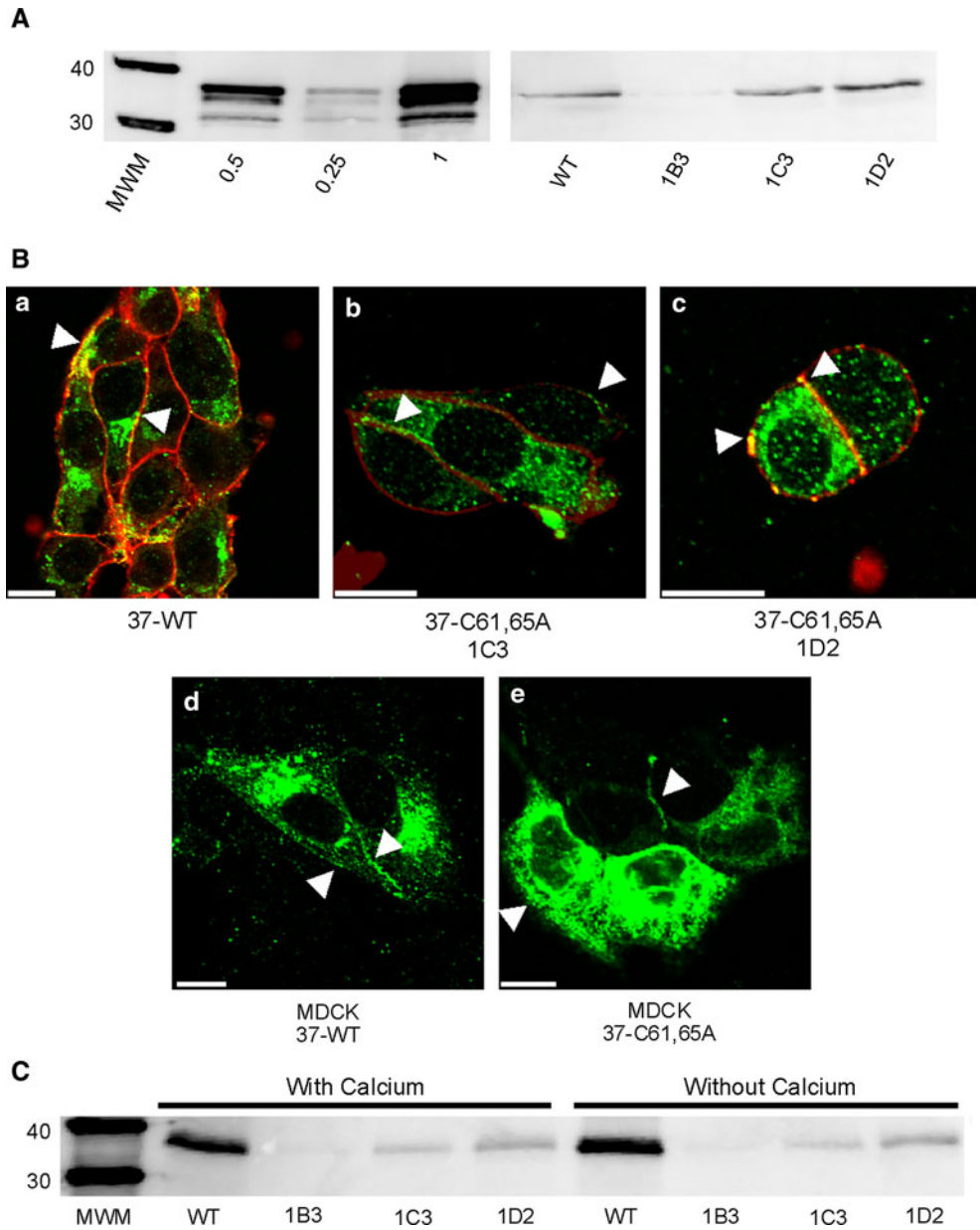

Fig. 1 Expression and localization of Cx37-C61,65A and Cx37-WT are comparable. **A** Western blots of GST-37CT loaded in different amounts (*left*) and total protein isolated from iRin37 and three clones (1B3, 1C3 and 1D2) of iRin37-C61,65A cells (*right*). iRin cells were induced for 24 h with 2 μg/ml doxycycline, whole-cell protein was isolated and 50 μg of total cell protein was loaded for each sample. Expression levels for each cell line, determined by comparing band intensities of the samples to the standard curve generated using GST-37CT, were 3.7, 4.5 and 5.1 pmol/mg of total cell protein for clones 1B3, 1C3 and 1D2, respectively, and 4.5 pmol/mg protein for iRin37 cells. **B** Confocal images of Cx37 (*green*) localization with biotinylated membrane proteins (*red*) in induced iRin37 (37-WT) (*a*), iRin37-C61,65A 1C3 (37-C61,65A 1C3) (*b*) and iRin37-C61,65A 1D2 (37-C61,65A 1D2) (*c*) cells showing the presence of punctate labeling at appositional and nonappositional membranes (*arrows*). Confocal images of Cx37 (*green*) localization in MDCK cells transiently transfected to express Cx37-WT (MDCK 37-WT) (*d*) or Cx37-C61,65A (MDCK 37-C61,65A) (*e*) also showing the presence of punctate labeling at appositional and nonappositional membranes (*arrows*). *Scale bars* = 10 μm. **C** Western blot of membrane localized Cx37 isolated from Cx37-WT or -C61,65A expressing iRin cells. Induced iRin37 (WT) and iRin37-C61,65A clones 1B3, 1C3 and 1D2 were DTT- and maleimide-biotin-treated and harvested, and protein was immunoprecipitated with streptavidin and immunoblotted with anti-Cx37 antibody. Solutions either contained or lacked calcium. Detected Cx37 indicates membrane insertion of this protein. Differences in band intensity in part reflect different cell densities in initial samples. Loaded 25 μl of each sample

Next, we determined whether expression of the Cx37-C61,65A protein altered the proliferative properties of iRin cells. The noninduced cells of all cell lines proliferated comparably (Fig. 2A). When iRin37 cells were induced to express Cx37-WT, proliferation over the 21-day period was significantly suppressed (Fig. 2B). In contrast, induced

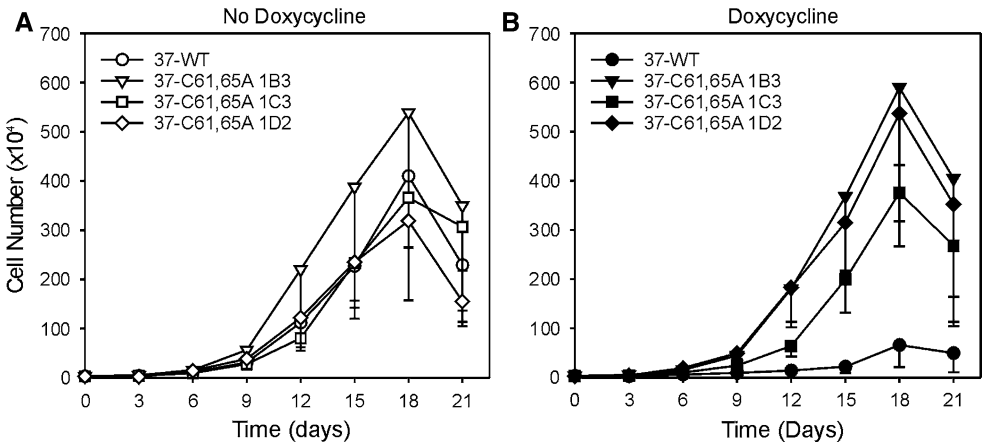

Fig. 2 Proliferation of Rin cells is suppressed by expression of Cx37-WT but not Cx37-C61,65A. **A** Proliferation was comparable between iRinCx37-WT and the three clones of iRinCx37-C61,65A when connexin expression was not induced. In contrast, proliferation of induced iRinCx37-WT cells (*filled circles*, **B**) was suppressed compared to the iRin clones with induced expression of Cx37-C61,65A. Four growth curves (with or without dox) were performed for each cell line except the iRin37-C61,65A-1C3 clone, for which five experiments were performed. Where *error bars* are not obvious, they are smaller than the size of the data point

expression of Cx37-C61,65A had no effect on Rin cell proliferation (Fig. 2B), even in the 1D2 clone with the highest level of expression. These results are similar to those obtained with the Cx37-T154A mutant (Good et al. 2011), which eliminates Cx37's growth-suppressive properties and, demonstrably, junctional channel formation. We therefore questioned whether Cx37-C61,65A formed functional hemichannels.

Initially, we determined whether the Cx37-C61,65A protein formed functional hemichannels using a dye-uptake strategy. Cx37 gap junction channels are cation-selective and readily permeated by the small cationic dye NBD-M-TMA$^+$ (Ek-Vitorín and Burt 2005), so this dye was selected to determine whether Cx37-C61,65A hemichannels would mediate dye uptake. A gap junction channel–impermeant dye (3,000-dalton rhodamine-labeled dextran) was included in all uptake experiments so that damaged cells (positive for rhodamine) would not be mistakenly counted as positive for hemichannel-mediated dye uptake. After washing Cx37-WT-expressing iRin cells with an EGTA–low-Ca^{2+} solution and performing the dye-uptake experiment in a low-[Ca^{2+}] dye solution, many more induced iRin37 cells were positive for NBD-M-TMA$^+$ than noninduced cells (compare panels a, b and c in Fig. 3B to panels d, e and f). Data from multiple experiments (quantified in Fig. 3A) showed that approximately 43 ± 4 % of Cx37-WT-expressing iRin cells ($n = 8$ wells) were positive for NBD-M-TMA$^+$ uptake and negative for rhodamine-dextran, a value significantly ($p < 0.001$) larger than the 10 ± 4 % observed for noninduced cells ($n = 7$ wells). Repetition of these procedures on induced versus noninduced iRin37-C61,65A cells (clone 1C3) revealed no significant differences in dye-positive cells (compare panels g, h and i in Fig. 3B to panels j, k and l). Of induced iRin-Cx37-C61,65A cells ($n = 10$ wells), 6 ± 1 % were NBD-M-TMA$^+$ positive compared to 6 ± 2 % of noninduced cells ($n = 9$ wells) (Fig. 3A). These results suggest that Cx37-C61,65A does not form a functional hemichannel; however, the dye-uptake approach is insensitive to the activity of dye-impermeant channels and to activity of individual channels, so we next turned to electrophysiological approaches.

To facilitate recognition of possible Cx37-C61,65A channel events, we first characterized the channels present in iRin parental cells and the channels formed by Cx37-WT. Parental iRin cells do not form functional gap junctions (data not shown). Using dual whole-cell voltage-clamp methods, the mean macroscopic conductance observed for induced iRin37 cells was 4 ± 1 nS ($n = 13$, including two cell pairs that showed no measurable coupling) (Fig. 4A). This level of coupling is comparable to previously reported data for this cell line (Burt et al. 2008; Good et al. 2011). In contrast, no electrical coupling could be detected in either induced ($n = 19$) or noninduced ($n = 9$) iRin37-C61,65A-expressing cells (Fig. 4A)—all values were below 0.3 nS and not different from system noise levels. Large-conductance single-channel events were observed in iRin37 cell pairs with naturally low coupling levels (Fig. 4B). In solutions containing 1 mM Ca^{2+} (Fig. 4B), gap junction channel events were between 250 and 350 pS and dwell times at any conductance level were very brief (flickering activity). In contrast, when in low $[Ca^{2+}]_0$ (Fig. 4C) channel conductances were larger, residual states evident and dwell times longer. As expected, comparable junctional channel activity was not seen in iRin37-C61,65A-expressing cell pairs ($n = 19$), indicating that this mutant does not form functional gap junction channels.

Based on the behavior of the Cx37-WT gap junction channel, hemichannel conductances were expected to be

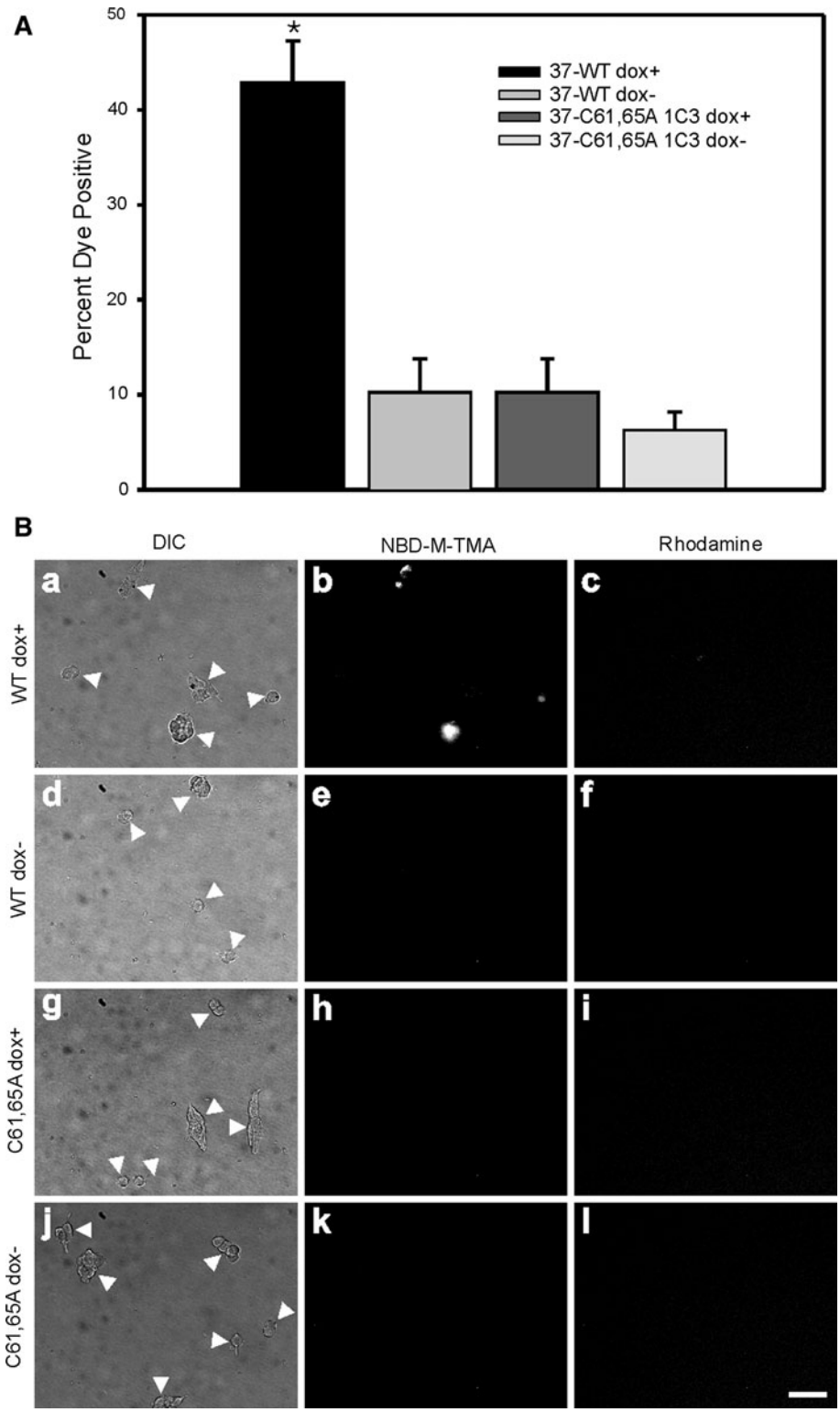

Fig. 3 Cx37-C61,65A does not form hemichannels able to mediate dye uptake. **A** The percent of cells positive for NBD-M-TMA uptake and negative for rhodamine dextran was compared to determine hemichannel function. In cells induced to express Cx37-WT, dye uptake was significantly more frequent (*$p < 0.001$) than in noninduced cells or cells induced to express Cx37-C61,65A. **B** Representative images of DIC (*arrows* indicate isolated cells or cell clusters), NBD-M-TMA and rhodamine dextran fields for iRin37 induced (*a–c*) and noninduced (*d–f*), iRin37-C61,65A 1C3 induced (*g–i*) and noninduced (*j–l*). *Scale bar* = 20 μm, applies to all images

quite large (500–700 pS, double the gap junction channel's conductance). Most voltage ramps performed on single Cx37-WT-expressing cells under normal external calcium conditions revealed no evidence of channel activity, but some showed activity at voltages incompatible with activity of Cx37-WT hemichannels, $V_m > \pm 70$ mV; the presence of these channels was confirmed and their amplitude (75–100 pS) documented with square pulses of $V_m > \pm 70$ mV (data not shown). Channels similar to these were also frequently observed in iRin parental cells (not

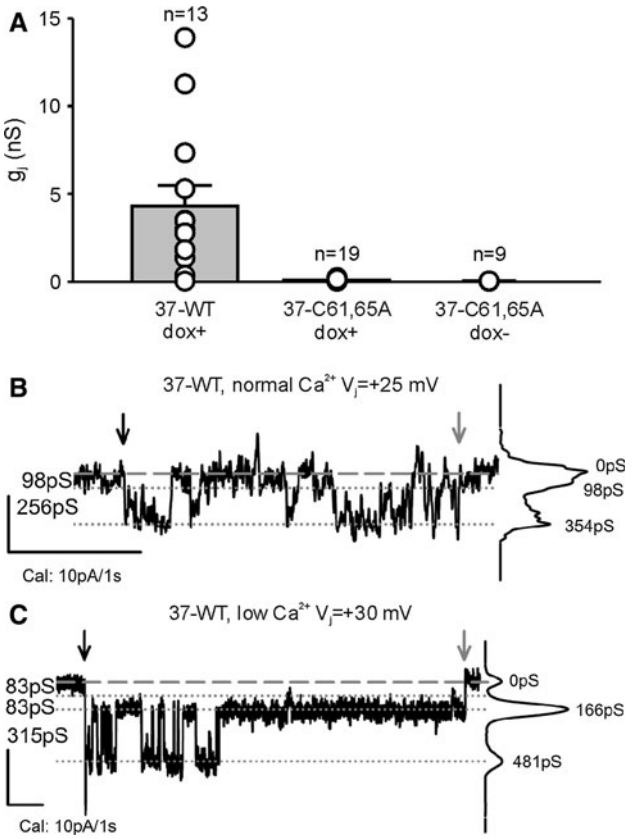

Fig. 4 Cx37-C61,65A does not form functional gap junction channels. **A** iRin cell pairs induced to express Cx37-WT (37-WT dox+) were variably coupled, with g_j commonly between 1 and 5 nS. In contrast, induced and noninduced iRin37-C61,65A cells were not detectably coupled (data from 1C3 and 1D2 clones). Notice that all of the iRin37-C61,65A cell pairs evaluated, whether induced or noninduced, had g_j values <0.3 nS, which is not different from electrical noise at these recording settings. **B**, **C** Single-channel events from iRin37 dox+ recorded in external solutions containing either normal (**B**) or low (**C**) calcium, as described in the dye-uptake protocol. Notice that channel flickering decreased upon introduction of low external calcium so that transitions corresponding to ~300 pS and substates corresponding to ~80 pS were readily apparent. *Downward black* and *gray arrows* indicate the start and end of the voltage pulse, respectively

transfected with any connexins) (Fig. 5A, B) and in both induced and noninduced iRin37-C61,65A cells (Fig. 5E, F). Thus, these events are unlikely to represent Cx37 hemichannel activity. On occasion (one in seven tested cells), voltage ramps performed in normal $[Ca^{2+}]_0$ on Cx37-WT-expressing cells revealed, transiently, activity in a V_m range (±20–50 mV) compatible with the opening of Cx37-WT hemichannels (Fig. 5C). Accordingly, in Cx37-WT-expressing cells, large-conductance (≥300 pS) transitions were observed during application of small V_m pulses (Fig. 5D) (one cell out of four tested, two successive pulses of many applied over more than 20 min in normal calcium). No similar activity was observed during either voltage ramps ($n = 28$ cells, Fig. 5E) or application of square pulses ($n = 7$ cells, recording from 10 to >25 min long; Fig. 5F) performed on Cx37-C61,65A mutant–expressing cells.

Since dye-uptake studies were successful only when the cells were washed with an EGTA-containing solution, we examined both Cx37-WT- and Cx37-C61,65A-expressing cells for electrophysiological evidence of hemichannel activity following a similar protocol. Hemichannel openings were transiently seen in two out of ten successive ramps implemented immediately following the lowering of external calcium with EGTA-containing solution in a Cx37-WT-expressing cell (Fig. 6A). In three out of six additional cells, similar, although shorter, duration openings were documented 5–20 min after lowering $[Ca^{2+}]_0$ (not shown). Hemichannel transitions of Cx37-WT were also seen under these low-$[Ca^{2+}]_0$ conditions during application of small V_m square pulses (channels transiently present within the first 5 min after lowering $[Ca^{2+}]_0$ in two of four cells; 20- to 30-min recordings; Fig. 6B). In contrast, comparable hemichannel activity was not observed in Cx37-C61,65A-expressing cells during application of ramps (six cells, 25- to 50-min records) or square pulses (five cells, 30- to 45-min records) in low $[Ca^{2+}]_0$ (Fig. 6C, D). Together the electrophysiology data strongly suggest either that Cx37-C61,65A does not form a functional hemichannel or that its open probability is sufficiently low under the conditions of our measurements that we could not detect it.

Discussion

Connexins form channels that serve (at least) two functions, transmembrane and intercellular signaling. In both cases the channels mediate the diffusive flux of ions and small molecules down their electrochemical gradients. While channel function is the best-described function of connexins, it is increasingly clear that the carboxy terminus of these proteins, through interaction with an array of intracellular proteins, also participates in cellular functions in a channel-independent manner. Several connexins have been demonstrated to participate in tumor suppression via both channel-dependent and channel-independent mechanisms (Kardami et al. 2007; King and Bertram 2005). We previously demonstrated that in Rin cells Cx37, but not Cx40 or Cx43, suppresses cell proliferation by prolonging all phases of the cell cycle, G_1 most prominently (Burt et al. 2008). To understand which properties of Cx37 are central to its growth-suppressive action, we first explored whether channel function was necessary for Cx37-mediated growth suppression. Since Cx40 and Cx43 form channels with a similar or less selective permeability profile than Cx37 (Ek-Vitorín and Burt 2005; Weber et al. 2004), we expected

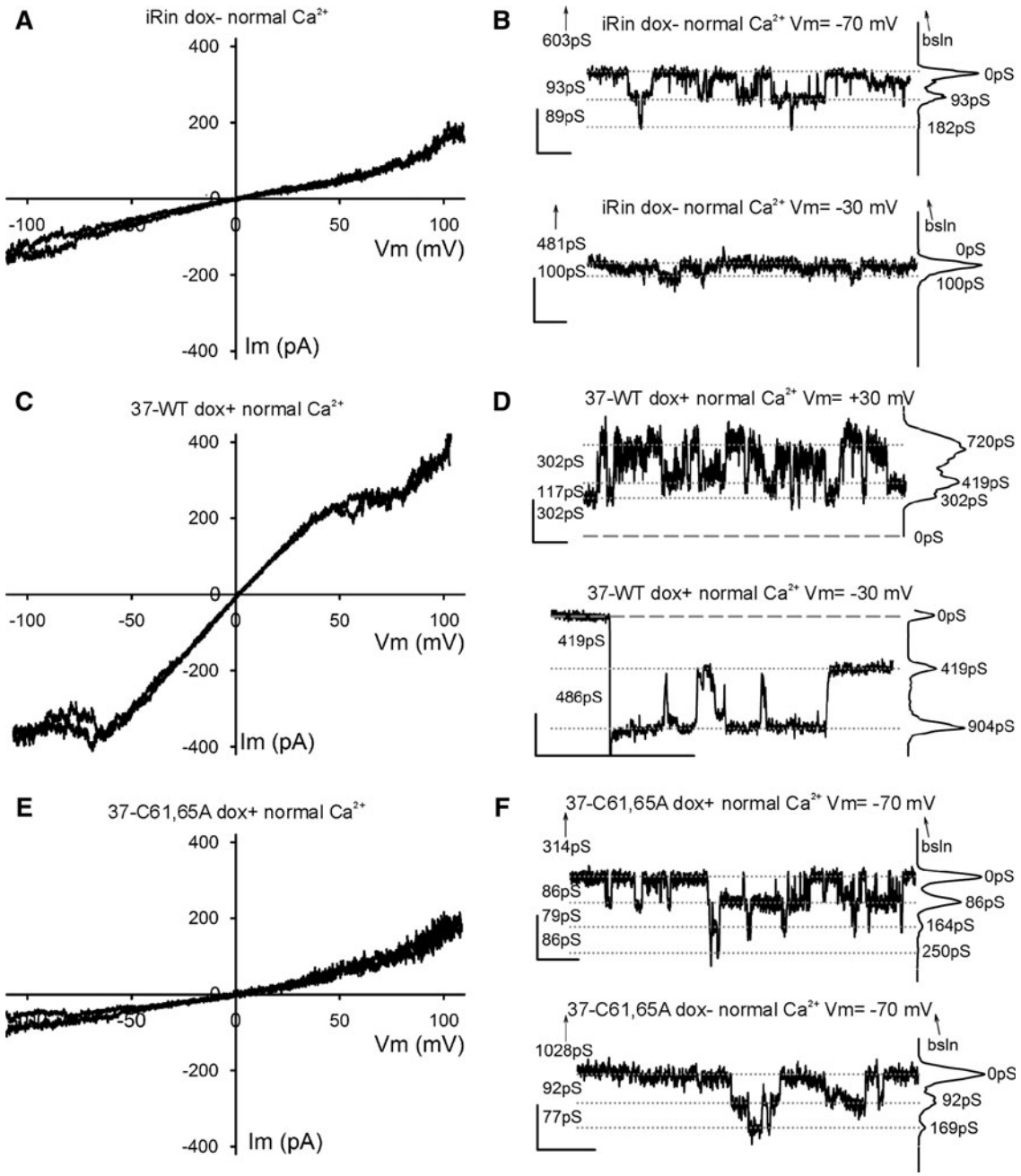

Fig. 5 Whole-cell voltage-clamp recordings obtained in normal external calcium concentration conditions. **A**, **C**, **E** Plots showing two exemplary traces of voltage ramps applied to parental iRin (not transfected with any Cx37) (**A**), iRin37 (**C**) and iRin37-C61,65A (**E**) cells bathed in solutions with normal external calcium content. In (**C**) the two representative traces were from a series of ten ramps from an iRin37 cell that showed current inactivation at high voltage values. **B**, **F** Transitions of membrane current (corresponding to 85–100 pS) appeared with square V_m pulses in iRin (**B**) and iRin37-C61,65A (**F**) induced (*top trace*) and noninduced (*bottom trace*) cells. Note that these current transitions are barely distinguishable from the noise at $V_m = -30$ mV (**B**, *bottom trace*); however, transitions of similar conductance were also observed at $V_m = -70$ mV. **D** Transitions of membrane current from single cells expressing Cx37-WT during ±30-mV square pulses in normal external calcium. Notice that recording is noisier at positive values; while these are contiguous recordings, transitions appear larger (>400 pS) at negative voltages. **B**, **D**, **F** All-points histograms are shown at the *right* of each trace, baseline is denoted by *dashed lines* and current levels by *dotted lines*, numbers on the *left* correspond to "between lines" conductance differences and numbers next to the histogram peaks indicate the cumulative conductance from the chosen zero current level; *upward-pointing arrows* indicate the distance (in pS) and direction of the true (zero current) baseline, when not displayed; *vertical/horizontal calibration bars* correspond to 10 pA and 1 s, respectively

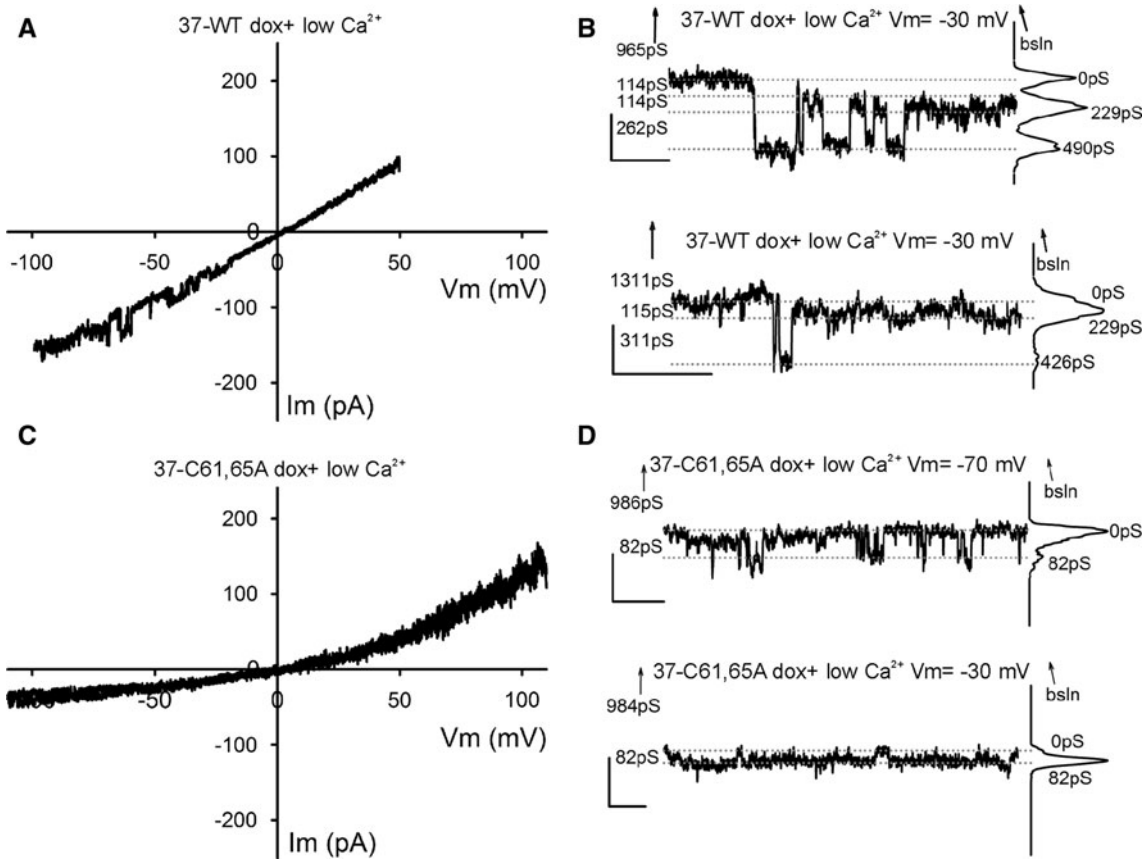

Fig. 6 Whole-cell voltage-clamp recordings obtained under conditions of low extracellular calcium concentration. **A**, **C** Plots showing one or two exemplary traces of ramps from iRin37 (**A**) and iRin37-C61,65A (**C**) cells. iRin37 cells (**A**) in low external calcium conditions show clear evidence of channel transitions in the V_m range of −20 to −60 mV (observed in two out of ten ramps, one shown), while Cx37-C61,65A-expressing cells (**c**) show no evidence of channel activity in any ramps in the V_m range −20 to −60 mV (see text for further details). **B** Transitions of membrane current (corresponding to conductances <400 pS) from single cells expressing Cx37-WT during −30 mV square pulses in low external calcium. Notice that most events appear to be smaller than observed in normal calcium, perhaps revealing more transitions to and from a substate. **D** Current transitions of Cx37-C61,65A-expressing cells. Notice transitions correspond to events of less than 100 pS. Traces are labeled as in Fig. 5 **B**, **D** and **F**

that channel function would not be necessary for Cx37-mediated growth suppression. Contrary to expectation, Cx37-T154A, which forms a nonfunctional gap junction channel, was not growth-suppressive, suggesting that channel functionality is necessary for Cx37-mediated growth suppression in Rin cells (Good et al. 2011). Although we did not test this mutant for hemichannel function, mutation of the corresponding highly conserved site in Cx50 renders both the hemichannel and gap junction channel nonfunctional (Beahm et al. 2006); thus, it is probable that Cx37-T154A hemichannels are also nonfunctional. Thus, the Cx37-T154A study did not permit us to discern whether functionality of hemichannels, gap junction channels or both is necessary for Cx37-mediated growth suppression.

In the current study we attempted to address the sufficiency of hemichannels in Cx37-mediated growth suppression, expecting that functional hemichannels would be sufficient and functional gap junction channels unnecessary for Cx37-mediated growth suppression. Three observations lead to this hypothesis. First, Cx37-WT-expressing Rin cells are growth-suppressed at all tested plating densities, even densities where cell–cell contact and, therefore, gap junction formation are rare (Burt et al. 2008). Second, Cx37 hemichannels appear to be functional under physiological conditions, at least in some cell types (Wong et al. 2006). Third, transmembrane gradients for ions and small molecules (e.g., calcium and ATP) are always present, whereas intercellular gradients are only transiently present because gap junction channels, by mediating diffusive exchange, tend to neutralize these gradients. Thus, opening of Cx37-WT hemichannels could mediate efflux or influx of critical signaling molecules that directly or indirectly regulate intracellular signaling processes involved in cell cycle progression.

To address whether Cx37 hemichannels might be sufficient to explain Cx37-mediated growth suppression, we created a mutant that we expected would support

hemichannel activity comparable to that displayed by Cx37-WT but not support gap junction channel formation. Available evidence suggested that mutation of one or more of the six highly conserved cysteines located in the extracellular loops of connexins would disable gap junction channel formation while preserving hemichannel functionality (Foote et al. 1998; Dahl et al. 1991, 1992; Bao et al. 2004; Tong et al. 2007). Consequently, we mutated the second and third cysteines in the first extracellular loop of Cx37 to alanines and stably transfected the encoding sequence into iRin cells, thereby creating the iRin37-C61,65A cell lines. Cx37 expression, localization to and insertion into the plasma membrane were comparable in iRin37-C61,65A and iRin37 cells. However, unlike the wild-type protein, the Cx37-C61,65A protein did not suppress the proliferation of iRin cells.

Failure of Cx37-C61,65A to growth-suppress prompted us to check whether the mutated protein formed functional hemichannels but nonfunctional gap junction channels. Cells expressing Cx37-C61,65A were never observed to take up NBD-M-TMA$^+$, a dye previously shown to readily permeate Cx37-WT gap junction channels (Ek-Vitorín and Burt 2005) and shown here to be taken up by iRin37 cells only when induced to express Cx37-WT protein and exposed to low-$[Ca^{2+}]_0$ conditions. In addition, using whole-cell voltage-clamp techniques, we detected functional Cx37-WT hemichannels and gap junction channels in both normal and low-$[Ca^{2+}]_0$ conditions but were unable to detect functional Cx37-C61,65A hemichannels or gap junction channels under comparable recording conditions. Thus, the failure of Cx37-C61,65A to suppress proliferation of Rin cells is entirely consistent with our previous studies demonstrating that channel functionality is necessary and proper localization of a normal carboxy terminus insufficient for Cx37-mediated growth suppression.

Failure of Cx37-C61,65A to form functional hemichannels suggests either that disruption of disulfide bond formation in the extracellular loops prevents the channel from adopting a (closed) configuration that can be triggered to open (by docking, exposure to low $[Ca^{2+}]_0$, mechanical stimulus or even phosphorylation-dependent regulation) or that the open configuration is blocked by the extracellular loops due to mutations there. Arguing against the possibility of channel block is the complete absence of hemichannel events and dye uptake in cells expressing the mutant protein, even when "triggered" to open by exposure to low-$[Ca^{2+}]_0$ conditions. Bao and colleagues (2004) and Tong and colleagues (2007) reported that Cx43 with all six cysteines in the extracellular loops mutated to alanine forms functional hemichannels with Ca^{2+}-sensitive open probability characteristics. Assuming similar behavior of other connexins, these observations collectively suggest that docking of hemichannels to form functional gap junction channels is blocked by mutation of even one cysteine in the extracellular loops (Dahl et al. 1992; Foote et al. 1998); and our data suggest that mutation of fewer than all six cysteines results in hemichannels that are closed and unable to be triggered open.

We expected the current study to distinguish whether Cx37 hemichannel activity, not gap junction channel activity, was sufficient to explain Cx37-mediated growth suppression of Rin cells and instead provide further evidence that an open channel configuration must be possible for growth suppression by Cx37 (Burt et al. 2008; Good et al. 2011). It remains unclear what, if anything, permeates the hemichannel/gap junction channel to influence cell cycle progression. Potentially germane to this issue, however, is the observation that the wild-type hemichannel opens in the presence of extracellular calcium ions, albeit with only modest probability. However, since culture medium contains "normal" levels of calcium and Cx37 is growth-suppressive at cell densities where gap junction channel formation is rare (Burt et al. 2008), hemichannels able to open could allow the influx (or efflux) of signaling molecules with a growth-regulatory effect.

In summary, we have demonstrated that mutation of the second and third cysteines in the first extracellular loop of Cx37 to alanines results in a protein that is no longer growth-suppressive to Rin cells. The absence of a growth-suppressive function is consistent with previous observations in which the capacity to form a functional channel was demonstrated as necessary for the growth-suppressive action of Cx37. Our data further suggest that disulfide bond formation between the extracellular loops is critical to the hemichannel's ability to adopt a conformation able to be triggered open as well as its ability to dock with another hemichannel to form a gap junction channel. Alternate (or additional) mutation sites will be necessary to create a Cx37 protein able to form functional hemichannels but unable to form functional gap junction channels. Thus, it remains to be determined whether transmembrane (hemichannel) or intercellular (gap junction channel) signaling, or both, is necessary for Cx37-mediated growth suppression and whether channel-independent properties of Cx37 might also be necessary.

Acknowledgments The authors acknowledge Dr. Ross Johnson for encouraging, in a hands-on manner and from a distance, our pursuit of hemichannel function. The authors also acknowledge the technical support of Tasha K. Nelson. These studies were supported by the National Institutes of Health, grants (to J.M.B.) R01HL057832, R01HL077675 and T32HL007249 (supporting M.E.G.).

References

Bao X, Chen Y, Reuss L, Altenberg GA (2004) Functional expression in *Xenopus* oocytes of gap-junctional hemichannels formed by a cysteine-less connexin 43. J Biol Chem 279:9689–9692

Beahm DL, Oshima A, Gaietta GM, Hand GM, Smock AE, Zucker SN, Toloue MM, Chandrasekhar A, Nicholson BJ, Sosinsky GE (2006) Mutation of a conserved threonine in the third transmembrane helix of alpha- and beta-connexins creates a dominant-negative closed gap junction channel. J Biol Chem 281:7994–8009

Bednarczyk D, Mash EA, Aavula BR, Wright SH (2000) NBD-TMA: a novel fluorescent substrate of the peritubular organic cation transporter of renal proximal tubules. Pflugers Arch 440:184–192

Burt JM, Fletcher AM, Steele TD, Wu Y, Cottrell GT, Kurjiaka DT (2001) Alteration of Cx43:Cx40 expression ratio in A7r5 cells. Am J Physiol Cell Physiol 280:C500–C508

Burt JM, Nelson TK, Simon AM, Fang JS (2008) Connexin 37 profoundly slows cell cycle progression in rat insulinoma cells. Am J Physiol Cell Physiol 295:C1103–C1112

Dahl G, Levine E, Rabadan-Diehl C, Werner R (1991) Cell/cell channel formation involves disulfide exchange. Eur J Biochem 197:141–144

Dahl G, Werner R, Levine E, Rabadan-Diehl C (1992) Mutational analysis of gap junction formation. Biophys J 62:172–180

Ek-Vitorín JF, Burt JM (2005) Quantification of gap junction selectivity. Am J Physiol Cell Physiol 289:C1535–C1546

Foote CI, Zhou L, Zhu X, Nicholson BJ (1998) The pattern of disulfide linkages in the extracellular loop regions of connexin 32 suggests a model for the docking interface of gap junctions. J Cell Biol 140:1187–1197

Good ME, Nelson TK, Simon AM, Burt JM (2011) A functional channel is necessary for growth suppression by Cx37. J Cell Sci 124:2448–2456

Goodenough DA, Paul DL (2003) Beyond the gap: functions of unpaired connexon channels. Nat Rev Mol Cell Biol 4:285–294

Harris AL (2001) Emerging issues of connexin channels: biophysics fills the gap. Q Rev Biophys 34:325–472

Kardami E, Dang X, Iacobas DA, Nickel BE, Jeyaraman M, Srisakuldee W, Makazan J, Tanguy S, Spray DC (2007) The role of connexins in controlling cell growth and gene expression. Prog Biophys Mol Biol 94:245–264

King TJ, Bertram JS (2005) Connexins as targets for cancer chemoprevention and chemotherapy. Biochim Biophys Acta 1719:146–160

Nakagawa S, Maeda S, Tsukihara T (2010) Structural and functional studies of gap junction channels. Curr Opin Struct Biol 20:423–430

Plum A, Hallas G, Magin T, Dombrowski F, Hagendorff A, Schumacher B, Wolpert C, Kim J-S, Lamers WH, Evert M, Meda P, Traub O, Willecke K (2000) Unique and shared functions of different connexins in mice. Curr Biol 10:1083–1091

Scherer SS, Xu YT, Nelles E, Fischbeck K, Willecke K, Bone LJ (1998) Connexin32-null mice develop demyelinating peripheral neuropathy. Glia 24:8–20

Simon AM, Goodenough DA, Li E, Paul DL (1997) Female infertility in mice lacking connexin 37. Nature 385:525–529

Simon AM, Chen H, Jackson CL (2006) Cx37 and Cx43 localize to zona pellucida in mouse ovarian follicles. Cell Commun Adhes 13:61–77

Sohl G, Willecke K (2004) Gap junctions and the connexin protein family. Cardiovasc Res 62:228–232

Solan JL, Lampe PD (2007) Key connexin 43 phosphorylation events regulate the gap junction life cycle. J Membr Biol 217:35–41

Sonntag S, Sohl G, Dobrowolski R, Zhang J, Theis M, Winterhager E, Bukauskas FF, Willecke K (2009) Mouse lens connexin23 (Gje1) does not form functional gap junction channels but causes enhanced ATP release from HeLa cells. Eur J Cell Biol 88:65–77

Tong D, Li TY, Naus KE, Bai D, Kidder GM (2007) In vivo analysis of undocked connexin43 gap junction hemichannels in ovarian granulosa cells. J Cell Sci 120:4016–4024

Weber PA, Chang HC, Spaeth KE, Nitsche JM, Nicholson BJ (2004) The permeability of gap junction channels to probes of different size is dependent on connexin composition and permeant-pore affinities. Biophys J 87:958–973

Wong CW, Christen T, Roth I, Chadjichristos CE, Derouette JP, Foglia BF, Chanson M, Goodenough DA, Kwak BR (2006) Connexin37 protects against atherosclerosis by regulating monocyte adhesion. Nat Med 12:950–954

J Membrane Biol (2012) 245:381–388
DOI 10.1007/s00232-012-9460-4

Regulation of Connexin43 Gap Junction Protein Triggers Vascular Recovery and Healing in Human Ocular Persistent Epithelial Defect Wounds

Susan Ormonde · Chi-Ying Chou · Lucy Goold · Con Petsoglou · Rasha Al-Taie · Trevor Sherwin · Charles N. J. McGhee · Colin R. Green

Received: 30 March 2012 / Accepted: 20 June 2012 / Published online: 15 July 2012

Abstract Transiently blocking the expression of the gap junction protein connexin43 using antisense oligodeoxynucleotides or blocking hemichannels with connexin mimetic peptides has been shown to significantly improve outcomes in a range of acute wound models. Less is known about their likely effects in nonhealing wounds. In the eye, prolonged inflammation and lack of epithelial recovery in nonhealing corneal epithelial wounds may lead to corneal opacity, blindness or enucleation. We report here the first human applications of antisense oligodeoxynucleotides that transiently block translation of connexin43 in a prospective study of five eyes with severe ocular surface burns (persistent epithelial defects), which were unresponsive to established therapy for 7 days to 8 weeks prior to treatment. Connexin43-specific antisense oligodeoxynucleotide was delivered in cold, thermoreversible Poloxamer407 gel under either an amniotic membrane graft or a bandage contact lens. The connexin43-specific antisense application reduced inflammation within 1–2 days, and in all five eyes complete and stable corneal reepithelialization was obtained. Recovery of the vascular bed and limbal reperfusion appeared to precede corneal epithelial recovery. We conclude that connexin modulation provides a number of benefits for nonhealing ocular burn wounds, one of which is to promote vascular recovery.

S. Ormonde · C.-Y. Chou · R. Al-Taie · T. Sherwin · C. N. J. McGhee · C. R. Green (✉)
Department of Ophthalmology, Faculty of Medical and Health Sciences, New Zealand National Eye Centre, University of Auckland, Private Bag 92019, Auckland, New Zealand
e-mail: c.green@auckland.ac.nz

L. Goold · C. Petsoglou
Save Sight Institute, GPO Box 4337, Sydney 2001, Australia

Keywords Gap junction · Connexin · Hemichannel · Wound healing · Cornea

Introduction

Gap junctional communication and hemichannel opening have been associated with the spread of cell death signals and lesion spread after tissue injury (Frantseva et al. 2002; Garcia-Dorado et al. 1997; Lin et al. 1998; Rawanduzy et al. 2009). In a number of preclinical models of tissue damage and wound repair, reducing protein translation of connexin43 (Cx43) with antisense oligodeoxynucleotides (Cx43AsODN) or hemichannel blockade has been demonstrated to limit inflammation, edema and lesion spread and to provide improved healing or functional outcomes. This has been noted in skin incision and excision wounds (Mori et al. 2006; Qiu et al. 2003), skin burns (Coutinho et al. 2005), the cornea of the eye (Grupcheva et al. 2012), cardiac ischemia (Hawat et al. 2010) and the central nervous system. Central nervous system models have encompassed injuries to the spinal cord (Cronin et al. 2008; Huang et al. 2012), optic nerve (Danesh-Meyer et al. 2008), retina (Danesh-Meyer et al. 2012a) and brain (Davidson et al. 2012). In the cornea of the eye, Cx43 AsODN treatment after epithelial scrape wounding or excimer laser ablation (as used for photorefractive keratectomy) significantly reduces edema and inflammation (myofibroblast differentiation) and speeds the rate of epithelial recovery (Grupcheva et al. 2012).

In the eye, chemical and thermal ocular burns can lead to nonhealing corneal epithelial wounds that pose a significant clinical challenge. Although the management of ocular surface burns has improved with the application of amniotic membrane grafts (Fernandes et al. 2005) and autologous

limbal tissue transplant (the limbus surrounding the cornea of the eye is said to contain stem cells) (Dua et al. 2010), severe chemical burns still have a poor visual prognosis. In this prospective observational study we report the first human use of gap junction Cx43-specific antisense oligodeoxynucleotides to treat five subjects with severe, nonhealing, ocular chemical or thermal burns. All subjects were treated under compassionate-use status when no corneal recovery was apparent 1–8 weeks postinjury, despite accepted best-practice clinical management. Secondary inflammatory changes in the vascular bed of the ocular surface were evident in all cases, and Cx43AsODN treatment resulted in a rapid reduction in inflammation and recovery of the vascular bed and limbal reperfusion. In all five subjects full restoration of the ocular surface integrity was achieved.

Subjects and Methods

Five subjects presenting with severe chemical or combined chemical and thermal burns (Table 1) had extensive 1- to 2-h normal saline irrigation of the ocular surface and fornices (the regions connecting the conjunctival membrane lining the inside of the eyelid with the conjunctival membrane covering the eyeball itself) on presentation until a stable, neutral pH was established. Subjects 1 and 2 in addition had cement debris removed under sedation in conjunction with other treatments. Subsequently, all subjects received the maximum current standard of care treatment for chemical injury, including, as appropriate, g. sodium ascorbate 10 %, g. sodium citrate 10 %, topical corticosteroid (g. prednisone phosphate 0.1 %, g. prednisone acetate 1.0 % or g. dexamethasone 0.1 %), g. chloramphenicol 0.5 %, g. cyclopentolate 1 %, g. atropine 1.0 % (all drops preservative-free where possible), oral doxycycline 100 mg and oral sodium ascorbate (vitamin C).

In all five subjects the initial ocular prognosis was extremely poor with an injury grade V–VI on the Dua classification of ocular burns scale at time of treatment (Dua et al. 2001). This grading was used as it has been shown to be of more predictive value in the case of severe ocular burns (Gupta et al. 2011). A grade V–VI burn is defined as having the entire limbus (12 clock hours) and total surface conjunctiva involved. After consulting Medsafe, the New Zealand Medicines and Medical Devices Safety Authority or the Australian Therapeutic Goods Administration as appropriate, Cx43AsODN was considered as a possible last resort and "urgent innovative treatment." An extensive informed consent process was undertaken with each patient.

Cx43AsODN (5-GTAATTGCGGCAGGAGGAATTG TTTCTGTC-3) has been shown to block translation of the

Table 1 Subject demographics, brief injury details and treatment regimes for each of the five patients treated with Cx43AsODN

	Patient demographics, injury and treatment details	Dua injury grade
1	25-year-old male. Cement from high-pressure hose into left eye. Complete corneal epithelial loss, 90 % bulbar and tarsal conjunctival epithelial loss, 360-degree moderate to severe limbal ischemia. Moderate full-thickness corneal haze, moderate cells in the anterior chamber. Contralateral eye had keratoconus with 6/15 spectacle-aided visual acuity.	V–VI
	Amniotic membrane applied day 5, Cx43AsODN treated day 9.	
2	27-year-old male. Cement from high-pressure hose into both eyes (right eye responded to conventional treatment). Severe conjunctival ischemia, 360-degree limbal ischemia in left eye.	VI
	Superficial tenonectomy day 5, amniotic membrane applied day 9, Cx43AsODN treated day 15.	
3	29-year-old male. Unknown chemical burn to both eyes. Presented 12 h after incident with 60 % corneal epithelial loss and 50 % of bulbar conjunctival injury. No response to intensive standard treatment and deteriorated further, with >90 % corneal epithelium and >75 % of bulbar conjunctival epithelium lost with 270 degrees of limbal ischemia.	IV at presentation but continued to deteriorate to VI
	Consecutive Cx43AsODN treatment given under a bandage contact lens on days 7 and 8.	
4	42-year-old male. Caustic alkali burn to left eye. Complete epithelial loss with severe 360-degree limbal ischemia. Slow recovery with protective Botox ptosis at day 14 and discharged with early corneal epithelial healing under way. Deteriorated and amniotic membrane applied at days 34 and 45 but both underwent rapid proteolytic degradation.	VI
	Double amniotic membrane and Cx43AsODN treated at day 58, amniotic membrane and second Cx43AsODN treatment at day 90.	
5	17-year-old male. Severe chemical and thermal burn from exploding firework. Complete epithelial loss, fusion of eyelids to ocular surface, significant globe injury with some sparing of inferior fornix only.	VI
	Amniotic membrane with Cx43AsODN treatment at days 8 and 42.	

Injury grade is based on the Dua classification of ocular burns scale. A grade of V or VI has very poor prognosis

Cx43 gap junction protein in a number of models (see e.g., Cronin et al. 2006; Green et al. 2001; Qiu et al. 2003), and the antisense oligomers were modified to match the equivalent human sequence and delivered (2 or 20 μM final concentration) in 100 μl ice-cold, filter-sterilized 25 % w/v Pluronic F-127 (Poloxamer407; BASF, Freeport, TX) gel, a thermoreversible gel that sets as it warms to physiological temperature. The gel provides sustained delivery for the unmodified oligonucleotides, which have a half-life of <20 min in cells (Wagner 1994). The half-life for unmodified oligonucleotides in serum is 1–2 min (Phillips and Zhang 1999), thus limiting possible spread of effect from the treatment site.

In each case the eye was prepared with local anesthesia, either topical benoxinate 0.4 %, subconjunctival lignocaine or sub-Tenons marcaine. To maximize and sustain surface contact, in four of the five subjects the gel (2 μM concentration) was injected beneath an amniotic membrane graft sutured to the corneal surface, using a precooled Rycroft cannula and syringe; in the remaining case the gel at 20 μM was applied under a 14-mm corneoscleral bandage contact lens. The eyelids were then closed and padded.

All other topical treatments were stopped after application of Cx43AsODN (except in the subject who had a bandage contact lens and hourly drops were continued) and then resumed 8–12 h later. The extent and rate of epithelial recovery were assessed by measuring the total area of corneal fluorescein dye staining.

Results

Prior to Cx43AsODN treatment the anterior segments of all eyes were ischemic with associated inflammation from the chemical/thermal burn (Fig. 1a, b). Figure 1a shows subject 1 after application of an amniotic membrane at day 5 after injury and prior to connexin antisense treatment on day 9. The blood vessels on the eye surface are poorly defined, and blood flow was stagnant, with 360 degrees of corneal limbus ischemia. In Fig. 1b the eye of subject 3 is shown on the third day after injury. The bulbar conjunctiva is inflamed and has lost blood vessel definition, and the limbus had 270 degrees of ischemia, with only a small (top left) segment retaining blood flow. Slit-lamp examination with fluorescein dye staining in this same eye (Fig. 1c) shows >60 % corneal epithelial loss with fluorescein penetration beneath the remaining epithelium, indicating poor adhesion and viability. This epithelium continued to deteriorate to >90 % loss by day 7 postinjury. There was in fact virtually no epithelial recovery on any of the corneas prior to Cx43AsODN treatment, and in two subjects the eyes were continuing to deteriorate clinically, despite maximal conventional treatment.

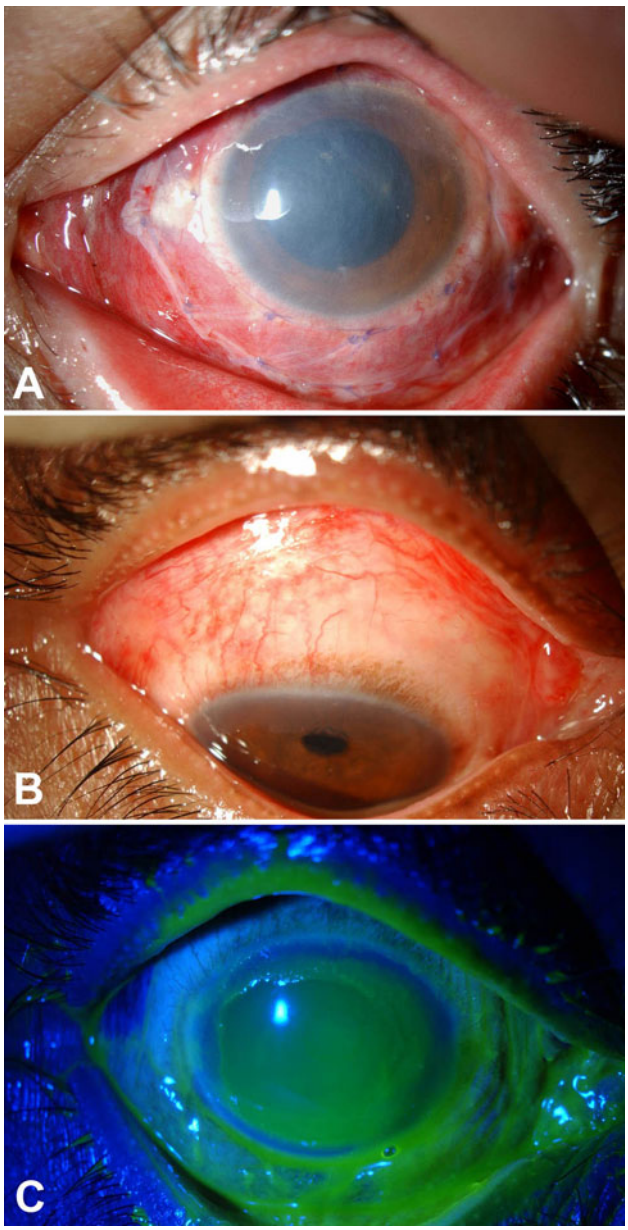

Fig. 1 Subjects presenting with severe ocular burns had ischemic or inflamed ocular surface and poor vascular definition. **a** Subject 1 after application of an amniotic membrane at day 5 after injury and prior to connexin antisense treatment on day 9. Blood vessels are poorly defined, and blood flow is stagnant, with 360 degrees of corneal limbus ischemia. **b** The eye of subject 3 on the third day after injury. The bulbar conjunctiva is inflamed but has lost blood vessel definition, and the limbus has 270 degrees of ischemia, with only a small supranasal segment retaining blood flow. Fluorescein staining (**c**) in this same eye shows >60 % corneal epithelial loss with fluorescein penetration beneath remaining epithelium, indicating poor adhesion and viability. This epithelium continued to deteriorate to over 90 % loss by day 7 postinjury, and the eye was then treated by Cx43AsODN application

In all five severe nonhealing corneal burns, treatment with Cx43AsODN reduced inflammation and a degree of limbal reperfusion was identified within 24–48 h. The most

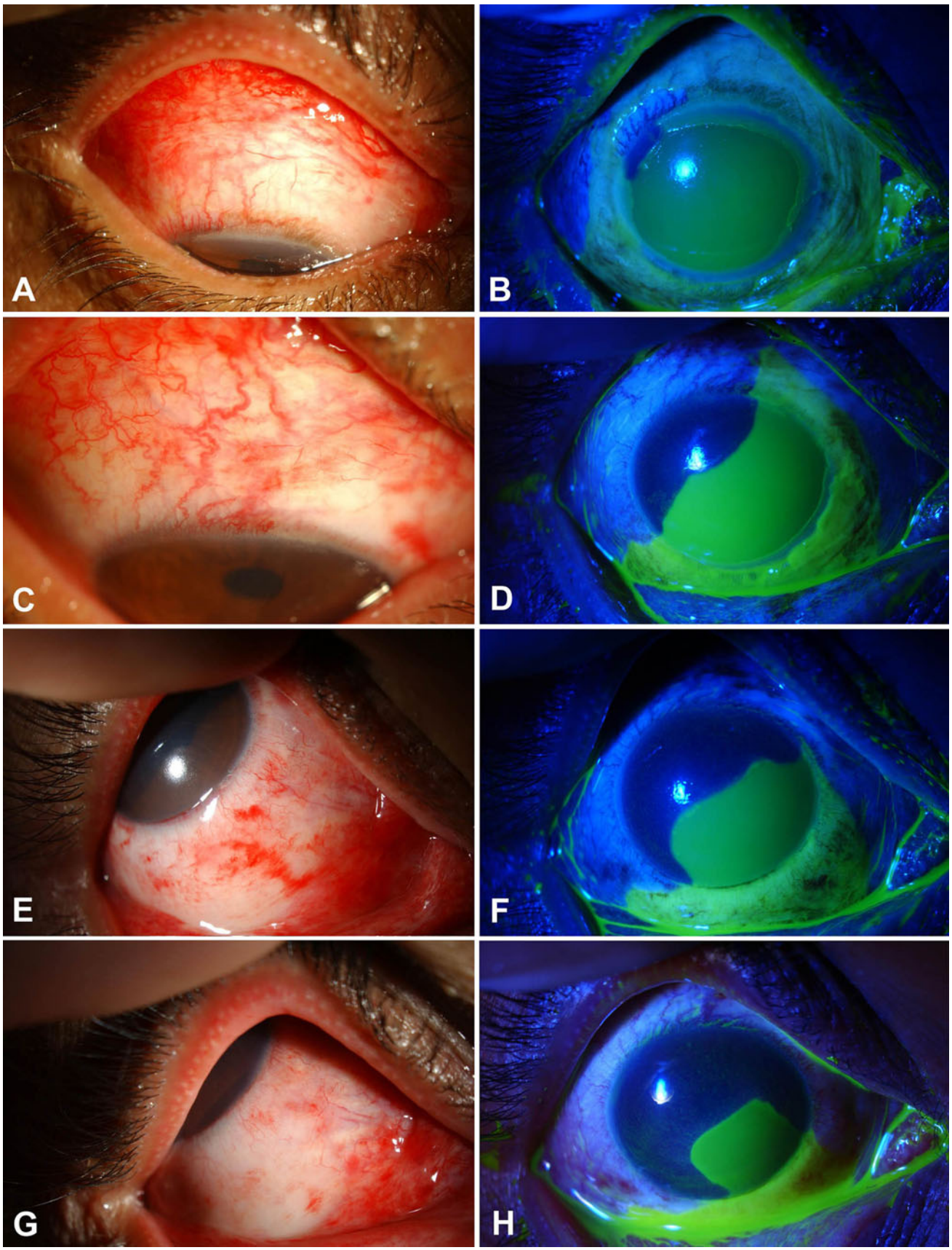
A
B
C
D
E
F
G
H

◀**Fig. 2** Recovery of the eye of subject 3 after connexin antisense treatment. On day 5 after presentation, a region of supranasal limbal perfusion is seen (**a**), and fluorescein drops revealed only a small area of epithelium remained viable (**b**). After Cx43AsODN treatment on days 7 and 8, more widespread limbal reperfusion occurred, preceding epithelial recovery in the nasal and supratemporal segments (**c** and **d** at day 2 after treatment, **e** and **f** 6 days after treatment). The last portion of the cornea to reepithelialize was the inferior-temporal region, where the limbus remained ischemic longest (**g** and **h** 8 days after treatment). Full epithelial recovery occurred within 11 days after treatment

severely injured eye (subject 5) showed a more delayed initial vascular recovery and epithelial healing 8 days after treatment. Corneal epithelial recovery typically appeared to parallel or follow limbal reperfusion in all eyes. This was highlighted by the response of subject 3. In this case limbal reperfusion and revascularization occurred in a stepwise fashion around the limbus over 8–11 days, with epithelial recovery apparent in successive corneal regions adjacent to areas where limbal reperfusion had first been restored (Fig. 2a–h). In Fig. 2a, b vessel recovery and epithelial healing are beginning at the top left (10 o'clock), but by Fig. 2c, d they have progressed between clock hours 9 and 1. In Fig. 2e and f vascular recovery and epithelial healing are evident between clock hours 7 and 2, and in Fig. 2g, h the last segment not yet showing epithelial recovery (clock hours 4–5) is also the region that remains ischemic at this point in time.

In all five cases complete ocular surface epithelial healing was attained with subsequent surface stability. Specific, brief details for each subject are given in Table 2, and epithelial recovery for each patient (based upon fluorescein staining) is graphed in Fig. 3. In all cases the connexin-specific antisense, applied at times ranging from 7 days to 8 weeks after the initial injury, is seen to have a rapid and positive effect on epithelial recovery. In two subjects reepithelialization reached a plateau, at approximately 80 % cover in one and 20 % in the other, but was retriggered with a second application of the connexin antisense, which then led to 100 % reepithelialization.

Discussion

Cx43 antisense oligonucleotides are designed to achieve transient knockdown in connexin expression followed by recovery of cell–cell coupling in order to allow normal tissue patterning and homeostasis to occur. Prior to the compassionate use in these human subjects animal studies had demonstrated efficacy for the Cx43AsODNs in aiding wound repair and improving epithelial recovery (Coutinho et al. 2005; Qiu et al. 2003).

Table 2 Specific outcomes for each subject treated with Cx43AsODN

Treatment outcomes for subjects 1–5	
1	Within 18 h of a single Cx43AsODN treatment evidence of early limbal vessel recovery through 360 degrees and corneal reepithelialization (Fig. 3a) extending 1 mm onto the cornea nasally, superiorly and temporally. Within 42 h 360 degrees of peripheral reepithelialization extending on average 3 mm onto the cornea. The eye was less inflamed, and the anterior chamber cellular reaction reduced. Six days after treatment with Cx43AsODN full reepithelialization of the cornea was attained. The ocular surface remained stable at 18 months, with the patient maintaining an unaided visual acuity of 6/9.
2	Dilatation of limbal vessels superiorly was evident within 24 h of Cx43AsODN application with commencement of local corneal reepithelialization. Corneal reepithelialization increased to 50 % by day 4 and 80 % by day 7 after treatment, healing slowing to reach 90 % by day 17 (Fig. 3b). Full corneal epithelial closure was reached 28 days after treatment. At 12 months the ocular surface remained stable, though extensive corneal vascularization limited visual acuity to 6/60 unaided.
3	Case treated by a single Cx43AsODN treatment under a 14-mm-diameter bandage contact lens on day 7 postinjury. Limbal vessel recovery was evident within 16 h, followed by ocular surface reepithelialization. A second application of Cx43AsODN was provided on day 8, and full corneal reepithelialization was achieved within 11 days posttreatment with minor conjunctival tissue growth into the cornea nasally, although the latter was not visually significant (Fig. 3c). Final visual acuity was 6/6 unaided.
4	Treated by Cx43AsODN 58 days after a severe ocular burn; limbal reperfusion was evident in the inferior 50 % of the limbus, associated with improvement to superior perfusion and early recovery of corneal epithelium within 48 h (Fig. 3d). By 18 days posttreatment the corneal epithelium had healed 70–80 %. However, 11 days later the defect size was unchanged but had developed rolled edges consistent with a persistent epithelial defect; therefore, a second Cx43AsODN treatment was given. Epithelial recovery progressed, and the defect proceeded to complete closure over the next 2 weeks. At 3 months after epithelial closure the corneal epithelial surface remained stable. Although some superficial blood vessel ingrowth onto the peripheral cornea was evident, there appeared to be moderate recovery of the limbal barrier. Final visual acuity was hand movements at 18 months.
5	Due to particularly extensive, severe and deep ocular surface damage and nonresponse to conventional treatment, Cx43AsODN was applied 9 days after injury. Progressive limbal reperfusion was noted from 8 days after treatment and reepithelialization followed. Corneal epithelial recovery reached a plateau at about 20 % coverage, and a second treatment was applied at day 42 with a rapid response (Fig. 3e). Recovery again slowed after about 80 % epithelial coverage but progressed to full, but rather conjunctivalized, corneal epithelial closure over the following 6 weeks. At 18 months postinjury, surgery to release tarsal attachment revealed a clear cornea beneath, and a good final visual outcome is expected.

The rate of epithelial recovery for each is shown graphically in Fig. 3

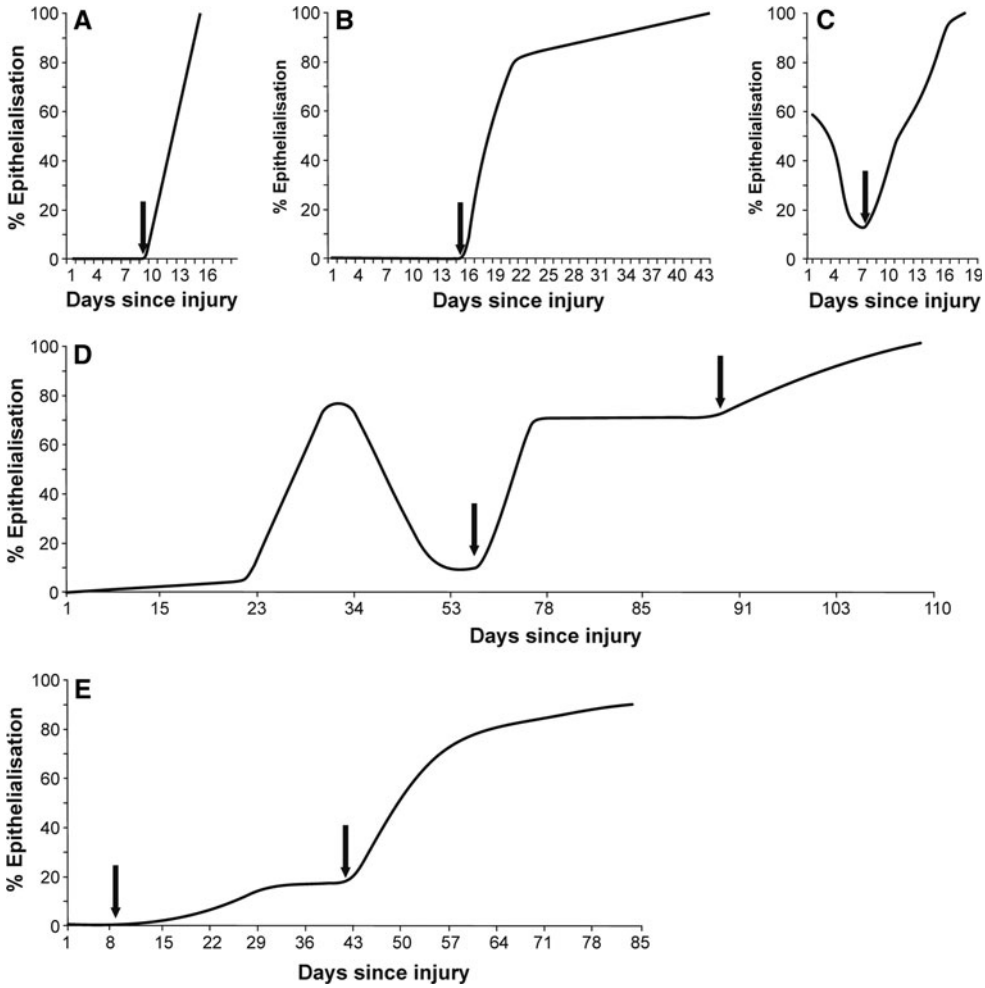

Fig. 3 Graphical representation of corneal epithelium recovery in the five subjects. In each case, points at which the antisense treatment was applied are shown by *arrows*. As subjects were not necessarily seen daily, the *graphs* are interpolated between visits. In all cases the connexin-specific antisense is seen to have a rapid and positive effect on epithelial recovery. Subject 3 (**c**) received two doses of connexin antisense 1 day apart. In subjects 4 (**d**) and 5 (**e**) reepithelialization reached a plateau but was retriggered with a second application of the connexin antisense

In skin wounds keratinocytes at the wound edge downregulate Cx43 in the first 24–48 h as they become migratory in order to close the wound. Cx43AsODNs speed this natural downregulation of Cx43, resulting in faster wound closure (Qiu et al. 2003). The same applies in the cornea of the eye where the corneal epithelium and underlying stroma are analogous to skin epithelium and dermis (Grupcheva et al. 2012). In the dermis of wounded skin and in spinal cord wounds Cx43 is rapidly upregulated after injury, notably in activated neutrophils and glial cells as part of the inflammatory response to injury (Coutinho et al. 2005; Cronin et al. 2008; Qiu et al. 2003). In the corneal stroma, Cx43 is also upregulated, correlating with the inflammatory response typified by differentiation and proliferation of myofibroblasts (Grupcheva et al. 2012). Cx43AsODN treatment in all cases dampens down the inflammatory response with benefits throughout the rest of the healing process.

In this study Cx43AsODNs were applied under compassionate use to one eye of five subjects presenting over a 3-year period with severe nonhealing chemical or thermal burns. Dua grade V–VI ocular surface chemical burns involving the entire limbus and conjunctiva have a very poor prognosis (Dua et al. 2001). All the injured eyes in this study were classified grade V–VI at the time of treatment. The presence of ocular surface inflammation affects the success of limbal transplant or amniotic membrane transplant in grade-VI burns (Gupta et al. 2011); for example, subject 4 had two amniotic membranes applied prior to connexin antisense treatment (under a third membrane), with the second membrane actually dissolving within 4 days, in large part due to the highly inflamed condition of the eye. Amniotic membrane (the inner of the three layers forming a fetal membrane) is used as an ocular burn dressing as it has anti-inflammatory and antiscarring effects and is proposed to contain growth factors that promote epithelial wound healing. In three of the five patients, prior treatment with amniotic membranes had provided no benefit, and in one patient a bandage contact lens was used rather than an amniotic membrane.

Prior to Cx43AsODN treatment and after a minimum of 7 days to more than 8 weeks of intensive, hospital-based, best-practice conventional treatment for a severe chemical or thermal burn injury, all five subjects showed marked

inflammation, limbal ischemia and no signs of ocular epithelial or limbal recovery. Indeed, in two subjects the involved eye was continuing to deteriorate clinically prior to treatment. Following a single low-dose or time-separated double application of Cx43AsODN in a slow-release formulation, the ocular surfaces in all five fully recovered, albeit with a degree of corneal vascularization that one might anticipate in such severe injuries.

The healing pattern in subject 3 (Fig. 2) was not unlike that previously reported for healing of ocular surface wounds involving the limbus (Dua et al. 1994), but our study suggests that an additional influence on the healing pattern may be the relationship with limbal reperfusion. In subjects with a grade-VI corneal burn there was no surviving corneal epithelium from which to trigger cell migration and healing by Cx43AsODN application. Instead, the effect of Cx43AsODN application appears to have been to reduce inflammation, wound edema and arterial insufficiency, also known to be features of some nonhealing wounds. Changes in the vascular bed of the ocular surface are readily discernible at the slit lamp, and in all subjects restoration of limbal perfusion and a general reduction in ocular inflammation appeared to precede full ocular epithelial recovery.

It has previously been reported that exogenous addition of proangiogenic growth factors (VEGF, FGF, PDGF) is not able to prevent vascular regression in wounds (Gosain et al. 2006). These authors concluded that "anti-angiogenic signals that mediate vessel regression in wounds are strongly dominant over pro-angiogenic factors" during the later stages of wound healing. One factor may be increased Cx43 expression. Cx43 is upregulated in the vascular bed of rodent skin wounds within 6 h of injury, contributing to a greater inflammatory response and reduced healing (Couthinho et al. 2003; Qiu et al. 2003). In damaged spinal cord upregulated Cx43 expression results in vascular leak up to 4 mm either side of the injury site, leading to edema, exudation, vessel wall permeability and neutrophil invasion (Cronin et al. 2008). The vascular leak is inhibited with Cx43AsODNs, resulting in reduced inflammation and lesion size. After retinal ischemia–reperfusion, an increase in Cx43 expression correlates with vascular leak, leading to downstream inflammation (astrocytosis) and subsequently neuronal (retinal ganglion cell) loss in the following 7–21 days (Danesh-Meyer et al. 2012). In that case, systemic delivery of hemichannel-blocking mimetic peptides ameliorated vascular leak, reduced inflammation and resulted in almost complete neuronal sparing.

In chronic neuroinflammatory diseases such as Alzheimer and Parkinson disease, morphological changes to the microvasculature indicate capillary dysfunction (Farkas and Luiten 2001). Certainly, a robust inflammatory response to injury can be detrimental to wound closure (Dovi et al. 2004; Ueno et al. 2005), and in humans epithelial wound healing frequently stalls in the chronic inflammation stage (Vuorisala et al. 2009). While bacterial load and poor moisture balance are also associated with nonhealing skin wounds, these are less likely to contribute to the nonhealing ocular cases we report here. Instead, somewhat paradoxically, arterial insufficiency and inflammatory edema of the limbus are possibly major causative factors in impaired corneal epithelial healing (in the context of the normally avascular cornea), as is the case for vascular skin ulcers where the quality of arterial flow or a perturbed venous system is prevalent (Gist et al. 2009; Vuorisala et al. 2009).

In this case series report it cannot be excluded that factors other than connexin modulation may be playing a role. As noted above, however, grade V–VI ocular surface chemical burns normally have a very poor prognosis (Dua et al. 2001); in all cases patients responded immediately to treatment, and in two cases the wounds were continuing to deteriorate prior to treatment. This does not exclude the possibility of vehicle effects, although the supporting literature in animal models, where vehicle and/or control oligonucleotides have no significant effect, would suggest a Cx43-specific mode of action and Pluronic gel is commonly used as a pharmaceutical carrier (Escobar-Chávez et al. 2006). Nonetheless, direct controls were not possible for the compasionate-use case series reported here.

We believe that this first therapeutic human use of Cx43 modulation in five subjects with severe, nonhealing ocular surface chemical/thermal injury indicates that modifying reperfusion and reducing inflammation has potential in the treatment of severe, often unresponsive injuries. While connexin modulation provides a number of benefits in wound healing, downregulation in Cx43 to enable vascular recovery may be a key factor in the treatment of wounds.

Acknowledgments We acknowledge support from the Royal Society of New Zealand Marsden Fund and the Maurice and Phyllis Paykel Trust for characterization work with the antisense oligonucleotides. We acknowledge the Wendy and Bruce Hadden Endowment for salary support (to C.R.G.).

References

Coutinho P, Qiu C, Frank S, Tamber K, Becker D (2003) Dynamic changes in connexin expression correlate with key events in the wound healing process. Cell Biol Int 27:525–541

Coutinho P, Qiu C, Frank S, Wang CM, Brown T, Green CR, Becker DL (2005) Limiting burn extension by transient inhibition of connexin43 expression at the site of injury. Br J Plastic Surg 58:658–667

Cronin M, Anderson PN, Green CR, Becker DL (2006) Antisense delivery and protein knockdown within the intact central nervous system. Front Biosci 11:2967–2975

Cronin M, Anderson PN, Cook JE, Green CR, Becker DL (2008) Blocking connexin43 expression reduces inflammation and improves functional recovery after spinal cord injury. Mol Cell Neurosci 39:152–160

Danesh-Meyer HV, Huang R, Nicholson LFB, Green CR (2008) Connexin43 antisense oligodeoxynucleotide treatment down-regulates the inflammatory response in an in vitro interphase organotypic culture model of optic nerve ischaemia. J Clin Neurosci 15:1253–1263

Danesh-Meyer HV, Kerr NM, Zhang J, Eady EK, O'Carroll SJ, Nicholson LF, Johnson CS, Green CR (2012) Connexin43 mimetic peptide reduces vascular leak and retinal ganglion cell death following retinal ischaemia. Brain 135:506–520

Davidson JO, Green CR, Nicholson LF, O'Carroll SJ, Fraser M, Bennet L, Gunn AJ (2012) Connexin hemichannel blockade improves outcomes in a model of fetal ischemia. Ann Neurol 71:121–132

Dovi JV, Szpaderska AM, DiPietro LA (2004) Neutrophil function in the healing wound: adding insult to injury? Thromb Haemost 92:275–280

Dua HS, Gomes JAP, Singh A (1994) Corneal wound healing. Br J Ophthalmol 78:401–408

Dua HS, King AJ, Joseph A (2001) A new classification of ocular surface burns. Br J Ophthalmol 85:1379–1383

Dua HS, Miri A, Said DG (2010) Contemporary limbal stem cell transplantation—a review. Clin Exp Ophthalmol 38:104–117

Escobar-Chávez JJ, López-Cervantes M, Naïk A, Kalia YN, Quintanar-Guerrero D, Ganem-Quintanar A (2006) Applications of thermo-reversible Pluronic F-127 gels in pharmaceutical formulations. J Pharm Pharmaceut Sci 9:339–358

Farkas E, Luiten PG (2001) Cerebral microvascular pathology in aging and Alzheimer's disease. Prog Neurobiol 64:575–611

Fernandes M, Sridhar MS, Sangwan VS, Rao GN (2005) Amniotic membrane transplantation for ocular surface. Cornea 24:643–653

Frantseva MV, Kokarovtseva L, Naus CG, Carlen PL, MacFabe D, Perez Velazquez JL (2002) Specific gap junctions enhance the neuronal vulnerability to brain traumatic injury. J Neurosci 22:644–653

Garcia-Dorado D, Inserte J, Ruiz-Meana M, Gonzalez MA, Solares J, Julia M, Barrabes JA, Soler-Soler J (1997) Gap junction uncoupler heptanol prevents cell-to-cell progression of hypercontracture and limits necrosis during myocardial reperfusion. Circulation 96:3579–3586

Gist S, Tio-Matos I, Falzgraf S, Cameron S, Beebe M (2009) Wound care in the geriatric client. Clin Interv Aging 4:269–287

Gosain A, Matthies AM, Dovi JV, Barbul A, Gamelli RL, DiPietro LA (2006) Exogenous pro-angiogenic stimuli cannot prevent physiologic vessel regression. J Surg Res 135:218–225

Green CR, Law L-Y, Lin JS, Becker DL (2001) Spatiotemporal depletion of connexins using antisense oligonucleotides. In: Bruzzone R, Giaume C (eds) Methods in molecular biology. Connexin methods and protocols, vol 154. Humana Press, Totawa, pp 175–185

Grupcheva CN, Laux WT, Rupenthal ID, McGhee J, McGhee CNJ, Green CR (2012) Improved corneal wound healing through modulation of gap junction communication using connexin43-specific antisense oligodeoxynucleotides. Invest Ophthalmol Vis Sci 53:1130–1138

Gupta N, Kalaivani M, Tandon R (2011) Comparison of prognostic value of Roper Hall and Dua classification systems in acute ocular burns. Br J Ophthalmol 95:194–198

Hawat G, Benderdour M, Rousseau G, Baroudi G (2010) Connexin 43 mimetic peptide Gap26 confers protection to intact heart against myocardial ischemia injury. Pflugers Arch 460:583–592

Huang C, Han X, Li X, Lam E, Peng W, Lou N, Torres A, Yang M, Garre JM, Tian GF, Bennett MV, Nedergaard M, Takano T (2012) Critical role of connexin 43 in secondary expansion of traumatic spinal cord injury. J Neurosci 32:3333–3338

Lin JH, Weigel H, Cotrina ML, Liu S, Bueno E, Hansen AJ, Hansen TW, Goldman S, Nedergaard M (1998) Gap-junction-mediated propagation and amplification of cell injury. Nat Neurosci 1:494–500

Mori R, Power KT, Wang CM, Martin P, Becker DL (2006) Acute downregulation of connexin43 at wound sites leads to reduced inflammatory response, enhanced keratinocyte proliferation and wound fibroblast migration. J Cell Sci 119:5193–5203

Phillips MI, Zhang YC (1999) Basic principles of using antisense oligonucleotides in vivo. Methods Enzymol 313:46–56

Qiu C, Coutinho P, Frank S, Franke S, Law L-y, Martin P, Green CR, Becker DL (2003) Targeting connexin43 expression accelerates the rate of wound repair. Curr Biol 13:1697–1703

Rawanduzy A, Hansen A, Hansen TW, Nedergaard M (2009) Effective reduction of infarct volume by gap junction blockade in a rodent model of stroke. J Neurosurg 87:916–920

Ueno M, Lyons BL, Burzenski LM, Gott B, Shaffer DJ, Roopenian DC, Shultz LD (2005) Accelerated wound healing of alkali-burned corneas in MRL mice is associated with reduced inflammatory signature. Invest Ophthalmol Vis Sci 46:4097–4106

Vuorisala S, Venermo M, Lepantalo M (2009) Treatment of diabetic foot ulcers. J Cardiovasc Surg 50:275–291

Wagner RW (1994) Gene inhibition using antisense oligodeoxynucleotides. Nature 372:333–335

J Membrane Biol (2012) 245:389–400
DOI 10.1007/s00232-012-9461-3

Degradation of Connexins Through the Proteasomal, Endolysosomal and Phagolysosomal Pathways

Vivian Su · Kimberly Cochrane · Alan F. Lau

Received: 3 April 2012 / Accepted: 20 June 2012 / Published online: 8 July 2012

Abstract Connexins comprise gap junction channels, which create a direct conduit between the cytoplasms of adjacent cells and provide for intercellular communication. Therefore, the level of total cellular connexin protein can have a direct influence on the level of intercellular communication. Control of connexin protein levels can occur through different mechanisms during the connexin life cycle, such as by regulation of connexin gene expression and turnover of existing protein. The degradation of connexins has been extensively studied, revealing proteasomal, endolysosomal and more recently autophagosomal degradation mechanisms that modulate connexin turnover and, subsequently, affect intercellular communication. Here, we review the current knowledge of connexin degradation pathways.

Keywords Connexin · Degradation · Proteasome · Lysosome · Autophagy

Introduction

Gap junctions are plasma membrane channels that allow the passive diffusion of molecules less than 1,000 daltons directly between the cytoplasms of neighboring cells (Goodenough et al. 1996). The molecules include secondary messengers (cAMP), small metabolites (ATP) and ions (Ca^{2+}). The regulation of gap junctions and gap junctional intercellular communication (GJIC) is critical as the channels contribute to the normal homeostasis of cells, tissues and organs, as well as being important during development (Vinken et al. 2006; Wei et al. 2004; White and Paul 1999). Furthermore, misregulation of gap junctions and the corresponding intercellular communication can result in a number of human diseases, including heart arrhythmias (Martin and Evans 2004; Severs et al. 2008; van Veen et al. 2001), developmental diseases (Laird 2008) and cancers (Naus and Laird 2010).

The complete gap junction channel is comprised of two hexameric structures (connexons or hemichannels), one contributed by each of the neighboring cells. Connexons contain six connexin proteins that form either homomeric oligomers or, in cells expressing more than one type of connexin, heteromeric oligomers if the expressed connexins are compatible. Connexins are four-pass transmembrane proteins, containing cytoplasmic N- and C-terminal domains, two extracellular loops and one intracellular loop. There are 21 members of the human connexin protein family, expressed to different degrees depending on the tissue or cell type. Of these, connexin43 (Cx43) has been the most widely studied family member. Generally, connexins are cotranslationally inserted into the endoplasmic reticulum (ER) membrane, where they undergo proper folding and are then transported through the Golgi network. During the ER to Golgi transport, a number of connexins have been demonstrated to oligomerize into hemichannels (Das et al. 2009; Das Sarma et al. 2002; Diez et al. 1999; Koval 2006; Maza et al. 2003, 2005). The hemichannels are then transported to the plasma membrane to dock with hemichannels on the neighboring cell surface to form the

V. Su (✉) · K. Cochrane · A. F. Lau
Cancer Biology Program, University of Hawaii Cancer Center, University of Hawaii at Manoa, 651 Ilalo Street, BSB 222, Honolulu, HI 96813, USA
e-mail: vsu@cc.hawaii.edu

K. Cochrane · A. F. Lau
Department of Cell and Molecular Biology, John A. Burns School of Medicine, University of Hawaii at Manoa, Honolulu, HI 96813, USA

gap junction channels. Large accretions of gap junctions may form between cells, which are generally known as gap junction plaques. Undocked hemichannels have more recently been shown to have their own activity, with important roles in cell death (Bargiotas et al. 2009; Contreras et al. 2003; Goodenough and Paul 2003; Sato et al. 2009; Stout et al. 2004) and tissue remodeling (Knight et al. 2009; Siller-Jackson et al. 2008). Hemichannels can be opened under specific conditions, such as membrane depolarization (Contreras et al. 2003), changes in ionic concentrations (Gómez-Hernández et al. 2003; Srinivas et al. 2006) and mechanical shear stress (Cherian et al. 2005; Siller-Jackson et al. 2008). All of these conditions can regulate the passage of ions and metabolites through the hemichannels (Anselmi et al. 2008; Cherian et al. 2005; Garré et al. 2010; Siller-Jackson et al. 2008).

From the plasma membrane, undocked hemichannels, intact gap junctions and even large sections of gap junction plaques are internalized and primarily degraded (Laird 2006). Remarkably, for transmembrane proteins, connexins have a short half-life of 1.5–5 h depending on the cell type (Beardslee et al. 1998; Darrow et al. 1995; Fallon and Goodenough 1981; Laird et al. 1991; Musil et al. 2000). The degradation mechanisms for connexins have been studied for years, with reports demonstrating the involvement of the proteasomal, lysosomal and autophagosomal degradation pathways (Beardslee et al. 1998; Fong et al. 2012; Girao and Pereira 2003; Guan and Ruch 1996; Hesketh et al. 2010; Kelly et al. 2007; Laing and Beyer 1995; Laing et al. 1997, 1998; Leithe et al. 2006; Leithe and Rivedal 2004a, b; Li et al. 2008; Lichtenstein et al. 2011; Musil et al. 2000; Qin et al. 2003; Su et al. 2010; Thomas et al. 2003; VanSlyke et al. 2000; VanSlyke and Musil 2002, 2005). Proper regulation of these pathways that are responsible for connexin turnover is essential as the amount of connexin protein can have a direct effect not only on the level of GJIC (Leithe et al. 2009; Leithe and Rivedal 2004a; Musil et al. 2000; VanSlyke and Musil 2003) but also on the activities of hemichannels and other functions of connexins, which are unrelated to intercellular communication (Goodenough and Paul 2003; Scemes et al. 2009; Stout et al. 2004). All of these connexin activities are critical for normal cellular and tissue functions.

Proteasomal Degradation

Protein degradation through the proteasomal pathway typically involves the 26S proteasome holoenzyme. This complex consists of the 20S core particle (CP) and the 19S regulatory particle (RP) (reviewed in Voges et al. 1999). The 20S CP consists of four rings stacked upon each other. Each ring contains seven individual protein subunits. The innermost two rings contain the proteolytic activity with the β-type subunits, while the α-type subunits comprise the outer two rings. The core is flanked on each side by one complete 19S RP, which is made up of the base and cap, also consisting of many protein subunits. The 19S RP subunits are classified as either ATPases (*Saccharomyces cerevisiae* Rpt proteins) or non-ATPases (*S. cerevisiae* Rpn proteins) (Glickman et al. 1998). The ATPase activity of the 19S subunit most likely is responsible for the unfolding of substrate proteins, to allow the polypeptide chain to enter the 20S CP for degradation.

The tag that marks a substrate for proteasomal degradation is often considered to be a polyubiquitin chain. Ubiquitin is a 76–amino acid protein that is highly conserved and expressed in all eukaryotes. The covalent linkage of ubiquitin to substrates occurs through a highly regulated process that is mediated by a number of enzymes (Fang and Weissman 2004). The E1 ubiquitin-activating enzyme, multiple E2 ubiquitin-conjugating enzymes and several E3 ubiquitin ligases facilitate the specific ubiquitination of cellular proteins. The E1 enzyme activates ubiquitin, enabling ubiquitin to be transferred to one of the E2 enzymes. The ubiquitin-loaded E2 then associates with an E3 ligase, which results in the covalent bonding of ubiquitin to the target protein or, alternatively, to another ubiquitin to create a polyubiquitin chain. Ubiquitination of proteins is a mechanism that provides for the selective degradation of cellular proteins. In fact, the 19S RP contains subunits that are ubiquitin-binding proteins, such as Rpn1, Rpn10 and Rpn13 (Deveraux et al. 1994; Elsasser et al. 2002; Husnjak et al. 2008). Almost all proteins known to be degraded by the 26S proteasome are ubiquitinated, with a small number of exceptions. It should be noted, however, that a large number of proteins, such as oxidized proteins, are able to be degraded without ubiquitination specifically through the 20S CP alone (Davies 2001; Ferrington et al. 2001; Grune et al. 1997; Jariel-Encontre et al. 2008; Orlowski and Wilk 2003; Shringarpure et al. 2003). Presumably, oxidation causes sufficient unfolding of the target protein to allow it to directly enter the 20S CP barrel without the unfolding activity of the ATPase activity resident in the 19S RP.

Cx43 Proteasomal Degradation

The first documented study of the involvement of proteasome degradation in connexin turnover came in 1995 by Laing and Beyer, who reported that pharmacological inhibition of proteasomal activity using ALLN resulted in increased levels and reduced turnover of Cx43 protein in Chinese hamster ovary (CHO) E36 and rat heart–derived BWEM cells, respectively. In addition, the authors used the ts20 cell line, which contains a thermolabile E1 enzyme

and where heat treatment inactivates the E1 activity, resulting in loss of the ubiquitination process. It was demonstrated that Cx43 required active ubiquitination in order to be degraded after heat treatment. Furthermore, sequential immunoprecipitation indicated that Cx43 was ubiquitinated. In a subsequent study, neonatal rat ventricular myocytes subjected to heat treatment displayed loss of Cx43, which was prevented with proteasomal inhibition using ALLN or lactacystin, further supporting a role for the proteasome in Cx43 degradation (Laing et al. 1998).

Proteasomal degradation is typically associated with ER-associated degradation (ERAD). During ERAD, misfolded or unfolded proteins are dislocated out of the ER and into the cytoplasm, where the proteins are thought to be polyubiquitinated (Smith et al. 2011). This ubiquitination then marks these proteins for proteasomal degradation. Studies have indicated that Cx43 can be degraded via ERAD. Treatment of BWEM cells with the fungal metabolite brefeldin A (BFA) to prevent transport of newly synthesized Cx43 to the plasma membrane, with a concurrent inhibition of proteasomal degradation using ALLN, resulted in increased intracellular pools of Cx43 (Laing et al. 1997). With the block in transport to the membrane, newly synthesized Cx43 would accumulate in the ER. Simultaneously blocking proteasomal degradation would then reveal the pool of Cx43 bound for ERAD. DTT treatment of CHO cells to prevent formation of the intramolecular Cx43 disulfide bonds necessary for function (in effect causing Cx43 to be misfolded) in combination with ALLN blockage of proteasomal degradation resulted in a dramatic increase of Cx43 protein levels (Musil et al. 2000). An analysis of cellular stress on Cx43 ER dislocation and degradation was conducted using multiple cell lines, where DTT treatment (an ER stressor) more than doubled the amount of cytoplasmic Cx43 present in BFA-treated cells (VanSlyke and Musil 2002). In the absence of BFA, little Cx43 was found in the cytoplasm, suggesting that DTT treatment/Cx43 protein unfolding resulted in enhanced dislocation of Cx43 from the ER. Additional proteasomal inhibition using ALLN or epoxomicin further increased the amount of cytoplasmic Cx43 that was reversed upon ALLN washout, suggesting that the ER-dislocated Cx43 was bound for proteasomal degradation and further supporting the concept that Cx43 is subject to ERAD.

The ubiquitin-like (UbL) and ubiquitin-associated (UBA) domain protein family has been documented to be involved in proteasomal degradation (reviewed in Su and Lau 2009). It is generally thought that these proteins act as shuttle or adaptor proteins to transport their substrates from the ER to the proteasome. The UBA domain can interact with ubiquitin and ubiquitinated proteins. The UbL domain of these proteins interacts with subunits of the 19S RP, specifically Rpn1 and Rpn10. These two domains provide these proteins with the proper interactions necessary to function as a shuttle factor that is involved in proteasomal degradation or ERAD. The identification of the UbL-UBA protein CIP75, which is able to interact with Cx43, provides further insight into the mechanisms that regulate Cx43 proteasomal degradation (Li et al. 2008). The CIP75 UBA domain interacted with a region of the Cx43 C-terminal tail, a domain that has been found to interact with many other proteins. In human HeLa and mouse S180 cells, the interaction between CIP75 and Cx43 affected the Cx43 half-life, where increased levels of CIP75 reduced Cx43 half-life, while siRNA knock-down of CIP75 had the opposite effect. The CIP75-facilitated degradation was inhibited with MG132, which blocks proteasomal degradation. Furthermore, the CIP75 UbL domain was demonstrated to interact with the Rpn1 and Rpn10 components of the 19S RP, supporting a role for CIP75 as an adaptor between Cx43 and the proteasome. Finally, colocalization of CIP75 and Cx43 at the ER indicated that the role of CIP75 in Cx43 proteasomal degradation might involve ERAD (Li et al. 2008). Interestingly, while almost all substrates of the 26S proteasome have been found to be ubiquitinated, the ubiquitination of Cx43 was demonstrated to be nonessential for interaction with CIP75. By using a series of Cx43 point mutants with mutations of the various lysine residues that could potentially serve as ubiquitin attachment sites, CIP75 was demonstrated to still be able to interact with the mutated Cx43 (Su et al. 2010). Significantly, this is one of the unique situations where a non-ubiquitinated substrate undergoes 26S proteasomal degradation as only a limited number of proteins have been conclusively demonstrated to also undergo ubiquitin-independent degradation by the proteasome holoenzyme (Bercovich et al. 1989; Glass and Gerner 1987; Jariel-Encontre et al. 1995, 2008; Murakami et al. 1992).

Proteasomal Degradation of Membrane-Localized Cx43

Many studies using proteasomal inhibitors have reported increased Cx43 at the plasma membrane. Treatment of BWEM cells with the inhibitor lactacystin, ALLN or MG132, concurrently with BFA or monensin (to disrupt Cx43 trafficking to the plasma membrane), resulted in increased cell surface Cx43 compared to treatment with BFA/monensin alone (Laing et al. 1997). Furthermore, treatment of gap junction assembly-inefficient CHO cells or serum-starved mouse S180L cells with ALLN resulted in the upregulation of gap junction assembly and GJIC (Musil et al. 2000). Additional studies also employed proteasomal inhibitors to demonstrate that proteasomal degradation is responsible for the turnover of Cx43 from the cell surface and the corresponding reduction in

intercellular communication (Fernandes et al. 2004; Girao and Pereira 2003, 2007; Kimura and Nishida 2010; Leithe and Rivedal 2004a, b; Simeckova et al. 2009; VanSlyke and Musil 2005). The observation of the ubiquitination of Cx43 localized in the gap junction plaques at the cell surface provided additional support of a role for the proteasome in regulating Cx43 at the plasma membrane (Leithe et al. 2009; Leithe and Rivedal 2004a, b; Rutz and Hülser 2001).

A recent report, however, has provided evidence for an indirect mechanism involving proteasomal degradation that influences the Cx43 protein level and localization at the plasma membrane (Dunn et al. 2012). By utilizing a Cx43 point mutant that cannot be ubiquitinated (containing lysine to arginine mutations of all the lysine residues that would act as ubiquitin acceptor sites), the proteasome was demonstrated to regulate the levels of Akt/protein kinase B which caused the resulting stabilization of Cx43 at the cell surface. Using canine MDCK and rat NRK cells expressing the Cx43 lysine mutant, the mutant Cx43 was found to traffic to the plasma membrane and to participate in channel formation and intercellular communication. Inhibiting proteasomal degradation with MG132 elicited an increase in Cx43 at the plasma membrane in cells expressing either the wild-type Cx43 or lysine mutant, which suggested a possible indirect effect on Cx43 stabilization that resulted from the proteasomal inhibition. Furthermore, these data demonstrate that the Cx43 that is localized to the plasma membrane and creates gap junctional channels is not necessarily ubiquitinated in order for the channels to be functional.

Internalization of connexins has been linked to post-translational modifications of connexins, including phosphorylation, ubiquitination, acetylation and SUMOylation (Colussi et al. 2011; Kjenseth et al. 2012; Leithe et al. 2012; Locke et al. 2009; Shearer et al. 2008; Solan and Lampe 2005, 2007, 2009; Su and Lau 2012). Cx43 phosphorylation at the serine^{255} and serine^{262} residues by the MAP kinase ERK can occur in response to epidermal growth factor (EGF) or 12-*O*-tetradecanoylphorbol 13-acetate (TPA) exposure, which is followed by internalization of Cx43 from the plasma membrane and subsequent lysosomal degradation (Leithe et al. 2006; Leithe and Rivedal 2004b; Sirnes et al. 2008, 2009). Akt had also previously been demonstrated to phosphorylate Cx43 (Park et al. 2007), and inhibition of Akt activity using Akt VIII treatment or expression of the dominant negative Akt-K179A mutant reduced the amount of Cx43 at the cell surface (Dunn et al. 2012). Furthermore, closer examination of Akt revealed an increase in ubiquitinated Akt and, in general, Akt kinase activity in response to MG132 treatment, blocking proteasomal degradation (Dunn et al. 2012), which has been demonstrated to increase Akt translocation to the plasma membrane and increased activity due to a phosphorylation event (Feng et al. 2004; Sarbassov et al. 2005). Furthermore, Akt-phosphorylated Cx43 was present at higher levels after MG132 treatment (Dunn et al. 2012). These results suggested that proteasomal degradation of ubiquitinated Cx43 at the cell surface is not the cause for the turnover of Cx43 gap junctions.

Cx32 Proteasomal Degradation

Similar to Cx43, Cx32 is also degraded by ERAD (Fig. 1). The degradation of Cx32 is of particular interest because of the identification of Cx32 mutations in the human peripheral neuropathy X-linked Charcot-Marie-Tooth disease (CMTX). Using rat pheochromocytoma PC12J cells stably expressing wild-type Cx32, significantly more Cx32 accumulation was detected upon proteasomal inhibition compared to blocking lysosomal degradation (VanSlyke et al. 2000). In NRK fibroblasts, Cx32 was also demonstrated to undergo ER dislocation (VanSlyke and Musil 2002), like Cx43; and accumulation of Cx32 following DTT treatment (inducing ER stress) occurred only after treatment with the proteasomal inhibitors epoxomicin and ZL_3VS (Kelly et al. 2007; VanSlyke and Musil 2002). Interestingly, a study, using the prostate cancer cell line LNCaP stably expressing exogenous wild-type Cx32, also demonstrated that Cx32 undergoes ERAD, which occurs at a faster rate after androgen depletion (Mitra et al. 2006). This degradation is rescued upon exposure to androgens, resulting in increased Cx32 trafficking to the plasma membrane and increased intercellular communication. Additional studies utilizing the Cx32 E208K mutant,

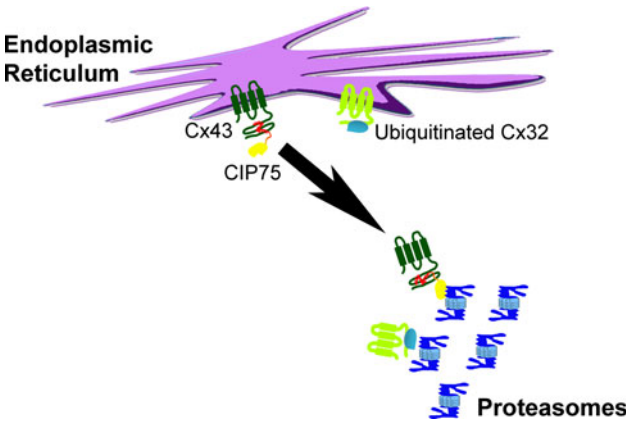

Fig. 1 Proteasomal degradation of connexins. During protein synthesis, connexins are cotranslationally inserted into the ER membrane, where the proteins undergo proper folding. Misfolded connexins can be polyubiquitinated and degraded by the proteasome through ERAD, as in the case of Cx32. Alternatively, nonubiquitinated Cx43 interacts with the accessory factor CIP75, which facilitates Cx43 ERAD by interacting with the proteins in the proteasome 19S RP

identified in CMTX patients (Fairweather et al. 1994), enabled further observation of Cx32 ERAD. This mutant exhibits an intracellular trafficking defect as it fails to form connexon hexamers and does not traffic to the plasma membrane (VanSlyke et al. 2000). Cx32 E208K localizes to the ER, and the degradation appeared to be affected by proteasomal inhibitors but not lysosomal inhibitors, indicating that turnover occurred via ERAD. The E208K mutant protein was detected in both polyubiquitinated and nonubiquitinated forms (Kelly et al. 2007). Significantly more polyubiquitinated E208K was detected than nonubiquitinated protein, particularly in the cytoplasm. These data indicated that, as is the general case for 26S proteasomal degradation, the pool of Cx32 that undergoes ER dislocation and ERAD via the proteasome is polyubiquitinated.

Lysosomal Degradation

While early reports suggested the involvement of proteasomes in the turnover of connexins from the plasma membrane, lysosomes have been demonstrated to directly facilitate the degradation of connexins internalized from the plasma membrane. Lysosomes are cytoplasmic membrane-enclosed intracellular vesicles whose low internal pH provides the optimal environment for acidic hydrolytic enzymes to function. Chloride and proton pumps (hydrogen ion ATPases) maintain the acidic environment by pumping H^+ ions into lysosomes (Saftig and Klumperman 2009). The hydrolytic enzymes are targeted to the Golgi-derived lysosomes by the addition of a mannose-6-phosphate tag following their synthesis in the ER (González-Noriega et al. 1980; Mari et al. 2008). These enzymes include glycosidases, proteases, lipidases, acid phosphatases and sulfatases that degrade proteins and other cellular debris taken up in vacuoles that fuse with lysosomes (Bright et al. 2005; Lubke et al. 2009). Products of lysosomal digestion can be reused to synthesize new cellular components following transport to the cytosol by solute transporters in the lysosomal membrane (Jeyakumar et al. 2005; Puri et al. 1999).

Endolysosomal Degradation of Cx43

Early studies identified gap junctions and, specifically, Cx43 in endosomal and lysosomal membrane compartments (Murray et al. 1981; Naus et al. 1993; Sasaki and Garant 1986). Multiple studies provided evidence that Cx43 at the cell surface undergoes internalization via the endocytic pathway. In human, rat and mouse cells, intracellular Cx43 was observed in endocytic compartments through colocalization with the endosomal markers EEA1, Rab5 and Rab7 (Boassa et al. 2010; Gilleron et al. 2008; Govindarajan et al. 2010; Leithe et al. 2006, 2009; Segretain et al. 2003). Furthermore, the delivery of connexins to lysosomes for degradation was demonstrated to be facilitated by interactions with proteins involved in endocytosis and intracellular trafficking. During endocytosis, clathrin is recruited to the membrane through interactions between proteins at the plasma membrane and clathrin adaptor proteins, such as adaptor protein complex-2 (AP-2) and Disabled-2 (Dab2). After endocytic vesicles, such as clathrin-coated pits, bud from the plasma membrane, the large GTPase dynamin protein is required for the endosome to pinch off into the cytoplasm. Cx43 colocalizes with clathrin, AP-2, Dab2 and dynamin2 at cell surface gap junction plaques (Gilleron et al. 2011; Gumpert et al. 2008; Piehl et al. 2007). Additionally, the loss of dynamin GTPase activity or the reduction of dynamin2, clathrin, AP-2 or Dab2 proteins inhibited the internalization of Cx43 as observed by a significant decrease in the number of annular gap junctions (AGJs). AGJs are cytoplasmically localized double-membrane structures containing intact gap junction channels that are derived from the membranes of both neighboring cells. These data indicate that the proteins involved in clathrin-mediated endocytosis are necessary for the internalization of gap junctions, which subsequently may be degraded by lysosomes. Additionally, the Cx43-interacting protein of 85 kDa, CIP85, is a Rab GTPase activating protein that was found to colocalize with Cx43 at the plasma membrane; and the interaction was required for Cx43 degradation by lysosomes (Lan et al. 2005).

The internalized AGJ structures and Cx43 were observed to be fused with structures resembling lysosomes by electron microscopy (Murray et al. 1981; Naus et al. 1993; Sasaki and Garant 1986), providing some of the initial evidence that internalized connexins associated with lysosomes. Laing and Beyer (1995) were the first to demonstrate that pharmacological inhibition of lysosomal function, using primaquine to treat E36 cells, resulted in a twofold accumulation in Cx43 levels and a minor prolongation of its half-life from 2.5 to 3 h. Additional studies in rat and human cells confirmed the role of lysosomes in the degradation of Cx43 internalized from the plasma membrane. These studies observed an increased accumulation of connexins in lysosomes and detected increased total levels of connexins, following treatment of cells with a wide variety of lysosomal inhibitors (Guan and Ruch 1996; Laing et al. 1997, 1998; Leithe et al. 2006; Qin et al. 2003; Simeckova et al. 2009; Thomas et al. 2003). Furthermore, biotinylated cell surface Cx43 degradation was blocked in S180 cells upon treatment with the lysosomal inhibitors chloroquine and, to a lesser extent, leupeptin, supporting the conclusion that intact gap junctions and undocked

hemichannels can be internalized and subsequently degraded by lysosomes (VanSlyke and Musil 2005). Other studies have demonstrated similar mechanisms for additional members of the connexin family. Cx32 was observed in endosome- and lysosome-containing subcellular fractions of rat liver cells (Rahman et al. 1993). Following treatment of HeLa cells with multiple lysosomal inhibitors, accumulation of Cx31 was observed (He et al. 2005). These results suggested that these connexins, and perhaps others, are internalized and can be degraded by endolysosomal mechanisms.

One area that is still unresolved is the molecular mechanism(s) responsible for the possible fusion of the double membrane of internalized AGJs with single-membrane endosome or lysosome compartments. Under physiological conditions, there is little evidence that intact gap junctions can be separated back into separate hemichannels on single membranes (Ghoshroy et al. 1995; Goodenough and Gilula 1974). However, there are electron microscopic observations of nonjunctional membrane domains within AGJs where the two membranes are not attached to each other (Fong et al. 2012; Leithe et al. 2012; Piehl et al. 2007). These membrane areas may provide AGJs an opportunity to fuse with other single-membrane vesicles. There is also evidence that the double-membrane structure of internalized AGJs becomes disrupted in coordination with the formation of single membranes and intraluminal vesicles. These multivesicular structures appeared to be able to fuse with other vesicles including lysosomes (Leithe et al. 2006, 2009).

While many reports have proposed an endocytic pathway of Cx43 internalization from the plasma membrane to the lysosome, an alternative mechanism for the delivery of Cx43 to the lysosome has been reported. One study using breast tumor cell lines found that blocking Cx43 trafficking to the plasma membrane from the Golgi with BFA did not affect the steady-state level of Cx43 that was otherwise significantly decreased by inhibiting protein synthesis with cycloheximide treatment (Qin et al. 2003). In addition, BFA treatment did not diminish the localization of Cx43 in lysosomal compartments. These results suggested that Cx43 might also be delivered directly to lysosomes from early secretory compartments (Fig. 2). A similar observation was made for the CMTX-linked Cx32 mutant R142W in PC12J cells (VanSlyke et al. 2000). As with the E208K mutant, the R142W Cx32 mutant does not traffic to the cell surface, although it can pass through the secretory pathway to reach the distal compartments of the Golgi. Inhibition of the lysosome with leupeptin increased Cx32 R142W levels in lysosomes despite the inability of the mutant to traffic through to the plasma membrane, which suggested the possibility of direct Cx32 transport from the secretory pathway to the lysosome (VanSlyke et al. 2000).

There is evidence that Cx43 internalized from the plasma membrane not only may be destined for lysosomal degradation but can be recycled back to the plasma membrane. First, dye coupling was observed to resume independently of de novo protein synthesis following Cx43 internalization and cell uncoupling that occurred during cytokinesis (Xie et al. 1997). Second, recycling of cell surface Cx43 was also demonstrated in experiments where S180 cells were first biotinylated, then treated with sodium 2-mercaptoethanesulfonate (MesNa) to strip the biotin label from the protein that had not been internalized. After a period of recovery, a subset of Cx43 was found to still be sensitive to MesNa, while control cells that were not allowed to resume vesicle-mediated recycling did not. These data suggested the possibility that intracellularly localized Cx43 was able to recycle back to the plasma membrane, where it became vulnerable to MesNa treatment (VanSlyke and Musil 2005). Third, using the tetracysteine/biarsenical labeling system with fluorescent FlAsH and ReAsH ligands to bind to internal tetracysteine tags in Cx43, the return of Cx43 to the plasma membrane after mitosis was demonstrated to result from Cx43 that was labeled prior to the onset of mitosis, instead of newly synthesized Cx43. This existing pool of Cx43 was responsible for reestablishing gap junctional communication following mitosis (Boassa et al. 2010). Finally, Cx43 in AGJs and vesicles which pinched off from AGJs were shown to colocalize with Rab11, a small GTPase involved in the recycling pathway (Gilleron et al. 2011). Taken together, these data indicate that not all internalized connexins are destined for degradation by lysosomes. Despite these reports, there is a general consensus that connexins can be internalized and degraded through the endolysosomal pathway (Berthoud et al. 2000; Leithe et al. 2012; Salameh 2006; Segretain and Falk 2004).

The molecular mechanisms that dictate the fate of connexin proteins are not clearly understood. Connexin posttranslational modifications are known to affect connexin function and localization. Of the various modifications, ubiquitination has been proposed to function as part of the internalization and, possibly, the subsequent intracellular trafficking mechanism of cell surface connexins. The ubiquitination of connexins has been discussed in depth by three recent reviews (Kjenseth et al. 2010; Leithe et al. 2012; Su and Lau 2012). These reviews cover the initial reports linking ubiquitination to connexin degradation (Laing and Beyer 1995; Laing et al. 1997), as well as later studies which revealed that connexin phosphorylation by MAP kinases resulted in multiple monoubiquitination events (Leithe and Rivedal 2004a, b). The monoubiquitination resulted in the targeting of Cx43 for internalization and degradation (Leithe and Rivedal 2004a, b), which differs from polyubiquitination associated with proteasomal

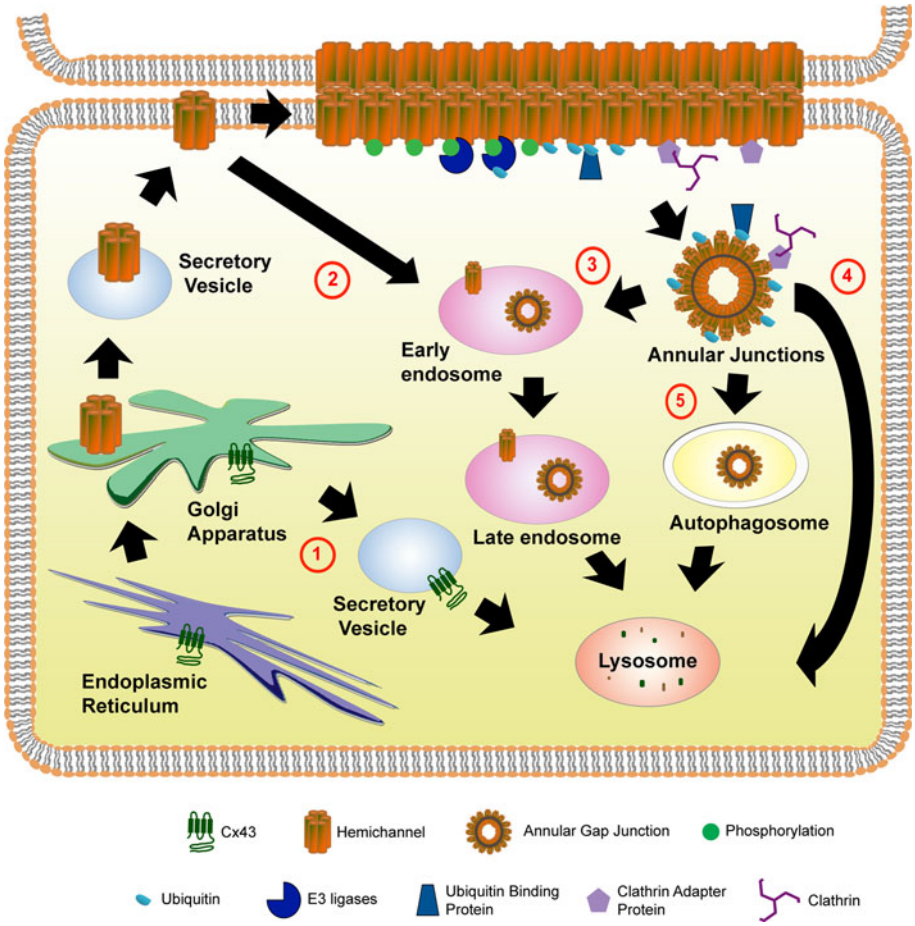

Fig. 2 Lysosomal degradation of connexins. Following synthesis in the ER, some new connexins may be transported directly to lysosomes via early secretory vesicles (*1*). Most connexins oligomerize in the Golgi to form hemichannels that are trafficked to the plasma membrane. Evidence suggests that nonjunctional hemichannels can be internalized and degraded via the endolysosomal pathway (*2*). Hemichannels that dock with hemichannels from adjacent cells to form gap junction channels will be incorporated into gap junction plaques. Phosphorylation and ubiquitination of connexins mediate gap junction internalization, which can involve the formation of AGJs. AGJs are internalized by a clathrin-dependent process and may fuse directly with early endosomes that will mature into late endosomes and fuse with lysosomes (*3*). Some observations suggest that AGJs can fuse directly with lysosomes (*4*). The direct fusion of AGJs with other vesicular membranes (*3–4*) could involve small areas of the outer AGJ membrane not occupied by gap junctions or the transformation of AGJs into single-membrane, multivesicular structures. Alternatively, phagophores may engulf AGJs into autophagosomes (*5*), which are able to fuse with lysosomes, resulting in degradation of their contents

degradation. Also, Cx43 has been found to interact with the ubiquitin-binding proteins Hrs (hepatocyte growth-factor regulated tyrosine kinase substrate), TSG101 (tumor susceptibility gene 101) and Eps15 (epidermal growth factor substrate 15), which mediate the ESCRT (endosomal sorting complex required for transport)–dependent endolysosomal trafficking of proteins (Auth et al. 2009; Girao et al. 2009; Leithe et al. 2009). Interestingly, a possible recycling of Cx43 back to the plasma membrane was observed when Hrs and TSG101 levels were reduced in siRNA-treated cells that were also treated with TPA to induce Cx43 internalization concurrently with a block in protein synthesis (Leithe et al. 2009). It has been proposed that Cx43 ubiquitination and perhaps the interactions with proteins of the ESCRT complexes dictate the trafficking of internalized Cx43, i.e., to the lysosome for degradation versus being recycled back to the cell surface.

Phagolysosomal Degradation of Cx43

Autophagy has long been recognized as a part of the connexin life cycle as a result of observations of gap junctions in autophagic structures by electron microscopy (Mazet et al. 1985; Sasaki and Garant 1986; Severs et al. 1989). Macroautophagy involves the degradation of cytoplasmic complex protein structures, where autophagic double-membrane compartments assemble de novo around protein complexes and engulf them along with surrounding cytoplasm. The engulfed proteins are subsequently degraded by acidic hydrolases following fusion of the outer

membrane of a completed phagophore with a lysosome (Yang and Klionsky 2009). AGJs, which are composed almost entirely of a double membrane fused by gap junctions, would be considered a complex protein structure that could be subject to macroautophagy. Despite previous observations of gap junctions in autophagosomes, only recently has autophagy received attention as an alternate means of delivering complex structures containing internalized connexins to lysosomes in studies that specifically investigated the role of autophagy degradation in the connexin life cycle (Fong et al. 2012; Hesketh et al. 2010; Lichtenstein et al. 2011). The most recent of these studies suggested that autophagy may be the most common pathway for degradation of internalized gap junctions (Fong et al. 2012).

Autophagy of Cx43 was observed in diseased cardiac cells (Hesketh et al. 2010). Cx43 localizes to the intercalated disc region of the plasma membrane in cardiomyocytes under normal conditions, where intact gap junction channels propagate the electrical signal required for the heart rhythm. Reduced electrical signaling in the failing heart has previously been linked to the relocalization of Cx43 from intercalated discs, which are located in the plasma membranes at the ends of cardiomyocytes, to lateral cell membranes (Beardslee et al. 2000; Peters et al. 1993; Severs et al. 2008; Smith et al. 1991). In failing canine heart myocardium, multilamellar membrane structures containing Cx43 were observed near the lateral membranes through electron microscopy. These Cx43-positive structures also colocalized with the autophagosome marker light chain 3 (LC3) (Hesketh et al. 2010). Another study demonstrated that internalized Cx43 and Cx50 colocalized with cup- or ring-shaped LC3-containing structures, which resembled autophagosomes and colocalized with p62 (Lichtenstein et al. 2011), which has been suggested to be a receptor for substrates in autophagic degradation (Komatsu and Ichimura 2010). Treatment of NRK and HeLa cells with the lysosomal inhibitor chloroquine during starvation, a condition known to induce autophagy, resulted in increased levels of Cx43 and Cx50, respectively, in autophagosomes (Lichtenstein et al. 2011). Most recently, AGJs have been demonstrated to be engulfed by autophagosomes prior to lysosomal degradation in HeLa cells (Fong et al. 2012). AGJ vesicles colocalized with the LC3 and p62 autophagic markers as well as the lysosomal markers LAMP-1 and LysoTracker. Electron microscopic studies identified the formation of phagophores around AGJ vesicles, which were subsequently degraded by lysosomal mechanisms. When autophagic degradation was inhibited or reduced, by treatment with either pharmacological agents or RNAi against requisite autophagic proteins, accumulation of total Cx43 protein in cells was observed (Fong et al. 2012). Thus, it appears that connexins that are internalized in AGJ vesicles can be targeted for degradation by autophagy. While there is significant evidence that both endolysosomal and phagolysosomal pathways participate in connexin degradation (Fig. 2), it is unclear whether these pathways are in fact part of the same overall mechanism that dictates the turnover of connexins from the cell surface or whether these pathways diverge at some point during the trafficking of connexins from the plasma membrane.

Regulation of Connexin Levels by Degradation—Relevance in Human Disease

There have been a number of reports suggesting that Cx43 degradation may play an important role in human diseases. A recent study analyzed the effect of Cx43 on cancer cell death when proteasomal degradation is inhibited (Huang et al. 2010). The rationale of studying proteasomal degradation in cancer arose from the use of the proteasomal inhibitor bortezomib as treatment for patients with multiple myeloma, among other cancers. Blocking degradation of Cx43 by the proteasome with MG132 also resulted in increased apoptosis of murine hepatoma Hepa-1c1c7 cells. Gap junction inhibitors flufenamic acid, 18-α glycyrrhetinic acid and carbenoxolone reduced the cell death induced by MG132. Using a gap junction–deficient cell line, porcine kidney epithelial LLC-PK1 cells, expression of wild-type Cx43 sensitized the cells to the apoptotic effects of MG132 that was blocked with treatment of gap junction inhibitors. Notably, expression of the Cx43 Δ130–137 deletion mutant, which does not create functional gap junctions, had the same effect as wild-type Cx43, suggesting that the apoptosis induced by MG132 was independent of the ability of Cx43 to establish GJIC. Induction of ER stress with treatment using tunicamycin and thapsigargin demonstrated a Cx43-dependent increase in cell death in response to stress (Huang et al. 2010). These observations indicated that Cx43 may have a critical role in the induction of cell death and may be an important component of successful cancer therapy.

Similarly, lysosomal degradation of connexins has been implicated as a potentially important mechanism in human cancer. The lysosome contributes to the downregulation of gap junctions at the plasma membrane in human tumors originating from human and mouse breast cancers, as well as in rat keratinocytes, rat C6 glioma cells and mouse testicular Leydig cells (Langlois et al. 2010; Naus et al. 1993; Qin et al. 2002, 2003; Segretain et al. 2003). Studies in breast tumor cells have linked decreased expression of Cx26 and Cx43 with increased tumor growth in mice and demonstrated that the connexins were localized preferentially to lysosomes in communication-deficient

MDA-MB-231 human breast tumor cells (Qin et al. 2002). Furthermore, delivery of Cx43 to lysosomes in MDA-MB-231 cells contributed to the loss of Cx43 from the cell surface, which was previously linked to tumor cell growth and the upregulation of genes involved in tumor growth and metastasis (Qin et al. 2003). Cx43 was also shown to function as a tumor-suppressor in rat endothelial keratinocyte cells (Langlois et al. 2010). Increased endolysosomal degradation of Cx43 in rat endothelial keratinocytes, following treatment with TPA or EGF, decreased Cx43 at the plasma membrane. This reduced the interaction of Cx43 with caveolin-1 and increased cell transformation (Langlois et al. 2010). Cx43 also exhibited anticancer activity in C6 glioma cells that express low endogenous levels of Cx43, where the overexpression of Cx43 resulted in reduced proliferation and tumorigenesis (Naus et al. 1993). This was linked to an increase in Cx43 and gap junction plaques observed at the surface of Cx43-overexpressing cells compared to untransfected cells, where distinctive gap junctional aggregates were not observed. In transfected as well as untransfected glioma cells, AGJs and Cx43 were both observed in lysosomes, indicating their involvement in Cx43 degradation (Naus et al. 1993).

Cx43 autophagy may also play an important role in heart disease and trauma. An elevation in autophagosomes containing Cx43 has been reported in failing canine myocardium (Hesketh et al. 2010), which suggests a potential mechanism for how Cx43 is removed from the intercalated disc region of cardiomyocytes, an observation commonly made in human heart disease.

Concluding Remarks

Aberrant connexin degradation clearly contributes to the impaired regulation of connexin functions that is associated with human diseases. These observations underscore the importance of fully elucidating the specific mechanisms of proteasomal, endolysosomal and phagolysosomal degradation pathways in connexin turnover. Recent studies demonstrating the involvement of autophagy in the degradation of internalized Cx43 reveal the need to reexamine the previous studies of connexin lysosomal degradation for the possible role of autophagy. Earlier reports proposed that lysosomal degradation occurred as part of the endosomal trafficking of Cx43. However, since lysosomal degradation is the end point for both endolysosomal and autophagic degradation, it is important to clarify whether these two pathways are separate and distinct processes or whether they are part of the same mechanism. In addition, further study of the factors that facilitate connexin proteasomal degradation is required to gain a better understanding of how the proteasome affects connexin-dependent processes as cellular and ER stresses, which influence proteasomal degradation, can have dramatic effects on connexin levels and trafficking. It has become evident that connexin turnover is controlled by a diverse array of physiological stimuli and posttranslational modifications. Understanding the molecular mechanisms by which these factors target connexins toward the different degradation pathways and influence their functioning may evoke novel approaches to restore connexin function in cells resulting from the aberrant degradation of connexins that can contribute to various pathological conditions.

Acknowledgements This work was supported by awards from the American Heart Association (11POST5460028, to V.S.), the Hawaii Community Foundation (11ADVC-49235, to V.S. and A.F.L.) and the National Cancer Institute, National Institutes of Health (CA052098-18, to A.F.L.).

References

Anselmi F, Hernandez VH, Crispino G, Seydel A, Ortolano S, Roper SD, Kessaris N, Richardson W, Rickheit G, Filippov MA, Monyer H, Mammano F (2008) ATP release through connexin hemichannels and gap junction transfer of second messengers propagate Ca^{2+} signals across the inner ear. Proc Natl Acad Sci USA 105:18770–18775

Auth T, Schluter S, Urschel S, Kussmann P, Sonntag S, Hoher T, Kreuzberg MM, Dobrowolski R, Willecke K (2009) The TSG101 protein binds to connexins and is involved in connexin degradation. Exp Cell Res 315:1053–1062

Bargiotas P, Monyer H, Schwaninger M (2009) Hemichannels in cerebral ischemia. Curr Mol Med 9:186–194

Beardslee MA, Laing JG, Beyer EC, Saffitz JE (1998) Rapid turnover of connexin43 in the adult rat heart. Circ Res 83:629–635

Beardslee MA, Lerner DL, Tadros PN, Laing JG, Beyer EC, Yamada KA, Kleber AG, Schuessler RB, Saffitz JE (2000) Dephosphorylation and intracellular redistribution of ventricular connexin43 during electrical uncoupling induced by ischemia. Circ Res 87:656–662

Bercovich Z, Rosenberg-Hasson Y, Ciechanover A, Kahana C (1989) Degradation of ornithine decarboxylase in reticulocyte lysate is ATP-dependent but ubiquitin-independent. J Biol Chem 264: 15949–15952

Berthoud VM, Tadros PN, Beyer EC (2000) Connexin and gap junction degradation. Methods 20:180–187

Boassa D, Solan JL, Papas A, Thornton P, Lampe PD, Sosinsky GE (2010) Trafficking and recycling of the connexin43 gap junction protein during mitosis. Traffic 11:1471–1486

Bright NA, Gratian MJ, Luzio JP (2005) Endocytic delivery to lysosomes mediated by concurrent fusion and kissing events in living cells. Curr Biol 15:360–365

Cherian PP, Siller-Jackson AJ, Gu S, Wang X, Bonewald LF, Sprague E, Jiang JX (2005) Mechanical strain opens connexin 43 hemichannels in osteocytes: a novel mechanism for the release of prostaglandin. Mol Biol Cell 16:3100–3106

Colussi C, Rosati J, Straino S, Spallotta F, Berni R, Stilli D, Rossi S, Musso E, Macchi E, Mai A, Sbardella G, Castellano S, Chimenti C, Frustaci A, Nebbioso A, Altucci L, Capogrossi MC, Gaetano C (2011) Nepsilon-lysine acetylation determines dissociation from GAP junctions and lateralization of connexin 43 in normal and dystrophic heart. Proc Natl Acad Sci USA 108:2795–2800

Contreras JE, Saéz JC, Bukauskas FF, Bennett MV (2003) Functioning of cx43 hemichannels demonstrated by single channel properties. Cell Commun Adhes 10:245–249

Darrow BJ, Laing JG, Lampe PD, Saffitz JE, Beyer EC (1995) Expression of multiple connexins in cultured neonatal rat ventricular myocytes. Circ Res 76:381–387

Das Sarma J, Wang F, Koval M (2002) Targeted gap junction protein constructs reveal connexin-specific differences in oligomerization. J Biol Chem 277:20911–20918

Das S, Smith TD, Sarma JD, Ritzenthaler JD, Maza J, Kaplan BE, Cunningham LA, Suaud L, Hubbard MJ, Rubenstein RC, Koval M (2009) ERp29 restricts connexin43 oligomerization in the endoplasmic reticulum. Mol Biol Cell 20:2593–2604

Davies KJ (2001) Degradation of oxidized proteins by the 20S proteasome. Biochimie 83:301–310

Deveraux Q, Ustrell V, Pickart C, Rechsteiner M (1994) A 26 S protease subunit that binds ubiquitin conjugates. J Biol Chem 269:7059–7061

Diez JA, Ahmad S, Evans WH (1999) Assembly of heteromeric connexons in guinea-pig liver en route to the Golgi apparatus, plasma membrane and gap junctions. Eur J Biochem 262:142–148

Dunn CA, Su V, Lau AF, Lampe PD (2012) Activation of Akt, not connexin 43 protein ubiquitination, regulates gap junction stability. J Biol Chem 287:2600–2607

Elsasser S, Gali RR, Schwickart M, Larsen CN, Leggett DS, Muller B, Feng MT, Tubing F, Dittmar GA, Finley D (2002) Proteasome subunit Rpn1 binds ubiquitin-like protein domains. Nat Cell Biol 4:725–730

Fairweather N, Bell C, Cochrane S, Chelly J, Wang S, Mostacciuolo ML, Monaco AP, Haites NE (1994) Mutations in the connexin 32 gene in X-linked dominant Charcot-Marie-Tooth disease (CMTX1). Hum Mol Genet 3:29–34

Fallon RF, Goodenough DA (1981) Five-hour half-life of mouse liver gap-junction protein. J Cell Biol 90:521–526

Fang S, Weissman AM (2004) A field guide to ubiquitylation. Cell Mol Life Sci 61:1546–1561

Feng J, Park J, Cron P, Hess D, Hemmings BA (2004) Identification of a PKB/Akt hydrophobic motif Ser-473 kinase as DNA-dependent protein kinase. J Biol Chem 279:41189–41196

Fernandes R, Girao H, Pereira P (2004) High glucose down-regulates intercellular communication in retinal endothelial cells by enhancing degradation of connexin 43 by a proteasome-dependent mechanism. J Biol Chem 279:27219–27224

Ferrington DA, Sun H, Murray KK, Costa J, Williams TD, Bigelow DJ, Squier TC (2001) Selective degradation of oxidized calmodulin by the 20 S proteasome. J Biol Chem 276:937–943

Fong JT, Kells RM, Gumpert AM, Marzillier JY, Davidson MW, Falk MM (2012) Internalized gap junctions are degraded by autophagy. Autophagy 8:794–811

Garré JM, Retamal MA, Cassina P, Barbeito L, Bukauskas FF, Saéz JC, Bennett MV, Abudara V (2010) FGF-1 induces ATP release from spinal astrocytes in culture and opens pannexin and connexin hemichannels. Proc Natl Acad Sci USA 107:22659–22664

Ghoshroy S, Goodenough DA, Sosinsky GE (1995) Preparation, characterization, and structure of half gap junctional layers split with urea and EGTA. J Membr Biol 146:15–28

Gilleron J, Fiorini C, Carette D, Avondet C, Falk MM, Segretain D, Pointis G (2008) Molecular reorganization of Cx43, Zo-1 and Src complexes during the endocytosis of gap junction plaques in response to a non-genomic carcinogen. J Cell Sci 121:4069–4078

Gilleron J, Carette D, Fiorini C, Dompierre J, Macia E, Denizot JP, Segretain D, Pointis G (2011) The large GTPase dynamin2: a new player in connexin 43 gap junction endocytosis, recycling and degradation. Int J Biochem Cell Biol 43:1208–1217

Girao H, Pereira P (2003) Phosphorylation of connexin 43 acts as a stimuli for proteasome-dependent degradation of the protein in lens epithelial cells. Mol Vis 9:24–30

Girao H, Pereira P (2007) The proteasome regulates the interaction between Cx43 and ZO-1. J Cell Biochem 102:719–728

Girao H, Catarino S, Pereira P (2009) Eps15 interacts with ubiquitinated Cx43 and mediates its internalization. Exp Cell Res 315:3587–3597

Glass JR, Gerner EW (1987) Spermidine mediates degradation of ornithine decarboxylase by a non-lysosomal, ubiquitin-independent mechanism. J Cell Physiol 130:133–141

Glickman MH, Rubin DM, Fried VA, Finley D (1998) The regulatory particle of the *Saccharomyces cerevisiae* proteasome. Mol Cell Biol 18:3149–3162

Gómez-Hernández JM, de Miguel M, Larrosa B, González D, Barrio LC (2003) Molecular basis of calcium regulation in connexin-32 hemichannels. Proc Natl Acad Sci USA 100:16030–16035

González-Noriega A, Grubb JH, Talkad V, Sly WS (1980) Chloroquine inhibits lysosomal enzyme pinocytosis and enhances lysosomal enzyme secretion by impairing receptor recycling. J Cell Biol 85:839–852

Goodenough DA, Gilula NB (1974) The splitting of hepatocyte gap junctions and zonulae occludentes with hypertonic disaccharides. J Cell Biol 61:575–590

Goodenough DA, Paul DL (2003) Beyond the gap: functions of unpaired connexon channels. Nat Rev Mol Cell Biol 4:285–294

Goodenough DA, Goliger JA, Paul DL (1996) Connexins, connexons, and intercellular communication. Annu Rev Biochem 65:475–502

Govindarajan R, Chakraborty S, Johnson KE, Falk MM, Wheelock MJ, Johnson KR, Mehta PP (2010) Assembly of connexin43 into gap junctions is regulated differentially by E-cadherin and N-cadherin in rat liver epithelial cells. Mol Biol Cell 21:4089–4107

Grune T, Reinheckel T, Davies KJ (1997) Degradation of oxidized proteins in mammalian cells. FASEB J 11:526–534

Guan X, Ruch RJ (1996) Gap junction endocytosis and lysosomal degradation of connexin43-P2 in WB-F344 rat liver epithelial cells treated with DDT and lindane. Carcinogenesis 17:1791–1798

Gumpert AM, Varco JS, Baker SM, Piehl M, Falk MM (2008) Double-membrane gap junction internalization requires the clathrin-mediated endocytic machinery. FEBS Lett 582:2887–2892

He LQ, Cai F, Liu Y, Liu MJ, Tan ZP, Pan Q, Fang FY, de Liang S, Wu LQ, Long ZG, Dai HP, Xia K, Xia JH, Zhang ZH (2005) Cx31 is assembled and trafficked to cell surface by ER-Golgi pathway and degraded by proteasomal or lysosomal pathways. Cell Res 15:455–464

Hesketh GG, Shah MH, Halperin VL, Cooke CA, Akar FG, Yen TE, Kass DA, Machamer CE, Van Eyk JE, Tomaselli GF (2010) Ultrastructure and regulation of lateralized connexin43 in the failing heart. Circ Res 106:1153–1163

Huang T, Zhu Y, Fang X, Chi Y, Kitamura M, Yao J (2010) Gap junctions sensitize cancer cells to proteasome inhibitor MG132-induced apoptosis. Cancer Sci 101:713–721

Husnjak K, Elsasser S, Zhang N, Chen X, Randles L, Shi Y, Hofmann K, Walters KJ, Finley D, Dikic I (2008) Proteasome subunit Rpn13 is a novel ubiquitin receptor. Nature 453:481–488

Jariel-Encontre I, Pariat M, Martin F, Carillo S, Salvat C, Piechaczyk M (1995) Ubiquitinylation is not an absolute requirement for degradation of c-Jun protein by the 26 S proteasome. J Biol Chem 270:11623–11627

Jariel-Encontre I, Bossis G, Piechaczyk M (2008) Ubiquitin-independent degradation of proteins by the proteasome. Biochim Biophys Acta 1786:153–177

Jeyakumar M, Dwek RA, Butters TD, Platt FM (2005) Storage solutions: treating lysosomal disorders of the brain. Nat Rev Neurosci 6:713–725

Kelly SM, VanSlyke JK, Musil LS (2007) Regulation of ubiquitin-proteasome system mediated degradation by cytosolic stress. Mol Biol Cell 18:4279–4291

Kimura K, Nishida T (2010) Role of the ubiquitin-proteasome pathway in downregulation of the gap-junction protein connexin43 by TNF-α in human corneal fibroblasts. Invest Ophthalmol Vis Sci 51:1943–1947

Kjenseth A, Fykerud T, Rivedal E, Leithe E (2010) Regulation of gap junction intercellular communication by the ubiquitin system. Cell Signal 22:1267–1273

Kjenseth A, Fykerud TA, Sirnes S, Bruun J, Kolberg M, Yohannes Z, Omori Y, Rivedal E, Leithe E (2012) The gap junction channel protein connexin43 is covalently modified and regulated by SUMOylation. J Biol Chem 287:15851–15861

Knight MM, McGlashan SR, Garcia M, Jensen CG, Poole CA (2009) Articular chondrocytes express connexin 43 hemichannels and P2 receptors—a putative mechanoreceptor complex involving the primary cilium? J Anat 214:275–283

Komatsu M, Ichimura Y (2010) Physiological significance of selective degradation of p62 by autophagy. FEBS Lett 584: 1374–1378

Koval M (2006) Pathways and control of connexin oligomerization. Trends Cell Biol 16:159–166

Laing JG, Beyer EC (1995) The gap junction protein connexin43 is degraded via the ubiquitin proteasome pathway. J Biol Chem 270:26399–26403

Laing JG, Tadros PN, Westphale EM, Beyer EC (1997) Degradation of connexin43 gap junctions involves both the proteasome and the lysosome. Exp Cell Res 236:482–492

Laing JG, Tadros PN, Green K, Saffitz JE, Beyer EC (1998) Proteolysis of connexin43-containing gap junctions in normal and heat-stressed cardiac myocytes. Cardiovasc Res 38:711–718

Laird DW (2006) Life cycle of connexins in health and disease. Biochem J 394:527–543

Laird DW (2008) Closing the gap on autosomal dominant connexin-26 and connexin-43 mutants linked to human disease. J Biol Chem 283:2997–3001

Laird DW, Puranam KL, Revel JP (1991) Turnover and phosphorylation dynamics of connexin43 gap junction protein in cultured cardiac myocytes. Biochem J 273(pt 1):67–72

Lan Z, Kurata WE, Martyn KD, Jin C, Lau AF (2005) Novel rab GAP-like protein, CIP85, interacts with connexin43 and induces its degradation. Biochemistry 44:2385–2396

Langlois S, Cowan KN, Shao Q, Cowan BJ, Laird DW (2010) The tumor-suppressive function of connexin43 in keratinocytes is mediated in part via interaction with caveolin-1. Cancer Res 70: 4222–4232

Leithe E, Rivedal E (2004a) Epidermal growth factor regulates ubiquitination, internalization and proteasome-dependent degradation of connexin43. J Cell Sci 117:1211–1220

Leithe E, Rivedal E (2004b) Ubiquitination and down-regulation of gap junction protein connexin-43 in response to 12-*O*-tetradecanoylphorbol 13-acetate treatment. J Biol Chem 279:50089–50096

Leithe E, Brech A, Rivedal E (2006) Endocytic processing of connexin43 gap junctions: a morphological study. Biochem J 393:59–67

Leithe E, Kjenseth A, Sirnes S, Stenmark H, Brech A, Rivedal E (2009) Ubiquitylation of the gap junction protein connexin-43 signals its trafficking from early endosomes to lysosomes in a process mediated by Hrs and Tsg101. J Cell Sci 122:3883–3893

Leithe E, Sirnes S, Fykerud T, Kjenseth A, Rivedal E (2012) Endocytosis and post-endocytic sorting of connexins. Biochim Biophys Acta 1818:1870–1879

Li X, Su V, Kurata WE, Jin C, Lau AF (2008) A novel connexin43-interacting protein, CIP75, which belongs to the UbL-UBA protein family, regulates the turnover of connexin43. J Biol Chem 283:5748–5759

Lichtenstein A, Minogue PJ, Beyer EC, Berthoud VM (2011) Autophagy: a pathway that contributes to connexin degradation. J Cell Sci 124:910–920

Locke D, Bian S, Li H, Harris AL (2009) Post-translational modifications of connexin26 revealed by mass spectrometry. Biochem J 424:385–398

Lubke T, Lobel P, Sleat DE (2009) Proteomics of the lysosome. Biochim Biophys Acta 1793:625–635

Mari M, Bujny MV, Zeuschner D, Geerts WJ, Griffith J, Petersen CM, Cullen PJ, Klumperman J, Geuze HJ (2008) SNX1 defines an early endosomal recycling exit for sortilin and mannose 6-phosphate receptors. Traffic 9:380–393

Martin PE, Evans WH (2004) Incorporation of connexins into plasma membranes and gap junctions. Cardiovasc Res 62:378–387

Maza J, Mateescu M, Das Sarma J, Koval M (2003) Differential oligomerization of endoplasmic reticulum–retained connexin43/connexin32 chimeras. Cell Commun Adhes 10:319–322

Maza J, Das Sarma J, Koval M (2005) Defining a minimal motif required to prevent connexin oligomerization in the endoplasmic reticulum. J Biol Chem 280:21115–21121

Mazet F, Wittenberg BA, Spray DC (1985) Fate of intercellular junctions in isolated adult rat cardiac cells. Circ Res 56:195–204

Mitra S, Annamalai L, Chakraborty S, Johnson K, Song XH, Batra SK, Mehta PP (2006) Androgen-regulated formation and degradation of gap junctions in androgen-responsive human prostate cancer cells. Mol Biol Cell 17:5400–5416

Murakami Y, Matsufuji S, Kameji T, Hayashi S, Igarashi K, Tamura T, Tanaka K, Ichihara A (1992) Ornithine decarboxylase is degraded by the 26S proteasome without ubiquitination. Nature 360:597–599

Murray SA, Larsen WJ, Trout J, Donta ST (1981) Gap junction assembly and endocytosis correlated with patterns of growth in a cultured adrenocortical tumor cell (SW-13). Cancer Res 41: 4063–4074

Musil LS, Le AC, VanSlyke JK, Roberts LM (2000) Regulation of connexin degradation as a mechanism to increase gap junction assembly and function. J Biol Chem 275:25207–25215

Naus CC, Laird DW (2010) Implications and challenges of connexin connections to cancer. Nat Rev Cancer 10:435–441

Naus CC, Hearn S, Zhu D, Nicholson BJ, Shivers RR (1993) Ultrastructural analysis of gap junctions in C6 glioma cells transfected with connexin43 cDNA. Exp Cell Res 206:72–84

Orlowski M, Wilk S (2003) Ubiquitin-independent proteolytic functions of the proteasome. Arch Biochem Biophys 415:1–5

Park DJ, Wallick CJ, Martyn KD, Lau AF, Jin C, Warn-Cramer BJ (2007) Akt phosphorylates connexin43 on Ser373, a "mode-1" binding site for 14–3-3. Cell Commun Adhes 14:211–226

Peters NS, Green CR, Poole-Wilson PA, Severs NJ (1993) Reduced content of connexin43 gap junctions in ventricular myocardium from hypertrophied and ischemic human hearts. Circulation 88:864–875

Piehl M, Lehmann C, Gumpert A, Denizot JP, Segretain D, Falk MM (2007) Internalization of large double-membrane intercellular vesicles by a clathrin-dependent endocytic process. Mol Biol Cell 18:337–347

Puri V, Watanabe R, Dominguez M, Sun X, Wheatley CL, Marks DL, Pagano RE (1999) Cholesterol modulates membrane traffic along the endocytic pathway in sphingolipid-storage diseases. Nat Cell Biol 1:386–388

Qin H, Shao Q, Curtis H, Galipeau J, Belliveau DJ, Wang T, Alaoui-Jamali MA, Laird DW (2002) Retroviral delivery of connexin genes to human breast tumor cells inhibits in vivo tumor growth by a mechanism that is independent of significant gap junctional intercellular communication. J Biol Chem 277:29132–29138

Qin H, Shao Q, Igdoura SA, Alaoui-Jamali MA, Laird DW (2003) Lysosomal and proteasomal degradation play distinct roles in the life cycle of Cx43 in gap junctional intercellular communication-deficient and -competent breast tumor cells. J Biol Chem 278: 30005–30014

Rahman S, Carlile G, Evans WH (1993) Assembly of hepatic gap junctions. Topography and distribution of connexin 32 in intracellular and plasma membranes determined using sequence-specific antibodies. J Biol Chem 268:1260–1265

Rutz ML, Hülser DF (2001) Supramolecular dynamics of gap junctions. Eur J Cell Biol 80:20–30

Saftig P, Klumperman J (2009) Lysosome biogenesis and lysosomal membrane proteins: trafficking meets function. Nat Rev Mol Cell Biol 10:623–635

Salameh A (2006) Life cycle of connexins: regulation of connexin synthesis and degradation. Adv Cardiol 42:57–70

Sarbassov DD, Guertin DA, Ali SM, Sabatini DM (2005) Phosphorylation and regulation of Akt/PKB by the rictor-mTOR complex. Science 307:1098–1101

Sasaki T, Garant PR (1986) Fate of annular gap junctions in the papillary cells of the enamel organ in the rat incisor. Cell Tissue Res 246:523–530

Sato M, Jiao Q, Honda T, Kurotani R, Toyota E, Okumura S, Takeya T, Minamisawa S, Lanier SM, Ishikawa Y (2009) Activator of G protein signaling 8 (AGS8) is required for hypoxia-induced apoptosis of cardiomyocytes: role of G betagamma and connexin 43 (Cx43). J Biol Chem 284:31431–31440

Scemes E, Spray DC, Meda P (2009) Connexins, pannexins, innexins: novel roles of "hemi-channels.". Pflugers Arch 457:1207–1226

Segretain D, Falk MM (2004) Regulation of connexin biosynthesis, assembly, gap junction formation, and removal. Biochim Biophys Acta 1662:3–21

Segretain D, Decrouy X, Dompierre J, Escalier D, Rahman N, Fiorini C, Mograbi B, Siffroi JP, Huhtaniemi I, Fenichel P, Pointis G (2003) Sequestration of connexin43 in the early endosomes: an early event of Leydig cell tumor progression. Mol Carcinog 38:179–187

Severs NJ, Shovel KS, Slade AM, Powell T, Twist VW, Green CR (1989) Fate of gap junctions in isolated adult mammalian cardiomyocytes. Circ Res 65:22–42

Severs NJ, Bruce AF, Dupont E, Rothery S (2008) Remodelling of gap junctions and connexin expression in diseased myocardium. Cardiovasc Res 80:9–19

Shearer D, Ens W, Standing K, Valdimarsson G (2008) Posttranslational modifications in lens fiber connexins identified by off-line-HPLC MALDI-quadrupole time-of-flight mass spectrometry. Invest Ophthalmol Vis Sci 49:1553–1562

Shringarpure R, Grune T, Mehlhase J, Davies KJ (2003) Ubiquitin conjugation is not required for the degradation of oxidized proteins by proteasome. J Biol Chem 278:311–318

Siller-Jackson AJ, Burra S, Gu S, Xia X, Bonewald LF, Sprague E, Jiang JX (2008) Adaptation of connexin 43-hemichannel prostaglandin release to mechanical loading. J Biol Chem 283:26374–26382

Simeckova P, Vondracek J, Andrysik Z, Zatloukalova J, Krcmar P, Kozubik A, Machala M (2009) The 2,2′,4,4′,5,5′-hexachlorobiphenyl-enhanced degradation of connexin 43 involves both proteasomal and lysosomal activities. Toxicol Sci 107:9–18

Sirnes S, Leithe E, Rivedal E (2008) The detergent resistance of connexin43 is lost upon TPA or EGF treatment and is an early step in gap junction endocytosis. Biochem Biophys Res Commun 373:597–601

Sirnes S, Kjenseth A, Leithe E, Rivedal E (2009) Interplay between PKC and the MAP kinase pathway in connexin43 phosphorylation and inhibition of gap junction intercellular communication. Biochem Biophys Res Commun 382:41–45

Smith JH, Green CR, Peters NS, Rothery S, Severs NJ (1991) Altered patterns of gap junction distribution in ischemic heart disease. An immunohistochemical study of human myocardium using laser scanning confocal microscopy. Am J Pathol 139:801–821

Smith MH, Ploegh HL, Weissman JS (2011) Road to ruin: targeting proteins for degradation in the endoplasmic reticulum. Science 334:1086–1090

Solan JL, Lampe PD (2005) Connexin phosphorylation as a regulatory event linked to gap junction channel assembly. Biochim Biophys Acta 1711:154–163

Solan JL, Lampe PD (2007) Key connexin 43 phosphorylation events regulate the gap junction life cycle. J Membr Biol 217:35–41

Solan JL, Lampe PD (2009) Connexin43 phosphorylation: structural changes and biological effects. Biochem J 419:261–272

Srinivas M, Calderón DP, Kronengold J, Verselis VK (2006) Regulation of connexin hemichannels by monovalent cations. J Gen Physiol 127:67–75

Stout C, Goodenough DA, Paul DL (2004) Connexins: functions without junctions. Curr Opin Cell Biol 16:507–512

Su V, Lau AF (2009) Ubiquitin-like and ubiquitin-associated domain proteins: significance in proteasomal degradation. Cell Mol Life Sci 66:2819–2833

Su V, Lau AF (2012) Ubiquitination, intracellular trafficking, and degradation of connexins. Arch Biochem Biophys 524:16–22

Su V, Nakagawa R, Koval M, Lau AF (2010) Ubiquitin-independent proteasomal degradation of endoplasmic reticulum–localized connexin43 mediated by CIP75. J Biol Chem 285:40979–40990

Thomas MA, Zosso N, Scerri I, Demaurex N, Chanson M, Staub O (2003) A tyrosine-based sorting signal is involved in connexin43 stability and gap junction turnover. J Cell Sci 116:2213–2222

van Veen AA, van Rijen HV, Opthof T (2001) Cardiac gap junction channels: modulation of expression and channel properties. Cardiovasc Res 51:217–229

VanSlyke JK, Musil LS (2002) Dislocation and degradation from the ER are regulated by cytosolic stress. J Cell Biol 157:381–394

VanSlyke JK, Musil LS (2003) Degradation of connexins from the plasma membrane is regulated by inhibitors of protein synthesis. Cell Commun Adhes 10:329–333

VanSlyke JK, Musil LS (2005) Cytosolic stress reduces degradation of connexin43 internalized from the cell surface and enhances gap junction formation and function. Mol Biol Cell 16:5247–5257

VanSlyke JK, Deschenes SM, Musil LS (2000) Intracellular transport, assembly, and degradation of wild-type and disease-linked mutant gap junction proteins. Mol Biol Cell 11:1933–1946

Vinken M, Vanhaecke T, Papeleu P, Snykers S, Henkens T, Rogiers V (2006) Connexins and their channels in cell growth and cell death. Cell Signal 18:592–600

Voges D, Zwickl P, Baumeister W (1999) The 26S proteasome: a molecular machine designed for controlled proteolysis. Annu Rev Biochem 68:1015–1068

Wei CJ, Xu X, Lo CW (2004) Connexins and cell signaling in development and disease. Annu Rev Cell Dev Biol 20:811–838

White TW, Paul DL (1999) Genetic diseases and gene knockouts reveal diverse connexin functions. Annu Rev Physiol 61: 283–310

Xie H, Laird DW, Chang TH, Hu VW (1997) A mitosis-specific phosphorylation of the gap junction protein connexin43 in human vascular cells: biochemical characterization and localization. J Cell Biol 137:203–210

Yang Z, Klionsky DJ (2009) An overview of the molecular mechanism of autophagy. Curr Top Microbiol Immunol 335: 1–32

J Membrane Biol (2012) 245:401–409
DOI 10.1007/s00232-012-9462-2

Connexin43 and Pannexin1 Channels in Osteoblasts: Who Is the "Hemichannel"?

Mia M. Thi · Shalena Islam · Sylvia O. Suadicani · David C. Spray

Received: 9 April 2012 / Accepted: 20 June 2012 / Published online: 15 July 2012

Abstract Osteoblasts sense and respond to mechanical stimuli in a process involving influx and release of large ions and signaling molecules. Unapposed gap junction hemichannels formed of connexin43 (Cx43) have been proposed as a major route for such exchange, in particular for release of ATP and prostaglandin E_2 (PGE_2) in osteocytes. However, we have found that Cx43-null osteoblasts have unaltered, mechanically induced PGE_2 release and ATP-induced YoPro dye uptake. In contrast, PGE_2 release in response to fluid shear stress is abolished in $P2X_7$ receptor ($P2X_7R$)–null osteoblasts, and ATP-induced dye uptake is attenuated following treatment of wild-type cells with a $P2X_7R$ or Pannexin1 (Panx1) channel blocker. These data indicate that Panx1 channels, in concert with $P2X_7R$, likely form a molecular complex that performs the hemichannel function in osteoblast mechanosignaling.

Keywords $P2X_7R$ · ATP · Osteoblast · Gap junction · Dye uptake

M. M. Thi (✉)
Department of Orthopedic Surgery, Albert Einstein College of Medicine, Bronx, NY 10461, USA
e-mail: mia.thi@einstein.yu.edu

M. M. Thi · S. O. Suadicani · D. C. Spray
Department of Neuroscience, Albert Einstein College of Medicine, Bronx, NY 10461, USA

S. Islam
Department of Biology, The City College of New York, New York, NY 10031, USA

S. O. Suadicani
Department of Urology, Albert Einstein College of Medicine, Bronx, NY 10461, USA

Introduction

Gap junctions are formed in vertebrates by connexins and in invertebrates by innexins; remarkably, these functionally equivalent proteins display no homology at the level of amino acid sequence; but, as shown 40 years ago by Ross Johnson, their intramembrane particles look pretty similar (Johnson and Sheridan 1971; Johnson et al. 1973). Pannexins were discovered in searches of the vertebrate genome for similarities to innexin cDNA sequences. In contrast to connexins and innexins, pannexins likely do not form junctional channels; however, at least one of the three pannexins, Pannexin1 (Panx1), forms large-conductance, mechanosensitive and highly permeable channels in non-junctional membranes of mammalian cells (for reviews, see Iglesias et al. 2009a; Sosinsky et al. 2011). Certain connexin hemichannels can also open when unpaired, forming pores permeable to large molecules, similar to Panx1 channels and gap junctions (Spray et al. 2006).

Thus, whereas both connexins and Panx1 are involved in intercellular communication, they appear to have different roles (Scemes et al. 2007). Connexins mainly provide junctional coupling, whereas Panx1 channels assist autocrine/paracrine signaling by providing a pathway for controlled release of signaling molecules such as ATP (Dahl and Locovei 2006; Scemes et al. 2007; MacVicar and Thompson 2010; Sosinsky et al. 2011). In this article we report largely unpublished studies of osteoblasts in vitro, focusing on these different roles of connexins and Panx1 in bone cells. We conclude that, under the conditions of our studies, functions previously attributed to connexin43 (Cx43) hemichannels are likely mediated by Panx1 channels instead.

Bone cells are coupled into a functional syncytium by gap junction channels formed mainly by Cx43 (Donahue

2000; Civitelli 2008). Intercellular signals transmitted through gap junction channels formed by these connexins are believed to play key roles in bone embryogenesis, differentiation and mineralization (Minkoff et al. 1994; Donahue 2000; Schiller et al. 2001; Civitelli 2008; Kar et al. 2012). Studies of Cx43-deficient mice (Lecanda et al. 2000; Civitelli 2008) and our recent study with immortalized wild-type and Cx43-null osteoblasts (Thi et al. 2010b) have clearly demonstrated that the presence of Cx43 is essential during early phases of osteoblast differentiation and maturation.

Signaling through gap junction channels is also believed to be essential in bone remodeling. This life-long process is crucial for maintenance of bone mass and integrity and consists of continuous bone resorption and deposition, whereby aging tissue is replaced and injuries are repaired. While it is well established that bone remodeling is regulated by the mechanical loading imposed on the bone by daily physical activity, it is still unclear how these load-generated mechanical signals are translated into the cellular and biochemical events that ultimately result in bone remodeling. There is accumulating evidence that non-junctional Cx43 could actively participate in these events, where Cx43 hemichannels would open in response to mechanical stimulation and provide an efflux pathway for mechanosignaling molecules, such as ATP and prostaglandin E_2 (PGE_2) (Romanello and D'Andrea 2001; Jiang and Cherian 2003; Cherian et al. 2005; Genetos et al. 2007). Cx43 hemichannels are not mechanosensitive, and their response to mechanical stimuli has been proposed to be mediated by their interaction with integrins (Batra et al. 2012a). Besides Cx43 hemichannels, a role for ATP receptors (ionotropic $P2X_7$ receptors) in bone cell mechanotransduction and signaling has also been proposed (Li et al. 2005). Activation of $P2X_7$ receptors ($P2X_7$Rs) has been shown to mediate ATP-induced ATP release from certain cell types (Anderson et al. 2004; Suadicani et al. 2006), and $P2X_7$R deletion abrogates PGE_2 release from osteoblasts in response to fluid shear stress (Li et al. 2005). Moreover, our studies and those of others have shown that $P2X_7$Rs functionally interact with Panx1 channels to provide the permeabilization pathway for $P2X_7$R-induced ATP and IL-1β release (Pelegrin and Surprenant 2006; Locovei et al. 2007). In addition, Panx1 channels possess both mechanosensitivity (Bao et al. 2004) and activation by extracellular K^+ (Silverman et al. 2009; Suadicani et al. 2012), both of which may be important in bone pathophysiology.

The main goal of the studies described here was to determine the relative role of Cx43 and Panx1 in bone cell mechanotransduction and formation of the ATP-induced dye-uptake pathway that facilitates PGE_2 release. Use of pharmacological approaches to discriminate the participation of connexin hemichannels and Panx1 channels is somewhat complicated by the overlapping effects of pharmacological blockers. In this study we combined use of these drugs with that of the newly generated MOB cell line (wild-type and Cx43-null) (Thi et al. 2010b), allowing us to specifically address the participation of Cx43 in fluid shear stress–induced PGE_2 release from osteoblasts and ATP-induced dye uptake.

Materials and Methods

Materials

Alpha-minimal essential medium (α-MEM), fetal bovine serum (FBS), penicillin–streptomycin and YoPro-1 iodide (491/509) were purchased from Invitrogen (Carlsbad, CA). Collagenase type II was purchased from Worthington Biochemical (Lakewood, NJ), protease inhibitor cocktail was purchased from Roche (Mannheim, Germany), nitrocellulose membranes were purchased from Whatman (Dassel, Germany) and the Immobilon Western detection kit was purchased from Millipore (Billerica, MA). All other chemicals were from Sigma-Aldrich (St. Louis, MO) unless otherwise stated.

Cell Line Culture

Osteoblastic MOB-C and 43KO-MOB-C cells (mouse osteoblast cell lines derived from wild-type and Cx43-null calvaria) (Thi et al. 2010b) and MC3T3-E1 cells (subclone 4) (ATCC, Manassas, VA) were cultured in α-MEM containing 1 % penicillin–streptomycin and 10 % FBS at 37 °C with 95 % air/5 % CO_2.

Primary Osteoblast Culture

As described in our previous work (Thi et al. 2010b), osteoblasts were isolated from calvaria of newborn (P0) and embryonic (E19–20) wild-type and Cx43-null mice obtained from in-house mating of Cx43 heterozygous mice (C57BL/6J-Gja1^{tm1Kdr}) (Reaume et al. 1995) and from newborn $P2X_7$R-null mice (B6.129P2-P2rx7^{tm1Gab}/J). All animal procedures and experimental protocols were approved by the Institute for Animal Studies of the Albert Einstein College of Medicine in accordance with NIH guidelines. Briefly, pups were killed by decapitation, and the periosteum and endosteum of individual calvaria were carefully removed, cleaned and thoroughly diced into small pieces, then pooled for each pup and digested in 1× PBS containing 4 mg/ml of collagenase type II at 37 °C for 10 min. Supernatant from the second and third sequential

digestions at 37 °C were collected. Cells were then collected by centrifugation, resuspended in α-MEM supplemented with 10 % FBS and 1 % penicillin–streptomycin and seeded in culture dishes. Primary osteoblasts isolated from wild-type and from Cx43-null and $P2X_7R$-null calvarial tissue were termed PMOB, 43KO-PMOB and $P2X_7$RKO-PMOB, respectively.

Pulsatile Fluid Shear Stress Treatment

For flow experiments the immortalized wild-type (MOB-C), Cx43-null (43KO-MOB-C) and MC3T3-E1 osteoblastic cell lines were seeded at 10^4 cells/cm^2 and primary osteoblasts were seeded at 2×10^4 cells/cm^2 and grown on glass slides for 3 days. The fluid flow setup consisted of a parallel plate flow chamber (Cytodyne, La Jolla, CA) and a recirculating flow circuit as previously described (Thi et al. 2010a). Briefly, the flow loop included a variable speed Masterflex pump (Cole-Palmer Instrument, Vernon Hills, IL) and a reservoir with culture medium (α-MEM + 1 % FBS) maintained at 37 °C with 95 % air/5 % CO_2. This system produces pulsatile flow over a cell monolayer with average shear stress of 10 dyne/cm^2 at 1 Hz frequency. Control cells were kept under static conditions at 37 °C with 95 % air/5 % CO_2.

Quantification of PGE_2 Release

Supernatants from control (static) and pulsatile flow–conditioned medium were collected immediately after 1-h exposure of cells to fluid shear stress. Supernatants were stored at –80 °C and then assayed for PGE_2 using a PGE_2 EIA Kit (Cayman, Ann Arbor, MI). Average OD values were acquired at wavelength 415 nm using a FLUOStar Omega plate reader (BMG Labtech, Ortenberg, Germany). PGE_2 concentrations in the medium were determined from the standard curve obtained for each set of experiments. The amount of PGE_2 release was normalized to respective cellular protein levels. Total protein concentration from the samples was determined using the BCA Assay Kit (Thermo Scientific, Waltham, MA).

Western Blot Analysis

Cells were seeded at 1,500 cells/cm^2 and cultured for 10 days. Cells were then harvested and sonicated in 70 µl of lysis buffer (1 mM $NaHCO_3$, 2 mM PMSF, 1 mM Na orthovanadate, 5 mm EDTA and 1× protease inhibitor), and Western blotting was performed as previously described (Thi et al. 2010b). Briefly, protein samples were loaded onto 10 % SDS-PAGE gels for separation and electrophoretically transferred to nitrocellulose membranes. Membranes were probed with primary polyclonal antibodies against Cx43 (1:10,000, Sigma-Aldrich), $P2X_7R$ (1:1,000; Alomone Labs, Jerusalem, Israel) and Panx1 (mid, 1:100; Invitrogen) and monoclonal antibody against β-actin (1:25,000, Sigma-Aldrich), followed by incubation with the secondary antibody, horseradish peroxidase–conjugated anti-rabbit IgG or anti-mouse IgG (Santa Cruz Biotechnology, Santa Cruz, CA). Protein bands were detected using the Immobilon Western detection kit and exposed on the In Vivo FX PRO imaging system (Carestream, Rochester, NY).

YoPro-1 Dye-Uptake Analysis

MOB-C, 43KO-MOB-C and MC3T3-E1 cells were seeded at 2,000 cells/cm^2 and grown for 3 days on MatTek glass-bottomed dishes (MatTek, Ashland, MA). All dye-uptake experiments were performed in low divalent cation PBS (LDPBS, Ca^{2+}/Mg^{2+}-free), a condition that has been routinely used in experiments with connexin hemichannels and $P2X_7$Rs to maximize channel activation (Liu et al. 1996; Virginio et al. 1997; North and Surprenant 2000; Contreras et al. 2003; Jiang and Cherian 2003; Parpura et al. 2004; Cherian et al. 2005; Burra et al. 2010; Batra et al. 2012a). Cells were pretreated with the $P2X_7R$ blocker brilliant blue G (BBG, Sigma-Aldrich) and the connexin/pannexin blockers carbenoxolone (CBX, Sigma-Aldrich) and mefloquine (QU-024, Bioblocks, San Diego, CA) in serum-free α-MEM at 37 °C for 20 min prior to application of 5 µM YoPro-1 (Invitrogen) dye in LDPBS with or without the P2 receptor agonist ATP (Sigma-Aldrich) for 10 min. YoPro-1 dye was used because it is nonfluorescent in solution and fluoresces only when permeating the cells and interacting with nucleic acids. Three to four images per treatment were taken from each set of experiments using a Nikon (Melville, NY) Eclipse TE300 microscope and a Spot-RT digital camera (Diagnostic Instruments, Sterling Heights, MI) with fixed gain and exposure time.

Statistical Analysis

YoPro uptake was quantified as the number of YoPro-positive cells divided by the total number of cells, then multiplied by 100 (percent YoPro-positive cells), and counted using ImageJ software (NIH, Maryland, MD). Data were analyzed from three to four independent sets of experiments using Prism 5 software (GraphPad, San Diego, CA). Statistical differences between PGE_2 released amounts and YoPro-1 dye uptake were determined by one-way ANOVA, followed by Tukey's multiple comparison test. $P < 0.05$ was considered statistically significant.

Results

Participation of Cx43 Hemichannels and $P2X_7Rs$ in Fluid Shear Stress–Induced PGE_2 Release from Osteoblasts

Most previous studies on the role of Cx43 hemichannels in shear-induced ATP or PGE_2 release have relied on the use of compounds that do not pharmacologically discriminate Cx43 from Panx1-$P2X_7R$ (Cherian et al. 2005; Genetos et al. 2007). Therefore, we used Cx43-null or $P2X_7R$-null osteoblasts to specifically address each channel's role. As shown in Fig. 1, significant PGE_2 is released from MC3T3-E1 cells, primary osteoblasts (PMOB), primary Cx43-null osteoblasts (43KO-PMOB) and hTERT-immortalized wild-type (MOB-C) and Cx43-null (43KO-MOB-C) osteoblasts in response to pulsatile fluid shear stress (PFSS). In contrast, PFSS-induced PGE_2 release was completely absent in primary osteoblasts lacking $P2X_7R$ ($P2X_7$RKO-PMOB), as shown previously by another group (Li et al. 2005). PGE_2 released amounts under static conditions were not significantly different among all the cell types. This finding shows that under these conditions $P2X_7R$, rather than Cx43, plays a crucial role in shear-induced PGE_2 release from osteoblasts.

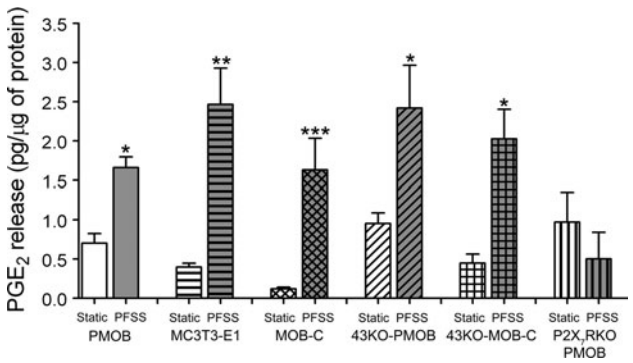

Fig. 1 Analysis of pulsatile fluid shear stress (*PFSS*)–induced PGE_2 release from MC3T3-E1 cells, primary osteoblast (*PMOB*), primary Cx43-null osteoblast (*43KO-PMOB*), $P2X_7R$-null osteoblasts (*$P2X_7$RKO-PMOB*) and hTERT-immortalized wild-type (*MOB-C*) and Cx43-null (*43KO-MOB-C*) osteoblasts. Supernatants from static and PFSS conditioned media were assayed for PGE_2 using the PGE_2 EIA kit. PGE_2 concentrations in the media were determined from standard curves obtained for each set of experiments, and the amount of PGE_2 release was normalized to respective cellular protein content. All data are presented as mean ± SEM, $n = 4$. P values were obtained using one-way ANOVA, followed by Tukey's multiple comparison test (***$P < 0.0005$, **$P < 0.005$, *$P < 0.05$ for static control vs. respective PFSS = 10 dyne/cm^2 at 1 Hz for 1 h)

To evaluate the extent to which the cell lines used in these studies express the channels of interest, we screened MC3T3-E1, MOB-C and 43KO-MOB-C cells for expression of Cx43, $P2X_7R$ and Panx1 using Western blot analysis. As shown in Fig. 2, all three lines expressed $P2X_7R$, as was expected from the well-established role of these receptors in bone resorption and mechanotransduction (Gallagher 2004; Li et al. 2005). In addition, Panx1 was found in all cell lines, consistent with its reported expression in primary osteoblasts (Penuela et al. 2007), and Cx43 was found in both MC3T3-E1 and MOB-C but not in 43KO-MOB-C (Thi et al. 2010b).

Cx43 Hemichannels Do Not Mediate Dye Uptake in Low Divalent Cation Solution

To study whether Cx43 was involved in dye uptake resulting from the mechanical stimulation induced by medium displacement in the imaging dish, we performed control basal level YoPro dye-uptake experiments in LDPBS, a condition reported to favor hemichannel opening (Contreras et al. 2003; Cherian et al. 2005; Burra et al. 2010; Batra et al. 2012a). Our results indicate that mechanically induced YoPro dye uptake in LDPBS solution was virtually identical in MC3T3-E1, MOB-C and 43KO-MOB-C cells and that this dye uptake was thus independent of whether Cx43 was present or absent (Fig. 3).

When we treated all three cell types with 1 mM ATP, YoPro uptake significantly increased (Fig. 4, solid gray bars), indicating that ATP could induce large pore formation in osteoblasts regardless of whether Cx43 was present or absent. Next, we examined the extent to which Cx43

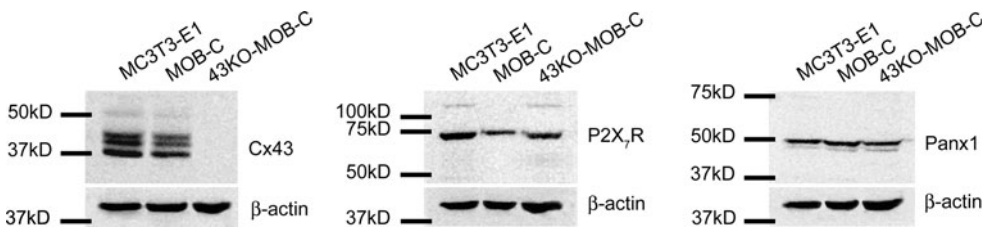

Fig. 2 Western blot assessment of Cx43, $P2X_7R$ and Panx1 expression levels in MC3T3-E1, MOB-C and 43KO-MOB-C cells. Equal amounts of protein from each cell type were used. Western blot analysis was performed using antibodies against Cx43, $P2X_7R$, Panx1 and β-actin. β-actin was used as a constitutively expressed protein for loading control

channel blockers inhibited dye uptake into MC3T3-E1, MOB-C and 43KO-MOB-C cells. For these studies, we used two compounds originally shown to block gap junction channels but subsequently found to be much more potent inhibitors of Panx1 channels at much lower concentrations. CBX is a widely used gap junction blocker, effective at concentrations of 100 μM and higher (Cherian et al. 2005; Batra et al. 2012a); we found a radical decrease in ATP-induced dye uptake not only in wild-type cells but also in Cx43-null cells, using a lower concentration that blocks Panx1 (20 μM) (see Bruzzone et al. 2005; Iglesias et al. 2008; Poornima et al. 2012) (Fig. 4, gray striped bars). This finding of blockade of dye uptake by low CBX concentration in both wild-type and Cx43-null osteoblast cells strongly suggests that Cx43 hemichannels do not play a critical role in large pore formation induced by ATP. This also suggests that a channel other than Cx43, likely Panx1, is responsible for the dye uptake.

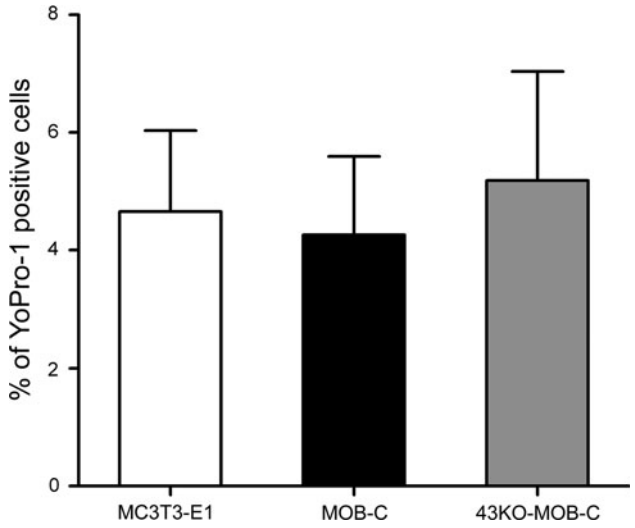

Fig. 3 Assessment of basal level YoPro-1 uptake resulting from the mechanical stimulation induced by medium displacement in the imaging dish with MC3T3-E1, MOB-C and 43KO-MOB-C cells. Cells were bathed in α-MEM at 37 °C for 20 min prior to 5 μM YoPro incubation for 10 min in low divalent cation PBS (*LDPBS*). Percent of YoPro-1-positive cells was calculated by normalizing dye-positive cells with total number of cells in each image field × 100. All data are presented as mean ± SEM, $n = 4$, for each cell type and compared using one-way ANOVA, followed by Tukey's multiple comparison test

To test the participation of Panx1 in ATP-induced pore formation, we also used mefloquine (MFQ). MFQ was originally shown to block gap junction channels [IC_{50} for Cx43–25 μM (Cruikshank et al. 2004)] but is now known to be a much more potent blocker for Panx1, being effective at submicromolar concentrations (Iglesias et al. 2009b). We used three low concentrations of MFQ (10, 50 and 90 nM) that were far below those with effects on Cx43 channels on other cell types (Cruikshank et al. 2004). We found that while MFQ only slightly inhibited basal dye influx in LDPBS (Fig. 5a–c, hatched bars), ATP-induced dye uptake was substantially reduced in MC3T3-E1 cells (Fig. 5a, gray hatched bars) and in both MOB-C and 43KO-MOB-C cells (Fig. 5c, gray hatched bars). In particular, ATP-induced dye uptake was completely eliminated in the presence of 90 nM MFQ in all cell lines. These results imply that Panx1, rather than Cx43, is the mechanosensitive channel being activated by ATP that provides the influx pathway for YoPro uptake.

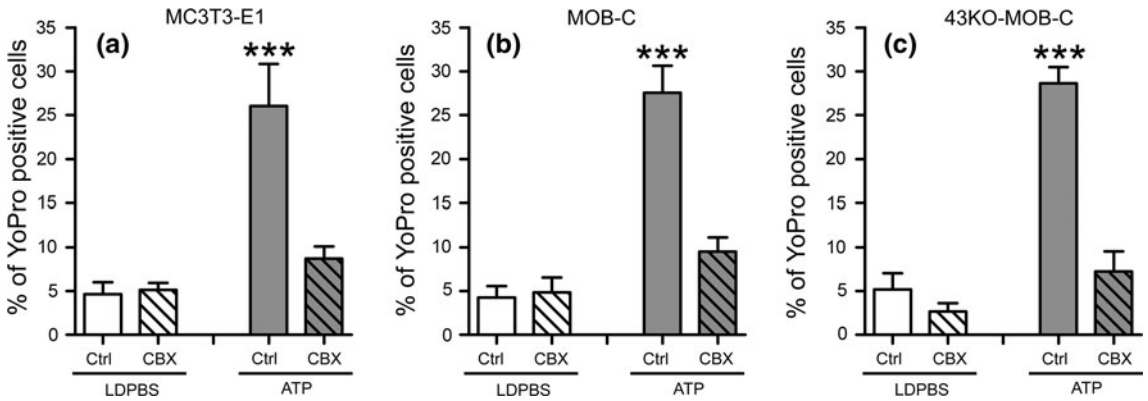

Fig. 4 Effects of carbenoxolone (*CBX*) treatment on YoPro-1 uptake induced either by mechanical stimulation caused by liquid displacement or by ATP application in **a** MC3T3-E1, **b** MOB-C and **c** 43KO-MOB-C osteoblasts. For these studies, cells were bathed in 5 μM YoPro-1 and the effects of 20 μM CBX were evaluated 20 min after treatment. For the ATP-stimulated group, 1 mM ATP was added 10 min after CBX. All experiments were performed in low divalent cation PBS (*LDPBS*). Percent of YoPro-1-positive cells was calculated by normalizing dye-positive cells with the total number of cells in each image field × 100. All data are presented as mean ± SEM, $n = 3$. *P* values were obtained using one-way ANOVA, followed by Tukey's multiple comparison test (***$P < 0.0005$, ATP-treated cells vs. all other treatments)

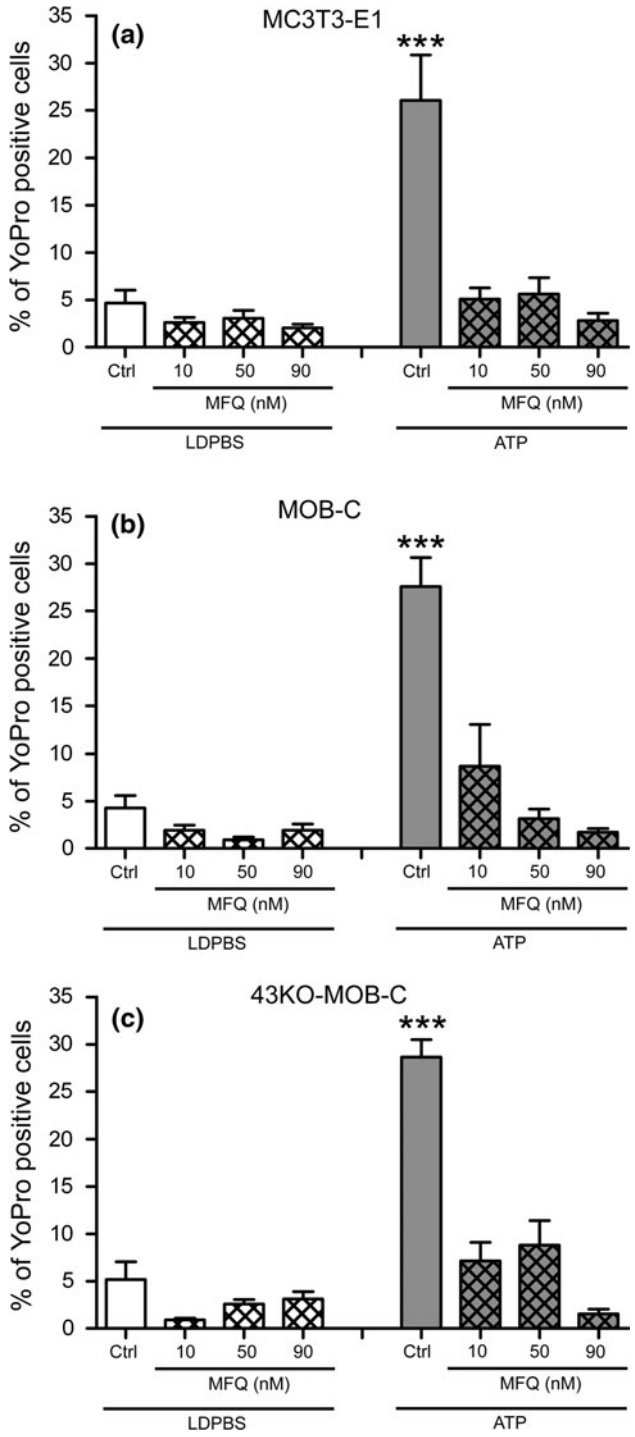

◀ **Fig. 5** Effects of mefloquine (*MFQ*) on YoPro-1 uptake induced either by mechanical stimulation caused by liquid displacement or by ATP application in **a** MC3T3-E1, **b** MOB-C and **c** 43KO-MOB-C osteoblasts. For these studies, cells were bathed in 5 μM YoPro-1 and the effects of three different concentrations of MFQ (10, 50 and 90 nM) were evaluated 20 min after treatment. For the ATP-stimulated group, 1 mM ATP was added 10 min after MFQ. All experiments were performed in low divalent cation PBS (*LDPBS*). Percent of YoPro-1-positive cells was calculated by normalizing dye-positive cells with the total number of cells in each image field × 100. All data are presented as mean ± SEM, $n = 3$. *P* values were obtained using one-way ANOVA, followed by Tukey's multiple comparison test (***$P < 0.0005$, ATP-treated cells vs. all other treatments)

Participation of the Panx1-P2X$_7$R Complex in ATP-Induced Dye Uptake

It has been shown that mice lacking P2X$_7$R have osteopenia in load-bearing bones, implying a critical role for P2X$_7$R as a key mediator in the skeletal response to mechanical loading (Ke et al. 2003). Moreover, ATP signaling through P2X$_7$R has been implicated in fluid shear stress–induced release of PGE_2 in bone cells (Li et al. 2005). There is accumulating evidence that P2X$_7$R functionally interacts with Panx1, providing a conduit for ATP-induced ATP release (Locovei et al. 2007; Iglesias et al. 2008). Therefore, to test the hypothesis that the P2X$_7$R-Panx1 complex in osteoblasts provides the pathway for ATP-induced dye influx, we tested the effects of BBG, a P2X$_7$R blocker. As shown in Fig. 6, all cell lines showed inhibition of ATP-induced dye uptake by BBG in a dose-dependent manner. At higher concentrations (5 and 10 μM) BBG completely abolished ATP-induced dye uptake in both wild-type osteoblastic cells and 43KO-MOB-C cells, demonstrating that P2X$_7$Rs play a role in such uptake. These collective findings strongly indicate that a pathway other than Cx43 hemichannels, likely the P2X$_7$R-Panx1 complex, participates in dye uptake under static conditions.

Discussion

There are several types of channels in osteoblasts and other cell types that are permeable to molecules as large as 1 kDa (Spray et al. 2006). The most prominent of those are channels formed by the gap junction protein Cx43 and the P2X$_7$R-Panx1 complex. Gap junction hemichannels have been proposed to underlie the large-conductance anion channel in skeletal myocytes and elsewhere (Blatz and Magleby 1983; Schwarze and Kolb 1984) and were thought to be responsible for permeabilization of J774 cells by high ATP concentration (Beyer and Steinberg 1991). This permeabilization by ATP now appears to be the result of P2X$_7$R activation in association with Panx1 (Pelegrin and Surprenant 2006; Locovei et al. 2007), and the permeability of these channels to fluorescent dyes has been shown to be very similar to that of gap junction channels (compare Flagg-Newton et al. 1979; Di Virgilio et al. 1996). Moreover, pharmacological blockade of connexins and Panx1 is achieved by most of the same agents. It is thus possible that roles attributed to one of these classes of molecules could be performed by the other.

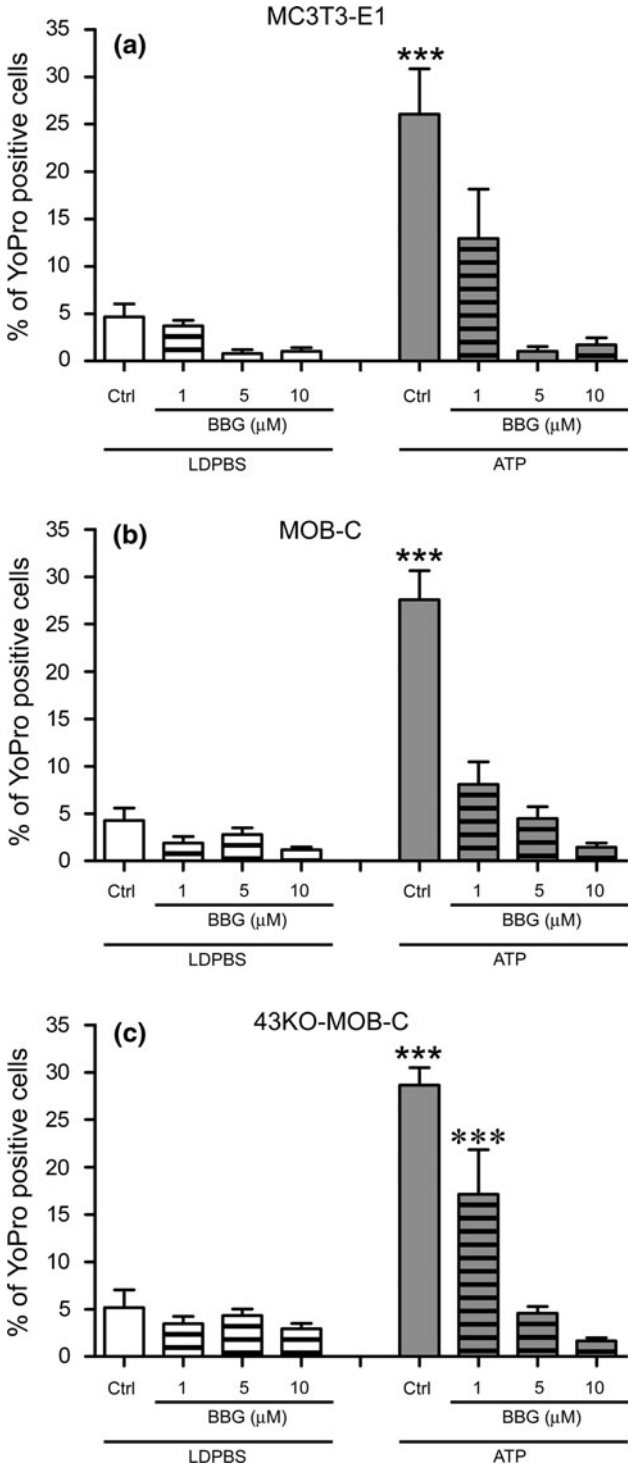

◀ **Fig. 6** Effects of brilliant blue G (*BBG*) treatment on YoPro-1 uptake induced either by mechanical stimulation caused by liquid displacement or by ATP application in **a** MC3T3-E1, **b** MOB-C and **c** 43KO-MOB-C osteoblasts. For these studies, cells were bathed in 5 μM YoPro-1 and the effects of three different concentrations of BBG (1, 5 and 10 μM) were evaluated 20 min after treatment. For the ATP-stimulated group, 1 mM ATP was added 10 min after BBG. All experiments were performed in low divalent cation PBS (*LDPBS*). Percent of YoPro-1-positive cells was calculated by normalizing dye-positive cells with the total number of cells in each image field × 100. All data are presented as mean ± SEM, $n = 3$. *P* values were obtained using one-way ANOVA, followed by Tukey's multiple comparison test (***$P < 0.0005$, ATP-treated cells vs. all other treatments, ***$P < 0.0005$, 1 μM BBG vs. 1 μM BBG + ATP)

In bone cells, fluid shear stress induces the release of extracellular mechanosignaling molecules such as PGE_2, nitric oxide (NO), ATP and VEGF that are essential for bone homeostasis (Reich and Frangos 1993; Klein-Nulend et al. 1995; Genetos et al. 2005; Thi et al. 2010a). However, the cellular pathways that are involved in the release of these substances are not well characterized in bone cells. Studies with other cell types suggest that Cx43 hemichannels, Panx1 channels and the ionotropic purinergic $P2X_7$ receptor (Fig. 7) most likely assist in the release of these substances (Cherian et al. 2005; Li et al. 2005; Locovei et al. 2006).

Despite the existence of a small pool of unpaired Cx43 connexons ("hemichannels") on the unopposed cell surface (Dermietzel et al. 2003), there is little evidence for opening of these channels under physiological conditions. Nevertheless, most reports of functional hemichannels use as evidence dye-uptake measurements at normal resting potentials, with or without divalent cation chelation, and validation by use of gap junction channel blockers (Hofer and Dermietzel 1998; Stout et al. 2002; Contreras et al. 2003; Goodenough and Paul 2003). However, dye uptake mediated by the $P2X_7R$-Panx1 complex is Ca^{2+} and mechanosensitive, increased by membrane depolarization and even more sensitive to blockade by CBX than are gap junctions (Bao et al. 2004; Suadicani et al. 2012). Activation of $P2X_7Rs$ was shown to mediate ATP release in astrocytes (Anderson et al. 2004; Suadicani et al. 2006), and PGE_2 release from osteoblasts in response to fluid shear stress is absent in $P2X_7R$-null mice (Li et al. 2005). Studies on cells in which Panx1 expression was manipulated have shown that Panx1 provides the channel for $P2X_7R$-induced release of ATP (Locovei et al. 2007), which has been confirmed using the Panx1-null mouse (Suadicani et al. 2012). Perhaps most interesting of all, activation of Panx1 channels has been shown to be mechanosensitive (Bao et al. 2004). Therefore, although Cx43 hemichannels have been the focus of many studies in bone mechanotransduction (Jiang and Cherian 2003; Cherian et al. 2005; Genetos et al. 2007; Burra et al. 2010; Batra et al. 2012b), we here provide evidence for $P2X_7R$-Panx1 complex involvement in mechanically induced ATP release from osteoblasts (as illustrated in Fig. 7) and PGE_2 release via an unidentified pathway that does not require Cx43.

The combined use of pharmacological blockers and of osteoblasts lacking Cx43 or $P2X_7R$ in the studies described here has allowed discrimination of the specific role of each

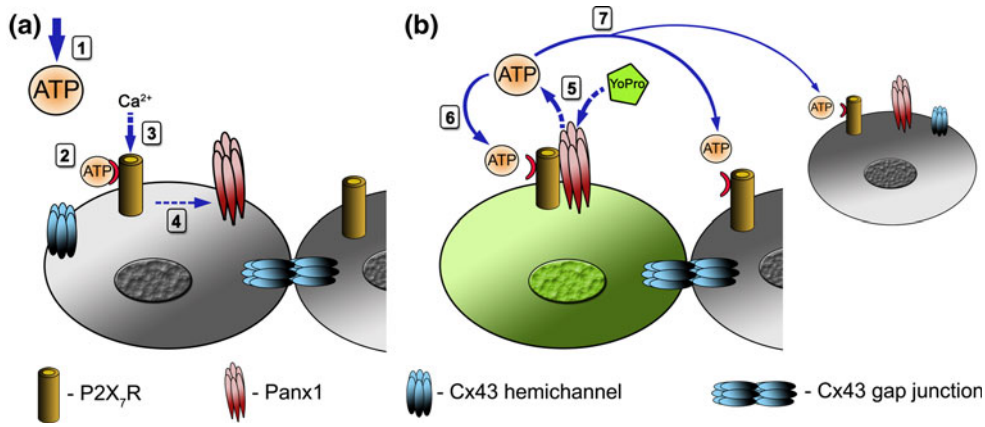

Fig. 7 Schematic diagram depicting the sequence of events triggered by ATP-induced activation of $P2X_7Rs$ in osteoblasts and the distribution of $P2X_7Rs$, Panx1 channels and Cx43 when forming gap junction channels and hemichannels. **a** Extracellular ATP (exogenously added or release from mechanically stimulated cells) diffuses (*1*), binds and activates ionotropic $P2X_7Rs$ (*2*), resulting in influx of Ca^{2+} (*3*) and $P2X_7R$ interaction with Panx1 channels (*4*). **b** P2X7 activation induces opening of Panx1 channels, providing a pathway for ATP efflux and for YoPro dye uptake (*5*). Autocrine $P2X_7R$ activation by released ATP triggers further ATP-induced ATP release from stimulated cells (*6*) and enhances paracrine signaling (*7*) to the neighboring cells. Gap junction channels formed of Cx43 also play a role in intercellular signaling through exchange of second messengers

of these molecular mediators of intercellular communication. While we find that mechanically induced PGE_2 release and ATP-induced dye uptake are not dependent on the presence or function of Cx43, further dissection of the roles of components of the $P2X_7R$-Panx1 complex await the use of Panx1-null osteoblastic cell lines, which are currently being generated in our laboratory.

Acknowledgments This work was supported by the National Institutes of Health, National Institute of Diabetes and Digestive and Kidney Disease [Grants DK091466 (to M.M.T.), DK081435 (to S.O.S.)] and the National Institute of Arthritis and Musculoskeletal and Skin Diseases [Grant AR057139 (to D.C.S)].

References

Anderson CM, Bergher JP, Swanson RA (2004) ATP-induced ATP release from astrocytes. J Neurochem 88:246–256

Bao L, Locovei S, Dahl G (2004) Pannexin membrane channels are mechanosensitive conduits for ATP. FEBS Lett 572:65–68

Batra N, Burra S, Siller-Jackson AJ, Gu S, Xia X, Weber GF, Desimone D, Bonewald LF, Lafer EM, Sprague E, Schwartz MA, Jiang JX (2012a) Mechanical stress–activated integrin alpha5beta1 induces opening of connexin 43 hemichannels. Proc Natl Acad Sci USA 109:3359–3364

Batra N, Kar R, Jiang JX (2012b) Gap junctions and hemichannels in signal transmission, function and development of bone. Biochim Biophys Acta 1818:1909–1918

Beyer EC, Steinberg TH (1991) Evidence that the gap junction protein connexin-43 is the ATP-induced pore of mouse macrophages. J Biol Chem 266:7971–7974

Blatz AL, Magleby KL (1983) Single voltage-dependent chloride-selective channels of large conductance in cultured rat muscle. Biophys J 43:237–241

Bruzzone R, Barbe MT, Jakob NJ, Monyer H (2005) Pharmacological properties of homomeric and heteromeric pannexin hemichannels expressed in *Xenopus* oocytes. J Neurochem 92:1033–1043

Burra S, Nicolella DP, Francis WL, Freitas CJ, Mueschke NJ, Poole K, Jiang JX (2010) Dendritic processes of osteocytes are mechanotransducers that induce the opening of hemichannels. Proc Natl Acad Sci USA 107:13648–13653

Cherian PP, Siller-Jackson AJ, Gu S, Wang X, Bonewald LF, Sprague E, Jiang JX (2005) Mechanical strain opens connexin 43 hemichannels in osteocytes: a novel mechanism for the release of prostaglandin. Mol Biol Cell 16:3100–3106

Civitelli R (2008) Cell–cell communication in the osteoblast/osteocyte lineage. Arch Biochem Biophys 473:188–192

Contreras JE, Saez JC, Bukauskas FF, Bennett MV (2003) Gating and regulation of connexin 43 (Cx43) hemichannels. Proc Natl Acad Sci USA 100:11388–11393

Cruikshank SJ, Hopperstad M, Younger M, Connors BW, Spray DC, Srinivas M (2004) Potent block of Cx36 and Cx50 gap junction channels by mefloquine. Proc Natl Acad Sci USA 101:12364–12369

Dahl G, Locovei S (2006) Pannexin: to gap or not to gap, is that a question? IUBMB Life 58:409–419

Dermietzel R, Meier C, Bukauskas F, Spray DC (2003) Following tracks of hemichannels. Cell Commun Adhes 10:335–340

Di Virgilio F, Ferrari D, Falzoni S, Chiozzi P, Munerati M, Steinberg TH, Baricordi OR (1996) P2 purinoceptors in the immune system. Ciba Found Symp 198:290–305

Donahue HJ (2000) Gap junctions and biophysical regulation of bone cell differentiation. Bone 26:417–422

Flagg-Newton J, Simpson I, Loewenstein WR (1979) Permeability of the cell-to-cell membrane channels in mammalian cell junction. Science 205:404–407

Gallagher JA (2004) ATP P2 receptors and regulation of bone effector cells. J Musculoskelet Neuronal Interact 4:125–127

Genetos DC, Geist DJ, Liu D, Donahue HJ, Duncan RL (2005) Fluid shear-induced ATP secretion mediates prostaglandin release in MC3T3-E1 osteoblasts. J Bone Miner Res 20:41–49

Genetos DC, Kephart CJ, Zhang Y, Yellowley CE, Donahue HJ (2007) Oscillating fluid flow activation of gap junction hemichannels induces ATP release from MLO-Y4 osteocytes. J Cell Physiol 212:207–214

Goodenough DA, Paul DL (2003) Beyond the gap: functions of unpaired connexon channels. Nat Rev Mol Cell Biol 4:285–294

Hofer A, Dermietzel R (1998) Visualization and functional blocking of gap junction hemichannels (connexons) with antibodies against external loop domains in astrocytes. Glia 24:141–154

Iglesias R, Locovei S, Roque A, Alberto AP, Dahl G, Spray DC, Scemes E (2008) P2X7 receptor-pannexin1 complex: pharmacology and signaling. Am J Physiol Cell Physiol 295:C752–C760

Iglesias R, Dahl G, Qiu F, Spray DC, Scemes E (2009a) Pannexin 1: the molecular substrate of astrocyte "hemichannels.". J Neurosci 29:7092–7097

Iglesias R, Spray DC, Scemes E (2009b) Mefloquine blockade of pannexin1 currents: resolution of a conflict. Cell Commun Adhes 16:131–137

Jiang JX, Cherian PP (2003) Hemichannels formed by connexin 43 play an important role in the release of prostaglandin E_2 by osteocytes in response to mechanical strain. Cell Commun Adhes 10:259–264

Johnson RG, Sheridan JD (1971) Junctions between cancer cells in culture: ultrastructure and permeability. Science 174:717–719

Johnson RG, Herman WS, Preus DM (1973) Homocellular and heterocellular gap junctions in *Limulus*: a thin-section and freeze-fracture study. J Ultrastruct Res 43:298–312

Kar R, Batra N, Riquelme MA, Jiang JX (2012) Biological role of connexin intercellular channels and hemichannels. Arch Biochem Biophys 524:2–15

Ke HZ, Qi H, Weidema AF, Zhang Q, Panupinthu N, Crawford DT, Grasser WA, Paralkar VM, Li M, Audoly LP, Gabel CA, Jee WSS, Dixon SJ, Sims SM, Thompson DD (2003) Deletion of the P2X7 nucleotide receptor reveals its regulatory roles in bone formation and resorption. Mol Endocrinol 17:1356–1367

Klein-Nulend J, Semeins CM, Ajubi NE, Nijweide PJ, Burger EH (1995) Pulsating fluid flow increases nitric oxide (NO) synthesis by osteocytes but not periosteal fibroblasts—correlation with prostaglandin upregulation. Biochem Biophys Res Commun 217:640–648

Lecanda F, Warlow PM, Sheikh S, Furlan F, Steinberg TH, Civitelli R (2000) Connexin43 deficiency causes delayed ossification, craniofacial abnormalities, and osteoblast dysfunction. J Cell Biol 151:931–944

Li J, Liu D, Ke HZ, Duncan RL, Turner CH (2005) The P2X7 nucleotide receptor mediates skeletal mechanotransduction. J Biol Chem 280:42952–42959

Liu TF, Li HY, Atkinson MM, Johnson RG (1996) Comparison of lucifer yellow leakage and cell-to-cell transfer following intracellular injection in normal and antisense Novikoff cells under treatment with low extracellular Ca^{2+}. Methods Find Exp Clin Pharmacol 18:493–497

Locovei S, Bao L, Dahl G (2006) Pannexin 1 in erythrocytes: function without a gap. Proc Natl Acad Sci USA 103:7655–7659

Locovei S, Scemes E, Qiu F, Spray DC, Dahl G (2007) Pannexin1 is part of the pore forming unit of the P2X7 receptor death complex. FEBS Lett 581:483–488

MacVicar BA, Thompson RJ (2010) Non-junction functions of pannexin-1 channels. Trends Neurosci 33:93–102

Minkoff R, Rundus VR, Parker SB, Hertzberg EL, Laing JG, Beyer EC (1994) Gap junction proteins exhibit early and specific expression during intramembranous bone formation in the developing chick mandible. Anat Embryol (Berl) 190:231–241

North RA, Surprenant A (2000) Pharmacology of cloned P2X receptors. Annu Rev Pharmacol Toxicol 40:563–580

Parpura V, Scemes E, Spray DC (2004) Mechanisms of glutamate release from astrocytes: gap junction "hemichannels," purinergic receptors and exocytotic release. Neurochem Int 45:259–264

Pelegrin P, Surprenant A (2006) Pannexin-1 mediates large pore formation and interleukin-1beta release by the ATP-gated P2X7 receptor. EMBO J 25:5071–5082

Penuela S, Bhalla R, Gong XQ, Cowan KN, Celetti SJ, Cowan BJ, Bai D, Shao Q, Laird DW (2007) Pannexin 1 and pannexin 3 are glycoproteins that exhibit many distinct characteristics from the connexin family of gap junction proteins. J Cell Sci 120: 3772–3783

Poornima V, Madhupriya M, Kootar S, Sujatha G, Kumar A, Bera AK (2012) P2X7 receptor-pannexin 1 hemichannel association: effect of extracellular calcium on membrane permeabilization. J Mol Neurosci 46:585–594

Reaume AG, de Sousa PA, Kulkarni S, Langille BL, Zhu D, Davies TC, Juneja SC, Kidder GM, Rossant J (1995) Cardiac malformation in neonatal mice lacking connexin43. Science 267: 1831–1834

Reich KM, Frangos JA (1993) Protein kinase C mediates flow-induced prostaglandin E_2 production in osteoblasts. Calcif Tissue Int 52:62–66

Romanello M, D'Andrea P (2001) Dual mechanism of intercellular communication in HOBIT osteoblastic cells: a role for gap-junctional hemichannels. J Bone Miner Res 16:1465–1476

Scemes E, Suadicani SO, Dahl G, Spray DC (2007) Connexin and pannexin mediated cell–cell communication. Neuron Glia Biol 3:199–208

Schiller PC, D'Ippolito G, Balkan W, Roos BA, Howard GA (2001) Gap-junctional communication is required for the maturation process of osteoblastic cells in culture. Bone 28:362–369

Schwarze W, Kolb HA (1984) Voltage-dependent kinetics of an anionic channel of large unit conductance in macrophages and myotube membranes. Pflugers Arch 402:281–291

Silverman WR, de Rivero Vaccari JP, Locovei S, Qiu F, Carlsson SK, Scemes E, Keane RW, Dahl G (2009) The pannexin 1 channel activates the inflammasome in neurons and astrocytes. J Biol Chem 284:18143–18151

Sosinsky GE, Boassa D, Dermietzel R, Duffy HS, Laird DW, MacVicar B, Naus CC, Penuela S, Scemes E, Spray DC, Thompson RJ, Zhao HB, Dahl G (2011) Pannexin channels are not gap junction hemichannels. Channels (Austin) 5:193–197

Spray DC, Ye ZC, Ransom BR (2006) Functional connexin "hemichannels": a critical appraisal. Glia 54:758–773

Stout CE, Costantin JL, Naus CC, Charles AC (2002) Intercellular calcium signaling in astrocytes via ATP release through connexin hemichannels. J Biol Chem 277:10482–10488

Suadicani SO, Brosnan CF, Scemes E (2006) P2X7 receptors mediate ATP release and amplification of astrocytic intercellular Ca^{2+} signaling. J Neurosci 26:1378–1385

Suadicani SO, Iglesias R, Wang J, Dahl G, Spray DC, Scemes E (2012) ATP signaling is deficient in cultured pannexin1-null mouse astrocytes. Glia 60:1106–1116

Thi MM, Suadicani SO, Spray DC (2010a) Fluid flow-induced soluble vascular endothelial growth factor isoforms regulate actin adaptation in osteoblasts. J Biol Chem 285:30931–30941

Thi MM, Urban-Maldonado M, Spray DC, Suadicani SO (2010b) Characterization of hTERT-immortalized osteoblast cell lines generated from wild-type and connexin43-null mouse calvaria. Am J Physiol Cell Physiol 299:C994–C1006

Virginio C, Church D, North RA, Surprenant A (1997) Effects of divalent cations, protons and calmidazolium at the rat P2X7 receptor. Neuropharmacology 36:1285–1294

J Membrane Biol (2012) 245:411–422
DOI 10.1007/s00232-012-9465-z

Cx43 Associates with $Na_v1.5$ in the Cardiomyocyte Perinexus

J. Matthew Rhett · Emily L. Ongstad · Jane Jourdan · Robert G. Gourdie

Received: 10 April 2012 / Accepted: 20 June 2012 / Published online: 19 July 2012

Abstract Gap junctions (GJs) are aggregates of channels that provide for direct cytoplasmic connection between cells. Importantly, this connection is thought responsible for cell-to-cell transfer of the cardiac action potential. The GJ channels of ventricular myocytes are composed of connexin43 (Cx43). Interaction of Cx43 with zonula occludens-1 (ZO-1) is localized not only at the GJ plaque, but also to the region surrounding the GJ, the perinexus. Cx43 in the perinexus is not detectable by immunofluorescence, yet localization of Cx43/ZO-1 interaction to this region indicated the presence of Cx43. Therefore, we hypothesized that Cx43 occurs in the perinexus at a lower concentration per unit membrane than in the GJ itself, making it difficult to visualize. To overcome this, the Duolink protein–protein interaction assay was used to detect Cx43. Duolink labeling of cardiomyocytes localized Cx43 to the perinexus. Quantification demonstrated that signal in the perinexus was lower than in the GJ but significantly higher than in nonjunctional regions. Additionally, Duolink of Triton X-100-extracted cultures suggested that perinexal Cx43 is nonjunctional. Importantly, the voltage gated sodium channel $Na_v1.5$, which is responsible for initiation of the action potential, was found to interact with perinexal Cx43 but not with ZO-1. This work provides a detailed characterization of the structure of the perinexus at the GJ edge and indicates that one of its potential functions in the heart may be in facilitating conduction of action potential.

Keywords Connexin43 · Duolink · Gap junction · Hemichannel · $Na_v1.5$ · Perinexus · Sodium channel

Introduction

The gap junction (GJ) is an aggregate of channels bridging the cytoplasms of adjacent cells. The channels of the GJ allow for passage of small molecules (less than ~1,000 Da) and electrotonic coupling between cells (Liu and Johnson 1999; Palatinus et al. 2012; Severs et al. 2008). Intercellular channels are formed by the interaction of half-channels (called connexons or hemichannels) contributed by each contacting cell (Koval 2006), and connexons are in turn composed of connexin subunit proteins (Evans and Martin 2002). Connexin43 (Cx43) is one of the more commonly expressed connexins in mammalian tissues, most notably in the ventricular myocardium (Beyer et al. 1987; Delmar and Liang 2012; Desplantez et al. 2007). In the ventricle, Cx43 underpins contraction synchronization by contributing to the mechanism of cell-to-cell propagation of action potential (Kleber and Rudy 2004; Severs et al. 2008).

The Cx43 life cycle begins with cotranslational insertion in the endoplasmic reticulum, after which oligomerization of connexons occurs in the Golgi (Musil and Goodenough 1993). Vesicles containing connexons are then thought to traffic to the plasma membrane along microtubules (Fort et al. 2011), although other work suggests that this pathway is only utilized in specialized conditions (Johnson et al. 2002). In the 2000s, it was shown that new Cx43 channels were predominately added from the edge of the GJ (Gaietta et al. 2002; Lauf et al. 2002). Work by Shaw and

Electronic supplementary material The online version of this article (doi:10.1007/s00232-012-9465-z) contains supplementary material, which is available to authorized users.

J. M. Rhett · E. L. Ongstad · J. Jourdan · R. G. Gourdie (✉)
Department of Regenerative Medicine, Medical University of South Carolina, 173 Ashley Ave, CRI Room 616, Charleston, SC 29425, USA
e-mail: gourdier@musc.edu

colleagues suggested a molecular linkage between delivery of Cx43 vesicles to the membrane and incorporation of connexons into the GJ. These studies showed that Cx43 was trafficked from microtubules directly to N-cadherin associated with GJs via EB1 binding of the p150(Glued)/dynein/dynactin complex (Shaw et al. 2007).

The Gourdie laboratory has provided evidence that the scaffolding protein zonula occludens-1 (ZO-1) localizes to the edge of GJs, where it regulates addition of new connexons to the plaque (Hunter et al. 2005). Subsequently, it was shown that ZO-1 interaction with undocked connexons in the plasma membrane regulated their transition to GJ intercellular channels (Rhett et al. 2011). In this work, subcellular localization of Cx43/ZO-1 interaction indicated a novel region of plasma membrane surrounding the GJ. This domain was termed the perinexus for its location next to (*peri-*) the junction (*-nexus*). Perinexal Cx43/ZO-1 interaction, in combination with functional assays, suggested that the perinexus functions as a staging area where ZO-1 served to sequester undocked connexons.

The identification of Cx43/ZO-1 interaction localized to the perinexus indicated the presence of Cx43 molecules, but Cx43 in this region was not detectable by standard immunofluorescence (IF). Others have identified putative Cx43 hemichannels in this region (Beahm et al. 2006; Johnson et al. 2012; Lal et al. 1995). Notably, Ross Johnson and colleagues (Johnson et al. 2012) have recently demonstrated that unaggregated connexons reside near newly forming GJs in the formation plaque (FP) by using sophisticated freeze-fracture replica immunogold labeling (FRIL) techniques. Here, we provide the first direct labeling of Cx43 in the perinexus. Using high-sensitivity Duolink labeling of Cx43–Cx43 interactions, we show that Triton X-100-soluble Cx43 localizes and concentrates in the perinexus of mature junctions. Moreover, we provide evidence that the myocardial perinexus may have unique constitutive functions that go beyond the transition of undocked connexons into the GJ. Specifically, we observe that nonjunctional Cx43 interacts with $Na_v1.5$ in the perinexus of cultured cardiomyocytes, indicating a possible role for $Na_v1.5$ in electrical conduction between cells. These results contribute to a viewpoint held by increasing numbers of workers in the field that cell-to-cell propagation of electrical impulse in the heart may be determined by nonelectrotonic mechanisms.

Materials and Methods

Animals

Cardiac myocytes were collected from freshly dissected ventricles of 1- to 2-day-old Sprague Dawley rats. Tissue sections were generated from hearts collected from 12–15-week-old female Sprague Dawley rats. All animal procedures were in accordance with the Medical University of South Carolina IACAUC and NIH Animal Welfare Assurance A3728–01.

Cell Culture

Freshly dissected ventricles were immediately placed in cold HBSS. The ventricles were finely minced and enzymatically dissociated into single cells at 37 °C with gentle rotation. The combined enzymatic fractions were layered onto a Percoll density gradient 1.080/1.060 for myocyte enrichment. Fibroblasts and myocyte layers were collected and washed. Myocytes were plated in M199/EBSS, 5 % NCS, 10 % HS, and antibiotics onto gelatin-coated dishes at 1.3×10^6 cells/35 mm MatTek plate, and 3×10^6 cells/60 mm culture plate. Cultures were attached 18–24 h at 37 °C/5 % CO_2. After overnight attachment, cultures were washed twice with DPBS Ca^{2+}/Mg^{2+}. Thereafter, fresh maintenance media was added every 2–3 days, and beating cultures were used for experiments 5 days after plating.

Triton Extraction and Fractionation

Neonatal rat heart ventricular myocyte (NRHM) cultures were subjected to in situ Triton X-100 extraction according to the method of Musil and Goodenough (1991). After the final wash step, plates were fixed and stained as described below, or the remaining cellular material was scraped into 1 ml of Triton X-100 extraction buffer for Western blot analysis. Triton fractionation was carried out as previously described (Rhett et al. 2011). Briefly, cells were lysed in the presence of 1 % Triton X-100 and centrifuged for 50 min at $100{,}000 \times g$. Supernatants and pellets were separated, and pellets were resolubilized in lysis buffer containing SDS (0.1 % final concentration was used in both fractions).

Immunocytochemistry

Immunofluorescent and Duolink staining was carried out as previously described (Rhett et al. 2011). For Cx43/ZO-1 interaction, primary antibodies used were mouse anti-Cx43 (Millipore MAB3067) and rabbit anti-ZO-1 (Invitrogen 617–300). In these cultures, goat anti-Cx43 (Abcam 87645) was used to detect Cx43 by standard IF. Cx43–Cx43-Duolink was performed both by dual and single primary detection. For dual detection, mouse anti-Cx43 (Millipore MAB3067) and rabbit anti-Cx43 (Sigma C-6219) were used for Duolink with goat anti-Cx43 (Abcam 87645) for detection by standard IF. For single-primary Duolink detection goat anti-Cx43 (Abcam 87645) was used with mouse anti-Cx43 (Millipore MAB3067) for detection by

standard IF. For standard IF labeling of NRHMs by Cx43, ZO-1 and $Na_v1.5$ goat anti-Cx43 (Abcam 87645), mouse anti-ZO-1 (Zymed 33–9100), and rabbit anti-$Na_v1.5$ (Alamone ASC-005) were used, respectively. For Cx43/$Na_v1.5$ Duolink labeling mouse anti-Cx43 (Millipore MAB3067) and rabbit anti-$Na_v1.5$ (Alamone ASC-005) were used along with goat anti-Cx43 (Abcam 87645) for detection of Cx43 by standard IF. For ZO-1/$Na_v1.5$ Duolink labeling mouse anti-ZO-1 (Zymed 33–9100) and rabbit anti-$Na_v1.5$ (Alamone ASC-005) were used along with goat anti-Cx43 (Abcam 87645) for detection of Cx43 by standard IF. Duolink reactions were carried out using appropriate PLA secondary antibodies according to the manufacturers instructions.

Western Blot Testing

For the Triton fractionation/extraction assay proteins were resolved on 10 % SDS-PAGE gels, followed by immunoblotting for Cx43 with rabbit anti-Cx43 (Sigma C-6219). For $Na_v1.5$ detection, Triton X-100 fractionated NRHM lysates were run on 7 % SDS-PAGE gels, followed by immunoblotting for $Na_v1.5$ (Sigma S0819).

Image Acquisition and Analysis

Confocal images were acquired on a TCS SP5 laser scanning confocal microscope equipped with a 63 ×/1.4 numerical aperture oil objective (Leica, Buffalo Grove, IL). Images were analyzed by ImageJ software (NIH, http://rsbweb.nih.gov/ij/). Measurements were performed on threshold versions of original images, and the same threshold settings were always used within a given experiment.

For Cx43-Duolink density measurements, Cx43 IF images were used to create a selected region of interest encircling GJs, and the integrated density of Cx43-Duolink labeling was measured within the GJ, a region expanded 250 μM from the GJ edge, a region expanded 500 μM from the GJ edge, and the entire image. The Cx43-Duolink density within each region described in the text was determined by subtraction.

For perinexus width measurements, ellipses were fit to all GJs >1 μM^2 in area (smaller junctions were not much bigger than individual Duolink labels), and the distance was measured from the edge of the GJ plaque to the end of Cx43-Duolink labeling along the major and minor axes. When the perinexus was continuous between two junctions along an axis, measurements could not be made accurately and were not used.

Statistical Analysis

Statistical analysis was carried out by GraphPad Prism software, version 5.0d for Mac OS X (GraphPad, San Diego, CA). Multiple comparisons were made using ANOVA with Tukey's multiple comparison test, and single comparisons used an unpaired *t*-test. *p*-values and numbers are indicated in the text and figure captions.

Results

Cx43 Is Concentrated in the Perinexus of Cardiomyocytes

Recent work with Cx43-expressing HeLa cells and rat epicardial cells has identified a region adjacent to GJs involved in regulating transition of connexons in the membrane to intercellular channels in the GJ plaque (Rhett et al. 2011). This region, termed the perinexus, was defined by Cx43/ZO-1 interaction as visualized by the Duolink assay. Cx43 is the primary isoform of connexin expressed in the working ventricular myocardium (Noorman et al. 2009), where it plays a critical role in propagation of the action potential (Severs et al. 2008). Therefore, we sought to determine if ventricular cardiomyocytes also displayed a perinexus. Figure 1a shows cultured NRHMs labeled for Cx43 by standard IF in green, and Cx43/ZO-1 interaction by Duolink in red. We found that nearly all Cx43-labeled GJ structures coincided with labeling for Cx43/ZO-1 interaction—both within GJ plaques and in the adjacent membrane, indicating that cardiomyocytes also possess a perinexus surrounding Cx43 GJs.

The detection of Cx43/ZO-1 interaction in the perinexus suggests the presence of Cx43 in this region. However, it does not yield information pertaining to the quantity of Cx43 within this region. Attempts have been made to visualize perinexal Cx43 by standard IF (Rhett et al. 2011), but this method is not optimal as it is difficult to determine whether this signal originates from perinexal Cx43 or out-of-focus light emanating from the nearby GJ. To avoid this issue, we used Duolink to detect Cx43–Cx43 interaction as a means to resolve Cx43 signals of lower intensity. The rationale for this methodology is that the readout of the Duolink assay is binary—i.e., a Duolink signal is either generated or not depending on whether protein interaction is detected or not—and therefore the number of Duolink signals, and not their intensity, varies with Cx43 concentration within a given region of the cell preparation. Figure 1b depicts neonatal rat heart ventricular myocytes labeled in this manner, with Cx43 labeled by standard IF in green and Cx43–Cx43 interaction by Duolink in red. Duolink signal labeled the GJ, as expected, and also appeared to intensely label the surrounding perinexal membrane, providing direct evidence of Cx43 molecules in the perinexus.

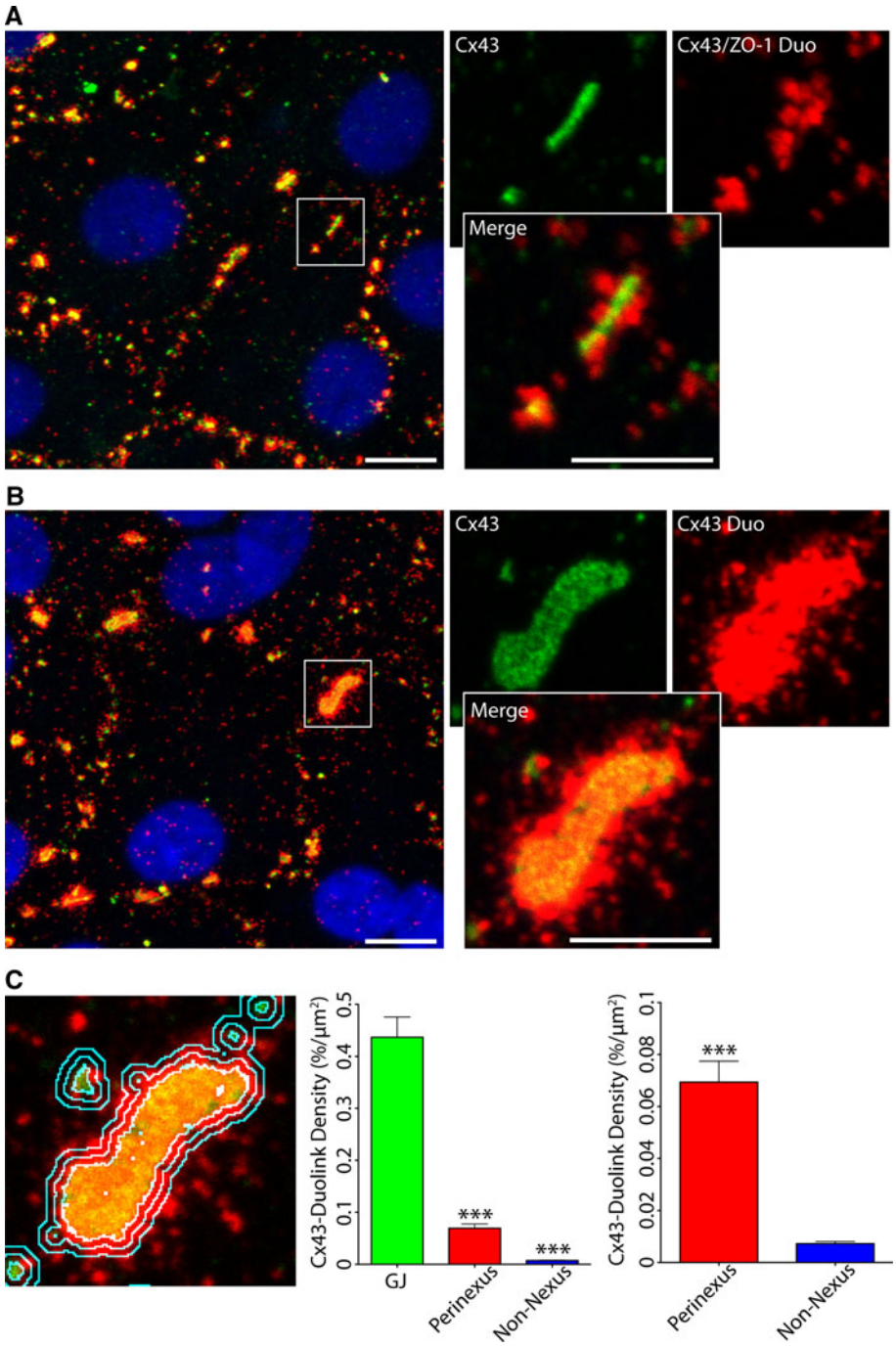

Fig. 1 NHRMs display a perinexus that contains concentrated Cx43 molecules. **a** Cultured NRHMs were labeled for Cx43 by standard IF (*green*), Cx43/ZO-1 interaction by Duolink (*red*), and the nucleus (*blue*). Note the preponderance of Duolink spots adjacent to the GJ plaque. **b** Cx43 is labeled in the perinexus by high-sensitivity Duolink. Cx43 is labeled both by standard IF (*green*) and by Duolink (*red*). The nucleus is labeled in *blue*. **c** Analysis of Duolink-labeled Cx43. The image shows the same GJ expanded in (**b**) with cyan lines demarcating the GJ perimeter (*innermost line*), and 250 and 500 nm from the perimeter (*middle* and *outer* lines, respectively). The graphs show averaged measurements of Cx43-Duolink density within the *innermost line* (GJ), between the *middle* and *outer lines* (Perinexus), and exterior to the *outermost line* (Non-Nexus). The *left* graph compares all three regions; the *right* graph limits the comparison to the perinexus and nonnexal regions (***$p < 0.001$ and ****$p < 0.0001$; $n = 5$). *Error bars* represent SEM; *scale bars* represent 10 μm in large images, and 5 μm in expanded images

Although inspection of the images labeled with Cx43–Cx43-Duolink clearly show interaction that occurs outside of but near the GJ edge, it is difficult to determine the relative amount of Cx43 in the perinexus by visual inspection as a result of the relatively large size of Duolink signals (~400–500 nm diameter). This effect results in highly concentrated signals originating at the GJ edge but extending as far as 250 nm into the perinexus. Thus, to determine the relative amount of Cx43 in the perinexus, measurements of Duolink signal density were performed in three separate regions of Cx43–Cx43-Duolink labeled images: the GJ plaque as defined by standard Cx43 IF (innermost cyan line in Fig. 1c), the perinexus limited to the region between 250 and 500 nm from the GJ edge (from the middle cyan line to the outer cyan line), and nonnexal regions of the cell (everything outside of the outer cyan, 500 nm perimeter line). The perinexal Cx43–Cx43-Duolink signal measured in this way could only have originated from outside of the of the GJ plaque edge.

It was found that the density of Cx43-Duolink signal in both the perinexus and nonnexal regions of the cell were significantly lower than within the GJ plaque (Fig. 1c, left). Importantly, the density of signal in the perinexus was approximately 10-fold lower than the GJ—as would be expected based on the IF signal. Additionally, comparison of the perinexus to nonnexus showed a significantly greater concentration of Cx43-Duolink signal in the perinexus (Fig. 1c, right). Despite the above-mentioned limitations of making similar measurements using IF, comparable levels of Cx43 density were ascertained with this method (Supplementary Material). Taken together, these results demonstrate the presence of Cx43 in the perinexus at a much lower concentration than the GJ plaque, but at a substantially higher concentration than the rest of the cell.

The Perinexus Has Variable Shape

Having defined the Cx43 composition of the perinexus, we next sought to analyze the distance that perinexal Cx43 signal extended from the GJ edge. Measurements were performed on images acquired from neonatal rat heart ventricular myocyte cultures by fitting ellipses to GJs, and measuring the distance from the edge of the GJ (labeled by standard Cx43 IF) to the end of contiguous Cx43-Duolink label along major and minor axes of the ellipse (Fig. 2). The method of fitting ellipses and using the major and minor axes as plumb lines along which to measure was done to introduce randomness in where the measurements were taken (i.e., we did not chose the location of the axes) and to ensure that the perinexus width was obtained as near as possible along a line emanating directly outward from the GJ.

It was determined that, after compensating for the size of individual Cx43-Duolink signals, the average width of the perinexus obtained from five separate experiments was 200.4 ± 28.4 nm (mean ± SEM; Fig. 2). We used SEM here to compare means between experiments because it reflects how accurately we know the "true" value of the average perinexus width. The relatively small SEM (i.e., 28.4 nm) indicated that our results were consistent between experiments. However, visual inspection indicated variation in the width of the perinexus for any given GJ (Fig. 2). To this end, we used the standard deviation of all the measurements *within* an experiment to determine the variability between individual perinexus width measurements. The large standard deviation for measurements within an experiment, 313.9 ± 20.4 nm (mean of all experiments ± SEM between experiments; Fig. 2) compared to the ~200 nm perinexus width confirmed our observations.

We did not find any correlation between perinexus width and GJ size as defined by either area or length (R^2 = 0.017 ± 0.015 and 0.033 ± 0.015, respectively), but it was determined that the percentage of measurements for which the perinexus width was recorded as 0 in each experiment was high: 42.4 ± 5.4 %. Furthermore, there was a relatively small percentage of perinexus width measurements over 500 nm (12.5 ± 2.6 %). However, fully 45.1 ± 3.7 % of measurements were between 0 and 500 nm, suggesting that many junctions displayed uniform Cx43-Duolink labeling in the perinexus but that perinexal Cx43 was often distributed in elongated projections from the GJ plaque edge. This could be confirmed by visual inspection of images (Figs. 1b, 2).

Cx43 in the Perinexus Is Nonjunctional

In recent work, correlative biochemical and functional data suggested that at least a portion of Cx43 present in the perinexus was in the form of functional hemichannels (Rhett et al. 2011). To further address the composition of perinexal Cx43 we used in situ Triton X-100 extraction. In this assay, a buffer containing 1 % Triton X-100 was applied to cultured NRHMs with mild agitation, followed by reclamation of the buffer (now containing Triton-soluble portions of the cells) and fixation, staining, and imaging

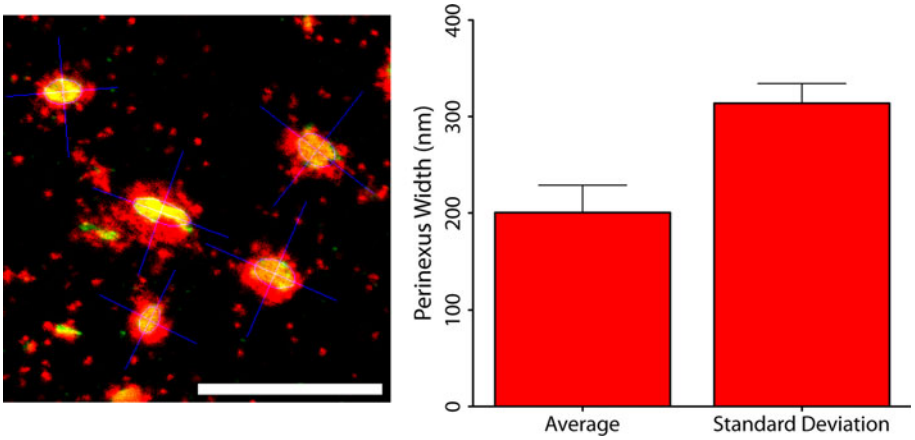

Fig. 2 The perinexus has a distinct shape. Confocal image of typical GJs and perinexi from cultured NRHMs. Cx43 is labeled by standard IF in *green*, Duolink in *red*, and fitted ellipses with major and minor axes are in *blue* (*left*). *Scale bar* 10 μm. The graph at *right* shows the perinexus width, averaged over 5 experiments, and the standard deviation for individual measurements within each experiment. *Error bars* represent SEM

of the remaining Triton-insoluble cellular components left on the culture plate.

To validate the assay, we compared the results of a Triton X-100 detergent extraction to NRHM lysates separated into Triton X-100-soluble (nonjunctional) and -insoluble (junctional) fractions by ultracentrifugation. In this instance of Triton extraction, the cell components remaining on the culture plate were scraped into an equivalent volume of extraction buffer as opposed to being fixed. We compared the two methodologies by Western blot analysis for Cx43 as shown in Fig. 3a. Similar to the results of others in cultured cardiomyocytes (Tence et al.

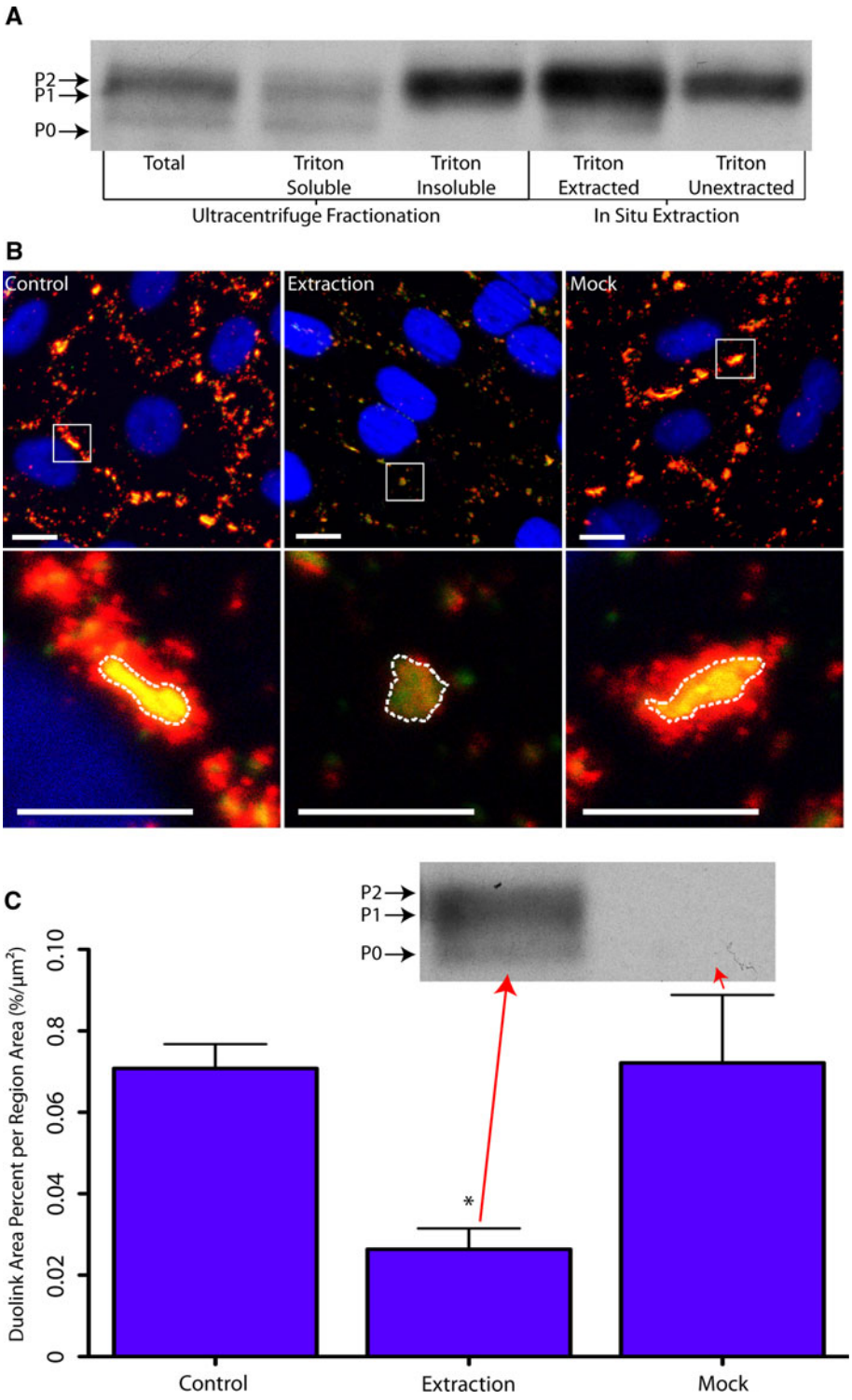

Fig. 3 Cx43 in the perinexus is nonjunctional. **a** Comparison of Cx43 Western blot banding pattern between cultured NRHM lysates subjected to Triton X-100 fractionation by ultracentrifugation, and cultured NRHMs extracted in situ with Triton X-100. Whole Cx43 lysates ("Total" lane) display the characteristic triple banding pattern corresponding to different phospho-isoforms of Cx43 (P0, P1, and P2). The Triton-soluble and -insoluble fractions of ultracentrifuged lysates display similar banding profiles to Cx43 extracted from NRHM cultures by Triton and the remaining unextracted protein, respectively. **b** Cx43 labeled in NRHM cultures by standard IF (*green*) and high-sensitivity Duolink (*red*). The nucleus is labeled in blue. "Control" cultures were not subjected to in situ Triton extraction; "Extraction" images represent the remaining unextracted protein in cultures treated with buffer containing 1 % Triton X-100 before fixation and staining; "Mock" cultures were treated with the same buffer without Triton before being fixed and stained. **c** Analysis of Duolink staining within the perinexus region (defined as 250–500 nm from the plaque edge) from the experiment in (**b**). Triton extracted cultures displayed a significantly reduced concentration of Cx43 in the perinexus (*$p < 0.05$ vs. "Control"; $n = 4$). The Western blot is labeled for Cx43, probing protein extracted from the cultures labeled in (**b**) in Triton extracted cultures (*left*), and mock extracted cultures (*right*). *Error bars* represent SEM, and *scale bars* represent 10 μm in large images, and 5 μm in expanded images

2012), separation of NRHM lysates by Triton X-100 fractionation resulted in a preponderance of the P1 and P0 phosphoisoforms accumulating in the detergent-soluble fraction, as well as a small amount of the P2 isoform (Fig. 3a, "Triton Soluble" lane).

In contrast, the Triton-insoluble fraction contained a large amount of the P2/P1 isoform, while the P0 isoform was absent (Fig. 3a, "Triton Insoluble" lane). In a similar result, the portion of the cell solubilized by Triton extraction contained all three isoforms of Cx43, but with a much larger amount of the P1 and P2 isoforms than obtained by fractionation (Fig. 3a, "Triton Extracted" lane). The Triton X-100-insoluble cellular remainder also compared favorably to the insoluble fraction obtained by ultracentrifugation in that it appeared to be composed solely of P2/P1 isoforms (Fig. 3a "Triton Unextracted" lane). We concluded from these results that Cx43 in NRHMs separated by the two methodologies yields similar separation of Cx43, with the primary exception that in situ extraction results in a larger amount of P1 and P2 isoforms segregating into the Triton X-100-soluble extract, suggesting that some of the junctional Cx43 on the culture plate was solubilized.

The fixed, stained, and imaged component of a Triton X-100-extracted NRHM culture is shown in Fig. 3b, "Extraction." As controls, NRHMs were fixed, labeled, and imaged without any extraction procedure (Fig. 3b, "Control") or after a mock extraction in which no Triton X-100 was added to the extraction buffer (Fig. 3b, "Mock"). The preparations were labeled for Cx43 both by standard IF in green and Duolink in red. By visual inspection, it appeared that Cx43-Duolink label colocalized with GJs, and extended well into the perinexal region in the controls (Fig. 3b, "Control" and "Mock"), similar to the results presented in Fig. 1. In contrast, the unextracted cellular remains of cultures exposed to Triton X-100 displayed little perinexal Cx43-Duolink label, indicating that Cx43 in the perinexus is Triton soluble (Fig. 3b, "Extraction").

To confirm this result, we measured Cx43-Duolink density (as described above) in the three treatments. We found that Cx43 was significantly reduced in the perinexus of Triton-extracted NRHMs when compared to the control (Fig. 3c). Importantly, the Triton-solubilized component could be demonstrated by Western blot analysis to contain Cx43 in a similar banding profile to that of the "Triton Soluble" fraction of ultracentrifuged lysates (cf. Western blot analysis in Fig. 3c to "Triton Soluble" lane in Fig. 3a), while the reclaimed buffer from mock extracted cultures contained no detectable Cx43. These results demonstrate that Cx43 in the perinexus is Triton X-100 soluble—i.e., nonjunctional—and therefore potentially in the form of undocked connexons/hemichannels. Moreover, the loss of Cx43 signals from around the GJ edge after detergent solubilization provided evidence that these signals were not accounted for by out-of-focus fluorescence and that the perinexus is a membrane structure with physical properties that distinguish it from the GJ proper.

Cx43 Interacts with $Na_v1.5$ in the Perinexus

Our next goal was to investigate other Cx43 protein partners and their relationship to the perinexus. Of particular interest was the voltage gated sodium channel $Na_v1.5$ as a result of its role in generating the cardiac action potential. It has previously been shown to localize to the intercalated disc (Cohen 1996; Colussi et al. 2010; Maier et al. 2002; Malhotra et al. 2004; Noorman et al. 2008; Petitprez et al. 2011; Stein et al. 2009) and interact with Cx43 (Malhotra et al. 2004). We first used a standard IF labeling and confocal imaging protocol to study the codistribution of the two proteins in NRHM cultures. Cell preparations were labeled with Cx43 in green, ZO-1 in red, and $Na_v1.5$ in blue (Fig. 4a). As has been previously described, ZO-1 localized to the GJ edge and surrounding area (Hunter et al. 2005; Hunter and Gourdie 2008; Palatinus et al. 2011; Zhu et al. 2005). In a result confirming that described by Yoram Rudy and coworkers (Kucera et al. 2002), we found a high degree of overlap between the Cx43 and $Na_v1.5$ signals (Fig. 4a). We further investigated the relationship between Cx43 and $Na_v1.5$ by performing a Duolink assay for Cx43/$Na_v1.5$ interaction. This determined that the Cx43/$Na_v1.5$ Duolink label closely resembled that of Cx43/ZO-1 interaction (cf. Figs. 4b, Fig. 1a), with Cx43/$Na_v1.5$ Duolink signal overlapping with Cx43 GJs labeled by standard IF, and more frequently localizing to the perinexus region (Fig. 4b). Because of the similarities between Cx43 and $Na_v1.5$ codistribution with ZO-1, and the resemblance of the Cx43/ZO-1 interaction pattern to that of Cx43/$Na_v1.5$, we also labeled NRHM cultures for ZO-1/$Na_v1.5$ interaction (Fig. 4c). Very few Duolink signals were generated with this protocol, indicating that ZO-1 and $Na_v1.5$ have little, if any, interaction in agreement with Abriel and coworkers (Petitprez et al. 2011).

The biochemical relationship between Cx43 and $Na_v1.5$ was addressed by Triton X-100 fractionation of NRHM lysates, followed by Western blot analysis of $Na_v1.5$ (Fig. 4d). For comparison, the Triton fractionated and extracted samples from Fig. 2 have been included. It was found that $Na_v1.5$ almost exclusively segregated into the Triton-soluble pool (Fig. 4d). On the basis of these results, we concluded that $Na_v1.5$ associates with nonjunctional Cx43 (connexons/hemichannels) in the perinexus.

Discussion

The purpose of this study was to characterize the composition and structure of the cardiomyocyte perinexus. This

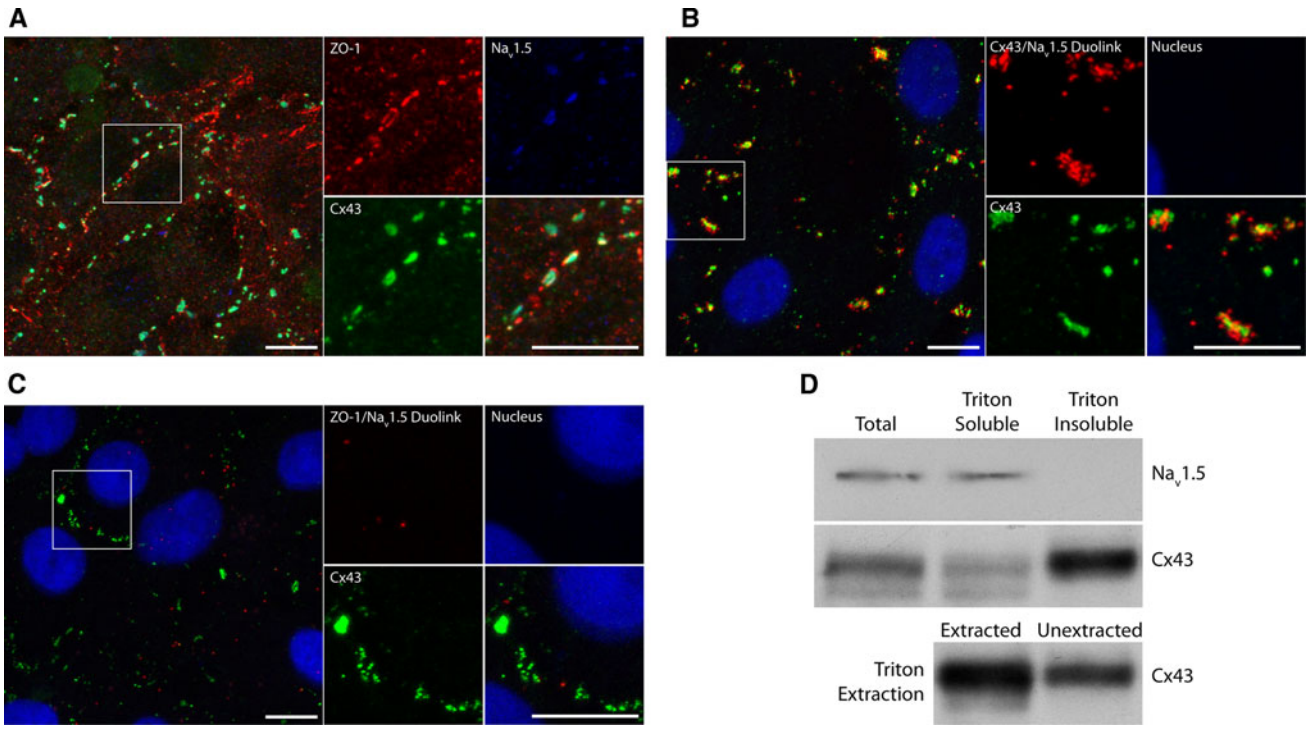

Fig. 4 $Na_v1.5$ interacts with Cx43, but not ZO-1, in the perinexus of cardiomyocytes. **a** Cultured NRHMs were labeled for Cx43 (*green*), ZO-1 (*red*), and $Na_v1.5$ (*blue*). Note the strong overlap of Cx43 and $Na_v1.5$ signal. **b** Duolink labeling shows Cx43/$Na_v1.5$ interaction at and surrounding GJs in NRHMs. Cx43 is labeled in *green,* Cx43/$Na_v1.5$ interaction is labeled by Duolink in *red,* and the nucleus is *blue.* **c** $Na_v1.5$ has little or no interaction with ZO-1. Cultured NRHMs were labeled for Cx43 (*green*), ZO-1/$Na_v1.5$ interaction by Duolink (*red*), and the nucleus (*blue*). **d** Triton X-100 fractionated NRHM lysates underwent Western blot analysis for $Na_v1.5$. Clear bands are visible in the whole lysate ("Total" lane) and detergent-soluble fraction ("Triton Soluble" lane), but not the detergent-insoluble fraction ("Triton Insoluble" lane). For comparison, the same Cx43 blots from Fig. 3 are provided, with the Triton fractionation portion being shown in the *middle row,* and the Triton extraction portion being shown in the *bottom row. Scale bars* represent 10 μm

study provides the first comprehensive depiction of the location, extent, and quantity of Cx43 in this specialized region of membrane. The canonical pathway for GJ accretion at the GJ edge was first introduced over 10 years ago (Gaietta et al. 2002; Lauf et al. 2002). In and of itself, this mechanism of GJ aggregation suggests the presence of Cx43 in the surrounding membrane. Our measurements describe a region surrounding the GJ plaque that contains nonuniformly distributed Cx43 molecules at a higher concentration than other nonjunctional regions of the cell.

Comparison of Confocal Cx43-Duolink Imaging to GJs Imaged by Electron Microscopy of Freeze-fracture Replicas

In freeze-fracture studies, Johnson et al. (2012) have reported immunogold detection of unaggregated, nonjunctional Cx43 particles (presumptive connexons) near GJs in the FP. At first glance, these data suggest that the FP and perinexus may be the same structure. However, several important distinctions must be made.

First, in Johnson's seminal work on the FP, the initiation of GJ formation is studied in a model system using reaggregated cells (Johnson et al. 1974). Electron microscopy of freeze-fracture replicas from cells within the first hour after reaggregation revealed the FP as a prominent structure. Over that time period, 9–11 nm intramembraneous particles (IMPs), presumptive connexin channels, displayed first as unaggregated, then "clustered" (i.e., associated but not packed in hexagonal arrays), and finally as GJ aggregates within the FP. However, at later time points (2–3 h), the FP reduced to a narrow, particle-free halo around the junction (Johnson et al. 1974). In contrast, the cardiomyocytes we labeled were cultured for nearly a week before fixation, and we observed perinexus widths as great as ~2.5 μM—as defined by the *presence* of Cx43.

Differentiation of the FP and perinexus on these criteria is supported by a detailed comparison of Cx36 GJs imaged by confocal vs. FRIL. Kamasawa et al. (2006) showed that by enhancing the "dark output" (i.e., low intensity Cx36 IF signals) of confocal images, smaller GJ punctae corresponding to string and ribbon GJs become visible. Similarly, we find that measurement of low-intensity IF signal in the perinexus indicates the presence of Cx43 in that region of the cell at a higher concentration than nonjunctional regions of the cell (Supplementary Material).

Corroboration of this result by Duolink confirms the findings of Kamasawa et al. on the limits of light microscopy. In addition, Kamasawa et al. show that confocal microscopy of Cx36 GJs overestimates the size of those junctions as compared to measurements made by electron microscopy of freeze-fracture replicas. If this relationship holds true for Cx43, then this would suggest that the ~200 nm average distance that we measure Cx43-Duolink signal emanating from the GJ edge actually underestimates the extent of the perinexus—again suggesting that in mature junctions, the perinexus extends far beyond the FP.

Second, in remarkable stereoscopic FRIL images of Cx36 in goldfish Mauthner cells, Flores et al. (2012) showed vesicles inserting putative hemichannels near mature GJs. Furthermore, "tall" IMPs in P-face images and immunogold labeling of Cx36 in E-face images of clustered particles adjacent to GJs suggest docking of connexons just before accretion in the GJ. Similar results were obtained by Johnson et al. (2012) for Cx43 in the FP of immature junctions. These data support a role for the perinexus in the constitutive transition of hemichannels to GJ intercellular channels in mature junctions that has been previously proposed (Rhett and Gourdie 2012; Rhett et al. 2011), and this is underscored by our finding that perinexal Cx43 is nonjunctional as defined by Triton X-100 solubility (Fig. 3).

Finally, one defining feature of the FP is the exclusion of IMPs other than the 9–11 nm connexin channels (Johnson et al. 1974, 2012). In contrast, we conceive of the perinexus not only as the region of membrane surrounding the GJ, but as a complex assemblage of channels (at least Cx43 and $Na_v1.5$ [Rhett and Gourdie 2012; Rhett et al. 2011]; Figs. 1, 4), scaffolding proteins (ZO-1 [Hunter et al. 2005; Rhett et al. 2011]; Fig. 1), junctional molecules (N-cadherin [Hunter and Gourdie 2008; and unpublished data]), and cytoskeletal elements (actin [Rhett and Gourdie 2012; Rhett et al. 2011; and unpublished data]). We envisage the perinexus as a constitutive structure, albeit dynamic, with ongoing homeostatic functions including hemichannel regulation, conduction, and GJ dynamics. The FP, as conceived by Johnson et al. (1974, 2002, 2012), seems to be a more transient construct that serves largely during the establishment and building of a GJ.

Despite these differences, it is undeniable that there are parallels between the FP and perinexus. Both are involved in the transition to and aggregation of GJ channels. During the building phase of immature GJs, the perinexus and FP are likely to be indistinguishable. One possibility that arises is that the FP is a temporal and spatial subset of the perinexus. Another, and perhaps more intriguing, possibility is that the perinexus is an exapted derivative of the FP—where the molecular machinery delivering connexons to the edge of the plaque may have assumed new functions and elaborated structure during evolution.

Interpretation of Perinexus Structure as Determined by Cx43-Duolink

Importantly, we did not find Cx43-Duolink labeling in the perinexus to be uniform. Rather, the labeling tended to cluster or shift to subdomains of the perinexus (Figs. 1b, 2). One possible explanation involves the size and efficiency of Duolink labeling. First, Duolink signals are limited in their ability to optically resolve structures by their size (up to 1 μm in diameter [Clausson et al. 2011; Jarvius et al. 2006]; 400–500 nm diameter in our hands). For this reason, it was impossible to precisely determine the exact density, extent, and shape of the perinexus. For example, we limited the region analyzed for Cx43 density in the perinexus to exclude the region 0–250 nm from the GJ edge in order to account for the 250 nm radius of a Duolink signal. In the future, a technique such as stimulated emission depletion microscopy could provide approaches to increasing resolution of perinexal Cx43.

In addition, the exact fraction of interaction events that Duolink labels varies from preparation to preparation, cell to cell, and probably even subcellular domain to subcellular domain (Clausson et al. 2011). Because of this it is difficult to be sure that variation in the shape of Cx43-Duolink labeling in the perinexus is a result of genuine clustering of Cx43 within the perinexus, steric hindrance of the ligation or PCR reaction by Cx43 molecular partners, an unknown feature of subcellular structure, or stochasticity inherent to Duolink labeling. However, these caveats being raised, the high consistency of labeling from experiment to experiment suggests that the Cx43-Duolink labeling pattern does reflect the actual location of Cx43 molecules in the perinexus. Moreover, the ability of the Duolink technology to provide strong signals from low density concentrations of Cx43 may be helpful in resolving areas of debate such as whether Cx43 is associated with subcellular structures such as microtubules and mitochondria (Rodriguez-Sinovas et al. 2006).

Given that the Cx43-Duolink labeling pattern authentically mirrors the nature of Cx43 in the perinexus, a biological explanation for this phenomenon could potentially be rooted in the mechanism of connexon delivery to the cell surface. It has been observed that N-cadherin labeling/area composita is/are coincident with the GJ edge (Delmar and Liang 2012; Palatinus et al. 2011). Shaw et al. (2007) reported that connexons are delivered along microtubules linked to adherens junctions via EB1 interaction with the p150(Glued)/dynein/dynactin complex. Here, we observed large extensions of the perinexus, sometimes extending as much as 2 μM from the plaque edge. Putting these ideas together, the possibility is suggested that the perinexus serves as the site of delivery of new, undocked connexons to the plasma membrane. This hypothesis is supported by

the above-mentioned work of Flores et al. (2012), in which vesicles inserting putative hemichannels adjacent to GJs were observed.

This exciting possibility leads to interesting questions about the molecular mechanics of GJ accretion. For example, phosphorylation on S365 and S325/S328/S330 have been associated with the incorporation of Cx43 into GJ plaques (Lampe et al. 2006; Solan and Lampe 2007; Solan et al. 2007). Future high-resolution/sensitivity studies of the subcellular localization of these Cx43 phosphoisoforms could yield insights into the role of phosphorylation state in GJ assembly.

Another possible interpretation of our observation of Cx43 concentrated in the perinexus is implicated by the work of Shaw and colleagues. Smyth et al. (2012) reported that actin also participates in anterograde trafficking of Cx43 to GJs in cardiomyocytes. They propose that vesicles containing Cx43 and associated with actin fibers might accumulate in the submembrane near GJs, awaiting transport to the GJ by transfer to the microtubule system. Therefore, it is possible to interpret the data provided in the present investigation as Cx43 in "intracellular reserves." Given that multiple lines of evidence support the existence of functional hemichannels (Li et al. 1996; Quist et al. 2000; Rhett et al. 2011; Saez et al. 2003; Thompson et al. 2006), it is unlikely that Cx43 in or near the plasma membrane only exists in either actin-sequestered vesicles or the GJ plaque. Therefore, a combination of models in which perinexal Cx43 represents an accumulation of undocked connexons both in intracellular vesicles and in the plasma membrane is more likely.

Finally, new work on the effects of G protein–coupled receptor agonists has shed light on the role of Cx43/ZO-1 interaction. Past studies have shown that endothelin-1 (ET-1) can regulate both GJ intercellular communication (GJIC; van Zeijl et al. 2007) and internalization (Baker et al. 2008). Importantly, both these studies showed a critical role for Cx43/ZO-1 interaction in mediating the effects of ET-1. In a detailed study, Tence et al. (2012) recently demonstrated in cultured astrocytes that Cx43/ZO-1 interaction increased and GJIC decreased in response to ET-1, in agreement with the previous reports. Notably, they also found that the pool of Cx43 interacting with ZO-1 in response to ET-1 became Triton X-100 soluble. Because Cx43/ZO-1 interaction is detected in the perinexus (Fig. 1a; Rhett et al. 2011) and the perinexus is likely to be composed of undocked connexons, it is interesting to speculate that the perinexus is involved in GJ internalization and reductions in GJIC associated with ET-1.

The Perinexus Indicates Noncanonical Roles for Cx43

In addition to trafficking, other roles for perinexal Cx43 are indicated. For example, the perinexus may represent a platform to regulate the balance between intercellular communication and hemichannel-mediated membrane permeability (Rhett et al. 2011). A means of rapid control over intercellular communication has obvious implications for excitable tissues, but the ability to quickly enhance or reduce hemichannel function could give cells the ability to regulate GJ-mediated adhesivity, volume (Quist et al. 2000), ATP signaling (Yuan et al. 2012), or cell death (Decrock et al. 2009; Shintani-Ishida et al. 2007), to name a few examples.

In addition to providing subcellular Cx43 localization in previously unparalleled detail, we show that Cx43 interacts with $Na_v1.5$ in the perinexus of cardiomyocytes (Fig. 4b). We also demonstrate that $Na_v1.5$ has, at best, a low level of interaction with ZO-1. The few Duolink labels that we did observe rarely coincided with the perinexus. These data suggest that there may be a complex pattern of association and segregation between molecular complexes in the perinexus. Indeed, if Cx43/ZO-1 interaction occurs in the perinexus (Fig. 1a), and if Cx43/$Na_v1.5$ interaction occurs in the perinexus but ZO-1/$Na_v1.5$ interaction does not, it suggests that Cx43 interaction with $Na_v1.5$ is mutually exclusive with Cx43/ZO-1 interaction.

Importantly, our finding that $Na_v1.5$ localizes to both the perinexus (Fig. 4b) and the GJ itself (Fig. 4a) places it in a region of close apposition between two cell membranes. Intriguingly, this nonjunctional location at the GJ edge would uniquely position sodium channels for participation nonelectrotonic mechanisms of propagation electrical excitation in the heart. Mori et al. (2008) have demonstrated in a 3-D electrodiffusion model of conduction that even in the absence of GJ coupling, conduction can occur between cells when their membranes are $\sim$2 to 7 nm apart via an electric field mechanism. Whether or not $Na_v1.5$ participates in coupling across narrow clefts in extracellular space occurring at GJs is not addressed by our data. Nonetheless, there is mounting evidence that Cx43 alone is insufficient and that both Cx43 and $Na_v1.5$ are necessary in the mechanism of cell-to-cell transmission of action potential (Gutstein et al. 2001; Jansen et al. 2012; Lin et al. 2011). Moreover, Poelzing and coworkers have shown that increasing interstitial volume reduces conduction velocity on a timescale incompatible with GJ remodeling (Veeraraghavan et al. 2012). Sites of high concentration of depolarizing currents and close membrane–membrane apposition raise the potential for electric field transmission at the GJ edge as an auxiliary conduction pathway.

Conclusion

The perinexus is a region of membrane involved in the regulation of GJIC and membrane permeability (Rhett et al. 2011). The data presented herein provide the first

direct measurement of concentrated Cx43 in the perinexus, in the form of undocked connexons, suggesting the possibilities that this specialized zone of the plasma membrane has functions in GJ assembly, hemichannel function, and signaling. In particular, the data we present here on Cx43/$Na_v1.5$ interaction in the perinexus indicates that this specialized domain of membrane could have assignments in impulse conduction. As such, the perinexus represents a new target for amelioration of arrhythmia via its potential role in novel pathways for electrical coupling between myocytes in the heart.

Acknowledgments This work was supported in part by grants from the National Institutes of Heath (RO1 HL56728-10A2 to RGG, RO11DE019355-1 RGG subcontract, F30 HL095320-01 RGG mentor, and 5P20RR016434-07 RGG mentor), and an AHA Grant-in-Aid (RGG).

References

Baker SM, Kim N, Gumpert AM, Segretain D, Falk MM (2008) Acute internalization of gap junctions in vascular endothelial cells in response to inflammatory mediator-induced G-protein coupled receptor activation. FEBS Lett 582:4039–4046

Beahm DL, Oshima A, Gaietta GM, Hand GM, Smock AE, Zucker SN, Toloue MM, Chandrasekhar A, Nicholson BJ, Sosinsky GE (2006) Mutation of a conserved threonine in the third transmembrane helix of alpha- and beta-connexins creates a dominant-negative closed gap junction channel. J Biol Chem 281:7994–8009

Beyer EC, Paul DL, Goodenough DA (1987) Connexin43: a protein from rat heart homologous to a gap junction protein from liver. J Cell Biol 105:2621–2629

Clausson CM, Allalou A, Weibrecht I, Mahmoudi S, Farnebo M, Landegren U, Wahlby C, Soderberg O (2011) Increasing the dynamic range of in situ PLA. Nat Methods 8:892–893

Cohen SA (1996) Immunocytochemical localization of rH1 sodium channel in adult rat heart atria and ventricle. Presence in terminal intercalated disks. Circulation 94:3083–3086

Colussi C, Berni R, Rosati J, Straino S, Vitale S, Spallotta F, Baruffi S, Bocchi L, Delucchi F, Rossi S, Savi M, Rotili D, Quaini F, Macchi E, Stilli D, Musso E, Mai A, Gaetano C, Capogrossi MC (2010) The histone deacetylase inhibitor suberoylanilide hydroxamic acid reduces cardiac arrhythmias in dystrophic mice. Cardiovasc Res 87:73–82

Decrock E, De Vuyst E, Vinken M, Van Moorhem M, Vranckx K, Wang N, Van Laeken L, De Bock M, D'Herde K, Lai CP, Rogiers V, Evans WH, Naus CC, Leybaert L (2009) Connexin 43 hemichannels contribute to the propagation of apoptotic cell death in a rat C6 glioma cell model. Cell Death Differ 16: 151–163

Delmar M, Liang FX (2012) Connexin43 and the regulation of intercalated disc function. Heart Rhythm 9:835–838

Desplantez T, Dupont E, Severs NJ, Weingart R (2007) Gap junction channels and cardiac impulse propagation. J Membr Biol 218: 13–28

Evans WH, Martin PE (2002) Gap junctions: structure and function (review). Mol Membr Biol 19:121–136

Flores CE, Nannapaneni S, Davidson KG, Yasumura T, Bennett MV, Rash JE, Pereda AE (2012) Trafficking of gap junction channels at a vertebrate electrical synapse in vivo. Proc Natl Acad Sci USA 109:E573–E582

Fort AG, Murray JW, Dandachi N, Davidson MW, Dermietzel R, Wolkoff AW, Spray DC (2011) In vitro motility of liver connexin vesicles along microtubules utilizes kinesin motors. J Biol Chem 286:22875–22885

Gaietta G, Deerinck TJ, Adams SR, Bouwer J, Tour O, Laird DW, Sosinsky GE, Tsien RY, Ellisman MH (2002) Multicolor and electron microscopic imaging of connexin trafficking. Science 296:503–507

Gutstein DE, Morley GE, Tamaddon H, Vaidya D, Schneider MD, Chen J, Chien KR, Stuhlmann H, Fishman GI (2001) Conduction slowing and sudden arrhythmic death in mice with cardiac-restricted inactivation of connexin43. Circ Res 88:333–339

Hunter AW, Gourdie RG (2008) The second PDZ domain of zonula occludens-1 is dispensable for targeting to connexin 43 gap junctions. Cell Commun Adhes 15:55–63

Hunter AW, Barker RJ, Zhu C, Gourdie RG (2005) Zonula occludens-1 alters connexin43 gap junction size and organization by influencing channel accretion. Mol Biol Cell 16:5686–5698

Jansen JA, Noorman M, Musa H, Stein M, de Jong S, van der Nagel R, Hund TJ, Mohler PJ, Vos MA, van Veen TA, de Bakker JM, Delmar M, van Rijen HV (2012) Reduced heterogeneous expression of Cx43 results in decreased Nav1.5 Expression and reduced sodium current which accounts for arrhythmia vulnerability in conditional Cx43 knockout mice. Heart Rhythm 9:600–607

Jarvius J, Melin J, Goransson J, Stenberg J, Fredriksson S, Gonzalez-Rey C, Bertilsson S, Nilsson M (2006) Digital quantification using amplified single-molecule detection. Nat Methods 3: 725–727

Johnson R, Hammer M, Sheridan J, Revel JP (1974) Gap junction formation between reaggregated Novikoff hepatoma cells. Proc Natl Acad Sci USA 71:4536–4540

Johnson RG, Meyer RA, Li XR, Preus DM, Tan L, Grunenwald H, Paulson AF, Laird DW, Sheridan JD (2002) Gap junctions assemble in the presence of cytoskeletal inhibitors, but enhanced assembly requires microtubules. Exp Cell Res 275:67–80

Johnson RG, Reynhout JK, TenBroek EM, Quade BJ, Yasumura T, Davidson KG, Sheridan JD, Rash JE (2012) Gap junction assembly: roles for the formation plaque and regulation by the C-terminus of connexin43. Mol Biol Cell 23:71–86

Kamasawa N, Furman CS, Davidson KG, Sampson JA, Magnie AR, Gebhardt BR, Kamasawa M, Yasumura T, Zumbrunnen JR, Pickard GE, Nagy JI, Rash JE (2006) Abundance and ultrastructural diversity of neuronal gap junctions in the OFF and ON sublaminae of the inner plexiform layer of rat and mouse retina. Neuroscience 142:1093–1117

Kleber AG, Rudy Y (2004) Basic mechanisms of cardiac impulse propagation and associated arrhythmias. Physiol Rev 84: 431–488

Koval M (2006) Pathways and control of connexin oligomerization. Trends Cell Biol 16:159–166

Kucera JP, Rohr S, Rudy Y (2002) Localization of sodium channels in intercalated disks modulates cardiac conduction. Circ Res 91: 1176–1182

Lal R, John SA, Laird DW, Arnsdorf MF (1995) Heart gap junction preparations reveal hemiplaques by atomic force microscopy. Am J Physiol 268:C968–C977

Lampe PD, Cooper CD, King TJ, Burt JM (2006) Analysis of connexin43 phosphorylated at S325, S328 and S330 in normoxic and ischemic heart. J Cell Sci 119:3435–3442

Lauf U, Giepmans BN, Lopez P, Braconnot S, Chen SC, Falk MM (2002) Dynamic trafficking and delivery of connexons to the plasma membrane and accretion to gap junctions in living cells. Proc Natl Acad Sci USA 99:10446–10451

Li H, Liu TF, Lazrak A, Peracchia C, Goldberg GS, Lampe PD, Johnson RG (1996) Properties and regulation of gap junctional hemichannels in the plasma membranes of cultured cells. J Cell Biol 134:1019–1030

Lin X, Liu N, Lu J, Zhang J, Anumonwo JM, Isom LL, Fishman GI, Delmar M (2011) Subcellular heterogeneity of sodium current properties in adult cardiac ventricular myocytes. Heart Rhythm 8:1923–1930

Liu TF, Johnson RG (1999) Effects of TPA on dye transfer and dye leakage in fibroblasts transfected with a connexin 43 mutation at ser368. Methods Find Exp Clin Pharmacol 21:387–390

Maier SK, Westenbroek RE, Schenkman KA, Feigl EO, Scheuer T, Catterall WA (2002) An unexpected role for brain-type sodium channels in coupling of cell surface depolarization to contraction in the heart. Proc Natl Acad Sci USA 99:4073–4078

Malhotra JD, Thyagarajan V, Chen C, Isom LL (2004) Tyrosine-phosphorylated and nonphosphorylated sodium channel beta1 subunits are differentially localized in cardiac myocytes. J Biol Chem 279:40748–40754

Mori Y, Fishman GI, Peskin CS (2008) Ephaptic conduction in a cardiac strand model with 3D electrodiffusion. Proc Natl Acad Sci USA 105:6463–6468

Musil LS, Goodenough DA (1991) Biochemical analysis of connexin43 intracellular transport, phosphorylation, and assembly into gap junctional plaques. J Cell Biol 115:1357–1374

Musil LS, Goodenough DA (1993) Multisubunit assembly of an integral plasma membrane channel protein, gap junction connexin43, occurs after exit from the ER. Cell 74:1065–1077

Noorman M, van Rijen HV, van Veen TA, de Bakker JM, Stein M (2008) Differences in distribution of fibrosis in the ventricles underlie dominant arrhythmia vulnerability of the right ventricle in senescent mice. Neth Heart J 16:356–358

Noorman M, van der Heyden MA, van Veen TA, Cox MG, Hauer RN, de Bakker JM, van Rijen HV (2009) Cardiac cell–cell junctions in health and disease: electrical versus mechanical coupling. J Mol Cell Cardiol 47:23–31

Palatinus JA, O'Quinn MP, Barker RJ, Harris BS, Jourdan J, Gourdie RG (2011) ZO-1 determines adherens and gap junction localization at intercalated disks. Am J Physiol Heart Circ Physiol 300:H583–H594

Palatinus JA, Rhett JM, Gourdie RG (2012) The connexin43 carboxyl terminus and cardiac gap junction organization. Biochim Biophys Acta 1818:1831–1843

Petitprez S, Zmoos AF, Ogrodnik J, Balse E, Raad N, El-Haou S, Albesa M, Bittihn P, Luther S, Lehnart SE, Hatem SN, Coulombe A, Abriel H (2011) SAP97 and dystrophin macromolecular complexes determine two pools of cardiac sodium channels Nav1.5 in cardiomyocytes. Circ Res 108:294–304

Quist AP, Rhee SK, Lin H, Lal R (2000) Physiological role of gap-junctional hemichannels. Extracellular calcium-dependent isosmotic volume regulation. J Cell Biol 148:1063–1074

Rhett JM, Gourdie RG (2012) The perinexus: a new feature of Cx43 gap junction organization. Heart Rhythm 9:619–623

Rhett JM, Jourdan J, Gourdie RG (2011) Connexin 43 connexon to gap junction transition is regulated by zonula occludens-1. Mol Biol Cell 22:1516–1528

Rodriguez-Sinovas A, Boengler K, Cabestrero A, Gres P, Morente M, Ruiz-Meana M, Konietzka I, Miro E, Totzeck A, Heusch G, Schulz R, Garcia-Dorado D (2006) Translocation of connexin 43 to the inner mitochondrial membrane of cardiomyocytes through the heat shock protein 90-dependent TOM pathway and its importance for cardioprotection. Circ Res 99:93–101

Saez JC, Contreras JE, Bukauskas FF, Retamal MA, Bennett MV (2003) Gap junction hemichannels in astrocytes of the CNS. Acta Physiol Scand 179:9–22

Severs NJ, Bruce AF, Dupont E, Rothery S (2008) Remodelling of gap junctions and connexin expression in diseased myocardium. Cardiovasc Res 80:9–19

Shaw RM, Fay AJ, Puthenveedu MA, von Zastrow M, Jan YN, Jan LY (2007) Microtubule plus-end-tracking proteins target gap junctions directly from the cell interior to adherens junctions. Cell 128:547–560

Shintani-Ishida K, Uemura K, Yoshida K (2007) Hemichannels in cardiomyocytes open transiently during ischemia and contribute to reperfusion injury following brief ischemia. Am J Physiol Heart Circ Physiol 293:H1714–H1720

Smyth JW, Vogan JM, Buch PJ, Zhang SS, Fong TS, Hong TT, Shaw RM (2012) Actin cytoskeleton rest stops regulate anterograde traffic of connexin 43 vesicles to the plasma membrane. Circ Res 110:978–989

Solan JL, Lampe PD (2007) Key connexin 43 phosphorylation events regulate the gap junction life cycle. J Membr Biol 217:35–41

Solan JL, Marquez-Rosado L, Sorgen PL, Thornton PJ, Gafken PR, Lampe PD (2007) Phosphorylation at S365 is a gatekeeper event that changes the structure of Cx43 and prevents down-regulation by PKC. J Cell Biol 179:1301–1309

Stein M, van Veen TA, Remme CA, Boulaksil M, Noorman M, van Stuijvenberg L, van der Nagel R, Bezzina CR, Hauer RN, de Bakker JM, van Rijen HV (2009) Combined reduction of intercellular coupling and membrane excitability differentially affects transverse and longitudinal cardiac conduction. Cardiovasc Res 83:52–60

Tence M, Ezan P, Amigou E, Giaume C (2012) Increased interaction of connexin43 with zonula occludens-1 during inhibition of gap junctions by G protein-coupled receptor agonists. Cell Signal 24:86–98

Thompson RJ, Zhou N, MacVicar BA (2006) Ischemia opens neuronal gap junction hemichannels. Science 312:924–927

van Zeijl L, Ponsioen B, Giepmans BN, Ariaens A, Postma FR, Varnai P, Balla T, Divecha N, Jalink K, Moolenaar WH (2007) Regulation of connexin43 gap junctional communication by phosphatidylinositol 4,5-bisphosphate. J Cell Biol 177:881–891

Veeraraghavan R, Salama ME, Poelzing S (2012) Interstitial volume modulates the conduction velocity–gap junction relationship. Am J Physiol Heart Circ Physiol 302:H278–H286

Yuan D, Wang Q, Wu D, Yu M, Zhang S, Li L, Tao L, Harris AL (2012) Monocyte–endothelial adhesion is modulated by Cx43-stimulated ATP release from monocytes. Biochem Biophys Res Commun 420:536–541

Zhu C, Barker RJ, Hunter AW, Zhang Y, Jourdan J, Gourdie RG (2005) Quantitative analysis of ZO-1 colocalization with Cx43 gap junction plaques in cultures of rat neonatal cardiomyocytes. Microsc Microanal 11:244–248

J Membrane Biol (2012) 245:423–436
DOI 10.1007/s00232-012-9485-8

REVIEW ARTICLES

Connexin- and Pannexin-Based Channels in Normal Skeletal Muscles and Their Possible Role in Muscle Atrophy

Luis A. Cea · Manuel A. Riquelme · Bruno A. Cisterna · Carlos Puebla · José L. Vega · Maximiliano Rovegno · Juan C. Sáez

Received: 27 April 2012 / Accepted: 28 June 2012 / Published online: 1 August 2012

Abstract Precursor cells of skeletal muscles express connexins 39, 43 and 45 and pannexin1. In these cells, most connexins form two types of membrane channels, gap junction channels and hemichannels, whereas pannexin1 forms only hemichannels. All these channels are low-resistance pathways permeable to ions and small molecules that coordinate developmental events. During late stages of skeletal muscle differentiation, myofibers become innervated and stop expressing connexins but still express pannexin1 hemichannels that are potential pathways for the ATP release required for potentiation of the contraction response. Adult injured muscles undergo regeneration, and connexins are reexpressed and form membrane channels. In vivo, connexin reexpression occurs in undifferentiated cells that form new myofibers, favoring the healing process of injured muscle. However, differentiated myofibers maintained in culture for 48 h or treated with proinflammatory cytokines for less than 3 h also reexpress connexins and only form functional hemichannels at the cell surface. We propose that opening of these hemichannels contributes to drastic changes in electrochemical gradients, including reduction of membrane potential, increases in intracellular free Ca^{2+} concentration and release of diverse metabolites (e.g., NAD^{+} and ATP) to the extracellular milieu, contributing to multiple metabolic and physiologic alterations that characterize muscles undergoing atrophy in several acquired and genetic human diseases. Consequently, inhibition of connexin hemichannels expressed by injured or denervated skeletal muscles might reduce or prevent deleterious changes triggered by conditions that promote muscle atrophy.

Keywords Gap junction · Cell–cell channel · Physiology of calcium channels in muscle · Pharmacology of muscle diseases

L. A. Cea · M. A. Riquelme · B. A. Cisterna · C. Puebla · J. L. Vega · M. Rovegno · J. C. Sáez (✉)
Departamento de Fisiología, Pontificia Universidad Católica de Chile, Alameda 340, Santiago, Chile
e-mail: jcsaezc@gmail.com

L. A. Cea
e-mail: lacea@uc.cl

C. Puebla · J. C. Sáez
Centro Interdisciplinario de Neurociencias de Valparaíso, Valparaiso, Chile

J. L. Vega
Laboratorio de Fisiología Experimental, Universidad de Antofagasta, Antofagasta, Chile

Connexin- and Pannexin-Based Channels

Connexins (Cxs) and pannexins (Panxs) constitute two families of integral membrane proteins that, in mammals, are composed of about 20 and 3 members, respectively. In most cells studied thus far, the pattern of Cx expression varies according to the species, cell type and physiological state (Gorbe et al. 2005; Račkauskas et al. 2010; Bedner et al. 2011). Similarly, Panxs are expressed in many different cell types, but Panx2 has been detected preferentially in the nervous system of vertebrate animals (Bruzzone et al. 2003; Li et al. 2011; Ray et al. 2006).

Since several investigators have been unable to find evidence of gap junctions formed by Panxs, it was recently proposed that Panxs only form hemichannels (HCs); thus, it was recommended to call them Panx channels (Sosinsky et al. 2011). However, Panx gap junction channels (GJCs) have been observed in exogenous expression systems, including *Xenopus* oocytes and mammalian cells, as well as

in endogenous expression systems such as osteoblasts (Baranova et al. 2004; Peñuela et al. 2007; Söhl and Willecke 2004), which suggests that further efforts to find GJCs made of Panxs are required. In spite of this discrepancy, it is clear that Cxs and Panxs present four transmembrane domains, one cytoplasmic and two extracellular loops, and the $–NH_2$ and –COOH termini are located at the cytoplasmic side of the cell membrane. Both Cxs and Panxs can form HCs, and at least Cxs can form GJCs (Bruzzone and Dermietzel 2006; Ishikawa et al. 2011; Solan and Lampe 2009); HCs are also called connexons or pannexons, if composed of connexins or pannexins, respectively. HCs are composed of six subunits (except for Panx2 HCs, which form octamers [Ambrosi et al. 2010]), and if they are constituted of the same or different subunits, they are homomeric or heteromeric, respectively.

HCs can be found either at unapposed cell surfaces or at the vicinity of gap junction plaques at cellular interfaces, where they serve as precursors of GJCs (Gaietta et al. 2002). GJCs commonly allow communication between the cytoplasms of adjacent cells, but in a few exceptions they can provide communication means within the cytoplasm of the same expressing cell, in which they are called reflexive gap junctions.

Transfer of ions and small molecules (e.g., amino acids, peptides, sugars and some lipophilic compounds such as PGE_2) across the cellular membrane was believed to take place mainly via selective ion channels and/or transporters or by simple diffusion due to their physicochemical features. However, data reported during the last decade indicate that HCs, which present rather low selectivity, particularly when compared with ion channels, may also serve as membrane pathways for diffusional transfer of ions and small molecules between the intra- and extracellular compartments (Sáez et al. 2005). HCs have been shown to mediate the release of ATP, NAD^+ and/or PGE_2 from cells (Bruzzone et al. 2001; Cherian et al. 2005; Orellana et al. 2012). Interestingly, several HCs are permeable to Ca^{2+} (Sánchez et al. 2009, 2010; Schalper et al. 2010; Vanden Abeele et al. 2006) and, thus, can contribute to diverse cell responses activated by rises in free intracellular Ca^{2+} concentration. However, kinetic permeability properties have been studied for only a few HC types (Orellana et al. 2011), and further studies are needed to understand what distinguishes HCs with different subunit compositions and/or covalent modifications.

HCs play relevant roles in autocrine and paracrine cell–cell signaling. Opening of Cx HCs can be enhanced by diverse conditions, including the reduction of extracellular divalent cation concentrations, positive membrane potentials, some polyunsaturated fatty acids and changes in covalent modifications (e.g., oxidation or dephosphorylation) (Retamal et al. 2011; Schalper et al. 2012), whereas opening of Panx1 HCs can be enhanced by membrane depolarization, mechanical and metabolic stress (Domercq et al. 2010; Thompson et al. 2006) and activation of purinergic $P2X_7$ or $P2Y_1$ and $P2Y_2$ receptors (Locovei et al. 2006b; Thompson et al. 2006). Cx and Panx HCs present some pharmacological differences. For example, Cx HCs are inhibited by octanol and La^{3+} and resistant to probenecid, while Panx HCs are resistant to octanol and La^{3+} and inhibited by probenecid (Schalper et al. 2008). Moreover, low carbenoxolone concentrations (<10 μM) inhibit Panx1 HCs but not Panx2 or Cx HCs (Ambrosi et al. 2010), and high carbenoxolone concentrations (>50 μM) inhibit Panx1, Panx3 and Cx HCs (Ambrosi et al. 2010; Ishikawa et al. 2011; Schalper et al. 2008); probenecid inhibits Panx1-based HCs but not Panx2-based HCs (Ambrosi et al. 2010). Notably, some cells do not form either Cx or Panx GJCs, such as erythrocytes, and the main functional role of Panx1 is as HCs (Locovei et al. 2006a). A similar situation might occur in adult skeletal muscles (see below). These and other demonstrations in normal cells (Orellana et al. 2011; Schalper et al. 2008) indicate that HC opening can be handled by normal cells. Moreover, several cellular functions previously thought to be mediated by GJCs need to be reevaluated because they might be partially or totally explained by changes in the functional state of HCs, as recently demonstrated in astrocyte death induced by hypoxia reoxygenation in high glucose (Orellana et al. 2010).

GJCs facilitate direct communication between adjacent cells (Solan and Lampe 2009) because they allow intercellular transfer of electrical and metabolic signals without leakage to the extracellular space and, thus, participate in numerous functions of most cell communities (Račkauskas et al. 2010). To date, GJCs formed by endogenously expressed Cxs are rapidly inhibited (from seconds to a few minutes) by most Cx HC blockers. Peptides that react with cytoplasmic domains of Cx43 block Cx43 HCs but do not affect Cx43 GJCs (Ponsaerts et al. 2010). Similarly, La^{3+} blocks Cx43 and other Cx HCs (Schalper et al. 2008) but does not affect Cx43 GJCs (Contreras et al. 2002). The available information on Panx GJCs is limited mostly to studies performed in exogenous expression systems (Bruzzone et al. 2005), and their pharmacological sensitivity is likely to be similar to that of Panx HCs. On the other hand, like HCs, GJCs are permeable to ions and small molecules; and to date, the permeability properties of these two channel types have been assumed to be similar, but no empirical demonstration has been reported.

Possible Role of GJCs and HCs in Myoblast Commitment Acquisition and Differentiation during Ontogeny

Myogenic development, from the acquisition commitment of mesenchymal stem cells to contractile myofiber

formation, is highly regulated and coordinated. Ultrastructural, functional and molecular studies suggest the involvement of gap junctions. Skeletal muscle ontogeny occurs via a series of cellular and molecular steps that lead to the formation of multinucleated myofibers. Members of the MyoD transcription factors family, including MyoD, Myf5, myogenin and MRF4/herculin/Myf6, are key regulators in skeletal muscle development (Molkentin and Olson 1996). Each myogenic determination factor is expressed at different stages during skeletal muscle differentiation and becomes a marker of the corresponding stage (Pownall et al. 2002). For example, MyoD and Myf5 are markers of myogenic commitment (Braun et al. 1992; Rudnicki et al. 1993; Weintraub 1993).

Gap junctions were detected by electron microscopy in myoblast cultures and during embryonic development of rat myofibers derived from diaphragm and extensor digitorum longus (EDL) muscles (Kalderon et al. 1977; Ling et al. 1992). From a functional point of view, communication between developing myofibers was found to expand, and even if one myofiber was stimulated, the response propagated to other fibers of the muscle (Dennis et al. 1981). Consequently, gap junctions were proposed to allow the passage of molecules and metabolites required for myogenic development (Kalderon et al. 1977; Dennis et al. 1981). Later, Cxs were detected in embryonic skeletal myoblasts (monucleated muscle cells) (Duxson and Usson 1989). So far, Cx43 has been found to participate in terminal differentiation of skeletal muscles because myoblasts deficient in Cx43 ($Cx43^{Cre\text{-}ER(T)/fl}$) are associated with a relevant reduction in MyoD and myogenin expression (Araya et al. 2005). Moreover, rat L6 myoblasts and primary cultures of mouse myoblasts express Cx43 at 24 and 48 h of differentiation (Araya et al. 2005; Balogh et al. 1993), and consistently, the coupling index between myoblasts of the C_2C_{12} cell line (mouse myoblast cell line) increases at 24 and 48 h of differentiation (Araya et al. 2005). In addition, the expression of dominant negative Cx43, which reduces intercellular coupling through GJCs, inhibits the formation of myotubes (multinucleated muscle cells) in primary cultures of myoblasts obtained from newborn rats, suggesting that Cx43 is relevant in the fusion process of myoblasts (Gorbe et al. 2007). In agreement with this interpretation, blockers of GJCs inhibit both the fusion of myoblasts and the increase in levels of transcription factors that regulate myogenesis, e.g., myogenin (Araya et al. 2003a; Proulx et al. 1997). Therefore, Cx GJCs have been proposed to play a relevant role in several physiological processes of skeletal muscle ontogeny, such as cell growth, acquisition of myogenic commitment and differentiation (Araya et al. 2004; Söhl and Willecke 2004; von Maltzahn et al. 2004).

Cx39 (orthologue of hCx40.1) is expressed in murine myotubes but not in myoblast cells (von Maltzahn et al. 2006), suggesting that this connexin is involved in skeletal muscle differentiation but not in the process of myogenic commitment acquisition. Myotubes also express Cx43 and Cx45 (Araya et al. 2003a) and form gap junctions with myoblasts (Araya et al. 2004). However, gap junctions are reduced near birth and are absent in 1-week postnatal mice (Ling et al. 1992; von Maltzahn et al. 2004). At that time, only the remaining mononucleated cells that correspond to resident stem cells (satellite cells) express Cxs. Both Cx43 and Cx45 are known to form functional GJCs and HCs (Barrio et al. 1997; Li et al. 1996; Moreno et al. 1995; Steinberg et al. 1994), but evidence of whether Cx39 forms functional GJCs and/or HCs is yet to be reported. Moreover, the expression of Panxs in myoblasts remains unknown.

The acquisition of myogenic commitment is triggered by increases in $[Ca^{2+}]_i$, which promotes activation of calcineurin, a Ca^{2+}-dependent protein phosphatase that induces expression of the transcription factor myf-5 (Friday and Pavlath 2001). Two main Ca^{2+} mobilizing systems coexist in the cell: (1) Ca^{2+} release from internal stores (Zhang et al. 2011) and (2) Ca^{2+} influx from the extracellular medium. Upon extracellular stimulation by various receptor agonists, including ATP, phospholipase-C (PLC) is activated and phosphatidylinositol 4,5-bisphosphate is hydrolyzed, generating IP_3. The latter binds to its receptors (IP_3Rs) located in the membrane of the endoplasmic reticulum, leading to Ca^{2+} release (Zhang et al. 2011). The Ca^{2+}-release activity of the IP_3R channel is regulated by many intracellular modulators such as ATP, Ca^{2+}, IP_3R-binding proteins and protein kinases (Berridge 1993; Foskett et al. 2007; Zhang et al. 2011). On the other hand, Ca^{2+} influx is not mediated by voltage-sensitive Ca^{2+} channels (Araya et al. 2003b) but could be mediated by other Ca^{2+}-permeable channels, including stretch-activated Ca^{2+} channels (Sonobe et al. 2008), capacitive Ca^{2+} channels (Okon et al. 2002), TRP channels like TRPV4 (Pritschow et al. 2011), P2X receptors (Banachewicz et al. 2005) and possibly by Cx and Panx HCs. Since most Cxs also form HCs, the relative role of HCs and GJCs in these events remains unknown.

In L6 cells, a cell line derived from rat myoblasts, treatment with β-glycyrrhetinic acid, a blocker of Cx GJCs and Cx or Panx HCs (Schalper et al. 2008), inhibits the expression of myogenin and MRF4, two transcription factors that promote myogenesis. Such treatment also inhibits the cellular fusion process that leads to myotube formation (Proulx et al. 1997). P2X receptors ($P2X_{1-7}$) are ionotropic and activated by purine triphosphate nucleotides. P2Y receptors ($P2Y_{1,2,4,6,11-14}$) are metabotropic, and most of them are coupled to G proteins activated by both di- and triphosphate purine or pyrimidine nucleotides (Araya et al. 2004; Burnstock 2007; North 2002). In addition, C_2C_{12} cells, a cell line derived from satellite myoblasts, express $P2Y_1$, $P2Y_2$,

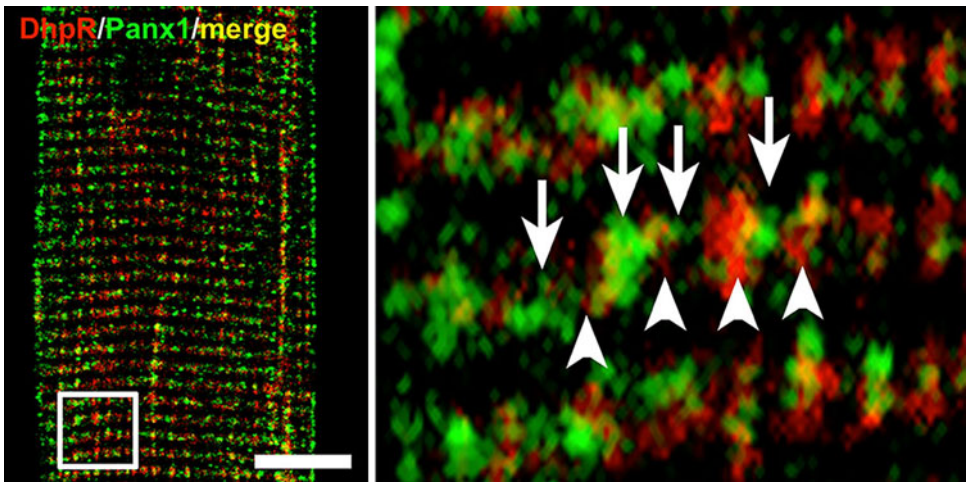

Fig. 1 Panx1 reactivity in rat skeletal muscle. Myofibers freshly isolated from flexor digitorum brevis (FDB) muscle were fixed with formaldehyde 4 % for 30 min, permeabilized (0.025 % Triton X-100) and double-labeled with rabbit anti-Panx1 antibody (*green*) designed by our group and directed to the nonconserved region of the C terminus of human, mouse and rat Panx1 (amino acid residues CNLGMIKMD). The antidihydropiridine receptor 1 (DhpR, *red*) was obtained from the Developmental Studies Hybridoma Bank developed under the auspices of the NICHD and maintained by the University of Iowa, Department of Biology (Iowa City, IA). *Left* Merged image of Panx1 (*green*, FitC) and DhpR (*red*, rhodamine) immunoreactivity. *Right* Magnification of the boxed region. Panx1 (*arrows*) was intercalated with DhpR (*arrowheads*) reactivity along transverse domains in the myofiber with little colocalization ($n = 4$). *Scale bar* = 10 μm

$P2Y_4$, $P2Y_6$ and $P2Y_{12}$ as well as $P2X_4$, $P2X_5$ and $P2X_7$ receptors (Banachewicz et al. 2005). Additionally, inhibition of P2 receptors prevents myoblast differentiation (Araya et al. 2004; Ryten et al. 2002). These findings suggest that myogenic commitment acquisition and differentiation require GJCs for intercellular propagation of a feed-forward mechanism generated in cells that express more P2 receptors. Immunohistochemical and in situ localization studies demonstrated that P2X receptors are expressed during skeletal muscle formation in vivo (Meyer et al. 1999; Ruppelt et al. 2001; Ryten et al. 2002). Moreover, it is possible that myoblasts express Panx or Cx HCs as membrane pathways for ATP release that modulates the intracellular free Ca^{2+} concentration required for muscle ontogeny. During late ontogeny, rat myotubes present functional Panx1 HCs (Buvinic et al. 2009) and nucleotide receptors ($P2X_4$, $P2X_5$, $P2X_7$, $P2Y_1$ and $P2Y_4$), and their activation of P2 receptors with exogenous nucleotides evokes Ca^{2+} transients (Buvinic et al. 2009; Deli et al. 2007). Moreover, tetanic stimuli (45 Hz, 400 1-ms pulses) evoke Ca^{2+} transients in myotubes that are inhibited by suramin, an inhibitor of P2 receptors, and apyrase, an ectonucleotidase that hydrolyzes ATP (Buvinic et al. 2009).

Possible Participation of HCs in Healthy Adult Skeletal Muscles

In rats, electrical coupling between skeletal myofibers disappears 1 week after birth (Dennis et al. 1981; Ling et al. 1992). In agreement, Cx expression has not been detected in normal adult skeletal muscles (Račkauskas et al. 2010). However, the presence of Panx1 mRNA (Baranova et al. 2004) and protein (Dvoriantchikova et al. 2006) has been demonstrated, suggesting that innervated myofibers might form Panx1 HCs. Moreover, we found that adult innervated myofibers present Panx1 reactivity side by side with dihydropyridine receptors (unpublished observation by Riquelme, Cea and Sáez; preliminary findings were presented at the Annual Meeting of the American Society for Cell Biology 2009) (Fig. 1), suggesting that Panx1 plays a relevant functional role in muscle physiology. Thus, it is possible that direct interaction between Panx1 HCs and P2 receptors plays a critical role in transduction processes, such as excitation–transcription coupling (Araya et al. 2003b). In support of this possibility, the dihydropyridine receptor coprecipitates with both the $P2Y_2$ receptor and Panx1 in homogenates of skeletal myotubes (Buvinic et al. 2009). However, similar studies in innervated skeletal muscles have not been reported yet. The above findings also indicate that the Panx1 expression of myotubes is not abrogated by innervation, but whether innervation up- or downregulates Panx1 expression remains to be studied.

The absence of Cx expression by adult rat skeletal muscles is in agreement with the proposal that Cx-based channels are not relevant for physiological muscle responses. This interpretation is consistent with the absence of functional Cx HCs in freshly isolated rat myofibers (Fig. 2). However, freshly isolated mouse myofibers show dye uptake through a membrane pathway inhibited by La^{3+} (Fig. 2). This finding suggests that normal mouse skeletal muscles might present Cx HCs on their surfaces. Clearly, a comparative study on Cx expression in skeletal muscles of

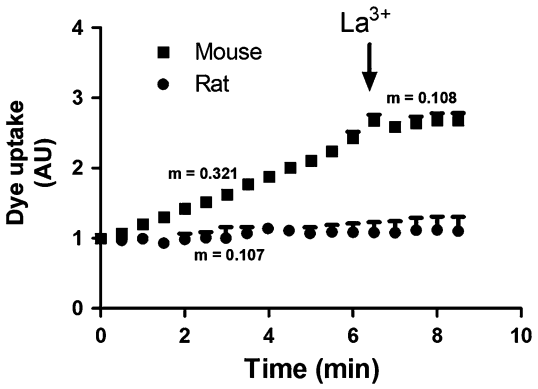

Fig. 2 Comparison of basal hemichannel activity between mouse and rat skeletal muscle fibers. We extracted the FDB skeletal muscle from rat and mouse and isolated the myofibers with collagenase type Ia (Sigma, St. Louis, MO). Then, we used the fibers for ethidium (5 μM) uptake assays in real time ($n = 6$). Fibers from mouse muscles showed a higher dye uptake rate than fibers from rats, and this increase was totally inhibited by La^{3+} (200 μM), an inhibitor of Cx-HCs

different mammalian species would contribute to resolving this apparent controversy.

As mentioned above, possible membrane receptors involved in $[Ca^{2+}]_i$ increments are P2 receptors activated by extracellular ATP/ADP (Araya et al. 2004; Buvinic et al. 2009; North 2002). Differentiated cells obtained from human skeletal muscle treated with exogenous P2Y receptor agonists show Ca^{2+} transients dependent on the IP_3 pathway but independent of ryanodine receptors (RyRs), which leads to ERK1/ERK2 activation (May et al. 2006).

P2Y receptors are likely to be expressed in fast skeletal muscles because potentiation of the contraction response occurs in the absence of extracellular Ca^{2+} (Louboutin et al. 1996). $P2X_4$ receptors are expressed in fast and slow skeletal muscles (Sandona et al. 2005). However, they participate in potentiation of muscle contraction only in slow muscles, where ectonucleotidases abrogate this response (Sandona et al. 2005). In the same line of thought, Panx1 HCs are permeable to Ca^{2+} (Vanden Abeele et al. 2006) and ^{10}panx1, a mimetic peptide that blocks Panx1 HCs, inhibits both the intracellular Ca^{2+} transients and the release of ATP to the extracellular milieu induced by tetanic stimulation in rat myotubes (Buvinic et al. 2009). The possible role of Panx1 HCs in ATP release and potentiation of muscle contraction needs to be demonstrated in fully differentiated (innervated) fast and slow skeletal muscles.

During repetitive skeletal muscle stimulation, extracellular ATP levels rise, causing activation of purinergic receptors that increase Ca^{2+} influx, potentiating the contraction force (Sandona et al. 2005; Zhi et al. 2005). In slow muscles, the potentiation response depends on the activation of purinergic $P2X_4$ receptors present in the T-tubule membrane as well as on the entry of extracellular Ca^{2+} (Sandona et al. 2005). In fast muscles, $P2X_4$ receptors are not found and potentiation occurs in the absence of extracellular Ca^{2+} (Louboutin et al. 1996; Sandona et al. 2005), suggesting the involvement of Ca^{2+} released from intracellular stores. Accordingly, potentiation of fast muscle contraction is blocked by extracellular ATPases, suggesting that extracellular ATP activates metabotropic P2 receptors linked to G proteins, leading to Ca^{2+} release from intracellular stores (Sandona et al. 2005). The three cloned IP_3Rs (IP_3R1, IP_3R2, IP_3R3) (Mikoshiba 2007) are present in adult muscles but in different intracellular locations (Casas et al. 2010). The rise in $[Ca^{2+}]_i$ increases the amount of calmodulin bound to Ca^{2+}, which activates calmodulin kinase II (CaMKII) and myosin light chain kinase. The latter phosphorylates the myosin regulatory protein kinase, enhancing Ca^{2+} affinity of the contractile machinery and increasing the twitch force (Zhi et al. 2005).

Skeletal muscle fibers release ATP during contraction (Cunha and Sebastião 1993; Sandona et al. 2005). In other cell types, ATP can be released via vesicles (Pangrsic et al. 2007) or through ATP permeable channels, including Cx and Panx HCs (Bao et al. 2004; Buvinic et al. 2009; Lu et al. 2012). In differentiated myoblast cultures, ATP release is inhibited by treatment with the Panx1 inhibitor ^{10}panx1, providing pharmacological evidence for a role of Panx1-based HCs in ATP release (Buvinic et al. 2009; Wang et al. 2007). It remains unknown, however, if innervation affects the expression of Panx1 in differentiated myofibers. Nevertheless, it is likely that innervated myofibers also express Panx1 because adult skeletal muscles express Panx1 and its transcript (Dvoriantchikova et al. 2006). Moreover, Panx1 might be located in T tubules because it can be coimmunoprecipitated with dihydropyridine receptors from total homogenates of myotubes (Buvinic et al. 2009). Since P2 receptors are present in adult myofibers, repetitive electrical stimulation could induce accumulation of intracellular Ca^{2+}. This would lead to activation of Panx1 HCs via a cytoplasmic mediator such as CaMKII, followed by ATP release via Panx1 HCs and activation of P2 receptors known to activate Panx1 HCs (Locovei et al. 2006b). This would then further increase ATP release and favor Ca^{2+} influx, which could contribute to potentiating the contraction force.

Cx Expression in Regenerating Skeletal Muscles

During skeletal muscle regeneration, satellite cells acquire myogenic commitment, reflected by the expression of myogenic determination factors, such as MyoD, Myf-5 and myogenin, transforming these cells into proliferative

myoblasts (Chargé and Rudnicki 2004). Moreover, adult regenerating mouse skeletal muscles present an increase in Cx43 and Cx45 levels after injection of $BaCl_2$, with highest expression at 5 and 3 days postinjection, respectively. At least, the absence of Cx43 delays the regeneration response (Araya et al. 2005). This process also occurs in adult rats, and the increase of Cx43 is accompanied by the synchronized exit of myoblasts from the cell cycle (Gorbe et al. 2005). In addition, a transient increase in Cx39 immunoreactivity was found through immunofluorescence analysis in regenerating adult skeletal muscle 2–10 days after injection of $BaCl_2$ into the tibialis anterior muscle of 6-week-old mice (von Maltzahn et al. 2004). However, muscles from mice deficient in Cx39 present an earlier myogenesis and accelerated regeneration after injection of $BaCl_2$, accompanied by higher levels of Cx43, probably compensating for the absence of Cx39 (von Maltzahn et al. 2011).

The above findings suggest that Cx-based channels expressed during regeneration play roles similar to those performed during the ontogeny of skeletal muscles.

Skeletal Muscle Atrophy and Hemichannels

Skeletal muscle atrophy can be defined as a decrease in mass, due to muscle wasting. It can occur in a variety of diseases associated with inflammatory responses and/or disuse (see below), trauma (tenotomy or denervation), prolonged immobilization, extended unloading (microgravity) or starvation or as a natural progression of aging. Denervation-induced atrophy involves the total disruption of trophic factors and nerve conduction, thus representing a model of acute acquired myopathy, which is frequently used in the study of muscle atrophy (Goldspink 1976; Goldspink et al. 1983).

Currently, it is difficult to establish the timing of different muscle changes associated with atrophy, mainly because the rate of atrophy varies among species, among individuals of the same species and among muscles of the same individual. For example, the weight of a rat muscle may be reduced by 50 % after 2 weeks of denervation, while in humans the same muscle suffers only a small loss of weight (Winlow and Usherwood 1975). Therefore, for practical purposes, variations in different muscle features are divided into early and late events linked to atrophy.

In the short term after skeletal muscle denervation, functional and structural changes can be observed. The distal segment of the motor neuron begins with Wallerian degeneration (Coleman 2005; Raff et al. 2002). Whereas muscles show a reduction in resting membrane potential (Albuquerque et al. 1971; Finol et al. 1981), there are increases in acetylcholine sensitivity at the extrajunctional

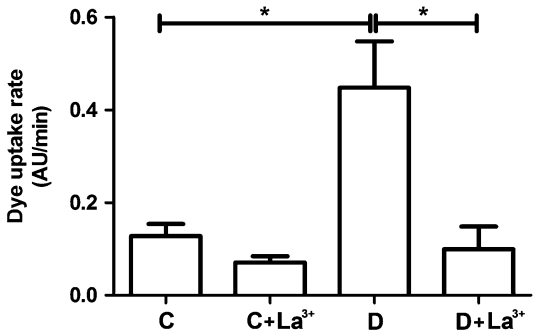

Fig. 3 Denervation induces an increase in membrane permeability in fast skeletal muscle fibers. At 6 days postdenervation we extracted the rat FDB skeletal muscle and isolated the myofibers. Then, we used the myofibers for ethidium (5 μM) uptake assays in real time ($n = 4$). Myofibers from denervated muscles showed a higher dye uptake rate (AU/min) than control fibers, and this increase was totally inhibited by La^{3+} (200 μM), an inhibitor of Cx-HCs. $*P < 0.05$, ANOVA with posttest. *C* control, *D* denervated

membrane (Lomo and Westgaard 1975), proliferation of satellite cells (Ontell 1974; Snow 1983) and increases in the expression of myogenic regulatory factors (MRFs) (Buonanno et al. 1992; Legerlotz and Smith 2008).

Since the mechanism that explains the reduction in membrane potential after denervation remains unidentified (Kotsias and Venosa 2001; Lenman 1965), we evaluated membrane permeability in skeletal muscle fibers under different experimental conditions that induce muscular atrophy, e.g., denervation and proinflammatory cytokine exposure. We isolated skeletal muscle fibers from rat denervated flexor digitorum brevis muscle from 6 days postdenervation and found that HC activity was higher in denervated fibers (approximately sixfold) (Fig. 3). We blocked the increase in permeability with La^{3+}, which is a Cx HC blocker. Additionally, we evaluated the influence of proinflammatory cytokines that induce muscular atrophy, such as TNF-α and IL-1β, in the membrane permeability of skeletal muscle fibers. We found that TNF-α itself induces an increase in ethidium uptake rates and that the combination of TNF-α and IL-1β induces a higher increase in membrane permeability, which is also blocked by La^{3+} (Fig. 4).

With regard to the mechanism that could explain the reduction in resting membrane potential, it is relevant to mention that intracellular levels of Na^+ and extracellular concentrations of K^+ are elevated compared to control muscles (Kotsias and Venosa 2001). However, Na^+ and K^+ channels show properties similar to normal muscles (Escobar et al. 1993; Kotsias and Venosa 2001). In contrast to a possible increase in Na^+ current, the number of TTX-sensitive Na^+ channels is reduced 3–10 days after denervation in rat skeletal muscles (Schmid et al. 1984). Moreover, a reduction in Na/K-ATPase activity has also been ruled

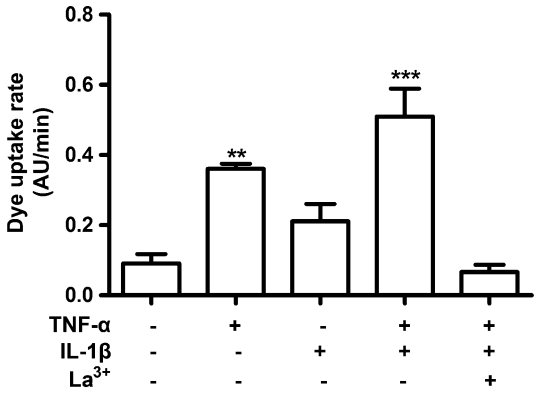

Fig. 4 Proinflammatory cytokines increase membrane permeability in fibers of fast skeletal muscles. Freshly isolated myofibers from rat FDB muscle were incubated for 3 h with either TNF-α (10 ng/ml) or IL-β (10 ng/ml) or with both cytokines. Membrane permeability was evaluated by ethidium (5 μM) uptake in time-lapse measurements ($n = 4$). TNF-α and IL-1β alone increased dye uptake, and treatment with both cytokines induced the summation response. Dye uptake induced by the cytokine mix was inhibited by La^{3+}. $^{**}P < 0.05$, $^{***}P < 0.001$ with respect to control uptake, ANOVA with posttest

out (Schmid et al. 1984). Since the increase in Cx HC levels occurs early after denervation, it is attractive to propose that a simultaneous increase in Na^+ influx and K^+ efflux mediated by Cx HCs might contribute to the reduction in resting membrane potential observed after denervation. Despite the low selectivity of HCs, it is conceivable that a new and lower resting membrane potential is established, mainly because intracellular negatively charged proteins are retained within the cells and, thus, reduce K^+ efflux.

The maintenance of muscle mass is regulated by a balance between protein synthesis and protein degradation pathways, which shift toward protein degradation during atrophy induced by denervation (Goldspink 1976, 1978). In addition, a net efflux of amino acids, such as glutamine, was detected after denervation (Hundal et al. 1990). Since Cx43 HCs, and most likely other Cx HCs (e.g., Cx39 and Cx45 HCs), are permeable to amino acids such as glutamate (Jiang et al. 2011), it is possible that they could disfavor protein synthesis by avoiding increases in intracellular concentrations of free amino acids required for protein synthesis, being that they would allow amino acid diffusion to the extracellular milieu.

Protein degradation is mainly mediated by four pathways: (1) calpains (Dargelos et al. 2008), (2) caspasas (Du et al. 2004), (3) cathepsins (Bechet et al. 2005), and (4) ubiquitin proteasome (Kandarian 2008). Many studies suggest that the latter plays a more significant role in protein degradation during muscle atrophy (Cao et al. 2005; Lecker 2003; Masiero et al. 2009; Ventadour and Attaix 2006). The major genes regulated during atrophy are *Fbxo32* and *Trim63*, which correspond to the ubiquitin ligases atrogin-1 and MuRF-1, respectively (Bodine et al. 2001), These genes show the greatest increase around 3 days after denervation, which is the time at which weight loss rates are higher in muscle (Sacheck et al. 2007). Overexpression of MuRF-1 in myotubes produces atrophy, whereas mice deficient in any of these ligases exhibit reduced atrophy after denervation (Bodine et al. 2001; Gomes et al. 2001; Rommel et al. 2001). During the second month of denervation, type II fibers show greater atrophy levels than type I fibers. From that point on, the observed atrophy is similar in all fibers and larger amounts of interstitial collagen are deposited (Lu et al. 1997).

Intracellular Ca^{2+} levels are higher in denervated than in normal skeletal muscles (Kirby and Lindley 1981; Picken and Kirby 1976; Shimizu and Kuriaki 1960). In addition, Ca^{2+} transport is slightly diminished in the sarcoplasmic reticulum of fast muscles, while Ca^{2+} transport of slow muscles is markedly increased (Marcreth et al. 1972). Accordingly, proteins involved in reducing intracellular Ca^{2+} levels are reduced; a reduced expression of fast SERCA1 Ca^{2+}-ATPase isoform, fast calsequestrin and fast parvalbumin occurs after denervation (Donoghue et al. 2004; Müntener et al. 1985) and possibly contributes to the persistent increase in free intracellular Ca^{2+} levels. Moreover, the denervated muscle contractile response depends on extracellular Ca^{2+} concentration (Picken and Kirby 1976). Since Cx43 HCs are permeable to Ca^{2+} (Schalper et al. 2010), it is possible that the higher free intracellular Ca^{2+} levels measured in denervated muscles are, in part, the consequence of enhanced Ca^{2+} influx via Cx HCs. Interestingly, protein degradation pathways can be activated by elevated free intracellular Ca^{2+} (Hussain et al. 1987), and thus, an increase in Cx HC activity in denervated muscles might be relevant in the development of muscle atrophy.

Other Pathological Conditions Associated with Muscular Atrophy

Other muscle diseases (i.e., myasthenia gravis) and different pathological conditions associated with inflammation (i.e., diabetes and septic shock) or chronic disuse (i.e., cancer) also develop muscle atrophy. However, all of these conditions may share some, but not all, etiological factors; and muscle atrophy is just a common characteristic developed by yet unknown factors.

Diseases of Neural Origin

Several diseases affect motor neurons and finally result in muscular atrophy. In this review, we focus on the most prevalent diseases, including spinal muscular atrophy. This is a neurodegenerative disease caused by mutations of the

survival motor neuron gene (D'Amico et al. 2011) that affects lower motor neurons, yielding progressive limb muscle weakness and paralysis. Motor neurons are also affected in spinal and bulbar muscular atrophy, which is a chromosome X–linked disease that affects lower motor neurons. It is caused by the expansion of CAG repeats, encoding the polyglutamine (polyQ) tract in the androgen receptor gene (Kennedy et al. 1968; Sobue et al. 1989). A normal individual possess 9–36 CAG repeats, and an affected individual has 38–62 repeats.

Another disease is amyotrophic lateral sclerosis, which is a progressive condition affecting upper and lower motor neurons and can either be of genetic origin or occur sporadically (Hama et al. 2012). A number of potential mechanisms have been proposed, including superoxidase dismutase type 1–mediated toxicity, excitotoxicity, cytoskeletal derangements, RNA processing and microglial activation (Rowland and Shneider 2001).

A classic denervation disease that affects lower motor neurons is Guillain-Barré syndrome. This is a group of acute immune-mediated polyneuropathies with several clinical forms. The most common variant is acute inflammatory demyelinating polyradiculoneuropathy, in 85–90 % of cases (Ropper 1992). Cardinal symptoms are progressive ascending weakness, which can compromise facial, oropharyngeal, oculomotor and respiratory muscles (Alshekhlee et al. 2008).

Diseases of Genetic Origin

There are several genetic diseases that induce skeletal muscle atrophy. The most prevalent of these is Duchenne muscular dystrophy (DMD), which is produced by a spontaneous mutation in the dystrophin gene, leading to muscular atrophy. Humans and dogs primarily show muscle atrophy. However, Mdx mice progress through an initial phase of muscle hypertrophy, followed by atrophy; and cats show persistent muscle hypertrophy (Kornegay et al. 2012). Dystrophin deficiency produces different responses depending on the species, individual and muscles. The reasons for phenotypic variation are not clear and raise questions about primary versus secondary effects of dystrophin deficiency. Other dystrophin mutations lead to attenuated expression of truncated protein and result in a milder phenotype referred to as Becker muscular dystrophy. Dystrophin is a member of the dystrophin-glycoprotein complex (DGC), a structural complex that anchors the cytoskeleton to the extracellular matrix. Alterations of dystrophin destabilize the DGC, thus compromising the cellular integrity and, finally, the structural and functional integrity of skeletal muscles. DMD patients report first weakness in the proximal lower limbs and then progress to the remaining ones. Onset of symptoms in humans occurs between 2 and 3 years of age. Muscle biopsies reveal myofiber necrosis, inflammatory cell infiltration, early muscle regeneration and fibrosis, which finally evolve to atrophy (Kornegay et al. 2012).

Acute Inflammatory Diseases

Sepsis and respiratory failure are two conditions of major risk for acquired weakness in critically ill patients. As a complication of critical illness, weakness of limb and respiratory muscles frequently slows and even dominates the course of recovery. Long-term consequences such as exercise limitation and low health-related quality of life sometimes persist for years (Herridge et al. 2003). Patients manifest both neuropathy and myopathy but with a common feature of muscle atrophy (Angel et al. 2007). There is a decrease in skeletal muscle protein synthesis and enhancement of catabolic degradation (Helliwell et al. 1998; Vary and Kimball 1992). However, sepsis induces early changes in contraction fiber properties, even without modifications in muscle mass (Callahan and Supinski 2009).

Chronic Inflammatory Diseases

Several chronic inflammatory diseases manifest a state called *cachexia*, which is defined as "a multifactorial syndrome characterized by an ongoing loss of skeletal muscle mass (with or without loss of fat mass) that cannot be fully reversed by conventional nutritional support and leads to progressive functional impairment" (Fearon et al. 2001). The molecular mechanism involves TNF-α, which activates NFκB, which in turn increases the levels of atrogin (Judge et al. 2007) and MurF1 (Adams et al. 2008; Cai et al. 2004), two E3 ligase proteins that belong to the ubiquitin-proteasome system, and favors a catabolic state leading to muscular atrophy (Foletta et al. 2011).

One of the most prevalent chronic diseases is diabetes (types 1 and 2). It presents serious complications including neuropathies, retinopathies, cardiovascular disease and muscular atrophy. Skeletal muscle wasting is one of the most common alterations, in which protein breakdown increases and protein synthesis decreases (Smith et al. 1989).

Another highly prevalent chronic disease is cancer, in which there is an increase in TNF-α levels (Tisdale 2008), which in turn activates NFκB, leading to muscular atrophy. However, other cytokines, such as IL-1β and IL-6, and several tumor-derived substances are involved in cancer cachexia (Davis et al. 2004). Cachexia is a common state in patients with advanced cancer and is associated with less treatment tolerance, reduction of response to therapy and lower survival rates (Fearon 2011). It occurs with reduced

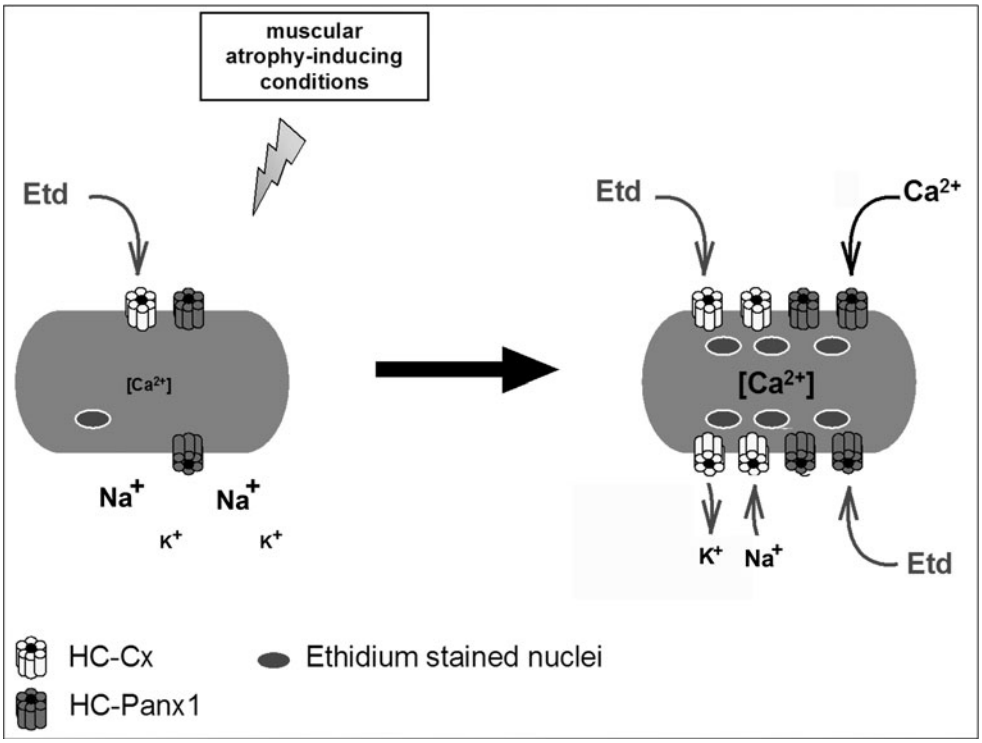

Fig. 5 Scheme showing possible membrane permeability changes in adult skeletal muscle undergoing atrophy. *Left* Normal skeletal muscle fibers have no or very low hemichannel activity. *Right* Conditions that induce muscular atrophy (i.e., proinflammatory cytokines) induce functional expression of connexin-based hemichannels that increase the membrane permeability to ions such as Na^+, K^+ and Ca^{2+}. Panx1 HCs are present in normal muscles, where most likely they are activated via extracellular ATP/P2 receptors and could also favor ion and small molecule fluxes in fibers undergoing atrophy

food intake and abnormal metabolism, which leads to a negative balance of energy and proteins. Moreover, this state is influenced by systemic inflammation (Zhou et al. 2010).

Muscular wasting is also present in nearly 20 % of patients with HIV/AIDS (Wanke et al. 2000). AIDS wasting syndrome is an involuntary weight loss >10 % of baseline body weight during the previous 12 months or a 5 % weight loss in the previous 6 months. Inflammatory myopathy resembling idiopathic polymyositis can occur in patients with HIV infection, as well as myopathy induced by treatment with nucleoside reverse transcriptase inhibitors, such as ziduvudine, lamivudine, abacabir and tenofovir (Moyle 2005).

In general, the paradigms of chronic inflammatory diseases that compromise muscle functions are the inflammatory myopathies, which share the common feature of autoimmune–mediated muscle injury. The most important subtypes include dermatomyositis, inclusion-body myositis, idiopathic polymyositis and overlap syndromes (with another systemic rheumatic disease). The exact pathogenic process differs, but they are all characterized by autoantibody production, inflammation, muscle weakness and immunity-independent NFκB activation such as endoplasmic reticulum stress by overload (Nagaraju et al. 2005).

Metabolic Myopathies

This group of diseases combines infrequent metabolic defects in energy production to muscle requirements. These include defects in lipid, glycogen and glucose metabolism as well organelle defects, namely, mitochondrial and lysosomal pathologies. Most patients report exercise intolerance, muscle pain and cramps rather than a fixed sense of weakness. However, some patients may develop muscular atrophy when experiencing fixed weakness. This evolution can occur in patients with acid maltase deficiency (Shea and Raben 2009), mitochondrial myopathies by mutations involving cytochrome *b*, cytochrome *c* oxidase (cox), MELAS A3260G mutation (Kollberg et al. 2005) and fatty acid oxidation defects (Hale and Bennett 1992). In the latter group, free fatty acids cannot be metabolized due to the existing metabolic block. As a result, they are stored in the cytoplasm as triglycerides, thereby resulting in progressive lipid storage myopathy with weakness,

hypertrophic and/or dilated cardiomyopathy and fatty liver (Treem 2000).

Concluding Remarks

Cx GJCs and HCs in ensemble with several membrane receptors, including P2 receptors, orchestrate numerous relevant steps in the muscle ontogeny process, including cell commitment to skeletal muscle lineage and differentiation. Moreover, in normal adult skeletal muscles Panx1 HCs may be key players in tissue responses, such as potentiation of muscle contraction. This is an example where Panx1 HCs do not coexist with Cx HCs.

Cxs are not expressed by normal adult skeletal muscles. However, under pathological conditions, such as denervation and inflammation, differentiated myofibers express functional Cx HCs (Fig. 5). Since Cx HCs are low-resistance membrane pathways with low selectivity, their functional expression in the cell membrane might lead to partial dissipation of the electrochemical gradient across the cellular membrane. Consequently, the increase in Cx HC activity offers a partial explanation for a number of cellular events that precede muscle atrophy, such as reduction in resting membrane potential and increases in protein degradation. Therefore, Cx HC blockers are expected to prevent or reduce skeletal muscle atrophy caused by different etiologies.

References

Adams V, Mangner N, Gasch A, Krohne C, Gielen S, Hirner S, Thierse HJ, Witt CC, Linke A, Schuler G, Labeit S (2008) Induction of MuRF1 is essential for TNF-alpha-induced loss of muscle function in mice. J Mol Biol 384:48–59

Albuquerque EX, Schuh FT, Kauffman FC (1971) Early membrane depolarization of the fast mammalian muscle after denervation. Pflügers Arch 328:36–50

Alshekhlee A, Hussain Z, Sultan B, Katirji B (2008) Guillain-Barré syndrome: incidence and mortality rates in US hospitals. Neurology 70:1608–1613

Ambrosi C, Gassmann O, Pranskevich JN, Boassa D, Smock A, Wang J, Dahl G, Steinem C, Sosinsky GE (2010) Pannexin1 and pannexin2 channels show quaternary similarities to connexons and different oligomerization numbers from each other. J Biol Chem 285:24420–24431

Angel MJ, Bril V, Shannon P, Herridge MS (2007) Neuromuscular function in survivors of the acute respiratory distress syndrome. Can J Neurol Sci 34:427–432

Araya R, Eckardt D, Riquelme MA, Willecke K, Sáez JC (2003a) Presence and importance of connexin43 during myogenesis. Cell Commun Adhes 10:451–456

Araya R, Liberona JL, Cárdenas JC, Riveros N, Estrada M, Powell JA, Carrasco MA, Jaimovich E (2003b) Dihydropyridine receptors as voltage sensors for a depolarization-evoked, IP3R-mediated, slow calcium signal in skeletal muscle cells. J Gen Physiol 121:3–16

Araya R, Riquelme MA, Brandan E, Sáez JC (2004) The formation of skeletal muscle myotubes requires functional membrane receptors activated by extracellular ATP. Brain Res Rev 47:174–178

Araya R, Eckardt D, Maxeiner S, Kruger O, Theis M, Willecke K, Sáez JC (2005) Expression of connexins during differentiation and regeneration of skeletal muscle: functional relevance of connexin43. J Cell Sci 118:27–37

Balogh S, Naus CC, Merrifield PA (1993) Expression of gap junctions in cultured rat L6 cells during myogenesis. Dev Biol 155: 351–360

Banachewicz W, Suplat D, Krzeminski P, Pomorski P, Baranska J (2005) P2 nucleotide receptors on C2C12 satellite cells. Purinergic Signal 1:249–257

Bao L, Locovei S, Dahl G (2004) Pannexin membrane channels are mechanosensitive conduits for ATP. FEBS Lett 572:65–68

Baranova A, Ivanov D, Petrash N, Pestova A, Skoblov M, Kelmanson I, Shagin D, Nazarenko S, Geraymovych E, Litvin O, Tiunova A, Born TL, Usman N, Staroverov D, Lukyanov S, Panchin Y (2004) The mammalian pannexin family is homologous to the invertebrate innexin gap junction proteins. Genomics 83: 706–716

Barrio LC, Capel J, Jarillo JA, Castro C, Revilla A (1997) Species-specific voltage-gating properties of connexin-45 junctions expressed in *Xenopus* oocytes. Biophys J 73:757–769

Bechet D, Tassa A, Taillandier D, Combaret L, Attaix D (2005) Lysosomal proteolysis in skeletal muscle. Int J Biochem Cell Biol 37:2098–2114

Bedner P, Steinhäuser C, Theis M (2011) Functional redundancy and compensation among members of gap junction protein families? Biochim Biophys Acta 1818:1971–1984

Berridge MJ (1993) Inositol trisphosphate, calcium signaling. Nature 361:315–325

Bodine SC, Latres E, Baumhueter S, Lai VK, Nunez L, Clarke BA, Poueymirou WT, Panaro FJ, Na E, Dharmarajan K, Pan ZQ, Valenzuela DM, DeChiara TM, Stitt TN, Yancopoulos GD, Glass DJ (2001) Identification of ubiquitin ligases required for skeletal muscle atrophy. Science 294:1704–1708

Braun T, Rudnicki MA, Arnold HH, Jaenish R (1992) Targeted inactivation of the muscle regulatory gene Myf-5 results in abnormal rib development and perinatal death. Cell 71:369–382

Bruzzone R, Dermietzel R (2006) Structure and function of gap junctions in the developing brain. Cell Tissue Res 326:239–248

Bruzzone S, Guida L, Zocchi E, Franco L, De Flora A (2001) Connexin 43 hemichannels mediate Ca^{2+}-regulated transmembrane NAD^{+} fluxes in intact cells. FASEB J 15:10–12

Bruzzone R, Hormuzdi SG, Barbe MT, Herb A, Monyer H (2003) Pannexins, a family of gap junction proteins expressed in brain. Proc Natl Acad Sci USA 100:13644–13649

Bruzzone R, Barbe MT, Jakob NJ, Monyer H (2005) Pharmacological properties of homomeric and heteromeric pannexin hemichannels expressed in *Xenopus* oocytes. J Neurochem 92:1033–1043

Buonanno A, Apone L, Morasso MI, Beers R, Brenner HR, Eftimie R (1992) The MyoD family of myogenic factors is regulated by electrical activity: isolation and characterization of a mouse Myf-5 cDNA. Nucleic Acids Res 20:539–544

Burnstock G (2007) Purine and pyrimidine receptors. Cell Mol Life Sci 64:1471–1483

Buvinic S, Almarza G, Bustamante M, Casas M, López J, Riquelme M, Sáez JC, Huidobro-Toro JP, Jaimovich E (2009) ATP released by electrical stimuli elicits calcium transients and gene expression in skeletal muscle. J Biol Chem 284:34490–34505

Cai D, Frantz JD, Tawa NE Jr, Melendez PA, Oh BC, Lidov HG, Hasselgren PO, Frontera WR, Lee J, Glass DJ, Shoelson SE

(2004) IKKbeta/NF-kappaB activation causes severe muscle wasting in mice. Cell 119:285–298
Callahan LA, Supinski GS (2009) Sepsis-induced myopathy. Crit Care Med 37:S354–S367
Cao PR, Kim HJ, Lecker SH (2005) Ubiquitin-protein ligases in muscle wasting. Int J Biochem Cell Biol 37:2088–2097
Casas M, Figueroa R, Jorquera G, Escobar M, Molgó J, Jaimovich E (2010) IP_3-dependent, post-tetanic calcium transients induced by electrostimulation of adult skeletal muscle fibers. J Gen Physiol 136:455–467
Chargé SB, Rudnicki MA (2004) Cellular and molecular regulation of muscle regeneration. Physiol Rev 84:209–238
Cherian PP, Siller-Jackson AJ, Gu S, Wang X, Bonewald LF, Sprague E, Jiang JX (2005) Mechanical strain opens connexin 43 hemichannels in osteocytes: a novel mechanism for the release of prostaglandin. Mol Biol Cell 16:3100–3106
Coleman M (2005) Axon degeneration mechanisms: commonality amid diversity. Nat Rev Neurosci 6:889–898
Contreras JE, Sánchez HA, Eugenin EA, Speidel D, Theis M, Willecke K, Bukauskas FF, Bennett MV, Sáez JC (2002) Metabolic inhibition induces opening of unapposed connexin 43 gap junction hemichannels and reduces gap junctional communication in cortical astrocytes in culture. Proc Natl Acad Sci USA 99:495–500
Cunha RA, Sebastião AM (1993) Adenosine and adenine nucleotides are independently released from both the nerve terminals and the muscle fibres upon electrical stimulation of the innervated skeletal muscle of the frog. Pflügers Arch 424:503–510
D'Amico A, Mercuri E, Tiziano FD, Bertini E (2011) Spinal muscular atrophy. Orphanet J Rare Dis 6:71–81
Dargelos E, Poussard S, Brule C, Daury L, Cottin P (2008) Calcium-dependent proteolytic system and muscle dysfunctions: a possible role of calpains in sarcopenia. Biochimie 90:359–368
Davis MP, Dreicer R, Walsh D, Lagman R, LeGrand SB (2004) Appetite and cancer-associated anorexia: a review. J Clin Oncol 22:1510–1517
Deli T, Szappanos H, Szigeti GP, Cseri J, Kovács L, Csernoch L (2007) Contribution from P2X and P2Y purinoreceptors to ATP-evoked changes in intracellular calcium concentration on cultured myotubes. Pflugers Arch 453:519–529
Dennis MJ, Ziskind-Conhaim L, Harris AJ (1981) Development of neuromuscular junctions in rat embryos. Dev Biol 81:266–279
Domercq M, Perez-Samartin A, Aparicio D, Alberdi E, Pampliega O, Matute C (2010) P2X7 receptors mediate ischemic damage to oligodendrocytes. Glia 58:730–740
Donoghue P, Ribaric S, Moran B, Cebasek V, Erzen I, Ohlendieck K (2004) Early effects of denervation on Ca^{2+}-handling proteins in skeletal muscle. Int J Mol Med 13:767–772
Du J, Wang X, Miereles C, Bailey JL, Debigare R, Zheng B, Price SR, Mitch WE (2004) Activation of caspase-3 is an initial step triggering accelerated muscle proteolysis in catabolic conditions. J Clin Invest 113:115–123
Duxson MJ, Usson Y (1989) Cellular insertion of primary and secondary myotubes in embryonic rat muscles. Development 107:243–251
Dvoriantchikova G, Ivanov D, Panchin Y, Shestopalov VI (2006) Expression of pannexin family of proteins in the retina. FEBS Lett 580:2178–2182
Escobar AL, Schinder AF, Biali FI, Nicola LC, Uchitel OD (1993) Potassium channels from normal and denervated mouse skeletal muscle fibers. Muscle Nerve 16:579–586
Fearon KC (2011) Cancer cachexia and fat–muscle physiology. N Engl J Med 365:565–567
Fearon KC, Barber MD, Moses AG (2001) The cancer cachexia syndrome. Surg Oncol Clin North Am 10:109–126
Finol HJ, Lewis DM, Owens R (1981) The effects of denervation on contractile properties or rat skeletal muscle. J Physiol 319:81–92
Foletta VC, White LJ, Larsen AE, Léger B, Russell AP (2011) The role and regulation of MAFbx/atrogin-1 and MuRF1 in skeletal muscle atrophy. Pflugers Arch 461:325–335
Foskett JK, White C, Cheung KH, Mak DO (2007) Inositol trisphosphate receptor Ca^{2+} release channels. Physiol Rev 87: 593–658
Friday BB, Pavlath GK (2001) A calcineurin- and NFAT-dependent pathway regulates Myf5 gene expression in skeletal muscle reserve cells. J Cell Sci 114:303–310
Gaietta G, Deerinck TJ, Adams SR, Bouwer J, Tour O, Laird DW, Sosinsky GE, Tsien RY, Ellisman MH (2002) Multicolor and electron microscopic imaging of connexin trafficking. Science 296:503–507
Goldspink DF (1976) The effects of denervation on protein turnover of rat skeletal muscle. Biochem J 156:71–80
Goldspink DF (1978) The effects of denervation on protein turnover of the soleus and extensor digitorum longus muscles of adult mice. Comp Biochem Physiol B Biochem Mol Biol 61: 37–41
Goldspink DF, Garlick PJ, McNurlan MA (1983) Protein turnover measured in vivo and in vitro in muscles undergoing compensatory growth and subsequent denervation atrophy. Biochem J 210:89–98
Gomes MD, Lecker SH, Jagoe RT, Navon A, Goldberg AL (2001) Atrogin-1, a muscle-specific F-box protein highly expressed during muscle atrophy. Proc Natl Acad Sci USA 98:14440–14445
Gorbe A, Becker DL, Dux L, Stelkovics E, Krenacs L, Bagdi E, Krenacs T (2005) Transient upregulation of connexin43 gap junctions and synchronized cell cycle control precede myoblast fusion in regenerating skeletal muscle in vivo. Histochem Cell Biol 123:573–583
Gorbe A, Krenacs T, Cook JE, Becker DL (2007) Myoblast proliferation and syncytial fusion both depend on connexin43 function in transfected skeletal muscle primary cultures. Exp Cell Res 313:1135–1148
Hale DE, Bennett MJ (1992) Fatty acid oxidation disorders: a new class of metabolic diseases. J Pediatr 121:1–11
Hama T, Hirayama M, Hara T, Nakamura T, Atsuta N, Banno H, Suzuki K, Katsuno M, Tanaka F, Sobue G (2012) Discrimination of spinal and bulbar muscular atrophy from amyotrophic lateral sclerosis using sensory nerve action potentials. Muscle Nerve 45:169–174
Helliwell TR, Wilkinson A, Griffiths RD, McClelland P, Palmer TE, Bone JM (1998) Muscle fibre atrophy in critically ill patients is associated with the loss of myosin filaments and the presence of lysosomal enzymes and ubiquitin. Neuropathol Appl Neurobiol 24:507–517
Herridge MS, Cheung AM, Tansey CM, Matte-Martyn A, Diaz-Granados N, Al-Saidi F, Cooper AB, Guest CB, Mazer CD, Mehta S, Stewart TE, Barr A, Cook D, Slutsky AS (2003) One-year outcomes in survivors of the acute respiratory distress syndrome. N Engl J Med 348:683–693
Hundal HS, Babij P, Watt PW, Ward MR, Rennie MJ (1990) Glutamine transport and metabolism in denervated rat skeletal muscle. Am J Physiol Endocrinol Metab 259:E148–E154
Hussain H, Dudley GA, Johnson P (1987) Effects of denervation on calpain and calpastatin in hamster skeletal muscles. Exp Neurol 97:635–643
Ishikawa M, Iwamoto T, Nakamura T, Doyle A, Fukumoto S, Yamada Y (2011) Pannexin 3 functions as an ER Ca^{2+} channel, hemichannel, and gap junction to promote osteoblast differentiation. J Cell Biol 193:1257–1274

Jiang S, Yuan H, Duan L, Cao R, Gao B, Xiong YF, Rao ZR (2011) Glutamate release through connexin 43 by cultured astrocytes in a stimulated hypertonicity model. Brain Res 1392:8–15

Judge AR, Koncarevic A, Hunter RB, Liou HC, Jackman RW, Kandarian SC (2007) Role for IkappaBalpha, but not c-Rel, in skeletal muscle atrophy. Am J Physiol Cell Physiol 292:C372–C382

Kalderon N, Epstein ML, Gilula NB (1977) Cell-to-cell communication and myogenesis. J Cell Biol 75:788–806

Kandarian S (2008) The molecular basis of skeletal muscle atrophy—parallels with osteoporotic signaling. J Musculoskelet Neuronal Interact 8:340–341

Kennedy WR, Alter M, Sung JH, Sung JH (1968) Progressive proximal spinal and bulbar muscular atrophy of late onset. A sex-linked recessive trait. Neurology 18:671–680

Kirby AC, Lindley BD (1981) Calcium content of rat fast and slow muscle after denervation. Comp Biochem Physiol A Physiol 70: 583–586

Kollberg G, Moslemi A-R, Lindberg C, Holme E, Oldfors A (2005) Mitochondrial myopathy and rhabdomyolysis associated with a novel nonsense mutation in the gene encoding cytochrome c oxidase subunit I. J Neuropathol Exp Neurol 64:123–128

Kornegay JN, Childers MK, Bogan DJ, Bogan JR, Nghiem P, Wang J, Fan Z, Howard JF Jr, Schatzberg SJ, Dow JL, Grange RW, Styner MA, Hoffman EP, Wagner KR (2012) The paradox of muscle hypertrophy in muscular dystrophy. Phys Med Rehabil Clin N Am 23:149–172

Kotsias BA, Venosa RA (2001) Sodium influx during action potential in innervated and denervated rat skeletal muscles. Muscle Nerve 24:1026–1033

Lecker SH (2003) Ubiquitin-protein ligases in muscle wasting: multiple parallel pathways? Curr Opin Clin Nutr Metab Care 6:271–275

Legerlotz K, Smith HK (2008) Role of MyoD in denervated, disused, and exercised muscle. Muscle Nerve 38:1087–1100

Lenman JA (1965) Effect of denervation on the resting membrane potential of healthy and dystrophic muscle. J Neurol Neurosurg Psychiatry 28:525–528

Li H, Liu TF, Lazrak A, Peracchia C, Goldberg GS, Lampe PD, Johnson RG (1996) Properties and regulation of gap junctional hemichannels in the plasma membranes of cultured cells. J Cell Biol 134:1019–1030

Li S, Bjelobaba I, Yan Z, Kucka M, Tomic M, Stojilkovic SS (2011) Expression and roles of pannexins in ATP release in the pituitary gland. Endocrinology 152:2342–2352

Ling Y, Appelt D, Kelly AM, Franzini-Armstrong C (1992) Differences in the histogenesis of EDL and diaphragm in rat. Dev Dyn 193:359–369

Locovei S, Bao L, Dahl G (2006a) Pannexin 1 in erythrocytes: function without a gap. Proc Natl Acad Sci USA 103:7655–7659

Locovei S, Wang J, Dahl G (2006b) Activation of pannexin 1 channels by ATP through P2Y receptors and by cytoplasmic calcium. FEBS Lett 580:239–244

Lomo T, Westgaard RH (1975) Further studies on the control of ACh sensitivity by muscle activity in the rat. J Physiol 252:603–626

Louboutin JP, Fichter-Gagnepain V, Noireaud J (1996) Effects of external calcium on contractile responses in rat extensor digitorum longus muscles after sciatic nerve injury at birth. Muscle Nerve 19:1421–1428

Lu DX, Huang SK, Carlson BM (1997) Electron microscopic study of long-term denervated rat skeletal muscle. Anat Rec 248:355–365

Lu D, Soleymani S, Madakshire R, Insel PA (2012) ATP released from cardiac fibroblasts via connexin hemichannels activates profibrotic P2Y2 receptors. FASEB J 26:2580–2591

Marcreth A, Salviati G, Dimauro S, Turati G (1972) Early biochemical consequences of denervation of fast and slow skeletal muscles and their relationship in neural control over muscle differentiation. Biochem J 126:1099–1110

Masiero E, Agatea L, Mammucari C, Blaauw B, Loro E, Komatsu M, Metzger D, Reggiani C, Schiaffino S, Sandri M (2009) Autophagy is required to maintain muscle mass. Cell Metab 10: 507–515

May C, Weigl L, Karel A, Hohenegger M (2006) Extracellular ATP activates ERK1/ERK2 via a metabotropic P2Y1 receptor in a Ca^{2+} independent manner in differentiated human skeletal muscle cells. Biochem Pharmacol 71:1497–1509

Meyer MP, Gröschel-Stewart U, Robson T, Burnstock G (1999) Expression of two ATP-gated ion channels, P2X5 and P2X6, in developing chick skeletal muscle. Dev Dyn 216:442–449

Mikoshiba K (2007) IP_3 receptor/Ca^{2+} channel: from discovery to new signaling concepts. J Neurochem 102:1426–1446

Molkentin JD, Olson EN (1996) Combinatorial control of muscle development by basic helix-loop-helix and MADS-box transcription factors. Proc Natl Acad Sci USA 93:9366–9367

Moreno AP, Laing JG, Beyer EC, Spray DC (1995) Properties of gap junction channels formed of connexin 45 endogenously expressed in human hepatoma (SKHep1) cells. Am J Physiol Cell Physiol 268:C356–C365

Moyle G (2005) Mechanisms of HIV and nucleoside reverse transcriptase inhibitor injury to mitochondria. Antivir Ther 10(Suppl 2):M47–M52

Müntener M, Berchtold MW, Heizmann CW (1985) Parvalbumin in cross-reinnervated and denervated muscles. Muscle Nerve 8: 132–137

Nagaraju K, Casciola-Rosen L, Lundberg I, Rawat R, Cutting S, Thapliyal R, Chang J, Dwivedi S, Mitsak M, Chen Y-W, Plotz P, Rosen A, Hoffman E, Raben N (2005) Activation of the endoplasmic reticulum stress response in autoimmune myositis: potential role in muscle fiber damage and dysfunction. Arthritis Rheum 52:1824–1835

North RA (2002) Molecular physiology of P2X receptors. Physiol Rev 82:1013–1067

Okon EB, Golbabaie A, van Breemen C (2002) In the presence of L-NAME SERCA blockade induces endothelium-dependent contraction of mouse aorta through activation of smooth muscle prostaglandin H_2/thromboxane A_2 receptors. Br J Pharmacol 137:545–553

Ontell M (1974) Muscle satellite cells: a validated technique for light microscopic identification and a quantitative study of changes in their population following denervation. Anat Rec 178:211–227

Orellana JA, Hernández DE, Ezan P, Velarde V, Bennett MV, Giaume C, Sáez JC (2010) Hypoxia in high glucose followed by reoxygenation in normal glucose reduces the viability of cortical astrocytes through increased permeability of connexin 43 hemichannels. Glia 58:329–343

Orellana JA, Díaz E, Schalper KA, Vargas AA, Bennett MV, Sáez JC (2011) Cation permeation through connexin 43 hemichannels is cooperative, competitive and saturable with parameters depending on the permeant species. Biochem Biophys Res Commun 409:603–609

Orellana JA, Sáez PJ, Cortés-Campos C, Elizondo RJ, Shoji KF, Contreras-Duarte S, Figueroa V, Velarde V, Jiang JX, Nualart F, Sáez JC, García MA (2012) Glucose increases intracellular free Ca^{2+} in tanycytes via ATP released through connexin 43 hemichannels. Glia 60:53–68

Pangrsic T, Potokar M, Stenovec M, Kreft M, Fabbretti E, Nistri A, Pryazhnikov E, Khiroug L, Giniatullin R, Zorec R (2007) Exocytotic release of ATP from cultured astrocytes. J Biol Chem 282:28749–28758

Peñuela S, Bhalla R, Gong XQ, Cowan KN, Celetti SJ, Cowan BJ, Bai D, Shao Q, Laird DW (2007) Pannexin 1 and pannexin 3 are glycoproteins that exhibit many distinct characteristics from the

connexin family of gap junction proteins. J Cell Sci 120:3772–3783

Picken JR, Kirby AC (1976) Denervated frog skeletal muscle: Calcium content and kinetics of exchange. Exp Neurol 53:64–70

Ponsaerts R, De Vuyst E, Retamal M, D'hondt C, Vermeire D, Wang N, De Smedt H, Zimmermann P, Himpens B, Vereecke J, Leybaert L, Bultynck G (2010) Intramolecular loop/tail interactions are essential for connexin 43-hemichannel activity. FASEB J 24:4378–4395

Pownall ME, Gustafsson MK, Emerson CP Jr (2002) Myogenic regulatory factors and the specification of muscle progenitors in vertebrate embryos. Annu Rev Cell Dev Biol 18:747–783

Pritschow BW, Lange T, Kasch J, Kunert-Keil C, Liedtke W, Brinkmeier H (2011) Functional TRPV4 channels are expressed in mouse skeletal muscle and can modulate resting Ca^{2+} influx and muscle fatigue. Pflugers Arch 461:115–122

Proulx AA, Merrifield PA, Naus CC (1997) Blocking gap junctional intercellular communication in myoblasts inhibits myogenin and MRF4 expression. Dev Genet 20:133–144

Račkauskas M, Neverauskas V, Skeberdis VA (2010) Diversity and properties of connexin gap junction channels. Medicina (Kaunas) 46:1–12

Raff MC, Whitmore AV, Finn JT (2002) Axonal self-destruction and neurodegeneration. Science 296:868–871

Ray A, Zoidl G, Wahle P, Dermietzel R (2006) Pannexin expression in the cerebellum. Cerebellum 5:189–192

Retamal MA, Evangelista-Martínez F, León-Paravic CG, Altenberg GA, Reuss L (2011) Biphasic effect of linoleic acid on connexin 46 hemichannels. Pflugers Arch 461:635–643

Rommel C, Bodine SC, Clarke BA, Rossman R, Nunez L, Stitt TN, Yancopoulos GD, Glass DJ (2001) Mediation of IGF-1-induced skeletal myotube hypertrophy by PI_3K/Akt/mTOR and PI_3K/Akt/GSK3 pathways. Nat Cell Biol 3:1009–1013

Ropper AH (1992) The Guillain-Barré syndrome. N Engl J Med 326:1130–1136

Rowland LP, Shneider NA (2001) Amyotrophic lateral sclerosis. N Engl J Med 344:1688–1700

Rudnicki MA, Schnegelsberg PN, Stead RH, Braun T, Arnold HH, Jaenisch R (1993) MyoD or Myf-5 is required for the formation of skeletal muscle. Cell 75:1351–1359

Ruppelt A, Ma W, Borchardt K, Silberberg SD, Soto F (2001) Genomic structure, developmental distribution and functional properties of the chicken $P2X_5$ receptor. J Neurochem 77:1256–1265

Ryten M, Dunn PM, Neary JT, Burnstock G (2002) ATP regulates the differentiation of mammalian skeletal muscle by activation of a P2X5 receptor on satellite cells. J Cell Biol 158:345–355

Sacheck JM, Hyatt JP, Raffaello A, Jagoe RT, Roy RR, Edgerton VR, Lecker SH, Goldberg AL (2007) Rapid disuse and denervation atrophy involve transcriptional changes similar to those of muscle wasting during systemic diseases. FASEB J 21:140–155

Sáez JC, Retamal MA, Basilio D, Bukauskas FF, Bennett MV (2005) Connexin-based gap junction hemichannels: gating mechanisms. Biochim Biophys Acta 1711:215–224

Sánchez HA, Orellana JA, Verselis VK, Sáez JC (2009) Metabolic inhibition increases activity of connexin-32 hemichannels permeable to Ca^{2+} in transfected HeLa cells. Am J Physiol Cell Physiol 297:C665–C678

Sánchez HA, Mese G, Srinivas M, White TW, Verselis VK (2010) Differentially altered Ca^{2+} regulation and Ca^{2+} permeability in Cx26 hemichannels formed by the A40 V and G45E mutations that cause keratitis ichthyosis deafness syndrome. J Gen Physiol 136:47–62

Sandona D, Danieli-Betto D, Germinario E, Biral D, Martinello T, Lioy A, Tarricone E, Gastaldello S, Betto R (2005) The T-tubule membrane ATP-operated P2X4 receptor influences contractility of skeletal muscle. FASEB J 19:1184–1186

Schalper KA, Palacios-Prado N, Orellana JA, Sáez JC (2008) Currently used methods for identification and characterization of hemichannels. Cell Commun Adhes 15:207–218

Schalper KA, Sánchez HA, Lee SC, Altenberg GA, Nathanson MH, Sáez JC (2010) Connexin 43 hemichannels mediate the Ca^{2+} influx induced by extracellular alkalinization. Am J Physiol Cell Physiol 299:C1504–C1515

Schalper KA, Riquelme MA, Brañes MC, Martínez AD, Vega JL, Berthoud VM, Bennett MV, Sáez JC (2012) Modulation of gap junction channels and hemichannels by growth factors. Mol Biosyst 8:685–698

Schmid A, Kazazoglou T, Renaud JF, Lazdunski M (1984) Comparative changes of levels of nitrendipine Ca^{2+} channels, of tetrodotoxin-sensitive Na^+ channels and of ouabain-sensitive ($Na^+ + K^+$)-ATPase following denervation of rat and chick skeletal muscle. FEBS Lett 172:114–118

Shea L, Raben N (2009) Autophagy in skeletal muscle: implications for Pompe disease. Int J Clin Pharmacol Ther 47(Suppl 1): S42–S47

Shimizu S, Kuriaki K (1960) Effect of denervation on the total metal content of skeletal muscle. Am J Physiol 198:943–944

Smith OL, Wong CY, Gelfand RA (1989) Skeletal muscle proteolysis in rats with acute streptozocin-induced diabetes. Diabetes 38: 1117–1122

Snow MH (1983) A quantitative ultrastructural analysis of satellite cells in denervated fast and slow muscles of the mouse. Anat Rec 207:593–604

Sobue G, Hashizume Y, Mukai E, Hirayama M, Mitsuma T, Takahashi A (1989) X-linked recessive bulbospinal neuronopathy. A clinicopathological study. Brain 112:209–232

Söhl G, Willecke K (2004) Gap junctions and the connexin protein family. Cardiovasc Res 62:228–232

Solan JL, Lampe PD (2009) Connexin43 phosphorylation: structural changes and biological effects. Biochem J 419:261–272

Sonobe T, Inagaki T, Poole DC, Kano Y (2008) Intracellular calcium accumulation following eccentric contractions in rat skeletal muscle in vivo: role of stretch-activated channels. Am J Physiol Regul Integr Comp Physiol 294:R1329–R1337

Sosinsky GE, Boassa D, Dermietzel R, Duffy HS, Laird DW, MacVicar B, Naus CC, Penuela S, Scemes E, Spray DC, Thompson RJ, Zhao HB, Dahl G (2011) Pannexin channels are not gap junction hemichannels. Channels 5:193–197

Steinberg TH, Civitelli R, Geist ST, Robertson AJ, Hick E, Veenstra RD, Wang HZ, Warlow PM, Westphale EM, Laing JG (1994) Connexin43 and connexin45 form gap junctions with different molecular permeabilities in osteoblastic cells. EMBO J 13:744–750

Thompson RJ, Zhou N, MacVicar BA (2006) Ischemia opens neuronal gap junction hemichannels. Science 312:924–927

Tisdale MJ (2008) Catabolic mediators of cancer cachexia. Curr Opin Support Palliat Care 2:256–261

Treem WR (2000) New developments in the pathophysiology, clinical spectrum, and diagnosis of disorders of fatty acid oxidation. Curr Opin Pediatr 12:463–468

Vanden Abeele F, Bidaux G, Gordienko D, Beck B, Panchin YV, Baranova AV, Ivanov DV, Skryma R, Prevarskaya N (2006) Functional implications of calcium permeability of the channel formed by pannexin 1. J Cell Biol 174:535–546

Vary TC, Kimball SR (1992) Sepsis-induced changes in protein synthesis: differential effects on fast- and slow-twitch muscles. Am J Physiol Cell Physiol 262:C1513–C1519

Ventadour S, Attaix D (2006) Mechanisms of skeletal muscle atrophy. Curr Opin Rheumatol 18:631–635

von Maltzahn J, Euwens C, Willecke K, Sohl G (2004) The novel mouse connexin39 gene is expressed in developing striated muscle fibers. J Cell Sci 117:5381–5392

von Maltzahn J, Wulf V, Willecke K (2006) Spatiotemporal expression of connexin 39 and -43 during myoblast differentiation in cultured cells and in the mouse embryo. Cell Commun Adhes 13:55–60

von Maltzahn J, Wulf V, Matern G, Willecke K (2011) Connexin39 deficient mice display accelerated myogenesis and regeneration of skeletal muscle. Exp Cell Res 317:1169–1178

Wang J, Ma M, Locovei S, Keane RW, Dahl G (2007) Modulation of membrane channel currents by gap junction protein mimetic peptides: size matters. Am J Physiol Cell Physiol 293:C1112–C1119

Wanke CA, Silva M, Knox TA, Forrester J, Speigelman D, Gorbach SL (2000) Weight loss and wasting remain common complications in individuals infected with human immunodeficiency virus in the era of highly active antiretroviral therapy. Clin Infect Dis 3:803–805

Weintraub H (1993) The MyoD family and myogenesis: redundancy, networks, and thresholds. Cell 75:1241–1244

Winlow W, Usherwood PN (1975) Ultrastructural studies of normal and degenerating mouse neuromuscular junctions. J Neurocytol 4:377–394

Zhang S, Fritz N, Ibarra C, Uhlén P (2011) Inositol 1,4,5-trisphosphate receptor subtype-specific regulation of calcium oscillations. Neurochem Res 36:1175–1185

Zhi G, Ryder JW, Huang J, Ding P, Chen Y, Zhao Y, Kamm KE, Stull JT (2005) Myosin light chain kinase and myosin phosphorylation effect frequency-dependent potentiation of skeletal muscle contraction. Proc Natl Acad Sci USA 102:17519–17524

Zhou X, Wang JL, Lu J, Song Y, Kwak KS, Jiao Q, Rosenfeld R, Chen Q, Boone T, Simonet WS, Lacey DL, Goldberg AL, Han HQ (2010) Reversal of cancer cachexia and muscle wasting by ActRIIB antagonism leads to prolonged survival. Cell 142: 531–543

J Membrane Biol (2012) 245:437–449
DOI 10.1007/s00232-012-9488-5

Manipulating Connexin Communication Channels: Use of Peptidomimetics and the Translational Outputs

W. Howard Evans · Geert Bultynck · Luc Leybaert

Received: 14 May 2012 / Accepted: 7 July 2012 / Published online: 11 August 2012

Abstract Gap junctions are key components underpinning multicellularity. They provide cell to cell channel pathways that enable direct intercellular communication and cellular coordination in tissues and organs. The channels are constructed of a family of connexin (Cx) membrane proteins. They oligomerize inside the cell, generating hemichannels (connexons) composed of six subunits arranged around a central channel. After transfer to the plasma membrane, arrays of Cx hemichannels (CxHcs) interact and couple with partners in neighboring attached cells to generate gap junctions. Cx channels have been studied using a range of technical approaches. Short peptides corresponding to sequences in the extra- and intracellular regions of Cxs were used first to generate epitope-specific antibodies that helped studies on the organization and functions of gap junctions. Subsequently, the peptides themselves, especially Gap26 and -27, mimetic peptides derived from each of the two extracellular loops of connexin43 (Cx43), a widely distributed Cx, have been extensively applied to block Cx channels and probe the biology of cell communication. The development of a further series of short peptides mimicking sequences in the intracellular loop, especially the extremity of the intracellular carboxyl tail of Cx43, followed. The primary inhibitory action of the peptidomimetics occurs at CxHcs located at unapposed regions of the cell's plasma membrane, followed by inhibition of cell coupling occurring across gap junctions. CxHcs respond to a range of environmental conditions by increasing their open probability. Peptidomimetics provide a way to block the actions of CxHcs with some selectivity. Furthermore, they are increasingly applied to address the pathological consequences of a range of environmental stresses that are thought to influence Cx channel operation. Cx peptidomimetics show promise as candidates in developing new therapeutic approaches for containing and reversing damage inflicted on CxHcs, especially in hypoxia and ischemia in the heart and in brain functions.

Keywords Connexin hemichannels · Peptidomimetics · Clinical translation

Dedicated to the memory of Tudor Griffith, 1951–2011.

W. H. Evans (✉)
Institute of Infection and Immunity, Cardiff University School of Medicine, Heath Park, Cardiff, Wales CF14 4XN, UK
e-mail: EvansWH@cf.ac.uk

G. Bultynck
Department of Cellular and Molecular Medicine, K. U. Leuven Campus Gasthuisberg, 3000 Leuven, Belgium

L. Leybaert
Department of Basic Medical Sciences, Physiology Group, Faculty of Medicine and Health Science, Ghent University, Ghent, Belgium

Introduction

Gap junctions are cell–cell connections that ensure harmonious integration, regulation and equalization of metabolic events and signaling in tissues and organs. Their role in the coordination of cell behavior is vividly illustrated in the heart, where gap junctions in the intercalated discs provide pathways that allow direct intercellular electrical communication essential for synchronous contraction of component myocytes and for generating waves of rhythmic contractions observed in arteries. Gap junctions are constructed of paired connexin hemichannels (CxHcs), each composed of six protein subunits arranged around a central pore, and occur at adhesive areas where plasma membranes

touch. Hcs are continuously recruited from surrounding unapposed plasma membrane areas and subsequently dock head to head with partners from adjacent cells and attach to the rims of preexisting gap junction plaques. The operational area and size of gap junction plaques where intercellular communication occurs are regulated by a balanced internalization and degradation of the dodecameric Cx channel units (Laird 2006; Goodenough and Paul 2009).

Many approaches have been applied to study the structure and function of gap junctions and their constituent CxHcs (Harris and Locke 2009). This account deals with the development of peptides that correspond to specific short Cx sequences that block widely the operation of gap junctions and CxHcs. The consequences ensuing from the actions of these peptides on Cx channels are allowing research to move forward into the realms of translational innovation across many fronts, especially in addressing the pathological consequences of ischemic stress that induces the channels to become leaky. Peptidomimetic approaches are complemented by gene knockout and antisense siRNA approaches to study Cx-based communication.

The development and application of short peptides mimicking sequences in various protein domains of Cxs, especially Cx43, initially focused on the two loops projecting outside the cell membrane; but peptides corresponding to sequences in the cytoplasmic intracellular loop and carboxyl tail are now finding application. Over the last 25 years, mimetic peptides have become important tools in elucidating a panoply of roles for gap junctions and their constituent CxHcs in a wide range of cells, tissues and organs. These are summarized in Tables 1, 2 and 3.

Development and Exploitation of Cx Mimetic Peptides

Following the deduction of the complete amino acid sequences especially of Cx32 and Cx43, two of the 20 members of the Cx family of proteins, a number of short mimetic peptides were chemically synthesized and coupled to immunogenic carriers to generate antibodies to target specific domains and epitopes. The two highly conserved extracellular loops of Cx have proven to be poorly immunogenic, and it has been difficult to generate antibodies to these domains. Nevertheless, antibodies to both extracellular loop domains have been used in studies of a wide range of functions underwritten by Cx channels. These include (1) the topographical arrangement of Cx proteins in the membrane (Zimmer et al. 1987), (2) the roles of gap junctions in the development of mouse embryos (Becker et al. 1995), (3) Ca^{2+} wave signaling across cell layers connected by gap junctions (Boitano et al. 1998), (4) subcellular assembly of gap junctions (Rahman et al. 1993), (5) coordination of Ca^{2+} transients in beating cardiac myocytes (Verma et al. 2009b), (6) Cx43 as a candidate component of the immunological synapse (Mendoza-Naranjo et al. 2011), (7) the functional importance of the two exposed extracellular loops (Goodenough et al. 1988), (8) CxHc organization in polarized cells (Clair et al. 2008) and (9) tracking conformational changes as Cx traffic from the Golgi apparatus to gap junctions (Sosinsky et al. 2007). Antibodies to peptides from intracellular regions have been used extensively as diagnostic immunological/analytical tools and are widely available from commercial sources.

Although reagents such as heptanol, octanol, oleamide, lithium ions, quinine derivatives, carbenoxolone, fenamates, anandamide, oleamide, triarylmethanes and glycyrrhetinic acid inhibited gap junctional communication (Herve and Dhein 2010; Juszczak and Swiergiel 2009; Bodendiek and Raman 2010), there remained a need for more specific reagents with a known mechanism of action. From early on, it became evident that Cx mimetic peptides used to generate the antibodies to gap junctions might prove useful as chemical tools to manipulate channel operation; it was argued that the utility of antibodies was restricted by their size and limited penetration across the cell membrane and into intercellular regions where gap junctions are located. Such drawbacks would be overcome by using small mimetic peptides that could penetrate into intercellular junctions, disrupt the docking and/or operation of hemichannels and, thus, target the gap junction (Fig. 1).

Two studies using model systems marked the beginning of the exploration of Cx mimetic peptides as tools to study gap junction functions. The first took advantage of the contractile behavior displayed by embryonic chick heart myoballs and known to require coordination provided by intercellular communication via gap junctions. The effects of a series of 15 Cx peptides, corresponding to short sequences mainly in intra- and extramembrane amino acid regions of the tetraspan membrane protein in delaying gap junction functions, were determined (Warner et al. 1995). A parallel study that used six dodecapeptide Cx mimetics to interrupt communication across gap junctions generated in *Xenopus* oocytes transfected with RNA to Cx32 (Dahl et al. 1994) likewise pointed to the potential of using short peptides to tamper with Cx-dependent intercellular communication. Warner et al. (1995) pinpointed motifs that included short sequence motifs, SRPTEK in extracellular loop 1 and SHVR in extracellular loop 2, as likely potent peptides for use in disrupting cell communication. These motifs were later incorporated into Gap26 and -27 mimetic peptides and their close homologues (see Tables 1, 2, 3). Kwak and Jongsma (1999) used dye coupling and dual patch-clamp approaches to study the inhibition of Cx channels using peptide mimetics from the second extracellular loop of Cx43 and Cx40. An extensive literature has

Table 1 Examples of the use of Gap26 and -27 mimetic peptides in studying the functions of gap junctions and connexin hemichannels in tissues/organs, cell layers and slices

Test model	Peptide	Effects	Reference
Arteries	Gap26/27	Block rhythmic contractions	Chaytor et al. (1997)
Mesenteric arteries	Gap27	Attenuates hyperpolarization	Dora et al. (1999)
Endothelium	Gap27	Attenuates Ach relaxations	Hutcheson et al. (1999)
Arteries	Gap26/27	Block EHF signaling	Chaytor et al. (2005)
Kidney	Gap27	Blocks renal vasodilatation	De Vriese et al. (2002)
Heart tissue	Gap26	Aids recovery after hypoxia	Hawat et al. (2010)
Heart lateral ventricle	Gap27[a]	Aids recovery after ischemia	Davidson et al. (2012)
Arteries	Gap27	Lowered intercell resistance	Matchkov et al. (2006)
Lung capillaries	Gap26/27	Inhibit Ca waves	Parthasarathi et al. (2006)
Trophoblasts/fibroblasts	Gap26/27	Block bilayer signaling and reduce DNA damage	Bhabra et al. (2009)
Various cell barriers	Gap27	Blocks signaling across barriers	Sood et al. (2011)
Brain endothelial and MDCK epithelial cells	Gap27	Inhibits Ca oscillations	De Bock et al. (2012)
Leukocytes	Gap27	Inhibits ATP release	Eltzschig et al. (2006)
Hippocampus	Gap27	Impairs learning, memory	Bissiere et al. (2011)
Hippocampus slices	Gap27	Inhibits epileptiform activity	Samoilova et al. (2008)
Rat amygdala	Gap27	Induces amnesia	Stehberg et al. (2012)
Spinal cord	Gap27[a]	Reduces swelling, reduces neuronal cell death	O'Carroll et al. (2008)
Optic nerve	Gap27	Attenuates CNS injury	Chew et al. (2010)
Hippocampus	Gap27[a]	Decreases cell death	Yoon et al. (2010)
Lung	Gap26	Reduces neutrophil transmigration	Sarieddine et al. (2009)
Various cells	Gap26	Blocks microtissue assembly	Bao et al. (2011)
Skin model systems	Gap27	Increased migration and proliferation	Pollok et al. (2011)

Gap26, VCYDKSFPISHVR; Gap27, SRPTEKTIFI

[a] Gap27 analogue. See Table 2 for sequence. A Gap27 acting on Cx40 channels (SRPTEKNVFIV) has been used on vascular tissues where this Cx is expressed

since built up around the study of Cx-dependent cell communication processes, especially with peptides mimicking sequences in Cx43 and, to a lesser extent, Cx40 and Cx37, which are widely expressed in the vascular system as well as with Cx32 (De Bock et al. 2011). Gap26 and -27 have emerged as mimetic peptide tools that have entered the literature in studies that explore the operation and function of Cx channels in several settings (Tables 1, 2). As discussed below, the blockage of direct cell coupling across gap junctions (Evans and Boitano 2001) is now likely to be a secondary event that follows initial interaction of the peptides with CxHcs. Recent work is increasingly focused on the translational and therapeutic possibilities offered by the action of the mimetic peptides, especially in averting or reversing tissue damage in ischemia and inflammation.

Gap Junctions and CxHcs

The view that CxHcs possess functions in their own right and are able to operate in different modes from gap junctions has now become generally accepted (Goodenough and Paul 2003; Bennett et al. 2003; Evans et al. 2006). CxHcs were detected in *Xenopus* oocytes (Ebihara and Steiner 1993), a test bed to study gap junction expression and function and where the channels were observed to open in low-Ca media. Hc opening was also detected in vertebrate retinal dendrites (Malchow et al. 1993). These early studies appeared against the background view that CxHcs sustained in open configuration in membranes would lead to potentially catastrophic cellular outcomes by allowing transmembrane escape from cells of small intracellular signaling molecules, e.g., ATP and glutamate, and would result in a collapse or dissipation of ionic gradients. The possible importance of CxHcs operating under normal physiological situations in cells and tissues was critically evaluated (Spray et al. 2006). Collateral evidence for the functional reality of CxHcs began to appear later for roles in pathology with, e.g., the demonstration that leaky mutated CxHcs in the ear were linked to deafness (Stong et al. 2006; Scott and Kelsell 2011) and a mutation in the intracellular loop of Cx43 that decreased single-channel conductance and is linked to neurological disturbances in oculodentodigital dysplasia (Lai et al. 2006). Reconstituted Hcs were used to

Table 2 Examples of use of Gap 26 and 27 mimetic peptides on various cells in culture

Test model/cells	Peptide	Effect	References
Skin fibroblasts, keratinocytes	Gap27	Increases migration in diabetes	Wright et al. (2012a, b)
HeLa Cx43 GFP	Gap26/27	Inhibit dye transfer	Berman et al. (2002)
Lymphocytes	Gap26/27	Inhibit transendothelial migration	Oviedo-Orta et al. (2002)
T/dendritic cells	Gap27	Cell sensitization abrogated	Ring et al. (2010)
Mesenteric smooth muscle	Gap27	Attenuates hyperpolerization	Dora et al. (1999)
Alveolar epithelial	Gap27	Inhibits Ca signaling	Boitano and Evans (2000)
Alveolar epithelial	Gap26/27	Inhibit dye transfer	Isakson et al. (2003)
Neonatal myocytes	Gap26	Inhibits ATP release in ischemia	Clarke et al. (2009)
HeLa/cardiac cells	Gap26/27	Inhibit Ca uptake and Ca waves	Verma et al. (2009b)
$CD4^+$ T lymphocytes	Gap27	Inhibits T-cell proliferation	Oviedo-Orta et al. (2010)
B and T lymphocytes	Gap26/27	Decrease antibody production	Oviedo-Orta et al. (2010)
Corneal	Gap26	ATP release and Ca waves blocked	Gomes et al. (2005)
Ganglia	Gap27[a]	Limits retinal ganglion injury	Danesh-Meyer et al. (2012)
Neural retinal	Gap26	Limits ATP release and development	Pearson et al. (2005)
Astrocytes	Gap27	Abolished NMDA excitotoxicity	Froger et al. (2010)
Astrocytes	Gap26	Blocks glutamate release	Jiang et al. (2011)
Astroglia	Gap26/27	Block glutamate release	Orellana et al. (2011)
Glioma	Gap26/27	Delay apoptosis, cell death	Decrock et al. (2009a, b)
Astroglia	Gap26	Influences neural inflammation	Karpuk et al. (2011)
Glia	Gap26/27	Inhibit ATP release	De Vuyst et al. (2009)
Astroglia	Gap26	Inhibits ATP release and activation of P2Y receptors	Orellana et al. (2012a)
Astrocytes	Gap26/27	Induce anhedonia, depression	Sun et al. (2012)
Blood–brain barrier endothelium	Gap27	Inhibits ATP release and permeability of endothelium	De Bock et al. (2011)
AT11	Gap27	Inhibits Ca waves	Isakson et al. (2001)
Endothelium	Gap26	Inhibits ATP release	Robertson et al. (2010)
Bladder cancer	Gap26/27	Inhibit ATP release	De Vuyst et al. (2006)
T lymphocytes	1,848[b]	Blocks GJ docking	Mendoza-Naranjo et al. (2011)
Cardiomyocytes	Gap26	Blocks CxHc in cardiac hypoxia	Shintani-Ishida et al. (2007)
Platelets	Gap27	Blocks Cx 43/37 channels	Vaiyapuri et al. (2012)
Bone marrow stem cells	Gap27	Confirms Cx channels absent	Yang et al. (2009)

[a] VDCFLSRPTEKT peptide 5 derived from extracellular loop 2 of CxHc43

[b] Sequence of the Cx mimetic peptide not disclosed

investigate the influence of Ca and atomic force microscopy, to study Hc pore opening (Thimm et al. 2005). It is now generally accepted that CxHcs open under environmental circumstances considered to be stressful to cells such as volume or osmotic changes; oxidative, metabolic and mechanical stresses; and especially hypoxia/ischemia.

If not contained, leaky CxHcs can lead to apoptosis and cell death (Saez et al. 2010; Decrock et al. 2009a, b). Binding of mimetic peptides such as extracellular loop peptides Gap26 and -27 to the extracellular face inhibited functions associated with CxHcs; these are also regulated by membrane depolarization, phosphorylation of several sites on the carboxyl tail of Cx43 (Solan and Lampe 2009), S-nitrosylation (Retamal et al. 2006) and SUMOylation of lysine residues in the intracellular loop (Kjenseth et al. 2012). The particle–receptor hypothesis (see below) explained the mechanics of gating in those Cxs with extended cytoplasmic tails such as Cx43, Cx40 and Cx45 (Delmar et al. 2004). Recent evidence suggests that mimetic peptide perturbation of intracellular domains, especially the interactive cytoplasmic loop (CL) and the carboxyl tail (CT), also influences Hc functions (Ponsaerts et al. 2010). CxHc gating is also conditioned by signaling cascades operating in subplasmalemmal environs (Fig. 2).

Besides structural differences, with Hcs being asymmetrical and gap junctions being symmetrical double channels, there are other important differences between the functions of these weakly selective channels. CxHcs stand out in being responsive to environmental changes and contingencies. Gap junction channels allow the cytoplasms of cells to be linked directly, whereas open CxHcs provide channels connecting the cell's external environment with

Table 3 Effects of various intracellular Cx mimetic and other short and mainly Cx43 peptides on gap junctions and hemichannels

Test model	Peptide	Effect	Reference
Brain synapses	Carboxyl tail	Prevents Cx36/GJ formation	Flores et al. (2012)
Bladder cancer	Gap24[a]	Inhibits ATP release	De Vuyst et al. (2006)
Mouse hearts	Carboxyl tail[b]	Increases Cx43 and ps368 phosphorylation and induces arrhythmia	O'Quinn et al. (2011)
Heart	Carboxyl tail	May open gap junctions	Lewandowski et al. (2008)
Heart	R, any amino acid	May open gap junctions	Verma et al. (2009b)
Cardiac mitochondria	Gap27	Inhibits Cx43	Rottlaender et al. (2012)
T lymphocytes	Gap20[c]	Ineffective on gap junctions	Mendoza-Naranjo et al. (2011)
Endothelium- denuded arteries	Gap20[c]	Ineffective on gap junctions	Chaytor et al. (1997)
C6 glioma cells	L2 segment nonapeptide	Blocks CxHc but not gap junctions	Wang et al. (unpublished)
Corneal endothelial and C6 glioma cells	TAT-L2	Blocks CxHc but not gap junctions	Ponsaerts et al. (2010)
Basolateral amygdala	Cx43-L2 TAT	Blocks gliotransmitter release	Stehberg et al. (2012)
MDCK	CT9 peptide[b] Carboxyl tail	Blocks Ca oscillations by removing high Ca closure	De Bock et al. (2012)

[a] Gap24: a Cx32 Gap20 homologue GHGDPLHLEEVK (from intracellular loop)

[b] Peptide RPRPDDLEI

[c] Gap20 EIKKFKYG

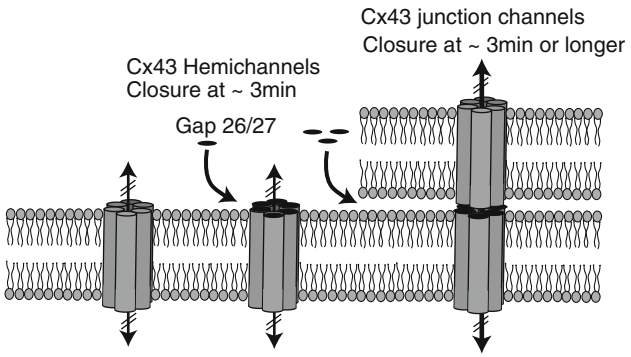

Fig. 1 Mechanism of action of Gap26 and -27 mimetic peptides. Peptides bind to extracellular loop regions one and two, respectively, of CxHc, causing closure of channels within minutes. At later time intervals (30 min or longer) and depending on factors such as cell confluency, tissue, organ, tissue slice origin and thickness and conditions of perfusion of various organs, peptides permeate into intercellular spaces in gap junctions, causing disruption and diminished cell coupling. CxHcs with attached peptide move laterally toward the rims of gap junction plaques as they assemble and are then internalized

the cytoplasmic mileu beneath the plasma membrane. In a cell-signaling context, changes in CxHc open probability provide a mechanism for paracrine intercellular communication by allowing small molecules such as ATP and K to exit and Ca to enter cells. ATP release underwrites purinergic intercellular signaling (Isakson et al. 2001; Paemeleire et al. 2000; Kang et al. 2008), a function shared with pannexin channels.

Gap junction channels exist normally in open mode, and an elevation in intracellular Ca^{2+} leads to closure (generally 500–2,000 nM). In contrast, CxHcs open at 500 nM (De Vuyst et al. 2006, 2009, 2011). Differences in Ca sensitivity of the two channel types may relate to their complementary roles in regulating intracellular Ca oscillations and the intercellular propagation of Ca waves (Verma et al. 2009a; Orellana et al. 2012b; De Bock et al. 2012). The various intracellular processes that influence the gating of Cx43Hcs are shown in Fig. 2b. Gap junctions and CxHcs respond differently to lipopolysaccharide and basic fibroblast growth factor, a consequence of their involvement in releasing ATP (De Vuyst et al. 2007); their channel functions also respond differently to many growth factors (Schalper et al. 2012).

Widespread Use of Gap26 and Gap27 Mimetic Peptides

Cx43 is by far the most widely distributed Cx in tissues and organs. It is therefore not surprising that Gap26 and -27, derived from Cx43 sequences, have found extensive use. A modified Gap27 peptide (Table 1) incorporating a sequence mimicking that in Cx40 has also proven useful in vascular tissues and other tissues where both Cxs are present (Chaytor et al. 1999; Wright et al. 2009). Early studies showed that inhibition by mimetic peptides was largely reversible as assessed by intercellular transfer of small fluorescent "reporter" dyes of varying size and by

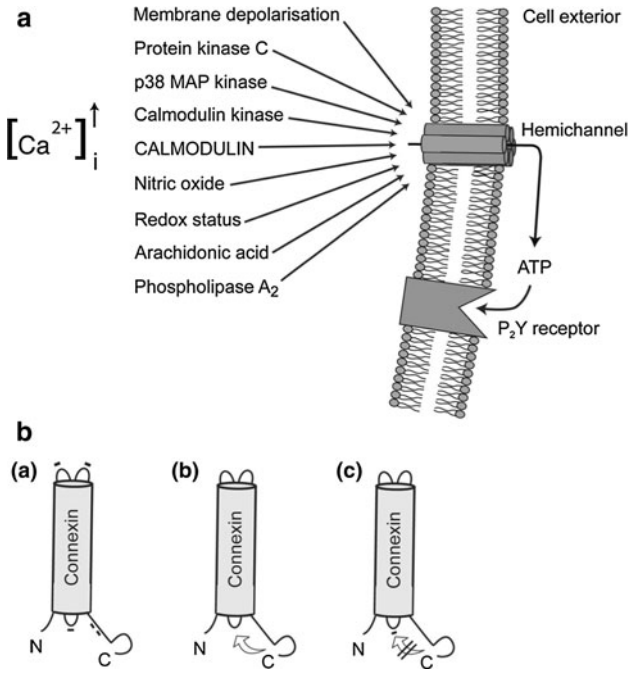

Fig. 2 **a** Several intracellular signals and events influence CxHc functions. Membrane depolarization above +30 V opens Hc. Several kinases may also be involved; PKC closes Hc, while p38MAPK and calmodulin kinases result in Hc opening. The cytoplasmic Ca concentration ($[Ca^{2+}]_i$) is also an important modulator; below 500 nM $[Ca^{+}]$ calmodulin is a key Ca binding protein and specific binding sites are present on Cx. An increase in intracellular Ca causes Hc opening, while Hc activation is lost at higher concentrations. Arachidonic acid stimulates Hc opening, and amino acid metabolites generated by PLA_2 activation may contribute to this. Nitric oxide and oxidative stress also result in opening of Hc. Figure modified from De Vuyst et al. (2009). **b** *a* Sites on the exposed extramembrane regions of Cx43 where the mimetic peptide sequences originated. *b* Proposed intramolecular mechanism of CxHc gating involving interaction of the carboxyl tail with the intracellular loop. *c* Binding of a nonapeptide mimetic derived from L2, the Cx43 intracellular loop region to a site on the carboxyl terminus regulates the closure of CxHc and leads to blockage of the channel

measuring the extent of Ca wave propagation over multiple rows of cells (Boitano and Evans 2000).

As the operational presence of CxHcs became evident, inhibition by mimetic peptides of ATP release in a wide range of tissues and cells (Tables 1, 2), of glutamate in astrocytes (Yang et al. 2009) and astrocytes/microglia (Orellana et al. 2011) and of ion trafficking, especially Ca^{2+} entry, were observed. Uptake of reporter dyes across CxHcs became a reliable and routine method to demonstrate open or leaky CxHcs (Li et al. 1996). A range of other effects were also noted on prolonged exposure (20 min or longer) to the mimetic peptides such as smooth muscle contraction in endothelium-denuded arteries (Chaytor et al. 1997; Hutcheson et al. 1999) and immunoglobulin production by lymphocytes (Oviedo-Orta et al. 2001). Subsequently, as the presence of CxHcs widened, it became increasingly clear that the primary action of Gap26 and -27 is in fact directed at CxHcs. Nevertheless, a combination of direct signaling across gap junctions and paracrine signaling acting through metabotropic purinergic receptors following release of ATP (Fig. 2) provides scope for complementary intercellular interplay involving both routes in several settings (Anselmi et al. 2008; Cotrina et al. 1998).

Initial experiments showing inhibition by mimetic peptides of CxHcs were carried out mainly using cultured cells (Table 2), followed by numerous examples in various tissues and organs, cell layers and thin tissue slices (Table 1). The growing attribution of nonjunctional properties to CxHcs (Cotrina et al. 2008; Kameritsch et al. 2011) has led to studies that attempt to unravel the potential functions in the realms of adhesion and cell movement. Enhancement of migration of dermal fibroblasts after treatment with Gap27 pointed to nonjunctional roles for CxHcs in cell movement and extending, e.g., to assessing their potential translational application in addressing their efficacy in accelerating wound healing in diabetes and in a range of micro-/macrovascular diseases (Wright et al. 2009, 2012a; Pollok et al. 2011). Gap27 increased migration of human keratinocytes and dermal fibroblasts, and the efficacy of the mimetic peptide was different in euglycemia and hyperglycemia (Wright et al. 2012b). Gene array approaches indicated that Gap27 induced upregulation of genes involved in extracellular matrix remodeling and cell adhesion. Exposure of cells to Gap27 may have effects on Cx43 phosphorylation, especially of serine 368; phosphorylation of this amino acid decreases Cx43 channel activity (Solan and Lampe 2009) and is a key process in the gating of Cx43 channels. Many of the effects of the mimetic peptides were seen after long-term exposures. Cx43 has been detected in the inner mitochondrial membrane of heart cells and has been implicated in cardiac preconditioning (Boengler et al. 2009; Rottlaender et al. 2012). The opening of mitochondrial CxHc influences K^{+} fluxes in processes that are linked to cardioprotection. The functions of Cx43Hc at this location are open to study using mimetic peptides developed to Cx43 cytoplasmic sequences (Verma et al. 2009a).

Mechanism of Action of Cx Mimetics

To further develop and refine the actions of Cx mimetics, it is important to gain insight into the mechanisms by which they block Cx channels. A major advance was the demonstration that the primary action of Gap26 and -27 was likely to be on CxHcs prior to blockage of gap junctions. With the acceptance that CxHcs and gap junctions were targets but in different time frames, the effects of the peptides on both were examined using electrophysiological approaches. These had already proven useful in studying

electrical coupling across gap junctions in cell pairs and the electrical properties of CxHcs (Harris 2001; Contreras et al. 2003; Saez et al. 2005). Using a voltage-clamp approach in nonconfluent and confluent HeLa cells expressing Cx43, Gap26 inhibited macroscopic currents through CxHcs in 2–3 min. In contrast, electrical coupling in cell pairs was delayed and completely inhibited after 30 min or more (Desplantez et al. 2012), indicating direct action of Gap26 on an exposed extracellular loop, as previously suggested by studies of CxHcs inserted into lipid bilayers (Liu et al. 2006). The extended time course of action on gap junctional electrical coupling suggests that longer diffusion pathways into plasma membrane junctional domains lead ultimately to blockage of gap junctional coupling (Fig. 1). The changes in conductance and voltage gating of CxHcs by Gap26 suggested interaction of the peptide at a consensus sequence in the first extracellular loop that may contribute to the inner wall of the pore (Sosinsky and Nicholson 2005), resulting in a decrease in channel diameter in the extracellular vestibule. Desplantez et al. (2012) also proposed that, of the two voltage gates controlling Hc, the slow gate is the more likely to be influenced by the binding of Gap26.

An expanded complementary study by Wang et al. (unpublished) examined the mechanism of action of Gap26 and -27 in HeLa cells stably transfected with Cx43 and in pig ventricular myocytes endogenously expressing Cx43 using a voltage-clamp approach. Both mimetic peptides inhibited Cx43Hc unitary currents within minutes. An important outcome of this study with cardiac translational implications was that unitary current activity was promoted by a moderate elevation of cytoplasmic Ca, an event observed in cardiac arrhythmogenesis.

Gap26 and -27 have been used mainly to inhibit Cx43 channels, but actions on other Cx channels have also been studied. For example, Wright et al. (2009) carried out an extensive study of the effects of Gap26 and -27 on dye coupling in cells expressing several human Cxs and found that Gap27 had broader Cx specificity than Gap26. In some situations where multiple Cxs are expressed, as in skin, broad specificity can be an advantage.

The precise protein domains to which Gap26 and -27 mimetic peptides attach and any conformational changes induced in Cx channels remain to be determined. Fluorescently labeled Gap26 and -27 are poorly soluble; but evidence points to attachment and retention at cell exteriors, and problems of image resolution could not answer the issue of whether attachment of a mimetic peptide ligand to a "channel receptor" sequence can lead to peptide internalization (Evans, unpublished work). Voltage-clamp approaches have been useful in deciphering the inhibitory action of these peptides on Cx channels and go a long way toward resolving questions concerning the specificity of mimetic peptide inhibitory effects. Cx mimetics have been claimed as effective inhibitors due to steric pore block (Wang et al. 2007). Steric block may indeed occur, but recent data indicate that it only occurs when peptides are used in the range of 1 mM and above (Wang et al. unpublished). The examples shown in Tables 1 and 2 used mainly protein concentrations of 100–250 μM. In the vast majority of these studies, investigators have used scrambled peptides or short peptides derived from regions believed not to be directly involved in channel operation (often internal sequences) as controls and, in each instance, they pointed to a high sequence dependence of mimetic peptide action in blocking gap junctional coupling and, more recently, ATP release or dye entry across CxHcs.

Pannexins, of which three are identified compared to around 22 in the Cx family of proteins, also form oligomeric channels with a similar tetraspan topographical arrangement in the membrane to CxHcs. However, these two protein families share no amino acid homology. Pannexins, unlike Cxs, are posttranslationally glycosylated (D'Hondt et al. 2009; Scemes et al. 2009) and are disinclined to dock with partner pannexins on neighboring cells. It follows that they are not expected to generate gap junction-like structures and, indeed, are found at higher levels inside cells (D'Hondt et al. 2011). In contrast, a recent report claims that they can form gap junctions and act as Ca leak channels in the endoplasmic reticulum (Ishikawa et al. 2011). Pannexins are relatively unaffected by changes in cytoplasmic Ca^{2+} levels and, unlike Cx, are calmodulin-insensitive. Pannexins are especially abundant in neural tissues. The action of Gap26 and -27 on pannexin channel currents has not yet been rigorously tested. It is worth noting that high sequence diversity occurs in the intracellular loop of Cx proteins; the carboxyl tail of larger Cx proteins also varies in length, sequence and the extent of posttranslational modification.

Small peptides generally have little structural organization but may assume some on binding to a target that then becomes subject to conformational change. Studies of the interaction of calmodulin with mimetic peptides from the intracellular loop of Cx43 demonstrate a way forward toward functionally dissecting this key region of Cxs (Myllykoski et al. 2009). A calmodulin binding region in Cx43 was located to amino acid residues 136–158 (Zhou et al. 2007). Clearly, further knowledge of the structural organization of Cx43Hc is awaited along the lines available on CxHc26 (Maeda et al. 2009; Oshima et al. 2011).

Table 3 lists the growing number of mimetic peptides derived from the CL and CT that act on CxHcs and gap junctions. Many of these peptides are not able to cross the plasma membrane. To gain access to their sites of action, many of these mimetics need to be attached first to "Trojan" cell-penetrating peptides that contain a

membrane-translocation motif (Jarver and Langel 2006). Intracellular loop mimetic peptides with a positive charge due to several lysine residues stand out as candidates, for they can, depending on length, gain access to intracellular targets without need for attachment of a membrane-penetrating peptide or by microinjection, as discussed below. Indeed, peptides of around 1 kDa or less may be able to access the cytoplasm via open CxHcs.

Mimetics and Other Cx Peptides as Agents to Address Pathology

In a cardiac context, blockage by Gap26 and -27 of gap junctional coupling between myocytes negated their candidacy for use, especially in therapeutic approaches to address cardiac arrhythmia, for the outcomes of peptide treatment were likely to compound the pathology. Consequently, studies in heart focused on nonmimetic hexapeptides shown to be prorhythmic, especially ZP123 derived from AAp10 and later renamed rotigaptide (Hagen et al. 2009; Herve and Dhein 2010). This hexapeptide promoted changes to Cx phosphorylation, increased gap junctional coupling (Clarke et al. 2006) and showed promise in animal models, where it prevented ventricular tachycardia in myocardial ischemia (Xing et al. 2003). However, following inconclusive clinical trials, rotigaptide was not developed further. Cellular studies showed that despite its prorhythmic action on gap junctions, ZP123 also led to the opening of CxHcs, causing ATP release. In a cardiac myocyte ischemia model, Gap26 blocked the release of ATP, whereas ZP123 enhanced its release across Cx43Hc (Clarke et al. 2009). Other antiarrhythmic peptides—such as Gap134, a prorhythmic dipeptide—were also developed (Hennan et al. 2009).

In the meantime, encouraging outcomes in addressing ischemic cardiomyopathy using Gap26 have appeared. These results can be explained by the direct action of this mimetic peptide on CxHc rendered open under hypoxic/ischemic conditions. Hawat et al. (2010) showed that following myocardial ischemic insult, Gap26 helped to confer protection through its binding to and blockage of Cx43Hc. Similar protection from hypoxic stress by these peptides has also been reported. Vascular leak and retinal ganglion cell death were reduced by application of a close homologue of Gap27 in an atrial ischemia model where Cx43Hc expression was increased (Danesh-Meyer et al. 2012). The same group also reported that infusion of Gap27 in a large animal model with cerebral injury delayed the onset of ischemic injury and suggested that Gap27 homologue peptides reduced inflammation. For example, mimetic peptide treatment reduced the spread of damage after traumatic spinal cord injury where Cx43Hc plays a critical role (O'Carroll et al. 2008; Huang et al. 2012). Such studies combine to show that Gap26 and -27 mimetic peptides acting on CxHc-related functions, especially in situations of tissue injury, show therapeutic potential. In brain, inhibition of inflammation-induced activation of Cx43Hc in astroglial cells was attenuated by treatment with Gap26 and -27, suggesting that the channels play a critical role in instigating neuronal death and pointing to a neuroprotective role for these mimetic peptides (Froger et al. 2010). Interaction of the mimetic peptides with CxHcs is also likely to modify intracellular signaling cascades in subplasma membrane environments (Fig. 2a).

The action of Gap26 and -27 on CxHcs and later at gap junctions encouraged the view that pathological outcomes could be fine-tuned if mimetic peptides were to become available that confined their blocking action on CxHcs resident in the plasma membrane. Attention had already focused on the intracellular loop region implicated in explaining gap junction gating in cardiac cells and involving intramolecular interaction of the carboxyl tail region with the intracellular loop L2 region (a region in Cx43 incorporating amino acids 119–144) and described as the particle–receptor hypothesis (Delmar et al. 2004). The role of the L2 domain as a key molecular determinant of Cx43 function originated from the acidification-related closure of gap junctions (Delmar et al. 2004), and the particle-receptor hypothesis has been proposed to explain Cx43 closure during acidification, with the CT moving as a flexible gating particle that binds to the L2 site at the intracellular vestibule and leading to closure of the gap junction pore. Because of the similarity to the inactivation of K^+ channels, this mechanism has also been called the ball and chain model of gap junction closure. A 34-amino acid nonmimetic peptide (RXP-E) and its derivatives were developed to target the Cx43CT (Shibayama et al. 2006; Lewandowski et al. 2008; Verma et al. 2009a). When coupled to cell-penetrating peptides, these composite peptides successfully restored gap junctional coupling and impulse propagation in cultured neonatal rat ventricular cardiomyocytes. Although the ability of L2 peptide to bind to the Cx43CT region has been intensively studied, less is known about how it is influenced by pH.

Loop–tail interactions also control Cx43Hc opening (Ponsaerts et al. 2010). The interaction of a cytoplasmic loop domain with the C-terminal region is an important requisite for the opening of Cx43Hc in response to stimuli such as lowering of extracellular Ca^{2+} or increasing intracellular Ca^{2+}. In contrast, Cx43 gap junctions behave in the opposite manner and are closed by intramolecular loop–tail interactions (Delmar et al. 2004; Hirst-Jensen et al. 2007). Interfering with loop–tail interactions can inhibit the operation of Cx43Hc. One way to suppress CxHc operation in response to high intracellular Ca^{2+} is to

activate the actomyosin contractile system, a process that appears to physically dislodge the CT from the CL region (Ponsaerts et al. 2012). Importantly, the selective myosin11-ATPase inhibitor blebbistatin restores Cx43Hc activity when cells are exposed to high intracellular Ca (Ponsaerts et al. 2012). The proteins involved in this mechanism linking Cx43Hc and the actomyosin contractile system have not been identified, but a likely target is the CT region of Cx43Hc, for Cx43 lacking the CT is inactive. Even in the absence of a functional actomyosin cytoskeleton, loop–tail interactions in Cx43Hc can be disrupted using mimetic peptides from the L2 region, and coupling the peptides to a TAT cell-penetrating sequence inhibits CxHc opening. An important interactive target of L2-region peptides is the last 10 amino acids of the carboxyl tail (CT10). Direct binding between the L2 domain and CT10 has been demonstrated by surface plasmon resonance. Thus, TAT-L2 allows exploitation of the opposite regulation of gap junctions and Cx43Hc and can provide a route to selectively inhibit Cx43Hc while maintaining gap junctional communication. The importance of the 10–amino acid terminal carboxyl domain has been studied in detail also using electrophysiological approaches in *Xenopus* oocytes where the TAT-L2 and TAT-CT10 peptide constructs have been crucial in analyzing and deciphering intramolecular loop–tail interactions (Ponsaerts et al. 2010, 2012). These studies illustrate how mimetic peptide approaches for selectively studying the physiological functions of Cx43Hc can complement knockdown/knockout approaches in, e.g., processes leading to cell death (Decrock et al. 2011) and in brain functions in the basolateral amygdala, where Cx mimetic peptides such as Gap27 demonstrate that Cx43Hc activities are implicated in amnesia (Stehberg et al. 2012).

A short nonmimetic peptide (designated RXP-E) that bound to the carboxyl tail of Cx43, derived from heart lysates and studied in animal and cellular models, prevented action potential block in the heart (Lewandowski et al. 2008). A series of nonmimetic peptides with a motif designated RXP and containing a predominance of basic amino acid increased the mean open time of gap junction channels; these peptides were proposed as potential functional regulators in ischemia-induced arrhythmias (Shibayama et al. 2006; Verma et al. 2009a).

Currently, the application of novel short peptides mimicking sequences in the L2 region of Cx43 (Delmar et al. 2004) where a putative calmodulin binding site is identified (Zhou et al. 2007) proceeds. One major aim is to design mimetic peptides that confine their blocking actions to CxHcs with no interference on gap junction functionality, thus avoiding pro-arrhythmic consequences and allowing the bound mimetic peptide to arrest, e.g., the loss of vital cell metabolites via CxHcs in cardiomyocytes subject to hypoxia or ischemia perfusion injury. A potential tool for more selective inhibition of Hcs without associated inhibition of gap junctions is a synthetic mimetic peptide corresponding to the L2 region that, when delivered into the cell by a whole-cell recording pipette, prevented gap junctional opening to the subconductance state at high transjunctional voltage and increased the channel open time (Ponsaerts et al. 2010). Also, L2 peptide linked to the TAT membrane translocation motif (TAT-L2) inhibited Cx43Hc activation, further suggesting that prevention of interaction of CT and CT suppresses Hc opening. Consequently, the particle–receptor hypothesis described above has an opposite outcome for Hcs compared to gap junctions. This raises questions concerning why this is so, for the composite proteins of the channels are identical but the Ca sensitivity of the Cx43Hc and gap junctions differs. It now appears that intracellular interactive partners may also be different at the cytoplasmic aspects of junctional and nonjunctional regions of the plasma membrane. One possible reason for these differences is that Hcs interact with the actomyosin contractile system, causing dynamic loop–tail interactions that control Hcs that differ from those occurring at gap junctions (Ponsaerts et al. 2012).

New mimetic peptides derived from the carboxyl tail of Cx43 are also being assessed. Here, peptide mimetic design has to deal with a region where the CT interacts with cytoskeletal elements (Herve et al. 2011; Palatinus et al. 2011). This region also incorporates several phosphorylation sites that condition channel gating (Solan and Lampe 2009). In the heart, the cytoskeletal adaptor protein ankyrin-G interacts with Cx43 and is a likely key intercalated disc complex in the pathophysiology of arrhythmias (Sato et al. 2011). A short Cx43-CT peptide incorporating the last nine amino acids and linked to a cell permeabilization sequence inhibited pathological changes at gap junctions that are related to ventricular arrhythmias (O'Quinn et al. 2011). This peptide disrupted the interaction between the PDZ domain of ZO1 and Cx43, thus accelerating assembly of gap junctions from a precursor pool of Hcs (Hunter et al. 2005; Rhett and Gourdie 2012). The peptide also enhanced PKC-epsilon-associated phosphorylation at the Cx43-S368 site, an effect that is activated in ischemic preconditioning and can reduce cardiac injury (Ek-Vitorin and Burt 2012; Srisakuldee et al. 2009). A similar peptide with the same sequence named CT9 prevented high Ca–induced closure of Cx43Hc (De Bock et al. 2012; Ponsaerts et al. 2012). In the same vein, a 15–amino acid mimetic peptide derived from a sequence in the CT of Cx36 modified gap junction conductance in goldfish electrical synapses, and this peptide was injected intradendritically (Flores et al. 2012).

Concluding Comments

Peptides that mimic short sequences in extramembrane domains of Cx proteins show huge potential in addressing Cx-based communicationopathies by pharmacological means. The functions attributed to Cx, especially Cx43, continue to expand and include not only roles in intercellular cell communication effected by CxHc and gap junctions but also cell adhesion, cell migration and mitochondrial inner membrane channel functions. It is likely that the range of Cx mimetics and their applications will increase, for they provide activation mechanisms for manipulation of intercellular signaling and communication. Furthermore, the peptides can also help cells protect themselves from events emanating from leaky channels, events that may ultimately lead to apoptosis. Intriguingly, in the brain the Gap26 and -27 mimetic peptides that act mainly on astrocyte Cx channels have been shown to affect depression (anhedonia), epileptiform activity, memory consolidation and amnesia, further emphasizing the importance of Cx-mediated communication and signaling in a wide range of settings.

Acknowledgements We thank Nan Wang for critically reading and commenting on the manuscript. Funding for L. L. was from the Fund for Scientific Research, Flanders (G.0140.08, 3G0134.09, G.0298.11N and 3G.057112N), and Belgian Science Policy projects P6/31 and P7. G. B. was supported by the Fund for Scientific Research, Flanders (G.0298.11N) and Belgian Science Policy projects P6/28 and P7. W. H. E. received support from the British Heart Foundation (PG/01/1298 and PG/05/051).

References

Anselmi F, Hernandez VH et al (2008) ATP release through connexin hemichannels and gap junction transfer of second messengers propagate Ca^{2+} signals across the inner ear. Proc Natl Acad Sci USA 105(48):18770–18775

Bao B, Jiang J et al (2011) Connexon-mediated cell adhesion drives microtissue self-assembly. FASEB J 25(1):255–264

Becker DL, Evans WH et al (1995) Functional analysis of amino acid sequences in connexin43 involved in intercellular communication through gap junctions. J Cell Sci 108(Pt 4):1455–1467

Bennett MV, Contreras JE et al (2003) New roles for astrocytes: gap junction hemichannels have something to communicate. Trends Neurosci 26(11):610–617

Berman RS, Martin PE et al (2002) Relative contributions of NO and gap junctional communication to endothelium-dependent relaxations of rabbit resistance arteries vary with vessel size. Microvasc Res 63(1):115–128

Bhabra G, Sood A et al (2009) Nanoparticles can cause DNA damage across a cellular barrier. Nature Nanotechnol 4(12):876–883

Bissiere S, Zelikowsky M et al (2011) Electrical synapses control hippocampal contributions to fear learning and memory. Science 331(6013):87–91

Bodendiek SB, Raman G (2010) Connexin modulators and their potential targets under the magnifying glass. Curr Med Chem 17(34):4191–4230

Boengler K, Stahlhofen S et al (2009) Presence of connexin43 in subsarcolemmal, but not in interfibrillar cardiomyocyte mitochondria. Basic Res Cardiol 104(2):141–147

Boitano S, Evans WH (2000) Connexin mimetic peptides reversibly inhibit Ca^{2+} signaling through gap junctions in airway cells. Am J Physiol Lung Cell Mol Physiol 279(4):L623–L630

Boitano S, Dirksen ER et al (1998) Sequence-specific antibodies to connexins block intercellular calcium signaling through gap junctions. Cell Calcium 23(1):1–9

Chaytor AT, Evans WH et al (1997) Peptides homologous to extracellular loop motifs of connexin43 reversibly abolish rhythmic contractile activity in rabbit arteries. J Physiol 503(Pt 1): 99–110

Chaytor AT, Martin PE et al (1999) The endothelial component of cannabinoid-induced relaxation in rabbit mesenteric artery depends on gap junctional communication. J Physiol 520(Pt 2): 539–550

Chaytor AT, Bakker LM et al (2005) Connexin-mimetic peptides dissociate electrotonic EDHF-type signalling via myoendothelial and smooth muscle gap junctions in the rabbit iliac artery. Br J Pharmacol 144(1):108–114

Chew SS, Johnson CS et al (2010) Role of connexin43 in central nervous system injury. Exp Neurol 225(2):250–261

Clair C, Combettes L et al (2008) Extracellular-loop peptide antibodies reveal a predominant hemichannel organization of connexins in polarized intestinal cells. Exp Cell Res 314(6): 1250–1265

Clarke TC, Thomas D et al (2006) The antiarrhythmic peptide rotigaptide (ZP123) increases gap junction intercellular communication in cardiac myocytes and HeLa cells expressing connexin43. Br J Pharmacol 147(5):486–495

Clarke TC, Williams OJ et al (2009) ATP release by cardiac myocytes in a simulated ischaemia model: inhibition by a connexin mimetic and enhancement by an antiarrhythmic peptide. Eur J Pharmacol 605(1–3):9–14

Contreras JE, Saez JC et al (2003) Gating and regulation of connexin43 (Cx43) hemichannels. Proc Natl Acad Sci USA 100(20):11388–11393

Cotrina ML, Lin JH et al (1998) Connexins regulate calcium signaling by controlling ATP release. Proc Natl Acad Sci USA 95(26): 1574–15735

Cotrina ML, Lin JH et al (2008) Adhesive properties of connexin hemichannels. Glia 56(16):1791–1798

Dahl G, Nonner W et al (1994) Attempts to define functional domains of gap junction proteins with synthetic peptides. Biophys J 67(5): 1816–1822

Danesh-Meyer HV, Kerr NM et al (2012) Connexin43 mimetic peptide reduces vascular leak and retinal ganglion cell death following retinal ischaemia. Brain 135(Pt 2):506–520

Davidson JO, Green CR et al (2012) Connexin hemichannel blockade improves outcomes in a model of fetal ischemia. Ann Neurol 71(1):121–132

De Bock M, Culot M et al (2011) Connexin channels provide a target to manipulate brain endothelial calcium dynamics and blood–brain barrier permeability. J Cereb Blood Flow Metab 31(9): 1942–1957

De Bock M, Wang N et al (2012) Connexin-43 hemichannels contribute to cytoplasmic Ca^{2+} oscillations by providing a bimodal Ca^{2+}-dependent Ca^{2+} entry pathway. J Biol Chem 287 (15):12250–12266

De Vriese AS, Van de Voorde J et al (2002) Effects of connexin-mimetic peptides on nitric oxide synthase– and cyclooxygenase-independent renal vasodilation. Kidney Int 61(1):177–185

De Vuyst E, Decrock E et al (2006) Intracellular calcium changes trigger connexin32 hemichannel opening. EMBO J 25(1):34–44
De Vuyst E, Decrock E et al (2007) Connexin hemichannels and gap junction channels are differentially influenced by lipopolysaccharide and basic fibroblast growth factor. Mol Biol Cell 18(1): 34–46
De Vuyst E, Wang N et al (2009) Ca^{2+} regulation of connexin43 hemichannels in C6 glioma and glial cells. Cell Calcium 46(3):176–187
De Vuyst E, Boengler K et al (2011) Pharmacological modulation of connexin-formed channels in cardiac pathophysiology. Br J Pharmacol 163(3):469–483
Decrock E, De Vuyst E et al (2009a) Connexin43 hemichannels contribute to the propagation of apoptotic cell death in a rat C6 glioma cell model. Cell Death Differ 16(1):151–163
Decrock E, Vinken M et al (2009b) Connexin-related signaling in cell death: to live or let die? Cell Death Differ 16(4):524–536
Decrock E, Vinken M et al (2011) Calcium and connexin-based intercellular communication, a deadly catch? Cell Calcium 50 (3):310–321
Delmar M, Coombs W et al (2004) Structural bases for the chemical regulation of connexin43 channels. Cardiovasc Res 62(2): 268–275
Desplantez T, Verma V et al (2012) Gap26, a connexin mimetic peptide, inhibits currents carried by connexin43 hemichannels and gap junction channels. Pharmacol Res 65(5):546–552
D'Hondt C, Ponsaerts R et al (2009) Pannexins, distant relatives of the connexin family with specific cellular functions? Bioessays 31(9):953–974
D'Hondt C, Ponsaerts R et al (2011) Pannexin channels in ATP release and beyond: an unexpected rendezvous at the endoplasmic reticulum. Cell Signal 23(2):305–316
Dora KA, Martin PE et al (1999) Role of heterocellular gap junctional communication in endothelium-dependent smooth muscle hyperpolarization: inhibition by a connexin-mimetic peptide. Biochem Biophys Res Commun 254(1):27–31
Ebihara L, Steiner E (1993) Properties of a nonjunctional current expressed from a rat connexin46 cDNA in *Xenopus* oocytes. J Gen Physiol 102(1):59–74
Ek-Vitorin JF, Burt JM (2012) Structural basis for the selective permeability of channels made of communicating junction proteins. Biochim Biophys Acta (in press)
Eltzschig HK, Eckle T et al (2006) ATP release from activated neutrophils occurs via connexin43 and modulates adenosine-dependent endothelial cell function. Circ Res 99(10):1100–1108
Evans WH, Boitano S (2001) Connexin mimetic peptides: specific inhibitors of gap-junctional intercellular communication. Biochem Soc Trans 29(Pt 4):606–612
Evans WH, De Vuyst E et al (2006) The gap junction cellular internet: connexin hemichannels enter the signalling limelight. Biochem J 397(1):1–14
Flores CE, Nannapaneni S et al (2012) Trafficking of gap junction channels at a vertebrate electrical synapse in vivo. Proc Natl Acad Sci USA 109(9):E573–E582
Froger N, Orellana JA et al (2010) Inhibition of cytokine-induced connexin43 hemichannel activity in astrocytes is neuroprotective. Mol Cell Neurosci 45(1):37–46
Gomes P, Srinivas SP et al (2005) ATP-dependent paracrine intercellular communication in cultured bovine corneal endothelial cells. Invest Ophthalmol Vis Sci 46(1):104–113
Goodenough DA, Paul DL (2003) Beyond the gap: functions of unpaired connexon channels. Nat Rev Mol Cell Biol 4(4):285–294
Goodenough DA, Paul DL (2009) Gap junctions. Cold Spring Harb Perspect Biol 1(1):a002576
Goodenough DA, Paul DL et al (1988) Topological distribution of two connexin32 antigenic sites in intact and split rodent hepatocyte gap junctions. J Cell Biol 107(5):1817–1824
Hagen A, Dietze A et al (2009) Human cardiac gap-junction coupling: effects of antiarrhythmic peptide AAP10. Cardiovasc Res 83(2): 405–415
Harris AL (2001) Emerging issues of connexin channels: biophysics fills the gap. Q Rev Biophys 34(3):325–472
Harris A, Locke D (eds) (2009) Connexins: a guide. Springer, New York
Hawat G, Benderdour M et al (2010) Connexin43 mimetic peptide Gap26 confers protection to intact heart against myocardial ischemia injury. Pflugers Arch 460(3):583–592
Hennan JK, Swillo RE et al (2009) GAP-134 ([2S,4R]-1-[2-aminoacetyl]4-benzamidopyrrolidine-2-carboxylic acid) prevents spontaneous ventricular arrhythmias and reduces infarct size during myocardial ischemia/reperfusion injury in open-chest dogs. J Cardiovasc Pharmacol Ther 14(3):207–214
Herve JC, Dhein S (2010) Peptides targeting gap junctional structures. Curr Pharm Des 16(28):3056–3070
Herve JC, Derangeon M et al (2011) Gap junctional channels are parts of multiprotein complexes. Biochim Biophys Acta 1818(8): 1844–1865
Hirst-Jensen BJ, Sahoo P et al (2007) Characterization of the pH-dependent interaction between the gap junction protein connexin43 carboxyl terminus and cytoplasmic loop domains. J Biol Chem 282(8):5801–5813
Huang C, Han X et al (2012) Critical role of connexin43 in secondary expansion of traumatic spinal cord injury. J Neurosci 32(10): 3333–3338
Hunter AW, Barker RJ et al (2005) Zonula occludens-1 alters connexin43 gap junction size and organization by influencing channel accretion. Mol Biol Cell 16(12):5686–5698
Hutcheson IR, Chaytor AT et al (1999) Nitric oxide-independent relaxations to acetylcholine and A23187 involve different routes of heterocellular communication. Role of gap junctions and phospholipase A_2. Circ Res 84(1):53–63
Isakson BE, Evans WH et al (2001) Intercellular Ca^{2+} signaling in alveolar epithelial cells through gap junctions and by extracellular ATP. Am J Physiol Lung Cell Mol Physiol 280(2):L221–L228
Isakson BE, Seedorf GJ et al (2003) Cell–cell communication in heterocellular cultures of alveolar epithelial cells. Am J Respir Cell Mol Biol 29(5):552–561
Ishikawa M, Iwamoto T et al (2011) Pannexin3 functions as an ER Ca^{2+} channel, hemichannel, and gap junction to promote osteoblast differentiation. J Cell Biol 193(7):1257–1274
Jarver P, Langel U (2006) Cell-penetrating peptides—a brief introduction. Biochim Biophys Acta 1758(3):260–263
Jiang S, Yuan H et al (2011) Glutamate release through connexin43 by cultured astrocytes in a stimulated hypertonicity model. Brain Res 1392:8–15
Juszczak GR, Swiergiel AH (2009) Properties of gap junction blockers and their behavioural, cognitive and electrophysiological effects: animal and human studies. Prog Neuropsychopharmacol Biol Psychiatry 33(2):181–198
Kameritsch P, Pogoda K et al (2011) Channel-independent influence of connexin43 on cell migration. Biochim Biophys Acta 1818 (8):1993–2001
Kang J, Kang N et al (2008) Connexin43 hemichannels are permeable to ATP. J Neurosci 28(18):4702–4711
Karpuk N, Burkovetskaya M et al (2011) Neuroinflammation leads to region-dependent alterations in astrocyte gap junction communication and hemichannel activity. J Neurosci 31(2):414–425

Kjenseth A, Fykerud TA et al (2012) The gap junction channel protein connexin43 is covalently modified and regulated by SUMOylation. J Biol Chem 287(19):15851–15861

Kwak BR, Jongsma HJ (1999) Selective inhibition of gap junction channel activity by synthetic peptides. J Physiol 516(Pt 3): 679–685

Lai A, Le DN et al (2006) Oculodentodigital dysplasia connexin43 mutations result in non-functional connexin hemichannels and gap junctions in C6 glioma cells. J Cell Sci 119(Pt 3):532–541

Laird DW (2006) Life cycle of connexins in health and disease. Biochem J 394(Pt 3):527–543

Lewandowski R, Procida K et al (2008) RXP-E: a connexin43-binding peptide that prevents action potential propagation block. Circ Res 103(5):519–526

Li H, Liu TF et al (1996) Properties and regulation of gap junctional hemichannels in the plasma membranes of cultured cells. J Cell Biol 134(4):1019–1030

Liu F, Arce FT et al (2006) Nanomechanics of hemichannel conformations: connexin flexibility underlying channel opening and closing. J Biol Chem 281(32):23207–23217

Maeda S, Nakagawa S et al (2009) Structure of the connexin26 gap junction channel at 3.5 A resolution. Nature 458(7238):597–602

Malchow RP, Qian H et al (1993) Evidence for hemi-gap junctional channels in isolated horizontal cells of the skate retina. J Neurosci Res 35(3):237–245

Matchkov VV, Rahman A et al (2006) Analysis of effects of connexin-mimetic peptides in rat mesenteric small arteries. Am J Physiol Heart Circ Physiol 291(1):H357–H367

Mendoza-Naranjo A, Bouma G et al (2011) Functional gap junctions accumulate at the immunological synapse and contribute to T cell activation. J Immunol 187(6):3121–3132

Myllykoski M, Kuczera K et al (2009) Complex formation between calmodulin and a peptide from the intracellular loop of the gap junction protein connexin43: molecular conformation and energetics of binding. Biophys Chem 144(3):130–135

O'Carroll SJ, Alkadhi M et al (2008) Connexin43 mimetic peptides reduce swelling, astrogliosis, and neuronal cell death after spinal cord injury. Cell Commun Adhes 15(1):27–42

O'Quinn MP, Palatinus JA et al (2011) A peptide mimetic of the connexin43 carboxyl terminus reduces gap junction remodeling and induced arrhythmia following ventricular injury. Circ Res 108(6):704–715

Orellana JA, Froger N et al (2011) ATP and glutamate released via astroglial connexin43 hemichannels mediate neuronal death through activation of pannexin1 hemichannels. J Neurochem 118(5):826–840

Orellana JA, Saez PJ et al (2012a) Glucose increases intracellular free Ca^{2+} in tanycytes via ATP released through connexin43 hemichannels. Glia 60(1):53–68

Orellana JA, Sanchez HA et al (2012b) Regulation of intercellular calcium signaling through calcium interactions with connexin-based channels. Adv Exp Med Biol 740:777–794

Oshima A, Tani K et al (2011) Asymmetric configurations and N-terminal rearrangements in connexin26 gap junction channels. J Mol Biol 405(3):724–735

Oviedo-Orta E, Gasque P et al (2001) Immunoglobulin and cytokine expression in mixed lymphocyte cultures is reduced by disruption of gap junction intercellular communication. FASEB J 15(3):768–774

Oviedo-Orta E, Errington RJ et al (2002) Gap junction intercellular communication during lymphocyte transendothelial migration. Cell Biol Int 26(3):253–263

Oviedo-Orta E, Perreau M et al (2010) Control of the proliferation of activated $CD4^+$ T cells by connexins. J Leukoc Biol 88(1):79–86

Paemeleire K, Martin PE et al (2000) Intercellular calcium waves in HeLa cells expressing GFP-labeled connexin43, 32, or 26. Mol Biol Cell 11(5):1815–1827

Palatinus JA, Rhett JM et al (2011) The connexin43 carboxyl terminus and cardiac gap junction organization. Biochim Biophys Acta 1818(8):1831–1843

Parthasarathi K, Ichimura H et al (2006) Connexin43 mediates spread of Ca^{2+}-dependent proinflammatory responses in lung capillaries. J Clin Invest 116(8):2193–2200

Pearson RA, Dale N et al (2005) ATP released via gap junction hemichannels from the pigment epithelium regulates neural retinal progenitor proliferation. Neuron 46(5):731–744

Pollok S, Pfeiffer AC et al (2011) Connexin43 mimetic peptide Gap27 reveals potential differences in the role of Cx43 in wound repair between diabetic and non-diabetic cells. J Cell Mol Med 15(4):861–873

Ponsaerts R, De Vuyst E et al (2010) Intramolecular loop/tail interactions are essential for connexin43-hemichannel activity. FASEB J 24(11):4378–4395

Ponsaerts R, Wang N et al (2012) The contractile system as a negative regulator of the connexin43 hemichannel. Biol Cell 104(7): 367–377

Rahman S, Carlile G et al (1993) Assembly of hepatic gap junctions. Topography and distribution of connexin32 in intracellular and plasma membranes determined using sequence-specific antibodies. J Biol Chem 268(2):1260–1265

Retamal MA, Cortes CJ et al (2006) S-Nitrosylation and permeation through connexin43 hemichannels in astrocytes: induction by oxidant stress and reversal by reducing agents. Proc Natl Acad Sci USA 103(12):4475–4480

Rhett JM, Gourdie RG (2012) The perinexus: a new feature of Cx43 gap junction organization. Heart Rhythm 9(4):619–623

Ring S, Karakhanova S et al (2010) Gap junctions between regulatory T cells and dendritic cells prevent sensitization of $CD8^+$ T cells. J Allergy Clin Immunol 125(1):237–246

Robertson J, Lang S et al (2010) Peptidoglycan derived from *Staphylococcus epidermidis* induces connexin43 hemichannel activity with consequences on the innate immune response in endothelial cells. Biochem J 432(1):133–143

Rottlaender D, Boengler K et al (2012) Glycogen synthase kinase 3beta transfers cytoprotective signaling through connexin43 onto mitochondrial ATP-sensitive K^+ channels. Proc Natl Acad Sci USA 109(5):E242–E251

Saez JC, Retamal MA et al (2005) Connexin-based gap junction hemichannels: gating mechanisms. Biochim Biophys Acta 1711 (2):215–224

Saez JC, Schalper KA et al (2010) Cell membrane permeabilization via connexin hemichannels in living and dying cells. Exp Cell Res 316(15):2377–2389

Samoilova M, Wentlandt K et al (2008) Connexin43 mimetic peptides inhibit spontaneous epileptiform activity in organotypic hippocampal slice cultures. Exp Neurol 210(2):762–775

Sarieddine MZ, Scheckenbach KE et al (2009) Connexin43 modulates neutrophil recruitment to the lung. J Cell Mol Med 13(11–12):4560–4570

Sato PY, Coombs W et al (2011) Interactions between ankyrin-G, plakophilin-2, and connexin43 at the cardiac intercalated disc. Circ Res 109(2):193–201

Scemes E, Spray DC et al (2009) Connexins, pannexins, innexins: novel roles of "hemi-channels". Pflugers Arch 457(6):1207–1226

Schalper KA, Riquelme MA et al (2012) Modulation of gap junction channels and hemichannels by growth factors. Mol Biosyst 8(3):685–698

Scott CA, Kelsell DP (2011) Key functions for gap junctions in skin and hearing. Biochem J 438(2):245–254

Shibayama J, Lewandowski R et al (2006) Identification of a novel peptide that interferes with the chemical regulation of connexin43. Circ Res 98(11):1365–1372

Shintani-Ishida K, Uemura K et al (2007) Hemichannels in cardiomyocytes open transiently during ischemia and contribute to reperfusion injury following brief ischemia. Am J Physiol Heart Circ Physiol 293(3):H1714–H1720

Solan JL, Lampe PD (2009) Connexin43 phosphorylation: structural changes and biological effects. Biochem J 419(2):261–272

Sood A, Salih S et al (2011) Signalling of DNA damage and cytokines across cell barriers exposed to nanoparticles depends on barrier thickness. Nat Nanotechnol 6(12):824–833

Sosinsky GE, Nicholson BJ (2005) Structural organization of gap junction channels. Biochim Biophys Acta 1711(2):99–125

Sosinsky GE, Solan JL et al (2007) The C-terminus of connexin43 adopts different conformations in the Golgi and gap junction as detected with structure-specific antibodies. Biochem J 408(3): 375–385

Spray DC, Ye ZC et al (2006) Functional connexin "hemichannels": a critical appraisal. Glia 54(7):758–773

Srisakuldee W, Jeyaraman MM et al (2009) Phosphorylation of connexin-43 at serine 262 promotes a cardiac injury-resistant state. Cardiovasc Res 83(4):672–681

Stehberg J, Moraga-Amaro R, Salazar C, Becerra A, Echeverría C, Orellana JA, Bultynck G, Ponsaerts R, Leybaert L, Simon F, Sáez JC, Retamal MA (2012) Release of gliotransmitters through astroglial connexin 43 hemichannels is necessary for fear memory consolidation in the basolateral amygdala. FASEB J. doi:10.1096/fj.11-198416

Stong BC, Chang Q et al (2006) A novel mechanism for connexin26 mutation linked deafness: cell death caused by leaky gap junction hemichannels. Laryngoscope 116(12):2205–2210

Sun JD, Liu Y et al (2012) Gap junction dysfunction in the prefrontal cortex induces depressive-like behaviors in rats. Neuropsychopharmacology 37(5):1305–1320

Thimm J, Mechler A et al (2005) Calcium-dependent open/closed conformations and interfacial energy maps of reconstituted hemichannels. J Biol Chem 280(11):10646–10654

Vaiyapuri S, Jones CI et al (2012) Gap junctions and connexin hemichannels underpin hemostasis and thrombosis. Circulation 125(20):2479–2491

Verma V, Larsen BD et al (2009a) Novel pharmacophores of connexin43 based on the "RXP" series of Cx43-binding peptides. Circ Res 105(2):176–184

Verma V, Hallett MB et al (2009b) Perturbing plasma membrane hemichannels attenuates calcium signalling in cardiac cells and HeLa cells expressing connexins. Eur J Cell Biol 88(2):79–90

Wang J, Ma M et al (2007) "Modulation of membrane channel currents by gap junction protein mimetic peptides: size matters. Am J Physiol Cell Physiol 293(3):C1112–C1119

Warner A, Clements DK et al (1995) Specific motifs in the external loops of connexin proteins can determine gap junction formation between chick heart myocytes. J Physiol 488(Pt 3):721–728

Wright CS, van Steensel MA et al (2009) Connexin mimetic peptides improve cell migration rates of human epidermal keratinocytes and dermal fibroblasts in vitro. Wound Repair Regen 17(2):240–249

Wright CS, Pollok S et al (2012a) The connexin mimetic peptide Gap27 increases human dermal fibroblast migration in hyperglycemic and hyperinsulinemic conditions in vitro. J Cell Physiol 227(1):77–87

Wright JA, Richards T, Becker DL (2012b) Connexins and diabetes. Cardiol Res Pract 2012:496904

Xing D, Kjolbye AL et al (2003) ZP123 increases gap junctional conductance and prevents reentrant ventricular tachycardia during myocardial ischemia in open chest dogs. J Cardiovasc Electrophysiol 14(5):510–520

Yang J, Darley RL et al (2009) Low connexin channel-dependent intercellular communication in human adult hematopoietic progenitor/stem cells: probing mechanisms of autologous stem cell therapy. Cell Commun Adhes 16(5–6):138–145

Yoon JJ, Green CR et al (2010) Dose-dependent protective effect of connexin43 mimetic peptide against neurodegeneration in an ex vivo model of epileptiform lesion. Epilepsy Res 92(2–3):153–162

Zhou Y, Yang W et al (2007) Identification of the calmodulin binding domain of connexin 43. J Biol Chem 282(48):35005–35017

Zimmer DB, Green CR et al (1987) Topological analysis of the major protein in isolated intact rat liver gap junctions and gap junction—derived single membrane structures. J Biol Chem 262 (16):7751–7763

J Membrane Biol (2012) 245:451
DOI 10.1007/s00232-012-9501-z

ERRATUM

Erratum to: Manipulating Connexin Communication Channels: Use of Peptidomimetics and the Translational Outputs

W. Howard Evans · Geert Bultynck · Luc Leybaert

Published online: 15 September 2012

Erratum to: J Membrane Biol
DOI 10.1007/s00232-012-9488-5

In the article Manipulating connexin communication channels; use of peptidomimetics and the translational outputs by W. Howard Evans et al., in Table 3, in mouse hearts test model, the effect of a carboxyl tail peptide should be; Increases Cx43 and ps368 phosphorylation and reduces induced arrhythmia. The reference remains as O'Quinn et al. (2011).

The online version of the original article can be found under doi:10.1007/s00232-012-9488-5.

W. H. Evans (✉)
Institute of Infection and Immunity, Cardiff University School of Medicine, Heath Park, Cardiff, Wales CF14 4XN, UK
e-mail: EvansWH@cf.ac.uk

G. Bultynck
Department of Cellular and Molecular Medicine, K. U. Leuven, Campus Gasthuisberg, 3000 Leuven, Belgium

L. Leybaert
Department of Basic Medical Sciences, Physiology Group, Faculty of Medicine and Health Science, Ghent University, Ghent, Belgium

J Membrane Biol (2012) 245:453–463
DOI 10.1007/s00232-012-9457-z

ORIGINAL ARTICLES

The N-Terminal Half of the Connexin Protein Contains the Core Elements of the Pore and Voltage Gates

Jack Kronengold · Miduturu Srinivas · Vytas K. Verselis

Received: 1 June 2012 / Accepted: 20 June 2012 / Published online: 24 July 2012

Abstract Connexins form channels with large aqueous pores that mediate fluxes of inorganic ions and biological signaling molecules. Studies aimed at identifying the connexin pore now include a crystal structure that provides details of putative pore-lining residues that need to be verified using independent biophysical approaches. Here we extended our initial cysteine-scanning studies of the TM1/E1 region of Cx46 hemichannels to include TM2 and TM3 transmembrane segments. No evidence of reactivity was observed in either TM2 or TM3 probed with small or large thiol-modifying reagents. Several identified pore residues in E1 of Cx46 have been verified in different Cx isoforms. Use of variety of thiol reagents indicates that the connexin hemichannel pore is large and flexible enough, at least in the extracellular part of the pore funnel, to accommodate uncommonly large side chains. We also find that that gating characteristics are largely determined by the same domains that constitute the pore. These data indicate that biophysical and structural studies are converging towards a view that the N-terminal half of the Cx protein contains the principal components of the pore and gating elements, with NT, TM1 and E1 forming the pore funnel.

J. Kronengold
Department of Pharmacology, Yale University School of Medicine, New Haven, CT 06520, USA

M. Srinivas
Department of Biological Sciences, State University of New York College of Optometry, New York, NY 10036, USA

V. K. Verselis (✉)
Dominick P. Purpura Department of Neuroscience, Albert Einstein College of Medicine, 1300 Morris Park Avenue, Bronx, New York, NY 10461, USA
e-mail: vytas.verselis@einstein.yu.edu

Keywords Channel pore · Voltage gating connexin · Cysteine scanning · Chimera · Hemichannels

Introduction

Connexins (Cxs) comprise a family of ion channels with large aqueous pores that can transmit a variety of biological signaling molecules including cyclic nucleotides, inositol 1,4,5-triphosphate (IP_3), ATP and, in some instances, small interfering RNAs (Evans et al. 2006; Harris 2001; Neijssen et al. 2005; Valiunas et al. 2005). It is now evident that Cx channels function in two configurations, as gap junction (GJ) or cell-cell channels formed by the head-to-head docking of two hemichannels (connexons), and as undocked hemichannels. The latter function like conventional membrane ion channels in that they mediate transmission of signals across the plasma membrane, but the signals transmitted extend beyond small inorganic ions. Tissue-specific Cx expression (Willecke et al. 2002) and the different reported selectivity profiles of Cxs (Goldberg et al. 2004; Harris 2001; Veenstra et al. 1995; Verselis and Veenstra 2000; Weber et al. 2004) suggest that that there are differences in the pores among Cx channels that can impact significantly on which signals are selected for transmission.

An interesting feature of Cx channels that originated from early studies in cell pairs is that GJ channels gate in response to the transjunctional voltage, V_j, the voltage difference between two cells, irrespective of the absolute membrane potentials that generate the V_j (Harris et al. 1981; Spray et al. 1981). This sensitivity suggests that the gating elements that sense voltage reside in the pore. Thus, differences in the pores among Cx that impact on selectivity may also impact on gating. Conserved gating

characteristics of GJ channels and undocked hemichannels indicate that there is conservation of voltage gating structures in both Cx channel configurations (Bukauskas and Verselis 2004; Verselis 2009).

Recently, a crystal structure of a Cx26 GJ channel was obtained at 3.5 Å resolution and shows an overall pore structure that has wide entrances at the cytoplasmic ends of the two opposed hemichannels, narrowing to a funnel shape through the transmembrane spans and then widening slightly again in the extracellular region (Maeda et al. 2009). The topology of a Cx subunit consists of four membrane spanning segments, TM1–TM4, with N-terminal (NT) and C-terminal (CT) domains located intracellularly and two extracellular loops, E1 and E2, connecting TM1–TM2 and TM3–TM4, respectively. In the crystal structure, the bulk of the putative pore proper, i.e. the so-called pore funnel, is formed by segments of NT, TM1 and E1 domains. The widest parts of the cytoplasmic entrances beyond the funnel are formed by parts of TM2 and TM3, which in Cx26 is rich in positively charged residues.

This assignment of NT, TM1 and E1 to the pore funnel essentially agrees with reports that preceded the crystal structure and deduced the pore configuration based on biophysical studies of gating in Cx32 and Cx26 GJ channels and substituted-cysteine accessibility studies in Cx46 and chimeric Cx32*43E1 hemichannels (Kronengold et al. 2003a; Oh et al. 2008; Purnick et al. 2000; Verselis 2009; Verselis et al. 1994; Zhou et al. 1997). However, the charge selectivity of Cx26, which is biased towards cations, is not wholly compatible with the crystal structure and cysteine accessibility studies of Cx32 GJ channels using a cut-open oocyte preparation reported that some residues in TM1 and TM2 contributed to the cytoplasmic end of the pore with the channel in closed and open states, respectively (Skerrett et al. 2002). The same study reported TM3 as the major pore-lining helix throughout the transmembrane span.

Given these contrasting data and the need to test the general validity of the crystal structure as representative of a functional Cx channel, we applied the substituted cysteine accessibility method (SCAM), to the entire span of TM2 and TM3 in Cx46 hemichannels to extend published data in TM1 and E1 in the same Cx. In a subset of residues we also applied SCAM to Cx50 hemichannels, a Cx that despite close primary sequence homology with Cx46, exhibits a substantially larger unitary conductance and different voltage-dependent gating properties (Srinivas et al. 2005). We also examined unitary conductance and gating properties of a number of chimeric hemichannels composed of interchanged segments of Cx46 and Cx50 to determine whether gating and selectivity properties segregate together. We find that both the SCAM and chimeric data point to NT, TM1 and E1 domains as the core elements that constitute the Cx pore as well as the essential components necessary for voltage-dependent gating.

Materials and Methods

Construction of Cysteine Substitutions in TM2 and TM3

The rat Cx46 coding sequence was cloned into EcoRI-Hind III of pGem7*zf*(+) (Promega, Madison, WI) and was used as a template to construct the mutants. For construction of the TM2 Cys substitutions we introduced new restriction sites through silent mutagenesis (ApaI, PstI, SspI, SalI and AvrII) and created a new wtCx46 cassette called rCx46-M2mut. The PCR generated fragments containing the individual Cys mutations were subcloned as follows: EcoRI/SalI (F77C-Q81C), PstI (I82C-T87C), SalI/BssHII (P88C-L90C) and EcoRI/PmlI (I91C-G94C). To make TM3 mutants we first introduced SalI and MscI sites by silent mutagenesis into the full length wtCx46. A SalI/BstXI 330 bp fragment was cloned into pGem7*zf*(+) to make an rCx46-M3mut cassette which would allow for unique cloning sites. Mutants were generated on this cassette using PshAI/PstI (F157C-T163C), MscI/PmlI (L164C-I170C) and PstI/PmlI (A171C-F175C). Cysteine mutants were then backcloned into wtCx46. All constructs were sequenced over the restriction sites used for cloning.

Construction of Chimeras Composed of Cx46 and Cx50

The mouse Cx50 coding sequence was subcloned into the SP64T transcription vector (generously provided by Dr. Thomas White, SUNY, Stony Brook, NY). We constructed chimeras that exchanged Cx50 and Cx46 sequence. The chimeras are designated first by the parent Cx followed by the donor Cx and the sequence replaced by the donor Cx. Thus, Cx50*46NT-CL, has the NT half of Cx50, NT through CL, replaced by Cx46 sequence. The chimeras were made using PshAI and BamHI as cloning sites for the respective gel purified inserts and vectors. The domains of the two Cxs based on the alignment published in Bennett et al. (1991) are as follows: for Cx46, NT(Met 1–Lys 23), TM1 (Val 24–Ala 41), E1(Glu 42–Arg 76), TM2 (Phe 77–Gly 94), CL (His 95–Val 156), TM3 (Phe 157–Phe 175), E2 (Leu 176–Thr 207), TM4 (Ile 208–Leu 226) and CT (Glu 227–Ile 416). For Cx50, NT (Met 1–Arg 23), TM1 (Val 24–Ala 41), E1 (Glu 42–Arg 76), TM2 (Leu 77–Gly 94), CL (His 95–Val 159), TM3 (Cys 160–Phe 178), E2 (Leu 179–Thr 210), TM4 (Ile 211–Met 229), CT (Glu 230–Ile 440). Both chimeras were sequenced over the sites used for cloning.

Expression of Hemichannels in Xenopus Oocytes

mRNA was prepared from appropriately linearized plasmid DNA with the mMessage mMachine T7 and SP6 RNA kits from Ambion (Austin, TX), according to the manufacturer's protocol. The mRNA was purified using QIAquick PCR purification columns from QIAGEN (Valencia, CA). mRNA bound to the column was eluted with 30–40 µl of an aqueous solution of DNA antisense to the endogenous *Xen*Cx38 (8 pmole/ml). We used the phosphorothioate antisense oligo 5′-GCT TTA GTA ATT CCC ATC CTG CCA TGT TTC-3′, which is complementary to *Xen*Cx38 commencing at NT -5 with respect to the ATG initiation codon. Preparation of *Xenopus* oocytes has been described previously (Trexler et al. 2000). Each oocyte was injected with 50–100 nl of the mRNA/antisense solution. Injected oocytes were kept at 18 °C in a standard ND96 solution containing (in mM) 88 NaCl, 1 KCl, 2 $MgCl_2$, 1.8 $CaCl_2$, 5 glucose, 5 HEPES, 5 pyruvate, pH adjusted to 7.6.

Preparation of Reagents

The methane thiosulfonate (MTS) reagents 2-trimethylammonioethylmethane thiosulfonate (MTSET) and 2-sulfonatoethylmethane thiosulfonate (MTSES) were purchased from Anatrace (Maumee, Ohio). 2-biotinoylaminoethylmethane thiosulfonate (MTSEA biotin) and 2-(6-biotinoylaminohexanoyl-aminoethylmethane thiosulfonate (MTSEA biotin-X) were purchased from Biotium (Hayward, CA). Aliquots of dry powder were prepared and stored in microcentrifuge tubes at −20 °C. Prior to each experiment aliquots of MTSET or MTSES were dissolved in distilled water, chilled on ice, and in the case of MTSEA biotin and MTSEA biotin-X were dissolved in DMSO, to stock concentrations of 250 mM. Dilutions were made into IPS just prior to application to the desired final concentration (typically 0.5 to 1 mM). Activity of MTS reagents were periodically checked using a TNB assay (Karlin and Akabas 1998).

Electrophysiological Recording and Analysis

Functional expression of Cys-substituted mutants was screened using two electrode voltage clamp recordings of macroscopic currents from single *Xenopus* oocytes using a GeneClamp 500 amplifier (Molecular Devices Corp, Sunnyvale CA). Oocytes were placed in ND96 solution and both current-passing and voltage-recording pipettes contained 1 M KCl.

For patch clamp recordings of single hemichannel currents, *Xenopus* oocytes were manually devitellinized in a hypertonic solution consisting of (in mM) 220 Na aspartate, 10 KCl, 2 $MgCl_2$, 10 HEPES and then placed in the ND96 solution for recovery. Oocytes were then individually moved to a recording chamber, (RC-28, Warner Instruments Corp.) containing the patch pipette solution (IPS) which consisted of (in mM) 140 KCl, 1 $MgCl_2$, 5 HEPES, 1 $CaCl_2$, 3 EGTA, and pH adjusted to 8.0 with KOH. The bath compartment was connected via a 3 M agar bridge to a ground compartment containing the same IPS solution. After excision of patches containing single hemichannels, instrumentation offsets were manually corrected in the absence of an applied voltage. Hemichannel activity at a fixed voltage was recorded to establish a baseline current after which the compartment was perfused with freshly prepared MTS reagent. Single hemichannel I–V curves were obtained before and after MTS application by applying 8 s voltage ramps from −70 to +70 mV. Unitary conductances plotted represent the slope conductances at $V_m = 0$ obtained from fitted open channel I–V relations.

In all electrophysiological experiments, data was acquired with AT-MIO-16X D/A boards from National Instruments (Austin, TX) using our own acquisition software (developed by E.B. Trexler). For macroscopic currents, currents were acquired at 2 kHz and filtered at 500 Hz. For patch clamp experiments, currents were filtered at 1 kHz and data were acquired at 10 kHz.

Results

Single Channel SCAM of TM2 and TM3 with MTSET

Previously we showed that the extracellular end of TM1 extending into E1 contributes to the pore in Cx46 hemichannels (Kronengold et al. 2003b). Results of SCAM studies of substituted Cys mutants in TM2 of Cx46 hemichannels are shown in Fig. 1. We individually substituted 18 residues, F77 through G94, which according to the original accepted membrane topology encompasses TM2 (Bennett et al. 1991). Cysteine substitutions at three positions in Cx46 (P88, L90 and Y92) failed to produce functional hemichannel currents when expressed in *Xenopus* oocytes. Substitutions at three additional positions, I82, I83 and V85, resulted in poor expression, evidenced by consistently small macroscopic currents, such that single channel recordings could not be reliably obtained. At the remaining positions, cysteine substitutions produced hemichannels with near wild-type unitary conductance values. At each of these positions, application of MTSET to the bath and subsequent patching did not show any substantial changes in unitary conductance (Fig. 1) or in open hemichannel rectification (data not shown).

In the same way, we applied SCAM to the entire putative TM3 domain, which included residues F157 through

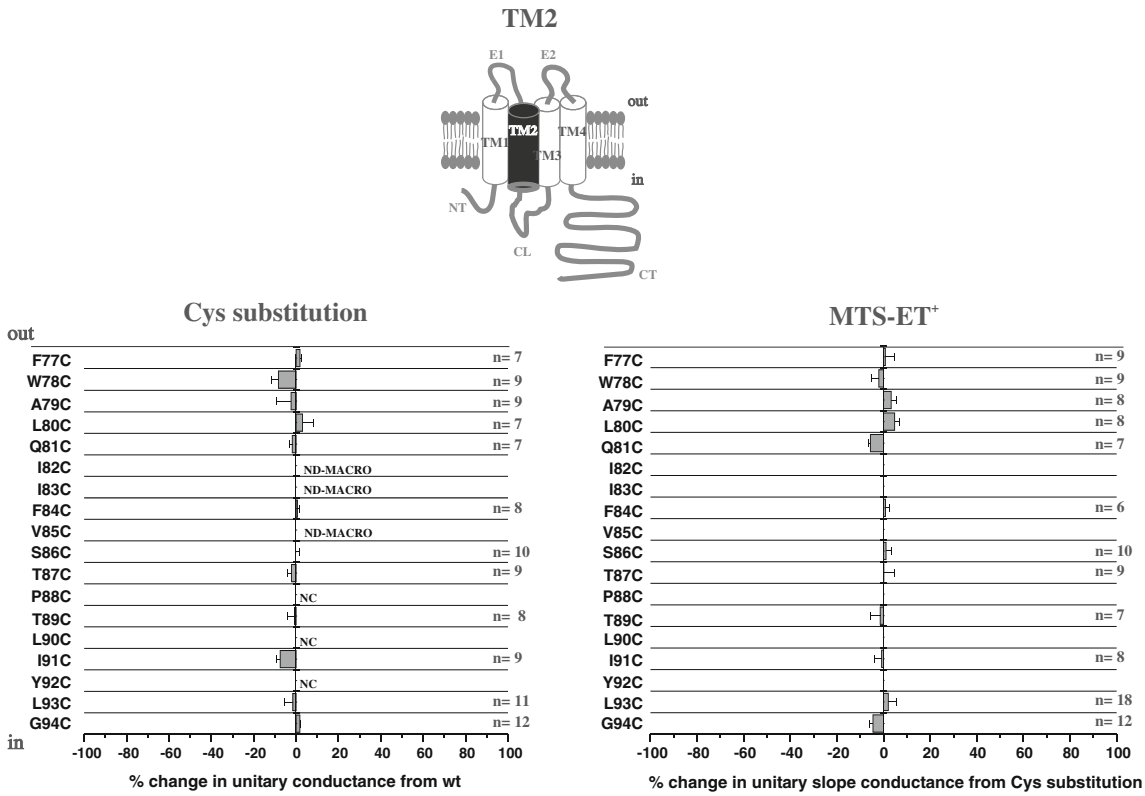

Fig. 1 TM2 does not contribute to the pore in open Cx46 hemichannels. Shown are effects of Cys substitutions for TM2 residues F77 through G94 (*left*) and SCAM results using MTSET (*right*). For the Cys substitutions, the change in unitary conductance represents the mean percentage change in the slope conductance compared with wt Cx46 measured at $V_m = 0$ from fitted open channel I–V relations. Of the 18 residues examined, only P88C, L90C and Y92C failed to form functional hemichannels. In addition, single hemichannels were not observed from oocytes injected with I82C and V85C due to consistently low expression levels. For the SCAM results, the change in unitary conductance represents the mean percentage change in the slope conductance relative to the Cys substituted mutant measured at $V_m = 0$ from fitted open channel I–V relations. No substantial changes were observed at any positions. NC denotes nonfunctional hemichannels. ND-MACRO denotes residues for which there was insufficient single-channel data for characterization but macroscopic data in ND96 with 2 and 0.2 mM Ca^{2+} showed no reactivity. *Error bars* represent standard deviations; $n \geq 8$ for each mutant

F175 (Fig. 2). Cys substitutions were generally well-tolerated throughout TM3 with Cys-substitutions at two positions (F165C and T163C) failing to produce functional hemichannels. As for TM2, application of MTSET did not show any substantial changes in single hemichannel properties at any of the positions. Data for the extracellular half, E166 to F175, probed with MTSET applied to extracellular and intracellular sides in excised patches was previously reported and showed no evidence of reactivity (Kronengold et al. 2003a, b).

SCAM Using a Large MTS Reagent, MTSEA Biotin-X

Assignment of TM3 to the pore in studies of Cx32 GJ channels used, maleimidobutyrylbiocytin (MBB) as the thiol reagent and use of a smaller thiol reagent could potentially fail to produce significant changes in unitary conductance in a large channel. Thus, we re-examined a subset of residues in TM3 at the single hemichannel level using a large MTS reagent, MTSEA biotin-X (MW = 485). Figure 3 shows an alignment of TM3 residues in Cx32, Cx46 and Cx50. Arrows indicate the 7 positions reported to be reactive in Cx32 GJs (Skerrett et al. 2002). We examined the corresponding positions in Cx46 hemichannels (boxed) using MTSEA biotin-X, which are Y155, I159, F161, L164, V167, F169 and A171 in Cx46. We also examined three corresponding positions in Cx50, Y158, V170 and F172 (boxed). No substantial changes in unitary conductance upon application of this reagent were found at any of the TM3 positions in Cx46 or Cx50 hemichannels, consistent with results obtained with MTSET. In contrast, results using a large MTSEA biotin-X reagent with a cysteine substituted at identified pore-lining positions showed large effects on conductance that differed from those observed using MTSET. In the example shown in Fig. 4, application of MTSEA biotin-X to an excised

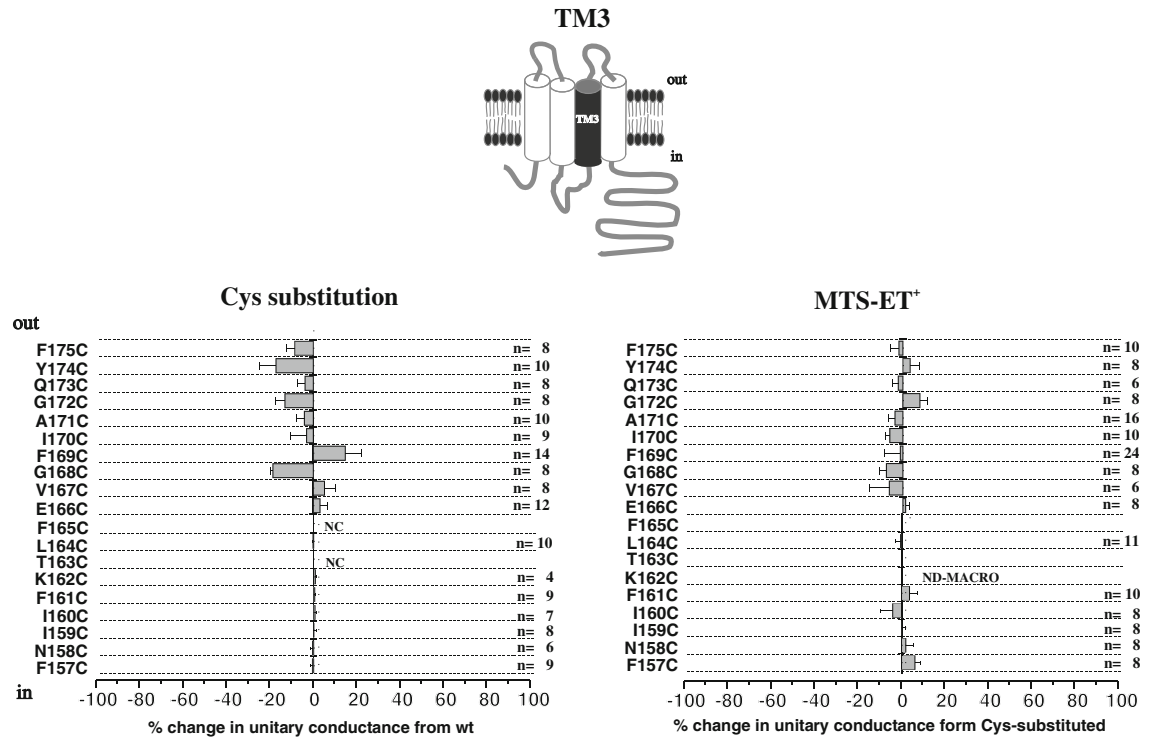

Fig. 2 TM3 does not contribute to the pore in open Cx46 hemichannels. Shown are effects of Cys substitutions for TM3 residues F157 through F175 (*left*) and SCAM results using MTSET (*right*). For the Cys substitutions, the change in unitary conductance represents the mean percentage change in the slope conductance compared with wt Cx46 measured at $V_m = 0$ from fitted open channel I–V relations. Of the 19 residues examined, only F163CF failed to form functional hemichannels and single hemichannels were not observed from oocytes injected with K162C due to consistently low expression levels. For the SCAM results, the change in unitary conductance represents the mean percentage change in the slope conductance relative to the Cys substituted mutant measured at $V_m = 0$ from fitted open channel I–V relations. No substantial changes were observed at any positions. NC denotes nonfunctional hemichannels. ND-MACRO denotes residues for which there was insufficient single-channel data for characterization but macroscopic data in ND96 with 2 and 0.2 mM Ca^{2+} showed no reactivity. *Error bars* represent standard deviations; $n \geq 8$ for each mutant

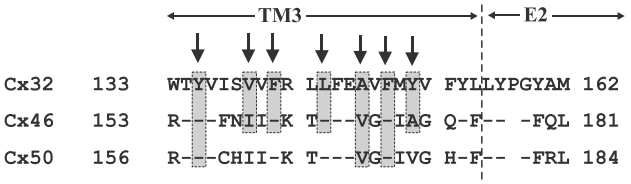

Fig. 3 SCAM of select TM3 residues using a large MTS reagent shows no evidence of reactivity. Shown is an alignment of Cx32, Cx46 and Cx50 sequence from the CL/TM3 border through the proximal portion of E2. Residues indicated by *arrows* in Cx32 were reported to be pore-lining in Cx32 GJ channels (Skerrett et al. 2002). *Boxed* residues in Cx46 and Cx50 were subjected to SCAM analysis using MTS biotin-X. These include Y155, I159, F161, V167, F169 and A171 in Cx46 and Y158, V170 and F172 in Cx50. No effects were observed at any of these positions

patch containing an F43C substitution at the TM1/E1 border of Cx50 resulted in a step-wise reduction in current that did not reverse upon wash-out of the reagent, indicative of covalent modification. The step-wise reduction in current occurred within seconds of application resulting in a final single channel current that was reduced by >90 % and displayed a very noisy, flickery behavior. Often 5 or 6 steps were discernible consistent with modification of most or all Cx subunits. In this example, 5 steps were visible and are illustrated at a higher time resolution below. These results indicate that the hemichannel pore is large enough and/or flexible enough to potentially accommodate all six biotin-X side chains. A bar graph showing the reductions in unitary current for four MTS reagents, MTSET and MTSES that differ in charge, and MTSEA biotin and MTSEA biotin-X that are large in size (Fig. 4b). The results show a large reduction for MTSET compared to MTSES and even larger reductions for the MTSEA biotin and MTSEA biotin–X reagents consistent with both electrostatic and steric effects on ion conduction. Moreover, the same results as shown in Fig. 4 could be obtained with reagent added from either extracellular or cytoplasmic sides of the hemichannel demonstrating that this large reagent is readily permeable.

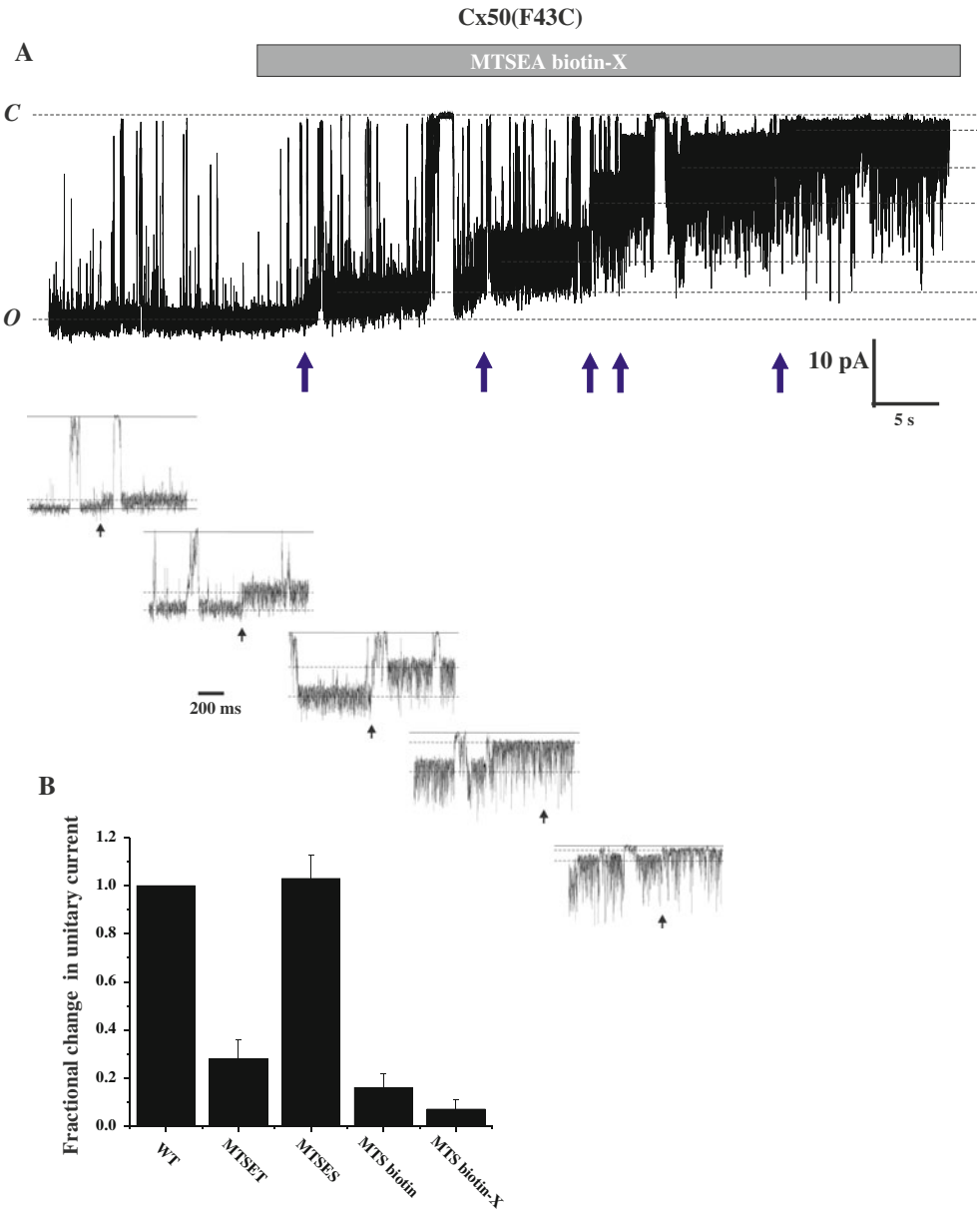

Fig. 4 Multiple subunits in a Cx pore are modified by large MTS reagents. **a** Example of MTSEA-biotin-X modification of a single F43C hemichannel recorded in the outside-out patch configuration. The membrane potential was held at −50 mV. Application of MTSEA biotin-X (100 μM) caused a stepwise reduction in the single hemichannel current (*arrows*). The final conductance is markedly reduced and shows substantial flicker. At least five distinct changes in current were observed indicating modification of individual cysteines. Each of the modifications is shown in an expanded time scale. The step changes in current are rapid, consistent with chemical modification and the hemichannel continues to gate even with multiple subunits modified. The degree of flicker increases with the number of modified subunits. **b** *Bar graph* summarizing reductions in current for in Cx50(F43C) hemichannels after modification with different MTS reagents. Currents were observed at a holding current of −40 or −50 mV and are expressed as fractional currents remaining relative to those before reaction. The data represent reductions of 72 % ($n = 8$), 84 % ($n = 5$) and 93 % ($n = 5$) for MTSET, MTSEA-biotin and MTSEA-biotin-X, respectively and a small increase (5 %, $n = 4$) for MTSES

Molecular Determinants of Single Hemichannel Conductance and Gating Reside Within the NT Half

To assess what parts of the Cx protein are important for determining Cx-specific conductance and gating properties, we utilized Cx46 and Cx50, which possess a high degree of sequence homology (White et al. 1992) yet exhibit substantially different unitary conductances and voltage gating characteristics (Srinivas et al. 2005). Unitary conductance measured as the slope conductance at $V_m = 0$ in 140 mM symmetric KCl was ∼290 pS for Cx46 and ∼470 pS for Cx50. As far as gating, closure at negative voltages, which is mediated by one of two intrinsic mechanisms termed loop or slow gating (Bukauskas and Verselis 2004; Trexler et al. 1996), is poorly sensitive to voltage in Cx50 when extracellular Ca^{2+} is chelated to sub-micromolar levels with EGTA and Mg^{2+} and maintained at physiological (1–2 mM) concentrations. Conversely, Cx46 hemichannels under these same conditions close steeply with voltages between −50 and −90 mV (Srinivas et al. 2005). Closure at positive voltages, mediated by another mechanism termed V_j or fast gating (Bukauskas and Verselis, 2004) is similar in both Cxs, albeit somewhat more sensitive in Cx50.

We constructed chimeras to exchange domains between Cx46 and Cx50 and examined the accompanying changes in unitary conductance and gating. Data are summarized in Figs. 5 and 6. For the most part, substitution of the NT half (NT-CL) of Cx46 with Cx50 sequence (Cx46*50NT-CL) and the reciprocal chimera, Cx50*46NT-CL, produced

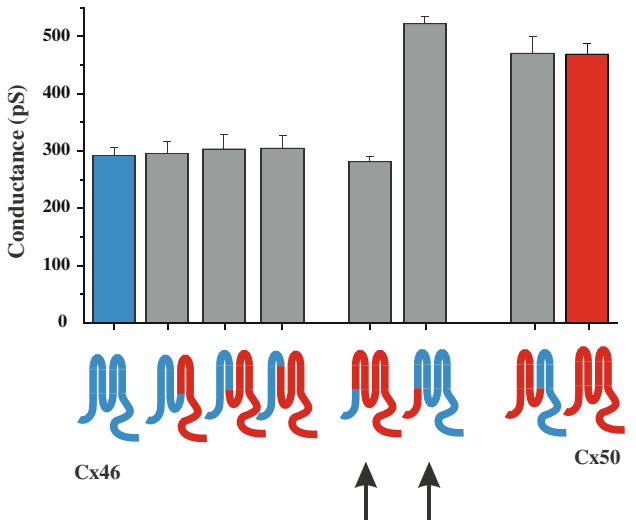

Fig. 5 Unitary conductances of Cx46 and Cx50 hemichannels are specified by NT, E1 and TM1 domains. Shown is a *bar graph* summarizing unitary conductances of WT Cx46 (blue Cx) and WT Cx50 (red Cx). Unitary conductances represent slope conductances at $V_m = 0$ from fits to open channel I–V relations obtained by applying 8 s ramps to patches containing single hemichannels. Sequence substituted in chimeras is indicated by color. *Arrows* denote substitutions of just NT domains

hemichannels that were indistinguishable from the donor Cxs, in terms of unitary conductance (Fig. 5). Open hemichannel rectification was also the same (not shown). Substitution of just the NT domain, to yield Cx46*50NT and Cx50*46NT chimeras (arrows), resulted in functional hemichannels with unitary conductances that were remarkably altered and closer in value to the respective donor Cxs (Fig. 5). Cx50*46NT-E1 and Cx50*46NT-TM2 were also similar to the donor Cx46. Thus, the NT, TM1 and E1 domains appear to be sufficient to specify unitary conductance and in the case of Cx46 sequence onto Cx50, and NT appears to be most responsible for the differences in their conductances. Unfortunately, the reciprocal chimeras, Cx46*50NT-E1 and Cx46*50NT-TM2 lacked function.

For gating, substitution of NT of Cx50 with Cx46 (Cx50*46NT) had little impact on loop gating, whereas the reciprocal chimera, Cx46*50NT, had a large impact (Fig. 6). The latter, however, appeared to open with hyperpolarizing voltages, unlike WT Cx50. The Cx50*46NT-E1 and Cx50*46NT-TM2 dramatically changed loop gating and actually made it more sensitive to voltage with faster kinetics of closure than WT Cx46. Finally, the reciprocal Cx46*50NT-CL and Cx50*46NT-CL chimeras, that exchanged domains NT through CL recapitulated the gating characteristics of the donor Cxs, Cx50 and Cx46 respectively. Thus, in order to fully reconstruct gating, sequence extending from NT and into the CL domain had to be included.

Discussion

There is now corroborating structural and electrophysiological evidence that the bulk of the Cx pore is formed by NT, TM1 and E1 domains. Our original SCAM study in Cx46 focused on TM1 and E1 domains and showed large effects on unitary conductance upon modification with MTS reagents (Kronengold et al. 2003b). Moreover, the effects differed upon modification with the positively and negatively charged MTS reagent MTSET and MTSES, respectively, consistent with the expected electrostatic effects on ion transport in a pore that better selects for cations over anions.

Here we applied SCAM to TM2 and TM3 domains of Cx46 hemichannels and extended the study to larger MTS reagents as well as to another Cx. Given the SCAM study on Cx32 that reported TM3 in GJs to be pore-lining using MBB, a large thiol reagent (Skerrett et al. 2002), we applied SCAM to hemichannels using a large MTS reagent with the idea that use of only smaller reagents could produce minimal effects, particularly at wider regions of the Cx pore. Using the criteria that modification must affect unitary conductance and occur with reagent added to either side of the membrane, we did not see evidence of accessibility in any of the residues in TM2 (F77–G94) or TM3 (F157–F175). Moreover, the subset of residues reported as pore-lining in TM3 of Cx32 GJs showed no reactivity in Cx46 when probed with the larger MTS biotin-X reagent. Several residues probed in Cx50 as well, showed no reactivity. In this study, we only screened TM2 and TM3 from the outside, i.e. we applied MTS reagents to extracellular side, but the lack of any effect fulfills the criteria for exclusion from the pore. These data indicate that either there is no exposure of TM2 and TM3 domains to the pore of open Cx46 hemichannels or that modifications are occurring, even with large thiol reagents, but that they constitute silent modifications. We reason that silent modifications are unlikely to occur if a residue is in the conducting pathway because placing 6 charges, even in a wide region, should alter the concentration of mobile counterions thereby affecting unitary conductance and rectification. Also, placing sufficient bulk that nearly occludes the hemichannel pore in the narrower regions, i.e. MTSEA biotin-X, would likely have some impact on conductance, at least in the form of open hemichannel noise. However, we cannot definitively rule out that silent modifications can occur. We did not check for effects on gating, which could produce changes in macroscopic currents as a result of changes in open probability irrespective of whether or not a residue resides in the pore.

An interesting observation is that most positions in TM2 and TM3 were remarkably well tolerated by Cys substitutions with no perceptible changes in open hemichannel

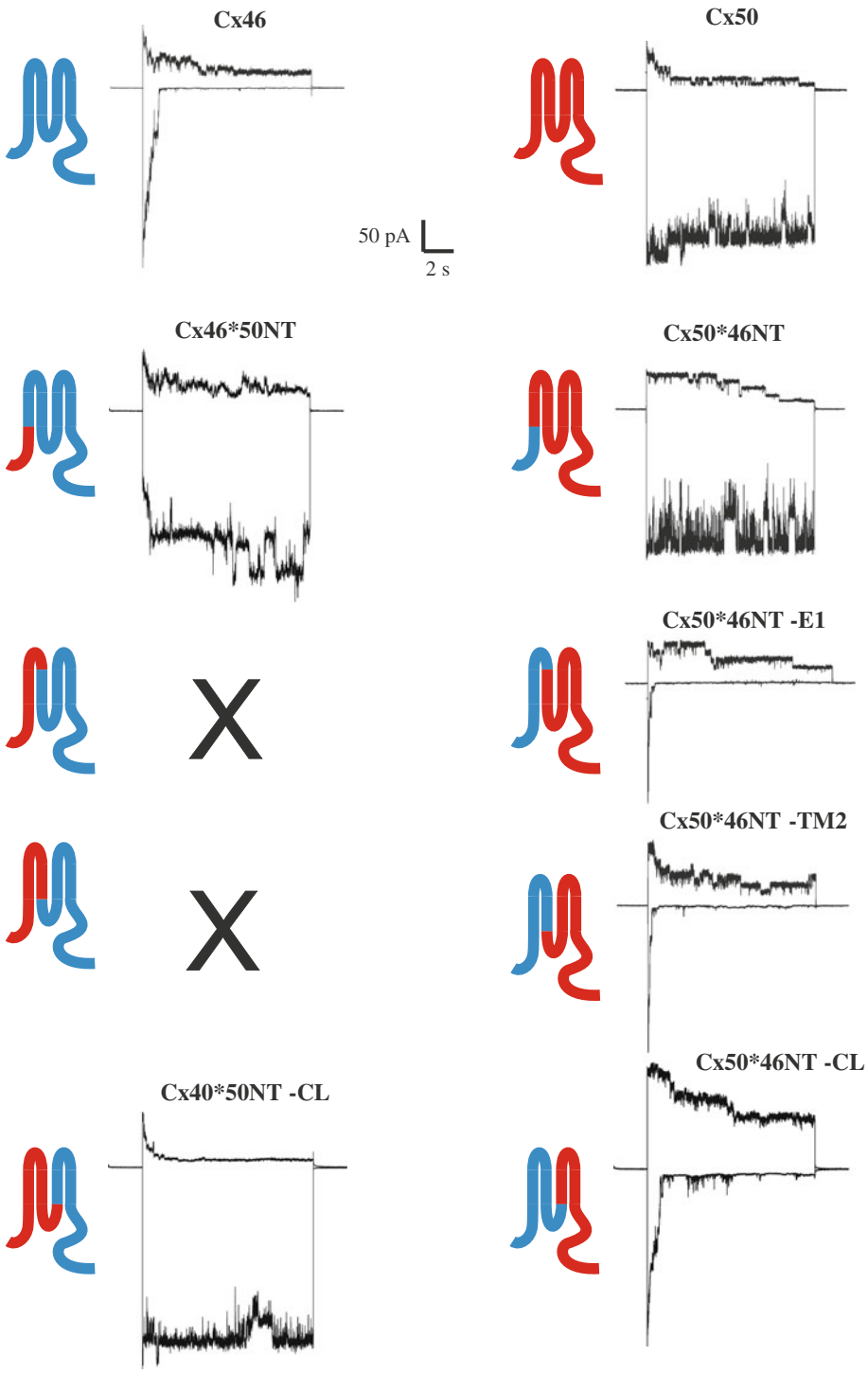

Fig. 6 Gating of Cx46 and Cx50 hemichannels is specified by NT half of the Cx protein, NT through CL. Shown are examples of currents obtained from patches containing multiple active hemichannels. Currents in response to positive (+40 mV) and negative (−90 mV) voltage steps are shown. WT Cx46 sequence is depicted in *blue* and WT Cx50 in *red*. Sequence substituted in the chimeras is indicated by color. Substitution of NT-E1 or NT-TM2 sequence of Cx50 onto Cx46 failed to form functional hemichannels

properties. Only a handful of Cys substitutions within these TM domains showed loss of function, which included P88C, L90C and Y92C in TM2 and T163C and F165C in TM3. P88 and nearby positions in TM2 have been shown to be important in gating via a proline-kink motif (Ri et al. 1999) and may disrupt channel function. It is unclear why T163 and F165 failed to function as hemichannels and we did not examine how these substitutions affected GJ channel function. Failure of both would suggest a more general disruption of structure, whether through changes helical structure and/or contacts with other helices. I82 and I83C in TM2 were functional, but displayed altered gating. With the exception of P88, none of these positions are associated with mutations that cause cataractogenesis.

Pore residues identified in E1 of Cx46 include E43, G46 and D51. These same residues are also reacted in SCAM studies of Cx50 (Verselis et al. 2009), although, perhaps, not surprising given the high degree of homology between Cx46 and Cx50. However, we recently demonstrated that the one of these homologous positions in Cx26, G45, is pore-lining (Sanchez et al. 2010) and the G45E mutation leads to a severe form of syndromic deafness (Janecke et al. 2005; Lee et al. 2009). Thus, there appears to be correspondence among distantly related Cxs, as well, an indication that overall pore structure may be conserved among all Cxs, although more members of the Cx family need to be examined. Systematic comparison of differences among all pore-lining residues, once identified, could provide a basis for Cx-specific differences in conductance and selectivity. However, the principal domains contributing to the pore, although conserved among Cxs, can undergo small perturbations in structure that can impart shifts in the positions of specific residues within pore-lining segments. Complicating this view is the possibility that post-translational modifications of key residues can modulate properties independent of whether coded sequence is conserved (Kwon et al. 2011; Locke et al. 2009).

At identified pore lining positions in Cx46 and Cx50, such E(F)43 or G46, modifications with different MTS reagents produce different effects on open hemichannel properties consistent with a strong impact of charge as well as size. The side chain that results from modification by MTSES is bulkier that that with MTSET, yet MTSES typically produced a small increase in unitary conductance. Thus, there is a considerable electrostatic effect on ion flux in this region of the pore. Introduction of a positive charge at one pore-lining position can reduce conductance substantially and in the case of Cx50, modification of F43 to a positive charge reduced conductance by $\sim$70 %. These electrostatic effects are consistent with a pore that is biased with negative charge, giving rise to a preferential flux of cations. Indeed, Cx46 and Cx50 have been shown to prefer cations over anions (Srinivas et al. 1999; Trexler et al. 1996, 2000). Modification of F43 with larger reagents, MTS biotin and MTS biotin-X produced even larger reductions in unitary conductance consistent with steric impedance to ion flux. The reductions were accompanied by large, noisy fluctuations, not resolvable by the patch clamp amplifiers that likely represent atomic motions of the biotin moieties. Perhaps surprising was that these large reagents produced 5 or 6 step-reductions in current consistent with modification of most or all six subunits. This result indicates that the F43 position, which is within the pore funnel identified by the Cx26 structure, allows sequential access of six MTS biotin-X molecules leading to six modified side chains. Thus, the pore must be quite wide and/or show enough flexibility to accommodate six large side chains. It will be interesting to determine whether other positions accommodate less molecules or show different degrees of noise, perhaps indicative of narrowed diameter and/or increased rigidity.

A potential link between selectivity and gating comes from the positioning of Cx voltage sensors within the pore. This arrangement comes from studies demonstrating sensitivity of GJ channels to V_j, irrespective of the absolute membrane potentials of the coupled cells (Harris et al. 1981; Spray et al. 1981). This arrangement applies to both intrinsic voltage gating mechanisms, loop or slow gating and V_j or fast gating (Bukauskas and Verselis 2004). In the absence of docking, the same sensors now respond to the membrane potential as the reference potential of the coupled cell is replaced by the extracellular milieu.

Knowing more about the pore structure, we examined chimeras that exchanged domains between Cx46 and Cx50, which exhibit substantially different loop gating characteristics and unitary conductances (Srinivas et al. 2005) despite close sequence homology. Reciprocally substituting just the NT domain had a huge impact on unitary conductance and rather than resulting in intermediate conductances, the Cx50*46NT and Cx46*50NT chimeras produced somewhat smaller and larger unitary conductances, respectively than the corresponding donor Cxs. Effects on loop gating were widely disparate, with minimal changes occurring when substituting NT of Cx46 on Cx50 (Cx50*46NT), but loss of the characteristically strong closure of the loop gate of Cx46 when substituting NT of Cx50 onto Cx46 (Cx46*50NT). Inclusion of more domains of Cx46 onto Cx50, *46NT-E1 and *46NT-TM2, remarkably converted the weak loop gating of Cx50 into one that resembled Cx46, except that closure was even more robust and displayed faster kinetics. Surprisingly, reciprocal chimeras were not functional. However, consistent with SCAM studies, the unitary hemichannel properties acquired all of the characteristics of the donor Cxs when the NT half (NT through CL) was substituted. Likewise, gating characteristics were also transferred. These data are consistent with mutational studies on chick homologs of Cx46 and Cx50 (Tong and Ebihara 2006; Tong et al. 2004) as well as chimeric studies that exchanged domains between Cx32 and Cx37 (Hu et al. 2006). Cx43 differs in that truncation of CT or tagging it with EGFP results in loss of V_j gating (Bukauskas et al. 2001; Moreno et al. 2002). NMR studies have shown that CT interacts with CL (Duffy et al. 2002), which may, in turn, interact with NT thereby affecting V_j gating. This property may be unique to Cx43 as tagging or truncating CT in other Cxs does not appear to affect gating.

Taken together, these data suggest that gating and conductance co-segregate, but that the relationship is, not surprisingly, complex. The disparate effects on loop gating

upon substitution of NT alone indicate that there is likely an intimate association of NT with other parts of protein, which in the case of Cx46 and Cx50 appears to occur within TM1 through E1. This observation is in support of the crystal structure that suggests there are interactions between NT and TM1 that keep the NT domain up against the channel wall, thereby keeping the pore unobstructed. It remains to be determined whether this specific interaction mediates gating. The lack of function for chimeras that substitute NT-E1 and NT-TM2 sequence of Cx50 onto Cx46 suggest that the putative interactions between NT and TM1 are very sensitive to structural perturbations, and may require inclusion of NT through CL. Although TM3, E2, TM4 and CT sequences may not contain the core elements that determine differences in conductance and gating properties among Cxs, helix packing can undoubtedly be disrupted with substitutions in these regions resulting in effects on channel properties. However, these will often lead to loss of function or effects that are not consistent among members of the Cx family.

In conclusion, biophysical and structural studies are converging towards a view that the Cx pore is principally formed by NT, TM1 and E1 domains and that this structure is conserved among all members of the Cx family. An additional contribution to the pore suggested by the crystal structure includes a region of positive charge in the CL region (now assigned as an extension of the TM2 helix) that resides at the cytoplasmic entrance. These charges are incompatible with the selectivity characteristics of Cx26 and an equilibrated structure of Cx26 resulting from molecular dynamics simulations suggest that neutralization of these charges is required to produce cation flux through the channel (Kwon et al. 2011). Moving forward, there is now a framework within which to continue testing and refining models of gating and permeability as functional studies test structural motifs and identified interactions. Agreement between structure and function will come by continued biophysical studies concomitant with higher resolution structures crystallized in various states.

Acknowledgments The authors wish to thank Dr. Ross Johnson for many thoughtful discussions and guidance over the years, particularly on critical evaluation of studies regarding connexin pores. This study was supported by NIH Grants GM54179 to V.K.V and EY13869 to M. S.

References

Bennett MV, Barrio LC, Bargiello TA, Spray DC, Hertzberg E, Saez JC (1991) Gap junctions: new tools, new answers, new questions. Neuron 6:305–320

Bukauskas FF, Verselis VK (2004) Gap junction channel gating. Biochim Biophys Acta 1662:42–60

Bukauskas FF, Bukauskiene A, Bennett MV, Verselis VK (2001) Gating properties of gap junction channels assembled from connexin43 and connexin43 fused with green fluorescent protein. Biophys J 81:137–152

Duffy HS, Delmar M, Spray DC (2002) Formation of the gap junction nexus: binding partners for connexins. J Physiol Paris 96:243–249

Evans WH, De Vuyst E, Leybaert L (2006) The gap junction cellular internet: connexin hemichannels enter the signalling limelight. Biochem J 397:1–14

Goldberg GS, Valiunas V, Brink PR (2004) Selective permeability of gap junction channels. Biochim Biophys Acta 1662:96–101

Harris AL (2001) Emerging issues of connexin channels: biophysics fills the gap. Q Rev Biophys 34:325–472

Harris AL, Spray DC, Bennett MV (1981) Kinetic properties of a voltage-dependent junctional conductance. J Gen Physiol 77:95–117

Hu X, Ma M, Dahl G (2006) Conductance of connexin hemichannels segregates with the first transmembrane segment. Biophys J 90:140–150

Janecke AR, Hennies HC, Gunther B, Gansl G, Smolle J, Messmer EM, Utermann G, Rittinger O (2005) GJB2 mutations in keratitis-ichthyosis-deafness syndrome including its fatal form. Am J Med Genet A 133:128–131

Karlin A, Akabas MH (1998) Substituted-cysteine accessibility method. Methods Enzymol 293:123–145

Kronengold J, Trexler EB, Bukauskas FF, Bargiello TA, Verselis VK (2003a) Pore-lining residues identified by single channel SCAM studies in Cx46 hemichannels. Cell Commun Adhes 10:193–199

Kronengold J, Trexler EB, Bukauskas FF, Bargiello TA, Verselis VK (2003b) Single-channel SCAM identifies pore-lining residues in the first extracellular loop and first transmembrane domains of Cx46 hemichannels. J Gen Physiol 122:389–405

Kwon T, Harris AL, Rossi A, Bargiello TA (2011) Molecular dynamics simulations of the Cx26 hemichannel: evaluation of structural models with Brownian dynamics. J Gen Physiol 138: 475–493

Lee JR, Derosa AM, White TW (2009) Connexin mutations causing skin disease and deafness increase hemichannel activity and cell death when expressed in Xenopus oocytes. J Invest Dermatol 129:870–878

Locke D, Bian S, Li H, Harris AL (2009) Post-translational modifications of connexin26 revealed by mass spectrometry. Biochem J 424:385–398

Maeda S, Nakagawa S, Suga M, Yamashita E, Oshima A, Fujiyoshi Y, Tsukihara T (2009) Structure of the connexin 26 gap junction channel at 3.5 A resolution. Nature 458:597–602

Moreno AP, Chanson M, Elenes S, Anumonwo J, Scerri I, Gu H, Taffet SM, Delmar M (2002) Role of the carboxyl terminal of connexin43 in transjunctional fast voltage gating. Circ Res 90: 450–457

Neijssen J, Herberts C, Drijfhout JW, Reits E, Janssen L, Neefjes J (2005) Cross-presentation by intercellular peptide transfer through gap junctions. Nature 434:83–88

Oh S, Verselis VK, Bargiello TA (2008) Charges dispersed over the permeation pathway determine the charge selectivity and conductance of a Cx32 chimeric hemichannel. J Physiol 586: 2445–2461

Purnick PE, Oh S, Abrams CK, Verselis VK, Bargiello TA (2000) Reversal of the gating polarity of gap junctions by negative charge substitutions in the N-terminus of connexin 32. Biophys J 79:2403–2415

Ri Y, Ballesteros JA, Abrams CK, Oh S, Verselis VK, Weinstein H, Bargiello TA (1999) The role of a conserved proline residue in mediating conformational changes associated with voltage gating of Cx32 gap junctions. Biophys J 76:2887–2898

Sanchez HA, Mese G, Srinivas M, White TW, Verselis VK (2010) Differentially altered Ca2+ regulation and Ca2+ permeability in Cx26 hemichannels formed by the A40 V and G45E mutations that cause keratitis ichthyosis deafness syndrome. J Gen Physiol 136:47–62

Skerrett IM, Aronowitz J, Shin JH, Cymes G, Kasperek E, Cao FL, Nicholson BJ (2002) Identification of amino acid residues lining the pore of a gap junction channel. J Cell Biol 159:349–360

Spray DC, Harris AL, Bennett MV (1981) Equilibrium properties of a voltage-dependent junctional conductance. J Gen Physiol 77: 77–93

Srinivas M, Costa M, Gao Y, Fort A, Fishman GI, Spray DC (1999) Voltage dependence of macroscopic and unitary currents of gap junction channels formed by mouse connexin50 expressed in rat neuroblastoma cells. J Physiol (Lond) 517:673–689

Srinivas M, Kronengold J, Bukauskas FF, Bargiello TA, Verselis VK (2005) Correlative studies of gating in Cx46 and Cx50 hemichannels and gap junction channels. Biophys J 88:1725–1739

Tong JJ, Ebihara L (2006) Structural determinants for the differences in voltage gating of chicken Cx56 and Cx45.6 gap-junctional hemichannels. Biophys J 91:2142–2154

Tong JJ, Liu X, Dong L, Ebihara L (2004) Exchange of gating properties between rat cx46 and chicken cx45.6. Biophys J 87:2397–2406

Trexler EB, Bennett MV, Bargiello TA, Verselis VK (1996) Voltage gating and permeation in a gap junction hemichannel. Proc Natl Acad Sci USA 93:5836–5841

Trexler EB, Bukauskas FF, Kronengold J, Bargiello TA, Verselis VK (2000) The first extracellular loop domain is a major determinant of charge selectivity in connexin46 channels. Biophys J 79: 3036–3051

Valiunas V, Polosina YY, Miller H, Potapova IA, Valiuniene L, Doronin S, Mathias RT, Robinson RB, Rosen MR, Cohen IS, Brink PR (2005) Connexin-specific cell-to-cell transfer of short interfering RNA by gap junctions. J Physiol 568:459–468

Veenstra RD, Wang HZ, Beblo DA, Chilton MG, Harris AL, Beyer EC, Brink PR (1995) Selectivity of connexin-specific gap junctions does not correlate with channel conductance. Circ Res 77:1156–1165

Verselis VK (2009) The connexin channel pore: pore-lining segments and residues. In: Harris AL, Locke D (eds) Connexins: a guide. Humana Press, New York, pp 77–102

Verselis VK, Veenstra R (2000) Gap junction channels permeability and voltage gating advances in molecular and cell biology. In: Hertzberg EL (ed) Gap junctions. Elsevier, Stamford, pp 129–192

Verselis VK, Ginter CS, Bargiello TA (1994) Opposite voltage gating polarities of two closely related connexins. Nature 368:348–351

Verselis VK, Trelles MP, Rubinos C, Bargiello TA, Srinivas M (2009) Loop gating of connexin hemichannels involves movement of pore-lining residues in the first extracellular loop domain. J Biol Chem 284:4484–4493

Weber PA, Chang HC, Spaeth KE, Nitsche JM, Nicholson BJ (2004) The permeability of gap junction channels to probes of different size is dependent on connexin composition and permeant-pore affinities. Biophys J 87:958–973

White TW, Bruzzone R, Goodenough DA, Paul DL (1992) Mouse Cx50, a functional member of the connexin family of gap junction proteins, is the lens fiber protein MP70. Mol Biol Cell 3:711–720

Willecke K, Eiberger J, Degen J, Eckardt D, Romualdi A, Guldenagel M, Deutsch U, Sohl G (2002) Structural and functional diversity of connexin genes in the mouse and human genome. Biol Chem 383:725–737

Zhou XW, Pfahnl A, Werner R, Hudder A, Llanes A, Luebke A, Dahl G (1997) Identification of a pore lining segment in gap junction hemichannels. Biophys J 72:1946–1953

J Membrane Biol (2012) 245:465–476
DOI 10.1007/s00232-012-9464-0

Degradation of Endocytosed Gap Junctions by Autophagosomal and Endo-/lysosomal Pathways: A Perspective

Matthias M. Falk · John T. Fong · Rachael M. Kells · Michael C. O'Laughlin · Tia J. Kowal · Anastasia F. Thévenin

Received: 29 March 2012 / Accepted: 13 June 2012 / Published online: 24 July 2012

Abstract Gap junctions (GJs) are composed of tens to many thousands of double-membrane spanning GJ channels that cluster together to form densely packed channel arrays (termed GJ plaques) in apposing plasma membranes of neighboring cells. In addition to providing direct intercellular communication (GJIC, their hallmark function), GJs, based on their characteristic double-membrane-spanning configuration, likely also significantly contribute to physical cell-to-cell adhesion. Clearly, modulation (up-/down-regulation) of GJIC and of physical cell-to-cell adhesion is as vitally important as the basic ability of GJ formation itself. Others and we have previously described that GJs can be removed from the plasma membrane via the internalization of entire GJ plaques (or portions thereof) in a cellular process that resembles clathrin-mediated endocytosis. GJ endocytosis results in the formation of double-membrane vesicles [termed annular gap junctions (AGJs) or connexosomes] in the cytoplasm of one of the coupled cells. Four recent independent studies, consistent with earlier ultrastructural analyses, demonstrate the degradation of endocytosed AGJ vesicles via autophagy. However, in TPA-treated cells others report degradation of AGJs via the endo-/lysosomal degradation pathway. Here we summarize evidence that supports the concept that autophagy serves as the cellular default pathway for the degradation of internalized GJs. Furthermore, we highlight and discuss structural criteria that seem required for an alternate degradation via the endo-/lysosomal pathway.

M. M. Falk (✉) · J. T. Fong · R. M. Kells · M. C. O'Laughlin · T. J. Kowal · A. F. Thévenin
Department of Biological Sciences, Lehigh University, 111 Research Drive, Iacocca Hall, D-218, Bethlehem, PA 18015, USA
e-mail: mmf4@lehigh.edu

Keywords Autophagy · Cell–cell junctions · Connexin 43 · Gap junctions · Protein degradation · Ubiquitin

Abbreviations

AGJ	Annular gap junction
CME	Clathrin mediated endocytosis
Cx	Connexin
DAG	Diacylglycerol
GFP	Green fluorescent protein
GJ	Gap junction
GJIC	Gap junction mediated intercellular communication
LAMP	Lysosomal associated membrane protein
LC3	Microtubule-associated protein light chain 3
PAEC	Pulmonary artery endothelial cell
PE	Phosphatidyl-ethanolamine
PKC	Protein kinase C
RNAi	RNA interference
SQSTM1	Sequestosome 1
SUMO	Small Ub-like modifier
TPA	12-O-tetradecanoylphorbol 13-acetate
Ub	Ubiquitin
WGA	Wheat germ agglutinin
YFP	Yellow fluorescent protein

Introduction

Direct cell-to-cell communication is a pivotal cellular function of multicellular organisms. It is established by gap junction (GJ) channels, that bridge apposing plasma membranes of neighboring cells. Typically, tens to thousands of GJ channels cluster into densely packed two-dimensional arrays, termed GJ plaques that can reach several micrometers in diameter. GJ channels are assembled from a

ubiquitously expressed class of four-pass trans-membrane proteins, termed connexins, with connexin 43 (Cx43) being the most abundantly expressed type. Six connexin polypeptides oligomerize into a ring to form a hexameric transmembrane structure with a central hydrophilic pore, called a hemi-channel or connexon. Once trafficked to the plasma membrane, two connexons, one provided by each of two neighboring cells, dock head-on in the extra-cellular space to form the complete double-membrane spanning GJ channel that is completely sealed-off to the extracellular space. Recruitment of additional GJ channels along the outer edge enlarges the GJ plaques, while simultaneous removal of older channels from plaque centers balances GJ channel turnover (Falk et al. 2009; Gaietta et al. 2002; Lauf et al. 2002). In addition to providing intercellular communication (their hallmark function), GJs, based on their characteristic double-membrane-spanning configuration and their tight extracellular head-to-head docking, are also likely to contribute significantly to physical cell-to-cell adhesion that generally is attributed to the adhesive force exerted by adherens- and tight junctions. Down-regulation of cell–cell adhesion contributes to many physiological and pathological conditions in which cells physically uncouple from their neighbors. For example, this uncoupling is seen during cell migration in development and wound healing, mitosis, apoptosis, leukocyte extravasation, ischemia, hemorrhage, edema, and cancer metastasis. Thus, to effectively reduce or abolish cell-to-cell adhesion under such conditions, all major types of cell–cell adhesion structures (including desmosomes, adherens, tight, and gap junctions) will either have to reduce their adhesive force, or will have to be removed from the plasma membrane.

GJ channels are known to gate such that physiological parameters including intracellular pH, Ca^{2+} concentration and Cx phosphorylation can modulate the status of GJ channels (opened, closed) and the extent of GJ-mediated intercellular communication (GJIC) (Delmar et al. 2004; Laird 2005; Lampe and Lau 2004; Moreno 2005; Pahujaa et al. 2007; Solan and Lampe 2009; Warn-Cramer and Lau 2004). Importantly, however, GJ channel gating (channel closure, not channel removal) is unlikely to significantly affect the level of GJ-mediated cell-to-cell adhesion. Alternatively, the extent of GJIC could also be regulated by splitting GJ channels (similar to adherens junctions), or by reducing the number of plasma membrane-located GJs. Both mechanisms also would contribute to a reduction in physical cell-to-cell adhesion. Goodenough and Gilula (1974) and Ghoshroy et al. (1995) reported that connexons, once docked, appear inseparable under physiological conditions, suggesting that GJs, especially under conditions where physical cell–cell adhesion needs to be reduced/abolished, will be removed from the plasma membrane. Here, we summarize recent findings that support the view that GJ removal from the plasma membrane is achieved by the internalization/endocytosis of GJs. Next, we will address two potential cellular degradation pathways, autophagosomal versus endo-/lysosomal, that both have been described recently to degrade endocytosed GJs (Fig. 1). We provide evidence that supports the concept that autophagy appears as the most likely cellular degradation pathway for removing internalized GJs from the cytoplasm. Finally, we discuss important structural criteria that may allow an alternate endo-/lysosomal degradation of internalized GJs.

Plasma Membrane-Located GJs are Endocytosed, Resulting in the Formation of Cytoplasmic Double-Membrane GJ Vesicles Termed AGJs or Connexosomes

We reported previously that cells continuously, -and effectively after treatment with natural inflammatory mediators-, internalize and turn over their GJs via a combined endo-/exocytic process (Baker et al. 2008; Falk et al. 2009; Gilleron et al. 2008; Gumpert et al. 2008; Piehl et al. 2007) (Fig. 1, steps 1–5). Internalization was found to occur preferentially into one of two coupled cells, indicating a highly regulated process (Falk et al. 2009; Piehl et al. 2007). The scaffolding protein, ZO-1, a well-known binding partner of Cx43 (Giepmans and Moolenaar 1998; Hunter et al. 2005; Toyofuku et al. 1998), was found to be displaced from GJ plaques on the side of plaque invagination (Baker et al. 2008; Gilleron et al. 2008). This observation suggests that ZO-1, not surprising for a scaffolding protein, may play multiple roles in GJ biosynthesis and function, including regulation of GJ plaque size (Hunter et al. 2005), accrual of channels to GJ plaques (Rhett and Gourdie 2011; Rhett et al. 2011), and defining directionality of GJ plaque internalization (Baker et al. 2008; Gilleron et al. 2008). Further analyses indicated that GJ internalization utilizes well-known components of the clathrin-mediated endocytosis (CME) machinery, including the classical endocytic coat protein clathrin, the clathrin-adaptors AP-2 and Dab2, the GTPase dynamin2, the retrograde actin motor myosin VI (myo6), as well as the process of actin polymerization (Gumpert et al. 2008; Piehl et al. 2007) (Fig. 1, steps 1–4). GJ internalization generates characteristic cytoplasmic double-membrane GJ vesicles, termed annular GJs (AGJs) or connexosomes. Note that the outer membrane of the generated AGJ vesicles corresponds to the plasma membrane of the host-cell, while the inner membrane and the vesicle lumen correspond to plasma membrane and cytoplasm of the neighboring donor cell (Fig. 1, steps 1–5). Others and we further found that internalization is highly regulated and can occur very efficiently. For example, acute GJ internalization can be seen in

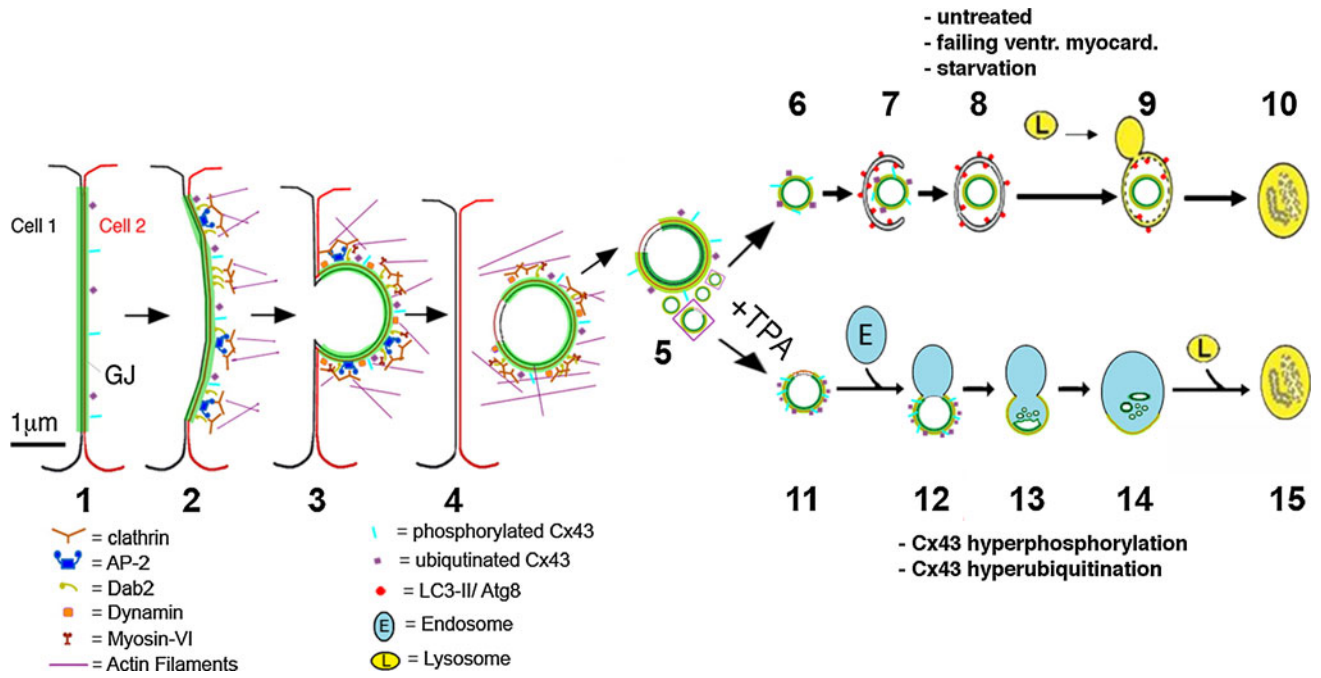

Fig. 1 Schematic representation of proposed steps that lead to GJ internalization (*steps 1–3*), cytoplasmic AGJ vesicle formation and fragmentation (*steps 4*, *5*), and AGJ vesicle degradation by phago-/lysosomal (*steps 6–10*) and endo-/lysosomal pathways (*steps 11–15*) based on the previous work by others and by us. Note the proposed nonjunctional membrane domains missing the green GJ label (shown in *steps 4*, *5*, *11*, *12*), and the increased phosphorylation and ubiquitination on AGJ vesicles that fuse with endosomes (*steps 11*, *12* vs. *6*, *7*). Adapted from Falk et al. (2009) and Fong et al. (2012)

primary porcine pulmonary artery endothelial cells (PAECs) exposed to natural inflammatory mediators such as thrombin and endothelin (Baker et al. 2008), well-known inhibitors of GJIC (Blomstrand et al. 2004; Postma et al. 1998; Spinella et al. 2003; van Zeijl et al. 2007), and in Cx43-GFP expressing NRK cells (Jordan et al. 2001). Efficient internalization of cell–cell junctions reduces/abolishes cell–cell adhesion, most likely allowing the endothelial cells to migrate to the inflamed tissue regions in order to aid in the healing process and to modulate endothelial barrier function (Baldwin and Thurston 2001; Falk 2010; Lum and Malik 1994; Wong et al. 2004). Efficient GJ internalization is also seen in Sertoli cells in response to treatment with the non-genomic carcinogen lindane (Gilleron et al. 2008), and it is seen under pathological conditions such as in the failing canine ventricular myocardium (Hesketh et al. 2010).

Continuous, as well as induced endocytosis of GJ plaques (consisting of double-membrane spanning GJ channels) is supported (I) by numerous earlier ultrastructural and live-cell based analyses that detected AGJ vesicles in the cytoplasm of cells in situ, especially occurring in differentiating tissues and sometimes, in association with lysosomes (Ginzberg and Gilula 1979; Hesketh et al. 2010; Jordan et al. 2001; Larsen et al. 1979; Leach and Oliphant 1984; Mazet et al. 1985; Pfeifer 1980; Severs et al. 1989); (II) the fundamental observation that connexons, once docked, are inseparable under physiological conditions (Ghoshroy et al. 1995; Goodenough and Gilula 1974); and (III) by the typical short half-life of connexins and GJ channels of only 1–5 h (Beardslee et al. 1998; Berthoud et al. 2004; Falk et al. 2009; Fallon and Goodenough 1981; Gaietta et al. 2002).

What Happens to Cytoplasmic AGJ Vesicles After Their Generation?

Four recent studies, Hesketh et al. (2010), Lichtenstein et al. (2011), Fong et al. (2012), and Bejarano et al. (2012) report the degradation of endocytosed AGJ vesicles via autophagy (Fig. 1, steps 6–10), while Leithe and colleagues (Leithe et al. 2009; Leithe and Rivedal 2004b; Fykerud et al. 2012) report degradation of endocytosed AGJ vesicles via the cellular endo-/lysosomal degradation pathway in cells that were treated with the phorbol ester, TPA (12-O-tetradecanoylphorbol 13-acetate), an analog of the secondary messenger DAG (diacylglycerol) (Fig. 1, steps 11–15). Hesketh et al. (2010) report loss of GJs from the plasma membrane, GJ endocytosis, and AGJ degradation by autophagy in pacing-induced failing canine ventricular myocardium. Lichtenstein et al. (2011) report that autophagy contributes to the degradation of endogenously (NRK cells and mouse embryonic fibroblasts) and exogenously (HeLa cells) expressed wild type Cx43 protein, and

of wild type and cataract-associated mutant Cx50 proteins in both un-induced cells and in cells in which autophagy was induced by starvation (Lichtenstein et al. 2011). Fong et al. (2012) report the autophagic degradation of AGJ vesicles in HeLa cells expressing exogenous fluorescently tagged Cx43, and in primary porcine pulmonary artery endothelial cells (PAECs) endogenously expressing Cx43. Bejarano et al. (2012) report the Nedd4-mediated ubiquitin-dependent autophagic degradation of internalized GJs in situ (mouse liver), as well as in starved and fed cultured cells expressing Cx43 endogenously and exogenously (mouse embryonic fibroblasts, NIH3T3, COS7, and NRK cells). In all four studies, cytoplasmic AGJ vesicles were detected inside phagophores by ultrastructural analyses, and AGJs were observed to colocalize with the most commonly used autophagy marker protein, LC3-II/Atg8 (Fig. 2). Autophagosomes exhibit a highly characteristic, clearly recognizable double-membrane structure on ultrathin sections, and thus conventional electron microscopy, as performed by Hesketh et al., Lichtenstein et al., Fong et al., and Bejarano et al. is still one of the best techniques for the characterization of autophagosomes (Mizushima 2004) (Fig. 2D–H). Microtubule-associated protein light chain 3 (LC3, the mammalian homolog of the yeast autophagic protein Atg8) is an abundant soluble cytoplasmic protein. It is proteolytically processed by the removal of a few N-terminal amino acid residues shortly after translation that generates LC3-I. LC3-I is recruited to developing phagophores, is covalently conjugated to phosphatidylethanolamine (PE) of the phagophore membrane (termed LC3-II), and remains on autophagosomes for most of their lifetime (Kabeya et al. 2000; Mizushima 2004). Thus, LC3 protein that was used by all four laboratories in colocalization studies is one of the most useful generic marker-proteins for the characterization of autophagosomes (Kabeya et al. 2000) (Fig. 2A).

Although the studies of Lichtenstein et al. and Bejarano et al. were aimed more broadly at a potential role of autophagy contributing to connexin and GJ degradation in general, the Fong et al., and the Hesketh et al. studies were aimed specifically at investigating the fate of internalized AGJ vesicles that others and we had characterized previously (Baker et al. 2008; Gumpert et al. 2008; Jordan et al. 2001; Piehl et al. 2007). To support their findings, Lichtenstein et al. and Bejarano et al., besides using other approaches, knocked down the autophagy-related proteins Atg5 and Atg7 in cells expressing either endogenous or exogenous Cx43, and used the drugs chloroquine and 3MA to inhibit autophagy. In contrast, Fong et al. knocked down expression of the autophagy related proteins, Beclin-1 (Atg6), LC3 (Atg8), LAMP-2, and p62/sequestosome 1 (SQSTM1) (Fig. 2B, C), and used the drugs 3MA, Wortmannin, and Bafilomycin A1 in Cx43-GFP expressing HeLa cells. Taken together, all four complementary studies (Bejarano et al. 2012; Fong et al. 2012; Hesketh et al. 2010; Lichtenstein et al. 2011) provide convincing evidence that under physiological, as well as pathological conditions, GJ plaques are endocytosed from the plasma membrane, and the resulting AGJ vesicles are degraded by autophagy (Figs. 1, 2). As mentioned above, in the Lichtenstein et al., Fong et al., and Bejarano et al. studies the ubiquitin-binding protein p62/SQSTM1 was identified as a protein that targets internalized GJs to autophagic degradation. Knocking down p62/SQSTM1 protein levels as performed by Fong et al. resulted in a significantly increased accumulation of cytoplasmic AGJs (av. 55 %, $n = 4$) and a significantly reduced colocalization (av. 69.5 %, $n = 3$) of AGJs with autophagosomes (Fig. 2C). Remarkably, although autophagic degradation of GJs had been described in several classical ultrastructural analyses of various cells and tissues in situ, including heart, dermis, and liver (Leach and Oliphant 1984; Mazet et al. 1985; Pfeifer 1980; Severs et al. 1989) (Fig. 2E, F, H), until recently, not much attention was attributed to this fundamental GJ degradation pathway. Autophagic degradation of GJs plays a significant role in the regulation of GJ function, as inhibition of cellular autophagy increases GJIC, prevents internalization of GJs, slows down the degradation of connexins, and causes cytoplasmic accumulation of internalized GJ vesicles in situ, as well as in cultured cells expressing either endogenous or exogenous connexin proteins (Bejarano et al. 2012; Fong et al. 2012; Lichtenstein et al. 2011). Some characteristics that aid in a better understanding of the autophagic degradation pathway will be described next.

(Macro)Autophagy

Cells have developed three principal degradation pathways: the proteasomal, the endo-/lysosomal, and the phago-/lysosomal system (termed macroautophagy or simply autophagy), and all three have been implicated previously at various steps in the regulation of GJ stability and connexin degradation (Hesketh et al. 2010; Laing et al. 1997; Leach and Oliphant 1984; Leithe and Rivedal 2004a; Musil et al. 2000; Pfeifer 1980; Qin et al. 2003). Although the two latter ones utilize the lysosome for final degradation and are designed for the degradation of protein aggregates, multiprotein complexes, and cytoplasmic organelles, the proteasomal system is designed for the degradation of single polypeptide chains that require unfolding to be inserted into the tubular core of the cytoplasmically located proteasome. Because AGJ vesicles are highly oligomeric multisubunit protein assemblies, their degradation by the proteasome appears unlikely, and to our knowledge, no evidence exists that would suggest proteasome-mediated degradation of assembled GJ plaques or of

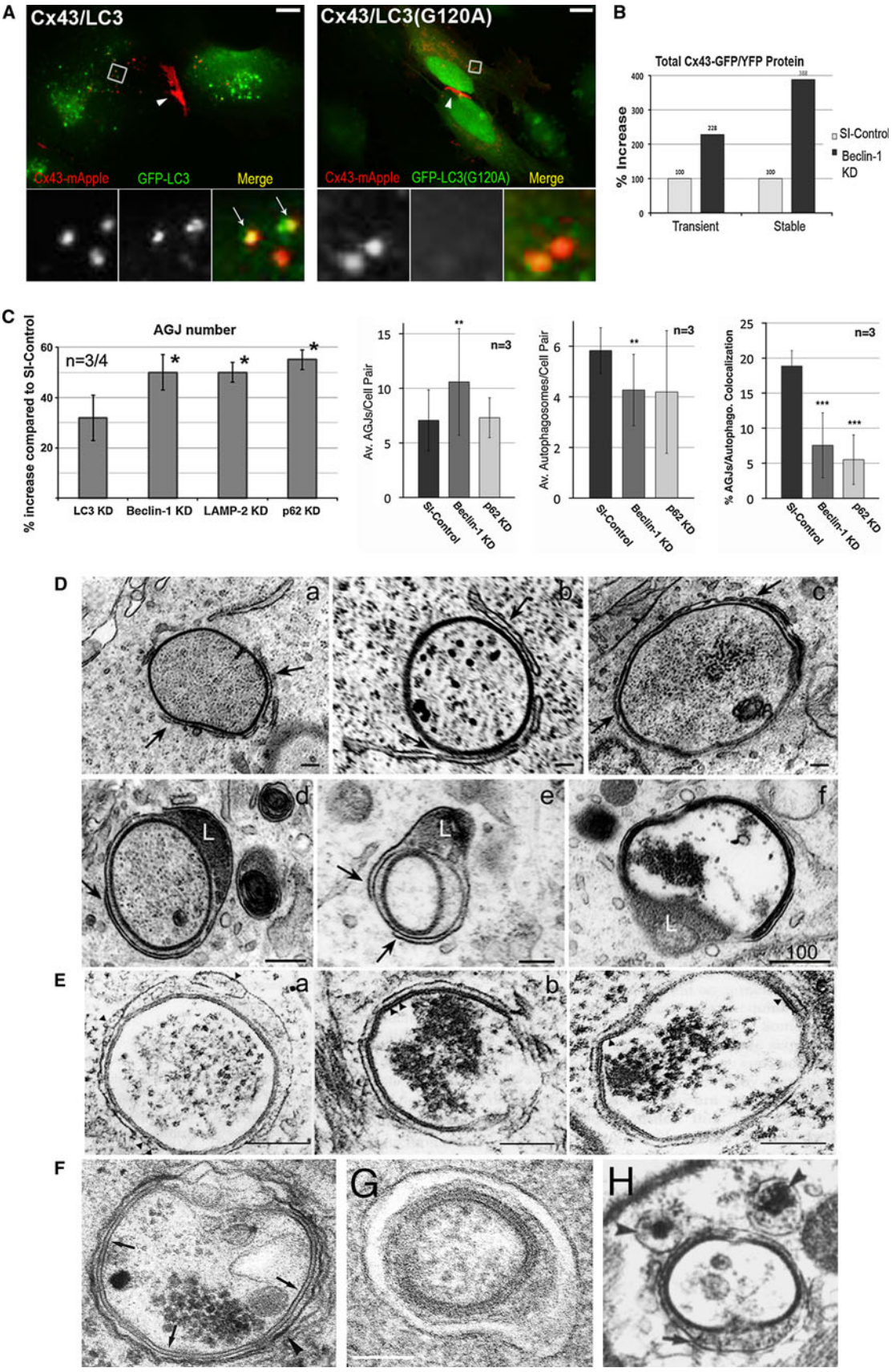
A
Cx43/LC3
Cx43-mApple
GFP-LC3
Merge
Cx43/LC3(G120A)
Cx43-mApple
GFP-LC3(G120A)
Merge
B
Total Cx43-GFP/YFP Protein
% Increase
Sl-Control
Beclin-1 KD
Transient
Stable
C
AGJ number
n=3/4
% increase compared to Sl-Control
LC3 KD
Beclin-1 KD
LAMP-2 KD
p62 KD
Av. AGJs/Cell Pair
Av. Autophagosomes/Cell Pair
% AGJs/Autophago. Colocalization
Sl-Control
Beclin-1 KD
p62 KD
D
a
b
c
d
e
f
L
100
E
a
b
c
F
G
H

Fig. 2 Evidence for autophagic AGJ vesicle degradation. **A** HeLa cells were cotransfected with Cx43-mApple and the mammalian autophagy marker protein GFP-LC3 (*left*) or the activation-deficient LC3 mutant GFP-LC3 (G120A) (*right*). In cells, a fraction of cytoplasmic LC3 (LC3-I) is covalently conjugated to phagophore membranes (LC3-II) that localizes to autophagosomes; LC3 (G120A) cannot be conjugated and remains cytoplasmic. Representative merged fluorescence images acquired 24 h after transfections are shown. Individual and merged fluorescence signals of the boxed areas are shown below at higher magnification. Robust colocalization of cytoplasmic AGJ vesicles present in Cx43-mApple expressing cells (red puncta) with GFP-LC3-II (green puncta) was observed in GFP-LC3 expressing cells, but not in GFP-LC3 (G120A) expressing cells. Representative colocalizing AGJ vesicles are marked with *arrows*; GJs are marked with *arrowheads*. *Scale bars* = 10 μm. **B** Western blot analyses of total Cx43-GFP, or Cx43-YFP protein in transiently and stably expressing HeLa cells 72 h after Beclin-1, a crucial autophagy protein, was depleted by RNAi-oligonucleotide transfection. SI control cells were transfected with a scrambled nontargeting RISC-activating control oligonucleotide. Cx43-GFP/YFP was detected by probing with polyclonal anti-Cx43 antibodies. Normalized quantitative analyses revealed a 2- to 3-fold accumulation of Cx43-GFP/YFP protein in Beclin-1-KD over RNAi-control cell. **C** Quantitative AGJ vesicle analyses performed 72 h after RNA oligonucleotide transfection indicated a significant cytoplasmic AGJ accumulation in Beclin-1/(Atg6), LAMP-2, and p62/SQSTM1 (all autophagy-related proteins) depleted cells (≥50 %, marked with *asterisks*) compared to RNAi control cells (*panel 1*, *left*). Less pronounced AGJ vesicle-accumulation was observed in LC3-depleted cells (32 %), and this was attributed to sufficient inactive LC3-I that may have remained in the LC3-KD cells and may have been converted into active LC3-II. In addition, quantitative analyses of AGJ vesicles (*panel 2*, *center left*), LC3-positive autophagosomes (*panel 3*, *center right*), and colocalizing AGJ/autophagosomes (*panel 4*, *right*) in Beclin-1 and p62/SQSTM1 knockdown cells revealed a significant increase of AGJs, a significant decrease of autophagosomes, and significantly reduced AGJ/autophagosome colocalization in 3 independent experiments (**$p < 0.01$; ***$p < 0.001$). **D** Multiple stages characteristic of progressive autophagosome formation and maturation that formed around AGJ vesicles revealed by ultrastructural analyses of Cx43-GFP expressing HeLa cell preparations. Double-membrane cisternae (presumably isolation membranes, marked with *arrows*) progressively encircled AGJ vesicles (**a**–**c**), coalesced into phagophores (**c**–**e**) and fused with lysosomes (**L**, **d, e**), resulting in AGJ degradation inside the phagosome (**f**). **A**–**D** Reproduced from Fong et al. (2012). **E**–**H** Autophagosomes presumably degrading endogenous AGJs in vivo, identified in the equine stratum spinosum (**E**, reproduced with permission of S. Karger AG, Basel from Leach and Oliphant 1984); rat liver (**F**, reproduced with permission of Elsevier from Pfeifer 1980); mouse embryonic fibroblasts (**G**, reproduced with permission of The Company of Biologists from Lichtenstein et al. 2011); and mammalian cardiomyocytes (**H**, reproduced with permission of Wolters Kluwer Health from Severs et al. 1989). *Scale bars* = 100 nm

AGJ vesicles. Also, it should be noted here that lysosomal inhibitors such as leupeptin, chloroquine, NH_4Cl, and E-64, that previously have been used to gain evidence for endo-/lysosomal degradation of GJs (Berthoud et al. 2004; Laing et al. 1997; Musil et al. 2000; Qin et al. 2003), will also inhibit autophagic GJ degradation, and thus obtained results may not have been accurately interpreted. Additional, future experiments that specifically target one or the other cellular degradation pathway may be required to clarify specific roles of both pathways in GJ degradation. GJ endocytosis, postendocytic sorting, and the role of Cx43 ubiquitination for proteasomal and endo-/lysosomal degradation of connexin polypeptides, connexons, nonaggregated GJ channels, and of GJ plaques has recently been extensively reviewed (Kjenseth et al. 2010; Leithe et al. 2011; Su and Lau 2012). Here, we therefore concentrate on the autophagosomal degradation of AGJs, and on addressing a few prerequisites and factors that appear crucial for allowing a potential alternate endo-/lysosomal degradation of AGJ vesicles (Fig. 1).

Historically, autophagy has been known as a lysosomal degradation pathway that is essential for cell survival after nutrient depletion. However, substantial research over the past decade has indicated that autophagy, beside its well-known function in organelle degradation during starvation, represents a much more common and highly conserved lysosome-based cellular degradation pathway that is specifically designed to remove and degrade protein aggregates, multiprotein complexes, organelles, and invading pathogens from the cytoplasm (Bjorkoy et al. 2005; Hung et al. 2009; Pohl and Jentsch 2009; Ravikumar et al. 2008). Recent studies have further shown that protein aggregates, such as the ones formed by huntingtin and β-amyloid protein, and cellular structures such as the midbody ring, a mitotic cytokinesis leftover multiprotein complex, are all degraded by autophagy (Bjorkoy et al. 2005; Hung et al. 2009; Pohl and Jentsch 2009; Ravikumar et al. 2008). Clearly, these cellular structures are degraded by autophagy independent of starvation. In addition, autophagosomal degradation of membranous/vesicular organelles, as for example, malfunctioning mitochondria, is common. Because the catabolic activity of lysosomes is used in this process, degradation-prone structures first need to be separated from the cytoplasm. This is due to the destructive activity of lysosomal enzymes, which cannot be released directly into the cytoplasm. Indeed, cytoplasmic structures targeted for degradation are engulfed in double-membraned vesicles called autophagosomes that allow lysosomal fusion, degradation, and subsequent recycling of the phagosome cargo and the phagosome membrane (Fig. 1, steps 6–8).

Autophagosomes are formed by the elongation and fusion of phagophore membrane cisternae, which are derived from preautophagosomal structures. The membrane origin of phagophores is still unclear and likely involves multiple sources, such as the plasma membrane (Ravikumar et al. 2010), outer mitochondrial membranes (Hailey et al. 2010), the endoplasmic reticulum (Matsunaga et al. 2010), and the Golgi apparatus (Yen et al. 2010; reviewed recently in Mari et al. 2011). A large number of proteins essential or relevant for autophagosome formation and autophagic degradation (termed Atg-proteins) have

been characterized and can be used as reliable markers for autophagic degradation. Of these, the ubiquitin-like proteins Atg12 (that is conjugated to Atg5) and LC3/Atg8, Atg7, and the PI3-kinase complex-component Beclin-1 (BECN1)/Atg6 (essential for phagophore nucleation, as described above) are especially important for autophagosome formation and autophagic degradation. All of them have been targeted in the four above-mentioned GJ/autophagy studies (Bejarano et al. 2012; Fong et al. 2012; Hesketh et al. 2010; Lichtenstein et al. 2011) (Fig. 2A–C).

Autophagosomal Degradation of AGJs

Because cytoplasmic vesicles in general can fuse with endosomes, at first glance, autophagic degradation of AGJ vesicles might not appear intuitive. However, considering the structural organization of AGJ vesicles, including the dense packing of channels that occupy most or even the entire surface of AGJs in a double-membrane arrangement and their cytoplasmic location, autophagic degradation of AGJ vesicles appears much more plausible. In addition, the two tightly bound membranes of AGJ vesicles may not easily allow their fusion with single-membraned endosomes. Because, as explained above, lysosomal enzymes cannot be released into the cytosol, it is likely that the isolation membrane (the phagophore) formed during the initial steps of autophagy is required to sequester and separate the AGJ vesicle from the cytoplasm, thus providing the sealed membrane container that is required for subsequent lysosome fusion and lysosomal-based AGJ degradation. Finally, the unique structural composition of AGJ vesicles with lumen and inner membrane derived from the neighboring cell (being foreign to the AGJ-receiving host cell) may further direct AGJs to autophagic degradation. Also, although cell–cell communication provided by GJs before endocytosis can only accommodate the diffusion of small molecules, ions, and secondary messengers across the connected plasma membranes, endocytosis of GJs and formation of AGJ vesicles could in addition allow the transfer of potentially harmful substances from cell to cell. Such substances, for example, could include unwanted regulatory proteins, other larger molecules (e.g., micro-RNAs), or even cytoplasmic pathogens that could get entrapped in the AGJ vesicle lumen, further requiring efficient AGJ degradation. Taken together, these structural and functional characteristics, in addition with the fact that autophagy serves as the generic pathway for cytoplasmically localized degradation products (organelles and protein-aggregates), renders autophagic degradation the most likely cellular pathway for AGJ degradation.

Signals that May Direct AGJs for Degradation

Posttranslational modification of proteins is a widespread mechanism to fine-tune the structure, function, and localization of proteins. One of the most versatile and intriguing protein-modifications is the covalent attachment of ubiquitin (Ub) or Ub-like modifications to target proteins. Ub is a 76-amino acid protein, and either single or multiple Ub moieties can be conjugated to lysine amino acid residues of target proteins. An incredible diversity of mono- and poly-Ub chains (in which Ub moieties can be linked to each other via the Ub residues Met1-, Lys6-, Lys11-, Lys27-, Lys29-, Lys33-, Lys48-, and Lys63-) conjugated to target proteins have been characterized, and can range in function from protein activation to protein degradation (see Fushman and Wilkinson 2011 for a recent review). Multiple mono-Ubs, and Lys48- and Lys63-linked poly-Ubs have been recognized as important signals for protein degradation. For example, conjugation of Ub moieties to proteins has been recognized as a signal for both proteasomal targeting (addition of Lys48-linked poly-Ub chains) and more recently, as a sorting signal for internalized vesicles of the late endocytic pathway. This is achieved through the addition of multiple mono-Ub moieties or of Lys63-linked poly-Ub chains which ultimately lead to degradation by lysosomes (Hicke 2001; Hicke and Dunn 2003; Schnell and Hebert 2003; Shih et al. 2002; Stahl and Barbieri 2002). In addition, Lys-63-linked poly-ubiquitination can act as an internalization signal for clathrin-mediated endocytosis (CME) (Belouzard and Rouille 2006; Geetha et al. 2005). In this process, multiple mono-Ub moieties are attached to the target protein and are recognized by specific CME-machinery protein-components that associate with a subset of Ub-binding proteins (specifically Epsin1 and Eps15) (Barriere et al. 2006; Hawryluk et al. 2006; Madshus 2006). Further work has shown that the Ub-binding protein, p62/SQSTM1, recognizes and interacts via its UBA-domain with poly-ubiquitinated proteins (Ciani et al. 2003; Seibenhener et al. 2004; Wilkinson et al. 2001) and delivers poly-ubiquitinated (Lys63-linked) oligomeric protein complexes to the autophagic degradation pathway (Bjorkoy et al. 2005; Pankiv et al. 2007). Ubiquitination of Cx43-based GJs has been described previously (Catarino et al. 2011; Girao et al. 2009; Leithe et al. 2009, 2011; Leithe and Rivedal 2004b; reviewed in Kjenseth et al. 2010; Leithe et al. 2011). The findings that Cx43-based GJs can become ubiquitinated, the known affinity of p62/SQSTM1 for ubiquitinated protein complexes, its colocalization with plasma membrane GJs in HeLa, COS7, and PAE cells (Bejarano et al. 2012; Fong et al. 2012; Lichtenstein et al. 2011), and its apparent involvement in targeting AGJ vesicles to autophagic degradation (Fong et al. 2012) suggest that ubiquitination of Cx43 (and at least Cx50), besides serving as a likely signal

for GJ internalization, may also serve as the signal for targeting AGJ vesicles to autophagic degradation. Future research will be required to determine the potentially numerous types (multiple mono-Ubs, Lys48- and Lys63-linked poly-Ubs, etc.) and functions of connexin ubiquitination (see Kjenseth et al. 2010; Leithe et al. 2011; Su and Lau 2012 for recent reviews that discuss Cx ubiqitination). Recently, Kjenseth et al. (2012) described an additional, Ub-like posttranslational modification of Cx43, SUMOylation (SUMO, small ubiquitin-like modifier) that appears to be involved in regulating GJ stability and turnover. The small Ub-like protein SUMO was found to be conjugated to lysines 144 and 237 of the Cx43-C-terminal domain further complicating the role of Ub and Ub-like signals in the maintenance and degradation of GJs.

Alternative, Endo-/lysosomal Degradation of AGJs

Interestingly, a recent paper by Leithe et al. (2009) reports that in TPA-treated cells [a structural analog of the secondary messenger molecule diacylglycerol (DAG)], internalized GJs appear to be degraded by the endo-/lysosomal and not the autophagosomal pathway (Fig. 1, steps 11–15). Very recently, the Leithe lab identified the protein Smurf2 (the HECT E3 ubiquitin ligase *sm*ad *u*biqitination *r*egulatory *f*actor-2) as a critical factor that regulates GJ internalization and endo-/lysosomal targeting in TPA-treated cells (Fykerud et al. 2012). DAG is a known potent activator of protein kinase C (PKC), and PKC is known to phosphorylate and promote ubiquitination of Cx43 (Leithe et al. 2009; Leithe and Rivedal 2004b; Postma et al. 1998). On the basis of these and our own results, it is tempting to speculate that cells might be able to regulate by which pathway (endo-/lysosomal vs. phago-/lysosomal) specific cargo is sequestered and processed (e.g., endo-/lysosomal and phago-/lysosomal pathways might process internalized GJs in different ways). Furthermore, the level of cargo-phosphorylation and/or ubiquitination might determine which of these pathways is ultimately chosen (basal phosphorylation/ubiquitination signaling autophagic AGJ vesicle degradation; elevated phosphorylation/ubiquitination signaling endo-/lysosomal AGJ vesicle degradation) (Fig. 1, steps 6–10 vs. 11–15). Such a regulation dependent on ubiquitin level has for example been shown for the endocytosis of the epidermal growth factor (EGF) receptor (Sigismund et al. 2005).

Endo-/lysosomal degradation of AGJs as observed in TPA-treated cells by Leithe et al. (2009) of course raises an important question: How is it structurally possible for a double-membrane vesicle that consists of tightly bonded membrane layers and densely packed GJ channels to fuse with a single-membrane endosome? The Rivedal and Leithe laboratories suggest that subsequent to GJ internalization and AGJ formation, the inner AGJ membrane splits and peels away from the outer AGJ membrane, generating a single-membraned cytoplasmic AGJ vesicle that then can fuse with a single-membraned endosome (Kjenseth et al. 2010, 2012; Leithe et al. 2009, 2011). However, because docked GJ channels can not split into undocked connexons under physiological conditions (Ghoshroy et al. 1995; Goodenough and Gilula 1974)—which appears to be the apparent reason for double-membrane GJ endocytosis—it is not clear how membrane separation could be initiated in the AGJ vesicles shortly after their generation. Clearly, low pH (a characteristic of late endosomes and lysosomes, and a potential initiator of GJ splitting), can be excluded because AGJ vesicle membrane-separation needs to occur before AGJ/endosome fusion. Su and Lau (2012) also do not speculate on how cytoplasmic AGJs may end up inside endosomes, as is suggested in their recent review article.

Interestingly, we found that AGJ vesicles examined by electron microscopy may include a small area where the two membranes are void of GJ channels and are not docked or linked to each other (Piehl et al. 2007) (Fig. 3a, and shown schematically in Fig. 1, steps 4, 5, 11 and 12). Similar small AGJ membrane separations were also observed in classical ultrastructural analyses of GJs and AGJ vesicles (see, e.g., Mazet et al. 1985). Possibly, these nonjunctional membrane domains consist of plasma membrane that is derived from both neighboring cells, and we postulate that these areas might originate from plasma membrane regions that were located immediately adjacent to the GJ plaques and were also internalized. To gain further support for this hypothesis, we incubated inducible stably Cx43-YFP expressing HeLa cells (described in Lauf et al. 2002) for 2–4 h with a fluorescently tagged lectin, Alexa594-wheat germ agglutinin (WGA), and examined AGJ vesicles by high-resolution fluorescence microscopy. WGA binds specifically to sialic acid and *N*-acetylglucosaminyl carbohydrate moieties commonly found on extracellular-exposed carbohydrate side-chains of plasma membrane proteins. Due to its relatively large size ($\sim$38 kDa), WGA is not able to traverse the plasma membrane in living cells. However, WGA will label the extracellular surface of plasma membranes and only subsequently will be endocytosed to also label intracellular membrane compartments (Wright 1984). Interestingly we found that a portion of cytoplasmic AGJ vesicles that were likely generated during the WGA-incubation period, exhibited red-fluorescent WGA-puncta (labeled with arrows in Fig. 3b). These results support our hypothesis that the un-docked membrane domains we detected by EM on AGJ vesicles indeed represent plasma membrane that was located in the immediate vicinity of GJ plaques and was concomitantly internalized in the AGJ endocytosis process. For us, it is tempting to speculate that this nonjunctional membrane domain could provide the single membrane area that would

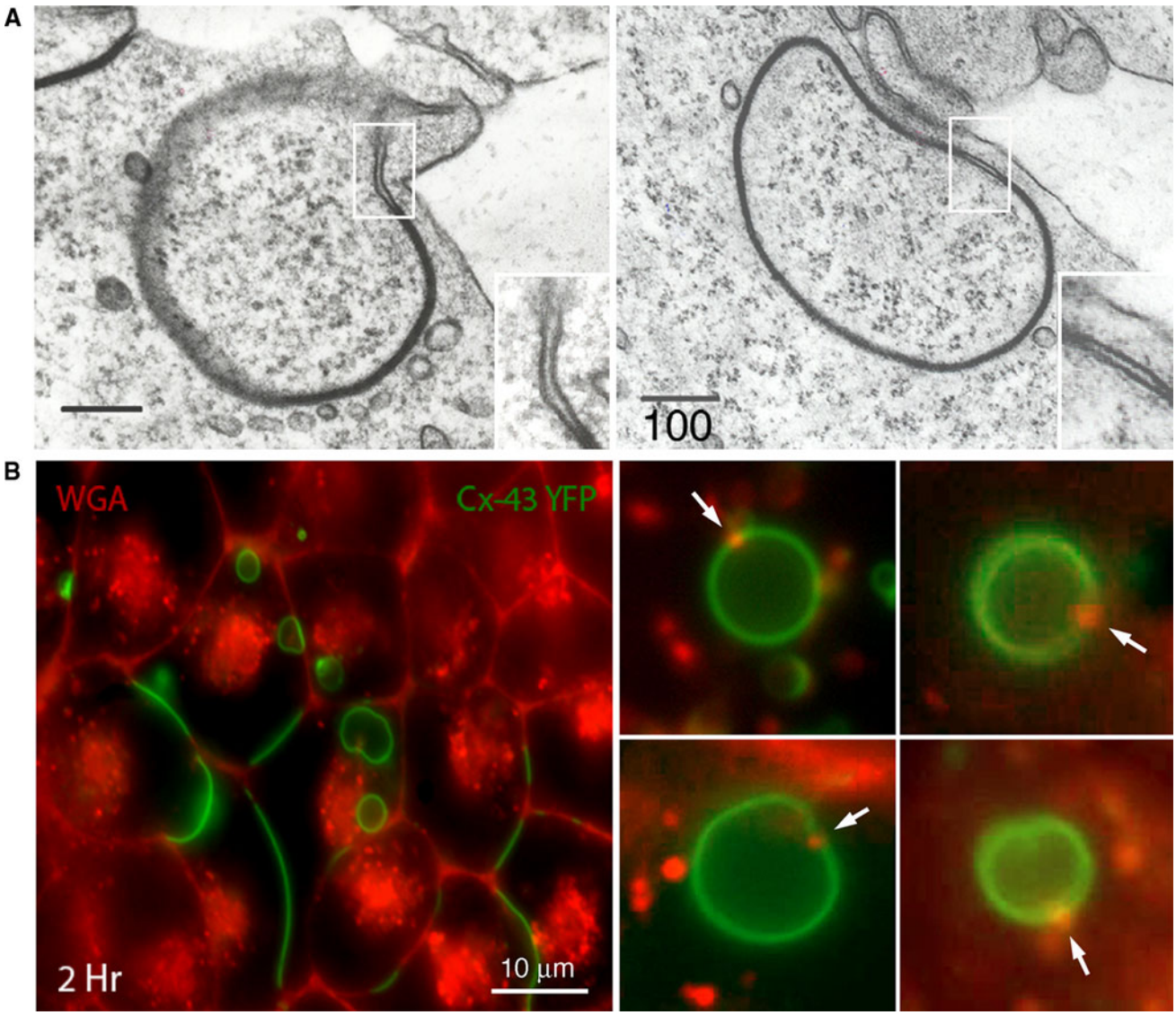

Fig. 3 Fine structure and composition of AGJ vesicles. **a** Double-membrane AGJ vesicles can contain a patch of nonjunctional membrane where the two membrane layers are separated (enlarged in *insets*). These nonjunctional membrane patches appear to be derived from plasma membrane that was located immediately adjacent to the GJ plaque and was concomitantly endocytosed. **b** These nonjunctional AGJ membrane domains label with extracellularly applied, fluorescence-labeled wheat germ agglutinin (WGA) (red puncta on green AGJ vesicles marked with *arrows*) in Cx43-YFP expressing cells. Stable Cx43-YFP expressing HeLa cells were incubated for 2–4 h with Alexa594-labeled WGA and examined by fluorescence microscopy. Low-magnification survey image (*panel 1*, *left*) and high-resolution images of internalized AGJ vesicles (*panels 2–5*, *right*) are shown (*scale bars* = nm in **a** and µm in **b**). **a** Adapted from Piehl et al. (2007)

allow double-membrane AGJ vesicles to fuse with single-membrane endosomes.

Conclusion

A number of recent and classic manuscripts describe the endocytosis of GJ plaques as double-membrane spanning structures (Baker et al. 2008; Falk et al. 2009; Ginzberg and Gilula 1979; Gumpert et al. 2008; Jordan et al. 2001; Larsen et al. 1979; Mazet et al. 1985; Piehl et al. 2007) and the autophagosomal, and potentially endo-/lysosomal degradation of the resulting cytoplasmic double-membrane AGJ vesicles (Bejarano et al. 2012; Fong et al. 2012; Hesketh et al. 2010; Leach and Oliphant 1984; Leithe et al. 2009; Lichtenstein et al. 2011; Pfeifer 1980; Severs et al. 1989). On the basis of the recent and classic observations described above, we hypothesize that double-membrane GJ endocytosis is the only practical means of how cells can efficiently remove plasma membrane-localized GJ plaques.

Potential GJ splitting, or GJ dispersion (Lane and Swales 1980) have not been observed by us in any of our multiple live-cell recordings and therefore are not considered efficient mechanisms of GJ removal. Furthermore, on the basis of the recently published evidence suggesting autophagosomal degradation of AGJ vesicles (Fong et al. 2012; Hesketh et al. 2010; Lichtenstein et al. 2011), the knowledge that autophagy serves as the generic pathway for the degradation of cytoplasmically localized organelles and protein-aggregates, and based on the known structural composition of AGJ vesicles consisting of tightly sealed-together membrane layers, we further hypothesize that the default degradation pathway for these cytoplasmic structures is (macro)autophagy. Alternatively, endo-/lysosomal AGJ degradation described to occur in TPA-treated cells may be achieved on the basis of the presence of AGJ membrane-domains where the two membrane-layers are not linked to each other (such as the ones we have characterized and described above, see Fig. 3), providing the structural prerequisite to allow single-membrane endosomes to fuse with double-membrane AGJ vesicles.

Finally, we speculate that the level of connexin phosphorylation and/or ubiquitination might allow cells to regulate by which pathway (endo-/lysosomal versus phago-/lysosomal), endocytosed AGJ vesicles are sequestered and processed; an interesting hypothesis considering that autophagosomal and endo-/lysosomal processing may render different (degradation) products. Future research will elucidate whether our hypotheses are correct, and if there are additional cellular pathways that may dictate the fate of endocytosed GJs.

Acknowledgments Work in the laboratory of M.M.F. is supported by NIHs NIGMS (grant GM55725) and by Lehigh University. We thank additional members of the Falk laboratory for critical comments. We wish to extend our sincere appreciation to Ross Johnson, whose dedication to gap junctions has revealed so many exciting aspects of this truly amazing cellular structure. His excitement and passion has fueled this research and will fuel the passion of many generations of researchers to come. Although we know so much about gap junctions, so much more still needs to be discovered! His contributions to this field have been significant.

References

Baker SM, Kim N, Gumpert AM, Segretain D, Falk MM (2008) Acute internalization of gap junctions in vascular endothelial cells in response to inflammatory mediator-induced G-protein coupled receptor activation. FEBS Lett 582:4039–4046

Baldwin AL, Thurston G (2001) Mechanics of endothelial cell architecture and vascular permeability. Crit Rev Biomed Eng 29:247–278

Barriere H, Nemes C, Lechardeur D, Khan-Mohammad M, Fruh K, Lukacs GL (2006) Molecular basis of oligoubiquitin-dependent internalization of membrane proteins in Mammalian cells. Traffic 7:282–297

Beardslee MA, Laing JG, Beyer EC, Saffitz JE (1998) Rapid turnover of connexin43 in the adult rat heart. Circ Res 83:629–635

Bejarano E, Girao H, Yuste A, Patel B, Marques C, Spray DC, Pereira P, Cuervo AM (2012) Autophagy modulates dynamics of connexins at the plasma membrane in a ubiquitin-dependent manner. Mol Biol Cell 23:2156–2169

Belouzard S, Rouille Y (2006) Ubiquitylation of leptin receptor OB-Ra regulates its clathrin-mediated endocytosis. EMBO J 25: 932–942

Berthoud VM, Minogue PJ, Laing JG, Beyer EC (2004) Pathways for degradation of connexins and gap junctions. Cardiovasc Res 62:256–267

Bjorkoy G, Lamark T, Brech A, Outzen H, Perander M, Overvatn A, Stenmark H, Johansen T (2005) p62/SQSTM1 forms protein aggregates degraded by autophagy and has a protective effect on huntingtin-induced cell death. J Cell Biol 171:603–614

Blomstrand F, Venance L, Siren AL, Ezan P, Hanse E, Glowinski J, Ehrenreich H, Giaume C (2004) Endothelins regulate astrocyte gap junctions in rat hippocampal slices. Eur J Neurosci 19:1005–1015

Catarino S, Ramalho JS, Marques C, Pereira P, Girao H (2011) Ubiquitin-mediated internalization of connexin43 is independent of the canonical endocytic tyrosine-sorting signal. Biochem J 437:255–267

Ciani B, Layfield R, Cavey JR, Sheppard PW, Searle MS (2003) Structure of the ubiquitin-associated domain of p62 (SQSTM1) and implications for mutations that cause Paget's disease of bone. J Biol Chem 278:37409–37412

Delmar M, Coombs W, Sorgen P, Duffy HS, Taffet SM (2004) Structural bases for the chemical regulation of connexin43 channels. Cardiovasc Res 62:268–275

Falk MM (2010) Adherens junctions remain dynamic. BMC Biol 8:34

Falk MM, Baker SM, Gumpert AM, Segretain D, Buckheit RW 3rd (2009) Gap junction turnover is achieved by the internalization of small endocytic double-membrane vesicles. Mol Biol Cell 20:3342–3352

Fallon RF, Goodenough DA (1981) Five-hour half-life of mouse liver gap-junction protein. J Cell Biol 90:521–526

Fong JT, Kells RM, Gumpert AM, Marzillier JY, Davidson MW, Falk MM (2012) Internalized gap junctions are degraded by autophagy. Autophagy 8:794–811

Fushman D, Wilkinson KD (2011) Structure and recognition of polyubiquitin chains of different lengths and linkage. F1000 Biol Rep 3:26

Fykerud TA, Kjenseth A, Schink KO, Sirnes S, Bruun J, Omori Y, Brech A, Rivedal E, Leithe E (2012) Smad ubiquitination regulatory factor-2 controls gap junction intercellular communication by modulating endocytosis and degradation of connexin43. J Cell Sci. doi:10.1242/j cs.093500

Gaietta G, Deerinck TJ, Adams SR, Bouwer J, Tour O, Laird DW, Sosinsky GE, Tsien RY, Ellisman MH (2002) Multicolor and electron microscopic imaging of connexin trafficking. Science 296:503–507

Geetha T, Jiang J, Wooten MW (2005) Lysine 63 polyubiquitination of the nerve growth factor receptor TrkA directs internalization and signaling. Mol Cell 20:301–312

Ghoshroy S, Goodenough DA, Sosinsky GE (1995) Preparation, characterization, and structure of half gap junctional layers split with urea and EGTA. J Membr Biol 146:15–28

Giepmans BN, Moolenaar WH (1998) The gap junction protein connexin43 interacts with the second PDZ domain of the zona occludens-1 protein. Curr Biol 8:931–934

Gilleron J, Fiorini C, Carette D, Avondet C, Falk MM, Segretain D, Pointis G (2008) Molecular reorganization of Cx43, Zo-1 and Src complexes during the endocytosis of gap junction plaques in response to a non-genomic carcinogen. J Cell Sci 121: 4069–4078

Ginzberg RD, Gilula NB (1979) Modulation of cell junctions during differentiation of the chicken otocyst sensory epithelium. Dev Biol 68:110–129

Girao H, Catarino S, Pereira P (2009) Eps15 interacts with ubiquitinated Cx43 and mediates its internalization. Exp Cell Res 315:3587–3597

Goodenough DA, Gilula NB (1974) The splitting of hepatocyte gap junctions and zonulae occludentes with hypertonic disaccharides. J Cell Biol 61:575–590

Gumpert AM, Varco JS, Baker SM, Piehl M, Falk MM (2008) Double-membrane gap junction internalization requires the clathrin-mediated endocytic machinery. FEBS Lett 582:2887–2892

Hailey DW, Rambold AS, Satpute-Krishnan P, Mitra K, Sougrat R, Kim PK, Lippincott-Schwartz J (2010) Mitochondria supply membranes for autophagosome biogenesis during starvation. Cell 141:656–667

Hawryluk MJ, Keyel PA, Mishra SK, Watkins SC, Heuser JE, Traub LM (2006) Epsin 1 is a polyubiquitin-selective clathrin-associated sorting protein. Traffic 7:262–281

Hesketh GG, Shah MH, Halperin VL, Cooke CA, Akar FG, Yen TE, Kass DA, Machamer CE, Van Eyk JE, Tomaselli GF (2010) Ultrastructure and regulation of lateralized connexin43 in the failing heart. Circ Res 106:1153–1163

Hicke L (2001) Protein regulation by monoubiquitin. Nat Rev Mol Cell Biol 2:195–201

Hicke L, Dunn R (2003) Regulation of membrane protein transport by ubiquitin and ubiquitin-binding proteins. Annu Rev Cell Dev Biol 19:141–172

Hung SY, Huang WP, Liou HC, Fu WM (2009) Autophagy protects neuron from Abeta-induced cytotoxicity. Autophagy 5:502–510

Hunter AW, Barker RJ, Zhu C, Gourdie RG (2005) Zonula occludens-1 alters connexin43 gap junction size and organization by influencing channel accretion. Mol Biol Cell 16:5686–5698

Jordan K, Chodock R, Hand AR, Laird DW (2001) The origin of annular junctions: a mechanism of gap junction internalization. J Cell Sci 114:763–773

Kabeya Y, Mizushima N, Ueno T, Yamamoto A, Kirisako T, Noda T, Kominami E, Ohsumi Y, Yoshimori T (2000) LC3, a mammalian homologue of yeast Apg8p, is localized in autophagosome membranes after processing. EMBO J 19:5720–5728

Kjenseth A, Fykerud T, Rivedal E, Leithe E (2010) Regulation of gap junction intercellular communication by the ubiquitin system. Cell Signal 22:1267–1273

Kjenseth A, Fykerud TA, Sirnes S, Bruun J, Kolberg M, Yohannes Z, Omori Y, Rivedal E, Leithe E (2012) The gap junction channel protein connexin43 is covalently modified and regulated by SUMOylation. J Biol Chem 287:15851–15861

Laing JG, Tadros PN, Westphale EM, Beyer EC (1997) Degradation of connexin43 gap junctions involves both the proteasome and the lysosome. Exp Cell Res 236:482–492

Laird DW (2005) Connexin phosphorylation as a regulatory event linked to gap junction internalization and degradation. Biochim Biophys Acta 1711:172–182

Lampe PD, Lau AF (2004) The effects of connexin phosphorylation on gap junctional communication. Int J Biochem Cell Biol 36:1171–1186

Lane NJ, Swales LS (1980) Dispersal of junctional particles, not internalization, during the in vivo disappearance of gap junctions. Cell 19:579–586

Larsen WJ, Tung HN, Murray SA, Swenson CA (1979) Evidence for the participation of actin microfilaments and bristle coats in the internalization of gap junction membrane. J Cell Biol 83:576–587

Lauf U, Giepmans BN, Lopez P, Braconnot S, Chen SC, Falk MM (2002) Dynamic trafficking and delivery of connexons to the plasma membrane and accretion to gap junctions in living cells. Proc Natl Acad Sci USA 99:10446–10451

Leach DH, Oliphant LW (1984) Degradation of annular gap junctions of the equine hoof wall. Acta Anat (Basel) 120:214–219

Leithe E, Rivedal E (2004a) Epidermal growth factor regulates ubiquitination, internalization and proteasome-dependent degradation of connexin43. J Cell Sci 117:1211–1220

Leithe E, Rivedal E (2004b) Ubiquitination and down-regulation of gap junction protein connexin-43 in response to 12-O-tetradecanoylphorbol 13-acetate treatment. J Biol Chem 279:50089–50096

Leithe E, Kjenseth A, Sirnes S, Stenmark H, Brech A, Rivedal E (2009) Ubiquitylation of the gap junction protein connexin-43 signals its trafficking from early endosomes to lysosomes in a process mediated by Hrs and Tsg101. J Cell Sci 122:3883–3893

Leithe E, Sirnes S, Fykerud T, Kjenseth A, Rivedal E (2011) Endocytosis and post-endocytic sorting of connexins. Biochim Biophys Acta 1818:1870–1879

Lichtenstein A, Minogue PJ, Beyer EC, Berthoud VM (2011) Autophagy: a pathway that contributes to connexin degradation. J Cell Sci 124:910–920

Lum H, Malik AB (1994) Regulation of vascular endothelial barrier function. Am J Physiol 267:L223–L241

Madshus IH (2006) Ubiquitin binding in endocytosis—how tight should it be and where does it happen? Traffic 7:258–261

Mari M, Tooze SA, Reggiori F (2011) The puzzling origin of the autophagosomal membrane. F1000 Biol Rep 3:25

Matsunaga K, Morita E, Saitoh T, Akira S, Ktistakis NT, Izumi T, Noda T, Yoshimori T (2010) Autophagy requires endoplasmic reticulum targeting of the PI3-kinase complex via Atg14L. J Cell Biol 190:511–521

Mazet F, Wittenberg BA, Spray DC (1985) Fate of intercellular junctions in isolated adult rat cardiac cells. Circ Res 56:195–204

Mizushima N (2004) Methods for monitoring autophagy. Int J Biochem Cell Biol 36:2491–2502

Moreno AP (2005) Connexin phosphorylation as a regulatory event linked to channel gating. Biochim Biophys Acta 1711:164–171

Musil LS, Le AC, VanSlyke JK, Roberts LM (2000) Regulation of connexin degradation as a mechanism to increase gap junction assembly and function. J Biol Chem 275:25207–25215

Pahujaa M, Anikin M, Goldberg GS (2007) Phosphorylation of connexin43 induced by Src: regulation of gap junctional communication between transformed cells. Exp Cell Res 313:4083–4090

Pankiv S, Clausen TH, Lamark T, Brech A, Bruun JA, Outzen H, Overvatn A, Bjorkoy G, Johansen T (2007) p62/SQSTM1 binds directly to Atg8/LC3 to facilitate degradation of ubiquitinated protein aggregates by autophagy. J Biol Chem 282:24131–24145

Pfeifer U (1980) Autophagic sequestration of internalized gap junctions in rat liver. Eur J Cell Biol 21:244–246

Piehl M, Lehmann C, Gumpert A, Denizot JP, Segretain D, Falk MM (2007) Internalization of large double-membrane intercellular vesicles by a clathrin-dependent endocytic process. Mol Biol Cell 18:337–347

Pohl C, Jentsch S (2009) Midbody ring disposal by autophagy is a post-abscission event of cytokinesis. Nat Cell Biol 11:65–70

Postma FR, Hengeveld T, Alblas J, Giepmans BN, Zondag GC, Jalink K, Moolenaar WH (1998) Acute loss of cell–cell communication caused by G protein-coupled receptors: a critical role for c-Src. J Cell Biol 140:1199–1209

Qin H, Shao Q, Igdoura SA, Alaoui-Jamali MA, Laird DW (2003) Lysosomal and proteasomal degradation play distinct roles in the life cycle of Cx43 in gap junctional intercellular communication-deficient and -competent breast tumor cells. J Biol Chem 278:30005–30014

Ravikumar B, Imarisio S, Sarkar S, O'Kane CJ, Rubinsztein DC (2008) Rab5 modulates aggregation and toxicity of mutant

huntingtin through macroautophagy in cell and fly models of Huntington disease. J Cell Sci 121:1649–1660

Ravikumar B, Moreau K, Jahreiss L, Puri C, Rubinsztein DC (2010) Plasma membrane contributes to the formation of pre-autophagosomal structures. Nat Cell Biol 12:747–757

Rhett JM, Gourdie RG (2011) The perinexus: a new feature of Cx43 gap junction organization. Heart Rhythm 9:619–623

Rhett JM, Jourdan J, Gourdie RG (2011) Connexin 43 connexon to gap junction transition is regulated by zonula occludens-1. Mol Biol Cell 22:1516–1528

Schnell DJ, Hebert DN (2003) Protein translocons: multifunctional mediators of protein translocation across membranes. Cell 112:491–505

Seibenhener ML, Babu JR, Geetha T, Wong HC, Krishna NR, Wooten MW (2004) Sequestosome 1/p62 is a polyubiquitin chain binding protein involved in ubiquitin proteasome degradation. Mol Cell Biol 24:8055–8068

Severs NJ, Shovel KS, Slade AM, Powell T, Twist VW, Green CR (1989) Fate of gap junctions in isolated adult mammalian cardiomyocytes. Circ Res 65:22–42

Shih SC, Katzmann DJ, Schnell JD, Sutanto M, Emr SD, Hicke L (2002) Epsins and Vps27p/Hrs contain ubiquitin-binding domains that function in receptor endocytosis. Nat Cell Biol 4: 389–393

Sigismund S, Woelk T, Puri C, Maspero E, Tacchetti C, Transidico P, Di Fiore PP, Polo S (2005) Clathrin-independent endocytosis of ubiquitinated cargos. Proc Natl Acad Sci USA 102:2760–2765

Solan JL, Lampe PD (2009) Connexin43 phosphorylation: structural changes and biological effects. Biochem J 419:261–272

Spinella F, Rosano L, Di Castro V, Nicotra MR, Natali PG, Bagnato A (2003) Endothelin-1 decreases gap junctional intercellular communication by inducing phosphorylation of connexin 43 in human ovarian carcinoma cells. J Biol Chem 278:41294–41301

Stahl PD, Barbieri MA (2002) Multivesicular bodies and multivesicular endosomes: the "ins and outs" of endosomal traffic. Sci STKE 2002:pe32

Su V, Lau AF (2012) Ubiquitination, intracellular trafficking, and degradation of connexins. Arch Biochem Biophys 524:16–22

Toyofuku T, Yabuki M, Otsu K, Kuzuya T, Hori M, Tada M (1998) Direct association of the gap junction protein connexin-43 with ZO-1 in cardiac myocytes. J Biol Chem 273:12725–12731

van Zeijl L, Ponsioen B, Giepmans BN, Ariaens A, Postma FR, Varnai P, Balla T, Divecha N, Jalink K, Moolenaar WH (2007) Regulation of connexin43 gap junctional communication by phosphatidylinositol 4,5-bisphosphate. J Cell Biol 177:881–891

Warn-Cramer BJ, Lau AF (2004) Regulation of gap junctions by tyrosine protein kinases. Biochim Biophys Acta 1662:81–95

Wilkinson CR, Seeger M, Hartmann-Petersen R, Stone M, Wallace M, Semple C, Gordon C (2001) Proteins containing the UBA domain are able to bind to multi-ubiquitin chains. Nat Cell Biol 3:939–943

Wong CW, Christen T, Kwak BR (2004) Connexins in leukocytes: shuttling messages? Cardiovasc Res 62:357–367

Wright CS (1984) Structural comparison of the two distinct sugar binding sites in wheat germ agglutinin isolectin II. J Mol Biol 178:91–104

Yen WL, Shintani T, Nair U, Cao Y, Richardson BC, Li Z, Hughson FM, Baba M, Klionsky DJ (2010) The conserved oligomeric Golgi complex is involved in double-membrane vesicle formation during autophagy. J Cell Biol 188:101–114

J Membrane Biol (2012) 245:477–482
DOI 10.1007/s00232-012-9466-y

The Noncanonical Functions of Cx43 in the Heart

Esperanza Agullo-Pascual · Mario Delmar

Received: 20 April 2012 / Accepted: 20 June 2012 / Published online: 24 July 2012

Abstract There is abundant evidence showing that connexins form gap junctions. Yet this does not exclude the possibility that connexins can exert other functions, separate from that of gap junction (or even a permeable hemichannel) formation. Here, we focus on these noncanonical functions of connexin43 (Cx43), particularly in the heart. We describe two specific examples: the importance of Cx43 on intercellular adhesion, and the role of Cx43 in the function of the sodium channel. We propose that these two functions of Cx43 have important repercussions on the propagation of electrical activity in the heart, irrespective of the presence of permeable gap junction channels. Overall, the gap junction–independent functions of Cx43 in cardiac electrophysiology emerge as an exciting area of future research.

Keywords Arrhythmia · Cell–cell adhesion · Connexin43 · Heart

Introduction

Sixty years ago, Silvio Weidmann published his classic article on "The Electrical Constants of Purkinje Fibers." In it, he beautifully demonstrated that electrotonic propagation in cardiac tissue extends well beyond the size of a single cell (Weidmann 1952). His observations provided the physiological evidence that cardiac cells are electrically coupled via low-resistive pathways. Electron microscopic observations followed, culminating with the elegant work of Revel and Karnovsky (1967) showing that at the site of close appositional membranes in the cardiac intercalated disc, the membranes were not fused. Instead, the membranes were separated by a gap, traversed by junctions. These findings led Revel to later coin the term *gap junctions*. The demonstration that gap junctions are formed by oligomerization of connexin proteins established gap junction formation as the key function of connexin molecules. Yet the fundamental importance of connexins in intercellular communication does not exclude the possibility that connexins may exert other functions, separate and independent from that of gap junction formation. This is hardly a novel concept. Twenty years ago, Ross Johnson and his colleagues reported a very important discovery: Fab fragments of antibodies to the extracellular domain of connexin43 (Cx43), the most abundant connexin in the heart, inhibits adherens junction assembly in cells in culture (Meyer et al. 1992). This unexpected finding has been followed by others, showing that Cx43 is not only a pore-forming protein that allows ions and small molecules to move between cells (see, e.g., Danik et al. 2008; Jansen et al. 2012a, b; Francis et al. 2011; Soder et al. 2009). Our understanding of the molecular nature of connexins and their function has expanded enormously since Ross Johnson, Weidmann, Revel, Bennett, Gilula, Goodenough, and many other giants of science first paved the way. Yet a number of interesting questions about the role of connexins in biology remain unanswered, while other concepts that seemed established are now challenged by novel experimental results

Here, we will dwell on what we call the noncanonical functions of Cx43—that is, functions that go beyond that of

E. Agullo-Pascual · M. Delmar (✉)
The Leon H. Charney Division of Cardiology, New York University School of Medicine, 522 First Avenue, Smilow 805, New York, NY 10016, USA
e-mail: Mario.Delmar@nyumc.org

E. Agullo-Pascual
e-mail: esperanza.agullo-pascual@nyumc.org

gap junction formation. Although our discussion will center on Cx43 and its role in heart function, these issues likely extend to the functions of other connexins and in other organs. Of the many interesting angles that apply to this topic, we will cover only two aspects: intercellular adhesion and sodium channel function. These functions are described from the point of view of Cx43 as a component of the protein interacting network (the interactome) that populates the cardiac intercalated disc.

The Intercalated Disc as the Site of a Protein Interacting Network

Cardiac myocytes are highly differentiated, specialized, and compartmentalized cells. Proteins organize in defined microdomains. Slight changes in the position of a protein within its domain can bring about a major disruption in function (see, e.g., Nikolaev et al. 2010). Connexins occupy a subcellular region called the intercalated disc. This electron dense structure is located at the point where two cardiac cells meet end to end. In its classical definition, the intercalated disc is composed of three electron dense structures: gap junctions, desmosomes, and adherens junctions. The latter two are involved in mechanical coupling between cells. Desmosomes couple to intermediate filaments (desmin, in the case of the heart), whereas adherens junctions anchor N-cadherins to the actin cytoskeleton. A mixed desmosome/adherens junction structure, dubbed the *area composita*, is also present in the adult mammalian heart (Franke et al. 2006). Originally these structures were considered separate and independent from each other. Recent data suggest this not to be the case. Furthermore, the advent of immunofluorescence techniques brought about the demonstration that other molecules, not classically considered junctional, are also present at the cell end and in fact colocalize with junctional molecules. Of particular interest are two ion channel proteins fundamental to normal cardiac electrophysiology: the sodium channel alpha subunit, Nav1.5, and the potassium channel protein $K_V1.5$. For a number of years, each of these channels, and their accessory proteins, were studied as independent entities. Yet recent data show that there is extensive cross-talk at the intercalated disc, and that this cross-talk extends to interactions between complexes previously seen as being independent (Fig. 1). As such, loss of expression of plakophilin-2 (PKP2), a desmosomal molecule, affects gap junction–mediated coupling (Oxford et al. 2007) as well as sodium channel function (Sato et al. 2009); loss of N-cadherin expression affects gap junctions (Li et al. 2005) and also the function of $K_V1.5$ channels (Cheng et al. 2011); loss of intercellular contact leads to a decrease in sodium current (Lin et al. 2011); expression of ankyrin-G (AnkG), a protein

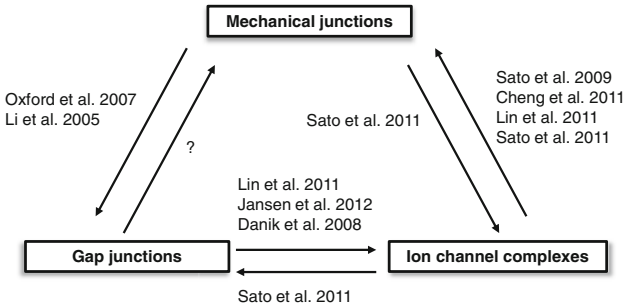

Fig. 1 Diagram indicating cross-talk between gap junctions, mechanical junctions, and ion channel complexes. Gap junctions refers to Cx43, while mechanical junctions includes desmosomes and adherens junctions (N-cadherin). Ion channel complexes refers primarily to sodium channel complex and $K_V1.5$. Citations correspond to experimental evidence in cardiac preparations that support the interaction described

associated with the sodium channel complex (Lowe et al. 2008), is necessary for proper intercellular adhesion strength and for proper electrical coupling (Sato et al. 2011); finally, expression of Cx43, a protein previously associated only with gap junctions, is in fact required for the normal function of sodium (Jansen et al. 2011) and potassium currents (Danik et al. 2008). When taken together, the evidence suggests that the intercalated disc is not a site where independent molecules reside, but rather the host of an interactome—a protein-interacting web that involves molecules relevant to excitability, propagation, and mechanical coupling between cells.

Cx43 and Intercellular Adhesion

The possible interaction between connexins and mechanical junctions in the heart was highlighted by the findings of Jeff Saffitz and his colleagues. These investigators examined the hearts of patients afflicted with arrhythmogenic right ventricular cardiomyopathy, a disease related to mutations in proteins of the desmosome, and demonstrated a consistent loss of gap junction plaques from the intercalated disc (Kaplan et al. 2004). Follow-up work showed that loss of expression of the desmosomal protein, PKP2, leads to a loss of Cx43 from the site of intercellular contact and an $\sim$50 % decrease in the extent of dye transfer between cells (Oxford et al. 2007). These and other studies strongly supported the notion that mechanical junctions affect gap junctions. On the basis of the early work of Meyer et al. (1992), we have now asked a reciprocal question: is Cx43 expression necessary to maintain intercellular adhesion strength? To address this question, we implemented a dispase assay, whereby the contact between the cells and the extracellular matrix is disrupted by the use of dispase. If adhesion between cells is strong, the layer

lifts as one sheet (cells remain attached to one another). If cell–cell adhesion is weaker, the sheet fragments. Thus, the more fragments, the weaker the mechanical coupling. Using this method, we recently showed that loss of Ank-G expression (a protein that scaffolds for the sodium channel complex) causes a decrease in mechanical coupling between cells (Sato et al. 2011). Here, we applied this method to compare two cell populations: HEK293 cells that endogenously express Cx43; and a stable HEK293 line where we used lentivirus to permanently silence Cx43 expression. Three groups are compared: untreated (UNT), treated with a virus that contains a nonsilencing construct (ϕshRNA-Cx43), and a third group where Cx43 expression was prevented (shRNA-Cx43). Western blot analysis revealed the loss of Cx43 expression in the corresponding group (Fig. 2), and loss of Cx43 expression brought about a loss of intercellular adhesion strength, represented by a significant increase in the number of fragments detected 90 min after dispase addition. Thus Cx43 expression is relevant to mechanical coupling. Whether this effect is consequent to gap junctions being a physical element that provides intercellular adhesion, or whether the result involves intermolecular interactions between Cx43 and components of the mechanical junctions, remains to be determined. The results do show that intercellular adhesion strength is a function of Cx43 that extends beyond the formation of a low-resistive pathway between cells.

Cx43 Is Necessary for Sodium Channel Function

Figure 1 also shows an arrow connecting Cx43 to the sodium channel complex. This is an exciting and novel finding regarding the noncanonical functions of Cx43 in the heart. Indeed, in the classical description, sodium channels provide the current that is necessary for the generation of an action potential in most cardiac cells, whereas Cx43 forms gap junctions, the channels that allow for that electrical charge to move between one cell and the next. This description then separates the type of channel, with its function: sodium channels are responsible for cell excitability; gap junctions allow cell–cell passage of charge. In a recent study, however, we reported that loss of Cx43 expression brings about a loss of sodium current amplitude (Jansen et al. 2012a). In other words, the molecule necessary for making the gap junctions is actually necessary to maintain the complex in charge of generating the action potential. This means that loss of Cx43 expression is in fact a double-edge sword: not only will the path between cells be disrupted, but also the amount of charge that is generating by the excited cell will decrease. Loss of Cx43 expression, as it happens in a number of pathological cardiac conditions (Desplantez et al. 2007; Akar et al. 2007; Chkourko et al. 2012; Kalcheva et al. 2007; Qu et al. 2009), can have complex deleterious effects on propagation.

Novel Roles of Cx43 in Cardiac Propagation: Sodium Current and the Intercellular Space

These findings come at a time when the classical description of cardiac propagation deserves to be reviewed. Early models based on the principles of continuous cable theory represented gap junctions as passive resistors providing the only means for passage of charge between cells. When incorporated into a model of cardiac propagation, these equations predicted that reductions in gap junction–mediated communication would bring about a concomitant reduction in conduction velocity. The first serious challenge to this notion came from experiments demonstrating that 50–80 % loss of Cx43 expression in the heart causes a decrease in junctional conductance between cells (Yao et al. 2003), but not a decrease in conduction velocity (Morley et al. 2000; Danik et al. 2004). Are gap junctions, then, the only path for transfer of charge between cardiac cells? What is the missing element (missing from the equations) that preserves propagation when gap junction–mediated conductance decreases?

Although a conclusive answer has not yet been found, it seems pertinent to remain open to models that, though less conventional, may better represent what happens at the site of contact between cells. We refer in particular to the proposed electrical field mechanism of cardiac propagation. This model postulates that the large inward sodium current in the proximal side of an intercellular cleft can generate a large negative extracellular potential within the cleft, effectively depolarizing the membrane of the distal cell, activating its sodium channels and allowing for propagation to continue downstream, even in the absence of functional gap junctions (Sperelakis 2002; Hand and Peskin 2010; Mori et al. 2008). Although this mechanism would play an insignificant role when gap junctions are present and functional, it would become crucial to maintain propagation when gap junctions close or when connexins are lost.

The effect of electric fields, also known as ephaptic interactions, has been extensively investigated in the nervous system. These nonsynaptic mechanisms play a significant role in neuronal function and can mediate neuronal synchrony on a fast scale compared to ionic and chemical mechanisms that operate on a much slower scale (Jefferys 1995). In this context, recent studies of the presence of electrical synapses in the mammalian central nervous system have described the chemical transmission through Cx36 in neurons of the mesencephalic trigeminal nucleus. Although in these cells the fraction of opened channels is small, the sodium and potassium conductances enhances

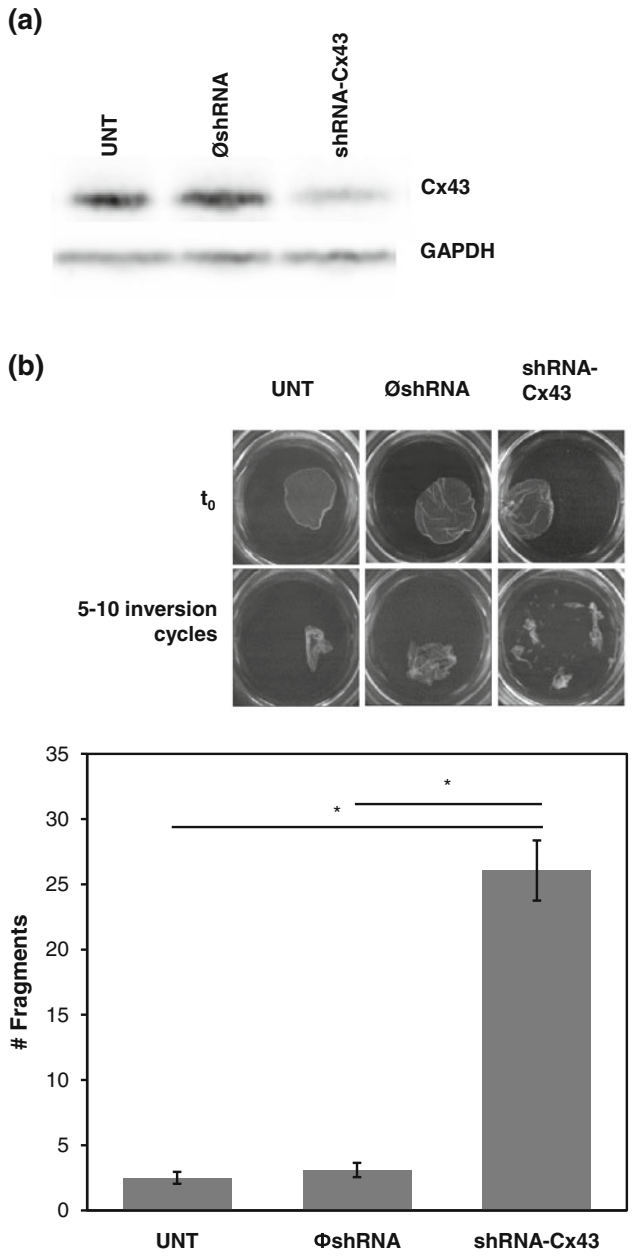

Fig. 2 Loss of Cx43 induces loss of intercellular adhesion strength. **a** Western blot for Cx43 in HEK293 cells untreated (UNT), treated with a virus that contains a nonsilencing construct (ϕshRNA-Cx43) and silenced for Cx43 (shRNA-Cx43). GAPDH was used as loading control. **b** Dispase assay. Cells were treated with 2.4 U/mL dispase for 90 min to disrupt attachment to extracellular matrix. Images were taken before (t_0) and after 5–10 inversion cycles. *Bars* show number of fragments after subjecting monolayers to 5–10 inversion cycles. $n = 10$–20, $p < 0.001$

the electrical coupling leading to a strong synchronization of these neurons (Curti et al. 2012).

Under the concept of the electric field mechanism, propagation is dependent on the subcellular distribution of sodium channels because their density, specifically at the intercalated disc, is critical to the generation of the electrical field in the intercellular cleft (Tsumoto et al. 2011). In this context, it is important to mention our recent results (Lin et al. 2011) showing that (a) sodium current amplitude is larger in the area of the intercalated disc; (b) steady-state inactivation of sodium channels located in the middle of the cell is shifted toward more negative values; as such, the burden of excitation during propagation falls on the channels at the intercalated disc; and (c) sodium current density is larger in cells that remain paired. These results are complementary to those of Petitprez et al. (2011), showing that there are two separate pools of Nav1.5 in the heart: one at the intercalated disc and a separate one associated with the costameres. Our data demonstrated that, together with the segregation of channels by subcellular regions, there is also a segregation of function; here, we further propose that the function of Nav1.5 at the intercalated disc is determined, at least in part, by Cx43.

The electric field mechanism also requires a preservation of the dimensions of the intercellular space. Experimental values for this variable are less solid. Currently, we are using high-pressure freezing methods and tomographic electron microscopy to obtain images of the intercellular space with a high level of structural preservation (Delmar and Liang 2012). Using these methods, we have began to collect images that allow us to make accurate measurements of the intercellular space under conditions where Cx43 is reduced, either by genetic manipulation (e.g., in Cx43-deficient hearts) or by disease. In this context, it seems pertinent to remind the reader of the discovery of Ross Johnson and his colleagues 20 years ago: connexins are important for intercellular adhesion (Fig. 2). It would follow that diseases that cause loss or remodeling of Cx43 would lead to an increased separation of the cells at the intercalated disc. From the point of view of electrophysiology, this would become an important challenge to the preservation of propagation between cells.

Conclusions

We have discussed two noncanonical functions of Cx43: preservation of cell–cell adhesion and preservation of sodium current amplitude in cardiac cells. We have also argued in favor of a model of cardiac propagation where cell–cell transfer of charge occurs not only by the flow of current through gap junction channels but also, by an electric field mechanism that relies on (a) a tight intercellular gap and (b) the accumulation of functional sodium channels at the intercalated disc. Thus, we speculate that under conditions of poor gap junction–mediated electrical coupling, propagation can be maintained via the electrical field mechanism, but only if sodium current properties, and a narrow cleft, are preserved. As such, we propose that the

Cx43-dependent loss of sodium current and perhaps a Cx43-dependent increase in the size of the intercellular gap are critical to propagation failure resulting from reduced Cx43 abundance. Cx43 may play a key role in intercellular communication not only directly, by forming gap junctions, but also indirectly, by maintaining a high sodium current density at the intercalated disc, and a narrow intercellular cleft for the transfer of activation. The gap junction–independent functions of Cx43 in cardiac electrophysiology emerge as an exciting area of future research.

References

Akar FG, Nass RD, Hahn S, Cingolani E, Shah M, Hesketh GG, DiSilvestre D, Tunin RS, Kass DA, Tomaselli GF (2007) Dynamic changes in conduction velocity and gap junction properties during development of pacing-induced heart failure. Am J Physiol Heart Circ Physiol 293:H1223–H1230

Cheng L, Yung A, Covarrubias M, Radice GL (2011) Cortactin is required for N-cadherin regulation of $K_V1.5$ channel function. J Biol Chem 286:20478–20489

Chkourko HS, Guerrero-Serna G, Lin X, Darwish N, Pohlmann JR, Cook KE, Martens JR, Rothenberg E, Musa H, Delmar M (2012) Remodeling of mechanical junctions and of microtubule-associated proteins accompany cardiac connexin 43 lateralization. Heart Rhythm 9:1133–1140

Curti S, Hoge G, Nagy JI, Pereda AE (2012) Synergy between electrical coupling and membrane properties promotes strong synchronization of neurons of the mesencephalic trigeminal nucleus. J Neurosci 32:4341–4359

Danik SB, Liu F, Zhang J, Suk HJ, Morley GE, Fishman GI, Gutstein DE (2004) Modulation of cardiac gap junction expression and arrhythmic susceptibility. Circ Res 95:1035–1041

Danik SB, Rosner G, Lader J, Gutstein DE, Fishman GI, Morley GE (2008) Electrical remodeling contributes to complex tachyarrhythmias in connexin43-deficient mouse hearts. FASEB J 22:1204–1212

Delmar M, Liang FX (2012) Connexin43 and the regulation of intercalated disc function. Heart Rhythm 9:835–838

Desplantez T, Dupont E, Severs NJ, Weingart R (2007) Gap junction channels and cardiac impulse propagation. J Membr Biol 218: 13–28

Francis R, Xu X, Park H, Wei CJ, Chang S, Chatterjee B, Lo C (2011) Connexin43 modulates cell polarity and directional cell migration by regulating microtubule dynamics. PloS One 6:e26379

Franke WW, Borrmann CM, Grund C, Pieperhoff S (2006) The area composita of adhering junctions connecting heart muscle cells of vertebrates. I. Molecular definition in intercalated disks of cardiomyocytes by immunoelectron microscopy of desmosomal proteins. Eur J Cell Biol 85:69–82

Hand PE, Peskin CS (2010) Homogenization of an electrophysiological model for a strand of cardiac myocytes with gap-junctional and electric-field coupling. Bull Mathemat Biol 72:1408–1424

Jansen JA, Noorman M, Musa H, Stein M, de Jong S, van der Nagel R, Hund TJ, Mohler PJ, Vos MA, van Veen TA, de Bakker JM, Delmar M, van Rijen HV (2011) Reduced heterogeneous expression of Cx43 results in decreased Nav1.5 expression and reduced sodium current which accounts for arrhythmia vulnerability in conditional Cx43 knockout mice. Heart Rhythm. S1547–5271(11)01360–9. doi:10.1016/j.hrthm.2011.11.025

Jansen JA, Noorman M, Musa H, Stein M, de Jong S, van der Nagel R, Hund TJ, Mohler PJ, Vos MA, van Veen TA, de Bakker JM, Delmar M, van Rijen HV (2012a) Reduced heterogeneous expression of Cx43 results in decreased Nav1.5 expression and reduced sodium current that accounts for arrhythmia vulnerability in conditional Cx43 knockout mice. Heart Rhythm 9:600–607

Jansen JA, van Veen TA, de Jong S, van der Nagel R, van Stuijvenberg L, Driessen H, Labzowski R, Oefner CM, Bosch AA, Nguyen TQ, Goldschmeding R, Vos MA, de Bakker JM, van Rijen HV (2012b) Reduced Cx43 expression triggers increased fibrosis due to enhanced fibroblast activity. Circ Arrhythmia Electrophysiol 5:380–390

Jefferys JG (1995) Nonsynaptic modulation of neuronal activity in the brain: electric currents and extracellular ions. Physiol Rev 75:689–723

Kalcheva N, Qu J, Sandeep N, Garcia L, Zhang J, Wang Z, Lampe PD, Suadicani SO, Spray DC, Fishman GI (2007) Gap junction remodeling and cardiac arrhythmogenesis in a murine model of oculodentodigital dysplasia. Proc Natl Acad Sci USA 104:20512–20516

Kaplan SR, Gard JJ, Protonotarios N, Tsatsopoulou A, Spiliopoulou C, Anastasakis A, Squarcioni CP, McKenna WJ, Thiene G, Basso C, Brousse N, Fontaine G, Saffitz JE (2004) Remodeling of myocyte gap junctions in arrhythmogenic right ventricular cardiomyopathy due to a deletion in plakoglobin (Naxos disease). Heart Rhythm 1:3–11

Li J, Patel VV, Kostetskii I, Xiong Y, Chu AF, Jacobson JT, Yu C, Morley GE, Molkentin JD, Radice GL (2005) Cardiac-specific loss of N-cadherin leads to alteration in connexins with conduction slowing and arrhythmogenesis. Circ Res 97:474–481

Lin X, Liu N, Lu J, Zhang J, Anumonwo JM, Isom LL, Fishman GI, Delmar M (2011) Subcellular heterogeneity of sodium current properties in adult cardiac ventricular myocytes. Heart Rhythm 8:1923–1930

Lowe JS, Palygin O, Bhasin N, Hund TJ, Boyden PA, Shibata E, Anderson ME, Mohler PJ (2008) Voltage-gated Nav channel targeting in the heart requires an ankyrin-G dependent cellular pathway. J Cell Biol 180:173–186

Meyer RA, Laird DW, Revel JP, Johnson RG (1992) Inhibition of gap junction and adherens junction assembly by connexin and A-CAM antibodies. J Cell Biol 119:179–189

Mori Y, Fishman GI, Peskin CS (2008) Ephaptic conduction in a cardiac strand model with 3D electrodiffusion. Proc Natl Acad Sci USA 105:6463–6468

Morley GE, Vaidya D, Jalife J (2000) Characterization of conduction in the ventricles of normal and heterozygous Cx43 knockout mice using optical mapping. J Cardiovasc Electrophysiol 11: 375–377

Nikolaev VO, Moshkov A, Lyon AR, Miragoli M, Novak P, Paur H, Lohse MJ, Korchev YE, Harding SE, Gorelik J (2010) Beta2-adrenergic receptor redistribution in heart failure changes cAMP compartmentation. Science 327(5973):1653–1657

Oxford EM, Musa H, Maass K, Coombs W, Taffet SM, Delmar M (2007) Connexin43 remodeling caused by inhibition of plakophilin-2 expression in cardiac cells. Circ Res 101:703–711

Petitprez S, Zmoos AF, Ogrodnik J, Balse E, Raad N, El-Haou S, Albesa M, Bittihn P, Luther S, Lehnart SE, Hatem SN, Coulombe A, Abriel H (2011) SAP97 and dystrophin macromolecular complexes determine two pools of cardiac sodium channels Nav1.5 in cardiomyocytes. Circ Res 108:294–304

Qu J, Volpicelli FM, Garcia LI, Sandeep N, Zhang J, Marquez-Rosado L, Lampe PD, Fishman GI (2009) Gap junction remodeling and spironolactone-dependent reverse remodeling in the hypertrophied heart. Circ Res 104:365–371

Revel JP, Karnovsky MJ (1967) Hexagonal array of subunits in intercellular junctions of the mouse heart and liver. J Cell Biol 33:C7–C12

Sato PY, Musa H, Coombs W, Guerrero-Serna G, Patino GA, Taffet SM, Isom LL, Delmar M (2009) Loss of plakophilin-2 expression leads to decreased sodium current and slower conduction velocity in cultured cardiac myocytes. Circ Res 105:523–526

Sato PY, Coombs W, Lin X, Nekrasova O, Green KJ, Isom LL, Taffet SM, Delmar M (2011) Interactions between ankyrin-G, plakophilin-2, and connexin43 at the cardiac intercalated disc. Circ Res 109:193–201

Soder BL, Propst JT, Brooks TM, Goodwin RL, Friedman HI, Yost MJ, Gourdie RG (2009) The connexin43 carboxyl-terminal peptide ACT1 modulates the biological response to silicone implants. Plastic Reconstr Surg 123:1440–1451

Sperelakis N (2002) An electric field mechanism for transmission of excitation between myocardial cells. Circ Res 91:985–987

Tsumoto K, Ashihara T, Haraguchi R, Nakazawa K, Kurachi Y (2011) Roles of subcellular Na^+ channel distributions in the mechanism of cardiac conduction. Biophys J 100:554–563

Weidmann S (1952) The electrical constants of Purkinje fibres. J Physiol 118:348–360

Yao JA, Gutstein DE, Liu F, Fishman GI, Wit AL (2003) Cell coupling between ventricular myocyte pairs from connexin43-deficient murine hearts. Circ Res 93:736–743

J Membrane Biol (2012) 245:483–493
DOI 10.1007/s00232-012-9497-4

Pannexin 1 Ohnologs in the Teleost Lineage

Stephen R. Bond · Nan Wang · Luc Leybaert · Christian C. Naus

Received: 12 April 2012 / Accepted: 31 July 2012 / Published online: 26 August 2012

Abstract Advances in genomic analysis indicate that the early chordate lineage underwent two whole-genome duplication events in fairly rapid succession around 400–600 million years ago, and that a third duplication event punctuated the radiation of ray-finned fishes (teleosts) around 320–350 million years ago. Connexin ohnologs have been disproportionately well maintained in the teleost genome following this third event, implying that gap junction proteins are amenable to neofunctionalization. A second family of gap junction–like proteins, the pannexins, is also present in chordates, but expansion of this family following the teleost whole-genome duplication has not been addressed in the literature. In the current study we report that ohnologs of *panx1* are expressed by zebrafish, and orthologs of these two genes can be found in various other teleost species. The genomic locality of each gene is described, along with sequence alignments that reveal conservation of classic pannexin-specific features/motifs. The transcripts were then cloned from cDNA for in vitro analysis, and both are shown to traffic to the plasma membrane when exogenously expressed. Furthermore, electrophysiological recordings show differences in the biophysical properties between the channels formed by these two proteins. Our results indicate that both copies of the ancestral teleost *panx1* gene were conserved following the last whole-genome duplication event and, following conventional zebrafish nomenclature, should now be referred to as *panx1a* and *panx1b*.

Keywords Pannexin · Teleost · R3 whole-genome duplication · Ohnolog · Neofunctionalization

Introduction

Early chordate evolution was punctuated by two whole-genome duplication (WGD) events (named "R1" and "R2") approximately 400–600 million years ago (MYA) (Dehal and Boore 2005; Putnam et al. 2008), with a third major WGD occurring in the ancestral teleost lineage (R3) between 320 and 350 MYA (Jaillon et al. 2004). These events were followed by significant reshuffling of the polyploid chromosomes via interchromosomal exchange, accompanied by massive loss of replicate genes through inactivation or deletion, and may have contributed to episodes of rapid speciation and radiation (Jaillon et al. 2004; Roth et al. 2007). While most duplicate genes derived from a WGD (i.e., ohnologs) are expected to be lost over time (Force et al. 1999), at least 3–4 % of the ohnologs created during the R3 WGD have been retained (Kassahn et al. 2009). Neofunctionalization and subfunctionalization are believed to be the primary drivers of duplicate gene retention because random mutation will eventually inactivate at least one copy, unless a selective advantage is gained from retaining both (Lynch et al. 2001). Gap junction genes (connexins) have been notably well

Electronic supplementary material The online version of this article (doi:10.1007/s00232-012-9497-4) contains supplementary material, which is available to authorized users.

S. R. Bond (✉) · C. C. Naus (✉)
Department of Cellular and Physiological Science, Life Sciences Institute, University of British Columbia, Vancouver, BC, Canada
e-mail: biologyguy@gmail.com

C. C. Naus
e-mail: cnaus@interchange.ubc.ca; christian.naus@ubc.ca

N. Wang · L. Leybaert
Department of Basic Medical Sciences–Physiology Group, Faculty of Medicine and Health Sciences, Ghent University, 9000 Ghent, Belgium

preserved in the teleosts following R3, with ~37 functional members present in most species versus ~21 mammalian members (Zoidl et al. 2008). Wagner (2002) has argued that overall functional complexity in a protein strongly correlates with the probability of both paralogs being retained if duplication occurs, or more specifically, that greater complexity increases the opportunity for subfunctionalization; mutations that ablate a different functional property from each copy can render both indispensable. Gap junction proteins are expressed by almost every vertebrate cell type, they interact with a diverse group of binding partners, and are involved in many physiological processes (Giepmans 2004; Willecke et al. 2002), so it is perhaps unsurprising that so much connexin diversity has been retained by the ray-finned fishes.

A second family of "gap junction–like" proteins also exists within vertebrates, named "pannexins" (Panchin et al. 2000). This small group of channel proteins (Panx1, -2 and -3) is homologous to the much larger innexin family, which are the invertebrate analogs of the vertebrate connexins. Innexins and connexins have a very similar structural topology and share many functional characteristics (Phelan 2005), yet it is unlikely these protein families are derived from a common ancestral gene that would have been classified as encoding a gap junction–forming monomer. Instead, they are believed to be the products of convergent evolution (Fushiki et al. 2010; Yen and Saier 2007). While it appears that pannexins are able to form intercellular gap junctions to a limited extent in overexpression systems (Bruzzone et al. 2003; Lai et al. 2007), under normal physiological conditions they are now understood to function as large unitary pores between the intra- and extracellular compartments (Boassa et al. 2007). As such, the "hemichannel" nomenclature often used to describe unpaired connexin or innexin channels has been deemed inaccurate when referring to pannexin channels (Sosinsky et al. 2011) and, thus, will not be used in this report. Regardless, the number of physiological processes in which pannexins have been implicated has rapidly grown in recent years (Penuela et al. 2012), with numerous studies having assessed the diversity of innexins and pannexins across many phyla (Baranova et al. 2004; Fushiki et al. 2010; Panchin 2005; Phelan 2005; Shestopalov and Panchin 2008; Yen and Saier 2007). Pannexin expression has even been studied specifically in fish (Prochnow et al. 2009a, b; Zoidl et al. 2007, 2008), but to date no one has determined if extra pannexins have been functionally preserved following R3.

Here, we report that *panx1* has in fact been retained as two independent ohnologs (*panx1a* and *panx1b*) and describe several features of the genes and EGFP-tagged versions of the gene products.

Materials and Methods

Phylogenetic Analysis

Pannexin coding sequences were downloaded from NCBI and Ensembl (see supplementary data, Table S1) and analyzed within the Geneious 4.8 bioinformatics platform (Drummond et al. 2009). Global alignment of protein sequences was executed using the Blosum45 cost matrix, with an open gap penalty of 11 and an extension penalty of 1. Consensus cladograms were generated with the Geneious Tree Builder, using the unweighted-pair group method with arithmetic mean (UPGMA) in conjunction with the Jukes-Cantor genetic distance model. Subsequently, bootstrapping with 1,000 replicates was used to estimate clade confidence (Felsenstein 1985). Syntenic gene blocks associated with *panx1* and shared between zebrafish and mouse were identified using the online synteny database (Catchen et al. 2009).

Real-Time Quantitative PCR

Twelve separate tissues were harvested from three individual zebrafish according to an approved University of British Columbia Animal Care protocol (A07-0288). Total RNA was isolated using Trizol reagent (Invitrogen, Carlsbad, CA), according to the manufacturer's directions, and treated with DNAseI to remove genomic contamination. Relative pannexin expression was measured between tissues using real-time quantitative PCR (qPCR) on a CFX96 real-time qPCR machine (Bio-Rad, Hercules, CA). Primers are listed in the supplementary data (Table S2), and 10 ng of total RNA was analyzed in duplicate 10-µl reactions using the iScript™ One-Step RT-PCR kit with SYBR® green (Bio-Rad). Expression levels were standardized against 18S rRNA (ΔC_T), and $\Delta\Delta C_T$ was dynamically based on the tissue with the lowest ΔC_T in a given experiment. The tissues from each animal were analyzed separately and then averaged.

Cloning Zebrafish Pannexins

Total zebrafish mRNA was reverse-transcribed with SuperScript III (Invitrogen), and each of the four pannexin cDNAs was PCR-amplified using primers containing 5′ *Eco*RI or *Eco*RV sites (supplementary Table S3). PCR products were digested and ligated into pBlueScript downstream of the T7 promoter. The four genes were then subcloned into pEGFP-N1 using an appropriate double digest and ligation (*panx1a*, *Hind*III/*Bam*HI; *panx1b*, *Kpn*I/*Bam*HI; *panx2*, *Hind*III/*Pst*I; *panx3*, *Hind*III/*Bam*HI), followed by restriction-free cloning to remove the stop codons

and to add a small linker sequence (GAAQSK) between the pannexins and EGFP (Bond and Naus 2012; Bryksin and Matsumura 2010).

Cell Culture

Human cervical carcinoma HeLa cells (American Type Culture Collection, Manassas, VA) were maintained in DMEM + 10 % FBS in a humidified 37 °C incubator with 5 % CO_2 and transfected with the pEGFP-N1 constructs using FuGENE6 (Roche, Indianapolis, IN) per the manufacturer's directions. To produce stable overexpression, the growth medium was supplemented with 500 µg/ml G418 and cells were subjected to fluorescence-activated cell sorting once per week for 4 weeks to enrich for EGFP expression.

Western Blot

Transfected HeLa cell lysates were collected with RIPA buffer (150 mM NaCl, 50 mM Tris-HCl [pH 8.0], 0.5 % Sarkosyl, 1 % IGEPAL, 0.1 % SDS) and separated on 10 % Tris-glycine SDS-PAGE gels. The protein was transferred to Immuno-Blot PVDF (Bio-Rad) and then blocked in 5 % nonfat milk + 0.1 % Tween20 (NFM-T). Membranes were probed with an HRP-linked α-GFP mouse monoclonal antibody (Santa Cruz Biotechnology, Santa Cruz, CA) diluted in 3 % NFM-T for 2 h at room temperature. HRP activity was visualized by treating the membrane with SuperSignal® West Pico Chemiluminescent Substrate (Pierce, Rockford, IL) and exposing/developing Bioflex® Econo Film (Clonex, Markham, Canada).

Visualizing Pannexin-EGFP

Pannexin-EGFP-transfected HeLa cells were grown in eight-well ibiTreat μ-Slides (Ibidi, Munich, Germany) for 12 h and supplemented with 20 mM HEPES buffer (pH 7.4) just prior to imaging. Confocal microscopy was performed on a Leica (Nussloch, Germany) TCS SP5II Basic VIS system, using the special photomultiplier R 9624 with low dark current. Time-lapse and z-stack images were analyzed with ImageJ (http://rsbweb.nih.gov/ij/).

Electrophysiological Recording

HeLa cells were bathed in a recording chamber filled with a modified Krebs-Ringer solution consisting of (in mM) 150 NaCl, 4 KCl, 2 $CaCl_2$, 2 $MgCl_2$, 2 CsCl, 1 $BaCl_2$, 2 pyruvate, 5 glucose and 5 HEPES (pH 7.4). The standard whole-cell recording pipette solution was composed of (in mM) 130 CsCl, 10 Na-aspartate, 0.26 $CaCl_2$, 1 $MgCl_2$, 2 EGTA, 5 tetraethylammonium (TEA)-Cl and 5 HEPES (pH 7.2). Pipette resistance was 3–4 MΩ.

Whole-cell recording was performed as described previously (Bukauskas et al. 2001) with an EPC7 PLUS patch-clamp amplifier (HEKA Elektronik, Lambrecht, Germany). All currents in whole-cell configuration were filtered at 1 kHz (7-pole Besselfilter). Data were acquired at 4 kHz using an NI USB-6221 data-acquisition device from National Instruments (Austin, TX) and software written by J. Dempster (University of Strathclyde, Glasglow, UK). Steady-state currents for *I–V* relations were measured between the ninth and tenth seconds of the 10-s membrane potential steps and are expressed as mean ± standard error of the mean (SEM).

For outside–out patch recording, the recording electrode was lifted and pulled away from the cell after establishment of whole-cell configuration, thus excising the membrane patch attached to the electrode.

Results and Discussion

At Least Four Pannexin Genes Are Present in the Teleost Lineage

As of Ensembl release 66 (February 2012), seven species of ray-finned fish have been annotated: zebrafish, stickleback, fugu, green spotted puffer, Atlantic cod, Nile tilapia and medaka. Each of these species has a single record for Panx2 and Panx3, and two listings for Panx1. The green spotted puffer is an exception, with three listings for Panx1. Within each species analyzed, the two Panx1 proteins share an average 55.0 % sequence identity (±6.9 %) and 67.6 % similarity (±7.3 %). They retain the classic innexin-specific P-X-X-X-W motif in the second transmembrane domain and two cysteine residues in each extracellular loop (Phelan 2005) (supplementary Fig. S1). They also contain a charged K or R residue relative to position 75 in the mouse, which is thought to be involved in ATP-mediated channel regulation (Qiu and Dahl 2009). Interestingly, we do not observe any conservation of the cysteine residue at position 282, previously reported to regulate channel activity of zebrafish Panx1 (Prochnow et al. 2009a). The authors of this study chose to use a bulky tryptophan residue to replace the native cysteine, which is a common practice when attempting to identify transmembrane residues with side chains that interact with the main body of the protein; it does not, however, reveal much about the actual function of the specific residue being replaced (Sharp et al. 1995). In this light, it seems that the impacts on channel activity are more likely to be a product of steric interference than ablation of a novel functional innovation associated with this particular cysteine.

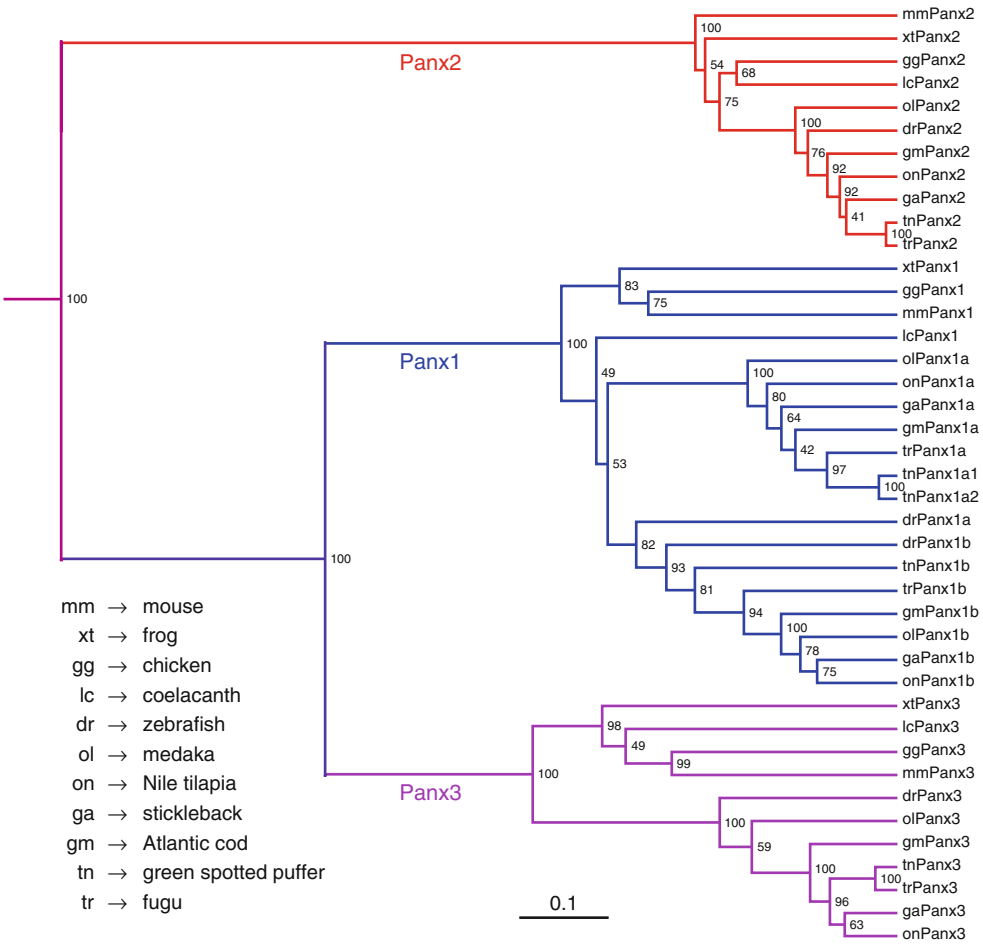

Fig. 1 Cladogram illustrating the phylogenetic relationship between pannexins. The tree was generated from aligned protein sequences using UPGMA and Jukes-Cantor genetic distance, with branch length proportional to genetic distance. *Bootstrap values* are indicated at branch points and were calculated through 1,000 replicates

The only exception to the aforementioned conserved features is the extra Panx1 sequence in the green spotted puffer, which appears to be the product of a partial duplication event that truncated the coding sequence immediately after the first cysteine residue in the second extracellular domain (C234). Even if this truncated protein is still actively translated, it is very unlikely it can participate in normal channel activity because all four extracellular loop cysteines are needed for formation of active channels (Bunse et al. 2011).

Multiple pairwise alignment splits the teleost Panx1 sequences roughly into two orthologous clades, and these groups combine into a single sister clade relative to Panx1 sequences from more distantly related vertebrates (Fig. 1). The zebrafish sequences complicate this phylogeny to some degree because both paralogs group into a single clade within the teleost Panx1 branch. This is probably due to the fact that the zebrafish belongs to the taxonomic group Otocephala, as opposed to the rest of the fish species in this study which belong to the Euteleostei, and these two lineages diverged approximately 250–300 MYA (Hedges et al. 2006). One of the sequences does, however, group more tightly with its respective clade, so this property

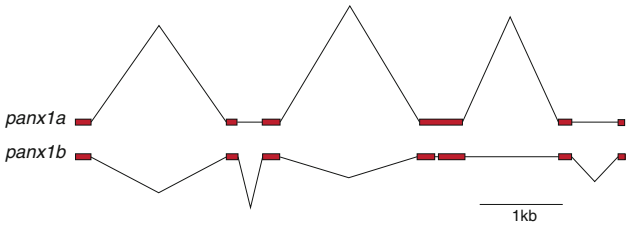

Fig. 2 Genomic architecture of the two zebrafish *panx1* genes. Exons are indicated by *red boxes*, with intronic regions represented by *thin lines*. Feature lengths are to scale (Color figure online)

along with genomic positioning will be utilized below for naming purposes.

The Two Teleost *panx1* Genes Likely Originate from the R3 WGD Event

Clupeocephala is the lowest taxonomic group to include all of the teleosts present in this study, so the most parsimonious time frame for the duplication of *panx1* precedes the Clupeocephala/Elopomorpha split 300–350 MYA (Hedges et al. 2006). Gene duplications occur through various processes, including retrotransposition, errors

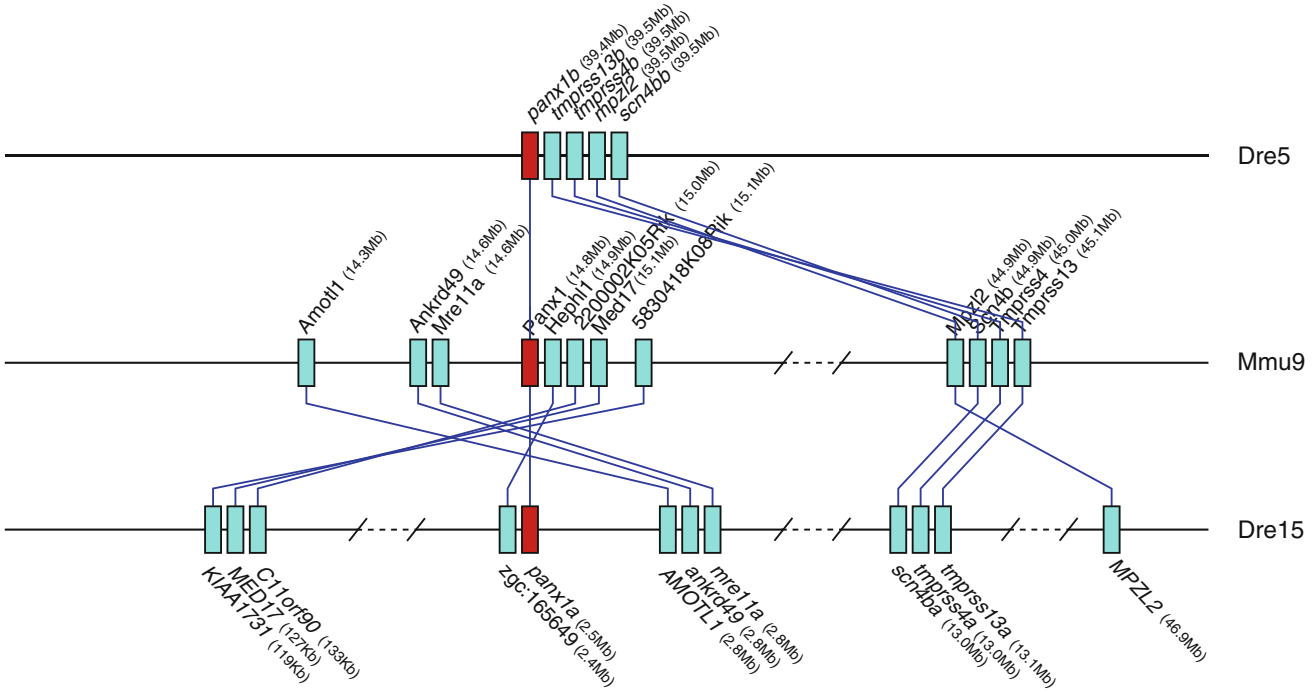

Fig. 3 Syntenic relationship between zebrafish and mouse chromosomal regions containing *panx1* genes. Individual genes are represented by *solid boxes* (*red* for *panx1*, *blue* for all others), and orthologous pairs are indicated with *connector lines* (Color figure online)

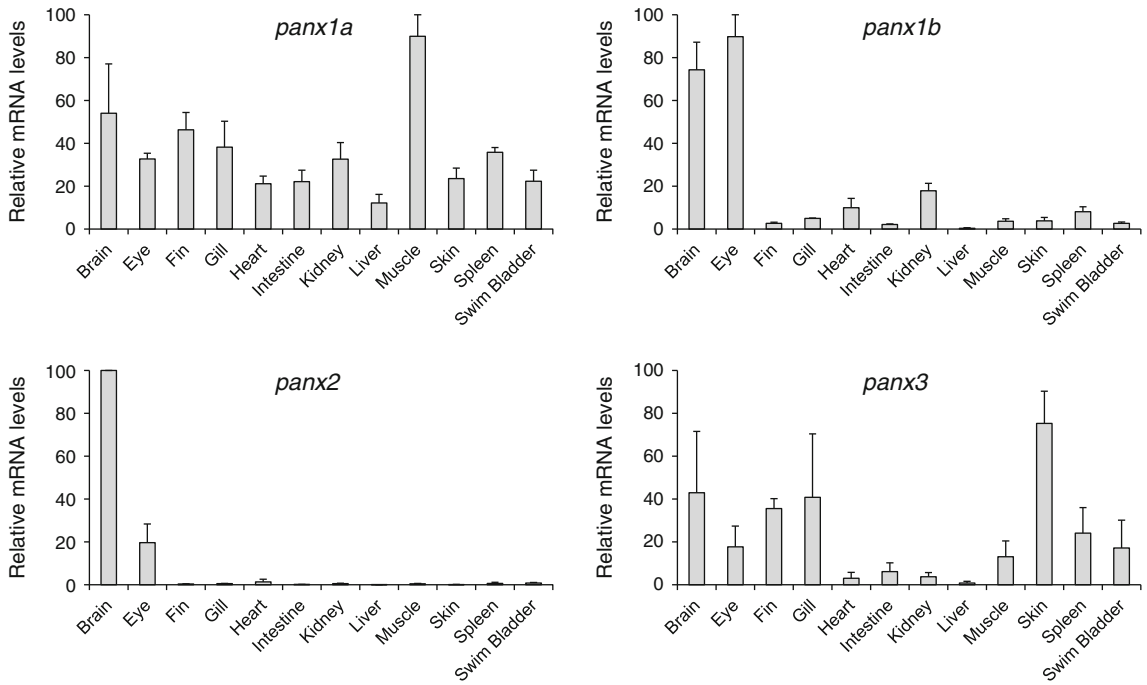

Fig. 4 Relative mRNA levels of pannexins expressed by zebrafish tissues, as measured by qPCR. Each graph is the average of three independent experiments, where $\Delta\Delta C_T$ was based on the tissue with the highest expression in a given experiment. *Error bars* represent standard error

during homologous recombination and whole-chromosome or -genome duplications (Hahn 2009). It is highly unlikely that the extra copy of *panx1* resulted from reintegration of a processed mRNA into the genome by a retrotransposon, because the exon architecture is nearly identical between the two genes (Fig. 2). Although not impossible, it is also unlikely that the duplication was the product of an unequal crossover event. These are usually characterized by a

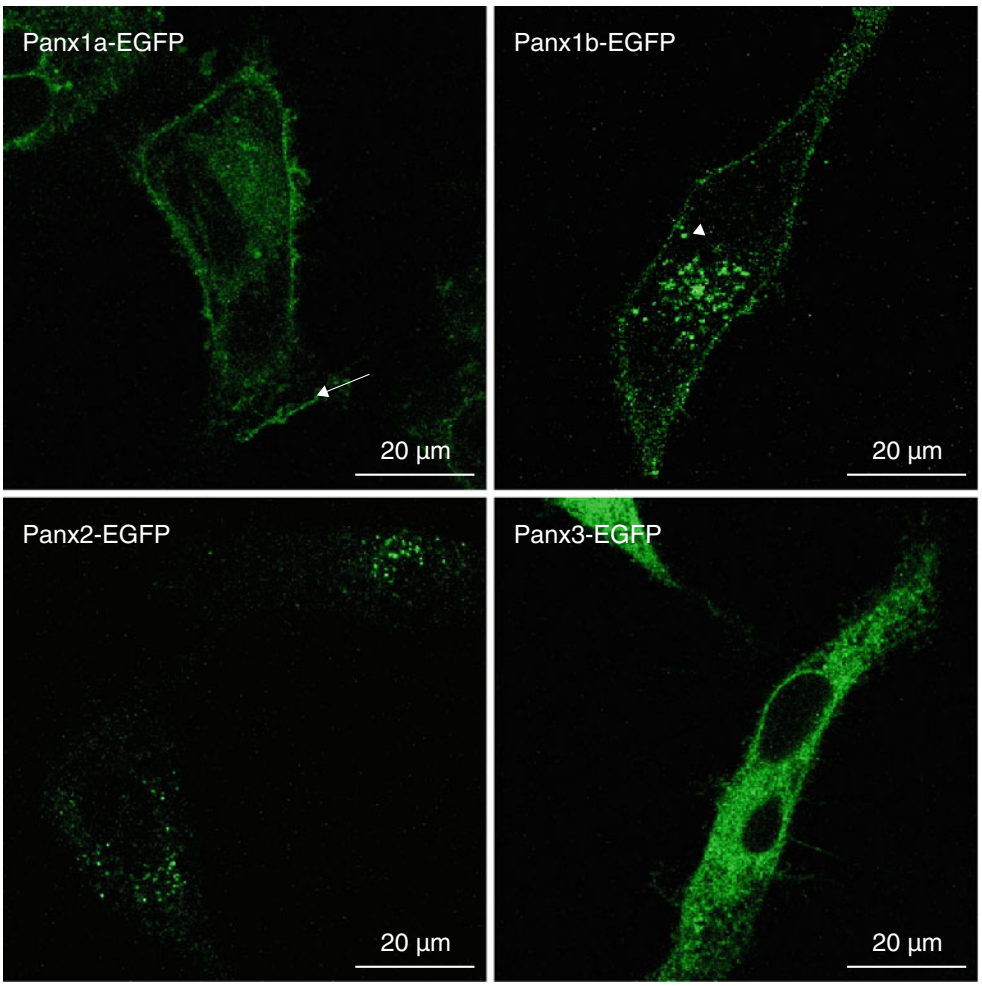

Fig. 5 Exogenous expression of EGFP-tagged zebrafish pannexins in HeLa cells. Panx1a localized to the cell membrane and was recruited to areas of membrane ruffling (*arrow*). Panx1b localized to the cell membrane as well but was also present in intracellular vesicles (*arrowhead*). Panx2 was exclusively observed in small intracellular vesicles, while Panx3 was more diffuse

tandem repeat pattern (Semple and Wolfe 1999), and the two *panx1* genes are located on separate chromosomes. For this process to have generated the current localization of the two *panx1* genes, a homologous recombination error would need to have been followed in relatively quick succession by an interchromosomal exchange and, depending on when this occurred relative to the WGD, either one or two extra panx1 paralogs must have then been deleted from the genome. A more parsimonious explanation is that the extra gene was produced during the R3 WGD.

The initial period following an instance of tolerated polyploidy (i.e., when the extrachromosomal load does not kill or sterilize the organism) is generally associated with genomic instability, and recombination shuffles alleles between all homologous chromosomes during meiosis (Cifuentes et al. 2010). Homologous recombination is also thought to facilitate rapid genomic downsizing of a neopolyploid species (Leitch and Bennett 2004), with deletions presumably remaining innocuous so long as the affected regions are present on the replicate chromosome. Eventually, sufficient divergence causes the karyotype to once again assume a diploid state, but two key signatures of the duplication will remain for a considerable time afterward. First, large syntenic regions can be expected to exist between the duplicated chromosomes, preserving gene order and orientation. Second, comparison against the genome of a related species that did not undergo WGD should reveal a pattern of gene interleaving between the duplicated chromosomes relative to the homologous outgroup chromosome (Jaillon et al. 2004). The chromosomal neighborhoods of the two zebrafish *panx1* genes contain signs of both synteny and gene interleaving. For example, the *panx1* gene on zebrafish chromosome 15 (Dre15) is flanked by the same set of genes observed on mouse chromosome 9 (Mmu9), while a block of genes adjacent to the *panx1* gene on zebrafish chromosome 5 (Dre5) is many megabases away on both Mmu9 and Dre15 (Fig. 3). The

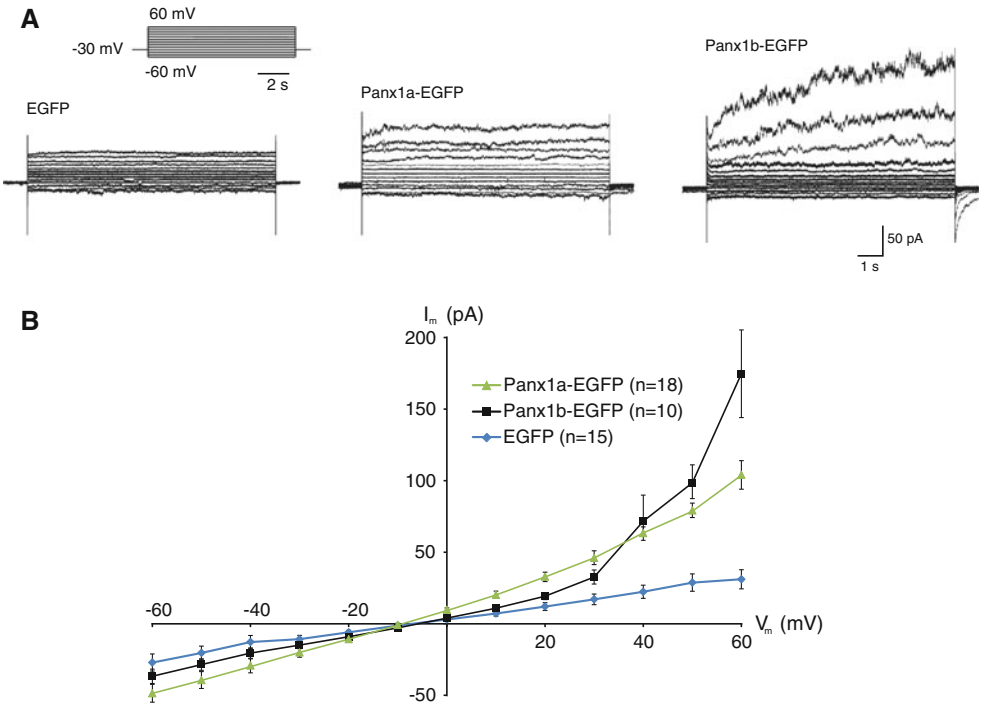

Fig. 6 Whole-cell voltage clamp of EGFP, Panx1a-EGFP and Panx1b-EGFP transfected HeLa cells. **a** The protocol included a brief holding potential of −30 mV, followed by 13 consecutive 10-s holding steps starting at −60 mV and increasing depolarization by 10 mV per step. Depolarization to positive membrane potentials evoked progressively increasing membrane currents from Panx1a-EGFP and Panx1b-EGFP compared to EGFP controls, but the activation time was much longer for Panx1b-EGFP than Panx1a-EGFP. **b** *I–V* plot demonstrating the voltage-gated pannexin currents, in contrast to the linear (background) *I–V* relationship recorded in HeLa cells expressing EGFP only

genes adjacent to *panx1* on Dre5 have been previously annotated as "b" ohnologs (e.g., *tmprss13b*, *tmprss4b* and *scn4bb*), while the genes on Dre15 are annotated "a." As such, the zebrafish *panx1* genes should now be referred to as *panx1a* and *panx1b* on Dre15 and Dre5, respectively. Furthermore, despite both of the zebrafish *panx1* gene products clustering into a single clade of the remaining teleost *panx1* sequences, *panx1b* shares greater similarity with that clade, so the genes for the other species included in Fig. 1 have been annotated accordingly.

Expression Profiles of *panx1a* and *panx1b* Are Distinct

To compare expression levels of each pannexin throughout the adult zebrafish, mRNA was prepared from 12 separate tissues and analyzed by real-time qPCR (Fig. 4). In line with previous studies, expression of *panx2* was primarily restricted to the eye and central nervous system (Bruzzone et al. 2003; Dvoriantchikova et al. 2006; Zoidl et al. 2008), and *panx3* was highest in skin (Celetti et al. 2010). The distribution of zebrafish *panx1a* has previously been reported in the central nervous system, muscle, heart, liver, kidney and retina (Prochnow et al. 2009b; Zoidl et al. 2008), similar to our observations here showing the near ubiquitous expression pattern characteristic of mammalian *panx1* (Bruzzone et al. 2003). Previous attempts to isolate or measure *panx1b* transcript were unsuccessful (Prochnow et al. 2009b), but we were able to observe robust expression in cDNA prepared from brain and eye with more modest relative levels of expression in heart, kidney and spleen.

Subcellular Dynamics and Localization of Zebrafish Pannexins

The coding sequences of all four zebrafish pannexin genes were amplified from a multitissue preparation of total cDNA and cloned into the expression vector pEGFP-N1, so trafficking of the proteins could be monitored live. HeLa cells were chosen for this study because they express very little endogenous connexin (Elfgang et al. 1995), and while reports on the expression of *panx1* in HeLa are mixed (Clair et al. 2008; Penuela et al. 2008; Zappala et al. 2006), we were unable to observe the protein by Western blot (data not shown). Western blot analysis of lysates taken from stably transfected HeLa cultures confirmed the presence of EGFP-tagged products of expected size for all constructs (supplementary Fig. S2).

Time-lapse imaging revealed distinct cellular distributions for each of the four pannexins (Fig. 5). A fraction of Panx1a localizes to the plasma membrane, with concentrations in areas of membrane ruffling (Fig. 5a, supplementary data 1 and 2). This is consistent with previous reports of Panx1 localizing to the leading edge of motile cells (Mayo et al. 2008), probably through direct interaction with filamentous actin (Bhalla-Gehi et al. 2010). Panx1b also localizes to the plasma membrane with recruitment to dynamic membrane ruffles, but most of the cells analyzed also had a fraction of the protein associated with mobile intracellular vesicles with diameters of about 200–500 nm (Fig. 5b, supplementary data 3 and 4). Many vesicles within the endocytic pathway are approximately this size (Geumann et al. 2008), but we observed no

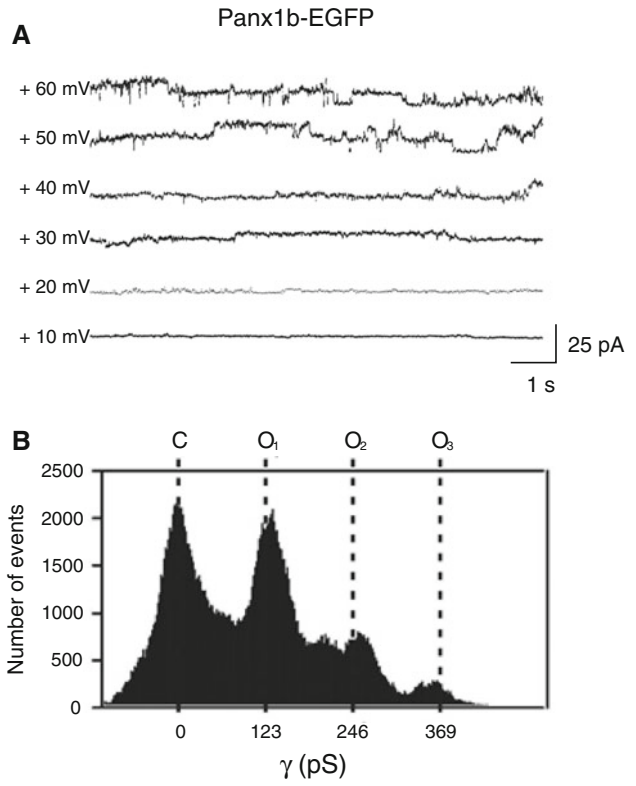

Fig. 7 Single-channel recordings of Panx1b-EGFP demonstrating unitary event activity and single-channel conductance. **a** Representative traces from excised outside–out patches reveal single-channel activity for Panx1b-EGFP channels at membrane potentials of +30 mV and above. **b** An all-point histogram representing all six example traces illustrates a unitary conductance of ~123 pS between the closed state (*C*) and fully open state (O_1). The peaks at O_2 and O_3 are both multiples of 123 pS and, thus, are most likely the result of multiple channels in the excised patch. The histogram shows some background activity that may be caused by subconductance states

colocalization between Panx1b and the early endosome marker EEA1 (data not shown); thus, the identity of these vesicles remains undetermined at this time. Mammalian Panx2 has been reported to localize primarily to small intracellular vesicles (Lai et al. 2009; Zappala et al. 2007), similar to what we observed with the zebrafish ortholog (Fig. 5c; supplementary data 5 and 6). Multiple splice variants exist for this protein however (Zoidl et al. 2008), of which we isolated only the "C" variant, while context-dependent depalmitoylation has been shown to facilitate trafficking of Panx2 to the plasma membrane (Swayne et al. 2010). Finally, Panx3 expression appeared to be primarily intracellular (Fig. 5d, supplementary data 7 and 8). "Normal" localization of Panx3 is variable in the literature, and it is also probably cell type–dependent and can be disrupted when tagged with GFP (Bhalla-Gehi et al. 2010; Iwamoto et al. 2010; Penuela et al. 2008). Given all these potentially confounding factors with regard to pannexin trafficking, we do not assume our results are necessarily equivalent to normal in vivo dynamics but instead hope to highlight the differences among the four proteins when expressed in a common environment, with particular emphasis on the two Panx1 proteins. According to the classic duplication–degeneration–complementation model (Force et al. 1999), we expect Panx1a and Panx1b to have undergone some degree of neofunctionalization at the transcriptional level and/or the physiological level. While the differences we have observed in relative mRNA expression and intracellular distribution of the EGFP-tagged proteins appear to support this position, the clearest evidence of neofunctionalization would be a measurable difference in channel properties.

Physiological Properties of Zebrafish Panx1 Channels

Individual Panx1a-EGFP, Panx1b-EGFP or EGFP control transfected HeLa cells were voltage-clamped at a holding potential of –30 mV for 1 s, followed by voltage steps of 10-s duration to potentials in the range of –60 to +60 mV in 10-mV increments (Fig. 6). Similar to previous reports for Panx1a (Prochnow et al. 2009a), the macroscopic currents from cells expressing our constructs were characterized by an outwardly rectifying, nonlinear current-to-voltage relationship (*I–V*) at positive potentials. Panx1b-EGFP appears to have a voltage threshold for activation (i.e., the point where *I–V* breaks from linearity) between +20 and +30 mV, which is higher than the 0 to +20 mV necessary to activate Panx1a currents. Panx1b also exhibits a longer activation time than Panx1a, requiring upward of 8 s to reach steady state upon membrane depolarization versus <250 ms for Panx1a. These results match reasonably well with those reported previously for Panx1a properties (Prochnow et al. 2009a, b). Recordings from outside–out patches of Panx1b-EGFP-transfected cells displayed unitary events upon stepping the membrane potential to +30 mV or above (Fig. 7a), and analysis of an all-event histogram indicates a Panx1b-EGFP single-channel conductance of ~123 pS (Fig. 7b). This is nearly fourfold lower than has previously been reported as the unitary conductance of fish or mammalian Panx1 (Bao et al. 2004; Prochnow et al. 2009a). Unexpectedly, unitary opening events could not be resolved from any excised outside–out patches taken from over 60 Panx1a-EGFP-transfected cells, and yet the increase in whole-cell currents at positive membrane potentials does still appear to be the result of pannexin channels because the current was completely inhibited by 25 μM carbenoxolone, returning the *I–V* plot to a linear relationship without affecting the steady-state currents at negative membrane potentials (Fig. 8). The addition of bulky tags like GFP to the carboxy terminus (CT) of connexin can alter channel gating properties and unitary conductance (Bukauskas et al.

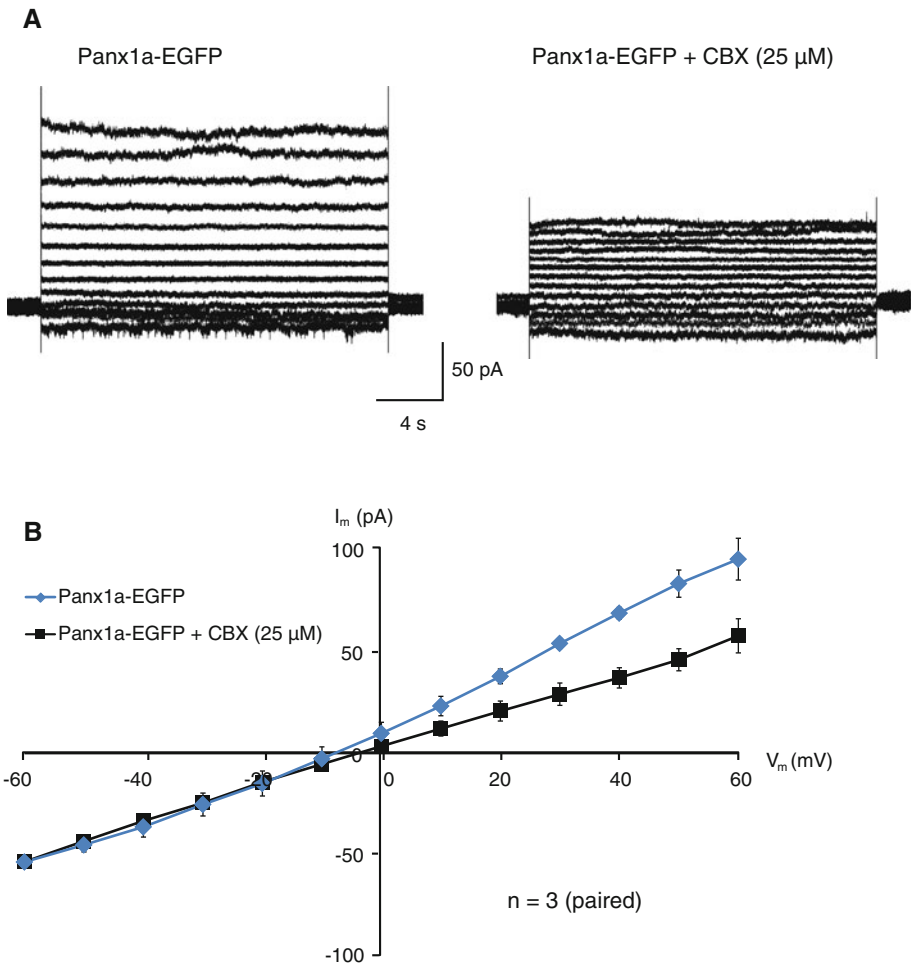

Fig. 8 Panx1a-EGFP is sensitive to carbenoxolone (CBX). **a** Representative traces from a single Panx1a-EGFP-expressing cell recorded in the whole-cell configuration and subjected to incremental 10-mV steps from −60 to +60 mV before (*left*) and after (*right*) treatment with carbenoxolone. **b** *I–V* plot illustrating the reduction in voltage-activated currents from Panx1a-EGFP-expressing cells following carbenoxolone treatment as well as the lack of effect on steady-state currents at negative membrane potentials

2000, 2001; Carnarius et al. 2012), and while CT tagging Panx1a with EYFP has been shown to have no untoward effect on unitary recordings (Prochnow et al. 2009a), the addition of an EGFP tag to the CT of human Panx1 completely blocked channel activity (Ma et al. 2009). As such, it is not unreasonable to speculate that the tag in our system could be causing a partial blockade and/or altering open probability, and indeed, closer examination of whole-cell currents taken from Panx1a-EGFP-transfected cells revealed infrequent but well-resolved unitary events of ~276 pS at potentials ≥+50 mV (data not shown). These events could represent the occasional transition of a partially open channel to a more fully open state, but further work with the untagged proteins will be required to properly resolve this issue.

Conclusion

In the current study we have demonstrated that a fourth pannexin gene is present and actively expressed in the ray-finned fishes. This gene is probably a holdover from the teleost R3 WGD event, representing a split of *panx1*. As such, the two *panx1* genes should now be referred to as *panx1a* and *panx1b*. These genes display distinct differences in tissue distribution, with the *panx1a* expression pattern mimicking the near ubiquity of mammalian *panx1*, while *panx1b* is heavily enriched in the brain and eye. Exogenous overexpression of the zebrafish ohnologs reveals potential differences in the intracellular vesicles with which each protein associates, but both clearly traffic to the plasma membrane, particularly to areas of cell ruffling. At the channel level the two proteins appear to have distinct physiological properties, in terms of both gating and conductance, although future electrophysiological characterization of the untagged versions of these channels will be needed to fully assess the extent of their differences. Taken together, our results indicate that the two *panx1* genes and gene products have undergone some degree of neofunctionalization or subfunctionalization, as would be expected according to conventional evolutionary theory. To our knowledge, this is the first time functional properties of *panx1b* have been reported.

Acknowledgement We thank Dr. Patricia Schulte for her kind assistance with obtaining zebrafish tissues and for critical review of the manuscript.

References

Bao L, Locovei S, Dahl G (2004) Pannexin membrane channels are mechanosensitive conduits for ATP. FEBS Lett 572:65–68

Baranova A, Ivanov D, Petrash N, Pestova A, Skoblov M, Kelmanson I, Shagin D, Nazarenko S, Geraymovych E, Litvin O, Tiunova A, Born TL, Usman N, Staroverov D, Lukyanov S, Panchin Y (2004) The mammalian pannexin family is homologous to the invertebrate innexin gap junction proteins. Genomics 83: 706–716

Bhalla-Gehi R, Penuela S, Churko JM, Shao Q, Laird DW (2010) Pannexin1 and pannexin3 delivery, cell surface dynamics, and cytoskeletal interactions. J Biol Chem 285:9147–9160

Boassa D, Ambrosi C, Qiu F, Dahl G, Gaietta G, Sosinsky G (2007) Pannexin1 channels contain a glycosylation site that targets the hexamer to the plasma membrane. J Biol Chem 282:31733–31743

Bond SR, Naus CC (2012) RF-Cloning.org: an online tool for the design of restriction-free cloning projects. Nucleic Acids Res 40:W209–W213

Bruzzone R, Hormuzdi SG, Barbe MT, Herb A, Monyer H (2003) Pannexins, a family of gap junction proteins expressed in brain. Proc Natl Acad Sci USA 100:13644–13649

Bryksin AV, Matsumura I (2010) Overlap extension PCR cloning: a simple and reliable way to create recombinant plasmids. Biotechniques 48:463–465

Bukauskas FF, Jordan K, Bukauskiene A, Bennett MV, Lampe PD, Laird DW, Verselis VK (2000) Clustering of connexin 43-enhanced green fluorescent protein gap junction channels and functional coupling in living cells. Proc Natl Acad Sci USA 97:2556–2561

Bukauskas FF, Bukauskiene A, Bennett MV, Verselis VK (2001) Gating properties of gap junction channels assembled from connexin43 and connexin43 fused with green fluorescent protein. Biophys J 81:137–152

Bunse S, Schmidt M, Hoffmann S, Engelhardt K, Zoidl G, Dermietzel R (2011) Single cysteines in the extracellular and transmembrane regions modulate pannexin 1 channel function. J Membr Biol 244:21–33

Carnarius C, Kreir M, Krick M, Methfessel C, Moehrle V, Valerius O, Bruggemann A, Steinem C, Fertig N (2012) Green fluorescent protein changes the conductance of connexin 43 (Cx43) hemichannels reconstituted in planar lipid bilayers. J Biol Chem 287:2877–2886

Catchen JM, Conery JS, Postlethwait JH (2009) Automated identification of conserved synteny after whole-genome duplication. Genome Res 19:1497–1505

Celetti SJ, Cowan KN, Penuela S, Shao Q, Churko J, Laird DW (2010) Implications of pannexin 1 and pannexin 3 for keratinocyte differentiation. J Cell Sci 123:1363–1372

Cifuentes M, Grandont L, Moore G, Chevre AM, Jenczewski E (2010) Genetic regulation of meiosis in polyploid species: new insights into an old question. New Phytol 186:29–36

Clair C, Combettes L, Pierre F, Sansonetti P, Tran Van Nhieu G (2008) Extracellular-loop peptide antibodies reveal a predominant hemichannel organization of connexins in polarized intestinal cells. Exp Cell Res 314:1250–1265

Dehal P, Boore JL (2005) Two rounds of whole genome duplication in the ancestral vertebrate. PLoS Biol 3:e314

Drummond AJ, A.B., Buxton S, Cheung M, Cooper A, Duran C, Field M, Heled J, Kearse M, Markowitz S, Moir R, Stones-Havas S, Sturrock S, Thierer T, Wilson A 2009. Geneious v4.8. http://www.geneious.com/

Dvoriantchikova G, Ivanov D, Panchin Y, Shestopalov VI (2006) Expression of pannexin family of proteins in the retina. FEBS Lett 580:2178–2182

Elfgang C, Eckert R, Lichtenberg-Frate H, Butterweck A, Traub O, Klein RA, Hulser DF, Willecke K (1995) Specific permeability and selective formation of gap junction channels in connexin-transfected HeLa cells. J Cell Biol 129:805–817

Felsenstein J (1985) Confidence limits on phylogenies—an approach using the bootstrap. Evolution 39:783–791

Force A, Lynch M, Pickett FB, Amores A, Yan YL, Postlethwait J (1999) Preservation of duplicate genes by complementary, degenerative mutations. Genetics 151:1531–1545

Fushiki D, Hamada Y, Yoshimura R, Endo Y (2010) Phylogenetic and bioinformatic analysis of gap junction-related proteins, innexins, pannexins and connexins. Biomed Res 31:133–142

Geumann U, Barysch SV, Hoopmann P, Jahn R, Rizzoli SO (2008) SNARE function is not involved in early endosome docking. Mol Biol Cell 19:5327–5337

Giepmans BN (2004) Gap junctions and connexin-interacting proteins. Cardiovasc Res 62:233–245

Hahn MW (2009) Distinguishing among evolutionary models for the maintenance of gene duplicates. J Hered 100:605–617

Hedges SB, Dudley J, Kumar S (2006) TimeTree: a public knowledge-base of divergence times among organisms. Bioinformatics 22:2971–2972

Iwamoto T, Nakamura T, Doyle A, Ishikawa M, de Vega S, Fukumoto S, Yamada Y (2010) Pannexin 3 regulates intracellular ATP/cAMP levels and promotes chondrocyte differentiation. J Biol Chem 285:18948–18958

Jaillon O, Aury JM, Brunet F, Petit JL, Stange-Thomann N, Mauceli E, Bouneau L, Fischer C, Ozouf-Costaz C, Bernot A, Nicaud S, Jaffe D, Fisher S, Lutfalla G, Dossat C, Segurens B, Dasilva C, Salanoubat M, Levy M, Boudet N, Castellano S, Anthouard V, Jubin C, Castelli V, Katinka M, Vacherie B, Biemont C, Skalli Z, Cattolico L, Poulain J, De Berardinis V, Cruaud C, Duprat S, Brottier P, Coutanceau JP, Gouzy J, Parra G, Lardier G, Chapple C, McKernan KJ, McEwan P, Bosak S, Kellis M, Volff JN, Guigo R, Zody MC, Mesirov J, Lindblad-Toh K, Birren B, Nusbaum C, Kahn D, Robinson-Rechavi M, Laudet V, Schachter V, Quetier F, Saurin W, Scarpelli C, Wincker P, Lander ES, Weissenbach J, Roest Crollius H (2004) Genome duplication in the teleost fish *Tetraodon nigroviridis* reveals the early vertebrate proto-karyotype. Nature 431:946–957

Kassahn KS, Dang VT, Wilkins SJ, Perkins AC, Ragan MA (2009) Evolution of gene function and regulatory control after whole-genome duplication: comparative analyses in vertebrates. Genome Res 19:1404–1418

Lai CP, Bechberger JF, Thompson RJ, Macvicar BA, Bruzzone R, Naus CC (2007) Tumor-suppressive effects of pannexin 1 in C6 glioma cells. Cancer Res 67:1545–1554

Lai CP, Bechberger JF, Naus CC (2009) Pannexin2 as a novel growth regulator in C6 glioma cells. Oncogene 28:4402–4408

Leitch IJ, Bennett MD (2004) Genome downsizing in polyploid plants. Biol J Linn Soc 82:651–663

Lynch M, O'Hely M, Walsh B, Force A (2001) The probability of preservation of a newly arisen gene duplicate. Genetics 159: 1789–1804

Ma W, Hui H, Pelegrin P, Surprenant A (2009) Pharmacological characterization of pannexin-1 currents expressed in mammalian cells. J Pharmacol Exp Ther 328:409–418

Mayo C, Ren R, Rich C, Stepp MA, Trinkaus-Randall V (2008) Regulation by P2X7: epithelial migration and stromal organization in the cornea. Invest Ophthalmol Vis Sci 49:4384–4391

Panchin YV (2005) Evolution of gap junction proteins—the pannexin alternative. J Exp Biol 208:1415–1419

Panchin Y, Kelmanson I, Matz M, Lukyanov K, Usman N, Lukyanov S (2000) A ubiquitous family of putative gap junction molecules. Curr Biol 10:R473–R474

Penuela S, Celetti SJ, Bhalla R, Shao Q, Laird DW (2008) Diverse subcellular distribution profiles of pannexin 1 and pannexin 3. Cell Commun Adhes 15:133–142

Penuela, S., Gehi, R., Laird, D.W. 2012. The biochemistry and function of pannexin channels. Biochim Biophys Acta (in press)

Phelan P (2005) Innexins: members of an evolutionarily conserved family of gap-junction proteins. Biochim Biophys Acta 1711:225–245

Prochnow N, Hoffmann S, Dermietzel R, Zoidl G (2009a) Replacement of a single cysteine in the fourth transmembrane region of zebrafish pannexin 1 alters hemichannel gating behavior. Exp Brain Res 199:255–264

Prochnow N, Hoffmann S, Vroman R, Klooster J, Bunse S, Kamermans M, Dermietzel R, Zoidl G (2009b) Pannexin1 in the outer retina of the zebrafish, *Danio rerio*. Neuroscience 162:1039–1054

Putnam NH, Butts T, Ferrier DE, Furlong RF, Hellsten U, Kawashima T, Robinson-Rechavi M, Shoguchi E, Terry A, Yu JK, Benito-Gutierrez EL, Dubchak I, Garcia-Fernandez J, Gibson-Brown JJ, Grigoriev IV, Horton AC, de Jong PJ, Jurka J, Kapitonov VV, Kohara Y, Kuroki Y, Lindquist E, Lucas S, Osoegawa K, Pennacchio LA, Salamov AA, Satou Y, Sauka-Spengler T, Schmutz J, Shin IT, Toyoda A, Bronner-Fraser M, Fujiyama A, Holland LZ, Holland PW, Satoh N, Rokhsar DS (2008) The amphioxus genome and the evolution of the chordate karyotype. Nature 453:1064–1071

Qiu F, Dahl GP (2009) A permeant regulating its permeation pore: inhibition of pannexin 1 channels by ATP. Am J Physiol Cell Physiol 296:C250–C255

Roth C, Rastogi S, Arvestad L, Dittmar K, Light S, Ekman D, Liberles DA (2007) Evolution after gene duplication: models, mechanisms, sequences, systems, and organisms. J Exp Zool B Mol Dev Evol 308:58–73

Semple C, Wolfe KH (1999) Gene duplication and gene conversion in the *Caenorhabditis elegans* genome. J Mol Evol 48:555–564

Sharp LL, Zhou J, Blair DF (1995) Features of MotA proton channel structure revealed by tryptophan-scanning mutagenesis. Proc Natl Acad Sci USA 92:7946–7950

Shestopalov VI, Panchin Y (2008) Pannexins and gap junction protein diversity. Cell Mol Life Sci 65:376–394

Sosinsky GE, Boassa D, Dermietzel R, Duffy HS, Laird DW, Macvicar B, Naus CC, Penuela S, Scemes E, Spray DC, Thompson RJ, Zhao HB, Dahl G (2011) Pannexin channels are not gap junction hemichannels. Channels (Austin) 5:193–197

Swayne LA, Sorbara CD, Bennett SA (2010) Pannexin 2 is expressed by postnatal hippocampal neural progenitors and modulates neuronal commitment. J Biol Chem 285:24977–24986

Wagner A (2002) Asymmetric functional divergence of duplicate genes in yeast. Mol Biol Evol 19:1760–1768

Willecke K, Eiberger J, Degen J, Eckardt D, Romualdi A, Guldenagel M, Deutsch U, Sohl G (2002) Structural and functional diversity of connexin genes in the mouse and human genome. Biol Chem 383:725–737

Yen MR, Saier MH Jr (2007) Gap junctional proteins of animals: the innexin/pannexin superfamily. Prog Biophys Mol Biol 94:5–14

Zappala A, Cicero D, Serapide MF, Paz C, Catania MV, Falchi M, Parenti R, Panto MR, La Delia F, Cicirata F (2006) Expression of pannexin1 in the CNS of adult mouse: cellular localization and effect of 4-aminopyridine-induced seizures. Neuroscience 141:167–178

Zappala A, Li Volti G, Serapide MF, Pellitteri R, Falchi M, La Delia F, Cicirata V, Cicirata F (2007) Expression of pannexin2 protein in healthy and ischemized brain of adult rats. Neuroscience 148:653–667

Zoidl G, Petrasch-Parwez E, Ray A, Meier C, Bunse S, Habbes HW, Dahl G, Dermietzel R (2007) Localization of the pannexin1 protein at postsynaptic sites in the cerebral cortex and hippocampus. Neuroscience 146:9–16

Zoidl G, Kremer M, Zoidl C, Bunse S, Dermietzel R (2008) Molecular diversity of connexin and pannexin genes in the retina of the zebrafish *Danio rerio*. Cell Commun Adhes 15:169–183

J Membrane Biol (2012) 245:495–506
DOI 10.1007/s00232-012-9500-0

Coregulation of Multiple Signaling Mechanisms in pp60v-Src-Induced Closure of Cx43 Gap Junction Channels

Siddhartha S. Mitra · Ji Xu · Bruce J. Nicholson

Received: 23 April 2012 / Accepted: 27 August 2012 / Published online: 11 September 2012

Abstract Attenuation in gap junctional coupling has consistently been associated with induction of rapid or synchronous cell division in normal and pathological conditions. In the case of the v-src oncogene, gating of Cx43 gap junction channels has been linked to both direct phosphorylation of tyrosines (Y247 and 265) and phosphorylation of the serine targets of Erk1/2 (S255, 279 and 282) on the cytoplasmic C-terminal domain of Cx43. However, only the latter has been associated with acute, rather than chronic, gating of the channels immediately after v-src expression, a process that is mediated through a "ball-and-chain" mechanism. In this study we show that, while ERK1/2 is necessary for acute closure of gap junction channels, it is not sufficient. Rather, multiple pathways converge to regulate Cx43 coupling in response to expression of v-src, including parallel signaling through PKC and MEK1/2, with additional positive and negative regulatory effects mediated by PI3 kinase, distinguished by the involvement of Akt.

S. S. Mitra · J. Xu · B. J. Nicholson (✉)
Department of Biochemistry, University of Texas Health Science Center at San Antonio, 7703 Floyd Curl Drive, San Antonio, TX 78229-3900, USA
e-mail: NicholsonB@uthscsa.edu

Present Address:
S. S. Mitra
Institute of Stem Cell Biology and Regenerative Medicine, Stanford University, Stanford, CA 09304, USA

Present Address:
J. Xu
Department of Physiology, David Geffen School of Medicine, University of California Los Angeles, Los Angeles, CA 90095, USA

Keywords Cx43 · Gap junction · v-Src · Erk1/2 · Signal transduction

Introduction

Mammalian gap junctions, composed of membrane proteins called connexins, represent arrays of transmembrane channels that allow low-molecular weight molecules and ions to move directly between the cytoplasm of opposed cells (Goldberg et al. 1998; Kumar and Gilula 1996). Reduced communication through gap junction channels has been frequently correlated with increases in cell proliferation of both normal and transformed cells (Berthoud et al. 1993; Cronier et al. 2009). An early response to the stimulation of many cells by growth factors in culture is a decrease in coupling just prior to initiation of mitosis (Lau et al. 1992). Similarly, several oncogenes have been shown to reduce coupling of cells, most notably $pp60^{v\text{-}src}$, which Ross Johnson first observed 31 years ago to acutely induce closure of gap junction channels (Atkinson et al. 1981). It has been proposed that this uncoupling could serve to isolate cells from the inhibitory signals of neighboring cells and/or enable the accumulation of positive stimuli within the cells that generate them (Loewenstein 1990). In the current work, we return to a more detailed analysis of the signals that link v-src expression to the closure of Cx43 gap junction channels, to compare the similarities and differences of the oncogenic process to that induced by normal growth factor signaling.

Several growth factors [EGF (Lau et al. 1992), PDGF (Hossain et al. 1998, 1999b), and insulin-like growth factor (Homma et al. 1998)] have been shown to cause acute closure of Cx43 gap junction channels, primarily associated with activation of ERK, and its direct phosphorylation of Cx43

(Kanemitsu and Lau 1993; Hossain et al. 1998). However, other kinase pathways, such as PKC (Hossain et al. 1998, 1999a, b), have also been implicated. Several phosphorylation sites for these and other kinases have been mapped on the C-terminal domain of Cx43 (Berthoud et al. 1993; Kanemitsu et al. 1998; Warn-Cramer et al. 1996; reviewed in Lampe and Lau 2004). Consistent with this, removal of the C-terminal domain was shown to ablate gating by insulin-like growth factor, which could then be rescued by addition of the C-terminal domain as a separate peptide (Homma et al. 1998). This led to the model that this phosphorylation-driven gating in response to growth factors occurs by a "ball-and-chain" mechanism, similar to what had been shown for pH gating of Cx43 (Ek-Vitorin et al. 1996; Morley et al. 1996) and much earlier for inactivation of K^+ channels (Hoshi et al. 1990). However, while these studies had focused on acute gating of the channels, there is also evidence that growth factors can more chronically induce internalization of gap junction structures over longer periods of time. Hence, the interaction of the cytoplasmic domain of Cx43 with various signaling [e.g., src via SH2 and 3 domains (Warn-Cramer et al. 1996)], adapter [e.g., ZO-1 via PDZ 1 (Giepmans and Moolenaar 1998; Toyofuku et al. 1998), and 14-3-3 protein (Park et al. 2007)] and cytoskeletal [e.g., tubulin (Giepmans et al. 2001)] elements may also be relevant to longer-term regulation of coupling by growth factors.

While the regulation of gap junctions by v-src was first studied 10 years before that with growth factors, the precise mechanism of how v-src induces loss of coupling either acutely or chronically has remained somewhat controversial. By analogy with the closure of Cx43 channels by growth factors described above, Zhou et al. (1999) demonstrated that v-src closure of Cx43 channels depended not on the direct src targets on Cx43 [Y265 and 247 (Swenson et al. 1990; Solan and Lampe 2008)] but on the presence of three ERK1/2 phosphorylation sites (S255, 279 and 282) mapped in the C-terminal domain by Warn-Cramer et al. (1996). The dependence on ERK activity was also demonstrated pharmacologically in normal rat kidney (NRK) cells expressing a temperature-sensitive (ts) pp60v-src. Consistent with this, Ito et al. (2006) implicated the Ras-Raf pathway, which directly activates ERK, in the gating of Cx43 gap junction channels by v-src. Others have also implicated Cas as being essential for src gating, although the mechanism of this effect remains unclear (Shen et al. 2007). Finally, truncations of the C-terminal domain led to a loss of response of Cx43 to v-src, which was restored by coexpression of the C-terminal domain as an independent polypeptide, consistent with the "ball and chain" mechanism implicated in growth factor gating of Cx43.

However, contrary results have been published by Swenson et al. (1990) and Lin et al. (2001), who showed that Y265 and Y247 are required for v-src-induced disruption of coupling in both *Xenopus* oocytes (Swenson et al. 1990) and a mouse Cx43 knockout cell line transfected with different Cx43 mutants (Lin et al. 2001). In the latter study, the ERK1/2 phosphorylation sites (S255, 279 and 282) were found not to be required for closure. The differences between these seemingly contradictory findings do not correlate with the expression system as both results have been reported in oocytes and mammalian cells. However, one consistent distinction is that ERK dependence was reported when src's effect was exerted on preformed Cx43 channels and was likely associated with initial gating immediately following v-src expression. This is likely to be similar to the transient closing of Cx43 channels in response to cytokines [PDGF (Hossain et al. 1998) and EGF (Kanemitsu and Lau 1993)]. By contrast, tyrosines were implicated when v-src was expressed prior to, or concurrently with, Cx43 and could represent a more chronic mechanism for closure of Cx43 channels that diverges from known growth factor pathways. Using phosphorylation state-specific antibodies, Solan and Lampe (2008) showed that, in LA-25 cells, tyrosine phosphorylation predominantly occurred in gap junction plaques when v-src was activated. They also showed increased phosphorylation of ERK and PKC sites in Cx43 upon *v-src* activation, suggesting a role of multiple signaling pathways in gap junction downregulation during src transformation. However, they were unable to address the issue of whether these phosphorylation sites were functionally required for gap junction closure, nor could they assess the timeline of these phosphorylation events following src expression. In most cell lines this poses a problem, unless src expression can be acutely activated, such as in ts mutants. Unfortunately, the better-characterized ts v-src constructs have often proven to be unstable.

An alternative model system is the *Xenopus* oocyte, where src can be acutely activated by injection of its encoding RNA, allowing the time course of the response to be followed. Most mitogenic signaling cascades are present and well characterized in *Xenopus* oocytes, and they have been used extensively in the electrophysiological characterization of gap junction channels. In this study, we employed this expression system to conduct a comprehensive analysis of the regulatory pathways that mediate the initial gating of Cx43 channels by v-src to explore the degree to which they may use similar or distinct pathways from those implicated in growth factor-mediated Cx43 gating.

Materials and Methods

cDNA Constructs

Rat Cx43 cDNA (provided by Dr. Eric Beyer, University of Chicago, Chicago, IL) was subcloned into the PGEM-7Zf$^+$

vector (Promega, Madison, WI) at the *Eco*RI site. All mutants were provided by Drs. Steve Taffet and Mario Delmar (State University of New York Health Science Center, Syracuse, NY). The cDNA for pp60v-src was provided by Dr. Marilyn Resh (Memorial Sloan-Kettering Cancer Center, New York, NY). The cDNA for constitutively active MEK1 (human CA-MEK1), a kind gift from Dr. Natalie Ahn (University of Colorado, Boulder, CO), was subcloned into the oocyte expression vector pBluescript MXT at the *Eco*RV and *Xba*I restriction sites. Constitutively active and dominant negative (DN) PKC (PKCα/ε) constructs (murine) were provided by Dr. Elissavet Kardami (University of Manitoba, Winnipeg, Canada) in the pSVK3 vector.

Preparation of cRNAs

All cRNAs were linearized and transcribed in vitro using Ampliscribe Transcription kits (Epicentre, Madison, WI) according to the manufacturer's recommendations. The resultant cRNAs were quantitated after DNase-1 (Sigma-Aldrich, St. Louis, MO) treatment by absorbance at 260 nm.

Xenopus Oocyte Expression System and Measurement of Junctional Conductance

Oocytes were unilaterally extracted from female *Xenopus laevis* toads and treated with 1 mg/ml collagenase (Sigma-Aldrich) to digest most of the follicular layer. Oocytes were preinjected with 40 nl of 0.2 μg/μl of an oligonucleotide complementary to *Xenopus* Cx38, 5′-75 GCTTTA GTAATTCCCATCCTGCCATGTTTC 45-3′, prior to injection with Cx43 cRNA (2 ng/oocyte) as described by Zhou et al. (1999). After final manual stripping of the vitelline membrane, oocytes were paired for ~16 h prior to measuring junctional currents (I_j) by dual-cell voltage clamp as described in Zhou et al. (1999). All experiments were carried out in oocyte batches from at least five different females, to account for differences in batch-specific physiological behavior.

Measure of Kinase Effects

About 16 h after pairing, oocytes were recorded for approximately 20 min to ensure stable conductance levels before secondary injection of cRNAs for the kinase of interest [i.e., v-src (8 ng), CA-PKC (8 ng) or CA-MEK (8 ng)]. The effects of secondary injection on gap junctional conductance were assessed after 6 h and expressed as fractional decrements of the conductance recorded from the same oocyte pair before introduction of the kinase cRNA. Thus, the effects of kinases were normalized within the same oocyte. In cases where DN constructs were used, the cRNAs encoding DN-PKAα (8 ng) and DN-PKCε (8 ng) were injected at the same time as v-src cRNA injection. Expression of each construct was tested by Western blot analysis in each batch of oocytes as described below.

Pharmacological Inhibitors

Bis(indolyl-1)maleamide (BIM; Calbiochem, La Jolla, CA) was added to 0.1 μm final concentration, U0126 and LY294002 (Cell Signaling technology, Beverly, MA) were added to 50 μm final concentration, wortmannin (Sigma-Aldrich) was added to 0.05 μm final concentration and Akt inhibitor VIII (Akti-1/2, Calbiochem) was added to 10 μm final concentration. All inhibitors were added to L-15 *Xenopus* oocyte incubation medium (Sigma-Aldrich) just before injection of the cRNA for pp60v-src, CA-MEK1/2 or CA-PKCε. The medium with the relevant inhibitor was changed every hour to ensure its full effect over the entire duration of the experiment.

Immunoprecipitation and Western Blot

Oocyte lysates were prepared from approximately 15–20 oocytes, injected with the same schedule as used in the functional assays. Lysates were prepared in modified RIPA buffer [1 % NP-40, 0.1 % SDS, 50 ml Tris (pH 7.4), 100 mM NaCl, 2 mM EDTA, 50 mM NaF, 40 mM β-glycerophosphate, 1 mM Na_2VO_4 and protease inhibitors]. The supernatant was collected from clarified lysates and immunoprecipitated with anti-Cx43 polyclonal antibody (1:200; Santa Cruz Biotechnology, Santa Cruz, CA) or anti-Erk1/2 polyclonal antibody (1:500; Upstate Biotechnology, Lake Placid, NY) overnight at 4 °C. For Western blot analysis of oocyte lysates, oocytes were lysed in 200 μl of RIPA buffer and clarified at 14,000 rpm for 30 min. Lysates were resolved on a 10 % SDS-polyacrylamide gel before transfer onto a PVDF membrane (Millipore, Billerica, MA). Since *Xenopus* oocytes express only Erk2 (Ferrell 1999), a single band is observed when probed for Erk1/2 or phospho-Erk1/2. For Cx43 detection, anti-Cx43 monoclonal antibody (Chemicon, Temecula, CA) targeted to the C-terminal tail of Cx43 was used as the primary antibody. To test for expression of kinase constructs, anti-avian Src antibody (clone EC10, 1:1,000; Upstate Biotechnology), anti-PKCε (Cell Signaling Technologies) and anti-PKCε mouse monoclonal antibody (1:1,000, Santa Cruz Biotechnology) were used.

Radiolabeled Assay for Cx43 Phosphorylation

To assay for MEK-induced Cx43 phosphorylation, ATP-γ32 (2–10 μCi/oocyte, 250 μCi/μl; Amersham Biosciences,

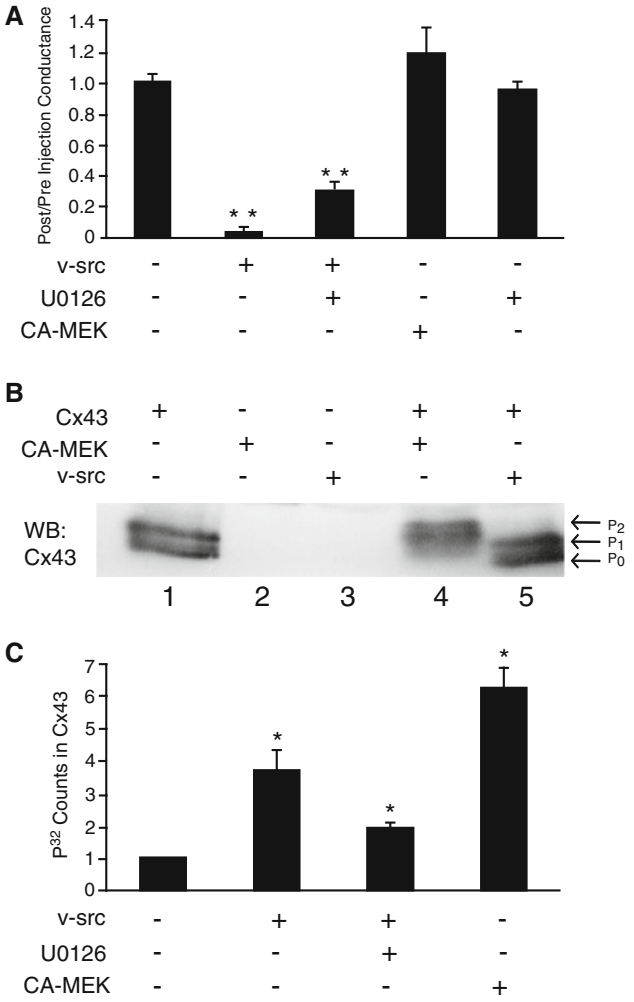

◀**Fig. 1** **a** ERK1/2 is necessary, but not sufficient, for v-src gating of Cx43. Cx43 paired oocytes were injected with water, v-src or CA-MEK1; and conductance 6 h postinjection was measured as a ratio of the preinjection conductance. v-src induced almost complete inhibition of coupling, which could be partially prevented by inhibition of MEK1/2 with U0126. However, CA-MEK1 injection alone had no significant effect on Cx43 coupling. U0126 alone had no effect on coupling. The data represent means of six separate experiments, each having a minimum of eight coupled oocyte pairs. Statistical analysis was performed using Student's *t* test, comparing each group to the Cx43-expressing oocytes (**$P < 0.001$). In this and all subsequent graphs, bars represent mean values, with standard errors indicated. **b** CA-MEK induces phosphorylation of Cx43. Cx43 coupled oocytes, subjected to various treatments as indicated, were lysed and then immunoprecipitated with anti-Cx43 polyclonal antibody, followed by analysis via western blot probed with a Cx43 monoclonal antibody. No bands were evident in the absence of Cx43 injection (*lanes 2* and *3*). A doublet corresponding to P_0 and P_1, a phosphorylated form, was found in cells injected with only Cx43 (*lane 1*). CA-MEK induced retardation in electrophoretic mobility of Cx43, producing a more highly phosphorylated P_2 form (*lane 4*). In contrast, v-src (*lane 5*) failed to induce a significant shift in mobility. **c** Src phosphorylation of Cx43 occurs partially through ERK but with low efficiency. Cx43 coupled oocytes were coinjected with ATP-γ^{32} and either v-src or CA-MEK1 cRNA. After 6 h of incubation, oocyte pairs were lysed, immunoprecipitated with anti-Cx43 antibody and separated by SDS-PAGE. Incorporated ^{32}P was quantitated by phosphoimage analysis. Src induced phosphorylation, which was about 50 % inhibited by the MEK inhibitor U0126. CA-MEK induced significantly higher phosphorylation levels than src. Data represent the mean ± SE from three separate experiments, with equal numbers of oocyte pairs in each set. Data were normalized and compared statistically to oocytes expressing only Cx43; statistical significance was determined by Student's *t* test (*$P < 0.05$)

Arlington Heights, IL) was injected along with CA-MEK1 mRNA into Cx43 coupled oocytes. After 6 h, oocytes were lysed as described in Zhou et al. (1999). Briefly, for each experiment, approximately six labeled oocytes were homogenized in 200 µl/oocyte of modified RIPA buffer. The homogenate was brought to 2 % Triton X-100 after boiling for 5 min and cleared in a microcentrifuge at 13,000 rpm for 5 min. One microliter of primary antibody/oocyte (crude rabbit antisera against Cx43 residues 302–319) was added to the supernatant and pulled down by preswollen protein A-Sepharose CL-4B beads (Sigma-Aldrich). The beads were washed three times in the same RIPA buffer used for oocyte lysis, before solubilization of the immunoprecipitated material by boiling for 10 min in 2× SDS sample buffer and subsequent separation by SDS-PAGE on a 10 % gel. The dried gel was analyzed by exposure to a PhosphoImaging cassette (model 425E using ImageQuant v.4.2 software; Molecular Dynamics, Sunnyvale, CA) for several hours, and then bands were quantitated after reading on a PhosphoImager.

Results

ERK1/2 is Necessary in v-src-Induced Acute Closure of Cx43 Gap Junctions

Oocytes have proven to be an effective system for analysis of acute gating of Cx43 channels by src, as the v-src protein can be expressed after Cx43 gap junction channels are stably established. This is in contrast to most mammalian cell studies where src is expressed concurrently with Cx43 and can affect many processes including assembly and degradation. We had previously shown a requirement for ERK phosphorylation of Cx43 for acute gating by src in oocytes. In mammalian cells, inhibition of both ERK (Zhou et al. 1999) and Ras (Ito et al. 2006) largely prevents src gating of Cx43, a result we now tested in oocytes. In the presence of the highly specific inhibitor of MEK1/2 activation, U0126 (Davies et al. 2000), we observed only a 2.5-fold drop in conductance of Cx43 coupled oocytes (Fig. 1a). This was slightly greater than the nonspecific effect of v-src on Cx43 with the ERK targets deleted, or on Cx32, which has no endogenous src or ERK kinase targets, and dramatically less than the 150-fold drop induced by v-src alone on Cx43. This indicated that the ERK was

required for src gating of Cx43, consistent with the previous observation that the consensus ERK phosphorylation sites on Cx43 are required for src gating (Zhou et al. 1999).

To test if it was also sufficient, CA-MEK1, which directly activates ERK1/2, was injected into Cx43 coupled oocytes, with no significant effect on gap junction coupling (Fig. 1a). This was not due to failure of expression or activity of CA-MEK1 in the oocyte system as CA-MEK1 induced both a significantly greater mobility shift of Cx43 in SDS polyacrylamide electrophoresis [this has been correlated with serine phosphorylation (Musil et al. 1990; Lampe et al. 2000) (Fig. 1b)] and ^{32}P incorporation into Cx43 (Fig. 1c) than was caused by v-src. About 50 % of src-induced phosphorylation of Cx43 could be attributed to ERK, as it could be blocked by U0126. However, the efficiency of the signal is less than that achieved by directly activating ERK through MEK. Thus, while ERK1/2 appears to be necessary for acute closure of gap junctions by v-src, it is not sufficient. We have also shown previously that direct gating of Cx43 channels by v-src is not dependent on the tyrosine targets of v-src on Cx43 (Zhou et al. 1999). Thus, it seems reasonable to deduce that other signaling pathways are likely to be involved in acute closure of Cx43 gap junctions.

PKC is Also Required for v-src-Induced Closure of Cx43 Gap Junctions

Given previous documentation of direct effects of PKC on Cx43 coupling (Moreno et al. 1994) and its implication in uncoupling Cx43 expressing cells in response to PDGF (Hossain et al. 1998) or v-src (Solan and Lampe 2008), we tested the effects of the broad-spectrum PKC inhibitor BIM. This significantly reduced the ability of v-src to close Cx43 gap junctions, although, as in the case of the MEK1/2 inhibitor U0126, this was not complete (Fig. 2a). When added together, the MEK1/2 (U0126) and PKC (BIM) inhibitors appeared to act in an additive fashion. In fact, the rescue of coupling to two-thirds of the level before src injection is comparable to that seen in src injections of Cx32 cells (a connexin that lacks src or ERK targets). This has been interpreted as reflecting non-gap junction-specific effects of src, possibly on cell adhesion. To assess if the role of PKC in v-src gating required direct phosphorylation of Cx43, the PKC targets on Cx43 were deleted. Cx43Δ363-373 removes PKC phosphorylation sites that have been definitively mapped [S368, S372 (Lampe et al. 2000)], while Cx43S262A and Cx43S297A delete serines within consensus PKCε phosphorylation sites (Doble et al. 2001). Neither the deletion nor site-specific mutants showed any significant effect on v-src gating of Cx43 (Fig. 2b), demonstrating that PKC must affect signaling pathways upstream of the channel itself. S297 appears to be

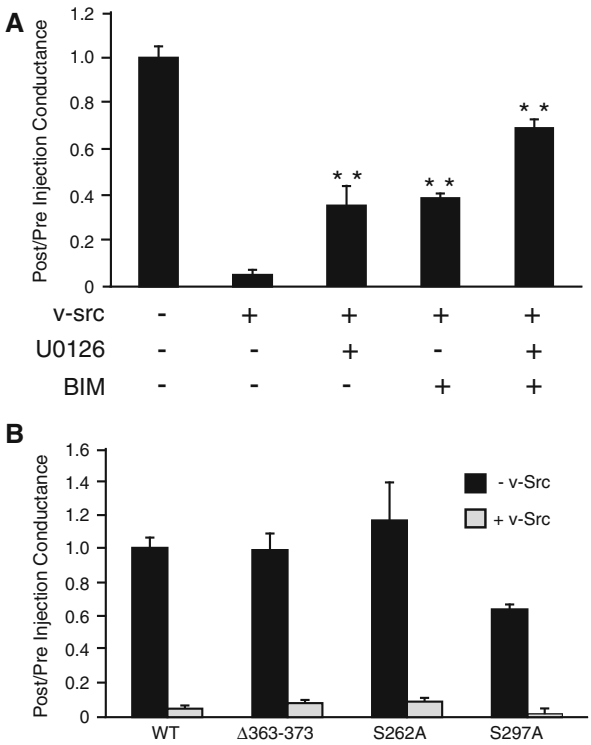

Fig. 2 **a** Both MEK1/2 and PKC play a role in v-src-induced Cx43 gating. Cx43 coupled oocytes were incubated in medium alone or in the presence of the PKC inhibitor BIM (0.1 μm), the MEK inhibitor U0126 (50 μm) or both. Individually, both U0126 and BIM decreased $pp60^{v\text{-}src}$-induced Cx43 closure. Combined treatment with both inhibitors showed an additive effect, indicating that MEK and PKC may act through parallel pathways. The data represent means of six separate experiments, each having a minimum of eight coupled oocyte pairs. Statistical analysis was performed by Student's *t* test, comparing each group to the Cx43 + src-injected oocytes (**$P < 0.001$). **b** PKC phosphorylation of Cx43 is not required for gating. Ablation of all documented PKC phosphorylation targets (Cx43Δ363-373) as well as consensus PKCε phosphorylation sites on Cx43 (S362A and S297A) failed to significantly affect v-src gating of the channels. The reduced coupling in Cx43S297A cells may reflect the independent role of this site in efficient Cx43 expression. *Gray bars* represent pre-/postconductance ratios in the absence of Src, and *black bars* represent conductance ratios pre- and post-v-src cRNA injection

required for optimal function of Cx43 as Cx43S297A expressing oocytes showed consistently lower coupling, despite injection of similar cRNA levels. However, the src gating response was not impacted (Fig. 2b).

PKC has been demonstrated in other systems to be required for optimal ERK1/2 activity in response to upstream signals (Schonwasser et al. 1998). To test this in the oocyte system, we first showed that direct activation of ERK1/2 by CA-MEK1, which caused a large increase in the phospho form, was unaffected by BIM (Fig. 3, lanes 1, 2). However, ERK2 activation by the upstream effector v-src (Fig. 3, lane 3) was substantially inhibited by BIM

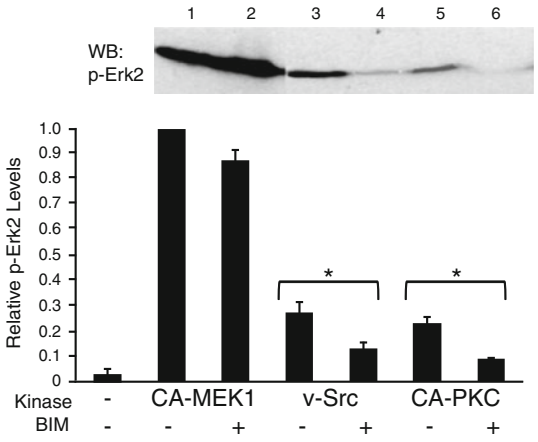

Fig. 3 ERK1/2 phosphorylation is regulated by PKC. Cx43 coupled oocytes were incubated in L-15 medium, with or without BIM (0.1 μm); subsequently injected with cRNA for $pp60^{v\text{-}src}$, CA-MEK1 or CA-PKC; and immunoblotted with anti-phospho-ERK1/2 antibody (*inset*). ERK1/2 activation was evident by all three kinases (*lanes 1*, *3* and *5*), although direct activation by MEK1/2 was by far the most effective. BIM did not affect ERK1/2 activation by CA-MEK1 (*lane 2*) but significantly inhibited its activation by $pp60^{v\text{-}src}$ and CA-PKC (*lanes 4* and *6*, respectively). Data are from three separate experiments, each having equal numbers of coupled oocyte pairs for each set ($n = 10$). Statistical significance of each treatment with or without src or with or without CA-PKC was assessed by Student's *t* test ($^*P < 0.05$)

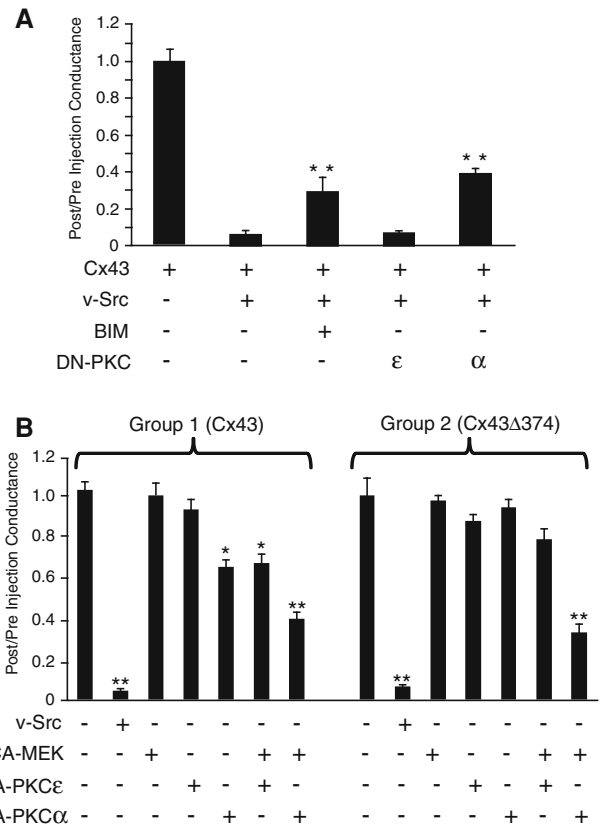

Fig. 4 **a** The PKCα isoform mediates v-src gating of Cx43 in oocytes. The effects of coinjection of DN isoforms of PKCα and PKCε on v-src-induced Cx43 gating were compared to those of the generic PKC inhibitor BIM. DN-PKCα showed similar effects to BIM, while DN-PKCε had no effect. Data represent means of six separate experiments, each having a minimum of eight coupled oocyte pairs. Statistical analysis was performed by Student's *t* test, comparing each treatment to the Cx43 + src group ($^{**}P < 0.001$). **b** PKCα, in conjunction with MEK, selectively inhibits Cx43 coupling, independent of the C-terminal binding domain for ZO-1. *Group 1* CA-PKCα, but not CA-PKCε, inhibited Cx43 coupling when injected into oocyte pairs. Uncoupling was enhanced by coinjection of CA-MEK, but this did not approach the degree of uncoupling generated by v-src. *Group 2* truncation of Cx43 at residue 374, removing the PDZ domain which mediates ZO-1 binding, eliminated the effect of CA-PKCα but did not change the combined MEK/PKC effect on coupling. Data represent means of six separate experiments, each having a minimum of eight coupled oocyte pairs. Statistical analysis was performed using Student's *t* test, comparing each group to oocytes expressing Cx43 only ($^{**}P < 0.001$, $^*P < 0.05$)

(Fig. 3, lane 4). Also, ERK1/2 can be directly activated by CA-PKC (Fig. 3, lane 5), which, as might be expected, was almost completed clocked by BIM (Fig. 3, lane 6).

While BIM is an effective inhibitor of many PKC isoforms, it also can have off-target effects against other kinases like MAP kinase-activated kinase, S6 kinase, GSK3 and PI-dependent protein kinase (Davies et al. 2000). DN PKC constructs represent more specific reagents, but these are isotype-specific. The two likely candidates in this case were PKCε and PKCα, since their direct phosphorylation sites on Cx43 have been identified (Doble et al. 2001; Lampe et al. 2000) and their activation by v-src is well documented (Zang et al. 1995). When DN constructs specific for each isoform were injected into oocytes, only DN-PKCα was effective, producing a similar level of inhibition of v-src gating of Cx43 as seen with BIM (Fig. 4a). Consistent with the isoform specificity of the DN constructs, only the α-isoform of CA-PKC induced partial closure of Cx43 channels (Fig. 4b, group 1). In conjunction with CA-MEK1 both isoforms had some effect on partially closing Cx43 channels, but this effect was larger for PKCα. However, the maximum reduction in coupling (~60 %) was still far less than that induced by v-src (>99 %) (Fig. 4b, group 1), indicating that additional pathways still need to be considered beyond PKC.

ZO-1 Binding Site on Cx43 Does Not Appear to Play a Role in v-src-Induced Closure of Cx43 Gap Junctions

Since v-src gating of Cx43 has been characterized as operating through a "ball-and-chain" mechanism, that would presumably require a free C terminus. Thus, we also investigated the potential role of ZO-1 binding to the C terminus as this would "tether" the tail to the cytoskeleton. This interaction, which occurs through a PDZ binding site at the C terminus of Cx43 (Giepmans and Moolenaar 1998;

Toyofuku et al. 1998), has been shown by Toyofuku et al. (2001) and Sorgen et al. (2004) to be disrupted by constitutively active c-src, invoking a possible direct role for src in gating other than through tyrosine phosphorylation. However, deletion of the ZO-1 binding site by truncation of the nine C-terminal residues (Cx43Δ374, a gift from Dr. M. Delmar) had no effect on the ability of v-src to close the channels and did not enhance the ability of MEK1 or CA-PKCα (separately or coordinately) to close the channel (Fig. 4b, group 2). The modest inhibition of wt Cx43 coupling observed with CA-PKCα alone (Fig. 4b, group 1) was not seen with this C-terminal truncation mutant (Fig. 4b, group 2), despite the fact that none of the consensus PKCα sites were directly eliminated.

Phosphatidylinositol-3-Kinase Plays a Complex Regulatory Role in v-src Closure of Cx43 Gap Junctions

Another potential pathway that has been implicated in src signaling is phosphatidylinositol-3-kinase (PI3K). To probe the role of this pathway in src gating of Cx43, we used two different PI3K inhibitors, reversible LY294002 and irreversible wortmannin. The former has a lower affinity and shows some cross-reactivity with casein kinase II and GSK3β, while the latter has a higher affinity and different cross-reactivity with smooth muscle myosin light chain kinase (Davies et al. 2000), likely not relevant in the current study. Despite the different properties of these two inhibitors, both caused similar inhibition ($P < 0.05$) of v-src gating (Fig. 5, groups 2 and 3, respectively), albeit less efficiently than we had observed with either the MEK1/2 (U0126) or PKC inhibitors (BIM) (Fig. 5, group 1; $P < 0.001$). No significant increase in inhibition was seen when either wortmannin or LY294002 was used in combination with BIM compared to BIM alone. However, the application of U0126 in concert with wortmannin or LY294002 caused an unexpected restoration of v-src gating of Cx43, reversing the inhibition seen with either inhibitor alone. The application of all three inhibitors caused a similar "annulment" of their individual effects and the synergistic effects of the PKC and ERK pathways and restored full closure of Cx43 channels by v-src. None of the inhibitors, alone or in combination, affected Cx43 coupling in the absence of v-src (Fig. 5, group 4), indicating no deleterious effects on oocytes from the combination of inhibitors used.

Further insights into the apparently antagonistic effects of wortmannin and U0126 were obtained by directly examining levels of activated ERK under the different treatments. Wortmannin treatment not only enhanced the activation of ERK1/2 following v-src treatment (Fig. 6, lanes 2 and 3; $P < 0.001$) but also reversed the reduction of src-induced ERK phosphorylation caused by U0126 (Fig. 6, lanes 4 and

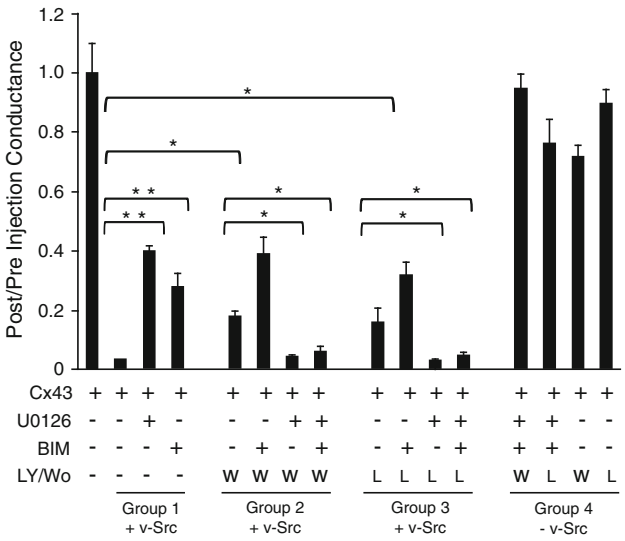

Fig. 5 PI3K plays a complex role in v-src-induced gating. Inhibition of PI3K by wortmannin or LY294002 partially blocked the ability of v-src to close Cx43 channels (compare first bars in group 2 or 3, respectively, with second bar in group 1). When added together with BIM, both wortmannin and LY294002 slightly enhanced the inhibition of v-src gating (*second bars*, *groups 2* and *3*), although this was significant only in the case of wortmannin. However, when wortmannin or LY294002 was added in conjunction with U0126, with or without BIM (*third and fourth bars*, *groups 2* and *3*), the effects of both inhibitors appeared to be annulled, restoring full closure of Cx43 by v-src. None of the inhibitors, alone or in combination, had a significant effect on Cx43 coupling in the absence of v-src (group 4). Data represent the mean ± SE from three separate experiments with an equal number of oocyte pairs in each set. *Brackets* indicate specific comparisons subjected to Student's *t* test, yielding differences at the $^{**}P < 0.001$ or the $^{*}P < 0.05$ level

5; $P < 0.05$). Thus, PI3K may play dual roles in the src gating of Cx43, facilitating the process, possibly through PKC, while also exerting an inhibitory influence through effects on ERK activation. In an effort to distinguish which aspects of the diverse PI3K pathways might mediate these apparently opposing effects on v-src gating, we tested the role of the major PI3K effector Akt. Akti, a highly specific inhibitor of both Akt isoforms 1 and 2 (Barrett et al. 2005), caused a similar level of inhibition of v-src gating as had the PI3K inhibitor LY294002 (Fig. 7). However, unlike the PI3K inhibitors, application of Akti in conjunction with the ERK inhibitor U0126 caused no restoration of v-src gating (Fig. 7). Thus, it appears that PI3K's role in contributing to v-src-induced closure of Cx43 channels is mediated by Akt, while its positive effects on Cx43 coupling through antagonism of the ERK pathway do not involve Akt.

Discussion

The mechanisms for inhibition of cell coupling during transformation remain unclear. Chronic uncoupling in

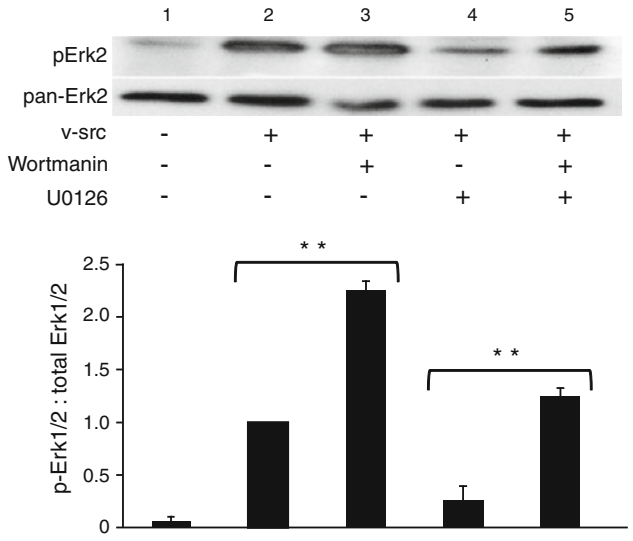

Fig. 6 PI3K activity inhibits phosphorylation of ERK1/2. Immunoblot, using anti-phospho ERK1/2 (*upper panel*) and pan-specific ERK1/2 (*lower panel*) antibodies, of lysates from Cx43 coupled, v-src injected cells (*lanes 2–5*) treated with either wortmannin (*lane 3*), U0126 (*lane 4*) or both (*lane 5*). In either the presence or the absence of the MEK1/2 inhibitor, wortmannin induced an increase in ERK phosphorylation. There was no significant change in the expression of ERK1/2 in response to the inhibitors. The density of the bands was measured from several experiments, expressed as a ratio of phospho- to total ERK1/2 levels and plotted in a histogram below the gel. *Brackets* indicate pairwise statistical comparisons of results from three independent experiments, yielding differences significant at the $^{**}P < 0.001$ or the $^{*}P < 0.05$ level; analysis was performed using Student's *t* test

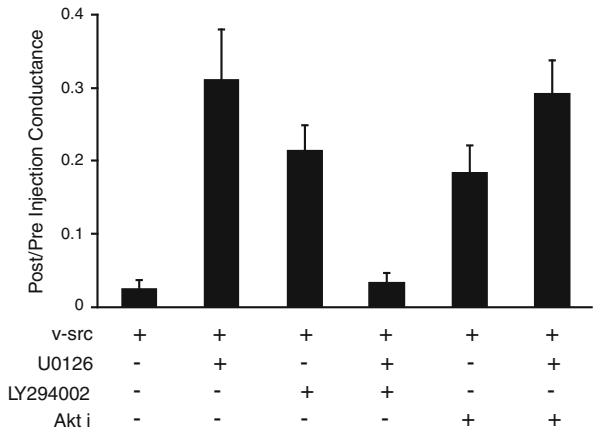

Fig. 7 The positive, but not the negative, regulatory effects of PI3K on src gating are mediated through Akt. As shown, inhibition of ERK by U0126 or PI3K by LY294002 each partially prevented v-src gating of Cx43. Inhibition of Akt by Akti had the same effect as PI3K inhibition, indicating that PI3K-induced closure of Cx43 is mediated through Akt. By contrast, the "rescue" of src gating by inhibition of both ERK and PI3K was not reproduced by a combination of ERK and Akt inhibition, indicating that the negative influence of PI3K on Cx43 gating by src is mediated through a pathway other than Akt

response to v-src has been consistently linked to direct phosphorylation of tyrosines in the C-terminal domain of Cx43, mapped to Y265, and a secondary site at Y247. Even after long-term expression of src, the phosphorylation of tyrosine in Cx43 remains in plaques (Solan and Lampe 2008); but it is not clear if the channels are gated or if other processes related to assembly are affected. Serine phosphorylation has also been associated with src expression but appears not to be required for long-term uncoupling (Lin et al. 2001). In contrast, the initial acute gating of Cx43 gap junction channels by src immediately after its expression has been linked to a "ball-and-chain" mechanism, triggered, not by tyrosine phosphorylation, but by ERK1/2 phosphorylation of serines in the C-terminal domain of Cx43 (Zhou et al. 1999). These specific sites were the same as those mapped by Warn-Cramer et al. (1996) in cellular responses to growth factors (i.e., serine S255, 279, 282), which suggests potential commonality in these gating mechanisms.

ERK Activation Alone Cannot Account for v-src Gating

In order to clearly dissect the temporal nature of src regulation of Cx43 and focus on the acute phase, which may be analogous to growth factor-induced gating of Cx43, we employed the *Xenopus* oocyte expression system. This allows for temporally controlled expression of the v-src kinase in cells that are already stably coupled by Cx43. Both mutation of ERK phosphorylation sites and inhibition of ERK activity (Zhou et al. 1999) (Fig. 1a) prevented v-src gating of Cx43, demonstrating the necessity of ERK for initial gating of Cx43 channels by v-src. However, we show here that this is not sufficient as activation of ERK by CA-MEK1 failed to close the Cx43 channels (Fig. 1c). This led us to investigate other pathways that could contribute to src gating. Our strategy was to combine the use of pharmacological blockers of different kinase pathways, which have been implicated in various studies of src action, with more specific knockouts of their target phosphorylation sites (in the case of ERK) or DN and constitutively active constructs (in the case of PKC). When these were not available, we used multiple inhibitors with different modes of action and specificities (in the case of PI3K). Using this double confirmation approach, we minimized the probability of off-target effects of the pharmacological agents alone (Davies et al. 2000; Anastassiadis et al. 2011).

Possible Roles for PKC in v-src Gating

Based on similar inhibitory effects of both BIM and an α-isotype-specific DN-PKC (Fig. 4a) on v-src gating of

Cx43, we concluded that closure of Cx43 channels by v-src also utilizes the PKC pathway. However, since deletion of all known PKC sites on Cx43 failed to affect gating (Fig. 2b), PKC must exert its effects on upstream events. This may be partially through interactions between PKC and ERK as we show that ERK phosphorylation is enhanced by CA-PKC and reduced by BIM (Fig. 3). However, all of PKC's effects cannot be mediated through ERK as CA-MEK1 induced significantly higher levels of ERK phosphorylation than either PKC isotype (Fig. 3) but with no effect on gating (Fig. 1a). In addition, both α and ε isotypes of PKC induced similar enhancement of ERK phosphorylation (data not shown), yet only the former affected gating (Fig. 4). The additive effect of U0126 and BIM (MEK and PKC inhibitors, respectively) on preventing v-src block of Cx43 (Fig. 2a) and the synergistic action of CA-MEK and CA-PKAα (Fig. 4b) suggest that MEK1/2 and PKC may affect closure of Cx43 channels through independent pathways. The specific PKC pathway remains to be elucidated, but it appears not to be mediated through direct phosphorylation of Cx43 on any of the identified consensus sites.

Complexity of PI3K Modulation of v-src Gating

PI3K, which is also known to be modulated by src activity (Penuel and Martin 1999), is involved in Cx43 gating, as inhibition of PI3K by two independent compounds attenuated v-src block of Cx43 (Fig. 5). This effect of PI3K appears to be mediated by Akt (Fig. 7), consistent with previous observations that have associated the PI3K-Akt pathway with both v-src and TNFα closure of Cx43 channels (Ito et al. 2010). In this previous case the effect was linked to Akt1. This is consistent with the effectiveness of Akti in preventing src gating, as this inhibitor targets Akts 1 and 2 (Barrett et al. 2005). Also, since inhibition of src gating by PKC was not further enhanced by inhibition of PI3K, these kinases may inhibit Cx43 through a common pathway. However, we also find that PI3K not only plays a role in promoting closure of the Cx43 channels by v-src, but also serves to antagonize this gating. This antagonistic effect appears not to involve Akt action, but to be mediated through ERK, as inhibition of PI3K caused an increase in ERK phosphorylation levels (Fig. 6) that may be sufficient to overcome the effects of MEK inhibition on src gating (Fig. 5).

An Integrated Model of v-src Gating of Cx43: A Delicate Balance

The same three pathways, Ras-Raf-ERK, PKC and PI3K, which we have identified as mediating initial v-src gating of Cx43, have frequently been implicated in many aspects of growth factor signaling, with growing evidence of cross-talk between them at several levels. This is specifically true for the effects of growth factors on Cx43 coupling (Warn-Cramer et al. 1996; Hossain et al. 1999a, b). Consistent with these known pathways and the results presented here, one possible model for how v-src may regulate Cx43 coupling is presented in Fig. 8. Based on the demonstrated Ras-independent means of activation of ERK1/2 by PKC (Schonwasser et al. 1998; Kolch 2000), PI3K could activate MEK via PKC. This could explain why PI3K inhibitors alone partially blocked closure of Cx43 channels by v-src and why these inhibitors could not further enhance the effects of inhibition of PKC. Akt1 has also been implicated in the PI3K component of the src gating response of Cx43 (Ito et al. 2010), consistent with our finding that Akti can partially prevent acute src closure of Cx43 channels. The mechanism of Akt action on Cx43 has yet to be resolved, although Akt has been shown to phosphorylate Cx43 at both S369 and 373, leading to association of 14-3-3 with the Cx43 C-terminal domain (Park et al. 2007). This might be expected to affect aspects of Cx43 trafficking, but in the oocyte studies presented here the gating effects are acute and could suggest a more direct role of this interaction, or other effects of Akt, on the open state of Cx43 channels.

The mechanism by which the PI3K pathway also exerts antagonistic effects on src gating are less clear, although it appears this may be mediated through suppression of ERK activation based on the hyperphosphorylation of ERK that is observed in response to wortmannin. PI3K has been shown to inhibit the Ras-Raf-MEK1/2-ERK pathway via an antagonistic influence of Akt (Moelling et al. 2002), but this appears not to be the pathway in this study as Akti had no effect on reestablishing src gating in the presence of MEK inhibitors. These schizophrenic effects of PI3K, as both an activator and an inhibitor of the MEK1/2 pathway, are likely to be a critical aspect of the fine-tuning of ERK activity that appears to control Cx43 function in response to different mitogenic signals through convergence of several major signaling networks. This balance may be required to avoid activation of the negative feedback loop that has been shown to operate through the serine phosphorylation of SOS by ERK (Langlois et al. 1995). However, artificial elevation of ERK activity through CA-MEK expression, which produces maximal Cx43 phosphorylation, still does not result in gating. Hence, ERK-independent pathways must also be required for closure of Cx43 gap junction channels. The nature of these pathways remains to be elucidated (indicated by dotted arrows in Fig. 8), although we have eliminated some possibilities, such as direct PKC phosphorylation of Cx43 (Fig. 2a) and binding events, like ZO-1, at the very C-terminal tail of Cx43 (Fig. 4b).

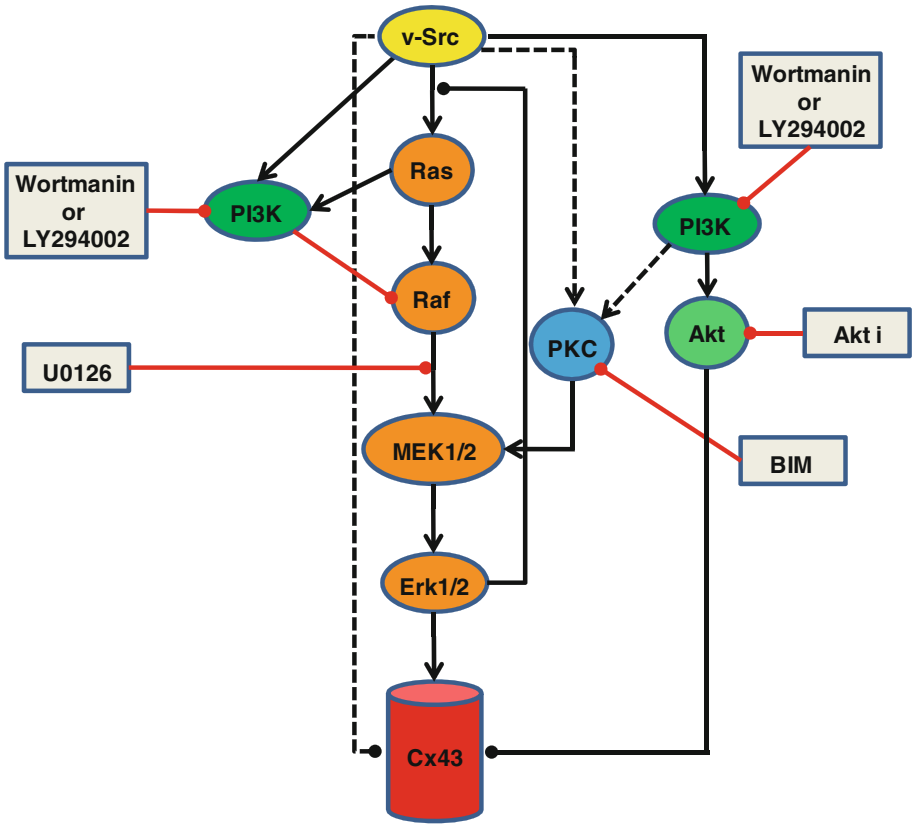

Fig. 8 Model for signaling pathways involved in v-src-induced initial closure of Cx43. The hypothetical model shown is based on the data presented here and established (*solid lines*) or proposed (*dashed lines*) connections from other studies (see text). We have noted only the simplest model consistent with the data and literature, and more complex connections are possible. Activating effects are indicated by *arrowheads* and inhibitory effects by lines with *solid circles*. The sites of action of the inhibitors (shown in *gray rectangles*) used in the current study are also indicated. The central player appears to be ERK1/2 (*orange pathway*). The PKC pathway (*blue*) can positively influence the activation of ERK1/2 but may also regulate Cx43 in a manner dependent on its very C-terminal ZO1 binding domain. PI3K (*green*) can contribute to src gating through PKC (and ERK?) or through Akt (*light green*), possibly by direct effects on Cx43 that have been reported. PI3K can also antagonize src gating of Cx43 in a yet to be defined pathway that inhibits ERK activation. Together, these pathways may serve to regulate the levels of ERK1/2 activation, perhaps keeping it within a defined range so as not to activate the negative feedback loop of ERK to the activator of Ras. However, since full activation of ERK by CA-MEK fails to induce channel closure, pathways independent of ERK are likely to present parallel mechanisms for channel closure (*dashed lines*)

Comparison of Acute v-src vs. Growth Factor-Induced Closure of Cx43 Channels

The data presented here suggest that the initial action of v-src on Cx43 gap junction channels is similar to that of growth factors, with multiple control pathways regulating the process. This is typical of the checks and balances seen in other aspects of the mitogenic response. This initial uncoupling may serve to isolate cells from potential mitogenic inhibitory signals from neighbors or to allow accumulation of promitogenic activators within the cell. The effects of v-src diverge from those of growth factors in that the suppression of coupling becomes chronic. This effect, which has been linked to tyrosine phosphorylation of Cx43 in several systems, is likely mediated by a mechanism distinct from that of the initial gating response to v-src studied here. Our analyses, including this distinction between acute and chronic gating, provide a basis for reconciliation of diverse reports in the literature. Chronic gating appears to be connected exclusively with tyrosine phosphorylation, while acute gating, which has been associated with Ras (Ito et al. 2006) and Cas (Shen et al. 2007) activity, appears to work through synergistic operation of the ERK, PKC and PI3K pathways.

Acknowledgments Te authors are grateful to Mario Delmar and Steve Taffett for providing various Cx43 mutants, Elissavett Kardami for the PKC constructs, Marilyn Resh for provision of the v-src construct and Natalie Ahn for providing the CA-MEK1 construct. The authors' thank Mary Merritt and Eileen Kasperek for technical assistance, Sandra A. Mathis for help in compiling the manuscript and Edward A. Kalmykov for assistance in preparing the figures for submission. This study was supported by National Institutes of Health grant CA048049 (to B. J. N.).

References

Anastassiadis T, Deacon SW, Devarajan K, Ma H, Peterson JR (2011) Comprehensive assay of kinase catalytic activity reveals features of kinase inhibitor selectivity. Nat Biotechnol 29:1039–1045

Atkinson MM, Menko SS, Johnson RG, Sheppard JR, Sheridan JD (1981) Rapid and reversible reduction of junctional permeability in cells infected with a temperature-sensitive mutant of avian sarcoma virus. J Cell Biol 91:573–578

Barrett SF, Defeo-Jones D, Fu S, Hancock PJ, Haskell KM, Jones RE, Kahana JA, Kral AM, Leander K, Lee LL, Malinowski J, McAvoy EM, Nahas DD, Robinson RG, Huber HE (2005) Identification and characterization of pleckstrin-homology-domain-dependent and isoenzyme-specific Akt inhibitors. Biochem J 385:399–408

Berthoud VM, Rook MB, Traub O, Hertzberg EL, Saez JC (1993) On the mechanisms of cell uncoupling induced by a tumor promoter phorbol ester in clone 9 cells, a rat liver epithelial cell line. Eur J Cell Biol 62:384–396

Cronier L, Crespin S, Strale PO, Defamie N, Mesnil M (2009) Gap junctions and cancer: new functions for an old story. Antioxid Redox Signal 11:323–338

Davies SP, Reddy H, Caivano M, Cohen P (2000) Specificity and mechanism of action of some commonly used protein kinase inhibitors. Biochem J 351:95–105

Doble BW, Ping P, Fandrich RR, Cattini PA, Kardami E (2001) Protein kinase C-epsilon mediates phorbol ester-induced phosphorylation of connexin-43. Cell Commun Adhes 8:253–256

Ek-Vitorin JF, Calero G, Morley GE, Coombs W, Taffet SM, Delmar M (1996) PH regulation of connexin43: molecular analysis of the gating particle. Biophys J 71:1273–1284

Ferrell JE Jr (1999) *Xenopus* oocyte maturation: new lessons from a good egg. BioEssays 21:833–842

Giepmans BN, Moolenaar WH (1998) The gap junction protein connexin43 interacts with the second PDZ domain of the zona occludens-1 protein. Curr Biol 8:931–934

Giepmans BN, Verlaan I, Hengeveld T, Janssen H, Calafat J, Falk MM, Moolenaar WH (2001) Gap junction protein connexin-43 interacts directly with microtubules. Curr Biol 11:1364–1368

Goldberg GS, Lampe PD, Sheedy D, Stewart CC, Nicholson BJ, Naus CC (1998) Direct isolation and analysis of endogenous trans-junctional ADP from Cx43 transfected C6 glioma cells. Exp Cell Res 239:82–92

Homma N, Alvarado JL, Coombs W, Stergiopoulos K, Taffet SM, Lau AF, Delmar M (1998) A particle-receptor model for the insulin-induced closure of connexin43 channels. Circ Res 83:27–32

Hoshi T, Zagotta WN, Aldrich RW (1990) Biophysical and molecular mechanisms of Shaker potassium channel inactivation. Science 250:533–538

Hossain MZ, Ao P, Boynton AL (1998) Platelet-derived growth factor–induced disruption of gap junctional communication and phosphorylation of connexin43 involves protein kinase C and mitogen-activated protein kinase. J Cell Physiol 176:332–341

Hossain MZ, Jagdale AB, Ao P, Boynton AL (1999a) Mitogen-activated protein kinase and phosphorylation of connexin43 are not sufficient for the disruption of gap junctional communication by platelet-derived growth factor and tetradecanoylphorbol acetate. J Cell Physiol 179:87–96

Hossain MZ, Jagdale AB, Ao P, Kazlauskas A, Boynton AL (1999b) Disruption of gap junctional communication by the platelet-derived growth factor is mediated via multiple signaling pathways. J Biol Chem 274:10489–10496

Ito S, Ito Y, Senga T, Hattori S, Matsuo S, Hamaguchi M (2006) v-Src requires Ras signaling for the suppression of gap junctional intercellular communication. Oncogene 25:2420–2424

Ito S, Hyodo T, Hasegawa H, Yuan H, Hamaguchi M, Senga T (2010) PI3K/Akt signaling is involved in the disruption of gap junctional communication caused by v-Src and TNF-α. Biochem Biophys Res Commun 400:230–235

Kanemitsu MY, Lau AF (1993) Epidermal growth factor stimulates the disruption of gap junctional communication and connexin43 phosphorylation independent of 12-*O*-tetradecanoylphorbol 13-acetate-sensitive protein kinase C: the possible involvement of mitogen-activated protein kinase. Mol Biol Cell 4:837–848

Kanemitsu MY, Jiang W, Eckhart W (1998) Cdc2-mediated phosphorylation of the gap junction protein, connexin43, during mitosis. Cell Growth Differ 9:13–21

Kolch W (2000) Meaningful relationships: the regulation of the Ras/Raf/MEK/ERK pathway by protein interactions. Biochem J 351(Pt 2):289–305

Kumar NM, Gilula NB (1996) The gap junction communication channel. Cell 84:381–388

Lampe PD, Lau AF (2004) The effects of connexin phosphorylation on gap junctional communication. Int J Biochem Cell Biol 36: 1171–1186

Lampe PD, TenBroek EM, Burt JM, Kurata WE, Johnson RG, Lau AF (2000) Phosphorylation of connexin43 on serine368 by protein kinase C regulates gap junctional communication. J Cell Biol 149:1503–1512

Langlois WJ, Sasaoka T, Saltiel AR, Olefsky JM (1995) Negative feedback regulation and desensitization of insulin- and epidermal growth factor–stimulated p21ras activation. J Biol Chem 270:25320–25323

Lau AF, Kanemitsu MY, Kurata WE, Danesh S, Boynton AL (1992) Epidermal growth factor disrupts gap-junctional communication and induces phosphorylation of connexin43 on serine. Mol Biol Cell 3:865–874

Lin R, Warn-Cramer BJ, Kurata WE, Lau AF (2001) v-Src phosphorylation of connexin 43 on Tyr247 and Tyr265 disrupts gap junctional communication. J Cell Biol 154:815–827

Loewenstein WR (1990) Cell-to-cell communication and the control of growth. Am Rev Respir Dis 142:S48–S53

Moelling K, Schad K, Bosse M, Zimmermann S, Schweneker M (2002) Regulation of Raf-Akt cross-talk. J Biol Chem 277:31099–31106

Moreno AP, Saez JC, Fishman GI, Spray DC (1994) Human connexin43 gap junction channels. Regulation of unitary conductances by phosphorylation. Circ Res 74:1050–1057

Morley GE, Taffet SM, Delmar M (1996) Intramolecular interactions mediate pH regulation of connexin43 channels. Biophys J 70:1294–1302

Musil LS, Cunningham BA, Edelman GM, Goodenough DA (1990) Differential phosphorylation of the gap junction protein connexin43 in junctional communication-competent and -deficient cell lines. J Cell Biol 111:2077–2088

Park DJ, Wallick CJ, Martyn KD, Lau AF, Jin C, Warn-Cramer BJ (2007) Akt phosphorylates connexin43 on Ser373, a "mode-1" binding site for 14-3-3. Cell Commun Adhes 14:211–226

Penuel E, Martin GS (1999) Transformation by v-Src: Ras-MAPK and PI3K-mTOR mediate parallel pathways. Mol Biol Cell 10:1693–1703

Schonwasser DC, Marais RM, Marshall CJ, Parker PJ (1998) Activation of the mitogen-activated protein kinase/extracellular signal-regulated kinase pathway by conventional, novel, and atypical protein kinase C isotypes. Mol Cell Biol 18:790–798

Shen Y, Khusial PR, Li X, Ichikawa H, Moreno AP, Goldberg GS (2007) SRC utilizes Cas to block gap junctional communication mediated by connexin43. J Biol Chem 282:18914–18921

Solan JL, Lampe PD (2008) Connexin 43 in LA-25 cells with active v-src is phosphorylated on Y247, Y265, S262, S279/282, and

S368 via multiple signaling pathways. Cell Commun Adhes 15:75–84

Sorgen PL, Duffy HS, Sahoo P, Coombs W, Delmar M, Spray DC (2004) Structural changes in the carboxyl terminus of the gap junction protein connexin43 indicates signaling between binding domains for c-Src and zonula occludens-1. J Biol Chem 279: 54695–54701

Swenson KI, Piwnica-Worms H, McNamee H, Paul DL (1990) Tyrosine phosphorylation of the gap junction protein connexin43 is required for the pp 60v-src-induced inhibition of communication. Cell Regul 1:989–1002

Toyofuku T, Yabuki M, Otsu K, Kuzuya T, Hori M, Tada M (1998) Direct association of the gap junction protein connexin-43 with ZO-1 in cardiac myocytes. J Biol Chem 273:12725–12731

Toyofuku T, Akamatsu Y, Zhang H, Kuzuya T, Tada M, Hori M (2001) c-Src regulates the interaction between connexin-43 and ZO-1 in cardiac myocytes. J Biol Chem 276:1780–1788

Warn-Cramer BJ, Lampe PD, Kurata WE, Kanemitsu MY, Loo LW, Eckhart W et al (1996) Characterization of the mitogen-activated protein kinase phosphorylation sites on the connexin-43 gap junction protein. J Biol Chem 271:3779–3786

Zang Q, Frankel P, Foster DA (1995) Selective activation of protein kinase C isoforms by v-Src. Cell Growth Differ 6:1367–1373

Zhou L, Kasperek EM, Nicholson BJ (1999) Dissection of the molecular basis of pp 60v-src induced gating of connexin 43 gap junction channels. J Cell Biol 144:1033–1045

J Membrane Biol (2012) 245:507–508
DOI 10.1007/s00232-012-9473-z

INTRODUCTION

Introduction for the special issue on electroporation

Damijan Miklavčič · Lluis M. Mir · P. Thomas Vernier

Received: 25 June 2012 / Accepted: 28 June 2012 / Published online: 11 August 2012

Following up on the success of the first special electroporation-based technologies and treatments issue of the Journal of Membrane Biology, this special issue brings to readers of the journal recent developments in the field of electroporation that were presented and discussed during the 5th International Workshop and Postgraduate Course on "Electroporation-Based Technologies and Treatments" (EBTT 2011) held in Ljubljana, November 13–19, 2011, gathering faculty members, six other recognized researchers in the field, and 32 students from 12 different countries. A complementary staff of 12 young investigators of the Laboratory of Biocybernetics of the Faculty of Electrical Engineering of the University of Ljubljana conducted practical training exercises during the afternoons. This school is a real platform for learning, extending, consolidating, and developing knowledge of electroporation mechanisms and applications.

D. Miklavčič
Faculty of Electrical Engineering, University of Ljubljana, Ljubljana, Slovenija

L. M. Mir
Université Paris-Sud, Laboratoire de Vectorologie et Thérapeutiques Anticancéreuses, UMR 8203, Orsay, France

L. M. Mir
CNRS, Orsay, Laboratoire de Vectorologie et Thérapeutiques Anticancéreuses, UMR 8203, Orsay, France

L. M. Mir
Institut Gustave Roussy, Laboratoire de Vectorologie et Thérapeutiques Anticancéreuses, UMR 8203, Villejuif, France

P. T. Vernier (✉)
University of Southern California, Los Angeles, CA, USA
e-mail: vernier@usc.edu

The field of cell and membrane electroporation continues to grow and expand. Electroporation is now performed in silico (using molecular dynamics approaches), in vitro (using lipid planar bilayers, or lipid vesicles, very often giant unicellular vesicles termed GUVs), on cells in culture (that is in vivo for the biochemists but still in vitro for the cell biologists) as well as in tissues (termed in vivo by the cells biologists, and more precisely ex vivo if the tissue is removed and treated outside the organism or in situ if the tissue is treated as part of the organism). The importance of electroporation, in research and in technological (biotechnological), medical, and industrial applications, has been recognized in 2012 at the highest political level since 22 countries have signed a Memorandum of Understanding to participate in a COST action at the European level (COST TD 1104 "European network for development of electroporation-based technologies and treatments"). The Electroporation-Based Technologies and Treatments (EBTT) meeting and school is one of the many activities of this EU action.

The peer-reviewed selection of articles presented in this special issue offers a wide-ranging view of the various aspects of present research in the field of cell electroporation. We wish to thank all the contributors for their efforts in presenting their recent results to the journal's readers who, whether new or old in the field, will find new data and interesting ideas in this special issue of the Journal of Membrane Biology.

Finally, we would like to express our sincere thanks to our scientific colleagues, to the agencies that have been sponsoring our research work for years, and to the Slovenian Research Agency, the Bioelectrochemical Society, and the Centre National de la Recherche Scientifique (CNRS). We also would like to thank BIA Separations (Slovenia), Bio-Rad Laboratories (USA), C3 M (Slovenia), IGEA (Italy),

Iskra Medical (Slovenia), Kemomed (Slovenia), Mediline (Slovenia) and Mikro + polo (Slovenia), whose financial support allowed us to assist many participating students by waiving their fee or providing them with lodging. The Bioelectromagnetics Society (BEMS) and the European Bioelectromagnetics Association (EBEA) have also contributed by providing travel grants and partial coverage of tuition fees for their student members. The Workshop and Postgraduate Course was conducted within the scope of the LEA EBAM (European Associated Laboratory on Pulsed Electric Fields Applications in Biology and Medicine).

J Membrane Biol (2012) 245:509–520
DOI 10.1007/s00232-012-9432-8

ORIGINAL ARTICLES

In Vivo Muscle Electroporation Threshold Determination: Realistic Numerical Models and In Vivo Experiments

Selma Čorović · Lluis M. Mir · Damijan Miklavčič

Received: 20 December 2011 / Accepted: 30 April 2012 / Published online: 24 May 2012

Abstract In vivo electroporation is used as an effective technique for delivery of therapeutic agents such as chemotherapeutic drugs or DNA into target tissue cells for different biomedical purposes. In order to successfully electroporate a target tissue, it is essential to know the local electric field distribution produced by an application of electroporation voltage pulses. In this study three-dimensional finite element models were built in order to analyze local electric field distribution and corresponding tissue conductivity changes in rat muscle electroporated either transcutaneously or directly (i.e., two-plate electrodes were placed either on the skin or directly on the skeletal muscle after removing the skin). Numerical calculations of electroporation thresholds and conductivity changes in skin and muscle were validated with in vivo measurements. Our model of muscle with skin also confirms the in vivo findings of previous studies that electroporation "breaks" the skin barrier when the applied voltage is above 50 V.

S. Čorović · D. Miklavčič (✉)
Faculty of Electrical Engineering, University of Ljubljana, Trzaska 25, 1000 Ljubljana, Slovenia
e-mail: damijan.miklavcic@fe.uni-lj.si

S. Čorović
e-mail: selma.corovic@fe.uni-lj.si

S. Čorović · L. M. Mir
UMR 8203 CNRS, Laboratoire de Vectorologie et Thérapeutiques Anticancéreuses, Institute Gustave-Roussy, 114 rue Edouard Vaillant, 94805, Villejuif Cedex, France
e-mail: luis.mir@igr.fr

S. Čorović · L. M. Mir
UMR 8203, University of Paris-Sud XI, Paris, France

Keywords Muscle electroporation · Skin electroporation · Electric field · Numerical model · Electrochemotherapy · Gene therapy · Vaccination

Introduction

Tissue electroporation (also termed "electropermeabilization") is a transient electrical increase of cell membrane permeability by means of local delivery of short and sufficiently intense voltage pulses (i.e., electroporation pulses) to the target tissue cells via properly selected electrodes (Miklavcic et al. 2000). In vivo electroporation is used as an effective technique for the delivery of a variety of therapeutic agents, such as chemotherapeutic drugs, DNA or other molecules which in normal conditions do not cross the cell membrane, into many different target tissue cells (Mir et al. 1995; Prud'homme et al. 2006). Skeletal muscle tissue is one of the most promising tissues for DNA delivery by electroporation for either local or systemic gene therapy and gene vaccination (Mir et al. 1999; Mathiesen 1999; Tevz et al. 2008; Hojman et al. 2009). Investigating in vivo muscle tissue electroporation is relevant to both clinical electrochemotherapy (Marty et al. 2006; Edhemovic et al. 2011) and transdermal drug delivery (Denet et al. 2004) for providing knowledge on the sensitivity of underlying muscle tissue to the electroporation procedure (Zupanic et al. 2007; Mali et al. 2008), as well as in various physiological and developmental studies (Breton and Mir 2011).

The key parameter in effective tissue electroporation is local electric field distribution, E (the symbol E refers to the magnitude of the vector of electric field intensity), established within the treated tissue due to the delivered electroporation pulses. Target tissue cells can be electroporated

in a reversible and safe way only within the tissue regions subjected to a local electric field (E) of a magnitude comprised between reversible (E_{rev}) and irreversible (E_{irrev}) electroporation thresholds (Miklavcic et al. 1998). The magnitude of E can be controlled by carefully choosing electroporation pulse amplitude and electrode configuration, given that the electroporation thresholds E_{rev} and E_{irrev} and the tissue's electrical and geometrical properties are known (Zupanic et al. 2008; Corovic et al. 2008; Kos et al. 2010). An important prerequisite for the determination of E_{rev} and E_{irrev} thresholds is the visualization of the local electric field distribution with numerical calculations in realistic tissue models which are validated with corresponding experimental observations and, thus, take into account realistic geometric and electrical properties of the tissues to be modeled (Miklavcic et al. 1998; Sel et al. 2005; Corovic et al. 2010). Since the electroporation thresholds (and thus the induced transmembrane potentials at these thresholds) are related to the cell size, density and orientation with respect to the electric field and to the parameters of the electroporation pulses, they have to be determined for each cell and tissue type (Pavlin et al. 2002; Valic et al. 2003). Theory and experiments also showed that when the cells are electroporated, their electrical properties change due to the increase in the cell membrane's conductivity, which is reflected in the bulk conductivity increase (Pavlin and Miklavcic 2003). It was previously suggested that tissue conductivity changes, as an indicator of the tissue electroporation level, can also be assessed by in vivo measurements of changes in tissue conductance (Davalos et al. 2002, 2004; Ivorra et al. 2009) and of the total current flowing through the treated tissues (Cukjati et al. 2007).

The protocols for in vivo muscle electroporation, for muscle electroporated either transcutaneously or directly (i.e., without skin), were established based on the ratio of the amplitude of applied electroporation pulses relative to the distance between the electrodes. Very few studies investigated the local electric field distribution in the muscle and its surrounding tissues (Gehl et al. 1999; Pavselj et al. 2005; Corovic et al. 2010). In most of the studies on skin electroporation, a pronounced change in skin resistance indicating skin electroporation was reported to occur at voltages above 50 V (Prausnitz et al. 1993; Pliquett et al. 1995).

The aim of our study was to develop realistic numerical models in order to investigate the E_{rev} and E_{irrev} thresholds and the electroporation process between these thresholds in skeletal muscle tissue electroporated either transcutaneously or directly. We numerically and experimentally investigated the local electric field distribution as well as the geometric and electrical properties of skin and muscle tissue electroporated separately and of muscle electroporated through the skin. We observed an influence on electroporation efficiency in muscle tissue due to the presence of skin.

We built three separate realistic numerical models of skinfold, muscle and muscle with skin. Changes in electrical properties resulting from electroporation were modeled by determining the functional dependence of tissue conductivity, σ (S/m), on local electric distribution (E) above the reversible electroporation threshold (E_{rev}) in each of the examined tissues. Using finite element methods, we calculated local electric field distribution and total electric current at voltages of equal amplitudes as the electroporation pulses that were applied in in vivo experiments.

In order to validate the realistic numerical models that we developed in this study, we mathematically interpreted the data collected during an extensive in vivo study on the response of the skin, muscle and muscle with skin to the electroporation pulses (Cukjati et al. 2007). We compared the results of our numerical simulations to the in vivo total current measurement and ^{51}CrEDTA-uptake results. From the numerical models validated on the experimentally obtained results we determined electroporation parameters such as reversible and irreversible electroporation threshold values, E_{rev} and E_{irrev}; the initial tissue conductivity (before the electroporation pulses were applied), σ_0; the conductivity of the same tissue modified due to the electroporation, σ_1; and the functional dependence of tissue conductivity on local electric field distribution, $\sigma(E)$, between the thresholds.

The same electroporation threshold values were found, as expected, for both muscle electroporated transcutaneously and directly since the electroporation threshold is a property of the tissue and cannot be affected by neighboring tissues. However, in order to electrically overcome the skin barrier, a higher voltage between the electrodes (i.e., amplitude of electroporation pulses applied) was required when the muscle was electroporated through the skin in contrast to electroporation directly on the muscle.

Methods

In Vivo Experiments

Animals

Female Wistar rats purchased from Janvier (Le Genest Saint Isle, France) were used for the experiments. Rats were anesthetized by intraperitoneal administration of ketamine (100 mg/kg; Panpharma, Frankfurt, Germany) and xylazine (10 mg/kg; Bayer, Leverkusen, Germany). Animals were handled according to recommended good

practices and standard institutional ethics rules for animal experimentation (UKCCCR 1998).

^{51}Cr-EDTA

To determine the electropermeabilization level of skin and muscle tissue when applying electroporation pulses directly or transcutaneously in vivo, we performed the quantitative uptake method using ^{51}Cr-EDTA as the indicator (Gehl and Mir 1999; Cukjati et al. 2007). Animals were given 200 µl of ^{51}Cr-EDTA (Amersham, Aylesbury, UK) with a specific activity of 3.7 MBq/ml intravenously 5 min before delivery of the electric pulses. The injected ^{51}Cr-EDTA distributes freely in the vascular and extracellular compartments and can enter the intracellular compartments only if access is provided (e.g., by electroporation). Animals were killed 24 h after injection, and tissues exposed to electric pulses were removed, weighed and counted in a Cobra 5002 gamma counter (Packard Instrument, Meriden, CT). Net ^{51}Cr-EDTA uptake as a result of electropermeabilization was calculated as the measured activity (converted to nanomoles of ^{51}Cr-EDTA) per gram of tissue exposed to the electric pulses. ^{51}Cr-EDTA-uptake values were then used to calculate mean values of uptake (±SEM) as a function of the ratio of the applied voltage to the electrodes' distance in the rat skeletal muscle electroporated transcutaneously or directly.

Electroporation Protocol

Electroporation pulses consisted of a train of eight square-wave and 100-µs-long pulses, delivered at a repetition frequency of 1 Hz. In all experiments the electric pulses were generated by a PS 15 electropulse generator (Jouan, St. Herblain, France) and delivered to the tissue through two parallel plate stainless-steel electrodes. The electrode dimensions used in our experiments are shown in Fig. 1a. The following three experiments were carried out: electroporation of skin tissue only (a skinfold was formed and placed between the electrodes, as shown in Fig. 1b), direct muscle electroporation (the skin was previously removed and the plate electrodes were placed directly on the muscle surface, Fig. 1c) and transcutaneous muscle electroporation (Fig. 1d). Electrodes were positioned on the tissue so that the electric field was perpendicular to the muscle fibers. We treated the triceps brachii muscle of the hind limb and the gastrocnemius medialis muscle of the forelimb. Electrodes were separated by 5.7 mm for the muscles electroporated directly and transcutaneously and by 2.8 mm for electroporation of the skinfold. Good contact between the electrodes and tissue was assured by the use of a gel (ultrasound transmission gel EKO-GEL; Camina, Egna, Italy). During the electroporation pulse delivery, the applied voltage and the actual current delivered were monitored and collected using a digital oscilloscope (Waverunner; LeCroy, Chestnut Ridge, NY).

The input used for in vivo experiments was the amplitude of the delivered electric pulses to the tissue. The output from the experiment was the measured electric current and the measured ^{51}CrEDTA absorption.

Numerical Modeling

Experimentally treated tissues were mathematically modeled as passive volume conductors in a quasi-stationary electric current field. Electric field distribution (i.e., local electric field, E [V/cm]) in the tissue models caused by electroporation pulses was determined by numerically solving Laplace's equation:

$$-\nabla\,(\sigma\cdot\nabla\varphi)=0 \qquad (1)$$

where σ and φ represent tissue conductivity (S/m) and electric potential (V), respectively. The calculated E in our models was used to calculate threshold values for

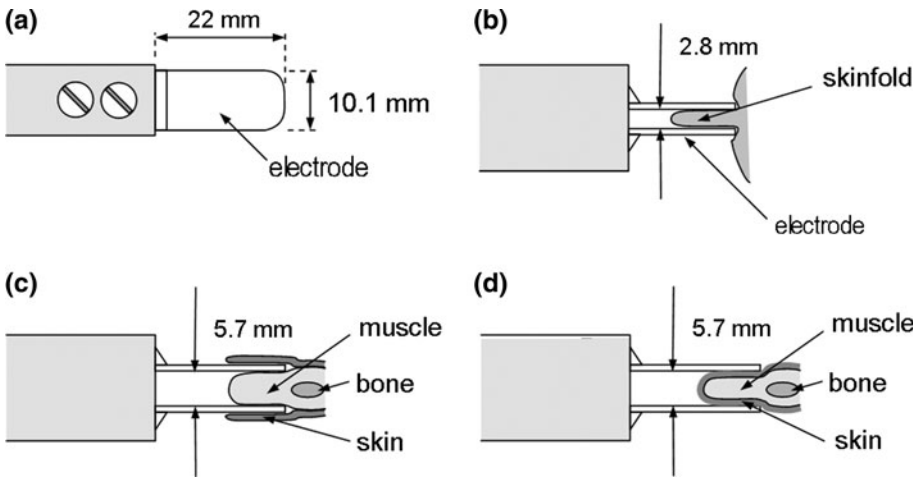

Fig. 1 Electrode dimensions used in experiments (**a**) and geometry of the measurement setup for skinfold electroporation (**b**) and muscle electroporated directly (**c**) and transcutaneously (**d**)

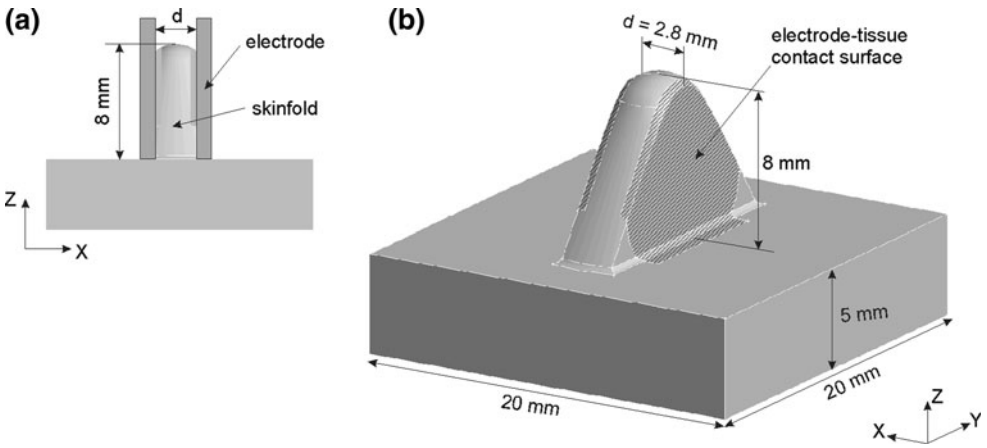

Fig. 2 Geometry of the skinfold finite element model in the *zx* cross-sectional plane (**a**) and in 3D (**b**). Patterned region represents the contact surface between the electrode and tissue geometry (i.e., electrode—tissue contact surface)

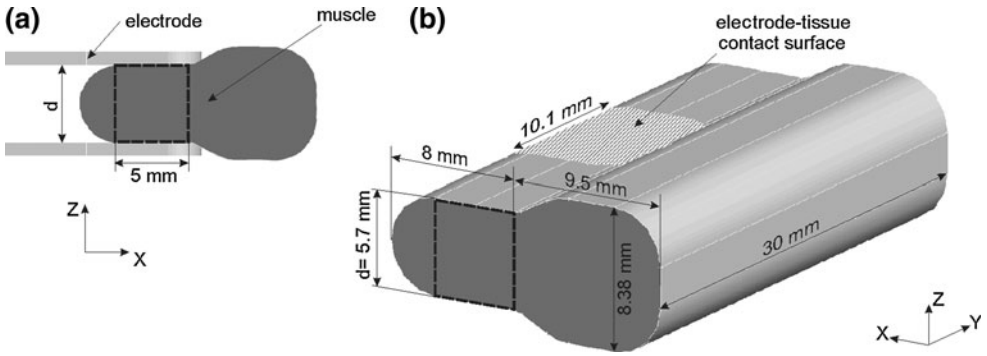

Fig. 3 Geometry of the muscle tissue finite element model (electroporated directly) in the *zx* cross-sectional plane (**a**) and in 3D (**b**). Patterned region represents the contact surface between the electrode and tissue geometry (i.e., electrode—tissue contact surface)

reversible (E_{rev}) and irreversible (E_{irrev}) tissue electroporation. Total electric current flowing through the 3D modeled tissues was then calculated according to Ohm's law. In the first stage of numerical modeling we built 3D models of the skinfold (Fig. 2), muscle tissue electroporated directly (Fig. 3) and muscle tissue electroporated transcutaneously (Fig. 4) using the commercial software package EMAS (Ansoft, Canonsburg, PA). Taking into account the fact that electric field distribution and total electric current flowing through the tissue depend strongly on the tissue geometry, we designed the geometry of our numerical models as accurately as possible. Applied voltage, U (V, model input), was modeled as Dirichlet's boundary condition on the contact surface between electrode and tissue geometry. For the model input values we used the amplitudes of the electroporation pulses applied in vivo (Cukjati et al. 2007). We mathematically separated the conductive segment from its surroundings by applying Neuman's boundary condition ($J_n = 0$, where J_n is the normal electric current density [A/m^2]) on all outer boundaries of the model.

Results of the calculated model outputs (total electric current, I, and local electric field distribution, E) were controlled for numerical errors by increasing the size of our model and increasing the mesh density until the electric insulation condition and error due to meshing irregularities

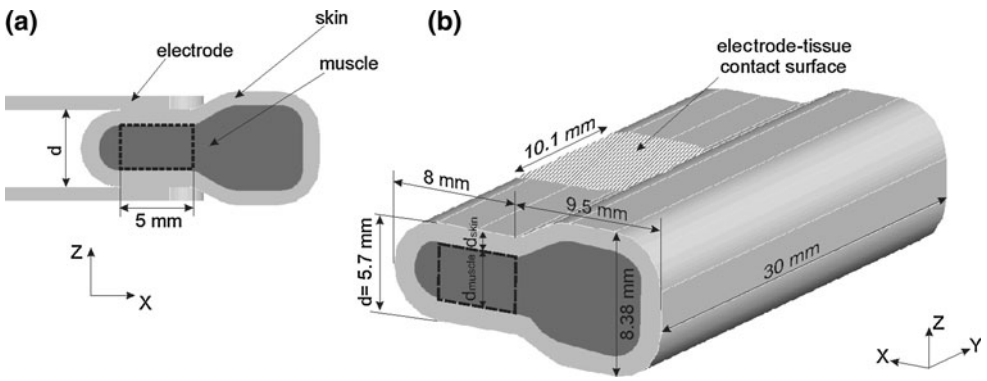

Fig. 4 Geometry of muscle electroporated transcutaneously in the *zx* cross-sectional plane (**a**) and in 3D (**b**). Patterned region represents the contact surface between the electrode and tissue geometry (i.e., electrode—tissue contact surface)

were insignificant—a further increase in domain size or mesh density only increased the computation time; however, the results changed by <0.5 %. The resulting models—mesh of skinfold, muscle and muscle electroporated transcutaneously—consisted of 4173, 7546 and 10074 tetrahedral finite elements, respectively.

Electric Properties of the Modeled Tissues and Electroporation Process Modeling

In our numerical models, ohmic tissue behavior was analyzed (i.e., skin and muscle conductivities, σ). Before applying electroporation pulses or if the amplitude of the applied electroporation pulses was too low to produce a local electric field above the reversible electroporation threshold ($E < E_{rev}$), the tissues were modeled as linear conductors with linear current–voltage, I (U), relationships due to the constant tissue conductivities. The initial prepulse values of conductivities (σ_0 corresponding to the $E < E_{rev}$ condition) used in numerical models were selected from the available literature (Miklavcic et al. 2006). Muscle tissue was considered an anisotropic conductor, being more conductive along the muscle fibers in the y axis compared to the two other perpendicular x and z axes (Table 1), while skin tissue was considered isotropic and homogeneous. Since the skin tissue was not the primary target of our investigation, different layers of skin were not modeled; thus, an average value for conductivity was assigned to skin tissues in our models (Table 1). Namely, large differences in skin layer geometries would unnecessarily increase the computational time of numerical simulations while not contributing to the accuracy of the electric field distribution in the muscle tissue (Pavselj et al. 2005).

If the local electric field in the tissues exceeded the E_{rev} value, the tissue electric properties changed (i.e., tissue conductivity increased due to the electroporation process). During the application of electroporation pulses, tissue conductivity increased according to the functional dependence of the tissue conductivity on the local electric field distribution, $\sigma(E)$, which in our study described the dynamics of the electroporation process. This subsequently resulted in a nonlinear dependence of the electric current as a function of the applied voltage $I(U)$. Thus, due to the change of σ, we detected the threshold electroporation E_{rev} as a result of the deviation of $I(U)$ from the linear relationship $I = U/R$ (where R [ohm] is tissue electric resistance).

The tissue electroporation dynamics were modeled based on the sequential permeabilization model proposed by Sel et al. 2005, where changes in tissue conductivity were used as an indicator of tissue permeabilization. For this purpose a sequence analysis subprogram (as an extension of EMAS) was developed to model the dynamics of electroporation as a sequence of static FEM models. The subprogram was developed so as to avoid the oscillations in electric conductivity and to allow only the local electric field intensity to change due to the conductivity increase. In each static description in the dynamic sequence of tissue changes, tissue conductivity was determined based on the electric field distribution from the previous step in the sequence, as described in the following equation:

$$\sigma(k) = f[E(k-1)] \tag{2}$$

where k stands for the number of static FEM steps in the sequence.

Model input is the applied voltage, U, and model outputs are the electric field distribution, E, and total electric current, I, in each specific sequence step, k. The modeled tissue behavior during the electroporation pulse delivery is illustrated in Fig. 5. In our models we took into account only the current measurement (I_k) at the end of the pulses, which corresponds to the value of the current calculated in the first sequence (I_5 in $k = 5$) in which the $\sigma(E)$ in our models stabilized. The output current from I_5 was then compared to the measured current at the end of the eighth pulse (i.e., output from the in vivo corresponding experiment).

The increase in electrical current I from I_0 to I_k simulates the tissue response in each discrete interval k during

Table 1 Electroporation parameters σ_o, σ_1, E_{rev} and E_{irrev} calculated in single models of skinfold and muscle tissue

Tissue	σ_0 (S/m)	σ_1 (S/m)	E_{rev} (V/cm)	E_{irrev} (V/cm)
Skin	0.008	20 σ_o	480	1,050
Muscle	x and y axes	3.5 σ_o	240	450
	0.135			
	z axis[a]			
	0.75			

[a] Numerical calculations showed that varying the factor σ_1/σ_o in z axis did not significantly change the $I(U)$ characteristic

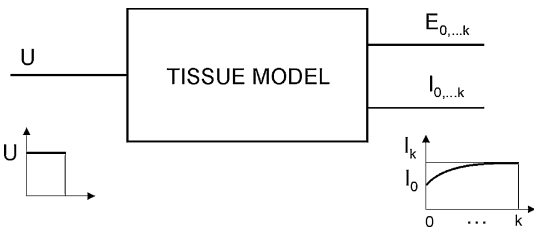

Fig. 5 Modeled tissue behavior during electroporation pulse delivery, where U is the amplitude of the electroporation pulses delivered to the tissues, E is the electric field strength, I is the total electric current calculated in each sequence step and k is the number of steps in the sequence corresponding to the duration of the electroporation pulses

the delivery of the electroporation pulses U to the tissue (due to the functional dependence of σ on the electric field distribution E). If electroporation does not occur, σ remains constant; thus, $I = I_0$. The sequence analysis subprogram gives us a choice of five different $\sigma(E)$ relationships given by Eqs. 3–7.

$$\sigma(E) = \begin{cases} \sigma_0, & E < E_{\text{rev}} \\ \sigma_1, & E \geq E_{\text{rev}} \end{cases} \tag{3}$$

$$\sigma(E) = \begin{cases} \sigma_0, & E < E_{\text{rev}} \\ \frac{\sigma_1 - \sigma_0}{E_{\text{irrev}} - E_{\text{rev}}} \cdot (E - E_{\text{rev}}) + \sigma_0, & E_{\text{rev}} \leq E < E_{\text{irrev}} \\ \sigma_1, & E \geq E_{\text{irrev}} \end{cases} \tag{4}$$

$$\sigma(E) = \begin{cases} \sigma_0, & E < E_{\text{rev}} \\ A \cdot \left(1 - \exp\left(\frac{E - E_{\text{rev}}}{B}\right)\right) + \sigma_0, & E_{\text{rev}} \leq E < E_{\text{irrev}} \\ \sigma_1, & E \geq E_{\text{irrev}} \end{cases} \tag{5}$$

$$\sigma(E) = \begin{cases} \sigma_0, & E < E_{\text{rev}} \\ A \cdot \left(\exp\left(\frac{E - E_{\text{irrev}}}{B}\right) - 1\right) + \sigma_1, & E_{\text{rev}} \leq E < E_{\text{irrev}} \\ \sigma_1, & E \geq E_{\text{irrev}} \end{cases} \tag{6}$$

$$\sigma(E) = \begin{cases} \sigma_0, & E < E_{rev} \\ \sigma_0 + \frac{\sigma_1 - \sigma_0}{\left(1 + \exp\left(-\frac{E - a}{B}\right)\right)}, & E_{\text{rev}} \leq E < E_{\text{irrev}} \\ \sigma_1, & E \geq E_{\text{irrev}} \end{cases} \tag{7}$$

where $A = \frac{\sigma_0 - \sigma_1}{\exp\left(\frac{E_{\text{rev}} - E_{\text{irrev}}}{B}\right) - 1}$ and $a = \frac{E_{\text{rev}} + E_{\text{irrev}}}{2}$

Parameters σ_0 and σ_1 represent the initial prepulse tissue conductivity and the conductivity of electroporated tissue, respectively; parameters E_{rev} and E_{irrev} stand for reversible and irreversible electroporation thresholds of the local electric field, respectively; and parameter B defines the shape of the exponential and sigmoid functions.

Single-Tissue Models—Skin and Muscle Tissue Models

First, we modeled the electroporation process in each of the tissue models separately: skinfold (Fig. 2) and muscle tissue (Fig. 3). The same values of applied voltages in vivo were applied to the contact surfaces of the single muscle and skin models as model inputs. A comparison of the current as a function of the voltage $I(U)$ to the measured ones in vivo was used to determine which of the functional dependencies given by Eqs. 3–7 best described the dynamics of the electroporation process in each of the tissues analyzed. Namely, in order to tune our single-tissue models for in vivo electroporation of skinfold (Fig. 1b) and for direct in vivo muscle electroporation (Fig. 1c) measurement, we varied different functional relationships (step [Eq. 3], exponential [Eqs. 4, 5], linear [Eq. 6], and sigmoidal [Eq. 7] functions) with different reversible and irreversible electroporation threshold values until good agreement between $I(U)$ obtained numerically and the $I(U)$ characteristic measured in vivo was established.

From the resulting numerical models, we collected the initial prepulse tissue conductivity, σ_0; the conductivity of the electroporated tissues, σ_1; and the $\sigma(E)$ relationships between the reversible and irreversible threshold values, E_{rev} and E_{irrev} (with the corresponding parameters a, A and B).

Complete Muscle Tissue Model—Model of Muscle Electroporated Transcutaneously

The $\sigma(E)$ relationships with E_{rev} and E_{irrev} obtained from single models of the skin (Fig. 2) and muscle (Fig. 3) were applied to the skin and muscle composing the complete model (model of muscle electroporated transcutaneously) (Fig. 4). The same values of voltages of transcutaneous muscle electroporation in vivo (Fig. 1d) were applied to the contact surfaces of the complete muscle with skin model (Fig. 4). In order to tune the intricate muscle model with the transcutaneously electroporated muscle in vivo, we also varied the thickness of the skin (d_{skin} parameter in Fig. 4) until the $I(U)$ relationship matched the measured one. In such a way we numerically detected the complete muscle tissue geometry that corresponded to realistic muscle with a skin layer treated in our experiments in vivo, and we validated the model parameters σ_0, the conductivity of σ_1 and the $\sigma(E)$ relationships with E_{rev} and E_{irrev} collected from the single-tissue electroporation modeling. In order to compare the conductivity change and geometry of skin layer numerically found in the intricate muscle model to the data from the published literature, we also calculated the complete muscle model resistance, R, for each of the voltages applied.

Analysis of the Influence of Skin Presence on Muscle Electroporation

In order to analyze the influence of the skin layer on muscle electroporation, we compared the local electric field distribution in muscle electroporated directly (Fig. 3) with the local electric field distribution obtained in the muscle only, inside the intricate muscle model with skin (Fig. 4). For this purpose, we wrote a program with Matlab7a to calculate the average local electric field at the end of the electroporation process (i.e., the final sequence FEM model for each voltage applied).

The average electric field intensities were calculated in the volumes between two plate electrodes (the regions between electrodes marked with a dashed square in Figs. 3, 4), where the local electric field (E) was the most homogeneous (i.e., equal to the applied voltage to the inter-electrode distance ratio [$E = U/d$]). In this way we numerically removed the skin layer from the complete

muscle model with skin shown in Fig. 4. The numerical results of E in the muscle from the complete model were then compared to the numerical results of E calculated in the numerical model of the directly electroporated muscle.

Results and Discussion

The aims of our study were to develop realistic numerical models in order to investigate the electroporation process in skeletal muscle tissue electroporated directly and transcutaneously and to examine the influence of the presence of the skin on the electroporation process in muscle tissue. For this purpose, we numerically and experimentally investigated the local electric field and the geometric and electrical properties of electroporated skinfold and muscle tissue electroporated directly and transcutaneously. Numerical calculations of the local electric field were performed by means of the finite element method and sequential modeling of tissue electroporation (Sel et al. 2005), taking into account realistic geometries and electrical properties of the examined tissues. Local electric field distribution was experimentally assessed by measurement of the total current and of ^{51}CrEDTA uptake in vivo. The 3D realistic models of skinfold and muscle electroporated directly and transcutaneously were then developed (based on good agreement between numerical calculations and experimental observations).

It has been previously demonstrated that tissue electroporation can be modeled as a conductivity (σ) change due to the tissue permeabilization (Sel et al. 2005). Accordingly, in our numerical models we took into consideration the mathematical relationship between the skin and muscle conductivities and the local electric field intensity in the following manner: a magnitude of E below the reversible threshold E_{rev} does not permeabilize the cell membranes, and therefore, no changes in conductivity are expected (σ is constant); when the local electric field intensity exceeds the E_{rev} threshold, the cell membrane is electropermeabilized and tissue conductivity increases according to the function $\sigma(E)$. In order to numerically study the electroporation process in a complete model that is composed of different tissues, the electroporation parameters σ_0, σ_1, E_{rev}, E_{irrev} and $\sigma(E)$ between the thresholds need to be determined in each of the single tissues separately, as previously demonstrated by Pavselj et al. (2005). Similarly, in order to numerically study the electroporation of muscle tissue electropulsed transcutaneously, we first built single models of skinfolds (Fig. 2) and muscle tissue (Fig. 3) separately and determined the corresponding electroporation parameters based on the analysis of a permeabilization sequence (Sel et al. 2005). The electroporation parameters for each of the tissues were determined considering that the acceptation criterion was that the output of the models using these parameters are those that best fit the experimental data (i.e., the electroporation parameters were varied until good agreement between the computed and measured current–voltage $I(U)$ relationship was obtained). We found that the $\sigma(E)$ function in the skinfold model was an exponential one (Eq. 6 with $B = 50{,}000$), while in the skeletal muscle model the function $\sigma(E)$ was sigmoid (Eq. 7 with $B = 10{,}000$). The electroporation parameters calculated for each of the tissues are listed in Table 1. The $\sigma(E)$ was chosen so that parameters such as E_{rev}, E_{irrev}, σ_o and σ_1 were as close as possible to the experimentally determined values. By varying all the functions of $\sigma(E)$, we noticed that $\sigma(E)$ can also be described with all the functions through proper adjustment of the electroporation parameters, which may be too far from the biologically justifiable values determined in the experiments, as previously suggested by Pavselj et al. (2005).

Different functions of $\sigma(E)$ are needed to describe the distribution of tissue electroporation in our models of muscle and skin tissue. This is probably due to differences in biological properties (i.e., cell size and distribution, electrical properties of intra- and extracellular media) of the tissues analyzed.

The $\sigma(E)$ functions with E_{rev} and E_{irrev} found in single models of skin (Fig. 2) and muscle (Fig. 3) were applied to the individual skin and muscle models composing the complete muscle model (Fig. 4). The same values of voltages of transcutaneous muscle electroporation in vivo (Fig. 1d) were applied to the contact surfaces of the complete muscle model (Fig. 4). In order to fine-tune the complete muscle model for the transcutaneously electroporated muscle in vivo, we also varied the thickness of the skin (d_{skin} parameter in Fig. 4) until the $I(U)$ relationship matched the measured one.

In our model of muscle with skin the skin layer takes into account the complex skin layer tissue. In the literature adult rat skin thickness was determined to be around 1 mm (Ngawhirunpat et al. 2002). However, our first calculations were made with a model in which the skin layer thickness was 0.5 mm. We changed the thickness of the skin layer from 0.5 to 1.4 mm. The calculations showed that in our models the smaller the thickness of the skin (i.e., lower resistance), the higher the electric current calculated. A skin thickness of 1.4 mm resulted in the best agreement between the measured and calculated currents, which was a very positive result since the thickness of the skinfold (two times the complex skin layer) of the same animals treated in the experiments was 2.8 mm (Fig.1b).

Since electric current gives quantitative information about tissue geometry and electric properties (i.e., tissue conductivity changes), good agreement between calculated and measured electric current at the end of electroporation

for the corresponding applied voltages validated our 3D finite element models. The agreement between calculated and measured current–voltage relationships obtained for the skinfold analysis is shown in Fig. 6a. The comparison of agreements between calculated and measured current–voltage relationships obtained for muscle and muscle with skin is shown in Fig. 6b.

At the lowest voltages the slope of the $I(U)$ curve is low and linear, meaning that electroporation does not yet occur. The value of U at which the $I(U)$ relationship starts to diverge from its linear curve indicates that the reversible threshold value of the local electric field for tissue electroporation has been obtained. The threshold value E_{rev} in the directly electroporated muscle model was obtained at $U = 136$ V and in the muscle model electroporated transcutaneously at $U = 252$ V. The local electric field distribution in both muscle models is displayed in Fig. 7 in the xy cross-sectional plane located in the middle of the two plate electrodes. To more precisely analyze the local electric field distribution around the reversible threshold obtained with the sequence analysis ($E_{rev} = 240$ V/cm), we visualized E in the range 0–250 V/cm for the first four applied voltages. The reversible threshold for muscle electroporation is obtained at a lower value of applied voltage ($U = 136$ V) in the model of directly electroporated muscle (Fig. 7a) than in the model of muscle electroporated through the skin ($U = 252$ V) (Fig. 7b) due to the high resistance of the skin layer that must be overcome

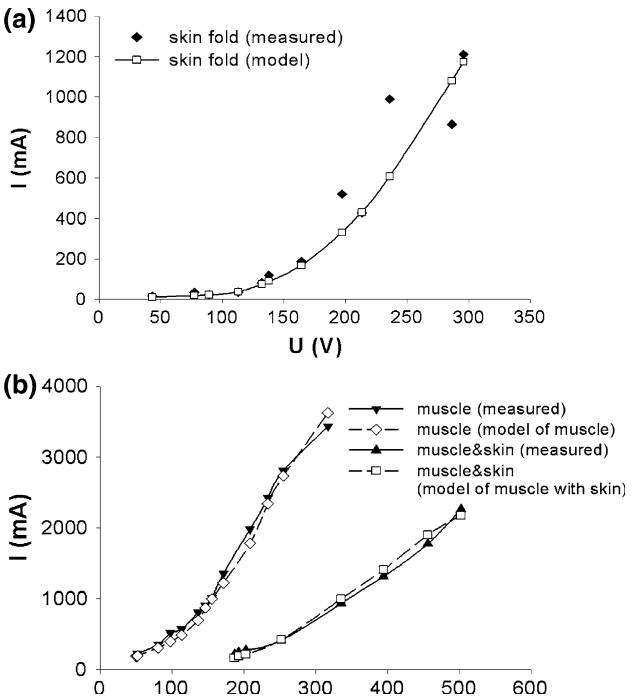

Fig. 6 Calculated and in vivo measured current–voltage relationships for **a** skinfold and **b** muscle and muscle with skin

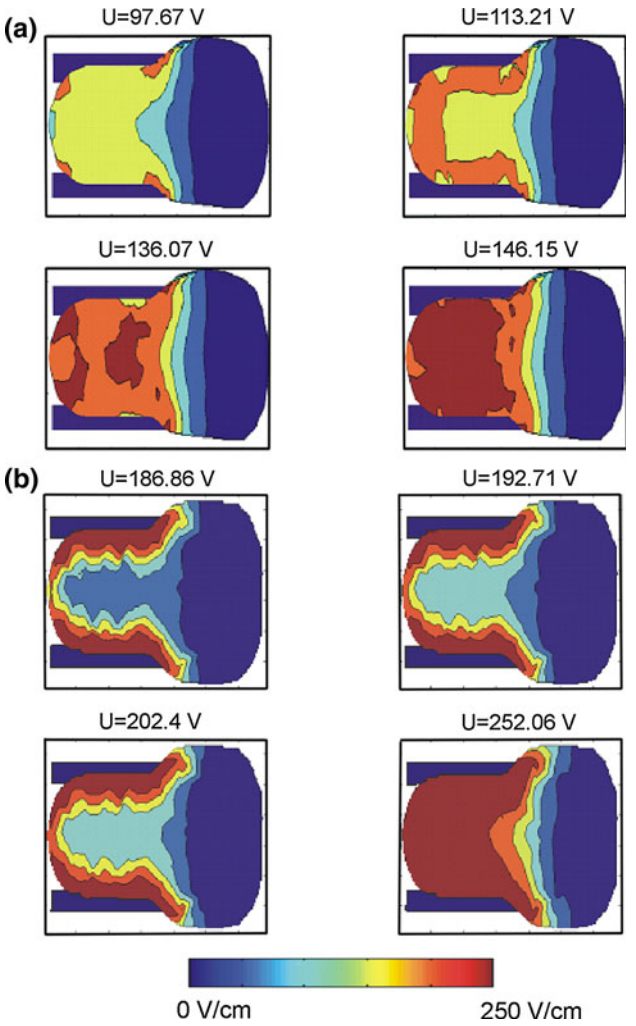

Fig. 7 Distribution of E in the model of muscle alone (**a**) and in the muscle model with skin (**b**)

by a higher U in order to target the underlying muscle tissue with $E > E_{rev}$. In other words, the reversible threshold value in muscle with skin was obtained at a higher U because the skin tissue needed to be permeabilized first. Namely, when U is applied, the electric field is distributed within the complex tissue according to its specific electric properties (acting as a voltage divider), meaning that the electric field is highest in the layer with the highest electric resistivity (i.e., lowest conductivity) (Pavselj and Miklavcic 2008). When the skin becomes permeabilized, its conductivity increases according to the function $\sigma(E)$, which leads to electric field redistribution in the skin and its underlying more conductive tissues (in our case muscle tissue), as shown in Fig. 7b. If U is too low, the highest electric field remains in the skin layer and does not reach the muscle.

Nonuniform distribution of tissue permeabilization also occurs in a single tissue (in our case muscle tissue) due to

an inhomogeneous E distribution. The increase in tissue conductivity, and thus tissue permeabilization, first occurs in close proximity to the electrodes (i.e., the region with the highest E). The conductivity increase causes a modification in E distribution according to $\sigma(E)$, which consequently causes another change in tissue conductivity and the distribution of muscle permeabilization away from the electrodes, toward the regions with lower initial E between the electrodes, as shown in Fig. 7a.

In most of the studies on skin electroporation (Prausnitz et al. 1993; Pliquett et al. 1995), a pronounced change in skin resistance was observed above 50 V for the experiments done through a single skin tissue layer. In order to compare our analysis on changes in electric properties in the skin layer in the complete muscle model to the data from the literature, we also calculated the resistance of the complete muscle model for each of the voltages applied as well as a few additional voltages ($U < 186.86$ V) that were not applied during in vivo experiments. The calculated resistance–voltage relationship, $R(U)$, is shown in Fig. 8. From the $R(U)$ curve it can be observed that a visible drop in skin resistance was obtained at $U > 100$ V, which is in agreement with the abovementioned studies, proved in our study by electroporation of the double skin layer. The increase in skin conductivity, thus the drop in skin resistance, in our skinfold (double skin layer) model was also observed at $U > 100$ V, as shown in Fig. 6a. In a similar experimental and numerical study on cutaneous tumor electroporation, pronounced changes in skin conductivity were also observed at 100 V of applied voltage (Pavselj et al. 2005). Therefore, the conductivity change and the geometry of the skin layer numerically found in our complete muscle model are in agreement with previous studies on skin.

In order to analyze the influence of the skin layer on muscle electroporation, we used in vivo experimental data of ^{51}Cr-EDTA uptake measured in muscle electroporated directly and transcutaneously. The ^{51}Cr-EDTA molecules from the extracellular compartments could enter only the electroporated cells. Both measurements were done at the same applied voltages as in the total current measurement in vivo. The experimentally obtained ^{51}Cr-EDTA (U/d) relationships for muscle electroporated directly and transcutaneously are shown in Fig. 9a. The start of the ^{51}Cr-EDTA-uptake increase should correspond to the start of reversible electroporation, the start of ^{51}Cr-EDTA-uptake decline should correspond to the point of irreversible electroporation.

We then analyzed the electroporation parameters of muscles electroporated directly and transcutaneously by comparing the local electric field distribution in the model of muscle without skin (Fig. 3) with the local electric field distribution obtained only in the muscle inside the

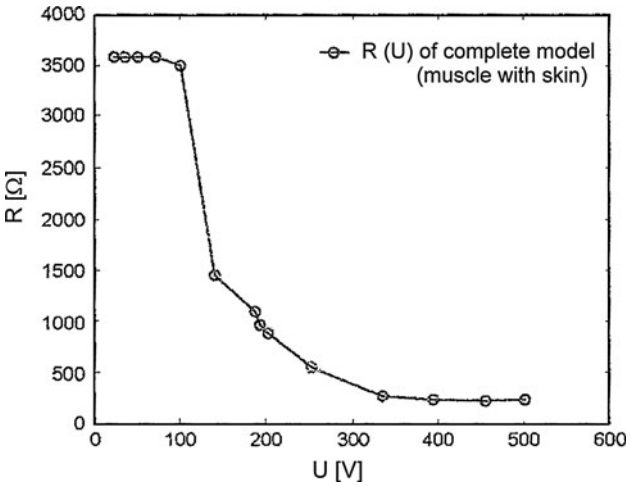

Fig. 8 Calculated resistance–voltage relationship for the complete model from Fig. 4 (muscle with skin)

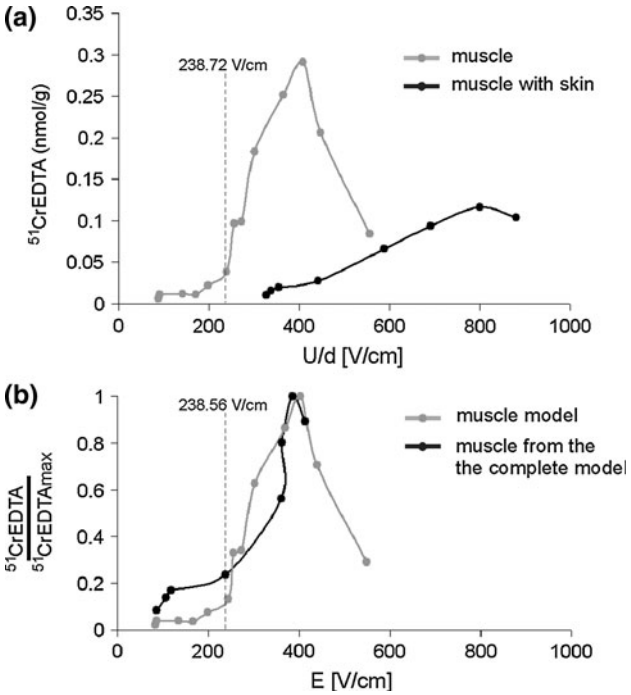

Fig. 9 **a** Measured ^{51}CrEDTA uptake (nmol/g) in muscle electroporated directly and transcutaneously (the skin is present) and **b** ^{51}CrEDTA uptake in muscle models electroporated directly and transcutaneously (skin is numerically removed from complete model). For muscle from the complete model we took into account the ^{51}CrEDTA uptake from the muscle with skin (**a**) and normalized the ^{51}CrEDTA-uptake values for both muscles (with and without skin) to the maximum uptake obtained in the directly electroporated muscle (^{51}CrEDTAmax = 0.29 nmol/g, as shown in **a**). (U values in **a** are normalized to the interelectrode distance ratio (U/d). The interelectrode distance used in all experiments was $d = 5.7$ mm. The E in **b** is the average local electric field calculated in the model of muscle electroporated directly and in the model of muscle from the complete model without skin [i.e., with skin numerically removed])

complete muscle model with skin (Fig. 4). The local electric field was analyzed at the end of the electroporation process (i.e., at the end of the sequence analysis). Namely, the average electric field intensities were calculated in the space between the two plate electrodes (the regions between electrodes marked with the dashed square in Figs. 3, 4), where the electric field was the most homogeneous (i.e., where the electric field approaches U/d). In this way we numerically removed the skin layer from the complete muscle model with skin shown in Fig. 4. The numerical results of E in the muscle from the complete model were then compared to the average E in the muscle electroporated directly, as shown in Fig. 9b. The maximum uptake of ^{51}CrEDTA in transcutaneously electroporated muscle was obtained at higher voltage applied compared to the maximum uptake obtained in directly electroporated muscle: 0.12 nmol/g ($U = 233$ V, $U/d = 409$ V/cm) versus 0.29 nmol/g ($U = 456$ V, $U/d = 800$ V/cm) (Fig. 9a). When we calculated the local electric field in the muscle models and numerically removed the skin from the complete model, we showed that uptake of ^{51}CrEDTA in muscle that was electroporated through the skin occurred at similar local electric fields as the uptake of ^{51}CrEDTA in directly electroporated muscle (Fig. 9b). The maximum uptakes in the muscle from the complete model (0.12 nmol/g) and the model of directly electroporated muscle (0.29 nmol/g) were obtained at $E = 386$ and 403 V/cm, respectively (Fig. 9b). In Fig. 9b the comparison of ^{51}CrEDTA uptake in both muscle models (directly electroporated muscle and the complete model of muscle with skin removed) is given for the ^{51}CrEDTA values normalized to the maximum uptake ^{51}CrEDTAmax obtained in the directly electroporated muscle (^{51}CrEDTAmax = 0.29 nmol/g).

The average value of E in the model of muscle alone calculated at $U = 136$ V ($U/d = 238.72$ V/cm) was $E_{rev} = 242$ V/cm, whereas the average E in muscle in the complete model with skin at the higher applied voltage $U = 252$ V ($U/d = 442$ V/cm) was calculated to be almost the same as in muscle without skin, $E_{rev} = 238.56$ V/cm, as shown in Fig. 9b. Similarly, the irreversible threshold values calculated as average local E for muscle alone and muscle with skin were $E_{irrev} = 443$ V/cm (at applied $U = 255$ V, $U/d = 447$ V/cm) and 414 V/cm (at applied $U = 502$ V, $U/d = 880$ V/cm), respectively. Based on these calculations, we conclude that the skin layer has, as expected, no influence on the thresholds of the local electric field needed to successfully electroporate muscle tissue. We did, however, find that the presence of skin affects ^{51}CrEDTA uptake into the muscle while being electroporated through the skin, which can be explained by the dependence of the electroporation level on the duration and the number of electroporation pulses. Namely, due to the presence of the skin, the effective duration of the electroporation pulses can be shorter, which consequently results in a lower ^{51}Cr-EDTA uptake in the muscle tissue (the maximum uptake of ^{51}CrEDTA in transcutaneously electroporated muscle was by a factor of 2.41 lower compared to the maximum uptake in directly muscle electroporated muscle, Fig. 9). It is well known that the molecular flux through the permeabilized membrane depends on the duration and number of electroporation pulses (Puc et al. 2003; Pucihar et al. 2008).

The threshold values calculated in both the model of muscle alone and the complete model with skin are similar to the threshold values obtained with sequence analysis in the model of muscle alone, $E_{rev} = 240$ and 450 V/cm, respectively. From Fig. 9 it can be seen that in muscle electroporated directly the average local electric field in the region between the electrodes (gray curve in Fig. 9b), where the tissue is (region marked with dashed square in Fig. 3), is almost equal to the voltage over the interelectrode distance ratio, U/d (gray curve in Fig. 9a), and is thus almost homogeneous. Consequently, the error we make using U/d values to approximately determine the threshold value of local electric field to successfully electroporate muscle without skin is acceptably small. However, for the precise determination of the local electric field threshold value needed for the electroporation of muscle inside a complex tissue, a realistic numerical model that takes into account realistic geometries, electric properties and electric field nonhomogeneities due to the tissue permeabilization of all the composing tissues needs to be used in combination with corresponding in vivo experiments.

Our results are comparable with data obtained in a similar numerical and in vivo study for the same type of pulses as those used in our study (eight pulses, 100 μs, 1 Hz) (Pavselj et al. 2005), where the E_{rev} and E_{irrev} for muscle electroporated directly were estimated to be 200 and 450 V/cm, respectively. In another study (Gehl et al. 1999), the combination of in vivo experiments (transcutaneous muscle electroporation using plate electrodes with $d = 4$ mm) and 2D numerical models resulted in a higher electroporation threshold (450 V/cm) compared to the one obtained in our study ($E_{rev} = 238$ V/cm) since in their study the tissue between electrodes was considered homogeneous in two dimensions, meaning that differences in skin and muscle electric conductivity and geometry were not taken into account.

A similar reversible electroporation threshold ($E_{rev} = 200$ V/cm) for muscle without skin and for the same orientation (perpendicular) of the applied electric field with respect to the muscle fibers was found in our previous study where thresholds in the two main muscle orientations (electrodes parallel or perpendicular to the main muscle fiber axes) were compared (Corovic et al. 2010).

Conclusion

In this study we present realistic numerical models of electroporated skinfold and skeletal muscle tissue electroporated directly and transcutaneously, which we developed in order to analyze the electroporation process in skin and muscle tissues in vivo. The models were developed by validating numerical calculations on in vivo experimental results. We determined how to map electropermeabilization by identifying the local electric field distribution in skin and muscle tissues. Namely, we found the functional dependence of tissue conductivity on electric field intensity, $\sigma(E)$, to be exponential for skin with electroporation thresholds $E_{rev} = 480$ V/cm and $E_{irrev} = 1{,}050$ V/cm and sigmoid for muscle tissue with $E_{rev} = 240$ V/cm and $E_{irrev} = 430$ V/cm. The same electroporation threshold values, E_{rev} and E_{irrev}, were found for both muscles electroporated directly and transcutaneously. We thus conclude that the skin layer has, as expected, no influence on the thresholds of the local electric field intensity needed for successful muscle tissue electroporation, but it does require higher voltage to be applied between the electrodes when muscle is electroporated transcutaneously. Our model of muscle with skin also confirms the in vivo findings of previous studies that electroporation "breaks" the skin barrier when the applied voltage is above 50 V.

We also showed that the error of an approximate estimation of electroporation threshold values in in vivo experiments by calculating the U/d ratio, without numerical calculations of local electric field distribution, is small enough only if the plate electrodes are used and only for one type of tissue placed between the electrodes. For more complex tissues with different geometric and electrical properties, a combination of realistic numerical modeling and in vivo experiments needs to be used for the precise determination of electroporation threshold values.

It is also important to note that the thresholds of the local electric field for tissue electroporation depend on the type of molecules used for the detection of in vivo tissue permeabilization (Kotnik et al. 2000) and electroporation pulse characteristics (i.e., duration and number of pulses as well as pulse repetition frequency). Thus, the threshold values determined in our study are relevant for the setting of eight pulses of 100-μs duration at a repetition frequency of 1 Hz. For the precise electroporation threshold determination for other pulse parameters, our numerical models remain valid, but additional in vivo experiments need to be done and the results included in the models.

The findings of our study carry important practical information for treatment planning in electroporation-mediated therapies such as gene electrotransfer into muscle, transdermal drug and gene delivery and clinical electrochemotherapy.

Acknowledgments This research was supported in part by the European Commission under the fifth framework (Grant Cliniporator QLK3-1999-00484), Slovenian Research Agency, CNRS (Centre National de la Recherche Scientifique), Institute Gustave-Roussy and Ad-Futura. This research was conducted in the scope of LEA EBAM. The authors thank Dr. David Cukjati and Dr. Danute Batiuskaite for the results of in vivo experiments performed in the lab of L. M. M. (Institut Gustave-Roussy, Villejuif, France) as well as Derek Snyder for help in proofreading and editing the text.

References

Breton M, Mir LM (2011) Microsecond and nanosecond electric pulses in cancer treatments. Bioelectromagnetics. doi:10.1002/bem.20692

Corovic S, Zupanic A, Miklavcic D (2008) Numerical modeling and optimization of electric field distribution in subcutaneous tumor treated with electrochemotherapy using needle electrodes. IEEE Trans Plasma Sci 36:1665–1672

Corovic S, Zupanic A, Kranjc S, Al Sakere B, Leroy-Willig A, Mir LM, Miklavcic D (2010) Influence of skeletal muscle anisotropy on electroporation: in vivo study and numerical modeling. Med Biol Eng Comput 48:637–648

Cukjati D, Batiuskaite D, André F, Miklavcic D, Mir LM (2007) Real time electroporation control for accurate and safe in vivo non-viral gene therapy. Bioelectrochemistry 70:501–507

Davalos R, Rubinsky B, Otten DM (2002) A feasibility study for electrical impedance tomography as a means to monitor tissue electroporation for molecular medicine. IEEE Trans Biomed Eng 49:400–403

Davalos RV, Otten DM, Mir LM, Rubinsky B (2004) Electrical impedance tomography for imaging tissue electroporation. IEEE Trans Biomed Eng 51:761–767

Denet AR, Vanbever R, Préat V (2004) Skin electroporation for transdermal and topical delivery. Adv Drug Deliv Rev 56:659–674

Edhemovic I, Gadzijev EM, Brecelj E, Miklavcic D, Kos B, Zupanic A, Mali B, Jarm T, Pavliha D, Marcan M, Gasljevic G, Gorjup V, Music M, Pecnik Vavpotic T, Cemažar M, Snoj M, Sersa G (2011) Electrochemotherapy: a new technological approach in treatment of metastases in the liver. Technol Cancer Res Treat 10:475–485

Gehl J, Mir LM (1999) Determination of optimal parameters for in vivo gene transfer by electroporation, using a rapid in vivo test for cell permeabilization. Biochem Biophys Res Commun 261:377–380

Gehl J, Sorensen TH, Nielsen K, Raskmark P, Nielsen SL, Skovsgaard T, Mir LM (1999) In vivo electroporation of skeletal muscle: threshold, efficacy and relation to electric field distribution. Biochim Biophys Acta 1428:233–240

Hojman P, Eriksen J, Gehl J (2009) In vivo imaging of far-red fluorescent proteins after DNA electrotransfer to muscle tissue. Biol Proc Online 11:253–262

Ivorra A, Al-Sakere B, Rubinsky B, Mir LM (2009) In vivo electrical conductivity measurements during and after electroporation of sarcomas: conductivity changes reflect treatment outcome. Phys Med Biol 54:5949–5963

Kos B, Zupanic A, Kotnik T, Snoj M, Sersa G, Miklavcic D (2010) Robustness of treatment planning for electrochemotherapy of deep-seated tumors. J Membr Biol 236:147–153

Kotnik T, Macek-Lebar A, Miklavcic D, Mir LM (2000) Evaluation of cell membrane electropermeabilization by means of non-permeant cytotoxic agent. Biotechniques 28:921–926

Mali B, Jarm T, Corovic S, Paulin-Kosir MS, Cemazar M, Sersa G, Miklavcic D (2008) The effect of electroporation pulses on functioning of the heart. Med Biol Eng Comput 46:745–757

Marty M, Sersa G, Garbay JR, Gehl J, Collins CG, Snoj M, Billard V, Geertsen PF, Larkin JO, Miklavcic D, Pavlovic I, Paulin-Kosir SM, Cemazar M, Morsli N, Soden DM, Rudolf Z, Robert C, O'Sullivan GC, Mir LM (2006) Electrochemotherapy—an easy, highly effective and safe treatment of cutaneous and subcutaneous metastases: results of ESOPE (European Standard Operating Procedures of Electrochemotherapy) study. Eur J Cancer Suppl 4:3–13

Mathiesen I (1999) Electropermeabilisation of skeletal muscle enhances gene electrotransfer in vivo. Gene Ther 6:508–514

Miklavcic D, Beravs K, Semrov D, Cemazar M, Demsar F, Sersa G (1998) The importance of electric field distribution for effective in vivo electroporation of tissues. Biophys J 74:2152–2158

Miklavcic D, Semrov D, Mekid H, Mir LM (2000) A validated model of in vivo electric field distribution in tissues for electrochemotherapy and for DNA electrotransfer for gene therapy. Biochim Biophys Acta 1523:73–83

Miklavcic D, Pavselj N, Hart FX (2006) Electric properties of tissues. In: Wiley encyclopedia of biomedical engineering. Wiley, New York

Mir LM, Orlowski S, Belehradek J Jr, Teissié J, Rols MP, Sersa G, Miklavcic D, Gilbert R, Heller R (1995) Biomedical applications of electric pulses with special emphasis on antitumor electrochemotherapy. Bioelectrochemistry 38:203–207

Mir LM, Bureau MF, Gehl J, Rangara R, Rouy D, Caillaud JM, Delaere P, Branellec D, Schwartz B, Scherman D (1999) High-efficiency gene transfer into skeletal muscle mediated by electric pulses. Proc Natl Acad Sci U S A 74:4262–4267

Ngawhirunpat T, Hatanaka T, Katayama K, Yoshikawa H, Kawakami J, Adachi I (2002) Changes in electrophysiological properties of rat skin with age. Biol Pharm Bull 25:1192–1196

Pavlin M, Miklavcic D (2003) Effective conductivity of a suspension of permeabilized cells: a theoretical analysis. Biophys J 85: 719–729

Pavlin M, Pavselj N, Miklavcic D (2002) Dependence of induced transmembrane potential on cell density, arrangement, and cell position inside a cell system. IEEE Trans Biomed Eng 49: 605–612

Pavselj N, Miklavcic D (2008) Numerical modeling in electroporation-based biomedical applications. Radiol Oncol 42:159–168

Pavselj N, Bregar Z, Cukjati D, Batiuskaite D, Mir LM, Miklavcic D (2005) The course of tissue permeabilization studied on a mathematical model of a subcutaneous tumor in small animals. IEEE Trans Biomed Eng 52:1373–1381

Pliquett U, Langer R, Weaver JC (1995) Changes in the passive electrical properties of human stratum corneum due to electroporation. BBA 1239:111–121

Prausnitz MR, Bose VG, Langer R, Weaver JC (1993) Electroporation of mammalian skin: a mechanism to enhance transdermal drug delivery. Proc Natl Acad Sci U S A 90:10504–10508

Prud'homme GJ, Glinka Y, Khan AS, Draghia-Akli R (2006) Electroporation enhanced nonviral gene transfer for the prevention or treatment of immunological, endocrine and neoplastic diseases. Curr Gene Ther 6:243–273

Puc M, Kotnik T, Mir LM, Miklavcic D (2003) Quantitative model of small molecules uptake after in vitro cell electropermeabilization. Bioelectrochemistry 60:1–10

Pucihar G, Kotnik T, Miklavčič D, Teissié J (2008) Kinetics of transmembrane transport of small molecules into electropermeabilized cells. Biophys J 95:2837–2848

Sel D, Cukjati D, Batiuskaite D, Slivnik T, Mir LM, Miklavcic D (2005) Sequential finite element model of tissue electropermeabilization. IEEE Trans Biomed Eng 52:816–827

Tevz G, Pavlin D, Kamensek U, Kranjc S, Mesojednik S, Coer A, Sersa G, Cemazar M (2008) Gene electrotransfer into murine skeletal muscle: a systematic analysis of parameters for long-term gene expression. Technol Cancer Res Treat 7(2):91–154

UKCCCR (1998) UKCCR guidelines for welfare of animals in experimental neoplasia (second edition). Br J Cancer 77:1–10

Valic B, Golzio M, Pavlin M, Schatz A, Faurie C, Gabriel B, Teissie J, Rols MP, Miklavcic D (2003) Effect of electric field induced transmembrane potential on spheroidal cells: theory and experiments. Eur Biophys J 32:519–528

Zupanic A, Ribaric S, Miklavcic D (2007) Increasing the repetition frequency of electric pulse delivery reduces unpleasant sensations that occur in electrochemotherapy. Neoplasma 54:246–250

Zupanic A, Corovic S, Miklavcic D (2008) Optimization of electrode position and electric pulse amplitude in electrochemotherapy. Radiol Oncol 42:93–101

J Membrane Biol (2012) 245:521–529
DOI 10.1007/s00232-012-9433-7

Electric Field Exposure Triggers and Guides Formation of Pseudopod-Like Blebs in U937 Monocytes

Mikhail A. Rassokhin · Andrei G. Pakhomov

Received: 21 December 2011 / Accepted: 30 April 2012 / Published online: 26 May 2012

Abstract We describe a new phenomenon of anodotropic pseudopod-like blebbing in U937 cells stimulated by nanosecond pulsed electric field (nsPEF). In contrast to "regular," round-shaped blebs, which are often seen in response to cell damage, pseudopod-like blebs (PLBs) formed as longitudinal membrane protrusions toward anode. PLB length could exceed the cell diameter in 2 min of exposure to 60-ns, 10-kV/cm pulses delivered at 10–20 Hz. Both PLBs and round-shaped nsPEF-induced blebs could be efficiently inhibited by partial isosmotic replacement of bath NaCl for a larger solute (sucrose), thereby pointing to the colloid-osmotic water uptake as the principal driving force for bleb formation. In contrast to round-shaped blebs, PLBs retracted within several minutes after exposure. Cells treated with 1 nM of the actin polymerization blocker cytochalasin D were unable to form PLBs and instead produced stationary, spherical blebs with no elongation or retraction capacity. Live cell fluorescent actin tagging showed that during elongation actin promptly entered the PLB interior, forming bleb cortex and scaffold, which was not seen in stationary blebs. Overall, PLB formation was governed by both passive (physicochemical) effects of membrane permeabilization and active cytoskeleton assembly in the living cell. To a certain extent, PLB mimics the membrane extension in the process of cell migration and can be employed as a nonchemical model for studies of cytomechanics, membrane–cytoskeleton interaction and cell motility.

M. A. Rassokhin (✉) · A. G. Pakhomov
Frank Reidy Research Center for Bioelectrics, Old Dominion University, 4211 Monarch Way, Suite 300, Norfolk, VA 23508, USA
e-mail: mrass002@odu.edu; medchel@gmail.com

Keywords Electroporation · Nanosecond pulsed electric field · Colloid-osmotic swelling · Blebbing · Membrane protrusion · Cell motility

Introduction

Permeabilization of the cellular membrane by pulsed electric field, including nanosecond pulsed electric field (nsPEF), triggers cell reshaping due to swelling and blebbing (Gass and Chernomordik 1990; Deng et al. 2003; André et al. 2010). Intact cells maintain osmotic equilibrium with extracellular buffer (Hoffmann et al. 2009), but electropermeabilized cells are unable to do that effectively. Swelling in such cells is caused by a colloid-osmotic mechanism (Kinosita and Tsong 1977; Saulis 1999; Pakhomov and Pakhomova 2010) that results from differential permeability of the electroporated membrane to extra- and intracellular solutes. In brief, pores formed in the cell membrane due to pulse application are permeable to small ions but not to larger molecules. Bath buffer contains predominantly small ions and molecules, while the cellular interior contains a fraction of large organic molecules and anions. After permeabilization, small ions like Na^+ and Cl^- enter the cell down their electrochemical gradients. Meanwhile, large pore-impermeant organic molecules and anions remain trapped inside. Osmolality created by organic molecules and entering ions becomes larger than osmolality of the bath buffer, which remains undisturbed due to its large volume. Such a mechanism generates osmotic gradient and drives water uptake.

Swelling in nsPEF-treated cells is often accompanied by formation of blebs, rounded membrane protrusions that appear on the cell surface in an apparently uncontrolled manner (Tekle et al. 2008; Pakhomov et al. 2009).

Currently, the mechanisms and implementations of blebbing for physiology of electroporated cells are not clear. Supposedly, blebbing is a by-product of PEF-induced cell damage (Tsong 1991); however, outside the research area of electroporation, blebbing is commonly seen in the life cycle of intact cells (Blaser et al. 2006). Such blebs form during cytokinesis (Tinevez et al. 2009), migration (Charras and Paluch 2008), in attaching cells (Bereiter-Hahn et al. 1990) and in response to physiological stimuli (Torgerson and McNiven 1998).

In early studies, blebs were described as "clear, round cytoplasmic protrusions" (Hogue 1919) and referred to as blisters (Zollinger 1948) or bubbles (Holtfreter 1944). At present, the term "blebbing" is also used to describe membrane evaginations during cell spreading (Norman et al. 2011) and cell division (Pletjushkina et al. 2001), as well as in necrotic (Barros et al. 2003) and apoptotic (Sebbagh et al. 2001) cell damage. "Membrane ballooning" is another term that illustrates terminal blebbing in necrotic cells (Petersen and Dailey 2004; Lang et al. 2011). Due to the lack of clear definition and classification, the term "bleb" may be confusing when used outside the context of physiological or pathological processes. In this article we will differentiate between reversible, nonlethal blebbing and stationary blebbing, which is a sign of cell damage (Fackler and Grosse 2008).

Modern knowledge about blebbing and its mechanisms comes from multiple sources. Reversible blebs and their life cycle were comprehensively studied in cell lines with defects in actin polymerization. Such cells exhibit intense and reversible blebbing due to weakening of membrane–cytoskeleton adhesion (Cunningham et al. 1992; Derivery et al. 2008). Another factor responsible for bleb formation is actomyosin contractility of cell cortex and resulting increase in cortical tension (Dai and Sheetz 1999). In general, bleb formation can also be triggered by local transmembrane ion transport and associated water uptake (Mitchison et al. 2008). As mentioned previously, in electropermeabilized cells the colloid-osmotic water uptake also results from increased inward ion transport (Pakhomov and Pakhomova 2010). Hence, blebs induced by nsPEF may not only resemble regular blebs morphologically but also form through similar mechanisms.

Reversible and stationary blebs nucleate on the cell surface and inflate while remaining attached to the cell body through the neck region. Expansion of blebs lasts several seconds or minutes and results in the formation of rounded, membrane-bound protrusions, the size of which may become comparable to the size of the cell body. At the early stage of formation, morphological distinctions between reversible and stationary blebs are negligible. Both bleb types are present as transparent, membrane-bound, rounded protrusions with no cytoskeleton or organelles (Cunningham 1995). However, upon maturation the interior of reversible blebs becomes filled with de novo forming actin fibrils (Charras et al. 2006) that participate in the organization of contractile bleb cortex. Cortex assembly is associated with reestablishment of membrane–cytoskeleton integrity and further bleb retraction. Cortex contractility in reversible blebs is attributed to the presence of actomyosin motors (Charras et al. 2005). In contrast, formation of actin scaffold or contractile cortex does not occur in stationary blebs formed during necrosis (Barros et al. 2003) or due to cytoskeletal toxin exposure (Charras 2008). Once inflation in such blebs stops, they remain stagnant and show no retraction.

Reversible blebbing passes through cycles of membrane expansion, reassembly of cortical cytoskeleton and retraction due to actomyosin contractility (Charras et al. 2006). Such a mechanism of membrane expansion may provide an alternative to actin-driven protrusion formation for cell locomotion (Keller and Eggli 1998; Maugis et al. 2010). In several works blebbing already has been established as a mechanism of cell migration (Fackler and Grosse 2008).

Typical blebs formed due to nsPEF exposure are stationary and reflect either apoptotic or necrotic cell transformation. However, we found an all new type of blebs that we called "pseudopod-like blebs" (PLBs). PLBs are characterized by elongated shape, fast directional growth toward anode and rapid retraction following nsPEF exposure. Some of these findings were reported previously in meeting proceedings (Rassokhin and Pakhomov 2010, 2011). This is the first systematic study of some PLB properties and the mechanisms that underlie their formation.

Materials and Methods

Cell Line and Propagation

This study was entirely performed on human suspension promonocytic U937 cells that were obtained from the ATCC (Mannanas, VA). Cells were propagated at 37 °C with 5 % CO_2 in air. In accordance with the supplier's recommendations, cells were maintained in RPMI 1640 growth medium containing L-glutamine and supplemented with 10 % fetal bovine serum and 1 % penicillin/streptomycin. Cell culture components were obtained from Atlanta Biologicals (Norcross, GA) or Mediatech Cellgro (Herndon, VA). Before the experiment, cells were transferred onto glass coverslips pretreated with poly-L-lysine (Sigma-Aldrich, St. Louis, MO). Cells were left in full growth medium for at least 30 min prior to experiments.

Cell Imaging and Image Analysis

For timelapse image recording a coverslip with attached cells was placed into a glass-bottomed chamber (Warner Instruments, Hamden, CT) mounted on an IX81 motorized inverted

microscope (Olympus, Center Valley, PA). Differential-interference contrast (DIC) and fluorescence imaging was performed using a 40 × dry objective (NA 0.95) or a 60 × oil objective (NA 1.42). Cell images were recorded using the FV 1000 confocal laser scanning system (Olympus).

Cell images were taken at regular intervals of 4–5 s. Typically, six or seven images were captured prior to exposure. nsPEF treatment started 30 s into the experiment and continued for 30, 60 or 120 s. All experiments were performed at room temperature.

DIC images were analyzed for blebbing probability, location and bleb size. PLBs were defined as longitudinal, anodotropic blebs with the length exceeding at least one cell diameter. For measurement of membrane permeability a fluorescent membrane integrity marker, propidium iodide (Sigma-Aldrich), was added to the exposure buffer at a concentration of 5 μg/ml (~7.5 μM). To avoid saturation of the fluorescent channel, the sensitivity of the detector was calibrated on cells permeabilized with 0.3 % digitonin (Sigma-Aldrich). In other experiments to visualize actin rearrangements caused by nsPEF, rhodamine-phalloidin conjugate (Cytoskeleton, Denver, CO) was added to the bath buffer at a concentration of 28 nM. Analyses of blebbing, propidium uptake and actin rearrangements were performed using MetaMorph 7.7 software (Molecular Devices, Sunnyvale, CA).

Experimental Chemicals and Buffers

All experiments, except with sucrose, were performed in a bath buffer that contained (in mM) 135 NaCl, 5 KCl, 4 $MgCl_2$, 3 HEPES, 2 Na-EGTA and 10 glucose at pH 7.4 (Nesin et al. 2011). In experiments on the verification of the colloid-osmotic mechanism, we replaced 22.5, 45 or 90 mM of NaCl with isosmotic amounts of sucrose (45, 90 and 180 mM, respectively). The final osmolality of all experimental buffers remained at ~290 mOsm/kg, as measured with a freezing point micro-osmometer (Advanced Instruments, Norwood, MA). Chemicals were purchased from Sigma-Aldrich unless stated overwise. Rhodamine-phalloidin (Cytoskeleton) was dissolved in 100 % methanol, while cytochalasin D was dissolved in 100 % DMSO. In experiments studying actin rearrangements, vehicle (0.001 % DMSO) was used as a negative control. Overall exposure of cells to cytochalasin D before image recording was kept to a minimum and did not exceed 5 min.

Pulse Stimulation and Local Electric Field Modeling

nsPEF exposure of individual cells was performed as described previously (Bowman et al. 2010). Pulses were delivered to a selected group of cells with a pair of custom tungsten rod electrodes (0.08 mm diameter, 0.15 mm gap). Using a robotic micromanipulator (MP-225; Sutter, Novato, CA), electrodes were positioned at 50 μm above the coverslip surface so that the selected cells were located between their tips. Nearly rectangular 60-ns pulses were generated in a transmission line-type circuit, by closing a MOSFET switch upon a timed delivery of a TTL trigger pulse from pClamp software via a Digidata 1322A output (MDS, Foster City, CA). The exact nsPEF delivery protocol and synchronization of nsPEF delivery with image acquisition were programmed in pClamp. The E-field between the electrodes was determined by a 3D simulation with a finite element Maxwell equation solver Amaze 3D (Field Precision, Albuquerque, NM). Exact EP shapes and amplitudes were captured and measured with a Tektronix (Beaverton, OR) TDS 3052 oscilloscope. Experiments included appropriate controls in which cells were subjected to identical manipulations but without nsPEF delivery ("sham" exposures).

Results

The Phenomenon of Pseudopod-Like Blebbing

Pseudopod-like blebbing was discovered when U937 cells were exposed to long trains of nanosecond pulses. PLB formation is illustrated in Fig. 1, which shows representative frames of PLB nucleation and directional growth during exposure to a train of 3,600 60-ns pulses (12.1 kV/cm, 20 Hz).

Bleb formation usually occurs with ~30-s delay after the onset of exposure. After this interval, small rounded blebs appear on the anode-facing cell pole. At this time, these blebs resemble typical blebs widely reported in the literature (Keller et al. 2002; Charras 2008). During the course of treatment, small blebs rapidly elongate toward the anode electrode and may exceed the size of cell diameter after 2 min of exposure. We define such blebs as PLBs. Although the size and growth velocity are distinctive features of PLBs, what makes these blebs unique is that they grow exclusively toward anode and assume an elongated sausage-like appearance. Even blebs nucleated away from anodic cell pole eventually "steer" toward anode. During growth the bleb tip retains its rounded shape and leaves behind the extended bleb body. Developed PLBs commonly have a sectioned appearance due to occasional transverse strictures. When pulse treatment is discontinued, the bleb growth stops promptly and changes to partial or complete retraction.

Role of Pulse Parameters in Triggering Pseudopod-Like Blebbing

For initiation of PLBs we used long trains of 60-ns pulses. At first we focused on the effect of pulse repetition rate and

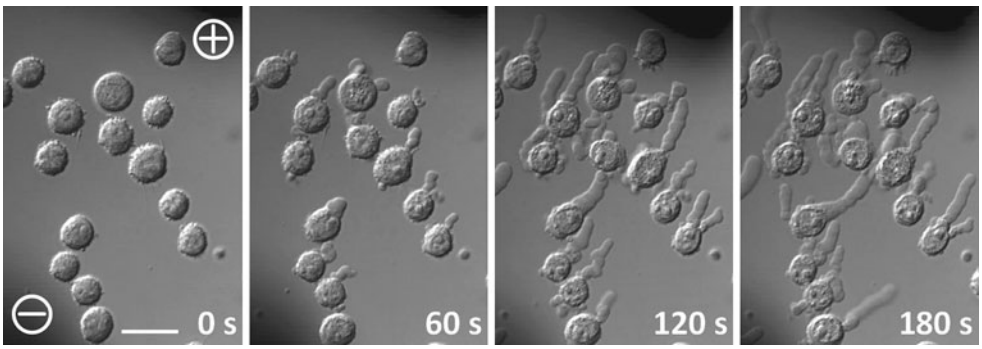

Fig. 1 Nanosecond pulsed electric field (nsPEF) exposure triggers and guides formation of anodotropic pseudopod-like blebs. Images show representative frames of time series illustrating U937 cells at different time points (60-s interval) during exposure to 60-ns pulses (12.1 kV/cm, 20 Hz, 3,600 pulses). Pulse treatment started at 0 s. Shadows at the *upper right* and *lower left* corners are those of nsPEF-delivering electrodes. Anode and cathode electrodes are identified by + and − signs, respectively. *Scale bar* = 20 μm

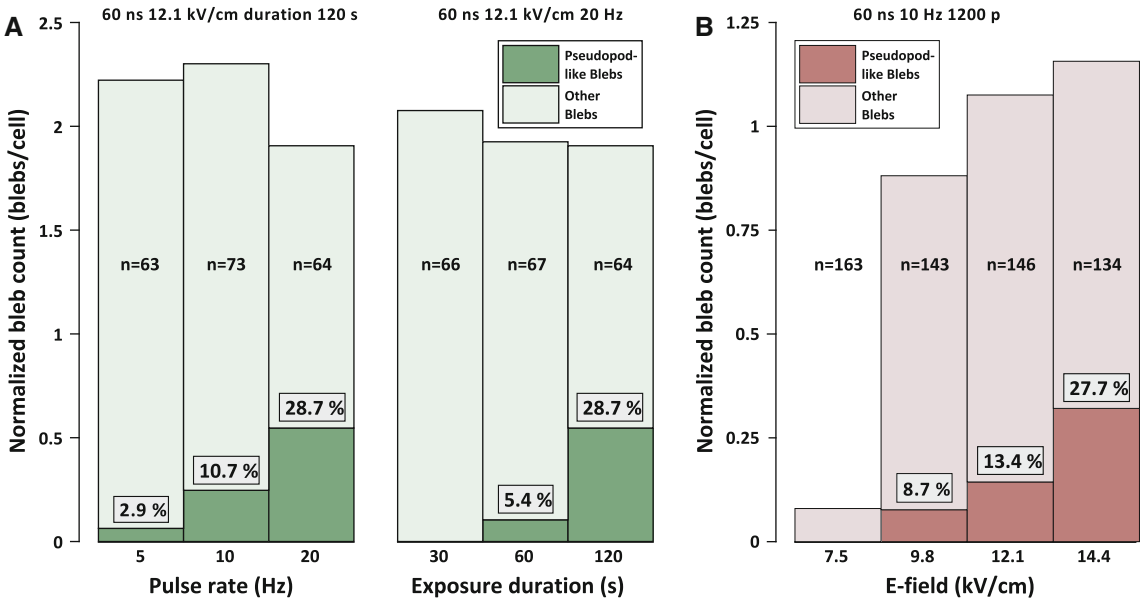

Fig. 2 Effect of the treatment parameters on formation of regular and pseudopod-like blebs. *Numbers* on the graphs indicate the number of analyzed cells and the percentage of pseudopod-like blebs in the overall bleb count. The set of parameters indicated above each chart was kept constant, while parameters below the charts were varied. **a** *Left panel* Pulse rate was varied while keeping other parameters constant. *Right panel* Exposure duration was varied while keeping other parameters constant. One group (20 Hz, 2,400 pulses) is shared between the two charts. **b** E-field was varied while all other parameters were constant. Plots **a** and **b** summarize the results of 8 and 15 independent treatments, respectively. Sham-exposed cells did not produce any blebs (not shown)

exposure duration while keeping amplitude fixed. Within the tested parameter range, the probability of bleb nucleation was relatively constant and remained at a level of 2–2.5 blebs per cell. However, the probability to form PLBs from regular blebs increased considerably with the increase in pulse rate from 5 to 20 Hz and increase in exposure duration from 30 to 120 s (Fig. 2a). Cells treated with rates of 5, 10 and 20 Hz produced PLBs from 2.9, 10.7 and 28.7 % of regular blebs, respectively. The plot in the right panel of Fig. 2a demonstrates the increase in PLB formation in response to increase in pulse-exposure duration. When other parameters were kept constant, the exposure duration of 30, 60 or 120 s produced 0, 5.4 or 28.7 % of PBLs, respectively.

In the second series of experiments, the E-field was varied from 7.5 to 14.4 kV/cm, while the pulse-repetition rate and exposure duration were fixed at 10 Hz and 120 s, respectively (Fig. 2b). Cell exposure to the lowest tested E-field of 7.5 kV/cm produced a very low regular bleb count of 0.1 blebs/cell and no PLBs. An E-field increase to 9.8 kV/cm resulted in a much higher bleb count of 0.9 blebs/cell but a low relative PLB count (8.7 %). The

E-field of 12.1 kV/cm resulted in a bleb count of 1.1 blebs/cell and formation of PLBs from 13.4 % of regular blebs. Exposure to the highest tested E-field of 14.4 kV/cm produced 1.2 blebs/cell, of which 27.7 % were PLBs.

Of note, although two exposure protocols with different frequencies (12.1 kV/cm, 20 Hz, 2,400 pulses in series A and 14.4 kV/cm, 10 Hz, 1,200 pulses in series B) were almost equally efficient at producing PLBs (28.7 and 27.7 %, respectively), we chose the 20-Hz over the 10-Hz protocol for subsequent experiments for the following reasons. First, the velocity of PLB growth at 20 Hz was higher than that at 10 Hz (data not shown). Second, the PLB yield of 10-Hz exposures in series A and B varied, while the PLB yield of the 20-Hz protocol remained steadily high. Based on the studied effects of pulse parameters, selection of 20 Hz seemed the most appropriate due to the maximal yield of PLBs.

Asymmetrical Nucleation of Blebs

In the next series we tested the effect of different pulse protocols on preferred location of bleb nucleation. The cell surface was separated into four sectors relative to position of pulse-delivering electrodes (anodic, cathodic and two sides). All nucleation events were assigned to one of four sectors according to their location. Each bar length in Fig. 3 indicates the percent fraction of nucleation events in the sector to the total number of nucleation events registered for the treatment protocol. In all tested protocols the preferred location of bleb nucleation ($\sim$60 %) was at the cell pole facing anode. Other locations displayed a low and nearly equal chance of nucleation. Different bar angles are used merely for convenience of presentation and do not correspond to actual direction of blebbing. Asymmetry of nucleation suggests that permeabilization plays a central role in determining bleb directionality.

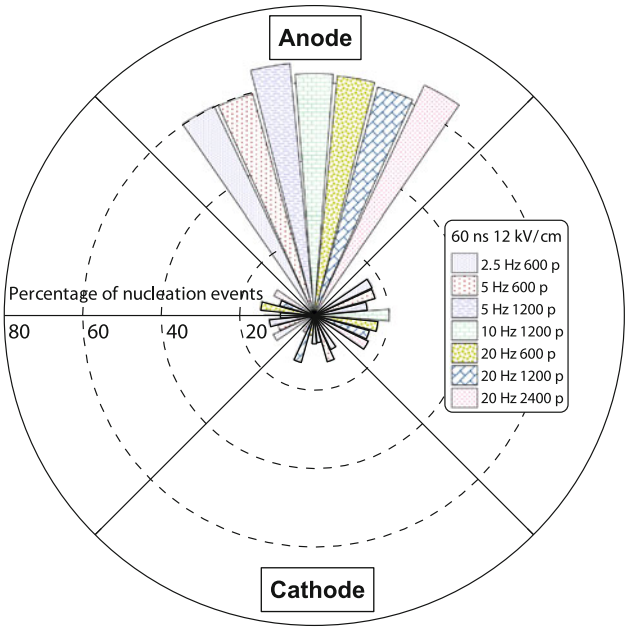

Fig. 3 Blebs are predominantly nucleated at the anodic cell pole. Bleb initiation was evaluated during exposure to one of the pulse protocols shown in the graph. For each treatment the number of nucleation events was measured in four 90° sectors of the cell surface (anodic, cathodic and two sides). The total number of nucleation events in each protocol was taken for 100 %. *Bars* encode the fraction of nucleation events and do not imply exact bleb position against the electrodes. Data summarize the results of eight experiments for each protocol

Evaluation of Propidium Uptake in Exposed Cells

The propidium emission of nsPEF-treated cells was compared to staining of dead cells which were present in all samples and constituted $\sim$1–2 % of the cell population. The results illustrated in Fig. 4 show that propidium uptake was at least 20-fold lower in nsPEF-exposed cells than in dead cells. This modest uptake level indicates that the membrane barrier function was only partially compromised by nsPEF. However, the long-term viability of PLB-forming cells was not studied.

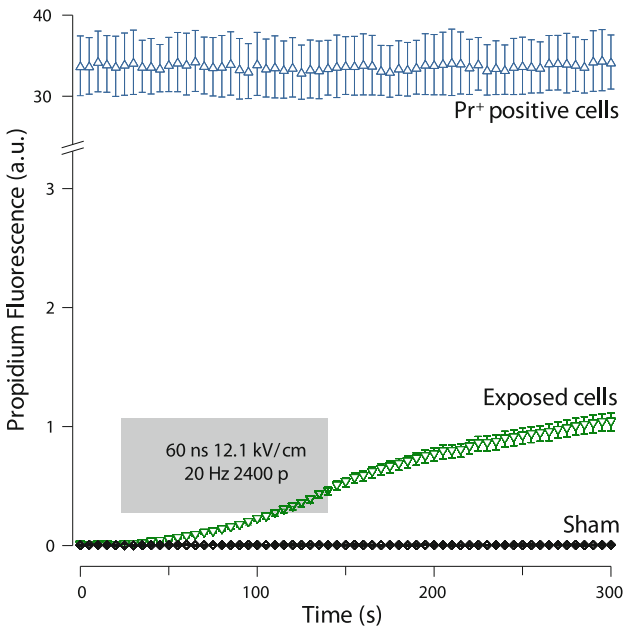

Fig. 4 Nanosecond pulsed electric field–triggered propidium uptake compared to uptake in sham-exposure cells and dead cells. Dead cells typically constitute $\sim$1–2 % of cell samples. Shading represents the exposure interval. Note the scale break on the fluorescence axis. The exposed group presents recordings of 53 cells in eight independent experiments

The Role of Colloid-Osmotic Swelling in PLB Growth

Once the optimal pulse parameters were explored, the mechanisms of PLB growth were addressed. Possible

candidates for processes driving bleb formation were electrophoresis, water uptake and cytoskeletal rearrangements. Electrophoretic drift of charged molecules inside the cell is a legitimate expectation during exposure to an electric field; however, a very small duty cycle employed in our treatments (1.2×10^{-6}) renders this unlikely. Presumably, the growth of some cell protrusions is driven by actin polymerization (Chhabra and Higgs 2007), but the growth rate and size of PLBs exceed that of protrusions formed via such mechanism (Pollard and Borisy 2003). Alternatively, PLB growth may be fueled by water uptake. As discussed previously, nsPEF-treated cells swell by a Donnan-type colloid-osmotic mechanism (Pakhomov and Pakhomova 2010; Nesin et al. 2011).

To test the role of the colloid-osmotic mechanism, we partially substituted NaCl for an equiosmolar amount of sucrose, which is a swelling inhibitor in nsPEF-treated cells (Nesin et al. 2011). Exposure buffers in this series contained 45, 90 or 180 mM of sucrose instead of a fraction of NaCl equal to 22.5, 45 or 90 mM, respectively. The results in Fig. 5 illustrate that such replacement is indeed effective against bleb formation. Partial substitution of NaCl for 45 mM of sucrose almost completely eliminated PLBs and modestly affected other bleb types. In the presence of 90 mM of sucrose, no PLBs developed, while formation of other blebs was considerably inhibited. Finally, NaCl replacement for 180 mM of sucrose prevented all types of blebbing. Sham-exposed cells did not produce blebs in any of the buffers.

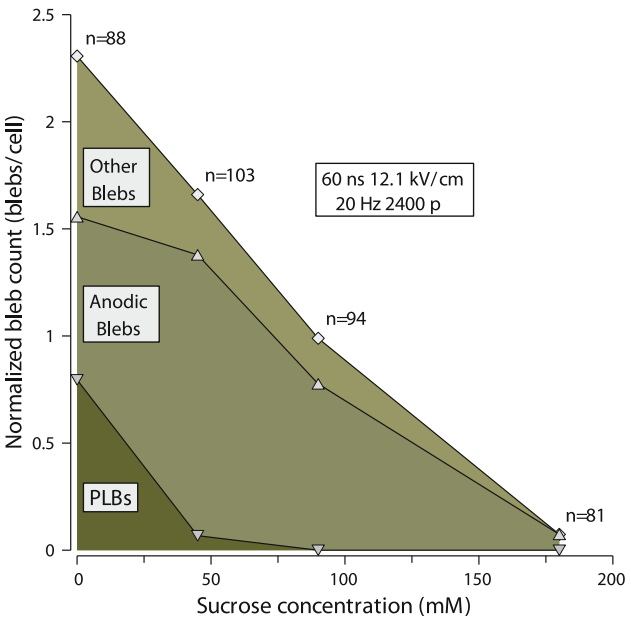

Fig. 5 Inhibition of nanosecond pulsed electric field–induced blebbing by isosmotic replacement of different fractions of NaCl for sucrose. Replacement of equiosmolar amount of NaCl for sucrose inhibits water uptake by electroporated cells and does not change the final buffer osmolality. The number of blebs per cell was plotted against the fraction of sucrose in the buffer (45, 90 and 180 mM). The cell count is the sum of eight independent experiments

These results showed that water uptake is indeed the driving mechanism of PLB growth. Thus, formation of both PLBs and regular blebs in nsPEF-treated cells relies on water inflow. However, the elongated shape that contrasts PLBs to regular rounded blebs suggests that other mechanisms, such as cytoskeletal rearrangements, may be involved in PLB formation.

Role of Actin Rearrangements in PLB Formation

In this series we focused on the mechanism responsible for the structural support and shape of PLBs. Considering their monocytic origin, U937 cells may have an advanced regulation of their cytoskeleton (Sheth et al. 1991). As noted above, PLBs commonly extend through the formation of smaller sections that constantly append at the anodic tip. As a result, these blebs commonly have transverse strictures located between two consecutive sections. This observation suggests a complex internal organization of PLBs. We hypothesized that PLB support is provided by formation of an actin scaffold.

In order to establish the role of the actin cytoskeleton, we used a fluorescent rhodamine-phalloidin conjugate. Conveniently, nsPEF treatment improved penetration of the conjugate inside the cell and enabled efficient actin visualization at a low dye concentration. The time series of DIC and corresponding actin staining images during PLB development are presented in Fig. 6a. PLB growth was accompanied by the accumulation of actin in the bleb interior. After nsPEF exposure, bleb growth stopped and concurrently the formation of an actin rim began along the bleb surface. The assembly of the actin cortex preceded partial PLB retraction. During the retraction, PLBs deflated and assumed a wrinkled appearance that corresponded to intense actin accumulation in the bleb body.

To verify the role of actin in support of the PLB shape, we inhibited actin polymerization by the addition of cytochalasin D (1 nM). The results in Fig. 6b show that in the presence of cytochalasin D nsPEF exposure induced formation of regular rounded blebs rather than PLBs. After pulse treatment, rounded blebs did not retract or develop an actin rim.

Overall, the inhibition of F-actin formation by cytochalasin D prevented formation of PLBs. Together with fluorescent labeling data, this demonstrates that actin polymerization is responsible for the unique PLB shape and its retraction.

In summary, we established that the driving force of PLB growth was Donnan-type colloid-osmotic water uptake, while the specific bleb shape arises due to formation of the actin cytoskeleton.

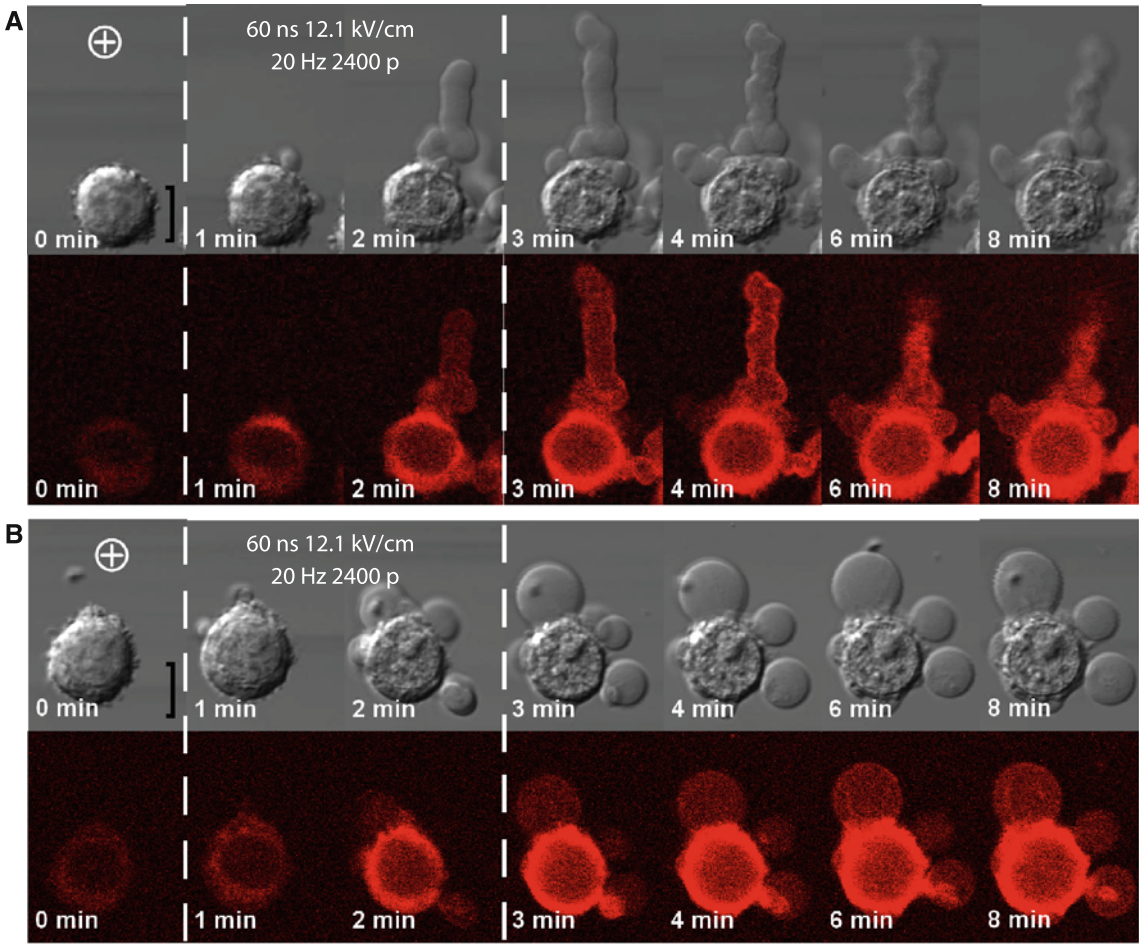

Fig. 6 Cytoskeleton formation in pseudopod-like blebs (PLBs) and the effect of F-actin inhibition on bleb shape and retraction. Representative frames of an image time series demonstrate blebs in U937 cells before, during and after nanosecond pulsed electric field treatment (started at 30 s). Pseudopod-like blebbing (**a**) is accompanied by formation of an actin rim and partial bleb retraction after exposure. The presence of cytochalasin D (**b**) inhibits PLB formation. Rounded blebs that form instead do not develop the actin rim and lack the retraction capability. *Dashed lines* enclose frames recorded during exposure. *Scale bar* = 10 μm

Discussion

The experiments above clearly define pseudopod-like blebbing as a phenomenon different from both apoptotic and necrotic blebbing, which are commonly associated with electric pulse exposure. PLBs exhibit distinctive features, like elongated shape and growth directionality, and to our best knowledge have not been reported previously. Whether PLBs are exclusive to nsPEF or can also be produced by longer pulses remains to be established.

PLBs form predominantly on the anode-facing cell surface during exposure to long trains of nanosecond pulses. During pulse application, the anodic pole is subject to the largest induced transmembrane voltage and most intense permeabilization (Frey et al. 2006; White et al. 2011). Prolonged permeabilization is an essential prerequisite for PLB formation. Water uptake in the permeabilized area driven by the colloid-osmotic gradient is the primary force for PLB nucleation and growth. Although water uptake starts immediately after permeabilization, PLB formation typically begins in about 30 s. We propose that this interval is required for water uptake and the corresponding increase in intracellular pressure that would result in bleb nucleation. Alternatively, based on the poroelastic cell concept (Charras et al. 2009), a 30-s interval may be required for buildup of the pressure locally. According to this hypothesis, the increase in local pressure may result from a slow pressure equilibration across the whole cell. In addition, we do not exclude the possibility of a direct impact of membrane depolarization or pulse damage on membrane–cytoskeleton interactions.

The growth of PLBs occurs exclusively during nsPEF treatment and is directed toward the anode electrode. Prolonged nsPEF treatment results in continual permeabilization on the anodic pole and formation of a bleb tip that migrates toward anode concurrently with bleb elongation. Continual permeabilization of the tip generates constant

influx of extracellular water and determines the direction of extension. According to this assumption, the anodotropic direction of PLB growth is not an effect of the electric field but rather a result of constant permeabilization of the anodic cell pole.

Although we demonstrated that the colloid-osmotic gradient is the driving mechanism of PBL extension, this does not explain the characteristic elongated shape of PLBs. We established that bleb elongation is accompanied by formation of an actin cytoskeleton in the bleb interior. Supposedly, prompt recruitment of actin into the bleb reinforces bleb walls and prevents bleb growth sideways. Meanwhile, continual permeabilization on the anodic pole promotes bleb growth toward the electrode. Polymerization of actin coupled with continual bleb formation at the growing tip may also be responsible for the sectioned PLB appearance. Blockage of actin polymerization permits bleb spreading in all directions, thereby inhibiting PLBs and resulting in the formation of stationary rounded blebs with no retraction capability. Such blebs are morphologically indistinguishable from terminal blebs formed in necrotic cells. Formation of the actin scaffold culminates in assembly of the bleb cortex and is responsible for PLB retraction when the exposure ends. Actin assembly and retraction of PLBs is an active process, suggesting that nsPEF treatment does not damage cells beyond their repair capacity. This assumption combined with a modest level of propidium uptake suggests that PLB formation is hardly a manifestation of cell necrosis. More likely such nsPEF-guided protrusive blebbing provides a mechanism to expand and retract the cell membrane in a controlled manner.

Protrusion formation is an essential part of cell migration (Bereiter-Hahn 2005). Accumulating evidence suggests that during protrusion formation, contrary to the traditional view (Pollard and Borisy 2003), water inflow (Loitto et al. 2002) and membrane evagination precede actin assembly (Yang et al. 2009) and not the opposite. Our experiments established that inhibition of water uptake is sufficient to inhibit nucleation of PLBs and other blebs, while inhibition of actin polymerization does not prevent nucleation. In view of these findings, it may be interesting to examine the role of water uptake in other types of cell protrusions. However, the relevance of pseudopod-like blebbing to cell protrusions in general, including blebbing associated with cell motility, remains to be established.

Within the range of tested pulse conditions, PLB formation was observed in U937 cells but not in several other cell types (CHO, Jurkat and GH3; data not presented here). This may indicate the lack of free actin monomers in these cells or suboptimal nsPEF treatment conditions. Although PLBs may be specific to a particular cell type, they may provide a valuable model for investigation of blebbing and other protrusions. Fast initiation, high yield and flexible control over pulse-exposure parameters make this phenomenon easy to manage. Further investigation of PLBs may provide insights into membrane trafficking, cytoskeletal rearrangements and transmembrane water transport not only in electroporated cells but also in cells studied in their physiological environment.

Acknowledgments The work was funded by R01CA125482 from the National Cancer Institute and R01GM088303 from the National Institute of General Medical Sciences.

References

André FM, Rassokhin MA, Bowman AM, Pakhomov AG (2010) Gadolinium blocks membrane permeabilization induced by nanosecond electric pulses and reduces cell death. Bioelectrochemistry 79(1):95–100

Barros LF, Kanaseki T, Sabirov R, Morishima S, Castro J, Bittner CX, Maeno E, Ando-Akatsuka Y, Okada Y (2003) Apoptotic and necrotic blebs in epithelial cells display similar neck diameters but different kinase dependency. Cell Death Differ 10(6):687–697

Bereiter-Hahn J (2005) Mechanics of crawling cells. Med Eng Phys 27(9):743–753

Bereiter-Hahn J, Luck M, Miebach T, Stelzer HK, Voth M (1990) Spreading of trypsinized cells: cytoskeletal dynamics and energy requirements. J Cell Sci 96(1):171–188

Blaser H, Reichman-Fried M, Castanon I, Dumstrei K, Marlow FL, Kawakami K, Solnica-Krezel L, Heisenberg CP, Raz E (2006) Migration of zebrafish primordial germ cells: a role for myosin contraction and cytoplasmic flow. Dev Cell 11(5):613–627

Bowman A, Nesin O, Pakhomova O, Pakhomov A (2010) Analysis of plasma membrane integrity by fluorescent detection of Tl^+ uptake. J Membr Biol 236(1):15–26

Charras GT (2008) A short history of blebbing. J Microsc 231(3):466–478

Charras G, Paluch E (2008) Blebs lead the way: how to migrate without lamellipodia. Nat Rev Mol Cell Biol 9(9):730–736

Charras GT, Yarrow JC, Horton MA, Mahadevan L, Mitchison TJ (2005) Non-equilibration of hydrostatic pressure in blebbing cells. Nature 435(7040):365–369

Charras GT, Hu C-K, Coughlin M, Mitchison TJ (2006) Reassembly of contractile actin cortex in cell blebs. J Cell Biol 175(3):477–490

Charras GT, Mitchison TJ, Mahadevan L (2009) Animal cell hydraulics. J Cell Sci 122(18):3233–3241

Chhabra ES, Higgs HN (2007) The many faces of actin: matching assembly factors with cellular structures. Nat Cell Biol 9(10):1110–1121

Cunningham CC (1995) Actin polymerization and intracellular solvent flow in cell surface blebbing. J Cell Biol 129(6):1589–1599

Cunningham CC, Gorlin JB, Kwiatkowski DJ, Hartwig JH, Janmey PA, Byers HR, Stossel TP (1992) Actin-binding protein requirement for cortical stability and efficient locomotion. Science 255(5042):325–327

Dai J, Sheetz MP (1999) Membrane tether formation from blebbing cells. Biophys J 77(6):3363–3370

Deng J, Schoenbach KH, Stephen Buescher E, Hair PS, Fox PM, Beebe SJ (2003) The effects of intense submicrosecond electrical pulses on cells. Biophys J 84(4):2709–2714

Derivery E, Fink J, Martin D, Houdusse A, Piel M, Stradal TE, Louvard D, Gautreau A (2008) Free brick1 is a trimeric precursor in the assembly of a functional wave complex. PLoS ONE 3(6):e2462

Fackler OT, Grosse R (2008) Cell motility through plasma membrane blebbing. J Cell Biol 181(6):879–884

Frey W, White JA, Price RO, Blackmore PF, Joshi RP, Nuccitelli R, Beebe SJ, Schoenbach KH, Kolb JF (2006) Plasma membrane voltage changes during nanosecond pulsed electric field exposure. Biophys J 90(10):3608–3615

Gass GV, Chernomordik LV (1990) Reversible large-scale deformations in the membranes of electrically-treated cells: electroinduced bleb formation. Biochim Biophys Acta 1023(1):1–11

Hoffmann EK, Lambert IH, Pedersen SF (2009) Physiology of cell volume regulation in vertebrates. Physiol Rev 89(1):193–277

Hogue MJ (1919) The effect of hypotonic and hypertonic solutions on fibroblasts of the embryonic chick heart in vitro. J Exp Med 30(6):617–648

Holtfreter J (1944) A study of the mechanics of gastrulation. J Exp Zool 95(2):171–212

Keller H, Eggli P (1998) Protrusive activity, cytoplasmic compartmentalization, and restriction rings in locomoting blebbing Walker carcinosarcoma cells are related to detachment of cortical actin from the plasma membrane. Cell Motil Cytoskelet 41(2):181–193

Keller H, Rentsch P, Hagmann J (2002) Differences in cortical actin structure and dynamics document that different types of blebs are formed by distinct mechanisms. Exp Cell Res 277(2):161–172

Kinosita K Jr, Tsong TT (1977) Hemolysis of human erythrocytes by transient electric field. Proc Natl Acad Sci USA 74(5):1923–1927

Lang TU, Khalbuss WE, Monaco SE, Michelow P, Pantanowitz L (2011) Review of HIV-related cytopathology. Pathol Res Int 2011:256083

Loitto V-M, Forslund T, Sundqvist T, Magnusson K-E, Gustafsson M (2002) Neutrophil leukocyte motility requires directed water influx. J Leukocyte Biol 71(2):212–222

Maugis B, Brugues J, Nassoy P, Guillen N, Sens P, Amblard F (2010) Dynamic instability of the intracellular pressure drives bleb-based motility. J Cell Sci 123(22):3884–3892

Mitchison TJ, Charras GT, Mahadevan L (2008) Implications of a poroelastic cytoplasm for the dynamics of animal cell shape. Semin Cell Dev Biol 19(3):215–223

Nesin OM, Pakhomova ON, Xiao S, Pakhomov AG (2011) Manipulation of cell volume and membrane pore comparison following single cell permeabilization with 60- and 600-ns electric pulses. Biochim Biophys Acta 1808(3):792–801

Norman L, Sengupta K, Aranda-Espinoza H (2011) Blebbing dynamics during endothelial cell spreading. Eur J Cell Biol 90(1):37–48

Pakhomov AG, Pakhomova ON (2010) Nanopores: a distinct transmembrane passageway in electroporated cells. In: Pakhomov AG, Miklavcic D, Markov MS (eds) Advanced electroporation techniques in biology and medicine. CRC Press, Boca Raton, pp 178–194

Pakhomov AG, Bowman AM, Ibey BL, Andre FM, Pakhomova ON, Schoenbach KH (2009) Lipid nanopores can form a stable, ion channel-like conduction pathway in cell membrane. Biochem Biophys Res Commun 385(2):181–186

Petersen MA, Dailey ME (2004) Diverse microglial motility behaviors during clearance of dead cells in hippocampal slices. Glia 46(2):195–206

Pletjushkina OJ, Rajfur Z, Pomorski P, Oliver TN, Vasiliev JM, Jacobson KA (2001) Induction of cortical oscillations in spreading cells by depolymerization of microtubules. Cell Motil Cytoskelet 48(4):235–244

Pollard TD, Borisy GG (2003) Cellular motility driven by assembly and disassembly of actin filaments. Cell 112(4):453–465

Rassokhin MA, Pakhomov AG (2010) Fast anodotropic expansion of cell membrane under exposure to high-rate nanosecond duration electric pulses (nsEP). In: The American society for cell biology 50th annual meeting, Philadelphia, PA, USA, 11–15 December 2010

Rassokhin MA, Pakhomov AG (2011) Cell reshaping triggered by nanosecond electric pulses (nsEP). In: 8th international bioelectrics symposium, Toulouse, France, 4–6 May 2011

Saulis G (1999) Cell electroporation: estimation of the number of pores and their sizes. Biomed Sci Instrum 35:291–296

Sebbagh M, Renvoize C, Hamelin J, Riche N, Bertoglio J, Breard J (2001) Caspase-3-mediated cleavage of ROCK I induces MLC phosphorylation and apoptotic membrane blebbing. Nat Cell Biol 3(4):346–352

Sheth B, Banks P, Burton DR, Monk PN (1991) The regulation of actin polymerization in differentiating U937 cells correlates with increased membrane levels of the pertussis-toxin-sensitive G-protein Gi2. Biochem J 275(Pt 3):809–811

Tekle E, Wolfe MD, Oubrahim H, Chock PB (2008) Phagocytic clearance of electric field induced "apoptosis-mimetic" cells. Biochem Biophys Res Commun 376(2):256–260

Tinevez J-Y, Schulze U, Salbreux G, Roensch J, Joanny J-F, Paluch E (2009) Role of cortical tension in bleb growth. Proc Natl Acad Sci 106(44):18581–18586

Torgerson RR, McNiven MA (1998) The actin-myosin cytoskeleton mediates reversible agonist-induced membrane blebbing. J Cell Sci 111(19):2911–2922

Tsong TY (1991) Electroporation of cell membranes. Biophys J 60(2):297–306

White J, Pliquett U, Blackmore P, Joshi R, Schoenbach K, Kolb J (2011) Plasma membrane charging of Jurkat cells by nanosecond pulsed electric fields. Eur Biophys J 40(8):947–957

Yang C, Hoelzle M, Disanza A, Scita G, Svitkina T (2009) Coordination of membrane and actin cytoskeleton dynamics during filopodia protrusion. PLoS ONE 4(5):e5678

Zollinger HU (1948) Cytologic studies with the phase microscope; morphologic changes associated with the death of cells in vitro and in vivo. Am J Pathol 24(5):1039–1053

J Membrane Biol (2012) 245:531–543
DOI 10.1007/s00232-012-9434-6

Molecular Dynamics Simulations of Lipid Membrane Electroporation

Lucie Delemotte · Mounir Tarek

Received: 22 December 2011 / Accepted: 30 April 2012 / Published online: 30 May 2012

Abstract The permeability of cell membranes can be transiently increased following the application of external electric fields. Theoretical approaches such as molecular modeling provide a significant insight into the processes affecting, at the molecular level, the integrity of lipid cell membranes when these are subject to voltage gradients under similar conditions as those used in experiments. This article reports on the progress made so far using such simulations to model membrane—lipid bilayer—electroporation. We first describe the methods devised to perform in silico experiments of membranes subject to nanosecond, megavolt-per-meter pulsed electric fields and of membranes subject to charge imbalance, mimicking therefore the application of low-voltage, long-duration pulses. We show then that, at the molecular level, the two types of pulses produce similar effects: provided the TM voltage these pulses create are higher than a certain threshold, hydrophilic pores stabilized by the membrane lipid headgroups form within the nanosecond time scale across the lipid core. Similarly, when the pulses are switched off, the pores collapse (close) within similar time scales. It is shown that for similar TM voltages applied, both methods induce similar electric field distributions within the membrane core. The cascade of events following the application of the pulses, and taking place at the membrane, is a direct consequence of such an electric field distribution.

Keywords Millisecond pulse · Nanopulse · Electric field · Nanopore

L. Delemotte · M. Tarek
UMR Structure et Réactivité des Systèmes Moléculaires Complexes, CNRS-Université de Lorraine, Vandoeuvre-lès-Nancy, Cedex, France

Present Address:
L. Delemotte
Institute for Computational Molecular Science, Temple University, Philadelphia, PA 19122, USA

M. Tarek (✉)
Unité Mixte de Recherches CNRS UHP 7565, Université de Lorraine, Campus Science Grignard BP 239, 54506 Vandoeuvre-lès-Nancy, Cedex, France
e-mail: mounir.tarek@univ-lorraine.fr

Introduction

Electroporation disturbs transiently or permanently the integrity of cell membranes (Eberhard et al. 1989; Nickoloff 1995; Li 2008). These membranes consist of an assembly of lipids, proteins and carbohydrates that self-organize into a thin barrier that separates the interior of cell compartments from the outside environment (Gennis 1989). The main lipid constituents of natural membranes are phospholipids that arrange themselves into a two-layered sheet (a bilayer). Experimental evidence suggests that the effect of an applied external electric field to cells is to produce aqueous pores specifically in the lipid bilayer (Abidor et al. 1979; Benz et al. 1979; Weaver and Chizmadzhev 1996; Weaver 2003; Chen et al. 2006). Information about the sequence of events describing the electroporation phenomenon can therefore be gathered from measurements of electrical currents through planar lipid bilayers along with characterization of molecular transport of molecules into (or out of) cells subjected to electric field pulses. It may be summarized as follows: the application of electrical pulses induces rearrangements of the membrane components (water and lipids) that ultimately lead to the formation of aqueous hydrophilic pores (Abidor et al. 1979; Benz et al. 1979; Weaver and Chizmadzhev 1996; Weaver 2003; Chen et al. 2006; Pucihar et al. 2006),

whose presence increases substantially the ionic and molecular transport through the otherwise impermeable membranes (Pucihar et al. 2008).

The key features of electroporation are based on theories involving stochastic pore formation (Chen et al. 2006). In erythrocyte membranes, large pores could be observed using electron microscopy (Chang 1992); but in general, direct observation of the formation of nano-sized pores is not possible with conventional techniques. Furthermore, due to the complexity and heterogeneity of cell membranes, it is difficult to describe and characterize their electroporation in terms of atomically resolved processes. Atomistic simulations in general, and molecular dynamics (MD) simulations in particular, have proven to be effective for providing insights into both the structure and the dynamics of model lipid membrane systems in general (Tieleman et al. 1997; Tobias et al. 1997; Forrest and Sansom 2000; Feller 2000, 2008; Tobias 2001; Mashl et al. 2001; Saiz and Klein 2002a; Anézo et al. 2003; Berkowitz et al. 2006; Lindahl and Sansom 2008; Edholm 2008; Marrink et al. 2009).

Recent studies have shown that the method is suitable for investigating electroporation phenomena. Several MD simulations have recently been conducted in order to model the effect of electric field on membranes (Hu et al. 2005; Tieleman 2004; Tarek 2005; Bockmann et al. 2008; Ziegler and Vernier 2008), providing perhaps the most complete molecular model of the electroporation process of lipid bilayers. This article reviews the progress made so far using such atomistic simulations to model lipid bilayer electroporation.

The effects of an electric field on a cell may be described considering the latter as a dielectric layer (cell surface membrane) embedded in conductive media (internal, cytoplasm; external, extracellular media). When relatively low-field pulses of microsecond or millisecond duration are applied to this cell (by placing, for instance, the cell between two electrodes and applying a constant voltage pulse), the resulting current causes accumulation of electrical charges at both sides of the cell membrane. The time required to charge the surface membrane is dependent upon the electrical parameters of the medium in which it is suspended. For a spherical cell it is estimated using equivalent network RC circuits in the 100-ns time scale (Hu et al. 2005; Beebe and Schoenbach 2005; Vasilkoski et al. 2006; Sundararajan 2009; Deng et al. 2003). A charging time constant in the range of hundreds of nanoseconds was also obtained from derivations based on the Laplace equation (see, e.g., Pauly and Schwan 1959 for the first-order analysis on a spherical vesicle; Kotnik et al. 1998 for the second-order analysis; and Kotnik and Miklavcic 2006 for the second-order analysis for two concentric spherical vesicles, i.e., modeling an organelle).

If, on the other hand, the pulse duration is short enough relative to the charging time constant of the resistive-capacitive network formed by the conductive intracellular and extracellular fluids and the cell membrane dielectric, which is the case for nanosecond pulses, the electric field acts directly and mainly on the cell membrane.

Simulations allow one to perform in silico experiments under both conditions, i.e., submitting the system either to nanosecond, megavolt-per-meter pulsed electric fields or to charge imbalance, mimicking therefore the application of low-voltage, long-duration pulses. Here, we describe the results of such simulations, after a brief general introduction to MD simulations of membranes.

Materials and Methods

MD Simulations

The MD simulation presented here was carried out using the program NAMD targeted for massively parallel architectures (Kalé et al. 1999; Bhandarkar et al. 2002). The systems were examined in the NPT (1 atm and 300 K) or NVT (300 K) ensembles employing Langevin dynamics and the Langevin piston method. The equations of motion were integrated using the multiple time-step algorithm. A time step of 2.0 fs was employed. Short- and long-range forces were calculated every two and four time steps, respectively. Chemical bonds between hydrogen and heavy atoms were constrained to their equilibrium value. Long-range, electrostatic forces were taken into account using a fast implementation of the particle mesh Ewald (PME) approach (Darden et al. 1993; Essmann et al. 1995), with a direct space sum tolerance of 10^{-6} and a spherical truncation of 11 Å.

Bond stretching, valence angle deformation, torsional and nonbonded parameters and nonbonded interaction were all extracted from the all-atom CHARMM force field (MacKerell et al. 1998). For the lipid palmitoyl-oleyl-phosphatidylcholine (POPC) we used the united atom representation for the acyl chains.

Electrostatic Properties

The electrostatic potential, $\phi(z)$, along the lipid bilayer normal, z, was derived from MD simulations using Poisson's equation and expressed as the double integral of $\rho(z)$, the molecular charge density distributions:

$$\phi(z) = \phi(z) - \phi_0 = \frac{-1}{\varepsilon_0} \int_0^Z \int \rho(z'') \mathrm{d}z'' \mathrm{d}z' \qquad (1)$$

As a reference, ϕ_0 is set to zero in the upper bulk. Finally, the transmembrane (TM) voltage was calculated as the difference between the electrostatic potentials measured at the upper and lower baths.

The electric field profiles deriving from the charge distribution, called here "local electric fields," were obtained from the electrostatic profiles using $\partial\phi(z)/\partial z$.

Three-dimensional (3D) maps of the electrostatic potential characterizing the systems were generated by solving numerically the Poisson equation. This calculation was performed employing the PMEPot module of the visualization program VMD (Humphrey et al. 1996). Instantaneous values of the electrostatic potential were averaged over 100-ps segments. The first derivative of the electrostatic potential was evaluated using OpenDX (http://www.opendx.org), an open–source visualization software package, to yield the 3D maps of the electric field. The electric properties of the bilayers described in this contribution were visualized with OpenDX and the CMSP Chemistry module (Gillilan and Wood 1995).

Modeling Membrane Electroporation

"Molecular dynamics" refers to a family of computational methods aimed at simulating macroscopic behavior through the numerical integration of the classical equations of motion of a microscopic, many-body system. Macroscopic properties are expressed as functions of particle coordinates and/or momenta, which are computed along a phase space trajectory generated by classical dynamics (Allen and Tildesley 1987; Leach 2001) When performed under conditions corresponding to laboratory scenarios, MD simulations can provide a detailed view of the structure and dynamics of a macromolecular system. They can also be used to perform "computer experiments" that cannot be carried out in the laboratory, either because they do not represent a physical behavior or because the necessary controls cannot be achieved. Simulations are usually performed on a small number of molecules (few tens to few hundred thousand atoms), the system size being limited, of course, by the speed of execution of the programs and the availability of computer power. In order to eliminate edge effects and to mimic a macroscopic system, simulations of condensed phase systems consider a small patch of molecules confined in a central simulation cell and replicate the latter using periodic boundary conditions (PBCs) in the three directions of Cartesian space. For membranes, for instance, the simulated system would correspond to a small fragment of either a black film, a liposome or multilamellar oriented lipid stacks deposited on a substrate (Lindahl and Edholm 2000; Marrink and Mark 2001).

Traditionally, phospholipids have served as models for investigating in silico the structural and dynamic properties of membranes. From both a theoretical and an experimental perspective, zwitterionic phosphatidylcholine (PC) lipid bilayers constitute the best-characterized systems (Chiu et al. 1999; Rög et al. 2002; Saiz and Klein 2001; Feller et al. 2002) (Fig. 1). More recent studies have considered a variety of alternative lipids, featuring different, possibly charged, headgroups (Berkowitz and Raghavan 1991; Damodaran and Merz 1994; Cascales et al. 1996; Mukhopadhyay et al. 2004; Chiu et al. 2003) and more recently mixed bilayer compositions (Pandit et al. 2003; Patel and Balaji 2008; Dahlberg and Maliniak 2008; Gurtovenko and Vattulainen 2008; Vacha et al. 2009; Rog et al. 2009; Li et al. 2009). Despite their simplicity, bilayers built from PC lipids represent remarkable test systems to probe the computation methodology and to gain additional insight into the physical properties of

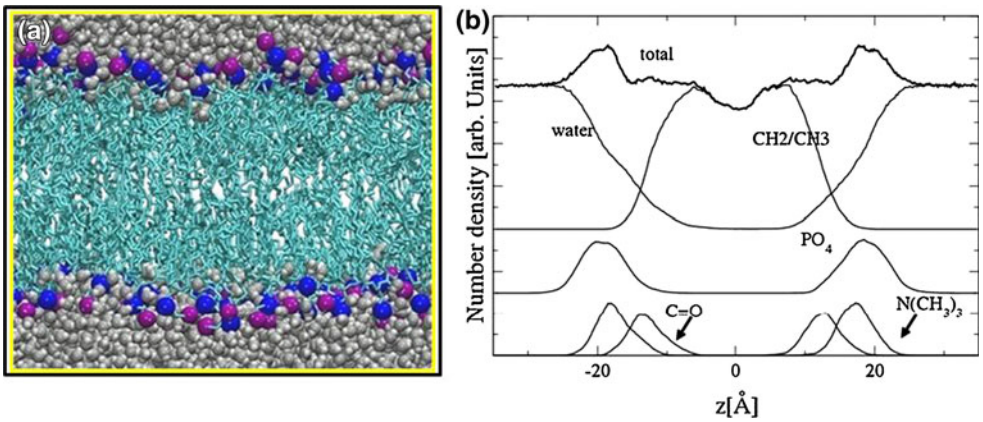

Fig. 1 **a** Configuration of a palmitoyl-oleyl-phosphatidylcholine (POPC)-hydrated bilayer system from a well-equilibrated, constant-pressure MD simulation performed at 300 K. Only the molecules in the simulation cell are shown. Water molecules (O, *gray*; H, *white*) and the phosphate (*blue*) and nitrogen (*purple*) atoms of the lipid headgroups are depicted by their van der Waals radii, and the acyl chains (*cyan*) are represented as sticks. **b** Number density profiles (arbitrary units) along the bilayer normal, z, averaged over 2 ns of the MD trajectory. The total density, water and hydrocarbon chain contributions are indicated, along with those from the POPC headgroup moieties. The bilayer center is located at $z = 0$ (Color figure online)

membranes (Tobias et al. 1997; Tobias 2001; Anézo et al. 2003; Chipot et al. 2005).

Up to recently, most membrane models consisted of simulating fully hydrated, pure phospholipid bilayers, without taking into account the effect of salt concentration (see sections below). For such systems, the average structure of the lipid–water interface at the atomic scale may be provided by the density distributions of different atom types along the bilayer normal (Fig. 1), which can be measured experimentally on multilamellar stacks by neutron and X-ray diffraction techniques (Wiener and White 1992) as well as calculated from MD simulations. These distributions highlight the composition and properties of the membrane that appears as a broad hydrophilic interface, with only a thin slab of pure hydrocarbon fluid in the middle (Fig. 1). They indicate clearly the roughness of the lipid headgroup area and how water density decays smoothly from the bulk value and penetrates deeply into the bilayer at a region delimiting the membrane–water interface.

Electroporation Induced by Direct Effect of an Electric Field

In the following we describe the methods/protocols and results obtained from modeling the effect of a direct electric field on lipid membranes. In simulations, it is possible to apply "directly" a constant electric field, $\vec{E}$, perpendicular to the membrane (lipid bilayer) plane. In practice, this is done by adding a force, $\vec{F} = q_i\vec{E}$, to all the atoms bearing a charge, q_i (Zhong et al. 1998; Yang et al. 2002; Tieleman et al. 2001; Crozier et al. 2001; Roux 2008). MD simulations adopting such an approach have been used to study membrane electroporation (Hu et al. 2005; Tieleman 2004; Tarek 2005; Bockmann et al. 2008; Ziegler and Vernier 2008) and lipid externalization (Vernier et al. 2006a), to activate voltage-gated K^+ channels (Treptow et al. 2004) and to determine the transport properties of ion channels (Aksimentiev and Schulten 2005; Khalili-Araghi et al. 2006; Sotomayor et al. 2007; Chimerel et al. 2008). Quite noticeably, these protocols were initially applied in simulations of membranes to study classical electroporation. It was only later that it became possible experimentally to use nanosecond pulses. It turns out that such protocols model rather the effects of nanosecond, megavolt-per-meter pulsed electric fields that are too short to charge the membrane capacitor. For practical reasons and in order to avoid charge (ions) accumulations when the field is applied, it is recommended that this method be used when modeling lipid bilayers in the absence of salts. Indeed, in contrast to experiments, because of the small size of the systems ($\sim$10 nm in the $\vec{E}$ field direction), even nanosecond pulses can induce "notable" charge reorganization.

The consequence resulting from high electric field application to the system stems from the properties of the membrane and from the simulations setup conditions: pure lipid membranes exhibit a heterogeneous atomic distribution across the bilayer, to which are associated charges and molecular dipole distributions. Phospholipid headgroups adopt in general a preferential orientation. For hydrated PC bilayers at temperatures above the gel to liquid crystal transition, the PC dipoles point on average 30° away from the membrane normal (Tobias 2001; Saiz and Klein 2002b). The organization of the phosphate (PO_4^-), choline ($N[CH_3]_3^+$) and carbonyl (C=O) groups of the lipid headgroup hence give rise to a permanent dipole, and the solvent (water) molecules bound to the lipid headgroup moieties tend to orient their dipoles to compensate the latter (Gawrisch et al. 1992). The electrostatic characteristics of the bilayer may be gathered from estimates of the electrostatic profile, $\phi(z)$, that stems from the distribution of all the charges in the system.

For lipid bilayers, most of which are modeled without consideration of a salt concentration, an applied electric field acts specifically and primarily on the interfacial water dipoles (small polarization of bulk water molecules). The reorientation of the lipid headgroups appears not to be affected at very short time scales (Tarek 2005; Vernier and Ziegler 2007) and not to exceed a few degrees toward the field direction at a longer time scale (Bockmann et al. 2008). Hence, within a very short time scale, typically few picoseconds (Tarek 2005), a transverse field, $\vec{E}$, induces an overall TM potential, ΔV (Fig. 2). It is very important to note here that, because of the MD simulation setup (and the use of PBCs), $\vec{E}$ induces a voltage difference, $\Delta V \approx |\vec{E}|.L_Z$, over the whole system, where L_z is the size of the simulation box in the field direction. In the example shown in Fig. 2, L_z is $\sim$10 nm. The electric field (0.1 V nm^{-1}) applied to the POPC bilayer induces $\Delta V \sim$ 1 V.

MD simulations of pure lipid bilayers have shown that the application of electric fields of high enough magnitude leads to membrane electroporation, with a rather common poration sequence: the electric field favors quite rapidly (within a few hundred picoseconds) formation of water defects and water wires deep into the hydrophobic core (Tieleman 2004). Ultimately, water fingers forming at both sides of the membrane join up to form water channels (often termed "prepores" or "hydrophobic pores") that span the membrane. Within nanoseconds, a few lipid headgroups start to migrate from the membrane–water interface to the interior of the bilayer, stabilizing hydrophilic pores ($\sim$1–3 nm diameter) (Fig. 3). All MD studies have reported pore expansion as the electric field was

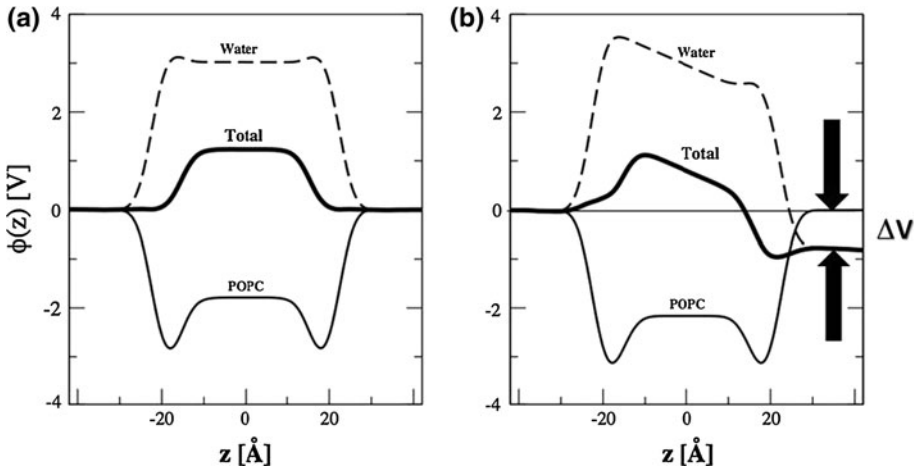

Fig. 2 Electrostatic potential profiles, $\phi(z)$, along the membrane normal, z, of a POPC lipid bilayer **a** at rest and **b** subject to a transverse electric field. Shown are the contributions from water, lipid and the total electrostatic profile. Note that the TM voltage, ΔV (potential difference between the upper and lower water baths), created under electric field (**b**) is mainly due to water dipole reorientation

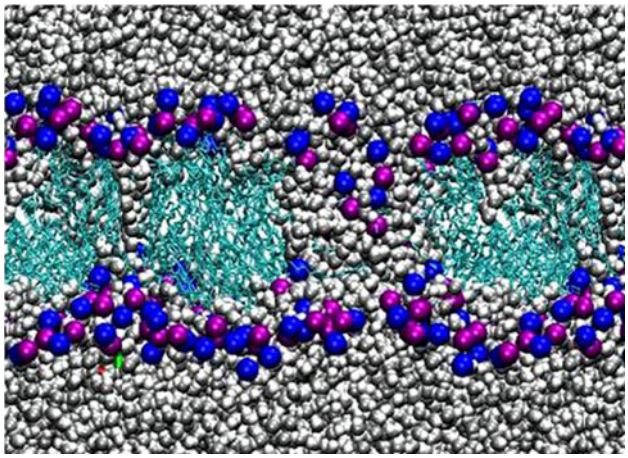

Fig. 3 Configuration taken from an MD simulation of a large POPC bilayer, subject to an electric field generating a TM potential of ~1.5 V after a 2 ns run. *Note* the simultaneous presence of water wires and of large water pores stabilized by lipid headgroups

maintained. In contrast, it was shown in one instance (Tarek 2005) that a hydrophilic pore could reseal within few nanoseconds when the applied field was switched off. Membrane complete recovery, i.e., migration of the lipid headgroups forming the hydrophilic pore toward the lipid–water interface, being a much longer process, was not observed.

For typical MD system sizes (128 lipids, 6 × 6 nm membrane cross section), most of the simulations reported a single pore formation at high field strengths. For much larger systems, multiple pore formation with diameters ranging from a few to 10 nm could be witnessed (Tieleman 2004; Tarek 2005). Such pores are in principle wide enough to transport ions and small molecules. One attempt has so far been made to investigate such a molecular transport under electroporation (Tarek 2005). In this simulation, partial transport of a 12 bp DNA strand across the membrane could be followed. The strand was considered diffused toward the interior of the bilayer when a pore was created beneath it and formed a stable DNA/lipid complex in which the lipid headgroups encapsulated the strand. The process provided support to the gene-delivery model proposed by Golzio et al. (2002), in which an "anchoring step" connecting the plasmid to permeabilized cell membranes takes place during DNA transfer assisted by electric pulses and agrees with the last findings from the same group (Paganin-Gioannia et al. 2011).

The electroporation process takes place much more rapidly under higher fields, without a major change in the pore-formation characteristics. The lowest voltages reported to electroporate a PC lipid bilayer are ~2 V (Bockmann et al. 2008; Vernier and Ziegler 2007). Ziegler and Vernier (2008) reported minimum poration external field strengths for four different PC lipids with different chain lengths and composition (number of unsaturations). The authors found a direct correlation between the minimum porating fields (ranging 0.26–0.38 V nm^{-1}) and the membrane thickness (ranging 2.92–3.92 nm). Note that estimates of electroporation thresholds from simulations should, in general, be considered only as indicative since they are related to the time scale the pore formation may take. A field strength threshold is "assumed" to be reached when no membrane rupture is formed within the 100 ns time scale.

Electroporation Induced by Ionic Salt Concentration Gradients

In this section, we describe the methods/protocols and results obtained from modeling the effect of a charge imbalance. Such protocols aim at mimicking the effects of low-field pulses of microsecond or millisecond duration that result in an accumulation of electrical charges at the cell membrane. Indeed, regardless of how low-intensity millisecond electrical pulses are applied, the ultimate step

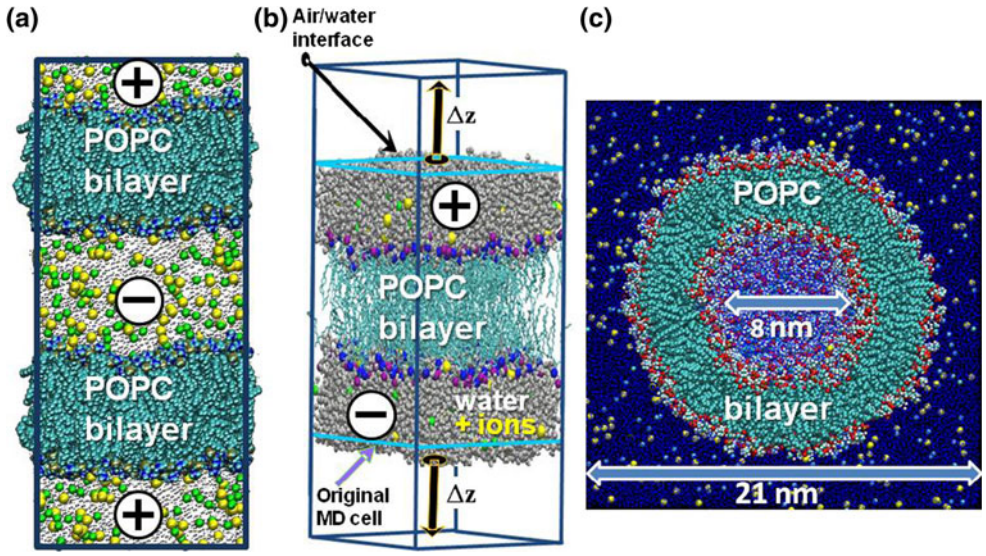

Fig. 4 MD simulation setups of three systems using the charge imbalance method. **a** The double bilayer setup: two lipid bilayers are separated by electrolyte baths at 1 M NaCl salt concentration. Note that due to the use of PBCs (*drawn box*) the upper and lower electrolytes are in contact. Q is imposed between the central water bath and the two others. **b** The single bilayer setup: here, one single bilayer is surrounded by water baths (maintained at 1 M NaCl). The original MD cell represented the classical setup and the large cell that allows for the creation of water–air interfaces. Q is imposed between the lower and upper baths. **c** The liposome setup: a small, spherical liposome is embedded in a 1 M NaCl electrolyte. Q is imposed between the inner and outer water baths and 3D PBCs (*drawn box*) are used

is the charging of the membrane due to ion flow. Note that here the "charging" of the membrane is not modeled. Rather, the simulations are initiated by assuming that the charging has already taken place, i.e., with a system already set at a specific (selected) charge imbalance. Evidently, in contrast to the previous protocol, here the bilayers need to be modeled at a given salt concentration. In a classical setup of membrane simulations and due to the use of 3D PBCs, the TM voltage cannot be controlled by imposing a charge imbalance across the bilayer, even when ions are present in the electrolytes. Several MD simulation protocols that can overcome this limitation have been recently devised (Fig. 4).

The Double Bilayer Setup

It was indeed shown that TM potential gradients can be generated by a charge imbalance across lipid bilayers by considering an MD unit cell consisting of three saltwater baths separated by two bilayers and 3D PBCs (Sachs et al. 2004) (Fig. 4a). Setting up a net charge imbalance, Q, between the two independent water baths at time $t = 0$ induces a TM voltage ΔV by explicit ion dynamics.

The Single Bilayer Setup

Delemotte et al. (2008) introduced a variant of this method where the double layer is not needed, avoiding therefore the overcost of simulating a large system. The method consists in considering a unique bilayer surrounded by electrolyte baths, each of them terminated by an air–water interface (Bostick and Berkowitz 2003). The system is set up as indicated in Fig. 4b. First, a hydrated bilayer is equilibrated at a given salt concentration using 3D PBCs. Air–water interfaces are then created on both sides of the membrane, and further equilibration is undertaken at constant volume, maintaining therefore a separation between the upper and lower electrolytes. A charge imbalance, Q, between the two sides of the bilayer is generated by simply displacing at time $t = 0$ an adequate number of ions from one side to the other. As far as the water slabs are thicker than 25–30 Å, the presence of air–water interfaces has no influence on the lipid bilayer properties and the membrane "feels" as if it is embedded in infinite baths whose characteristics are those of the modeled finite solutions. This method was recently successfully applied to study transport in ion channels (Delemotte et al. 2010, 2011; Treptow et al. 2009).

Extension to Liposomes

The availability of large computer resources has extended the realm of simulations of membrane electroporation to study systems large enough to allow modeling of small liposomes. Figure 4c represents such a liposome constructed from a POPC bilayer and equilibrated in a

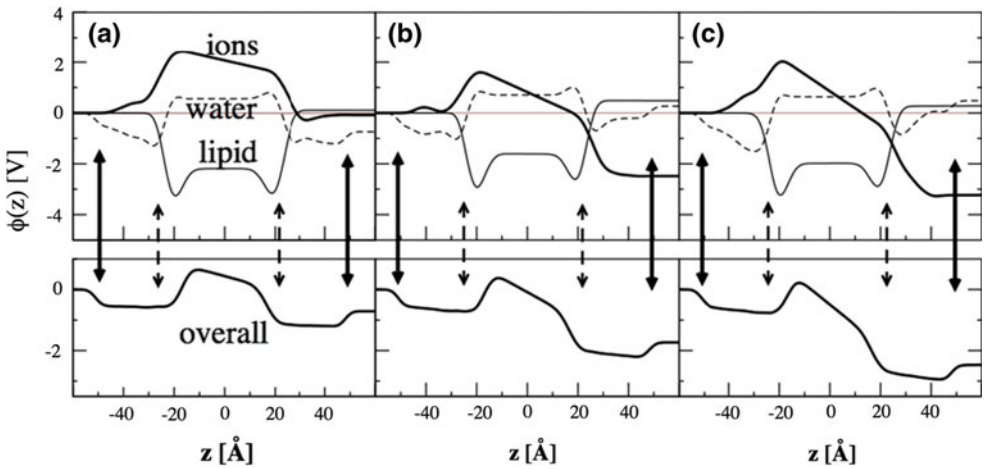

Fig. 5 Components of the electrostatic potential profiles, $\phi(z)$, along the lipid bilayer normal, z, of a POPC membrane estimated from the initial stage of MD simulations of the system at 1 M NaCl salt concentration using the single bilayer method. $z = 0$ represents here the center of the lipid bilayer, *broken arrow* indicates the location of the bilayer–water interfaces and *solid arrows* show the locations of the air–water interfaces. From **a** to **c** increasing amounts of net charge imbalance Q between the lower and upper electrolytes induce TM voltages (that may be estimated from the difference between the electrostatic potentials of the two water baths) of increasing amplitudes. Shown in the *top panels* are the contributions from lipid, water and ions and in the *lower panels* the total electrostatic potential. Note that the most of the TM voltage is due to the contribution from ions

200 mM NaCl salt solution. The system contains over 1,400 lipid molecules, forming a liposome of internal diameter of 8 nm. The system size ($210 \times 210 \times 210$ Å^3) was chosen to be large enough to avoid interaction between the central liposome and its replica, resulting in an overall number of $\sim$890,000 atoms. In such a setup a charge imbalance, Q, was imposed after the system equilibration between the inner and outer sides of the liposome.

Figure 5 reports the electrostatic potential profiles along the normal to the membrane generated from MD simulations of a POPC bilayer in contact with 1 M NaCl saltwater baths set at three increasing charge imbalances, Q, using the single bilayer method. Here, the electrostatic profiles are computed by considering also the charges of ions present in the system. For all simulations, the profiles computed at the initial stage show plateau values in the aqueous regions and, for increasing Q, an increasing potential difference ΔV between the two electrolytes indicative of a TM potential.

Quite interestingly, the profiles show clearly that, in contrast to the electric field case where the TM voltage is mainly due to the water dipole reorientation (Fig. 2), most of the voltage drop in the charge imbalance method is due to a contribution from the ions. Indeed, the sole collapse of the electrostatic potential due to the charge imbalance separation by the membrane lipid core accounts for the largest part of ΔV.

Using the charge imbalance setup, it was possible for the first time to directly demonstrate in silico that the simulated lipid bilayer behaves as a capacitor (Delemotte et al. 2008) (Fig. 6). Simulations at various charge imbalances, Q, show a linear variation of ΔV from which the capacitance can be estimated as $C = Q_s.\Delta V^{-1}$, where Q_s is the charge imbalance per unit area. The capacitance values extracted from simulations are expected to depend on the lipid composition (charged or not) and on the force-field parameters used and as such constitutes a supplementary way of checking the accuracy of lipid force-field parameters used in the simulation. Here, in the case of POPC bilayers embedded in a 1 M solution of NaCl (Delemotte et al. 2008), the capacitance, C, amounts to 0.85 μF cm^{-2}, which is in reasonable agreement with the value usually assumed in the literature, e.g., 1.0 μF cm^{-2} (Roux 1997; Sachs et al. 2004) and with recent measurements for planar POPC lipid bilayers in a 100 mM KCl solution (0.5 μF cm^{-2}).

For large enough induced TM voltages, the three protocols lead to electroporation of the lipid bilayer. As in the case of the electric field method, for ΔV above 1.5–2.5 volts, the electroporation process starts with the formation of water fingers that protrude inside the hydrophobic core of the membrane. Within nanoseconds, water wires bridging the two sides of the membrane under voltage stress appear. If the simulations are further expended, lipid headgroups migrate along one wire and form a hydrophilic connected pathway (Fig. 7).

Because salt solutions are explicitly considered in these simulations, ion conduction through the hydrophilic pores occurred following electroporation of the lipid bilayers. Details about the ionic transport through the pores formed within the bilayer core upon electroporation could be gathered (Gurtovenko et al. 2010). The MD simulations of the double bilayer system (Gurtovenko and Vattulainen

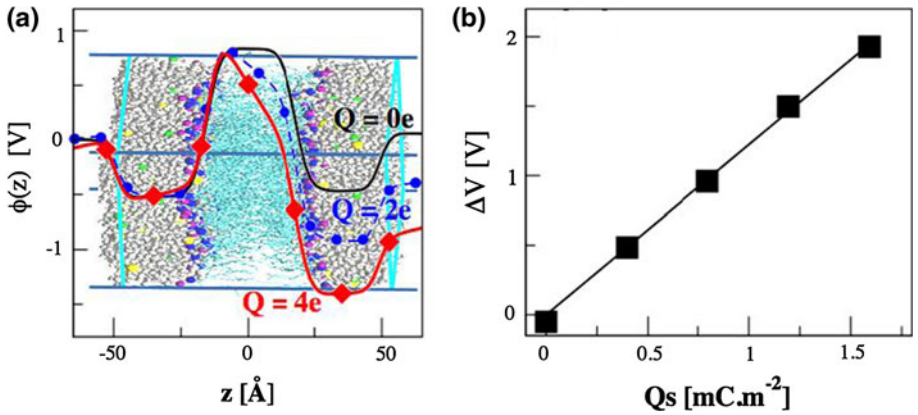

Fig. 6 **a** Electrostatic potential, $\phi(z)$, across a POPC lipid bilayer for different net charge imbalances, Q, between the upper and lower electrolytes from MD simulations considering the setup of Fig. 5. $\phi(z)$ is estimated as an in-plane average of the EP distributions (Eq. 1). As a reference it was set to zero in the lower electrolyte. **b** TM potential, ΔV, as a function of the charge imbalance, Q_s, per unit area. The capacitance (C) of the bilayer can be derived from the slope of the curve

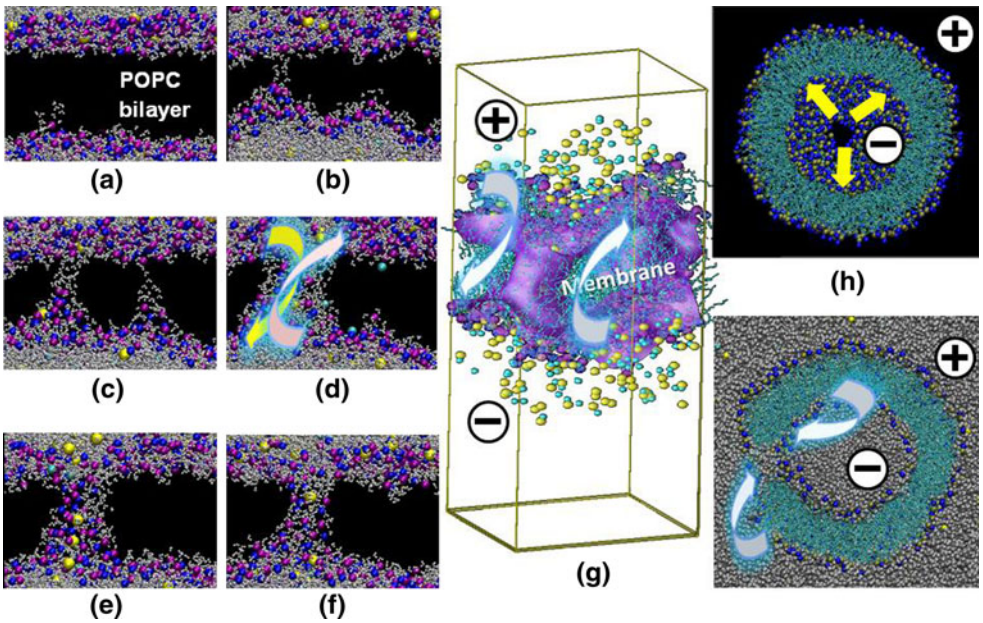

Fig. 7 Sequence of events following the application of a TM voltage to a POPC lipid bilayer using the charge imbalance method (**a–f**). Note the migration of Na^+ (*yellow*) and Cl^- (*cyan*) ions through the formed hydrophilic pores that are lined with lipid phosphate (*magenta*) and nitrogen (*blue*) headgroup atoms. **f** The state of a nonconducting pore reached when the exchange of ions between the two baths lowered Q and therefore ΔV to values $\approx$200 mV is shown. Topology of the nanometer-wide hydrophilic pores formed under high ΔV imposed by the charge imbalance method in the planar bilayer (**g**) and in the liposome (**h**). *Blue arrows* highlight the subsequent ionic flow through the pores, and the *yellow one* indicates the expansion of the pore as ΔV is maintained (Color figure online)

2005; Kandasamy and Larson 2006), and the results presented here for the single bilayer setup and for the liposome (Fig. 7) show that both cations and anions exchange through the pores between the two baths, with an overall flux of charges directed toward a decrease of the charge imbalance. Ion translocation through the pores from one bulk region to the other lasts from a few tens to a few hundreds of picoseconds and leads to a decrease of the charge imbalance and, hence, to the collapse of ΔV. Hence, for all systems, when the charge imbalance reached a level where the TM voltage was down to a couple of hundred millivolts, the pores "closed" or "collapsed" in the sense that no more ionic translocation occurred (Fig. 7f). The final topology of the pores toward the end of the simulations remained stable for time spans exceeding the 10-ns scale, showing as reported in previous simulations (Tarek 2005) that complete recovery of the original bilayer structure requires a much longer time scale.

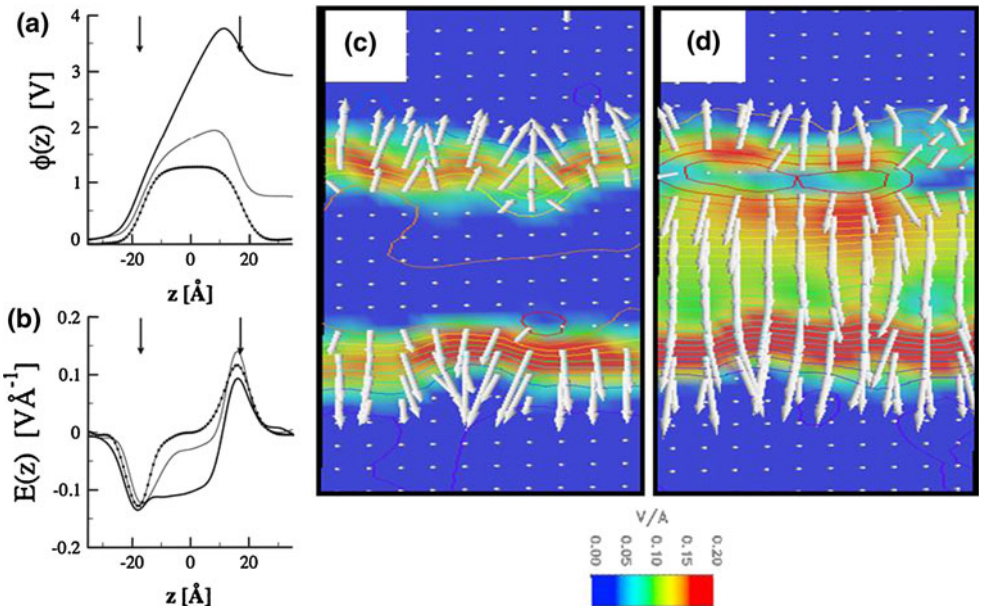

Fig. 8 **a** Electrostatic potential profiles, $\phi(z)$, across a lipid bilayer subject to electric fields of 0.0 $V\text{Å}^{-1}$ (*dotted line*), 0.6 $V\text{Å}^{-1}$ (*thin line*) and 3.0 $V\text{Å}^{-1}$ (*bold line*). *Black arrows* point to the location of the lipid headgroups–water interface. **b** Corresponding electric field profiles derived as $\partial\phi(z)/\partial z$. **c** Two-dimensional (*out of plane*) map of the electric field distribution at 0.0 $V\text{Å}^{-1}$. The local electric field direction and strength are displayed as *white arrows*. Note that the larger fields are located at the lipid–water interfaces and oriented toward the solvent. **d** Two-dimensional (out of plane) map of the electric field distribution at 3.0 $V\text{Å}^{-1}$. *Note* the large fields located in the lipid core

Note that in order to maintain ΔV constant the modeler needs to maintain the initial charge imbalance by "injecting" charges (ions) in the electrolytes at a pace equivalent to the rate of ion translocation through the hydrophilic pore. This protocol is, particularly for the single bilayer setup, adequate for performing simulations under constant voltage (low voltage, millisecond duration) or constant current conditions, which is suitable for comparison to experiments undertaken under similar conditions (Kutzner et al. 2011).

Discussion

MD simulations of lipid bilayers subject to high enough TM voltages, regardless of how the latter are generated, i.e., either by a direct electric field effect or by charging of the membranes, undergo a similar cascade of events: within a very short (nanosecond) time scale a defect in the membrane manifested by the protrusion of water fingers from the lipid headgroups/solvent forms in the lipid core. When the TM voltage is maintained, these fingers span the entire hydrophobic core, forming hydrophilic pores that are later stabilized by lipid headgroups. The time scales associated with each of these processes appear to be similar in both protocols. Finally, when the pulses are switched off, the pores collapse (close) within the same time scales. Accordingly, the MD simulations show clearly that, at the membrane level, the effects of nanosecond, megavolt-per-meter pulsed electric fields and of low-voltage, millisecond pulses are very similar. In the following we further investigate the molecular reasons leading to such similarities.

In order to determine the detailed mechanism of the pore creation, it is helpful to probe the electric field distribution across the bilayer, both at rest and under the effect of a TM voltage. Figure 8a displays the electrostatic potential profiles for a lipid bilayer subject to increasing electric fields that generate TM potentials ranging from 0 to $\sim$3 V. At 0 V, the lipid bilayer is at rest and the profiles reveal, in agreement with experiments (Liberman and Topaly 1969), the existence of a positive potential difference between the membrane interior and the adjacent aqueous phases.

At rest, the voltage change across the lipid–water interfaces, the so-called dipole potential (Fig. 1), gives rise locally to large electric fields. The latter, estimated simply as $\partial\phi(z)/\partial z$ (in the present case up to 1.5 V nm^{-1}), is oriented toward the bulk, while at the center of the bilayer the local electric field is null (Fig. 8b, c). When external electric fields of magnitudes, respectively, of 0.06 and 0.30 V nm^{-1} are applied, reorientation of the water molecules gives rise to TM potentials of $\sim$0.75 and 3 V. Figure 8b, c reveals the incidence of such reorganization on the local electric field both at the interfacial region and within the bilayer core. In particular one notes that the field in the membrane core has

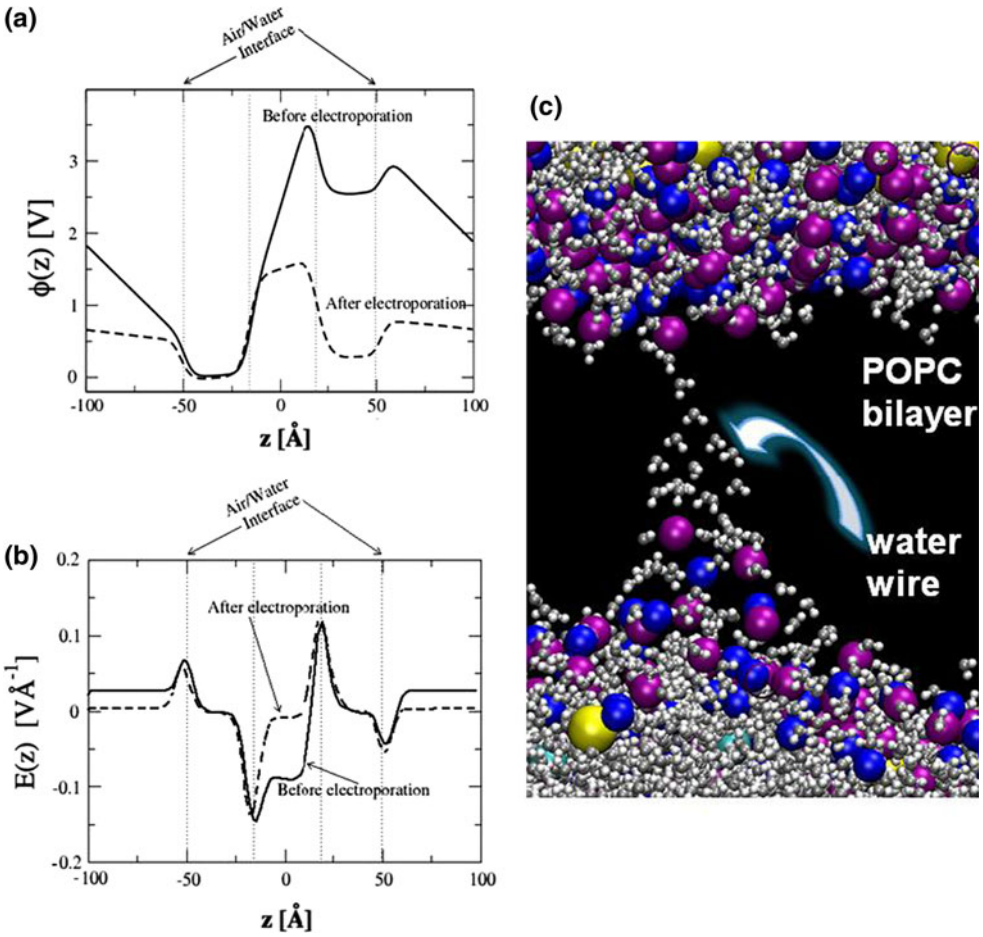

Fig. 9 **a** Electrostatic potential profiles, $\phi(z)$, across a POPC lipid membrane subject to a charge imbalance (single bilayer setup) before (*solid line*) and after (*broken line*) electroporation. **b** Corresponding electric field profiles. **c** Snapshot taken from the MD simulation of the lipid bilayer subject to a TM voltage taken at the early stage of the pore formation showing the configuration of water molecules represented as balls and sticks (oxygen, *gray*) and (hydrogen, *white*) forming a continuous wire through the hydrophobic core of the membrane

risen to a value of ~ 1 V nm^{-1} for the highest ΔV imposed. For the charge imbalance method, the overall picture is similar (Fig. 9a, b), where again the TM voltages created give rise to large electric fields within the membrane core, oriented perpendicular to the bilayer.

Qualitatively, the electric field method and the charge imbalance method result in a similar cascade of events that take place at the membrane, which is a direct consequence of such a field distribution. Indeed, water molecules, initially restrained to the interfacial region as they randomly percolate down within the membrane core, are subject to a high electric field and therefore inclined to orient their dipole along this local field. These molecules can easily hydrogen-bond among themselves, which results in the creation of water files. Such fingers protrude through the hydrophobic core from both sides of the membrane. Finally, these fingers meet up to form water channels (often termed "prepores" or "hydrophobic pores") that span the membrane (Fig. 9c). As the TM voltage is maintained, these water wires appear to be able to overcome the free energy barrier associated with the formation of a water molecule file that spans the bilayer (estimated to be ~ 108 kJ/mol in the absence of external electric field (Marrink et al. 1996). As the electrical stress is maintained, lipid headgroups migrate along the stable water wires and participate in the formation of larger "hydrophilic pores," able to conduct ions and larger molecules as they expand. Evidently, reorientation of the lipids depends not only on the net charges their headgroup carries, as has been shown for negatively charged phosphatidylserines that can move from one leaflet of the bilayer to the other, but also on the nature of the tails (Vernier et al. 2009).

Conclusion

Currently, computational approaches remain potentially the only techniques able to follow, at the atomic scale, the local perturbation lipid membranes undergo when they are subjected to external electric field. The results obtained so far are believed to capture the essence of several aspects of the electroporation phenomena in bilayer membranes and could serve as an additional, complementary source of information to the current arsenal of experimental tools. At rest, i.e., before membrane breakdown, many characteristics of the bilayer (e.g., hydrophobic core thickness, area

per lipid, intrinsic dipole potential, capacitance) are in satisfactory agreement with experiments which indicate that the force fields and protocols used in MD simulations of lipid bilayers are rather well optimized. Despite their intrinsic differences, all MD simulations of lipid bilayers subjected to high enough TM voltages, regardless of how the latter are generated, provide support to the stochastic pore-formation theories in which the stress imposed on the membrane is released thanks to formation of nanometer-scale hydrophilic pores that span the lipid core. Quite interestingly, it was shown that pore time formation is similar for the electric field method and the charge imbalance method (Vernier et al. 2006b). Hence, MD simulations show clearly that at the membrane level the effects of nanosecond, megavolt-per-meter pulsed electric fields and of low-voltage, millisecond pulses are very similar.

There are several points that need further investigation. Perhaps the most important one is the interplay between pore densities (number of hydrophilic pores per unit area that can form) and transport rate that can be maintained at a given imposed voltage or current condition. Simulations have shown (Tarek 2005), as predicted (Lewis 2003), that upon pore creation the electric field induces a significant lateral stress, of the order of 1 mN m^{-1}. It is unclear how the induced lateral tension relaxes in a macroscopic system when a voltage pulse is applied, which may have an incidence on the density of pores that could nucleate. Regardless of the topology of the bilayer, i.e., in planar lipid membranes or in a liposome, one expects a strong correlation between the size of the defect created, the density of pores and the maintained electrical stress. Simulations of very large systems or those of liposomes should in principle help us to characterize better such a correlation.

It is undeniable that much more effort is still needed in order to determine the cascade of events involved in more complex events such as the transport of large molecules across the membranes.

Acknowledgments The research was conducted in the scope of the EBAM European Associated Laboratory (LEA). Simulations were performed using HPC resources from GENCI-CINES (grant 2010-2011 075137). M. T. acknowledges the support of the French Agence Nationale de la Recherche (grant ANR-10_BLAN-916-03-INTCELL).

References

Abidor IG, Arakelyan VB, Chernomordink LV, Chizmadzhev YA, Pastushenko VF, Tarasevich MR (1979) Electrical breakdown of BLM: main experimental facts and their qualitative discussion. Bioelectrochem Bioenerg 6:37–52

Aksimentiev A, Schulten K (2005) Imaging α-hemolysin with molecular dynamics: ionic conductance, osmotic permeability, and the electrostatic potential map. Biophys J 88:3745–3761

Allen MP, Tildesley DJ (1987) Computer simulation of liquids. Clarendon Press, Oxford

Anézo C, Vries AHd, Höltje HD, Tieleman DP, Marrink SJ (2003) Methodological issues in lipid bilayer simulations. J Phys Chem B 107:9424–9433

Beebe SJ, Schoenbach KH (2005) Nanosecond pulsed electric fields: a new stimulus to activate intracellular signaling. J Biomed Biotechnol 4:297–300

Benz R, Beckers F, Zimmerman U (1979) Reversible electrical breakdown of lipid bilayer membranes—a charge-pulse relaxation study. J Membr Biol 48:181–204

Berkowitz ML, Raghavan MJ (1991) Computer simulation of a water/membrane interface. Langmuir 7:1042–1044

Berkowitz ML, Bostick DL, Pandit S (2006) Aqueous solutions next to phospholipid membrane surfaces: insights from simulations. Chem Rev 106(4):1527–1539

Bhandarkar M, Brunner R, Chipot C, Dalke A, Dixit S, Grayson P, Gullinsrud J, Gursoy A, Humphrey W, Hurwitz D, Krawetz N, Nelson M, Phillips J, Shinozaki A, Zheng G, Zhu F (2002) NAMD version 2.4. http://wwwksuiucedu/Research/namd

Bockmann RA, de Groot BL, Kakorin S, Neumann E, Grubmuller H (2008) Kinetics, statistics, and energetics of lipid membrane electroporation studied by molecular dynamics simulations. Biophys J 95:1837–1850

Bostick D, Berkowitz ML (2003) The implementation of slab geometry for membrane-channel molecular dynamics simulations. Biophys J 85:97–107

Cascales JJL, Berendsen HJC, de la Torre JG (1996) Molecular dynamics simulation of water between two charged layers of dipalmitoylphosphatidylserine. J Phys Chem 100:8621–8627

Chang DC (1992) Structure and dynamics of electric field-induced membrane pores as revealed by rapid-freezing electron microscopy. In: Guide to electroporation and electrofusion. Academic Press, Orlando, pp 9–27

Chen C, Smye SW, Robinson MP, Evans JA (2006) Membrane electroporation theories: a review. Med Biol Eng Comput 44:5–14

Chimerel C, Movileanu L, Pezeshki S, Winterhalter M, Kleinekathofer U (2008) Transport at the nanoscale: temperature dependence of ion conductance. Eur Biophys J 38:121–125

Chipot C, Klein ML, Tarek M (2005) Modeling lipid membranes. In: Yip S (ed) Handbook of materials modeling. Springer, Dordrecht, pp 929–958

Chiu SW, Clark M, Jakobsson E, Subramaniam S, Scott HL (1999) Optimization of hydrocarbon chain interaction parameters: application to the simulation of fluid phase lipid bilayers. J Phys Chem B 103:6323–6327

Chiu SW, Vasudevan S, Jakobsson E, Mashl RJ, Scott HL (2003) Structure of sphingomyelin bilayers: a simulation study. Biophys J 85:3624–3635

Crozier PS, Henderson D, Rowley RL, Busath DD (2001) Model channel ion currents in NaCl extended simple point charge water solution with applied-field molecular dynamics. Biophys J 81:3077–3089

Dahlberg M, Maliniak A (2008) Molecular dynamics simulations of cardiolipin bilayers. J Phys Chem B 112:11655–11663

Damodaran KV, Merz KM (1994) A comparison of DMPC and DLPE-based lipid bilayers. Biophys J 66:1076–1087

Darden T, York D, Pedersen L (1993) Particle mesh ewald—an N log(N) method for Ewald sums in large systems. J Chem Phys 98:10089–10092

Delemotte L, Dehez F, Treptow W, Tarek M (2008) Modeling membranes under a transmembrane potential. J Phys Chem B 112:5547–5550

Delemotte L, Treptow W, Klein ML, Tarek M (2010) Effect of sensor domain mutations on the properties of voltage-gated ion channels: molecular dynamics studies of the potassium channel Kv1.2. Biophys J 99(9):L72–L74

Delemotte L, Tarek M, Klein ML, Amaral C, Treptow W (2011) Intermediate states of the Kv1.2 voltage sensor from atomistic molecular dynamics simulations. Proc Natl Acad Sci USA 108(15):6109–6114

Deng J, Schoenbach KH, Buescher ES, Hair PS, Fox PM, Beebe SJ (2003) The effects of intense submicrosecond electrical pulses on cells. Biophys J 84:2709–2714

Eberhard N, Sowers AE, Jordan CA (1989) Electroporation and electrofusion in cell biology. Plenum Press, New York

Edholm O (2008) Time and length scales in lipid bilayer simulations. In: Feller SE (ed) Computational modeling of membrane bilayers, vol 60. Current topics in membranes. Elsevier, London, pp 91–110

Essmann U, Perera L, Berkowitz ML, Darden T, Pedersen LG (1995) A smooth particle mesh Ewald method. J Chem Phys 103: 8577–8593

Feller SE (2000) Molecular dynamics simulations of lipid bilayers. Curr Opin Colloid Interface Sci 5:217–223

Feller SE (2008) Computational modeling of membrane bilayers, vol 60. current topics in membranes. Elsevier, London

Feller SE, Gawrisch K, MacKerell AD (2002) Polyunsaturated fatty acids in lipid bilayers: intrinsic and environmental contributions to their unique physical properties. J Am Chem Soc 124:318–326

Forrest LR, Sansom MSP (2000) Membrane simulations: bigger and better. Curr Opin Struct Biol 10:174–181

Gawrisch K, Ruston D, Zimmerberg J, Parsegian V, Rand R, Fuller N (1992) Membrane dipole potentials, hydration forces, and the ordering of water at membrane surfaces. Biophys J 61:1213–1223

Gennis RB (1989) Biomembranes: molecular structure and function. Springer, Heidelberg

Gillilan RE, Wood F (1995) Visualization, virtual reality, and animation within the data flow model of computing. Comput Graph 29:55–58

Golzio M, Teissie J, Rols M-P (2002) Direct visualization at the single-cell level of electrically mediated gene delivery. Proc Natl Acad Sci USA 99:1292–1297

Gurtovenko AA, Vattulainen I (2005) Pore formation coupled to ion transport through lipid membranes as induced by transmembrane ionic charge imbalance: atomistic molecular dynamics study. J Am Chem Soc 127:17570–17571

Gurtovenko AA, Vattulainen I (2008) Effect of NaCl and KCl on phosphatidylcholine and phosphatidylethanolamine lipid membranes: insight from atomic-scale simulations for understanding salt-induced effects in the plasma membrane. J Phys Chem B 112:1953–1962

Gurtovenko AA, Jamshed Anwar J, Vattulainen I (2010) Defect-mediated trafficking across cell membranes: insights from in silico modeling. Chem Rev 110:6077–6103

Hu Q, Viswanadham S, Joshi RP, Schoenbach KH, Beebe SJ, Blackmore PF (2005) Simulations of transient membrane behavior in cells subjected to a high-intensity ultrashort electric pulse. Phys Rev E 71:031914

Humphrey W, Dalke A, Schulten K (1996) VMD—visual molecular dynamics. J Mol Graph 14:33–38

Kalé L, Skeel R, Bhandarkar M, Brunner R, Gursoy A, Krawetz N, Phillips J, Shinozaki A, Varadarajan K, Schulten K (1999) Namd2: greater scalability for parallel molecular dynamics. J Comp Phys 151:283–312

Kandasamy SK, Larson RG (2006) Cation and anion transport through hydrophilic pores in lipid bilayers. J Chem Phys 125:074901

Khalili-Araghi F, Tajkhorshid E, Schulten K (2006) Dynamics of K^+ ion conduction through Kv1.2. Biophys J 91:L72–L74

Kotnik T, Miklavcic D (2006) Theoretical evaluation of voltage inducement on internal membranes of biological cells exposed to electric fields. Biophys J 90(2):480–491

Kotnik T, Miklavcic D, Slivnik T (1998) Time course of transmembrane voltage induced by time-varying electric fields—a method for theoretical analysis and its application. Bioelectrochem Bioenerg 45(1):3–16

Kutzner C, Grubmüller H, de Groot BL, Zachariae U (2011) Computational electrophysiology: the molecular dynamics of ion channel permeation and selectivity in atomistic detail. Biophys J 101:809–817

Leach AR (2001) Molecular modelling: principles and applications, 2nd edn. Prentice Hall, Englewood Cliffs

Lewis TJ (2003) A model for bilayer membrane electroporation based on resultant electromechanical stress. IEEE Trans Dielectr Electr Insul 10:769–777

Li S (2008) Electroporation protocols: preclinical and clinical gene medicine, vol 423. Methods in molecular biology. Humana Press, Totowa

Li Z, Venable RM, Rogers LA, Murray D, Pastor RW (2009) Molecular dynamics simulations of PIP2 and PIP3 in lipid bilayers: determination of ring orientation, and the effects of surface roughness on a Poisson-Boltzmann description. Biophys J 97:155–163

Liberman YA, Topaly VP (1969) Permeability of biomolecular phospholipid membranes for fat-soluble ions. Biophysics USSR 14:477

Lindahl E, Edholm O (2000) Mesoscopic undulations and thickness fluctuations in lipid bilayers from molecular dynamics simulations. Biophys J 79:426–433

Lindahl E, Sansom MSP (2008) Membrane proteins: molecular dynamics simulations. Curr Opin Struct Biol 18:425–431

MacKerell AD Jr, Bashford D, Bellott M, Dunbrack RL Jr, Evanseck J, Field MJ, Fischer S, Gao J, Guo H, Ha S, Joseph-McCarthy D, Kuchnir L, Kuczera K, Lau FTK, Mattos C, Michnick S, Ngo T, Nguyen DT, Prodhom B, Reiher WE III, Roux B, Schlenkrich M, Smith JC, Stote R, Straub J, Watanabe M, Wiorkiewicz-Kuczera J, Yin D, Karplus M (1998) All-atom empirical potential for molecular modeling and dynamics studies of proteins. J Phys Chem B 102:3586–3616

Marrink SJ, Mark AE (2001) Effect of undulations on surface tension in simulated bilayers. J Phys Chem B 105:6122–6127

Marrink SJ, Jähniga F, Berendsen HJ (1996) Proton transport across transient single-file water pores in a lipid membrane studied by molecular dynamics simulations. Biophys J 71:632–647

Marrink SJ, de Vries AH, Tieleman DP (2009) Lipids on the move: simulations of membrane pores, domains, stalks and curves. Biochim Biophys Acta Biomembr 1788:149–168

Mashl RJ, Scott HL, Subramaniam S, Jakobsson E (2001) Molecular simulation of dioleylphosphatidylcholine bilayers at differing levels of hydration. Biophys J 81:3005–3015

Mukhopadhyay P, Monticelli L, Tieleman DP (2004) Molecular dynamics simulation of a palmitoyl-oleoyl phosphatidylserine bilayer with Na^+ counterions and NaCl. Biophys J 86:1601–1609

Nickoloff JA (1995) Animal cell electroporation and electrofusion protocols, vol 48. Methods in molecular biology. Humana Press, Totowa

Paganin-Gioannia A, Bellarda E, Escoffrea JM, Rols MP, Teissié J, Golzio M (2011) Direct visualization at the single-cell level of siRNA electrotransfer into cancer cells. Proc Natl Acad Sci USA 108:10443–10447

Pandit SA, Bostick D, Berkowitz ML (2003) Mixed bilayer containing dipalmitoylphosphatidylcholine and dipalmitoylphosphatidylserine: lipid complexation, ion binding, and electrostatics. Biophys J 85:3120–3131

Patel RY, Balaji PV (2008) Characterization of symmetric and asymmetric lipid bilayers composed of varying concentrations of ganglioside GM_1 and DPPC. J Phys Chem B 112:3346–3356

Pauly H, Schwan HP (1959) Uber die Impedanz Einer Suspension von Kugelformigen Teilchen mit Einer Schale—Ein Modell fur das Dielektrische Verhalten von Zellsuspensionen und von Proteinlosungen. Z Naturforsch B 14(2):125–131

Pucihar G, Kotnik T, Valic B, Miklavcic D (2006) Numerical determination of transmembrane voltage induced on irregularly shaped cells. Ann Biomed Eng 34:642–652

Pucihar G, Kotnik T, Miklavcic D, Teissié J (2008) Kinetics of transmembrane transport of small molecules into electropermeabilized cells. Biophys J 95:2837–2848

Rog T, Martinez-Seara H, Munck N, Oresic M, Karttunen M, Vattulainen I (2009) Role of cardiolipins in the inner mitochondrial membrane: insight gained through atom-scale simulations. J Phys Chem B 113:3413–3422

Rög T, Murzyn K, Pasenkiewicz-Gierula M (2002) The dynamics of water at the phospholipid bilayer: a molecular dynamics study. Chem Phys Lett 352:323–327

Roux B (1997) Influence of the membrane potential on the free energy of an intrinsic protein. Biophys J 73:2980–2989

Roux B (2008) The membrane potential and its representation by a constant electric field in computer simulations. Biophys J 95:4205–4216

Sachs JN, Crozier PS, Woolf TB (2004) Atomistic simulations of biologically realistic transmembrane potential gradients. J Chem Phys 121:10847–10851

Saiz L, Klein ML (2001) Structural properties of a highly polyunsaturated lipid bilayer from molecular dynamics simulations. Biophys J 81:204–216

Saiz L, Klein ML (2002a) Computer simulation studies of model biological membranes. Acc Chem Res 35:482–489

Saiz L, Klein ML (2002b) Electrostatic interactions in a neutral model phospholipid bilayer by molecular dynamics simulations. J Chem Phys 116:3052–3057

Sotomayor M, Vasquez V, Perozo E, Schulten K (2007) Ion conduction through MscS as determined by electrophysiology and simulation. Biophys J 92:886–902

Sundararajan R (2009) Nanosecond electroporation: another look. Mol Biotechnol 41:69–82

Tarek M (2005) Membrane electroporation: a molecular dynamics simulation. Biophys J 88:4045–4053

Tieleman DP (2004) The molecular basis of electroporation. BMC Biochem 5:10

Tieleman DP, Marrink SJ, Berendsen HJC (1997) A computer perspective of membranes: molecular dynamics studies of lipid bilayer systems. Biochim Biophys Acta 1331:235–270

Tieleman DP, Berendsen JHC, Sansom MSP (2001) Voltage-dependent insertion of alamethicin at phospholipid/water and octane water interfaces. Biophys J 80:331–346

Tobias DJ (2001) Membrane simulations. In: Becker OH, Roux B, Watanabe M (eds) Computational biochemistry and biophysics. Marcel Dekker, New York

Tobias DJ, Tu K, Klein ML (1997) Atomic-scale molecular dynamics simulations of lipid membranes. Curr Opin Colloid Interface Sci 2:15–26

Treptow W, Maigret B, Chipot C, Tarek M (2004) Coupled motions between pore and voltage-sensor domains: a model for *Shaker* B, a voltage-gated potassium channel. Biophys J 87:2365–2379

Treptow W, Tarek M, Klein ML (2009) Initial response of the potassium channel voltage sensor to a transmembrane potential. J Am Chem Soc 131:2107–2110

Vacha R, Berkowitz ML, Jungwirth P (2009) Molecular model of a cell plasma membrane with an asymmetric multicomponent composition: water permeation and ion effects. Biophys J 96:4493–4501

Vasilkoski Z, Esser AT, Gowrishankar TR, Weaver JC (2006) Membrane electroporation: the absolute rate equation and nanosecond time scale pore creation. Phys Rev E 74:021904

Vernier PT, Ziegler MJ (2007) Nanosecond field alignment of head group and water dipoles in electroporating phospholipid bilayers. J Phys Chem B 111:12993–12996

Vernier PT, Ziegler MJ, Sun Y, Chang WV, Gundersen MA, Tieleman DP (2006a) Nanopore formation and phosphatidylserine externalization in a phospholipid bilayer at high transmembrane potential. J Am Chem Soc 128:6288–6289

Vernier PT, Ziegler MJ, Sun Y, Gundersen MA, Tieleman DP (2006b) Nanopore-facilitated, voltage-driven phosphatidylserine translocation in lipid bilayers—in cells and in silico. Phys Biol 3:233–247

Vernier PT, Levine ZA, Wu H-S, Joubert V, Ziegler MJ, Mir LM, Tieleman DP (2009) Electroporating fields target oxidatively damaged areas in the cell membrane. PLoS ONE 4:e7966

Weaver JC (2003) Electroporation of biological membranes from multicellular to nano scales. IEEE Trans Dielectr Electr Insul 10:754–768

Weaver JC, Chizmadzhev YA (1996) Theory of electroporation: a review. Bioelectrochem Bioenerg 41:135–160

Wiener MC, White SH (1992) Structure of fluid dioleylphosphatidylcholine bilayer determined by joint refinement of X-ray and neutron diffraction data. III. Complete structure. Biophys J 61:434–447

Yang Y, Henderson D, Crozier P, Rowley RL, Busath DD (2002) Permeation of ions through a model biological channel: effect of periodic boundary condition and cell size. Mol Phys 100: 3011–3019

Zhong Q, Moore PB, Newns DM, Klein ML (1998) Molecular dynamics study of the LS3 voltage-gated ion channel. FEBS Lett 427:267–270

Ziegler MJ, Vernier PT (2008) Interface water dynamics and porating electric fields for phospholipid bilayers. J Phys Chem B 112: 13588–13596

J Membrane Biol (2012) 245:545–554
DOI 10.1007/s00232-012-9435-5

In Vivo Molecular Imaging and Histological Analysis of Changes Induced by Electric Pulses Used for Plasmid DNA Electrotransfer to the Skin: A Study in a Dorsal Window Chamber in Mice

Bostjan Markelc · Elisabeth Bellard · Gregor Sersa · Sandrine Pelofy · Justin Teissie · Andrej Coer · Muriel Golzio · Maja Cemazar

Received: 14 January 2012 / Accepted: 30 April 2012 / Published online: 27 May 2012

Abstract Electropermeabilization/electroporation (EP) is a physical method that by application of electric pulses to cells increases cell membrane permeability and enables the introduction of molecules into the cells. One of the uses of EP in vivo is plasmid DNA electrotransfer to the skin for DNA vaccination. EP of tissues induces reduction of blood flow and, in combination with plasmid DNA, induction of an immune response. One of the EP protocols for plasmid DNA electrotransfer to the skin is a combination of high-voltage (HV) and low-voltage (LV) pulses. However, the effects of this pulse combination on skin-vessel blood flow are not known. Therefore, using intravital microscopy in a dorsal window chamber in mice and fluorescently labeled dextrans, the effects of one HV and eight LV pulses on skin vasculature were investigated. In addition, a detailed histological analysis was performed. Image analysis of fluorescence intensity changes demonstrated that EP induces a transient constriction and increased permeability of blood vessels as well as a "vascular lock." Histological analysis revealed rounding up of endothelial cells and stacking up of erythrocytes at 1 h after EP. In addition, extravasation of erythrocytes and leukocyte infiltration accompanied by edema were determined up to 24 h after EP. In conclusion, our results show that blood flow modifying effects of EP in skin contribute to the infiltration of immune cells in the exposed area. When combined with plasmid DNA for vaccination, this could enable the initial and prolonged contact of immune cells with encoded therapeutic proteins.

Keywords Electropermeabilization · Electroporation · Blood vessel · Permeability · Vasoconstriction · Vascular lock · Immune cell infiltration · Plasmid DNA

B. Markelc · G. Sersa · M. Cemazar (✉)
Department of Experimental Oncology, Institute of Oncology Ljubljana, Zaloska 2, 1000 Ljubljana, Slovenia
e-mail: mcemazar@onko-i.si

E. Bellard · S. Pelofy · J. Teissie · M. Golzio
IPBS (Institut de Pharmacologie et de Biologie Structurale), CNRS, 205 route de Narbonne, BP 64182, 31077 Toulouse, France

E. Bellard · S. Pelofy · J. Teissie · M. Golzio
IPBS (Institut de Pharmacologie et de Biologie Structurale), Université de Toulouse, UPS (Université Paul Sabatier), BP 64182, 31077 Toulouse, France

A. Coer · M. Cemazar
Faculty of Health Sciences, University of Primorska, Polje 42, 6310 Izola, Slovenia

Introduction

The use of plasmid DNA as a vaccine is a promising alternative to traditional vaccines that are based on live or attenuated viruses (Tang et al. 1992; Rice et al. 2008; Ingolotti et al. 2010; Ferraro et al. 2011). The possibility of delivering a vaccine without inducing antiviral immunity, the ability to formulate multicomponent vaccines (Hirao et al. 2011; Sardesai and Weiner 2011), the stability of DNA at room temperature and the safety of production compared to viral vaccines make plasmid DNA vaccination especially attractive. Proper design of plasmid DNA can lead to enhanced expression of antigen, targeted expression in the cell (cytosol or endoplasmic reticulum) and induction of $CD4^+$ T-helper cells, among other things, which leads to an increased immune response (Rice et al. 2008). The initial problems with the delivery of DNA vaccines to cells in vivo and induction of a potent immune response of the host have been successfully surmounted by using electropermeabilization/electroporation (EP) as a delivery system (Drabick et al. 2001; Pavselj and

Preat 2005; Rice et al. 2008; Donate et al. 2011; Sardesai and Weiner 2011). EP is a physical method where the application of external electric pulses directly to living cells induces a local increase in transmembrane potential difference. This consequently enables the introduction of molecules into the cells (Miklavcic and Towhidi 2010). The method was first described by Neumann et al. (1982) for the introduction of DNA into cells in vitro; however, clinical use was first achieved for the delivery of cancer chemotherapeutic drugs with EP, such as bleomycin or cisplatin (electrochemotherapy) (Marty et al. 2006; Sersa et al. 2008b). Nowadays, EP is increasingly used for the delivery of different nucleic acids (plasmid DNA, siRNA, miRNA, shRNA, etc.) into cells in vitro and different tissues, including muscle, skin and tumors, in vivo (Rols et al. 1998; Gehl and Mir 1999; Cemazar et al. 2006; Aung et al. 2009; Mir 2009; Escoffre et al. 2010; Vidic et al. 2010). Effective use of EP for enhancement of plasmid DNA vaccination was first reported 10 years ago (Kadowaki et al. 2000; Widera et al. 2000; Drabick et al. 2001) and has already reached the clinical trial stage (van Drunen Littel-van den Hurk and Hannaman 2010; Ferraro et al. 2011; Vasan et al. 2011; El-Kamary et al. 2012). The success of EP for plasmid DNA vaccination was attributed to the fact that EP enhances delivery of plasmid DNA into the cells, where it is expressed for a long time (several months) (Widera et al. 2000; Cemazar et al. 2006; Escoffre et al. 2010), and thus induces a potent immune response of the host to the introduced encoded antigen (Drabick et al. 2001; Liu et al. 2008; Roos et al. 2009; Xing et al. 2012). Furthermore, EP was demonstrated to be safe and well tolerated in preclinical as well as clinical studies (Vanbever and Preat 1999; Sardesai and Weiner 2011; El-Kamary et al. 2012).

The best results were obtained when plasmid DNA vaccination was performed in muscle or skin (Sardesai and Weiner 2011). One of the EP protocols for plasmid DNA electrotransfer used a combination of one short (100 μs) high-voltage (HV) pulse and one or more long (several milliseconds) low-voltage (LV) pulses, the voltage being chosen from the electrode design and the tissue being pulsated. In this setting EP increased DNA expression up to 100-fold in muscle and skin. Also, a higher infiltration of immune cells into the EP area was present, consequently enabling the contact of more antigen-presenting cells (APCs) with encoded antigens (Roos et al. 2009; Tevz et al. 2009; Lee et al. 2011). It was shown that EP induces vascular changes in muscle, which could contribute to the observed immune effects (Gehl et al. 2002). However, the vascular and blood-modifying effects of the HV–LV pulse combination that was used for plasmid DNA electrotransfer to the skin are not known.

Therefore, the aim of the present study was to determine the effects of an HV–LV pulse combination on skin and subcutaneous blood vessels. For this purpose we used in vivo optical imaging in a dorsal window chamber (DWC) (Jain et al. 2002; Dreher et al. 2006; Palmer et al. 2011) in mice together with histological characteristic evaluation: edema, blood-vessel changes and immune cell infiltration at different times after the HV–LV pulse combination.

Materials and Methods

Reagents

We resuspended 2,000 kDa fluorescein isothiocyanate (FITC) labeled dextran (Sigma-Aldrich, St. Louis, MO) in phosphate-buffered saline (PBS). To remove any free FITC or low-molecular weight contaminants, the 2,000 kDa FITC-labeled dextran was washed two times for 2 h through a 1,000 kDa Vivaspin ultrafiltration spin column (Sartorius Stedim Biotech, Goettingen, Germany). The high-molecular weight component was then resuspended in PBS to a final concentration of 37.5 mg/ml.

Animals

In the experiments 6–8 week-old female C57Bl/6 mice weighing 20–24 g were used. Mice were kept under specific pathogen-free conditions at a constant room temperature (21 °C) and humidity and a 12 h light/dark cycle. Food and water were provided ad libitum. Animals were subjected to an adaptation period of 14 days before experiments. All animal experiments were conducted in accordance with the guidelines for animal experiments of the EU directives, the French procedural guidelines for animal handling with the approval of the Regional Ethical Review Committee in Midi-Pyrénées (MP/02/36/10/10) and permission from the Ministry of Agriculture, Forestry and Food of the Republic of Slovenia (permission 34401-12/2009/6). For each experimental condition three to five mice were randomly assigned, out of which two to four mice were selected for histological analysis. Only one experiment was performed on each mouse.

Preparation of the DWC in Mice

The DWC model in mice is a chronic model where a dorsal skinfold is sandwiched between two symmetrical frames. It allows direct visual access to the normal vasculature of the skin through a standard microscopy cover glass and enables repetitive high-resolution imaging of the exposed vasculature in the same mouse over a period of 2–3 weeks (Palmer et al. 2011). For DWC implantation mice were first anesthetized with an intraperitoneal injection of ketamine (1 mg/ml, Narketan®; Vetoquinol, Ittigen, Switzerland), xylazine (5 mg/ml, Chanazine; Chanelle Pharmaceuticals, Loughrea, Ireland) and acepromazine (0.4 mg/ml, Promace; Fort Dodge

Animal Health, IA); then, the back of the mouse was shaved and depilated with depilatory cream (Veet; Reckitt Benckiser, Slough, UK). DWC (APJ Trading, Ventura, CA) consisting of two titanium frames was surgically implanted onto the extended double layer of the skin with stainless-steel screws and sutures. Subsequently, one layer of the skin was excised to expose the vasculature of the lower layer of skin. From the lower layer of skin all fat and connective tissues were dissected away to ensure optimal microscopic observation. The DWC was filled with 0.9 % NaCl solution and closed with a 12 mm cover glass (Glaswarenfabrik Karl Hecht, Sondheim, Germany). After the surgery and for the following 2 days, butorphanol (0.3 mg/kg, Torbugesic; Fort Dodge Animal Health) was injected intramuscularly once per day.

Electropermeabilization

EP was performed 3–7 days after the implantation of DWC in mice. The pulsing parameters used were one HV pulse (voltage-to-distance ratio 1,000 V/cm, duration 100 μs) followed by a 1 s lag and eight LV pulses (voltage-to-distance ratio 140 V/cm, duration 50 ms, repetition frequency 1 Hz) (Andre et al. 2008). Pulses were generated by Cliniporator™ (Igea, Carpi, Italy) and delivered by two parallel stainless-steel rods (length 5 mm, width 1.3 mm) 4 mm apart (Mazeres et al. 2009). The electrodes were placed on the skin on the opposite side of the cover glass, where the epidermis was intact. Good contact between the electrodes and the skin was ensured by means of a conductive gel (P. J. Dahlhausen, Cologne, Germany). To determine the leakage of FITC-labeled dextran from the vessels, EP was performed 2 min after FITC-labeled dextran injection, when all vessels were completely filled, or at different times before FITC-labeled dextran injection to determine resealing of the vessel wall and duration of the "vascular lock."

Intravital Microscopy and Image Acquisition

For intravital microscopy an upright "Macrofluo" fluorescence microscope (Leica Microsystems, Rueil-Malmaison, France) equipped with a Cool Snap HQ Camera (Roper Scientific, Ottobrunn, Germany) and Metamorph (Molecular Devices, Sunnyvale, CA) image acquisition software were used. Animals were first anesthetized with inhalation anesthesia (Isofluran; Nicholas Piramal India, London, UK) and placed on a custom-designed holder, which enabled fixation of the DWC during image acquisition and therefore prevented the artifacts caused by movement due to breathing. Blood vessels were visualized by fluorescence (excitation filter, BP 480/40 nm; emission filter, LP 510 nm) after injection of 100 μl of FITC-labeled dextran (3.75 mg/mouse). To ensure that the vessels were completely filled up, a series of images every 20 s for 2 min was acquired when FITC-labeled dextran was injected before EP. Immediately after EP (<10 s) a second series of images every 20 s for the first 8 min and every 2 min for the next 22 min was acquired. When FITC-labeled dextran was injected after EP, only the second series of images was acquired. Images were analyzed offline with image analysis software (AxioVision; Zeiss, Jena, Germany).

Data Analysis

To determine the increase in fluorescence intensity inside and outside the vessels, a differential approach was used, which was adapted from Reyes-Aldasoro et al. (2008), followed by specific image analysis. Briefly, after i.v. injection of FITC-labeled dextran, a series of images was acquired during the first 2 min before EP and 30 min after EP. Then, a mask of the blood-vessel network was created and the mean fluorescence intensity determined in the vascular compartment and in the tissue. For measurement of blood-vessel diameters, at least five venules (diameters 20–250 μm) and arterioles (10–100 μm) were selected from each mouse. The narrow, straight, fast-flowing vessels with few branches were defined as arterioles and the rest as venules. The diameter of the vessels was measured in each image of the recorded series and normalized to the value before EP.

Histology

The circular part of the skin inside the DWC that was monitored through the cover glass was excised at 1, 12, 24, or 48 h after EP. The skin was then fixed in formalin for 24 h and stored in 70 % ethanol until it was embedded in paraffin in such orientation that sections were cut perpendicular to the skin layers encompassing both parts of the skin where electrodes were placed. From each DWC preparation, 9–12 sections of 5 μm thickness were cut and stained with hematoxylin and eosin. Slides were observed with a BX-51 microscope (Olympus, Hamburg, Germany) coupled with a DP72 digital camera (Olympus).

Statistical Analysis

For statistical analysis Sigma Plot software (Systat Software, London, UK) was used. For comparison of the control and EP groups, a Student *t*-test or one-way ANOVA followed by a Holm-Sidak test was used. A value of $p < 0.05$ was considered statistically significant.

Results

EP Induces Constriction of Blood Vessels

To determine the effect of EP on vessel morphology, the diameters of arterioles and venules were measured for the

first 30 min after EP. Application of electric pulses resulted in an immediate constriction of the arterioles and venules (Fig. 1). The statistically significant constriction of arterioles (~70 %) was more pronounced than the constriction of venules (~30 %) and lasted longer (Fig. 1). In comparison to the control, the diameters of arterioles remained statistically significantly smaller during the entire observation period (30 min), whereas the diameters of venules returned to pre-EP values 14 min after EP (Fig. 1). The diameters of arterioles and venules in control mice remained constant during the entire observation time (20–250 μm for venules and 10–100 μm for arterioles).

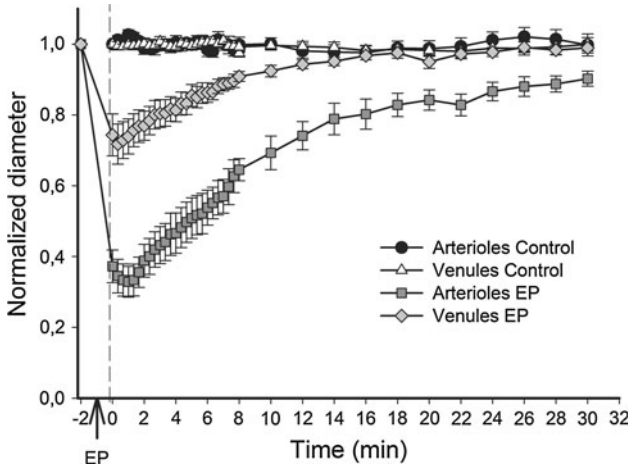

Fig. 1 Constriction of blood vessels after EP. Diameters of vessels were measured after i.v. injection of FITC-labeled dextran. Pulsing parameters when EP was applied: one pulse of voltage-to-distance ratio 1,000 V/cm, 100 μs, 1s pause; eight pulses of voltage-to-distance ratio 140 V/cm, 50 ms, 1 Hz. Diameters were normalized to the value 2 min after i.v. injection of FITC-labeled dextran. Normalized diameters of arterioles and venules after EP ($n = 3$) are represented as a function of time in comparison to control ($n = 3$). Diameters were statistically significantly smaller for the first 14 min for venules and throughout the observation time for arterioles ($p < 0.05$). Student's t test was used for comparison of each time point of the EP group to the same time point of the control group

EP Induces a "Vascular Lock"

EP induced transient obstruction of blood flow, a "vascular lock" in the skin, which resulted in slowed filling up of vessels in comparison to the control group, where complete filling up of vessels was achieved within 2 min after FITC-labeled dextran i.v. injection (Fig. 2a). When FITC-labeled dextran was injected 0.5, 1, and 5 min after EP, the filling up of all pulsed vessels was completed ~10 min after i.v. injection (Figs. 2,3). When FITC-labeled dextran was injected 10 or 30 min after EP, the filling up of vessels was completed within 3 min after i.v. injection (Fig. 2). The maximal variation of mean fluorescence intensity per second was also statistically significantly decreased at 0.5, 1, and 5 min after EP (Fig. 2b). This demonstrates that the EP-induced "vascular lock" in the skin is transient and lasts ~10 min after EP.

EP Increases the Permeability of Blood Vessels

To determine the effect of EP on the permeability of blood vessels, the relative variation of the mean fluorescence intensity in the tissue neighboring the blood vessel due to FITC-labeled dextran leakage from the pulsed blood vessels was measured (Fig. 3). A statistically significant increase of the mean fluorescence intensity was determined after EP in comparison to the control. For the first 8 min

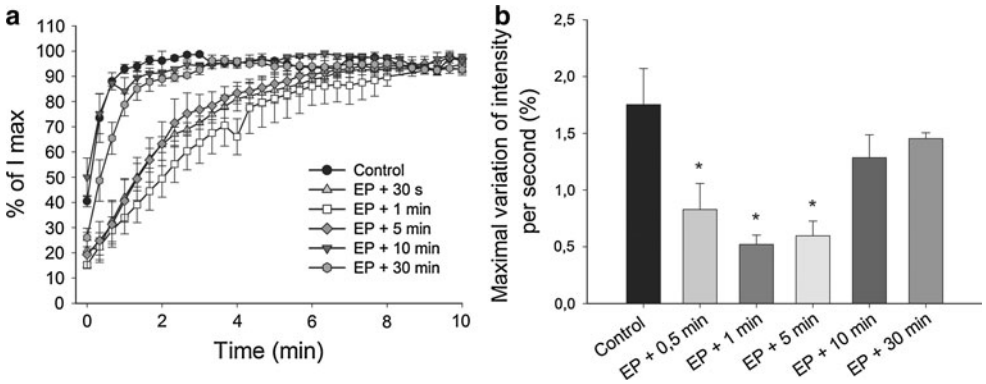

Fig. 2 Time course of filling up of blood vessels after EP. Kinetics of filling up of vessels was determined after i.v. injection of FITC-labeled dextran at different times after EP (0.5, 1, 5, 10, and 30 min). Pulsing parameters when EP was applied: one pulse of voltage-to-distance ratio 1,000 V/cm, 100 μs, 1s pause; eight pulses of voltage-to-distance ratio 140 V/cm, 50 ms, 1 Hz. **a** Filling up of vessels is expressed as a percent of maximum mean fluorescence intensity in vessels (I_{max}) after i.v. injection of FITC-labeled dextran. **b** Maximal variation of intensity per second calculated from the filling up curves. The filling up of vessels was slowed down when dextran was i.v. injected 0.5, 1, and 5 min after EP and returned to control levels when the interval between EP and i.v. -injection was 10 and 30 min ($n = 3$–5). A one-way ANOVA followed by a Holm-Sidak test were used for statistical analysis. *$p < 0.05$ in comparison to the control. *Error bars* indicate SEM

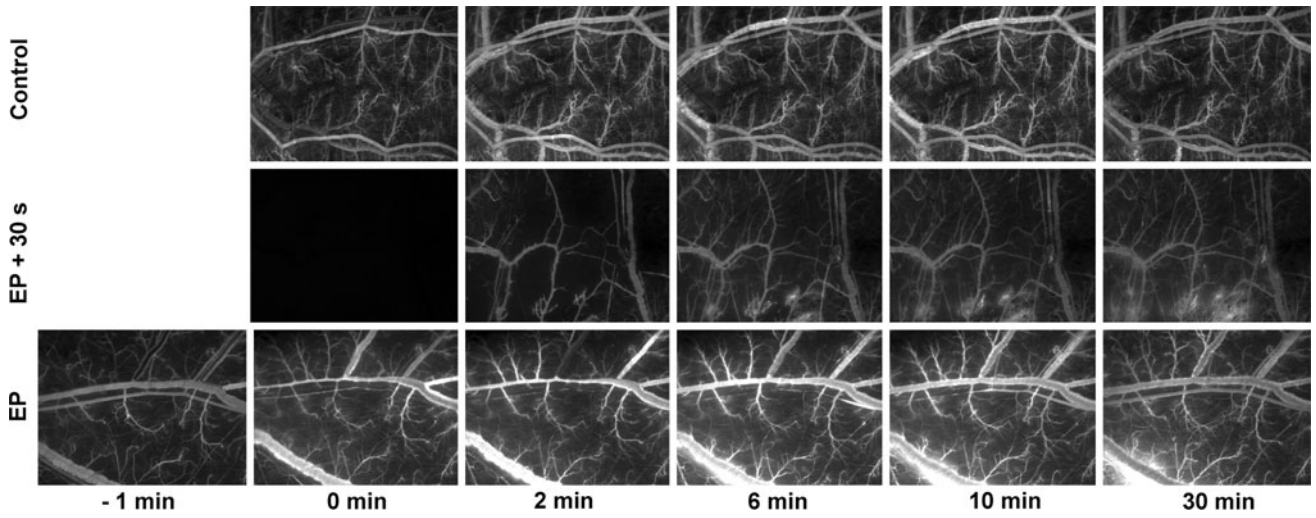

Fig. 3 Illustration of "vascular lock" and dextran leakage into the tissue after EP. Pulsing parameters when EP was applied: one pulse of voltage-to-distance ratio 1,000 V/cm, 100 μs, 1s pause; eight pulses of voltage-to-distance ratio 140 V/cm, 50 ms, 1 Hz. "Vascular lock" was determined when FITC-labeled dextran was i.v. -injected 0.5 min after EP (*EP + 30 s*), where the filling up of vessels was completed ~10 min after EP, whereas leakage of FITC-labeled dextran was observed earlier (~6 min after EP). Leakage of FITC-labeled dextran into the tissue was measured when FITC-labeled dextran was i.v. -injected 2 min before EP (*EP*), and then relative variation of mean fluorescence intensity was determined for the next 30 min. In the control group (*Control*) filling up of vessels was completed within 2 min after i.v. injection of FITC-labeled dextran, and there was no leakage of dextran into the tissue

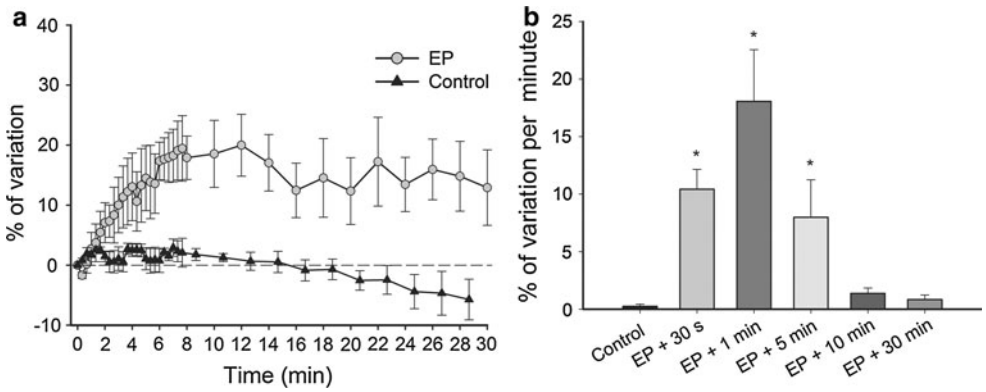

Fig. 4 Increased permeability of blood vessels and duration of increased permeability. Pulsing parameters when EP was applied: one pulse of voltage-to-distance ratio 1,000 V/cm, 100 μs, 1s pause; eight pulses of voltage-to-distance ratio 140 V/cm, 50 ms, 1 Hz. **a** Measure of relative mean fluorescence intensity changes in DWC tissues outside the vessels as a function of time after EP in comparison to the control group without EP. **b** Measure of relative mean fluorescence intensity changes per minute in DWC tissues outside the vessels when FITC-labeled dextran was injected at different times after EP ($n = 3$–5). A one-way ANOVA followed by a Holm-Sidak test were used for statistical analysis. *$p < 0.05$ in comparison to control. *Error bars* indicate SEM

after EP, the increase of relative variation of fluorescence intensity was linearly dependent on time, after which it reached a plateau (Fig. 4a). In the control group the relative variation of mean fluorescence intensity in the tissue decreased slightly during the observation time (Fig. 4a).

To evaluate the duration of increased permeability of the pulsed blood vessels, FITC-labeled dextran was i.v.-injected at different times after EP and the relative increase of mean fluorescence in the tissue per minute was determined thereafter (Figs. 3, 4b). Statistically significant values were determined for the injection of FITC-labeled dextran 0.5, 1, and 5 min after EP; then, the relative variation of mean fluorescence intensity per minute decreased and reached values similar to the control group when injection of FITC-labeled dextran was performed 30 min after EP (Fig. 4b). For the calculations, only the first 8 min after FITC-labeled dextran injection were relevant due to the fact that during this time interval after EP the FITC-labeled dextran leakage from blood vessels into the tissue was linearly dependent on time (Fig. 4a).

EP-Induced Histological Changes of the Skin

Histological changes of the skin after EP were determined 1, 12, 24, and 48 h after EP. In the slides, sections of the skin consisting of epidermis, dermis with hair follicles, subcutaneous tissues with blood vessels and a thin striated muscle layer are presented (Fig. 5a). Rounding up of vessel endothelial cells, narrowing of vessel lumen and stacking of erythrocytes in vessels were present at 1 h after EP (Fig. 5d–f) but were not present anymore at later time points. The extravasation of erythrocytes; increased presence and marginalization of leukocytes, which was accompanied by extravasation; and increased infiltration of leukocytes into the tissue between the electrodes was observed at 1 and 12 h after EP (Fig. 5d–i). Infiltration of leukocytes was also observed at 24 h after EP, which decreased at 48 h after EP (Fig. 5j–o). Infiltration was accompanied by edema, which was present in the connective tissue under the epidermis at all time points, except at 48 h after EP, when it was already resolved (Fig. 5). All of these features were more pronounced closer to the negative electrode than under the positive one or between the electrodes. In addition, at all time points the damage to the epidermis, vessels and hair follicles was much more evident under the negative electrode, where even destruction of different tissue structures was observed (Fig. 5). Recovery of the epidermis and underlying tissue under the electrodes was evident at 24 and 48 h after EP (Fig. 5g–o). All of the above-mentioned features were observed in all samples at specific time points.

Fig. 5 EP-induced changes in skin. Representative images of tissue sections which were exposed to EP and stained with hematoxylin and eosin (pulsing parameters: one pulse of voltage-to-distance ratio 1,000 V/cm, 100 μs, 1s pause; eight pulses of voltage-to-distance ratio 140 V/cm, 50 ms, 1 Hz). **a** *E* epidermis, *D* dermis with hair follicles, *S* subcutaneous tissues with blood vessels, *M* a thin striated muscle layer; **b** *arrow* blood vessels; **c** *arrow* intact epidermis, *arrowhead* hair follicle; **d** *arrow* stacking of erythrocytes; **e** *arrow* rounding up of endothelial cells in the venule, *arrowhead* rounding up of endothelial cells in the arteriole; **f** *thick arrow* damaged keratinocytes under the electrode, *arrowhead* marginalization of immune cells (prominent nuclei are present) in the blood vessel, *thin arrow* damaged hair follicle; **g** *arrow* extravasation of erythrocytes; **h** *arrow* infiltration of immune cells; **i** *arrow* damaged keratinocytes under the electrode, *arrowhead* damaged hair follicle; **j** *arrow* edema; **k** *arrow* infiltration of immune cells; **l** *arrow* recovery of epidermis, *arrowhead* damaged keratinocytes under the electrode; **m** *arrow* recovered/normal blood vessels; **n** *arrow* infiltration of immune cells; **o** *arrow* recovery of epidermis, *arrowhead* damaged keratinocytes under the electrode. *Scale bar* 50 μm

Discussion

The results of this study show that application of an HV–LV pulse combination used for plasmid DNA electrotransfer to the skin induces a transient constriction of blood vessels, "vascular lock" and increased permeability of blood vessels. Already within 1 h after EP rounding up of endothelial cells and stacking up of erythrocytes can be observed in the area of the tissue exposed to EP. In addition, extravasation of erythrocytes into the tissue and leukocyte infiltration with edema were observed. Damage to the epidermis and the tissue beneath the electrodes was repaired within 48 h after EP.

Several studies have reported that different HV–LV combinations of pulses are very effective for plasmid DNA electrotransfer to the skin, inducing a better immune response and longer gene expression in comparison to HV or LV pulses alone (Pavselj and Preat 2005; Andre et al. 2008; Roos et al. 2009; Brave et al. 2010; Gothelf et al. 2011). Concerning the safety of the methods, regardless of the electrodes used, the application of pulses to the skin results in a slight and transient disruption of the skin barrier function, slight and transient erythema and upregulation of genes involved in the immune response (Dujardin et al. 2002; Pavselj and Preat 2005; Roos et al. 2009). However, there have been no reports on the effects of EP on the vasculature of the skin and detailed histological analysis of these effects. Our study is the first to provide direct observations of the effects of an HV–LV combination of pulses on normal vasculature in the skin.

First, the effects of EP on blood vessels in the skin from our direct observation extended the models of vascular response observed in studies done on muscle and tumors (Gehl et al. 2002; Sersa et al. 2008a). The vascular response was described as a two-phase phenomenon, where the first short phase is quick and was attributed to sympathetically mediated vasoconstriction of afferent arterioles, whereas the second slower phase is of much longer duration (up to 30 min in the case of muscle) and supposed to follow the kinetics of cell membrane resealing after EP and changes of endothelial cell shape (Gehl et al. 2002; Jarm et al. 2010). Our data on measurement of blood-vessel diameters are in agreement with this hypothesis. The immediate constriction of blood vessels after EP was more pronounced for arterioles ($\sim$70 %) than for venules ($\sim$30 %). The constriction of arterioles also lasted longer (throughout the observation period) than the constriction of venules ($\sim$15 min). The bigger impact of EP on the diameter of arterioles can be explained by differences in the structure of the blood-vessel wall, where the smooth muscle of the tunica media is more abundant in the wall of arterioles compared to venules (Seeley et al. 2000). The observed constriction of the blood vessels resulted in a "vascular lock" (Gehl et al. 2002; Sersa et al. 2008a) (Fig. 2). The filling up of the vessels was statistically significantly slower for the first 5 min after EP. For example, when FITC-labeled dextran was injected immediately after EP (0.5 min), the filling up of the blood vessels

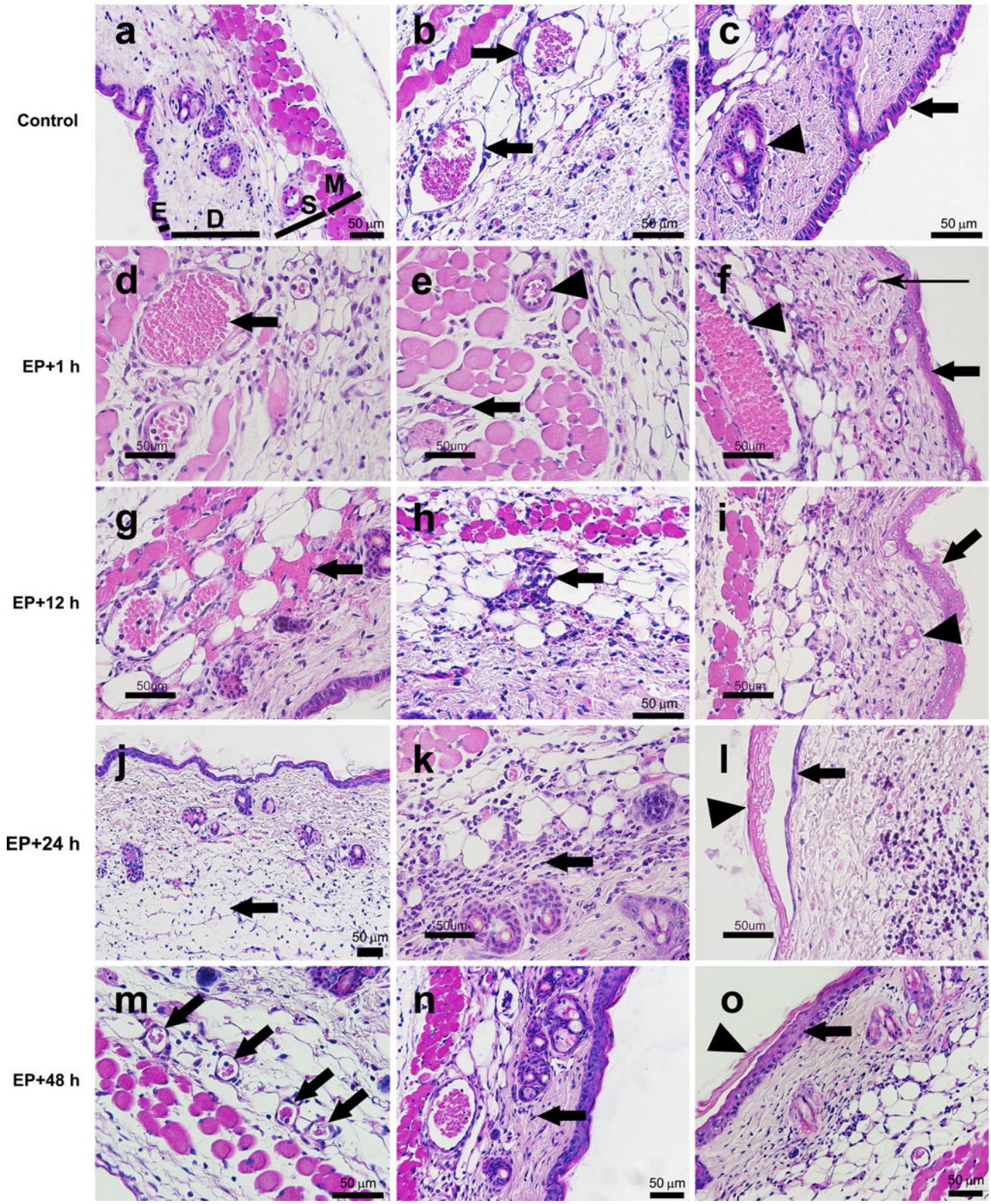

was completed ~10 min after the injection. Direct in vivo experimental support for the second phase of the proposed vascular effects was demonstrated in our study by increased permeability of the blood vessels after EP for 2,000 kDa FITC-labeled dextran. Its size was chosen as being approximately the size of plasmid DNA (Paganin-Gioanni et al. 2011). The increased permeability of the blood vessels for 2,000 kDa FITC-labeled dextran lasted for 5–10 min and

gradually returned to pre-EP values 30 min after EP. The second phase was mainly attributed to disruption of the cellular cytoskeleton and junctional integrity of the blood-vessel endothelium (Kanthou et al. 2006; Jarm et al. 2010). The increased permeability of the blood vessels for 2,000 kDa FITC-labeled dextran returned to control levels only 30 min after EP, indicating that restoration of the blood-vessel endothelium is slow and, thus, enables leakage of large molecules for an extended period of time.

Second, EP also has other effects on the target tissue besides vascular effects, and very little is known about these effects. It is now known that application of electric pulses to tissues affects not only the permeability of cell membranes but also the distribution of DNA and other molecules in the tissues (Zaharoff et al. 2002; Henshaw et al. 2007, 2011). One of the hallmarks of DNA vaccination combined with EP is that EP significantly enhances the immunogenicity of DNA vaccines relative to DNA injection alone also in human clinical trials (Hirao et al. 2010; Livingston et al. 2010; Sardesai and Weiner 2011; Vasan et al. 2011). This was concluded by measuring different features of the immune response, but the underlying mechanisms remain poorly understood. DNA vaccination, regardless of the therapeutic gene used, combined with EP increased the excretion of interferon-gamma from antigen-specific $CD8^+$ cells, increased the number of antigen-specific $CD4^+$ cells and several other types of immune cells compared to injection of DNA alone or another type of vaccination (Rosati et al. 2009; Belisle et al. 2011; Brave et al. 2011; Kulkarni et al. 2011; Lee et al. 2011; Sardesai and Weiner 2011). The results of our study demonstrate that the effects of EP on skin blood vessels can contribute to the immune response observed in other studies when EP was combined with DNA vaccines. Namely, the observed effects of EP, i.e., increased permeability of blood vessels and "vascular lock," cause a small and reversible tissue damage that is enough to lead to inflammation and increased infiltration of immune cells. Specifically, EP induces increased permeability of the blood vessels for at least 30 min, which enables protein leakage outside the vessels, leading to a decrease in the pressure between the intra- and extra-vascular compartments and to extravasation of fluids. The results are development of interstitial edema, increased interstitial fluid pressure and decreased intravascular pressure, which all contribute to compromised blood flow, i.e. "vascular lock," in addition to vasoconstriction. Furthermore, although the observed "vascular lock" was short-lived, it can still result in ischemia–reperfusion injury (van den Heuvel et al. 2009). Moreover, it was shown in our previous studies that EP causes the formation of reactive oxygen species in vitro, which was indirectly shown also in vivo in mouse muscle (Gabriel and Teissie 1995; Markelc et al. 2012). All of these effects of EP on skin and subcutaneous vasculature observed by in vivo imaging were confirmed by histological analysis performed at different times after EP. Increased permeability of the blood vessels was demonstrated by rounding up of endothelial cells, extravasation of erythrocytes and edema present in the connective tissue below the epidermis. Furthermore, attraction of immune cells was demonstrated by the marginalization of leukocytes in the vessels and by pronounced infiltration seen only in the areas between the electrodes, which were present for at least 24 h. Therefore, taken collectively, in case of plasmid DNA vaccine combined with EP, we can predict that the cells transfected with plasmid DNA are in contact with numerous immune cells for at least 24 h. Thus, the plasmid DNA has enough time to translate into an antigenic protein, which can react with immune cells, leading to a pronounced immune response, both cellular and humoral. It is also worth mentioning that the effects of EP on histological changes (tissue damage, lymphocyte infiltration, etc.) were more pronounced at the negative electrode. The reason for this observation is not known, but it could be ascribed to the electrolytic chemical reaction of reduction at the negative electrode, leading to formation of different chemicals, mainly sodium hydroxide (Wagner et al. 1985).

One of the aspects dealing with translation of plasmid DNA vaccination combined with EP to more widespread use in humans is the standardization of EP parameters. From the tissue effects of EP that were shown in previous studies in muscle, tumors and our study on the skin, it is obvious that the EP parameters optimized for therapeutic effects are dependent on the tissue's structural characteristics and blood-vessel morphology. Therefore, further studies are needed to evaluate the tissue effect of EP, which will bring plasmid DNA vaccination combined with EP into wider clinical use.

Acknowledgments The authors acknowledge financial support from the state budget through the Slovenian Research Agency (program P3-0003), French–Slovenian Scientific Cooperation (PROTEUS and PICS) and Région Midi Pyrénées. Research was conducted in the scope of EBAM European Associated Laboratory (LEA). The authors thank Toulouse Réseau Imagerie core facilities at the IPBS. The authors declare no conflict of interest.

References

Andre FM, Gehl J, Sersa G, Preat V, Hojman P, Eriksen J, Golzio M, Cemazar M, Pavselj N, Rols MP, Miklavcic D, Neumann E, Teissie J, Mir LM (2008) Efficiency of high- and low-voltage

pulse combinations for gene electrotransfer in muscle, liver, tumor, and skin. Hum Gene Ther 19:1261–1271

Aung W, Hasegawa S, Koshikawa-Yano M, Obata T, Ikehira H, Furukawa T, Aoki I, Saga T (2009) Visualization of in vivo electroporation-mediated transgene expression in experimental tumors by optical and magnetic resonance imaging. Gene Ther 16:830–839

Belisle SE, Yin J, Shedlock DJ, Dai A, Yan J, Hirao L, Kutzler MA, Lewis MG, Andersen H, Lank SM, Karl JA, O'Connor DH, Khan A, Sardesai N, Chang J, Aicher L, Palermo RE, Weiner DB, Katze MG, Boyer J (2011) Long-term programming of antigen-specific immunity from gene expression signatures in the PBMC of rhesus macaques immunized with an SIV DNA vaccine. PLoS ONE 6:e19681

Brave A, Gudmundsdotter L, Sandstrom E, Haller BK, Hallengard D, Maltais AK, King AD, Stout RR, Blomberg P, Hoglund U, Hejdeman B, Biberfeld G, Wahren B (2010) Biodistribution, persistence and lack of integration of a multigene HIV vaccine delivered by needle-free intradermal injection and electroporation. Vaccine 28:8203–8209

Brave A, Nystrom S, Roos AK, Applequist SE (2011) Plasmid DNA vaccination using skin electroporation promotes poly-functional CD4 T-cell responses. Immunol Cell Biol 89:492–496

Cemazar M, Golzio M, Sersa G, Rols MP, Teissie J (2006) Electrically-assisted nucleic acids delivery to tissues in vivo: where do we stand? Curr Pharm Des 12:3817–3825

Donate A, Coppola D, Cruz Y, Heller R (2011) Evaluation of a novel non-penetrating electrode for use in DNA vaccination. PLoS ONE 6:e19181

Drabick JJ, Glasspool-Malone J, King A, Malone RW (2001) Cutaneous transfection and immune responses to intradermal nucleic acid vaccination are significantly enhanced by in vivo electropermeabilization. Mol Ther 3:249–255

Dreher MR, Liu W, Michelich CR, Dewhirst MW, Yuan F, Chilkoti A (2006) Tumor vascular permeability, accumulation, and penetration of macromolecular drug carriers. J Natl Cancer Inst 98:335–344

Dujardin N, Staes E, Kalia Y, Clarys P, Guy R, Préat V (2002) In vivo assessment of skin electroporation using square wave pulses. J Control Release 79:219–227

El-Kamary SS, Billington M, Deitz S, Colby E, Rhinehart H, Wu Y, Blackwelder W, Edelman R, Lee A, King A (2012) Safety and tolerability of the easy Vax clinical epidermal electroporation system in healthy adults. Mol Ther 20:214–220

Escoffre JM, Teissie J, Rols MP (2010) Gene transfer: how can the biological barriers be overcome? J Membr Biol 236:61–74

Ferraro B, Morrow MP, Hutnick NA, Shin TH, Lucke CE, Weiner DB (2011) Clinical applications of DNA vaccines: current progress. Clin Infect Dis 53:296–302

Gabriel B, Teissie J (1995) Spatial compartmentation and time resolution of photooxidation of a cell membrane probe in electropermeabilized Chinese hamster ovary cells. Eur J Biochem 228:710–718

Gehl J, Mir LM (1999) Determination of optimal parameters for in vivo gene transfer by electroporation, using a rapid in vivo test for cell permeabilization. Biochem Biophys Res Commun 261:377–380

Gehl J, Skovsgaard T, Mir LM (2002) Vascular reactions to in vivo electroporation: characterization and consequences for drug and gene delivery. Biochim Biophys Acta 1569:51–58

Gothelf A, Mahmood F, Dagnaes-Hansen F, Gehl J (2011) Efficacy of transgene expression in porcine skin as a function of electrode choice. Bioelectrochemistry 82:95–102

Henshaw JW, Zaharoff DA, Mossop BJ, Yuan F (2007) Electric field-mediated transport of plasmid DNA in tumor interstitium in vivo. Bioelectrochemistry 71:233–242

Henshaw J, Mossop B, Yuan F (2011) Enhancement of electric field-mediated gene delivery through pretreatment of tumors with a hyperosmotic mannitol solution. Cancer Gene Ther 18:26–33

Hirao LA, Wu L, Satishchandran A, Khan AS, Draghia-Akli R, Finnefrock AC, Bett AJ, Betts MR, Casimiro DR, Sardesai NY, Kim JJ, Shiver JW, Weiner DB (2010) Comparative analysis of immune responses induced by vaccination with SIV antigens by recombinant Ad5 vector or plasmid DNA in rhesus macaques. Mol Ther 18:1568–1576

Hirao LA, Draghia-Akli R, Prigge JT, Yang M, Satishchandran A, Wu L, Hammarlund E, Khan AS, Babas T, Rhodes L, Silvera P, Slifka M, Sardesai NY, Weiner DB (2011) Multivalent smallpox DNA vaccine delivered by intradermal electroporation drives protective immunity in nonhuman primates against lethal monkeypox challenge. J Infect Dis 203:95–102

Ingolotti M, Kawalekar O, Shedlock DJ, Muthumani K, Weiner DB (2010) DNA vaccines for targeting bacterial infections. Expert Rev Vaccines 9:747–763

Jain RK, Munn LL, Fukumura D (2002) Dissecting tumour pathophysiology using intravital microscopy. Nat Rev Cancer 2:266–276

Jarm T, Cemazar M, Miklavcic D, Sersa G (2010) Antivascular effects of electrochemotherapy: implications in treatment of bleeding metastases. Expert Rev Anticancer Ther 10:729–746

Kadowaki S, Chen Z, Asanuma H, Aizawa C, Kurata T, Tamura S (2000) Protection against influenza virus infection in mice immunized by administration of hemagglutinin-expressing DNAs with electroporation. Vaccine 18:2779–2788

Kanthou C, Kranjc S, Sersa G, Tozer G, Zupanic A, Cemazar M (2006) The endothelial cytoskeleton as a target of electroporation-based therapies. Mol Cancer Ther 5:3145–3152

Kulkarni V, Jalah R, Ganneru B, Bergamaschi C, Alicea C, von Gegerfelt A, Patel V, Zhang GM, Chowdhury B, Broderick KE, Sardesai NY, Valentin A, Rosati M, Felber BK, Pavlakis GN (2011) Comparison of immune responses generated by optimized DNA vaccination against SIV antigens in mice and macaques. Vaccine 29:6742–6754

Lee IH, Park JB, Cheong M, Choi YS, Park D, Sin JI (2011) Antitumor therapeutic and antimetastatic activity of electroporation-delivered human papillomavirus 16 e7 DNA vaccines: a possible mechanism for enhanced tumor control. DNA Cell Biol 30:975–985

Liu J, Kjeken R, Mathiesen I, Barouch DH (2008) Recruitment of antigen-presenting cells to the site of inoculation and augmentation of human immunodeficiency virus type 1 DNA vaccine immunogenicity by in vivo electroporation. J Virol 82:5643–5649

Livingston BD, Little SF, Luxembourg A, Ellefsen B, Hannaman D (2010) Comparative performance of a licensed anthrax vaccine versus electroporation based delivery of a PA encoding DNA vaccine in rhesus macaques. Vaccine 28:1056–1061

Markelc B, Tevz G, Cemazar M, Kranjc S, Lavrencak J, Zegura B, Teissie J, Sersa G (2012) Muscle gene electrotransfer is increased by the antioxidant tempol in mice. Gene Ther 19:312–320

Marty M, Sersa G, Garbay JR, Gehl J, Collins CG, Snoj M, Billard V, Geertsen PF, Larkin JO, Miklavcic D, Pavlovic I, Paulin-Kosir SM, Cemazar M, Morsli N, Soden DM, Rudolf Z, Robert C, O'Sullivan GC, Mir LM (2006) Electrochemotherapy—an easy, highly effective and safe treatment of cutaneous and subcutaneous metastases: results of ESOPE (European standard operating procedures of electrochemotherapy) study. EJC Suppl 4:3–13

Mazeres S, Sel D, Golzio M, Pucihar G, Tamzali Y, Miklavcic D, Teissie J (2009) Noninvasive contact electrodes for in vivo localized cutaneous electropulsation and associated drug and nucleic acid delivery. J Control Release 134:125–131

Miklavcic D, Towhidi L (2010) Numerical study of the electroporation pulse shape effect on molecular uptake of biological cells. Radiol Oncol 44:34–41

Mir LM (2009) Nucleic acids electrotransfer-based gene therapy (electrogenetherapy): past, current, and future. Mol Biotechnol 43:167–176

Neumann E, Schaefer-Ridder M, Wang Y, Hofschneider PH (1982) Gene transfer into mouse lyoma cells by electroporation in high electric fields. EMBO J 1:841–845

Paganin-Gioanni A, Bellard E, Escoffre JM, Rols MP, Teissie J, Golzio M (2011) Direct visualization at the single-cell level of siRNA electrotransfer into cancer cells. Proc Natl Acad Sci USA 108:10443–10447

Palmer GM, Fontanella AN, Shan S, Hanna G, Zhang G, Fraser CL, Dewhirst MW (2011) In vivo optical molecular imaging and analysis in mice using dorsal window chamber models applied to hypoxia, vasculature and fluorescent reporters. Nat Protoc 6:1355–1366

Pavselj N, Preat V (2005) DNA electrotransfer into the skin using a combination of one high- and one low-voltage pulse. J Control Release 106:407–415

Reyes-Aldasoro CC, Wilson I, Prise VE, Barber PR, Ameer-Beg M, Vojnovic B, Cunningham VJ, Tozer GM (2008) Estimation of apparent tumor vascular permeability from multiphoton fluorescence microscopic images of P22 rat sarcomas in vivo. Microcirculations 15:65–79

Rice J, Ottensmeier CH, Stevenson FK (2008) DNA vaccines: precision tools for activating effective immunity against cancer. Nat Rev Cancer 8:108–120

Rols MP, Delteil C, Golzio M, Dumond P, Cros S, Teissie J (1998) In vivo electrically mediated protein and gene transfer in murine melanoma. Nat Biotechnol 16:168–171

Roos AK, Eriksson F, Timmons JA, Gerhardt J, Nyman U, Gudmundsdotter L, Brave A, Wahren B, Pisa P (2009) Skin electroporation: effects on transgene expression, DNA persistence and local tissue environment. PLoS ONE 4:e7226

Rosati M, Bergamaschi C, Valentin A, Kulkarni V, Jalah R, Alicea C, Patel V, von Gegerfelt AS, Montefiori DC, Venzon DJ, Khan AS, Draghia-Akli R, Van Rompay KK, Felber BK, Pavlakis GN (2009) DNA vaccination in rhesus macaques induces potent immune responses and decreases acute and chronic viremia after SIVmac251 challenge. Proc Natl Acad Sci USA 106:15831–15836

Sardesai NY, Weiner DB (2011) Electroporation delivery of DNA vaccines: prospects for success. Curr Opin Immunol 23:421–429

Seeley R, Stephens T, Tate P (2000) Anatomy and physiology, 5th edn. McGraw-Hill, New York

Sersa G, Jarm T, Kotnik T, Coer A, Podkrajsek M, Sentjurc M, Miklavcic D, Kadivec M, Kranjc S, Secerov A, Cemazar M (2008a) Vascular disrupting action of electroporation and electrochemotherapy with bleomycin in murine sarcoma. Br J Cancer 98:388–398

Sersa G, Miklavcic D, Cemazar M, Rudolf Z, Pucihar G, Snoj M (2008b) Electrochemotherapy in treatment of tumours. Eur J Surg Oncol 34:232–240

Tang DC, DeVit M, Johnston SA (1992) Genetic immunization is a simple method for eliciting an immune response. Nature 356:152–154

Tevz G, Kranjc S, Cemazar M, Kamensek U, Coer A, Krzan M, Vidic S, Pavlin D, Sersa G (2009) Controlled systemic release of interleukin-12 after gene electrotransfer to muscle for cancer gene therapy alone or in combination with ionizing radiation in murine sarcomas. J Gene Med 11:1125–1137

van den Heuvel MG, Buurman WA, Bast A, van der Hulst RR (2009) Ischaemia–reperfusion injury in flap surgery. J Plast Reconstr Aesthet Surg 62:721–726

van Drunen Littel-van den Hurk S, Hannaman D (2010) Electroporation for DNA immunization: clinical application. Expert Rev Vaccin 9:503–517

Vanbever R, Preat VV (1999) In vivo efficacy and safety of skin electroporation. Adv Drug Deliv Rev 35:77–88

Vasan S, Hurley A, Schlesinger SJ, Hannaman D, Gardiner DF, Dugin DP, Boente-Carrera M, Vittorino R, Caskey M, Andersen J, Huang Y, Cox JH, Tarragona-Fiol T, Gill DK, Cheeseman H, Clark L, Dally L, Smith C, Schmidt C, Park HH, Kopycinski JT, Gilmour J, Fast P, Bernard R, Ho DD (2011) In vivo electroporation enhances the immunogenicity of an HIV-1 DNA vaccine candidate in healthy volunteers. PLoS ONE 6:e19252

Vidic S, Markelc B, Sersa G, Coer A, Kamensek U, Tevz G, Kranjc S, Cemazar M (2010) MicroRNAs targeting mutant K-ras by electrotransfer inhibit human colorectal adenocarcinoma cell growth in vitro and in vivo. Cancer Gene Ther 17:409–419

Wagner RF Jr, Tomich JM, Grande DJ (1985) Electrolysis and thermolysis for permanent hair removal. J Am Acad Dermatol 12:441–449

Widera G, Austin M, Rabussay D, Goldbeck C, Barnett SW, Chen M, Leung L, Otten GR, Thudium K, Selby MJ, Ulmer JB (2000) Increased DNA vaccine delivery and immunogenicity by electroporation in vivo. J Immunol 164:4635–4640

Xing X, Sha S, Li Y, Zong L, Jiang T, Cao Y (2012) Immunization with a new DNA vaccine for Alzheimer's disease elicited Th2 immune response in BALB/c mice by in vivo electroporation. J Neurol Sci 313:17–21

Zaharoff DA, Barr RC, Li CY, Yuan F (2002) Electromobility of plasmid DNA in tumor tissues during electric field-mediated gene delivery. Gene Ther 9:1286–1290

J Membrane Biol (2012) 245:555–564
DOI 10.1007/s00232-012-9467-x

Destabilizing Giant Vesicles with Electric Fields: An Overview of Current Applications

Thomas Portet · Chloé Mauroy · Vincent Démery · Thibault Houles · Jean-Michel Escoffre · David S. Dean · Marie-Pierre Rols

Received: 14 December 2011 / Accepted: 24 June 2012 / Published online: 5 August 2012

Abstract This review presents an overview of the effects of electric fields on giant unilamellar vesicles. The application of electrical fields leads to three basic phenomena: shape changes, membrane breakdown, and uptake of molecules. We describe how some of these observations can be used to measure a variety of physical properties of lipid membranes or to advance our understanding of the phenomena of electropermeabilization. We also present results on how electropermeabilization and other liposome responses to applied fields are affected by lipid composition and by the presence of molecules of therapeutic interest in the surrounding solution.

Keywords Deformation · Electric field · Fusion · Giant unilamellar vesicle · Poration

Introduction

Our conception of the role of lipid molecules in biological membranes has dramatically evolved over the past few decades. The lipid membrane was first considered as a purely passive barrier and a substrate to house membrane proteins that carried out the biological functions of the cell membrane. However, it is now widely accepted that lipids play an active role in a number of biological processes. Their physicochemical properties, conferred by their structure and their amphiphilic nature, have consequences well beyond their self-assembly and ability to form a barrier. However, the study of the behavior of lipid molecules in a complex environment, such as a living cell, turns out to be a very difficult task as a result of the presence of other cell constituents such as the cytoskeleton and organelles, and also because of the large number of different lipid species present. Another source of complexity emerges from the presence of various membrane proteins and the cell glycocalyx.

Fortunately, we are now able to form cell-sized artificial membranes with well controlled compositions. These objects are called giant unilamellar vesicles (GUVs), also referred to as giant vesicles or giant liposomes. Their study has become increasingly popular in chemistry, biology and physics laboratories. Their primary interest is probably their size which, ranging from a few to hundreds micrometers in diameter, allows their direct observation via optical microscopy techniques. During the 1980s, Angelova and Dimitrov developed an efficient protocol for GUV production known as electroformation (Angelova and Dimitrov 1986; Mathivet et al. 1996), which was later shown to indeed produce unilamellar vesicles (Rodriguez et al. 2005). Because of the ease of their fabrication and their rich phenomenology, artificial vesicles have received an ever growing interest from the scientific community, as attested by the increasing number of studies using GUVs as membrane model systems. We anticipate that this tendency could even accelerate in the future, as a number of obstacles in the preparation of giant liposomes under physiological conditions have recently been overcome (Estes and Mayer 2005; Horger et al. 2009; Montes et al. 2007; Pott et al. 2008).

Thomas Portet and Chloé Mauroy contributed equally to this review.

T. Portet · V. Démery · D. S. Dean
Laboratoire de Physique Théorique, CNRS UMR 5152, Université Paul Sabatier, Toulouse, France

T. Portet · C. Mauroy · T. Houles · J.-M. Escoffre · M.-P. Rols (✉)
Institut de Pharmacologie et de Biologie Structurale, Centre National de la Recherche Scientifique, UMR 5089 and Université Paul Sabatier, 205 route de Narbonne, BP 64182, 31077 Toulouse, France
e-mail: rols@ipbs.fr; Marie-Pierre.Rols@ipbs.fr

Here we aim to introduce the various phenomena that occur when GUVs are subjected to electric fields. Dimova and colleagues have written comprehensive reviews about the effects of electric fields on GUVs (Dimova et al. 2007, 2009) and about the physics of GUVs in general (Dimova et al. 2006). The present paper is a natural sequel to these articles. It reviews newer results published after 2009, with an emphasis on works from our group. As review paper, it naturally suffers from certain subjectivity and is obviously not exhaustive; however, we hope it will be of use to newcomers in the field or to people familiar with Dimova et al.'s reviews and who wish to know about the most recent developments. It is organized in the following way: we first describe results on the influence of electric fields on giant liposomes, along with their theoretical explanations when they exist. We then describe some applications resulting from these behaviors. In addition, we present some preliminary results on the effect of lipid composition and the presence of poloxamers on the electropermeabilization of GUVs. Some results on the electromediated uptake of DNA by GUVs are also described.

Some Effects of Electric Fields on Giant Vesicles

Both direct current (DC) square pulses and alternating current (AC) sinusoidal fields can strongly destabilize giant vesicles and influence their behavior. Depending on the parameters of the applied field (amplitude, frequency, and number and duration of pulses), giant vesicles can porate, fuse, deform, or even exhibit domain motion in the case of multicomponent liposomes. The purpose of this section is to present these phenomena.

Deformation

To our knowledge, the deformation of giant vesicles by electric fields (or electrodeformation) was first extensively studied by Kummrow and Helfrich (1991). The authors applied sinusoidal AC electric fields of ~ 1 kHz frequency and amplitudes ranging up to 100 V/cm, and found that spherical liposomes deformed into prolate ellipsoids oriented in the field direction, the degree of deformation increasing with the magnitude of the applied field. Ellipsoidal deformation of spherical vesicles in water by AC and DC electric fields had already been predicted earlier (Winterhalter and Helfrich 1988). Monitoring the relative area dilation of the membrane yielded an experimental estimate for the bending rigidity k_c of the lipid bilayer. A few years later, Mitov et al. (1993) explained theoretically and observed experimentally a prolate to oblate shape transition when increasing the field frequency above a few kilohertz. However, these experiments were limited to vesicles in pure water (internal–external conductivity ratio $x = \lambda_{in}/\lambda_{out} \approx 1$), and to AC field frequencies in the kHz range. An extensive study of the influence of the media's electrical conductivities ($x > 1$ or $x < 1$) in a wider range of frequencies f (from 10^2 to 10^8 Hz) was published 15 years later (Aranda et al. 2008). Aranda et al. observed that GUVs could attain oblate, prolate or spherical shapes upon varying x or f, and were able to construct a morphological phase diagram describing four different transitions whose characteristic frequencies depend on the conductivity ratio x. At high frequencies (several MHz), all vesicles were found to adopt spherical shapes. At low frequencies ($f <$ a few kHz), all vesicles deformed into prolate ellipsoids, as predicted in (Winterhalter and Helfrich 1988). The prolate to oblate transition happens at intermediate frequencies for $x < 1$, i.e., when there is more salt outside the liposomes than inside. Another transition of this type could also be triggered at a fixed frequency f by varying x, for example by adding pure water to the sample and thus increasing the conductivity ratio. These behaviors can be qualitatively understood if one considers the motion of ions and the distance they travel in presence of an AC electric field. If the field frequency is large they are virtually immobile, while if the frequency is lowered they can be pushed against the membrane and then modify the vesicle shape. Nevertheless, at that time there was no theory able to fully describe these four transitions as a function of f and x. Winterhalter and Helfrich's (1988) theory did not account for the recovery of the spherical shape at high frequencies, and Mitov's theory could not either (Mitov et al. 1993). A theory explaining the morphological diagram of (Aranda et al. 2008) was developed in (Vlahovska et al. 2009). In this approach, vesicle shape was determined by balancing electric, hydrodynamic, bending and tension stresses exerted on the membrane. This force balance approach also provides information about the kinetics of liposome deformation, unlike the former theories based on energy minimization (Mitov et al. 1993; Winterhalter and Helfrich 1988). A more recent theoretical study (Yamamoto et al. 2010), despite not considering the effect of the electric double layer, provides an explanation for all the features of the morphological diagram of (Aranda et al. 2008). Rigorous evaluation of the work done by the Maxwell stresses, for different frequency and salt conditions, finally enabled to clarify the molecular mechanisms underlying the morphological transitions.

Winterhalter and Helfrich's (1988) model also predicted that DC pulses should deform spherical vesicles into prolate ellipsoids too. However, DC pulses usually have durations of the order of several tens or hundreds of microseconds, or at most of some milliseconds. Imaging at such high rates is impossible with classical video cameras, so if one wants to get insight at what happens during an

electric pulse application, one has to work with a fast imaging setup allowing image acquisition at several thousand frames per second. This approach was first applied by Riske and Dimova (2005), and they indeed found that GUVs deformed into prolate ellipsoids upon the application of electric pulses of 50–300 μs duration and 1–3 kV/cm amplitude. They worked with salt-free solutions, but still at a conductivity ratio of $x \approx 1.3$, meaning that the solution inside the vesicle was more conductive that the outer one. Later, when the same authors wanted to work in conditions closer to physiological ones and to investigate the role of salts in the exterior medium, it was somewhat surprisingly found, that vesicles subjected to electric pulses in salt solutions always adopted cylindrical shapes, irrespective of their ionic content (and thus of the conductivity ratio) (Riske and Dimova 2006). This finding still lacks a quantitative theoretical explanation.

Electropermeabilization

Electric pulses may also have much more dramatic effects on lipid bilayers than simple deformation. They can sufficiently disrupt the membrane as to allow the uptake of otherwise nonpermeant molecules such as Propidium Iodide, plasmid DNA, poloxamer, bleomycin or cisplatin. Depending on the field strength used this can occur in a reversible manner and without affecting cell viability (Neumann et al. 1989). This process, called electropermeabilization, has led to biomedical applications in the fight against cancer, or in the field of gene therapy (Belehradek et al. 1993; Escoffre et al. 2009). Despite its increasing popularity among physicians, biologists and oncologists, no one knows for sure what really happens when subjecting a living cell to a permeabilizing electric pulse. Uptake mechanisms are triggered by the electric potential difference across the membrane $\Delta\Psi$ induced by the field and seem to be dependent on the size and charge of the transferred compounds. Electric potential difference across the membrane is among others influenced also by both membrane surface potentials (inner and outer) which depends on the physical properties of the electric double layer at both sides of the membrane (McLaughlin 1989).

No consensus exists on the way the membrane reorganizes at the molecular level and this question still remains a challenge. Here again, GUVs are convenient tools to investigate these questions. Some studies have been performed and have shown that indeed, giant vesicles can be permeabilized by electric pulses. By coupling electropermeabilization and the micropipette aspiration technique, it was shown that the critical membrane voltage $\Delta\Psi_c$ required for breakdown ranged from 1.1 to 1.8 V, depending on membrane composition (Needham and Hochmuth 1989). It was also observed that a macropore of several micrometers size could be induced (Zhelev and Needham 1993). It was later shown by Tekle et al. (2001) that the mechanism of pore formation is asymmetric. A macropore is formed on the cathode-facing side of the vesicle, whereas the presence of many smaller pores on the other hemisphere can be inferred from the size decrease of the liposome after pulse application. This phenomenon of GUVs shrinkage during electropulsation was then extensively studied by our team (Portet et al. 2009). By applying a sequence of long (5 ms) electric pulses, we found that vesicles shrank, down to a critical radius beyond which their size no longer changed. We identified three mechanisms for the lipid loss: formation of macropores on the cathode-facing side as already reported (Tekle et al. 2001), formation of tubular structures on the anode facing side, and formation of small vesicles at both poles. These three features should probably not be considered as distinct mechanisms. Macropore and tubules formation probably reflect the same phenomena, as they were found to occur together. Small vesicles expulsion can be understood as another way of expelling lipids, and may under certain conditions be more energetically favorable than tubule formation. While assuming that the area lost per pulse was proportional to the permeabilized area (the area on the vesicle where the induced transmembrane voltage $\Delta\Psi = (3/2)\mathrm{RE}\cos(\theta)$ exceeded the critical transmembrane voltage $\Delta\Psi_c$, R denoting the radius of the vesicle, E the pulse amplitude and θ the angle with respect to the field direction), we were able to analytically predict the decrease of the GUV radius as a function of the number of applied pulses. We fitted our experimental data with the appropriate formula (equation (10) in Portet et al. 2009), and finally obtained the values of $\Delta\Psi_c$ for DOPC and EggPC vesicles, 0.85 and 1 V, respectively. Later on, we conducted the same experiments with liposomes of another composition: DOPC/Sphingomyelin/Cholesterol (2/2/1, mol/mol/mol) [unpublished results]. We found $\Delta\Psi_c \approx 0.4$ V for this composition closer to the actual lipidic composition of a real cell membrane. This finding is interesting, as to our knowledge, such a low value for permeabilization threshold of GUVs has never previously been found. Typical values are about 1 V for giant liposomes containing a single phosphatidylcholine, or a simple two component mixture, while typical critical transmembrane voltages are about 0.2 V for many cell types (Teissie and Rols 1993). Our results thus indicate that the reason for this discrepancy with respect to the case of simple model membranes may be the result of the presence of several lipid phases. Macropore formation was also studied by Riske and Dimova (2005). The pulses they applied were shorter and more intense than ours, but could still cause macropore formation. It was shown that poration of the vesicles affected the membrane relaxation dynamics, and that the initial membrane tension had a strong influence on the critical potential difference for porating the GUV.

Another study reported that the presence of anionic lipid species in the membrane could cause vesicle bursting, whereas simple phosphatidylcholine membranes usually reseal after a permeabilizing electric pulse (Riske et al. 2009). More recently, the same group investigated the electropermeabilization of GUVs in the gel phase (Knorr et al. 2010). Wrinkling patterns of the membrane were reported, along with poration thresholds 10 times higher than those typically measured with fluid membranes. It was also observed that the macropores created by the electric pulse did not reseal in these gel phase vesicles; the pores were stable for several minutes.

Motion of Domains

Increasing the membrane complexity by addition of different phospholipids and cholesterol leads to phenomena that cannot be observed in single component GUVs. Staykova et al. (2008) managed to monitor the motion of liquid ordered domains in giant vesicles made of DOPC/DPPC/cholesterol (different molar ratios were explored) subjected to AC electric fields of $\approx$500 V/cm amplitude in the kHz frequency range. They report that this movement had characteristic features depending on the field parameters, and that it was caused by the inhomogeneous surface tension induced by the field because of the chamber geometry. It was the first time this phenomenon of induced charge electroosmosis was observed and studied on a lipid membrane.

Fusion

Membrane fusion is a key process of life. It is one of the most common ways for molecules to enter or exit cells. The process of fusion occurs in a variety of important biological processes such as nerve signal transmission provided by the fusion of synaptic vesicles to the outer membranes of nerve cells. Other processes where fusion occurs are intracellular trafficking (Eitzen 2003; Hay 2007) and viral infection by membrane-enclosed viruses (Kielian and Rey 2006; Weissenhorn et al. 2007).

However, membrane fusion does not occur spontaneously because of large energetic barriers in biological membranes. These energetic barriers are caused by Van der Waals, electrostatic and steric repulsions and by strong hydration (Helm et al. 1992; Kozlovsky and Kozlov 2002). To promote membrane fusion it is essential to overcome these barriers. In biological membrane systems this process occurs via fusion proteins (Carr and Kim 1993; Yu et al. 1994) in a multistep process. For most viruses, a fusion event is achieved in two steps. First, fusion proteins recognize a site for fusion on the membrane of the host cell. Then, the hydrophobic domain of the fusion protein inserts itself into the membrane of the host cell.

Studies of the fusion pathway have shown two important types of intermediate structures in the fusion mechanism: hemifusion structures and fusion pores (Lentz et al. 2000). Hemifusion structures form a connection between outer leaflets but not between inner leaflets which remain distinct. They are transient structures that either dissociate to give two independent membranes or induce fusion pores (Lentz et al. 2000). Fusion pores are connections between both outer and inner leaflets, they form an aqueous connection between the two aqueous compartments. The propensity to obtain these two intermediates depends on lipid composition, as fusion depends on the ability of the membrane to bend into these states and thus on the spontaneous curvature and bending rigidity of the associated monolayers and bilayers (Chernomordik and Kozlov 2003). It has been recently shown that the stability of the fusion pore may strongly depend on the anisotropic, intrinsic shape of lipids in the fusion pore (Jorgacevski et al. 2010). Obviously another condition to induce fusion is the establishment of a sufficiently close interbilayer proximity. As hydration forces contribute to the repulsion between membranes, the fusogenic state can be induced via bilayer dehydration (Lentz 1994). In biological systems dehydration can be induced by calcium ions that neutralize the negatively charged phospholipid head groups, reducing electrostatic repulsion between membranes, and/or help the formation of Ca^{2+}-phosphate bridges between opposing bilayers (Jeremic et al. 2004). Dehydration can also be induced by the application of an electric field on membrane systems, which can rearrange the interfacial water molecule network (Lopez et al. 1988).

Electrofusion is a very convenient way to control, both spatially and temporally, fusion events. It is thus possible to trigger and observe the whole fusion process to study the underlying mechanisms. To occur, electrofusion requires two conditions: (a) electropermeabilization and (b) contact between lipid membranes. When the two membranes are close enough and lipid perturbation is high enough, fusion occurs; for cells this was demonstrated by Zimmermann (1982). It has been shown that membrane fusion can be obtained, not only by pulsing cells already in close contact, but also by bringing them into close contact after their permeabilization (Rols and Teissie 1989; Sowers 1986; Teissie and Rols 1986). Electropermeabilized membranes are thus fusogenic. For a better understanding of the fundamental processes involved in membrane fusion, lipid vesicles are often used as model systems (Neumann et al. 1989; Tamm et al. 2003). An AC field can be used to align vesicles in the field direction and bring two vesicles into contact. A subsequent application of a DC pulse induces the permeabilization of the two vesicles and if permeabilization is induced in the contact area fusion is induced. Membrane fusion is a fast process. It has been shown that

the fusion process occurs within two stages (Haluska et al. 2006). The first stage is the opening of the fusion neck with an average expansion velocity of about 2 cm/s. In the second stage, the neck-expansion velocity slows down until complete opening of the fusion neck. In the absence of salt, the fusion typically occurs at several contact points of the vesicles. In the case of several contact points (more than two), the coalescence of these fusion necks can lead to small vesicles enclosed in the contact zone. In the presence of salt in the solution outside of the vesicles, the DC pulse induces vesicles deformation and the vesicles are pushed together and form a at contact zone. As no enclosed vesicles are observed, one may infer that only one fusion neck or a small number of such necks has been formed.

In summary, it is possible to control and observe vesicle fusion by the method of electrofusion. Vesicle fusion has applications that we discuss below.

Some Applications

In the last section, we have reviewed the various possible responses of GUVs subjected to different kinds of electric fields. These phenomena have led to applications, which we describe in this section. We first describe how shape analysis of giant liposomes in an AC field can allow the measurement of the lipid bilayer bending rigidity k_c. Then we show how electric pulses can be used to efficiently load GUVs with nonpermeant molecules. Below we highlight some applications of membrane fusion. Finally we explain how to measure the edge or line tension γ of lipid membranes, and how electric fields can be used to improve the current measurement methods.

Measuring Bending Rigidities

The bending rigidity k_c is a material property of lipid membranes introduced by Helfrich (1973) in his theory of the elasticity of lipid bilayers. It has the dimensions of energy and, roughly speaking, can be related to the energy price one has to pay in order to bend a membrane. It plays a role in the control of the membrane shape, in the determination of the amplitude of thermal fluctuations, or in the modulation of membrane proteins activity, and thus being able to measure it is of interest in the understanding of various biological events. Here we will just describe the k_c measurement method on the basis of electrodeformation. There exist other ways of measuring bending rigidities which are described in the review of Marsh (2006).

In the first bending rigidity measurements via electrodeformation, giant vesicles were exposed to AC fields of a few kHz frequency and $\approx$100 V/cm amplitude, and shapes were recorded while increasing the field amplitude (Kummrow and Helfrich 1991). The liposomes deformed gradually into a more and more elongated prolate ellipsoid, and also changed their apparent surface area as a result of the flattening of thermal fluctuations. The basic idea of the method is first to calculate the lateral tension σ induced by the field. To do so, one combines the Laplace relation at the pole and the equator for a vesicle with uniform internal pressure, which yields: $\sigma(c_1 + c_2)_e - (T_{rr})_e = \sigma(c_1 + c_2)_p - (T_{rr})_p$, where c_1 and c_2 are the principal curvatures of the ellipsoid (computed from the measured values of the axes of the ellipsoid), T_{rr} is the stress exerted on the outer surface of the vesicle by the field which gives rise to the deformation and the flattening of undulations, and the subscripts e and p indicate that the associated quantities are calculated at the equator and the poles of the vesicle, respectively. The difference between the equatorial and polar stresses is proportional to the square of the magnitude of the applied field. The tension σ can then be obtained on the basis of the known value of the applied field and the observed shape of the GUV. After that, the relative area change α should be computed using the measured values of the axes of the ellipsoid. This relative area change is given by $(k_BT/8\pi k_c)\ln(\sigma/\sigma_0)$, where k_BT is the thermal energy and σ_0 a positive parameter obtained by extrapolation to $\alpha = 0$. Note that this parameter is not necessarily the tension at zero field, but is not required to determine k_c by fitting a straight line to the logarithmic plot of α as a function of σ. This method for measuring k_c was later applied by Gracia et al. (2010) in order to study the influence of cholesterol on the rigidity of membranes of various compositions. The authors also used another measurement method for k_c on the basis of the analysis of membrane fluctuations (see, e.g., Faucon et al. 1989; Milner and Safran 1987; Schneider et al. 1984). It was found that the electrodeformation method leads to slightly lower k_c values than the fluctuation method (as noted in Kummrow and Helfrich 1991). Nevertheless, both methods give the same trends and reproducible results. The results suggest that the effect of cholesterol addition on the membrane bending rigidity is concentration dependent, but is also highly influenced by the lipid type to which cholesterol is added (Gracia et al. 2010). An important point to keep in mind is that the electrodeformation method using the theoretical analysis described above cannot be applied if one works in salt solutions or with charged lipid species.

Loading Vesicles

As previously stated, DC pulses are useful tools to enable the entry of nonpermeant molecules into cells. They can thus also enable one to load a vesicle with compounds of interest. This has applications in drug delivery, where lipid vesicles play the role of cargo carriers, but is also of interest in fundamental research, for example when trying

to understand the nature of the DNA/membrane interaction occurring during cell electropermeabilization (Golzio et al. 2002). As far as we know, very few papers focusing on the electromediated DNA uptake by liposomes have been published. Chernomordik et al. (1990) applied a single electric pulse of 12.5 kV/cm amplitude and 300 μs duration to large unilamellar vesicles (≈100 nm size, two orders of magnitude smaller than GUVs) composed of DPPC/cholesterol (7/3, mol/mol) in the presence of high molecular mass DNA of size similar to that of the plasmid DNA usually used in gene transfer protocols. They claim that the uptake mechanism took place via the electrostimulated formation of endosome-like vesicles rather than via electropores. These conclusions were questioned 10 years later by Lurquin and Athanasiou (2000), who found that DNA could enter DPPC GUVs under free form by a mechanism involving electro-induced membrane pores. They used longer pulses (12 ms) of smaller amplitude (1,500 V/cm), but which caused greater induced transmembrane voltages than those of Chernomordik et al. (1990).

In order to resolve these conflicting results, we carried out DNA loading experiments on DOPC GUVs. Our results clearly favor the second mechanism involving DNA entry via electropores. As can be seen on Fig. 1, showing a vesicle before (left) and a few seconds after (right) electric treatment (15 pulses of 5 ms duration, 370 V/cm amplitude and 0.33 Hz frequency), plasmid DNA stays trapped inside the vesicle, mostly under free form and not in endocytosis-like vesicles. Tubules and small vesicles associated with lipid loss and vesicle shrinkage, as described in 2.2, can also be observed. The small vesicles may contain some DNA, but DNA entry under free form is the predominant mechanism. The tubules appear to stay mostly attached to the vesicle and diffuse along the vesicle surface after the pulses application. The encapsulation is stable; DNA stays trapped in the GUVs several minutes after the electric treatment. The extent of lipid loss was comparable to the one reported in Portet et al. (2009); about 30 % of the permabilized area was lost, per pulse. No macropores were detected in these experiments, but this is not surprising because the temporal resolution of our setup was 3 s whereas the macropores typically reseal within a few hundred milliseconds. Using confocal microscopy, we were able to quantify the amount of DNA entering the liposome after each pulse, and have developed a theoretical model able to account for the increase of DNA concentration inside the GUV (Portet et al. 2011).

Applications of Fusion

Because membrane fusion induces a mixing of the lipids initially present in each membrane and a mixing of the aqueous compartments, electrofusion could be used to introduce molecules into a membrane or into an aqueous compartment. In the case of the fusion of two vesicles having different lipid compositions, it is possible to produce multicomponent vesicles of well-defined composition (Dimova et al. 2007; Riske et al. 2006). This provides the possibility of studying the dynamics of domain formation and stability. When giant vesicles are prepared directly with a multicomponent lipid mixture, the compositions of the different vesicles are dispersed about the composition of the initial lipid mixture. Electrofusion of two vesicles

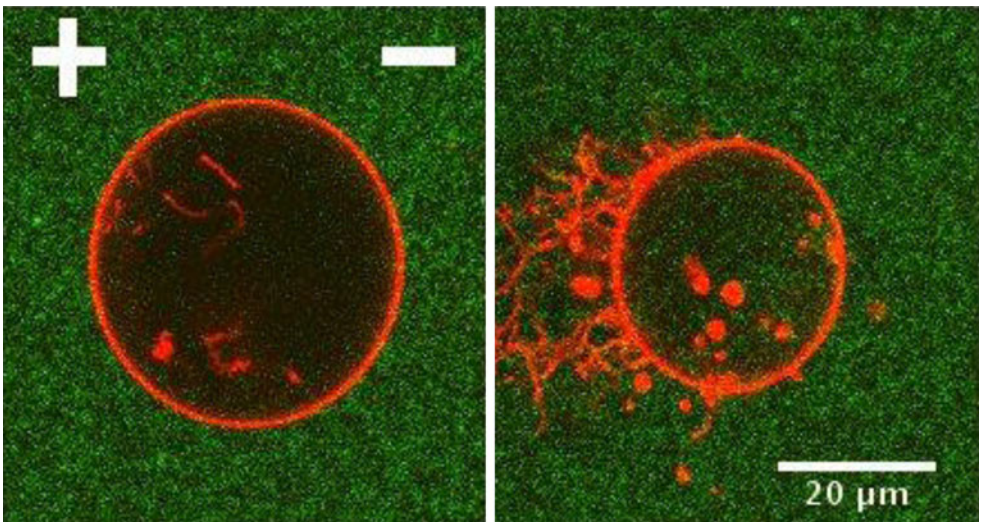

Fig. 1 Confocal microscopy image of a DOPC GUV fluorescently labeled with rhodamine-PE (*red*) in the presence of plasmid DNA labeled with TOTO-1 (*green*). *Left* There is no DNA present inside the liposome before electric treatment. *Right* A few seconds after electropermeabilization, the vast majority of electrotransferred DNA is under free form and not enclosed in endocytosis-like vesicles. Tubules and small vesicles associated with lipid loss can also be observed. Field polarity is indicated on the *left*

each made of different components thus allows one to obtain vesicles with a well specified composition. Fusing two vesicles of nonmiscible lipid composition produces microdomains in the resulting vesicle's membrane.

The fusion of two vesicles of different content is a realization of a microreactor. It has been shown that two vesicles can encapsulate one or more reagent molecules (Chiu et al. 1999). When electrofusion is induced between these two vesicles, the contents of the two vesicles are mixed and a chemical reaction between the two reagent molecules can occur. This method needs one condition to be efficient: the lipid membranes of the two compartments have to be impermeable to the reactants. The first use of vesicles as microreactors was demonstrated with a chemical reaction between the calcium sensitive fluorescent dye Fluo-3 and Ca^{2+} (Chiu et al. 1999). A batch of vesicles was loaded with Fluo-3 and another was loaded with Ca^{2+}. The two types of containers were mixed, electrofusion was induced, and fluorescence enhancement due to the formation of a complex between Fluo-3 and Ca^{2+} was observed. The method of electrofusion provides a promising tool for studying and following one chemical reaction at a time where spatial and temporal localization can be precisely controlled. Furthermore, the small volume used in this technique could also provide a general chemical or biochemical delivery system.

On the basis of this previous experiment, electrofusion has been used as a method for nanoparticle synthesis in vesicles (Yang et al. 2009). In this case, one vesicle is loaded with Na_2S and the other one with $CdCl_2$. The application of an AC field allows the bringing of vesicles into contact, DC pulse application then induces fusion and as a consequence mixing of the two compartments. Fluorescence in the interior of the resulting vesicles indicates the formation of CdS nanoparticles. Thanks to this approach it is possible to observe and monitor the whole reaction with an optical microscope. This experiment suggests that nanoparticles could be synthesized in biological compartments even without the intervention of macromolecules.

Measuring Edge/Line Tensions

The hydrocarbon chains of lipids are hydrophobic and the energy cost per unit length for leaving the hydrophobic core of a membrane in contact with water is called the line or edge tension γ. It is often hypothesized that for large edges the lipid heads can bend over the edge to make the edge hydrophilic; however, there is still an edge tension due to the bending energy associated with this lipid rearrangement. The edge tension is a lipid material property and depends on the external medium. It is the edge tension that makes a membrane patch embedded in an aqueous environment spontaneously bend to form a vesicle, and it also generates the force driving pore closure in lipid bilayers (Fromherz et al. 1986; Sandre et al. 1999). Roughly speaking, the higher the edge tension, the faster the pore closes and one can deduce γ from the evaluation of the corresponding pore closure times.

We put this idea into practice while studying the influence of a poloxamer molecule on EggPC GUVs. It was seen in Sharma et al. (1996) that poloxamers could modify lipid membrane properties under electric pulses. We explored the effect of the presence of poloxamer in the surrounding solution. Using poloxamer L64 at concentrations of 2.5 and 5 g/L, we first observed no effect on giant liposomes at rest. Then we applied porating electric pulses of 5 ms duration and $\approx$500 V/cm amplitude to these liposomes, and with a fast EMCCD camera we were able to measure the size of the pores and their closure time. We saw no difference of the pore size between liposomes with or without poloxamer, regardless of the concentration. A study of pore closure shows a strong effect: the average measured closure time without poloxamer is 0.2 s while it is 0.4 s with poloxamer, and we did not detect any effect of the concentration of poloxamer. Pore closure is thus twice as slow with poloxamer, and this seems to indicate that L64 reduces the edge tension of EggPC membranes, hence helping to maintain the membrane in a permeabilized state. Because the above results come from very few measurements (6 without poloxamer and 2 for each poloxamer concentration) they are only preliminary and still need to be corroborated.

It is possible to go beyond these qualitative observations and to accurately measure edge tension values. Harbich and Helfrich (1979) observed open cylindrical EggPC giant vesicles in AC fields and then deduced a value of 20 pN for γ. Zhelev and Needham (1993) obtained values in the same range for SOPC and SOPC/cholesterol (1/1, mol/mol) liposomes while coupling the electroporation technique and micropipette aspiration. A more recent edge tension measurement method emerged from the theoretical work by Brochard-Wyart et al. (2000). Considering a spherical vesicle of size R, it was shown that in the limit corresponding to experiments on giant vesicles, a pore of radius r spent the vast majority of its lifetime in a so-called slow closure stage during which the quantity $R^2 \ln(r)$ decreased linearly with time, the coefficient of proportionality being equal to $(-2\gamma/3\pi\eta_0)$, where η_0 denotes the external medium viscosity. The same group later applied this method to pure DOPC GUVs and also to systems containing cholesterol or a surfactant, opening pores via intense visible light illumination. Adding glycerol to the aqueous solutions caused slowing down of the dynamics, and they were thus able to measure the pore size during the slow closure stage using classical fluorescence microscopy. They obtained values of

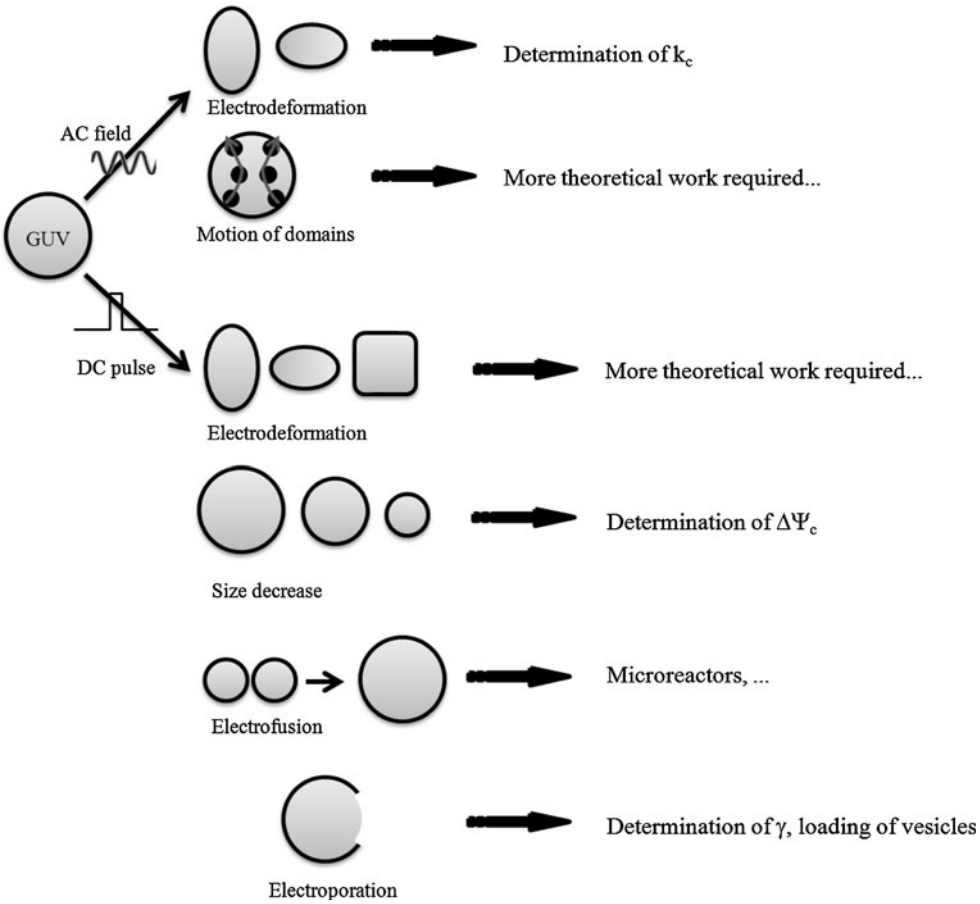

Fig. 2 Diagram summarizing the influence of electric fields on giant lipid vesicles and their practical uses. The mention "More theoretical work required…" means that the current understanding of the phenomenon does not allow us to design practical uses yet, and that deeper knowledge is still needed to fully exploit this effect of the electric field. Indeed, further identification of gaps and opportunities in the field should be exploited

γ for their different vesicle compositions, and found that cholesterol caused an increase of γ whereas the surfactant led to a decrease (Karatekin et al. 2003). The main problem of this approach is that glycerol influences the lipid bilayer organization, and that fluorescent dyes embedded in the membrane behave as impurities and may hence lead to inaccurate edge tension measurements. We thus proposed an improvement of Brochard-Wyart's method based on the application of an electric pulse to porate the vesicle and on ultrafast phase contrast imaging to monitor pore size evolution (Portet and Dimova 2010). This method is easy to implement, requires little equipment, and does not suffer from the drawbacks related to the presence of glycerol and fluorescent dye. We confirmed that the addition of cholesterol increased the edge tension of a bare DOPC membrane, and surprisingly, we found that DOPE addition to a DOPC bilayer caused a decrease of γ.

Conclusions

Giant vesicles provide a useful model system for measuring a variety of physical properties of lipid membranes and for improving our understanding of the electropermeabilization and electrofusion phenomena. In this review, we have summarized the presently known effects of electric fields on giant vesicles and some of their practical applications, and presented current research topics covered by our group. Subjecting GUVs to DC pulses or alternating AC fields can destabilize the lipid bilayer, inducing different behavior such as deformation of the vesicles, poration, motion of domains, or fusion. An outline of these various behaviors and their uses is presented in Fig. 2.

It is now known that the deformation of the vesicles depends not only on the frequency and the intensity of the applied field, but also on the solutions conductivities. Furthermore, the deformations are not exactly the same, depending on the presence or not of salt in the external medium and on the shape of the applied electric field (AC or DC). By monitoring the relative area dilatation of the membrane, it is possible to estimate the bending rigidity k_c of the lipid bilayer.

Electric pulses have more dramatic consequences than just deformation. With suitable parameters for the electric field, it is possible to electropermeabilize the membrane. This effect can lead to exchange of molecules between the

inside and the outside of the vesicle. If the electropermeabilization is strong enough, membrane macropores can be visualized via optical microscopy. When a sequence of pulses is used, such observations are in general accompanied by loss of lipid membrane material and a subsequent GUV size decrease allowing the determination of a critical transmembrane voltage. Moreover, by monitoring the evolution of the pore radius it is possible to measure another lipid material property, the edge or line tension γ.

When two vesicles are in close contact, electropermeabilizing them with suitably chosen electric field parameters can induce their fusion. This electrofusion method allows the control and observation of vesicle fusion and is thus useful for insertion of molecules into the membrane or for mixing different chemicals in the resulting vesicle, thus giving a microreactor.

Acknowledgments We acknowledge financial support from the Institut Universitaire de France, ANR-PCV (project CMIDT-139888), and the Association Française contre les Myopathies. We thank our colleagues C. Favard, J. Tessié, L. Wasungu, N. Mignet, M. Bureau, and D. Scherman for many useful discussions and interactions on the subjects discussed in this review.

References

Angelova MI, Dimitrov DS (1986) Liposome electroformation. Biophys J 81:303–311

Aranda S, Riske KA, Lipowsky R, Dimova R (2008) Morphological transitions of vesicles induced by alternating electric fields. Biophys J 95:L19–L21

Belehradek M, Domenge C, Luboinski B, Orlowski S, Belehradek J Jr, Mir LM (1993) Electrochemotherapy, a new antitumor treatment. First clinical phase I–II trial. Cancer 72:3694–3700

Brochard-Wyart F, de Gennes PG, Sandre O (2000) Transient pores in stretched vesicles: role of leak-out. Phys A 278:32–51

Carr CM, Kim PS (1993) A spring-loaded mechanism for the conformational change of influenza hemagglutinin. Cell 73: 823–832

Chernomordik LV, Kozlov MM (2003) Protein-lipid interplay in fusion and fission of biological membranes. Annu Rev Biochem 72:175–207

Chernomordik LV, Sokolov AV, Budker VG (1990) Electrostimulated uptake of DNA by liposomes. Biochim Biophys Acta 1024:179–183

Chiu DT, Wilson CF, Ryttsen F, Stromberg A, Farre C, Karlsson A, Nordholm S, Gaggar A, Modi BP, Moscho A, Garza-Lopez RA, Orwar O, Zare RN (1999) Chemical transformations in individual ultrasmall biomimetic containers. Science 283:1892–1895

Dimova R, Aranda S, Bezlyepkina N, Nikolov V, Riske KA, Lipowsky R (2006) A practical guide to giant vesicles. Probing the membrane nanoregime via optical microscopy. J Phys Condens Matter 18:S1151–S1176

Dimova R, Riske KA, Aranda S, Bezlyepkina N, Knorr RL, Lipowsky R (2007) Giant vesicles in electric fields. Soft Matter 3:817–827

Dimova R, Bezlyepkina N, Domange Jordo M, Knorr RL, Riske KA, Staykova M, Vlahovska PM, Yamamoto T, Yang P, Lipowsky R (2009) Vesicles in electric fields: some novel aspects of membrane behavior. Soft Matter 5:3201–3212

Eitzen G (2003) Actin remodeling to facilitate membrane fusion. Biochim Biophys Acta 1641:175–181

Escoffre JM, Portet T, Wasungu L, Teissie J, Dean D, Rols MP (2009) What is (still not) known of the mechanism by which electroporation mediates gene transfer and expression in cells and tissues. Mol Biotechnol 41:286–295

Estes DJ, Mayer M (2005) Giant liposomes in physiological buffer using electroformation in a flow chamber. Biochim Biophys Acta 1712:152–160

Faucon JF, Mitov MD, Méléard P, Bivas I, Bothorel P (1989) Bending elasticity and thermal fluctuations of lipid membranes. Theoretical and experimental requirements. J Phys 50:2389–2414

Fromherz P, Röcker C, Rüppel D (1986) From discoid micelles to spherical vesicles. The concept of edge activity. Faraday Discuss Chem Soc 81:39–48

Golzio M, Teissie J, Rols MP (2002) Direct visualization at the single-cell level of electrically mediated gene delivery. Proc Natl Acad Sci U S A 99:1292–1297

Gracia RS, Bezlyepkina N, Knorr RL, Lipowsky R, Dimova R (2010) Effect of cholesterol on the rigidity of saturated and unsaturated membranes: fluctuation and electrodeformation analysis of giant vesicles. Soft Matter 6:1472–1482

Haluska CK, Riske KA, Marchi-Artzner V, Lehn JM, Lipowsky R, Dimova R (2006) Time scales of membrane fusion revealed by direct imaging of vesicle fusion with high temporal resolution. Proc Natl Acad Sci U S A 103:15841–15846

Harbich W, Helfrich W (1979) Alignment and opening of giant lecithin vesicles by electric fields. Z Naturforsch 34:1063–1065

Hay JC (2007) Calcium: a fundamental regulator of intracellular membrane fusion? EMBO Rep 8:236–240

Helfrich W (1973) Elastic properties of lipid bilayers: theory and possible experiments. Z Naturforsch C 28:693–703

Helm CA, Israelachvili JN, McGuiggan PM (1992) Role of hydrophobic forces in bilayer adhesion and fusion. Biochemistry 31:1794–1805

Horger KS, Estes DJ, Capone R, Mayer M (2009) Films of agarose enable rapid formation of giant liposomes in solutions of physiologic ionic strength. J Am Chem Soc 131:1810–1819

Jeremic A, Kelly M, Cho JA, Cho SJ, Horber JK, Jena BP (2004) Calcium drives fusion of SNARE-apposed bilayers. Cell Biol Int 28:19–31

Jorgacevski J, Fosnaric M, Vardjan N, Stenovec M, Potokar M, Kreft M, Kralj-Iglic V, Iglic A, Zorec R (2010) Fusion pore stability of peptidergic vesicles. Mol Membr Biol 27:65–80

Karatekin E, Sandre O, Guitouni H, Borghi N, Puech PH, Brochard-Wyart F (2003) Cascades of transient pores in giant vesicles: line tension and transport. Biophys J 84:1734–1749

Kielian M, Rey FA (2006) Virus membrane-fusion proteins: more than one way to make a hairpin. Nat Rev Microbiol 4:67–76

Knorr RL, Staykova M, Gracia RS, Dimova R (2010) Wrinkling and electroporation of giant vesicles in the gel phase. Soft Matter 6:1990–1996

Kozlovsky Y, Kozlov MM (2002) Stalk model of membrane fusion: solution of energy crisis. Biophys J 82:882–895

Kummrow M, Helfrich W (1991) Deformation of giant lipid vesicles by electric fields. Phys Rev A 44:8356–8360

Lentz BR (1994) Polymer-induced membrane fusion: potential mechanism and relation to cell fusion events. Chem Phys Lipids 73:91–106

Lentz BR, Malinin V, Haque ME, Evans K (2000) Protein machines and lipid assemblies: current views of cell membrane fusion. Curr Opin Struct Biol 10:607–615

Lopez A, Rols MP, Teissie J (1988) ^{31}P NMR analysis of membrane phospholipid organization in viable, reversibly electropermeabilized Chinese hamster ovary cells. Biochemistry 27:1222–1228

Lurquin PF, Athanasiou K (2000) Electric field-mediated DNA encapsulation into large liposomes. Biochem Biophys Res Commun 267:838–841

Marsh D (2006) Elastic curvature constants of lipid monolayers and bilayers. Chem Phys Lipids 144:146–159

Mathivet L, Cribier S, Devaux PF (1996) Shape change and physical properties of giant phospholipid vesicles prepared in the presence of an AC electric field. Biophys J 70:1112–1121

McLaughlin S (1989) The electrostatic properties of membranes. Annu Rev Biophys Biophys Chem 18:113–136

Milner ST, Safran SA (1987) Dynamical fluctuations of droplet microemulsions and vesicles. Phys Rev A 36:4371–4379

Mitov MD, Meleard P, Winterhalter M, Angelova MI, Bothorel P (1993) Electric-field-dependent thermal fluctuations of giant vesicles. Phys Rev E Stat Phys Plasmas Fluids Relat Interdiscip Topics 48:628–631

Montes LR, Alonso A, Goni FM, Bagatolli LA (2007) Giant unilamellar vesicles electroformed from native membranes and organic lipid mixtures under physiological conditions. Biophys J 93:3548–3554

Needham D, Hochmuth RM (1989) Electro-mechanical permeabilization of lipid vesicles. Role of membrane tension and compressibility. Biophys J 55:1001–1009

Neumann E, Sowers A, Jordan C (1989) Electroporation and electrofusion in cell biology. Plenum, New York

Portet T, Dimova R (2010) A new method for measuring edge tensions and stability of lipid bilayers: effect of membrane composition. Biophys J 99:3264–3273

Portet T, Camps i Febrer F, Escoffre JM, Favard C, Rols MP, Dean DS (2009) Visualization of membrane loss during the shrinkage of giant vesicles under electropulsation. Biophys J 96:4109–4121

Portet T, Favard C, Teissie J, Dean DS, Rols MP (2011) Insights into the mechanisms of electromediated gene delivery and application to the loading of giant vesicles with negatively charged macromolecules. Soft Matter 7:3872–3881

Pott T, Bouvrais H, Meleard P (2008) Giant unilamellar vesicle formation under physiologically relevant conditions. Chem Phys Lipids 154:115–119

Riske KA, Dimova R (2005) Electro-deformation and poration of giant vesicles viewed with high temporal resolution. Biophys J 88:1143–1155

Riske KA, Dimova R (2006) Electric pulses induce cylindrical deformations on giant vesicles in salt solutions. Biophys J 91: 1778–1786

Riske KA, Bezlyepkina N, Lipowsky R, Dimova R (2006) Electrofusion of model lipid membranes viewed with high temporal resolution. Biophys Rev Lett 1:387–400

Riske KA, Knorr RL, Dimova R (2009) Bursting of charged multicomponent vesicles subjected to electric pulses. Soft Matter 5:1983–1986

Rodriguez N, Pincet F, Cribier S (2005) Giant vesicles formed by gentle hydration and electroformation: a comparison by fluorescence microscopy. Colloids Surf B Biointerfaces 42:125–130

Rols MP, Teissie J (1989) Ionic-strength modulation of electrically induced permeabilization and associated fusion of mammalian cells. Eur J Biochem 179:109–115

Sandre O, Moreaux L, Brochard-Wyart F (1999) Dynamics of transient pores in stretched vesicles. Proc Natl Acad Sci U S A 96:10591–10596

Schneider MB, Jenkins JT, Webb WW (1984) Thermal fluctuations of large cylindrical phospholipid vesicles. Biophys J 45:891–899

Sharma V, Stebe K, Murphy JC, Tung L (1996) Poloxamer 188 decreases susceptibility of artificial lipid membranes to electroporation. Biophys J 71:3229–3241

Sowers AE (1986) A long-lived fusogenic state is induced in erythrocyte ghosts by electric pulses. J Cell Biol 102:1358–1362

Staykova M, Lipowsky R, Dimova R (2008) Membrane flow patterns in multicomponent giant vesicles induced by alternating electric fields. Soft Matter 4:2168–2171

Tamm LK, Crane J, Kiessling V (2003) Membrane fusion: a structural perspective on the interplay of lipids and proteins. Curr Opin Struct Biol 13:453–466

Teissie J, Rols MP (1986) Fusion of mammalian cells in culture is obtained by creating the contact between cells after their electropermeabilization. Biochem Biophys Res Commun 140: 258–266

Teissie J, Rols MP (1993) An experimental evaluation of the critical potential difference inducing cell membrane electropermeabilization. Biophys J 65:409–413

Tekle E, Astumian RD, Friauf WA, Chock PB (2001) Asymmetric pore distribution and loss of membrane lipid in electroporated DOPC vesicles. Biophys J 81:960–968

Vlahovska PM, Gracia RS, Aranda-Espinoza S, Dimova R (2009) Electrohydrodynamic model of vesicle deformation in alternating electric fields. Biophys J 96:4789–4803

Weissenhorn W, Hinz A, Gaudin Y (2007) Virus membrane fusion. FEBS Lett 581:2150–2155

Winterhalter M, Helfrich W (1988) Deformation of spherical vesicles by electric fields. J Colloid Interface Sci 122:583–586

Yamamoto T, Aranda-Espinoza S, Dimova R, Lipowsky R (2010) Stability of spherical vesicles in electric fields. Langmuir 26: 12390–12407

Yang P, Lipowsky R, Dimova R (2009) Nanoparticle formation in giant vesicles: synthesis in biomimetic compartments. Small 5:2033–2037

Yu YG, King DS, Shin YK (1994) Insertion of a coiled-coil peptide from influenza virus hemagglutinin into membranes. Science 266:274–276

Zhelev DV, Needham D (1993) Tension-stabilized pores in giant vesicles: determination of pore size and pore line tension. Biochim Biophys Acta 1147:89–104

Zimmermann U (1982) Electric field-mediated fusion and related electrical phenomena. Biochim Biophys Acta 694:227–277

J Membrane Biol (2012) 245:565–571
DOI 10.1007/s00232-012-9468-9

Chemically Modified Oligonucleotide–Increased Stability Negatively Correlates with Its Efficacy Despite Efficient Electrotransfer

Sandrine Pelofy · Justin Teissié · Muriel Golzio · Sophie Chabot

Received: 19 December 2011 / Accepted: 24 June 2012 / Published online: 15 July 2012

Abstract Despite great potential for disease treatment, small interfering RNA (siRNA) development has been hampered due to its poor stability and the lack of efficient delivery method. To overcome the sensitivity, new generations of chemically modified oligonucleotides have been developed such as the locked nucleic acid (LNA). LNA substitution in an siRNA sequence (siLNA) is supposed to increase its stability and its affinity for its complementary sequence. The purpose of this study was to evaluate the potential benefit of an anti-GFP siLNA using the biophysical delivery method electropermeabilization. We used two types of electrical conditions: electrochemotherapy (ECT), a condition for efficient transfer of small molecules in clinics, and electrogenotherapy (EGT), a condition for efficient transfer of macromolecules. We first confirmed that siLNA was indeed more stable in mouse serum than unmodified siRNA. After determining the ECT and EGT optimal electrical parameters for a human colorectal carcinoma cell line (HCT-116) expressing eGFP, we showed that modifications of siRNA do not interfere with electrotransfer efficiency. However, despite its higher stability and its high electrotransfer efficacy, siLNA was less efficient for eGFP silencing compared to the electrotransferred, unmodified siRNA regardless of the electrical conditions used. Our study highlighted the care that is needed when designing chemically modified oligonucleotides.

Keywords Electropermeabilization · Electroporation · Gene silencing · siRNA · siLNA · Locked nucleic acid · Chemically modified oligonucleotide

Introduction

RNA interference (RNAi) is a natural process that allows gene silencing at the transcriptional level (Fire et al. 1998). Short interfering RNAs (siRNAs) are doubled-stranded, noncoding RNAs that, once introduced into cells, are loaded into the cytoplasmic RNA–induced silencing complex (RISC). The complex binds targeted RNA messenger (mRNA), leading to its cleavage (Moazed 2009). Therefore, siRNA offers the possibility to silence the expression of any pathological protein in a specific way. However, its clinical success has been hampered by its poor cellular uptake and stability. To overcome these problems, progress has been made in developing new technologies to optimize the siRNA chemistry, on the one hand, and to achieve its effective delivery, on the other hand (Whitehead et al. 2009).

Electropermeabilization (EP) is a physical delivery method which consists of the application of controlled electric field pulses to induce cell permeabilization (Teissie et al. 2011). Since the first report in 2002 (Hu et al. 2002), numerous publications have demonstrated the potency of this technique for siRNA delivery (Calegari et al. 2002; Pekarik et al. 2003; Golzio et al. 2007; Lewis et al. 2002; Matsuda and Cepko 2004; Paganin-Gioanni et al. 2008). Recently, we demonstrated by time-lapse microscopy that siRNA electrotransfer depends on both the

M. Golzio and S. Chabot contributed equally to this study.

S. Pelofy · J. Teissié · M. Golzio (✉) · S. Chabot
CNRS (Centre National de la Recherche Scientifique), IPBS (Institut de Pharmacologie et de Biologie Structurale), BP 64182, 205 route de Narbonne, 31077 Toulouse, France
e-mail: muriel.golzio@ipbs.fr

S. Pelofy · J. Teissié · M. Golzio · S. Chabot
IPBS, Université Paul Sabatier de Toulouse, 31077 Toulouse, France

permeabilization of the cell membrane and the electrophoretic drag of the negatively charged oligonucleotide (Paganin-Gioanni et al. 2011). In addition, we showed that, contrary to most of the carrier systems (Decuzzi and Ferrari 2008), EP allows siRNA to enter directly into the cell, avoiding endolysosomal compartmentalization and keeping it localized in the cytoplasm, where its enzymatic machinery and mRNA target are located (Paganin-Gioanni et al. 2011). Therefore, EP is particularly well adapted for siRNA use. Several electric settings have been described in the literature as efficiently electrotransferring siRNA. Basically, two major electric conditions exist for EP supporting oligonucleotide delivery. The first one, electrochemotherapy (ECT), is commonly used in clinics and mainly allows transfer of small hydrophilic molecules (Mir et al. 1997). It corresponds to pulse duration in the microsecond range. The second electric condition is electrogenotherapy (EGT) and usually leads to a more efficient plasmid DNA electrotransfer. It is based on the application of pulses with duration in the millisecond range (Aihara and Miyazaki 1998; Rols and Teissie 1998).

Despite efficient siRNA electrodelivery, its silencing effect is transient and short (25 days for electrotransferred muscle and 2–4 days for in vitro and in vivo electrotransferred tumor cells) (Golzio et al. 2005, 2007; Paganin-Gioanni et al. 2008). The transient effect of siRNA could be mainly explained by its low biostability as it is quickly degraded by extra- and intracellular ribonucleases (Layzer et al. 2004; Raemdonck et al. 2006).

To address this problem and improve siRNA potency and efficacy, approaches based on the introduction of chemical modifications in its sequence have been developed. Locked nucleic acid (LNA) containing a methylene bridge that connects the 2′-carbon of the ribose with the 4′-carbon (Kumar et al. 1998) is the third generation of such nucleotide analogues. Due to its methylene bridge, the sugar moiety is conformationally locked in an RNA/mimicking C3′endo/N-type conformation that preorganizes the base for hybridization (Petersen et al. 2000). Consequently, oligonucleotides containing LNA nucleotides exhibit very high thermal stability when hybridized with its RNA target molecule (Braasch and Corey 2001) and improved mismatch discrimination compared to unmodified oligonucleotides (Kaur et al. 2007). In addition, oligonucleotides containing LNA nucleotides are highly resistant to nuclease degradation (Crinelli et al. 2002) and display low toxicity in biological systems (Wahlestedt et al. 2000). Therefore, LNA-modified siRNA (siLNA) appears to be a promising tool for siRNA therapeutic application.

The goal of the present study was to evaluate the potential benefit of siLNA compared to unmodified siRNA using the EP technique. Electrotransfer efficiency was quantified using cyanine 5 (Cy5)–labeled oligonucleotides. To analyze electrotransferred oligonucleotide silencing potency, we targeted enhanced green fluorescent protein (eGFP) because it allows a simple quantitative readout for gene-specific knockdown over time. We first confirmed that LNA substitutions in the oligonucleotide sequence increased half-life in serum. After determining the optimal electrical parameters, we showed that siLNA and siRNA were equivalently electrotransferred using Cy5-labeled oligonucleotides. However, we observed that electrotransferred siLNA was less efficient for eGFP silencing than electrotransferred siRNA in vitro. Our study highlighted the care that is needed when designing chemically modified oligonucleotides.

Materials and Methods

Cell Culture

HCT-GFP cells are HCT-116 cells (human colorectal carcinoma) expressing eGFP that have been transferred by retroviral transduction. HCT-GFP cells were maintained in DMEM, 4.5 g/l of D-glucose, L-glutamine, 110 mg/l of sodium pyruvate (GIBCO-Invitrogen, Grand Island, NY), containing 1 % antibiotic penicillin/streptavidin (GIBCO-Invitrogen) supplemented with 10 % inactivated fetal calf serum (Boehringer Ingelheim, Paris, France) in a 5 % CO_2 humidified incubator at 37 °C.

Oligonucleotides

Cy5-labeled and unlabeled siRNA and siLNA directed against eGFP mRNA were purchased from Qiagen Xeragon (Germantown, MD) and Ribotask (Odense, Denmark), respectively. The siLNA sequences were, sense, 5′-GcaagcugacccugaaguucaTT-3′ and, antisense, 5′-gaacuucagggucagcuugcCG-3′ (LNA nucleotides are depicted in uppercase letters). The position of LNA was chosen with respect to previous results (Mook et al. 2007). The same exact sequences were used for siRNA as previously described (Caplen et al. 2001). To determine oligonucleotide uptake, Cy5-labeled siRNA (Cy5-siRNA) and Cy5-siLNA were used. Labeling of siRNA does not modify its global negative charge.

Stability Test

We incubated siRNA or siLNA (10 µM) at 37 °C in 30 µl of PBS or in 30 µl of fresh mouse serum. Aliquots of 4 µl were withdrawn after 1, 2, 3, 4 and 7 days of incubation and stored at −20 °C until used. Samples were analyzed on 2 % agarose gel. Oligonucleotides were visualized with ethidium bromide (Sigma-Aldrich, St. Louis, MO) staining.

Electropermeabilization

Cell suspension (5×10^5) in 100 µl of pulsing buffer (10 mM phosphate, 1 mM $MgCl_2$, 250 mM sucrose, pH 7.4) containing 100 µM of propidium iodide (Sigma-Aldrich) was placed in an electropulsation chamber, which was designed using stainless-steel parallel plate electrodes (10 mm length, 0.5 mm thickness and 4 mm interelectrode distance; IGEA, Carpi, Italy) brought into contact with the bottom of a 35-mm Petri dish (Nunc, Roskilde, Denmark). Electropulsation was operated using the S20u electropulsator (βtech, l'Union, France), which delivered square-wave electric pulses. The βtech monitored pulse shape online on its integrated display. A uniform electric field was generated when the voltage pulse was delivered (Gehl et al. 1999). Pulses with controlled duration and frequency of 1 Hz were applied at preset electric field intensities at room temperature (25 °C). Cells were analyzed by flow cytometry using a FACScalibur (Becton Dickinson, Franklin Lakes, NJ) to determine the percentage of permeablized cells (i.e., propidium iodide–positive cells). A minimum of 10^4 events were acquired on the FL-2 channel and analyzed with Cellquest software (Becton Dickinson).

Cell Viability Analysis

Cell viability was determined by the ability of cells to grow and divide over 24 h (Gabriel and Teissie 1995). Viability was measured by counting cells by crystal violet staining (Merck, Darmstadt, Germany). Briefly, cells were stained with 1 ml crystal violet (0.1 % in pulsing buffer) for 20 min, rinsed with PBS and then lysed with 500 µl acetic acid (10 %) for 5 min. Cell density was evaluated by 595 nm OD measurement. Nonpulsed cells were referred to as 100 % viable cells.

Confocal Fluorescence Microscopy

For fluorescence microscopy, cells (8×10^4) were seeded on a glass coverslip chamber (Nalge Nunc, Illkirch, France) overnight at 37 °C in a humidified atmosphere with 5 % CO_2. The electropulsation chamber was designed using two stainless-steel parallel rods (1 mm diameter, 10 mm length, 5 mm interelectrode distance) that were connected to the electropulsator. The chamber was set on the stage of an inverted confocal microscope (Zeiss LSM510; Carl Zeiss MicroImaging, Göttingen, Germany) equipped with a 40 × Zeiss objective (1.3 numerical aperture, oil immersion). Adherent cells were then electrotransfected in 500 µl of pulsing buffer in the presence of 250 nM (final) Cy5-labeled siLNA using the following electrical parameters: 300 V/cm, 10 pulses of 5 ms, 1 Hz. Cy5 was visualized using a 633-nm laser (emission filter 640–710 nm). Eight-bit images were recorded with Zeiss LSM510 software (EMBL, Heidelberg, Germany). LSM images were processed with ImageJ software (NIH, Bethesda, MD) as described in Paganin-Gioanni et al. (2011).

Electrotransfer of Oligonucleotides

Cells were pulsed or not in the presence of oligonucleotides (2 µg), as described above, using optimal electric parameters as determined by cell permeabilization and viability analysis. After 5-min incubation at room temperature, cells were analyzed by flow cytometry or recultivated in 35-mm Petri dishes, supplemented with 2 ml of DMEM and then incubated for 24 h to 7 days at 37 °C under 5 % CO_2. To determine oligonucleotide uptake, the percentage of $Cy5^+$ cells was quantified (FL-4 channel). To determine the efficiency of electrotransferred oligonucleotides, the percentage of cells expressing eGFP was analyzed (FL-1 channel).

Statistical Analyses

Quantitative data (presented as means ± SD) were analyzed with GraphPad (San Diego, CA) Prism 4 software. Before carrying out statistical tests, we determined whether the data were normally distributed and evaluated their variance. We then carried out appropriate tests as indicated. We report the actual P value for each test. For in vitro time course experiments, we used two-way ANOVA with the Bonferroni post hoc test. $P < 0.05$ was considered statistically significant.

Results

Oligonucleotide Stability

We first compared siRNA and siLNA stability. For that purpose, oligonucleotides were incubated at 37 °C in saline buffer or in fresh mouse serum. In PBS, both oligonucleotides were detectable for at least 7 days (Fig. 1a). However, in serum, siRNA was undetectable within 2 days of incubation, while siLNA was detectable for 3 days (Fig. 1b). Our result confirmed that siLNA was more stable in mouse serum than the unmodified siRNA.

Optimal Electric Parameter Determination

EP is modulated by the electric parameters used and may vary as a function of cell type. Therefore, we determined the optimal electric parameters (i.e., high transfection level in accordance with good cell viability) for HCT-GFP cells

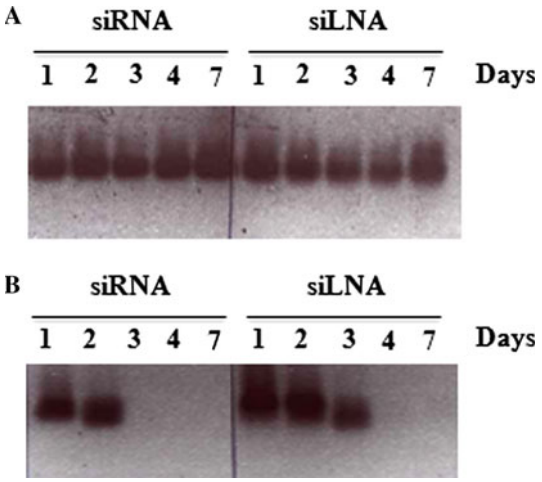

Fig. 1 Oligonucleotide stability. SiRNA and siLNA were incubated at 37 °C in PBS (**a**) or in fresh mouse serum (**b**) for the indicated times. Oligonucleotide electrophoresis was run on an agarose gel and visualized with ethidium bromide staining. This gel is representative of three independent experiments

for the two main EP conditions. Permeabilization was analyzed by entry of propidium iodide. Cell viability was analyzed 24 h later by crystal violet staining.

In both conditions, an increase of EP was induced by an increase of the field intensity. On the contrary, cell viability decreased as the field intensity increased. In ECT condition, we obtained 81 ± 5 % of viable cells for 84 ± 1 % of permeabilized cells at 1,500 V/cm. Thus, the optimal electric parameter (eight pulses of 100 µs duration with a field intensity of 1,500 V/cm at 1 Hz frequency) led to 65 ± 7 % of viable and permeabilized HCT-GFP cells (Fig. 2a). Under the EGT condition, we obtained 71 ± 7 % of viable cells for 71 ± 6 % of permeabilized cells at 600 V/cm. Optimal electric parameters (10 pulses of 5 ms duration at 1 Hz frequency and a field intensity of 600 V/cm) led to 42 ± 10 % of viable and permeabilized HCT-GFP cells (Fig. 2b). The percentage of viable permeabilized cells was determined under the assumption that dead cells must have been permeabilized: [permeabilization (%) + viability (%)] − 100 (Gabriel and Teissie 1997).

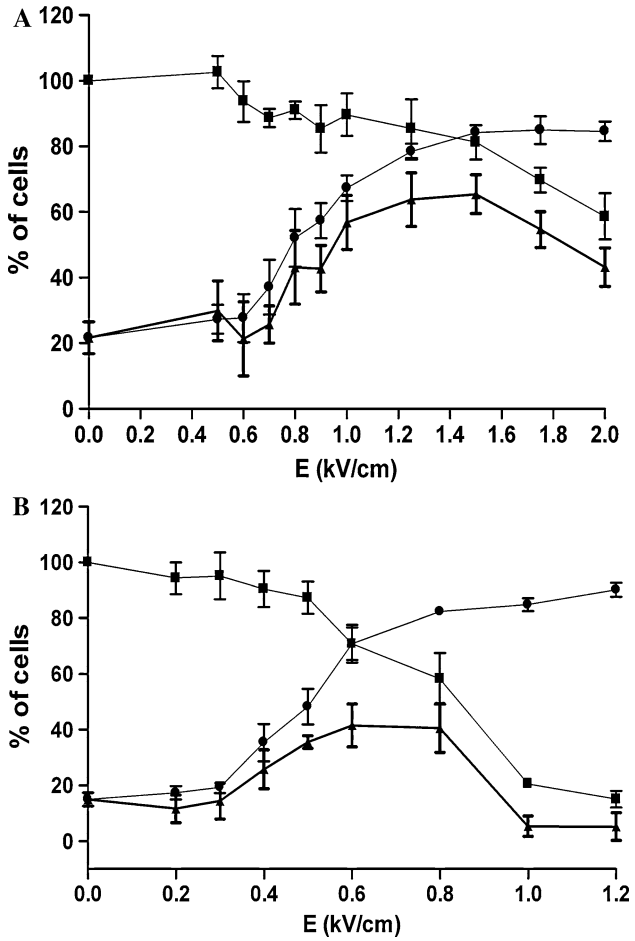

Fig. 2 Optimal electric parameter determination. Percentages of viable cells and permeabilized cells were plotted as a function of the electric field intensity according to (**a**) ECT condition (eight pulses of 100 µs duration at 1 Hz) and (**b**) EGT condition (10 pulses of 5 ms duration at 1 Hz). Permeabilization was assayed by propidium iodide entry into cells and analyzed by flow cytometry (*filled circle*). Cell viability was determined 24 h after EP by crystal violet staining (*filled square*). Values are means ± SD of three experiments

Oligonucleotide Electrotransfer Efficiency

We first visualized the electrotransferred siLNA at the single-cell level, as we previously did for siRNA (Paganin-Gioanni et al. 2011). We observed that, just after pulse application, siLNA is dispersed in the cytoplasm of the electrotransfected cells (Fig. 3a) in the same way as siRNA (Paganin-Gioanni et al. 2011). We then compared siRNA and siLNA electrotransfer efficiency in ECT (1,500 V/cm, 8 × 100 µs, 1 Hz) and EGT (600 V/cm, 10 × 5 ms, 1 Hz) conditions, using Cy5-labeled oligonucleotides. A nonsignificant 10 % augmentation of $Cy5^+$ cells was observed for EGT condition (Fig. 3b), and the cell-associated Cy5 fluorescence intensity was doubled for this electrical condition (Fig. 3c). In ECT condition, 67 ± 7 and 73 ± 6 % of cells were $Cy5^+$ when siRNA or siLNA was present in the pulsing buffer, respectively (Fig. 3b). In EGT conditions, we observed that 79 ± 5 and 83 ± 4 % of cells were $Cy5^+$ when pulsed in the presence of siRNA or siLNA, respectively (Fig. 3b). No significant difference was observed between the two oligonucleotides (Fig. 3b, c). Both electrical conditions led to efficient oligonucleotide electrotransfer, with similar efficiencies for both constructs.

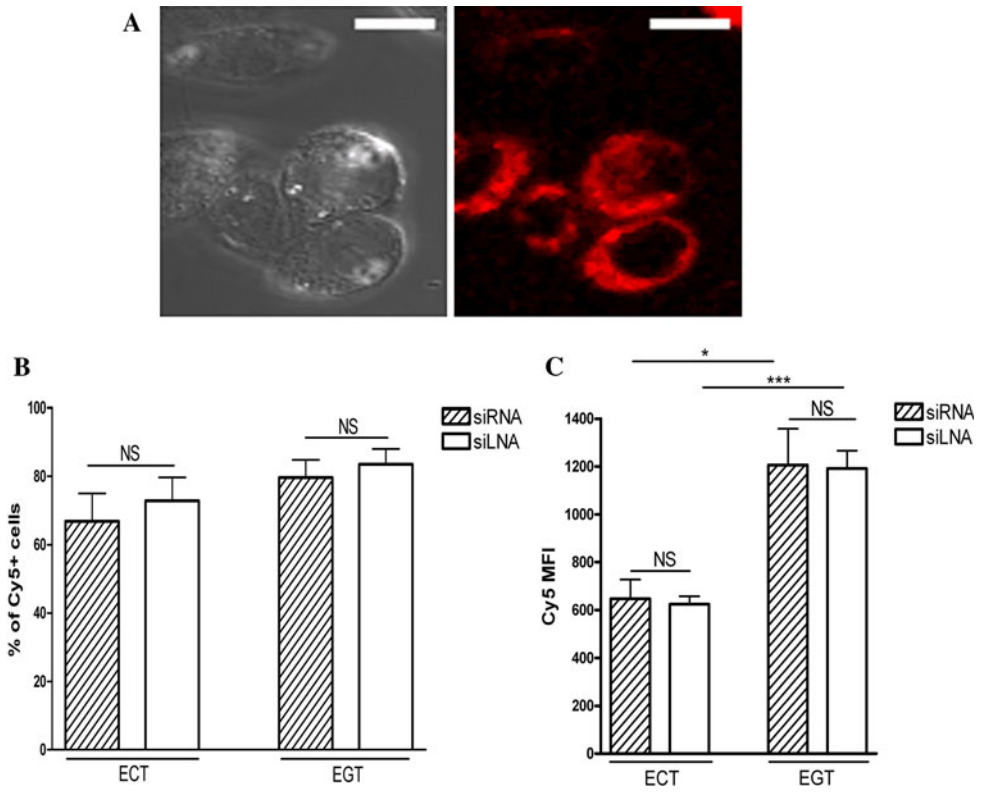

Fig. 3 Oligonucleotide electrotransfer efficiency. **a** Visualization of Cy5-siLNA electrotransfer by confocal fluorescence microscopy. Plated cells were pulsed on a coverslip under a confocal microscope in EGT (300 V/cm, 10 pulses of 5 ms, 1 Hz) condition in the presence of Cy5-siLNA (250 nM). Acquisition was performed after pulse application. *Left* Light transmission acquisition. *Right* Cy5 fluorescence acquisition. Scale bar = 10 µm. **b**, **c** HCT-GFP cells were pulsed in the presence of Cy5-siRNA or Cy5-siLNA using ECT condition (eight pulses of 100 µs duration, 1,500 V/cm at 1 Hz) and EGT condition (10 pulses of 5 ms duration, 600 V/cm at 1 Hz). The percentage of Cy5-positive cells was determined by flow cytometry a few minutes after the electrotransfer (**b**), and the cell-associated Cy5 mean fluorescence intensity was determined (**c**). Values are means ± SD of three experiments. *NS* nonsignificant; $*P = 0.0175$, $***P = 0.0004$ (Student's *t*-test)

Silencing Efficacy of Electrotransferred Oligonucleotides

Finally, we compared the silencing efficacy of electrotransferred siRNA and siLNA under ECT and EGT conditions. For both conditions, maximal eGFP silencing was observed at day 3 for the electrotransferred siRNA and at day 2 for the electrotransferred siLNA (Fig. 4). Using the ECT condition, we obtained 46 ± 4 and 66 ± 3 % of GFP^+ cells with electrotransferred siRNA and siLNA, respectively (Fig. 4a). In the EGT condition, we obtained 38 ± 6 and 63 ± 4 % of GFP^+ cells with electrotransferred siRNA and siLNA, respectively (Fig. 4b). One week after oligonucleotide electrotransfer, the percentage of eGFP-expressing cells returned to its control value. In summary, we observed a transient decreased eGFP expression with both electrotransferred anti-eGFP oligonucleotides, this effect being larger under the EGT conditions. However, in both electric conditions, electrotransferred siLNA led to a significantly weaker time effect of eGFP silencing compared to the unmodified, electrotransferred siRNA ($P < 0.001$, two-way ANOVA). In conclusion, electrotransferred siLNA was around 20 % less effective and its maximal silencing effect was shorter (2 vs. 3 days) compared to unmodified, electrotransferred siRNA.

Discussion

LNA nucleotides are proposed to offer a high resistance to nucleases. We indeed observed that siLNA was more stable in mouse serum than unmodified siRNA (Fig. 1). We then determined the optimal electric parameters (i.e., high transfection level in accordance with good cell viability) for HCT-GFP electrotransfer as follows: eight pulses of 100 µs duration at 1,500 V/cm for ECT condition and 10 pulses of 5 ms duration at 600 V/cm for EGT condition (Fig. 2). We observed for both oligonucleotides a significant increase in the cell-associated Cy5 fluorescence intensity with EGT parameters compared to ECT (Fig. 3c). This increase could be explained by the electric drift,

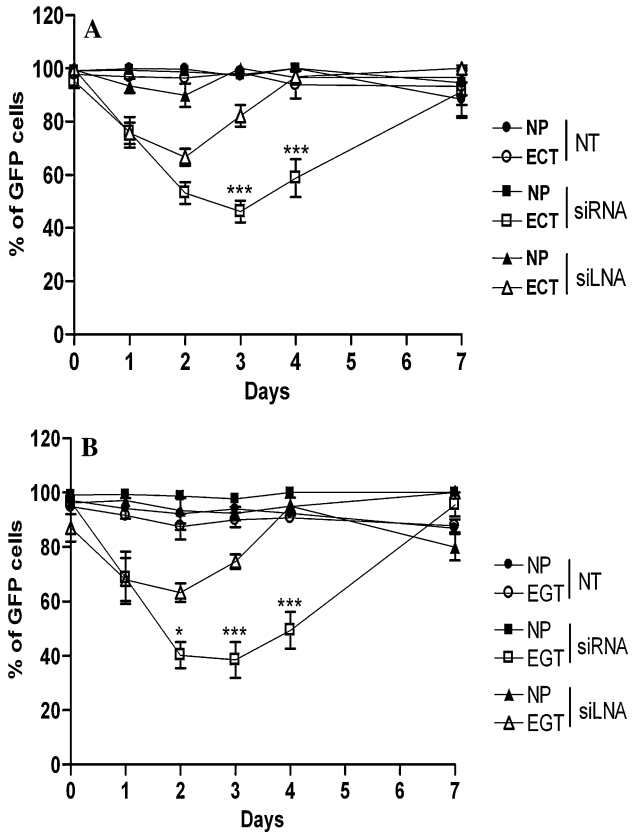

Fig. 4 Silencing efficiency of electrotransferred oligonucleotides. HCT-GFP cells were pulsed or not (*NP*) in the presence of siRNA or siLNA or not untreated (*NT*) using (**a**) the optimal ECT condition (eight pulses of 1.5 kV/cm, 100 µs, 1 Hz) and (**b**) the optimal EGT condition (10 pulses of 0.6 kV/cm, 5 ms, 1 Hz). The percentage of eGFP-positive cells was analyzed over time by flow cytometry. Values are means ± SD of three experiments. $*P \leq 0.05$ and $***P \leq 0.001$ (two-way ANOVA)

which is more important with EGT parameters compared to ECT parameters. In consequence, electrophoretic movement of the electrotransferred, negatively charged oligonucleotide during the pulse is more important and therefore could lead to its more efficient uptake. We further showed that siRNA and siLNA were equivalently electrotransferred, although a slight but nonsignificant increase was observed with siLNA in both ECT and EGT conditions (Fig. 3b). Despite these positive results, electrotransferred siLNA was less efficient for eGFP silencing regardless of the electric conditions that were used (Fig. 4).

The positioning and number of LNA nucleotides in the oligonucleotide sequence are crucial for siLNA activity (Kauppinen et al. 2006). As internal modification in the antisense strand may hamper siLNA activity (Elmen et al. 2005), we designed a gapmers endblock siLNA, meaning that LNA substitutions were located at the extremities of the oligonucleotides. The 3′-end LNA modifications in both the sense and antisense strands have been described as increasing oligonucleotide stability (Elmen et al. 2005), as confirmed by our result (Fig. 1). A limitation in siRNA use is that both strands might be incorporated into the RISC. Loading of the sense strand leads to unwanted off-target effects. LNA substitution could also be useful in this context as LNA modification in the sense strand 5′ end favors loading of the antisense strand. In fact, the thermodynamic stabilities of the 5′ ends of the two siRNA strands in the duplex determine the identity of the guide strand and the passenger strands (Schwarz et al. 2003). The guide strand directs the silencing, whereas the passenger strand is ultimately destroyed. Considering these data, the 5′ end of the antisense strand of our siLNA was devoid of LNA nucleotides, and LNA substitutions were added in the 5′ end of the sense strand. This design was thought to increase the binding energy of the sense 5′ base pair, preventing its loading into the RISC. In addition, the 5′ end LNA in the sense strand impaired nucleotide phosphorylation and, thus, RISC activation (Kaur et al. 2007). Thus, according to published data, our construct should encourage antisense strand loading and increase eGFP silencing. This was not supported by the experiments; we found that electrotransferred siLNA was less efficient for eGFP silencing (Fig. 4). More surprising, despite an enhanced serum half-life, the siLNA effect was less sustained compared to unmodified siRNA. Thus, the lowered siLNA efficacy was not compensated for by its increased stability, contrasting with previous suggestions (Mook et al. 2007). The lowered siLNA efficacy may be due to its less efficient recruitment by the RISC complex and/or its low processing as suggested by Bramsen et al. (2007). An interesting alternative will be the use of small internally segmented interfering RNAs (Bramsen et al. 2007).

It is noteworthy that the EGT condition that led to a slightly better cellular uptake of both oligonucleotides was associated with a better oligonucleotide eGFP silencing efficacy.

To conclude, we demonstrated that increased stability and efficient electrotransfer did not correlate with chemically modified oligonucleotide gene silencing efficacy.

Acknowledgement This work was supported by grants of the Ligue contre le Cancer, CNRS and FP7 Oncomirs (Grant 201102). Flow cytometry was performed at the TRI (funded by the region Midi-Pyrénées, the communauté du Grand Toulouse and the FEDER) platform at the IPBS. We thank Bettina Couderc (Institut National de la Santé et de la Recherche Médicale U563, Toulouse) for providing the HCT-GFP cell lines.

References

Aihara H, Miyazaki J (1998) Gene transfer into muscle by electroporation in vivo. Nat Biotechnol 16:867–870

Braasch DA, Corey DR (2001) Locked nucleic acid (LNA): fine-tuning the recognition of DNA and RNA. Chem Biol 8:1–7

Bramsen JB, Laursen MB, Damgaard CK, Lena SW, Babu BR, Wengel J, Kjems J (2007) Improved silencing properties using small internally segmented interfering RNAs. Nucleic Acids Res 35:5886–5897

Calegari F, Haubensak W, Yang D, Huttner WB, Buchholz F (2002) Tissue-specific RNA interference in postimplantation mouse embryos with endoribonuclease-prepared short interfering RNA. Proc Natl Acad Sci USA 22:14236–14240

Caplen NJ, Parrish S, Imani F, Fire A, Morgan RA (2001) Specific inhibition of gene expression by small double-stranded RNAs in invertebrate and vertebrate systems. Proc Natl Acad Sci USA 98:9742–9747

Crinelli R, Bianchi M, Gentilini L, Magnani M (2002) Design and characterization of decoy oligonucleotides containing locked nucleic acids. Nucleic Acids Res 30:2435–2443

Decuzzi P, Ferrari M (2008) The receptor-mediated endocytosis of nonspherical particles. Biophys J 94:3790–3797

Elmen J, Thonberg H, Ljungberg K, Frieden M, Westergaard M, Xu Y, Wahren B, Liang Z, Orum H, Koch T, Wahlestedt C (2005) Locked nucleic acid (LNA) mediated improvements in siRNA stability and functionality. Nucleic Acids Res 33:439–447

Fire A, Xu S, Montgomery MK, Kostas SA, Driver SE, Mello CC (1998) Potent and specific genetic interference by double-stranded RNA in *Caenorhabditis elegans*. Nature 391:806–811

Gabriel B, Teissie J (1995) Control by electrical parameters of short- and long-term cell death resulting from electropermeabilization of Chinese hamster ovary cells. Biochim Biophys Acta 1266:171–178

Gabriel B, Teissie J (1997) Direct observation in the millisecond time range of fluorescent molecule asymmetrical interaction with the electropermeabilized cell membrane. Biophys J 73:2630–2637

Gehl J, Sorensen TH, Nielsen K, Raskmark P, Nielsen SL, Skovsgaard T, Mir LM (1999) In vivo electroporation of skeletal muscle: threshold, efficacy and relation to electric field distribution. Biochim Biophys Acta 1428:233–240

Golzio M, Mazzolini L, Moller P, Rols MP, Teissie J (2005) Inhibition of gene expression in mice muscle by in vivo electrically mediated siRNA delivery. Gene Ther 12:246–251

Golzio M, Mazzolini L, Ledoux A, Paganin A, Izard M, Hellaudais L, Bieth A, Pillaire MJ, Cazaux C, Hoffmann JS, Couderc B, Teissie J (2007) In vivo gene silencing in solid tumors by targeted electrically mediated siRNA delivery. Gene Ther 14:752–759

Hu WY, Myers CP, Kilzer JM, Pfaff SL, Bushman FD (2002) Inhibition of retroviral pathogenesis by RNA interference. Curr Biol 15:1301–1311

Kauppinen S, Vester B, Wengel J (2006) Locked nucleic acid: high-affinity targeting of complementary RNA for RNomics. Handb Exp Pharmacol 173:405–422

Kaur H, Babu BR, Maiti S (2007) Perspectives on chemistry and therapeutic applications of locked nucleic acid (LNA). Chem Rev 107:4672–4697

Kumar R, Singh SK, Koshkin AA, Rajwanshi VK, Meldgaard M, Wengel J (1998) The first analogues of LNA (locked nucleic acids): phosphorothioate-LNA and 2'-thio-LNA. Bioorg Med Chem Lett 8:2219–2222

Layzer JM, McCaffrey AP, Tanner AK, Huang Z, Kay MA, Sullenger BA (2004) In vivo activity of nuclease-resistant siRNAs. RNA 10:766–771

Lewis DL, Hagstrom JE, Loomis AG, Wolff JA, Herweijer H (2002) Efficient delivery of siRNA for inhibition of gene expression in postnatal mice. Nat Genet 32:107–108

Matsuda T, Cepko CL (2004) Electroporation and RNA interference in the rodent retina in vivo and in vitro. Proc Natl Acad Sci USA 101:16–22

Mir LM, Devauchelle P, Quintin-Colonna F, Delisle F, Doliger S, Fradelizi D, Belehradek J Jr, Orlowski S (1997) First clinical trial of cat soft-tissue sarcomas treatment by electrochemotherapy. Br J Cancer 76:1617–1622

Moazed D (2009) Small RNAs in transcriptional gene silencing and genome defence. Nature 457:413–420

Mook OR, Baas F, de Wissel MB, Fluiter K (2007) Evaluation of locked nucleic acid-modified small interfering RNA in vitro and in vivo. Mol Cancer Ther 6:833–843

Paganin-Gioanni A, Bellard E, Couderc B, Teissie J, Golzio M (2008) Tracking in vitro and in vivo siRNA electrotransfer in tumor cells. J RNAi Gene Silenc 4:281–288

Paganin-Gioanni A, Bellard E, Escoffre JM, Rols MP, Teissie J, Golzio M (2011) Direct visualization at the single-cell level of siRNA electrotransfer into cancer cells. Proc Natl Acad Sci USA 108:10443–10447

Pekarik V, Bourikas D, Miglino N, Joset P, Preiswerk S, Stoeckli ET (2003) Screening for gene function in chicken embryo using RNAi and electroporation. Nat Biotechnol 21:93–96

Petersen M, Nielsen CB, Nielsen KE, Jensen GA, Bondensgaard K, Singh SK, Rajwanshi VK, Koshkin AA, Dahl BM, Wengel J, Jacobsen JP (2000) The conformations of locked nucleic acids (LNA). J Mol Recognit 13:44–53

Raemdonck K, Remaut K, Lucas B, Sanders NN, Demeester J, De Smedt SC (2006) In situ analysis of single-stranded and duplex siRNA integrity in living cells. Biochemistry 45:10614–10623

Rols MP, Teissie J (1998) Electropermeabilization of mammalian cells to macromolecules: control by pulse duration. Biophys J 75:1415–1423

Schwarz DS, Hutvagner G, Du T, Xu Z, Aronin N, Zamore PD (2003) Asymmetry in the assembly of the RNAi enzyme complex. Cell 115:199–208

Teissie J, Escoffre JM, Paganin A, Chabot S, Bellard E, Wasungu L, Rols MP, Golzio M (2011) Drug delivery by electropulsation: recent developments in oncology. Int J Pharm 423(1):3–6

Wahlestedt C, Salmi P, Good L, Kela J, Johnsson T, Hokfelt T, Broberger C, Porreca F, Lai J, Ren K, Ossipov M, Koshkin A, Jakobsen N, Skouv J, Oerum H, Jacobsen MH, Wengel J (2000) Potent and nontoxic antisense oligonucleotides containing locked nucleic acids. Proc Natl Acad Sci USA 97:5633–5638

Whitehead KA, Langer R, Anderson DG (2009) Knocking down barriers: advances in siRNA delivery. Nat Rev Drug Discov 8:129–138

J Membrane Biol (2012) 245:573–582
DOI 10.1007/s00232-012-9469-8

Adhesion Signals of Phospholipid Vesicles at an Electrified Interface

Nadica Ivošević DeNardis · Vera Žutić · Vesna Svetličić · Ruža Frkanec

Received: 23 December 2011 / Accepted: 24 June 2012 / Published online: 19 July 2012

Abstract General adhesion behavior of phospholipid vesicles was examined in a wide range of potentials at the mercury electrode by recording time-resolved adhesion signals. It was demonstrated that adhesion-based detection is sensitive to polar headgroups in phospholipid vesicles. We identified a narrow potential window around the point of zero charge of the electrode where the interaction of polar headgroups of phosphatidylcholine vesicles with the substrate is manifested in the form of bidirectional signals. The bidirectional signal is composed of the charge flow due to the nonspecific interaction of vesicle adhesion and spreading and of the charge flow due to a specific interaction of the negatively charged electrode and the most exposed positively charged choline headgroups. These signals are expected to appear only when the electrode surface charge density is less than the surface charge density of the choline groups at the contact interface. In comparison, for the negatively charged phosphatidylserine vesicles, we identified the potential window at the mercury electrode where charge compensation takes place, and bidirectional signals were not detected.

Keywords Adhesion signal · Choline headgroup · Electrified interface · Mercury electrode · Phospholipid vesicle

N. I. DeNardis (✉) · V. Žutić · V. Svetličić
Ruđer Bošković Institute, P.O. Box 180, 10002 Zagreb, Croatia
e-mail: ivosevic@irb.hr

R. Frkanec
Institute of Immunology, P.O. Box 266, 10000 Zagreb, Croatia

Introduction

Lipids can be classified according to their biological activity. Lipids that perform regulatory functions have a distinct residual charge distribution. Residual charge distribution is one of the factors of intermolecular recognition, leading to a specific interaction of lipid molecules with the selected proteins in various processes, particularly those involved in signal-transduction pathways (Testa et al. 1997). Charge distribution within the membrane interface determines the distribution and hydration of ions in the vicinity. Intermolecular interactions within the interface should therefore be treated as a combination of electrostatic force and hydration, along with static and dynamic steric constraints (Israelachvili 1992). The lipid composition is important for the functional requirements of the membrane. Phosphatidylcholine (PC), phosphatidylethanolamine (PE) and sphingomyelin (SM) are the most abundant lipid species in biological membranes (Gennis 1989). As the major components of the surface matrix, they determine the surface global properties that characterize its environment; but they do not interfere in membrane-associated processes, requiring them to be biologically passive. Phospahtidylserine (PS) in biological membranes plays a dual role, depending on its location. When situated on the inner surface of the plasma membrane, it interacts with a variety of proteins. The presence of PS on the plasma membrane outer surface is sporadic and has important consequences, such as in the stage preceding apoptosis (Bennet et al. 1995). Vernier and coworkers (2004) identified a specific and physiologically significant molecular event: translocation of PS from the inner leaflet of the cell membrane to the exterior face of the cell that is induced by application of ultrashort (nanosecond) and high-field (mV/m) electric pulses. One of the interesting features of the cell membrane

is the presence of surface molecules that act like a "signature" for a cell. The interaction of protein ovalbumin and biologically active adamantyltripeptides with phospholipids in the liposomal bilayers has been described (Frkanec et al. 2003; Brgles et al. 2007).

The phospholipids deposited on a mercury electrode surface, either by extruding the drop of mercury through a monolayer spread on a gas–solution interface or by unilamellar vesicle fusion, have been extensively studied (Nelson and Benton 1986; Nelson and Auffret 1988; Leermarkers and Nelson 1990; Nelson and Leermarkers 1990; Bizzotto and Nelson 1998; Stauffer et al. 2001). Such a system can be used as a model to study the effect of an electric field on membrane stability, properties of voltage-gated membrane proteins as well as lipid–lipid and lipid–protein interactions (Guidelli et al. 2001). Mercury, with its atomically smooth surface, allows study of the surface properties of such a film and the charge transfer across a film modified by incorporated proteins (Bizzoto and Nelson 1998; Nelson and Bizzoto 1999; Guidelli et al. 2001).

The adsorption of various physical forms of PC onto a mercury electrode was extensively studied using electrochemical and optical techniques (Stauffer et al. 2001; Agak et al. 2004; Bizzotto et al. 2004). The spreading of liposomes onto the mercury surface at constant potential yields a monolayer of adsorbed PC that is identical to the layer adsorbed from the G–S interface. This monolayer undergoes several phase transitions, two of which correspond to the change in the adsorbed state and one that corresponds to the adsorption–desorption process. Nelson and Leermakers (1990) stated that competition between the heads and the tail for access to the electrode interface was detected through the existence of a capacitance peak at the negatively charged mercury electrode. The headgroup of PS has less specific surface interaction with the mercury electrode than the PC headgroup. Thus, the conformation of PS polar heads with the two negative charges and the one positive charge on the same plane parallel to the lipid layer is not as electrostatically favored as the conformation assumed by zwitterionic lipids such as PC (Moncelli et al. 1998). Lipkowski's group studied the behavior of phospholipid bilayers with and without the incorporated peptides in an electric field using the Au(111) electrode (Zawisza et al. 2003; Burgess et al. 2004, 2005; Xu et al. 2004; Sek et al. 2009). They found that the ingress of electrolytes is accompanied by electric field–induced changes in the orientation of the phospholipid on the electode (Bin and Lipkowski 2006). Electroporation of membranes could be likened to the ingress of the electrolyte into the phospholipid layer at the electrode (Nelson 2010). Molecular dynamic simulation of mixed zwitterionic–anionic, asymmetric phospholipid bilayers with monovalent and divalent cations demonstrates electrostatic and entropy-driven association of calcium and sodium ions with polar groups in the bilayer interface in terms of spatial distribution profiles and a change in the orientation of the phospholipid headgroup (Vernier et al. 2009).

While capacitance measurements in liposome suspensions generally reveal properties of the already formed monolayers at the mercury interface, time-resolved adhesion signals trace the transformation of a single liposome to a film of finite surface area. The kinetics of an adhesion event of a single liposome at the mercury electrode became accessible through signal analysis using empirical equations (Hellberg et al. 2005; Hernandez and Scholz 2006; Žutić et al. 2007) and derived analytical solutions for the reaction kinetics model (Ružić et al. 2009, 2010). The adhesion signal of a liposome reflects the dynamics of liposome adhesion by tracing the continuous transformation from the initial intact state to the intermediate deformed state and the final state of the lipid monolayer. The recently developed reaction kinetics and mechanical models (Ivoševic DeNardis et al. 2012) indicate that all three states evolve stimultaneously from the onset of the adhesion process. Apart from the force generated by adhesion, which drives the motion of the liposome and causes it to spread on the electrode, the main elements of the equation of motion in the mechanical model are the inertial term and the damping term associated with the release of liposome content across the membrane. The mechanical model advances the understanding of the physics of the adhesion event and offers an interpretation of the three states identified by the reaction kinetics model. In particular, it suggests that the intermediate state consists of a spherical cap containing the remaining unreleased content of the liposome and a flat annular skirt closely bound to the electrode. The main conclusion is that the liposome content is released through transient pores formed in the cap membrane.

Adhesion signals of single liposomes at the dropping mercury electrode (DME) in air-saturated suspensions were detected in a broad potential range (Ivošević DeNardis et al. 2007), while the adhesion signals recorded in deaerated liposome suspension indicated the significance of a specific interaction of phospholipid polar headgroups in close molecular contact with the mercury electrode (Žutić et al. 2007; Ivošević DeNardis et al. 2009). Here, our aim was to demonstrate that adhesion-based detection at the mercury electrode is sensitive to the polar headgroups of phospholipid vesicles. We present a study of vesicles formed from PC and PS lipids.

PC is a zwitterionic lipid, with the headgroup consisting of two oppositely charged residues: phosphate and trimethylammonium groups. On the other hand, the resulting net charge for PS is negative. PS has three residual charges: two are negative and associated with the phosphate and

carboxyl groups, while the third, positive charge, is within the ammonium group.

Materials and Methods

The electrochemical measurement technique was based on measuring the displacement of the surface charge of the mercury electrode by adhesion and spreading of deformable particles and living cells (Žutić et al. 1993; Svetličić et al. 2000). The key ingredient in such measurement is the versatile potentiostatic control of adhesion forces by changing the surface charge and tension at the electrode–aqueous suspension interface. The adhesion force can be fine-tuned to study the interplay of the complex processes involved in a deformable particle–electrode double-layer interaction. In particular, the signature of a single adhesion event at the mercury electrode is the spike-shaped current transient (adhesion signal), which is consistent with the classical model of the electrical double-layer at the electrode–solution interface. The flow of double-layer charge displacement current reflects the dynamics of adhesive contact formation of the deformable particle with the electrode and the subsequent rupture and spreading of particle constituents to a film of the finite surface area at the millisecond time scale:

$$I_{\mathrm{D}} = \frac{\mathrm{d}A}{\mathrm{d}t}\sigma_{12} \tag{1}$$

where I_{D} is the displacement current, A is the area of the interacting interface, t is time and σ_{12} is the surface charge density of the mercury electrode–aqueous electrolyte interface (Žutić et al. 1993). At a given potential, the current amplitude reflects the size of the adhered particle, while the signals frequency reflects the particle concentration in the suspension (Žutić et al. 1993; Svetličić et al. 2000; Ivošević DeNardis et al. 2007). The adhesion signals are defined by maximum signal amplitude ($I_{\max}$), signal duration (τ) and displaced charge (q_{D}). The displaced double-layer charge (q_{D}) is obtained by integrating the area under the adhesion signal.

$$q_{\mathrm{D}} = \int_{t_1}^{t_1+\tau} I\mathrm{d}t \tag{2}$$

If a complete charge displacement takes place, as in the case of nonpolar droplets of organic liquids, the area of the contact interface (A_{c}) is

$$A_{\mathrm{c}} = \frac{q_{\mathrm{D}}}{\sigma_{12}} \tag{3}$$

The general mechanism established for adhesion of hydrocarbon droplets and living cells is expected to be valid as well for liposome adhesion within the wide range of surface charge densities (Ivošević DeNardis et al. 2009). Dispersion of hexadecane droplets was selected as a simple and well-defined reference system due to the fact that hexadecane is the highest saturated *n*-alkane that is fluid at room temperature and it has a large set of calculations and experimental data on surface and interfacial tension (Fowkes 1963; Ribarsky and Landman 1992). Interaction of oil droplets at the mercury–water interface is defined according to the modified Young–Dupré equation. The total Gibbs energy of interaction between a droplet and the aqueous mercury interface is

$$-\Delta G = A(\gamma_{12} - \gamma_{23} - \gamma_{13}) \tag{4}$$

where γ_{12}, γ_{13} and γ_{23} are the interfacial energies at mercury–water, mercury–organic liquid and water–organic liquid interfaces, respectively. The expression in parentheses is the spreading coefficient (S_{132}) at the three-phase boundary (Israelachvili 1992). When $S_{132} > 0$ attachment and spreading are spontaneous processes, while when $S_{132} < 0$ spreading is not spontaneous. The critical interfacial tension of adhesion $(\gamma_{12})_c$ defined by $S_{132} = 0$ will be $(\gamma_{12})_{\mathrm{c}} = \gamma_{13} + \gamma_{23}$. In the case of nonpolar organic liquids, the critical interfacial tensions of adhesion at the positively and negatively charged interfaces are the same, showing good agreement with the calculated values (Ivošević et al. 1994, 1999) according to Young–Dupré and Good–Girifalco–Fowkes relationships (Fowkes 1962, 1963). With increasing chain length and increasing polarity of molecules, the potential range of adhesion becomes wider as the critical interfacial tension of adhesion decreases.

Hexadecane Droplet Dispersion

The aqueous dispersion of *n*-hexadecane (99 % GC; Aldrich, Milwaukee, WI) was prepared by shaking 50 µl of organic liquid in 250 ml of phosphate-buffered saline (PBS, 0.15 M), pH 7.47, at 300 rpm for 1 h.

Vesicle Suspensions

1,2-Dioleoyl-*sn*-glycero-3-phosphocholine (DOPC, ≥99 %) and PS (1,2-diacyl-*sn*-glycero-3-phospho-L-serine, from bovine brain, ≥97 %) were purchased from Sigma (St. Louis, MO) and used as received. The fatty acid composition and positional distribution in glycerophosphatides of bovine gray matter are given in Yabuuchi and O'Brien (1968). Multilamellar DOPC and PS vesicles were prepared by dissolving 10 mg of lipid in 2 ml of chloroform. After rotary evaporation of the solvent, the remaining lipid film was dried in vacuum for 1 h and dispersed by gentle hand shaking in 1 ml of PBS. The solution was left

overnight at 4 °C to swell and stabilize. The suspension submitted for electrochemical measurements was characterized by a Coulter counter to determine vesicle concentration and size distribution using a 100-μm-diameter sampling orifice tube. The normal-size distribution was fairly reproducible and stable throughout the electrochemical experiment. Vesicle suspension of 2×10^8/l contains predominantly size fractions in the range 3.2–16 μm.

Unilamellar DOPC vesicle suspensions were prepared according to Moscho and coworkers (1996). The lipid was dissolved in chloroform (0.1 M), and 20 μl of this solution was added to a 50 ml round-bottomed flask containing 920 μl of chloroform and 150 μl of methanol. The aqueous phase (7 ml of PBS) was carefully added along the flask walls. Organic solvents were removed in a rotary evaporator under 240–300 mmHg pressure at 40–43 °C. After evaporation for a couple of minutes, an opalescent fluid was obtained with a volume of approximately 6.5 ml. The suspension was characterized by a Coulter counter using a 140-μm-diameter sampling orifice tube, where particle size distribution was in the range 2–60 μm.

Electrochemical Measurements

DME had a drop-life of 2.0 s, a flow rate of 6.0 mg/s and a maximum surface area of 4.57 mm^2. All potentials were referred to an Ag/AgCl (0.1 M NaCl) reference electrode, which was separated from the measured dispersion by a ceramic frit. Its potential was +2 V versus calomel electrode (1 M KCl). Electrochemical measurements were performed using a 174A Polarographic Analyzer (Princeton Applied Research, Oak Ridge, TN) interfaced to a computer. Analogous data acquisition was performed with a DAQ card-AI-16-XE-50 (National Instruments, Austin, TX) input device, and the data were analyzed using the application developed in LabView 6.1 software (National Instruments). The current–time (*I–t*) curves over 50 mercury drop lives were recorded at constant potentials, with a time resolution of 50 μs. Signal frequency is expressed as number of adhesion event over 100 s. The aliquot of liposome suspension was added in deaerated PBS under purging with nitrogen at 25 °C.

Results

Hexadecane Droplets

The adhesion behavior of hexadecane droplets at the charged DME interface is presented as the dependence of signal frequency and maximum signal amplitude on electrode potential (Fig. 1). The adhesion signal frequency of

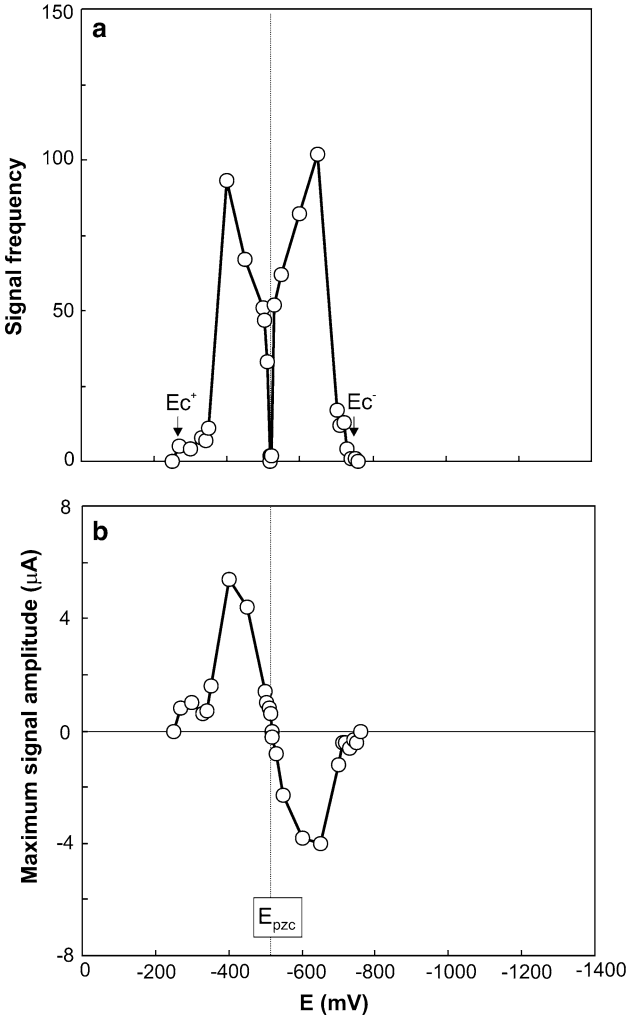

Fig. 1 The reference system: dispersion of *n*-hexadecane droplets (180 mg/l) in PBS. Dependence of signal frequency (**a**) and maximum signal amplitude (**b**) on electrode potential. E_c^+ and E_c^- denote critical potentials of adhesion at the positively and negatively charged mercury/PBS interfaces, respectively

hexadecane droplets was detected in the potential range from −270 to −730 mV in PBS. These experimentally determined potentials are referred to as critical potentials of adhesion (E_c^+ and E_c^-). The difference between the critical interfacial tensions of hexadecane adhesion at the positively and negatively charged electrodes corresponds to 1.3 mJ/m^2 due to the specific adsorption of chloride and phosphate anions of the supporting electrolyte at the positively charged mercury electrode (Ivošević et al. 1999). At the potentials positive to −270 mV or negative to −730 mV, adhesion of hexadecane droplets was not detected and droplets behaved as inert particles due to the stronger interaction of mercury with water and electrolyte ions than the interaction with the droplets. The signal frequency of hexadecane droplets changes by scanning the potential, creating a butterfly-shaped dependence. At the

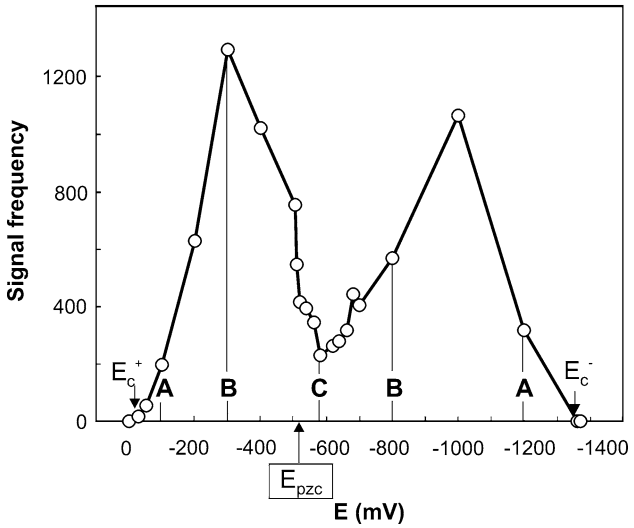

Fig. 2 Potential dependence of the signal frequency of multilamellar DOPC vesicles in PBS. Characteristic potential points are indicated: *A* high σ_{12} and low S_{132} values, *B* moderate values of σ_{12} and S_{132} and *C* with $\sigma_{12} < 0$ and close to the highest S_{132}values

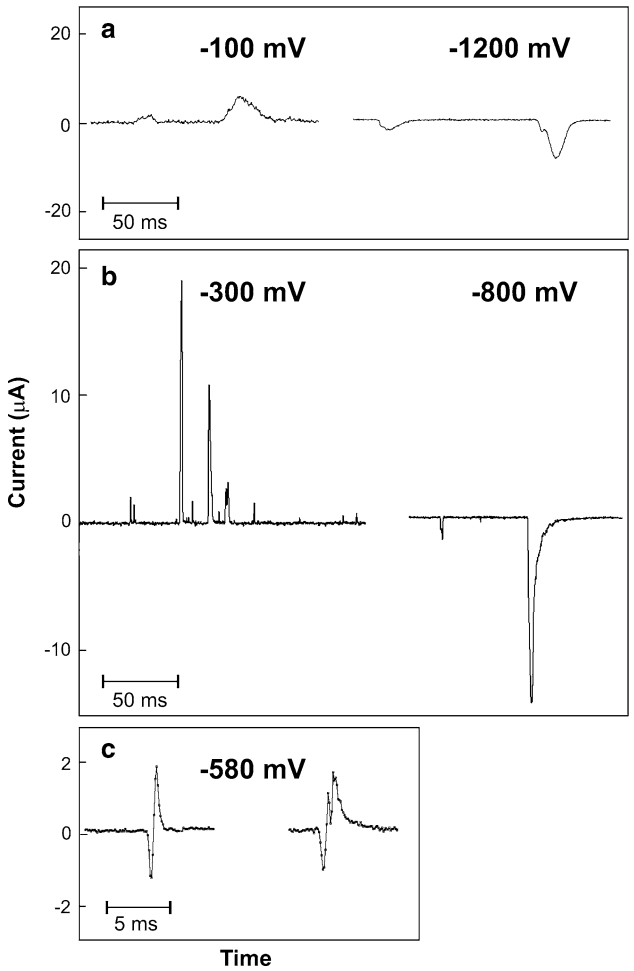

Fig. 3 Characteristic shapes of adhesion signals at the potential points *A, B, C* defined in Fig. 2: unidirectional signals corresponding to the displacement of negative or positive charges of the electrode at **a** high σ_{12} but low S_{132} value and **b** moderate values of σ_{12} and S_{132}. Bidirectional signals occur only in a narrow potential region **c** with $\sigma_{12} < 0$ and close to the highest S_{132}value

potential of zero charge of the mercury electrode (E_{pzc}), signal frequency is zero as there is no electrode double-layer charge to be displaced. The maximum signal amplitude of hexadecane droplets varies as well by changing the potential. The signal amplitude depends on the droplet size as well as on the polarity and the surface charge density of the mercury electrode. In particular, the signal amplitude is positive at a positively charged mercury electrode, i.e., at the potentials $E > E_{pzc}$. Signal amplitude displays a negative sign at a negatively charged electrode, i.e., at the potentials $E < E_{pzc}$. Only simple unidirectional signals of hexadecane droplets are recorded at the positively and negatively charged electrodes. At the E_{pzc} maximum signal amplitude is zero.

Multilamellar DOPC Vesicles

The effect of the potential at the DME–PBS interface on the adhesion behavior of multilamellar DOPC vesicles in terms of signal frequency and signal shape is presented in Figs. 2 and 3. The adhesion behavior of zwitterionic DOPC vesicles differs from that of nonpolar hexadecane droplets based on (1) a wider potential range of adhesion, i.e., from −20 to −1360 mV; (2) signal frequency at E_{pzc}; (3) positive direction of the signal at E_{pzc}; (4) shifts of minimum signal frequency from E_{pzc}; (5) critical interfacial tensions of adhesion; and (6) the appearance of bidirectional signals. The difference between the critical interfacial tensions of DOPC vesicle adhesion at the positively and negatively charged electrodes corresponds to 27.5 mJ/m^2. The value of critical interfacial tension at the negatively charged electrode for adhesion of DOPC vesicles is significantly smaller than the value at the positively charged electrode due to the strong and specific electrostatic interaction between the positively charged choline groups and the negatively charged mercury electrode.

Figure 3 shows the selected adhesion signals of DOPC vesicles captured with a time resolution of 50 μs at the selected potential points. At characteristic potential region A being placed in the vicinity of the critical potentials of adhesion (high σ_{12} and low S_{132}), the adhesion signals show a drawn-out shape, while signal direction depends on the polarity of the surface charge of the electrode. Signal durations are in the range of 5–200 ms at the potential of −100 mV depending upon vesicle size. At potential region B (moderate values of σ_{12} and S_{132}), adhesion signals of DOPC vesicles become sharp and narrow. Signal durations are in the range 0.5–10 ms at the potential of −300 mV. The dependence of signal duration on the spreading

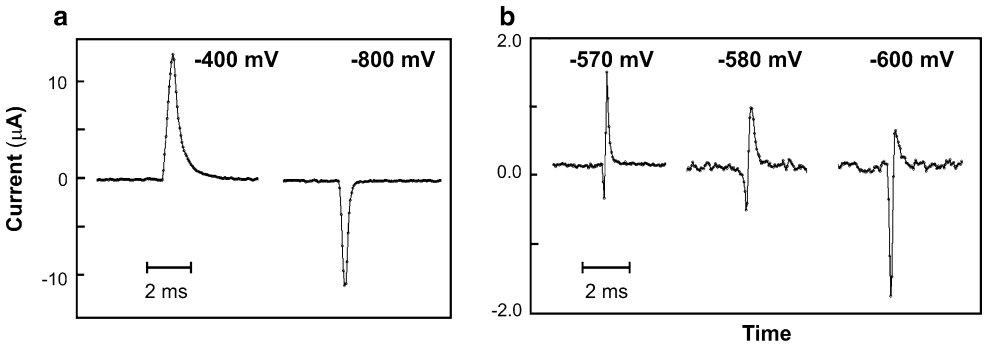

Fig. 4 Adhesion signals of unilamellar DOPC vesicles in PBS. Unidirectional adhesion signals were recorded at −400 mV ($\sigma_{12} = 3.31\ \mu C/cm^2$) and −800 mV ($\sigma_{12} = -7.13\ \mu C/cm^2$) (**a**). Bidirectional signals were recorded at −570 mV ($\sigma_{12} = -1.85\ \mu C/cm^2$), −580 mV ($\sigma_{12} = -2.09\ \mu C/cm^2$) and −600 mV ($\sigma_{12} = -2.59\ \mu C/cm^2$), i.e., potential region with $\sigma_{12} < 0$ and close to the highest S_{132} (**b**)

coefficient was determined for hydrocarbon droplets irrespective of the polarity of the electrode charge, proving that interfacial energy governs the rate of spreading (Ivošević and Žutić 2002). Only simple unidirectional signals of DOPC vesicles are recorded at potential regions A and B. At potential region C (with $\sigma_{12} < 0$ and close to the highest S_{132}), complex bidirectional signals of DOPC vesicles were recorded only in a narrow potential range.

Unilamellar DOPC Vesicles

We performed closer examination of the adhesion behavior of PC vesicles by scanning the electrode potential in a suspension of unilamellar DOPC. In general, the potential range of adhesion at the DME and the adhesion signal feature in suspension of unilamellar DOPC resemble those recorded in the suspension of multilamellar DOPC. Figure 4a illustrates the shape of adhesion signals and the direction of flow of the compensating current at the positive and negative surface charge densities, respectively. The smallest signal of DOPC vesicles measured at the potential of −400 mV that is detected beyond the noise level has an amplitude of 0.18 μA, signal duration of 1 ms and displaced charge of 49 pC, which corresponds to the contact area of 1484 μm^2. This signal was recorded at a drop lifetime of the mercury electrode of 0.26 s, and the resulting portion of occupied electrode surface area is 0.13 %. If the surface area of the DOPC molecule in the bilayer (72.5 Å) (Lagüe et al. 2001) is the same as in the monolayer on the positively charged electrode with the hydrophobic tails oriented perpendicularly to the electrode, the radius of the unilamellar vesicle in solution would be 7 μm. However, in the case of multilamellar vesicles, only the radius of an equivalent unilamellar vesicle could be evaluated from the displaced charge, assuming a successive peel off, rupture and spreading of bilayers to the phospholipid monolayer, which is the only stable structure

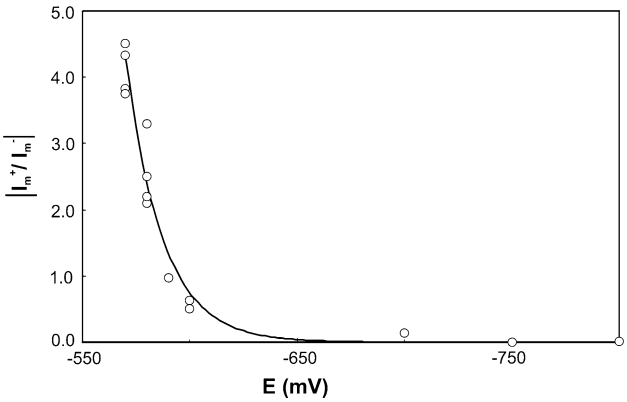

Fig. 5 Potential dependence of peak heights ratio $|I_m^+/I_m^-|$ of bidirectional signals of unilamellar DOPC vesicles in PBS

at the aqueous mercury interface at potentials of strong adhesion.

Scanning the electrode potential around E_{pzc} (potential region C) reveals the characteristic bidirectional adhesion signals (Fig. 4b). Bidirectional signals of DOPC vesicles appear in the narrow potential range from −570 to −700 mV, which corresponds to a surface charge density $-1.85 \geq \sigma_{12} \geq -5.08$. This type of adhesion signal was first reported for multilamellar egg-PC liposomes, showing that bidirectional signals originate from a specific interaction of positively charged choline groups of phospholipid polar heads when in immediate contact with the negatively charged mercury electrode (Žutić et al. 2007). Here, we show that the phenomenon of bidirectional signals is characteristic of PC vesicles irrespective of their lamellarity. We confirmed the appearance of bidirectional signals of vesicles around the E_{pzc} of the mercury electrode as well as in the systems of DMPC vesicles in PBS at 25 °C and DPPC vesicles in PBS at 45 °C (Ivošević et al. 2009). The ratio of the positive portion peak to the negative portion peak of the bidirectional signal shows potential

dependence (Fig. 5). Attenuation of the positive portion peak with increasing negative potential is due to the charge flow associated with vesicle spreading, which dominates over the charge flow associated with a specific interaction of choline groups.

Multilamellar PS Vesicles

The effect of potential at the DME on the adhesion behavior of multilamellar PS vesicles in terms of signal frequency was examined in potential region C, to trace a specific behavior of the serine polar headgroup. The behavior observed was quite different from that of the choline group, which is characterized by bidirectional signals. Although PS adhesion signals had the same appearance for potential regions A and B, no signals were observed in region C, i.e., in the range from −520 to −560 mV (Fig. 6). At pH 7.5 the polar head of PS is negatively charged (Moncelli et al. 1998). The absence of adhesion signals more negative than E_{pzc} indicated overall interaction of the positively charged vesicles. Since measured double-layer charge displacement takes place at a distance of less than 10 Å, it is possible to detect the charge corresponding to the ammonium group. Kotyńska and Figaszewski (2005) studied the effect of the adsorption of ions (H^+, Na^+, OH^-, Cl^-) present in the solution upon the electric charge of the liposome membrane formed of PC vesicles. The surface charge density of the membrane was determined as a function of pH and of electrolyte concentration obtained with electrophoretic mobility measurements. For high concentration of sodium chloride (0.1 M) at pH 7, competition in the adsorption between the

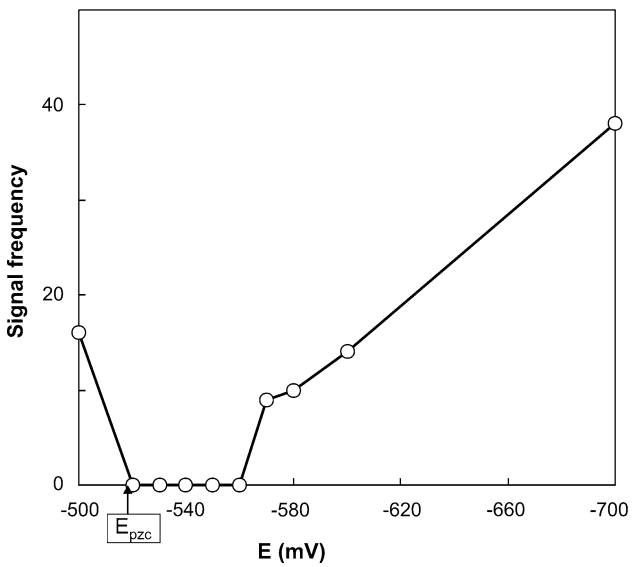

Fig. 6 Potential dependence of signal frequency of multilamellar PS vesicles in PBS

H^+ and Na^+ ions takes place. The increase in Na^+ ion concentration causes a decrease in the negative charge, proving the adsorption of Na^+. The confined range of surface charge densities of the mercury electrode in which electrostatic interaction was identified is from −0.55 to −1.50 μC/cm^2. Our results are in agreement with the capacitance measurements, where the determined charge density on PS-coated mercury electrode in 0.1 M KCl at constant applied potential of −0.5 V/vs. SCE and at pH 7.5 was around −0.49 μC/cm^2 (Moncelli et al. 1998).

Discussion

The bidirectional signal is composed of the charge flow due to the nonspecific charge displacement at the initial contact of a liposome with the electrode (negative portion of the signal) and of the charge flow due to a specific interaction of positively charged choline groups of phospholipid polar heads that form a direct contact with the electrode surface (positive portion of the signal). The lipid vesicle first establishes the adhesion contact through displacement of the ions situated in the inner Helmholtz plane (IHP, the initial negative portion of the peak) in such a way that the polar headgroups of still intact vesicles come in direct (molecular) contact with the mercury electrode and charge transfer takes place due to a specific electrostatic interaction of the positively charged choline groups of phospholipids and the negatively charged electrode, forming a surface complex with a partial charge transfer (positive portion of the peak). With increasing negative potential, the compensating charge flow due to the spreading of vesicle dominates over the charge flow due to a specific electrostatic interaction of choline groups because the increased surface charge density of the electrode compensates for the positive charge. For potentials where the electrode surface charge is close to, equal to or exceeds the charge density created by the choline groups, the positive portion of the bidirectional signal attenuates and finally disappears.

Our interpretation of the bidirectional signal origin is in agreement with studies of potential-dependent fluorescence of DOPC on the mercury surface by Stoodley and Bizzotto (2003). They provided evidence of polar lipid headgroup–mercury electrode interaction based on fluorescein chromophores residing in the lipid headgroup/aqueous region. Around the E_{pzc} lipids are closer to the electrode and form the preadsorbed state, effectively quenching fluorescence. By scanning the potential negatively from the E_{pzc}, fluorescence increases and the lipid layer desorbs and remains close to the electrode surface. High affinity of tetraalkylammonium cations for interaction with the negatively charged mercury electrode is well known in the electrochemical literature (Ryan et al. 1987). Choline methyl

groups are hydrophobic, and adjacent water molecules are hydrogen-bonded between themselves, forming a clathrate shell around the PC headgroup. It is estimated that about 25–30 water molecules are needed to fully hydrate the choline headgroup (Damodaran and Merz 1993, 1994). The lack of hydrogen bonds enables the choline moiety to rotate freely (Israelachvili 1992). The range of the surface charge densities where specific electrostatic interaction of choline and mercury electrode was identified is from −1.85 to −5.08 μC/cm^2. The σ_{12} value at which the positive portion of the bidirectional signal disappears is the surface charge density of the mercury electrode needed to compensate for the charge of the choline groups. From this value, we can calculate the area at the electrode surface occupied by one positive charge of the choline group, which corresponds to 315 Å^2. This indicates a flat orientation of lipid molecule in the monolayer formed after liposome spreading over the electrode, although some other orientations of PC lipid molecule at the mercury electrode have been proposed (Hellberg et al. 2005; Hernandez and Scholz 2006; Nelson 2010).

Another piece of evidence for such an orientation of lipid molecules at the negatively charged electrode is found by analysis of the adhesion signal of a single DMPC liposome (Hernandez and Scholz 2006), where for the unilamellar liposome the surface area occupied by one lipid molecule in the monolayer is 230 Å^2 compared to the surface area occupied by a headgroup, which equals 65 Å^2. In the pH range 4–9, the PC film is uncharged and does not contain partially protonated ionizable groups. Over this pH range the conformation of the PC polar head with the P-N dipoles aligned head to tail in the direction parallel to the monolayer is the most energetically favored arrangement from the electrostatic viewpoint (Moncelli et al. 1998).

Finally, the orientation of DMPC molecules at the Au(111) electrode surface observed at a charge density close to zero was visualized by STM with high molecular resolution. The images of flat-lying DMPC molecules with acyl chains oriented parallel to the surface and assembled into an oriented monolayer could be observed in dilute vesicle solution but only during a short period of time after vesicle deposition. With time, the molecules reorient and the monolayer is transfomed into a hemimicelar film (Xu et al. 2004).

Conclusions

We demonstrated that adhesion-based detection is sensitive to polar headgroups in phospholipid vesicles. By studying the effect of potential on adhesion signals of PC and PS vesicles at the DME, we have identified the potential window of the interaction of lipid polar headgroups with the substrate. Thus, for PC vesicles the interaction is manifested in the form of bidirectional signals. The bidirectional signal is composed of (1) the charge flow due to vesicle adhesion and spreading (displacement of ions from the electrode IHP), yielding the negative portion of bidirectional signal, and (2) the charge flow due to a specific interaction of the negatively charged electrode and the most exposed charged group of the phospholipid polar head, i.e., the positively charged trimethylammonium group, yielding the positive portion of the bidirectional signal. Therefore, bidirectional signals are expected to appear only when the electrode surface charge density is less than the surface charge density of the choline groups at the contact interface.

We conclude that the major distinction between phospholipid vesicles and oil droplets is manifested as (1) the difference between the critical interfacial tensions of adhesion at the positively and negatively charged electrodes, (2) the appearance of specific bidirectional signals at the low surface charge density and (3) the molecular orientation in the monolayer. In order to derive molecular-level imaging and to gain information about the phospholipid orientation with respect to the potential stimuli, further research should employ computer simulation methods to model such a membrane system.

Acknowledgements This study was supported by the Croatian Ministry of Science, Education and Sports, projects 098-0982934-2744 and 021-0212432-2431. Special thanks are due to Ivica Ružić for help with charge density calculations.

References

Agak JO, Stoodley R, Retter U, Bizzotto D (2004) On the impendance of a lipid-modified Hg/electrolyte interface. J Electroanal Chem 562:135–144

Bennet MR, Gibson DF, Schwartz SM, Tait JF (1995) Binding and phagocytosis of apoptotic vascular smooth muscle cells is mediated in part by exposure of phosphatidylserine. Circ Res 77:1136–1145

Bin X, Lipkowski J (2006) Electrochemical and PM-IRRAS studies of the effect of cholesterol on the properties of the headgroup of a DMPC bilayer supported at a Au(111) electrode. J Phys Chem B 110:26430–26441

Bizzotto D, Nelson A (1998) Continuing electrochemical studies of phospholipid monolayers of dioleoyl phosphatidylcholine at the mercury–electrolyte interface. Langmuir 14:6269–6273

Bizzotto D, Yang Y, Shepherd JL, Stoodley R, Agak J, Stauffer V, Lathuilliere M, Akhtar AS, Chung E (2004) Electrochemical and spectroelectrochemical characterization of lipid organization in an electric field. J Electroanal Chem 574:167–184

Brgles M, Mirosavljević K, Noethig-Laslo V, Frkanec R, Tomašić J (2007) Spin-labelling study of interactions of ovalbumin with multilamellar liposomes and specific anti-ovalbumin antibodies. Int J Biol Macromol 40:312–318

Burgess I, Li M, Horswell SL, Szymanski G, Lipkowski J, Majewski J, Satija S (2004) Electric field-driven transformations of a

supported model biological membrane—an electrochemical and neutron reflectivity study. Biophys J 86:1763–1776
Burgess I, Li M, Horswell SL, Szymanski G, Lipkowski J, Satija S, Majewski J (2005) Influence of the electric field on a biomimetic film supported on a gold electrode. Colloids Surf B 40:117–122
Damodaran KV, Merz KM (1994) A comparison of DMPC- and DLPE-based lipid bilayers. Biophys J 66:1076–1087
Damodoran KV, Merz KM (1993) Headgroup–water interactions in lipid bilayers: a comparison between DMPC- and DLPE-based lipid bilayers. Langmuir 9:1179–1183
Fowkes FM (1962) Ideal two-dimensional solutions. III. Penetration of hydrocarbons in monolayers. J Phys Chem 66:1863–1866
Fowkes FM (1963) Additivity of intermolecular forces at interfaces. I. Determination of the contribution to surface and interfacial tensions of dispersion forces in various liquids. J Phys Chem 67:2538–2541
Frkanec R, Noethig Laslo V, Vranešić B, Mirosavljević K, Tomašić J (2003) A spin labelling study of immunomodulating peptidoglycan monomer and adamantyltripeptides entrapped into liposomes. Biochim Biophys Acta 1611:187–196
Gennis RB (1989) Biomembranes: molecular structure and function. Springer, Heidelberg
Guidelli R, Aloisi G, Becucci L, Dolfi A, Monicelli R, Buoninegni FT (2001) Bioelectrochemistry at metal–water interfaces. J Electroanal Chem 504:1–28
Hellberg D, Scholz F, Schubert F, Lovrić M, Omanović D, Hernandez VA, Thede R (2005) Kinetics of liposome adhesion on a mercury electrode. J Phys Chem B 109:14715–14726
Hernandez VA, Scholz F (2006) Kinetics of the adhesion of DMPC liposomes on a mercury electrode: effect of lamellarity, phase composition, size and curvature of liposomes and presence of the pore forming peptide mastoparan X. Langmuir 22:10723–10731
Israelachvili JN (1992) Intermolecular forces & surface forces. Academic Press, New York
Ivošević DeNardis N, Žutić V, Svetličić V, Frkanec R, Tomašić J (2007) In situ amperometric characterization of liposome suspensions with concomitant oxygen reduction. Electroanal 19:2444–2450
Ivošević DeNardis N, Žutić V, Svetličić V, Frkanec R (2009) Amperometric adhesion signals of liposomes, cells and droplets. Chem Biochem Eng Q 23:87–92
Ivošević DeNardis N, Ružić I, Pečar-Ilić J, El Shawish S, Ziherl P (2012) Reaction kinetics and mechanical models of liposome adhesion at charged interface. Bioelectrochemistry 88:48–56
Ivošević N, Žutić V (2002) Effect of electrical potential on adhesion, spreading and detachment of organic droplets at an aqueous electrolyte/metal interface. In: Mittal K (ed) Contact angle, wettability and adhesion. VSP, Zeist, pp 549–561
Ivošević N, Tomaić J, Žutić V (1994) Organic droplets at an electrified interface: critical potentials of wetting measured by polarography. Langmuir 10:2415–2418
Ivošević N, Žutić V, Tomaić J (1999) Wetting equilibria of hydrocarbon droplets at an electrified interface. Langmuir 15:7063–7068
Kotyńska J, Figaszewski ZA (2005) Adsorption equilibria between liposome membrane formed phosphatidylcholine and aqueous sodium chloride solution as a function of pH. Biochim Biophys Acta 1720:22–27
Lagüe P, Zuckermann MJ, Roux B (2001) Lipid-mediated interactions between intrinsic membrane proteins: dependence on protein size and lipid composition. Biophys J 81:276–284
Leermakers FAM, Nelson A (1990) Substrate-induced structural changes in electrode-adsorbed lipid layers: a self-consistent field theory. J Electroanal Chem 278:53–72
Moncelli MR, Becucci L, Tadini Buoninsegni F, Guidelli R (1998) Surface dipole potential at the interface between water and self-assembled monolayers of phosphatidylserine and phosphatidic acid. Biophys J 74:2388–2397
Moscho A, Orwar O, Chiu DT, Modi BP, Zare RN (1996) Rapid preparation of giant unilamellar vesicles. Proc Natl Acad Sci USA 93:11443–11447
Nelson A (2010) Electrochemistry of mercury supported phospholipid monolayers and bilayers. Curr Opin Colloid Interface Sci 15:455–466
Nelson A, Auffret N (1988) Phospholipid monolayers of di-oleoyl lecithin at the mercury/water interface. J Electroanal Chem 244:99–113
Nelson A, Benton A (1986) Phospholid monolayers at the mercury/water interface. J Electroanal Chem 202:253–270
Nelson A, Bizzotto D (1999) Chronoamperometric study of TI(I) reduction at gramacidin-modified phospholipid-coated mercury electrodes. Langmuir 15:7031–7039
Nelson A, Leermakers FAM (1990) Substrate-induced structural changes in electrode-adsorbed lipid layers: experimental evidence from the behavior of phospholipid layers on the mercury–water interface. J Electroanal Chem 278:73–83
Ribarsky MW, Landman U (1992) Structure and dynamics of *n*-alkanes confined by solid surfaces. I. Stationary crystalline boundaries. J Chem Phys 97:1937–1949
Ružić I, Ivošević DeNardis N, Pečar-Ilić J (2009) Kinetics of the liposome adhesion on a mercury electrode: testing of a mathematical model. Int J Electrochem Sci 4:787–793
Ružić I, Pečar-Ilić J, Ivošević DeNardis N (2010) Mathematical model for kinetics of organic particle adhesion at an electrified interface. J Electroanal Chem 642:120–126
Ryan CM, Svetličić V, Kariv-Miller E (1987) Electrogenerated $R_4N(Hg)_5$ films: stoichiometry and substituent effects. J Electroanal Chem 219:247–258
Sek S, Laredo T, Dutcher JR, Lipkowski J (2009) Molecular recognition imaging of an antibiotic peptide in a lipid matrix. J Am Chem Soc 131:6439–6444
Stauffer V, Stoodley R, Agak JO, Bizzotto D (2001) Adsorption of DOPC onto Hg G/S interface a liposomal suspension. J Electroanal Chem 516:73–82
Stoodley R, Bizzotto D (2003) Epi-fluorescence microscopic characterization of potential-induced changes in a DOPC monolayer on a Hg drop. Analyst 128:552–561
Svetličić V, Ivošević N, Kovač S, Žutić V (2000) Charge displacement by adhesion and spreading of a cell: amperometric signals of living cells. Langmuir 16:8217–8220
Testa B, Kier LB, Carrupt PA (1997) A system approach to molecular structure, intermolecular recognition, and emergence-dissolvence in medical research. Med Res Rev 17:303–326
Vernier PT, Sun Y, Marcu L, Craft CM, Gundersen M (2004) Nanoelectropulse-induced phosphatidylserine translocation. Biophys J 86:4040–4048
Vernier PT, Ziegler MJ, Dimova R (2009) Calcium binding and headgroup dipole angle in phosphatidylserine–phosphatidylcholine bilayers. Langmuir 25:1020–1027
Xu S, Szymanski G, Lipkowski J (2004) Self-assembly of phospholipid molecules at a Au(111) electrode surface. J Am Chem Soc 126:12276–12277
Yabuuchi H, O'Brien JS (1968) Positional distribution of fatty acids in glycerophosphatides of bovine grey matter. J Lipid Res 9:65–67
Zawisza I, Lachenwitzer A, Zamlynny V, Horswell SL, Goddard JD, Lipkowski J (2003) Electrochemical and photon polarization modulation infrared reflection absorption spectroscopy study of the electric field driven transformations of a phospholipid bilayer supported at a gold electrode surface. Biophys J 85:4055–4075

Žutić V, Kovač S, Tomaić J, Svetličić V (1993) Heterocoalescence between dispersed organic microdroplets and a charged conductive interface. J Electroanal Chem 349:173–186

Žutić V, Svetličić V, Hozić Zimmermann A, Ivošević DeNardis N, Frkanec R (2007) Comment on "liposomes on a mercury electrode. effect of lamellarity, phase composition, size and curvature of liposomes, and presence of the pore forming peptide mastoparan X". Langmuir 23:8647–8649

J Membrane Biol (2012) 245:583–590
DOI 10.1007/s00232-012-9470-2

The Systematic Study of the Electroporation and Electrofusion of B16-F1 and CHO Cells in Isotonic and Hypotonic Buffer

Marko Usaj · Masa Kanduser

Received: 15 January 2012 / Accepted: 24 June 2012 / Published online: 29 July 2012

Abstract The fusogenic state of the cell membrane can be induced by external electric field. When two fusogenic membranes are in close contact, cell fusion takes place. An appropriate hypotonic treatment of cells before the application of electric pulses significantly improves electrofusion efficiency. How hypotonic treatment improves electrofusion is still not known in detail. Our results indicate that at given induced transmembrane potential electroporation was not affected by buffer osmolarity. In contrast to electroporation, cells' response to hypotonic treatment significantly affects their electrofusion. High fusion yield was observed when B16-F1 cells were used; this cell line in hypotonic buffer resulted in 41 ± 9 % yield, while in isotonic buffer 32 ± 11 % yield was observed. Based on our knowledge, these fusion yields determined in situ by dual-color fluorescence microscopy are among the highest in electrofusion research field. The use of hypotonic buffer was more crucial for electrofusion of CHO cells; the fusion yield increased from below 1 % in isotonic buffer to 10 ± 4 % in hypotonic buffer. Since the same degree of cell permeabilization was achieved in both buffers, these results indicate that hypotonic treatment significantly improves fusion yield. The effect could be attributed to improved physical contact of cell membranes or to enhanced fusogenic state of the cell membrane itself.

M. Usaj · M. Kanduser (✉)
Faculty of Electrical Engineering, University of Ljubljana, Trzaska cesta 25, 1000 Ljubljana, Slovenia
e-mail: masa.kanduser@fe.uni-lj.si

M. Usaj
e-mail: marko.usaj@fe.uni-lj.si

Keywords Electroporation · Electrofusion · Isotonic buffer · Hypotonic buffer · B16-F1 · CHO · Fluorescence microscopy

Introduction

According to current opinions in cell biology, cell fusion is the beginning and end, the alpha and omega, of all living beings. A human life starts with the fusion of two cells. However, recently published data also indicate that uncontrolled fusion of healthy cells results in cancer (Duelli and Lazebnik 2003, 2007). Furthermore, cell fusion is suggested to be one of the major mechanisms of the metastasis formation (Larsson et al. 2008; Lu and Kang 2009). Cell fusion is of interest not only as a fundamental biological process but also as a useful experimental tool in biotechnology, medicine and biology. For therapeutic purposes, we can use cell fusion to investigate and treat different diseases like diabetes (McClenaghan 2007), to regenerate axons of the central nervous system (Sretavan et al. 2005) and to produce cells with desired properties, such as reprogrammed progenitors for stem cell therapy (Yamanaka and Blau 2010). Even more, cell fusion also holds great promise in transplantation medicine (Sullivan and Eggan 2006). The most-know applications of cell fusion are the production of monoclonal antibodies in hybridoma technology (vor dem Esche et al. 2011; Trontelj et al. 2008) and the production of cell vaccines for cancer immunotherapy (Koido et al. 2010).

However, the success of the methods based on cell fusion depends on the number of fused and functional cells, which is not a trivial task to achieve. For this reason, an universal tool which will reliably produce a high fusion yield has been sought for almost 30 years. Among the physical, viral,

chemical and even genetic methods (Gottesman et al. 2010), cell fusion using electric pulses, known as "electrofusion," is the most promising one. However, its status as a routine tool for cell fusion has yet to be established. The method is relatively simple, is potentially highly efficient and enables a fusion of a large number of cells at the same time. In studies where the chemical method of cell fusion (PEG) was compared to electrofusion, the authors reported that electrofusion was more efficient (Hui and Stenger 1993; Karsten et al. 1988; Yu et al. 2008). Electrofusion also holds the great promise in the clinical environment since it does not include any viral or chemical additives.

The reason electrofusion is not already a universal tool for cell fusion is that all parameters and mechanisms are not yet completely known and optimized. It was shown that, even with modern microfluidic devices developed recently, fusion yields can still be very low (up to 5 %) (Ju et al. 2009). From the literature we can see that there are many factors which affect electrofusion, but no systematic study has been performed to clarify the influential parameters and to suggest directions for further studies.

By definition, electrofusion is a two-condition process: (1) a cell membrane has to be brought into a fusogenic state and (2) close physical contact between two fusogenic membranes has to be established (Teissie and Rols 1986). The fusogenic state of the cell membrane is achieved by electric pulse application, resulting in electroporation that causes a dramatic increase in membrane permeability after the cell is exposed to short and intense electric pulses. The energy for membrane permeability based on rearrangement of lipid molecules in the cell membrane is obtained by induced transmembrane voltage (ITV) (Neumann et al. 1989). In general, it is accepted that at higher ITV higher electroporation efficiency is achieved. The change in cell membrane permeability is not the only consequence of electric pulse application; such a membrane is also brought into a fusogenic state (Teissie and Ramos 1998). Therefore, for effective electrofusion, adequate electric field parameters have to be selected (Trontelj et al. 2008).

Close physical contact between cells is the second condition required for effective cell fusion; it is important to note that the contact has to be established while cell membranes are in the fusogenic state. Electrofusion is a considerably more complex process than electroporation due to the fact that cell contact is crucial and that the physiology of the cell is involved in the postpulse process leading to effective cell fusion. No theoretical descriptions yet exist which would predict a fusion yield. Even more, a fusion yield varies tremendously between different cell lines (Salomskaite-Davalgiene et al. 2009; Usaj et al. 2010). Thus, the mechanisms involved in efficient cell fusion and optimization of parameters involved in the process still require further studies. While part of the difference in electrofusion behavior can be attributed to cell size, an important part is governed by biological characteristics and the response of cells to the treatment (Glaser and Donath 1987; Neil and Zimmermann 1993). One of the earliest approaches proposed to improve electrofusion efficiency was the use of hypotonic buffers (Klock et al. 1992; Schmitt and Zimmermann 1989; Vienken and Zimmermann 1985). How hypotonic treatment improves electrofusion is still not known in detail. In the literature to date (Ahkong and Lucy 1986; Perkins et al. 1991; Reuss et al. 2004; Stenger et al. 1988; Sukhorukov et al. 1993, 2005, 2006; Zimmermann et al. 1990; Zimmermann and Neil 1996) we find only a few hypotheses, which can be divided into two groups: (1) a hypotonic treatment enhances the electroporation itself and (2) a hypotonic treatment improves cell contact and, by that, fusion yield. It is also possible that an improved fusion yield is the consequence of both phenomena. This questions cannot be answered only by analyzing the data already published since there is no systematic study where both phenomena, i.e., electroporation and electrofusion, were investigated in parallel using isotonic and hypotonic buffers with the same cell line, buffer composition, electric field parameters, method for establishing cell contact and temperature.

The aim of our study was to investigate electroporation and electrofusion in isotonic and hypotonic buffers for two cell lines using the same experimental conditions to enable us to separate the effects of cell membrane permeabilization and cell fusion. For electroporation we tested different electric pulse amplitudes. We used electric field amplitudes that resulted in comparable transmembrane potentials in isotonic and hypotonic buffers in order to exclude the influence of cell size (or ITV) on electroporation and electrofusion. Thus, from the data obtained we could separately evaluate the effect of hypotonic treatment on electroporation and electrofusion beyond the effect of the cell size. In our previously study (Usaj et al. 2010) we described a modified adherence method to efficiently perform cell fusion in hypotonic buffer. In this study we focused on the comparison of the electroporation and electrofusion in isotonic and hypotonic buffers, an aspect that was only briefly addressed in our previous work. Besides we described a simple but very effective modification of our electrofusion method, which gives a three times higher electrofusion yield compared to our previously published study.

Materials and Method

Chemicals, Cell Culture Media

Dulbecco's minimal essential medium (DMEM), Ham's Nutrient Mixtures (F-12 HAM), fetal bovine serum (FBS), L-glutamine, sucrose, dipotassium hydrogen phosphate

(K_2HPO_4), potassium dihydrogen phosphate (KH_2PO_4), magnesium chloride ($MgCl_2$), trypsin and EDTA were obtained from Sigma-Aldrich (Taufkirchen, Germany). Antibiotics (crystacillin and gentamicin) were obtained from Lek (Ljubljana, Slovenia). Propidium iodide, CMFDA and CMRA cell trackers were obtained from Molecular Probes/Invitrogen (Carlsbad, CA).

Cell Culture and Electroporation Buffer

Cell lines were cultured in humidified atmosphere at 37 °C and 5 % CO_2 in the following culture media: mouse melanoma (B16-F1) in DMEM supplemented with 10 % FBS, antibiotics (gentamicin, crystacillin) and L-glutamine; Chinese hamster ovary cells (CHO) in F-12 HAM supplemented with 10 % FBS, antibiotics and L-glutamine. Cells were grown in a 25 cm^2 culture flask (TPP, Trasadingen, Switzerland) to 70–80 % confluence. Iso- and hypotonic potassium phosphate buffer (KPB; 10 mM KH_2PO_4/K_2HPO_4, 1 mM $MgCl_2$) with 250 or 75 mM sucrose corresponding to osmolarities of 260 and 93 mOsm [mOsmol/kg, determined by Knauer vapor pressure osmometer (K-7000; Knauer, Wissenschaftliche Geratebau, Germany)] were used in the experiments. The conductivity of both buffers was 1.62 mS/cm and pH 7.2.

Electroporation

Cell suspensions were prepared on the day of the experiment by 0.25 % trypsin/EDTA solution. Trypsin solution was then removed and replaced by 5 ml of culture medium, and a homogenous cell suspension was prepared. For electroporation we used an electric pulse generator (Cliniporator; IGEA, Carpi, Italy) and 4 mm gap cuvettes (Eppendorf, Hauppauge, NY). The electric field was calculated as $E = U/d$, where U is applied voltage and d is distance between electrodes (4 mm). Aliquots of 1.5×10^5 cells for B16-F1 (or 3×10^5 cells for CHO) were prepared, centrifuged ($290\times g$, 5 min, 4 °C) and kept at 4 °C. Supernatant was carefully removed, and cells were resuspended in 270 µl of hypotonic buffer. Electroporation was performed 2 min after hypotonic buffer was added as it was shown previously that cells are close to their maximal size induced by hypotonic cell swelling (Usaj et al. 2009). Propidium iodide (30 µl, 1.5 mM) was added to the cell suspension 15 s before pulse application, and the cell suspension was then transferred to an electroporation cuvette. The same procedure was used for isotonic buffer. Electroporation was performed by application of eight rectangular pulses with pulse duration 100 µs, repetition frequency of 1 Hz and different pulse amplitudes from 0 V (0 V/cm, negative control) to 640 V (1,600 V/cm, positive control) for hypotonic buffer or 800 V (2,000 V/cm, positive control) for isotonic buffer, in 80 V (200 V/cm) steps. Electroporation efficiency was determined spectrofluorometrically by means of propidium iodide uptake in a microplate reader (Infinite M200; Tecan, Mannedorf, Switzerland) at 535 nm excitation and 617 nm emission wavelength, 3 min after pulse application. The percentage of propidium iodide uptake was then calculated. The value obtained from the negative control was subtracted from the value of the treated sample and then divided by that of the positive control. Mean values (±SD) for given pulse amplitudes were calculated from at least four independent experiments. The differences between electroporation in isotonic and hypotonic buffers at the same applied voltage (electric field amplitude) for each cell line were statistically tested using the independent samples t test (SPSS Statistic; SPSS, Inc., Chicago, IL).

Calculation of Maximal Induced Transmembrane Voltage

For ITV calculation we used an equation for induced transmembrane voltage of spherical cells

$$ITV = -1.5rE\cos\varphi \quad (1)$$

where r is the radius of the cell, E is the strength of the external electric field and φ is the angle between the direction of the external applied electric field and the normal from the center of the cell to the point of interest on the cell surface (Kotnik et al. 1997; Neumann et al. 1989; Pucihar et al. 2009). The hypotonic treatment used in our experiments induces swelling of the cells and, therefore, affects the maximum induced transmembrane voltage (ITV_{max}) and putatively the efficiency of electroporation/electrofusion. The cell radii for B16-F1 and CHO before and 2 min after the start of hypotonic treatment were determined in our previous studies (Usaj et al. 2009, 2010). The cell radii of B16-F1 in isotonic and hypotonic buffers were 8.1 ± 1.1 and 9.3 ± 1.8 µm, while those for CHO were 6.1 ± 0.6 and 7.7 ± 0.4 µm, respectively. An independent samples t test showed us that B16-F1 cells were significantly larger than CHO cells in isotonic buffer ($P < 0.05$). However, this difference was not statistically significant after the cells were maintained in hypotonic buffer for 2 min. A paired samples t test made on the sizes of the same cells in isotonic buffer and after 2 min in hypotonic buffer revealed that the increase in cell size due to hypotonic swelling was statistically significant for both cell lines ($P < 0.05$).

Electrofusion

Fluorescence microscopy was used for the detection and quantification of fused cells as described previously (Trontelj et al. 2010; Usaj et al. 2010). Cells in one flask

were stained with green CMFDA, while cells in the other flask were stained with red CMRA at 7 μM loading solution. The cells were then trypsinized and mixed together at a ratio of 1:1.

Close cell–cell contacts were established by a modified adherence method (Trontelj et al. 2010). Here has been made a simple but efficient improvement of the method since our first publication (Usaj et al. 2010). Instead of plating the whole microplate well with 1 ml of cells in suspension (Usaj et al. 2010), we placed only a 40 μl drop of cells in suspension in the middle of the well. Doing so, the cell contact is much more controllable since cells stay in the area between electrodes and do not distribute to the edge of the microplate well, where they are not exposed to electric pulse treatment. Thus, a 40 μl drop of cell suspension containing 2×10^6 cells/ml for B16-F1 and 4×10^6 cells/ml for CHO was placed in each well of a 24-multiwell plate (TPP). Cells were incubated in 5 % CO_2 at 37 °C for 20 min to slightly attach to the surface of the well. Before electroporation, cells were washed with isotonic buffer and 350 μl of hypotonic or isotonic buffer was added. Two minutes later, electric pulses (8 × 100 μs at 1 Hz) were delivered using two parallel wire electrodes (Pl/Ir = 90/10) with a 5 mm gap. Electric field amplitudes were selected in order to induce the same ITVs in isotonic and hypotonic buffers (see Eq. 1). After delivery of pulses, cells were left undisturbed for 10 min for cell fusion to take place. The fusion yield was determined by dual-color fluorescence microscopy (Jaroszeski et al. 1998; Trontelj et al. 2010). We used two emission filters, the first at 535 nm (HQ535/30 m, for CMFDA) and the second at 510 nm (D510/40 m, for CMRA) (both from Chroma, Brattleboro, VT), and a monochromator (Polychrome IV; Visitron, Puchheim, Germany). Cells were observed under an inverted fluorescence microscope (Axiovert 200; Zeiss, Oberkochen, Germany) with ×20 objective magnification. Three images (phase contrast, red and green fluorescence) were acquired from five randomly chosen fields in each well using a cooled CCD video camera (VisiCam 1280, Visitron) and PC software MetaMorph 7.1 (Molecular Devices, Palo Alto, CA).

For each parameter an image triplet composed of phase contrast, red fluorescent and green fluorescent images was created. The image-processing software ImageJ (NIH Image, Bethesda, MD) was used to create three channel images (Fig. 2) from each image triplet (phase contrast, red and green fluorescence). Cells were manually counted, and the fusion yield was calculated as a percentage of double-labeled fused (or polynucleated) cells: $(N_{double}/N_{total}) \times 100$. The fusion yield is presented as an average value (±SD) for a given cell line and the ITV_{max} obtained from at least three independent experiments. Differences between electrofusion in isotonic and hypotonic buffers at the same ITV for each cell line were statistically tested using the independent samples *t* test.

Results

Electroporation

We investigated the electroporation of B16-F1 and CHO cells in isotonic and hypotonic buffers at different electric field amplitudes. The results are shown in Fig. 1a, b. At first sight the hypotonic buffer enhanced cell electroporation. Propidium iodide uptake was higher in hypotonic buffer than in isotonic buffer at the same electric field amplitudes for both cell lines. Consequently, saturation was achieved at lower electric field amplitudes in hypotonic than in isotonic buffer. The apparent threshold for electroporation was lower in hypotonic buffer, 200–400 V/cm, than in isotonic buffer, 400–600 V/cm; however, the resolution of data points around the electroporation threshold was too low to more accurately confirm this visual observation and to more accurately determine the exact value of the electroporation threshold.

To gain insight into the effect of the hypotonic buffer, we calculated ITV_{max}. By doing so we excluded the effect of cell size on cell electroporation caused by hypotonic cell swelling. The radii of B16-F1 cells in isotonic and hypotonic buffers were 8.1 ± 1.1 and 9.3 ± 1.8 μm, while those for CHO cells were 6.1 ± 0.6 and 7.7 ± 0.4 μm, respectively. Based on these cell sizes, ITV_{max} values were calculated for both cell lines. The percentages of propidium iodide uptake by cells were then plotted against ITV_{max} values and are presented in Fig. 1c, d. No apparent differences in electroporation efficiency at any of the ITV_{max} values were found. More than 50 % of cells were permeabilized at ITV_{max} values of 0.8–0.9 V, while at 1.25–1.5 V all cells were permeabilized. The differences in electroporation efficiencies between the two cell lines and isotonic and hypotonic buffers are within the standard deviation of the experiments.

Electrofusion

In the second part of the study we investigated the electrofusion of B16-F1 and CHO cells in isotonic and hypotonic buffers at different electric field amplitudes. Based on the difference in cell size, we chose such electric field amplitudes that the ITV values were the same in isotonic and hypotonic buffers. In Fig. 2 micrographs of control and electrofused B16-F1 and CHO cells in hypotonic and isotonic buffer are presented. In Figs. 3 and 4 the percentage of fusion yields in isotonic and hypotonic buffers for B16-F1 and CHO cells are presented. The highest fusion

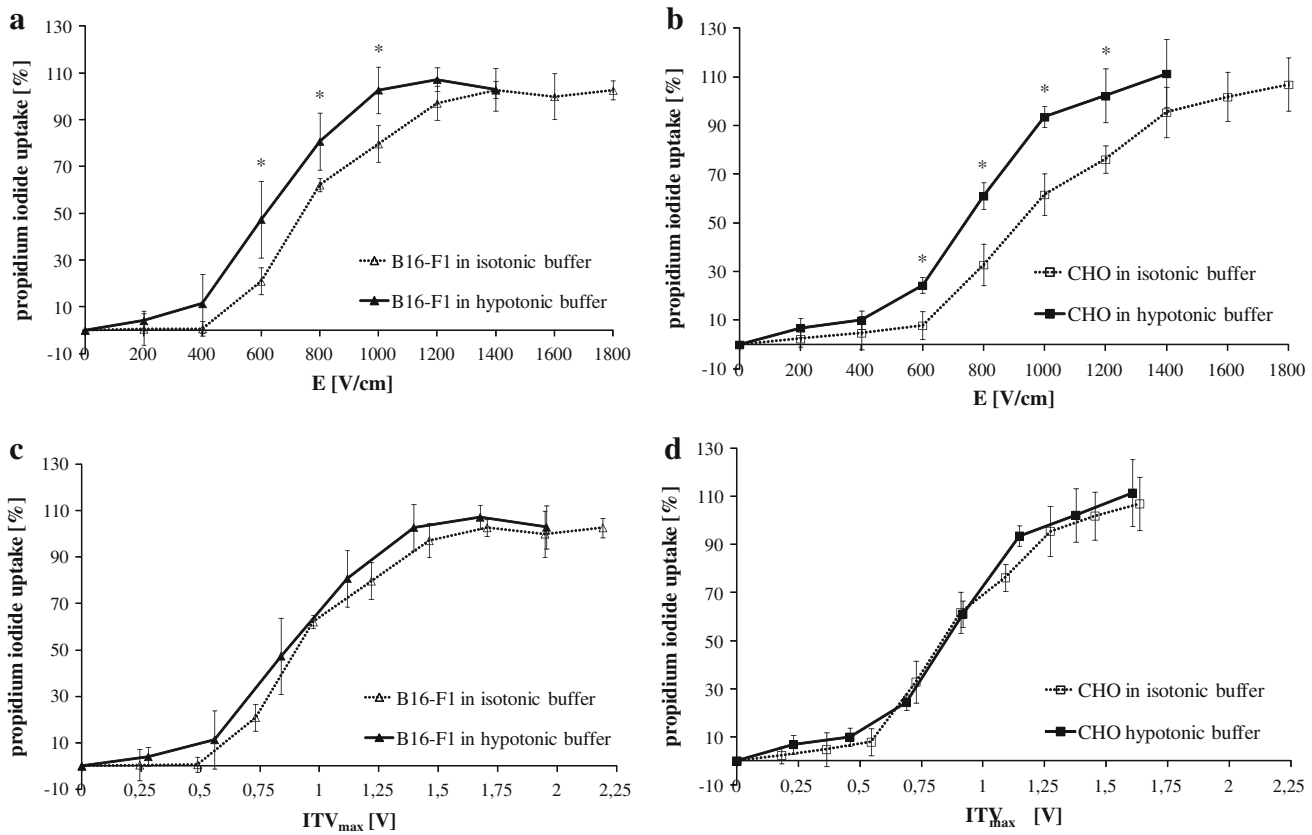

Fig. 1 Electroporation efficiency determined by propidium iodide uptake. Cells were electroporated 2 min after hypotonic or isotonic treatment with a train of pulses (8 × 100 µs, 1 Hz) at different electric field amplitudes. The percentage of propidium iodide uptake versus electric field amplitudes is presented for **a** B16-F1 and **b** CHO cells. Values of ITV$_{max}$ were then calculated based on cell radii and applied electric field amplitudes using Eq. 1 for **c** B16-F1 and **d** CHO cells. *Asterisks* represent statistically significant differences ($P < 0.05$). Each data point represents the average ± SD of at least four independent experiments

yield was obtained in hypotonic buffer with B16-F1 cells (up to 41 ± 9 %, Fig. 3). Nevertheless, a reasonably good fusion yield (32 ± 11 %) of B16-F1 cells was also found in isotonic buffer (Fig. 3). In contrast to B16-F1, when fusion was performed with CHO cells, <1 % of the fused cells were observed in isotonic buffer (Fig. 4). The hypotonic treatment increased the fusion of CHO cells up to 10 % (Fig. 4), suggesting that the hypotonic treatment plays a critical role in electrofusion of CHO cells.

Discussion

In this article a systematic comparison of cell electroporation and electrofusion in isotonic and hypotonic buffers using two cell lines (CHO and B16-F1) is presented. The main question was how hypotonic treatment affects cell fusion. Does it affect cell membrane permeabilization or the contact between cells? In our recent study (Usaj et al. 2010) we found that electrofusion efficiency in hypotonic buffer was considerably affected by the cell line used, suggesting that the biological characteristics of cells have a significant impact on cell electrofusion. Here, we extended our previous study (Usaj et al. 2010) and compared the effect of isotonic and hypotonic treatments on electroporation and electrofusion efficiency using two cell lines with different fusogenic abilities. In both isotonic and hypotonic buffers an increase in electric field amplitude led to an increase in electroporation efficiency. However, lower electric field amplitudes were required for electroporation in hypotonic buffer, while the shape of the curve was not affected (Fig. 1a, b). This is in accordance with the published literature, where a similar effect of hypotonic treatment has been reported (Barrau et al. 2004; Rols and Teissie 1990; Wang and Lu 2006). In order to exclude the effect of hypotonic treatment on cell size, which affects the ITV and therefore cell electroporation (Kinosita and Tsong 1979; Weaver and Chizmadzhev 1996), we calculated ITV$_{max}$ values (Fig. 1c, d). The results show that electroporation is not affected by buffer osmolarity and biological characteristics of the cells. This is in accordance with the study of Golzio et al. (1998), who did not find any significant effect of the hypotonic buffer on cell electroporation. We have to mention here that our experimental

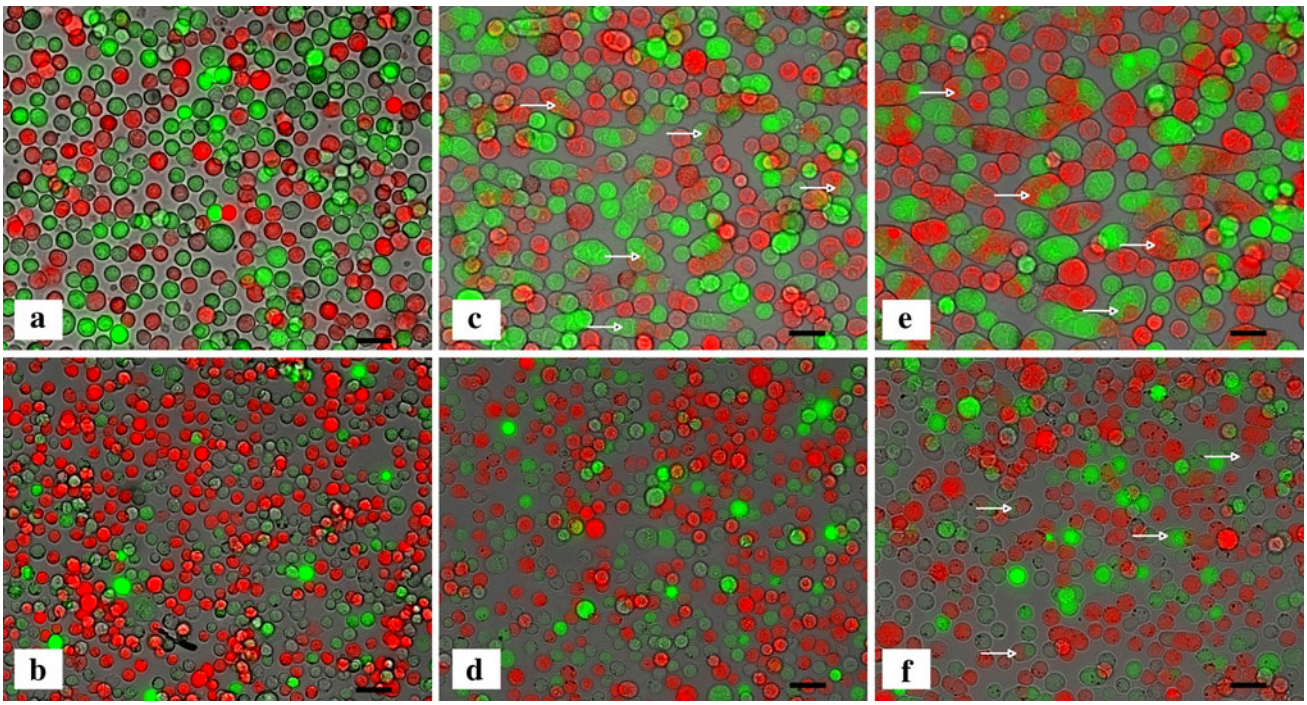

Fig. 2 Three-channel microscopic images of cell electrofusion: B16-F1 control cells (**a**) and fused cells at $ITV_{max} = 1.68$ V in isotonic (**c**) and hypotonic (**e**) buffer as well as CHO control (**b**) and fused at $ITV_{max} = 1.84$ V in isotonic (**d**) and hypotonic (**f**) buffer. Images of cell electrofusion were captured 10 min after electric pulse treatment under ×20 objective magnification. In order to keep images clearer, only a few fused cells are marked with *arrows*. <1 % of fused CHO cells were obtained in isotonic buffer. *Bars* = 30 μm

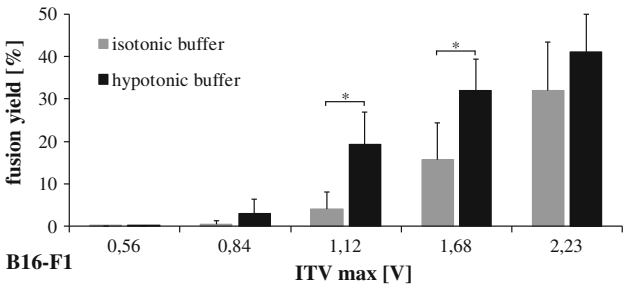

Fig. 3 Electrofusion efficiency in isotonic and hypotonic buffer of B16-F1 cells for different ITVs. The increase in ITV improves the fusion yield in hypotonic and isotonic buffer; however, higher fusion yields are observed in hypotonic buffer. *Asterisks* represent statistically significant differences ($P < 0.01$). Columns represent the average ± SD of at least three independent experiments

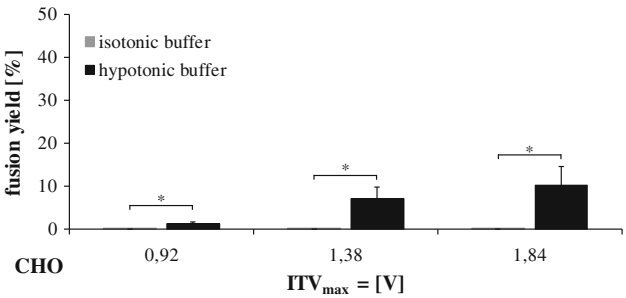

Fig. 4 Electrofusion efficiency in isotonic and hypotonic buffer of CHO cells for different ITVs. The increase in ITV improves the fusion yield only in hypotonic buffer, whereas in isotonic buffer <1 % of fused cells were obtained. *Asterisks* represent statistically significant differences ($P < 0.01$). Columns represent the average ± SD of four independent experiments

protocol was slightly different. In the study of Golzio et al. (1998) the electroporation was performed on cells after the regulatory volume decrease (RVD) induced in hypotonic buffer took place and the cells were back to their initial size. In our study electroporation was performed when cells reached their maximal size before RVD was activated. Therefore, the only effect observed in hypotonic buffer was cell electroporation at lower electric field amplitudes caused by cell swelling itself (Fig. 1a, b). Another effect of the hypotonic buffer on cell electroporation was proposed by Barrau et al. (2004), who suggested that cell swelling causes an increase in cell surface area, which requires the unfolding of undulations and envaginations of the cell membrane and increases membrane lateral tension. It was calculated that ≈100 mV lower ITV is needed to trigger cell membrane electroporation in hypotonic buffer (Barrau et al. 2004). However in our study (Fig. 1c, d) this was not observed due to low data resolution around the electroporation threshold.

In contrast to electroporation, cell physiology and the cell response to stress induced by hypotonic treatment seem to play crucial roles in electrofusion. It is interesting

to note that different degrees of electroporation are needed for electrofusion of B16-F1 and CHO cells. For example, in hypotonic buffer considerably higher electroporation efficiency (70 ± 11 %, at $ITV_{max} = 0.92$ V) is needed for CHO cells to start to fuse (fusion yield = 1.2 ± 0.4 %) than for B16-F1 cells (electroporation efficiency = 44 ± 8 %, at $ITV_{max} = 0.84$, fusion yield = 3.1 ± 3.2 %).

The hypotonic treatment improves cell fusion in both cell lines. The fusion yield of the more fusogenic cell line B16-F1 in hypotonic buffer was up to 41 ± 9 %. As far as we know this is one of the highest reported in situ electrofusion efficiencies determined by fluorescence microscopy (Gabrijel et al. 2004). We should not forget that not all of the fused cells can be detected by dual-color fluorescence microscopy. If we take into account (Scott-Taylor et al. 2000) that only one-half of fused cells can be detected by this method, then our total fusion yield exceeds 80 %. Here, we have to mention that our approach for fusion yield determination does not distinguish between binucleated cells as a result of the fusion between two cells and polynucleated cells as a result of multiple fusion events. From this point of view our fusion yields are underevaluated since polynucleated cells were often obtained. Such high fusion yields were obtained with a simple but efficient modification, described in "Materials and Methods", of our adherence method published previously (Usaj et al. 2010).

However, even with the highly efficient method for cell electrofusion, we did not obtain high electrofusion of CHO cells. The difference between the highly fusogenic B16-F1 and the poorly fusogenic CHO cells still exists. This different electrofusion ability of the two lines was described in our previous work (Usaj et al. 2010). The improved electrofusion method presented here results in a good fusion yield (32 ± 11 %) of B16-F1 cells even in isotonic buffer at the highest ITV_{max}. In contrast to B16-F1 cells, we obtained <1 % of fused CHO cells in isotonic buffer even at the highest electric field amplitude used (2,000 V/cm, $ITV_{max} = 1.84$ V). The use of hypotonic buffer improved the fusion yield of both cell lines. In our experimental conditions the hypotonic treatment seems to be crucial for CHO cells, where up to 10 ± 4 % of fused cells were observed. Compared with our previous study (Usaj et al. 2010), we improved the electrofusion of CHO cells on average by 67 %. Our results are in agreement with previous studies, where it was reported that the use of hypotonic treatment improves electrofusion efficiency (Perkins et al. 1991; Rols and Teissie 1990; Schmitt and Zimmermann 1989; Sukhorukov et al. 2006; Zimmermann et al. 1990). Several explanations were proposed, as discussed in our previous report (Usaj et al. 2010). Also, cell membrane fluidity alternation caused by a hypotonic environment should be considered as a possible explanation for the effect of the hypotonic treatment on cell electrofusion (Toplak et al. 1990).

From our results we can confirm that the better fusion yield in hypotonic buffer is not caused by the effect of the hypotonic treatment on cell electroporation since the same degree of cell permeabilization was achieved in both isotonic and hypotonic buffers for a given ITV. These results suggest that the beneficial effect of hypotonic treatment is indeed caused by membrane–membrane interactions due to improved physical cell contacts or due to enhanced fusogenic state of the cell membrane itself. Further studies and analyses are, however, needed to specify and evaluate one or both hypotheses, especially to determine the role of the cell cytoskeleton and membrane fluidity in cell electrofusion.

Acknowledgement This research was supported by the Slovenian Research Agency under research programs P2-0249 and MRIC UL IP-0510. Research was conducted in the scope of the EBAM European Associated Laboratory. The authors thank Barbara Mali for her help with statistics.

References

Ahkong QF, Lucy JA (1986) Osmotic forces in artificially induced cell fusion. Biochim Biophys Acta 858:206–216

Barrau C, Teissie J, Gabriel B (2004) Osmotically induced membrane tension facilitates the triggering of living cell electropermeabilization. Bioelectrochemistry 63:327–332

Duelli D, Lazebnik Y (2003) Cell fusion: a hidden enemy? Cancer Cell 3:445–448

Duelli D, Lazebnik Y (2007) Cell-to-cell fusion as a link between viruses and cancer. Nat Rev Cancer 7:968–976

Gabrijel M, Repnik U, Kreft M et al (2004) Quantification of cell hybridoma yields with confocal microscopy and flow cytometry. Biochem Biophys Res Commun 314:717–723

Glaser RW, Donath E (1987) Hindrance of red-cell electrofusion by the cytoskeleton. Stud Biophys 121:37–43

Golzio M, Mora M-P, Raynaud C et al (1998) Control by osmotic pressure of voltage-induced permeabilization and gene transfer in mammalian cells. Biophys J 74:3015–3022

Gottesman A, Milazzo J, Lazebnik Y (2010) V-fusion: a convenient, nontoxic method for cell fusion. Biotechniques 49:747–750

Hui SW, Stenger DA (1993) Electrofusion of cells: hybridoma production by electrofusion and polyethylene glycol. Methods Enzymol 220:212–227

Jaroszeski MJ, Gilbert R, Heller R (1998) Flow cytometric detection and quantitation of cell–cell electrofusion products. In: Jaroszeski MJ, Heller R (eds) Flow cytometry protocols. Humana Press, New York, pp 149–156

Ju J, Ko J-M, Cha H-C et al (2009) An electrofusion chip with a cell delivery system driven by surface tension. J Micromech Microeng 19:015004

Karsten U, Stolley P, Walther I et al (1988) Direct comparison of electric field-mediated and PEG-mediated cell fusion for the generation of antibody producing hybridomas. Hybridoma 7:627–633

Kinosita K, Tsong TY (1979) Voltage-induced conductance in human erythrocyte membranes. Biochim Biophys Acta 554:479–497

Klock G, Wisnewski AV, el-Bassiouni EA et al (1992) Human hybridoma generation by hypo-osmolar electrofusion: characterization of human monoclonal antibodies to *Schistosoma mansoni* parasite antigens. Hybridoma 11:469–481

Koido S, Homma S, Hara E et al (2010) Regulation of tumor immunity by tumor/dendritic cell fusions. Clin Dev Immunol 2010:516768

Kotnik T, Bobanovic F, Miklavcic D (1997) Sensitivity of transmembrane voltage induced by applied electric fields—a theoretical analysis. Bioelectrochem Bioenerg 43:285–291

Larsson LI, Bjerregaard B, Talts JF (2008) Cell fusions in mammals. Histochem Cell Biol 129:551–561

Lu X, Kang Y (2009) Cell fusion as a hidden force in tumor progression. Cancer Res 69:8536–8539

McClenaghan NH (2007) Physiological regulation of the pancreatic β-cell: functional insights for understanding and therapy of diabetes. Exp Physiol 92:481–496

Neil GA, Zimmermann U (1993) Electrofusion. Methods Enzymol 220:174–196

Neumann E, Sowers AE, Jordan CA (1989) Electroporation and electrofusion in cell biology. Plenum Press, New York

Perkins S, Zimmermann U, Foung SK (1991) Parameters to enhance human hybridoma formation with hypoosmolar electrofusion. Hum Antibodies Hybrid 2:155–159

Pucihar G, Miklavcic D, Kotnik T (2009) A time-dependent numerical model of transmembrane voltage inducement and electroporation of irregularly shaped cells. IEEE Trans Biomed Eng 56:1491–1501

Reuss R, Ludwig J, Shirakashi R et al (2004) Intracellular delivery of carbohydrates into mammalian cells through swelling-activated pathways. J Membr Biol 200:67–81

Rols MP, Teissie J (1990) Modulation of electrically induced permeabilization and fusion of Chinese hamster ovary cells by osmotic pressure. Biochemistry 29:4561–4567

Salomskaite-Davalgiene S, Cepurniene K, Satkauskas S et al (2009) Extent of cell electrofusion in vitro and in vivo is cell line dependent. Anticancer Res 29:3125–3130

Schmitt JJ, Zimmermann U (1989) Enhanced hybridoma production by electrofusion in strongly hypo-osmolar solutions. Biochim Biophys Acta 983:42–50

Scott-Taylor TH, Pettengell R, Clarke I et al (2000) Human tumour and dendritic cell hybrids generated by electrofusion: potential for cancer vaccines. Biochim Biophys Acta 1500:265–279

Sretavan DW, Chang W, Hawkes E et al (2005) Microscale surgery on single axons. Neurosurgery 57:635–646

Stenger DA, Kubiniec RT, Purucker WJ et al (1988) Optimization of electrofusion parameters for efficient production of murine hybridomas. Hybridoma 7:505–518

Sukhorukov VL, Arnold WM, Zimmermann U (1993) Hypotonically induced changes in the plasma membrane of cultured mammalian cells. J Membr Biol 132:27–40

Sukhorukov VL, Reuss R, Zimmermann D et al (2005) Surviving high-intensity field pulses: strategies for improving robustness and performance of electrotransfection and electrofusion. J Membr Biol 206:187–201

Sukhorukov VL, Reuss R, Endter JM et al (2006) A biophysical approach to the optimisation of dendritic-tumour cell electrofusion. Biochem Biophys Res Commun 346:829–839

Sullivan S, Eggan K (2006) The potential of cell fusion for human therapy. Stem Cell Rev 2:341–349

Teissie J, Ramos C (1998) Correlation between electric field pulse induced long-lived permeabilization and fusogenicity in cell membranes. Biophys J 74:1889–1898

Teissie J, Rols MP (1986) Fusion of mammalian cells in culture is obtained by creating the contact between cells after their electropermeabilization. Biochem Biophys Res Commun 140:258–266

Toplak H, Batchiulis V, Hermetter A et al (1990) Effects of culture and incubation conditions on membrane fluidity in monolayers of cultured cells measured as fluorescence anisotropy using trimethylammoniumdiphenylhexatriene (TMA-DPH). Biochim Biophys Acta 1028:67–72

Trontelj K, Rebersek M, Kanduser M et al (2008) Optimization of bulk cell electrofusion in vitro for production of human-mouse heterohybridoma cells. Bioelectrochemistry 74:124–129

Trontelj K, Usaj M, Miklavcic D (2010) Cell electrofusion visualized with fluorescence microscopy. J Vis Exp 41:e1991

Usaj M, Trontelj K, Hudej R et al (2009) Cell size dynamics and viability of cells exposed to hypotonic treatment and electroporation for electrofusion optimization. Radiol Oncol 43:108–119

Usaj M, Trontelj K, Miklavcic D, Kanduser M (2010) Cell–cell electrofusion: optimization of electric field amplitude and hypotonic treatment for mouse melanoma (B16–F1) and Chinese hamster ovary (CHO) cells. J Membr Biol 236:107–116

Vienken J, Zimmermann U (1985) An improved electrofusion technique for production of mouse hybridoma cells. FEBS Lett 182:278–280

vor dem Esche U, Huber M, Zgaga-Griesz A et al (2011) Passive vaccination with a human monoclonal antibody: generation of antibodies and studies for efficacy in *Bacillus anthracis* infections. Immunobiology 216:847–853

Wang H-Y, Lu C (2006) High-throughput and real-time study of single cell electroporation using microfluidics: effects of medium osmolarity. Biotechnol Bioeng 95:1116–1125

Weaver JC, Chizmadzhev YA (1996) Theory of electroporation: a review. Bioelectrochem Bioenerg 41:135–160

Yamanaka S, Blau HM (2010) Nuclear reprogramming to a pluripotent state by three approaches. Nature 465:704–712

Yu X, McGraw PA, House FS, Crowe JE (2008) An optimized electrofusion-based protocol for generating virus-specific human monoclonal antibodies. J Immunol Methods 336:142–151

Zimmermann U, Neil GA (1996) Electromanipulation of cells. CRC Press, Boca Raton

Zimmermann U, Gessner P, Schnettler R et al (1990) Efficient hybridization of mouse-human cell lines by means of hypoosmolar electrofusion. J Immunol Methods 134:43–50

J Membrane Biol (2012) 245:591–598
DOI 10.1007/s00232-012-9493-8

ORIGINAL ARTICLES

Network for Development of Electroporation-Based Technologies and Treatments: COST TD1104

Damijan Miklavčič

Received: 28 June 2012 / Accepted: 24 July 2012 / Published online: 25 August 2012

Abstract Exposure of biological cells to a sufficiently strong external electric field results in increased permeability of cell membranes, referred to as "electroporation." Since all types of cells (animal, plant and microorganism) can be effectively electroporated, electroporation is considered to be a universal method and a platform technology. Electroporation has become a widely used technology applicable to, e.g., cancer treatment, gene transfection, food and biomass processing and microbial inactivation. However, despite significant progress in electroporation-based applications, there is a lack of coordination and interdisciplinary exchange of knowledge between researchers from different scientific domains. Thus, critical mass for new major breakthroughs is missing. This is why we decided to establish cooperation between research groups working in different fields of electroporation. Cooperation in Science and Technology (COST), which funds networking and capacity-building activities, presents a perfect framework for such scientific cooperation. This COST action aims at (1) providing necessary steps toward EU cooperation of science and technology to foster basic understanding of electroporation; (2) improving communication between research groups, resulting in streamlining European research and development activities; and (3) enabling development of new and further development of existing electroporation-based applications by integrating multidisciplinary research teams, as well as providing comprehensive training for early-stage researchers. Results of this COST action will provide multiple societal, scientific and technological benefits from improving existing electroporation-based applications to adding new ones in the fields of medicine, biotechnology and environmental preservation.

Keywords Electroporation · Cancer treatment · Pulsed electric field · Microbial inactivation · Food processing and preservation · Electrochemotherapy

D. Miklavčič (✉)
Faculty of Electrical Engineering, University of Ljubljana, Tržaška 25, 1000 Ljubljana, Slovenia
e-mail: damijan.miklavcic@fe.uni-lj.si

Introduction

Exposure of biological cells to a sufficiently strong external electric field results in transiently or permanently increased permeability of cell membranes, referred to as "electroporation." Since all types of cells (animal, plant and microorganism) can be effectively electroporated, without addition of viral or chemical compounds, electroporation is considered to be a universal method and a platform technology. As such, it presents a common link to research areas in medicine, biotechnology, the environment and energy. The efforts needed to develop these applications and to address diverse aspects of electroporation (biological, chemical, physical, material science, modeling) are thus multidisciplinary. Therefore, to be efficient and successful, strong links need to be established between physicians, engineers and scientists working in different scientific domains. Electroporation is currently used in food and biomass processing (Martin-Belloso and Sobrino-Lopez 2011; Toepfl et al. 2007; Sack et al. 2010) and as a local treatment of cancer (Sersa et al. 2012; Testori et al. 2012). Preservation of food by electroporation was demonstrated to maintain color, flavor and levels of antioxidants, while destroying microorganisms. Recently, extraction of intracellular components from plants (Sack et al. 2010) as well as cryopreservation using electroporation (Phoon et al. 2008) have been

demonstrated. Electroporation is also used for local cancer treatment of skin metastases, a treatment called "electrochemotherapy" (Marty et al. 2006). Since 2006, more than 4,000 patients in Europe have been successfully treated. The objective response rate of all tumors that were treated in these clinical trials was 78 %, with complete response of 52 % (Sersa et al. 2012). Clinical centers are already working on three innovative systems for drug delivery to the colorectal system, the brain, bone and liver metastases (Soden et al. 2007; Edhemovic et al. 2011; Mahmood and Gehl 2011; Agerholm-Larsen et al. 2011; Fini et al. 2010). However, for treatment of deep-seated tumor nodules, further technological developments are needed (Pavliha et al. 2012). Electroporation has shown potential in pretreatment of sludge and other substrates, leading to increased biogas production. Other applications, such as water treatment (Rieder et al. 2008; Gusbeth et al. 2009), extraction of oil from algae and of sugar from sugar beets (Loginova et al. 2011), gene therapy (Andre et al. 2008), DNA vaccination (Vandermeulen et al. 2009), cell fusion for systemic cancer treatment and human monoclonal antibody production (Usaj et al. 2010) are just a few of the foreseeable new applications.

Despite significant progress and increased use of electroporation-based applications, as well as the existence of a large number of nationally funded research projects, there is a lack of coordination and interdisciplinary exchange of knowledge between researchers from different scientific domains. Thus, critical mass in the form of human resources, knowledge from different domains and research facilities for major breakthroughs is often missing. Therefore, Cooperation in Science and Technology (COST) Action TD1104 has been prepared, which will provide the necessary steps toward cooperation in science and technology to foster basic understanding of electroporation and to enable further development of new and existing electroporation-based applications through integrating multidisciplinary research teams, as well as provide comprehensive training for students and early-stage researchers.

Classical EU-funded projects (e.g., EU FP, ERC, ESF, EUREKA) mainly support research and development, either basic or specific application-oriented. In contrast, COST funds networking and capacity-building activities, thereby representing a perfect framework for interdisciplinary international collaboration in electroporation research, which is at its current stage characterized by a relatively high level of national (54 %) and private (21 %) funding. Coordination of research in this action will at least partially address some of the global challenges (according to the Millennium Project, http://www.unmillenniumproject.org) associated with science and technology, health issues, long-term perspective, clean water and energy. Concrete societal, scientific and technological benefits from the action will arise in medicine (e.g., cancer treatment), biotechnology (e.g., extraction from algae and other cell cultures, improvement of industrial processes), environment preservation (e.g., wastewater treatment, biogas production, energy harvest from biomass) and food processing (e.g., extending shelf life of food, development of novel foods, obtaining new ingredients).

About COST

COST was the first and is thus the oldest European network to coordinate nationally funded research activities. COST today covers 35 European member countries and is organized in nine scientific domains (for more details, see http://www.cost.esf.org/about_cost). The main goal of COST is to strengthen Europe in research through the support of cooperation and interaction between researchers. It has in all these years grown largely from being a European networking mechanism to being a wider, even worldwide, cooperation framework. COST provides funds for coordination of research through COST actions, such as this one on electroporation, while research remains funded on a national level. COST actions are thus networking activities based on predominantly nationally funded research projects on a research topic that is of interest to at least five COST countries. There is a great emphasis on gender balance and inclusion of young scientists. It also allows all interested scientists from countries who sign the Memorandum of Understanding (MoU, http://w3.cost.eu/fileadmin/domain_files/BMBS/Action_TD1104/mou/TD1104-e.pdf) to join the activities even after the start of the action.

The process of getting a specific COST action running involves several steps. Based on a call, which is announced twice per year, a researcher (the proposer was the author of this article) on behalf of other researchers interested in a topic submits a proposal for a COST action on a specific topic from one of eight domains. If the proposal spans multiple domains (like electroporation), then it is considered a transdomain proposal and is evaluated as such. In the call where the COST action "European network for development of electroporation-based technologies and treatments" was submitted more than 90 proposals were received. After the first evaluation, 11 proposers were asked to submit a full proposal. After the second evaluation, five proposers were invited to a hearing in front of the representatives of the domain committees, after which three proposals were selected for funding, for a success rate of little more than 3 %. The COST action on electroporation was submitted as a transdomain action spanning different domains from biomedicine and molecular biosciences; food and agriculture; information and communication technologies; material, physics and nanosciences; and earth systems science and

environmental management (ESSEM) to chemistry and molecular sciences and technologies—thus a truly multidisciplinary, i.e., transdomain, COST action.

The networking activities within the COST action include scientific and administrative meetings, short-term scientific missions and organization of training schools. Meetings can be organized in the form of a management committee (i.e., administrative meeting), as a workshop on a specific topic or as a conference. Funding is available for the travel and subsistence costs of participants and for partial coverage of the organizing costs of the meeting. Short-term scientific missions are exchange visits of up to 3 months, aiming at strengthening collaboration between researchers from different countries. Emphasis is on supporting young researchers to learn new methods and perform experiments and measurements with equipment not available at their home institution. Training schools are intended for dissemination of research activities of the COST action and have to provide intensive training for young scientists in one of the laboratories but are also intended for retraining as a part of life-long learning. Funds are also available for dissemination of research results and publication through regular scientific publishing channels, such as peer-review journals, workshop and conference proceedings and books, but also general-information leaflets and brochures.

Reasons for the Action

Despite significant progress and increased use of electroporation-based applications, there is a lack of coordination and interdisciplinary exchange of knowledge between researchers from different scientific domains. Furthermore, research and development of electroporation, even if funded within the EU program, is currently fragmented as it is very often only "a service" in developing new applications—critical mass is thus missing. In order to obtain the most from this platform technology and to avoid the same research being replicated and funded more than once, it is important to establish cooperation between research groups from different domains. This is why it is necessary to establish a coordination of research and network. The main reason for this action is to enable cross-fertilization of different areas that will allow exchange of experience and knowledge. This will facilitate collaboration of different specialists from engineering, physics, chemistry, biology and medicine, thus providing a multidisciplinary approach and critical mass for further improvement of existing and development of new electroporation-based applications in medicine, biotechnology, energy harvest from biomass and the food industry.

Immediate and future benefits of the action:

- New knowledge, closing the gap between basic research and applications
- Improving communication and avoiding duplication of research efforts
- New and improved medical treatments (cancer treatment, DNA vaccination, gene therapy)
- Safer and healthier food
- Savings in natural resources, development of energy-efficient processes
- Opening new markets and creating new jobs

Envisaged electroporation based applications developed within the action:

- New approaches in gene therapy for cancer treatment and DNA vaccination for the medical device industry
- In food processing, extraction of valuable ingredients, development of novel foods and improvement of industrial food processes in terms of food safety and food quality
- Microbial inactivation and biomass preprocessing in wastewater treatment, biogas production and energy production

Planning and Preparing the Proposal

Experts working on electroporation and electroporation-based applications from different domains have been in contact, working occasionally on developing treatment or processing protocols but usually only on a national level and only exceptionally internationally within EU FP projects. Considerable efforts have been made in the past few years to bring together experts working with electroporation in different areas such as food processing, cancer treatment, pulsed power electronics and energy efficiency. However, the success was limited. Experts were meeting at conferences that were specialized, e.g., in cancer treatment in general, in food quality and processing or in bioelectrochemistry; but none of them gave the opportunity to focus on electroporation as a technology platform. Few experts in the field made an attempt to bridge the gap between different disciplines, but funding has been obtained predominantly on the national level, which potentially leads to funding duplication, poor coordination of research and difficulties in exploiting the results.

Establishing a new professional organization dedicated to the promotion of electroporation and electroporation-based applications through organization of dedicated conferences did not seem to be adequate at this stage of development and at this level of collaboration. Therefore, the COST action seems a perfect way to help the electroporation community to develop stronger links, exchange

experience and bring together forces through establishing a communication platform including regular meetings.

During the COST action proposal an extensive questionnaire was prepared in order to collect relevant information regarding research groups and their funding. The questionnaire was divided into seven sections:

1. Introduction—Questionnaire for a new COST action
2. Personal and academic information
3. Scientific expertise
4. Facts and figures of laboratory/department
5. Participation in COST actions and other international cooperation
6. Expected results and benefits of the COST action
7. Additional information

This allowed us not only to prepare a high-quality proposal but also to collect data on existing projects on national, international and EU levels (Fig. 1a). The collected data will serve as a reference level for future research activities in the field of electroporation, against which the success of this COST action will be measured through the years of the action and at the end of the action.

A total of 73 experts from 25 countries participated in the preparation of this proposal. According to the data collected through the questionnaire, in the last 3 years these experts worked on a total of 229 projects related to electroporation, 152 of which were funded on a national level, with 26 EU projects and 51 other international projects. The funding of participating research groups comes predominantly from national (54 %), private (21 %) and EU (10 %) sources (Fig. 1b).

According to the responses to the questionnaire, it was established that 293 researchers and 115 PhD students are currently working in COST country laboratories. In addition to 56 research groups from 19 COST countries, 13 research groups with 56 researchers were from countries with reciprocal agreements (Argentina, Australia and New Zealand) and non-COST countries (Russian Federation, Ukraine and United States), and they also participated actively in the preparation of the action (see Fig. 2 for participant structure). In these research groups, 152 national and 51 international research projects in the field of electroporation were funded in the last 3 years. The groups also participated in 26 EU FP projects in the last 3 years. This alone provides the COST action with great potential for coordination of these projects, thus providing better use of resources, avoiding duplication of research and allowing synergistic effects to take place.

The number of countries (19 COST and 6 non-COST countries) that have actively participated in the preparation of the proposal clearly demonstrates the extent of existing research and the need for coordination of this research, which is predominantly funded on a national level (54 %). Starting the COST action will allow also "smaller" groups that are working "alone" or are just starting their research on a national level to join the network. Until the kick-off meeting that took place on April 10, 2012, in Brussels already 21 COST countries had signed the Memorandum of Understanding and had nominated national representatives.

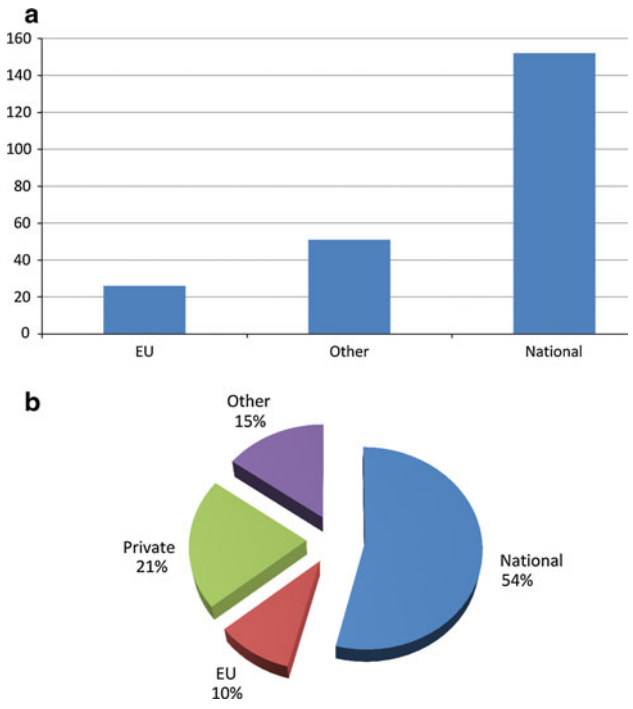

Fig. 1 Number of projects on electroporation by type (**a**) and by sources of funding (**b**) conducted by project proposers in the last 3 years

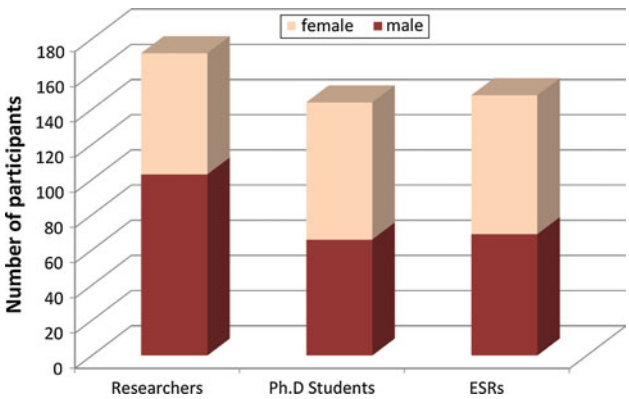

Fig. 2 Number of individual researchers and their representation by sex and years in research

Work Plan of the Project

Improving existing and developing new applications of electroporation will be the topics of the research. Coordination of national and international projects will allow collaborations not only between teams working in specific fields of electroporation but also among partners from different disciplines by using multidisciplinary approaches. In particular, focus will be given to linking theoretical efforts (e.g., analytical and numerical modeling of electroporation) with experimental results to develop basic knowledge of this phenomenon, which will be incorporated into electroporation-based applications. Modeling efforts on different levels—from the molecular level (molecular dynamics simulations) to the cell and tissue level (finite element modeling)—will be linked vertically and validated with experimental results.

The work plan of the action consists thus of investigating the basic mechanisms of electroporation and optimizing protocols in different electroporation-based applications, with special emphasis on food and biomass processing, medical applications and sustainable energy production (Fig. 3). Optimized protocols will allow technology development and transfer. The most important research tasks coordinated by the action are briefly described below.

1. Establishment of a close collaboration between researchers in biology, chemistry, physics, mathematics, informatics and engineering to enhance our understanding of electroporation and its associated processes. This will start immediately after approval of the action and will cover the first 3 years of the cooperative program. Emphasis will be on modeling the cell membrane with a goal of identifying the underlying processes of membrane electroporation and the associated phenomena (membrane destabilization, cytoskeleton reorganization, transmembrane pathways, etc.). Theoretical and modeling results will be compared to experimental data.
2. Optimizing electroporation protocols for industrial applications (e.g., food and biomass processing, microbial inactivation). Conditions used in these applications so far have only been determined empirically, while the latest developments, such as intracellular manipulation by nanosecond pulses, have not been implemented yet. Based on recent studies on a cellular level and basic research, processing conditions for industrial applications will be optimized with respect to low energy consumption. The knowledge about the impact of processing conditions on electroporation efficacy will be reviewed, taking into account specific industrial requirements (large-scale processing, high throughput, environmental and economic issues). General and application-oriented electroporation protocols for food and biomass processing will be gathered in a database. This will allow simple parameter selection for nonexperts and industrial end-users and provide an easy-to-access knowledge base for regulatory bodies.
3. Development of equipment design guidelines. Based on electroporation protocols, the guidelines for design of electroporation equipment (generators, electrode

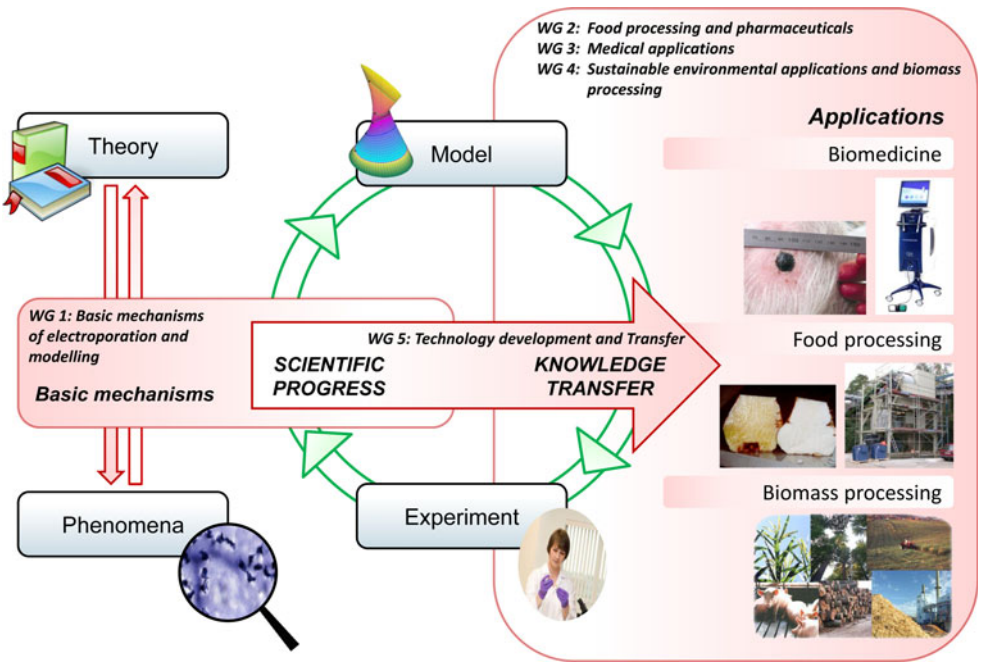

Fig. 3 Diagram illustrating the research processes and knowledge transfer within the action, emphasizing the process of translating basic research into applications. The working groups (WGs) facilitate all stages of the process

systems, microchambers) will be elaborated with the aim of achieving optimal treatment homogeneity, food safety and hygienic design. In addition, a database of applications already investigated and/or transferred into industry will be generated. The available scientific literature will be screened and information will be collected on equipment suppliers (e.g., product type, type of equipment, processing parameters). The database, accessible to COST partners via a Web site, will allow the selection of suitable, commercially viable application areas in food and biomass processing and the identification of new application fields.

4. Process monitoring. In the food industry, typically hazard analysis and critical control points concepts have to be followed to ensure food safety, where at critical points processing conditions are recorded. For electroporation, such protocols and suitable sensors still have to be developed. The identification of suitable monitoring techniques will be a key requirement for a broader application. Electrochemical reactions and electrode erosion should be minimized with regard to food safety. The impact of pulse wave shape and frequencies as well as other pulse characteristics and material-related effects will have to be determined to develop optimal equipment and select optimal processing conditions.
5. Development of electrochemotherapy (ECT) for cancer treatment. The development of electrodes for use in internal organs, identification and testing of new cancer drugs suitable for ECT and expansion of pulse parameters to increase versatility of ECT are challenges that still need to be addressed and that require future efforts. Clinical centers are already working on three innovative systems for drug and gene delivery to the colorectal system, the brain, bone and liver metastases. Several centers have worked with drugs other than conventional chemotherapeutic agents, and expansion of the spectrum of such drugs would be advantageous. The extension of attainable pulse parameter ranges should increase the flexibility of electroporation used in clinics in achieving both reversible electroporation (as used for drug delivery) and irreversible electroporation (with the aim of causing cell death by electroporation alone).
6. Expansion of delivery technology for large molecules, with a focus on end products such as DNA vaccines. Use of electroporation to transfer nucleic acids to various tissues (e.g., skeletal muscle, tumors, skin, liver) has benefited from the electrodes, generators and knowledge accumulated in the development of ECT protocols. In vivo, combinations of electroporating and electrophoretic pulses have been shown to be highly efficient, and clinical studies have demonstrated their safety compared to classical viral methods for gene therapy. The results of the clinical trials must now be promoted, and the researchers should dedicate their efforts to finding optimal protocols, developing adequate electrodes and generators, etc. The first clinical trials of gene electrotransfer (EGT) either have recently finished or are in progress. The range of applications of EGT is broad, and particularly promising are its applications in the treatment of cancer and infectious diseases. Development of nonviral EGT is a collective task, and the COST action will impact its emergence by gathering scientists with different expertise.
7. Identification of new effects of interaction of short electric pulses with biological matter and their possible applications. In particular, emphasis will be placed on the use of pulses with extremely short duration and high voltage. Recently, experimental evidence for growth stimulation of plants and fungi after treatment with pulses of nanosecond duration and sublethal amplitude was found, which promises applications in biomass production and conditioning. Within this task, further basic research demands will be identified.
8. Identification of synergetic process combinations. A combination of thermal and electroporation treatments has been shown to increase the microbial inactivation performance of electroporation-based treatment. In case of wastewater disinfection, the inactivation rate of the combined process was also higher than the sum of the rates of the single processes. Possibilities of synergetic process combinations for other applications will be investigated with regard to saving processing energy and simplifying existing processes.

Organization and Implementation of the Project

The research work in the COST action will be conducted by partners and financed predominantly through various research agencies and grants, while COST will provide the necessary coordination. The action is coordinated by the management committee (MC, Fig. 4). The MC supervises and coordinates implementation of the action. According to the rules of procedure for the MC, the chair and vice chair of the action were appointed at the kick-off meeting by the MC. The MC also established working groups (WGs) according to the scientific plan and appointed their leaders. The MC will meet once a year to set priorities, plan meetings and distribute funds to WG programs. The MC will summarize the WGs results and produce action reports, which will be posted on a dedicated Web site (www.electroporation.net).

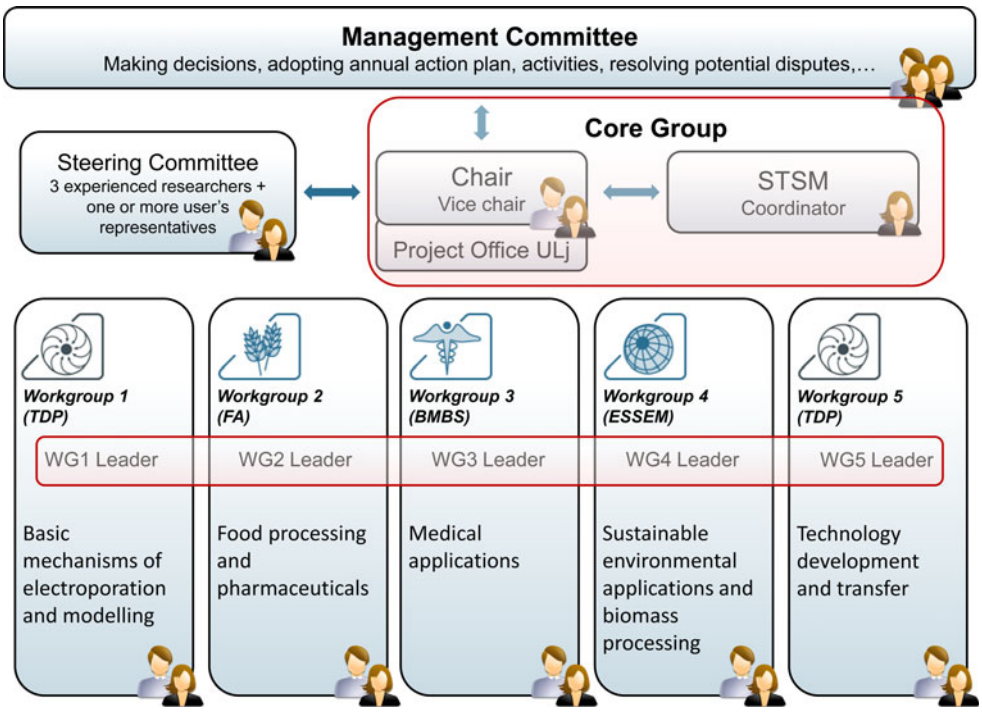

Fig. 4 COST Action TD1104 management structure diagram identifying the key management entities and their interactions. *TDP* transdomain proposal, *FA* food and agriculture, *BMBS* biomedicine and molecular biosciences, *ESSEM* earth system science and environmental management, *STSM* short-term scientific mission

Steering of the action will be further ensured by the steering committee, to which the MC appointed three experienced researchers from different WGs and at least one representative of potential users, e.g., an industry representative. A core group, composed of the chair, vice chair, WG leaders and short-term scientific missions (STSM) coordinator, will further ensure effective and continuous steering for the action by maintaining regular periodic contacts by means of conference calls, videoconferences and meetings every 4 months or more frequently when deemed necessary. The STSM coordinator will put emphasis on the effective use of STSM as an instrument of collaboration and training, with priority given to early-stage researchers, who will be encouraged to also apply for COST conference grants.

Five WGs have been established following the scientific plan: WG 1, Basic Mechanisms of Electroporation and Modeling; WG 2, Food Processing and Pharmaceuticals; WG 3, Medical Applications; WG 4, Sustainable Environmental Applications and Biomass Processing; and WG 5, Technology Development and Transfer. Specific objectives of each of these WG will be as follows

WG 1 Basic Mechanisms of Electroporation and Modeling to obtain in-depth knowledge of the biological, physical and chemical mechanisms underlying electroporation

WG 2 Food Processing and Pharmaceuticals to gain knowledge on process–product interactions in food and pharmaceutical applications involving electroporation and combine it with the latest findings in other application areas to improve equipment and process design

WG 3 Medical Applications to disseminate present clinical applications, develop new applications and standardize clinical protocols

WG 4 Sustainable Environmental Applications and Biomass Processing to improve the economic and technological efficiency of environmental and biomass applications of electroporation

WG 5 Technology Development and Transfer to exchange technical knowledge on development of safe and reliable electroporation systems for industrial applications and clinical use.

Each WG will have a leader appointed by the MC who will be responsible for organization, program preparation and reporting to the MC. The organization of work and coordination in these five WGs will allow members to focus on specific scientific questions and research, facilitating coordination and preparation of annual programs and activities of the action, which will be prepared by the WGs and submitted for approval to the MC.

Expected Results

Electroporation requires multidisciplinary research, integrating efforts of experts from different domains, from basic research to applications and from life sciences to engineering sciences. As experience from the past shows, interdisciplinary research, i.e., collaboration of a mixed group of experts from different fields, allows us to address even the most important world challenges, such as health

issues, clean water, science and technology and energy sources.

Electroporation has a direct impact on health (cancer treatment, DNA vaccination) and environmental (water disinfection) issues. Huge benefits may be expected from applications in food preservation that increases nutritional value but also in reducing the waste from agricultural resources by improving extraction efficiency and reducing energy demand. Positive effects on the environment can also be expected in biomass processing (e.g., economic algae processing for use as an energy source) and wastewater treatment.

It is exactly through the mechanisms of networking and coordination activities provided within the COST TD1104 Action that synergies are expected, offering the possibility to improve the existing and develop new electroporation-based applications. These synergies will result in new spin-off project proposals, new processes and products achieved by means of international collaboration, multidisciplinary approach and reaching the critical mass in human resources and equipment. For example, in food processing optimization toward highest energy efficiency and low operation and investment costs is required to allow for further development of technology. Making use of the extensive amount of research performed in the medical sector, this COST action will allow a knowledge transfer and a significant step toward a broader use of electroporation in other industry sectors including the food processing industry and pharmacy.

Acknowledgement The author is presenting this COST action on behalf of the consortium consisting of 73 researchers from 25 countries. In particular I thank for help in preparing this proposal the members of the Laboratory of Biocybernetics at the University of Ljubljana (Igor Marjanovic, Tadej Kotnik and Gorazd Pucihar); the project office for EU projects at the University of Ljubljana (Tjasa Nabergoj and Staska Mrak Jamnik); as well as Wolfgang Frey, Stefan Toepfl, Gregor Sersa, Marie Pierre Rols, Lluis M. Mir and Julie Gehl.

References

Agerholm-Larsen B, Iversen HK, Ibsen P, Moller JM, Mahmood F, Jensen KS, Gehl J (2011) Preclinical validation of electrochemotherapy as an effective treatment for brain tumors. Cancer Res 71:3753–3762

Andre FM, Gehl J, Sersa G, Preat V, Hojman P, Eriksen J, Golzio M, Cemazar M, Pavselj N, Rols M-P, Miklavcic D, Neumann E, Teissie J, Mir LM (2008) Efficiency of high- and low-voltage pulse combinations for gene electrotransfer in muscle, liver, tumor, and skin. Hum Gene Ther 19:1261–1271

Edhemovic I, Gadzijev EM, Brecelj E, Miklavcic D, Kos B, Zupanic A, Mali B, Jarm T, Pavliha D, Marcan M, Gasljevic G, Gorjup V, Music M, Vavpotic TP, Cemazar M, Snoj M, Sersa G (2011) Electrochemotherapy: a new technological approach in treatment of metastases in the liver. Technol Cancer Res Treat 10:475–485

Fini M, Tschon M, Ronchetti M, Cavani F, Bianchi G, Mercuri M, Alberghini M, Cadossi R (2010) Ablation of bone cells by electroporation. J Bone Joint Surg Br 92B:1614–1620

Gusbeth C, Frey W, Volkmann H, Schwartz T, Bluhm H (2009) Pulsed electric field treatment for bacteria reduction and its impact on hospital wastewater. Chemosphere 75:228–233

Loginova KV, Vorobiev E, Bals O, Lebovka NI (2011) Pilot study of countercurrent cold and mild heat extraction of sugar from sugar beets, assisted by pulsed electric fields. J Food Eng 102:340–347

Mahmood F, Gehl J (2011) Optimizing clinical performance and geometrical robustness of a new electrode device for intracranial tumor electroporation. Bioelectrochemistry 81:10–16

Martin-Belloso O, Sobrino-Lopez A (2011) Combination of pulsed electric fields with other preservation techniques. Food Bioprocess Technol 4:954–968

Marty M, Sersa G, Garbay JR, Gehl J, Collins CG, Snoj M, Billard V, Geertsen PF, Larkin JO, Miklavcic D, Pavlovic I, Paulin-Kosir SM, Cemazar M, Morsli N, Rudolf Z, Robert C, O'Sullivan GC, Mir LM (2006) Electrochemotherapy—an easy, highly effective and safe treatment of cutaneous and subcutaneous metastases: results of ESOPE (European Standard Operating Procedures of Electrochemotherapy) study. EJC Suppl 4:3–13

Pavliha D, Kos B, Zupanic A, Marcan M, Sersa G, Miklavcic D (2012) Patient-specific treatment planning of electrochemotherapy: procedure design and possible pitfalls. Bioelectrochemistry. doi:10.1016/j.bioelechem.2012.01.007

Phoon PY, Galindo FG, Vicente A, Deimek P (2008) Pulsed electric field in combination with vacuum impregnation with trehalose improves the freezing tolerance of spinach leaves. J Food Eng 88:144–148

Rieder A, Schwartz T, Schoen-Hoelz K, Marten S-M, Suess J, Gusbeth C, Kohnen W, Swoboda W, Obst U, Frey W (2008) Molecular monitoring of inactivation efficiencies of bacteria during pulsed electric field treatment of clinical wastewater. J Appl Microbiol 105:2035–2045

Sack M, Sigler J, Frenzel S, Eing C, Arnold J, Michelberger T, Frey W, Attmann F, Stukenbrock L, Mueller G (2010) Research on industrial-scale electroporation devices fostering the extraction of substances from biological tissue. Food Eng Rev 2:147–156

Sersa G, Cufer T, Paulin SM, Cemazar M, Snoj M (2012) Electrochemotherapy of chest wall breast cancer recurrence. Cancer Treat Rev 38:379–386

Soden D, Sadadcharam M, Piggott J, Morrissey A, Collins CG, O'Sullivan GC (2007) An endoscopic system for gene & drug delivery directly to intraluminal tissue. In: Jarm T, Kramar P, Zupanic A, Magjarevic R (eds) 11th mediterranean conference on medical and biomedical engineering and computing. IFMBE proceedings. Springer, Berlin, p 628

Testori A, Rossi CR, Tosti G (2012) Utility of electrochemotherapy in melanoma treatment. Curr Opin Oncol 24:155–161

Toepfl S, Heinz V, Knorr D (2007) High intensity pulsed electric fields applied for food preservation. Chem Eng Process 46:537–546

Usaj M, Trontelj K, Miklavcic D, Kanduser M (2010) Cell–cell electrofusion: optimization of electric field amplitude and hypotonic treatment for mouse melanoma (B16-F1) and Chinese hamster ovary (CHO) cells. J Membr Biol 236:107–116

Vandermeulen G, Staes E, Vanderhaeghen M-L, Bureau MF, Scherman D, Preat V (2009) Optimisation of intradermal DNA electrotransfer for immunisation. Mol Ther 17:S60–S61

J Membrane Biol (2012) 245:599–610
DOI 10.1007/s00232-012-9471-1

Calcium and Phosphatidylserine Inhibit Lipid Electropore Formation and Reduce Pore Lifetime

Zachary A. Levine · P. Thomas Vernier

Received: 15 January 2012 / Accepted: 24 June 2012 / Published online: 20 July 2012

Abstract Molecular dynamics simulations of electroporation of homogeneous phospholipid bilayers show that the pore creation time is strongly dependent on the magnitude of the applied electric field. Here, we investigated whether heterogeneous bilayers containing phospholipids with zwitterionic and anionic headgroups exhibit a similar dependence. To facilitate this analysis we divide the life cycle of an electropore into several stages, marking the sequence of steps for pore creation and pore annihilation (restoration of the bilayer after removal of the electric field). We also report simulations of calcium binding isotherms and the effects of calcium ions on the electroporation of heterogeneous lipid bilayers. Calcium binding simulations are consistent with experimental data using a 1:2 Langmuir binding isotherm. We find that calcium ions and phosphatidylserine increase pore creation time and decrease pore annihilation time. For all systems tested, pore creation time was inversely proportional to the bilayer internal electric field.

Z. A. Levine
Department of Physics and Astronomy, Dornsife College of Letters, Arts & Sciences, University of Southern California, Los Angeles, CA, USA

Z. A. Levine (✉) · P. T. Vernier
MOSIS, Information Sciences Institute, Viterbi School of Engineering, University of Southern California, 4676 Admiralty Way, Marina del Rey, CA 90292, USA
e-mail: zlevine@mosis.com

P. T. Vernier
Ming Hsieh Department of Electrical Engineering, Viterbi School of Engineering, University of Southern California, Los Angeles, CA, USA

Keywords Electropermeabilization · Electroporation · Molecular dynamics · Pore life cycle · Pore creation · Pore annihilation · Calcium · Phosphatidylserine

Introduction

Lipid membranes play many fundamental roles in cell biology, one of which is the partitioning of interior cellular components from the outside world. This barrier function can be disrupted with the application of a sufficiently high external electric field, which permeabilizes the membrane, a process referred to as "electropermeabilization" or "electroporation" (Hamilton and Sale 1967; Rols and Teissie 1990). Within a few nanoseconds of applying such a field, increases in membrane electrical conductance can be detected (Benz and Zimmermann 1980), and normally impermeant molecules which were previously excluded from the cell are able to penetrate the membrane (Neumann et al. 1982; Rols et al. 1992; Mir et al. 1999). Fluorescent dyes which interact only with intracellular material can be used as indicators of the extent of permeabilization, but the mechanisms and physical structures associated with electropermeabilization are far from being completely understood and not easily accessible by experiment (Teissie et al. 2005). Since the first reports of reversible and irreversible modifications of membrane conductance by electric fields (Stampfli and Willi 1957; Coster 1965; Hamilton and Sale 1967), steady progress has been made toward a phenomenological understanding of the nature of the permeabilized membrane and the processes that restructure the phospholipid bilayer in an externally applied electric field (Zimmerman et al. 1974; Abidor et al. 1979; Chizmadzhev and Abidor 1980). Observational studies have been enhanced and guided by the development

of continuum electrophysical models of electroporation (Sugar and Neumann 1984; Popescu et al. 1991; Weaver and Chizmadzhev 1996; DeBruin and Krassowska 1998; Neu and Krassowska 1999; Weaver 2003; Vasilkoski et al. 2006), which in turn have contributed to experimental designs and perspectives.

Furthermore, many biological processes are significantly affected by small changes in the local energy landscape, as is the case when an asymmetric distribution of charge is present; thus, a mechanistic understanding of electropermeabilization cannot be restricted to simple, homogeneous lipid bilayer systems. It becomes necessary then to take into account also the effects of inorganic ions which may, for instance, cause membrane lipids to aggregate (Ziegler and Vernier 2008; Boettcher et al. 2011), possibly modifying local surface tensions. Similarly, the behavior of heterogeneous phospholipid bilayers, which may have not only zwitterionic but also anionic and cationic headgroups, must be considered since these additions further perturb the electrochemical landscape and greatly increase the required complexity of analytical models.

Recent advances in high-performance computing have enhanced studies of electropermeabilization using molecular dynamics (MD) simulations of phospholipid bilayers. These simulations suggest that electropermeabilization results at least in part from the formation of discrete, nanoscale electropores that develop in a characteristic sequence: (1) appearance of an electric field–driven water column across the bilayer interior, a process dominated by the energy minimization of interfacial water molecules under an applied electric field (Tieleman 2004; Ziegler and Vernier 2008); (2) construction of a bridge of hydrophilic lipid headgroups and additional hydrating water molecules; and (3) expansion of the pore while the external field continues to be applied (Tieleman et al. 2003; Tieleman 2004; Tarek 2005; Bockmann et al. 2008). Previously, we proposed definitions for these individual stages in pore formation, which we called "pore initiation," "pore construction" and "pore maturation," respectively (Levine and Vernier 2010). In this article we refine the nomenclature for these steps.

We have also observed that homogeneous, zwitterionic (containing phosphatidylcholine [PC]) bilayers with varying degrees of hydrocarbon saturation require different "minimum" external electric fields to form pores within a finite period of time (Ziegler and Vernier 2008), which indicates, not surprisingly, that pore formation is affected by lipid properties. Because anionic lipids such as phosphatidylserine (PS) can form complexes in the presence of calcium ions (Vernier et al. 2009), it is reasonable to expect that the incorporation of PS into phospholipid bilayers and the inclusion of Ca^{2+} in the system will also affect pore formation and annihilation. We present here a description of the electropore life cycles of PC:PS bilayers with and without calcium, extending the analysis we developed for homogeneous PC bilayers (Levine and Vernier 2010).

MD simulations of electropermeabilization must be verified by alignment with existing continuum theories (Weaver and Chizmadzhev 1996) and experiments (Sinn et al. 2006). For validating MD representations of calcium binding to phospholipid bilayers, stoichiometric or coordination complex measurements have been used as a metric (Bockmann and Grubmuller 2004; Vernier et al. 2009; Porasso and Cascales 2009). Here, we propose using binding isotherms as an additional metric to describe the concentration of adsorbed ions at an interface relative to the total ion concentration. At low calcium concentrations one would expect to see linear 1:1 binding, implying that every added calcium ion binds to the interface. At higher calcium concentrations, however, one expects to observe a Langmuir binding isotherm, which is characterized by a transition from linear ion binding to a fixed amount of ion binding when the interface becomes saturated, as others have reported (Bockmann and Grubmuller 2004; Sinn et al. 2006). We compare our simulated calcium binding isotherms with existing experimental and theoretical binding constants for PC:PS bilayers and Ca^{2+}.

Materials and Methods

Simulation Conditions

All simulations were performed using the GROMACS set of programs, version 4.0.5 (Hess et al. 2008), on the University of Southern California High Performance Computing and Communications Linux cluster (http://www.usc.edu/hpcc/). Lipid topologies were derived from OPLS united-atom parameters (Berger et al. 1997), and the simple point charge water model was implemented (Berendsen et al. 1981). Each system was coupled to a temperature bath at 310 K with a relaxation time of 0.1 ps and a pressure bath at 1 bar with a relaxation time of 1 ps, each using a weak coupling algorithm (Berendsen et al. 1984). Pressure was coupled semi-isotropically (using a compressibility of 4.5×10^{-5} bar^{-1}) normal to and in the plane of the membrane. Bond lengths were constrained using the LINCS algorithm (Hess et al. 1997) for lipids and SETTLE (Miyamoto and Kollman, 1992) for water. Short-range electrostatic and Lennard-Jones interactions were cut off at 1.0 nm. Long-range electrostatics were calculated by the PME algorithm (Essmann et al. 1995) using fast Fourier transforms and conductive boundary conditions. Reciprocal-space interactions were evaluated on a 0.12-nm grid with fourth-order B-spline interpolation. Periodic boundary conditions were employed to mitigate system size effects.

Systems and Structures

All systems contain a total of 128 lipids—either 1-palmitoyl-2-oleoyl-*sn*-glycero-3-phosphatidylcholine (POPC) or 1-palmitoyl-2-oleoyl-*sn*-glycero-3-phosphatidylserine (POPS)—and about 9,000 water molecules ($\sim$70 waters/lipid), which resulted in an initial system box size of approximately $7 \times 7 \times 10$ nm. Homogeneous bilayers consist only of POPC. Heterogeneous bilayers were obtained by replacing 20 POPC molecules on a single leaflet with 20 (anionic) POPS molecules and 20 sodium counterions in the bulk water, followed by equilibration until the total area per lipid became constant. Simulations with multiple trials were run in parallel, starting from the same initial positions. To ensure that each trial was independent, every atom was assigned a randomized velocity with a Maxwell distribution at the beginning of the simulation (a built-in function of GROMACS). All systems were equilibrated for a constant area per lipid. Pore creation times were measured for three values of applied external electric field—400, 500 and 600 MV/m—with three independent trials at each electric field strength. Note that 600 MV/m in vacuum corresponds to an effective electric field in aqueous media of about 8 MV/m due to their relative dielectric permittivities. Following pore formation, the external field was removed from a randomly selected simulation, and three independent trials were run to track the annihilation of that single pore. Additionally, we extracted calcium binding coefficients and pore creation times in the presence of calcium from systems where the GROMACS function "genion" was used to replace bulk water molecules with one calcium ion and two chloride counterions. Calcium binding coefficients were extracted after 150 ns, to allow the system to reach equilibrium after calcium addition. Binding coefficients were determined using a 1:2 Langmuir isotherm. Pore radius measurements were obtained by first identifying a pore axis which passes directly through the pore in the z dimension (based on perpendicular x and y water density profiles). Then, bins were assigned between mean lipid phosphorus planes where, for each bin, maximally distant water molecules were identified relative to the pore axis in x and y to obtain local semimajor and semiminor pore diameters. Following this, the semimajor and semiminor pore diameters were averaged together in each bin, and finally all local pore diameters were averaged together to obtain an average pore diameter or pore radius. Pore creation times for systems with calcium present were observed after an electric field was applied to the equilibrated system.

Electropore Life Cycle

The life cycle of an electropore can be divided broadly into a pore creation step and a pore annihilation step, as described previously (Levine and Vernier 2010). Pore creation (Fig. 1) consists of three stages: initiation, construction and expansion (defined below). Pore annihilation begins when the external electric field is removed from an expanded pore and proceeds through settling, stabilization, deconstruction and dissolution.

Pore Creation

Pore initiation begins with the application of an external electric field and ends when the two groups of water molecules initially separated by the bilayer merge to become a single group (nonzero water density in every 0.1-nm slice between the two mean planes of phosphorus atoms). In some simulations the combined water groups split again <400 ps after the joining. These transient events are not counted as mergers. Pore construction begins with formation of the membrane-spanning water column (hydrophobic pore [Abidor et al. 1979]), which marks the merger of the water groups and ends when the phosphorus groups that are initially found on the two leaflets of the bilayer follow the water into the membrane interior and merge into a single phosphorus group. (A phosphorus group is defined as a set of atoms, each separated by a maximum distance of 1.2 nm [Sengupta et al. 2008].) Because water and the charged phospholipid headgroups now bridge the membrane interior, this structure is comparable to what is sometimes called a hydrophilic pore (Weaver and Mintzer 1981; Glaser et al. 1988; Leontiadou et al. 2004). Continued application of the porating electric field results in an evolution, or expansion, of the hydrophilic pore. We define an expanded pore arbitrarily as a hydrophilic pore in which at least 10 phosphorus atoms from the initial anodic leaflet are found within 1.2 nm of phosphorus atoms from the cathodic leaflet.

Pore Annihilation

Pore settling, the first stage of pore annihilation, is the quasi-stable period after the field is removed during which the number of anode-to-cathode phosphorus connections fluctuates around the expanded pore criterion (10 connections). Pore stabilization begins when the number of anode-to-cathode phosphorus connections drops below 10 and ends when there is only one anode-to-cathode phosphorus connection. The pore radius decreases around this time to a minimum, about 0.4–0.6 nm. We note that these so-called minimal pores remain hydrophilic and facilitate the conduction of sodium ions when very small external electric fields remain, consistent with theoretical models such as the asymptotic model of electroporation (Neu and Krassowska 1999) which also identify a minimum hydrophilic pore radius of about 0.5 nm. Pore deconstruction, another quasi-stable period, terminates when the single phosphorus group

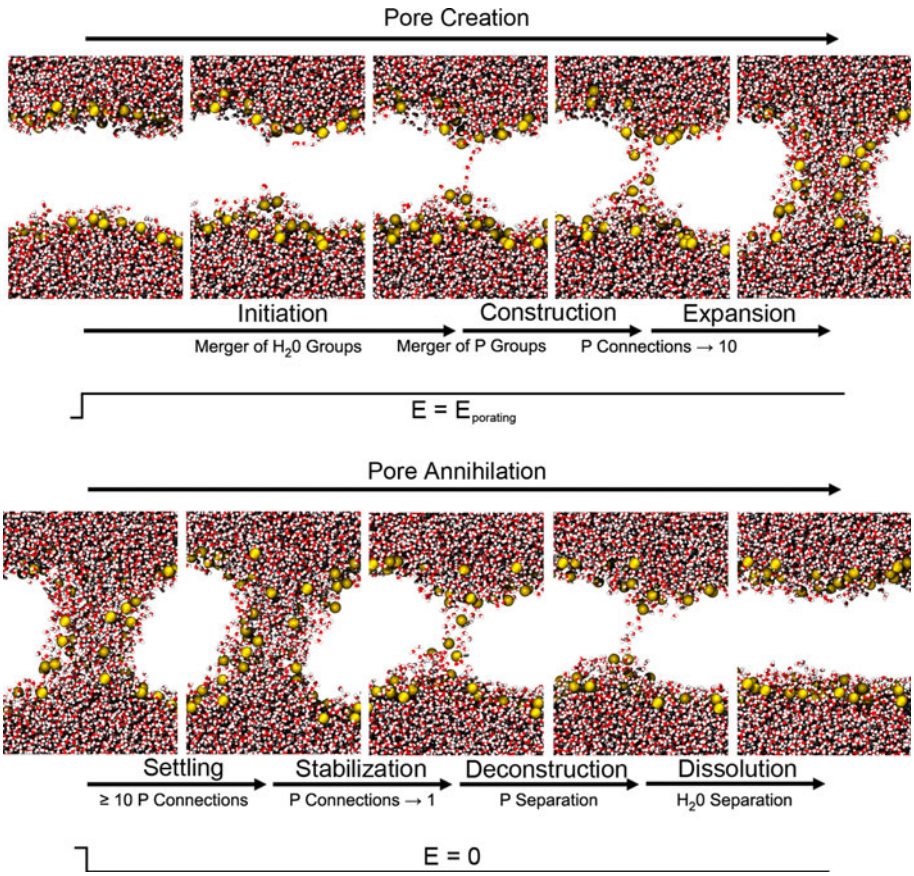

Fig. 1 Phospholipid electropore life cycle. Structurally distinct steps in pore creation and annihilation as observed in molecular dynamics simulations. Details in "Materials and Methods" section

of the porated bilayer splits into two groups, which remain separate for the remainder of the simulation. At the end of pore deconstruction only the water column remains. We call the disassembly of the water column "pore dissolution."

Individual pore life cycle times were calculated using a custom Perl program, which codifies the stage boundaries described above. The average value of the electric field at the bilayer midplane (membrane internal electric field) was extracted using the GROMACS function "g potential" over the period from 100 ps after the external electric field was applied to 100 ps before pore construction began. As in our previous work, "internal electric field" was used as a normalizing term (Levine and Vernier 2010).

Images

Molecular graphics images were generated with visual MD (Humphrey et al. 1996).

Results

A complete summary of the pore life cycle results reported here can be found in Figs. 2 and 3 and in Tables 1, 2, 3, 4, 5, 6, 7 and 8. Details are described below.

Pore Creation—Pure POPC and POPC:POPS

At smaller external electric fields, POPC:POPS bilayers have pore creation times that are, on average, slightly longer than homogeneous POPC bilayers (Fig. 2), primarily because of an increase in the pore initiation time, the time it takes water to bridge the membrane interior. The area per lipid, which is strongly correlated with membrane permeability (Mathai et al. 2007), in POPC:POPS systems was about 0.60 compared to 0.66 nm^2 for POPC bilayers. At higher applied electric fields the differences in pore creation time become minimal and mixed bilayers have pore creation times which are not significantly different from those for homogenous bilayers. Pore initiation times for POPC:POPS are inversely related to the externally applied electric field, and pore construction times remain constant over all electric fields sampled, similar to what we previously reported for homogeneous POPC bilayers (Levine and Vernier 2010). Pore expansion times decrease slightly as higher external electric fields are applied.

Pore Creation—Calcium and POPC

POPC bilayer systems containing calcium ions have, at small external electric fields, pore creation times which are

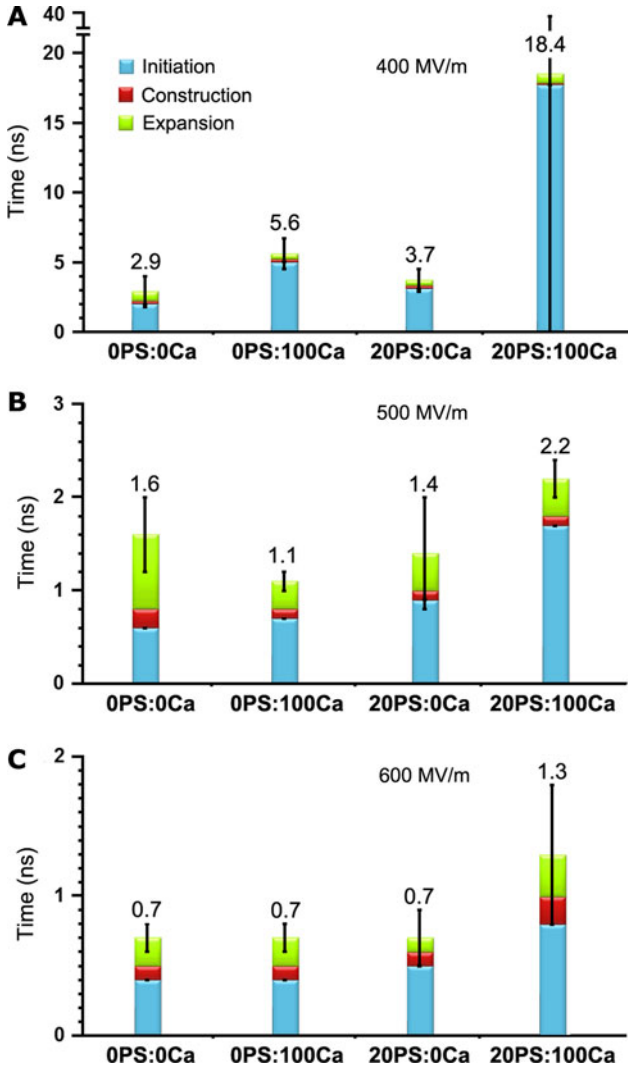

Fig. 2 Pore creation times for three different porating electric fields (400, 500, 600 MV/m) for bilayers consisting of 128 POPC (0PS:0Ca), 128 POPC saturated with calcium (0PS:100Ca), 108 POPC and 20 POPS on a single leaflet without calcium present (20PS:0Ca), and bilayers containing both PS and Ca^{2+} (20PS:100Ca). Systems containing 20 PS also contain 20 Na^{+} as counter ions, and systems containing Ca^{2+} contain two chloride counter ions for every calcium ion. Systems which contain both PS and Ca^{2+} have both sodium and chloride counter ions present. Ca^{2+} and POPS in the bilayer increase the pore initiation time

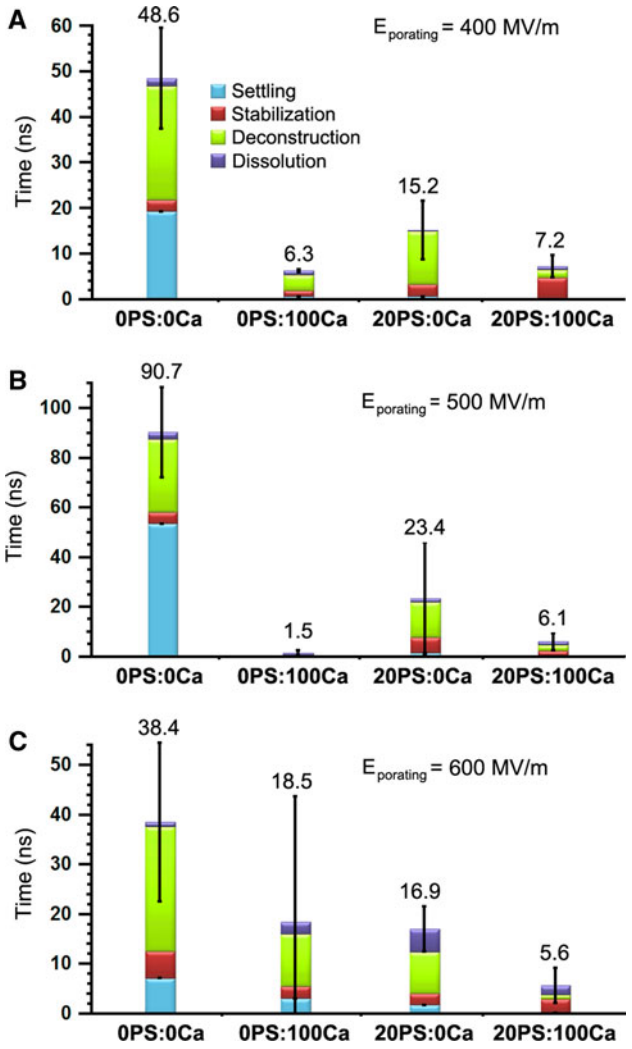

Fig. 3 Pore annihilation times after pore formation in the same systems shown in Fig. 2. Ca^{2+} and POPS in the bilayer decrease the pore annihilation time

about twice as long as systems without calcium and about one and a half times as long as those in mixed (POPC:-POPS) bilayers (Fig. 2). As with systems containing PS, when the external electric field is increased, pore creation times of pure POPC systems with calcium and those without calcium are not significantly different. The convergent area per lipid of POPC bilayers with calcium is about 0.56 nm^2, a value significantly smaller than the area per lipid without calcium reported above. Again, as with systems containing PS, we observed an inverse relationship between externally applied electric field and pore initiation time and pore expansion time for POPC bilayer systems containing calcium. Pore construction times remain constant at all electric fields applied.

Pore Creation—Calcium and POPC:POPS

POPC:POPS bilayers containing calcium have pore creation times which are significantly longer than those for pure POPC systems, with or without calcium, and longer than POPC:-POPS systems without calcium (Fig. 2). This is true for all electric fields applied, even very high fields where for all of the systems described above the pore creation times were not significantly different. The average area per lipid of POPC:-POPS bilayers with calcium was about 0.55 nm^2 before a field was applied, slightly smaller than the area per lipid of POPC bilayers with calcium. As with all other systems reported here, both pore initiation times and pore expansion times decrease

Table 1 POPC pore creation times without PS and without Ca^{2+} Levine and Vernier (2010)

Applied field (MV/m)	Average internal field (MV/m)	Initiation		Construction		Expansion		Creation	
		Time (ns)	Mean (ns)	Time (ns)	Mean (ns)	Time (ns)	Mean (ns)	Time (ns)	Mean (ns)
		2.8		0.0		0.5		3.3	
400	1,630	2.3	2.0 ± 1.0	0.3	0.2 ± 0.2	1.1	0.8 ± 0.3	3.7	2.9 ± 1.1
		0.8		0.2		0.7		1.7	
		0.9		0.1		1.0		2.0	
500	2,180	0.6	0.6 ± 0.3	0.2	0.2 ± 0.1	0.5	0.8 ± 0.3	1.3	1.6 ± 0.4
		0.4		0.3		0.9		1.6	
		0.5		0.1		0.1		0.7	
600	2,347	0.5	0.4 ± 0.2	0.0	0.1 ± 0.1	0.3	0.2 ± 0.1	0.8	0.7 ± 0.1
		0.2		0.2		0.2		0.6	

Table 2 POPC pore creation times without PS and with 100 Ca^{2+}

Applied field (MV/m)	Average internal field (MV/m)	Initiation		Construction		Expansion		Creation	
		Time (ns)	Mean (ns)	Time (ns)	Mean (ns)	Time (ns)	Mean (ns)	Time (ns)	Mean (ns)
		6.2		0.1		0.5		6.8	
400	1,373	4.6	5.0 ± 1.0	0.1	0.2 ± 0.1	0.4	0.4 ± 0.2	5.1	5.6 ± 1.1
		4.3		0.3		0.2		4.8	
		0.9		0.1		0.2		1.2	
500	1,837	0.8	0.8 ± 0.2	0.1	0.1 ± 0.0	0.2	0.3 ± 0.1	1.1	1.1 ± 0.1
		0.6		0.1		0.4		1.1	
		0.4		0.2		0.2		0.8	
600	2,292	0.4	0.4 ± 0.0	0.1	0.1 ± 0.1	0.2	0.2 ± 0.0	0.7	0.7 ± 0.1
		0.4		0.1		0.2		0.7	

Table 3 POPC pore creation times with PS and without Ca^{2+}

Applied field (MV/m)	Average internal field (MV/m)	Initiation		Construction		Expansion		Creation	
		Time (ns)	Mean (ns)	Time (ns)	Mean (ns)	Time (ns)	Mean (ns)	Time (ns)	Mean (ns)
		2.2		0.3		0.4		2.9	
400	1,707	3.2	3.1 ± 0.9	0.1	0.2 ± 0.1	0.4	0.4 ± 0.0	3.7	3.7 ± 0.8
		3.9		0.2		0.4		4.5	
		0.5		0.2		0.2		0.9	
500	1,930	1.4	0.9 ± 0.5	0.1	0.1 ± 0.1	0.5	0.4 ± 0.2	2.0	1.4 ± 0.6
		0.9		0.1		0.4		1.4	
		0.2		0.2		0.2		0.6	
600	2,197	0.3	0.4 ± 0.3	0.1	0.1 ± 0.1	0.1	0.1 ± 0.1	0.5	0.7 ± 0.2
		0.7		0.1		0.1		0.9	

as the external electric field increases, while pore construction times are similar for all values of electric field applied in these simulations.

Pore Annihilation—Pure POPC and POPC:POPS

POPC:POPS bilayers have pore annihilation times about three times smaller than pure POPC bilayers (Fig. 3). All pore annihilation stages except stabilization are shortened relative to pure POPC, and this is true regardless of the value of the electric field used to create the pore. The average pore radius at the start of the annihilation step was about 2.3 nm for POPC:POPS systems, similar to the average pore radius for pure PC bilayers, 2.2 nm. Also, pure POPC bilayer pore annihilation times are dominated by pore settling and pore deconstruction.

Table 4 POPC pore creation times with PS and with 100 Ca^{2+}

Applied field (MV/m)	Average internal field (MV/m)	Initiation		Construction		Expansion		Creation	
		Time (ns)	Mean (ns)	Time (ns)	Mean (ns)	Time (ns)	Mean (ns)	Time (ns)	Mean (ns)
		8.9		0.0		0.6		9.5	
400	1,417	5.1	17.7 ± 18.6	0.1	0.1 ± 0.1	0.9	0.7 ± 0.2	6.0	18.4 ± 18.5
		39.0		0.0		0.6		39.6	
		1.5		0.1		0.3		1.9	
500	1,833	1.8	1.7 ± 0.1	0.2	0.1 ± 0.1	0.3	0.4 ± 0.1	2.3	2.2 ± 0.2
		1.7		0.1		0.5		2.3	
		1.0		0.4		0.4		1.8	
600	2,230	0.8	0.9 ± 0.1	0.0	0.2 ± 0.2	0.1	0.3 ± 0.2	0.9	1.3 ± 0.5
		0.8		0.1		0.3		1.2	

Table 5 POPC pore annihilation times without PS and without Ca^{2+} Levine and Vernier (2010)

Field During Poration (MV/m)	Settling		Stabilization		Deconstruction		Dissolution		Annihilation	
	Time (ns)	Mean (ns)	Time (ns)	Mean (ns)	Time (ns)	Mean (ns)	Time (ns)	Mean (ns)	Time (ns)	Mean (ns)
	7.3		3.0		24.6		2.9		37.8	
400	29.2	19.4 ± 11.1	3.7	2.5 ± 1.5	25.9	25.0 ± 0.8	1.1	1.7 ± 1.0	59.9	48.6 ± 11.1
	21.6		0.8		24.6		1.1		48.1	
	84.4		7.5		17.3		1.4		110.6	
500	17.3	53.7 ± 33.9	4.0	4.7 ± 2.5	49.8	29.3 ± 17.8	4.2	2.9 ± 1.4	75.3	90.7 ± 18.1
	59.5		2.7		20.9		3.0		86.1	
	11.4		1.0		8.1		1.5		22.0	
600	3.8	7.1 ± 3.9	6.4	5.4 ± 4.0	28.5	25.1 ± 15.5	0.7	0.9 ± 0.6	39.4	38.4 ± 16.0
	6.2		8.7		38.6		0.4		53.9	

Table 6 POPC pore annihilation times without PS and with 100 Ca^{2+}

Field during poration (MV/m)	Settling		Stabilization		Deconstruction		Dissolution		Annihilation	
	Time (ns)	Mean (ns)	Time (ns)	Mean (ns)	Time (ns)	Mean (ns)	Time (ns)	Mean (ns)	Time (ns)	Mean (ns)
	0.0		0.4		4.6		1.0		6.0	
400	0.0	0.6 ± 1.0	2.3	1.4 ± 1.0	3.3	3.3 ± 1.3	0.7	1.0 ± 0.3	6.3	6.3 ± 0.3
	1.7		1.6		2.1		1.2		6.6	
	0.1		0.1		1.2		0.5		1.9	
500	0.0	0.1 ± 0.1	0.1	0.1 ± 0.0	0.1	0.5 ± 0.6	0.2	0.9 ± 0.9	0.4	1.5 ± 0.9
	0.0		0.1		0.1		1.9		2.1	
	0.0		0.5		2.3		2.7		5.5	
600	9.0	3.0 ± 5.2	5.4	2.4 ± 2.6	28.8	10.6 ± 15.8	4.4	2.4 ± 2.1	47.6	18.5 ± 25.3
	0.0		1.3		0.8		0.2		2.3	

POPC:POPS bilayers exhibit very short pore settling times and significantly reduced pore deconstruction times compared to POPC systems, reducing the overall time required to annihilate POPC:POPS electropores. An initial decrease in pore radius occurs immediately after the field is removed in both POPC and POPC:POPS bilayers, from about 2.3 to about 0.5 nm over the first few nanoseconds. This initial reduction of the pore radius does not appear to be correlated with pore settling time (Fig. 4).

Table 7 POPC pore annihilation times with PS and without Ca^{2+}

Field during poration (MV/m)	Settling		Stabilization		Deconstruction		Dissolution		Annihilation	
	Time (ns)	Mean (ns)	Time (ns)	Mean (ns)	Time (ns)	Mean (ns)	Time (ns)	Mean (ns)	Time (ns)	Mean (ns)
	0.8		2.8		4.9		0.1		8.6	
400	0.3	0.6 ± 0.3	3.7	2.7 ± 1.1	16.7	11.6 ± 6.0	0.7	0.3 ± 0.3	21.4	15.2 ± 6.4
	0.8		1.6		13.1		0.1		15.6	
	3.2		0.6		2.4		3.1		9.3	
500	0.9	1.5 ± 1.5	1.8	6.1 ± 8.5	8.7	14.2 ± 15.3	0.1	1.6 ± 1.5	11.5	23.4 ± 22.5
	0.3		15.9		31.4		1.7		49.3	
	1.1		1.5		13.8		3.6		20.0	
600	1.0	1.7 ± 1.1	1.2	2.3 ± 1.7	7.2	8.3 ± 5.1	9.5	4.7 ± 4.4	18.9	16.9 ± 4.5
	2.9		4.2		3.8		0.9		11.8	

Table 8 POPC pore annihilation times with PS and with 100 Ca^{2+}

Field during poration (MV/m)	Settling		Stabilization		Deconstruction		Dissolution		Annihilation	
	Time (ns)	Mean (ns)	Time (ns)	Mean (ns)	Time (ns)	Mean (ns)	Time (ns)	Mean (ns)	Time (ns)	Mean (ns)
	0.0		7.1		2.5		0.2		9.8	
400	0.1	0.1 ± 0.1	2.3	4.7 ± 2.4	2.0	1.7 ± 1.0	0.6	0.8 ± 0.7	5.0	7.2 ± 2.4
	0.0		4.8		0.5		1.5		6.8	
	0.0		1.7		1.5		1.6		4.8	
500	0.1	0.1 ± 0.1	1.9	2.2 ± 0.8	0.4	2.3 ± 2.4	1.0	1.5 ± 0.4	3.4	6.1 ± 3.5
	0.1		3.1		5.0		1.8		10.0	
	0.1		4.5		1.2		3.7		9.5	
600	0.2	0.1 ± 0.1	3.0	2.8 ± 1.8	0.2	0.8 ± 0.5	1.1	1.9 ± 1.6	4.5	5.6 ± 3.5
	0.0		0.9		0.9		0.9		2.7	

Pore Annihilation—Calcium and POPC

Pure POPC systems containing calcium have dramatically reduced pore annihilation times compared to POPC systems without calcium (Fig. 3). For pores created at 400 and 500 MV/m, POPC–Ca^{2+} systems exhibit virtually no pore settling, while all remaining stages take no more than a few nanoseconds to complete. For pores created at 600 MV/m, calcium still significantly reduces the pore annihilation time but the variation from simulation to simulation is large. As with POPC:POPS and pure POPC bilayers without calcium, the pore radius is reduced in POPC systems containing calcium to 0.5 nm after only a few nanoseconds but with calcium present the initial pore radius immediately after the external field is removed is 1.7 nm, about 0.6 nm smaller than the pores in the annihilation simulations without calcium.

Pore Annihilation—Calcium and POPC:POPS

POPC:POPS systems with calcium have pore annihilation times which are also significantly shorter than those for pure POPC bilayers and POPC:POPS systems without calcium. POPC:POPS–Ca^{2+} annihilation times are comparable to those for POPC–Ca^{2+} and POPC:POPS (no

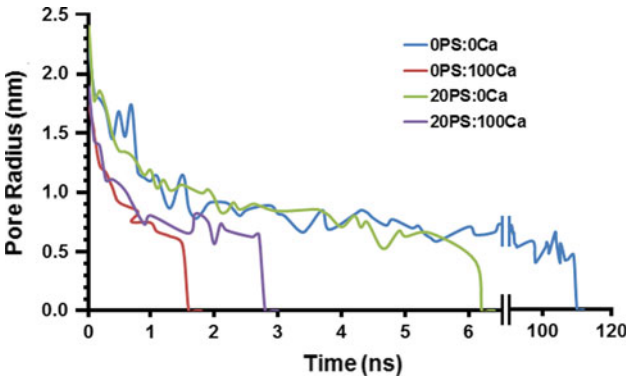

Fig. 4 Evolution of pore radius after removal of the porating electric field for the same systems shown in Fig. 2. This example, from a simulation in which $E_{porating} = 500$ MV/m, is representative of pore annihilation behavior for all values of $E_{porating}$ examined in this work. Average initial pore radii are 2.2 nm for 0PS:0Ca systems, 2.4 nm for 20PS:0Ca systems, 1.7 nm for 0PS:100Ca systems, and 1.9 nm for 20PS:100Ca systems

calcium) systems. For pores created at the highest electric field, POPC:POPS–Ca^{2+} systems have the shortest pore annihilation times of all systems sampled. Pore settling time for these systems is too short to measure in about half of the trials; the longest settling time measured for POPC:POPS–Ca^{2+} is 200 ps. Stabilization is the dominant step in pore annihilation for these systems, and the variance in pore annihilation time is much smaller than for pure POPC systems without calcium. As with POPC–Ca^{2+} systems, the initial pore radius for POPC:POPS–Ca^{2+} systems after the porating field is removed is about 1.8 nm. As soon as the pore radius decreases to about 0.5 nm in the POPC:POPS–Ca^{2+} systems, the pores dissipate quickly, in contrast with pure POPC bilayers without calcium, where pores remain open with a radius around 0.5 nm for many tens of nanoseconds.

Calcium Binding

To assess the validity of our calcium ion models in POPC:POPS systems, we constructed a binding isotherm (Fig. 5), which plots the amount of bound calcium ions against the bulk calcium ion concentration. Our data can be described by a 1:2 Langmuir binding isotherm between calcium and phospholipid (Altenbach and Seelig 1984) and with binding isotherms taken from experiments with pure and mixed vesicles (Sinn et al. 2006). Additionally, for small calcium concentrations we see linear 1:1 binding. Calcium appears to bind preferentially to PS carboxyl and PC:PS phosphoryl oxygens. From systems equilibrated for 150 ns (Vernier et al. 2009) we extracted a calcium binding coefficient, $K = 2.56\ \mathrm{M}^{-1}$.

Discussion

Electropore Life Cycle for POPC:POPS Bilayers

We have shown that incorporation of the anionic phospholipid POPS into a POPC (zwitterionic) bilayer slightly increases the time required for pore creation at lower external electric fields and drastically decreases the time required for pore annihilation for electropores created at all external electric fields. PS bilayers have a smaller area per lipid (Mukhopadhyay et al. 2004) compared to PC bilayers, and changes in surface tension, which may be affected by locally varying area per lipid, have been shown to affect pore formation (Lewis 2003; Tieleman et al. 2003; Tieleman 2004).

At higher electric fields pore creation times for POPC:POPS bilayers are similar to those for pure POPC bilayers. As previous studies have shown, interfacial water is a dominant component of pore formation (Tieleman

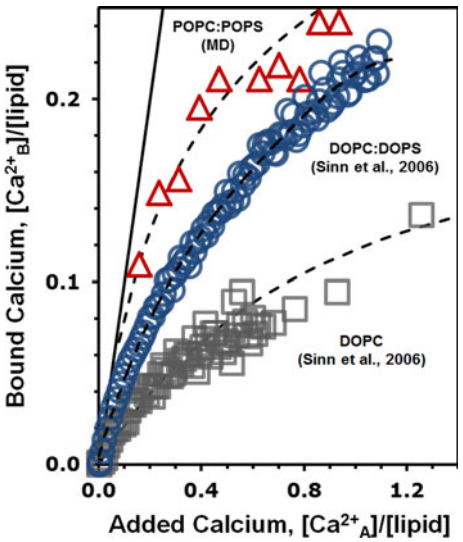

Fig. 5 Calcium binding curves show rough correspondence between experimental and simulated results. The data can be described by a 1:2 Langmuir binding isotherm, consistent with formation of $Ca:PS_2$ complexes

2004; Tarek 2005; Ziegler and Vernier 2008), and we can speculate that the formation of bilayer-spanning water bridges in the strong interfacial electric field gradients that result from application of large external electric fields is only weakly influenced by PS or PC interactions. This is consistent with the stochastic pore hypothesis for electropermeabilization (Sugar and Neumann 1984; Popescu et al. 1991; Neu and Krassowska 1999; Weaver 2003) and previous observations (Levine and Vernier 2010), in which pore creation time was inversely correlated with the magnitude of the applied electric field. In this scheme our highest external electric field, 600 MV/m, is at or near a saturating value for porating fields for POPC and POPC:POPS bilayers. In this saturation range electropores are created in similar, asymptotically convergent times. We also observe comparable pore radii for POPC:POPS and pure POPC bilayers at the end of the pore creation step, despite small differences in area per lipid, suggesting that the radius of an electropore is only partially dependent on phospholipid areal density.

Effects of Calcium on Pore Life Cycle

Calcium in pure POPC bilayer systems delays pore creation at lower external electric fields and greatly reduces the time required for pore annihilation. POPC:POPS systems containing calcium have even longer pore creation times at lower electric fields. The pore radius after creation is lower in both POPC and POPC:POPS systems containing calcium than for systems without calcium. As indicated above, this may be partially associated with significantly smaller area per lipid values found both experimentally (Mattai et al. 1989) and in

simulations (Bockmann and Grubmuller 2004) when calcium is present.

Even though the area per lipid is similar for POPC–Ca^{2+} and POPC:POPS–Ca^{2+} systems, it has been shown experimentally and in MD simulations that calcium binds with more affinity to PC:PS vesicles than to pure PC vesicles (Sinn et al. 2006; Vernier et al. 2009), forming Ca^{2+}–PS complexes involving PS carboxyl and phosphoryl oxygens. By increasing the total number of calcium-lipid complexes, we are effectively decreasing the area per lipid of our system and thus increasing membrane surface tension. Until the molecular-level details of water intrusion and bridge construction across the bilayer have been fully explained, we can only presume that increases in surface tension associated with the presence of Ca^{2+} and PS lead to increases in the energy barrier for interfacial water entry into the bilayer interior and an associated increase in pore creation times. Alternatively, when the external field is removed, a change in surface tension would result in a change in the pore edge tension since the two quantities are related (Ryham et al. 2011); thus, we would expect to see modified pore annihilation times for systems with PS and/or Ca^{2+} present compared to systems without PS and Ca^{2+}.

In addition, POPC:POPS–Ca^{2+} systems exhibit very short pore annihilation times (a few nanoseconds), similar to the time scale of pore creation. This is an order of magnitude faster than pure POPC systems, which have pore annihilation times that are tens of nanoseconds or even more than 100 ns in simulations (Levine and Vernier 2010). These timescales are similar to the resealing timescales reported in other MD simulations (Tarek 2005); however, a large discrepancy still exists between simulated pore annihilation times and experimental resealing times, which occur on timescales of milliseconds (Melikov et al. 2001) to hundreds of seconds (Koronkiewicz et al. 2002). These long-lasting pores occur in living cell membranes, not simple phospholipid bilayers, suggesting that some membrane restructuring beyond lipid nanopore formation occurs and that the permeabilizing structures in cell membranes have significantly stabilizing features.

Molecular and Continuum Models of Lipid Electropores

Our results agree (Fig. 6) with numerical models which predict an exponential relationship between transmembrane potential and pore creation (Neu and Krassowska 1999) for all configurations tested. (Note that there is a direct relationship between the internal electric field and the transmembrane potential.) The electric field is the dominant term for pore creation, and although we see variations in pore creation time at smaller fields for POPC versus POPC:POPS or with the introduction of calcium ions, pore creation occurs at similar

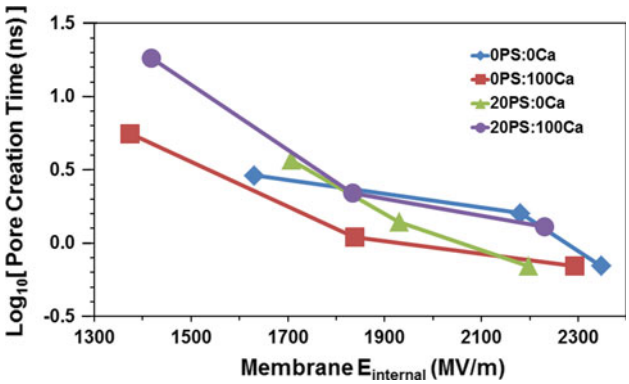

Fig. 6 Lipid electropore creation time as a function of bilayer internal electric field for the systems shown in Fig. 2. The log scale reflects the exponential dependence of the probability of pore formation on the applied electric field. Internal electric field is used here as a normalizing quantity

times for very high electric fields. Pore annihilation is a stochastic process in some models (Weaver and Chizmadzhev 1996), and indeed we see large variances in the pore annihilation time, which suggests that local fluctuations and dynamics strongly influence restructuring of the bilayer.

Our simulations of calcium binding to POPC and POPC:POPS bilayers provide support for the validity of the calcium ion model we are using. Our binding isotherm for POPC:POPS bilayers is similar to experimental data for dioleoyl-phosphatidycholine:phosphosphatidylserine (DOPC:DOPS) vesicles (Sinn et al. 2006) using a 1:2 Langmuir isotherm. The binding coefficient extracted from our simulations is 2.56 M^{-1}, in the range of the measured value of 13.8 M^{-1} (Altenbach and Seelig 1984), although experiments at different NaCl and Ca^{2+} concentrations are difficult to compare directly. Better models may lead to increased accuracy in determining proper binding coefficients.

Although our simple, largely intuitive characterization of the stages in the lipid electropore life cycle provides a useful scheme for analysis of pore creation and pore annihilation, a more sophisticated approach will build on this foundation to incorporate systematic measurements of the pore radius and pore energies (Neu and Krassowska 1999) and to include the atomic-scale electric field landscape and the interactions of water oxygen and hydrogen with the electron-dense acyl oxygens deep in the phospholipid bilayer interface. Once these key components of the molecular structure of electropores are accurately represented, the additional complexities of lipid heterogeneity, membrane proteins and cytoskeletal and glycocalyx attachments can be added to the model one by one, until we approach a useful representation of the living cell membrane in a porating electric field.

Acknowledgements We thank Rumiana Dimova for stimulating discussions and insightful input on calcium binding. Computing

resources were provided by the USC Center for High Performance Computing and Communications (http://www.usc.edu/hpcc/). This work was made possible in part by the Air Force Office of Scientific Research and by MOSIS, Information Sciences Institute, Viterbi School of Engineering, University of Southern California.

References

Abidor IG, Arakelyan VB, Chernomordik LV et al (1979) Electric breakdown of bilayer lipid-membranes. 1. Main experimental facts and their qualitative discussion. Bioelectrochem Bioenerg 6:37–52

Altenbach C, Seelig J (1984) Calcium binding to phosphatidylcholine bilayers as studied by deuterium magnetic resonance. Evidence for the formation of a calcium complex with two phospholipid molecules. Biochemistry 23(17):3913–3920

Benz R, Zimmermann U (1980) Pulse-length dependence of the electrical breakdown in lipid bilayer-membranes. Biochim Biophys Acta 597:637–642

Berendsen HJC, Postma JPM, van Gunsteren WF et al (1981) Interaction models for water in relation to protein hydration. In: Pullman B (ed) Intermolecular forces. Reidel, Dordrecht, pp 331–342

Berendsen HJC, Postma JPM, van Gunsteren WF et al (1984) Molecular-dynamics with coupling to an external bath. J Chem Phys 81:3684–3690

Berger O, Edholm O, Jahnig F (1997) Molecular dynamics simulations of a fluid bilayer of dipalmitoylphosphatidylcholine at full hydration, constant pressure, and constant temperature. Biophys J 72:2002–2013

Bockmann RA, Grubmuller H (2004) Multistep binding of divalent cations to phospholipid bilayers: a molecular dynamics study. Angew Chem 43(8):1021–1024

Bockmann RA, de Groot BL, Kakorin S et al (2008) Kinetics, statistics, and energetics of lipid membrane electroporation studied by molecular dynamics simulations. Biophys J 95:1837–1850

Boettcher JM, Davis-Harrison RL, Clay MC et al (2011) Atomic view of calcium-induced clustering of phosphatidylserine in mixed lipid bilayers. Biochemistry 50:2264–2273

Chizmadzhev YA, Abidor IG (1980) Bilayer lipid-membranes in strong electric-fields. Bioelectrochem Bioenerg 7:83–100

Coster HGL (1965) A quantitative analysis of voltage-current relationships of fixed charge membranes and associated property of punch-through. Biophys J 5:669

DeBruin KA, Krassowska W (1998) Electroporation and shock-induced transmembrane potential in a cardiac fiber during defibrillation strength shocks. Ann Biomed Eng 26:584–596

Essmann U, Perera L, Berkowitz ML et al (1995) A smooth particle mesh Ewald method. J Chem Phys 103:8577–8593

Glaser RW, Leikin SL, Chernomordik LV et al (1988) Reversible electrical breakdown of lipid bilayers: formation and evolution of pores. Biochim Biophys Acta 940:275–287

Hamilton WA, Sale AJH (1967) Effects of high electric fields on microorganisms. 2. Mechanism of action of lethal effect. Biochim Biophys Acta 148:789–800

Hess B, Bekker H, Berendsen HJC et al (1997) LINCS: a linear constraint solver for molecular simulations. J Comput Chem 18:1463–1472

Hess B, Kutzner C, van der Spoel D et al (2008) GROMACS 4: algorithms for highly efficient, load-balanced, and scalable molecular simulation. J Chem Theory Comput 4(3):435–447

Humphrey W, Dalke A, Schulten K (1996) VMD: visual molecular dynamics. J Mol Graph 14:33–38

Koronkiewicz S, Kalinowski S, Bryl K (2002) Programmable chronopotentiometry as a tool for the study of electroporation and resealing of pores in bilayer lipid membranes. Biochim Biophys Acta Biomembr 1561:222–229

Leontiadou H, Mark AE, Marrink SJ (2004) Molecular dynamics simulations of hydrophilic pores in lipid bilayers. Biophys J 86:2156–2164

Levine ZA, Vernier PT (2010) Life cycle of an electropore: field-dependent and field- independent steps in pore creation and annihilation. J Membr Biol 236:27–36

Lewis TJ (2003) A model for bilayer membrane electroporation based on resultant electromechanical stress. IEEE Trans Dielect Elect Insul 10:769–777

Mathai JC, Tristram-Nagle S, Nagle JF et al (2007) Structural determinants of water permeability through the lipid membrane. J Gen Physiol 131:69–76

Mattai J, Hauser H, Demel RA et al (1989) Interactions of metal ions with phosphatidylserine bilayer membranes: effect of hydrocarbon chain unsaturation. Biochemistry 28(5):2322–2330

Melikov KC, Frolov VA, Shcherbakov A, Samsonov AV, Chizmadzhev YA, Chernomordik LV (2001) Voltage-induced nonconductive pre-pores and metastable single pores in unmodified planar lipid bilayer. Biophys J 80:1829–1836

Mir LM, Bureau MF, Gehl J et al (1999) High-efficiency gene transfer into skeletal muscle mediated by electric pulses. Proc Natl Acad Sci USA 96:4262–4267

Miyamoto S, Kollman PA (1992) Settle: an analytical version of the shake and rattle algorithm for rigid water models. J Comput Chem 13:952–962

Mukhopadhyay P, Monticelli L, Tieleman DP (2004) Molecular dynamics simulation of a palmitoyl-oleoyl phosphatidylserine bilayer with Na^+ counterions and NaCl. Biophys J 86(3):1601–1609

Neu JC, Krassowska W (1999) Asymptotic model of electroporation. Phys Rev E 59:3471–3482

Neumann E, Schaeferridder M, Wang Y et al (1982) Gene-transfer into mouse lyoma cells by electroporation in high electric-fields. EMBO J 1:841–845

Popescu D, Rucareanu C, Victor G (1991) A model for the appearance of statistical pores in membranes due to self oscillations. Bioelectrochem Bioenerg 25:91–103

Porasso RD, Cascales JJL (2009) Study of the effect of Na^+ and Ca^{2+} ion concentration on the structure of an asymmetric DPPC/DPPC + DPPS lipid bilayer by molecular dynamics simulation. Colloids Surf B Biointerfaces 73:42–50

Rols MP, Teissie J (1990) Electropermeabilization of mammalian cells—quantitative analysis of the phenomenon. Biophys J 58:1089–1098

Rols MP, Coulet D, Teissie J (1992) Highly efficient transfection of mammalian cells by electric-field pulses: application to large volumes of cell culture by using a flow system. Eur J Biochem 206:115–121

Ryham R, Berezovik I, Cohen FS (2011) Aqueous viscosity is the primary source of friction in lipidic pore dynamics. Biophys J 101:2929–2938

Sengupta D, Leontiadou H, Mark AE et al (2008) Toroidal pores formed by antimicrobial peptides show significant disorder. Biochim Biophys Acta Biomembr 1778:2308–2317

Sinn CG, Antonietti M, Dimova R (2006) Binding of calcium to phosphatidylcholine: phosphatidylserine membranes. Colloids Surf A Physicochem Eng Asp 282:410–419

Stampfli R, Willi M (1957) Membrane potential of a ranvier node measured after electrical destruction of its membrane. Experientia 13:297–298

Sugar IP, Neumann E (1984) Stochastic model for electric field-induced membrane pores. Electroporation. Biophys Chem 19:211–225

Tarek M (2005) Membrane electroporation: a molecular dynamics simulation. Biophys J 88:4045–4053

Teissie J, Golzio M, Rols MP (2005) Mechanisms of cell membrane electropermeabilization: a minireview of our present (lack of?) knowledge. Biochim Biophys Acta 1724:270–280

Tieleman DP (2004) The molecular basis of electroporation BMC. Biochem 5:10

Tieleman DP, Leontiadou H, Mark AE et al (2003) Simulation of pore formation in lipid bilayers by mechanical stress and electric fields. J Am Chemical Soc 125:6382–6383

Vasilkoski Z, Esser AT, Gowrishankar TR, Weaver JC (2006) Membrane electroporation: the absolute rate equation and nanosecond time scale pore creation. Phys Rev E 74:021904

Vernier PT, Ziegler MJ, Dimova R (2009) Calcium binding and head group dipole angle in phosphatidylserine: phosphatidylcholine bilayers. Langmuir 25(2):1020–1027

Weaver JC (2003) Electroporation of biological membranes from multicellular to nano scales. IEEE Trans Dielect Elect Insul 10:754–768

Weaver JC, Chizmadzhev YA (1996) Theory of electroporation: a review. Bioelectrochem Bioenerg 41:135–160

Weaver JC, Mintzer RA (1981) Decreased bilayer stability due to transmembrane potentials. Phys Lett A 86:57–59

Ziegler MJ, Vernier PT (2008) Interface water dynamics and porating electric fields for phospholipid bilayers. J Phys Chem B 112:13588–13596

Zimmerman U, Pilwat G, Riemann F (1974) Dielectric breakdown of cell membranes. Biophys J 14:881–899

J Membrane Biol
DOI 10.1007/s00232-012-9472-0

Enhanced Killing Effect of Nanosecond Pulse Electric Fields on PANC1 and Jurkat Cell Lines in the Presence of Tween 80

Gaurav Basu · Bhargava Subhash Kalluri · Ahmet Can Sabuncu · Christopher J. Osgood · Michael W. Stacey

Received: 16 January 2012 / Accepted: 24 June 2012

Abstract We investigated the effects of nanosecond pulse electric fields (nsPEFs) on Jurkat and PANC1 cells, which are human carcinoma cell lines, in the presence of Tween 80 (T80) at a concentration of 0.18 % and demonstarted an enhanced killing effect. We used two biological assays to determine cell viability after exposing cells to nsPEFs in the presence of T80 and observed a significant increase in the killing effect of nsPEFs. We did not see a toxic effect of T80 when cells were exposed to surfactant alone. However, we saw a synergistic effect when cells exposed to T80 were combined with the nsPEFs. Increasing the time of exposure for up to 8 h in T80 led to a significant decrease in cell viability when nsPEFs were applied to cells compared to control cells. We also observed cell type–specific swelling in the presence of T80. We suggest that T80 acts as an adjuvant in facilitating the effects of nsPEFs on the cell membrane; however, the limitations of the viability assays were addressed. We conclude that T80 may increase the fragility of the cell membrane, which makes it more susceptible to nsPEF-mediated killing.

Keywords Nanosecond pulse electric field · Tween 80 · PANC1 cell · Jurkat cell

G. Basu and B. S. Kalluri contributed equally to this work

G. Basu · B. S. Kalluri · A. C. Sabuncu · C. J. Osgood · M. W. Stacey (✉)
Frank Reidy Research Center for Bioelectrics, Old Dominion University, 4211 Monarch Way, STE-300, Norfolk, VA 23508, USA
e-mail: mstacey@odu.edu

Introduction

The use of nanosecond pulse electric fields (nsPEFs) for the treatment of tumors is a relatively new and exciting field which is being explored by a number of groups around the world. The charging time constant for a typical mammalian cell (of 10 μm diameter) is in the order of 100 ns (Schwan et al. 1985). PEF exposures with durations of <100 ns can effectively penetrate into a mammalian cell. These ultrashort electric pulses are known as nsPEFs and have been shown to induce apoptosis in HCT116 human colon carcinoma cells, Jurkat cells, B10-2 fibrosarcoma tumors (Beebe et al. 2003a, b) and calcium bursts in Jurkat cells (Vernier et al. 2003). It has been observed that when high-voltage electric pulses of short time intervals (12 kV/cm, 60 ns) were applied to Jurkat, GH3 and PC-12 cells, there was a significant decrease in the membrane potential and increased cell death (Pakhomov et al. 2007). The major advantage of nsPEFs is their unique ability to noninvasively induce apoptosis without generating any huge thermal effect (Nuccitelli et al. 2006). Although nsPEFs significantly decrease tumor volume by 80 % in mice, histological results have shown significant damage to the healthy peripheral skin due to application of high electric fields (Chen et al. 2009). Increases in heart and respiratory rates were also observed when nsPEFs were applied to treat melanomas in mice (Chen et al. 2009). Keeping these characteristics in mind, nsPEFs provide a new approach to physically target tumor cells.

Polysorbate 80 is a nonionic surfactant which is commercially known as Tween 80 (T80) (Zheng and Obbard 2002) and has been used as an adjuvant along with different cancer-treating drugs (Tsujino et al. 1999). The killing effect shown by actinomycin-D and daunomycin on drug-resistant Chinese hamster cells was directly

Published online: 21 July 2012

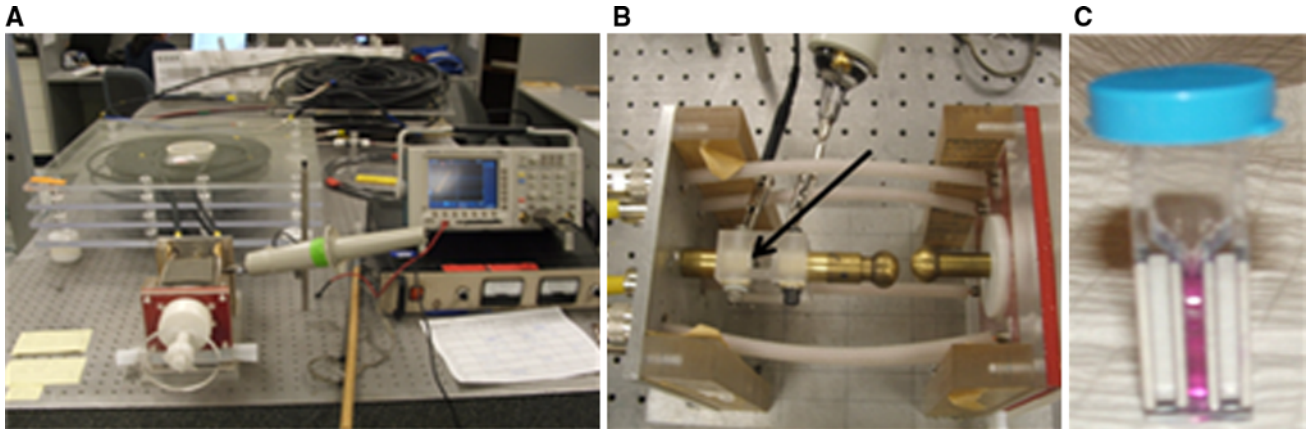

Fig. 1 Experimental setup for nsPEF treatment. **a** Sixty-nanosecond pulse generator. **b** The delivery chamber where electroporation cuvettes are inserted (*arrow*). **c** The 0.2-cm-wide cuvette with cell culture media

proportional to the concentration of adjuvant (T80) used (Riehm and Biedler 1972). T80 also enhances the chemotherapeutic efficiency of drugs such as doxorubicin (Adriamycin) (Chitnis et al. 1984; Parris et al. 1987), VP16 (Tsujino et al. 1999), ethoglucid (Epodyl), mitomycin-C and thiotepa (Parris et al. 1987) by altering the permeability of the plasma membranes of cancer cells in vitro (Riehm and Biedler 1972). These studies show the significance of T80 as an adjuvant in effectively killing cancer cells.

Our present work focuses on enhancing the killing efficiency of nsPEFs by (using T80 as an adjuvant) exposing PANC1 and Jurkat cells to T80. We believe that exposure of cells to T80 compromises the integrity of the plasma membrane of cells, thereby increasing the effect of nsPEFs on intracellular structures of cells (as discussed above). The use of two separate viability assays confirms increased cell killing; however, the limitations of these viability assays will be addressed.

Materials and Methods

Cells and Cell Culture

The PANC1 and Jurkat cells used in the study were purchased from American Type Culture Collection (Manassas, VA). PANC1 (human pancreatic carcinoma cell line) was chosen as an adherent cell line, whereas Jurkat (human T-lymphocyte cell line) was chosen as a nonadherent cell line. Cells were maintained at 5 % CO_2 and 37 °C in a humidified cell culture incubator. Dulbecco's modified Eagle medium (DMEM, American Type Culture Collection) supplemented with 10 % fetal calf serum, 2 mM L-glutamine and 2 % penicillin and streptomycin was used for culturing PANC1 cells, while Roswell Park Memorial Institute medium (RPMI, American Type Culture Collection) supplemented with 10 % fetal calf serum, 2 mM L-glutamine and 2 % penicillin and streptomycin was used for culturing Jurkat cells. Exponentially growing cells were used for all experiments.

Nanosecond Pulse Generator

A transmission line pulse generator was used to deliver electric pulses of 60-ns duration (as shown in Fig. 1) (Kolb et al. 2006). The pulse amplitude could be adjusted by varying the gap distance of any spark gap operated in open (atmospheric pressure) air.

Experimental Setup for Exposure to Ultrashort Electric Pulses

An optimal amount of T80 at 0.18 % was used for good dispersion, which had the least toxic effect on PANC1 and Jurkat cells (Sabuncu et al. 2010). Cell concentration was adjusted to 1×10^6/ml, and 900 µl of medium with suspended cells was used for experiments. To these cells, 200 µl of 1 % T80 was added, to bring the final concentration to 0.18 %; 400 µl of sample was exposed to 12 pulses of 30 kV/cm (60 ns, 3.2 joules) using electroporation cuvettes (BioSmith Biotech, San Diego, CA). After exposure, cell viability was analyzed using the trypan blue exclusion method (Tennant 1964) and WST-1 cell viability assay (Peskin and Winterbourn 2000) immediately after exposure to nsPEFs and after 8 h.

Cell Viability Assays

Cells exposed to nsPEFs were diluted at a concentration of 1:1 with 0.4 % trypan blue solution (Sigma, St. Louis, MO). Viable cells were counted using a hemacytometer (Hausser Scientific, Horsham, PA). The trypan blue assay is based on uptake of the dye by the cell membrane of dead

cells; however, it is not able to differentiate between apoptotic and necrotic cells. For the WST-1 cell viability assay 100 µl of each sample (8 x 10^4 cells) was transferred into each well of a 96-well plate and 10 µl of WST-1 (Roche Applied Sciences, Indianapolis, IA) reagent was added to each well and incubated for 1 h. After incubation, the 96-well plate was read using a microplate reader at 450 nm. The WST-1 cell viability assay is based on cleavage of the water-soluble tetrazolium salt WST-1 into a soluble formazan dye by a complex cell surface mechanism of metabolically active and live cells. The optical density of the formazan dye is measured to obtain an estimate of live cells.

Cell Size Measurement Using Microscopy

PANC1 and Jurkat cells were viewed under a bright field microscope (Olympus, Center Valley, PA) before and after exposure (5 min) to nsPEFs. Images were captured using a DP71 CCD camera with DP controller software. Cell sizes were measured and analyzed using Image J software (NIH, Bethesda, MD).

Statistical Analysis

Cell viability assays were performed in triplicate, and results are shown as mean ± standard error of the mean (SEM). Statistical analysis was performed using GraphPad Prism™ (GraphPad Software, La Jolla, CA). Two-way ANOVA was used to demonstrate the significance among triplicate samples, and a two-tailed paired *t* test (95 % confidence interval) was used to detect significant differences between any two different samples. For all statistical analyses, $P < 0.05$ was considered significant.

Results

Viability of Jurkat and PANC1 cells was analyzed immediately after exposure to nsPEFs and 8 h postexposure. Cell viability after exposure was compared to cells that were not exposed to T80 or nsPEFs (control) and cells exposed to nsPEF only (control exposure).

The viability of Jurkat cells which were exposed to nsPEFs in the presence of 0.18 % T80 was assessed by trypan blue exclusion and WST-1 cell viability assay (Fig. 2). The results of trypan blue exclusion (Fig. 2a) and the WST-1 viability assay (Fig. 2b) immediately after exposure to nsPEFs demonstrate that there was no toxic effect of T80 on Jurkat cells compared to control cells. The trypan blue exclusion results also indicate that the cell viability decreased by 73 % in Jurkat cells that were exposed to nsPEFs in the presence of T80, which was highly significant compared to control exposed cells without T80 ($P < 0.01$, respectively), whereas WST-1 viability assay results of Jurkat cells (Fig. 2b) indicated that there was no significant difference in cell viability after exposure to T80 alone compared to control cells. Also, there was a significant decrease in cell viability by 68 % after exposure to nsPEFs in the presence of T80 compared to control exposed cells ($P < 0.01$). When exposed to nsPEFs for longer periods (8 h) Jurkat cells (Fig. 2c) demonstarted a significant effect of T80 alone on cell viability (without exposure to nsPEFs) ($P < 0.05$). These results also demonstrate that cell viability decreased significantly by 88 % in Jurkat cells that were exposed to nsPEFs in the presence of T80 compared to control exposed cells ($P < 0.001$). The WST-1 cell viability assay results of Jurkat cells 8 h after exposure to nsPEFs (Fig. 2d) demonstrate that there was no significant toxic effect of T80 on Jurkat cells compared to control cells in the absence of T80. It can be inferred from the results that there was a significant decrease in cell viability by 60 % in cells exposed to nsPEFs in the presence of T80 compared to control exposed cells ($P < 0.01$).

PANC1 cells that were exposed to nsPEFs in the presence of T80 were assessed just after exposure to nsPEFs (0 h) and after 8 h by trypan blue exclusion (Fig. 3a, c) and WST-1 cell viability assay (Fig. 3b, d). Trypan blue exclusion demonstrated that cell viability decreased significantly by 40 % in PANC1 cells which were exposed to nsPEFs in the presence of T80 compared to control exposed cells ($P < 0.01$). There was no significant toxic effect of T80 alone on PANC1 cells (Fig. 3a). WST-1 cell viability assay results demonstrate that there was a significant decrease in cell viability by 42 % in cells exposed to nsPEFs in the presence of T80 (Fig. 3b) compared to control exposed cells ($P < 0.01$). Analyzing 8 h after exposure to nsPEFs, trypan blue exclusion method results indicate that there was a highly significant decrease in cell viability by 95 % in cells exposed to nsPEFs in the presence of T80 (Fig. 3c) compared to control exposed cells ($P < 0.001$). The WST-1 cell viability results of PANC1 (Fig. 3d) indicate that there was no significant toxic effect of T80 alone. There was a very significant decrease in the cell viability by 50 % in cells that were exposed to nsPEFs in the presence of T80 compared to control exposed cells ($P < 0.001$).

We also measured the size of Jurkat and PANC1 cells (Fig. 4) prior to and postexposure to nsPEFs (5 min). We observed that the size of Jurkat cells (Fig. 4a) increased significantly in the presence of 0.18 % T80 ($P < 0.05$). There was a significant change in the size of Jurkat cells in the presence of 0.18 % T80 before compared to after exposure to nsPEFs ($P < 0.05$). There was no significant difference in PANC1 cell size postexposure to nsPEFs in the presence of 0.18 % T80 or cell culture medium (Fig. 4b).

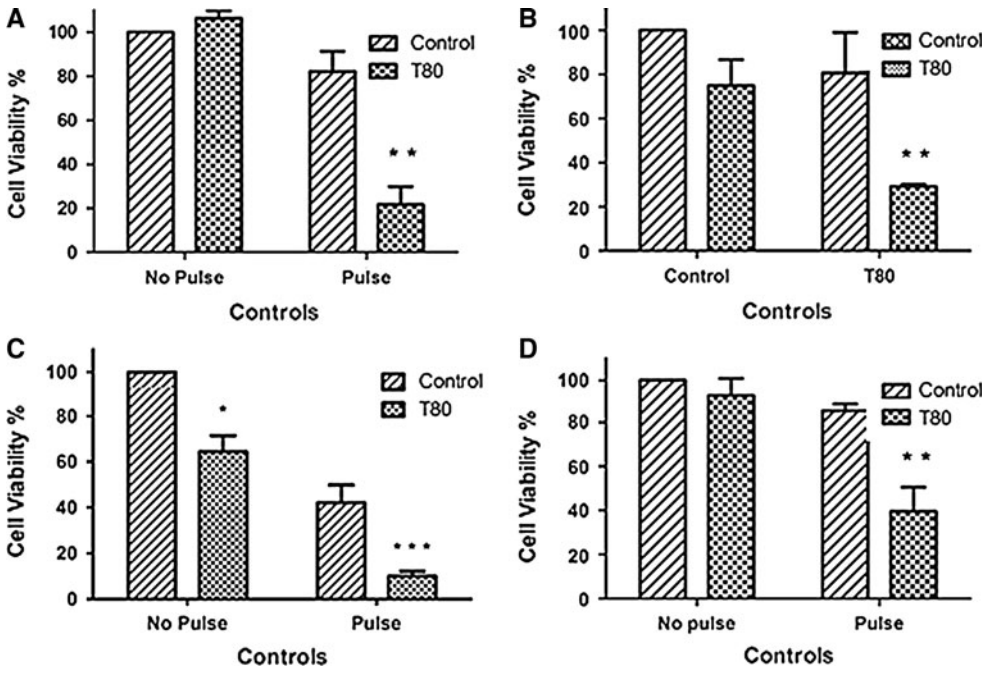

Fig. 2 Viability results of Jurkat cells after exposure to nsPEFs. **a** trypan blue assay results of Jurkat cells immeadiately after exposure to nsPEFs. **b** WST-1 cell viability assay results of Jurkat cells immeadiately after exposure to nsPEFs. **c** trypan blue assay results of Jurkat cells 8 h after exposure to nsPEF pulses. **d** WST-1 cell viability assay results of Jurkat cells 8 h after exposure to nsPEF pulses. $^{*}P < 0.05$, $^{**}P < 0.01$, $^{***}P < 0.001$

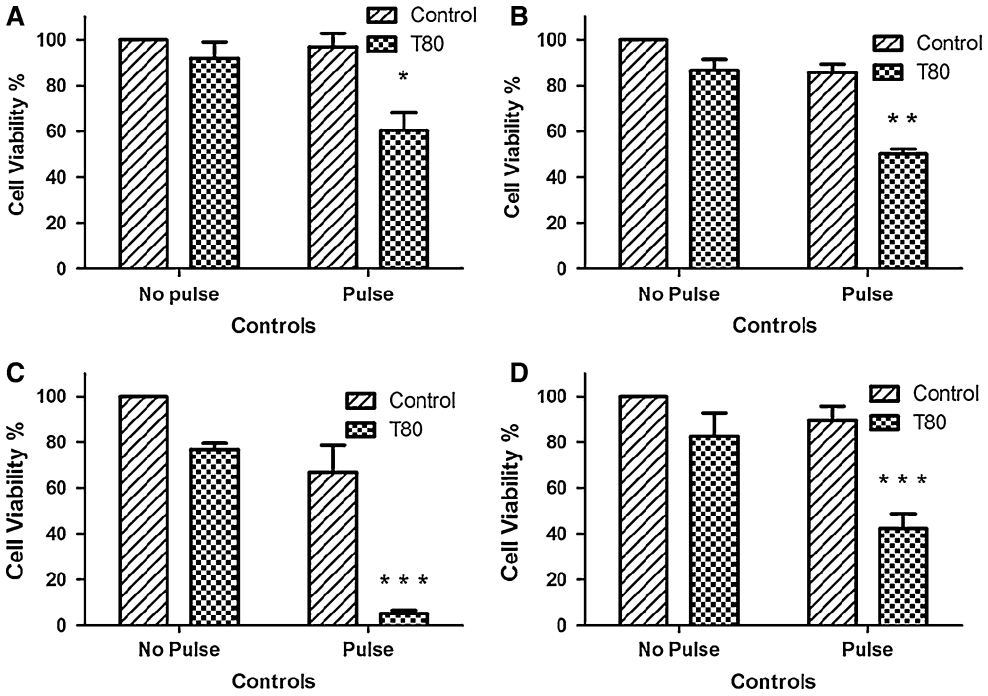

Fig. 3 Viability results of PANC1 cells (trypan blue assay and WST-1 cell viability assay) after exposure to nsPEFs. **a** trypan blue assay results of PANC1 cells immediately after exposure to nsPEFs. **b** WST-1 cell viability assay of PANC1 cells soon after exposure to nsPEFs. **c** trypan blue assay results of PANC1 cells 8 h after pulsing. **d** WST-1 cell viability assay results of PANC1 cells (8 h after pulsing). $^{*}P < 0.05$, $^{**}P < 0.01$, $^{***}P < 0.001$

Discussion

Our results clearly indicate that there was no immediate significant toxic effect of 0.18 % T80 on the viability of Jurkat and PANC1 cells; however, after 8-h exposure Jurkat cells showed increased sensitivity. There was a significant reduction in the viability of PANC1 and Jurkat cells when exposed to nsPEFs in the presence of 0.18 % T80 (Figs. 2a, b, 3a, b). The decrease in cell viability was even higher 8 h after exposure to nsPEFs in the presence of 0.18 % T80 (Figs. 2c, d, 3c, d). It has been shown in the past that T80 has similar adjuvant activity with regard to drugs such as doxorubicin, ethoglucid, mitomycin-C and thiotepa in treating superficial bladder cancer (Parris et al. 1987) and increasing the antitumor efficiency of hyperthermia in treating B16 melanoma cells in BALB/C mice (Yaoqin et al. 1996). It has also been shown that T80 decreases drug resistance in actinomycin-D and daunomycin-resistant Chinese hamster cells (Riehm and Biedler 1972) and daunorubicin-resistant Ehrlich ascites cells

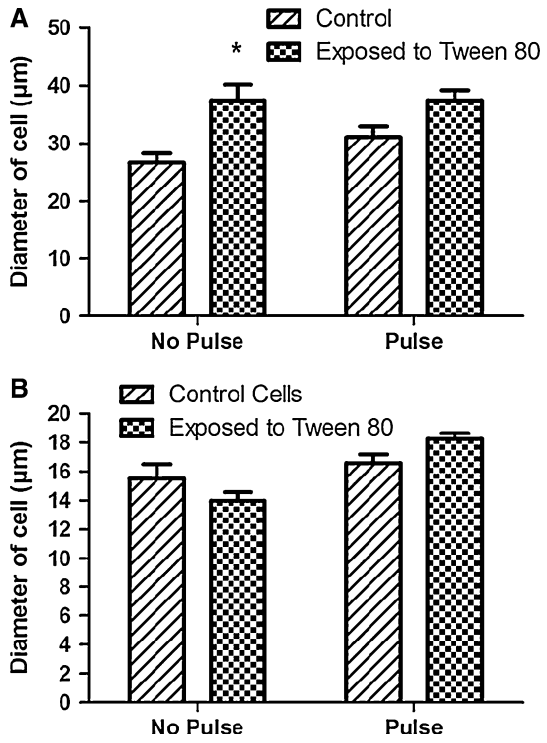

Fig. 4 Size variation in PANC1 and Jurkat cells in the presence of T80 and nsPEFs. **a** Change in Jurkat cell size when exposed to T80 alone, nsPEFs alone and both nsPEFs and T80. **b** Change in PANC1 cell size when exposed to T80 alone, nsPEFs only and both nsPEFs and T80

(Sehested et al. 1989). In all of these cases, T80 acted as a solubilizing agent to the plasma membrane of cells (Jones 1999) as well as in increasing membrane fluidity (Basrur et al. 1983; Chitnis et al. 1984; Tsujino et al. 1999; Coors et al. 2005). This increase in membrane fluidity could have significantly enhanced the poration (nano) effect of nsPEFs where stable poration is seen for minutes (Bowman et al. 2010). Better formulation of the possible effects of increased membrane fluidity in nsPEFs according to the reported effects in microsecond pulses is necessary (Kandušer et al. 2006). Another possible mechanism could be pore-induced changes in the osmotic pressure of cells, leading to an increase in the size of cells (Fig. 4), by the presence of T80. This effect, however, appeared to be cell type-specific, with Jurkat cells showing significant swelling. Jurkat cells are nonadherant and have reduced supporting cytoskeletal networks compared to adherent cells. The nsPEF-induced cytoskeletal damage (Stacey et al. 2011) along with T80-induced membrane fluidity may disrupt electrolyte balance, followed by water uptake, thus making Jurkat cells more susceptible to osmotic swelling.

Even though trypan blue and WST-1 cell viability assay results measured a significant killing effect of nsPEFs in the presence of 0.18 % T80, the difference in the cell viability results of these assays is primarily dependent on the cell component involved with the assay. The trypan blue exclusion assay is based on uptake of the dye by dead cells only, whereas the WST-1 cell viability assay is based on cleavage of WST-1 into a soluble formazan dye by mitochondrial dehydrogenase of metabolically active and live cells. T80 (0.5 %) (Wallace et al. 1968) has been implicated in mitochondrial and membrane biogenesis in yeast, a factor that was not investigated in these studies but which may influence both assay outcomes through different mechanisms. The plasma membrane is significantly affected after exposure to nsPEFs (André et al. 2010) measured by propidium iodide uptake across the cell membrane. The trypan blue assay is an assay based on the integrity of the plasma membrane. Therefore, with viability assays that may be compromised by T80 or membrane permeability, the results of WST-1 cell viability and trypan blue assays may be expected to differ from each other.

Conclusion

Based on our results, it can be concluded that T80 plays a major role in enhancing the killing effect of nsPEFs, which could be due to an adjuvant effect on PANC1 and Jurkat cells. We believe that T80 may increase the cell membrane permeability/fluidity, leading to increased fragility of the cell membrane. Further investigation is necessary to understand the mechanism of T80 as an adjuvant in enhancing the killing effect of nsPEFs. We also conclude that cell viability depends upon the protocol employed and may be indicative of different biological mechanisms that respective cell viability assays measure as a means to determine cell viability.

Acknowledgement We acknowledge the support of the Breeden Adams Foundation. The study sponsors had no role in the study design, data collection, data analysis, compiling the manuscript or the decision to submit it for publication.

References

André FM, Rassokhin MA, Bowman AM et al (2010) Gadolinium blocks membrane permeabilization induced by nanosecond electric pulses and reduces cell death. Bioelectrochemistry 79:95–100

Basrur V, Chitnis M, Menon R (1983) Differential agglutination of P388 Adriamycin-sensitive and P388 Adriamycin-resistant leukemia cells. Oncology 40:202–204

Beebe S, White J, Blackmore P et al (2003a) Diverse effects of nanosecond pulsed electric fields on cells and tissues. DNA Cell Biol 22:785–796

Beebe SJ, Fox PM, Rec LJ et al (2003b) Nanosecond, high-intensity pulsed electric fields induce apoptosis in human cells. FASEB J 17:1493–1495

Bowman A, Nesin O, Pakhomova O et al (2010) Analysis of plasma membrane integrity by fluorescent detection of Tl^+ uptake. J Membr Biol 236:15–26

Chen X, James Swanson R, Kolb J et al (2009) Histopathology of normal skin and melanomas after nanosecond pulsed electric field treatment. Melanoma Res 19:361–371

Chitnis M, Menon R, Gude R (1984) Effect of Tween 80 on Adriamycin cytotoxicity in murine P388 leukemia. Tumori 70:313

Coors E, Seybold H, Merk H et al (2005) Polysorbate 80 in medical products and nonimmunologic anaphylactoid reactions. Ann Allergy Asthma Immunol 95:593–599

Jones M (1999) Surfactants in membrane solubilisation. Int J Pharm 177:137–159

Kandušer M, Šentjurc M, Miklavcic D (2006) Cell membrane fluidity related to electroporation and resealing. Eur Biophys J 35(3): 196–204

Kolb J, Kono S, Schoenbach K (2006) Nanosecond pulsed electric field generators for the study of subcellular effects. Bioelectromagnetics 27:172–187

Nuccitelli R, Pliquett U, Chen X et al (2006) Nanosecond pulsed electric fields cause melanomas to self-destruct. Biochem Biophys Res Commun 343:351–360

Pakhomov A, Kolb J, White J et al (2007) Long-lasting plasma membrane permeabilization in mammalian cells by nanosecond pulsed electric field (nsPEF). Bioelectromagnetics 28:655–663

Parris C, Masters J, Walker M et al (1987) Intravesical chemotherapy: combination with Tween 80 increases cytotoxicity in vitro. Urol Res 15:17–20

Peskin A, Winterbourn C (2000) A microtiter plate assay for superoxide dismutase using a water-soluble tetrazolium salt (WST-1). Clin Chim Acta 293:157–166

Riehm H, Biedler J (1972) Potentiation of drug effect by Tween 80 in Chinese hamster cells resistant to actinomycin D and daunomycin. Cancer Res 32:1195

Sabuncu A, Kalluri B, Qian S et al (2010) Dispersion state and toxicity of mwCNTs in cell culture medium with different T80 concentrations. Colloids Surf B Biointerfaces 78:36–43

Schwan H, Chiabrera C, Nicolini C (1985) Interactions between electromagnetic fields and cells. Plenum Press, New York, pp 173–191

Sehested M, Jensen P, Skovsgaard T et al (1989) Inhibition of vincristine binding to plasma membrane vesicles from daunorubicin-resistant Ehrlich ascites cells by multidrug resistance modulators. Br J Cancer 60:809

Stacey M, Fox P, Buescher S, Kolb J (2011) Nanosecond pulsed electric field induced cytoskeleton, nuclear membrane and telomere damage adversely impact cell survival. Bioelectrochemistry 82:131–134

Tennant J (1964) Evaluation of the trypan blue technique for determination of cell viability. Transplantation 2:685

Tsujino I, Yamazaki T, Masutani M et al (1999) Effect of Tween-80 on cell killing by etoposide in human lung adenocarcinoma cells. Cancer Chemother Pharmacol 43:29–34

Vernier P, Sun Y, Marcu L et al (2003) Calcium bursts induced by nanosecond electric pulses. Biochem Biophys Res Commun 310:286–295

Wallace PG, Huang M, Linnane AW (1968) The biogenesis of mitochondria: II. The influence of medium composition on the cytology of anaerobically grown *Saccharomyces cerevisiae*. J Cell Biol 37:207–220

Yaoqin Y, Huchuan Y, Huihong T et al (1996) The enhancement of Tween-80 on the antitumor effect of the hyperthermia 41 °C in tumor-bearing mice. Chin J Cancer Res 8:168–173

Zheng Z, Obbard J (2002) Evaluation of an elevated non-ionic surfactant critical micelle concentration in a soil/aqueous system. Water Res 36:2667–2672

J Membrane Biol (2012) 245:617–624
DOI 10.1007/s00232-012-9474-y

Design and Implementation of a Microelectrode Assembly for Use on Noncontact In Situ Electroporation of Adherent Cells

Tomás García-Sánchez · Beatriz Sánchez-Ortiz · Ingrid Vila · Maria Guitart · Javier Rosell · Anna M. Gómez-Foix · Ramón Bragós

Received: 16 December 2011 / Accepted: 30 June 2012 / Published online: 24 July 2012

Abstract In situ electroporation of adherent cells provides significant advantages with respect to electroporation systems for suspension cells, such as causing minimal stress to cultured cells and simplifying and saving several steps within the process. In this study, a new electrode assembly design is shown and applied to in situ electroporate adherent cell lines growing in standard multiwell plates. We designed an interdigitated array of electrodes patterned on copper with printed circuit board technology and covered with nickel/gold. Small interelectrode distances were used to achieve effective electroporation with low voltages. Epoxy-based microseparators were constructed to avoid direct contact with the cells and to create more uniform electric fields. The device was successful in the electropermeabilization of two different adherent cell lines, C2C12 and HEK 293, as assessed by the intracellular delivery of the fluorescent dextran FD20S. Additionally, as a collateral effect, we observed cell electrofusion in HEK 293 cells, thus making this device also useful for performing cell fusion. In summary, we show the effectiveness of this minimally invasive device for electroporation of adherent cells cultured in standard multiwell plates. The cheap technologies used in the fabrication process of the electrode assembly indicate potential use as a low-cost, disposable device.

Keywords In situ electroporation · Noncontact · Microelectrode · Adherent cell

T. García-Sánchez (✉) · J. Rosell · R. Bragós
Electronic and Biomedical Instrumentation Group, Department of Electrical Engineering, Universitat Politecnica de Catalunya, Barcelona, Spain
e-mail: tomas.garcia.sanchez@upc.edu

B. Sánchez-Ortiz · I. Vila · M. Guitart · A. M. Gómez-Foix
Departament de Bioquímica i Biologia Molecular, IBUB, Universitat de Barcelona, Barcelona, Spain

A. M. Gómez-Foix
CIBER de Diabetes y Enfermedades Metabólicas (CIBERDEM), Barcelona, Spain

Introduction

Nowadays, electroporation, also known as "electropermeabilization," is a useful technique to introduce foreign impermeable material into the cell cytoplasm. A state of high permeability to ions and macromolecules is achieved by exposing cell membranes to short (microsecond–millisecond) high-electric field pulses (Neumann et al. 1982; Weaver and Chizmadzhev 1996; Teissie et al. 2005). This state can be either temporary (reversible electroporation) or permanent (irreversible electroporation) as a function of the electric field parameters (Wolf et al. 1994; Rols and Teissié 1998; Hui 1995; Lebar et al. 2002). Typical reversible applications comprise drug delivery (Dev et al. 2000), gene therapy (Wolf et al. 1994; Zheng and Chang 1991; Stopper et al. 1987) and introduction of fluorescent probes used in research and functional proteomic treatment (Lambert et al. 1990) as the main representative examples.

The technique can be applied to a wide spectrum of biological preparations, ranging from single cells (Wang et al. 2010) up to whole tissues such as liver, lung and muscle (Dev et al. 2000) and both in vitro and in vivo. Traditional in vitro equipment performs electroporation in cuvettes where cells are suspended in order to apply electric field pulses (Raptis and Firth 2008). Particularly, when adherent cells are electroporated a previous trypsinization process needs to be carried out. However, trypsinizing adherent cells causes an additional stress to the cells that

may affect both the electroporation efficiency and the invasiveness of the operation (Zheng and Chang 1991). As explained in Chang et al. (1992), there are several reasons to believe that in situ electroporation is more suitable for high-efficacy transfection in adherent cells maintaining a reasonable viability.

Some microfabricated devices have been designed to apply electric field pulses directly to the adherent cell monolayer, where cells commonly grow onto the microelectrode surface (Raptis and Firth 2008; Olbrich et al. 2008; Wegener et al. 2002). Some approaches make use of interdigitated microelectrodes deposited into planar glass surfaces with microfabrication techniques to apply the pulses (Huang et al. 2011; Lin et al. 2003). These devices allow lowering of the required voltages to reach the high-intensity electric fields (1–10 kV/cm) due to the small interelectrode distance. For example, in Lin et al. (2003) an electroporation microchip successfully transfected adherent cells using <2 V. The reduction in the required amplitude to create membrane poration reduces the complexity and cost of pulse generators used in traditional systems as well as the requirements for electrical safety of the devices. There are also reports of many single-cell devices that introduce silicon fabrication technology (Braeken et al. 2010) or microfluidics (Geng et al. 2010). However, all the devices described above are custom-built setups and are not suitable for direct use in standard multiwell plates. In addition, in most of them, cells are not attached to a standard cell growing surface; on the contrary, they are in contact with the electrodes or other nonstandard surfaces that may interfere with normal development. Some other commercially available devices have been designed to apply electroporation pulses to cells growing in standard culture plates; these approaches make use of big, flat or wire electrodes positioned above the monolayer very similarly to a cell suspension with relatively high electrode distances (Deora et al. 2007; Raptis and Firth 2008).

In the present report a new electroporation device is described. The electrode assembly proposed was initially designed to monitor the state of cell monolayers with a minimally invasive method by means of electrical bioimpedance spectroscopic measurements. We show the functionality of this electrode system also for in situ electroporation of C2C12 and HEK 293 adherent cells cultured in standard multiwell plates, making use of low voltages.

Materials and Methods

Electrode Assembly

The electrodes were conceived and designed taking into account the principle of in situ use with adherent cell monolayers growing in standard multiwell plates. The main goal was to reduce the invasiveness of the operation in order not to interfere in the regular behavior of cultured cells.

The electrode geometric design was based on an interdigitated structure consisting of six independent lines forming three arrays of electrodes. This design enables bioimpedance measurements in different configurations and, in the case of electroporation, configures three active areas. Each line in the active pairs connected alternately to +V or −V terminals of the pulse generator. Some different designs were tested using different electrode width and spacing (see Fig. 1). In this study the final dimensions were 75 and 150 μm width and spacing, respectively. Electrodes were patterned on copper with printed circuit board technology using as substrate 1-mm-thick FR4 discs with diameter compatible with the dimensions of standard 24-multiwell plates. Due to the toxicity of copper (Cu), once the electrode structure was patterned, a final nickel (Ni)/hold (Au) plating was deposited using the electroless nickel immersion gold technique.

Following the idea of in situ application to cell monolayers, small microseparations were created, to avoid direct contact between the electrodes and the monolayer which could cause mechanical stress or damage to the cells. Noncontact electroporation allows us to minimize the invasiveness of the operation. These separations were constructed using a final photosensible epoxy layer with thickness of 10 μm deposited on the border areas of the surface of the electrodes. Six circular microseparators were patterned on the surface of the electrodes that were equally distributed along the perimeter of the discs. The thickness of cell monolayers is usually 3–8 μm in most cell lines attached to a surface (Durante et al. 1993; Bettega et al. 1998); consequently, 10 μm is enough to avoid direct

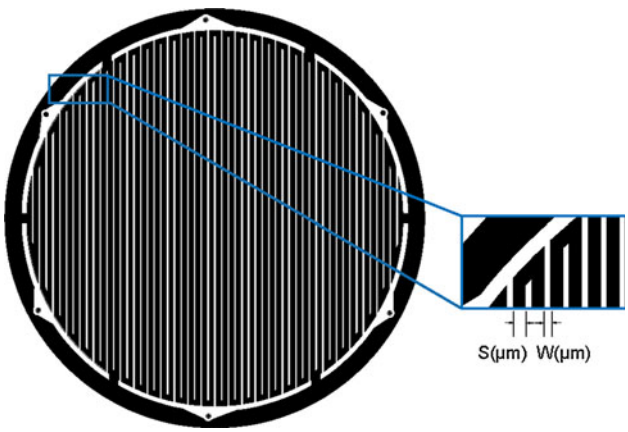

Fig. 1 Interdigitated geometry of the electrodes and detailed view. Six different *lines* are connected to the stimulator terminals. Different separations between electrodes (*S*) and different electrode widths (*W*) were tested

contact with the electrodes. Figure 2a depicts the in situ placement of the electrode assembly above the bottom surface of a culture well, and Fig. 2b is a detailed view of the microseparations described above.

In addition, considerably higher and irregular electric fields are presented in the border areas of microelectrodes that could irreversibly damage cell membranes near these areas. More uniform electric fields are created a short distance from the electrode surface (Lin et al. 2003; Lisen et al. 2007). A 2D simplification of the structure was simulated to study the electric field distribution. Simulations were made using commercial software (COMSOL Multiphysics 3.5; COMSOL, Burlington, MA). The conductivity values used for the different parts were $\sigma = 0.004$ S/m for the FR4 substrate, $\sigma = 5.998e^{7}$ S/m for copper electrodes and $\sigma = 0.16$ S/m for poration media. Boundary conditions in the electrodes were set to fixed current ports or ground alternatively. In Fig. 3a the current density distribution is shown. As pointed out above, more uniform distribution is present a short distance from the surface of the electrodes. In Fig. 3b and c cross-sectional plots are shown. Figure 3b depicts the electric field values along a horizontal line separated 15 μm from the electrodes. From this plot it can be stated that cells under the center of the electrodes will not be electroporated because the electric field intensity in these areas will not be high enough. On the other hand, the effect in the areas where the electric field is over the threshold will be very uniform, only 4 % of variation as indicated in the plot. In Fig. 3c the electric field values along a vertical line are plotted. As shown in the figure, there is an electric field reduction in the vertical direction with a maximum decrease of 10 % between the highest and lowest points of the line. From these simulations it can be concluded that the use of microseparations has the advantage of applying more uniform electric fields but that, due to the relative distance between the electrodes and the cell surface, higher voltages need to be applied to obtain suitable electric field intensities for electroporation.

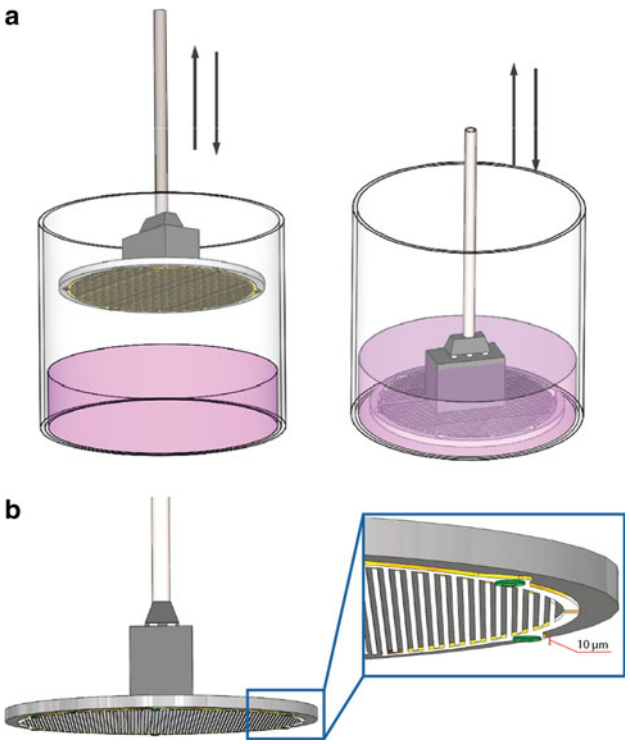

Fig. 2 Illustration of the electrode setup. **a** Representation of the principle of operation, showing how electrodes are placed in the bottom surface of the multiwell plates. **b** Detailed view of the microseparations used to avoid contact between electrodes and cells

Once the microelectrodes were fabricated and tested, the next step was to adapt them for in situ application. A biocompatible acrylic adhesive (LOCTITE 3555™; Henkel, Dusseldorf, Germany) was used to seal the soldering areas between the pads and the connector. Connection wires were introduced in a biomedical silicone tube whose flexibility allowed the discs to be settled uniformly parallel to the bottom surface of the multiwell plates when the assembly was leaned against the surface, and consequently, the electrodes were uniformly parallel to the cell monolayer. The electrode assembly is automatically positioned using a self-constructed positioner which ensures that the same vertical force was applied in all experiments. In addition, using this automatic system, the displacement speed can be controlled, ensuring that with slow enough speed fluid displacement does not harm the monolayer. This electrode assembly is in the patent process.

Electric Field Pulse Delivery

Electric field pulses were delivered using a biphasic stimulator developed in our laboratory and first conceived for long-term contraction of cultured muscle cells. The stimulator generates bipolar pulses acting as a fixed current source with intensities (A) ranging from 1 to 800 mA, minimal duration (D) of each part of the bipolar signal of 100 μs and minimal period (T) of 1 ms. There is an additional parameter (T_t) that allows one to set the time separation between the positive and negative parts of the pulse (minimum value 100 μs). The device is fully programmable by an RS-232 connection to a PC. As previously studied by other authors, the use of bipolar pulses enhances transfection efficiency (De Vuyst et al. 2008; Ephrem Tekle and Bonn Chock 1991) and reduces electrolytic gas bubble formation in metal electrodes (Ziv et al. 2009).

Cells and Chemicals

The C2C12 mouse myogenic cell line and the HEK 293 human embryonic kidney cell line were cultured as a

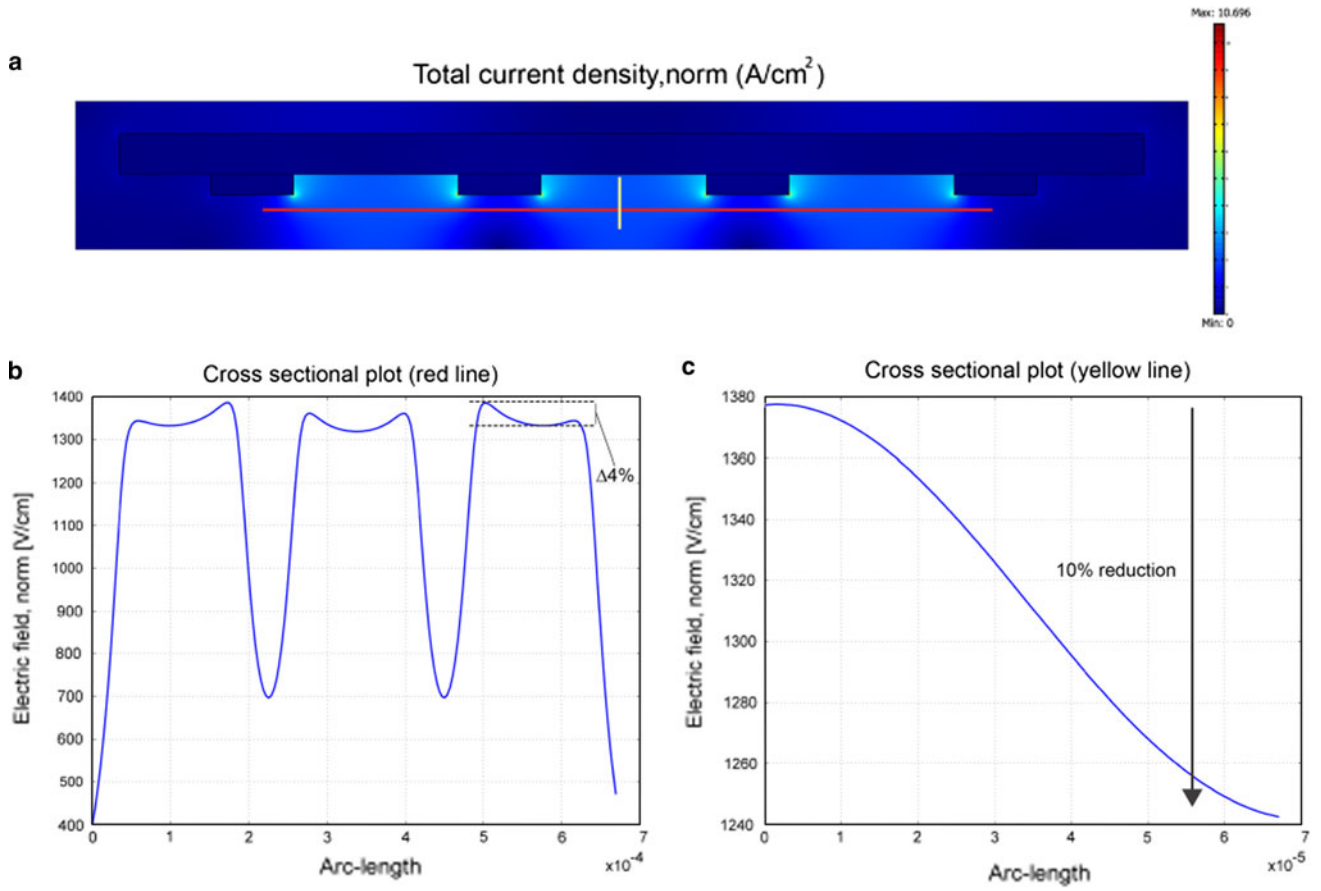

Fig. 3 Electric field simulations run on COMSOL Multiphysics 3.5. **a** The 2D simplification simulated is shown and the total current density is plotted. **b** A cross-sectional *plot* of the electric field distribution along a *horizontal line* 15 μm from the surface of the electrodes (*red line* in **a**). **c** A cross-sectional *plot* of the electric field distribution along a vertical line (*yellow line* in **a**) (Color figure online)

monolayer in Dulbecco's modified Eagle medium (DMEM) supplemented with 10 % fetal bovine serum and supplemented with penicillin, streptomycin and fungizone.

Low-conductivity electroporation buffer (LCEB) was used in the experiments. LCEB consisted of 10 mM Na_2HPO_4 (pH 7.4), 1 mM $MgCl_2$ and 250 mM sucrose. Conductivity was 1.6 mS/cm. When started, 2.5 mg/ml fluorescein isothiocyanate-dextran, average molecular weight 20,000 Da (FD20S; Sigma-Aldrich, Madrid, Spain) was added to the LCEB as a fluorescence electropermeabilization probe.

Electroporation Procedure

Both C2C12 and HEK 293 cell lines were plated in 24-multiwell plates at cell concentrations of 5×10^4/well and 7×10^4/well, respectively. Plates were cultured at 37 °C in a humidified 5 % CO_2 incubator for approximately 24 h, to reach 50–60 % confluence.

Before application of electric pulses, cells were rinsed with phosphate-buffered saline (PBS); and then 150 μl of LCEB were added to each well. The electrode assembly was sterilized with a 70 % ethanol solution, rinsed with sterile distilled water and finally immersed in LCEB before use. Immediately, the electrode assembly was placed above the cell monolayer and electric field pulses were applied, configuring the biphasic stimulator via RS-232. Eight biphasic pulses, with duration (D) of 100 μs, time separation between the positive and negative parts of the pulse (T_t) of 100 μs and frequency repetition of 1 Hz were applied with different current intensities (A) to create electric fields of 1.2, 1.6, 2 and 2.2 kV/cm in the surface of the electrodes, taking into consideration that the electric field affecting cell membranes is lowered about 10 % because of the relative distance between electrodes and cells. In control cells, no electric pulses were applied, but the electrode was positioned above the cell monolayer for an equivalent period of time. After the electroporation procedure, cells were incubated for an additional 30-min period in the incubator. After this period, the electroporation buffer was removed and cells were rinsed twice with PBS, medium was replaced with fresh culture medium and

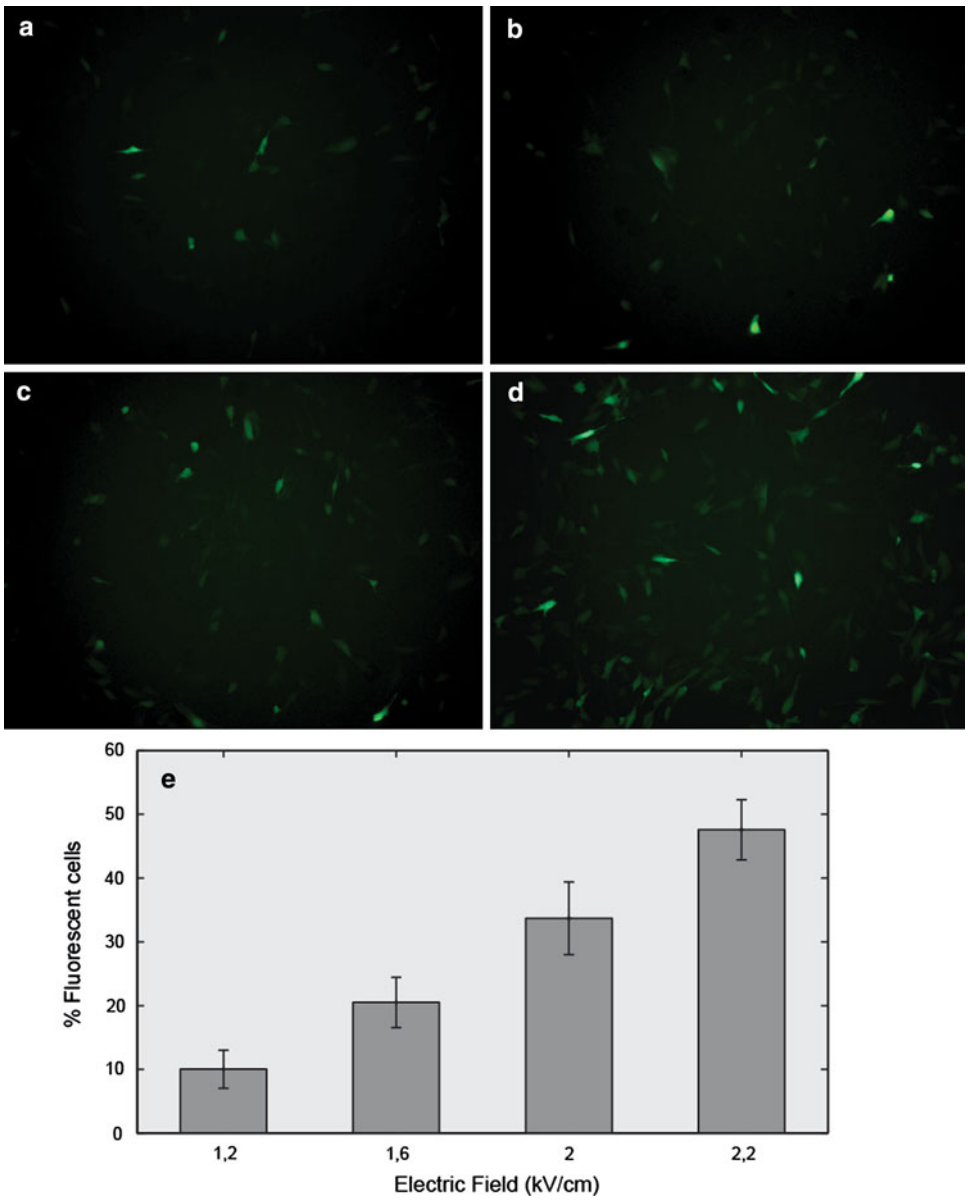

Fig. 4 *Micrograph* of C2C12 cells after electroporation. Cells were electroporated in the presence of FD20S at different electric field intensities: **a** 1.2 kV/cm, **b** 1.6 kV/cm, **c** 2 kV/cm and **d** 2.2 kV/cm. After cell electroporation and recovery, as described in "Materials and Methods" section, images of cell monolayers were taken at ×10 magnification. A representative *image* is shown. **e** Quantitative analysis of the results calculated as the percentage of fluorescent cells. Results are expressed in mean ± SD of at least five measurements

cells were left for 2 h in the incubator for complete resealing. Then, cells were examined under a Leica (Wetzlar, Germany) DMI 4000B inverted microscope for fluorescence, to detect FD20S, which has an excitation wavelength of 485 nm and emission at 510 nm. Images were taken with a digital camera (Leica DFC 300x).

Results and Discussion

The objective of this study was to test the use of an electrode assembly for in situ electropermeabilization of adherent cells growing in standard multiwell plates with minimal invasiveness of the operation. For that purpose two different cell lines, C2C12 myoblasts and HEK 293 epithelial cells, were subjected to electroporation with this system for intracellular delivery of fluorescent dextran FD20S, which has a molecular radius of 3.2 nm (Ambati et al. 2000). We first performed several tests, in which the duration and amplitude of pulses were varied, to find the optimal electric field parameters that caused effective reversible electroporation. Among the conditions tested for the bipolar pulses, we determined that a fixed, short-duration pulse of 100 μs avoided bubble gas formation caused by electrolysis of water. In addition, we observed that, due to the small distance between cells and electrodes, the cell monolayer detached when bubbles appeared, caused by both pH changes and mechanical stress of the bubbles themselves. In consequence, in the following experiments, we varied the amplitude of pulses at this fixed duration.

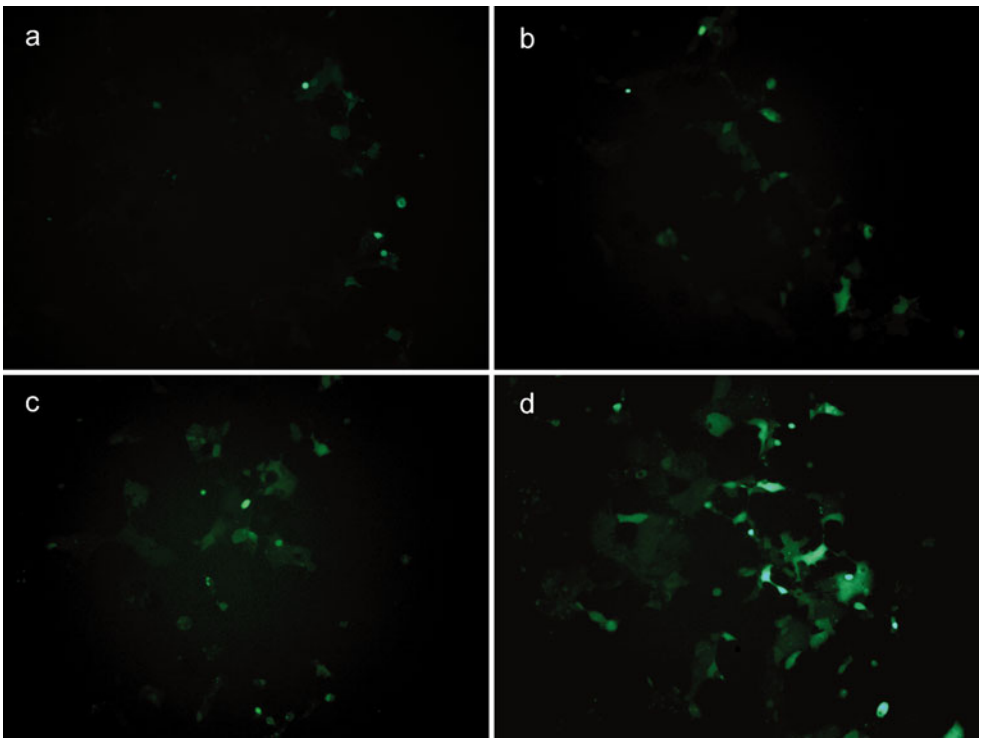

Fig. 5 *Micrograph* of HEK 293 cells after electroporation. Cells were electroporated in the presence of FD20S at different voltages: **a** 1.2 kV/cm, **b** 1.6 kV/cm, **c** 2 kV/cm and **d** 2.2 kV/cm. After cell electroporation and recovery, as described in "Materials and Methods" section, *images* of cell monolayers were taken at ×10 magnification. A representative *image* is shown

In Fig. 4, we show an electric field-dependent fluorescent label of C2C12 myoblasts. Very few fluorescent cells were observed after application of electric fields of 1.2 kV/cm (Fig. 4a). Data also reveal that the permeabilization yield increased with increasing electric field amplitude and reached a maximum when the electric field at the electrode surface was 2.2 kV/cm. Figure 4e shows the quantification of the results as a percentage of fluorescent cells calculated with respect to the total number of cells 2 h after application of the treatment. Thus, these results indicate uptake of FD20S into adhered C2C12 electroporated cells, with up to 50 % efficiency for the best case. C2C12 is a hard-to-transfect cell line with DNA plasmids and usually resistant to chemical methods. These results indicate the potential utility of electroporation as a feasible option when other methods are not suitable.

In Fig. 5 the effect of treatment of cell line HEK 293 with four different electric field amplitudes, 1.2, 1.6, 2 and 2.2 kV/cm, is shown. The micrographs also show, as expected, an increase in the number of fluorescent cells as a function of electric field intensity. On the other hand, in electroporated HEK 293 cells (see Fig. 5c, d) we observed giant cells, which suggests that cell fusion took place with the highest electric fields applied. As also known to those skilled in the field, the application of high electric field pulses can induce fusion of a wide variety of cells under certain conditions. One of the main conditions to achieve cell electrofusion is the establishment of contact between cell membranes. In our case, adherence of cells to the culture plate facilitated cell contact for fusion. Other methods classically forced cell–cell contact by dielectrophoresis, chemicals or centrifugation. The observation of cell fusion in HEK 293 cells but not in C2C12 cells may be due to the fact that the extent of cell electrofusion in vitro and in vivo is cell line-dependent and involves cell type-specific membrane properties and/or secretion of proteases (Salomskaite-Davalgiene et al. 2009). In contrast, in our study conditions for electropermeabilization of both adherent cell lines were very similar. Likewise, relatively little difference in electropermeabilization of plated CHO and B16F1 cells was reported, whereas significant differences were observed between the two cell lines in a suspension (Marjanovič et al. 2010).

In C2C12 or HEK 293 cells, we observed no alteration of the characteristics of the cell monolayer in the course of 24 h after positioning of electrodes in control cells (data not shown), indicating that the device does not cause a major mechanical stress or toxicity that affects cell viability.

Our observations reinforce the principle of minimal invasiveness of the device. An advantage of the system is its in situ application to multiwell plates where cells had

been initially grown, avoiding additional stress to the cell culture by trypsinization or other posttreatment steps.

Conclusions

In this study we tested a new electrode assembly design, based on the principle of in situ electroporation of adherent cell monolayers growing in standard multiwell plates. Using microelectrodes with small distances between adjacent lines, we achieved effective electroporation making use of low voltages. The use of microseparations between the electrodes and the bottom surface of the growing plates provided a significant advantage, avoiding contact with the cell monolayer, thus causing minimal stress to the cell culture. Furthermore, in situ treatment of cells simplified the process and saved several harvesting and processing steps, usually necessary in traditional systems, which may have contributed to improving the yield of the process.

This device was successful in introducing FD20S into two different cell lines with minimal invasiveness of the operation. The success in the electroporation of C2C12 cells, usually resistant to chemical gene transfer methods, suggests it may be valuable to deliver other macromolecules such as drugs, DNA or antibodies. Additionally, as a collateral effect, we observed electrofusion in HEK 293 cells, thus making this device also useful to induce cell fusion.

When compared to the available commercial electroporation equipment, this device has the advantages of simpler cell culturing and preparation processes because of the use of standard culturing plates. Additionally, the cheap technology used in the fabrication of the electrodes and the low voltages needed implies a significant reduction in costs both of the electrodes and of the pulse generator. Once the initial concept has been demonstrated to be feasible, future work will deal with the introduction of active molecules such as DNA plasmids, siRNAs and proteins, and several different cell lines will be tested.

Acknowledgments This study was supported by project VALTEC09-1-0061 from the Generalitat de Catalunya, ACC1Ó. We thank Anna Orozco and Alfonso Mendez for unconditional assistance.

References

Ambati J et al (2000) Diffusion of high molecular weight compounds through sclera. Investig Ophthalmol Vis Sci 41:1181–1185

Bettega D, Calzolari P, Doglia SM, Dulio B, Tallone L, Villa AM (1998) Cell thickness measurements by confocal fluorescence microscopy on C3H10T1/2 and V79 cells. Int J Radiat Biol 74(3):397–403

Braeken D, Huys R et al (2010) Single-cell stimulation and electroporation using a novel 0.18 μm CMOS chip with subcellular-sized electrodes. Engineering in Medicine and Biology Society (EMBC), 2010 annual international conference of the IEEE, Buenos Aires, Argentina, 31 August–4 September

Chang DC, Chassy BM, Saunders JA, Sowers AE (eds) (1992) Guide to electroporation and electrofusion. Academic Press, New York, pp 201–207

De Vuyst E et al (2008) In situ bipolar electroporation for localized cell loading with reporter dyes and investigating gap junctional coupling. Biophys J 94(2):469–479

Deora AA, Diaz F, Schreiner R, Rodriguez-Boulan E (2007) Efficient electroporation of DNA and protein into confluent and differentiated epithelial cells in culture. Traffic 8:1304–1312

Dev SB, Rabussay DP et al (2000) Medical applications of electroporation. IEEE Trans Plasma Sci 28(1):206–223

Durante M et al (1993) Thickness measurements on living cell monolayers by nuclear methods. Nucl Instrum Methods Phys Res B 73(4):543–549

Ephrem Tekle RDA, Bonn Chock P (1991) Electroporation by using bipolar oscillating electric field: an improved method for DNA transfection of NIH 3T3 cells. Proc Natl Acad Sci USA 88: 4230–4234

Geng T, Zhan Y et al (2010) Flow-through electroporation based on constant voltage for large-volume transfection of cells. J Control Release 144(1):91–100

Huang H, Wei Z et al (2011) An efficient and high-throughput electroporation microchip applicable for siRNA delivery. Lab Chip 11(1):163–172

Hui SW (1995) Effects of pulse length and strength on electroporation efficiency. Anim Cell Electroporation Electrofusion Protoc 48: 29–40

Lambert H, Pankov R, Gauthier J, Hancock R (1990) Electroporation-mediated uptake of proteins into mammalian cells. Biochem Cell Biol 68:729–734

Lebar AM, Troiano GC et al (2002) Inter-pulse interval between rectangular voltage pulses affects electroporation threshold of artificial lipid bilayers. IEEE Trans Nanobiosci 1(3):116–120

Lin Y-C, Li M et al (2003) A microchip for electroporation of primary endothelial cells. Sens Actuators A 108(1–3):12–19

Lisen W, Flanagan L, Lee AP (2007) Side-wall vertical electrodes for lateral field microfluidic applications. J Microelectromech Syst 16(2):454–461

Marjanovič I, Haberl S, Miklavčič D, Kandušer M, Pavlin M (2010) Analysis and comparison of electrical pulse parameters for gene electrotransfer of two different cell lines. J Membr Biol 236: 97–105

Neumann E, Schaefer-Ridder M et al (1982) Gene transfer into mouse lyoma cells by electroporation in high electric fields. EMBO J 1(7):841–845

Olbrich M, Rebollar E et al (2008) Electroporation chip for adherent cells on photochemically modified polymer surfaces. Appl Phys Lett 92(1):013901–013903

Raptis L, Firth KL (2008) Electrode assemblies used for electroporation of cultured cells. Methods Mol Biol 423:61–76

Rols M-P, Teissié J (1998) Electropermeabilization of mammalian cells to macromolecules: control by pulse duration. Biophys J 75:1415–1423

Salomskaite-Davalgiene S et al (2009) Extent of cell electrofusion in vitro and in vivo is cell line dependent. Anticancer Res 29(8): 3125–3130

Stopper H, Jones H, Zimmermann U (1987) Large scale transfection of mouse L-cells by electropermeabilization. Biochim Biophys Acta 900:38–44

Teissie J, Golzio M et al (2005) Mechanisms of cell membrane electropermeabilization: a minireview of our present (lack of ?) knowledge. Biochim Biophys Acta 1724(3):270–280

Wang M, Orwar O et al (2010) Single-cell electroporation. Anal Bioanal Chem 397(8):3235–3248

Weaver JC, Chizmadzhev YA (1996) Theory of electroporation: a review. Bioelectrochem Bioenerg 41(2):135–160

Wegener J, Keese CR, Giaever I (2002) Recovery of adherent cells after in situ electroporation monitored electrically. Biotechniques 33:348–357

Wolf H, Rols MP et al (1994) Control by pulse parameters of electric field-mediated gene transfer in mammalian cells. Biophys J 66(2, pt 1):524–531

Zheng Q, Chang DC (1991) High-efficiency gene transfection by in situ electroporation of cultured cells. Biochim Biophys Acta 1088:104–110

Ziv R et al (2009) Micro-electroporation of mesenchymal stem cells with alternating electrical current pulses. Biomed Microdevices 11(1):95–101

J Membrane Biol (2012) 245:625–632
DOI 10.1007/s00232-012-9476-9

System for Measuring Planar Lipid Bilayer Properties

Andraž Polak · Boštjan Mulej · Peter Kramar

Received: 20 December 2011 / Accepted: 30 June 2012 / Published online: 19 July 2012

Abstract We present a system for measuring planar lipid bilayer properties. The system is composed of a control unit, an output stage, an LCR meter, pumps for filling reservoirs, a bath with temperature regulation and a measurement chamber with four electrodes. The planar lipid bilayer is automatically formed using a folding method on apertures of different sizes. The automatization is assured by two syringes, which are clamped in actuators. Actuators are driven and controlled by a control unit via RS-232 communication. The temperature of the planar lipid bilayer can be regulated between 15 and 55 °C. The regulation is assured by insertion of the measurement chamber into the temperature-regulated bath. Different shapes of voltage- or current-clamp signals can be applied to the planar lipid bilayer. By measuring the response of the planar lipid bilayer to the applied signal, the capacitance and breakdown voltage of the planar lipid bilayer can be determined. The cutoff frequencies of the system output stage for voltage- and current-clamp methods are 11 and 17 kHz, respectively.

Keywords Electroporation · Capacitance · Breakdown voltage · Temperature regulation

Introduction

Electroporation is a phenomenon that describes the occurrence of structural changes in biological membranes as a consequence of applied electric pulses (Chen et al. 2006; Kotnik et al. 1997; Weaver and Chizmadzhev 1996). These structural changes are most often named "pores" and present an increase in cell membrane permeability. Electroporation is nowadays used in different fields like biology, medicine and biotechnology. Electroporation is divided into two different fields: irreversible electroporation and reversible electroporation. In irreversible electroporation, the cell membrane does not reseal pores after applied voltage and the cell dies. Irreversible electroporation is used in food production and preservation (Golberg et al. 2010), water cleaning (Vernhes et al. 2002) and tissue ablation (Davalos et al. 2005; Maor et al. 2009). In reversible electroporation, the cell membrane pores are resealed after application of electric pulses. It can be used to introduce substances into the cell. The best-known applications of reversible electroporation are electrochemotherapy (Sersa et al. 2008), transdermal drug delivery (Denet et al. 2004; Prausnitz 1999), gene therapy (Daud et al. 2008), cell fusion (Mekid and Mir 2000; Ogura et al. 1994) and insertion of proteins into membranes (Ouagari et al. 1995; Teissié 1998). The principles of pore formation are not yet fully elucidated. Recently, studies based on molecular dynamics proved that pores are formed in a lipid bilayer (Tieleman et al. 2003). When a lipid bilayer is exposed to an electric field, water wires are formed across the membrane. Then, the water wires expand into the water-filled pores, which are stabilized by reorganization of lipid molecules in the lipid bilayer (Levine and Vernier 2010). It is believed that the general picture of electroporation is the same for the planar lipid bilayer and biological cell membrane (Tarek 2005). Therefore, the lipid bilayer is considered the most important part of the cell membrane for studying pore formation.

Synthetic liposomes and vesicles are the simplest model of the biological cell membrane. They mimic the geometry of the biological cell membrane, but they do not have inner

A. Polak (✉) · B. Mulej · P. Kramar
Faculty of Electrical Engineering, University of Ljubljana, Tržaška 25, 1000 Ljubljana, Slovenia
e-mail: andraz.polak@fe.uni-lj.si

P. Kramar
e-mail: peter.kramar@fe.uni-lj.si

structures (Tekle et al. 2001). In comparison to synthetic liposomes and vesicles, planar lipid bilayers can have trapped solvent between the two bilayer leaflets. These can lead to differences in measured electrical properties and influences on pore formation in the lipid bilayer (White 1974, 1978). The planar lipid bilayer formed between two liquid solutions mimics a small fraction of the cell membrane, and it is accessible from both sides; therefore, the experiments are simpler than experiments on synthetic liposomes and vesicles (Benz et al. 1975; Huang et al. 1964; Mueller et al. 1963; Ottova and Tien 2002). Moreover, due to similar geometry usually modeled in molecular dynamic simulations, the results of both research methods can be combined and compared. Electroporation on small vesicles can also be performed using the molecular dynamic simulation.

Through the years, many planar lipid bilayer formation techniques between two liquid solutions have been developed: the tip-dip method (Coronado and Latorre 1983), the double-well chip method (Funakoshi et al. 2006), the cross-channel chip method (Funakoshi et al. 2006), the painting method (Mueller et al. 1963) and the folding method (Montal and Mueller 1972). The folding method is faster than other methods and can be easily automated. In the folding method, the lipid solution is spread on the liquid solution surface at each reservoir. In a few minutes, monolayers on the liquid solution surfaces are formed. After monolayer formation, the liquid solution levels in both reservoirs are raised. When the liquid solution surfaces cross the aperture between the reservoirs, the planar lipid bilayer is formed. This method is simple and quick and formation can be automated by computer-controlled syringe pumps.

From the electrical point of view, the planar lipid bilayer is considered a capacitor and resistor in parallel configuration. The capacitance and resistance are the most frequently measured electrical properties of a planar lipid bilayer. An additional electrical property of a planar lipid bilayer is breakdown voltage. It is one of the most important properties of a lipid bilayer when electroporation is under consideration. The capacitance is also a reference that the planar lipid bilayer is formed. If the capacitance of the planar lipid bilayer is lower than the expected value, then either multiple layers are formed or the planar lipid bilayer is not formed at all. Electrical properties of planar lipid bilayers are usually measured by two types of methods: voltage clamp and current clamp (Kramar et al. 2010). In the voltage-clamp method, a voltage signal is applied to the planar lipid bilayer and current, which flows through planar lipid bilayer, is measured. In the current-clamp method, a current signal is applied to the planar lipid bilayer and the voltage across the planar lipid bilayer is measured. The two methods use different-shaped signals like pulses, linear rising signals, sinusoids or triangular signals. Planar lipid bilayer capacitance, for example, is mostly measured using a discharge method (Kramar et al. 2010), a capacitance to period conversion method (Kalinowski and Figaszewski 1995) or an LCR meter (Punnamaraju and Steckl 2010).

Lipid bilayers can exist in a gel or liquid phase. The phase is defined by the mobility of the lipid molecules, which changes with temperature. The mobility of lipid molecules is higher in the liquid phase than in the gel phase; therefore, a lipid bilayer is in liquid phase at higher temperatures and in gel phase at lower temperatures. At a given temperature, a lipid bilayer can exist in either a liquid or a gel phase. With the phase transition also the thickness of the lipid bilayer is changed (Katsaras and Gutberlet 2010; Luckey 2008; Tokumasu et al. 2002). Because the capacitance of the planar lipid bilayer is inversely proportional to its thickness, also changes of the planar lipid bilayer capacitance have been observed (Antonov et al. 2003; Boheim et al. 1980). Moreover, Basu et al. (2001) showed that the conductance of the planar lipid bilayer is temperature-dependent.

To study the phenomenon of electroporation at various temperatures and provoked by various electrical signals, we developed a new system for measuring the properties of planar lipid bilayers. In the system, the folding method for forming planar lipid bilayers is implemented. The folding method is automated by two syringes, which raise and lower liquid solution levels in the measurement chamber. The temperature in the measurement chamber can be maintained at a constant value, which can be changed during the experiment. The system can be used to determine the planar lipid bilayer capacitance and breakdown voltage. The breakdown voltage can be measured by the voltage- or current-clamp method using a broad spectrum of signal shapes.

System Architecture

The system is composed of a control unit, an output stage, an LCR meter, pumps for filling reservoirs, a bath with temperature regulation and a measurement chamber with four electrodes. The control unit consists of an embedded PC, a control circuit, a digital to analog converter and an analog to digital converter (Figs. 1, 2).

Control Unit

The control unit consists of an embedded PC, a control circuit, an analog to digital converter and a digital to analog converter. This part of the system controls all switches, actuators and generators and acquires signals from sensors.

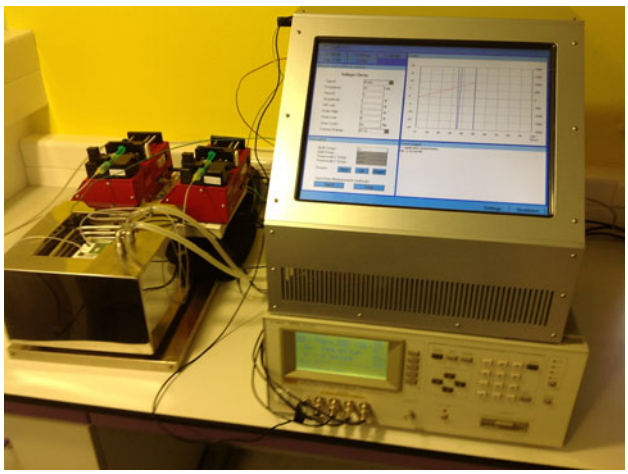

Fig. 1 The photography of the system for measuring the properties of planar lipid bilayers. On the left are two pumps for filling reservoirs and the bath with temperature regulation. The measurement chamber with four electrodes is inserted into the bath. The cables from the electrodes lead to the control unit, which is on the right. Below the control unit is the LCR meter

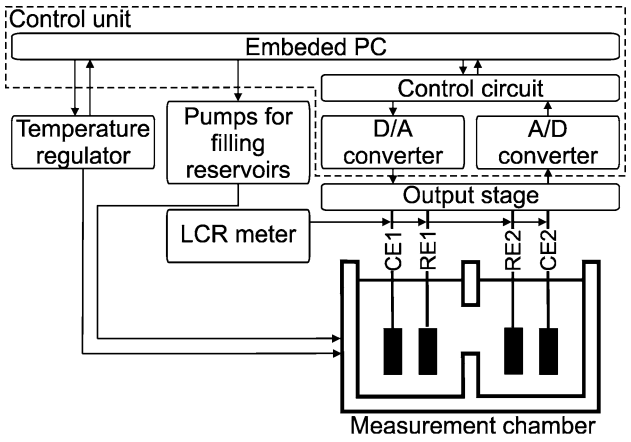

Fig. 2 The system for measuring the properties of planar lipid bilayer consists of the control unit, the LCR meter, the output stage, the pumps for filling reservoirs, the measurement chamber with four electrodes and the bath with temperature regulation. The control unit consists of the embedded PC, the control circuit, the digital to analog converter and the analog to digital converter

An embedded PC (Windows CE) is used as an interface between the human and the device. It has a graphical user interface, which allows setting of measurement method parameters and temperature. It also displays measured data and temperatures in both reservoirs and the bath. All acquired data are saved on a disc and can be accessible through Ethernet. By the press of a button, we can form planar lipid bilayers and start the measurement with the selected method.

The converters are a bridge between the analog and digital parts of the system. The digital to analog converter converts a digital signal from the control circuit to an analog signal, which is used by the output stage. The conversion is made at a frequency of 48 MHz with 14-bit resolution. It generates a bipolar signal between -2 and 2 V. These properties show that the generated signal is smooth and can contain high frequencies. The analog to digital converter converts an analog signal from the output stage to a digital signal, which is acquired by the control circuit. The conversion is made at a frequency of 150 kHz with 12-bit resolution. The analog voltage input can vary between -2 and 2 V. Both analog signals range between -2 and 2 V because the breakdown voltages of already measured planar lipid bilayers from the literature are in this range.

LCR Meter

The capacitance of a planar lipid bilayer is measured by an Agilent (Santa Clara, CA, USA) LCR meter 4284A. The LCR meter is connected directly to electrodes in the measurement chamber. The Agilent LCR meter 4284A can measure capacitance and resistance in different formations (parallel and serial). The LCR meter applies the sinus signal to the load and measures the response. We can set the parameters of the agitating sinus signal like frequency from 20 Hz to 1 MHz and the effective value from 0.005 to 2 V.

Output Stage

The output stage is a circuit, which combines the voltage- and current-clamp measuring circuits. The output stage has an input and an output that are connected to converters and four connectors for electrodes. Two of them are current electrodes (CE1 and CE2) and other two are reference electrodes (RE1 and RE2).

The voltage- and current-clamp methods that are implemented in our system are designed similarly. Both circuits have a current source and differential amplifier. The voltage-clamp method has closed-loop regulation, and the current-clamp method has open-loop regulation. The idea for the circuits was found in the literature (Kalinowski and Figaszewski 1995); our system has an additional resistor connected to the current electrodes for current source stabilization. The current source in our system generates current, which flows through an added resistor and planar lipid bilayer.

In the voltage-clamp method (Fig. 3a), the voltage is applied to the planar lipid bilayer and the current through the planar lipid bilayer and parallel resistor is measured. The differential amplifier measures the transmembrane voltage. The single-ended output of the differential amplifier is compared to the input voltage. The difference between the signals drives the current source, which forces

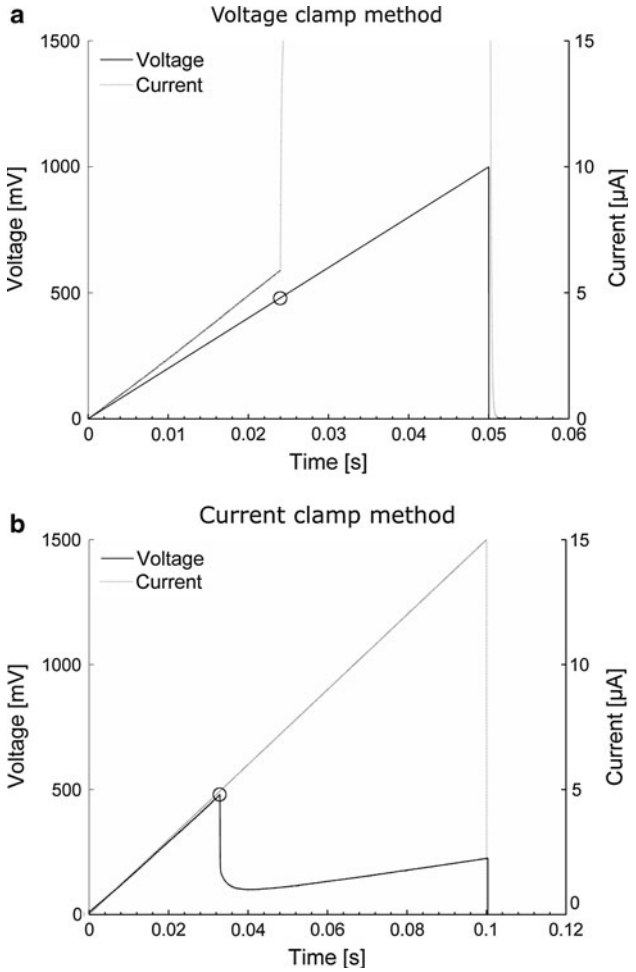

Fig. 3 The scheme of the circuit for the voltage-clamp method (**a**) and the scheme of the circuit for the current-clamp method (**b**). Both circuits consist of a differential amplifier and current source. The difference is only in the realization of the feedback loop. In the voltage-clamp method, the voltage is applied to the planar lipid bilayer and the current, which flows through the planar lipid bilayer and the resistor, is measured. In the current-clamp method, the current through the planar lipid bilayer and the resistor R_{I2} is forced and the voltage difference on the planar lipid bilayer is measured

current through the planar lipid membrane and resistor R_{I2}. The voltage at the output of the operational amplifier, which drives the current source, is proportional to the current which is forced through the planar lipid bilayer and resistor R_{I2}. The generated current is equal to the quotient between the driving voltage and resistor R_{I1}. The resistors R_{I1} and R_{I2} have a value of 100 kΩ. Capacitors C_{I1} and C_{I2} and resistor R_{I2} are added to the circuit to stabilize the current source and prevent oscillations. Capacitors C_{I1} and C_{I2} have a capacity of 33 and 100 pF, respectively.

The current-clamp method (Fig. 3b) is used to observe the transmembrane voltage response caused by forced current. The input voltage drives a current source, which forces current through the current electrodes and resistor R_{I2}. The voltage response on the planar lipid bilayer is measured by reference electrodes.

In both methods, different shapes of signals can be used, e.g., pulse, step change, linear rising signal or arbitrarily shaped signal. In the voltage-clamp method the output voltage range is between −1.5 and 1.5 V, with accuracy of 1 mV; the measured current ranges from −15 to 15 μA, with accuracy of 0.05 μA. In the current-clamp method, the output current range is between −15 and 15 μA, with accuracy 0.02 μA; the measured voltage ranges from −1.5 to 1.5 V, with accuracy 4 mV.

Pumps for Filling Reservoirs

The measurement chamber has two channels for filling reservoirs. Into each channel, a pipeline is inserted. Pipelines connect the reservoirs with the syringe filled with liquid solution. The syringes are clamped into actuators (Aladin-1000; World Precision Instruments, Sarasota, FL, USA). The Aladin-1000 is a syringe pump that can be driven via RS-232 communication. The syringe pumps are driven by an embedded PC, where we can set the volume which will be pumped into each reservoir. Each pump can be driven separately; therefore, we can avoid errors of liquid solution levels caused by asymmetry of the reservoirs. On the other hand, if asymmetric filing of the reservoirs is needed, the system allows setting this condition. Our system enables us to form planar lipid bilayers by the folding method by one press of a button.

Measurement Chamber

The measurement chamber is made of Teflon because it is highly resistant to chemicals and has a hydrophobic surface. The hydrophobic surface favors contact with lipid hydrophobic tails (Montal and Mueller 1972); therefore, the boundaries of the planar lipid bilayer can be linked to the edge of the aperture on the measurement chamber. The measurement chamber has two cubed reservoirs, which are connected with a round aperture. Each reservoir is made of a separate piece of Teflon. The round hole with a diameter of 3 mm connects the two reservoirs. Between the two reservoirs is a 25.40 μm-thin Teflon sheet with a round aperture of different sizes. The aperture is placed in the center of the connecting hole between the two reservoirs. The measurement chamber has two channels to each reservoir (Fig. 4a). In one channel the temperature probe is inserted, and in the other channel the pipe for filling the reservoir is inserted. The pipes are connected to the pumps, which fill or empty reservoirs.

Four electrodes made from Ag–AgCl (E255; IVM, Healdsburg, CA, USA) are inserted into the measurement chamber as shown in Fig. 4b. Two are current electrodes

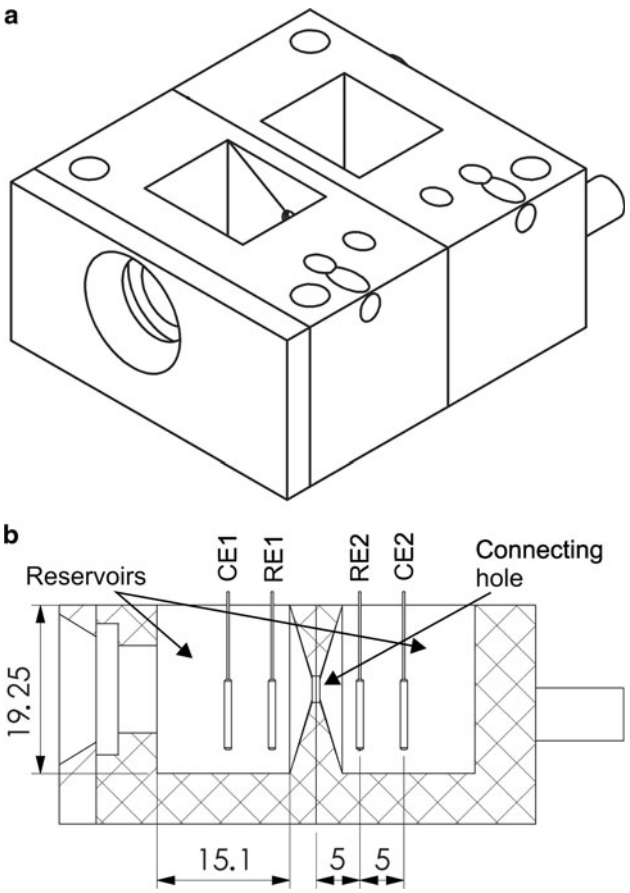

Fig. 4 The measurement chamber for formation of the planar lipid bilayer by the folding method. Perspective view reveals the construction of the measurement chamber (**a**). The Teflon sheet with aperture is inserted between the reservoirs. Lateral cut of the measurement chamber (**b**) reveals details and dimensions of the measurement chamber. *CE1*, *RE1*, *RE2* and *CE2* are Ag–AgCl electrodes. Chamber dimensions and electrode positions are in millimeters. The dimension of the reservoir perpendicular to the sketch is 17.8 mm. The hole, which connects the reservoirs, has a diameter of 3 mm

(CE1 and CE2), and the other two are reference electrodes (RE1 and RE2).

Temperature Regulation

The temperature of a planar lipid bilayer is ensured by a temperature-regulated bath. The bath is constructed of stainless steel. The inside dimensions of the bath are 150 × 150 × 100 mm. The bath is surrounded with 40-mm-thick insulation, and the bath cover has 20 mm of insulation. The coil, which is inserted into the bath, is used to heat or cool the medium and air in the bath. Through the coil flows medium with precisely regulated temperature. Regulation of the medium temperature is made by a Solid State (Wappingers Falls, NY, USA) ThermoCube 300. This

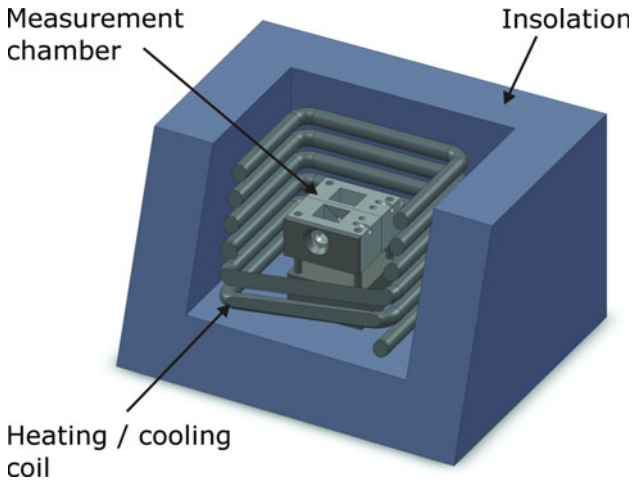

Fig. 5 The temperature-regulated bath with the measurement chamber. The bath is constructed of stainless steel and insolation. The heating coil and the measurement chamber are inserted into the bath

device can regulate medium temperature between 5 and 65 °C. The liquid solution that is in contact with the planar lipid bilayer can, however, achieve a temperature of 15–55 °C, which can be measured with an accuracy of 0.5 °C.

The measurement chamber is inserted in the temperature-regulated bath (Fig. 5). The temperature of the planar lipid bilayer is measured by two K-type thermocouple probes. They are inserted as close as possible to the planar lipid bilayer; therefore, the probes are inserted into reservoirs through the channels. One additional thermocouple probe is inserted into the bath. On the user interface, we set the temperature of the coil and measure the temperatures in the bath and both reservoirs.

System Evaluation

The system for measuring the properties of a planar lipid bilayer was evaluated using the frequency characteristic of the output stage, comparison of the measurement chambers with two sizes of the aperture and comparison of the voltage- and current-clamp measurement methods.

Chemicals

Lipids were prepared from 60 % lecithin (Fluka Analytical, Seelze, Germany), which was dissolved in a solution of hexane and ethanol at a ratio of 9:1. The mixture of hexadecane and pentane at a ratio of 3:7 was used for torus formation. The liquid solution consisted of 0.1 M KCl and 0.01 M HEPES in the same proportion. NaOH was added to obtain pH 7.4.

Methods

To evaluate the output stage, the electrode outputs, which lead into the same reservoir, were connected together (Fig. 4); the CE1 and RE1 outputs were connected together and the CE2 and RE2 outputs were connected together. On the input of the output stage, we applied the sinus signal with amplitude 1 V and frequencies from 1 Hz to 18 kHz generated by the Function/Arbitrary Waveform Generator 33250A. The input and output signals of the output stage were measured by a Tektronix (Beaverton, OR, USA) MSO4104 oscilloscope. We calculated gain and phase between output and input signals. Acquired data were analyzed using MATLAB software (Mathworks, Natick, MA, USA).

The parallel capacitance of the measurement chamber with and without formed lecithin planar lipid bilayers on two apertures with diameters of 126 and 197 μm was measured by the Agilent LCR meter 4284A. Measurements were done at 50 mV effective voltage, 1 kHz frequency and 25 °C temperature. The lecithin planar lipid bilayer is in liquid phase due to its mixture of unsaturated lipids, which have phase transition at low temperatures. At each aperture diameter, we performed 100 measurements. The difference between capacitances when the lecithin planar lipid bilayer was formed and when it was not present is the capacitance of the planar lipid bilayer. This value of the capacitance was divided by the area of the aperture. The result is specific capacitance of the lecithin planar lipid bilayer. At this point, it is not considered that the planar lipid bilayer has the Plateau-Gibbs border; therefore, the specific capacitance can be loaded with an error.

Voltage- and current-clamp methods to measure planar lipid bilayer breakdown voltage were tested on lecithin planar lipid bilayers formed on an aperture with a diameter of 126 μm at temperature 25 °C. During this test, we measured also the capacitance of each planar lipid bilayer to prove its correct formation. In the voltage-clamp method, we used linear rising voltage with slope 20 V/s. In the current-clamp method, we used a linear rising current with slope 150 μA/s. In each method, we performed three measurements. The mean values of breakdown voltage were calculated. Finally, the breakdown voltages obtained by the two methods were compared.

Results

Evaluation of the output stage has shown that, in the voltage-clamp and current-clamp methods, gain and phase between the output and input signals are close to 0 dB and 0° for frequencies from 1 Hz to 1 kHz. At higher frequencies, the gain and phase start to increase in the voltage-clamp method and decrease in the current-clamp method. This is expected because these two methods have inverted inputs and outputs. The voltage-clamp circuit reaches 3 dB gain at 11.0 kHz. The current-clamp circuit has −3 dB gain at 17 kHz. The phase of the circuits never reaches values of −45° or 45°. The frequency when the gain reaches −3 dB is called a "cutoff frequency." In our system, the voltage-clamp method has a lower cutoff frequency. The frequency characteristics for voltage and current clamp are shown in Fig. 6.

The lecithin planar lipid bilayer-specific capacitances were measured at 0.386 ± 0.027 and 0.381 ± 0.021 μF/cm^2 for apertures with diameters of 126 and 197 μm, respectively. The values are similar to the data reported in the literature (Naumowicz et al. 2003). The results also show that aperture size does not affect the specific capacitance.

The breakdown voltage was measured by applying linearly rising current or linearly rising voltage on the planar lipid bilayer. In the voltage-clamp method (Fig. 7a), planar lipid bilayer breakdown is detected by a dramatic increase of the current, while in the current-clamp method (Fig. 7b), planar lipid bilayer breakdown is detected by a sudden voltage drop. The breakdown voltage detected using the voltage-clamp method was 480.0 ± 5.0 mV. The breakdown voltage measured using the current-clamp method was 480.50 ± 6.5 mV. The specific capacitances of all formed planar lipid bilayers were 0.38 ± 0.01 μF/cm^2. The predominant species in lecithin is 1-palmitoyl-2-oleoyl-*sn*-glycero-3-phosphocholine (POPC). It was determined that the breakdown voltage of the POPC planar lipid membrane is 400 ± 6 mV in 100 mM KCl surrounding medium and use of voltage pulses (Meier et al. 2000). Using a linear rising signal to determine breakdown voltage can avoid multiple exposures to an applied signal. Kramar et al.

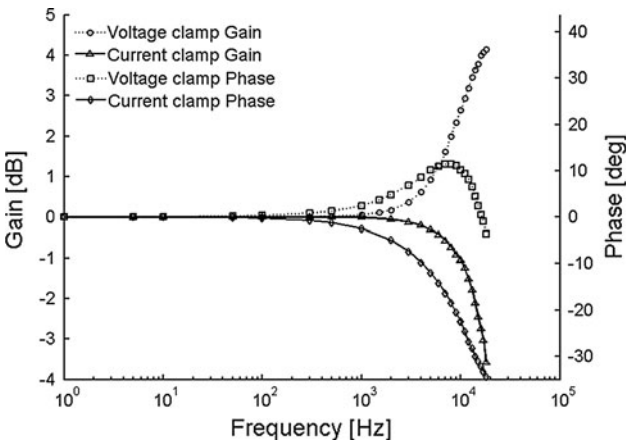

Fig. 6 Frequency characteristics for the voltage- and current-clamp circuits. The gain and phase for both circuits are shown for frequencies from 1 Hz to 18 kHz

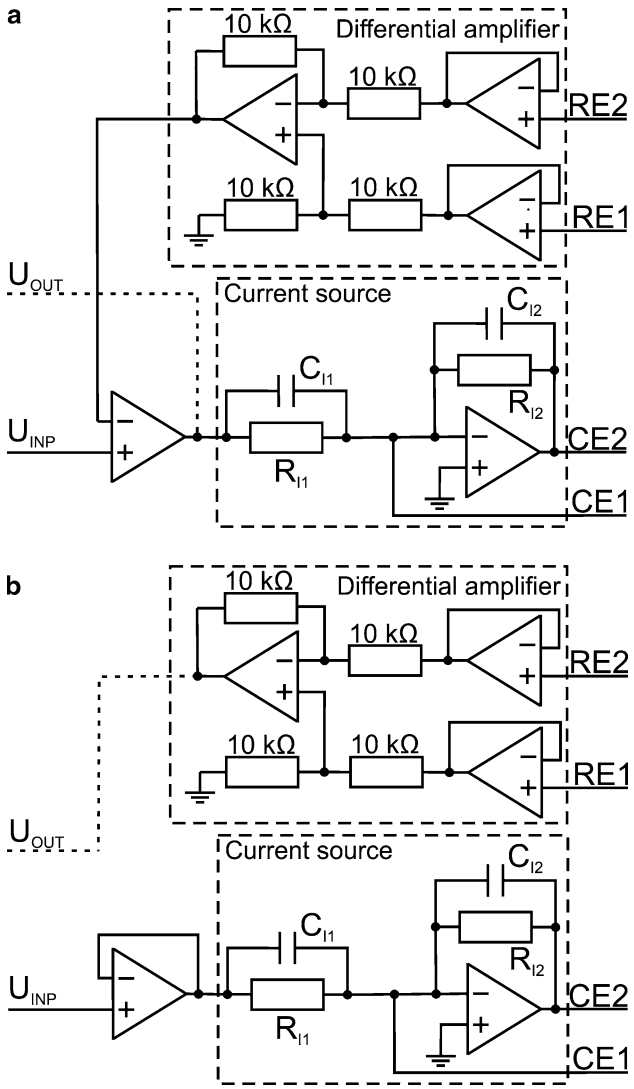

Fig. 7 The voltage and current signals acquired from the voltage- (**a**) and current- (**b**) clamp methods. In the voltage-clamp method, the rising voltage signal is applied. The current response is measured. At the beginning, the current rises proportionally to the applied voltage. When the current starts to increase more than before and goes out of the measured range, the planar lipid bilayer is broken. The value of voltage when this happens is voltage breakdown. In the current-clamp method the rising current signal is applied. The voltage response is measured, and it is proportional to the applied current. The planar lipid bilayer is broken when the measured voltage drops. The voltage value before the planar lipid bilayer is broken is breakdown voltage

(2007) found that breakdown voltage increases with increasing slope of the linear rising voltage signal. These measurements were performed using linear rising voltage signals with slopes from 4.8 to 48 kV/s. The minimum breakdown voltage of POPC in this study was 490 mV. In our experiment, we used a linear rising signal with slope of 20 V/s, due to expected lower values of the breakdown voltages. The measured breakdown voltages of the lecithin planar lipid bilayer using our new system are in the same range as the breakdown voltages of planar lipid bilayers using the other systems.

Discussion

We developed a system for formation of planar lipid bilayers and measuring planar lipid bilayer properties. The system allows the formation of planar lipid bilayers by the folding method. The electrical properties of a planar lipid bilayer which can be measured by this system are capacitance and breakdown voltage. Breakdown voltage can be determined by the voltage- and current-clamp methods. Using the voltage-clamp method we can generate voltage signals with 1 mV accuracy, while in the current-clamp method the system is able to measure voltage with 4 mV accuracy. The voltage and current signals can be generated as pulse, step change, linear rising signal or arbitrarily shaped signals. The cutoff frequencies of the system output stage are 11 and 17 kHz for the voltage-clamp and current-clamp methods, respectively. These two values show the dynamics of our system with open connectors. The voltage- and current-clamp methods were compared by measuring the breakdown voltage of lecithin planar lipid bilayers. In both cases, a linear raising signal was used to determine the breakdown voltage (Kramar et al. 2007). The results show that the two methods give similar breakdown voltages in similar conditions.

Planar lipid bilayers are automatically formed by the folding method. The automation is implemented by precise regulation of the liquid level in each reservoir. In this way, we are able to have the same hydrostatic pressure on both sides of the planar lipid bilayer, and each planar lipid bilayer is exposed to the same pressure conditions. This automation allows reproducible planar lipid bilayer formation and measurements at constant conditions. The measurement of planar lipid bilayer capacitance was tested on lecithin planar lipid bilayers at 25 °C. They were formed on apertures with diameters of 126 and 197 μm. The specific capacitances were 0.386 ± 0.027 and 0.381 ± 0.021 μF/cm^2, respectively. These values are similar to the literature data (Naumowicz et al. 2003). The results show that aperture size has no effect on measured specific capacitance.

The measurement chamber in our system is designed to form planar lipid bilayers by the folding method. The size of the aperture between the reservoirs, where the planar lipid bilayer is formed, is defined by the size of the aperture in the thin Teflon sheet which is inserted between the two parts of the chamber before experiments. Therefore, the size of the aperture can be easily changed by changing the Teflon sheet. The planar lipid bilayer can be formed on the aperture automatically. Moreover, we are able to have

the same pressure condition on a planar lipid bilayer at each formation by precisely regulating the liquid level in each reservoir.

Preliminary results confirm that the measuring system allows a broad spectrum of measurements. In particular, the temperature regulation can give new insights into planar lipid bilayer electroporation studies.

Acknowledgments This work was supported by the Slovenian Research Agency. The research was conducted in the scope of the EBAM European Associated Laboratory.

References

Antonov VF, Anosov AA, Norik VP et al (2003) Electrical capacitance of lipid bilayer membranes of hydrogenated egg lecithin at the temperature phase transition. Eur Biophys J 32:55–59

Basu R, De S, Ghosh D, Nandy P (2001) Nonlinear conduction in bilayer lipid membranes—effect of temperature. Phys A 292: 146–152

Benz R, Fröhlich O, Läuger P, Montal M (1975) Electrical capacity of black lipid films and of lipid bilayers made from monolayers. Biochim Biophys Acta 394:323–334

Boheim G, Hanke W, Eibl H (1980) Lipid phase transition in planar bilayer membrane and its effect on carrier- and pore-mediated ion transport. Proc Natl Acad Sci USA 77:3403–3407

Chen C, Smye SW, Robinson MP, Evans JA (2006) Membrane electroporation theories: a review. Med Biol Eng Comput 44:5–14

Coronado R, Latorre R (1983) Phospholipid bilayers made from monolayers on patch-clamp pipettes. Biophys J 43:231–236

Daud AI, DeConti RC, Andrews S et al (2008) Phase I trial of interleukin-12 plasmid electroporation in patients with metastatic melanoma. J Clin Oncol 26:5896–5903

Davalos RV, Mir LM, Rubinsky B (2005) Tissue ablation with irreversible electroporation. Ann Biomed Eng 33:223–231

Denet AR, Vanbever R, Préat V (2004) Skin electroporation for transdermal and topical delivery. Adv Drug Deliv Rev 56: 659–674

Funakoshi K, Suzuki H, Takeuchi S (2006) Lipid bilayer formation by contacting monolayers in a microfluidic device for membrane protein analysis. Anal Chem 78:8169–8174

Golberg A, Fischer J, Rubinsky B (2010) The use of irreversible electroporation in food preservation. In: Rubinsky B (ed) Irreversible electroporation. Springer, Berlin, pp 273–312

Huang C, Wheeldon L, Thompson TE (1964) The properties of lipid bilayer membranes separating two aqueous phases: formation of a membrane of simple composition. J Mol Biol 8:148–160

Kalinowski S, Figaszewski Z (1995) A 4-electrode potentiostat–galvanostat for studies of bilayer lipid membranes. Meas Sci Technol 6:1050–1055

Katsaras J, Gutberlet T (2010) Lipid bilayers: structure and interactions. Springer, Berlin

Kotnik T, Bobanovic F, Miklavcic D (1997) Sensitivity of transmembrane voltage induced by applied electric fields—a theoretical analysis. Bioelectrochem Bioenerg 43:285–291

Kramar P, Miklavcic D, Lebar AM (2007) Determination of the lipid bilayer breakdown voltage by means of linear rising signal. Bioelectrochemistry 70:23–27

Kramar P, Miklavcic D, Kotulska M, Lebar AM (2010) Voltage- and current-clamp methods for determination of planar lipid bilayer properties. Academic Press, San Diego, pp 29–69

Levine ZA, Vernier PT (2010) Life cycle of an electropore: field-dependent and field-independent steps in pore creation and annihilation. J Membr Biol 236:27–36

Luckey M (2008) Membrane structural biology: with biochemical and biophysical foundations. Cambridge University Press, New York

Maor E, Ivorra A, Rubinsky B (2009) Nonthermal irreversible electroporation: novel technology for vascular smooth muscle cell ablation. PLoS One 4:e4757

Meier W, Graff A, Diederich A, Winterhalter M (2000) Stabilization of planar lipid membranes: a stratified layer approach. Phys Chem Chem Phys 2:4559–4562

Mekid H, Mir LM (2000) In vivo cell electrofusion. Biochim Biophys Acta 1524:118–130

Montal M, Mueller P (1972) Formation of bimolecular membranes from lipid monolayers and a study of their electrical properties. Proc Natl Acad Sci USA 69:3561–3566

Mueller P, Rudin DO, Tien HT, Wescott WC (1963) Methods for the formation of single bimolecular lipid membranes in aqueous solution. J Phys Chem 67:534–535

Naumowicz M, Petelska A, Figaszewski Z (2003) Capacitance and resistance of the bilayer lipid membrane formed of phosphatidylcholine and cholesterol. Cell Mol Biol Lett 8:5–8

Ogura A, Matsuda J, Yanagimachi R (1994) Birth of normal young after electrofusion of mouse oocytes with round spermatids. Proc Natl Acad Sci USA 91:7460–7462

Ottova A, Tien H (2002) The 40th anniversary of bilayer lipid membrane research. Bioelectrochemistry 56:171–173

Ouagari KE, Teissié J, Benoist H (1995) Glycophorin A protects K562 cells from natural killer cell attack. J Biol Chem 270: 26970–26975

Prausnitz MR (1999) A practical assessment of transdermal drug delivery by skin electroporation. Adv Drug Deliv Rev 35:61–76

Punnamaraju S, Steckl AJ (2010) Voltage control of droplet interface bilayer lipid membrane dimensions. Langmuir 27:618–626

Sersa G, Miklavcic D, Cemazar M et al (2008) Electrochemotherapy in treatment of tumours. Eur J Surg Oncol 34:232–240

Tarek M (2005) Membrane electroporation: a molecular dynamics simulation. Biophys J 88:4045–4053

Teissié J (1998) Transfer of foreign receptors to living cell surfaces: the bioelectrochemical approach. Bioelectrochem Bioenerg 46:115–120

Tekle E, Astumian RD, Friauf WA, Chock PB (2001) Asymmetric pore distribution and loss of membrane lipid in electroporated DOPC vesicles. Biophys J 81:960–968

Tieleman DP, Leontiadou H, Mark AE, Marrink S-J (2003) Simulation of pore formation in lipid bilayers by mechanical stress and electric fields. J Am Chem Soc 125:6382–6383

Tokumasu F, Jin AJ, Dvorak JA (2002) Lipid membrane phase behaviour elucidated in real time by controlled environment atomic force microscopy. J Electron Microsc (Tokyo) 51:1–9

Vernhes MC, Benichou A, Pernin P et al (2002) Elimination of free-living amoebae in fresh water with pulsed electric fields. Water Res 36:3429–3438

Weaver JC, Chizmadzhev YA (1996) Theory of electroporation: a review. Bioelectrochem Bioenerg 41:135–160

White SH (1974) Temperature-dependent structural changes in planar bilayer membranes: solvent "freeze-out". Biochim Biophys Acta 356:8–16

White SH (1978) Formation of "solvent-free" black lipid bilayer membranes from glyceryl mono oleate dispersed in squalene. Biophys J 23:337–347

J Membrane Biol (2012) 245:633–642
DOI 10.1007/s00232-012-9479-6

2-NBDG, a Fluorescent Analogue of Glucose, as a Marker for Detecting Cell Electropermeabilization In Vitro

Elham Raeisi · Lluis M. Mir

Received: 14 January 2012 / Accepted: 30 June 2012 / Published online: 11 August 2012

Abstract This study investigated whether molecules spontaneously transported inside cells, like glucose derivatives, can also be used as electropermeabilization markers. Uptake of a fluorescent deoxyglucose derivative (2-NBDG) by normal and electropermeabilized cells in culture was analyzed. 2-NBDG was added to DC-3F cell suspensions and cells, exposed or not to eight square-wave electric pulses of 100-μs duration and of appropriate field amplitude at a repetition frequency of 1 Hz or 5 kHz, were incubated at 37 °C. 2-NBDG uptake was temperature-, concentration- and time-dependent in cells submitted or not to the electric pulses. In spite of significant uptake of 2-NBDG mediated by GLUT transporters into nonpermeabilized cells, the electric pulses significantly increased about ten to hundred times the 2-NBDG uptake into the cells. The increase in the field amplitude from 900 to 1,500 V/cm resulted in a progressive increase of 2-NDBG. Our results show that under the conditions of in vivo exposure duration to FDG and the physiological concentration of D-glucose, electric pulses increased 2-NBDG uptake into electropermeabilized cells. Under our experimental conditions, the percentage of permeabilized cells within the population of cells exposed to electric pulses remained at the same level regardless of the pulse frequency used, 1 Hz or 5 kHz. The findings showed that glucose derivatives can also be used to detect electropermeabilized cells exposed to electric pulses.

Keywords 2-NBDG · FDG · PET scan · Electropermeabilization · Flow cytometry · Tumor cell

E. Raeisi
Department of Medical Physics, Faculty of Medical Sciences, Tarbiat Modares University, Tehran, Iran

E. Raeisi · L. M. Mir
Laboratoire de Vectorologie et Thérapeutiques Anticancéreuses, CNRS, UMR 8203, 91405 Orsay Cedex, France

E. Raeisi · L. M. Mir
Laboratoire de Vectorologie et Thérapeutiques Anticancéreuses, Université Paris-Sud, UMR 8203, 91405 Orsay Cedex, France

E. Raeisi
Biomedical Center, European Scientific Institute, Technopole, 74166 Archamps, France

E. Raeisi
Faculty of Science, University of Geneva, Geneva, Switzerland

L. M. Mir (✉)
UMR 8203 CNRS, Institute Gustave Roussy, 114 rue E. Vaillant, 94805 Villejuif cedex, France
e-mail: luismir@igr.fr

Introduction

Cell electropermeabilization or electroporation is a physical method that uses short and intense electric pulses to increase cell membrane permeability (Neumann et al. 1982) and, therefore, increase the uptake of molecules such as DNA, antibodies and oligonucleotides into the cells (Mir 2001).

Electroporation can also facilitate the crossing of the cell membrane and the cellular uptake of drugs, for molecules that are hydrophilic and lack transport systems or for low-permeant molecules that poorly cross the plasma membrane (Orlowski et al. 1988; Sersa et al. 2003; Silve and Mir 2011). Several chemotherapeutic drugs were tested in vitro for potential application in combination with cell electroporation, and an increase of thousands of times was demonstrated for bleomycin and one of several times for cisplatin (Melvik et al. 1986; Orlowski et al. 1988; Sersa et al. 1995; Kambe et al. 1996; Cemazar et al. 1998, 2001;

Gehl et al. 1998; Jaroszeski et al. 2000; Kuriyama et al. 2000; Breton and Mir 2012). Therefore, the selection is limited to those drugs that are hydrophilic and lack transport systems in the membrane.

To monitor in vitro the permeability of cells, classical approaches rely on the uptake of fluorescence markers such as Lucifer yellow (Mir et al. 1988) and propidium iodide (Djuzenova et al. 1996) or on the release of previously loaded fluorescent markers, all of them being nonpermeant molecules that cannot diffuse through the membrane of intact cells (Silve and Mir 2011).

Glucose is a permeant molecule taken up by cells through different glucose transporters that specifically internalize the glucose molecules. Once in the cells, glucose is phosphorylated by the hexose kinases and the phosphorylated molecules cannot be transported back to the extracellular medium. We analyzed whether glucose derivatives can be used to detect cell electropermeabilization. Indeed, our final purpose was to evaluate whether ^{18}F-fluorodeoxyglucose (FDG), a radioactive glucose derivative used for clinical investigations and for diagnosis, staging and monitoring of the treatment of cancers by positron emission tomography (PET) (Hoh et al. 1993; Bomanji et al. 2001; Reske and Kotzerke 2001; Chin and Chang 2006), could have the potential for imaging permeabilized cells and mapping electropermeabilized tissues in vivo by PET. To survey the ability of FDG PET for monitoring the efficacy of electric pulses in experiments in vivo, the first mandatory step was to establish the feasibility of this approach in in vitro studies.

Because of limitations to the use of FDG in vitro, like the very short half-time of ^{18}Fluor, the need for protection in wet labs and the high cost, the use of this molecule is not easy to implement. Fluorescence-labeled deoxyglucose molecules (like 2-NDBG) can replace radioactive glucose derivatives (Nitin et al. 2009). 2-NBDG has been used to evaluate glucose metabolism in different model systems like *Escherichia coli* (Natarajan and Srienc 1999), yeast (Oh and Matsuoka 2002), pancreatic islet cells and neurons (Itoh et al. 2004) as well as in various cancer cell lines (O'Neil et al. 2005; Cheng et al. 2006). As 2-NBDG is a fluorescent analogue of D-glucose, it is transported like FDG into cells by glucose transporters (GLUTs), which are located at the cell membrane and cause facilitated transport of glucose across the membrane (Yoshioka et al. 1996a, 1996b, 1996c; Lloyd et al. 1999; Yamada et al. 2000; Zhang et al. 2004; Cheng et al. 2006; Iori et al. 2006; Nitin et al. 2009). Although six isoforms (GLUT1–GLUT5 and GLUT7) of these transporters have been identified (Pauwels et al. 2000), 2-NBDG is incorporated into the pancreatic ß-cells through GLUT1 and GLUT2 (Yamada et al. 2000). GLUT1 is widely expressed in cancer cells (Younes et al. 1996) such as MCF-7 and HepG2 cells (Chen et al. 2002). Consequently, 2-NBDG uptake in tumor cells should be facilitated by this glucose transporter (O'Neil et al. 2005). Therefore, there is spontaneous uptake of 2-NBDG in the absence of any cell membrane permeabilization. As electroporation-based therapies, like electrochemotherapy (ECT), are based on the increase of drug uptake into tumor cells caused by transient permeabilization of the cell membrane, we studied the effect of electric pulses on the uptake of 2-NBDG in DC-3F cells. In particular, we explored whether the uptake by transiently electropermeabilized cells could be larger than the spontaneous uptake for a period of time compatible with those of the usual PET investigations.

Materials and Methods

Cells

DC-3F cells are spontaneously transformed Chinese hamster fibroblasts (Biedler and Riehm 1970). They were grown in minimum essential medium (SMEM) supplement with 10 % fetal bovine serum (FBS) and 1 % penicillin/streptomycin solution (all from Life Technologies, Carlsbad, CA). Cells were detached with trypsin/EDTA (life technologies), counted and seeded in new flasks using standard protocols.

Cell Electropermeabilization

After trypsinization, cells were centrifuged for 10 min at 1,000 rpm at 4 °C and suspended in phosphate-buffered saline (PBS) to obtain 5×10^5 cells per 45 µl ($\sim 10^7$ cells/ml). For each experiment, 5 µl of NBDG (MW 342.26) (Molecular Probes, Eugene, OR) were added to the 45 µl of cell suspension. Immediately after, the 50 µl of cells in the presence of NBDG were placed in a sterile electroporation cuvette (Cell Projects, Kent UK; with a 1-mm gap between the electrodes). Eight square-wave electric pulses of appropriate voltage and of 100-µs duration were delivered at a repetition frequency of 1 Hz or 5 kHz using a Cliniporator (IGEA, Carpi, Italy).

In competition experiments, after trypsinization, cells were suspended in PBS containing 5.5, 11 or 27.5 mM D-glucose (Merck, Darmstadt, Germany). All experiments were performed at 22 or 37 °C as explained in the text.

Flow Cytometry

In all experiments, 2-NBDG uptake was stopped by diluting the cells with 15 ml of precooled PBS. Cells were subsequently resuspended in 500 µl precooled PBS and maintained at 4 °C before flow cytometric analysis.

For each measurement, fluorescence was measured with a FACScan flow cytometer (Becton Dickinson Immunocytometry Systems, San Jose, CA). Cells were excited at 488 nm, and the emitted 2-NBDG fluorescence was collected at 640 nm. Data from each flow cytometric measurement (relative scatter light or fluorescence intensity of each event) were stored under flow cytometry standard format. Controls (no 2-NBDG and no pulse in the presence of 2-NBDG) were included in all experiments.

Data Processing

All experiments were repeated at least three times on different days. Results are presented as the relative difference in the peak channel of the fluorescence intensity between each group and the corresponding control performed in the same experiment. Results are also presented as the percentage of events in the most fluorescent part of the cell population exposed to 2-NBDG and to the electric pulses (which should correspond to the percentage of reversibly permeabilized cells detected by 2-NBDG uptake). ANOVA and paired Student's *t*-test were used to evaluate the statistical significance of differences between the experimental and control groups. $p < 0.05$ was considered significant.

Results

Temperature Dependence of 2-NBDG Uptake

As spontaneous uptake is mediated by the activity of glucose transporters, we first analyzed the uptake temperature dependence with and without pulses, using typical electrical parameters for the reversible electropermeabilization of DC-3F cells (eight electric pulses of 1,200 V/cm and 100-μs duration delivered at a repetition frequency of 1 Hz). Cells were put in the presence of 300 μM 2-NBDG, immediately subjected to electric pulses (or not in the controls) and incubated for 5 more min at 22 or 37 °C (Table 1). Uptake of 2-NBDG was sensitive to temperature. In nonelectroporated cells, 2-NBDG uptake was larger at 37 °C than at 22 °C (Table 1). This difference was significant ($p < 0.01$). In samples treated with electric pulses a large increase in 2-NBDG uptake was observed for incubations of just 5 min, the time for the cells to reseal according to previous experience with these cells (Orlowski et al. 1988). Actually, a biphasic distribution was found, corresponding to the fluorescence of the transiently permeabilized cells and of the nonpermeabilized cells (in spite of their exposure to the electric pulses). Uptake in permeabilized cells was much more important than that in nonpermeabilized cells. Moreover, fluorescence was significantly ($p < 0.001$) higher at 37 °C with respect to uptake at 22 °C (mean peak channel increased from 2,951 to 3,918). Because in all cases uptake at 37 °C was higher than at 22 °C and since 37 °C is close to the physiological body temperature in most mammals, it was decided that all further experiments would be performed at 37 °C.

It must also be noted that at 22 °C 2-NBDG uptake was very low as there was almost no increase in cell fluorescence compared to the autofluorescence of those cells (Table 1, Fig. 1). At 37 °C, a net increase in fluorescence was found, which was the consequence of the increase in the cell basal metabolism as a result of exposure of cells at 37 °C physiological temperature.

2-NBDG Uptake Dependence on Its Concentration

To assess the optimal 2-NBDG concentration to be used in further experiments, cells were incubated in the presence of 10, 20, 40, 80, 160, 240 and 300 μM of 2-NBDG for 10 min after applying electric pulses at zero (controls no pulse), 1,000 or 1,200 V/cm (Fig. 2). In all cases, cell fluorescence increased with respect to the controls incubated in the absence of 2-NBDG ($p < 0.001$). In samples exposed to electric pulses, there was a large increase in uptake ($p < 0.001$), by two orders of magnitude, in electropermeabilized cells (Fig. 2). The highest 2-NBDG uptake was obtained at 300 μM, but the working concentration of 240 μM was chosen because the percentage of events in the part of the cell population that was electropermeabilized was higher in the presence of 240 μM 2-NBDG (data not

Table 1 Effect of electric pulses on uptake of 2-NBDG at an external concentration of 300 μM

Group	Peak channel of M_1 or M_2 region (means ± SD)		
	22 (°C)	37 (°C)	37/22 (°C)
No 2-NBDG (Autofluorescence)	18 ± 8	18 ± 8	1.0
2-NBDG alone	47 ± 30	76 ± 1.5[a]	1.6
2-NBDG + electric pulses	2,952 ± 501	3,918 ± 104[a]	1.3

The changes in the value of the peak channel of the high-fluorescence cell population (M_2) are reported in the table. Cells were incubated with 300 μM 2-NBDG for 5 min at room temperature (22 °C) or at 37 °C and exposed to eight pulses of 100 μs and 1,000 V/cm at a repetition frequency of 1 Hz

[a] Difference statistically significant for 2-NBDG uptake at 37 °C with respect to 22 °C, $p < 0.05$

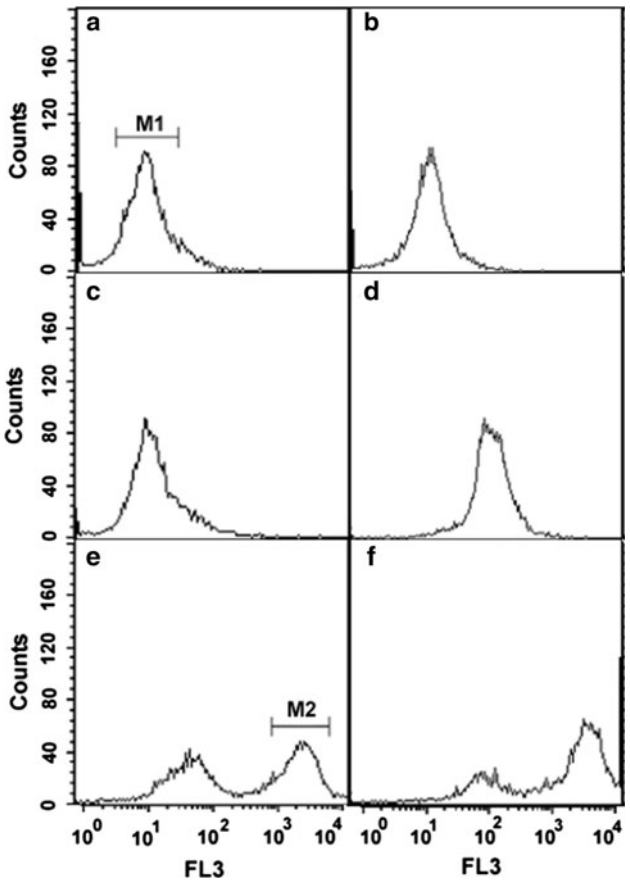

Fig. 1 Flow cytometric histograms of DC-3F cells: autofluorescence (**a**, **b**), 2-NBDG alone (**c**, **d**) and 2-NBDG together with electric pulses (**e**, **f**) of cells incubated at 22 °C (**a**, **c** and **e**) or at 37 °C (**b**, **d** and **f**) during incubation with 2-NBDG (**c**–**f**) or without 2-NBDG (**a**, **b**, autofluorescence, control). The effect of eight electric pulses of 100 μs, 1 Hz at 1,200 V/cm on uptake of 2-NBDG was studied (at an external concentration of 300 μM) into DC-3F cells exposed or not to the electric pulses

shown). This could mean that uptake in the presence of 300 μM 2-NBDG is toxic to electropermeabilized cells, and therefore, this high concentration was not used in subsequent experiments, to avoid such potentially toxic effects. It can also be noted that uptake with pulses of 1,200 V/cm was higher than uptake with pulses of 1,000 V/cm and that at the lowest concentration tested (10 μM 2-NBDG) spontaneous uptake by transporters was equally intense as uptake by electroporation (data not shown). Interestingly, at concentrations as low as 20 μM, the fluorescence intensity in samples with pulses was already higher than that in the corresponding controls: the electric pulses caused an increased of fluorescence from 12 to 79 and from 8.5 to 117.5 at 1,000 and 1,200 V/cm, respectively ($p < 0.001$). Therefore, the electric pulses moderately enhanced uptake of 2-NDBG at low concentration (20 μM) and highly increased it at higher concentrations.

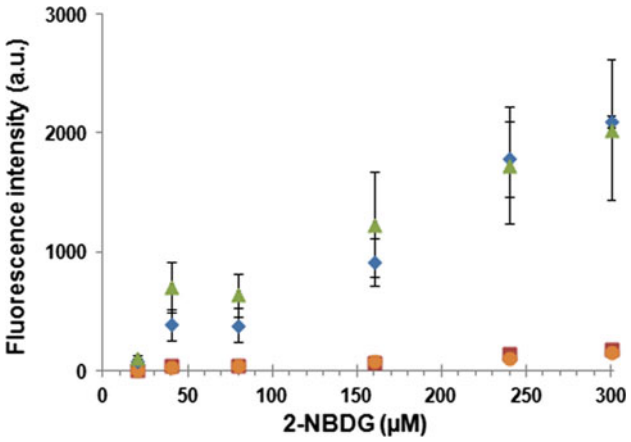

Fig. 2 Changes in the peak channel of monodistributed fluorescent cells not exposed to the electric pulses or changes in the value of the peak channel of the high-fluorescence cell population exposed after electric pulses (eight pulses of 100 μs, 1 Hz at 1,000 or 1,200 V/cm) in cells. Cells were incubated for 10 min at 37 °C. Data are means ± SD of at least three independent experiments. *filled square*, *filled circle* no electric pulses; *filled diamond* electric pulses at 1,000 V/cm; *filled triangle* electric pulses at 1,200 V/cm

2-NBDG Uptake as a Function of Pulse Amplitude

In the analysis of 2-NBDG uptake as a function of pulse amplitude, electric pulses with amplitudes of 900; 1,000; 1,100; 1,200; 1,300; 1,400 or 1,500 V/cm were delivered. Cells were pulsed immediately after the addition of the fluorescent marker and after the pulses; they were incubated at 37 °C for 10 min in a water bath to ensure that they were incubated at 37 °C. Two values were considered: the percentage of actually permeabilized cells and the peak channel of their fluorescence, which indicates the level of 2-NBDG uptake by these cells. 2-NBDG uptake increased with the field amplitude applied (Fig. 3a). Field amplitudes higher than 1,500 V/cm were not tested as it was known that they were highly toxic for the cells (induction of irreversible permeabilization and, thus, of cell death). As expected, the percentage of events in the population of cells permeabilized due to electric pulses started to decrease below this field amplitude (Fig. 3b). The highest convenient uptake was obtained using electric pulses of 1,200 V/cm, but the maximum percentage of highly fluorescent cells was reached at 1,000 V/cm ($p < 0.01$). Thus, 1,000 V/cm was considered to be the optimal electric field amplitude for the next part of this study.

2-NBDG Uptake in the Presence of D-Glucose

The previous experiments were performed in the absence of external glucose competing with 2-NBDG uptake. The effect of the presence of different concentrations of normal D-glucose on 2-NBDG uptake in DC-3F cells was

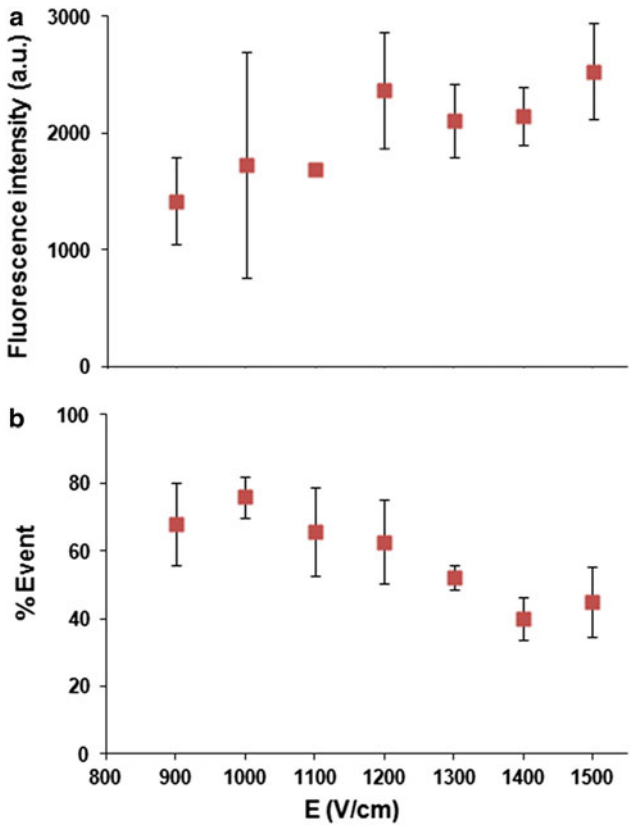

Fig. 3 **a** Changes in the value of the peak channel of the high-fluorescence cell population as a function of the pulse field amplitude, E (in V/cm). **b** Percentage of highly fluorescent (permeabilized) cells after incubation with 240 μM 2-NBDG for 10 min at 37 °C. Data are means ± SD of at least three independent experiments

examined to evaluate the potential reduction of fluorescence accumulation in the cells, particularly in the presence of the physiological external concentration of glucose (5.5 mM). Cells were thus incubated with 240 μM 2-NBDG or with 2-NBDG and 5.5, 11 or 27.5 mM glucose, together with the delivery or not of eight electric pulses of 100 μs and 1,000 V/cm at a repetition frequency of 1 Hz. Cells were incubated for 10 min at 37 °C after pulse delivery. Glucose, at all concentrations, affected 2-NBDG uptake by cells that were not exposed to electric pulses. However, only partial competition was found at 5.5 mM as the fluorescence of only a fraction of the cells decreased (creating a shoulder in the cell distribution, see Fig. 4c). However, the peak channel value was not affected (Fig. 4). At 11 mM, a small majority of the cells showed reduced fluorescence uptake, while the "fluorescent" cells remained at the control level. At 27 mM, competition was complete as even the more "fluorescent" fraction of the cells showed a decrease in individual fluorescence (peak channel at a value of 118, significantly different [$p < 0.05$] from the peak channel values of the other groups, at about a value of 150).

In cells that were treated with the electric pulses in the presence of different concentrations of external D-glucose, again there was an increase in uptake by two orders of magnitude in the part of the cell population exposed to electric pulses (Fig. 4) ($p < 0.001$).

When cells were exposed to electric pulses, the peak channel value of the highly fluorescent cell population did not significantly increase in the presence of additional external D-glucose ($p = 0.659$ with respect to the control with no added D-glucose). In addition, the percentage of events displaying high fluorescence values decreased at the highest concentrations of D-glucose, 11 or 27.5 mM (Fig. 5). This could reflect partial competition between 2-NBDG and D-glucose to enter the cells, but the difference was not statistically significant ($p = 0.126$).

Time Course of 2-NBDG Uptake

To analyze the time dependence of 2-NBDG uptake, cells were incubated with 240 μM of 2-NBDG at 37 °C for 0, 2, 5, 10, 20, 40 or 60 min in PBS (no D-glucose) after applying (or not) electric pulses at 1,000 V/cm. In the absence of D-glucose and in the absence of pulse delivery, uptake of 2-NBDG increased in a time-dependent manner (Fig. 6). It reached a maximum after 60 min of incubation. In samples exposed to the electric pulses, an increase in uptake by two orders of magnitude in the part of the cell population permeabilized by electric pulses was again observed, even at the maximum incubation time of 60 min (longer times were not tested as cells did not support longer incubations in the PBS buffer) (Fig. 6). Changes in fluorescence intensity showed significant differences during the different incubation times after the application of electric pulses ($p < 0.001$). At 60 min electroporation-based uptake (which does not seem to be modified during the incubation) is completed by the transport-mediated uptake (which increases during this time). In addition, there was always a significant difference in fluorescence intensity between the two experimental groups and between each of the experimental groups and the control without 2-NBDG ($p < 0.001$). This difference remained significant for up to 60 min of incubation ($p < 0.05$).

Time-dependence experiments were also performed in the presence of 5.5 mM of D-glucose (Fig. 6). Cells were manipulated under the same conditions except that after trypsinization they were suspended in modified PBS that contained 5.5 mM of D-glucose. In the absence of electric pulses, fluorescence increased regularly with time. Statistical analysis revealed no significant differences between the uptake of 2-NBDG alone in the presence or in the absence of D-glucose in all periods examined (2–60 min) in the absence of electric pulses.

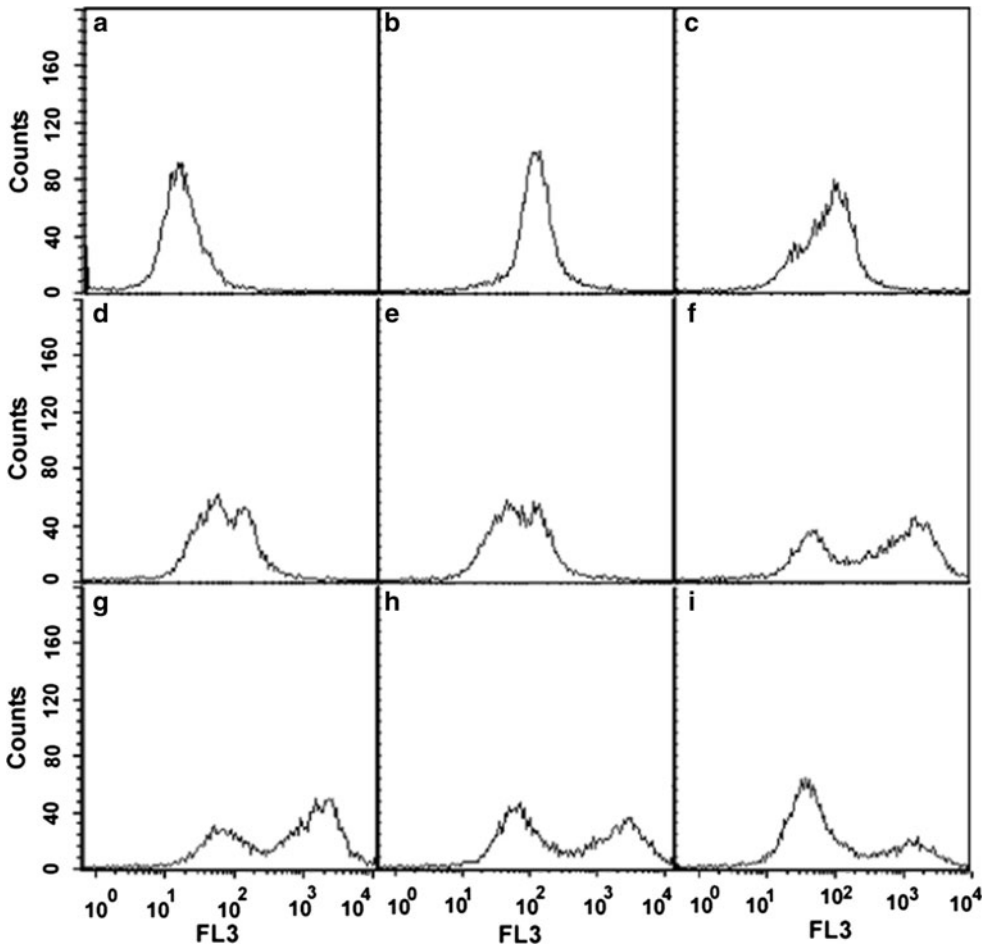

Fig. 4 Flow cytometric histograms of DC-3F cells treated **a** with no 2-NBDG (absolute control); **b–e** with 2-NBDG alone in the presence of 0, 5.5, 11 or 27.5 mM D-glucose; and **f–i** with 2-NBDG and electric pulses (eight pulses of 100 μs, 1 Hz at 1,000 V/cm) in the presence of 0, 5.5, 11 or 27.5 mM D-glucose, respectively

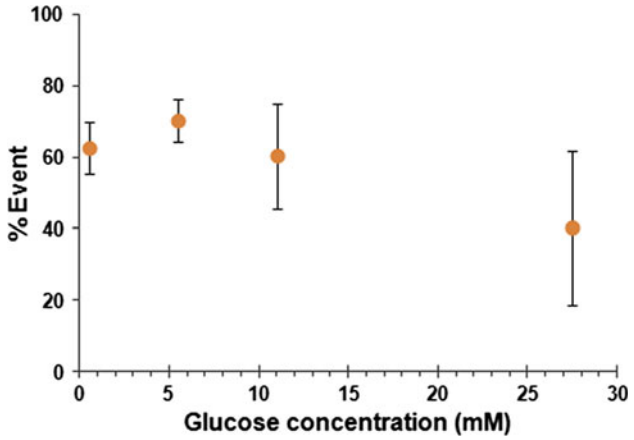

Fig. 5 Percentage of highly fluorescent (permeabilized) cells after exposure of cells to eight pulses of 100 μs and 1,000 V/cm and incubation with 240 μM 2-NBDG for 10 min at 37 °C in the presence of 0, 5.5, 11 or 27.5 mM of D-glucose. Data are means ± SD of at least three independent experiments

In the presence of the electric pulses and 5.5 mM D-glucose, a significant increase in uptake in electropermeabilized cells, by about two orders of magnitude, was again observed, even at 60 min (Fig. 6). Values of fluorescence intensity were similar in the presence and in the absence of D-glucose, except at 20 or 60 min, when significantly higher uptake was recorded in the presence of D-glucose ($p < 0.05$).

2-NBDG Uptake as a Function of Electric Pulses at 1 Hz and 5 kHz Repetition Frequencies

Finally, the effect of a 5-kHz repetition frequency during the delivery of the eight electric pulses on 2-NBDG uptake into electropermeabilized cells was evaluated in comparison to the effects of pulses delivered at the usual 1-Hz repetition frequency. Cells were incubated with 240 μM 2-NBDG for 10 min after applying eight (or no) electric pulses of 100 μs and 1,000 or 1,200 V/cm at repetition frequencies of 1 Hz or 5 kHz. In the absence of D-glucose a difference in uptake by electropermeabilized cells was indeed found (Fig. 7a). Fluorescence intensity was significantly higher when pulses were delivered at a repetition frequency of 1 Hz ($p < 0.001$). However, the same data showed no significant change in the percentage of permeabilized cells ($p = 0.898$) (Fig. 7b).

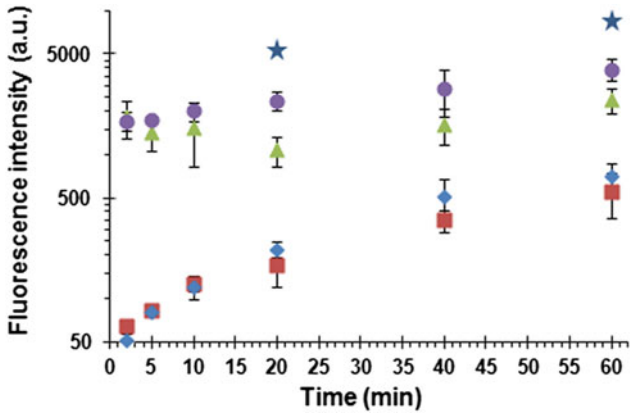

Fig. 6 Changes in the peak channel of monodistributed fluorescent cells not exposed to the electric pulses or changes in the value of the peak channel of the high-fluorescent cell population after electric pulse delivery. Cells were incubated in the absence or presence of a physiological glucose concentration (5.5 mM) for 2–60 min, always in the presence of 240 μM 2-NBDG and with or without the delivery of electric pulses (eight pulses of 100 μs, 1 Hz at 1,000 V/cm). Data are means ± SD of at least three independent experiments. *Stars* denote the only values in which a statistically significant difference was recorded between the absence and the presence of the external 5.5 mM D-glucose. *filled square* 2-NBDG, *filled diamond* 2-NBDG + 5.5 mM D-glucose, *filled triangle* electric pulses, *filled circle* electric pulses + 5.5 mM D-glucose

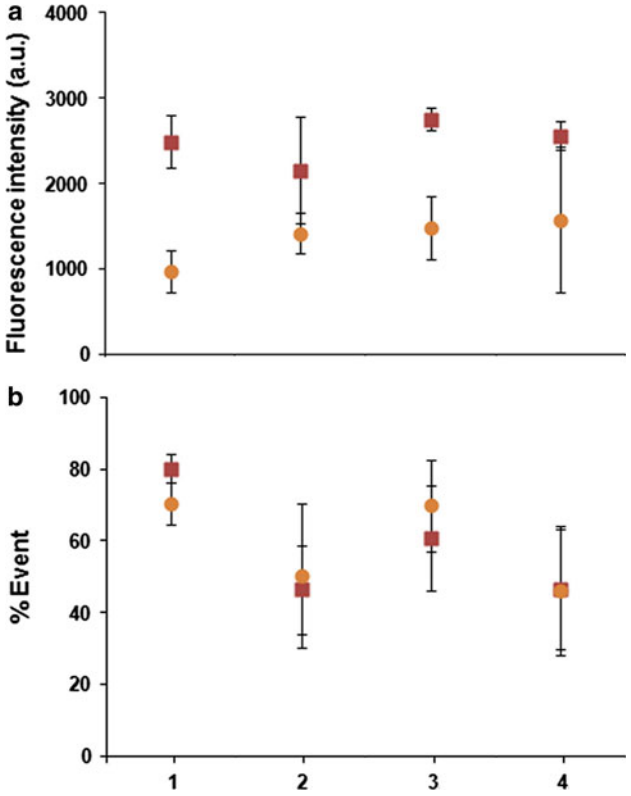

Fig. 7 **a** Changes in the value of the peak channel of the high-fluorescence cell population. **b** Percentage of highly fluorescent (permeabilized) cells after application of electric pulses (eight pulses of 100 μs, 1 Hz or 5 kHz at 1,000 or 1,200 V/cm). Cells were incubated for 10 min at 37 °C in the absence or presence of physiological glucose solution (5.5 mM). *1* 1,000 V/cm, *2* 1,000 V/cm + 5.5 mM D-glucose, *3* 1,200 V/cm, *4* 1,200 V/cm + 5.5 mM D-glucose, *filled square* electric pulses 1 Hz, *filled circle* electric pulses 5 kHz

As the data also show, there was no significant difference between 2-NBDG uptake in the absence or the presence of 5.5 mM D-glucose. Thus, a significant difference was also found in 2-NBDG uptake after application of electric pulses at 1-Hz or 5-kHz repetition frequencies in the presence of 5.5 mM D-glucose ($p < 0.001$) (Fig. 7a), while no significant change was observed in the percentage of cells permeabilized due to the delivery of electric pulses at either 1 Hz or 5 kHz ($p < 0.007$) (Fig. 7b).

Discussion

We have described for the first time the effect of electric pulses on the uptake of 2-NBDG (2-[*N*-(7-nitrobenz-2-oxa-1,3-diazol-4-yl)amino]-2-deoxy-D-glucose), a fluorescent derivative of D-glucose.

As stated in the Introduction, 2-NBDG is a marker of glucose uptake in cells of various origins and should have characteristics similar to those of FDG, which has been widely used in PET. In spite of high uptake of 2-NBDG by GLUT transporters into tumor cells, electroporation significantly increases 2-NBDG uptake into the tumor cells used in this study (DC-3F).

Indeed, in the present study, we show that 2-NBDG is rapidly taken up by, and accumulated in, DC-3F tumor cells in the absence of electric pulses. Our results are consistent with previous investigations that have used this molecule as a fluorescent marker for monitoring glucose uptake into malignant tumor cells (O'Neil et al. 2005; Cheng et al. 2006). Because of the aggressive growth patterns of the tumor cells, uptake of 2-NBDG by tumor cells is high. However, enhanced accumulation or trapping of 2-NBDG phosphorylated forms as a result of an increase of hexokinase activity has also been reported (Flier et al. 1987; Aloj et al. 1999).

Our study demonstrates that, after application of permeabilizing electric pulses, uptake of 2-NBDG is actually increased in the fraction of cells that are electropermeabilized by the electric pulses. The fluorescence of these cells is about 10–100 times larger than that of cells not exposed to electric pulses, whatever the experimental conditions used (with external glucose added or not, for example), resulting in the reversible electropermeabilization of a fraction of the treated cells.

In the initial experiments, we determined the experimental conditions. Uptake of 2-NBDG was higher at 37 °C, with or without pulses, than at room temperature

(22 °C). Our results are in agreement with previous studies showing that in the absence of electric pulses and in the presence of 600 μM 2-NBDG, uptake into MIN6 cells was temperature-dependent, the initial velocity of 2-NBDG uptake at 37 °C being twice that at 25 °C (Yamada et al. 2000). We then determined that 240 μM 2-NBDG seemed to be a convenient concentration that results in reproducible experimental results with the cells used in the present study. It can be seen in Fig. 2 that the uptake of 2-NBDG remarkably increased by exposing cells to electric pulses at all concentrations examined except at the lowest one, 10 μM. Membrane electropermeabilization opened new ways for the penetration of 2-NBDG inside cells, aside from its general uptake by the GLUT transporters described in the Introduction. This is the reason for the increased 2-NBDG accumulation inside electroporated cells. Contrary to facilitated transport, the rate of which is driven mainly by the number and activity of the transporters located at the cell surface, uptake through the electroporated membrane is proportional to the external concentration as clearly shown with typical nonpermeant molecules (Orlowski et al. 1988; Silve and Mir 2011). The same rule has been observed with 2-NBDG, the electroporation of the cell membrane leading to the highest uptake per cell at the highest concentrations tested, 240 and 300 μM. However, at 300 μM the percentage of cells in the electropermeabilized fraction slightly decreased, reflecting a potential toxicity on the electroporated cells of 2-NBDG at the high internalized concentration in the presence of 300 μM external 2-NBDG.

As 2-NBDG is normally transported into cells by the glucose transporters, this uptake should be inhibited by a high external concentration of unlabeled D-glucose competing with 2-NBDG to interact with the transporters. Previous studies demonstrated that 2-NBDG uptake was indeed inhibited in the presence of D-glucose. There is competition between 2-NBDG and D-glucose for the facilitated transporters to enter the cell in single vascular smooth muscle cells (Lloyd et al. 1999), *E. coli* cells (Yoshioka et al. 1996a), yeast *Candida albicans* (Oh et al. 2002) and tumor cells (MCF-7, HepG2, M-1 and U87MG) (O'Neil et al. 2005; Cheng et al. 2006). Moreover, other studies have reported that a high external concentration of D-glucose partially blocks uptake of 2-NBDG in other cells (Iori et al. 2006). For example, 2-NBDG uptake is inhibited about 70 % in the presence of 22 mM D-glucose in pancreatic ß-cells and 37 and 52 % in the presence of 5.6 and 11.2 mM of D-glucose, respectively (neurons, human erythrocytes) (Yamada et al. 2000). However, the exact mechanism of 2-NBDG transport is not known as it has not been determined whether all six types of glucose transporter can facilitate 2-NBDG uptake or not.

We analyzed the effect of the presence in the medium of D-glucose on 2-NBDG uptake by DC-3F cells, with or without electric pulses. Four different concentrations of D-glucose (0, 5.5, 11 or 27.5 mM) were tested. Competitive inhibition, increasing with the increased concentration of the added glucose, was found; but at 5.5 and 11 mM it affected only some of the cells in the absence of electric pulses. This result is consistent with previous studies that reported partial blocking of 2-NBDG uptake at high concentrations of D-glucose (Yamada et al. 2000; Iori et al. 2006). Nevertheless, our results are extremely relevant as the final aim of the study was to analyze whether, by studying NDBG uptake in vitro, we could determine whether FDG could be used to image electropermeabilized tissues in vivo by a technique like PET. Indeed, we show here that competition between 2-NBDG and glucose is minimal under physiological conditions (that is, with the 5.5 mM concentration) in the absence of electric pulses and that in the presence of the electric pulses there is, as expected, no detectable competition (which is in agreement with the mechanism of diffusion through the electropermeabilized membrane, which is not saturable like transport through transporters). Moreover, at the different concentration of D-glucose, there was increasing 2-NBDG uptake into electroporated cells.

The time course of 2-NBDG uptake into DC-3F cells, in the presence or absence of glucose and with or without pulse application, was also analyzed. Indeed, in PET analysis images are taken some minutes after the injection of FDG into the body. Therefore, it was necessary to ascertain that the differences observed after 10 min of incubation (most of the experiments reported) were also observed for longer incubation times. In the absence of the electric pulses, our results are in agreement with a study that measured 10 μM 2-NBDG uptake at 37 °C for 0, 15, 30, 60, 120 or 180 min in HepG2 human hepatocarcinoma cells and L6 rat skeletal muscle cells (Zou et al. 2005). According to these results, the highest uptake increases were observed from 0 to 60 min after the beginning of incubation. Interestingly, the results of this experiment confirm that in electropermeabilized cells there is no competition between 2-NBDG and glucose at the physiological concentration (5.5 mM). Moreover, the fluorescence taken up by electropermeabilized cells a short time after the pulse delivery (before the cells reseal) is not lost during the prolonged incubation of cells, and the difference from nonpermeabilized cells remains high for all of the times. As some more uptake can also occur in these cells after their resealing by the GLUT transporters, as in the cells not exposed to electric pulses, it is understandable that the difference is relatively maintained with respect to nonpermeabilized cells, at least during the 60 min of

incubation during which changes were followed in the experiments reported here.

In this study, the effect of the 1-Hz and 5-kHz pulse frequencies on 2-NBDG uptake into electropermeabilized cells was also examined. Indeed, the clinical protocols for electrochemotherapy (Marty et al. 2006; Mir 2006) often use trains of eight pulses delivered at a repetition frequency of 5 kHz. This repetition frequency has several advantages. When pulses are delivered close to muscles, a single muscle contraction is provoked at 5 kHz instead of eight muscle contractions when pulses are delivered at 1 Hz. Moreover, treatment is much faster: the train of pulses between a pair of electrodes is delivered in 1.5 ms instead of about 8 s. The results reported here show that, in the absence of externally added D-glucose, the application of electric pulses highly increased 2-NBDG uptake with noticeable differences as a function of the repetition frequency of the electric pulses. Indeed, if the percentage of electropermeabilized cells is the same at 1-Hz and 5-kHz pulse frequencies, the fluorescence intensity of the permeabilized cells was significantly lower at 5 kHz than at 1 Hz. A study by Pucihar et al. (2002) showed that Lucifer yellow uptake into the same type of cells (DC-3F) followed the same trend. Indeed, to maintain the uptake of Lucifer yellow at the same level, the increase of the repetition frequency (from 1 Hz to 8.3 kHz) imposed an increase in the amplitude of the electric pulses applied, which means that the pulses at the highest repetition frequency were less efficient at permeabilizing the cells. If we consider that in our study the effect of the 1-Hz and 5-kHz pulse frequencies was tested at the same amplitude in the absence or presence of physiological D-glucose, our results are indeed in agreement with these previous results. It is interesting that these two markers give the same result as the Lucifer yellow is a completely nonpermeant molecule, while 2-NBDG would also be a nonpermeant molecule if no GLUT transporters actively transported it inside the cells. The reduced effectiveness of the 5-kHz pulses is thus corroborated by molecules with different behaviors, considering their ability to cross the plasma membrane. Simultaneously, these similarities also confirm that the mechanism of drug uptake in electropermeabilized cells is diffusion across the permeabilized membranes.

The results of our in vitro studies highlight the ability of glucose derivatives as markers for monitoring the electropermeabilization of cells exposed to adequate electric pulses. Until now, only strictly nonpermeant molecules like Lucifer Yellow or bleomycin were used as cell electropermeabilization markers (Mir et al. 1998; Pron et al. 1999; Pucihar et al. 2002; Silve and Mir 2011). As FDG is a radioactive glucose derivative used for clinical investigations, the results reported here with 2-NBDG provide a preliminary step toward in vivo studies of FDG PET imaging in combination with electroporation. Considering the common applications of FDG, PET could be a useful means to probe electroporated cells in vivo, which provides a noninvasive way to monitor tissue electropermeabilization in living laboratory animals. FDG PET could then become a very attractive technique for the accurate detection of electropermeabilization efficacy in vivo. Further in vivo studies are thus necessary to assess the potential of this technique.

Conclusions

We investigated the potential of 2-NBDG, a fluorescent analogue of glucose, to reveal the electropermeabilization of cells after delivery of electric pulses in vitro. Based on the results, it can be suggested that FDG PET imaging could have potential to measure the electropermeabilization of cells in vivo.

Acknowledgements This research was conducted in the scope of the European Associated Laboratory "Electroporation in Medicine and Biology" (LEA EBAM). E. R. thanks the staff of the Laboratoire de Vectorologie et Thérapeutiques Anticancéreuses, UMR 8203 CNRS Université Paris-Sud, Institute Gustave-Roussy, Villejuif, France, for their hospitality during this research and the Biomedical Center of the European Scientific Institute, Archamps, France, for partial financial support. E. R. also thanks Dr. Malihe Nasiri, Biostatistics Department, Tarbiat Modares University, Tehran, Iran, for helping with the statistical tests.

References

Aloj L, Caraco C, Jagoda E, Eckelman WC, Neumann RD (1999) Glut-1 and hexokinase expression: relationship with 2-fluoro-2-deoxy-D-glucose uptake in A431 and T47D cells in culture. Cancer Res 59:4709–4714

Biedler JL, Riehm H (1970) Cellular resistance to actinomycin D in Chinese hamster cells in vitro: cross-resistance, radioautographic, and cytogenetic studies. Cancer Res 30:1174–1184

Bomanji JB, Hyder SW, Gaze MN, Gacinovic S, Costa DC, Coulter C, Ell PJ (2001) Functional imaging as an aid to decision-making in metastatic paraganglioma. Br J Radiol 74:266–269

Breton M, Mir LM (2012) Microsecond and nanosecond electric pulses in cancer treatments. Bioelectromagnetics 33:106–133

Cemazar M, Sersa G, Miklavcic D (1998) Electrochemotherapy with cisplatin in the treatment of tumor cells resistant to cisplatin. Anticancer Res 18:4463–4466

Cemazar M, Miklavcic D, Mir LM, Belehradek J Jr, Bonnay M, Fourcault D, Sersa G (2001) Electrochemotherapy of tumors resistant to cisplatin: a study in a murine tumor model. Eur J Cancer 37:1166–1672

Chen CP, Li XX, Zhang LR, Min JM, Chan JY, Fung KP, Wang SQ, Zhang LH (2002) Synthesis of antisense oligonucleotide-peptide conjugate targeting to GLUT-1 in HepG-2 and MCF-7 cells. Bioconjug Chem 13:525–529

Cheng Z, Levi J, Xiong Z, Gheysens O, Keren S, Chen X, Gambhir SS (2006) Near-infrared fluorescent deoxyglucose analogue for tumor optical imaging in cell culture and living mice. Bioconjug Chem 17:662–669

Chin BB, Chang PP (2006) Gastrointestinal malignancies evaluated with ^{18}F-fluoro-2-deoxyglucose positron emission tomography. Best Pract Res Clin Gastroenterol 20:3–21

Djuzenova CS, Zimmermann U, Frank H, Sukhorukov VL, Richter E, Fuhr G (1996) Effect of medium conductivity and composition on the uptake of propidium iodide into electropermeabilized myeloma cells. Biochim Biophys Acta 1284:143–152

Flier J, Mueckler M, Usher P, Lodish H (1987) Elevated levels of glucose transport and transporter messenger RNA are induced by ras and sarc oncogenes. Science 235:1492–1495

Gehl J, Skovsgaard T, Mir LM (1998) Enhancement of cytotoxicity by electropermeabilization: an improved method for screening drugs. Anticancer Drugs 9:319–325

Hoh CK, Hawkins RA, Glaspy JA, Dahlbom M, Tse NY, Hoffman EJ, Schiepers C, Choi Y, Rege S, Nitzsche E, Maddahi Y, Phelps ME (1993) Cancer detection with whole-body PET using 2-[^{18}F] fluoro-2-deoxy-D-glucose. J Comput Assist Tomogr 17:582–589

Iori I, Satoshi W, Yutaka K (2006) Mapping of odor-related neuronal activity using a fluorescent derivative of glucose. Neurosci Lett 398:224–229

Itoh Y, Abe T, Takaoka R, Tanahashi N (2004) Fluorometric determination of glucose utilization in neurons in vitro and in vivo. J Cereb Blood Flow Metab 24:993–1003

Jaroszeski MJ, Dang V, Pottinger C, Hickey J, Gilbert R, Heller R (2000) Toxicity of anticancer agents mediated by electroporation in vitro. Anticancer Drugs 11:201–208

Kambe M, Arita D, Kikuohi H, Funato T, Tezuka F, Gamo M, Murakawa Y, Kanamaru R (1996) Enhancing the effect of anticancer drugs against the colorectal cancer cell line with electroporation. Tahoku J Exp Med 180:161–171

Kuriyama S, Matsumoto M, Mitoro A, Tsujinoue H, Nakatani T, Fukui H, Tsujii T (2000) Electrochemotherapy for colorectal cancer with commonly used chemotherapeutic agents in a mouse model. Dig Dis Sci 45:1568–1577

Lloyd PG, Hardin CD, Sturek M (1999) Examining glucose transport in single vascular smooth muscle cells with a fluorescent glucose analog. Physiol Res 48:401–410

Marty M, Sersa G, Garbay JR, Gehl J, Collins CG, Snoj M, Billard V, Geetsen PF, Larkin JO, Miklavcic D, Pavlovic I, Paulin-Kosir SM, Cemazar M, Morsli N, Soden DM, Rudolf Z, Robert C, O'Sullivan G, Mir LM (2006) Electrochemotherapy—an easy, highly effective and safe treatment of cutaneous and subcutaneous metastases: results of ESOPE (European standard operating procedures of electrochemotherapy) study. Eur J Cancer Suppl 4:3–13

Melvik JE, Pettersen EO, Gordon PB, Seglen PO (1986) Increase in *cis*-dichlorodiammineplatinum (II) cytotoxicity upon reversible electropermeabilization of the plasma membrane in cultured human NHIK 3025 cells. Eur J Cancer Clin Oncol 22:1523–1530

Mir LM (2001) Therapeutic perspectives of in vivo cell electropermeabilization. Bioelectrochemistry 53:1–10

Mir LM (2006) Bases and rationale of the electrochemotherapy. Eur J Cancer Suppl 4:38–44

Mir LM, Banoun H, Paoletti C (1988) Introduction of definite amounts of nonpermanent molecules into living cells after electropermeabilization: direct access to the cytosol. Exp Cell Res 175:15–25

Natarajan A, Srienc F (1999) Dynamics of glucose uptake by single *Escherichia coli* cells. Metab Eng 1:320–333

Neumann E, Schaeter-Ridder M, Wang Y, Hofshneider PH (1982) Gene transfer into mouse lyoma cells by electroporation in high electric fields. EMBO J 7:841–845

Nitin N, Carlson AL, Muldoon T, El-Naggar AK, Gillenwater A, Richards-Kortum R (2009) Molecular imaging of glucose uptake in oral neoplasia following topical application of fluorescently labeled deoxy-glucose. Int J Cancer 124:2634–2642

O'Neil RG, Wu L, Mullani N (2005) Uptake of a fluorescent deoxyglucose analog (2-NBDG) in tumor cells. Mol Imaging Biol 7:388–392

Oh KB, Matsuoka H (2002) Rapid viability assessment of yeast cells using vital staining with 2-NBDG, a fluorescent derivative of glucose. Int J Food Microbiol 76:47–53

Orlowski S, Belehradek J Jr, Paoletti C, Mir LM (1988) Transient electropermeabilization of cells in culture. Increase of the cytotoxicity of anticancer drugs. Biochem Pharmacol 37: 4727–4733

Pauwels EKJ, Sturm EJC, Bombardieri E, Cleton V, Stokkel MPM (2000) Positron-emission tomography with [^{18}F]fluorodeoxyglucose. Part I. Biochemical uptake mechanism and its implication for clinical studies. J Cancer Res Clin Oncol 126:549–559

Pron G, Mahrour N, Orlowski S, Tounekti O, Poddevin B, Belehradek Jr J, Mir LM (1999) Internalization of the bleomycin molecules responsible for bleomycin cytotoxicity: a receptor-mediated endocytosis mechanism. Biochem Pharmacol 57:45–56

Pucihar G, Mir LM, Miklavcic D (2002) The effect of pulse repetition frequency on the uptake into electropermeabilized cells in vitro with possible applications in electrochemotherapy. Bioelectrochemistry 57:167–172

Reske S, Kotzerke J (2001) FDG-PET for clinical use. Eur J Nucl Med 28:1707–1723

Sersa G, Cemazar M, Miklavcic D (1995) Antitumor effectiveness of electrochemotherapy with *cis*-diamminedichloroplatinum (II) in mice. Cancer Res 55:3450–3455

Sersa G, Cemazar M, Rudolf Z (2003) Electrochemotherapy: advantages and drawbacks in treatment of cancer patients. Cancer Ther 1:133–142

Silve A, Mir LM (2011) Cell electropermeabilization and cellular uptake of small molecules: the ECT concept. In: Kee ST, Gehl J, Lee EW (eds) Clinical aspects of electroporation. Springer, New York, pp 69–82

Yamada K, Nakata V, Horimoto N, Saito M, Matsuoka H, Inagaki N (2000) Measurement of glucose uptake and intracellular calcium concentration in single, living pancreatic b-cells. J Biol Chem 275:22278–22283

Yoshioka K, Takahashi H, Omma T, Sato M, Ki Bong O, Nemoto Y, Matsuoka HK (1996a) A novel fluorescent derivative of glucose applicable to the assessment of glucose uptake activity of *Escherichia coli*. Biochim Biophys Acta 1289:5–9

Yoshioka K, Saito M, Oh KB, Nemoto Y, Matsuoka H, Natsume M, Abe H (1996b) Intracellular fate of 2-NBDG, a fluorescent probe for glucose uptake activity in *Escherichia coli* cells. Biosci Biotech Biochem 60:1899–1901

Yoshioka K, Oh KB, Saito M, Nemoto Y, Matsuoka V (1996c) Evaluation of 2-[*N*-(7-nitrobenz-2-oxa-1,3-diazol-4-yl)amino]-2-deoxy-D-glucose, a new fluorescent derivative of glucose, for viability assessment of yeast *Candida albicans*. Appl Microbiol Biotechnol 46:400–404

Younes M, Lechago LV, Somoana JR, Mosharaf M, Leechago J (1996) Wide expression of the human erythrocyte glucose transporter GLUT1 in human cancers. Cancer Res 56:1164–1167

Zhang Z, Li H, Liu Q, Zhou L, Zhang M, Luo Q, Glickson J, Chance B, Zheng G (2004) Metabolic imaging of tumors using intrinsic and extrinsic fluorescent markers. Biosens Bioelectron 20: 643–650

Zou C, Wang Y, Shen Z (2005) 2-NBDG as a fluorescent indicator for direct glucose uptake measurement. J Biochem Biophys Methods 64:207–215

J Membrane Biol (2012) 245:643–650
DOI 10.1007/s00232-012-9481-z

Combination of Microsecond and Nanosecond Pulsed Electric Field Treatments for Inactivation of *Escherichia coli* in Water Samples

Maj Kobe Žgalin · Duša Hodžić · Matej Reberšek · Maša Kandušer

Received: 31 January 2012 / Accepted: 30 June 2012 / Published online: 3 August 2012

Abstract Inactivation of microorganisms with pulsed electric fields is one of the nonthermal methods most commonly used in biotechnological applications such as liquid food pasteurization and water treatment. In this study, the effects of microsecond and nanosecond pulses on inactivation of *Escherichia coli* in distilled water were investigated. Bacterial colonies were counted on agar plates, and the count was expressed as colony-forming units per milliliter of bacterial suspension. Inactivation of bacterial cells was shown as the reduction of colony-forming units per milliliter of treated samples compared to untreated control. According to our results, when using microsecond pulses the level of inactivation increases with application of more intense electric field strengths and with number of pulses delivered. Almost 2-log reductions in bacterial counts were achieved at a field strength of 30 kV/cm with eight pulses and a 4.5-log reduction was observed at the same field strength using 48 pulses. Extending the duration of microsecond pulses from 100 to 250 μs showed no improvement in inactivation. Nanosecond pulses alone did not have any detectable effect on inactivation of *E. coli* regardless of the treatment time, but a significant 3-log reduction was achieved in combination with microsecond pulses.

Keywords Inactivation · Bacteria · Nanosecond · Microsecond · Electric pulse · Pulsed electric field treatment · Electroporation · *E. coli* · Water

M. K. Žgalin · D. Hodžić · M. Reberšek · M. Kandušer (✉)
Faculty of Electrical Engineering, University of Ljubljana, Tržaška cesta 25, 1000 Ljubljana, Slovenia
e-mail: masa.kanduser@fe.uni-lj.si

M. K. Žgalin
e-mail: kobemaj@gmail.com

Introduction

Electroporation is a method for cell membrane permeabilization. Its effect is a significant increase in electrical conductivity and permeability of the membrane, caused by externally applied electrical pulses. When cells are exposed to an external electric field of sufficient amplitude and duration, the cell membrane is electroporated. Aqueous pores are assumed to be induced in the cell membrane, and they increase in size and number with pulse duration (Neumann and Rosenheck 1972; Chang and Reese 1990; Weaver 2003; Saulis 2010). This is just one of various theoretical models that have been proposed to explain electroporation, with structural reorganization and creation of hydrophilic pores remaining directly unobserved (Rols 2006). Depending on the parameters of the electric pulses, the membrane can become either transiently or permanently permeable, thus making electroporation either reversible or irreversible. When electric pulse parameters are below the threshold of electroporation, the pores in the cell membrane can reseal and the cell survives. With electric pulse parameters exceeding critical threshold, the size and number of the induced pores achieve a critical value. Through these pores, the cell loses internal components, which leads to its death (Gusbeth et al. 2009; Saulis 2010).

Reversible electroporation requires the cell to survive exposure to an external electric field and return to its natural state afterward. It is most widely used in biotechnology and medicine for electrofusion and electrotransfer of drugs, genes and other large molecules to cells, both as a research tool and as a clinical technique. One such clinical technique is electrochemotherapy, where cancer cells are treated by permeabilizing the cell membrane and allowing chemotherapeutic agents to enter at greater concentrations

and kill the targeted cells (Marty et al. 2006; Bertacchini et al. 2007; Sersa et al. 2008). A new and developing field of research is the application of drugs and genes to brain tissue in humans (Agerholm-Larsen et al. 2011), where the blood–brain barrier could theoretically be overcome with the use of reversible electroporation.

In addition to reversible electroporation, electric pulses can be used for inactivation of microorganisms, where all biological activities in the cell are terminated. This has been extensively studied since the beginning of the electric power industry, with the first studies dating as far back as the nineteenth century (Fuller 1898). Irreversible electroporation uses an electric field to directly destroy cells. The pores created by the applied electric field are unable to reseal, which prevents maintenance of homeostasis (Rubinsky 2007). In medicine, the effects of irreversible electroporation are being clinically used as a method for tissue ablation (Davalos et al. 2005). This has the potential to become an alternative method of ablation for solid tumors (Lee et al. 2010). However, irreversible electroporation reaches far beyond medical purposes. It has found its way into the food industry, where it is used as a non-thermal method for inactivating microorganisms in liquid food products (pasteurization). Pulsed electric field (PEF) technology utilizes short electric pulses to preserve the food. The main advantage over other methods is that food products are treated at lower temperatures, so they retain nutritional and organoleptic characteristics. Irreversible electroporation is also more cost-effective than conventional systems (Barbosa-Cánovas et al. 1999). In industry it is also used to treat different water samples, for example, hospital wastewaters (Rieder et al. 2008; Gusbeth et al. 2009) that are usually contaminated with pathogenic bacteria (Kümmerer 2001). The main advantages of PEF technology in water treatment are less unwanted by-products compared to other inactivation techniques such as chlorination, ozonation and UV irradiation (Rook 1977; Paraskeva and Graham 2002; Schwartz et al. 2003) and no developed adaptation to electric field by the descendants of treated bacteria (Gusbeth et al. 2009).

Several studies have investigated the inactivation of bacteria predominantly in relation to microbial inactivation in liquid food (Calderon-Miranda et al. 1999; Heinz et al. 2002; Wu et al. 2005) and wastewater (Rieder et al. 2008). Results of those studies showed significant inactivation but with variable results depending on the microorganisms, the medium in which they were treated and the different electrical parameters that were used. Electrical field strengths ranged from 10 to 40 kV/cm, with pulse duration from 1 μs to 100 ms (Hamilton and Sale 1967; Teissié et al. 2002; Mosqueda-Melgar et al. 2007). Besides microsecond and millisecond electric pulses used for electroporation of cell membranes, Schoenbach et al. (2000) reported that nanosecond pulse durations can be used to efficiently eradicate bacteria from liquid samples. However, reduction of pulse duration from micro- to nanoseconds must be compensated by an increase in the electric field intensity (Schoenbach et al. 2000; Kotnik and Miklavcic 2006; Saulis 2010). When exposing bacterial cells to nanosecond pulses, electric field strength is around 100 kV/cm and pulse duration is in the range of tens of nanoseconds (Schoenbach et al. 2000; Perni et al. 2007). The mechanism of inactivation with nanosecond pulses is different from that caused by reversible and irreversible electroporation with micro- and millisecond pulses (Schoenbach et al. 2000; Weaver 2003). Micro- and millisecond pulse durations induce a voltage on the cell plasma membrane which reduces the energy necessary for membrane lipid rearrangements, leading to cell membrane permeabilization. Exposure of the cell to an external electric field also induces voltage on cell organelles that is several orders of magnitude smaller than the voltage on the cell membrane. Such voltage is too low to induce organelle membrane permeabilization. In nanosecond pulse application, the pulse duration is shorter than the charging time of the outer membrane, for bacteria typically less than 10 ns; besides the effects on cell membrane integrity, additional disruption of internal cell organization is observed (Schoenbach et al. 2000; Perni et al. 2007). Theoretical evaluation of such effects of nanosecond electric pulses was presented for mammalian cells containing organelles by Kotnik and Miklavcic (2006); however, it cannot be directly applied to bacteria due to different internal organization of eukaryotic and prokaryotic cells.

Our study concentrated on inactivation of bacteria in water samples. The aim was to investigate how different electrical pulse parameters affect the inactivation efficiency. We used different protocols, applying microsecond and nanosecond pulses and systematically changing only one parameter at a time, to ascertain the parameters that crucially contribute to the best inactivation results. Microsecond and nanosecond pulses were also used in combination for a potential synergistic effect between the two different pulse protocols.

Materials and Methods

Preparation of Water Samples with Bacterial Culture

The *Escherichia coli* K12 ER1821 strain (New England BioLabs, Frankfurt am Main, Germany) was used as a test microorganism. Luria broth (Sigma-Aldrich, Munich, Germany) was inoculated with *E. coli* cells in an Erlenmeyer flask and incubated for 16–18 h with continuous shaking at 37 °C. In order to prepare samples for the

experiments, a given volume of broth was centrifuged at 4,200 RCF for 30 min at 4 °C. Supernatant was carefully removed, and the cell pellet was resuspended in distilled water, to obtain a final concentration of about 2×10^9 CFU/ml, from which serial dilutions ranging from 10^{-1} to 10^{-7} were prepared. The negative control was the untreated suspension of bacteria. Samples for treatment were diluted suspensions (10^{-1}) of bacterial culture.

Electroporation Protocols

Suspension of bacteria in water was electroporated in cuvettes with integrated aluminum electrodes (Eppendorf, Hamburg, Germany) with a 1- or 2-mm gap. For our experiment, we used different pulsing protocols, which consisted of microsecond, nanosecond and a combination of these pulses. To generate different sequences of microsecond pulses, we used the electric pulse generator HVP-VG (Igea, Carpi, Italy). Nanosecond pulses were generated by a custom-designed high-voltage nanosecond generator built in the Laboratory of Biocybernetics at the Faculty of Electrical Engineering of the University of Ljubljana. The nanosecond generator was built as a diode opening switch generator (Reberšek and Miklavčič 2011) with air-core inductors (Sanders et al. 2009). The electrical field strength (E) was evaluated as

$$E = \frac{U}{d} \quad (1)$$

where U is the applied voltage of the pulses (1,500 and 3,000 V) and d is the gap between electrodes in the cuvettes (1 and 2 mm).

For electroporation with microsecond pulses at different electrical field strengths (7.5, 15, 30 kV/cm) we used eight rectangular unipolar pulses with pulse duration of 100 µs and repetition frequency 1 Hz (Fig. 1a). The correlation between the number of pulses and inactivation was determined by using 8-, 24- and 48-µs pulses at 15 and 30 kV/cm, with pulse duration of 100 µs. The effect of two different pulse durations was determined by comparison of 100 and 250 µs at 30 kV/cm.

Nanosecond pulses were delivered in trains ranging from 10 to 1,000 pulses at 10-Hz frequency, with pulse duration of 10 ns and electrical field strength of 80 kV/cm (Fig. 1b).

The combination of microsecond and nanosecond pulses started with application of 8 × 100-µs pulses ($E = 30$ kV/cm, 1-Hz repetition frequency) followed by 1,000 × 10-ns pulses at 10-Hz repetition frequency, with pulse duration of 10 ns and electrical field strength of 80 kV/cm (Fig. 1c). We also studied the possible effect of the time gap between applying microsecond and nanosecond pulses. In the first set of experiments, there was a 5-s time gap between sets of pulses. A second set of experiments had a time gap of 1 min. All experiments were repeated with pulses delivered in reverse order, applying first nanosecond and then microsecond pulses (Fig. 1d).

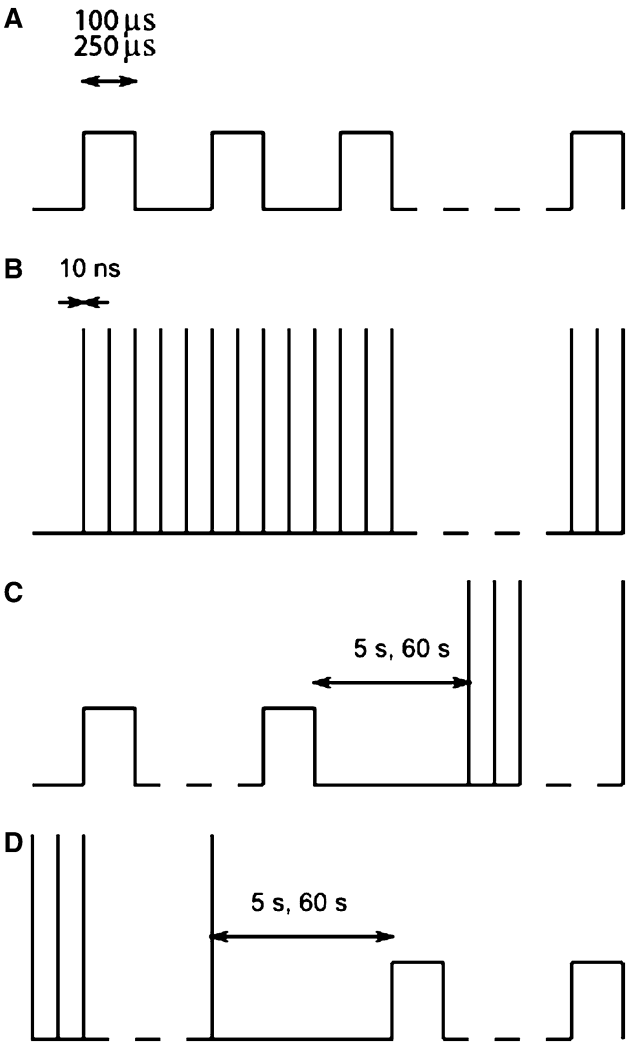

Fig. 1 Schematic representation of different pulsing protocols used in our experiments. Microsecond pulses (**a**), nanosecond pulses (**b**), combination of microsecond and nanosecond pulses (**c**) and combination of nanosecond and microsecond pulses (**d**)

Viable Cell Count

The plate count method (Reasoner 2004) was used to determine cell viability in negative controls (untreated samples) and treated samples. Serial dilutions of each sample were evenly spread using a spread plate technique on Luria agar (Sigma-Aldrich). Plates were incubated for 24 h at 37 °C. Bacterial colonies were counted manually, and the count was expressed as colony-forming units per milliliter of sample. To test the possible toxic effect of

treatment medium on bacteria at chosen electrical parameters, we electroporated the distilled water in cuvettes without bacterial cells and added it to untreated bacterial suspension at a ratio of 1:1, while we did a parallel experiment with untreated distilled water.

The inactivation level of bacterial cells was determined by calculating the $\log_{10}$ of the survival fraction ($S = N/N_0$). N is the number of colony-forming units per milliliter of treated sample, and N_0 is the number of colony-forming units per milliliter of untreated sample. The results are mean values from at least three experiments, with standard deviations shown by error bars. The number of experiments was higher for the most crucial pulse parameters: 8 × 100 µs, 30 kV/cm, where ten experiments were performed; 1,000 × 10-ns pulses, where five experiments were performed; and combination of 8 × 100 µs, 30 kV/cm and 1,000 × 10 ns pulses, where five experiments were performed.

Statistics

Statistical tests were performed on all results (SigmaPlot 11.0; Systat Software, Richmond, CA). A paired *t*-test was performed on results obtained from the same sample and on normalized results if they were obtained from different samples. Respectively, if the normality test (Shapiro-Wilk) failed, the Wilcoxon signed rank test and Mann–Whitney rank sum test were used instead. Results were considered statistically different at $P > 0.05$.

Results

Microsecond Pulses

The effect of different electrical field strengths on the inactivation curve of *E. coli* is shown in Fig. 2a. Electrical field strengths were 7.5, 15 and 30 kV/cm. The inactivation level increased with applied electrical field strengths, for 7.5 ($P = 0.039$), 15 ($P = 0.041$) and 30 ($P < 0.001$) kV/cm compared to control samples not exposed to electric pulses.

Increasing the pulse number from eight to 48 at electrical field strengths of 15 kV/cm, we achieved an almost 2.5-log reduction, which was not statistically significant ($P > 0.05$). For electric field amplitude 30 kV/cm, increasing the pulse number from eight to 24 resulted in significant inactivation ($P = 0.014$), and a similar effect was obtained when comparing eight and 48 pulses ($P = 0.014$). With 48 pulses and 30 kV/cm, a more than 4.5-log reduction was observed.

With eight microsecond pulses of 100 µs we were able to achieve an almost 2-log reduction of *E. coli* ($P < 0.001$).

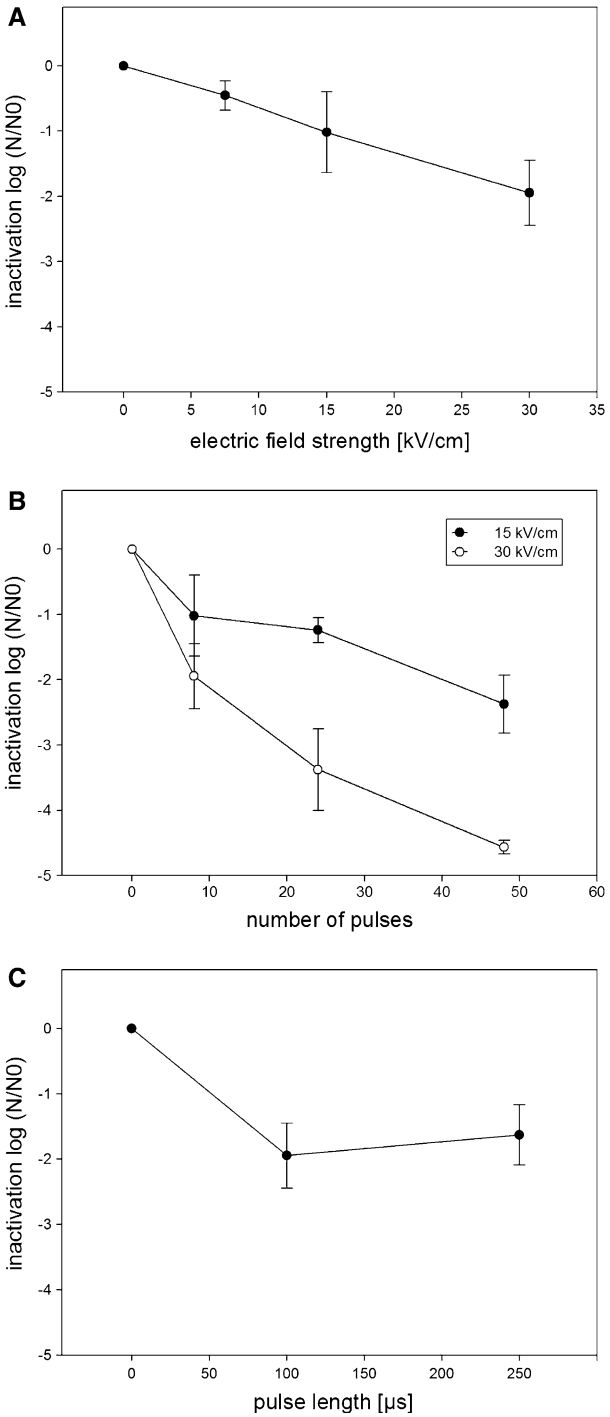

Fig. 2 Inactivation curve of *E. coli* cells by microsecond electric pulses at different electrical field strengths (7.5, 15, 30 kV/cm) with eight pulses of 100 µs (**a**), with different numbers of 100-µs pulses at 15 kV/cm (*filled circle*) and 30 kV/cm (*open circle*) (**b**) and with two different pulse durations, 100 and 250 µs. A train of eight pulses with a repetition frequency of 1 Hz and electrical field strength of 30 kV/cm was applied (**c**). Inactivation is presented as a log N/N_0, where N is the number of colony-forming units per milliliter of treated sample and N_0 is the number of colony-forming units per milliliter of untreated sample. Results are means from at least three experiments, with standard deviations shown by *error bars*

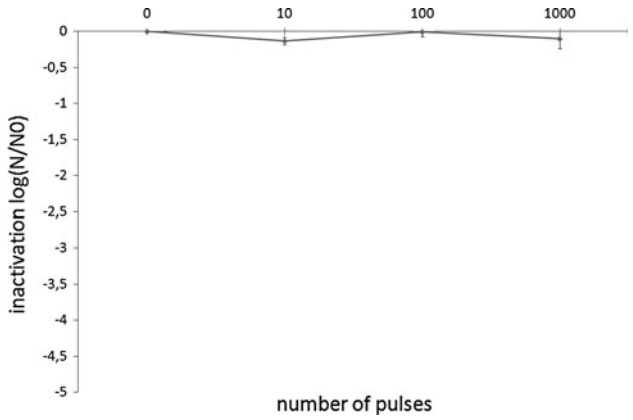

Fig. 3 Inactivation curve of *E. coli* with nanosecond pulses for different numbers of pulses (10, 100, 1,000). Pulse duration was 10 ns and electrical field strength was 80 kV/cm at 10-Hz frequency. Inactivation is presented as a log N/N_0, where N is the number of colony-forming units per milliliter of treated sample and N_0 is the number of colony-forming units per milliliter of untreated sample. Results are means from at least three experiments with standard deviations shown by *error bars*

Increasing pulse duration to 250 µs achieved the same inactivation as 100-µs pulses ($P = 0.353$), as shown in Fig. 2c.

Nanosecond Pulses

The results obtained by treating cell suspensions of *E. coli* with a train ranging from 10 to 1,000 pulses at 10-Hz repetition frequency (10 ns, $E = 80$ kV/cm) are shown in Fig. 3. Nanosecond pulses with these parameters did not have any effect ($P > 0.05$) on inactivation of *E. coli* regardless of the number of pulses delivered.

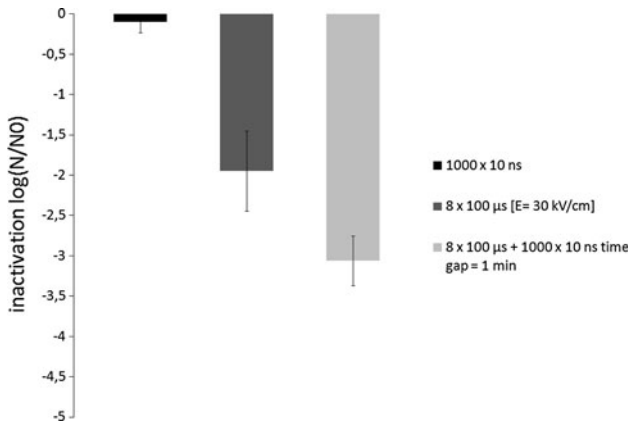

Fig. 4 Comparison of inactivation of *E. coli* using a combination of nano- and microsecond pulses. The pulsing protocol consisted of 1,000 pulses of 10 ns ($E = 80$ kV/cm), eight pulses of 100 µs ($E = 30$ kV/cm) and a combination of eight pulses of 100 µs ($E = 30$ kV/cm) followed by 1,000 pulses of 10 ns ($E = 80$ kV/cm). Inactivation is presented as a log N/N_0, where N is the number of colony-forming units per milliliter of treated sample and N_0 is the number of colony-forming units per milliliter of untreated sample. Results are means from at least three experiments, with standard deviations shown by *error bars*

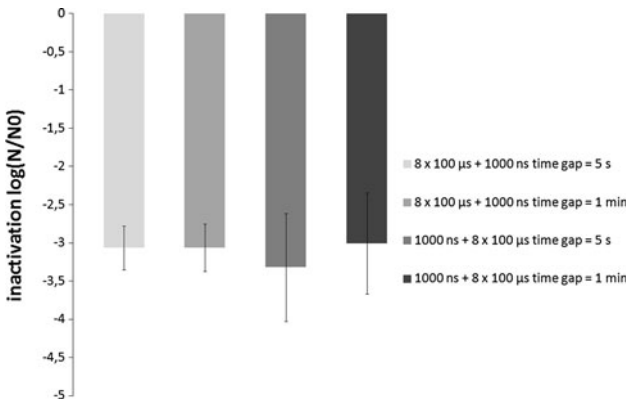

Fig. 5 Effect of the time gap and order of application of nanosecond and microsecond pulses on the inactivation of *E. coli*. Nanosecond pulses consisted of 1,000 pulses of 10 ns ($E = 80$ kV/cm), while microsecond pulses were applied as a train of eight pulses of 100 µs ($E = 30$ kV/cm). The time gap between nanosecond and microsecond pulses was 5 s and 1 min, respectively. Nanosecond pulses were delivered in two different sequences: microsecond pulses, followed by nanosecond pulses or in the reverse order. Inactivation is presented as a log N/N_0, where N is the number of colony-forming units per milliliter of treated sample and N_0 is the number of colony-forming units per milliliter of untreated sample. Results are means from at least three experiments, with standard deviations shown by *error bars*

Combination of Microsecond and Nanosecond Pulses

Using a combination of microsecond and nanosecond pulses resulted in a pronounced reduction (three log) in the bacterial count compared to using only microsecond ($P = 0.003$) or nanosecond ($P = 0.008$) pulses (Fig. 4). Extending the time gap between electroporation from 5 s to 1 min did not seem to have any effect on inactivation of cells. Changing the order in which the microsecond and nanosecond pulses were delivered also had no effect on inactivation ($P > 0.05$) (Fig. 5).

Discussion

Based on experimental work, this study presents inactivation of bacteria in water samples with microsecond pulses, nanosecond pulses and a combination of both protocols. We investigated how various field amplitudes, increasing number of pulses and different pulse durations affected the inactivation of *E. coli*.

Inactivation of bacteria with microsecond pulses increases with higher electric field amplitudes (Fig. 2a). These results are in agreement with the findings of other authors (Hülsheger et al. 1981; Schoenbach et al. 2000; Álvarez et al.

2003; Pataro et al. 2011). A theoretical explanation is available for the effects of microsecond pulses on bacterial inactivation. Transmembrane potential induced on the cell membrane by external electric pulses leads to creation of small, metastable, hydrophilic pores and pore evolution in terms of pore size enlargement and increase in the number of pores. The rate of pore formation depends strongly on transmembrane potential and electric field amplitude. It is important to note that for bacterial inactivation postpulse events in the cell are also important. Namely, cell viability is strongly related to the pore resealing process and to leaking of material out of the cell as the majority of transport occurs after electric pulse application (Saulis 2010). Even though electric pulse duration is one of the factors affecting cell survival, in our study extending the duration of microsecond pulses from 100 to 250 μs did not affect the inactivation of *E. coli*, which is consistent with the theory of electroporation that indicates that increasing electric pulse amplitude is more effective than lengthening treatment time (Saulis 2010). However, results show that microbial inactivation rate increased with increasing number of pulses (Fig. 2b). Authors working with different microorganisms report similar results (Hülsheger et al. 1981; Jayaram et al. 1992; Martín-Belloso et al. 1997; Calderon-Miranda et al. 1999). Regarding pulse parameters affecting bacterial inactivation caused by micro- and millisecond pulse duration, lipid rearrangements leading to cell membrane permeabilization (Kotnik and Miklavcic 2006) and postpulse resealing (Saulis 2010) are the main factors involved in the process. Besides, when a large number of or long pulses are applied, PEF treatment can produce toxic side products due to electrochemical reactions such as electrolysis of the media, release of the ions from electrodes and generation of free radicals. Bacterial inactivation could be caused by those toxic products, which was not the case in our study as additional experiments were performed. Only the electroporation medium was exposed to PEF treatment and added to intact bacteria, which then grew just as well as bacteria exposed to untreated electroporation medium. No effect on bacterial viability was detected, indicating that in our case no toxic products which would affect bacterial inactivation were formed.

In case of nanosecond pulse application the microbial inactivation observed could not be due only to the effects caused on the cell membrane level (Schoenbach et al. 2000; Perni et al. 2007). In our study, when nanosecond pulses were used to inactivate *E. coli*, no effect was observed regardless of the number of pulses (ranging 10–1,000) to which the samples were exposed (Fig. 3). However, Perni et al. (2007) reported an almost 2-log reduction for *E. coli*. The electric pulse parameters used for this effect were 32-ns pulses at field strength of 100 kV/cm and 30-Hz frequency. Samples were treated for 300 s, receiving 9,000 pulses in total (Perni et al. 2007). The differences between our results and those reported by Perni and coworkers can be attributed to the different electric pulse protocols used. In our study lower field strength (80 kV/cm), shorter pulse duration (10 ns) applied at lower frequencies (10 Hz) and lower number of pulses (maximal 1,000) were used. It is therefore possible that the overall treatment with our nanosecond pulse parameters was not severe enough to reduce the viability of treated bacteria (Fig. 3). Perni et al. (2007) observed that at the end of the treatment only approximately 1 % of the surviving populations remained uninjured. They assumed that the mechanism of bacterial inactivation with such short pulses may have affected the internal structures of bacterial cells (Perni et al. 2007), as proposed earlier by Schoenbach et al. (2000). Theoretical evaluation of the effect of microsecond and nanosecond electroporation of mammalian cells containing organelles showed that the cell membrane is affected by nanosecond electric pulses and that organelles are permeabilized if the electric properties of the cytosol and the organelle interior are different (Kotnik and Miklavcic 2006). However, the theoretical findings on mammalian cells cannot be directly applied to bacteria due to the different internal organization of eukaryotic and prokaryotic cells, and currently only experimental evidence on the effect of nanosecond pulses on bacteria is available. A large majority of theoretical studies are devoted to explaining the mechanism involved in the electroporation of eukaryotic cells, while the pathways leading to microbial inactivation remain obscure (Saulis 2010). Nevertheless, some experimental evidence is available. Effects of PEF treatment on internal cell structures were observed when bacteria were exposed to microsecond pulses. Electron microscopy revealed that approximately 25 % of the *E. coli* cells exposed to PEF treatment at 30 kV/cm, 20 pulses and 4-μs duration had an altered internal organization, while rupture of cell membranes could not be confirmed by use of transmission electronic microscopy (Aronsson et al. 2001). The critical pulse duration that results in intracellular effects is for bacteria in the range of tens of nanoseconds (Schoenbach et al. 2000). From this point of view it is interesting that Aronsson et al. (2001) observed alterations in intracellular structures with longer microsecond pulses that should have had a main effect at the cell membrane level. From the data available in the literature (Schoenbach et al. 2000; Weaver 2003; Kotnik and Miklavcic 2006; Perni et al. 2007; Saulis 2010) we can expect that microsecond pulses affect cell membrane integrity, while nanosecond pulses additionally affect internal organization. Since a wide variety of microbial inactivation processes are known to cause death through injury accumulation (Perni et al. 2007), we decided to combine microsecond and nanosecond pulses. Our results

suggest a great synergistic effect between microsecond and nanosecond pulses, with a more than 3-log reduction for *E. coli*. According to our results (Figs. 2b, 4), using only microsecond pulses, 20 × 100-μs pulses would be needed to achieve the same level of inactivation as eight microsecond pulses in combination with 1,000 nanosecond pulses. The combination of nanosecond and microsecond pulses is a unique method of inactivation and has two main advantages, energy efficiency and less joule heating, compared to microsecond pulses. We roughly estimated the electrical energy needed for each type of electric pulse. Supposing that the electrical pulses are rectangular and that the electric field in cuvettes is homogeneous allows us to use the following equation to estimate the pulse energy,

$$Wp = E^2 \times \sigma \times V \times t_p \quad (2)$$

where W_p is the pulse energy, E is the electric field intensity between the electrodes, σ is the electrical conductivity of cell suspension, V is the volume of suspension and t_p is the pulse duration. The ratio between the energy of one 100-μs pulse (W_μ) and the energy of one 10-ns pulse (W_n) is 1,400. One 100-μs pulse equals 1,400 × 10-ns pulses from the pulse energy point of view.

Although nanosecond pulses alone have no effect on inactivation, the results of combining them with microsecond pulses suggest that there clearly is some mechanism involved in which nanosecond pulses contribute to inactivation. The effect of the time gap from 5 s up to 1 min between applying microsecond and nanosecond pulses as well as the order in which the pulses were delivered showed no difference in inactivation.

In conclusion, our results confirm that bacterial inactivation is affected by electric pulse parameters such as pulse amplitude and number of pulses when we applied only microsecond pulses. A synergistic effect was observed when nanosecond and microsecond pulses were combined even though nanosecond pulses alone did not affect bacterial inactivation. Further studies are needed to determine the exact mechanisms of action of such a pulse combination on bacteria.

Acknowledgements The authors thank Prof. Dr. Damijan Miklavčič, who read the manuscript and provided comments and insights that improved it. This research was supported by the Slovenian Research Agency under research program P2-0249, MRIC UL IP-0510 and research project L2-4314. The research was conducted in the scope of EBAM, European Associated Laboratory.

References

Agerholm-Larsen B, Linnert M, Iversen HK, Gehl J (2011) Drug and gene electrotransfer to the brain. In: Kee ST, Gehl J, Lee EW (eds) Clinical aspect of electroporation. Springer, New York, pp 129–135

Álvarez I, Pagán R, Condón S, Raso J (2003) The influence of process parameters for the inactivation of *Listeria monocytogenes* by pulsed electric fields. Int J Food Microbiol 87:87–95

Aronsson K, Lindgren M, Johansson BR, Rönner U (2001) Inactivation of microorganisms using pulsed electric fields: the influence of process parameters on *Escherichia coli*, *Listeria innocua*, *Leuconostoc mesenteroides* and *Saccharomyces cerevisiae*. Innov Food Sci Emerg Technol 2:41–54

Barbosa-Cánovas G, Góngora-Nieto M, Pothakamury U, Swanson B (1999) Preservation of foods with pulsed electric fields. Academic Press, San Diego

Bertacchini C, Margotti PM, Bergamini E, Lodi A, Ronchetti M, Cadossi R (2007) Design of an irreversible electroporation system for clinical use. Technol Cancer Res Treat 6:313–320

Calderon-Miranda ML, Barbosa-Canovas GV, Swanson BG (1999) Inactivation of *Listeria innocua* in liquid whole egg by pulsed electric fields and nisin. Int J Food Microbiol 51:7–17

Chang DC, Reese TS (1990) Changes in membrane structure by electroporation as revealed by rapid-freezing electron microscopy. Biophys J 58:1–12

Davalos RV, Mir LM, Rubinsky B (2005) Tissue ablation with irreversible electroporation. Ann Biomed Eng 33:223–231

Fuller GW (1898) Report on the investigations into the purification of the Ohio River water at Louisville Kentucky. D. Van Nostrand, New York

Gusbeth C, Frey W, Volkmann H, Schwartz T, Bluhm H (2009) Pulsed electric field treatment for bacteria reduction and its impact on hospital wastewater. Chemosphere 75:228–233

Hamilton WA, Sale AJH (1967) Effects of high electric fields on microorganisms: I. Killing of bacteria and yeast. Biochim Biophys Acta 148:781–788

Heinz V, Alvarez L, Angersbach A, Knorr D (2002) Preservation of liquid foods by high intensity pulsed electric fields—basic concepts for process design. Trends Food Sci Technol 12:103–111

Hülsheger H, Pottel J, Niemann E (1981) Killing of bacteria with electric pulses of high field strength. Radiat Environ Biophys 20:53–65

Jayaram S, Castle G, Margaritis A (1992) Kinetics of sterilization of *Lactobacillus brevis* by the application of high voltage pulses. Biotech Bioeng 40:1412–1420

Kotnik T, Miklavcic D (2006) Theoretical evaluation of voltage inducement on internal membranes of biological cells exposed to electric fields. Biophys J 90:480–491

Kümmerer K (2001) Drugs in the environment: emission of drugs, diagnostic aids and disinfectants into wastewater by hospitals in relation to other sources—a review. Chemosphere 45:957–969

Lee EW, Chen C, Prieto VE, Dry SM, Loh CT, Kee ST (2010) Advanced hepatic ablation technique for creating complete cell death: irreversible electroporation. Radiology 255:426–433

Martín-Belloso O, Qin B, Chang F, Barbosa-Cánovas G, Swanson B (1997) Inactivation of *Escherichia coli* in skim milk by high intensity pulsed electric fields. J Food Process Eng 20:317–336

Marty M, Sersa G, Rémi Garbay J, Gehl J, Collins CG, Snoj M, Billard V, Geersten PF, Larkin JO, Miklavcic D, Pavlovic I, Paulin-Kosir SM, Cemazar M, Norsli N, Soden DM, Rudolf Z, Robert C, O'Sullivan GC, Mir LM (2006) Electrochemotherapy—an easy, highly effective and safe treatment of cutaneous and subcutaneous metastases: results of ESOPE (European standard operating procedures of electrochemotherapy) study. EJC Suppl 4:3–13

Mosqueda-Melgar J, Raybaudi-Massilia RM, Martín-Belloso O (2007) Influence of treatment time and pulse frequency on *Salmonella enteritidis*, *Escherichia coli* and *Listeria monocytogenes* populations inoculated in melon and watermelon juices treated by pulsed electric fields. Int J Food Microbiol 117:192–200

Neumann E, Rosenheck K (1972) Permeability changes induced by electric impulses in vesicular membranes. J Membr Biol 14:194–196

Paraskeva P, Graham NJ (2002) Ozonation of municipal wastewater effluents. Water Environ Res 74:569–581

Pataro G, Senatore B, Donsi G, Ferrari G (2011) Effect of electric and flow parameters on PEF treatment efficiency. J Food Eng 105:79–88

Perni S, Charlise PR, Shama G, Kong MG (2007) Bacterial cells exposed to nanosecond pulsed electric fields show lethal and sublethal effects. Int J Food Microbiol 120:311–314

Reasoner DJ (2004) Heterotrophic plate count methodology in the United States. Int J Food Microbiol 92:307–315

Reberšek M, Miklavčič D (2011) Advantages and disadvantages of different concepts of electroporation pulse generation. Automatika 52:12–19

Rieder A, Schwartz T, Schön-Hölz K, Marten S, Süss J, Gusbeth C, Kohnen W, Svoboda W, Obst U, Frey W (2008) Molecular monitoring of inactivation efficiencies of bacteria during pulsed electric field treatment of clinical wastewater. J Appl Microbiol 105:2035–2045

Rols MP (2006) Electropermeabilization, a physical method for the delivery of therapeutic molecules into cells. Biochim Biophys Acta 1758:423–428

Rook JJ (1977) Chlorination reactions of fulvic acids in natural waters. Environ Sci Technol 11(5):478–482

Rubinsky B (2007) Irreversible electroporation in medicine. Technol Cancer Res Treat 6:255–259

Sanders JM, Kuthi A, Wu Y, Vernier PT, Gundersen MA (2009) A linear, single-stage, nanosecond pulse generator for delivering intense electric fields to biological loads. IEEE Trans Dielectr Electr Insul 16:1048–1054

Saulis G (2010) Electroporation of cell membranes: the fundamental effects of pulsed electric fields in food processing. Food Eng Rev 2:52–73

Schoenbach KH, Joshi RP, Stark RH (2000) Bacterial decontamination of liquids with pulsed electric fields. IEEE Trans Dielectr Electr Insul 7:637–645

Schwartz T, Hoffman S, Obst U (2003) Formation of natural biofilms during chlorine dioxide and UV disinfection in a public drinking water distribution system. J Appl Microbiol 95:591–601

Sersa G, Miklavcic D, Cemazar M, Rudolf Z, Pucihar G, Snoj M (2008) Electrochemotherapy in treatment of tumors. Eur J Surg Oncol 34:232–240

Teissié J, Eynard N, Vernhes MC, Bénichou A, Ganeva V, Galutzov B, Cabanes PA (2002) Recent biotechnological developments of electropulsation. A prospective review. Bioelectrochemistry 55:107–112

Weaver JC (2003) Electroporation of biological membranes from multicellular to nano scales. IEEE Trans Dielectr Electr Insulation 10:754–768

Wu Y, Mittal GS, Griffiths MW (2005) Effect of pulsed electric field on the inactivation of microorganisms in grape juices with and without antimicrobials. Biosyst Eng 90:1–7

J Membrane Biol (2012) 245:651–659
DOI 10.1007/s00232-012-9487-6

Molecular-Level Characterization of Lipid Membrane Electroporation using Linearly Rising Current

Peter Kramar · Lucie Delemotte · Alenka Maček Lebar · Malgorzata Kotulska · Mounir Tarek · Damijan Miklavčič

Received: 19 December 2011 / Accepted: 5 July 2012 / Published online: 11 August 2012

Abstract We present experimental and theoretical results of electroporation of small patches of planar lipid bilayers by means of linearly rising current. The experiments were conducted on ~120-μm-diameter patches of planar phospholipid bilayers. The steadily increasing voltage across the bilayer imposed by linearly increasing current led to electroporation of the membrane for voltages above a few hundred millivolts. This method shows new molecular mechanisms of electroporation. We recorded small voltage drops preceding the breakdown of the bilayer due to irreversible electroporation. These voltage drops were often followed by a voltage re-rise within a fraction of a second. Modeling the observed phenomenon by equivalent electric circuits showed that these events relate to opening and closing of conducting pores through the bilayer. Molecular dynamics simulations performed under similar conditions indicate that each event is likely to correspond to the opening and closing of a single pore of about 5 nm in diameter, the conductance of which ranges in the 100-nS scale. This combined experimental and theoretical investigation provides a better quantitative characterization of the size, conductance and lifetime of pores created during lipid bilayer electroporation. Such a molecular insight should enable better control and tuning of electroporation parameters for a wide range of biomedical and biotechnological applications.

Keywords Planar lipid bilayer · Linear rising current · Molecular dynamics simulation

P. Kramar · A. Maček Lebar · D. Miklavčič (✉)
Faculty of Electrical Engineering, University of Ljubljana, Trzaska 25, 1000 Ljubljana, Slovenia
e-mail: damijan.miklavcic@fe.uni-lj.si

L. Delemotte · M. Tarek (✉)
UMR Structure et Réactivité des Systèmes Moléculaires Complexes, Centre National de la Recherche Scientifique, Université de Lorraine, Nancy, France
e-mail: mounir.tarek@univ-lorraine.fr

M. Kotulska
Institute of Biomedical Engineering and Instrumentation, Wroclaw University of Technology, Wybrzeze Wyspianskiego 27, 50-350 Wroclaw, Poland

Introduction

Electroporation is a process in which lipid membranes, the cell envelopes, are permeabilized when subjected to high electric fields (Neumann and Rosenheck 1972). Under specific conditions, Electroporation may be reversible, in which case membranes and cells recover their initial state when the applied field is turned off (Zimmermann et al. 1976; Glaser et al. 1988). Electroporation is widely used in biomedicine and biotechnology to enhance the transport of molecules across the plasma membrane (Prausnitz et al. 1993), a technique also known as electropermeabilization (Mir et al. 1988; Teissie et al. 1999). Applications range from in vitro DNA plasmids and siRNA cell delivery (Golzio et al. 2002; Villemejane and Mir 2009) to clinical electrochemotherapy (Marty et al. 2006), where delivery of drugs, e.g., bleomycin and cisplatinum, to cancer cells is enhanced (Mir et al. 1995; Sersa et al. 1995; Heller et al. 1999). It is now well established that the efficiency of such applications depends on the intensity, duration and number of electric pulses applied (Rols and Teissie 1998; Pucihar et al. 2002; Teissie et al. 2008). Better control and tuning of the method require full understanding and quantitative characterization of the molecular-level processes taking place during and after electroporation.

Low-intensity electric fields normal to the membrane induce, through Maxwell-Wagner polarization (Kotnik et al. 1997), a transmembrane voltage. When the voltage reaches a certain value characteristic of the membrane composition, water wires form within the bilayer. This is followed by the appearance of hydrophilic pores that disrupt the membrane integrity, as suggested by early molecular dynamics (MD) simulations (Tieleman et al. 2003; Tarek 2005). Electroporation voltage thresholds are most often determined in experiments where electric pulses or linearly increasing voltage signal is applied to planar lipid bilayers (Kramar et al. 2007) or on cells in vitro using fluorescent dyes (Teissie and Rols 1993) or cytotoxic drugs (Kotnik et al. 2000). However, most often, such techniques do not allow characterization of structural and dynamic properties of the putative pores formed during the membrane electroporation, such as pore size, conductance and lifetime. As an alternative, electroporation under constant current conditions has been proposed (Genco et al. 1993; Kalinowski et al. 1998). This method allows the maintenance of long-lived fluctuating pores, as shown for planar membranes of lecithin (Koronkiewicz and Kalinowski 2004; Kotulska et al. 2004, 2007).

Here, we report on electroporation of planar lipid bilayer patches by another experimental protocol, based on exposure to linearly rising current (Koronkiewicz et al. 2002). We studied the appearance of pores and investigated the molecular mechanism of electroporation. Exposing lipid bilayers to a linearly increasing current builds voltage across the membrane and induces events indicative of poration and subsequent resealing of the bilayer. In order to characterize these changes on a molecular scale, we carried out MD simulations under similar conditions. Combined together, the theoretical and experimental investigations allowed a quantitative estimation of the properties of the created pores.

Materials and Methods

Experiments on Planar Lipid Bilayer

Experiments under current-controlled conditions (i.e., current clamp) were performed using a measuring system (Fig. 1), as described by Kalinowski and Figaszewski (1995a, b) and Kalinowski et al. (1998), with four Ag–AgCl electrodes (two current electrodes and two reference electrodes). The measuring system consisted of two modules. The first one was a capacity to period converter, used for measuring the bilayer's capacitance; the second was a potentiostat-galvanostat for current-controlled planar lipid bilayer studies.

The chamber where planar lipid bilayers are formed consists of two 5.3-cm^3 reservoirs made of Teflon. Between the two compartments, a thin Teflon sheet with a

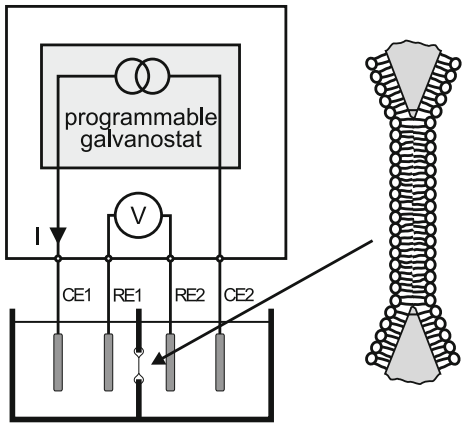

Fig. 1 Measurement system with a programmable galvanostat and a voltameter with four Ag–AgCl electrodes, two current electrodes (*CE*) and two reference electrodes (*RE*) plunged into the Teflon chamber compartments

117-μm diameter, round aperture was inserted (Kramar et al. 2009). Planar lipid bilayers were formed by the Montal–Mueller method (Montal and Mueller 1972).

We studied bilayers prepared from 1-pamitoyl 2-oleoyl phosphatidylcholine (POPC) (Avanti Polar-Lipids, Alabaster, AL). Lipid powder was dissolved in a 9:1 hexane/ethanol solution. A 3:7 mixture of hexadecane and pentane was used for torus formation. The salt solution consisted of 0.1 M KCl and 0.01 M HEPES in the same proportion. We added 1 M NaOH to obtain a neutral pH (7.4).

Measuring protocols consisted of two parts: capacitance measurement and lipid bilayer breakdown voltage measurement. Membrane capacitance was measured with the capacitance to period converting principle described in detail by Kalinowski and Figaszewski (1995a) and then normalized to the surface area of the bilayer to calculate the specific capacitance (C_{BLM}). We then determined the breakdown voltage (U_{br}) of each lipid bilayer by applying linear rising current signals (of slope k). Nine different slopes were selected: 0.03, 0.05, 0.1, 0.2, 0.5, 4, 8, 10 and 20 μA/s. U_{br} was defined as the voltage at t_{br}, when an abrupt voltage drop due to lipid bilayer rupture was detected (Fig. 2).

Electrical Model of Experimental Setup

The whole measuring system was modeled by an equivalent electrical circuit (Fig. 3). We used Spiceopus software (http://www.spiceopus.com/) to simulate the equivalent electrical circuit behavior under our specific experimental conditions (Tuma and Buermen 2009). In the Spiceopus model (Fig. 3) current was applied by current generator I_0. In Fig. 3, C_{BLM} is the capacitance of the planar lipid bilayer, R_{BLM} is the resistance of the planar lipid bilayer,

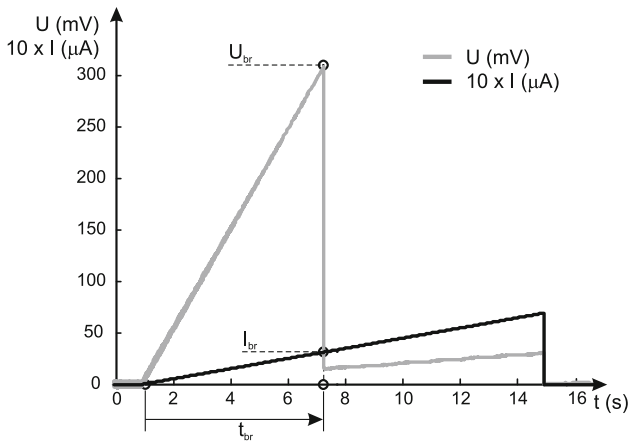

Fig. 2 Breakdown voltage U_{br} determination by means of linear rising current signal

C_{sys} is the capacitance of the chamber, R_{sys} is the resistance of the chamber and R_P is resistance of the pores.

Spiceopus software uses node-voltage analysis. To measure the currents flowing through various parallel branches of the circuit, an independent voltage source ($V = 0$) was added in series with the element of the branch (Fig. 3) according to recommendations. The appearance of pores (R_P) in the planar lipid bilayer was simulated by introducing a voltage-controlled switch in the R_P branch. An intact planar lipid bilayer was represented by an open switch, while a porated planar lipid bilayer was represented by a closed switch.

The value of R_{BLM} was set to 10^8 Ω, which is the typical value found in the literature (Tien 1974). The value of membrane capacitance was estimated to be 0.51 μF/cm^2 as an average of the experimentally measured values. Values for C_{sys} and R_{sys} were obtained by optimization in Spiceopus software. The values that gave the best fit are $C_{sys} = 105 \pm 54$ nF and $R_{sys} = 100 \pm 5$ kΩ. Finally, R_P, i.e., the conductance of pores ($1/R_P$) value in the model, was adjusted to each of 44 experimentally obtained voltage drops.

MD Simulations

The membrane model used for this study is an equilibrated fully hydrated POPC bilayer and was built by replication of a previous well-equilibrated smaller system (Delemotte et al. 2008). It consists of 1,152 lipid units and 58,304 water molecules organized in two lamellae above and below the lipids. At the temperature set for the study, i.e., 300 K, the bilayer was in the biologically relevant liquid crystal Lα phase. The solvent contained 560 Na^+ and 560 Cl^- ions. The final dimensions of the system before extending it in the z direction were 168 × 183 × 110 Å^3 and the total number of atoms was 261,280.

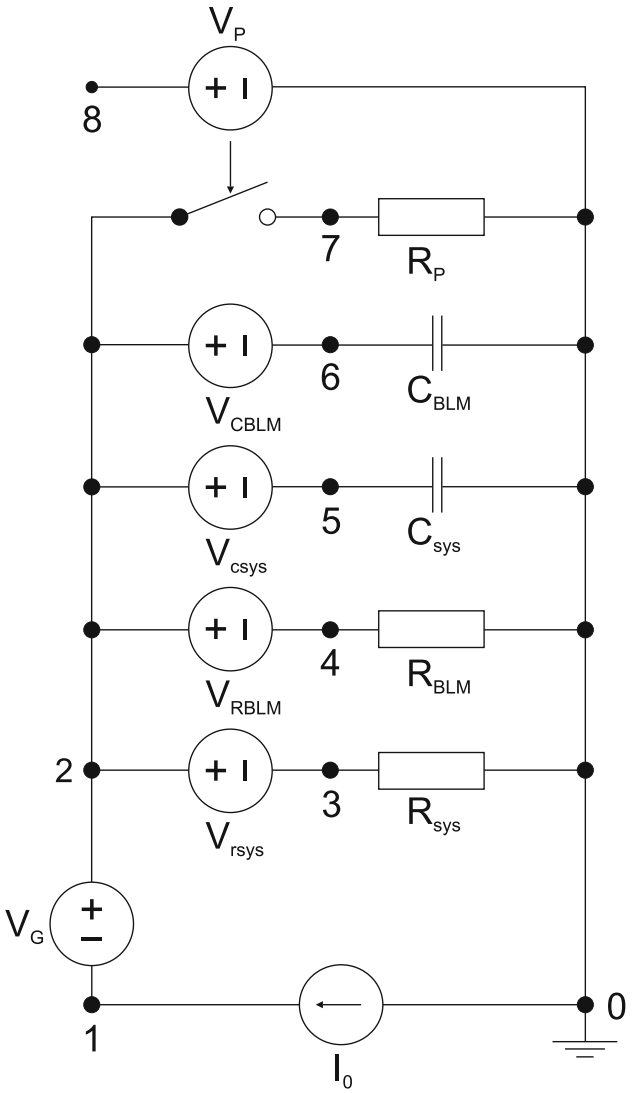

Fig. 3 Equivalent electrical circuit representing the measurement chamber (R_{sys}, C_{sys}) and the planar lipid bilayer (R_{BLM}, C_{BLM}) used for the SPICE model. The current source I_0 was used to simulate current-clamp conditions. A voltage control switch (V_P) was used to simulate a pore on the planar lipid bilayer. Voltage generators V_G, V_{rsys}, V_{RBLM}, V_{csys} and V_{CBLM} with voltage set to zero were introduced to measure the current trough in each branch

The MD simulation was carried out using the program NAMD targeted for massively parallel architectures (Kale et al. 1999; Phillips et al. 2005). The systems were examined at constant pressure and constant temperature (1 atm and 300 K) or at constant volume and constant temperature (300 K) employing Langevin dynamics and the Langevin piston method. The equations of motion were integrated using the multiple time-step algorithm. A time step of 2.0 fs was employed. Short- and long-range forces were calculated every two and four time steps, respectively. Chemical bonds between hydrogen and heavy atoms were constrained to their equilibrium value. Long-range,

electrostatic forces were taken into account using a fast implementation of the particle mesh Ewald (PME) method (Darden et al. 1993; Essmann et al. 1995), with a direct space sum tolerance of 10^{-6} and a spherical truncation of 11 Å. Water molecules were described using the TIP3P model (Jorgensen et al. 1983), and a united-atom representation was adopted for the acyl chains of the POPC lipid molecules (Henin et al. 2008).

The system was first equilibrated for tens of nanoseconds at constant temperature (300 K) and constant pressure (1 atm), as in the simulations of multilamellar stacks of lipids. Following this equilibration, the initial salt concentration (~530 mM, counting only the fraction of ions) went down in the bulk, because of accumulation of charges near the zwitterionic lipid headgroup interface, to 490 mM. The system size was then extended in the z direction ($L_z = 200$ Å), creating therefore an air–water interface. Subsequent simulations were run at constant volume, using 3D periodic boundary conditions, the thickness of the vacuum slab created above and below the solvent (>40 Å each) being large enough to prevent significant interactions between the original cell and its replicas in the z direction, i.e., perpendicular to the bilayer (Fig. 4).

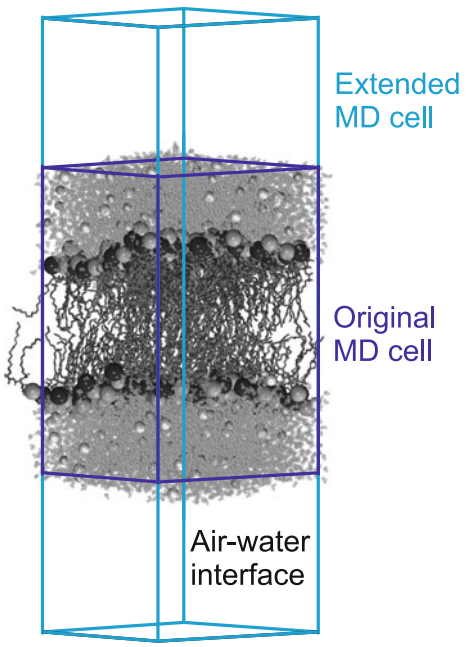

Fig. 4 MD simulation setup: configuration of a hydrated POPC lipid bilayer embedded in a ~500-mM NaCl electrolyte solution. Lipid tails are depicted as *purple sticks*, and headgroup atoms are represented as *large spheres* (*cyan* choline, *blue* phosphate). Water molecules are represented as *gray* and Cl^- and Na^+ ions as, respectively, *cyan* and *yellow small spheres*. The extension of the simulation cell (from *purple* to *blue box*) creates air–water interfaces that permit induction of a transmembrane voltage by imposing a net charge imbalance across the bilayer (Color figure online)

Further simulations were performed using the standard "electric field method" for which a constant electric field, $\vec{E}$, normal to the bilayer, was applied on the "nonextended" systems (i.e., original MD cell) using 3D periodic boundary conditions. Under $E \sim 0.2$ V Å^{-1}, the applied voltage is $U = E{\cdot}L_z$, where L_z is the length of the simulation box along the normal to the bilayer and amounts here to ~2 V. For an MD simulation under such conditions lasting about 2 ns, the diameter of the hydrophilic pore increased to ~50 Å.

The one-dimensional electrostatic potential profile along the membrane normal was derived directly from the MD simulations as a double integral of the charge distribution of all atoms averaged over the membrane planes, $\rho(z)$, as

$$\Phi(z) - \Phi(0) = -\varepsilon_0^{-1} \int \int \rho(z'')dz''dz'$$

As a reference, $\Phi(z)$ was set to zero in the upper electrolyte. Considering the present protocol, $\Phi(z)$ showed plateau values in the aqueous regions. The difference between the plateau values at the two electrolytes corresponds to the transmembrane potential, ΔV.

Results

We performed 63 experiments at nine different slopes of linearly rising current (0.03, 0.05, 0.1, 0.2, 0.5, 4, 8, 10 and 20 μA/s) during which the transmembrane voltage, U, across the planar lipid bilayer was monitored. For each bilayer, the capacitance was first estimated from measurements of the whole system capacitance with and without bilayer formed (Kramar et al. 2009; Benz and Janko 1976), using the capacitance to period converter method (Kalinowski and Figaszewski 1995b).

A typical trace of the voltage measured across the bilayer, corresponding to the applied current, is presented in Fig. 5a. As expected, at a certain U_{br}, high enough transmembrane voltage, the voltage collapses, indicating a breakdown of the planar lipid bilayer. In about half of the experiments, at some voltage level U_d below U_{br}, the transmembrane voltage suddenly drops for a few millivolts (within the experimental time resolution of either 1 or 10 ms). Afterwards, the voltage either continues rising with the same slope as previously before reaching U_{br} and collapsing to ~0 mV or, after increasing steadily for a while, jumps back to a higher value and then exhibits the same rise as before U_d (Fig. 5a). Interestingly, as opposed to the constant current-clamp method for which we previously observed only fluctuations in the transmembrane voltage (Kotulska et al. 2004, 2007, 2010), this new linearly rising current excitation enables observation of well-defined and reproducible events.

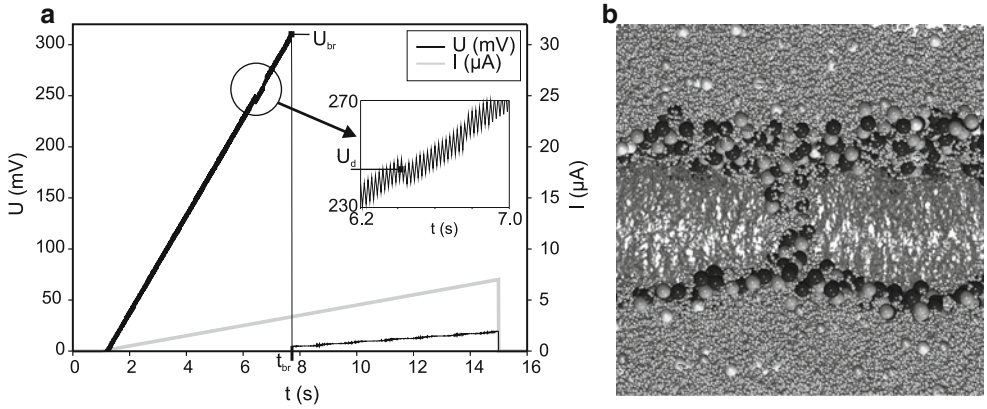

Fig. 5 **a** Trace of the measured transmembrane voltage (U) under linearly rising current (I) conditions. U_{br} is the voltage at which bilayer breakdown occurs, and the *arrow* points at a transient voltage drop. After this event, the bilayer appears to recover completely within a fraction of the second. **b** MD simulation snapshot of the hydrophilic pore created in the POPC bilayer subject to high transmembrane voltages induced by ionic imbalance. Same color code as Fig. 4

Out of these 63 experiments, small voltage drops (as examples indicated by arrows in Fig. 6) were observed in 31 experiments. Mostly we observed a single voltage drop, but even up to three separate drops were observed in these experiments. All together, we recorded 44 small voltage drops. According to their shape, they were divided into two categories: (1) drop only and (2) drop and reseal (Table 1). At drop only (Fig. 6a) the voltage drops to a finite value of U_d and does not rise back. At drop and reseal (Fig. 6b) the voltage drops for a finite value of U_d; after a certain time interval t event, the voltage rises back to a value of U_{rise}, continuing on the same slope as before the drop.

In order to quantify these voltage drop events and to discriminate between the contribution of the measurement chamber and that of the bilayer, it was necessary to model the whole system using an equivalent electrical circuit. A SPICE model including five parallel branches connected to a current generator (Fig. 3) was used to model the changes in the recorded voltage of all 63 performed experiments. Two branches of the circuit describe the measurement system, as a capacitor C_{sys} in parallel with a resistor R_{sys}. The values for C_{sys} and R_{sys} were iteratively optimized to fit the experimental curves obtained in the experiments, where poration events occurred at U_d and equalled 105 ± 54 nF and 100 ± 5 kΩ, respectively. The three other branches were introduced to describe the membrane as (1) a capacitor (C_{BLM}), (2) a resistor (R_{BLM}) and (3) a resistor (R_P) and a switch in series. This last branch models the bilayer in either an intact or porated state, which corresponds to the switch being opened or closed, respectively. An average value of ∼0.51 μF/cm^2 obtained from all measurements on the lipid membrane was considered for the membrane capacitance (C_{BLM}), and the membrane resistance (R_{BLM}) was ∼10^8 Ω, a value commonly used in the literature to describe membranes (Tien 1974). Finally, the R_P values were adjusted to model the voltage drops occurring at U_d (Table 2; Fig. 7). Using the traces of the recorded voltages, the spice model allowed us to estimate the conductance ($G_P = 1/R_P$) of the pores created at U_d, the distribution of which is reported in Fig. 8.

Quite interestingly, the conductances recorded for planar lipid membranes are much larger than those reported using other protocols, such as current clamp or rising voltage, which range from a fraction of a nanoSiemens (Kotulska et al. 2010; Melikov et al. 2001) to a few tens of nanoSiemens (Kalinowski et al. 1998).

In order to gain insight into the corresponding process taking place at the molecular level, we carried out fully atomistic MD simulations under conditions similar to the experiment. We considered a POPC planar lipid bilayer embedded in a 150 mM NaCl solution. Overall, the system consisted of 1,152 lipids, 58,304 water molecules, 560 sodium ions and 560 chloride ions (a total of 261,280 atoms). The bilayer was first replicated in 3D and equilibrated at a constant pressure (1 atm) and temperature (300 K). Then, it was extended in the z direction (16.8 × 18.3 × 20.1 nm^3) in order to create air (vacuum)–water interfaces (Fig. 4). This setup (Delemotte et al. 2008) enables the generation of a transmembrane voltage by imposing a charge imbalance between the solutions on either side of the membrane. MD simulations performed at different transmembrane voltages (charge imbalances, Q_s) showed that, as such, the POPC membrane behaves as a capacitor (Delemotte et al. 2008). Its capacitance, estimated by $V = Q_s/C$ amounts to 0.85 μF/cm^2.

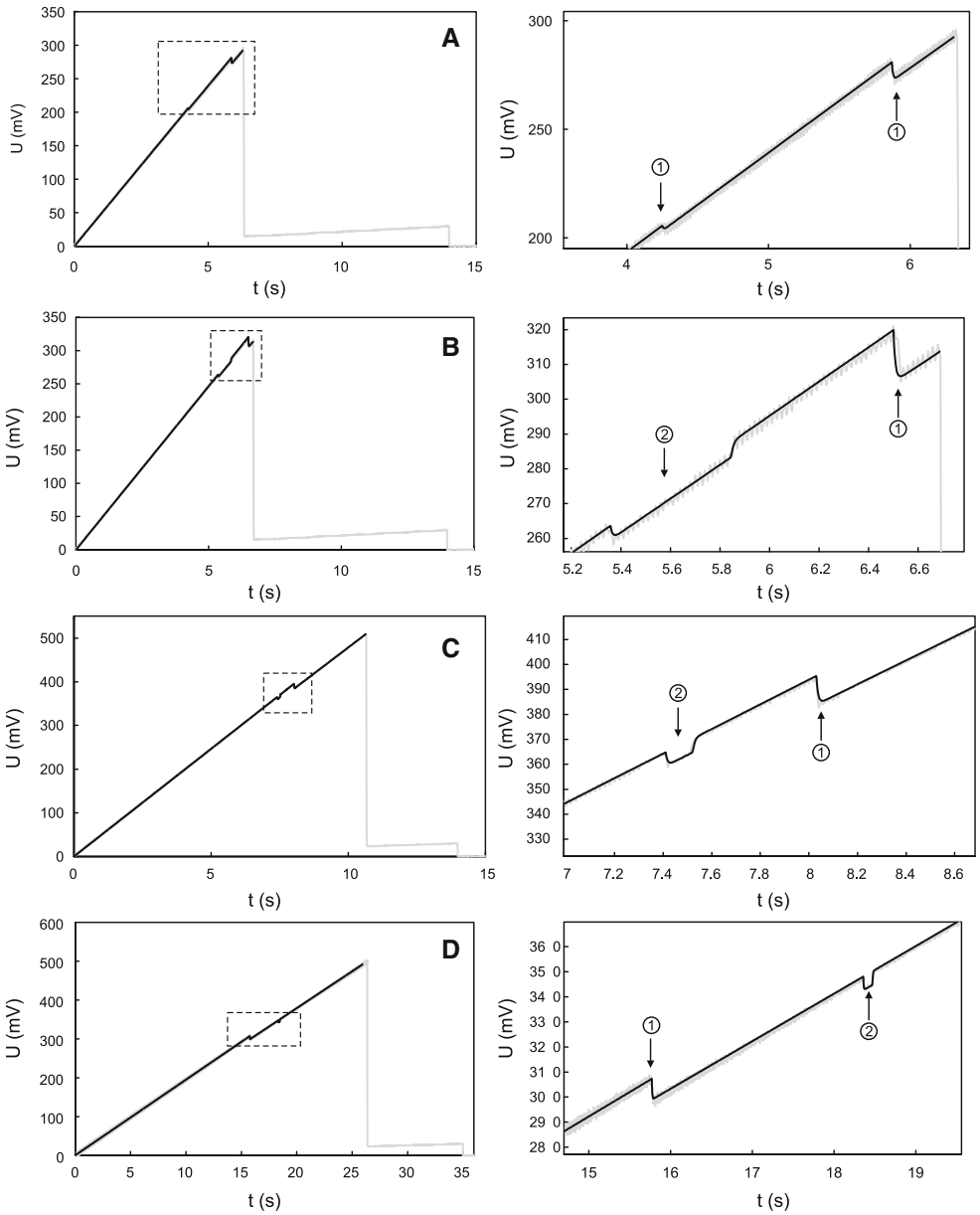

Fig. 6 Experimentally obtained voltage traces (*light lines*) and best fits (*bold lines*) obtained with the SPICE model. The entire voltage traces are presented in the *left column* and a zoom on the event(s) on the *right*

Discussion

As we were mainly interested in characterizing the voltage drop events (Fig. 6, 7), the MD simulations were carried out in order to follow the dynamics of pore creation. Accordingly, we generated systems at transmembrane voltages (ΔV) high enough to induce electroporation, mimicking therefore the experimental event starting at U_d. Using the SPICE model, the intensity of the current applied to the membrane was estimated to be in the order of a few picoamperes (Table 2). Considering the ratio between the sizes of the simulation and experimental membrane patches, this is equivalent to charging the MD patch at a rate of $\sim 10^{-7}$ elementary charges per picosecond. On the simulation time scale (tens of nanoseconds), one should therefore not expect a voltage buildup. Accordingly, the initial charge imbalance imposed to create ΔV was not modified during the simulation run.

Comparison of capacitances estimated in MD simulations (0.85 μF/cm^2) to the experimental values (0.51 μF/cm^2) indicates that the setup and the MD force field we used yielded good agreement with the experiment.

For ΔV above a threshold of 1.5 V, the bilayer undergoes a drastic change in terms of its molecular structure, which is comparable to what was observed when applying an electric field to MD bilayer setups (Tarek 2005;

Table 1 Voltage drops as a function of the linearly rising current slopes

I slopes (k) (μA/s)	Experiments	Total drop events	Drop only	Drop and reseal
0.03	4	4	6	0
0.05	9	6	3	5
0.1	5	1	0	1
0.2	8	3	2	3
0.5	13	10	6	8
4	5	4	5	1
8	5	3	2	2
10	6	0	0	0
20	8	0	0	0

The number of measurements for each current slope, the number of experiments that exhibit voltage drops, including the number of drop-only events and the number of drop-and-reseal events are presented

Table 2 Parameters of the trace (fit) shown in Fig. 7

	t_1	t_2	t_3	t_4	t_5	t_6
t (s)	5.40	5.42	5.57	5.72	5.74	5.84
U (mV)	265.96	264.92	271.65	279.23	282.30	287.91
I (μA)	2.70	2.71	2.78	2.86	2.87	2.92
I_{RSYS} (μA)	2.69	2.68	2.75	2.83	2.86	2.92
I_{RBLM} (pA)	2.66	2.65	2.72	2.79	2.82	2.88
I_{CSYS} (nA)	6.20	2.49	6.14	6.14	13.00	6.20
I_{CBLM} (pA)	2.71	1.09	2.68	2.68	5.68	2.71
I_P (nA)	0.00	26.49	27.17	27.92	0.00	0.00

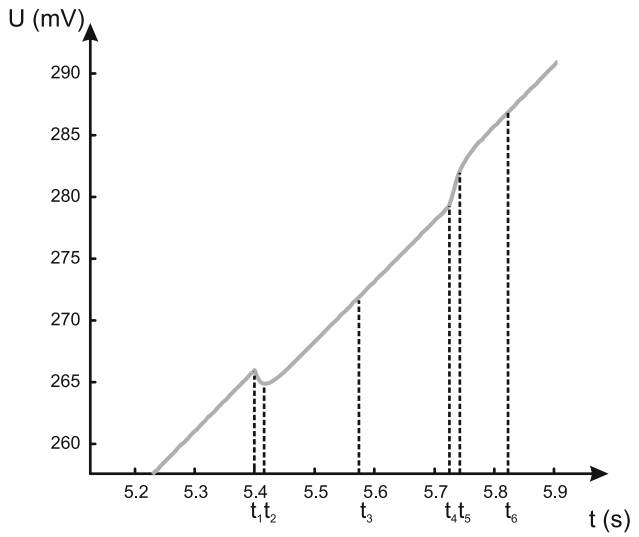

Fig. 7 Example of fit to the recorded traces of voltage (V) as a function of time (s) for event 2 in Fig. 6c

Tieleman 2004; Bockmann et al. 2008; Ziegler and Vernier 2008) or with the charge imbalance method (Gurtovenko and Vattulainen 2005; Kandasamy and Larson 2006; Tarek and Delemotte 2010). See Gurtovenko et al. (2010) for a review. Indeed, within a few nanoseconds, water fingers started protruding from both sides of the membrane, until a water wire connected the two baths. During the next step, lipid headgroups dived along the sides of these water wires, thus forming a hydrophilic pore. The diameter of the created hydrophilic pore ($\sim$20 Å) was large enough to enable conduction of Na^+ and Cl^- ions from one side of the bilayer to the other, releasing the electrical stress imposed by the ionic imbalance. Accordingly, the initial charge imbalance decreased, leading to a decrease of the transmembrane voltage. When the latter reached values of a few hundred millivolts, the pore stopped conducting ions and the water within the pore retracted toward the external baths, leading to a collapse of the hydrophilic pore. The final topology of the pore toward the end of the simulations remained stable for time spans exceeding 10 ns. It was probably because, as reported in previous simulations, complete recovery of the membrane requires a much longer time scale. We estimated the conductance of the pore, $G_{pMD} = I/U$, where I is the total number of ion translocations over the time elapsed during the simulation. Here, 20 elementary charges were conducted over 10 ns, leading to a value of $I \sim 320$ pA. During these translocations, the voltage dropped from 2 V to 200 mV, leading to values of G_{pMD} ranging from $\sim$160 pS to 1.6 nS in the case of the higher estimate.

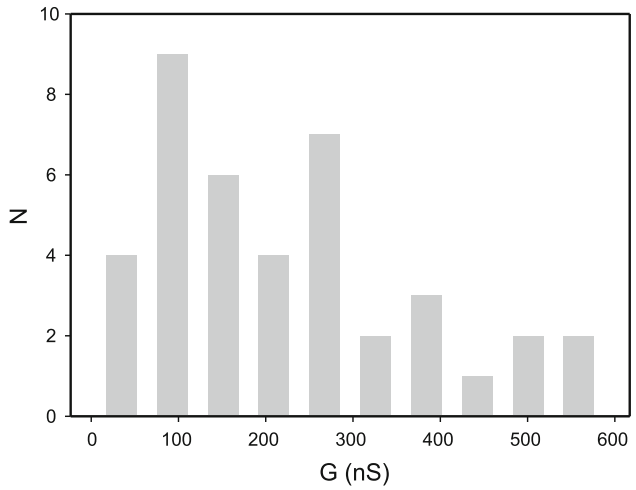

Fig. 8 Distributions of pores conductance $G_P = 1/R_p$ extracted from the SPICE model

Now, what is the most likely explanation, based on the simulation results, for what happens to the bilayer patch at and above the voltage U_d in the experiment? The estimated pore conductance values, obtained in experiments, are in the 100-nS range (Fig. 8). This leads to two hypotheses that may rationalize the observed voltage drops. (1) Multiple pores, such as those observed in MD, are created. The ratio

between experimental and simulation conductance values yields numbers ranging between $\sim$60 and $\sim$600 pores in the experimental patch, which corresponds to pore densities of $\sim 600 \times 10^8$ pore/m^2. Interestingly, a similar pore density was estimated from earlier measurements assuming the formation of hydrophilic pores of 1-nm diameter (Glaser et al. 1988). (2) At each drop event, a single pore is created in the experimental patch, the topology of which is different from the one obtained in the simulation. Its size allows for a conductance 60–600 times larger than that of the MD simulations. The single pore would then enable conduction of 120 elementary charges over 1 ns. In order to see if this is merely within the realm of what is conceivable, we carried out additional simulations, trying to characterize the conductance of larger pores. These were generated by performing simulations under a constant electric field, $\vec{E}$, perpendicular to the membrane patch, inducing a voltage of 2 V. For an MD run lasting about 2 ns, the diameter of the hydrophilic pore increased to $\sim$5 nm, enabling the conduction of $\sim$100 ions. This shows that it is indeed possible that the voltage drop events we observed in the experimental setup were due to the formation of a single pore, provided the latter has a diameter of a few nanometers.

Considering the experimental recordings (Fig. 5a) and given the shape of the voltage drops (and subsequent resealing), it seems more likely, however, that only a single pore is involved. The other alternative (hundreds of small pores within the experimental patch) would require that multiple pores would all open at the same time (on the millisecond time scale). There is even less rationale for the multiple pores to close all at the same time (millisecond time scale) while the transmembrane voltage keeps rising, i.e., as the electrical stress is becoming greater. On the contrary, if the events are due to a single pore, when the stress is relieved due to local ionic conduction in the region around the pore, the latter would close while the voltage keeps rising in the rest of the membrane. Such a scenario would lead eventually to breakdown of the planar lipid bilayer at U_{br}.

Electroporation is herein induced in the MD simulations by ionic salt concentration gradients between the two sides of the lipid bilayer patch, i.e., imposing a charge imbalance across the bilayer. One way of doing so is to consider in the MD simulation cell three salt baths separated by two bilayers and the use of 3D periodic boundary conditions at constant pressure. Accordingly, the overall lateral pressure on the system is zero. However, only one bilayer undergoes electroporation in such setups, and the influence of such asymmetry on the exact tension of the latter is not clear. Here, we performed a simulation considering a single bilayer and the air–water interface. In such a setup the simulation is carried out at constant volume, and therefore, a surface tension builds as the bilayer undergoes electroporation. We should note, however, that while this may be considered more appropriate for comparison to the planar lipid bilayer experimental setup, it is very difficult to estimate the lateral tension that builds up in the much larger bilayer patch.

In summary, we applied linear rising currents on planar POPC bilayers to observe well-defined voltage drops due to poration of the membrane. The use of theoretical tools, such as SPICE modeling and MD simulations, helped us to understand and characterize the phenomena occurring on a molecular scale and indicate that the observed voltage drops in bilayer patches are likely due to the opening and resealing of a single pore, a few tens of angstroms wide and of $\sim$100 nS conductance. Such a molecular understanding should enable better control and tuning of electroporation parameters to a wide range of biomedical and biotechnological applications.

Acknowledgements This work was in part supported by various grants from the Slovenian Research Agency and bilateral cooperation programs between Poland and Slovenia and between France and Slovenia (PROTEUS). The research was conducted in the scope of the EBAM European Associated Laboratory. Simulations were performed using HPC resources from GENCI-CINES (Grant 2010-075137). We thank A. Burmen for valuable discussion regarding SPICE modeling. M. T. acknowledges the support of the French Agence Nationale de la Recherche (Grant ANR-10_BLAN-916-03-INTCELL).

References

Benz R, Janko K (1976) Voltage-induced capacitance relaxation of lipid bilayer membranes: effects of membrane composition. Biochim Biophys Acta 455:721–738

Bockmann RA, de Groot BL, Kakorin S et al (2008) Kinetics, statistics, and energetics of lipid membrane electroporation studied by molecular dynamics simulations. Biophys J 95:1837–1850

Darden T, York D, Pedersen L (1993) Particle mesh Ewald—an n.log(n) method for Ewald sums in large systems. J Chem Phys 98:10089–10092

Delemotte L, Dehez F, Treptow W, Tarek M (2008) Modeling membranes under a transmembrane potential. J Phys Chem B 112:5547–5550

Essmann U, Perera L, Berkowitz M et al (1995) A smooth particle mesh Ewald method. J Chem Phys 103:8577–8593

Genco I, Gliozzi A, Relini A et al (1993) Electroporation in symmetric and asymmetric membranes. Biochim Biophys Acta 1149:10–18

Glaser R, Leikin S, Chernomordik L et al (1988) Reversible electrical breakdown of lipid bilayers—formation and evolution of pores. Biochim Biophys Acta 940:275–287

Golzio M, Teissie J, Rols M (2002) Direct visualization at the single-cell level of electrically mediated gene delivery. Proc Natl Acad Sci USA 99:1292–1297

Gurtovenko A, Vattulainen I (2005) Pore formation coupled to ion transport through lipid membranes as induced by transmembrane

ionic charge imbalance: atomistic molecular dynamics study. J Am Chem Soc 127:17570–17571
Gurtovenko A, Anwar J, Vattulainen I (2010) Defect-mediated trafficking across cell membranes: insights from in silico modeling. Chem Rev 110:6077–6103
Heller R, Gilbert R, Jaroszeski M (1999) Clinical applications of electrochemotherapy. Adv Drug Deliv Rev 35:119–129
Henin J, Shinoda W, Klein ML (2008) United-atom acyl chains for CHARMM phospholipids. J Phys Chem B 112:7008–7015
Jorgensen W, Chandrasekhar J, Madura J et al (1983) Comparison of simple potential functions for simulating liquid water. J Chem Phys 79:926–935
Kale L, Skeel R, Bhandarkar M et al (1999) NAMD2: greater scalability for parallel molecular dynamics. J Comput Phys 151: 283–312
Kalinowski S, Figaszewski Z (1995a) A 4-electrode system for measurement of bilayer lipid membrane capacitence. Meas Sci Technol 6:1043–1049
Kalinowski S, Figaszewski Z (1995b) A 4-electrode potentiostat-galvanostat for studies of bilayer lipid membranes. Meas Sci Technol 6:1050–1055
Kalinowski S, Ibron G, Bryl K, Figaszewski Z (1998) Chronopotentiometric studies of electroporation of bilayer lipid membranes. Biochim Biophys Acta 1369:204–212
Kandasamy SK, Larson RG (2006) Cation and anion transport through hydrophilic pores in lipid bilayers. J Chem Phys 125: 074901
Koronkiewicz S, Kalinowski S (2004) Influence of cholesterol on electroporation of bilayer lipid membranes: chronopotentiometric studies. Biochim Biophys Acta 1661:196–203
Koronkiewicz S, Kalinowski S, Bryl K (2002) Programmable chronopotentiometry as a tool for the study of electroporation and resealing of pores in bilayer lipid membranes. Biochim Biophys Acta 1561:222–229
Kotnik T, Bobanovic F, Miklavcic D (1997) Sensitivity of transmembrane voltage induced by applied electric fields—a theoretical analysis. Bioelectrochem Bioenerg 43:285–291
Kotnik T, Macek-Lebar A, Miklavcic D, Mir L (2000) Evaluation of cell membrane electropermeabilization by means of a nonpermeant cytotoxic agent. Biotechniques 28:921–926
Kotulska M, Koronkiewicz S, Kalinowski S (2004) Self-similar processes and flicker noise from a fluctuating nanopore in a lipid membrane. Phys Rev E 69:031920
Kotulska M, Kubica K, Koronkiewicz S, Kalinowski S (2007) Modeling the induction of lipid membrane electropermeabilization. Bioelectrochemistry 70:64–70
Kotulska M, Basalyga J, Derylo M, Sadowski P (2010) Metastable pores at the onset of constant-current electroporation. J Membr Biol 236:37–41
Kramar P, Miklavcic D, Lebar AM (2007) Determination of the lipid bilayer breakdown voltage by means of linear rising signal. Bioelectrochemistry 70:23–27
Kramar P, Miklavcic D, Lebar AM (2009) A system for the determination of planar lipid bilayer breakdown voltage and its applications. IEEE Trans Nanobiosci 8:132–138
Marty M, Sersa G, Garbay JR et al (2006) Electrochemotherapy—an easy, highly effective and safe treatment of cutaneous and subcutaneous metastases: results of ESOPE (European Standard Operating Procedures of Electrochemotherapy) study. EJC Suppl 4:3–13
Melikov K, Frolov V, Shcherbakov A et al (2001) Voltage-induced nonconductive pre-pores and metastable single pores in unmodified planar lipid bilayer. Biophys J 80:1829–1836
Mir LM, Banoun H, Paoletti C (1988) Introduction of definite amounts of nonpermeant molecules into living cells after electropermeabilization—direct access to the cytosol. Exp Cell Res 175:15–25
Mir L, Orlowski S, Belehradek J et al (1995) Biomedical applications of electric pulses with special emphasis on antitumor electrochemotherapy. Bioelectrochem Bioenerg 38:203–207
Montal M, Mueller P (1972) Formation of bimolecular membranes from lipid monolayers and a study of their electrical properties. Proc Natl Acad Sci USA 69:3561–3566
Neumann E, Rosenheck K (1972) Permeability changes induced by electric impulses in vesicular membranes. J Membr Biol 10: 279–290
Phillips J, Braun R, Wang W et al (2005) Scalable molecular dynamics with NAMD. J Comput Chem 26:1781–1802
Prausnitz MR, Bose VG, Langer R, Weaver JC (1993) Electroporation of mammalian skin—a mechanism to enhance transdermal drug-delivery. Proc Natl Acad Sci USA 90:10504–10508
Pucihar G, Mir L, Miklavcic D (2002) The effect of pulse repetition frequency on the uptake into electropermeabilized cells in vitro with possible applications in electrochemotherapy. Bioelectrochemistry 57:167–172
Rols M, Teissie J (1998) Electropermeabilization of mammalian cells to macromolecules: control by pulse duration. Biophys J 75:1415–1423
Sersa G, Cemazar M, Miklavcic D (1995) Antitumor effectiveness of electrochemotherapy with *cis*-diamminedichloroplatinum(II) in mice. Cancer Res 55:3450–3455
Tarek M (2005) Membrane electroporation: a molecular dynamics simulation. Biophys J 88:4045–4053
Tarek M, Delemotte L (2010) Electroporation of lipid membranes. In: Pakhomov A, Miklavčič D, Markov M (eds) Advanced electroporation techniques in biology and medicine. Taylor and Francis/CRC Press, Boca Raton, FL
Teissie J, Rols M (1993) An experimental evaluation of the critical potential difference inducing cell-membrane electropermeabilization. Biophys J 65:409–413
Teissie J, Eynard N, Gabriel B, Rols M (1999) Electropermeabilization of cell membranes. Adv Drug Deliv Rev 35:3–19
Teissie J, Escoffre JM, Rols MP, Golzio M (2008) Time dependence of electric field effects on cell membranes. A review for a critical selection of pulse duration for therapeutical applications. Radiol Oncol 42:196–206
Tieleman D (2004) The molecular basis of electroporation. Biophys J 86:371A–372A
Tieleman D, Leontiadou H, Mark A, Marrink S (2003) Simulation of pore formation in lipid bilayers by mechanical stress and electric fields. J Am Chem Soc 125:6382–6383
Tien HT (1974) Bilayer lipid membranes. Marcel Dekker, New York
Tuma T, Buermen Á (2009) Circuit simulation with SPICE OPUS: theory and practice. Birkhäuser, Boston
Villemejane J, Mir LM (2009) Physical methods of nucleic acid transfer: general concepts and applications. Br J Pharmacol 157: 207–219
Ziegler MJ, Vernier PT (2008) Interface water dynamics and porating electric fields for phospholipid bilayers. J Phys Chem B 112:17003
Zimmermann U, Pilwat G, Beckers F, Riemann F (1976) Effects of external electrical fields on cell-membranes. Bioelectrochem Bioenerg 3:58–83

J Membrane Biol
DOI 10.1007/s00232-012-9475-x

Electric Field Orientation for Gene Delivery Using High-Voltage and Low-Voltage Pulses

J. Orio · M. Coustets · C. Mauroy · J. Teissie

Received: 19 December 2011 / Accepted: 30 June 2012

Abstract Electropermeabilization is a biological physical process in response to the presence of an applied electric field that is used for the transfer of hydrophilic molecules such as anticancer drugs or DNA across the plasma membranes of living cells. The molecular processes that support the transfer are poorly known. The aim of our study was to investigate the effect of high-voltage and low-voltage (HVLV) pulses in vitro with different orientations on cell permeabilization, viability and gene transfection. We monitored the permeabilization with unipolar and bipolar HVLV pulses with different train repetition pulses, showing that HVLV pulses increase cell permeabilization and cell viability. Gene transfer was also observed by measuring green fluorescent protein (GFP) expression. The expression was the same for HVLV pulses and electrogenotherapy pulses for in vitro experimentation. As the viability was better preserved for HVLV-pulsed cells, we managed to increase the number of GFP-expressing cells by up to 65 % under this condition. The use of bipolar HVLV train pulses increased gene expression to a higher extent, probably by affecting a larger part of the cell surface.

Keywords High-voltage and low-voltage pulses · Electropermeabilization · CHO cell · Electrotransfection · Field orientation · Gene transfer

J. Orio (✉) · M. Coustets · C. Mauroy · J. Teissie
Centre National de la Recherche Scientifique,
Institut de Pharmacologie et de Biologie Structurale,
UMR 5089, 205 Route de Narbonne, BP 64182,
31077 Toulouse Cedex, France
e-mail: orio@ipbs.fr

J. Orio · M. Coustets · C. Mauroy · J. Teissie
Université Paul Sabatier, UMR 5089, Toulouse III, France

Introduction

The cell membrane represents a physical barrier which isolates the cell content from the external medium. A calibrated electric field pulse (electropulsation) can be applied to cells in suspension to induce a permeabilization of the cell membrane (electropermeabilization). This permeabilized state is obtained when the field strength is higher than a threshold function to the cell size, shape and orientation (Bellard and Teissie 2009; Valic et al. 2003).

Plasmid electrotransfer and resulting expression (electrotransfection) was first described 30 years ago (Neumann et al. 1982). Because electropermeabilization represents an efficient and safe method for transmembrane transfer, it is now a routine technique for the delivery of various types of molecules (RNA, DNA, drugs, etc.). Gene delivery is a complex phenomenon which is still poorly understood, with pertinent studies performed in the 1990s (Neumann et al. 1999; Smith et al. 2004; Sukharev et al. 1992). Intense activity is still present, combining biophysical and cellular approaches (Pavlin et al. 2010, 2012; Wu and Yuan 2011; Yu et al. 2012). Gene delivery is not the result of direct plasmid diffusion into the cytoplasm. DNA molecules are accumulated by electrophoretic forces at the membrane level, where they remain trapped after pulse application and then are slowly translocated into the cytoplasm. Due to the electrophoretic drift of DNA, this accumulation is present only on the cell side facing the cathode (Escoffre et al. 2011; Golzio et al. 2002). Changing the orientation of the electric field was indeed described to increase the interaction surface between DNA and the membrane (Faurie et al. 2004). As a consequence, a higher level of expression was observed.

Several studies have shown the crucial role of electrophoretic forces in gene transfer, but alone those forces do

Published online: 27 July 2012

not provide any transfection (Cepurniene et al. 2010): electropermeabilization must be present. For a given electrode width, using high-voltage, short pulses followed by a low-voltage, long pulse (HVLV), gene expression is observed in vivo (Andre et al. 2008). After an HV pulse, all cells are permeabilized and the LV pulse brings plasmids into contact with cells due to electrophoretic forces. This double-pulse method was shown to be valid in vitro when using suboptimal plasmid concentration (Kandušer et al. 2009). In the present study we observed the effect of electric field orientation using HVLV pulse trains with different modulations of the pulse polarities.

Materials and Methods

Cell Culture

Chinese hamster ovary (CHO) cells in early passage were used. The WTT clone was selected for its ability to grow in suspension or plated. Cells were grown in minimum Eagle's medium (MEM) supplemented with 8 % fetal calf serum. Cells were mycoplasma-free.

Plasmid

A 4.7-kbp plasmid (pEGFP-C1; Clontech, Mountain View, CA) carrying the gene of the green fluorescent protein (GFP) controlled by the CMV promoter was used. It was prepared from transfected *Escherichia coli* cells using the Maxiprep DNA purification system according to the manufacturer's instructions (Qiagen, Valencia City, CA).

Electropulsation Device

A S20b pulse generator was used (Betatech, L'Union, France). The output was connected to a pulse polarity inverter, which was controlled by the pulse generator through a TTL signal. The double pulse from the S20b kept the same polarity as for the classical HVLV protocol. But in a train of pulses, an inversion can be obtained between each (HVLV) pulse couple (Fig. 1).This was called "bipolar" HVLV pulses. The output was controlled at two levels: either directly on the internal monitor of the S20b or by a current follower (Chauvin Arnoux, Paris, France) on a laptop using a Picoscope (Pico Technology, St. Neots, UK) to follow the polarity.

Electropermeabilization

Cells were cultured by plating in a flask (Easy Flask; Nunc, Rochester, NY), and just before the experiment cells were trypsinized and counted with a Neubauer chamber. Cells were centrifugated at $800 \times g$ for 5 min at room temperature. Culture medium was removed. Cells were resuspended in an electropulsation buffer (10 mM phosphate, 1 mM $MgCl_2$, 250 mM sucrose, pH 7.4) complemented with propidium iodide (100 μM) (Sigma-Aldrich, St. Louis, MO) at 5×10^6 cells/ml. Penetration of the propidium iodide was used to monitor cell permeability (Kennedy et al. 2008). This suspension (100 μl) was poured between two plated parallel stainless-steel electrodes (distance between electrodes 4 mm). After electropulsation, this suspension was transferred in a culture chamber (Lab-Tek I system, Nunc) and observed under an inverted digitized video fluorescence microscope (DMIRB; Leica, Wetzlar, Germany). Several images of each condition were taken and treated with ImageJ (ImageJ 1.4n; Wayne Rasband, NIH, Bethesda, MD).

Electrotransfection

The same protocol was applied for the electrotransfection test. Cells were resuspended in a pulsation buffer complemented with 5 μg/ml of plasmid pEGFP-C1. After pulse delivery, 1 ml of complete culture medium was added, and the cells were incubated for 24 h in an incubator at 37 °C, 5 % CO_2. Cells were trypsinized and analyzed by flow cytometry (BD Biosciences, San Jose, CA; FACScalibur) to determine the percentage of transfected cells and the fluorescence intensity (average value) of the expression of GFP.

Viability

For viability experiments, cells were imaged 24 h after treatment by bright field illumination under an inverted digitized video microscope (DMIRB). We acquired six random images. Adherent and morphologically nonaffected cells were counted for each condition and expressed as the relative percentage to the counting of nonpulsated cells.

Statistical Analysis

Statistical analysis was carried out using statistical software (Prism 4.01; GraphPad Software, San Diego, CA). Each experiment under the different pulsing conditions was performed three times. Errors bars represent the standard error of the mean. The statistical significance of differences between the means was evaluated by two-sided, unpaired Student's *t* test (NS = nonspecific, $*P < 0.05$, $**P < 0.01$).

Results and Discussion

Pulse parameters were selected by taking into account previous data (Faurie et al. 2010). This reference was our

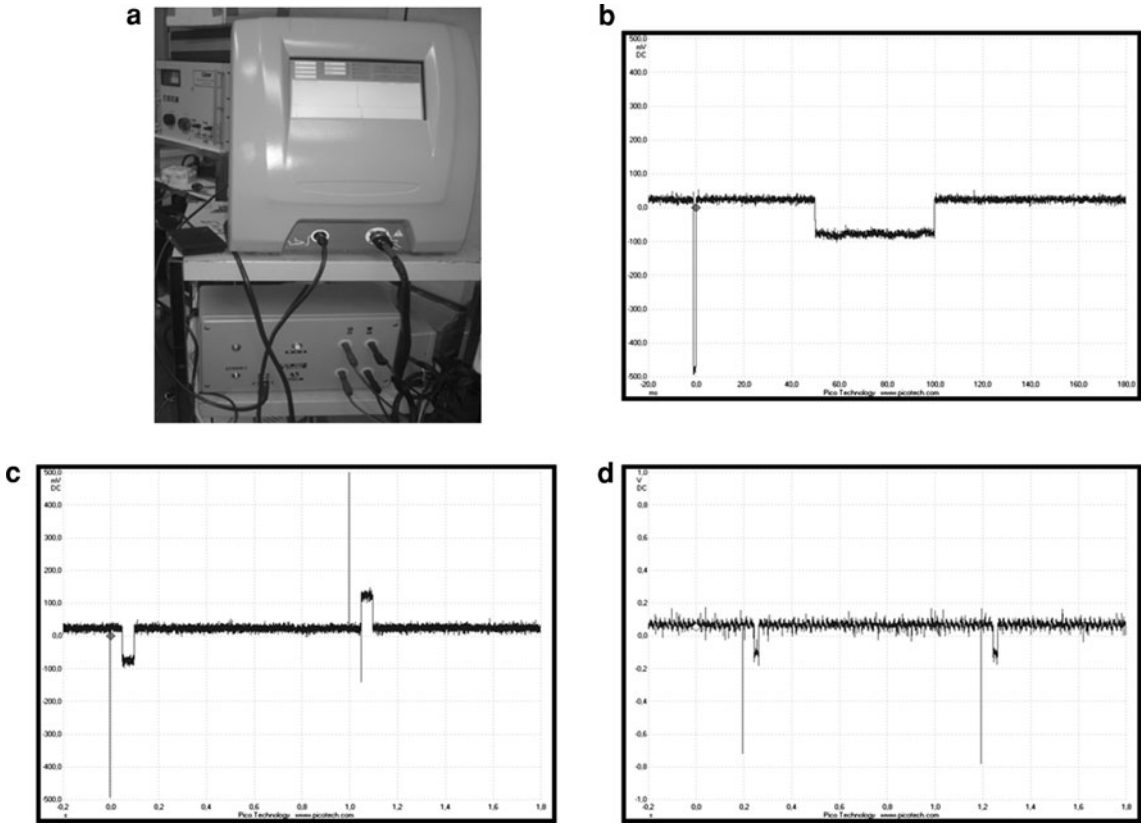

Fig. 1 Multipolarity pulse generator. A bipolar Betatech S20b was coupled to a homemade automatic pulse inverter (*gray box* on the stage below the pulse generator) (**a**). The output (*black* and *grey* banana plugs) was connected to plate parallel electrodes (not shown). View on the picoscope of one single HVLV pulse current (one HV, $E = 1{,}300$ V/cm, $t = 0.1$ ms, followed by one LV of $E = 150$ V/cm, $t = 50$ ms after a delay of 50 ms) (**b**). A train of two pulses (each was as displayed in **b**) in a bipolar sequence. A polarity inversion is present. The delay was 1 s (**c**). A train of two pulses (each was as displayed in **b**) in a unipolar sequence. The pulse polarity is conserved. The delay was 0.5 s (**d**)

guideline for the choice in the delay between successive pulses in a train for the pulse polarity inversion. We therefore selected 1-s delay. For technical reasons (the present specifications of the S20b pulsator), the LV (150 V/cm) pulse duration remained limited to 50 ms, but this second pulse was nevertheless delivered only 50 ms after the HV (1,300 V/cm, duration 0.1 ms) one. Pulse parameters were therefore slightly different from in previous reports (Cepurniene et al. 2010; Kandušer et al. 2009). We compared the effect of the polarity inversion in trains of HVLV pulses, bipolar (Fig. 1c) and unipolar trains (Fig. 1d), to a train of electrogenotherapy (EGT) "classical" pulses (long-lasting pulse with a medium voltage, 700 V/cm) on the permeabilization, viability and transfection.

Permeabilization was quantified by monitoring propidium iodide uptake in CHO cells (Kennedy et al. 2008). We observed a higher rate of permeabilized cells with HVLV pulses when compared to classical pulses (EGT) (Fig. 2a). Fluorescence intensity was also measured (Fig. 2b). Whatever the number of train repetitions, HVLV pulses provided a higher fluorescence level ("higher" permeabilization). Using HVLV pulses increased the percentage of propidium iodide-positive cells and the entry of small molecules. The EGT conditions were selected to preserve the viability, so the field strength was reduced. The consequence was permeabilization of only a subpopulation, due to the size selectivity by the electric field strength, which affected only the largest cells. The HV pulse affected all cells (whatever their size) and the LV electrophoretically accumulated the dye (Pucihar et al. 2008).

When the viability 24 h after electric pulses (Fig. 3) was observed, as already known, classical electric pulses (EGT) reduced the number of viable cells. Furthermore, HVLV pulses (with and without polarity inversion) do not affect the viability of CHO cells even for an eight-repetition train. As after the electric pulse, cells have to keep their integrity to express the transfected gene. This is a clear advantage of using HVLV pulses.

Taking into account previous results, a suboptimal concentration of plasmid was used (Kandušer et al. 2009). Cells electropulsated with eight HVLV pulses with no polarity inversion provide a more efficient transfer of

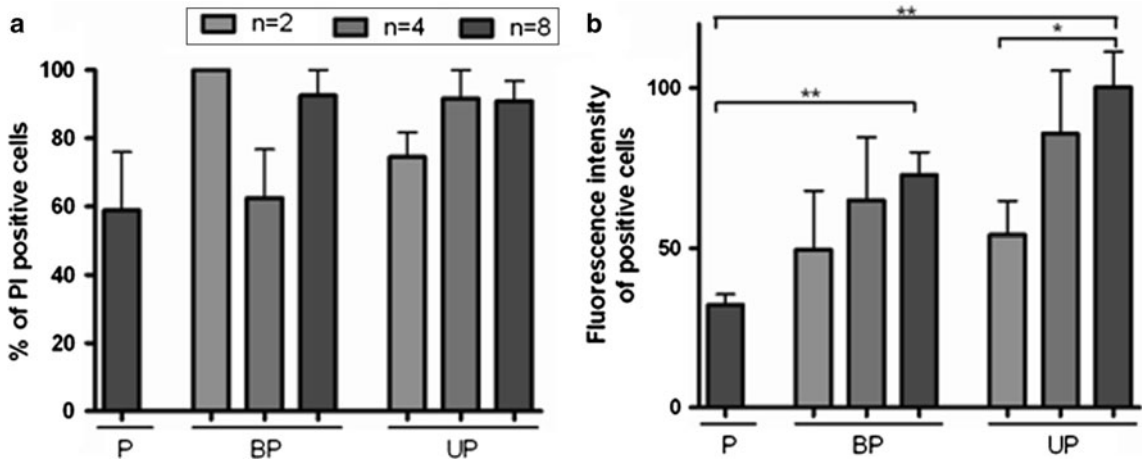

Fig. 2 Effect of high- and low-voltage pulses on cell permeabilization. CHO cells were pulsed with electric pulses of $E = 700$ V/cm, $t = 5$ ms, $n = 8$, $F = 1$ Hz (*P*); with bipolar trains of two, four or eight HVLV pulses (*BP*); or with unipolar trains of two, four or eight HVLV pulses (*UP*) in the presence of propidium iodide to monitor the permeabilization. We observed the percentage of permeabilized cells (**a**) and the associated mean fluorescence level of propidium iodide-positive cells (**b**) by microscopy

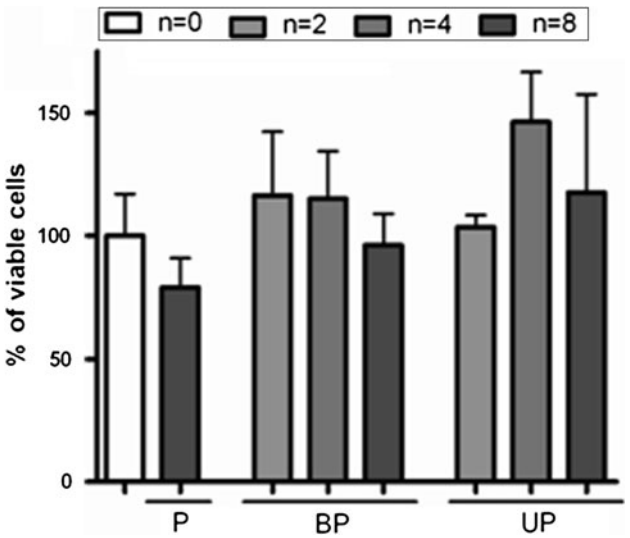

Fig. 3 Viability of CHO cells after electropulsation. CHO cells were pulsed with electric pulses of $E = 700$ V/cm, $t = 5$ ms, $n = 8$, $F = 1$ Hz (*P*); with bipolar trains of two, four or eight HVLV pulses (*BP*); or with unipolar trains of two, four or eight HVLV pulses (*UP*). Cells were counted 24 h after electropulsation under the microscope

plasmid than classical (EGT) pulses (Fig. 4a) as reported (Cepurniene et al. 2010; Kandušer et al. 2009; Pavlin et al. 2010). But the pulse duration, sequence and shape (a sharper voltage rise time [200 ns], a delay of 50 ms is delivered by the S20b) were different from these published data (several microseconds with a Cliniporator used by Kandušer et al., the delay between HV and LV pulses was 1 s in Cepurniene et al.'s experiments). This is strongly illustrative of the flexibility of the approach. Taking into account the key role of the electric field pulse-induced electrophoretic drift of DNA in electrotransfection, this was tentatively explained in the 2009 study by the hypothesis that LV pulses could bring the plasmid in the neighborhood of the membrane due to electric forces (Pavlin et al. 2010). This effect was masked by an excess of plasmid in the cell suspension (Kandušer et al. 2009) but detected with a suboptimal concentration.

Our technology (giving a polarity inversion in the HVLV train delivery) (Fig. 1) allows us to show that bipolar HVLV pulses bring a higher level of plasmid expression than unipolar HVLV pulses (Fig. 4b). Under EGT conditions, polarity inversion was previously shown to provide DNA–membrane interaction on a larger part of the cell surface (Faurie et al. 2004) and more plasmid transfer to the cytoplasm. This was proposed to explain the higher expression of GFP. Again, under the bipolar train condition, DNA would interact on both sides of the cell membrane, facing the electrodes. A larger part of the cell surface acts in the DNA transfer across the plasma membrane to the cytoplasm. As expected, the number of GFP-positive cells increased with the number of pulse couples and was larger under the bipolar condition.

The mean GFP fluorescence level was only slightly lower than under the EGT conditions (in a nonstatistically significant way). Nevertheless, the computed electrophoretic DNA accumulation at the cell surface was always larger under the HVLV conditions. It is proportional to ETN (E = field strength, t = pulse duration, n = cumulated number of pulses). In all HVLV conditions, mean fluorescence was observed to fairly increase linearly with the number of pulses, in agreement with a key role of the electrophoretic DNA drift in the control of expression. Another key feature of the HVLV train is that cell viability appears not to be affected by the electrical treatment. From the initial population, EGT conditions bring a 17 % value

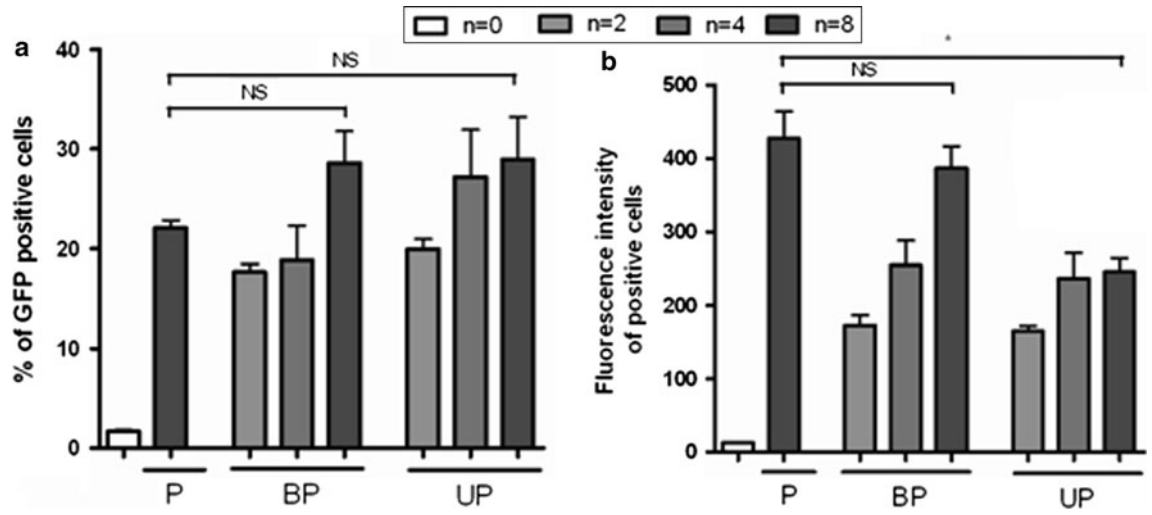

Fig. 4 Effect of unipolar and bipolar pulse trains on CHO cell gene transfection. Percentage of transfected cell with plasmid pEGFP-C1 (**a**) and the associated median fluorescence level of GFP-expressing cells (**b**). CHO cells were pulsed with electric pulses of $E = 700$ V/cm, $t = 5$ ms, $n = 8$, $F = 1$ Hz (*P*); with bipolar trains of two, four or eight HVLV pulses (*BP*); or with unipolar trains of two, four or eight HVLV pulses (*UP*). GFP expression was assayed 24 h after electropulsation and analyzed by flow cytometry

of GFP-positive cells (from Figs. 3, 4), while eight-train bipolar HVLV conditions give 28 % (i.e., a 65 % increase).

As a final conclusion, the LV pulse in the HVLV couple acts on the DNA–membrane interaction under nonpermeabilizing conditions (Rols and Teissie 1990). Under our conditions, the interaction can occur up to 100 ms after the permeabilizing HV pulse (50-ms delay and 50-ms duration). The use of bipolar conditions brings this interaction to a larger part of the cell surface and results in higher expression. This improvement is associated with preserving the viability of the pulsed population.

Acknowledgments This work was supported by the European Union project OncomiR (Grant 201102). The authors thank Betatech for the joint development of generators and the TRI (Toulouse Réseau d'Imagerie) platform at the IPBS (funded by the region Midi-Pyrénées, the Communauté du Grand Toulouse and the FEDER) for providing access to the flow cytometer.

References

Andre FM, Gehl J, Sersa G, Preat V, Hojman P, Eriksen J, Golzio M, Cemazar M, Pavselj N, Rols MP, Miklavcic D, Neumann E, Teissie J, Mir LM (2008) Efficiency of high- and low-voltage pulse combinations for gene electrotransfer in muscle, liver, tumor, and skin. Hum Gene Ther 19:1261–1271

Bellard E, Teissie J (2009) Double pulse approach of electropulsation: a fluorescence analysis of the nucleus perturbation at the single cell level. IEEE Trans Dielectr Electr Insul 16:1267–1272

Cepurniene K, Ruzgys P, Treinys R, Satkauskiene I, Satkauskas S (2010) Influence of plasmid concentration on DNA electrotransfer in vitro using high-voltage and low-voltage pulses. J Membr Biol 236:81–85

Escoffre JM, Portet T, Favard C, Teissie J, Dean DS, Rols MP (2011) Electromediated formation of DNA complexes with cell membranes and its consequences for gene delivery. Biochim Biophys Acta 1808:1538–1543

Faurie C, Phez E, Golzio M, Vossen C, Lesbordes J-C, Delteil C, Teissie J, Rols M-P (2004) Effect of electric field vectoriality on electrically mediated gene delivery in mammalian cells. Biochim Biophys Acta 1665:92–100

Faurie C, Rebersek M, Golzio M, Kanduser M, Escoffre J-M, Pavlin M, Teissie J, Miklavcic D, Rols M-P (2010) Electro-mediated gene transfer and expression are controlled by the life-time of DNA/membrane complex formation. J Gene Med 12:117–125

Golzio M, Teissie J, Rols MP (2002) Direct visualization at the single-cell level of electrically mediated gene delivery. Proc Natl Acad Sci USA 99:1292–1297

Kandušer M, Miklavčič D, Pavlin M (2009) Mechanisms involved in gene electrotransfer using high- and low-voltage pulses—an in vitro study. Bioelectrochemistry 74:265–271

Kennedy SM, Ji Z, Hedstrom JC, Booske JH, Hagness SC (2008) Quantification of electroporative uptake kinetics and electric field heterogeneity effects in cells. Biophys J 94:5018–5027

Neumann E, Schaefer-Ridder M, Wang Y, Hofschneider PH (1982) Gene transfer into mouse lyoma cells by electroporation in high electric fields. EMBO J 1:841–845

Neumann E, Kakorin S, Toensing K (1999) Fundamentals of electroporative delivery of drugs and genes. Bioelectrochem Bioenerg 48:3–16

Pavlin M, Flisar K, Kanduser M (2010) The role of electrophoresis in gene electrotransfer. J Membr Biol 236:75–79

Pavlin M, Pucihar G, Kanduser M (2012) The role of electrically stimulated endocytosis in gene electrotransfer. Bioelectrochemistry 83:38–45

Pucihar G, Kotnik T, Miklavcic D, Teissie J (2008) Kinetics of transmembrane transport of small molecules into electropermeabilized cells. Biophys J 95:2837–2848

Rols MP, Teissie J (1990) Electropermeabilization of mammalian cells. Quantitative analysis of the phenomenon. Biophys J 58:1089–1098

Smith KC, Neu JC, Krassowska W (2004) Model of creation and evolution of stable electropores for DNA delivery. Biophys J 86:2813–2826

Sukharev SI, Klenchin VA, Serov SM, Chernomordik LV, Chizmadzhev Yu A (1992) Electroporation and electrophoretic DNA transfer into cells. The effect of DNA interaction with electropores. Biophys J 63:1320–1327

Valic B, Golzio M, Pavlin M, Schatz A, Faurie C, Gabriel B, Teissie J, Rols MP, Miklavcic D (2003) Effect of electric field induced transmembrane potential on spheroidal cells: theory and experiment. Eur Biophys J 32:519–528

Wu M, Yuan F (2011) Membrane binding of plasmid DNA and endocytic pathways are involved in electrotransfection of mammalian cells. PLoS ONE 6:e20923

Yu M, Lin H, Tan W (2012) A stochastic model for DNA translocation through an electropore. Biochim Biophys Acta

J Membrane Biol (2012) 245:667–674
DOI 10.1007/s00232-012-9425-7

ORIGINAL ARTICLES

Expression, Purification and Functional Reconstitution of Slack Sodium-Activated Potassium Channels

Yangyang Yan · Youshan Yang · Shumin Bian · Fred J. Sigworth

Received: 13 January 2012 / Accepted: 15 March 2012 / Published online: 23 June 2012

Abstract The *slack* (*slo*2.2) gene codes for a potassium-channel α-subunit of the 6TM voltage-gated channel family. Expression of *slack* results in Na^+-activated potassium channel activity in various cell types. We describe the purification and reconstitution of Slack protein and show that the Slack α-subunit alone is sufficient for potassium channel activity activated by sodium ions as assayed in planar bilayer membranes and in membrane vesicles.

Keywords Artificial planar membrane · Ion channel expression and reconstitution · Patch clamp · Potassium ion channel

Introduction

First identified by Kameyama et al. (1984) in cardiac myocytes, sodium-activated potassium channels have been found in many cell types. In neurons (Bhattacharjee and Kaczmarek 2005; Budelli et al. 2009; Yang et al. 2007) they control bursting and the adaptation of firing rates of action potentials; they may also be involved in protection from ischemia (Ruffin et al. 2008). Na^+-activated K^+ channels are found as well in diverse tissues such as kidney (Paulais et al. 2006) and smooth muscle (Kim et al. 2007; Zhang and Paterson 2007). Na^+-activated K^+ channels can be formed from Slack (also called Slo2.2) subunits (Joiner et al. 1998; Yuan et al. 2003) and from the related gene product Slick (Slo2.1) (Bhattacharjee et al. 2003). Slack and Slick are expressed widely and in varying proportions in the central nervous system (Bhattacharjee et al. 2002, 2005). The longer splice variant of Slack, Slack-B (Brown et al. 2008) forms heteromeric channels with distinct properties when coexpressed with Slick (Chen et al. 2009). Slack-A, on the other hand, has a shorter N-terminal sequence and does not coassemble with Slick subunits.

The structure and function of Slack channels are gradually becoming clear. A site of Na^+ sensing has been identified in the large intracellular C-terminal region of Slack (Zhang et al. 2010). The C-terminal region forms a "gating ring" whose X-ray structure, solved at low resolution, is quite similar to that of the gating ring of the BK (Slo1) Ca^{2+}-activated K^+ channel. This similarity was sufficient to allow the molecular replacement procedure to be employed in deducing the quaternary structure of the BK gating ring (Yuan et al. 2010). Slack channels are modulated by phosphorylation (Santi et al. 2006) and participate in protein–protein interactions (Uchino et al. 2003) including the RNA-binding protein FMRP and others which depend on the state of activation of the channel (Brown et al. 2010; Fleming and Kaczmarek 2009). A goal in our laboratory is to study Slack channels and their protein complexes by cryo-EM methods (Cong and Ludtke 2010; Wang and Sigworth 2009). We therefore sought to establish a system for the expression, purification and reconstitution of Slack protein. Here, we describe these methods as well as the results from functional assays of reconstituted Na^+-activated K^+ channels.

Yangyang Yan and Youshan Yang contributed equally to this work.

Y. Yan · Y. Yang · S. Bian · F. J. Sigworth (✉)
Department of Cellular and Molecular Physiology, Yale University, 333 Cedar Street, New Haven, CT 06520-8026, USA
e-mail: fred.sigworth@yale.edu

Experimental Procedures

Molecular Biology

The Slack-B cDNA sequence (1,237 amino acids) has a short, alternatively spliced N-terminal region. A FLAG epitope tag was inserted at the C terminus through ligation of a construct in the pcDNA3 vector (Joiner et al. 1998). Another construct was made in the pEGFP-C1 vector (Clontech, Mountain View, CA) so that the EGFP sequence was fused to the N terminus of Slack-B. All constructs were confirmed by restriction digestion and sequencing.

Establishing Slack Stable Cell Lines

Constructs were transfected into HEK293 cells using Superfect (Qiagen, Valencia, CA) or Lipofectamine 2000 (Invitrogen, Carlsbad, CA). Cells were cultured in a low-sodium medium containing 500 ml DMEM (GIBCO, Grand Island, NY) plus 250 ml Leibovitz's L-15, 15 ml 0.5 M HEPES and 235 ml H_2O, pH 7.3. Stable cell lines were selected by G418 sulfate (GIBCO) at 600 μg/ml. Anti-FLAG Western blotting was used to confirm the presence of Slack protein in monoclonal stable cell lines, and patch-clamp recordings were made from these lines.

Protein Purification

Cells were harvested from 10–20 dishes (150 mm diameter, approximately 0.1 g cells per dish) in cell storage buffer (10 ml/g cells) containing (in mM) 10 Tris, 5 KCl, 1 $MgCl_2$, 1 EGTA, 1:100 diluted protease inhibitor cocktail (PI; P 8340; Sigma, St. Louis, MO) and 5 EDTA. All buffers and recording solutions were titrated to pH 7.4. Cells were stored at −80 °C and, upon thawing, broken using a Dounce tissue grinder on ice. After centrifugation at 2,000×*g* for 15 min at 4 °C, the supernatant was collected; then after centrifugation at 141,000×*g* for 1 h at 4 °C, the membrane pellet was collected and resuspended in membrane storage buffer (0.5 ml/g cells) containing (in mM) 250 sucrose, 5 KCl, 10 Tris, 1:100 diluted PI and 5 EDTA. The membrane preparation was stored at −80 °C.

Membranes were incubated in solubilization buffer (1.5 ml/g cells) containing 150 KCl, 50 Tris, 5 EDTA, 1:100 PI and either 16 mM Cymal-5 (Anatrace, Maumee, OH) or 10–16 mM dodecylmaltoside (Calbiochem, San Diego, CA) for 2 h at 4 °C with rotation. After removing the insoluble material by centrifugation (16,000×*g* for 20 min at 4 °C), an equal volume of the solubilization buffer but without detergent was added and subsequently anti-FLAG affinity beads (0.3 ml beads/g cells, Sigma A2220). The mixture was rotated at 4 °C for 2 h; beads were collected in a 10 ml column and washed three times with equal volumes of wash buffer (same as the solubilization buffer but with only 5 mM detergent), and protein was eluted with three 150 μl applications at 20 min intervals of wash buffer with 500 μg/ml FLAG peptide added. A spin column (Bio-Rad, Hercules, CA; 732-6204) was used to extract the eluate. The final protein concentration was approximately 70 ng/μl, as quantified by fluorescence of the GFP-fusion protein; kept at 4 °C; and used immediately for assays or reconstitution. For gel electrophoresis, protein was incubated in 8 M urea buffer overnight at room temperature and run on 8 % polyacrylamide gels.

Slack Channel Reconstitution

Slack protein was reconstituted into liposomes containing POPC, POPE and POPS. The final protein to lipid ratio was about 0.3 Slack tetramer per 50,000 lipid molecules in a 40 nm liposome.

Mixed lipids, 3.6, 1 and 0.8 mg of POPC, POPE and POPS, respectively, were dried by argon and vortexed with 450 μl of reconstitution buffer (150 KCl, 30 TRIS, 5 EGTA, pH 7.4) for 15 min, followed by 10 freeze–thaw cycles using liquid nitrogen and a 40 °C water bath and 60 s sonication. Detergent (Cymal-5 or DM) was added to a 3:1 detergent to lipid ratio, vortexed for 30 min and sonicated for 30 s, then left on ice for about 3 h. The final lipid concentration was 12.8 mM.

Of the protein solution, 100 μl was mixed with 100 μl of solubilized lipids with a rotator at 4 °C for 3 h. The mixture was then loaded into dialysis tubing Spectra/Por Dialysis Membrane (MWCO: 25 kDa; Spectrum, Rancho Dominguez, CA), followed by 36 h of dialysis at 4 °C in buffer (450 KCl, 4 *N*-methyl D-glucamine [NMDG], 20 TRIS, pH 7.4) to form lipid vesicles. A Nycodenz (NYC; Progen Biotechnik, Heidelberg, Germany) discontinuous gradient was used to collect vesicles containing protein. Initial gradient layers were 100 μl 40 % NYC, 200 μl 30 % (containing 100 μl protein liposomes) and 200 μl each for 20, 15, 3 and 1 % NYC concentrations. After 3 h at 214,000×*g*, a liposome band was visible at the top of the 15 % NYC layer and collected. The presence of Slack protein in vesicles was confirmed by Western blotting with the anti-Flag M2 antibody (Sigma).

Patch-Clamp and Bilayer Experiments

Inside–out patch-clamp recordings were carried out with the EPC-9 patch-clamp amplifier and PULSE acquisition program (HEKA Instruments, Lambrecht, Germany). The SF-77B step perfusion system (Warner Instruments, Hamden, CT) controlled by PULSE was used for fast internal solution perfusion. For Na^+ dose-response measurements the pipette solution contained (in mM) 160 KCl,

1 $MgCl_2$, 140 NMG aspartate, 1 EGTA and 10 HEPES, while the bath (internal) solution contained 50 K^+, 100 Cl^-, 200 aspartate$^-$, 10 HEPES and variable concentrations of Na^+ and $NMDG^+$ summing to 250 mM.

Bilayer experiments were carried out using reconstituted vesicles obtained as above with a bilayer recording system (Warner Instruments). Lipids (Avanti, Birmingham, AL; 25 mg/ml) POPE:POPG = 18 µl:6 µl and POPE:-POPC = 16 µl:4 µl were dried by argon and washed with an equal volume of pentane. Hexadecane (Sigma) was then added to yield a final lipid concentration of 10 µg/µl. Two different initial solution configurations were used for our experiments. *Cis* and *trans* buffers were 350 KCl, 30 NaCl, 10 MOPS and 100 KCl, 6 HEPES and 0.6 EGTA or alternatively 100 KCl, 150 NaCl, 5 MOPS and 20 KCl, 30 NaCl and 5 MOPS, respectively. After formation of the bilayer, Slack protein vesicles were added to the *cis* chamber; then after the appearance of channel events, the *cis* solution was exchanged to one with lower osmolarity. An EPC-9 patch amplifier and PULSE software were used for recording.

JC-1 Fluorescence Measurements

The fluorescent dye JC-1 (Molecular Probes, Eugene, OR) was used for monitoring changes in vesicle membrane potential. Slack protein was purified in the presence of Cymal-5 and reconstituted into liposomes with dialysis against 1,000 ml of reconstitution buffer (150 KCl, 30 TRIS, 5 EGTA, pH 7.4) for 36 h at 4 °C with one buffer exchange. Vesicles were collected after centrifugation at 214,000×*g*, and 10 µl of vesicles were resuspended in 1 ml buffer containing 3 mM K^+ (150 NMG-Cl, 10 HEPES, 1 EGTA, 3 KOH, pH 7.4). After taking baseline spectra with

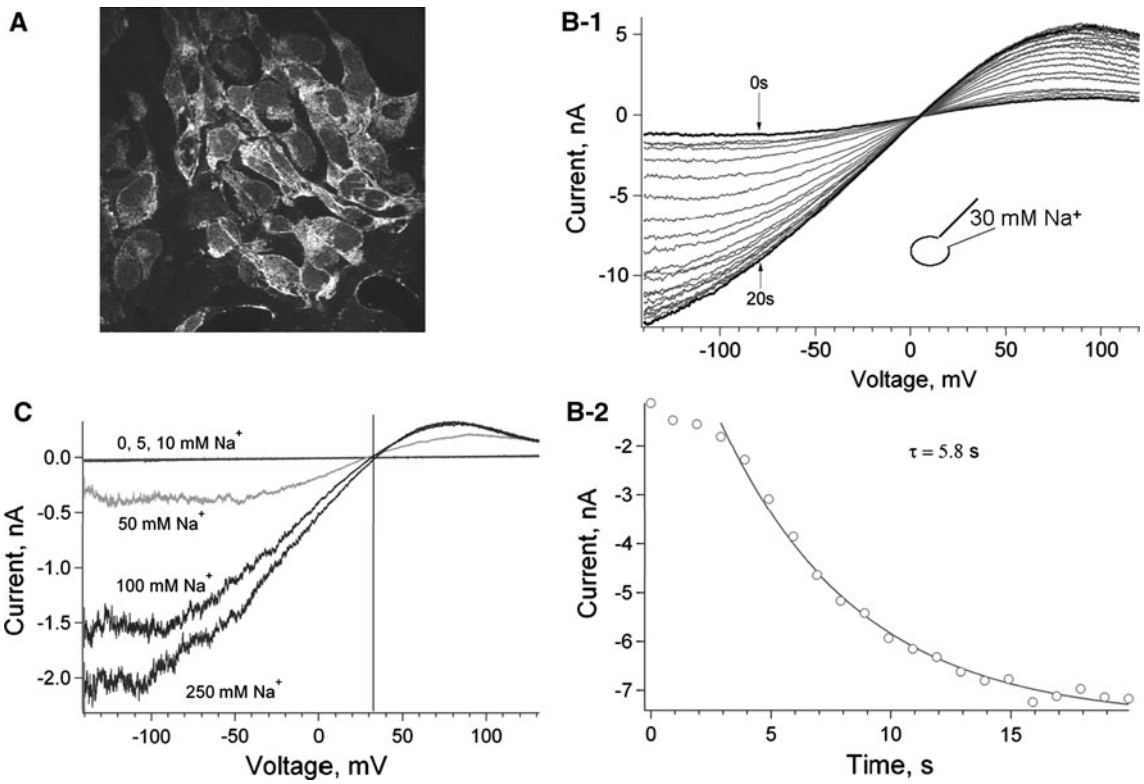

Fig. 1 HEK 293 stable cell lines express functional Slack protein. **a** Fluorescence of HEK cells expressing the N-terminal EGFP-Slack fusion construct. **b-1** Whole-cell recording made from a cell expressing wt-Slack with 30 mM Na^+ in the pipette [pipette solution (in mM): 30 NaCl, 100 KCl, 5 EGTA, 10 HEPES; bath solution: 160 KCl, 1 EGTA, 10 HEPES, 1 $MgCl_2$]. Shown are 22 current traces evoked by voltage ramps from −100 to +120 mV recorded immediately after establishing the whole-cell recording configuration; currents increased as Na^+ diffused from the pipette into the cell. **b-2** Time course of the development of inward currents from the cell shown in **b-1**, measured at −60 mV. The time constant is about 6 s. **c** An inside–out patch was perfused with various Na^+ concentrations (0, 5, 10, 50, 100, 250 mM) while keeping the potassium and chloride gradients constant. The calculated equilibrium potential, E_K, was +30 mV and E_{Cl} was −12 mV, while E_{Na} varied from 0 (at 5 mM internal Na^+) to −100 mV (at 250 mM internal Na^+). The measured reversal potential of the currents was near +30 mV, indicating that K^+ conductance was predominant. Pipette solution (in mM): 160 KCl, 1 $MgCl_2$, 140 NMG-aspartate, 1 EGTA, 10 HEPES; perfused solution (cytoplasmic side): 50 K^+, 100 Cl^-, 200 aspartate$^-$, $[Na^+] + [NMG^+] = 250$

a FluoroMax-3 spectrofluorimeter (Horiba Scientific, Edison, NJ), 3 μM JC-1 was added to the cuvette. The excitation wavelength was 465 nm, and emission at wavelengths of 530 nm (JC-1 monomer) and 590 nm (JC-1 aggregate) was recorded. The emission ratio at 590 and 530 nm was used as an indicator of membrane potential.

Cryo-EM Imaging

Reconstituted vesicle suspension, 3–4 μl having an approximate concentration of 1.9 mg/ml lipid, was applied to a home-made holey carbon film (Chester et al. 2007); blotted manually; and plunge-frozen in liquid ethane. Imaging was performed at liquid N_2 temperature in a Tecnai F20 microscope (FEI, Hillsboro, OR).

Results

Making Stable Cell Lines Expressing Slack-GFP and Slack

Transient transfection of a SlackB construct with an N-terminal GFP fusion into HEK293 cells yielded clear membrane-associated fluorescence (Fig. 1a) as well as Na^+-activated K^+ currents as measured in whole-cell and inside–out patch recordings. However, when we attempted to grow these cells either in normal medium or with selection, the cells survived for no more than 3–4 days after transfection. We noticed in whole-cell recordings from transfected cells the activation of K^+ current by extracellular Na^+ and reasoned that either an intrinsic external Na^+ sensitivity or an Na^+ leak that increases internal Na^+ was allowing Slack channels to be activated, yielding excessive K^+ conductance. We modified the growth medium, which is based on DMEM, to reduce the Na^+ concentration from 155 to 112 mM and found that this medium allowed growth even under selection with G-418. After successfully establishing the SlackB-GFP stable cell line, we also made stable cell lines expressing SlackB alone. Data shown in the rest of this article were obtained from these "native" SlackB channels.

Stabilized Slack on HEK293 Cells Preserves Its Na^+ Gating Properties

In a whole-cell recording, rupture of the patch membrane allows Na^+ to diffuse into the cell, yielding an increase in current as Na^+ equilibrates in a few seconds (Fig. 1b).

To evaluate the sodium dependence of the expressed channels, we used inside–out patches with a fixed gradient for potassium ($[K]_i = 50$ mM, $[K]_o = 160$ mM) and chloride ($[Cl]_i = 100$ mM, $[Cl]_o = 162$ mM), with equilibrium potentials $E_K = +30$ mV and $E_{Cl} = -12$ mV. The bath (intracellular) Na^+ concentration was varied while keeping the sum of Na^+ and N-methylglucamine (NMG^+) concentrations equal to 250 mM. Figure 1c shows the currents evoked by voltage ramps as the bath Na^+ concentration was changed with a rapid perfusion system. The currents increased steeply with Na^+ concentration, but the reversal potentials remained very close to E_K, regardless of the Na^+ concentration.

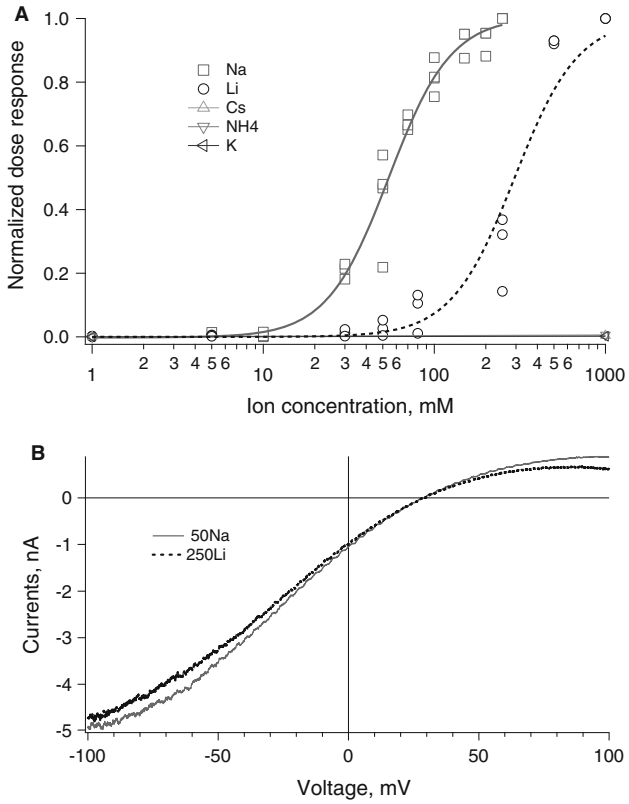

Fig. 2 Dose-response of ion activation of Slack channels. **a** Inward currents activated by internal Na^+ and Li^+ were measured from an inside–out patch at −80 mV while keeping potassium and chloride gradients unchanged. K_d for Na^+ was about 54 mM and the Hill coefficient, $n_H = 2.4$ (pipette: 160 KCl, 1 $MgCl_2$, 140 NMG-aspartate, 1 EGTA, 10 HEPES; perfused [internal] solution: 50 K^+, 100 Cl^-, 200 $aspartate^-$, $Na^+ + NMG^+ = 250$). Saturation was not attained in the lithium dose response, but the *dashed curve* shows the same function as fitted for Na^+ but with $K_d = 295$ mM. Cs^+, NH_4^+ and K^+ did not measurably open Slack channels at concentrations up to 1 M. **b** Very similar current traces are evoked by 50 mM Na^+ (*solid curve*) or 250 mM Li^+ (*dotted curve*). A voltage ramp from −100 to +100 mV was applied to an inside–out patch with intracellular solutions containing 50 mM K^+, 100 Cl^-, 200 $aspartate^-$ and either 200 $NMG^+ + 50$ Na^+ or 250 Li^+, respectively. The pipette contained 160 mM K^+ (160 KCl, 1 $MgCl_2$, 140 NMG-aspartate, 1 EGTA, 10 HEPES)

Lithium Opens Slack Channels But Is About Six Times Less Potent than Sodium

Zhang et al. (2010) have shown that, unlike larger ions, Li^+ is able to activate Slack channels expressed in *Xenopus* oocytes, although at lower potency. We obtained dose-response relationships with internal potassium, lithium, cesium and ammonium ions in inside–out patches from our cells. Responses at −80 mV are plotted in Fig. 2a, with the responses from each patch normalized to the response of the same patch to 250 mM internal Na^+. At a concentration of 1 M, cesium and ammonium produced <0.6 % of maximal activation. Li^+ (1 M) was capable of inducing a nearly saturating current, but its affinity was about six times lower than that of Na^+. The sodium dose response was fitted with $K_{1/2} = 54$ mM with the Hill slope $n_H = 2.4$. When the Li^+ data were fitted with the constraint $n_H = 2.4$, the estimated $K_{1/2}$ was 294 mM. Figure 2b shows the nearly identical currents evoked by a voltage ramp in the presence of 50 mM Na^+ or 250 mM Li^+ in the internal solution.

Purification and Reconstitution

Expression of Slack protein is only a few micrograms per 150 mm dish of cells; however, for some purposes, such as single-particle cryo-EM studies, quantities of ~10 µg protein are sufficient. The membrane fraction isolated from cells was solubilized in dodecylmaltoside or Cymal-5. Purification made use of the C-terminal FLAG tag on the expressed protein, with an anti-FLAG affinity column and elution with FLAG peptide. The resulting protein ran at the expected size of 136 kDa on an SDS-PAGE gel (Fig. 3a).

The protein was reconstituted into membranes by first mixing with detergent-solubilized lipids and then removing the detergent by dialysis. The vesicle fraction was enriched by density-gradient centrifugation, and cryo-EM revealed that the resulting vesicles were unilamellar and 25–50 nm in size (Fig. 3b). Successful reconstitution of the protein was assayed by resolubilizing the vesicles and running an SDS-PAGE gel. Western blotting with anti-FLAG showed recovery of the 136 kDa protein band (Fig. 3c).

Assay for Functional Channels after Reconstitution

Reconstituted vesicles were fused with planar bilayers for single-channel recordings. No channel currents were seen in the absence of Na^+ on the *cis* side (from which the vesicles were added), but channel activity was reversibly seen when a solution containing 100 mM Na^+ was perfused (Fig. 4a). Under the recording conditions (100 mM K^+ on the *trans* side), the single-channel conductance was 270 pS.

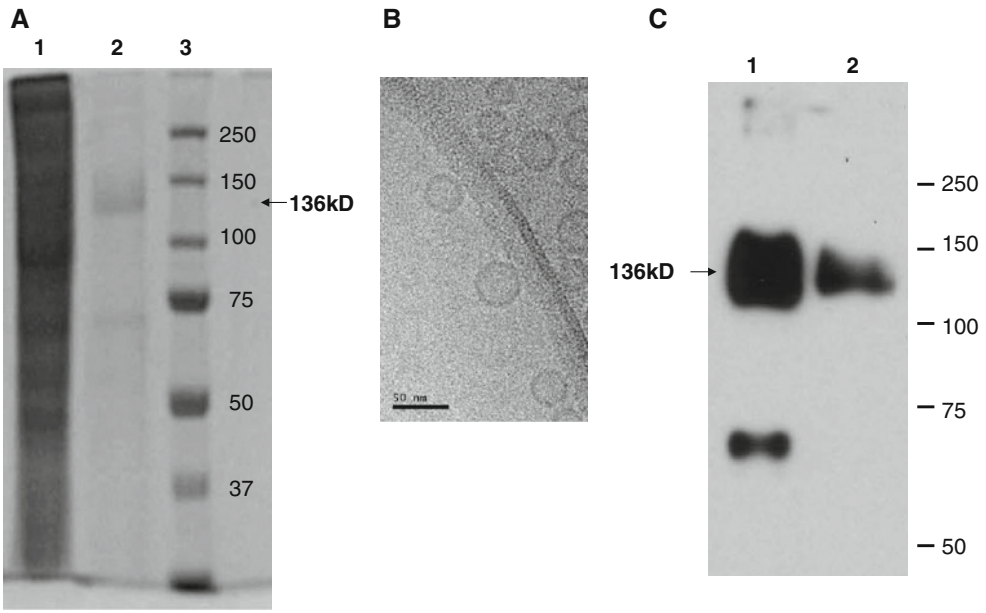

Fig. 3 Slack protein purification and liposome reconstitution. **a** Coomassie-stained protein gel made with 8 % polyacrylamide. *Lane 1*, cell lysate; *lane 2*, affinity-purified Slack protein; *lane 3*, protein molecular-weight markers. The purification yield was about 2 µg protein per 150 mm dish from 0.1 g cells. The ~70 kDa contaminant was not always present and appears to come from the antibody beads. **b** Examination of the reconstituted preparation by cryo-EM shows overwhelmingly unilamellar vesicles. The image shows the edge of a hole in the carbon film. The image was recorded with 2 µm underfocus at 200 keV. **c** Western blot probed with anti-FLAG antibody. *Lane 1*, Slack protein (monomer 136 kDa) as solubilized with Cymal-5 and purified; *lane 2*, protein extracted from liposomes after reconstitution. A 70 kDa band is again present in *lane 1*. It appears in control Western blots and appears to come from the antibody beads; note that it is absent from *lane 2*

Figure 4c shows another bilayer recording with 100 mM K^+ in the *cis* solution and 20 mM K^+ *trans*. The recording from a voltage ramp (bottom trace) shows a reversal potential of −45 mV, while the theoretical E_K was −42 mV. The single-channel conductance was 244 pS under these conditions.

Bilayer experiments demonstrate the presence of individual Na^+-activated channels but do not assay the population of reconstituted channels. We used the fluorescent dye JC-1 to measure Na^+-activated membrane potential changes driven by a K^+ diffusion potential. JC-1 in its monomeric form emits at 530 nm, but at high concentration it forms aggregates with a red-shifted fluorescence at 590 nm. As JC-1 is positively charged and membrane-permeable, it serves as a "slow" voltage indicator. Based on quantitative fluorometry of the Slack-GFP fusion construct, we were able to define a protein-to-lipid ratio in the reconstitution process of approximately one Slack tetramer to 50,000 lipid molecules. This ratio corresponds to approximately 0.3 tetrameric channels per 40 nm lipid vesicle, typical for the vesicle sizes we observed (Fig. 3b). Vesicles containing 160 mM K^+ were diluted into a solution with 3 mM K^+. Addition of 30 mM NaCl to the outside solution resulted in a 6 % increase in the ratio of intensity at 590 nm relative to 530 nm (Fig. 4d). This change reflects the establishment of a negative membrane

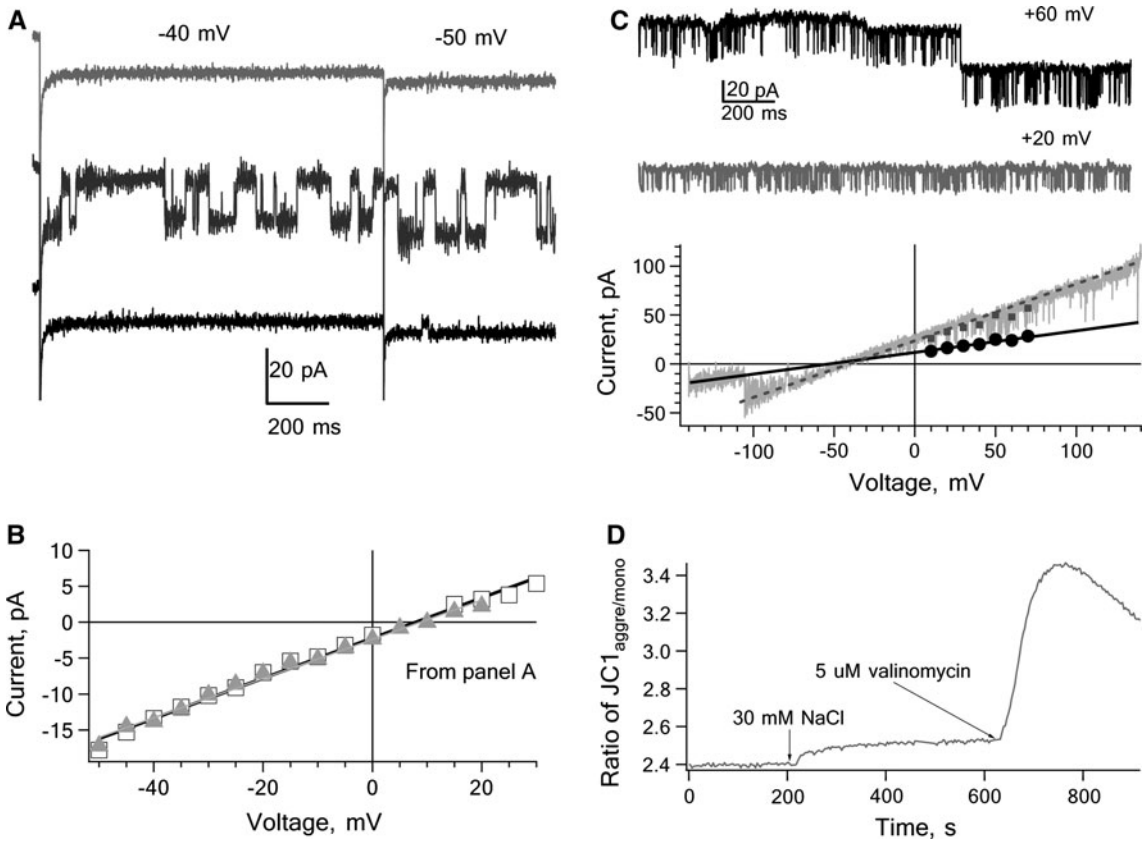

Fig. 4 Reconstituted Slack forms Na^+-activated K^+ channels. **a** Slack-containing vesicles formed from Cymal-5 solution were fused with a POPE:POPC = 4:1 bilayer membrane. Each sweep shows a recording at −40 mV followed by a step to −50 mV. After vesicles were added to the *cis* side and channel events were first observed, the hypertonic solution on the *cis* side (1 ml volume) was replaced by perfusion of 10 ml K buffer: 160 KCl, 10 HEPES, 1 EGTA (*top trace*), followed by 10 ml Na buffer, 100 mM NaCl, 10 HEPES, 1 EGTA (*middle trace*) and then another 10 ml K buffer (*bottom trace*). Solution on the *trans* side was 100 KCl, 6 HEPES and 0.6 EGTA. **b** The single-channel conductance was calculated to be 270 pS from a linear fit of unitary current amplitudes from the experiment in **a**, with a reversal potential of +10 mV. This reversal potential differs from the theoretical E_K consistent with the possibility that the 160 K^+ on the *cis* side was not completely replaced by perfusion. **c** Recording from a POPE:POPG = 3:1 bilayer in which the ion concentrations on both sides were fixed. *Cis* side: 100 KCl, 150 NaCl, 5 MOPS; *trans* side: 20 KCl, 30 NaCl, 5 MOPS. Vesicles were formed from the same lipid mixture using DM. Recordings at +20 and +60 mV show two active channels (*openings are upward*). Unitary current values (*black dots*) are plotted along with the current from a voltage ramp. The fitted line corresponds to a single-channel conductance of 244 pS and reversal potential of −45 mV; *dashed line and filled squares* indicate twice the conductance when two channels are active. The theoretical E_K was −42 mV under these conditions. **d** Flux assay for potassium transport. Reconstituted vesicles loaded with 150 mM K^+ were diluted into a solution containing 3 K^+ and 150 NMG^+. Addition of 30 mM Na^+ evoked a 5 % increase in the ratio of fluorescence at 595 and 540 nm. Subsequent addition of 5 μM valinomycin caused a further 36 % increase in the ratio, consistent with about 15 % of the liposomes containing channels that were activated by external Na^+

potential in a fraction of vesicles. Subsequent addition of 5 μM valinomycin, which is expected to produce a K^+ diffusion potential in every vesicle, yielded a peak increase of 36 % in the ratio. These results show that a substantial fraction of vesicles, roughly 16 %, have a K^+ permeability that is activated by external Na^+, presumably from inside–out Slack channels.

If we assume that channel reconstitution has no bias for orientation and assume a reconstituted density of roughly 0.3 tetrameric channels per vesicle, then the total yield of inside–out channels should be about 15 %, consistent with the result from the JC-1 fluorescence measurement and implying a high specific activity of reconstituted channels.

Discussion

The Slack Na^+-activated potassium channel is a member of the six-transmembrane-segment ion channel superfamily, which also includes the voltage-gated channels. Voltage gating of Slack channels is very weak (Yuan et al. 2003), as seen in Fig. 2, which would be expected from the absence of charged residues in the primary voltage-sensing S4 helix (Joiner et al. 1998). However, Slack activity is very sensitive to Na^+ concentrations in the range of tens of millimoles. This sensitivity is appropriate for a channel that responds to action potential–induced fluxes in neurons and muscle cells as well as providing Na^+-activated fluxes in other cells. Here, we describe the establishment of a stable cell line expressing Slack and show that the Slack protein can be purified on an antibody-affinity column. The purified protein can be reconstituted to form Na^+-activated and K^+-selective channels as detected in a planar lipid bilayer assay. Also, using a flux assay based on a potential-sensitive dye, we found that the fraction of vesicle-enclosed volume that participated in Na^+-activated K^+ flux was essentially equal to the number of vesicles containing inside–out Slack channels, assuming random orientation. Thus, the size of the flux signal was consistent with a high specific activity of the channel protein.

Acknowledgments We are grateful to Drs. David Chester and Yufeng Zhou for their advice and patient instruction in cryo-EM and reconstitution techniques. This work was supported by NIH grant NS21501 to F.S.

References

Bhattacharjee A, Kaczmarek LK (2005) For K^+ channels, Na^+ is the new Ca^{2+}. Trends Neurosci 28:422–428

Bhattacharjee A, Gan L, Kaczmarek LK (2002) Localization of the Slack potassium channel in the rat central nervous system. J Comp Neurol 454:241–254

Bhattacharjee A, Joiner WJ, Wu M, Yang Y, Sigworth FJ, Kaczmarek LK (2003) Slick (Slo2.1), a rapidly-gating sodium-activated potassium channel inhibited by ATP. J Neurosci 23:11681–11691

Bhattacharjee A, von Hehn CAA, Mei X, Kaczmarek LK (2005) Localization of the Na^+-activated K^+ channel Slick in the rat central nervous system. J Comp Neurol 484:80–92

Brown MR, Kronengold J, Gazula VR, Spilianakis CG, Flavell RA, von Hehn CA, Bhattacharjee A, Kaczmarek LK (2008) Amino-termini isoforms of the Slack K^+ channel, regulated by alternative promoters, differentially modulate rhythmic firing and adaptation. J Physiol 586:5161–5179

Brown MR, Kronengold J, Gazula V-R, Chen Y, Strumbos JG, Sigworth FJ, Navaratnam D, Kaczmarek LK (2010) Fragile X mental retardation protein controls gating of the sodium-activated potassium channel Slack. Nat Neurosci 13:819–821

Budelli G, Hage TA, Wei A, Rojas P, Jong Y-JI, Oandapos-Malley K, Salkoff L (2009) Na^+-activated K^+ channels express a large delayed outward current in neurons during normal physiology. Nat Neurosci 12:745–750

Chen H, Kronengold J, Yan Y, Gazula V-R, Brown MR, Ma L, Ferreira G, Yang Y, Bhattacharjee A, Sigworth FJ, Salkoff L, Kaczmarek LK (2009) The N-terminal domain of Slack determines the formation and trafficking of Slick/Slack heteromeric sodium-activated potassium channels. J Neurosci 29:5654–5665

Chester DW, Klemic JF, Stern E, Sigworth FJ, Klemic KG (2007) Holey carbon micro-arrays for transmission electron microscopy: a microcontact printing approach. Ultramicroscopy 107:685–691

Cong Y, Ludtke SJ (2010) Single particle analysis at high resolution. Methods Enzymol 482:211–235

Fleming MR, Kaczmarek LK (2009) Use of optical biosensors to detect modulation of Slack potassium channels by G protein-coupled receptors. J Recept Signal Transduct Res 29:173–181

Joiner WJ, Tang MD, Wang LY, Dworetzky SI, Boissard CG, Gan L, Gribkoff VK, Kaczmarek LK (1998) Formation of intermediate-conductance calcium-activated potassium channels by interaction of Slack and Slo subunits. Nat Neurosci 1:462–469

Kameyama M, Kakei M, Sato R, Shibasaki T, Matsuda H, Irisawa H (1984) Intracellular Na^+ activates a K^+ channel in mammalian cardiac cells. Nature 309:354–356

Kim YC, Sim JH, Kang TM, Suzuki H, Kim SR, Kwon SC, Xu WX, Lee SJ, Kim KW (2007) Sodium-activated potassium current in guinea pig gastric myocytes. J Korean Med Sci 22:57–62

Paulais M, Lachheb S, Teulon J (2006) A Na^+- and Cl^--activated K^+ channel in the thick ascending limb of mouse kidney. J Gen Physiol 127:205–215

Ruffin VA, Gu XQ, Zhou D, Douglas RM, Sun X, Trouth CO, Haddad GG (2008) The sodium-activated potassium channel Slack is modulated by hypercapnia and acidosis. Neuroscience 151:410–418

Santi CM, Ferreira G, Yang B, Gazula V-R, Butler A, Wei A, Kaczmarek LK, Salkoff L (2006) Opposite regulation of Slick and Slack K^+ channels by neuromodulators. J Neurosci 26:5059–5068

Uchino S, Wada H, Honda S, Hirasawa T, Yanai S, Nakamura Y, Ondo Y, Kohsaka S (2003) Slo2 sodium-activated K^+ channels bind to the PDZ domain of PSD-95. Biochem Biophys Res Commun 310:1140–1147

Wang L, Sigworth FJ (2009) Structure of the BK potassium channel in a lipid membrane from electron cryomicroscopy. Nature 461(7261):292–295

Yang B, Desai R, Kaczmarek LK (2007) Slack and Slick K(Na) channels regulate the accuracy of timing of auditory neurons. J Neurosci 27:2617–2627

Yuan A, Santi CM, Wei A, Wang ZW, Pollak K, Nonet M, Kaczmarek L, Crowder CM, Salkoff L (2003) The sodium-activated potassium channel is encoded by a member of the Slo gene family. Neuron 37:765–773

Yuan P, Leonetti MD, Pico AR, Hsiung Y, MacKinnon R (2010) Structure of the human BK channel Ca^{2+}-activation apparatus at 3.0 Å resolution. Science 329:182–186

Zhang Y, Paterson WG (2007) Functional evidence for Na^+-activated K^+ channels in circular smooth muscle of the opossum lower esophageal sphincter. Am J Physiol Gastrointest Liver Physiol 292:G1600–G1606

Zhang Z, Rosenhouse-Dantsker A, Tang Q-Y, Noskov S, Logothetis DE (2010) The RCK2 domain uses a coordination site present in Kir channels to confer sodium sensitivity to Slo2.2 channels. J Neurosci 30:7554–7562

J Membrane Biol (2012) 245:675–681
DOI 10.1007/s00232-012-9436-4

Oxidative Parameters in the Rat Brain of Chronic Mild Stress Model for Depression: Relation to Anhedonia-Like Responses

Chao Wang · He-ming Wu · Xiao-rong Jing · Qiang Meng · Bei Liu · Hua Zhang · Guo-dong Gao

Received: 18 January 2012 / Accepted: 30 April 2012 / Published online: 8 July 2012

Abstract The chronic mild stress (CMS) protocol is widely used to evoke depression-like behaviors in the laboratory. Some animals exposed to CMS are resistant to the development of anhedonia, whereas the remaining are responsive, CMS-resilient and CMS-sensitive, respectively. The aim of this study was to examine the effects of chronic stress on oxidative parameters in the rat brain. The consumption of sweet food, protein and lipid oxidation levels and superoxide dismutase and catalase activities in the rat hippocampus, cortex and cerebellum were assessed. We found a significant increase in protein peroxidation (hippocampus and cortex), a significant increase in catalase activity (cortex, hippocampus and cerebellum) and a decrease in superoxide dismutase activity (cortex, hippocampus and cerebellum) in the CMS-sensitive group compared to the CMS-resilient group and normal controls as well as an increase in lipid peroxidation (cerebellum) in the CMS-sensitive and CMS-resilient groups compared to normal controls. However, there was no significant difference in protein peroxidation (cerebellum) and lipid peroxidation (cortex and hippocampus) among the three groups. In conclusion, our results indicate that the segregation into CMS-sensitive and -resilient groups based on sucrose intake is paralleled by significant differences in oxidative parameters. CMS induces oxidative damage and alterations in the activity of antioxidants which may lead to increased oxidative damage, irrespective of the anhedonia-like status of the stressed animals.

Keywords Anhedonia · Oxidative parameter · Stress · Anhedonia-like response

Introduction

Chronic stress is an etiological factor in anxiety disorder and depression, and therefore, based on this observation, the chronic mild stress (CMS) animal model has been developed to mimic the development and progress of clinical depression. In the CMS model, one of the main symptoms of major depression, anhedonia, is mimicked (Willner et al. 1992). Anhedonia has been widely measured as decreased consumption of and preference for palatable sweet solutions, indicating decreased responsiveness to rewarding stimuli as a consequence of sequential exposure to a variety of mild stressors (Henningsen et al. 2009; Moreau et al. 1995; Papp et al. 1991; Willner 1997). The decrease in sweet consumption does not occur in all animals exposed to CMS; i.e., a group of rats are stress-resistant or -resilient (Bergstrom et al. 2007; Bisgaard et al. 2007; Jayatissa et al. 2006; Strekalova et al. 2004). Previous studies have shown that rats subjected to CMS segregate into two subgroups: a group that develops anhedonia-like symptoms (CMS-sensitive) and a group that appears to be resilient to the influence of chronic stress on hedonic status (CMS-resilient) as assessed by sucrose-intake profiles (Bergstrom et al. 2008). This segregation was confirmed by a place preference conditioning test and on the molecular level by global gene and protein expression analysis (Bisgaard et al. 2007). Additionally, studies have implied that the HPA axis is activated in both

C. Wang, H. Wu and X. Jing have contributed equally to this work.

C. Wang · H. Wu · X. Jing · Q. Meng · B. Liu · H. Zhang · G. Gao (✉)
Department of Neurosurgery, Institute of Functional Brain Disorders of PLA, Tangdu Hospital, The Fourth Military Medical University, 1 Xin'shi Road, Xi'an 710032, China
e-mail: konglingmin81@163.com

CMS-sensitive and CMS-resilient animals, hence indicating other processes as responsible for the development of, and resistance to, anhedonia. In particular, this would argue for some protective mechanism only in CMS-resilient animals (Bergstrom et al. 2008).

The brain metabolizes 20 % of total-body oxygen and has a limited amount of antioxidant capacity, so it is very vulnerable to reactive oxygen species (ROS) production. In the CMS model, the generation of free radicals can exceed the capacity of antioxidant defense in the brain. And oxidative stress, which results from increased production of ROS, decreased antioxidant defense or failure to repair oxidative damage, may lead to membrane degradation, cellular dysfunction and apoptosis. Recent studies have consistently reported increased ROS in plasma of patients with major depression, especially with melancholia associated (Bilici et al. 2001). Recent studies also have shown the effects of the CMS paradigm on lipid and protein oxidation levels (markers of oxidative stress) and on superoxide dismutase (SOD) and catalase (CAT) activities (the major antioxidant enzymes) in the rat brain, and it is believed that stress produces oxidants and an imbalance between SOD and CAT activities that contributes to stress-related diseases such as depression (Lucca et al. 2009a). But the relationship between oxidative parameters and an anhedonia-like state remains unknown.

In the present study, we analyzed possible differences in the oxidative parameters among CMS-resilient, CMS-sensitive and normal control rats in the cortex, hippocampus and cerebellum to investigate if any alteration of oxidative stress was specific for the anhedonia-like state and the relationship between them.

Materials and Methods

Subjects

We used adequate measures to minimize pain or discomfort of the rats. The research was conducted in accordance with the guidelines published in the NIH *Guide for the Care and Use of Laboratory Animals* and the principles presented in the "Guidelines for the Use of Animals in Neuroscience Research" by the Society for Neuroscience. All experimental protocols were approved by the Review Committee for the Use of Human or Animal subjects of the Fourth Military Medical University.

Male Wistar rats were purchased from the animal center of the Fourth Military Medical University. Animal weight was approximately 220 g when adaptation for sucrose consumption was initiated and approximately 340 g at the start of the stress regime. Animals were singly housed, except when grouping was applied as a stress parameter. Food and water were available ad libitum except when food and/or water deprivation was applied as a stress parameter. The standard 12-h light/dark cycle, with lights on from 6:00 a.m. to 6:00 p.m., was changed only in the course of the stress regime.

Sucrose-Consumption Test

Animals were first trained to consume a palatable sucrose solution (1.5 %). Training lasted 5 weeks. In this period, the sucrose test was made twice a week during the first 3 weeks and once a week during the last 2 weeks. Animals were food- and water-deprived 14 h before the test. The test consisted of 1-h exposure to a bottle with sucrose solution. During the stress period the sucrose-consumption test was performed once a week.

CMS Protocol and Study Design

On the basis of sucrose intake in the three final baseline tests, animals were divided into two matched groups and placed in separate rooms. One group was exposed to an initial 2 weeks of chronic mild stressors and the other was left undisturbed. The unchallenged group was food- and water-deprived 14 h before the sucrose-consumption test; otherwise, food and water were freely available. The stress procedure is a slight modification of the protocol developed by Papp (Garcia et al. 2008; Sanchez et al. 2003). It consisted of seven different stressors: one period of intermittent illumination, stroboscopic light, grouping and food or water deprivation; two periods of soiled cage and no stress; and three periods of 45° cage tilting. All stressors lasted from 10 to 14 h. Stress was continued during the entire period of treatment. Based on end-point sucrose intake, animals were finally subdivided in three groups: normal controls ($n = 7$), CMS-sensitive ($n = 7$) and CMS-resilient ($n = 10$). At the end of the experiment, all rats were handled and accustomed to the environment where the killing was to be performed. All subjects were removed from their home cages and killed by decapitation. The hippocampus, cortex and cerebellum were immediately isolated and stored at −80 °C for posterior analyses for oxidative parameters.

Oxidative Stress Parameters

In order to assess oxidative damage, the formation of thiobarbituric acid-reactive species (TBARS) was measured during an acid-heating reaction (Esterbauer and Cheeseman 1990; Lucca et al. 2009a). Samples were mixed with 1 ml of trichloroacetic acid (TCA) 10 % and 1 ml of thiobarbituric acid 0.67 % and then heated in a boiling water bath for 15 min. TBARS were determined by

absorbance at 535 nm. Oxidative damage to proteins was measured by quantification of carbonyl groups based on the reaction with dinitrophenylhydrazine (DNPH), as previously described (Levine et al. 1994). Proteins were precipitated by the addition of 20 % TCA and redissolved in DNPH; absorbance was read at 370 nm. To determine CAT activity, brain tissue was sonicated in 50 mmol/l phosphate buffer (pH 7.0), and the resulting suspension was centrifuged at 3,000×g for 10 min. The supernatant was used for enzyme assay. CAT activity was measured by the rate of decrease in hydrogen peroxide absorbance at 240 nm (Aebi 1984). SOD activity was assayed by measuring the inhibition of adrenaline auto-oxidation, as previously described (Bannister and Calabrese 1987). All biochemical measures were normalized to the protein content, with bovine albumin as standard (Lowry et al. 1951).

Statistical Analysis

Results were presented as mean ± SEM. Statistical analysis of data was performed with SPSS 11.0 (SPSS, Inc., Chicago, IL). Data were analyzed by one-way ANOVA followed by a pairwise multiple comparison test (Student–Newman–Keul). The significance level was set at $p < 0.05$.

Results

CMS: Sucrose Intake as a Measure of Anhedonia

Sucrose consumption was monitored once a week throughout the experiments, and the results are shown in Table 1. Based on end-point sucrose intake, animals were subdivided into three groups: normal controls ($n = 7$), CMS-sensitive ($n = 7$) and CMS-resilient ($n = 10$). This segregation lasted throughout the experiment. An anhedonia-like state (CMS-sensitive) was defined as a minimum of 40 % reduction in sucrose intake in response to stress. CMS resilience was defined as remaining on a sucrose-intake level corresponding to the baseline level. Normal control animals did not decrease sucrose intake. No significant difference among the three groups was present at baseline. The segregation was significant through the entire period ($p < 0.05$). The normal control group was significantly different from the CMS-sensitive ($p < 0.05$), but not from the CMS-resilient, animals ($p > 0.05$). The segregation was evident already after 7 days of exposure to CMS and persistent after 14 days.

Effects of CMS on Oxidative Stress Variables in Rat Brain

As shown in Fig. 1, protein peroxidation and carbonyl in the cortex and hippocampus were significantly higher in the CMS-sensitive group compared to the CMS-resilient group (cortex $F_{2,21} = 179.244$, $p = 0.000$; hippocampus $F_{2,21} = 234.557$, $p = 0.000$) and to normal controls (cortex $F_{2,21} = 179.244$, $p = 0.000$; hippocampus $F_{2,21} = 234.557$, $p = 0.000$). Compared with normal controls, protein peroxidation and carbonyl in the cortex and hippocampus were also significantly higher in the CMS-resilient group (cortex $F_{2,21} = 179.244$, $p = 0.000$; hippocampus $F_{2,21} = 234.557$, $p = 0.000$). In the cerebellum, there was no significant main effect of groups for protein peroxidation and carbonyl ($F_{2,21} = 4.588$, $p = 0.055$).

We also measured the lipid peroxidation–TBARS variation (Fig. 2). No significant differences were found for lipid peroxidation–TBARS in the cortex ($F_{2,21} = 0.966$, $p = 0.403$) and hippocampus ($F_{2,21} = 0.966$, $p = 0.095$). In the cerebellum, lipid peroxidation–TBARS was significantly increased in CMS-sensitive ($F_{2,21} = 50.867$, $p = 0.000$) and CMS-resilient ($F_{2,21} = 50.867$, $p = 0.000$) compared to normal controls. No differences were found between CMS-sensitive and CMS-resilient animals ($F_{2,21} = 50.867$, $p = 0.127$).

Effects of CMS on Antioxidant Variables in Rat Brain

As shown in Fig. 3, SOD activity in the cortex and hippocampus was significantly higher in normal controls compared to the CMS-sensitive group (cortex $F_{2,21} = 47.175$, $p = 0.001$; hippocampus $F_{2,21} = 39.527$, $p = 0.001$) and to the CMS-resilient group (cortex $F_{2,21} = 47.175$, $p = 0.007$;

Table 1 Sucrose consumption (mean ± SD) in the chronic mild stress model in three groups: CMS-sensitive ($n = 7$), CMS-resilient ($n = 10$) and normal control ($n = 7$)

	Baseline	1 week	2 weeks	3 weeks	4 weeks	5 weeks
Normal control	10.53 ± 1.29	12.38 ± 2.03	13.78 ± 2.95	14.45 ± 2.38	14.92 ± 3.41	14.73 ± 2.55
CMS-resilient	10.12 ± 1.37	11.47 ± 2.56	12.41 ± 2.12	13.87 ± 2.54	13.68 ± 2.49	14.21 ± 2.37
CMS-sensitive	10.92 ± 1.45	9.14 ± 1.12[a,b]	7.34 ± 0.86[a,b]	6.02 ± 0.93[a,b]	5.32 ± 0.74[a,b]	5.45 ± 0.83[a,b]

[a] Significant difference between normal control and CMS-sensitive ($p < 0.05$)

[b] Significant difference between CMS-sensitive and CMS-resilient ($p < 0.05$)

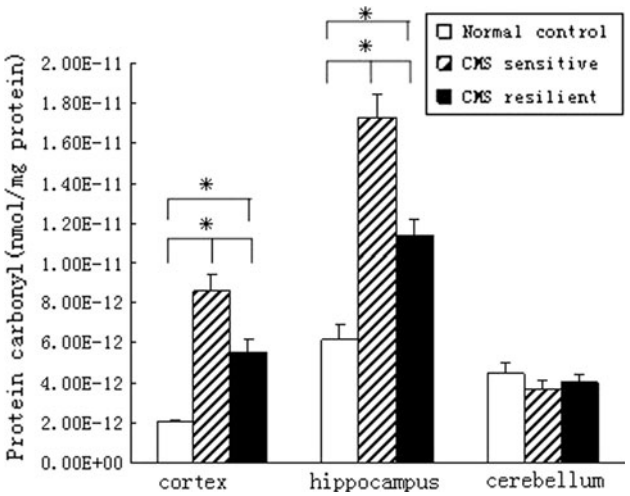

Fig. 1 Effect of the CMS paradigm on protein peroxidation in brain of normal control, CMS-sensitive and CMS-resilient rats. *Bars* represent mean ± SEM. *Vertical lines above bars* indicate standard deviation. $^*p < 0.05$

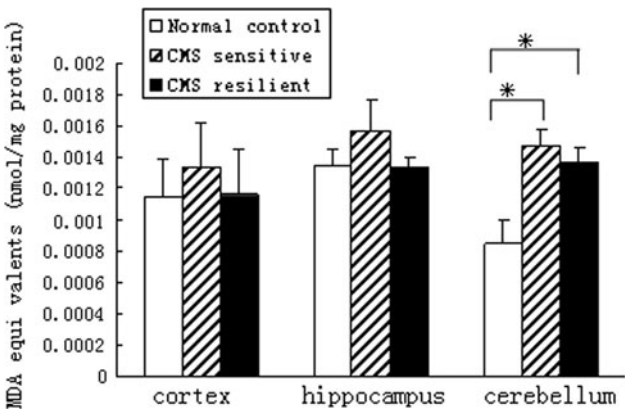

Fig. 2 Effect of the CMS paradigm on lipid peroxidation in brain of normal control, CMS-sensitive and CMS-resilient rats. *Bars* represent mean ± SEM. *Vertical lines above bars* indicate standard deviation. $^*p < 0.05$

hippocampus $F_{2,21} = 39.527$, $p = 0.007$). Compared with the CMS-sensitive group, protein SOD activity in the cortex and hippocampus was also significantly higher in the CMS-resilient group (cortex $F_{2,21} = 47.175$, $p = 0.000$; hippocampus $F_{2,21} = 39.527$, $p = 0.002$). Compared with the CMS-sensitive group, SOD activity in the cerebellum was significantly higher in normal controls ($F_{2,21} = 12.776$, $p = 0.005$) and the CMS-resilient group ($F_{2,21} = 12.776$, $p = 0.032$). No differences were found between normal controls and the CMS-resilient group ($F_{2,21} = 12.776$, $p = 0.110$).

In Fig. 4, CAT activity in the hippocampus and cerebellum was significantly higher in the CMS-sensitive group compared to the CMS-resilient group (hippocampus

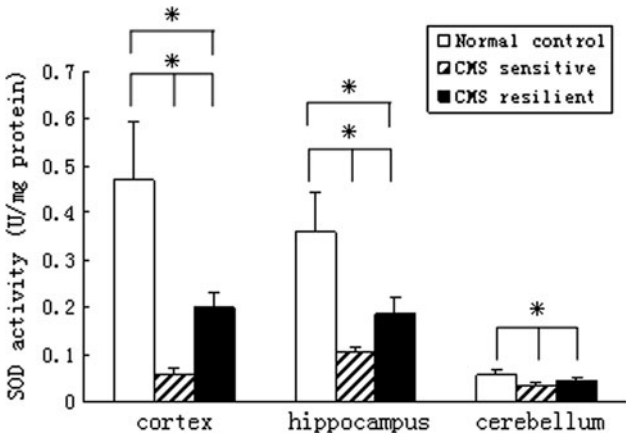

Fig. 3 Effect of the CMS paradigm on superoxide dismutase activity in brain of normal control, CMS-sensitive and CMS-resilient rats. *Bars* represent mean ± SEM. *Vertical lines above bars* indicate standard deviation. $^*p < 0.05$

$F_{2,21} = 50.967$, $p = 0.001$; cerebellum $F_{2,21} = 55.264$, $p = 0.001$) and to normal controls (hippocampus $F_{2,21} = 50.967$, $p = 0.000$; cerebellum $F_{2,21} = 55.264$, $p = 0.000$). Compared with normal controls, CAT activity in the hippocampus and cerebellum was also significantly higher in the CMS-resilient group (hippocampus $F_{2,21} = 50.967$, $p = 0.000$; cerebellum $F_{2,21} = 55.264$, $p = 0.000$). In the cortex, CAT activity was significantly increased in the CMS-sensitive group compared to the CMS-resilient group ($F_{2,21} = 20.841$, $p = 0.000$) and compared to normal controls ($F_{2,21} = 20.841$, $p = 0.001$). No differences were found between the CMS-resilient group and normal controls ($F_{2,21} = 20.841$, $p = 0.499$).

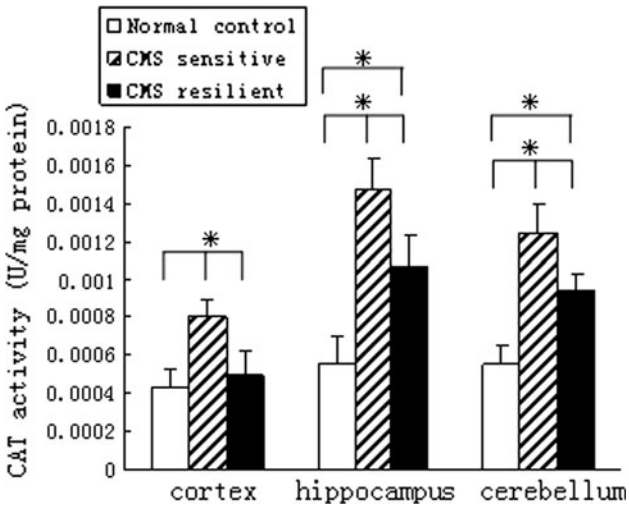

Fig. 4 Effect of the CMS paradigm on catalase activity in brain of normal control, CMS-sensitive and CMS-resilient rats. *Bars* represent mean ± SEM. *Vertical lines above bars* indicate standard deviation. $^*p < 0.05$

Discussion

The CMS model, originally described by Willner et al. (1992), is a model of depression that employs chronic unpredictable mild stressors. Most of the symptoms of depression have been modeled and mimicked in the CMS rats. In this model reduced consumption of sucrose solution as well as decreased intracranial self-stimulation behavior serve as markers of a decrease in reward sensitivity and may simulate anhedonia (Bekris et al. 2005; Bergstrom et al. 2008; Gamaro et al. 2003).

This is the first study to demonstrate a clear difference in distinct oxidative parameters between CMS-resilient and CMS-sensitive animals, which could be involved in the pathogenesis of depression. We segregated animals exposed to CMS into the above two groups, decreasing and not decreasing sucrose intake, respectively. This was paralleled by significant differences in oxidative parameters. We found a significant increase of protein peroxidation in the hippocampus and cortex in the CMS-sensitive group compared to the CMS-resilient group and normal controls. Increased lipid peroxidation in the cerebellum was also observed in the CMS-sensitive and CMS-resilient groups compared to normal controls. Moreover, we found a significant increase of CAT activity and a decrease of SOD activity in the cortex, hippocampus and cerebellum in the CMS-sensitive group compared to the CMS-resilient group and normal controls. However, there was no difference in protein peroxidation in the cerebellum and lipid peroxidation in the cortex and hippocampus among the three groups.

In a previous study an animal model of repeated restraint stress showed that this kind of model induced an increase in TBARS levels in the hippocampus (Fontella et al. 2005). In another study it was demonstrated that, compared to unstressed controls, an animal model of immobilization stress caused significant increases in lipid peroxidation in the cerebral cortex, cerebellum and hippocampus and significant increases in levels of protein oxidation in the cortex, hypothalamus and striatum (Liu et al. 1996). In humans, it was demonstrated that ROS was elevated in the plasma of patients with major depression, especially in those with melancholic type (Bilici et al. 2001). Moreover, in a previous study it was demonstrated that CMS induced an increase in protein peroxidation (prefrontal, hippocampus, striatum and cortex) and lipid peroxidation (cerebellum and striatum) and an increase in CAT (cerebellum, hippocampus, striatum and cortex) and a decrease in SOD (prefrontal, hippocampus, striatum and cortex) activities in stressed rats compared with normal controls (Lucca et al. 2009a). Therefore, our findings in this study are consistent with previous results suggesting that oxidative stress is crucially involved in the pathophysiology of depression.

There are four major sources of ROS: (1) oxidative burst, (2) oxidative processes, (3) lipid peroxidation and (4) oxidative stress. Studies have reported numerous oxidative disturbance parameters in patients with major depression, including oxidative damage in erythrocytic membranes (Peet et al. 1998) as well we elevated superoxide anion generation and lipid peroxidation products (Sarandol et al. 2007). And it is believed that stress in adult male rats which were immobilized for 6 h per day over 21 days inhibits the activities of the first complexes of the mitochondrial respiratory chain, which may potentiate the formation of peroxynitrite, leading to depletion of antioxidant defenses and increased lipid peroxidation (Darley-Usmar et al. 1992). Lipid peroxidation can cause structural damage to membranes, including those which form the mitochondria, further potentiating their dysfunction (Darley-Usmar et al. 1992; Lucca et al. 2009b). Our results also demonstrated increased protein peroxidation in the cortex and hippocampus, but not in the cerebellum, of CMS rats compared to controls. An increase in lipid peroxidation was also detected in the cerebellum, but not in the hippocampus and cortex, of CMS rats. These discrepancies may reflect the fact that basal activities of diverse antioxidant enzymes, such as SOD, CAT, and glutathione reductase, are highly variable across brain regions (Carvalho et al. 2001). However, since repeated restraint stress showed an increase in TBARS levels in the hippocampus and immobilization stress caused significant increases in lipid peroxidation in the cerebral cortex and hippocampus (Fontella et al. 2005; Liu et al. 1996), this may reflect that the stressors in our setting were too mild to cause changes in lipid peroxidation in the cortex and hippocampus. There was also significantly higher lipid peroxidation (cortex and hippocampus) in CMS-sensitive than in CMS-resilient rats. This demonstrated that the CMS-resilient group experienced lower oxidative stress than the CMS-sensitive group. The CMS-resilient group may be prone to neuroprotective support of the neurons in the brain and the CMS-sensitive group may be more prone to brain damage.

SOD is an enzyme that uses the superoxide anion as substrate and produces hydrogen peroxide. This molecule is a substrate to the peroxidases, such as CAT, which is one of the most important peroxidases in the organs. In situations of SOD overactivation without a compensatory increase in the peroxidases, the excess of hydrogen peroxide could react with metal ions and generate hydroxyl radicals, which are thought to be the most dangerous radicals. CAT metabolizes the excess of H_2O_2, producing $O_2 + H_2O$ and then decreasing the intracellular redox status. The brain is particularly prone to oxidative damage due to its relatively high content of peroxidizable fatty acids and limited antioxidant capacity (Floyd 1999).

Recently, studies have demonstrated in patients that major depression, especially with melancholia, is associated

with elevated CAT and SOD (antioxidative enzyme) activities in the plasma. And there was a significant positive correlation between SOD activity and Hamilton Depression Rating Scale score (Bilici et al. 2001). In this study, CMS had a marked effect on CAT and SOD activities, with both CMS-sensitive and resilient rats showing significant increases of CAT activity in the cortex and hippocampus and decreased SOD activity in the hippocampus and cerebellum compared with normal controls. In situations where SOD levels are increased without a concomitant CAT increase, the intermediate product hydrogen peroxide may accumulate and generate hydroxyl radicals, which may lead to lipid and protein oxidation (oxidative damage). This effect was evident for both CMS-sensitive and CMS-resilient rats, suggesting that chronic unpredictable stress has a detrimental effect on generating dangerous radicals, regardless of whether the stressed animals developed anhedonia-like responses. And the differences are also paralleled with the segregation of CMS. Hence, the CMS-resilient group may in fact be stressed, as the presence of different oxidative parameters would argue, which may be induced by some protective responses in the brain. But this kind of protective response does not occur in the CMS-sensitive group.

In conclusion, this study has shown that segregation of animals exposed to CMS into sensitive and resilient groups is paralleled by significant differences in oxidative parameters in the hippocampus, cortex and cerebellum. CMS induces oxidative damage and alterations in the activity of antioxidants, which may lead to increased oxidative damage, irrespective of the anhedonia-like status of the stressed animals. Further investigation of essential mechanisms underlying the development of oxidative damage during CMS administration will be necessary for a better understanding of the relationship between oxidative stress and anhedonia-like.

Acknowledgments This work was supported by the Institute of Functional Brain Disorders of PLA.

References

Aebi H (1984) Catalase in vitro. Methods Enzymol 105:121–126

Bannister JV, Calabrese L (1987) Assays for superoxide dismutase. Methods Biochem Anal 32:279–312

Bekris S, Antoniou K, Daskas S, Papadopoulou-Daifoti Z (2005) Behavioural and neurochemical effects induced by chronic mild stress applied to two different rat strains. Behav Brain Res 161:45–59

Bergstrom A, Jayatissa MN, Thykjaer T, Wiborg O (2007) Molecular pathways associated with stress resilience and drug resistance in the chronic mild stress rat model of depression: a gene expression study. J Mol Neurosci 33:201–215

Bergstrom A, Jayatissa MN, Mork A, Wiborg O (2008) Stress sensitivity and resilience in the chronic mild stress rat model of depression: an in situ hybridization study. Brain Res 1196:41–52

Bilici M, Efe H, Koroglu MA, Uydu HA, Bekaroglu M, Deger O (2001) Antioxidative enzyme activities and lipid peroxidation in major depression: alterations by antidepressant treatments. J Affect Disord 64:43–51

Bisgaard CF, Jayatissa MN, Enghild JJ, Sanchez C, Artemychyn R, Wiborg O (2007) Proteomic investigation of the ventral rat hippocampus links DRP-2 to escitalopram treatment resistance and SNAP to stress resilience in the chronic mild stress model of depression. J Mol Neurosci 32:132–144

Carvalho F, Fernandes E, Remiao F, Gomes-Da-Silva J, Tavares MA, Bastos MD (2001) Adaptative response of antioxidant enzymes in different areas of rat brain after repeated D-amphetamine administration. Addict Biol 6:213–221

Darley-Usmar VM, Hogg N, O'Leary VJ, Wilson MT, Moncada S (1992) The simultaneous generation of superoxide and nitric oxide can initiate lipid peroxidation in human low density lipoprotein. Free Radic Res Commun 17:9–20

Esterbauer H, Cheeseman KH (1990) Determination of aldehydic lipid peroxidation products: malonaldehyde and 4-hydroxynonenal. Methods Enzymol 186:407–421

Floyd RA (1999) Antioxidants, oxidative stress, and degenerative neurological disorders. Proc Soc Exp Biol Med 222:236–245

Fontella FU, Siqueira IR, Vasconcellos AP, Tabajara AS, Netto CA, Dalmaz C (2005) Repeated restraint stress induces oxidative damage in rat hippocampus. Neurochem Res 30:105–111

Gamaro GD, Manoli LP, Torres IL, Silveira R, Dalmaz C (2003) Effects of chronic variate stress on feeding behavior and on monoamine levels in different rat brain structures. Neurochem Int 42:107–114

Garcia R, Spennato G, Nilsson-Todd L, Moreau JL, Deschaux O (2008) Hippocampal low-frequency stimulation and chronic mild stress similarly disrupt fear extinction memory in rats. Neurobiol Learn Mem 89:560–566

Henningsen K, Andreasen JT, Bouzinova EV, Jayatissa MN, Jensen MS, Redrobe JP, Wiborg O (2009) Cognitive deficits in the rat chronic mild stress model for depression: relation to anhedonia-like responses. Behav Brain Res 198:136–141

Jayatissa MN, Bisgaard C, Tingstrom A, Papp M, Wiborg O (2006) Hippocampal cytogenesis correlates to escitalopram-mediated recovery in a chronic mild stress rat model of depression. Neuropsychopharmacology 31:2395–2404

Levine RL, Williams JA, Stadtman ER, Shacter E (1994) Carbonyl assays for determination of oxidatively modified proteins. Methods Enzymol 233:346–357

Liu J, Wang X, Shigenaga MK, Yeo HC, Mori A, Ames BN (1996) Immobilization stress causes oxidative damage to lipid, protein, and DNA in the brain of rats. FASEB J 10:1532–1538

Lowry OH, Rosebrough NJ, Farr AL, Randall RJ (1951) Protein measurement with the Folin phenol reagent. J Biol Chem 193: 265–275

Lucca G, Comim CM, Valvassori SS, Reus GZ, Vuolo F, Petronilho F, Dal-Pizzol F, Gavioli EC, Quevedo J (2009a) Effects of chronic mild stress on the oxidative parameters in the rat brain. Neurochem Int 54:358–362

Lucca G, Comim CM, Valvassori SS, Reus GZ, Vuolo F, Petronilho F, Gavioli EC, Dal-Pizzol F, Quevedo J (2009b) Increased oxidative stress in submitochondrial particles into the brain of rats submitted to the chronic mild stress paradigm. J Psychiatr Res 43:864–869

Moreau JL, Scherschlicht R, Jenck F, Martin JR (1995) Chronic mild stress-induced anhedonia model of depression: sleep abnormalities and curative effects of electroshock treatment. Behav Pharmacol 6:682–687

Papp M, Willner P, Muscat R (1991) An animal model of anhedonia: attenuation of sucrose consumption and place preference conditioning by chronic unpredictable mild stress. Psychopharmacology (Berl) 104:255–259

Peet M, Murphy B, Shay J, Horrobin D (1998) Depletion of omega-3 fatty acid levels in red blood cell membranes of depressive patients. Biol Psychiatry 43:315–319

Sanchez C, Gruca P, Papp M (2003) R-Citalopram counteracts the antidepressant-like effect of escitalopram in a rat chronic mild stress model. Behav Pharmacol 14:465–470

Sarandol A, Kirli S, Akkaya C, Altin A, Demirci M, Sarandol E (2007) Oxidative–antioxidative systems and their relation with serum S100 B levels in patients with schizophrenia: effects of short term antipsychotic treatment. Prog Neuropsychopharmacol Biol Psychiatry 31:1164–1169

Strekalova T, Spanagel R, Bartsch D, Henn FA, Gass P (2004) Stress-induced anhedonia in mice is associated with deficits in forced swimming and exploration. Neuropsychopharmacology 29: 2007–2017

Willner P (1997) Validity, reliability and utility of the chronic mild stress model of depression: a 10-year review and evaluation. Psychopharmacology (Berl) 134:319–329

Willner P, Muscat R, Papp M (1992) Chronic mild stress-induced anhedonia: a realistic animal model of depression. Neurosci Biobehav Rev 16:525–534

J Membrane Biol (2012) 245:683–690
DOI 10.1007/s00232-012-9437-3

Isolation of Chromatin DNA Tightly Bound to the Nuclear Envelope of HeLa Cells

Vasily Vladimirovich Kuvichkin

Received: 2 February 2012 / Accepted: 30 April 2012 / Published online: 30 May 2012

Abstract Recent discovery of the role of nuclear pores in transcription, predicted by our early DNA-membrane complex (DMC) model, makes membrane-bound DNA (MBD) isolation from the cell nucleus and analysis of the MBD actual. The method of MBD isolation proposed by us retains DMC integrity during isolation. We used HeLa cells for DMC extraction. Changing the ionic composition of the isolation medium and replacing DNase I, used commonly for chromatin destruction, with a set of restriction enzymes allowed us to isolate the MBD. Treatment of a nuclear membrane with proteinase K and ultrasound has been used to increase the yield of MBD. Electron microscopic analysis of the purified fraction of isolated DMC supports our previous model of nuclear envelope lipid–chromatin interaction in the nuclear pore assembly.

Keywords Lipid–protein interaction · Membrane assembly · Membrane biophysics · Membrane fusion

Introduction

The question about chromatin DNA binding with the nuclear envelope (NE) has been discussed for more than 40 years (Moyer 1980). Comings (1968) suggested that DNA attaches to the nuclear membrane at the site of pore complexes. Later investigations confirmed that DNA binds with a nuclear pore (Riley and Keller 1978; Arlucea et al. 1998; Ishii et al. 2002) and that nuclear pores participate in transcriptional activity (Akhtar and Gasser 2007; Capelson et al. 2010; Van de Vosse et al. 2011; Mendjan et al. 2006). Nevertheless, many details of DNA interaction with the NE remain unclear.

In the past 40 years, attempts to isolate the DNA-membrane complex (DMC) from eukaryotic cells have been undertaken. The DMC fraction obtained contained all nascent DNA. As a result, it was concluded that DNA replication initiation also occurs at sites of DNA contact with a membrane (Crabb et al. 1980; Leno 1992; Infante et al. 1976; Sinha and Mizuno 1977; Kaufman et al. 1983).

However, many methods used for DMC isolation had an essential fault, namely, the possibility of artifact attachment of total-genome DNA to the DMC. Isolation from the cells of the nuclear matrix fraction (NM) has shifted the attention of researchers to a search for points of contact of chromatin DNA with NM. Later, the existence of NM in the nucleus was questioned (Cook 1988).

Several authors continued to try to isolate DMC; but no differences between DNA from this fraction and total DNA were revealed, or these differences were insignificant (Dvorkin et al. 1977; Prusov et al. 1980, 1982). Shabarina et al. (2006) found a unique DNA sequence in DMC, but in our opinion the method used for the isolation of this sequence is not applicable to membrane-bound DNA (MBD) isolation.

We have made one other attempt to isolate DMC from HeLa cells based on current data on structure and the possible functions of DNA–lipid interactions (Manzoli et al. 1974; Shabarshina et al. 1979; Sukhorukov et al. 1980; Kuvichkin and Sukhomudrenko 1987; Kuvichhkin 2002, 1983, 2010, 2011; Kuvichkin et al. 1999).

V. V. Kuvichkin
Department of Reception Mechanisms, Institute of Cell Biopysics, Russian Academy of Sciences, 3, Institutskaya, Pushchino, Moscow region 142290, Russia

V. V. Kuvichkin (✉)
Genome and Gene Expression Data Analysis Division, Bioinformatic Institute, 30 Biopolis Street, 07-01, Singapore 138671, Singapore
e-mail: VVKuvichkin@gmail.com

According to the biophysical data available, the DMC model (a nuclear pore) has been proposed based on direct interactions between DNA and zwitterionic lipids in the presence of bivalent metal cations (Kuvichhkin 2002, 2009, 2010, 2011).

Four Principles of DMC Isolation

It should be noted that factors that destroy ternary complexes: DNA–phosphatidylcholine liposomes–Mg^{2+} (Kuvichkin and Sukhomudrenko 1987) also influence the stability and structure of the NE. Agutter (1972) showed the necessity of a small percent of DNA to the structural integrity of the NE. The presence of a minimal amount of DNA in a nuclear membrane protects the NE from disintegration into membrane vesicles, maintaining a constant number of nuclear pores (Agutter 1972).

The main conditions necessary for NE isolation, at which DNA–lipid interactions and "membrane" DNA are kept, have been suggested as follows:

1. The absence of large concentrations of univalent cations (K^+ ≤0.1 M, Na^+ ≤0.2 M)
2. The presence of at least insignificant concentrations of bivalent metal cations (≥1 mM Ca^{2+}, Mg^{2+}) and the complete lack of chelating agents (EDTA, etc.)
3. The absence of enzymes able to destroy single-stranded DNA
4. The absence of ionic or non-ionic detergents that are capable of destroying the lipid bilayer; accordingly, DNA–lipid interactions are also desirable

Having analyzed methods for isolating MBD and the NE from the cell nucleus (Prusov et al. 1980, 1982; Shabarina et al. 2006; Matunis 2006), we came to the conclusion that in almost all techniques most of the conditions mentioned above were not taken into consideration. DNase I was used as the basic enzyme for destruction of chromatin DNA. DNase I is known to destroy double-stranded DNA as well as single-stranded DNA, resulting in detachment of MBD from the NE. In many techniques, EDTA, high NaCl and KCl concentrations and detergents were also used. None of these researchers discussed the maintenance of DNA–lipid interactions during the isolation procedure. As a result, the DNA had already detached from the membrane at the stage of NE isolation, and the nuclear membrane was composed only of proteins of lamina and intramembrane proteins. Nucleoporins, linked to each other and to nuclear membranes by protein–protein and protein–lipid interactions, likely retain the shape of DNA-free nuclear pores. According to our DMC model (Kuvichkin 1983), DNA is an important structural element of the nuclear pore and participates in both transcription and replication. We

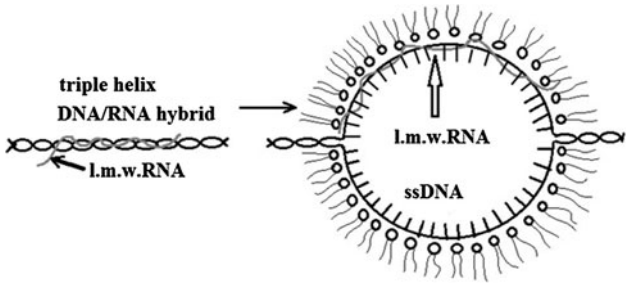

Fig. 1 Model DMC (nuclear pore complex). DNA–RNA hybrids located on chromatin fuse two membrane vesicles and form nuclear pores at the intersection of fused vesicles with the NE. The triple-stranded hybrid of DNA—l.m.w. RNA untwists at DMC formation up to hybrid DNA–RNA and single-stranded DNA (Kuvichkin 2010)

assume that the DMC structure is more complex and includes DNA–RNA hybrids and single-stranded DNA arising at the unwinding of the triple-stranded DNA–RNA hybrid (Fig. 1) (Kuvichhkin 2002, 2010, 2011).

With the aim of isolating MBD, the new isolation method must be in agreement with the four principles stated above. It is rather easy to lower the concentration of univalent cations, add a little Mg^{2+} and not use EDTA and detergents. What can be substituted for DNase I, if all known DNases that are able to destroy double-stranded DNA digest single-stranded DNA in a nonspecific manner too? Therefore, we had to use a specific enzyme in this work—to be more precise, a set of four restriction enzymes, typically used in genetic engineering. Four enzymes digested double-stranded DNA as effectively as DNase I did and did not disturb single-stranded DNA. As a result, we first isolated the fragments of the MBD-containing NE from the nucleus of HeLa cells and then separately isolated the MBD.

Methods and Results

Reagents

Calf thymus DNA, deoxyribonuclease I from bovine pancreas, ribonuclease H (RNase H) from *Escherichia coli* H 560 pol A1, proteinase K from *Tritirachium album*, protease inhibitor cocktail, HEPES, sucrose (SigmaUltra), Triton X-100, DL-dithiothreitol, chloroform and magnesium chloride hexahydrate were from Sigma-Aldrich (St. Louis, MO). Restriction enzymes *Bam*HI, *Nco*I, *Nhe*I and *Pst*I were from New England Biolabs (Hitchin, UK).

Equipment

We used the 5402 Eppendorf (Hamburg, Germany) Vacufuge Concentrator and the Thermo Scientific (Waltham, MA) Sorvall ST 40. Equipment for agarose gel electrophoresis included a Midi horizontal electrophoresis unit

(Sigma-Aldrich, St. Louis, MO), the Micro-Volume UV-Vis Spectrophotometer NanoDrop 2000 (NanoDrop, Wilmington, DE) and ultrasonic disintegrator Dailymag Magnetic Technology (Ningbo, Zhejiang, China). We also used the CKX31 compact inverted microscope (Olympus, Tokyo, Japan), the FEI (Hillsboro, OR) Tecnai T12 and the JEOL (Tokyo, Japan) JEM 1220 transmission electron microscopes as well as the JEOL JSM-5200 scanning electron microscope (JEOL, Tokyo, Japan).

MBD Isolation

The isolation of MBD consists of three stages: (1) isolation of nuclei from HeLa cells, (2) isolation of DMC from nuclei and (3) isolation of MBD from DMC. Nuclei were isolated from HeLa cells by the technique developed by the Collas lab (Department of Biochemistry, Institute of Basic Medical Sciences, University of Oslo, Norway; http://www.collaslab.com/UserFiles/File/Isolation%20of%20somatic%20cell%20nuclei.pdf). The isolation procedure was controlled by means of an inverted microscope for cells in culture. Isolated nuclei were frozen in the presence of 50 % glycerol and stored at −80 °C. The DMC was isolated according to a considerably modified version of the procedure of NE isolation using animal cells. First, DNase I was replaced by a set of four restriction enzymes. This set may include different restriction enzymes, provided that each of the enzymes works well in the buffer used for isolation, maintaining at least 75 % of its maximal activity. The buffer for restriction enzymes (NEB 2) also was selected to conform with the four principles set forth above. Thus, the procedure for NE isolation from HeLa cells was as follows.

Preparation of NEs from Somatic Nuclei

This protocol was adapted from the procedure developed by Dwyer and Blobel (1976). This procedure entails only one digestion step. "Classical" protocols include two digestion steps.

Working Solutions

Prepare the following solutions before starting isolation or washing nuclei. Alternatively, thaw these solutions outside of the freezer. All solutions should contain 1 mM PMSF (10 µl/ml solution) and 1 mM DTT (1 µl/ml solution), added to an aliquot just prior to use. Solutions should be kept on ice at all times.

1. TKM buffer (pH 7.9) at 25 °C
2. Tris–HCl (pH 7.5, 2.5 ml of 1 M stock), KCl 25 mM (0.4 ml of 3 M stock), $MgCl_2$ 5 mM (0.25 ml of 1 M stock), H_2O 47 ml

Table 1 Comparison of two types of digestion solutions

Collas lab solution (50 ml)	NeB buf2
10 % sucrose, 7.8 ml of 2 M stock	50 mM NaCl
20 mM Tris (pH 7.5), 1 ml 1 M stock Tris–HCl (pH 7.5)	10 mM Tris–HCl
H_2O 41.2 ml	10 mM $MgCl_2$
1 mM DTT, PMSF	1 mM DTT
pH 7.5	pH 7.9 at 25 °C

3. $MgCl_2$ solution: 1 mM (10 µl of 1 M $MgCl_2$ stock into 10 ml H_2O)
4. Digestion solution (50 ml): NeB buffer 2 (right row in Table 1) instead of the Collas lab digestion solution (left row)
5. Restriction enzyme mixture prepared by mixing 10 µl of each enzyme in the next step
6. *Bam*HI, *Eco*RI, *Nco*I and *Nhe*I, keeping 100 % enzyme activity, and *Pst*I, 75 %, in NEB 2 buffer
7. Sucrose cushion (50 ml): 25 % sucrose, 19.5 ml of 2 M stock; 20 mM Tris (pH 7.5), 1 ml of 1 M stock; H_2O 29.5 ml

Procedure

- Start with 1–2 ml of packed purified nuclei.
- Wash nuclei in 5 ml of TKM buffer at 1,000 rpm (200×*g*), 10 min, 4 °C.
- Decant supernatant.
- While vortexing, add 4 ml of 1 mM $MgCl_2$ solution. It is important to vortex or else nuclei cannot be resuspended.
- Add 12 ml of digestion solution (NEB 2) and mix by inversion.
- Add 10 µl of each of restriction enzyme and mix well by inversion at room temperature.
- Incubate for 20 min at room temperature, then make 50 strokes with a glass Dounce pestle B in a sterile environment. The nuclear suspension becomes very viscous at first but clarifies over time as the DNA is digested. Repeat these steps two to three times, if necessary, until the solution turns clear. After this step, cool samples on ice and work subsequently at +4 °C.
- Transfer the solution into two 10-ml clean plastic centrifuge tubes (2 × 6 ml).
- Underlay solution with a 3-ml sucrose cushion.
- Centrifuge at 10,000×*g* in a Sorvall or Beckman centrifuge for 15 min. The NE pellet will be concentrated at the bottom of the tube.
- Remove the supernatant, wash the walls of the tube and remove all supernatant.
- Resuspend the NE pellet in 500 µl of TKM buffer.
- Keep on ice until use or freeze in TKM buffer.

For MBD isolation from the NE, it is possible to use standard techniques, but we conducted several experiments to increase the yield of DNA and DNA purity on the basis of our DMC model and interphase chromosome structure.

Model of Interphase Chromatin Organization in the Nucleus

To formulate a research program and understand the results, it is necessary to choose one of two possible ways to characterize DNA interaction with the nuclear membrane: the standard mode, in which the interaction occurs by means of proteins, or the mode developed by this study's author, in which DNA directly interacts with membrane lipids as the DNA simultaneously unwinds. The latter does not exclude but assumes that MBD interacts with nucleoporins. Since we work with cells but not with DNA in vitro, we suppose that not double-stranded DNA but rather the triple-stranded hybrid of DNA and low-molecular weight RNA interacts with the nuclear membrane (Fig. 1).

The temperature of this transition is considerably lower than the temperature of DNA melting, which results in the preferential attachment of triple-stranded hybrids to the NE. Acceptance of this precondition allows us to formulate a research program and to explain the results obtained. We would propose the real arrangement of chromatin DNA in an interphase nucleus as represented in Fig. 2.

Here, DNA is attached to nuclear pores not as a double helix but in the form of hybrid DNA–RNA and single-stranded DNA located on the periphery of a nuclear pore annulus. As can be seen, several nuclear pores close located on one DNA chain form linear clusters (the long black arrows).

Nucleases as a Tool for Study of MBD and Interphase Chromatin Structure in the Nucleus

Based on this structure of the cellular nucleus and with a set of restriction enzymes instead of DNase I during DMC isolation, it is possible to isolate a real MBD and "tails" of genome DNA not removed by restriction enzymes. After isolation of a fraction of the NE with DMC, the following nucleases were added to equal volumes of the fraction: S1-endonuclease, RNase H, RNase H + nuclease S1 and DNase I. After reaction with the enzymes for 20 min (in the buffer recommended by the nuclease manufacturer), MBD was isolated from each fraction and then analyzed by horizontal agarose electrophoresis (Fig. 3).

Figure 3 shows that the molecular weight of DNA isolated from DMC is abnormally large, about 12 kDa, instead of the expected 500–1,000 Da. We can assume that the rest of the genome DNA, which is present at the ends of "membrane" DNA after genome treatment by restriction enzymes, is too long. Nevertheless, the nuclease action on "membrane" DNA needs to be explained. S1 nuclease (lane 2) and DNase I (lane 5) destroy MBD completely. RNase H (lane 3) also strongly disturbs MBD. At the same time that DMC is treated with RNase H and nuclease S1 sequentially, a portion of "membrane" DNA remains undamaged. DNase I was observed by completely removing DNA from the nuclear membrane. Therefore, when techniques for NE isolation are used for DNase I treatment, nuclear membranes can be isolated but without MBD. The fact that the effect of nuclease S1 is similar shows that in the area of DNA attachment to the NE, sites where the double helix opens exist. These sites keep DNA in contact with the nuclear membrane.

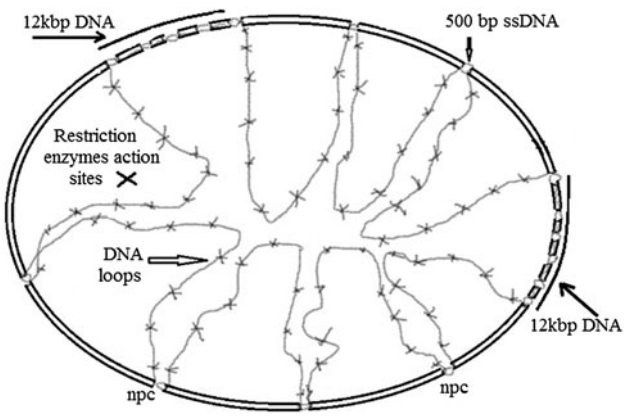

Fig. 2 DNA structure in an interphase nucleus. DNA is attached to the nuclear pores, forming big intranuclear loops of DNA (*white arrow*). In addition to single pores (*npc*) there exist pore clusters 12 kbp in length (*long black arrows*). *Crosses* indicate where genome DNA is cut by restriction enzyme

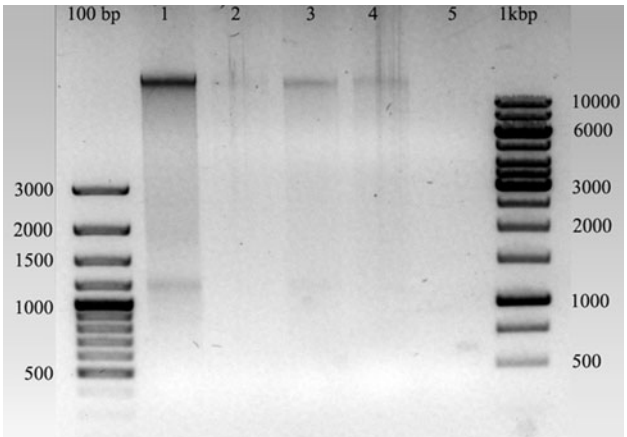

Fig. 3 Electrophoresis of MBD after treatment of NE by nucleases: *lane 1* NE without nucleases, *lane 2* NE treated by nuclease S1, *lane 3* NE after treatment with RNase H, *lane 4* NE treated RNase H + nuclease S1, *lane 5* NE treatment with DNase I

The ability of RNase H to destroy DMC is observed due to the presence of the DNA–RNA hybrid in the area where DNA is attached to the nuclear membrane. Destruction of this hybrid can lead to recovery of the DNA double helix and its detachment from a membrane (Fig. 1). Partial recovery of the DNA double helix with the action of RNase H in combination with nuclease S1 may result in a weakened destructive effect of nuclease S1 on DMC (lane 5).

Thus, it is possible to conclude that double-stranded DNA or the DNA–RNA hybrid easily detaches from DMC. Apparently, double-stranded DNA after replication also detaches from nuclear pores, although pores keep their shapes because of interaction between nucleoporins. Pore complexes lose any matrix activity and keep only their transport functions. Pore complexes without DNA are most likely unstable and quickly disassembled. This assumption is supported by their full disappearance from the NE in the beginning of mitosis (Chatel and Fahrenkrog 2011).

MBD and Linear Pore Clusters

The above-mentioned data on the structure and sensitivity of DMC to nucleases give us the basis to consider our DMC model to be true (Figs. 1, 2), taking into account the following remarks. We assume that usually DNA is attached to a membrane at one site (single nuclear pore), with the formation of big loops of DNA between these pores. In rare instances linear pore clusters exist (Fig. 2, long black arrows). These clusters are formed when pores are too closely located to each other along one DNA thread. In this case, the DNA segment that connects these pores is so short that it is located in the perinuclear space (Fig. 2).

The occurrence of such pore clusters can be explained by the presence of highly repeated sequences in DNA that have enhanced affinity to the membrane vesicles from which the NE is formed. The DNA-induced fusion membrane of these vesicles leads to formation of "string of pearls"—type structures on a DNA thread (Shaulov and Harel 2012) and then nuclear pore clusters, according to the model described earlier (Kuvichkin 2011). Electron microscopic data about the existence of linear pore clusters at the NE are available (Fiserova et al. 2009).

Provided that the size of the DNA site connected with one pore is 400–500 bp and the length of DNA between pores in the cluster is the same, to obtain a DNA cluster size around 10 kbp, the average number of pores in the cluster should be equal to 10, as observed in previous experiments (Fiserova et al. 2009).

Our technique is also used while isolating "membrane" DNA from a single pore, but it is accompanied by big losses. If the fragment of the membrane connected with a pore is insignificant, because of insignificant density, it can be lost at the last stage of isolation through a sucrose gradient. Therefore, the band of 10 kbp observed in our experiments is connected with a large fragment of an NE and belongs to nuclear pore clusters where interpore DNA sites are located in the perinuclear space. Our task is to find a way of isolating the "membrane" or "pore" DNA from these clusters. For this purpose, we studied how to increase the yield of cluster DNA by treatment of DMC with various enzymes and ultrasound for MBD isolation.

Furthermore, we compared the isolation of cluster and "membrane" DNA, in which phenol and a mix of chloroform-isoamyl alcohol (24:1) were used as extracting substances at the last stage of isolation. The DMC fraction was exposed to ultrasound or treated with proteinase K or a combination of these two factors (Fig. 4).

As seen in Fig. 4, phenol or chloroform cannot extract DNA from membrane fractions (lanes 1, 2). Ultrasound also fails to detach DNA from DMC (lanes 5, 6). However, proteinase K and subsequent treatment with phenol or chloroform greatly increased the yield of cluster DNA (lanes 7, 8). Proteinase K action and the subsequent ultrasound led to the appearance of a fraction of MBD 500 bp in length. This was most likely a consequence of destruction of the cluster DNA band (10–12 kbp), the residues of which are visible in Fig. 4 (lanes 3, 4).

Electron Microscopic View of the NE with DMC

We tried to observe DMC isolated with our method by electronic microscopy (a method of negative contrast). In Fig. 5, it is possible to see nuclear pores in the DMC fraction, which still have a hole; however, annuli and edges of

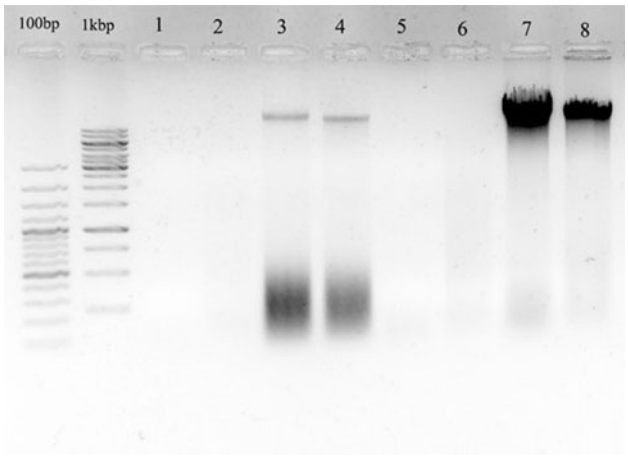

Fig. 4 Effect of NE treatment with chloroform and phenol. *Lanes 1* extraction by chloroform, *2* extraction by phenol, *3* proteinase K + ultrasound 5 min (extraction chloroform), *4* same as lane 3 with phenol extraction, *5* ultrasound 5 min with chloroform extraction, *6* same as lane 5 with phenol extraction, *7* proteinase K with chloroform extraction, *8* same as lane 7 with phenol extraction. The 100-bp and 1-kbp DNA ladders are the same as in Fig. 3

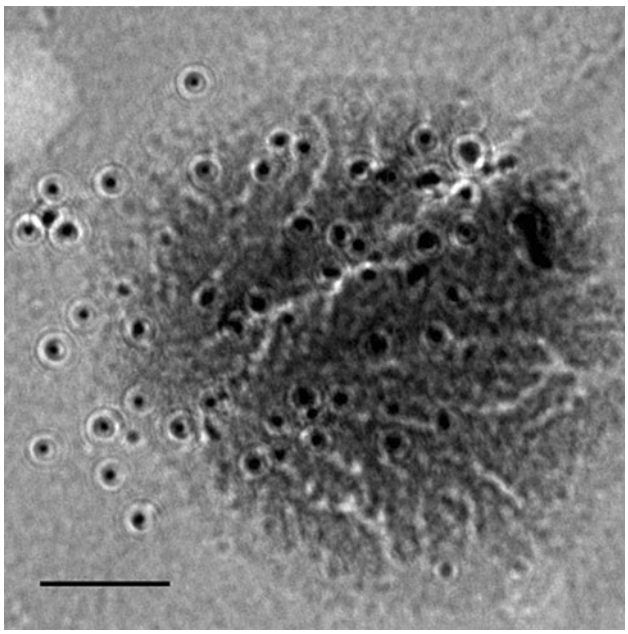

Fig. 5 Nuclear pore structure after NE isolation with restriction enzymes and 30 min proteinase K treatment. *Bar* = 50 nm

Fig. 6 NE fragments isolated with restriction nuclease enzymes and proteinase K (*arrows* show the double membrane of NE). *Bar* = 50 nm

pores are smooth. Octagonal symmetry and other structural peculiarities of pore complexes were not observed. Apparently, this is the result of proteinase K action. Annuli of pores are connected to each other by the threads of DNA that branch from the annuli in opposite directions.

The elements of a double nuclear membrane and MBD connected with it are more clearly shown in Fig. 6. In Fig. 6, we can see the inner and outer nuclear membranes (white arrows). The density of a nuclear pore on fragments of the NE is very high, which confirms that DMC remains in the course of isolation of the nuclear membranes by our method. At the same time, several areas were observed where the NE split into two membranes. The increased fragment of the NE with sharply visible MBD is shown in Fig. 7.

Based on the thickness of fibrils in Figs. 6, 7, the DNA is presented in a complex with lipids and proteins partially destroyed by proteinase K. Numerous zones of the DNA–RNA hybrids opening (R-loops) in the area of nuclear pores are observed (arrows).

Scanning electron microscopic data showed high packaging of nuclear pores in our samples of NE prepared after ultrasonic and proteinase K treatment of NE (Fig. 8).

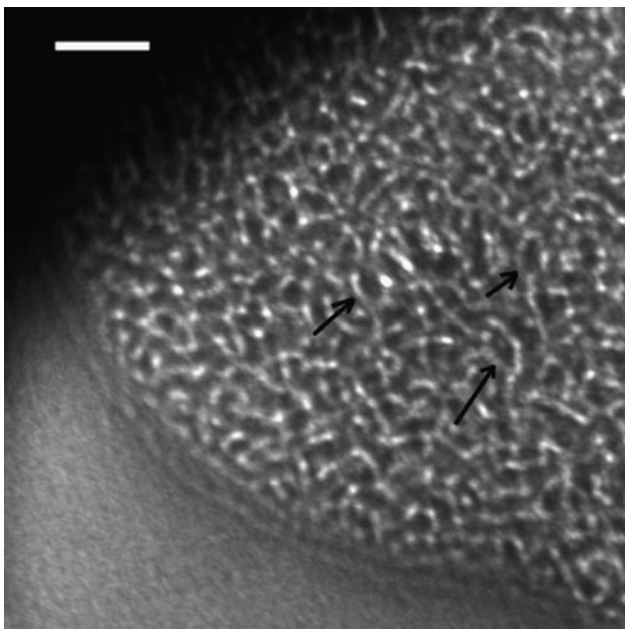

Fig. 7 NE fragment with two nuclear membranes (*arrows*) and MBD. *Bar* = 50 nm

MBD Extraction

Thus, the final stage of MBD isolation, taking into account the investigations performed, is as follows. The DNA extraction protocol utilized the fresh, native NE containing membrane DNA. Preparation was started with 50–500 µl of an NE sample.

We added 1–10 µl of proteinase K (10 mg/ml) to 50–500 µl of NE, held for 30 min on ice, then sonicated for 5 min at 0 °C. DNA was extracted with an equal volume of chloroform/isoamyl alcohol (Sigma, 24:1) and centrifuged for 15 min at 12,800×*g* (eppendorf centrifuge) at 4 °C. The aqueous phase was transferred into a new eppendorf

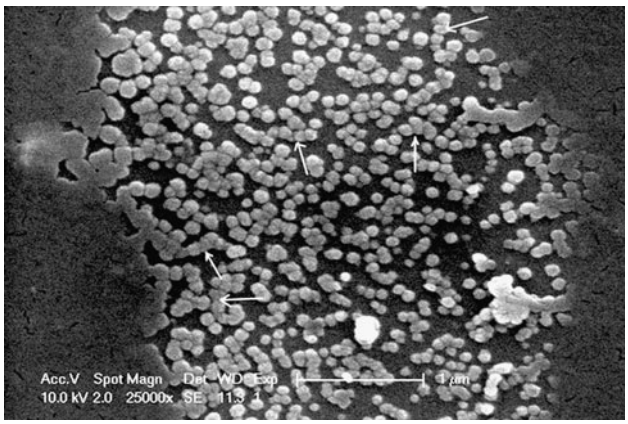

Fig. 8 Scanning electron microscopic image of NE fragments isolated with restriction nuclease enzymes and proteinase K (*arrows* show probable nuclear pore clusters). *Bar* = 1 µm

tube and extracted repeatedly with chloroform/isoamyl alcohol (24:1).

The clear supernatant was concentrated to two times less volume in a vacuum concentrator. During this procedure, most of the chloroform-isoamyl alcohol removed from DNA samples. DNA concentrations were measured by UV spectroscopy (NanoDrop), and their concentrations were 20–30 ng/µl (optimal for agarose electrophoresis).

Conclusion

A variety of factors—DNase I, high ionic force, the presence of EDTA, detergents, etc.—can destroy a complex of DNA with lipids. Based on our DMC model (Fig. 1), we selected the conditions that protect MBD and the DNA complex with membrane lipids from destruction in the course of isolation.

The isolation techniques of nucleoid (Risley et al. 1986) and nuclear matrix (Nickerson 2001) should be reconsidered because none of the authors who described such techniques for the NE (Agutter 1972; Rout and Blobel 1993; Matunis 2006) or MBD (Prusov et al. 1980, 1982; Shabarina et al. 2006) took lipid–nucleic acid interactions into account.

Acknowledgement The author would like to express thanks to Dr. Vladimir Kuznetsov the Head of Genome and Gene Expression Data Analysis Division of the Bioinformatics Institute (BII), Singapore for help in organisation of his fellowsip in BII and discussion and so resarchers of BII and the Institute of Molecular and Cell Biology (IMCB), Singapore for technical assistance.

References

Agutter PS (1972) The isolation of the envelopes of rat liver nuclei. Biochim Biophys Acta 255:397–401

Akhtar A, Gasser SM (2007) The nuclear envelope and transcriptional control. Nat Rev Genet 8:507–517

Arlucea J, Andrade R, Alonso R, Arachaga J (1998) The nuclear basket of the nuclear pore complex is part of a higher-order filamentous network that is related to chromatin. J Struct Biol 124:51–58

Capelson M, Liang Y, Schulte R, Mair W, Wagner U, Hetzer MW (2010) Chromatin-bound nuclear pore components regulate gene expression in higher eukaryotes. Cell 140:372–383

Chatel G, Fahrenkrog B (2011) Nucleoporins: leaving the nuclear pore complex for a successful mitosis. Cell Signal 23:1555–1562

Comings D (1968) The rationale for an ordered arrangement of chromatin in the interphase nucleus. Am J Hum Genet 20:440–460

Cook R (1988) The nucleoskeleton: artifact, passive framework or active site? J Cell Sci 90(Pt 1):1–6

Crabb WD, Firshein W, Infante AA (1980) A potential DNA replication complex isolated from sea urchin embryos by renografin gradient centrifugation. Biochim Biophys Acta 609:456–463

Dvorkin VM, Prusov AN, Fais D, Kir'ianov GI, Vaniushin BF (1977) DNA from chromatin-nuclear membrane complex: reassociation kinetics at different stages of the cell cycle (in Russian). Biokhimiia 42:74–78

Dwyer N, Blobel G (1976) A modified procedure for the isolation of a pore complex-lamina fraction from rat liver nuclei. J Cell Biol 70:581–591

Fiserova J, Kiseleva E, Goldberg MW (2009) Nuclear envelope and nuclear pore complex structure and organization in tobacco BY-2 cells. Plant J 59:243–255

Infante AA, Firshein W, Hobart P, Murray L (1976) A nuclear membrane-associated DNA complex in cultured mammalian cells capable of synthesizing DNA in vitro. Biochemistry 15:4810–4817

Ishii K, Arib G, Lin C, Van Houwe G, Laemmli UK (2002) Chromatin boundaries in budding yeast: the nuclear pore connection. Cell 109:551–556

Kaufman DG, Cordeiro-Stone M, Rude TH, Nelson KG, Kaufmann WK (1983) Fractionation and characterization of DNA at sites of replication from rat liver nuclei. Exp Cell Res 146:339–347

Kuvichhkin VV (2002) Lipid–nucleic acids interactions in vitro and in vivo. Bioelectrochemistry 58:3–12

Kuvichkin VV (1983) Theoretical model of DNA-membrane contacts. Biofizika 28:771–775

Kuvichkin VV (2009) Investigation of ternary complexes: DNA–phosphatidylcholine liposomes–Mg^{2+} by freeze-fracture method and their role in the formation of some cell structures. J. Membrane Biol 231:29–34

Kuvichkin VV (2010) Lipid–nucleic acids interactions as base for organization and expression of cellular genome. Int J Quant Chem 110:120–126

Kuvichkin VV (2011) The mechanism of a nuclear pore assembly: a molecular biophysics view. J Membr Biol 241:109–116

Kuvichkin VV, Sukhomudrenko AG (1987) Interaction of natural and synthetic polynucleotides with liposomes in the presence of divalent cations (in Russian). Biofizika 32:628–633

Kuvichkin VV, Kuznetsova SM, Emeljanenko VI, Zhdanov RI, Petrov AI (1999) Calorimetric study of the complexes: polyA*polyU-phosphatidylcholine liposomes-Mg^{2+}. Biofizika 44:430–435

Leno GH (1992) DNA replication by the nuclear envelope. Semin Cell Biol 3:237–243

Manzoli FA, Muchmore JH, Capitani S, Bonora B, Bartoli S (1974) Lipid–DNA interactions: II. Phospholipids, cholesterol, glycerophosphorylcholine, sphingosine and fatty acids. Biochim Biophys Acta 340:1–15

Matunis MJ (2006) Isolation and fractionation of rat liver nuclear envelopes and nuclear pore complexes. Methods 39:277

Mendjan S, Taipale M, Kind J, Holz H, Gebhardt P, Schelder M, Vermeulen M, Buscaino A, Duncan K, Mueller J, Wilm M, Stunnenberg HG, Saumweber H, Akhtar A (2006) Nuclear pore components are involved in the transcriptional regulation of dosage compensation in *Drosophila*. Mol Cell 21:811–823

Moyer MP (1980) The association of DNA and RNA with membranes. Int Rev Cytol 61:1–61

Nickerson JA (2001) Experimental observations of a nuclear matrix. J Cell Sci 114:463–474

Prusov AN, Fais D, Polyakov VY, Vanyushin BF (1980) Chromatin–nuclear envelope complex from rat liver: isolation and purification. Cell Biol Int Rep 4:391–398

Prusov AN, Fais D, Poliakov VIu, Vaniushin BF (1982) Properties of rat liver chromatin bound to the nuclear membrane. Biokhimiia 47:502–510

Riley DE, Keller JM (1978) The Ultrastructure of non-membranous nuclear ghosts. J Cell Sci 32:249–268

Risley MS, Einheber S, Bumcrot DA (1986) Changes in DNA topology during spermatogenesis. Chromosoma (Berl) 94:217–227

Rout MP, Blobel G (1993) Isolation of the yeast nuclear pore complex. J Cell Biol 123:771–783

Shabarina AN, Prilepa EI, Glazkov MV (2006) Unusual nucleotide sequence of a DNA fragment isolated from nuclear envelopes of mouse hepatocytes. Genetika 42:879–886

Shabarshina LI, Sukhorukov BI, Kuvichkin VV (1979) Infrared spectroscopic study of DNA–lipid interactions. DNA compacting on disperse particles. Biofizika 24:990–994

Shaulov L, Harel A (2012) Improved visualization of vertebrate nuclear pore complexes by field emission scanning electron microscopy. Structure 20:407–413

Sinha AA, Mizuno NS (1977) DNA synthesis associated with a DNA-nuclear-membrane complex from rat liver. Cell Tissue Res 183:191–201

Sukhorukov BI, Kuvichkin VV, Shabarchina LI (1980) Structure and function of DNA-membrane contact in cells. Biofizika 25:270–275

Van de Vosse DW, Wan Y, Wozniak RW, Aitchison JD (2011) Role of the nuclear envelope in genome organization and gene expression. Wiley Interdiscip Rev Syst Biol Med 3:147–166

J Membrane Biol (2012) 245:691–696
DOI 10.1007/s00232-012-9438-2

Effect of Mixed-Phospholipid Layer on Phospholipase D Reaction-induced Vesicle Rupture

Jin-Won Park

Received: 4 February 2012 / Accepted: 17 April 2012 / Published online: 25 May 2012

Abstract Spherical phospholipid bilayers, or vesicles, were prepared layer by layer using a double-emulsion technique, which allows the outer layer of the vesicles to be formed with two phospholipids that have different head groups: phosphatidylcholine (PC) and phosphatidylethanolamine. At the outer layer of the vesicles, the phospholipase D (PLD) catalyzed for the conversion of PC to phosphatidic acid. The reaction caused by PLD induced the curvature change of the vesicles, which eventually led to the rupture of the vesicles. Before the investigation, the ratio of dioleoylphosphatidylethanolamine to oleoylhydroxyphosphatidylethanolamine was found as a condition such that the vesicles made with the mixed lipids were as stable as those made with pure dioleoylphosphatidylcholine. Response time from the PLD injection to vesicle rupture was monitored by the composition of the outer layer by the fluorescence intensity change of pH-sensitive dye encapsulated in the vesicles. The response time began to be slowed at approximately 30 % PC. The response times for the compositions were associated with the surface density of PC at the outer layer. These results also seem to be determined by the size of PLD, specifically the PLD active site.

Keywords Biophysics · Fluorescence techniques · Lipid protein interactions · Measurement · Membrane biophysics · Membrane vesicles

J.-W. Park (✉)
Department of Chemical and Biomolecular Engineering, College of Energy and Biotechnology, Seoul National University of Science and Technology,
172 Gongreung 2-dong, Nowon-gu, Seoul 139-743, South Korea
e-mail: jwpark@seoultech.ac.kr

Phospholipase D (PLD) is membrane-active enzyme involved in a variety of cellular function, including membrane/vesicle trafficking, actin cytoskeleton rearrangements, glucose transport, superoxide production, secretion, cellular proliferation, and apoptosis (McDermott et al. 2004; Exton 2002). As a result, PLD is implicated in a range of diseases, including cancer, inflammation, and myocardial disease (Huang and Frohman 2007; Tappia et al. 2006; Scott et al. 2009; Brown et al. 2007). By PLD action upon phosphatidylcholine (PC), PC is cleaved into alcohol and phosphatidic acid (PA, a potent mitogen), which may be essential for the formation of certain types of transport vesicles or which may be constitutive vesicular transport-to-signal transduction pathways. This hydrolysis leads to changes in the lipid content of membranes that could also play a role. PLD may have a physiological function through the further metabolism of PA to diacylglycerol and lysophosphatidic acid (McDermott et al. 2004; Brown et al. 2007).

Lipid layers are widely used models for cell-surface analyses and for investigating molecular events in membranes because the preparation methodology for the layers has been well established, and sensitive analytical techniques can be applied to investigate the events (New 1990; McConnell et al. 1986; Sackmann 1996; Brian and McConnell 1984). The lipid layers have been applied to many areas of biomedical research, such as cell recognition, membrane-mediated catalysis, effects of anesthetics, and antimicrobial peptides (Giesen et al. 1991; Mou et al. 1994; Miszta et al. 2008; Fang et al. 2000; Cheow and Hadinoto 2011). This layer has been used to investigate the phospholipases, i.e., the effect of the enzymes on the wetting properties of the lipid layers and the configuration of the layers, as well as the activity of the enzymes (Jurak and Chibowski 2010; Chen et al. 2009; Chemburu et al. 2008).

Hydrolysis triggered by PLD is a critical step for the fusion essential for the cellular processes. This hydrolysis is found to induce a change in the composition of the membranes that eventually induces the rupture of the vesicles. The change in composition means that the geometry of the vesicle components is changed: the head groups of the components become smaller. Therefore, hydrolysis leads to a decrease in curvature, and rupture is finally reached. Recently, it has been found how the PLD-induced-vesicle rupture occurred with respect to the phase of the vesicle layers (Park 2011). However, little is known about how the composition of the outer layer affects the properties of the biological membranes caused by hydrolysis. Investigating this effect may contribute to an understanding of the physical behavior of these enzymes in terms of quantitative analysis. In this work, we aim to investigate the effect of the composition of the lipid outer layer on vesicle rupture.

Experiments

Dioleoylphosphatidylethanolamine (DOPE), oleoylhydroxyphosphatidylethanolamine (OHPE), dioleoylphosphatidylcholine (DOPC), and dipalmitoylphosphatidic acid (DPPA) were purchased from Avanti Polar Lipids (Alabaster, AL) and used without further purification. The DPPA was dissolved in 10 ml of *tert*-butyl methyl ether at 10 mg/ml, followed by adding 100 µl DI water of 5 mM pyranine, 50 mM NaCl, and 1 mM $CaCl_2$ at pH 9.0. Therefore, the micelles with DPPA were prepared by extrusion through the 50 nm pores of 78-mm diameter PTFE membranes above the transition temperature of the DPPA. Several drops (<10 µl) of the micelle solution and the 10 mg/ml *tert*-butyl methyl ether solution of a desired ratio of DOPC, DOPE, or OHPE were continuously added through a 22-gauge needle inserted into 10 ml aqueous solutions of 50 mM NaCl and 1 mM $CaCl_2$ at pH 9.0. The final lipid concentration of the aqueous solution was 1 mg/ml. During the addition, the aqueous solution was magnetically stirred, and a nitrogen stream was injected into the aqueous solution. The solution was centrifuged ($3700 \times g$) to remove the phospholipids that did not form the vesicles. The liposome solution was acquired from the supernatant of the solution. These procedures are well known as a methodology to prepare vesicles (New 1990). For the confirmation of the vesicle formation, the diameter of the micelles was measured (ELS-8000; Otsuka Electronics, Osaka, Japan) before the micelles were transferred to the aqueous solution. For the measurement, the viscosity and the refractive index of the *tert*-butyl methyl ether were 0.23 cP and 1.3686, respectively (Lide 2005). After the transfer of the micelles into the aqueous solution, the diameter of the vesicles was measured. The diameters of the micelles and the vesicles were 75 ± 10 and 80 ± 10 nm, respectively. These results were consistent with the expectation that the lipid layer formed on the micelle surface. Besides the change in the diameter, no leakage of the pyranine molecules indicated that each layer was not disturbed. Otherwise, the fluorescence intensity at 510 nm would be changed tremendously when several drops of aqueous solutions of 50 mM NaCl and 1 mM $CaCl_2$ at pH 3.0 were added to the vesicle solution.

Phospholipiase D (PLD) was purchased from Sigma Aldrich (St. Louis, MO). One nanomole was selected as a PLD concentration because recent results indicated that more than 1 nM of PLD concentration had little effect on the rupture's response time (Park 2011). Because it was known that the reaction causes the rupture of the vesicles and the pyranine (pH-sensitive fluorescence dye) was encapsulated inside the vesicles, the fluorescence intensity was monitored in real time with a Wallac Victor3 multiwell fluorometer (Perkin Elmer, Waltham, MA). Because the pyranine molecules have different fluorescence intensities when they are exposed to the different pH solutions within the rupture, the tremendous change in the intensity difference between the vesicle solution with the PLD injection and with only the buffer solution injection means that the vesicles rupture. Therefore, the intensity was observed to investigate the effect of the composition on the vesicle rupture on the PLD reaction. For each phospholipid ratio, we measured when the rupture occurred from the injection of the PLD molecules.

The high-performance liquid chromatography (HPLC) analyzer consisted of a Gel Silica 60 column (particle size 5 µl; inner diameter 47 mm; length 15 cm; Tosoh, Tokyo, Japan) and an HPLC system (Waters Associates, Milford, MA) containing a type 600 solvent delivery system, a type U6K injector, a type 490 variable wavelength detector, and a type 740 data module. Elution was performed with a solution of acetonitrile–methanol–85 % phosphoric acid (130:5:1.7, v/v/v) at a flow rate of 1 ml/min at room temperature. Phospholipid solutions were dissolved in 100 µl of methylene chloride, and 10 µl of the solution was injected into the HPLC system.

Results and Discussion

For the investigation of the PLD reaction on the lipid layer, the pyranine molecules were dissolved only inside of the vesicles. The encapsulation of the molecules was confirmed via fluorometry (Perkin Elmer, Boston, MA) with 460 nm excitation and 520 nm emission wavelengths. The fluorescence intensity was changed with Tween-20 treatment. Without the treatment, the intensity was not changed after the addition of pH 3 DI water drops. The results are

provided in Fig. 1. Encapsulation was successfully achieved.

The desired ratio of the phospholipids at the outer layer was confirmed by HPLC. The peak area of each component was compared for the solution before centrifugation and for the supernatant after centrifugation (Fig. 2). Although the areas for every component after the centrifugation were reduced except PA, the degree of the decrease was proportional. The proportional decrease means that the ratio of the phospholipids at the outer layer are still almost identical with that of the DOPC, DOPE, and OHPE solution added for liposome preparation. As expected, the retention time for OHPE was longest, the result of its molecular weight. It was also expected that the more negative component would correspond to the shorter retention as a result of the surface interaction with the silica spheres, the surfaces of which had inherently negative dipoles. The order of the peak for each component was consistent with that previously described (Kurumi et al. 1991; Singleton and Stikeleather 1995). PA peak after centrifugation varied little. From this invariance, we found that the inner layer made with PAs remained during the centrifugation. This result is consistent with a confirmation of encapsulation.

Apart from the composition, there are other factors that influence the reaction—for example, the vesicle number, the PLD concentration, the ionic concentration of the vesicle solution, the phase of the inner layer, the vesicle radius, and the vesicle stability. Therefore, these factors were determined before the composition experiments. The concentration of the phospholipids and the radius of the vesicles were constant in this research, and it is known that 10 mg/ml of the phospholipids correspond to the 10^7–10^8 quantity of the vesicles (Park 2007). Previous research

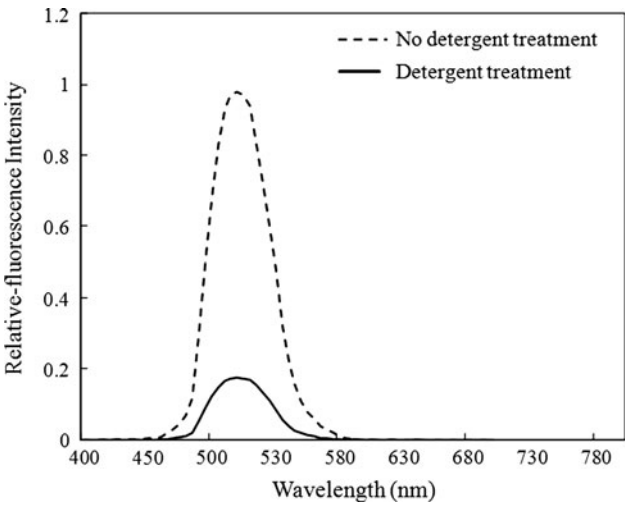

Fig. 1 Fluorescence intensity change after the addition of pH 3 DI water drops

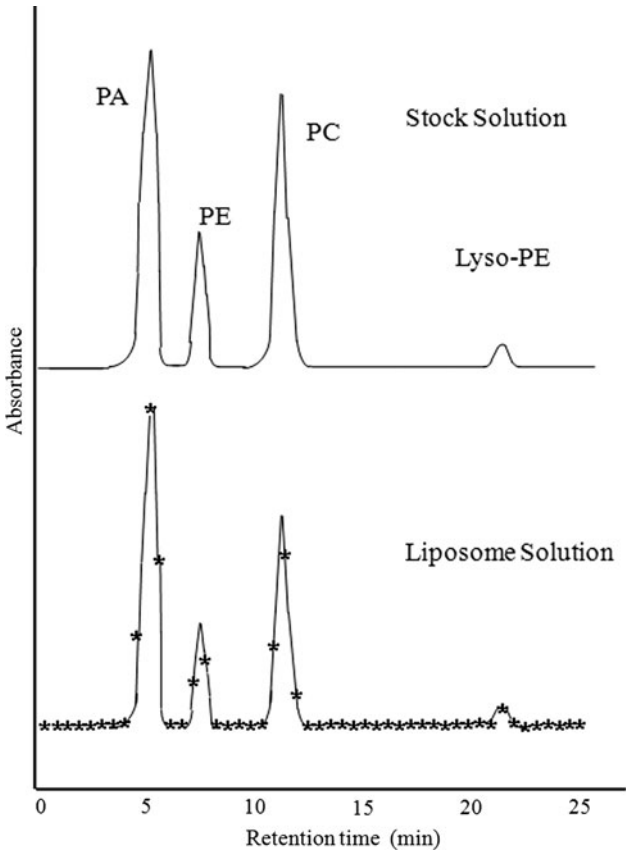

Fig. 2 HPLC peaks for each component: lipid solution before centrifugation (*top*) and supernatant of solution after centrifugation (*bottom*)

found effects of the other factors (Park 2011). At the 1 mg/ml solution of phospholipids, 1–10 nM PLD concentration led to little change in the reactivity. Fifty micromoles of NaCl and 1 mM $CaCl_2$, one of the biomimetic conditions, were selected for the ionic concentration because the reactivity was dependent on a concentration less than that (Brown et al. 2007; Webb et al. 2010; Cheow et al. 2010; Furt and Moreau 2009). Under the conditions described above, it was found that the reactivity was independent of the inner-layer phase. Because the solid phase is known to be more stable, DPPA was used instead of DOPA at room temperature (Park 2010a). The phase of the lipid layers was made with the phospholipids whose transition temperature was considered (Park and Ahn 2008). Dioleoyl lipids were used for the liquid phase because their transition temperature was much lower than room temperature. However, dipalmitoyl lipids were solid at room temperature. The stability was adjusted identically for the vesicle of each composition. Stability depended on the composition of the vesicles. Except for the composition of the outer layer, all the factors were decided.

As components for the outer layer, PC and phosphatidylethanolamine (PE) were selected because only PC was

reacted by PLD. However, if DOPC was replaced with DOPE only, the radius of the vesicles would be increased as a result of the difference in the geometries between DOPC and DOPE. Therefore, OHPE, lyso-PE, was utilized for the vesicle preparation with DOPC and DOPE so that the radius could be kept constant. The schematic diagrams for the vesicles made with different components are presented in Fig. 3. Because the PLD reaction was based on the curvature change of the vesicles, it was essential that the radius remain constant. The introduction of OHPE allowed only the composition effect on the PLD reaction found. In terms of the PE:PC ratio that was important for the PLD reaction, 11 conditions (pure PE to pure PC by 10 %) were considered. However, at a specific PE, it was also necessary to determine the amounts of DOPE and OHPE that might influence the stability of the vesicles. Therefore, the composition of the mixed outer layer was adjusted because the vesicles of each composition were necessarily found to be as stable as the vesicles made with pure DOPC. To find out the composition resulting in identical stability, we observed permeability at 5:1, 10:1, and 15:1 ratios of DOPE to OHPE for each PE condition, measuring the fluorescence intensity change with respect to time (Fig. 4). The ratio of PE to PC at a specific ratio of DOPE to OHPE had little effect on the stability. It was found that the stability of the vesicles at 15:1 of DOPE to OHPE was almost identical with that of the vesicles made with pure DOPC. This result was consistent with the expectation from the geometries of the lipids in that the ratios of lipid volume to head group area and lipid length were 0.5–1, 1, and less than 0.33333 for DOPC, DOPE, and OHPE, respectively (Cevc and Marsh 1987).

Reactivity was monitored at the various composition conditions by fluorescence response time. The time of pure DOPC vesicles was consistent with the previous result (Park 2011). A 30 % PC to non-PC condition led to a gradual increase in the response time (Table 1), which means that the reactivity was decreased gradually from a 30 % PC to a non-PC condition. Because the vesicles of the outer layer made with only PE included OHPE of less than 7 %, the mean molecular area of the outer layer was presumably $\sim$0.8 nm^2 (Park and Ahn 2008; Park 2010b). Therefore, the density of PC on the outer layer made with 30 % PC was one PC molecule per 2.7 nm^2. Considering that the PLD gyration radius is known to be approximately 4 nm, the value of the PLD area calculated with the radius is much higher than the area necessary to find one PC molecule in the case where the outer layer of the vesicles was made with even 10 % PC (Brown et al. 1995). The density of PC on the outer layer made with 10 % PC was one PC molecule per 8 nm^2. Therefore, it was expected

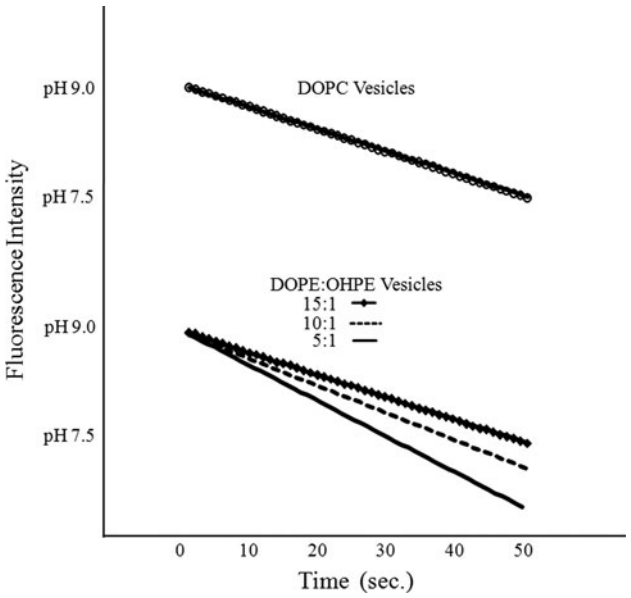

Fig. 4 Fluorescence intensity change with respect to time for the vesicles of the outer layer made with pure DOPC (*top*) and made with a mixture of DOPC, DOPE, and OHPE at different DOPE:OHPE ratios (*bottom*)

Table 1 Response time from PLD injection to vesicle rupture[a]

DOPC and PE	Response time (s)
Pure DOPC	0.7
90 % DOPC, 10 % PE	0.7
80 % DOPC, 20 % PE	0.7
70 % DOPC, 30 % PE	0.7
60 % DOPC, 40 % PE	0.7
50 % DOPC, 50 % PE	0.7
40 % DOPC, 60 % PE	0.7
30 % DOPC, 70 % PE	0.9
20 % DOPC, 80 % PE	1.3
10 % DOPC, 90 % PE	2.7
Pure PE	50

[a] PE consisted of DOPE:OHPE at a 15:1 ratio

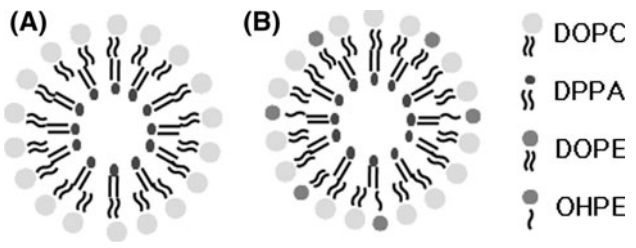

Fig. 3 Schematic diagram for the vesicles made with different components. **a** Vesicles of the outer layer made with pure DOPC. **b** Vesicles made with mixture of DOPC, DOPE, and OHPE

that the response time would be little changed from the vesicles of the outer layer made with 10 % PC. This discrepancy might be due to the size of the PLD active site. Leiros et al. (2000) noted that PLD had a PC hydrolysis site with an area of 1.5–2 nm^2. Therefore, if the average area to find one PC molecule was decreased to less than 2 nm^2, the reactivity remained. From 30 % PC to non-PC, the reactivity began to be reduced.

In conclusion, in this study, the effect of mixed lipid layer on the PLD-induced hydrolysis was investigated by fluorescence intensity change. Before the investigation, the ratio of DOPE to OHPE was found to be a condition such that the vesicles made with the mixed lipids were as stable as those made with pure DOPC. Monitoring revealed that the rupture caused by the PLD reaction could be interpreted with respect to the composition of each layer, especially the PC density on the outer layer of the vesicles. It was observed that the vesicles made with more than 30 % PC at the layer showed identical reactivity as to PLD reaction. However, from 30 % PC to non-PC at the layer, the reactivity of the vesicles was reduced. These results seem to be caused by not only the density of PC on the layer, but also the size of PLD, specifically the PLD active site.

Acknowledgments This study was financially supported by Seoul National University of Science and Technology. We thank all of members of Department of Chemical Engineering at the Seoul National University of Technology for help and valuable discussions. We thank Prof. D. J. Ahn, Dr. G. S. Lee, Mr. H. Choi, and Mr. C. S. Choi at the Korea University for valuable help.

References

Brian AA, McConnell HM (1984) Allogeneic stimulation of cytotoxic T-cells by supported planar membranes. Proc Natl Acad Sci USA 81:6159–6163

Brown HA, Gutowski S, Kahn RA, Sternweis PC (1995) Partial purification and characterization of Arf-sensitive phospholipase D from porcine brain. J Biol Chem 270:14935–14943

Brown HA, Henage LG, Preininger AM, Xiang Y, Exton JH (2007) Chapter 4 Biochemical Analysis of Phospholipase D. In: Brown HA (ed) Lipidomics and bioactive lipids: lipids and cell signaling. Academic Press, New York, pp 49–88

Cevc G, Marsh D (1987) Phospholipid bilayers: physical principles and methods. John Wiley and Sons, New York

Chemburu S, Ji E, Casana Y, Wu Y, Buranda T, Schanze KS, Lopez GP, Whitten DG (2008) Conjugated polyelectrolyte supported bead based assays for phospholipase a(2) activity. J Phys Chem B 112:14492–14499

Chen CH, Malkova S, Pingali SV, Long F, Garde S, Cho W, Schlossman ML (2009) Configuration of PKC alpha-C2 domain bound to mixed SOPC/SOPS lipid monolayers. Biophys J 97:2794–2802

Cheow WS, Hadinoto K (2011) Factors affecting drug encapsulation and stability of lipid-polymer hybrid nanoparticles. Colloids Surf B Biointerfaces 85:214–220

Cheow WS, Chang MW, Hadinoto K (2010) Antibacterial efficacy of inhalable antibiotic-encapsulated biodegradable polymeric nanoparticles against *E. coli* biofilm cells. J Biomed Nanotechnol 6:391–403

Exton JH (2002) Phospholipase D: structure, regulation and function. Rev Physiol Biochem Pharmacol 144:1–94

Fang HH, Chan PK-Y, Xu L-C (2000) Quantification of bacterial adhesion forces using atomic force microscopy (AFM). J Microbiol Methods 40:89–97

Furt F, Moreau P (2009) Importance of lipid metabolism for intracellular and mitochondrial membrane fusion/fission processes. Int J Biochem Cell Biol 41:1828–1836

Giesen PL, Willems GM, Hemker HC, Hermens WT (1991) Membrane-mediated assembly of the prothrombinase complex. J Biol Chem 266:18720–18725

Huang P, Frohman MA (2007) The potential for phospholipase D as a new therapeutic target. Expert Opin Ther Targets 11: 707–716

Jurak M, Chibowski E (2010) Influence of (phospho) lipases on properties of mica supported phospholipid layers. Appl Surf Sci 256:6304–6312

Kurumi Y, Adachi Y, Ito T, Kobayashi H, Nanno T, Yamamoto T (1991) Novel high-performance liquid chromatography for determination of membrane phospholipid composition of rat hepatocytes. J Gastroenterol 26:628–632

Leiros I, Secundo F, Zambonelli C, Servi S, Hough E (2000) The first crystal structure of a phospholipase D. Structure 8:655–667

Lide DR (2005) CRC handbook of chemistry and physics: a ready-reference book of chemical and physical data, 85th edn. CRC Press, Boca Raton

McConnell HM, Watts TH, Weis RM, Brian AA (1986) Supported planar membranes in studies of cell–cell recognition in the immune system. Biochim Biophys Acta 864:95–106

McDermott M, Wakelam MJ, Morris AJ (2004) Phospholipase D. Biochem Cell Biol 82:225–253

Miszta A, Machan R, Benda A, Ouellette AJ, Hermens WT, Hof M (2008) Combination of ellipsometry, laser scanning microscopy and Z-scan fluorescence correlation spectroscopy elucidating interaction of cryptdin-4 with supported phospholipid bilayers. J Pept Sci 14:503–509

Mou JX, Yang J, Huang C, Shao Z (1994) Alcohol induces interdigitated domains in unilamellar phosphatidylcholine bilayers. Biochemistry 33:9981–9985

New RRC (1990) Liposomes: a practical approach. Academic Press, New York

Park J-W (2007) Nanoliter reactor arrays for antibiotic study. Bull Korean Chem Soc 28:1709–1714

Park J-W (2010a) Probe chemistry effect on surface properties of asymmetric-phase lipid bilayers. Colloids Surf B Biointerfaces 75:290–293

Park J-W (2010b) First-leaflet phase effect on properties of phospholipid bilayer formed through vesicle adsorption on LB monolayer. J Membr Biol 237:107–114

Park J-W (2011) Effect of phospholipid bilayer phase asymmetry on phospholipase d reaction-induced vesicle rupture. J Membr Biol 244:55–59

Park J-W, Ahn DJ (2008) Temperature effect on nanometer-scale physical properties of mixed phospholipid monolayers. Colloids Surf B Biointerfaces 62:157–161

Sackmann E (1996) Supported membranes: scientific and practical applications. Science 271:43–48

Scott SA, Selvy PE, Buck JR, Cho HP, Criswell TL, Thomas AL, Armstrong MD, Arteaga CL, Lindsley CW, Brown HA (2009) Design of isoform-selective phospholipase D inhibitors

that modulate cancer cell invasiveness. Nat Chem Biol 5: 108–117

Singleton JA, Stikeleather LF (1995) High-performance liquid chromatography analysis of peanut phospholipids. II. Effect of postharvest stress on phospholipid composition. J Am Oil Chem Soc 72:485–488

Tappia PS, Dent MR, Dhalla NS (2006) Oxidative stress and redox regulation of phospholipase D in myocardial disease. Free Radic Biol Med 41:349–361

Webb LM, Arnholt AT, Venable ME (2010) Phospholipase D modulation by ceramide in senescence. Mol Cell Biochem 337:153–158

J Membrane Biol (2012) 245:697–705
DOI 10.1007/s00232-012-9441-7

The Effects of Atorvastatin Therapy on Rheological Characteristics of Erythrocyte Membrane, Serum Lipid Profile and Oxidative Status in Patients with Dyslipidemia

Hüseyin Avni Uydu · Sermet Yıldırmış · Cihan Örem · Mustafa Calapoglu · Ahmet Alver · Birgül Kural · Asım Örem

Received: 7 October 2011 / Accepted: 1 June 2012 / Published online: 16 June 2012

Abstract The statins, most commonly used in the treatment of hyperlipidemia, have certain beneficial effects including improved endothelial function, plaque stability and decreased oxidative stress and inflammation, beyond their lipid-lowering effect in plasma. We evaluated the pleiotropic impact of atorvastatin on erythrocyte structural/mechanical properties and lipid peroxidation in dyslipidemics. The study group included 44 patients with dyslipidemia and was divided into subgroups according to triglyceride and cholesterol levels as hypercholesterolemic ($n = 29$) and mixed-type hyperlipidemic ($n = 15$). Subjects were given 10 mg atorvastatin per day for 12 weeks. Changes in serum lipid composition, lipid contents, Na^+/K^+-ATPase activity and osmotic fragility in erythrocytes and oxidative stress parameters of erythrocytes and plasma were studied. Atorvastatin therapy improved the serum lipid profile of both subgroups. This alteration was accompanied by a decreased level of cholesterol in erythrocyte membranes. Moreover, enhanced activity of Na^+/K^+-ATPase in erythrocytes reflected the improvements in membrane lipids of both subgroups. However, a significant change was observed in osmotic fragility values of the mixed-typed dyslipidemic group. This treatment lowered the lipid peroxidation in plasma and erythrocytes and increased plasma total antioxidant capacity in all groups. The present study shows that the use of atorvastatin reversed the structural and functional features of erythrocyte membranes in dyslipidemic subjects. Also, hypolipidemic therapy had a beneficial impact on a balance between oxidant and antioxidant systems.

Keywords Atorvastatin · Dyslipidemia · Erythrocyte lipid · Na^+/K^+-ATPase · Osmotic fragility · TBARS · TAS

H. A. Uydu (✉)
Department of Medical Biochemistry, Faculty of Medicine, Recep Tayyip Erdoğan University, Rize, Turkey
e-mail: hauydu@hotmail.com

S. Yıldırmış
Department of Chemistry, Faculty of Pharmacia, Karadeniz Technical University, Trabzon, Turkey

C. Örem
Faculty of Medicine, Department of Cardiology, Karadeniz Technical University, Trabzon, Turkey

M. Calapoglu
Faculty of Science, Department of Chemistry, Suleyman Demirel University, Isparta, Turkey

A. Alver · B. Kural · A. Örem
Department of Medical Biochemistry, Faculty of Medicine, Karadeniz Technical University, Trabzon, Turkey

Introduction

Dyslipidemia is one of the most common and important risk factors for developing of atherosclerosis and the resulting cardiovascular diseases. This lipid disorder, viewed as a lipid triad, is characterized by increased triglyceride (TG) and low-density lipoprotein cholesterol (LDL-C) and decreased high-density lipoprotein cholesterol (HDL-C) (Austin et al. 2000; Orem et al. 2002). Hypercholesterolemia and mixed-type hyperlipidemia are the most common forms of atherogenic dyslipidemia. Numerous clinical trials have focused on the effect of atherogenic lipids on hemorheological factors associated with cardiovascular diseases (Kanakaraj and Singh 1989; Koter et al. 2004; Saklamaz et al. 2005; De Queiroz Mello et al. 2010). Cholesterol is an essential and functional

component of cell membranes, and any change in erythrocyte membrane cholesterol levels reflects substantial modification of the serum lipid profile because of not having de novo cholesterol synthesis in the cell (Dwight et al. 1996; Calişkan et al. 2000; Uyuklu et al. 2007). Cholesterol enrichment in erythrocytes results in decreased deformability and fluidity of these cells. This may cause impairment of functional properties including membrane-bound enzymes and rheological behaviors such as osmotic fragility that can promote atherosclerotic lesions (Ramanadham and Kaplay 1982; Kanakaraj and Singh 1989; Koter et al. 2004; Vayá et al. 2008). Besides the effect of hypercholesterolemia on erythrocyte rheological characteristics, recent studies have indicated that the free cholesterol in erythrocyte membrane could structurally contribute to plaque formation as well as serum lipoprotein fractions (Mason et al. 2006; Vayá et al. 2008). On the other hand, oxidative stress is the underlying cause of many diseases and closely associated with cardiovascular risk factor (Koter et al. 2004). Free radicals, the mediators of oxidative stress, primarily attack membrane lipids and lead to irreversible functional and structural disorders including membrane-bound ion transport proteins and other proteins involved in signal-transduction pathways (Koter et al. 2004; Mason et al. 2006). As a result of lipid peroxidation, the crystallized cholesterol formed in the extracellular milieu of the plasma membrane contributes directly to the pathogenesis of cardiovascular diseases by leading to cell death and inflammation. Free cholesterol exchange between erythrocytes and lipoprotein fractions can easily occur despite the crystallized form being insensitive to pharmacologic intervention or reverse cholesterol transport mechanisms (Mason et al. 2006).

Statins are commonly used to lower high blood cholesterol levels. They are competitive inhibitors of 3-hydroxy-3-methylglutaryl coenzyme A (3-HMG-CoA) reductase, which catalyzes the conversion of HMG-CoA to mevalonate, the early rate-limiting step in the biosynthesis of cholesterol (Dwight et al. 1996; Calişkan et al. 2000; Koter et al. 2002). A number of clinical studies have demonstrated that treatment of dyslipidemic patients with HMG-CoA reductase inhibitors such as lovastatin and simvastatin caused a decrement in serum and cellular cholesterol levels, despite some reports showing no significance (Levy et al. 1992; Rabini et al. 1993; Martinez et al. 1996; Lijnen et al. 1996; Dwight et al. 1996; Uyuklu et al. 2007). Evidence concerning the hypolipidemic effect of statin-derived agents indicates that this therapy can lead to plaque stabilization, decreased platelet aggregation (Koter et al. 2002) and improvement in erythrocyte hemorheological action (Martinez et al. 1996) as well as antioxidant (Mason et al. 2006; Bełtowski et al. 2009; Chopra and Flanders 2009). Among statin-derived drugs, atorvastatin is a synthetic inhibitor of HMG-CoA and more effective than other statins. Experimental studies on the pleiotropic effects of atorvastatin have increased in recent years.

In the present study, the efficiency of atorvastatin therapy concerning the serum lipid profile and the structural and functional properties of erythrocyte membranes in individuals with dyslipidemia were researched. Also, the antioxidative potency of the therapy on erythrocytes and serum was examined.

Materials and Methods

Patients and Treatment Organization

The study involved 44 patients (23 men and 21 women, aged 30–76 years, average 54) with dyslipidemia. They were recruited via the Cardiology Department of the Medical Faculty at Karadeniz Technical University in Turkey. The research was approved by the local ethics committee at the Medical Faculty, and all patients gave informed consent before entering the study. Because of the strong interrelationships between elevated TG and LDL-C and reduced HDL-C, patients were classified into two groups according to their serum total cholesterol (TC) levels as 29 hypercholesterolemic (with cholesterol levels >240 mg/dl) and serum TC and TG levels as 15 mixed-type hyperlipidemic (with cholesterol and TG above 240 and 200 mg/dl, respectively). Patients were eligible to take part in the study if they met the criteria of the National Cholesterol Education Program-Adult Treatment Panel 2 (NCEP-ATP2) and were not receiving lipid-lowering therapy before entry into the study. All undertook a screening program consisting of medical history, examination and full hematologic and biochemical profiles. Patients with any of the following conditions were excluded: hypothyroidism, diabetes mellitus, nephrotic syndrome, renal insufficiency, hepatic dysfunction, malignant diseases, immune disorders, uncontrolled hypertension and coronary artery disease; also, cigarette smokers were excluded. The study lasted 16 weeks. Patients were started on atorvastatin (10 mg/day) and evaluated at 6–12 weeks to assess therapeutic efficacy. Patients were also assigned to a hypolipidemic diet regimen according to NCEP step 1 during the treatment. This diet limits cholesterol intake to <300 mg/day and total fats to 30 % of total calories, with <10 % of total calories from saturated fats, 10 % from polyunsaturated fats and 10–15 % from monounsaturated fats. All manual measurements were made in triplicate.

Measurement of Serum Lipids and Lipoproteins

Blood samples were drawn after an overnight fast of 12 h, and sera were separated by low-speed (2,500×*g*) centrifugation for 15 min. Levels of TC and TG were estimated with enzymatic methods using a Hitachi (Tokyo, Japan) 917 autoanalyzer with Boehringer Mannheim (Mannheim, Germany) original reagents. HDL-C was measured by the dextran sulfate-Mg^{2+} precipitation method. LDL-C was calculated by Friedewald's formula. Apolipoprotein A-I (Apo A-I) and apoprotein B (Apo B) levels were assessed by immunonephelometry using Date Behring (BN II, Marburg, Germany) and its original reagent. Results were expressed as milligrams per deciliter of serum.

Erythrocyte Preparation, Extraction and Measurement of Membrane Lipids

Erythrocytes were separated from blood plasma and leukocytes by means of centrifugation (3,000×*g*, 10 min) at 4 °C and washed three times with phosphate-buffered saline (PBS). Membrane lipids were extracted using the procedure of Rose and Oklander (1965), in which lipids are extracted from an aliquot of erythrocyte membrane suspension with chloroform-isopropanol (7:11, v/v) using a single extraction tube. Membrane cholesterol was assayed by the cholesterol oxidase method with a high-performance Monotest kit (Boehringer Mannheim) (Ott et al. 1982). Membrane total phospholipid phosphorus was estimated according to Findlay and Evans (1987). To prevent autooxidation, butylated hydroxytoluene (0.001 %, w/v) as antioxidant was added to all solvents.

Measurement of Na^+/K^+-ATPase Activity

For ATPase activity, erythrocyte membranes were prepared according to Dodge et al. (1963). The method described by Charalambous and Mir (1982) was used to assay Na^+/K^+-ATPase activity. It is based on the measurement of orthophosphate released from ATP during incubation of membrane suspensions with a medium containing (in mM) 2 ATP, 10 $MgCl_2$, 30 Tris-EGTA buffer (pH 7.4, 0.1 mM EGTA), 10 NaCN and 0.1 ouabain. Enzyme activity was expressed as the difference in the inorganic phosphate (P_i) released in the presence and absence of ouabain. Na^+/K^+-ATPase activity was expressed as micromoles P_i per hour per milligram membrane protein.

Measurement of Osmotic Fragility

The test was performed by the method of Parpart et al. (1947). Calibration for percentage hemolysis was performed with the same groups by mixing 0.1 % saline solution with 0.02 ml packed cells. This reading was treated as 100 % hemolysis, and distilled water was used as a blank for calibration.

Measurements of Lipid Peroxidation in Plasma and Erythrocytes

Plasma concentrations of thiobarbituric acid reactive substances (TBARS) were measured according to method of Yagi (1994). Lipids and proteins were precipitated using 10 % phosphotungstic acid and 0.04 M sulfuric acid (w/v). The sediment was resuspended in distilled water, and thiobarbituric acid (TBA) was added to the mixture. The reaction mixture was heated to 95 °C for 60 min. TBARS were extracted with *n*-butanol. After centrifugation, the butanol layer was taken for fluorometric measurements at 515 nm excitation and 553 nm emission.

Erythrocyte TBARS was estimated according to the method described by Stocks and Dormandy (1971). Cell suspension (3 ml) was added to trichloroacetic acid-arsenite solution (2 ml). Supernatant (3 ml) was transferred to TBA solution (1 ml) following centrifugation of the mixture for 10 min. An air condenser was fitted to the tube, and the mixture was incubated for exactly 15 min in a boiling water bath. The tube was cooled. The absorption spectrum of the mixture between 500 and 600 nm was plotted by a recording spectrophotometer. The formula ($OD_{532} - OD_{600}$) × 900 gave the TBARS concentration in nanomoles per gram Hb. Mean hemoglobin concentration was measured by a Coulter (Hialeah, FL) analyzer.

Measurement of Total Antioxidant Status in Plasma

Total antioxidant status (TAS) was assayed using the method of Miller et al (1993). In this method, metmyoglobin reacts with hydrogen peroxide to form ferrylmyoglobin, a free radical species. All reagent and calibrator/control materials were supplied by Randox Laboratories (Antrim, UK). The within-run coefficient of variance (CV) for the control was 4.8 % ($n = 10$).

Statistical Analysis

All results are expressed as means ± SD. Comparisons for serum lipids, lipoproteins, membrane lipids, ATPase activity, osmotic fragility, TBARS and TAS levels before and after lipid-lowering therapy were performed with the paired *t*-test for normally distributed data or Wilcoxon's signed-rank test for non-normally distributed data. The unpaired *t*-test or Mann–Whitney *U*-test was used to compare parameters between subgroups. Relationships among variables were assessed by Spearman's rank or

Pearson's correlation coefficient. $p < 0.05$ was considered significantly different. The SPSS 16.0 software package (SPSS, Inc., Chicago, IL) was used in all statistical analyses.

Results

The demographic, clinical and treatment data of the dyslipidemic groups are given in Table 1. In our study population 29 (66 %) were hypercholesterolemic and 15 (34 %) were mixed-type hyperlipidemic subjects. Of the participants, 21 (48 %) were hypertensive, 13 (30 %) were current smokers, 10 (23 %) had obesity and 16 (36 %) had a family history of dyslipidemia. There was no statistically significant difference among experimental groups in demographic features (Table 1). Higher TG and lower LDL-C and HDL-C levels of mixed-type hyperlipidemics compared to hypercholesterolemics were found in the pretreatment period, but no difference was observed in other parameters. The dyslipidemic subgroups showed similar responses to atorvastatin treatment concerning the studied parameters. As expected, atherogenic lipid components (TC, LDL-C and TG) and Apo B level significantly decreased, while HDL-C and Apo A-I levels increased in both groups after treatment. No significant change was found in Lp (a) level in all groups after the therapy. Table 2 presents membrane cholesterol, phospholipids levels, C/P ratio, Na^+/K^+-ATPase activity and osmotic fragility before and after treatment with atorvastatin in the two groups. Erythrocyte membranes from the atorvastatin-treated group contained lower concentrations of cholesterol and a lower C/P ratio than those of the untreated group ($p < 0.001$, $p < 0.01$ in hypercholesterolemic group and $p < 0.05$, $p < 0.05$ in mixed-type dyslipidemic group, respectively). Following the therapy, there was a significant increase in phospholipid level in erythrocytes of subjects with dyslipidemia. Erythrocyte Na^+/K^+-ATPase activity was also enhanced during the lipid-lowering therapy in hypercholesterolemics and mixed-type dyslipidemics ($p < 0.001$ and $p < 0.05$, respectively). Following the treatment, the osmotic fragility of erythrocytes showed a significant increasing trend in the mixed-type hyperlipidemic group, while there was an insignificant rise in the hypercholesterolemic group. Our finding showed that the balance between the oxidant and antioxidant

Table 1 Distribution of demographic features in patients with hypercholesterolemia and mixed-type hyperlipidemia and lipid profiles in the dyslipidemic groups before and after lipid-lowering therapy

Parameters	Patients with hypercholesterolemia ($n = 29$, mean ± SD)	Patients with mixed-typed hyperlipidemia ($n = 15$, mean ± SD)
Gender, male, *n* (%)	18 (62)	5 (33)
Hypertension, *n* (%)	13 (45)	8 (53)
Smoking, *n* (%)	10 (35)	3 (20)
Obesity, *n* (%)	6 (21)	4 (27)
Familiy history, *n* (%)	12 (41)	4 (27)
Age (years)	54 ± 12	54 ± 9
BMI (kg/m^2)	29 ± 5	27 ± 3
Treatment dosage (mg/day)	10	10

Parameters	Patients with hypercholesterolemia ($n = 29$, mean ± SD)		Patients with mixed-typed hyperlipidemia ($n = 15$, mean ± SD)	
	Before treatment	After treatment	Before treatment	After treatment
TG (mg/dl)	132 ± 39	112 ± 39[a,***]	311 ± 84[c,***]	199 ± 79[a,***]
TC (mg/dl)	282 ± 33	205 ± 37[a,***]	290 ± 26	209 ± 36[a,***]
LDL-C (mg/dl)	210 ± 30	134 ± 34[a,***]	190 ± 33[c,*]	129 ± 39[a,***]
HDL-C (mg/dl)	43 ± 8	47 ± 9[a,***]	38 ± 5[c,*]	41 ± 6[a,**]
Apo A-I (mg/dl)	122 ± 20	136 ± 17[a,***]	123 ± 11	134 ± 14[a,**]
Apo B (mg/dl)	132 ± 16	101 ± 12[b,***]	142 ± 27	108 ± 21[b,***]
Lp (a) (mg/dl)	21 ± 31	19 ± 29	21 ± 22	17 ± 24

TC total cholesterol, *TG* triglyceride, *LDL-C* low-density lipoprotein cholesterol, *HDL-C* high-density lipoprotein cholesterol, *Apo* apoprotein

[a,b] According to paired *t*-test[a] and Wilcoxon test[b] for comparison of plasma lipid parameters before and after treatment with atorvastatin

[c] According to paired *t*-test for comparison of plasma lipid parameters between hypercholesterolemic and mixed-type hyperlipidemic groups

* $p < 0.05$, ** $p < 0.01$, *** $p < 0.001$

Table 2 Na^+/K^+-ATPase activity, osmotic fragility and levels of plasma membrane lipid in patients with hypercholesterolemia and mixed-type hyperlipidemia before and after lipid-lowering therapy

Parameters	Patients with hypercholesterolemia ($n = 29$, mean ± SD)		Patients with mixed-typed hyperlipidemia ($n = 15$, mean ± SD)	
	Before treatment	After treatment	Before treatment	After treatment
Cholesterol (μmol/mg Prt)	0.33 ± 0.12	0.22 ± 0.06***	0.31 ± 0.12	0.24 ± 0.05*
Phospholipid (μmol/mg Prt)	0.55 ± 0.17	0.75 ± 0.30*	0.58 ± 0.21	0.83 ± 0.33*
Cholesterol/phospholipid	0.64 ± 0.33	0.34 ± 0.13**	0.62 ± 0.37	0.32 ± 0.10*
Na^+/K^+-ATPase activity (μmol P_i/h/mg Prt)	0.79 ± 0.30	0.93 ± 0.36***	0.61 ± 0.18	0.81 ± 0.14*
Osmotic fragility[a] (g/l)	4.03 ± 0.27	4.14 ± 0.34	3.96 ± 0.18	4.26 ± 0.26*

[a] NaCl concentration giving 50 % hemolysis

* $p < 0.05$, ** $p < 0.01$, *** $p < 0.001$, according to paired *t*-test

Table 3 Lipid peroxidation intensity of erythrocyte and plasma and plasma TAS values in patients with hypercholesterolemia and mixed-type hyperlipidemia before and after lipid-lowering therapy

Parameters	Patients with hypercholesterolemia ($n = 29$, mean ± SD)		Patients with mixed-typed hyperlipidemia ($n = 15$, mean ± SD)	
	Before treatment	After treatment	Before treatment	After treatment
TBARS in the whole erythrocyte (nmol/g hemoglobin)	276 ± 94	233 ± 82*	265 ± 79	191 ± 42**
TBARS in plasma (nmol/ml)	5.63 ± 1.81	3.69 ± 0.80***	6.64 ± 3.32	4.02 ± 1.28***
TAS (mmol/l)	1.41 ± 0.09	1.51 ± 0.09***	1.38 ± 0.11	1.49 ± 0.09**

TBARS thiobarbituric acid reactive substances, *TAS* total antioxidant status

* $p < 0.05$, ** $p < 0.01$, *** $p < 0.001$, according to paired *t*-test

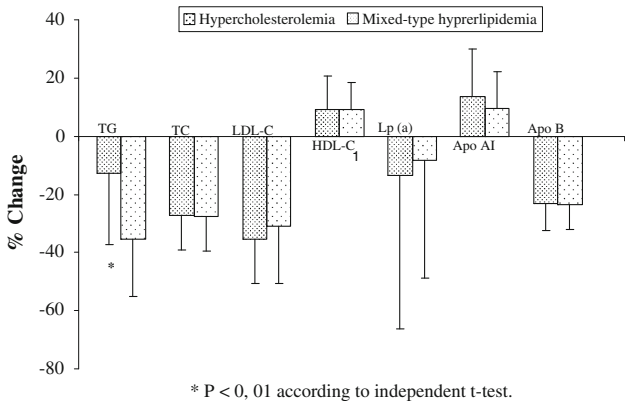

Fig. 1 Comparison of percent changes in plasma lipid profile in patients with hypercholesterolemia and mixed-type hyperlipidemia after 12-week atorvastatin therapy

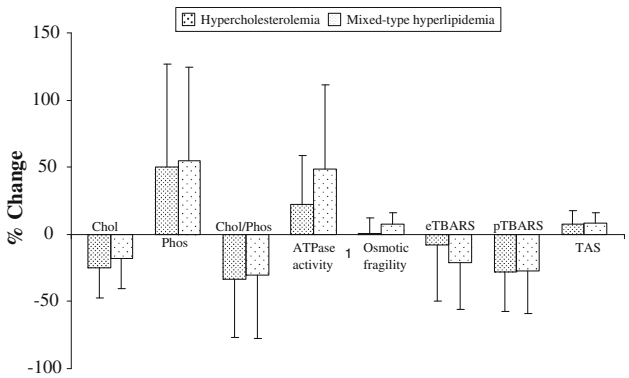

Fig. 2 Comparison of percent changes in erythrocyte membrane lipid composition and in lipid peroxidation products in erythrocyte and plasma of patients with hypercholesterolemia and mixed-type hyperlipidemia after 12-week atorvastatin therapy. *eTBARS* and *pTBARS* Thiobarbituric acid reactive substances in erythrocyte and plasma, respectively

systems was affected by atorvastatin therapy. In all study groups, the lower TBARS levels in erythrocytes and plasma were obviously estimated after this treatment. Also, plasma TAS values of the two subgroups compared to baseline were higher after the therapy (Table 3). The percentage changes in serum lipid profile and in erythrocyte lipid composition, Na^+/K^+-ATPase activity, osmotic fragility and components of the oxidant and antioxidant systems are given in Figs. 1 and 2. As can be seen in these figures, the degree of change in all of these parameters, except for triglyceride, was similar in both subgroups. In addition, Fig. 3 indicates the relationship between the percentage changes of C/P ratio and Na^+/K^+-ATPase activity in erythrocytes of hypercholesterolemics ($r = -0.786$, $p < 0.02$). The enzyme activity of erythrocyte membranes was enhanced according to the decrease in

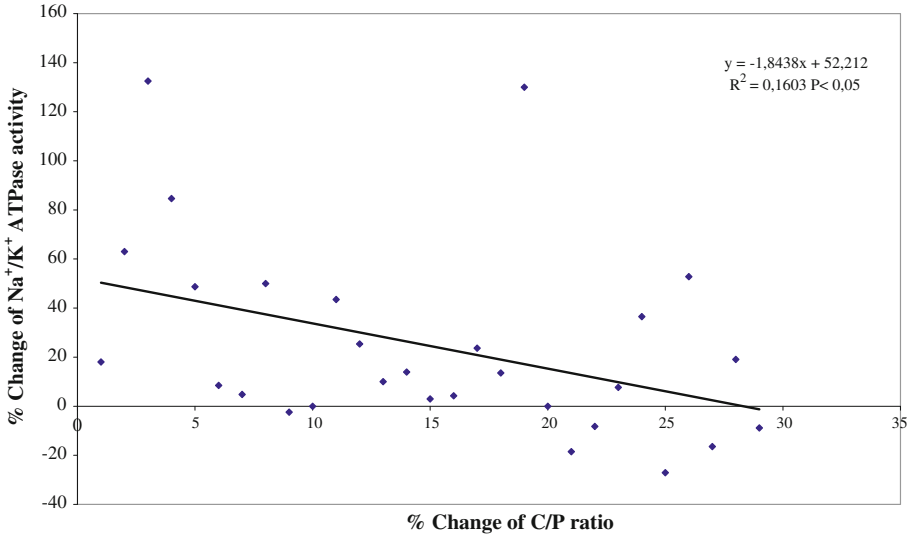

Fig. 3 Relationship between percent changes of Na^+/K^+-ATPase activity and C/P ratio of erythrocytes in subjects with dyslipidemia

membrane C/P ratio of both groups. Also, it was estimated that there was a negative correlation between the percentage change of erythrocyte TBARS amount and the C/P ratio and plasma TAS level in subjects with dyslipidemia ($r = -0.714$, $p < 0.047$ and $r = -0.424$, $p < 0.022$, respectively).

Discussion

Our findings show that short-term therapy with low-dose atorvastatin in subjects with dyslipidemia was efficient at reducing the serum concentration of TC, LDL-C, TG and Apo B and at increasing HDL-C and Apo AI, while the Lp (a) level was not changed. All these changes were independent of possible cofounders such as gender, family history, obesity, smoking and hypertension. The changes in these parameters were similar to the results obtained by many studies (Koter et al. 2002; Uyuklu et al. 2007; Koh et al. 2010; Jones et al. 2010, Arsenault et al. 2011; Thongtang et al. 2011; Athyros et al. 2011). Also, we demonstrated that there was no statistical difference between baseline lipid and apolipoprotein characteristics of the dyslipidemic groups except for TG and HDL-C. This indicated that the study groups had the proper demographic characteristics. The effects of statins on HDL-C levels have been controversial. Some studies have shown a marked elevation in levels of serum HDL-C during atorvastatin treatment (Barter et al. 2010; Arsenault et al. 2011) and others no change (Rabini et al. 1993; Lijnen et al. 1996; Koter et al. 2002; Arsenault et al. 2011). The lipid-lowering effect of atorvastatin, as for other statins on serum lipid, is due to a competitive inhibition of the rate-limiting enzyme 3-HMG CoA reductase in the intracellular biosynthesis of cholesterol, subsequently leading to induction of receptor production and catabolic rate of LDL-C (Rubenfire et al. 1991; Lijnen et al. 1996). In both dyslipidemic groups, there were close correlations between reduced Apo B levels, increased Apo A-I levels and plasma levels of LDL-C and HDL-C. In general, an unchanged serum Lp (a) level has been reported during statin-derived drug treatment of hypercholesterolemic patients (Miller et al. 1993; Bełtowski et al. 2009). A number of studies have shown that alterations in the serum lipid composition were accompanied by changes in erythrocyte lipid content (Lijnen et al. 1996; Martinez et al. 1996; Koter et al. 2002), but not all agree (Dwight et al. 1996; Tziakas et al. 2008). In the present study, a significant decrement in erythrocyte membrane cholesterol in subjects with hypercholesterolemia and mixed-type hyperlipidemia after atorvastatin therapy was clearly observed. After a 12-week therapy, serum concentrations of TC and LDL-C in the subgroups were similarly lowered. Also, the percent change of erythrocyte C/P ratio was positively correlated with that of serum LDL-C. There are some reports that conflict with our finding. Of these, Dwight et al. (1996) indicated that 8-week treatment with simvastatin in low doses altered membrane acyl chain composition and serum cholesterol but had no effect on erythrocyte cholesterol content. In contrast to the mentioned studies, there are many more studies showing that the short- and long-term statin therapies resulted in decreased erythrocyte cholesterol and C/P ratio (Rabini et al. 1993; Martinez et al. 1996; Koter et al. 2004; Vayá et al. 2008). The lipid-lowering impact of atorvastatin as well other statins was thought to result from an influence on cholesterol exchange by binding to the plasma membrane and displacing cholesterol between the lipoproteins and the erythrocytes in which the rate of

cholesterol synthesis is relatively insignificant (Garnier et al. 1988; Lijnen et al. 1996; Martinez et al. 1996). One of the most important determinants of erythrocyte function and survival throughout the blood circulation is its deformability property, which is determined by some factors: membrane viscoelasticity, intracellular viscosity and area to volume ratio of the cell surface causing the membrane C/P ratio and a younger cell population. Na^+/K^+ pump activity and osmotic fragility are perfect indices of cell age (Ramanadham and Kaplay 1982). The reduction in C/P ratio of the erythrocyte membrane was associated with a significant enhancement of erythrocyte membrane Na^+/K^+ pump activity. This was obviously shown by our study. Recently, many reports have demonstrated that erythrocyte Na^+/K^+ pump activity is inversely related to its membrane contents of cholesterol, polyunsaturated fatty acid and particularly phospholipid subclasses (Uyuklu et al. 2007). Increased Na^+/K^+-ATPase activity in both dyslipidemic groups may be evident only in the presence of an elevation in membrane fluidity, depending on the reduction of erythrocyte C/P ratio after atorvastatin treatment. This is consistent with previous reports suggesting that the improved membrane fluidity by hypolipidemic therapy enhanced pump activity in subjects with dyslipidemia (Rabini et al. 1993; Lijnen et al. 1996; Martinez et al. 1996; Koter et al. 2004).

Serum lipid composition could change the osmotic fragility of erythrocytes by disrupting phospholipid compounds and the cholesterol content of cell membranes (Kanakaraj and Singh 1989). Even though the erythrocyte Na^+/K^+ pump activity and C/P ratio altered in both groups after treatment, increased osmotic resistance to hypotonic hemolysis was significant only in the mixed-type hyperlipidemic group. This behavior in the mixed-type group only may be a consequence of the small size of the population. There have been a number of studies showing that the erythrocytes of hypercholesterolemics were osmotically more resistant to lysis in a hypotonic medium (Kanakaraj and Singh 1989; Özdemirler et al. 2001). In the present study, the unaltered osmotic fragility values of the hypercholesterolemic group after treatment are, however, consistent with the finding that Dwight and colleagues (1996) obtained in 2-month simvastatin therapy of individuals with a clinical history of atherosclerosis. After atorvastatin treatment, the increment in osmotic fragility may be due to lost cholesterol or acquired phospholipid content of erythrocytes, particularly phosphatidylcholine.

On the basis of the literature data, clinical trials have shown that dyslipidemia contributes to the development of cardiovascular diseases and that this course is amplified by oxidative stress, resulting in the formation of atheromatous plaque (Koter et al. 2004; De Freitas et al. 2010; Barter et al. 2010). Erythrocytes are more susceptible to the free radicals which cause structural and functional disorders in the cell membrane, including reduced enzyme activities, essential fatty acid content and membrane rigidity, thus decreasing the cell's ability to deform (Koter et al. 2004). As a measurement of oxidative stress, TBARS level in the erythrocyte and plasma of the study groups was estimated during pre- and posttreatment periods. There was a highly significant decrease in TBARS values in both erythrocyte and plasma of subgroups compared to baseline. Our results were confirmed by the report of Koter et al. (2004), showing that TBARS concentrations in erythrocyte and plasma of hypercholesterolemic subjects were notably lowered after 12 weeks of atorvastatin treatment. Given the fact that statins indicate pleiotropic effects, their antioxidant activity may be to bind to the phospholipids of erythrocyte membranes and lipoprotein fractions, thereby preventing the diffusion of free radicals generated under oxidative stress (Bellosta et al. 2000). In addition, Mason and colleagues (2006) propounded that when comparing other statins the higher antioxidant potency of atorvastatin resulted from the *o*-hydroxy metabolite form, about 70 % presented in serum. The metabolite protects the lipid moiety against free radical attack. This protective mechanism is due to electron donation and proton stabilization associated with its phenoxy group located in the membrane lipid core. Correlatively, total plasma antioxidant status, an indication of antioxidant capacity, was higher in both dyslipidemic groups after treatment; and all these data clearly confirm the antioxidative action of this antilipidemic agent.

In the present research study, we have shown that treating dyslipidemic patients with atorvastatin not only causes favorable changes in serum, erythrocyte lipid profile and some aspects of cell deformability related to membrane components but also leads to an antioxidative impact against oxidative stress beyond cholesterol lowering. However, further studies are needed to elucidate the molecular mechanisms underlying the changes in lipid composition of erythrocyte membrane and the balance between oxidant and antioxidant status changed by atorvastatin therapy.

Acknowledgements This work was supported by Grants from the Karadeniz Technical University Research Foundation.

References

Arsenault BJ, Barter P, DeMicco DA, Bao W, Preston GM, LaRosa JC, Grundy SM, Deedwania P, Greten H, Wenger NK, Shepherd J, Waters DD, Kastelein JJ, TNT Study Investigators (2011) Prediction of cardiovascular events in statin-treated stable coronary patients by lipid and nonlipid biomarkers. J Am Coll Cardiol 57(1):63–69

Athyros VG, Tziomalos K, Karagiannis A, Mikhailidis DP (2011) Dyslipidaemia of obesity, metabolic syndrome and type 2

diabetes mellitus: the case for residual risk reduction after statin treatment. Open Cardiovasc Med J 5:24–34

Austin MA, McKnight B, Edwards KL, Bradley CM, McNeely MJ, Psaty BM, Brunzell JD, Motulsky AG (2000) Cardiovascular disease mortality in familial forms of hypertriglyceridemia: a 20-year prospective study. Circulation 101(24):2777–2782

Barter PJ, Brandrup-Wognsen G, Palmer MK, Nicholls SJ (2010) Effect of statins on HDL-C: a complex process unrelated to changes in LDL-C: analysis of the VOYAGER database. J Lipid Res 51(6):1546–1553

Bellosta S, Ferri N, Bernini F, Paoletti R, Corsini A (2000) Non-lipid-related effects of statins. Ann Med 32(3):164–176

Bełtowski J, Wójcicka G, Jamroz-Wiśniewska A (2009) Adverse effects of statins: mechanisms and consequences. Curr Drug Saf 4(3):209–228

Calişkan S, Calişkan M, Kuralay F, Onvural B (2000) Effect of simvastatin therapy on blood and tissue ATP levels and erythrocyte membrane lipid composition. Res Exp Med (Berl) 199(4):189–194

Charalambous BM, Mir MA (1982) An improved procedure for the preparation and measurement of (Na^+/K^+)-ATPase in human erythrocytes. Biochim Biophys Acta 691:71–82

Chopra V, Flanders SA (2009) Does statin use improve pneumonia outcomes? Chest 136(5):1381–1388

De Freitas MV, de Oliveira MR, dos Santos DF, de Cássia Mascarenhas Netto R, Fenelon SB, Penha-Silva N (2010) Influence of the use of statin on the stability of erythrocyte membranes in multiple sclerosis. J Membr Biol 233(1–3): 127–134

De Queiroz Mello AP, da Silva IT, Oliveira AS, Nunes VS, Abdalla DS, Gidlund M, Damasceno NR (2010) Electronegative low-density lipoprotein is associated with dense low-density lipoprotein in subjects with different levels of cardiovascular risk. Lipids 45(7):619–625

Dodge JT, Mitchell C, Hanahan DJ (1963) The preparation and chemical characteristics of hemoglobin-free ghosts of human erythrocytes. Arch Biochem Biophys 100:119–130

Dwight JF, Mendes Ribeiro AC, Hendry BM (1996) Effects of HMG-CoA reductase inhibition on erythrocyte membrane cholesterol and acyl chain composition. Clin Chim Acta 256(1):53–63

Findlay JB, Evans WH (1987) Biological membranes. Oxford University Press, New York, pp 119–121

Garnier M, Perret G, Pilardeau P, Vaysse J, Rolland Y, Uzzan B, Vassy R (1988) Effect of diosmin upon red blood cell deformability and osmotic fragility. Relationship with lipid content. Methods Find Exp Clin Pharmacol 10(4):259–262

Jones PH, Goldberg AC, Knapp HR, Kelly MT, Setze CM, Stolzenbach JC, Sleep DJ (2010) Efficacy and safety of fenofibric acid in combination with atorvastatin and ezetimibe in patients with mixed dyslipidemia. Am Heart J 160(4):7 59–766

Kanakaraj P, Singh M (1989) Influence of hypercholesterolemia on morphological and rheological characteristics of erythrocytes. Atherosclerosis 76(2–3):209–218

Koh KK, Quon MJ, Han SH, Lee Y, Kim SJ, Shin EK (2010) Atorvastatin causes insulin resistance and increases ambient glycemia in hypercholesterolemic patients. J Am Coll Cardiol 55(12):1209–1216

Koter M, Broncel M, Chojnowska-Jezierska J, Klikczynska K, Franiak I (2002) The effect of atorvastatin on erythrocyte membranes and serum lipids in patients with type-2 hypercholesterolemia. Eur J Clin Pharmacol 58(8):501–506

Koter M, Franiak I, Strychalska K, Broncel M, Chojnowska-Jezierska J (2004) Damage to the structure of erythrocyte plasma membranes in patients with type-2 hypercholesterolemia. Int J Biochem Cell Biol 36(2):205–215

Levy Y, Leibowitz R, Aviram M, Brook JG, Cogan U (1992) Reduction of plasma cholesterol by lovastatin normalizes erythrocyte membrane fluidity in patients with severe hypercholesterolaemia. Br J Clin Pharmacol 34(5):427–430

Lijnen P, Echevaría-Vázquez D, Petrov V (1996) Influence of cholesterol-lowering on plasma membrane lipids and function. Methods Find Exp Clin Pharmacol 18(2):123–136

Martinez M, Vaya A, Marti R, Gil L, Lluch I, Carmena R, Aznar J (1996) Effect of HMG-CoA reductase inhibitors on red blood cell membrane lipids and haemorheological parameters, in patients affected by familial hypercholesterolemia. Haemostasis 26(Suppl 4):171–176

Mason RP, Walter MF, Day CA, Jacob RF (2006) Active metabolite of atorvastatin inhibits membrane cholesterol domain formation by an antioxidant mechanism. J Biol Chem 281(14):9337–9345

Miller NJ, Rice-Evans C, Davies MJ, Gopinathan V, Milner A (1993) A novel method for measuring antioxidant capacity and its application to monitoring antioxidant status in premature neonates. Clin Sci 34:407–412

Orem C, Orem A, Uydu HA, Celik S, Erdöl C, Kural BV (2002) The effects of lipid-lowering therapy on low-density lipoprotein autoantibodies: relationship with low-density lipoprotein oxidation and plasma total antioxidant status. Coron Artery Dis 13(1):65–71

Ott P, Binggeli Y, Brodbeck U (1982) Rapid and sensitive assay for determination of cholesterol in membrane lipid extracts. BBA Biomembr 685:211–213

Özdemirler G, Küçük S, Orhan Y, Aykaç-Toker G, Uysal M (2001) Lipid and protein oxidation in erythrocyte membranes of hypercholesterolemic subjects. Clin Biochem 34(4):335–339

Parpart AK, Lorenz PB, Parpart ER, Gregg JR, Chase AM (1947) The osmotic resistance (fragility) of human red cells. J Clin Invest 26(4):636–640

Rabini RA, Polenta M, Staffolani R, Tocchini M, Signore R, Testa I, Mazzanti L (1993) Effect of hydroxymethylglutaryl-CoA reductase inhibitors on the functional properties of erythrocyte membranes. Exp Mol Pathol 59(1):51–57

Ramanadham M, Kaplay SS (1982) Erythrocyte osmotic fragility in protein-energy malnutrition: cholesterol, phospholipid, and Ca^{2+}, Mg^{2+} adenosine triphosphatase. Biochem Med 27: 226–231

Rose HG, Oklander M (1965) Improved procedure for the extraction of lipid from human erythrocytes. J Lipid Res 6:428–431

Rubenfire M, Maciejko JJ, Blevins RD, Orringer C, Kobylak L, Rosman H (1991) The effect of pravastatin on plasma lipoprotein and apolipoprotein levels in primary hypercholesterolemia. The Southeastern Michigan Collaborative Group. Arch Intern Med 151(11):2234–2240

Saklamaz A, Comlekci A, Temiz A, Caliskan S, Ceylan C, Alacacioglu A, Yesil S (2005) The beneficial effects of lipid-lowering drugs beyond lipid-lowering effects: a comparative study with pravastatin, atorvastatin, and fenofibrate in patients with type IIa and type IIb hyperlipidemia. Metabolism 54(5): 677–681

Stocks J, Dormandy TL (1971) The autoxidation of human red cell lipids induced by hydrogen peroxide. Br J Haematol 20:95–111

Thongtang N, Ai M, Otokozawa S, Himbergen TV, Asztalos BF, Nakajima K, Stein E, Jones PH, Schaefer EJ (2011) Effects of maximal atorvastatin and rosuvastatin treatment on markers of glucose homeostasis and inflammation. Am J Cardiol 107(3):387–392

Tziakas DN, Chalikias GK, Stakos D, Tentes IK, Chatzikyriakou SV, Mitrousi K, Kortsaris AX, Boudoulas H, Kaski JC (2008) Cholesterol composition of erythrocyte membranes and its association with clinical presentation of coronary artery disease. Coron Artery Dis 19(8):583–590

Uyuklu M, Meiselman HJ, Baskurt OK (2007) Effect of decreased plasma cholesterol by atorvastatin treatment on erythrocyte mechanical properties. Clin Hemorheol Microcirc 36(1):25–33

Vayá A, Martínez Triguero M, Réganon E, Vila V, Martínez Sales V, Solá E, Hernández Mijares A, Ricart A (2008) Erythrocyte membrane composition in patients with primary hypercholesterolemia. Clin Hemorheol Microcirc 40(2):289–294

Yagi K (1994) Lipid peroxides and related radicals in clinical medicine. In: Free radicals in diagnostic medicine. Pleneum Press, New York, pp 1–15

J Membrane Biol (2012) 245:707–716
DOI 10.1007/s00232-012-9442-6

Preparation and Characterization of Collagen–Chitosan–Chondroitin Sulfate Composite Membranes

Wang Kangjian · Dan Nianhua · Xiao Shiwei · Ye Yichun · Dan Weihua

Received: 20 October 2011 / Accepted: 25 May 2012 / Published online: 22 June 2012

Abstract Collagen (Col)–chitosan (Chi) membrane was modified by a hot dehydrogenation cross-linking method. Carbodiimide was added for further crossing modification. Chondroitin sulfate (CS) was added so that Col–Chi sulfate composite membranes were prepared. The structure of the composite membranes was characterized by Fourier transform infrared spectroscopy and X-ray photoelectron spectroscopy, and its mechanical properties, degradation, and cytotoxicity were characterized. The composite membrane was applied to a full-thickness skin injury in animal experiments performed in rabbits. Strong interactions and good compatibility among Col, Chi, and CS in the composite membrane were present. The good mechanical properties, biocompatibility, digestion resistance, and wound healing promotion of the composite membrane make it a potential wound dressing or skin scaffold for tissue engineering.

Keywords Chitosan · Chondroitin sulfate · Collagen · Medical composite membrane · Wound repair

Biomedical membrane is an important kind of biomedical material for tissue-engineering scaffolds, wound dressings, and hemostatic products, and it has been a high-priority research topic for the past few decades (Wang et al. 2011).

W. Kangjian · Y. Yichun · D. Weihua (✉)
National Engineering Laboratory for Clean Technology of Leather Manufacture, Sichuan University, Chengdu 610065, China
e-mail: sculeather415@yahoo.com.cn

D. Nianhua · X. Shiwei
Research Center of Biomedicine Engineering, Sichuan University, Chengdu 610065, China

Wound healing comprises a complicated sequence of cellular and biochemical events involving inflammation, migration, and proliferation of a variety of cell types; production of extracellular matrix (ECM) and proteins; and neovascularization (Chen et al. 2006).

It has been demonstrated that the ECM, including such elements as collagen (Col) and glycosaminoglycans (GAGs), plays an important role in the process of injury repair. In particular, Col has been demonstrated to be a good ECM substitute in injury repair (Bissell 2001; Midwood 2004). Col can identify the specific molecular signal and mediate cell adhesion and migration. It also has low immunogenicity and good histocompatibility. In addition, its small-chain polypeptide of protein and amino acid in the catabolite could be used as the nutrient component of tissue-engineered cells. However, Col has several negative effects when extracted, including overall structure change, diminished intensity, and degradation of collagenase in vivo. Wound repair materials that use Col as a membrane have been extensively studied during the past few years (Braga-Vilela et al. 2008; Rho et al. 2006). Various technologies and methods have been applied to increase the intensity of Col and to control its degradation in vivo. In particular, Col may be mixed with chitosan (Chi) and GAGs.

Chi is a natural polysaccharide that is structurally similar to GAGs. It consists of β-(1-4) linked D-glucosamine residues with a variable number of randomly located *N*-acetyl-glucosamine groups. It has been reported to be nontoxic and biocompatible, and it promotes wound healing (Francis and Howard 2000). Furthermore, the incorporation of Chi into a Col scaffold is known to increase its mechanical strength, as it forms an ionic complex between the positively charged Chi and the negatively charged Col (Taravel and Domard 1996). In addition, the biodegradable

Chi itself provides bacteriostatic and fungistatic activities (Tomihata and Ikada 1997). For these reasons, Chi has been an important biomaterial for wound management. A novel asymmetric Chi membrane has been prepared by an immersion–precipitation phase-inversion method and evaluated as a wound covering (Mi et al. 2001).

GAGs, including hyaluronan and chondroitin sulfate (CS), are amino-sugar-containing polysaccharides in the ECM of all vertebrates. CS is composed of alternating units of β-1,3-linked glucuronic acid and (β-1,4)-*N*-acetyl-galactosamine (GalNAc), and it is sulfated in either the 4 or 6 position of the GalNAc residues (Kirker et al. 2002). Furthermore, CS has biocharacteristics that include the binding and modulation of growth factors and cytokines, and CS is involved in the adhesion, migration, proliferation, and differentiation of cells (Pieper et al. 2000; Lee et al. 2004).

By dehydrothermal treatment (DHT) modification and an EDC (1-ethyl-3-(3-dimethyl aminopropyl)carbodiimide) cross-linking method (Ma et al. 2004), following the Col–Chi preparation technology, CS was introduced to combine with the composite membrane in order to provide the biological activity of polysaccharides and to further improve its stability and biocompatibility (Ye et al. 2007a, b). The purpose of this study was to develop a composite membrane for tissue-engineered skin scaffolding or wound dressing.

Experimental Materials

Materials and Reagents

The following chemicals, all of analytical grade and used as received without any further purification, were purchased: 2-*N*-morpholino ethanesulfonic acid (Amresco, Dallas, TX); carbodiimide (EDC, Yanchang Biochemistry Company, Shang Hai, China); *N*-hydroxysuccinimide (NHS; Yanchang Biochemistry Company); Chi (degree of deacetylation >87 %, Cheng Du Kelong Chemical Reagents, Chengdu, China); cartilage (CS, Sigma, St. Louis, MO); ninhydrin (Merck, Darmstadt, Germany); lysozyme (Cheng Du Tian Tai Life Sciences, Chengdu, China); glycine (Amresco); and recombinant human basic fibroblast growth factor (bFGF; Sigma). Col was obtained in our laboratory (molecular weight 300,000 Da).

The following experimental apparatuses were used: lyophilizer (Freeze 6; Labconco, Kansas City, MO); CO_2 cell incubator (Sanyo, Tokyo, Japan); inverted phase contrast microscope (Olympus IX70; Olympus, Tokyo, Japan); centrifuge (Varifuge 3.0RS; Thermo Scientific Heraeus, Hanau, Germany); and scanning electron microscope (SEM; JSM-5900LV; JEOL, Tokyo, Japan).

Methods

Preparation of DHT-EDC-Modified Col–Chi–CS Membrane

The membrane was prepared by blending 0.5 mol/L aqueous HAc at a given ratio (Col/Chi = 1:1). After freeze-drying, the unmodified membrane was vacuumed at room temperature, then treated for 2 h after increasing the temperature to 110 °C. The resulting membrane was soaked for 30 min in 40 ml 40 % ethanol solution (pH 5.0–6.0) containing 50 mM 2-*N*-morpholino ethanesulfonic acid, then soaked for 4 h at room temperature in 40 % ethanol solution that contained 50 mM 1-ethyl-3-(3-dimethylaminopropyl) carbodiimide, EDC, 20 mM *N*-hydroxysuccinimide, NHS, and 1 % CS. Next 0.1 M Na_2HPO_4 solution (pH 9.1) was introduced to wash the composite scaffold for 4 h. The material was washed overnight in different concentrations of NaCl (aq) and neutralized to pH 7.0 via freeze-drying. This process completed the preparation of the DHT-EDC composite modified membrane.

After EDC modification, the Col–Chi–CS membrane was washed thoroughly with 0.1–1.0 M Na_2HPO_4 (aq) (pH 8.0–9.1), 1–2 M NaCl (aq), 5–50 mM glycine, and double-distilled water. The self-made bFGF controlled microsphere dispersed with phosphate-buffered saline (PBS) was evenly sprayed onto the surface of the membrane. After drying, the wound healing membrane based on Col was obtained. It was stored it in a medical package that was irradiation-sterilized by a ^{60}Co irradiation apparatus with 25 kGy before further evaluation.

Structure Characterization of Modified Col–Chi–CS Membrane

X-ray Photoelectron Spectroscopy X-ray photoelectron spectroscopy (XPS) was performed regulated with a standard sample by the XSAM800 ESCA system Au (Au4f = 84.0 eV) and Ag (Ag3d = 386.3 eV).

Determination of Free Amino Groups and Modification Index We drew standard curves with the ninhydrin colorimetry method. We then calculated the modification index by the equation $[(M_0 - M_1)/M_0]$, where M_0 is the free amino group amount before modification and M_1 is the free amino group amount after modification.

Fourier Transform Infrared Spectroscopy The modified Col–Chi–CS membrane was analyzed by Fourier transform infrared spectroscopy (FTIR) with the KBr pellet pressing method. The accompanying scanning wave number was

450 ~ 4,000 cm^{-1} and the resolving power was 2 cm^{-1}. Each scan was repeated 15 times.

Properties of Modified Col–Chi–CS Membrane

Tensile Strength Dumbbell-shaped membrane was prepared and put in the condition (temperature 20 ± 2 °C, relative humidity 65 ± 2 %) for 48 h. The tensile strength was determined on a tensile testing machine with a velocity of 10 mm/min; each sample was tested five times and the average value calculated.

Degradation Test Vacuum-dried membrane samples (10 × 25 mm) were stored in test tubes after being precisely weighed. The samples were then soaked with 5 ml lysozyme degradation solution (1.0 mg/ml PBS). After putting the sealed test tubes in a bath rotator (fixed rotation speed 80 rpm), samples were withdrawn for testing at 1, 2, 3, 5, 8, 12, and 15 days. The degradation solution was replaced every 72 h to maintain enzyme activity. Samples were washed with deionized water and dried to a constant weight. The degree of degradation was characterized by the decrease in weight.

Cytotoxic Test The membrane samples were cut into small samples of 1 cm^2. Extracted fluid was withdrawn daily after soaking the samples in 4 ml of culture medium at 37 °C for 3 days. Fibroblast cells were cultured in extracted fluid for 3 days, then tested by MTT (3-(4,5-dimethylthiazol-2-yl)-2,5-diphenyltetrazolium bromide) and observed via optical microscope.

Cell Culture The Col–Chi–CS membrane was cut and placed into a 24-well culture plate. Fibroblast suspension (5 × 10^4 cells/ml) was then placed on the membrane and cultured under 37 °C 5 % CO_2 for 2 h. Three milliliters of culture medium was added, and it was allowed to sit for another 3 days. The results were observed by SEM.

Wound Healing Test Twenty New Zealand rabbits were selected, 10 each male and female, weighing 1.5–2.0 kg. General anesthetized rabbits were dehaired and sterilized on two sides of their backs to permit full-layer wounds 3 × 4 cm in size. In the experimental group, the wounds on the left side were covered with Col–Chi–CS membrane; in the control group, they were not. Then all the wounds were swabbed with oil and stitched. After 1 week, the dressing was removed. Each rabbit was injected with veterinary-quality ampicillin trihydrate 0.25 g for 3 days. We then recorded the amount of bleeding, the duration of the healing period, and the appearance of the wounds.

Results and Discussion

XPS Analysis

The composite membrane was prepared by introducing CS during EDC modification. To find out whether the CS had combined with the membrane or whether it was easily washed away during the follow-up processes (to ensure that the Col–Chi–CS membrane was firmly formed), XPS was performed to analyze elements of the membrane surface (Fig. 1). There was an S-element peak at 167.8 eV in the Col–Chi–CS membrane, while there was only a signal peak in the Col–Chi membrane (Fig. 2). We speculate that CS bonded with the Col–Chi membrane. The element content of the two different membranes is listed in Table 1. Although there was 0.2 % S in the Col–Chi–CS membrane, there was none detected in the Col–Chi membrane; in addition, an increase in O and a decrease in N and C were also measured. CS belongs to the polysaccharides, which contain large amount of SO_4 and –OH, leading to the appearance of S and the increase in O detected in the Col–Chi–CS membrane. This element change further clarified the existence of CS.

The C1s peak was fitted and separated into several peaks: C–H, C–OH, C–NH_2, and C=O (Fig. 3; Table 2). The Col–Chi–CS membrane has more C–OH and C–NH_2 polar groups and fewer C–H nonpolar groups than the Col–Chi membrane. The change in the content of the polar and nonpolar groups indicated a change in the hydrophilic and hydrophobic abilities of the membrane surface. Compared with the Col–Chi membrane, the Col–Chi–CS membrane maintained a higher hydrophilic but a lower hydrophobic performance, which simultaneously affected the cell adhesion and biocompatibility, resulting in a marked application difference.

Free Amino and Modification Index Analysis

CS contains large amounts of hydroxide radicals, carboxyl groups, sulfate radicals, and so on. During EDC modification, an amino link or ester bond was generated by the reaction of the carboxyl group from CS with a hydroxide radical or an amino group from the composite membrane, respectively. A hydrogen or ester bond was generated by the reaction of the hydroxide radical of CS with the amino group or the carboxyl group from the composite membrane, respectively. As a bridge, not only were the active groups of the binary membrane (Col–Chi) cross-linked with CS, but also the distant nonactive groups, thus improving its performance. The ternary membrane (Col–Chi–CS) cross-link reaction degree was determined by the analysis of free amino content. At the same condition of

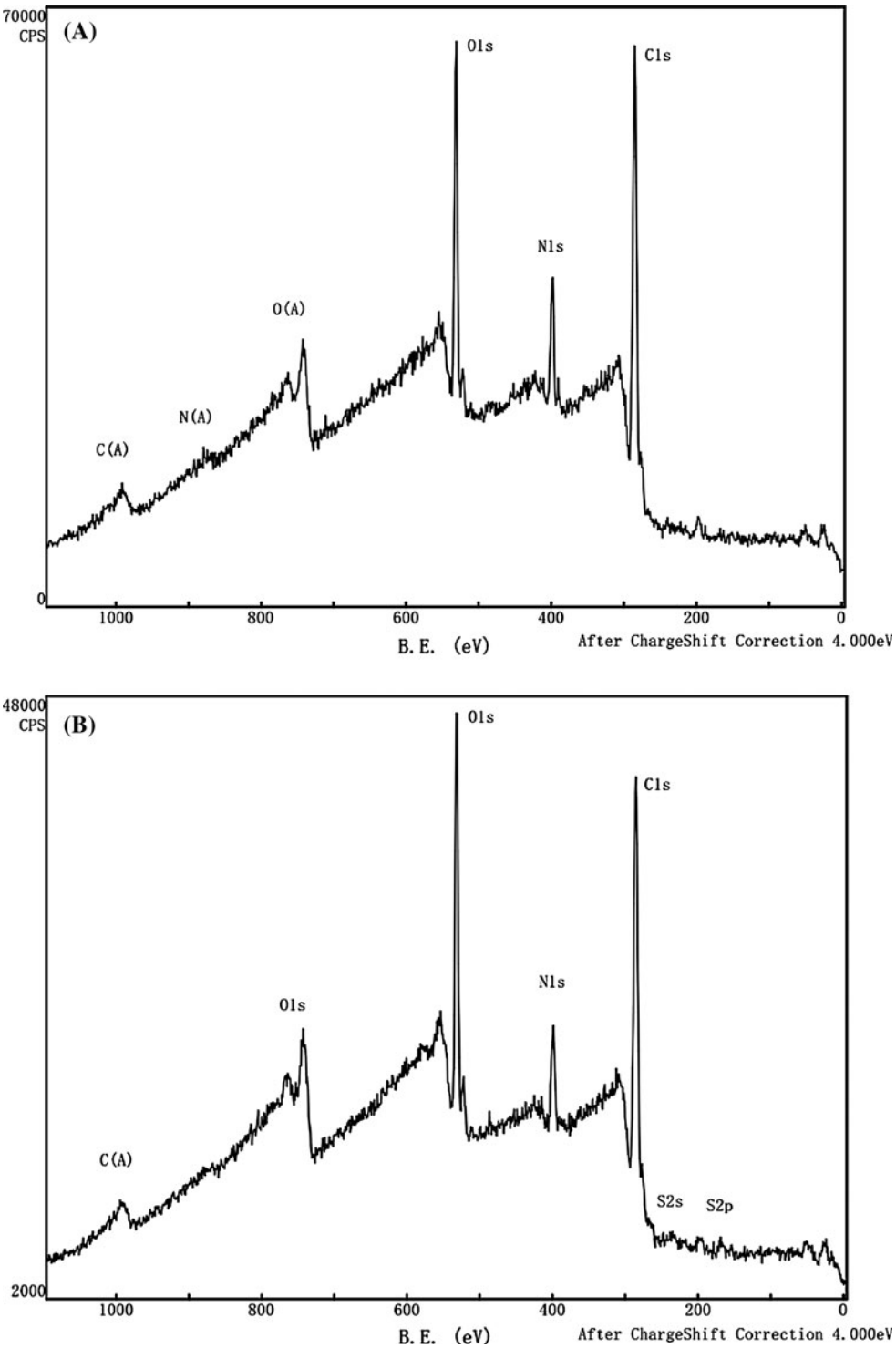

Fig. 1 XPS of composite membrane. **a** Col–Chi membrane. **b** Col–Chi–CS membrane

EDC modification compared with two-component membrane, the cross-linking index of the three-component membrane was larger, which, as a result of the bridge function of CS combined the distant active groups, accordingly improved the degree of the cross-link reaction (Fig. 4).

FTIR Analysis

Figure 5 shows the FTIR curves of the Col–Chi and Col–Chi–CS membranes. A blueshift occurred in the Col–Chi–CS membrane (amide 1,658.80 cm^{-1}) compared to that of Col–Chi membrane (1,658.62 cm^{-1}). The peak at around

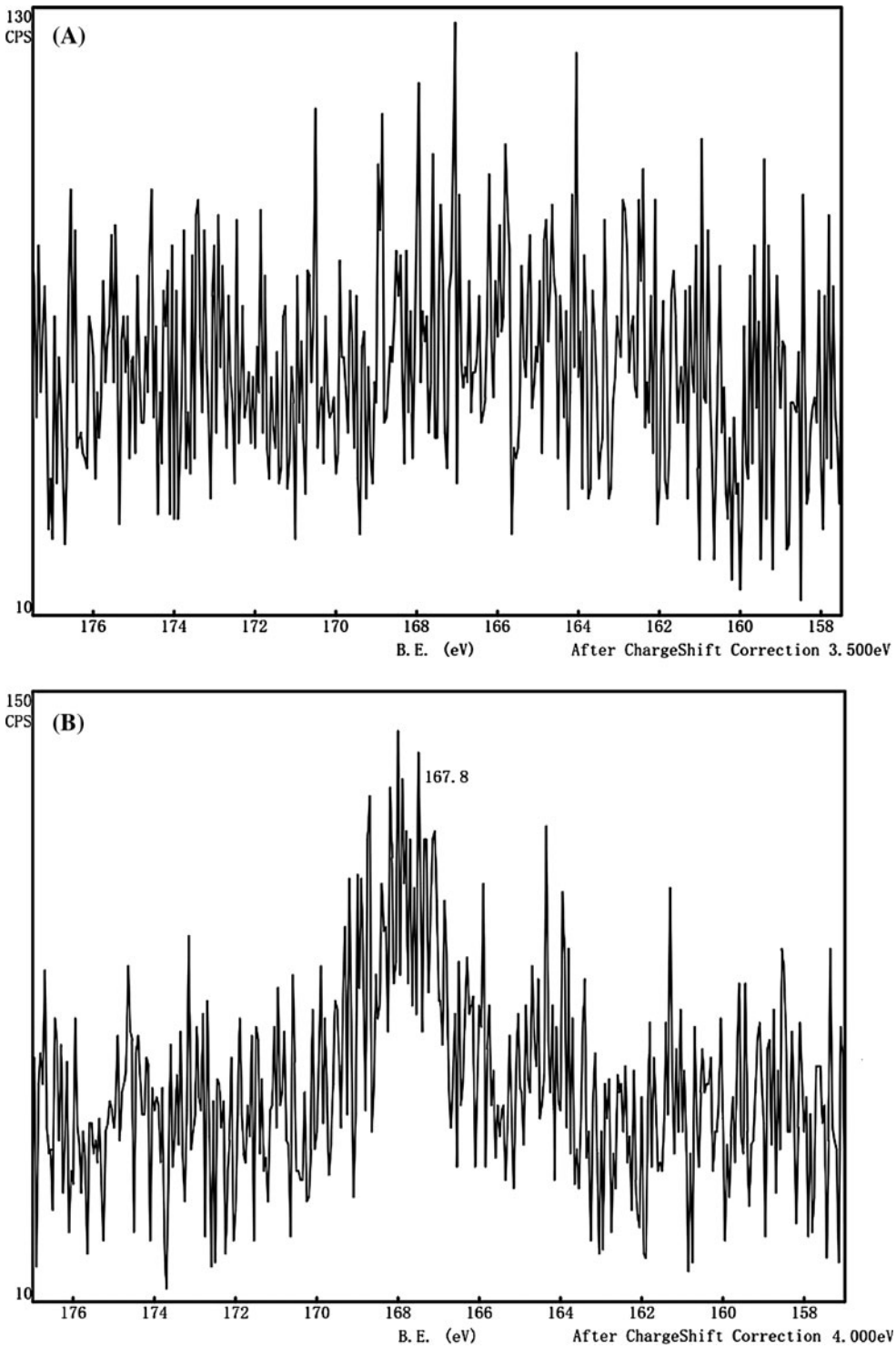

Fig. 2 S energy spectra of XPS. **a** Col–Chi membrane. **b** Col–Chi–CS membrane

Table 1 Content of surface element of Col-based membrane

	C	O	N	S
Col–Chi	66.9	22.8	10.3	0
Col–Chi–CS	65.2	25.9	8.7	0.2

620 cm^{-1} was attributed to an out-of-plane deformation vibration of the primary amine. The *D* value between intensities of deformation vibration and amide to some extent reflects the content of the primary amine in these materials. According to our calculations, the *D* values of

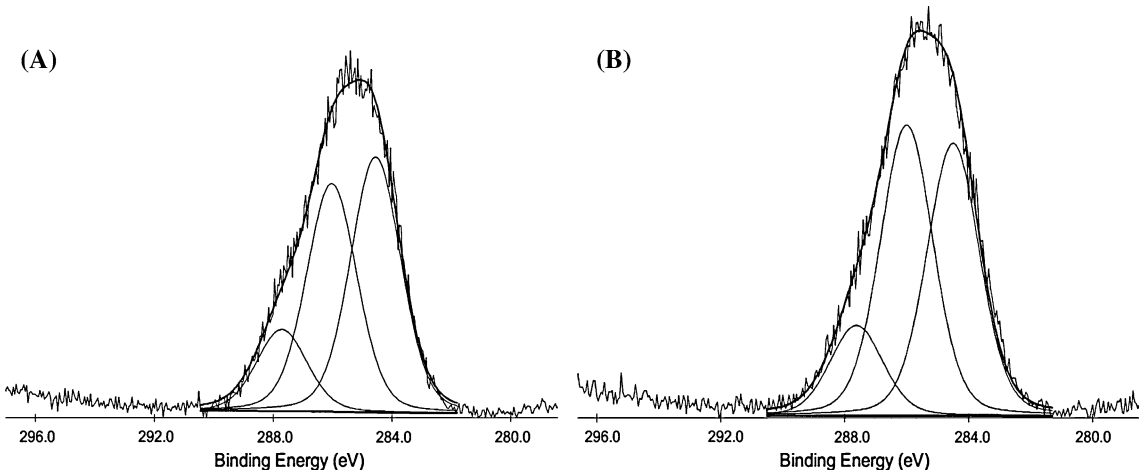

Fig. 3 Fitting *curves* of C1s energy spectrum of blended membrane surfaces. **a** Col–Chi membrane. **b** Col–Chi–CS membrane

Table 2 Content of C1s energy spectra (%)

	C–H	C–OH, C–NH_2	C=O
Col–Chi	45.20	40.36	14.44
Col–Chi–CS	41.68	44.51	13.81

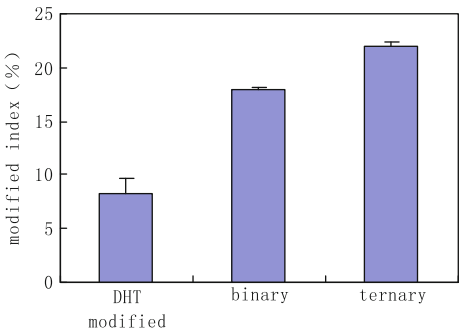

Fig. 4 Contrast of cross-linking index of modified Col-based membrane

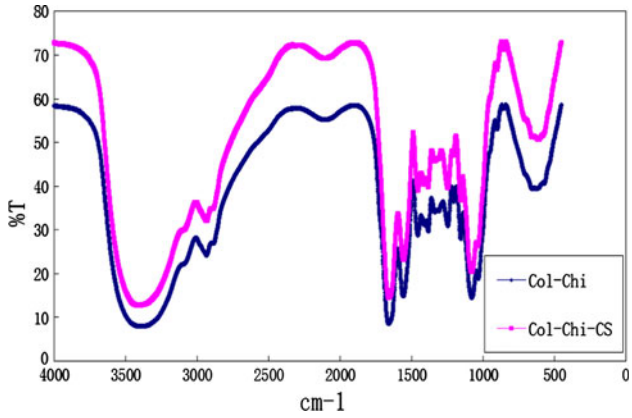

Fig. 5 FTIR spectra of Col-based membrane

the Col–Chi and Col–Chi–CS membranes were 30.89 and 36.60, respectively. Compared to the Col–Chi membrane, the higher *D* value of the Col–Chi–CS membrane indicated a lower content of primary amine. It was thus clear that the number of unreacted amino groups of the Col–Chi–CS membrane was less than that of the Col–Chi membrane, which suggested that the degree of cross-linking of the former was much higher than that of the latter. This finding was in agreement with the measured results of the free amino group.

Tensile Strength

The tensile strength of EDC modified Col–Chi membrane was 1.06 MPa, while that of the EDC modified Col–Chi–CS membrane was 1.19 MPa, which can account for the higher mechanical strength of three-component membrane. This result was related to the modification index.

Degradation Test

Figure 6 shows the degradation of modified membrane in lysozyme solution. When modified and unmodified membrane are compared, the modified one performed better in degradation. After soaking in the solution for 15 days, the remaining quality of EDC-modified two- and three-component membrane was 89.74 and 93.02 %, respectively, of the initial weight, while it was less than 60 % of that of the unmodified one. These indicate the capability of improving the cross-link degree and the antizymohydrolysis ability of the EDC modification technology. EDC-modified membrane has a superior performance. By introducing CS, the antizymohydrolysis ability of this composite membrane was improved.

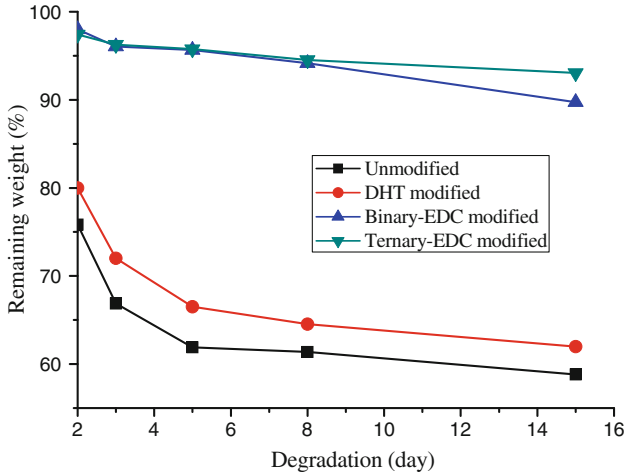

Fig. 6 Degradation of Col-based membrane in lysozyme solution

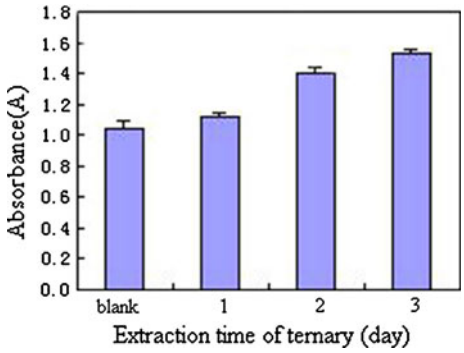

Fig. 7 MTT results of fibroblast culture in extracted solution of Col–Chi–CS membrane

Cytotoxic Test

The cytotoxic test was carried out by culturing fibroblast cells in the fluid extracted from Col–Chi–CS membrane, which contained sustained-release bFGF microspheres, for 1, 2, and 3 days, and a control group; the experimental and control cells were then tested by MTT. More cells were reproduced in the three experimental groups than in the control group (Fig. 7). The cell amount increased with the duration of the extraction period. The extracted fluid was noncytotoxic and promoted cell proliferation. Figure 8 illustrates control and experimental fibroblast cells cultivated for 3 days; cells in the experimental groups grew faster than controls and covered almost the whole culture plate. The reason cell proliferation was promoted may be related to the sustained-release bFGF microspheres. With longer extraction periods, the bFGF amount was enhanced and the cell proliferation rate increased.

Cell Culture

SEM results are shown in Fig. 9 for the self-made bFGF-controlled microsphere-containing Col–Chi–CS membrane cultured for 3 days. The bFGF-controlled microspheres, which were of uniform size, were evenly distributed on the membrane. The three-dimensional structure of membrane was preserved even after soaking for 3 days, which permitted cell proliferation. Figure 10 shows the adhesion growth of the fibroblasts on the membrane, which indicated that the membrane worked well for cell adhesion and growth.

Wound Healing Test

As a holder for cells, membrane based on Col can induce cell proliferation, differentiation, and migration. This membrane is an effective wound healing material that can absorb tissue exudate and adhere to the wound to maintain certain humidity and to avoid mechanical injury and resulting bacterial infection. A novel dressing was created by combining bFGF-controlled microspheres with Col membrane and applied to a rabbit model to observe the wound healing process.

Figure 11 shows the wound reconstruction process. Figure 12 shows the wound covered by composite

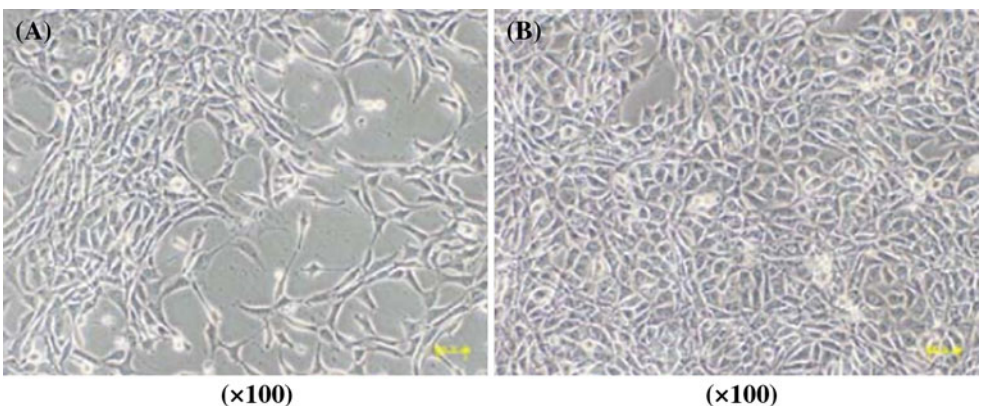

Fig. 8 Fibroblast. **a** Culture medium. **b** Extracted solution of Col–Chi–CS membrane

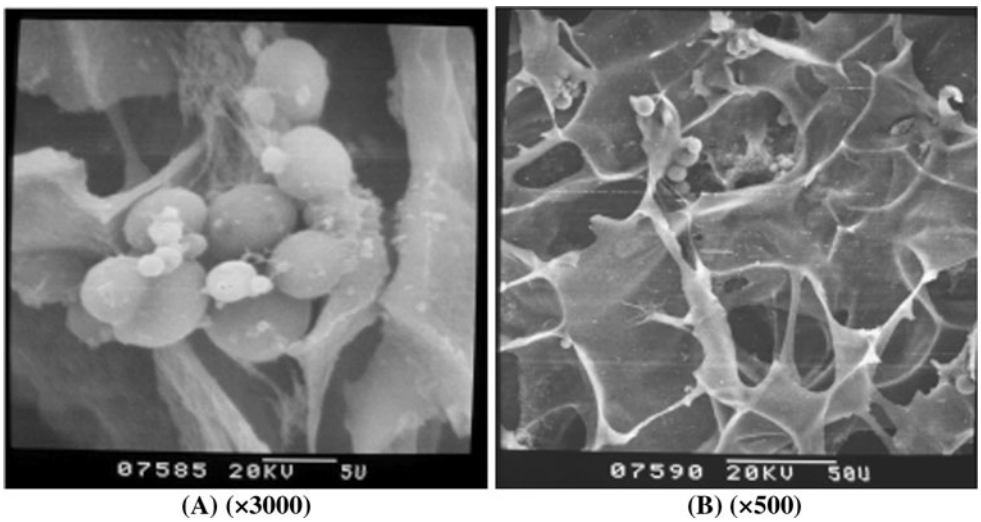

Fig. 9 SEM of Col–Chi–CS membrane impregnated microsphere after 3 days in culture medium

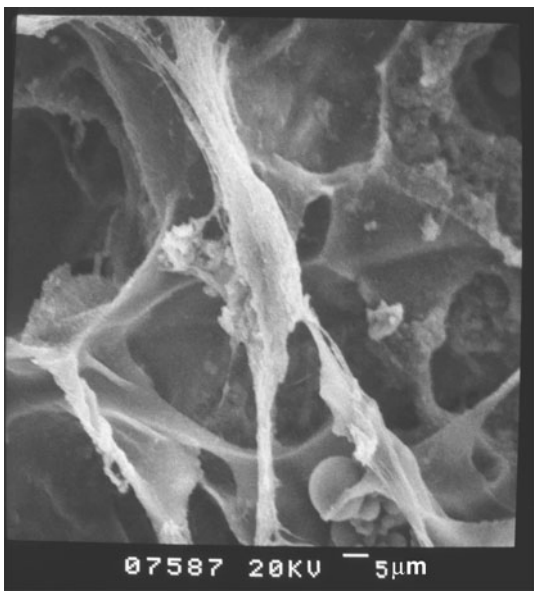

Fig. 10 SEM of fibroblast culture on the Col-based membrane (original magnification, ×3,000)

membrane and an oil swab. After being covered by the composite membrane, tissue exudate and blood were absorbed, and the membrane smoothly adhered to the wound, creating a good microenvironment for the wound healing process. Three days after the wounds were inflicted, the experimental group wound was dry. The wound adhered closely to the membrane, with no adhesion to the paraffin gauze dressings and with no erythema; in addition, no allergy occurred. In the wounds in the control group, on the other hand, tissue exudate and adhesion to the paraffin gauze dressings were observed. Figure 13 illustrates the wound healing of a rabbit 3 weeks after surgery.

Wound healing status and healing are listed in Table 3. There were six cases of bleeding (30 %) in the control group, whereas in the experimental group, there was only one (5 %). There was one case of wound infection in the control group but none in the experimental group. It took 20.76 days of the control group for wound healed but only 18.00 days compared to experimental one. The wounds in the experimental group clearly healed better and faster, and for less cost.

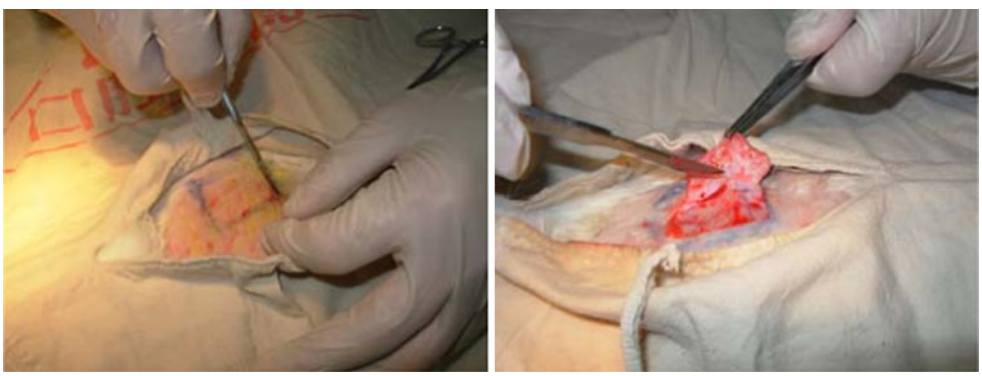

Fig. 11 Establishment of whole-layer skin wound

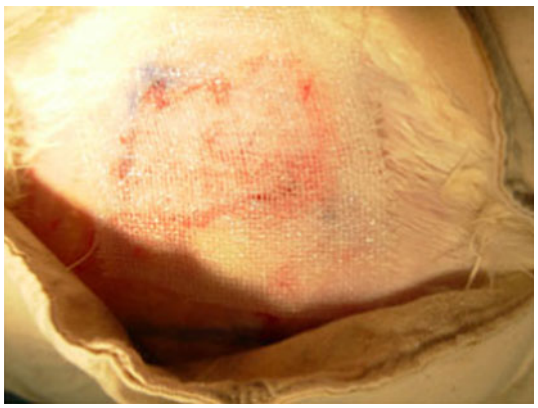

Fig. 12 Wound after covering with repair membrane

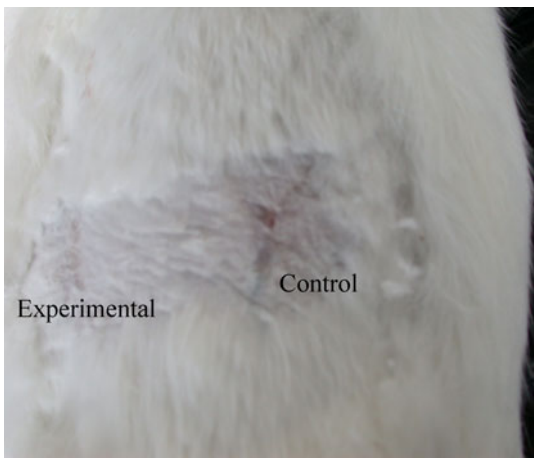

Fig. 13 Wound healing after 3 weeks. The experimental wound is on the *left side* of the rabbit back, and the control wound is on the *right side*. Compared to control wound, which was not fully healed and had a small scab, the experimental wound was entirely healed; regenerated tissue knitted with the surrounding tissue, leaving no scab

Table 3 Observations of wound repairing in rabbits

Wound	Experimental ($n = 10$)	Control ($n = 10$)
Wound bleeding	1	6
Wound with gauze adhesion	0	13
Wound infection	0	1
Average healing time (days)	18.00 ± 1.93	20.73 ± 1.95

The membrane based on Col that we prepared was bonded with histocompatible and biodegradable CS and Chi. Along with cross-linking modified by EDC, the stability and biocompatibility of this composite membrane were improved. We found the novel healing material to be bacteriostatic, hemostatic, and analgesic, and it accelerated the tissue's wound healing abilities.

In this study of Col membrane combined with sustained-release bFGF microspheres, we found that the composite membrane can be used to cover the wound, thus creating a scaffold to assist the migration and proliferation of epidermal cells and granulation tissue. In addition, the wound healing period was markedly shortened, and we found excellent sustained-release function of bFGF microspheres. The primary benefits of this novel composite membrane include protecting the wound, decreasing the amount of exudates, and permitting water-spreading properties. The animal defect model experiment indicated that the membrane based on Col combined with sustained-release bFGF microspheres performs well in terms of wound healing, skin regeneration, hemostasis, antiadhesion, and distinctive knitting abilities.

Conclusions

(1) XPS observation revealed that after EDC modification, CS was firmly bonded in the Col–Chi membrane. Col–Chi–CS membrane of a different polarity was collected.
(2) The modification index of DHT-EDC-modified Col–Chi–CS membrane was higher than that of the Col–Chi membrane, and the tensile strength and degradation of the modified Col–Chi–CS membrane were distinctly higher. The EDC modification technology and the introduction of CS improved the antienzymolysis ability of the composite membrane.
(3) Fibroblast culture experiments indicated the membrane was nontoxic and good for cell proliferation and adhesion.
(4) Wound healing tests suggest the feasibility of promoting the wound healing process and tissue regeneration, as well as promoting hemostasis and preventing postoperative adhesion abilities.

Acknowledgments This research was supported by Science and Technology Bureau of Chengdu (Grant 10GGYB345SW-023).

References

Bissell DM (2001) Chronic liver injury, TGF-beta, and cancer. Exp Mol Med 33:179–190

Braga-Vilela AS, Pimentel ER, Marangoni S, Toyama MH, de Campos Vidal B (2008) Extracellular matrix of porcine pericardium: biochemistry and collagen architecture. J Membr Biol 221:15–25

Chen RN, Wang GM, Chen CH, Ho HO, Sheu MT (2006) Development of N,O-(carboxymethyl)chitosan/collagen matrixes as a wound dressing. Biomacromolecules 7:1058–1064

Francis Suh JK, Howard WT (2000) Application of chitosan-based polysaccharide biomaterials in cartilage tissue engineering: a review. Biomaterials 21:2589–2598

Kirker KR, Luo Y, Nielson JH, Shelby J, Prestwich GD (2002) Glycosaminoglycan hydrogel films as bio-interactive dressings for wound healing. Biomaterials 23:3661–3671

Lee JE, Kim KE, Kwon IC, Ahn HJ, Lee SH, Cho H, Kim HJ, Seong SC, Lee MC (2004) Effects of the controlled-released TGF-β1 from chitosan microspheres on chondrocytes cultured in a collagen/chitosan/glycosaminoglycan scaffold. Biomaterials 25: 4163–4173

Ma L, Gao C, Mao Z, Zhou J, Shen J (2004) Enhanced biological stability of collagen porous scaffolds by using amino acids as novel cross-linking bridges. Biomaterials 25:2997–3004

Mi FL, Shyu SS, Wu YB, Lee ST, Shyong JY, Huang RN (2001) Fabrication and characterization of a sponge-like asymmetric chitosan membrane as a wound dressing. Biomaterials 22:165–173

Midwood KS (2004) Tissue repair and the dynamics of the extracellular matrix. Int J Biochem Cell Biol 36:1031–1037

Pieper JS, van Wachem PB, van Luyn MJA, Brouwer LA, Hafmans T, Veerkamp JH, van Kuppevelt TH (2000) Attachment of glycosaminoglycans to collagenous matrices modulates the tissue response in rats. Biomaterials 21:1689–1699

Rho KS, Jeong L, Lee G, Seo BM, Park YJ, Hong SD, Roh S, Cho JJ, Park WH, Min BM (2006) Electrospinning of collagen nanofibers: effects on the behavior of normal human keratinocytes and early-stage wound healing. Biomaterials 27:1452–1461

Taravel MN, Domard A (1996) Collagen and its interactions with chitosan, III: some biological and mechanical properties. Biomaterials 17:451–455

Tomihata K, Ikada Y (1997) In vitro and in vivo degradation of films of chitin and its deacetylated derivatives. Biomaterials 18: 567–573

Wang K, Dan N, Lin H, Hu Y, Yi Q, Dan W (2011) Preparation and characterization of CS/PVA/SiO_2 composite membrane. In: China and Finland workshop on biomanufacturing and evaluation techniques, pp 304–308

Ye Y, Dan W, Zeng R, Lin H, Dan N, Guan L, Mi Z (2007a) Miscibility studies on the blends of collagen/chitosan by dilute solution viscometry. Eur Polym 43:2066–2071

Ye Y, Lin H, Zeng R, Dan N, Mi Z, Wang K, Dan W (2007b) The preparation and characterization of collagen–chitosan composite membranes. Funct Mater 38:1843–1847

J Membrane Biol (2012) 245:717–730
DOI 10.1007/s00232-012-9452-4

Ser/Thr Motifs in Transmembrane Proteins: Conservation Patterns and Effects on Local Protein Structure and Dynamics

Coral del Val · Stephen H. White · Ana-Nicoleta Bondar

Received: 5 February 2012 / Accepted: 4 June 2012 / Published online: 27 July 2012

Abstract We combined systematic bioinformatics analyses and molecular dynamics simulations to assess the conservation patterns of Ser and Thr motifs in membrane proteins, and the effect of such motifs on the structure and dynamics of α-helical transmembrane (TM) segments. We find that Ser/Thr motifs are often present in β-barrel TM proteins. At least one Ser/Thr motif is present in almost half of the sequences of α-helical proteins analyzed here. The extensive bioinformatics analyses and inspection of protein structures led to the identification of molecular transporters with noticeable numbers of Ser/Thr motifs within the TM region. Given the energetic penalty for burying multiple Ser/Thr groups in the membrane hydrophobic core, the observation of transporters with multiple membrane-embedded Ser/Thr is intriguing and raises the question of how the presence of multiple Ser/Thr affects protein local structure and dynamics. Molecular dynamics simulations of four different Ser-containing model TM peptides indicate that backbone hydrogen bonding of membrane-buried Ser/Thr hydroxyl groups can significantly change the local structure and dynamics of the helix. Ser groups located close to the membrane interface can hydrogen bond to solvent water instead of protein backbone, leading to an enhanced local solvation of the peptide.

Keywords Bioinformatics · Molecular dynamics · Molecular transporters and receptors · Ser/Thr motifs · Transmembrane proteins

Electronic supplementary material The online version of this article (doi:10.1007/s00232-012-9452-4) contains supplementary material, which is available to authorized users.

C. del Val (✉)
Department of Computer Science and Artificial Intelligence, University of Granada, 18071 Granada, Spain
e-mail: C.DelVal@decsai.ugr.es

C. del Val
CITIC-UGR, Centro de Investigación en Tecnologías de la Información y de las Comunicaciones de la Universidad de Granada, 18071 Granada, Spain

S. H. White · A.-N. Bondar
Department of Physiology and Biophysics, University of California, Irvine, Medical Sciences I, D-374, Irvine, CA 92697-4560, USA

Present Address:
A.-N. Bondar (✉)
Theoretical Molecular Biophysics, Department of Physics, Freie Universität Berlin, Arnimallee 14, Berlin-Dahlem, DE 14195, Germany
e-mail: nbondar@zedat.fu-berlin.de

Hydrophilic amino acids of transmembrane (TM) proteins can have important structural and functional roles. For example, hydrophilic amino acids can contribute to the association of TM segments via hydrogen-bonding or salt-bridging interactions (Hermansson and von Heijne 2003; Zhou et al. 2000, 2001), influence the boundary of the insertion of membrane proteins into the lipid bilayer (Krishnakumar and London 2007), reduce (via salt bridging) the free energy of membrane partitioning of a helix (Chin and von Heijne 2000), and can influence ligand binding (Junne et al. 2007) or participate in chemical reactions of the TM protein (Metz et al. 1991). Ser and Thr groups are distinguished from other polar side chains by their ability to compete with the backbone groups for intrahelical hydrogen bonding. Such hydrogen bonding may have important consequences for the structure and function of the membrane protein. To understand the conservation patterns of Ser/Thr groups in membrane proteins, and the effect of Ser/Thr groups on the local protein structure and

dynamics, here we combined extensive bioinformatics analyses with molecular dynamics simulations.

Regardless of whether the residue is buried or solvent-accessible, the side chains of the polar amino acids Ser and Thr have a high propensity for intrahelical hydrogen bonding (Gray and Matthews 1984); this intrahelical hydrogen bonding can be either with a backbone amide or with a backbone carbonyl group (Gray and Matthews 1984; Presta and Rose 1988; Richardson and Richardson 1988). Hydrogen bonding to the backbone amide is observed when Ser/Thr are located in the position immediately preceding the N terminus of α-helices (N-cap) (Doig et al. 1997; Kumar and Bansal 1998; Vijayakumar et al. 1999) and in membrane proteins (Eilers et al. 2000).

The interior location preferred by Ser/Thr in membrane proteins (Pilpel et al. 1999) was associated with the high packing values of these amino acids (Eilers et al. 2000); statistical analysis suggested that Ser/Thr whose hydroxyl groups hydrogen bond to the backbone of the TM helix can induce a small local bending of the helix (Ballesteros et al. 2000). When associated with Pro in the TM segment sequence, a Ser/Thr can modulate significantly the structural deformation of the helix induced by Pro (Deupi et al. 2004). The preference of Ser/Thr amino acids for intrahelical hydrogen bonding with the backbone could also be responsible for the lack of a significant contribution of Ser/Thr to the association of TM segments (Zhou et al. 2001). But, when specific Ser/Thr motifs are present at the interface of TM helices, they can drive oligomerization of the helices via interhelical hydrogen bonding (Dawson et al. 2002).

The competition with backbone groups for hydrogen bonding may be related to the low propensity of these amino acids in the middle of α-helices (Vijayakumar et al. 1999). Nevertheless, the frequency of occurrence of Thr/Ser at buried sites within TM segments of helical is higher than that of other polar and charged amino acids (Gratkowski et al. 2001). At buried sites in proteins, Ser/Thr tend to hydrogen bond (Worth and Blundel 2008).

Given the expectation that Ser/Thr are relatively infrequent in a TM α-helical segment, we were intrigued by our observations that multiple Ser/Thr are present within TM segments of membrane proteins with different function, particularly in functionally important regions of several molecular transporters and receptors. In what follows we discuss briefly several such examples.

The analysis of sequences of retinal proteins indicates the presence of a TT motif at the heart of the protein; the TT motif is largely conserved as TT, ST, or TC (Nack et al. 2012). In the bacteriorhodopsin proton pump the two Thr are present at position 89 and 90 (i.e., close to the primary proton acceptor D85), and the Thr90Ala mutation has profound effects on the reaction cycle (Perálvarez et al. 2001). G-protein-coupled receptors squid and bovine rhodopsin contain several Ser/Thr motifs along the TM segments—for example, $\mathbf{S}_{79}$DF$\mathbf{T}_{82}$, $\mathbf{S}_{122}$IM$\mathbf{T}_{125}$ and $\mathbf{S}_{263}$IVIV**S**QFL**S**W$\mathbf{S}_{275}$ in squid rhodopsin (pdb 2Z73, Murakami and Kouyama 2008), and $\mathbf{T}_{58}$LIV$\mathbf{T}_{62}$, $\mathbf{T}_{92}$**TT**LY$\mathbf{TS}_{98}$, and $T_{297}S_{298}$ in bovine rhodopsin (pdb 1U19, Okada et al. 2004). S122 of squid rhodopsin is part of the hydrogen-bonded network that may be involved in signal relay (Murakami and Kouyama 2008, Jardon-Valadez et al. 2010), and bovine rhodopsin T94 is involved in controlling the protonation state of the retinal Schiff base (Buss et al. 2003). The conserved squid rhodopsin Y315 makes potentially important hydrogen bonds with water (Sugihara et al. 2011); Y315 is located on the cytoplasmic side of a TM helix, near the loop segment $\mathbf{S}_{316}$V$\mathbf{S}_{318}$.

In the GlpG intramembrane protease, helix TM3 that interconnects distant hydrogen-bonding clusters contains the sequence $\mathbf{S}_{171}$GKLIVI**T**LI**S**AL$\mathbf{S}_{185}$ (Bondar et al. 2009); another intramembrane protease, FlaK, also has a TM helix that contains three closely spaced Thr/Ser groups ($\mathbf{T}_{710}$L**S**YLV$\mathbf{T}_{716}$) (pdb 3S0X, Hu et al. 2011). In the *Thermotoga maritima* SecY TM7, a helix thought to be critical for the translocon function (Plath et al. 1998; van den Berg et al. 2004; Du Plessis et al. 2009), contains the sequence $\mathbf{S}_{277}$AIV**S**IP**S**AIA**S**I$\mathbf{T}_{290}$; the hydroxyl groups of the four Ser amino acids and of the Thr hydrogen bond to backbone carbonyl groups of other TM7 amino acids (Bondar et al. 2010). The corresponding region of the *Escherichia coli* translocon contains three Ser and one Thr groups in the sequence $\mathbf{S}_{281}\mathbf{S}_{282}$IILFPA$\mathbf{T}_{288}IA\mathbf{S}_{291}$ (Bondar et al. 2010). Mutation of the *E. coli* S282 to Arg leads to the *prl*A401 phenotype (Osborne and Silhawy 1993) thought to be characterized by the destabilization of the closed state of the translocon (Smith et al. 2005); adding one more Thr that replaces I290 reduced export of staphylokinase by the translocon (Sako 1991; Osborne and Silhavy 1993). Arrangements of Ser/Thr separated by two or three residues, with the Ser/Thr side chains largely on one side of the TM helix, are also observed in the P-type proton pump AHA2 from *Arabidopsis thaliana*—$\mathbf{T}_{686}$IM$\mathbf{T}_{689}$, $\mathbf{S}_{762}$II$\mathbf{S}_{765}$, or $\mathbf{S}_{827}$IV$\mathbf{T}_{830}$ (pdb 3B8C, Pedersen et al. 2007); the $\mathbf{T}_{686}$IM$\mathbf{T}_{689}$ segment within TM6 is very close to the primary proton donor/acceptor D684. The membrane-embedded region of the α subunit of the nicotinic acethylcholine receptor consists of four helices, each with at least one Ser/Thr motif; helix M2 contains three Thr and six Ser groups (Unwin 2005). Finally, the TM segment of the amyloid precursor protein has two Thr amino acids separated by two VI pairs, the N-terminal Thr being at the γ42 cleavage site (see e.g., Munter et al. 2007).

Because Thr/Ser have positive free energies of insertion in the membrane hydrophobic core (Hessa et al. 2005; Moon and Fleming 2011), and weakly inhibit membrane insertion (Xie et al. 2007)—although the context of the amino acid in the

TM segment is also very important for its recognition by the protein translocon (Hessa et al. 2005), it is indeed plausible, as some of the examples above may suggest, that the presence of Ser/Thr motifs in TM segments may be important for the structural and/or functional role of the protein.

We revisit here the presence of Ser/Thr amino acids in TM proteins and their effect on the local structure and dynamics of model TM protein segments. We performed systematic bioinformatics analyses of a data set consisting of 339 unique sequences of protein chains that contain α-helical and β-barrel TM segments. We find that, within the data sets analyzed here, about half of the sequences of the α-helical membrane proteins have at least one Ser/Thr motif, although sequences containing a large number of motifs are a minority. In the α-helical membrane proteins, Ser/Thr motifs can be present not only along the TM helices, but also in solvent-exposed regions of the protein—which may contain β-strands. On the basis of the bioinformatics analyses and visual inspection of protein structures we could identify membrane transporters that have a remarkable number of Ser/Thr groups along TM helices (see examples in Fig. S1). To assess how various Ser/Thr motifs affect the local structure and dynamics of α-helical TM segments, we carried out molecular dynamics (MD) simulations of four model single-spanning α-helical TM segments, including TM7 of *T. maritima* SecY. The MD simulations indicate that presence of Ser/Thr motifs can affect the local structure, dynamics, and solvation of TM helices. We thus conclude that the presence of multiple Ser/Thr motifs along the TM helices of a protein, although a relatively infrequent event, likely has significant implications for the structure and dynamics of the protein.

Methods

Bioinformatics Analyses

TM protein sequence chains were selected from the Protein Data Bank of Transmembrane Proteins (PDB_TM, Tusnády et al. 2005a), which is based on scanning all PDB entries with the TMDET algorithm (Tusnády et al. 2005b). Only nonredundant sequences were selected from the complete PDB_TM data set. The sequences are classified into two subsets: chains containing α-helical TM segments, and chains containing β-barrel TM segments; these two data sets are denoted here as, respectively, data-α (291 unique sequences) and data-β (48 unique sequences).

For the protein sequences in the both data-α and data-β sets, we analyzed the presence of the following specific motifs (denoted in what follows as Signatures) containing Ser/Thr amino acids: SS, ST, TT, SxxS, SxxxS, SxxT, SxxxT, TxxT, and TxxxT, where "x" denotes any amino acid. For the Signature analysis of the protein sequences, we used the program Preg (Rice et al. 2000). The search for Signatures included the entire protein chain—that is, regions of the protein that may not be within the lipid membrane region are also included in the search.

The statistical analysis of the sequences was performed using the R software (R Development Core Team 2010). Using R, we first tested the normality of the data-α and data-β samples using the Shapiro–Wilk normality test (Shapiro and Wilk 1965; Royston and Remark 1995). To compare the results for the different Signatures in data-α and data-β, we used the nonparametric (i.e., distribution-free) statistical hypothesis Mann–Whitney *U*-test, also called the Wilcoxon rank-sum test (Mann and Whitney 1947).

To cluster the data-α and data-β Sequences according to the number and type of Signatures, we proceeded as follows. The results of the Signature analysis described above were used to derive the Signature number information per sequence (that is, the number of SS, ST, TT, SxxS, SxxS, TxxT, TxxxT, SxxT and SxxxT per sequence) for each data set. For each Signature, all counts were normalized between 0 (no Signature) and 1 (the highest number of Signatures in each column). The Signature data were analyzed using unsupervised cluster learning methods. We used two distinct clustering methods: hierarchical clustering (Mitchell 1997; Jain et al. 1999), and k-means clustering (MacQueen 1967). The hierarchical clustering was performed using the Euclidean distance and the complete linkage approach. The number of clusters was calculated using the inconsistency threshold and coefficient (Bezdek and Pal 1998) as validity indices. The Euclidian space was used for the k-means clustering. In order to reduce the sensitivity of the algorithm to the initial random cluster centroids, we repeated each of the k-means runs 10 times and chose the best solution. We used the silhouette method (Rousseeuw 1987) to estimate the number of clusters. The potentially optimal number of k-means clusters was then chosen in order to maximize the average distance between silhouette means. Unless indicated otherwise, all functions used are part of the Matlab Statistics Toolbox (Jones 1993).

Molecular Dynamics Simulations

We investigated the structure and dynamics of four model peptides that contain different types and numbers of Ser/Thr Signatures (Table 1). The peptide in Sim1 consists of the seventh TM helix of the SecYEG protein translocon from *T. maritima* (Zimmer et al. 2008), and a fragment of the loop that connects the seventh and eighth TM helices of the *T. maritima* translocon (for a total of 27 amino acids); there are four Ser groups and one Thr in this peptide, separated by one, two, or three amino acids that are hydrophobic (Ile, Phe, or Val), or mildly hydrophobic (Ala). Sim2 and Sim3

Table 1 Summary of the MD simulations performed

Simulation	Peptide sequence	Simulation length (ns)[a]	Average RMSD (Å)[b]
Sim1	$VIPIIPAS_{277}AIVS_{281}IPS_{284}A$ $IAS_{288}IT_{290}AAET_{294}LK$	34	2.7 ± 0.1[c]
Sim2	$(L)_3$-$(SL)_2$-$(L)_{13}$	49	2.0 ± 0.1
Sim3	$(L)_3$-$(SL)_4$-$(L)_9$	34	1.8 ± 0.1
Sim4	L-$(SLL)_4$-$(L)_7$	34	1.8 ± 0.1

[a] The simulation length denotes the length of the trajectory without any constraints

[b] The average RMSD and standard deviation values were computed from the last 20 ns of the trajectory without constraints (2000 frames). Time series of the RMSD values computed from Sim1–Sim4 are provided in Fig. S10

[c] For the TM helical segment of the peptide in Sim1, the average RMSD is 1.3 ± 0.2 Å (see also Fig. S2A)

are on peptides that contain two (Sim2) or four (Sim3) SerLeu stretches. In Sim4 we consider a model peptide that has four Ser groups within three SLLS repeats. The sequences of all peptides used in the MD simulations are given in Table 1. The simulation systems contained the TM peptide embedded in the center of hydrated palmitoyloleoyl phosphatidylethanolamine (POPE) hydrated lipid membrane, for a total of ~72,600 atoms (~280 lipid molecules, and ~12670 water molecules).

Coordinates for the peptide in Sim1 were taken from the crystal structure of Zimmer et al. (2008). The helical model peptides investigated in Sim2–Sim4 were constructed using the CHARMM software (Brooks et al. 1983). The protonatable amino acid residues in Sim1 were considered in their standard protonation states (Glu—negatively charged, and Lys—positively charged).

MD simulations were performed using the NAMD software (Kalé et al. 1999; Phillips et al. 2005) with the CHARMM22 force field for the protein atoms (MacKerell et al. 1998), CHARMM27 for lipids (Feller and MacKerell 2000), and the TIP3P model for the water molecules (Jorgensen et al. 1983). We cut off the short-range real-space interactions at 12 Å using a switching function between 8 and 12 Å. The smooth particle mesh Ewald summation (Darden et al. 1993; Essmann et al. 1995) was used to compute the Coulombic interactions. To maintain a constant temperature of 310 K and the pressure at 1 barr we used a Langevin dynamics scheme and a Nosé-Hoover Langevin piston (Feller et al. 1995; Martyna et al. 1994).

In the initial stages of the MD simulation the system was subject to weak harmonic constraints, as follows. During minimization, heating, and the first 1.5 ns of the equilibration, we used harmonic constraints of 5 kcal mol^{-1} $Å^{-2}$ for the peptide atoms, and 2 kcal mol^{-1} $Å^{-2}$ for the lipid and water molecule atoms. The constraints on the lipid atoms were then switched off, and we continued with 1 ns of equilibration with the constraints on the peptide and water atoms unchanged. The constraints on the peptide atoms were set to 2 kcal mol^{-1} $Å^{-2}$ for the subsequent 1 ns of the equilibration. We then switched off the constraints on the peptide, and continued the equilibration with a constraint of 2 kcal mol^{-1} $Å^{-2}$ on the water atoms only. All harmonic constraints were switched off for the remaining part of the simulations.

During the equilibration with harmonic constraints, and for the first 1 ns of the MD simulation without constraints, we used an integration step of 1 fs. For the remaining part of the simulation we used the reversible multiple time-step algorithm (Grubmüller et al. 1991; Tuckerman and Berne 1992) with time steps of 1 fs for the bonded forces, 2 fs for the short-range nonbonded forces, and 4 fs for the long-range electrostatic forces. The lengths of the bonds to hydrogen atoms were constrained using SHAKE (Ryckaert et al. 1977).

We used VMD (Humphrey et al. 1996) for molecular graphics, inspection of selected structures (e.g., Fig. S1), and trajectory analysis.

Results

Bioinformatics Analysis of the Sequences of TM Proteins

The statistical analysis of the sequences showed that they mostly did not follow a normal distribution; this made necessary the use of nonparametric tests to address the differences in the number of Signatures in data-α and data-β. The nonparametric tests showed significant differences in the number of Signatures appearing in data-α and data-β when using the Wilcoxon rank-sum test (Table 2, Figs. 1, S2–S4). The meaning of the box plots is illustrated in Fig. 1a. A summary of the statistical analyses of the sequences is given in Fig. S4. The Shapiro test is summarized in Fig. S5.

On average, most proteins from data-β contain Ser/Thr Signatures (Table 2, Figs. S2 and S3). Only 15–25 % of these sequences do not have any Signature (Table 2). We

Table 2 Summary of the percentage of data-α and data-β sequences that contain given numbers of specific Signatures [a]

Motif	No. of Signatures					
	0	1	2	3	4	5
Data-α						
SS	47.4	23	13.4	8.9	1.7	3.1
SxxS	55	22	9	8	4	1
SxxxS	45	29	13	7	3	1
ST	52.9	25.1	12	4.8	3.1	0.7
SxxT	49	22	17	7	3	1
SxxxT	58	23	12	4	2	1
TT	55.3	25.1	13.1	3.8	0.3	0.7
TxxT	53	30	11	4	1	1
TxxxT	57	25	9	6	2	0
Data-β						
SS	5	16	11	23	23	9
SxxS	20	25	35	12	2	4
SxxxS	23	21	15	9	8	8
ST	7	21	16	12	21	15
SxxT	19	25	17	21	14	2
SxxxT	15	21	29	6	13	8
TT	12	12	19	14	11	14
TxxT	25	31	6	15	11	4
TxxxT	19	21	13	21	8	6

[a] For a graphical representation of the Signature analysis here summarized, and for further details, see Figs. S2 and S3

note significant differences between the distributions of Ser/Thr Signatures separated by two amino acids. Two SxxS Signatures are present in a large part of the sample (35 %), whereas TxxT is present in just 6 %; the presence of SxxT has an intermediate value of 17 % (Table 2; Fig. S3B, E, H).

The number of Signatures in data-α is significantly smaller than in data-β (Fig. 1). In data-α SxxxS (55 %) and SxxT (51 %) remain prevalent, although most often just one Signature is present (Fig. S2C, E); TxxT, SxxxT, TxxxT, and SxxS are found in, respectively, 47, 42, 43, and 45 % of the sequences (Table 2; Fig. S2H, F, I, B).

For a certain Signature, the amino acid sequence encompassed by Ser/Thr can be different for the two classes of TM proteins sequences considered here. Whereas in data-α SxxxS appears most often as SLxxS or SVxxS—that is, with a bulky hydrophobic amino acid (Fig. S6g–i), in data-β the preferred SxxxS sequences are SYxxS and SAxxS (Fig. S7b). Leu and Val are also associated with most of the TxxxT Signatures in data-α (Fig. S6p–s); in data-β, most common TxxxT motifs are TGxxT and TSxxT (Fig. S7e). Signatures SxxxT, SxxT, and SxxS have the same motifs in the both data sets, respectively, SAxxT and SLxxT, SVxT and SGxT, and SSxS and STxS (Figs. S6d–f, j–e, a–c, S7a, c, f) (Fig. 2).

Our preliminary analysis of a possible relationship between noticeable numbers of Signatures and the molecular function of the protein indicates that, within the data sets considered here, the proteins with large numbers of Signatures tend to be transporters or receptors. Below we discuss briefly several such examples.

Identification of Molecular Transporters and Receptors with Significant Numbers of Ser/Thr Motifs

Visual inspection of data-α molecular transporters with a large number of Signatures (Fig. S8) indicates that the Signatures can be present not only in the membrane-embedded region of the protein, but also on solvent-exposed regions—loops, or larger soluble domains. The inclusion in the analysis of solvent-exposed parts of TM proteins is a limitation of the data sets used for the current analysis that leads to an over-estimation of the number of Ser/Thr Signatures. Below we discuss briefly examples of molecular transporters that contain large numbers of Signatures in the TM and/or solvent-exposed domains. In the discussion and in the Supplementary Information files the proteins are identified by the Protein Data Bank (PDB, Berman et al. 2003) chain used in the bioinformatics analysis; for example, 1f6g_A indicates that we used chain A from PDB 1f6g.

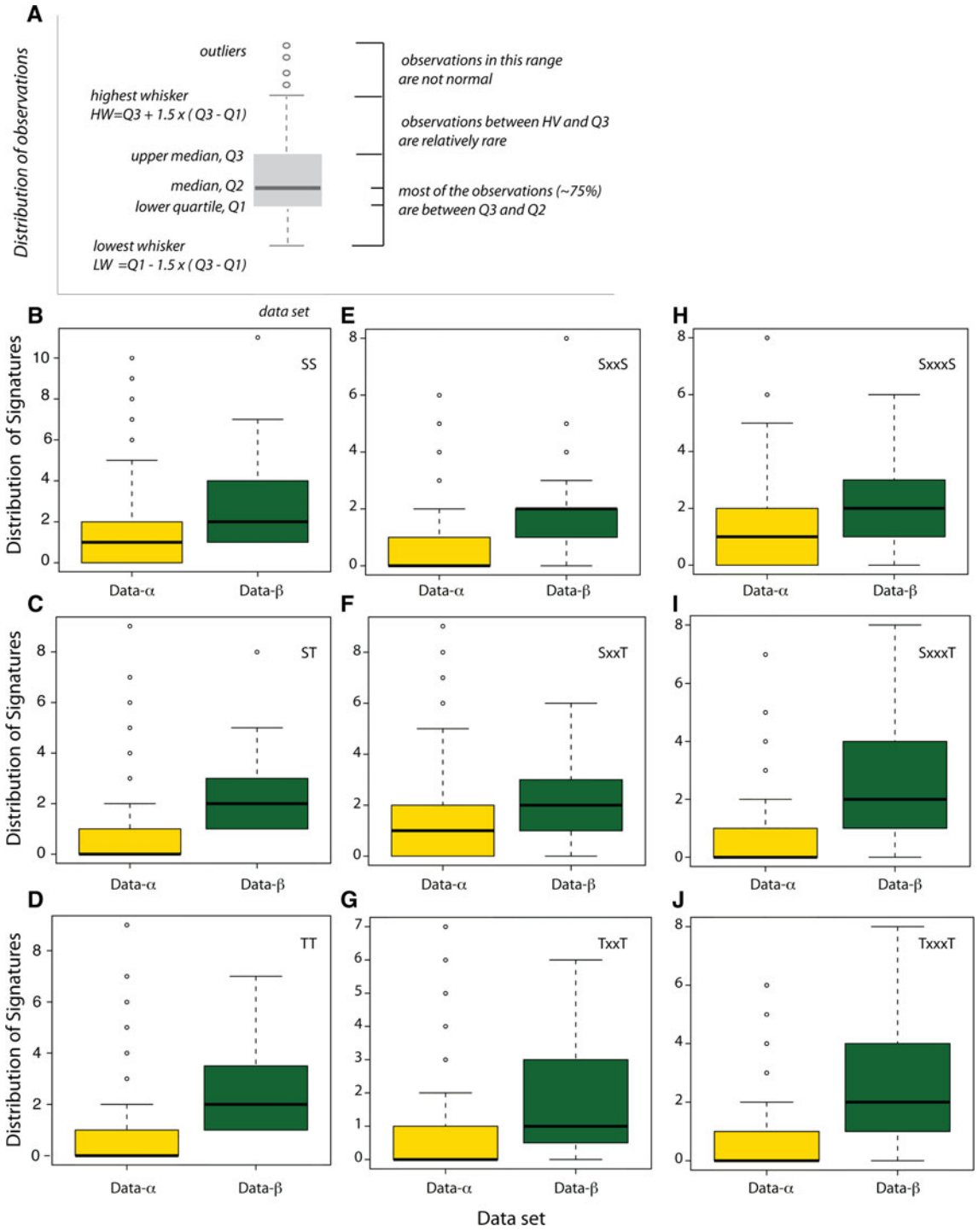

Fig. 1 Box-and-whisker plots illustrating the distribution of Signatures in data-α and data-β. Box-and-whisker plots are nonparametric representations of the distribution of the data within the sample assessed. The principles of a box plot are illustrated in (**a**). For example, the *yellow box* in (**b**) (for SS Signatures in data-α) indicates that (1) the median number of SS Signatures in the data-α set is 1; (2) approximately half of the sequences have no Signature; (3) about a quarter of the sequences have one SS Signature; and (4) outliers more than 5 SS Signatures are not normal within the data-α set. For information about the number of specific Signatures for each of the data-α and data-β sets, see Figs. S2–S5. Details of the statistical analyses and the results of the Shapiro test are given in Figs. S6 and S7

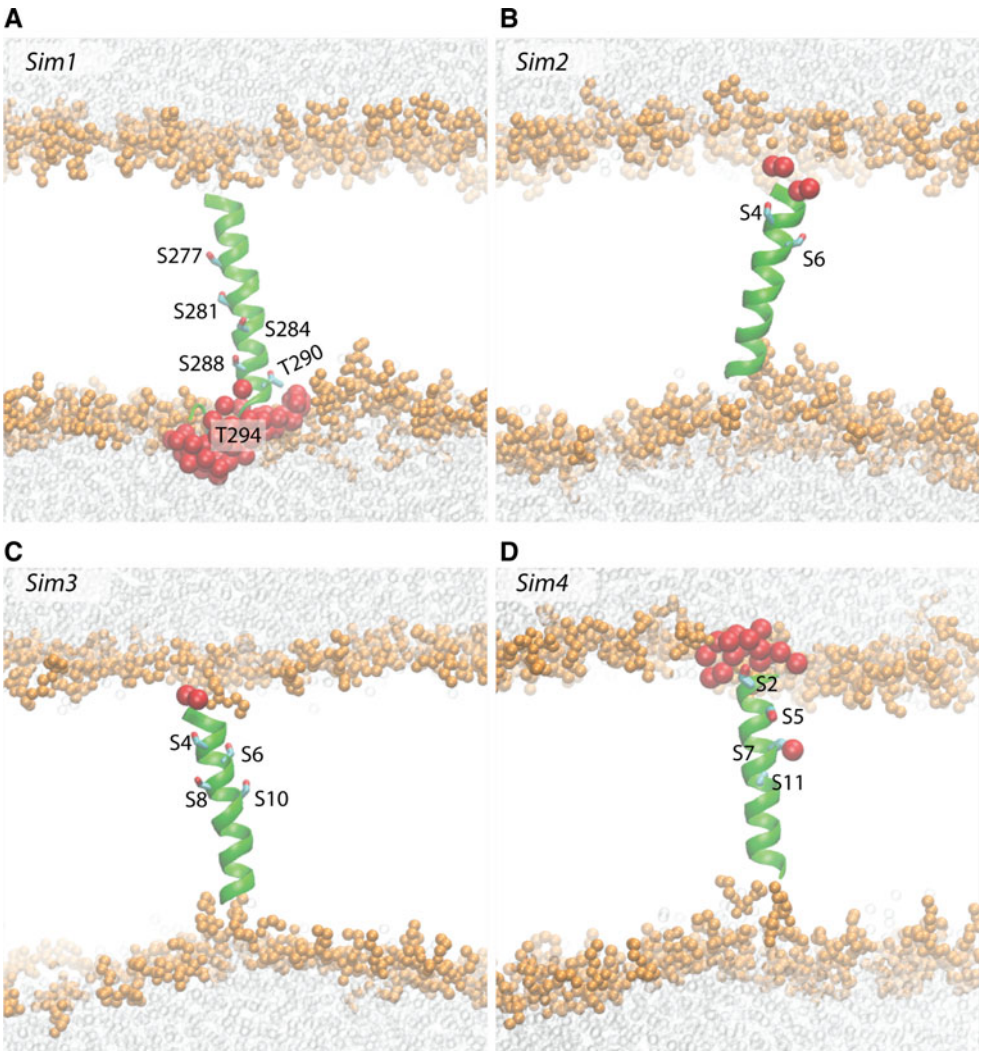

Fig. 2 Schematic representations of Sims1–4. Coordinate snapshots from the end of Sim1 (**a**), Sim2 (**b**), Sim3 (**c**), and Sim4 (**d**) are shown as cutaway views with heavy atoms of lipid glycerol, phosphate, and choline groups depicted as van der Waals spheres scaled down by 40 %, and solvent water oxygen atoms depicted as transparent van der Waals spheres (also scaled down by 40 %). Water oxygen atoms within 6 of any Ser/Thr atom are shown as large spheres (van der Waals spheres enlarged by 20 %). The Ser/Thr side chains are shown as bonds. VMD (Humphrey et al. 1996) was used to prepare molecular graphics images

The AMPA subtype ionotropic glutamate receptor (Sobolevsky et al. 2009) has numerous Ser/Thr groups that give rise to sixteen SxxxS Signatures, nine SxxT, and smaller numbers of other Signatures—although most of the groups are solvent exposed (3kg2_A, Fig. S1A). The full-length potassium channel KcsA (1f6g_A; Cortes et al. 2001) (Fig. S1B), and the P-type ATPases AHA2–proton pump (3b8c_A, Pedersen et al. 2007) (Fig. S1C), sarcoplasmic reticulum Ca^{2+} pump (Obara et al. 2005) (2agv_A, Fig. S1D), and the *Neurospora* proton pump (1mhs_A; Kühlbrandt et al. 2002) (Fig. S1E) have Ser/Thr Signatures in the both TM and solvent-exposed regions.

Solvent-exposed domains of the TM protein may contain β-strand domains where most of the Ser/Thr Signatures are found, such as entry 3h9v_A, corresponding to the ATP-gated P2X4 ion channel from Kawate et al. 2009) (Fig. S1F). The structure of the KirBac3.4 potassium channel from Gulbis et al. (n.d.) (pdb entry 1XL4) has Signatures in the both TM helices and solvent-exposed β-strands (Fig. S1G). The polysaccharides translocon Wza (2j58_A; Dong et al. 2006) has 12 Signatures, of which three (two TxT and one SxxxT) are within the C-terminal D4 helical segment thought to be embedded in the outer membrane, and the remaining Signatures are in solvent-exposed α-helical or β-strand segments (Fig. S1H). A stunning example of a molecular transporter with solvent-exposed helical and β-strand segments and a large number of Signatures is mouse P-glycoprotein (3g5u_A; Aller et al. 2009), which has numerous SxxxS and ST Signatures, and at least one from each of the other Signatures (Figs. S1I, S8–J).

There are other examples of data-α transporters containing a remarkable number of Signatures within the TM region. In the putative ammonium channel *Nitrosomonas europaea* Rh50 (data-α entry 3b9w_A; Lupo et al. 2007), some of the Ser/Thr amino acid residues are part of TT (4), SxxS (2), TxxT (16), or TxxxT (1) Signatures, and a

single TM helix can have up to five Ser/Thr groups (Fig. S1R). Alignment of the sequences of *N. europaea* Rh50 and the *E. coli* ammonium transporter AmtB (Lupo et al. 2007) indicates that some of the Ser/Thr Signatures are conserved, whereas others are present only in *N. europaea* Rh 50. For example, the **S**$_{44}$A**T**$_{46}$**T**$_{47}$G**T**$_{49}$YLV Rh50 segment of TM2 corresponds to **S**$_{43}$ML**T**$_{46}$QV**T**$_{49}$V**T**$_{51}$ in AmtB. In Rh50, F86 and F194 are thought to form a gate in the substrate transport path (Lupo et al. 2007). F194 is part of a **S**F$_{194}$A**T** segment in TM6, and this sequence is present as **S**FN**S** in human Rhesus RhD and RhAG—two membrane proteins whose molecular function is not entirely clear, though RhAG may participate in ammonium transport (van Kim et al. 2006). TM6 of Rh50 also contains the SxxxS Signature **S**$_{180}$MLG**S**$_{184}$ (Lupo et al. 2007) S$_{180}$ being part of the pore-lining amino acid residues (Hub et al. 2010). The arginine-agmatine antiporter (AdiC, data-α entry 3hqk_A; Fang et al. 2009) has a total of 14 Signatures, of which four are SS, and the remaining are one or two of the ST, TT, T/SxxxT/S or SxxT Signatures (Fig. S1J). Aquaporin AQP1 (data-α entry 1J4N_A; Sui et al. 2001) has Ser/Thr Signatures (mostly with Ser) both along TM helices and solvent-exposed loops (Fig. S1K).

We also identified membrane proteins with signal-transducing activities that have Ser/Thr Signatures in regions of the protein known to be critical for function, or have numerous Signatures. Thus, we found that bovine rhodopsin has 14 Signatures, four of which TT (Fig. S1L; 3cgl_A, Stenkamp 2008). The muscarinic M3 receptor (2amk_A, Han et al. 2005; Li et al. 2005), has numerous Ser/Thr along the TM helices (Fig. S1M).

From the data-β set, the outer membrane heme transporter ShuA (data-β entry 3fhh_A, Brillet et al. n.d.) is loaded with Ser and Thr groups: the structure depicted in Fig. S1N has 111 Ser/Thr groups, which is approximately 18 % of the 621 amino acids. This significant number of Ser/Thr gives rise to 11 SS Signatures and 29 other Signatures, SxxT being the least represented—just one Signature. Another example of a data-β protein with numerous Signatures is the hemophore receptor (and transporter) HasR (Krieg et al. 2009) (data-β entry 3csl_A, Figs. S1O, S9); this protein structure has 115 Ser/Thr groups, accounting for 15 % of the total amino acids. The protein has seven SS Signatures, eight SxxS, and between three and six from each of the other Signatures. At the other extreme in terms of number of Signatures for a data-β protein we mention the outer membrane porin OmpG (data-β entry 2f1c_X; Subbarao and van der Berg 2006). Out of the 286 amino acids, 27 ($\sim$9 %) are Ser/Thr (Fig. S1P), but there are only six Signatures: one ST, one TT, two TxxxT, one SxxxT, and one TxxT Signature (Fig. S9).

Structure and Dynamics of Model TM Peptides

The root mean squared differences (RMSD) relative to the starting coordinates has reached plateau values for all four model peptides considered here (Table 1; Fig. S10). The MD simulations (Sim1-Sim4) indicate that the presence of Ser/Thr amino acids within the membrane-embedded peptide segment has a significant effect on the structure and dynamics of the TM helix.

In Sim1, T290 and each of the four Ser amino acids hydrogen bond to the carbonyl group of the fourth amino acid downstream the sequence; in addition to the stable *i-4* hydrogen bond, each of the two central Ser groups have a transient hydrogen bond with the carbonyl group of amino acid *i-3* (Fig. 3a, c–e, g). Competition of the Ser hydroxyls with the amide groups for hydrogen bonding to the carbonyl groups (Fig. 3d, g) induces local kinks in the helix (Fig. 3b, d), and an enhanced dynamics of this region. Indeed, the root-mean-squared-fluctuation (rmsf) profile indicates high mobility for the groups close to S281 and S284, in particular upstream the sequence where the backbone hydrogen bonding is most perturbed (Fig. 3d–f).

SecY-TM7, the TM peptide investigated in Sim1, contains four Ser/Thr Signatures in which Ser/Thr are separated by 1, 2, or 3 amino acid residues (Table 1; Fig. 3a); of the amino acids that separate Ser/Thr in these four Signatures, Ile and Ala are each present in three Signatures (Ile: S273xxxS277, S281xxS284, S284xxxS288, and S288 xS290; Ala: S273xxxS277, S284xxxS288, and T290xxx T294) (Table 1; Fig. 3a). The presence of Ile in the Ser Signatures of SecY-TM7 is consistent with the observation from the bioinformatics analysis above that in data-α; these Signatures are often associated with a bulky hydrophobic amino acid. In Sim2–Sim4 we explore further the structure and dynamics of Ser-containing TM segments by considering peptides with different numbers of Ser amino acid residues, and with different numbers of Leu separating the Ser groups (Table 1).

The results on the three Ser-containing poly-Leu model peptides tested in Sim2–Sim4 indicate that the dynamics and hydrogen-bonding interactions of the peptides depend on the number and location of the Ser groups. In Sim2, the two Ser at positions 4 and 6 in the sequence (Table 1; Fig. 4a) hydrogen bond to, respectively, the *i-3* and *i-4* backbone carbonyls (Fig. 4f, g); S4 can also interact with water (Fig. 4a).

Compared to Sim2, the peptide in Sim3 has two additional Ser groups at positions 8 and 10 in the sequence (Table 1; Fig. 4b). Hydrogen bond dynamics of S4 is similar in Sim2 and Sim3—during the first $\sim$30 ns of the simulations the S4 hydroxyl: L1 backbone hydrogen bond breaks and reforms, and then stabilizes to $\sim$3.4 Å. S10, located deep in the membrane core, is mostly hydrogen

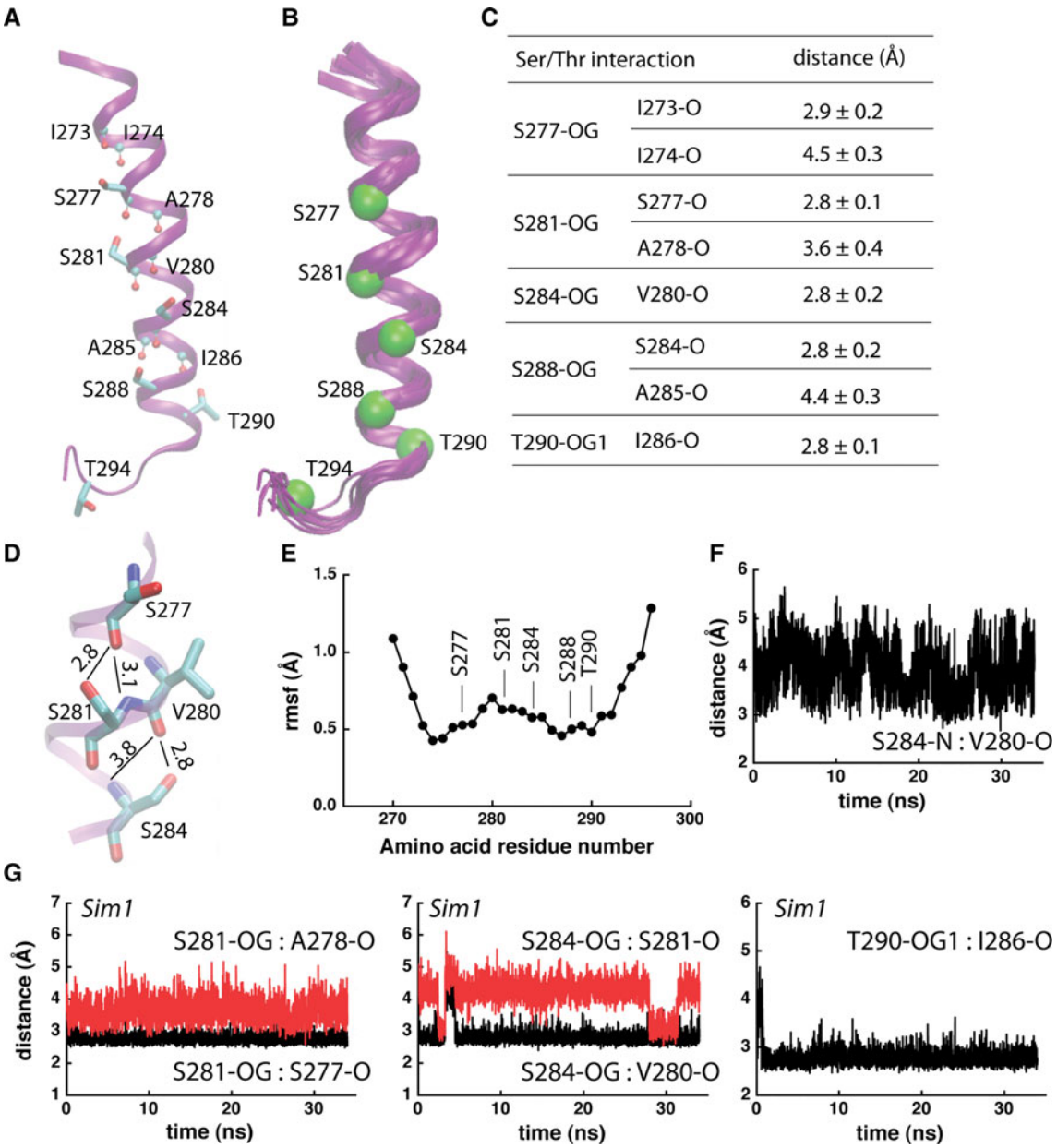

Fig. 3 Intrahelical hydrogen bonding in Sim1. **a** Each of the Ser amino acids from the TM helical part of peptide 1 (Table 1) engages in at least 1 intrahelical hydrogen bond. Ser/Thr groups are shown as bonds, and Leu backbone groups that hydrogen bond with Ser/Thr are shown with atoms as small spheres. **b** Overlap of 10 snapshots of the last 10 ns of Sim1 taken at every 1 ns. Cα atoms of the Ser/Thr amino acid residues at the end of Sim1 are shown as Van der Waals spheres. **c** Average distances between Ser/Thr hydroxyl oxygen atoms and their interaction partners. Average and standard deviation values were computed from the last 10 ns of Sim1 (1000 coordinate sets). **d** Close view of hydrogen bonding in the middle segment of peptide 1. Thin lines with numbers indicate hydrogen bonding and the corresponding distances in Å. The standard deviations for the side chain distances are given in (**c**); for the backbone S281-N:S277-O, and S284-N:V280-O distances, the standard deviations are ±0.3 Å and ±0.5 Å, respectively. **e** Cα-rmsf profile of peptide 1, computed from the last 10 ns segment of Sim1. The rmsf profile and the overlap of structural snapshots in (**b**) would suggest an enhanced flexibility of the Ser/Thr-rich TM helix. **f** Time series of the S284-N:V280-O distance. **g** Examples of distances (in Å) between Ser/Thr hydroxyl groups and backbone carbonyl groups monitored during Sim1. For all time series presented here and in Fig. 4, the origin of the time axis corresponds to all harmonic constraints being switched off

bonded to the S6 backbone carbonyl (Fig. 4g); S8 hydrogen bonds to the S4 carbonyl (Fig. 4b). The presence of S8 and S10 in Sim3 is associated with the middle segment of the peptide being more flexible than in Sim2 (Fig. 4e).

The 4 Ser groups of peptide in Sim4 are separated by short LL stretches (Table 1; Fig. 4c, d). That is, unlike in Sims 2 and 3, where the Ser side chains are distributed approximately symmetrically around the helix (Fig. 4a, b),

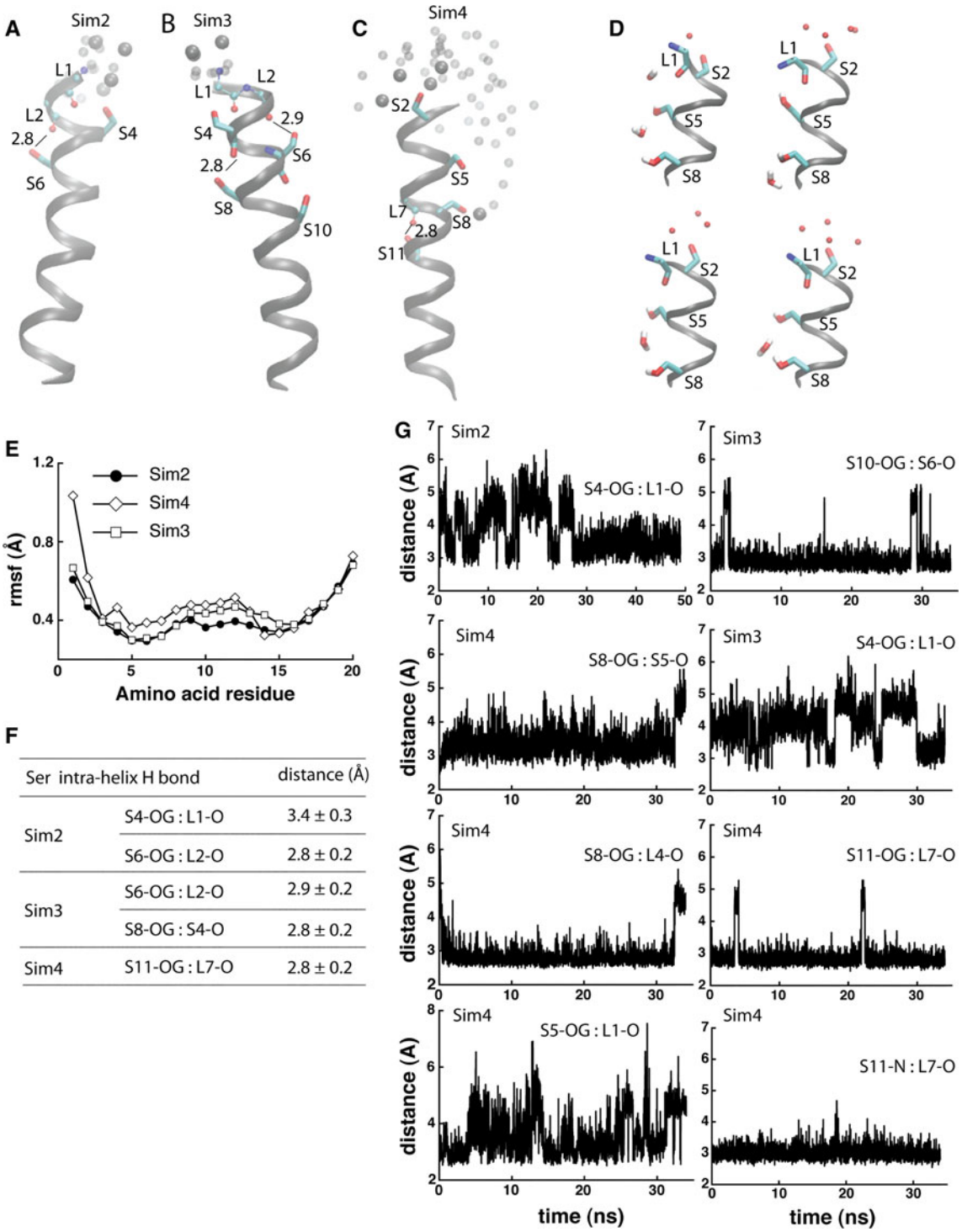

Ser intra-helix H bond		distance (Å)
Sim2	S4-OG : L1-O	3.4 ± 0.3
	S6-OG : L2-O	2.8 ± 0.2
Sim3	S6-OG : L2-O	2.9 ± 0.2
	S8-OG : S4-O	2.8 ± 0.2
Sim4	S11-OG : L7-O	2.8 ± 0.2

Fig. 4 Dynamics and hydrogen bonding of Ser-containing poly-Leu peptides. **a**, **b** Coordinate snapshots from Sim2–Sim4 showing the peptide and specific amino acids at the end of the Sims. Ser side chains are shown as bonds; atoms of backbone groups involved in Ser hydrogen bonding are shown as small spheres. Oxygen atoms of water molecules within 6 Å from Ser groups are shown as van der Waals spheres for the snapshot at the of the Sims, and as small transparent spheres for 2 coordinate snapshots taken 2 and 1 ns before the end of the Sims, respectively. For simplicity, in panels **a**-**c** hydrogen are not shown. In Sim4, water molecules penetrate into the lipid bilayer, forming hydrogen bonds with S8 and/or S5. **d** Snapshots from the last ~1 ns segment of Sim4 illustrating hydrogen bonding between Ser side chains and water molecules; selected hydrogen atoms are depicted for examples of hydrogen bonding. **e** Rmsf (Å) computed from the last 10 ns of Sim2–Sim4. **f** Selected Ser hydrogen-bond distances measured during the last 10 ns segments of Sim2–Sim4. **g** Examples of time series of Ser hydrogen-bond distances in Sim2–Sim4

in Sim4 the Ser side chains are roughly on the same side of the helix turns, leading to an imbalanced polarity of the helix (Fig. 4c, d). Toward the end of Sim4, we observe water molecules penetrating the lipid bilayer, where they hydrogen bond with S5 and S8 (Fig. 4d, c). That water molecules enter the lipid membrane to solvate the Ser groups in a peptide containing SLLS Signatures (Fig. 4c) is compatible with previous experiments on synthetic $(LSSLLSL)_3$ peptides in diphytanol phosphatodylcholine lipid membranes: such peptides oligomerized and gave rise to ionic currents (Lear et al. 1998).

Upon hydrogen bonding to water S8 no longer hydrogen bonds to the backbone carbonyls of L4 and S5 (Fig. 4d, g); we also observe geometries in which the side chains of S5 and S8 are bridged via a water molecule (Fig. 4d). Backbone hydrogen bonding of S11 is largely stable (Fig. 4c, g). The presence in Sim4 of more Ser side chains that can interact with backbone or water molecules is associated with the flexibility of the middle segment of the peptide being larger than that observed for the peptides in Sim2 and Sim3 (Fig. 4e).

Discussion

We have revisited the conservation patterns of Ser/Thr motifs in α-helical and β-barrel TM proteins using a data set of 339 unique chain sequences. The bioinformatics analyses indicate the noticeable presence of Ser/Thr Signatures in both β-barrel and α-helical membrane proteins (Table 2, Figs. S1–S3). There is, however, a significant difference between these two classes of proteins: whereas just ~20 % of the β-barrel protein sequences analyzed here do not have any Ser/Thr Signature, in the α-helical TM proteins set the percentage of such sequences is 45–58 % (Table 2, Figs. S2, S3). The finding that within the data sets used here, proteins having more than two Ser/Thr Signatures are a minority (Table 2; Fig. 1) is consistent with Ser/Thr being relatively little represented in the single transmembrane helices analyzed in (Landolt-Marticorena et al. 1993), and with the expectation from the kPROT analysis that the probability of finding multiple Ser groups within the same TM segment degreases rapidly from ~20 % for two Ser groups, to ~0 for 5–6 groups (Pilpel et al. 1999). It is important to note here that the results on the frequency of Ser/Thr motifs depend on the protein sequences included in the data sets for bioinformatics analyses. Further work is necessary to understand whether the number and identity of Ser/Thr motifs within the TM domain of a TM protein depend on the structural details of the protein—e.g., on the number of TM helices or β-sheets.

Although multiple Ser/Thr motifs are relatively rare in TM proteins, we identified intriguing examples of α-helical TM proteins that contain multiple Ser/Thr groups within their TM helices (Fig. S1), including in regions that are important for function (Fig. S1R). The bioinformatics analysis further indicates that some Signatures are clearly preferred: compared to other Ser/Thr Signatures, the SxxS Signatures are disfavored in the β-barrel TM proteins set; such Signatures are also infrequent in the α-helical TM proteins. The SxxxS Signature, present in 55 % of the data-α TM proteins analyzed here, is often associated with a bulky hydrophobic side chain (e.g., SLxxS or SVxxS).

The MD simulations on model Ser-containing α-helical TM segments suggest that SxxS motifs may be disfavored because the energetic cost for hydrogen bonding to the helix backbone such buried Ser hydroxyl groups may be too high. In the simulation on the model peptide that contains four Ser groups each separated by two Leu (Sim4), water molecules enter the lipid bilayer and solvate all except for the deepest buried Ser (Fig. 4c, d). Penetration of water molecules into the hydrophobic core of the lipid bilayer had been observed in previous MD simulations on the partitioning of charged and polar amino acid models (MacCallum et al. 2008).

The side chains of all five Ser/Thr groups of the seventh TM helix of the *T. maritima* translocon hydrogen bond to the carbonyl group of the *i-4* amino acid (Fig. 4a, c). In addition to the *i-4* hydrogen bond, the two central Ser hydroxyl groups hydrogen bond transiently to the *i-3* backbone carbonyls (Fig. 4a, g). Rh50 was identified here as a transporter with Ser/Thr Signatures within the TM region. In the 1.3 Å resolution structure of Rh50 (Lupo et al. 2007), T46 and T47 of the $T_{46}T_{47}xT_{49}$ motif have the side chains on the membrane-facing side of a TM helix, whereas T49 faces the protein interior. Each of the three threonine hydroxyl groups is hydrogen bonded to backbone carbonyls from the same TM helix: T47 and T49 hydrogen bond to the *i-4* carbonyl, whereas T46 has two hydrogen bonds, with the *i-4* (2.9 Å) and *i-3* (3.2 Å) carbonyl groups. Hydrogen bonding of Ser/Thr hydroxyl groups with the backbone carbonyl of the *i-4* amino acid was also observed in previous MD simulations on model GGPG-flanked α-helical TM peptides in hydrated DMPC lipid bilayers (Johansson and Lindahl 2006). Hydrogen bonding to the backbone stabilizes the Ser/Thr hydroxyl groups within the hydrophobic membrane environment without the need of water entering the bilayer. That is, whether or not water molecules penetrate into the membrane to solvate buried hydroxyl groups depends on the sequence context.

The hydroxyl groups of Ser/Thr compete with backbone amide groups for hydrogen bonding to the carbonyls, and their backbone amide groups can hydrogen bond to the *i-4* carbonyls (Fig. 3d). In the case of the peptide in Sim1, the maximum perturbation of the backbone amide:carbonyl hydrogen bond is observed for the central S284:V280

interaction (Fig. 3d, f). Perturbation of the backbone hydrogen bonding appears associated with an enhanced flexibility of the peptide (Fig. 4e). Although the details are expected to depend somewhat on how many motifs are present and where these motifs are located within the sequence, the computations on the model peptides considered here support a model in which Ser/Thr intrahelical hydrogen bonding can have significant effects on the local structure, dynamics, and water interactions of a TM α-helix.

The influence of the Ser/Thr Signatures on the local structure, dynamics, and solvation of the TM helices could be interpreted to suggest that such Signatures may have important functional roles. For example, Ser/Thr motifs may be used by the protein to shape the local structure by inducing local kinks (Fig. 3d), to enhance solvation (Fig. 4a–d) or flexibility (Fig. 4e). Within the data set considered here, proteins having significant numbers of Ser/Thr Signatures include molecular transporters and receptors. Examples of transporters and receptors containing Ser/Thr groups that are part of Signatures and known as functionally important include squid rhodopsin—S_{122}, part of a SxxT motif, which contributes to a hydrogen-bonded network along the signal relay path (Jardon-Valadez et al. 2010); bacteriorhodopsin—the Thr90Ala mutation in the $T_{89}T_{90}$ Signature has drastic effects on the kinetics of the reaction cycle (Perálvarez et al. 2001); and SecY—the *E. coli* S282R mutation in the $\mathbf{S}_{281}\mathbf{S}_{282}$II-LFPA$\mathbf{T}_{288}IA\mathbf{S}_{291}$ sequence destabilizes the translocon (Smith et al. 2005).

As another implication of the results here on the Ser/Thr motifs, we suggest the possibility that the interpretation of serine scanning mutagenesis as tool for assessing the structure–function relationship in membrane proteins may be complicated by the introduction, through mutation, of Ser/Thr Signatures. A recent example of a serine-scanning investigation in which Ser/Thr Signatures have been introduced is the investigation by Miranda et al. (2011) of the structure–function relationship in TM6 of the yeast H^+ ATPase Pma1. The yeast Pma1 has a Thr at position 733; the A732S and A735S mutations, which introduce ST and, respectively, TxS Signatures, led to a reduction in the proton pumping activity (Miranda et al. 2011). In the absence of detailed information about the structure, dynamics, and water interactions of the mutant proteins, the molecular origin of the mutation effect is unclear. But the consequences of removing from or inserting a Signature-related Ser/Thr group are likely due to a complex set of factors that would include not only the loss/addition of a hydrogen-bonding hydroxyl group, but also modification of the structure (e.g., releasing/promoting a kink), changes in the local dynamics, and reducing/enhancing the local hydration. In multipass TM proteins, Ser/Thr groups could also be involved in interhelical hydrogen bonds (Adamian and Liang 2002; Dawson et al. 2002); changes in the interhelical hydrogen bonds via mutation could affect significantly the conformational dynamics of the protein.

Acknowledgements This research was supported in part by Grant GM-74637 from the National Institute of General Medical Sciences (to S.H.W), the Spanish Ministerio de Ciencia e Innovación (project TIN-2009-13950), the Consejería de Innovación, Investigación y Ciencia de la Junta de Andalucía (project TIC-02788) (to C.M.D.V.), the Marie Curie International Reintegration Award IRG276920/BiolTransp-Comput (to A.-N.B), and an allocation of computer time from the National Science Foundation through the TeraGrid resources.

References

Adamian L, Liang J (2002) Interhelical hydrogen bonds and spatial motifs in membrane proteins: polar clamps and serine zippers. Prot Struct Funct Gen 47:209–218

Aller SG, Yu J, Ward A, Weng Y, Chittaboina S, Zhuo R, Harrel PM, Trinh YT, Zhang Q, Urbatsch IL, Chang G (2009) Structure of P-glycoprotein reveals a molecular basis for poly-specific drug binding. Science 323:1718–1722

Ballesteros JA, Deupi X, Olivella M, Haaksma EEJ, Pardo L (2000) Serine and threonine residues bend a-helices in the $\chi_1 = g^-$ conformation. Biophys J 79:2754–2760

Berman HM, Heinrick K, Nakamura H (2003) Announcing the worldwide Protein Data Bank. Nat Struct Biol 10:980

Bezdek JC, Pal NR (1998) Some new indexes of cluster validity. IEEE Trans Syst Man Cybern B Cybern 28:301–315

Bondar A-N, del Val C, White SH (2009) Rhomboid protease dynamics and lipid interactions. Structure 17:395–405

Bondar A-N, del Val C, Freites JA, Tobias JA, White SH (2010) Dynamics of SecY translocons with translocation-defective mutations. Structure 18:847–857

Brillet K, Meksem A, Cobessi D (n.d.) Crystal structure of the heme/hemoglobin outer membrane transporter ShuA from *Shigella dysenteriae*. Protein Data Bank. doi:10.2210/pdb3fhh/pdb

Brooks BR, Bruccoleri RE, Olafson BD, States DJ, Swaminathan S, Karplus M (1983) CHARMM: a program for macromolecular energy, minimization, and dynamics. J Comput Chem 4:187–217

Buss V, Sugihara M, Entel P, Hafner J (2003) Thr94 and wat2b effect protonation on the retinal chromophore in rhodopsin. Angew Chem Int Ed 42:3245–3247

Chin CN, von Heijne G (2000) Charge pair interactions in a model transmembrane helix in the ER membrane. J Mol Biol 303:1–5

Cortes DM, Cuello LG, Perozo E (2001) Molecular architecture of full-length KcsA: role of cytoplasmic domains in ion permeation and activation gating. J Gen Physiol 117:165–180

Darden T, York D, Pedersen L (1993) Particle mesh Ewald: an $\mathbf{N}\cdot\log(\mathbf{N})$ method for Ewald sums in large systems. J Chem Phys 98:10089–10092

Dawson JP, Weinger JS, Engelman DM (2002) Motifs of serine and threonine can drive association of transmembrane helices. J Mol Biol 316:799–805

Deupi X, Olivella M, Govaerts C, Ballesteros JA, Campillo M, Pardo L (2004) Ser and Thr residues modulate the conformation of Pro-kinked transmembrane α-helices. Biophys J 86:105–115

Doig AJ, Malcolm WM, Stapley BJ, Thornton JM (1997) Structures of N-termini of helices in proteins. Prot Sci 6:147–155

Dong C, Beis K, Nesper J, Brunkan-LaMontagne AL, Clarke BR, Whitfiled C, Naismith JH (2006) Wza the translocon for *E. coli*

capsular polysaccharides defines a new class of membrane protein. Nature 444:226–229
Du Plessis DJF, Berrelkamp G, Nouwen N, Driessen AJM (2009) The lateral gate of SecYEG opens during protein translocation. J Biol Chem 284:15805–15814
Eilers M, Shekar SC, Shieh T, Smith SO, Fleming PJ (2000) Internal packing of helical membrane proteins. Proc Natl Acad Sci U S A 97:5796–5801
Essmann U, Perera L, Berkowitz ML, Darden T, Lee H, Pedersen LG (1995) A smooth particle mesh Ewald method. J Chem Phys 103:8577–8593
Fang Y, Jayaram H, Shane T, Kolmakova-Partensky L, Wu F, Williams C, Xiong Y, Miller C (2009) Structure of a prokaryotic virtual proton pump at 3.2 Å resolution. Nature 460:1040–1043
Feller SE, MacKerell AD Jr (2000) An improved empirical potential energy function for molecular simulations of phospholipids. J Phys Chem B 104:7510–7515
Feller SE, Zhang Y, Pastor RW, Brooks BR (1995) Constant pressure molecular dynamics simulation: the Langevin piston method. J Chem Phys 103:4613–4621
Gratkowski H, Lear JD, DeGrado WF (2001) Polar side chains drive the association of model transmembrane peptides. Proc Natl Acad Sci U S A 98:880–885
Gray TM, Matthews BW (1984) Intrahelical hydrogen bonding of serine, threonine and cysteine residues within α-helices and its relevance to membrane-bound proteins. J Mol Biol 175:75–81
Grubmüller H, Heller H, Windemuth A, Schulten K (1991) Generalized Verlet algorithm for efficient molecular dynamics simulations with long-range interactions. Mol Simul 6:121–142
Gulbis JM, Kuo A, Smith B, Doyle DA, Edwards A, Arrowsmith C, Sundstrom M (n.d.) Intermediate gating structure 1 of the inwardly rectifying K^+ channel KirBac3.1. Protein Data Bank. doi:10.2210/pdb1xl4/pdb
Han S-J, Hamdan FF, Kim S-K, Jacobson KA, Brichta L, Bloodworth LM, Li JH, Wess J (2005) Pronounced conformational changes following agonist activation of the M3 muscarinic acethylcholine receptor. J Biol Chem 280:24870–24879
Hermansson M, von Heijne G (2003) Inter-helical hydrogen bond formation during membrane protein integration into the ER membrane. J Mol Biol 334:803–809
Hessa T, Kim H, Bihlmaier K, Lundin C, Boekel J, Andersson H, Nilsson I, White SH, von Heijne G (2005) Recognition of transmembrane helices by the endoplasmic reticulum translocon. Nature 433:377–381
Hu J, Xue Y, Lee S, Ha Y (2011) The crystal structure of GxxGD membrane protease FlaK. Nature 475:528–531
Hub JS, Winkler FK, Merrick M, de Groot BL (2010) Potentials of mean force and permeabilities for carbon dioxide, ammonia, and water flux across the Rhesus protein channel and lipid membranes. J Am Chem Soc 132:13251–13263
Humphrey W, Dalke W, Schulten K (1996) VMD: visual molecular dynamics. J Mol Graph 14:33–38
Jain AK, Murty MN, Flynn PJ (1999) Data clustering: a review. ACM Comput Surv 31:264–323
Jardon-Valadez E, Bondar A-N, Tobias DJ (2010) Coupling of retinal, protein, and water dynamics in squid rhodopsin. Biophys J 99:2200–2207
Johansson ACV, Lindahl E (2006) Amino-acid solvation structure in transmembrane helices from molecular dynamics simulations. Biophys J 91:4450–4463
Jones B (1993) MATLAB statistics toolbox: computation, visualization, programming: user's guide. MathWorks, Natick
Jorgensen WL, Chandrasekhar J, Madura JD, Impey RW, Klein ML (1983) Comparison of simple potential functions for simulating liquid water. J Chem Phys 79:926–935
Junne T, Schwede T, Goder V, Spiess M (2007) Mutations in the Sec61p channel affecting signal sequence recognition and membrane protein topology. J Biol Chem 282:33201–33209
Kalé L, Skeel R, Bhandarkar M, Brunner R, Gursoy A, Krawetz N, Phillips J, Shinozaki A, Varadarajan K, Schulten K (1999) NAMD2: greater scalability for parallel molecular dynamics. J Comput Phys 151:283–312
Kawate T, Michel JC, Birdsong WT, Gouaux E (2009) Crystal structure of the ATP-gated $P2X_4$ ion channel in the closed state. Nature 460:592–598
Krieg S, Huché F, Diederichs K, Izadi-Pruneyre N, Lecroisey A, Wandersman C, Delepelaire P, Welte W (2009) Heme uptake across the outer membrane as revealed by crystal structures of the receptor-hemophore complex. Proc Natl Acad Sci U S A 106:1045–1050
Krishnakumar SS, London E (2007) The control of transmembrane helix transverse position in membranes by hydrophilic residues. J Mol Biol 374:1251–1269
Kühlbrandt W, Zeelen J, Dietrich J (2002) Structure, mechanism, and regulation of the Neurosphora plasma membrane H^+-ATPase. Science 297:1692–1696
Kumar S, Bansal M (1998) Dissecting α-helices: position-specific analysis of α-helices in globular proteins. Prot Struct Funct Gen 31:460–476
Landolt-Marticorena C, Williams KA, Deber CM, Reithmeier RAF (1993) Non-random distribution of amino acids in the transmembrane segments of human type I single span membrane proteins. J Mol Biol 229:602–608
Lear JD, Wasserman ZR, DeGrado WF (1998) Synthetic peptide models for protein ion channels. Science 240:1177–1181
Li B, Nowak NM, Kim SK, Jacobson KA, Bagheri A, Schmidt C, Wess J (2005) Random mutagenesis of the M3 muscarinic acetylcholine receptor. J Biol Chem 280:5664–5675
Lupo D, Li X-D, Durand A, Tomizaki T, Cherif-Zahar B, Matassi G, Merrik M, Winkler FK (2007) The 1.3 Å resolution structure of *Nitrosomonas europaea* Rh50 and mechanistic implications for NH3 transport by Rhesus family proteins. Proc Natl Acad Sci U S A 104:19303–19308
MacCallum JL, Benett WFD, Tieleman DP (2008) Distribution of amino acids in a lipid bilayer from computer simulations. Biophys J 94:3393–3404
MacKerell AD Jr, Bashford D, Bellott M, Dunbrack RL Jr, Evanseck JD, Field MJ, Fischer S, Gao J, Guo H, Ha S et al (1998) All-atom empirical potential for molecular modeling and dynamics studies of proteins. J Phys Chem B 102:3586–3616
MacQueen JB (1967) Some methods for classification and analysis of multivariate observations, vol 1. University of California Press, Berkeley
Mann HB, Whitney DR (1947) On a test of whether one of two random variables is stochastically larger than the other. Ann Math Stat 18:50–60
Martyna GJ, Tobias DJ, Klein ML (1994) Constant-pressure molecular dynamics algorithms. J Chem Phys 101:4177–4189
Metz G, Siebert F, Engelhard M (1991) Asp85 is the only internal aspartic acid that gets protonated in the M intermediate and the purple-to-blue transition in bacteriorhodopsin. FEBS Lett 303: 237–241
Miranda M, Pardo JP, Petrov VV (2011) Structure–function relationships in membrane segment 6 of the yeast plasma membrane Pma1 H^+-ATPase. Biochim Biophys Acta 1808:1781–1789
Mitchell TM (1997) Machine learning. McGraw-Hill Higher Education, New York
Moon CP, Fleming KG (2011) Side-chain hydrophobicity scale derived from transmembrane protein folding into lipid bilayers. Proc Natl Acad Sci U S A 108:10174–10177

Murakami M, Kouyama T (2008) Crystal structure of squid rhodopsin. Nature 453:363–367

Munter L-M, Voigt P, Harmeier A, Kaden D, Gottschalk KE, Weise C, Pipkorn R, Schaefer M, Langosch D, Multhaup G (2007) GxxxG motifs within the amyloid precursor transmembrane sequence are critical for the etiology of Aβ42. EMBO J 26: 1702–1712

Nack M, Radu I, Schultz B-J, Resler T, Schlesinger R, Bondar A-N, del Val C, Abbruzzetti S, Viappiani C, Bamann C, Bamberg E, Heberle J (2012) Kinetics of proton release and uptake by channelrhodopsin-2. FEBS Lett 586:1344–1348

Obara K, Miyashita N, Xu C, Toyoshima I, Sugita Y, Inesi G, Toyoshima C (2005) Structural role of countertransport revealed in Ca^{2+} pump crystal structure in the absence of Ca^{2+}. Proc Natl Acad Sci U S A 102:14489–14496

Okada T, Sugihara M, Bondar A-N, Elstner M, Entel P, Buss V (2004) The retinal conformation and its environment in rhodopsin in light of a new 2.2 Å crystal structure. J Mol Biol 342:571

Osborne RS, Silhawy TJ (1993) PrlA suppressor mutations cluster in regions corresponding to three distinct topological domains. EMBO J 12:3391–3398

Pedersen BP, Buch-Pedersen MJ, Morth JP, Palmgren MG, Nissen P (2007) Crystal structure of the plasma membrane proton pump. Nature 450:1111–1114

Perálvarez A, Barnadas R, Sabés M, Querol E, Padrós E (2001) Thr90 is a key residue of the bacteriorhodopsin proton pumping mechanism. FEBS Lett 508:399–402

Phillips JC, Braun B, Wang W, Gumbart J, Tajkhorshid E, Villa E, Chipot C, Skeel RD, Kale L, Schulten K (2005) Scalable molecular dynamics with NAMD. J Comput Chem 26:1781–1802

Pilpel Y, Ben-Tal N, Lancet D (1999) kPROT: a knowledge-based scale for the propensity of residue orientation in transmembrane segments. Application to membrane protein structure prediction. J Mol Biol 294:921–935

Plath K, Mothes W, Wilkinson BM, Stirling CJ, Rapoport TA (1998) Signal sequence recognition in posttranslational protein transport across the yeast ER membrane. Cell 94:795–807

Presta LG, Rose GD (1988) Helix signals in proteins. Science 240:1632–1641

Rice P, Longden I, Bleasby A (2000) EMBOSS: the European molecular biology open software suite. Trends Genet 16:276–277

Richardson JS, Richardson DC (1988) Amino acid preferences for specific location at the ends of helices. Science 240:1648–1652

Rousseeuw P (1987) Silhouettes: a graphical aid to the interpretation and validation of cluster analysis. J Comput Appl Math 20:53–65

Royston P, Remark AS (1995) R94: a remark on algorithm AS 181: the W test for normality. Appl Stat 44:547–551

Ryckaert J-P, Ciccotti G, Berendsen HJC (1977) Numerical integration of the Cartesian equations of motion of a system with constraints: molecular dynamics of **n**-alkanes. J Comput Phys 23:327–341

Sako T (1991) Novel prlA alleles defective in supporting staphylokinase processing in *Escherichia coli*. J Bacteriol 173:2289–2296

Shapiro SS, Wilk MB (1965) An analysis of variance test for normality (complete samples). Biometrika 52:591–611

Smith MA, Clemmons WM Jr, DeMars CJ, Flower AN (2005) Modelling the effects of prl mutations on the *Escherichia coli* SecY complex. J Bacteriol 187:6454–6465

Sobolevsky AI, Rosconi MP, Gouaux E (2009) X-ray structure, symmetry and mechanism of an AMPA-subtype glutamate receptor. Nature 462:745–756

Stenkamp RE (2008) Alternative models for two crystal structures of bovine rhodopsin. Acta Crystallogr D64:902–904

Subbarao GV, van der Berg B (2006) Crystal structure of the monomeric porin OmpG. J Mol Biol 360:750–759

Sugihara M, Fujibuchi W, Suwa M (2011) Structural elements of the signal propagation pathway in squid rhodopsin and bovine rhodopsin. J Phys Chem B 115:6172–6179

Sui H, Han B-G, Lee JK, Wallan P, Jap BK (2001) Structural basis of water-specific transport through the AQP1 water channel. Nature 414:872–878

R Develompment Core Team (2010) R: a language and environment for statistical computing. R Foundation for Statistical Computing, Vienna, Austria. http://www.R-project.org

Tuckerman M, Berne BJ (1992) Reversible multiple time scale molecular dynamics. J Chem Phys 97:1990–2001

Tusnády GE, Dosztányi ZS, Simon I (2005a) PDB_TM: selection and membrane localization of transmembrane proteins in the protein data bank. Nucleic Acids Res 33:D275–D278

Tusnády GE, Dosztányi ZS, Simon I (2005b) TMDET: web server for detecting transmembrane domains by using 3D structure of proteins. Bioinformatics 21:1276–1277

Unwin N (2005) Refined structure of the nicotinic acethylcholine receptor at 4Å resolution. J Mol Biol 346:967–989

van den Berg B, Clemons WM Jr, Collinson I, Modis Y, Hartmann E, Harrison SC, Rapoport T (2004) X-ray structure of a protein conducting channel. Nature 427:36–44

van Kim CL, Colin Y, Cartron J-P (2006) Rh proteins: key structural and functional components of the red cell membrane. Blood Rev 20:93–110

Vijayakumar M, Qian H, Zhou H-X (1999) Hydrogen bonds between short polar side chains and peptide backbone: prevalence in proteins and effects on helix-forming pepensities. Prot Struct Funct Gen 34:497–507

Worth CL, Blundell TL (2008) Satisfaction of hydrogen-bonding potential influences the conservation of polar sidechains. Proteins 75:413–429

Xie K, Hessa T, Seppälä S, Rapp M, von Heijne G, Dalbey RE (2007) Features of transmembrane segments that promote the lateral release from the translocase into the lipid phase. Biochem 46:15153–15161

Zhou FX, Cocco MJ, Russ WP, Brunger AT, Engelman DM (2000) Interhelical hydrogen bonding drives strong interactions in membrane proteins. Nat Struct Biol 7:154–160

Zhou FX, Merianos HJ, Brunger AT, Engelman DM (2001) Polar residues drive association of polyleucine transmembrane helices. Proc Natl Acad Sci U S A 98:2250–2255

Zimmer J, Nam Y, Rapoport TA (2008) Structure of a complex of the ATPase SecA and the protein-translocation channel. Nature 455:936–943

J Membrane Biol (2012) 245:731–745
DOI 10.1007/s00232-012-9463-1

STRA6-Catalyzed Vitamin A Influx, Efflux, and Exchange

Riki Kawaguchi · Ming Zhong · Miki Kassai · Mariam Ter-Stepanian · Hui Sun

Received: 18 March 2012 / Accepted: 23 June 2012 / Published online: 20 July 2012

Abstract Vitamin A has diverse biological functions and is essential for human survival. STRA6 is the high-affinity membrane receptor for plasma retinol binding protein (RBP), the principle and specific carrier of vitamin A (retinol) in the blood. It was previously shown that STRA6 couples to lecithin retinol acyltransferase (LRAT) and cellular retinol binding protein I (CRBP-I), but poorly to CRBP-II, for retinol uptake from holo-RBP. STRA6 catalyzes both retinol release from holo-RBP, which is responsible for its retinol uptake activity, and the loading of free retinol into apo-RBP, which can cause retinol efflux. Although STRA6-catalyzed retinol efflux into apo-RBP can theoretically deplete cells of retinoid, it is unclear to what extent this efflux happens and in what context. We show here that STRA6 can couple strongly to both CRBP-I and CRBP-II for retinol efflux to apo-RBP. Strikingly, pure apo-RBP can cause almost complete depletion of retinol taken up by CRBP-I in a STRA6-dependent manner. However, if STRA6 encounters both holo-RBP and apo-RBP (as in blood), holo-RBP blocks STRA6-mediated retinol efflux by competing with apo-RBP's binding to STRA6 and by counteracting retinol efflux with influx. We also found that STRA6 catalyzes efficient retinol exchange between intracellular CRBP-I and extracellular RBP, even in the presence of holo-RBP. STRA6's retinol exchange activity may serve to refresh the intracellular retinoid pool. This exchange is also a previously unknown function of CRBP-I and distinguishes CRBP-I from LRAT.

Keywords Membrane receptor · Membrane transport · Retinoid · Vitamin A transport

Vitamin A performs diverse physiological functions including its essential roles in vision (Crouch et al. 1996; Dowling 1966; Travis et al. 2007; Wald 1968), embryonic development (Niederreither and Dolle 2008), immune cell maturation (Stephensen 2001), and the adult nervous system (Drager 2006; Maden 2007). Vitamin A mediates these physiological functions through its derivatives called retinoids (Evans 1994; Mark et al. 2006; Napoli 1999). Despite the ability of free vitamin A and most of its derivatives to diffuse systemically, virtually all vitamin A in the blood under physiological conditions is bound to plasma retinol binding protein (RBP), the principle and specific high-affinity carrier of vitamin A (Blomhoff et al. 1990; Goodman 1984; Newcomer and Ong 2000; Quadro et al. 2003, 2005; Zanotti and Berni 2004). RBP mediates vitamin A transport from sites of storage (especially the liver) to target organs. Unlike other retinoids in the blood, which fluctuate depending on dietary intake, vitamin A–bound RBP (holo-RBP) is maintained stably at micromolar concentrations and serves as a buffer for fluctuations in dietary intake of retinoids to maintain a stable supply for tissues that depend on vitamin A (Blomhoff et al. 1990).

Although free vitamin A can diffuse through membranes as a result of its hydrophobic nature, vitamin A bound to RBP becomes membrane impermeable. It was first proposed in the 1970s that there exists an RBP receptor that mediates cellular vitamin A uptake (Heller 1975; Heller and Bok 1976; Rask and

Electronic supplementary material The online version of this article (doi:10.1007/s00232-012-9463-1) contains supplementary material, which is available to authorized users.

R. Kawaguchi · M. Zhong · M. Kassai · M. Ter-Stepanian · H. Sun (✉)
Department of Physiology, Jules Stein Eye Institute and Howard Hughes Medical Institute, David Geffen School of Medicine, University of California, Los Angeles, CA, USA
e-mail: hsun@mednet.ucla.edu

Peterson 1976). Despite strong evidence accumulated over three decades for the existence of this receptor, this hypothesis was heatedly debated as a result of a belief that RBP can freely release retinol, which can pass through membrane without a receptor (Noy 2000). This belief that supports the nonexistence of the RBP receptor suggests that retinol acutely mixed with RBP is identical to holo-RBP. Because free retinol can diffuse through membranes, there is indeed no need for the RBP receptor to exist if this belief is true.

The RBP receptor was recently identified as a multitransmembrane domain protein called STRA6 through unbiased biochemical purification and mass spectrometry (Kawaguchi et al. 2007). The fact that STRA6 promotes cellular vitamin A uptake from holo-RBP (Golczak et al. 2008; Isken et al. 2008; Kawaguchi et al. 2007) strongly argues against the belief that the RBP receptor does not exist and that retinol can freely be released by RBP. STRA6 was originally known as a retinoic acid-stimulated cell-surface protein in cancer cells (Bouillet et al. 1997; Szeto et al. 2001). STRA6 has nine transmembrane domains (Kawaguchi et al. 2008b) and an essential RBP binding domain on an extracellular loop (Kawaguchi et al. 2008a). In addition to RBP binding, STRA6 catalyzes both retinol release from holo-RBP, which is responsible for its retinol uptake activity, and the highly efficient loading of free retinol into apo-RBP in the absence of LRAT or CRBP-I (Kawaguchi et al. 2011). STRA6-mediated retinol uptake is perhaps most similar to Scavenger Receptor Class B Type I (SR-BI)-mediated cholesterol uptake from high-density lipoprotein (HDL) (Acton et al. 1996) because both membrane proteins take up molecules bound to extracellular carrier proteins while the carrier proteins remain outside of the cell after uptake. STRA6 and SR-BI have no similarity in sequence, and STRA6 has nine transmembrane domains (Kawaguchi et al. 2008b), while SR-BI has two (Babitt et al. 1997; Connelly et al. 2001). Although a few possible mechanisms have been proposed for SR-BI (Connelly 2009; Connelly and Williams 2004), STRA6's vitamin A uptake mechanism is different from these mechanisms.

LRAT is known to enhance STRA6's vitamin A uptake activity (Golczak et al. 2008; Isken et al. 2008; Kawaguchi et al. 2007). However, it has been shown that the reverse reaction of vitamin A loading into apo-RBP still happens in cells that express both STRA6 and LRAT to lead to cellular retinol loss (Isken et al. 2008). This suggests the possibility that STRA6 can cause retinol efflux (Isken et al. 2008). It was also found that apo-RBP efficiently takes up retinol in a STRA6-dependent manner in the absence of LRAT (Kawaguchi et al. 2011). This activity is consistent with the hypothesis that STRA6 might mediate cellular retinol efflux by loading retinol into extracellular apo-RBP. SR-BI, the HDL receptor, is known to mediate cellular cholesterol loss (Connelly and Williams 2004). Can the RBP receptor STRA6 mediate cellular retinol loss, in analogy to HDL receptor-mediated cholesterol loss?

Although apo-RBP in the blood is removed by kidney filtration, blood still contains a small fraction of apo-RBP in addition to holo-RBP (Mills et al. 2008). If STRA6 encounters both holo-RBP and apo-RBP, does it mediate cellular vitamin A uptake or loss? Does retinol efflux mediated by apo-RBP happen in human blood? If STRA6 mediates cellular vitamin A loss when it is exposed to the blood, how does it function as the RBP receptor to mediate cellular vitamin A uptake?

Excessive RBP in the blood has also been found to be a signal in insulin resistance (Yang et al. 2005). The average RBP level in healthy people is 2.67 μM (Mills et al. 2008), and this level does not cause insulin resistance. What is the signaling receptor that senses RBP levels in excess of 2.67 μM to cause insulin resistance? It was hypothesized that STRA6, the nanomolar affinity RBP receptor that mediates vitamin A uptake (Kawaguchi et al. 2007), is also the signaling receptor that mediates insulin resistance, and that holo-RBP, but not apo-RBP, binds to STRA6 to initiate the signaling (Berry et al. 2011). This study was based on a commercial antibody that does not correctly recognize STRA6 (Supplementary Fig. 1) and the belief that retinol acutely mixed with RBP is identical to holo-RBP. A subsequent report reached the opposite conclusion that apo-RBP, not holo-RBP, binds to STRA6 to initiate signal transduction (Chen et al. 2012). Does STRA6 bind only holo-RBP or only apo-RBP or both? If it binds both, can its interaction with holo-RBP influence its interaction with apo-RBP?

We show here that both holo-RBP and apo-RBP bind to STRA6. Holo-RBP inhibits STRA6-catalyzed retinol loading into apo-RBP. Although STRA6 couples to CRBP-I and LRAT (but poorly to CRBP-II) in retinol uptake from holo-RBP, STRA6 couples to both CRBP-I and CRBP-II (but poorly to LRAT) in retinol efflux to pure apo-RBP. Despite the ability of pure apo-RBP to cause retinol efflux, STRA6 mediates retinol uptake, not retinol loss, when exposed to the blood, which contains both holo-RBP and apo-RBP. We also found that STRA6 catalyzes retinol exchange between intracellular holo-CRBP-I and extracellular holo-RBP and between RBP molecules. These findings reveal new biochemical activities of STRA6, in addition to its role as the RBP receptor to mediate retinol uptake.

Materials and Methods

Production of Holo-RBP, Apo-RBP, and ^{3}H-retinol/RBP

Holo-RBP was produced, refolded, and purified as described (Kawaguchi et al. 2007). It is necessary to use high-

performance liquid chromatography (HPLC) in order to remove imperfectly folded RBP, and to purify holo-RBP 100 % loaded with retinol. High quality holo-RBP is essential because poorly folded holo-RBP has low affinity for retinol and can release retinol easily. Apo-RBP was prepared from holo-RBP by extracting retinol as described (Heller and Horwitz 1973). For production of ^{3}H-retinol/RBP, ^{3}H-retinol (PerkinElmer) was incubated with apo-RBP (with 6XHis tag at the N-terminus) overnight at 4 °C. ^{3}H-retinol/RBP was incubated with Ni-NTA resin (Qiagen) for 3 h. After three washes with phosphate-buffered saline (PBS), the complex was eluted by 100 mM imidazole in PBS. The eluted ^{3}H-retinol/RBP was used immediately for cellular uptake assays.

Assays for ^{3}H-retinol Uptake or Efflux Using ^{3}H-retinol/RBP

The COS-1 cell is chosen for this assay because it adheres to the cell culture dish strongly and does not detach during repeated washes and media changes in this live cell assay. The other commonly used cell type HEK293 cell is not useful for this assay because of its weak adherence that can cause complete cell loss after a few washes. Transfected COS-1 cells or untransfected control cells were washed once with Hanks balanced salt solution (HBSS) and incubated in serum-free medium (SFM) 24 h after transfection. Cellular ^{3}H-retinol uptake assay from ^{3}H-retinol/RBP was performed 48 h after transfection. Cells were incubated with ^{3}H-retinol/RBP diluted in SFM for 1 h at 37 °C. To assay for retinol efflux into apo-RBP or normal human serum (NHS) (Innovative Research), the cells were then washed with HBSS and incubated with SFM for 2 h to dissociate cell-surface-bound RBP. Apo-RBP or NHS diluted in SFM was then added to the cells for an additional 2 h of incubation. Bovine serum albumin (BSA), a nonspecific retinol binding protein, was used as a control. After a further HBSS wash, the cells were solubilized in 1 % Triton X-100 in PBS. ^{3}H-retinol remaining in the cells was measured with a scintillation counter. All experiments were done in triplicate. Conditions specific to each experiment are described in the figure captions.

Assays for ^{3}H-retinol Efflux into Apo-RBP or Human Serum Using Free ^{3}H-retinol

For experiments involving cells that cannot effectively take up retinol from holo-RBP due to the absence of STRA6 (e.g., CRBP-I-only cells or CRBP-II-only cells), free ^{3}H-retinol was loaded to the cells instead of ^{3}H-retinol/RBP. Loading cells with free ^{3}H-retinol makes it possible to demonstrate STRA6-independent ^{3}H-retinol efflux. After cells were loaded with free ^{3}H-retinol for 2 h, the cells were washed with HBSS before apo-RBP or NHS was added to cause ^{3}H-retinol efflux. BSA was used as a negative control. After a further HBSS wash, the cells were solubilized in 1 % Triton X-100 in PBS. ^{3}H-retinol remaining in cells was measured with a scintillation counter. All experiments were done in triplicate. Conditions specific to each experiment are described in the figure captions.

HPLC-based Assay for Retinol Uptake from Human Serum and Efflux into Extracellular Apo-RBP

For retinol uptake assay using human serum as the source of holo-RBP, we first incubated COS-1 cells transfected with STRA6/CRBP-I or STRA6/LRAT with 25 % NHS diluted in SFM for 4 h. To assess the ability of apo-RBP to extract retinol taken up by cells, 1 μM of apo-RBP in SFM, 25 % NHS in SFM or SFM alone was added to HBSS-washed cells and incubated for another 4 h. At the end of each experiment, cells were washed once with HBSS and collected for HPLC analysis, as described below.

Production and Purification of Enhanced Green Fluorescent Protein-RBP Fusion Protein (EGFP-RBP)

It was known previously that N-terminal tagging of RBP does not interfere with its binding to its receptor (Kawaguchi et al. 2007). To create EGFP-tagged RBP, EGFP was tagged to the N-terminus of RBP right after the secretion signal (EGFP is connected to RBP through a 3-glycine linker). A 6XHis tag was also added to the protein to allow nickel affinity purification. Six hours after transfection with the expression plasmid, COS-1 cells were washed with HBSS, and the culture medium was changed to SFM. The medium containing secreted EGFP-RBP was collected 24 h later. After concentrating the medium, EGFP-RBP was purified using Ni-NTA resin (Qiagen).

HPLC Analysis of Vitamin A Uptake from Human Serum

Retinol from cells was extracted using hexane containing 1 mM 2,6-Di-tert-butyl-4-methylphenol (BHT). Retinol was dried under nitrogen and resolubilized in 100 % methanol. Before HPLC analysis, 10 % water was added to the solution. Samples were analyzed on the Agilent 1100 series liquid chromatography system with a photo-diode array detector. Retinol was separated using a Zorbax Rx-SIL column (Agilent) and using 90 % methanol as the mobile phase. Retinyl ester was extracted by adding methanol containing 1 mM BHT. Retinyl ester was separated using a Zorbax Eclipse EDB-C18 column (Agilent). The isopropanol concentration was increased from 0 to 100 % against methanol during the 10 min run, followed by a 5 min wash with 100 % isopropanol. Both retinol and retinyl esters were detected by absorbance at 325 nm.

Fluorescence Assay for STRA6-Catalyzed Retinol Loading into Apo-RBP and Retinol Release from Holo-RBP

Real-time monitoring of retinol fluorescence was measured using POLARstar Omega (BMG Labtech) with the excitation filter 320ex and the emission filter 460–10. The black Microfluor-2 plate (Thermo) was coated with Blocker Casein (Pierce) overnight at 4 °C and was washed once with PBS before addition of membrane suspension to prevent nonspecific sticking of holo-RBP to the plastic wall. Membranes resuspended in PBS and mixed with various proteins were transferred to the plate for fluorescent measurement. The signal from each time points is the average of 10 measurements. Samples were shaken for 10 s at 500 rpm using double-orbital shaking before each measurement. The fluorescent signals before the addition of retinol or holo-RBP at 0 min are considered background signals and were subtracted from the final fluorescence signals at each time point.

Fluorescence Resonance Transfer Assay for STRA6-Catalyzed Retinol Transfer between RBP Molecules

To study retinol transfer between RBP molecules, we tagged EGFP to the N-terminus of RBP right after its natural secretion signal to create N-EGFP-RBP. The fluorescence resonance transfer (FRET) between retinol and EGFP has been demonstrated previously (Kawaguchi et al. 2011). The transfer reaction was initiated by adding holo-RBP to N-EGFP-RBP premixed with membrane purified from STRA6 expressing COS-1 cells. Membranes from COS-1 cells expressing both STRA6 and LRAT and cells that express neither STRA6 nor LRAT were used as controls. Real-time retinol-EGFP FRET was measured with the excitation filter 320ex and the emission filters 460–10 and 510–10 using simultaneous duel emission optics in POLARstar Omega. The signal from each time point of each reaction was the average of 10 measurements. The fluorescence of each reaction was measured before holo-RBP was added at 0 min to initiate the reaction. The

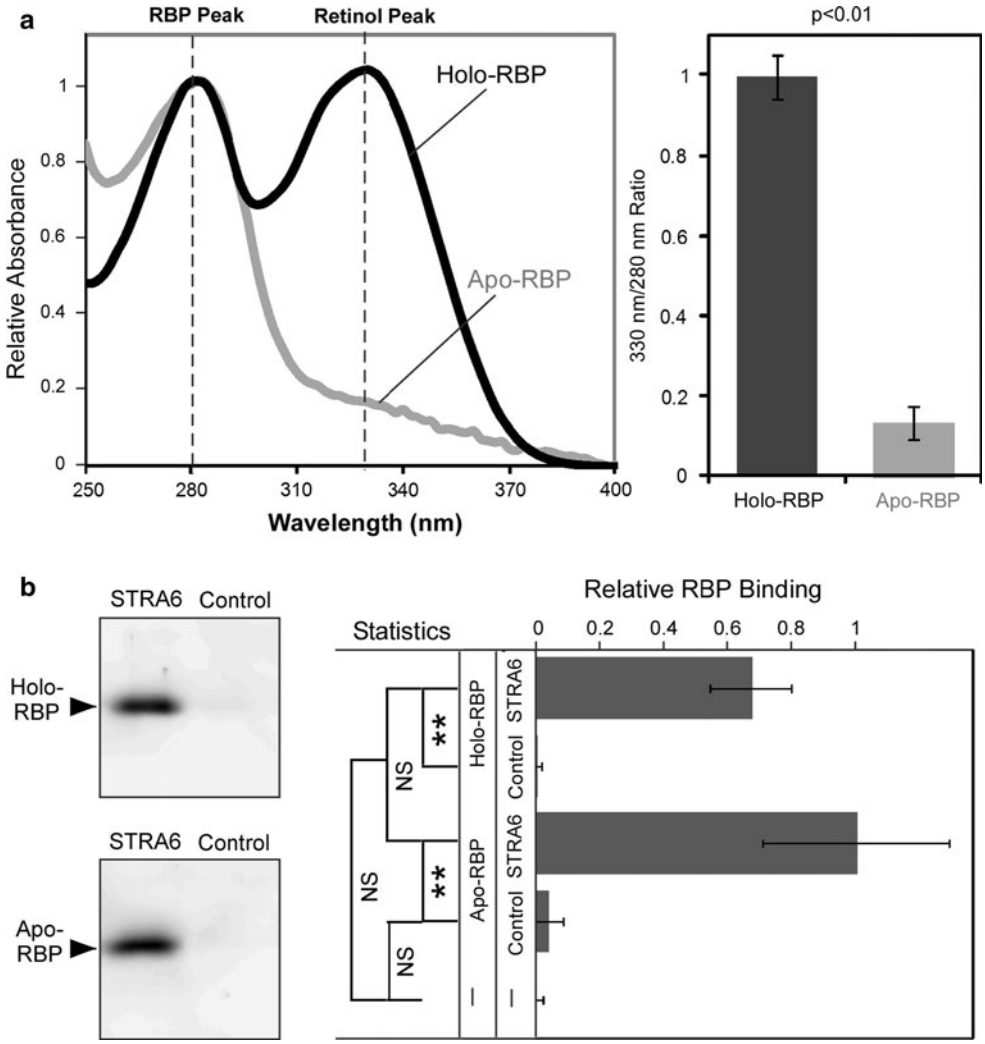

Fig. 1 Both holo-RBP and apo-RBP bind to STRA6. **a** Absorption spectra of HPLC-purified holo-RBP fully loaded with retinol and apo-RBP produced from fully loaded RBP. The absorption at 280 nm is defined as 1. Statistical analysis of the difference between holo-RBP and apo-RBP in 330/280 nm ratio is shown on the *right. Error bars* indicates standard deviation ($n = 3$) for the ratio of absorption at 330 and 280 nm. Statistical significance is determined by Student's t test with equal variance. **b** Both holo-RBP and apo-RBP bind to STRA6. Holo-RBP (0.2 μM) or apo-RBP (0.2 μM) was incubated with STRA6-expressing cells or control cells that do not express STRA6. After 1 h binding, the cells were washed twice to remove unbound proteins. RBP associated with cells was detected by Western blot analysis. Western blot was recorded using Fujifilm LAS3000 Luminescent Image Analyzer and analyzed by Multi-Gauge software. Statistical analysis ($n = 3$) was conducted by Tukey's multiple comparison test (**$p < 0.01$; *NS* not significant)

equation to calculate this ratio is $[(510_t - 510_b)/(460_t - 460_b)]$, where 510_t, 510_b, 460_t, and 460_b represent emissions at 510 nm after initiation of the reaction (t = time point), at 510 nm before holo-RBP is added (b = background), at 460 nm after initiation of the reaction (t = time point), and at 460 nm before holo-RBP is added (b = background), respectively.

Statistical Analysis of Experimental Results

All statistical analysis was performed by Minitab 15 software. Student's *t* test was used for a single set of comparison. The data sets containing multiple data points were analyzed by one-way ANOVA followed by Tukey's multiple comparison (1 and 5 % error rate were used).

Results

Both Holo-RBP and Apo-RBP Bind STRA6

Because both retinol influx and retinol efflux mediated by STRA6 theoretically depend on STRA6 interacting with holo-RBP and apo-RBP, it is imperative to confirm these interactions. Two previous reports reached opposite conclusions on the interactions of holo-RBP and apo-RBP with STRA6 (Berry et al. 2011; Chen et al. 2012). To resolve the issue of STRA6's interaction with RBP, we used HPLC to purify correctly folded and fully loaded holo-RBP (as demonstrated by the retinol peak similar in height as the protein peak in the absorption spectrum), and produced apo-RBP from this correctly folded RBP (Fig. 1a). These reagents are different from the previous reports, which used either free retinol mixed with apo-RBP in solution (not holo-RBP) (Berry et al. 2011) or urine RBP combined with retinoic acid as holo-RBP (Chen et al. 2012). Using these reagents, we compared the binding of holo-RBP and apo-RBP to STRA6 and found that they both bind to STRA6 (Fig. 1b).

STRA6 Catalyzes Retinol Transport from CRBP-I to Apo-RBP

It was previously shown that STRA6 couples to CRBP-I for retinol uptake from holo-RBP. Can STRA6 also mediate retinol efflux into apo-RBP if retinol is bound to CRBP-I intracellularly? To test this possibility, we first incubated STRA6/CRBP-I cells with holo-RBP to allow retinol uptake by CRBP-I and then incubated the cells with pure apo-RBP. Interestingly, apo-RBP did cause retinol efflux and an almost complete loss of retinol taken up by CRBP-I (Fig. 2). This effect is apo-RBP dependent because BSA, a nonspecific retinol binding protein, did not have this effect. As a control, apo-RBP removed little retinol from STRA6/LRAT cells. This result revealed a difference in retinol uptake mediated by CRBP-I from retinol uptake mediated by LRAT in that retinol taken up through CRBP-I can be much more readily lost to extracellular apo-RBP.

Comparison of STRA6 Catalyzed Retinol Efflux from Retinol/CRBP-I and Retinol/CRBP-II

In contrast to CRBP-I, CRBP-II couples poorly to STRA6 in mediating cellular retinol uptake from holo-RBP (Kawaguchi et al. 2011). Can STRA6 mediate retinol efflux to extracellular apo-RBP from retinol taken up by CRBP-II? To compare CRBP-I and CRBP-II in retinol efflux, we first loaded cells with free ^{3}H-retinol as has been done to study STRA6/LRAT in efflux previously (Isken et al. 2008) and then compared the ability of apo-RBP to cause retinol efflux from different cells. This method effectively loads cells with retinol in the absence of STRA6 and overcomes the difficulty of CRBP-II's ineffectiveness in coupling to STRA6 to take up retinol from ^{3}H-retinol/RBP and CRBP-I's dependence on STRA6 to efficiently take up retinol from ^{3}H-retinol/RBP. This method of loading retinol makes it possible to study STRA6 dependence of retinol efflux. Interestingly, STRA6 mediates retinol efflux from both STRA6/CRBP-I cells and STRA6/CRBP-II cells (Fig. 3). In addition, CRBP-II cells lose retinol to extracellular apo-RBP more readily than CRBP-I in the absence of STRA6. These experiments offer unique insight into the relationship between cellular retinol binding proteins and STRA6-mediated retinol efflux and the difference in STRA6-mediated retinol influx and efflux.

Apo-RBP to Holo-RBP Ratio Affects STRA6-mediated Retinol Efflux from Retinol/CRBP-I

It was also shown previously that pure apo-RBP can cause a fraction of retinol to be lost from STRA6/LRAT cells (Isken et al. 2008). The above experiments showed that STRA6 can cause strong retinol efflux from retinol/CRBP-I to pure apo-RBP and an almost complete loss of retinol taken up by CRBP-I. However, the blood is known to contain only a small fraction of apo-RBP compared to holo-RBP. Whether apo-RBP causes retinol efflux in the presence of holo-RBP has not been studied. When we added holo-RBP in apo-RBP-dependent retinol efflux reactions, net flux depended on the ratio of holo-RBP to apo-RBP (Fig. 4). Retinol efflux only happened when there was an overwhelming amount of apo-RBP relative to holo-RBP. When the holo-RPB concentration was similar to or higher than the apo-RBP concentration, retinol influx instead of efflux happened. The effect of holo-RBP on

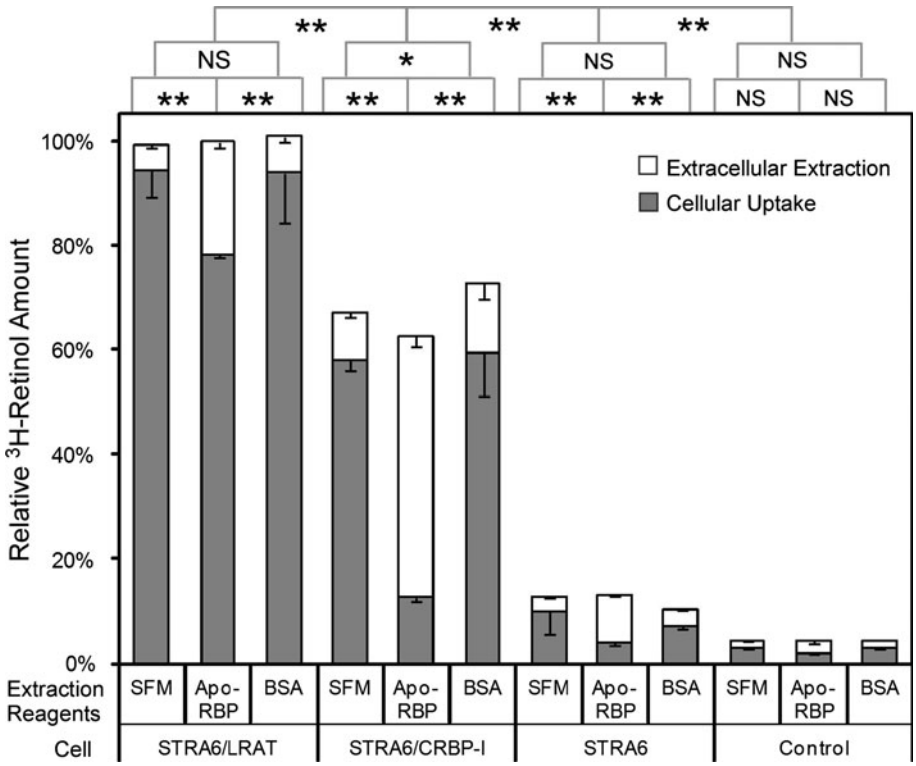

Fig. 2 Preferential loss of retinol taken up by STRA6/CRBP-I cells in an apo-RBP-dependent manner. After cells take up ^{3}H-retinol from ^{3}H-retinol/RBP for 1 h, incubation with apo-RBP for 1 h can remove more ^{3}H-retinol from STRA6/CRBP-I than STRA6/LRAT or STRA6-only cells. BSA and SFM were used as controls for apo-RBP. ^{3}H-retinol extracted during the 1 h incubation with apo-RBP, BSA, or SFM is shown in the *white column.* ^{3}H-retinol remaining in the cells after extraction is shown in the *gray column.* The total amount of ^{3}H-retinol taken up by cells after the first 1 h incubation is represented by combining the *white column* and *blue column* for each reaction. The highest activity by STRA6/LRAT cells is defined as 100 %. Statistical significance of the comparison of the extracted ^{3}H-retinol is shown on the *top* of the graph ($n = 3$). Statistical significance was determined by Tukey's multiple comparison test ($*p < 0.05$; $**p < 0.01$; *NS* not significant)

STRA6-catalyzed retinol efflux is likely the combined result of holo-RBP's competition with apo-RBP in binding to STRA6 and the counteracting effect of STRA6-mediated retinol influx.

STRA6-Catalyzed Retinol Loading Is Inhibited by Holo-RBP and STRA6-Catalyzed Retinol Release Is Inhibited by Apo-RBP

It was previously known that STRA6 catalyzes efficient loading of retinol into apo-RBP in the absence of LRAT or CRBP-I. How is this loading reaction affected by holo-RBP? Using a retinol fluorescence assay established previously (Kawaguchi et al. 2011), we found that holo-RBP inhibits STRA6-catalyzed retinol loading into apo-RBP, although STRA6 catalyzes retinol loading into pure apo-RBP (Fig. 5a). This is consistent with results above using radioactive assays. When STRA6 is exposed to a mixture of RBP with a holo-RBP to apo-RBP ratio similar to that of the blood, STRA6 catalyzes net retinol release not loading. Conversely, apo-RBP inhibits STRA6-catalyzed retinol release from holo-RBP (Fig. 5b). In this experiment, we also examined a long time course of STRA6-catalyzed retinol loading and STRA6-catalyzed retinol release involving the same concentrations of retinol and RBP. STRA6-catalyzed retinol loading is not simply a mirror image of STRA6-catalyzed retinol release. These fundamental properties of STRA6's interactions with holo-RBP and apo-RBP determine STRA6-mediated retinol release and loading in the presence of a mixture of holo-RBP and apo-RBP. These experiments are consistent with the previous experiment (Fig. 1b) showing that both holo-RBP and apo-RBP bind to STRA6.

STRA6 Catalyzes Retinol Exchange Between Intracellular Holo-CRBP-I and Extracellular Holo-RBP

There are two possible mechanisms to explain the lack of net retinol efflux caused by apo-RBP in the presence of holo-RBP. It is possible that retinol efflux does not happen

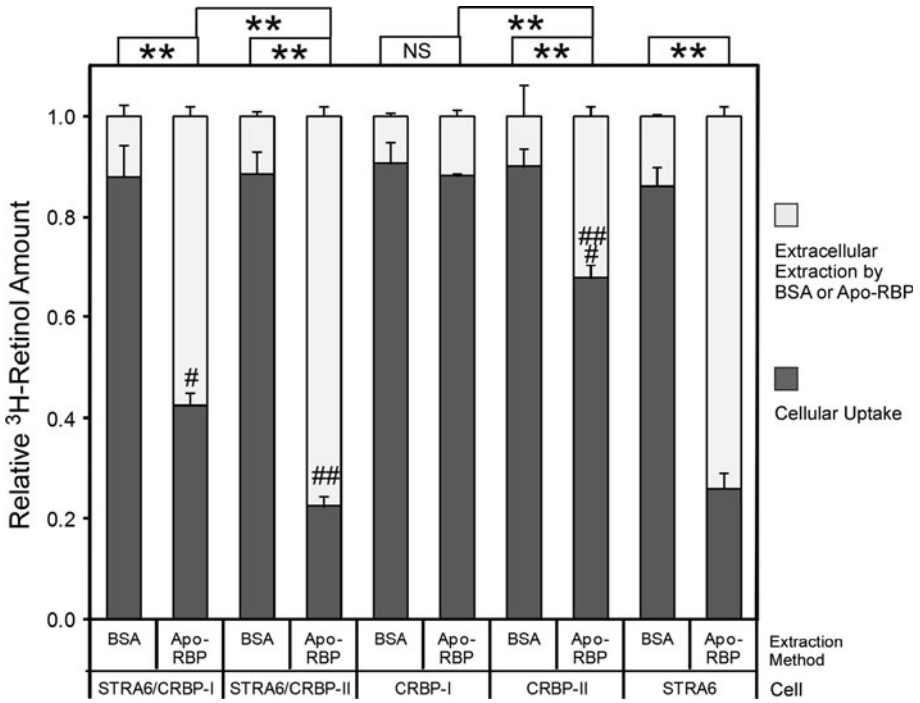

Fig. 3 Comparison of CRBP-I and CRBP-II in STRA6-mediated retinol efflux. After cells were loaded with free ^{3}H-retinol for 2 h, 1 μM of apo-RBP was added to cause ^{3}H-retinol depletion for 2 h. BSA (1 μM) of was used as a control. ^{3}H-retinol extracted during the 2-h incubation with apo-RBP or BSA is shown in the *white column.* ^{3}H-retinol remaining in the cells after extraction is shown in the *dark gray column.* The total amount of ^{3}H-retinol taken up by cells before the extraction is represented by combining the *white column* and *dark gray column* and is defined as 100 % for each reaction. Apo-RBP caused strong ^{3}H-retinol depletion of both STRA6/CRBP-I cells (#) and STRA6/CRBP-II cells (##). In contrast to CRBP-I, CRBP-II loses retinol more readily to extracellular apo-RBP independently of STRA6 (###). Statistical significance of the comparison of the extracted ^{3}H-retinol is shown on the *top* of the graph ($n = 3$). Statistical significance was determined by Tukey's multiple comparison test (**$p < 0.01$; *NS* not significant)

in the presence of holo-RBP, but it is more likely that retinol influx counteracts retinol efflux to prevent net retinol loss in the presence of holo-RBP. To test the second possibility, we distinguished intracellular retinol from the extracellular retinol by preloading STRA6/CRBP-I cells with ^{3}H-retinol from ^{3}H-retinol/RBP and then incubating cells with cold holo-RBP or apo-RBP (Fig. 6a). Amazingly, intracellular retinol clearly still gets out of the cell in a STRA6- and RBP-dependent manner in the presence of holo-RBP. Cold holo-RBP is as effective as apo-RBP in causing retinol efflux from STRA6/CRBP-I cells (Fig. 6a). This experiment demonstrates that retinol efflux still happens in the presence of holo-RBP. Although retinol influx in the presence of holo-RBP prevents net retinol efflux, the efflux reaction can exchange retinol between intracellular CRBP-I and extracellular RBP. The existence of the retinol exchange activity suggests that cold holo-RBP causes ^{3}H-retinol loss from STRA6 expressing cells not only by removing ^{3}H-retinol/RBP bound to cell-surface STRA6 but also through retinol exchange between ^{3}H-retinol and cold retinol. To further demonstrate the existence of retinol exchange, we added unlabeled retinol before addition of holo-RBP but after STRA6 cells were incubated with ^{3}H-retinol/RBP. Indeed, unlabeled retinol blocked the ability of holo-RBP to remove ^{3}H-retinol from STRA6 cells (Fig. 6b). This result is consistent with the occurrence of retinol exchange.

STRA6 Catalyzes Net Retinol Influx, Not Efflux in the Presence of Human Serum

Human serum contains RBP in the form of holo-RBP/Transthyretin (TTR) complex and a fraction of apo-RBP (Mills et al. 2008; Zanotti and Berni 2004). Does the apo-RBP in human serum cause retinol efflux from STRA6/LRAT or STRA6/CRBP-I cells? Using HPLC assays, we found that strong retinol efflux to pure extracellular apo-RBP did happen for STRA6/CRBP-I cells that have taken retinol from human serum (Fig. 7a). However, human serum, which contains both holo-RBP and apo-RBP, caused net retinol influx, not retinol efflux for either STRA6/LRAT cells or STRA6/CRBP-I cells that have previously taken up retinol (Fig. 7a, b). This result is consistent with the inhibitory effect of holo-RBP on apo-RBP-mediated retinol efflux from STRA6-expressing cells.

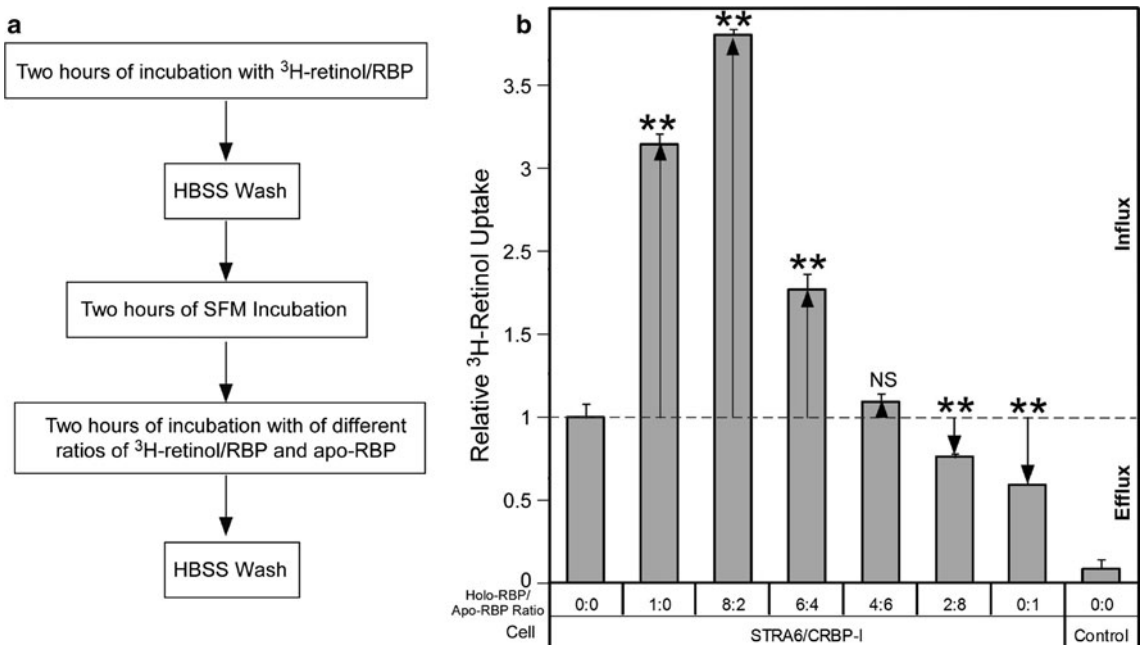

Fig. 4 The ratio of holo-RBP and apo-RBP determines the ability of apo-RBP to cause net retinol efflux from STRA6/CRBP-I cells. **a** Diagram of experimental design. After taking up ^{3}H-retinol from ^{3}H-retinol/RBP for 2 h, the cells were washed with HBSS and incubated with SFM for 2 h to dissociate cell-surface bound RBP. Apo-RBP with different amounts of ^{3}H-retinol/RBP was incubated with the cells for 2 h. After a further HBSS wash, the ^{3}H-retinol remaining in cells was counted. **b** Effect of different ratios of holo-RBP to apo-RBP on the ability of apo-RBP to cause retinol efflux. Holo-RBP to apo-RBP ratio is shown on the X-axis. For all reactions in which apo-RBP was added ("8:2," "6:4," "4:6," "2:8," "0:1" reactions), the same amount of apo-RBP (0.12 μM) was used. Reaction "0:0" means neither holo-RBP nor apo-RBP was added, while "1:0" means only holo-RBP was added and "0:1" means only apo-RBP was added. The *dashed line* indicates basal level of ^{3}H-retinol uptake without efflux or influx after the 2-h uptake (no additional apo-RBP or holo-RBP added). This basal level of ^{3}H-retinol uptake is defined as 1. The *downward arrow* indicates net retinol efflux. The *upward arrow* indicates net retinol influx. Statistical analysis ($n = 3$) was determined by Tukey's multiple comparison test against the control reaction without holo-RBP/apo-RBP added in the last 2 h as indicated by "0:0" (**$p < 0.01$; *NS* not significant)

STRA6 Catalyzes Retinol Exchange between CRBP-I and Human Serum

Given the retinol exchange reaction mentioned above, is it possible that intracellular retinol exchanges with retinol in human serum despite the ability of serum to cause net retinol influx in STRA6-expressing cells? To study retinol exchange, we preloaded cells with ^{3}H-retinol and found that human serum does cause strong STRA6-dependent ^{3}H-retinol efflux from STRA6/CRBP-I cells (Fig. 8a), consistent with STRA6-catalyzed retinol exchange between intracellular CRBP-I and extracellular RBP. This STRA6-dependent ^{3}H-retinol efflux is much more efficient from STRA6/CRBP-I cells than STRA6/LRAT cells. This experiment demonstrates that STRA6 mediates retinol exchange between intracellular CRBP-I and the serum, although holo-RBP in the serum prevents net retinol efflux from cells. We also compared the ability of serum in causing ^{3}H-retinol efflux from intracellular CRBP-I and CRBP-II. Although STRA6 promotes ^{3}H-retinol efflux from both CRBP-I and CRBP-II cells, ^{3}H-retinol efflux caused by human serum is much less STRA6-dependent for CRBP-II cells than CRBP-I cells (Fig. 8b).

STRA6 Catalyzes Retinol Exchange between RBP Molecules

Given the mechanism of STRA6's action, its abilities to catalyze retinol release from RBP and loading into RBP should be responsible for its ability to catalyze retinol exchange between RBP and CRBP-I. If that is the case, the exchange reaction should also apply to RBP molecules. To test this possibility, we used fluorescence resonance transfer (FRET) between retinol and EGFP by tagging RBP with EGFP. The FRET pair of retinol and EGFP has been demonstrated previously (Kawaguchi et al. 2011). We tagged EGFP at the N-terminus of RBP because we found previously that N-terminus tag does not interfere with RBP's binding to STRA6 (Kawaguchi et al. 2007). By incubating untagged holo-RBP with EGFP-RBP, we found that STRA6 indeed catalyzes retinol transport between RBP molecules as shown by the time-dependent and STRA6-dependent increase in retinol-EGFP FRET signals

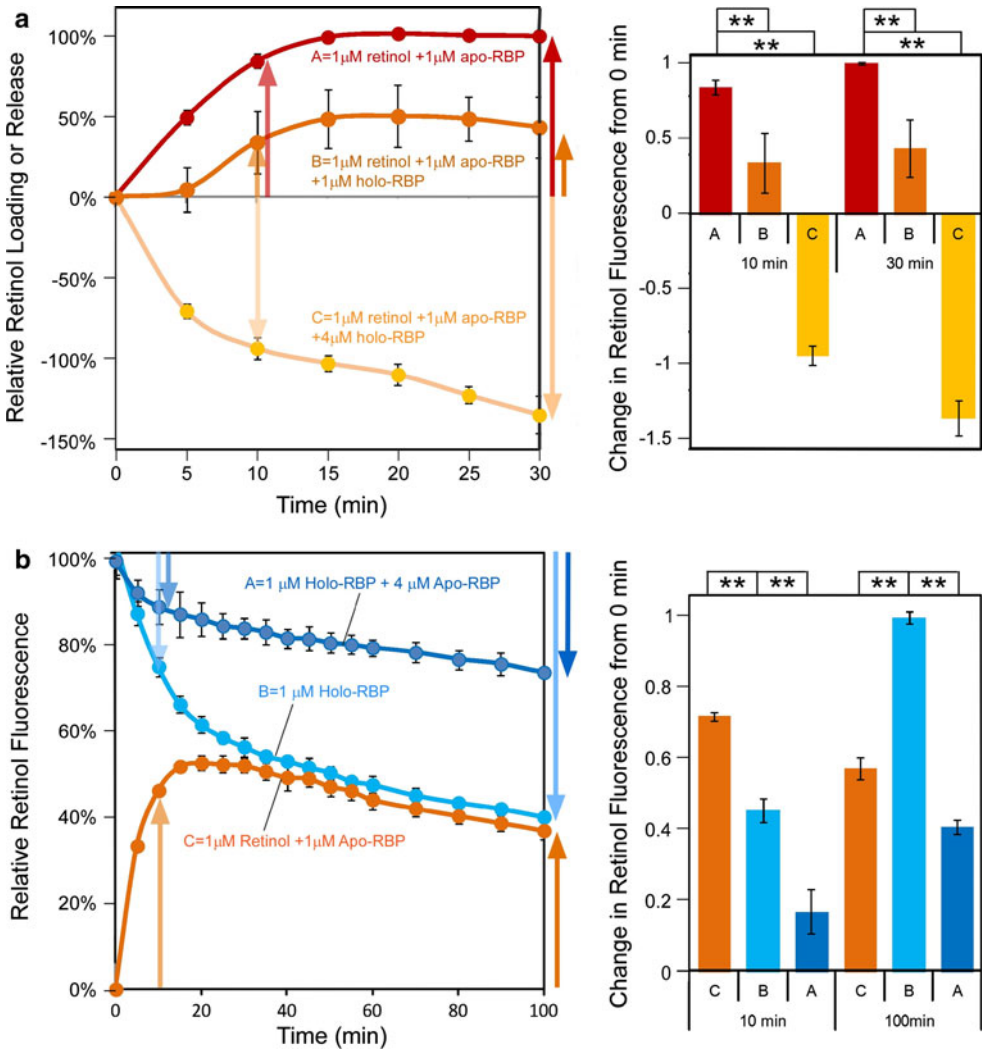

Fig. 5 Inhibition of STRA6-catalyzed retinol loading into apo-RBP by holo-RBP and inhibition of STRA6-catalyzed retinol release from holo-RBP by apo-RBP. **a** Although STRA6-catalyzed retinol loading into pure apo-RBP and caused an increase in retinol fluorescence (reaction A), the presence of holo-RBP inhibited net retinol loading (reactions B and C). When holo-RBP to apo-RBP ratio approached that of blood (reaction C), STRA6 catalyzed net retinol release, not retinol loading. To visualize and compare time-dependent changes, retinol fluorescence at time 0 min is defined as 0 for all reactions, and the highest retinol fluorescence change achieved in the retinol loading reaction (*red reaction*) is defined as 100 %. Statistical significance of the 10 min and 30 min data points ($n = 3$) was determined by Tukey's multiple comparison test ($^{**}p < 0.01$). **b** Apo-RBP inhibits STRA6-catalyzed retinol release. STRA6 catalyzed retinol release from 1 μM holo-RBP (reaction A) is strongly inhibited by the presence of 4 μM apo-RBP (reaction B). STRA6-catalyzed retinol loading (reaction C) is not a mirror image of STRA6-catalyzed retinol release (reaction B), although they contain the same concentration of retinol and RBP. For all reactions, fluorescence before the addition of holo-RBP or apo-RBP is defined as 0. Retinol fluorescence of 1 μM holo-RBP is defined as 100 %. Statistical significance of the 10 and 100 min data points ($n = 3$) was determined by Tukey's multiple comparison test ($^{**}p < 0.01$)

(Fig. 9). LRAT suppresses this retinol transfer. This experiment revealed another perspective of STRA6's function in vitamin A uptake. STRA6 constantly catalyzes retinol exchange between holo-RBP and apo-RBP. During this exchange reaction, holo-RBP becomes apo-RBP and apo-RBP becomes holo-RBP. LRAT couples to STRA6 for vitamin A uptake by stopping this exchange reaction. This retinol exchange activity is a further support of the proposed mechanism of STRA6 (Kawaguchi et al. 2011) and argues against the absolute dependence of STRA6 for LRAT or CRBP-I for its activity.

Discussion

LRAT was the first protein shown to enhance STRA6's vitamin A uptake activity (Golczak et al. 2008; Isken et al. 2008; Kawaguchi et al. 2007). It was also shown that the

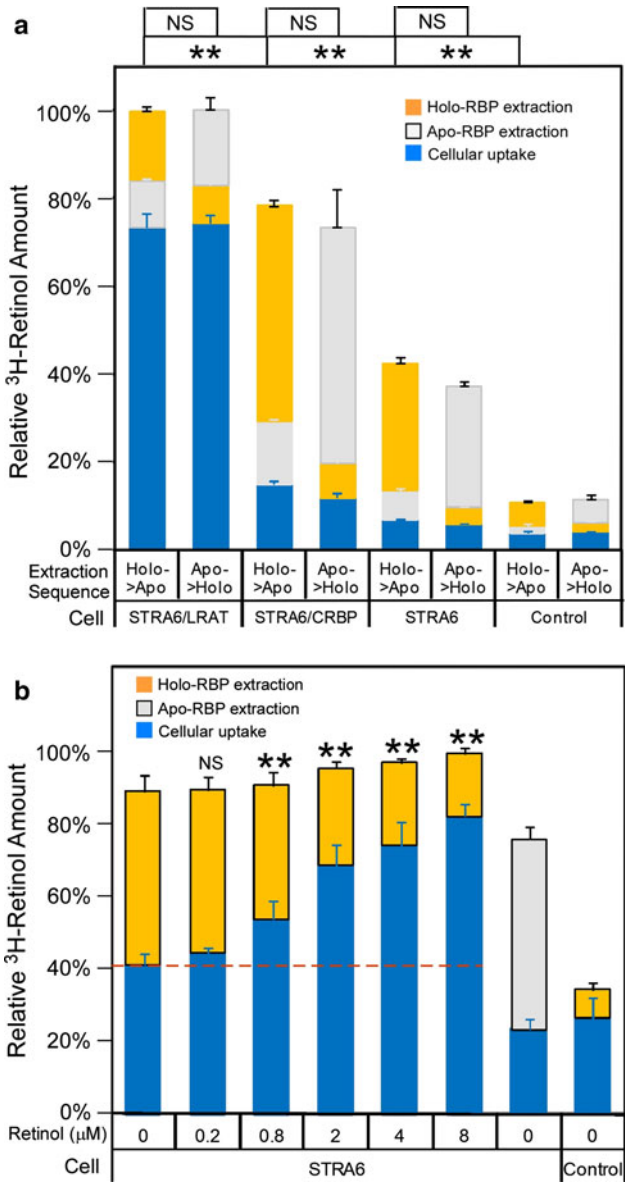

◀ **Fig. 6** STRA6-catalyzed retinol exchange. **a** Holo-RBP and apo-RBP are similarly effective in their abilities to remove ^{3}H-retinol from STRA6/CRBP-I cells. Both apo-RBP and cold holo-RBP extract much more ^{3}H-retinol from STRA6/CRBP-I cells than from STRA6/LRAT cells. After cells took up ^{3}H-retinol from ^{3}H-retinol/RBP for 1 h, unlabeled holo-RBP and apo-RBP were sequentially added to cells (1 h incubation each) to extract ^{3}H-retinol. The amounts of ^{3}H-retinol extracted by holo-RBP (*yellow column*), ^{3}H-retinol extracted by apo-RBP (*white column*), or ^{3}H-retinol remaining in cells (*blue column*) are shown for each reaction. The sequence of addition is indicated on the *bottom* of each reaction. The total amount of ^{3}H-retinol taken up by cells after the first 1 h incubation is represented by combining the *white*, *yellow*, and *blue columns* for each reaction. The highest total activity by STRA6/LRAT cells is defined as 100 %. Statistical significance ($n = 3$) of the comparison between the first extraction by holo-RBP or apo-RBP was determined by Tukey's multiple comparison test (**$p < 0.01$; *NS* not significant). **b** Unlabeled retinol suppressed the ability of unlabeled holo-RBP to extract ^{3}H-retinol. After cells took up ^{3}H-retinol from ^{3}H-retinol/RBP for 1 h, they were washed with SFM. Different amounts of cold retinol were added to cells incubated in SFM for 10 min. After removal of medium, unlabeled holo-RBP or apo-RBP was added to cells (1 h incubation) to extract ^{3}H-retinol. The amount of ^{3}H-retinol extracted by holo-RBP (*yellow column*), ^{3}H-retinol extracted by apo-RBP (*white column*), or ^{3}H-retinol remaining in cells (*blue column*) are shown. The total amount of ^{3}H-retinol taken up by cells after the first 1 h incubation is represented by combining extracted amount (*yellow* or *white column*) with cellular uptake after extraction (*blue column*) for each reaction. The highest activity by STRA6 cells is defined as 100 %. Statistical significance of the comparison between the retinol addition reactions and the control reaction with no retinol added ($n = 3$) was determined by Tukey's multiple comparison test (**$p < 0.01$; *NS* not significant)

reverse reaction of vitamin A loading into apo-RBP still happens in cells that express both STRA6 and LRAT to lead to cellular retinol loss (Isken et al. 2008). This finding suggests that STRA6's action can lead to retinol efflux (Isken et al. 2008). The activity of STRA6-catalyzed retinol loading into apo-RBP is much stronger without LRAT (Kawaguchi et al. 2011). Can STRA6 mediate both retinol uptake and retinol efflux, analogous to the role of HDL receptor SR-BI's role in cholesterol uptake and efflux (Connelly and Williams 2004)? If STRA6 can do both, what are the factors that determine these activities? If STRA6 mediates retinol efflux to cause vitamin A loss, how does it function to take up vitamin A?

To answer these questions, we systematically examined the roles of individual components involved in these activities to dissect STRA6's mechanism (Table 1). For example, natural blood contains both holo-RBP and apo-RBP. If only natural blood is used as a source of RBP (no purified component), it is not possible to evaluate apo-RBP's binding to STRA6, to study apo-RBP's role in retinol efflux, to compare STRA6's binding to holo-RBP and apo-RBP, or to reveal their mutual competition during STRA6-mediated retinol influx and efflux. Using this strategy, we found that STRA6's ability to mediate retinol efflux is determined by both RBP species (apo-RBP to holo-RBP ratio) and intracellular retinol storage mechanisms (CRBP-I or LRAT) (Table 1; Fig. 10). Holo-RBP inhibits STRA6-mediated retinol efflux by apo-RBP. Similarly, apo-RBP inhibits STRA6-mediated retinol influx from holo-RBP. However, holo-RBP permits retinol exchange between intracellular CRBP and extracellular RBP (Table 1). In addition, experiments presented here (e.g., STRA6-catalyzed retinol exchange between RBP molecules) provide further support for the proposed mechanism of STRA6 (Kawaguchi et al. 2011) and argue against the alternative models. For example, they argue against the models that propose a strict dependence of STRA6 on CRBP-I or LRAT for its activity. Lastly, this study also helps to explain the opposite conclusions of STRA6's interaction with holo-RBP and apo-RBP from two previous reports (Berry et al. 2011; Chen et al. 2012) (Supplementary Discussion and Supplementary Fig. 1).

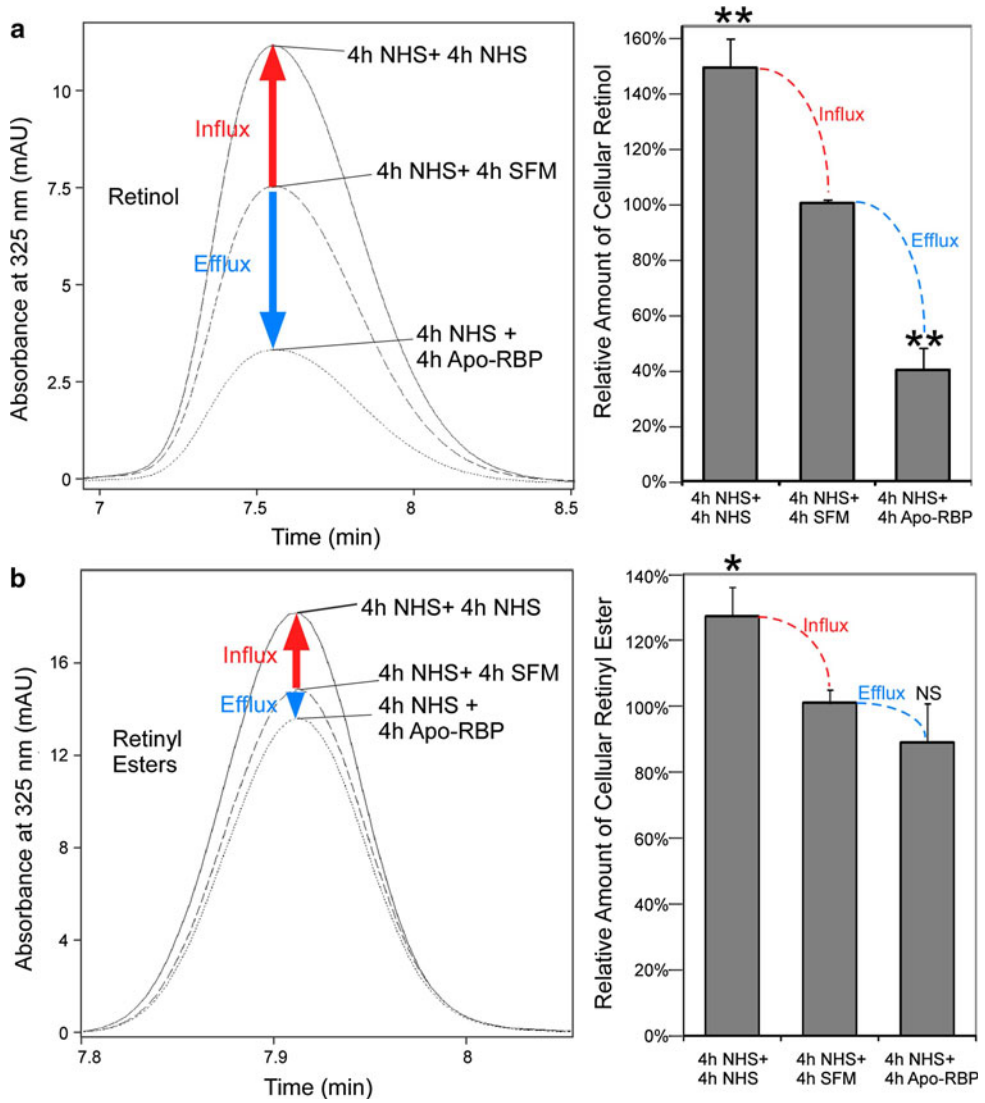

Fig. 7 HPLC analyses demonstrating that STRA6 mediates net vitamin A influx not efflux when exposed to serum. **a** HPLC assays for retinol efflux from STRA6/CRBP-I cells. After STRA6/CRBP-I cells took up retinol from NHS for 4 h, they are further incubated with SFM, NHS, or 1 μM apo-RBP for another 4 h. Although apo-RBP caused significant retinol loss compared to the SFM control, NHS caused further retinol uptake, not loss. *Left* representative retinol peaks from the HPLC analyses. *Right* average data from 3 independent experiments. Statistical significance ($n = 3$) of the comparison between SFM incubation with apo-RBP incubation (efflux) or with NHS incubation (influx) was determined by Tukey's multiple comparison test ($^{**}p < 0.01$). The retinol level in the SFM control is defined as 100 %. **b** HPLC assays for retinol efflux from STRA6/LRAT cells. After STRA6/LRAT cells took up retinol from NHS for 4 h, they are further incubated with SFM, NHS, or 1 μM apo-RBP for another 4 h. *Left panel* shows representative retinyl ester peaks from the HPLC analyses. *Right panel* shows the average data from three independent experiments. The level of retinyl ester in the SFM control is defined as 100 %. Statistical significance ($n = 3$) of the comparison between SFM incubation with apo-RBP incubation (efflux) or with NHS incubation (influx) was determined by Tukey's multiple comparison test ($^{*}p < 0.05$; *NS* not significant)

There are three major findings of this study. First, pure extracellular apo-RBP can effectively cause retinol efflux from STRA6/CRBP-I cells and can deplete almost all retinol taken up by STRA6/CRBP-I cells. A simple hypothesis to explain the previous finding that CRBP-I effectively couples to STRA6 for retinol uptake from holo-RBP is that CRBP-I's affinity for retinol is higher (or much higher) than that of RBP bound to STRA6. This hypothesis is consistent with STRA6's ability to catalyze retinol release from holo-RBP and suggests that STRA6 may simply functions like a "bottle opener" (if RBP is analogous to a "bottle" that holds vitamin A) to let retinol out. However, STRA6's ability to catalyze retinol efflux from CRBP-I to apo-RBP, as shown in the study, argues against this hypothesis and suggests that CRBP-I's affinity for retinol is similar to that of RBP bound to STRA6. The structural basis of STRA6's ability to fine-tune the transport of retinol into and out of RBP so that it catalyzes both retinol

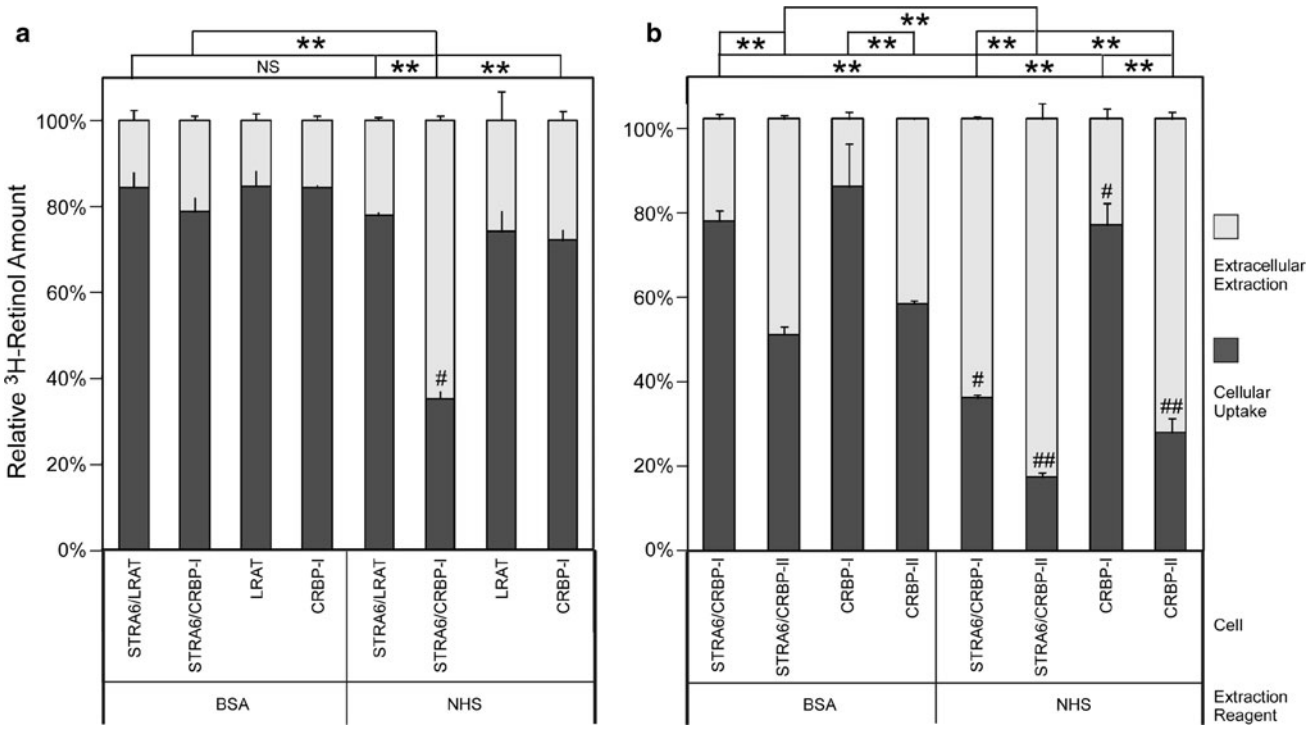

Fig. 8 STRA6 catalyzes retinol exchange between intracellular CRBP and the serum. To study retinol exchange, intracellular retinol is distinguished from extracellular retinol using ^{3}H-retinol. **a** After cells were loaded with free ^{3}H-retinol for 2 h, NHS or BSA was added to cause ^{3}H-retinol depletion. NHS caused strong ^{3}H-retinol depletion of STRA6/CRBP-I cells (#), as compared to STRA6/LRAT cells. The strong ^{3}H-retinol depletion from CRBP-I expression cells is both STRA6 dependent and NHS dependent (the control is 5 mg/ml BSA). **b** Comparison of CRBP-I and CRBP-II in retinol efflux. After cells were loaded with free ^{3}H-retinol (2 h), NHS or BSA was added to cause ^{3}H-retinol depletion (2 h). Although NHS-mediated depletion of CRBP-I cells is dependent on STRA6 (compare the 2 reactions marked with #), NHS can strongly deplete ^{3}H-retinol from CRBP-II cells with or without STRA6 (compare the 2 reactions marked with ##). Even BSA (5 mg/ml) is sufficient to cause large ^{3}H-retinol efflux from CRBP-II-expressing cells. In both (**a**) and (**b**), ^{3}H-retinol extracted by NHS or BSA is shown in the *white column* and ^{3}H-retinol remaining in the cells after extraction is shown in the *dark gray column*. The total activity of each reaction before extraction is defined as 100 %. Statistical significance ($n = 3$) of the extracted ^{3}H-retinol was determined by Tukey's multiple comparison test. Comparison is shown on the *top* of each figure (**$p < 0.01$; *NS* not significant)

influx from RBP to CRBP-I and retinol efflux from CRBP-I to RBP is still unknown.

CRBP-I's behavior is certainly not the only possible scenario of how cellular retinol binding proteins may couple to STRA6. Unlike the more widely expressed CRBP-I, CRBP-II is most highly expressed in the small intestine and functions to facilitate the uptake of free retinol by enterocytes (Harrison 2005). Because both CRBP-I and CRBP-II are cellular retinol binding proteins and CRBP-II binds retinol with lower affinity (Ong 1994), we included CRBP-II here and in a previous study (Kawaguchi et al. 2011) as a control for CRBP-I. CRBP-II couples poorly with STRA6 in taking up retinol from holo-RBP, but it can couple to STRA6 for retinol efflux into apo-RBP.

The effective coupling of LRAT and CRBP-I to STRA6 for retinol influx distinguishes them from CRBP-II, but the effective coupling of CRBP-I and CRBP-II to STRA6 for retinol efflux distinguishes them from LRAT and the degree of dependence on STRA6 distinguishes CRBP-I from CRBP-II in retinol efflux (CRBP-II depends less on STRA6 for retinol efflux). Although retinyl ester formation by LRAT prevents STRA6-catalyzed retinol efflux into apo-RBP, it is possible that there exist a still unidentified complex regulatory mechanism that promotes retinol efflux into apo-RBP by native cells that express both STRA6 and LRAT. This mechanism needs to balance retinyl ester formation, which prevents retinol efflux, and retinyl ester hydrolysis, which prevents vitamin A storage as retinyl esters.

Second, holo-RBP inhibits STRA6-mediated retinol efflux into apo-RBP. Holo-RBP promotes STRA6-mediated retinol release, which counteracts retinol loading. For healthy individuals, the blood contains on average 2.67 μM RBP, which includes about 90 % holo-RBP and 10 % apo-RBP (Mills et al. 2008). It was also known previously that the residence time for RBP uncomplexed with TTR is only 1.2–1.3 h in the blood (Vahlquist et al. 1973). We have shown that holo-RBP inhibits

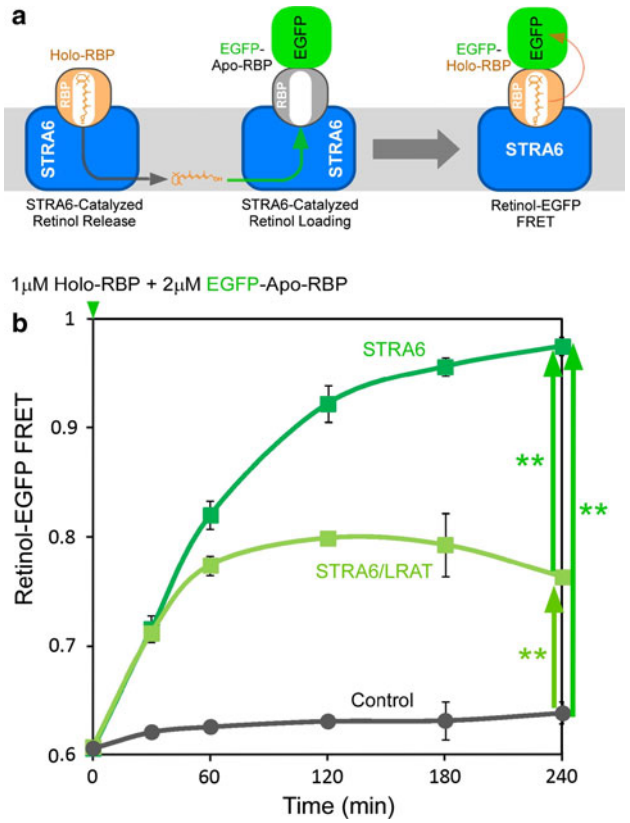

Fig. 9 Retinol-EGFP FRET demonstrating STRA6-catalyzed retinol exchange between RBP molecules. **a** Schematic diagram of the proposed mechanism of STRA6-catalyzed retinol exchange between RBP molecules. To demonstrate STRA6-catalyzed exchange between RBP molecules, apo-RBP is tagged with EGFP. Retinol binding to EGFP-RBP would lead to fluorescence resonance energy transfer between retinol and EGFP. **b** STRA6 catalyzes the transfer of retinol from untagged holo-RBP to EGFP-apo-RBP in a time-dependent manner (*dark green*), as shown by the increase in retinol-EGFP FRET. This transfer reaction does not happen in the absence of STRA6 (*black*) and is suppressed by LRAT (*light green*). Statistical significance ($n = 3$) was determined by Tukey's multiple comparison test ($^{**}p < 0.01$)

STRA6-catalyzed retinol loading into apo-RBP. At the ratio of holo-RBP to apo-RBP found in the blood, STRA6 mediates net retinol release from RBP, not retinol loading into RBP. In the presence of human serum, STRA6 mediates net vitamin A uptake (not loss), despite the presence of a small fraction of apo-RBP in serum.

Consistent with STRA6's function in vitamin A uptake, retinoid analyses have shown that STRA6 knockdown in zebrafish (Isken et al. 2008) or STRA6 knockout in mice (Ruiz et al. 2012) both lead to loss of tissue vitamin A uptake, not excessive vitamin A accumulation. If STRA6's primary function is retinol efflux, excessive vitamin A accumulation is expected. STRA6 knockout in mice leads to a loss of more than 90 % of retinyl ester, the major form of stored vitamin A, in the retinal pigment epithelium (RPE), the primary cell type responsible for vitamin A

Table 1 Summary of key experimental conditions to dissect STRA6-dependent retinol influx, efflux, and exchange

Extracellular		Intracellular			STRA6-dependent retinol transport
Holo-RBP	Apo-RBP	Holo-CRBP-I	Apo-CRBP-I	LRAT	
+	−	−	+	−	Influx
−	+	+	−	−	Efflux
+	−	+	−	−	Exchange
+	−	−	−	+	Influx
+[a]	+	−	+	−	Influx
+[a]	+	−	−	+	Influx
+[a]	+	+	−	−	Exchange
+	+	−	−	−	Exchange

[a] Holo-RBP to apo-RBP ratio similar to that of blood

uptake for vision (Ruiz et al. 2012). Because RPE-specific knockout of LRAT leads to a similar decrease in retinyl ester levels in the RPE (LRAT-independent retinyl ester in the RPE is a result of cellular uptake of retinyl ester directly) (Ruiz et al. 2007), STRA6 is responsible for virtually all retinol from the blood that is accessible to LRAT in the RPE. To prevent excessive accumulation of cellular retinoid, it is possible that there exist unknown cellular proteins that might mediate retinol efflux into extracellular apo-RBP with or without STRA6's involvement.

Third, STRA6 catalyzes efficient retinol exchange between extracellular RBP molecules and between extracellular RBP and intracellular CRBP-I. Unlike apo-RBP-dependent retinol efflux, STRA6-catalyzed retinol exchange between intracellular CRBP-I and extracellular RBP applies to holo-RBP and is not inhibited by holo-RBP. We have demonstrated that the exchange happens in human serum, which consists largely of holo-RBP. It is likely that this retinol exchange between extracellular and intracellular binding proteins functions to "refresh" the intracellular stores of retinol to guard against depletion due to gradual oxidation occurring during long-term storage. The CRBP-I and STRA6-dependent retinol exchange is a newly identified role of CRBP-I in retinol homeostasis and distinguishes CRBP-I from LRAT although both proteins can couple to STRA6 for retinol uptake.

This finding may also help to explain a few interesting and puzzling earlier findings on vitamin A transport. Kinetic models of vitamin A metabolism predicted that 50–70 % of the total input of retinol into the circulation comes from extrahepatic tissues (Blomhoff et al. 1991). This result is seemingly counterintuitive given the role of the liver as the major site of holo-RBP secretion. Another interesting puzzle is that muscle-expressed human RBP can rescue RBP null mice's vision defect (Quadro et al. 2002), although muscle-expressed human RBP cannot mobilize

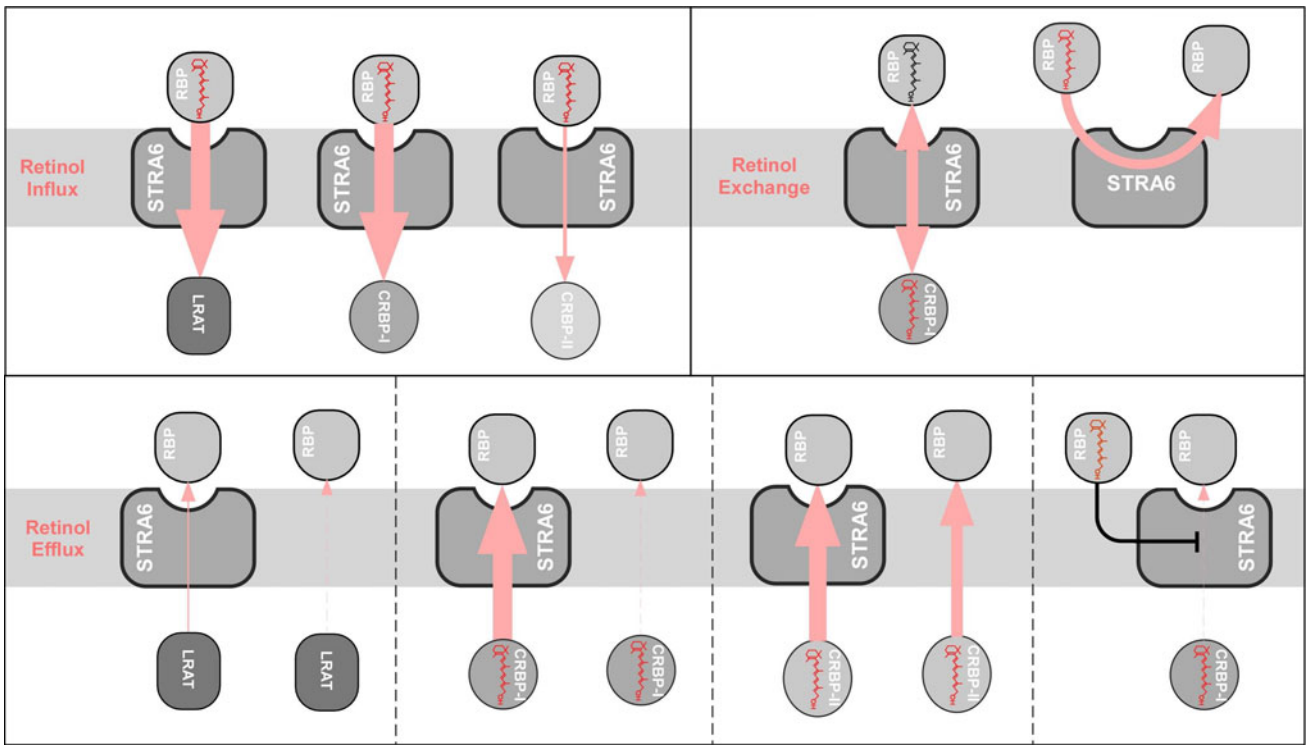

Fig. 10 Schematic diagrams comparing STRA6-mediated retinol influx with STRA6-mediated retinol exchange and retinol efflux. The directions of retinol transport are indicated by *light red arrows*. The efficiency of retinol transport is indicated by the thickness of each arrow (the thicker the arrow, the stronger the flow)

liver stored vitamin A (Quadro et al. 2004). STRA6's potent retinol exchange activity between RBP and CRBP-I discovered in this study is a likely source of retinol input from extrahepatic tissues and may contribute to the retinol in human RBP that rescues the vision defect.

Acknowledgments Supported by National Institutes of Health Grant 5R01EY018144.

References

Acton S, Rigotti A, Landschulz KT, Xu S, Hobbs HH, Krieger M (1996) Identification of scavenger receptor SR-BI as a high density lipoprotein receptor. Science 271:518–520

Babitt J, Trigatti B, Rigotti A, Smart EJ, Anderson RG, Xu S, Krieger M (1997) Murine SR-BI, a high density lipoprotein receptor that mediates selective lipid uptake, is N-glycosylated and fatty acylated and colocalizes with plasma membrane caveolae. J Biol Chem 272:13242–13249

Berry DC, Jin H, Majumdar A, Noy N (2011) Signaling by vitamin A and retinol-binding protein regulates gene expression to inhibit insulin responses. Proc Natl Acad Sci USA 108:4340–4345

Blomhoff R, Green MH, Berg T, Norum KR (1990) Transport and storage of vitamin A. Science 250:399–404

Blomhoff R, Green MH, Green JB, Berg T, Norum KR (1991) Vitamin A metabolism: new perspectives on absorption, transport, and storage. Physiol Rev 71:951–990

Bouillet P, Sapin V, Chazaud C, Messaddeq N, Decimo D, Dolle P, Chambon P (1997) Developmental expression pattern of Stra6, a retinoic acid–responsive gene encoding a new type of membrane protein. Mech Dev 63:173–186

Chen CH, Hsieh TJ, Lin KD, Lin HY, Lee MY, Hung WW, Hsiao PJ, Shin SJ (2012) Increased unbound retinol binding protein 4 concentration induced apoptosis through its receptor-mediated signaling. J Biol Chem 287:9694–9707

Connelly MA (2009) SR-BI-mediated HDL cholesteryl ester delivery in the adrenal gland. Mol Cell Endocrinol 300:83–88

Connelly MA, Williams DL (2004) Scavenger receptor BI: a scavenger receptor with a mission to transport high density lipoprotein lipids. Curr Opin Lipidol 15:287–295

Connelly MA, de la Llera-Moya M, Monzo P, Yancey PG, Drazul D, Stoudt G, Fournier N, Klein SM, Rothblat GH, Williams DL (2001) Analysis of chimeric receptors shows that multiple distinct functional activities of scavenger receptor, class B, type I (SR-BI), are localized to the extracellular receptor domain. Biochemistry 40:4259–5259

Crouch RK, Chader GJ, Wiggert B, Pepperberg DR (1996) Retinoids and the visual process. Photochem Photobiol 64:613–621

Dowling JE (1966) Night blindness. Sci Am 215:78–84

Drager UC (2006) Retinoic acid signaling in the functioning brain. Sci STKE 2006:pe10

Evans RM (1994) The molecular basis of signaling by vitamin A and its metabolites. Harvey Lect 90:105–117

Golczak M, Maeda A, Bereta G, Maeda T, Kiser PD, Hunzelmann S, von Lintig J, Blaner WS, Palczewski K (2008) Metabolic basis of visual cycle inhibition by retinoid and nonretinoid compounds in the vertebrate retina. J Biol Chem 283:9543–9554

Goodman DS (1984) Plasma retinol-binding protein. In: Sporn MB, Boberts AB, Goodman DS (eds) The Retinoids. Academic Press, New York, pp 41–88

Harrison EH (2005) Mechanisms of digestion and absorption of dietary vitamin A. Annu Rev Nutr 25:87–103

Heller J (1975) Interactions of plasma retinol-binding protein with its receptor. Specific binding of bovine and human retinol-binding protein to pigment epithelium cells from bovine eyes. J Biol Chem 250:3613–3619

Heller J, Bok D (1976) Transport of retinol from the blood to the retina: involvement of high molecular weight lipoproteins as intracellular carriers. Exp Eye Res 22:403–410

Heller J, Horwitz J (1973) Conformational changes following interaction between retinol isomers and human retinol-binding protein and between the retinol-binding protein and prealbumin. J Biol Chem 248:6308–6316

Isken A, Golczak M, Oberhauser V, Hunzelmann S, Driever W, Imanishi Y, Palczewski K, von Lintig J (2008) RBP4 disrupts vitamin A uptake homeostasis in a stra6-deficient animal model for Matthew-Wood syndrome. Cell Metab 7:258–268

Kawaguchi R, Yu J, Honda J, Hu J, Whitelegge J, Ping P, Wiita P, Bok D, Sun H (2007) A membrane receptor for retinol binding protein mediates cellular uptake of vitamin A. Science 315: 820–825

Kawaguchi R, Yu J, Wiita P, Honda J, Sun H (2008a) An essential ligand-binding domain in the membrane receptor for retinol-binding protein revealed by large-scale mutagenesis and a human polymorphism. J Biol Chem 283:15160–15168

Kawaguchi R, Yu J, Wiita P, Ter-Stepanian M, Sun H (2008b) Mapping the membrane topology and extracellular ligand binding domains of the retinol binding protein receptor. Biochemistry 47:5387–5395

Kawaguchi R, Yu J, Ter-Stepanian M, Zhong M, Cheng G, Yuan Q, Jin M, Travis GH, Ong D, Sun H (2011) Receptor-mediated cellular uptake mechanism that couples to intracellular storage. ACS Chem Biol 6:1041–1051

Maden M (2007) Retinoic acid in the development, regeneration and maintenance of the nervous system. Nat Rev Neurosci 8: 755–765

Mark M, Ghyselinck NB, Chambon P (2006) Function of retinoid nuclear receptors: lessons from genetic and pharmacological dissections of the retinoic acid signaling pathway during mouse embryogenesis. Annu Rev Pharmacol Toxicol 46:451–480

Mills JP, Furr HC, Tanumihardjo SA (2008) Retinol to retinol-binding protein (RBP) is low in obese adults due to elevated apo-RBP. Exp Biol Med (Maywood) 233:1255–1261

Napoli JL (1999) Interactions of retinoid binding proteins and enzymes in retinoid metabolism. Biochim Biophys Acta 1440: 139–162

Newcomer ME, Ong DE (2000) Plasma retinol binding protein: structure and function of the prototypic lipocalin. Biochim Biophys Acta 1482:57–64

Niederreither K, Dolle P (2008) Retinoic acid in development: towards an integrated view. Nat Rev Genet 9:541–553

Noy N (2000) Retinoid-binding proteins: mediators of retinoid action. Biochem J 348(pt 3):481–495

Ong DE (1994) Cellular transport and metabolism of vitamin A: roles of the cellular retinoid-binding proteins. Nutr Rev 52:S24–S31

Quadro L, Blaner WS, Hamberger L, Van Gelder RN, Vogel S, Piantedosi R, Gouras P, Colantuoni V, Gottesman ME (2002) Muscle expression of human retinol-binding protein (RBP). Suppression of the visual defect of RBP knockout mice. J Biol Chem 277:30191–30197

Quadro L, Hamberger L, Colantuoni V, Gottesman ME, Blaner WS (2003) Understanding the physiological role of retinol-binding protein in vitamin A metabolism using transgenic and knockout mouse models. Mol Aspects Med 24:421–430

Quadro L, Blaner WS, Hamberger L, Novikoff PM, Vogel S, Piantedosi R, Gottesman ME, Colantuoni V (2004) The role of extrahepatic retinol binding protein in the mobilization of retinoid stores. J Lipid Res 45:1975–1982

Quadro L, Hamberger L, Gottesman ME, Wang F, Colantuoni V, Blaner WS, Mendelsohn CL (2005) Pathways of vitamin A delivery to the embryo: insights from a new tunable model of embryonic vitamin A deficiency. Endocrinology 146:4479–4490

Rask L, Peterson PA (1976) In vitro uptake of vitamin A from the retinol-binding plasma protein to mucosal epithelial cells from the monkey's small intestine. J Biol Chem 251:6360–6366

Ruiz A, Ghyselinck NB, Mata N, Nusinowitz S, Lloyd M, Dennefeld C, Chambon P, Bok D (2007) Somatic ablation of the *lrat* gene in the mouse retinal pigment epithelium drastically reduces its retinoid storage. Invest Ophthalmol Vis Sci 48:5377–5387

Ruiz A, Mark M, Jacobs H, Klopfenstein M, Hu J, Lloyd M, Habib S, Tosha C, Radu RA, Ghyselinck NB, Nusinowitz S, Bok D (2012) Retinoid content, visual responses and ocular morphology are compromised in the retinas of mice lacking the retinol-binding protein receptor, STRA6. Invest Ophthalmol Vis Sci 53: 3027–3039

Stephensen CB (2001) Vitamin A, infection, and immune function. Annu Rev Nutr 21:167–192

Szeto W, Jiang W, Tice DA, Rubinfeld B, Hollingshead PG, Fong SE, Dugger DL, Pham T, Yansura DG, Wong TA, Grimaldi JC, Corpuz RT, Singh JS, Frantz GD, Devaux B, Crowley CW, Schwall RH, Eberhard DA, Rastelli L, Polakis P, Pennica D (2001) Overexpression of the retinoic acid–responsive gene Stra6 in human cancers and its synergistic induction by Wnt-1 and retinoic acid. Cancer Res 61:4197–4205

Travis GH, Golczak M, Moise AR, Palczewski K (2007) Diseases caused by defects in the visual cycle: retinoids as potential therapeutic agents. Annu Rev Pharmacol Toxicol 47:469–512

Vahlquist A, Peterson PA, Wibell L (1973) Metabolism of the viatmin A transporting protein complex. I. Turnover studies in normal persons and in patients with chronic renal failure. Eur J Clin Invest 3:352–362

Wald G (1968) Molecular basis of visual excitation. Science 162: 230–239

Yang Q, Graham TE, Mody N, Preitner F, Peroni OD, Zabolotny JM, Kotani K, Quadro L, Kahn BB (2005) Serum retinol binding protein 4 contributes to insulin resistance in obesity and type 2 diabetes. Nature 436:356–362

Zanotti G, Berni R (2004) Plasma retinol-binding protein: structure and interactions with retinol, retinoids, and transthyretin. Vitam Horm 69:271–295

J Membrane Biol (2012) 245:747–757
DOI 10.1007/s00232-012-9477-8

Escherichia coli Membranes Depleted of SecYEG Elicit SecA-Dependent Ion-Channel Activity but Lose Signal Peptide Specificity

Bor-Ruei Lin · Ying-Hsin Hsieh · Chun Jiang · Phang C. Tai

Received: 30 December 2011 / Accepted: 30 June 2012 / Published online: 2 August 2012

Abstract We have developed a sensitive method to detect the opening of SecA-dependent, protein-conducting channels in *Xenopus* oocytes. In this study, we determined the ionic current activities of the SecA-dependent channel from membrane vesicles depleted of SecYEG. We found that these SecYEG-depleted membranes produced SecA-dependent ionic currents in the oocytes, as did membranes containing SecYEG. However, reconstituted membranes depleted of SecYEG required higher concentrations of SecA to elicit ionic currents like those in membranes containing SecYEG. In contrast to membranes containing SecYEG, the proofreading capacity of signal peptides was lost for those membranes lacking SecYEG. These findings are consistent with loss of signal peptide specificity in channel activity from membranes of SecY suppressor or SecY plug domain mutants. The signal peptide specificity of the reconstituted membranes, like SecA-liposomes, can be restored by the addition of SecYEG proteoliposomes. On the other hand, the channel activity efficiency of reconstituted membranes was fully restored, while SecA-liposomes could only be partially enhanced by the addition of SecYEG, indicating that, in addition to SecYEG, other membrane proteins contribute to the efficiency of channel activity. The SecA-dependent channels in membranes that lacked SecYEG also lost ion selectivity to monovalent cations but retained selective permeability to large anions. Thus, the electrophysiological evidence presented here indicates that SecYEG is not obligatory for the channel activity of *Escherichia coli* membranes, as previously shown for protein translocation, and that SecYEG is important for maintenance of the efficiency and specificity of SecA-dependent channels.

Keywords Electrophysiology · Ion channel · Mechanism of transport protein · Biochemistry/Molec. Biology

B.-R. Lin and Y.-H. Hsieh contributed equally to this work.

Electronic supplementary material The online version of this article (doi:10.1007/s00232-012-9477-8) contains supplementary material, which is available to authorized users.

B.-R. Lin · Y.-H. Hsieh · C. Jiang · P. C. Tai (✉)
Department of Biology, Petit Science Center, Georgia State University, 161 Jesse Hill Dr., Suite 490, Atlanta, GA 30303, USA
e-mail: biopct@gsu.edu

Y.-H. Hsieh
e-mail: yhsieh3@student.gsu.edu

Introduction

The characteristics of the SecA and SecYEG complex involved in *Escherichia coli* protein translocation have been studied extensively over the last few decades. SecA has been widely viewed as a peripheral ATPase protein that is able to cycle on and off the membranes during protein translocation. By hydrolyzing ATP as the energy source, it has been shown that SecA inserts part of its domain into the SecYEG protein-conducting channel and thereby drives precursors across the translocase complex (Manting and Driessen 2000; Mori and Ito 2001; Veenendaal et al. 2004). However, the centrality of the SecYEG complex as the only protein-conducting channel has also been brought into question. It has been found that certain precursor proteins can be translocated in vitro with membranes depleted of either SecY or SecE (Watanabe et al. 1990; Yang et al. 1997a, b) or reconstituted membranes with the removal of SecYEG (Hsieh et al. 2011). Moreover, the SecYEG complex may not form a pore large enough for protein translocation (Van den Berg et al. 2004).

The roles of SecA in protein-conducting channels have been evaluated by different research groups. Studies have shown that SecA is permanently embedded in *E. coli* cytoplasmic membranes (Chen et al. 1996) and capable of forming ring-like pore structures in the presence of anionic phospholipids (Wang et al. 2003). Through the in vivo use of sulfhydryl domain-specific labeling, the membrane-embedded SecA has been shown to possess multiple domains that are oriented toward, and exposed to, the periplasmic side of the membrane (Jilaveanu and Oliver 2007). It has also been demonstrated that the concentration of SecA is increased in cells to compensate for several defects in protein translocation (Cabelli et al. 1988; Fandl et al. 1988; Fandl and Tai 1987; Kusters et al. 1992). More recent in vitro studies have shown that SecA may function as a dimer for protein translocation (Jilaveanu and Oliver 2006; Jilaveanu et al. 2005; Wang et al. 2008). Recently, we reported that SecA liposomes alone without SecYEG participate in ion-channel activity (and protein translocation), indicating that SecA is essential and sufficient for channel activity (Hsieh et al. 2011). However, this channel activity is less efficient than that of *E. coli* membranes with SecYEG and requires more SecA and additional ATP, suggesting that other membrane components may contribute to the SecA/liposomal protein-conducting channel.

We have recently developed a sensitive method to measure the activity of protein-conducting channels in *E. coli* membranes by injecting inverted bacterial membrane vesicles into *Xenopus* oocytes (Lin et al. 2006). In so doing, we have found that ionic currents through such membranes were strictly SecA-dependent and could be blocked by SecA inhibitors such as sodium azide and nonhydrolyzable ATP analogs. Using this electrophysiological method, we were able to examine the central components of protein-conducting channels in bacterial membranes and determine the function of Sec proteins at various steps in protein translocation.

In this study, we provide new evidence for the SecA-mediated, protein-conducting channel in the absence of the SecYEG complex using similar electrophysiological measurements. Ionic currents were recorded from oocytes injected with *E. coli* membrane vesicles in which SecYEG were depleted or removed. The currents were inhibited by puromycin, which removed nascent peptides in the oocytes, and subsequently restored by addition of either wild-type LamB signal peptides or proOmpA precursor proteins. Defective LamB signal peptides or unfolded mature OmpA protein were also capable of producing the ionic currents in membranes lacking SecYEG. The observations are consistent with our previous findings in membranes containing SecY mutants (Hsieh et al. 2011), suggesting a loss of proofreading function for signal sequences in the absence of SecY. Moreover, such proofreading capability can be fully restored by supplementing purified SecYEG. Taken together, the electrophysiological studies presented here, when combined with previous biochemical and physical evidence (Chen et al. 1996, 2007; Wang et al. 2003; Yang et al. 1997a, b), indicate that SecYEG is not obligatory for SecA-dependent ionic currents. The data further suggest an important role of SecYEG in the maintenance of protein channel efficiency and specificity.

Materials and Methods

Bacterial Strains *E. coli*

K12 strain MC4100 was from J. Beckwith (Silhavy and Beckwith 1983), and BA13, a derivative of MC4100, was from D. Oliver (Oliver and Beckwith 1982a). MC1000 was from J. Beckwith (Chen et al. 1996). BL21(DE3)/pT7-SecA, for overproducing the SecA protein by the T7 promoter expression system, was from D. Oliver (Cabelli et al. 1988). *E. coli* strains D10-1 and D10-3 are lab stocks as described (Fandl et al. 1988). PrlA665 was a gift from T. Silhavy (Emr et al. 1981). All cells were grown in a buffered Luria–Bertani medium LinA with 0.5 % glucose with aeration (Tai et al. 1991).

Reagents and Chemicals

All chemicals are of reagent grade and were obtained from Sigma-Aldrich (St. Louis, MO) or other commercial sources.

Purification of SecA, proOmpA and LamB Signal Peptides

SecA was purified from BL21 (DE3)/pT7-SecA as described (Cabelli et al. 1988). Purified proOmpA and OmpA were prepared as described (Chen et al. 1987, 1996). Protein amounts were determined using a Bio-Rad (Richmond, CA, USA) assay kit with bovine serum albumin as standard. Wild-type LamB signal peptide (MMITLRKLPLA VAVAAGVMSAQAMA) and LamB deletion mutant signal peptide (MMITLRKLP—VAAGVMSAQAMA) were gifts from Lila Gierasch (Lin et al. 2006).

Preparation of SecYEG-Depleted Membranes

Membranes from wild-type *E. coli* MC1000, MC4100 (Oliver and Beckwith 1982b) and D10-3 lacking F_1F_o-ATPase and OmpT were prepared as described (Tai et al. 1991). SecA-depleted membrane vesicles from the *secA* amber mutant strain BA13 were prepared as described (Tai

et al. 1991). SecYEG$^-$ membrane vesicles were prepared from strain PS289 according to the procedures described by Yang et al. (1997b). The residual amount of SecYEG used in this study is <1 %.

Removal of SecYEG from Reconstituted Membranes

Reconstituted membranes were prepared as described previously, which resulted in the removal of >99 % of the SecY (Nicchitta and Blobel 1990; Watanabe et al. 1990) with modifications. Cytoplasmic membranes were obtained from either the *E. coli* strain D10-3 or BA13 by two layers of sucrose gradients (Tai et al. 1991), washed by high-salt buffer (0.4 M sucrose, 1 M potassium acetate, 20 mM triethanolamine hydrochloride [pH 7.5], 1.5 M magnesium acetate and 1 mM EDTA) and resuspended at a final concentration of 3–4 mg/ml. Sodium cholate was added at a final concentration of 1 %. The mixture was incubated on ice for 1 h and then centrifuged in a Beckman (Fullerton, CA, USA) TLA-100.3 rotor at 90,000 rpm for 30 min. The supernatant was collected and treated with 0.75 % sodium cholate in at least double volume of high-salt buffer and then placed on ice for 1 h, followed by centrifugation in the TLA-100.3 rotor at 90,000 rpm for 30 min. The supernatant was collected and dialyzed with a Spectra-Por 1 dialysis membrane (Spectrum Medical Industries, Houston, TX) at room temperature against 500–1,000 volumes of dialysis buffer (0.25 M sucrose, 0.4 M potassium acetate, 20 mM triethanolamine hydrochloride [pH 7.5], 1.5 mM magnesium acetate and 1 mM EDTA) overnight. The dialysis membrane was first boiled for 10 min in 1 % $NaHCO_3$ and 1 mM EDTA, then boiled in deionized H_2O for 10 min and cooled on ice before use. After dialysis, reconstituted membrane vesicles were collected by centrifugation in the TLA-100.3 rotor at 90,000 rpm for 15 min. Pellets were suspended with stirring in DTK buffer (1 mM dithiothreitol, 10 mM Tris–HCl [pH 7.6], 50 mM KCl), and the concentration was determined by measuring the OD_{280}/OD_{260} ratio with the Bio-Rad SmartSpec 3000. Such reconstituted membranes contained <1 % SecYEG.

Xenopus Oocyte Preparation and Injection

Oocytes were obtained from *Xenopus laevis* (Mao et al. 2004; Xu et al. 2001). Frog surgery and sample injection were performed as described previously (Lin et al. 2006). Samples containing *E. coli* membranes, SecA and precursors were premixed together and then injected into the dark side of oocytes by the Nanojector II microinjection system (Drummond Scientific, Broomall, PA, USA). Injected oocytes were incubated at 23 °C for 2.5–3.0 h, and outward currents were recorded at room temperature with the two-electrode voltage-clamp technique using KCl as the major conducting ion in the bath solution, unless indicated otherwise. The final amounts or concentrations of sample injected were membranes (60 ng), wild-type and defective LamB signal peptides (1 pmol) and puromycin (4 mM) as standardized concentrations unless otherwise indicated. Estimates of injected sample concentrations in oocytes were made based on the average volume of oocytes at 500- and 50-nl injection volumes (Lin et al. 2006).

Voltage-Clamp Measurements

Ionic currents were recorded using the two-electrode voltage-clamp technique, as previously described (Lin et al. 2006). In brief, whole-cell currents were studied on oocytes 3 h after injection. Two-electrode voltage-clamp measurements were performed using an amplifier (Geneclamp 500; Axon Instruments, Foster City, CA) at room temperature (~24 °C). Cells were impaled using electrodes filled with 3 M KCl. One of the electrodes (1.0–2.0 MΩ) served as a voltage recorder and was connected to the HS-2 x1L headstage, while the other electrode (0.3–0.6 MΩ) was used for current recording and connected to the HS-2 x10MG headstage. Oocytes were accepted for further experimentation only if they did not show leakage in membrane currents. Current records were low pass-filtered (Bessel, 4-pole filter, 3 dB at 5 kHz), digitized at 5 kHz (12-bit resolution) and stored on a computer disk for later analysis (pClamp 6.0.3, Axon Instruments). Junction potentials between bath and pipette solutions were appropriately nulled before impaling the cell.

Data Analysis

Data are presented as mean ± SE. Differences in means were tested with Student's t test for a pair of data and ANOVA for three groups or more. Differences were accepted as significant at $p \leq 0.05$.

Results

Detection of Ionic Currents from Injection of Membranes Depleted of SecYEG

Ionic currents were studied with and without SecYEG-depleted membranes. In these membranes, SecYEG proteins were below detectable levels and SecA was elevated by sixfold as determined immunologically (Yang et al. 1997b; Yi et al. 2003). Concentration-dependent increases in ionic currents were produced with increased amount of membranes under the condition of SecYEG depletion (Fig. 1a). In comparison with wild-type membranes, these currents saturated at 6.6 ± 0.8 μA ($n = 10$) remained blocked by AMP-PCP, a nonhydrolyzable ATP analog for

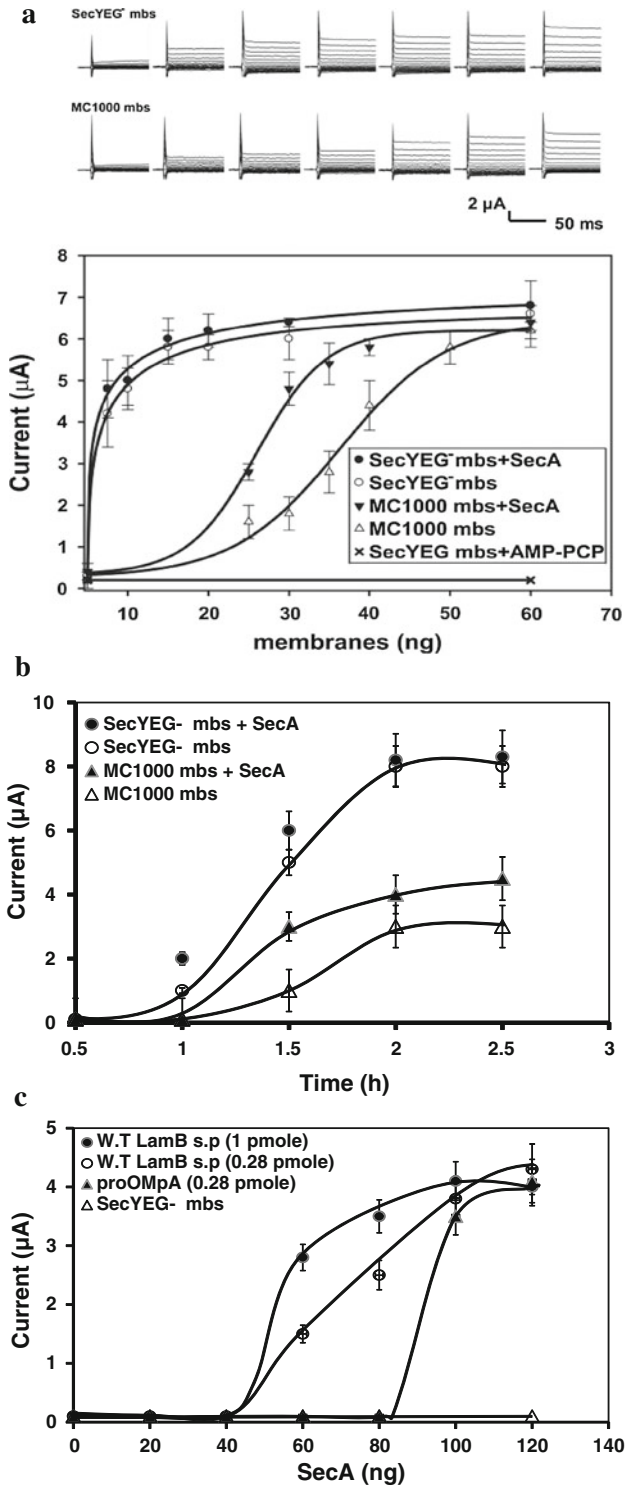

Fig. 1 Channel activities of SecYEG$^-$ and MC1000 membranes. **a** Ionic currents were measured from different amounts of SecYEG$^-$ or MC1000 membranes injected into oocytes, and SecA (5 ng) or AMP-PCP (4 mM) was coinjected with membranes where indicated. Tracings of current recording of different amounts of injected membranes are shown above with the same scale. **b** SecYEG$^-$ or MC1000 membranes (30 ng) were injected with or without SecA in the time-course experiment in the absence of puromycin. **c** Different amounts of SecA were coinjected with SecYEG$^-$ membranes and wild-type LamB signal peptides or pOmpA in the presence of puromycin, which acts to block the oocyte-endogenous signal peptides

inhibition of SecA activity (Fig. 1a), and were enhanced with the additional SecA (Fig. 1b). Indeed, the SecYEG$^-$ membranes showed even higher current activity compared to wild-type MC1000 membranes (Fandl et al. 1988).

We found that oocyte-endogenous signal peptides can open protein-conducting channels in *E. coli* membranes and that such activity can be inhibited by puromycin, which functions to block the synthesis of oocyte-endogenous precursor proteins bearing signal peptides (Lin et al. 2006). Similarly, there were no detectable ionic currents in the presence of puromycin (Fig. 1c). In our previous finding, 20 ng of SecA was sufficient to recover the ionic currents with wild-type LamB signal peptides in wild-type *E. coli* membranes (Lin et al. 2006). However, higher concentrations of exogenous SecA were needed to restore ionic currents in SecYEG$^-$ membranes with either LamB signal peptides or OmpA precursor proteins (Fig. 1c).

SecA Stimulates Ionic Currents on Reconstituted Membranes with SecYEG Removed In Vitro

Although SecYEG$^-$ membranes are good for studying channel activity without SecYEG, it is likely that stress components were induced during their depletion in cells (Ruiz and Silhavy 2005). Thus, we reconstituted SecYEG$^-$ membranes from *E. coli* D10-3, which was an OmpT$^-$ strain, and SecY was removed by sodium cholate precipitation (Watanabe et al. 1990; Zhong et al. 1996). The reconstituted membranes contained a negligible amount (<1 %) of SecYEG, while other Sec proteins, SecD, SecF and YidC, were all retained (Fig. 2a). To determine the role of SecA in the reconstituted membranes, we prepared reconstituted membranes lacking SecA as well as those lacking SecYEG (RE-BA13). We were able to detect ionic currents from these membranes only in the presence of additional exogenous SecA (Fig. 2b). The recording of currents from SecYEG$^-$ reconstituted membranes (RE-BA13) required higher amounts of SecA (at least 60 ng) than those SecYEG$^-$ membranes, suggesting that these ionic currents are strictly SecA-dependent and that the SecA-dependent currents are less efficient in the absence of SecYEG (Hsieh et al. 2011). The sharp rise of channel activity with increasing SecA further suggested a cooperative aspect to the ability of SecA to conduct current at critical concentrations.

Loss of Channel Proofreading and Efficiency in the Absence of SecYEG

SecY is suggested to provide the proofreading function for the signal peptides (Osborne and Silhavy 1993). We

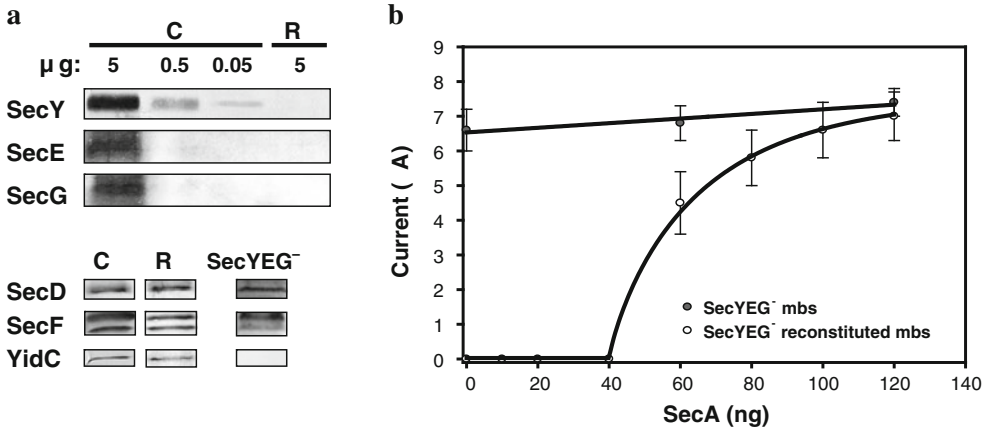

Fig. 2 Reconstituted SecYEG$^-$ membranes are active. **a** SecY, SecE and SecG were examined by Western blot analysis with *E. coli* strain D10-3 crude membrane extracts and reconstituted membranes. Reconstituted membranes contained <1 % of SecY content and nondetectable SecE and SecG. Antibodies against SecD, SecF and YidC were also used for these two membrane preparations. SecYEG$^-$ membranes = 5 μg. *C* crude membranes, *R* reconstituted membranes. **b** Different amounts of SecA were injected with SecYEG$^-$ reconstituted membranes or SecYEG$^-$ membranes in the absence of puromycin

investigated whether removal of SecYEG in the membranes had any effect upon the proofreading function of the ion channel activity in the oocyte system. In our previous study, neither mature OmpA protein nor defective LamB signal peptides were capable of stimulating channel activity from wild-type membranes containing SecYEG (Lin et al. 2006). Here, we find that the ionic currents elicited by proOmpA or wild-type LamB signal peptides were almost as effective in both the SecYEG-depleted membranes (Fig. 3a) and reconstituted BA13 membranes (Fig. 3b) as they were in wild-type MC4100 membranes. Moreover, membranes lacking SecYEG also produced ionic currents that responded to unfolded mature OmpA as well as defective Lam B signal peptide stimulation to remove oocyte endogenous nascent peptides, even in the presence of puromycin (Fig. 3a, b). These results suggest that the proofreading function in these membranes had been lost. Similar results were also observed in SecY suppressor mutant PrlA665 membranes (Supplemental Fig. 1) and the SecY plug mutant (Hsieh et al. 2011). The increased channel activity that was induced by the mature OmpA protein or LamB defective mutant is in accordance with previous in vitro translocation assay results (Emr et al. 1981) and with SecA-liposomal assays (Hsieh et al. 2011).

SecYEG Fully Restored Channel Specificity and Efficiency

Having shown that membranes without SecYEG lost their ability to proofread signal peptides, the next question was whether this proofreading function could be restored in either SecYEG-depleted membranes or reconstituted BA13 membranes by coinjection of purified SecYEG proteoliposomes. In addressing this question, we found that such reconstituted membranes when coinjected with SecYEG proteoliposomes in the presence of puromycin (Fig. 4a, b) failed to produce ionic currents unless SecA was also added, along with the wild-type precursors (pOmpA) or wild-type LamB signal peptide (LamB WT). Moreover, there were no detectable ionic currents when mature OmpA or LamB defective mutant (LamB DM) was added, indicating that these reconstituted membranes had regained their signal peptide specificity following the addition of SecYEG.

We also used reconstituted PrlA665 membranes (RE-PrlA665) or reconstituted SecY plug mutant membranes (RE-SecY plug mutant) in which the SecY variants had been removed to investigate if the proofreading function of these membranes could be restored by exogenous SecYEG proteoliposomes. Both unfolded mature OmpA and defective LamB signal peptides elicited ionic currents from these membranes (Fig. 5a, b), which proved to be as active as proOmpA or wild-type LamB signal peptides. Addition of SecYEG proteoliposomes with SecA to the RE-PrlA665 membranes or RE-SecY plug mutant membranes restored their proofreading ability to discriminate between proOmpA and mature OmpA as well as wild-type and defective LamB signal peptides (Fig. 5a, b), indicating that such membranes were no longer responsive to mature OmpA or defective signal peptide.

Furthermore, the addition of SecYEG proteoliposomes was also shown to increase ionic currents in reconstituted BA13 membranes (Fig. 6). Indeed, the presence of SecA RE-BA13 membranes with added SecYEG proteoliposomes was able to restore channel activity almost to the same level as wild-type BA13 membranes containing intrinsic SecYEG. Similarly, addition of SecYEG proteoliposomes elicited higher ionic currents to RE-BA13 membranes (Fig. 6).

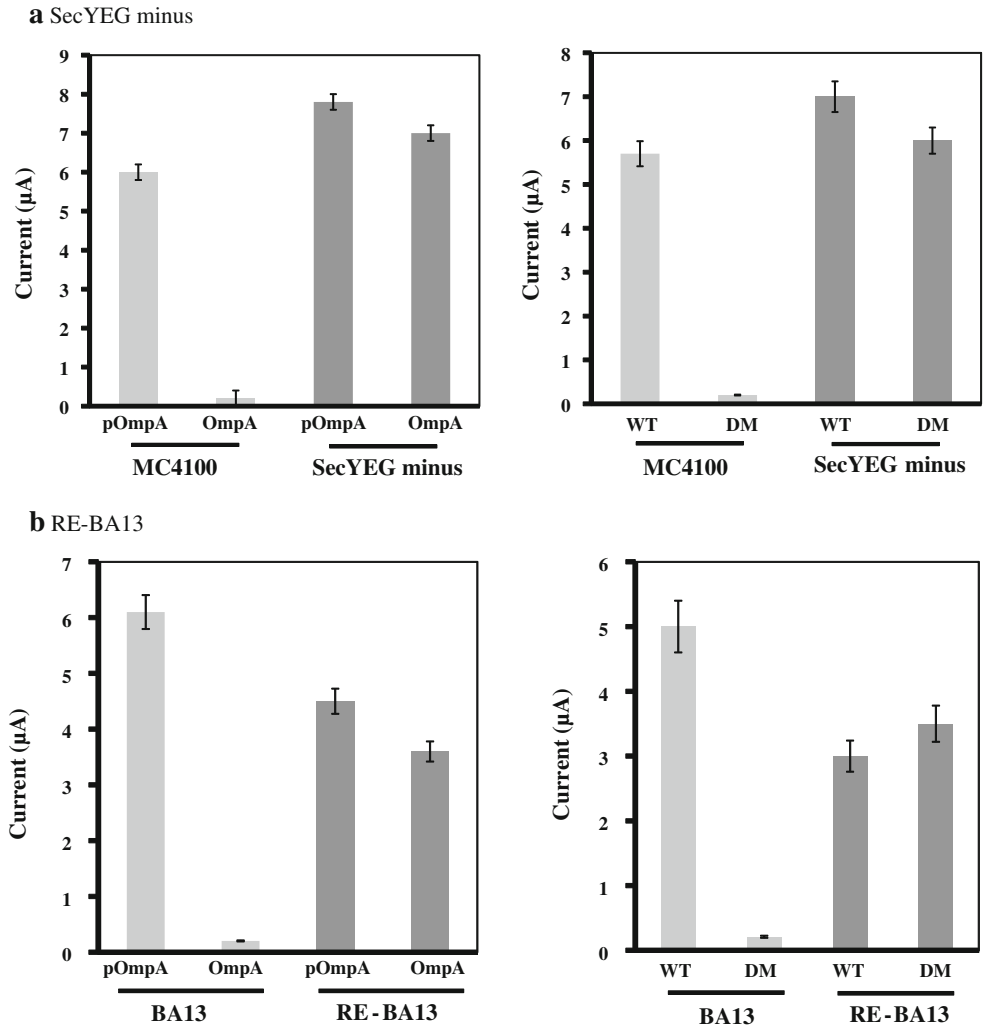

Fig. 3 Loss of proofreading function for SecYEG$^-$ membranes and reconstituted BA13 membranes. **a** SecYEG$^-$ membranes or (**b**) reconstituted BA13 membranes (*RE-BA13*) were injected with precursors (*pOmpA*), mature precursors (*OmpA*), wild-type LamB signal peptides (*WT*) or defective mutant LamB signal peptides (*DM*) in the presence of SecA (60 ng) and puromycin

These results suggest that the proofreading function of membranes lacking SecYEG can be restored by exogenous SecYEG proteoliposomes and that SecYEG is not only responsible for proofreading ability but also important for the efficiency of channel activity. Similar results were found when SecA liposomes were coinjected with SecYEG proteoliposomes, although more SecA was needed for active ionic currents and the restoration of activity was not nearly to the same extent (Fig. 6). These findings indicate that membrane proteins other than SecA/SecYEG also contribute to the higher efficiency of channel activity.

The Protein-Conducting Channel without SecYEG Loses Selectivity for Monovalent Cations

We have previously shown that the protein-conducting channels of wild-type membranes have the capability to discriminate ions according to size (Lin et al. 2006). To examine the effect of SecYEG on ion selectivity, we performed experiments in which the K^+ or Cl^- in the extracellular solution was replaced with Na^+, *N*-methyl-D-glucamine ($NMDG^+$), glutamate$^-$ or gluconate$^-$. The molecular weights of these cations and anions were K^+ (39.1 Da), Na^+ (23.0 Da), $NMDG^+$ (195.2 Da), Cl^- (35.5 Da), glutamate$^-$ (147.1 Da) and gluconate$^-$ (198.8 Da). Membranes depleted of SecYEG$^-$ or reconstituted membranes without SecYEG were injected with SecA and wild-type LamB signal peptides, and the reversal potentials and current amplitude were measured for each conductive ion in the bath solution 2–3 h after injection. According to the direction of ionic movements, inward currents were studied for cations, while outward currents were examined for anions.

Complete replacement of K^+ in the extracellular solution with Na^+ demonstrated only moderate changes in both

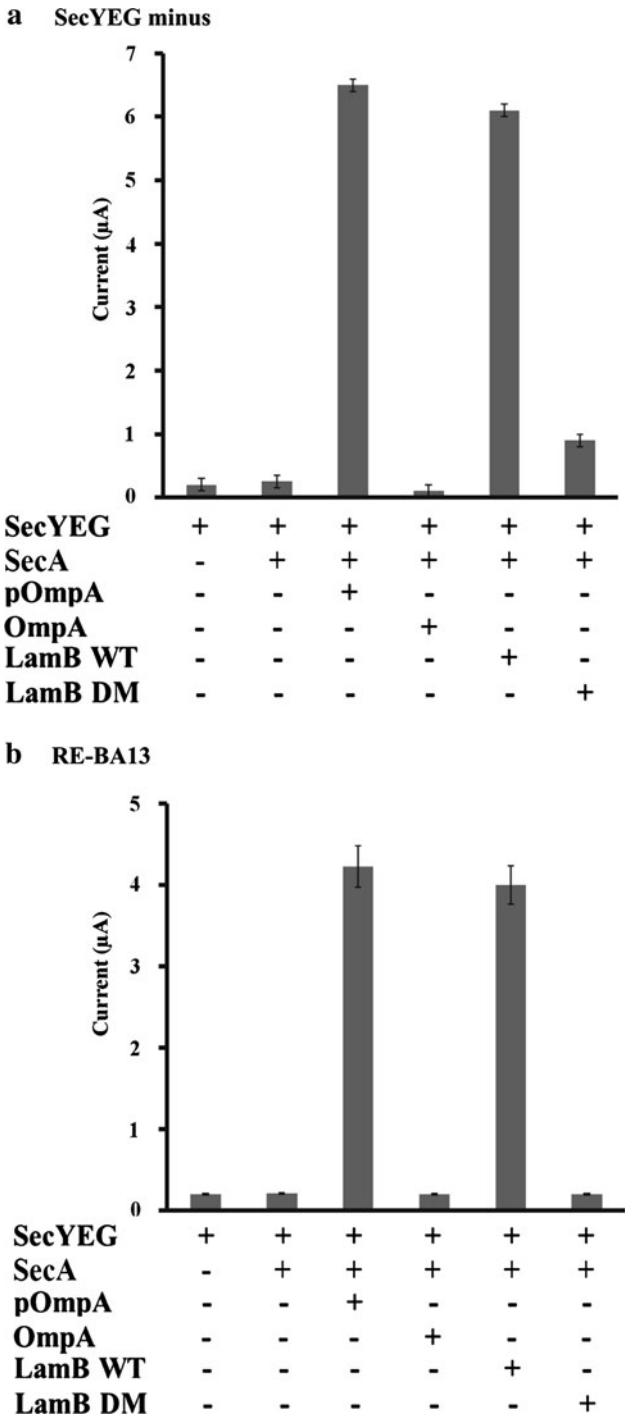

Fig. 4 Restoration of proofreading function of SecYEG$^-$ membranes or reconstituted BA13 membranes by SecYEG proteoliposomes. SecYEG proteoliposomes (30 ng) were coinjected with (**a**) SecYEG$^-$ or (**b**) reconstituted BA13 membranes (*RE-BA13*) and SecA, proOmpA, OmpA, wild-type LamB or defective mutant of LamB signal peptides where indicated in the presence of puromycin

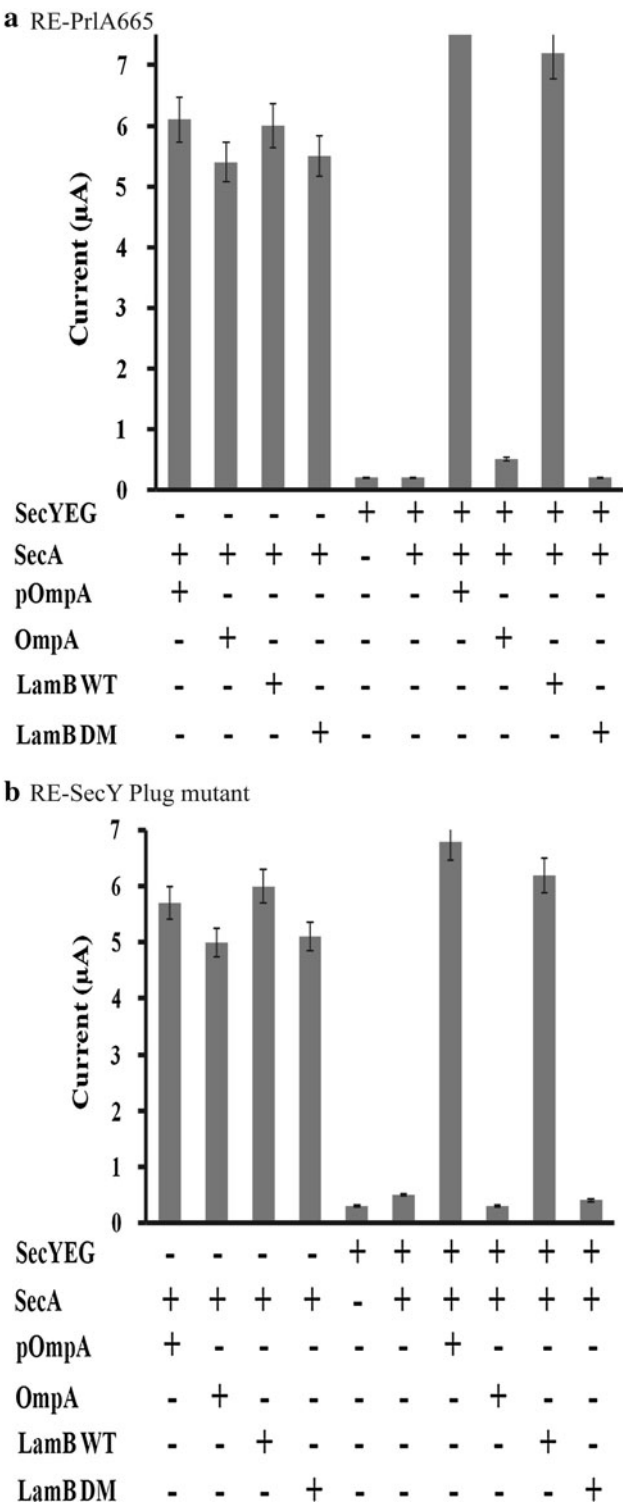

Fig. 5 Restoration of proofreading function in reconstituted membranes of SecY mutants. SecYEG proteoliposomes (30 ng) were coinjected with SecA, precursors or signal peptides with reconstituted membranes of **a** SecY suppressor mutant PrlA665 or **b** SecY plug-deletion mutant in the presence of puromycin

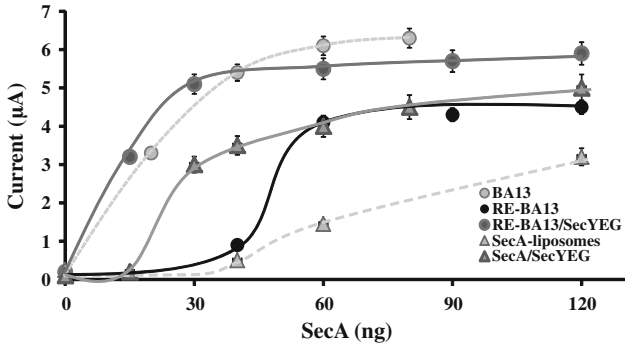

Fig. 6 SecYEG increases channel activity efficiency in reconstituted BA13 membranes or in SecA liposomes. Different amounts of SecA were injected with BA13 membrane (*gray circle*), RE-BA13 (*black circle*) or RE-BA13 membranes plus SecYEG proteoliposomes (*dark gray circles*). SecA liposomes (*light gray triangles*) were prepared by sonication of *E. coli* total lipid extracts. SecA liposomes together with SecYEG proteoliposomes (*dark gray triangles*) were injected with ATP (2 mM) and Mg^{2+} (1 mM) in the presence of SecA and the precursors

reversal potentials and current amplitudes in either the SecYEG$^-$ membranes or the reconstituted SecYEG$^-$ membranes (Table 1; Supplemental Fig. 2a, b), suggesting that all the channels are about equally permeable to K^+ and Na^+. A clear shift in the reversal potential and a reduction in the current amplitude occurred in wild-type membranes when $NMDG^+$ was substituted for K^+ (Table 1). However, no major change in reversal potentials and current amplitude were observed in SecYEG$^-$ membranes or in reconstituted SecYEG$^-$ membranes under similar ion substitution conditions (Table 1; Supplemental Fig. 2a, b). Since the extracellular Cl^- concentration remained the same, these results indicate that, in the absence of SecYEG, the SecA-dependent channels lost selective permeability to the tested cations. Similar ion substitution experiments were performed for other anions. The results showed that the SecA-dependent, protein-conducting channels without SecYEG showed a clear shift in reversal potentials when Cl^- was replaced by glutamate$^-$ or gluconate$^-$ (Table 1).

Based on these reversal potentials, we calculated the relative ion permeability of each of the different cations and anions that were tested (Table 2). The relative permeability of $NMDG^+$ to K^+ is close to 1 for the SecYEG-depleted membranes and reconstituted SecYEG membranes, suggesting that both these membranes become less selective for cations. In contrast, the SecYEG-depleted membranes and reconstituted SecYEG membranes remained selectively permeable to Cl^- over glutamate$^-$ or gluconate$^-$ (Table 2).

Discussion

We have shown that ionic currents can be observed through membranes in the absence of detectable SecYEG

Table 1 Reversal potentials and ionic currents measured from different cations or anions

	MC4100 mbs[a]		SecYEG$^-$ mbs		Reconstituted SecYEG$^-$ mbs	
	Reversal potential (mV)	Current (μA)	Reversal potential (mV)	Current (μA)	Reversal potential (mV)	Current (μA)
Cations						
K^+	−20.2 ± 2.0 (n = 8)	1.5 ± 0 1 (n = 8)	−21.3 ± 3.1 (n = 20)	1.9 ± 0.1 (n = 13)	−32.4 ± 0.1 (n = 15)	2.2 ± 0.1 (n = 10)
Na^+	−21.2 ± 2.1 (n = 8)	1.1 ± 0.3 (n = 8)	−22.3 ± 2.6 (n = 11)	2.0 ± 0.1 (n = 12)	−32.7 ± 0.4 (n = 12)	2.4 ± 0.1 (n = 10)
$NMDG^+$	−27.2 ± 2.1 (n = 8)	0.4 ± 0.2 (n = 8)	−24.4 ± 2.2 (n = 12)	1.3 ± 0.1 (n = 14)	−34.6 ± 0.2 (n = 9)	2.0 ± 0.1 (n = 8)
Anions						
Cl^-	−20.2 ± 2.0 (n = 8)	10.2 ± 0.5 (n = 8)	−21.3 ± 3.1 (n = 20)	6.8 ± 0.2 (n = 15)	−32.4 ± 0.1 (n = 15)	11 ± 0.2 (n = 10)
Glutamate$^-$	−14.4 ± 2.1 (n = 8)	7.0 ± 0.4 (n = 10)	−14.6 ± 3.3 (n = 15)	3.0 ± 0.2 (n = 20)	−27.6 ± 0.8 (n = 9)	7.4 ± 0.2 (n = 11)
Gluconate$^-$	−9.9 ± 1.1 (n = 8)	4.3 ± 0.3 (n = 10)	−13.6 ± 3.2 (n = 15)	2.5 ± 0.1 (n = 20)	−27.2 ± 0.2 (n = 10)	6.9 ± 0.2 (n = 10)

Reversal potentials were analyzed by CLAMPFIT 6 (Axon Instruments). Ionic currents were recorded and calculated by CLAMPEX 5 (Axon Instruments). Data are presented as mean ± standard error (n for numbers of oocytes). Typical recording tracings of currents versus reversal potential and figures of ionic currents in Table 1 are provided in Supplementary Figure 2

[a] The data were adapted from Lin et al. (2006)

Table 2 Relative permeability of cations to K^+ or anions to Cl^-

	MC4100 mbs[a]	SecYEG$^-$ mbs	Recon. SecYEG$^-$ mbs
Na^+/K^+	0.96	0.96	0.99
$NMDG^+/K^+$	0.76	0.89	0.92
Glutamate$^-$/Cl^-	0.77	0.74	0.81
Gluconate$^-$/Cl^-	0.63	0.71	0.79

The relative permeability ratio P_A/P_B was calculated according to the Nernst equation: $E_{rev} = \frac{RT}{zF} \ln \frac{P_A[A]_0}{P_B[B]_0}$, where the gas constant $R = 8.3145$ J mol^{-1} K^{-1}, T is absolute temperature = 297 K (24 °C), z is the charge of the ion, F (Faraday constant) = 96,500 C mol^{-1}. Ion concentrations: K^+ (90 mM), Na^+ (90 mM), $NMDG^+$ (90 mM), Cl^- (90 mM), glutamate$^-$ (80 mM), gluconate$^-$ (80 mM). When the extracellular solution was replaced by glutamate$^-$ or gluconate$^-$, the 10 mM Cl^- remained in the bath solution

[a] The data were adapted from Lin et al. (2006)

using electrophysiological studies with *Xenopus* oocytes. In our previous report, as little as 5 ng of SecA could stimulate ionic currents in *E. coli* wild-type membranes with or without coinjected proOmpA (Lin et al. 2006). However, in membranes depleted of SecYEG from cells or by cholate precipitation, higher amounts of SecA (60–120 ng of current saturation) were needed to stimulate the ionic currents in the oocytes (Fig. 2). LamB signal peptides or precursor proteins can induce the opening of SecA-dependent channels in SecYEG$^-$ membranes in the presence of puromycin, albeit requiring additional SecA, indicating that SecA is sufficient for ion channel activities, even in the absence of detectable SecYEG. This conclusion is further supported by similar findings that SecA liposomes alone can promote protein translocation and channel activity (Hsieh et al. 2011). These data together indicate that SecY is not essential for protein translocation, as determined in both biochemical and electrophysiological studies. Compared to the simpler SecA-liposomal systems (Hsieh et al. 2011), the channel activity of reconstituted membranes is higher and does not require additional ATP (other than those already present in the oocytes). This observation suggests that some other Sec components (e.g., SecDF) or other factors in the membrane can contribute to maintaining the higher channel activity than SecA liposomes alone (Fig. 6). Interestingly, we noted that more SecA was required to recover the ionic currents without SecYEG in either reconstituted membranes or SecA liposomes. It has been reported that SecY contains a high-affinity binding site for SecA (Kim et al. 1994) and a "plug domain" to gate the channel (Li et al. 2007; Tam et al. 2005; Dalal and Duong 2009). The sharp increase in channel activity following the addition of increasing amounts of SecA (Figs. 1c, 2b) suggests a critical concentration for SecA to function in the absence of SecYEG, presumably to form the "low-affinity" SecA channel at higher concentrations (Wang et al. 2003; Hsieh et al. 2011). Such higher SecA concentrations are still within the physiological ranges observed in the cells (as discussed in Hsieh et al. 2011).

Our results show that the SecYEG complex is not essential for the opening of the SecA-dependent channel but is required for efficiency and signal peptide specificity. Proofreading of signal sequences is one of the functions that SecY fulfills in the early stage of protein translocation (Maillard et al. 2007). Wild-type membranes having functional SecYEG rejected the mature precursors' or defective LamB signal peptides' ability to open the protein-conducting channel. Defective LamB signal peptides and OmpA can bypass such recognition and were able to induce the opening of protein-conducting channels without SecYEG. The crystal structure of SecY from *Methanococcus jannaschii* (Bostina et al. 2005; Van den Berg et al. 2004) suggests that SecY possesses a plug domain that is not essential for cell viability in either *E. coli* (Li et al. 2007; Maillard et al. 2007) or yeast (Junne et al. 2006). This SecY plug might be involved in channel gating and specificity of signal peptides (Li et al. 2007; Maillard et al. 2007). Indeed, studies have shown that removal of half or the complete plug domain suppresses the effects of a defective signal sequence of alkaline phosphatase (Li et al. 2007). We have also shown that the channels of these plug mutant membranes lose channel signal peptide specificity (Hsieh et al. 2011). However, in our studies, the proofreading function of the protein-conducting channel cannot be bypassed by a folded OmpA or PhoA or nonspecific unfolded protein (data not shown), indicating that these channels in the absence of SecYEG retain some degree of specificity for secretory proteins. These observations indicate that the gating mechanism is not totally dependent on SecY and may engage other accessory proteins (e.g., SecDFYajC and YidC, which are still present in the membranes we used here). Alternatively, a global structural discrimination by the channel of secretory proteins might be involved. Taken together, our results suggest that SecY does represent a checkpoint for signal sequences or precursor proteins and selects the entrance of the protein-conducting channel proficiently before protein translocation is initiated.

The conductance and ion selectivity of the *E. coli* protein-conducting channels have previously been revealed in several studies (Dalal and Duong 2009; Park and Rapoport 2011; Saparov et al. 2007; Schiebel and Wickner 1992). We have shown that SecA-dependent ion channels in *E. coli* wild-type membrane exhibit selective permeability to monovalent cations and anions. They are more permeable to K^+ and Na^+ than to $NMDG^+$ (Lin et al. 2006). Our

present study shows that the cationic selectivity of the SecA-dependent channels is lost in membranes without SecYEG, suggesting that SecYEG is likely involved in the maintenance of pore sizes or the recognition of ion charges. Interestingly, the anionic permeability is maintained in membranes with or without SecYEG (Tables 1, 2). These data suggest that the SecA protein-conducting channel in the absence of SecYEG may constitute an aqueous environment that is more sensitive to anions than cations during the channel opening, which is similar to SecY plug mutants (Dalal et al. 2010; Dalal and Duong 2009). In addition, the selective ion permeability of the SecA-dependent protein-conducting channels suggests that the interaction of the secretory proteins and the conducting pore could be disrupted in the absence of SecYEG and that SecYEG may play a role in such interaction or in the maintenance of the pore conformations necessary for ion selectivity.

In this report, we provide additional evidence that membranes in the absence of SecYEG are active for the SecA-dependent ion channel but lose the efficiency and specificity of the proofreading function of signal peptides, similar to the SecA-liposome system. However, compared to the SecA liposomes which require additional ATP to function, the channel activity in reconstituted membranes can be fully restored by addition of the SecYEG complex, suggesting that other membrane proteins may contribute to the efficiency of the channel. SecD-SecF-YajC or other membrane proteins may be involved in this apparatus, supporting the basic SecA channel structure for active protein translocation. The use of sensitive assays of electrophysiological voltage-clamping techniques on reconstituted proteoliposomes provides another perspective for studying this dynamic system.

Acknowledgments We thank J. Houghton for the comments and edits on the manuscript. We also thank L. Gierasch for signal peptides and comments and C. Murphy, J. Beckwith, T. Silhavy and D. Oliver for strains and plasmids. We thank X. Chen for purified proOmpA and H. Yang for purified SecA. SecYEG$^-$ membranes were a gift of Dr. You in this lab. This work was supported in part by NIH research grants GM034766 (to P. C. T.) and equipment facility grants by Georgia Research Alliance. B.-R. L. and Y.-H. H. were fellows of the Molecular Basis of Disease Program at GSU.

References

Bostina M, Mohsin B, Kuhlbrandt W, Collinson I (2005) Atomic model of the *E. coli* membrane-bound protein translocation complex SecYEG. J Mol Biol 352:1035–1043

Cabelli RJ, Chen L, Tai PC, Oliver DB (1988) SecA protein is required for secretory protein translocation into *E. coli* membrane vesicles. Cell 55:683–692

Chen L, Tai PC, Briggs MS, Gierasch LM (1987) Protein translocation into *Escherichia coli* membrane vesicles is inhibited by functional synthetic signal peptides. J Biol Chem 262:1427–1429

Chen X, Xu H, Tai PC (1996) A significant fraction of functional SecA is permanently embedded in the membrane. SecA cycling on and off the membrane is not essential during protein translocation. J Biol Chem 271:29698–29706

Chen Y, Tai PC, Sui SF (2007) The active ring-like structure of SecA revealed by electron crystallography: conformational change upon interaction with SecB. J Struct Biol 159:149–153

Dalal K, Duong F (2009) The SecY complex forms a channel capable of ionic discrimination. EMBO Rep 10:762–768

Dalal K, Bao H, Duong F (2010) Modulation of the SecY channel permeability by pore mutations and trivalent cations. Channels (Austin) 4:83–86

Emr SD, Hanley-Way S, Silhavy TJ (1981) Suppressor mutations that restore export of a protein with a defective signal sequence. Cell 23:79–88

Fandl JP, Tai PC (1987) Biochemical evidence for the *secY24* defect in *Escherichia coli* protein translocation and its suppression by soluble cytoplasmic factors. Proc Natl Acad Sci USA 84:7448–7452

Fandl JP, Cabelli R, Oliver D, Tai PC (1988) SecA suppresses the temperature-sensitive SecY24 defect in protein translocation in *Escherichia coli* membrane vesicles. Proc Natl Acad Sci USA 85:8953–8957

Hsieh Y-h, Zhang H, Lin B-r, Cui N, Na B, Yang H, Jiang C, Sui S-f, Tai PC (2011) SecA alone can promote protein translocation and ion channel activity. J Biol Chem 286:44702–44709

Jilaveanu LB, Oliver D (2006) SecA dimer cross-linked at its subunit interface is functional for protein translocation. J Bacteriol 188:335–338

Jilaveanu LB, Oliver DB (2007) In vivo membrane topology of *Escherichia coli* SecA ATPase reveals extensive periplasmic exposure of multiple functionally important domains clustering on one face of SecA. J Biol Chem 282:4661–4668

Jilaveanu LB, Zito CR, Oliver D (2005) Dimeric SecA is essential for protein translocation. Proc Natl Acad Sci USA 102:7511–7516

Junne T, Schwede T, Goder V, Spiess M (2006) The plug domain of yeast Sec61p is important for efficient protein translocation, but is not essential for cell viability. Mol Biol Cell 17:4063–4068

Kim YJ, Rajapandi T, Oliver D (1994) SecA protein is exposed to the periplasmic surface of the *E. coli* inner membrane in its active state. Cell 78:845–853

Kusters R, Huijbregts R, de Kruijff B (1992) Elevated cytosolic concentrations of SecA compensate for a protein translocation defect in *Escherichia coli* cells with reduced levels of negatively charged phospholipids. FEBS Lett 308:97–100

Li W, Schulman S, Boyd D, Erlandson K, Beckwith J, Rapoport TA (2007) The plug domain of the SecY protein stabilizes the closed state of the translocation channel and maintains a membrane seal. Mol Cell 26:511–521

Lin BR, Gierasch LM, Jiang C, Tai PC (2006) Electrophysiological studies in *Xenopus* oocytes for the opening of *Escherichia coli* SecA-dependent protein-conducting channels. J Membr Biol 214:103–113

Maillard AP, Lalani S, Silva F, Belin D, Duong F (2007) Deregulation of the SecYEG translocation channel upon removal of the plug domain. J Biol Chem 282:1281–1287

Manting EH, Driessen AJ (2000) *Escherichia coli* translocase: the unravelling of a molecular machine. Mol Microbiol 37:226–238

Mao J, Wang X, Chen F, Wang R, Rojas A, Shi Y, Piao H, Jiang C (2004) Molecular basis for the inhibition of G protein-coupled inward rectifier K^+ channels by protein kinase C. Proc Natl Acad Sci USA 101:1087–1092

Mori H, Ito K (2001) An essential amino acid residue in the protein translocation channel revealed by targeted random mutagenesis of SecY. Proc Natl Acad Sci USA 98:5128–5133

Nicchitta CV, Blobel G (1990) Assembly of translocation-competent proteoliposomes from detergent-solubilized rough microsomes. Cell 60:259–269

Oliver DB, Beckwith J (1982a) Identification of a new gene (*secA*) and gene product involved in the secretion of envelope proteins in *Escherichia coli*. J Bacteriol 150:686–691

Oliver DB, Beckwith J (1982b) Regulation of a membrane component required for protein secretion in *Escherichia coli*. Cell 30: 311–319

Osborne RS, Silhavy TJ (1993) PrlA suppressor mutations cluster in regions corresponding to three distinct topological domains. EMBO J 12:3391–3398

Park E, Rapoport TA (2011) Preserving the membrane barrier for small molecules during bacterial protein translocation. Nature 473:239–242

Ruiz N, Silhavy TJ (2005) Sensing external stress: watchdogs of the *Escherichia coli* cell envelope. Curr Opin Microbiol 8:122–126

Saparov SM, Erlandson K, Cannon K, Schaletzky J, Schulman S, Rapoport TA, Pohl P (2007) Determining the conductance of the SecY protein translocation channel for small molecules. Mol Cell 26:501–509

Schiebel E, Wickner W (1992) Preprotein translocation creates a halide anion permeability in the *Escherichia coli* plasma membrane. J Biol Chem 267:7505–7510

Silhavy TJ, Beckwith J (1983) Isolation and characterization of mutants of *Escherichia coli* K12 affected in protein localization. Methods Enzymol 97:11–40

Tai PC, Tian G, Xu H, Lian JP, Yu JN (1991) In vitro protein translocation into *Escherichia coli* inverted membrane vesicles. Methods Cell Biol 34:167–187

Tam PC, Maillard AP, Chan KK, Duong F (2005) Investigating the SecY plug movement at the SecYEG translocation channel. EMBO J 24:3380–3388

Van den Berg B, Clemons WM Jr, Collinson I, Modis Y, Hartmann E, Harrison SC, Rapoport TA (2004) X-ray structure of a protein-conducting channel. Nature 427:36–44

Veenendaal AK, van der Does C, Driessen AJ (2004) The protein-conducting channel SecYEG. Biochim Biophys Acta 1694: 81–95

Wang HW, Chen Y, Yang H, Chen X, Duan MX, Tai PC, Sui SF (2003) Ring-like pore structures of SecA: implication for bacterial protein-conducting channels. Proc Natl Acad Sci USA 100:4221–4226

Wang H, Na B, Yang H, Tai PC (2008) Additional in vitro and in vivo evidence for SecA functioning as dimers in the membrane: dissociation into monomers is not essential for protein translocation in *Escherichia coli*. J Bacteriol 190:1413–1418

Watanabe M, Nicchitta CV, Blobel G (1990) Reconstitution of protein translocation from detergent-solubilized *Escherichia coli* inverted vesicles: PrlA protein-deficient vesicles efficiently translocate precursor proteins. Proc Natl Acad Sci USA 87: 1960–1964

Xu H, Cui N, Yang Z, Wu J, Giwa LR, Abdulkadir L, Sharma P, Jiang C (2001) Direct activation of cloned K_{ATP} channels by intracellular acidosis. J Biol Chem 276:12898–12902

Yang YB, Lian J, Tai PC (1997a) Differential translocation of protein precursors across SecY-deficient membranes of *Escherichia coli*: SecY is not obligatorily required for translocation of certain secretory proteins in vitro. J Bacteriol 179:7386–7393

Yang YB, Yu N, Tai PC (1997b) SecE-depleted membranes of *Escherichia coli* are active. SecE is not obligatorily required for the in vitro translocation of certain protein precursors. J Biol Chem 272:13660–13665

Yi L, Jiang F, Chen M, Cain B, Bolhuis A, Dalbey RE (2003) YidC is strictly required for membrane insertion of subunits a and c of the F_1F_0ATP synthase and SecE of the SecYEG translocase. Biochemistry 42:10537–10544

Zhong X, Kolter R, Tai PC (1996) Processing of colicin V-1, a secretable marker protein of a bacterial ATP binding cassette export system, requires membrane integrity, energy, and cytosolic factors. J Biol Chem 271:28057–28063

J Membrane Biol (2012) 245:759–760
DOI 10.1007/s00232-012-9439-1

LETTER TO THE EDITOR

Endosis and Exosis: New Names for Fusion and Budding

David D. Busath · Dixon J. Woodbury · Adam Frost

Received: 16 April 2012 / Accepted: 30 April 2012 / Published online: 1 June 2012

To the Editor,

Endocytosis and exocytosis are named for the fact that vesicle action (-osis) is movement into (endo-) or out of (exo-) the cell (-cyt-). Vesicle budding and fusion of extracellular vesicles to cells are also commonplace processes in biology (Mause and Weber 2010; Nabhan et al. 2012) but lack formal names. For instance, budding occurs from cells infected by enveloped viruses or undergoing apoptosis and from apocrine glands and megakaryocytes. The products of budding are sometimes referred to as "exosomes" (Keller et al. 2006). Fusion of external vesicles to a cell is exemplified by HIV fusion to natural killer cells. Budding and subsequent fusion of exosomal vesicles containing fibroblast growth factor-2 may illustrate both processes (Taverna et al. 2003).

Topologically, these processes are distinct from endocytosis and exocytosis. They are not inversely related or mirror images, as they would be if the cell membrane were simply a plane, because the cell membrane is closed, encompassing the cell contents, so prefixation based on the inverse (in-) or opposite (anti-) nature of the processes would not be appropriate. They could be referred to jointly as the converse (con-) of endocytosis and exocytosis in the sense that the processes are reversed: they involve outward rather than inward bending of the cell membrane.

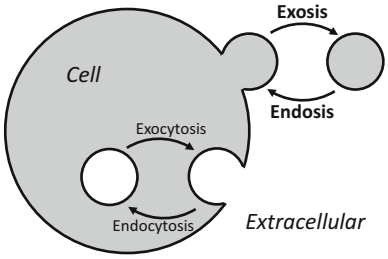

Fig. 1 Proposed terms for budding (exosis) and fusion (endosis)

Alternatively, names could be based on vesicles moving away from (ab-) or toward (ad-) the plasmalemma or as external instead of internal processes. However, each of these leads to cumbersome terminology.

Instead "budding" could be called "exosis" and "fusion" "endosis" (see Fig. 1). These terms are memorable and simultaneously convey symmetry and contrast with the terms endocytosis and exocytosis. They lack the root that refers to the cell, which is appropriate because these processes are extracellular actions of vesicles rather than intracellular. Furthermore, they complement the established nomenclature that endocytosis leads to endosomes and budding to exosomes. The complementation would be perfect if endosomes were instead called "endocytosomes."

D. D. Busath (✉) · D. J. Woodbury
Department of Physiology and Developmental Biology, Brigham Young University, Provo, UT 84602, USA
e-mail: david_busath@byu.edu

A. Frost
Department of Biochemistry, University of Utah, Salt Lake City, UT 84112, USA

References

Keller S, Sanderson MP, Stoeck A, Altevogt P (2006) Exosomes: from biogenesis and secretion to biological function. Immunol Lett 107:102–108

Mause SF, Weber C (2010) Microparticles: protagonists of a novel communication network for intercellular information exchange. Circ Res 107:1047–1057

Nabhan JF, Hu R, Oh RS, Cohen SN, Lu Q (2012) Formation and release of arrestin domain-containing protein 1-mediated microvesicles (ARMMs) at plasma membrane by recruitment of TSG101 protein. Proc Natl Acad Sci USA 109:4146–4151

Taverna S, Ghersi G, Ginestra A, Rigogliuso S, Pecorella S, Alaimo G, Saladino F, Dolo D, Dell'Era P, Pavan P, Pizzolanti G, Mignatti P, Presta M, Vittorelli ML (2003) Shedding of membrane vesicles mediates fibroblast growth factor-2 release from cells. J Biol Chem 278:51911–51919

J Membrane Biol (2012) 245:761
DOI 10.1007/s00232-012-9430-x

RETRACTION NOTE

RETRACTED ARTICLE: Deprotonation of Arginines in S4 is Involved in NaChBac Gating

Tzur Paldi

Received: 26 January 2012 / Accepted: 1 April 2012 / Published online: 18 April 2012

Article retracted due to disputed authorship.

T. Paldi (✉)
Department of Plant Molecular Biology and Ecology,
George S. Wise Faculty of Life Sciences, Tel Aviv University,
Ramat Aviv, Tel Aviv 69978, Israel
e-mail: tzur.paldi@gmail.com